

Short Communication/Kurze Mitteilung

Cytoplasmic Microtubules in Strial Marginal Cells

Joseph Santos-Sacchi

Dept. of Speech Pathology and Audiology, Teachers College, Columbia University,
120 Street and Broadway, New York, N.Y. 10027, USA

It has been known for some time that primary glutaraldehyde fixation and primary osmium fixation may offer different ultrastructural detail (Merck et al., 1974; Santos-Sacchi, 1977). Of significance is the almost selective ability of glutaraldehyde fixation to preserve labile cytoplasmic microtubules (CMT). In fact, Behnke and Forer (1967) reported that CMT of Crane-fly spermatids would not have been discovered if glutaraldehyde fixation were not employed. Apparently, CMT depolymerise during primary osmication.

The ubiquity of CMT within eukaryote cells is well acknowledged. They have been implicated in cytoskeletal support (Tilney, 1968), cellular morphologic maturation (Heywood et al., 1975), intracytoplasmic transport (La Vail and La Vail, 1974), secretion (Le Marchand et al., 1975), and organelle stratification (Neve et al., 1975).

Most research on the fine structure of the stria vascularis has employed primary osmium fixation (Smith, 1957; Hinojosa and Rodriguez-Echandia, 1966; Sugar et al., 1972). Generally, the cytoplasm of the marginal cells has been described as having a dense matrix. CMT have been reported rarely. However, recently Hilding and Ginsberg (1977) while studying melanogenesis in the stria reported the presence of cross-sectioned CMT within the marginal cell basal processes. Primary aldehyde fixation was employed. Their cross-sectioned CMT were identical to the 200 Å vesicles found within the marginal cell processes by Spondlin (1967).

The presumed secretory or absorptive function and the tenuous anatomy of the strial cells make them likely candidates for CMT inclusions. It is the purpose of this short communication to report upon the marginal cell microanatomy following glutaraldehyde fixation, with special reference to CMT.

Procedure

Cochleae of young adult albino mice were fixed by immersion either in 1% OsO₄ or 2% glutaraldehyde in 0.1 M cacodylate buffer at 4° C for 2 h. Post-osmication for 2 h followed glutaraldehyde fixation. The cochleae were dehydrated in graded series of acetone, the stria dissected free and embedded in

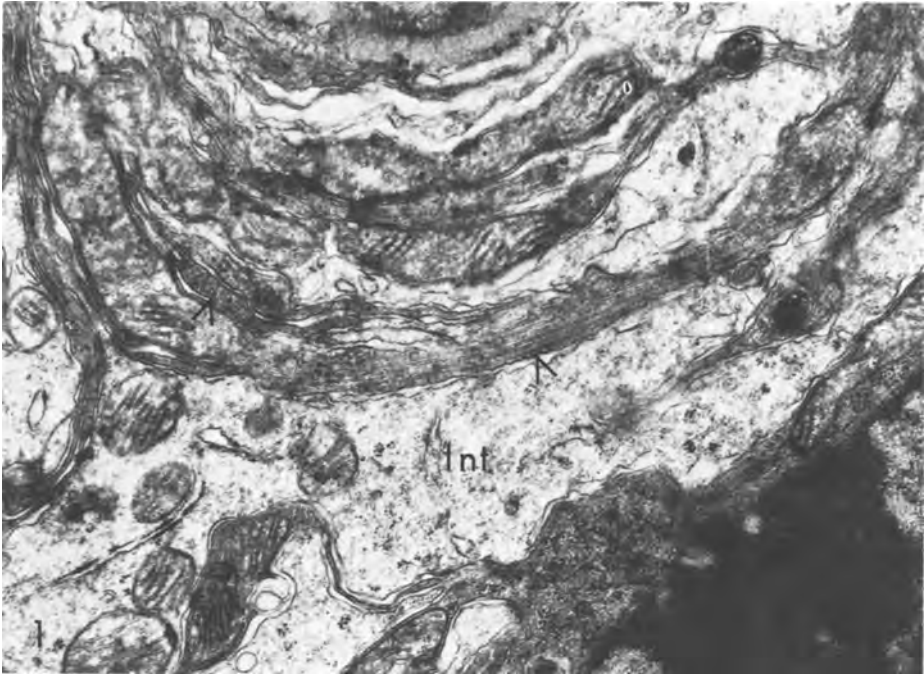


Fig. 1. Cytoplasmic microtubules (arrows) in the cell processes of the marginal cells of the stria vascularis. Longitudinal and cross sectioned tubules are visible. Intermediate cell process (Int.) $\times 23,703$

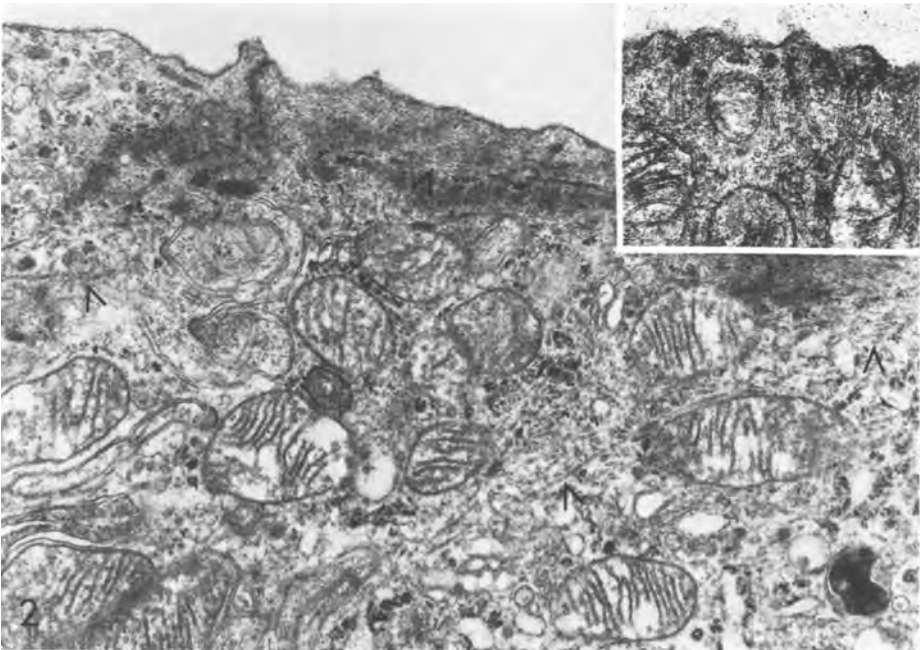


Fig. 2. Cytoplasmic microtubules in the apical cytoplasm of the stria vascularis ($\times 21,960$). Insert: Microtubules approaching apical membrane perpendicularly ($\times 29,822$)

Epon at 60° C. Ultrathin sections were stained with saturated uranyl acetate and lead citrate, and were examined with a Zeiss 9S-2 EM.

Results

In all animals, abundant numbers of CMT were present in the marginal cells only after primary fixation in glutaraldehyde. Only a dense cytoplasmic matrix was visible after primary osmication. Marginal cell CMT were seen both in cross and longitudinal section in the cell processes (Fig. 1). They extended parallel to each other for several microns and filled most of the cytoplasm not occupied by other organelles. CMT were also abundant in the apical cytoplasm (Fig. 2). They were observed coursing perpendicular, oblique, and parallel to the endolymphatic surface. CMT and apical membrane contacts were seen, as well as occasional associations with apical vesicles.

Discussion

CMT have not been reported within the marginal cells to the extent observed in this report. Apparently, the dense cytoplasmic matrix of the marginal cells reported in the past was due to the depolymerisation of CMT during primary osmication. The preservation of CMT by glutaraldehyde is thought to be due to the fixative's superior cross-linking of protein.

Speculative roles for marginal cell CMT are numerous. For example, they may play a role in the development of strial interdigitations, since during early development, marginal cells form a single layer of cuboidal epithelium which proceeds to send out basal processes (Kikuchi and Hilding, 1966). Indeed, the regression of adult strial tissue to early developmental forms as a result of various toxic materials may be due to CMT disruption. CMT inhibitors have been known to cause the retraction of cellular processes (Tilney, 1968). Also, the secretory or absorptive nature of the stria may be linked to CMT, since a correlation between secretion and microtubule numbers has been suggested (Sloper and Grainger, 1975). Marginal cell CMT-vesicle interactions may be important for apical vesicle transport.

Certainly, the vast number of CMT present in the marginal cells argues for roles similar to those observed in other cells, viz., cytoskeletal support and intracytoplasmic transport. The study of these structures in pathologic states may prove fruitful.

Acknowledgements. Thanks to Dr. W. F. Marovitz, Dept. of Otolaryngology, Mt. Sinai School of Medicine, for guidance and the use of his laboratory facilities. Also thanks to Celeste Conway for help in the preparation of this manuscript.

References

- Behnke, O., Forer, A.: Evidence for four classes of microtubules in individual cells. *J. Cell Sci.* **2**, 169 (1967)
- Heywood, P., Van de Water, T., Hilding, D., Ruben, R.: Distribution of microtubules and microfilaments in developing vestibular sensory epithelium of mouse otocysts grown in vitro. *J. Cell Sci.* **17**, 171 (1975)
- Hilding, D., Ginzberg, R.: Pigmentation of the stria vascularis. *Acta Otolaryngol.* **84**, 24 (1977)
- Hinojosa, R., Rodriguez-Echandia, E.: The fine structure of the stria vascularis of the cat inner ear. *Am. J. Anat.* **118**, 631 (1966)
- Kikuchi, K., Hilding, D.: The development of the stria vascularis in the mouse. *Acta Otolaryngol.* **62**, 277 (1966)
- La Vail, J., La Vail, M.: The retrograde intraaxonal transport of horse radish peroxidase in the chick visual system: a light and electron microscopic study. *J. Comp. Neurol.* **157**, 303 (1974)
- Le Marchand, Y., Singh, A., Patzelt, C., Orci, L., Jeanrenaud, B.: In vivo and in vitro evidences for the role of microtubules in the secretory processes of liver, p. 153. In: Borgers, M., De Brabander, M. (eds.): *Microtubules and microtubular inhibitors*. Amsterdam: North-Holland 1975
- Merck, W., Sparwald, E., Cürten, I.: Über den Einfluß verschiedener Fixationsmethoden und Fixationsmittel auf die electronenmikroskopische Struktur der Stria vascularis, prominentia spiralis und des Ligamentum spirale beim Meerschweinchen. *Arch. Oto-Rhino-Laryng.* **206**, 299 (1974)
- Neve, P., Rocmans, P., Ketelbant-Balasse, P.: Microtubules and microtubule inhibitors and cytochalasin in the thyroid gland, p. 177. In: Borgers, M., De Brabander, M. (eds.): *Microtubules and microtubular inhibitors*. Amsterdam: North Holland 1975
- Santos-Sacchi, J.: Differential effects of primary fixation with glutaraldehyde and osmium upon the membranous systems of the strial and external sulcus cells (acc. for publication, *Acta Otolaryngol.* [1977])
- Sloper, J., Grainger, F.: Quantitation of microtubules in secretory neurons, p. 281. In: Borgers, M., De Brabander, M. (eds.): *Microtubules and microtubular inhibitors*. Amsterdam: North Holland 1975
- Smith, C.: Structure of the stria vascularis and spiral prominence. *Ann. Otol.* **66**, 521 (1957)
- Spoendlin, H.: Stria vascularis. In: Iurato, S. (ed.): *Submicroscopic structure of the inner ear*. New York: Pergamon Press 1967
- Sugar, J., Engstrom, H., Stahle, J.: Stria vascularis. *Acta Otolaryngol., Suppl.* **301**, 61 (1972)
- Tilney, L.: IV. The effect of colchicine on the formation and maintenance of the axopodia and redevelopment of pattern in *Actinosphaerium nucleofilum*. *J. Cell Sci.* **3**, 549 (1968)

Received October 12, 1977

Developmental Expression of the Outer Hair Cell Motor Prestin in the Mouse

Takahisa Abe · Seiji Kakehata · Rei Kitani ·
Shin-ichiro Maruya · Dhasakumar Navaratnam ·
Joseph Santos-Sacchi · Hideichi Shinkawa

Received: 11 July 2006 / Accepted: 22 January 2007 / Published online: 6 April 2007
© Springer Science+Business Media, LLC 2007

Abstract The development of motor protein activity in the lateral membrane of the mouse outer hair cell (OHC) from postnatal day 5 (P5) to P18 was investigated under whole-cell voltage clamp. Voltage-dependent, nonlinear capacitance (C_v), which represents the conformational fluctuations of the motor molecule, progressively increased during development. At P12, the onset of hearing in the mouse, C_v was about 70% of the mature level. C_v saturated at P18 when hearing shows full maturation. On the other hand, C_{lin} , which represents the membrane area of the OHC, showed a relatively small increase with development, reaching steady state at P10. This early maturation of linear capacitance is further supported by morphological estimates of surface area during development. These results, in light of recent prestin knockout experiments and our results with quantitative polymerase chain reaction, suggest that, rather than the incorporation of new motors into the lateral membrane after P10, molecular motors mature to augment nonlinear capacitance. Thus, current estimates of motor protein density based on charge movement may be exaggerated. A corresponding indicator of motor maturation, the motor's operating voltage mid-

point, V_{pkcm} , tended to shift to depolarized potentials during postnatal development, although it was unstable prior to P10. However, after P14, V_{pkcm} reached a steady-state level near -67 mV, suggesting that intrinsic membrane tension or intracellular chloride, each of which can modulate V_{pkcm} , may mature at P14. These developmental data significantly alter our understanding of the cellular mechanisms that control cochlear amplification and provide a foundation for future analysis of genetic modifications of mouse auditory development.

Keywords Development · Mouse outer hair cell · Motor protein · Hearing · Cochlear amplification

Introduction

The organ of Corti, the auditory sensory epithelium of the mammal, has two types of hair cells, the inner hair cell (IHC) and the outer hair cell (OHC). In mammals, the OHC can contract and elongate at acoustic frequencies upon electrical stimulation (Brownell et al. 1985; Ashmore 1987; Santos-Sacchi 1992; Dallos and Evans 1995; Frank, Hemmert and Gummer 1999). Such voltage-dependent length change is termed “electromotility” and is thought to provide a means for improving mammalian cochlear sensitivity and frequency selectivity (Dallos 1992). Recently, on the basis of subtractive cloning between motile OHCs and nonmotile IHCs, a cDNA clone that is specifically expressed in OHCs was isolated and termed “Prestin” (Zheng et al. 2000b). The expressed motor protein prestin, which resides exclusively in the lateral membrane (Belyantseva et al. 2000), is likely key to cochlear amplification (Zheng et al. 2000b; Liberman et al. 2002). It is common practice to evaluate OHC motor activity either by

T. Abe · S. Kakehata (✉) · R. Kitani · S.-i. Maruya ·
H. Shinkawa

Department of Otorhinolaryngology, Hirosaki University School
of Medicine, Hirosaki 036-8562, Japan
e-mail: seijik@cc.hirosaki-u.ac.jp

D. Navaratnam
Department of Neurology and Neurobiology, Yale University
School of Medicine, New Haven, Connecticut 06510, USA

J. Santos-Sacchi
Department of Otolaryngology and Neurobiology, Yale
University School of Medicine, New Haven, Connecticut 06510,
USA

measuring changes in OHC length or motor-derived nonlinear capacitance (C_v), both being inextricably related (Santos-Sacchi and Dilger 1988; Ashmore 1987, 1990; Santos-Sacchi 1990, 1991). GLUT5, another protein initially considered a motor candidate (Geleoc et al. 1999) that also resides within the lateral membrane, does not express nonlinear capacitance (Ludwig et al. 2001). In the OHC, then, membrane capacitance (C_m) is the sum of motor-derived capacitance and capacitance resulting from the intrinsic capacity of membrane, i.e., surface area (Santos-Sacchi and Navarrete 2002).

The onset of hearing in the mouse is approximately at postnatal day 12 (P12), and full maturation is at P18 (Ehret 1976; Steel and Bock 1980). While the mouse is currently an important model for studies on hearing and the genetics of hearing, there is no information on the development of OHC motor activity in this species. However, OHC motor development has been studied in two other species, the rat and gerbil (He, Evans and Dallos 1994; Oliver and Fakler 1999; Belyantseva et al. 2000). He et al. (1994) reported that postnatal OHCs of gerbils begin to acquire electromotile properties at P7 in the basal cochlear turn and at P8 in the apical turn, reaching adult characteristics at about P13–14. In rat OHCs, the density of motor protein matured near P11 (Oliver and Fakler 1999; Belyantseva et al. 2000); Oliver and Fakler (1999) further concluded that the increase in membrane capacitance after P11 was due to an increase in membrane area containing the same density of motor proteins. Here, we investigated the density of the motor protein in the lateral membrane of the mouse OHC during development and demonstrate that, whereas cell size of OHCs matures at P12, voltage-dependent capacitance increases continuously up to P18. We argue that this increase, in the face of fixed surface area, derives from maturation of motor activity and not from additional motor incorporation. These observations impact on basic mechanisms of motor development as well as interpretation of genetic manipulations of the motor protein prestin.

Materials and Methods

OHCs were obtained from acutely dissected organs of Corti from C57BL/6J mice. Though this strain exhibits age-related hearing loss, normal hearing persists to 2 months of age (Wu et al. 2004). Additionally, we limited our cell harvesting to low-frequency regions (middle to apical turn) that remain normal well beyond that time. The persistence of normal cochlear amplification into adulthood indicates that development occurs normally in this strain. We additionally used this strain in order to make direct comparisons with the prestin knockout results (Liberman et al. 2002). The mice were killed in accordance with the

Guidelines for Animal Experimentation, Hiroasaki University. Cochleae were dissected, and the organs of Corti were separated from the modiolus and stria vascularis. The organs were then digested with trypsin (1 mg/ml) in external solution for 10–12 min at room temperature and transferred into 35-mm plastic dishes (Falcon, Lincoln Park, NJ) with 2 ml external solution. OHCs were isolated by gentle trituration. The dish was mounted on an inverted microscope (IX71; Olympus, Tokyo, Japan).

The external solution contained (mM) 100 NaCl, 20 tetraethylammonium, 20 CsCl, 2 CoCl₂, 1.52 MgCl₂, 10 4-(2-hydroxyethyl)-1-piperazineethanesulfonic acid (HEPES) and 5 dextrose (pH 7.2), 300 mosmol • liter⁻¹, in order to block ionic conductances. The patch pipette solution contained (mM) 140 CsCl, 2 MgCl₂, 10 ethyleneglycoltetraacetic acid (EGTA), 10 HEPES (pH 7.2), 300 mosmol • liter⁻¹ (adjusted with dextrose).

The cells were whole-cell voltage-clamped with an Axon (Burlingame, CA) 200B amplifier using patch pipettes having initial resistances of 3–5 MΩ. Series resistances, which ranged 5–20 MΩ, remained uncompensated for C_m measurements, though corrections for series resistance voltage errors were made offline. All data acquisition and analyses were performed with the Windows-based patch-clamp program jClamp (SciSoft, New Haven, Connecticut).

C_m functions were obtained 1 min after establishment of the whole-cell configuration, following sufficient time for wash-in of pipette solutions in these small cells. C_m was assessed using a continuous high-resolution (2.56 ms sampling) two-sine voltage stimulus protocol (10 mV peak at both 390.6 and 781.2 Hz) superimposed onto a voltage ramp (200 ms duration) from -150 to +150 mV (Santos-Sacchi 2004; Santos-Sacchi, Kakehata and Takahashi 1998). Capacitance data were fit to the first derivative of a two-state Boltzmann function (Santos-Sacchi 1991).

$$C_m = Q_{\max} \frac{ze}{kT} \frac{b}{(1+b)^2} + C_{lin}$$

$$b = \exp\left(\frac{-ze(V_m - V_{pkcm})}{kT}\right)$$

where Q_{\max} is the maximum nonlinear charge moved, V_{pkcm} is voltage at peak capacitance or half-maximum charge transfer, V_m is membrane potential, z is valence, C_{lin} is linear membrane capacitance, e is electron charge, k is Boltzmann's constant, and T is absolute temperature. Density was calculated as $d = (Q_{\max}/e)/(C_{lin}/0.008)$, i.e., based on a conversion of 0.008 pF/μm² (as measured directly, see Results). This conversion factor is within the range of factors commonly used (Solsona, Innocenti and Fernandez 1998). A further discussion of OHC linear capacitance can be found in Santos-Sacchi and Navarrete

(2002). For analyses, we quantified C_v , an estimate of voltage-dependent, nonlinear capacitance (NLC), as the absolute peak capacitance minus linear capacitance. In order to estimate surface area (A_{ohc}), we modeled the OHC as a cylinder composed of three pieces, the cuticular plate area (A_{cut}), the lateral membrane area (A_{lat}) and the basal area (A_{bas}). Cell width was determined at three equidistant positions along the cells' length.

$$A_{ohc} = A_{lat} + A_{cut} + A_{bas}$$

where

$$A_{lat} = 2\pi r(L - r)$$

$$A_{cut} = \pi r^2$$

$$A_{bas} = \frac{\pi(2r)^2}{2}$$

For P5–8 (see Fig. 1B), where the length and width were similar and the cell appeared more spherical, area was calculated as a sphere with an average diameter: (width + length)/2. Cell width for this age group was measured at the cell's midpoint. Dimensions were measured at 1 min following membrane patch rupture. On average, cell

lengths are compressed 5.99% after the whole-cell configuration. OHC images were captured by a digital charge-coupled device camera and recorded with AQUA-Lite (version 1.2; Hamamatsu, Shizuoka, Japan). All data are given as mean \pm standard error of the mean (SEM). Fits to the data were made with a sigmoidal logistic function (Sigma Plot 9.0; Systat, San Jose, California). All electrophysiological and morphometric measures were made on each cell for direct comparison.

To estimate the prestin mRNA level during development, a two-step reverse transcription (RT) and quantitative polymerase chain reaction (QPCR) was employed. Total RNA was extracted from the organ of Corti at P5, P8, P10 and P15, using TRI reagent and reverse-transcribed using random decamers according to the manufacturer's instructions (Invitrogen, Carlsbad, CA). QPCR was done using a 1:10 dilution of cDNA. QPCR was performed with a Brilliant SYBR Green qPCR kit and Stratagene MX3000 (both from Stratagene, La Jolla, CA). Each amplification was done in duplicate. Amplification conditions were 94°C for 30 s, 60°C for 30 s and 72°C for 1 min. Primer sequences were as follows: prestin, TGGGGTCAAAA-CAAAGCGG and GCAAACCAAAAACCATCAGGC (spanning intron between exons 8 and 9); glyceraldehyde-3-phosphate dehydrogenase (GAPDH), AGGTCCGGTGTGAACGGATTG and TGTAGACCATGTAGTTGAGGTCA. Amplification specificity was confirmed by melting curve analysis and agarose gel electrophoresis (Metaphor; ICN, Irvine, CA). Data were normalized to GAPDH expression.

Results

The signature electrical response of an adult OHC is a bell-shaped, voltage-dependent capacitance. In postnatal OHCs, C_m showed bell-shaped voltage dependence from P7; C_v was not detectable at either P5 or P6. Examples of the change of C_m functions with development are shown in Figure 1A. Examples of digitally captured phase-contrast images of developing OHCs are shown in Figure 1B. From such data we determined estimates of the cells' linear capacitance (a correlate of membrane surface area), which increased slightly from P5 to P9, thereafter remaining stable (Fig. 2A, colored symbols). In that same figure, surface area estimates (see Materials and Methods) correspond to measures of C_{lin} . Linear capacitance measures more accurately assess the surface area since these measures are not dependent on geometrical models. Although surface area remains fixed after P9, dimensions change, with cell width decreasing and cell length increasing. A plot of their correspondence (Fig. 2B) shows this inverse relationship and indicates that after OHCs attain about

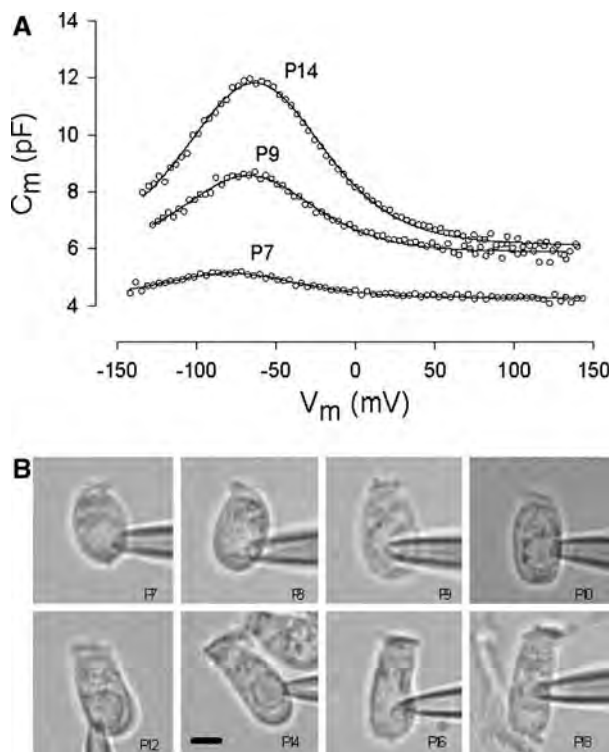


Fig. 1 (A) Examples of C_m functions from three postnatal days. In addition to an increase in peak capacitance, note the shift in V_{pkcm} to the right during maturation. Fitted parameters were $Q_{max} = 0.091$ pC, $z = 0.89$ at P7; $Q_{max} = 0.263$ pC, $z = 0.95$ at P9; $Q_{max} = 0.542$ pC, $z = 0.89$ at P14. (B) Images of patch-clamped OHCs from P7 to P18. Scale bar (7.5 μ m) in P14 figure applies to all images

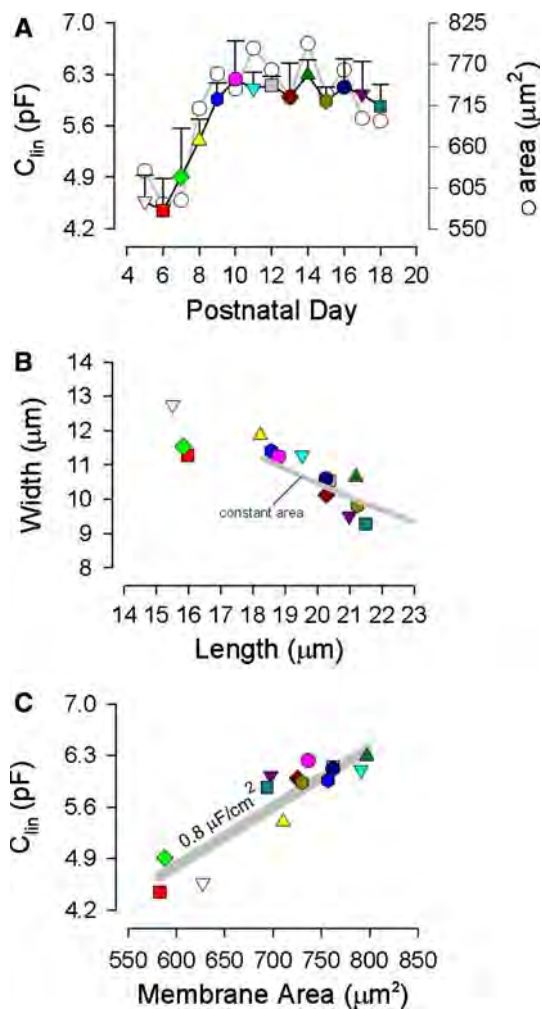


Fig. 2 Cell dimensions as a function of postnatal day. (A) Linear capacitance (with standard error bars) and surface area as a function of postnatal day. Note saturation of each measure at P10. (B) Inverse relationship between measured length and width of OHCs. *Solid gray line* denotes constant surface area constraint on width vs. length for the cylindrical model (see Materials and Methods). Surface area was constrained at 740 μm² (P10). (C) Relationship between linear capacitance and calculated surface area. *Solid gray line* denotes a specific membrane capacitance of 0.008 pF/μm²

18 μm in length, dimensional changes are constrained by constant surface area (solid gray line). That is, length and width of the cylindrical cell continue to change during development but do so while maintaining a fixed surface area. A specific membrane capacitance of 0.008 pF/μm² characterizes the plasma membrane of developing OHCs (Fig. 2C).

NLC, unlike linear capacitance, increases throughout the developmental time period studied. Figure 3A shows the sigmoidal rise of C_v (colored symbols), reaching a saturating level (7.66 pF) at P18. Correspondingly, the unitary charge density (open circles) increases to saturation (10,956 e⁻/μm²) but, being determined by the surface area (which remains fixed above P9), shows a relative boost,

over C_v , as maturation advances. The bimodal change in C_v vs. C_{lin} is highlighted in Figure 3B, where both C_v and C_{lin} increase linearly between P5 and P10 but, following that, only C_v increases. The changes in capacitance that occur early (P6–P10) are accompanied by a highly variable operating voltage range (V_{pkcm} , Fig. 4); however, when C_v is solely on the rise (>P10), V_{pkcm} shifts rightward to more stably occupy a voltage near -67 mV. The voltage sensitivity or valence, z , remained stable from P6 to P18 (0.875 ± 0.014).

Figure 5 shows the expression of prestin and GAPDH using a two-step RT-QPCR. Both the absolute and normalized levels of prestin RNA peaked near P10, consistent with our electrophysiological results. Absolute prestin RNA levels at P5, P8 and P15 were, respectively, 18%, 32% and 58% of that at P10. Similarly, prestin RNA levels at P5, P8 and P15, normalized to GAPDH RNA expression, were, respectively, 66%, 66% and 30% of that at P10. These quantitative data wholly support our electrophysiological conclusions that prestin expression matures at P10.

Discussion

Hearing in altricial mammals develops following birth. The mouse is first capable of detecting sounds as early as P12 (Ehret 1976; Steel and Bock 1980). However, this rudimentary ability does not benefit from the enhanced fine tuning and sensitivity afforded by cochlear amplification, the result of active, electromechanical feedback into the basilar membrane by mature OHCs. During the next several days, sensitivity and frequency tuning mature until at P18 the hearing organ is fully mature as measured by masked auditory brainstem response tuning curves (Song, McGee and Walsh 2006). Here, we provide the first detailed developmental study of mouse OHC motor protein expression in order to assess the OHCs' contribution toward the development of cochlear amplification (Zheng et al. 2000a; Liberman et al. 2002). Our data bear not only on this developing contribution toward mature audition but also on molecular mechanisms of motor maturation itself.

OHC Maturation

Certain characteristics of mouse OHC maturation correlate well with the development of hearing, though it should be kept in mind that the attainment of adult cochlear function undoubtedly profits from a concerted developmental contribution from a variety of cellular and acellular structures (Shnerson, Devigne and Pujol 1981; Shnerson and Pujol 1981; Souter and Forge 1998; Forge, Souter and Denman Johnson 1997; Souter, Nevill and Forge 1995). Nevertheless, considering the unusually important contribution of

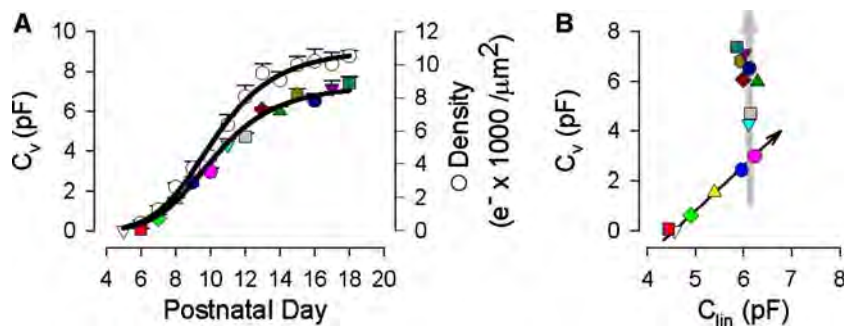


Fig. 3 (A) NLC (C_v , colored symbols) and unitary charge density (open circles) as a function of postnatal day. Each function saturates at P18. Charge density was computed using C_{lin} to calculate surface area with the specific membrane capacitance of $0.008 \text{ pF}/\mu\text{m}^2$. Logistic fits were made with C_v or density = $\max/[1+(\text{day}/\text{mid}) \times b]$.

Charge density fit (max, b, mid): 10,956, -5.65 , 10.22. C_v : 7.66, -5.33 , 10.66. The number of cells was (from P5 to P18) 2, 5, 5, 9, 5, 6, 10, 9, 5, 10, 6, 9, 5 and 5. Standard error is plotted. (B) Relationship between C_v and C_{lin} . Note the continued increase in C_v after C_{lin} (or surface area) saturates

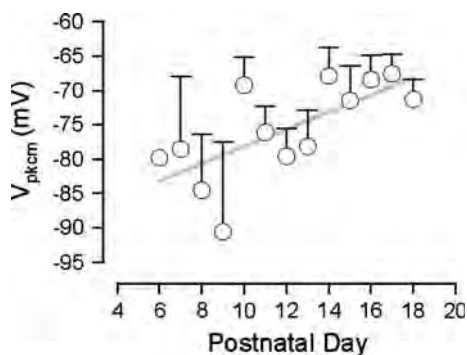


Fig. 4 Voltage at peak capacitance (V_{pkcm}) changes during development. Note variability during early stages and eventual shift toward depolarized voltages, stabilizing near -67 mV

OHCs to cochlear amplification, the development of OHC electromotility is considered one of the key features in this process. Our data show that motor activity (C_v or NLC) of the mouse OHC reaches adult levels at P18, having its onset at P7. Marcotti and Kros (1999) studied OHC motility and capacitance. However, they measured capacitance only at a fixed membrane voltage of -84 mV ; therefore, they could not detect linear and nonlinear capacitance. In addition, they did not study beyond P12. Similar results have been found in other altricial species, including the gerbil, guinea pig and rat (Pujol et al. 1991; He et al. 1994; Oliver and Fakler 1999; Belyantseva et al. 2000). In the rat, NLC matures at P17 (Belyantseva et al. 2000) and is detectable as early as P0 in apical turn OHCs (Oliver and Fakler 1999). Interestingly, for apical turn OHCs, Oliver and Fakler (1999) found a growth correspondence in linear capacitance and NLC for P10–14, which differs from our measures that show saturation of linear capacitance in the face of increasing NLC. Consequently, we find an increasing charge density out to adult performance times (P18, Fig. 3A), whereas they calculate a saturated charge density after P11. While species differences must be considered, methodological differences in measuring NLC may play a role. Our methodology provides unbiased estimates of C_m in the face of changing voltage-dependent impedance (Santos-Sacchi 2004); however, the stair-step protocol employed by Oliver and Fakler (1999) could have been influenced by the inability of the fixed (5 ms) voltage step protocol to adequately evaluate charge transfer across the range of OHC voltage-dependent time constants evoked by the wide-ranging voltage ramp. Their early developmental data for linear capacitance (P0–10) show a saturating increase from P0, which is stable from P4 to P11. Thus, we speculate that the abrupt increase in linear capacitance that they found after P11 obscures a continuing increase in charge density out to later days.

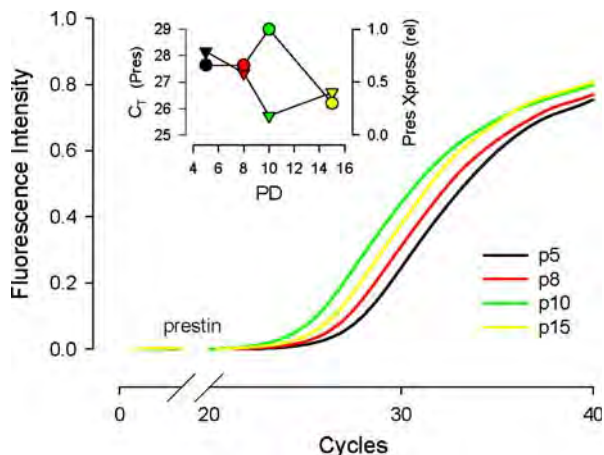


Fig. 5 Expression of prestin changes with development and peaks at P10. QPCR amplification of cDNA from cochlea RNA obtained on P5 (black), P8 (red), P10 (green) and P15 (yellow) are shown. Inset shows the C_t values of prestin and the relative amplification of prestin corrected for GAPDH expression at P5, P8, P10 and P15. The lower C_t value (triangles) at P10 confirms the highest expression at this time point. The relative expression (circles) of prestin is compared to expression at P10

Supporting this contention, Belyantseva et al. (2000) found nonlinear charge density to increase beyond P17 in the rat, and He et al. (1994) found an inverse relationship between length and width of developing gerbil OHCs, similar to what we found. We should also note that the developmental shift of V_{pkcm} that we observed, though similar in direction to that observed by Oliver and Fakler (1999), matured at a potential more negative than their value, i.e., near -67 mV, the resting potential found in adult guinea pig OHCs *in vivo* (Dallos, Santos-Sacchi and Flock 1982).

OHC Motor Maturation

Though we find that OHC motor activity saturates at P18, which is coincident with the attainment of mature hearing in the mouse, our data actually indicate that this saturation does not directly reflect the attainment of adult motor density in the lateral membrane. Instead, our data likely characterize the maturation of an already fixed pool of membrane motor proteins at P10 that we have measured with QPCR. Indeed, prestin expression in the rat has also been shown to plateau after P10 in the rat, confirming our results (Reisinger et al. 2005). These direct measures are additionally supported by the observation that motor protein membrane residence contributes to membrane surface area in the OHC. In fact, not only does prestin occupy space in the OHC membrane but the amount of surface area it occupies is voltage-dependent (Kalinec et al. 1992; Iwasa 1994; Santos-Sacchi 1993; Santos-Sacchi and Navarrete 2002). Thus, in prestin knockout mice, it was shown that the length of OHCs diminished relative to the length of normal OHCs in the control C57BL/6J mouse (Lieberman et al. 2002). From Lieberman et al.'s morphometric data on OHCs isolated from the apical region of the cochlea, the length reduction corresponds to about $134 \mu\text{m}^2$ surface area occupancy by prestin. Our data show that from P6 to P10 surface area increases by about $165 \mu\text{m}^2$, remaining fixed thereafter (Fig. 2A). This increase in surface area is coterminous with the increase in C_v that accompanies prestin expression; thus, we hypothesize that from P6 to P10 a full complement of motor proteins is expressed in mouse OHCs. Our hypothesis is strongly supported by our and others' (Reisinger et al. 2005) QPCR data, which show prestin expression to plateau at p10. Previous studies have concluded that the saturation of motor activity in the OHC represents the attainment of adult levels of motor protein density in the lateral membrane. For example, Belyantseva et al. (2000) found a correlated development of motor charge density and prestin antibody fluorescence in the lateral membrane. Souter et al. (1995) also found that the density of intramembranous particles (a presumed ultrastructural correlate of the motors) in the lateral membrane matures at P16 in the gerbil. How could the density of motors increase in the

lateral membrane given our observation that a fixed pool of motors resides within the OHC following P10? In tackling this question, it must be realized that all motor charge data arise from measures of the whole OHC membrane. Recently, it has been shown that during development of rat OHCs prestin is initially expressed throughout the basolateral membrane and subsequently redistributes only to the lateral membrane between days P7 and P12 (Weber et al. 2002). Thus, it is possible for the density of motors in the lateral membrane to increase over time by redistribution into the lateral membrane, where, in the adult, motor activity is restricted (Kalinec et al. 1992; Huang and Santos-Sacchi 1993a). However, it is not clear that a simple redistribution of motors within the membrane would have an effect on the magnitude of motor charge movement. So, in the face of a fixed pool of motors following P10, how might C_v increase? It is well established that prestin-derived NLC can be modulated by a variety of biophysical forces, perhaps these forces themselves being developmentally regulated.

Two of the most significant biophysical influences on the OHC motor are its sensitivity to membrane tension and chloride ions (Iwasa 1993; Gale and Ashmore 1994; Kakehata and Santos-Sacchi 1995; Oliver et al. 2001; Rybalchenko and Santos-Sacchi 2003; Song, Seeger and Santos-Sacchi 2005), each capable of shifting V_{pkcm} and modulating the magnitude of C_v . The simultaneous changes in V_{pkcm} and C_v that we find during maturation at P10–18 may thus result from developmental changes in membrane tension and/or intracellular chloride activity. It is well known that changes in intracellular chloride levels during development can alter the anion's equilibrium potential, bringing about significant changes in inhibitory neurotransmitter response characteristics (Rivera et al. 1999). In the OHC, development of the adult architecture of the lateral wall, including the cortical cytoskeleton and its interaction with the lateral membrane, could alter membrane tension. Additionally, the increasing density of motors could alter motor-motor interactions, leading to the maturation of motor-derived tension within the membrane. Such motor interactions have been modeled to account for prepulse effects on NLC V_{pkcm} within the OHC lateral membrane and prestin transfected cells (Santos-Sacchi et al. 1998, 2001). Finally, it may be that other factors can influence the maturation of motor activity, including second messenger/phosphorylation effects on the motor itself or on associated cytoskeletal elements (Huang and Santos-Sacchi 1993b; Frolenkov et al. 2000; Deak et al. 2005).

Acknowledgement This work was supported by Grants-in-Aid for Scientific Research from the Ministry of Education, Culture, Sports, Science and Technology of Japan (to S. K., H. S.), NIH grants DC00273 (to J. S.-S.) and K08 DC05352 (to D. N.).

References

- Ashmore JF (1987) A fast motile response in guinea-pig outer hair cells: The cellular basis of the cochlear amplifier. *J Physiol* 388:323–347
- Ashmore JF (1990) Forward and reverse transduction in the mammalian cochlea. *Neurosci Res Suppl* 12:S39–S50
- Belyantseva IA, Adler HJ, Curi R, Frolenkov GI, Kachar B (2000) Expression and localization of prestin and the sugar transporter GLUT-5 during development of electromotility in cochlear outer hair cells. *J Neurosci* 20:RC116
- Brownell WE, Bader CR, Bertrand D, de Ribaupierre Y (1985) Evoked mechanical responses of isolated cochlear outer hair cells. *Science* 227:194–196
- Dallos P (1992) The active cochlea. *J Neurosci* 12:4575–4585
- Dallos P, Evans BN (1995) High-frequency motility of outer hair cells and the cochlear amplifier. *Science* 267:2006–2009
- Dallos P, Santos-Sacchi J, Flock A (1982) Intracellular recordings from cochlear outer hair cells. *Science* 218:582–584
- Deak L, Zheng J, Orem A, Du GG, Aguinaga S, Matsuda K, Dallos P (2005) Effects of cyclic nucleotides on the function of prestin. *J Physiol* 563:483–496
- Ehret G (1976) Development of absolute auditory thresholds in the house mouse (*Mus musculus*). *J Am Audiol Soc* 1:179–184
- Forge A, Souter M, Denman Johnson K (1997) Structural development of sensory cells in the ear. *Semin Cell Dev Biol* 8:225–237
- Frank G, Hemmert W, Gummer AW (1999) Limiting dynamics of high-frequency electromechanical transduction of outer hair cells. *Proc Natl Acad Sci USA* 96:4420–4425
- Frolenkov GI, Mammano F, Belyantseva IA, Coling D, Kachar B (2000) Two distinct Ca^{2+} -dependent signaling pathways regulate the motor output of cochlear outer hair cells. *J Neurosci* 20:5940–5948
- Gale JE, Ashmore JF (1994) Charge displacement induced by rapid stretch in the basolateral membrane of the guinea-pig outer hair cell. *Proc R Soc Lond B Biol Sci* 255:243–249
- Geleoc GS, Casalotti SO, Forge A, Ashmore JF (1999) A sugar transporter as a candidate for the outer hair cell motor. *Nat Neurosci* 2:713–719
- He DZ, Evans BN, Dallos P (1994) First appearance and development of electromotility in neonatal gerbil outer hair cells. *Hear Res* 78:77–90
- Huang G, Santos-Sacchi J (1993a) Mapping the distribution of the outer hair cell motility voltage sensor by electrical amputation. *Biophys J* 65:2228–2236
- Huang G-J, Santos-Sacchi J (1993b) Metabolic control of OHC function: Phosphorylation and dephosphorylation agents shift the voltage dependence of motility related capacitance. *Assoc Res Otolaryngol Abs* 16:464
- Iwasa KH (1993) Effect of stress on the membrane capacitance of the auditory outer hair cell. *Biophys J* 65:492–498
- Iwasa KH (1994) A membrane motor model for the fast motility of the outer hair cell. *J Acoust Soc Am* 96:2216–2224
- Kakehata S, Santos-Sacchi J (1995) Membrane tension directly shifts voltage dependence of outer hair cell motility and associated gating charge. *Biophys J* 68:2190–2197
- Kalinec F, Holley MC, Iwasa KH, Lim DJ, Kachar B (1992) A membrane-based force generation mechanism in auditory sensory cells. *Proc Natl Acad Sci USA* 89:8671–8675
- Lieberman MC, Gao J, He DZ, Wu X, Jia S, Zuo J (2002) Prestin is required for electromotility of the outer hair cell and for the cochlear amplifier. *Nature* 419:300–304
- Ludwig J, Oliver D, Frank G, Klockner N, Gummer AW, Fakler B (2001) Reciprocal electromechanical properties of rat prestin: The motor molecule from rat outer hair cells. *Proc Natl Acad Sci USA* 98:4178–4183
- Marcotti W, Kros CJ (1999) Developmental expression of the potassium current $I_{K,n}$ contributes to maturation of mouse outer hair cells. *J Physiol* 520:653–660
- Oliver D, Fakler B (1999) Expression density and functional characteristics of the outer hair cell motor protein are regulated during postnatal development in rat. *J Physiol* 519(pt 3):791–800
- Oliver D, He DZ, Klockner N, Ludwig J, Schulte U, Waldegger S, Ruppersberg JP, Dallos P, Fakler B (2001) Intracellular anions as the voltage sensor of prestin, the outer hair cell motor protein. *Science* 292:2340–2343
- Pujol R, Zajic G, Dulon D, Raphael Y, Altschuler RA, Schacht J (1991) First appearance and development of motile properties in outer hair cells isolated from guinea-pig cochlea. *Hear Res* 57:129–141
- Reisinger E, Zimmermann U, Knipper M, Ludwig J, Klockner N, Fakler B, Oliver D (2005) Cod106, a novel synaptic protein expressed in sensory hair cells of the inner ear and in CNS neurons. *Mol Cell Neurosci* 28:106–117
- Rivera C, Voipio J, Payne JA, Ruusuvauro E, Lahtinen H, Lamsa K, Pirvola U, Saarma M, Kaila K (1999) The K^+/Cl^- co-transporter KCC2 renders GABA hyperpolarizing during neuronal maturation. *Nature* 397:251–255
- Rybalchenko V, Santos-Sacchi J (2003) Cl^- flux through a non-selective, stretch-sensitive conductance influences the outer hair cell motor of the guinea-pig. *J Physiol* 547:873–891
- Santos-Sacchi J (1990) Fast outer hair cell motility: How fast is fast? In: Dallos P, Geisler CD, Matthews JW, Ruggero MA, Steele CR, editors. *The Mechanics and Biophysics of Hearing*. Springer-Verlag, Berlin, pp. 69–75
- Santos-Sacchi J (1991) Reversible inhibition of voltage-dependent outer hair cell motility and capacitance. *J Neurosci* 11:3096–3110
- Santos-Sacchi J (1992) On the frequency limit and phase of outer hair cell motility: Effects of the membrane filter. *J Neurosci* 12:1906–1916
- Santos-Sacchi J (1993) Harmonics of outer hair cell motility. *Biophys J* 65:2217–2227
- Santos-Sacchi J (2004) Determination of cell capacitance using the exact empirical solution of dY/dC_m and its phase angle. *Biophys J* 87:714–727
- Santos-Sacchi J, Dilger JP (1988) Whole cell currents and mechanical responses of isolated outer hair cells. *Hear Res* 35:143–150
- Santos-Sacchi J, Kakehata S, Takahashi S (1998) Effects of membrane potential on the voltage dependence of motility-related charge in outer hair cells of the guinea-pig. *J Physiol* 510(pt 1):225–235
- Santos-Sacchi J, Navarrete E (2002) Voltage-dependent changes in specific membrane capacitance caused by prestin, the outer hair cell lateral membrane motor. *Pfluegers Arch* 444:99–106
- Santos-Sacchi J, Shen WX, Zheng J, Dallos P (2001) Effects of membrane potential and tension on prestin, the outer hair cell lateral membrane motor protein. *J Physiol* 531:661–666
- Shnerson A, Devigne C, Pujol R (1981) Age-related changes in the C57BL/6J mouse cochlea. II. Ultrastructural findings. *Brain Res* 254:77–88
- Shnerson A, Pujol R (1981) Age-related changes in the C57BL/6J mouse cochlea. I. Physiological findings. *Brain Res* 254:65–75
- Solsona C, Innocenti B, Fernandez JM (1998) Regulation of exocytotic fusion by cell inflation. *Biophys J* 74:1061–1073
- Song L, McGee J, Walsh EJ (2006) Frequency- and level-dependent changes in auditory brainstem responses (ABRs) in developing mice. *J Acoust Soc Am* 119:2242–2257
- Song L, Seeger A, Santos-Sacchi J (2005) On membrane motor activity and chloride flux in the outer hair cell: Lessons learned

- from the environmental toxin tributyltin. *Biophys J* 88:2350–2362
- Souter M, Forge A (1998) Intercellular junctional maturation in the stria vascularis: Possible association with onset and rise of endocochlear potential. *Hear Res* 119:81–95
- Souter M, Nevill G, Forge A (1995) Postnatal development of membrane specialisations of gerbil outer hair cells. *Hear Res* 91:43–62
- Steel KP, Bock GR (1980) The nature of inherited deafness in deafness mice. *Nature* 288:159–161
- Weber T, Zimmermann U, Winter H, Mack A, Kopschall I, Rohbock K, Zenner HP, Knipper M (2002) Thyroid hormone is a critical determinant for the regulation of the cochlear motor protein prestin. *Proc Natl Acad Sci USA* 99:2901–2906
- Wu X, Gao J, Guo Y, Zuo J (2004) Hearing threshold elevation precedes hair-cell loss in prestin knockout mice. *Brain Res Mol Brain Res* 126:30–37
- Zheng J, Shen W, He D, Long K, Madison L, Dallos P (2000a) Prestin is the motor protein of cochlear outer hair cells. *Nature* 405:149–155
- Zheng J, Shen W, He DZ, Long KB, Madison LD, Dallos P (2000b) Prestin is the motor protein of cochlear outer hair cells. *Nature* 405:149–155



The remarkable cochlear amplifier

J. Ashmore^{a,1}, P. Avan^b, W.E. Brownell^{c,2}, P. Dallos^d, K. Dierkes^e, R. Fettiplace^{f,3}, K. Grosh^{g,h}, C.M. Hackneyⁱ, A.J. Hudspeth^j, F. Jülicher^e, B. Lindner^e, P. Martin^k, J. Meaud^g, C. Petit^{l,4}, J.R. Santos Sacchi^{m,5}, B. Canlon^{n,*}

^a Department of Neuroscience, Physiology and Pharmacology and UCL Ear Institute, Gower Street, London WC1E 6BT, UK

^b Laboratoire de Biophysique Sensorielle, Faculté de Médecine, Université d'Auvergne, 28 place Henri-Dunant, F-63001 Clermont-Ferrand, France

^c Department of Otolaryngology – Head & Neck Surgery, Baylor College of Medicine, Houston, TX, USA

^d Departments of Neurobiology and Physiology and Communication Sciences and Disorders, The Hugh Knowles Center, Northwestern University Evanston, IL 60208, USA

^e Max Planck Institute for the Physics of Complex Systems, Nöthnitzer Straße 38, 01187 Dresden, Germany

^f Department of Physiology, University of Wisconsin Medical School, Madison, WI 53706, USA

^g Department of Mechanical Engineering, University of Michigan, MI 48109, USA

^h Department of Biomedical Engineering, University of Michigan, MI 48109, USA

ⁱ Department of Biomedical Science, University of Sheffield, Sheffield S10 2TN, UK

^j Howard Hughes Medical Institute and Laboratory of Sensory Neuroscience, The Rockefeller University, 1230 York Avenue, New York, NY 10065-6399, USA

^k Laboratoire Physico-Chimie Curie, CNRS, Institut Curie, UPMC, 26, Rue d'Ulm, F-75248 Paris Cedex 05, France

^l Unité de Génétique et Physiologie de l'Audition, Inserm UMRS 587, UPMC-Université Pierre et Marie Curie, Collège de France, Institut Pasteur, 25 rue du Dr Roux, F-75724 Paris 15, France

^m Otolaryngology, Cellular and Molecular Physiology, and Neurobiology, Yale University School of Medicine, 333 Cedar St., New Haven, CT 06510, USA

ⁿ Karolinska Institutet, Department of Physiology and Pharmacology, von Eulers väg 8, 171 77 Stockholm, Sweden

ARTICLE INFO

Article history:

Received 29 December 2009

Accepted 6 May 2010

ABSTRACT

This composite article is intended to give the experts in the field of cochlear mechanics an opportunity to voice their personal opinion on the one mechanism they believe dominates cochlear amplification in mammals. A collection of these ideas are presented here for the auditory community and others interested in the cochlear amplifier. Each expert has given their own personal view on the topic and at the end of their commentary they have suggested several experiments that would be required for the decisive mechanism underlying the cochlear amplifier. These experiments are presently lacking but if successfully performed would have an enormous impact on our understanding of the cochlear amplifier.

© 2010 Elsevier B.V. All rights reserved.

Introduction

by Barbara Canlon

Mechano-electrical transduction in the mammalian cochlea occurs due to vibrations of the basilar membrane that cause the stereocilia of the outer hair cells to deflect resulting in the gating of mechanosensitive transducer channels. There is an active mechanical response that amplifies low-level and compresses high-level basilar membrane displacements. The amplification is frequency

dependent and results in high auditory sensitivity and an extended dynamic range.

The idea of an active process in the cochlea was first proposed by Gold, 1948, and has been the focus of intense research for more than many decades. In 1983 Hallowell Davis wrote, "We are in the midst of a major breakthrough in auditory physiology. Recent experiments force us, I believe, to accept a revolutionary new hypothesis concerning the action of the cochlea namely, that an active process increases the vibration of the basilar membrane (BM) by energy provided somehow in the organ of Corti". In his insightful paper he describes a cochlear model to include an active process and its underlying properties.

Numerous scientific reports have been aimed at characterizing the biophysical, biochemical and molecular properties of the active process. Two main mechanisms have been put forth to explain the mechanism underlying the cochlear amplifier. In brief, one is a voltage-dependent somatic motility resulting from the activity of the motor protein prestin in the lateral membrane of the outer hair cells. The other is dependent on hair-bundle motility driven by calcium currents. There is a continuum of articles being published

* Corresponding author. Tel.: +46 8524 87248.

E-mail addresses: j.ashmore@ucl.ac.uk (J. Ashmore), brownell@bcm.tmc.edu (W.E. Brownell), p-dallos@northwestern.edu (P. Dallos), fettiplace@physiology.wisc.edu (R. Fettiplace), julicher@mpipks-dresden.mpg.de (F. Jülicher), pascal.martin@curie.fr (P. Martin), jmeaud@umich.edu (J. Meaud), christine.petit@pasteur.fr (C. Petit), joseph.santos-sacchi@yale.edu (J.R. Santos Sacchi), barbara.canlon@ki.se (B. Canlon).

¹ Tel.: +44 20 7679 2141.

² Tel.: +1 713 798 8540.

³ Tel.: +1 608 262 9320.

⁴ Tel.: +33 145688890.

⁵ Tel.: +1 203 785 7566.

regarding the role of stereocilia versus somatic motility as the mechanism for the active process and these publications often spark up intense discussions among the auditory community.

There are two main mechanisms discussed in these commentaries (somatic and stereocilia based active processes) and several authors are suggesting that mechanical amplification is driven by both somatic and stereocilia contributions. However, all authors are in agreement that further experimentation is needed to be fully convinced of the mechanistic basis of outer hair cell motility. There are still many basic questions that remain to be answered before the basis of the cochlear amplifier or amplifiers is fully understood. As mentioned in the commentaries, some basic experiments that are needed include determining the characteristics of amplification along the basilar membrane (high versus low frequencies); dissecting the contribution of somatic motility from hair-bundle motility via genetic modifications and finally targeted biophysical experiments to alter ion channels and protein levels in hair cell membranes and in stereocilia. Hopefully the suggested experiments will soon be tested by inquisitive scientists to help generate a full characterization of the cochlear amplifier. There is most probably no definitive experiment but a combination of studies that will help solved the many years of debate and controversy around the cochlear amplifier.

Cochlear amplification – Somatic or stereociliar forces? A first-person response

by Jonathan Ashmore

It is always said that experimental artefacts are the most convincing of results. From the moment that Brownell and colleagues in Geneva reported that when an outer hair cell was depolarised it shortened (Brownell et al., 1985), there was always a nagging doubt that this was an epiphenomenon – a consequence of doing the experiments in a particular way. The Geneva finding used Ake Flock's earlier (re-)discovery at the Karolinska Institute of how to produce good-looking isolated OHCs. Ian Russell and I even took some home-built equipment to Stockholm in late 1982 to measure isolated cell resting potentials. We always found that the electrical V–I curves were difficult to record at hyperpolarised potentials. As a good electrophysiologist, straight from working in the retina, I did not think to look down the microscope while

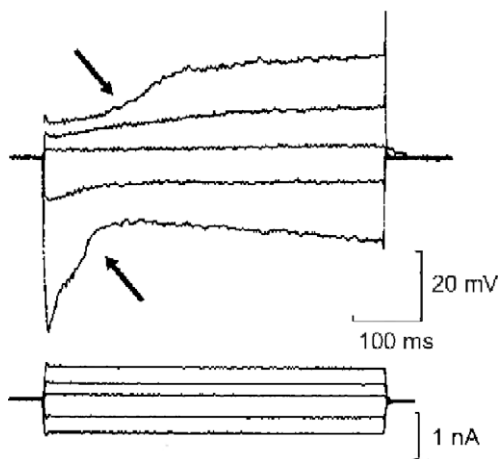


Fig. 1. Current-induced OHC movement. A microelectrode recording of potentials in an isolated guinea pig OHC during current injection, ca. 1983. Allowing for a low resting potential (ca. -30 mV), the voltage–current curves match data subsequently obtained by patch clamp recordings. The voltage distortions during current injection (arrowed) are almost certainly the result of the OHC changing length during the commands (Ashmore, unpublished).

recording data. Of course I know now, in retrospect, that the records were contaminated by the cell expanding off the microelectrode (Fig. 1). Reliable recordings of the cell biophysics required patch clamp techniques, but that came three years later. So why do I still think that OHC motility underlies the cochlear amplifier?

It is a robust mechanism: OHC motility has been recorded in so many laboratories with so many different techniques that it is hard to believe any more that it is an artefact. The cells produce forces and motility is a robust phenomenon. This seems to me to be a necessary condition for its involvement in amplifying sound in the cochlea, or more specifically for injecting power into basilar membrane mechanics. The cochlea itself needs to be built with components which withstand some, if not all, the vicissitudes of life. I also like the idea that the sensor and the effector should be distinct and separated components of the cell. I do not think such arguments are foolproof, but experiments which point to hair-bundle forces are technically difficult to carry out. Although not ruled out for this reason, bundle forces appear to be much less robust.

It is fast: We now know that OHC length changes can be driven experimentally at acoustic speeds to over 70 kHz, (Frank et al., 1999). Bill Brownell and I managed to convince ourselves that OHCs could be driven faster than 1 kHz one December day in 1985 by using a photosensor and a huge, hardwired signal averager called a Biomac (serial number 5, since you asked, and whose 60 discrete component circuit boards I came to know intimately). But to relate these results to *in vivo* cochleas, it is necessary to argue around the ‘RC-time constant problem’ where any potential changes are filtered out by the membrane at acoustic frequencies. The host of ingenious resolutions of this problem, (including bundle forces), all involve some sort of cochlear modelling. I think that some of the most physiologically convincing (and most intuitively accessible) models which resolve the problem invoke larger transducer currents in basal cochlear OHCs to offset the membrane filter. Recent work with Pavel Mistrik also leads me to think that current flow along the cochlea, through the gap junctions, enhances the extracellular potentials with the correct phase so that the potentials driving prestin are further increased at high frequencies. In brief, there are cochlear models which seem to work.

It can be knocked out: Sydney Brenner once declared that if you delete a gene and something happens you have a party; if you delete a gene and nothing happens, you still have a party as it means that your gene is so important there is compensation. With prestin knocked out, auditory thresholds rise (Liberman et al., 2002); so there is a phenotype and you can have a party. The data is compelling, although there is still room for doubt as prestin may have other regulatory roles in the cell, for example, by controlling cell pH and metabolism (Ikeda et al., 1992). Mutated or absent prestins could easily distort other, non-motor, aspects of OHC physiology. There may be an opportunity for bundle mechanisms to steal in here, but the window is a small one.

What experiments might change my mind?

No effect of ‘clean’ prestin motor alterations: I would like to see more experiments to decouple transduction from the action of the prestin motor. There are some of these experiments under way, for example in a knockin mouse where the prestin voltage dependence is altered by a minimal peptide mutation (Dallos et al., 2008). It would also be good to design ‘gain of function’ mutations in prestin making a situation where the motor forces are enhanced. But what I would like to see most would be acute, reversible, experiments where the basilar membrane mechanics is measured during instantaneous inhibition of prestin – a ‘caged salicylate’, suddenly released, might be an attractive way to do this. And then to be surprised when nothing happened.

Convincing hair-bundle movements in the kilohertz range: I would like to see bundle force measurements carried out on mammalian hair bundles at frequencies over 5 kHz. For technical reasons, many of the arguments advanced so far for stereocilia forces are extrapolations from the data. To be convinced I would like to see measurements of the magnitude and the phase of real bundle forces from real mammalian cells. Moreover these need to be made from cells taken from different cochlear positions, for models predict that bundle forces should depend upon cochlear position before they contribute to the cochlear amplifier.

Top connectors of the hair-bundle are required for waveform distortion and suppression masking but not cochlear amplification

by Paul Avan, Christine Petit*

Several major properties of sound perception rest upon the pre-processing of sound by the outer hair cells (OHC) in the mammalian inner ear, that is, one stage ahead of the mechano-electrical transduction eventually achieved by inner hair cells (IHC). Those OHCs are the key element of a feedback loop whereby sound stimuli are mechanically amplified in a widely popular view (Davis, 1983; Gold, 1948). It is the most common explanation brought forward for explaining why the auditory system of mammals is sensitive enough to detect sound power levels hardly an order of magnitude above the thermal noise. Moreover, the fine tonotopy observed in the cochlea and reflected in the remarkable ability to discriminate two sounds with slightly different pitches, is also attributed to the regenerative amplifier with feedback, working through OHCs and that operates in a frequency-selective manner.

Natural sounds pose an additional challenge: several frequency components are presented simultaneously instead of sequentially. Spectral complexity increases in the presence of competing sound sources or background acoustic noise. In such cases, if applied indiscriminately to all spectral lines, gain would be inadequate because, acting equally on signal and noise, it would leave the latter swamp neural messages. Because the gain produced by OHCs is accompanied by filtering, but also because the nonlinearities it entails generate suppressive masking interactions, acoustic messages can be cleaned up.

The place of cochlear nonlinearities in the analysis of frequency mixtures deserves to be specifically examined. The concept of non-linearity is very general, applying to any system whose response to two simultaneously presented signals is not the arithmetic sum of its responses to either signal when presented alone: instead, when mixed up, some components increase at the expense of others. Masking is a typically nonlinear psychophysical event defined by the fact that the loudness of one sound decreases or even vanishes when another sound interferes. Its cochlear correlate is suppressive masking whereby the mechanical or electrical response to a test tone decreases in the presence of a masking tone. This phenomenon, felt as a nuisance when it is the signal of interest that gets masked, globally turns as an advantage in that it allows the dominant frequency component at one place in the cochlea to become even more dominant by exerting a masking effect on competing, weaker signals. Therefore, suppressive masking can enhance contrasts.

There is now no doubt that cochlear mechanics is far from linear and it can express its nonlinearities in several ways. Besides suppressive masking, another example is that contrary to high-fidelity devices, OHC operation introduces conspicuous waveform distortions. These distortions are large enough to be heard although not being present in the initial sound stimulus (e.g., Tartini, 1754; Goldstein, 1967). In response to bitonal stimuli at frequencies f_1 and f_2 , distortion of their waveforms generates combination

tones at arithmetic combinations of f_1 and f_2 – hence the best known cubic difference tone at $2f_1 - f_2$, assuming $f_2 > f_1$. Not only does the cochlea produce audible sound distortion but it also re-emits them as one category of otoacoustic emissions, namely distortion-product otoacoustic emissions (DPOAE) (Kim et al., 1980). Otoacoustic emissions have become a prominent tool for achieving neonatal hearing screening: when by being absent they signal OHC dysfunction and, according to the most popular interpretation, failure of the cochlear amplifier, inner hair cells also happen to be impaired in many cases, owing to the structural and functional kinship of the two types of sensory cells. Sensorineural deafness is then a likely diagnosis.

In summary, the currently accepted picture is that gain and filtering are two closely associated properties ensured by OHCs and that their way of operating induces strong waveform distortions coming out as non-invasively detectable DPOAEs. Last, the very mechanism that leads to instantaneous distortion of sound waveforms is likely strong enough to contribute to suppressive masking. This holistic view placing OHCs and their nonlinear behavior at the heart of the concept of cochlear amplifier and of many perceptive phenomena does not allow for the fact that the nonlinearities produced by OHCs do not share the same meaning and may thus have different structural or functional origins – e.g., the mechanotransduction channel for some of them, other molecules or substructures in the stereocilia bundle or cell body for others. Some types of nonlinearities in current use in electroacoustic amplifiers do not produce instantaneous waveform distortion, as is the case for compressive devices in hearing aids. Conversely, other types of nonlinearities do not need gain to generate waveform clipping.

Until now holistic models posited that at the core of OHC ability to produce gain, and the combination of filtering, and waveform distortion, and masking that comes with gain, is a common source, i.e., the intrinsic properties of the mechanotransduction channels.

A common explanation might be inherent to the mandatory nonlinearity associated with the thermodynamics of the mechanotransduction channel. This channel exists in at least two states, open and closed. Its opening probability relates to stereocilia deflection according to Boltzmann's law accounting for the different energies associated with the opened and closed states. Boltzmann's law is a sigmoid instead of a straight line, thus when stereocilia bundles are deflected by the sinusoidal pressure wave of a pure tone coming from outside, the current through mechanotransduction channels, proportional to the opening probability, exhibits a distorted waveform. The resulting mechanical feedback exerted through bi-directional transduction thus injects distortion into the initially sinusoidal sound wave. It was thought that waveform distortion, Tartini tones and DPOAEs were produced in this manner by OHCs. Simple mathematics then shows that waveform distortion generates suppressive masking (Engebretson and Eldredge, 1968).

This view of mechanotransduction channel properties as a central player in all aspects of sound pre-processing by OHCs suggested that OHCs ensured, in a remarkably parsimonious manner, a whole set of functions sharing a common origin. As a counterpart, failure of this intrinsic property of channels should also result in hearing impairment in relation to loss of cochlear amplification, and in the concomitant loss of all other beneficial aspects of cochlear pre-processing of sound.

A recent study of a mutant strain of mice in which the gene coding for stereocilin is inactivated has shown that the aforementioned holistic view seems not valid (Verpy et al., 2008). When these mutant mice are young enough (around 14–15 postnatal days, P14–15), their cochlear sensitivity is normal, as illustrated by the fact that across the whole frequency spectrum auditory brainstem evoked (ABR) and compound action potential (CAP) thresholds do not statistically differ in mutant mice and wild-type

littermates. Cochlear filtering is also normal in mutant mice, as indicated by the normal Q10s of their CAP masking tuning curves. Mechano-electrical transduction currents derived from round-window measurements of cochlear microphonics are normal as well. These characteristics indicate the presence of a full supply of normally functioning mechanotransduction channels. Their thermodynamics thus obeys a normal Boltzmann law and the curve relating the transduction current to stereocilia deflection must be the same sigmoid as in normal ears. Yet in the absence of stereocilin, mice no longer distort waveforms, and for example their cochlear microphonics in response to loud tones remain sinusoidal up to 100 dB SPL. The electrical cochlear response to pure tones does not contain harmonics. Likewise, DPOAEs are totally absent. Furthermore, with even more significant perceptive consequences, when these mutant mice are exposed to a mixture of sounds, suppressive masking is absent or strongly diminished. The level of a masking tone must be about 20 dB louder than in a normal ear for the CAP response to a probe tone to decrease. CAP masking tuning curves can still be plotted; however, because the line-busy neural mechanism of masking, alone, persists: this is what allowed Q10s to be found similar in mutants and controls. Therefore, in the presence of a mixture of sounds, the mutant cochlea is no longer able to significantly act on the contrasts among components.

Stereocilin enters in the composition of hair-bundle fibrous links, the top connectors, bonding the apexes of stereocilia inside the bundle. In mutant mice, top connectors are absent and the tips of stereocilia in OHCs are more remote than in non-mutant mice.

So, suppressive masking and waveform distortion come with each other and can vanish even though OHC mechanotransduction channels provide normal amplification and filtering. This unusual experimental situation leads to conclude that the top connectors, and possibly the stereocilin-mediated contact of the stereocilia bundle to the tectorial membrane contribute to a major cause of distortion, larger than that in relation to the Boltzmann statistics of mechanotransduction channels. Stereocilin-dependent connectors could distort either as a result of an intrinsic property or indirectly by a constraint they might exert on the displacement of the stereocilia bundle or on the response to sound of some of its components.

We thus propose that in mutant mice as well as in normal ones, the operating curve of OHC mechanotransduction channels relating displacement to current exhibits a normal sigmoid shape because its becoming straighter would affect cochlear gain by negatively affecting channel sensitivity, which was not the case. Likely, this nonlinearity, on its own, is not large enough to generate measurable distortion. In normal mice, it is the presence of top connectors that enables waveform distortions, DPOAEs and suppressive masking to show up in standard measurements. In mutant mice, the same measurements detect none of these properties even though the cochlear amplifier works, thanks to a normally nonlinear mechanotransduction in OHCs.

Stereocilin mutants show that dissociation between normal auditory thresholds and missing DPOAEs is possible, if not commonplace. Previous work on acute cochlear ischemia has shown, conversely, that DPOAEs can persist and keep many of their normal properties although cochlear gain has vanished (Avan et al., 2003). Put together, these observations should warn clinicians against too systematic attempts at interpreting DPOAEs in terms of cochlear amplification and hearing sensitivity.

Membrane-based amplification in hearing

by William E. Brownell*

Acoustic vibrations enter and neuronal action potentials leave the inner ear. An interplay of mechanical and electrical energy re-

sults in hair-cell receptor potentials that ultimately trigger neurotransmitter release at the afferent synapse. The diffusion of neurotransmitter across the synaptic cleft depolarizes 8th nerve terminals and initiates action potentials that travel to the central nervous system. The action potentials encode information about the spectral and temporal content of environmental sounds. The ability to localize predator or prey is improved by analyzing sounds over a wide range of frequencies resulting in an evolutionary selection pressure for detecting ever higher frequencies. Nature has incorporated diverse strategies to overcome physical constraints for high-frequency hearing. The constraints include: (1) viscous damping by inner ear fluids; (2) electrical filtering by cell membranes; and (3) temporal limitations imposed by chemical cascades at the synapse. The mechanisms that overcome viscous damping have been called the “cochlear amplifier” in mammalian ears and an “active process” in vestibular and other hair cell systems. These must work in concert with mechanisms for increasing membrane bandwidth and assuring the temporal precision of afferent fiber action potentials if high-frequency hearing is to be achieved.

It is likely that the cochlear amplifier originated in the stereocilia bundle of early vertebrates. Several mechanisms for bundle motility have been proposed but it is the one responsible for fast voltage-dependent bundle movement or flicks (Cheung and Corey, 2006) that suggests an evolutionary origin for the voltage-dependent somatic motility of the outer hair cell. In order for high-frequency voltage-dependent electromechanical transduction to take place in either the bundle or the soma there must be a mechanism that increases the electrical bandwidth of the membrane. Membrane flexoelectricity and converse flexoelectricity are suited for high-frequency bundle and somatic motility as well as increasing membrane bandwidth. A flexoelectric based “synaptic amplifier” may also help to assure the temporal precision of afferent fiber action potentials.

When outer hair cell electromotility was first observed (Brownell et al., 1985) it was a strong candidate for the mammalian cochlear amplifier. The OHC is unique to the mammalian cochlea and is perhaps the most exotically specialized hair cell (see Fig. 2). Morphological and molecular features of its lateral wall endow it with the ability to generate mechanical force at high frequencies (Frank et al., 1999). The force generating mechanism is located in the lateral wall plasma membrane where the transmembrane electric field is converted directly into mechanical force. Biological membranes are soft, thin ensembles of lipids, proteins, and other molecules. The proportions of the components vary but lipids dominate reaching 10^2 lipid molecules for every protein in some membranes. Membrane constituents diffuse freely within the plane of the membrane unless they are anchored to the cytoskeleton. Membranes are very thin (typically ~ 5 nm) yet cover large surface areas ($>10^3 \mu\text{m}^2$ in the case of the plasma membrane). Living cells expend metabolic energy to sustain electrochemical gradients (~ 100 mV) across their membranes and the associated transmembrane electric field is large (>10 MV/m – compare to the ~ 3 MV/m fields associated with atmospheric lightning). Living cells also expend energy to maintain a characteristic asymmetry in the number of lipid associated fixed charges on the inner and outer surfaces of their membranes. Integral membrane proteins can contribute to the electrical charge difference at the two surfaces. The net charge asymmetry of the membrane gives rise to an intrinsic electrical polarization that sets the stage for a piezoelectric-like force generation (Brownell, 2006). The electrical field is converted directly into mechanical stress and charge displacement is converted into mechanical strain. Experimental evidence demonstrates that electromechanical coupling occurs naturally in lipid bilayers where it is called the flexoelectric effect (Petrov, 2006; Sachs et al., 2009). This phenomenon is an analogue of the electromechanical

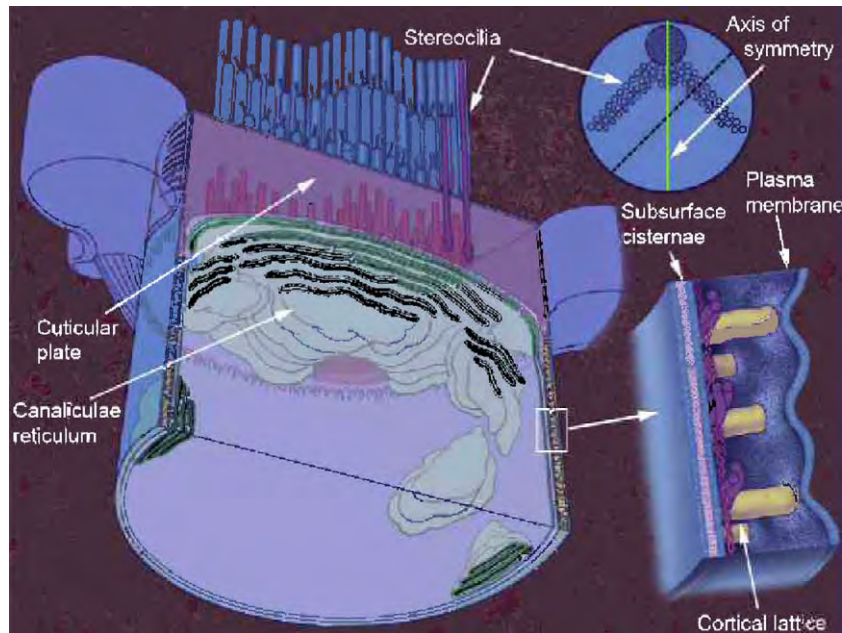


Fig. 2. Membrane organization of the outer hair cell stereocilia bundle and lateral wall. Both the apical pole and the lateral wall are composed of three layers. The plasma membrane is the outermost layer in both locations. The innermost layer is composed of a membrane bound organelle called the canalicular reticulum in the apex and the subsurface cisterna in the lateral wall. In between outer and inner membrane layers is a cytoskeletal structure called the cuticular plate at the apex and the cortical lattice in the lateral wall. Insert on the right portrays a high power rendering of the outer hair cell lateral wall. Insert at upper right is a view of the apical end showing the plane at which the outer hair cell has been opened. Adapted from Fig. 1 in Brownell, 2002.

behavior of piezoelectric crystals. Two kinds of flexoelectricity are typically discussed: (1) the direct flexoelectric effect describes changes in the electrical polarization of the membrane resulting from changes in curvature; and (2) the converse flexoelectric effect is the reciprocal phenomena in which the membrane curvature changes in response to applied electric fields. Both somatic (Raphael et al., 2000) and stereocilia bundle (Breneman et al., 2009) motility have been modeled to arise from converse flexoelectricity.

While membranes can produce high-frequency mechanical force (Anvari et al., 2007; Frank et al., 1999; Ludwig et al., 2001; Zhang et al., 2007) in response to experimentally applied electric fields the functional significance of this ability has been questioned because commonly studied cell membranes are considered to be low-pass electrical filters and therefore unable to sustain transmembrane receptor potentials at high frequencies. A solution for the low-pass constraint is provided by coupling electrical and mechanical energy. The ready conversion of one form of energy to the other endows the membrane with a biological piezoelectricity that pushes the cell membrane cutoff frequency to higher frequencies (Rabbitt et al., 2009; Spector et al., 2003; Weitzel et al., 2003).

Prestin is an integral membrane protein belonging to the Slc26A family of anion transporters that enhances the piezoelectric properties of transfected test cells (Ludwig et al., 2001; Zhang et al., 2007; Zheng et al., 2000). Prestin-associated charge movement is at least three orders of magnitude larger and qualitatively different than the nonlinear charge movement of untransfected cells (Farrell et al., 2006). Electromotile force production, in contrast, is increased by well under an order of magnitude (Anvari et al., 2007; Ludwig et al., 2001). The large prestin-associated non-ohmic, reactive displacement currents are thought to arise from the movement of cytoplasmic anions such as chloride and bicarbonate into and out the membrane. A model of the electrodiffusion of anions into a model protein is able to quantitatively reproduce several features of this charge movement (Sun et al., 2009). Prestin may help overcome the low-pass problem by facilitating a phaseshifted

charge movement that compensates for membrane capacitance in a manner similar to the negative-capacitance circuits found in voltage-clamp amplifier headstages.

Both outer hair cell electromotility and neurotransmission at the inner hair cell synapse are rapid, membrane-based, mechanical events that are controlled by the hair cell receptor potential. Since neurotransmitter release can be synchronized to high frequencies (approaching 10 kHz) in some species, broad-band electrical properties are also required to allow synaptic stimulation. The magnitude of inner hair cell receptor potentials varies with stimulus intensity yet the timing of neural discharge is intensity invariant for both clicks and best frequency tones (if neurotransmitter release were only a function of current it would occur at different times as the intensity changed). Temporal invariance in the presence of receptor potentials of increasing magnitude argues for a feedback mechanism resembling that of the cochlear amplifier on basilar-membrane vibrations. OHC mechanical feedback preserves the temporal fine structure of basilar-membrane vibrations throughout a wide range of intensities (Shera, 2001). Temporal shifts of basilar-membrane vibration zero-crossings and local peaks and troughs would occur in the absence of mechanical feedback and these shifts are not observed experimentally (Recio and Rhode, 2000). Membrane flexoelectric mechanisms could provide an electromechanical feedback to exocytosis at the afferent synapse and help to insure intensity independent temporal precision (Brownell et al., 2003). The cochlear amplifier, broad-band electrical properties and the synaptic amplifier could all benefit from membrane electromechanics.

There are several experiments whose results could validate or disprove the flexoelectric concepts presented in this section. High-frequency axial displacements of the stereocilia bundle similar to those observed in membrane tethers (Zhang et al., 2007) is required to determine if converse flexoelectricity is contributing to the bundle motor. Experimental confirmation of the inverse relation between the radius of curvature of the membrane and electromechanical force production by the membrane is also

required. Such an experiment would require ultramicroscopic measures of the curvature. High resolution structural information for prestin is required to unravel its precise role in the outer hair cell somatic motor. The existence of acoustically evoked, non-ohmic, displacement currents in cochlear fluids is predicted by the prestin-associated charge movement measured in isolated cells. Experimental confirmation of cochlear displacement currents could explain the discrepancy between maximal hair cell receptor currents in isolated hair cells and those predicted from earlier cochlear current density measures (Zidanic and Brownell, 1990).

Feedback in the cochlea

by Peter Dallos

Science thrives on controversy and scientists love a good clean fight. Students of how mammalian “cochlear amplification” comes about have been in the ring for more than 30 years; more than 60 if we consider Gold’s (1948) initial suggestions. The development of two schools of thought, championing outer hair cell (OHC) somatic motility and OHC ciliary motility as the means of amplification, is amply documented and need no review here (Dallos, 2008; Hudspeth, 2008). The common thread, that OHCs are the amplifier elements, arose early on the basis of experiments with chemical ablation of OHCs using ototoxic agents and the examination of resulting behavioral threshold shifts and alterations of neural tuning curves (Ryan and Dallos, 1975; Dallos and Harris, 1978; Liberman and Dodds, 1987). Inner hair cell (IHC) stereocilia have no firm contact with the tectorial membrane (Lim, 1980), consequently these cells are unlikely to participate in mechanical amplification.

Here I briefly list a few items that have been adduced as supportive or contrary to either amplifier schemes, which I consider to be less than deal breakers.

Probably the most often cited problem with somatic motility being the amplifier is its voltage dependence (Santos-Sacchi and Dilger, 1988). Inasmuch as the passive OHCs’ lateral membranes are electrical low-pass filters with low cutoff frequencies (<1 kHz; Housley and Ashmore, 1992; Preyer et al., 1996) the receptor potential, which presumably drives electromotility, is attenuated at high frequencies. This seemingly fatal problem for electromotility-based amplification has been attacked by a whole host of schemes. These are in four major categories. One approach is to see if gross cochlear potentials might be sufficient to provide the voltage gradients for OHCs at high frequencies (Dallos and Evans, 1995; Fridberger et al., 2004; Iwasa and Sul, 2008), or if the cochlear electroanatomy is sufficiently influential (Mistik et al., 2009). The second is based on the realization that the OHC is a reciprocal electromechanical system (Weiss, 1982). As a consequence, its effective time constant is not what is simply measured by electrical means in an isolated cell, but one modified by the reflection of the mechanical elements upon the electrical side of the network during contractile activity (Mountain and Hubbard, 1994; Spector et al., 2003; Ramamoorthy et al., 2007). The third possibility is that the collective action of a group of OHCs in a negative feedback circuit provides amplification at high frequencies even if individual OHCs are limited in their frequency response range (Lu et al., 2006 b). Finally, local activation of motor molecules by basolateral ionic current has been proposed as a means of avoiding the low-pass filter conundrum (Rybalchenko and Santos-Sacchi, 2003; Spector et al., 2005). While full experimental verification of any of these schemes is yet forthcoming, they, individually or collectively in some combinations, are sufficiently compelling as to render the principal objection to the somatic motility mechanism much less troublesome. The speed of stereociliary motility has been addressed as well. While the forward mechanotransducer channel activation is extremely fast (Corey

and Hudspeth, 1983), fast adaptation of the channel, which is associated with the fast feedback process, is slower (Ricci et al., 2005). The development of force associated with OHC transducer channel activity has been measured (Kennedy et al., 2005). Negative stiffness (departure from linear stiffness) develops over time, but, while not proven, it is possible that *in vivo* the time course is adequately fast.

The second widely cited objection to the dominant role of somatic motility is that this process itself is not tuned. The context of this issue is the often-stated question: what tells an OHC to provide amplification for a given stimulus? The usual formulation is to postulate a need for a second system of graded filters, different from the traveling wave, which would provide the input to appropriately located amplifying OHCs. Tectorial membrane resonance is one of the favored means of such filtering (Allen, 1980; Zwislocki and Kletschy, 1979; Gummer et al., 1996). Another possibility is to enlist the inherent band-pass nature of the ciliary amplifier as a pre-filter to somatic motility (Ricci, 2003; Hudspeth, 2008). Tuning of ciliary motile processes (Martin and Hudspeth, 1999) may be a significant advantage, by itself, to this means of amplification.

One question raised about ciliary amplification pertains to the adequacy of the force that this source can deliver into the cochlear mechanical load. It is now reasonably certain that the collective action of circumscribed groups of OHCs can produce enough force to displace the cochlear partition, including the basilar membrane (Hudspeth, 2008; Dierkes et al., 2008). While the force produced by somatic motility is significantly greater, this should not preclude ciliary motility as a mechanism for amplification.

Are there definitive experiments that rule out the contribution of either candidate mechanism in the mammal? The short answer is no. There *are* experiments that suggest some combined operation of the two systems (Kennedy et al., 2006). The work of Chan and Hudspeth, 2005 intimates that ciliary motility is sufficient to provide cycle-by-cycle amplification, with slow somatic motility serving as an adjustor of the former system’s operating point. A difficult problem in all experiments that attempt to parcel the process into its two possible components is eliminating one while sustaining the other. *In vitro*, the complete suppression of either process is difficult and may not have been achieved. *In vivo*, inasmuch as the cochlea operates as a feedback system any alteration of the feedback loop will affect the response of all components. Thus the difficulty of interpreting the results derived from mouse models in which the OHC motor molecule (prestin) was absent has been appreciated. In the absence of prestin from OHCs in the prestin knockout mouse, the cells become shorter and more compliant (Liberman et al., 2002; Cheatham et al., 2004; Dallos et al., 2008). Consequently, raised thresholds and lack of tuning in these mice could result from non-existing somatic motility, altered ciliary motility due to changed mechanical load, or a combination. While the model does not yield unequivocal results, the electrophysiological phenotype is essentially the same as one obtains in the absence of OHCs. In order to overcome incidental changes attendant to the lack of prestin, a mouse model was developed that incorporated the V499G/Y501H mutation in its prestin molecules (Dallos et al., 2008). OHCs in 499/501 mice have normal lengths and stiffnesses, but the prestin-produced somatic motility is more than 90% reduced. These animals have hearing loss and lack of tuning, not unlike the knockout mice. It was concluded that the presence of functional prestin is essential for the full expression of cochlear feedback. The result could be explained two ways. Somatic motility is the entire feedback amplifier and its elimination negates all gain. Alternatively, ciliary motility produces the feedback, but it is under tight control by somatic motility. At this time, further experimental refinement of the choice is lacking. The ubiquity of ciliary feedback-based amplification among vertebrates and indeed in some insects speaks for the primacy of this mechanism (Manley, 2001:

Hudspeth, 2008). Its suggested control by somatic motility in the mammal is more problematic. The commonly postulated low-frequency adjustment of the ciliary amplifier by somatic motility (e.g., Chan and Hudspeth, 2005) is not likely to occur due to the fact that, at low-levels, where amplification is most pronounced, the high-pass filter nature of mechanotransducer-channel fast-adaptation should virtually eliminate DC mechanical inputs to OHCs. Simply stated, the putative controlling DC signal in cochlear mechanics is significantly reduced. Of course, one should also ask what evolutionary pressure could have produced the voltage-activated prestin motor that has the demonstrated and unique capability of operating at ultrasonic frequencies (Frank et al., 1999), if its function would be effective only at DC?

Bottom lines: Prestin-based somatic motility and ciliary motility may both contribute to the total cochlear feedback. Examination of the cochlear output of genetically modified mice suggests that without functional prestin essentially all amplification is eliminated. The many suggested schemes to counteract OHC membrane filtering of receptor potentials suggest the possibility that the filter is not a necessary impediment to somatic motility providing the feedback at any frequency. It is unlikely that OHCs can provide DC control of a ciliary amplifier.

Coupled hair-bundles could endow the cochlear amplifier with sharp frequency tuning and nonlinear compression

by Kai Dierkes, Benjamin Lindner, Frank Jülicher*

The key signatures of the auditory amplifier are (i) a frequency tuned and sensitive response to weak stimuli, (ii) a compressive nonlinear response over a large amplitude range, and (iii) spontaneous otoacoustic emissions (Dallos, 1992; Hudspeth, 2008). These signatures are reflected in observed basilar-membrane vibrations (Robles and Ruggero, 2001) and can be understood as the consequence of the presence of nonlinear dynamic oscillators operating in a critical regime (Camalet et al., 2000; Eguiluz et al., 2000; Duke and Jülicher, 2003). This suggests that the working of the cochlear amplifier is based on nonlinear oscillators. It is commonly thought that that active amplification is mediated by mechano-sensory hair cells (Dallos, 1992; Hudspeth, 1997; Manley et al., 2001; Fettiplace and Hackney, 2006). Two important features of hair cells have been suggested to contribute: (i) outer hair cell electromotility can provide mechanical feedback to the basilar-membrane vibrations (Brownell et al., 1985; Santos-Sacchi, 2003; Ashmore, 2008; Dallos et al., 2008) and (ii) mechanosensitive hair-bundles have been shown to be active elements which can generate spontaneous movements and noisy oscillations (Crawford and Fettiplace, 1985; Martin and Hudspeth, 1999; Martin et al., 2001; Kennedy et al., 2005). Individual hair bundles can act as nonlinear oscillators capable to amplify stimuli (Martin and Hudspeth, 1999; Martin and Hudspeth, 2001) albeit with restricted performance which is limited by intrinsic noise at the cellular scale (Nadrowski et al., 2004). This limitation as well as the small forces associated with movements of individual hair-bundles have put doubts on the role of active hair-bundle motility for the cochlear amplifier.

In many vertebrate inner ear organs hair-bundles are linked to overlying elastic membrane structures, such as otolithic and tectorial membranes (see Fig. 3a) and (Freeman et al., 2003). This introduces the possibility that the cooperation of hair-bundles plays a role to enhance the properties of hair-bundle-mediated amplification (Manley and Köppl, 2008). Recently, we have shown that small groups of hair bundles which are coupled by elastic elements can respond much more sensitively to periodic stimuli than isolated hair-bundles. Furthermore, such groups of hair-bundles display spontaneous movements with sharply peaked power spectra and behave as sharply tuned amplifiers that exhibit compressive nonlinearities over a wide range of signal amplitudes (Dierkes et al., 2008).

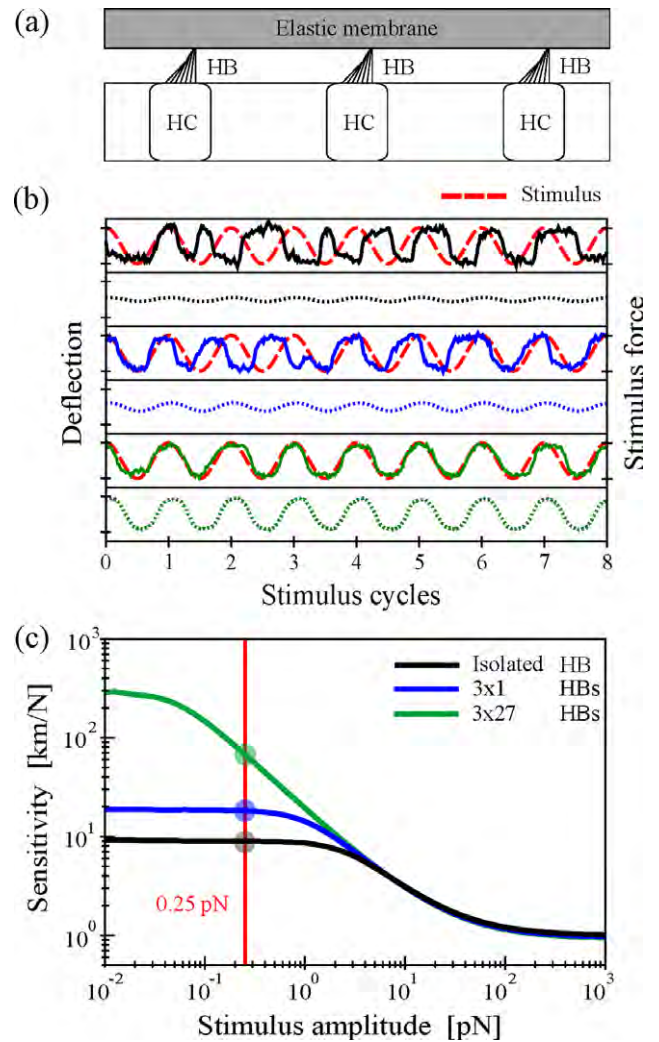


Fig. 3. (a) Schematic of three hair cells (HC) with their hair-bundles (HB) coupled elastically via an overlying membrane. (b) Illustration of phase-locking for an isolated hair-bundle (black) and the central hair-bundle of groups of coupled hair-bundles (3×1 HBs, blue; 3×27 HBs, green). Sample trajectories of simulation results (solid lines) are shown together with the periodic stimulus force $F(t) = A \cos(2\pi f_0 t)$ with $A = 0.25$ pN (broken red line) for coupling stiffness matched to stereociliar pivotal stiffness, $K = K_{sp} = 0.6$ pN/nm. Each system is driven at its characteristic frequency f_0 ($f_0 = 8.91$ Hz (1×1), 9.90 Hz (3×1), 10.54 Hz (3×27)). The respective time-dependent average responses over many repetitions of the stimulus are shown as dotted lines below. Distance between ticks is 40 nm for deflection and 0.5 pN for stimulus force. (c) Nonlinear response of coupled hair-bundles. For the three systems studied in (b) the sensitivity (average response amplitude divided by stimulus amplitude) is displayed as a function of stimulus amplitude. The red vertical line indicates the stimulus force used in (b). Note that the sensitivity to weak stimuli and the amplitude range of nonlinear compression increase with increasing system size.

sive nonlinearities over a wide range of signal amplitudes (Dierkes et al., 2008).

In our study we employed a model of the single hair-bundle that can account quantitatively for its active mechanical properties and the stochastic features of hair-bundle motility (Nadrowski et al., 2004; Tinevez et al., 2007). The model incorporates stereociliar pivotal stiffness, channel gating elasticity, the properties of adaptation motors, as well as calcium feedback on these motors. Fluctuations reflecting thermal interactions of the hair-bundle with the surrounding fluid, stochastic transitions of transducer channels and adaptation motors are also taken into account. Limitations of the single hair bundle's ability to respond faithfully to an external stimulus (see Fig. 3b, broken red lines) are consequences

of these fluctuations (see Fig. 3b, black solid line). Fluctuations thereby limit the detector's sensitivity to weak stimuli and also the sharpness of frequency tuning, as well as the amplitude range over which nonlinear amplification occurs.

Our results were obtained by considering groups of $N \times M$ hair-bundles that are arranged on a square lattice with their excitatory directions aligned along the same lattice axis. Coupling is described by linear springs of stiffness K that connect nearest neighbors including diagonal connections. Homogeneous systems of identical hair-bundles as well as heterogeneous systems of hair-bundles with varying characteristic frequency were considered. In the homogeneous case the quality of spontaneous oscillations exhibits a threshold-like dependence on coupling strength K . A sudden increase of quality occurs for $K \approx K_{SP}$, with K_{SP} denoting the stereociliar pivotal stiffness. When a group of hair-bundles is driven by a weak periodic stimulus at the characteristic frequency (see Fig. 3b, broken red lines), the system shows an enhanced phase-locking to the external signal (see Fig. 3b, cf. blue and green solid lines to black solid line). This higher degree of phase-locking leads to an increase of the time-dependent average of the response amplitude (see Fig. 3b, dotted lines). Thus coupling of hair-bundles increases the sensitivity (defined as the ratio of the mean response amplitude to the stimulus amplitude) in response to a weak stimulus (see Fig. 3c). For increasing stimulus amplitude, the sensitivity decreases, indicative of the compressive nonlinear response of the system. The range of stimulus amplitudes over which this nonlinear response is observed increases for increasing system size (see Fig. 3c). The response to strong stimuli is determined by the passive stiffness of the single hair-bundles and does not depend on system size. As a consequence the amplification gain, which is the ratio of sensitivities to weak and strong stimuli, increases almost linearly with system size. For a system of 81 hair bundles a gain of up to 400 is obtained for optimal coupling strength.

In the mammalian cochlea, nonlinear compression of the basilar-membrane vibration amplitude in response to stimuli at the local characteristic frequency have been reported, that range up to four orders of magnitude of sound pressure amplitude (Robles and Ruggero, 2001). The corresponding amplification gains are of the order of 1000 (Robles and Ruggero, 2001). These properties can be understood as resulting from the combination of a global excitation of the basilar membrane (the traveling wave) and the effects of nonlinear active elements which govern the basilar-membrane vibration in the vicinity of the characteristic place (Nobili and Mammano, 1996; Duke and Jülicher, 2003). While the properties of the active elements in the cochlea exceed by far the abilities of an isolated hair-bundle, our work suggests that groups of coupled hair-bundles can approach their performance.

In the mammalian cochlea the basilar membrane exhibits a graded profile of characteristic frequencies and the sensory hair cells display a morphological gradient (Dallos et al., 1996). This raises the question whether enhanced signal detection due to coupling can also work in heterogeneous systems. We thus performed simulations of systems of 3 times 27 hair-bundles (representing three rows of outer hair cells) with varying intrinsic frequencies, resulting from a gradient of pivotal stiffness. For intermediate coupling strength $K \approx \bar{K}_{SP}$, where \bar{K}_{SP} is the average pivotal stiffness of the hair-bundles, the amplification gain is still enhanced by coupling, while a frequency gradient is also maintained (Dierkes et al., 2008). This implies that in order to make use of mechanical coupling in the cochlea the elasticity of the overlying membrane has to be locally adjusted to the hair-bundle pivotal stiffness. It has been shown that hair-bundle stiffness as well as tectorial membrane stiffness vary gradually along the cochlea in such a way that coupling strength and the stereociliar stiffness could indeed be matched (Strelioff and Flock, 1984; Gueta et al., 2006; Richter et al., 2007).

What does the above imply about the cochlear amplifier? There is strong evidence that outer hair cell electromotility plays an important role in cochlear amplification (Dallos et al., 2008). Electromotility introduces an electromechanical feedback that couples hair-bundle movements back to basilar-membrane vibrations (Ashmore, 2008; Nowotny and Gummer, 2006). However, electromotility does not exhibit significant nonlinearities for physiological voltage variations and it does not show frequency tuning (Ashmore, 2008). In contrast, small groups of hair bundles do show all the necessary features: sharp frequency tuning, high sensitivity and compressive nonlinearity (Dierkes et al., 2008). However, there are two limitations. Firstly, the high amplification gain observed in the cochlea is not easily reached in our model if at the same time a frequency gradient is maintained. Secondly, hair-bundle movements may be inefficient to significantly drive basilar-membrane vibrations. These issues could be resolved by regarding the cochlear amplifier as a combination of outer hair cell electromotility and active motility of locally coupled hair-bundles. In this scenario, the frequency selectivity and the compressive nonlinear properties of the cochlear amplifier are provided by coupled hair-bundles. Outer hair cell electromotility is a largely linear element that may allow hair-bundle movements to efficiently drive basilar-membrane vibrations. By varying properties of the electromotile feedback the sensitivity and amplification gain of the amplifier could be adjusted. Careful regulation of nonlinear amplification is important to guarantee the stable operation of nonlinear oscillators in the inner ear (Camalet et al., 2000) and thereby to enhance the detection of complex sounds in varying environments. The electromotile feedback is well suited to mediate such a regulation. This may explain why outer hair cells receive signals from the brain via efferent fibers which could influence electromotility.

The origin of the cochlear amplifier

by Robert Fettiplace*, Carole M. Hackney

The mammalian cochlea is a unique cellular array the properties of which vary systematically along the organ. These range from the stiffness and size of gross features such as the basilar and tectorial membrane and the dimensions of the outer hair cells (OHCs) (Lim, 1986) to the amplitude of the mechanotransducer channels (Beurg et al., 2006). All features must ultimately conspire to establish the tonotopic map. Passive mechanical tuning is augmented by the cochlear amplifier which endows sharp frequency selectivity and accounts for the 20–60 dB of extra tip to the tuning curves measured for vibrations of the mammalian basilar membrane (Robles and Ruggero, 2001). The amplifier incorporates a compressive nonlinearity such that the gain and sharpness of tuning are diminished at higher sound levels. The underlying process is thought to involve electromechanical feedback by the OHCs probably through a filter whose frequency characteristics change along the tonotopic axis (Fig. 4). Work over the past 20 years has demonstrated voltage-dependent contractility of the OHCs underpinned by aggregation of the motile protein, prestin, in the lateral membrane (Zheng et al., 2000). However, somatic deformation of the OHC is only one step in a feedback pathway that also includes motion of the tectorial membrane and hair-bundles, mechano-electrical transduction and generation of a receptor potential to drive the prestin motor. It is assumed that OHC contractions supply force to boost the vibrations of the basilar membrane. A primary argument for the somatic motor is that molecular modifications or knock out of prestin largely abolish amplification (Lieberman et al., 2002; Dallos et al., 2008). A criticism of this approach is that interfering with prestin merely alters a feedback loop, any part of which could be the site of amplification. For example, knock out of the mechanotransducer channel protein (although not currently feasible) would presum-

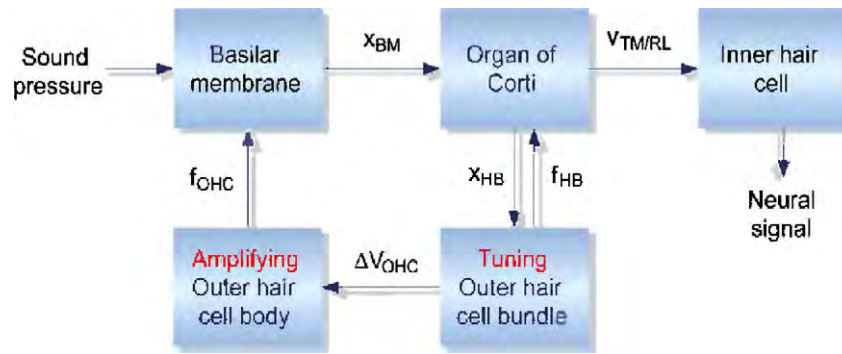


Fig. 4. Process involved in the cochlear amplifier. Sound causes displacements of the basilar membrane, x_{BM} , and organ of Corti leading to deflection of the OHC hair-bundle, x_{HB} . Activation and adaptation of the mechanotransducer channels generate a tuned transducer current culminating in a change in OHC membrane potential, ΔV_{OHC} , that drives the somatic motor. The force, f_{OHC} , produced by OHC electromotility augments basilar membrane motion and may also deform the organ of Corti (Mammano and Ashmore, 1993). Gating of the mechanotransducer channels may generate sufficient force, f_{HB} , to move the hair-bundles (the hair-bundle motor) and the organ of Corti. The inner hair cell bundles are stimulated by the relative velocity, $v_{TM/RL}$.

ably also eliminate amplification. An alternative view is that amplification is linked to active hair-bundle motion, powered by calcium influx promoting fast adaptation of the mechanotransducer channels (Ricci et al., 2000). To appreciate the contributions of the different processes, it is necessary to understand the micromechanics of the organ of Corti and how forces generated by the OHC somatic and hair bundle motors vibrate the basilar membrane and are transmitted to inner hair cells that also exhibit similar sharp tuning.

The prevailing view, that the somatic motor is at the heart of cochlear amplification, is strongly endorsed by recent work mutating prestin or proteins of the tectorial membrane (Dallos et al., 2008; Mellado Lagarde et al., 2008). However, there are several details not fully explained. How is the somatic motor controlled on a cycle-by-cycle basis at high frequencies where the periodic component of the receptor potential will be filtered by the OHC time constant? Several solutions have been proposed (summarized in Ashmore, 2008) but none has been fully confirmed experimentally. How does the somatic motor supply frequency selective feedback? In many attempts to simulate the sharp basilar membrane tuning, an additional filter or phase shift is introduced to match simulations with experimental results but somatic motility itself is not inherently frequency selective. The extra filter invoked in modeling is often assigned to a resonant tectorial membrane (Nobili and Mammano, 1996). Although the properties of the tectorial membrane, both stiffness and mass, change substantially along the cochlea (Richter et al., 2007), the evidence for membrane resonance is controversial. Finally, how do OHC properties change to generate the necessary forces at high frequencies to counter the increase in viscous load and basilar membrane stiffness? Again in simulations, the force achieved by OHC contraction is assumed to increase (sometimes >100-fold; Lu et al., 2006a) in progressing from the low- to high-frequency end of the cochlea. However, there is no evidence for such an increase in force generation (Iwasa and Adachi, 1997) and if the prestin concentration in the OHC lateral membrane shows little variation with cochlear location (Mahendrasingam et al., 2008), force production remains constant despite different cellular dimensions. Most of the direct evidence for performance of the somatic motor has accrued from measurements on isolated OHCs which invariably lack forward transduction. The operation of the motor may be clarified by studying OHC mechanics in an intact organ of Corti preparation.

The case for a role of the hair-bundle motor is based on its properties in non-mammals. In those animals it can amplify the extrinsically induced hair-bundle vibrations in a frequency-selective manner (Martin et al., 2000; Ricci et al., 2000). The frequency selec-

tivity stems at least partly from tonotopic variation in the fast adaptation time constant for mechanotransduction. Why should it be less important in mammals? Perhaps the bandwidth of the process is insufficient to cope with the extension of the frequency range in mammals. A similar problem exists with electrical tuning of the receptor potential based on gating of potassium channels which is the major source of auditory frequency selectivity in non-mammals (Fettiplace and Fuchs, 1999). Although there is no direct evidence, it seems likely that hair-bundle amplification is employed in the high-frequency region of the avian cochlea, up to 9 kHz in owls (Köppl and Yates, 1999), in which short hair cells (analogous to OHCs) lack prestin or somatic contractility (He et al., 2003). Because the hair-bundle motor is driven by gating of the mechanotransducer channels, it does not suffer the frequency dependent attenuation imposed by the membrane time constant. The mechanotransducer channels must open and close on a microsecond time scale to explain transduction in animals such as bats and cetaceans that hear up to 120 kHz. However, the hair-bundle motor is thought to be coupled to fast channel adaptation (Ricci et al., 2000) which may itself be frequency limited due to the kinetics of calcium binding and unbinding (Nam and Fettiplace, 2008). Speed restrictions to the process remain an open question because attempts to measure active hair-bundle motion in mammalian preparations are currently limited by the bandwidth of force delivery using flexible fiber stimulation (Beurg et al., 2008). Nevertheless, amplification mediated by calcium influx via mechanotransducer channels has been observed in an isolated mammalian cochlea (Chan and Hudspeth, 2005). To fully characterize the hair-bundle motor in OHCs, the speed of the measurement techniques must be improved to ascertain whether the primary mechanical event is a recoil (negative feedback; Ricci et al., 2000) or a release (positive feedback; Martin et al., 2003; Kennedy et al., 2005) synchronous with fast adaptation. A drawback of the hair-bundle motor is the small force it can generate, a few hundred pN at most, more than 10-fold less than the prestin motor. Nevertheless, the feedback can be frequency tuned unlike that for the somatic motor. Furthermore, the force developed will increase with location due to a decrease in height and increase in number of stereocilia per bundle (Lim, 1986). Such frequency selectivity may be enhanced by tight coupling of the hair-bundles to the tectorial membrane (Nam and Fettiplace, 2008).

The most reasonable conclusion is that both somatic and hair-bundle motors collaborate to produce cochlear amplification and that the hair bundle motor has not been discarded but rather supplemented in extending the frequency range. Mechano-electrical transduction in the hair-bundle may largely confer frequency

selectivity and the compressive nonlinearity, whereas the somatic motor may be the major force generator (Fig. 4). However, the relative importance of the two mechanisms may change between base and apex which differ in the shapes of their basilar membrane tuning curves and degree of low-level amplification and nonlinearity (Robles and Ruggero, 2001). To apportion the contributions of the two motors, the most promising experimental approach is to assay hair cell responses and cochlear mechanics in an *in vivo* preparation (Nuttall et al., 2009). However, these techniques may still have insufficient resolution to define the motion at specific points within the organ of Corti. In the long run, an understanding of the micromechanics will be needed to determine the efficacies of the two motors in vibrating the basilar membrane at both low- and high-frequency locations.

A critical need in hearing

by Pascal Martin*, A.J. Hudspeth

One may investigate the basis of the active process in either of two ways. Most studies have focused on the subcellular and molecular details of the candidate mechanisms, membrane-based electromotility and active hair-bundle motility. Despite the present uncertainties in the field, such detailed mechanistic investigations must ultimately reveal the origins of the four cardinal aspects of the active process: amplification, frequency tuning, compressive nonlinearity, and spontaneous otoacoustic emission (Manley, 2000).

A second approach is to inquire, not about mechanistic details, but instead about the principles underlying the active process. What feature of the active process accounts for the unusual phenomena associated with hearing? What is the connection between the four manifestations of the active process observed in amphibians, reptiles including birds, and mammals? We contend that the answers to these questions are the same: critical oscillation at a Hopf bifurcation.

A physical system displays a Hopf bifurcation when its behavior changes abruptly from quiescence to spontaneous oscillation as the value of a control parameter varies (Strogatz, 1997). If the control parameter is poised at or near the critical value at which spontaneous oscillation emerges, the system is termed a critical oscillator. Any critical oscillator is endowed with generic properties that do not depend on the specific mechanism that produces the oscillatory instability (Choe et al., 1998; Camalet et al., 2000; Eguiluz et al., 2000; Jülicher et al., 2001; Duke and Jülicher, 2008).

Precisely what phenomena can be explained by a critical oscillator?

- (i) A critical oscillator can mobilize internal resources of energy to compensate for frictional losses and provide power gain, the defining feature of the cochlear amplifier.
- (ii) The amplification of a critical oscillator is tuned to a narrow band of frequencies centered at the characteristic frequency of spontaneous oscillation. In addition, the bandwidth of this active resonance is inversely related to the intensity of the stimulus; weak stimuli are amplified with sharper frequency selectivity.
- (iii) As observed in basilar-membrane recordings (Ruggero et al., 1997), the response of a critical oscillator to sinusoidal stimuli near resonance displays a compressive nonlinearity such that the amplification preferentially boosts weak signals. In contrast, the response is linear for stimulus frequencies that differ significantly from the characteristic frequency of critical oscillation.
- (iv) As it traverses the Hopf bifurcation, a critical oscillator becomes unstable and enters into limit-cycle oscillation, a likely cause of spontaneous otoacoustic emission.

- (v) Like the human ear (Goldstein, 1967), a critical oscillator displays “essential” nonlinearity in the sense that distortion products persist even for weak acoustic stimuli, decreasing more-or-less linearly with the amplitude of stimulation until they reach the threshold of detectability.
- (vi) The responsiveness of a critical oscillator to a sinusoidal stimulus is diminished by the presence of a second stimulus at a nearby frequency, a phenomenon akin to psychoacoustical masking, or two-tone suppression, in the human ear.

A ubiquitous feature of vertebrate hair cells, active hair-bundle motility has been observed *in vitro* in the eel (Rüsch and Thurm, 1990), frog (Benser et al., 1996; Martin et al., 2003; Tinevez et al., 2007), turtle (Crawford and Fettiplace, 1985; Ricci et al., 2002), chicken (Hudspeth et al., 2000), and rat (Kennedy et al., 2005). In the frog’s sacculus, active hair-bundle motility exhibits each of the six characteristics listed above (Martin and Hudspeth, 2001; Martin et al., 2001; Barral and Martin, unpublished observations). If intrinsic hair-bundle fluctuations are taken into account, a simple critical-oscillator model quantitatively emulates the observed behaviors (Nadrowski et al., 2004). Although intrinsic noise seriously limits amplification at the single-cell level, most hair-bundles are mechanically coupled by overlying membranous structures. By effectively reducing noise, cooperation among a few tens of neighboring hair-bundles apparently allows active hair-bundle motility to achieve a dynamic range of responsiveness compatible with that of hearing (Dierkes et al., 2008). The functional unit of the active process may thus comprise a small cluster of coupled hair cells with similar characteristics, which together achieve critical oscillation at a particular frequency.

Precisely because critical oscillation is generic, any dynamical system operating near a Hopf bifurcation must display the same properties. The mammalian lineage, which diverged from those of the other amniotes some 320 million years ago, has had ample opportunity to find novel ways of achieving critical oscillation. The phenomenon of membrane-based somatic electromotility, which is unique to mammalian outer hair cells, has been implicated in the production of active basilar-membrane movements (Dallos et al., 2008; Mellado Lagarde et al., 2008). Electromotility cannot operate alone, however, for this process is nearly linear over a physiological range of membrane potentials and lacks frequency selectivity (Ashmore, 2008). The nonlinearity and frequency selectivity of the cochlear amplifier are usually thought to emerge from respectively the saturating nonlinearity of mechano-electrical transduction by the hair-bundle and passive mechanical resonance within the cochlear partition (Nobili and Mammano, 1996). Modeling studies suggest that electromotility can provide negative friction to turn each segment of the cochlear partition, described as a spring-mass system, into a highly tuned resonator (Nobili et al., 1998). If negative damping overcomes passive sources of friction, the system is expected to become unstable and oscillate spontaneously. We suspect that successful cochlear models have been adjusted to operate in a stable regime near an unrecognized Hopf bifurcation. If the simulated behaviors are generic, the success of a given model does not necessarily validate the underlying assumptions; this difficulty may explain why no particular model of cochlear amplification has yet been accepted as definitive.

Models that rely only on passive resonance to set the characteristic frequency of each segment of the cochlear partition confront an important problem. The measured range of stiffness along the cochlear partition does not suffice to account for the thousandfold frequency range of mammalian hearing (Naidu and Mountain, 1998). It is more likely that the frequency is set, at least in part, by the local active process (Duke and Jülicher, 2003). Active hair-bundle motility, which occurs in the mammalian cochlea (Chan and Hudspeth, 2005; Kennedy et al., 2005), may provide both the

necessary nonlinearity and the frequency selectivity of the active process.

The critical-oscillator hypothesis also bears on the propagation of signals within the cochlea. The cochlear partition may be viewed as a set of oscillator modules with characteristic frequencies tonotopically distributed along the longitudinal axis of the cochlea. Although the traveling wave that results from hydrodynamic coupling of these modules is doubtlessly important in distributing sound energy to appropriately tuned hair cells, critical oscillators can account for the sharp peaking of the wave at the characteristic place. When critical oscillation is invoked, relatively simple models of cochlear hydrodynamics suffice to capture the known qualitative features of the traveling wave (Duke and Jülicher, 2003; Kern and Stoop, 2003; Magnasco, 2003).

The actual behavior of the mammalian cochlea differs in four ways from the abstract representation of a single critical oscillator (Fig. 5). First, the presence of intrinsic noise limits the amplification of faint stimuli; the gain saturates at a constant value below some threshold level, whereas the gain of a critical oscillator formally diverges at resonance for vanishingly small stimuli. Next, the restricted dynamic range of some process, perhaps active hair-bundle motility, implies that amplification wanes at very high stimulus levels. Third, by curtailing responsiveness to stimuli above the characteristic frequency, the traveling-wave mechanism introduces a sharp asymmetry in real tuning curves. Finally, longitudinal shifts of the tuning curve at increasing stimulus levels, as well as nonlinear modifications of the pressure stimulus traveling from the cochlear base to the characteristic place, can distort the power-law behaviors that are typical of the compressive nonlinearity generated by a single critical oscillator. We expect generic behaviors to emerge most clearly by following the peak of basilar-membrane response and relating the magnitude of this response to the local pressure.

The wealth of experimental observations on mammalian hearing implies that few experimentally accessible tests of the critical-oscillation hypothesis remain to be performed. Put another way, the strength of the hypothesis lies less in its predictive ability than in its capacity to accommodate a broad range of existing observations in a unified model. There are nevertheless striking predictions from the hypothesis that could lead to its falsification. Because the various manifestations of the active process are posited to emerge together from critical oscillation, they should be coupled obligatorily. If a control parameter can be adjusted systematically, for example by pharmacological manipulations (Martin et al., 2003) or genetic engineering (Holt et al., 2002), the strengths of the several effects should rise or fall together. More-

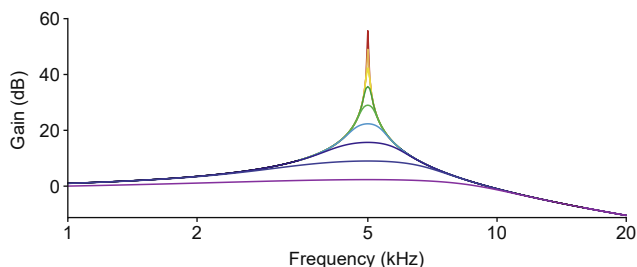


Fig. 5. The characteristic features of a critical oscillator emerge in a doubly logarithmic plot of the relation between stimulus frequency and gain for a series of sinusoidal stimuli. Gain is defined as the ratio of the oscillator's sensitivity to a given stimulus to that evoked by intense stimulation at the same frequency. A weak stimulus evokes a sharply tuned response with high gain. As the stimulus level rises in 10-dB increments, the gain at the characteristic frequency of 5 kHz declines as the two-thirds power of the stimulus amplitude and the bandwidth of amplification increases. Although the system displays compressive nonlinearity near resonance, its behavior remains linear for stimulus frequencies that differ significantly from the characteristic frequency of the critical oscillator.

over, if conditions can be found in which some features of the active process are definitely suppressed while others clearly persist, the critical-oscillator hypothesis must be modified or abandoned.

Predicting the role of OHC somatic motility and HB motility in cochlear amplification using a mathematical model

by Julien Meaud*, Karl Grosh

Introduction

Outer hair cells (OHC) have been shown experimentally to exhibit somatic electromotility at frequencies covering the entire mammalian frequency range (Frank et al., 1999). To predict the high sensitivity of the mammalian cochlea to low-level acoustic stimulus, previous mathematical models have included OHC somatic motility as in Mammano and Nobili, 1993 and Ramamoorthy et al., 2007. These models can predict the high gain as well as the sharp tuning of the frequency response of the basilar membrane (BM) to low-level acoustic input. When these models were developed there was no experimental evidence of active hair-bundle (HB) motion in the mammalian cochlea. However, activity (as evidenced by distortion products and spontaneous otoacoustic emissions) and amplification without any OHC somatic motility in the hearing organ of non-mammalian vertebrates have been demonstrated. Experimental and theoretical studies have shown that the non-mammalian HB can produce a force due to the action of a calcium dependent process. This active force production is linked to the fast adaptation of the transduction current (Ricci et al., 2000) and can amplify an external stimulus (Martin and Hudspeth, 1999). Moreover, recent experiments show that the mammalian HB also exhibits fast adaptation of the transduction current (Kennedy et al., 2003) and can produce a force in a submillisecond time scale (Kennedy et al., 2005). This new evidence provides an alternative to the prevailing theory that somatic motility is the basis of the cochlear amplifier. In our mathematical model, we selectively include OHC somatic motility, HB motility and a combination of both, with the goal of understanding the role of these two active sources in the mammalian cochlea.

Model

Our mathematical model is based on a box model of the guinea pig cochlea with a 3 D representation of the fluid, as described in Ramamoorthy et al., 2007. Viscous dissipation in the subreticular space is included. The BM interacts with the fluid via linearized Euler relation and with the organ of Corti which is coupled to the tectorial membrane (TM). Each cross-section of the TM is modeled as a rigid body with two degrees of freedom corresponding to the motions in a transverse and radial direction (see Fig. 3 in Ramamoorthy et al., 2007). Electrical conduction in the scalae of the cochlea is represented by longitudinal cables which allow current to pass down the length of the cochlea as well as into the transduction channels of the OHC (see Fig. 2 in Ramamoorthy et al., 2007). The system is linearized about the stationary point to predict the response of the system to low-level acoustic stimulation. We consider time harmonic vibrations ($e^{-i\omega t}$ time dependence). Somatic electromotility is modeled by linearized piezoelectric relations between the OHC deformation, $u_{\text{OHC}}^{\text{comp}}$, the fluctuating part of the transmembrane voltage, $\Delta\phi_{\text{OHC}}$, the OHC force (per unit length of the BM), F_{OHC} , and the current (per unit length of the BM), I_{OHC} , which

$$F_{\text{OHC}} = K_{\text{OHC}} u_{\text{OHC}}^{\text{comp}} + \epsilon_3 \Delta\phi_{\text{OHC}} \quad (1)$$

$$I_{\text{OHC}} = \frac{\Delta\phi_{\text{OHC}}}{Z_m} - i\omega\epsilon_3 u_{\text{OHC}}^{\text{comp}} \quad (2)$$

where K_{OHC} is the stiffness (per unit length of the BM) of the OHC, ϵ_3 is the electromechanical coupling coefficient of the OHC and Z_m is the impedance of the basolateral portion of the OHC.

In a nonlinear physiological model of HB transduction and motility, the dynamics of the HB are fairly complicated. In the linearization of such a model the properties are expected to be frequency dependent (as discussed in Ricci et al., 2000). Here, however, we use frequency independent properties and assume the transduction channel conductivity to be directly proportional to the stereocilia deflection, u_{HB} . Further the HB force is taken to be proportional to the HB deflection u_{HB} and velocity $-i\omega u_{\text{HB}}$. In this simple model, if the HB is to add energy to the system in a cycle-by-cycle manner, the real part of the HB impedance must be negative (i.e., some form of negative damping). Hence the HB force in the shear or radial direction is:

$$F_{\text{HB}} = k_{\text{HB}}u_{\text{HB}} - i\omega c_{\text{HB}}^{\text{act}}u_{\text{HB}} \quad (3)$$

where k_{HB} is the HB stiffness and $c_{\text{HB}}^{\text{act}}$ is the (negative) active damping coefficient. The constant is chosen to provide forces and energies that are in the physiologically relevant ranges, limited by experimental evidence given in Kennedy et al., 2005 and Choe et al., 1998, respectively. The energy is assumed to arise from a calcium binding event that is not included in other models (Mammano and Nobili, 1993; Ramamoorthy et al., 2007).

Results

The response of the BM to acoustic stimulation is plotted as a function of frequency in Fig. 6. The green dashed line represents the response of the BM in the passive system, i.e., neither somatic nor HB motility are included. It compares very well to the experimental measurements of de Boer and Nuttall, 2000 at 100 dB SPL (shown in blue dashed line).

When we add somatic motility to the model (thick blue dashed line), we see an increase in the gain and in the sharpness of the tuning and a shift of about half an octave in the peak frequency

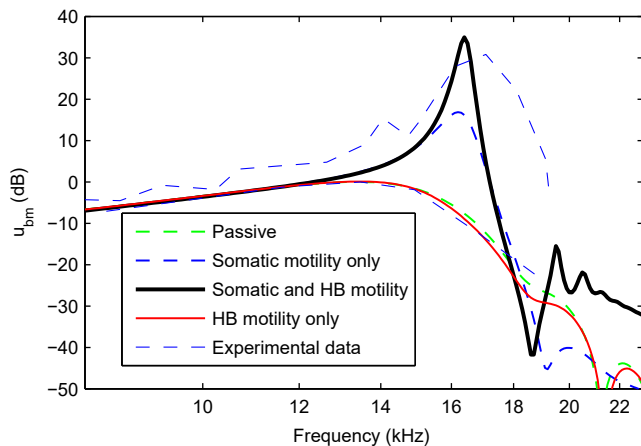


Fig. 6. Response of the BM to acoustic stimulation at the 17 kHz best place. The responses are normalized to the maximum passive BM response. The model predictions are compared to measurements from de Boer and Nuttall, 2000 at 20 and 100 dB SPL (thin blue dashed lines). The parameters used in the simulations are, for OHC somatic motility, $\epsilon_3 = -8.4 \times 10^6$ N/m/mv and for HB motility $c_{\text{act}}^{\text{HB}} = -3.15 \times 10^{-8}$ N/m/s. The passive model prediction (thick green dashed line) follows closely the measurements at 100 dB SPL. When somatic motility is included (thick blue dashed line), the peak gain is about 20 dB higher than in the passive case and the tuning of the response is sharper as in the experimental data at 20 dB SPL. When somatic motility and HB motility are included (thick solid black line), the gain is about 10 dB higher than in the previous case. For the case when only HB motility is included (red solid line), the response is almost the same as the passive model response.

as seen in the experimental data at 10 dB SPL. In the results presented here, the electromechanical coupling coefficient was chosen such that the model that includes both somatic and HB motility is stable. With this value of ϵ_3 , the predicted magnitude of the BM gain of the model only including somatic motility is lower than the experimental value. However, if we use a slightly higher value for ϵ_3 (about 16% higher), the prediction for the magnitude of the BM gain when only somatic motility is included can match the experimental value as shown in Ramamoorthy et al., 2007. Despite the basolateral RC filtering of the transmembrane voltage, somatic electromotility can amplify the BM motion thanks to an electromechanical resonance in the organ of Corti and the high sensitivity of the transduction channels.

If we add HB motility to somatic motility (thick black solid line), there is another 10 dB increase in the gain. For a 0.5 nm displacement (which corresponds approximately to a 20 dB acoustic input), the magnitude of the OHC somatic force is about 60 pN (on the order of magnitude predicted by Iwasa and Adachi, 1997) and the power added to the system by HB motility is about 60zJ, which is lower than the maximum value postulated by Choe et al. (about 2000zJ, Choe et al., 1998). For this case (somatic motility and HB motility) as well as the previous one (somatic motility only), the tuning of the response is not due to an intrinsic tuning of somatic or HB motility, but to an electromechanical resonance in the organ of Corti.

However, when only HB motility is included (red solid line) using the same active damping coefficient, $c_{\text{act}}^{\text{HB}}$, as in the previous calculations, the response is similar to the passive model response, with a low gain and broad tuning. When the active damping coefficient is increased, the model becomes unstable before the maximum gain of the BM reaches the experimental value for low-level sounds.

Conclusions

In these preliminary results with a simple HB model, OHC somatic motility is necessary for cochlear amplification whereas HB motility is not. This is consistent with measurements on prestin-knockin mice (Dallos et al., 2008) which also show that prestin-based somatic motility is necessary for normal cochlear function. With the parameters used here and the current experimental data, HB motility does not appear to be necessary to predict the BM gain to acoustic stimulus. However, as our results suggest, HB motility could still play a significant role and work in synergy with somatic motility to provide a higher BM gain and sharper tuning than with OHC motility alone. A more realistic HB model needs to be developed in order to make more conclusive remarks about the relative roles of OHC somatic and HB motility.

New experiments needed to change or elaborate our claims

- *In vitro* measurements of the mechanical response of mammalian HB to a stimulus more rapid than the time course of adaptation: The mechanical response of mammalian HB have only been measured with a stimulus having a time constant similar to or greater than the adaptation time constant. Measurements of HB with a faster time scale and/or with a small harmonic stimulation in the 5–20 kHz frequency range would help to find realistic parameters for a linearized HB model in the mammalian auditory frequency range, which are needed for a more precise prediction of the role of HB motility.
- *In vivo* measurements of the BM response to acoustic input in a cochlea perfused with salicylate: Current evidence that prestin somatic motility is necessary for normal cochlear function is based on prestin-knockin mice. The transduction channel of

these mutant mice appear to be normal. However the genetic mutation could affect other properties of the mouse cochlea during the development of the animal. Moreover data is only available for mice since genetic mutation have only performed on mice. Measurements of the BM response in a cochlea perfused with salicylate could be another way to block somatic motility while not affecting HB motility. It could potentially validate or invalidate the claim that prestin is necessary for cochlear amplification.

- Measurements of the BM frequency response to acoustic stimulation with endolymph with reduced calcium concentration: Using a perfusing scheme similar to Zheng et al., 2007, a controlled alteration of the endolymphatic calcium concentration can be reversibly applied. Reduction of the calcium concentration should slow down adaptation, increase the transduction current and reduce the magnitude of the active HB force. Because of the increase in the transduction current, it should also increase the magnitude of the OHC somatic force. Since OHC somatic motility is the main source of cochlear amplification according to our present model, we expect a net increase of the gain of the BM (provided the phase of the increased current is not deleteriously altered).
- *In vivo* measurements simultaneous measurements of the motion of the BM, the TM and the different structures of the organ of Corti in response to acoustic stimulation: Our mathematical model of the cochlea predicts the relative amplitude of the motion of the TM and the BM that are difficult to verify due to the lack of experimental data. In our results the gain of the BM and TM are similar. If HB motility had a greater effect than what we predict, we should expect the TM to have a much higher gain than the BM since the HBs are attached directly to the TM and can apply a force in the TM shear direction.

The mammalian cochlear amplifier done

by J. Santos-Sacchi

Introduction

I think we all agree that mammalian cochlear amplification must arise from the activity of OHCs, and that such activity must be physically coupled to the cochlear partition. The upshot of this is that (1) the evolution of OHCs to perform this special job arguably might have included a design to improve on extant mechanisms, namely, to recruit a new cellular component or modify an existing one, and (2) whether a somatic or stereociliar mechanism, it must link to the partition. Indeed, stereocilia embed in the tectorial membrane and the OHC soma join apically to the reticular lamina and basally to the basilar membrane via Deiters' cells. These required connections potentially allow OHC mechanical activity to provide a boost of stimulus to the inner hair cell stereocilia. Methods to uncouple these links or immobilize the underlying mechanics will tell which rules in the mammal.

Stereocilia drive the mammalian cochlear amplifier ... not

There are clear examples showing that prestin generated mechanical responses underlie mammalian amplification. Included are (1) our results (Santos-Sacchi et al., 2006) that BM sensitivity and tuning is modulated by anion control of prestin, and (2) definitive knockout results from the Dallos lab (Dallos et al., 2008). Another key observation is that when the coupling between stereocilia and the tectorial membrane is abolished, the BM behavior characteristic of normal amplification evoked by electrical stimulation is unaffected (Mellado Lagarde et al., 2008). Furthermore, it is not clear to me that evidence for bundle contributions (Chan and

Hudspeth, 2005; Kennedy et al., 2005; Kennedy et al., 2006) cannot be explained by underlying prestin-based mechanisms (Jia and He, 2005). I note that the use of salicylate as a tool to remove prestin effects is not absolute, as we have previously shown that residual mechanical responses remain in OHCs after such treatments (Kakehata and Santos-Sacchi, 1996). Given that the preponderance of evidence indicates that a prestin-based mechanism is responsible for mammalian amplification, we hope to put this issue to rest and focus on how this amazing protein prestin works at the cellular and molecular level.

Anions work as prestin's voltage sensor ... not

The initial suggestion that anions influence the electrical signature of prestin, nonlinear capacitance (NLC), because they subserve voltage sensation by a dysfunctional prestin transporter (Oliver et al., 2001) is not supported by many pieces of data. These include (1) conformational state of the motor is altered by anions at fixed voltage, (2) effects on the motor depend not simply on the presence of anions, but also on anion species and structure, (3) there is not the expected relationship between anion valence and motor unitary charge, (4) prestin is an anion transporter, (5) intrinsic amino acid residue charge contributes to voltage sensing, and (6) mutations of prestin can divorce NLC and anion transport capabilities (Bai et al., 2009; Rybalchenko and Santos-Sacchi, 2003; Rybalchenko and Santos-Sacchi, 2008; Song et al., 2005). We view the effects of anions working in an allosteric fashion, just as allosteric actions of voltage and Ca^{2+} ions control the behavior of the Ca-K channel, for example (Horrigan et al., 1999). For the OHC, this allosteric mechanism may rival the well known allosteric effects of Ca^{2+} on the stereociliar MET conductance (Fettiplace and Ricci, 2003).

How I envision the ear's works working

Enhanced tuning exists within cochleae that possess prestin-endowed OHCs; however, how such sharpening occurs requires more than amplification of a passive travelling wave. We suggested that interactions among coupled OHCs could provide such sharpening and give rise to nonlinearities characteristic of the amplifier (Zhao and Santos-Sacchi, 1999). Interestingly, a recent model of coupled hair-bundle activity suggests that improvements in tuning and amplification can result from interacting adjacent hair cell bundles (Dierkes et al., 2008). I think that just as the generic Hopf bifurcation model for bundle function can be usurped to understand the action of the electromotility nonlinearity, so too can this new coupling model. In fact, I think there are many analogies between proposed bundle mechanisms of amplification and prestin-driven amplification. Ironically, work on the bundle may help us understand how electromotility might work! One notable hypothesis that we suggested was the possible action of an ion underlying the mechanical event that drives amplification. Thus, in analogy with the process whereby Ca^{2+} influx through the molecularly-identified transduction channel conductance (G_{met}) drives bundle movements, we suggested that Cl^- could be fluxed via the molecularly-identified, mechanically-active lateral membrane conductance (G_{metL}) to effect prestin conformation change (Rybalchenko and Santos-Sacchi, 2003). We have shown that manipulation of Cl^- flux across the lateral membrane can reversibly alter cochlear amplification on the BM *in vivo* (Santos-Sacchi et al., 2006). Clearly, if such flux could be effected at acoustic rates, such a mechanism would bypass the membrane filter problem identified as a consequence of the voltage-dependence and nonlinear nature of electromotility (Santos-Sacchi, 1989). In this regard, we did show that G_{metL} is gated at acoustic rates (Rybalchenko and Santos-Sacchi, 2003), and it was shown that

deformations of the OHC soma occur during acoustic stimulation (Fridberger and De Monvel, 2003) – a possible stimulus for G_{metL} .

I am now captivated by a possibility that stereocilia and the prestin-based mechanism may team up to overcome the membrane time constant problem intrinsic to the conventional concept of prestin activation (Fig. 7). Interestingly, a correspondence between apical and lateral membrane activities has been observed *in vivo*, where bundle biasing and other manipulations appeared to affect OHC mechanical activity (Kirk, 2001; Kirk and Yates, 1998). Possible mechanisms included an alteration of intracellular chloride levels. Could the bundle influence cochlear amplification in a manner unrelated to active bundle mechanics and not due to the direct action of voltage on the motors? Could this involve chloride? I see two possibilities in this regard. One challenging dogma and another recently identified.

Here is the first scenario. Ion channels are characterized by their selectivity, their ability to pass particular ions over others based on size and/or charge. For all channels, the selectivity is not perfect, and ranges from extremely poor selectivity (e.g., (Oliver et al., 2001; Singh et al., 2007; Uhl et al., 1988)), to high selectivity (e.g., K channels).

Still, the most select ones can pass small amounts of ions that are generally considered impermeable (e.g., <1%). It is true that the bundle channel is nonselective for cations (Corey and Hudspeth, 1979; Crawford et al., 1991; Ohmori, 1985), but even though the replacement of chloride with sulfate has no apparent effects on cation currents (Valli et al., 1979), detailed anion selectivity has never been studied. It may sound like heresy today, but concessions that anion selectivity of the transduction channel require further investigation have been made (Hudspeth, 1983; Ohmori, 1985), and I am unaware of any further investigations on this topic since that time, especially in OHCs. Interestingly, one of the most

abundant proteins in stereocilia, CLIC5 (Gagnon et al., 2006), only nominally an intracellular chloride channel, has recently been shown to form channels in bilayers (Singh et al., 2007). Selectivity for charge is mildly cationic, with poor specificity, and measured multi-conductance levels of ~ 105 and ~ 17 pS. OHC MET channel conductance is about 110 pS (Geleoc et al., 1997). Imagine if CLIC5 were the MET channel! It is modulated by F-actin (Singh et al., 2007), making it potentially sensitive to Ca^{2+} and tension. It would be ironic should hair cells use only a few of an abundant supply of molecules – what redundancy for a critical mission! Let's check these ideas!

The second scenario involves an observation (Furness et al., 2008) made this past year showing that stereociliar rootlets insert into the junctional region of the apical lateral membrane. The potential for mechanical perturbation of the lateral membrane by the bundle therefore exists. Thus, bundle displacement, via the rootlets, is hypothesized to mechanically activate G_{metL} , promoting a flux of Cl^- at the apical region of the OHC. One further exciting prediction arises – a travelling wave of chloride flux along the apical to basal extent of the lateral membrane. This will occur because activation of G_{metL} causes a local flux of Cl^- which in turn causes the motor to change conformation, thereby mechanically triggering adjacent G_{metL} conductances to gate. A regenerative wave of activity should spread basally down the lateral membrane! An anion permeant MET channel could do the same. Let's measure it!

Finally, we should remember that efferent control of the cochlear amplification may also benefit from the modulation of chloride levels via GABA receptors at the cell's base (Maison et al., 2003; Plinkert et al., 1993). Here I can imagine a reverse travelling wave of contracture moving apically! Let's look for it!

Summary

Here, in this short space, I have revealed some of my inner most thoughts on mammalian cochlear amplification and associated problems. I have touched on why I think prestin rules, but offer up as consolation that the bundle may work with prestin. We need bold ideas like this and others (electro-osmosis, flexoelectricity) in our field to drive us to uncover the truth – to truly understand how hearing happens.

Acknowledgements

Paul Avan, Christine Petit, "Top connectors of the hair-bundle are required for waveform distortion and suppression masking but not cochlear amplification." This work was supported by the European Commission FP6 Integrated Project EuroHear.

William E. Brownell, "Membrane-based amplification in hearing." Work supported by research grants R01-DC002775 and DC000354 from NIDCD.

Peter Dallos, "Feedback in the cochlea." Supported by NIH Grant DC00089-38.

Robert Fettiplace, Carole M. Hackney, "The origin of the cochlear amplifier." Work supported by NIH-NIDCD R01 DC01362. Thanks to Jong-Hoon Nam for helpful discussions and for Fig. 1.

Julien Meaud, Karl Grosh, "Predicting the role of OHC somatic motility and HB motility in cochlear amplification using a mathematical model." This research was supported by NIH-NIDCD R01-04084.

J. Santos-Sacchi, "The mammalian cochlear amplifier done." Supported by NIDCD DC00273, DC008130 and DC009913.

References

Allen, J.B., 1980. Cochlear micromechanics – a physical model of transduction. *J. Acoust. Soc. Am.* 68, 1660–1670.

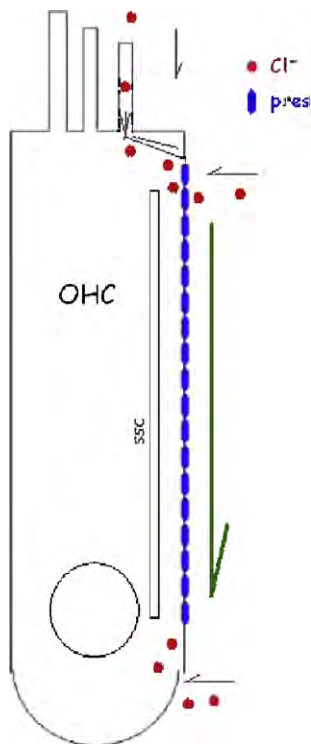


Fig. 7. The OHC is anion driven. The schematic illustrates the possible routes that chloride may take to alter prestin activity intracellularly. We have already shown that the expanse of the lateral membrane fluxes chloride via the mechanically active G_{metL} (Rybalchenko and Santos-Sacchi, 2003). Other proposed routes are through the stereociliary MET channel directly, or via rootlet perturbations of G_{metL} . Chloride may also flux during efferent activation of GABA receptors.

- Anvari, B., Zhang, R., Qian, F., Rajagopalan, L., Pereira, F.A., Brownell, W.E., 2007. Effects of prestin on membrane mechanics and electromechanics. *Conf. Proc. IEEE Eng. Med. Biol. Soc.* 68, 5384–5386.
- Ashmore, J., 2008. Cochlear outer hair cell motility. *Physiol. Rev.* 88, 173–210.
- Avan, P., Bonfils, P., Gilain, L., Mom, T., 2003. Physiopathological significance of distortion-product otoacoustic emissions at 2f₁-f₂ produced by high- versus low-level stimuli. *J. Acoust. Soc. Am.* 113, 430–441.
- Bai, J.P., Surguchev, A., Montoya, S., Aronson, P.S., Santos-Sacchi, J., Navaratnam, D., 2009. Prestin's anion transport and voltage-sensing capabilities are independent. *Biophys. J.* 96 (8), 3179–3186. available from: PM:19383462.
- Benser, M.E., Marquis, R.E., Hudspeth, A.J., 1996. Rapid, active hair bundle movements in hair cells from the bullfrog's sacculus. *J. Neurosci.* 16, 5629–5643.
- Beurg, M., Evans, M.G., Hackney, C.M., Fettiplace, R., 2006. A large-conductance calcium-selective mechanotransducer channel in mammalian cochlear hair cells. *J. Neurosci.* 26, 10992–11000.
- Beurg, M., Nam, J.-H., Crawford, A.C., Fettiplace, R., 2008. The actions of calcium on hair bundle mechanics in mammalian cochlear hair cells. *Biophys. J.* 94, 2639–2653.
- Breneman, K.D., Brownell, W.E., Rabbitt, R.D., 2009. Hair cell bundles: flexoelectric motors of the inner ear. *PLoS ONE* 4, e5201.
- Brownell, W.E., 2002. On the origins of the outer hair cell electromotility. In: Berlin, C.I., Hood, L.J., Ricci, A. (Eds.), *Hair Cell Micromechanics and Otoacoustic Emissions*. Delmar Learning, Clifton Park, NJ, pp. 25–45.
- Brownell, W.E., 2006. The piezoelectric outer hair cell: bidirectional energy conversion in membranes. In: Nuttall, A.L., Gillespie, P., Ren, T., Grosh, K., de Boer, E. (Eds.), *Auditory Mechanisms: Processes and Models*. World Scientific, Singapore, pp. 176–186.
- Brownell, W.E., Bader, C.R., Bertrand, D., de Ribaupierre, Y., 1985. Evoked mechanical responses of isolated cochlear outer hair cells. *Science* 227, 194–196.
- Brownell, W.E., Farrell, B., Raphael, R.M., 2003. Membrane electromechanics at hair cell synapses. In: Gummer, A.W. (Ed.), *Biophysics of the Cochlea: From Molecule to Model*. World Scientific, Singapore, pp. 169–176.
- Camalet, S., Duke, T., Jülicher, F., Prost, J., 2000. Auditory sensitivity provided by self-tuned critical oscillations of hair cells. *Proc. Natl. Acad. Sci. USA* 97, 3183–3188.
- Chan, D.K., Hudspeth, A.J., 2005. Ca²⁺ current-driven nonlinear amplification by the mammalian cochlea in vitro. *Nat. Neurosci.* 8 (2), 149–155. available from: PM:15643426.
- Cheatham, M.A., Huynh, K.H., Gao, J., Zuo, J., Dallos, P., 2004. Cochlear function in Prestin knockout mice. *J. Physiol. (Lond.)* 560, 821–830.
- Cheung, E.L., Corey, D.P., 2006. Ca²⁺ changes the force sensitivity of the hair-cell transduction channel. *Biophys. J.* 90, 124–139.
- Choe, Y., Magnasco, M.O., Hudspeth, A.J., 1998. A model for amplification of hairbundle motion by cyclical binding of Ca²⁺ to mechano-electrical-transduction channels. *Proc. Natl. Acad. Sci. USA* 95, 15321–15326.
- Corey, D.P., Hudspeth, A.J., 1979. Ionic basis of the receptor potential in a vertebrate hair cell. *Nature* 281 (5733), 675–677. available from: PM:000045121.
- Corey, D.P., Hudspeth, J.A., 1983. Kinetics of the receptor current in bullfrog saccular hair-cells. *J. Neurosci.* 3, 962–976.
- Crawford, A.C., Fettiplace, R., 1985. The mechanical properties of ciliary bundles of turtle cochlear hair-cells. *J. Physiol.* 364, 359–379.
- Crawford, A.C., Evans, M.G., Fettiplace, R., 1991. The actions of calcium on the mechano-electrical transducer current of turtle hair cells. *J. Physiol. (Lond.)* 434, 369–398. available from: PM:0001708822.
- Dallos, P., 1992. The active cochlea. *J. Neurosci.* 12, 4575–4585.
- Dallos, P., 2008. Cochlear amplification, outer hair cells and prestin. *Curr. Opin. Neurobiol.* 18, 370–376.
- Dallos, P., Evans, B.N., 1995. High frequency motility of outer hair cells and the cochlear amplifier. *Science* 267, 2006–2009.
- Dallos, P., Harris, D., 1978. Properties of auditory nerve responses in the absence of outer hair cells. *J. Neurophysiol.* 41, 365–383.
- Dallos, P., Popper, A.N., Fay, R.R. (Eds.), 1996. *The Cochlea*. Springer-Verlag, New York.
- Dallos, P., Wu, X., Cheatham, M.A., Gao, J., Zheng, J., Anderson, C.T., Jia, S., Wang, X., Cheng, W.H., Sengupta, S., He, D.Z., Zuo, J., 2008. Prestin-based outer hair cell motility is necessary for mammalian cochlear amplification. *Neuron* 58 (3), 333–339. available from: PM:18466744.
- Davis, H., 1983. An active process in cochlear mechanics. *Hear. Res.* 9, 79–90.
- de Boer, E., Nuttall, A.L., 2000. The mechanical waveform of the basilar membrane. III: intensity effects. *J. Acoust. Soc. Am.* 107 (3), 1497–1507.
- Dierkes, K., Lindner, B., Jülicher, F., 2008. Enhancement of sensitivity gain and frequency tuning by coupling of active hair bundles. *Proc. Natl. Acad. Sci. USA* 105 (48), 18669–18674. available from: PM:19015514.
- Duke, T., Jülicher, F., 2003. Active traveling wave in the cochlea. *Phys. Rev. Lett.* 90, 158101.
- Duke, T., Jülicher, F., 2008. Critical oscillators as active elements in hearing. In: Manley, G.A., Popper, A.N., Fay, R.R. (Eds.), *Active Processes and Otoacoustic Emissions*. Springer, New York, pp. 63–92.
- Eguiluz, V.M., Ospeck, M., Choe, Y., Hudspeth, A.J., Magnasco, M.O., 2000. Essential nonlinearities in hearing. *Phys. Rev. Lett.* 84, 5232–5235.
- Engbreton, A.M., Eldredge, D.H., 1968. Model for the nonlinear characteristics of cochlear potentials. *J. Acoust. Soc. Am.* 44, 548–554.
- Farrell, B., Do Shope, C., Brownell, W.E., 2006. Voltage-dependent capacitance of human embryonic kidney cells. *Phys. Rev. E Stat. Nonlin. Soft Matter Phys.* 73, 041930.
- Fettiplace, R., Fuchs, P.A., 1999. Mechanisms of hair cell tuning. *Ann. Rev. Physiol.* 61, 809–834.
- Fettiplace, R., Hackney, C.M., 2006. The sensory and motor roles of auditory hair cells. *Nat. Rev. Neurosci.* 7, 19–29.
- Fettiplace, R., Ricci, A.J., 2003. Adaptation in auditory hair cells. *Curr. Opin. Neurobiol.* 13 (4), 446–451. available from: PM:12965292.
- Frank, G., Hemmert, W., Gummer, A.W., 1999. Limiting dynamics of high-frequency electromechanical transduction of outer hair cells. *Proc. Natl. Acad. Sci. USA* 96, 4420–4425.
- Freeman, D.M., Masaki, K., McAllister, A.R., Wei, J.L., Weiss, T.F., 2003. Static material properties of the tectorial membrane: a summary. *Hear. Res.* 180, 11–27.
- Fridberger, A., De Monvel, J.B., 2003. Sound-induced differential motion within the hearing organ. *Nat. Neurosci.* 6 (5), 446–448. available from: PM:12692558.
- Fridberger, A., Boutet de Monvel, J., Zheng, J., Hu, N., Zou, Y., Ren, T., Nuttall, A., 2004. Organ of Corti potentials and the motion of the basilar membrane. *J. Neurosci.* 24, 10057–10063.
- Furness, D.N., Mahendrasingam, S., Ohashi, M., Fettiplace, R., Hackney, C.M., 2008. The dimensions and composition of stereociliary rootlets in mammalian cochlear hair cells: comparison between high- and low-frequency cells and evidence for a connection to the lateral membrane. *J. Neurosci.* 28 (25), 6342–6353. available from: PM:18562604.
- Gagnon, L.H., Longo-Guess, C.M., Berryman, M., Shin, J.B., Saylor, K.W., Yu, H., Gillespie, P.G., Johnson, K.R., 2006. The chloride intracellular channel protein CLIC5 is expressed at high levels in hair cell stereocilia and is essential for normal inner ear function. *J. Neurosci.* 26 (40), 10188–10198. available from: PM:17021174.
- Geleoc, G.S., Lennan, G.W., Richardson, G.P., Kros, C.J., 1997. A quantitative comparison of mechano-electrical transduction in vestibular and auditory hair cells of neonatal mice. *Proc. R. Soc. Lond. B Biol. Sci.* 264 (1381), 611–621. available from: PM:9149428.
- Gold, T., 1948. Hearing. II. The physical basis of the action of the cochlea. *Proc. R. Soc. Lond. B Biol. Sci.* 135, 492–498.
- Goldstein, J.L., 1967. Auditory nonlinearity. *J. Acoust. Soc. Am.* 41, 676–689.
- Gueta, R., Barlam, D., Shneck, R.Z., Rouso, I., 2006. Measurement of the mechanical properties of isolated tectorial membrane using atomic force microscopy. *Proc. Natl. Acad. Sci. USA* 103, 14790–14795.
- Gummer, A.W., Hemmert, W., Zenner, H.P., 1996. Resonant tectorial membrane motion in the inner ear: its crucial role in frequency tuning. *Proc. Natl. Acad. Sci. USA* 93, 8727–8732.
- He, D.Z., Beisel, K.W., Chen, L., Ding, D.L., Jia, S., Fritzsche, B., Salvi, R., 2003. Chick hair cells do not exhibit voltage-dependent somatic motility. *J. Physiol.* 546, 511–520.
- Holt, J.R., Gillespie, S.K., Provance, D.W., Shah, K., Shokat, K.M., Corey, D.P., Mercer, J.A., Gillespie, P.G., 2002. A chemical-genetic strategy implicates myosin-1 c in adaptation by hair cells. *Cell* 108, 371–381.
- Horrigan, F.T., Cui, J., Aldrich, R.W., 1999. Allosteric voltage gating of potassium channels I. Mslo ionic currents in the absence of Ca(2+). *J. Gen. Physiol.* 114 (2), 277–304. available from: PM:10436003.
- Housley, G.D., Ashmore, J.F., 1992. Ionic currents of outer hair cells isolated from the guinea-pig cochlea. *J. Physiol. (Lond.)* 448, 73–98.
- Hudspeth, A.J., 1983. Mechano-electrical transduction by hair cells in the acousticolateralis sensory system. *Annu. Rev. Neurosci.* 6, 187–215. available from: PM:6301349.
- Hudspeth, A.J., 1997. Mechanical amplification of stimuli by hair cells. *Curr. Opin. Neurobiol.* 7, 480–486.
- Hudspeth, A.J., 2008. Making an effort to listen: mechanical amplification in the ear. *Neuron* 59, 530–545.
- Hudspeth, A.J., Choe, Y., Mehta, A.D., Martin, P., 2000. Putting ion channels to work: mechano-electrical transduction, adaptation, and amplification by hair cells. *Proc. Natl. Acad. Sci. USA* 97, 11765–11772.
- Ikeda, K., Saito, Y., Nishiyama, A., Takasaka, T., 1992. Intracellular pH regulation in isolated cochlear outer hair cells of the guinea-pig. *J. Physiol.* 447, 627–648.
- Iwasa, K.H., Adachi, M., 1997. Force generation in the outer hair cell of the cochlea. *Biophys. J.* 73, 546–555.
- Iwasa, K.H., Sul, B., 2008. Effect of the cochlear microphonic on the limiting frequency of the mammalian ear. *J. Acoust. Soc. Am.* 124, 1607–1612.
- Jia, S., He, D.Z., 2005. Motility-associated hair-bundle motion in mammalian outer hair cells. *Nat. Neurosci.* 8 (8), 1028–1034. available from: PM:16041370.
- Jülicher, F., Andor, D., Duke, T., 2001. Physical basis of two-tone interference in hearing. *Proc. Natl. Acad. Sci. USA* 98, 9080–9085.
- Takehata, S., Santos-Sacchi, J., 1996. Effects of salicylate and lanthanides on outer hair cell motility and associated gating charge. *J. Neurosci.* 16 (16), 4881–4889. available from: PM:0008756420.
- Kennedy, H.J., Evans, M.G., Crawford, A.C., Fettiplace, R., 2003. Fast adaptation of mechano-electrical transducer channels in mammalian cochlear hair cells. *Nat. Neurosci.* 6 (8), 832–836.
- Kennedy, H.J., Crawford, A.C., Fettiplace, R., 2005. Force generation by mammalian hair bundles supports a role in cochlear amplification. *Nature* 433 (7028), 880–883. available from: PM:15696193.
- Kennedy, H.J., Evans, M.G., Crawford, A.C., Fettiplace, R., 2006. Depolarization of cochlear outer hair cells evokes active hair bundle motion by two mechanisms. *J. Neurosci.* 26 (10), 2757–2766. available from: PM:16525055.
- Kern, A., Stoop, R., 2003. Essential role of couplings between hearing nonlinearities. *Phys. Rev. Lett.* 91, 128101.

- Kim, D.O., Molnar, C.E., Matthews, J.W., 1980. Cochlear mechanics: nonlinear behavior in two-tone responses as reflected in cochlear-nerve-fiber responses and in ear-canal sound pressure. *J. Acoust. Soc. Am.* 67, 1704–1721.
- Kirk, D.L., 2001. Effects of 4-aminopyridine on electrically evoked cochlear emissions and mechano-transduction in guinea pig outer hair cells. *Hear. Res.* 161 (1–2), 99–112. available from: PM:11744286.
- Kirk, D.L., Yates, G.K., 1998. Enhancement of electrically evoked oto-acoustic emissions associated with low-frequency stimulus bias of the basilar membrane towards scala vestibuli. *J. Acoust. Soc. Am.* 104 (3 Pt. 1), 1544–1554. available from: PM:9745737.
- Köppl, C., Yates, G., 1999. Coding of sound pressure level in the barn owl's auditory nerve. *J. Neurosci.* 19, 9674–9686.
- Liberman, M.C., Dodds, L.W., 1987. Acute and chronic effects of acoustic trauma: serial-section reconstruction of stereocilia and cuticular plates. *Hear. Res.* 26, 45–64.
- Liberman, M.C., Gao, J., He, D.Z., Wu, X., Jia, S., Zuo, J., 2002. Prestin is required for electromotility of the outer hair cell and for the cochlear amplifier. *Nature* 419, 300–304.
- Lim, D.J., 1980. Cochlear anatomy related to cochlear micromechanics. *J. Acoust. Soc. Am.* 67, 1686–1695.
- Lim, D.J., 1986. Functional structure of the organ of Corti: a review. *Hear. Res.* 22, 117–146.
- Ludwig, J., Oliver, D., Frank, G., Klocker, N., Gummer, A.W., Fakler, B., 2001. Reciprocal electromechanical properties of rat prestin: the motor molecule from rat outer hair cells. *Proc. Natl. Acad. Sci. USA* 98, 4178–4183.
- Lu, T.K., Zhak, S., Dallos, P., Sarpeshkar, R., 2006a. Fast cochlear amplification with slow outer hair cells. *Hear. Res.* 214, 45–67.
- Lu, T.K., Zhak, S., Dallos, P., Sarpeshkar, R., et al., 2006b. Negative feedback enables fast cochlear amplification with slow outer hair cells. *Hear. Res.* 241, 45–67.
- Magnasco, M.O., 2003. A wave traveling over a Hopf instability shapes the cochlear tuning curve. *Phys. Rev. Lett.* 90, 058101.
- Mahendrasingam, S., Furness, D.N., Fettiplace, R., Hackney, C.M., 2008. Prestin distribution in rat outer hair cells: an ultrastructural study. In: Cooper, N.P., Kemp, D.T. (Eds.), *Concepts and Challenges in the Biophysics of Hearing*. World Scientific, Singapore, pp. 407–412.
- Maison, S.F., Adams, J.C., Liberman, M.C., 2003. Olivocochlear innervation in the mouse: immunocytochemical maps, crossed versus uncrossed contributions, and transmitter colocalization. *J. Comp. Neurol.* 455 (3), 406–416. available from: PM:12483691.
- Mammano, F., Ashmore, J.F., 1993. Reverse transduction measured in the isolated cochlea by laser Michelson interferometry. *Nature* 365, 838–841.
- Mammano, F., Nobili, R., 1993. Biophysics of the cochlea: linear approximation. *J. Acoust. Soc. Am.* 93, 3320–3332.
- Manley, G.A., 2000. Cochlear mechanisms from a phylogenetic viewpoint. *Proc. Natl. Acad. Sci. USA* 97, 11736–11743.
- Manley, G.A., 2001. Evidence for an active process and a cochlear amplifier in nonmammals. *J. Neurophysiol.* 86, 541–549.
- Manley, G.A., Köppl, C., 2008. What have lizard ears taught us about auditory physiology? *Hear. Res.* 238, 3–11.
- Manley, G.A., Kirk, D.L., Köppl, C., Yates, G.K., 2001. In vivo evidence for a cochlear amplifier in the hair-cell bundle of lizards. *Proc. Natl. Acad. Sci. USA* 98, 2826–2831.
- Martin, P., Hudspeth, A.J., 1999. Active hair-bundle movements can amplify a hair cell's response to oscillatory mechanical stimuli. *Proc. Natl. Acad. Sci. USA* 96, 14306–14311.
- Martin, P., Hudspeth, A.J., 2001. Compressive nonlinearity in the hair bundle's active response to mechanical stimulation. *Proc. Natl. Acad. Sci. USA* 98, 14386–14391.
- Martin, P., Mehta, A.D., Hudspeth, A.J., 2000. Negative hair-bundle stiffness betrays a mechanism for mechanical amplification by the hair cell. *Proc. Natl. Acad. Sci. USA* 97, 12026–12031.
- Martin, P., Hudspeth, A.J., Jülicher, F., 2001. Comparison of a hair bundle's spontaneous oscillations with its response to mechanical stimulation reveals the underlying active process. *Proc. Natl. Acad. Sci. USA* 98, 14380–14385.
- Martin, P., Bozovic, D., Choe, Y., Hudspeth, A.J., 2003. Spontaneous oscillation by hair bundles of the bullfrog's sacculus. *J. Neurosci.* 23, 4533–4548.
- Mellado Lagarde, M.M., Drexler, M., Lukashkina, V.A., Lukashkin, A.N., Russell, I.J., 2008. Outer hair cell somatic, not hair bundle, motility is the basis of the cochlear amplifier. *Nat. Neurosci.* 11 (7), 746–748. available from: PM:18516034.
- Mistrik, P., Mullaney, C., Mammano, F., Ashmore, J., 2009. Three-dimensional current flow in a large-scale model of the cochlea and the mechanisms of amplification of sound. *J. Roy. Soc. Interface* 6, 279–291.
- Mountain, D.C., Hubbard, A.E., 1994. A piezoelectric model of outer hair cell function. *J. Acoust. Soc. Am.* 95, 350–354.
- Nadrowski, B., Martin, P., Jülicher, F., 2004. Active hair-bundle motility harnesses noise to operate near an optimum of mechanosensitivity. *Proc. Natl. Acad. Sci. USA* 101, 12195–12200.
- Naidu, R.C., Mountain, D.C., 1998. Measurements of the stiffness map challenge a basic tenet of cochlear theories. *Hear. Res.* 124, 124–131.
- Nam, J.-H., Fettiplace, R., 2008. Theoretical conditions for high-frequency hair bundle oscillations in auditory hair cells. *Biophys. J.* 95, 4948–4962.
- Nobili, R., Mammano, F., 1996. Biophysics of the cochlea II: stationary nonlinear phenomenonology. *J. Acoust. Soc. Am.* 99, 2244–2255.
- Nobili, R., Mammano, F., Ashmore, J., 1998. How well do we understand the cochlea? *Trends Neurosci.* 21, 159–167.
- Nowotny, M., Gummer, A.W., 2006. Nanomechanics of the subtectorial space caused by electromechanics of cochlear outer hair cells. *Proc. Natl. Acad. Sci. USA* 103, 2120–2125.
- Nuttall, A.F., Zheng, J., Chen, F., Choudhury, N., Jacques, S., 2009. Sound-evoked vibrations in the basilar membrane and reticular lamina of living guinea pigs using optical coherence tomography. *ARO Abstr.* 32, 253.
- Ohmori, H., 1985. Mechano-electrical transduction currents in isolated vestibular hair cells of the chick. *J. Physiol. (Lond.)* 359, 189–217. available from: PM:0002582113.
- Oliver, D., He, D.Z., Klocker, N., Ludwig, J., Schulte, U., Waldegger, S., Ruppersberg, J.P., Dallos, P., Fakler, B., 2001. Intracellular anions as the voltage sensor of prestin, the outer hair cell motor protein. *Science* 292 (525), 2340–2343. available from: PM:11423665.
- Petrov, A.G., 2006. Electricity and mechanics of biomembrane systems: flexoelectricity in living membranes. *Anal. Chim. Acta* 568, 70–83.
- Plinkert, P.K., Gitter, A.H., Mohler, H., Zenner, H.P., 1993. Structure, pharmacology and function of GABA-A receptors in cochlear outer hair cells. *Eur. Arch. Otorhinolaryngol.* 250 (6), 351–357. available from: PM:8260146.
- Preyer, S., Renz, S., Hemmert, W., Zenner, H.P., Gummer, A.W., 1996. Receptor potential of outer hair cells isolated from base to apex of the adult guinea-pig cochlea: implications for cochlear tuning mechanisms. *Aud. Neurosci.* 2, 145–157.
- Rabbitt, R.D., Clifford, S., Breneman, K.D., Farrell, B., Brownell, W.E., 2009. Power efficiency of outer hair cell somatic electromotility. *PLoS Comput. Biol.* 5 (7), e1000444. Epub 2009 Jul 24.
- Ramamoorthy, S., Deo, N.V., Grosh, K., 2007. A mechano-electro-acoustical model for the cochlea: response to acoustic stimuli. *J. Acoust. Soc. Am.* 121, 2758–2773.
- Raphael, R.M., Popel, A.S., Brownell, W.E., 2000. A membrane bending model of outer hair cell electromotility. *Biophys. J.* 78, 2844–2862.
- Recio, A., Rhode, W.S., 2000. Basilar membrane responses to broadband stimuli. *J. Acoust. Soc. Am.* 108, 2281–2298.
- Ricci, A., 2003. Active hair bundle movements and the cochlear amplifier. *J. Am. Acad. Audiol.* 14, 325–338.
- Ricci, A.J., Crawford, A.C., Fettiplace, R., 2000. Active hair bundle motion linked to fast transducer adaptation in auditory hair cells. *J. Neurosci.* 20, 7131–7142.
- Ricci, A.J., Crawford, A.C., Fettiplace, R., 2002. Mechanisms of active hair bundle motion in auditory hair cells. *J. Neurosci.* 22, 44–52.
- Ricci, A.J., Kennedy, H.J., Crawford, A.C., Fettiplace, R., 2005. The transduction channel filter in auditory hair cells. *J. Neurosci.* 25, 7831–7839.
- Richter, C.P., Emadi, G., Getnick, G., Quesnel, A., Dallos, P., 2007. Tectorial membrane stiffness gradients. *Biophys. J.* 93, 2265–2276.
- Robles, L., Ruggero, M.A., 2001. Mechanics of the mammalian cochlea. *Physiol. Rev.* 81, 1305–1352.
- Ruggero, M.A., Rich, N.C., Robles, L., 1997. Basilar-membrane responses to tones at the base of the chinchilla cochlea. *J. Acoust. Soc. Am.* 104, 2151–2163.
- Rüsch, A., Thurm, U., 1990. Spontaneous and electrically induced movements of ampullary kinocilia and stereovilli. *Hear. Res.* 48, 247–263.
- Ryan, A., Dallos, P., 1975. Absence of cochlear outer hair cells: effect on behavioural auditory threshold. *Nature* 253, 44–46.
- Rybalchenko, V., Santos-Sacchi, J., 2003. Cl⁻ flux through a non-selective, stretch-sensitive conductance influences the outer hair cell motor of the guinea-pig. *J. Physiol.* 547 (Pt. 3), 873–891. available from: PM:12562920.
- Rybalchenko, V., Santos-Sacchi, J., 2008. Anion control of voltage sensing by the motor protein prestin in outer hair cells. *Biophys. J.* 95 (9), 4439–4447. available from: PM:18658219.
- Sachs, F., Brownell, W.E., Petrov, A.G., 2009. Membrane electromechanics in biology, with a focus on hearing. *MRS Bull.* 34 (9), 665.
- Santos-Sacchi, J., 1989. Asymmetry in voltage-dependent movements of isolated outer hair cells from the organ of Corti. *J. Neurosci.* 9 (8), 2954–2962. available from: PM:0002769373.
- Santos-Sacchi, J., 2003. New tunes from Corti's organ: the outer hair cell boogie rules. *Curr. Opin. Neurobiol.* 13, 459–468.
- Santos-Sacchi, J., Dilger, J.P., 1988. Whole cell currents and mechanical responses of isolated outer hair-cells. *Hear. Res.* 35, 143–150.
- Santos-Sacchi, J., Song, L., Zheng, J., Nuttall, A.L., 2006. Control of mammalian cochlear amplification by chloride anions. *J. Neurosci.* 26 (15), 3992–3998. available from: PM:16611815.
- Shera, C.A., 2001. Intensity-invariance of fine time structure in basilar-membrane click responses: implications for cochlear mechanics. *J. Acoust. Soc. Am.* 110, 332–348.
- Singh, H., Cousin, M.A., Ashley, R.H., 2007. Functional reconstitution of mammalian 'chloride intracellular channels' CLIC1, CLIC4 and CLIC5 reveals differential regulation by cytoskeletal actin. *FEBS J.* 274 (24), 6306–6316. available from: PM:18028448.
- Song, L., Seeger, A., Santos-Sacchi, J., 2005. On membrane motor activity and chlorine flux in the outer hair cell: lessons learned from the environmental toxin tributyltin. *Biophys. J.* 88 (3), 2350–2362. available from: PM:15596517.
- Spector, A.A., Brownell, W.E., Popel, A.S., 2003. Effect of outer hair cell piezoelectricity on high-frequency receptor potentials. *J. Acoust. Soc. Am.* 113, 453–461.
- Spector, A.A., Popel, A.S., Eatock, R.A., Brownell, W.E., 2005. Mechanosensitive channels in the lateral wall can enhance the cochlear outer hair cell frequency response. *Ann. Biomed. Eng.* 33, 991–1002.
- Strelhoff, D., Flock, A., 1984. Stiffness of sensory-cell hair bundles in the isolated guinea pig cochlea. *Hear. Res.* 15, 19–28.

- Strogatz, S.T., 1997. *Nonlinear Dynamics and Chaos*, seventh ed. Addison-Wesley, Reading, MA.
- Sun, S.X., Farrell, B., Chana, M.S., Oster, G., Brownell, W.E., Spector, A.A., 2009. Voltage and frequency dependence of prestin-associated charge transfer. *J. Theor. Biol.* 260 (1), 137–144. Epub 2009 May 31.
- Tartini, G., 1754. *Trattato di musica secondo la vera scienza dell'armonia*, G. Manfrè, Padova.
- Tinevez, J.Y., Jülicher, F., Martin, P., 2007. Unifying the various incarnations of active hair-bundle motility by the vertebrate hair cell. *Biophys. J.* 93, 4053–4067.
- Uhl, J., Murer, H., Kolb, H.A., 1988. Ion channels activated by osmotic and mechanical stress in membranes of opossum kidney cells. *J. Membr. Biol.* 104 (3), 223–232. available from: PM:2463364.
- Valli, P., Zucca, G., Casella, C., 1979. Ionic composition of the endolymph and sensory transduction in labyrinthine organs. *Acta Otolaryngol.* 87 (5–6), 466–471. available from: PM:313653.
- Verpy, E., Weil, D., Leibovici, M., Goodyear, R.J., Hamard, G., Houdon, C., Lefevre, G.M., Hardelin, J.P., Richardson, G.P., Avan, P., Petit, C., 2008. Stereocilindifferent mice reveal the origin of cochlear waveform distortions. *Nature* 456, 255–258.
- Weiss, T.F., 1982. Bidirectional transduction in vertebrate hair cells: a mechanism for coupling mechanical and electrical vibrations. *Hear. Res.* 7, 353–360.
- Weitzel, E.K., Tasker, R., Brownell, W.E., 2003. Outer hair cell piezoelectricity: frequency response enhancement and resonance behavior. *J. Acoust. Soc. Am.* 114, 1462–1466.
- Zhang, R., Qian, F., Rajagopalan, L., Pereira, F.A., Brownell, W.E., Anvari, B., 2007. Prestin modulates mechanics and electromechanical force of the plasma membrane. *Biophys. J.* 93, L07–L09.
- Zhao, H.B., Santos-Sacchi, J., 1999. Auditory collusion and a coupled couple of outer hair cells. *Nature* 399 (6734), 359–362. available from: PM:0010360573.
- Zheng, J., Shen, W., He, D.Z., Long, K.B., Madison, L.D., Dallos, P., 2000. Prestin is the motor protein of cochlear outer hair cells. *Nature* 405, 149–155.
- Zheng, J., Deo, N., Zou, Y., Grosh, K., Nuttall, A.L., 2007. Chlorpromazine alters cochlear mechanics and amplification: in vivo evidence for organ of corti stiffness modulation. *J. Neurophysiol.* 97, 994–1004.
- Zidanic, M., Brownell, W.E., 1990. Fine structure of the intracochlear potential field. I. The silent current. *Biophys. J.* 57, 1253–1268.
- Zwislocki, J.J., Kletsky, E.J., 1979. Tectorial membrane: a possible effect on frequency analysis in the cochlea. *Science* 204, 639–641.

Prestin's Anion Transport and Voltage-Sensing Capabilities Are Independent

Jun-Ping Bai,[†] Alexei Surguchev,^{†‡} Simone Montoya,^{†‡} Peter S. Aronson,^{§¶} Joseph Santos-Sacchi,^{‡¶||} and Dhasakumar Navaratnam^{†||*}

[†]Department of Neurology, [‡]Division of Otolaryngology, Department of Surgery, [§]Department of Internal Medicine, [¶]Department of Cellular and Molecular Physiology, and ^{||}Department of Neurobiology, Yale University School of Medicine, New Haven, Connecticut

ABSTRACT The integral membrane protein prestin, a member of the SLC26 anion transporter family, is responsible for the voltage-driven electromotility of mammalian outer hair cells. It was argued that the evolution of prestin's motor function required a loss of the protein's transport capabilities. Instead, it was proposed that prestin manages only an abortive hemicycle that results in the trapped anion acting as a voltage sensor, to generate the motor's signature gating charge movement or nonlinear capacitance. We demonstrate, using classical radioactive anion (¹⁴C]formate and [¹⁴C]oxalate) uptake studies, that in contrast to previous observations, prestin is able to transport anions. The prestin-dependent uptake of both these anions was twofold that of cells transfected with vector alone, and comparable to SLC26a6, prestin's closest phylogenetic relative. Furthermore, we identify a potential chloride-binding site in which the mutations of two residues (P328A and L326A) preserve nonlinear capacitance, yet negate anion transport. Finally, we distinguish 12 charged residues out of 22, residing within prestin's transmembrane regions, that contribute to unitary charge movement, i.e., voltage sensing. These data redefine our mechanistic concept of prestin.

INTRODUCTION

It is now well established that prestin drives voltage-dependent electromotility in mammalian outer hair cells (1–4). Although its primary sequence places it in the SLC26 family of anion transporters, two early findings suggested that prestin (SLC26a5) was different from other members of this family. First, prestin uniquely imparts voltage-dependent mechanical activity and its corresponding electrical signature, gating charge movements, or nonlinear capacitance (NLC) (1,2). Second, unlike its nonmammalian orthologs and mammalian family members, prestin reportedly cannot transport anions (6,7). An attempt to discover how prestin senses voltage led to mutation analyses of 21 charged residues found in prestin that are not conserved in SLC26a6, its closest phylogenetic-related protein that lacks NLC (8). Such mutations failed to alter the Boltzmann parameter that corresponds to a voltage-evoked unitary gating charge (α or z). These observations led Oliver et al. (8) to invoke an incomplete transport cycle (with a hemimovement of anions within the intramembranous protein) as the mechanism by which prestin achieves its voltage sensitivity, thereby underlying the generation of NLC (8). This is generally known as the extrinsic voltage sensor or partial anion transporter hypothesis. Evidence was presented against this hypothesis, and in favor of the argument that anions work allosterically, by modifying the energy profile of the intramembranous motor protein, prestin (9–11).

Here we test key premises underlying the extrinsic voltage sensor hypothesis, i.e., that prestin is not an anion

transporter, and that prestin lacks an intrinsic voltage sensor. We show that: 1), prestin transports anions; 2), intrinsic charged residues contribute to voltage sensing; and 3), by mutation, these two functions of prestin can be divorced. These observations, in conjunction with others (9,10,12), cast doubt on a simple extrinsic voltage-sensing scheme.

METHODS

The assumption that mammalian prestin is unable to transport anions is based, in part, on a reported failure of anion transport in oocytes (7), involving data that we have replicated (J.-P. Bai and D. Navaratnam, unpublished observations). Therefore, we chose to use heterologous expression in Chinese hamster ovary (CHO) cells to evaluate prestin's ability to transport [¹⁴C]formate and [¹⁴C]oxalate. CHO cells were used extensively to characterize prestin's NLC.

We fused YFP (in eYFPN1, Clontech, Mountain View, CA) to the C-terminus of prestin (including all mutants), as previously described (13). This step allowed us to verify that transfection efficiency was comparable, and to identify cells transfected with prestin for electrophysiological recording. We expressed murine SLC26a6 (14) in pcDNA 3.1, which contains the identical cytomegalovirus promoter. We mutated individual residues using the Quikchange mutagenesis kit (Stratagene, La Jolla, CA). Mutagenesis was confirmed by sequencing the entire transcript.

Each transport experiment was performed using a 24-well plate (Costar/Corning, Lowell, MA). Cells were plated at a concentration of 200,000 cells per well, and transfected with lipofectamine 24 h after plating (as previously described) (13). Each experimental variable was evaluated in triplicate wells. Each experiment included three wells transfected with empty vector (negative control), and three wells transfected with prestin (positive control) to control for experimental variables (e.g., transfection/plating efficiency). We used 0.8 μ g of DNA and 1.6 μ L of lipofectamine per well. Formate or oxalate uptake was assayed 24 h after transfection. Cells were incubated with 120 mM NaCl, 20 mM HEPES, 5 mM KCl, 5 mM glucose, 2 mM CaCl₂, and 1 mM MgCl₂ (pH 7.4) for 30 min. After aspiration of the NaCl solution, cells were incubated in 130 mM K gluconate, 20 mM HEPES, and 5 mM glucose (pH 7.4), containing 20 μ M of [¹⁴C]formate

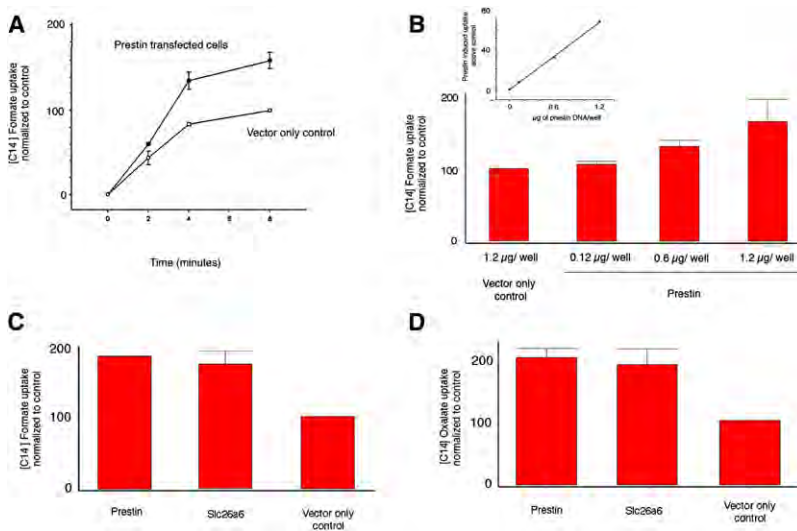
Submitted September 26, 2008, and accepted for publication December 23, 2008.

*Correspondence: dhasakumar.navaratnam@yale.edu

Editor: Tzyh-Chang Hwang.

© 2009 by the Biophysical Society
0006-3495/09/04/3179/8 \$2.00

doi: 10.1016/j.bpj.2008.12.3948



control (YFP vector only). The plot shows mean uptake per 200,000 cells contained in a well (of a 24-well plate) \pm SE. Data were normalized to vector-only controls ($n = 3$, in each case). Controls were assigned a value of 100. The uptake of [^{14}C]formate by prestin and Slc26a6 was 183 (± 0.7) and 171 (± 17.3), respectively, i.e., significantly different from controls ($p < 0.01$, one-way ANOVA). The uptake of [^{14}C]oxalate by prestin and Slc26a6 was 198 (± 13.5) and 187 (± 24.0), respectively, i.e., significantly different from vector-only controls ($p < 0.05$, one-way ANOVA). The absolute prestin-induced uptake of oxalate was 1.5-fold greater than formate uptake; this was obscured by normalization. Uptake is denoted in relative counts (see Methods).

(or [^{14}C]oxalate) for 8 min (in the standard assay, or at other time points indicated in timed experiments). Cells were washed three times with ice-cold 130 mM K gluconate, 20 mM HEPES, and 5 mM glucose. Cells were then lysed with 0.2 mL of 0.5 M NaOH, neutralized with 0.5 M HCl, and [^{14}C]formate (or [^{14}C]oxalate) uptake was determined by liquid scintillation counting. All data are reported as [^{14}C]formate (or [^{14}C]oxalate) uptake per 200,000 cells, and are mean values from 3–4 experiments (\pm SE) that were normalized to vector-only controls. Thus, uptake in the figures is denoted in relative counts. Each experiment, in turn, represents the mean of triplicate wells. The absolute mean uptake of [^{14}C]formate and [^{14}C]oxalate in a given control well across a number of experiments was ~ 20 pmol and 28 pmol per 200,000 cells, respectively. In independent experiments, we established by both protein and DNA assays that transfection with different plasmids did not affect the cell number within the first 24 h. Knowing the intracellular concentration of transported anions would be important in evaluating the actual fluxes that may occur in vivo. We are aware of no data concerning intracellular concentrations of oxalate or formate, or methods for their measurement. Fortunately, we are simply making a determination here that anion transport occurs, and this determination is independent of intracellular concentrations. Confocal microscopy was performed as previously described, using YFP fusions of each mutant (13).

Whole-cell patch clamp recordings were performed at room temperature, using an Axon 200B amplifier (Axon Instruments, Union City, CA), as described previously (13). Cells were recorded 48 h after transfection, to allow for stable measurements of nonlinear capacitance. Ionic blocking solutions were used to isolate capacitive currents. The bath solution contained (in mM): TEA 20, CsCl 20, CoCl₂ 2, MgCl₂ 1.47, HEPES 10, NaCl 99.2, and CaCl₂ \cdot 2H₂O 2, pH 7.2, and the pipette solution contained (in mM): CsCl 140, EGTA 10, MgCl₂ 2, and HEPES 10, pH 7.2. Osmolarity was adjusted to 300 ± 2 mOsm with dextrose. Command delivery and data collections were performed with a Windows-based whole-cell voltage-clamp program, jClamp (Sciosoft, New Haven, CT), using an NI PCI 6052E interface (National Instruments). We corrected for the effects of series resistance. Capacitance was evaluated with a continuous high-resolution, two-sine wave technique fully described elsewhere (15,16). Capacitance data were fitted to the first derivative of a two-state Boltzmann function, to extract Boltzmann parameters (17). A two-state Boltzmann model adequately describes prestin's charge movement (18,19)

FIGURE 1 Prestin-transfected CHO cells indicate anion transport. (A) CHO cells transfected with prestin show a time-dependent uptake of [^{14}C]formate that was greater than that of CHO cells transfected with empty vector alone (control). Uptake of [^{14}C]formate by prestin-transfected cells at 2, 4, and 8 min was 60 (± 8.2), 135 (± 10.4), and 160 (± 9.5), respectively. In contrast, the uptake of control cells at corresponding time points was 44 (± 8.2), 84 (± 2.2) and 100 ($n = 3$). Data were normalized to vector-only controls at 8 min, which was given a value of 100. (B) There is a dose-dependent increase in [^{14}C]formate uptake in cells transfected with increasing quantities of prestin-YFP plasmid. The mean uptake for cells transfected with 0.12 μg , 0.6 μg , and 1.2 μg of prestin plasmid DNA were 107 (± 4), 131 (± 8.5), and 166 (± 31), respectively. Control wells were transfected with 1.2 μg of YFP plasmid DNA ($n = 3$). (Inset) Linear relationship between transport induced by prestin (after subtracting background) and amount of DNA used in transfection. (C and D) CHO cells transfected with prestin and Slc26a6 show increased uptake of [^{14}C]formate (C) and [^{14}C]oxalate (D) compared with

$$C_m = Q_{\max} \frac{ze}{kT} \frac{b}{(1+b)^2} + C_{lin}, \quad (1)$$

where

$$b = \exp\left(\frac{-ze(V_m - V_h)}{kT}\right).$$

Q_{\max} is the maximum nonlinear charge transfer, V_h is the voltage at peak capacitance or half-maximal nonlinear charge transfer, V_m is the membrane potential, C_{lin} is the linear capacitance, z is the unitary charge movement or valence (also a metric of voltage sensitivity), e is the electron charge, k is Boltzmann's constant, and T is the absolute temperature. Q_{\max} is reported as Q_{sp} , the specific charge density, i.e., the total charge moved, normalized to linear capacitance. Student's t -test and analyses of variance (ANOVAs) were used to evaluate the effects of mutations on different parameters of NLC and transport.

RESULTS

Prestin is an anion transporter

Although prestin-induced anion transport is not demonstrable in oocytes, it is possible that transport occurs in other systems. To test whether prestin transports anions in alternative expression systems, we transfected CHO cells with prestin (*Meriones unguiculatus*), and compared anion transport in these cells and in CHO cells transfected with empty vector. As shown in Fig. 1 A, CHO cells transfected with prestin showed a time-dependent increase in [^{14}C]formate uptake, compared with cells transfected with vector alone. The CHO cells possess an intrinsic anion-uptake mechanism that accounts for the levels of [^{14}C]formate uptake in cells transfected with empty vector alone. As expected, we also found that the accumulation of [^{14}C]formate was dose-dependent, i.e.,

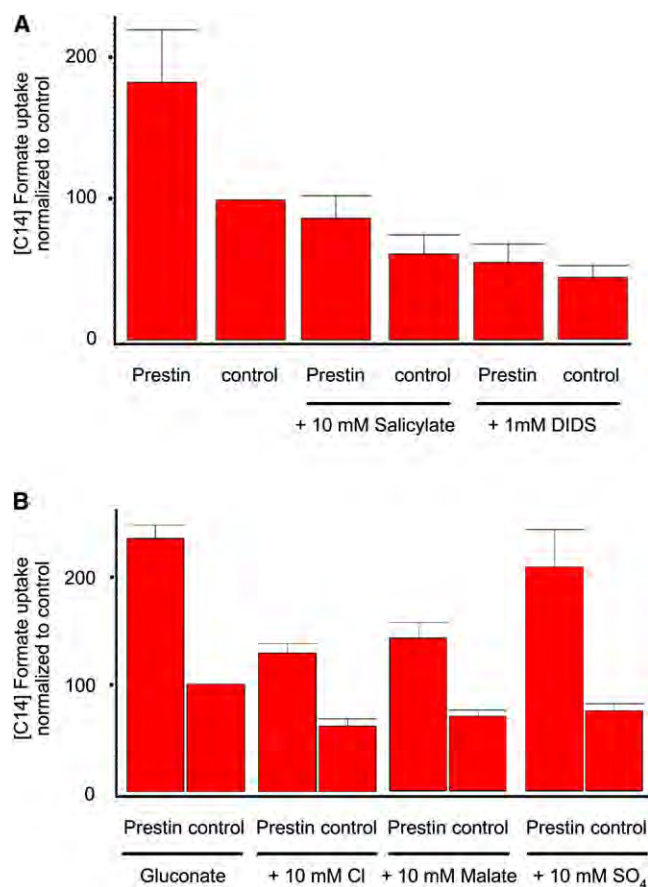


FIGURE 2 Prestin-induced uptake of [¹⁴C]formate can be blocked. (A) [¹⁴C]formate uptake in cells transfected with prestin and vector only, and similarly transfected cells treated with 10 mM salicylate and 1 mM DIDS in incubation/preincubation medium. Prestin-induced uptake of [¹⁴C]formate was reduced by both agents. Mean values for the six groups were: prestin, 183 (±37); control, 100, prestin with salicylate, 87 (±16); control with salicylate, 61 (±13.0); prestin with DIDS, 53.9 (± 13.0); and control with DIDS, 44 (±8.5) (*n* = 3). (B) Effects of various test anions on prestin-induced uptake of [¹⁴C]formate. Prestin-transfected cells were incubated with Na gluconate and Na gluconate to which various indicated test anions were then added. Both chloride and malate decreased prestin uptake, whereas SO₄²⁻ had minimal effects on prestin-induced [¹⁴C]formate uptake. Mean values for the eight groups were: prestin, 237 (±11.8); control, 100; prestin + chloride, 130 (±8.6); control + chloride, 61 (±6.7); prestin + malate, 142 (±15); control + malate, 70 (±5.7); prestin + SO₄²⁻, 209 (±35); and control + SO₄²⁻, 75 (±6.5). Uptake of [¹⁴C]formate by prestin was significantly reduced by chloride and malate (*p* < 0.05, one-way ANOVA), but not by SO₄²⁻ (*p* > 0.05) (*n* = 3). Data were normalized to vector-only controls. Uptake is denoted in relative counts (see Methods).

the amount of prestin plasmid used for transfection correlated with [¹⁴C]formate accumulation (Fig. 1 B). We then compared the uptake of prestin with SLC26a6, a member of the SLC26 anion transporter family that is most closely related to prestin. As indicated in Fig. 1 C, cells transfected with prestin showed a marked increase in [¹⁴C]formate uptake that was comparable to that of CHO cells similarly transfected with SLC26a6. The uptake induced by transfected transporters was significantly greater than that for cells transfected

with vector only (*p* < 0.01, ANOVA). Fig. 1 D summarizes similar positive transport studies with [¹⁴C]oxalate. SLC26a6 has a preferred affinity for the oxalate anion, and knockouts of SLC26a6 have defective epithelial Cl-oxalate exchange, leading to oxalate urinary calculi (14,20). The absolute prestin-induced uptake of oxalate was 1.5-fold greater than formate uptake, and is not reflected in the figures, which were normalized to our controls. As noted above, we reinvestigated anion transport in oocytes using [¹⁴C]formate and [¹⁴C]oxalate uptake, and in contrast to our data with CHO cells, we failed to demonstrate an uptake of these anions by prestin. At best, we found an inconsistent increase in uptake, even when we attempted to maximize translation by using unidirectionally capped cRNA at a concentration of 50 ng per oocyte. These results are consistent with other work in the field, and may result from an absence of an associated cofactor for prestin in oocytes, which is present in CHO cells. Because we lack a quantitative mechanism for determining the expression of prestin on the cell surface, we cannot ascertain if the absence of transport in oocytes results from inadequate surface expression.

Prestin's anion transport is similar to SLC26 family-member anion transporters

The uptake of [¹⁴C]formate induced by prestin in CHO cells was blocked by 1 mM 4,4'-diisothiocyanatostilbene-2,2'-disulfonic acid (DIDS), a well-characterized blocker of anion transport (Fig. 2 A) (14). Anion transport by other members of the SLC26 anion transporter family was shown to require up to 1 mM DIDS to completely block anion transport. Furthermore, anion transport was also blocked by 10 mM salicylate, which is known to block prestin's NLC (Fig. 2 A) (21,22).

After establishing that prestin mediates formate and oxalate transport, we tested the ability of other anions to compete for formate uptake. Anion transporters of the SLC26 family have a variable ability to transport different anions that is, in part, explained by their relative affinity for these anions (23,24). Fig. 2 B summarizes experiments where [¹⁴C]formate uptake by prestin-transfected CHO cells was measured in the presence of competing extracellular (10 mM) test anions. As is evident, both chloride and malate were able to inhibit the uptake of formate (*p* < 0.01, ANOVA), whereas the divalent anion sulfate had minimal effects on formate uptake (*p* > 0.05, ANOVA). The result with sulfate is interesting, because sulfate was originally thought not to support NLC (8), but was subsequently shown to support robust NLC and electromotility in outer hair cells (9–11,25,26).

Prestin's anion-transporter function can be separated from NLC: the role of a potential chloride-binding site

Chloride plays an important role in generating NLC, whether as its extrinsic voltage sensor or as an intracellular allosteric

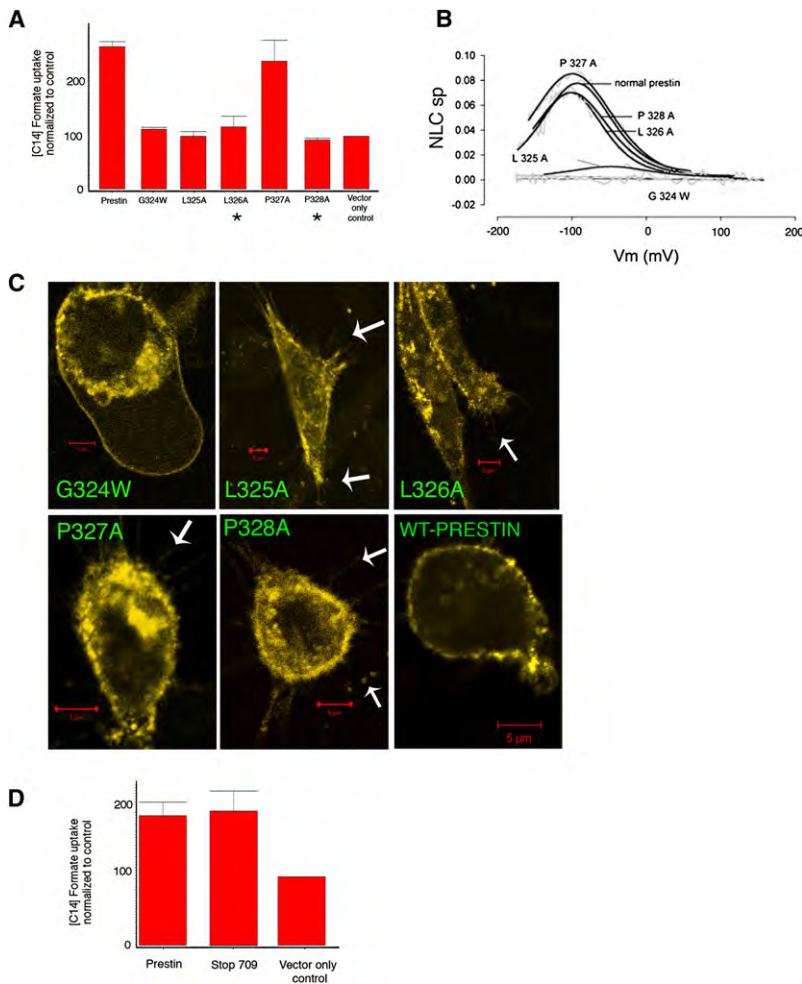


FIGURE 3 Effects of truncations and mutations in prestin on prestin-induced uptake of [^{14}C]formate. (A) Single mutations in potential chloride-binding motif decrease anion transport. All mutants except P327A show decreased anion transport. Mean uptake of [^{14}C]formate of prestin, G324W, L325A, L326A, P327A, P328A, and vector-only control cells were 269 (± 9), 113 (± 3), 100 (± 9), 117 (± 20), 241 (± 40), 93 (± 3.5), and 100, respectively. The uptake of [^{14}C]formate by prestin and P327A-transfected cells was significantly greater than in controls ($p < 0.05$, one-way ANOVA) ($n = 4$). (B) Effects of these mutations on NLC. Two mutants P328A and L326A show preserved NLC but decreased anion transport (indicated by asterisk in A). P327A has preserved NLC and anion transport, whereas remaining mutants eliminated (G324W) or significantly decreased (L325A) NLC, while also decreasing anion transport. (C) Confocal microscopy of YFP fusions of prestin and individual mutants (G324W, L325A, L326A, P327A, and P328A) shows membrane targeting. Arrows indicate filopodia containing prestin-YFP fluorescence. (D) Truncation of C-terminus at amino acid 709 (stop 709) that eliminates NLC shows preserved anion transport. Mean [^{14}C]formate uptake values for prestin, stop 709, and vector-only control were 188 (± 18), 197 (± 28), and 100, respectively. The [^{14}C]formate uptakes in prestin and stop 709-transfected cells were significantly greater than in controls ($p < 0.05$) ($n = 3$). Uptake is denoted in relative counts (see Methods).

modulator (8–10). In seeking to understand the action of intracellular chloride, we identified one potential chloride-binding motif in prestin, based on its homology with a proven chloride-binding site (GXXXP) in the bacterial CLC channel (27), where it is thought to bind chloride ions traversing the channel's pore. In prestin, this sequence, GLLPP (amino acids 324–328), lies on the predicted intracellular surface of the protein between transmembrane loops 6 and 7 of the 10-transmembrane model (13). We mutated individual amino acids in this motif, and determined their effects on NLC and anion transport. Four mutations (G324W, L325A, L326A, and P328A) abolished prestin-induced anion transport ($p < 0.01$, one-way ANOVA; Fig. 3 A). Correspondingly, one mutation (G324W) abolished NLC, and another (L325A) profoundly reduced NLC, whereas three mutations (L326A, P327A, and P328A) had normal NLC (Fig. 3 B). Consequently, two of our mutants (L326A and P328A) exerted differential effects on NLC and anion transport, each preserving the former and reducing the latter. As shown in Fig. 3 C, confocal imaging confirmed that all these mutants were targeted to the plasma membrane, even showing an unequivocal fluorescence of filopodia, processes that lack

confounding intramembranous organelles. Of course, plasmalemmal targeting was expected for mutations showing NLC, because NLC (or transport) was observed in these mutants, and such functional activity could only have occurred if the proteins were targeted to the membrane where they could sense voltage or mediate the cellular transport of anions.

Although these data clearly show a divorce between transport and NLC, we sought unequivocal corroboration. In previous studies, we and others showed that serial truncations of prestin's C-terminus reduce and then abolish NLC (13,28). Truncation of the C-terminus at amino acid 709 results in a loss of NLC. We tested anion transport (Fig. 3 D) in this mutant lacking NLC (stop 709), and found that it had preserved anion transport, equivalent to normal prestin and statistically greater than in cells transfected with control YFP vector alone ($p < 0.05$). We previously demonstrated via confocal microscopy and flow cytometry that this mutant was targeted to the plasma membrane. These transport data confirm the truncation's proper membrane targeting. Clearly, the demonstration of preserved anion transport with this NLC-incompetent mutant confirms that anion transport can be separated from NLC.

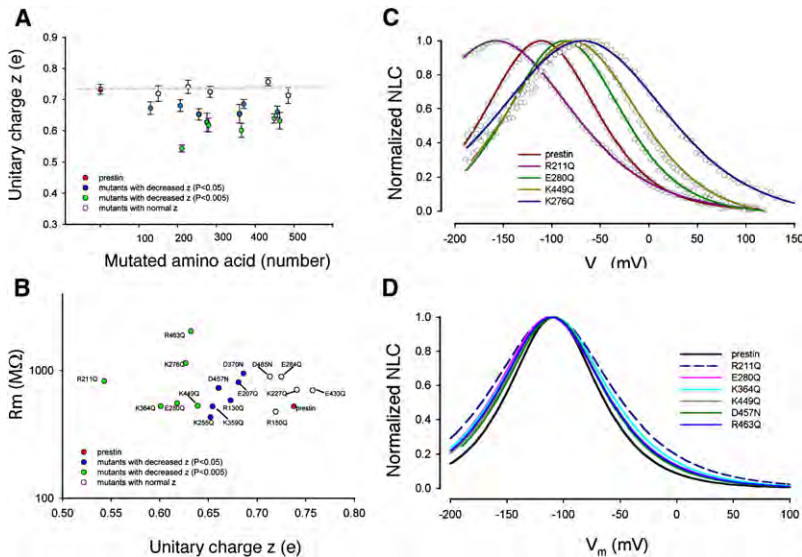


FIGURE 4 Effects of single amino-acid substitutions of charged residues that are within or in close proximity to predicted membrane-spanning regions. (A) Effects on unitary charge (z) are shown and plotted against amino-acid position. Data include only those mutants that showed nonlinear capacitance. Residues are grouped according to how significantly different their z values were, compared with wild-type prestin (*red*). Those residues are in blue where $p < 0.05$ (R130Q, R211Q, K255Q, K359Q, D269N, and D457N), and in green where $p < 0.005$ (E207Q, K276Q, E280Q, K364Q, K449Q, and R463Q). (B) Average membrane resistance of prestin and prestin mutants in A. These data confirm that changes in z were independent of membrane resistance. (C) Normalized examples of NLC of prestin and four mutants that showed a reduction in z . Data points are fitted with Eq. 1. (D) Normalized average fits of individual mutants are aligned to wild-type prestin's V_h , for a better demonstration of decrease in voltage sensitivity evidenced by a broadening of the functions.

Prestin has an intrinsic voltage sensor

Our results so far provide evidence that key components of the extrinsic voltage-sensor hypothesis (i.e., that transport is absent, along with the reasonable inference that NLC arises from the loss of a full transport cycle) are untenable. Although these results do not disprove the extrinsic-voltage hypothesis, they warrant a reexploration of the model. Moreover, these results beget the question: is there an alternative or additional mechanism whereby prestin senses voltage? We sought to determine if charged residues in prestin's transmembrane domains contribute to its gating charge movement. To do so, we neutralized 22 charged residues that were predicted to lie in its transmembrane regions by site-directed mutagenesis, and determined the effects on the unitary charge movement, z . In contrast to findings by Oliver et al. (8), all these residues were conserved between prestin and its closest relative, SLC26a6. We relied on measures of unitary charge derived from the traditional two-state Boltzmann function as a metric of charge movement within a single motor. It is our best (and only) estimate of charge movement within a single motor. Moreover, empirical data as they relate to prestin function (both charge and electromotility) fit exceedingly well with the two-state Boltzmann function (17–19). Of 22 mutated, charged residues, we found a subset of 12 that significantly reduced z (Fig. 4 A and Table 1). We were careful to exclude potential alterations in membrane resistance characteristics in our evaluations, because membrane resistance remained equivalent to controls (Fig. 4 B). The reduced z , evidence of altered voltage-sensing as reflected by reduced voltage sensitivity (i.e., broader NLC functions), is most readily seen in the normalized NLC traces in Fig. 4, C and D.

In Fig. S1 of the Supporting Material, we show representative C-V functions from all 12 mutants. These 12 residues that affected z are located across the entire span of the

transmembrane core of prestin (Fig. 5, A and B). Of the remaining 10 residues, mutations of five residues failed to affect z (R150, K227, E284, E433, and D485); mutations of four residues (D83, E293, E374, and E404) resulted in absent NLC; and the mutation of one residue (R399) resulted in a V_h shift to an extreme negative range, making the estimation of z impossible. The mutations of the four residues that showed absent NLC were likely attributable to poor membrane-targeting, as evidenced by confocal imaging (data not shown). Of the residues that affected z , four were negatively charged (E207, E280, D370, and D457), and eight residues were positively charged (R130, R211, K255, K276, K359, K364, K449, and R463). The effects on z of all these charged residues varied. These mutations also affected the operating voltage of the protein (V_h), although there was no relationship between z and V_h (Fig. 6). As expected, there was a correlation between z and the total

TABLE 1 Z values (\pm SE) of individual mutations, p values of a t -test compared with wild-type prestin, and number of cells recorded

Amino acid position	z		Number of cells recorded
	z	p	
Wild-type prestin	0.73 ± 0.02		19
R130Q	0.67 ± 0.02	<0.05	11
E207Q	0.68 ± 0.02	<0.05	10
R211Q	0.54 ± 0.01	<0.00000001	15
K255Q	0.65 ± 0.02	<0.01	8
K276Q	0.63 ± 0.03	<0.001	9
E280Q	0.62 ± 0.02	<0.0001	11
K359Q	0.65 ± 0.03	<0.01	11
K364Q	0.60 ± 0.02	<0.0001	9
D370N	0.69 ± 0.01	<0.05	10
K449Q	0.64 ± 0.01	<0.001	10
D457N	0.66 ± 0.02	<0.01	9
R463Q	0.63 ± 0.03	<0.005	9

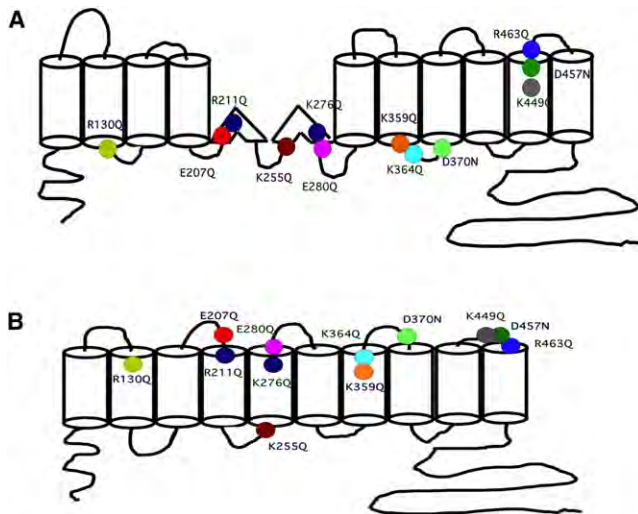


FIGURE 5 Residue locations. Placement of charge residue mutations in 12 (A) and 10 (B) transmembrane models of the protein. The residues and their traces in Fig. S1 are correspondingly color-coded. Also indicated are specific amino-acid numbers, which in turn are color-coded as in Fig. 4 A, to indicate residues and their effects on z .

charge movement in prestin and all of its point mutations that affected z (Fig. 7).

DISCUSSION

Here we unequivocally showed that prestin, in contrast to our previous understanding, is an anion transporter, much like its closest relative, SLC26a6. Moreover, our results are consistent with the concept of prestin's voltage sensitivity deriving at least in part (and perhaps even entirely) from intrinsic charged residues in the protein. Finally, we were able to separate these two functional characteristics of prestin by mutations to residues within a putative anion-binding site.

The widely accepted notion of an absence of intrinsic voltage-sensing in prestin followed experiments by Oliver et al. (8), who failed to find a change in unitary gating charge after mutating charged residues in prestin that were absent in SLC26a6 (the closest relative that does not exhibit gating charge movement). They reasoned that the gating charge in prestin was attributable to newly acquired charged residues in prestin. In reviewing their mutagenesis experiments, we noted that a significant number (10/21) of charged residues that were different between the two proteins lay outside its predicted transmembrane domain, and therefore could not have sensed transmembrane voltage. Indeed, we mutated charged residues in the intracellular C-terminus, and found that such mutations did not alter the unitary charge relative to controls (29). To test fully for intrinsic voltage-sensing, we mutated every charged residue in prestin that lies within or in very close proximity to the predicted transmembrane segments (of both the 10-transmembrane and 12-transmembrane models; Fig. 5, A and B), and determined the effect on unitary charge (z). We identified a large number of charged residues (12 out of 22)

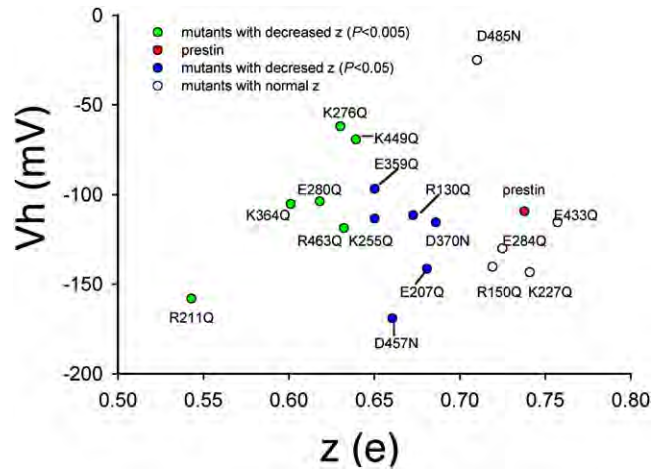


FIGURE 6 Relationship between voltage of peak capacitance (V_h) and unitary charge (z). There is no relationship between z values and V_h , although most of the mutants caused a negative shift in V_h .

within prestin's transmembrane domains that are also conserved in SLC26a6, and that contribute to the generation of NLC. These data require a fundamental rethinking of how prestin brings about electromotility.

Three features of the identified residues and their relationship to voltage sensitivity are noteworthy. First, prestin shows much less voltage sensitivity than conventional ion channels. Thus, the unitary charge per motor in prestin amounts to $\sim 0.74 e$, and contrasts with values of 13.6e for Shaker potassium channels, 10e for sodium channels, and 2.6e for large-conductance, calcium-activated potassium channels (30–33). Second, mutations that produced a reduction in z , although they were as low as 0.55, clustered around a mode of 0.65e, indicating that these residues contributed a similar amount of charge to the total gating-charge movement. Third, all of these residues are conserved between prestin and SLC26a6, which does not exhibit gating-charge movement (8) (J.-P. Bai and D. Navaratnam, unpublished observations).

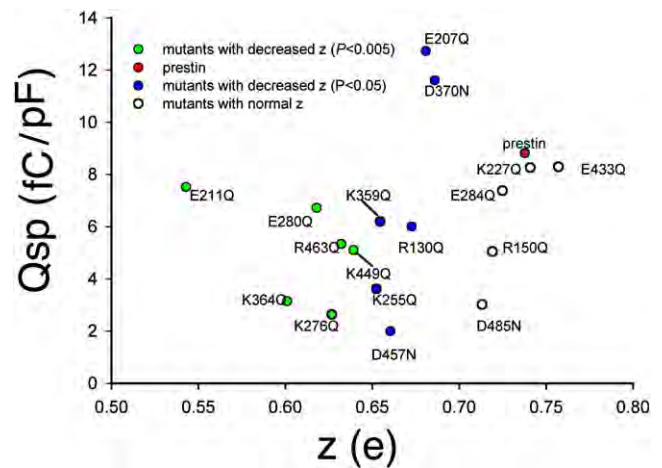


FIGURE 7 Relationship between unitary charge z and specific capacitance. There is a positive trend between z and Q_{sp} ($Q_{max}/\text{linear capacitance}$).

Why should conserved residues generate a charge movement in one family member but not the other? There are parallels in ion channels where residues that contribute to gating charge and voltage sensitivity in one protein are conserved in a related orthologous protein, yet do not contribute to gating charge or voltage sensitivity in the orthologous protein. For example, the Shab delayed rectifier potassium channel and its mammalian homolog Kv2.1 have the same number of charged residues in their voltage sensors, yet carry different gating charges (7.5e and 12.5e, respectively) (34). Similarly, the gating charge in mSlo channels (2.6e) is fivefold less than that in Shaker channels (13e), although mSlo contains three of the five residues most important for gating charges (33). According to a widely held consensus, these differences are likely attributable to a smaller movement of these residues in both mSlo and Shab (33–35). A similar mechanism could explain the apparent discrepancy between prestin's gating-charge movement and its absence in SLC26a6, which has the same residues implicated in prestin's charge movement. Alternatively, there may be a movement of charged residues of opposite polarity neutralizing their effects in SLC26a6. In any event, the movement of charge through the voltage field in prestin and the contribution from each of these residues to total charge movement are small, when compared with voltage-gated ion channels. In this respect, prestin differs from voltage-gated ion channels, where a few charged residues account for the majority of voltage sensitivity.

Perhaps more germane to the workings of prestin, a member of a transporter family, is the observation that in some transporters, when substrate is removed, presteady-state currents are revealed (36–38). Transient, presteady-state currents are equivalent to the gating-charge movements or NLC measured in prestin, and represent voltage-sensor activity. For example, in line with our determinations for prestin, the voltage-sensing mechanisms in the Na⁺-glucose transporter were shown to involve intrinsic charge movements of the protein, rather than only Na⁺ binding/unbinding to sites within the protein's membrane field (38,39). Interestingly, the charge valence *z* of 1e is close to that of prestin. Similarly, it is known that the GABA transporter's charge movement is derived from extrinsic (chloride) and intrinsic charge (36). Indeed, even the chloride dependence of gating in CLC channels is known to arise because of competition with a glutamate gate charge, rather than functioning as a mobile extrinsic voltage sensor (40). Thus, the use of intrinsic charged residues is clearly a general mechanism of voltage-sensing proteins, and prestin is no different (41).

Our data showing separated NLC and anion transport by mammalian prestin contain several implications. First, our data extend work showing that nonmammalian orthologs of prestin are able to transport anions in an electrogenic manner (6). In that study (6), electrophysiological methodology was used solely to assess electrogenic transport, and the authors reasoned that electrogenic transport in mam-

lian prestin does not occur. Interestingly, however, some electrophysiological characteristics of mammalian prestin were successfully modeled as a result of the exact type of electrogenic transport found in nonmammalian orthologs of prestin (25). Our data cannot resolve this controversy, because the classic transport techniques that we used, although thoroughly sufficient for the demonstration of anion transport, cannot assess electrogenicity. Second, our data suggest that the advent of NLC/electromotility occurs independent of anion transport, and is not coincident with its loss, as previously suggested. Indeed, an evolutionary analysis suggests that SLC26a6, which lacks the ability to generate NLC or electromotility, arose from SLC26a5 (Dr. Kirk Beisel, Creighton University, personal communication, 2008). Third, because each outer hair cell is estimated to contain up to 10 million prestin motors (42,43), our data imply the presence of a powerful homeostatic mechanism for controlling anion concentration in these cells. This is especially the case in light of ample data showing that prestin's operating voltage range is affected by intracellular anion concentration (10,12,44). Fourth, our data showing intrinsic voltage-sensor activity in prestin establish an alternative or additional molecular mechanism for voltage-sensing in the outer hair cell motor. The original extrinsic voltage-sensor or partial anion-transporter model of prestin voltage-sensing, where monovalent chloride anions serve as sources of voltage-sensor charge movement or NLC (8), has received serious challenges. For example, whereas sulfate anions were found to abolish NLC in prestin-transfected cells (8), several groups showed that sulfate supports NLC and electromotility in OHCs (10,11,25,26). Furthermore, anion-charge valence does not dictate gating-charge valence, as would be expected in the extrinsic voltage-sensor model (9). We suggested that anions serve as allosteric modulators, because the conformational state of prestin depends not only on the concentration of intracellular anions, but on their structure as well (9). In this regard, it is interesting that alkylsulfonic anions of differing hydrocarbon chain lengths variably shift prestin's operating voltage range, conceivably because of interactions with the different voltage-sensing residues that we identified here.

Finally, our data raise an important question. Because the advent of the outer hair cell motor is thought to be a recent evolutionary event, and because the residues in prestin responsible for sensing voltage are also present in SLC26a6, what additional features in prestin allow these charged residues to move in response to changes in transmembrane voltage?

SUPPORTING MATERIAL

A figure is available at [http://www.biophysj.org/biophysj/supplemental/S0006-3495\(09\)00470-6](http://www.biophysj.org/biophysj/supplemental/S0006-3495(09)00470-6).

The authors thank Dr. Fred Sigworth for suggestions, discussions about the data, and critical reading of the manuscript.

Support was provided by National Institutes of Health National Institute on Deafness and Other Communication Disorders grants DC 000273 (to J.S.S.) and DC 008130 (to J.S.S. and D.N.).

REFERENCES

- Zheng, J., W. Shen, D. He, K. Long, L. Madison, et al. 2000. Prestin is the motor protein of cochlear outer hair cells. *Nature*. 405:149–155.
- Santos-Sacchi, J., W. X. Shen, J. Zheng, and P. Dallos. 2001. Effects of membrane potential and tension on prestin, the outer hair cell lateral membrane motor protein. *J. Physiol. (Lond.)*. 531:661–666.
- Ludwig, J., D. Oliver, G. Frank, N. Klocker, A. W. Gummer, et al. 2001. Reciprocal electromechanical properties of rat prestin: the motor molecule from rat outer hair cells. *Proc. Natl. Acad. Sci. USA*. 98:4178–4183.
- Liberman, M. C., J. Gao, D. Z. He, X. Wu, S. Jia, et al. 2002. Prestin is required for electromotility of the outer hair cell and for the cochlear amplifier. *Nature*. 419:300–304.
- Reference deleted in proof.
- Schaechinger, T. J., and D. Oliver. 2007. Nonmammalian orthologs of prestin (SLC26A5) are electrogenic divalent/chloride anion exchangers. *Proc. Natl. Acad. Sci. USA*. 104:7693–7698.
- Dallos, P., and B. Fakler. 2002. Prestin, a new type of motor protein. *Nat. Rev. Mol. Cell Biol.* 3:104–111.
- Oliver, D., D. Z. He, N. Klocker, J. Ludwig, U. Schulte, et al. 2001. Intracellular anions as the voltage sensor of prestin, the outer hair cell motor protein. *Science*. 292:2340–2343.
- Rybalchenko, V., and J. Santos-Sacchi. 2008. Anion control of voltage sensing by the motor protein prestin in outer hair cells. *Biophys. J.* 95:4439–4447.
- Rybalchenko, V., and J. Santos-Sacchi. 2003. Cl⁻ flux through a non-selective, stretch-sensitive conductance influences the outer hair cell motor of the guinea-pig. *J. Physiol.* 547:873–891.
- Rybalchenko, V., and J. Santos-Sacchi. 2003. Allosteric modulation of the outer hair cell motor protein prestin by chloride. In *Biophysics of the Cochlea: From Molecules to Models*. A. Gummer, editor. World Scientific Publishing, Singapore. 116–126.
- Song, L., A. Seeger, and J. Santos-Sacchi. 2005. On membrane motor activity and chloride flux in the outer hair cell: lessons learned from the environmental toxin tributyltin. *Biophys. J.* 88:2350–2362.
- Navaratnam, D., J. P. Bai, H. Samaranyake, and J. Santos-Sacchi. 2005. N-terminal-mediated homomultimerization of prestin, the outer hair cell motor protein. *Biophys. J.* 89:3345–3352.
- Jiang, Z., I. I. Grichtchenko, W. F. Boron, and P. S. Aronson. 2002. Specificity of anion exchange mediated by mouse Slc26a6. *J. Biol. Chem.* 277:33963–33967.
- Santos-Sacchi, J. 2004. Determination of cell capacitance using the exact empirical solution of dY/dCm and its phase angle. *Biophys. J.* 87:714–727.
- Santos-Sacchi, J., S. Kakehata, and S. Takahashi. 1998. Effects of membrane potential on the voltage dependence of motility-related charge in outer hair cells of the guinea-pig. *J. Physiol.* 510:225–235.
- Santos-Sacchi, J. 1991. Reversible inhibition of voltage-dependent outer hair cell motility and capacitance. *J. Neurosci.* 11:3096–3110.
- Santos-Sacchi, J. 1993. Harmonics of outer hair cell motility. *Biophys. J.* 65:2217–2227.
- Scherer, M. P., and A. W. Gummer. 2005. How many states can the motor molecule, prestin, assume in an electric field? *Biophys. J.* 88:L27–L29.
- Jiang, Z., J. R. Asplin, A. P. Evan, V. M. Rajendran, H. Velazquez, et al. 2006. Calcium oxalate urolithiasis in mice lacking anion transporter Slc26a6. *Nat. Genet.* 38:474–478.
- Tunstall, M. J., J. E. Gale, and J. F. Ashmore. 1995. Action of salicylate on membrane capacitance of outer hair cells from the guinea-pig cochlea. *J. Physiol.* 485:739–752.
- Kakehata, S., and J. Santos-Sacchi. 1996. Effects of salicylate and lanthanides on outer hair cell motility and associated gating charge. *J. Neurosci.* 16:4881–4889.
- Markovich, D., and P. S. Aronson. 2006. Specificity and regulation of renal sulfate transporters. *Annu. Rev. Physiol.* 69:361–375.
- Mount, D. B., and M. F. Romero. 2004. The SLC26 gene family of multifunctional anion exchangers. *Pflugers Arch.* 447:710–721.
- Muallem, D., and J. Ashmore. 2006. An anion antiporter model of prestin, the outer hair cell motor protein. *Biophys. J.* 90:4035–4045.
- Kennedy, H. J., M. G. Evans, A. C. Crawford, and R. Fettiplace. 2006. Depolarization of cochlear outer hair cells evokes active hair bundle motion by two mechanisms. *J. Neurosci.* 26:2757–2766.
- Estevez, R., and T. J. Jentsch. 2002. CLC chloride channels: correlating structure with function. *Curr. Opin. Struct. Biol.* 12:531–539.
- Zheng, J., G. G. Du, K. Matsuda, A. Orem, S. Aguinaga, et al. 2005. The C-terminus of prestin influences nonlinear capacitance and plasma membrane targeting. *J. Cell Sci.* 118:2987–2996.
- Bai, J. P., D. Navaratnam, H. Samaranyake, and J. Santos-Sacchi. 2006. En bloc C-terminal charge cluster reversals in prestin (SLC26A5): effects on voltage-dependent electromechanical activity. *Neurosci. Lett.* 404:270–275.
- Aggarwal, S. K., and R. MacKinnon. 1996. Contribution of the S4 segment to gating charge in the Shaker K⁺ channel. *Neuron*. 16:1169–1177.
- Seoh, S. A., D. Sigg, D. M. Papazian, and F. Bezanilla. 1996. Voltage-sensing residues in the S2 and S4 segments of the Shaker K⁺ channel. *Neuron*. 16:1159–1167.
- Yang, N., A. L. George, Jr., and R. Horn. 1996. Molecular basis of charge movement in voltage-gated sodium channels. *Neuron*. 16:113–122.
- Horrigan, F. T., J. Cui, and R. W. Aldrich. 1999. Allosteric voltage gating of potassium channels I. Mslo ionic currents in the absence of Ca(2+). *J. Gen. Physiol.* 114:277–304.
- Islas, L. D., and F. J. Sigworth. 1999. Voltage sensitivity and gating charge in Shaker and Shab family potassium channels. *J. Gen. Physiol.* 114:723–742.
- Ma, Z. M., X. J. Lou, and F. T. Horrigan. 2006. Role of charged residues in the S1–S4 voltage sensor of BK channels. *J. Gen. Physiol.* 127:309–328.
- Sacher, A., N. Nelson, J. T. Ogi, E. M. Wright, D. D. Loo, et al. 2002. Presteady-state and steady-state kinetics and turnover rate of the mouse gamma-aminobutyric acid transporter (mGAT3). *J. Membr. Biol.* 190:57–73.
- Hazama, A., D. D. Loo, and E. M. Wright. 1997. Presteady-state currents of the rabbit Na⁺/glucose cotransporter (SGLT1). *J. Membr. Biol.* 155:175–186.
- Loo, D. D., B. A. Hirayama, A. Cha, F. Bezanilla, and E. M. Wright. 2005. Perturbation analysis of the voltage-sensitive conformational changes of the Na⁺/glucose cotransporter. *J. Gen. Physiol.* 125:13–36.
- Aronson, P. S. 1978. Energy-dependence of phlorizin binding to isolated renal microvillus membranes. Evidence concerning the mechanism of coupling between the electrochemical Na⁺ gradient the sugar transport. *J. Membr. Biol.* 42:81–98.
- Dutzler, R., E. B. Campbell, and R. MacKinnon. 2003. Gating the selectivity filter in CIC chloride channels. *Science*. 300:108–112.
- Bezanilla, F. 2008. How membrane proteins sense voltage. *Nat. Rev. Mol. Cell Biol.* 9:323–332.
- Huang, G. J., and J. Santos-Sacchi. 1993. Mapping the distribution of the outer hair cell motility voltage sensor by electrical amputation. *Biophys. J.* 65:2228–2236.
- Gale, J. E., and J. F. Ashmore. 1997. The outer hair cell motor in membrane patches. *Pflugers Arch.* 434:267–271.
- Santos-Sacchi, J., L. Song, J. Zheng, and A. L. Nuttall. 2006. Control of mammalian cochlear amplification by chloride anions. *J. Neurosci.* 26:3992–3998.

OPEN

Prestin kinetics and corresponding frequency dependence augment during early development of the outer hair cell within the mouse organ of Corti

Jun-Ping Bai⁴, Dhasakumar Navaratnam^{1,3,4} & Joseph Santos-Sacchi^{1,2,3*}

Several studies have documented the early development of OHC electromechanical behavior. The mechanical response (electromotility, eM) and its electrical correlate (nonlinear capacitance, NLC), resulting from prestin's voltage-sensor charge movement, increase over the course of several postnatal days in altricial animals. They increase until about p18, near the time of peripheral auditory maturity. The correspondence of auditory capabilities and prestin function indicates that mature activity of prestin occurs at this time. One of the major requirements of eM is its responsiveness across auditory frequencies. Here we evaluate the frequency response of prestin charge movement in mice over the course of development up to 8 months. We find that in apical turn OHCs prestin's frequency response increases during postnatal development and stabilizes when mature hearing is established. The low frequency component of NLC, within *in situ* explants, agrees with previously reported results on isolated cells. If prestin activity is independent of cochlear place, as might be expected, then these observations suggest that prestin activity somehow influences cochlear amplification at high frequencies in spite of its low pass behavior.

The outer hair cell (OHC) enhances cochlear sensitivity up to 3 orders of magnitude, and the cellular basis of this feat resides within the OHCs that populate the organ of Corti. OHCs are electro-motile, responding to transmembrane current perturbations with changes in cell length, termed electromotility (eM)^{1,2}. Though the pertinent electromechanical characteristics (e.g., voltage-dependence, and magnitude) of OHC eM had been studied since the mid-80s^{3,4}, the identification of the membrane protein, SLC26a5 (prestIn), driving this response required over a decade⁵. Various candidates were considered along the way, similar to the quest for the stereociliar MET channel⁶.

Prestin drives OHC electromotility (eM), known to be responsible for cochlear amplification (CA) in mammals⁷. The electrical signature of eM is a bell-shaped nonlinear capacitance (NLC), the first derivative of prestin sensor charge vs. membrane voltage (dQ_p/dV_m), which peaks at a characteristic membrane voltage (V_h)^{8,9}. We have previously studied the development of NLC in OHCs of the mouse¹⁰. Those studies demonstrated that increases in prestin charge (Q_{max}) continued after stabilization of linear capacitance (at p10), which corresponds to total membrane surface area (sum of membrane and embedded prestin surface area). Thus, though the number of prestin molecules appeared to stabilize, additional changes in NLC characteristics ensued, indicating some sort of maturational events. Here we study, in developing OHCs, the maturation of prestin kinetics, which has recently been shown to possess low pass characteristics in adult guinea pig OHCs¹¹. We find that during development the frequency response of NLC increases, stabilizing near 6 kHz in adults at the apical turn of the cochlea at room temperature. We also find that linear capacitance decreases with aging, and is indicative of reduced prestin

¹Department of Surgery (Otolaryngology), Yale University School of Medicine, 333 Cedar St, New Haven CT, USA.

²Department of Cellular and Molecular Physiology, Yale University School of Medicine, 333 Cedar St, New Haven CT, USA. ³Department of Neuroscience, Yale University School of Medicine, 333 Cedar St, New Haven CT, USA.

⁴Department of Neurology, Yale University School of Medicine, 333 Cedar St, New Haven CT, USA. *email: joseph.santos-sacchi@yale.edu

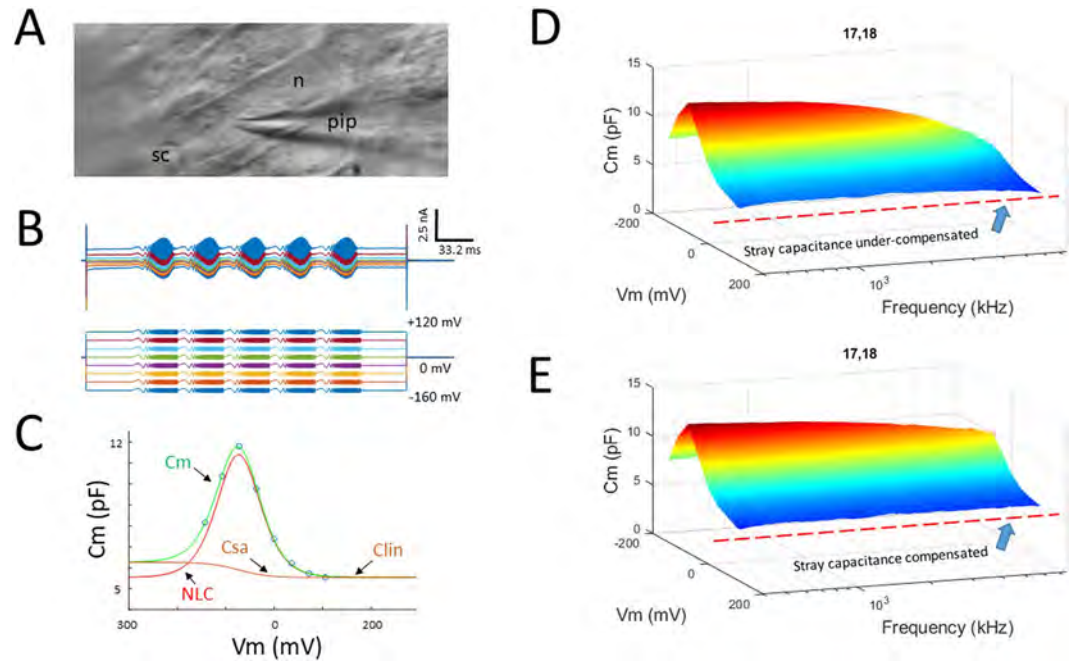


Figure 1. High frequency measurement of OHC NLC in organ of Corti explants. (A) Light micrograph of an *in situ* patch clamped OHC. sc, stereocilia; n, nucleus; pip, patch pipette. (B) Whole cell currents induced by chirp voltage protocol. (C) Derived voltage-dependent capacitance (circles) at each frequency (see methods) was fit to extract NLC and its Boltzmann parameters. (D,E) Surface plots of raw C_m data before (D) and after (E) correction for residual stray capacitance effects on high frequency measures. Note frequency independence of C_{lin} following correction.

insertion in the membrane. Nevertheless, specific motor charge density (a metric for prestin density within the membrane) remains fairly constant.

Methods

C57/B6 pups aged postnatal days 6–18, and months 2 and 8 were used. All experimental protocols were approved by the Yale Animal Care and Use Committee, and were in accordance with relevant guidelines and regulations. Apical turns of the organ of Corti were dissected out and recorded with ionic current blocking solutions, thereby removing interference on measures of membrane capacitance. The extracellular solution contained (in mM): 100 NaCl, 20 tetraethylammonium (TEA)-Cl, 20 CsCl, 2 CoCl₂, 1 MgCl₂, 1 CaCl₂, 10 HEPES, pH 7.2. The intracellular solution contained (in mM): 140 CsCl, 2 MgCl₂, 10 HEPES, and 10 EGTA, pH 7.2. Pipettes were coated with M-coat to reduce stray capacitance, and had resistances of 3–5 MΩ. Gigohm seals were made and stray capacitance was balanced out with amplifier circuitry prior to establishing whole-cell conditions. A Nikon Eclipse E600-FN microscope with 40× water immersion lens was used to observe cells during voltage clamp. Whole cell voltage clamp recordings were performed from all rows of outer hair cells (OHCs) of whole mount organ of Corti. We limited the recording area within 1/4 turn. OHCs were recorded at room temperature using jClamp software and an Axopatch 200B amplifier. Data were low pass filtered at 10 kHz and digitized at 100 kHz with a Digidata 1320 A.

Chirp voltage stimuli were delivered across frequency and analyzed within 300–7000 Hz, where stray capacitance was removed. The voltage chirps were generated in jClamp using the Matlab logarithmic “chirp” function (10 mV pk; pts = 4096; F0 = 24.4141 Hz; F1 = 50 kHz; t1 = 0.04095 s). Chirp responses were not averaged at each voltage step (−160 to +120 in 40 mV steps). Cell currents were either averaged for analysis (6–8 cells/group) for surface plot presentations or analyzed individually for statistical measures. Detailed analysis of C_m was performed in Matlab. Capacitance was measured using dual-sine analysis at harmonic frequencies (Santos-Sacchi *et al.*, 1998; Santos-Sacchi, 2004). Briefly, real and imaginary components of membrane current at harmonic frequencies were determined by FFT in jClamp, corrected for the roll-off of recording system admittance¹² and residual stray capacitance¹³. R_s , R_m and C_m were extracted using the dual-sine, 3-parameter solution of the standard patch clamp model^{14,15}, based on the original single sine solution¹⁶. In order to extract Boltzmann parameters, capacitance-voltage data were fit to the first derivative of a two-state Boltzmann function.

$$C_m = NLC + C_{sa} + C_{lin} = Q_{max} \frac{ze}{k_B T} \frac{b}{(1+b)^2} + C_{sa} + C_{lin} \quad (1)$$

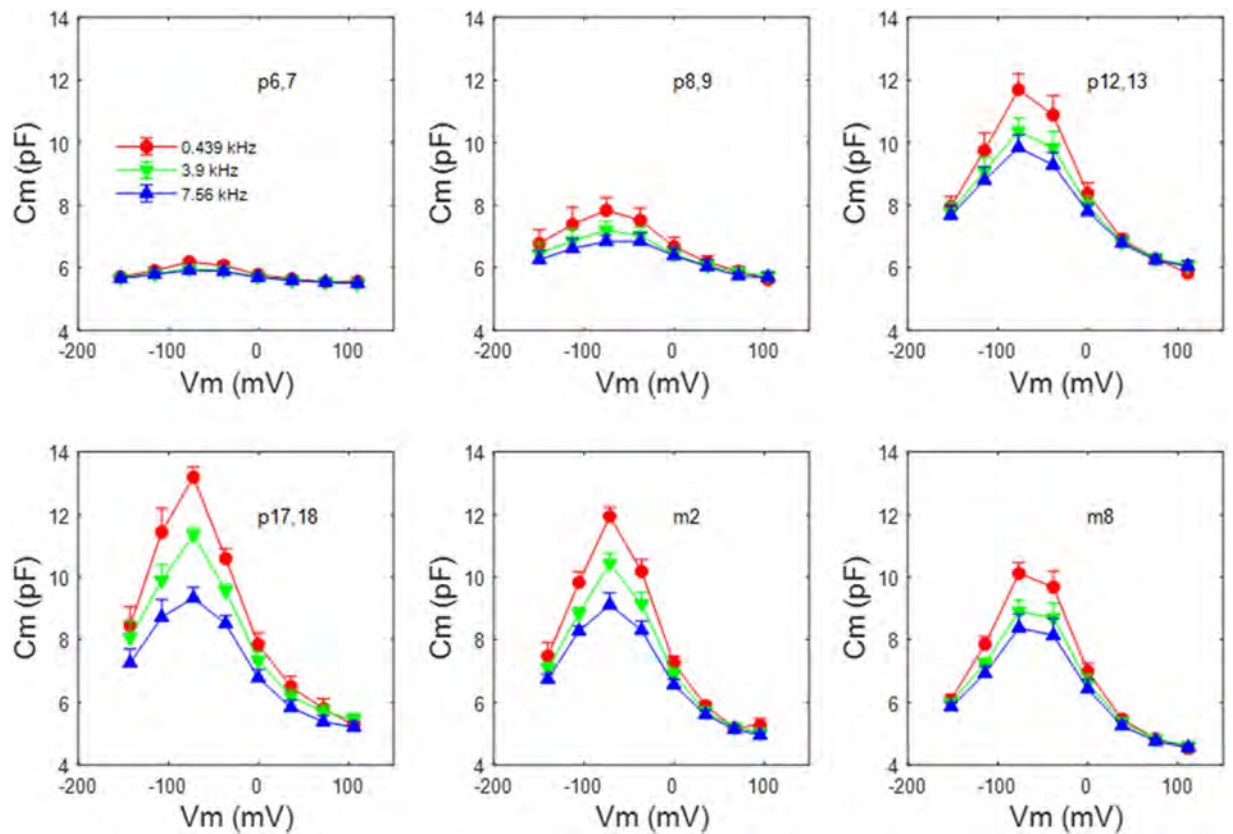


Figure 2. NLC (mean \pm se) as a function of postnatal age at select stimulating frequencies. Peak NLC reaches maximal values at p17/18 across frequency. C_{lin} increases until p12/13 as a result of surface area increase, but decreases thereafter. NLC also reduces following p17/18. By 8 months, C_{lin} has markedly decreased. P6,7 n = 7; p8,9 n = 7; p12,13 n = 6; p17,18 n = 8; 2 month n = 8; 8 month n = 9.

$$\text{where } b = \exp\left(-ze\frac{V_m - V_h}{k_B T}\right), C_{sa} = \frac{\Delta C_{sa}}{(1 + b^{-1})}$$

Q_{max} is the maximum nonlinear charge moved, V_h is voltage at peak capacitance or equivalently, at half-maximum charge transfer, V_m is R_s -corrected membrane potential, z is valence, C_{lin} is linear membrane capacitance, e is electron charge, k_B is Boltzmann's constant, and T is absolute temperature. C_{sa} is a component of capacitance that characterizes sigmoidal changes in specific membrane capacitance¹⁷. ΔC_{sa} is the total sum of unitary changes per prestin motor protein. Q_{sp} denotes charge density, namely Q_{max}/C_{lin} .

A Lorentzian function (or the sum of two Lorentzians) (Gale and Ashmore, 1997; Santos-Sacchi and Tan, 2018) was used to fit NLC across frequency.

$$NLC(f) = NLC_0/[1 + (2\pi f\tau)^2]^{1/2} \quad (2)$$

where NLC_0 is the zero frequency component, and $\tau = 1/F_c$, the cut-off frequency. Additionally, a power fit of NLC across frequency was performed.

$$NLC(f) = NLC_0 + a * f^b \quad (3)$$

where NLC_0 is the zero frequency component, and a and b control the frequency response.

Results

Figure 1 illustrates our methodology to measure NLC across frequency. With our Boltzmann fit (Eq. 1) we obtain the usual Boltzmann parameters while extracting NLC, and additionally determine C_{sa} , a component of capacitance that we believe arises from changes in membrane surface area or membrane thickness as prestin alters its conformational state across voltage^{17–20}.

Figure 2 shows mean (\pm se) NLC at 3 selected frequencies within our measurement bandwidth, as a function of postnatal age. As determined previously, NLC reaches maximal values at p17/18 in rodents^{10,21}. Here we find the same pattern across frequencies. C_{lin} increases until p12/13 as a result of surface area increase as the cells mature, lengthen and express increasing amounts of prestin within the membrane. However, C_{lin} decreases

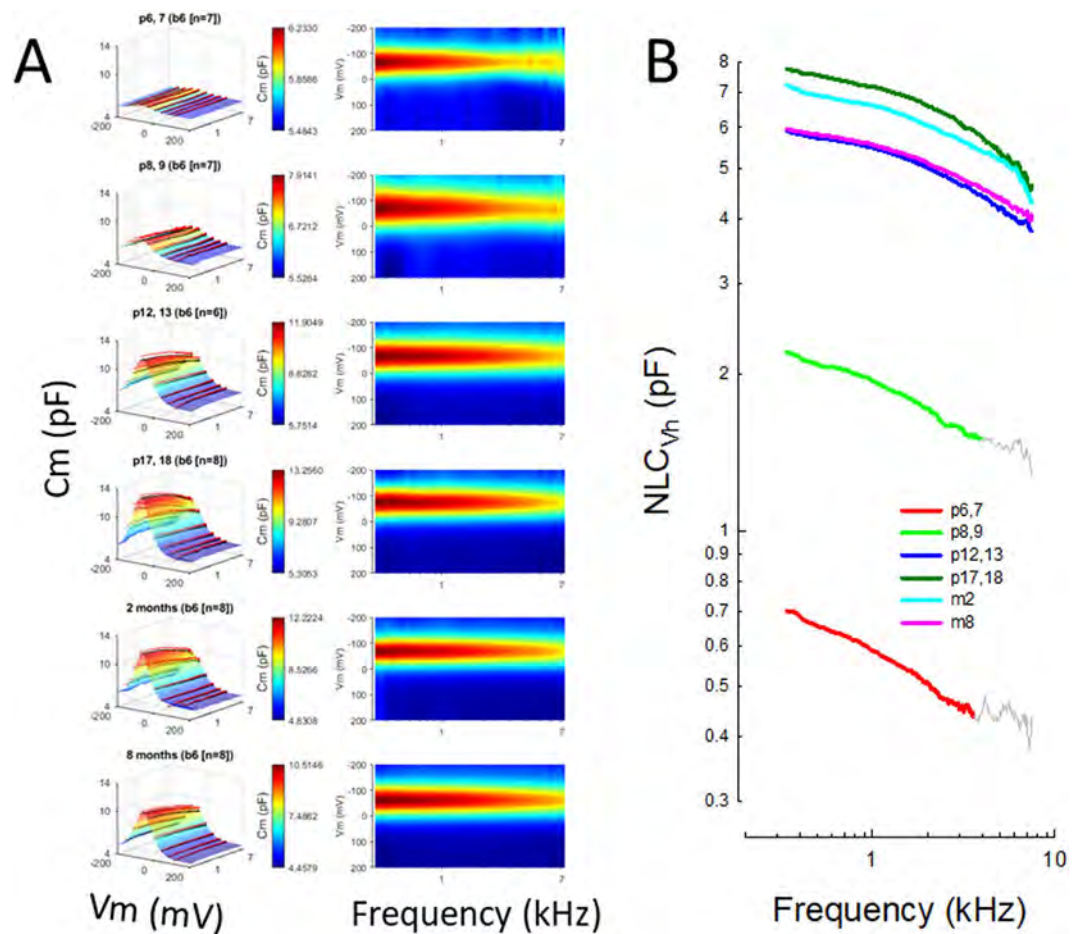


Figure 3. (A) Left panels show full NLC spectrum (0.39–7 kHz) surface plots as a function of postnatal age, illustrating the bell-shaped NLC and its roll-off with increasing frequency. Black dots indicate means and pink dots are \pm se, which sit atop the Boltzmann fits. The panels on the right show the same data top-down, and provide a clearer view of the frequency response changes during aging. (B) NLC_{V_h} for each age group is log-log plotted to more clearly show the low-pass behavior that changes during aging. The colored points were used for fitting in Fig. 5. For the 2 youngest groups grey lines show regions omitted from fits because of noise at high frequencies.

thereafter at all frequencies. By 8 months, C_{lin} has decreased by more than 25%. NLC also reduces following p17/18. The plots also highlight a substantial roll-off of peak NLC across frequency, which we investigate in more detail further below.

Because we limited our recordings to a quarter turn of the apical coil of the cochlea, we determined whether the variability in hair cell length within that region could impact our C_{lin} data. OHC lengths in different rows of the cochlear apex are indistinguishable²². In the mouse strain we used, they determined that OHC lengths from middle (17.3 μm) and apical (21.3 μm) turn regions differed by 4 μm . Assuming that this progression will translate into our quarter turn (as their plots suggest) we would maximally expect about a 1 μm length variability in our hair cell recordings. Given the cylindrical geometry of the OHC and its diameter in mice ($\sim 7 \mu\text{m}$), we calculate an expected maximal variability in linear capacitance (based on surface area arising from our measured membrane specific capacitance of 0.08 $\text{pF}/\mu\text{m}^2$ ²⁰ of 0.26 pF. This is well below our finding of -1.6 pF (25% reduction from p12/13) during aging. Utilizing a more stringent estimate of 0.05 $\text{pF}/\mu\text{m}^2$ for specific membrane capacitance²³, giving 0.165 pF variability, our results are even less likely to be influenced by sampling within the quarter turn. We conclude that the C_{lin} changes during aging are real.

In Fig. 3 we show the NLC recorded between 0.39 and 7 kHz at 24 Hz resolution. The data show that NLC is maximal at low frequencies and decreases at higher frequencies, depending on the age of the animal. In Fig. 3A, the 3D plots on the left highlight the voltage dependence of NLC (mean \pm se of the data overlies the smooth Boltzmann fits), whereas those 2D plots on the right highlight the frequency response of NLC. In Fig. 3B, we plot NLC at V_h , illustrating the changing frequency dependence as animals age. The low pass nature of NLC at all ages is apparent. A quantification of this roll-off is supplied below. Nonetheless, the representations in Fig. 3 provide a rich picture of the magnitude, voltage-dependence and frequency extent of NLC across age.

Boltzmann parameters (mean \pm se) for three disparate bandwidths are plotted in Fig. 4 as a function of age. A comparison to our previous isolated cell mouse data¹⁰ obtained at low frequency (dotted lines) is made.

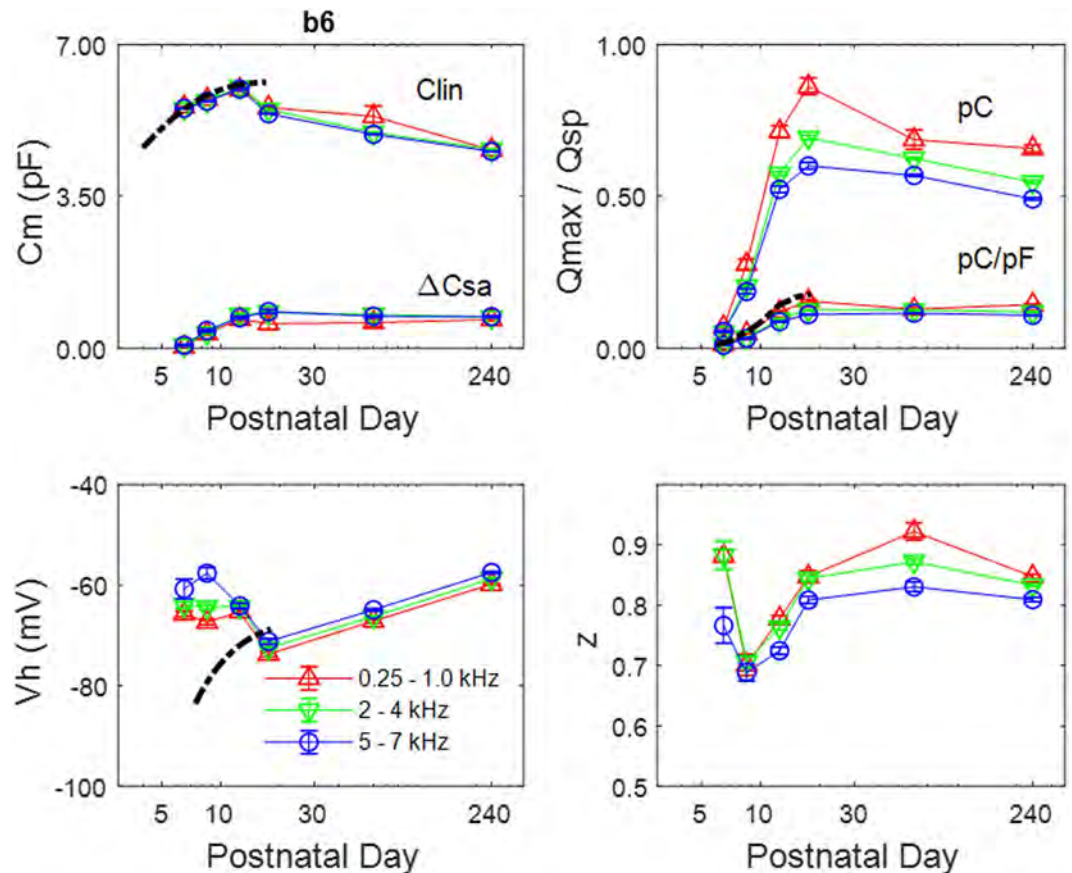


Figure 4. Boltzmann characteristics (mean \pm se) for selected bandwidths. The dashed line denotes NLC measured at low frequencies from isolated OHCs (Abe *et al.*, 2010). Note abrupt decline of C_{lin} , while C_{sa} remains steady. V_h is initially at a more positive potential than isolated cells. Q_{max} (pC) and Q_{sp} (pC/pF) increase rapidly during development. Q_{max} decreases after p17/18, with a clear difference between low and high frequencies, but Q_{sp} stabilizes because of the C_{lin} drop. Following some variability at p6/7, z increases with age, and also tends to be smaller at higher frequencies. P6/7 n = 7; p8,9 n = 7; p12,13 n = 6; p17,18 n = 8; 2 month n = 8; 8 month n = 9.

Quantification of Q_{max} and C_{lin} confirms their initial rise between p6/7 to p12/13 as the cells increase in surface area, and mirror measures made in isolated cells. The development of Q_{sp} in the low frequency region also corresponds to measures from isolated cells. After p17/18, Q_{max} decreases, while Q_{sp} appears to stabilize, due to simultaneous decrease in C_{lin} . The additional frequency information provided by chirp analysis shows that both Q_{max} and Q_{sp} following p17/18 depend on frequency, with higher frequencies showing reduced values. Interestingly, V_h within the explant differs from isolated cells during early development, and may result from forces that normally exist in the organ of Corti, e.g., membrane tension. It is well known that many factors can influence V_h , including membrane tension and intracellular Cl^- ,^{14,24–30}. The Boltzmann parameter z , which characterizes the voltage sensitivity of prestin or the distance sensor charge is moved within the membrane field, is variable in p6/7 animals, but clearly increases after this time period over age. Some frequency dependence of z in the adult is evident, and reduction in z at high frequencies in the adult guinea pig was originally noted by Gale and Ashmore³¹.

Finally, in Fig. 5 we explore the changes in frequency cut-off (F_c) of NLC at V_h . Since the reduction of NLC _{V_h} across frequency is clearly not a simple process, three methods of fitting were evaluated to estimate frequency roll-off (Fig. 5A). We provide fits to average data. Examples of the 3 fit types for p17/18 OHCs are shown, including single Lorentzian, dual Lorentzian (sum of 2 Lorentzians) and power fits. The blue line depicts the fit and red lines show 95% confidence predictions of the fits (fitting performed in Sigmaplot). The poorest fit is with a single Lorentzian, followed by dual Lorentzian and power fits. In regard to the power fit, we have previously found evidence of multi/stretched exponential behavior in NLC^{32,33}. The stretched exponential (known as the Kohlrausch-Williams-Watts [KWW] relaxation function), first devised by Kohlrausch (1854) to describe the behavior of capacitor discharge in a Leyden jar, is also applicable to the viscoelastic behavior of glasses³⁴, and other systems where time-dependent behavior results from overcoming a multitude of energy barriers. Interestingly, cytoskeletal dynamics is one such system³⁵. The KWW function has a related counterpart in the frequency domain³⁶, termed the Havriliak-Negami [HN] relaxation function. Fitting our data with that counterpart, we obtain similar quality fits to the power functions (for example, at p17,18 the fit R^2 is 0.9975 and 0.9974 for power and HN). Since the power function fit has fewer parameters (one less) than HN, we have chosen to

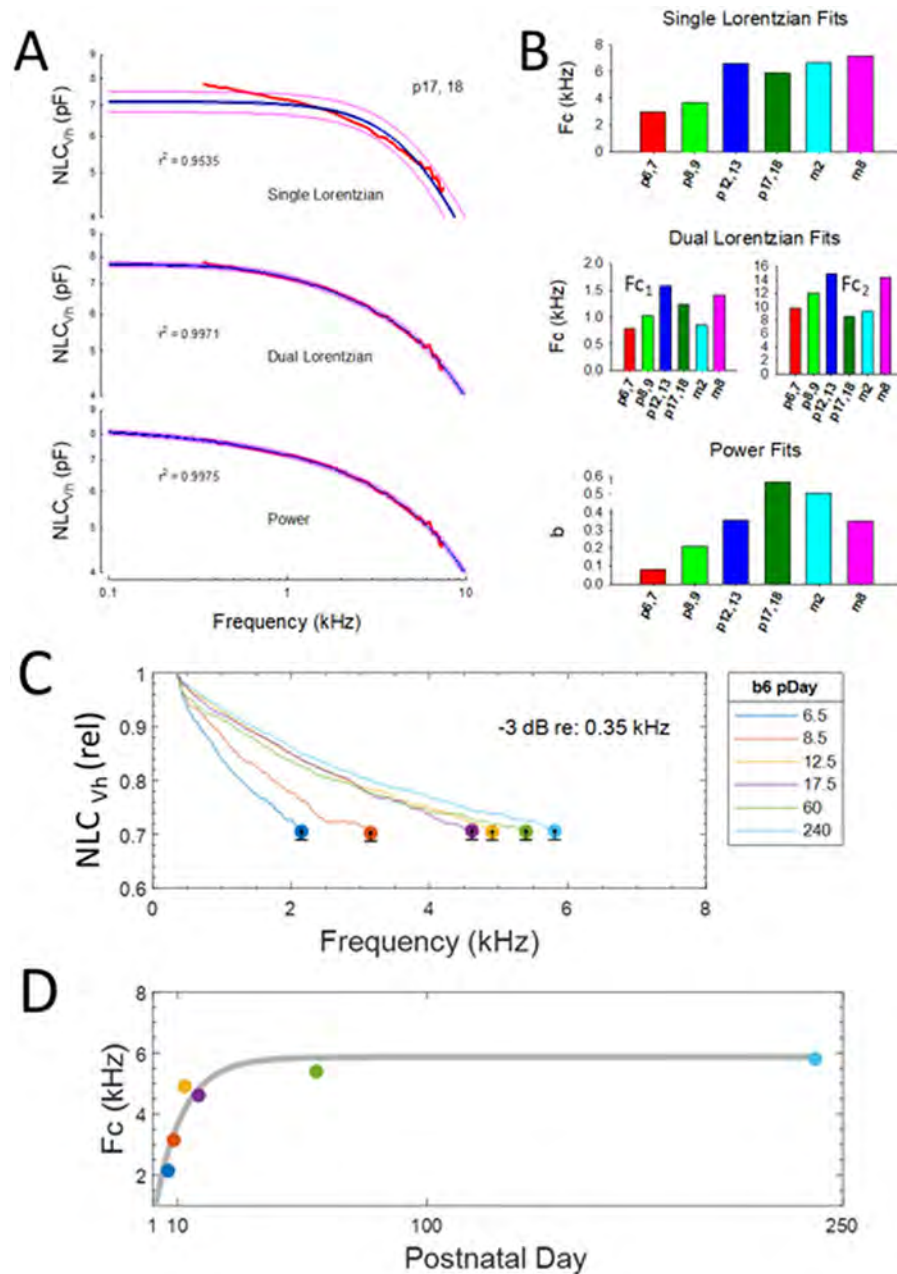


Figure 5. Changes in frequency response of NLC during aging. **(A)** Three types of fits to mean NLC_{vh} were performed to estimate frequency roll-off. Examples of the 3 fits for p17/18 OHCs are shown. Blue line is fit and red lines are 95% confidence predictions of the fits (done in Sigmaplot). The poorest fit is with a single Lorentzian, followed by dual Lorentzian and power fits (f in kHz). Nevertheless, each provides evidence for increases in frequency responsiveness during development. The $\langle a \rangle$ parameter, as all others, was not constrained, but was not age-dependent and similar for all fits [p6,7 - m8: $-1.4055, -1.3548, -1.5980, -1.1960, -1.1552, -1.5031$; mean \pm se $-1.369 (0.07)$]. The small se indicates little variability. **(B)** Bar plots of frequency cut-off parameters of the fits. **(C)** Another metric of frequency response roll-off was to determine the -3 dB magnitude of NLC_{vh} relative to 350 Hz values, denoted here with circles. It should be noted that the F_c 's simply reflect the relative roll-off during aging, and their absolute values will differ depending on the cut-off frequency. During the life span, F_c increases. The se indicates the variability at the cut-off frequencies. **(D)** The F_c data were fit to a power law function in Matlab (grey line; $F_c = a \cdot (1 - b \cdot \text{pDay})$, where $a = 5.867$ and $b = 0.9065$; $R^2 = 0.849$), and indicates a stabilization near 6 kHz. P6,7 n = 7; p8,9 n = 7; p12,13 n = 6; p17,18 n = 8; 2 month n = 8; 8 month n = 9.

illustrate power fits. The usage of the term *low-pass* for the power function should not be construed in a strict engineering sense, but here denotes domination of low pass components whose slope changes over maturation. Figure 5B shows that regardless of the utilized fitting function, each provides evidence for increases in frequency responsiveness during development, as indicated by the bar plots. The dual Lorentzian gives dubious F_{c2} cut-offs

since they are above the sampled frequency. In Fig. 5C, we provide another metric of frequency response roll-off by finding the -3dB magnitude of NLC_{V_h} relative to 350 Hz. During the life span, F_c increases and appears to stabilize near 6 kHz in our older animals. Interestingly, the cut-offs roughly correspond to those of the single Lorentzian fits. We are cognizant that these cut-off estimates cannot be considered true cut-off frequencies, but only indicate that the NLC response has lost much of its steady state magnitude even at low frequencies. That is, the F_c 's simply reflect the relative roll-off among aging groups, and their absolute values will differ depending on the reference frequency. Thus, all methods to quantify roll-off indicate that frequency responsiveness increases with age. Possible reasons for this are discussed below.

Discussion

Studying the development of OHC function can reveal important determinants of adult auditory function. A variety of OHC characteristics mature during the course of post-natal development in altricial animals, including stereociliar transduction and eM. By using such animals, these characteristics can be conveniently studied in isolated cells or explants following birth. The development of eM and its corresponding electrical correlate, nonlinear membrane capacitance (NLC), have been found to reach maturity near p18 in the rodent^{10,21,37}, close to the onset of hearing. These studies did not include an assessment of prestin frequency dependence during development, a likely important factor for OHC performance in the adult animal's acoustic environment. Here we evaluated the development of NLC frequency response in the *in situ* mouse cochlea, and find that its frequency cut-off (F_c) increases from p6 to p18, thereafter stabilizing out to 8 months at about 6 kHz at room temperature. Assuming that the frequency response is solely limited by the kinetics of prestin (however, see below) and given a Q_{10} of 2³⁸, the F_c would approach 15 kHz. The data indicate that the F_c is lower pass in nature than the full auditory capabilities of the mouse, since prestin's intrinsic kinetics is likely place independent. That is, prestin's molecular structure, molecular interactions, and especially molecular behavior have yet to show significant differences among OHCs from various turns of the cochlea^{39,40}.

Importantly, most developmental prestin characteristics measurable within the *in situ* organ of Corti correspond to those measures obtained in isolated cells^{10,21}, i.e., at low measurement frequencies. However, we find that V_h in young animals differs from isolated cell studies, and this may be due, for example, to changes in turgor pressure or membrane tension upon isolation. It is notable that for a simple two-state voltage-dependent protein, V_h is determined by the ratio of forward and backward transition rates of conformational change. Thus, V_h alterations may inform on changes in prestin kinetics. Considering the differences of V_h *in situ* vs. in isolated cells, it may be desirable to analyze the effects of prestin mutations, e.g. the "499" knock-in mutation⁷ in the explant, rather than isolated cells.

We find that C_{in} decreases following the attainment of mature NLC. The decrease corresponds to a decrease in Q_{max} , indicating that the absolute number of prestin motors in OHCs decreases with age. This result implies that the surface area of the cells decrease because prestin occupies less surface area, and this is expected since in the prestin KO OHC surface area/length is markedly reduced⁴¹. The reduction of surface area and prestin in OHCs may have influential effects on the mechanical properties of the cochlear partition. Indeed, in the prestin KO mouse, Mellado Lagarde *et al.* have found that frequency tuning of the partition changes⁴². Thus, we might expect altered hearing in the aging mouse based on the reduction of prestin content that we find.

Why does the frequency response of prestin change during aging? Several possibilities exist. Prestin function itself could change during maturation due to changes in 1) phosphorylation or glycosylation^{43,44}; 2) multimerization^{45–47}; or 3) molecular crowding within the lateral membrane. Extrinsic influences may also change; for example, during the development of the spaces of Nuel supporting cell rearrangements may occur, and less cell-cell contact could reduce interactive mechanical constraints. Certainly, such types of interactions can affect auditory performance⁴⁸. Finally, cytoskeletal influences on prestin^{49,50} may change during development. We recently, determined that MAP1S, a small microtubule binding protein interacts with both actin and prestin, and co-expression in heterologous cells promotes targeting and alteration in prestin characteristics⁵¹. Cytoskeletal forces acting on prestin may work to influence conformational switching by the well-known piezoelectric nature of the protein^{27,28,30}, which has been extensively modelled^{52–54}. Thus, there may well be mechanical filtering of prestin performance depending on whole-cell mechanics that simultaneously impacts the F_c of both NLC and eM, as the two are well coupled^{55,56}. In any case, whatever mechanisms that enhance prestin's frequency response during the developmental likely limits its frequency response in adults. Interestingly, quite low pass estimates ($F_c \sim 1.5\text{ kHz}$) of adult OHC eM frequency response have been found in the high frequency region of the living gerbil using optical coherence microscopy (OCT) vibrometry⁵⁷. Thus, at this point, the mechanism whereby OHC eM influences very high frequency hearing is under question.

Received: 30 May 2019; Accepted: 25 October 2019;

Published online: 11 November 2019

References

1. Kachar, B., Brownell, W. E., Altschuler, R. & Fex, J. Electrokinetic shape changes of cochlear outer hair cells. *Nature* **322**, 365–368 (1986).
2. Brownell, W. E., Bader, C. R., Bertrand, D. & de Ribaupierre, Y. Evoked mechanical responses of isolated cochlear outer hair cells. *Science* **227**, 194–196 (1985).
3. Ashmore, J. F. A fast motile response in guinea-pig outer hair cells: the cellular basis of the cochlear amplifier. *J. Physiol.* **388**, 323–347 (1987).
4. Santos-Sacchi, J. & Dilger, J. P. Whole cell currents and mechanical responses of isolated outer hair cells. *Hear. Res.* **35**, 143–150 (1988).
5. Zheng, J. *et al.* Prestin is the motor protein of cochlear outer hair cells. *Nature* **405**, 149–155 (2000).
6. Corey, D. P. What is the hair cell transduction channel? *J. Physiol.* **576**, 23–28 (2006).

7. Dallos, P. *et al.* Prestin-based outer hair cell motility is necessary for mammalian cochlear amplification. *Neuron* **58**, 333–339 (2008).
8. Ashmore, J. F. Forward and reverse transduction in the mammalian cochlea. *Neurosci. Res. Suppl.* **12**, S39–S50 (1990).
9. Santos-Sacchi, J. Reversible inhibition of voltage-dependent outer hair cell motility and capacitance. *J. Neurosci.* **11**, 3096–3110 (1991).
10. Abe, T. *et al.* Developmental expression of the outer hair cell motor prestin in the mouse. *J. Membr. Biol.* **215**, 49–56 (2007).
11. Santos-Sacchi, J. & Song, L. Chloride anions regulate kinetics but not voltage-sensor Q_{max} of the solute carrier SLC26a5. *Biophys. J.* **110**, 1–11 (2016).
12. Gillis, K. D. In *Single Channel Recording* (eds Sakmann, B. & Neher, E.) Ch. 7, 155–198 (Plenum Press, 1995).
13. Santos-Sacchi, J. High frequency measures of OHC nonlinear capacitance (NLC) and their significance: Why measures stray away from predictions. *AIP Conference Proceedings* **1965**, 060004-060001–060004-060005 (2018).
14. Santos-Sacchi, J., Kakehata, S. & Takahashi, S. Effects of membrane potential on the voltage dependence of motility-related charge in outer hair cells of the guinea-pig. *J. Physiol.* **510**(Pt 1), 225–235 (1998).
15. Santos-Sacchi, J. Determination of cell capacitance using the exact empirical solution of dY/dCm and its phase angle. *Biophys. J.* **87**, 714–727 (2004).
16. Pusch, M. & Neher, E. Rates of diffusional exchange between small cells and a measuring patch pipette. *Pflugers Arch.* **411**, 204–211 (1988).
17. Santos-Sacchi, J. & Navarrete, E. Voltage-dependent changes in specific membrane capacitance caused by prestin, the outer hair cell lateral membrane motor. *Pflugers Arch.* **444**, 99–106 (2002).
18. Chessum, L. *et al.* Helios is a key transcriptional regulator of outer hair cell maturation. *Nature* **563**, 696–700 (2018).
19. Duret, G., Pereira, F. A. & Raphael, R. M. Diflunisal inhibits prestin by chloride-dependent mechanism. *PLoS One* **12**, e0183046 (2017).
20. Harasztosi, C. & Gummer, A. W. The chloride-channel blocker 9-anthracenecarboxylic acid reduces the nonlinear capacitance of prestin-associated charge movement. *Eur. J. Neurosci.* **43**, 1062–1074 (2016).
21. Oliver, D. & Fakler, B. Expression density and functional characteristics of the outer hair cell motor protein are regulated during postnatal development in rat [In Process Citation]. *J. Physiol. (Lond)* **519**(Pt 3), 791–800 (1999).
22. Keiler, S. & Richter, C. P. Cochlear dimensions obtained in hemicochleae of four different strains of mice: CBA/CaJ, 129/CD1, 129/SvEv and C57BL/6J. *Hear. Res.* **162**, 91–104 (2001).
23. Solsona, C., Innocenti, B. & Fernandez, J. M. Regulation of exocytotic fusion by cell inflation. *Biophys. J.* **74**, 1061–1073 (1998).
24. Santos-Sacchi, J., Navaratnam, D., Raphael, R. & Oliver, D. *The Cochlea Chapter 5: Prestin - molecular mechanisms underlying outer hair cell electromotility. Springer Handbook Of Auditory Research.* Vol. The Cochlea (Springer, 2017).
25. Rybalchenko, V. & Santos-Sacchi, J. Cl⁻ flux through a non-selective, stretch-sensitive conductance influences the outer hair cell motor of the guinea-pig. *J. Physiol.* **547**, 873–891 (2003).
26. Oliver, D. *et al.* Intracellular anions as the voltage sensor of prestin, the outer hair cell motor protein. *Science* **292**, 2340–2343 (2001).
27. Iwasa, K. H. Effect of stress on the membrane capacitance of the auditory outer hair cell. *Biophys. J.* **65**, 492–498 (1993).
28. Gale, J. E. & Ashmore, J. F. Charge displacement induced by rapid stretch in the basolateral membrane of the guinea-pig outer hair cell. *Proc. R. Soc. Lond. B. Biol. Sci.* **255**, 243–249 (1994).
29. Rybalchenko, V. & Santos-Sacchi, J. Anion control of voltage sensing by the motor protein prestin in outer hair cells. *Biophys. J.* **95**, 4439–4447 (2008).
30. Kakehata, S. & Santos-Sacchi, J. Membrane tension directly shifts voltage dependence of outer hair cell motility and associated gating charge. *Biophys. J.* **68**, 2190–2197 (1995).
31. Gale, J. E. & Ashmore, J. F. An intrinsic frequency limit to the cochlear amplifier. *Nature* **389**, 63–66 (1997).
32. Santos-Sacchi, J., Navarrete, E. & Song, L. Fast electromechanical amplification in the lateral membrane of the outer hair cell. *Biophys. J.* **96**, 739–747 (2009).
33. Santos-Sacchi, J. & Song, L. Chloride-driven Electromechanical Phase Lags at Acoustic Frequencies Are Generated by SLC26a5, the Outer Hair Cell Motor Protein. *Biophys. J.* **107**, 126–133 (2014).
34. Langer, J. S. Shear-transformation-zone theory of viscosity, diffusion, and stretched exponential relaxation in amorphous solids. *Phys. Rev. E Stat. Nonlin. Soft Matter Phys.* **85**, 051507 (2012).
35. Lieleg, O., Kayser, J., Brambilla, G., Cipelletti, L. & Bausch, A. R. Slow dynamics and internal stress relaxation in bundled cytoskeletal networks. *Nat Mater* **10**, 236–242 (2011).
36. Alvarez, F., Alegria, A. & Colmenero, J. Relationship between the time-domain Kohlrausch-Williams-Watts and frequency-domain Havriliak-Negami relaxation functions. *Physical Review B* **44**, 7306–7312 (1991).
37. He, D. Z., Evans, B. N. & Dallos, P. First appearance and development of electromotility in neonatal gerbil outer hair cells. *Hear. Res.* **78**, 77–90 (1994).
38. Okunade, O. & Santos-Sacchi, J. IR laser-induced perturbations of the voltage-dependent solute carrier protein SLC26a5. *Biophys. J.* **105**, 1822–1828 (2013).
39. Santos-Sacchi, J., Kakehata, S., Kikuchi, T., Katori, Y. & Takasaka, T. Density of motility-related charge in the outer hair cell of the guinea pig is inversely related to best frequency. *Neurosci. Lett.* **256**, 155–158 (1998).
40. Mahendrasingam, S., Beurg, M., Fettiplace, R. & Hackney, C. M. The ultrastructural distribution of prestin in outer hair cells: a post-embedding immunogold investigation of low-frequency and high-frequency regions of the rat cochlea. *Eur. J. Neurosci.* **31**, 1595–1605 (2010).
41. Liberman, M. C. *et al.* Prestin is required for electromotility of the outer hair cell and for the cochlear amplifier. *Nature* **419**, 300–304 (2002).
42. Mellado Lagarde, M. M., Drexler, M., Lukashkin, A. N., Zuo, J. & Russell, I. J. Prestin's role in cochlear frequency tuning and transmission of mechanical responses to neural excitation. *Curr. Biol.* **18**, 200–202 (2008).
43. Rajagopalan, L. *et al.* Glycosylation regulates prestin cellular activity. *J. Assoc. Res. Otolaryngol.* **11**, 39–51 (2010).
44. Deak, L. *et al.* Effects of cyclic nucleotides on the function of prestin. *J. Physiol.* **563**, 483–496 (2005).
45. Hallworth, R., Stark, K., Zholudeva, L., Currall, B. B. & Nichols, M. G. The conserved tetrameric subunit stoichiometry of SLC26 proteins. *Microsc. Microanal.* **19**, 799–807 (2013).
46. Navaratnam, D., Bai, J. P., Samaranyake, H. & Santos-Sacchi, J. N-terminal-mediated homomultimerization of prestin, the outer hair cell motor protein. *Biophys. J.* **89**, 3345–3352 (2005).
47. Detro-Dassen, S. *et al.* Conserved dimeric subunit stoichiometry of SLC26 multifunctional anion exchangers. *J. Biol. Chem.* **283**, 4177–4188 (2008).
48. Lukashkina, V. A., Yamashita, T., Zuo, J., Lukashkin, A. N. & Russell, I. J. Amplification mode differs along the length of the mouse cochlea as revealed by connexin 26 deletion from specific gap junctions. *Sci. Rep.* **7**, 5185 (2017).
49. Keller, J. P. *et al.* Functional regulation of the SLC26-family protein prestin by calcium/calmodulin. *J. Neurosci.* **34**, 1325–1332 (2014).
50. Zhang, M., Kalinec, G. M., Urrutia, R., Billadeau, D. D. & Kalinec, F. ROCK-dependent and ROCK-independent control of cochlear outer hair cell electromotility. *J. Biol. Chem.* **278**, 35644–35650 (2003).
51. Bai, J. P. *et al.* Prestin surface expression and activity are augmented by interaction with MAP1S, a microtubule-associated protein. *J. Biol. Chem.* **285**, 20834–20843 (2010).

52. Spector, A. A., Brownell, W. E. & Popel, A. S. Effect of outer hair cell piezoelectricity on high-frequency receptor potentials. *J. Acoust. Soc. Am.* **113**, 453–461 (2003).
53. Rabbitt, R. D., Clifford, S., Breneman, K. D., Farrell, B. & Brownell, W. E. Power efficiency of outer hair cell somatic electromotility. *PLoS Comput. Biol.* **5**, e1000444 (2009).
54. Iwasa, K. H. A two-state piezoelectric model for outer hair cell motility. *Biophys. J.* **81**, 2495–2506 (2001).
55. Santos-Sacchi, J. & Tan, W. The Frequency Response of Outer Hair Cell Voltage-Dependent Motility Is Limited by Kinetics of Prestin. *J. Neurosci.* **38**, 5495–5506 (2018).
56. Dong, X. X. & Iwasa, K. H. Tension sensitivity of prestin: comparison with the membrane motor in outer hair cells. *Biophys. J.* **86**, 1201–1208 (2004).
57. Vavakou, A., Cooper, N. P. & van der Heijden, M. The frequency limit of outer hair cell motility measured *in vivo*. *Elife* **8**, e47667 (2019).

Acknowledgements

This work was supported by National Institutes of Health–National Institute on Deafness and Other Communication Disorders Grants R01 DC000273 (JSS), R01 DC016318 (JSS), and R01 DC008130 (JSS and DN).

Author contributions

All authors contributed to the design and analysis of experiments. J.S.S. wrote the manuscript; J.P.B. and D.N. edited the manuscript.

Competing interests

The authors declare no competing interests.

Additional information

Correspondence and requests for materials should be addressed to J.S.-S.

Reprints and permissions information is available at www.nature.com/reprints.

Publisher's note Springer Nature remains neutral with regard to jurisdictional claims in published maps and institutional affiliations.



Open Access This article is licensed under a Creative Commons Attribution 4.0 International License, which permits use, sharing, adaptation, distribution and reproduction in any medium or format, as long as you give appropriate credit to the original author(s) and the source, provide a link to the Creative Commons license, and indicate if changes were made. The images or other third party material in this article are included in the article's Creative Commons license, unless indicated otherwise in a credit line to the material. If material is not included in the article's Creative Commons license and your intended use is not permitted by statutory regulation or exceeds the permitted use, you will need to obtain permission directly from the copyright holder. To view a copy of this license, visit <http://creativecommons.org/licenses/by/4.0/>.

© The Author(s) 2019

Prestin Surface Expression and Activity Are Augmented by Interaction with MAP1S, a Microtubule-associated Protein*

Received for publication, February 25, 2010, and in revised form, March 26, 2010 Published, JBC Papers in Press, April 23, 2010, DOI 10.1074/jbc.M110.117853

Jun-Ping Bai^{†1}, Alexei Surguchev^{§1}, Yudelca Ogando[‡], Lei Song[§], Shumin Bian[§], Joseph Santos-Sacchi^{§¶||}, and Dhasakumar Navaratnam^{§¶2}

From the Departments of [‡]Neurology, [¶]Neurobiology, ^{||}Cellular and Molecular Physiology, and [§]Surgery (Otolaryngology), Yale University School of Medicine, New Haven, Connecticut 06510

Prestin is a member of the SLC26 family of anion transporters that is responsible for outer hair cell (OHC) electromotility. Measures of voltage-evoked charge density (Q_{sp}) of prestin indicated that the protein is highly expressed in OHCs, with single cells expressing up to 10 million molecules within the lateral membrane. In contrast, charge density measures in transfected cells indicated that they express, at best, only a fifth as many proteins on their surface. We sought to determine whether associations with other OHC-specific proteins could account for this difference. Using a yeast two-hybrid technique, we found microtubule-associated protein 1S (MAP1S) bound to prestin. The interaction was limited to the STAS domain of prestin and the region connecting the heavy and light chain of MAP1S. Using reciprocal immunoprecipitation and Forster resonance energy transfer, we confirmed these interactions. Furthermore, co-expression of prestin with MAP1S resulted in a 2.7-fold increase in Q_{sp} in single cells that was paralleled by a 2.8-fold increase in protein surface expression, indicating that the interactions are physiological. Quantitative PCR data showed gradients in the expression of prestin and MAP1S across the tonotopic axis that may partially contribute to a previously observed 6-fold increase in Q_{sp} in high frequency hair cells. These data highlight the importance of protein partner effects on prestin.

Prestin is a member of the SLC26 family of anion transporters that is responsible for outer hair cell (OHC)³ electromotility, the basis of mammalian cochlear amplification (1–4). Prestin is found in the lateral membrane of the OHC (5, 6) and has piezoelectric properties, deriving from reciprocal voltage and mechanical sensitivity (7–10). The voltage sensor of the protein, which is integral to electromotility, generates charge movement that can be detected as a nonlinear capacitance (NLC) (11, 12). NLC parallels electromotility and has been established as an excellent surrogate marker for electromotility (11). There are three commonly described attributes of NLC as

follows: V_h , the voltage of peak capacitance; z , an estimate of charge carried by a single motor; and Q_{sp} the charge moved across a unit of membrane. V_h reflects the steady state energy profile of the protein, and Q_{sp} provides an estimate of the density of the protein in the plasma membrane.

Prestin in OHCs exists in very high density. It is estimated that OHCs contain up to 10 million of these molecules in the lateral membrane of a given cell (13, 14). Measures of NLC in transfected cells, however, have not yielded this high density of prestin. Measures of Q_{sp} can reach 5 fC/pF in transiently transfected CHO cells (15) but contrasts with a Q_{sp} of 220 fC/pF in the mature OHC (16). Although differences in transcription could account for this change, we have been unable to induce OHC-like prestin expression levels in the membrane in transfected cells using the best available promoters, including cytomegalovirus and the tetracycline-inducible promoter. Moreover, mRNA expression in OHCs is not as robust as would be expected for a protein with such high levels of expression (17), indicating low turnover of prestin that is stable in the membrane. In contrast, exogenous expression of prestin using a cytomegalovirus promoter in chick hair cells results in NLC measures that were significantly increased compared with CHO cells.⁴ These data have led us to speculate on the existence of post-translational mechanisms or protein associations in hair cells that are absent in transfected cells. We have other reasons to hypothesize post-translational mechanisms or associations that modulate prestin activity. For instance, whereas prestin possesses many of the major features of the OHC motor, there were notable discrepancies in the behavior of the OHC motor and that of prestin in transfected cells. For example, the magnitude of the effects of prior (prepulse) voltage and membrane tension is somewhat less than found with the native OHC motor (18). These data prompted us to seek other additional mechanisms that would modify prestin activity.

It is evident over the last 15 years that many membrane proteins, including ion channels and receptors, interact with other proteins to form large complexes. The components of these complexes affect the delivery of these proteins to the surface as well as their function. For instance, there is substantial literature showing the effect of ancillary proteins on ion channels and receptors (19–21). In view of these findings, we sought to find proteins that interacted with prestin. We used the yeast two-hybrid technique to identify proteins that interacted with prestin. We used the intracellular C terminus of prestin in a Gal-4-

* This work was supported, in whole or in part, by National Institutes of Health Grants DC 007894, DC 000273, and DC 0081130 from NIDCD.

¹ Both authors contributed equally to this work.

² To whom correspondence should be addressed: LCI 703, 310 Cedar St., New Haven, CT 06510. Tel.: 203-785-5755; Fax: 203-785-7826; E-mail: Dhasakumar.Navaratnam@Yale.Edu.

³ The abbreviations used are: OHC, outer hair cell; PBS, phosphate-buffered saline; FRET, Forster resonance energy transfer; CHO, Chinese hamster ovary; NLC, nonlinear capacitance; CFP, cyan fluorescent protein; YFP, yellow fluorescent protein; qPCR, quantitative PCR; fC, femtocoulomb; pF, picofarad.

⁴ J.-P. Bai and D. Navaratnam, unpublished observations.

based yeast two-hybrid technique to probe a brain cDNA library. We identified several proteins that interacted with prestin. Here, we describe the interaction between one of these proteins, microtubule-associated protein 1-S (MAP1S), and prestin, and we explore its physiological consequences.

EXPERIMENTAL PROCEDURES

Yeast Two-hybrid Experiments—Yeast two-hybrid experiments were done as described previously (49). Briefly, the C terminus of prestin (amino acids 491–744) was subcloned into pGBKT7 and used as bait to interrogate a rat brain cDNA library in pGAD T7 (Clontech). AH109 cells were serially transfected with both constructs and plated on drop out medium lacking histidine, adenine, tryptophan, and leucine. Single colonies were isolated and serially re-plated in similar conditions on plates containing 5-bromo-4-chloro-3-indolyl- β -D-galactopyranoside (X-gal). Cultures from single isolated colonies were used for yeast mini preps. Plasmid was electroporated into DH101 *Escherichia coli*, grown in ampicillin and plasmid DNA isolated for sequencing.

DNA Constructs and Transfection—Gerbil prestin and MAP1S sequences used were as described previously (1, 38). For NLC recording, transient co-transfection of prestin (0.8 μ g per well of 24-well plate) and MAP1S-CFP (or CFP) (0.8 μ g per well of 24-well plate) into CHO cells was achieved with Lipofectamine (Invitrogen) in accordance with the manufacturer's recommendations. We identified MAP1S-CFP (or CFP)-transfected cells with CFP fluorescence for electrophysiological recording, and only cells that showed NLC were analyzed. We were thus able to determine with certainty that these cells contained both plasmids. For co-immunoprecipitation, FLAG-MAP1S-CFP was transfected into a prestin-Myc stable line in human embryonic kidney (HEK) cells established in our laboratory⁵ or HEK cells with Lipofectamine.

Prestin Surface Expression and Western Blots—Surface expression of prestin alone or with MAP1S was determined using a surface biotinylation assay (Thermo Scientific/Pierce, Rockford, IL). Transiently transfected CHO cells were washed with PBS and incubated in the presence of sulfo-NHS-biotin (sulfo-succinimidyl-2-(biotinamido) ethyl-1,3-dithiopropionate) for 30 min at 4 °C. Free sulfo-NHS-biotin was quenched by washing cells in 140 mM Tris-Cl, and the cells were lysed in lysis buffer containing the following (in mM): 20 Tris, pH 8.0, 137 NaCl, 5 NaEDTA, 5 NaEGTA, 10% glycerol, 0.5% Triton X-100, 0.2 phenylmethylsulfonyl fluoride, 50 NaF, 20 benzamide. The lysates were cleared by centrifugation, and its protein concentration was assayed (Bio-Rad) and equalized with sample buffer. Streptavidin-agarose was added, and the mixtures were incubated for 1 h at room temperature with constant agitation. After centrifugation at 1000 \times g, the beads were washed with washing buffer. The bound surface proteins were released by the addition of 50 mM dithiothreitol and analyzed by SDS-PAGE and Western blotting. Lysates or eluates of surface-labeled proteins were separated on a precast 4–15% Tris-HCl SDS-polyacrylamide gel (Bio-Rad). Proteins were transferred by wet transfer to polyvinylidene fluoride membrane (Roche

Applied Science). Western blots were probed with anti-prestin N20 (Santa Cruz Biotechnology, Santa Cruz, CA) at a 1:500 dilution and then with horseradish peroxidase-conjugated bovine anti-goat secondary antibody (Santa Cruz Biotechnology) at 1:5000 dilution with five washes in TBST between each step. The presence of horseradish peroxidase-conjugated antibody was detected using SuperSignal[®] West Dura extended duration Substrate (Thermo Scientific/Pierce).

Co-immunoprecipitation—Reciprocal immunoprecipitation was done with anti-FLAG (MAP1S-CFP) antibody and anti-Myc (prestin-YFP) antibody using immunoprecipitation kits purchased from Sigma. In brief, membrane-enriched protein lysates were generated 48 h after transfection. 60 μ l of anti-FLAG M2-agarose or 60 μ l of anti-c-Myc-agarose was added to the lysates. The mixtures were incubated with constant agitation for 2 h at 4 °C. Following this binding step, the beads were washed seven times with washing buffer. To elute the FLAG fusion protein (MAP1S) or Myc fusion protein (prestin), 100 μ l of 5 μ g/ml FLAG peptide or c-Myc peptide (Sigma) was added to the resin. The samples were incubated with constant agitation for 30 min at 4 °C and then eluted by centrifugation. The eluted samples were boiled with loading buffer and 6% β -mercaptoethanol for 5 min and then were separated on a precast 4–15% Tris-HCl SDS-polyacrylamide gel (Bio-Rad). Proteins were transferred by wet transfer to polyvinylidene fluoride membrane (Roche Applied Science). Western blots were probed with anti-c-Myc antibody-peroxidase conjugate (1:3000) or anti-FLAG M2 antibody-peroxidase conjugate (1:4000) (Sigma) for 1 h at room temperature. Immunoreactive proteins were detected using SuperSignal[®] West Dura extended duration substrate (Thermo Scientific/Pierce).

Isolation of Individual OHCs from Guinea Pig Cochlea—Hartley albino guinea pigs (~200 g) were sacrificed with halothane (2-bromo-2-chloro-1,1,1-trifluoroethane, Halocarbon Labs, River Edge, NJ), and the temporal bones were dissected in PBS. Four turns of the cochlea were separated and hair cells dislodged by mechanical trituration in PBS and dispersed in Petri dishes to allow cells to settle.

Individual OHCs were captured using a pipette (~30- μ m tip) attached to a micro-manipulator (Scientifica, Uckfield, UK) with the cells visualized using a Nikon Eclipse 600 FN microscope (Nikon, Melville, NY). The tips were silanized with trimethylchlorosilane (Fluka, St. Louis, MO) to prevent cell adhesion to the pipette wall. Cells were aspirated into the pipette using gentle suction. Isolated cells were expelled into Eppendorf tubes and stored in a -80 °C freezer.

Quantitative Immunofluorescence—Quantitative immunofluorescence was done as described previously (50), with modifications. In particular, we used a confocal microscope to obtain images and used the attendant Zeiss LSM software to analyze and extract data. Cochlea were isolated from mice euthanized by CO₂ asphyxiation. Cochlea were dissected from these animals and fixed in 4% paraformaldehyde, PBS for 1 h. The cochlea were washed in PBS (three times) and placed in blocking solution (PBS, 1% bovine serum albumin, 5% horse serum, 0.1% Tween 20). Tissue was incubated in 1:500 anti-prestin antibody in blocking solution overnight (N20 prestin) (Santa Cruz Biotechnology) at 4 °C. After washing in PBS, 0.1% Tween

⁵ S. Bian, manuscript in preparation.

MAP1S Interacts with Prestin

20 (three times), the tissue was incubated with Alexa 648-conjugated horse anti-goat antibody (1:1000) for 1 h at room temperature. The tissue was washed again in wash buffer (three times) and incubated with a 1:50 dilution of mouse anti-MAP1S antibody (Abnova, 00055201B01) for 1 h at room temperature. Alexa 488 goat anti-mouse antibody (1:1000) was added after washing the tissue. The tissue was dissected, and the three turns of the cochlea were separated after a further three washes. Tissue was then mounted using Vectorshield, and viewed using a Zeiss 510 meta confocal microscope. Sixteen bit images were acquired using a 40× water immersion lens (N.A. 1.2), with fixed laser settings, a scan rate of 6.4 μs/pixel, a pinhole aperture of 1.0 Airy units, and fixed detector gain. Regions of interest identified as horizontal sections of circumscribed hair cells in the most basal and apical ends of the cochlea were identified, and fluorescence data were extracted. We established that the fluorescence intensity was within the linear range and used mean fluorescence density as a measure of protein concentration. Surrounding supporting cells, where there is minimal prestin and MAP1S expression, were used to subtract background fluorescence. Cells from four individual cochlea were used for these analyses. The specificity of the antibodies was established by Western blots of cell lysates from cells with the respective constructs. Both antibodies identified bands of the expected size with minimal additional bands.

Single Cell Nested PCR from OHC—cDNAs from each cell were synthesized as described previously in a total volume of 20 μl (51). Nested PCR was performed in two steps. 35 cycles of PCR amplification were performed (94 °C for 30 s, 55 °C for 1 min, and 68 °C for 3 min) using 5 μl of cDNA and MAP1S outer primers (MAP1SOUTF, AACTTCTTCCTGCGTGTGCG; MAP1SOUTR, ATGCGTCTCCTCATAACCTGTG). A second nested PCR amplification was then done using 5 μl of the initial PCR as template. This second PCR step involved 30 cycles of amplification using MAP1S inner primers as follows: MAP1SINF, GTGTGCGTGCACTCTGCTAT; MAP1SINR, TCACTGCAGAGTCGAAGGTG. Both steps used Expand High Fidelity PCR enzyme (Roche Applied Science). PCR fragments were analyzed on a 1% agarose gel. These primers spanned an intron of 501 bp. Control PCRs included aliquots from isolated cells to which no reverse transcriptase was added (no cDNA).

Quantitative (q) PCR—Organs of Corti were peeled off of each turn of the cochlea, and total RNA was isolated using the RNAqueous kit (Ambion, Austin, TX) following the manufacturer's instructions. cDNAs was synthesized using oligo(dT) primers and random hexamers as described previously (51). Triplicate qPCR amplifications using 1 μl of cDNA from each turn of the cochlea were performed using the IQ SYBR Green super mix (Bio-Rad). The reaction mixtures were set up in 96-well thin wall plates (Bio-Rad) and run on either C1000 thermal cycler with a CFX96 optical reaction module (Bio-Rad) or Mx3000P QPCR system (Stratagene, La Jolla, CA). The parameters were 95 °C for 30 s, 55 °C for 1 min, and 72 °C for 30 s for 35 cycles. Amplification data were analyzed using CFX Manager software (Bio-Rad) and normalized to 18 S RNA.

The primer sequences were as follows: prestin, PRQ96F, CAG-CAGTTGACTGCCCTGTA, and PRQ276R, ACGTGGTAC-

TTCTGGGTTGC; MAP1S, MAP1Q2945F, GAGTTCTAGC-CCCACACTGC, and MAP1Q3105R, TCTGCCTCTCCAAC-CTGAGT; and 18 S, 18 S344F, AGAAACGGCTCCACATCC-AAG, and 18 S493R, TCAAAGTCCCTCCAATGGTCC.

Electrophysiological Recording—Whole-cell patch clamp recordings were performed at room temperature using an Axon 200B amplifier (Axon Instruments) as described previously (15). Cells were recorded 48 h after transfection to allow for stable measurement of nonlinear capacitance. Ionic blocking solutions were used to isolate capacitive currents. The bath solution contained the following (in mM): tetraethyl ammonium 20, CsCl 20, CoCl₂ 2, MgCl₂ 1.47, Hepes 10, NaCl 99.2, CaCl₂·2H₂O 2, pH 7.2, and the pipette solution contained the following (in mM): CsCl 140, EGTA 10, MgCl₂ 2, Hepes 10, pH 7.2. Osmolarity was adjusted to 300 ± 2 mosM with dextrose. Command delivery and data collections were carried out with a Windows-based whole-cell voltage clamp program, jClamp (Scisoft, CT), using a Digidata 1322A interface (Axon Instruments). Capacitance was evaluated with a continuous high resolution 2-sine wave technique fully described elsewhere (52, 53). Capacitance data were fitted to the first derivative of a two-state Boltzmann function to extract Boltzmann parameters (11); a two-state Boltzmann model adequately describes charge movement of prestin (54, 55) as shown in Equations 1 and 2,

$$C_m = Q_{\max} \frac{ze}{kT} \frac{b}{(1+b)^2} + C_{\text{lin}} \quad (\text{Eq. 1})$$

where

$$b = \exp\left(\frac{-ze(V_m - V_h)}{kT}\right) \quad (\text{Eq. 2})$$

where Q_{\max} is the maximum nonlinear charge transfer; V_h is the voltage at peak capacitance or half-maximal nonlinear charge transfer; V_m is the membrane potential; C_{lin} is linear capacitance; z is the unitary charge movement or valence (also a metric of voltage sensitivity); e is electron charge; k is the Boltzmann constant, and T is absolute temperature. Q_{\max} is reported as Q_{sp} , the specific charge density, *i.e.* total charge moved normalized to linear capacitance. A Student's *t* test was used to evaluate the effects of mutants on the different parameters of NLC.

RESULTS

Yeast Two-hybrid Results Show That Prestin Interacts with MAP1S—In seeking to find binding partners to prestin, we used the C terminus of prestin as bait in a Gal-4-based yeast two-hybrid screen. The Gal-4-based method requires soluble (non-membrane-bound) protein, and we used the intracellular hydrophilic C terminus of prestin for this experiment. We subcloned cDNA encoding amino acids 488–744 of prestin into the pGBK-T7 vector and screened a rat brain cDNA library. Of several clones identified, one encoded the C terminus of MAP1S from amino acids 720–972. The interaction was detectable even in the most stringent conditions. Thus, yeast containing both of these constructs grew in the absence of histidine and adenine and expressed β-galactosidase.

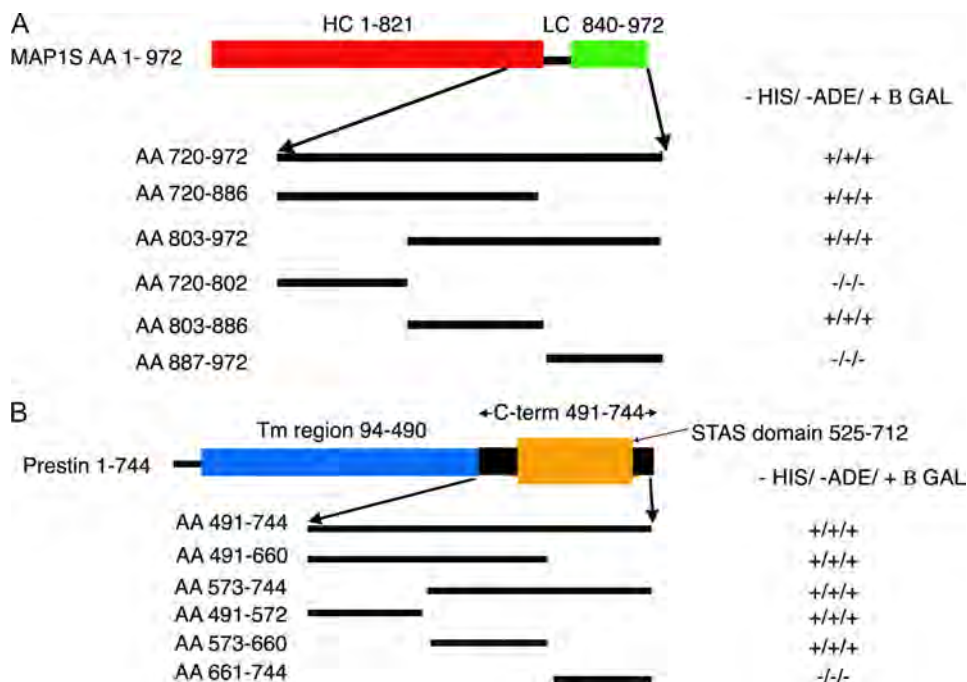


FIGURE 1. Yeast two-hybrid experiments detect interactions between prestin and MAP1S, which is restricted to specific domains. Initial yeast two-hybrid screening using the C terminus of prestin as bait revealed MAP1S as a binding partner. This clone extended from residues 720 to 972. Subsequently, we used several truncations of these constructs in a yeast two-hybrid assay to clarify the specific domains involved in this interaction. *A*, initial screening using three equal parts of the protein revealed the interacting domain to lie within the middle fragment (amino acids (AA) 803–886). Subsequent yeast two-hybrid assays (data not shown) using 15–16-amino acid fragments within this region confirmed that the interaction with prestin was mediated by amino acids 819–835 in MAP1S, which lacks predicted secondary structure, contains a large number of proline residues, and lies between the heavy (HC) and light chains (LC) of the protein. Also indicated are the heavy chain (red) and light chain (green) regions of MAP1S relative to the region in MAP1S identified in the yeast two-hybrid screen. *B*, in a similar approach, we used three equal fragments of the C terminus of prestin in a yeast two-hybrid assay to determine areas that were important in interactions with MAP1S(720–972). We determined that the interacting domains in prestin extended across residues 491–655, which includes parts of the STAS domain and included the entire IVS subdomain within it. We have also shown in schematic form the transmembrane region (blue) of the prestin, its C terminus (black), and the STAS domain (orange) within the C terminus.

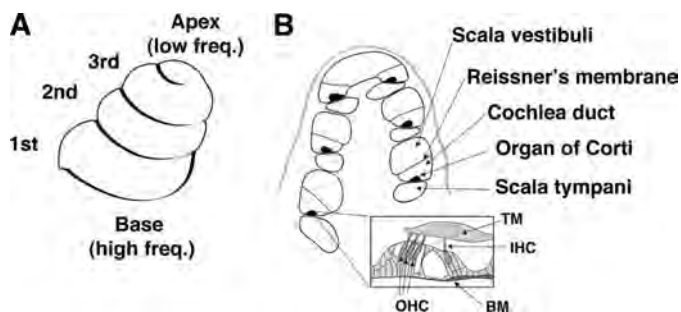


FIGURE 2. Anatomy of the cochlea. OHCs are arranged tonotopically along the three turns of the cochlea. *A*, schematic of the external appearance of the cochlea shows its three turns. Hair cells in these turns are arranged tonotopically with cells at the base responding to high frequency (Freq) sounds and cells at the apex responding to low frequency sound. Notably, hair cells in the 1st, 2nd, and 3rd turns of the cochlea respond to sound of decreasing frequency. *B*, section across the cochlea reveals the organ of Corti to be compartmentalized. An expanded view of the organ of Corti reveals it to contain three rows of OHCs and one row of inner hair cells. TM, transmembrane; IHC, inner hair cell; BM, basilar membrane.

Interactions between MAP1S and Prestin Is Limited to Specific Regions—We attempted to isolate the regions of MAP1S that interacted with prestin (Fig. 1A). We divided the MAP1S amino acid sequence from 720 to 972 into approximately three equal segments and used these three segments (encoding

amino acids 720–802, 803–886, and 887–972) to test if they interacted with prestin using the yeast two-hybrid assay. In this instance, MAP1S cDNA fragments were subcloned into pGADT7 and used in a complementation assay with the C terminus of prestin (amino acids 488–744) in pGBK-T7. Interactions were detected using the middle segment encoding amino acids 802–886. This region was further subdivided into five segments of ~16 amino acids each, and interactions with the C terminus of prestin were assayed using the yeast two-hybrid assay. This third more focused complementation assay (again using MAP1S fragments in pGAD-T7 and amino acids 488–744 of prestin in pGBK-T7) revealed that MAP1S interacted with a short segment limited to amino acids 819–835. These 17 residues are not predicted to contain a specific secondary structure, but rather they contain a large number of proline residues. Moreover, these 17 amino acids lie in a region between the purported heavy and light chains of the protein. The heavy and light chains of the better studied MAP1B has been defined as extending from residues 1 to 2185 and 2210 to 2459, respectively. The corresponding residues in MAP1S

are 1–821 and 840–972. A search using the FingerPRINTScan revealed two other proteins containing a similar sequence, Kv3.3 and Atrophin.

We next attempted to determine the interacting sites within prestin responsible for binding to MAP1S (Fig. 1B). Here too we used a similar strategy of using the yeast two-hybrid assay to ascertain interactions of three equal regions of the C terminus of prestin with amino acids 720–972 of MAP1S. In these experiments, these smaller fragments of cDNA were subcloned into pGBKT7. As shown in Fig. 1B, regions of prestin that are important for interacting with MAP1S extended across amino acids 491–660. This region includes parts of the STAS domain (525–712) and encompasses almost the entirety of the IVS region of the STAS domain.

MAP1S Is Expressed in OHC and Shows a Tonotopic Gradient—To determine whether the interaction between MAP1S and prestin is physiologically significant, we sought to ascertain if MAP1S existed in OHCs from guinea pig cochlea (the species in which there is the most amount of physiological data). A schematic of the guinea pig cochlea along with the tonotopic axis is shown in Fig. 2. We isolated individual OHCs and performed single cell PCRs from these cells. As evident in Fig. 3, OHCs contained MAP1S. Single cell nested PCR from

MAP1S Interacts with Prestin

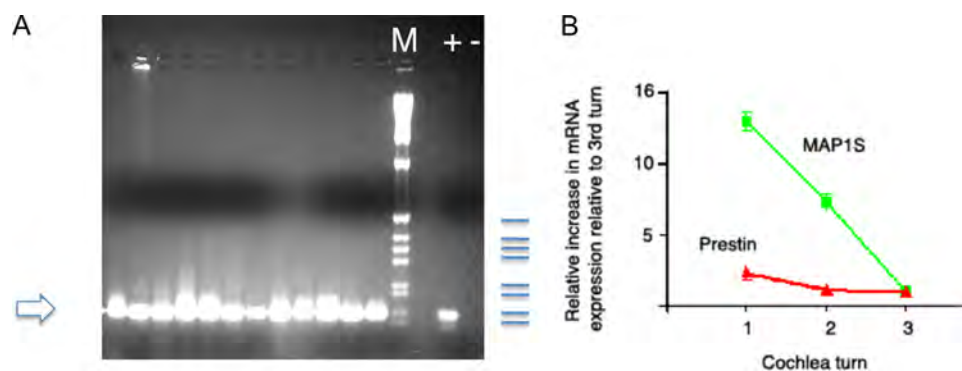


FIGURE 3. MAP1S is expressed in individual hair cells, and its mRNA shows a marked gradient in expression across the tonotopic axis. *A*, MAP1S was detected in 12 individual OHCs by nested PCR using cDNA from single cells. The product of 147 bp is the expected product of the inner primer pair. The products were separated on a 2% agarose gel. Also included are DNA size markers (*M*); a positive control (+, using plasmid containing MAP1S cDNA as template), and negative control (–, no reverse transcriptase). The sizes of the markers indicated in blue are 506, 398, 356, 298, 220, 203, 154, and 134 bp. *B*, shown in graph form are the fold change of prestin and MAP1S mRNA determined by qPCR across the organ of Corti from the three turns of the cochlea compared with the 3rd turn of the cochlea. The expression of each mRNA species was normalized to the expression of the 18 S subunit of ribosomal RNA. As is evident, although prestin shows an almost 3-fold increase in expression from the third to the basal (first) turn of the cochlea, MAP1S shows a more dramatic 13-fold increase in expression from the third to the basal (first) turn of the cochlea. The error bars are \pm S.E., $n = 4$.

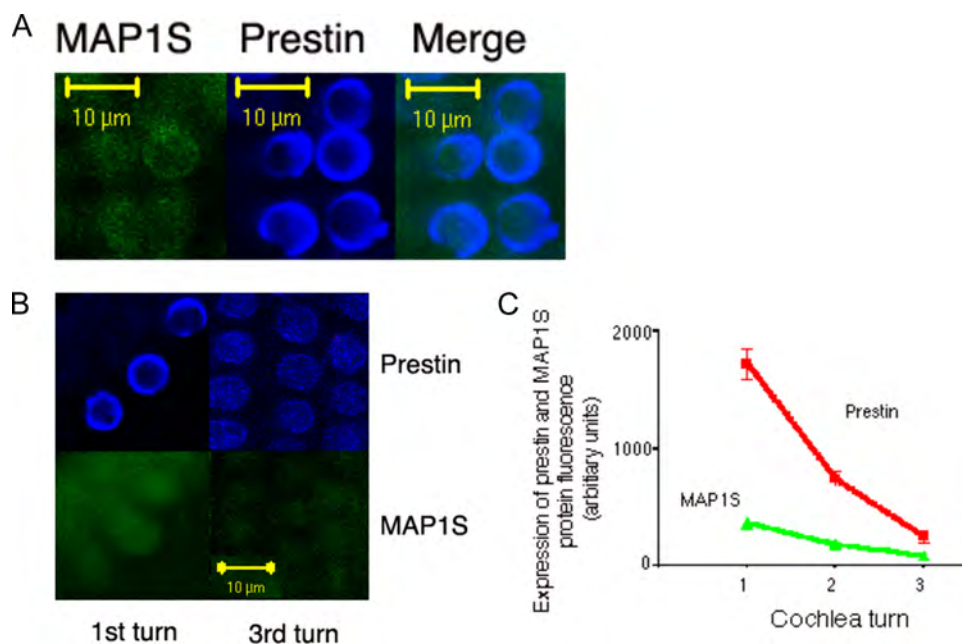


FIGURE 4. MAP1S co-localizes with prestin in mouse OHC and, along with prestin, shows a gradient in expression across the tonotopic axis. *A*, prestin co-localizes with MAP1S. Shown are mouse OHCs labeled consecutively with antibodies against MAP1S (*left*) and prestin (*middle*). There is co-localization of the two proteins in these cells (*right*). *B*, OHCs from the most apical (*left*) and basal (*right*) portions of the mouse cochlea were labeled with antibodies to prestin (*upper*) and MAP1S (*lower*). As is evident, these two proteins are abundant in OHCs of the basal turn. Contrast in the *right* panel was increased post hoc to better show the expression of MAP1S and prestin. *C*, these findings were confirmed using quantitative immunofluorescence. OHCs from the most basal and apical portions of the mouse cochlea together with cells from the midpoint between these two extremes were tested for the expression of prestin and MAP1S. The mean fluorescence density (\pm S.E.) of MAP1S in the apical, mid, and basal hair cells are 88 (± 14 , $n = 6$), 183 (± 28 , $n = 12$), and 371 (± 48 , $n = 6$). Similarly, values for prestin are 257 (± 53 , $n = 6$), 744 (± 60 , $n = 12$), and 1723 (± 130 , $n = 6$). These quantitative data confirm a 7-fold increase in prestin expression and a 3.5-fold increase in MAP1S expression from the most apical to basal ends of the mouse cochlea.

OHCs from the three turns of the cochlea all revealed MAP1S. We then attempted to quantify the expression of MAP1S and prestin across the tonotopic axis using qPCR. As shown in Fig. 3, prestin mRNA expression is increased 1.2-fold in the middle turn compared with the 3rd turn and 2.8-fold in the basal turn

compared with the 3rd turn. In contrast, MAP1S expression is increased 7-fold in the middle turn compared with the third turn and 13-fold in the basal turn compared with the third turn.

We attempted to confirm our protein data using antibodies to these proteins in the guinea pig. However, because of poor antibody recognition of MAP1S in this species, we were unable to confirm or refute our qPCR data. We were able, however, to use mouse cochlea to confirm our PCR data from the guinea pig cochlea. As shown in Fig. 4, mouse OHCs demonstrate co-localization of these two proteins. Moreover, there is an apical to basal gradient in the expression of prestin and MAP1S. Thus, prestin showed a 7-fold increase in expression in the most basal hair cells, whereas MAP1S increased 3.5-fold in these cells compared with those from the apex.

In Vivo Interactions between MAP1S Are Confirmed by Immunoprecipitation—Although the interaction between prestin and MAP1S was suggested by the yeast two-hybrid experiments done under stringent conditions, it is widely believed that the yeast two-hybrid assay can be erroneous, yielding false positives from non-specific interactions. To confirm interactions between prestin and MAP1S, we performed a reciprocal immunoprecipitation using prestin and MAP1S in its entirety tagged with c-Myc and FLAG tags, respectively. FLAG-MAP1S was transfected into cells constitutively expressing prestin-YFP-c-Myc. Immunoprecipitation and wash steps were stringent and included high salt and detergent (0.05% Triton X-100). As shown in Fig. 5, prestin and MAP1S could reciprocally immunoprecipitate the other protein. Together with our showing interactions between prestin

and MAP1S using the yeast two-hybrid system, these data argue for a robust interaction between the two proteins. Interestingly, the form of MAP1S that was immunoprecipitated by prestin was the entire coding sequence and not the heavy chain, although there was evidence of the protein being cleaved into

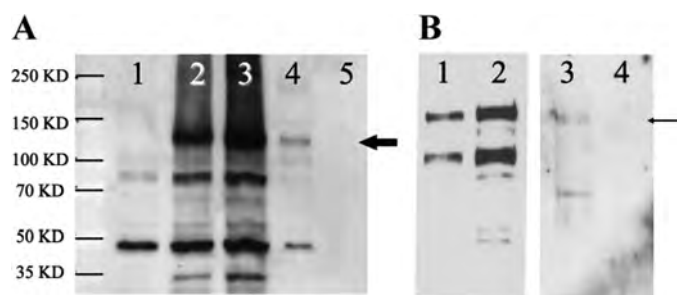


FIGURE 5. Reciprocal immunoprecipitations confirm the interaction between prestin and MAP1S. A permanent cell line expressing prestin-YFP-myc was transfected with FLAG-MAP1S-CFP. A, immunoprecipitations were performed with anti-FLAG (MAP1S) antibody and the presence of prestin in the immunoprecipitate detected on Western blots with anti-Myc antibody. Lanes 1–3 are control crude lysates of untransfected HEK cells, cells expressing prestin-YFP-myc, and cells expressing prestin-YFP-myc and FLAG-MAP1S-CFP, respectively. Lane 4 is an immunoprecipitate with FLAG antibody of lysates from HEK cells expressing prestin-YFP-myc together with FLAG-MAP1S-CFP. Prestin-YFP-myc is indicated by the thick arrow. Lane 5 is an anti-FLAG immunoprecipitate of HEK cells expressing prestin-YFP-myc. The absence of prestin in this lane confirms the specificity of the immunoprecipitating antibody. B, reciprocal experiment was performed to further confirm the interactions. Immunoprecipitation of cell lysates was done using anti-Myc antibody, and the presence of MAP1S in the immunoprecipitate was detected by Western blotting using anti-FLAG antibody. Lanes 1 and 2 are crude cell lysates of HEK cells expressing FLAG-MAP1S-CFP and HEK cells expressing prestin-YFP-myc together with FLAG-MAP1S-CFP, respectively. Lane 3 is the Myc immunoprecipitate of cells expressing prestin-YFP-myc and FLAG-MAP1S-CFP. FLAG-MAP1S-CFP is indicated by the thin arrow. Lane 4 is a Myc immunoprecipitate of cells expressing FLAG-MAP1S-CFP alone. The absence of prestin in lane 4 confirms the specificity of the immunoprecipitating Myc antibody. Although lanes 1–4 were separated on a single gel and transferred to the same blot, lanes 1 and 2 have been separated from lanes 3 and 4 in the figure for reasons of clarity. Lanes 1 and 2 are a shorter exposure and lanes 3 and 4 a longer exposure of the same blot. The experiments were repeated three times.

heavy and light chains in these cells. Consistent with these data, our yeast two-hybrid assay identified the interacting domain within MAP1S as restricted to an area between the heavy and light chains of the protein.

Physiological Interaction between MAP1S Confirmed by Förster Resonance Energy Transfer (FRET)—Our immunoprecipitation data strongly argue for an interaction between prestin and MAP1S. We next sought to determine that such an interaction took place *in vivo* (and prior to cell lysis in the immunoprecipitation assay). We chose to use FRET to demonstrate these interactions. Prestin and MAP1S were tagged at their C termini with YFP and cyan fluorescent protein (CFP). cDNA encoding these two fused proteins were inserted into an internal ribosome entry site vector and expressed in CHO cells. As evident in Fig. 6, cells transfected with this construct and expressing both these fused proteins show FRET. FRET efficiency was measured after acceptor photobleaching and showed values similar to what we have previously found in prestin-prestin interactions (15). FRET efficiency after photobleaching in Prestin-YFP/MAP1S-CFP was $2.8 (\pm 0.9 \text{ S.E.})$ and contrasts with $-36 (\pm 11 \text{ S.E.})$ in prestin-YFP/CFP. In contrast, the FRET efficiency of a construct in which CFP and YFP were in tandem separated by three amino acids was $35 (\pm 10 \text{ S.E.})$. These results argue that the distance between MAP1S and prestin is proximate to that between two molecules of prestin. These results also argue that interactions between prestin and MAP1S are likely physiological.

MAP1S Increases NLC—Having established a likely physiological interaction between prestin and MAP1S, we sought to ascertain if MAP1S affected prestin function. CHO cells were transfected with $0.8 \mu\text{g}$ of prestin and $0.8 \mu\text{g}$ of MAP1S fused to CFP per well in a 24-well plate. The control group was transfected with $0.8 \mu\text{g}$ of prestin and $0.8 \mu\text{g}$ of CFP. We assayed the physiological function of prestin by determining NLC in cells from these two groups. As shown in Fig. 7, cells transfected with prestin and MAP1S showed a 2.7-fold excess in NLC compared with cells that were transfected with prestin and CFP together. Prestin and MAP1S-transfected cells showed Q_{sp} of 6.38 fC/pF , which compared with 2.34 fC/pF in cells transfected with prestin and CFP alone (Table 1). In contrast, MAP1S did not affect other aspects of NLC function. Thus, cells transfected with prestin and MAP1S had mean V_h and z values of -120 mV and $0.63e$ and contrasted with values of -119 mV and $0.6e$ in cells transfected with prestin and CFP alone (Table 1). It should be noted that the Q_{sp} values obtained in these experiments were 50% of those that we normally achieve in CHO cells. Most likely, this results from the use of half the relative amount of prestin plasmid in each transfection that we normally use, necessitated by the need to co-transfect MAP1S at the same time.

MAP1S Increases Surface Expression of Prestin—Our data showing increased charge movement in the membrane of cells expressing MAP1S and prestin could be due to an increased number of molecules delivered to the membrane or as a result of an allosteric effect on each molecule at the surface of the cell. Our estimates of z , the charge carried by individual motors, were unchanged in cells transfected with prestin and MAP1S and argue against an allosteric effect. Rather our electrophysiological data argue for an increased number of motors delivered to the surface of the cell. To test this possibility, we assayed prestin expression in the membrane using a surface biotinylation assay. As shown in Fig. 8, there was a 2.8-fold increase in surface expression of prestin induced by MAP1S. This increase corresponded well with our electrophysiological findings that showed a 2.7-fold increase in specific charge, Q_{sp} . Because MAP1S binds tubulin, and because there is evidence that microtubule-associated mechanisms are important for surface expression of cell surface proteins, we sought to determine whether tubulin disruption affected prestin surface expression. In several experiments, cells were treated with and without $10 \mu\text{M}$ colchicine soon after transfection with prestin-YFP and $10 \mu\text{M}$ colchicine maintained in culture for 48 h. NLC in these cells was assayed at 48 h and showed no difference in the two groups (Table 2).

DISCUSSION

Our data show for the first time an interaction between prestin and MAP1S and evinces a physiological role for this interaction. The initial yeast two-hybrid data showing an interaction between these proteins are substantiated by the immunoprecipitation data. Subsequently, we demonstrate that the interaction is physiological with FRET, and electrophysiological recordings show an enhanced amount of prestin on the surface of the cell in the presence of MAP1S. The latter finding is further confirmed by biochemical means. Finally, we show that

MAP1S Interacts with Prestin

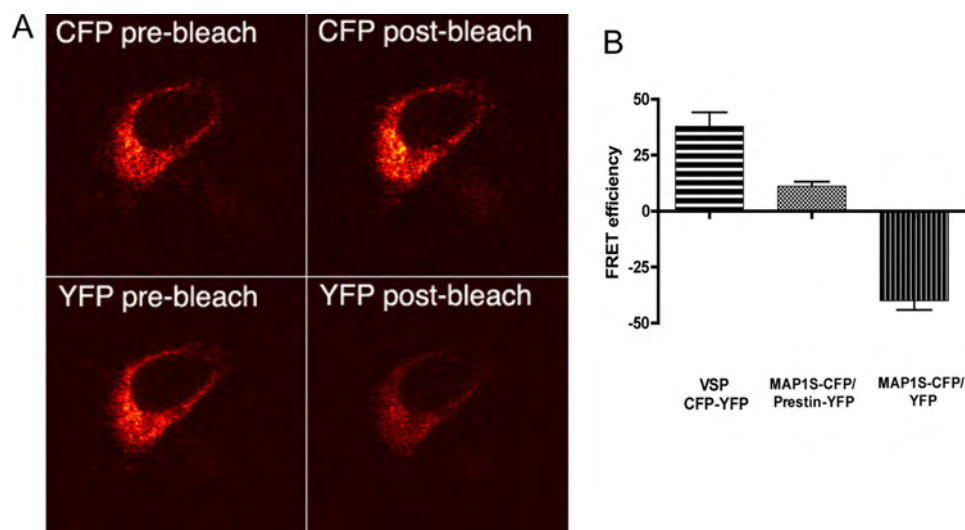


FIGURE 6. FRET experiments using acceptor photobleaching confirm *in vivo* interactions between prestin and MAP1S. *A*, photomicrographs of a CHO cell expressing prestin-YFP and MAP1S-CFP in an internal ribosome entry site vector are shown. The cell was excited with an argon laser at 458 nm, and the CFP emission in the bandwidth from 476 to 485 nm was recorded with a meta detector (upper two panels). The cell was also excited at 514 nm, and YFP emission at 536–545 nm was recorded (lower two panels). YFP was photobleached by continuous excitation at 514 nm for 1 min. Emission of CFP after photobleaching (right upper panel) shows an increase compared with CFP emission before photobleaching (left upper panel). In contrast, YFP emission (left lower panel) shows a decrease after photobleaching (right lower panel) compared with YFP emission before photobleaching (left lower panel). *B*, CFP FRET efficiency was measured after photobleaching as described previously (15). The MAP1S-CFP and prestin-YFP pair shows an increase in FRET efficiency after photobleaching (mean 11.02 ± 2.0 S.E., $n = 8$) and contrasts with MAP1S-CFP and YFP pair that shows a decrease in FRET efficiency (mean -40.0 ± 4.6 S.E., $n = 7$). Also included is a positive control that has CFP and YFP in tandem separated by one amino acid and fused to the C terminus of the membrane-spanning voltage-sensing phosphatase from *Nematostella vectensis*. This construct yielded higher FRET efficiency (mean 37.87 ± 6.26 S.E., $n = 4$).

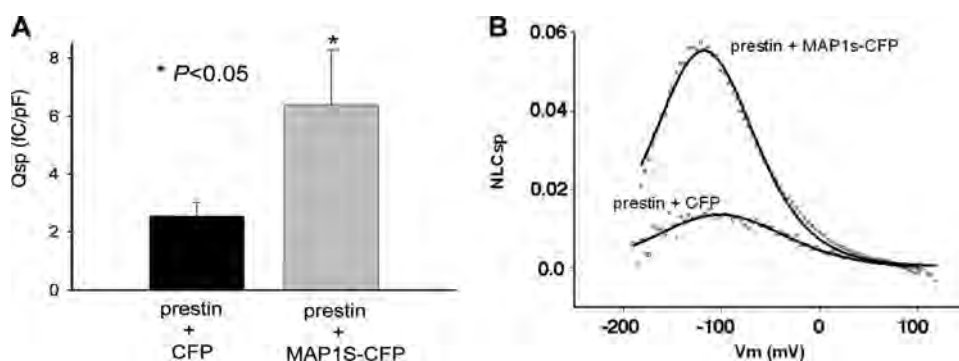


FIGURE 7. MAP1S increases Q_{sp} . *A*, CHO cells transiently transfected with prestin and MAP1S-CFP showed a statistically significant ($p < 0.05$, *t* test) increase in Q_{sp} (mean 6.38 ± 1.89 S.E.) compared with cells transfected with prestin and CFP (mean 2.34 ± 0.47 S.E.). *B*, shown are two representative NLC_{sp} (defined as NLC (pF)/linear capacitance (pF) to correct for effects of cell size) traces from two comparable cells transfected with the combination of plasmids prestin/CFP and prestin/MAP1S-CFP. There is a notable increase in peak NLC_{sp} in the cell transfected with the plasmid combination prestin/MAP1S-CFP compared with the plasmid combination prestin/CFP.

TABLE 1

MAP1S increases Q_{sp} but does not affect other measures of NLC (V_h and z)

Shown are values of NLC in cells transfected with the combination of plasmids prestin/MAP1S-CFP or prestin/CFP. Although Q_{sp} is significantly increased, both the voltage of peak capacitance (V_h) and estimates of the charge carried by a single motor z are comparable.

	Q_{sp}	V_h	z	n
	fC/pF	mV		
0.8 μ g of normal prestin + 0.8 μ g of CFP	2.34 ± 0.47	-119.29 ± 3.17	0.60 ± 0.02	11
0.8 μ g of normal prestin + 0.8 μ g of MAP1S-CFP	6.38 ± 1.89	-120.47 ± 3.61	0.63 ± 0.04	10

there is a gradient in the expression of prestin and MAP1S along the tonotopic axis. This gradient may partially explain the increase in charge density in high frequency OHCs.

Interaction between MAP1S and Prestin Is Restricted to Specific Regions of the Proteins

The interaction between these two proteins occurs in the region between the heavy and light chain in MAP1S and the proximal portion of the STAS domain in prestin. Although it is possible that interactions with prestin may extend into the loops connecting consecutive transmembrane domains, our current approaches limit our exploration of this possibility. To date there has been no evidence that the region between the heavy and light chain of MAP1S is involved in interactions with other proteins (22). Consistent with these results, our immunoprecipitation data show that prestin interacts with the holoprotein and not its component heavy and light chains. The cleavage site between the heavy and light chains of MAP1S lies in the region between them and coincides with the prestin-binding site (22). The light and heavy chains of the molecule have been shown to bind different elements of the cytoskeleton (22). Thus, the N terminus of the light chain binds tubulin, and the more C-terminally placed MH3 domain binds actin. In contrast, the heavy chain interferes with the interaction between the light chain and tubulin. In this respect, our data that show no effect on surface expression of prestin by colchicine is consistent with the result that prestin surface expression is mediated by the holo-

protein, which does not interact with tubulin.

Other data from the yeast two-hybrid experiments show that amino acids involving the STAS domain of prestin are involved in the interaction with MAP1S. Specifically, the sequence extends across the first three β -strands, the first α -helix, and the intervening IVS region of the purported STAS domain in prestin determined by molecular modeling (22, 23). The STAS domain resembles the bacterial SPOIIAA transcription factor, the crystal and NMR structure of which has been determined (24, 25). The SPOIIAA transcription factor is involved in protein-protein interactions with the anti- σ factor SPOIIB. Bind-

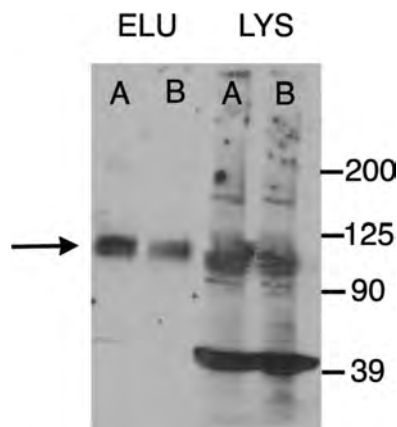


FIGURE 8. MAP1S increases surface expression of prestin. CHO cells were transfected with prestin/MAP1S CFP and separately prestin/CFP plasmids. Proteins on the surface of the cell were labeled with sulfo-succinimidyl-2-(biotinamido)ethyl-1,3-dithiopropionate and isolated using a Neutravidin resin. The surface proteins were eluted using 50 mM dithiothreitol and separated by SDS-PAGE, and the presence of prestin was detected by Western blotting (left two lanes). The amount of surface protein loaded in each lane has been normalized to the total protein in the cell lysate. As is evident, cells expressing prestin and MAP1S-CFP (A) demonstrate an increase (2.8-fold \pm 0.9 S.E., $n = 4$) in surface expression of prestin when compared with cells expressing prestin and CFP (B). The comparable expressions of prestin in the corresponding cell lysates are shown in the two right lanes confirming that the total amounts of prestin in these cells were equivalent. The prestin band is shown by an arrow. The numerous other bands in the lysates (for example, the band at 39 kDa) are nonspecific and detected in untransfected HEK cells probed with the secondary antibody alone (data not shown). ELU, eluate; LYS, lysate.

TABLE 2

Colchicine has no effect on the Q_{sp}

The table shows the effects of treating cells with 10 μ M colchicine for 48 h after transfection. Measures of NLC, including Q_{sp} , V_h , and z , were unchanged by treatment with this drug. It should be noted that because treatment with this drug is cytotoxic, we incorporated in our data analysis only those cells that showed good seal resistance, using it as a surrogate marker for the well being of cells.

	Q_{sp}	V_h	z	n
	fC/pF	mV		
Prestin	7.35 ± 0.42	-110.03 ± 3.00	0.71 ± 0.02	5
Prestin + 10 μ M colchicine	7.33 ± 1.88	-107.70 ± 10.24	0.69 ± 0.03	5

ing of these two proteins results in σ factor release from SPOIIB, which in turn triggers transcription (26–28). Mutations within the STAS domain of SLC26A2, SLC26A3, and SLC26A4 and the *Arabidopsis thaliana* sulfate transporter Sultr 1.2 have been shown to alter anion transport function (29–34). Moreover, the STAS domain in SLC26A3 also interacts with cystic fibrosis transmembrane regulator, and this interaction reciprocally modulates cystic fibrosis transmembrane regulator channel function as well as SLC26A3 transporter function (35). In contrast, cystic fibrosis transmembrane regulator interacts with the STAS domain of SLC26A9 and inhibits Cl^- currents as well as its Cl^- - HCO_3^- exchange (36). Given these data, it was our expectation that MAP1S would modulate NLC. However, we did not note an alteration in measures of prestin “kinetics.” Both V_h and z , reflecting the steady state energy profile and unitary charge movement, were unchanged in cells co-transfected with MAP1S. In contrast, we noted increased delivery of prestin to the surface of the cell. Several mutations in the STAS domain resulted in altered delivery of SLC26A3, a related protein, to the surface of the cell (32). Taken together, these data suggest that modulation of the

STAS domain may affect surface delivery of SLC26 proteins (prestin), in addition to affecting the kinetics of the protein (SLC26A3). Efforts are currently underway in our laboratory to determine how MAP1S affects prestin anion transport (37), especially given the data that mutations in the STAS domain have been shown to affect anion transport in members of the SLC26 family of proteins. Furthermore, given the sequence homology in this region between the different members of the SLC26 family of proteins, and the ubiquitous distribution of MAP1S, we would anticipate that these anion transporters also will interact with MAP1S (38). In this regard, the yeast two-hybrid experiments identifying residues 491–572, which is conserved between prestin and other SLC26 members, could suggest homologous regions from other SLC26 members as also interacting with MAP1S. In contrast, it is possible that residues 573–660, which has little homology in other SLC26 family members, confers specificity to the interactions with prestin.

Increase in Q_{sp} Is Likely Brought About by Increased Amounts of Prestin on the Surface of the Cell—As noted above, our data on measures of NLC show that MAP1S affects Q_{sp} but not other measures of NLC, including z and V_h . Theoretically, Q_{sp} could be increased by increasing the number of functional motors in the membrane or by increasing the net charge carried by each motor. However, given that z , our best estimate of charge carried by an individual motor, was unchanged in the presence of MAP1S, it is most likely that the number of motors delivered to the surface is increased. This conclusion is borne out by our determination of surface expression of prestin in the presence and absence of MAP1S. The biotinylation assay revealed a 2.8-fold increase in surface expression of prestin that compared with a 2.7-fold increase in Q_{sp} . Thus, there was good concordance between our biochemical assays of surface expression and electrophysiological determination of surface expression. How is this increase in surface expression brought about? Three possibilities are suggested as follows: increased delivery of newly synthesized protein to the surface, decreased degradation of the protein, or increased recycling of the protein that is endocytosed from the surface. Although we have no experimental data to discern these possibilities at present, we expect that MAP1S will likely deliver more newly synthesized protein to the surface. Previous experiments in our laboratory indicate that turnover rates of prestin may be slow; in the presence of brefeldin A, a blocker of newly synthesized protein delivery into the surface membrane, OHCs in culture maintained robust NLC for up to 7 days.⁶

MAP1S has been shown to interact with the NR3A *N*-methyl-D-aspartic acid receptor subunit, the fibroblast growth factor-associated protein LRPPRC, the tumor suppressor protein RASSF1A, and the sperm protein VCY2 that has been implicated in azoospermia (39–43). However, in all these instances there were no clearly observed consequences of the interactions. Thus, the functional effect of MAP1S on prestin expression appears to be the first direct demonstration of any functional effect by MAP1S. In the case of the NR3A receptor and MAP1S, there was sharp co-localization of the two proteins in

⁶ E. Navarrete and J. Santos-Sacchi, unpublished data.

MAP1S Interacts with Prestin

dendritic spines that led the authors to speculate that MAP1S was important for localizing NR3A receptors to dendritic spines (41). However, there were no direct tests of this possibility. In the related MAP1B protein, early data suggested that MAP1B was important for targeting γ -aminobutyric acid type C receptors to specific subcellular locales (44). These two proteins co-localize in retinal bipolar cells (44). Heterologous expression of the two proteins in COS cells resulted in an altered distribution of the γ -aminobutyric acid type C receptor. However, subsequent MAP1B knock-out experiments were confounding with normal γ -aminobutyric acid type C clustering in bipolar cells (45).

There are a number of reports suggesting a role for the microtubule-associated motors in directing organelles and proteins to subcellular sites, including dendritic shafts (46–48). Given the known associations between MAP1S and tubulin, an obvious mechanism for prestin delivery to the surface of the cell would be through its association via MAP1S with microtubules and their motors. However, we show that continued disruption of microtubules (after transfection) with 10 μ M colchicine had no effect on Q_{sp} .

Interactions between Prestin and MAP1S Likely Has Physiological Significance—Our data showing a graded tonotopic expression of prestin and MAP1S have bearing on physiological findings in the cochlea. Prior work has compared Q_{sp} in guinea pig OHCs isolated from regions along the tonotopic axis and found an ~5–6-fold increase in Q_{sp} in the lateral membrane of OHC responding to high frequency sound compared with OHC responding to low frequency sound (13). However, prestin mRNA expression increases 1.2-fold from the 3rd turn to the 2nd turn and 2.8-fold from the third turn to the basal turn. Thus, the prestin expression increase in high frequency cells is less than the increase in Q_{sp} . Whether the even greater increase in MAP1S expression that we find contributes to the excess increase in Q_{sp} remains to be investigated. In the mouse where physiological data are unavailable, but antibodies to MAP1S and prestin are available, there is a 7-fold increase in prestin protein expression from the most apical to the most basal hair cells. Similarly, there is also a smaller 3.5-fold increase in protein expression of MAP1S. This is an important issue, because the increase in Q_{sp} in high frequency cells has been proposed to be a mechanism that provides a constant electrical energy to these cells, which may help circumvent the low pass filter effects of the cell membrane (13).

In conclusion, we show for the first time an interaction between prestin and the microtubule-associated protein MAP1S. The interaction is confirmed by immunoprecipitation and FRET. Our data from FRET suggest that the relative distance between MAP1S and prestin is proximate to the distances between two molecules of prestin. The interaction results in an increased amount of prestin on the surface of the cell that accounts for the increase in Q_{sp} brought about by MAP1S. We demonstrate the presence of MAP1S in individual OHCs and confirm a gradient in the expression of prestin and MAP1S along the tonotopic axis. This gradient of both proteins could explain the increase in charge movement density (Q_{sp}) seen in OHCs from higher frequencies.

Acknowledgment—We thank Dr. Fritz Probst for the MAP1S constructs and for critical reading of this manuscript.

REFERENCES

1. Zheng, J., Shen, W., He, D. Z., Long, K. B., Madison, L. D., and Dallos, P. (2000) *Nature* **405**, 149–155
2. Liberman, M. C., Gao, J., He, D. Z., Wu, X., Jia, S., and Zuo, J. (2002) *Nature* **419**, 300–304
3. Santos-Sacchi, J., Song, L., Zheng, J., and Nuttall, A. L. (2006) *J. Neurosci.* **26**, 3992–3998
4. Dallos, P., Wu, X., Cheatham, M. A., Gao, J., Zheng, J., Anderson, C. T., Jia, S., Wang, X., Cheng, W. H., Sengupta, S., He, D. Z., and Zuo, J. (2008) *Neuron* **58**, 333–339
5. Zheng, J., Madison, L. D., Oliver, D., Fakler, B., and Dallos, P. (2002) *Audiol. Neurootol.* **7**, 9–12
6. Belyantseva, I. A., Adler, H. J., Curi, R., Frolenkov, G. I., and Kachar, B. (2000) *J. Neurosci.* **20**, RC116
7. Iwasa, K. H. (1993) *Biophys. J.* **65**, 492–498
8. Iwasa, K. H. (2001) *Biophys. J.* **81**, 2495–2506
9. Gale, J. E., and Ashmore, J. F. (1994) *Proc. R. Soc. Lond. B Biol. Sci.* **255**, 243–249
10. Kakehata, S., and Santos-Sacchi, J. (1995) *Biophys. J.* **68**, 2190–2197
11. Santos-Sacchi, J. (1991) *J. Neurosci.* **11**, 3096–3110
12. Ashmore, J. F. (1989) in *Mechanics of Hearing* (Kemp, D., and Wilson, J. P., eds) pp. 107–113, Plenum Publishing Corp., New York
13. Santos-Sacchi, J., Kakehata, S., Kikuchi, T., Katori, Y., and Takasaka, T. (1998) *Neurosci. Lett.* **256**, 155–158
14. Gale, J. E., and Ashmore, J. F. (1997) *Pflugers Arch.* **434**, 267–271
15. Navaratnam, D., Bai, J. P., Samaranyake, H., and Santos-Sacchi, J. (2005) *Biophys. J.* **89**, 3345–3352
16. Huang, G., and Santos-Sacchi, J. (1993) *Biophys. J.* **65**, 2228–2236
17. Abe, T., Kakehata, S., Kitani, R., Maruya, S., Navaratnam, D., Santos-Sacchi, J., and Shinkawa, H. (2007) *J. Membr. Biol.* **215**, 49–56
18. Santos-Sacchi, J., Shen, W., Zheng, J., and Dallos, P. (2001) *J. Physiol.* **531**, 661–666
19. Pocklington, A. J., Cumiskey, M., Armstrong, J. D., and Grant, S. G. (2006) *Mol. Syst. Biol.* **2**, 1–14
20. Pocklington, A. J., Armstrong, J. D., and Grant, S. G. (2006) *Brief. Funct. Genomic Proteomic* **5**, 66–73
21. Vacher, H., Mohapatra, D. P., and Trimmer, J. S. (2008) *Physiol. Rev.* **88**, 1407–1447
22. Rouached, H., Berthomieu, P., El Kassis, E., Cathala, N., Catherinot, V., Labesse, G., Davidian, J. C., and Fourcroy, P. (2005) *J. Biol. Chem.* **280**, 15976–15983
23. Bai, J. P., Navaratnam, D., Samaranyake, H., and Santos-Sacchi, J. (2006) *Neurosci. Lett.* **404**, 270–275
24. Seavers, P. R., Lewis, R. J., Brannigan, J. A., Verschuere, K. H., Murshudov, G. N., and Wilkinson, A. J. (2001) *Structure* **9**, 605–614
25. Kovacs, H., Comfort, D., Lord, M., Campbell, I. D., and Yudkin, M. D. (1998) *Proc. Natl. Acad. Sci. U.S.A.* **95**, 5067–5071
26. Diederich, B., Wilkinson, J. F., Magnin, T., Najafi, M., Errington, J., and Yudkin, M. D. (1994) *Genes Dev.* **8**, 2653–2663
27. Clarkson, J., Campbell, I. D., and Yudkin, M. D. (2003) *Biochem. J.* **372**, 113–119
28. Kroos, L., Zhang, B., Ichikawa, H., and Yu, Y. T. (1999) *Mol. Microbiol.* **31**, 1285–1294
29. Taylor, J. P., Metcalfe, R. A., Watson, P. F., Weetman, A. P., and Trembath, R. C. (2002) *J. Clin. Endocrinol. Metab.* **87**, 1778–1784
30. Karniski, L. P. (2001) *Hum. Mol. Genet.* **10**, 1485–1490
31. Karniski, L. P. (2004) *Hum. Mol. Genet.* **13**, 2165–2171
32. Dorwart, M. R., Shcheynikov, N., Baker, J. M., Forman-Kay, J. D., Muallem, S., and Thomas, P. J. (2008) *J. Biol. Chem.* **283**, 8711–8722
33. Shibagaki, N., and Grossman, A. R. (2004) *J. Biol. Chem.* **279**, 30791–30799
34. Shibagaki, N., and Grossman, A. R. (2006) *J. Biol. Chem.* **281**, 22964–22973

35. Ko, S. B., Zeng, W., Dorwart, M. R., Luo, X., Kim, K. H., Millen, L., Goto, H., Naruse, S., Soyombo, A., Thomas, P. J., and Muallem, S. (2004) *Nat. Cell Biol.* **6**, 343–350
36. Chang, M. H., Plata, C., Sindic, A., Ranatunga, W. K., Chen, A. P., Zandi-Nejad, K., Chan, K. W., Thompson, J., Mount, D. B., and Romero, M. F. (2009) *J. Biol. Chem.* **284**, 28306–28318
37. Bai, J. P., Surguchev, A., Montoya, S., Aronson, P. S., Santos-Sacchi, J., and Navaratnam, D. (2009) *Biophys. J.* **96**, 3179–3186
38. Orbán-Németh, Z., Simader, H., Badurek, S., Tranciková, A., and Propst, F. (2005) *J. Biol. Chem.* **280**, 2257–2265
39. Liu, L., Vo, A., Liu, G., and McKeegan, W. L. (2005) *Cancer Res.* **65**, 4191–4201
40. Liu, L., Vo, A., Liu, G., and McKeegan, W. L. (2005) *Biochem. Biophys. Res. Commun.* **332**, 670–676
41. Eriksson, M., Samuelsson, H., Samuelsson, E. B., Liu, L., McKeegan, W. L., Benedikz, E., and Sundström, E. (2007) *Biochem. Biophys. Res. Commun.* **361**, 127–132
42. Wong, E. Y., Tse, J. Y., Yao, K. M., Lui, V. C., Tam, P. C., and Yeung, W. S. (2004) *Biol. Reprod.* **70**, 775–784
43. Song, M. S., Chang, J. S., Song, S. J., Yang, T. H., Lee, H., and Lim, D. S. (2005) *J. Biol. Chem.* **280**, 3920–3927
44. Pattnaik, B., Jellali, A., Sahel, J., Dreyfus, H., and Picaud, S. (2000) *J. Neurosci.* **20**, 6789–6796
45. Meixner, A., Haverkamp, S., Wässle, H., Führer, S., Thalhammer, J., Kropf, N., Bittner, R. E., Lassmann, H., Wiche, G., and Propst, F. (2000) *J. Cell Biol.* **151**, 1169–1178
46. Allan, V. J., Thompson, H. M., and McNiven, M. A. (2002) *Nat. Cell Biol.* **4**, E236–E242
47. Murray, J. W., and Wolkoff, A. W. (2003) *Adv. Drug Deliv. Rev.* **55**, 1385–1403
48. Zheng, Y., Wildonger, J., Ye, B., Zhang, Y., Kita, A., Younger, S. H., Zimmerman, S., Jan, L. Y., and Jan, Y. N. (2008) *Nat. Cell Biol.* **10**, 1172–1180
49. Navaratnam, D. S. (2009) *Methods Mol. Biol.* **493**, 257–268
50. Blot, V., and McGraw, T. E. (2008) *Methods Mol. Biol.* **457**, 347–366
51. Navaratnam, D. S., Bell, T. J., Tu, T. D., Cohen, E. L., and Oberholtzer, J. C. (1997) *Neuron* **19**, 1077–1085
52. Santos-Sacchi, J. (2004) *Biophys. J.* **87**, 714–727
53. Santos-Sacchi, J., Kakehata, S., and Takahashi, S. (1998) *J. Physiol.* **510**, 225–235
54. Santos-Sacchi, J. (1993) *Biophys. J.* **65**, 2217–2227
55. Scherer, M. P., and Gummer, A. W. (2005) *Biophys. J.* **88**, L27–L29

Combinatorial Cysteine Mutagenesis Reveals a Critical Intramonomer Role for Cysteines in Prestin Voltage Sensing

Jun-Ping Bai,[†] Alexei Surguchev,[†] Shumin Bian,[†] Lei Song,[†] Joseph Santos-Sacchi,^{†§¶*} and Dhasakumar Navaratnam^{††}

[†]Department of Neurology, ^{††}Department of Neurobiology, [§]Department of Cellular and Molecular Physiology, and [¶]Department of Surgery (Otolaryngology), Yale University School of Medicine, New Haven, Connecticut

ABSTRACT Prestin is a member of the SLC26 family of anion transporters and is responsible for electromotility in outer hair cells, the basis of cochlear amplification in mammals. It is an anion transporting transmembrane protein, possessing nine cysteine residues, which generates voltage-dependent charge movement. We determine the role these cysteine residues play in the voltage sensing capabilities of prestin. Mutations of any single cysteine residue had little or no effect on charge movement. However, using combinatorial substitution mutants, we identified a cysteine residue pair (C415 and either C192 or C196) whose mutation reduced or eliminated charge movement. Furthermore, we show biochemically that surface expression of mutants with markedly reduced functionality can be near normal; however, we identify two monomers of the protein on the surface of the cell, the larger of which correlates with surface charge movement. Because we showed previously by Förster resonance energy transfer that monomer interactions are required for charge movement, we tested whether disulfide interactions were required for dimerization. Using Western blots to detect oligomerization of the protein in which variable numbers of cysteines up to and including all nine cysteine residues were mutated, we show that disulfide bond formation is not essential for dimer formation. Taken together, we believe these data indicate that intramembranous cysteines are constrained, possibly via disulfide bond formation, to ensure structural features of prestin required for normal voltage sensing and mechanical activity.

INTRODUCTION

Prestin (SLC26A5) is a member of the SLC26 family of anion transporters (1). It is now well established that this protein is responsible for electromotility in mammalian outer hair cells (OHC), which are believed to be responsible for cochlear amplification (2–5). Prestin is a membrane protein of 744 amino acids (1). A large central core of the protein is predicted to traverse the membrane multiple times based on hydrophobicity analysis (1,6). The number of predicted transmembrane regions varies (10 or 12), and is dependent on the different prediction paradigms (1,6–8). It also has a small N-terminus and a larger C-terminus that are thought to be intracellular (6,9). Prestin has piezoelectric properties; membrane voltage controls its conformation (10–13). Its voltage sensitivity arises from voltage sensor charge movement within the membrane that can be measured as a nonlinear capacitance (NLC) (14–16).

Prestin contains nine cysteine residues (1). Of these nine residues, six (C192, C196, C260, C381, C395, and C415) lie in areas that are potential transmembrane regions (1,6,7). Of the remaining three, two (C52 and C679) are located in the intracellular N- and C-termini, respectively, whereas the remaining cysteine (C124) residue lies in a loop connecting two potential transmembrane regions (Fig. 1). Cysteine residues, because of their ability to form disulfide bonds, can play a number of roles in a protein's function (17,18).

Disulfide bond formation is a covalent posttranslational modification that occurs concurrent with translation. Disulfide bonds can be structural, catalytic, or allosteric (17–19). Structural bonds stabilize the structure of the protein by decreasing the entropy of the unfolded (denatured) protein (18). Catalytic disulfide bonds help in catalyzing enzyme reactions. The best known of these is found in oxidoreductases where a catalytic disulfide bond is found in its thioredoxin-like fold. Allosteric disulfide bonds, in contrast, modulate a protein's function (19). Cleavage of allosteric disulfide bonds results in a change in the protein's tertiary or quaternary structure and its function (19).

Tests for disulfide bond formation often involve functional assays of proteins, for example, membrane transport (20). In native OHCs, measures of NLC or mechanical activity have been used (21,22). Preliminary exploration of disulfide bonds in the structure and function of prestin has provided a number of insights. It has been reported that mutation of individual cysteine residues did not adversely affect its charge movement (23,24). Other work has implicated disulfide bonds formed by one or more cysteine residues in the transmembrane regions of prestin as important for dimerization of the protein (25). Here, we systematically mutated cysteine residues individually and in combination, and then determined how mutations affect characteristics of NLC (see **Materials and Methods**). These characteristics include the density of voltage sensor charge (Q_{sp}), the voltage at peak capacitance (V_h), and unitary charge valence (z). Q_{sp} is an estimate of functional motors within a unit membrane surface area, V_h is a metric of the steady-state

Submitted May 18, 2009, and accepted for publication March 19, 2010.

[†]Jun-Ping Bai and Alexei Surguchev contributed equally to this work.

*Correspondence: santos-sacchi@yale.edu

Editor: Francisco Bezanilla.

© 2010 by the Biophysical Society
0006-3495/10/07/0085/10 \$2.00

doi: 10.1016/j.bpj.2010.03.066

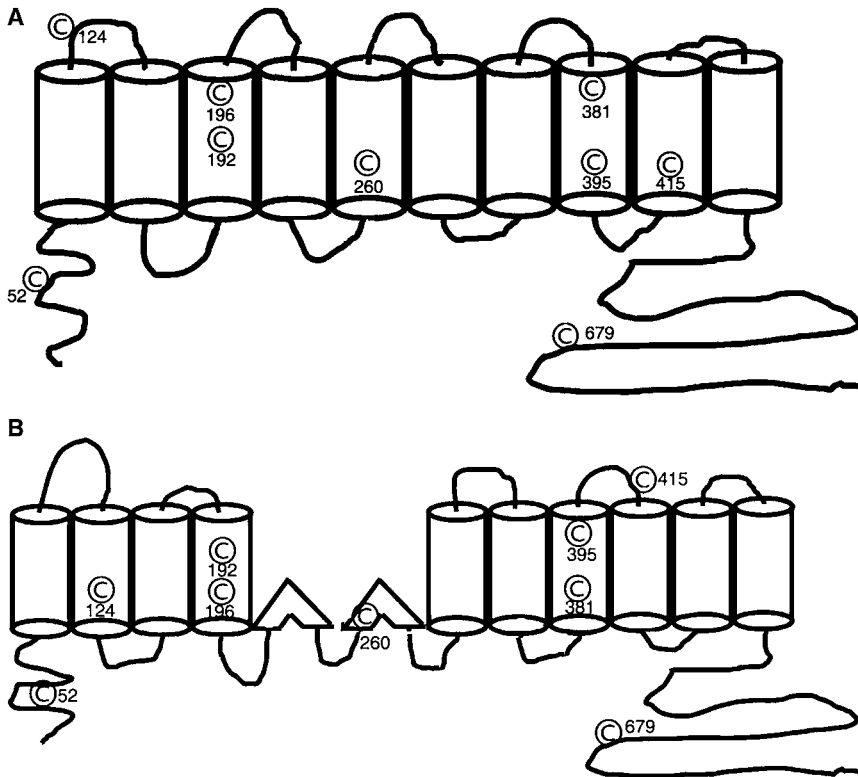


FIGURE 1 Nine cysteine residues are distributed throughout the protein. A cartoon of the two different transmembrane models are shown along with the position of individual cysteine residues in these two models. (A) Ten transmembrane model. (B) Twelve transmembrane model. Six of these residues (C192, C196, C260, C381, C395, C415) lie within hydrophobic transmembrane regions of the protein. Two residues (C52 and C679) lie in the predicted intracellular amino and carboxy termini of the protein, respectively, and the last residue (C124) lies in a loop connecting two transmembrane regions in the 10 transmembrane model.

energy profile, and z is an estimate of charge moved within an individual motor. We also explored the role of these cysteine residues in the formation of prestin multimers. Our data show that mutation of individual cysteine residues has little or no effect on the function of prestin. However, our combinatorial data show profound changes in the function of prestin, providing evidence that cysteine residues (namely, C415 and either C192 or C196) in prestin potentially form disulfide bonds. Finally, we show that disulfide bond formation is not necessary for the formation of prestin multimers.

MATERIALS AND METHODS

cDNA constructs and generation of mutants

Single or multiple amino acid substitutions were generated using QuickChange II or QuickChange II Multi site-directed mutagenesis kits (Stratagene, La Jolla, CA) with a gerbil prestin-YFP in pEYFPN1 vector (Clontech, Mountain View, CA) as a template. All mutations were confirmed by DNA sequencing, including the entire coding region.

Transient transfections in Chinese hamster ovary cells

For electrophysiological recordings 100,000 Chinese hamster ovary (CHO) cells were transfected in 24-well plates with the cysteine mutants using Lipofectamine (Invitrogen, Carlsbad, CA) as described previously (7).

Electrophysiological recording

Cells were recorded by whole-cell patch clamp configuration at room temperature using an Axon 200B amplifier (Axon Instruments, Sunnyvale,

CA), as described previously (7). Cells were recorded 24–48 h after transfection to allow for stable measurement of NLC. Ionic blocking solutions were used to isolate capacitive currents. The bath solution contained (in mM): TEA 20, CsCl 20, CoCl₂ 2, MgCl₂ 1.47, Hepes 10, NaCl 99.2, CaCl₂·2H₂O 2, pH 7.2, and the pipette solution contained (in mM): CsCl 140, EGTA 10, MgCl₂ 2, Hepes 10, pH 7.2. Osmolarity was adjusted to 300 ± 2 mOsm with dextrose. Command delivery and data collections were carried out with a Windows-based whole-cell voltage clamp program, jClamp (Sciosoft, Ridgefield, CT), using a Digidata 1322A interface (Axon Instruments).

Capacitance was evaluated using a continuous high-resolution 2-sine wave technique, fully described elsewhere (26,27). Capacitance data were fitted to the first derivative of a two-state Boltzmann function (16):

$$C_m = Q_{\max} \frac{ze}{kT} \frac{b}{(1+b)^2} + C_{\text{lin}},$$

where

$$b = \exp\left(\frac{-ze(V - V_{\text{pkCm}})}{kT}\right).$$

Q_{\max} is the maximum nonlinear charge transfer, V_h the voltage at peak capacitance or half-maximal nonlinear charge transfer, V_m the membrane potential, C_{lin} linear capacitance, z the valence (a metric of voltage sensitivity), e the electron charge, k the Boltzmann constant, and T the absolute temperature. Q_{\max} is reported as Q_{sp} the specific charge density, i.e., total charge moved normalized to linear capacitance. Where necessary we increased the range of voltage commands to test mutants in which V_h was extreme. A Student's t -test was used to evaluate the effects of mutants on the different parameters of NLC. In mutants where Q_{sp} was immeasurable, namely zero, we state, for presentation purposes, that the significance of differences with prestin that had NLC was <0.01 , although the probability of a difference between these data would be infinitely small.

It should be noted that measures of Q_{sp} , V_h , and z in CHO cells are in line with our previous work. Measures of Q_{sp} in CHO cells are in the lower range

of that recorded in HEK cells. However, V_h in CHO cells (-120 to -100 mV) is significantly negative compared to prestin expressed in HEK cells (-50 to -70 mV).

Western blots

Crude lysates were generated from transiently transfected CHO cells after 24–48 h. Lysates were separated on a precast 4–15% Tris-HCl SDS-PAGE gel (Bio-Rad, Hercules, CA) or a 5–8% urea-SDS PAGE containing 6 M urea. Samples were incubated with and without reducing agents where indicated. Two reducing agents, β -mercaptoethanol and ethanedithiol (EDT), were added to the samples at final concentrations of 200 mM and 600 mM, respectively. Proteins were transferred by wet transfer to polyvinylidene fluoride membrane (Roche, Indianapolis, IN). Western blots were probed with anti-prestin-N20 (Santa Cruz, Santa Cruz, CA) at a 1:500 dilution and then with horseradish peroxidase (HRP) conjugated bovine anti-goat secondary antibody (Santa Cruz) at 1:5000 dilution with TBST washing ($\times 5$) in between. The presence of HRP conjugated antibody was detected using SuperSignal West Dura Extended Duration Substrate (ThermoScientific/Pierce, Rockford, IL). Where indicated, the blots were stripped using Restore plus Western stripping buffer and reprobed with prestin C-16 antibody (Santa Cruz) at a 1:500 dilution and HRP conjugated bovine anti-goat secondary antibody at a 1:5000 dilution.

Prestin surface expression

Surface expression of prestin was determined using a surface biotinylation assay (ThermoScientific/Pierce). Transiently transfected CHO cells were analyzed 24 h after transfection. These cells were washed with PBS, and incubated in the presence of sulfo-NHS-biotin for 30 min at 4°C. Free sulfo-NHS-biotin was quenched by washing cells in 140 mM Tris-Cl, and the cells lysed in lysis buffer containing (mM): Tris 20, pH 8.0, NaCl 137, NaEDTA 5, NaEGTA 5, 10% glycerol, 0.5% Triton X-100, PMSF 0.2, NaF 50, benzamidine 20. The lysates were cleared by centrifugation, and its protein concentration assayed (Bio-Rad) and equalized. Streptavidin agarose was added in the mixtures, incubated 1 h at room temperature with constant agitation. After centrifugation at $1000 \times g$ the beads were washed with washing buffer. The bound surface proteins were released by addition of 50 mM dithiothreitol and analyzed by SDS-PAGE and Western blotting as described above. In several experiments we also sorted cells by fluorescent activated cell sorting and determined that there was no consistent difference in transfection efficiency between different mutants. Similarly, there was no difference in the ratio between the upper to lower monomer within a given mutant irrespective of whether or not cells were sorted before labeling of cell surface proteins.

RESULTS

Substitution of single cysteine residues did not abolish NLC

To ascertain which cysteine residues are important for the structure and function of prestin, we substituted each of the nine individual cysteine residues with a serine residue. We reasoned that substituting cysteine with a serine residue, which has the identical side chain length (thereby minimizing confounding effects from side chain interactions), was a good method to determine the role of disulfide bonds in the function of the protein. NLC characteristics of three single point cysteine mutations differed significantly from wild-type prestin (Table 1). These were C415S which had a significant change in Q_{sp} (2.45 ± 0.81 fC/pF vs. 7.88 ± 1.26 fC/pF),

TABLE 1 Mean NLC parameters of single cysteine to serine mutations and number of cells recorded for each mutant

Single mutants	NLC parameter			n
	Q_{sp}	V_h	z	
Wild-type prestin	7.88 ± 1.26	-111.30 ± 2.94	0.72 ± 0.01	25
C52S	6.49 ± 0.92	-111.03 ± 4.31	0.70 ± 0.05	5
C124S	10.18 ± 4.03	-111.05 ± 4.30	0.68 ± 0.03	6
C192S	5.87 ± 0.74	-109.72 ± 6.41	0.70 ± 0.02	6
C196S	6.50 ± 1.00	$-130.14 \pm 3.22^*$	0.68 ± 0.01	8
C260S	4.16 ± 0.49	-110.11 ± 5.43	0.68 ± 0.05	4
C381S	8.72 ± 1.06	-97.07 ± 7.39	0.66 ± 0.03	5
C395S	5.37 ± 0.82	$-58.51 \pm 4.68^*$	0.66 ± 0.03	7
C415S	$2.45 \pm 0.81^*$	-117.11 ± 9.47	0.71 ± 0.06	7
C679S	7.64 ± 1.54	-107.78 ± 9.57	0.73 ± 0.03	5

Values that show statistically significant differences from wild-type prestin are indicated.

* $p < 0.05$.

and C196S and C395S that had changes in V_h (-130.14 ± 3.22 mV and -58.51 ± 4.68 mV, respectively, versus -111.30 ± 2.94 mV in control).

Substitution of two or more cysteine residues does not alter prestin surface expression, but rather folding of monomers with adverse affects on Q_{sp}

Our data that mutations of individual cysteine residues do not eliminate NLC suggest several possibilities. First, there may be no disulfide bonds. Second, disulfide bonds are not crucial for the generation of NLC. Third, one disulfide bond is able to compensate for the loss of another disulfide bond. Our experiments thus far are unable to rule out the first two possibilities. Attempts in our lab to purify adequate amounts of prestin expressed in mammalian expression systems for analysis by mass spectrometry have not been successful. To test the third possibility, we mutated cysteine residues in varying combinations and determined their effects on NLC (Fig. 2 and Table 2). These data show that mutation of more than one cysteine residue in the nontransmembrane regions had no effect on NLC. Thus, the combination of mutations C52S, C124S, and C679S has preserved NLC (namely, no significant changes in Q_{sp} , and z, although there were some significant effects on V_h). In contrast, several combinations of two or more transmembrane cysteine mutations could abolish NLC.

Two opposing transmembrane models for prestin exist for which structural data are of insufficient resolution to choose between (6–8,28). Interestingly, our observations on transmembrane cysteine mutations might help to choose between models, because the 10- and 12-transmembrane models predict potential physical approximations of different cysteine residues, with the implication that they could more likely form disulfide bonds (Fig. 1). An attempt to rationalize our

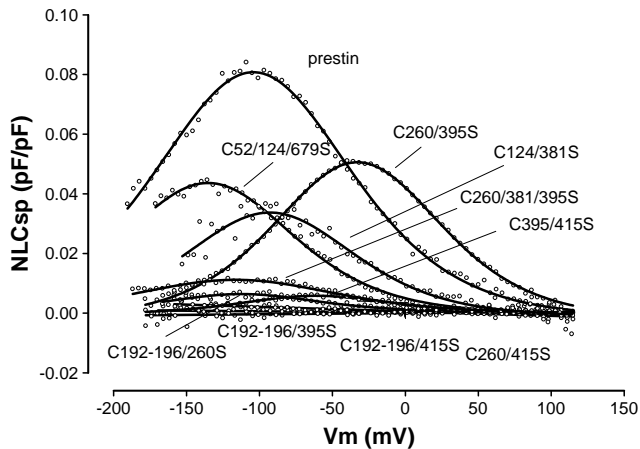


FIGURE 2 Representative NLC traces of wild-type prestin and several combinatorial cysteine mutants. These individual combinations are representative of the variable effects on different aspects of NLC produced by these mutants. Only select combinations were able to markedly reduce NLC (see text and Table 2 for details).

data given the constraints of either model was not definitive, however, and we expect that higher resolution structural studies will be needed to answer this question.

We also used our mutational data to model the formation of disulfide bonds removed from the spatial constraints of the two transmembrane models. Thus, the combinations C260S/C415S and C192S–C196S/C395S that both lost NLC raised the possibility that residue C260 could form a disulfide bond with C192–C196 or C395, and C415 form a second disulfide bond with the remaining cysteine residue (either C192–C196 or C395). To test this hypothesis we made the following combination of mutants: C260S/C395S, C395S/C415S, C192S–C196S/C260S and C192S–196S/C415S. Of these combinations, only the latter abolished NLC. This result is consistent with the possible formation of disulfide bonds between C415 and C395, and separately C192–C196 and C260. However, the preserved NLC in C260S/C395S (and reduced NLC in C192S–C196S/260S, and separately, C395S/C415S) rules out this possibility.

We reasoned that the loss of NLC in prestin mutants could result from inadequate surface expression of the mutated protein, subtle alterations in structure in a protein adequately expressed on the surface of the cell, or a combination thereof. We used a surface biotinylation assay to determine surface expression of prestin in wt prestin and several mutants that showed variation in Q_{sp} . In this procedure, prestin or individual mutants of prestin were expressed transiently in CHO cells, and surface proteins labeled using Sulfo-NHS-SS-Biotin, a cell impermeable cleavable biotinylation reagent. Surface labeled proteins were isolated from the lysed cells and the presence of prestin detected by Western blot (Fig. 3). Wild-type prestin contained dimeric protein and two forms of monomeric protein with the larger form of the monomer dominating. In contrast, all the mutants that had reduced Q_{sp}

showed both monomers with the smaller form dominating in those mutants where Q_{sp} was most decreased. Indeed, in mutants that lacked NLC there was a profound decrease in the larger monomeric form. Moreover, there was a linear relationship between Q_{sp} of individual mutants and their respective ratios of the upper monomeric form to the lower monomeric form (Fig. 3). Both monomers were detected with antibodies to the N-terminus of prestin and after stripping and reprobing with antibodies to the C-terminus of prestin (data not shown), suggesting that the smaller form of the protein was misfolded, not truncated. Importantly, when we used fluorescence activated cell sorting to isolate transfected cells we noted no difference in prestin expression determined by YFP fluorescence between mutants with reduced or absent NLC and wt-prestin (data not shown). Moreover, there were similar levels of prestin expression on the membrane of mutants with reduced NLC (Fig. 3). The remarkable difference in these mutants, as noted above, was that they predominantly expressed the smaller monomer. Together these data suggest a subtle misfolding of the protein, but not inadequate surface expression, as a cause for reduced Q_{sp} in these mutants.

Line scan maps suggest the presence of three dimers (potentially from upper monomer–upper monomer, upper monomer–lower monomer, and lower monomer–lower monomer). However, although there was an impression that the ratio of the three different dimers in the different mutants related to that of the two monomers, the gels had insufficient resolution to consistently separate the different bands with three distinct peaks. We are therefore unable to quantify the expression of different prestin dimers and their relationship to Q_{sp} . This is unfortunate because other work indicates that dimers form the functional motor subunit of the protein (7,29).

Cysteine 192 substitutes for cysteine 196, suggesting the formation of disulfide bonds

The two residues C192 and C196 lie in an α helix and would therefore be predicted to lie in close proximity to one another in 3D space. We therefore hypothesized that C192 could substitute for C196 (and vice-versa) in forming disulfide bonds. NLC in C192S/C395S and C196S/C395S mutants (as pointed out above C192S–C196S/C395S lacked NLC) was assayed. As shown in Fig. 4, mutation of C395S with either C192S or C196S resulted in a recovery in NLC. Similarly, there was recovery of NLC when C381S was mutated with either C192S or C196S; in contrast, C381S/C192S–C196S had severely decreased NLC (Table 2). In keeping with this pattern, two other combinations of mutants (C192S–C196S/C260S and C192S–C196S/C415S) that had reduced or absent NLC, showed recovery in Q_{sp} when mutated with either C192 or C196, alone. Thus C192S/C260S, C196S/C260S, C192S/C415S, C196S/C415S all restored Q_{sp} (Fig. 4). We interpret these data to signify the formation of disulfide bonds by either C192 or C196. C192S–C196S was the only mutant that showed significant

TABLE 2 Mean NLC parameters of the different combinatorial cysteine mutants and number of cells recorded for each mutant

Mutants	NLC parameter			<i>n</i>
	Q_{sp}	V_h	z	
Wild-type prestin	7.88 ± 1.26	-111.30 ± 2.94	0.72 ± 0.01	25
C192/196/395S	0			20
C192/196/415S	0			11
C260/415S	0			18
C381/415S	0			15
C192/196S	1.97 ± 0.22*	-127.58 ± 3.49*	0.60 ± 0.03*	6
C192/196/381S	0.89 ± 0.09*	-123.36 ± 12.48	0.69 ± 0.08	4 (18)
C192/381S	5.11 ± 1.16	-118.12 ± 7.34	0.65 ± 0.04	6
C196/381S	3.49 ± 0.66	-119.37 ± 7.27	0.69 ± 0.04	7
C192/395S	1.98 ± 0.58*	-77.94 ± 9.63 [†]	0.68 ± 0.04	7
C196/395S	3.35 ± 0.73	-90.29 ± 6.01*	0.67 ± 0.04	7
C192/196/260S	1.55 ± 0.32*	-119.20 ± 2.91	0.62 ± 0.04*	6 (16)
C192/260S	3.78 ± 0.58	-107.03 ± 4.15	0.70 ± 0.02	7
C196/260S	4.14 ± 0.75	-119.35 ± 3.26	0.67 ± 0.02	7
C192/415S	1.00 ± 0.26*	-141.90 ± 5.72 [†]	0.63 ± 0.05*	5 (16)
C196/415S	1.24 ± 0.47*	-125.59 ± 8.08	0.63 ± 0.02 [†]	6 (21)
C192/196/124S	1.20 ± 0.24*	-124.29 ± 1.62*	0.66 ± 0.04	6
C381S/C415A	5.78 ± 1.56	-90.24 ± 6.87 [†]	0.76 ± 0.03	6
C395/415S	0.86 ± 0.16*	-56.46 ± 3.36 [†]	0.70 ± 0.02	5 (20)
C395S/C415A	3.67 ± 0.66	-31.99 ± 8.03 [†]	0.62 ± 0.02 [†]	8
C192S/C196S/C415A	1.83 ± 0.46*	-100.06 ± 4.1	0.69 ± 0.04	5
C52/124/679S	5.21 ± 1.38	-136.00 ± 7.28*	0.65 ± 0.02	5
C260/381/395S	1.62 ± 0.20*	-102.85 ± 9.52	0.50 ± 0.02 [†]	7
C260/381S	3.36 ± 0.44	-115.18 ± 7.44	0.64 ± 0.03	6
C260/395S	5.44 ± 1.25	-53.04 ± 4.38 [†]	0.70 ± 0.03	12
C260S/C415A	4.22 ± 0.80	-86.47 ± 5.18 [†]	0.72 ± 0.04	6
C124/260S	6.99 ± 1.20	-110.82 ± 6.12	0.72 ± 0.03	6
C124/381S	3.21 ± 0.75	-115.88 ± 9.27	0.67 ± 0.06	7
C124/395S	6.33 ± 1.54	-66.10 ± 4.59 [†]	0.66 ± 0.03	5

In mutants where the percentage of transfected cells that showed NLC was <90%, the fraction of cells with demonstrable NLC is shown. Values that show statistically significant differences from wild-type prestin are indicated. Because z the estimated charge carried by a single motor is not significantly changed, the reduction in Q_{sp} (representing the total charge carried by all the motors per unit area of membrane) suggests that the total number of functional motors on the surface is reduced.

* $p < 0.05$.

[†] $p < 0.01$.

alteration in Q_{sp} , V_h , and z . Moreover, any combinatorial mutation that included C192S–C196S showed absent or significantly reduced Q_{sp} . These data reinforce our conclusion that either residue C192 or C196 forms a disulfide bond.

Cysteine 415 likely forms a disulfide bond

The only single cysteine mutation that resulted in a significant reduction in Q_{sp} was C415S. In this regard, C415S was similar to the single mutation equivalent of C192S–C196S, and suggested that C415 should be as influential as the C192–C196 pair. As suspected, mutation of C415S in combination with another cysteine residue posited to lie within the transmembrane segments also resulted in a loss or near loss of NLC. These include C192S–C196S/C415S, C260S/C415S, C381S/C415S (abolished NLC), and C395S/C415S (greatly reduced NLC). One possibility was that C415 formed a disulfide bond that was critical in maintaining tertiary structure of the protein important for generating NLC. Alternatively, because disulfide bonded cysteine resi-

dues are sterically constrained by the bond, in contrast to the side chain of an unbonded serine residue, we hypothesized that changes in NLC were because the more freely mobile serine residue interfered with prestin function. To test this possibility we mutated C415 to alanine, which has a shorter side chain and would be predicted to minimally disrupt secondary structure, and tested NLC of this mutant. Additionally, C415A was mutated in combination with each of the following substitutions: C192S–C196S, C260S, C381S, and C395S. The C415A mutant alone or in combination with the other cysteine mutations resulted in significant NLC (Fig. 5). Taken together these data argue that C415 forms a disulfide bond.

Substitution of all nine cysteine residues did not hinder dimerization of the protein

Our data suggest that cysteine residues are important for the generation of NLC. In addition, there is compelling indirect evidence that cysteine residues in prestin form disulfide

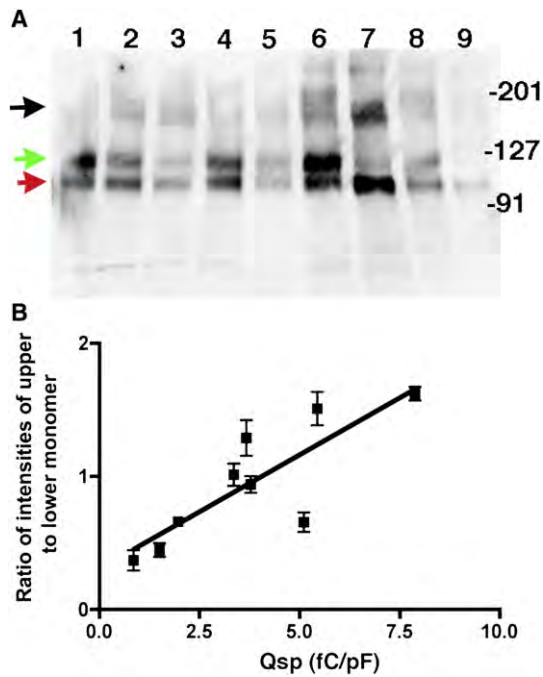


FIGURE 3 Prestin and nonfunctional cysteine mutants of prestin are expressed on the surface of the cell. (A) To ascertain if mutations in cysteine residues allowed surface expression, we assayed prestin expressed on the surface of the cell using a surface biotinylation assay. CHO cells were transiently transfected with prestin-YFP constructs. Plasma membrane proteins in these cells were labeled using the cell impermeable amino reactive agent, Sulfo-NHS-SS-Biotin. Surface proteins were isolated using avidin Sepharose beads and the avidin bound protein released by cleavage with dithiothreitol. The released surface proteins were separated by SDS-PAGE and the presence of prestin detected by Western blots using an antibody to an epitope in prestin's N-terminus (and separately to its C-terminus; data not shown). The total protein loaded on each column was the same. The lanes from left to right along with their respective Q_{sp} values and ratios of upper to lower monomer intensities \pm SE ($n = 3$) are: 1), wt-prestin (7.88 fC/pF; 1.62 ± 0.09); 2), C192S/C381S (5.11 fC/pF; 0.67 ± 0.12); 3), C192S/C196S (1.97 fC/pF, 0.66 ± 0.04); 4), C260S/C381S (3.36 fC/pF, 1.01 ± 0.14); 5), C192S/ C260S (3.78 fC/pF, 0.94 ± 0.1); 6), C260S/C395S (5.44 fC/pF, 1.51 ± 0.22); 7), C395S/C415S (0.86 fC/pF, 0.37 ± 0.13); 8), C395S/C415A (3.67 fC/pF, 1.28 ± 0.23), and 9), C192S/C196S/C260S (1.5 fC/pF, 0.447 ± 0.09). The positions of the molecular weight markers are indicated on the right. As is evident, there are two monomeric forms of prestin-YFP at ~ 120 kD in wild-type prestin and the multiple cysteine mutants, although the relative proportions between the two monomeric forms varied in the different cysteine mutants. The upper functional monomer is indicated by a green arrow, whereas the lower nonfunctional monomer is indicated by the red arrow. Prestin dimers shown in black (at ~ 250 kD) were present in all the mutants. Furthermore, the total amount of prestin monomers and dimers on the surface of the cell were similar, suggesting that there were no deficiencies in trafficking to the surface. (B) Plot of the relationship between Q_{sp} of individual mutants and the ratio between the upper and lower monomers. The intensities of the different bands were quantified using a BioRad ChemiDoc XRS imaging system. The ratios represent the average of three experiments.

bonds. Given the importance of multimerization in prestin function (7), we then sought to determine if any of these cysteine residues were important in multimerization of the protein. Work by Zheng et al. (25) showed that the addition

of the hydrophobic reducing agent EDT resulted in a reduction in the amount of dimeric prestin relative to its monomeric form. Data hitherto mutating several cysteine residues in combination had no effect on dimerization (Fig. 3). We also assayed dimerization in prestin-YFP in which all nine cysteine residues were mutated to serine (ALL9). Cell lysates from this mutant and from wt-prestin-YFP were separated by SDS-PAGE. Prestin was detected by Western blotting using an antibody to its N terminus (Fig. 6). Two features of the mutant were evident. First, dimers of prestin were evident in both wt-prestin as well as prestin in which all nine cysteine residues were mutated. Second, removal of all nine cysteine residues resulted in a notable apparent reduction in molecular weight of prestin monomers (and dimers). Because disulfide bonds were not necessary for prestin dimerization we then separated the protein using Urea-SDS gels, attempting to disrupt potential hydrophobic interactions between monomers of the protein. As is evident in Fig. 6 this approach also failed to disrupt dimer formation. Unexpectedly, monomers of prestin were seen to separate into several closely interspersed discrete bands. These bands were detected on Western blots using antibodies to the N-terminus of prestin, and after stripping and reprobing with antibodies to YFP (because YFP was fused to the C-terminus of prestin), suggesting that the smaller forms of prestin were not due to significant proteolytic cleavage (data not shown). Finally, we note that higher multimers of prestin are likely not detected because we did not boil our preparations before running gels.

DISCUSSION

Prestin is a protein that underlies cochlea amplification, in turn responsible for the high sensitivity of mammalian hearing (2,4). It is an anion transporter (SLC26a5) that is voltage-dependent, as well (14). Intrinsic charged residues are displaced during membrane voltage perturbations to effect conformational changes that drive a robust somatic motility that provides a boost in signal to the sensory inner hair cells within the cochlea (16,31). We showed previously that monomer interactions determined by FRET were required for normal voltage sensing, because very short truncations of the N-terminus, but not the C-terminus, abolished FRET and NLC, the electrical signature of OHC electromotility (7). Additionally, sulfhydryl reagents have been shown to significantly alter NLC and mechanical activity in native OHCs (21,22). These data raised the possibility that voltage sensing and multimerization in prestin require disulfide bond formation.

Combinatorial cysteine substitutions reveal critical residues for voltage sensing and are likely involved in disulfide bond formation

We have attempted to discern the role of cysteine residues in prestin by mutating these residues both individually and in

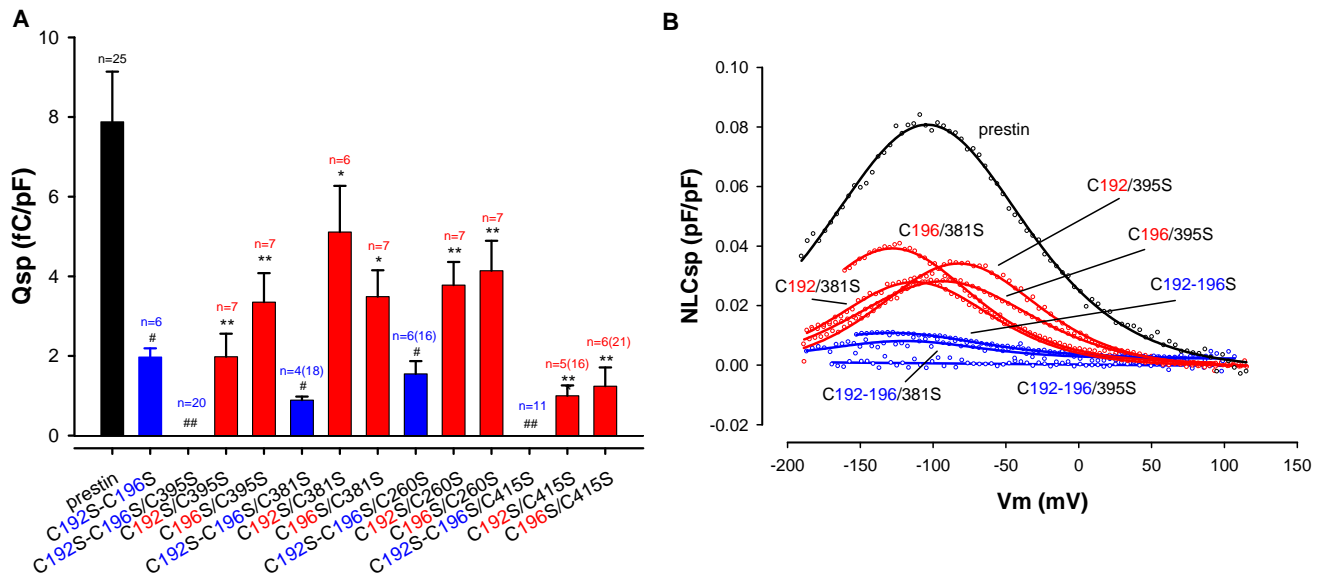


FIGURE 4 C192 and/or C196 play a key role in generating NLC. (A) Q_{sp} values of C192S–C196S related mutants are shown. Mutating C192S–C196S together markedly decreases Q_{sp} compared to control. Moreover, mutating them in combination with other transmembrane cysteine to serine residues reduces Q_{sp} even further (blue). Separate back mutation, either S192C or S196C (red), recovers Q_{sp} , suggesting that C192 and C196 are able to compensate for each other. For instance, C192S–C196S/C395S and C192S–C196S/C415S (blue) fully abolish NLC. Nevertheless, C395S (or C415S) in combination with either C192S or C196S alone (red) partially recovers Q_{sp} . Similar patterns were found in C260S combined with C192S and/or C196S, and C381S combined with C192S and/or C196S, although C192S–C196S/C260S and C192S–C196S/C381S decrease (but do not abolish) Q_{sp} . Reduction of Q_{sp} in these C192S–C196S mutants were statistically significantly different from wild-type prestin ($^{\#}p < 0.05$; $^{\#\#}p < 0.01$). Similarly, recovery of Q_{sp} with back mutation of either S192C or S196C alone was also statistically significant ($^*p < 0.05$; $^{**}p < 0.01$). n is number of cells that evidenced NLC and were used for statistics; parentheses enclose the total number of cells recorded. (B) Representative NLC traces from wild-type prestin and mutants.

combination, and then determining their effects on NLC. Earlier work had shown that individual mutations only slightly affected measures of NLC, in line with our results. However, Zheng et al. (25) raised the possibility that disulfide bonds between cysteine residues in the transmembrane domains were important for oligomer formation. Disulfide bond prediction programs, which use a host of algorithms, largely predict an absence of cysteine bonding (A. Surguchev and D. S. Navaratnam, unpublished observation). However, two caveats apply to these programs; they are based largely on soluble proteins, and a number of them rely on empirically established cysteine residue interactions in homologous proteins (17). Thus, the use of these algorithms for prestin analysis is limited, because six of the nine cysteine residues reside in predicted hydrophobic transmembrane regions. Moreover, there is scarce literature on cysteine residue interactions in prestin homologs.

Our data provide indirect evidence that residues C415 and either C192 or C196 are involved in disulfide bond formation. Our reasoning for imputing the formation of disulfide bonds for each differs. In the case of C192–C196, the formation of disulfide bonds by one of these residues is indicated by the two residues being able to substitute for one another. In the case of C415, bond formation is indicated based on the ability of alanine substitution to rescue effects produced by C415S. We hypothesize that the unconstrained side chain of the serine residue interferes with prestin function.

In contrast, the naturally occurring cysteine residue, with an identical side chain length, is disulfide bonded and therefore sterically constrained. We reason that this sterically constrained side chain is unable to interfere with NLC. Similarly, we reason that the shortened side chain in C415A is incapable of interfering with prestin function.

It might be argued that differences in hydrophobicity of alanine, cysteine, and serine, rather than disulfide bond formation promote NLC generation. However, it is not clear that hydrophobicity differences between cysteine and the two substitutes are significant. In fact, the differences between the hydrophobicity of serine, cysteine, and alanine are small (32). Of the >30 tabulations of hydrophobicity the placement of these residues by relative hydrophobicity are interchangeable. In part, this is because cysteine residues form disulfide bonds and are prone to lie on the internal surface of the protein. Some tabulations use position of the residue on 3D structure as a measure of hydrophobicity. However, others that use only the physical/chemical properties of the amino acid find it to be less hydrophobic. Furthermore, the relevance of an amino acid’s hydrophobicity to structure is questionable (33). To reiterate, we suggest that disulfide bond formation constrains C415 and allows for NLC generation.

An obvious pairing would be for C415 to form a disulfide bond with C192 or C196. However, individual mutations of these residues do not produce mirror effects on measures of

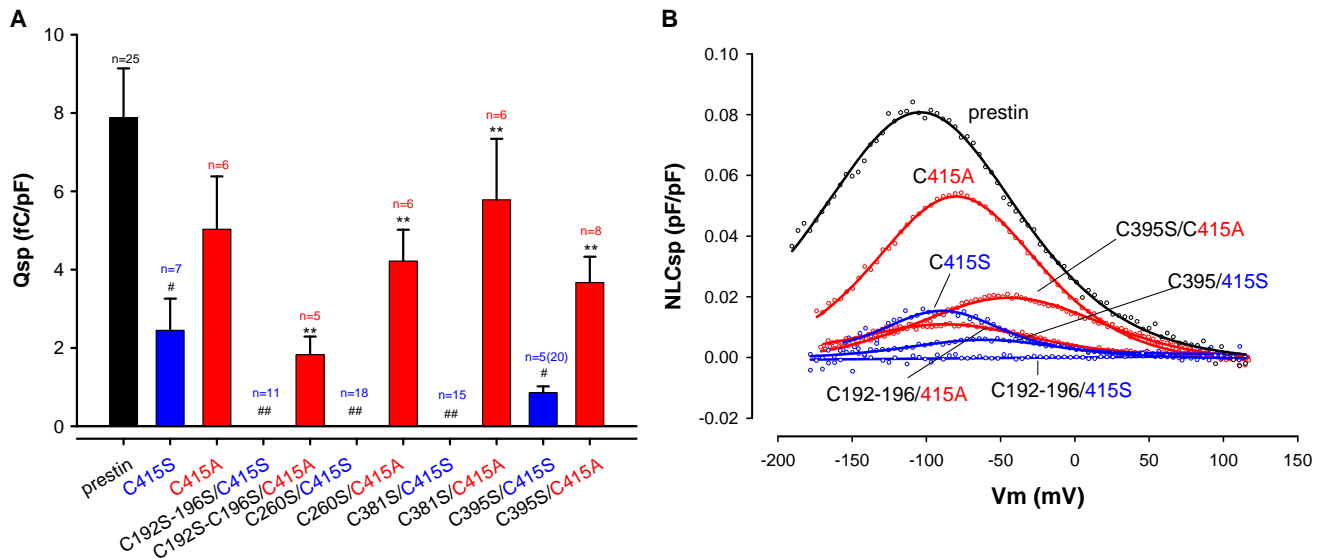


FIGURE 5 C415S plays a key role in generating NLC. (A) Q_{sp} values of C415S related mutants are shown. C415S (blue) alone markedly decreases Q_{sp} . In addition, C415S in combination with other transmembrane cysteine mutants reduces Q_{sp} even further. In contrast, the back mutation C415A alone or in combination with other cysteine mutants evidenced recovery of Q_{sp} (red). Thus, C192S–C196S/C415S, C260S/C415S, and C381S/C415S completely eliminate NLC, and C395S/C415S markedly reduced NLC. In contrast, C192S–C196S/C415A, C260S/C415A, C381S/C415A, and C395S/C415A all showed significantly improved or recovered Q_{sp} . Residue side chain length and spatial constraint may underlie these differences (see text for details). Q_{sp} in C415S mutants was statistically significantly different from wild-type prestin ($^{\#}p < 0.05$; $^{\#\#}p < 0.01$). Similarly, recovery of Q_{sp} with back mutation of S415A was statistically significant ($*p < 0.05$; $**p < 0.01$). n is number of cells that evidenced NLC and were used for statistics; parentheses enclose the total number of cells recorded. (B) Representative NLC traces from wild-type prestin and mutants.

NLC (V_h , Q_{sp} , and z), as might be expected. The reason for this could be due to C192 substituting for C196, with mutation of both residues (C192 and C196) producing additional effects on measures of NLC. Should there be formation of disulfide bonds between C415 and C192 or C196, we would anticipate a physical approximation of the two residues, a feature not especially obvious in the current transmembrane models of the protein. Other data indicate that a disulfide bond between C415 and C192 (or C196) is unlikely. For instance, Q_{sp} was significantly decreased when C415S (or C192S–C196S) was combined with other transmembrane cysteine residues, but not when combined with nontransmembrane cysteine residues (C52S, C124S, and C679S). Thus, given that intra membranous disulfide bonds are formed in these cases, the occurrence of a bond between C415 and C192 or C196 is unfeasible.

Evolutionarily new cysteine residues are among those residues critical for NLC generation

Of the nine cysteine residues four, C52, C381, C395, and C679, are conserved between nonmammalian vertebrates and eutherian mammals (34). In contrast, cysteines in positions 124, 192, 196, 260, and 415 are not conserved. Cysteine residues could be important for determining electromotility, a feature of mammalian prestin but not its nonmammalian counterparts (35,36). It could be reasoned that these nonconserved, and evolutionarily newly acquired,

cysteine residues would be more important than cysteine residues that are conserved between prestin from mammals and nonmammalian vertebrates. It is interesting that both C415 and C192–C196 are not found in prestin from nonmammalian vertebrates, reinforcing the view that these newly acquired cysteine residues are important for the structural features in prestin responsible for generating characteristics of gating charge movement that underlie electromotility. The data suggesting that these residues are involved in disulfide bond formation lead us to predict that these disulfide bonds are structural (instead of allosteric or catalytic disulfide bonds). The increased amounts of misfolded protein on the surface of the cell where these cysteines have been modified corroborate this prediction. It should be noted that the removal of cysteines does not predicate misfolding of the protein but rather increases the probability of misfolding suggested by a fraction of wt-prestin that is also misfolded (albeit to a smaller degree).

Alterations in Q_{sp} produced by different cysteine mutants is due to subtle alteration in folding and not due to reduced surface expression

The effects of cysteine mutations on prestin could be due to inadequate surface expression, changes in tertiary/quaternary structure or a combination of the two. There was no relationship between transfection and expression efficiencies of the different mutants and its effects on Q_{sp} . Both the expression

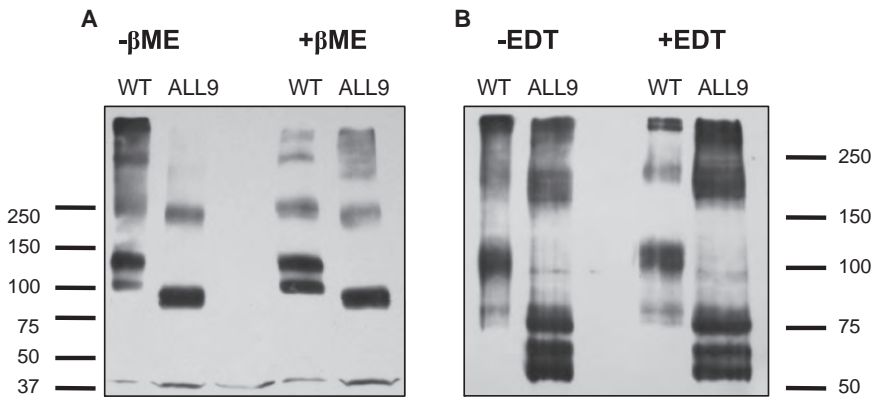


FIGURE 6 Prestin dimerization does not require cysteine residues. Cell lysates of CHO cells transiently transfected with prestin-YFP or prestin-YFP where all nine cysteine residues were mutated to serine (ALL9) were separated by SDS-PAGE and prestin was detected by Western blotting using an antibody to its N-terminus. The position of molecular weight markers is shown. (A) The absence of all nine cysteine residues does not influence the formation of prestin dimers (~250 kD) in lysates separated by standard SDS-PAGE in the presence or absence of 5% β -mercaptoethanol. Prestin monomers and dimers were apparently smaller in the ALL9 cysteine mutants. (B) Separation on SDS-PAGE gels containing 6 M urea before Western blotting did not alter the identification of dimers. Prestin dimers in both wild-type

prestins and ALL9 mutants were still detectable in the presence of 6 M urea (and 600 mM EDT), signifying that the formation of dimers did not require disulfide bonds and resulted from strong hydrophobic bonds. Moreover, the smaller prestin monomers and dimers in the ALL9 mutant were resolved into several discrete bands. These bands were also detected after stripping and reprobing the blots with antibodies to tagged YFP (data not shown) indicating that altered folding rather than proteolytic cleavage was responsible for the observed difference in molecular weight between prestin and the ALL9 mutant.

of YFP tagged protein in the cell determined by fluorescent activated cell sorting and the total expression of prestin on the surface of the cell determined by surface biotinylation had no relationship to Q_{sp} , the electrophysiological measure of functional prestin on the surface of the cell. Rather, a linear correlation between the ratio of the upper monomer to lower monomer and Q_{sp} suggests that the cell expresses a functional monomer and that Q_{sp} is a measure of this functional monomer. Why does the ratio of upper to lower monomer correlate with Q_{sp} ? We reason that the misfolded lower band interferes with prestin function, in a dominant negative manner, possibly during dimerization of the two forms. In this way, the absolute amount of upper band monomer may not necessarily correlate with prestin function.

Although it is known that SLC26A3 can be cleaved at its N-terminus to produce two bands detectable with C-terminal antibodies on Western blotting (17), we conclude that the observed differences in prestin monomers are due to changes in folding because the two monomers are detected with antibodies to both the N- and C-terminus of prestin. An alternate possibility that the lower molecular form represents a nonglycosylated protein is unlikely. For one, both forms of the protein would have been exposed to the glycosylation machinery before insertion into the plasma membrane. For another, prior experiments have shown absent glycosylation of prestin in CHO cells (7). Moreover, removal of glycosylation results in a functional protein. Importantly, these data question the use of prestin surface expression determined by fluorescence as a measure of adequate surface delivery, as has been done by many groups including ours. Our data suggest an alternative and more accurate test—adequate surface delivery of properly folded protein. Conversely, we believe the data in this study substantiate the idea that Q_{sp} , in the absence of significant changes in z , to be a good measure of functional protein on the surface of the cell.

Dimer formation is a result of strong van der Waals forces and does not require disulfide bonds

Previous experiments by Zheng et al. (25) suggested that disulfide bonds were important in the formation of prestin dimers. However, the formation of prestin dimers in the absence of all nine cysteine residues leads us to conclude that disulfide bonds are not essential for the formation of prestin dimers, in line with another recent study (29). The presence of prestin dimers in multiple cysteine mutations involving different cysteine residues further validates our reasoning. We think it unlikely the alternative explanation that mutation of all nine cysteines resulted in a misfolding of the protein that then led to dimerization of this misfolded protein through interactions of novel exposed hydrophobic surfaces. On the other hand, although not essential for dimer formation, we are unable to confirm if disulfide bonds contribute to prestin dimer maintenance. For instance, disulfide bonds stabilize dimers in the enzyme acetylcholinesterase, but are not required for their formation (37). In any case, the presence of dimers in 6 M urea in mutants lacking all nine cysteine residues implies very strong hydrophobic interactions between prestin monomers. In the absence of evidence showing intermolecular disulfide bond formation in prestin, we posit that cysteine residues are constrained by intramolecular disulfide bonds that are important for normal voltage sensing and mechanical activity in prestin.

This work was supported by the National Institute on Deafness and Other Communication Disorders (DC007894 to D.S.N., DC00273 to J.S.S., and DC0008130 to D.S.N. and J.S.S.).

REFERENCES

1. Zheng, J., L. D. Madison, ..., P. Dallos. 2002. Prestin, the motor protein of outer hair cells. *Audiol. Neurootol.* 7:9–12.

2. Dallos, P., X. Wu, ..., J. Zuo. 2008. Prestin-based outer hair cell motility is necessary for mammalian cochlear amplification. *Neuron*. 58:333–339.
3. Liberman, M. C., J. Gao, ..., J. Zuo. 2002. Prestin is required for electromotility of the outer hair cell and for the cochlear amplifier. *Nature*. 419:300–304.
4. Santos-Sacchi, J., L. Song, ..., A. L. Nuttall. 2006. Control of mammalian cochlear amplification by chloride anions. *J. Neurosci*. 26:3992–3998.
5. Brownell, W. E., C. R. Bader, ..., Y. de Ribaupierre. 1985. Evoked mechanical responses of isolated cochlear outer hair cells. *Science*. 227:194–196.
6. Zheng, J., K. B. Long, ..., P. Dallos. 2001. Prestin topology: localization of protein epitopes in relation to the plasma membrane. *Neuroreport*. 12:1929–1935.
7. Navaratnam, D., J. P. Bai, ..., J. Santos-Sacchi. 2005. N-terminal-mediated homomultimerization of prestin, the outer hair cell motor protein. *Biophys. J.* 89:3345–3352.
8. Deak, L., J. Zheng, ..., P. Dallos. 2005. Effects of cyclic nucleotides on the function of prestin. *J. Physiol.* 563:483–496.
9. Ludwig, J., D. Oliver, ..., B. Fakler. 2001. Reciprocal electromechanical properties of rat prestin: The motor molecule from rat outer hair cells. *Proc. Natl. Acad. Sci. USA*. 98:4178–4183.
10. Gale, J. E., and J. F. Ashmore. 1994. Charge displacement induced by rapid stretch in the basolateral membrane of the guinea-pig outer hair cell. *Proc. R. Soc. Lond. B. Biol. Sci.* 255:243–249.
11. Kakehata, S., and J. Santos-Sacchi. 1995. Membrane tension directly shifts voltage dependence of outer hair cell motility and associated gating charge. *Biophys. J.* 68:2190–2197.
12. Iwasa, K. H. 2001. A two-state piezoelectric model for outer hair cell motility. *Biophys. J.* 81:2495–2506.
13. Iwasa, K. H. 1993. Effect of stress on the membrane capacitance of the auditory outer hair cell. *Biophys. J.* 65:492–498.
14. Bai, J. P., A. Surguchev, ..., D. Navaratnam. 2009. Prestin's anion transport and voltage-sensing capabilities are independent. *Biophys. J.* 96:3179–3186.
15. Ashmore, J. F. 1989. Transducer motor coupling in cochlear outer hair cells. In *Mechanics of Hearing*. D. Kemp and J. P. Wilson, editors. Plenum Press, New York. 107–113.
16. Santos-Sacchi, J. 1991. Reversible inhibition of voltage-dependent outer hair cell motility and capacitance. *J. Neurosci.* 11:3096–3110.
17. Singh, R. 2008. A review of algorithmic techniques for disulfide-bond determination. *Brief. Funct. Genomic. Proteomic.* 7:157–172.
18. Wedemeyer, W. J., E. Welker, ..., H. A. Scheraga. 2000. Disulfide bonds and protein folding. *Biochemistry*. 39:4207–4216.
19. Hogg, P. J. 2003. Disulfide bonds as switches for protein function. *Trends Biochem. Sci.* 28:210–214.
20. Dorn, M., M. Weiwad, ..., E. Bosse-Doenecke. 2009. Identification of a disulfide bridge essential for transport function of the human proton-coupled amino acid transporter hPAT1. *J. Biol. Chem.* 284:22123–22132.
21. Santos-Sacchi, J., and M. Wu. 2004. Protein- and lipid-reactive agents alter outer hair cell lateral membrane motor charge movement. *J. Membr. Biol.* 200:83–92.
22. Kalinec, F., and B. Kachar. 1993. Inhibition of outer hair cell electromotility by sulfhydryl specific reagents. *Neurosci. Lett.* 157:231–234.
23. McGuire, R., F. Pereira, and R. M. Raphael. 2008. Effects of cysteine mutations on prestin function and oligomerization. *Assoc. Res. Otolaryngol. Abs.* 675.
24. McGuire, R., F. Pereira, and R. M. Raphael. 2007. Modulation of prestin function due to cysteine point mutations. *Assoc. Res. Otolaryngol. Abs.* 1039.
25. Zheng, J., G. G. Du, ..., M. Cheatham. 2006. Analysis of the oligomeric structure of the motor protein prestin. *J. Biol. Chem.* 281:19916–19924.
26. Santos-Sacchi, J. 2004. Determination of cell capacitance using the exact empirical solution of dY/dCm and its phase angle. *Biophys. J.* 87:714–727.
27. Santos-Sacchi, J., S. Kakehata, and S. Takahashi. 1998. Effects of membrane potential on the voltage dependence of motility-related charge in outer hair cells of the guinea-pig. *J. Physiol.* 510:225–235.
28. Mio, K., Y. Kubo, ..., C. Sato. 2008. The motor protein prestin is a bullet-shaped molecule with inner cavities. *J. Biol. Chem.* 283:1137–1145.
29. Detro-Dassen, S., M. Schanzler, ..., C. Fahlke. 2008. Conserved dimeric subunit stoichiometry of SLC26 multifunctional anion exchangers. *J. Biol. Chem.* 283:4177–4188.
30. Reference deleted in proof.
31. Ashmore, J. F. 1990. Forward and reverse transduction in the mammalian cochlea. *Neurosci. Res. Suppl.* 12:S39–S50.
32. Wolfenden, R., L. Andersson, ..., C. C. Southgate. 1981. Affinities of amino acid side chains for solvent water. *Biochemistry*. 20:849–855.
33. Charton, M., and B. I. Charton. 1982. The structural dependence of amino acid hydrophobicity parameters. *J. Theor. Biol.* 99:629–644.
34. Okoruwa, O. E., M. D. Weston, ..., K. W. Beisel. 2008. Evolutionary insights into the unique electromotility motor of mammalian outer hair cells. *Evol. Dev.* 10:300–315.
35. He, D. Z., K. W. Beisel, ..., R. Salvi. 2003. Chick hair cells do not exhibit voltage-dependent somatic motility. *J. Physiol.* 546:511–520.
36. Albert, J. T., H. Winter, ..., D. Oliver. 2007. Voltage-sensitive prestin orthologue expressed in zebrafish hair cells. *J. Physiol.* 580:451–461.
37. Bon, S., F. Coussen, and J. Massoulié. 1997. Quaternary associations of acetylcholinesterase. II. The polyproline attachment domain of the collagen tail. *J. Biol. Chem.* 272:3016–3021.

SCIENTIFIC REPORTS



OPEN

Current carried by the Slc26 family member prestin does not flow through the transporter pathway

Jun-Ping Bai¹, Iman Moeini-Naghani¹, Sheng Zhong², Fang-Yong Li³, Shumin Bian¹, Fred J. Sigworth⁴, Joseph Santos-Sacchi^{2,4,5} & Dhasakumar Navaratnam^{1,2,5}

Received: 04 November 2016

Accepted: 21 March 2017

Published: 19 April 2017

Prestin in the lateral membrane of outer hair cells, is responsible for electromotility (EM) and a corresponding nonlinear capacitance (NLC). Prestin's voltage sensitivity is influenced by intracellular chloride. A regulator of intracellular chloride is a stretch-sensitive, non-selective conductance within the lateral membrane, G_{metL} . We determine that prestin itself possesses a stretch-sensitive, non-selective conductance that is largest in the presence of thiocyanate ions. This conductance is independent of the anion transporter mechanism. Prestin has been modeled, based on structural data from related anion transporters (SLC26Dg and UraA), to have a 7 + 7 inverted repeat structure with anion transport initiated by chloride binding at the intracellular cleft. Mutation of residues that bind intracellular chloride, and salicylate treatment which prevents chloride binding, have no effect on thiocyanate conductance. In contrast, other mutations reduce the conductance while preserving NLC. When superimposed on prestin's structure, the location of these mutations indicates that the ion permeation pathway lies between the core and gate ring of helices, distinct from the transporter pathway. The uncoupled current is reminiscent of an omega current in voltage-gated ion channels. We suggest that prestin itself is the main regulator of intracellular chloride concentration via a route distinct from its transporter pathway.

Outer hair cell (OHC) electromotility is at the heart of cochlear amplification, a mechanism responsible for the mammal's ability to hear sounds of extremely low intensity^{1,2}. Prestin is a member of the SLC26 anion transporter family that now includes 10 members, and was initially identified in a search for the OHC lateral membrane motor³⁻⁵. Subsequent experiments have confirmed that prestin (SLC26a5) is required for electromotility and has all the properties including electromotility (EM) and non-linear capacitance (NLC) of the voltage-driven motor in OHCs⁶⁻⁹, expanding and contracting up to several thousand Hz¹⁰. Recent modeling and experimental data have established that it most likely has a structure similar to the distantly related bacterial uracil transporter UraA^{11,12}, and this is now corroborated by the crystal structure of the more closely related bacterial homologue SLC26Dg¹³. This modeling experiment, that shows prestin with a 7 + 7 inverted repeat structure, supersedes previous models suggesting similarity of the SLC26 family to the ClC bacterial chloride transporter/ion channel family^{12,14,15}.

Intracellular chloride anions play a critical role in prestin's function¹⁶, setting, in an allosteric-like manner, its operating voltage range and affecting transition rates between expanded and contracted states^{17,18}. How intracellular chloride levels are regulated in OHCs remains largely unknown. A dominant stretch-sensitive, non-selective conductance, G_{metL} , has been observed in the lateral membrane of OHCs, and awaits molecular identification¹⁹. An obvious candidate would be prestin itself, although its ability to transport anions has been controversial. An initial model suggested a complete absence of transmembrane ion flux; instead, chloride movement in a truncated cycle of transport was hypothesized to act as the protein's voltage sensor¹⁶. Many subsequent observations have challenged this hypothesis^{17,19-24}. Additionally, experiments have shown formate and oxalate uptake based on isotopic flux²⁰ (although one report failed to do so²⁵), and $\text{HCO}_3^-/\text{Cl}^-$ exchange at a 2:1 ratio generating small

¹Dept. of Neurology, Yale School of Medicine, 333 Cedar Street, New Haven, CT, 06510 USA. ²Dept. of Surgery, Yale School of Medicine, 333 Cedar Street, New Haven, CT, 06510 USA. ³Yale Center for Analytical Sciences, Yale School of Public Health, 300 George St., Ste Suite 555, New Haven, CT 06511, USA. ⁴Dept. of Cellular and Molecular Physiology, Yale School of Medicine, 333 Cedar Street, New Haven, CT, 06510, USA. ⁵Dept. of Neuroscience, Yale School of Medicine, 333 Cedar Street, New Haven, CT, 06510, USA. Correspondence and requests for materials should be addressed to D.N. (email: Dhasakumar.Navaratnam@Yale.Edu)

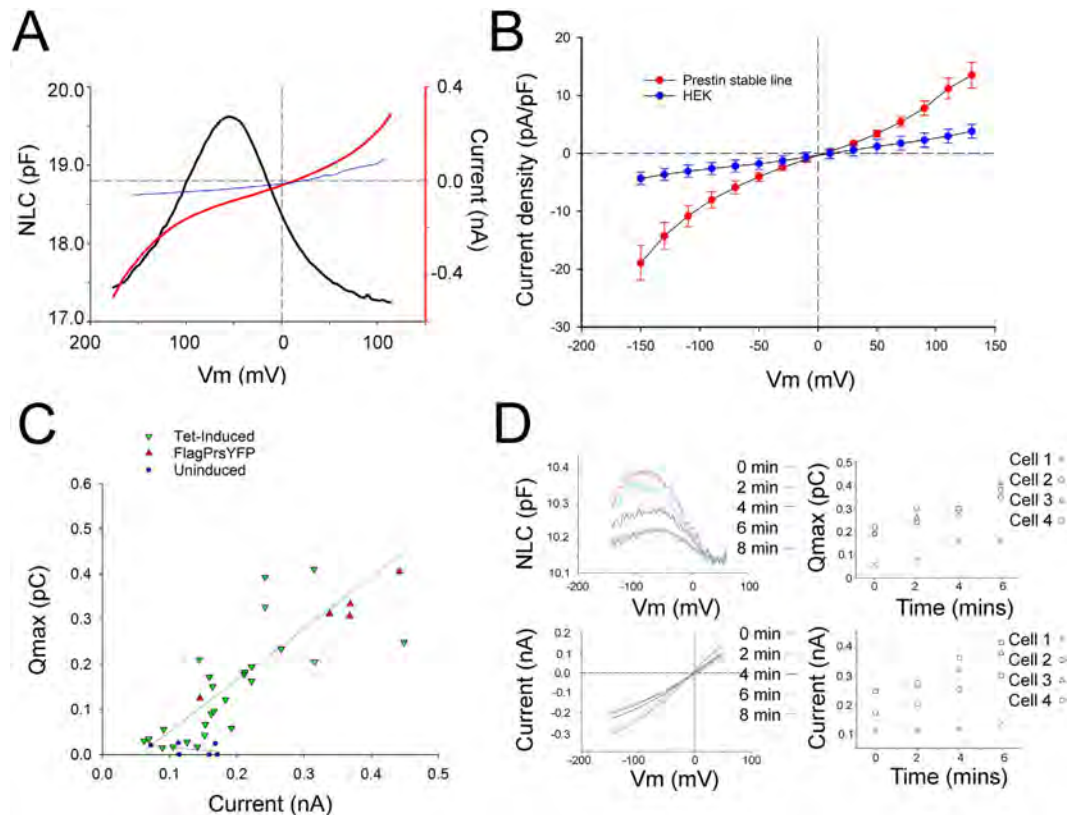


Figure 1. Prestin expression induces a current. (A) Voltage dependence of gating charge (NLC) and current, recorded in the presence of Cl⁻ after tetracycline induction of prestin expression in a HEK cell. There is a large non-linear capacitance (left axis, with a Q_{\max} of 302 fC, z of 0.81e) accompanied by a voltage dependent current (right axis, current, in red, of 0.64 nA for voltage range of -160 mV to 110 mV. In blue is the current of a control cell). (B) I-V relationship of average currents of cells after tetracycline induced prestin expression ($n = 16$) is compared to native HEK cells ($n = 10$). Prestin expression is associated with a significant increase in voltage dependent current ($p < 0.001$, mixed model analysis for correlated measures). Pipette solution contained 100 mM KCl, 20 mM TEACl, 20 mM CsCl, 2 mM CoCl₂, 2 mM MgCl₂, 5 mM Hepes, pH 7.2 and the bath solution contained 100 mM NaCl, 20 mM CsCl, 5 mM EGTA, 2 mM MgCl₂, 10 mM Hepes, pH 7.2. Error bars are standard error. (C) There is a linear relationship between size of prestin induced currents and NLC. The difference in current at 110 mV and -150 mV is plotted against total charge movement (Q_{\max}) of individual cells. Green triangles are cells after tetracycline induction ($n = 27$), red triangles are from cells stably expressing high levels of prestin ($n = 5$) and circles are currents from untransfected HEK cells ($n = 6$). The line represents a simple linear regression in tetracycline induced cells ($R = 0.78$, $n = 27$). (D) Increased surface expression of prestin after Golgi release is temporally associated with an increase in current. Inducible cell lines were maintained at 22 °C for 24 hours to allow accumulation of prestin in the Golgi immediately after tetracycline induction. Cells were then continuously recorded using a two-sine protocol and the bath temperature raised to 37 °C. There is increasing prestin expression on the surface of the cell evidenced by time dependent increase in NLC (upper left, single cell; upper right, four cells) that is correlated with increasing currents (lower left, single cell; lower right, four cells).

transporter currents²⁶. Interestingly, large currents associated with prestin expression arise in the presence of the pseudohalide thiocyanate, similar to uncoupled currents in SLC26a6 and SLC26a3^{14,15,27}. In this paper we show that prestin itself has a tension-sensitive, non-selective leakage conductance similar to G_{metl} that operates independently of its putative transporter pathway.

Results

Schänzler and Fahlke²⁷ demonstrated an uncoupled conductance for SCN⁻ ions that correlates with the expression of prestin. We find that expression of prestin induces currents in the absence of SCN⁻, as well. In the presence of Cl⁻, we observed a current in tet-inducible, prestin expressing HEK cells²⁸, which is significantly larger than currents in untransfected or uninduced HEK cells (Fig. 1A,B). The current, several hundred pA per cell in symmetrical chloride solutions, shows a non-linear voltage dependence, similar to the non-selective current (I_{metl}) observed within the lateral membrane of OHCs²⁹. The size of the current correlates with the magnitude of prestin-associated, voltage-dependent NLC, the electrical signature of OHC mechanical activity, indicating that the current is associated with prestin successfully expressed on the surface of the HEK cell (Fig. 1C). Further evidence that prestin carries this current is shown by the parallel increases of current and NLC magnitudes upon

delivery of prestin to the plasma membrane after release of low-temperature Golgi block (Fig. 1D)³⁰. This effect was clearly demonstrated in 8 cells (four cells are shown in Fig. 1D).

Absence of ion selectivity of the conductance was shown by substitution of anions and cations in both the intracellular and extracellular solutions; no substitutions resulted in clear change in the size of these currents, except for the large cation NMDG⁺ (Fig. 2A, B). Moreover, there was no change in the I-V relationships (Fig. 2A, B). The anion substitution data also suggest that the current was uncoupled: extracellular substitution of Cl⁻ with the anion malate did not affect the size of the current or its reversal potential (Fig. 2A). A similar effect was seen with oxalate, IO₃⁻, and methanesulfonate (data not shown). Each of these ion replacements is known to cause a shift of up to 50 mV in the NLC voltage operating range¹⁷. Similarly, substitutions of intracellular and extracellular K⁺ and Na⁺ with other ions (Na⁺, K⁺ or Tris⁺) did not affect the size of the current or its reversal potential (Fig. 2B). In contrast, when extracellular Na⁺ was replaced with NMDG⁺, we note a significant decrease in the size of the current (Fig. 2B). NMDG⁺ substitution affected both outward and inward currents, as might be expected from a pore-block mechanism. Further confirming the non-selective nature of the conductance, we observed a decrease in the size of the current at both depolarizing and hyperpolarizing voltages when extracellular KCl was decreased from 140 to 14 mM (the pipette solution contained 140 mM KCl, setting the intracellular concentrations) while 300 mOsm extracellular osmolarity was maintained with sucrose. The reversal potential shifted by -15 mV + /- 2 mV with 14 mM extracellular KCl, and is consistent with a calculated permeability ratio of 0.45 for Cl⁻ relative to K⁺ (2C,D). Consistent with the current being carried by a non-selective "open pore", we note that cells expressing prestin show significant depolarization, relative to controls, in resting membrane potential, determined immediately after establishing the whole cell configuration under current clamp (Fig. 2E).

Similar to the Schänzler and Fahlke observation²⁷, we find larger uncoupled currents (nA magnitude) in prestin-expressing cells in the presence of thiocyanate (Fig. 2F), also akin to the effect observed in Slc26a3 and Slc26a6^{14,15,27}. As expected for a current predominantly carried by SCN⁻, the current was directed outward with extracellular thiocyanate and inward with intracellular thiocyanate. The reversal potential with extracellular SCN⁻ (in millimolar: 100 SCN⁻ and 44 Cl⁻ in the bath; 122 Cl⁻ in the pipette with Na⁺ as the counterion in the pipette and bath solutions), was -29 ± 2 mV. We calculate a permeability ratio of 0.27 for Na⁺ and 0.11 for Cl⁻ relative to SCN⁻. These permeability ratios are underestimates, and most probably they are discordant due to the background conductances that are also seen in control HEK cells (Fig. 2).

In the presence of thiocyanate, voltage step-induced currents were instantaneous in onset and showed no deactivation (Fig. 2F, inset). We observe a similar instantaneous onset with no deactivation with Cl⁻ substitution (data not shown). The shape of the I-V relationship is similar to that observed with Cl⁻ as the dominant intra and extracellular anion, with increasing slope upon both depolarization and hyperpolarization. This I-V relationship would be expected from a channel having a large central energy barrier and whose currents are sufficiently small to exclude diffusion limitation. A symmetrical, single-barrier channel model, which yields a hyperbolic sine I-V relationship, fits the data well (Fig. 3) but with a reduced voltage dependence, obtained by setting the valence to 0.75 instead of unity. This effect could arise from a broadened central barrier, or from the presence of barriers at slightly different locations for different ion species and polarities. According to the fitted model with external SCN⁻ and internal Cl⁻ the ratio of permeabilities $P \approx 6$.

As shown in Figs 2 and 4, a similar but smaller whole-cell current was observed when cyanate replaced thiocyanate. These anion substitutions were notable for effects on the Boltzmann parameter V_h of NLC: while small shifts in V_h were noted when switching from chloride to thiocyanate, much larger effects on V_h were found with cyanate; on the other hand, significant effects on Qmax were found with both anions (Fig. 4B, Table 1).

Notably, currents in the presence of thiocyanate and extracellular Cl⁻ were unaffected by application of salicylate that, however, eliminated NLC (Fig. 4C,D, and Supplementary Figure 1). These data argue against a transporter mechanism as the origin of the current since salicylate binds to the intracellular Cl⁻ binding site and has been shown to reduce transporter currents³¹ and inhibit NLC^{32,33}. Consistent with this observation, the use of 1 mM DIDS, the well-established blocker of anion transport³⁴⁻³⁶, did not affect the size of these currents in the presence of thiocyanate, nor did it affect NLC (Fig. 4C,D). Application of membrane tension by exposing the cell to a fluid jet of extracellular solution resulted in a decrease in the size of the current in the presence of thiocyanate and an increase in the size of the current in the presence of chloride and cyanate (Fig. 4E,F, for comparison see Supplementary Figure 2 for the size of effects of pressure on currents of HEK cells not expressing prestin). We observed a similar effect in guinea pig OHCs with large outward currents in the presence of extracellular thiocyanate that decreased in size in the presence of fluid jet stimulation (data not shown).

An estimate of the unitary current of a prestin-associated channel can be obtained as the whole-cell current normalized by the number of prestin molecules. This number can be derived from the magnitude of NLC³⁷. In this way we estimate that at +50 mV the unitary currents are 0.010 fA and 0.062 fA with extracellular Cl⁻ and thiocyanate, respectively.

Another approach to determining the size of unitary currents is fluctuation analysis. Schänzler and Fahlke²⁷ observed fluctuations in thiocyanate currents having a 1/f spectral density in whole-cell recordings. Because, however, the variance of the fluctuations had no clear relationship to the mean current, they concluded that the unitary currents were too small to be estimated with any reliability. We chose instead to record currents in excised patches to obtain higher sensitivity. Individual patch experiments (with patches of 1-2 mm²) from prestin expressing cells demonstrate an increase in average current of +11.94 pA (+50 mV) and -12.56 pA (-50 mV), and +7.73 pA (+50 mV) and -10.36 pA (+50 mV) over HEK cells in the presence of thiocyanate and chloride, respectively.

In the presence of Cl⁻ and SCN⁻ we also observed fluctuations with a power-law frequency dependence, approximately 1/f, whose magnitude clearly depended on membrane potential (Fig. 5A,C). The variance of the fluctuations was computed in two steps. First, the spectral density at 0 mV applied potential was taken to be the background spectrum, and was subtracted from spectra obtained at +50 mV or -50 mV (Fig. 5B,D). The

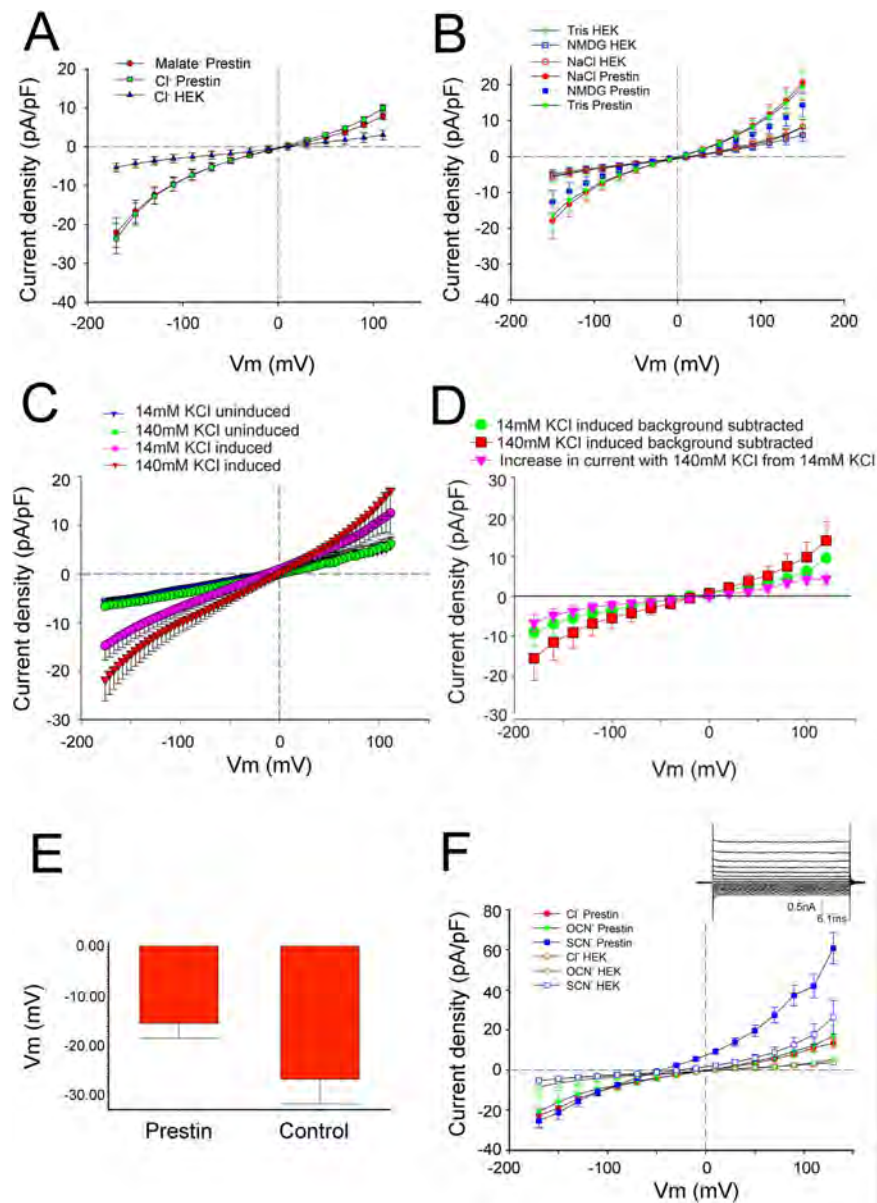


Figure 2. Prestin expression is associated with a non-selective current that is augmented with thiocyanate. (A) Substitution of extracellular NaCl with NaMalate did not affect the size of the current ($P > 0.05$, $n = 7$) or affect the reversal potential. (B) Extracellular substitution of Na^+ with NMDG $^+$ significantly reduced the size of the currents ($P < 0.001$, $n = 10$). In contrast, substitution with Tris^+ did not affect the current size or shift reversal potential. (C) Prestin associated currents are non-selective. In prestin expressing cells the substitution of 14 mM extracellular KCL with 140 mM KCL, while maintaining pipette (intracellular) KCL at 140 mM, results in an increase in the size of the whole-cell current at both depolarizing and hyperpolarizing voltages ($p < 0.05$, $n = 7$; $+/-$ SEM). In induced cells the reversal potential is 1.2 mV ($+/-$ 3.6, $n = 7$) with symmetrical 140 mM KCl and -14.7 mV ($+/-$ 3.9, $n = 7$) with 14 mM extracellular KCl. These data are consistent with permeability ratios for $\text{K}^+ : \text{Cl}^-$ of 1: 0.45. (D) Subtraction of baseline currents in uninduced cells from currents after prestin induction confirms the non-selective nature of the prestin associated current. (E) Resting membrane potentials recorded in current clamp mode immediately after achieving the whole cell configuration show significant depolarization in prestin expressing cells to -15.4 mV ($+/-$ 2.9 SE, $n = 11$) compared to -26 mV ($+/-$ 4.8 SE $n = 7$) in uninduced HEK cells ($p < 0.05$, students t test). (F) I-V relationships show a non-linear voltage dependent current with cyanate and thiocyanate. Average currents corrected for the size of the cell after induced expression of prestin in HEK cells are compared with currents in uninduced HEK cells before and after perfusion with 100 mM NaOCN, and 100 mM NaSCN ($+/-$ SE). Currents increase significantly in prestin expressing cells compared to HEK cells in the presence of extracellular Cl^- ($P < 0.001$, $n = 16$ prestin, $n = 5$ HEK), OCN^- ($p < 0.001$, $n = 3$ prestin, $n = 5$ HEK) and SCN^- ($p < 0.001$, $n = 17$ prestin, $n = 5$ HEK) with the largest effects seen with SCN^- . Inset: Thiocyanate current activates instantaneously and shows no deactivation. Prestin currents were recorded in a cell perfused with 100 mM NaSCN (holding at 0 mV, -150 to $+150$ mV with 20 mV steps of 50 ms duration).

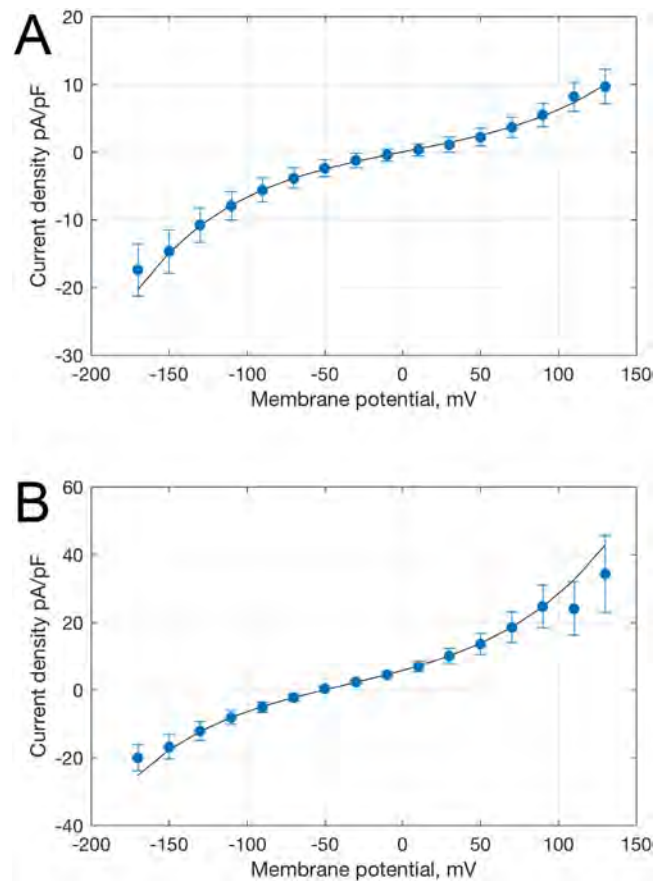


Figure 3. Single-barrier model I-V fits. Plotted is whole-cell current density in prestin-induced cells ($n = 19$) after subtraction of the corresponding current in control HEK cells ($n = 19$) in (A) symmetrical 140 mM KCl⁻ or (B) with extracellular SCN⁻ replacing Cl⁻ (+/-SEM). Curves are fitted with a single-barrier current-voltage relationship.

variance was then calculated as the integral of the subtracted spectrum over the frequency bandwidth of 0.1 to 1000 Hz. Very rough estimates of the unitary current can be made from the ratio of the variance to the mean current, yielding values of about ± 2 fA at ± 50 mV driving force in chloride solutions, and about 5 fA for outward current carried by SCN⁻ at +50 mV (Table 2).

This simple estimation of the elementary current magnitude is very approximate because it is based on several assumptions. First, it assumes switching between open and closed states, with a low probability of the open state. Second it is assumed that the fluctuations are approximately confined to the 0.1 to 1000 Hz frequency band. Finally, the use of the spectral density at 0 mV as the background estimate is not strictly correct for currents having a nonzero reversal potential. However, as the variance depends quadratically on the current, which is small at 0 mV, the error from this approximation is probably smaller than the errors arising from the other assumptions.

The power spectrum of current fluctuations in well-behaved transporters and gated ion channels typically shows one or more Lorentzian components^{38–43}. A power-law decay, like the one observed here over a range of four orders of magnitude in frequency, is instead consistent with fluctuations having a broad distribution of relaxation times. The estimated unitary currents are far too small to be visible in patch recordings, and consistent with this, no channel events were visible in the traces recorded at ± 50 mV. However, at large voltages such as +120 mV, channel-like activity could be seen (Fig. 5E). We assume that these very large currents arise from different channels than those under study here.

To date there are scant structural data on eukaryotic Slc26 transporters. However, recently, prestin was modeled, with confirmatory molecular dynamics simulations and experimental evidence, to closely fit the crystal structure of a bacterial uracil transporter, UraA, that is distantly related to the SLC26 family^{11,12}. A recent paper has observed an almost identical 7 + 7 inverted repeat structure in the more closely related bacterial homologue SLC26Dg, a facilitator of proton-coupled fumarate symport from *Deinococcus geothermalis*¹³. For our analyses, we use the 3D crystal structure of UraA as the template (see Supplementary Figure 3 for the sequence alignment using HHpred), as there are better structure-function correlates in UraA than in SLC26Dg. Several key residues in UraA that bind to uracil and are critical for transport are conserved in prestin, including S398 and F137 based on hidden Markov model homology (HHpred). Of these residues E290 in UraA, corresponding to S398 in prestin, is modeled to bind to uracil close to its intracellular cleft. Similarly, F73 in UraA, corresponding to F137 in prestin, binds to uracil and acts as a barrier for its escape to the periplasmic surface¹². We reasoned that mutation of these residues in prestin would reduce the easily measurable thiocyanate currents if prestin were to mediate

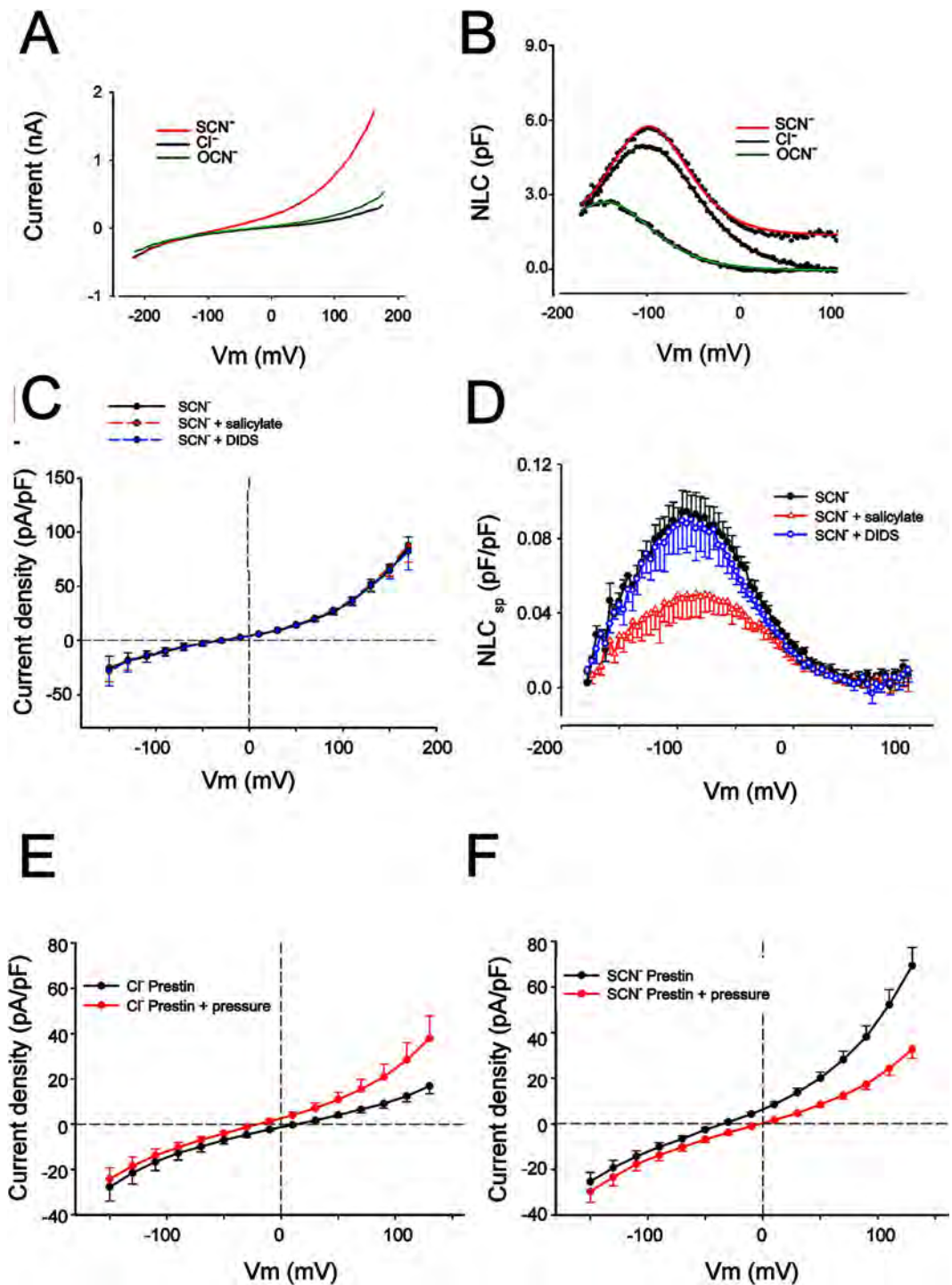


Figure 4. Currents and NLC associated with prestin are separable. (A,B). Shown are NLC (A) and currents (B) in a single cell perfused with extracellular Cl⁻, OCN⁻ and SCN⁻. SCN⁻ increases current significantly and affects gating charge, while OCN⁻ causes a slight increase in current while causing a hyperpolarizing shift in V_h. (C,D) Extracellular salicylate (20 mM) has no effect on currents (C) in the presence of extracellular SCN⁻, while reducing NLC (D). 1 mM DIDS does not affect NLC or SCN⁻ current. Shown are average tracings from three cells (+/-SEM). (E,F) The effects of fluid-jet pressure on the size of the current are dependent on the conducting anion. With Cl⁻ in the bath solution there is an increase in the size of the current with exposure of the cell to a fluid jet (E). In contrast, in the presence of extracellular SCN⁻, the size of the current decreases with exposure to a fluid jet (F). Shown are average tracings from 10 cells (+/-SEM).

these currents via its transporter pathway. However, mutation of these residues to alanine had little effect on the size of thiocyanate currents but they did shift V_h of NLC (F137A did not have detectable NLC likely since V_h was so shifted; membrane targeting was confirmed by confocal microscopy (Supplementary Figure 4)). We interpret

Prestin stable line	Q_{sp} (fC/pF)	V_h (mV)	z	n
extracellular Cl^-	20.32+/-2.21	-96.26+/-3.37	0.74+/-0.02	19
extracellular SCN^-	15.32+/-1.68	-101.34+/-2.49	0.81+/-0.02	19
extracellular OCN^-	9.08+/-1.74	-141.72+/-3.94	0.76+/-0.02	6

Table 1. Effects of extracellular substitution with the pseudohalides OCN^- and SCN^- on parameters of NLC in tetracycline inducible HEK cell line. Specific capacitance was reduced by both extracellular OCN^- and SCN^- with V_h shifted to more hyperpolarizing voltages. The effects were more pronounced with OCN^- . Additionally, SCN^- also increased estimates of single charge movement (z).

these data as consistent with a model of Na^+ , Cl^- and thiocyanate movement through the protein independent of its transporter pathway (Fig. 6A). We note that mutation of F137A did produce a positive shift in SCN^- reversal potential, although an increase SCN^- conductance is not borne out in the size of SCN^- currents at -130 mV. One possible explanation for the shift in reversal potential is of a decrease in cation conductance in the presence of thiocyanate.

In contrast to the absence of effects on thiocyanate or chloride currents from mutation of residues corresponding to those in the UraA binding pocket, we note marked reductions in SCN^- currents with charge neutralizing mutations of several charged residues in prestin's transmembrane domains (Fig. 6B). The side chains of these residues reside at the interface between the core and gate domain (Fig. 6D–F). These mutations (K227Q, K359Q and D485N) in three widely separated alpha helical transmembrane domains 5, 8 and 14, preserved NLC (Table 3, Fig. 6C), thus confirming surface expression of functional molecules. Examining the modeled structure of prestin reveals a potential accessory pathway, which links these widely separated residues that lie in physical proximity in its tertiary structure, independent of the suspected substrate binding site between the alpha-helical regions of TM3 and 10. Indeed, this pathway allows access to the inner membrane surface while access to the external surface is partially obstructed by a loop linking transmembrane domains 3 and 4. Significantly, an additional mutation, R463Q, that also reduced SCN^- currents, lies in an unstructured loop linking transmembrane domains 12 and 13. It lies at the intracellular cleft of the transporter and is in a potential pathway linking the extracellular medium and the envisaged accessory pathway. Note however, that our model is based on the structure of UraA and SLC26dg both of which capture a single state, namely an inside open conformation. Determining the exact pathway of the non-selective conductance will require more structural data particularly of the outside open and other intermediary conformations.

Discussion

Prestin has evolved to facilitate hearing in mammals by enhancing auditory thresholds by up to 1000 fold, through cochlear amplification^{1,2}. Since it is a member of the SLC26 anion transporter family, it is no surprise that anions, chiefly intracellular chloride, control many of its biophysical characteristics^{16–18}. It is paramount that intracellular chloride homeostasis be understood, since chloride manipulations have been shown to reversibly abolish cochlear amplification⁴⁴. Here we present evidence that prestin, itself, provides a stretch-sensitive leakage pathway for anions that is independent of its transporter pathway, thereby providing a potential feedback system driven by the protein's voltage-induced mechanical activity. A similar non-selective current, GmetL, has been observed along the lateral wall of outer hair cells¹⁹. Initially, we believed these currents were independent of prestin since the current in outer hair cells had different voltage sensitivity than NLC^{17,29}. However, our new data require that we reexamine the role of prestin in the non-selective currents observed along the lateral wall of outer hair cells^{19,29}.

Previous studies have characterized an ionic conductance in the SLC26 transporter family in the presence of SCN^- . In prestin, we find that this conductance is also demonstrable in the presence of Cl^- as the main anion. Our major findings can be summarized as follows. First, there is clear evidence to associate this conductance with prestin: 1) in individual cells the conductance increases with prestin expression and is proportional to NLC. 2) the conductance appears with the same time course as NLC upon release of Golgi block. 3) Mutations in prestin affect the current. An alternative possibility that a prestin associated protein contributes to the current could account for the first two observations. However, the third observation strongly suggests that the current is carried by prestin itself. Moreover, two other SLC26 family members have been demonstrated to have an uncoupled current in the presence of SCN^- ^{14,15}.

Our second major finding is that the conductance is carried by a pathway different from the Cl^- transport pathway in prestin. Evidence for this is: 1) mutation of residues that are modeled to bind intracellular Cl^- , the first essential step in the transporter cycle, do not affect the size of the current. 2) salicylate, which in non-mammalian homologs has been shown to block the transporter current while simultaneously blocking NLC, has no effect on the size of the current. 3) single point mutations have effects on the size of the current or on NLC but not both. Since mutation of F137, that we speculate based on homology to UraA to be involved in the transporter cycle, changed the reversal potential in the presence of SCN^- , it is possible that the alternative leakage pathway shares some commonality with the transporter pathway. In this context, owing to data that prestin and many similar transporter proteins form dimers and since the charge mutations that affected current are in proximity to its dimer interface, it is possible that the leakage pathway may in fact lie within the dimer interface^{45–50}.

The unusual current-voltage relationship can be explained by a channel having a high central energy barrier to ion transport. Consistent with this possibility we note small unitary currents in the fA range. We conclude that prestin forms at least part of an independent pathway for ions to cross the membrane. Mutations suggest that the pathway is located between the core and gate domains of the 7 + 7 inverted repeat structure. In this way

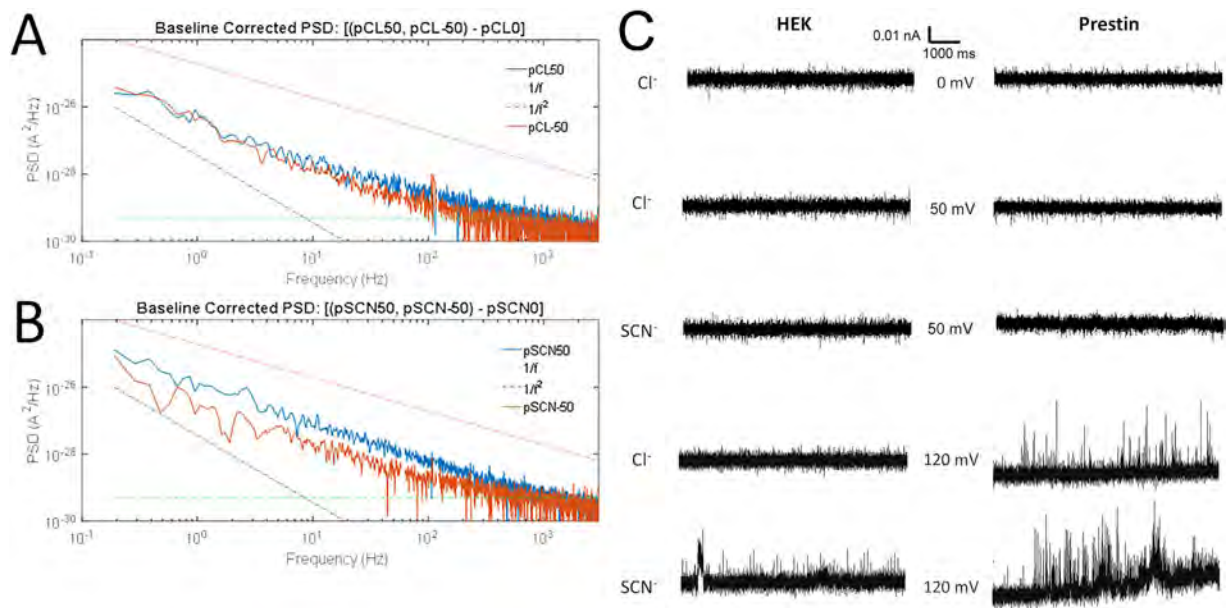


Figure 5. Noise analysis of currents in prestin expressing cells. (A) Currents in inside-out patches from prestin-expressing cells were recorded in symmetrical 140 mM Cl^- solutions at -50 mV (red line), 0 mV and $+50$ mV (blue line) for 10 seconds. Spectra from 11 patches were averaged. Spectra are plotted after subtraction of the 0 mV background spectrum. The frequency dependence is well described by a power-law decay plus a shot-noise (constant, green dotted lines) component with no apparent Lorentzian components. (B) Corresponding averaged, subtracted spectra obtained from same inside-out patches with 100 mM NaSCN on the intracellular side. As expected, noise is larger for currents at $+50$ mV where, by convention, the movement of SCN^- current is inward, although the size of the mean patch current at $+50$ mV (Table 2) is similar to that at -50 mV (Table 2). Reference lines of $1/f$ and $1/f^2$ slopes accompany data plots as visual aids. (C) Consistent with the small unitary currents estimated from the noise variance, no ion-channel events were visible except at extreme potentials such as $+120$ mV. Representative recordings are shown from excised inside out patches of HEK cells (left) and HEK cells with prestin expression (right) held at 0, 50 and 120 mV in the presence of 140 mM Cl^- and 100 mM $\text{SCN}^-/40\text{mMCl}^-$.

	Variance, σ^2 (A^2)	Mean patch current, $\langle I \rangle$ (pA)	Estimate of single channel current $\sigma^2/\langle I \rangle$ (fA)	n
-50 mV Cl^-/Cl^-	$1.66\text{e-}26$	-11.9 ± 5.5	-1.40	11
$+50$ mV Cl^-/Cl^-	$2.40\text{e-}26$	12.6 ± 5.6	1.91	11
-50 mV Cl^-/SCN^-	$1.58\text{e-}26$	-16.3 ± 5.4	-0.97	11
$+50$ mV Cl^-/SCN^-	$7.19\text{e-}26$	14.8 ± 5.3	4.87	11

Table 2. Noise analysis of inside out patches demonstrate increased variance with SCN^- during depolarization. Inside out patches from induced HEK cells expressing prestin were recorded for 10 seconds in each condition. The table lists variance of currents, σ^2 (A^2) with symmetrical Cl^- and after perfusing with SCN^- (with Cl^- inside the electrode) at -50 mV and $+50$ mV. Also shown are mean currents, $\langle I \rangle$ (re: 0 mV), and estimates ($\sigma^2/\langle I \rangle$) of single channel currents in each of the conditions.

the pathway is reminiscent of the omega current pathway in voltage gated channels. There a nonselective cation current is carried by voltage-sensor domains, in a structure entirely separate from the ion-selective pore of these channels.

Our whole cell and patch analyses provide disparate estimates of unitary currents. One explanation could be that only a fraction of prestin molecules show a leakage conductance, as our whole-cell estimates are based on normalization with the total population of prestin molecules derived from NLC. By contrast, the noise analysis provides estimates solely from active channels within a patch (without normalization to NLC as above). We also note that the relative conductances for Cl^- and SCN^- differed between whole cell recordings and excised patches. These discrepancies between recording approaches could very well be explained by the effects of an increase in membrane tension in excised patches, given the conductance's tension dependence (Fig. 4E and F).

The non-selective nature of the prestin associated currents and its small size is somewhat at odds given our current understanding of the selectivity filters in ion channels. Perhaps the mechanical model gleaned from structural data of the unrelated EAAT transporter that has a similar leakage conductance (albeit limited to anions) has

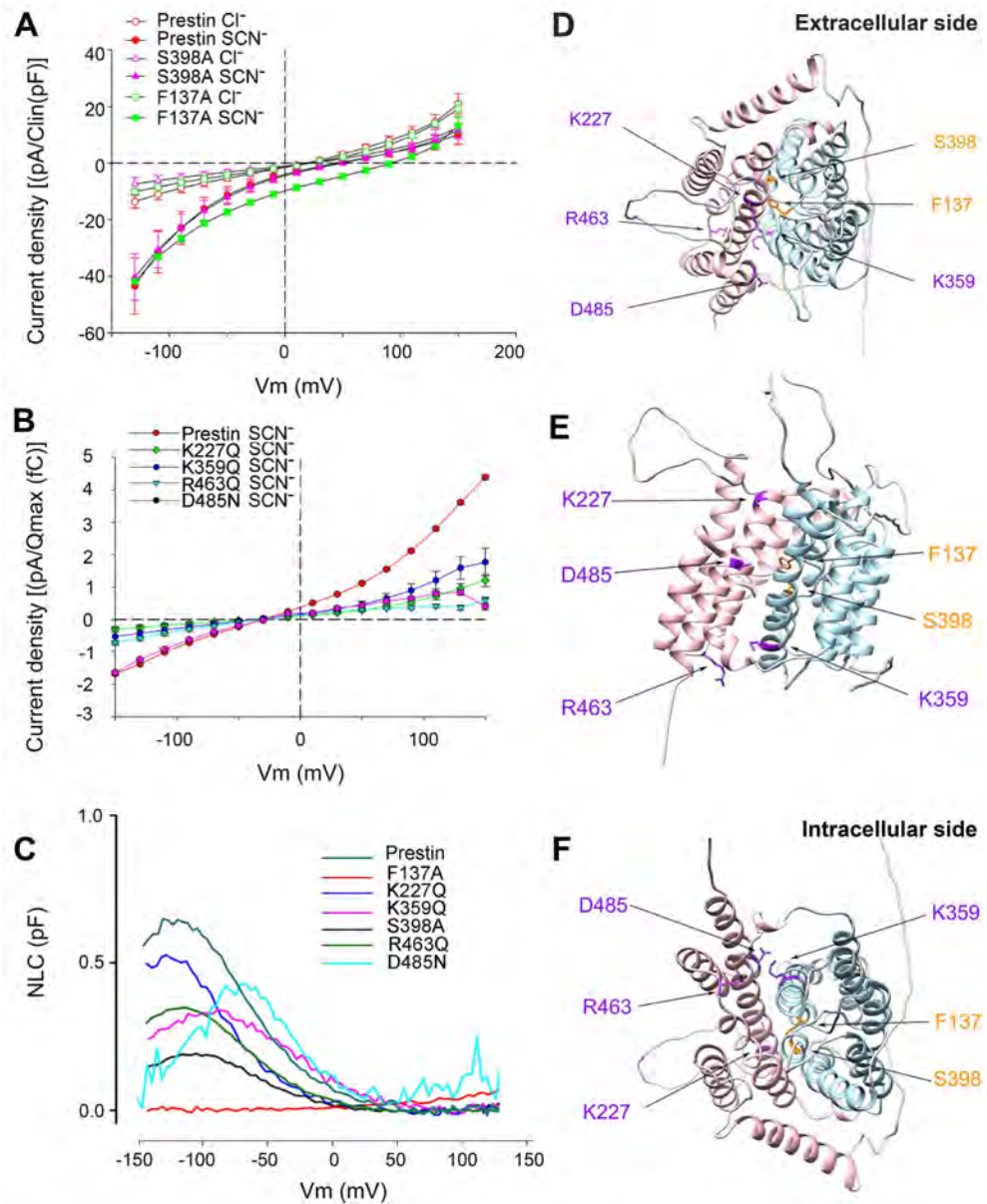


Figure 6. SCN^- currents in prestin suggest an ancillary pathway independent of the transporter pathway.

(A) Mutation of residues critical for Cl^- binding, the first step in transport, has no effects on SCN^- currents. Average currents of CHO cells expressing prestin ($n = 5$), F137A ($n = 4$) and S398A ($n = 7$) show no differences (\pm SEM). Currents, after correction for background currents, were divided by linear capacitance to correct for differences in cell size and plotted against voltage (F137A did not have easily measurable NLC, so the more rigorous normalization to NLC was not possible). Cells show large inward currents in the presence of intracellular SCN^- (100 mM) at depolarizing voltages. Intracellular SCN^- was used since the residue corresponding to S398 lies closer to the inner cleft of the transporter pathway and binds to intracellular uracil in UraA; the residue corresponding to F137 acts as a barrier to the diffusion of uracil to the exterior surface. (B) Neutralization of charged residues lying outside the transporter pathway reduce SCN^- currents. Average currents of CHO cells expressing K227Q ($n = 7$), K359Q ($n = 7$), R463Q ($n = 9$), and D485N ($n = 18$) show significantly reduced currents in the presence of extracellular SCN^- ($p < 0.001$). To account for variations in expression, current averages for each mutant construct, after correction of average background currents, were normalized by the NLC charge Q_{max} and plotted against voltage. (C) NLC traces from residues (K227Q, K359Q, R463Q and D485N) where mutation affected SCN^- currents but had measurable NLC, and of mutations in the transporter pathway (F137A and S398A). (D–F) The location of residues that line a potential accessory pathway are shown on the structure of prestin modeled on the crystal structure of the bacterial uracil transporter UraA rendered with Chimera^{11,12}. The core domains are colored blue and the gate domains colored in pink. (D–F) are the molecule viewed from above, the side and below respectively. In the potential accessory pathway lined by alpha helices 5, 8 and 14, the contained amino acids K227, K359 and D485, and R463, that lies in the loop connecting helices 12 and 13, are colored purple. Residues modeled to bind intracellular chloride (F137 and S398) are colored orange.

	Q_{sp} (fC/pF)	V_h (mV)	z	n
Prestin (wt)	8.79+/-2.28	-127.69+/-6.31	0.70+/-0.02	8
S398A	4.99+/-0.90	-107.73+/-2.21	0.71+/-0.008	9
F137A	—	—	—	5
K227Q	13.08+/-5.32	-146.12+/-6.27	0.67+/-0.03	7
K359Q	5.76+/-0.47	-98.01+/-3.71	0.57+/-0.02	7
R463Q	7.61+/-1.50	-114.32+/-5.62	0.70+/-0.03	9
D485N	6.3+/-1.4	-63.06+/-7.6	1.00+/-0.06	21

Table 3. Effects of neutralizing charge substitutions along a potential accessory pathway on gating charge parameters on transiently transfected CHO cells. Almost all these mutations decreased Q_{sp} (except K227Q) and affected the direction of V_h variably. Effects on unitary z were variable and consistent with previous data²⁰.

bearing⁵¹. In this transporter, the anion leakage pathway is not evident in the crystal structures of the many permutations of the transporter cycle including inside open, outside open and several intermediate states. Molecular dynamics simulations, however, show a conductance pathway that opens several 100s of nanoseconds after application of voltage. Experimental observations confirm such a pathway. The absence of an anion leakage pathway in the many conformations of the transporter cycle of EAAT crystal structures suggests that the pathway is a transient opening. In prestin, as well, the even smaller size of unitary currents may represent much briefer openings in the leakage pathway. In this respect, the block of the non-selective current in prestin by charge neutralization of both positive and negatively charged residues may result from reduced hydrophilicity, preventing water movement that is modeled to precede ionic movements in EAAT.

Our data suggest that currents carried by prestin's leakage conductance could affect Cl^- in OHCs. A similar conductance in the lateral membrane of OHCs has been demonstrated, and Cl^- ions have been shown to affect the voltage sensitivity and affect the speed of transitions from expanded to contracted states of prestin. Although the current carried by individual molecules of prestin is small, the presence of large numbers of prestin in the lateral membrane of OHCs (estimated to be upwards of 10^6 per OHC) likely makes this current important. Consistent with this possibility, expression of prestin at high levels in HEK cells has a major effect on its resting potential. A similar role has been established in the leakage conductance of EAAT1/2 in glial cells in the cerebellum, that show developmental expression, reducing intracellular chloride⁵².

Methods

Cell culture. Chinese hamster ovary (CHO) cells were cultured in Hams-F12 medium (high glucose), containing 50 U/ml each of penicillin and streptomycin, 10% fetal bovine serum, 2 mM L-glutamine at 37 °C in a CO_2 incubator (5%).

HEK293 cells were cultured in Dulbecco's modified Eagle's medium (DMEM, high glucose) containing 50 U/ml each of penicillin and streptomycin, 10% fetal bovine serum at 37 °C in a CO_2 incubator (5%).

The tetracycline-inducible, highly-expressing monoclonal prestin HEK 293 cell lines were reported previously²⁸. Cells were cultured in modified DMEM mentioned above. In addition, 4 μ g/ml of blasticidin and 130 μ g/ml of zeocin were supplemented in the growth media to maintain prestin expression. Tetracycline (1 μ g/ml) was added to the cell growth medium to induce prestin expression. Cells were recorded after 24 to 72 h after tetracycline-induction.

Mutagenesis. Single amino acid substitutions were generated using QuickChange II site-directed mutagenesis kit (Stratagene, La Jolla, CA) with a gerbil prestin (genbank AF230376³)-YFP in pEYFPN1 vector (Clontech, Mountain View, CA) as a template. All mutations were confirmed by DNA sequencing.

Transient transfection in CHO cells. Transfection of constructs into CHO cells (CHO-K1.ATCC[®] CCL-61[™]) was done using Fugene 6 (Promega, Madison, WI) according to the manufacturer's instructions, in 24-well plates. Cells were recorded 24–72 h after transfection.

Electrophysiological Recording. Prestin stably expressed in a tetracycline inducible HEK line or transiently transfected into CHO cells were recorded using a whole-cell configuration at room temperature using an Axon 200B amplifier (Molecular Devices, Sunnyvale, CA), as described previously²⁸. Cells were recorded 24–72 h after tetracycline induction or transfection to allow for stable measurement of current and NLC. A series of bath solutions with different anions/cations were used. The standard base solution components were (in mM): TEACl 20, CsCl 20, $CoCl_2$ 2, $MgCl_2$ 2, Hepes 5, pH 7.2. In addition, for anion substitutions the following were added (separately) to the base solution (in mM): NaCl 100, NaSCN 100, NaOCN 100, $NaIO_3$ 100, Na Methanesulfonate 100, Na_2 Malate 60, or Na_2 Oxalate 60. Similarly, for cation substitutions the following were added separately to the base solution (in mM): KCl 100, NMDG-Cl 100, or Tris-Cl 100, separately. The pipette solution contains (in mM): NaCl 100/NaSCN 100, CsCl 20, EGTA 5, $MgCl_2$ 2, Hepes 10, pH 7.2. Osmolarity was adjusted to 300 ± 2 mOsm with dextrose. After whole cell configuration was achieved in extracellular NaCl and a ramp protocol recorded to confirm baseline NLC and currents. Extracellular anion and cation substitutions were then made by local extracellular perfusion of each individual cell followed by recording a ramp protocol.

Command delivery and data collections were carried out with a Windows-based whole-cell voltage clamp program, jClamp (Scisoft, Ridgefield, CT), using a Digidata 1322A (Axon Instruments).

A continuous high-resolution 2-sine voltage command was used, cell capacitance and current being extracted synchronously. Capacitance data were fitted to the first derivative of a two-state Boltzmann function:

$$C_m = Q_{max} \frac{ze}{kT} \frac{b}{(1+b)^2} + C_{lin} \quad (1)$$

where

$$b = \exp \left(-\frac{ze(V_m - V_{vh})}{kT} \right) \quad (2)$$

Q_{max} is the maximum nonlinear charge transfer, V_h the voltage at peak capacitance or half-maximal nonlinear charge transfer, V_m the membrane potential, C_{lin} linear capacitance, z the unitary charge (a metric of voltage sensitivity), e the electron charge, k the Boltzmann constant, and T the absolute temperature. Q_{sp} the specific charge density, is the total charge moved (Q_{max}) normalized to linear capacitance. Capacitive currents (Icap) generated by our ramp protocol were removed to reveal ionic currents. In order to estimate Icap (from both linear and NLC), we modelled the patch clamp-cell in Matlab and extracted membrane capacitive currents arising from averaged values of linear capacitance and NLC. In all figures, individual I-V plots were corrected based on averages from the inclusive cells. Reversal potentials, thus, arise from ionic current contributions only. Separately, in specific experiments currents were also determined after voltage steps (50 ms duration) from -150 mV to 150 mV, with 20 mV step increments. Where cations and anions were substituted, local perfusion of the cells were estimated to give rise to small junctional potentials (JPCalc function in pClampEx). These varied from $+1.1$ mV (SCN⁻) to -5.4 mV (Methanesulfonate) with anion substitutions. Cation substitutions also were estimated to give rise to small junctional potentials varying from -0.8 mV (KCl) to $+6.8$ mV (NMDG⁺). Since these numbers were small no corrections were made to the IV plots. For fluid jet experiments we used a QMM perfusion system (ALA Scientific, Instruments, Westbury, NY). The manifold's output tip was $200 \mu\text{m}$ placed 1 mm from the cell, and the flow rate increased by an applied pressure of approximately 20 kPa. Significance of the size of currents at different voltage steps from experimental perturbations were determined using a mixed model analysis of correlated measures (MMACM). Statistical analysis was done with SAS software (SAS Institute Inc, NC).

Inside-out patch recording (noise analysis). Thick wall glass pipettes were pulled using same puller as described above, and coated with sylgard. The initial resistances of the pipettes are 13 – 15 M Ω . Pipette solution contains (in mM): NaCl 100, CsCl 20, EGTA 5, MgCl₂ 2, Hepes 10, pH 7.2. Bath solution contains (in mM): NaCl/NaSCN 100, TEACl 20, CsCl 20, CoCl₂ 2, MgCl₂ 2, Hepes 5, pH 7.2. Osmolarity was adjusted to 300 ± 2 mOsm with dextrose. Inside-out patches were obtained from control HEK cells or the tetracycline-induced prestin stable line. Data acquisition was done with the same interface and amplifier described above. Continuous 10 second commands at desired holding potentials were delivered during recording.

Noise analysis. PSD analyses of excised patch currents from prestin transfected cells, filtered with a 10 kHz, 4 pole Bessel filter and Hamming windowed, were derived from 10 second recordings held at -50 , 0 , and $+50$ mV potentials. In some cases, voltages up to ± 120 mV were analyzed. Some patch records were excluded because of seal loss during recording. Number of patches from separate cells: 11 for symmetrical chloride condition; and 11 for chloride/SCN⁻ conditions 5 for symmetrical chloride of HEK cells and 5 for chloride/SCN⁻ conditions in HEK cells. Spectra were taken for each individual patch recording (1,061,306 pts at $10 \mu\text{s}$ sampling, with a frequency resolution of 0.095 Hz), averaged and plotted out to 3 kHz. Data are presented following subtraction of baseline spectra at 0 mV. Variance was determined by integration of spectra between 0.1 Hz and 1 kHz after subtraction of calculated shot noise ($2ie_0$). Analyses were made with a custom written MATLAB application.

$$I = g \frac{kT}{q[(P-1)\delta + 1]} \left[P \exp\left(\frac{q\delta E}{kT}\right) - \exp\left(\frac{-q(1-\delta)E}{kT}\right) \right] \quad (3)$$

where g is the slope conductance at $E = 0$, q is the apparent charge, is the electrical distance of the barrier, and P is the relative permeability of ions carrying outward current compared to those carrying inward current; if the current were entirely anion selective P would be the permeability ratio P_{SCN^-}/P_{Cl^-} . For Cl⁻ as the external anion the values were $P = 1$, $\delta = 0.467$, $q(e_0) = 0.75$ and g (pS/pF) = 46.3 . For SCN⁻ as the anion the values were $P = 6.18$, $\delta = 0.339$, $q(e_0) = 0.75$ and g (pS/pF) = 92.8 . The values that differ for the two anion species, and the value of q smaller than the elementary charge, are consistent with a distribution of barrier locations, for example distinct barrier locations for anions and cations.

References

- Brownell, W. E., Bader, C. R., Bertrand, D. & de Ribaupierre, Y. Evoked mechanical responses of isolated cochlear outer hair cells. *Science* **227**, 194–196 (1985).
- Davis, H. An active process in cochlear mechanics. *Hear Res* **9**, 79–90, doi: 10.1016/0378-5955(83)90136-3 (1983).
- Zheng, J. *et al.* Prestin is the motor protein of cochlear outer hair cells. *Nature* **405**, 149–155, doi: 10.1038/35012009 (2000).
- Mount, D. B. & Romero, M. F. The SLC26 gene family of multifunctional anion exchangers. *Pflugers Arch* **447**, 710–721, doi: 10.1007/s00424-003-1090-3 (2004).
- Dorwart, M. R., Shcheynikov, N., Yang, D. & Muallem, S. The solute carrier 26 family of proteins in epithelial ion transport. *Physiology* **23**, 104–114, doi: 10.1152/physiol.00037.2007 (2008).
- Lieberman, M. C. *et al.* Prestin is required for electromotility of the outer hair cell and for the cochlear amplifier. *Nature* **419**, 300–304, doi: 10.1038/nature01059 (2002).

7. Santos-Sacchi, J., Shen, W., Zheng, J. & Dallos, P. Effects of membrane potential and tension on prestin, the outer hair cell lateral membrane motor protein. *J Physiol* **531**, 661–666 (2001).
8. Ludwig, J. *et al.* Reciprocal electromechanical properties of rat prestin: The motor molecule from rat outer hair cells. *Proc. Natl. Acad. Sci. USA* **98**, 4178–4183 (2001).
9. Meltzer, J. & Santos-Sacchi, J. Temperature dependence of non-linear capacitance in human embryonic kidney cells transfected with prestin, the outer hair cell motor protein. *Neuroscience letters* **313**, 141–144 (2001).
10. Frank, G., Hemmert, W. & Gummer, A. W. Limiting dynamics of high-frequency electromechanical transduction of outer hair cells. *Proc. Natl. Acad. Sci. USA* **96**, 4420–4425 (1999).
11. Gorbunov, D. *et al.* Molecular architecture and the structural basis for anion interaction in prestin and SLC26 transporters. *Nature communications* **5**, 3622, doi: 10.1038/ncomms4622 (2014).
12. Lu, F. *et al.* Structure and mechanism of the uracil transporter UraA. *Nature* **472**, 243–246, doi: 10.1038/nature09885 (2011).
13. Geertsma, E. R. *et al.* Structure of a prokaryotic fumarate transporter reveals the architecture of the SLC26 family. *Nature structural & molecular biology*, doi: 10.1038/nsmb.3091 (2015).
14. Ohana, E., Shcheynikov, N., Yang, D., So, I. & Muallem, S. Determinants of coupled transport and uncoupled current by the electrogenic SLC26 transporters. *The Journal of general physiology* **137**, 239–251, doi: 10.1085/jgp.201010531 (2011).
15. Shcheynikov, N. *et al.* Coupling modes and stoichiometry of Cl⁻/HCO₃⁻ exchange by slc26a3 and slc26a6. *The Journal of general physiology* **127**, 511–524, doi: 10.1085/jgp.200509392 (2006).
16. Oliver, D. *et al.* Intracellular anions as the voltage sensor of prestin, the outer hair cell motor protein. *Science* **292**, 2340–2343, doi: 10.1126/science.1060939 (2001).
17. Rybalchenko, V. & Santos-Sacchi, J. Anion control of voltage sensing by the motor protein prestin in outer hair cells. *Biophys J* **95**, 4439–4447, doi: 10.1529/biophysj.108.134197 (2008).
18. Santos-Sacchi, J. & Song, L. Chloride-driven electromechanical phase lags at acoustic frequencies are generated by SLC26a5, the outer hair cell motor protein. *Biophys J* **107**, 126–133, doi: 10.1016/j.bpj.2014.05.018 (2014).
19. Rybalchenko, V. & Santos-Sacchi, J. Cl⁻ flux through a non-selective, stretch-sensitive conductance influences the outer hair cell motor of the guinea-pig. *J Physiol* **547**, 873–891, doi: 10.1113/jphysiol.2002.036434 (2003).
20. Bai, J. P. *et al.* Prestin's anion transport and voltage-sensing capabilities are independent. *Biophys J* **96**, 3179–3186, doi: 10.1016/j.bpj.2008.12.3948 (2009).
21. Song, L. & Santos-Sacchi, J. Conformational state-dependent anion binding in prestin: evidence for allosteric modulation. *Biophys J* **98**, 371–376, doi: 10.1016/j.bpj.2009.10.027 (2010).
22. Song, L. & Santos-Sacchi, J. Disparities in voltage-sensor charge and electromotility imply slow chloride-driven state transitions in the solute carrier SLC26a5. *Proc Natl Acad Sci USA* **110**, 3883–3888, doi: 10.1073/pnas.1218341110 (2013).
23. Song, L., Seeger, A. & Santos-Sacchi, J. On membrane motor activity and chloride flux in the outer hair cell: lessons learned from the environmental toxin tributyltin. *Biophys J* **88**, 2350–2362, doi: 10.1529/biophysj.104.053579 (2005).
24. Santos-Sacchi, J. & Song, L. Chloride anions regulate kinetics but not voltage-sensor Q_{max} of the solute carrier SLC26a5. *Biophys. J.* **110**, 1–11 (2016).
25. Tan, X. *et al.* From zebrafish to mammal: functional evolution of prestin, the motor protein of cochlear outer hair cells. *J Neurophysiol* **105**, 36–44, doi: 10.1152/jn.00234.2010 (2011).
26. Mistrik, P., Daudet, N., Morandell, K. & Ashmore, J. F. Mammalian prestin is a weak Cl⁽⁻⁾/HCO₃⁽⁻⁾ electrogenic antiporter. *J Physiol* **590**, 5597–5610, doi: 10.1113/jphysiol.2012.241448 (2012).
27. Schanzler, M. & Fahlke, C. Anion transport by the cochlear motor protein prestin. *J Physiol* **590**, 259–272, doi: 10.1113/jphysiol.2011.209577 (2012).
28. Bian, S., Koo, B. W., Kelleher, S., Santos-Sacchi, J. & Navaratnam, D. S. A highly expressing Tet-inducible cell line recapitulates *in situ* developmental changes in prestin's Boltzmann characteristics and reveals early maturational events. *Am J Physiol Cell Physiol* **299**, C828–835, doi: 10.1152/ajpcell.00182.2010 (2010).
29. Santos-Sacchi, J., Rybalchenko, V., Bai, J. P., Song, L. & Navaratnam, D. On the temperature and tension dependence of the outer hair cell lateral membrane conductance G_{metL} and its relation to prestin. *Pflügers Arch* **452**, 283–289, doi: 10.1007/s00424-005-0037-2 (2006).
30. Bian, S., Navaratnam, D. & Santos-Sacchi, J. Real time measures of prestin charge and fluorescence during plasma membrane trafficking reveal sub-tetrameric activity. *PLoS One* **8**, e66078, doi: 10.1371/journal.pone.0066078 (2013).
31. Schaechinger, T. J. & Oliver, D. Nonmammalian orthologs of prestin (SLC26A5) are electrogenic divalent/chloride anion exchangers. *Proc Natl Acad Sci USA* **104**, 7693–7698, doi: 10.1073/pnas.0608583104 (2007).
32. Kakehata, S. & Santos-Sacchi, J. Effects of salicylate and lanthanides on outer hair cell motility and associated gating charge. *J. Neurosci.* **16**, 4881–4889 (1996).
33. Tunstall, M. J., Gale, J. E. & Ashmore, J. F. Action of salicylate on membrane capacitance of outer hair cells from the guinea-pig cochlea. *J. Physiol.* **485** (Pt 3), 739–752 (1995).
34. Alper, S. L. The band 3-related anion exchanger (AE) gene family. *Annual review of physiology* **53**, 549–564, doi: 10.1146/annurev.ph.53.030191.003001 (1991).
35. Shami, Y., Carver, J., Ship, S. & Rothstein, A. Inhibition of Cl⁻ binding to anion transport protein of the red blood cell by DIDS (4, 4'-diisothiocyano-2, 2'-stilbene disulfonic acid) measured by [³⁵S]NMR. *Biochemical and biophysical research communications* **76**, 429–436 (1976).
36. Wang, T., Giebisch, G. & Aronson, P. S. Effects of formate and oxalate on volume absorption in rat proximal tubule. *The American journal of physiology* **263**, F37–42 (1992).
37. Huang, G. & Santos-Sacchi, J. Mapping the distribution of the outer hair cell motility voltage sensor by electrical amputation. *Biophys J* **65**, 2228–2236, doi: 10.1016/S0006-3495(93)81248-7 (1993).
38. Cherny, V. V., Murphy, R., Sokolov, V., Levis, R. A. & DeCoursey, T. E. Properties of single voltage-gated proton channels in human eosinophils estimated by noise analysis and by direct measurement. *The Journal of general physiology* **121**, 615–628, doi: 10.1085/jgp.200308813 (2003).
39. Larsson, H. P., Picaud, S. A., Werblin, F. S. & Lecar, H. Noise analysis of the glutamate-activated current in photoreceptors. *Biophys J* **70**, 733–742, doi: 10.1016/S0006-3495(96)79613-3 (1996).
40. Sigworth, F. J. The variance of sodium current fluctuations at the node of Ranvier. *The Journal of physiology* **307**, 97–129 (1980).
41. Wadiche, J. I., Amara, S. G. & Kavanaugh, M. P. Ion fluxes associated with excitatory amino acid transport. *Neuron* **15**, 721–728 (1995).
42. Wadiche, J. I. & Kavanaugh, M. P. Macroscopic and microscopic properties of a cloned glutamate transporter/chloride channel. *The Journal of neuroscience: the official journal of the Society for Neuroscience* **18**, 7650–7661 (1998).
43. Alvarez, O., Gonzalez, C. & Latorre, R. Counting channels: a tutorial guide on ion channel fluctuation analysis. *Advances in physiology education* **26**, 327–341 (2002).
44. Santos-Sacchi, J., Song, L., Zheng, J. & Nuttall, A. L. Control of mammalian cochlear amplification by chloride anions. *J. Neurosci.* **26**, 3992–3998 (2006).
45. Alguel, Y. *et al.* Structure of eukaryotic purine/H⁽⁺⁾ symporter UapA suggests a role for homodimerization in transport activity. *Nature communications* **7**, 11336, doi: 10.1038/ncomms11336 (2016).

46. Alguet, Y., Cameron, A. D., Diallinas, G. & Byrne, B. Transporter oligomerization: form and function. *Biochem Soc Trans* **44**, 1737–1744, doi: 10.1042/BST20160217 (2016).
47. De Zutter, J. K., Levine, K. B., Deng, D. & Carruthers, A. Sequence determinants of GLUT1 oligomerization: analysis by homology-scanning mutagenesis. *J Biol Chem* **288**, 20734–20744, doi: 10.1074/jbc.M113.469023 (2013).
48. Kilic, F. & Rudnick, G. Oligomerization of serotonin transporter and its functional consequences. *Proc Natl Acad Sci USA* **97**, 3106–3111, doi: 10.1073/pnas.060408997 (2000).
49. Tao, Y. *et al.* Structure of a eukaryotic SWEET transporter in a homotrimeric complex. *Nature* **527**, 259–263, doi: 10.1038/nature15391 (2015).
50. Zhen, J. *et al.* Dopamine transporter oligomerization: impact of combining protomers with differential cocaine analog binding affinities. *Journal of neurochemistry* **133**, 167–173, doi: 10.1111/jnc.13025 (2015).
51. Machtens, J. P. *et al.* Mechanisms of anion conduction by coupled glutamate transporters. *Cell* **160**, 542–553, doi: 10.1016/j.cell.2014.12.035 (2015).
52. Untiet, V. *et al.* Glutamate transporter-associated anion channels adjust intracellular chloride concentrations during glial maturation. *Glia* **65**, 388–400, doi: 10.1002/glia.23098 (2017).

Acknowledgements

We wish to thank Youshan Yang and Yangyang Yan for help with excised patch recording in noise free environment.

Author Contributions

D.S.N., F.J.S. and J.S.S. wrote the main manuscript text. J.P.B., I.M.N., S.B., and D.S.N. performed experiments. F.Y.L., J.P.B., J.S.S. and D.S.N. performed statistical analysis. J.P.B., I.M.N., S.Z., J.S.S., F.J.S. and D.S.N. prepared Figures 1–6. All authors reviewed the manuscript

Additional Information

Supplementary information accompanies this paper at <http://www.nature.com/srep>

Competing Interests: The authors declare no competing financial interests.

How to cite this article: Bai, J.-P. *et al.* Current carried by the Slc26 family member prestin does not flow through the transporter pathway. *Sci. Rep.* **7**, 46619; doi: 10.1038/srep46619 (2017).

Publisher's note: Springer Nature remains neutral with regard to jurisdictional claims in published maps and institutional affiliations.



This work is licensed under a Creative Commons Attribution 4.0 International License. The images or other third party material in this article are included in the article's Creative Commons license, unless indicated otherwise in the credit line; if the material is not included under the Creative Commons license, users will need to obtain permission from the license holder to reproduce the material. To view a copy of this license, visit <http://creativecommons.org/licenses/by/4.0/>

© The Author(s) 2017

En block C-terminal charge cluster reversals in prestin (SLC26A5): Effects on voltage-dependent electromechanical activity

Jun-Ping Bai^b, Dhasakumar Navaratnam^a, Haresha Samaranayake^a, Joseph Santos-Sacchi^{b,*}

^a Neurology and Neurobiology, Yale University School of Medicine, BML 246, 333 Cedar Street, New Haven, CT 06510, USA

^b Otolaryngology Neurobiology, and Cellular and Molecular Physiology, Yale University School of Medicine, BML 246, 333 Cedar Street, New Haven, CT 06510, USA

Received 18 August 2005; received in revised form 8 May 2006; accepted 9 May 2006

Abstract

Prestin, the transmembrane motor protein is a novel protein underlying the motility of the outer hair cells. Nonlinear capacitance (NLC) or gating charge current, which can be observed in both auditory and transfected non-auditory cells, is the electrical signature of prestin's electromechanical activity. To test the functional role of the C-terminus of prestin, several charged residue clusters were reversed en-block by site-directed mutagenesis. They are D/E to K at 516, 518, 522, 524, 527, 528 and 531 (*cluster a*); R/K to D at 571, 572, 573, 576, 577 and 580 (*cluster b*); R to D at 571; and E/D to K at 608, 609, 610, 611, 612 and 613 (*cluster c*). These constructs were transfected into Chinese hamster ovary cells (CHO) and NLC recordings were performed to evaluate the effects of these charge substitutions. All of the mutants showed NLC. Charge *cluster a* reversal significantly reduced the maximum charge movement (Q_{max}). All but one mutation (charge *cluster c* reversal) shifted V_h , indicative of the operating voltage range, in the depolarizing direction. None of the mutations affected unitary charge movement (z). These data suggest that the C-terminus of prestin lies outside the membrane voltage field, and may play an important role in controlling the operating voltage range through control of the protein's conformational energy profile via allosteric means.

© 2006 Elsevier Ireland Ltd. All rights reserved.

Keywords: Capacitance; Outer hair cell; Prestin; SLC26

Two types of receptor cells populate the mammalian organ of Corti, the inner hair cell (IHC) and the outer hair cell (OHC). IHCs serve only as sensory receptors by transducing basilar membrane vibrations into electrical signals. However, OHCs function both as receptors and effectors, possessing both electro-mechanical and mechano-electrical activities, thereby enabling amplification of the auditory stimulus to the IHCs [2,5,21]. Voltage-dependent mechanical activity of the OHC is detectable by whole-cell patch clamp recording as a nonlinear capacitance (NLC), or equivalently, a gating charge current [3,25]. Recently, the motor protein, prestin, which resides in the OHC lateral membrane [4], was found to underlie OHC electro-mechanical activity and mammalian cochlear amplification [12,31,24]. Transfection of the gene into non-auditory cells results in electro-mechanical characteristics similar to that observed in the native outer hair cell [15,26,31]. Topology studies of this 744 amino acid protein, a member of the anion

transporter family SLC26, show that its C- and N-termini reside within the cytoplasm [6,15,16,18,30]. Interestingly, intracellular chloride was found to play a key role in influencing NLC in both OHCs and prestin-transfected cells, but whether chloride itself is an intrinsic voltage sensor or an allosteric modulator is still debated [18,20]. We have found that removal of intracellular chloride by substitution with other anions causes shifts in prestin's operating voltage range, in addition to altering the protein's nonlinear charge transfer or NLC, indicating that anions modulate energy barriers controlling prestin's conformational state [20,27]. Additionally, we recently observed prestin–prestins interactions via their intracellular termini [17]. Such results may indicate that charged residues within prestin may interact with intracellular anions or influence interactions with other proteins. Many charged residues within the putative transmembrane regions of prestin have been manipulated [18]; however, little data are available on the role played by charged residues found within the cytoplasmic termini, structures which are unlikely to house the molecule's voltage sensor. Here we evaluate the effects of several C-terminal charge cluster reversals on prestin's electromechanical activity in order to gauge

* Corresponding author. Tel.: +1 203 785 5407; fax: +1 203 737 2502.
E-mail address: joseph.santos-sacchi@yale.edu (J. Santos-Sacchi).

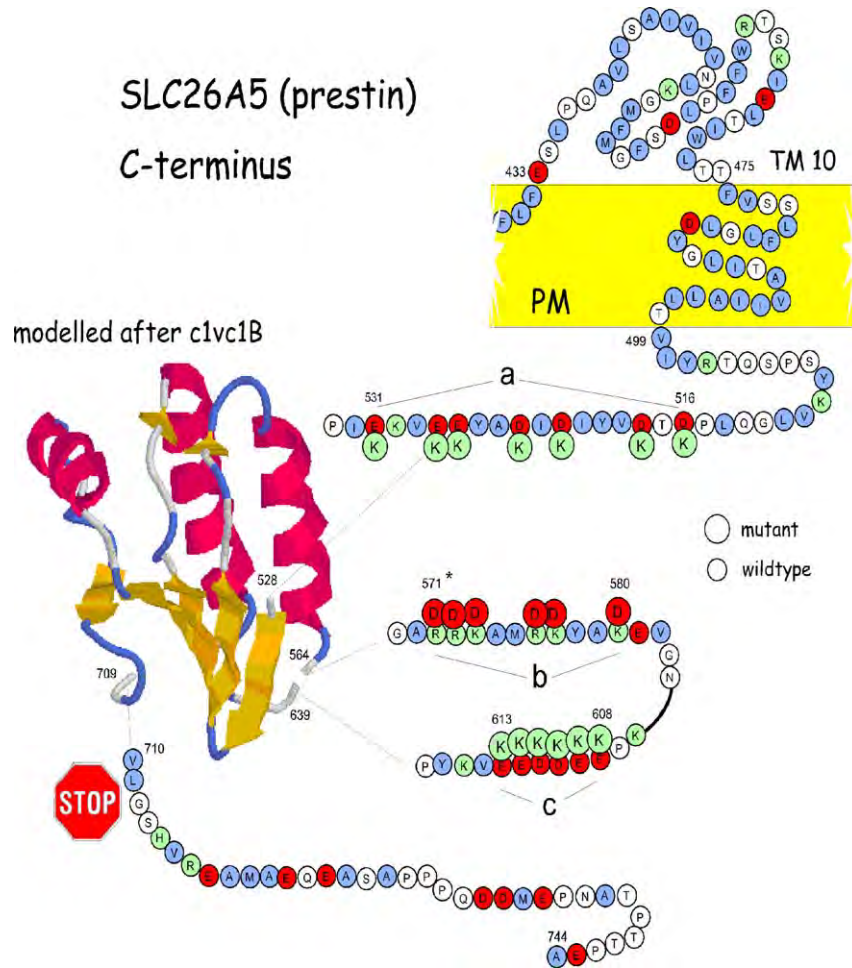


Fig. 1. C-terminal cartoon of gerbil prestin. Indicated are the charged clusters (a–c) which were mutated to residues of opposite polarity (large circles). The final transmembrane domain from the topology model of Navaratnam et al. [18] is shown along with the intracellular residues that were not captured in the model based on 3D structure of the sequence of c1vc1B, the putative anti-sigma factor antagonist tm1442. The model gives an excellent prediction of prestin’s C-terminal structure, but nearly all of the charged clusters we mutated reside in regions with no clear secondary structure. The residues 569–617 though present in prestin, are absent in c1vc1B. Parameters of the model fit: 19% i.d., 100% precision and a 6.4e-7 E value. The stop indicates the position (709) of the C-terminal truncation that results in a loss in NLC [18].

the C-terminal contribution to allosteric modulation of motor function.

The gerbil prestin sequence [31] was submitted to Quick Phyre (<http://www.sbg.bio.ic.ac.uk/~phyre/>) fold facility for 3D structural modeling and the C-terminal region of prestin was best fit with the structure encoded by the putative anti-sigma factor antagonist tm1442 (PDBcode: 1vc1_B; characteristic of the STAS domain [1]), at 19% i.d., 100% precision and a 6.4e-7 E value. The structure is shown in Fig. 1 along with noted mutations that we made in the prestin sequence. Though the STAS domain stretches from 525–711, the model is more limited.

We changed two negatively charged clusters to positive (residues 516–531 and 608–613; designated as charge clusters a and c, respectively), and changed one positively charged cluster to negative (571–580; cluster b). Additionally, a single site charge substitution was made at residue 571, denoted by “*” in Fig. 1. Charged amino acids were mutated en-block using the megaprimer PCR amplification method. Amplification by PCR was done using Hi-Fidelity DNA polymerase (Roche). The parameters were: 10 cycles of 94 °C for 40 s, 55 °C for 2 min,

68 °C for 6 min; 30 cycles of 94 °C for 40 s, 55 °C for 2 min, 68 °C for 6 min with 20 s extension for every cycle. A clone of gerbil prestin served as the template (courtesy of Zheng et al. [31]). Amplified products were purified, and ligated into PCDNA 3.1. Each of the clones generated were sequenced to exclude the possibility of PCR generated errors. Transient co-transfection with EGFP into Chinese hamster ovary cells (CHO) was achieved with Lipofectamine in accordance with the manufacturer’s recommendations. The ratio of prestin to EGFP plasmid (2:1) was kept constant in all the experimental groups. All cells showing NLC were included in our analyses.

Cells were recorded by whole-cell patch clamp configuration at room temperature using an Axon 200A amplifier (Axon Instruments, CA, USA), as described previously [25]. Expression levels, as evidenced by NLC measures, were stable from 24–72 h after transfection in control group. All statistical analyses of the mutants were performed at the 48 h time period following transfection. The bath solution contained (in mM): TEA 20, CsCl 20, CoCl₂ 2, MgCl₂ 1.47, Hepes 10, NaCl 99.2, CaCl₂·2H₂O 2, pH 7.2, and the pipette solution contained (in

mM): CsCl 140, EGTA 10, MgCl₂ 2, Hepes 10, pH 7.2. These conditions ensured that prestin-chloride interactions were maximal [18,20]. Osmolarity was adjusted to 300 ± 2 mOsm with dextrose. Command delivery and data collections were carried out with a Windows-based whole-cell voltage clamp program, jClamp (Scisoft, CT, USA), using a NI PCI 6052E interface (National Instruments Co., USA).

Capacitance was evaluated with a continuous high-resolution 2-sine wave technique fully described elsewhere [22,25]. Capacitance data were fitted to the first derivative of a two-state Boltzmann function:

$$C_m = Q_{\max} \frac{ze}{kT} \frac{b}{(1+b)^2} + C_{\text{lin}} \quad (1)$$

where

$$b = \exp\left(\frac{-ze(V_m - V_h)}{kT}\right)$$

Q_{\max} is the maximum nonlinear charge transfer, V_h the voltage at peak capacitance or half-maximal nonlinear charge transfer, V_m the membrane potential, C_{lin} linear capacitance, z the valence (a metric of voltage sensitivity), e the electron charge, k the Boltzmann's constant and T the absolute temperature. Q_{\max} is reported as Q_{sp} the specific charge density, i.e. total charge moved normalized to linear capacitance. A student's t -test was used to evaluate the effects of mutations on the different parameters of NLC.

FACS analysis of the different mutants and prestin were done to determine levels of surface expression exclusively [17]. Two antibodies to prestin peptides (aa 274–290 and 359–375) that we model to lie on the outer surface of the membrane were used to live stain transfected CHO cells [17]. Staining was performed as previously described except that the secondary antibody used was an Alexa 488 labeled goat anti-rabbit antibody. There was good concordance between the two antibodies used to separately stain transfected cells, results that internally validated our data (see Fig. 4). We have previously established that prestin surface expression in CHO cells were unchanged between 24–72 h after transfection by both FACS analysis and measurement of NLC [17]. The percentage of cells expressing prestin on its surface and the magnitude in NLC in CHO cells are similar to that obtained by other investigators [17,18].

Fig. 1 depicts the structural features of prestin's C-terminus. Large circles indicate the charge reversals that were made and confirmed by sequencing. All charge substitution mutants displayed NLC, and did not affect unitary charge movement z . Q_{\max} , was significantly different only with mutation of residues 516–531 (charge cluster *a*), which reduced Q_{\max} . Fig. 2 shows an example of a NLC capacitance function obtained from this mutation and a control cell. For presentation purposes, we averaged fitted Boltzmann parameters, presented in Table 1, and constructed average NLC functions of each mutation based on their average values (Fig. 3). The mutation of cluster *a* had a significant decrease of Q_{\max} , but unitary charge movement (z) remained normal, indicating that the mutated protein's voltage sensor remained unaltered, and only the number of functional proteins decreased. We confirmed that the levels of prestin surface expression in this (and other) mutant(s) were similar to

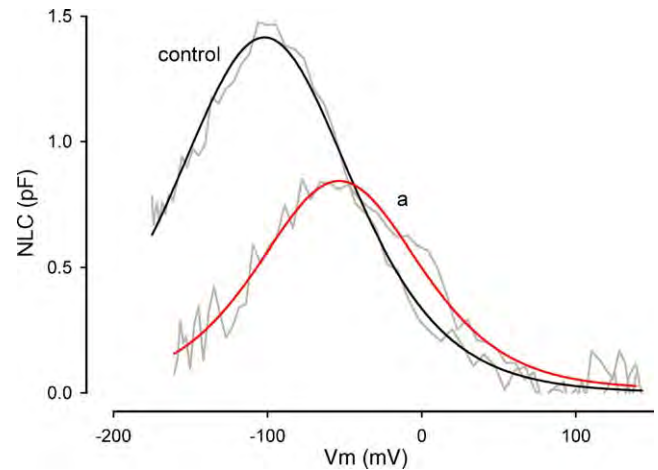


Fig. 2. NLC traces from prestin transfected CHO cells. CHO cells were transfected with constructs containing normal prestin (control) or the reversal of charge cluster *a* as indicated in Fig. 1. The solid traces are fitted curves. V_h of the reversal mutation shifts in the depolarizing direction along the voltage axis, and Q_{\max} significantly decreases.

Table 1
Average fitted Boltzmann parameters

	Q_{sp} (fC/pF) ± S.E.	z ± S.E.	V_h (mV) ± S.E.
Control ($n=15$)	6.15 ± 0.71	0.58 ± 0.03	-99.85 ± 2.51
Cluster <i>a</i> ($n=5$)	2.90 ± 0.58	0.53 ± 0.04	-57.41 ± 5.51
Cluster <i>b</i> ($n=6$)	6.23 ± 1.50	0.52 ± 0.04	-67.93 ± 1.73
Cluster <i>c</i> ($n=5$)	5.10 ± 0.38	0.71 ± 0.01	-108.20 ± 6.45
Residue 571 ($n=7$)	4.86 ± 0.63	0.65 ± 0.05	-90.19 ± 0.97

controls by FACS analysis (Fig. 4). z (and Q_{\max}) remained stable in the other mutations too, confirming that these residues, as expected, do not serve as charge carriers through the membrane. Some substitutions significantly affected V_h , with opposite charge substitutions changing V_h in the same depolarizing direction. For example, a change of negative charge in cluster *a* to

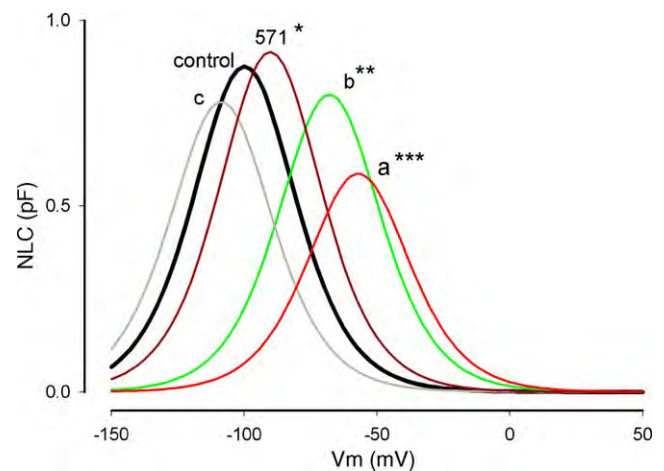


Fig. 3. C-terminal charge reversals predominately alter prestin's operating voltage range. For visual clarity, we averaged fitted parameters from each mutation, presented in Table 1, and constructed NLC functions of each based on their average values. Traces from each mutation are indicated as *a*, *b*, *c* and 571, and show some significant differences from control NLC, namely, for V_h and Q_{sp} (* $P_{V_h} < 0.05$; ** $P_{V_h} < 0.05$; *** $P_{V_h} < 0.05$; $P_{Q_{\text{sp}}} < 0.05$, respectively. The trace from control cells is the heavy black line.

positive, and a change in positive charge in *cluster b* to negative resulted in a depolarizing shift in V_h to -57.41 ± 5.51 ($n = 5$) and -67.93 ± 1.73 mV ($n = 6$), respectively. These effects on prestin activity are likely due to changes in the steady state energy profile of prestin, i.e. an allosteric effect possibly through interference with interacting proteins or anions (see discussion). Interestingly, mutation of charge *cluster c* within the most distal charged cluster, showed little difference from controls. Finally, the single charge substitution at residue 571 showed only minor changes.

The topology of prestin (SLC26A5) has received much attention, as has that of the other family members of SLC26

[6,13–19,30]. Initial efforts indicated that the protein consists of 12 transmembrane domains (TM), with both C- and N-terminal regions residing intracellularly [6,15,16,18,29,30]. Though the location of these termini are fairly certain, various prediction programs provide a confusing profile of TM domains. Even so, epitope tagging and the putative location of reactive residues have narrowed our view. One of the popular maps places two N-glycosylation sites on the second extracellular loop [16], but we have since observed that this site may not reside extracellularly, but instead intracellularly [17]. Though our new model flips the protein within the plane of the membrane, while conserving the

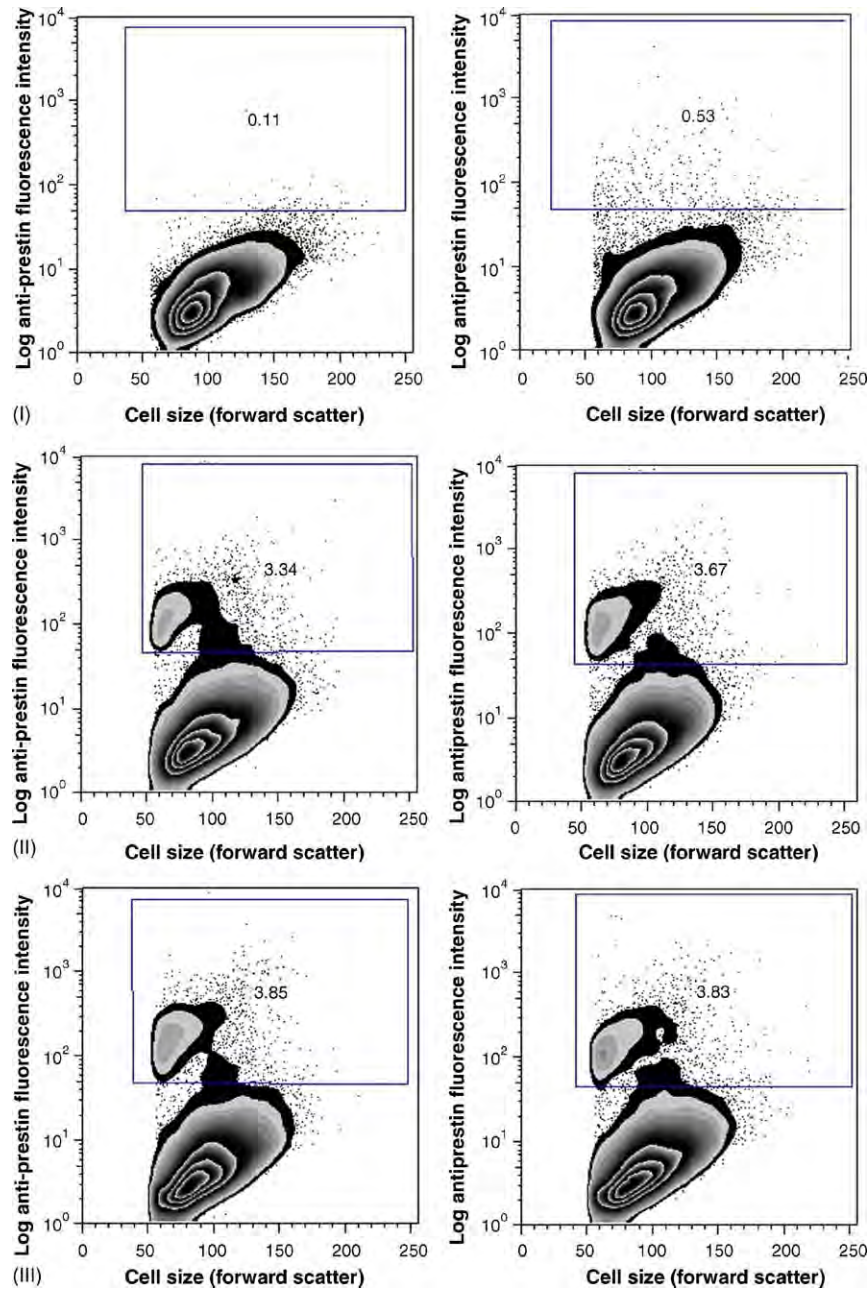


Fig. 4. Surface expression of cells transfected with normal prestin and mutant prestin were similar. Shown above are FACS plots of cells transfected with empty vector (I), normal prestin (II), charge cluster reversal a (III), charge cluster reversal b (IV) and charge cluster reversal c (V). The cells were live-stained with two antibodies against two peptides that we model to lie on the outer surface of the cell [18]. The percentage of cells with prestin surface expression (boxed area) reflecting efficiencies of transfection (inset) varied from 3.5 to 8.0% and are in line with results obtained by other groups (Oliver and Zheng, personal communication, see also [18]). The intensities of fluorescence between the different groups were similar confirming similar levels of surface expression.

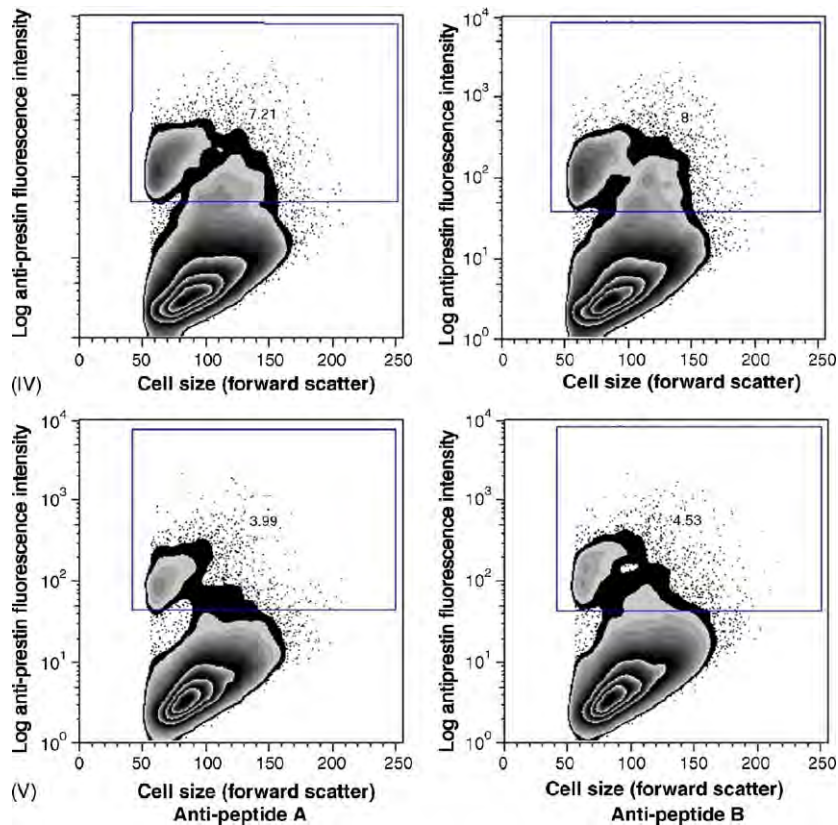


Fig. 4. (Continued).

intracellular termini and reversing the resident milieu of the non membrane bound loops, it maintains the intracellular location of a cGMP phosphorylation site proposed by Dallos and coworkers [6]; their modified model required a reentrant loop to intracellularly expose their previously predicted extracellular location of the site. Our model predicts simple TM transits. Clearly, the controversy over prestin's membrane topology indicates a complex interaction with the plasma membrane, which structural studies must finally divulge.

More germane to the present work, despite the seemingly clear localization of the C-terminus intracellularly, there are some observations which indicate that this domain is not simply accessible to attempted perturbations made intracellularly, outside the lipid bilayer. For example, the lack of an effect of intracellular trypsin or pronase treatment on OHC and transfected cell NLC indicates that prestin's termini are somehow protected [7–9,28]. We would therefore expect that deletion of either the C- or N-terminus would abolish NLC, a view that has been confirmed by mutational analysis (see Fig. 1); [17,29]. Interestingly, in channel forming bacterial colicins an intracellular hydrophilic group of residues (or even larger appended tags) can be moved across the membrane in response to changes in voltage [10,11], a mechanism that could also operate in prestin since these charged clusters may be constrained close to the PM within the restricted sub-plasmalemmal space bounded by the subsurface cisternae. Indeed, this type of mechanism that colicin employs has been offered as a possible mechanism to account for area changes evoked by prestin activation [23]. Thus, we

have no direct empiric evidence that the C-terminus of prestin is statically placed outside the bilayer. Nevertheless, our current work bears on this issue, since mutating charged residues in prestin that do not reside within the membrane field should not directly alter unitary charge movement. We found with our charge reversal mutations that, in no case, was the unitary charge of prestin's voltage altered, implying that these residues lie outside the membrane field. However, clear effects on voltage sensing were observed, with three mutations, *a*, *b* and *R571D* showing significant changes in V_h . We interpreted these results to indicate a shift in the steady state energy profile of the protein. Since both mutations of *cluster a* and *b* (which have opposite charge) shift V_h in the same direction, it is possible that simultaneous mutations of both could produce an augmented shift. Additionally, one mutant (*charge cluster a* that is most proximal to the membrane) shows a significant decrease in the total charge moved. We interpret this to mean that the number of functional motors in this mutant has decreased. This view is additionally supported by similar levels of surface targeting of prestin determined by FACS in cells transfected with this mutant compared to normal prestin. Moreover, this observation is also in line with our previous work on truncations at the most distal section of the C-terminus, where the number of functional motors within the membrane decreased as stop codons were successively placed within the residue range of 715 to 710. Truncations at residues more proximal to 710 produced non-functional motors despite proper membrane targeting. We additionally showed in that work that homo-multimerization occurs among prestin molecules, and

hypothesized that obligate interactions underlie prestin's motive force. It may be that our charge reversals also interfere with interactions of other proteins at the C-terminus.

One other possibility arises. It is known that Cl^- interactions with intracellular moieties of prestin are crucial for prestin function, and we have proposed that, in contrast to models suggesting extrinsic voltage sensing by Cl^- , Cl^- serves as an allosteric modulator of prestin. For this reason, it may be that anions might interact with the C-terminal charge clusters, at least with those two clusters which reside most proximal to the membrane (*clusters a, b*), since only those showed substantial shifts in voltage sensing. Recently, manipulation of the STAS domain, which is conserved within the C-terminus among SLC26 transporter family members has been shown to inhibit sulfate transport in SULTR1.2 [19]. This was observed in the presence of normal membrane targeting. We are currently investigating whether our charge reversal mutants alter multimerization and Cl^- sensitivity in prestin.

In sum, we hypothesize that the C-terminal charged clusters of prestin, while not interacting with the membrane field to alter unitary charge movements in prestin, may work by intracellular interactions with either other proteins or anions, namely via allosteric means.

Acknowledgements

Support was provided by NIH NIDCD grants DC 000273 (JSS) and K08 (DN). We thank Peter Dallos and colleagues for the gerbil prestin clone, and Margaret Mazzucco for technical help.

References

- [1] L. Aravind, E.V. Koonin, The STAS domain—a link between anion transporters and antisigma-factor antagonists, *Curr. Biol.* 10 (2000) R53–R55.
- [2] J.F. Ashmore, A fast motile response in guinea-pig outer hair cells: the cellular basis of the cochlear amplifier, *J. Physiol. (Lond.)* 388 (1987) 323–347.
- [3] J.F. Ashmore, Forward and reverse transduction in the mammalian cochlea, *Neurosci. Res.* 12 (Suppl.) (1990) S39–S50.
- [4] I.A. Belyantseva, H.J. Adler, R. Curi, G.I. Frolenkov, B. Kachar, Expression and localization of prestin and the sugar transporter GLUT-5 during development of electromotility in cochlear outer hair cells, *J. Neurosci.* 20 (2000) RC116.
- [5] W.E. Brownell, C.R. Bader, D. Bertrand, Y. de Ribaupierre, Evoked mechanical responses of isolated cochlear outer hair cells, *Science* 227 (1985) 194–196.
- [6] L. Deak, J. Zheng, A. Orem, G.G. Du, S. Aguinaga, K. Matsuda, P. Dallos, Effects of cyclic nucleotides on the function of prestin, *J. Physiol.-Lond.* 563 (2005) 483–496.
- [7] X.X. Dong, K.H. Iwasa, Tension sensitivity of prestin: comparison with the membrane motor in outer hair cells, *Biophys. J.* 86 (2004) 1201–1208.
- [8] G. Huang, J. Santos-Sacchi, Motility voltage sensor of the outer hair cell resides within the lateral plasma membrane, *Proc. Natl. Acad. Sci. USA* 91 (1994) 12268–12272.
- [9] S. Kakehata, J. Santos-Sacchi, Membrane tension directly shifts voltage dependence of outer hair cell motility and associated gating charge, *Biophys. J.* 68 (1995) 2190–2197.
- [10] P.K. Kienker, K.S. Jakes, R.O. Blaustein, C. Miller, A. Finkelstein, Sizing the protein translocation pathway of colicin Ia channels, *J. Gen. Physiol.* 122 (2003) 161–176.
- [11] P.K. Kienker, X. Qiu, S.L. Slatin, A. Finkelstein, K.S. Jakes, Transmembrane insertion of the colicin Ia hydrophobic hairpin, *J. Membr. Biol.* 157 (1997) 27–37.
- [12] M.C. Liberman, J. Gao, D.Z. He, X. Wu, S. Jia, J. Zuo, Prestin is required for electromotility of the outer hair cell and for the cochlear amplifier, *Nature* 419 (2002) 300–304.
- [13] H. Lohi, M. Kujala, E. Kerkela, U. Saarialho-Kere, M. Kestila, J. Kere, Mapping of five new putative anion transporter genes in human and characterization of SLC26A6, a candidate gene for pancreatic anion exchanger, *Genomics* 70 (2000) 102–112.
- [14] H. Lohi, M. Kujala, S. Makela, E. Lehtonen, M. Kestila, U. Saarialho-Kere, D. Markovich, J. Kere, Functional characterization of three novel tissue-specific anion exchangers SLC26A7, -A8, and -A9, *J. Biol. Chem.* 277 (2002) 14246–14254.
- [15] J. Ludwig, D. Oliver, G. Frank, N. Klocker, A.W. Gummer, B. Fakler, Reciprocal electromechanical properties of rat prestin: the motor molecule from rat outer hair cells, *Proc. Natl. Acad. Sci. USA* 98 (2001) 4178–4183.
- [16] K. Matsuda, J. Zheng, G.-G. Du, L. Deak, E. Navarrete, P. Dallos, Protein kinase C and voltage-dependent capacitance in prestin-transfected TSA cells, *Assoc. Res. Otolaryngol. Abs.* (2003) 105.
- [17] D.S. Navaratnam, J.-P. Bai, H. Samaranyake, J. Santos-Sacchi, N-terminal mediated homo-multimerization of prestin, the outer hair cell motor protein, *Biophys. J.* 89 (2005) 3345–3352.
- [18] D. Oliver, D.Z. He, N. Klocker, J. Ludwig, U. Schulte, S. Waldegger, J.P. Ruppersberg, P. Dallos, B. Fakler, Intracellular anions as the voltage sensor of prestin, the outer hair cell motor protein, *Science* 292 (2001) 2340–2343.
- [19] H. Rouached, P. Berthomieu, E. El Kassis, N. Cathala, V. Catherinot, G. Labesse, J.C. Davidian, P. Fourcroy, Structural functional analysis of the C-terminal STAS (sulfate transporter and anti-sigma antagonist) domain of the Arabidopsis thaliana sulfate transporter SULTR1.2, *J. Biol. Chem.* 280 (2005) 15976–15983.
- [20] V. Rybalchenko, J. Santos-Sacchi, Cl^- flux through a non-selective, stretch-sensitive conductance influences the outer hair cell motor of the guinea-pig, *J. Physiol.* 547 (2003) 873–891.
- [21] J. Santos-Sacchi, J.P. Dilger, Whole cell currents and mechanical responses of isolated outer hair cells, *Hear. Res.* 35 (1988) 143–150.
- [22] J. Santos-Sacchi, S. Kakehata, S. Takahashi, Effects of membrane potential on the voltage dependence of motility-related charge in outer hair cells of the guinea-pig, *J. Physiol.* 510 (Pt 1) (1998) 225–235.
- [23] J. Santos-Sacchi, E. Navarrete, Voltage-dependent changes in specific membrane capacitance caused by prestin, the outer hair cell lateral membrane motor, *Pflugers Arch.* 444 (2002) 99–106.
- [24] J. Santos-Sacchi, New tunes from Corti's organ: the outer hair cell boogie rules, *Curr. Opin. Neurobiol.* 13 (2003) 459–468.
- [25] J. Santos-Sacchi, Reversible inhibition of voltage-dependent outer hair cell motility and capacitance, *J. Neurosci.* 11 (1991) 3096–3110.
- [26] J. Santos-Sacchi, W.X. Shen, J. Zheng, P. Dallos, Effects of membrane potential and tension on prestin, the outer hair cell lateral membrane motor protein, *J. Physiol.-Lond.* 531 (2001) 661–666.
- [27] L. Song, A. Seeger, J. Santos-Sacchi, On membrane motor activity and chloride flux in the outer hair cell: Lessons learned from the environmental toxin tributyltin, *Biophys. J.* 88 (2005) 2350–2362.
- [28] S. Takahashi, J. Santos-Sacchi, Non-uniform mapping of stress-induced, motility-related charge movement in the outer hair cell plasma membrane, *Pflugers Arch.* 441 (2001) 506–513.
- [29] J. Zheng, G.G. Du, K. Matsuda, A. Orem, S. Aguinaga, L. Deak, E. Navarrete, L.D. Madison, P. Dallos, The C-terminus of prestin influences nonlinear capacitance and plasma membrane targeting, *J. Cell Sci.* 118 (2005) 2987–2996.
- [30] J. Zheng, K.B. Long, W. Shen, L.D. Madison, P. Dallos, Prestin topology: localization of protein epitopes in relation to the plasma membrane, *Neuroreport* 12 (2001) 1929–1935.
- [31] J. Zheng, W. Shen, D. He, K. Long, L. Madison, P. Dallos, Prestin is the motor protein of cochlear outer hair cells, *Nature* 405 (2000) 149–155.

A highly expressing Tet-inducible cell line recapitulates in situ developmental changes in prestin's Boltzmann characteristics and reveals early maturational events

Shumin Bian,^{4,1} Bon W. Koo,¹ Stephen Kelleher,¹ Joseph Santos-Sacchi,^{4,3}
and Dhasakumar S. Navaratnam^{1,2}

Departments of ¹Neurology, ²Neurobiology, ³Cellular and Molecular Physiology, and ⁴Surgery (Otolaryngology), Yale University School of Medicine, New Haven, Connecticut

Submitted 17 May 2010; accepted in final form 8 July 2010

Bian S, Koo BW, Kelleher S, Santos-Sacchi J, Navaratnam DS. A highly expressing Tet-inducible cell line recapitulates in situ developmental changes in prestin's Boltzmann characteristics and reveals early maturational events. *Am J Physiol Cell Physiol* 299: C828–C835, 2010. First published July 14, 2010; doi:10.1152/ajpcell.00182.2010.—Prestin is the motor protein within the lateral membrane of outer hair cells (OHCs), and it is required for mammalian cochlear amplification. Expression of prestin precedes the onset of hearing in mice, and it has been suggested that prestin undergoes a functional maturation within the membrane coincident with the onset of hearing. We have developed a tetracycline-inducible prestin-expressing cell line that we have used to model prestin's functional maturation. We used prestin's voltage-dependent nonlinear charge movement (or nonlinear capacitance) as a test of function and correlated it to biochemical measures of prestin expressed on the cell surface. An initial stage of slow growth in charge density is accompanied by a rapid increase in our estimate of charge carried by an individual motor. A rapid growth in charge density follows and strongly correlates with an increasing ratio between an apparently larger and smaller monomer, suggesting that the latter exerts a dominant-negative effect on function. Finally, there is a gradual depolarizing shift in the voltage of peak capacitance, similar to that observed in developing OHCs. This inducible system offers many opportunities for detailed studies of prestin.

development; prestin; cell lines

MAMMALIAN OUTER HAIR CELLS (OHCs) are electromotile, and this property is believed to underlie cochlear amplification, a process that enhances mammalian frequency tuning and sensitivity (4, 5, 16). Prestin, a member of the SLC26 anion transporter family, has been identified as the protein responsible for electromotility (15, 20). In these and other studies, voltage-dependent charge movement of prestin's voltage sensor, detected as a nonlinear capacitance (NLC), has been shown to strongly correlate with electromotility. Thus, NLC can be used as a proxy measure of electromotility. The Boltzmann characteristics of NLC include the density of voltage sensor charge (Q_{sp}), the voltage at peak capacitance (V_h), and unitary charge valence (z). Q_{sp} is an estimate of the number of functional motors within a unit area of surface membrane, V_h is a metric of the steady-state energy profile, and z is an estimate of charge moved within an individual motor. Both electromotility and NLC show a developmental maturation in the OHCs (1, 2, 7, 13). In gerbils, electromotility is first detected at postnatal day P8 and P7 in OHCs from the apical

and basal turns, respectively; thereafter it stabilizes at P17–P19 (7), coincident with maturation of hearing (11). In contrast, NLC can be detected as early as P0 in OHCs from the rat apical turn (13). In that study, specific NLC was found to stabilize at P11 well before maturation of hearing in rats (3). However, in mice, linear capacitance (an indicator of both cell surface area and prestin deposition into the membrane) and prestin RNA levels asymptote at about P10, whereas specific NLC continued to increase until P18 (1), which coincides with maturation in hearing (17). The results of Abe et al. (1) strongly suggest a maturation process for the motor protein itself, although the nature of this maturation has yet to be determined. To gain insight into the possible mechanisms underlying this phenomenon, we used a tetracycline-inducible, prestin-expressing stable cell line of human embryonic kidney (HEK) cells to study aspects of NLC as they relate to expression of prestin. Our results demonstrate that maturation following induction involves an increasing incorporation of two monomeric forms of prestin into the cell membrane, with one form exerting a dominant-negative effect on the other. Functional correlates of maturation show early and prolonged time course components following induction, with z increasing during the first few hours, and both Q_{sp} and V_h changing over tens of hours. These data substantiate observations about the maturation of electromotility in OHCs. They also provide insights that cannot be gleaned from OHC measures alone and underscore the utility of this inducible cell line.

MATERIALS AND METHODS

Prestin gene constructs. Plasmid pcDNA6/TR is from Invitrogen with selective antibiotic blasticidin. This construct codes for a tetracycline operon (TO) repressor that works with the second plasmid, pcDNA4/TO/*myc*-HisC, to create a tetracycline-inducible system for protein expression. pcDNA4/TO/*myc*-HisC is also from Invitrogen and is selective by antibiotic zeocin. The gerbil prestin gene (a gift from J. Zheng and P. Dallos) tagged with enhanced yellow fluorescent protein (EYFP) was inserted into the multiple cloning site of pcDNA4/TO/*myc*-HisC. This construct (gPrestin-YFP4TOMycHisC) contains a 2× tetracycline operon that works with the first construct to create inducible prestin expression. When tetracycline is absent, the repressor binds to the tetracycline operon, keeping the gene downstream from being expressed. When tetracycline is present, it binds to the repressor, releasing the tetracycline operon and allowing the prestin gene to be expressed. The *myc*-His tags in the construct are for detection and purification purposes. pEYFP-N1 vector (Clontech) was used to construct the noninducible prestin-YFP-expressing vector with a Flag tag added to the NH₂ terminus. This vector uses antibiotic G418 for selecting stable cell lines.

Address for reprint requests and other correspondence: D. S. Navaratnam, Dept. of Neurology, Yale School of Medicine, New Haven, CT 06520 (e-mail: dhasakumar.navaratnam@yale.edu).

Cell culture and transfection. HEK293 cells (American Type Culture Collection ATCC, Manassas, VA) were cultured in Dulbecco's modified Eagle's medium (DMEM, high glucose) medium containing 50 U/ml each of penicillin and streptomycin, 10% fetal bovine serum at 37°C in a CO₂ incubator (5%). Transfection of constructs into these cells was done using Superfect reagent (Qiagen) according to the manufacturer's instructions for stable transfection. To produce inducible prestin cell lines, pcDNA6/TR was first transfected and selected with 8 µg/ml blasticidin for monoclonal stable cell lines (293-pcDNA6/TR). Then the gPrestin-YFP4TomyHisC construct was transfected to stabilized 293-pcDNA6/TR cells, and selected with 280 µg/ml zeocin. Stabilized monoclonal prestin-YFP-mycHis expression was initially screened by using fluorescence microscopy 1 or 2 days after addition of 1 µg/ml tetracycline to the growth medium. Culturing of these cell lines (293-TRxST-gPrestin-YFP4TomyHisC) was in DMEM base medium supplemented with 4 µg/ml blasticidin and 130 µg/ml zeocin. Selection of the Flag-prestin-YFP-N1 construct was done by adding 1,200 µg/ml G418 (geneticin) to these cells. G418 concentration in the growth medium was reduced to 600 µg/ml for stable cell lines.

Patch-clamp electrophysiology. Intracellular solution (pipette solution) contained (in mM) 136 KCl, 1 CaCl₂, 1 MgCl₂, 10 HEPES buffer, and 5 EGTA, pH 7.28. Osmolarity was adjusted to 299 ± 2 mosM using glucose for all solutions. Extracellular solution (bath solution) contained (in mM) 20 TEA, 20 CsCl, 2 CoCl₂, 1.47 MgCl₂, 10 HEPES buffer, 99.2 NaCl, 2 CaCl₂, and 2 BaCl₂, pH 7.28. Glass pipettes were pulled using a P-2000 laser-heating pipette puller (Sutter Instruments). All pipettes have initial resistances of about 2.5 MΩ. All patches were made on single cells growing on a coverslip at different time points after tetracycline induction. A Nikon Eclipse FNI upright microscope equipped with a ×40 water immersion lens and a green fluorescent protein (GFP) UV light filter was used for cell observation,

and an EXFO motorized manipulator by Burleigh (PCS-6000) was used for pipette manipulation. Data acquisition was done with a Digidata 1322A A/D converter and an Axonpatch 200B Integrating Patch clamp (Axon Instruments). Cell capacitance was measured under whole cell configuration using the jClamp software (<http://www.scisoftco.com/>). For time course studies with tetracycline-inducible cell lines, 4–11 cells were averaged for each time point. NLC from two inducible cell lines was measured separately, and the results are comparable. Only one is presented in this study.

The NLC traces show the change of membrane capacitance C_m in response to voltage across the membrane V_m . Each trace can be fitted according to Eq. 1 using four parameters:

$$C_m = Q_{\max} \frac{ze}{kT} \frac{b}{(1+b)^2} + C_{\text{lin}}$$

where

$$b = \exp \left[\frac{-ze(V_m - V_h)}{kT} \right] \quad (1)$$

Q_{\max} is maximum nonlinear charge transfer, V_h is voltage at peak capacitance or half-maximal nonlinear charge transfer, V_m is membrane potential, C_{lin} is linear capacitance proportional to cell surface area, z is valence (a metric of voltage sensitivity), e is electron charge, k is Boltzmann's constant, and T is absolute temperature. Q_{\max} is reported as Q_{sp} , the specific charge density, i.e., total charge moved normalized to linear capacitance. Similarly, specific nonlinear capacitance NLC_{sp} refers to $(C_m - C_{\text{lin}})/C_{\text{lin}}$.

Confocal fluorescence imaging. Tetracycline (1 µg/ml) was added to the cell growth medium 1 day after the cells were plated on coverslips. After incubation for 24 to 48 h for tetracycline-induced

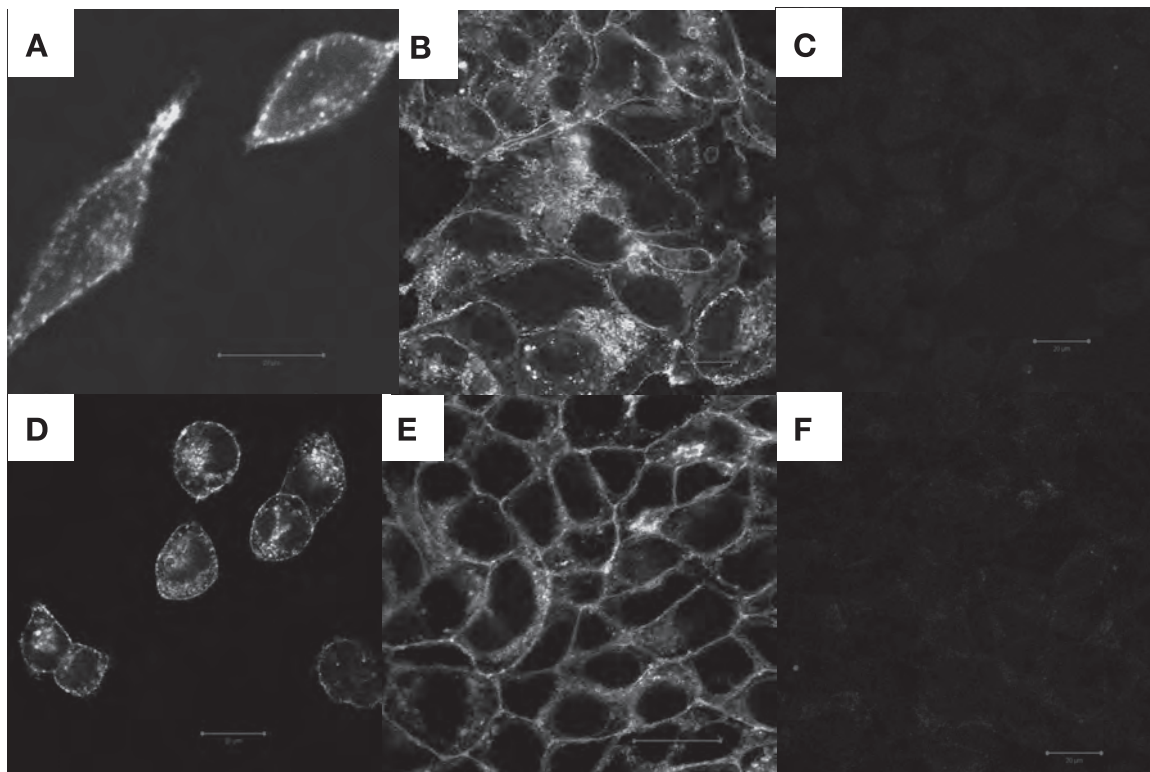


Fig. 1. Prestin-yellow fluorescent protein (YFP) is localized to the membrane. Prestin-YFP expression in human embryonic kidney (HEK) 293 cell lines characterized by confocal imaging of YFP fluorescence is shown. *A* and *B*: a HEK293 cell line stably expressing a Flag-tagged prestin-YFP construct. *C*: untransfected HEK293 cells as negative control. *D–F*: a tetracycline-inducible HEK293 cell line expressing prestin-YFP with a mycHis6 tag at its COOH terminus. *D* and *E*: 24 h after addition of 1 µg/ml tetracycline to the growth media. *F*: no tetracycline added as negative control. Scale bar, 20 µm.

expression of prestin-YFP, cells were washed briefly with PBS, then fixed in 3% formaldehyde in PBS for 20 min at room temperature. Following a wash in PBS, cells were mounted with VectaShield mounting media for confocal microscope observation. All confocal experiments were done on a Zeiss LSM 510 Meta confocal microscope using a 514 nm laser line. Image analysis was done using LSM Image browser.

To analyze fluorescence intensity of cell surface prestin versus total prestin expression using YFP fluorescence imaging, individual cells from the 293-Flag-prestin-YFP cell line were analyzed using Photoshop's histogram utility. The integrated fluorescence intensity is the product of mean pixel intensity, after subtracting mean background intensity, times total pixel numbers in the region of interest (ROI). By demarcating the outer edge of the whole cell as the ROI, we obtained total integrated pixel intensity. We then obtained intracellular intensity by applying the same algorithm defining the ROI within the inner aspect of the cell membrane. Surface intensity was obtained by subtracting the intracellular intensity from the total cell intensity.

Electron microscopy of nanogold-labeled prestin-YFP. Electron microscopy immunohistochemistry was done at the Yale Center for Cell and Molecular Imaging using a Tecnai 12 Bio Twin Transmission Electron Microscope. All images were taken at the same calibrated magnification ($\times 43,000$). Fifty images were taken randomly from HEK cells expressing prestin-YFP, as well as 20 images from a control sample (untransfected HEK cells) for quantification and statistics. For all images included in this analysis, the anti-GFP primary antibody conjugated with 10-nm nanogold was used at a 1:50 dilution for maximum labeling efficiency. Background labeling as seen in

mitochondria and nucleus was very low. Quantification of surface prestin and total prestin expression was done by counting the nanogold particles either on plasmic membrane only or everywhere in the cell.

Surface protein labeling. Cell surface protein labeling was done according to the manufacturer's instructions (Pierce Biotech, EZ-link Sulfo-NHS-SS-Biotin surface protein isolation kit). Briefly, cells grew on 10-cm culture plates, and 1 $\mu\text{g/ml}$ tetracycline was added at different time points to give different incubation times at harvest. Cell surface proteins were labeled after a brief wash in cold PBS at 4°C on a flat shaker. The reaction was quenched using quenching solution after 30 min, and cells harvested by using a scraper. Cells were spun down and briefly washed in Tris-buffered saline before addition of lysis buffer supplemented with protease inhibitors (Roche Complete protease inhibitors). Cells were lysed at 4°C for 30 min with end-to-end rotation, and total protein was quantified using Bio-Rad Protein Assay kit (500-0006); 2,500 μg of total protein from each sample was mixed with 250 μl NeutrAvidin Gel and incubated for 1 h at room temperature. Following steps of washing and centrifugation, plasma membrane proteins were purified and eluted from the gel using SDS sample buffer with 100 mM DTT. Two microliters of each eluted surface protein was loaded onto a Bio-Rad 4-15% Tris-glycine gradient gel. Lysate loading was also quantified to have 0.75 μg of total protein for each lane. In total, three rounds of surface labeling were done, each followed by Western blot and densitometry measurements, and the results were averaged. To avoid signal saturation on the film, and to minimize the subjectivity in assigning the boundaries between the bands, different exposures that gave clearly identifiable

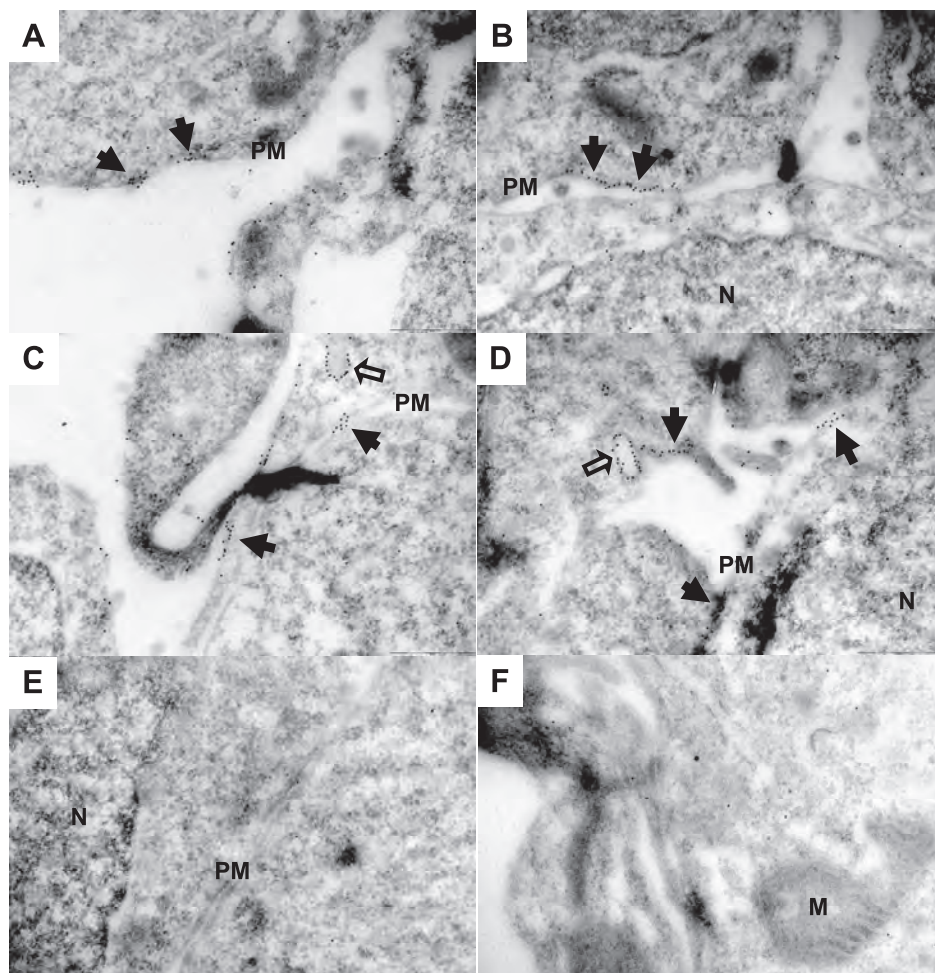


Fig. 2. Immunogold labeling localizes prestin to the plasma membrane. Electron microscopy (EM) images of a HEK293 cell line expressing Flag-tagged prestin-YFP are shown. Cells were grown to a monolayer in culture dishes, fixed, embedded, thin-sectioned, labeled with anti-green fluorescent protein (GFP) antibody (that cross-reacts with YFP) conjugated with 10 nm nanogold particles, stained, and imaged using a Tecnai 12 Bio Twin transmission electron microscope. *A–D*: samples from cells expressing prestin-YFP. Nanogold labeling is clearly seen on the plasma membrane (filled arrows), indicating proper trafficking and targeting of prestin molecules to the cell membrane. Notice also scattered labeling in the cytoplasm and on some intracellular vesicles as pointed out by hollow arrows. *E* and *F*: in the untransfected HEK293 cells, very small amount of labeling was observed. N, nucleus; PM, plasma membrane; M, mitochondria. Scale bar, 250 nm.

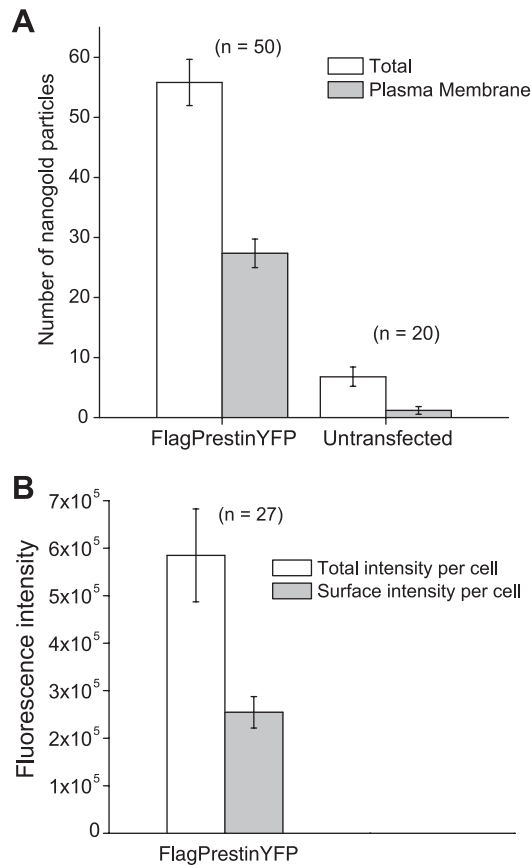


Fig. 3. Equivalent amounts of prestin are found in the plasma membrane and cytoplasm. Quantitative analysis on the distribution of prestin molecules in a Flag-tagged prestin-YFP stable cell line is shown. *A*: nanogold particle counting from EM images. Individual particles were counted from each micrograph, and the particles on the plasma membrane were subtracted from the total. As shown here, on average there are 56 gold particles in each micrograph of transfected cells, out of which 27 are localized on the cell membrane ($\sim 50.6 \pm 2.5\%$). *B*: the intensity of fluorescence was assayed on Flag-tagged prestin-YFP-expressing cells. The localization of YFP fluorescence was quantified in the plasma membranes of these cells. The plasma membranes of these cells contained $48.6 \pm 1.9\%$ of the total fluorescence signal (\pm SE).

and separate bands were used. To allow comparison between different exposures, data were normalized to several bands in the middle lanes with expression levels that were intermediate.

RESULTS

We have established several inducible and noninducible HEK cell lines stably expressing the motor protein prestin. When making these cell lines, we used a number of prestin constructs where prestin was variably tagged to YFP, and the c-myc and FLAG epitopes. We have studied the distribution of prestin expression in these cells by electron microscopic immunogold labeling and confocal imaging. Using our tetracycline-inducible cell line, we investigated the development of the motor protein by measuring NLC and correlated these data with biochemical measures of prestin surface expression in these cells.

Prestin is targeted to the surface membrane in HEK cells. With both inducible and noninducible cell lines expressing prestin-YFP, we observed that YFP fluorescence was localized to the plasma membrane, but significant amounts remained

intracellularly (Fig. 1). In inducible cell lines, YFP was observed at very low levels before induction (Fig. 1*F*) but showed a dramatic increase after induction (Fig. 1, *D* and *E*).

We also attempted to better localize prestin in these cell lines by using nanogold labeling with an antibody to GFP that also recognizes YFP with high fidelity (Fig. 2). In these experiments, we noted that nanogold particles were localized on the plasma membrane and within the cell. A quantitative morphometric analysis where individual particles were counted in 50 photomicrographs revealed that about half of the particles were on the surface membrane of the cell (Fig. 3*A*). These data are congruent with measurement of fluorescence in YFP-tagged prestin-expressing cells. In these cells, $\sim 50\%$ of the fluorescence signal was localized to the surface of the cell (Fig. 3*B*).

Nonlinear capacitance characterization of stable cell lines. Fluorescence measurements indicate that our stable cell lines have high levels of prestin-YFP located in the cell plasma membrane. We then tested these cell lines for functional expression of prestin, by determining NLC in several representative cells from each cell line.

Under whole cell voltage-clamp configuration, we were able to record large NLC in most of our HEK cell lines expressing prestin (Fig. 4). For example, a Flag-tagged noninducible cell line (termed G) exhibits a peak NLC of 3.7 pF (Fig. 4, *top* trace), while the tetracycline-inducible line (termed 16c) has a peak NLC of 2.8 pF (*bottom* trace). NLC values of these cell lines are summarized in Table 1. These typical values are higher than values seen in transiently transfected Chinese hamster ovary cells, which exhibit peak capacitance of about 1 pF; expression levels in these lines are also higher than other stable prestin cell lines (9).

Development of NLC in a tetracycline-inducible prestin cell line. We used tetracycline-inducible cell lines to analyze time-dependent changes in NLC. Typical traces of NLC from different time points after addition of tetracycline to the growth

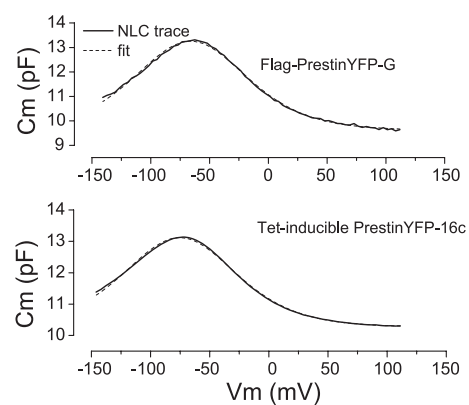


Fig. 4. Large nonlinear capacitance (NLC) is generated in cell lines expressing prestin. Shown are typical traces of NLC from two stable cell lines expressing prestin-YFP. The data were fitted according to Eq. 1. *Top*: trace from a noninducible HEK293 cell line (termed G) expressing Flag-tagged prestin-YFP. The fitting parameters were as follows: peak capacitance voltage (V_h) = -66.1 mV, unitary charge valence (z) = 0.801, maximum nonlinear charge (Q_{max}) = 0.468 pC, and linear capacitance (C_{lin}) = 9.61 pF. C_m , membrane capacitance. *Bottom*: NLC trace from a tetracycline (Tet)-inducible HEK293 cell line expressing prestin-YFP tagged with mycHis6. Tetracycline (1 μ g/ml) was added to the growth media, and NLC was measured 34 h after tetracycline induction. Fitting parameters were as follows: V_h = -75.3 mV, z = 0.804, Q_{max} = 0.365 pC, and C_{lin} = 10.3 pF. V_m , cell membrane potential.

Table 1. Nonlinear capacitance parameters from representative prestin cell lines

Cell Line	Q_{sp} , fC/pF	V_h , mV	z	n	Notes
Flag-prestin-YFP-G*	20.1 ± 2.7	-106 ± 7.0	0.78 ± 0.04	5	
Prestin-YFP-myc-His-15b†	14.1 ± 1.4	-93.9 ± 5.2	0.70 ± 0.02	7	30 h Tet
Prestin-YFP-myc-His-16c†	20.6 ± 1.3	-77.0 ± 7.9	0.76 ± 0.01	8	28 h Tet
HEK transiently transfected cells (18)	$\sim 11 \pm 4$	-70 ± 18	0.82	10	
CHO cell line (8)	~ 6	-75			

Values are means \pm SE of nonlinear capacitance parameters in one noninducible (*) and two tetracycline (Tet)-inducible (†) monoclonal cell lines we have developed. For inducible cell lines 15b and 16c, values were chosen from specific time points after induction, since their specific charge density (Q_{sp}) as well as unitary charge valence (z) and voltage at peak capacitance (V_h) change with time of incubation. These cells have a range of Q_{sp} values, all of which are higher than either typical transiently transfected human embryonic kidney (HEK) cells or other stable cell lines developed previously. YFP, yellow fluorescent protein; CHO, Chinese hamster ovary cells. Reference numbers are in parentheses.

media are shown in Fig. 5. When no tetracycline is added, little or no NLC is observed. With 1 μ g/ml tetracycline, NLC becomes readily measurable as early as 2 h after addition.

We also assayed three different parameters of NLC, Q_{sp} , z , and V_h , to further delineate prestin function. Q_{sp} , charge movement per unit of membrane surface, increases with time in a sigmoidal manner (Fig. 6A). The inset in Fig. 6A shows the growth phase in the first 6 h after addition of tetracycline. This phase was characterized by a steady, yet slow increase of Q_{sp} , to about one-tenth of the asymptotic value. This is followed by a rapid increase in Q_{sp} from 6 h to about 20 h after tetracycline induction, where Q_{sp} increases to $\sim 60\%$ of the asymptotic value. Following this rapid increase there is again a phase of slow increase in Q_{sp} to its mature level over a further period of 72–96 h.

In contrast to Q_{sp} , which takes over 60 h to reach its asymptotic level, z , an estimate of charge carried by an individual motor, reaches a maximum level of $0.8e$ 6 h after induction (Fig. 6B).

We also looked at changes in V_h over the time course of prestin expression. As shown in Fig. 6C, even though V_h values fluctuate, there was a general trend for these values to reach

more depolarized potentials with time. V_h settles near -80 mV at ~ 30 h after tetracycline induction.

Development of surface prestin expression in a tetracycline-inducible cell line. We undertook quantitative surface protein labeling experiments using a tetracycline-inducible cell line to determine the expression of prestin on the cell surface. We used a cell surface protein labeling method with cleavable water-soluble Sulfo-NHS-SS-Biotin reagent that then allows for the isolation of surface-labeled protein through its binding to avidin-Sepharose beads. The amount of prestin in these surface-labeled preparations was then determined using Western blotting.

Prestin expressed on the cell surface reaches an asymptotic level at 18–20 h (Fig. 7, B and D). In contrast, the total amount of prestin in the cell continues to increase throughout the sampling period after induction, albeit more slowly after 22 h (Fig. 7, A and C). In these experiments, we observed two major monomeric forms of prestin in both total cell lysate and the cell surface components. The upper monomer has a molecular mass of ~ 125 kDa, and the lower monomer a mass of ~ 100 kDa. There is also a broad multimeric form of prestin, which was first detected at ~ 4 h after induction. The upper monomeric form is the predominant component in both cell lysates and plasma membranes. When plotting Q_{sp} against the intensity of the upper monomer alone, we obtained a linear correlation (adjusted $R^2 = 0.83$). However, this relationship was attenuated at higher Q_{sp} values, when the amount of upper monomer remained stable with continued increase in Q_{sp} (Figs. 7D and 8A). At higher Q_{sp} values, there was a decrease in the lower monomer (Fig. 7D). Concordant with these data, we observed a strong linear relationship (with adjusted $R^2 = 0.92$, Fig. 8A), when we plotted Q_{sp} against the ratio of the upper to lower monomer. These results corroborate our previous assertion (9) that the lower monomer has a dominant-negative effect on the upper monomer. Interestingly, there is also a linear correlation between the initial rapid rise in z and the shift toward more depolarizing voltages in V_h (Fig. 8B). We note that this particular correlation was not an artifact of different initial fitting parameters. That is, we tested a range of voltages used to bracket NLC and established that V_h was not changed by the limits of the voltage range set when establishing a fit.

DISCUSSION

We have developed and used an inducible HEK cell line as a model system to understand prestin's maturation that has been observed in OHCs (1, 13). We used a combination of imaging, electrophysiological recording, and protein labeling

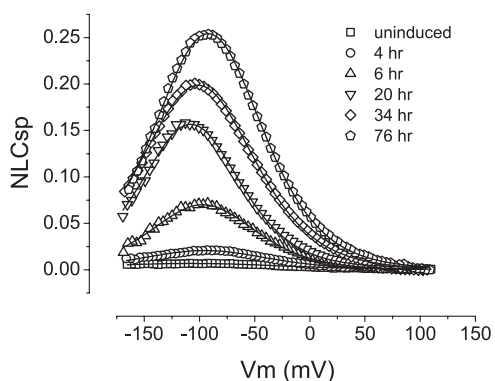


Fig. 5. NLC increases as a function of time in inducible cell lines expressing prestin. Shown are representative NLC curves from a tetracycline-inducible HEK293 cell line (16c). Specific NLC (NLC_{sp}) was used as a means to normalize data to cell size [$NLC_{sp} = (C_m - C_{lin})/C_{lin}$]. Without tetracycline added to the growth media (uninduced), prestin expression is repressed, resulting in minimal measurement of NLC. As the incubation time with tetracycline lengthens, the cells develop higher NLC as a result of either more prestin expression and/or prestin maturation on the cell membrane. Fitting parameters according to Eq. 1 were the following: for 4 h, V_h (mV) = -93.8 , $z = 0.697$, Q_{max} (pC) = 0.045 , C_{lin} (pF) = 18.0 ; for 6 h, $V_h = -97.3$, $z = 0.799$, $Q_{max} = 0.213$, $C_{lin} = 23.7$; for 20 h, $V_h = -108$, $z = 0.855$, $Q_{max} = 0.270$, $C_{lin} = 14.6$; for 34 h, $V_h = -101$, $z = 0.753$, $Q_{max} = 0.528$, $C_{lin} = 19.5$; and for 76 h, $V_h = -92.2$, $z = 0.780$, $Q_{max} = 0.548$, $C_{lin} = 16.5$.

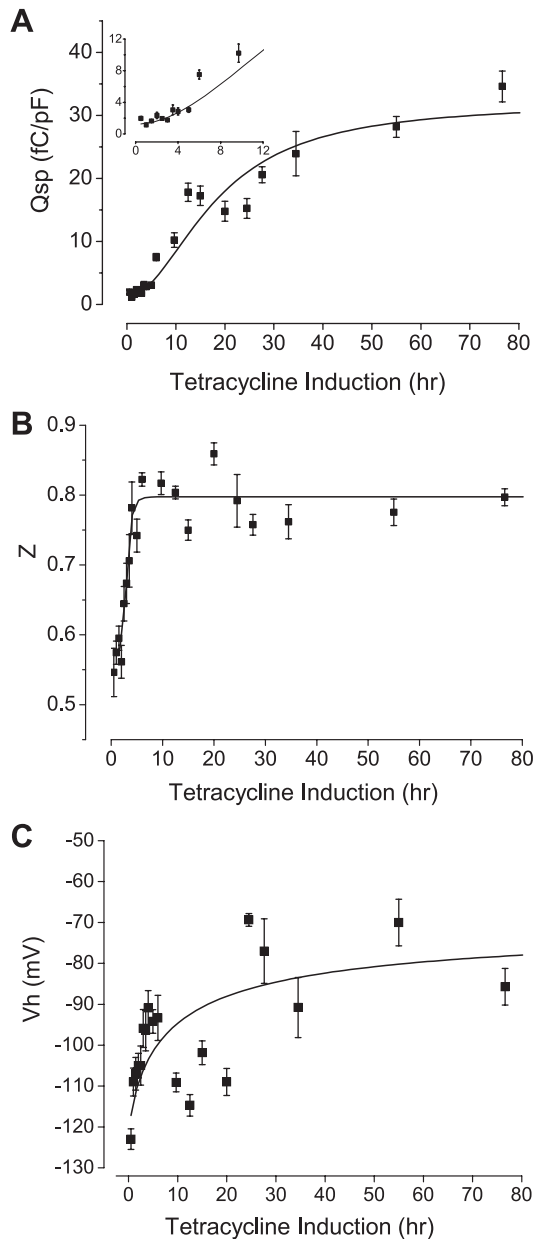


Fig. 6. NLC parameters change as a function of time after induction. *A*: development of specific charge density (Q_{sp}) after induction in a representative tetracycline-inducible prestin cell line (16c) with time. Q_{sp} increase shows a sigmoidal pattern with time and stabilizes at 30+ h. The number of cells patched for each point ranged from 4 to 11. Error bars are \pm SE. Data were fitted to a Hill equation [$y = \text{start} + (\text{end} - \text{start}) \times x^n / (k^n + x^n)$] with the following parameters: start = 1.23; end = 32.0; $k = 18.3$; $n = 2.0$. *B*: development of unitary charge valence (z) in a tetracycline-inducible cell line as a function of time after induction. z shows a rapid increase over several hours to reach its plateau at 6–8 h. z values did not change significantly, remaining stable after this time point. Fitting parameters were as follows: start = 0.58; end = 0.80; $k = 3.0$; $n = 6.8$. *C*: development of voltage dependence of peak NLC (V_h) as a function of time after induction. While there was considerable variation in V_h values, there was a clear trend in the development of V_h values toward more depolarizing voltages with time. Fitting parameters were as follows: start = -123 ; end = -69.4 ; $k = 8.6$; $n = 0.74$.

to ascertain aspects of prestin's development. Both confocal fluorescence and electron microscopy techniques show prestin to be efficiently targeted to the surface of the cell, with approximately half of the expressed prestin found on the cell

surface. Immunogold labeling and fluorescence quantifications were equivalent.

We also observed a relationship between aspects of prestin biochemistry and function. Increase in Q_{sp} , which corresponds to electromotility, clearly correlates to an increase in the level of prestin expression on cell surface (Fig. 8A). Moreover, consistent with our prior data in transiently transfected cells (9), we observed a strong linear relationship between Q_{sp} and the ratio of the upper and lower forms of prestin monomer. These data indicate that the lower prestin monomer has a dominant-negative effect on the upper monomer. It also means that the lower monomer is a less functional or nonfunctional variant of prestin. Moreover, because they imply interactions between upper and lower forms, these data are indirect evidence that the functional unit of the protein is a dimer, in line with previous suggestions (6, 12, 14, 19).

Our data raise questions as to the nature of the two monomers of prestin that we identified. Three scenarios are conceivable. First, it may be that the two monomers are differentially folded forms of the protein, with the smaller being misfolded and migrating faster on SDS-PAGE. This possibility is supported by our previous data showing increasing amounts of the lower monomer with cysteine mutants that are likely important for the structural integrity of the protein (9). The second scenario, that the lower monomer represents proteolytic cleavage of the protein, is untenable since antibodies to both NH₂- and COOH-terminal tags of the protein identify both monomers (data not shown). Lastly, it is also possible that these two monomers represent effects of differential glycosylation (10) with the upper and lower monomer representing glycosylated and unglycosylated forms of the protein, respectively. However, since we and others have previously shown that wild-type prestin and prestin in which the two potential *N*-glycosylation sites (N163 and N166) were mutated differ minimally in function (10, 12), this possibility will not explain the dominant-negative effect of the lower monomer on prestin function (Fig. 8A).

Our hypothesis that the lower monomer represents a misfolded form raises mechanistic questions concerning prestin turnover. Induction results in a continuous production of prestin that continues in time beyond asymptotic measures of prestin activity (Q_{sp}), indicating a mechanism of prestin removal. Since the ratio of upper to lower monomer changes with time until steady state, we reason that the rates of production and/or removal of these two forms of the monomer must be different during the early and late stages following induction. This possibility is substantiated by the differing rates of change in upper and lower monomers that occur over time in total cell lysates versus that in the plasma membrane (Fig. 7, *C* and *D*).

We noted an early increase in z after induction (Fig. 6*B*), indicating that the unitary charge carried by a functional motor changes with time. Since there are data supporting the role of the dimer as the functional unit (6, 12, 14, 19), an obvious possibility is that the increase in z represents a rapid increase of dimers on the cell surface in the initial hours of induction. We were unable to substantiate this possibility owing to technical difficulties in detecting prestin dimer in the very early stages after induction (0–4 h), when z shows its greatest change.

Our detection of a progressive depolarizing shift in V_h is similar to that observed in OHCs (1, 13). It had been suggested

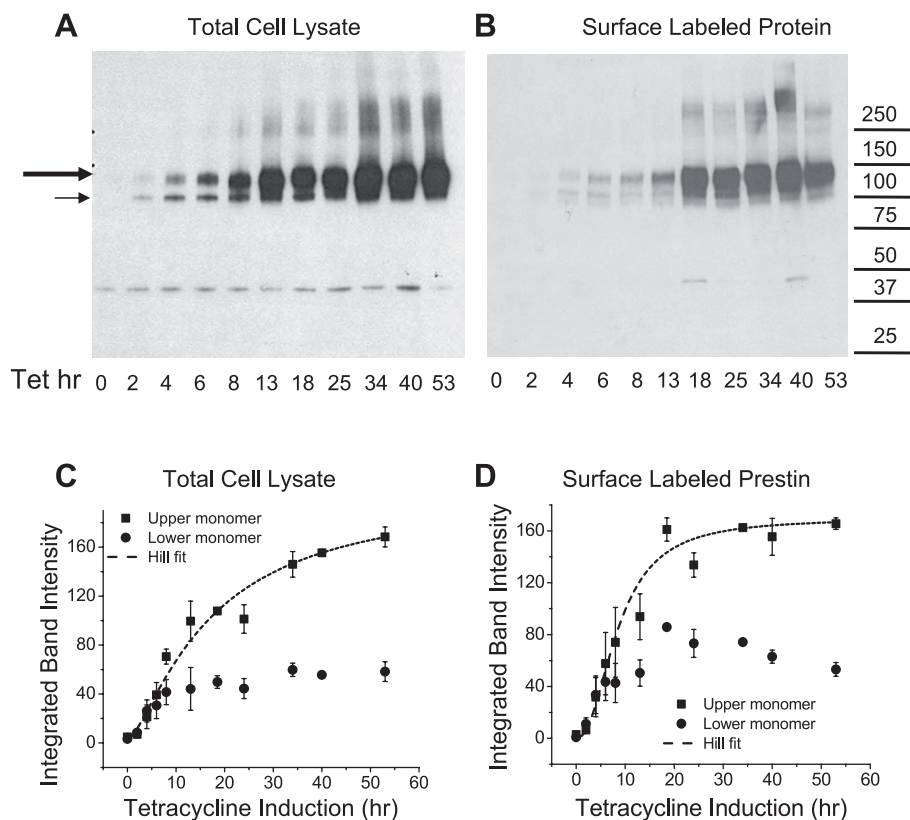


Fig. 7. Two monomers and multimers of prestin develop differentially as a function of time after induction (cell line 16c). *A*: Western blot of total cell lysate probed with anti-prestin N-20 antibody. Each lane has 0.75 μg of total protein as determined by protein assay. The large and small arrows indicate the upper (dominant) and lower monomers of prestin-YFP, respectively. A dimeric form of the protein is identifiable at 250 kDa. Prolonged incubation with tetracycline causes total cell prestin expression to increase steadily. The band at ~ 40 kDa is a nonspecific artifact, because it appears also in untransfected HEK293 cells (data not shown). *B*: Western blot of surface-labeled prestin-YFP obtained from cells at different time points after induction with 1 $\mu\text{g}/\text{ml}$ tetracycline. Each lane has 2 μl of the 250 μl surface-purified eluate from NeutrAvidin beads after binding to 2.7 mg of total protein. Each lane was derived from and corresponds to cell lysates in *A*. As with total cell lysates, prestin has at least two monomers and a broad dimeric form. The monomers in particular are detectable at the earliest time point (2 h) at which NLC is detectable. *C* and *D*: densitometric quantification of monomers of prestin from Western blots reveals a sigmoidal increase in the upper larger monomer of prestin. The surface expression of this monomer, however, stabilizes earlier than the monomer in cell lysates, with an asymptotic value achieved at 20 h after induction. The lower monomer expressed on the surface in contrast shows a small but persistent decrease in the asymptotic value with time. Hill fitting parameters for lysate (*C*) were as follows: start = 1; end = 205; $k = 17.2$; $n = 1.4$. Hill fitting parameters for surface prestin (*D*) were as follows: start = 0; end = 169; $k = 8.6$; $n = 2.2$. Data are averages from three batches of surface labeling experiments. Error bars are \pm SE.

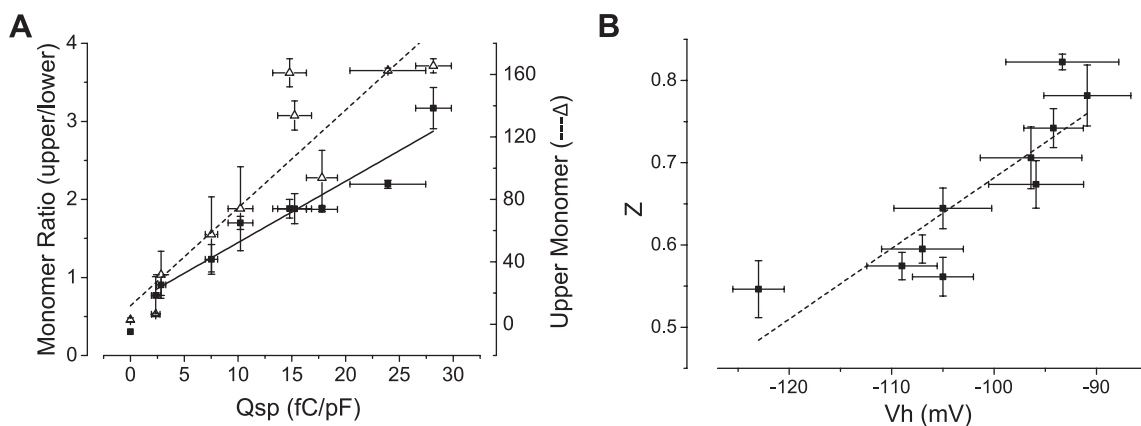


Fig. 8. Prestin's lower monomer exerts a dominant-negative effect on the upper functional monomer. *A*: the relationship between Q_{sp} and the densitometric ratio of the upper to lower prestin monomer expressed on the surface of the cell is linear ($Q_{sp} = -8.35 + 11.12 \times \text{ratio}$; adjusted $R^2 = 0.93$). Data were obtained from cells at variable time points after induction. Taken together, these data would suggest that the lower monomer exerts a dominant-negative effect on the function of the molecule. Also shown is the relationship between the upper monomer intensity and Q_{sp} . There is an initial correlation between the two that decreases with higher Q_{sp} values. *B*: correlation of z and V_h in the initial phase after induction where there is a rapid increase in z that correlates with a change in V_h .

that this shift might represent development of other unique molecular structures within the OHC, such as subsurface cisternae, pillars, and cortical cytoskeleton (1). Since a similar developmental event is unlikely in HEK cells, a more plausible explanation is that this change in V_h represents a maturation process that is intrinsic to the protein. It is interesting that in the first 6 h after induction, this shift in V_h coincides with the rapid increase in z (Fig. 8B). This suggests that charge valence and sensitivity to voltage is coupled in the initial stages of prestin's maturation.

In conclusion, we have developed several stable cell lines that have functional expression of prestin up to four times that of transiently transfected cells and have focused on a tetracycline-inducible line to elucidate the molecular events that underlie the development of prestin's NLC characteristics. Our data suggest that two prestin monomers are expressed on the cell surface, only one form being functional. Our data also suggest that dimerization of prestin may be associated with increases in prestin's voltage sensitivity (z values). Finally, our data suggest that prestin undergoes an intrinsic maturation that results in a shift in its voltage operating range to more depolarizing levels. Clearly, these cell lines will be useful as model systems for studying other aspects of prestin activity, including trafficking and turnover.

GRANTS

This work was supported by National Institute on Deafness and Other Communication Disorders Grants DC-007894, DC-00273, and DC-008130.

DISCLOSURES

No conflicts of interest, financial or otherwise, are declared by the authors.

REFERENCES

1. Abe T, Kakehata S, Kitani R, Maruya S, Navaratnam D, Santos-Sacchi J, Shinkawa H. Developmental expression of the outer hair cell motor prestin in the mouse. *J Membr Biol* 215: 49–56, 2007.
2. Belyantseva IA, Adler HJ, Curi R, Frolenkov GI, Kachar B. Expression and localization of prestin and the sugar transporter GLUT-5 during development of electromotility in cochlear outer hair cells. *J Neurosci* 20: RC116, 2000.
3. Blatchley BJ, Cooper WA, Coleman JR. Development of auditory brainstem response to tone pip stimuli in the rat. *Brain Res* 429: 75–84, 1987.
4. Brownell WE, Bader CR, Bertrand D, de Ribaupierre Y. Evoked mechanical responses of isolated cochlear outer hair cells. *Science* 227: 194–196, 1985.
5. Dallos P, Wu X, Cheatham MA, Gao J, Zheng J, Anderson CT, Jia S, Wang X, Cheng WH, Sengupta S, He DZ, Zuo J. Prestin-based outer hair cell motility is necessary for mammalian cochlear amplification. *Neuron* 58: 333–339, 2008.
6. Detro-Dassen S, Schanzler M, Lauks H, Martin I, zu Berstenhorst SM, Nothmann D, Torres-Salazar D, Hidalgo P, Schmalzing G, Fahlke C. Conserved dimeric subunit stoichiometry of SLC26 multifunctional anion exchangers. *J Biol Chem* 283: 4177–4188, 2008.
7. He DZ, Evans BN, Dallos P. First appearance and development of electromotility in neonatal gerbil outer hair cells. *Hear Res* 78: 77–90, 1994.
8. Iida K, Tsumoto K, Ikeda K, Kumagai I, Kobayashi T, Wada H. Construction of an expression system for the motor protein prestin in Chinese hamster ovary cells. *Hear Res* 205: 262–270, 2005.
9. Bai JP, Surguchev A, Bian S, Song L, Santos-Sacchi J, Navaratnam D. Combinatorial cysteine mutagenesis reveals a critical intra-monomer role for cysteines in prestin's voltage sensing. *Biophys J*. In press.
10. Matsuda K, Zheng J, Du GG, Klocker N, Madison LD, Dallos P. N-linked glycosylation sites of the motor protein prestin: effects on membrane targeting and electrophysiological function. *J Neurochem* 89: 928–938, 2004.
11. McFadden SL, Walsh EJ, McGee J. Onset and development of auditory brainstem responses in the Mongolian gerbil (*Meriones unguiculatus*). *Hear Res* 100: 68–79, 1996.
12. Navaratnam D, Bai JP, Samaranayake H, Santos-Sacchi J. N-terminal-mediated homomultimerization of prestin, the outer hair cell motor protein. *Biophys J* 89: 3345–3352, 2005.
13. Oliver D, Fakler B. Expression density and functional characteristics of the outer hair cell motor protein are regulated during postnatal development in rat. *J Physiol* 519: 791–800, 1999.
14. Pasqualetto E, Seydel A, Pellini A, Battistutta R. Expression, purification and characterisation of the C-terminal STAS domain of the SLC26 anion transporter prestin. *Protein Expr Purif* 58: 249–256, 2008.
15. Santos-Sacchi J, Shen W, Zheng J, Dallos P. Effects of membrane potential and tension on prestin, the outer hair cell lateral membrane motor protein. *J Physiol* 531: 661–666, 2001.
16. Santos-Sacchi J, Song L, Zheng J, Nuttall AL. Control of mammalian cochlear amplification by chloride anions. *J Neurosci* 26: 3992–3998, 2006.
17. Song L, McGee J, Walsh EJ. Development of cochlear amplification, frequency tuning, and two-tone suppression in the mouse. *J Neurophysiol* 99: 344–355, 2008.
18. Sturm AK, Rajagopalan L, Yoo D, Brownell WE, Pereira FA. Functional expression and microdomain localization of prestin in cultured cells. *Otolaryngol Head Neck Surg* 136: 434–439, 2007.
19. Zheng J, Du GG, Anderson CT, Keller JP, Orem A, Dallos P, Cheatham M. Analysis of the oligomeric structure of the motor protein prestin. *J Biol Chem* 281: 19916–19924, 2006.
20. Zheng J, Shen W, He DZ, Long KB, Madison LD, Dallos P. Prestin is the motor protein of cochlear outer hair cells. *Nature* 405: 149–155, 2000.

Sakaorat Blasits · Steffen Maune
Joseph Santos-Sacchi

Nitric oxide uncouples gap junctions of supporting Deiters cells from Corti's organ

Received: 24 March 2000 / Received after revision: 3 May 2000 / Accepted: 10 May 2000 / Published online: 29 June 2000
© Springer-Verlag 2000

Abstract Supporting cells of Corti's organ are electrically coupled via gap junctions. They probably serve to maintain the unique cochlear environment that is required for normal sensory function. In this study we used input capacitance measurements under whole-cell voltage-clamp conditions to evaluate the effects of nitric oxide on gap junctional communication between pairs of isolated supporting Deiters cells. We show that the nitric oxide (NO) donor sodium nitroprusside causes the uncoupling of Deiters cells, and that an NO synthase inhibitor blocks the effect. The cGMP analogue 8-bromo-cGMP also uncouples Deiters cells. With either treatment, the input capacitance of pairs of Deiters cells drops to single-cell levels within minutes of application, indicative of electrical uncoupling. We surmise that the NO/cGMP pathway may serve to modulate normal cochlear homeostasis and possibly plays a role in ototoxic mechanisms.

Key words Calcium · cGMP · Gap junctions · Membrane capacitance · Supporting cells

Introduction

The mammalian organ of Corti is comprised of sensory (inner and outer hair cells) and supporting cells, e.g., Hensen, Deiters, and Pillar cells. The supporting cells are structurally and electrically coupled together by gap junctions, which permit the direct cellular exchange of ions, dyes, and metabolites [5]. Cochlear homeostasis is believed to rely on intercellular coupling [4]. Coupling in the organ can be modulated by changes in intracellular

pH and Ca^{2+} , temperature, membrane voltage (junctional and non-junctional), and membrane tension (e.g., [8]). Recently, free radicals have been shown to uncouple Henson cells [7].

An understanding of nitric oxide's (NO) role in inner ear function is presently limited, but evolving (see [1] for review). The Ca^{2+} -dependent constitutive isoforms of nitric oxide (NO) synthase (NOS), neuronal bNOS (NOS I) and endothelial eNOS (NOS III) are found in the inner ear [2]. More specifically, Hess et al. [2] showed that bNOS is present in Deiters cells and in efferent nerve fibers, while eNOS is found in afferent nerve fibers and synaptic endings. The inducible Ca^{2+} -independent iNOS (NOS II) is a third isoform that has not been found in the cochlea under normal conditions but can be stimulated by bacterial lipopolysaccharides (LPS) and tumor necrosis factor α (TNF- α) [2]. In the present study we investigate the effects of NO on the electrical coupling between supporting cells. We show that the generation of NO can uncouple gap junctions of Deiters cells, and that the effect probably occurs through the NO/cGMP pathway.

Materials and methods

Guinea pigs were killed by decapitation. The organ of Corti was dissected from the temporal bone in Ca^{2+} -free Leibovitz medium (NaCl 142.2 mM, KCl 5.37 mM, MgCl_2 1.48 mM, HEPES 10.0 mM, dextrose 5.0 mM, pH 7.2, 300 mosmol/l). Pairs of Deiters cells were obtained by agitating the organ of Corti in Ca^{2+} -free Leibovitz medium containing 1 mg/ml trypsin for 10 min. The cell-enriched supernatant was then transferred to a 700- μ l perfusion chamber, and the cells were allowed to settle and attach to the untreated glass bottom of the chamber at room temperature for 15 min. An ionic blocking solution [tetraethylammonium (TEA) 20.0 mM, CsCl 20.0 mM, CoCl_2 2.0 mM, MgCl_2 1.47 mM, HEPES 10.0 mM, NaCl 99.2 mM, 2 mM $\text{CaCl}_2 \cdot 2\text{H}_2\text{O}$, pH 7.2, 300 mosmol/l] was used as the normal extracellular perfusate in order to block outward (K) and inward (K, Ca) currents. The use of ionic blocking solutions has no effect on gap junctional coupling in supporting cells [4, 8], and is simply used so that capacitive currents can be evaluated in isolation. Better voltage control is an additional benefit. CaCl_2 was included to facilitate pipette seal formation and cell attachment to the chamber bottom. Before starting an experi-

S. Blasits · J. Santos-Sacchi (✉)
Sections of Otolaryngology and Neurobiology,
Yale University School of Medicine, 333 Cedar St., New Haven,
CT 06510, USA
Tel.: +1-203-7857566; +1-203-7855407

S. Blasits · S. Maune
Department of Otorhinolaryngology, Head and Neck Surgery,
University of Kiel, Germany

ment, enzyme and cell debris were removed by perfusing for 15 min. The bath perfusion was continued for the whole of each experiment. Patch electrodes were made from borosilicate glass capillaries. The initial resistance was 3–5 M Ω , corresponding to tip sizes of 1–2 μ m in diameter. The pipette solution was composed of 140 mM CsCl, 1 mM EGTA, 2 mM MgCl₂, 10 mM HEPES, pH 7.2, 300 mosmol/l. In some experiments, 10 mM BAPTA replaced EGTA to more efficiently limit intracellular Ca²⁺ activity. Electrical coupling between isolated pairs of Deiters cells was evaluated by monitoring the input capacitance obtained by the whole-cell voltage clamp of one cell in the pair. This method is a sensitive indicator of junctional coupling [4, 8]. All data collection and analysis were performed with the software program jClamp (www.med.yale.edu/surgery/otolar/santos/jclamp.html).

A 1 mM sodium nitroprusside (SNP) solution (Sigma, St. Louis, Mo., USA) and a 1 mM 8-bromo-guanosine 3', 5'-cyclic monophosphate (cGMP) solution (Calbiochem, La Jolla, Calif., USA) were freshly prepared in the normal medium prior to each experiment. Each solution was locally delivered to the cells via Y-tube microperfusion while the normal bath perfusion continued. This was done to limit the treatment effect to the cell pair under study. NOS activity was blocked by a 500- μ M solution of *S*-methyl-L-thiocitrulline (MTC, Sigma), a competitive NOS inhibitor.

Results and discussion

Deiters cells are intimately associated with outer hair cells, providing a cellular buffer between the outer hair cell and the basilar membrane. Additionally, via their apical processes, they contribute to the formation of the reticular lamina, a boundary between endolymph and perilymph. These cells are strategically placed to support the normal function of the outer hair cell, which serves as the basis of the "cochlear amplifier". Pairs of Deiters cells are readily isolated from Corti's organ, and remain electrically well coupled (Fig. 1). This coupling effectively provides contiguity of the plasma membrane among Deiters cells, as evidenced by measurements of input capacitance. Figure 1A shows the input capacitance of a pair of Deiters cells where octanol is used reversibly to uncouple the cells. Input capacitance decreases to single-cell values during uncoupling and increases during washout with normal solution. Isolated pairs of Hensen cells show similar responses [4], and indeed this supporting cell type has been used to confirm the utility of input capacitance measures in coupling studies. For example, visually confirmed single cells, pairs and triplets have average input capacitances of 31.0, 64.8, and 104 pF, respectively [8]. In the present study, the input capacitance of single Deiters cells was 42.4 \pm 7.4 pF ($n=12$).

In order to evaluate the effects of NO on the coupling of Deiters cells, we perfused solutions containing the NO donor SNP (1 mM) during electrical recording. Figure 2A illustrates that SNP reduces the input capacitance of cell pairs to single-cell levels, indicating that gap junctional communication was disrupted. This type of result was obtained in 11 of 13 cell pairs. For those pairs that uncoupled, the initial input capacitance averaged 101.3 \pm 9.9 pF (mean \pm SE). The time course of effects was variable, but, on average, input capacitance was reduced to 75% after 493 \pm 97 s following the start of SNP perfusion. The minimum input capacitance ultimately

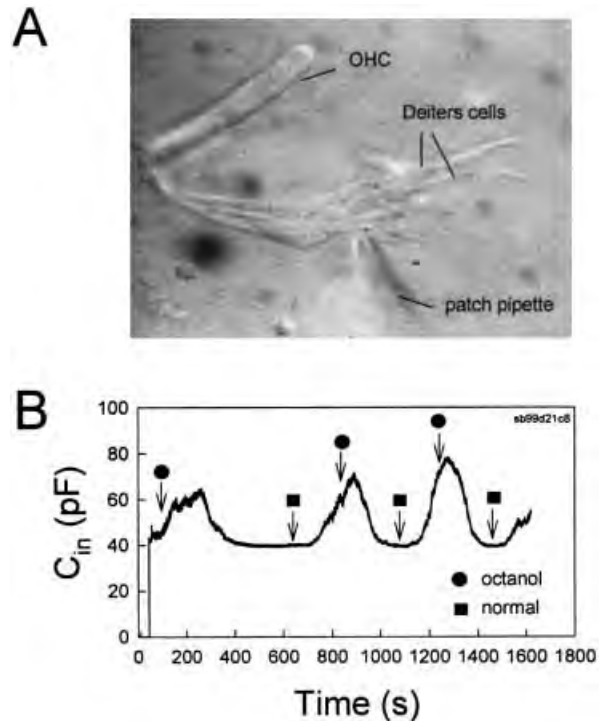


Fig. 1 **A** Digitally captured image of an isolated pair of Deiters cells, one of which is whole-cell voltage clamped. An outer hair cell (OHC) remains attached to the apical processes. **B** Effect of octanol on the input capacitance (C_{in}) of a pair of Deiters cells. After about 30 s, the pipette-membrane seal was ruptured and C_{in} jumped to 43 pF; initially, coupling was slight, but increased over the course of a few minutes, i.e., as C_{in} increased. The application of octanol (\approx 1 mM) via Y-tube perfusion uncoupled the cells as indicated by a drop of capacitance to single-cell levels. After washout of octanol, re-coupling occurred. The effects were repeatable. The absence of an immediate effect upon the initial application of octanol is probably due to perfusion blockage, as subsequently, and in previous studies (e.g. [4]), octanol uncouples supporting cells within tens of seconds

reached was 50.6 \pm 7.4 pF. In some cells, re-coupling occurred following the washout of SNP. In an additional ten pairs, the NOS inhibitor MTC (0.5 mM) was perfused continuously during SNP delivery (Fig. 2B). In eight of ten cells no reduction of input capacitance to single-cell levels was observed; in two cases where input capacitance dropped to single-cell levels, the quality of the cells may have been low since the recordings were made at the end of an experimental session.

Many of the effects of NO are mediated by activation of soluble guanylate cyclase (sGC) and the subsequent action of cyclic guanosine monophosphate (cGMP) [3]. sGC is found in supporting cells, including Deiters cells [1]. We tested the possibility that NO acts via the cGMP pathway by treating coupled Deiters cells with a membrane-permeant form of cGMP (1 mM). Fig. 2C illustrates that 8-bromo cGMP causes Deiters cells to uncouple. As with SNP treatment, input capacitance drops to single-cell levels following treatment. All six cell pairs tested evidenced uncoupling. The initial input capacitance averaged 112.6 \pm 18.2 pF (mean \pm SE). Similar to

Table 1 The input capacitance of a pair of Deiters cells and the effects of altering gap junctional communication between them. (*cGMP* 8-Bromo-guano-sine 3', 5'-cyclic monophosphate, *MTC* S-methyl-L-thiocit-rulline, *SNP* sodium nitroprus-side.) Single-cell values were 42.4 ± 7.4 pF ($n=12$; mean \pm SD)

Treatment	Initial C_{in} (pF)	Time (s) to 75% C_{in}	Ultimate C_{in} (pF)	% decrease
SNP ($n=11$)	101 \pm 9.9	493 \pm 97	50.6 \pm 7.4	50
SNP + MTC ($n=7^*$)	90.6 \pm 20.4	–	79.3 \pm 13.4	88
cGMP ($n=6$)	112 \pm 18	908 \pm 163	46.2 \pm 13.6	41

*Only seven of the eight pairs that did not reduce to single-cell levels were perfused with MTC throughout the recording period. In the other pair, MTC was washed out and subsequently SNP did reduce C_{in} to single-cell levels

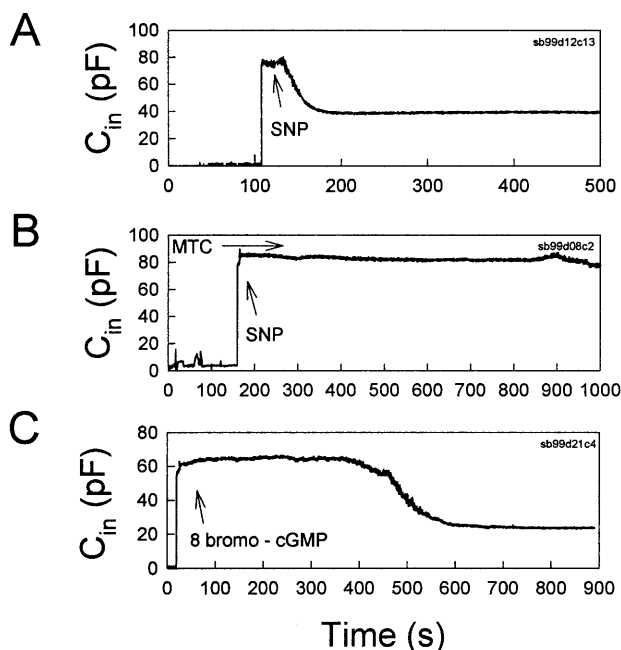


Fig. 2 **A** After about 110 s, the whole-cell configuration was established, indicated by the jump in capacitance (C_{in}). Perfusion of 1 mM sodium nitroprusside (SNP) caused the cell pair to rapidly uncouple, indicated by the drop in capacitance to a single-cell value of 40 pF. **B** Perfusion of the nitric oxide synthase (NOS) inhibitor MTC (0.5 mM) started before the whole-cell configuration was established, and continued during application of SNP. C_{in} remained fairly constant throughout the recording period. **C** Treatment with 8-bromo cGMP (1 mM) uncoupled this pair of Deiters cells after about 7 min

SNP, the time course of effects was variable, but, on average, input capacitance was reduced to 75% after 908 ± 163 s following the start of 8-bromo-cGMP perfusion. The minimum input capacitance ultimately reached was 46.2 ± 13.6 pF. Our results are summarized in Table 1.

The susceptibility of supporting cell gap junctions to intracellular calcium is well documented (see [5]), and, indeed, second messenger mechanisms that elevate intracellular calcium levels, e.g., inositol 1,4,5-trisphosphate or IP_3 , can uncouple supporting cells [6]. In preliminary tests, we found that replacing the patch pipette solution Ca^{2+} chelator EGTA (1 mM) with the more effective chelator BAPTA (10 mM) blocked the effect of SNP on supporting cell coupling (six cell pairs). The enzyme probably responsible for NO generation is one of the Ca^{2+} -dependent constitutive ones, because of the rapidity of the

uncoupling effects. Consequently, it might be that Ca^{2+} sequestration interferes with NO generation. Alternatively, it is conceivable that NO is generated within the adjacent un-patched cell, or other cells within the perfusion area, and that it is the buffering of Ca^{2+} within the immediate vicinity of gap junctions that maintains coupling. BAPTA, based on molecular weight, can traverse gap junctions into adjacent Deiters cells so as to maintain low Ca^{2+} levels within the vicinity of gap junctions. Further studies are required to resolve the mechanism of BAPTA's effects.

Among other possibilities, we have suggested that coupling between supporting cells provides for the spatial buffering of potassium ions within the organ of Corti, which otherwise would compromise the normal activity of hair cell and neural elements [4]. The present results may underscore a mechanism for the physiological control of ionic buffering within the organ of Corti. Additionally, the potential for damage caused by free radicals subsequent to NO generation may have a bearing on the detrimental affects of bacterial toxins [2] and ototoxic drugs [7] on cochlear function.

Acknowledgements This work was supported by NIH-NIDCD grant DC00273 to J.S.S., and a Boehringer Scholarship to S.B. We thank Margaret Mazzucco for technical help.

References

- Fessenden JD, Schacht J (1998) The nitric oxide/cyclic GMP pathway: a potential major regulator of cochlear physiology. *Hear Res* 118:168–176
- Hess A, Bloch W, Huverstuhl J, Su J, Stennert E, Addicks K, Michel O (1999) Expression of inducible nitric oxide synthase (iNOS/NOS II) in the cochlea of guinea pigs after intratympanic endotoxin-treatment. *Brain Res* 830:113–122
- Murad F (1994) The nitric oxide-cyclic GMP signal transduction system for intracellular and intercellular communication. *Recent Prog Horm Res* 49:239–248
- Santos-Sacchi J (1991) Isolated supporting cells from the organ of Corti: some whole cell electrical characteristics and estimates of gap junctional conductance. *Hear Res* 52:89–98
- Santos-Sacchi J (2000) Cell coupling in Corti's organ. *Brain Res Reviews* 32:167–171
- Sato Y, Oku Y, Orita Y, Santos-Sacchi J (1996) Effect of IP_3 on gap junction conductance of supporting cells of the organ of Corti. *Midwinter Meeting of the Association for Research in Otolaryngology*, Feb. 4–8, 1996. Abstracts, p 520
- Todt I, Ngezahayo A, Ernst A, Kolb HA (1999) Inhibition of gap junctional coupling in cochlear supporting cells by gen-tamicin. *Pflügers Arch.* 438:865–867
- Zhao HB, Santos-Sacchi J (1998) Effect of membrane tension on gap junctional conductance of supporting cells in Corti's organ. *J Gen Physiol* 112:447–455

PART IV: ANIMAL RESEARCH IN PERIPHERAL AUDITORY PHYSIOLOGY

Joseph Santos-Sacchi

BACKGROUND

Cataloging the microanatomy of the auditory end organ provided an important start for understanding the physiology of the peripheral auditory system. These anatomical studies, conducted on a variety of species, began in earnest following the development of the compound light microscope in the 1700s. The detail in some of the original work of such pioneers as Alfonso Corti is remarkable (see Hawkins (2001) and references within), but alas, the microscopic structures were necessarily altered by the decay following extirpation and dissection. As we shall see, this decay had a major impact on our understanding of cochlear physiology as well. Whereas the development of fixatives proved a boon for anatomists, physiologists did not benefit directly, but belatedly profited from histologists' appreciation of the need to preserve the natural state.

The cochlea, we now know, is a remarkable electromechanical device. Prior to the discovery of animal electricity and the means to measure it, only the mechanical components of cochlea function could be investigated. Thus, the microscopic structures in the inner ear were used to deduce the mechanical foundation of cochlea function; for example, Helmholtz postulated his resonance theory based on the changing length (hence mechanical properties) of radial basilar membrane fibers. Clearly, in mammals, the basilar membrane, with its varying dimensions and stiffness, would be a prime candidate for the basis of hearing. Indeed, von Bekesy's (1960) studies confirmed the importance of the basilar membrane's mechanical qualities by demonstrating tuned traveling waves evoked by basilar membrane disturbances. von Bekesy used a variety of animal models, mainly the human temporal bone, but also mouse to elephant, to assess the sharpness of tuning in the cochlea. While the data he obtained contributed immensely to our understanding of cochlea mechanics and won him the Nobel prize in 1961, unforeseen factors worked to stymie an understanding of the true sensitivity and tuning of the mammalian cochlea. These factors were the same that stymied early anatomists, namely the difficult-to-avoid decay of normal cellular structure and function after death. These problems, though acknowledged by von Bekesy, were argued away, so that for many years auditory aficionados were led to believe that his data were gold. In fact, there were serious problems with his experiments, which when ultimately realized and solved, helped elucidate the roles of the two types of hair cells; the inner and outer hair cells, that the early anatomists identified with the aid of improved fixation techniques. To improve on the work of von Bekesy, models other than the human would be required.

WHY DO WE STUDY ANIMAL MODELS?

There are two main reasons for the study of peripheral auditory physiology, namely 1) the quest to understand and cure auditory dysfunction, and 2) simply to understand how our, and other animals', ears work. Clearly, study based on the former rationale would benefit from direct investigations on humans. Unfortunately, though, immense difficulties are associated with human experimentation on the auditory periphery. These problems include limited numbers of specimens, inability to control for pathological effects, and the inevitable problem of tissue destruction caused by delays in getting access to the cochlea (caused by dissection difficulties due to the dense temporal bone and delays in acquisition following death). Thus, for many reasons and regardless of the clinical vs. scientific rationales, animal models are best for studies on cochlear physiology. The major hurdle in rationalizing a particular animal model is its validity and generality. Most investigators believe that a range of small mammals, including the cat, chinchilla, guinea pig, rat, and mouse are appropriate for providing insight into the human condition. Of course, one or another species may prove better for particular experimental questions. In general, however, these small animals are particularly well suited, since the cochlea structures can be easily accessed. This enhanced accessibility (and heightened concern for better physiological status) has led directly to enhancements of the findings of von Bekesy.

BASILAR MEMBRANE TUNING

The data on basilar membrane movement that von Békésy obtained indicated that the response of the basilar membrane was linear, i.e., the magnitude of the displacement response grew linearly with the stimulus level. By extrapolating down to threshold levels, it was argued that basilar membrane movements at the threshold of hearing were a fraction of an atom's width. Tuning of the basilar membrane was also observed to be not as good as psychophysical measures, and von Békésy sought reasons beyond the basilar membrane to explain how we hear so well. With the aid of animal models, these notions would dramatically change.

Using the squirrel monkey, Rhode and colleagues (Rhode 1974; Rhode and Robles 1974) first noticed that, in some animals, a nonlinear growth in basilar membrane motions occurred as stimulation levels were changed. Importantly, this compressive nonlinearity of the basilar membrane response was vulnerable to the animal's status. Only when extreme care was used to maintain a healthy preparation did the response remain nonlinear, otherwise it resembled the data of von Békésy. We know now that tuning on the basilar membrane is far sharper than the data that von Békésy showed, indicating that his human temporal bone preparation and his animal preparations were working in a passive, damaged mode. Of course, the new Mossbauer measurement tool that Rhode and colleagues (Rhode 1974; Rhode and Robles 1974) used helped to record at lower stimulus levels than von Békésy could when using stroboscopic illumination. Today, it is clear that the sharp tuning found in the eighth nerve has its direct counterpart in basilar membrane motion (Narayan et al 1998). This turnaround in the description of basilar membrane tuning highlights the caveat that while animal models have the potential to provide valid data, care must be exercised in order to attain validity.

THE COCHLEA IS ELECTRIC

In the 1700s, electricians (as serious students of electricity were then called) often relied on themselves or acquaintances to serve as subjects. Indeed, Volta perceived a deafening blast as a result of self-inflicted aural electrocution (Piccolino 2000). Despite this early indication, it would be nearly two centuries after the controversial discovery of animal electricity that the electrical nature of audition would be confirmed. The discovery had to wait for the invention of the vacuum tube and oscilloscope, but once in hand, Wever and Bray (1930) demonstrated the "cochlear microphonic", an electrical response of the hair cells (which they mistakenly took as eighth nerve firings) measured from electrodes placed on a decerebrate cat's eighth nerve. The response mimicked the acoustic stimulus, and they confirmed this finding in a number of animal species, including turtles and insects.

The study of the electrical activity of the cochlea took off, and small mammals were perfect models since their cochleae were easily exposed for electrode implantations. Extracellular (from scala media and the perilymphatic scalae) electrical recordings were made of the resting (e.g., endolymphatic potential) and sound-evoked potentials (cochlea microphonic, summing potential, and even action potentials; see Dallos (1973)), but eventually these were usurped by intracellular recording directly from hair cells (Dallos et al 1982; Russell and Sellick 1978) after the high impedance electrode was devised. The clear correspondence of electrical activity within the auditory periphery with hearing capabilities would place this measure above that of histopathologic determination of auditory insult and recovery.

ANIMAL MODELS OF CLINICAL IMPORTANCE

The anatomical identification and characterization of cochlear dysfunction is time-consuming. The classic histological work on otopathology (see Schuknecht 1974), while quite informative, could not be used with high efficiency, simply because the animal or human temporal bone had to be removed and processed after death. The use of electrical measures to determine auditory sensitivity, especially those that were noninvasive (e.g., auditory brainstem response [ABR], compound action potential [CAP]) permitted ongoing and quantitative studies on the effects of noise exposure, ototoxic drug exposure, and hazardous chemicals (e.g., see Henderson et al 1999). As a direct result of animal experimentation, we would no longer have to experience devastation such as that caused by the first uses of the ototoxic antibiotic, dihydrostreptomycin (Shambaugh et al 1959). Nevertheless, while animal models have contributed significantly toward our understanding of pathologies that afflict humans, we must remain cognizant of species-specific differences.

One of the hottest areas of current research is that of hair cell regeneration (see Warchol 2001). Mammalian hair cells do not regenerate following destruction, as do those of some lower vertebrates. Thus, unlike some

tissues that can be interrogated via cell culture, mammalian inner ears must be harvested for each new experiment. Perhaps some day, if the key that controls hair cell production is found, hair cell cultures may reduce the need for animal sacrifice.

In the heyday of electron microscopy, transport of electron-dense markers into various compartments of the inner ear was studied. These studies included, for example, movements of molecules out of the vasculature and into cochlea scalae, thus identifying the blood–labyrinthine barriers (Duvall and Klinkner 1983; Hukee and Duvall 1985; Santos-Sacchi and Marovitz 1980) and movements of molecules across the round window membrane into the scala tympani (Schachern et al 1987). The latter experiments contributed to the scientific basis for the currently popular clinical approach of intratympanic drug delivery, notably used to deliver gentamycin for control of intolerable vertigo. This type of approach heralds a new era where the otologist will successfully treat previously inaccessible structures of the inner ear and will ultimately do so with the new tools of molecular biology. In cochlear implant research, animal models helped in facilitating assessment of the reversibility of deafness-associated changes at the level of the cochlea. The feasibility of using clinical devices in the animal models is a great asset in evaluation and study of such devices in the present and future (Kretzmer et al 2004).

FROM MOLECULES TO EAR

Some very important advances in auditory physiology have been made in recent years using the techniques of molecular biology. Two of them are especially dear to my heart, namely, the determination that mutations of the connexon 26 gene result in nonsyndromic deafness (Kelsell et al 1997) and the identification of the protein responsible for the mechanical activity of the outer hair cell (Zheng et al 2000).

Connexons are proteins that form gap junction channels between adjacent cells, in the ear's case, allowing ionic and metabolic communication between supporting cells (Santos-Sacchi and Dallos 1983). These channels were proposed to aid in the removal of harmful extracellular potassium away from active hair cells (Santos-Sacchi 2000), and this is a likely reason for the mutation's devastation of hearing.

The mammalian outer hair cell has long been known to dance wildly in response to electrical stimulation (Brownell et al 1985; Ashmore 1987; Santos-Sacchi and Dilger 1988); this mechanical activity is believed to promote the sharp tuning and nonlinearity that Rhode and colleagues (Rhode 1974; Rhode and Robles 1974) found in the basilar membrane. Finally, after nearly two decades, the motor responsible for the outer hair cell (OHC) boogie was molecularly identified as the protein, prestin (Zheng et al 2000). The story is a continuing one that is full of twists (Santos-Sacchi 2003), but most recently, a knockout of the prestin gene in the mouse seriously interfered with normal auditory function (Liberman et al 2002), and a mutation of the gene was shown to cause deafness in humans (Liu et al 2003). In the end, it will likely be the mouse model that holds the key to our interests in the ear, as this small prolific rodent is a perfect molecular biology laboratory. But let us not forget the guinea pig, which is a classic model in auditory research; indeed, this animal has helped show that gene transfection (of Math1 transcription factor) into the intact cochlea can induce new hair cell growth (Kawamoto et al 2003). Imagine, the future otologist growing some new hair cells for us hard-of-hearing baby boomers — thanks to animal research.

HERE AND NOW

Well, some 14 years have passed since the short review given above, and one thing remains clear – animal modelling enjoys tremendous popularity in otolaryngological research, especially in auditory physiology. We have not yet made enough progress to understand basic physiological mechanisms so that mathematical models can fully supplant experiment. Importantly, however, experiments on animals and their cells, often are simultaneously accompanied by mathematical models of identified processes, leading the way to limit the use of animals in the future.

What has become of the hope that the otologist could grow and insert new hair cells to alleviate deafness? Well, as I see it, though progress to the bedside has not been as rapid as initially anticipated, things are picking up. One of the promising bases for potential treatments involves manipulating signaling pathways to promote proliferation of stem cells that can then be triggered to differentiate into hair cells – methods that have been established in the mouse (McLean et al., 2017). Several clinical trials are now underway to help regenerate hair cells. Most trials include molecular biological approaches that have directly benefited from animal experiments. Even methods of treatment delivery, e.g., transtympanic or systemic, have been evaluated using animal models.

In the meantime, the cochlear implant remains the prime treatment for severe deafness, but even this established approach is benefiting from animal experiments aimed at prolonging spiral ganglion cell and neurite survival (Jolly et al., 2010). Such experiments often use guinea pigs (because of the large size of the cochlea) to study the effects of drug delivery (e.g., steroids) via the implant.

For the auditory physiologist, the animal model of choice is now clearly the mouse, although the zebrafish is far more amenable to molecular manipulations on a more rapid time scale. To be sure, the zebrafish has been instrumental in understanding certain aspects of auditory and vestibular development, and sensory function (Nicolson, 2005). In fact, the lateral line, in particular, has been a popular model for studying hair cell function, and the ability to now patch clamp from these cells (Ricci et al., 2013) is a boon for the auditory electrophysiologist. However, the usefulness of this species will never surpass the mouse. Below, I touch on a couple of significant observations that have benefited from mouse experimentation.

The elucidation of the molecular nature of the vertebrate hair cell stereociliar transduction channel has been a persistent challenge over the years, with many suggestions made (Corey et al., 2004), but all failing to materialize (Corey, 2006). Recently, however, several investigations have honed in on the TMC protein as being a major component of the channel, and these efforts have benefited from studies in the mouse (Beurg et al., 2018 ; Pan et al., 2018). The Pan et al. experiments showed that single channel characteristics of the stereociliar transduction channel could be manipulated following cysteine mutagenesis of the presumed pore-forming region of TMC1, pointing towards its central role in transduction. However, since such channel characteristics are also altered by membrane lipid modifications of PIP2 (Effertz et al., 2017) in the presence of normal TMC1. This indicates that the mere alteration of single channel characteristics does not guarantee the identification of a pore-forming region in a membrane protein. Thus, expression of the TMC1 protein in heterologous cells is required to fully confirm that it is indeed the transduction channel. Currently, TMC1 is unable to be transfected into non-auditory cells. Nevertheless, we are now closer than ever to solving this puzzle.

Alluded to above, prestin is the identified motor protein that accounts for electromotility and cochlear amplification. This protein exclusively resides in the outer hair cell membrane, and in no other cell type in the organ of Corti. Nevertheless, Chessum et al. (Chessum et al., 2018) have identified a key regulator of OHC maturation (Helios) that dictates the localized expression of prestin, and knockout mice of the gene encoding Helios produces deafness and reduction of prestin expression. Surprisingly, the ectopic expression of this gene regulator in mouse inner hair cell results in prestin expression and electromotility in inner hair cells! I believe that the mouse is truly a molecular laboratory destined to tell us how the ear's works really works.

REFERENCES

1. Hawkins, J.E., Auditory physiological history: a surface view, in *Physiology of the Ear*, Jahn, A.F. and Santos-Sacchi, J., Eds., Raven Press, New York, 2001.
2. Von Bekesy, G., *Experiments in Hearing*, McGraw-Hill, New York, 1960.
3. Rhode, W.S., Measurement of vibration of the basilar membrane in the squirrel monkey, *Ann. Oto. Rhino. Laryngol.*, 83, 619, 1974.
4. Rhode, W.S. and Robles, L., Evidence from Mossbauer experiments for nonlinear vibration in the cochlea, *J. Acoust. Soc. Am.*, 55, 588, 1974.
5. Narayan, S.S., Temchin, A.N., Recio, A., and Ruggero, M.A., Frequency tuning of basilar membrane and auditory nerve fibers in the same cochleae, *Science*, 282, 1882, 1998.
6. Piccolino, M., The bicentennial of the Voltaic battery (1800--2000): the artificial electric organ, *Trends Neurosci.*, 23, 147, 2000.
7. Wever, E.G. and Bray, C., Action currents in the auditory nerve in response to acoustic stimulation, *PNAS*, 16, 344, 1930.
8. Dallos, P., *The Auditory Periphery*, Academic Press, New York, 1973.
9. Dallos, P., Santos-Sacchi, J., and Flock, A., Intracellular recordings from cochlear outer hair cells, *Science*, 218, 582, 1982.
10. Russell, I.J. and Sellick, P.M., Intracellular studies of hair cells in the mammalian cochlea, *J. Physiol.*, 284, 261, 1978.
11. Schuknecht, H.F., *Pathology of the Ear*, Harvard University Press, Cambridge, MA, 1974.
12. Henderson, D., Salvi, R.J., Quaranta, A., McFadden, S.L., and Burkard, R.F., *Ototoxicity: Basic Science and Clinical Applications*, New York Academy of Sciences, New York, 1999.
13. Shambaugh, G.E., Jr., Derlacki, E.I., Harrison, W.H., House, H., House, W., Hildyard, V., Schuknecht, H., and Shea, J.J., Dihydrostreptomycin deafness, *J. Am. Med. Assoc.*, 170, 1657, 1959.
14. Warchol, M.E., Regeneration of cochlear hair cells, in *Physiology of the Ear*, Jahn, A.F. and Santos-Sacchi, J., Eds., Raven Press, New York, 2001.
15. Duvall, A.J., III and Klinkner, A., Macromolecular tracers in the mammalian cochlea, *Am. J. Otolaryngol.*, 4, 400, 1983.
16. Hukee, M.J. and Duvall, A.J., III, Cochlear vessel permeability to horseradish peroxidase in the normal and acoustically traumatized chinchilla: a reevaluation, *Ann. Oto. Rhino. Laryngol.*, 94, 297, 1985.
17. Santos-Sacchi, J. and Marovitz, W.F., An evaluation of normal stria! capillary transport using the electron-opaque tracers ferritin and iron dextran, *Acta Otolaryngol.*, 89, 12, 1980.
18. Schachern, P.A., Paparella, M.M., Goycoolea, M.V., Duvall, A.J., III, and Choo, Y.B., The permeability of the round window membrane during otitis media, *Arch. Otolaryngol. Head Neck Surg.*, 113, 625, 1987.
19. Kelsell, D.P., Dunlop, J., Stevens, H.P., Lench, N.J., Liang, J.N., Parry, G., Mueller, R.F., and Leigh, I.M., Connexin 26 mutations in hereditary nonsyndromic sensorineural deafness, *Nature*, 387, 80, 1997.
20. Zheng, J., Shen, W., He, D.Z., Long, K.B., Madison, L.D., and Dallos, P., Prestin is the motor protein of cochlear outer hair cells, *Nature*, 405, 149, 2000.

21. Santos-Sacchi, J. and Dallas, P., Intercellular communication in the supporting cells of the organ of Corti, *Hear. Res.*, 9, 317, 1983.
22. Santos-Sacchi, J., Cell coupling in Corti's organ, *Brain Res. Brain Res. Rev.*, 32, 167, 2000.
23. Brownell, W.E., Bader, C.R., Bertrand, D., and de Ribaupierre, Y., Evoked mechanical responses of isolated cochlear outer hair cells, *Science*, 227, 194, 1985.
24. Ashmore, J.F., A fast motile response in guinea-pig outer hair cells: the cellular basis of the cochlear amplifier, *J. Physiol. (Lond.)*, 388, 323, 1987.
25. Santos-Sacchi, J. and Dilger, J.P., Whole cell currents and mechanical responses of isolated outer hair cells, *Hear. Res.*, 35, 143, 1988.
26. Santos-Sacchi, J., New tunes from Corti's organ: the outer hair cell boogie rules, *Curr. Opin. Neuro-biol.*, 13, 459, 2003.
27. Liberman, M.C., Gao, J., He, D.Z., Wu, X., Jia, S., and Zuo, J., Prestin is required for electromotility of the outer hair cell and for the cochlear amplifier, *Nature*, 419, 300, 2002.
28. Liu, X.Z., Ouyang, X.M., Xia, X.J., Zheng, J., Pandya, A., Li, F., Du, L.L., Welch, K.O., Petit, C., Smith, R. J., Webb, B.T., Yan, D., Amos, K.S., Corey, D., Dallas, P., Nance, W.E., and Chen, Z.Y., Prestin, a cochlear motor protein, is defective in nonsyndromic hearing loss, *Hum. Mot. Genet.*, 12, 1155, 2003.
29. Kawamoto, K., Ishimoto, S., Minoda, R., Brough, D.E., and Raphael, Y., Math 1 gene transfer generates new cochlear hair cells in mature guinea pigs *in vivo*, *J. Neurosci.*, 23, 4395, 2003.

- Beurg M, Cui R, Goldring AC, Ebrahim S, Fettiplace R, Kachar B (2018) Variable number of TMC1-dependent mechanotransducer channels underlie tonotopic conductance gradients in the cochlea. *Nat Commun* 9:2185.
- Chessum L et al. (2018) Helios is a key transcriptional regulator of outer hair cell maturation. *Nature* 563:696-700.
- Corey DP (2006) What is the hair cell transduction channel? *J Physiol* 576:23-28.
- Corey DP, Garcia-Anoveros J, Holt JR, Kwan KY, Lin SY, Vollrath MA, Amalfitano A, Cheung EL, Derfler BH, Duggan A, Geleoc GS, Gray PA, Hoffman MP, Rehm HL, Tamasauskas D, Zhang DS (2004) TRPA1 is a candidate for the mechanosensitive transduction channel of vertebrate hair cells. *Nature* 432:723-730.
- Effertz T, Becker L, Peng AW, Ricci AJ (2017) Phosphoinositol-4,5-Bisphosphate Regulates Auditory Hair-Cell Mechanotransduction-Channel Pore Properties and Fast Adaptation. *J Neurosci* 37:11632-11646.
- Jolly C, Garnham C, Mirzadeh H, Truy E, Martini A, Kiefer J, Braun S (2010) Electrode features for hearing preservation and drug delivery strategies. *Adv Otorhinolaryngol* 67:28-42.
- McLean WJ, Yin X, Lu L, Lenz DR, McLean D, Langer R, Karp JM, Edge ASB (2017) Clonal Expansion of Lgr5-Positive Cells from Mammalian Cochlea and High-Purity Generation of Sensory Hair Cells. *Cell Rep* 18:1917-1929.
- Nicolson T (2005) The genetics of hearing and balance in zebrafish. *Annu Rev Genet* 39:9-22.
- Pan B, Akyuz N, Liu XP, Asai Y, Nist-Lund C, Kurima K, Derfler BH, Gyorgy B, Limapichat W, Walujkar S, Wimalasena LN, Sotomayor M, Corey DP, Holt JR (2018) TMC1 Forms the Pore of Mechanosensory Transduction Channels in Vertebrate Inner Ear Hair Cells. *Neuron* 99:736-753 e736.
- Ricci AJ, Bai JP, Song L, Lv C, Zenisek D, Santos-Sacchi J (2013) Patch-clamp recordings from lateral line neuromast hair cells of the living zebrafish. *J Neurosci* 33:3131-3134.

male was silenced or the subordinate males were deafened, the results were very similar.

A dominant male that was audible to his subordinates devoted less time to fighting and more to courting and, consequently, had a higher rate of copulation. Our study, as well as more detailed studies of female behavior (5), indicates that male chirping does not affect female behavior directly. We conclude that acoustic signals influence male mating success because inaudible males are interrupted by other males more often during courtship than are audible males. The structural similarity in chirps produced during courtship and during aggression may reflect a convergence of function: no matter what the context, male chirps signal an aggressive warning to other males.

The chirps of many species of crickets have a different structure for each of several contexts (13). Most species of field crickets are solitary, and the males produce loud species-specific "calling" songs that attract females from a distance and possibly serve a role in the territorial spacing of neighboring males (3). The less intense "courtship" chirps of solitary males are audible to females in the immediate vicinity, but may not be detectable by other males (5); female field crickets discriminate against males that do not chirp during courtship (4). "Aggressive" chirps usually have yet another structure (13). A gregarious cricket such as *Amphiacusta maya* need not produce a calling song but is very likely to be interrupted during courtship. Thus a male in a gregarious species, at risk of constant interruptions and fights, produces "war propaganda" whenever he chirps.

CHRISTINE R. B. BOAKE*

ROBERT R. CAPRANICA

Section of Neurobiology and
Behavior, Cornell University,
Ithaca, New York 14853

References and Notes

1. R. A. Fisher, *The Genetical Theory of Natural Selection*, (Dover, New York, ed. 2, 1958), p. 155.
2. L. Fairchild, *Science* **212**, 950 (1981); R. D. Howard, *Evolution* **32**, 850 (1978); M. J. Ryan, *Science* **209**, 523 (1980).
3. R. D. Alexander, in *Insects, Science, and Society*, D. Pimentel, Ed. (Academic Press, New York, 1975), p. 35; P. D. Bell, *Can. J. Zool.* **58**, 1861 (1980); W. Cade, *Science* **190**, 1312 (1975); in *Sexual Selection and Reproductive Competition in Insects*, M. S. Blum and N. A. Blum, Eds. (Academic Press, New York, 1979); D. J. Campbell and E. Shipp, *Z. Tierpsychol.* **51**, 260 (1979); A. V. Popov and V. F. Shuvalov, *J. Comp. Physiol.* **119**, 111 (1977); S. M. Ulagaraj and T. J. Walker, *Science* **182**, 1278 (1973).
4. T. Burk, thesis, University of Oxford (1979); in *Orthopteran Mating Systems: Sexual Competition in a Diverse Group of Insects*, D. T. Gwynne and G. K. Morris, Eds. (Westview, Boulder, Colo., in press).
5. C. R. B. Boake, thesis, Cornell University (1982).
6. Another gregarious Phalangopsine cricket, *Phaeophilacris spectrum*, communicates with infrasound rather than with audible signals. The same signal is produced during courtship and aggression, but a second signal is added in high-intensity aggressive interactions [M. von Dambach and L. Lichtenstein, *Z. Tierpsychol.* **46**, 14 (1978)].
7. Three marked males were housed in each cage. One female was put in immediately before observations began. Most aggressive interactions occurred in the vicinity of the female, when a male was interrupted during courtship. The interactions varied in intensity from one male antennating the other and displacing him, to fights in which both males stood on their hind legs, hit each other with their front legs, tried to bite, and chirped continuously. All aggressive interactions [described in (5)] and all attempts to copulate were recorded for 0.5 hour. If the female had mated during this period, she was removed; otherwise, she was left in the cage for another 0.5 hour. The ranks of males were assigned on the basis of the number of aggressive interactions that each male won during each observation session. A cage was observed only once per day.
8. Fifty cages each containing three males were observed for one to four sessions each (7). If mating in this species occurs by chance alone, then each male should have achieved approximately 0.33 of the copulations in his cage. To test this hypothesis, one day on which just one copulation occurred was chosen at random for each cage, and the number of times that the dominant or a subordinate male copulated was compared with an expected value of the dominant male copulating in 0.33 of the cases and the subordinates in 0.67. Dominant males copulated in 39 cases and subordinates in 11 ($\chi^2 = 45$, d.f. = 1, $P \ll .001$).
9. Males were silenced by first anesthetizing them with CO₂ or N₂ or restraining them, then waxing the stridulatory file on the underside of the right wing. This allowed them to move their wings normally but they were unable to produce sound. Control males were anesthetized or restrained similarly and in the second experiment a drop of wax was put on their pronota.
10. Seven of 40 copulations in 57 observations were made by silent males.
11. Fisher test, not significant, 14 experimental and 9 control cages.
12. Subordinate males were deafened by tearing the tympana on their prothoracic legs. The dominant males were handled in similar fashion except that the analogous sites on their metathoracic legs were scratched rather than their prothoracic tympana. All of the males walked normally after this operation.
13. R. D. Alexander, *Evolution* **16**, 443 (1962).
14. We thank R. Hoy and G. Hausfater for advice at many stages in this research and writing; S. Arnold, L. Heisler, R. Jaeger, and M. Wade for suggestions about the manuscript; and J. Altman and B. Jones for computer time. Parts of this research were supported by NINCDS grant 09244 to R.R.C. and by the Organization for Tropical Studies, the George F. Harris Foundation, Sigma Xi, and NSF BNS77-09447. While writing this report, C.R.B.B. was supported by PHS training grant MH-15181.

* Send requests for reprints to Allee Laboratory of Animal Behavior, University of Chicago, 940 East 57 Street, Chicago, Ill. 60637.

29 March 1982; revised 15 June 1982

Intracellular Recordings from Cochlear Outer Hair Cells

Abstract. *Intracellular recordings were made from outer hair cells in the third turn of the guinea pig cochlea, and the electrical characteristics of the cells were compared to those of inner hair cells, supporting cells, and extracellular spaces from the same recording region. Outer hair cells have higher membrane potentials than do inner hair cells, but they produce smaller a-c receptor potentials. The frequency response characteristics of both types of hair cells are probably not significantly different. In the frequency region where tuning is optimal, both cell types produce depolarizing d-c receptor potentials, but outer hair cells also generate hyperpolarizing responses at low frequencies.*

The most advanced auditory organs have two morphologically distinct sensory receptors. Electrical characteristics of individual mammalian receptors have been described only for one type, the inner hair cell (1). We now describe results of a 4-year study of cochlear outer hair cells (2). Information from single outer hair cells may explain some central questions of cochlear physiology, such as the role of this receptor cell in hearing and the types of interaction, if any, that occur between outer and inner hair cells.

Anesthetized guinea pigs were maintained at a constant core temperature and their heart rates were monitored; in later experiments, exhaled CO₂ was also measured. To assess the normalcy of the ear, a wire electrode was placed in the scala tympani of the first cochlear turn, and tone-burst-generated compound action potentials were recorded. In preparing for the recording of hair cell potentials a fenestra (~ 0.3 by 0.5 mm) was made in the bone over the stria vas-

cularis in the third turn of the cochlea. Microelectrodes were introduced through the stria and aimed at the organ of Corti. The cochlea was back-lighted with a fiber optics illuminator, so that the shadow of the organ of Corti could be seen through the fenestra. Attempts were made to insert the electrodes so that they would travel parallel with the reticular lamina (3) (Fig. 1A). Electrodes were driven by a motorized microdrive in increments of multiples of 2 μ m (4). Only responses obtained with tone-burst stimuli are presented.

The continuous recording of electrode position and a characteristic sequence of d-c potential changes (Fig. 1B) help identify the location of the electrode tip within the organ of Corti. Cell types may be identified by a combination of recording depth, membrane potential, and response magnitude. In all supporting cell types the membrane potential is high (steady-state values range up to -100 mV) and electrical responses are smaller, at any frequency, than those mea-

sured in scala media or in the extracellular spaces in the organ of Corti. Inner hair cells ($N = 19$ stable recordings) are characterized by low steady-state membrane potentials (median, -20 mV; highest, -47 mV) and large receptor potentials (up to 25 mV, peak to peak). At the best frequency of the cell, these responses can be up to a hundred times larger than the corresponding extracellular response. These findings are in harmony with the observations of Russell and Sellick on first-turn inner hair cells (1). Outer hair cells ($N = 22$) can be recognized from their large steady-state membrane potentials (median, -71 mV; highest, -94 mV) and large receptor potentials (up to 15 mV, peak to peak) (5). The cell's a-c response is between 3 and 15 times greater than the extracellular potential. Response patterns at various electrode locations are shown in Fig. 1C.

We compared observations made among a-c response magnitudes recorded at various locations in the same organ of Corti (Fig. 2A). All functions, except the scala media plot (6), depict bandpass filter characteristics. Around the best frequency there is a relatively sharply tuned tip segment with a high frequency slope of more than 40 dB per octave. The low frequency slope flattens out in a tail section which begins about 10 dB below the maximum at the tip. Direct comparison between the inner and outer hair cells in the same cochlea show that the tuning characteristics are comparable, even though the tip-to-tail ratio tends to be smaller in outer hair cells. This ratio, however, is highly variable among animals, ranging from 0 to 20 dB. Higher ratios probably correspond to better preparations.

When a-c and d-c receptor potentials recorded from an outer hair cell are compared, several striking observations can be made. First, outer hair cells produce both depolarizing and hyperpolarizing d-c responses, whereas the d-c output of inner hair cells is always positive (1). Second, the d-c response of outer hair cells appears to be much more sharply tuned than the a-c component. Third, around the best frequency of the cell, the a-c and d-c response magnitudes are commensurate. The behavior of the d-c receptor potential is similar to the patterns described for the gross summing potential (7), which also undergoes a polarity reversal along the frequency axis. In addition, we have shown that the summing potential is much better tuned than the gross cochlear microphonic (8), further suggesting a similarity between intracellular responses of outer hair cells and the gross cochlear poten-

tials. Both a-c and d-c intracellular responses are largest at the same frequency when measured at low sound levels. With an increase in the magnitude of the stimulus both types of responses saturate, and the a-c response peak shifts to lower frequencies. Thus, for example, at 70 dB (Fig. 2B) the a-c maximum occurs at 600 Hz even though at low sound levels it is at 800 Hz, the same frequency at which the d-c maximum is maintained over the whole range of intensities.

Our results reveal some potentially significant similarities, as well as differences, between the electrical characteristics of inner and outer hair cells. The a-c potential produced by either the inner or outer hair cells peaks at the same frequency which is determined by the cell's location along the cochlear spiral. In other words, there does not appear to be a systematic tuning disparity between the two types of receptors located at the same place. The sharpness of tuning

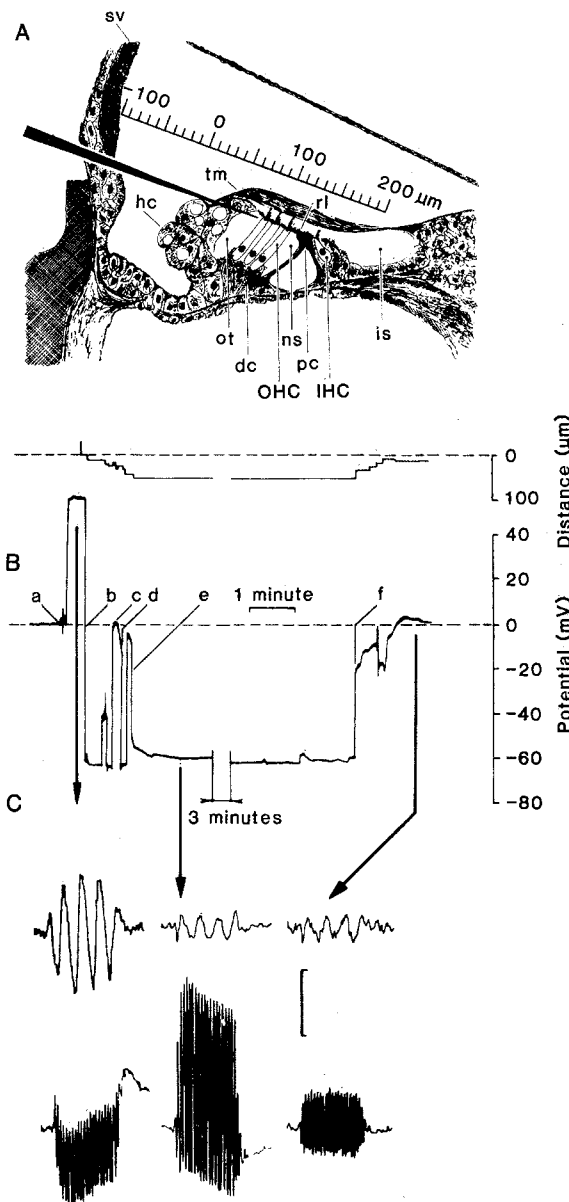
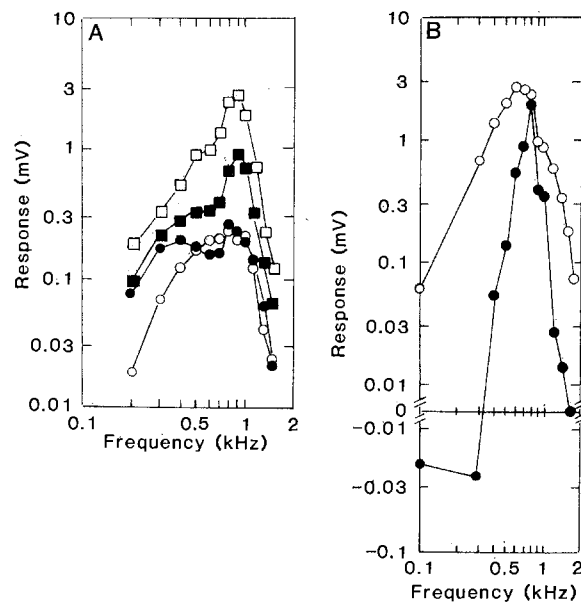


Fig. 1. (A) Cross-section of the third turn of a guinea pig cochlea. The recording electrode was inserted through the stria vascularis by a fenestra in the cochlear bone. The optimal electrode path is parallel to the reticular lamina and situated just below it. OHC, outer hair cell; IHC, inner hair cell; sv, stria vascularis; hc, Hensen's cell; tm, tectorial membrane; rl, reticular lamina; ot, outer tunnel; dc, Deiters' cell; ns, Nuel space; pc, pillar cell; and is, inner sulcus. (B) The d-c potentials measured during a typical electrode track through the cochlear scala. The appearance of a potential can be correlated with the location of the electrode tip with the aid of the distance scale provided. Electrode tip potentials are balanced to zero on the outer surface of the tissue lining the cochlear duct. At point *a* the electrode penetrates the stria vascularis and enters the endolymphatic space. This is signaled by the positive endocochlear potential (EP = 57 mV). After encountering the EP, the electrode travels within the endolymph from 80 to 180 μ m, depending on its position and orientation, before reaching the organ of Corti. Hensen's cells are contacted first, and their penetration is clearly marked by a d-c shift from positive to negative of up to 180 mV (point *b*). A further advance of the electrode traverses the Hensen's cell layer and locates the tip within the outer tunnel of Corti (point *c*). The d-c potential in the outer tunnel or in any fluid space (12) within the spiral organ is zero or slightly negative (less than -10 mV). At electrode location *d* a cell is registered; it is, however, quickly lost. This is probably a third-row outer hair cell. At a depth of 50 μ m another cell is penetrated (point *e*) and held with a stable membrane potential. (The range of holding times for outer hair cells is from 1.2 to 33 minutes; the many cells that were lost before a minute are not considered.) This is another outer hair cell. At marker *f* contact is lost with the hair cell in which the electrode dwelled for 7.5 minutes. A 3 -minute segment of recording is omitted. (C) Averaged responses ($N = 32$) to tone bursts from various electrode locations. Two stimulus frequencies were used (100 and 600 Hz), and all presentations are at the same sound level (70 dB with respect to 20 μ Pa). The vertical bar represents 1 mV, except for the two, top right-hand traces, for which it is 0.2 mV. The recording electronics is a-c coupled with a low frequency cutoff of 1 Hz. Recording electrodes typically possess a bandwidth extending to 1700 Hz (upon optimal capacitance compensation).

Fig. 2. (A) Peak-to-peak a-c response magnitude as a function of stimulus frequency, recorded from various locations within the same organ of Corti. Sound pressure is constant at 40 dB (with respect to 20 μ Pa); at this level the responses are linear. Inner hair cells (\square), outer hair cells (\blacksquare), scala media (\bullet), and organ of Corti fluid space (\circ). (B) Comparison of the frequency dependence of the a-c and d-c receptor potential components from one outer hair cell. Data are obtained from averaged responses with tone-burst stimuli having a constant sound level of 70 dB (with respect to 20 μ Pa); a-c responses are peak-to-peak magnitude, and d-c responses are measured between prestimulus baseline and half the excursion of the a-c waveform; a-c (\circ) and d-c (\bullet).



appears to be similar in both types of cells. Although some evidence suggests that inner hair cells can be better tuned, tuning appears to vary more from animal to animal than from cell to cell in a particular animal. This variation most likely reflects the nonuniformity of physiological conditions among our subjects. We have compared equal intensity response curves with single auditory nerve fiber rate functions obtained at the same sound level from fibers (recorded from chinchillas in our laboratory) for which the best frequency matched those of our hair cells. The range of tuning for these single fibers encompassed our sample, but our best tuned hair cell is not as sharply tuned as the best nerve fiber; it is much better tuned, however, than the poorest one. Since single fiber tuning itself is relatively shallow in the frequency range of interest (600 to 1000 Hz), quantitative comparisons between fiber and hair cell tuning are not particularly revealing. Our data therefore support the suggestion that the sharpness of tuning seen in single fiber discharge patterns is already established at the hair cell level, and the degree of sharpness is probably determined by the mechanical tuning of the basilar membrane-organ of Corti complex (9).

In agreement with work (1) on inner hair cells, we find that the magnitude of a-c and d-c receptor potentials is remarkably large. The responses of inner hair cells appear to be about three times greater than the ones recorded from outer hair cells. There also does not appear to be a systematic difference in sensitivity between the two types of hair cells. Thus schemes that assign different operating regions of sound intensity for outer

and inner hair cells are not supported by these data. At their best frequency the operation of both inner and outer hair cells becomes markedly nonlinear above approximately 50 dB. The nonlinearity is manifested by saturation and production of harmonics and of a d-c component. Although it has been suggested that outer and inner hair cells operate in phase opposition (10), we find no evidence to support such a contention. At the best frequency the a-c receptor potentials produced by the two sensory cell types are approximately in phase, and, as was mentioned above, the d-c receptor potentials are depolarizing. Thus the intrinsic electrical behavior of the two hair cell types is similar around their best frequency.

The most striking difference between the electrical characteristics of outer and inner hair cells is in their resting membrane potentials: the inner hair cells appear to operate at about half the membrane potential of the outer hair cells, and thus resemble supporting cells in this respect. There is no readily evident explanation for this difference in resting potentials. Although the input resistance of our receptor cells is highly variable, the two cell types show overlapping distributions ranging between 10 and 34 megohms (11).

PETER DALLOS

JOSEPH SANTOS-SACCHI

*Auditory Physiology Laboratory and
Department of Neurobiology and
Physiology, Northwestern University,
Evanston, Illinois 60201*

ÅKE FLOCK

*Department of Physiology II,
Karolinska Institute,
Stockholm, Sweden*

References and Notes

1. I. J. Russell and P. M. Sellick, *J. Physiol. (London)* **284**, 261 (1978); P. M. Sellick and I. J. Russell, *Hearing Res.* **1**, 277 (1979); *ibid.* **2**, 439 (1980).
2. P. Dallos and J. Santos-Sacchi, papers presented at the meetings of the Association for Research in Otolaryngology, St. Petersburg, Fla., January 1981 and January 1982; P. Dallos, A. Flock, J. Santos-Sacchi, paper presented at the meeting of the European Inner Ear Biology Workshop, Montpellier, France, September 1981.
3. Initially electrodes filled with aqueous solutions of Niagara sky blue, Procion yellow, or Lucifer yellow were used to mark the cells. Dye injection followed recording and was accomplished by passing a 1 to 5 nA negative current through the cell. After the experiments, the cochleas were perfused with 4 percent glutaraldehyde buffered to pH 7, removed from the animal, and stored in the perfusing solution. Subsequently the ears were dehydrated, embedded in Epon or Spurr, and sectioned in 10- μ m increments. Dye-filled cells were identified under epifluorescent illumination, and 4 inner hair cells, 13 outer hair cells, 28 Deiters' cells, 41 pillar cells, 19 Hensen's cells, and a small assortment of other supporting cell types were recovered. Once the electrical characteristics of various cell types had been clarified, only 3M KCl-filled pipettes (tip, 0.1 μ m in diameter with 120 to 200-megohm resistance) were used for recording.
4. There may be interference with cochlear partition movement when an electrode is introduced into the organ of Corti. It may be questioned if our approach (with an electrode track roughly parallel to the basilar membrane instead of perpendicular to it) compounds the problem. To study this issue we recorded gross receptor potentials from a third turn scala vestibuli electrode during various stages of microelectrode penetration. In most cases no changes were observed in the gross potential, either in its waveform or its spectral content.
5. All organ of Corti cells, including outer hair cells, had negative membrane potentials. This is in contrast to the report of Y. Tanaka, A. Asanuma, and K. Yanagisawa [*Hearing Res.* **2**, 431 (1980)].
6. The observation that in some cases (for example, see Fig. 1C at 100 Hz) the scala media potential can be larger than the intracellular outer hair cell response appears disturbing, since gross potentials are largely produced by outer hair cells [P. Dallos and M. A. Cheatham, *J. Acoust. Soc. Am.* **60**, 510 (1976)]. We have shown that the low frequency lobe of the scala media response function does not represent a locally produced electrical activity. Instead, these responses are conducted from more apical regions of the cochlea which are tuned to the low frequencies and produce much larger potentials. When the fourth turn of the cochlea is amputated, the large, low frequency response disappears, and the scala media function assumes the form of the organ of Corti gross response, without a change in its magnitude at the best frequency.
7. H. Davis, B. H. Deatherage, D. H. Eldredge, C. A. Smith, *Am. J. Physiol.* **195**, 251 (1958); T. Konishi and T. Yasuno, *J. Acoust. Soc. Am.* **35**, 1448 (1963); V. Honrubia and P. Ward, *ibid.* **45**, 1443 (1969); P. Dallos, Z. G. Schoeny, M. A. Cheatham, *Acta Oto-Laryngol. Suppl.* **302**, 1 (1972).
8. P. Dallos, in *Basic Mechanisms in Hearing*, A. Møller, Ed. (Academic Press, New York, 1973), p. 335.
9. S. M. Khanna and D. G. B. Leonard, *Science* **215**, 305 (1982); P. M. Sellick, I. J. Russell, R. Patuzzi, B. M. Johnstone, *J. Acoust. Soc. Am.* **70**, S51 (1981).
10. J. J. Zwislocki, *Audiology* **14**, 443 (1975); V. Honrubia, D. Strelloff, S. T. Sitko, *Ann. Otol. Rhinol. Laryngol.* **85**, 697 (1976); M. Pierson and A. Møller, *Hearing Res.* **2**, 135 (1980).
11. Input impedance of cells was measured with a single-electrode bridge-balance technique.
12. In contrast to the fluid spaces within the organ of Corti proper, in the inner spiral sulcus and in the subreticular space the resting potential is identical to the positive endocochlear potential.
13. We thank M. A. Cheatham, B. Flock, W. Lutz, and E. Relkin for their contributions. This work was supported by grant NS 08635 from the National Institute of Neurological Communicative Disorders and Stroke, a Guggenheim fellowship to P.D., and the Swedish Medical Research Council.

16 March 1982; revised 4 June 1982

Modulators of Kv3 Potassium Channels Rescue the Auditory Function of Fragile X Mice

Lynda El-Hassar,¹ Lei Song,^{2,6,7,8}  Winston J.T. Tan,² Charles H. Large,⁵ Giuseppe Alvaro,⁵  Joseph Santos-Sacchi,^{2,3,4} and  Leonard K. Kaczmarek^{1,4}

Departments of ¹Pharmacology, ²Surgery, ³Neuroscience, ⁴Cellular and Molecular Physiology, Yale University School of Medicine, New Haven, Connecticut 06520, ⁵Autifony Therapeutics Limited, Stevenage Bioscience Catalyst, Stevenage SG1 2FX, United Kingdom, ⁶Department of Otolaryngology-Head and Neck Surgery, Shanghai Ninth People's Hospital, Shanghai Jiao Tong University School of Medicine, Shanghai 200011, P. R. China, ⁷Ear Institute, Shanghai Jiao Tong University School of Medicine, Shanghai 200125, P.R. China, and ⁸Shanghai Key Laboratory of Translational Medicine on Ear and Nose Diseases, Shanghai 200125, P. R. China

Fragile X syndrome (FXS) is characterized by hypersensitivity to sensory stimuli, including environmental sounds. We compared the auditory brainstem response (ABR) recorded *in vivo* in mice lacking the gene (*Fmr1*^{-/-}) for fragile X mental retardation protein (FMRP) with that in wild-type animals. We found that ABR wave I, which represents input from the auditory nerve, is reduced in *Fmr1*^{-/-} animals, but only at high sound levels. In contrast, wave IV, which represents the activity of auditory brainstem nuclei is enhanced at all sound levels, suggesting that loss of FMRP alters the central processing of auditory signals. Current-clamp recordings of neurons in the medial nucleus of the trapezoid body in the auditory brainstem revealed that, in contrast to neurons from wild-type animals, sustained depolarization triggers repetitive firing rather than a single action potential. In voltage-clamp recordings, K⁺ currents that activate at positive potentials (“high-threshold” K⁺ currents), which are required for high-frequency firing and are carried primarily by Kv3.1 channels, are elevated in *Fmr1*^{-/-} mice, while K⁺ currents that activate near the resting potential and inhibit repetitive firing are reduced. We therefore tested the effects of AUT2 [((4-({5-[(4R)-4-ethyl-2,5-dioxo-1-imidazolidinyl]-2-pyridinyl}oxy)-2-(1-methylethyl) benzonitrile], a compound that modulates Kv3.1 channels. AUT2 reduced the high-threshold K⁺ current and increased the low-threshold K⁺ currents in neurons from *Fmr1*^{-/-} animals by shifting the activation of the high-threshold current to more negative potentials. This reduced the firing rate and, *in vivo*, restored wave IV of the ABR. Our results from animals of both sexes suggest that the modulation of the Kv3.1 channel may have potential for the treatment of sensory hypersensitivity in patients with FXS.

Key words: auditory brainstem response; AUT2; fragile X; high- and low-threshold potassium channels; medial nucleus of the trapezoid body; potassium channels

Significance Statement

mRNA encoding the Kv3.1 potassium channel was one of the first described targets of the fragile X mental retardation protein (FMRP). Fragile X syndrome is caused by loss of FMRP and, in humans and mice, causes hypersensitivity to auditory stimuli. We found that components of the auditory brain response (ABR) corresponding to auditory brainstem activity are enhanced in mice lacking FMRP. This is accompanied by hyperexcitability and altered potassium currents in auditory brainstem neurons. Treatment with a drug that alters the voltage dependence of Kv3.1 channels normalizes the imbalance of potassium currents, as well as ABR responses *in vivo*, suggesting that such compounds may be effective in treating some symptoms of fragile X syndrome.

Introduction

Fragile X syndrome (FXS) is a genetic disease caused by a silencing mutation of the *FMRI* gene. In the majority of cases, this is

caused by an expansion of the CGG repeats in the promoter region of the *FMRI* gene, which leads to a lack of fragile X mental retardation protein (FMRP; Oberlé et al., 1991; Verkerk et al., 1991). FMRP is a mRNA binding protein that controls the func-

Received March 30, 2018; revised March 15, 2019; accepted March 26, 2019.

Author contributions: L.E.-H. and L.K.K. designed research; L.E.-H. and W.J.T.T. performed research; L.S., C.H.L., G.A., and J.S.-S. contributed unpublished reagents/analytic tools; L.E.-H. analyzed data; L.E.-H. wrote the paper.

This work was supported by grants from Autofony Therapeutics Limited; the FRAXA Research Foundation; and National Institutes of Health Grants DC-01919 (to L.K.K.), and DC-000273, DC-008130 and DC-016318 (to J.S.-S.).

C.H.L. is a director of Autofony Therapeutics Limited. G.A. is a full-time employee of Autofony Therapeutics Limited. We thank Dr. Nigel Bamford for support and use of electrophysiological equipment.

Correspondence should be addressed to Leonard K. Kaczmarek at leonard.kaczmarek@yale.edu.
<https://doi.org/10.1523/JNEUROSCI.0839-18.2019>

Copyright © 2019 the authors

tion and expression level of a variety of proteins including several ion channels (Darnell et al., 2011). Patients with FXS experience multiple symptoms such as hypersensitivity to sensory stimuli, hyperactivity, susceptibility to seizures, intellectual disability, anxiety, and social and memory impairment (Garber et al., 2008; Chonchaiya et al., 2009). Some of these symptoms have been replicated in fragile X mice in which the gene for FMRP has been deleted (*Fmr1*^{-/-} mice; Michalon et al., 2012; Curia et al., 2013; Rotschafer and Razak, 2014; Myrick et al., 2015; Bostrom et al., 2016; Aloisi et al., 2017; Pyronneau et al., 2017; Sinclair et al., 2017). In humans, early intervention, such as drug treatment, speech therapy, schooling, and social integration, are believed to improve cognition in patients with FXS (Lozano et al., 2016). This offers hope that further effective treatments for fragile X symptoms will emerge if the appropriate targets for therapeutic agents can be identified.

One symptom that is relevant to this study is the hypersensitivity of patients with FXS to auditory stimuli (Arinami et al., 1988; Roberts et al., 2005). Physiological levels of sound evoke abnormal elevation of the cortical auditory response in patients with FXS (St Clair et al., 1987; Rojas et al., 2001; Castrén et al., 2003; Van der Molen et al., 2012), and ordinary environmental sounds can become unbearable for patients with FXS. In addition to this hypersensitivity to auditory stimuli, patients with fragile X syndrome have difficulties in discriminating the timing of auditory stimuli, which renders them unable to localize sounds in space (Hall et al., 2009; Rotschafer and Razak, 2014). Both the elevated cortical responses to sound stimuli and the deficits in temporal processing are likely to be influenced by alterations in subcortical networks such as those in the auditory brainstem that compute sound localization. These include the anteroventral cochlear nucleus (AVCN) and the medial nucleus of the trapezoid body (MNTB), as well as the medial and lateral superior olivary nuclei to which the AVCN and MNTB project. This conclusion is supported by the finding that the auditory brainstem response (ABR) recorded *in vivo* is altered in adult *Fmr1*^{-/-} mice, and this may result, in part, from an alteration in the balance of excitation and inhibition (Rotschafer et al., 2015; Garcia-Pino et al., 2017; McCullagh et al., 2017).

The intrinsic excitability of neurons is determined by the ion channels they express. The mRNAs for several ion channels bind FMRP (Darnell et al., 2011), and in several cases the loss of FMRP has been demonstrated to alter levels of ion channel proteins in neurons (Brager and Johnston, 2014; Frick et al., 2017). Moreover, a subset of these ion channel proteins bind FMRP directly, altering the amplitude, gating, or trafficking of the channels (Brown et al., 2010; Zhang et al., 2012; Deng et al., 2013, 2019; Ferron et al., 2014; Myrick et al., 2015; Yang et al., 2018). Previous studies have demonstrated that currents corresponding to some of these ion channels are altered in the auditory brainstem MNTB neurons of *Fmr1*^{-/-} mice (Brown et al., 2010; Strumbos et al., 2010b). We have now analyzed the effects of the loss of FMRP on the intrinsic excitability of auditory brainstem MNTB neurons *in vitro* and compared this to alterations in auditory brainstem responses *in vivo*, in *Fmr1*^{-/-} and wild-type (WT) mice. We have also characterized the actions of a small molecule, AUT2 [(4-({5-[(4R)-4-ethyl-2,5-dioxo-1-imidazolidinyl]-2-pyridinyl}oxy)-2-(1-methylethyl) benzonitrile; Brown et al., 2016], which modulates Kv3.1 potassium channels, and found that this compound was able to normalize both the firing patterns of MNTB neurons and the ABR of *Fmr1*^{-/-} mice.

Materials and Methods

AUT compound. AUT2 (Autifony Therapeutics) is a small molecule modulator of human and rodent Kv3.1 and Kv3.2 channels. Some of the electrophysiological actions of AUT2 have been described previously (Brown et al., 2016). AUT2 is a cell-permeant small molecule, which modulates human recombinant Kv3.1 channels by shifting the voltage dependence of activation and inactivation to negative potentials (EC_{50} , 0.9 μ M; Brown et al., 2016). AUT2 (10 mM stock solution) was dissolved in DMSO (0.1%), and the final concentration used in the recording chamber was 10 μ M for *in vitro* recordings. A 10 μ M concentration of AUT2 has previously been shown to strongly modulate the recombinant Kv3.1 channel, causing a 28 mV leftward shift in the V_{1/2} of activation (Brown et al., 2016). For testing the effects of AUT2 on auditory brainstem response *in vivo*, we prepared a vehicle containing 12.5% of Captisol, mixed with 0.5% HPMC (hydroxypropylmethylcellulose) K15M and 0.5% Tween 80 in sterile water. The AUT2 drug suspension was then prepared by dissolving AUT2 compound in the vehicle solution, which was used at a final concentration of 30 mg/kg and dosed by the intraperitoneal route 20 min before testing. While formal pharmacokinetic studies have not been conducted with this compound in the mouse, a dose of 30 mg/kg AUT2 administered orally to rats gave brain concentrations of ~3500 mg/ml 2 h after dosing (Autifony Therapeutics, unpublished data). Taking into account brain tissue binding, this is expected to be equivalent to a free brain concentration of ~0.5 μ M. The brain concentration of AUT2, 20 min after 30 mg/kg, i.p., administration, might be expected to be in the range of 0.5–1 μ M.

Electrophysiological recordings from MNTB brain slices. Both male and female WT (FVB.129P2-*Pde6b*⁺*Tyr^{c-ctd}*/Ant) and *Fmr1*^{-/-} (FVB.129P2-*Fmr1*^{tm1Cgr/J}) mice were purchased from The Jackson Laboratory. All data represent the mean \pm SE. The number of neurons or animals is represented by “n” or “N” respectively.

All procedures described followed National Institutes of Health guidelines outlined in *Preparation and Maintenance of Higher Animals during Neuroscience Experiments* (publication 91–3207). Procedures were approved by the Institutional Animal Care and Use Committee at the Yale University School of Medicine. The auditory brainstem including the MNTB was extracted from 15-d-old wild-type (Fvbn129) and *Fmr1*^{-/-} mice of either sex. Acute transverse slices of the auditory brainstem were cut to a thickness of 250 μ m using procedures described previously (Yang and Wang, 2006). Recordings were performed in a chamber continuously perfused (1–2 ml/min) with oxygenated and warmed (31–33°C) artificial CSF containing the following (in mM): 124 NaCl, 2.5 KCl, 25 NaHCO₃, 1.25 NaH₂PO₄, 2 MgCl₂, 2 CaCl₂, and 10 glucose. Whole-cell patch-clamp recordings were made from visualized MNTB neurons using an upright Zeiss Axioskop 2 FS microscope with differential interference contrast optics. Patch pipettes (3–5 M Ω) were pulled from borosilicate glass tubing (outer diameter, 2.0 mm; wall thickness, 0.5 mm) and filled with the following intracellular solution (in mM): 32.5 KCl, 97.5 K-gluconate, 5 EGTA, 10 HEPES, and 1 MgCl₂, pH 7.2 (Macica et al., 2003). Voltage-clamp recordings were made using EPC-7 (HEKA Elektronik) or Multiclamp 700B (Molecular Devices) amplifiers. Tetrodotoxin (1 μ M) and CdCl₂ (20 μ M) were used to suppress Na⁺- and Ca²⁺-activated K⁺ channels, respectively. Current-clamp recordings were made in bridge mode using an SEC 05L amplifier (npi electronic). Neurons with resting potentials more positive than –50 mV were discarded, regardless of treatment. The junction potential was not corrected. Uncompensated series resistances were on average 13.12 \pm 0.31 M Ω (n = 77 cells, N = 52 cells). Series resistance was compensated at 50–70%. Access resistance and holding current were continuously monitored for stability; >20% variation led to a rejection of the cell.

Data acquisition and analysis were performed using software that was either custom written in the Igor Pro programming environment (WaveMetrics) or using pCLAMP version 9.2 (Molecular Devices). Conductance values were obtained by dividing the current by the electrochemical driving force, as follows: $I_K/(V_m - E_K)$, where I_K is the K⁺ current, V_m is the membrane potential and E_K is the reversal potential for K⁺ ions. For voltage dependence of activation experiments, normalized conductance–voltage plots were obtained by normalizing conductance

(G) to that measured at +60 mV (G_{+60}) for each recording and fit using the sigmoidal function: $y = A_2 + (A_1 - A_2)/(1 + e^{(x-x_0)/k})$, where A_1 and A_2 represent the initial and final values of the y abscise, respectively; k is the slope factor; and x_0 is the half-maximal value. For the voltage dependence of inactivation, normalized conductance–voltage plots were fitted by normalizing currents to the maximum obtained by stepping from -100 mV and fitted using the same function. These fits were not used to calculate $V_{1/2}$ values, which were instead determined for each cell by direct determination of the potential at which conductance was 0.5 of the maximal value at +60 mV. In current-clamp recordings, input resistance was calculated by applying a train of three hyperpolarizing current pulses (250 pA, 300 ms duration, at 0.3 Hz), and comparing the mean maximal voltage deflection during these pulses to the baseline membrane potential 20 ms before current injections.

ABR. Animals (15 d old) were anesthetized with 480 mg/kg, i.p., chloral hydrate, and all recordings were conducted in a sound-attenuating chamber (Industrial Acoustics). A customized TDT3 system (Tucker-Davis Technologies) was used for ABR recordings. Subdermal needle electrodes (Rochester Electro-Medical) were positioned at the vertex (active, noninverting), the infra-auricular mastoid region (reference, inverting), and the neck region (ground). Differentially recorded scalp potentials were bandpass filtered between 0.05 and 3 kHz over a 15 ms epoch. A total of 400 trials was averaged for each waveform for each stimulus condition.

Symmetrically shaped tone bursts were 3 ms long (1 ms raised cosine on/off ramps and 1 ms plateau). All acoustic stimuli were delivered free field via a speaker (Part FF1 2021, Tucker-Davis Technologies) positioned 10 cm from the vertex. Stimulus levels were calibrated using a 0.5 inch condenser microphone (model 4016, ACO Pacific) positioned at the approximate location of the animal's head during recording sessions and are reported in decibels of sound pressure level (SPL; referenced to 20 μ Pa). Stimuli of alternating polarity were delivered at a rate of \sim 20/s. Tone burst responses were collected in half-octave steps ranging from 32 to 2.0 kHz. The effects of level were determined by decreasing stimulus intensity in 5 or 10 dB steps. A maximum stimulus level of 90 dB SPL was used first to avoid overstimulation. The ABR threshold was defined as the lowest intensity of sound level capable of evoking a reproducible, visually detectable response (Song et al., 2006). Latencies and amplitudes of the initial four ABR peaks were measured from sound stimuli delivered at a rate of 20/s and at a frequency of 11.3 kHz, one of the most sensitive frequency ranges of hearing in mice. The analysis was performed off-line in BioSig (BioSig Technologies) on traces with visible peaks by setting cursors at the maxima and minima of the peaks. Latency was defined as the time from the onset of the stimulus to the peak, while amplitude was measured by taking the mean of the ΔV of the positive and negative deflections of the ABR wave (Tan et al., 2017).

Experimental design and statistical analysis. All data were collected from different littermates and used both males and females. Data analysis was performed using Igor, Clampfit, and BioSig software. For whole-cell voltage-clamp experiments, evoked currents were quantified by measuring the mean current between 50 ms after the onset of a test pulse and 50 ms before the end of the pulse. The interval between each pulse protocol ranged from 3 to 5 min in control conditions. When waiting for drugs to take effect, cells were held at resting membrane potentials for 10–15 min. The analyses used either a paired two-tailed t test (for comparison between $Fmr1^{-/-}$ mice before and after AUT2 treatment) or unpaired two-tailed t test for comparison between wild-type and $Fmr1^{-/-}$ mice (with Welch's correction). In some cases, for example, when a comparison of ABR amplitude and/or latency with genotype (or with AUT2 treatment) across sound level intensity was performed, we used a two-way ANOVA that considered a full set of variances. Similarly, for data comparing the number of action potentials between genotypes across stimulus frequencies or the magnitude of potassium current between genotypes across membrane voltages, we performed a two-way ANOVA followed by a *post hoc* multiple comparison using Bonferroni–Dunn or Holm–Sidak method. A value of $p < 0.05$ was considered significant for all tests. Statistical analysis was conducted using GraphPad Prism 8 and Origin software.

Results

Loss of FMRP alters central processing of auditory information

To investigate how loss of FMRP impacts the processing of auditory information early in development, we compared the *in vivo* ABR of 15-d-old wild-type and $Fmr1^{-/-}$ mice, corresponding to 3–5 d after the onset of hearing. The ABR is characterized by a series of electrical waves, labeled as waves I to V (Jewett and Williston, 1971; Song et al., 2006), representing the progressive transfer of the auditory signal from the periphery to the CNS. Wave I represents the summated response from the spiral ganglion and auditory nerve, while waves II to V represent responses from the ascending auditory pathway (Akil et al., 2016).

We first determined that the threshold for detecting an electrophysiological response (ABR threshold) was not altered in $Fmr1^{-/-}$ mice at all sound frequencies tested from 2 to 32 kHz (Fig. 1A). ABRs were then recorded in response to an 11.3 kHz stimulus lasting 3 ms at intensities up to 90 dB (Fig. 1B). A two-way ANOVA with mean comparison using Bonferroni's test was performed to compare the effects of genotype (WT or $Fmr1^{-/-}$ mice) and of sound levels (from 40 to 90 dB) on the amplitude of the ABR response. We found that the amplitude of wave I was significantly reduced in $Fmr1^{-/-}$ mice compared with WT mice ($F_{(1,353)} = 15.44$, $p = 0.0002$). We also found a significant interaction effect between the genotype and sound level on the amplitude of wave I ($F_{(10,353)} = 2.4$; $p = 0.01$). When this analysis was followed by a simple test effect that corrected for multiple comparisons using Bonferroni–Dunn method, we found that the amplitude of wave I was significantly smaller in $Fmr1^{-/-}$ animals at higher intensities of sound levels (Fig. 1C: 85 dB, $*p = 0.002$; $*90$ dB, $p = 0.0009$).

In contrast, the amplitude of wave IV, which reflects the synchronous activity of the auditory brainstem nuclei including the MNTB, was significantly enhanced in $Fmr1^{-/-}$ mice ($F_{(1,301)} = 30.33$, $p < 0.0001$). The intensity of sound level had a significant effect on the amplitude of wave IV ($F_{(10,301)} = 10.20$, $p < 0.0001$), and the interaction of both genotype and sound levels also had an effect on the amplitude of wave IV ($F_{(10,301)} = 2.23$, $p = 0.01$; Fig. 1C). We thus performed a simple effects test and found that the amplitude of wave IV was significantly higher at 75, 80, 85, and 90 dB ($p = 0.0001$, Bonferroni–Dunn method).

We then analyzed the latency of each wave to investigate any potential changes in the rate of propagation through the nervous system. Although the latency of waves I appeared slightly prolonged in $Fmr1^{-/-}$ mice compared with wild-type mice, this difference was not statistically significant ($F_{(1,340)} = 2.213$, $p = 0.13$). In addition, the latency of wave IV was not significantly different between WT and $Fmr1^{-/-}$ mice ($F_{(10,285)} = 0.3$, $p = 0.98$).

Firing patterns of MNTB neurons are disrupted in $Fmr1^{-/-}$ mice

To determine whether the loss of FMRP alters the firing patterns of MNTB neurons, we performed *in vitro* recordings from principal neurons of the MNTB in brainstem slices from 15-d-old mice. We first used a whole-cell current-clamp configuration to record the response of cells to a series of sustained hyperpolarizing and depolarizing current pulses (200 ms square current pulses, -250 to $+350$ pA). As has been found in previous studies (Wang et al., 1998a), we found that in response to a 250 or 350 pA depolarizing current injection, MNTB neurons from wild-type mice fire only at the onset of the depolarization, and never fire more than one or two action potentials (Fig. 2A). In contrast,

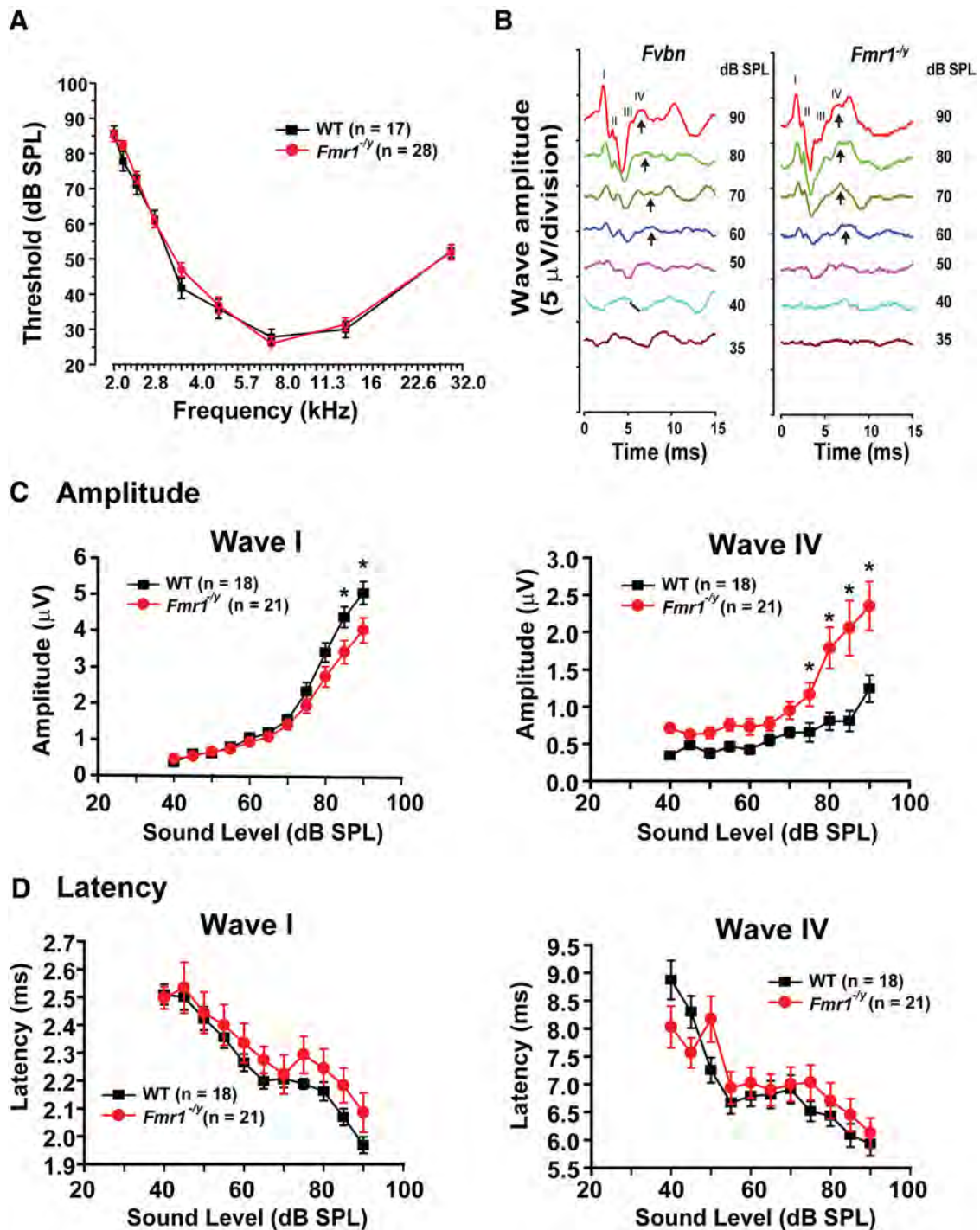


Figure 1. Loss of FMRP alters the central processing of auditory signals. **A**, Plots of the ABR thresholds for wild-type mice ($N = 17$ animals) and *Fmr1*^{-/-} mice ($N = 28$ animals). **B**, ABR wave recordings from WT and *Fmr1*^{-/-} mice stimulated at 11.3 kHz at different sound levels (35–90 dB). Arrows indicate wave IV of the ABR response. **C, D**, Plots of the amplitudes (**C**) and latencies (**D**) of ABR waves I and IV as a function of sound levels (40–90 dB). The magnitude of wave I is decreased for high sound levels ($p = 0.0002$) only, and there is a significant increase in wave IV amplitude in *Fmr1*^{-/-} mice at most sound levels tested ($p < 0.0001$) without significant change in the ABR latencies. Error bars indicate the mean \pm SEM. In **C**, asterisks indicate statistical significance (two-way ANOVA followed by Bonferroni–Dunn post-test).

MNTB neurons from *Fmr1*^{-/-} mice fire repetitively throughout the sustained depolarizations (Fig. 2*A, B*). Overall, the number of action potentials evoked by the 200 ms, 250 pA depolarizing current pulse was significantly greater in neurons from *Fmr1*^{-/-} mice (5.82 ± 1.48 , $n = 27$ cells, $N = 9$ animals; Fig. 2*A, B*) than in those from wild-type animals (0.33 ± 0.11 , $n = 18$ cells, $N = 7$ animals; $p = 0.002$, Student's unpaired t test with Welch's correction; $t = 1.713$, $df = 3.041$).

The input resistances and resting membrane potentials of MNTB neurons from *Fmr1*^{-/-} mice (88.70 ± 5.42 M Ω and -60.76 ± 1.44 mV, $n = 18$, $N = 11$) were not different from those of wild-type mice [90.65 ± 9.67 M Ω and -59.92 ± 0.39 mV, $n = 18$, $N = 15$; $p = 0.23$ for the input resistance comparison (Student's unpaired t test with Welch's correction, $t = 1.239$, $df = 22.76$); and $p = 0.87$ for the resting membrane potential comparison (Student's unpaired t test with Welch's correction

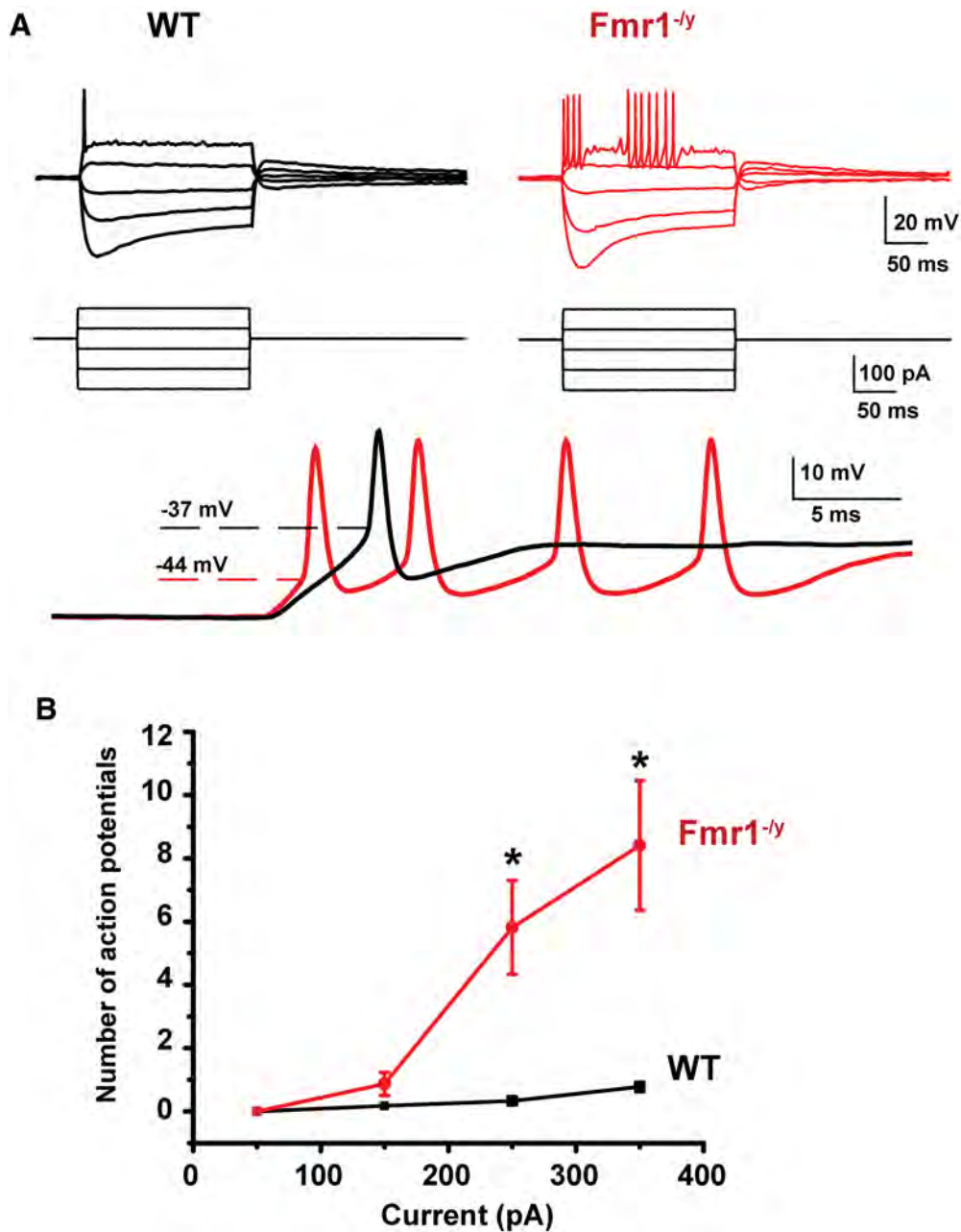


Figure 2. MNTB neurons from *Fmr1*^{-/-} mice are hyperexcitable. **A**, Current-clamp recordings of action potentials in response to a series of sustained hyperpolarizing and depolarizing current pulses (200 ms square current pulses, -250 to +350 pA). Note the repetitive firing and the shorter latency firing of MNTB neurons from *Fmr1*^{-/-} mice compared with the WT mice, which never fired more than one or two action potentials. **B**, Group data showing a significant increase in number of action potentials evoked in neurons from *Fmr1*^{-/-} mice in response to currents of increasing amplitude (Asterisks indicate statistical significance. *p* = 0.002, Student’s unpaired *t* test with Welch’s correction).

Table 1. Electrical parameters of MNTB neurons from wild type and *Fmr1*^{-/-} animals

Condition	Input resistance (MΩ)	Resting membrane potential (mV)	Rheobase (pA)	First action potential latency (ms)	Spike threshold (mV)
Wild type	90.65 ± 9.67 (18)	-59.92 ± 0.39 (18)	450 ± 49.25(18)**	3.67 ± 0.24 (18)	-37.28 ± 1.35(18)**
<i>Fmr1</i> ^{-/-}	88.70 ± 5.42 (18)	-60.76 ± 1.44 (18)	255.55 ± 20.56(18)**	3.48 ± 0.32 (18)	-44.21 ± 1.37(18)**

***p* = 0.001.

(*t* = 0.1649, *df* = 12.7)]. We found, however, a significant difference in the spike threshold between the two groups of mice [wild-type mice: -37.3 ± 1.35 mV, *n* = 18, *N* = 15; vs *Fmr1*^{-/-} mice: -44.2 ± 1.37 mV, *n* = 18, *N* = 11; *p* = 0.001, Student’s unpaired *t* test with Welch’s correction (*t* = 3.59, *df* = 31.92)]. This is consistent with a significant decrease of

the rheobase from 450 ± 49.25 pA in wild-type mice to 255 ± 20.56 pA in *Fmr1*^{-/-} mice (Table 1; *p* = 0.001, Student’s unpaired *t* test, with Welch’s correction; *t* = 3.643, *df* = 21.45). We found, however, no statistical difference in action potential height between the wild-type mice (43.51 ± 3.73 mV, *n* = 18, *N* = 15) and the *Fmr1*^{-/-} mice (42.11 ± 2.57 mV, *n* = 18,

$N = 11$, $p = 0.8$; Student's unpaired t test, with Welch's correction, $t = 0.3085$, $df = 15.63$).

In response to high rates of stimulation, MNTB neurons are capable of locking their action potentials to stimuli at rates of up to several hundred hertz (Macica et al., 2003; Song et al., 2005; Kopp-Scheinflug et al., 2011). We therefore compared the ability of MNTB neurons from wild-type and $Fmr1^{-/-}$ mice to follow repetitive stimuli of brief and subthreshold current pulses (1 nA, 0.3 ms, 20 stimuli) applied at rates from 50 to 600 Hz. Consistent with their enhanced excitability in response to sustained depolarization, we found that MNTB neurons from $Fmr1^{-/-}$ mice fired more action potentials compared with WT mice. For example, at 200 Hz, the number of spikes elicited by a train of 20 stimuli was 14.38 ± 1.43 ($n = 10$, $N = 9$ animals) in $Fmr1^{-/-}$ mice compared with 8.66 ± 1.92 ($n = 13$, $N = 10$ animals) in wild-type mice ($p = 0.04$, Student's unpaired t test with Welch's correction; $t = 2.381$, $df = 10.71$). A two-way ANOVA was further performed to examine changes in the number of spikes in relation to both variables: the genotype of animals (WT or $Fmr1^{-/-}$ mice) and the frequency of stimulation. We found that the genotype had a stronger impact on the number of spikes ($F_{(1,75)} = 16.88$, $p = 0.0001$; Fig. 3A,B). The stimulus frequency also had an effect on the number of evoked spikes ($F_{(3,75)} = 2.81$, $p = 0.04$), but no significant interaction effect was found between the genotype and the stimulus frequency on the number of action potentials ($F_{(3,75)} = 2.81$, $p = 0.3$). *Post hoc* tests that corrected for multiple comparisons showed that this increase in spike number in $Fmr1^{-/-}$ mice was significant for 50, 200, and 400 Hz ($p = 0.0005$, $p = 0.04$, $p = 0.04$) but not for 600 Hz ($p = 0.5$, Holm–Sidak method; Fig. 3B, asterisk).

Multiple potassium currents are altered in MNTB neurons of $Fmr1^{-/-}$ mice.

Several different types of voltage-dependent K^+ currents have been described in MNTB neurons. Some of these activate only at positive potentials and contribute primarily to the rapid repolarization of action potentials. These include currents attributed to the Kv3.1 and Kv2.2 channels (Macica et al., 2003; Steinert et al., 2011). Several other components of K^+ current activate near the resting potential and are required to maintain accurate temporal locking of action potentials to incoming stimuli. These include subunits of the Kv1, Kv11, and K_{Na} subfamilies (Brew and Forsythe, 1995; Grigg et al., 2000; Dodson et al., 2002; Yang et al., 2007; Hardman and Forsythe, 2009; Mathews et al., 2010). To evaluate the effect of loss of FMRP on intrinsic excitability, we performed voltage-clamp experiments using protocols that differentiate between these two components of current in postnatal day 15 wild-type and $Fmr1^{-/-}$ mice. Because several K^+ subunits have a tonotopic distribution in the MNTB (Li et al., 2001; Bhat-tacharjee et al., 2002, 2005; Brew and Forsythe, 2005; Strumbos et al., 2010a), we confined our recordings to cells in the lateral region of the MNTB.

We first recorded K^+ currents that activate at positive potentials by holding the membrane potential at -40 mV for 2 min before applying test pulses between -30 and $+60$ mV in 10 mV increments (Fig. 4A). This holding potential causes the inactivation of most components of K^+ current that activate at more negative potentials, and 80–90% of the current evoked under these conditions represents the Kv3.1 current (Wang et al., 1998a; Macica et al., 2003). The amplitude of these currents at $+60$ mV, which we will term “high-threshold” K^+ currents, was significantly higher in MNTB neurons from $Fmr1^{-/-}$ mice than in wild-type mice (Figs. 4A, 5.90 ± 0.40 vs 3.99 ± 0.66 nA, respectively,

$p = 0.02$; Student's unpaired t test with Welch's correction: $t = 2.493$, $df = 14.87$). A two-way ANOVA test revealed that both the genotype ($F_{(1,150)} = 22.02$, $p < 0.0001$) and the membrane voltage ($F_{(9,150)} = 45.54$, $p < 0.0001$) had a significant impact on the magnitude of high-threshold K^+ currents. Using a *post hoc* test that corrected for multiple comparisons, we found that the high-threshold K^+ currents were significantly increased in neurons from $Fmr1^{-/-}$ mice at 40 mV ($p = 0.01$), 50 mV ($p = 0.003$), and 60 mV ($p = 0.0007$; Fig. 4A).

When the normalized conductance was plotted as a function of membrane voltage (Fig. 4A, right), we found no significant change in the conductance between WT and $Fmr1^{-/-}$ groups of mice. The half-activation potential ($V_{1/2 \text{ max}}$) for the WT group was -1.05 ± 3.8 ($n = 9$, $N = 7$) compared with 6.25 ± 2.2 mV in the $Fmr1^{-/-}$ group ($p = 0.16$, $n = 7$, $N = 7$; Student's unpaired t test with Welch's correction: $t = 1.47$, $df = 12.94$).

For the second protocol, the membrane potential was held at -80 mV, and currents were evoked by potentials between -70 to $+60$ mV in 10 mV increments. This evokes currents that activate near the resting potential and action potential threshold (-60 to -20 mV, low-threshold currents) as well as the high-threshold K^+ currents (Fig. 4B). Under these conditions, the currents recorded at $+60$ mV were significantly lower in MNTB neurons from $Fmr1^{-/-}$ mice: 7.71 ± 0.31 nA ($n = 7$, $N = 7$ animals) than in those from wild-type mice vs 9.51 ± 0.47 nA ($n = 9$, $N = 7$ animals, $p = 0.007$, Student's unpaired t test with Welch's correction: $t = 3.535$, $df = 8.506$). Additional two-way ANOVA revealed a significant main effect of the genotype on the amplitude of low-threshold K^+ current ($F_{(2,139)} = 56.30$, $p < 0.0001$). Using a *post hoc* test that corrected for multiple comparisons, we found that the low-threshold K^+ currents were significantly decreased in $Fmr1^{-/-}$ mice at membrane voltages from -10 to $+60$ mV (-10 mV: $p = 0.006$; 0 mV: $p = 0.0005$; 10 mV: $p = 0.00002$; 20 – 50 mV: $p < 0.0001$; 60 mV: $p < 0.0001$; Fig. 4B).

When the normalized conductance was plotted as a function of membrane voltage (Fig. 4B), there was a significant decrease in the conductance in the $Fmr1^{-/-}$ group of mice. The $V_{1/2 \text{ max}}$ for the WT group was -34.15 ± 1.4 mV compared with -20.12 ± 1.23 mV in the $Fmr1^{-/-}$ group ($p = 0.01$, Student's unpaired t test with Welch's correction; $t = 5.88$, $df = 6.99$).

These findings indicate that the high-threshold and low-threshold K^+ currents are altered in opposite directions by loss of FMRP. Both of these changes are consistent with the increased excitability of MNTB neurons in $Fmr1^{-/-}$ mice. Increased Kv3.1-like high-threshold currents increase the ability of neurons to fire at high rates, while reduced low-threshold K^+ currents, which dominate total current in steps from -80 mV, lower the threshold for action potentials and promote repetitive firing (Gan and Kaczmarek, 1998; Rudy and McBain, 2001; Zhang et al., 2012).

Actions of the Kv3.1 channel modulator AUT2 on K^+ currents in MNTB neurons from $Fmr1^{-/-}$ mice

AUT2 is an imidazolidinedione derivative that modulates Kv3.1 channels (Brown et al., 2016; Fig. 5A). In mammalian cells transfected with human Kv3.1 channels, AUT2 shifts the voltage dependence of activation toward more negative potentials. This may cause Kv3.1 channels to activate at potentials that normally only activate low-threshold K^+ channels. In addition, AUT2 also shifts the voltage dependence of steady-state inactivation to more negative potentials, reducing the amount of current that can be activated by depolarization to positive potentials. We investigated the effects of AUT2 on the high- and low-threshold components of current in MNTB neurons of $Fmr1^{-/-}$ mice.

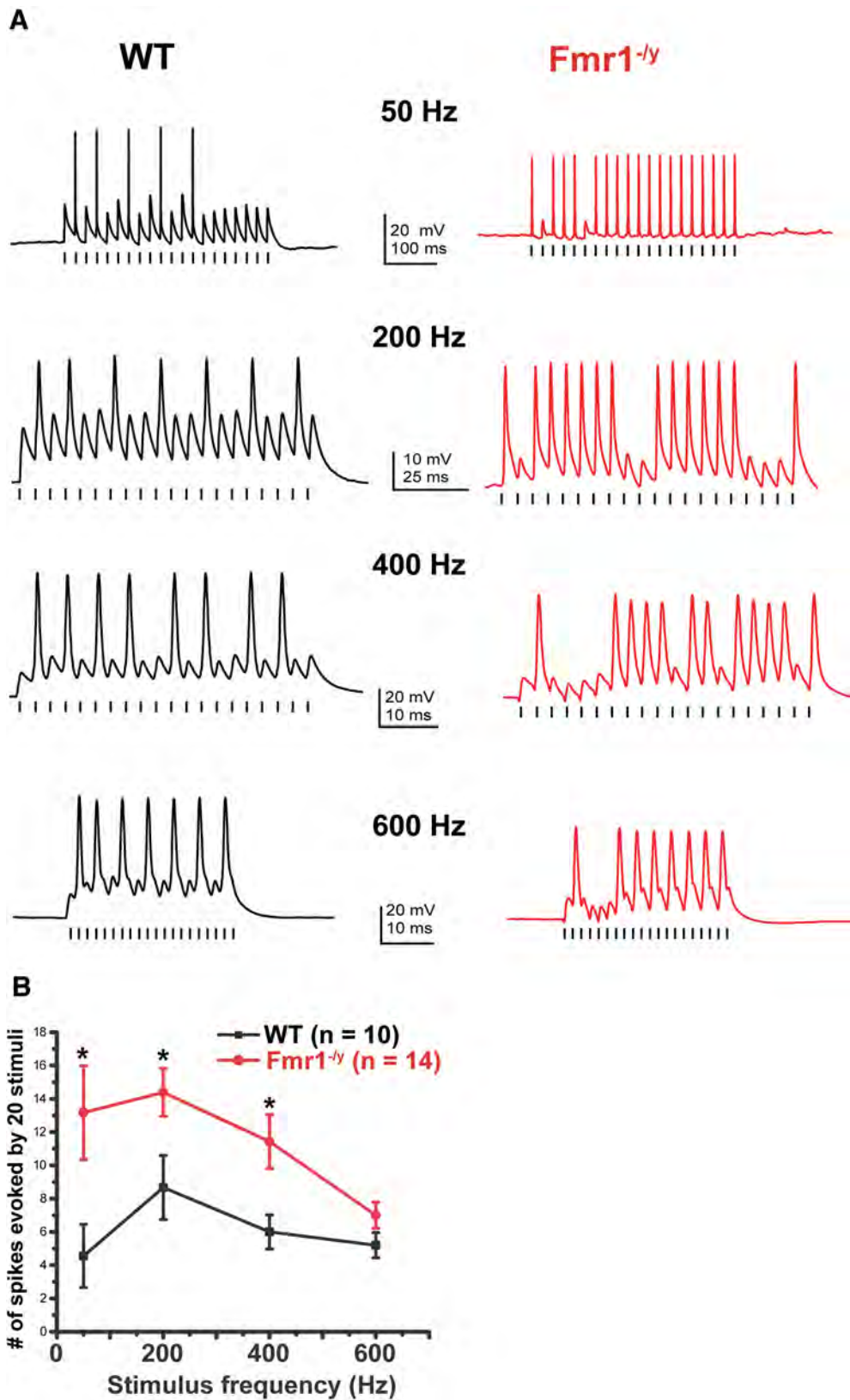


Figure 3. MNTB neurons from *Fmr1*^{-/-} mice fire more action potentials in response to repetitive stimulation. **A**, Current-clamp recordings of action potentials in response to repetitive stimulation with brief current pulses (1 nA, 0.3 ms, 20 stimuli) applied at rates from 50 to 600 Hz. **B**, Group data showing that MNTB neurons from *Fmr1*^{-/-} mice fire more action potentials at all stimulus frequencies up to 400 Hz. Asterisks indicate significant differences (two-way ANOVA followed by Holm–Sidak post-test).

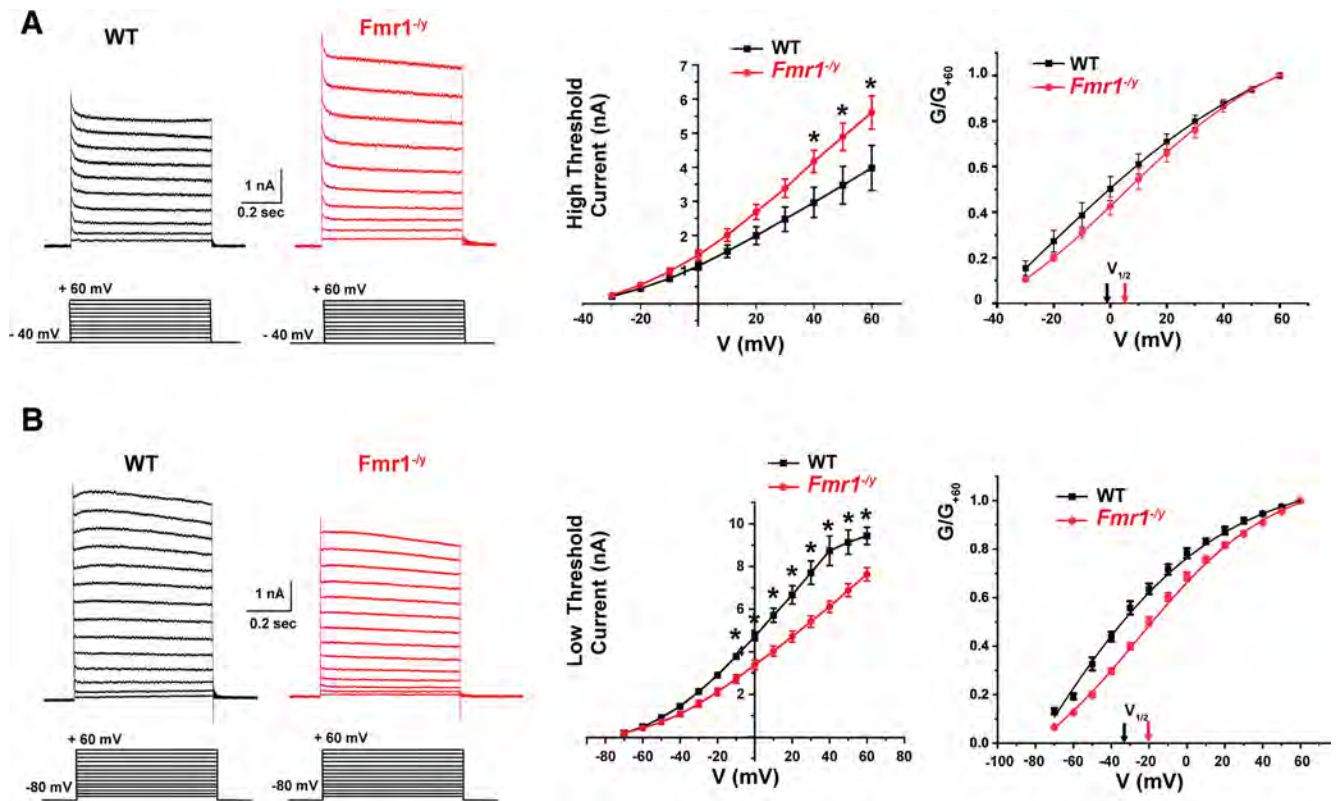


Figure 4. High- and low-threshold potassium currents are altered in MNTB neurons of *Fmr1*^{-/-} mice. **A**, Representative whole-cell patch-clamp recordings of high-threshold potassium current evoked by holding the membrane potential at -40 mV for 2 min before stepping to test potentials between -30 and $+60$ mV in 10 mV increments. Middle, Plot shows that the amplitude of high-potassium current was significantly higher in MNTB neurons from *Fmr1*^{-/-} mice compared with wild-type mice (two-way ANOVA, $p < 0.0001$). Right, Plot shows the corresponding normalized conductance that was not significantly ($p = 0.16$) different between WT and *Fmr1*^{-/-} mice. **B**, Representative whole-cell patch-clamp recordings of low-threshold potassium current by holding the membrane potential at -80 mV before stepping to test potentials from -70 to $+60$ mV in 10 mV increments. Middle, Plots show that the peak amplitude of low-potassium current was significantly reduced in *Fmr1*^{-/-} mice compared with WT mice ($p < 0.0001$, two-way ANOVA). Plot on the right shows a significant shift in voltage dependence of the low-threshold K⁺ conductance in *Fmr1*^{-/-} mice ($p = 0.01$, Student's unpaired *t* test with Welch's correction). In the *I*-*V* plots, asterisks indicate statistical significance in post-test results for multiple comparisons (Holm–Sidak method).

Application of AUT2 reduced the amplitude of the high-threshold component of currents that could be evoked from a holding potential of -40 mV to a test potential of $+60$ mV in MNTB neurons from *Fmr1*^{-/-} mice. At 60 mV, the amplitude of the high-threshold potassium currents decreased from 4.82 ± 0.54 to 2.24 ± 0.22 nA ($n = 4$, $N = 4$ animals, $p = 0.0006$, Student's paired *t* test; Fig. 5A). Using a two-way ANOVA with *post hoc* correction for multiple comparisons, we found that AUT2 had a main effect on high-threshold current ($F_{(1,130)} = 54.66$, $p < 0.0001$). Because we found a significant interaction between AUT2 treatment and membrane voltage on the amplitude of high-threshold potassium currents ($F_{(9,130)} = 3.20$, $p = 0.001$), we then performed a simple effects test and found that the high-threshold K⁺ currents recorded in *Fmr1*^{-/-} mice were significantly decreased by AUT2 treatment at membrane voltages from 20 to 60 mV (20 mV: $p = 0.01$; 30 mV: $p = 0.002$; 40 mV: $p = 0.0001$; 50 and 60 mV; $p < 0.0001$; Fig. 5A).

When the normalized conductance was plotted as a function of membrane voltage (Fig. 5A), we found no significant change in voltage dependence after the addition of AUT2. The $V_{1/2 \max}$ for the *Fmr1*^{-/-} group of mice was 0.67 ± 3.59 mV compared with -2.53 ± 5.72 mV with AUT2 treatment ($p = 0.84$, $n = 4$, $N = 4$ animals; Student's paired *t* test, $t = 0.2$, $df = 6$).

When the holding potential was maintained at -80 mV, allowing for evaluation of combined low-threshold and high-threshold components of evoked K⁺ currents, AUT2 produced a

significant increase in current. For example, the current at $+60$ mV was increased from 6.64 ± 0.57 nA in MNTB neurons from *Fmr1*^{-/-} mice to 8.43 ± 0.4 nA ($p = 0.031$, $n = 4$, $N = 4$ animals Student's paired *t* test; Fig. 5B). Using a two-way ANOVA with *post hoc* correction for multiple comparisons, we found that AUT2 had a main effect on low-threshold current ($F_{(2,209)} = 61.65$, $p < 0.0001$). Because we found a significant interaction between the drug treatment and membrane voltage ($F_{(26,209)} = 2.14$, $p = 0.001$), we performed a simple effects test and found that the increase of low-threshold potassium current by AUT2 was significant at membrane voltages from -20 to $+60$ mV (-20 mV: $p = 0.01$; -10 mV: $p = 0.002$; 0 mV: $p = 0.0004$; 10 – 60 mV: $p < 0.0001$; Fig. 5B).

The voltage dependence of the low-threshold currents was also altered by AUT2. When the normalized conductance was plotted as a function of membrane voltage (Fig. 5B), we found a significant shift of the $V_{1/2 \max}$ toward hyperpolarized potentials after AUT2 treatment. Values of $V_{1/2 \max}$ shifted from 8.42 ± 3.33 mV before AUT2 to -3.82 ± 0.65 mV after AUT2 application ($p = 0.004$, $n = 4$, $N = 4$ animals; Student's paired *t* test, $t = 5$; $df = 5$).

We have previously described that application of AUT2 alters also the voltage dependence of inactivation of Kv3.1 channels when expressed in mammalian cells (Brown et al., 2016). To test further whether the same concentration of AUT2 used previously ($10 \mu\text{M}$) can also change the inactivation curve of the high-

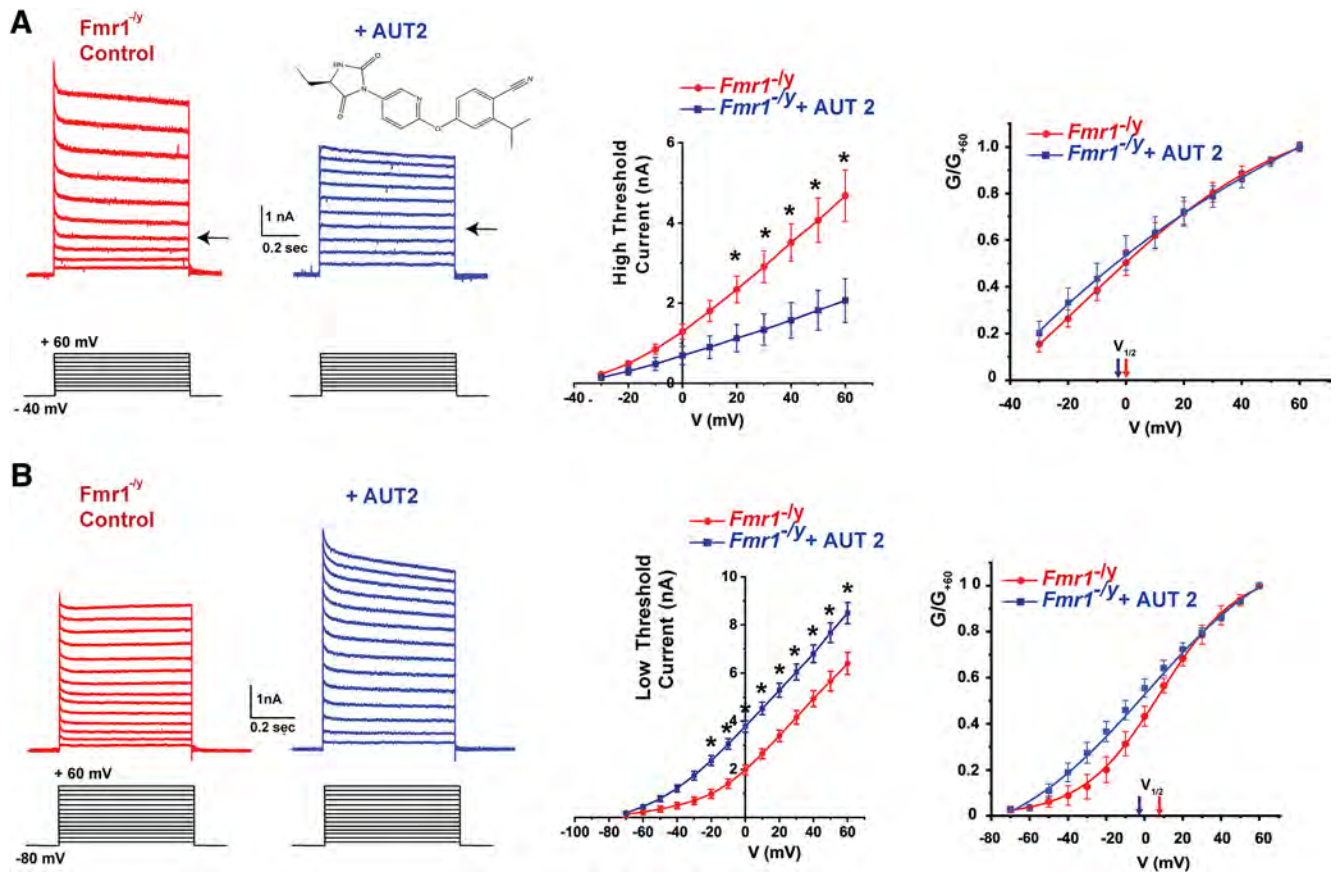


Figure 5. AUT2 decreases high-threshold potassium current and increases low-threshold potassium current of MNTB neurons from *Fmr1*^{-/-} mice. **A**, Representative traces of high-threshold potassium current evoked by holding the membrane potential at -40 mV and stepping to test potentials from -30 and +60 mV in 10 mV increments before and after the addition of 10 μM AUT2. The chemical structure of AUT2 is shown above the right-hand current traces. Middle, Group data for the effects of AUT2 on current amplitude at different voltages. Right, group data for conductance-voltage relations normalized to maximal value at +60 mV (G/G_{+60}), indicating that AUT2 did not produce a significant change of the voltage-dependent activation of high-threshold potassium currents. **B**, Representative whole-cell patch-clamp recordings of low-threshold potassium current evoked by holding the membrane potential at -80 mV and applying test potentials from -70 to +60 mV in 10 mV increments before and after addition of AUT2 (10 μM). Panels at center and right show group data for current amplitudes and conductance-voltage relations, demonstrating that AUT2 significantly increased the low-threshold potassium currents in *Fmr1*^{-/-} mice. Asterisks in **A** and **B** indicate statistical significance in post-test results of the simple effect test for multiple comparison (Holm-Sidak method).

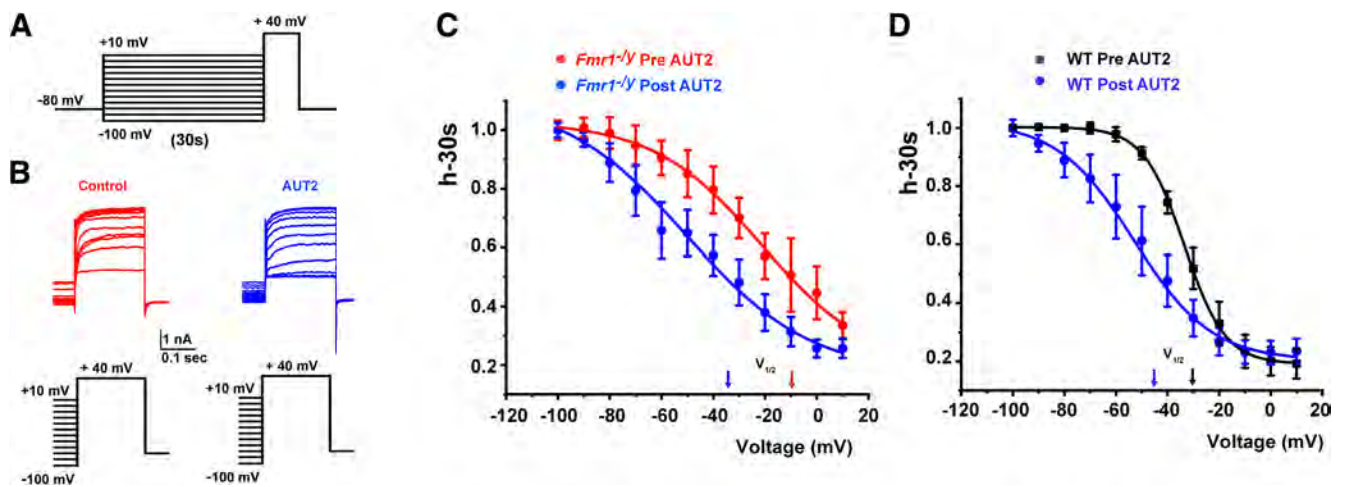


Figure 6. Addition of AUT2 produces a left shift in the voltage dependence of inactivation of high-threshold potassium currents in wild-type and *Fmr1*^{-/-} mice. **A**, Standard voltage-clamp protocol to assess the inactivation of K⁺ currents. Cells were held at potentials between -100 and +10 mV for 30 s before a test pulse to +40 mV. **B**, Representative traces of the outward current recorded in neurons from *Fmr1*^{-/-} mice at a test potential of +40 mV before and after AUT2 (10 μM). **C**, **D**, Plots of steady-state inactivation as a function of a 30 s prepulse to potentials between -100 and +10 mV in *Fmr1*^{-/-} (**C**) and WT (**D**) mice.

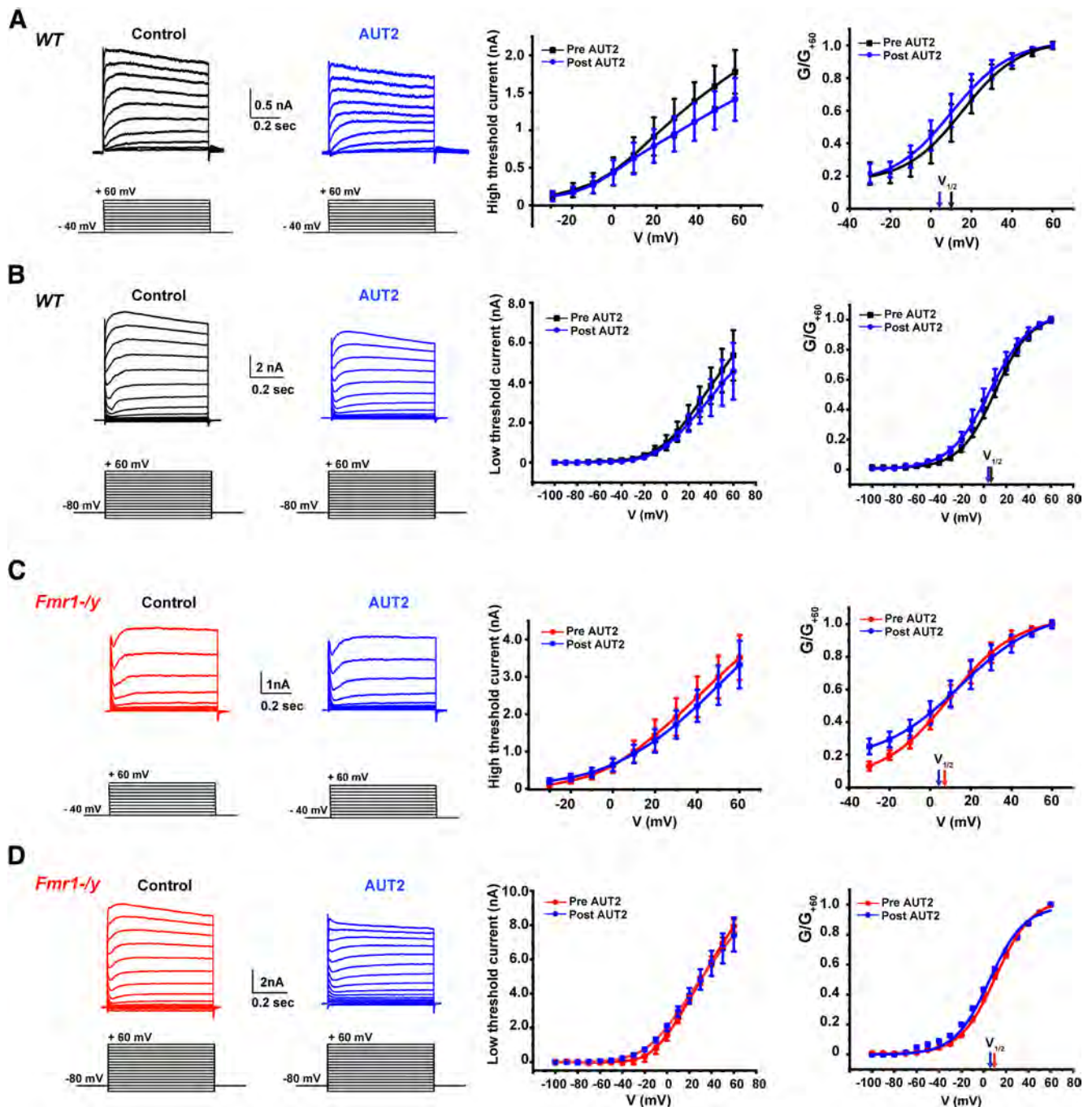


Figure 7. AUT2 fails to alter high- and low-threshold K^+ currents in the presence of the Kv3 channel blocker TEA. **A–D**, Voltage-clamp recordings of the high-threshold (**A, C**) and low-threshold (**B, D**) potassium currents in wild-type and in *Fmr1*^{-/-} mice. Panels on the right show the current–voltage and the conductance–voltage (normalized to maximal value at +60 mV; G/G_{+60}) curves for high- and low-threshold K^+ currents before and after AUT2, in the presence of the Kv3 channels blocker TEA (1 mM). AUT2 failed to alter the magnitude and the conductance of both high- and low-threshold potassium currents in these conditions.

threshold of K^+ currents in MNTB neurons, we used a standard protocol to assess the inactivation of K^+ currents. Neurons were held at potentials between -100 and $+10$ mV for 30 s before a test pulse to $+40$ mV, before and after the application of AUT2 to MNTB neurons from brain slices of either WT or *Fmr1*^{-/-} mice (Fig. 6A). Consistent with our previous results, we found that AUT2 compound produced a significant shift of the half-inactivation potential toward hyperpolarization potentials in both genotypes. In *Fmr1*^{-/-} mice, AUT2 shifted $V_{1/2 \max}$ from -10.17 ± 3.82 to -35.21 ± 3.42 mV ($p = 0.041$, $t_{(5)} = 2.72$, two-tailed paired Student's t test; $n = 5$, $N = 5$ animals; Fig.

6B, C). In WT mice, AUT2 shifted $V_{1/2 \max}$ from -30.51 ± 0.37 to -44.36 ± 1.86 mV ($p = 0.043$, $t_{(4)} = 2.85$; $n = 5$, $N = 5$ animals two-tailed paired Student's t test; Fig. 6D).

To exclude the possibility that AUT2 may have affected other type of channels in MNTB neurons, we repeated the experiments described in Figure 5 in the presence of a low concentration of tetraethylammonium (TEA; 1 mM), which selectively eliminates the component of current carried by Kv3 channels in these cells (Wang et al., 1998a). We found that, in the presence of TEA, AUT2 did not change the magnitude or the voltage dependence of either low- or high-threshold K^+ currents when tested in both

WT and *Fmr1*^{-/-} mice. Using a two-way ANOVA (with Bonferroni's *post hoc*) to analyze the effect of AUT2 on the amplitude of both high- and low-threshold potassium currents, we found no significant effect in WT mice (high *Kv*: $F_{(1,60)} = 2.32$, $p = 0.13$; low *Kv*: $F_{(1,102)} = 4.07$, $p = 0.35$; Figure 7*A,B*, middle panels). AUT2 also failed to change the amplitude of potassium currents in *Fmr1*^{-/-} mice (high *Kv*: $F_{(1,26)} = 0.99$, $p = 0.32$; low *Kv*: $F_{(1,102)} = 1.77$, $p = 0.18$; Figure 7*C,D*, middle panels). When the normalized conductance of the high-threshold currents in WT mice was plotted as a function of membrane voltage, there was no significant shift of the $V_{1/2}$ after AUT2 treatment (10 μM): $V_{1/2}$ was 10.11 ± 6.30 mV and changed to 5.2 ± 5.4 after AUT2 application ($p = 0.42$, $n = 3$, $N = 3$ animals, Student's paired *t* test; Fig. 7*A*, right). Similarly, AUT2 failed to change the voltage dependence of activation of low-threshold K^+ currents in the presence of TEA ($V_{1/2 \text{ max}}$ for WT mice before AUT2 was 8.52 ± 0.8 mV and 5.40 ± 1.07 mV after AUT2 application; $p = 0.09$, $n = 3$, $N = 3$ animals, paired *t* test; Fig. 7*B*, right).

The conductance of both high- and low-threshold potassium currents in *Fmr1*^{-/-} mice, in the presence of TEA, was also unaffected by AUT2 [$V_{1/2 \text{ max}}$ for high-threshold currents: 9.42 ± 0.40 mV before AUT2; 4.82 ± 0.63 mV after AUT2; $p = 0.12$, $n = 4$, $N = 4$ animals, Student's paired *t* test (Fig. 7*C*, right); $V_{1/2 \text{ max}}$ for low-threshold currents: 10.00 ± 1.72 mV before AUT2; 5.16 ± 0.35 mV after AUT2; $p = 0.36$, $n = 4$, $N = 4$ animals, Student's paired *t* test (Fig. 7*D*, right)].

These changes in amplitude and voltage dependence of the high- and low-threshold currents in normal conditions and the absence of these changes in the presence of the selective inhibitor of Kv3 channels (TEA) are entirely consistent with that expected from the effects of AUT2 observed on recombinant human Kv3.1 currents in transfected cells (Brown et al., 2016). A shift in steady-state inactivation to more negative potentials would be expected to reduce maximal currents evoked by the high-threshold voltage protocol. With the more negative holding potential, however, the shift in activation of Kv3.1 to more negative potentials would be expected to increase evoked currents, particularly at those negative test potentials where Kv3.1 channels are not normally activated.

AUT2 reduces the hyperexcitability of MNTB neurons in *Fmr1*^{-/-} mice

The effects of AUT2 on high- and low-threshold components of K^+ currents are directly opposite to those produced by loss of FMRP (Fig. 4). In particular, the increase in current that activates close to the resting potential would be expected to limit the generation of action potentials by increasing spike threshold. We therefore performed current-clamp recordings of MNTB neurons from *Fmr1*^{-/-} mice to determine the effects of AUT2 on their firing patterns evoked by repetitive stimulation with brief current pulses (1 nA, 0.3 ms, 20 stimuli) applied at rates from 50 to 300 Hz (Fig. 8). We found that AUT2 (10 μM) decreased the number of action potentials of MNTB neurons at all frequencies tested. Using two-way ANOVA and the Holm-Sidak method for *post hoc* correction, we found that the effect of AUT2 treatment was significant ($F_{(1,14)} = 29.32$, $p < 0.0001$) and that AUT2 decreased the number of spikes at all stimulus frequencies tested (50 Hz: $p = 0.002$; 200 Hz: $p = 0.02$; and 300 Hz: $p = 0.0006$, Holm-Sidak method; Fig. 8*A,B*).

AUT2 rescues the ABR of *Fmr1*^{-/-} mice

Because AUT2 reversed some of the effects of loss of FMRP on K^+ currents and firing patterns of MNTB neurons in brainstem

slices, we tested the effects of AUT2 on auditory function in *Fmr1*^{-/-} mice *in vivo*. As shown in Figure 1, the magnitude of wave IV of the ABR of 15-d-old mice was significantly enhanced in *Fmr1*^{-/-} animals compared with wild-type mice of the same age, which is consistent with the increased excitability of MNTB neurons. We found that intraperitoneal administration of AUT2 (30 mg/kg, 20 min before testing) significantly reduced the magnitude of wave IV in five of five mice without changing the magnitude of wave I (Fig. 9*A,B*). For sounds delivered at 80 dB, the amplitude of wave IV decreased from 1.24 ± 0.10 to 0.9 ± 0.07 μV after AUT2 treatment ($p = 0.001$, two-way ANOVA; $N = 5$ *Fmr1*^{-/-} mice) without changing the ABR threshold. The two-way ANOVA revealed no significant interaction between wave IV amplitudes before and after AUT2 treatment with the intensity of sound level ($F_{(5,59)} = 0.478$, $p = 0.8$). We found, however, a significant difference in the effect of sound level on wave IV amplitude before and after AUT2 ($F_{(1,59)} = 11.26$, $p = 0.001$).

AUT2 failed to change the magnitude of wave I ($p = 0.3$, two-way ANOVA). Although AUT2 slightly increased the latency of wave I at 80 and 90 dB, this effect was not statistically significant ($p = 0.1$, two-way ANOVA with multiple comparisons using the Holm-Sidak method; Fig. 9*B*). When the vehicle was administered alone (without AUT2) in another group of mice, the magnitudes of wave I and IV were unchanged. For example, at a sound level of 85 dB, the amplitude of wave IV was 1.78 ± 0.57 μV in *Fmr1*^{-/-} mice before the administration of the vehicle compared with 1.52 ± 0.64 μV 20 min after the vehicle administration ($N = 4$ animals; $p = 0.99$, two-way ANOVA; Fig. 10*A*). At the same sound level, the administration of the vehicle to *Fmr1*^{-/-} mice did not change the amplitude of wave I (before vehicle: 2.00 ± 0.49 μV ; vs after vehicle: 1.90 ± 0.45 μV ; $N = 4$ animals; $p = 0.99$, two-way ANOVA; Fig. 10*A*). Similarly, the latencies of waves I and IV were also unchanged by the administration of the vehicle. At a sound level of 85 dB, the latency of wave I was 2.42 ± 0.28 ms before and 2.55 ± 0.23 ms after vehicle administration and the latency of wave IV was 6.47 ± 0.30 ms before and 6.072 ± 0.238 ms after the administration of vehicle ($N = 4$ animals; $p = 0.98$ and $p = 0.90$, respectively, two-way ANOVA; Fig. 10*A*).

We also tested the effect of AUT2 on wild-type mice and found no significant changes in the amplitude of waves I or IV, perhaps because levels of Kv3.1 are lower in wild-type mice (Fig. 10*B,C*). Together, these data suggest that AUT2 rescues the auditory function of *Fmr1*^{-/-} mice by changing the voltage dependence of Kv3-like, high-threshold K^+ channels, thereby reducing excitability and restoring brainstem responses *in vivo* to those of wild-type animals.

Discussion

Our findings suggest that one mechanism by which the loss of FMRP alters the processing of auditory information is by altering the expression and activity of K^+ channels. Our results with *Fmr1*^{-/-} mice are consistent with the clinical observation that patients with fragile X syndrome experience a hypersensitivity to sound and impairment of auditory processing (St Clair et al., 1987; Arinami et al., 1988; Ferri, 1989; Wisniewski et al., 1991; Rojas et al., 2001; Castrén et al., 2003; Van der Molen et al., 2012; Garcia-Pino et al., 2017). Most of these studies show a prolonged latency of the ABR response in humans, particularly for waves III and V and for interpeak intervals III–V and I–V, suggesting a central, as opposed to a peripheral, dysfunction of auditory pathways (Arinami et al., 1988). Consistent with these findings, the marked increase in the magnitude of wave IV in *Fmr1*^{-/-} mice in

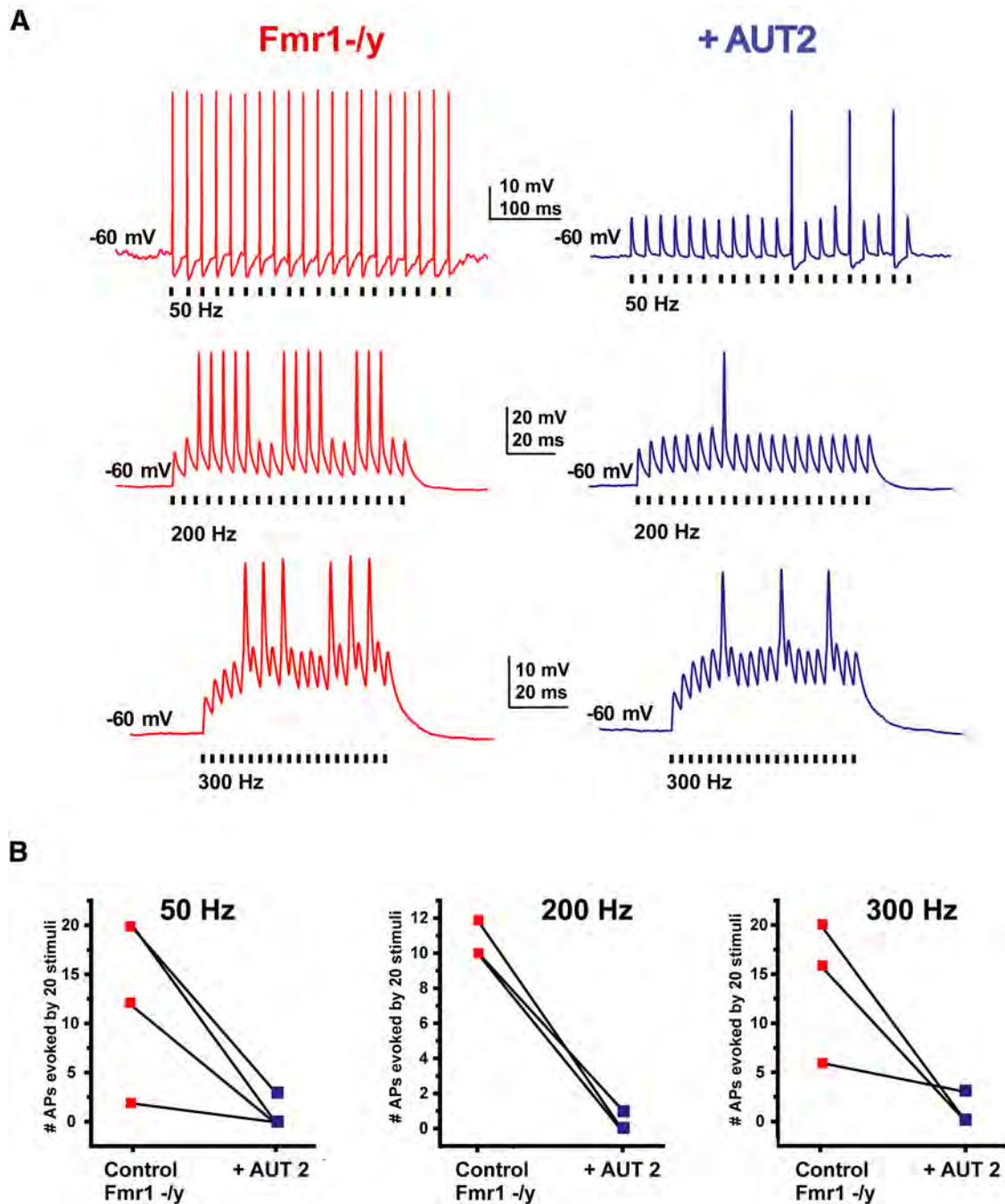


Figure 8. AUT2 reduces the firing rate of MNTB neurons of *Fmr1*^{-/-} mice. **A**, Current-clamp recordings of action potentials evoked by 20 consecutive stimuli of intracellular current pulses (2 nA, 0.3 ms) in MNTB neurons applied at 50, 200, or 300 Hz before and after application of AUT2 (10 μ M). **B**, Plots of the numbers of action potentials evoked by repetitive stimulation at 50, 200, and 300 Hz in different experiments before and after AUT2 application. AUT2 decreased the number of evoked action potentials in MNTB neurons at all frequencies tested ($n = 3$, $N = 3$ animals; $p < 0.0001$, two-way ANOVA followed by Holm–Sidak post-test).

the present study also suggests that changes in the excitability of brainstem nuclei are more pronounced than those in auditory afferents as there is little or no change in wave I amplitude compared with that of wave IV.

We have demonstrated that in neurons of the MNTB in *Fmr1*^{-/-} mice, low-threshold K⁺ currents, which activate near the resting potential, are significantly decreased. The K⁺ channels that contribute to these currents in the MNTB of mice have been identified, and include Kv1.1, Kv1.2, Kv1.6, Kv11.1, Kv11.3, K_{Na}1.1, and K_{Na}1.2 channel subunits (Dodson et al., 2002; Brew et al., 2003; Kopp-Scheinplüg et al., 2003; Yang et al., 2007;

Hardman and Forsythe, 2009; Brown et al., 2010). In the neurons of wild-type mice, these channels, particularly Kv1.1. and Kv1.2, serve to limit the response to sustained depolarization to a single action potential at the onset of the depolarization. A reduction in the low-threshold K⁺ current is therefore consistent with the repetitive firing of MNTB neurons of *Fmr1*^{-/-} mice evoked by depolarization. The mRNA for three of the low-threshold K⁺ subunits are targets of FMRP (Darnell et al., 2011). Moreover, two of these subunits, K_{Na}1.1 (Slack) and Kv1.2, directly bind FMRP itself (Brown et al., 2010; Zhang et al., 2012; Yang et al., 2018). In MNTB neurons, the Slack-FMRP interaction stimulates

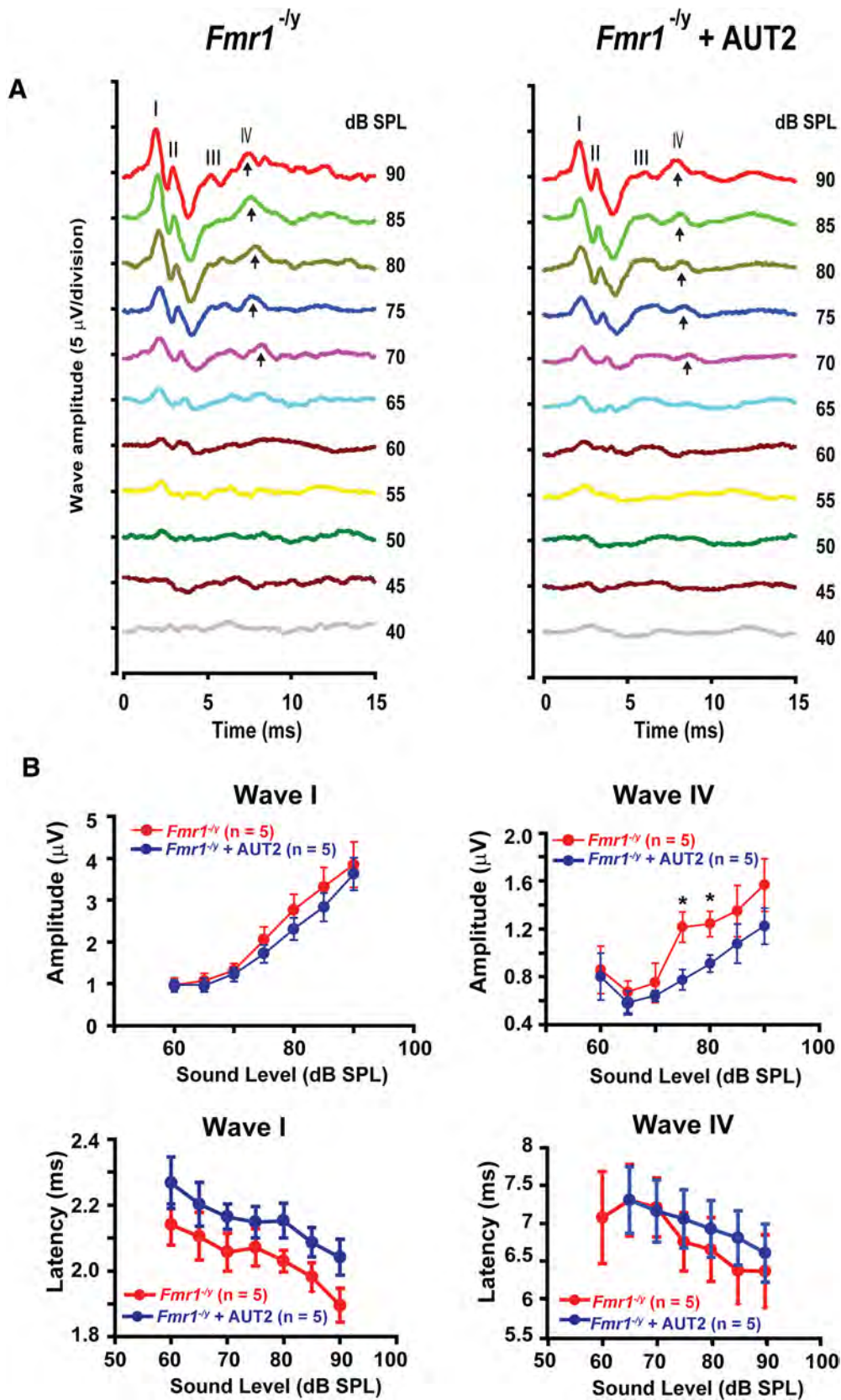


Figure 9. AUT2 rescues the auditory function of *Fmr1*^{-/-} mice. **A**, Representative ABR traces recorded from *Fmr1*^{-/-} mice before and 20 min after intraperitoneal injection of AUT2 (30 mg/kg). Arrows indicate wave IV of the ABR response. **B**, Plots of the amplitudes and latencies of ABR waves I and IV as a function of sound level before and after injection of AUT2. The group data show a significant decrease in the amplitude of ABR wave IV after AUT2 injection ($p = 0.001$) with no change in the amplitude of wave I ($p = 0.3$). In **B**, asterisks indicate statistical significance (two-way ANOVA followed by Holm–Sidak post-test).

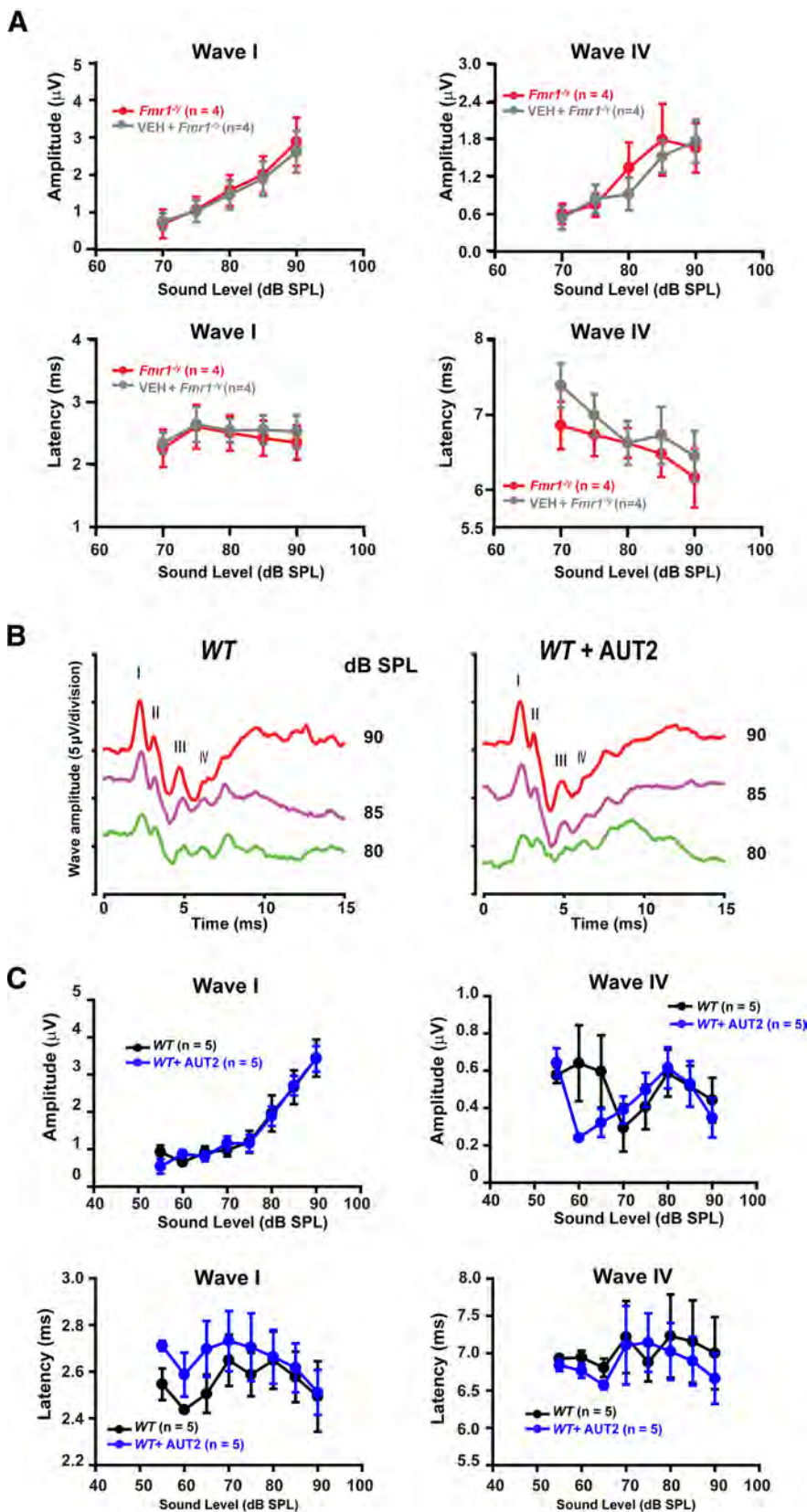


Figure 10. Administration of vehicle does not alter ABR waves in $Fmr1^{-/-}$ mice, and AUT2 does not alter auditory function in wild-type mice. **A**, Plots of the amplitudes and latencies of ABR waves I and IV as a function of sound level before and after the administration of vehicle to $Fmr1^{-/-}$ mice. No statistical differences in the magnitude of wave I and IV ($p = 0.99$ for both) or in the latencies of wave I and IV ($p = 0.98$ and $p = 0.90$, respectively) were found after vehicle injection (two-way ANOVA followed by Holm–Sidak post-test). **B**, Representative ABR traces recorded from WT mice before and 20 min after intraperitoneal injection of AUT2 (30 mg/kg). Traces represent responses to sounds delivered at 80, 85, and 90 dB. **C**, Plots of the amplitudes and latencies of ABR waves I and IV as a function of sound level before and after injection of AUT2. The group data show no significant changes in

channel activity, and the Na^+ -dependent K^+ current is reduced in these neurons in $Fmr1^{-/-}$ mice (Brown et al., 2010). Such a reduction in K_{Na} current is expected to reduce the temporal accuracy of firing (Yang et al., 2007).

Our findings also indicate that, in contrast to the low-threshold currents, high-threshold K^+ currents are enhanced in the MNTB of $Fmr1^{-/-}$ mice relative to those in wild-type animals. The dominant channel responsible for the high-threshold current in MNTB neurons is Kv3.1b , and this current is reduced by >80% in $\text{Kv3.1}^{-/-}$ mice (Wang et al., 1998a; Macica et al., 2003). Our present recordings are also consistent with this identification in that Kv3.1 currents can have a phase of rapid partial inactivation that was also seen in many of the present recordings of high-threshold current. This transient component can be detected in some but not all Kv3.1 -expressing transfected cells and in native neurons (Critz et al., 1993; Kanemasa et al., 1995; Wang et al., 1998b; McCrossan et al., 2003). The transient component, which is regulated by auxiliary subunits, can be attributed, at least in part, to the rapid accumulation of external K^+ ions (Critz et al., 1993; Wang et al., 1998b; McCrossan et al., 2003). Nevertheless, although Kv3.1 appears to be the dominant channel contributing to high-threshold currents, Kv2.2 can become the dominant subunit responsible for action potential repolarization with stimulation at low rates (Steinert et al., 2008, 2011).

Numerous studies have demonstrated that Kv3.1 channels promote the ability of neurons to fire at high rates (Rudy and McBain, 2001; Gu et al., 2012; Kaczmarek and Zhang, 2017). mRNA for Kv3.1 was one of the first mRNAs to be recognized as a target of FMRP (Darnell et al., 2001; Strumbos et al., 2010b; Darnell et al., 2011), and our present findings are consistent with those of previous studies demonstrating that Kv3.1 currents are enhanced in $Fmr1^{-/-}$ mice (Strumbos et al., 2010b). Another possibility is that Kv3.4 channels, which are located both presynaptically and postsynaptically in the brainstem region (Brooke et al., 2004) may contribute to the hyperexcitability of MNTB neurons in $Fmr1^{-/-}$ mice either by

←

the amplitude of ABR waves I and IV ($p = 0.92$, $p = 0.3$ respectively) after AUT2 injection. Similarly, AUT2 did not change the latencies of waves I and IV ($p = 0.8$ and $p = 0.46$, respectively, two-way ANOVA by Holm–Sidak post-test).

speeding the repolarization rate of action potentials or by enhancing glutamatergic synaptic transmission (Muqem et al., 2018).

Our studies were performed using 15-d old mice. This allows a direct comparison of ABR responses *in vivo* with recordings of K^+ currents in MNTB neurons from brainstem slices before the onset of myelination, which hampers patch-clamp recordings at later stages. We found no change in the ABR threshold in the *Fmr1*^{-/-} mice but did find an increase in the magnitude of wave IV, a finding consistent with the increase in the intrinsic excitability of different types of brainstem and midbrain nuclei, particularly the MNTB. ABR recordings reflect the passage of auditory information along diverse anatomical pathways, and the high- and low-threshold potassium channels studied here are widely expressed in cells of the auditory system. Thus, it is possible that changes in the amplitude of wave IV captured in this study may result from increased excitability or synchrony in other nuclei such as the inferior colliculus, and the medial and/or lateral superior olive.

We also found that, in *Fmr1*^{-/-} mice, the magnitude of wave I was decreased at higher sound levels (85–90 dB), further reinforcing the concept that auditory hyperexcitability in fragile X syndrome results from changes in central rather than peripheral pathways. Another study of *Fmr1*^{-/-} mice, which used adult animals, found an imbalance of glutamatergic and GABAergic inputs within the MNTB (Rotschafer et al., 2015; McCullagh et al., 2017). This study, however, also found a different pattern of changes in the ABR, specifically that while the amplitudes of the early waves I and III were reduced, the later waves IV and V were unchanged. This apparent discrepancy may reflect adaptive changes that occur during early life. Both the ABR waveform threshold and latency are subject to changes during development (Song et al., 2006). Moreover, it has been established that, at least for Kv3.1 channels, the maintenance of channel expression is very markedly altered by ongoing auditory activity (von Hehn et al., 2004; Leão et al., 2010; Strumbos et al., 2010a,b). Thus, our present findings are most likely to be relevant to the effects of the loss of FMRP early in development.

We found that the imbalance of low- to high-threshold K^+ currents in MNTB neurons of *Fmr1*^{-/-} mice could, in large part, be corrected by treatment with AUT2, a modulator of Kv3 family channels. AUT2 is one of a number of agents that have been found to shift the voltage dependence of activation of Kv3.1 and Kv3.2 channels to more negative potentials, increasing the amount of K^+ current activated by depolarization to voltages closer to the resting potential (Rosato-Siri et al., 2015; Taskin et al., 2015; Brown et al., 2016; Boddum et al., 2017). AUT2 also produces a negative shift in the voltage dependence of steady-state inactivation, reducing the amount of current activated by depolarizations to more positive membrane potential (e.g., +30 mV). A consequence of this is to reduce high-voltage activated K^+ current. These changes also reduce the firing rate of MNTB neurons in wild-type mice (Brown et al., 2016). Thus, AUT2 appears to reduce the intrinsic excitability of MNTB neurons by increasing the low-threshold component and reducing the high-threshold component of K^+ currents. The finding that AUT2 normalizes ABR responses in *Fmr1*^{-/-} mice *in vivo* is therefore consistent with the suggestion that the enhancement of wave IV in *Fmr1*^{-/-} animals reflects increased intrinsic excitability of auditory brainstem neurons. It is possible, however, that AUT2 has additional biophysical effects that have not been captured in the present analyses.

Increased neuronal excitability is detected in a variety of brain regions in *Fmr1*^{-/-} mice, including the auditory cortex and the lateral superior olive (Kim et al., 2013; Rotschafer and Razak, 2014; Garcia-Pino et al., 2017), as well as the barrel and prefrontal cortex (Zhang et al., 2012, 2014; Gonçalves et al., 2013; Hébert et al., 2014; Kalmbach et al., 2015; Deng and Klyachko, 2016a,b). In some of these areas, alterations in K^+ channels such as Kv1.2, Kv4.2, and $K_{Ca}1.1$ (BK) have been implicated in the hyperexcitability of fragile X mice (Zhang et al., 2014; Kalmbach et al., 2015). The function and/or the expression of these channels is regulated by FMRP either through mRNA binding or through protein–protein interactions with the channels themselves. (Frick et al., 2017). Given the large number of FMRP targets that control multiple aspects of neuronal function, including synaptic transmission, signal transduction, and neuronal development, it is likely that multiple therapeutic strategies will be required to reduce the broad range of symptoms of patients with fragile X syndrome. However, our results suggest that the hypersensitivity to sound observed in a large proportion of patients with FXS may be ameliorated by drugs that modulate Kv3.1 channels.

References

- Akil O, Oursler AE, Fan K, Lustig LR (2016) Mouse auditory brainstem response testing. *Bio Protoc* 6:e1768.
- Aloisi E, Le Corf K, Dupuis J, Zhang P, Ginger M, Labrousse V, Spatuzza M, Georg Haberl M, Costa L, Shigemoto R, Tappe-Theodor A, Drago F, Vincenzo Piazza P, Mülle C, Groc L, Ciranna L, Catania MV, Frick A (2017) Altered surface mGluR5 dynamics provoke synaptic NMDAR dysfunction and cognitive defects in *Fmr1* knockout mice. *Nat Commun* 8:1103.
- Arinami T, Sato M, Nakajima S, Kondo I (1988) Auditory brain-stem responses in the fragile X syndrome. *Am J Hum Genet* 43:46–51.
- Bhattacharjee A, Gan L, Kaczmarek LK (2002) Localization of the Slack potassium channel in the rat central nervous system. *J Comp Neurol* 454:241–254.
- Bhattacharjee A, von Hehn CA, Mei X, Kaczmarek LK (2005) Localization of the Na⁺-activated K⁺ channel Slick in the rat central nervous system. *J Comp Neurol* 484:80–92.
- Boddum K, Hougaard C, Xiao-Ying Lin J, von Schoubye NL, Jensen HS, Grunnet M, Jespersen T (2017) Kv3.1/Kv3.2 channel positive modulators enable faster activating kinetics and increase firing frequency in fast-spiking GABAergic interneurons. *Neuropharmacology* 118:102–112.
- Bostrom C, Yau SY, Majaess N, Vetri M, Gil-Mohapel J, Christie BR (2016) Hippocampal dysfunction and cognitive impairment in fragile-X syndrome. *Neurosci Biobehav Rev* 68:563–574.
- Brager DH, Johnston D (2014) Channelopathies and dendritic dysfunction in fragile X syndrome. *Brain Res Bull* 103:11–17.
- Brew HM, Forsythe ID (1995) Two voltage-dependent K⁺ conductances with complementary functions in postsynaptic integration at a central auditory synapse. *J Neurosci* 15:8011–8022.
- Brew HM, Forsythe ID (2005) Systematic variation of potassium current amplitudes across the tonotopic axis of the rat medial nucleus of the trapezoid body. *Hear Res* 206:116–132.
- Brew HM, Hallows JL, Tempel BL (2003) Hyperexcitability and reduced low threshold potassium currents in auditory neurons of mice lacking the channel subunit Kv1.1. *J Physiol* 548:1–20.
- Brooke RE, Atkinson L, Batten TF, Deuchars SA, Deuchars J (2004) Association of potassium channel Kv3.4 subunits with pre- and post-synaptic structures in brainstem and spinal cord. *Neuroscience* 126:1001–1010.
- Brown MR, Kronengold J, Gazula VR, Chen Y, Strumbos JG, Sigworth FJ, Navaratnam D, Kaczmarek LK (2010) Fragile X mental retardation protein controls gating of the sodium-activated potassium channel slack. *Nat Neurosci* 13:819–821.
- Brown MR, El-Hassar L, Zhang Y, Alvaro G, Large CH, Kaczmarek LK (2016) Physiological modulators of Kv3.1 channels adjust firing patterns of auditory brain stem neurons. *J Neurophysiol* 116:106–121.
- Castrén M, Pääkkönen A, Tarkka IM, Ryyänen M, Partanen J (2003) Augmentation of auditory N1 in children with fragile X syndrome. *Brain Topogr* 15:165–171.

- Chonchaiya W, Schneider A, Hagerman RJ (2009) Fragile X: a family of disorders. *Adv Pediatr* 56:165–186.
- Critz SD, Wible BA, Lopez HS, Brown AM (1993) Stable expression and regulation of a rat brain K⁺ channel. *J Neurochem* 60:1175–1178.
- Curia G, Gualtieri F, Bartolomeo R, Vezzali R, Biagini G (2013) Resilience to audiogenic seizures is associated with p-ERK1/2 dephosphorylation in the subiculum of *Fmr1* knockout mice. *Front Cell Neurosci* 7:46.
- Darnell JC, Jensen KB, Jin P, Brown V, Warren ST, Darnell RB (2001) Fragile X mental retardation protein targets G quartet mRNAs important for neuronal function. *Cell* 107:489–499.
- Darnell JC, Van Driesche SJ, Zhang C, Hung KY, Mele A, Fraser CE, Stone EF, Chen C, Fak JJ, Chi SW, Licatalosi DD, Richter JD, Darnell RB (2011) FMRP stalls ribosomal translocation on mRNAs linked to synaptic function and autism. *Cell* 146:247–261.
- Deng PY, Klyachko VA (2016a) Increased persistent sodium current causes neuronal hyperexcitability in the entorhinal cortex of *Fmr1* knockout mice. *Cell Rep* 16:3157–3166.
- Deng PY, Klyachko VA (2016b) Genetic upregulation of BK channel activity normalizes multiple synaptic and circuit defects in a mouse model of fragile X syndrome. *J Physiol* 594:83–97.
- Deng PY, Rotman Z, Blundon JA, Cho Y, Cui J, Cavalli V, Zakharenko SS, Klyachko VA (2013) FMRP regulates neurotransmitter release and synaptic information transmission by modulating action potential duration via BK channels. *Neuron* 77:696–711.
- Deng PY, Carlin D, Mi Oh YM, Myrick LK, Warren ST, Cavalli V, Klyachko VA (2019) Voltage-independent SK-channel dysfunction causes neuronal hyperexcitability in the hippocampus of *Fmr1* knock-out mice. *J Neurosci* 39:28–43.
- Dodson PD, Barker MC, Forsythe ID (2002) Two heteromeric Kv1 potassium channels differentially regulate action potential firing. *J Neurosci* 22:6953–6961.
- Ferri R (1989) Brain-stem auditory evoked potentials in the fragile X syndrome. *Am J Hum Genet* 45:977–979.
- Ferron L, Nieto-Rostro M, Cassidy JS, Dolphin AC (2014) Fragile X mental retardation protein controls synaptic vesicle exocytosis by modulating N-type calcium channel density. *Nat Commun* 5:3628.
- Frick A, Ginger M, El-Hassar L, Kaczmarek L (2017) Ion channel dysfunction and FXS. In: *Fragile X syndrome: from genetics to targeted treatment* (Willemsen R, Kooy RF, eds), pp 323–340. London: Academic.
- Gan L, Kaczmarek LK (1998) When, where, and how much? expression of the Kv3.1 potassium channel in high-frequency firing neurons. *J Neurobiol* 37:69–79.
- Garber KB, Visootsak J, Warren ST (2008) Fragile X syndrome. *Eur J Hum Genet* 16:666–672.
- Garcia-Pino E, Gessele N, Koch U (2017) Enhanced excitatory connectivity and disturbed sound processing in the auditory brainstem of fragile X mice. *J Neurosci* 37:7403–7419.
- Gonçalves JT, Anstey JE, Golshani P, Portera-Cailliau C (2013) Circuit level defects in the developing neocortex of fragile X mice. *Nat Neurosci* 16:903–909.
- Grigg JJ, Brew HM, Tempel BL (2000) Differential expression of voltage-gated potassium channel genes in auditory nuclei of the mouse brainstem. *Hear Res* 140:77–90.
- Gu Y, Barry J, McDougel R, Terman D, Gu C (2012) Alternative splicing regulates kv3.1 polarized targeting to adjust maximal spiking frequency. *J Biol Chem* 287:1755–1769.
- Hall SS, Walter E, Sherman E, Hoefl F, Reiss AL (2009) The neural basis of auditory temporal discrimination in girls with fragile X syndrome. *J Neurodev Disord* 1:91–99.
- Hardman RM, Forsythe ID (2009) Ether-a-go-go-related gene K⁺ channels contribute to threshold excitability of mouse auditory brainstem neurons. *J Physiol* 587:2487–2497.
- Hébert B, Pietropaolo S, Mème S, Laudier B, Laugeray A, Doisne N, Quartier A, Lefevre S, Got L, Cahard D, Laumonier F, Crusio WE, Pichon J, Menuet A, Perche O, Briault S (2014) Rescue of fragile X syndrome phenotypes in *Fmr1* KO mice by a BKCa channel opener molecule. *Orphanet J Rare Dis* 9:124.
- Jewett DL, Williston JS (1971) Auditory-evoked far fields averaged from the scalp of humans. *Brain* 94:681–696.
- Kaczmarek LK, Zhang Y (2017) Kv3 channels: enablers of rapid firing, neurotransmitter release, and neuronal endurance. *Physiol Rev* 97:1431–1468.
- Kalmbach BE, Johnston D, Brager DH (2015) Cell-type specific channelopathies in the prefrontal cortex of the *fmr1-/-* mouse model of fragile X syndrome. *eNeuro* 2:ENEURO.0114–15.2015.
- Kanemasa T, Gan L, Perney TM, Wang LY, Kaczmarek LK (1995) Electrophysiological and pharmacological characterization of a mammalian shaw channel expressed in NIH 3T3 fibroblasts. *J Neurophysiol* 74:207–217.
- Kim H, Gibboni R, Kirkhart C, Bao S (2013) Impaired critical period plasticity in primary auditory cortex of fragile X model mice. *J Neurosci* 33:15686–15692.
- Kopp-Scheinpflug C, Fuchs K, Lippe WR, Tempel BL, Rübsamen R (2003) Decreased temporal precision of auditory signaling in *Kcna1*-null mice: an electrophysiological study *in vivo*. *J Neurosci* 23:9199–9207.
- Kopp-Scheinpflug C, Steinert JR, Forsythe ID (2011) Modulation and control of synaptic transmission across the MNTB. *Hear Res* 279:22–31.
- Leão KE, Leão RN, Deardorff AS, Garrett A, Fyffe R, Walmsley B (2010) Sound stimulation modulates high-threshold K⁺ currents in mouse auditory brainstem neurons. *Eur J Neurosci* 32:1658–1667.
- Li W, Kaczmarek LK, Perney TM (2001) Localization of two high-threshold potassium channel subunits in the rat central auditory system. *J Comp Neurol* 437:196–218.
- Lozano R, Azarang A, Wilaisakditipakorn T, Hagerman RJ (2016) Fragile X syndrome: A review of clinical management. *Intractable Rare Dis Res* 5:145–157.
- Macica CM, von Hehn CA, Wang LY, Ho CS, Yokoyama S, Joho RH, Kaczmarek LK (2003) Modulation of the Kv3.1b potassium channel isoform adjusts the fidelity of the firing pattern of auditory neurons. *J Neurosci* 23:1133–1141.
- Mathews PJ, Jercog PE, Rinzel J, Scott LL, Golding NL (2010) Control of submillisecond synaptic timing in binaural coincidence detectors by K(v)1 channels. *Nat Neurosci* 13:601–609.
- McCrossan ZA, Lewis A, Panaghie G, Jordan PN, Christini DJ, Lerner DJ, Abbott GW (2003) MinK-related peptide 2 modulates Kv2.1 and Kv3.1 potassium channels in mammalian brain. *J Neurosci* 23:8077–8091.
- McCullagh EA, Salcedo E, Huntsman MM, Klug A (2017) Tonotopic alterations in inhibitory input to the medial nucleus of the trapezoid body in a mouse model of fragile X syndrome. *J Comp Neurol* 525:3543–3562.
- Michalon A, Sidorov M, Ballard TM, Ozmen L, Spooren W, Wettstein JG, Jaeschke G, Bear MF, Lindemann L (2012) Chronic pharmacological mGlu5 inhibition corrects fragile X in adult mice. *Neuron* 74:49–56.
- Muqem T, Ghosh B, Pinto V, Lepore AC, Covarrubias M (2018) Regulation of nociceptive glutamatergic signaling by presynaptic Kv3.4 channels in the rat spinal dorsal horn. *J Neurosci* 38:3729–3740.
- Myrick LK, Deng PY, Hashimoto H, Oh YM, Cho Y, Poidevin MJ, Suhl JA, Visootsak J, Cavalli V, Jin P, Cheng X, Warren ST, Klyachko VA (2015) Independent role for presynaptic FMRP revealed by an FMR1 missense mutation associated with intellectual disability and seizures. *Proc Natl Acad Sci U S A* 112:949–956.
- Oberlé I, Rousseau F, Heitz D, Kretz C, Devys D, Hanauer A, Boué J, Bertheas MF, Mandel JL (1991) Instability of a 550-base pair DNA segment and abnormal methylation in fragile X syndrome. *Science* 252:1097–1102.
- Pyronneau A, He Q, Hwang JY, Porch M, Contractor A, Zukin RS (2017) Aberrant Rac1-cofilin signaling mediates defects in dendritic spines, synaptic function, and sensory perception in fragile X syndrome. *Sci Signal* 10:eaan0852.
- Roberts J, Hennon EA, Anderson K, Roush J, Gravel J, Skinner M, Misener J, Reitz P (2005) Auditory brainstem responses in young males with fragile X syndrome. *J Speech Lang Hear Res* 48:494–500.
- Rojas DC, Benkers TL, Rogers SJ, Teale PD, Reite ML, Hagerman RJ (2001) Auditory evoked magnetic fields in adults with fragile X syndrome. *Neuroreport* 12:2573–2576.
- Rosato-Siri MD, Zambello E, Mutinelli C, Garbati N, Benedetti R, Aldegheri L, Graziani F, Virginio C, Alvaro G, Large CH (2015) A novel modulator of Kv3 potassium channels regulates the firing of parvalbumin-positive cortical interneurons. *J Pharmacol Exp Ther* 354:251–260.
- Rotschafer SE, Razak KA (2014) Auditory processing in fragile x syndrome. *Front Cell Neurosci* 8:19.
- Rotschafer SE, Marshak S, Cramer KS (2015) Deletion of *Fmr1* alters function and synaptic inputs in the auditory brainstem. *PLoS One* 10:e0117266.
- Rudy B, McBain CJ (2001) Kv3 channels: voltage-gated K⁺ channels designed for high-frequency repetitive firing. *Trends Neurosci* 24:517–526.

- Sinclair D, Featherstone R, Naschek M, Nam J, Du A, Wright S, Pance K, Melnychenko O, Weger R, Akuzawa S, Matsumoto M, Siegel SJ (2017) GABA-B agonist baclofen normalizes auditory-evoked neural oscillations and behavioral deficits in the *Fmr1* knockout mouse model of fragile X syndrome. *eNeuro* 4:ENEURO.0380–16.2017.
- Song L, McGee J, Walsh EJ (2006) Frequency- and level-dependent changes in auditory brainstem responses (ABRS) in developing mice. *J Acoust Soc Am* 119:2242–2257.
- Song P, Yang Y, Barnes-Davies M, Bhattacharjee A, Hamann M, Forsythe ID, Oliver DL, Kaczmarek LK (2005) Acoustic environment determines phosphorylation state of the Kv3.1 potassium channel in auditory neurons. *Nat Neurosci* 8:1335–1342.
- St Clair DM, Blackwood DH, Oliver CJ, Dickens P (1987) P3 abnormality in fragile X syndrome. *Biol Psychiatry* 22:303–312.
- Steinert JR, Kopp-Scheinflug C, Baker C, Challiss RA, Mistry R, Haustein MD, Griffin SJ, Tong H, Graham BP, Forsythe ID (2008) Nitric oxide is a volume transmitter regulating postsynaptic excitability at a glutamatergic synapse. *Neuron* 60:642–656.
- Steinert JR, Robinson SW, Tong H, Haustein Martin D, Kopp-Scheinflug C, Forsythe ID (2011) Nitric oxide is an activity-dependent regulator of target neuron intrinsic excitability. *Neuron* 71:291–305.
- Strumbos JG, Polley DB, Kaczmarek LK (2010a) Specific and rapid effects of acoustic stimulation on the tonotopic distribution of Kv3.1b potassium channels in the adult rat. *Neuroscience* 167:567–572.
- Strumbos JG, Brown MR, Kronengold J, Polley DB, Kaczmarek LK (2010b) Fragile X mental retardation protein is required for rapid experience-dependent regulation of the potassium channel Kv3.1b. *J Neurosci* 30:10263–10271.
- Tan WJT, Song L, Graham M, Schettino A, Navaratnam D, Yarbrough WG, Santos-Sacchi J, Ivanova AV (2017) Novel role of the mitochondrial protein Fus1 in protection from premature hearing loss via regulation of oxidative stress and nutrient and energy sensing pathways in the inner ear. *Antioxid Redox Signal* 27:489–509.
- Taskin B, von Schoubye NL, Sheykhzade M, Bastlund JF, Grunnet M, Jespersen T (2015) Biophysical characterization of KV3.1 potassium channel activating compounds. *Eur J Pharmacol* 758:164–170.
- Van der Molen MJ, Van der Molen MW, Ridderinkhof KR, Hamel BC, Curfs LM, Ramakers GJ (2012) Auditory and visual cortical activity during selective attention in fragile X syndrome: a cascade of processing deficiencies. *Clin Neurophysiol* 123:720–729.
- Verkerk AJ, Pieretti M, Sutcliffe JS, Fu YH, Kuhl DP, Pizzuti A, Reiner O, Richards S, Victoria MF, Zhang FP (1991) Identification of a gene (FMR-1) containing a CGG repeat coincident with a breakpoint cluster region exhibiting length variation in fragile X syndrome. *Cell* 65:905–914.
- von Hehn CA, Bhattacharjee A, Kaczmarek LK (2004) Loss of Kv3.1 tonotopicity and alterations in cAMP response element-binding protein signaling in central auditory neurons of hearing impaired mice. *J Neurosci* 24:1936–1940.
- Wang LY, Gan L, Forsythe ID, Kaczmarek LK (1998a) Contribution of the Kv3.1 potassium channel to high-frequency firing in mouse auditory neurons. *J Physiol* 509:183–194.
- Wang LY, Gan L, Perney TM, Schwartz I, Kaczmarek LK (1998b) Activation of Kv3.1 channels in neuronal spine-like structures may induce local potassium ion depletion. *Proc Natl Acad Sci U S A* 95:1882–1887.
- Wisniewski KE, Segan SM, Miezieski CM, Sersen EA, Rudelli RD (1991) The Fra(X) syndrome: neurological, electrophysiological, and neuropathological abnormalities. *Am J Med Genet* 38:476–480.
- Yang B, Desai R, Kaczmarek LK (2007) Slack and Slick K(Na) channels regulate the accuracy of timing of auditory neurons. *J Neurosci* 27:2617–2627.
- Yang YM, Wang LY (2006) Amplitude and kinetics of action potential-evoked Ca²⁺ current and its efficacy in triggering transmitter release at the developing calyx of Held synapse. *J Neurosci* 26:5698–5708.
- Yang YM, Arsenault J, Bah A, Krzeminski M, Fekete A, Chao OY, Pacey LK, Wang A, Forman-Kay J, Hampson DR, Wang LY (2018) Identification of a molecular locus for normalizing dysregulated GABA release from interneurons in the Fragile X brain. *Mol Psychiatry*. Advance online publication. Retrieved April 2, 2019. doi:10.1038/s41380-018-0240-0.
- Zhang Y, Brown MR, Hyland C, Chen Y, Kronengold J, Fleming MR, Kohn AB, Moroz LL, Kaczmarek LK (2012) Regulation of neuronal excitability by interaction of fragile X mental retardation protein with Slack potassium channels. *J Neurosci* 32:15318–15327.
- Zhang Y, Bonnan A, Bony G, Ferezou I, Pietropaolo S, Ginger M, Sans N, Rossier J, Oostra B, LeMasson G, Frick A (2014) Dendritic channelopathies contribute to neocortical and sensory hyperexcitability in *Fmr1*^(-/-) mice. *Nat Neurosci* 17:1701–1709.

Lecture Notes in Biomathematics

Managing Editor: S. Levin

87

P. Dallos C.D. Geisler J.W. Matthews
M.A. Ruggero C.R. Steele (Eds.)

The Mechanics and Biophysics of Hearing

Proceedings, Madison, WI, 1990



Springer-Verlag Berlin Heidelberg GmbH

FAST OUTER HAIR CELL MOTILITY: HOW FAST IS FAST?

J. Santos-Sacchi

*Laboratory of Otolaryngology
New Jersey Medical School, Newark N. J. 07103*

Introduction

Recent experiments have implicated transmembrane voltage as the driving force of OHC motility (Santos-Sacchi and Dilger, 1988a,b; Iwasa and Kachar, 1989). A voltage dependence of OHC motility clearly implies that a charged voltage sensing particle must reside in the OHC membrane, and as was predicted for voltage dependent ionic channels (Hodgkin and Huxley, 1952), particle movement should occur under an applied transmembrane voltage. Gating currents associated with the movement of the presumed voltage sensor in OHCs have been described by Ashmore (1989).

However, two lines of evidence argue against a voltage-dependent motility mechanism in OHCs. The first is the inability of the OHC to faithfully follow a voltage stimulus in time or frequency; i.e., the speed of the movements have been reported to be unrelated to the time course of voltage clamp stimuli (Ashmore, 1987). The second is the poor temperature dependence of the rate of OHC movement (Ashmore and Holley, 1988). If OHC motility is coupled to a voltage-dependent charge movement across the OHC membrane (hence the observed gating currents), then a temperature dependence with a Q_{10} greater than 2 might be expected as occurs for sodium channel gating currents (Bezanilla and Taylor, 1978; Collins and Rojas, 1982).

This work attempts to explain these discrepancies in the voltage dependency hypothesis of OHC motility.

Methods

OHCs were obtained from the apical turns of the guinea pig cochlea by simple mechanical dissociation. Temperature was adjusted with a Peltier device and measured with a probe placed within 500 μm of the cells studied. Voltage step studies were performed with an Axon Instruments A/D and D/A board (Axolab 1100) with associated software (P-Clamp, sampling period down to 3 μs). AC studies were performed using a digital signal processing board with custom software (DSP-16; Ariel Corp., NJ), capable of delivering and analyzing pure tone or swept frequency stimuli. Filtered current records were saved to disk for off-line analysis.

Patch electrodes (flint or borosilicate glass) had initial resistances of 3-6 Mohm. The series resistance, i.e., the actual electrode resistance obtained upon establishment of whole cell configuration, typically ranged from 4 to 12 Mohm, and was reduced further by electronic compensation; care was taken to maintain low series resistance values during recording by delivering transient positive or negative pressure into the electrode to maintain an unobstructed orifice. The resistance values are estimated from current transients initiated at the onset of voltage pulses and are corrected for during analysis, so that actual voltages imposed upon the cell are known (Marty and Neher, 1983). The program Clampex (Axon Instruments) was modified to provide a continuous display of clamp time constant, cell capacitance and resistance, and series resistance between data collections. Pipette solutions were composed of 140 mM CsCl, 10 mM EGTA, 2 mM MgCl₂, and 5 mM HEPES buffered to pH 7.2. Gigohm seals were obtained at the nuclear level of the cell membrane and electrode capacitance was compensated prior to whole cell recording. Generally, single cells were clamped to holding potentials near -70 to -80 mV using a Dagan patch clamp amplifier. OHC gating currents (nonlinear capacitive currents) were measured by averaging current responses elicited by voltage pulses of alternating polarity (40 mV magnitude) about the holding potential of -80 mV, or by using a P/5 protocol at a holding potential of -120 mV.

Fast OHC movements elicited by voltage clamp with short duration or high frequency stimuli (below video detectability) were measured with a differential photodiode onto which the image of the cuticular plate from the microscope was projected. The frequency response of the differential photodiode is flat out to 2 kHz (measured with a light emitting diode or piezoelectric bimorph). Absolute calibration of cell movements is determined by measuring off the video monitor the cell movement in response to a large steady state or low frequency voltage stimulus.

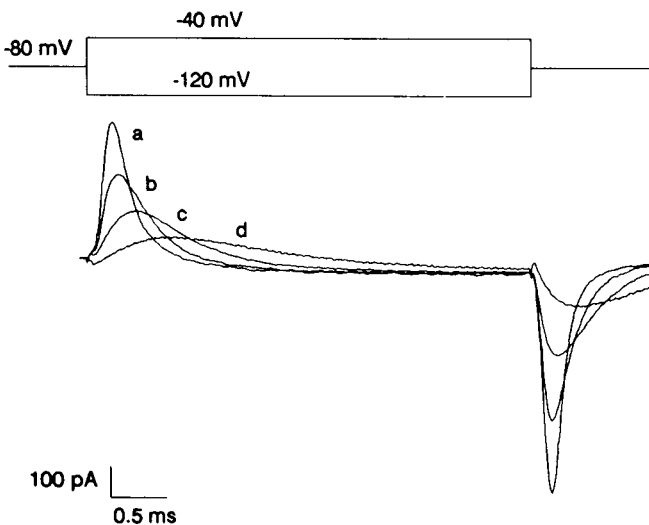


FIGURE 1 Nonlinear capacitive currents generated at the onset and offset of depolarizing voltage step. Linear capacitive currents were removed by averaging 100 X alternating steps of 40 mV above and below a holding level of -80 mV. Cell resistance was 140 Mohm. Charge movement indicates a nonlinear capacitance of 4.5 pF under these conditions. Clamp time constant was varied by adjusting series resistance compensation. Clamp time constant (ms), gate-on time constant (ms): a) 0.08, 1.38, 0.22; b) 0.15, 4.0, 0.37; c) 0.25, 7.83, 0.52; d) 0.36, 11.8, 1.1. Note parallel shift of gating time constant as clamp time constant is changed. Extracellular solution: 10 mM TEA, 300 nM TTX.

Results

OHCs exhibit a nonlinear charge movement which can be seen under voltage clamp as a transient outward current upon depolarization from negative holding potentials, and an inward current upon repolarization (Fig. 1). Charge movement for the cell in Fig. 1 was equal at the onset and offset of the voltage step, being about 185 fC. The time constants associated with the decaying phase of on and off currents differ, with the off tau being of similar magnitude to the clamp time constant, and the on tau being roughly twice in magnitude. Both time constants are directly dependent upon the clamp time constant, indicating that the kinetics of the gating current are faster than the time limitations imposed by the voltage clamp amplifier. Because of the apical OHC's large capacitance (Santos-Sacchi, 1989b), clamp time constants of only around 100 μ s have been achieved.

These results may indicate that the speed of OHC mechanical responses are dependent upon the ability of the clamp amplifier to charge the membrane. This is the case, and is demonstrated in the time domain in Fig. 2. The OHC was induced to contract with depolarizing steps to +40 mV from a holding potential of -80 mV, before and after electronically compensating the series resistance. The attendant changes in the clamp time constant is reflected in the rate of onset of the mechanical response, the slower clamp time constant charging the OHC membrane more slowly than the faster clamp time constant. Hence, it would be expected that the mechanical response of the OHC in the frequency domain will display a similar dependence upon clamp characteristics. Fig. 3 illustrates the mechanical response of two OHCs which have been voltage clamped

FIGURE 2 An OHC was held at a potential of -80 mV and stepped to +40 mV for 5 ms duration. Current and mechanical response records were recorded simultaneously, being averaged 200 X. Collections were made with different clamp time constants: a) clamp tau was 0.4 ms; b) clamp tau was 0.19 ms. Boxed portion of traces are enlarged and fitted with single exponentials (smooth curves). a) fitted tau was 0.37 ms; b) fitted tau was 0.23 ms. Scales refer to traces on right.

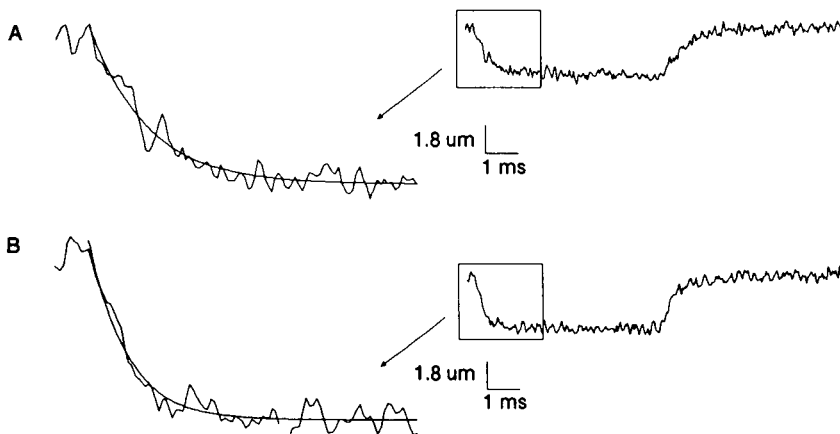
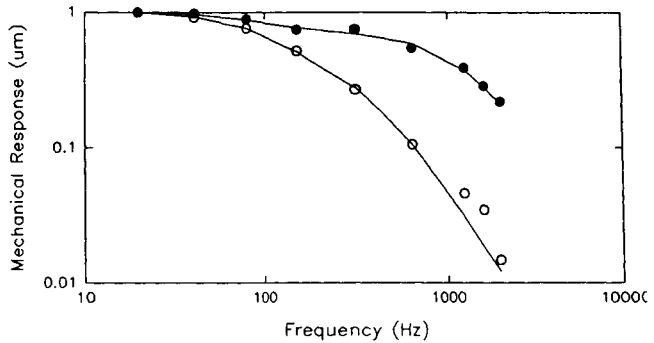


FIGURE 3 Two OHC's were clamped at -80 mV and stimulated with sinusoidal voltage bursts. The fundamental magnitude was obtained by FFT. Open circle (50 mV Pk) data were collected with a clamp tau of 1 ms, and were fit with the sum of two Lorentzians, with time constants of 1.7 and 0.5 ms. Closed circle (40 mV Pk) data clamp tau was 0.2 ms and fit with taus of 1.87 ms and 0.12 ms. Note improved frequency response associated with faster clamp time constant. 20 mM TEA.



at a holding potential of -80 mV and stimulated with superimposed sinusoidal voltages of varying frequency. The clamp time constant dictates the frequency response of each cell's mechanical response. The cell clamped with the poorer time constant displays a precipitous drop in mechanical response as frequency increases. The other cell displays a much better frequency response, the response measuring about 13 dB down at 2 kHz.

The temperature dependence of the gating current time constant was studied in order to determine if it behaves similar to sodium channel gating currents. Figure 4 shows the change in gate-on time constants for two OHCs as the temperature is varied from about 20 to 5°C. At first glance it appears that gating kinetics are slowed down as the temperature is decreased, with a Q₁₀ of about 1.5 (Fig. 4a); however, when one takes into account the dependency of gate time constant upon clamp time constant, no relation is apparent (Fig. 4b).

DISCUSSION

The limitations imposed by the whole cell voltage clamp technique can provide us with a distorted picture of some of the properties of the OHC. The apical OHC has a

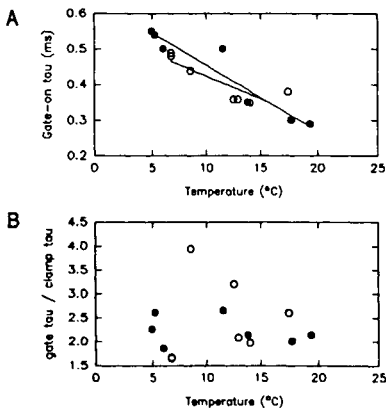


FIGURE 4 Two OHCs were voltage clamped at -80 mV and the single exponential time constant of the non-linear capacitive on current was determined as in Fig. 1. The temperature was varied from about 20 to 5°C and the effects on gate time constant plotted. In Fig. 4a it appears that temperature reduction slows down the kinetics of the gating currents, as is known to occur with sodium channel gating. However, the Q₁₀ is only about 1.5. Fig. 4b demonstrates that when the dependence of gate time constant upon clamp time constant is taken into account the temperature dependence is difficult to observe. It appears that cooling the OHC down to 5°C does not slow the gating kinetics sufficiently to overcome its dependence upon clamp characteristics. 20 mM TEA, 20 mM CsCl, 2 mM CoCl₂, no added calcium.

fairly large capacitance, a substantial portion of which is due to a nonlinear voltage-dependent component. The nonlinear contribution saturates with depolarization at about 30% of the cells' linear capacitance when the P/5 protocol at -120 mV holding potential is used (Santos-Sacchi, 1990). Even at a holding potential near the cell's normal resting potential (-70 mV; Dallos, Santos-Sacchi and Flock, 1982), there is a substantial nonlinear contribution. The OHC's capacitance in conjunction with the series resistance limits the voltage clamp's ability to rapidly alter the cell's transmembrane voltage (Santos-Sacchi, 1989b). The fact that the time and frequency response of OHC motility is dependent upon the clamp's ability to charge the membrane indicates that the actual mechanical capabilities of the OHC have yet to be determined. In this regard it is interesting to note that *in vivo* measures of electrically evoked oto-acoustic emissions, presumably due to the activity of OHCs, have been measured in pass bands up to several kHz (Hubbard and Mountain, 1990). Although these investigators suggest, based on Ashmore's data (1987), that the OHC length changes are too low-pass to account for such high frequency phenomena, the data presented here indicate that this may not be the case.

The fact that the time course of the nonlinear capacitive currents is imposed by those of the voltage clamp, also indicates that the kinetics of charge movement in the OHC membrane are faster than can be observed presently. Indeed, an attempt to slow down this charge movement by cooling to 5°C proved unsuccessful. This may indicate that these currents are artifacts of the technique used to collect the data; however, the clearest evidence against this is that Deiter cells possess no nonlinear capacitance. Lower temperatures are being investigated. Nevertheless, if these charge movements are related to the mechanical responses, then it is clear that clamp time constants down to 80 usec with associated fast gating constants (Fig. 1) still cannot validly investigate OHC mechanical capabilities. Ashmore (1989) reported gate time constants ranging from 1 to 2 ms, which is probably indicative of a large series resistance, with attendant slow clamp time constants. Under such clamp conditions (Ashmore and Holley, 1988), it would be difficult to measure a temperature dependent *increase* from 20 to 37°C in the rate of OHC movement that was due to an effect on the OHC, since the clamp imposes its temporal characteristics.

The OHC appears to alter its length in response to a change in transmembrane voltage. The underlying mechanism may involve the movement of membrane bound molecules bearing charged moieties which is somehow translated into longitudinal forces. This membrane phenomenon can be interfered with, for example, by treatment of the cells with gadolinium ions, which rapidly and reversibly reduce or abolish OHC gating currents and motility (Santos-Sacchi, 1989a; 1990). However, the coupling between membrane phenomena and these longitudinal forces is clearly dependent upon cytosolic volume -- cell turgor. This is demonstrated by several means. Prolonged depolarizations or treatment of OHCs with salicylates produces a slow loss of cell volume, with accompanying reduction of the magnitude of longitudinal motility (Brownell, Shehata, and Imredy, 1989; Brownell, Imredy, and Shehata, 1989; Brownell, 1990). I have observed similar effects during prolonged whole cell voltage clamping, even though cells were maintained at a potential near -70 to -80 mV. In fact, very rapid reversible changes in cell volume can be produced using large tipped patch pipettes. Voltage-dependent longitudinal motility is rapidly abolished during loss of cell turgor

and is restored upon cell volume replacement (Santos-Sacchi, 1990). In sum, the capability of OHCs to mechanically follow transmembrane voltage alterations may be limited by a number of factors including the strength of hydrodynamic coupling between membrane phenomena and longitudinal displacement. As yet, an estimate of this limit is difficult to make with the presently used technology, and it must be concluded that OHC motility is faster than has been reported.

Acknowledgements: Supported by a Research Career Development Award from NIDCD, and NIH grant DC00273. I thank John Callahan and Janet Santos for assistance.

References

- Ashmore, J.F. (1989) Transducer motor coupling in cochlear outer hair cells. In: *Mechanics of Hearing* (Eds: Kemp, D. and Wilson, J.P.) Plenum Press, New York, pp. 107-113.
- Ashmore, J.F. (1987) A fast motile response in guinea-pig outer hair cells: The cellular basis of the cochlear amplifier. *J. Physiol. (Lond.)*, 388, 323-347.
- Ashmore, J.F. and Holley, M.C. (1988) Temperature-dependence of a fast motile response in isolated outer hair cells of the guinea-pig cochlea. *Quart. J. Exper. Physiol.*, 73, 143-145.
- Bezanilla, F. and Taylor, R. (1978) Temperature effects on gating currents in the squid giant axon. *Biophys. J.*, 23, 479-484.
- Brownell, W.E. (1990) Outer hair cell electromotility and otoacoustic emissions. *Ear and Hearing*, 11, 82-92.
- Brownell, W.E., Imredy, J.B. and Shehata, W. (1989) Stimulated volume changes in mammalian outer hair cells. *Proc. Ann. Int. Cong. IEEE-Eng. Med. Biol. Soc.*, 11, 1344-1345.
- Brownell, W.E., Shehata, W. and Imredy, J.B. (1989) Slow electrically and chemically evoked volume changes in guinea pig outer hair cells. In: *Biomechanics of Active Movement and Deformation of Cells* (Ed: Akas, N.) Springer-Verlag, New York, pp. 493-498.
- Collins, C.A. and Rojas, E. (1982) Temperature dependence of the sodium channel gating kinetics in the node of Ranvier. *Quart. J. Exper. Physiol.*, 67, 41-55.
- Dallos, P., Santos-Sacchi, J. and Flock, A. (1982) Intracellular recordings from outer hair cells. *Science*, 218, 582-584.
- Hodgkin, A.L. and Huxley, A.F. (1952) A quantitative description of membrane current and its application to conduction and excitation in nerve. *J. Physiol.*, 117, 500-544.
- Hubbard, A.E. and Mountain, D.C. (1990) Haircell forward and reverse transduction: Differential suppression and enhancement. *Hear. Res.* 43, 269-272.
- Iwasa, K.H. and Kachar, B. (1989) Fast in vitro movement of outer hair cells in an external electric field: effect of digitonin, a membrane permeabilizing agent. *Hear. Res.*, 40, 247-254.
- Marty, A. and Neher, E. (1983) Tight-seal whole-cell recording. In: *Single channel recording* (Eds: Sakmann, B. and Neher, E.) Plenum Press, New York, pp. 107-122.
- Santos-Sacchi, J. (1990) Reversible inhibition of voltage-dependent outer hair cell motility: effects of gadolinium ions and cytosolic volume alterations. In preparation.

Santos-Sacchi, J. (1989a) Gadolinium ions reversibly block voltage dependent movements of isolated outer hair cells. 19th Annual Meeting, Soc. for Neurosci., Phoenix, AZ, October.

Santos-Sacchi, J. (1989b) Asymmetry in voltage dependent movements of isolated outer hair cells from the organ of Corti. *J. Neurosci.*, 9, 2954-2962.

Santos-Sacchi, J. and Dilger, J.P. (1988a) Whole cell currents and mechanical responses in outer hair cells. Midwinter Meeting, Assoc. for Res. in Otolaryngol., Clearwater, FL, February.

Santos-Sacchi, J. and Dilger, J.P. (1988b) Whole cell currents and mechanical responses of isolated outer hair cells. *Hear. Res.*, 35, 143-150.

Maturation of Voltage-induced Shifts in SLC26a5 (Prestin) Operating Point during Trafficking and Membrane Insertion

Feng Zhai,^{a,e} Lei Song,^{a,f} Jun-Ping Bai,^c Chunfu Dai,^g Dhasakumar Navaratnam^{a,b,c} and Joseph Santos-Sacchi^{a,b,d,*}

^a Department of Surgery (Otolaryngology), Yale University School of Medicine, New Haven, CT, USA

^b Department of Neuroscience, Yale University School of Medicine, New Haven, CT, USA

^c Department of Neurology, Yale University School of Medicine, New Haven, CT, USA

^d Department of Cellular and Molecular Physiology, Yale University School of Medicine, New Haven, CT, USA

^e Department of Otolaryngology, Shanghai Children's Medical Center, Shanghai Jiao Tong University School of Medicine, Shanghai 200127, China

^f Department of Otolaryngology-Head and Neck Surgery, Shanghai Ninth People's Hospital, Shanghai Jiao Tong University School of Medicine, Shanghai 200011, China

^g Department of Otolaryngology and Skull Base Surgery, Eye Ear Nose and Throat Hospital, Fudan University, Shanghai, China

Abstract—Prestin (SLC26a5) is an integral membrane motor protein in outer hair cells (OHC) that underlies cochlear amplification. As a voltage-dependent protein, it relies on intrinsic sensor charge to respond to transmembrane voltage (receptor potentials), thereby effecting conformational changes. The protein's electromechanical activity is experimentally monitored as a bell-shaped nonlinear capacitance (NLC), whose magnitude peaks at a characteristic voltage, V_h . This voltage denotes the midpoint of prestin's charge–voltage (Q – V) Boltzmann distribution and region of maximum gain of OHC electromotility. It is an important factor in hearing capabilities for mammals. A variety of biophysical forces can influence the distribution of charge, gauged by shifts in V_h , including prior holding voltage or membrane potential. Here we report that the effectiveness of prior voltage augmentations during the delivery of prestin to the membranes in an inducible HEK cell line. The augmentation coincides with an increase in prestin density, maturing at a characteristic membrane areal density of 870 functional prestin units per square micrometer, and is likely indicative of prestin–prestins cooperative interactions. © 2020 IBRO. Published by Elsevier Ltd. All rights reserved.

Key words: nonlinear capacitance, prestin cell line, voltage clamp, molecular memory, prestin density.

INTRODUCTION

Prestin (SLC26a5) is a protein (Zheng et al., 2000) that is housed in abundance within the lateral membrane of outer hair cells (OHC) in the organ of Corti. The protein imparts robust electromechanical activity to the cell that is unlike any other form of cellular motility, notably associated with a voltage-dependent, bell-shaped nonlinear capacitance (NLC) that reports on conformational changes in the protein (Ashmore, 1990; Santos-Sacchi, 1991). This mechanical activity, termed electromotility, driven by receptor potentials (Evans and Dallos, 1993), is believed to feed back into the acoustically-driven vibration of the cochlear partition, thereby enhancing the

mechanical stimulus that the inner hair cells (IHC) sense and transmit to the CNS (Ashmore et al., 2010). This process is called cochlear amplification, amounting to 40–60 dB of gain.

One of the interesting features of prestin is the protein's ability to alter its state differentially depending upon initial voltage conditions, i.e., it shows hysteresis. Simply put, the protein's operating voltage range (conveniently characterized by V_h , the voltage at peak NLC, where half of its sensor charge is moved across the membrane field, and where electromotility gain is maximal) shifts depending upon prior holding potentials. This phenomenon has been measured in OHCs and in prestin-transfected cells (Santos-Sacchi et al., 1998, 2001). In OHCs, the voltage at peak capacitance (namely, V_h) differs by about 20 mV between pre-pulse holding potentials of ± 100 mV. Besides magnitude of holding voltage, the shift depends on the polarity direction of voltage prior to the measurement of NLC. Finally, the shift evolves over time in a stretched exponential fashion, ranging from sub-milliseconds to seconds

*Correspondence to: J. Santos-Sacchi, Dept. of Surgery (Otolaryngology), Yale University School of Medicine, BML 224, 333 Cedar Street, New Haven, CT 06510, USA. Tel: +1-203-785-5407; fax: +1-203-737-2502.

E-mail address: joseph.santos-sacchi@yale.edu (J. Santos-Sacchi).
Abbreviations: IHC, inner hair cells; NLC, nonlinear capacitance; OHC, outer hair cells.

(Santos-Sacchi et al., 2009); thus, the duration of prior holding potential influences the amplitude of the V_h shift. This phenomenon likely reflects interactions among adjacent prestin molecules within the local membrane environment, just as ion channels show cooperative effects when expressed at high areal densities within the membrane (Molina et al., 2006). Here we denote this phenomenon observed in prestin Boltzmann characteristics as “molecular memory”, realizing that it may not be an intrinsic property of the protein prestin itself, but instead an interaction of prestin with itself and its local microenvironment (lipid, cytoskeletal) within the membrane. In mice, having an appropriate V_h value is critically important for normal hearing. In prestin knock-ins that have altered V_h , or with cochlear perilymphatic alterations of chloride that alter V_h , profound deafness ensues, the latter in a reversible manner (Santos-Sacchi et al., 2006; Dallos et al., 2008).

The development of prestin function has been studied in immature hair cells and in prestin-transfected cells (Oliver and Fakler, 1999; Abe et al., 2007; Bian et al., 2010, 2013; Seymour et al., 2016; Bai et al., 2019). We recently established a HEK cell line where prestin expression is tetracycline-inducible (Bian et al., 2010). We have already reported on some component Boltzmann characteristics of NLC maturation over hours following induction, and during the first few minutes following release of membrane trafficking block from low temperature (Bian et al., 2013). Prestin insertion into the membrane followed a sigmoidal function of time following induction. Here we utilize our model system to follow the maturation of prestin’s molecular memory as prestin density increases post-induction. We find that mature function arises after about 12 h following induction, that is, when prestin charge density is greater than 11.1 fC/pF, or equivalently about 870 functional prestin units/ μm^2 . We suggest that protein–protein interactions are optimized at and above this molecular density, such that negative cooperative effects among prestin units are maximized.

EXPERIMENTAL PROCEDURES

Experiments were performed on OHCs and HEK cells. Full details on OHC measurements have been reported previously (Santos-Sacchi et al., 2009). Full details on cell culture and induction of our tetracycline-inducible, highly-expressing monoclonal prestin HEK 293 cell lines have been reported previously (Bian et al., 2010, 2013). Briefly, cells were cultured in Dulbecco’s modified Eagle’s medium (DMEM) containing 50 U/ml each of penicillin and streptomycin, 10% fetal bovine serum at 37 °C in a 5% CO₂ incubator. 4 $\mu\text{g}/\text{ml}$ of blasticidin and 130 $\mu\text{g}/\text{ml}$ of zeocin were supplemented in the growth media. Induction was begun by treating with 1.0 $\mu\text{g}/\text{ml}$ tetracycline. At time point 2, 4, 6, 10 and 24 h, coverslips of grown cells were transferred to recording media (see below).

Whole cell patch-clamp measurements were made with an Axopatch 200B patch clamp amplifier (Axon Instruments) and a Digidata 1322A digitizer, with sampling rates of 10 μs . Experiments were performed at room temperature. Blocking solutions were used to remove ionic currents, limiting confounding effects on

NLC determination and voltage delivery under voltage clamp (Santos-Sacchi, 1991; Santos-Sacchi and Song, 2016). Extracellular solution was (in mM): NaCl 100, TEA-Cl 20, CsCl 20, CoCl₂ 2, MgCl₂ 1, CaCl₂ 1, Hepes 10. Intracellular solution was (in mM): CsCl 140, MgCl₂ 2, Hepes 10 and EGTA 10. All chemicals were purchased from Sigma-Aldrich.

Pipettes had initial resistances of about 2.5 M Ω . Stray capacitance was compensated with amplifier controls prior to whole-cell establishment. Corrections for series resistance were made post-hoc. For our HEK cell studies, following establishment of whole-cell recording conditions, cells were held at 0 mV. Thirty second pre-pulse holding potential steps to -100 or $+50$ mV preceded NLC collections. Whole cell recordings were made on single cells growing on a coverslip at 2 h, 4 h, 6 h, 10 h and 24 h after tetracycline induction. The number of cells recorded for each time point was 9, 9, 10, 10 and 9, respectively.

Membrane capacitance was measured with jClamp software (Scisoft, CT; www.SciSoftCo.com) using a continuous high resolution (2.56 ms sampling) two-sine stimulus protocol (10 mV peak at both 390.6 and 781.2 Hz) superimposed onto the voltage ramp (Santos-Sacchi et al., 1998; Santos-Sacchi, 2004). Briefly, real and imaginary components of membrane current at harmonic frequencies were determined by FFT in jClamp, corrected for the roll-off of recording system admittance (Gillis, 1995). R_s , R_m and C_m were extracted using the dual-sine, 3-parameter solution of the standard patch clamp model (Santos-Sacchi et al., 1998; Santos-Sacchi, 2004), based on the original single sine solution (Pusch and Neher, 1988). In order to extract Boltzmann parameters, capacitance–voltage data were fit to the first derivative of a two-state Boltzmann function.

$$C_m = NLC + C_{sa} + C_{lin} = Q_{max} \frac{ze}{k_B T} \frac{b}{(1+b)^2} + C_{sa} + C_{lin}$$

$$\text{where } b = \exp\left(-ze \frac{V_m - V_h}{k_B T}\right), C_{sa} = \frac{\Delta C_{sa}}{(1+b^{-1})}$$

Q_{max} is the maximum nonlinear charge moved, V_h is voltage at peak capacitance or equivalently, at half-maximum charge transfer, V_m is R_s -corrected membrane potential, z is valence, C_{lin} is linear membrane capacitance, e is electron charge, k_B is Boltzmann’s constant, and T is absolute temperature. C_{sa} is a component of capacitance that characterizes sigmoidal changes in specific membrane capacitance (Santos-Sacchi and Navarrete, 2002; Santos-Sacchi and Song, 2014). ΔC_{sa} is the total sum of unitary changes per prestin motor protein. Q_{sp} denotes charge density, namely Q_{max}/C_{lin} .

The time-dependent change in Q_{sp} in Fig. 3B is fit by a sigmoidal function, $f = a/(1 + \exp(-(x - x0)/b))$, as we have done previously (Bian et al., 2010), where x is time, $x0$ is the midpoint, b is the slope indicator, and a is the asymptotic value. Two parameter exponential fits were made using the formula $f = a*(1 - \exp(-b * x))$, where x is time for Fig. 3A, and x is Q_{sp} for Fig. 4. The parameter a denotes the asymptotic value of either Q_{sp} or ΔV_h (see plots). The parameter $1/b$ is the characteristic “time constant” to achieve the final value a . For Fig. 4, to estimate

charge density at “steady state”, we use the value reached at five times the “time constant”.

RESULTS

The voltage range over which prestin works is not fixed, but shifts depending on previous state of the protein/membrane environment set by holding voltage. This is most apparent in native isolated OHCs. Fig. 1 illustrates the effect of prior holding voltage on prestin’s state/charge distribution as revealed through capacitance measures in the guinea pig OHC. In this case, dual sine stimuli were superimposed on a slow sinusoidal holding voltage (Fig. 1b), which spanned from -150 to $+150$ mV. The direction of holding potential change over time influences the position of V_h along the voltage axis (Fig. 1a); in the hyperpolarizing direction (blue lines), V_h is shifted towards depolarized voltages and vice versa (red lines). Steady state pre-pulse voltages can likewise cause shifts in V_h .

Our HEK cell line allows us to monitor NLC characteristics over the course of prestin insertion into the membrane. Thirty seconds holding potential pre-pulses to either -100 or $+50$ mV were used to gauge the molecular memory of prestin in our HEK cell line. Following these pre-pulses, NLC was measured. Fig. 2 illustrates the dependence of V_h on post-induction time. Here we average our voltage protocol-generated currents prior to C_m determination. Clear differences are found between 2 and 24 h post-induction. Analysis of cells on an individual basis allowed statistical comparisons. At 2 h post induction, the average difference in V_h between 2 and 24 h pre-pulse protocols

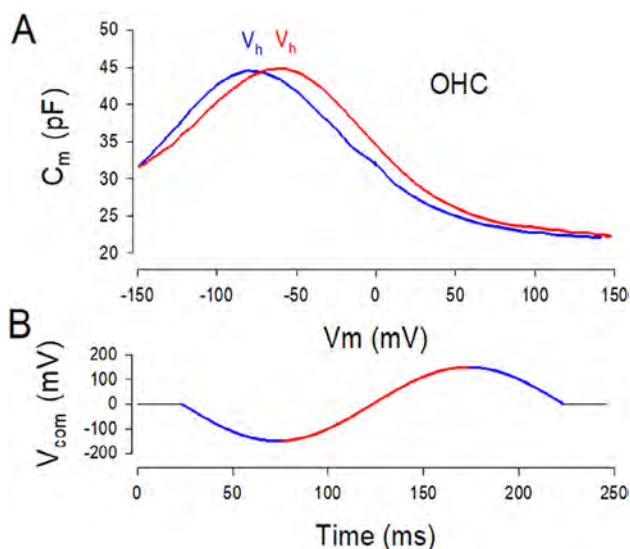


Fig. 1. Prestin state memory. **(A)** NLC functions in a guinea pig OHC measured during hyperpolarizing direction (blue) and depolarizing direction (red) of sinusoidal change in holding potential. Prior hyperpolarizations cause movements of V_h in the opposite direction. The shift in voltage at peak capacitance (V_h) indicates redistribution of charge as a function of prior voltage. **(B)** Holding potential sinusoid. Two sine stimuli have been removed. (For interpretation of the references to colour in this figure legend, the reader is referred to the web version of this article.)

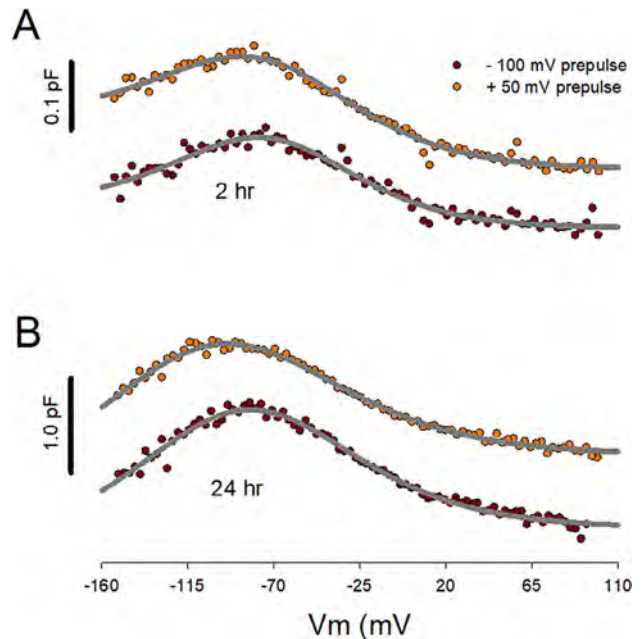


Fig. 2. Illustration of post-induction time dependence of V_h on steady state holding potential. Individual cell currents were averaged prior to C_m determination from averaged currents. **(A)** At 2 h post tetracycline induction, 0.5 min prepulse to -100 or $+50$ mV has smaller effects on V_h than at 24 h post induction **(B)**. V_h for fits at 2 h, -100 mV prepulse: -73.3 mV; $+50$ mV prepulse: -76.4 mV. Fits at 24 h, -100 mV prepulse: -84.7 mV; $+50$ mV prepulse: -102.3 mV. Traces offset for visual clarity.

(ΔV_h) is smaller than that measured after 24 h post induction (unpaired t -test, $p = 0.02$). The average difference (mean \pm SEM) at 2 h was 7.39 ± 1.32 mV ($n = 9$) and that at 24 h was 12.97 ± 1.70 mV ($n = 9$). Fig. 3A plots results for 2, 4, 6, 12, and 24 h post induction (mean \pm SEM). ΔV_h rises exponentially over induction time, with a time constant of 2.2 h. Along with the growth of molecular memory, the density of prestin, gauged as Q_{sp} , increases more slowly in a sigmoidal fashion (Fig. 3B), with a time at half magnitude of 7.3 h and reaching an asymptotic value of 16.0 fC/ μm^2 based on the fit. This is in line with our previous observations over this time course (Bian et al., 2010). Clearly, while the density of prestin continues to rise, ΔV_h asymptotes during the early phase of prestin delivery to the membrane. The Boltzmann parameter, z , on the other hand is stable after 4 h post induction near 0.8 (Fig. 3C).

In order to relate prestin density and ΔV_h , we plot the two against each other in Fig. 4. The relation shows an exponential growth in ΔV_h as density increases, reaching at five times the characteristic “time constant”, $1/b$ ($5 * 2.2$ fC/pF = 11.1 fC/pF), the value of 12.6 mV. The number of prestin units per square micrometer is determined by $Q_{sp}/(z * e)$, where e is electron charge. Taking the classical value for linear membrane capacitance of $1 \mu\text{F}/\text{cm}^2$ (Hille, 1992), $1 \text{ pF} = 100 \mu\text{m}^2$, and based on 11.1 fC/pF, we estimate that beyond a critical density of about 870 functional units of prestin per square micrometer, ΔV_h has matured. The nonlinear relationship between charge density and ΔV_h we take to

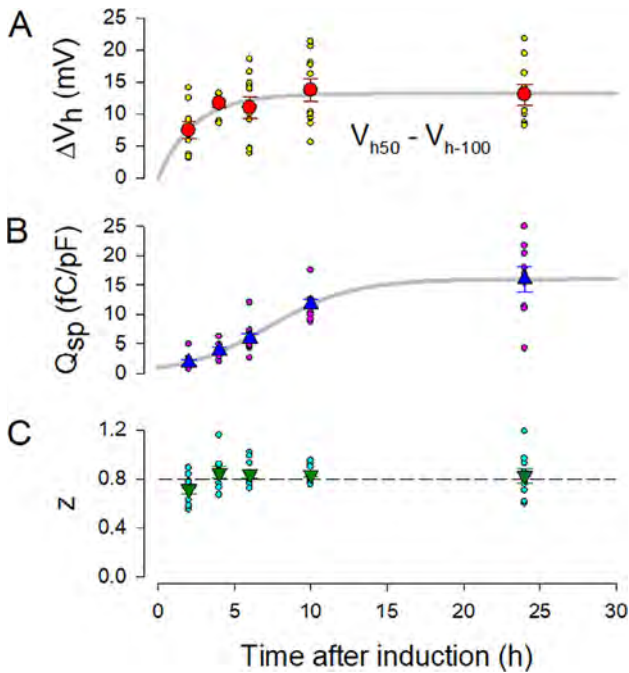


Fig. 3. Prestin behavior alters over post-induction time. **(A)** The magnitude of V_h change (ΔV_h) increases in an exponential manner over time. Fitted exponential parameters: $a = 12.6$ mV, $1/b = 1.9$ h (see Experimental procedures). R^2 : (correlation coefficient of variation): 0.89. **(B)** Prestin charge density also increases in an exponential manner. Fitted exponential parameters: $a = 20.1$ fC/pF, $1/b = 14.9$ h (see Methods). R^2 : 0.99. **(C)** On the other hand, the Boltzmann parameter z , which increases very early following induction (Bian et al., 2010), is stable after 4 h. Error bars are SEM.

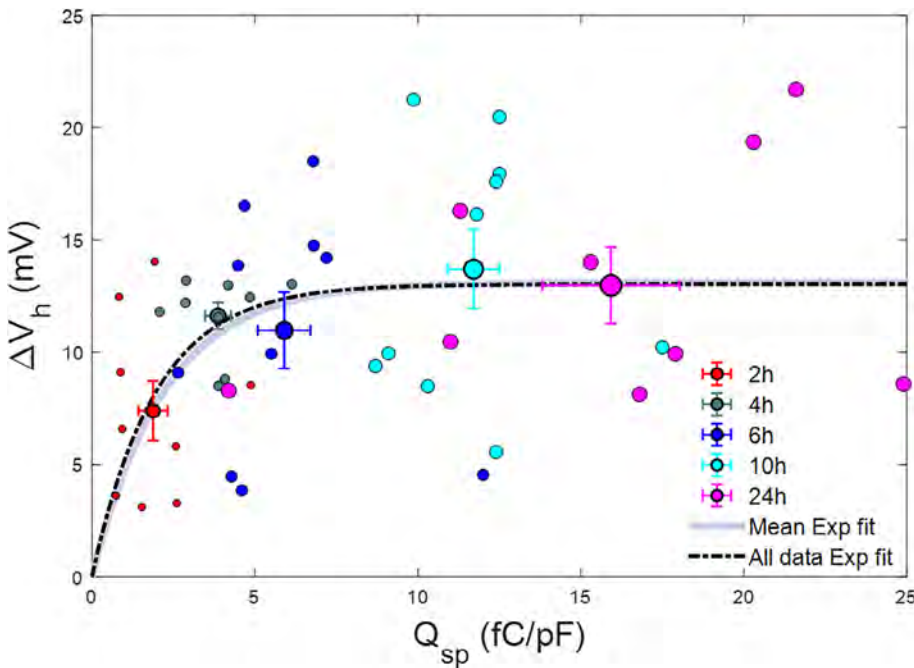


Fig. 4. Relationship between susceptibility to voltage pre-pulse (ΔV_h) versus prestin charge density (Q_{sp}). ΔV_h increases exponentially with charge density, reaching at 11.1 fC/pF at five times $1/b$, the characteristic “time constant”. Fitted exponential parameters of the mean data points: $a = 13.11$ mV, $1/b = 2.2$ fC/pF (see Experimental procedures). R^2 : 0.89. Error bars are SEM. All data points were used for an exponential fit, as well. Fitted exponential parameters are similar: $a = 13.02$ mV, $1/b = 2.0$ fC/pF.

mean that above this critical density, interactions among prestin molecules are likely.

DISCUSSION

All hair cells utilize apical membrane components (stereocilia) for forward transduction of sound into receptor potentials that evoke neurotransmitter release onto afferent nerve fibers (Flock, 1965). However, in addition, the OHC has evolved special lateral membrane components to reverse transduce those receptor potentials into mechanical energy, a process called electromotility (Evans and Dallos, 1993).

The responsible molecular motor was identified in 2000 (Zheng et al., 2000), and remarkably was found to be a solute carrier of the SLC26 family. Named as prestin, for its presumed fast kinetics (electromotility was measured beyond 80 kHz (Frank et al., 1999)), the protein has been studied extensively. Recently, this ultrafast capability of electromechanical activity has been challenged (Santos-Sacchi and Tan, 2018; Santos-Sacchi, 2019; Santos-Sacchi et al., 2019). Regardless, prestin is a voltage-dependent protein (Santos-Sacchi and Dilger, 1988) that has been successfully modelled with modifications of a two-state Boltzmann process, where motors are either in an expanded or compact state. Displacement currents or correspondingly a NLC arises from these conformational changes (Ashmore, 1990; Santos-Sacchi, 1990, 1991). Based on these measures, membrane density of the motor in the OHC lateral membrane has been estimated to be up to $11000/\mu\text{m}^2$ (Huang and Santos-Sacchi, 1993; Gale and Ashmore, 1997; Mahendrasingam et al., 2010; Santos-Sacchi and Tan, 2020). Specific membrane sensor charge correlates well with biochemical measures of membrane content (Bian et al., 2010; Seymour et al., 2016). Interestingly, as might be expected of an anion solute carrier, anion binding plays a pivotal role in its function (Oliver et al., 2001; Rybalchenko and Santos-Sacchi, 2003), though it likely does not work solely as an extrinsic voltage sensor (Song and Santos-Sacchi, 2010; Santos-Sacchi and Song, 2016). Concerning our present work, we have previously shown that chloride effects on prestin do not underlie its molecular memory (Santos-Sacchi et al., 2009).

In our current experiments we have employed our tetracycline-inducible prestin cell line which provides specific nonlinear charge (sensor charge/linear capacitance) values of up to 20 fC/pF after 24 h, far greater than transient transfection can provide (Bian et al., 2010). This efficiency allows

us to monitor characteristics of NLC resulting during prestin delivery and insertion into the plasma membrane. Specifically, we used this approach to study the development of prestin's ability to respond to its prior state, established by pre-pulse holding voltage. We find that ΔV_h , a metric for prestin's molecular memory, increases as post-induction time and the number of membrane-bound prestin molecules increase. The correspondence between areal density and ΔV_h indicates that at a critical density of prestin within the membrane, namely, about 870 functional prestin units per square micrometer, molecular memory matures. If maturation were simply a consequence of time spent within the membrane, we would not have expected asymptotic behavior, because insertion of new proteins into the membrane continues well beyond the observed maturation. The exponential fit of ΔV_h as charge density increases is simply used to provide an estimate of the asymptotic behavior; earlier time point measures of this phenomenon could reveal non-exponential behavior, just as charge density itself matures in a sigmoidal fashion (Fig. 2B) (Bian et al., 2010). Nevertheless, the identification of asymptotic behavior within our evaluated time points would not be changed by including earlier time points of ΔV_h , which would be exceedingly difficult to measure. Interestingly, we recently have found that prestin kinetics augments, that is, the frequency response of NLC increases, during early development of mouse OHCs in organ explants (Bai et al., 2019). However, it is unlikely that development of prestin density may be a controlling factor in prestin's ability to alter conformation at kilohertz rates. In that study, the estimated frequency cut-off (F_c) was found to asymptote beyond postnatal day p17–18, where charge density has also matured – a density well beyond maturation of molecular memory. Of course, for OHCs, other factors beyond prestin kinetics could be at play. For example, not only intrinsic (e.g., membrane components or cytoskeleton) but also extrinsic (e.g., viscoelastic interactions with supporting cells within the organ) mechanical loads could influence our frequency response measures, as we have recently observed (Santos-Sacchi et al., 2019). These mechanical impediments to charge movement have as their basis prestin's piezoelectric-like behavior, where load can influence prestin's state (Iwasa, 1993; Gale and Ashmore, 1994; Kakehata and Santos-Sacchi, 1995).

The piezoelectric-like mechanical sensitivity of prestin may also underlie its molecular memory, and result from interactions among functional prestin units within the membrane. Indeed, we previously modelled molecular memory as resulting from such behavior (Santos-Sacchi et al., 1998), where the voltage-induced conformational changes in one unit could directly affect those of adjacent units through the viscoelastic plasma membrane. We reasoned that when prestin moves from an extended state to a compact state, forces generated within the plane of the membrane will influence the state in adjacent molecules, as lipid redistributes around compact prestin and acts on neighbors. Recapitulation of experimental data with the model was successful (Santos-Sacchi et al., 1998). Of course, the effectiveness of such negative cooperativ-

ity will depend upon intermolecular distances. At a critical density of about 870 functional units per square micrometer, intermolecular distances would be on the order of 34 nm, assuming a uniform distribution. Physiological evidence for dimerization has been obtained for prestin (Navaratnam et al., 2005; Detro-Dassen et al., 2008), and recent cryo-EM observations on SLC26a9, a family member of prestin, also suggests dimerization. Given that the widest dimension of a prestin dimer within the membrane may be 10 nm based on SLC26a9 cryo-EM structure, the closest proximity of adjacent molecular edges would be 17 nm. Of course, this is founded on a uniform distribution, but local, restricted diffusion cannot be discounted (Santos-Sacchi and Zhao, 2003; Organ and Raphael, 2007; Yamashita et al., 2015), nor can subsequent clustering be ignored. To be sure, in our cell line prestin-fused YFP often presents as visible fluorescent patches within the membrane. Modelling of ion channels indicates that at areal densities greater than $10^3/\mu\text{m}^2$, close to our observed critical prestin density, cooperative viscoelastic interactions are possible (Ursell et al., 2007). Indeed, clustering in a variety of ion channels can impact on channel activity (see (Molina et al., 2006)). Thus, for the OHC, where densities of prestin are up to 11,000/ μm^2 (Huang and Santos-Sacchi, 1993; Gale and Ashmore, 1997; Mahendrasingam et al., 2010; Santos-Sacchi and Tan, 2020), the ensemble might be considered one huge cluster permitting negative cooperativity among molecules spanning across several molecular distances. These interactions are expected to impact OHC influence on cochlear amplification and hearing, since those resulting V_h shifts may be viewed as amplificatory in nature (Santos-Sacchi et al., 2009).

ACKNOWLEDGEMENTS

This research was supported by NIH-NIDCD R01 DC000273, R01 DC016318 and R01 DC008130 to JSS and DN, and a National Natural Science Foundation of China NSFC81900939 grant to FZ.

REFERENCES

- Abe T, Kakehata S, Kitani R, Maruya S, Navaratnam D, Santos-Sacchi J, Shinkawa H (2007) Developmental expression of the outer hair cell motor prestin in the mouse. *J Membr Biol* 215:49–56.
- Ashmore J, Avan P, Brownell WE, Dallos P, Dierkes K, Fettiplace R, Grosh K, Hackney CM, Hudspeth AJ, Juelicher F, Lindner B, Martin P, Meaud J, Petit C, Sacchi JRS, Canlon B (2010) The remarkable cochlear amplifier. *Hear Res* 266:1–17.
- Ashmore JF (1990) Forward and reverse transduction in the mammalian cochlea. *Neurosci Res Suppl* 12:S39–S50.
- Bai J-P, Navaratnam D, Santos-Sacchi J (2019) Prestin kinetics and corresponding frequency dependence augment during early development of the outer hair cell within the mouse organ of Corti. *Sci Rep.* in press.
- Bian S, Navaratnam D, Santos-Sacchi J (2013) Real time measures of prestin charge and fluorescence during plasma membrane trafficking reveal sub-tetrameric activity. *PLoS One* 8 e66078.
- Bian S, Koo BW, Kelleher S, Santos-Sacchi J, Navaratnam DS (2010) A highly expressing Tet-inducible cell line recapitulates in situ developmental changes in prestin's Boltzmann characteristics and reveals early maturational events. *Am J Physiol Cell Physiol* 299:C828–C835.

- Dallos P, Wu X, Cheatham MA, Gao J, Zheng J, Anderson CT, Jia S, Wang X, Cheng WH, Sengupta S, He DZ, Zuo J (2008) Prestin-based outer hair cell motility is necessary for mammalian cochlear amplification. *Neuron* 58:333–339.
- Detro-Dassen S, Schanzler M, Lauks H, Martin I, zu Berstenhorst SM, Nothmann D, Torres-Salazar D, Hidalgo P, Schmalzing G, Fahlke C (2008) Conserved dimeric subunit stoichiometry of SLC26 multifunctional anion exchangers. *J Biol Chem* 283:4177–4188.
- Evans BN, Dallos P (1993) Stereocilia displacement induced somatic motility of cochlear outer hair cells. *Proc Natl Acad Sci U S A* 90:8347–8351.
- Flock A (1965) Transducing mechanisms in the lateral line canal organ receptors. *Cold Spring Harb Symp Quant Biol* 30:133–145.
- Frank G, Hemmert W, Gummer AW (1999) Limiting dynamics of high-frequency electromechanical transduction of outer hair cells. *Proc Natl Acad Sci U S A* 96:4420–4425.
- Gale JE, Ashmore JF (1994) Charge displacement induced by rapid stretch in the basolateral membrane of the guinea-pig outer hair cell. *Proc R Soc Lond B Biol Sci* 255:243–249.
- Gale JE, Ashmore JF (1997) The outer hair cell motor in membrane patches. *Pflugers Arch* 434:267–271.
- Gillis KD (1995) Techniques for membrane capacitance measurements. In: Sakmann B, Neher E, editors. *Single channel recording*. New York: Plenum Press. p. 155–198.
- Hille B (1992) *Ionic channels of excitable membranes*. 2nd ed. Sunderland, Mass: Sinauer Associates.
- Huang G, Santos-Sacchi J (1993) Mapping the distribution of the outer hair cell motility voltage sensor by electrical amputation. *Biophys J* 65:2228–2236.
- Iwasa KH (1993) Effect of stress on the membrane capacitance of the auditory outer hair cell. *Biophys J* 65:492–498.
- Kakehata S, Santos-Sacchi J (1995) Membrane tension directly shifts voltage dependence of outer hair cell motility and associated gating charge. *Biophys J* 68:2190–2197.
- Mahendrasingam S, Beurg M, Fettiplace R, Hackney CM (2010) The ultrastructural distribution of prestin in outer hair cells: a post-embedding immunogold investigation of low-frequency and high-frequency regions of the rat cochlea. *Eur J Neurosci* 31:1595–1605.
- Molina ML, Barrera FN, Fernandez AM, Poveda JA, Renart ML, Encinar JA, Riquelme G, Gonzalez-Ros JM (2006) Clustering and coupled gating modulate the activity in KcsA, a potassium channel model. *J Biol Chem* 281:18837–18848.
- Navaratnam D, Bai JP, Samaranayake H, Santos-Sacchi J (2005) N-terminal-mediated homomultimerization of prestin, the outer hair cell motor protein. *Biophys J* 89:3345–3352.
- Oliver D, Fakler B (1999) Expression density and functional characteristics of the outer hair cell motor protein are regulated during postnatal development in rat [In Process Citation]. *J Physiol (Lond)* 519(Pt 3):791–800.
- Oliver D, He DZ, Klocker N, Ludwig J, Schulte U, Waldegger S, Ruppertsberg JP, Dallos P, Fakler B (2001) Intracellular anions as the voltage sensor of prestin, the outer hair cell motor protein. *Science* 292:2340–2343.
- Organ LE, Raphael RM (2007) Application of fluorescence recovery after photobleaching to study prestin lateral mobility in the human embryonic kidney cell. *J Biomed Opt* 12 021003.
- Pusch M, Neher E (1988) Rates of diffusional exchange between small cells and a measuring patch pipette. *Pflugers Arch* 411:204–211.
- Rybalchenko V, Santos-Sacchi J (2003) Cl⁻ flux through a non-selective, stretch-sensitive conductance influences the outer hair cell motor of the guinea-pig. *J Physiol* 547:873–891.
- Santos-Sacchi J (1990) Fast outer hair cell motility: how fast is fast? In: Dallos P, Geisler CD, Matthews JW, Ruggero MA, Steele CR, editors. *The mechanics and biophysics of hearing*. Berlin: Springer-Verlag. p. 69–75.
- Santos-Sacchi J (1991) Reversible inhibition of voltage-dependent outer hair cell motility and capacitance. *J Neurosci* 11:3096–3110.
- Santos-Sacchi J (2004) Determination of cell capacitance using the exact empirical solution of dY/dCm and its phase angle. *Biophys J* 87:714–727.
- Santos-Sacchi J (2019) The speed limit of outer hair cell electromechanical activity. *HNO* 67:159–164.
- Santos-Sacchi J, Dilger JP (1988) Whole cell currents and mechanical responses of isolated outer hair cells. *Hear Res* 35:143–150.
- Santos-Sacchi J, Navarrete E (2002) Voltage-dependent changes in specific membrane capacitance caused by prestin, the outer hair cell lateral membrane motor. *Pflugers Arch* 444:99–106.
- Santos-Sacchi J, Zhao H-B (2003) Excitation of fluorescent dyes inactivates the outer hair cell integral membrane motor protein prestin and betrays its lateral mobility. *Pflugers Arch*. in press.
- Santos-Sacchi J, Song L (2014) Chloride and salicylate influence prestin-dependent specific membrane capacitance: support for the area motor model. *J Biol Chem*.
- Santos-Sacchi J, Song L (2016) Chloride anions regulate kinetics but not voltage-sensor Q_{max} of the solute carrier SLC26a5. *Biophys J* 110:1–11.
- Santos-Sacchi J, Tan W (2018) The frequency response of outer hair cell voltage-dependent motility is limited by kinetics of prestin. *J Neurosci* 38:5495–5506.
- Santos-Sacchi J, Tan W (2020). Complex nonlinear capacitance in outer hair cell macro-patches: effects of membrane tension. arXiv:2001.10118v3 [physics.bio-ph]. <https://arxiv.org/abs/2001.10118v3>.
- Santos-Sacchi J, Kakehata S, Takahashi S (1998) Effects of membrane potential on the voltage dependence of motility-related charge in outer hair cells of the guinea-pig. *J Physiol* 510(Pt 1):225–235.
- Santos-Sacchi J, Navarrete E, Song L (2009) Fast electromechanical amplification in the lateral membrane of the outer hair cell. *Biophys J* 96:739–747.
- Santos-Sacchi J, Iwasa KH, Tan W (2019) Outer hair cell electromotility is low-pass filtered relative to the molecular conformational changes that produce nonlinear capacitance. *J Gen Physiol*. in press.
- Santos-Sacchi J, Shen W, Zheng J, Dallos P (2001) Effects of membrane potential and tension on prestin, the outer hair cell lateral membrane motor protein. *J Physiol* 531:661–666.
- Santos-Sacchi J, Song L, Zheng J, Nuttall AL (2006) Control of mammalian cochlear amplification by chloride anions. *J Neurosci* 26:3992–3998.
- Seymour ML, Rajagopalan L, Duret G, Volk MJ, Liu H, Brownell WE, Pereira FA (2016) Membrane prestin expression correlates with the magnitude of prestin-associated charge movement. *Hear Res* 339:50–59.
- Song L, Santos-Sacchi J (2010) Conformational state-dependent anion binding in prestin: evidence for allosteric modulation. *Biophys J* 98:371–376.
- Ursell T, Huang KC, Peterson E, Phillips R (2007) Cooperative gating and spatial organization of membrane proteins through elastic interactions. *PLoS Comput Biol* 3 e81.
- Yamashita T, Hakizimana P, Wu S, Hassan A, Jacob S, Temirov J, Fang J, Mellado-Lagarde M, Gursky R, Horner L, Leibiger B, Leijon S, Centonze VE, Berggren PO, Frase S, Auer M, Brownell WE, Fridberger A, Zuo J (2015) Outer hair cell lateral wall structure constrains the mobility of plasma membrane proteins. *PLoS Genet* 11 e1005500.
- Zheng J, Shen W, He DZ, Long KB, Madison LD, Dallos P (2000) Prestin is the motor protein of cochlear outer hair cells. *Nature* 405:149–155.

Gene Expression Gradients along the Tonotopic Axis of the Chicken Auditory Epithelium

COREY S. FRUCHT^{1,2}, MOHAMED UDUMAN^{3,4}, STEVEN H. KLEINSTEIN^{3,4}, JOSEPH SANTOS-SACCHI^{5,6}, AND DHASAKUMAR S. NAVARATNAM^{7,8}

¹*Medical Scientist Training Program, Yale School of Medicine, New Haven, CT, USA*

²*Interdepartmental Neuroscience Program, Yale University, New Haven, CT, USA*

³*Interdepartmental Program in Computation Biology and Bioinformatics, Yale University, New Haven, CT, USA*

⁴*Department of Pathology, Yale School of Medicine, New Haven, CT, USA*

⁵*Division of Otolaryngology, Department of Surgery, Yale School of Medicine, New Haven, CT, USA*

⁶*Department of Cellular and Molecular Physiology, Yale School of Medicine, New Haven, CT, USA*

⁷*Department of Neurobiology, Yale School of Medicine, New Haven, CT, USA*

⁸*Department of Neurology, Yale School of Medicine, New Haven, CT, USA*

Received: 11 November 2010; Accepted: 24 January 2011; Online publication: 12 March 2011

ABSTRACT

There are known differences in the properties of hair cells along the tonotopic axis of the avian auditory epithelium, the basilar papilla (BP). To determine the genetic basis of these differences, we compared gene expression between the high- (HF), middle-, and low-frequency (LF) thirds of 0-day-old chick auditory epithelia. RNA amplified from each sample was hybridized to whole-genome chicken arrays and GeneSpring software was used to identify differentially expressed genes. Two thousand six hundred sixty-three genes were found to be differentially expressed between the HF and LF segments, using a fold-change cutoff of 2 and a *p* value of 0.05. Many ion channel genes were differentially expressed between the HF and LF regions of the BP, an expression pattern that was previously established for some but not all of these genes. Quantitative PCR was used to verify tonotopic expression of 15 genes, including *KCNMA1* (Slo) and its alternatively spliced

STREX exon. Gene set enrichment analyses (GSEA) were performed on the microarray data and revealed many microRNA gene sets significantly enriched in the HF relative to the LF end, suggesting a tonotopic activity gradient. GSEA also suggested differential activity of the kinases protein kinase C and protein kinase A at the HF and LF ends, an interesting corollary to the observation that there is tonotopic expression of the STREX exon that confers on Slo sensitivity to the activity of kinases. Taken together, these results suggest mechanisms of induction and maintenance of tonotopicity and enhance our understanding of the complex nature of proximal–distal gene expression gradients in the chicken BP.

Keywords: cochlea, development, stem cells, kinases

Electronic supplementary material The online version of this article (doi:10.1007/s10162-011-0259-2) contains supplementary material, which is available to authorized users.

Correspondence to: Dhasakumar S. Navaratnam · Department of Neurobiology · Yale School of Medicine · New Haven, CT, USA; email: dhasakumar.navaratnam@yale.edu

INTRODUCTION

The basilar papilla (BP), the chicken auditory epithelium, is tonotopically organized much like its mammalian counterpart the organ of Corti. Hair cells residing at specific locations along the apical-basal axis are maximally responsive to sounds at a particular frequency. In non-mammalian vertebrates such as turtles (Crawford

and Fettiplace 1981) and birds (Fuchs et al. 1988), this tuning seems to be largely mediated by intrinsic electrical resonance properties of hair cells. Electrical resonance in these cells is mediated by interplay between a depolarizing voltage-gated calcium current through calcium channels and a hyperpolarizing calcium-sensitive potassium current through BK channels.

Both hair cell physiological activity and gene expression are known to vary along the tonotopic axis of auditory epithelia. There are also differences in the properties of the transduction apparatus along the tonotopic axis. The mechanotransduction channels at the HF end of the turtle BP pass more current per channel than those in the LF end, allowing for faster adaptation (Ricci et al. 2003). As another example, there are changes in the electrical tuning apparatus along the length of the BP. Both models and data confirm the expression of inward and delayed rectifying potassium channels in hair cells in the low-frequency portion of the sensory epithelium, while BK channels and L-type calcium channels are present in higher density in hair cells in the high-frequency region (Art et al. 1995; Wu et al. 1995; Samaranayake et al. 2004). Differences in the density and properties of these channels are believed to give rise to the higher resonant frequency of cells in the HF end of the BP (Navaratnam et al. 1997; Rosenblatt et al. 1997; Samaranayake et al. 2004). Specifically, the higher resonant frequency of HF hair cells seems to be partly due to an increase in calcium influx and an increase in potassium efflux through an increased number of potassium and calcium channels (Art et al. 1995; Wu et al. 1995; Tucker et al. 1996).

In light of what is known about tonotopic gradients of gene expression and hair cell physiology, we endeavored to use a genome-wide comparison of gene expression between the high-frequency (HF), middle-frequency (MF), and low-frequency (LF) segments of the post-hatch chicken BP to identify tonotopically expressed genes. Genes found to have this expression pattern may be functionally significant and may therefore provide new insight into BP structure and function. Specifically, tonotopically expressed genes may represent differences in development, susceptibility to injury, or regenerative capacity along the tonotopic axis. We expected that such a data set would identify gene expression regulators such as transcription factors and microRNAs (miRNA) that are important for the development and/or maintenance of these transcriptional gradients. Affymetrix whole-genome chicken microarrays were therefore used to compare transcription profiles between the HF (basal), MF, and LF (apical) thirds of the post-hatch chicken BP. Many of the genes found to be differentially expressed between the two extreme ends of the epithelium were ion channels, some known to

be tonotopically expressed and others with a previously uncharacterized pattern of expression. Given limitations in sensitivity and specificity of microarrays, gene set enrichment analyses (GSEA) were also performed. These analyses complement the microarray results as they are more specific and are less susceptible to systematic bias from false results. The GSEA results suggested tonotopic gradients of activity of a number of miRNAs and kinases, as well as expression of genes associated with the hematopoietic stem cell phenotype.

METHODS

Basilar papilla tissue preparation

Animals were treated in accordance with policies established by the Yale Institutional Animal Care and Use Committee (protocol number 2007–10439). Cochlear ducts were carefully dissected out of 0-day-old chicks. The tegmentum vasculosum and tectorial membrane were immediately dissected off to expose the auditory epithelium, which was delicately freed from the basement membrane resting on cartilaginous plates using a tuberculin needle. The entire epithelium was then sectioned into even HF, MF, and LF thirds (Fig. 1). Three segments from three different BPs went into each sample to produce a total of three HF samples, three MF samples, and three LF samples. Samples were frozen at -80°C until RNA isolation could be performed.

RNA isolation

Frozen samples were removed from the -80°C freezer and immediately placed in the lysis buffer from the RNAqueous[®] Kit (Ambion, Austin, TX). The tissue was not actively homogenized or disrupted given the small amount of tissue. Total RNA isolation was performed as per the manufacturer's instructions. The quality of each sample was confirmed by gel and Bioanalyzer analysis. All samples had an A260/A280 ratio of at least 1.9, as well as 18S and 28S bands with no obvious evidence of degradation or genomic contamination and RNA integrity numbers (based on 28S/18S ratio and other parameters) of at least 9 on a ten-point scale (Schroeder et al. 2006). Total RNA concentration was determined by measuring absorbance at 260 nm on a spectrophotometer.

Microarray hybridizations

Microarray hybridizations were performed as previously reported (Frucht et al. 2010). Briefly, double-stranded cDNA and biotin-labeled cRNA were synthesized from 1 to 5 μg of total RNA using a two-cycle target labeling kit (Affymetrix 2004). Biotin-labeled cRNA was purified using the GeneChip Cleanup Module prior to fragment-

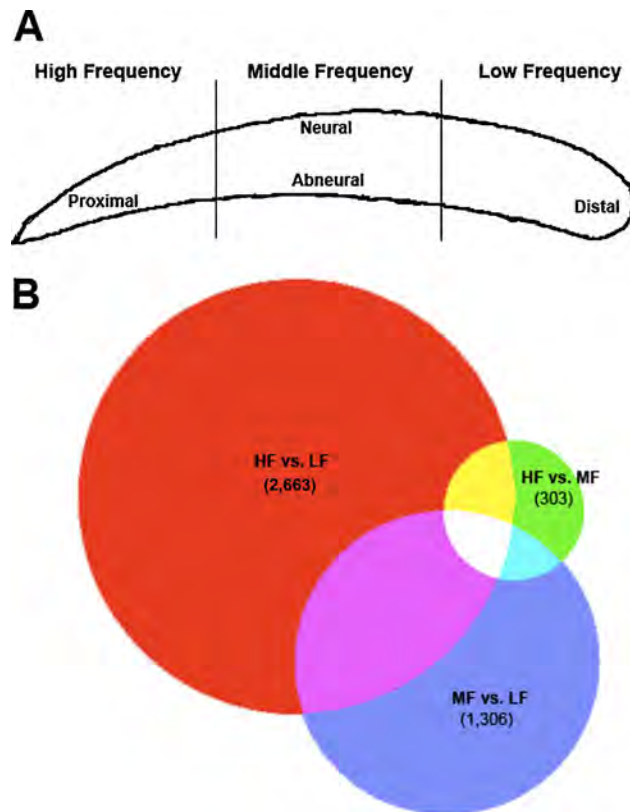


FIG. 1. Shown in panel **A** is a schematic diagram showing the manner in which the auditory epithelia were sectioned. Low-, middle-, and high-frequency segments were pooled as described in the text to allow for comparison of genome-wide expression across the three indicated regions. Shown in panel **B** is a proportional Venn diagram representing overlap of differentially expressed genes for the high- versus low-frequency (HF vs. LF; 2,663), high- versus middle-frequency (HF vs. MF; 303), and middle- versus low-frequency (MF vs. LF; 1,306) comparisons. Far more genes are differentially expressed between the HF and LF segments than either of the middle-frequency comparisons, suggesting that many of the HF vs. LF genes are expressed in a gradient along the tonotopic axis of the basilar papilla.

ing to a size of 35–200 bases. Hybridization of the samples with Affymetrix whole-genome chicken microarrays was then performed at the Yale University Keck Facility according to the manufacturer's protocol (Affymetrix 2009). This array contains many internal controls, including negative hybridization controls that serve to minimize the detection of signals resulting from nonspecific binding to probes. All microarray data is MIAME-compliant and has been uploaded to the EMBL-EBI ArrayExpress database (<http://www.ebi.ac.uk/arrayexpress/>) along with extensive annotations on both experimental and analytical methods as well as all raw and normalized data (accession: E-MEXP-2806).

Differential gene expression analysis

Gene expression analyses were performed using GeneSpring GX 9.0 software (Agilent Technologies,

Santa Clara, CA). After GC-RMA normalization without baseline transformation, the microarray data were then filtered by expression (20–100% in at least one of the three samples from each segment of the BP) to exclude genes expressed only at very low levels in all samples. In cases of probeset redundancy, median expression values were used. Differentially expressed genes were identified by using a fold-change cutoff of 2 and then performing an unpaired *t* test ($p < 0.05$) after Benjamini–Hochberg correction for multiple comparisons. R version 2.10.1 (www.r-project.org) was used to generate a heat map using the HeatPlus add-on in the Bioconductor package.

Quantitative PCR validation of microarray expression data

In order to validate the microarray data, quantitative PCR was performed on 15 detected genes. Six of these genes were upregulated in the HF relative to the LF region, and nine were upregulated in the LF relative to the HF region. The differentially expressed genes validated by quantitative PCR (qPCR) were highly expressed in at least one region and chosen to span a range in fold-change differences between the HF and LF regions, from 2.33 to 30.61.

The 15 genes that were validated are brain-derived neurotrophic factor, glutamate receptor 2, medium neurofilament, aquaporin 5, chordin-like 1, docking protein 7, ret proto-oncogene, SLIT, and NTRK-like family member 4, wnt inhibitory factor 1, integrin A1, potassium large conductance calcium-activated channel, subfamily M, alpha member 1 (KCNMA1, Slo; total and STREX exon), potassium voltage-gated channel, shaker-related subfamily, beta member 1 (KCNAB1), potassium voltage-gated channel, shaker-related subfamily, beta member 2 (KCNAB2), transient receptor potential cation channel, subfamily C, member 1 (TRPC1), and sodium channel, voltage-gated, type II, alpha subunit (SCN2A). The RNA samples were the same ones used for microarray analysis for all genes except KCNMA1 (total and STREX containing only) and TRPC1. Total Slo (KCNMA1) expression and expression of the Slo exon STREX were determined in the HF, MF, and LF segments of the BP to assess for expression gradients. At least three samples, each comprised of three BP segments, were used. Expression of the 18S ribosomal subunit was also assessed to allow for normalization of total RNA levels between samples using the $2^{-\Delta\Delta C_T}$ method (Schmittgen and Livak 2008). Primer 3 (Rozen and Skaletsky 2000) was used to design intron spanning primer pairs that were validated by melting curve analysis.

Five micrograms of RNA was isolated from each sample as described above and used to create first-strand cDNA using oligo-dT primers. Because exten-

sive genomic contamination was made unlikely by the use of oligo-dT primers and confirmed not to be present by Bioanalyzer measurements, RNA samples were not treated with DNase. qPCR was performed using the SYBR Green Supermix reagent (Bio-Rad, Hercules, CA) on an iCycler system (Bio-Rad, Hercules, CA). To establish the sensitivity of our qPCR methodology, reactions were run with serial dilutions of amplified 18S cDNA of known concentrations to ensure that the correct product (i.e., by band size and melting temperature) could be amplified with only several copies in a well. Each reaction was run in triplicate, and the data was averaged for each cDNA sample and primer pair combination. Only those fold-changes with a 95% confidence interval that did not include the value 1 were considered significant. A fold-change of 1 between two conditions would indicate that the expression level is exactly the same in both conditions, the null hypothesis of this test. Therefore, one can conclude with 95% certainty that a fold-change interval that does not overlap with a value of 1 represents a real change in gene expression.

Gene set descriptions

GSEA was performed to gain insights into the functional relevance of tonotopic gene expression gradients using GSEA version 2 software (Subramanian et al. 2005). In a GSEA, genes are first ranked by their association with the class distinction of the comparison being made (e.g., HF versus LF). In other words, the genes most consistently overexpressed in the HF samples were ranked at one end of the list, and those most overexpressed in the LF samples were ranked at the other end. GSEA asks whether the genes that make up a particular gene set are overrepresented at either end of the list, rather than randomly distributed throughout. This question was answered by calculating for every gene set a running sum statistic known as the enrichment score (ES). The ES can be thought of as a running tally that is proportional to the number of genes in a set that are upregulated with

a particular manipulation. Each ES was normalized to gene set size to produce a normalized enrichment score (NES). The statistical significance of each NES was determined by comparing that NES to the distribution of ESs generated by randomly permutating the genotype class labels. Both the p value and false discovery rate (FDR, q value) were calculated for each set. Gene sets whose NES had an associated FDR less than 0.25 and a p value less than 0.05 were considered significantly enriched.

The GeneSpring processed data from the 38,535 original probes was collapsed into 13,159 genes based on gene symbols. Some genes were assigned to one or multiple gene sets downloaded with the GSEA package. The mammalian gene set package included 837 gene sets, 50 of which were excluded by gene set size criteria (15–50), leaving 783 to be included in our analysis. One thousand one hundred ninety-seven out of the 1,892 curated gene sets also met this criterion (Table 1). The GSEA parameters used were as follows: metric=signal to noise; permutation number=1,000; gene size minimum=15; gene size maximum=500; enrichment statistic=classic; permutation type=gene set.

Gene set descriptions

Two different gene set packages were used, both of which were downloaded directly from the Broad Institute Website (www.broad.mit.edu/gsea). To assess for tonotopic gradients in miRNA and transcription factor activity in the chicken gene expression data, a GSEA was performed using a gene set package called “c3.all.v2.5.symbols,” which was obtained from the BROAD Institute Website (Xie et al. 2005). This package includes gene sets defined by the presence of transcription factor motifs and predicted miRNA binding sites. Because the genes in each set of this package share regulatory motifs that are conserved across human, mouse, rat, and dog genomes, they will be referred to as the “mammalian gene sets.” The motifs used come from Xie et al. (2005) and the TRANSEAC database and include sets of genes sharing particular 3'-UTR miRNA binding motifs.

TABLE 1

Shown are the number of mammalian and curated gene sets that were significantly enriched ($p < 0.05$ and false discovery rate < 0.25) in the high-frequency (HF), middle-frequency (MF), or low-frequency (LF) segments of the basilar papilla for the HF vs. LF, HF vs. MF, and MF vs. LF comparisons

	<i>HF vs. LF</i>		<i>HF vs. MF</i>		<i>MF vs. LF</i>	
	<i>Up in HF</i>	<i>Up in LF</i>	<i>Up in HF</i>	<i>Up in MF</i>	<i>Up in MF</i>	<i>Up in LF</i>
Mammalian	56/783	18/783	1/783	66/783	163/783	13/783
Curated	293/1,197	82/1,197	170/1,197	123/1,197	231/1,197	91/1,197

There are 783 mammalian gene sets and 1,197 curated gene sets that met the size criteria indicated in the text

To assess the functional relevance of the pattern of differential gene expression, GSEA was performed using a gene set package called “c2.all.v2.5.symbols” which was also downloaded from the BROAD Institute Website. This package defines curated sets of genes based on specific experimental findings from experiments on human and animal model tissue. This package includes both canonical pathways and chemical/genetic perturbations based gene sets. These gene sets will be referred to as the “curated gene sets.” References for all curated gene sets are provided on the BROAD Website.

To ascertain whether any of the tonotopic gene expression gradient is attributable to protein kinase activation, two additional GSEAs were performed by generating gene sets from available data sets. To assess for tonotopic activity of protein kinase A (PKA), a set of genes putatively upregulated with increased PKA activity was used. Specifically, the data used was raw Affymetrix whole-genome microarray data from a previously reported experiment describing gene expression differences in the chicken BP after 24-h exposure to forskolin (100 μ M), an adenylate cyclase activator which increases intracellular cAMP levels and therefore PKA activity (Frucht et al. 2010). These data were processed to generate a list of significantly (fold-change > 2, p value < 0.05) differentially expressed genes. The list of 39 affected genes was used for GSEA. A different data set was processed in the same fashion to produce a set of genes whose expression is putatively affected by protein kinase C (PKC) for use in a GSEA. This particular data set was from a previously reported experiment in which transcription was profiled with and without PMA-induced activation of PKC in human MM6 cells (Yu et al. 2008). The set of 3,456 genes that were differentially expressed (fold-change > 2, p value < 0.05) following PMA activation was used in a GSEA to look for evidence of tonotopic PKC activity.

RESULTS

Gene expression analysis statistics

We report here a systematic comparison of genome-wide expression along the tonotopic axis of the chicken auditory epithelium using Affymetrix whole-genome chicken microarrays. Zero-day-old chickens were used because this developmental time point succeeds the onset of hearing (Gottlieb 1965). The complete data set (included as [Supplemental Data](#)) should therefore be of interest to those studying expression and functional gradients along the tonotopic axis of the inner ear.

To examine gene expression gradients along the tonotopic axis of BPs, cochlear ducts were explanted and sensory epithelia were immediately isolated, microdissected, and sectioned into HF, MF, and LF segments (Fig. 1). Out of the 38,535 probe sets on the Affymetrix chicken array, 2,663 were differentially expressed between the HF and LF segments; 303 were differentially expressed between the HF and MF segments, and 1,306 genes were differentially expressed between the MF and LF segments. The complete list of differentially expressed genes for each of the three comparisons (i.e., HF vs. LF, HF vs. MF, MF vs. LF) are included as [Supplemental Data](#). A proportional Venn diagram clearly indicates that far more genes are differentially expressed between the two extreme ends of the epithelium than between the MF segment and either of the two extremes (Fig. 1). This is consistent with the notion that most genes are being expressed differentially along the tonotopic axis in an apical-to-basal gradient. Gene expression data for all genes on the array (Tables S1, S2, and S3) as well as only the subset of genes identified as differentially expressed (Tables S4, S5, and S6) are included as supplementary material.

qPCR confirms microarray data

qPCR was performed on select genes in order to validate the microarray data. Primers were designed for 15 genes, six of which were upregulated in the HF segment and nine of which were upregulated in the LF segment (Table 2). These genes were selected to span a range of fold-changes in both directions based on their high level of expression in at least one segment of the BP. Some genes were selected because they are specifically known to have an important role in the inner ear and are known to be tonotopically expressed in the BP (e.g., *KCNMA1*). However, most of the genes chosen were selected because their expression pattern in the BP was previously uncharacterized. Out of the 15 genes examined, qPCR confirmed the directionality of all 15. The fold-changes of 12 of these 15 genes (80%) were significantly different from a value of 1 (Table 2), confirming their differential expression as detected by microarray. These findings validate the microarray results, so further analyses were performed on the gene expression data set.

Slo (*KCNMA1*) and its alternatively spliced STREX exon were tested by qPCR in the HF, MF, and LF segments of the BP (Fig. 2). Both showed a clear tonotopic expression gradient with higher expression in the LF than in the MF or HF segments (one-way ANOVA, $p < 0.05$). Slo expression at the HF end was

TABLE 2

qPCR validation of gene expression data

Gene symbol	Gene name	Microarray		qPCR	
		Average fold-change (HF/LF)	Corrected p value	Average fold-change (HF/LF)	Significant (?)
AQP5	Aquaporin 5	1/14.84	0.011	1/1.40	No
		1/23.84	0.013		
		1/15.83	0.041		
BDNF	Brain-derived neurotrophic factor	1/17.49	0.0027	1/2.42	Yes
GRIA2	Glutamate receptor, ionotropic, AMPA 2	1/4.95	0.006	1/2.58	Yes
		1/2.51	0.0068		
KCNAB1	Potassium voltage-gated channel, shaker-related subfamily, beta member 1	1/9.46	0.0023	1/2.67	Yes
KCNAB2	Potassium voltage-gated channel, shaker-related subfamily, beta member 2	1/2.73	0.002	1/2.27	Yes
KCNMA1 (Slo)	Potassium large conductance calcium-activated channel, subfamily M, alpha member 1	1/6.82	0.025	1/2.94	Yes
NEFM	Neurofilament, medium polypeptide 150 kDa	1/21.75	0.0029	1/7.09	Yes
		1/25.90	0.020		
SCN2A	Sodium channel, voltage-gated, type II, alpha subunit	1/2.33	0.015	1/1.31	No
		1/8.55	0.0028		
TRPC1	Transient receptor potential cation channel, subfamily C, member 1	1/2.77	0.035	1/2.54	Yes
CHRD1	Chordin-like 1	7.039	0.0032	2.86	Yes
DOK7	Docking protein 7	6.18	0.0034	1.43	Yes
ITGA1	Integrin, alpha 1	30.61	0.0034	1.01	No
RET	ret Proto-oncogene	8.00	0.012	7.11	Yes
		6.22	0.014		
SLITRK4	SLIT and NTRK-like family, member 4	6.18	0.0077	3.54	Yes
		6.69	0.009		
WIF1	WNT inhibitory factor 1	18.24	0.011	1.74	Yes

Shown are qPCR and microarray data for genes selected for qPCR validation

Genes were selected to span a range of fold-change differences between the low- and high-frequency segments of the basilar papilla in both directions. Multiple microarray values represent redundant probe sets for the same gene. Significant fold-changes by qPCR have a 95% confidence interval excluding 1

34.1% of that at the LF end, whereas HF expression of STREX was 10.7% of that at the LF end. These results show a steeper tonotopic gradient for STREX than for Slo, suggesting that the proportion of Slo transcripts including the STREX exon decreases going from the LF to HF segments.

Tonotopic expression of structural proteins

Among the 2,663 genes found to be differentially expressed between the HF and LF segments were some genes known to have important functions in the inner ear, as well as many other genes whose functional significance is unknown (Table 3). As shown in Table 3, there was differential expression of the actin cross-linkers plastin 1 (up in LF) and plastin 2 (up in HF). Interestingly, some myosin transcripts were also tonotopically expressed. Myosin XVa expression was

higher in the LF end of the BP while myosin IIIa transcription was higher in the HF end.

Tonotopic expression of sodium, potassium, and calcium channels

Many sodium, potassium, and calcium channels were differentially transcribed between the HF and LF ends (Table 4). An expression heat map shows that most of these genes are expressed in a gradient along the tonotopic axis (Fig. 3). Interestingly, the expression patterns of most of these channels have not been previously described. Specifically, multiple calcium-gated (i.e., KCNMA1, KCNMB4), voltage-gated (i.e., KCNQ2, KCNG4, KCNF1, KCND2, KCNAB1, KCNAB2), and inward-rectifying (i.e., KCNJ2, KCNJ15) potassium channels were all upregulated in the LF end. There was also differential expression of

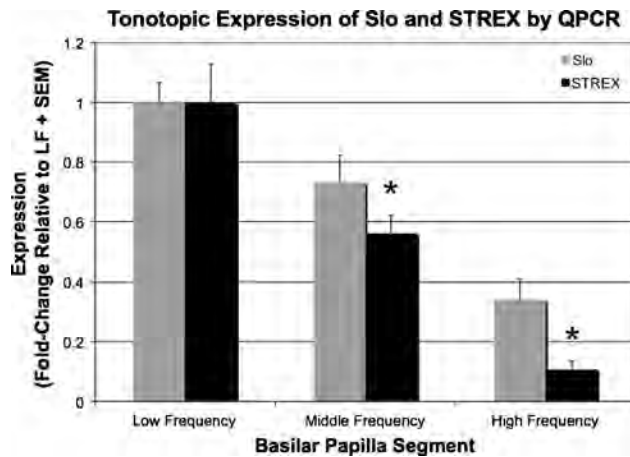


FIG. 2. Slo and the Slo exon STREX are transcribed tonotopically. Shown are the relative expression levels of both Slo and its alternatively spliced STREX exon in the low- (LF, $n=3$), middle- (MF, $n=3$), and high-frequency (HF, $n=4$) segments of the post-hatch chicken basilar papilla as determined by qPCR. Expression levels were normalized first to 18S expression, then respectively to Slo and STREX expression levels in the LF segment. A clear tonotopic gradient can be appreciated for both Slo and STREX with expression that significantly decreased from the LF region to the HF region (one-way ANOVA, $p<0.05$). The fold-change differences of LF versus MF and LF versus HF were significantly different between STREX and Slo, indicating a steeper gradient for STREX than for Slo (t tests, $p<0.05$).

voltage-gated calcium channels (i.e., *CACNA1B* was up in the LF end; *CACNA2D1* was up in the HF end) between the two ends of the BP. Additionally, there were sodium channels found by microarray differentially expressed between the HF and LF segments; *SCN2A* (voltage-gated) and *SCNN1A* (nonvoltage-gated) were up in the HF end of the BP, whereas *SCN3B* (voltage-gated) was up in the LF end. However, *SCN2A* was found by qPCR to not

be differentially expressed. Finally, three transient receptor potential (TRP) channels were found to be tonotopically expressed. *TRPC1* transcription was higher at the LF end, a finding confirmed by qPCR (Table 2). *TRPC3* and *TRPM3* were found by microarray to be upregulated in the HF end, but were undetectable by qPCR. These observations suggest important functional roles for some of these channels in the chicken inner ear.

Gene set enrichment analysis results

In order to determine the large-scale functional significance of differential gene expression, a GSEA was performed using manually curated gene sets downloaded from the Broad Institute Website. This package contains gene sets comprised of genes found by individual experiments to be associated with specific phenotypes in a variety of systems. Of the 1,197 gene sets included in this package, 293 were significantly enriched in the HF end whereas 82 were enriched in the LF end (Table 1). Interestingly, many gene sets comprised of genes associated with hematopoietic stem cells (HSC) are significantly enriched in the HF end of the BP, while only one HSC gene set is enriched in the LF end (Table 5). This finding is suggestive of a subpopulation of cells with HSC-like gene expression patterns in the HF end of the chick BP. GSEA statistics for all curated gene sets are included as supplemental material (Tables S7, S8, and S9).

To determine whether any miRNAs or transcription factors are differentially active between the HF and LF segments, an additional GSEA was performed using a gene set package with gene sets comprised of

TABLE 3

Shown are some of the genes possibly related to the transduction apparatus (*PCDH15*, *TRPC1*, *TRPC3*, *TRPM3*), genes known to interact with actin (*PLS1*, *PLS3*, *RCJMB04_3e19*), and myosins (*MYO3A*, *MYO15A*) found by microarray to be differentially expressed (fold-change>2, p value<0.05) between the high- and low-frequency segments of the basilar papilla

Gene symbol	Gene name	Average fold-change (HF/LF)	Corrected p value
MYO15A	Myosin XVA	1/2.33	0.0072
MYO3A	Myosin IIIA	3.34	0.049
PCDH15	Protocadherin 15	1/2.28	0.027
PLS1	Plastin 1 (I isoform)	1/2.87	0.0029
		3.12	0.0078
PLS3	Plastin 3 (T isoform)	2.81	0.0078
RCJMB04_3e19	Twinfilin, actin-binding protein, homolog 2 (<i>Drosophila</i>)	2.43	0.0059
		2.93	0.0051
TRPC1	Transient receptor potential cation channel, subfamily C, member 1	1/2.77	0.035
TRPC3	Transient receptor potential cation channel, subfamily C, member 3	3.55	0.023
TRPM3	Transient receptor potential cation channel, subfamily M, member 3	24.24	0.003

Multiple values are displayed for the probesets with redundancy

TABLE 4

Shown are some of the genes found by microarray to be differentially expressed (fold-change > 2, *p* value < 0.05) between the high- and low-frequency segments of the basilar papilla that are ion channels

<i>Gene symbol</i>	<i>Gene name</i>	<i>Average fold-change (HF/LF)</i>	<i>Corrected p value</i>
CACNA1B	Calcium channel, voltage-dependent, N type, alpha 1B subunit	1/2.46	0.036
CACNA2D1	Calcium channel, voltage-dependent, alpha 2/delta subunit 1	2.96	0.028
KCNAB1	Potassium voltage-gated channel, shaker-related subfamily, beta member 1	1/9.46	0.0023
KCNAB2	Potassium voltage-gated channel, shaker-related subfamily, beta member 2	1/2.73	0.0020
KCND2	Potassium voltage-gated channel, Shal-related subfamily, member 2	1/2.59	0.030
KCNF1	Potassium voltage-gated channel, subfamily F, member 1	1/61.46	0.0035
KCNG4	Potassium voltage-gated channel, subfamily G, member 4	1/7.53	0.0056
KCNJ15	Potassium inwardly rectifying channel, subfamily J, member 15	1/40.82 1/26.59	0.0019 0.0012
KCNJ2	Potassium inwardly rectifying channel, subfamily J, member 15	1/69.27	0.0035
KCNK5	Potassium channel, subfamily K, member 5	1/3.86	0.0093
KCNMA1	Potassium large conductance calcium-activated channel, subfamily M, alpha member 1	1/6.82	0.025
KCNMB4	Potassium large conductance calcium-activated channel, subfamily M, beta member 4	1/2.27	0.0045
SCN2A	Sodium channel, voltage-gated, type II, alpha subunit	2.33/1 8.55/1	0.015 0.0027
SCN3B	Sodium channel, voltage-gated, type III, beta	1/3.58	0.020
SCNN1A	Sodium channel, nonvoltage-gated 1 alpha	2.85/1 2.62/1	0.020 0.015
TRPC1	Transient receptor potential cation channel, subfamily C, member 1	1/2.77	0.035
TRPC3	Transient receptor potential cation channel, subfamily C, member 3	3.55	0.022
TRPM3	Transient receptor potential cation channel, subfamily M, member 3	24.24	0.0030

Multiple values are displayed for the probesets with redundancy. Various sodium, potassium, and calcium channels are all differentially expressed along the tonotopic axis of the chick basilar papilla. Three of the genes in this table were also tested by qPCR (KCNAB1, KCNAB2, SCN2A; see Table 2). Of these three genes, two are also found to be differentially expressed by qPCR (fold-change 95% confidence interval does not include 1)

genes containing particular transcription factor and miRNA recognition sites. Fifty-six out of 783 of the gene sets in this set are enriched in the HF end, whereas 18 of the gene sets are significantly upregulated in the LF end (Table 1). Interestingly, many of the differentially expressed gene sets are miRNA ("MIR") gene sets (Table 6). These results suggest tonotopic expression and therefore some functional relevance of these particular miRNAs in the chicken inner ear. GSEA statistics for all of these motif-based gene sets are included as supplemental material (Tables S10, S11, and S12).

GSEA was also performed using a PKC-based gene set and a PKA-based gene set as described in the [Methods](#). A set of genes found to be differentially

expressed following activation of PKC using PMA in human MM6 cells was significantly enriched in the HF end of the BP (Table 5; FDR < 0.001). Additionally, a set of genes differentially expressed in the chicken BP after 24 h of forskolin-induced PKA activation were significantly enriched in the LF end (Table 5; FDR = 0.002). These results suggest differential activation and/or expression of these kinases themselves along the tonotopic axis of the chicken BP.

DISCUSSION

Reported here are 2,663 genes that are differentially expressed between the HF (i.e., proximal) and LF

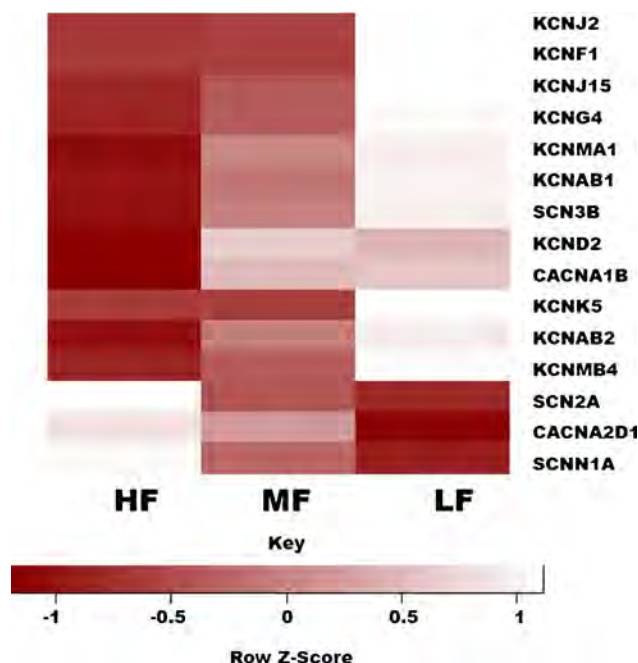


FIG. 3. Many ion channels are expressed in a gradient along the tonotopic axis of the chicken basilar papilla. Shown is a heat map showing normalized expression levels in the high- (HF), middle- (MF), and low-frequency (LF) segments of the basilar papilla for 15 ion channel genes. The depicted expression values are all normalized relative to the average for each row (i.e., the average expression for a particular gene across all three segments). As shown in the color key, *light rectangles* represent higher expression levels than *dark rectangles*. Most of the genes shown appear to be expressed in a gradient along the tonotopic axis.

(i.e., distal) thirds of the BP. Among the list of genes found to be differentially expressed are many that would be predicted to show this pattern, as well as many with a previously uncharacterized pattern of

expression or functional activity in the BP. Our data revealed that two inward-rectifying potassium channels (KCNJ2, KCNJ15) are transcribed at higher levels at the apical end, an interesting observation given that previous work has shown preferential expression of inward-rectifying potassium channels at the LF end of the BP (Fuchs et al. 1990; Fuchs 1992; Navaratnam et al. 1995; Wu et al. 1996). Also suggested by our microarray data is relative upregulation of a number of voltage-gated potassium channels in the LF end (Table 4), confirming physiological data on the presence of voltage-gated potassium currents preferentially found in LF hair cells of the turtle BP (Fuchs et al. 1990; Goodman and Art 1996). KCNMA1 was identified by our microarray data to be upregulated in the LF end of the BP, confirming recently reported results (Miranda-Rottmann et al. 2010). Similarly, there were increased amounts of the sodium channel transcript SCN3B in the LF end and of SCNN1A in the HF end. While sodium channels have not been observed in the chicken, hair cells from the LF end of alligator BP were found to contain TTX-sensitive currents (Evans and Fuchs 1987). Actin was detected by our array but found not to be tonotopically expressed (data not shown), a finding that is intuitive given that the total amount of actin per hair cell does not vary tonotopically in chickens (Tilney and Tilney 1988). The calcium binding protein calbindin was previously found to be expressed at higher levels in basal than in apical hair cells (Navaratnam et al. 1995; Navaratnam et al. 1997; Hiel et al. 2002), a finding that was not confirmed by our microarray data. However, this observation is likely the result of the 3' bias of the Affymetrix chicken array. The NCBI

TABLE 5

Shown are all hematopoietic stem cell (HSC) and protein kinase gene sets that were significantly enriched ($p < 0.05$, false discovery rate {FDR} < 0.25) in the high-frequency (HF) versus low-frequency (LF) curated gene set enrichment analysis

Gene set	P value	FDR	Up in HF or LF
STEMCELL_COMMON_UP	<0.001	<0.001	HF
HSC_EARLYPROGENITORS_SHARED	0.0020	0.0037	HF
HSC_EARLYPROGENITORS_FETAL	<0.001	0.0049	HF
HSC_EARLYPROGENITORS_ADULT	<0.001	0.0051	HF
HSC_LATEPROGENITORS_SHARED	<0.001	0.0087	HF
HSC_MATURE_ADULT	<0.001	0.0098	HF
HSC_MATURE_FETAL	<0.001	0.016	HF
HADDAD_HSC_CD7_UP	0.0021	0.018	HF
HSC_LATEPROGENITORS_ADULT	0.0041	0.018	HF
HSC_HSCANDPROGENITORS_SHARED	0.0098	0.040	HF
HSC_HSCANDPROGENITORS_FETAL	0.0064	0.044	HF
HSC_MATURE_SHARED	0.0080	0.046	HF
HSC_HSCANDPROGENITORS_ADULT	0.0058	0.050	HF
BYSTRYKH_HSC_BRAIN_TRANS_GLOCUS	0.0060	0.13	LF
BYSTRYKH_HSC_CIS_GLOCUS	0.049	0.23	LF
PKC	<0.001	<0.001	HF
PKA	0.002	0.002	LF

There are far more HSC gene sets associated with the HF end of the basilar papilla. The PKC and PKA gene sets shown here are as described in [Methods](#)

TABLE 6

Shown are all miRNA (MIR) gene sets that were significantly enriched ($p < 0.05$, false discovery rate {FDR} < 0.25) in the high-frequency (HF) versus low-frequency (LF) mammalian gene set enrichment analysis

Gene set	P value	FDR	Up in HF or LF
ATGTACA,MIR-493	<0.0001	0.0013	HF
GTGCAAA,MIR-507	<0.0001	0.17	HF
TCTATGA,MIR-376A,MIR-376B	0.0039	0.13	HF
AAGCCAT,MIR-135A,MIR-135B	0.0043	0.18	HF
ATGTTAA,MIR-302C	0.0019	0.17	HF
TTTGCAAG,MIR-518A-2	0.0021	0.16	HF
GCACCTT,MIR-18A,MIR-18B	0.0098	0.16	HF
TTTGTAG,MIR-520D	0.0080	0.15	HF
GTGCCAA,MIR-96	0.00763	0.19	HF
ATATGCA,MIR-448	0.0059	0.18	HF
TGCCTTA,MIR-124A	0.0077	0.18	HF
ATACCTC,MIR-202	0.016	0.19	HF
ACTGTGA,MIR-27A,MIR-27B	0.014	0.20	HF
ACACTAC,MIR-142-3P	0.016	0.20	HF
TCTGATC,MIR-383	0.018	0.21	HF
AACTGAC,MIR-223	0.0060	0.23	HF
CAAGGAT,MIR-362	0.014	0.23	HF
CAGTATT,MIR-200B,MIR-200C,MIR-429	0.024	0.24	HF
TGTTTAC,MIR-30A-5P,MIR-30C,MIR-30D,MIR-30B,MIR-30E-5P	0.027	0.25	HF
GTGCCTT,MIR-506	0.024	0.25	HF
TTGCCAA,MIR-182	0.027	0.25	HF
AACTGGA,MIR-145	0.027	0.25	HF

No miRNA gene sets were significantly enriched in the LF end of the basilar papilla. These results suggest that the above miRNAs are upregulated in the LF end, causing downregulation of their targets in the LF end, therefore relative HF upregulation

Module Maker lists all chicken calbindin mRNAs (*Gallus gallus* Build 2.1, Chromosome: 2, Contig: NW_001471651.1) including ESTs, the vast majority of which (24/25) do not contain the sequence targeted by the calbindin probeset on this array. In contrast, previous work showing tonotopicity of calbindin expression used qPCR primers designed to amplify a portion of the transcript that is present in all 25 variants, and these results are therefore much more reliable (Navaratnam et al. 1995, 1997; Hiel et al. 2002). That calbindin was not found by microarray to be tonotopically expressed therefore likely reflects the spatial distribution of an exceedingly rare splice variant. Despite the known limitations of microarrays, these observations and the good correlation with qPCR serve to instill confidence that this data set generally reflects actual gene expression levels.

Among the genes examined here are genes whose products are known components of stereocilia tip-links. For example, the stereocilia tip-link protein protocadherin-15 was found by microarray to be upregulated in the LF end of the BP. However, protocadherin-15 was not detectable by qPCR (data not shown), suggesting that its identification by microarray was likely a false-positive result. Previous work has also shown a temporal but no appreciable spatial gradient of protocadherin-15 in the postnatal mouse organ of Corti (Lelli et al. 2009). The same study showed that protocadherin-15 expression is

relatively high in embryonic mice, but drops to extremely low levels after birth. Our data suggest that protocadherin-15 is expressed at extremely low levels in the post-hatch chicken BP as well. Further work should aim to further characterize the spatiotemporal expression gradient of protocadherin-15 in BPs from animals of different ages to determine whether the pattern mirrors that seen in mammals.

KCNMA1, the transcript encoding the BK calcium-activated potassium channel, was upregulated in the LF end of the BP, confirming recently reported data (Miranda-Rottmann et al. 2010). However, the results from both studies are in apparent disagreement with both protein expression (Samaranayake et al. 2004) and electrophysiological data (Art et al. 1986, 1995) suggesting higher BK protein expression in the HF end of the BP. This discrepancy is likely due to post-transcriptional control of KCNMA1 (Bai et al. 2010, under review). There is precedent for this observation, as previous work has shown dissociation between mRNA expression and protein levels (Gygi et al. 1999; Ghaemmaghami et al. 2003). We have since established that Slo delivery to the surface of the cell is inhibited by beta-1 and beta-4 subunits (Bai et al. 2010, under review), which are expressed at higher levels in LF hair cells (Ramanathan et al. 1999, 2000; Bai et al. 2010, under review).

The TRP channel TRPC1 was found by qPCR to be upregulated in the LF end of the BP by both micro-

array and qPCR. Differential expression of TRP channels along the tonotopic axis is of particular interest given that they are among a small subset of channel families thought to possess the characteristics required of the as yet unidentified mechanoelectrical transduction (MET) channel in the inner ear (reviewed in Fettiplace 2009). Members of the TRP family are known to act as mechanically gated ion channels in a variety of species (reviewed in Christensen and Corey 2007). TRP proteins are capable of forming heteromultimeric channels with conductances that vary with channel composition (Bai et al. 2008; Köttgen et al. 2008). Channel composition may therefore partly give rise to the tonotopic gradient in MET channel conductance that is seen along the BP (Ricci et al. 2003). The present findings suggest closer examination of TRPC1 as a potential component of the transduction apparatus, especially in light of this protein's known expression in the organ of Corti (Cuajungco et al. 2007).

Given the limitations of microarray data sets, GSEA was performed to gain more meaningful insight into the spatial patterns of gene expression in the BP. Previous work has confirmed the utility of using GSEA to identify biologically important players in the BP (Frucht et al. 2010). One advantage of this approach is that gene sets found to be significantly enriched can be interpreted with confidence as they are not systematically biased by false-positives and false-negatives, which serve only to increase background noise in the data and decrease the sensitivity of this computational approach. Therefore, some genes sets that are actually enriched may be missed, but positive GSEA results are likely to reflect real gene expression patterns.

The GSEA results described here shed new light on the intricacy of tonotopicity in the post-hatch chicken BP. Interestingly, many sets of genes associated with HSC were enriched in the HF end of the BP. This finding suggests that there may exist a subpopulation of cells in the BP with properties similar to those of HSCs in the BP. HSCs, much like non-mammalian vertebrate hair cells, are quiescent until stimulated by external cues to divide and differentiate into new hair cells (Ryals and Rubel 1988; Jude et al. 2008; Narbonne and Roy 2008). The tonopocity of this pattern of gene expression is interesting, given that the HF end of the BP is more susceptible than the LF end to death following ototoxic insult (Matz et al. 1965; Johnstone and Boyle 1967). It may be more than merely coincidental that HSC genes are enriched in the HF end of the BP, which is the end of the BP that is most susceptible to damage by ototoxins. In birds, following ototoxic or traumatic injury, the entire auditory sensory epithelium regenerates so that morphology and architecture are almost

completely restored (reviewed in Stone and Cotanche 2007). The present results therefore beg the question, are there as yet unobserved differences in regenerative mechanisms and/or capacity along the tonotopic axis of the BP? Further experimentation will be required to definitively answer this question.

In addition to the HSC gene sets, GSEA revealed that many sets of predicted targets of specific miRNAs were enriched in the HF end of the BP, suggesting upregulation of these miRNAs in the LF end. It is striking that all 22 miRNA gene sets that were significantly enriched showed this directionality. Myriad miRNA have already been shown not only to be expressed in the inner ear (Weston et al. 2006; Sacheli et al. 2009; Wang et al. 2010), but also to play an important role in inner ear development (Friedman et al. 2009; Soukup 2009; Soukup et al. 2009), function (Lewis et al. 2009; Mencia et al. 2009), and hair cell regeneration (Frucht et al. 2010). The present results suggest a tonotopic gradient in activity and accordingly expression in the chicken BP. Tonopocity of miRNA activity in the post-hearing onset chicken suggest a role for these specific miRNAs in inner ear function.

GSEA of tonotopic data were consistent with increased activity of PKA at the low-frequency end of the papilla and PKC activity at the high-frequency end of the BP. These findings have implications for electrical tuning. The primary determinant of changing oscillatory frequency in membrane potential is the changing kinetic properties of the BK channel (Art et al. 1986, 1995). Specifically, deactivation times in response to a step voltage decreases with increase in characteristic frequency (Art et al. 1986, 1995). Thus, the inclusion of the STREX exon, which is preferentially expressed in LF hair cells, prolongs BK channel deactivation times consistent with native BK channels at this location (Art et al. 1986, 1995; Xie and McCobb 1998). Similarly, the presence of increased PKA activity in low-frequency hair cells is consistent with the longer deactivation times produced by addition of PKA (with the STREX exon and the beta-4 subunit) in heterologous expression systems (Petrik and Brenner 2007). The inference that PKC is increased in high-frequency hair cells corroborates the physiological finding of shorter open times in higher-frequency hair cells (Art et al. 1995). PKC has been shown to shorten BK channel open time (Zhou et al. 2010).

It is worth emphasizing that all of these experiments were performed on tissue from 0-day-old chickens. This age was selected for study because, unlike in mammals, there is much evidence that, in chickens, this time point is preceded by both acquisition and maturation of hearing. This observation is confirmed by behavioral (i.e., whole animal), physiological, and molecular evidence. For example, not

only do chickens at embryonic day 19 have evoked cochlear nuclei responses (Saunders et al. 1973, 1974), but the frequency tuning and threshold levels of embryonic chickens resemble those of adult animals (Rebillard and Rubel 1981). Furthermore, acquisition of BK currents necessary for electrical tuning is measurable in embryonic chickens and is coincident with hearing onset (Sokolowski et al. 1993). Interestingly, recent work suggests that part of this maturation process may involve developmental switching in the splice variants of BK channel subunit transcripts (Kim et al. 2010). Moreover, work in our lab has confirmed an identical spatial expression pattern of transcripts encoding KCNMA1 and its related proteins between 0-day-old and 14-day-old chickens (Bai and Navaratnam, unpublished observations). It therefore seems unlikely that genes found to be differentially expressed here represent transient developmental changes rather than true stable tonotopic expression, but this possibility cannot be definitively excluded. Future work should therefore aim to characterize these expression gradients in more mature BPs as well. An additional point that requires consideration is that, as was likely the case with calbindin, the microarray probesets may only be detecting a specific transcript variant when in reality there may be many additional variants in this tissue, perhaps some of which are tonotopically expressed. Therefore, in addition to the well-known methodological limitations of microarrays, there are also biological implications to the sensitivity of the approach.

In summary, the present results suggest that 2,663 genes are differentially expressed between the HF and LF thirds of the post-hatch chicken BP. While many of these genes likely reflect tonotopic differences in hair cells, which are known to have varying properties, some of these genes may reflect tonotopic differences in non-sensory supporting cells as well. Among those genes identified as differentially expressed were many potassium, calcium, and sodium channels, the inner ear expression patterns of which have not been previously described. Given the large number of genes found to be differentially expressed between the HF and LF ends of the BP, there must be gene expression regulatory mechanisms underlying this expression pattern. The present results point to specific miRNA and transcription factors that may play an important role in the maintenance of these gene expression gradients. Because the frequency selectivity properties of hair cells in non-mammalian vertebrates seem to be attributable more to the physiological properties of individual cells than to physical properties of the basilar membrane, it would be interesting to eventually determine whether transfection with pre-miRNAs and/or transcription factors can alter the tonotopic axis.

ACKNOWLEDGMENTS

This work is part of a dissertation submitted to fulfill in part the requirements for the degree of Doctor of Philosophy at Yale University.

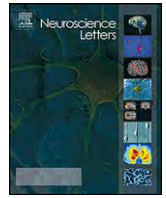
CSF was supported by NIH MSTP TG 2T32GM07205 and an Ohse Grant for Surgical Research at Yale School of Medicine. CSF, JSS, and DSN were supported by NIH/NIDCD grants DC 007894, DC 000273, and DC 008130. The authors would like to acknowledge the support of the National Organization for Hearing Research, which provided seed funding for this project to DSN. MU was supported by NIH Grant T15 LM07056 from the National Library of Medicine.

We thank Adam Thornberg and Shrikant Mane, PhD, Yale Keck Facility, for assistance with the RNA amplification and microarray hybridizations.

REFERENCES

- AFFYMETRIX I (2004) EUKARYOTIC SAMPLE AND ARRAY PROCESSING. GeneChip expression analysis technical manual. Santa Clara, CA, Affymetrix, Inc. 701021 Rev. 5:2.1.3–2.3.18
- AFFYMETRIX I (2009) GENECHIP. Expression analysis technical manual.
- ART JJ, CRAWFORD AC ET AL (1986) ELECTRICAL RESONANCE AND MEMBRANE CURRENTS IN TURTLE COCHLEAR HAIR CELLS. *Hear Res* 22:31–36
- ART JJ, WU YC ET AL (1995) THE CALCIUM-ACTIVATED POTASSIUM CHANNELS OF TURTLE HAIR CELLS. *J Gen Physiol* 105(1):49–72
- BAI C-X, GIAMARCHI A ET AL (2008) FORMATION OF A NEW RECEPTOR-OPERATED CHANNEL BY HETEROMERIC ASSEMBLY OF TRPP2 AND TRPC1 SUBUNITS. *EMBO Rep* 9(5):472–479
- BAI JP, SURGUCHEV A ET AL (2010) THE BETA-4 SUBUNIT INCREASES SLO RESPONSIVENESS TO PHYSIOLOGICAL CA²⁺ CONCENTRATIONS AND TOGETHER WITH BETA-1 REDUCES SURFACE EXPRESSION OF SLO IN HAIR CELLS. *Am J Physiol Cell Physiol* under review.
- CHRISTENSEN AP, COREY DP (2007) TRP CHANNELS IN MECHANOSENSATION: DIRECT OR INDIRECT ACTIVATION? *Nat Rev Neurosci* 8(7):510–521
- CRAWFORD AC, FETTIPLACE R (1981) AN ELECTRICAL TUNING MECHANISM IN TURTLE COCHLEAR HAIR CELLS. *J Physiol (Lond)* 312:377–412
- CUAJUNGCO MP, GRIMM C ET AL (2007) TRP CHANNELS AS CANDIDATES FOR HEARING AND BALANCE ABNORMALITIES IN VERTEBRATES. *Biochim Biophys Acta* 1772(8):1022–1027
- EVANS MG, FUCHS PA (1987) TETRODOTOXIN-SENSITIVE, VOLTAGE-DEPENDENT SODIUM CURRENTS IN HAIR CELLS FROM THE ALLIGATOR COCHLEA. *Biophys J* 52(4):649–652
- FETTIPLACE R (2009) DEFINING FEATURES OF THE HAIR CELL MECHANOELECTRICAL TRANSDUCER CHANNEL. *Pflugers Arch - Eur J Physiol* 458(6):1115–1123
- FRIEDMAN LM, DROR AA ET AL (2009) MICRORNAs ARE ESSENTIAL FOR DEVELOPMENT AND FUNCTION OF INNER EAR HAIR CELLS IN VERTEBRATES. *Proc Natl Acad Sci USA* 106(19):7915–7920
- FRUCHT CS, UDUMAN M ET AL (2010) GENE EXPRESSION ANALYSIS OF FORSKOLIN TREATED BASILAR PAPILLAE IDENTIFIES MICRORNA181A AS A MEDIATOR OF PROLIFERATION. *PLoS ONE* 5(7):e11502
- FUCHS PA (1992) IONIC CURRENTS IN COCHLEAR HAIR CELLS. *Prog Neurobiol* 39(5):493–505
- FUCHS PA, NAGAI T ET AL (1988) ELECTRICAL TUNING IN HAIR CELLS ISOLATED FROM THE CHICK COCHLEA. *J Neurosci* 8(7):2460–2467
- FUCHS PA, EVANS MG ET AL (1990) CALCIUM CURRENTS IN HAIR CELLS ISOLATED FROM THE COCHLEA OF THE CHICK. *J Physiol (Lond)* 429:553–568

- GHAEMMAGHAMI S, HUH W-K ET AL (2003) GLOBAL ANALYSIS OF PROTEIN EXPRESSION IN YEAST. *Nature* 425(6959):737–741
- GOODMAN MB, ART JJ (1996) VARIATIONS IN THE ENSEMBLE OF POTASSIUM CURRENTS UNDERLYING RESONANCE IN TURTLE HAIR CELLS. *J Physiol (Lond)* 497(Pt 2):395–412
- GOTTLIEB G (1965) PRENATAL AUDITORY SENSITIVITY IN CHICKENS AND DUCKS. *Science* 147:1596–1598
- GYGI SP, ROCHON Y ET AL (1999) CORRELATION BETWEEN PROTEIN AND mRNA ABUNDANCE IN YEAST. *Mol Cell Biol* 19(3):1720–1730
- HIEL H, NAVARATNAM DS ET AL (2002) TOPOLOGICAL AND DEVELOPMENTAL GRADIENTS OF CALBINDIN EXPRESSION IN THE CHICK'S INNER EAR. *J Assoc Res Otolaryngol* 3(1):1–15
- JOHNSTONE BM, BOYLE AJ (1967) BASILAR MEMBRANE VIBRATION EXAMINED WITH THE MÖSSBAUER TECHNIQUE. *Science* 158(799):389–390
- JUDE CD, GAUDET JJ ET AL (2008) LEUKEMIA AND HEMATOPOIETIC STEM CELLS: BALANCING PROLIFERATION AND QUIESCENCE. *Cell Cycle* 7(5):586–591
- KIM J-M, BEYER R ET AL (2010) EXPRESSION OF BK-TYPE CALCIUM-ACTIVATED POTASSIUM CHANNEL SPICE VARIANTS DURING CHICK COCHLEAR DEVELOPMENT. *J Comp Neurol* 518(13):2554–2569
- KÖTTGEN M, BUCHHOLZ B ET AL (2008) TRPP2 AND TRPV4 FORM A POLYMODAL SENSORY CHANNEL COMPLEX. *J Cell Biol* 182(3):437–447
- LELLI A, ASAI Y ET AL (2009) TONOTOPIC GRADIENT IN THE DEVELOPMENTAL ACQUISITION OF SENSORY TRANSDUCTION IN OUTER HAIR CELLS OF THE MOUSE COCHLEA. *J Neurophysiol* 101(6):2961–2973
- LEWIS MA, QUINT E ET AL (2009) AN ENU-INDUCED MUTATION OF miR-96 ASSOCIATED WITH PROGRESSIVE HEARING LOSS IN MICE. *Nat Genet* 41(5):614–618
- MATZ GJ, WALLACE TH ET AL (1965) THE OTOTOXICITY OF KANAMYCIN. A comparative histopathological study. *The Laryngoscope* 75(11):1690–1698
- MENCÍA A, MODAMIO-HØYBJØR S ET AL (2009) MUTATIONS IN THE SEED REGION OF HUMAN miR-96 ARE RESPONSIBLE FOR NONSYNDROMIC PROGRESSIVE HEARING LOSS. *Nat Genet* 41(5):609–613
- MIRANDA-ROTTMANN S, KOZLOV AS ET AL (2010) HIGHLY SPECIFIC ALTERNATIVE SPLICING OF TRANSCRIPTS ENCODING BK CHANNELS IN THE CHICKEN'S COCHLEA IS A MINOR DETERMINANT OF THE TONOTOPIC GRADIENT. *Mol Cell Biol* 1–45
- NARBONNE P, ROY R (2008) GENES THAT AFFECT BOTH CELL GROWTH AND POLARITY MEDIATE STEM CELL QUIESCENCE. *Front Biosci* 13:995–1002
- NAVARATNAM DS, ESCOBAR L ET AL (1995) PERMEATION PROPERTIES AND DIFFERENTIAL EXPRESSION ACROSS THE AUDITORY RECEPTOR EPITHELIUM OF AN INWARD RECTIFIER K⁺ CHANNEL CLONED FROM THE CHICK INNER EAR. *J Biol Chem* 270(33):19238–19245
- NAVARATNAM DS, BELL TJ ET AL (1997) DIFFERENTIAL DISTRIBUTION OF Ca²⁺-ACTIVATED K⁺ CHANNEL SPICE VARIANTS AMONG HAIR CELLS ALONG THE TONOTOPIC AXIS OF THE CHICK COCHLEA. *Neuron* 19(5):1077–1085
- PETRIK D, BRENNER R (2007) REGULATION OF STREX EXON LARGE CONDUCTANCE, CALCIUM-ACTIVATED POTASSIUM CHANNELS BY THE BETA4 ACCESSORY SUBUNIT. *Neuroscience* 149(4):789–803
- RAMANATHAN K, MICHAEL TH ET AL (1999) A MOLECULAR MECHANISM FOR ELECTRICAL TUNING OF COCHLEAR HAIR CELLS. *Science* 283(5399):215–217
- RAMANATHAN K, MICHAEL TH ET AL (2000) BETA SUBUNITS MODULATE ALTERNATIVELY SPLICED, LARGE CONDUCTANCE, CALCIUM-ACTIVATED POTASSIUM CHANNELS OF AVIAN HAIR CELLS. *J Neurosci* 20(5):1675–1684
- REBILLARD G, RUBEL EW (1981) ELECTROPHYSIOLOGICAL STUDY OF THE MATURATION OF AUDITORY RESPONSES FROM THE INNER EAR OF THE CHICK. *Brain Res* 229(1):15–23
- RICCI AJ, CRAWFORD AC ET AL (2003) TONOTOPIC VARIATION IN THE CONDUCTANCE OF THE HAIR CELL MECHANOTRANSDUCER CHANNEL. *Neuron* 40(5):983–990
- ROSENBLATT KP, SUN ZP ET AL (1997) DISTRIBUTION OF Ca²⁺-ACTIVATED K⁺ CHANNEL ISOFORMS ALONG THE TONOTOPIC GRADIENT OF THE CHICKEN'S COCHLEA. *Neuron* 19(5):1061–1075
- ROZEN S, SKALETSKY HJ (EDS) (2000) PRIMER3 ON THE WWW FOR GENERAL USERS AND FOR BIOLOGIST PROGRAMMERS. *Bioinformatics methods and protocols: methods in molecular biology*. Humana Press, Totowa, NJ
- RYALS BM, RUBEL EW (1988) HAIR CELL REGENERATION AFTER ACOUSTIC TRAUMA IN ADULT COTURNIX QUAIL. *Science* 240(4860):1774–1776
- SACHELI R, NGUYEN L ET AL (2009) EXPRESSION PATTERNS OF miR-96, miR-182 AND miR-183 IN THE DEVELOPING INNER EAR. *Gene Expression Patterns* 9(5):364–370
- SAMARANAYAKE H, SAUNDERS JC ET AL (2004) Ca²⁺ AND K⁺ (BK) CHANNELS IN CHICK HAIR CELLS ARE CLUSTERED AND COLOCALIZED WITH APICAL-BASAL AND TONOTOPIC GRADIENTS. *J Physiol (Lond)* 560(Pt 1):13–20
- SAUNDERS JC, COLES RB ET AL (1973) THE DEVELOPMENT OF AUDITORY EVOKED RESPONSES IN THE COCHLEA AND COCHLEAR NUCLEI OF THE CHICK. *Brain Res* 63:59–74
- SAUNDERS JC, GATES GR ET AL (1974) BRAIN-STEM EVOKED RESPONSES AS AN INDEX OF HEARING THRESHOLDS IN ONE-DAY-CHICKS AND DUCKLINGS. *J Comp Physiol Psychol* 86(3):426–431
- SCHMITTGEN TD, LIVAK KJ (2008) ANALYZING REAL-TIME PCR DATA BY THE COMPARATIVE C(T) METHOD. *Nat Protoc* 3(6):1101–1108
- SCHROEDER A, MUELLER O ET AL (2006) THE RIN: AN RNA INTEGRITY NUMBER FOR ASSIGNING INTEGRITY VALUES TO RNA MEASUREMENTS. *BMC Mol Biol* 7:3
- SOKOLOWSKI BH, STAHL LM ET AL (1993) MORPHOLOGICAL AND PHYSIOLOGICAL DEVELOPMENT OF VESTIBULAR HAIR CELLS IN THE ORGAN-CULTURED OTOCYST OF THE CHICK. *Dev Biol* 155(1):134–146
- SOUKUP GA (2009) LITTLE BUT LOUD: SMALL RNAs HAVE A RESOUNDING AFFECT ON EAR DEVELOPMENT. *Brain Res* 1277:104–114
- SOUKUP GA, FRITZSCH B ET AL (2009) RESIDUAL MICRORNA EXPRESSION DICTATES THE EXTENT OF INNER EAR DEVELOPMENT IN CONDITIONAL DICER KNOCKOUT MICE. *Dev Biol* 328(2):328–341
- STONE J, COTANCHE D (2007) HAIR CELL REGENERATION IN THE AVIAN AUDITORY EPITHELIUM. *Int J Dev Biol* 51(6–7):633–647
- SUBRAMANIAN A, TAMAYO P ET AL (2005) GENE SET ENRICHMENT ANALYSIS: A KNOWLEDGE-BASED APPROACH FOR INTERPRETING GENOME-WIDE EXPRESSION PROFILES. *Proc Natl Acad Sci U S A* 102(43):15545–15550
- TILNEY LG, TILNEY MS (1988) THE ACTIN FILAMENT CONTENT OF HAIR CELLS OF THE BIRD COCHLEA IS NEARLY CONSTANT EVEN THOUGH THE LENGTH, WIDTH, AND NUMBER OF STEREOCILIA VARY DEPENDING ON THE HAIR CELL LOCATION. *J Cell Biol* 107(6 Pt 2):2563–2574
- TUCKER T, ART JJ ET AL (1996) ROUTES OF CALCIUM ENTRY AND EXTRUSION IN TURTLE HAIR CELLS. *Ann N Y Acad Sci* 781:123–137
- WANG X-R, ZHANG X-M ET AL (2010) MICRORNA EXPRESSION IN THE EMBRYONIC MOUSE INNER EAR. *NeuroReport* 21(9):611–617
- WESTON MD, PIERCE ML ET AL (2006) MICRORNA GENE EXPRESSION IN THE MOUSE INNER EAR. *Brain Res* 1111(1):95–104
- WU YC, ART JJ ET AL (1995) A KINETIC DESCRIPTION OF THE CALCIUM-ACTIVATED POTASSIUM CHANNEL AND ITS APPLICATION TO ELECTRICAL TUNING OF HAIR CELLS. *Prog Biophys Mol Biol* 63(2):131–158
- WU YC, TUCKER T ET AL (1996) A THEORETICAL STUDY OF CALCIUM MICRODOMAINS IN TURTLE HAIR CELLS. *Biophys J* 71(5):2256–2275
- XIE J, MCCOBB DP (1998) CONTROL OF ALTERNATIVE SPLICING OF POTASSIUM CHANNELS BY STRESS HORMONES. *Science* 280(5362):443–446
- XIE X, LU J ET AL (2005) SYSTEMATIC DISCOVERY OF REGULATORY MOTIFS IN HUMAN PROMOTERS AND 3' UTRS BY COMPARISON OF SEVERAL MAMMALS. *Nature* 434(7031):338–345
- YU W, RAMAKRISHNAN R ET AL (2008) CYCLIN T1-DEPENDENT GENES IN ACTIVATED CD4 T AND MACROPHAGE CELL LINES APPEAR ENRICHED IN HIV-1 CO-FACTORS. *PLoS ONE* 3(9):e3146
- ZHOU X-B, WULFSEN I ET AL (2010) DUAL ROLE OF PROTEIN KINASE C ON BK CHANNEL REGULATION. *Proc Natl Acad Sci USA* 107(17):8005–8010



MicroRNA181a plays a key role in hair cell regeneration in the avian auditory epithelium

Corey S. Frucht^{a,b,*}, Joseph Santos-Sacchi^{c,d}, Dhasakumar S. Navaratnam^{e,f}

^a Medical Scientist Training Program, Yale School of Medicine, 367 Cedar Street, Room 316 ESH, New Haven, CT 06522, USA

^b Interdepartmental Neuroscience Program, Yale University, New Haven, CT 06522, USA

^c Division of Otolaryngology, Department of Surgery, BML 234, 333 Cedar Street, Yale School of Medicine, New Haven, CT 06522, USA

^d Department of Cellular and Molecular Physiology, Yale School of Medicine, New Haven, CT 06522, USA

^e Department of Neurobiology, Yale School of Medicine, 15 York Street, LLCI 703, New Haven, CT 06522, USA

^f Department of Neurology, Yale School of Medicine, New Haven, CT 06522, USA

ARTICLE INFO

Article history:

Received 3 January 2011

Received in revised form 4 February 2011

Accepted 7 February 2011

Keywords:

Hair cell
Regeneration
MicroRNA181a
MicroRNA
Inner ear
Hearing

ABSTRACT

Specialized sensory-transducing hair cells regenerate in response to injury in non-mammalian vertebrates such as birds and fish but not in mammals. Previous work has shown that overexpression of microRNA181a (miR181a) in cultured chicken basilar papillae, the avian counterpart of the cochlea, is sufficient to stimulate proliferation with production of new hair cells. The present study investigates the role of miR181a in hair cell regeneration after injury in explants of chicken auditory epithelia. Basilar papillae were explanted from 0-day-old chickens and transfected with either anti-miR181a, which knocks down endogenous miR181a, or a non-targeting miRNA and cultured with streptomycin to eliminate all hair cells from the epithelium. Labeling with BrdU was used to quantify proliferation. Explants exposed to streptomycin and transfected with anti-miR181a had significantly fewer BrdU positive cells than basilar papillae treated with streptomycin and transfected with a non-targeting miRNA. Activated caspase-3 and myosin VI labeling were used to show that the pattern of hair cell death and loss, respectively, were not affected by anti-miR181a transfection. MiR181a downregulation therefore seems to diminish the proliferative component of hair cell regeneration rather than prevent hair cell death following ototoxic injury.

© 2011 Elsevier Ireland Ltd. All rights reserved.

Auditory hair cells are highly specialized mechanosensitive sensory cells in the inner ear that respond to acoustic stimulation. These cells can be damaged or lost as a result of infection, chemical insult, aging, acoustic trauma, or genetic causes. These cells cannot regenerate in the mammalian organ of Corti, where hearing impairment resulting from their loss is irreversible. In contrast, non-mammalian vertebrates such as birds are able to regenerate hair cells after injury [22] by both mitotic [6,19,23] and non-mitotic mechanisms [1,3,18,2,17,24,7]. As yet, little is known about the molecular signals that underlie this phenomenon. A better understanding of the cellular signals for regeneration in the avian ear might point to rational targets for reversing sensorineural hearing loss in humans.

Previous work has shown that many genes are differentially expressed between proliferating and quiescent cultured chicken auditory epithelia [10]. Given this observation, a computational approach called gene set enrichment analysis was used to identify regulatory molecules and events that might be responsible for the complex changes in transcriptional profile that occur with proliferation and new hair cell production. This analysis identified myriad microRNAs (miRNA) that were predicted to play a role in this process. One particular miRNA, miR181a, was selected for functional studies and was found to stimulate proliferation and produce new hair cells when overexpressed in undamaged chicken auditory epithelia *in vitro*.

The present study addresses the question of whether endogenous miR181a plays a role in auditory hair cell regeneration after injury in the chicken inner ear. Cochlear ducts containing the basilar papilla (BP), the avian counterpart of the cochlea, were explanted from 0-day-old chickens and immediately transfected with either a nontargeting miRNA or anti-miR181a, which knocks down endogenous miR181a. The explants were then cultured with streptomycin to eradicate all hair cells and the thymidine analog BrdU to assay for proliferation. The tissue was then fixed and labeled for BrdU. BPs transfected with anti-miR181a had signif-

Abbreviations: BP, basilar papilla.

* Corresponding author at: 333 Cedar Street, New Haven, CT 06522 USA. Tel.: +1 203 785 5755; fax: +1 203 785 7826.

E-mail addresses: corey.frucht@yale.edu (C.S. Frucht), joseph.santos-sacchi@yale.edu (J. Santos-Sacchi), dhasakumar.navaratnam@yale.edu (D.S. Navaratnam).

icantly fewer BrdU positive cells than tissue transfected with a nontargeting miRNA, indicating that endogenous miR181a is necessary for the proliferative component of hair cell regeneration after injury in the chicken inner ear. Additionally, the pattern of hair cell loss is unaffected by anti-miR181a transfection, so the decreased rate of BrdU labeling seems to represent direct inhibition of proliferation rather than cytoprotection. Quantitative PCR (qPCR) was used to measure expression of miR181a, which did not increase after exposure to streptomycin, suggesting that the functional effect of miR181a in hair cell regeneration is not primarily mediated by expression level, but rather by regulation of its activity.

Animals were treated in accordance with policies set forth by the Yale Institutional Animal Care and Use Committee (protocol number 2007-10439). Cochlear ducts containing the BPs were explanted from 0-day-old chicks and then transfected with either anti-miR181a or a non-targeting miRNA (Ambion, Austin, TX) as described below. Explants were then cultured for 48 h with or without streptomycin (78 μ M) and BrdU (0.01%, to allow for quantification of proliferation) in DMEM with 10% FBS at 37 °C with 5% CO₂. BPs were then transfected again with either anti-miR181a or a non-targeting miRNA (pre-miR negative control #1, Ambion), and then cultured for an additional 48 h with BrdU but no streptomycin to allow recovery. The anti- and non-targeting miRNAs were transfected at a final concentration of 100 nM using the lipid-based X-tremeGENE SiRNA Transfection Reagent (Roche, Indianapolis, IN). This, and all subsequent reagent kits were used per the manufacturer's instructions. The efficacy of this transfection reagent in the chicken auditory epithelium has been previously established [10].

BPs were fixed in 4% PFA in PBS for 30 min. Between each step three 5-min PBS washes were performed. All BrdU labeling steps were performed at room temperature. The tissue was blocked and permeabilized using a solution of PBS with FBS (10%) and Triton-X (0.1%) for 1 h. Each BP was then incubated with mouse anti-BrdU antibodies (1:40, BD, Franklin Lakes, NJ) in PBS for 1 h. Alkaline phosphatase-conjugated goat anti-mouse IgG (1:400, Santa Cruz, Santa Cruz, CA) in PBS with Triton-X (0.1%) was applied for 1 h. Alkaline phosphatase substrate was produced using the NBT/BCIP Reagent Kit (Invitrogen, Carlsbad, CA) and then added to the tissue for approximately 5 min.

BPs immunohistochemically labeled for BrdU were viewed using brightfield microscopy and were analyzed following digitization. The borders of the sensory epithelium were easily appreciated by direct microscopy. Only those nuclei that were clearly within the epithelium were counted. Unpaired Student's *t*-tests were performed to determine the statistical significance of the comparisons discussed in the text using a cut-off of $p < 0.05$.

Explanted BPs cultured with or without streptomycin (78 μ M) for 48 h. These conditions cause a complete loss of hair cells in the proximal (i.e., high frequency) segment of the BP [20]. The CaspaTag kit (Millipore, Billerica, MA) was then used to label for activated caspase-3. The BPs were then fixed, permeabilized and incubated with rabbit anti-myosin VI (1:350, Proteus, Ramona, CA) in blocking solution for 1 h and then incubated in Alexa Fluor 546 conjugated anti-rabbit secondary antibodies (1:1,000, Invitrogen, Carlsbad, CA) with Alexa Fluor 633-conjugated phalloidin (1:100, Invitrogen, Carlsbad, CA) for 1 h. Sections were mounted on glass slides in Vectashield fluorescent mounting medium (Vector Laboratories, Burlingame, CA). Images were captured using a Zeiss LSM 510 confocal microscope.

Some BPs were microdissected after 24, 48, or 72 h in culture with or without 78 μ M streptomycin. Total plus small RNA isolation was performed using the MiRNEasy kit (Qiagen, Duesseldorf, Germany). Reverse transcription and qPCR were performed using the TaqMan MicroRNA Reverse Transcription Kit and Taq-

Man MicroRNA Assay for miR181a (Applied Biosystems, Foster City, CA).

Amplification was performed using the SYBR Green Supermix kit (Bio-Rad, Hercules, CA) on an iCycler system (Bio-Rad, Hercules, CA). Expression levels were normalized to the total RNA concentration. Three replicates were performed and the data averaged for each cDNA sample and primer pair combination. Those fold-changes with a 95% confidence interval excluding a fold-change of one (which would represent no change) were considered significant.

To determine miR181a's role in hair cell regeneration in the post-hatch chicken inner ear, BPs were cultured for 48 h with streptomycin to cause hair cell death, and then for an additional 48 h recovery period without streptomycin [20]. The explanted tissue was also transfected with either anti-miR181a, to knock down endogenous miR181a, or a nontargeting miRNA at 0 and 48 h of exposure to streptomycin. Also present in the culture medium was BrdU, a thymidine analog that is incorporated into the nuclei of cells entering S-phase. At the end of the entire 4-day culture duration, BPs were fixed and labeled for BrdU to quantify proliferation.

BPs injured with streptomycin and transfected with the nontargeting miRNA had an average of 353.1 (\pm SEM = 56.5) BrdU positive cells (Fig. 1). In contrast, anti-miR181a transfection and subsequent culture alone apparently does not cause much injury to the epithelium, as these BPs had on average 5.3 (\pm SEM = 2.6) BrdU positive cells. Similarly, BPs that were neither transfected nor exposed to streptomycin all had fewer than 10 BrdU positive cells per epithelium (data not shown). Explants that were cultured with streptomycin and transfected with anti-miR181a had on average 149.9 (\pm SEM = 14.5) BrdU positive cells per epithelium, significantly fewer than epithelia exposed to streptomycin and transfected with the non-targeting miRNA ($p < 0.01$).

The BrdU labeling data suggest that endogenous miR181a plays a crucial role in the post-injury proliferative response in the chicken auditory epithelium but does not exclude the possibility that anti-miR181a transfection simply prevents cell death. To address this issue it was necessary to compare the patterns of hair cell loss after streptomycin exposure with and without prior anti-miR181a transfection. BPs were therefore transfected with either anti-miR181a or a non-targeting miRNA and then cultured for 48 h with 78 μ M streptomycin, before fixation and labeling for the apoptosis marker activated caspase-3 [11], the hair cell marker myosin VI, and the major hair bundle component actin (Fig. 2). Streptomycin treatment causes complete hair cell loss at the high frequency segment of the BP (Fig. 2). Accordingly there are many activated caspase-3 positive cells in BPs exposed to streptomycin, but not in those cultured without streptomycin. This pattern of cell death and hair cell loss is consistent regardless of anti-miR181a transfection, where there is still hair cell loss and caspase-3 activation at the high frequency end of the BP. At the low frequency end, there is less of a loss of hair cells and accordingly less caspase-3 activation (data not shown). This pattern is also independent of anti-miR181a transfection, mirroring the data from the high frequency BP segment. It therefore appears as though the reduction in BrdU labeling with anti-miR181a transfection of streptomycin treated BPs is due to direct inhibition of the regenerative response, rather than cytoprotection with a resulting decrease in the number of cells damaged by streptomycin.

QPCR was used to ascertain whether expression of mature miR181a increases following exposure to streptomycin. BPs were cultured in streptomycin for 24, 48 or 72 h, at which point the sensory epithelium was isolated by microdissection. After RNA isolation, first-strand-synthesis and qPCR was performed using primers for miR181a. At none of these time points were there significant miR181a expression level differences (Fig. 3). Therefore, while knocking down endogenous miR181a interferes with post-

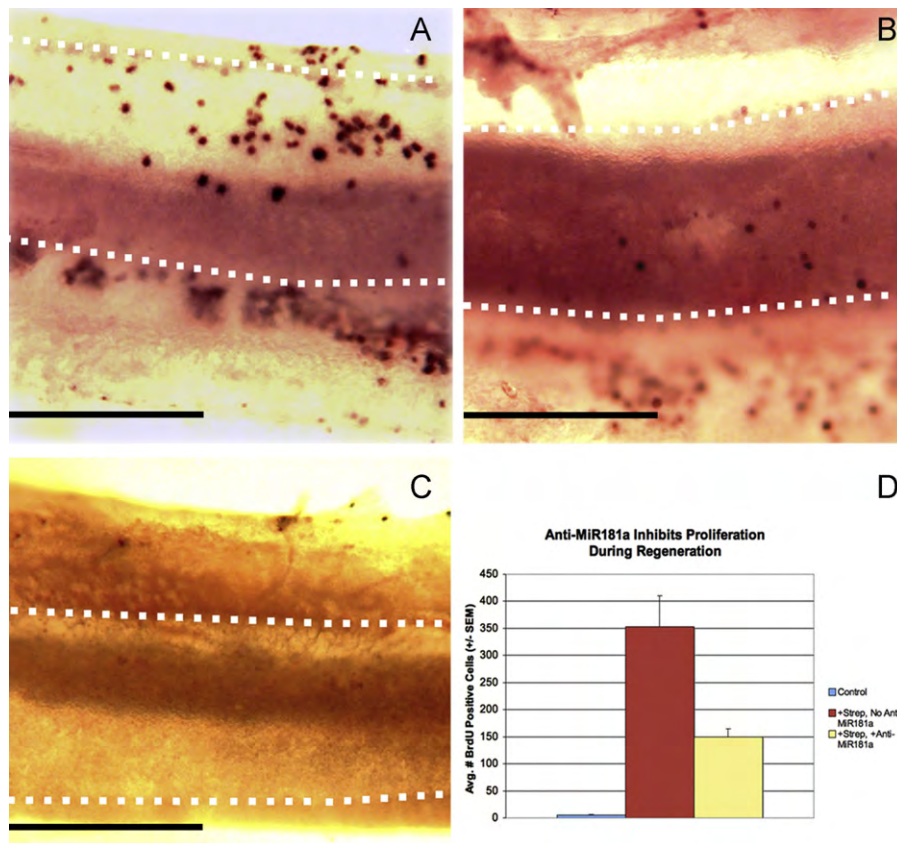


Fig. 1. Suppression of endogenous miR181a expression with anti-miR181a blunts proliferation during hair cell regeneration after streptomycin exposure. Basilar papillae from 0-day-old post-hatch chickens were transfected with either anti-miR181a or a non-targeting miRNA and then cultured with BrdU and streptomycin (78 μ M) or in drug-free medium ($n = 7$) as described in the text. There were a total of 7 BPs in each condition. After culture, explants were immunolabeled for BrdU to assay for proliferation. Panels A–C show basilar papillae labeled for BrdU, with the sensory epithelia outlined with dotted white lines. The neural edges of the epithelia are toward the bottom, and the proximal ends are to the left. Epithelia exposed to streptomycin exhibit far more proliferation when transfected with a non-targeting miRNA (A) than anti-miR181a (B). Epithelia transfected with a non-targeting miRNA and cultured in the absence of streptomycin typically have very few BrdU positive cells (C). Shown in D is the average number of BrdU positive cells per epithelium in each condition. All pair wise comparisons are statistically significant (t -test, $p < 0.05$). Scale bars in A–C = 0.2 mm.

injury hair cell regeneration, it appears as though an increase of activity rather than expression level mediates this miRNA's role in regeneration.

Presented here is the first direct functional biological evidence for the role of a specific miRNA in auditory hair cell regeneration after injury. Previously, there was limited, indirect evidence that the let-7 family of miRNA play a role in hair cell regeneration in the newt inner ear [25]. The present observation that transfection with anti-miR181a results in a markedly blunted regenerative response suggests that miR181a plays a key role in hair cell regeneration in the chicken inner ear. This finding agrees with a previous study showing that miR181a overexpression in the uninjured chicken BP can stimulate proliferation with the production of new hair cells [10]. Additionally, miR181a has a pro-proliferative role in cultured human myeloid leukemia cells that seems to be mediated at least partly by repressing expression of the cell cycle inhibitor p27 [26]. This is worth pointing out given that p27 is thought to represent a significant barrier to regeneration in the mammalian inner ear [15,12]. Further experiments will be necessary to determine whether miR181a's ability to stimulate proliferation in the chicken inner ear involves targeted downregulation of p27 expression.

The observation that miR181a expression does not increase during regeneration despite its clear role in this process suggests regulation of its activity mediates this effect. It is possible that upregulation of miR181a occurs earlier than 24 h after onset of exposure, or transiently between 24, 48 or 72 h, but these possibilities seem unlikely given the sustained nature of the regenerative

response. Our understanding of the mechanisms of control of miRNA biogenesis is more detailed than that of the ways in which miRNA biological activity is controlled [5]. miRNA activity can be modulated by different mechanisms including association with RNA-binding factors that influence miRNA-target interactions [4]. Unfortunately, there are presently no methods for directly assaying miRNA activity. One indirect method would be to look at changes in expression of predicted miR181a targets with exposure to streptomycin once such targets have been validated in chickens. Future studies on changes in expression of predicted miR181a targets in regeneration may be helpful in elucidating the precise mechanism of this miRNA's role in hair cell regeneration.

It also bears mentioning that miR181a is not the only miR181 family miRNA expressed in chickens. MiR181b is also expressed in chickens, and its sequence differs from that of miR181a by 4 bases. (www.mirbase.org). It is theoretically possible that the anti-miR181a may also cause downregulation of miR181b, but this seems highly unlikely given evidence that there is a significant decrease in anti-miRNA activity with just one mismatch and a complete lack of activity with as few as three mismatches [8]. Once there are known, biologically validated targets of both miR181a and miR181b in chickens, experiments should aim to confirm the predicted specificity of anti-miR181a.

Though presented here is the first functional evidence for a role for a specific miRNA in hair cell regeneration, previous work has shown that certain miRNAs are not only expressed in the mammalian inner ear [28,27], but are also important for the proper

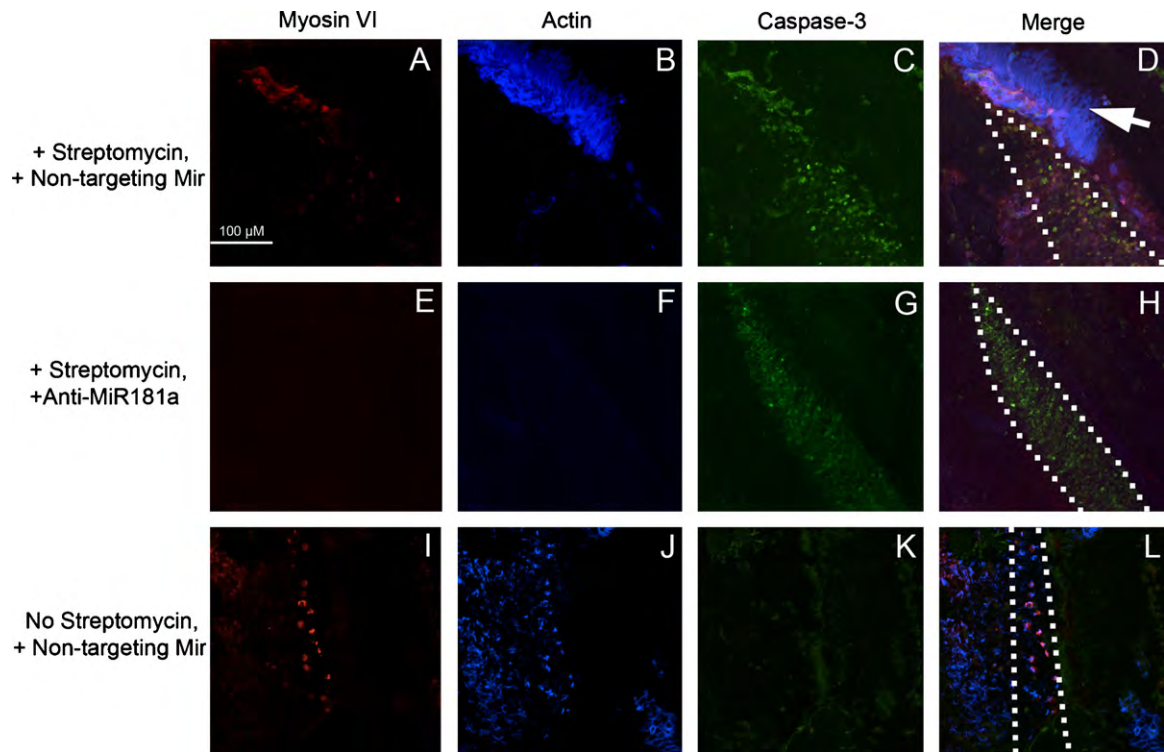


Fig. 2. Anti-miR181a transfection does not prevent hair cell death after streptomycin exposure. Basilar papillae were cultured with streptomycin for 48 h following transfection with either a non-targeting miRNA (A–D) or anti-miR181a (E–H). Whole-mounts were then labeled for the hair cell marker myosin VI, stereocilia bundle component actin, and the early cell death marker caspase-3. Hair cells were completely eliminated from the high frequency segment of basilar papillae exposed to streptomycin, regardless of transfection with anti-miR181a (A, B, E and F). Further, streptomycin exposure triggers extensive cell death with or without anti-miR181a transfection (C and G). In contrast, epithelia transfected with a non-targeting miRNA and unexposed to streptomycin retain hair cells (I and J) and do not show extensive apoptosis (K). The neural edge is to the right of each panel, and the proximal segment is to the top. The arrow in panel D shows what are likely homogeneous cells remaining after microdissection. The scale bar in A also applies to B–L.

function and/or development of this structure. For example, conditional *Dicer* knockout mouse embryos that are depleted of all inner ear miRNA develop grossly malformed inner ears [21]. Similarly, mice with conditionally silenced *Dicer* expression in hair cells only are deaf and have markedly aberrant hair cell morphology [9]. Interestingly, mutations in the target-defining seed region of miR96 cause a progressive hearing loss in both mice [13] and humans [16]. These results suggest inter-species similarities in ear miRNA function, at least within the class of mammals and therefore raise hopes that insights into the role of miRNA in hair cell regeneration in birds may shed light on why the mammalian auditory epithelium lacks regenerative capacity.

There are as yet very few studies that have directly examined the role of specific miRNAs in development, function, or regeneration of the inner ear. The miR183 family (miR96, miR182, miR183) have been examined closely following the observation that miR96 mutations are associated with progressive hearing loss. Specifically, miR183 is expressed in mammalian hair cells and spiral and vestibular ganglia [28]. Interestingly, overexpression of miR96 or miR182 causes production of ectopic hair cells in the zebrafish embryo [14]. In light of existing expression and functional data, it is clear that the miR183 family is important for inner ear development across species. These observations affirm that miRNA may prove to be suitable targets for rational therapies to reverse hearing loss.

In addition to miR181a, other miRNAs have been identified whose roles in hair cell regeneration warrant further investigation [10]. Increasing evidence suggests this is a promising avenue of investigation for those interested in developing rational therapies for sensorineural hearing loss. It is attractive to consider the possibility of miRNA based therapeutics, specifically, in light of the

transient nature of their overexpression which may result in side effect profiles that are more favorable than those of hypothetical DNA-based gene therapies for hearing loss. Further functional studies are necessary to test the hypothesis that miRNA transfection, perhaps with a carefully chosen combination of miRNA, can result in the production of new hair cells in the mammalian inner ear, and may therefore result in alleviation of sensorineural hearing loss.

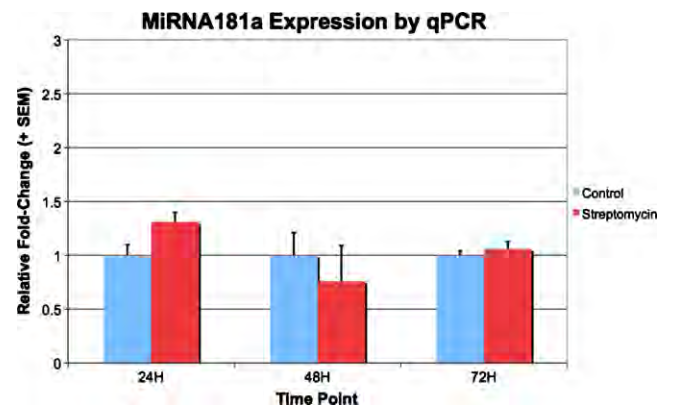


Fig. 3. MiR181a expression does not increase after exposure to streptomycin for 24, 48 or 72 h. Basilar papillae were cultured with 78 μ M streptomycin for 24, 48, or 72 h, and sensory epithelia were isolated by microdissection ($n = 3$ in each condition). Shown are relative fold-changes of miR181a expression with exposure to streptomycin, as detected by qPCR. The fold-changes shown are relative to expression in untreated controls. There was no significant difference in miR181a expression between the basilar papillae that were and were not treated with streptomycin at any of the three time points (t -test, $p < 0.05$).

Acknowledgements

This work is part of a dissertation submitted to fulfill the requirements for the degree of Doctor of Philosophy at Yale University.

The authors wish to thank Jennifer Stone, PhD, University of Washington, for helpful technical advice and critical feedback on this manuscript.

CSF was supported by NIH MSTP TG 2T32GM07205 and an Ohse Grant for Surgical Research at Yale School of Medicine. CSF, JSS and DSN were supported by NIH/NIDCD grants DC 007894, DC 000273 and DC 008130.

References

- [1] H.J. Adler, Y. Raphael, New hair cells arise from supporting cell conversion in the acoustically damaged chick inner ear, *Neurosci. Lett.* 205 (1996) 17–20.
- [2] R.A. Baird, M.D. Burton, A. Lysakowski, D.S. Fashena, R.A. Naeger, Hair cell recovery in mitotically blocked cultures of the bullfrog sacculle, *Proc. Natl. Acad. Sci. U.S.A.* 97 (2000) 11722–11729.
- [3] R.A. Baird, P.S. Steyger, N.R. Schuff, Mitotic and nonmitotic hair cell regeneration in the bullfrog vestibular otolith organs, *Ann. N.Y. Acad. Sci.* 781 (1996) 59–70.
- [4] K. Breving, A. Esquela-Kerscher, The complexities of microRNA regulation: mirandering around the rules, *Int. J. Biochem. Cell Biol.* 42 (2010) 1316–1329.
- [5] Y. Cai, X. Yu, S. Hu, J. Yu, A brief review on the mechanisms of miRNA regulation, *Genomics Proteomics Bioinformatics* 7 (2009) 147–154.
- [6] J.T. Corwin, D.A. Cotanche, Regeneration of sensory hair cells after acoustic trauma, *Science* 240 (1988) 1772–1774.
- [7] L.J. Duncan, D.A. Mangiardi, J.I. Matsui, J.K. Anderson, K. McLaughlin-Williamson, D.A. Cotanche, Differential expression of unconventional myosins in apoptotic and regenerating chick hair cells confirms two regeneration mechanisms, *J. Comp. Neurol.* 499 (2006) 691–701.
- [8] C.C. Esau, Inhibition of microRNA with antisense oligonucleotides, *Methods* 44 (2008) 55–60.
- [9] L.M. Friedman, A.A. Dror, E. Mor, T. Tenne, G. Toren, T. Satoh, D.J. Biesemeier, N. Shomron, D.M. Fekete, E. Hornstein, K.B. Avraham, MicroRNAs are essential for development and function of inner ear hair cells in vertebrates, *Proc. Natl. Acad. Sci. U.S.A.* 106 (2009) 7915–7920.
- [10] C.S. Frucht, M. Uduman, J.L. Duke, S.H. Kleinstein, J. Santos-Sacchi, D.S. Navaratnam, Gene expression analysis of Forskolin treated basilar papillae identifies MicroRNA181a as a mediator of proliferation, *PLoS One* 5 (2010) e11502.
- [11] C. Kaiser, B. Chapman, J. Guidi, C. Terry, D. Mangiardi, D. Cotanche, Comparison of activated caspase detection methods in the gentamicin-treated chick cochlea, *Hear. Res.* 240 (2008) 1–11.
- [12] Y.S. Lee, F. Liu, N. Segil, A morphogenetic wave of p27Kip1 transcription directs cell cycle exit during organ of Corti development, *Development* 133 (2006) 2817–2826.
- [13] M.A. Lewis, E. Quint, A.M. Glazier, H. Fuchs, M.H. De Angelis, C. Langford, S. Van Dongen, C. Abreu-Goodger, M. Piipari, N. Redshaw, T. Dalmay, M.A. Moreno-Pelayo, A.J. Enright, K.P. Steel, An ENU-induced mutation of miR-96 associated with progressive hearing loss in mice, *Nat. Genet.* 41 (2009) 614–618.
- [14] H. Li, W. Kloosterman, D.M. Fekete, MicroRNA-183 family members regulate sensorineural fates in the inner ear, *J. Neurosci.* 30 (2010) 3254–3263.
- [15] H. Lowenheim, D.N. Furness, J. Kil, C. Zinn, K. Gultig, M.L. Fero, D. Frost, A.W. Gummer, J.M. Roberts, E.W. Rubel, C.M. Hackney, H.P. Zenner, Gene disruption of p27(Kip1) allows cell proliferation in the postnatal and adult organ of corti, *Proc. Natl. Acad. Sci. U.S.A.* 96 (1999) 4084–4088.
- [16] A. Mencía, S. Modamio-Høybjør, N. Redshaw, M. Morin, F. Mayo-Merino, L. Olavarrieta, L.A. Aguirre, I. Del Castillo, K.P. Steel, T. Dalmay, F. Moreno, M.A. Moreno-Pelayo, Mutations in the seed region of human miR-96 are responsible for nonsyndromic progressive hearing loss, *Nat. Genet.* 41 (2009) 609–613.
- [17] D.W. Roberson, J.A. Alosi, D.A. Cotanche, Direct transdifferentiation gives rise to the earliest new hair cells in regenerating avian auditory epithelium, *J. Neurosci. Res.* 78 (2004) 461–471.
- [18] D.W. Roberson, C.S. Kreig, E.W. Rubel, Light microscopic evidence that direct transdifferentiation gives rise to new hair cells in regenerating avian auditory epithelium, *Aud. Neurosci.* 2 (1996) 195–205.
- [19] B.M. Ryals, E.W. Rubel, Hair cell regeneration after acoustic trauma in adult Coturnix quail, *Science* 240 (1988) 1774–1776.
- [20] J. Shang, J. Cafaro, R. Nehmer, J. Stone, Supporting cell division is not required for regeneration of auditory hair cells after ototoxic injury in vitro, *J. Assoc. Res. Otolaryngol.* (2010).
- [21] G.A. Soukup, B. Fritsch, M.L. Pierce, M.D. Weston, I. Jahan, M.T. McManus, B.D. Harfe, Residual microRNA expression dictates the extent of inner ear development in conditional Dicer knockout mice, *Dev. Biol.* 328 (2009) 328–341.
- [22] J. Stone, D. Cotanche, Hair cell regeneration in the avian auditory epithelium, *Int. J. Dev. Biol.* 51 (2007) 633–647.
- [23] J.S. Stone, D.A. Cotanche, Identification of the timing of S phase and the patterns of cell proliferation during hair cell regeneration in the chick cochlea, *J. Comp. Neurol.* 341 (1994) 50–67.
- [24] R.R. Taylor, A. Forge, Hair cell regeneration in sensory epithelia from the inner ear of a urodele amphibian, *J. Comp. Neurol.* 484 (2005) 105–120.
- [25] P. Tsonis, M. Call, M. Grogg, M. Sartor, R. Taylor, A. Forge, R. Fyffe, R. Goldenberg, R. Cowpersallari, C. Tomlinson, MicroRNAs and regeneration: let-7 members as potential regulators of dedifferentiation in lens and inner ear hair cell regeneration of the adult newt, *Biochem. Biophys. Res. Commun.* 362 (2007) 940–945.
- [26] X. Wang, E. Gocek, C.-G. Liu, G.P. Studzinski, MicroRNAs 181 regulate the expression of p27Kip1 in human myeloid leukemia cells induced to differentiate by 1,25-dihydroxyvitamin D3, *Cell Cycle* 8 (2009) 736–741.
- [27] X.-R. Wang, X.-M. Zhang, J. Zhen, P.-X. Zhang, G. Xu, H. Jiang, MicroRNA expression in the embryonic mouse inner ear, *Neuroreport* 21 (2010) 611–617.
- [28] M.D. Weston, M.L. Pierce, S. Rocha-Sanchez, K.W. Beisel, G.A. Soukup, MicroRNA gene expression in the mouse inner ear, *Brain Res.* 1111 (2006) 95–104.

Gene Expression Analysis of Forskolin Treated Basilar Papillae Identifies MicroRNA181a as a Mediator of Proliferation

Corey S. Frucht^{1,2}, Mohamed Uduman^{3,4}, Jamie L. Duke^{3,4}, Steven H. Kleinstein^{3,4}, Joseph Santos-Sacchi^{5,6,7}, Dhasakumar S. Navaratnam^{7,8*}

1 Medical Scientist Training Program, Yale School of Medicine, New Haven, Connecticut, United States of America, **2** Interdepartmental Neuroscience Program, Yale University, New Haven, Connecticut, United States of America, **3** Interdepartmental Program in Computation Biology and Bioinformatics, Yale University, New Haven, Connecticut, United States of America, **4** Department of Pathology, Yale School of Medicine, New Haven, Connecticut, United States of America, **5** Division of Otolaryngology, Department of Surgery, Yale School of Medicine, New Haven, Connecticut, United States of America, **6** Department of Cellular and Molecular Physiology, Yale School of Medicine, New Haven, Connecticut, United States of America, **7** Department of Neurobiology, Yale School of Medicine, New Haven, Connecticut, United States of America, **8** Department of Neurology, Yale School of Medicine, New Haven, Connecticut, United States of America

Abstract

Background: Auditory hair cells spontaneously regenerate following injury in birds but not mammals. A better understanding of the molecular events underlying hair cell regeneration in birds may allow for identification and eventually manipulation of relevant pathways in mammals to stimulate regeneration and restore hearing in deaf patients.

Methodology/Principal Findings: Gene expression was profiled in forskolin treated (i.e., proliferating) and quiescent control auditory epithelia of post-hatch chicks using an Affymetrix whole-genome chicken array after 24 (n = 6), 48 (n = 6), and 72 (n = 12) hours in culture. In the forskolin-treated epithelia there was significant (p < 0.05; > two-fold change) upregulation of many genes thought to be relevant to cell cycle control and inner ear development. Gene set enrichment analysis was performed on the data and identified myriad microRNAs that are likely to be upregulated in the regenerating tissue, including microRNA181a (miR181a), which is known to mediate proliferation in other systems. Functional experiments showed that miR181a overexpression is sufficient to stimulate proliferation within the basilar papilla, as assayed by BrdU incorporation. Further, some of the newly produced cells express the early hair cell marker myosin VI, suggesting that miR181a transfection can result in the production of new hair cells.

Conclusions/Significance: These studies have identified a single microRNA, miR181a, that can cause proliferation in the chicken auditory epithelium with production of new hair cells.

Citation: Frucht CS, Uduman M, Duke JL, Kleinstein SH, Santos-Sacchi J, et al. (2010) Gene Expression Analysis of Forskolin Treated Basilar Papillae Identifies MicroRNA181a as a Mediator of Proliferation. PLoS ONE 5(7): e11502. doi:10.1371/journal.pone.0011502

Editor: Timothy Ravasi, King Abdullah University of Science and Technology, Saudi Arabia

Received: March 19, 2010; **Accepted:** June 15, 2010; **Published:** July 9, 2010

Copyright: © 2010 Frucht et al. This is an open-access article distributed under the terms of the Creative Commons Attribution License, which permits unrestricted use, distribution, and reproduction in any medium, provided the original author and source are credited.

Funding: CSF was supported by NIH MSTP TG 2T32GM07205 and an Ohse Grant for Surgical Research at Yale School of Medicine. CSF, JSS and DSN were supported by NIH/NIDCD grants DC 007894, DC 000273 and DC 008130. The authors would like to acknowledge the support of the National Organization for Hearing Research, which provided seed funding for this project to DSN. MU and JLD were supported by NIH Grant T15 LM07056 from the National Library of Medicine. The funders had no role in study design, data collection and analysis, decision to publish, or preparation of the manuscript.

Competing Interests: The authors have declared that no competing interests exist.

* E-mail: Dhasakumar.Navaratnam@Yale.edu

Introduction

Sensorineural hearing loss represents a major public health concern. Approximately 300 million people worldwide have moderate to profound hearing loss in both ears [1]. Loss of inner ear hair cells, which serve to transduce sound into neural impulses, is responsible for the majority of hearing loss. In humans, and other mammals, loss of hair cells is permanent since these organisms have no capacity for hair cell regeneration. In contrast, other non-mammalian vertebrates such as birds, reptiles, amphibian and fish are able to replace lost hair cells.

The basilar papilla, the avian auditory epithelium, is able to regenerate hair cells in response to hair cell loss (reviewed in [2]). However, the auditory epithelium shows no mitotic activity normally, a feature that is reminiscent of the mammalian auditory

epithelium, and contrasts with the chick vestibular epithelium which shows continuous mitotic activity [3]. Thus, the avian auditory epithelium can be viewed as an intermediary in the evolution from the fish to the mammal, and we reason that the study of this epithelium will provide insight into why the mammalian auditory epithelium shows mitotic quiescence at rest (similar to the avian auditory epithelium), but is unable to proliferate in response to damage (in contrast to the avian auditory epithelium).

The basilar papilla is comprised of both sensory transducing hair cells and supporting cells. Following injury, it is the supporting cells which give rise to new hair cells [4,5]. For example, exposure of birds to intense noise causes some supporting cells to leave growth-arrest, re-enter the cell cycle and ultimately differentiate into hair cells [6,7,8,9]. New hair cells are first seen 4–5 days after the onset of

exposure to an intense sound [6,10] and undergo maturation so that by 20–28 days after stimulus onset they are virtually indistinguishable from unaffected cells [11]. In addition, some new hair cells arise from direct differentiation of supporting cells without an intervening mitotic step [12,13,14,15,16,17,18,19]. After acoustic or ototoxic insult, birds initially have increased hearing thresholds, which eventually return nearly to baseline confirming that newly produced hair cells are functional [20]. It is believed that this recovery of function results from both regeneration of new hair cells as well as repair of those that have survived [21].

Though the intracellular pathways required for hair cell regeneration have not yet been fully elucidated, various pathways and signaling cascades have been implicated in this process. For example, it has been shown that treatment of the chick basilar papilla with forskolin, a potent adenylate cyclase activator that increases intracellular cAMP levels, causes a robust and widespread proliferation of supporting cells, leading to the production of new hair cells [22]. This effect is first seen after 72 hours in culture, occurs without upregulation of markers of apoptosis, and is significantly blocked by protein kinase A inhibitors. It therefore appears as though activation of this pathway can stimulate growth of new hair cells with limited cell injury. Forskolin also appears to have a mitogenic effect in the mammalian vestibular system, in which brief treatment with this compound results in an increase in supporting cell S-phase entry [23]. Moreover, the same study found that this effect is blocked by brief treatment with forskolin in the presence of monensin or bafilomycin, which inhibit recycling of membrane receptors. Increased cAMP levels may therefore lead to proliferation by causing upregulation of tyrosine kinase growth factor receptors. With age-related hearing loss in humans there is a substantial loss of hair cells within the organ of Corti [24], so it is likely that a robust proliferative process that produces new hair cells is what will ultimately lead to maximal recovery of function in hearing impaired patients. In the present study, microarrays were used to analyze gene expression in forskolin treated basilar papillae given the robustness of this effect.

In other systems, microarray analysis of differing phenotypes has revealed complex differences in mRNA expression. These complex differences are likely brought about by the combined activity of transcription factors and microRNAs (miRNAs) that regulate expression of multiple genes and specific genetic programs. In fact, a study of transcription factor expression in regenerating versus non-regenerating chicken basilar papillae revealed a number of transcription factors that were differentially expressed [25].

MiRNAs are a species of small regulatory RNA that bind to complementary sequences in mRNA and decrease gene expression by increasing degradation and blocking translation (reviewed in [26]). Though each miRNA binds a specific sequence, these molecules are promiscuous in that their complementary sequences are found in a number of different mRNAs [27]. As a result, miRNA expression may represent a way in which cells can rapidly and in a coordinated fashion up- or downregulate a large number of genes. Some miRNAs are known to be important for inner ear development [28,29,30,31] and may play a role in hair cell regeneration, where there is presumably some reiteration of developmental events. However there have been few published studies on the role of miRNAs in auditory hair cell regeneration, specifically. One study revealed that the *let-7* family of miRNA are downregulated in the newt inner ear after hair cell injury [32]. This particular study underscores the importance of examining more closely the role of miRNA in hair cell regeneration.

In order to gain insight into the molecular events which underlie auditory hair cell regeneration in chicken, we compared gene

expression in forskolin treated (i.e., proliferating) and control (i.e., quiescent) auditory epithelia using Affymetrix whole genome chicken microarrays. The microarray data were validated by quantitative PCR. Gene set enrichment analyses were performed to identify miRNAs and transcription factors that may be important for hair cell regeneration. Many sets of genes representing predicted targets of specific miRNAs were found to be significantly enriched among genes downregulated in the forskolin-treated sensory epithelia after 72 hours, suggesting that these miRNAs were likely upregulated in the proliferating tissue. One of these microRNAs, miR181a, was selected for functional experiments given its role in proliferation and suppression of the cell cycle inhibitor p27 in human myeloid leukemia cells [33]. P27 is thought to represent a key barrier to hair cell regeneration in the mammalian inner ear [34,35]. Basilar papillae transfected with a miR181a precursor had increased numbers of BrdU positive cells than epithelia that were transfected with a non-targeting miRNA. Some cells labeling for BrdU also expressed the early hair cell marker myosin VI, indicating that overexpression of miR181a is capable of producing proliferation with production of new hair cells.

Materials and Methods

Basilar papilla explant cultures

Animals were treated in accordance with policies set forth by the Yale Institutional Animal Care and Use Committee (protocol number 2007-10439). Under sterile conditions, cochlear ducts containing the basilar papillae were carefully dissected out of 0-day-old chicks and then individually cultured in DMEM with 10% fetal bovine serum with or without forskolin (final concentration 100 μ M, delivered in 1% DMSO) for either 24, 48, or 72 hours at 37°C with 5% CO₂. Control samples received DMSO at 1% as a vehicle control. At the end of 72 hours, the tegmentum vasculosum was dissected off to expose the auditory epithelium, which was delicately freed from the underlying cartilaginous plates. All explants were kept in culture for 72 hours because new hair cells are first seen in basilar papillae treated with forskolin after ~72 hours of exposure to the small molecule [22]. Therefore, at even earlier time points in culture the molecular events that underlie hair cell proliferation are well underway. Each sample was comprised of three auditory epithelia from three different chicks and were put in 100 μ L of DMEM and then immediately frozen at –80°C until RNA isolation could be performed. There were a total of 24 samples in this experiment: three 24-hour forskolin, three 24-hour control, three 48-hour forskolin, three 48-hour control, six 72-hour forskolin and six 72-hour control.

RNA isolation

Immediately upon removal of the frozen epithelia samples from the –80°C freezer, the lysis buffer from the RNAqueous® Kit (Ambion, Austin, TX) was added. Given the small amount of tissue and relatively large surface area to size ratio, no measures to actively disrupt or homogenize the tissue in each sample were necessary. Total RNA isolation then proceeded as directed by the RNAqueous® Kit manual. Sample quality was confirmed by gel analysis.

Microarray experiments

Double-stranded cDNA and biotin-labeled cRNA were synthesized from 1 to 5 μ g of total RNA using a two-cycle target labeling kit [36]. Biotin-labeled cRNA was purified using the GeneChip Cleanup Module prior to fragmenting to a size of 35–200 bases by

incubating at 94°C for 35 minutes in fragmentation buffer (40 mM Tris-acetate, pH 8.1, 100 mM potassium acetate, 30 mM magnesium acetate). Hybridization of the samples with Affymetrix chicken arrays was then performed at the Yale University Keck Facility according to the manufacturer's protocol [37]. All microarray data is MIAME compliant and has been uploaded to MIAMEExpress (ArrayExpress accession: E-MEXP-2642, username = Reviewer_E-MEXP-2642, password = 1269882335242).

Differential gene expression analysis

The microarray gene expression analysis was performed using GeneSpring GX 9.0 software (Agilent Technologies, Santa Clara, CA). The data were GC-RMA normalized without baseline transformation, and then filtered by expression (20%–100% in at least one of the six or twelve samples at each time point) to exclude genes expressed only at very low levels in all samples. Median expression values were used for redundant probe sets. Genes differentially expressed were identified by using a fold-change cutoff of 2 and then performing an unpaired t-test after Benjamini-Hochberg correction for multiple comparisons ($p < 0.05$). Heat maps were generated using R version 2.10.1 (www.r-project.org) using the HeatPlus add-on in the Bioconductor package.

Quantitative PCR validation of microarray gene expression data

In order to validate the microarray data, twelve genes were selected to be verified by qPCR. Seven of the genes selected were upregulated and five were downregulated in the forskolin condition. The upregulated genes validated by qPCR were highly expressed in at least one condition and chosen to span a range in fold-change differences between the two experimental conditions at 72 hours, from 2.0 to 64.3. The 12 genes that were validated are BECN1, CCNI, CDKN1B (p27), CDKN2B, DPM1, EME1, FBXO8, ITGA4, NLGN1, OCM, PIGW, SNX1. Additionally, expression of the 18S ribosomal subunit was also assessed to allow for normalization of total RNA levels between samples using the $2^{-\Delta\Delta C_T}$ method [38]. Primers were designed using MacVector (MacVector, Cary, NC) software and Primer 3 [39] and were validated by melting curve analysis. 5 μ g of RNA was isolated from each sample as described above and was used to create first-strand cDNA using random hexamers and reverse transcriptase (Superscript II; Invitrogen, Carlsbad, CA), according to the manufacturer's instructions. Amplification was performed using the SYBR Green Supermix kit (Bio-Rad, Hercules, CA) on an iCycler system (Bio-Rad, Hercules, CA). Three replicates were performed and the data averaged for each cDNA sample and primer pair combination. Those fold-changes with a 95% confidence interval excluding one were considered significant.

Gene sets used for enrichment analyses

Gene set enrichment analysis (GSEA) was performed to analyze the pattern of differential gene expression between forskolin treated and control basilar papillae using GSEA version 2 software [40]. Three different gene set packages were used, two of which were downloaded directly from the Broad institute website (www.broad.mit.edu/gsea).

To identify transcription factors which may be important for hair cell regeneration, a GSEA was performed using a gene set package called “c3.all.v2.5.symbols,” which was obtained from the BROAD Institute website. This package contains a series of gene sets defined by the presence of transcription factor motifs and predicted miRNA binding sites. The genes in each set of this package therefore share a *cis*-regulatory motif that is conserved across human, mouse, rat, and

dog genomes and will be referred to hereafter as the “mammalian gene sets.” The motifs used come from Xie et al. (2005) and the TRANSFAC database and include sets of genes sharing a 3'-UTR miRNA binding motif [41]. Even though these gene sets are not based on the chicken genome, we reasoned that these results would be of interest given the known conservation of miRNA targets among mammals [42]. We further surmised that if the conservation of miRNA targets is poorly conserved between mammals and non-mammalian vertebrates then an enrichment analysis might produce no statistically significant results. Any significant findings, however, would warrant further examination.

In order to validate the GSEA results from the analyses performed using the mammalian gene sets, GSEA was also run using a gene set package that was generated by scanning the portions of the chicken genome that are conserved with frog (*Xenopus tropicalis*) to identify gene sets sharing particular transcription factor motifs defined in the TRANSFAC database. These gene sets will hereafter be referred to as the “chicken/frog conservation gene sets.” Only conserved regions were used to reduce the number of false positives, as there is evidence to suggest that transcription factor recognition sites tend to be enriched in conserved portions of the genome [43]. However, recent genome-wide studies have demonstrated that many transcription factor binding sites are not conserved [44,45] and are also found outside of the proximal promoter region [44,46]. Thus, our approach should be considered to be conservative in the sense that some true binding sites may be overlooked, but those that are identified have a higher likelihood of being functional. The frog genome in particular was used in light of this organism's close evolutionary relationship to chickens. The use of conservation between more distantly related organisms, such as chicken and mammals, would be very strict and would result in the omission of many potentially significant positive results. To create these gene sets we downloaded the transcription start site for all chicken RefSeq genes, defined by the May 2008 RefGene table [47] using the UCSC Genome Bioinformatics site (genome.ucsc.edu). The region 2 kilobases around each transcription start site was identified within the May 2006 genome-wide multiple alignment of 6 vertebrate species to the chicken genome [48], also available through UCSC Genome Bioinformatics site. In order to identify putative transcription factor binding sites, the chicken sequences, along with aligned regions from frog, were analyzed using the TRANSFAC MATCH algorithm with a cutoff chosen to minimize the sum of false positives and false negatives [49]. The analysis was performed for all vertebrate transcription factor matrices in the 2009.1 release of TRANSFAC [50], and putative binding sites were considered to be evolutionarily conserved if matches were also found at the aligned positions in both chicken and frog sequences and had no gaps present in the multiple alignment of these species.

To assess the functional relevance of the pattern of differentially expressed genes across a variety of organisms and systems, GSEA was performed using a gene set package called “c2.all.v2.5.symbols” which was also downloaded from the BROAD Institute website. This package defines curated sets of genes based on specific experimental findings from experiments on human and model animal tissue, which includes canonical pathways and chemical/genetic perturbations based gene sets. These gene sets will hereafter be referred to as the “curated gene sets.” The relevant reference is given on the BROAD website for each curated gene set for assessment of relevance.

Gene set enrichment analysis

The GeneSpring processed data from the 38,535 original probes was collapsed into 13,159 genes based on gene symbols. Some genes were assigned to one or multiple gene sets

downloaded with the GSEA package. There are a total of 837 gene sets in the mammalian gene sets package, 50 of which were excluded by gene set size criteria (15–50), leaving 783 to be included in our analysis. 359 of the 566 chicken/frog conservation gene sets met this size threshold criterion, as did 1,197 out of the 1,892 curated gene sets (Table 1).

Genes were first ranked by their signal-to-noise ratio between the forskolin and control groups. In other words, the genes most consistently overexpressed in the forskolin samples were ranked at one end of the list and those most underexpressed in this group were ranked at the other end. GSEA asks whether the genes that make up a particular gene set are randomly distributed throughout the ranked list of genes, or whether they have a tendency to cluster at the top or bottom of the list. This question was answered by calculating for every gene set a running sum statistic, the maximum of which is referred to as the enrichment score (ES). Each ES is then normalized to the size of its corresponding gene set to produce a normalized enrichment score (NES). Statistical significance of each NES is determined by comparing that NES to the distribution of ESs generated by randomly permutating the genotype class labels of the data set. Therefore, the null hypothesis of a GSEA is that the distribution of a gene set throughout the ranked list of genes is random with regards to the two treatment conditions being compared. The alternative hypothesis is that location of genes in a set is associated with the treatment conditions. Both the p-value and false discovery rate (FDR; q-value) were calculated for each set. Gene sets with a FDR less than 0.25 and a p-value less than 0.05 were considered differentially expressed. The GSEA parameters used were as follows: metric = signal to noise; permutation number = 1,000; gene size minimum = 15; gene size maximum = 500; enrichment statistic = classic; permutation type = phenotype. One GSEA was performed using the 24-hour control data and 72-hour control data to negatively control for gene expression changes occurring with culture duration, as well as false positives not reflective of the treatment condition.

Pre-microRNA181a and anti-microRNA181a transfection

For functional miR181a experiments, basilar papilla explants from 0-day-old chicks were cultured with or without forskolin for 72 hours as described above. Basilar papillae from both conditions were also transfected with either a miR181a precursor (Ambion, Austin, TX) or a non-targeting miRNA which served as a negative

control (Ambion, Austin, TX) at a final concentration of 100 nM. Transfections were performed for six hours in serum-free medium which was eventually replaced with regular medium. BrdU was present at a concentration of 0.01% for the entire culture duration, except for the six-hour transfection. Some basilar papillae were also cultured for 24 hours with forskolin as described above and then transfected with anti-miR181a (Ambion, Austin, TX) to suppress endogenous miR181a. Transfections were performed using the lipid-based X-tremeGENE SiRNA Transfection Reagent (Roche, Indianapolis, IN) per the manufacturer's instructions.

Antibody labeling

After 72 hours in culture basilar papillae were fixed in 4% PFA in PBS for 30 minutes. All fixative was removed by three 5-minute washes in PBS. The tissue was blocked and permeabilized using a solution of PBS with FBS (10%) and Triton-X (0.1%) for one hour. Each basilar papilla was then incubated with mouse anti-BrdU antibodies (1:40, BD, Franklin Lakes, NJ) in PBS for one hour. After washing with PBS, alkaline phosphatase-conjugated goat anti-mouse IgG (1:400, Santa Cruz, Santa Cruz, CA) in PBS with Triton-X (0.1%) was added for one hour. After washing in PBS, alkaline phosphatase substrate was produced using the NBT/BCIP Reagent Kit (Invitrogen, Carlsbad, CA) per the manufacturer's instructions and then added to the tissue for approximately five minutes. All substrate was then thoroughly washed with PBS.

Statistics

Basilar papillae immunohistochemically labeled for BrdU were viewed using brightfield microscopy and were imaged using a digital camera attached to a Zeiss Stemi SV 11 stereoscope. The borders of the sensory epithelium were easily viewed both by direct microscopy and in the captured images. The intraepithelial location of BrdU positive nuclei was confirmed through focal plane adjustments. Only those nuclei which were clearly within the epithelium were counted. Unpaired Student's t-tests were performed to determine the statistical significance of the comparisons discussed in the text using a cut-off of $p < 0.05$.

Co-labeling experiments

To determine whether any newly produced BrdU positive cells express the early hair cell marker myosin VI, some basilar papillae were transfected with pre-miR181a as described above and

Table 1. Gene set enrichment analysis results.

Gene Set Package	Statistic Description	24H FSK	24H CTL	48H FSK	48H CTL	72H FSK	72H CTL
Mammalian	Up/Total	407/783	376/783	512/783	271/783	146/783	636/783
	$p < 0.05$	72	26	165	29	37	210
	$q < 0.25$	66	0	198	5	41	331
Conservation	Up/Total	323/359	36/359	256/359	103/359	219/359	140/359
	$p < 0.05$	176	2	127	22	95	31
	$q < 0.25$	230	0	162	53	128	45
Curated	Up/Total	691/1,197	507/1,197	778/1,197	419/1,197	695/1,197	502/1,197
	$p < 0.05$	240	136	364	94	231	216
	$q < 0.25$	323	152	495	114	285	346

The number of mammalian miRNA/transcription factor motif based ("Mammalian"), chicken/frog conservation transcription factor motif based gene sets ("Conservation"), and curated gene sets from the BROAD Institute ("Curated") meeting the criteria $p < 0.05$ and q (false discovery rate) < 0.25 for forskolin (FSK) and control (CTL) samples after 24, 48, or 72 hours in culture.

doi:10.1371/journal.pone.0011502.t001

cultured for 72 hours. At the end of the culture duration, the tegmentum vasculosum and tectorial membranes were removed prior to fixation in 4% PFA for 30 minutes. Basilar papillae were cryoprotected overnight in 30% sucrose and then embedded in PBS with 1% low melting point agarose and 18% sucrose. The tissue was cryosectioned at 10 μ m and then blocked and permeabilized as described above. Sections were labeled for both myosin VI and BrdU as previously described [12]. Sections were then incubated with rabbit anti-myosin VI (1:350, Proteus, Ramona, CA) in blocking solution for one hour. After washing, sections were then incubated in Alexa Fluor 546 conjugated anti-rabbit secondary antibodies (1:1,000, Invitrogen, Carlsbad, CA) for one hour. After washing, basilar papilla sections were post-fixed in 4% PFA for one hour. The cryosections were then washed in PBS before 20 minute 2M HCl treatment to expose BrdU. After thorough washing, sections were incubated with mouse anti-BrdU antibodies (1:40, BD, Franklin Lakes, NJ) for one hour. After 3 additional PBS washes, sections were incubated with Alexa Fluor 647 conjugated anti-mouse secondary antibodies (Cell Signaling Technology, Danvers, MA) for one hour. After thorough washing, sections were mounted on glass slides in Vectashield fluorescent mounting medium (Vector Laboratories, Burlingame, CA). Images were captured using a Zeiss LSM 510 confocal microscope.

Results and Discussion

Differential expression of genes in the forskolin and control groups increases as a function of time

We report here a systematic comparison of genome-wide expression between proliferating and non-proliferating chick auditory epithelia using Affymetrix whole genome chicken microarrays. The forskolin-induced proliferation paradigm was chosen for this study given the robustness of the effect, which we reasoned would facilitate identification of the molecular events resulting in the production of new hair cells. RNA was isolated from control and forskolin-treated samples cultured for 24, 48 and 72 hours. BrdU incorporation, a marker for S-phase entry, is seen at 72 hours in the forskolin paradigm. Since S-phase entry is the

criterion that distinguishes the avian epithelium from that in mammals, we have concentrated our analysis on this time point.

The isolated RNA from proliferating and non-proliferating auditory epithelia was amplified, biotinylated, hybridized to Affymetrix chicken arrays and scanned as described. The normalized data were then filtered by expression to exclude all probes that were expressed below 20% of the maximum expression level in at least one of the samples at each time point. This measure was taken to ensure that differential expression of genes expressed at very low levels were not assigned a disproportionate amount of significance. 32,509 out of 38,535 probes in the microarray met this initial criterion in the 72-hour samples (Table 2). Of the 32,509 filtered probes, 5,032 had a corrected p-value less than 0.05 at 72 hours. Of these 5,032 genes, 2,824 had at least a two-fold change in expression, which was used as a criterion for functional significance. The same statistics from the 24- and 48-hour samples are also shown in Table 2. A proportional Venn diagram clearly shows differential expression of far more genes at 72 hours than at 24 or 48 hours, but expression of most of the genes differentially expressed at the two earlier time points are also affected at 72 hours (Figure 1). It is not surprising that far fewer genes are differentially expressed at 24 and 48 hours than at 72 hours, given that there must be some latency following exposure to forskolin before gene expression is affected. A heat map revealed that directionality of fold-changes for specific genes remained fairly consistent at 24, 48, and 72 hours (Figure 2). There also appeared to be a general trend toward larger fold-change differences at the two later time points.

Many genes thought to be related to cellular proliferation and inner ear development were differentially expressed between the two conditions at multiple time points (Table 3). The complete lists of genes differentially expressed between the control and forskolin conditions at 24, 48, and 72 hours are included as Supporting Information (Tables S1, S2, and S3, respectively). Given that cellular proliferation is first observed in the basilar papilla at 72 hours in culture with forskolin, the following discussion will focus on data from this particular time point. One gene that is differentially expressed after 72 hours of exposure to forskolin is cyclin I (CCNI), a cell cycle regulator, which is over three-fold

Table 2. Microarray analysis statistics.

Statistical Filtering	24 H			48 H			72 H		
	Number of Probe Sets	Probe Sets F>C	Probe Sets F<C	Number of Probe Sets	Probe Sets F>C	Probe Sets F<C	Number of Probe Sets	Probe Sets F>C	Probe Sets F<C
Total	38,535			38,535			38,535		
Expression above background ^a	31,692			31,793			32,509		
Corrected $p < 0.05$	46			25			5,032		
>1.5-fold (of $p < 0.05$ list)	41	9	32	25	7	18	4,313	2,236	2,077
>2-fold (of $p < 0.05$ list)	39	9	30	24	6	18	2,824	1,291	1,533
>3-fold (of $p < 0.05$ list)	28	3	25	20	2	18	1,302	432	870
>4-fold (of $p < 0.05$ list)	26	3	23	18	1	17	760	194	566

^aThe entire gene expression data set was filtered to exclude probes whose expression was not at least 20% in at least one out of the six 24-hour samples (24 H), six 48-hour samples (48 H), or twelve 72-hour samples (72 H). The statistics reported are based only on those probes that met this criterion. Half of the samples from each time point were treated with forskolin (F) and the remainder served as controls (C). Shown in boldface are the statistics for the list of genes defined to be differentially expressed using $p < 0.05$ and fold-change > 2 .

doi:10.1371/journal.pone.0011502.t002

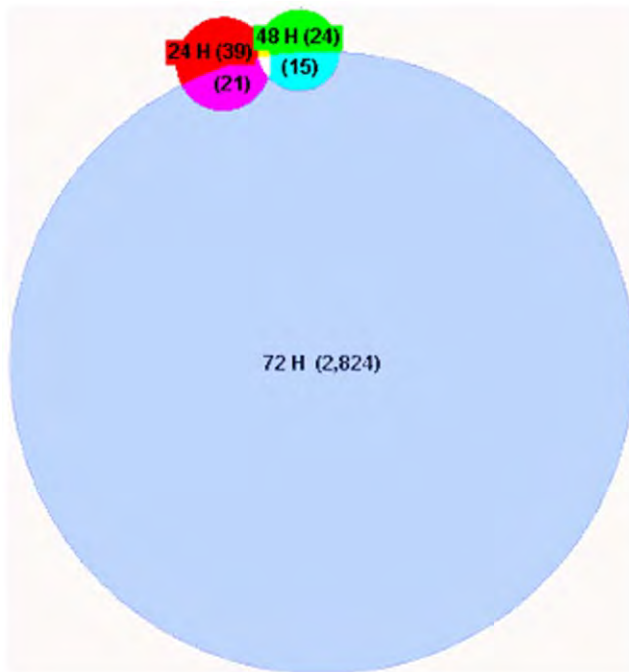


Figure 1. Far more genes were differentially expressed at 72 hours than at 24 or 48 hours of exposure to forskolin. Shown is a proportional Venn diagram indicating the number of genes significantly ($p < 0.05$ and fold change > 2) differentially expressed at 24, 48, and 72 hours of exposure to forskolin. The number of genes in each category is indicated in parentheses. Far more genes are affected at 72 hours than at either of the two earlier time points. A little over half of the genes differentially expressed at 24 or 48 hours are also differentially expressed at 72 hours. Only one gene, AMPH, was affected at all three time points.
doi:10.1371/journal.pone.0011502.g001

underexpressed in the forskolin samples at 72 hours and is downregulated in proliferating murine cardiomyocytes (Table 3) [51]. Wnt5a is underexpressed in regenerating tissue, a noteworthy observation as inactivation of this gene has been linked to cellular proliferation in a particular form of leukemia [52]. Wnt proteins are also thought to play a role in the development of the lateral line in zebrafish (reviewed in [53]) and chicken inner ears [54,55,56]. Frizzled homolog 10, a gene likely to play a role in cellular proliferation, is over 15-fold overexpressed in proliferating versus non-proliferating tissue after 72 hours in culture [57].

Differential gene expression is confirmed by qPCR

Quantitative PCR (qPCR) was performed on select genes in order to validate the microarray data. Primers were designed for twelve genes that were found by microarray to be differentially expressed between the two conditions at 72 hours; seven genes were upregulated and five were downregulated in the forskolin condition. QPCR confirmed the directionality of the microarray findings for nine out of the twelve genes tested (75%). The fold-changes of these nine genes were all significantly different from one (95% confidence interval, data not shown), confirming their differential expression as detected by microarray. These findings validate the initial microarray results, so further analyses were performed on the gene expression data set.

Curated gene set enrichment results

Our initial analysis of expression of individual genes that were differentially expressed revealed that many are known to be

involved in control of the cell cycle and hair cell differentiation. To more systematically identify genes that were correlated with specific phenotypes, we used gene set enrichment analysis (GSEA), a computational method to determine the expression of genes associated with specific empirically determined phenotypes. Gene sets packages were downloaded from the Broad Institute website and were used for GSEAs on the Affymetrix expression data from 24, 48, and 72 hours (Table 1). An additional GSEA was performed comparing the microarray data from the 24-hour control samples to that in the 72-hour control samples to serve as a negative control for changes in gene expression resulting from the culture conditions rather than exposure to forskolin. This GSEA produced no significantly (FDR < 0.25 and p -value < 0.05) enriched gene sets for any of the three gene set packages used (data not shown).

To assess the functional relevance of the genes that were differentially expressed, a GSEA was performed using manually curated gene sets downloaded from the Broad Institute website. This package contains sets of genes found by individual experiments to be associated with specific phenotypes. The complete GSEA results for all utilized gene sets in this and all subsequent GSEAs are included as Supporting Information (Tables S4, S5, S6, S7, S8, S9, S10, S11, S12). Consistent with our observation of individual gene expression, the GSEA performed using curated gene sets showed that in forskolin treated basilar papillae many gene sets associated with cell cycle control are significantly enriched at various time points. For example, at 24, 48, and 72 hours there is enrichment of the following gene sets: SERUM_FIBROBLAST_CELL_CYCLE [58], HSA04110_CELL_CYCLE [59], [60,61], CELL_CYCLE [62], CELL_CYCLE_KEGG [59,60,61], GOLDRATH_CELL_CYCLE [63], CELL_CYCLE_CHECKPOINT, G1_TO_S_CELL_CYCLE_REACTOME [64], and BRENTANI_CELL_CYCLE [65] in explants exposed to forskolin (Table 4). The enrichment statistics for all gene sets used in this GSEA are included as Supporting Information (Tables S4, S5, S6). These findings are expected and instill confidence about the rest of the enrichment analysis results, given that forskolin treatment is known to stimulate S-phase entry in normally quiescent cells [22,23].

The GSEA based on the curated gene sets also revealed that targets of E2F1, a transcription factor known to be important for cell cycle control, in human primary fibroblast cells identified by ChIP analysis (REN_E2F1_TARGETS [66]) are enriched in the proliferating auditory epithelia at both 48 and 72 hours. Further, a set of genes in the retinoblastoma pathway identified by microarray analysis in human cell lines (VERNELL_PRB_CLSTR1 [67]) was found to be significantly enriched after 24, 48, and 72 hours in culture with forskolin. These findings further underscore the potentially important role of the E2F1 transcription factor and the retinoblastoma protein pathway in auditory hair cell regeneration.

A particularly interesting result of the GSEA using the curated gene sets is the observation that a set of genes found to be upregulated in mouse embryonic, neural and hematopoietic stem cells (HSC) relative to differentiated brain and bone marrow cells (STEMCELL_COMMON_UP [68]) is also enriched in the basilar papilla after culture with forskolin for 24, 48, or 72 hours. Further, a set of genes found to be downregulated in stem cells (STEMCELL_COMMON_DN [68]) in the same study were also enriched in the quiescent tissue relative to proliferating tissue after 48 or 72 hours in culture, suggesting that genes downregulated in stem cells are also downregulated in the proliferating basilar papilla.

Though not widely accepted, there is evidence for the existence of stem cells within the postnatal organ of Corti [69]. Additionally, approximately 4% of supporting cells show stem cell-like behavior

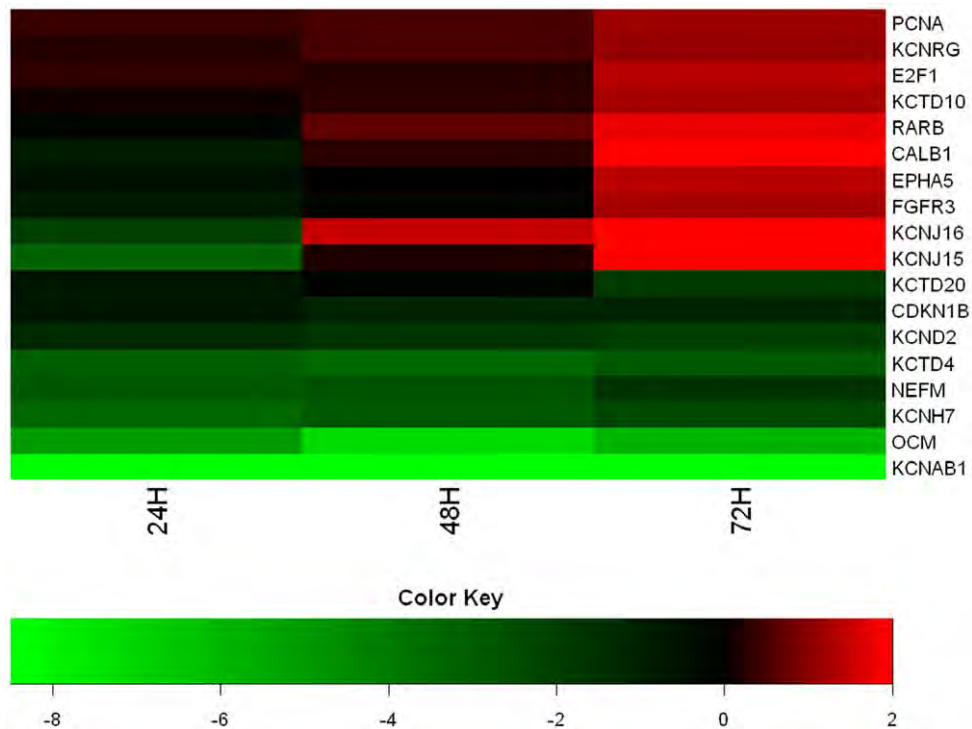


Figure 2. Fold-change differences of selected genes of interest remain stable at 24, 48, and 72 hours. Shown is a heat map depicting fold-changes between the forskolin and control conditions for a set of genes of interest the three time points indicated. The genes shown were selected because of their known expression in the inner ear (i.e., RARB, CALB1, OCM), ion channel identity (e.g., KCNAB1, KCNJ15), or relevance to the present study (i.e., E2F1). The genes span a range of fold-changes and are both up and downregulated with forskolin treatment. Fold-changes are given as $\log_2(\text{expression in forskolin}/\text{expression in control})$. The directionality of fold-changes was fairly consistent across time points, but there was a slight general trend toward increasing fold-change values from 24 to 72 hours. doi:10.1371/journal.pone.0011502.g002

in that they undergo multiple rounds of division [70]. Recent work has shown that murine embryonic and induced pluripotent stem cells retain the capacity to differentiate into mechanosensitive cells which resemble immature hair cells [71]. It is interesting that genes found to be upregulated in HSCs specifically are also upregulated in proliferating basilar papillae given that HSCs are thought to remain in a state of quiescence until stimulated to proliferate by external signals [72,73]. The chick basilar papilla is also quiescent until injury stimulates regeneration of hair cells by signals that have not yet been identified. It is therefore very interesting that proliferating basilar papillae overexpress genes that are also overexpressed in HSCs [68]. If the basilar papilla does in fact possess stem cells that share some properties with HSCs then it may be possible to stimulate the production of new hair cells using signals known to induce normally quiescent HSCs to proliferate. These results are consistent with the hypothesis that in forskolin treated basilar papillae some supporting cells are stimulated to dedifferentiate and express stem cell markers, prior to division and production of new hair cells.

It is worth noting that at 24 and 48 hours after exposure to forskolin, there is enrichment of the following curated gene sets, all of which are associated with cell death and/or apoptosis: BRENTANI_DEATH [65], HSA04210_APOPTOSIS [59,60,61], APOPTOSIS [64], APOPTOSIS_GENMAPP [64]. There is also enrichment of the gene set PASSERINI_APOPTOSIS [74] after 48 hours of exposure to forskolin. It is believed that forskolin induces proliferation in the inner ear without injury and subsequent regeneration, but this has never been definitively proven. However, the proliferation that is seen in the basilar papilla following exposure to forskolin is more

robust than that seen following exposure to gentamicin, which causes hair cell death and regeneration [22]. Unpublished experiments performed for the same paper also did not show a qualitative loss of hair cells at 24, 48, or 72 hours, whereas hair cell ejection from the basilar papilla is seen as early as 30 hours following subcutaneous administration of gentamicin [75]. Markers of cell death in avian hair cells can appear even earlier following injury and begin with TIAR translocation as early as 12 hours after injury, before caspase activation which can occur as early as 30 hours after injury [76,2]. Our gene expression data do not show differential expression of key markers of hair cell death such as caspase-3 and caspase-9 [76]. Regardless, the GSEA results suggest a possible contribution of apoptosis in forskolin induced proliferation in the avian inner ear. As the aim of the present study was to identify novel genes and pathways important for the production of new hair cells in deafened animals, the reported findings are of considerable interest regardless of a possible contribution of injury with subsequent regeneration in the forskolin-induced proliferation model of hair cell regeneration. Additional work will be needed to determine just how much, if any, of this proliferation is in fact the result of injury to the auditory epithelium.

Mammalian gene set enrichment results

To determine which miRNAs were likely upregulated to give rise to the observed pattern of differential gene expression detected by microarray, an additional GSEA was performed using the mammalian gene sets which are based on genomic conservation between the human, rat, mouse, and dog genomes. These gene sets were used on our chicken gene expression data because they included not only transcription factor binding site, but also

Table 3. QPCR validation of gene expression data.

<i>Gene symbol</i>	Microarray 24 Hours		Microarray 48 Hours		Microarray 72 Hours		qPCR 72 Hours
	Median Fold- Change (F/C)	Corrected <i>p</i> Value	Median Fold- Change (F/C)	Corrected <i>p</i> Value	Median Fold- Change (F/C)	Corrected <i>p</i> Value	Average Fold- Change (F/C)
CCNI	1/1.68	0.26	1/2.46	0.28	1/3.00	5.22E-05	1/1.54
	1/2.24	0.27	1/4.59	0.25	1/3.31	0.0017	
	1/2.57	0.23	1/3.32	0.33	1/3.44	0.0035	
	1/2.27	0.23	1/2.90	0.34	1/4.21	3.63E-04	
WNT5a	1/3.88	0.15	1/2.56	0.41	1/2.31	0.017	
WNT3	1.26	0.40	1.90	0.41	2.81	.023	
FZD10	1.28	0.86	1/1.34	0.88	15.48	0.0092	
BECN1	1.05	0.88	1.65	0.37	2.04	0.051	1.66
	1.39	0.27	1.37	0.50	1.61	0.15	
CDC45L	3.15	0.34	6.19	0.51	3.16	0.14	
DPM1	1.10	0.79	1.51	0.19	2.40	5.00E-04	1/1.11
	1.17	0.52	1.47	0.51	2.15	0.0024	
SNX1	1.69	0.21	1.22	0.39	2.65	7.07E-04	5.62
EME1	1.03	0.27	1.03	0.65	5.29	0.0032	1.38
	1.99	0.25	3.52	0.36	1.08	0.31	
FBXO8	1.03	0.27	2.02	0.22	3.42	0.0072	1.96
	1/1.99	0.25	2.05	0.37	2.16	0.031	
PIGW	2.09	0.041	2.58	0.33	4.30	6.38E-04	1.64
CDH20	1/1.11	0.87	1/1.28	0.56	1/8.20	0.0018	1/8.11
	1.13	0.89	1/2.19	0.51	1/22.25	4.52E-05	
ITGA4	1.09	0.36	1/1.18	0.51	1/1.06	0.47	1/3.67
	1/1.87	0.080	1/1.40	0.49	1/2.08	0.089	
	1.16	0.47	1/1.42	0.51	1/2.28	0.055	
NLGN1	1.06	0.30	1/1.12	0.51	1.02	0.43	1/1.46
	1.08	0.27	1/1.08	0.51	1/1.01	0.87	
	1/5.92	0.23	1/3.90	0.15	1/1.25	0.45	
	1/2.58	0.27	1/3.08	0.51	1/2.11	0.0046	
CDKN1B (p27)	1.06	0.28	1/1.05	0.51	1/2.99	0.011	2.64
	1/1.27	0.30	1/2.97	0.49	1/2.12	0.015	
	1/1.77	0.15	1/1.72	0.22	1/2.21	9.92E-04	
OCM	1/1.27	0.307	1/153.66	0.14	1/64.33	1.81E-04	1/13.45

QPCR and microarray data for individual genes of interest and genes selected for qPCR validation as described in the text. Multiple microarray values represent different probe sets for the same gene.

doi:10.1371/journal.pone.0011502.t003

miRNA binding sites, which are fairly well conserved between species [42]. Using these mammalian gene sets and a false discovery rate cut-off of 0.25 as suggested by [40], 210 out of 783 gene sets were significantly enriched in the control condition and 37 in the forskolin condition at 72 hours (Table 1). As a negative control, enrichment of predicted targets of the transcription factor PAX6 was examined, given its known role in retinal development [77,78] and absence of expression in the developing chicken inner ear [79]. That a pathway thought not to be important in the inner ear was not activated by forskolin exposure underscores that significantly enriched gene sets reflect real changes in gene expression (Supporting Information).

The difference in the number of gene sets associated with the control and forskolin conditions is striking, and it is worth pointing

out that many of the gene sets associated with the control condition are miRNA gene sets, each of which represents a group of genes that are predicted targets of a specific miRNA. The association of these sets with the control condition implies that the miRNA target genes are down-regulated following forskolin treatment. Thus, we hypothesize that these miRNAs are upregulated in the forskolin group. We put forward this entire set of miRNAs as candidates whose role in hair cell regeneration and cellular proliferation warrants further investigation. Specific miRNAs and transcription factors of interest based on our analysis using the mammalian gene sets are presented in Table 5. A complete list of all significantly enriched gene sets from this analysis are included in the Supporting Information section (Tables S7, S8, S9).

Table 4. Curated gene set enrichment analysis results.

Gene Set	Enriched at 24H	24H P-Value	24H FDR	Enriched at 48H	48H P-Value	48H FDR	Enriched at 72H	72H P-Value	72H FDR
SERUM_FIBROBLAST_CELLCYCLE	<i>Forskolin</i>	0.012	0.053	<i>Forskolin</i>	<0.001	<0.001	<i>Forskolin</i>	<0.001	<0.001
HSA04110_CELL_CYCLE	<i>Forskolin</i>	0.002	0.014	<i>Forskolin</i>	<0.001	<0.001	<i>Forskolin</i>	<0.001	<0.001
CELL_CYCLE	<i>Forskolin</i>	<0.001	0.004	<i>Forskolin</i>	<0.001	<0.001	<i>Forskolin</i>	<0.001	<0.001
CELL_CYCLE_KEGG	<i>Forskolin</i>	<0.001	0.004	<i>Forskolin</i>	<0.001	<0.001	<i>Forskolin</i>	<0.001	<0.001
GOLDRATH_CELLCYCLE	<i>Forskolin</i>	0.018	0.061	<i>Forskolin</i>	<0.001	<0.001	<i>Forskolin</i>	<0.001	0.002
CELL_CYCLE_CHECKPOINT	<i>Forskolin</i>	<0.001	0.003	<i>Forskolin</i>	0.002	0.008	<i>Forskolin</i>	<0.001	0.003
G1_TO_S_CELL_CYCLE_REACTOME	<i>Forskolin</i>	<0.001	0.002	<i>Forskolin</i>	0.006	0.023	<i>Forskolin</i>	0.013	0.054
BRENTANI_CELL_CYCLE	<i>Forskolin</i>	<0.001	0.004	<i>Forskolin</i>	<0.001	<0.001	<i>Forskolin</i>	0.018	0.059
HSA04330_NOTCH_SIGNALING_PATHWAY	<i>Forskolin</i>	0.577	0.679	<i>Forskolin</i>	0.037	0.084	<i>Forskolin</i>	0.896	0.949
STEMCELL_COMMON_UP	<i>Forskolin</i>	<0.001	0.001	<i>Forskolin</i>	<0.001	<0.001	<i>Forskolin</i>	<0.001	<0.001
STEMCELL_COMMON_DN	Control	0.107	0.294	Control	<0.001	0.022	Control	<0.001	0.008
REN_E2F1_TARGETS	<i>Forskolin</i>	0.141	0.278	<i>Forskolin</i>	0.002	0.007	<i>Forskolin</i>	<0.001	0.001
VERNELL_PRB_CLSTR1	<i>Forskolin</i>	0.006	0.054	<i>Forskolin</i>	<0.001	<0.001	<i>Forskolin</i>	<0.001	<0.001
BRENTANI_DEATH	<i>Forskolin</i>	<0.001	0.004	<i>Forskolin</i>	0.039	0.094	<i>Forskolin</i>	0.853	0.914
HSA04210_APOPTOSIS	<i>Forskolin</i>	<0.001	0.017	<i>Forskolin</i>	0.004	0.012	<i>Forskolin</i>	0.016	0.049
APOPTOSIS	<i>Forskolin</i>	0.002	0.010	<i>Forskolin</i>	0.004	0.044	Control	0.308	0.454
APOPTOSIS_GENMAPP	<i>Forskolin</i>	0.016	0.052	<i>Forskolin</i>	0.002	0.019	<i>Forskolin</i>	0.146	0.256
PASSERINI_APOPTOSIS	<i>Forskolin</i>	0.085	0.207	<i>Forskolin</i>	0.015	0.034	Control	0.045	0.132

Shown are the curated gene set enrichment analysis results for selected gene sets of interest at 24, 48, and 72 hours. The gene sets shown here were downloaded from the BROAD Institute website and represent empirically defined sets of genes. References for each gene set are provided in the text. Italicized are those gene sets with p-value <0.05 and false discovery rate (FDR) <0.25, which are taken as significant. Gene sets are directly as they appear in the Molecular Signatures Database on the Broad Institute website.

doi:10.1371/journal.pone.0011502.t004

Table 5. Mammalian gene set enrichment analysis results.

Gene Set	Enriched at 24H	24H P-Value	24H FDR	Enriched at 48H	48H P-Value	48H FDR	Enriched at 72H	72H P-Value	72H FDR
TGAATGT,MIR-181A,MIR-181B,MIR-181C,MIR-181D	<i>Forskolin</i>	0.475	1	<i>Forskolin</i>	0.001	0.009	Control	<0.001	0.001
ACTGTGA,MIR-27A,MIR-27B	<i>Forskolin</i>	0.238	1	<i>Forskolin</i>	0.406	1	Control	0.002	0.042
CAGTGTT,MIR-141,MIR-200A	Control	0.683	1	<i>Forskolin</i>	0.017	0.648	Control	0.002	0.031
V\$E2F_Q6	<i>Forskolin</i>	0.033	0.273	<i>Forskolin</i>	0.001	0.015	<i>Forskolin</i>	0.004	0.035
V\$E2F1_Q6	<i>Forskolin</i>	0.003	0.009	<i>Forskolin</i>	0.003	0.102	<i>Forskolin</i>	<0.001	0.034
V\$E2F_Q4	<i>Forskolin</i>	0.014	0.064	<i>Forskolin</i>	0.002	0.056	<i>Forskolin</i>	0.008	0.064
V\$E2F_Q4_01	<i>Forskolin</i>	0.014	0.064	<i>Forskolin</i>	0.001	0.003	<i>Forskolin</i>	0.019	0.121
V\$E2F1_Q3	<i>Forskolin</i>	0.126	0.994	<i>Forskolin</i>	0.014	0.53	<i>Forskolin</i>	0.006	0.121
SGCGSSAAA_V\$E2F1DP2_01	<i>Forskolin</i>	0.056	0.733	<i>Forskolin</i>	0.008	0.301	<i>Forskolin</i>	0.014	0.121
V\$E2F1DP2_01	<i>Forskolin</i>	0.055	0.549	<i>Forskolin</i>	0.001	0.016	<i>Forskolin</i>	0.031	0.14
V\$E2F1_Q4_01	<i>Forskolin</i>	0.254	1	<i>Forskolin</i>	0.001	0.016	<i>Forskolin</i>	0.016	0.142
V\$E2F4DP1_01	<i>Forskolin</i>	0.055	0.677	<i>Forskolin</i>	0.002	0.062	<i>Forskolin</i>	0.016	0.137
V\$E2F_Q2	<i>Forskolin</i>	0.056	0.601	<i>Forskolin</i>	0.001	0.016	<i>Forskolin</i>	0.016	0.132
V\$E2F1DP1RB_01	<i>Forskolin</i>	0.033	0.35	<i>Forskolin</i>	0.001	0.003	<i>Forskolin</i>	0.02	0.14
V\$E2F1DP1_01	<i>Forskolin</i>	0.055	0.771	<i>Forskolin</i>	0.001	0.018	<i>Forskolin</i>	0.024	0.139
V\$E2F1_Q6_01	<i>Forskolin</i>	0.003	0.009	<i>Forskolin</i>	0.007	0.256	<i>Forskolin</i>	0.073	0.224
V\$E2F_Q3	<i>Forskolin</i>	0.194	1	<i>Forskolin</i>	0.002	0.069	<i>Forskolin</i>	0.068	0.227

Shown are the mammalian gene set enrichment analysis results for selected gene sets of interest at 24, 48, and 72 hours. Italicized are those gene sets with p-value < 0.05 and false discovery rate (FDR) <0.25, which are taken as significant. Gene sets are directly as they appear in the Molecular Signatures Database on the Broad Institute website.

doi:10.1371/journal.pone.0011502.t005

Some of the miRNAs identified by enrichment analysis are interesting candidates for further study given what is already known about their function. For example, miR141 and miR200a are expressed in the chicken inner ear epithelium, and are important regulators of epithelial-mesenchymal transition [30,80]. It is also interesting that the miR27 family showed up as one of the most significant gene sets in this particular analysis given the known role of this miRNA in cellular proliferation. Specifically, downregulation of this miRNA seems to decrease proliferation in the context of hepatic stellate cell activation, an early event in liver fibrosis [81]. MiR27a is overexpressed in human gastric adenocarcinoma, and inhibition of this miRNA limits proliferation [82]. Another study has also shown that the oncogenic activity of miR27a in human breast cancer cells is likely due to downregulation of genes controlling the G2-M cell-cycle checkpoint [83]. MiR181a is known to be expressed in the mammalian inner ear [28], and has a pro-proliferative role in human leukemia cells, which appears to be mediated by suppression of the cell cycle inhibitor p27 [33]. Given the abundance and nature of evidence for a role of miR181a, miR27a, and miR141/miR200a in cellular proliferation or inner ear development, we put these forward as particularly intriguing candidates for further study within the context of auditory hair cell regeneration.

Chicken/frog gene set enrichment analysis

While the primary goal of the GSEA with the mammalian gene sets was to identify miRNAs that may be important for hair cell regeneration, interestingly some transcription factor gene sets were found to be up- and downregulated in the forskolin condition. This was surprising in light of the fact that these sets were based on portions conserved across only selected mammalian genomes, which were expected to differ significantly from gene sets based on the chicken genome. To verify the up- and downregulation of these gene sets in the chicken inner ear an additional GSEA was performed using gene sets based on scanning the portions of the chicken genome that are conserved with frog (*Xenopus tropicalis*) to look for enrichment of sets of genes sharing particular transcrip-

tion factor recognition sites obtained from the TRANSFAC database. Using a q-value cutoff of 0.25 there were 41 gene sets associated with forskolin treatment, and 331 gene sets associated with forskolin treatment (see Table 1). The enrichment statistics for all gene sets included in this analysis are presented as Supporting Information (Tables S10, S11, S12). Of the six gene sets that were significantly enriched in the forskolin condition, four are sets of genes that share known E2F1 binding sites (Table 6). Additionally, some E2F1 gene sets are significantly enriched in forskolin treated tissue at 24 and 48 hours relative to untreated controls (Table 6), suggesting that upregulation of predicted E2F1 targets occurs early after forskolin treatment and is sustained until 72 hours in culture, when new cells are first seen [22]. Many E2F/E2F1 gene sets are also enriched in the forskolin treated tissue when the mammalian gene sets (Table 5) are used to compare the expression data from forskolin samples fixed after 24 and 72 hours in culture, suggesting agreement between the GSEAs performed using the mammalian gene sets and chicken/frog conservation gene sets. The identification of E2F/E2F1 by both analyses strongly suggests a role for this transcription factor in forskolin induced proliferation in the chicken inner ear.

E2F1 is an intriguing candidate for further study given its known role in cell cycle control (reviewed in [84]) and potential role in inner ear development (reviewed in [85]). E2Fs bind hypophosphorylated pRBs which then sequester these factors. pRBs can be phosphorylated by cyclin-dependent kinases (CDKs), rendering these proteins unable to bind E2Fs thereby releasing these factors which then become transcriptionally active [86,87,88]. Interestingly, overexpression of E2F1 has been shown to induce quiescent REF-52 cells to enter S-phase [89]. E2F1 forms part of an 'activating' E2F complex that can interact with pocket proteins (pRBs) to control the cell cycle [90]. E2F1 exclusively binds the pRB RB1, and peaks in expression during the G1-S checkpoint [90]. Given the central role of E2Fs in cell cycle control, our finding that genes targeted by E2F1 are enriched among the genes that are overexpressed in the proliferating chick inner ear suggests a role for this transcription factor in hair cell regeneration.

Table 6. Conservation gene set enrichment analysis results.

Gene Set	Enriched at 24H	24H P-Value	24H FDR	Enriched at 48H	48H P-Value	48H FDR	Enriched at 72H	72H P-Value	72H FDR
V\$E2F_Q2	<i>Forskolin</i>	<0.001	<0.001	<i>Forskolin</i>	0.006	0.016	<i>Forskolin</i>	<0.001	0.003
V\$E2F1_Q3_01	<i>Forskolin</i>	0.038	0.066	<i>Forskolin</i>	0.017	0.063	<i>Forskolin</i>	0.024	0.415
V\$E2F_Q3	<i>Forskolin</i>	0.099	0.176	<i>Forskolin</i>	0.071	0.144	<i>Forskolin</i>	0.012	0.038
V\$E2F1DP1RB_01	<i>Forskolin</i>	0.793	0.840	<i>Forskolin</i>	0.905	0.933	<i>Forskolin</i>	0.019	0.057
V\$E2F1_Q4_01	<i>Forskolin</i>	0.345	0.430	<i>Forskolin</i>	0.573	0.639	<i>Forskolin</i>	0.041	0.096
V\$E2F_Q3	<i>Forskolin</i>	0.342	0.416	<i>Forskolin</i>	0.418	0.532	<i>Forskolin</i>	0.038	0.101
V\$E2F_Q3_01	<i>Forskolin</i>	0.681	0.734	<i>Forskolin</i>	0.416	0.483	<i>Forskolin</i>	0.038	0.108
V\$E2F_Q4	<i>Forskolin</i>	0.175	0.249	<i>Forskolin</i>	0.365	0.456	<i>Forskolin</i>	0.040	0.108
V\$E2F1_Q6_01	<i>Forskolin</i>	0.422	0.477	<i>Forskolin</i>	0.245	0.332	<i>Forskolin</i>	0.058	0.115
V\$E2F1_Q3	<i>Forskolin</i>	0.511	0.564	Control	0.306	0.437	<i>Forskolin</i>	0.077	0.155
V\$E2F_Q6	<i>Forskolin</i>	0.964	0.965	Control	0.714	0.832	<i>Forskolin</i>	0.073	0.155
V\$E2F1_Q6	<i>Forskolin</i>	0.330	0.395	<i>Forskolin</i>	0.245	0.332	<i>Forskolin</i>	0.079	0.152

Shown are the results of the conservation gene set enrichment analysis performed on gene expression data from 24, 48, and 72 hours in culture. These analyses were performed using gene sets based on transcription factor motifs in regions conserved between the chicken and frog genomes. The gene sets shown here were downloaded from the BROAD Institute website and represent empirically defined sets of genes. References for each gene set are provided in the text. Italicized are those gene sets with p-value <0.05 and false discovery rate (FDR) <0.25, which are taken as significant. Gene sets are directly as they appear in the Molecular Signatures Database on the Broad Institute website.

doi:10.1371/journal.pone.0011502.t006

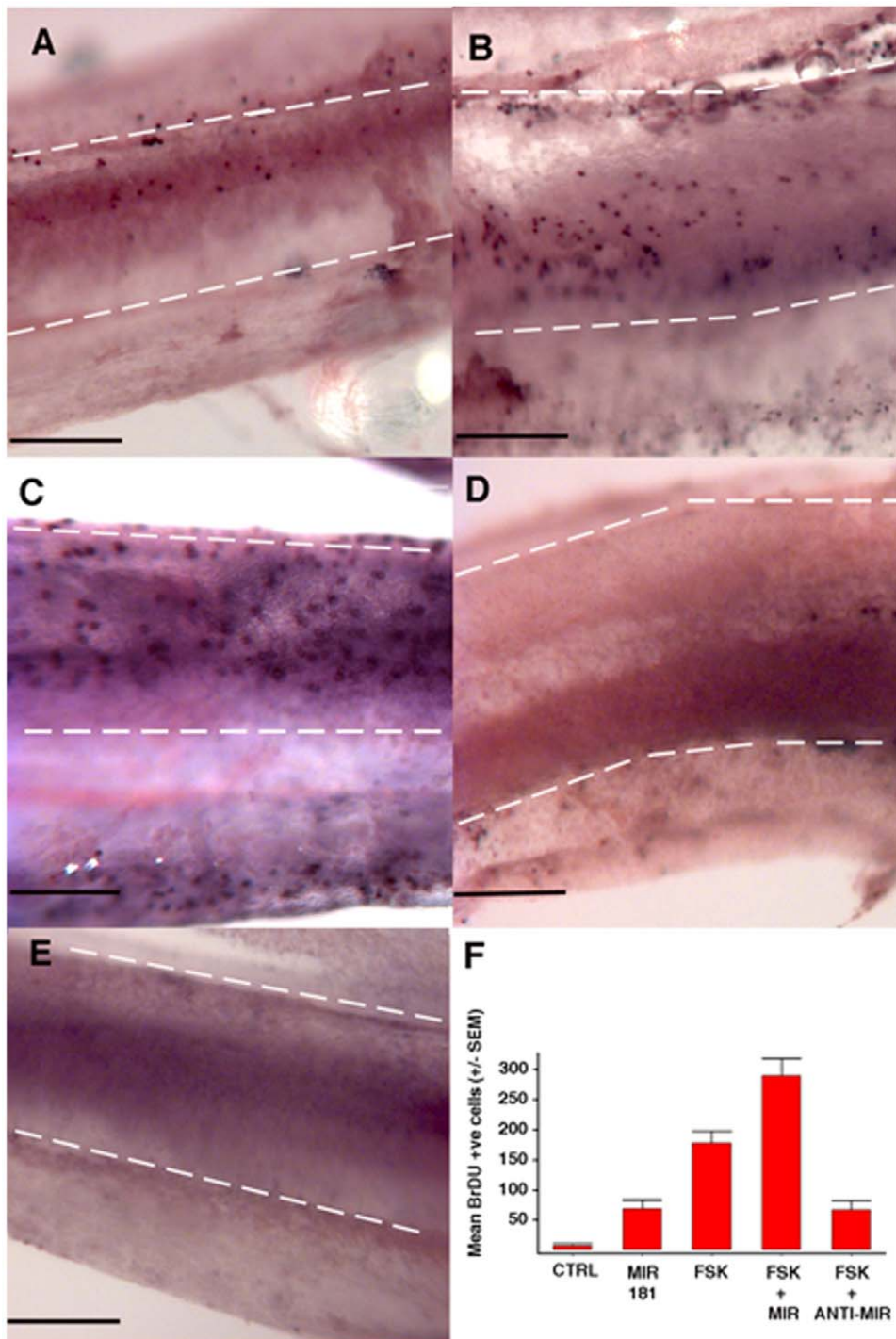


Figure 3. MicroRNA181a overexpression produces proliferation in the chicken basilar papilla. Basilar papillae from 0-day-old chicks were cultured for 72 hours in the presence of BrdU, the nuclear incorporation of which was detected by antibody labeling. In A–E sensory epithelia are outlined with dashed white lines. The neural edge of each epithelium is at the bottom, the abneural edge is at the top, the distal end is to the right and the proximal end is to the left of the image. BrdU-positive (i.e., recently divided) cells are immunohistochemically labeled and appear as purple dots. Individual cochleas were treated with 100 nM pre-miR181a (A), 100 μM forskolin (FSK) (B), FSK + 100 nM pre-miR181a (C), 100 μM FSK + 100 nM anti-miR181a (D), or DMSO as a vector control (E). A pro-proliferative effect of miR181a can be appreciated. Further, knocking down endogenous miR181a appears to have a large suppressive effect on forskolin induced proliferation. Transfection was achieved in the first 24 hours of culture using X-tremeGENE siRNA Transfection Reagent in accordance with the manufacturer's instructions (Roche, Indianapolis, IN). The miRNA containing media was removed after 24 hours and replaced with normal medium. The summary of the average number of BrdU positive cells for the control (n=7), miR181a (n=8), forskolin (n=8), forskolin + miR181a (n=8), and forskolin + anti-miR181a (n=3) conditions. The following comparisons were all statistically significant: control versus miR181a ($p=0.001$), control versus forskolin ($p<0.001$), miR181a versus forskolin ($p<0.001$), forskolin versus forskolin plus anti-miR181a ($p=0.008$) and forskolin versus forskolin plus miR181a ($p=0.005$). Scale bars in panels A–E=0.2 mm. doi:10.1371/journal.pone.0011502.g003

Functional microRNA181a studies

Of all the miRNAs whose predicted targets were significantly enriched in control relative to forskolin treated basilar papillae, miR181a was specifically selected for functional studies in light of its high level of statistical significance, known expression in the developing mammalian inner ear [28], and pro-proliferative role in human leukemia cells, which appears to be mediated by suppression of the cell cycle inhibitor p27 [33]. To test whether miR181a overexpression is sufficient to stimulate proliferation, chick basilar papilla explants were transfected with either pre-miR181a, which is converted to mature miR181a within cells, or a non-targeting negative control miRNA. Incorporation of the thymidine analog BrdU was used to assay proliferation. Basilar papillae transfected with pre-miRNA had on average 68.75 (\pm SEM = 13.54) BrdU positive cells, significantly more than organs transfected with a non-targeting miRNA which averaged only 7.00 (\pm SEM = 10.23) BrdU positive cells ($p < 0.01$, Figure 3). MiR181a overexpression is therefore sufficient to stimulate proliferation in the normally quiescent chick auditory epithelium.

Basilar papillae cultured with forskolin for 72 hours and transfected with a non-targeting miRNA had on average 178.25 (\pm SEM = 19.02) BrdU positive cells, significantly more than is seen with miR181a overexpression ($p < 0.05$) which suggests that miR181a upregulation may account for only a portion of forskolin's mitogenic effect (Figure 3). To determine whether miR181a expression is necessary for forskolin induced proliferation, some basilar papillae were cultured with forskolin for 24 hours, then transfected with anti-miR181a to suppress endogenous miR181a, then cultured with forskolin for an additional 24 hours. Basilar papillae transfected with only anti-miR181a without forskolin treatment had an average of only 14

(\pm SEM = 3.06) BrdU positive cells per epithelium, not significantly different from controls. Basilar papillae exposed to forskolin and transfected with anti-miR181a had an average of 67.33 (\pm SEM = 13.38) BrdU positive cells, significantly less than the basilar papillae that were cultured with forskolin and transfected with a negative control miRNA ($p < 0.01$), suggesting that endogenous miR181a contributes to the pro-proliferative effect of forskolin in the chick inner ear.

To see whether miR181a could enhance the already robust pro-proliferative effect of forskolin, basilar papillae were transfected with pre-miR181a and cultured in the presence of forskolin for 72 hours. These basilar papillae averaged 289.63 (\pm SEM = 28.04) BrdU positive cells per basilar papilla, which is significantly higher than the forskolin effect alone ($p < 0.01$). This observation reaffirms the finding that endogenous miR181a is an important mediator of forskolin induced proliferation in the chick inner ear and is limited in part by the ability of forskolin to stimulate upregulation of miR181a.

Given the observation that miR181a overexpression is sufficient to stimulate proliferation in the chick auditory epithelium, basilar papillae were transfected with pre-miR181a or nontargeting negative control miRNA and then cryosectioned and labeled for BrdU and the early myosin VI to determine whether any of the newly produced BrdU positive cells express the early hair cell marker. As is seen in Figure 4, some cells labeling for BrdU 72 hours after transfection with pre-miR181a are located at the most apical portion of the basilar papilla, an area occupied by only hair cells and thin supporting cell processes. Further, some cells with nuclear BrdU labeling also have cytoplasmic myosin VI labeling. No such co-labeling cells were observed in basilar papillae transfected with a non-targeting miRNA. These results

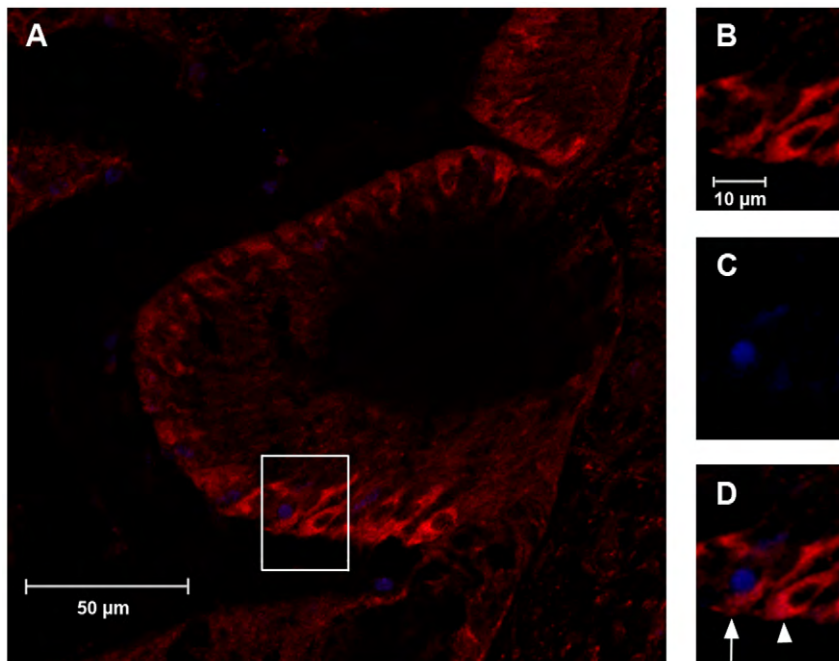


Figure 4. Some new cells produced by miR181a transfection express the early hair cell marker myosin VI. Shown is a confocal image of a basilar papillae that was transfected with pre-miR181a, cultured for 72 hours, then cryosectioned and labeled for BrdU (blue) and the early hair cell marker myosin VI (red) (A). The apical surface of hair cells is to the left of the image and the neural edge of the basilar papillae is toward the bottom. The tectorial membrane has been removed to allow for antibody labeling. The inset of A is also shown in panels B (myosin VI), C (BrdU) and D (merge). The arrow in D shows a cell that expresses myosin VI and has a BrdU positive nucleus, whereas the arrowhead shows a cell that is labeling for myosin VI but not BrdU. The double-labeled cell is one that has been stimulated to divide and subsequently begin differentiating toward a hair cell phenotype. The scale bar in B also applies to C and D. doi:10.1371/journal.pone.0011502.g004

suggest that miR181a overexpression results in the production of new hair cells.

It is not surprising that a single miRNA is able to stimulate S-phase entry in the avian auditory epithelium given the mounting evidence that miRNAs can affect cell cycle regulation in a variety of systems. MiR181a specifically has been shown to have a proliferative effect in human myeloid leukemia cells [33]. Interestingly, this effect appears to be mediated in part by producing downregulation of p27, which may represent a barrier to hair cell regeneration in the mammalian cochlea [34,35,91,92]. There is also evidence that many different miRNAs, including miR181a, are expressed in the developing mouse inner ear [28]. Despite these findings, studies on the role of miRNA in hair cell regeneration are limited in number and scope. One study revealed that the let-7 family of miRNA is downregulated in the regenerating newt auditory epithelium [32]. An interesting translational correlate to this finding is that let-7 reduces tumor growth in a rodent model of lung cancer, providing additional evidence for the antiproliferative effects of this particular family of miRNA [93]. Studies such as these underscore the importance of examining more closely the role of miRNA in hair cell regeneration, as induced underexpression of antiproliferative genes may ultimately allow regeneration of hair cells in mammals.

In summary, we have identified a possible role for miR181a in avian auditory hair cell regeneration. We have further identified additional miRNAs and transcription factors as candidates that warrant further investigation as potential targets for therapeutics aimed at replacing lost hair cells. Presented additionally are results suggestive of the presence of stem cells with properties similar to HSCs in the regenerating chick inner ear. Of all the candidates identified miR181a is specifically put forward for further study in *in-vivo* mammalian models of induced hearing loss in light of its demonstrated proliferative effect in the chicken inner ear as well as the fact that a miRNA based therapeutic could potentially be locally delivered to the middle ear and passively absorbed through the round window. This scenario seems plausible given that small molecules such as gentamicin can be delivered to the inner ear of patients in this fashion [94]. Computational analyses of our gene expression data suggest that the transcription factor E2F1 may also play a role in hair cell regeneration when many normally quiescent supporting cells are stimulated to re-enter the cell cycle and divide prior to differentiating into new hair cells. Additional functional studies will be necessary to ultimately determine what ability, if any, these players have to replace lost hair cells and result in recovery of compromised hearing thresholds in mammals.

Supporting Information

Table S1 Genes differentially expressed ($p < 0.05$, fold-change > 2) between control and forskolin treated basilar papillae after 24 hours in culture.

Found at: doi:10.1371/journal.pone.0011502.s001 (0.02 MB XLS)

Table S2 Genes differentially expressed ($p < 0.05$, fold-change > 2) between control and forskolin treated basilar papillae after 48 hours in culture.

Found at: doi:10.1371/journal.pone.0011502.s002 (0.03 MB XLS)

Table S3 Genes differentially expressed ($p < 0.05$, fold-change > 2) between control and forskolin treated basilar papillae after 72 hours in culture.

Found at: doi:10.1371/journal.pone.0011502.s003 (0.52 MB XLS)

Table S4 Gene set enrichment analysis statistics. Curated gene sets enriched in the control and forskolin samples after 24 hours.

Found at: doi:10.1371/journal.pone.0011502.s004 (0.25 MB XLS)

Table S5 Gene set enrichment analysis statistics. Curated gene sets enriched in the control and forskolin samples after 48 hours.

Found at: doi:10.1371/journal.pone.0011502.s005 (0.25 MB XLS)

Table S6 Gene set enrichment analysis statistics. Curated gene sets enriched in the control and forskolin samples after 72 hours.

Found at: doi:10.1371/journal.pone.0011502.s006 (0.25 MB XLS)

Table S7 Gene set enrichment analysis statistics. Mammalian gene sets enriched in the control and forskolin samples after 24 hours.

Found at: doi:10.1371/journal.pone.0011502.s007 (0.19 MB XLS)

Table S8 Gene set enrichment analysis statistics. Mammalian gene sets enriched in the control and forskolin samples after 48 hours.

Found at: doi:10.1371/journal.pone.0011502.s008 (0.19 MB XLS)

Table S9 Gene set enrichment analysis statistics. Mammalian gene sets enriched in the control and forskolin samples after 72 hours.

Found at: doi:10.1371/journal.pone.0011502.s009 (0.20 MB XLS)

Table S10 Gene set enrichment analysis statistics. Chicken/frog conservation gene sets enriched in the control and forskolin samples after 24 hours.

Found at: doi:10.1371/journal.pone.0011502.s010 (0.15 MB XLS)

Table S11 Gene set enrichment analysis statistics. Chicken/frog conservation gene sets enriched in the control and forskolin samples after 48 hours.

Found at: doi:10.1371/journal.pone.0011502.s011 (0.15 MB XLS)

Table S12 Gene set enrichment analysis statistics. Chicken/frog conservation gene sets enriched in the control and forskolin samples after 72 hours.

Found at: doi:10.1371/journal.pone.0011502.s012 (0.15 MB XLS)

Acknowledgments

We thank Jennifer Stone, PhD, University of Washington, for reviewing the manuscript and providing helpful suggestions.

We thank Adam Thornberg and Shrikant Mane, PhD, Yale Keck Facility, for assistance with the RNA amplification and microarray hybridizations.

We thank Guy Richardson, PhD, University of Sussex, for helpful technical advice.

Author Contributions

Conceived and designed the experiments: CSF SHK JSS DSN. Performed the experiments: CSF DSN. Analyzed the data: CSF MU SHK JSS DSN. Contributed reagents/materials/analysis tools: MU JLD. Wrote the paper: CSF SHK JSS DSN.

References

- WHO (2005) WHO | Deafness and hearing impairment World Health Organization.
- Stone J, Cotanche D (2007) Hair cell regeneration in the avian auditory epithelium. *Int J Dev Biol* 51: 633–647.
- Jorgensen JM, Mathiesen C (1988) The avian inner ear. Continuous production of hair cells in vestibular sensory organs, but not in the auditory papilla. *Naturwissenschaften* 75: 319–320.
- Warchol ME, Corwin JT (1996) Regenerative proliferation in organ cultures of the avian cochlea: identification of the initial progenitors and determination of the latency of the proliferative response. *J Neurosci* 16: 5466–5477.
- Balak KJ, Corwin JT, Jones JE (1990) Regenerated hair cells can originate from supporting cell progeny: evidence from phototoxicity and laser ablation experiments in the lateral line system. *J Neurosci* 10: 2502–2512.
- Stone JS, Cotanche DA (1994) Identification of the timing of S phase and the patterns of cell proliferation during hair cell regeneration in the chick cochlea. *J Comp Neurol* 341: 50–67.
- Raphael Y (1992) Evidence for supporting cell mitosis in response to acoustic trauma in the avian inner ear. *J Neurocytol* 21: 663–671.
- Corwin JT, Cotanche DA (1988) Regeneration of sensory hair cells after acoustic trauma. *Science* 240: 1772–1774.
- Ryals BM, Rubel EW (1988) Hair cell regeneration after acoustic trauma in adult Coturnix quail. *Science* 240: 1774–1776.
- Stone JS, Cotanche DA (1992) Synchronization of hair cell regeneration in the chick cochlea following noise damage. *J Cell Sci* 102 (Pt 4): 671–680.
- Lee KH, Cotanche DA (1996) Localization of the hair-cell-specific protein fimbrin during regeneration in the chicken cochlea. *Audiol Neurootol* 1: 41–53.
- Shang J, Cafaro J, Nehmer R, Stone J (2010) Supporting Cell Division Is Not Required for Regeneration of Auditory Hair Cells After Ototoxic Injury In Vitro. *J Assoc Res Otolaryngol*.
- Adler HJ, Raphael Y (1996) New hair cells arise from supporting cell conversion in the acoustically damaged chick inner ear. *Neurosci Lett* 205: 17–20.
- Baird RA, Burton MD, Lysakowski A, Fashena DS, Naeger RA (2000) Hair cell recovery in mitotically blocked cultures of the bullfrog saccule. *Proc Natl Acad Sci USA* 97: 11722–11729.
- Baird RA, Steyger PS, Schuff NR (1996) Mitotic and nonmitotic hair cell regeneration in the bullfrog vestibular otolith organs. *Annals of the New York Academy of Sciences* 781: 59–70.
- Taylor RR, Forge A (2005) Hair cell regeneration in sensory epithelia from the inner ear of a urodele amphibian. *J Comp Neurol* 484: 105–120.
- Duncan IJ, Mangiardi DA, Matsui JI, Anderson JK, McLaughlin-Williamson K, et al. (2006) Differential expression of unconventional myosins in apoptotic and regenerating chick hair cells confirms two regeneration mechanisms. *J Comp Neurol* 499: 691–701.
- Roberson DW, Alosi JA, Cotanche DA (2004) Direct transdifferentiation gives rise to the earliest new hair cells in regenerating avian auditory epithelium. *J Neurosci Res* 78: 461–471.
- Roberson DW, Kreig CS, Rubel EW (1996) Light microscopic evidence that direct transdifferentiation gives rise to new hair cells in regenerating avian auditory epithelium. *Aud Neurosci* 2: 195–205.
- Saunders SS, Salvi RJ (1995) Pure tone masking patterns in adult chickens before and after recovery from acoustic trauma. *J Acoust Soc Am* 98: 1365–1371.
- Gale JE, Meyers JR, Periasamy A, Corwin JT (2002) Survival of bundleless hair cells and subsequent bundle replacement in the bullfrog's saccule. *J Neurobiol* 50: 81–92.
- Navaratnam DS, Su HS, Scott SP, Oberholtzer JC (1996) Proliferation in the auditory receptor epithelium mediated by a cyclic AMP-dependent signaling pathway. *Nat Med* 2: 1136–1139.
- Montcouquiol M, Corwin JT (2001) Brief treatments with forskolin enhance s-phase entry in balance epithelia from the ears of rats. *J Neurosci* 21: 974–982.
- Schuknecht HF (1964) Further Observations on the Pathology of Presbycusis. *Arch Otolaryngol* 80: 369–382.
- Hawkins RD, Bashiardes S, Powder KE, Sajan SA, Bhonagiri V, et al. (2007) Large scale gene expression profiles of regenerating inner ear sensory epithelia. *PLoS ONE* 2: e525.
- Jackson RJ, Standart N (2007) How do microRNAs regulate gene expression? *Sci STKE* 2007: re1.
- Dalmay T (2008) Identification of genes targeted by microRNAs. *Biochem Soc Trans* 36: 1194–1196.
- Weston MD, Pierce ML, Rocha-Sanchez S, Beisel KW, Soukup GA (2006) MicroRNA gene expression in the mouse inner ear. *Brain Res* 1111: 95–104.
- Sacheli R, Nguyen L, Borgs L, Vandenbosch R, Bodson M, et al. (2009) Expression patterns of miR-96, miR-182 and miR-183 in the developing inner ear. *Gene Expression Patterns* 9: 364–370.
- Soukup GA (2009) Little but loud: Small RNAs have a resounding affect on ear development. *Brain Research* 1277: 104–114.
- Friedman LM, Dror AA, Mor E, Tenne T, Toren G, et al. (2009) MicroRNAs are essential for development and function of inner ear hair cells in vertebrates. *Proc Natl Acad Sci USA* 106: 7915–7920.
- Tsonis PA, Call MK, Grogg MW, Sartor MA, Taylor RR, et al. (2007) MicroRNAs and regeneration: Let-7 members as potential regulators of dedifferentiation in lens and inner ear hair cell regeneration of the adult newt. *Biochem Biophys Res Commun* 362: 940–945.
- Wang X, Gocek E, Liu CG, Studzinski GP (2009) MicroRNAs181 regulate the expression of p27Kip1 in human myeloid leukemia cells induced to differentiate by 1,25-dihydroxyvitamin D3. *Cell Cycle* 8: 736–741.
- Lee YS, Liu F, Segil N (2006) A morphogenetic wave of p27Kip1 transcription directs cell cycle exit during organ of Corti development. *Development* 133: 2817–2826.
- Lowenheim H, Furness DN, Kil J, Zinn C, Gultig K, et al. (1999) Gene disruption of p27(Kip1) allows cell proliferation in the postnatal and adult organ of corti. *Proc Natl Acad Sci U S A* 96: 4084–4088.
- Affymetrix I (2004) Eukaryotic sample and array processing. *GeneChip Expression Analysis Technical Manual*. Santa Clara, CA: Affymetrix, Inc. pp 2.1.3–2.3.18.
- Affymetrix I (2009) *GeneChip Expression Analysis Technical Manual*.
- Schmittgen TD, Livak KJ (2008) Analyzing real-time PCR data by the comparative C(T) method. *Nat Protoc* 3: 1101–1108.
- Rozen S, Skaletsky H (2000) Primer3 for the WWW for general users and for biologist programmers. *Methods Mol Biol* 132: 365–386.
- Subramanian A, Tamayo P, Mootha VK, Mukherjee S, Ebert BL, et al. (2005) Gene set enrichment analysis: a knowledge-based approach for interpreting genome-wide expression profiles. *Proc Natl Acad Sci U S A* 102: 15545–15550.
- Xie X, Lu J, Kulbokas EJ, Golub TR, Mootha V, et al. (2005) Systematic discovery of regulatory motifs in human promoters and 3' UTRs by comparison of several mammals. *Nature* 434: 338–345.
- Friedman RC, Farh KK, Burge CB, Bartel DP (2009) Most mammalian mRNAs are conserved targets of microRNAs. *Genome Res* 19: 92–105.
- Wasserman WW, Palumbo M, Thompson W, Fickett JW, Lawrence CE (2000) Human-mouse genome comparisons to locate regulatory sites. *Nat Genet* 26: 225–228.
- Schmidt D, Wilson MD, Ballester B, Schwalie PC, Brown GD, et al. Five-Vertebrate ChIP-seq Reveals the Evolutionary Dynamics of Transcription Factor Binding. *Science*.
- Borneman AR, Gianoulis TA, Zhang ZD, Yu H, Rozowsky J, et al. (2007) Divergence of transcription factor binding sites across related yeast species. *Science* 317: 815–819.
- Hua S, Kallen CB, Dhar R, Baquero MT, Mason CE, et al. (2008) Genomic analysis of estrogen cascade reveals histone variant H2A.Z associated with breast cancer progression. *Mol Syst Biol* 4: 188.
- Pruitt KD, Tatusova T, Maglott DR (2005) NCBI Reference Sequence (RefSeq): a curated non-redundant sequence database of genomes, transcripts and proteins. *Nucleic Acids Res* 33: D501–504.
- Blanchette M, Kent WJ, Riemer C, Elnitski L, Smit AF, et al. (2004) Aligning multiple genomic sequences with the threaded blockset aligner. *Genome Res* 14: 708–715.
- Kel AE, Gossling E, Reuter I, Cheremushkin E, Kel-Margoulis OV, et al. (2003) MATCH: A tool for searching transcription factor binding sites in DNA sequences. *Nucleic Acids Res* 31: 3576–3579.
- Matys V, Fricke E, Gelfers R, Gossling E, Haubrock M, et al. (2003) TRANSFAC: transcriptional regulation, from patterns to profiles. *Nucleic Acids Res* 31: 374–378.
- Liu Y, Tang MK, Cai DQ, Li M, Wong WM, et al. (2007) Cyclin I and p53 are differentially expressed during the terminal differentiation of the postnatal mouse heart. *Proteomics* 7: 23–32.
- Roman-Gomez J, Jimenez-Velasco A, Cordeu L, Vilas-Zornoza A, San Jose-Eneriz E, et al. (2007) WNT5A, a putative tumour suppressor of lymphoid malignancies, is inactivated by aberrant methylation in acute lymphoblastic leukaemia. *Eur J Cancer* 43: 2736–2746.
- Ma EY, Raible DW (2009) Signaling Pathways Regulating Zebrafish Lateral Line Development. *Current Biology* 19: R381–R386.
- Sienknecht UJ, Fekete DM (2008) Comprehensive Wnt-related gene expression during cochlear duct development in chicken. *J Comp Neurol* 510: 378–395.
- Sienknecht UJ, Fekete DM (2009) Mapping of Wnt, frizzled, and Wnt inhibitor gene expression domains in the avian otic primordium. *J Comp Neurol* 517: 751–764.
- Stevens CB, Davies AL, Battista S, Lewis JH, Fekete DM (2003) Forced activation of Wnt signaling alters morphogenesis and sensory organ identity in the chicken inner ear. *Developmental Biology* 261: 149–164.
- Yang-Snyder J, Miller JR, Brown JD, Lai CJ, Moon RT (1996) A frizzled homolog functions in a vertebrate Wnt signaling pathway. *Curr Biol* 6: 1302–1306.
- Chang HY, Sneddon JB, Alizadeh AA, Sood R, West RB, et al. (2004) Gene expression signature of fibroblast serum response predicts human cancer progression: similarities between tumors and wounds. *PLoS Biol* 2: E7.
- Kanehisa M, Araki M, Goto S, Hattori M, Hirakawa M, et al. (2008) KEGG for linking genomes to life and the environment. *Nucleic Acids Res* 36: D480–484.
- Kanehisa M, Goto S (2000) KEGG: kyoto encyclopedia of genes and genomes. *Nucleic Acids Research* 28: 27–30.
- Kanehisa M, Goto S, Hattori M, Aoki-Kinoshita KF, Itoh M, et al. (2006) From genomics to chemical genomics: new developments in KEGG. *Nucleic Acids Research* 34: D354–357.

62. Ashburner M, Ball CA, Blake JA, Botstein D, Butler H, et al. (2000) Gene ontology: tool for the unification of biology. *The Gene Ontology Consortium. Nat Genet* 25: 25–29.
63. Goldrath AW, Luckey CJ, Park R, Benoist C, Mathis D (2004) The molecular program induced in T cells undergoing homeostatic proliferation. *Proc Natl Acad Sci USA* 101: 16885–16890.
64. Doniger SW, Salomonis N, Dahlquist KD, Vranizan K, Lawlor SC, et al. (2003) MAPPFinder: using Gene Ontology and GenMAPP to create a global gene-expression profile from microarray data. *Genome Biol* 4: R7.
65. Brentani H, Caballero OL, Camargo AA, da Silva AM, da Silva WA, et al. (2003) The generation and utilization of a cancer-oriented representation of the human transcriptome by using expressed sequence tags. *Proc Natl Acad Sci USA* 100: 13418–13423.
66. Ren B, Cam H, Takahashi Y, Volkert T, Terragni J, et al. (2002) E2F integrates cell cycle progression with DNA repair, replication, and G(2)/M checkpoints. *Genes Dev* 16: 245–256.
67. Vernell R, Helin K, Müller H (2003) Identification of target genes of the p16INK4A-pRB-E2F pathway. *J Biol Chem* 278: 46124–46137.
68. Ramalho-Santos M, Yoon S, Matsuzaki Y, Mulligan RC, Melton DA (2002) “Stemness”: transcriptional profiling of embryonic and adult stem cells. *Science* 298: 597–600.
69. Oshima K, Grimm CM, Corrales CE, Senn P, Martinez Monedero R, et al. (2007) Differential distribution of stem cells in the auditory and vestibular organs of the inner ear. *J Assoc Res Otolaryngol* 8: 18–31.
70. Stone JS, Rubel EW (1999) Delta expression during avian hair cell regeneration. *Development* 126: 961–973.
71. Oshima K, Shin K, Diensthuber M, Peng AW, Ricci AJ, et al. (2010) Mechanosensitive Hair Cell-like Cells from Embryonic and Induced Pluripotent Stem Cells. *Cell* 141: 704–716.
72. Jude CD, Gaudet JJ, Speck NA, Ernst P (2008) Leukemia and hematopoietic stem cells: balancing proliferation and quiescence. *Cell Cycle* 7: 586–591.
73. Narbonne P, Roy R (2008) Genes that affect both cell growth and polarity mediate stem cell quiescence. *Front Biosci* 13: 995–1002.
74. Passerini AG, Polacek DC, Shi C, Francesco NM, Manduchi E, et al. (2004) Coexisting proinflammatory and antioxidative endothelial transcription profiles in a disturbed flow region of the adult porcine aorta. *Proc Natl Acad Sci USA* 101: 2482–2487.
75. Mangiardi DA, McLaughlin-Williamson K, May KE, Messana EP, Mountain DC, et al. (2004) Progression of hair cell ejection and molecular markers of apoptosis in the avian cochlea following gentamicin treatment. *J Comp Neurol* 475: 1–18.
76. Mangiardi DA, McLaughlin-Williamson K, May KE, Messana EP, Mountain DC, et al. (2004) Progression of hair cell ejection and molecular markers of apoptosis in the avian cochlea following gentamicin treatment. *J Comp Neurol* 475: 1–18.
77. Ashery-Padan R, Gruss P (2001) Pax6 lights-up the way for eye development. *Curr Opin Cell Biol* 13: 706–714.
78. Kumar JP (2001) Signalling pathways in Drosophila and vertebrate retinal development. *Nat Rev Genet* 2: 846–857.
79. Heanue TA, Davis RJ, Rowitch DH, Kispert A, McMahon AP, et al. (2002) Dach1, a vertebrate homologue of Drosophila dachshund, is expressed in the developing eye and ear of both chick and mouse and is regulated independently of Pax and Eya genes. *Mech Dev* 111: 75–87.
80. Gregory PA, Bracken CP, Bert AG, Goodall GJ (2008) MicroRNAs as regulators of epithelial-mesenchymal transition. *Cell Cycle* 7: 3112–3118.
81. Ji J, Zhang J, Huang G, Qian J, Wang X, et al. (2009) Over-expressed microRNA-27a and 27b influence fat accumulation and cell proliferation during rat hepatic stellate cell activation. *FEBS Lett* 583: 759–766.
82. Liu T, Tang H, Lang Y, Liu M, Li X (2009) MicroRNA-27a functions as an oncogene in gastric adenocarcinoma by targeting prohibitin. *Cancer Lett* 273: 233–242.
83. Mertens-Talcott S, Chintharlapalli S, Li X, Safe S (2007) The Oncogenic microRNA-27a Targets Genes That Regulate Specificity Protein Transcription Factors and the G2-M Checkpoint in MDA-MB-231 Breast Cancer Cells. *Cancer Res* 67: 11001–11011.
84. Johnson DG, Degregori J (2006) Putting the Oncogenic and Tumor Suppressive Activities of E2F into Context. *Curr Mol Med* 6: 731–738.
85. Rocha-Sanchez SM, Beisel KW (2007) Pocket proteins and cell cycle regulation in inner ear development. *Int J Dev Biol* 51: 585–595.
86. Cobrinik D (2005) Pocket proteins and cell cycle control. *Oncogene* 24: 2796–2809.
87. Dannenberg JH, Schuijff L, Dekker M, van der Valk M, te Riele H (2004) Tissue-specific tumor suppressor activity of retinoblastoma gene homologs p107 and p130. *Genes Dev* 18: 2952–2962.
88. Li JM, Hu PP, Shen X, Yu Y, Wang XF (1997) E2F4-RB and E2F4-p107 complexes suppress gene expression by transforming growth factor beta through E2F binding sites. *Proc Natl Acad Sci U S A* 94: 4948–4953.
89. Johnson DG, Schwarz JK, Cress WD, Nevins JR (1993) Expression of transcription factor E2F1 induces quiescent cells to enter S phase. *Nature* 365: 349–352.
90. Dyson N (1998) The regulation of E2F by pRB-family proteins. *Genes Dev* 12: 2245–2262.
91. Chen P, Segil N (1999) p27(Kip1) links cell proliferation to morphogenesis in the developing organ of Corti. *Development* 126: 1581–1590.
92. White PM, Doetzlhofer A, Lee YS, Groves AK, Segil N (2006) Mammalian cochlear supporting cells can divide and trans-differentiate into hair cells. *Nature* 441: 984–987.
93. Esquela-Kerscher A, Trang P, Wiggins JF, Patrawala L, Cheng A, et al. (2008) The let-7 microRNA reduces tumor growth in mouse models of lung cancer. *Cell Cycle* 7: 759–764.
94. Nedzelski JM, Chiong CM, Fradet G, Schessel DA, Bryce GE, et al. (1993) Intratympanic gentamicin instillation as treatment of unilateral Menière’s disease: update of an ongoing study. *The American journal of otology* 14: 278–282.

Expression in cochlea and retina of myosin VIIa, the gene product defective in Usher syndrome type 1B

TAMA HASSON*[†], MATTHEW B. HEINTZELMAN*, JOSEPH SANTOS-SACCHI^{§¶}, DAVID P. COREY^{||},
AND MARK S. MOOSEKER*^{†‡}

Departments of *Biology, [†]Cell Biology, [‡]Pathology, [§]Surgery (Otolaryngology), and [¶]Neurobiology, Yale University, New Haven, CT 06520; and ^{||}Howard Hughes Medical Institute, Massachusetts General Hospital and Program in Neuroscience, Harvard Medical School, Boston, MA 02114

Communicated by Frank H. Ruddle, Yale University, New Haven, CT, July 17, 1995

ABSTRACT Myosin VIIa is a newly identified member of the myosin superfamily of actin-based motors. Recently, the myosin VIIa gene was identified as the gene defective in shaker-1, a recessive deafness in mice [Gibson, F., Walsh, J., Mburu, P., Varela, A., Brown, K. A., Antonio, M., Beisel, K. W., Steel, K. P. & Brown, S. D. M. (1995) *Nature (London)* 374, 62–64], and in human Usher syndrome type 1B, an inherited disease characterized by congenital deafness, vestibular dysfunction, and retinitis pigmentosa [Weil, D., Blanchard, S., Kaplan, J., Guilford, P., Gibson, F., Walsh, J., Mburu, P., Varela, A., Leveilliers, J., Weston, M. D., Kelley, P. M., Kimberling, W. J., Wagenaar, M., Levi-Acobas, F., Larget-Piet, D., Munnich, A., Steel, K. P., Brown, S. D. M. & Petit, C. (1995) *Nature (London)* 374, 60–61]. To understand the normal function of myosin VIIa and how it could cause these disease phenotypes when defective, we generated antibodies specific to the tail portion of this unconventional myosin. We found that myosin VIIa was expressed in cochlea, retina, testis, lung, and kidney. In cochlea, myosin VIIa expression was restricted to the inner and outer hair cells, where it was found in the apical stereocilia as well as the cytoplasm. In the eye, myosin VIIa was expressed by the retinal pigmented epithelial cells, where it was enriched within the apical actin-rich domain of this cell type. The cell-specific localization of myosin VIIa suggests that the blindness and deafness associated with Usher syndrome is due to lack of proper myosin VIIa function within the cochlear hair cells and the retinal pigmented epithelial cells.

Myosin VIIa is a newly identified member of the myosin superfamily of actin-based motors (1–3). The gene encoding myosin VIIa is responsible for human Usher syndrome type 1B (USH1B) (4), a disease characterized by sensorineural hearing loss, absence of vestibular function, and a progressive retinal degeneration termed retinitis pigmentosa. It affects ≈4.4 per 100,000 in the total United States population and 3–6% of deaf children (5, 6) and is the most frequent cause of deaf-blindness. Mutations in the myosin VIIa gene are also responsible for a recessive deafness in mice termed shaker-1 (*sh1*) (7). *sh1* mice exhibit hearing loss following early degeneration of the sensory epithelium in the cochlea, and head tossing behavior due to vestibular dysfunction (8). We have cloned a large portion of the human myosin VIIa heavy-chain cDNA** and have generated antibodies specific to a tail domain of myosin VIIa. Myosin VIIa heavy chain is a 240-kDa polypeptide and its expression is restricted to retinal pigmented epithelial (RPE) cells, cochlear hair cells, and certain cells of the testis, lung, and kidney. These results provide compelling evidence that the blindness and deafness phenotypes associated with Usher disease are due to the lack of functional myosin VIIa polypeptide within a specific subset of retinal

and cochlear cells and suggest a role for myosin VIIa heavy chain in the development and maintenance of these sensory organs.

MATERIALS AND METHODS

Isolation of Human and Porcine Myosin VIIa cDNAs. The 130-bp PCR products encoding a portion of myosin VIIa identified from human and porcine cell lines and tissues (ref. 1; EMBL accession nos. L29145 and L29133, respectively) were used to screen a number of cDNA libraries. Screening of a human liver λZAPII cDNA library (provided by James Anderson, Yale Medical School) and a human testis λgt10 cDNA library (Clontech) resulted in nine overlapping clones, one of which, clone 10C, was found to encode the entire N-terminal 1075 aa of human myosin VIIa (GenBank accession no. U34227). Screening of a λgt10 cDNA library prepared from LLC-PK₁ porcine kidney cells (provided by Robert Reilly, Yale Medical School) resulted in two clones, one of which, 14C, encompassed the N terminus of porcine myosin VIIa (aa 1–566; GenBank accession no. U34226).

Preparation of Myosin VIIa-Specific Antibodies. A *HindIII*–*EcoRI* fragment encoding aa 877–1075 of human myosin VIIa was cloned into pGEX2-T (Amrad, Melbourne, Australia) to produce a 49-kDa glutathione S-transferase/myosin VIIa tail fusion protein. This insoluble fusion protein was extracted from the cell pellet with 0.5% (wt/vol) sodium *N*-lauroylsarcosine, diluted 1:10, brought to 1% (vol/vol) Triton X-100, and purified over a glutathione-Sepharose column. Rabbits were immunized with two 300-μg injections of purified fusion protein spaced 3 weeks apart and were bled 10 days after the second injection. To allow for affinity purification of serum, the same *HindIII*–*EcoRI* fragment was cloned into pQE-30 (Qiagen, Chatsworth, CA) and the resultant His₆-tagged myosin VIIa tail peptide was purified over a nickel-agarose column (Qiagen). The His₆-tagged myosin VIIa peptide was dialyzed into carbonate buffer containing 0.1% SDS and coupled to cyanogen bromide-activated Sepharose (Pharmacia). Rabbit serum was applied to the myosin-VIIa-tail affinity column and bound antibodies were eluted with low pH and dialyzed into phosphate-buffered saline (PBS: 10 mM sodium phosphate/137 mM NaCl, pH 7.4).

Immunoblot Analysis. Protein samples were homogenized in 5% (wt/vol) trichloroacetic acid and standardized for protein concentration by quantitation in the bicinchoninic acid (BCA) assay (Pierce). The trichloroacetic acid precipitation pellet was washed once with water before reconstitution in boiling 5× SDS/PAGE sample buffer to a final protein concentration of 0.9 mg/ml. After SDS/PAGE separation, proteins were transferred to poly(vinylidene difluoride) membrane and incubated with affinity-purified myosin-VIIa anti-

The publication costs of this article were defrayed in part by page charge payment. This article must therefore be hereby marked "advertisement" in accordance with 18 U.S.C. §1734 solely to indicate this fact.

Abbreviations: DIC, differential interference contrast; RPE, retinal pigmented epithelial.

**The sequences reported in this paper have been deposited in the GenBank data base (accession nos. U34226 and U34227).

bodies, and the bound antibodies were visualized with a chemiluminescence kit (Boehringer Mannheim).

Immunolocalization Studies. Guinea pig temporal bones were rapidly removed into PBS containing 50 mM EGTA (PBS/EGTA). The round window membrane and stapes footplate were removed, and a small fenestra was made in the apical cochlear bony capsule in order to rapidly and directly perfuse the cochlear scalae with 4% paraformaldehyde in PBS/EGTA. After 5 min of initial perfusion, the remaining bony capsule was chipped away, the spiral ligament and stria vascularis were peeled away, and the cochlea were immersed in fixative for an additional 15 min. Half-turns of the cochlea spiral were cut free, and nonspecific binding sites were blocked in PBS/EGTA/5% bovine serum albumin for 20 min. Affinity-purified anti-myosin-VIIa or control nonimmune IgG was added at a concentration of 10 μ g/ml in PBS/EGTA/0.1% bovine serum albumin/1% normal goat serum for 1 hr at room temperature. Samples were washed with PBS/EGTA for 20 min before incubation for 1 hr at room temperature with a 1:150 dilution of rhodamine-conjugated goat anti-rabbit antibodies (Cappel) and 40 nM fluorescein-labeled phalloidin (Molecular Probes) in PBS/EGTA/0.1% bovine serum albumin/5% normal goat serum. Samples were washed with PBS/EGTA and placed in PBS/glycerol mounting medium (Citifluor, Kent, England). Samples were observed with a Bio-Rad MRC600 laser scanning confocal microscope.

Rat retina was excised and fixed for 5 min on ice in 4% paraformaldehyde in PBS/EGTA. Samples were quenched, cryoprotected, embedded for frozen sectioning, and prepared for immunostaining as described (9). Antibody incubations were as described above but were done for 20 min. Mounted slides were observed with a Nikon Diaphot 300 light microscope equipped with epifluorescence and differential interference contrast (DIC) imaging.

RESULTS

A 130-bp PCR fragment encoding a portion of the motor domain of human myosin VIIa near the ATP binding site (1) was successfully used to screen a human testis λ gt10 cDNA library. The isolated 3.5-kb cDNA encodes a myosin-like molecule (GenBank accession no. U34227) that has a 730-aa N-terminal motor domain, a 130-aa neck domain containing five light-chain binding repeats ("IQ" motifs; ref. 10), and a 210-aa tail. This tail is made up of two domains, a region of \approx 70 aa predicted to form an α -helical coiled coil (11) and a unique C-terminal globular domain. The human myosin VIIa testis cDNA is 99% identical at the nucleotide level to the 1547-nt fragment of human myosin VIIa cDNA (ref. 4; GenBank accession no. U17180). The testis cDNA sequence differs from the U17180 sequence at 11 sites (Fig. 1), reflecting a frameshift (nt 1433–1440; U17180) and three single-base-pair discrepancies. These differences in the human myosin VIIa cDNA result in changes in the predicted amino acid sequence that match the murine ortholog at those sites (7). Human myosin VIIa is 96% identical to cloned portions of both mouse (7) and porcine (GenBank accession no. U34226) myosin VIIa at the amino acid level and is 83% identical to the frog homolog (2) (Fig. 1). By comparison, human myosin VIIa is only 25–40% identical to the motor domain of members of other unconventional myosin classes. In particular, the N-terminal 100 aa and the C-terminal tail of myosin VIIa are unique to this motor.

Repeated attempts to isolate the entire tail domain of myosin VIIa have been unsuccessful. Since the known portion of the myosin VIIa tail domain is novel, we generated antibodies directed against a bacterially expressed fusion protein containing the available myosin VIIa tail. These

affinity-purified antibodies were used in immunoblot studies to analyze the expression profile of this protein. A 240-kDa polypeptide was detected in rat retina, kidney, temporal bone, and testis, while a 200-kDa polypeptide was detected in lung (Fig. 2). No expression was observed in rat liver, muscle, intestine, stomach, or brain. This finding is consistent with the mRNA expression data of Gibson *et al.* (7), which showed a 9.5-kb transcript in mouse kidney and testis and a slightly smaller species in lung. The antibodies did not recognize myosins II, I, or VI, all of which are known to be expressed within these tissues and which exhibit molecular weights different from that seen with the myosin VIIa-specific antibodies.

PCR evidence suggests that another member of the myosin VIIa family is expressed in humans, myosin VIIb (1). Myosin VIIb has not been cloned, so we cannot specifically compare it with myosin VIIa. Several lines of evidence suggest that myosin VIIa-specific probes do not recognize myosin VIIb. cDNA probes directed against either the conserved motor domain or the novel tail domains of myosin VIIa recognize a single mRNA of \approx 9.5 kb in human testis by Northern blot analysis (data not shown). Screening of additional human and porcine cDNA libraries derived from liver, lung, small intestine, testis, and kidney tissues did not identify myosin VIIb clones when either motor- or tail-specific probes for myosin VIIa were used. When the 3.5-kb myosin VIIa cDNA clone was used as a probe for fluorescence *in situ* hybridization, it hybridized specifically to human chromosome 11q13–15, the position of *USH1B*, but not to additional loci (N. Mokady, T.H., and D. Ward, unpublished data). These examples of lack of cross-hybridization suggest that myosin VIIa and myosin VIIb are not highly homologous at the nucleotide level. The antibodies to myosin VIIa recognize appropriately sized polypeptides only in tissues known to express this motor as judged by Northern blot analysis (7) and by reverse transcription-PCR analysis (4) in human and mouse tissues. Taken together, these results suggest that myosin VIIa-directed probes are specific for this motor and do not recognize myosin VIIb.

An indirect-immunofluorescence study was undertaken to determine the cell-specific localization of myosin VIIa within the cochlea. Half-turns of guinea pig cochlear tissue were double-labeled with antibodies to myosin VIIa and with fluorescein-conjugated phalloidin and visualized as a whole mount by laser scanning confocal microscopy. Optical sections through the organ of Corti showed that myosin VIIa was concentrated within the outer and inner hair cells of the sensory epithelium (Fig. 3). It was detected within the stereocilia at the apex of the hair cell (Fig. 3 *a* and *b*) and within the cuticular plate which anchors the bases of the stereocilia (Fig. 3 *c* and *d*). Myosin VIIa was also present within the cytoplasm of the hair cells (Fig. 3 *e* and *f*), although this region is not enriched in F-actin. No myosin VIIa was detected within Hensen's cells or the pillar cells, two cell types within the organ of Corti that are enriched in F-actin. Nonimmune control experiments indicated that the staining of the stereocilia was not simply due to bleedthrough of the phalloidin signal. Also, no bleedthrough was seen from the bright phalloidin staining of the actin ring at the zona adherens (Fig. 3 *a* and *b*) or staining of the Hensen's cells and pillar cells (Fig. 3 *c–f*). Similar results were obtained with frozen sections of isolated cochlea and whole temporal bone (data not shown), indicating that this staining pattern was not dependent on the method of staining. No myosin VIIa-specific labeling was observed within any supporting cells or nerve cells within the cochlea. Similarly, no myosin VIIa-specific staining of the stria vascularis or other vascular tissue was seen. The image shown in Fig. 3 reflects the pattern of myosin VIIa expression along the entire length of the cochlea, with the staining intensity higher in inner hair cells than in outer hair cells. Labeling was not brighter at the tips

DISCUSSION

Our data establish that myosin VIIa is present within the hair cells of the cochlea and the pigmented epithelium cells of the retina, two tissues known to be affected in Usher disease. Some patients with Usher disease exhibit abnormal sperm cells (13) and defects in bronchial function (14); in keeping with this, myosin VIIa was also found to be expressed in the testis and lung. Myosin VIIa is also expressed in the kidney, but kidney problems have not been reported in Usher patients. The kidney, and in particular the proximal-tubule epithelial cells contains a number of myosins, including two myosins II, at least four myosins I, and myosin VI (reviewed in ref. 9). In addition, at least six other unconventional myosins are expressed within this cell type (1). Perhaps these myosins serve overlapping functions in the kidney, masking the loss of myosin VIIa in Usher patients and *sh1* mice.

sh1 mice exhibit degeneration of the organ of Corti and the afferent spiral ganglion neurons in the first few weeks after birth, at a time when the organ of Corti is normally still developing (8). Hair cells are first detectably abnormal within 3 days after birth. Spiral ganglion neurons are also abnormal at 3 days. Little is known of the histopathology of type 1 Usher patients, as existing studies are apparently on usher types 2 or 3. Given the restricted localization of myosin VIIa to the hair cells, we suggest that the defect lies within this cell type and that the degeneration of the afferent neurons is secondary.

Usher syndrome type 1 is also characterized by absence of vestibular function. Although we have not located myosin VIIa

in the vestibular system, amphibian myosin VIIa was identified in the sensory epithelium of the bullfrog sacculus (2), suggesting that myosin VIIa may be expressed in mammalian vestibular hair cells as well. Gillespie *et al.* (15) identified three myosin-like proteins in bullfrog saccular stereocilia by photoaffinity labeling with uridine nucleotides; one of them had an apparent molecular mass of 230 kDa. In addition, Walker *et al.* (16) identified a 240-kDa calmodulin-binding protein in saccular hair bundles which may be the same protein and, perhaps, myosin VIIa. The neck domain sequence of myosin VIIa has five light-chain-binding IQ repeats. These repeats have been shown to bind calmodulin in other unconventional myosins (10).

The primary cause of the retinal degeneration observed in Usher disease is not known. The problem could lie in the photoreceptors themselves or in the RPE cells, which support the photoreceptors and function in photoreceptor renewal by phagocytosing disks shed by the rod outer segments (17). Myosin VIIa expression is restricted to the pigmented epithelium, suggesting that defects in these cells are the cause of the retinitis pigmentosa in Usher type 1B. One animal model of retinitis pigmentosa, the RCS rat, provides supportive evidence. In these animals, the RPE layer is defective in phagocytosis (18). Cellular debris accumulates in the intercellular space between the outer segments and the RPE layer, leading to photoreceptor cell death. The genetic defect in the RCS rat is not known, but studies in chimeric animals have determined that the cellular defect lies in the RPE layer itself (19).

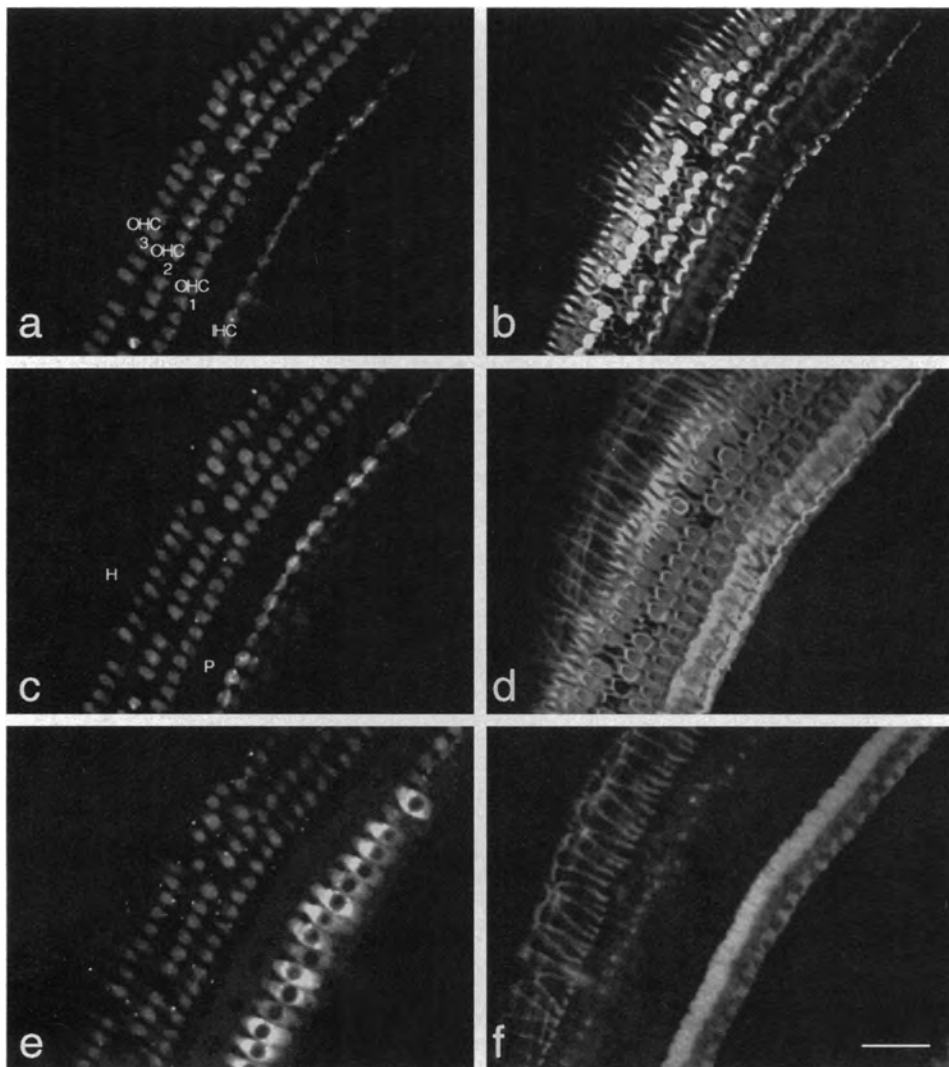


FIG. 3. Localization of myosin VIIa and F-actin in guinea pig cochlea. Immunofluorescence micrographs show optical sections through the organ of Corti perpendicular to the cochlear axis stained for myosin VIIa (*a*, *c*, and *e*) and F-actin (*b*, *d*, and *f*). (*a* and *b*) Apical domain of the organ of Corti. The locations of the inner hair cell (IHC) and three outer hair cell (OHC) rows are marked. The stereocilia are clearly visible as V-shaped, brightly stained bundles in the OHC and as a row of brightly stained material in the IHC. (*c* and *d*) Optical section 2.4 μm lower, at the level of the cuticular plate. The location of the actin-rich pillar cells (P) and Hensen's cells (H) are shown. (*e* and *f*) Optical section 7.8 μm lower, at the level of the IHC nuclei. (Bar = 50 μm .)

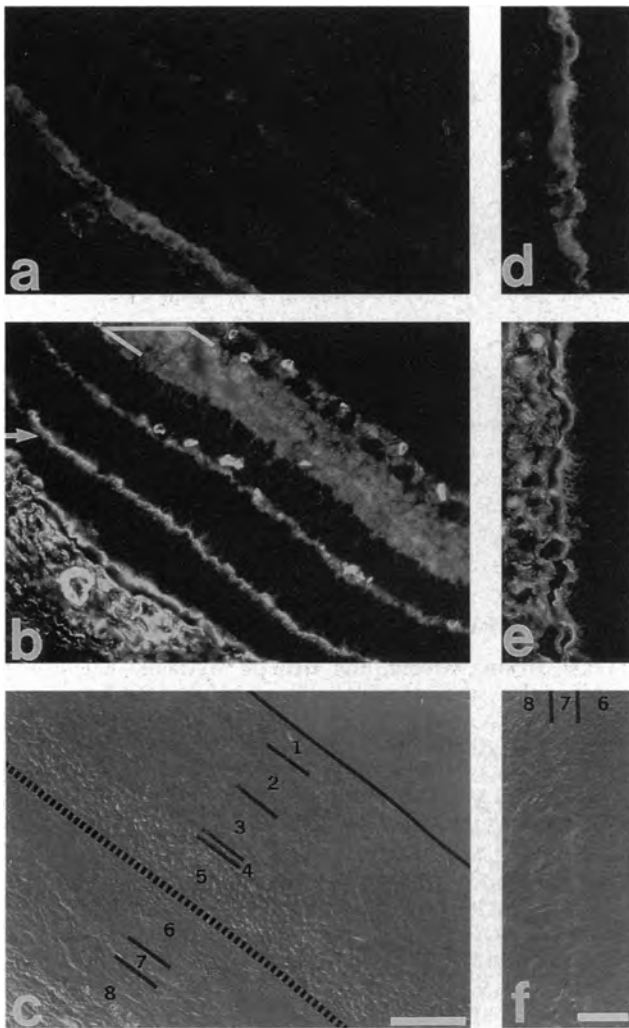


FIG. 4. Adult rat retina stained with myosin VIIa (*a* and *d*) and F-actin (*b* and *e*) and visualized by DIC optics (*c* and *f*). Retinal layers (demarcated in *c* and *f*) are as follows: solid line, inner limiting membrane; broken line, external limiting membrane; 1, ganglion cell layer; 2, inner plexiform layer; 3, inner nuclear layer; 4, outer plexiform layer; 5, outer nuclear layer; 6, rod and cone outer segments; 7, pigmented epithelium; 8, choroid layer. In *b*, the external limiting membrane is marked by an arrow, and the inner plexiform layer by a bracket. (Bar in *c* = 50 μ m; bar in *f* = 25 μ m.)

sh1 mice do not exhibit retinitis pigmentosa. As discussed by Weil *et al.* (4), this may reflect the type of myosin VIIa mutation observed within the *sh1* mice. The three *sh1* mutations identified by Gibson *et al.* (7) reflected two different single amino acid changes and a 10-aa deletion. All mutants expressed myosin VIIa at the mRNA level and therefore may express the mutant protein (7). A human recessive nonsyndromic deafness locus (*DFNB2*) also maps to 11q13 (20). Perhaps this human deafness is more closely related to *sh1*. Alternatively, another unconventional myosin could be compensating for the lack of myosin VIIa in the *sh1* retina.

Unconventional myosins have been shown to be associated with numerous actin-based motilities, such as phagocytosis, endocytosis, chemotactic movement, and vesicular transport (21, 22). Perhaps myosin VIIa serves a similar role in membrane movements in sensory hair cells and in the RPE cells. Both cell types undergo continuous and essential membrane movements—specifically, phagocytosis in the retina and re-

lease of transmitter-containing vesicles at the afferent hair-cell synapses (17, 23). Outer hair cells exhibit a much lower level of constitutive transmitter release than inner hair cells (24), consistent with the differential levels of expression of myosin VIIa between these two hair-cell types. Our results, showing a specific location of myosin VIIa within the cochlea and retina, should allow for an enhanced understanding of the molecular causes of blindness and deafness in Usher patients.

We thank N. Mokady and D. C. Ward for mapping the human myosin VIIa gene and we thank Spyridon Artavanis-Tsakonas for the use of his confocal microscope. Meena Ramakrishnan and Marc Schwartz provided excellent technical help in cloning and sequencing myosin VIIa. This work was supported by Grant PF-3659 from the American Cancer Society (T.H.), National Institutes of Health Program Project Grant DK38979 (T.H. and M.S.M.), and National Institutes of Health Grant DK25387, a basic research grant from the Muscular Dystrophy Association, and Yale Liver Center Pilot Project Grant DK34989 (M.S.M.). J.S.-S. and D.P.C. were supported by National Institute on Deafness and Other Communication Disorders Grants DC00273 and DC02281, respectively. D.P.C. is an Associate Investigator of the Howard Hughes Medical Institute.

- Bement, W. M., Hasson, T., Wirth, J. A., Cheney, R. E. & Mooseker, M. S. (1994) *Proc. Natl. Acad. Sci. USA* **91**, 6549–6553.
- Solc, C. F., Derfler, B. H., Duyk, G. M. & Corey, D. P. (1994) *Auditory Neurosci.* **1**, 63–75.
- Cheney, R. E., Riley, M. A. & Mooseker, M. S. (1993) *Cell Motil. Cytoskel.* **24**, 215–223.
- Weil, D., Blanchard, S., Kaplan, J., Guilford, P., Gibson, F., Walsh, J., Mburu, P., Varela, A., Levilliers, J., Weston, M. D., Kelley, P. M., Kimberling, W. J., Wagenaar, M., Levi-Acobas, F., Larget-Piet, D., Munnich, A., Steel, K. P., Brown, S. D. M. & Petit, C. (1995) *Nature (London)* **374**, 60–61.
- Boughman, J. A., Vernon, M. & Shaver, K. A. (1983) *J. Chronic Dis.* **36**, 595–603.
- Vernon, M. (1969) *J. Chronic Dis.* **22**, 133–151.
- Gibson, F., Walsh, J., Mburu, P., Varela, A., Brown, K. A., Antonio, M., Beisel, K. W., Steel, K. P. & Brown, S. D. M. (1995) *Nature (London)* **374**, 62–64.
- Schnerson, A., Lenoir, M., Van de Water, T. R. & Pujol, R. (1983) *Dev. Brain Res.* **9**, 305–315.
- Hasson, T. & Mooseker, M. S. (1994) *J. Cell Biol.* **127**, 425–440.
- Cheney, R. E. & Mooseker, M. S. (1992) *Curr. Opin. Cell Biol.* **4**, 27–35.
- Lupas, A., VanDyke, M. & Stock, J. (1991) *Science* **252**, 1162–1164.
- Howard, J. & Hudspeth, A. J. (1987) *Proc. Natl. Acad. Sci. USA* **84**, 3064–3068.
- Hunter, D. G., Fishman, G. A., Mehta, R. S. & Kretzer, F. L. (1986) *Arch. Ophthalmol.* **104**, 385–389.
- Bonneau, D., Raymon, F., Kremer, C., Klossek, J.-M., Kaplan, J. & Patte, F. (1993) *J. Med. Genet.* **30**, 253–254.
- Gillespie, P. G., Wagner, M. C. & Hudspeth, A. J. (1993) *Neuron* **11**, 581–594.
- Walker, R. G., Hudspeth, A. J. & Gillespie, P. G. (1993) *Proc. Natl. Acad. Sci. USA* **90**, 2807–2811.
- Heckenlively, J. R. (1988) *Retinitis Pigmentosa* (Lippincott, Philadelphia), pp. 1–67.
- Bok, D. & Hall, M. O. (1971) *J. Cell Biol.* **49**, 664–682.
- Mullen, R. J. & La Vail, M. M. (1976) *Science* **192**, 799–801.
- Guilford, P., Ayadi, H., Blanchard, S., Chaib, H., Le Paslier, D., Weissenbach, J., Drira, M. & Petit, C. (1994) *Hum. Mol. Genet.* **3**, 989–993.
- Pollard, T. D., Doberstein, S. K. & Zot, H. G. (1991) *Annu. Rev. Physiol.* **53**, 653–681.
- Hasson, T. & Mooseker, M. S. (1995) *Curr. Opin. Cell Biol.* **7**, 587–594.
- Siegel, J. H. & Brownell, W. E. (1986) *J. Neurocytol.* **15**, 311–328.
- Dodson, H. C., Bannister, L. H. & Douek, E. E. (1992) *J. Anat.* **180**, 535–544.

Tuning in to the Amazing Outer Hair Cell: Membrane Wizardry with a Twist and Shout

D.Z.Z. He¹, J. Zheng², F. Kalinec³, S. Kakehata⁴, J. Santos-Sacchi⁵

¹Hair Cell Biophysics Laboratory, Dept. of Biomedical Sciences, Creighton University School of Medicine, Omaha, NE 68178, USA

²Department of Communication Sciences and Disorders, Northwestern University, Evanston, IL 60208, USA

³Section on Cell Structure and Function, Gonda Department of Cell and Molecular Biology, House Ear Institute, Los Angeles, CA 90057, USA

⁴Department of Otorhinolaryngology, Hirosaki University School of Medicine, Hirosaki, Japan

⁵Otolaryngology, Neurobiology and Cellular and Molecular Physiology, Yale University School of Medicine, BML 246, 333 Cedar Street, New Haven, CT 06510, USA

Received: 15 December 2005

From Basilar to Plasma Membrane

Over 40 years ago the auditory community rejoiced that frequency tuning in the auditory periphery had been understood, and was proud that von Békésy received the Nobel Prize for showing us how the basilar membrane (BM) traveling wave provides for mechanical Fourier analysis (von Békésy, 1960). However, as soon as new techniques were devised to measure smaller movements of the BM than Békésy could imagine, curious incongruities arose concerning the significance of Békésy's measurements. Von Békésy made much of his measures on preparations that were compromised in a way unknown to him. Thus, the linear extrapolations from his high-intensity measures, which put auditory threshold movements below the diameter of an atom, were becoming unraveled. The problem turns out to be an inherent nonlinearity in the motion of the basilar membrane that is lost upon the slightest insult to the organ of Corti, that sensory epithelium of hair cells which is stimulated by BM movements. This remarkable observation of a compressive nonlinearity was made by Rhode (Rhode, 1971; Rhode & Robles, 1974), and has revolutionized our thinking on the micro mechanics of the inner ear. We now know that BM vibration is as sharply tuned to frequency as the eighth nerve fiber activity it evokes (Narayan et al., 1998). But what drives this nonlinearity? Why is it so vulnerable to insult? The answer is that it depends on the proper functioning of a particularly fragile cell

type within the organ, the outer hair cell (OHC) (Dallos & Harris, 1978; Ryan & Dallo, 1975).

The OHC is one of the two types of hair cells present in the organ of Corti. The other hair cell type is the inner hair cell (IHC) which receives up to 95% of the auditory nerve's afferent innervation (Spoendlin, 1988), but is fewer in number than OHCs by a factor of 3–4. Two decades ago, Brownell (Brownell, 1984; Brownell et al., 1985; Kachar et al., 1986) discovered that OHCs are capable of electrically evoked mechanical activity. Again, a revolution in our thinking began. The bottom line, after years of study, is that though both inner and outer hair cells respond to sound by generating receptor potentials (Russell & Sellick, 1978; Dallos, Santos-Sacchi & Flock, 1982), the OHCs alone are both receptor and effector – incredibly fast, at that. (You can view a movie of the OHC dance at www.YaleEarLab.org). Currently, the consensus is that OHCs provide a frequency-dependent boost to BM motion, which enhances the mechanical input to IHCs, thereby promoting enhanced tuning and amplification. Indeed, the term “cochlear amplifier” is commonly used to describe the work of the OHC (Davis, 1983). This review will summarize much of what we know about the OHC's electro-mechanical capabilities — phenomena which largely result from properties intrinsic to its plasma membrane (PM) and associated structures.

OHC Somatic Electromotility and Its Electrical Signature

The OHC is a cylindrically shaped cell whose length varies from short (~10–20 μm) to long (> 80 μm)

Correspondence to: J. Santos-Sacchi; email: joseph.santos-sacchi@yale.edu

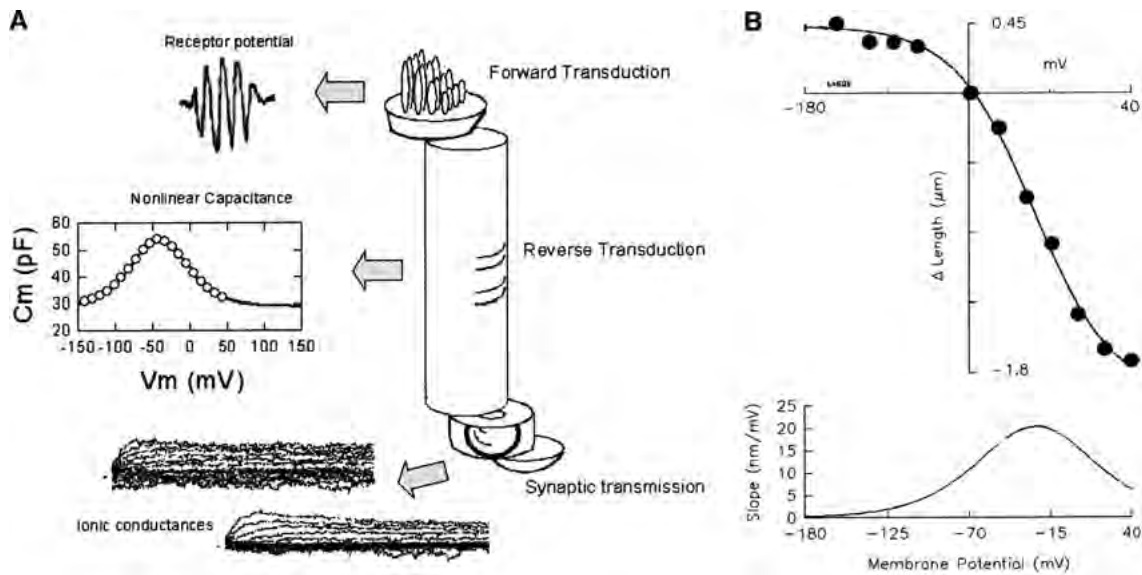


Fig. 1. (A) The OHC has a highly partitioned membrane. Apical, lateral and basal membranes possess characteristic integral membrane constituents with measurable electrical correlates. The apical stereocilia channels work to produce receptor potentials; the basal membrane houses the voltage-dependent ion channels; the lateral membrane houses the molecular motors (prestin), whose electrical signature is a nonlinear, voltage-dependent capacitance (NLC). Fits of the capacitance with the first derivative of a two-state Boltzmann provides information on the motors' operating range (characterized by $V_{1/2}$, the voltage at peak capacitance) and the sensitivity of the motors to voltage (an estimate of elementary motor charge, typically about 0.75). (B) The mechanical response (filled circles) of the OHC can also be fit by a two-state Boltzmann function. The first derivative defines the mechanical gain of the cell at a particular resting potential.

along the length of the basilar membrane, with short cells residing at the basal high-frequency regions of the cochlear spiral. While initial investigations did not identify OHC electrically evoked length changes as resulting from voltage or current flow across the PM, it soon became clear that this robust mechanical response, amounting to about 5% of the cell length, was evoked by voltage. This was indicated by the persistence of mechanical responses in spite of the block of a variety of membrane conductances, and the identification of gating-like currents or a nonlinear capacitance (NLC), which is characteristic of voltage-sensor activity that underlies membrane-based voltage-dependent processes. Consequently, OHCs contract with depolarization and elongate with hyperpolarization (Santos-Sacchi and Dilger 1988; Santos-Sacchi, 1990, 1991; Ashmore, 1989, 1990) Significantly, in isolated OHCs contraction/expansion cycles can be elicited by ciliary displacement (Evans & Dallos, 1993). OHC electromotility is independent of ATP, calcium, and the microtubule or actin system (Brownell et al., 1985; Kachar et al., 1986; Ashmore, 1987; Holley & Ashmore 1988b; Santos-Sacchi 1989; Kalinec et al., 1992). Motile responses can be seen at very high frequencies (Dallos and Evans 1995; Gale & Ashmore 1997; Frank, Hemmert & Gummer 1999). The mechanical response is sigmoidal and corresponds inextricably with those characteristics of the nonlinear charge movement (Fig. 1). Both the mechanical response

and its associated charge movement can be fit well with simple two-state Boltzmann functions and each share indistinguishable fitted parameters; namely, slope factors are near 30 mV per e-fold changes in charge or mechanical response, and operating voltage ranges have their midpoints ($V_{1/2}$) near negative 30–40 mV. Maximum charge movement in OHCs ranges up to about 3 pC, and early on it was observed that treatments that reduce this charge transfer or shift its operating voltage range correspondingly affect the mechanical response amplitude and its voltage activation range (Santos-Sacchi, 1991; Wu & Santos-Sacchi, 1998; Kakehata and Santos-Sacchi, 1995, 1996). Most investigators study charge movement in OHCs by measuring the NLC, which is bell-shaped (the first derivative of charge movement) with respect to voltage. Peak NLC can be greater than the cell's linear capacitance, the latter corresponding to the cell's surface area.

There are several perturbations that can influence the OHC motor mechanism, including membrane tension, temperature, and initial (resting) voltage conditions (Iwasa, 1993; Gale & Ashmore, 1994; Takahashi and Santos-Sacchi, 2001; Zhao and Santos-Sacchi 1998; Kakehata & Santos-Sacchi, 1995). In addition, lanthanides and salicylate can block to some extent NLC and somatic electromotility (Tunstall, Gale & Ashmore 1995; Kakehata & Santos-Sacchi 1996; Santos-Sacchi, 1991). The most

common effect on motor activity is a shift of the operating voltage range, indicative of a shift in the state probability of motor molecules residing in a contracted or expanded state. Additionally, maximum charge movement is also susceptible to external perturbations (*see* Santos-Sacchi, 2003, for a more detailed review). It was the electro-mechanical characteristics of the OHC motor that ultimately enabled the identification of the protein responsible for the unique function of the OHC.

The OHC Motor Protein Prestin

Although the existence of a unique motor protein embedded in the OHC's PM was proposed as early as 1992 (Kalinec et al., 1992), it was not until five years ago that the molecular nature of the OHC motor was revealed (Zheng et al., 2000). The basic strategy of this identification was based on the fact that inner hair cells IHCs do not show somatic electromotility but share many similarities with OHCs. An OHC-IHC subtracted cDNA library was created aiming to isolate the OHC-specific genes that are abundantly expressed only in OHCs and not in IHCs (Zheng et al., 2002a). The OHC motor protein was identified in this library and named prestin. Prestin is localized to the PM where the motor was known to be located (Hallworth, Evans & Dallos, 1993; Huang & Santos-Sacchi, 1993, 1994). When prestin was heterologously expressed in several cell lines, the transfected cells exhibited behaviors that are normally observed only in OHCs: voltage-dependent NLC and shape changes (Zheng et al., 2000); electro-mechanical reciprocity (Santos-Sacchi et al., 2001; Dong & Iwasa, 2004); temperature sensitivity (Meltzer & Santos-Sacchi, 2001), and mechanical force generation with constant amplitude and phase up to a stimulating frequency of at least 20 kHz (Ludwig et al., 2001). Ontogenic expressions of the *prestin* gene (Zheng et al., 2000) and prestin protein (Belyantseva et al., 2000a) are the same as that of electromotility (He, Evans & Dallos, 1994). In addition, the electromotile responses in prestin-transfected kidney cells can be blocked by salicylate (Zheng et al., Oliver et al., 2001), an inhibitor of somatic electromotility in OHCs (Shehata, Brownell & Dieler, 1991; Tunstall et al., 1995; Kakehata & Santos-Sacchi, 1996). Furthermore, OHCs from prestin-null mice lack somatic electromotility, and those mice also lose 40–60 dB of hearing sensitivity (Liberman et al., 2002) and lack frequency selectivity (Cheatham et al., 2004). A splicing mutation in *prestin* gene causes non-syndromic deafness (Liu et al., 2003). Collectively, these results are consistent with the idea that prestin is the motor protein of cochlear OHCs.

Prestin's Gene and Its Expression

Prestin belongs to a distinct anion transporter family called solute carrier protein 26 (SLC26) (Zheng et al., 2002b). At present, eleven members of this family have been identified (Mount & Romero 2004). Several proteins in this family, including prestin, are involved in human diseases (for review, *see* Dawson and Markovich, 2005). The human Prestin gene contains 21 exons crossing more than 90 kb in chromosome 7q22 (Liu et al., 2003), a location near to those of other important SLC26 members, such as PDS (SLC26A4) (Everett et al., 1997) and DRA (SLC26A3) (Haila et al., 1998). The mouse Prestin gene has 20 exons spanning nearly 55 kb in chromosome 5 (Zheng et al., 2003). Eighteen of these exons code for prestin amino acids in both hPrestin and mPrestin. Among coding exons, 12 exons are exactly the same sizes as in other members of the SLC26 family, such as Pendrin, DRA and CFEX (Zheng et al., 2003), indicating high homologies among these genes. Several prestin isoforms have also been found in different stages of human cochlear development (Liu et al., 2003). However, these isoforms were not found in mature mouse cochleae (Zheng and colleagues, *unpublished data*). The function of these predicted human prestin isoforms was not further studied. Prestin mRNA was also found in testis, brain and vestibular system through either RT-PCR or in situ experiments (Adler et al., 2003; Zheng et al., 2003). Anti-prestin labeling was found in the cytoplasm of vestibular hair cells, but not in the PM (Adler et al., 2003). The behavior endowed by prestin, somatic motile activity, was never found in vestibular hair cells (Adler et al., 2003). Overall, prestin is abundantly expressed only in OHCs, where somatic motile activity is observed. The time course of prestin mRNA and protein synthesis in OHCs corresponds to the emergence of somatic motile activity in OHCs (Belyantseva et al., 2000a; Zheng et al., 2000). Furthermore, a prominent longitudinal and radial gradient of prestin expression, ranging from base-to-apex and first-to-third row of OHCs, was also observed (Judice et al., 2002). Such tight regulation of prestin mRNA expression is not fully understood. Thyroid hormone was reported to regulate prestin mRNA expression (Weber et al., 2002). In spite of the fact that prestin's promoter and other regulating regions have not been precisely identified (Weber et al., 2002; Zheng, Richter & Cheatham 2003), the prestin gene has been modified to create transgenic mice that are useful for studying hair-cell-specific gene targeting (Tian et al., 2004).

Prestin is a highly conserved protein among different mammalian species. So far, the full-length prestin protein has been identified from four species including gerbil (Zheng et al., 2000), mouse (Adler et al., 2003; Zheng et al., 2003), rat (Ludwig et al.,

2001) and human (Liu et al., 2003). Among these four, 92.7 % of amino acids are identical and 6% show some similarity. Only 10 amino acids (1.3%) were different as determined by the CLUSTALW multiple alignment analysis (Thompson, Higgins & Gibson 1994). Prestin-related SLC26 proteins were also reported in non-mammalian vertebrates and insects (Weber et al., 2002). The closest one (AY278118) related to mammalian prestin was found in the Zebrafish's auditory organ. This prestin-related gene has ~ 15 exons with 49.8% amino acids identical to mammalian prestin. The function of Zebrafish prestin is not fully investigated. The key question, whether zPrestin demonstrates somatic motile activity, has not been answered yet. Therefore, whether non-mammalian prestin has a similar function and role in non-mammalian hearing needs further investigation.

Prestin Protein's Structure and Its Modification

Prestin appears to share the overall structure and specific protein domains of the SLC26 family: a highly conserved central core of hydrophobic amino acids (~ 400 amino acids) predicted to form 10–12 transmembrane domains according to the topology prediction programs chosen for the analysis (Oliver et al., 2001; Zheng et al., 2001; Deak et al., 2005; Navaratnam et al., 2005b). It is generally agreed that Prestin can be divided into three domains: N-terminus (~100 a.a.), hydrophobic core (~400 a.a.) interacting with lipids of the PM, and C-terminus domain (~240 a.a.) as shown in Fig. 2. Through immunofluorescence experiments, the N- and C-termini were shown to be located on the cytoplasmic side of the PM (Ludwig et al., 2001; Zheng et al., 2001). The "sulfate transporter signature" is present in the hydrophobic core, while a STAS (sulfate transporter and antisigma-factor antagonist) motif (Aravind & Koonin, 2000) is located in the C-terminus (a.a. 634–710). There are two predicted N-glycosylation sites in the hydrophobic core region: N163 and N166. While two sets of experiments suggest that these two sites are glycosylated, indicating that prestin is a glycoprotein (Matsuda et al., 2004; Iida et al., 2003), there are contrary data (Navaratnam et al., 2005b).

Aside from possible glycosylation, prestin can also be phosphorylated by cGMP-dependent kinase at S238 and T560 (Deak et al., 2005). Phosphorylation at these sites not only affects the operating voltage range of prestin's NLC (such as S238A), but also significantly changes the slope of voltage dependence (S238D) (Deak et al., 2005). There are several other phosphorylation sites affecting prestin's function, such as PKC-dependent phosphorylation (Matsuda et al., 2003). How these different phosphorylation sites cooperate with each other to

regulate motor function *in vivo* needs further investigation.

Prestin has 744 amino acids. The estimated size of a prestin monomer is too small to form the 10-nm particle originally found in the OHC's lateral membrane (Gulley & Reese 1977; Kalinec et al., 1992; Santos-Sacchi et al., 1998). Hence, the possibility of prestin's oligomerization has been studied through both genetic, biophysical and biochemical methods. Data from FRET and FRAP experiments obtained by several groups demonstrated that prestin can bind to itself (Kural et al., 2004; Greeson, Organ & Raphael 2005; Navaratnam et al., 2005b). In order to investigate the possibility of higher-order oligomers, we examined the quaternary structures of prestin by LDS/PAGE, PFO/PAGE, a membrane-based yeast two-hybrid system, and chemical cross-linker experiments. Our data suggest that prestin forms a high-order oligomer such as tetramer in OHCs (Zheng et al., 2005b). Using a protein density calculation method described by Fischer et al., (Fischer, Polikarpov and Craievich 2004), we estimate a tetramer of prestin transmembrane domains to be on the order of ~11 nm in diameter. Furthermore, 8–13 nm particles (likely to be prestin) were observed through atomic force microscopy in prestin-transfected CHO cells (Murakoshi, 2005). This size is consistent with the motor protein complex observed in the lateral membrane of OHCs (Gulley & Reese 1977; Kalinec et al., 1992; Santos-Sacchi et al., 1998). How prestin forms tetramers and what amino acids are involved in the formation of these structures is still unknown, though N-terminal-based interactions of prestin appear required for such homomeric relations (Navaratnam et al., 2005b).

Molecular Mechanism of Prestin Function

Prestin shows the greatest sequence similarity to PAT1 (putative anion exchanger 1, SLC26A6) (Dallos & Fakler, 2002). Based on early indications that no anion transport was associated with prestin function (Dallos & Fakler 2002), prestin was thought to behave as an incomplete anion transporter. Thus, although prestin demonstrates voltage-dependent charge transfer manifest as NLC, other members of the SLC26A family, such as SLC26A4 and SLC26A6, do not show NLC under similar conditions (Zheng et al., 2000; Oliver et al., 2001). How membrane potential changes across the OHC membrane result in conformational changes in prestin, corresponding to its motor function, is not understood. In order to find the voltage sensor of prestin, the nonconserved charged amino acids (R, K, D and E) between prestin and SLC26A6 in the hydrophobic core region were changed to neutral amino acids as shown in Fig. 2. However, all mutants continued to show NLC even

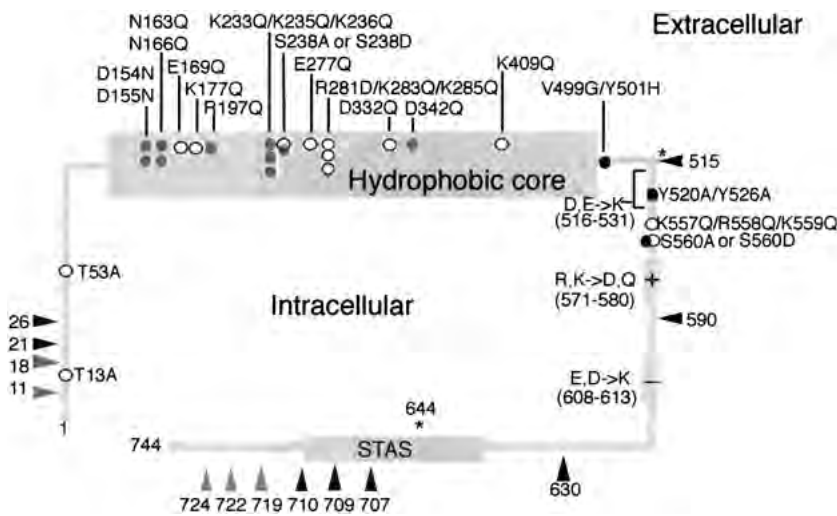


Fig. 2. Effects of mutated amino acids in prestin sequence on prestin's NLC function. *Open circles* are the point mutants that maintain prestin's normal function. *Black dots* are point mutants that produce total loss of prestin's function. *Grey dots* are point mutants that maintain NLC but with significant changes in properties such as voltage dependence. *Grey arrows* indicate truncation mutants (deleted at either the N-terminus or C-terminus end) that maintain prestin's NLC function. *Black arrows* are truncation mutants without NLC. *Asterisks* mark positions where prestin-pendrin, and prestin-pat1 chimeras were switched.

though the parameter values in some mutants were changed (Oliver et al., 2001; Bai et al., 2003). For example, mutant D154N (*grey dot*) has $V_{1/2}$ at -146.7 mV in contrast to -70 mV in wild-type prestin. There are also negative and positive charge clusters in prestin's C-terminus, as shown in Fig. 2. Changing charged amino acids in the C-terminus to either the opposite charge (R, K \rightarrow D, E, D \rightarrow K) or a neutral amino acid (Q), does not abolish NLC function either (Oliver et al., 2001; Bai et al., 2003). It thus appears that these charged amino acids in prestin do not play a primary role as voltage sensors. Subsequent experiments suggested that intracellular anions play a crucial role either as extrinsic voltage sensors (Oliver et al., 2001) or allosteric modulators of the voltage sensor (Oliver et al., 2001; Rybalchenko & Santos-Sacchi 2003). Chloride, in particular, has profound effects on NLC and the motor's operating voltage range (Oliver et al., 2001; Song, Seeger & Santos-Sacchi, 2005; Rybalchenko & Santos-Sacchi, 2003). Most recently, prestin transfected into CHO cells has been shown to exchange extracellular C^{14} formate for intracellular chloride; this transport, which is blocked by salicylate and DIDS, is competitively inhibited by extracellular malate and chloride, but not sulfate (Navaratnam et al., 2005a). Additionally, there is evidence that prestin also provides electrogenic transport of bicarbonate and chloride, and to transport sugar (Chambard & Ashmore, 2003; Ashmore, 2005). This recently observed capability of prestin to transport anions, and the ineffectiveness of anion valence to alter the elementary charge movement underlying NLC (Rybalchenko & Santos-Sacchi, 2003), seriously challenges the extrinsic voltage sensor model (Oliver et al., 2001), and suggests that the effect of anions on prestin activity results from allosteric modulation of the protein's conformation within the lateral membrane. The identity of the charged voltage sensor, however, remains elusive.

Amino acids in the hydrophobic core are near 100% identical among human, mouse, rat and gerbil prestin (only one amino acid is different). Since the function of prestin is directly associated with an increase and decrease of PM area (Kalinec et al., 1992; Santos-Sacchi, 1993; Iwasa, 1994; Santos-Sacchi & Navarrete, 2002), it is logical to assume that the hydrophobic core (embedded in the membrane) is more important for NLC than either the N- and C-termini, since it alone should sense the membrane field. Nevertheless, deletion of N- and C-terminus sections has been shown to be lethal for prestin's function. In fact, deletions of more than 21 amino acids at the N-terminus, or more than 32 amino acids at the C-terminus result in loss of prestin function (*filled arrow* in Fig. 2) (Navaratnam et al., 2005b). There is conflicting evidence whether the loss of function in truncated proteins is due to a lack of membrane insertion (Zheng et al., 2005c) or other causes (Navaratnam et al., 2005b). Replacing the C-terminus of prestin (at position 515 or 644 indicated as "*" in Fig. 2) with the analogous C-terminus portion of one of two closely related SLC26A proteins, Pendrin or PAT1, does not rescue the electrophysiological function of prestin. However, these chimera mutants are not delivered into the PM (Zheng et al., 2005c). In addition, mutating some of the non-charged amino acids in the C-terminus results in loss of electrophysiological function. Some of these mutants, e.g., Y520A/Y52A shown in Fig. 2, lose the ability to reach the PM. Other mutants, e.g., V499G/Y501H, can reach the PM; yet still lose function (Zheng et al., 2005c). These data suggest that the C-terminus plays an important role in both regulating membrane targeting and overall prestin function (Zheng et al., 2005c). Similar results are also found for the N-terminus (Navaratnam et al., 2005b). Together, these data suggest that both N- and C-termini play critical roles for the motor protein's function.

Prestin-Associated Proteins

The PM of OHCs is enriched with protein components. There is also a complicated structural network underlying the PM, including a cortical lattice and cisternal membranes. Although prestin is the key player in somatic electromotility, evidence suggests that other proteins are involved in modifying OHC electromotility. The neurotransmitter acetylcholine (Dallos et al., 1997; Kalinec et al., 2000) and secondary messengers such as cyclic GMP, can modify OHC motor function (Szonyi et al., 1999). An aquaporin-like protein has also been linked to OHC motor function (Belyantseva et al., 2000b). Sugar carrier Glut5 is associated with OHC length changes in a voltage-dependent fashion (Geleoc et al., 1999). Interestingly, Glut5 protein is absent in OHCs of prestin knockout mice (Wu, 2004). The relationship between prestin and Glut5 is still being investigated.

It is of interest to identify the prestin-associated proteins. Several groups used the yeast two-hybrid system to screen prestin-associated proteins. In this system, the C-terminus of prestin was used as “bait” to identify prestin-associated proteins. Couplin was first suggested as a novel protein that binds to both prestin and actin (Dougherty et al., 2003). A transcriptional repressor, promyelocytic leukemia zinc-finger protein (PLZF) was also identified as a protein interacting with prestin in OHCs (Nagy et al., 2005). PLZF gene produces a POZ/domain Kruppel-type zinc-finger transcription factor reported to have pro-apoptotic and anti-proliferative function. Currently, it is not clear how and where PLZF may affect prestin’s function. Other interacting proteins include VCY2-IP1, whose sequence shows homology to MAP1A and MAP1B, and the Na/K ATPase beta 1 subunit (Navaratnam et al., 2005c). Cystic fibrosis transmembrane conductance regulator (CFTR) was reported to activate several of the SLC26 family membrane proteins including DRA, Pendrin and PAT1 via interaction between the STAS domain of SLC26 and the R domain of CFTR (Ko et al., 2004). Prestin contains the conserved STAS domain like other SLC26 family members. Preliminary data also suggest that co-expressing CFTR with prestin in TSA cells could enhance prestin’s function (Zheng et al., 2005a). These observations indicate that the motor does not normally act in isolation in the intact OHC and indeed there are elaborate structural details within the sub-membrane spaces. To be sure, the motor must work in concert with these structures.

Development of Structural and Mechanical Characteristics of the OHC

The OHC lateral wall is a unique trilaminar structure consisting of the PM, the cortical lattice, and

subsurface cisternae. Like the PM of other cell types, the OHC PM has three main components: the lipids, the proteins, and the glycocalyx. A high density of integral membrane proteins in the lateral PM is one of the distinguishing features of OHCs. When the membrane bilayer is fractured using the freeze fracture technique, a dense array of particles can be seen on the inner surface of the cytoplasmic leaflet (Gulley & Reese 1977). The particles are about 10 nm in diameter and the packing density has been estimated to be from 2500–3000/μm² (Saito, 1983; Kalinec et al., 1992; Santos-Sacchi et al., 1998) to as much as 7000/μm² (Forge, 1991; Koppl, Forge & Manley, 2004). These values are much higher than those of inner hair cells (1900–2800/μm², (Koppl et al., 2004)), non-mammalian hair cells (1880–2360/μm², (Koppl et al., 2004)) and axolemma of peripheral myelinated fibers (1300–2500/μm²). The density of cochlear apical and basal turn cells appears to be the same (Forge & Richardson 1993). These particles in OHCs may include many of the normal membrane proteins, such as non-voltage-dependent ion channels and structural links with the cytoskeleton. However, it was suggested the motor protein might account for a major fraction (Kalinec et al., 1992), and as noted above, it is likely that prestin multimers comprise these structures. Indeed, when the PM of gerbil OHCs between 2 and 16 days after birth (DAB) is examined using replicas of the freeze fracture, the particles are found to be present at low density at 2 DAB and increased in density from 2200/μm² at 2 DAB to 4131/μm² at 8 DAB, and continue to increase in density until mature values are attained at 16 DAB (Souter, Nevill & Forge 1995). The increase in density of the particles during this time period matches the appearance and development of OHC motility in the same species (He et al., 1994). Since OHC somatic motility is required for normal hearing, it might be expected that development of motility would correspond in time to the development of hearing. Both measures of OHC length changes and NLC have been used to get at this issue.

To date, OHC motor development has been studied in three species, namely, rat, gerbil and mouse (He et al., 1994; Oliver & Fakler 1999; Belyantseva et al., 2000a; Abe et al., 2005). In these species, slight differences in the development of hearing are found. Hearing onset and maturation in mouse are observed at P10–12 and P18, respectively (Ehret, 1976; Steel & Bock, 1980). In rats and gerbils, these periods are somewhat extended, onset being P12 and P12–14, and maturation being P25 and P21 for rats and gerbils, respectively. He et al., (1994) reported that the electromotile response elicited using a whole-cell microchamber technique was detectable at P7 in cells from the basal cochlear turn and at P8 from the apical turn. All OHCs tested showed detectable responses at P12 and the threshold of detectable response reached

adult levels at about P12. Percentage ratios of maximal response amplitudes and cell lengths reached adult levels of 1.3% at P15 in the basal turn and at P17 apically. On the other hand, OHC cell length of the apical turn continued to elongate until P17 with decreasing cell width, while in basal cells only minimal changes were found. In apical OHCs, voltage-induced length change increased as the cell length elongated. These results suggest that the density of the motor in the longitudinal direction continued to increase until maturation of somatic motility.

In the rat, NLC is detectable as early as P0 in apical turn OHCs (Oliver & Fakler 1999). Oliver and Fakler measured NLC from P0 to P14, demonstrating that NLC increased up to P14, the oldest day they measured, while linear capacitance (C_{lin}) showed saturation between P3 and P11, but suddenly increased from P13. Thus, the calculated value of charge density displayed saturation after P11 because C_{lin} continued to increase after P11. The authors concluded that motor protein density matured at P11 and that the increase in NLC after P11 was due to an increase in membrane area containing the same density of motor proteins. They further concluded that characteristics of the OHC motor reach adult level at the onset of hearing, P12, substantially before the maturation of the hearing of P25 in rat. On the contrary, the developmental time course of NLC and intensity of immunolabeling of rat OHC lateral wall with anti-prestin antibodies correlates well and matures at P17 (Belyantseva et al., 2000a).

Marcotti and Kros (1999) studied somatic motility and capacitance of the OHCs from Swiss CD-1 mice. They measured capacitance at a fixed membrane voltage of -84 mV, and therefore could not detect linear and nonlinear capacitance separately. Total capacitance saturated beyond P16. All the cells tested showed detectable motile response at P12 (they recorded somatic electromotility at P6, 8, 9 and 12). In C57BL/6J mice, Abe and coworkers measured NLC to investigate the development of motor protein activity of apical OHCs each postnatal day from P5 to P18 (Abe et al., 2005). It was found that surface area or C_{lin} of OHCs mature at p10, whereas prestin activity – gauged as NLC – increased until p18. These and other data (prestin qPCR) were interpreted as evidence for a completed population of prestin molecules within the PM early on, whereas prestin function continues to mature, possibly through heteromeric formations, changing chloride sensitivity, establishment of other protein interactions or phosphorylation effects. Such maturation may correspond to ultrastructural particle formation in the PM, as noted above. Of course, it should be noted that the attainment of adult cochlear function undoubtedly profits from a concerted developmental contribution from a variety of cellular and acellular structures that work with the motors.

OHC Stiffness, Forces and Lateral Wall Structure

Little is known of the lipid content of the PM in OHCs, but it seems to include high levels of cholesterol that may reduce its flexibility and fluidity (Forge, 1991). Lipid lateral diffusion in the OHC PM is a function of transmembrane potential and bathing medium osmolality. Cell depolarization, hyposmotic challenge, and amphipathic drugs reduce membrane fluidity (Oghalai et al., 2000). The dynamic changes in membrane fluidity may represent the modulation of membrane tension by lipid-protein interactions. This and the high protein content should mean that the PM is relatively stiff. Indeed, the relatively high stiffness of the PM is important for the expression of somatic motility (Holley & Ashmore, 1988a; Tolomeo, Steele & Holley, 1996; He, Jia & Dallos 2003).

About 25 nm beneath the PM there is an elaborate and highly structured cortical network called the cortical lattice. The cortical lattice appears to be composed of two distinct types of filament (Holley & Ashmore 1990b; Holley, Kalinec & Kachar 1992). The most obvious of these is the 6–7-nm diameter actin filaments that follow a circumferential path around the cell. Adjacent circumferential filaments are from 30 to 80 nm apart, and they are held in parallel arrays by thinner cross-links (2–3 nm in diameter) that may appear single or branched. These thinner cross-links appear to be spectrin (Holley & Ashmore, 1990b). These arrays form discrete domains that vary from just a few parallel filaments only 200 nm long to at least 10 filaments of up to 1 μ m long. Their mean angle to the transverse axis of the cell is about 5° – 15° with significant variability ((Kalinec & Kachar 1995; Holley et al., 1992; Holley & Ashmore, 1990a). This wide range of orientations suggests that the mechanical response of the OHC lateral wall could be locally modulated. In this regard, the OHC motor appears to be able to be modulated by local stresses and conditions (Santos-Sacchi, 2002). The Young's modulus of the circumferential filamentous components of the lattice were calculated to be 1×10^7 N/m². The axial cross-links, believed to be a form of spectrin, were calculated to have a Young's modulus of 3×10^6 N/m² (Tolomeo et al., 1996). The lattice is sufficient to retain the shape of the cell following demembranization and mechanical deformation. The structure of the lattice allows it to be described as a coiled helical spring but with longitudinal stiffness primarily determined by the crosslinks. The axial and circumferential stiffness moduli for the cortical lattice measured in OHCs without PM are 5×10^{-4} N/m and 3×10^{-3} N/m, respectively (Tolomeo et al., 1996). Thus the cortical lattice is a highly orthotropic structure. Its axial stiffness is small compared with that of the intact cell, but its circumferential stiffness is within the same

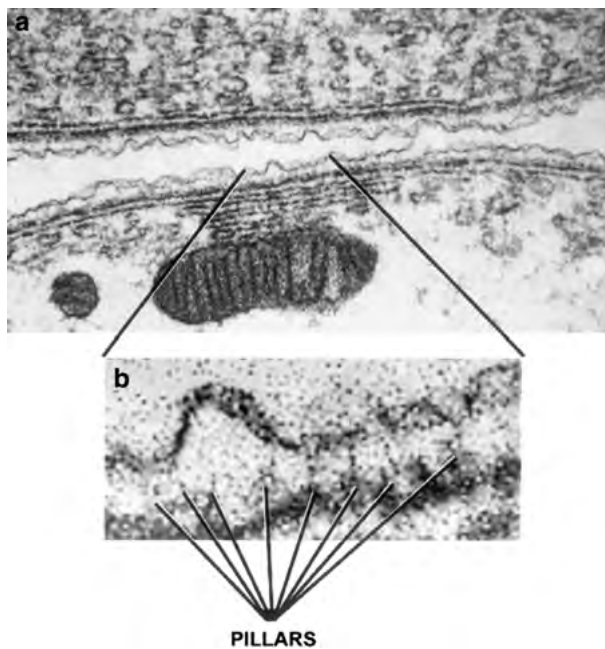


Fig. 3. (a) An electron micrograph of a section of a guinea pig organ of Corti showing two neighboring OHCs (separated by the Nuel space), showing a “rippled” plasma membrane. Beneath the PM is the continuous first sheet of subsurface cisternae. In places where the pillars look intact, the PM appears to be flat, whereas its bending is pronounced in regions where the pillars are disrupted (b). Note the variability in appearance and number of cytoplasmic cisterna, adjacent to the mitochondrion.

order of magnitude. Direct measurements of longitudinal stiffness indicate that the lattice contributes only a fraction of the overall stiffness of OHCs (Holley & Ashmore, 1988a; Tolomeo et al., 1996; He et al., 2003). These measurements support the theory that the cortical cytoskeleton directs electrically driven length changes along the longitudinal axis of the cell. The cortical lattice is connected to the PM by electron-dense “pillars” 7–10 nm in diameter and 25 nm long (Flock, Flock & Ulfendahl, 1986; Arima et al., 1991) that are attached specifically to the circumferential filaments at intervals of about 30 nm (Holley et al., 1992).

The lateral cisternae are a specialized and substantial fraction of the endoplasmic membrane within the OHC (Gulley & Reese, 1977; Saito, 1983). They form multiple, highly ordered layers that line the lateral cytoplasmic surface of the PM (Gulley & Reese, 1977). The number of layers and the morphology of these membranes vary considerably among different mammals, and between apical and basal turn OHCs, and even at different regions of the same cell (Fig. 3). In the guinea pig, as many as 12 layers have been reported (Evans, 1990; Forge et al., 1993), whereas in rats, only one layer is found in the apical turn OHCs (Raphael & Wroblewski, 1986). Modeling work suggests that the subsurface cisterna may influence the electrical properties of OHCs (Halter

et al., 1997) A reduction in the width of the extracisternal space decreases the whole-cell conductance and capacitance. It is unclear whether the lateral cisternae play an important role in the mechanism of somatic motility (beyond that of structural maintenance). Indeed, SSC are not required for normal prestin activity, since disruption of the cisternae with intracellular enzymatic treatments or expression into cells lacking the SSC, shows unmodified NLC (Huang & Santos-Sacchi, 1994; Zheng et al., 2000). Nevertheless, developmental studies show that the appearance of the first layer of the cisternae (Pujol et al., 1991; He, 1997) occurs at the same time when neonatal OHCs begin to exhibit somatic electromotility. The stiffness of the structurally irregular lateral cisternae is very unlikely to contribute significantly to that of the intact OHCs.

Under the influence of the cell’s turgor pressure, the PM, the cortical lattice, and the subsurface cisternae contribute to the global axial stiffness of OHCs. The static axial stiffness of OHCs has been measured by compressing the cell with a fine, vibrating glass probe of known stiffness. The stiffness value obtained by different studies from guinea pig OHCs varies from 0.5 to 5 mN/m (Holley & Ashmore, 1990a; Zenner et al., 1992; Gitter, Rudert & Zenner, 1993; Hallworth 1995, 1997; Iwasa & Adachi 1997; Ulfendahl et al., 1998; He & Dallos, 2000). Although the axial stiffness of OHCs varies significantly among different studies, stiffness of short OHCs from the basal turn is found to be much greater than that of long OHCs from the apical turn (Holley & Ashmore, 1988a; Hallworth, 1995; Russell & Schauz, 1996). OHCs are capable of producing an average maximum axial isometric (stall) force of ~ 5 nN (He & Dallos 2000; Iwasa & Adachi, 1997). From the number of molecules producing this force it can be estimated that the individual molecular stall force is on the order of 2.4 pN. In comparison, the stall force of kinesin is 5–6 pN (Svoboda & Block, 1994). The force generated per mV of command at the cell membrane is estimated to be around 0.1 nN/mV (Hallworth, 1995; Iwasa & Adachi, 1997).

Static stiffness and force of OHCs can also be manipulated by various means (Hallworth, 1997). Axial stiffness and electromotile forces are reduced by 65% when 5 mM salicylate is applied to the cell (Russell & Schauz, 1996). Dallos et al. (1997) demonstrated that delivery of the OHC’s efferent neurotransmitter acetylcholine (ACh) to the cell’s synaptic pole also decreases the axial stiffness. Quinine at 5.0 mM concentration can also substantially affect the cell mechanics and decrease active force generation in isolated OHCs (Jarboe & Hallworth 1999).

While the axial stiffness of OHCs has been studied, relative stiffness of the lateral wall components is still somewhat controversial. Some studies suggest that the PM appears to be relatively stiff and may be the

dominant contributor to the axial stiffness of intact cells (Holley & Ashmore 1990a; Tolomeo et al., 1996; He & Dallos 1999; He et al., 2003), while a study by Oghalai et al., (1998) indicates that the cortical lattice may account for ~70% of the axial stiffness. In addition, Adachi and Iwasa (1997) also show that diamide can reduce the axial stiffness of OHCs by 65%. Diamide presumably affects spectrin in the cortical lattice. Functionally, the stiffness of the PM must be at least within the same order of magnitude as that of the rest of the cell cortex. If it were not sufficiently stiff, most of the energy associated with conformational change of the motor protein would be stored in the PM itself as strain energy, whereas a stiffer cell cortex would resist the deformation. With the PM dominating the lateral wall stiffness, one hypothesis to explain OHC force coupling is the cytoskeletal spring model proposed by Holley and Ashmore (1988). In this model the molecular motors rest within the PM, and the cortical lattice is less stiff than the PM. When the motors change in dimensions, they push against themselves and their surrounding phospholipids, summing their forces and creating cell length changes. Hence, by this model, force coupling occurs within the PM because the PM has a high stiffness. An alternative possibility, suggested by Iwasa (1994) and further discussed by Tolomeo et al. (1996), is that motors in the PM transmit their force down the pillars to the cortical lattice, which then orients the forces. Because an equal and opposite force would be required to hold the motors in place within the PM, the PM must be stiffer than the cortical lattice in this theory, as well.

He and Dallos (1999, 2000) discovered that the axial stiffness of isolated OHCs is also voltage-dependent. They showed that cell stiffness increases upon hyperpolarization and decreases when the cell is depolarized. The stiffness change can be quite large — on the order of 100%. The stiffness change and somatic electromotility appear to co-vary if manipulated (He & Dallos, 2000). The general covariance of stiffness and length changes suggests that they may arise from a common mechanism, the motor protein (He et al., 2003). Existing standard area models (Iwasa, 1994, 2000) of OHC somatic electromotility do not automatically yield stiffness changes of the type that He and Dallos (1999, 2000) observed. Two generic models (Dallos & He, 2000) have been proposed to explain both phenomena via a single mechanism. The first model assumes that molecular motors change both their axial dimension and stiffness upon a voltage-dependent conformational shift. In the second model, only a stiffness change is associated with elementary motors. Corresponding cell-length change is obtained if the quiescent cell is preloaded so that in its resting state it is shorter than its natural length. This model suggests that somatic motility may simply be a consequence of stiffness change. This would then render voltage-dependent stiffness the primary

mechanism, with length change being an epiphenomenon (He & Dallos, 1999).

Honing in on the Role of the Cortical Actin-Spectrin Cytoskeleton in OHC Somatic Motility

A well-known paradigm establishes that even the simplest support system must be adapted to resist tension, compression and bending, three very different kinds of forces (Wainwright et al., 1982). The relative amount of each type of force, together with its intended function, will determine the particular support system for a given cell type. Cell's shape, in turn, will largely be an expression of this mechanical support system. Cochlear OHCs are a unique example of this paradigm.

OHCs possess a hydraulic support system consisting of a fluid under pressure (the cytoplasm), which acts as a compression-resisting component, and the container, which only resists tension (Brownell, 1990). Like OHCs, organisms with a fluid support system are either cylindrical or subcylindrical (Wainwright et al., 1982). However, while the walls of plant cells are rigid enough to support the cylinder at zero pressure, animal hydrostats are flabby and collapse without a positive internal pressure (Wainwright et al., 1982). For a cylindrical vessel closed at its ends — like an OHC — the stress in the longitudinal direction is

$$\sigma_L = pR/2t \quad (t = \text{membrane thickness}; \\ p = \text{external cell radius}).$$

The stress in the circumferential direction, in turn, is

$$\sigma_H = pR/t = 2\sigma_L$$

This means that if slight increases in internal pressure are not to cause disproportionate increase in body diameter, the cylinder wall must be reinforced in order to control the change of shape with changes in pressure. Because of that, lateral walls in pressurized cells are usually reinforced by helically oriented fibers. This is precisely the case in OHCs.

As noted above, OHCs possess a membrane skeleton — the cortical lattice (CL) — composed of relatively long, helically oriented actin filaments cross-linked by spectrin tetramers (Holley & Ashmore 1990a; Holley et al., 1992; Holley, 1996). The cortical actin-spectrin cytoskeleton is a structure common to every known cell population, although its molecular organization, extension and function are cell-specific.

Red blood cells (RBCs) and OHCs, in particular, expose two extreme cases of the functional adaptation of this structure. RBCs, like OHCs, possess a very well developed cortical actin-spectrin cytoskeleton (Bennett, 1990; Matsuoka, Li & Bennet, 2000; Bennet & Gilligan 1993). However, because of the particular

mechanical requirements in each case, they are structurally different. Healthy RBCs are highly deformable, a crucial requirement for cells that need to flow smoothly along very narrow capillary vessels. Consequently, the cytoskeleton is composed of five or six spectrin molecules linked to very short actin filaments, forming a highly flexible “spider-web” sheet underlying the plasma membrane. This arrangement ensures that any stress, in any direction, will actually be resisted by the highly deformable spectrin molecules rather than the practically inextensible actin filaments. In OHCs, in contrast, the cytoskeleton must primarily provide mechanical stability to the cells, and deformations are desirable only in the longitudinal direction and in a controlled way. This is provided by orienting the very long actin filaments in a near circular pattern and the spectrin molecules near parallel to the OHC’s longitudinal axis, facilitating the cell’s changes in length while maintaining the cylindrical shape. Interestingly, the connection between spectrin abundance, localization and particular spatial orientation in OHCs and one of the non-structural functions of these molecules has not been explored yet. Spectrin molecules have been described as “protein-sorting machines” that sort the proteins to be incorporated in plasma membranes (Beck & Nelson 1996), as well as “protein accumulators” because they can trap and stabilize particular protein species at specific points on cell surfaces (Hammarlund, Davis & Jorgensen, 2000; Moorthy, Chen & Bennet, 2000; Dubreuil et al., 2000). Thus, spectrin could be involved in the sorting, accumulation and organization of prestin molecules in the lateral plasma membrane of OHCs and, consequently, in the genesis of the OHC’s motor action.

The orientation and mechanical properties of the circumferential filaments and their cross-links could determine the nature of the shape changes observed in isolated cells (Holley and Ashmore 1988a). Wainwright and co-workers (Wainwright et al., 1982) mentioned as one of the “design principles for biological structural systems” that: “*Thin-walled cylinders are most effectively reinforced against explosion and buckling by crossed-helicallly wound fibers. As the cylinder changes shape, the fiber angle changes. For instance, if the cylinder becomes short and fat the angle increases, and vice-versa.*” In a closed, fiber-wound cylinder like an OHC, the circumferential and longitudinal stresses will be balanced when the fiber angle is $35^{\circ} 16'$ with respect to the transversal axis of the cell ($55^{\circ} 44'$ with respect to the longitudinal axis (Clark & Cowey 1958; Wainwright et al., 1982)

$$\sigma_H/\sigma_L = 2 = [\tan^2(35^{\circ}16')]^{-1}$$

For angles smaller than $35^{\circ}16'$, a given increase in pressure would produce an even larger increase in σ_H than in σ_L . For angles bigger than $35^{\circ} 16'$, the opposite will be true. Interestingly, cell volume would

be maximum for a fiber angle of $35^{\circ} 16'$, and would decrease for smaller or larger angles (Clark & Cowey, 1958; Wainwright et al., 1982). Therefore, the near inextensible actin filaments should be forming an angle smaller than 35° with the transversal axis of the cell in order to keep the cell cylindrical. It should be noted that a mechanism capable of controlling the angle of the helically oriented actin filaments could preserve the OHC’s cylindrical shape and at the same time modulate the amplitude of OHC motility by regulating the longitudinal component of the membrane-generated forces, cell stiffness, and membrane tension.

The question, of course, is which could be the mechanism capable of dynamically controlling the angle of actin filaments in the OHC cortical cytoskeleton. The answer could be in the modular organization of this structure.

The pillars have an important role in the recently proposed “membrane bending model of outer hair cell motility” (Raphael, Popel & Brownell 2000; Oghalai et al., 2000; Brownell et al., 2001; Morimoto et al., 2002). This model is based on the following three considerations (Raphael et al., 2000):

1. Membranes are thin structures in which bending deformations play a pivotal role in the response to external forces.
2. Membranes are liquid crystals and exhibit flexoelectricity.
3. The plasma membrane and the cytoskeleton are tightly associated.

Clearly, consideration number 3 is absolutely dependent on the presence as well as the structural and functional properties of the pillars. In addition, there are two points that, in our opinion, deserve a more detailed discussion. The first and third considerations should always be put in the context of the molecular scale of the OHC lateral wall. In many publications, either the membrane is represented thinner than the CL and/or the separation between the pillars is exaggerated. Although a conventional lipid bilayer may be modeled as ~ 8 nm-thick, a normal plasma membrane also includes a high concentration of integral membrane proteins and glycoproteins — with entire hydrophilic regions protruding from both surfaces of the bilayer — as well as plenty of extrinsic proteins adsorbed to the cytoplasmic side of the bilayer with strong interactions with plasma membrane lipids, proteins or both. Without considering the membrane glycocalyx — which in OHCs could be at least 100–200 nm thick — the actual thickness of a typical plasma membrane should be realistically assumed to be ~ 25 nm. This value is more than twice the pillar’s diameter, thrice the CL thickness, and nearly identical to the average separation between pillars along the actin filaments! From that point of

view, plasma membranes are hardly “thin structures”, and membrane bending would not be an easy task.

However, a significant increase in the distance between pillars — together with a positive cell turgor — could make a significant difference in the mechanical properties of the OHC lateral wall. For instance, as already emphasized by Brownell and coworkers, electron microscopy images of the OHC lateral wall frequently show a plasma membrane “rippling” (Fig. 3 *a*). A careful study of this membrane rippling, however, suggests that it is associated with regions of the lateral wall where the pillar-mediated connection between the CL and the plasma membrane is disrupted (Fig. 3*b*). Moreover, experiments with activators and inhibitors of Rho GTPases, which control the dynamics of the cytoskeleton, indicate that the extension and size of membrane rippling is correlated to the integrity of the pillar system (Kalinec et al., *unpublished*). Thus, not only the transmission but even the generation of forces in the OHC plasma membrane by prestin molecules and/or flexoelectricity could be somewhat regulated by the association between the plasma membrane and the CL via pillars.

It is clear, then, that some data suggest that the structure of the CL, the orientation of actin and spectrin molecules, and the integrity of the pillars could be important for the OHC electromotile response. We did not mention, however, how the CL structure, actin and spectrin molecular orientation, and pillar-mediated PM-CL connection — and consequently OHC somatic motility — could be regulated. From numerous studies in other cellular systems, it is currently accepted that the organization and dynamics of the cytoskeleton and associated molecules is mainly regulated by small GTPases of the Rho family (Van Aelst & D’Souza-Schorey, 1997; Hall, 1998). The existence of a cellular mechanism of homeostatic control of OHC motility involving small GTPases of the Rho family and Rho-mediated cytoskeletal changes has been already suggested (Kalinec et al., 2000). It has also been demonstrated that the molecular machinery underlying this mechanical homeostatic process requires the activation of Rho-Kinases (ROCK) as well as ROCK-dependent and ROCK-independent signaling pathways downstream RhoA and Rac1 (Zhang et al., 2003).

A potential problem with experiments aimed at elucidating the role of the cytoskeleton in the regulation of OHC somatic electromotility is that the results could be “contaminated” with slow, prestin-independent motile responses. For example, since electromotile amplitude is proportional to OHC total length, changes in the performance of the prestin-dependent mechanism could be exacerbated — or masked — by changes in total cell length. Recently reported studies, however, described a simple approach — based on continuous measurement of changes in cell length and longitudinal section area —

to evaluate the individual contribution of prestin-dependent and prestin-independent mechanisms to the total motile response of OHCs (Matsumoto & Kalinec, 2005). It was demonstrated that if the relative change in OHC length (L) during the motile response is expressed as $L = A^2 \times V^{-1}$ (with A and V being the relative changes in longitudinal section area and volume, respectively), A^2 will describe the contribution of the prestin-dependent, while V^{-1} will describe the contribution of the prestin-independent mechanisms. Thus, relative changes in any two of these cellular morphological parameters (L , A or V) would be necessary and sufficient for characterizing any OHC motile response. This simple approach may become an important tool for increasing our understanding of the cellular and molecular mechanisms of OHC somatic motility.

Putting the OHC into Action

It is certain that the evolution of the OHC was designed to enhance basilar membrane motion in order to amplify the mechanical input to the IHC, thereby providing improved hearing capabilities for mammals, which must register high-frequency sounds. The apparent voltage-dependent nature of OHC somatic electromotility necessarily encumbers the effectiveness of the presumed stimulus — voltage — in driving high-frequency mechanical activity. This conundrum derives from the low-pass filter effect of the cell’s plasma membrane (Santos-Sacchi, 1992; Santos-Sacchi, 1989). Consequently, receptor potentials generated by stereociliary transduction elements will be reduced at high acoustic frequency, resulting in diminished feedback into the basilar membrane. In addition to the several proposals advanced to explain how the OHC might deal with this difficulty (Santos-Sacchi et al., 1998; Kakehata and Santos-Sacchi, 1995; Dallos & Evans, 1995; Spector et al., 2003), a stretch-and voltage-activated conductance in the lateral membrane of the OHC, G_{metL} , was recently shown to be permeable to chloride anions (Song et al., 2005; Rybalchenko & Santos-Sacchi, 2003). Because the state of prestin is sensitive to the concentration of chloride near the inner leaflet aspect of prestin, chloride itself by fluctuating across the membrane could “gate” motor activity in a manner which circumvents the low-pass membrane characteristic (Rybalchenko & Santos-Sacchi, 2003; Santos-Sacchi, 2003). Whether such a scheme works in vivo remains to be determined. Nevertheless, we have recently found that modulating extracellular chloride levels in the perilymph bathing OHCs in the living animal (or other manipulations that alter the chloride gradient across the OHC membrane) can drastically alter cochlear amplification in a reversible manner (Nuttall, Zheng

& Santos-Sacchi 2005, Santos-Sacchi et al., 2006). Because intracellular chloride activity is below 10 mM (Santos-Sacchi & Song 2005), and perilymph is about 140 mM, modulation of the chloride gradient could alter the gain of the cochlear amplifier. In fact, changes in intracellular chloride concentration (Song et al., 2005) shift the operating voltage range of somatic electromotility. However, independent of how modulation occurs, it is clear that anions play a powerful physiological role in vivo.

Summary

In an attempt to expand on the pioneering work of the latter part of the last century, a feverish quest continues to uncover the events that lead to cochlear amplification in mammals. The role of the OHC is certainly paramount, and we now have identified many of its membrane constituents that form the basis of the cell's unique contribution. As this review intimates, the motor protein prestin and its interaction with other players within and beneath the plasma membrane drive the cell's augmentation of mammalian hearing acuity. Nevertheless, we are far from understanding the full complement of cellular elaborations that define the cell's mechanical capabilities. Surely, the next quarter century will tell more.

This work was supported by grants NIDCD DC006412 (JZ), NIDCD DC 006496 (DZZH), NIDCD DC05220 and House Ear Institute (FK), Grants-in-Aid for Scientific Research from the Ministry of Education, Culture, Sports, Science and Technology of Japan (SK), NIDCD DC00273 (JSS). We thank Peter Dallos and MaryAnn Cheatham for their comments on manuscript.

References

- Abe, T., Kakehata, S., Kitani, R., Santos-Sacchi, J., Shinkawa, H. 2005. Developmental expression of the outer hair cell motor in the mouse. *42nd. Workshop on Inner Ear Biology* Sept.: 138
- Adachi, M., Iwasa, K.H. 1997. Effect of diamide on force generation and axial stiffness of the cochlear outer hair cell. *Biophys. J.* **73**:2809–2818
- Adler, H.J., Belyantseva, I.A., Merritt, R.C. Jr, Frolenkov, G.I., Dougherty, G.W., Kachar, B. 2003. Expression of prestin, a membrane motor protein, in the mammalian auditory and vestibular periphery. *Hear. Res.* **184**:27–40
- Aravind, L., Koonin, E.V. 2000. The STAS domain—a link between anion transporters and antisigma- factor antagonists. *Curr Biol* **10**:53–55
- Arima, T., Kuraoka, A., Toriya, R., Shibata, Y., Uemura, T. 1991. Quick-freeze, deep-etch visualization of the 'cytoskeletal spring' of cochlear outer hair cells. *Cell Tissue Res.* **263**:91–97
- Ashmore, J. 2005. Prestin is an electrogenic anion transporter. *42nd. Workshop on Inner Ear Biology* Sept.:138
- Ashmore, J.F. 1987. A fast motile response in guinea-pig outer hair cells: the cellular basis of the cochlear amplifier. *J. Physiol.* **388**:323–347
- Ashmore JF. 1989. Transducer motor coupling in cochlear outer hair cells. *Mechanics of Hearing*. Kemp, D., Wilson, J.P., editors pp 107–113, Plenum Press, New York
- Ashmore, J.F. 1990. Forward and reverse transduction in the mammalian cochlea. *Neurosci. Res. Suppl.* **12**:39–50
- Bai, J.B., Samaranyake, H.S., Navaratnam, D.S., Santos-Sacchi, J. 2003. Carboxy-Terminal Truncations and Mutations of Prestin; Effects on NLC. *26th Meeting of the Assoc. Res. Otolaryngol. Daytona, FL Abst.* 1871
- Beck, K.A., Nelson, W.J. 1996. The spectrin-based membrane skeleton as a membrane protein-sorting machine. *Am. J. Physiol.* **270**:C1263–C1270
- Belyantseva, I.A., Adler, H.J., Curi, R., Frolenkov, G.I., Kachar, B. 2000a. Expression and localization of prestin and the sugar transporter GLUT-5 during development of electromotility in cochlear outer hair cells. *J. Neurosci.* **20**:RC116
- Belyantseva, I.A., Frolenkov, G.I., Wade, J.B., Mammano, F., Kachar, B. 2000b. Water permeability of cochlear outer hair cells: characterization and relationship to electromotility [In Process Citation]. *J. Neurosci.* **20**:8996–9003
- Bennet, V., Gilligan, D.M. 1993. The spectrin-based membrane skeleton and micron-scale organization of the plasma membrane. *Annu. Rev. Cell Biol.* **9**:7–66
- Bennett, V. 1990. Spectrin-based membrane skeleton: A multipotential adaptor between plasma membrane and cytoplasm. *Physiol. Rev.* **70**:1029–1065
- Brownell, W.E. 1984. Microscopic observation of cochlear hair cell motility. *Scan. Electron Microsc.* 3:1
- Brownell, W.E. 1990. Outer hair cell electromotility and otoacoustic emissions. *Ear. Hear.* **11**:82–92
- Brownell, W.E., Bader, C.R., Bertrand, D., Ribaupierre, Y. 1985. Evoked mechanical responses of isolated cochlear outer hair cells. *Science* **227**:194–196
- Brownell, W.E., Spector, A.A., Raphael, R.M., Popel, A.S. 2001. Micro- and nanomechanics of the cochlear outer hair cell. *Annu. Rev. Biomed. Eng.* **3**:169–194
- Chambard, J.M., Ashmore, J.F. 2003. Sugar transport by members of the SLC26 superfamily of anion-bicarbonate exchangers. *J. Physiol.* **550**:667–677
- Cheatham, M.A., Huynh, K.H., Gao, J., Zuo, J., Dallos, P. 2004. Cochlear function in Prestin knockout mice. *J. Physiol.* **560**:821–830
- Clark, R.B., Cowey, J.B. 1958. Factors controlling the change of shape of some worms. *J. Exp. Biol.* **35**:731–748
- Dallos, P., Evans, B.N. 1995. High-frequency motility of outer hair cells and the cochlear amplifier. *Science* **267**:2006–2009
- Dallos, P., Fakler, B. 2002. Prestin, a new type of motor protein. *Nat. Rev. Mol. Cell Biol.* **3**:104–111
- Dallos, P., Harris, D. 1978. Properties of auditory nerve responses in absence of outer hair cells. *J. Neurophysiol.* **41**:365–383
- Dallos, P., He, D.Z. 2000. Two models of outer hair cell stiffness and motility. *J. Assoc. Res. Otolaryngol.* **1**:283–291
- Dallos, P., He, D.Z., Lin, X., Sziklai, I., Mehta, S., Evans, B.N. 1997. Acetylcholine, outer hair cell electromotility, and the cochlear amplifier. *J. Neurosci.* **17**:2212–2226
- Dallos, P., Santos-Sacchi, J., Flock, A. 1982. Intracellular recordings from cochlear outer hair cells. *Science* **218**:582–584
- Davis, H. 1983. An active process in cochlear mechanics. *Hear. Res.* **9**:79–90
- Dawson, P.A., Markovich, D. 2005. Pathogenetics of the human SLC26 transporters. *Curr. Med. Chem.* **12**:385–396
- Deak, L., Zheng, J., Orem, A., Du, G.G., Aguinaga, S., Matsuda, K., Dallos, P. 2005. Effects of cyclic nucleotides on the function of prestin. *J. Physiol.* **563**:483–496
- Dong, X.X., Iwasa, K.H. 2004. Tension sensitivity of prestin: comparison with the membrane motor in outer hair cells. *Bioophys. J.* **86**:1201–1208
- Dougherty, G., Adler, H.J., Merritt, R., Rzdzińska, A., de Azevedo, R., Frolenkov, G., Belyantseva, I., Pompeia, C.,

- Kachar, B. 2003. Couplin, a novel 27 kDa protein, links prestin to the actin-spectrin cytoskeleton in auditory outer hair cells. *Assoc. Res. Otolaryngol. 2003 Abs.* 208
- Dubreuil, R.R., Wang, P.Y., Dahl, S., Lee, J., Goldstein, L.S.B. 2000. *Drosophila* β -spectrin functions independently of α -spectrin to polarize the Na, K ATPase in epithelial cells. *J. Cell Biol.* **149**:647–656
- Ehret, G. 1976. Development of absolute auditory thresholds in the house mouse (*Mus musculus*). *J. Am. Audiol. Soc.* **1**:179–184
- Evans, B.N. 1990. Fatal contractions: ultrastructural and electro-mechanical changes in outer hair cells following transmembrane electrical stimulation. *Hear. Res.* **45**:265–282
- Evans, B.N., Dallos, P. 1993. Stereocilia displacement induced somatic motility of cochlear outer hair cells. *Proc. Natl. Acad. Sci. USA* **90**:8347–8351
- Everett, L.A., Glaser, B., Beck, J.C., Idol, J.R., Buchs, A., Heyman, M., Adawi, F., Hazani, E., Nassir, E., Baxevanis, A.D., Sheffield, V.C., Green, E.D. 1997. Pendred syndrome is caused by mutations in a putative sulphate transporter gene (PDS). *Nat. Genet.* **17**:411–422
- Fischer, H., Polikarpov, I., Craievich, A.F. 2004. Average protein density is a molecular-weight-dependent function. *Protein Sci.* **13**:2825–2828
- Flock, A., Flock, B., Ulfendahl, M. 1986. Mechanisms of movement in outer hair cells and a possible structural basis. *Arch. Otorhinolaryngol.* **243**:83–90
- Forge, A. 1991. Structural features of the lateral walls in mammalian cochlear outer hair cells. *Cell Tissue Res.* **265**:473–483
- Forge, A., Richardson, G. 1993. Freeze fracture analysis of apical membranes in cochlear cultures: differences between basal and apical-coil outer hair cells and effects of neomycin. *J. Neurocytol.* **22**:854–867
- Forge, A., Zajic, G., Li, L., Nevill, G., Schacht, J. 1993. Structural variability of the sub-surface cisternae in intact, isolated outer hair cells shown by fluorescent labelling of intracellular membranes and freeze-fracture. *Hear. Res.* **64**:175–183
- Frank, G., Hemmert, W., Gummer, A.W. 1999. Limiting dynamics of high-frequency electromechanical transduction of outer hair cells. *Proc. Natl. Acad. Sci. USA* **96**:4420–4425
- Gale, J.E., Ashmore, J.F. 1994. Charge displacement induced by rapid stretch in the basolateral membrane of the guinea-pig outer hair cell. *Proc. R. Soc. Lond. B.* **255**:243–249
- Gale, J.E., Ashmore, J.F. 1997. An intrinsic frequency limit to the cochlear amplifier. *Nature* **389**:63–66
- Geleoc, G.S., Casalotti, S.O., Forge, A., Ashmore, J.F. 1999. A sugar transporter as a candidate for the outer hair cell motor. *Nat. Neurosci* **2**:713–719
- Gitter, A.H., Rudert, M., Zenner, H.P. 1993. Forces involved in length changes of cochlear outer hair cells. *Pfluegers Arch.* **424**:9–14
- Greenson J., Organ L., Raphael R. 2005. Advanced Optical Techniques for Investigating Outer Hair Cell Plasma Membranes. *Abstract of 28rd Meeting of the Assoc. Res. Otolaryngol. New Orleans, LA*
- Gulley, R.S., Reese, T.S. 1977. Regional specialization of the hair cell plasmalemma in the organ of Corti. *Anat. Rec.* **189**:109–124
- Hall, A. 1998. Rho GTPases and the actin cytoskeleton. *Science* **279**:509–514
- Hallworth, R. 1995. Passive compliance and active force generation in the guinea pig outer hair cell. *J. Neurophysiol.* **74**:2319–2328
- Hallworth, R. 1997. Modulation of outer hair cell compliance and force by agents that affect hearing. *Hear. Res.* **114**:204–212
- Hallworth, R., Evans, B.N., Dallos, P. 1993. The location and mechanism of electromotility in guinea pig outer hair cells. *J. Neurophysiol.* **70**:549–558
- Halter, J.A., Kruger, R.P., Yium, M.J., Brownell, W.E. 1997. The influence of the subsurface cisterna on the electrical properties of the outer hair cell. *Neuroreport* **8**:2517–2521
- Hammarlund, M., Davis, W.S., Jorgensen, E.M. 2000. Mutations in β -spectrin disrupt axon outgrowth and sarcomere structure. *J. Cell Biol.* **149**:931–942
- He, D.Z.Z. 1997. Relationship between the development of outer hair cell electromotility and efferent innervation: a study in cultured organ of Corti of neonatal gerbils. *J. Neurosci.* **17**:3634–3643
- He, D.Z., Dallos, P. 1999. Somatic stiffness of cochlear outer hair cells is voltage-dependent. *Proc. Natl. Acad. Sci. USA* **96**:8223–8228
- He, D.Z., Dallos, P. 2000. Properties of voltage-dependent somatic stiffness of cochlear outer hair cells. *J. Assoc. Res. Otolaryngol.* **1**:64–81
- He, D.Z., Evans, B.N., Dallos, P. 1994. First appearance and development of electromotility in neonatal gerbil outer hair cells. *Hear. Res.* **78**:77–90
- He, D.Z., Jia, S., Dallos, P. 2003. Prestin and the dynamic stiffness of cochlear outer hair cells. *J. Neurosci.* **23**:9089–9096
- Holley M.C. 1996. Outer hair cell motility. In: The Cochlea. Dallos, P., Popper, A., Fay, R., editors pp. 386–434, Springer Verlag, New York
- Holley, M.C., Ashmore, J.F. 1988a. A cytoskeletal spring in cochlear outer hair cells. *Nature* **335**:635–637
- Holley, M.C., Ashmore, J.F. 1988b. On the mechanism of a high-frequency force generator in outer hair cells isolated from the guinea pig cochlea. *Proc. R. Soc. Lond. B.* **232**:413–429
- Holley, M.C., Ashmore, J.F. 1990a. A cytoskeletal spring for the control of cell shape in outer hair cells isolated from the guinea pig cochlea. *Eur. Arch. Otorhinolaryngol.* **247**:4–7
- Holley, M.C., Ashmore, J.F. 1990b. Spectrin, actin and the structure of the cortical lattice in mammalian cochlear outer hair cells. *J. Cell Sci.* **96**:283–291
- Holley, M.C., Kalinec, F., Kachar, B. 1992. Structure of the cortical cytoskeleton in mammalian outer hair cells. *J. Cell Sci.* **102**:569–580
- Huang, G., Santos-Sacchi, J. 1993. Mapping the distribution of the outer hair cell motility voltage sensor by electrical amputation. *Biophys. J.* **65**:2228–2236
- Huang, G., Santo-Sacchi, J. 1994. Motility Voltage Sensor of the outer hair cell resides within the lateral plasma membrane. *Proc. Natl. Acad. Sci. USA* **91**:12268–12272
- Iida, K., Konno, K., Oshima, T., Tsumoto, K., Ikeda, K., Kumagai, I., Kobayashi, T., Wada, H. 2003. Stable expression of the motor protein prestin in Chinese hamster ovary cells. *Jsm International Journal Series C-Mechanical Systems Machine Elements and Manufacturing* **46**:1266–1274
- Iwasa, K.H. 1993. Effect of stress on the membrane capacitance of the auditory outer hair cell. *Biophys. J.* **65**:492–498
- Iwasa, K.H. 1994. A membrane motor model for the fast motility of the outer hair cell. *J. Acoust. Soc. Am.* **96**:2216–2224
- Iwasa, K.H. 2000. Effect of membrane motor on the axial stiffness of the cochlear outer hair cell. *J. Acoust. Soc. Am.* **107**:2764–2766
- Iwasa, K.H., Adachi, M. 1997. Force generation in the outer hair cell of the cochlea. *Biophys. J.* **73**:546–555
- Jarboe, J.K., Hallworth, R. 1999. The effect of quinine on outer hair cell shape, compliance and force. *Hear. Res.* **132**:43–50
- Judice, T.N., Nelson, N.C., Beisel, C.L., Delimont, D.C., Fritzsche, B., Beisel, K.W. 2002. Cochlear whole mount in situ hybridization: identification of longitudinal and radial gradients. *Brain Res. Brain Res. Protoc.* **9**:65–76

- Kachar, B., Brownell, W.E., Altschuler, R., Fex, J. 1986. Electrokinetic shape changes of cochlear outer hair cells. *Nature* **322**:365–368
- Takehata, S., Santos-Sacchi, J. 1995. Membrane tension directly shifts voltage dependence of outer hair cell motility and associated gating charge. *Biophys. J.* **68**:2190–2197
- Takehata, S., Santos-Sacchi, J. 1996. Effects of salicylate and lanthanides on outer hair cell motility and associated gating charge. *J. Neurosci.* **16**:4881–4889
- Kalincic, F., Holley, M.C., Iwasa, K.H., Lim, D.J., Kachar, B. 1992. A membrane-based force generation mechanism in auditory sensory cells. *Proc. Natl. Acad. Sci. USA* **89**:8671–8675
- Kalincic, F., Kachar, B. 1995. Structure of the electromechanical transduction mechanism in mammalian outer hair cells. In: Active Hearing Flock, Å, Ottoson, D, Ulfendahl, M., (editors) . pp 179–191, Elsevier Science, Oxford, England
- Kalincic, F., Zhang, M., Urrutia, R., Kalincic, G. 2000. Rho GTPases mediate the regulation of cochlear outer hair cell motility by acetylcholine. *J. Biol. Chem.* **275**:28000–28005
- Ko, S.B., Zeng, W., Dorwart, M.R., Luo, X., Kim, K.H., Millen, L., Goto, H., Naruse, S., Soyombo, A., Thomas, P.J., Muallem, S. 2004. Gating of CFTR by the STAS domain of SLC26 transporters. *Nat. Cell Biol.* **6**:343–350
- Koppl, C., Forge, A., Manley, G.A. 2004. Low density of membrane particles in auditory hair cells of lizards and birds suggests an absence of somatic motility. *J. Comp. Neurol.* **479**:149–155
- Kural C., Aguiaga S., Zheng J., Dallos P., Selvin P. 2004. FRET studies on Prestin, a new type of molecular motor. 48th Biophys. Soc.Mtg: Abstr.538
- Lieberman, M.C., Gao, J., He, D.Z., Wu, X., Jia, S., Zuo, J. 2002. Prestin is required for electromotility of the outer hair cell and for the cochlear amplifier. *Nature* **419**:300–304
- Liu, X.Z., Ouyang, X.M., Xia, X.J., Zheng, J., Pandya, A., Li, F., Du, L.L., Welch, K.O., Petit, C., Smith, R.J., Webb, B.T., Yan, D., Arnos, K.S., Corey, D., Dallos, P., Nance, W.E., Chen, Z.Y. 2003. Prestin, a cochlear motor protein, is defective in non-syndromic hearing loss. *Hum. Mol. Genet.* **12**:1155–1162
- Ludwig, J., Oliver, D., Frank, G., Klocker, N., Gummer, A.W., Fakler, B. 2001. Reciprocal electromechanical properties of rat prestin: the motor molecule from rat outer hair cells. *Proc. Natl. Acad. Sci. USA* **98**:4178–4183
- Marcotti, W., Kros, C.J. 1999. Developmental expression of the potassium current $I_{K,n}$ contributes to maturation of mouse outer hair cells. *J. Physiol.* **520**:653–660
- Matsuda, K., Zheng, J., Du, G.-G., Deak, L., Navarrete, E., Dallos, P. 2003. Protein kinase C and voltage-dependent capacitance in Prestin-transfected TSA cells. *Abstract of 26rd Meeting of the Assoc. Res. Otolaryngol. Daytona, FL*
- Matsuda, K., Zheng, J., Du, G.G., Klocker, N., Madison, L.D., Dallos, P. 2004. N-linked glycosylation sites of the motor protein prestin: effects on membrane targeting and electrophysiological function. *J. Neurochem.* **89**:928–938
- Matsumoto, N., Kalincic, F. 2005. Extraction of Prestin-Dependent and Prestin-Independent Components from Complex Motile Responses in Guinea Pig Outer Hair Cells. *Biophys. J.* **89**:4343–4351
- Matsuoka, Y., Li, X., Bennet, V. 2000. Adducin: structure, function and regulation. *Cell. Mol. Life Sci.* **57**:884–895
- Meltzer, J., Santos-Sacchi, J. 2001. Temperature dependence of non-linear capacitance in human embryonic kidney cells transfected with prestin, the outer hair cell motor protein. *Neurosci. Lett.* **313**:141–144
- Moorthy, S., Chen, L., Bennet, V. 2000. Caenorhabditis elegans β -G spectrin is dispensable for establishment of epithelial polarity, but essential for muscular and neuronal function. *J. Cell Biol.* **149**:915–930
- Morimoto, N., Raphael, R.M., Nygren, A., Brownell, W.E. 2002. Excess plasma membrane and effects of ionic amphipaths on mechanics of outer hair cell lateral wall. *Am. J. Physiol.* **282**:C1076–C1086
- Mount, D.B., Romero, M.F. 2004. The SLC26 gene family of multifunctional anion exchangers. *Pfluegers Arch.* **447**:710–721
- Murakoshi M.T.G.H.W. 2005. Imaging of the cytoplasmic face of the Prestin-expressing CHO cell membrane by atomic force microscopy. *Abstract of 28rd Meeting of the Assoc. Res. Otolaryngol. New Orleans, LA, Abstr. p.216*
- Nagy, I., Bodmer, M., Schmid, S., Bodmer, D. 2005. Promyelocytic leukemia zinc finger protein localizes to the cochlear outer hair cells and interacts with prestin, the outer hair cell motor protein. *Hear. Res.* **204**:216–222
- Narayan, S.S., Temchin, A.N., Redo, A., Ruggero, M.A. 1998. Frequency tuning of basilar membrane and auditory nerve fibers in the same cochlea. *Science* **282**:1882–1884
- Navaratnam, D., Bai, J.-P., Samaranayake, H., Aronson, P.S., Santos-Sacchi, J. 2005a. Prestin is an anion transporter. *Neuron Satellite Symposium, SFN Meeting, Washington, D.C.*
- Navaratnam, D., Bai, J.P., Samaranayake, H., Santos-Sacchi, J. 2005b. N-terminal mediated homo-multimerization of prestin, the outer hair cell motor protein. *Biophys. J.* **90**:967–974
- Navaratnam, D.S., Bai, J.-P., Samaranayake, H., Santos-Sacchi, J. 2005c. Prestin's partners: Molecular interactions a Go-Go! *Abstract of 28th Meeting of the Assoc. Res. Otolaryngol. New Orleans, LA, Abstr.p.366.*
- Nuttall, A.L., Zheng, J., Santos-Sacchi, J. 2005. Modulation of cochlea amplification by tributyltin and salicylate. *28th Mtg. Assoc. Res. Otolaryngol. Abs. p. 117*
- Oghalai, J.S., Patel, A.A., Nakagawa, T., Brownell, W.E. 1998. Fluorescence-imaged microdeformation of the outer hair cell lateral wall. *J. Neurosci.* **18**:48–58
- Oghalai, J.S., Zhao, H.B., Kutz, J.W., Brownell, W.E. 2000. Voltage- and tension-dependent lipid mobility in the outer hair cell plasma membrane. *Science* **287**:658–661
- Oliver, D., Fakler, B. 1999. Expression density and functional characteristics of the outer hair cell motor protein are regulated during postnatal development in rat. *J. Physiol.* **519**:791–800
- Oliver, D., He, D.Z., Klocker, N., Ludwig, J., Schulte, U., Waldegger, S., Ruppertsberg, J.P., Dallos, P., Fakler, B. 2001. Intracellular anions as the voltage sensor of prestin, the outer hair cell motor protein. *Science* **292**:2340–2343
- Pujol, R., Zajic, G., Dulon, D., Raphael, Y., Altschuler, R.A., Schacht, J. 1991. First appearance and development of motile properties in outer hair cells isolated from guinea-pig cochlea. *Hear. Res.* **57**:129–141
- Raphael, R.M., Popel, A.S., Brownell, W.E. 2000. A membrane bending model of outer hair cell electromotility. *Biophys. J.* **78**:2844–2862
- Raphael, Y., Wroblewski, R. 1986. Linkage of sub-membrane cisterns with the cytoskeleton and the plasma membrane in cochlear outer hair cells. *J. Submicrosc. Cytol.* **18**:731–737
- Rhode, W.S. 1971. Observations of the vibration of the basilar membrane in squirrel monkeys using the Mossbauer technique. *J. Acoust Soc. Am.* **49**:1218–1231
- Rhode, W.S., Robles, L. 1974. Evidence from Mossbauer experiments for nonlinear vibration in the cochlea. *J. Acoust Soc. Am.* **55**:588–596
- Russell, I.J., Schanz, C. 1996. Salicylate ototoxicity: Effects on the stiffness and electromotility of outer hair cells isolated from the guinea pig cochlea (vol 1, pg 309,1996). *Auditory Neuroscience* **2**:193

- Russell, I.J., Sellick, P.M. 1978. Intracellular studies of hair cells in the mammalian cochlea. *J. Physiol.* **284**:261–290
- Ryan, A., Dallos, P. 1975. Effect of absence of cochlear outer hair cells on behavioural auditory threshold. *Nature* **253**:44–46
- Rybalchenko, V., Santos-Sacchi, J. 2003. Cl⁻ flux through a non-selective, stretch-sensitive conductance influences the outer hair cell motor of the guinea-pig. *J. Physiol.* **547**:873–891
- Saito, K. 1983. Fine structure of the sensory epithelium of guinea-pig organ of Corti: subsurface cisternae and lamellar bodies in the outer hair cells. *Cell Tissue Res.* **229**:467–481
- Santos-Sacchi, J., Song, L. 2005. Salicylate bears OHC chloride activity. Society. for. *Neuroscience Meeting, November Prog.* #849.6
- Santos-Sacchi, J. 1989. Asymmetry in voltage-dependent movements of isolated outer hair cells from the organ of Corti. *J. Neurosci.* **9**:2954–2962
- Santos-Sacchi J. 1990. Fast outer hair cell motility: how fast is fast? In: *The Mechanics and Biophysics of Hearing*. Dallos P, Geisler CD, Matthews JW, Ruggiero MA, Steele CR, editors, pp 69–75, Springer-Verlag, Berlin
- Santos-Sacchi, J. 1991. Reversible inhibition of voltage-dependent outer hair cell motility and capacitance. *J. Neurosci.* **11**:3096–3110
- Santos-Sacchi, J. 1992. On the frequency limit and phase of outer hair cell motility: effects of the membrane filter. *J. Neurosci.* **12**:1906–1916
- Santos-Sacchi, J. 1993. Harmonics of outer hair cell motility. *Biophys. J.* **65**:2217–2227
- Santos-Sacchi, J. 2002. Functional motor microdomains of the outer hair cell lateral membrane. *Pfluegers Arch. Eur. J. Physiol.* **445**:331–336
- Santos-Sacchi, J. 2003. New tunes from Corti's organ: the outer hair cell boogie rules. *Curr. Opin. Neurobiol.* **13**:459–468
- Santos-Sacchi, J., Dilger, J.P. 1988. Whole cell currents and mechanical responses of isolated outer hair cells. *Hear. Res.* **35**:143–150
- Santos-Sacchi, J., Kakehata, S., Kikuchi, T., Katori, Y., Takasaka, T. 1998. Density of motility-related charge in the outer hair cell of the guinea pig is inversely related to best frequency. *Neurosci. Lett.* **256**:155–158
- Santos-Sacchi, J., Navarrete, E. 2002. Voltage-dependent changes in specific membrane capacitance caused by prestin, the outer hair cell lateral membrane motor. *Pfluegers Arch. Eur. J. Physiol.* **444**:99–106
- Santos-Sacchi, J., Shen, W.X., Zheng, J., Dallos, P. 2001. Effects of membrane potential and tension on prestin, the outer hair cell lateral membrane motor protein. *J. Physiol.* **531**:661–666
- Santos-Sacchi, J., Song, L., Zheng, J., Nuttall, A.L. 2006. Control of mammalian cochlear amplification by chloride anions. *J. Neurosci.* In press
- Shehata, W.E., Brownell, W.E., Dieler, R. 1991. Effects of salicylate on shape, electromotility and membrane characteristics of isolated outer hair cells from guinea pig cochlea. *Acta Otolaryngol.* **111**:707–718
- Song, L., Seeger, A., Santos-Sacchi, J. 2005. On membrane motor activity and chloride flux in the outer hair cell: Lessons learned from the environmental toxin tributyltin. *Biophys. J.* **88**:2350–2362
- Souter, M., Nevill, G., Forge, A. 1995. Postnatal development of membrane specialisations of gerbil outer hair cells. *Hear. Res.* **91**:43–62
- Spector A, Popel, AS, Brownell W 2003. Piezoelectric properties enhance outer hair cell high-frequency response. In: *Biophysics of the Cochlea: From Molecules to Models*. Gummer A, editor Singapore: World Scientific Publishing
- Spoendlin H, 1988. Neural anatomy of the inner ear. In: *Physiology of the Ear*. Jahn, A.F. Santos-Sacchi, J. eds. pp.201–219 Raven Press, New York
- Steel, K.P., Bock, G.R. 1980. The nature of inherited deafness in deafness mice. *Nature* **288**:159–161
- Svoboda, K., Block, S.M. 1994. Force and velocity measured for single kinesin molecules. *Cell* **77**:773–784
- Szonyi, M., He, D.Z., Ribari, O., Sziklai, L., Dallos, P. 1999. Cyclic GMP and outer hair cell electromotility. *Hear. Res.* **137**:29–42
- Takahashi, S., Santos-Sacchi, J. 2001. Non-uniform mapping of stress-induced, motility-related charge movement in the outer hair cell plasma membrane. *Pfluegers Arch.* **441**:506–513
- Thompson, J.D., Higgins, D.G., Gibson, T.J. 1994. CLUSTAL W: improving the sensitivity of progressive multiple sequence alignment through sequence weighting, position-specific gap penalties and weight matrix choice. *Nucleic Acids Res.* **22**:4673–4680
- Tian, Y., Li, M., Fritsch, B., Zuo, J. 2004. Creation of a transgenic mouse for hair-cell gene targeting by using a modified bacterial artificial chromosome containing Prestin. *Dev. Dyn.* **231**:199–203
- Tolomeo, J.A., Steele, C.R., Holley, M.C. 1996. Mechanical properties of the lateral cortex of mammalian auditory outer hair cells. *Biophys. J.* **71**:421–429
- Tunstall, M J., Gale, J.E., Ashmore, J.F. 1995. Action of salicylate on membrane capacitance of outer hair cells from the guinea-pig cochlea. *J. Physiol.* **485**:739–752
- Ulfendahl, M., Chan, E., McConnaughey, W.B., Prost-Domasky, S., Elson, E.L. 1998. Axial and transverse stiffness measures of cochlear outer hair cells suggest a common mechanical basis. *Pfluegers Arch.* **436**:9–15
- Van Aelst, L. Van , D'Souza-Schorey, C. 1997. Rho GTPases and signaling networks. *Genes & Development* **11**:2295–2322
- von Bekesy, G. 1960. *Experiments in Hearing*. McGraw-Hill, New York
- Wainwright, SA, Biggs, WD, Currey, JD, Gosline, JM. 1982. *Mechanical Design in Organisms*. Princeton University Press, Princeton, NJ
- Weber, T., Gopfert, M.C., Winter, H., Zimmermann, U., Kohler, H., Meier, A., Hendrich, O., Rohbock, K., Robert, D., Knipper, M. 2003. Expression of prestin-homologous solute carrier (SLC26) in auditory organs of nonmammalian vertebrates and insects. *Proc. Natl. Acad. Sci. USA* **100**:7690–7695
- Weber, T., Zimmermann, U., Winter, H., Mack, A., Kopschall, I., Rohbock, K., Zenner, H.P., Knipper, M. 2002. Thyroid hormone is a critical determinant for the regulation of the cochlear motor protein prestin. *Proc. Natl. Acad. Sci. USA* **99**:2901–2906
- Wu, M., Santos-Sacchi, J. 1998. Effects of lipophilic ions on outer hair cell membrane capacitance and motility. *J. Membrane Biol.* **166**:111–118
- Wu, X., Gao, J., Zuo, J. 2003. Apoptotic cell death in the organ of corti and absence of Glut5 in outer hair cells in Prestin knock-out mice. *26th Mtg. Assoc. Res. Otolaryngol.* Absr. 1530
- Zenner, H.P., Gitter, A.H., Rudert, M., Ernst, A. 1992. Stiffness, compliance, elasticity and force generation of outer hair cells. *Acta Otolaryngol.* **112**:248–253
- Zhang, M., Kalinec, G.M., Urrutia, R., Billadeau, D.D., Kalinec, F. 2003. ROCK-dependent and ROCK-independent control of cochlear outer hair cell electromotility. *J. Biol. Chem.* **278**:35664–356650
- Zhao, H.B., Santos-Sacchi, J. 1998. Mechano-electrical coupling among outer hair cells of Corti's organ. *Biophys. J.* **74**:A246
- Zheng, J., Shen, W., He, D., Long, K., Madison, L., Dallos, P. 2000. Prestin is the motor protein of cochlear outer hair cells. *Nature* **405**:149–155

- Zheng, J., Aguinaga, C., Anderson, C., Miller, K., Dallos, P. 2005a. Prestin's Interaction with CFTR Enhances Its Function. *Abstract of 28rd Meeting of the Assoc. Res. Otolaryngol. New Orleans, LA, Abstr.p.365*
- Zheng, J., Du, G.-G., Anderson, C., Orem, A., Dallos, P. 2005b. Prestin is an oligomer. *Abstract of the 42nd Workshop on Inner Ear Biology, Tübingen, Germany*
- Zheng, J., Du, G.G., Matsuda, K., Orem, A., Aguinaga, S., Deak, L., Navarrete, E., Madison, L.D., Dallos, P. 2005c. The C-terminus of prestin influences nonlinear capacitance and plasma membrane targeting. *J. Cell Sci.* **118**:2987–2996
- Zheng, J., Long, K.B., Matsuda, K.B., Madison, L.D., Ryan, A.D., Dallos, P.D. 2003. Genomic characterization and expression of mouse prestin, the motor protein of outer hair cells. *Mamm. Genome* **14**:87–96
- Zheng, J., Long, K.B., Robison, D.E., He, D.Z., Cheng, J., Dallos, P., Madison, L.D. 2002a. Identification of differentially expressed cDNA clones from gerbil cochlear outer hair cells. *Audiol. Neurootol.* **77**:277–288
- Zheng, J., Long, K.B., Shen, W., Madison, L.D., Dallos, P. 2001. Prestin topology: localization of protein epitopes in relation to the plasma membrane. *Neuroreport* **2**:1929–1935
- Zheng, J., Madison, L.D., Oliver, D., Fakler, B., Dallos, P. 2002b. Prestin, the motor protein of outer hair cells. *Audiol. Neurootol.* **7**:9–12
- Zheng, J., Richter, C.P., Cheatham, M.A. 2003. Prestin expression in the cochlea of the reeler mouse. *Neurosci. Lett.* **347**:13–16

Mapping the Distribution of the Outer Hair Cell Motility Voltage Sensor by Electrical Amputation

Guojie Huang and J. Santos-Sacchi

Sections of Otolaryngology and Neurobiology, Yale University School of Medicine, New Haven, Connecticut 06510 USA

ABSTRACT The outer hair cell (OHC) possesses a nonlinear charge movement whose characteristics indicate that it represents the voltage sensor responsible for OHC mechanical activity. OHC mechanical activity is known to exist along a restricted extent of the cell's length. We have used a simultaneous partitioning microchamber and whole cell voltage clamp technique to electrically isolate sections of the OHC membrane and find that the nonlinear charge movement is also restricted along the cell's length. Apical and basal portions of the OHC are devoid of voltage sensors, corresponding to regions of the cell where the subsurface cisternae and/or the mechanical responses are absent. We conclude that the physical domain of the motility voltage sensor corresponds to that of the mechanical effector and speculate that sensor and effector reside within one intra-membranous molecular species, perhaps an evolved nonconducting or poorly conducting voltage-dependent ion channel.

INTRODUCTION

The peripheral auditory system is responsible for the initial decoding of spectral information within acoustic stimuli. In the mammal, frequency selectivity and sensitivity afforded by Bekesy's basilar membrane traveling wave is enhanced by a metabolically labile process which involves one of the two types of sensory cells which populate the organ of Corti, the outer hair cells (OHC). Following the discovery of electrically induced OHC motility (Brownell et al., 1985), evidence has accumulated that the mechanical activity of the OHC alters basilar membrane motion in such a way as to enhance the tuning characteristics of inner hair cells and eight nerve fibers (Ruggero, 1992).

OHC motility is transmembrane voltage-dependent (Santos-Sacchi and Dilger, 1988; Iwasa and Kachar, 1989). Hyperpolarization elongates and depolarization shortens the cylindrically shaped cell. The mechanism underlying this shape change which can occur at acoustic frequencies is unknown. However, it is not based on typical cellular mechanisms of motility (Kachar et al., 1986; Santos-Sacchi and Dilger, 1988; Holley and Ashmore, 1988). In fact, recent evidence indicates that the force generating mechanism may reside within the plasma membrane itself, possibly corresponding to 8–10-nm intramembranous particles observed ultrastructurally in the lateral plasmalemma (Kalinec et al., 1992).

Nonlinear charge movement in the OHC, which is believed to be indicative of a motility voltage sensor, has been studied (Ashmore, 1989, 1992; Santos-Sacchi, 1990, 1991a, 1992), and many characteristics of the mechanical response and charge movement coincide. Recently, Dallos et al. (1991) have utilized a partitioning microchamber to map the distribution of the mechanical response along the length of the cylindrical OHC, and found that it resides within a central

region, roughly corresponding to the extent of the subsurface cisternae, an intracellular membranous system lying beneath the plasma membrane. Ashmore (1992) presented preliminary evidence that the nonlinear charge movement measured in cell-attached patches exists on the lateral portion of the cell, but is absent on the basal end. We have evaluated the extent of the motility voltage sensor using a combined microchamber and whole cell voltage clamp technique which enables us to electrically amputate portions of the OHC. We conclude that the distribution of the motility voltage sensor corresponds to the extent of the mechanical responses observed with the partitioning microchamber (Dallos et al., 1991), that is, that sensor and effector mechanisms colocalize.

A preliminary account of this work has been presented (Santos-Sacchi and Huang, 1993).

MATERIALS AND METHODS

General

Guinea pigs were overdosed with halothane. The temporal bones were removed, the apical two turns of the organ of Corti were microdissected free, and OHCs were isolated enzymatically with collagenase (0.3 mg/ml for 10 min followed by gentle reflux through a tapered polyethylene pipette tip) in Medium 199 with Hanks' salts (GIBCO). The cell-enriched supernatant was then transferred to a 700- μ l perfusion chamber, and the cells were permitted to settle onto the cover glass bottom. All experiments were performed at room temperature (\sim 23°C). A Nikon Diaphot inverted microscope with Hoffmann optics was used to observe the cells during electrical recording. Experiments were videotaped. A modified Leibovitz medium (100 mM NaCl, 5.37 mM KCl, 2.0 mM CoCl₂, 1.48 mM MgCl₂, 20 mM tetra ethyl ammonium, 2 μ M tetrodotoxin, 20 mM CsCl, 5.0 mM 4-(2-hydroxyethyl)-1-piperazineethanesulfonic acid, 5.0 mM dextrose, pH 7.2) was used in order to block ionic conductances (outward and inward K⁺, Ca²⁺, Na⁺) which might otherwise interfere with capacitive current measures. OHCs maintained normal appearance in this solution for up to an hour. Osmolarity was adjusted to 300 mOsm with dextrose.

Electrical Recording

OHCs were whole cell voltage-clamped with a Dagan 8900 patch clamp amplifier at a holding potential of -80 mV, similar to the potential recorded

Received for publication 26 April 1993 and in final form 26 July 1993.

Address reprint requests to Joseph Santos-Sacchi, PhD.

© 1993 by the Biophysical Society

0006-3495/93/11/2228/09 \$2.00

in vivo (Dallos et al., 1982). Pipette solutions were composed of 140 mM CsCl, 10 mM EGTA, 5 mM tetra ethyl ammonium, 2 mM MgCl₂, and 5 mM 4-(2-hydroxyethyl)-1-piperazineethanesulfonic acid buffered to pH 7.2. Osmolarity was adjusted to 300 mOsm with dextrose. Gigohm seals were obtained either at the nuclear level of the cell membrane or just beneath the cuticular plate depending upon experimental intent; electrode capacitance and series resistance were compensated prior to whole cell recording. A modified version of Clampex (Axon Instruments, CA) utilizing the Labmaster board was used to collect data which were saved to disk for off-line analysis. Current was filtered at 5 kHz with an eight-pole Bessel filter.

Determination of nonlinear capacitance

The electrical characteristics of the voltage-clamped OHC when ionic conductances are blocked can be modeled most simply as an electrode resistance (access resistance, R_s) in series with a parallel combination of a membrane resistance (R_m), a linear membrane capacitance (C_{lin}), and a voltage-dependent membrane capacitance (C_v) (Fig. 1 A). The total membrane capacitance (C_m) at any given voltage is the sum of the linear and nonlinear capacitances,

$$C_m = C_v + C_{lin}, \quad (1)$$

where C_v , which results from the nonlinear charge movement associated with the motility voltage sensor, is defined as the first derivative of the two-state Boltzmann function ($Q_v = Q_{max}/(1 + \exp(-ze(V_m - V_h)/kT))$) which has been shown to adequately relate OHC nonlinear charge movement and membrane voltage ($C_v = dQ_v/dV_m$; see Santos-Sacchi (1991a)). Thus,

$$C_v = \frac{\left(Q_{max} \frac{ze}{kT} \right)}{\exp\left(\frac{ze}{kT} (V_m - V_h) \right) \left[1 + \exp\left(\frac{-ze}{kT} (V_m - V_h) \right) \right]^2}, \quad (2)$$

where V_m is the membrane potential, V_h is voltage at half-maximal nonlinear charge transfer, e is electron charge, k is Boltzmann's constant, T is absolute temperature, z is the valence, and Q_{max} is maximum nonlinear charge transfer. Fits of the measured capacitance data with this equation permit the estimation of nonlinear charge characteristics, similar to measures of these characteristics determined by subtraction techniques (e.g., *P/-4*) which have been utilized previously (Santos-Sacchi, 1991a).

The method employed to estimate membrane capacitance (C_m) and series resistance (R_s) is based on a linearized circuit at small excitation voltage steps (V_c). It is robust despite filter settings and accurately takes into account the effects of series resistance on capacitance measures (Santos-Sacchi, 1993).

For each response at a given step voltage (Fig. 1, *b* and *c*; see Appendix),

$$C_m = \left(\frac{R_{in}}{R_m} \right)^2 \frac{Q}{V_c} \quad (3)$$

$$R_s = \frac{R_m \tau V_c}{Q R_{in} + \tau V_c}, \quad (4)$$

where

$$R_{in} = R_m + R_s, \quad (5)$$

the input resistance readily obtained at steady state. V_c is the raw command voltage. The time constant (τ) is a single exponential fit to the decaying capacitive current induced by the voltage step, and the charge (Q) is obtained by integration (Fig. 1 D). Eq. 3 had been identified and used by Mathias et al. (1981) to evaluate alternative explanations of nonlinear gating charge movement. It is the proper evaluation of cell capacitance for the cell model when the ratio of R_s and R_m does not approach zero. In this report, voltage and charge were corrected for residual series resistance effects. Furthermore, to account for voltage step size, the voltages used in the fits of the capacitance data to Eq. 1 were taken to be the corrected voltage prior to the step plus one-half the corrected step voltage, i.e., the average voltage,

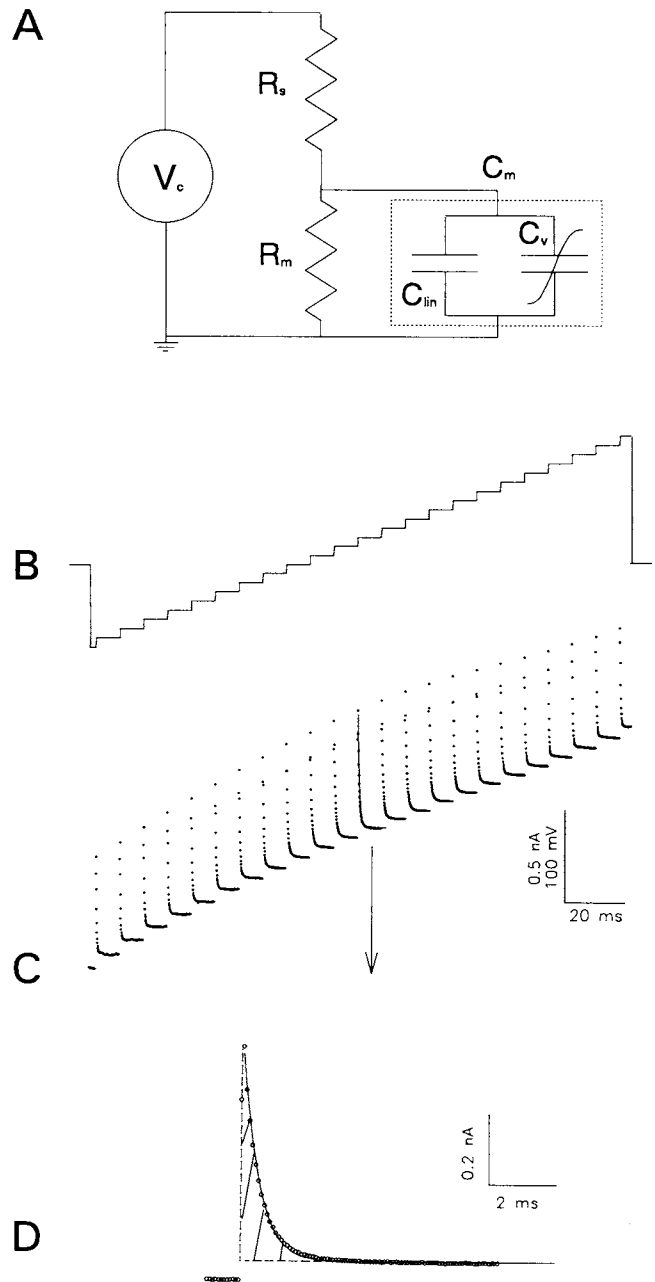


FIGURE 1 (A) Schematic of the OHC under voltage clamp. R_s , series resistance; R_m , membrane resistance; C_m , membrane capacitance composed of the parallel combination of a voltage-dependent capacitance (C_v) and linear capacitance (C_{lin}). (B) Voltage stair protocol. Holding potential was -80 mV. (C) Typical current record obtained from an OHC. For illustration, only one transient response is fitted to the extent of ten times its time constant. (D) Data and single exponential fit from above with expanded time scale. Charge was determined by integration of the shaded region.

as is predicted through modeling. All data analysis was performed with the software package MATLAB (Mathworks, Natick, MA). Fits of the data to Eq. 1 were made with the Nelder-Mead simplex algorithm.

The voltage protocol was a stair stimulus (2048 pts) whose nominal step size was 10 mV (Fig. 1 B), and whose step length was automatically adjusted to 10 times the previously determined time constant at the holding potential of -80 mV. Current records are averages of 20 collections. Since the time constant at each step potential is influenced by the OHC's nonlinear capacitance and any residual nonlinear leakage conductance, it was impossible

to guarantee that the decaying current trace would reach steady state for each step potential (Fig. 1 C). In order to overcome this limitation, the length of the exponential fit was extended to 10 times the fitted time constant and the fit was used for Q determination. The exponential fit was not extended back to zero onset time but only to peak current time. However, integration was performed back to zero onset time, utilizing pre-peak data points (Fig. 1 D). The position of peak current is due to the filtering effects of the clamp amplifier, and, as such, charge should be redistributed in time but not reduced.

RESULTS

OHCs possess a membrane capacitance which depends upon transmembrane voltage. In addition, despite efforts to block nonlinear voltage-dependent conductances, a residual nonlinearity remains. Fig. 2 illustrates the voltage dependence of the membrane capacitance and demonstrates the necessity of correcting for series resistance effects. In this example, a cell was chosen for which the series resistance and membrane resistance were relatively high, 27 and 281 Mohm, respectively (ratio of 0.096). Consequently, the time constants of the capacitive current decay are very large at potentials where the voltage-dependent capacitance is greatest. The series resistance-corrected membrane capacitance (Fig. 2, *solid downward triangles*) is plotted as a function of membrane voltage and fitted (*solid line*) with Eq. 1. The open downward triangles represent apparent capacitance estimates (Q/V_c), i.e., no series resistance corrections were made. Note the large differences in magnitude and voltage dependence between membrane and apparent capacitance. For comparison, the upward triangles represents a model simulation (that of Fig. 1 A) utilizing the parameters obtained from the fit to the corrected membrane capacitance data and a linear average membrane resistance. It is clear that the membrane capacitance estimates of the model and the data superimpose, how-

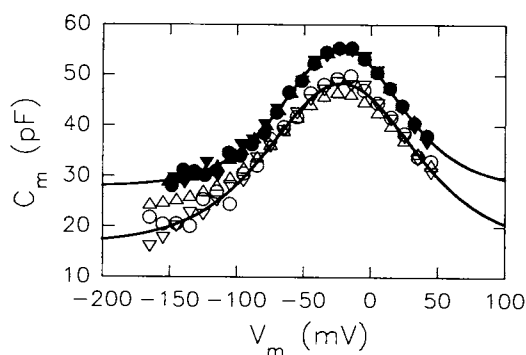


FIGURE 2 voltage-dependent capacitance of guinea pig OHC. Closed symbols indicate the membrane capacitance at each voltage step after correction for series resistance effects. Biophysical data (*downward triangles*), electrical model using fitted parameters of the biophysical data and a linear membrane resistance (*upward triangles*), model incorporating residual nonlinear membrane resistance of the biophysical data (*circles*). The solid line through these data points is a fit with Eq. 1 of the biophysical data (V_h , -27.33 mV; z , 0.829 ; Q_{max} , 2.66 pC; C_{lin} , 23.24 pF). The open symbols depict the apparent capacitance (Q/V_c) at each step, i.e., no series resistance corrections were made. The solid line through these data points is a fit with Eq. 1 of the biophysical data (V_h , -23.97 mV; z , 0.667 ; Q_{max} , 3.89 pC; C_{lin} , 14.75 pF). Note the requirement for series resistance correction in order to obtain correct estimates of the membrane capacitance.

ever, apparent capacitance estimates differ somewhat. Finally, the circles illustrate results when the nonlinear leakage conductance found in the biophysical data is included. Again the corrected capacitance data closely corresponds to the biophysical data, but now the apparent capacitance does as well. Simply modeling the cell with only a nonlinear leakage conductance does not generate an artifactual voltage-dependent capacitance. This exercise demonstrates that the method for estimating membrane capacitance (*filled symbols* in Fig. 2) is robust despite the existence of residual nonlinear leakage conductance and indicates that the correction for series resistance is required to obtain accurate estimates of membrane capacitance.

An additional 12 cells were recorded from in which the ratio of series resistance to average membrane resistance was fairly low, namely 0.057. Fits to the data indicate that the average maximum nonlinear charge transfer (Q_{max}) is 2.4 pC per cell, with a valence (z) of 0.92 . This corresponds to a peak nonlinear capacitance of 21.55 pF at -34.8 mV, riding upon a linear capacitance of 22.7 pF. The linear capacitance corresponds to the estimated whole cell surface area (based on a cylindrical model of the OHC) with the ratio of about 0.01 pF/ μm^2 (Fig. 3; however, see Discussion). It should be noted that nonlinear charge movement similar to that representing the motility voltage sensor is not demonstrable in supporting cells and is measurable in OHCs from species other than the guinea pig, e.g., mouse (Fig. 4).

In order to determine whether the motility voltage sensor is distributed within a restricted region of the OHC, a double voltage clamp protocol using two independent clamp amplifiers was employed. That is, utilizing the partitioning microchamber of Evans et al. (1989), in combination with whole cell voltage clamp we are able to electrically amputate that portion of the OHC housed within the chamber (Fig. 5). When identical voltage clamp stimuli are simultaneously delivered to the microchamber and the cell interior, only that portion of the membrane outside the chamber is excited.

The efficiency of this amputation technique is dependent upon the seal (shunt resistance, R_{sh}) which the microchamber makes with the OHC. This is illustrated in Fig. 6, where an

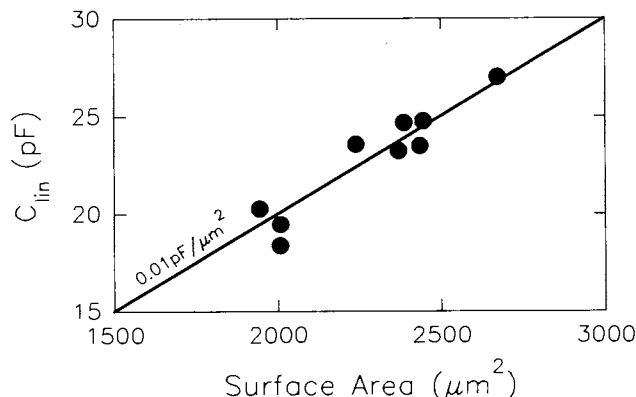


FIGURE 3 Linear capacitance (C_{lin}) versus estimated surface area of OHCs for nine cells.

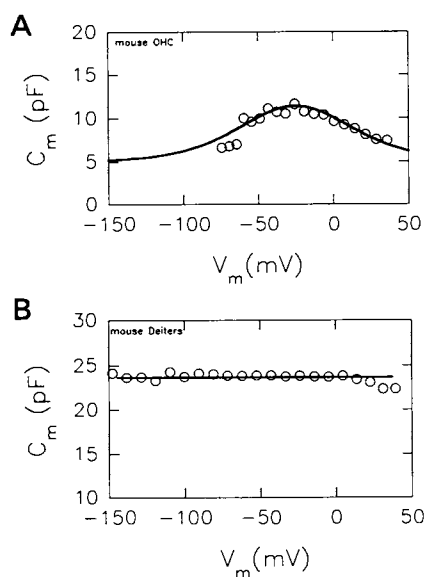


FIGURE 4 (A) Nonlinear membrane capacitance of a mouse OHC as a function of membrane potential. Mechanical responses were observed as well. (B) Membrane capacitance of a mouse Deiters cell demonstrates no voltage dependence.

electrical model of the double voltage clamp is evaluated with a model cell partitioned half-way. It is shown that when the shunt resistance is zero (or the chamber voltage is clamped to zero, i.e., ground), the system performs as a simple whole cell voltage clamp, measuring the parallel combination of the internal and external membrane capacitance. A shunt resistance above 5–10 Mohm, which is typical with the technique, provides good estimates of only the external membrane capacitance. By altering the partitioning of an OHC, it is possible to measure changes in linear and nonlinear capacitance utilizing the voltage stair protocol.

Fig. 7 presents the results from an individual OHC for which it was possible to obtain capacitance measures under three partitioning conditions and the whole cell condition. As the cell is extruded from the chamber, both the linear and nonlinear capacitance increase, because increasingly more membrane is exposed to the voltage stimulus (Fig. 7 A). Under the assumption that the change in linear capacitance and nonlinear charge (or nonlinear capacitance) is colinear as a function of cell extrusion, that is, that the voltage sensors are evenly distributed within the membrane, a linear fit to the partition data points provides evidence for the existence of a restricted, voltage-sensing region within the OHC (Fig. 7 B). The motility data of Dallos et al. (1991) indicates that the motor elements are evenly distributed along the length of the cell. It is likely, therefore, that motility voltage sensors are as well. The linear fit indicates that when the nonlinear charge movement (Q_{max}) reaches zero, linear capacitance is still measurable. That is, as the extent of cell inclusion is increased, a point is reached where nonlinear capacitance is absent, but linear capacitance exists and would continue to decrease with further inclusion. Similarly, as the cell is extruded, Q_{max} reaches a maximum but linear capacitance con-

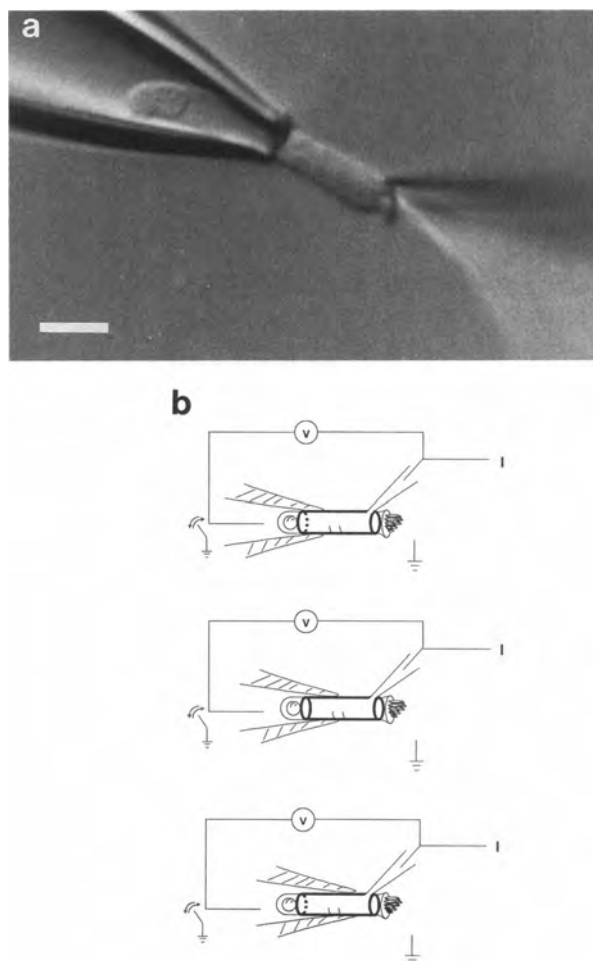


FIGURE 5 (A) Photomicrograph of a guinea pig OHC under double voltage clamp condition. Basal region of cell is within microchamber, and whole cell recording is established at the apical region. Scale is 20 μm . (B) Diagrammatic representation of the double voltage clamp with the OHC under three different conditions of cell extrusion.

tinues to increase with further extrusion. The slope of the fitted line indicates a charge density of $12,373 e^-/0.01 \text{ pF}$ within the voltage-sensing region. As expected, the portion of the cell within the microchamber which experiences no transmembrane voltage drop demonstrates no mechanical response, whereas the portion outside the chamber does (data not shown). However, upon grounding the chamber voltage, mechanical responses of that portion of the cell within the chamber are evident. Thus, the amputation technique also confirms the distributed nature of the mechanical effector (Dallos et al., 1991).

It is extremely difficult to maintain the preparation during changes in partitioning. Nevertheless, it was possible to obtain data on six additional OHCs where at least two partitioning conditions and the whole cell condition were achieved. The average linear capacitance in the apical region of the cells ($n = 7$) where no voltage sensors exist was 4.38 pF. In the base the average was 1.85 pF. The average charge density of the voltage-sensing region for these cells was $10,669 e^-/0.01 \text{ pF}$. The average R_s/R_m ratio for these cells was 0.24.

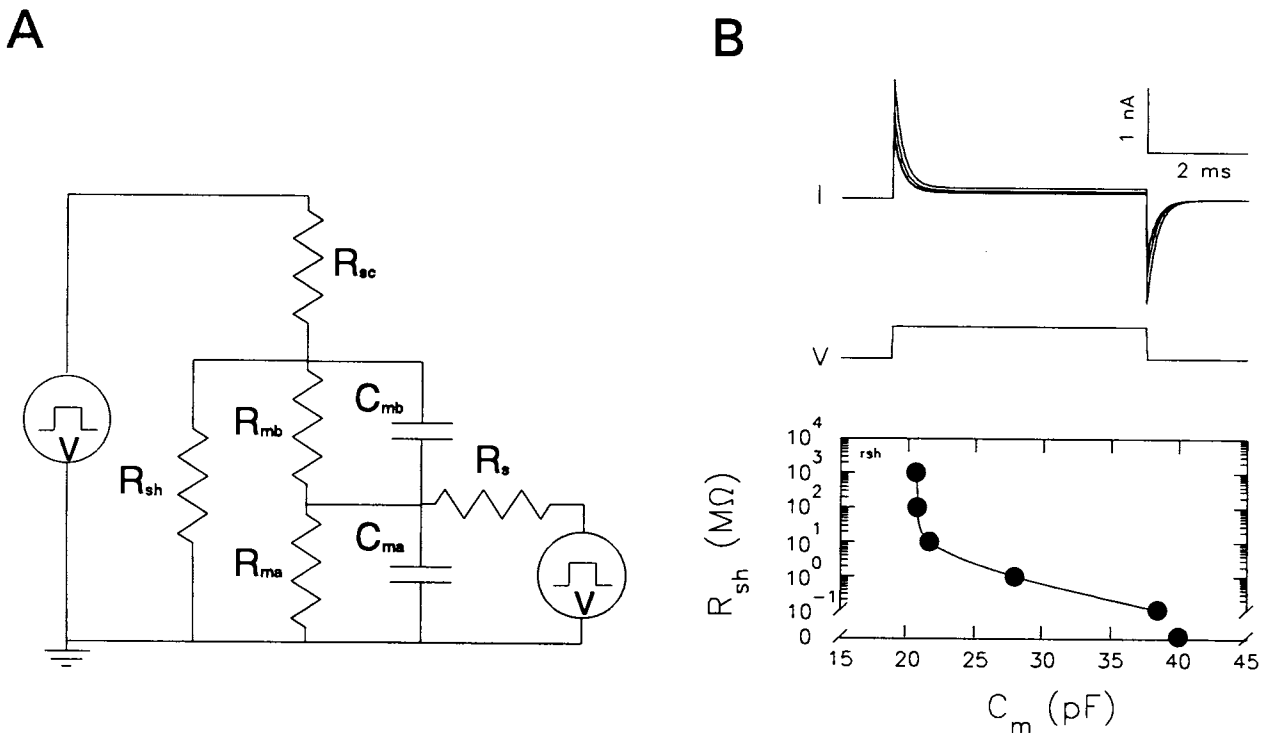


FIGURE 6 (A) Electrical model of double voltage clamp. R_{sc} , chamber series resistance; R_s , patch electrode series resistance; R_{sh} , shunt resistance between chamber electrode and ground; R_{mb} , membrane resistance of inserted portion of cell; C_{mb} , membrane capacitance of inserted portion of cell; R_{ma} , membrane resistance of extruded portion of cell; C_{ma} , membrane capacitance of extruded portion of cell. (B) The above model was numerically evaluated with parameters representing a cell inserted half way into the chamber, and the shunt resistance was varied to observe the effects on the efficiency of electrical amputation of the inserted portion. R_{sc} , 0.5 $M\Omega$; R_s , 5 $M\Omega$; R_{mb} and R_{ma} , 100 $M\Omega$; C_{mb} and C_{ma} , 20 pF. Current traces (I) in response to a 10 mV (V) step were used to determine input capacitance (see Methods) as a function of R_{sh} . When R_{sh} is zero the system functions as a simple whole cell voltage clamp, indicating a capacitance of 40 pF. Above 5–10 $M\Omega$, the system provides good indications of that capacitance of the extruded portion of the cell, 20 pF.

DISCUSSION

Several lines of evidence indicate that the mechanical response of the OHC is voltage-dependent (Santos-Sacchi and Dilger, 1988; Iwasa and Kachar, 1989; Ashmore, 1989; Santos-Sacchi, 1991a, 1992). The nonlinear charge movement, which presents itself as a voltage-dependent capacitance, is believed to represent the activity of the OHC's motility voltage sensor. Indeed, many of the characteristics of the nonlinear charge movement correspond to those of the OHC mechanical response, including extent and slope of voltage dependence, kinetics (which have yet to be fully described due to the limitations of the clamp time constant), block by gadolinium ions, and susceptibility to charge screening (Ashmore, 1992; Santos-Sacchi, 1991a, 1992). The present results indicate that the OHC nonlinear capacitance is restricted along the length of the cell, just as the mechanical response is restricted (Dallos et al., 1991).

Estimation of membrane capacitance and nonlinear charge

Under whole cell voltage clamp, OHCs from the apical turn of the cochlea possess a fairly low membrane resistance. Original estimates were between 20 to 40 $M\Omega$ (Ashmore and Meech, 1986). More recent average estimates are between 75

and 100 $M\Omega$ (Santos-Sacchi and Dilger, 1988; Housley and Ashmore, 1992). Because the ratio of series resistance to membrane resistance under whole cell voltage clamp is not ideal, i.e., zero, it is necessary to correct for series resistance effects. In the present report, membrane capacitance measures were corrected for such effects, and the efficacy of the correction procedure was verified through modeling. Corrections were especially important for those cells partitioned with the microchamber, where the membrane resistance was low (and the R_s/R_m ratio high) as a result of the physical trauma necessarily imposed upon the cell. Eq. 3 indicates that not only corrections to steady state voltage ($V_c \times R_m/R_{in}$) are required, but also corrections to charge magnitude ($Q \times R_{in}/R_m$) are required. In a previous study by Santos-Sacchi (1991), steady state voltage corrections were used to correct voltage dependence measures of nonlinear charge movement; however, corresponding corrections to the charge magnitudes were not made. In that study, average maximum charge movement (2 pC) was probably underestimated. The average Q_{max} in the present study was 2.59 pC ($n = 19$).

Area of OHC devoid of voltage sensors

A linear fit to the partition data points provided average estimates of linear capacitance in the sensor-devoid basal and

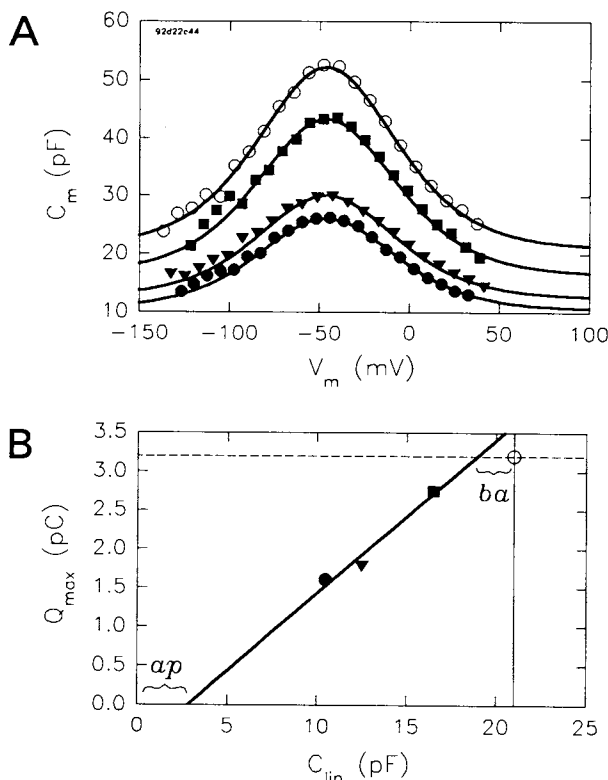


FIGURE 7 (A) The voltage-dependent membrane capacitance of a single OHC was evaluated at three levels of partitioning (*closed symbols*) and the whole cell condition (*open symbols*). Linear and nonlinear capacitance decrease as the cell inclusion is increased. The whole cell data were fit using the Nelder-Mead simplex algorithm. Partition data were fit by eye while holding z constant and varying Q_{\max} : z : 1. V_h of whole cell data: -46 mV, others shifted to coincide; filled squares, triangles, and circles were -51 , -53 , and -48 mV, respectively. (B) Relation between C_{lin} and Q_{\max} determined from above fits for the different levels of partitioning. Linear fit to the partition points indicates the extent of the OHC motility voltage sensor along the length of the cell. The vertical line indicates whole cell linear capacitance; the horizontal dotted line indicates whole cell Q_{\max} . Linear capacitance denoted by *ap* (2.65 pF) represents the area of the apical portion of the cell devoid of voltage sensors; that denoted by *ba* (2.06 pF) represents the area of the basal portion of the cell devoid of voltage sensors. Slope of fitted line indicates a charge density of $12,373 e^-/0.01$ pF within the sensing region. Ratio of R_s to R_m : 0.19.

apical regions of the OHC. The values were 1.85 and 4.38 pF, respectively. The actual membrane surface area of the OHC is greater than that estimated with light microscopy by a factor of about 1.3 (due to lateral membrane surface crenulation; see Dallos (1983)). This indicates that the linear specific capacitance measures obtained in the present study should be corrected¹ to a value of about 0.008 pF/ μm^2 . Consequently, the above capacitance values translate to areas of 231 and 547 μm^2 , respectively. It is possible to compare

these results with the surface areas of OHC plasmalemma which lack adjacent subsurface cisternae and/or mechanical responses.

Microchamber analysis of OHC motility demonstrates that a mechanical response is absent in the cell's most basal region (7 μm in length (B. Evans, personal communication)). The subsurface cisternae are poorly developed or absent in this region, as well. By modeling this basal region of the OHC as a half sphere of 5 - μm radius, with a 2 - μm cylindrical extension, an area of 220 μm^2 is obtained. This compares favorably with the present estimate of basal surface area lacking voltage sensors. At the apical region of the cell, substantial amounts of subsurface cisternae do not arise until about 5 μm from the top of the cell (Ades and Engstrom, 1974; Saito, 1983). The apical region of the OHC is oddly shaped (Fig. 5 *a*); however, if this portion is modeled as a simple single-ended cylinder (which is likely to underestimate its actual area) with a radius of 5 μm and length of 5 μm , then the calculated surface area is 236 μm^2 . Accounting for stereociliar surface area² (average of 50 per cell, with a radius of 0.15 μm and length of 6 μm ; B. Evans, personal communication), the total apical area increases to 518 μm^2 , which is similar to the present estimate of apical surface area lacking voltage sensors. These calculations provide strong support for the notion that the regions of the OHC which lack motility voltage sensors correspond to those which lack subsurface cisternae and/or voltage-dependent mechanical responses. Ultrastructural studies also indicate that only the lateral portion of the OHC plasmalemma possesses dense arrays of intramembranous particles (Saito, 1983; Kalinec et al., 1992).

The correspondence of the nonlinear capacitance with plasmalemmal regions bordering subsurface cisternae may imply some sort of electrical interaction between plasma and subsurface membrane. Such a possibility was considered by Santos-Sacchi (1991a) to account for nonlinear capacitance in this cell. That is, electrical interactions between the two membranous systems might affect capacitance measures, as occurs for input capacitance measures in inner ear supporting cells which are coupled via gap junctions (Santos-Sacchi, 1991b). Recently, however, it has been demonstrated that, following disruption of OHC subsurface structures with intracellularly applied trypsin, mechanical responses of the plasma membrane remain (Kalenic et al., 1992). This indicates that the mechanical effector resides within the plasma membrane. Similar treatments do not abolish the nonlinear capacitance (Huang and Santos-Sacchi, unpublished results), which implies a colocalization of motility voltage sensor and effector within the plane of the plasma membrane. Nevertheless, it is interesting that the subsurface cisternae and voltage sensors coincide, and it is possible that the subsurface

¹The correction is based on the assumption that the linear-specific capacitance is the same in sensor-containing and sensor-devoid membranes. It is possible that the sensor-containing region has a somewhat higher specific capacitance due to a higher dielectric of the protein particles residing therein. The corrected value should be considered approximate.

²While it was often noted that stereocilia were absent in isolated OHCs, it is possible that the isolation procedure caused resorption of the structures. For example, hair cell trauma often causes fusion and clumping of stereocilia (Engstrom, 1983). We never observe isolated stereocilia which may have been sheared off during isolation.

membrane represents a normal molecular turnover route for the motility voltage sensor and/or effector.

Uniform nature of voltage sensors within the OHC

It has previously been noted that some of the nonlinear charge movement in OHCs should be due to gating of voltage-dependent ionic channels (Santos-Sacchi, 1991a). However, while the supporting cells undoubtedly possess channel gating charge, charge movement of the magnitude recorded in OHCs is not seen. It appears that the charge moved by the motility voltage sensor far outweighs that contributed by channel gating, indicating that the characteristics of the nonlinear charge movement in the OHC overwhelmingly reflect that of the motility mechanism. Using similar logic, Fernandez et al. (1983) were able to evaluate characteristics of the membrane bound charge movement produced by the lipophilic molecule DpA^- despite the existence of smaller channel gating charge.

Some aspects of the nature of the voltage sensors along the length of the OHC can be gleaned from the results of the partitioning experiments. That is, it is possible to determine whether sensor characteristics (e.g., voltage sensitivity) along the extent of the active, voltage-sensing region vary from the average obtained under whole cell conditions. The only factor which changed significantly during changes in the degree of partitioning was the value of Q_{max} (except for the linear capacitance, of course). That is, the same nonlinear capacitance function (namely, z kept constant) which fit the whole cell data could adequately describe capacitance measures obtained from increasingly smaller portions of the cell. V_h was seen to vary sometimes, and may be due to charge screening effects, or changes in the metabolic state of cells during the course of the experiments. For example, it is known that phosphorylating agents can shift V_h without altering other parameters of the OHC nonlinear capacitance function (Huang and Santos-Sacchi, 1993). The maintenance of the form of the C_v function during successive amputations indicates that the nature of the voltage sensor along the extent of the OHC is constant, and that partitioning simply alters the number of sensors which are activated. That is, the voltage sensors (and possibly effectors) are probably of one type along their extent.

Density of voltage sensors

The number of independent elementary charges moved per square micrometer has previously been estimated to be about 4000 (Santos-Sacchi, 1991a), based on a Q_{max} of 2 pC and a total surface area of a model OHC of 70- μm length. In the present report, the linear capacitance values obtained in whole cell configuration translate to an average membrane surface area of 2917 μm^2 ($n = 19$). Thus, with the present Q_{max} value of 2.59 pC, an average charge density of 5542 $e^-/\mu\text{m}^2$ is obtained. However, it is now clear that the extent of the OHC motility voltage sensors is restricted along the

length of the cell. It is necessary, therefore, to compute charge density based on surface area estimates for that portion of the OHC which possesses the motility voltage sensors. After removing the average surface area of the OHC devoid of voltage sensors (sum of apex and base: 6.23 pF or 778 μm^2 ($n = 7$)) from the total average surface area, we obtain an average charge density of 7558 $e^-/\mu\text{m}^2$. Since the voltage dependence of the nonlinear charge movement and motility are comparable (z close to 1 (Ashmore, 1992; Santos-Sacchi, 1991a)), it is concluded, based on a two-state model, that about 7500 $e^-/\mu\text{m}^2$ independent elementary charged particles control the mechanical activity of the OHC. It is tempting to attribute the measured charge movement to integral membrane proteins represented by the membrane particles observed in the lateral plasmalemma of the OHC (Gulley and Reese, 1977; Saito, 1983; Forge, 1991; Kalinec et al., 1992). In a similar fashion, Roberts et al., (1990) suggested, based on colocalizing ultrastructural and electrophysiological evidence, that membrane particles located at synaptic areas of the hair cell may represent K^+ and Ca^{2+} channels. One possible interpretation of the colocalization of sensor and effector along the length of the OHC is that the sensor and effector reside within one molecular species, similar to ionic channels where sensor movement in an electrical field is believed to promote gating via a conformational change of the channel protein.

However, the present charge density estimate is no longer in line with the suggestion of Santos-Sacchi (1991a) that the number of elementary charges corresponds to the number of particles observed ultrastructurally in the OHC lateral membrane. Recent estimates of the number of membrane particles indicate about 2500/ μm^2 (Holley et al., 1992). It may be that each membrane particle possesses three charges which must each independently move between two states to effect a mechanical response. An interesting reinterpretation of the OHC charge data may be made by utilizing the electrodiffusion model of Neumcke et al. (1978), in which charge movement is viewed as a multistate phenomenon. For example, using this Langevin type fit to their data, they determined that the valence (z) of Na^+ channel nonlinear charge movement was about three times that of a two-state model. The multistate model more accurately accounted for Na^+ channel gating and conductance characteristics. Drews (1988) reached a similar conclusion. Under such an interpretation, the valence (z) of OHC charge movement would be closer to 3, and this might suggest that three charges correspond to each ultrastructurally observed membrane particle, all charges needing to traverse a characteristic distance across the membrane before a mechanical effect ensues. The multistate model would predict that the onset of the mechanical response would be delayed following a step voltage stimulus, and this type of response has been observed (Ashmore, 1987; Santos-Sacchi, 1992). However, because of the limitations of clamp amplifier speed, the true time course of the OHC mechanical response is not known (Santos-Sacchi, 1992). In addition, a loss of OHC cell turgor (known to interfere with OHC motility (Holley and Ashmore, 1988;

Santos-Sacchi, 1991a)) which necessarily accompanies whole cell voltage clamp configuration, may also contribute to a delayed response. It cannot be judged at this point whether charge movement in the OHC is two-state or multistate.

APPENDIX

For the model (Fig. 1 A), the steady state (I_∞) and instantaneous (I_0) current responses to a voltage step are defined as

$$I_\infty = \frac{V_c}{R_s + R_m}, I_0 = \frac{V_c}{R_s} \quad (6)$$

with the exponentially decaying capacitive current given as

$$I_{C_m} = (I_0 - I_\infty)e^{-\frac{t}{\tau}}, \quad (7)$$

where

$$\tau = R_{||}C_m, \quad (8)$$

$$R_{||} = \frac{R_m R_s}{R_{in}}, \quad (9)$$

and

$$R_{in} = R_m + R_s, \quad (10)$$

the input resistance readily obtained at steady state.

The charge moved is then obtained by integration

$$\int_0^\infty I_{C_m} dt = Q = \frac{C_m R_m^2 V_c}{R_{in}^2}. \quad (11)$$

Solving for C_m ,

$$C_m = \frac{R_{in}^2 Q}{R_m^2 V_c}, \quad (12)$$

and utilizing Eqs. 4 and 8, we obtain

$$R_s = \frac{R_{in} \tau V_c}{QR_{in} + \tau V_c}. \quad (13)$$

The time constant (τ) of the exponentially decaying current, and the charge moved (Q) are little affected by filter settings as low as 2 kHz (eight-pole Bessel).

We thank Frank N. Tilley III for technical assistance. Thanks also to Dr. H. Sontheimer for comments on the manuscript, and Drs. F. Bezanilla and K. Chandler for many helpful discussions.

This work was supported by National Institutes of Health-National Institute of Deafness and other Communication Disorders grant DC00273.

REFERENCES

Ades, H. W., and H. Engstrom. 1974. Anatomy of the inner ear. *In Handbook of Sensory Physiology*, Vol. V/1. W. D. Keidel and W. D. Neff, editors. 125-158.

- Ashmore, J. F. 1987. A fast motile response in guinea-pig outer hair cells: the cellular basis of the cochlear amplifier. *J. Physiol. (Lond.)* 388: 323-347.
- Ashmore, J. F. 1989. Transducer motor coupling in cochlear outer hair cells. *In Mechanics of Hearing*. D. Kemp and J. P. Wilson, editors. Plenum Press, New York. 107-113.
- Ashmore, J. F. 1992. Mammalian hearing and the cellular mechanisms of the cochlear amplifier. *In Sensory Transduction*. D. P. Corey, and S. D. Roper, editors. Rockefeller University Press, New York, p. 395-412.
- Ashmore, J. F., and R. W. Meech. 1986. Ionic basis of the resting potential in outer hair cells isolated from the guinea pig cochlea. *Nature*. 322: 368-371.
- Brownell, W. E., C. R. Bader, D. Bertrand, and Y. de Ribaupierre. 1985. Evoked mechanical responses of isolated cochlear outer hair cells. *Science (Wash. DC)*. 227:194-196.
- Dallos, P., J. Santos-Sacchi, and Å. Flock. 1982. Intracellular recordings from outer hair cells. *Science (Wash. DC)*. 218:582-584.
- Dallos, P. 1983. Some electrical circuit properties of the organ of Corti. I. Analysis without reactive elements. *Hear. Res.* 12:89-119.
- Dallos P., B. N. Evans, and R. Hallworth. 1991. On the nature of the motor element in cochlear outer hair cells. *Nature (Lond.)*. 350:155-157.
- Drews, G. 1988. Effects of aconitine and batrachotoxin on Na currents and gating currents in the frog node of Ranvier. *Pflugers Arch. Eur J. Physiol.* 411:491-499.
- Engstrom, B. 1983. Stereocilia of sensory cells in normal and hearing impaired ears. *Scand. Audiol. Suppl.* 19:1-34.
- Evans, B. N., P. Dallos, and R. Hallworth. 1989. Asymmetries in motile responses of outer hair cells in simulated in vivo conditions *In Mechanics of Hearing*. D. Kemp, and J. P. Wilson, editors. Plenum Press, New York. 205-206.
- Fernandez, J. M., R. E. Taylor, and F. Bezanilla. 1983. Induced capacitance in the squid giant axon. Lipophilic ion displacement currents. *J. Gen. Physiol.* 82:331-346.
- Forge, A. 1991. Structural features of the lateral walls in mammalian cochlear outer hair cells. *Cell Tissue Res.* 265:473-483.
- Gulley, R. L., and T. S. Reese. 1977. Regional specialization of the hair cell plasmalemma in the organ of Corti. *Anat. Rec.* 189:109-124.
- Holley, M. C., and J. F. Ashmore. 1988. On the mechanism of a high-frequency force generator in outer hair cells isolated from the guinea pig cochlea. *Proc. R. Soc. Lond. Ser. B Biol. Sci.* 232: 413-429.
- Holley, M. C., F. Kalenic, and B. Kachar. 1992. Structure of the cortical cytoskeleton in mammalian outer hair cells. *J. Cell Sci.* 102:569-580.
- Housley, G. D., and J. F. Ashmore. 1992. Ionic currents of outer hair cells isolated from the guinea-pig cochlea. *J. Physiol. (Lond.)*. 448:73-98.
- Huang, G., and J. Santos-Sacchi. 1993. Metabolic control of OHC function: phosphorylation and dephosphorylation agents shift the voltage dependency of motility related capacitance. *Proceedings of Midwinter Meeting of the Association for Research in Otolaryngology*, St. Petersburg, FL, February.
- Iwasa, K. H., and B. Kachar. 1989. Fast in vitro movement of outer hair cells in an external electric field: effect of digitonin, a membrane permeabilizing agent. *Hear. Res.* 40:247-254.
- Kalinez, F., M. C. Holley, K. H. Iwasa, D. J. Lim, and B. Kachar. 1992. A membrane-based force generation mechanism in auditory sensory cells. *Proc. Natl. Acad. Sci. USA.* 89:8671-8675.
- Mathias, R. T., R. A. Levis, and R. S. Eisenberg. 1981. An alternative interpretation of charge movement in muscle. *In The Regulation of Muscle Contraction: Excitation-Contraction Coupling*. A. D. Grinnell and M. A. B. Brazier, editors. Academic Press, New York. 39-52.
- Neumcke B., W. Nonner, and R. Stampfli. 1978. Gating currents in excitable membranes. *International Review of Biochemistry*, 19, 129-155.
- Roberts, W. M., R. A. Jacobs, and A. J. Hudspeth. 1990. Colocalization of ion channels involved in frequency selectivity and synaptic transmission at presynaptic active zones of hair cells. *J. Neurosci.* 10:3664-3684.
- Ruggero, M. A. 1992. Responses to sound of the basilar membrane of the mammalian cochlea. *Current Opinion in Neurobiology* 2:449-456.
- Saito, K. 1983. Fine structure of the sensory epithelium of guinea pig organ of Corti: subsurface cisternae and lamellar bodies in the outer hair cells. *Cell Tissue Res.* 229:467-481.
- Santos-Sacchi, J. 1990. Fast outer hair cell motility: how fast is fast? *In The*

- Mechanics and Biophysics of Hearing. P. Dallos, C. D. Geisler, J. W. Matthews, M. A. Ruggero, C. R. Steele, editors. Springer-Verlag, Berlin. 69–75.
- Santos-Sacchi, J. 1991a. Reversible inhibition of voltage-dependent outer hair cell motility and capacitance. *J. Neurosci.* 11:3096–3110.
- Santos-Sacchi, J. 1991b. Isolated supporting cells from the organ of Corti: some whole cell electrical characteristics and estimates of gap junctional conductance. *Hear. Res.* 52:89–98.
- Santos-Sacchi, J. 1992. On the frequency limit and phase of outer hair cell motility: effects of the membrane filter. *J. Neurosci.* 12:1906–1916.
- Santos-Sacchi, J. 1993. Voltage-dependent ionic conductances of Type I spiral ganglion cells from the guinea pig inner ear. *J. Neurosci.* 13:3599–3611.
- Santos-Sacchi, J., and J. P. Dilger. 1988. Whole cell currents and mechanical responses of isolated outer hair cells. *Hear. Res.* 35:143–150.
- Santos-Sacchi, J. and Huang, G.-J. 1993. Characterizing the extent of the OHC motility voltage sensor with an electrical guillotine: evidence that ends don't meet. Symposium on the Biophysics of hair cell sensory systems. Paterswolde, The Netherlands, June.

Motility voltage sensor of the outer hair cell resides within the lateral plasma membrane

GUOJIE HUANG AND JOSEPH SANTOS-SACCHI*

Sections of Otolaryngology and Neurobiology, Yale University School of Medicine, New Haven, CT 06510

Communicated by Jozef J. Zwislocki, August 25, 1994

ABSTRACT The outer hair cell (OHC) from the organ of Corti is believed to be responsible for the mammal's exquisite sense of hearing. A membrane-based motile response of this cell underlies the initial processing of acoustic energy. The voltage-dependent capacitance of the OHC, possibly reflecting charge movement of the motility voltage sensor, was measured in cells during intracellular dialysis of trypsin under whole cell voltage clamp. Within 10 min after dialysis, light and electron microscopic examination revealed that the subplasmalemmal structures, including the cytoskeletal framework and subsurface cisternae, were disrupted and/or detached from adjacent plasma membrane. Dialysis of heat-inactivated trypsin produced no changes in cell structure. Simultaneous measures of linear and nonlinear membrane capacitance revealed minimal changes, indicating that contributions by subsurface structures to the generation of the nonlinear capacitance are unlikely. This study strongly suggests that voltage-dependent charge movement in the OHC reflects properties of the force generator's voltage sensor and that the sensor/motor resides solely within the lateral plasma membrane.

The mammalian outer hair cell (OHC) possesses a unique transmembrane voltage-driven mechanical response that can occur at acoustic frequencies (1–5). This mechanical activity is believed to underlie the enhanced ability of the inner ear to detect and analyze sound (6) and is especially interesting since it is not directly dependent upon Ca^{2+} or metabolic substrates (3, 7, 8). A nonlinear charge movement, or corresponding voltage-dependent capacitance, has been observed in this cell and it probably reflects the activity of the motility voltage sensor, as many of its characteristics and those of the mechanical response coincide (9–12). Recently, the mechanical response and the extent of the nonlinear capacitance have been mapped along the central portion of the cylindrical OHC (13, 14); each corresponds roughly to the extent of subplasmalemmal structures, the cortical network of cytoskeletal filaments, and the subsurface cisternae. It is of interest to determine whether such structures contribute to the motile mechanism or nonlinear charge movement or if the cell's plasma membrane alone is responsible for these phenomena. The experiments of Kalinec *et al.* (15) have shown that intracellular dialysis of trypsin does not abolish OHC membrane movements. However, no electron microscopic analysis of the effects of the trypsin treatment was performed, so it is unclear whether the plasma membrane was totally isolated from intracellular structures in their experiments. We report here that following intracellular trypsin treatments, most of the plasma membrane is isolated from subsurface structures as evidenced electron microscopically. Furthermore, the nonlinear charge movement remains intact during such treatments, indicating that the motility voltage sensor, as well as the motor, reside within the plane of the OHC plasma membrane.

MATERIALS AND METHODS

General. Guinea pigs were euthanized with halothane overdose. The isolated organ of Corti was treated with collagenase (0.3 mg/ml for 10 min) and triturated gently within a polyethylene pipette in medium 199 with Hanks' salts (GIBCO). The OHC-enriched supernatant was then transferred to a 700- μl perfusion chamber. Experiments were performed at room temperature (22°C).

Electrical Recording. OHCs were whole cell voltage clamped with a Dagan 8900 patch clamp amplifier at a holding potential of -80 mV. Cells were bathed in a modified Leibovitz medium (in mM: NaCl 110, KCl 5.37, CoCl_2 2, MgCl_2 1.48, tetraethylammonium chloride 20, CsCl 20, Hepes 5, and dextrose 5; 300 mosM, pH 7.2) in order to block ionic conductances. Pipette solutions were composed of (mM) CsCl 140, EGTA 10, tetraethylammonium chloride 5, MgCl_2 2, and Hepes 5 (300 mosM, pH 7.2). Gigaohm seals were obtained at the middle portion of the lateral wall. In order to introduce trypsin into the cell, relatively large patch pipette tips were used (1.5- to 2- μm inner diameter; series resistance, 2–3 M Ω). For trypsin treatments, 300 μg of trypsin (source: bovine pancreas, M_r 23,281; Calbiochem) was dissolved in 1 ml of pipette solution and the osmolarity and pH were readjusted to 300 mosM and pH 7.2. As a control, heat-inactivated trypsin (enzyme pipette solution heated for 30 min in 56°C water bath) was also used. Electrode capacitance was compensated after gigaohm seal formation, and series resistance compensation was used in whole cell configuration. A modified version of Clampex (Axon Instruments, Burlingame, CA) was used to apply voltage stimuli and collect data that were saved on disk for off-line analysis. Current was filtered at 5 kHz with an eight-pole Bessel filter. All experiments were videotaped.

Three methods were used to evaluate the effects of trypsin treatment on cell capacitance. The first method simply measured cell capacitance near the cell's normal *in vivo* resting potential. The cell was nominally held at -80 mV and a -10 mV step command voltage (4 ms) was applied repeatedly over time. At this potential both linear and a substantial amount of nonlinear capacitance contributes to the generation of a transient capacitive current (12). From averaged ($\times 20$) current records, an on-line analysis of membrane capacitance (C_m), membrane resistance (R_m), and series resistance (R_s) was performed and saved to disk. The transient analysis calculations have been published elsewhere (16).

The second method evaluated the voltage dependence of nonlinear capacitance using a voltage stair protocol. The technique has been fully described elsewhere (14). Briefly, the cell was stair-stepped from a holding potential of -170 mV to voltages between -160 mV and $+50$ mV, in increments of 10 mV. From each step response, C_m , R_m , and R_s were calculated as a function of membrane voltage. The

The publication costs of this article were defrayed in part by page charge payment. This article must therefore be hereby marked "advertisement" in accordance with 18 U.S.C. §1734 solely to indicate this fact.

Abbreviation: OHC, outer hair cell.

*To whom reprint requests should be addressed.

measured membrane capacitance has two components, a linear one, which is a function of the total cell membrane area, and a nonlinear one, which is a measure of the charge movement of the motility voltage sensor. The total membrane capacitance (C_m) at any given voltage is the sum of the linear (C_{lin}) and nonlinear (C_v) capacitance. The nonlinear capacitance (C_v) can be described as the first derivative of a two-state Boltzmann function relating nonlinear charge movement to voltage, and such a fit provides estimates of the charge characteristics, including the voltage at half-maximal nonlinear charge transfer (V_h), and charge valence (z) (see Fig. 3 and ref. 14 for further details). Measures were made at 1- to 5-min intervals following whole cell configuration.

The third method was used to overcome potential harmful effects of the large voltages of the stair protocol. To estimate maximal nonlinear capacitance, a software tracking protocol using step analysis was developed to monitor peak capacitance by iteratively adjusting the holding potential to maintain the cell at V_h —i.e., the voltage at which nonlinear capacitance is greatest. Should V_h change during an experiment, the tracking technique, utilizing -10 mV steps, will continue to determine peak capacitance.

Electron Microscopy. Following single cell capacitance evaluations, primary fixation was accomplished by slowly perfusing the recording chamber with 0.75% glutaraldehyde in 0.1 M sodium cacodylate buffer with 2 mM CaCl_2 (300 mosM, pH 7.3). The perfusion rate was about 0.05 ml/min in order to minimize distortion of the cell. After perfusion for 30 min, cells were washed with buffer for 10 min and released from recording pipettes by gently breaking the tip on the chamber floor. To continue processing without losing the cell, a microchamber embedding method was devised. A polypropylene disposable pipette (Fisher) was heated and pulled to approximately 20- to 30- μm internal radius and 10- to 15- μm wall thickness. Under a dissecting microscope, the tube was shoed to the tip of a glass pipette. Cells were gently sucked into the microchamber, and the microchamber was affixed to the bottom of a new perfusion dish. Cells were postfixated with 1% OsO_4 in 0.1 M sodium cacodylate buffer (pH 7.3, 300 mosM) for 30 min, followed by dehydration in a graded series of ethanol up to 100%. Cells were stained with 2% uranyl acetate (while in 70% ethanol) for 30 min in the dark.

Poly Bed 812 was prepared according to the Mollenhauer mixture 1 formula (Polyscience). Three changes in graded concentrations of Poly Bed 812 (epoxy resin/ethanol, 1:3, 1:1, 3:1; 4 hr each) were followed by three changes in pure Poly Bed 812 (4 hr each). Polymerization was at 60°C overnight. The plastic microchamber was then cut out and reembedded in an Epon block. Ultrathin sections (70–80 nm) were taken at various points through the cell extent, placed on Formavar-coated 200-mesh copper grids, and stained with uranyl acetate (10 min) and lead citrate (2 min). Sections were observed with a Phillips 300 electron microscope at 60 kV.

RESULTS

During the course of whole cell electrical recording, trypsin enters the OHC and alters the cell's normal cylindrical structure. In a group of 15 OHCs, simultaneous capacitance measures were obtained at a nominal holding potential of -80 mV. Within 3–23 min (10.2 ± 6.7 min; mean \pm SD), these cells were transformed into spherical structures, which appeared at the light microscopic level to have undergone an involution and separation of the cell's subplasmalemmal structures from the plasma membrane. Fig. 1 illustrates the progression of this phenomenon. After the OHCs became fully spherical, the cells were fixed for electron microscopy. However, in some cells that were not fixed, continued dialysis eventually caused dissolution of the nucleus and

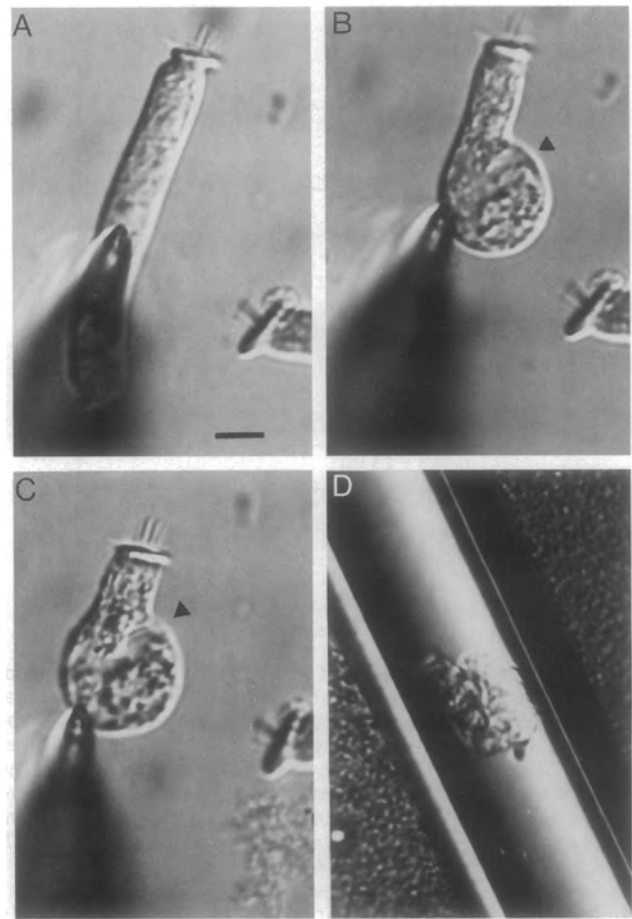


FIG. 1. Light microscopy of an OHC during the course of trypsin treatment and capacitance measurement, illustrating the loss of the cell's cylindrical shape and involution of intracellular cortical structures. (A) Cell 5 min after established whole cell configuration. (B and C) At the 12th and 16th min, respectively. The arrowheads indicate the area where the cortical structures began separation from the plasma membrane. This cell eventually became fully spherical at the 20th min and was then fixed. (D) Cell within a plastic microchamber, prior to embedding. (Bar = 10 μm .)

much of the cuticular plate. Although dramatic alterations in cell structure were observed, C_m at -80 mV did not decrease, as might have been expected if subplasmalemmal structures were requisite for the nonlinear capacitance component. Average data are presented in Fig. 2 and show that C_m actually increased in this sample from an initial value of about 35 pF to 39 pF. R_m decreased during the recording to about 75% of the initial 103 $\text{M}\Omega$ average. The electrode series resistance remained constant at about 6 $\text{M}\Omega$, indicating that efficient dialysis was maintained throughout the recording period.

During capacitance measures obtained at a fixed holding potential, it is possible that either holding potential changed, as a consequence of changes in the ratio of series resistance to membrane resistance (the voltage divider effect), or V_h changed, as a consequence of trypsin treatment. Such occurrences could account for the observed change in total membrane capacitance in Fig. 2. In fact, using the stair-step voltage protocol, it was determined that V_h shifts occurred in some cells. Fig. 3 illustrates the data obtained using the stair protocol. The results from a single cell are presented in Fig. 3 Upper and the average capacitance for 9 cells is presented in Fig. 3 Lower. In each panel, the voltage-dependent capacitance was measured within a minute after cell entry (closed circles) and after the cells had become spherical (open

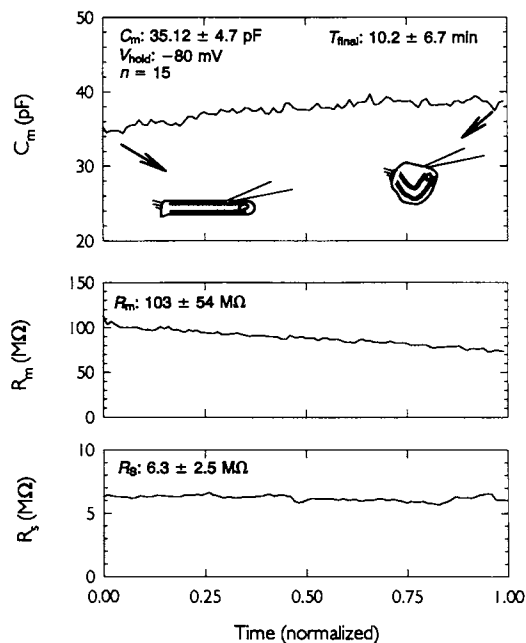


FIG. 2. Average C_m , R_m , and R_s of 15 OHCs during treatment with trypsin. The cells changed shape from cylindrical to spherical during the trypsin treatment, but the time to reach a spherical shape varied among cells, with an average time of 10 ± 6.7 min. Two other cells spontaneously burst at the nuclear pole during recording. The data were normalized by decimation along the time dimension to provide an end point corresponding to the time of sphere formation. Initial values were as follows: C_m , 35.12 ± 4.7 pF; R_m , 103 ± 54 M Ω ; R_s , 6.3 ± 2.5 M Ω . Note a slight increase in C_m .

circles). The data indicate that despite changes in V_h in some cells (average shift of -11 mV; see legend to Fig. 3), voltage-dependent characteristics of the nonlinear capacitance remained near normal, as did peak capacitance values. We have recently observed that a reduction of membrane tension, caused by reduced intracellular pressure, increases nonlinear capacitance and shifts V_h in the negative direction—up to a limiting voltage approaching the membrane potential of OHCs *in vivo*—namely, -70 mV (S. Kakehata and J.S.-S., unpublished observations). We speculate that trypsin treatment reduces tension on the membrane by destroying cortical cytoskeletal interactions with the membrane, causing a negative shift of V_h , and probably accounting for the increase of OHC C_m observed at a holding potential of -80 mV (Fig. 2).

We also confirm the results of Kalinec *et al.* (15), since we observe robust mechanical responses under this voltage protocol despite the fact that the plasma membrane appears divorced from intracellular structures. Nevertheless, the motility that remains in trypsin-treated cells is not the same as in normal cells. This results from the disruption of the cell's normal cytoarchitecture and mechanical properties that provide for the normal longitudinal length changes. Thus, despite the fact that the cell continues to respond to voltage changes by modifying its shape, motility characteristics (e.g., frequency response) may be altered and require further evaluation.

The stair protocol subjects the cells to very large, rapid voltage changes, which, over repeated application, tend to damage the cell or electrode seal. This is especially the case for trypsin-treated cells, which are by definition already compromised. In fact, many spherical cells were lost during such collections. In 19 cells that underwent the stair protocol, the electrode seal was lost in 10 cells, and in another 2 cells the membrane burst at locations remote from the electrode location, near the nuclear pole. Therefore, estimates of peak

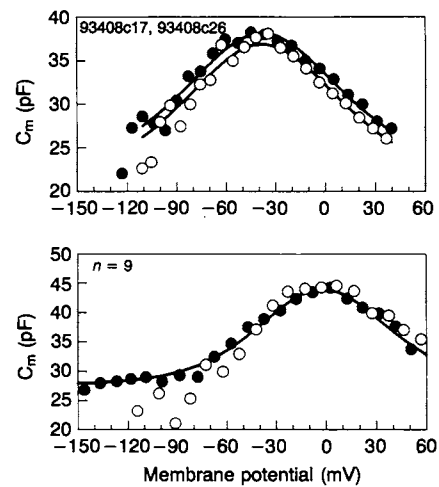


FIG. 3. Voltage-dependent capacitance of OHCs measured with the stair-step protocol during trypsin treatment. The voltage-dependent capacitance rides upon a linear membrane capacitance ($C_m = C_v + C_{lin}$). ●, C_m recorded immediately after the establishment of whole cell configuration; ○, data obtained after the OHCs became spherical. During stimulation, OHCs responded with robust motility, either before or after trypsin effects were evident. (Upper) Results from a single OHC. In this case, the voltage at peak capacitance (V_h) remained constant before and after trypsin treatment. Fits of the data to the first derivative (with respect to membrane voltage) of a two-state Boltzmann function [$Q(v) = Q_{max}/1 + \exp(-ez(V_m - V_h)/kT)$, where e , k , and T have their usual meanings] are indicated by the solid lines, with an additional linear capacitance added (C_{lin}). For the control condition (●), $z = 0.82$, $Q_{max} = 1.97$ pC, $V_h = -38$ mV, and $C_{lin} = 22.4$ pF. The fit through the open circles is the same, with C_{lin} reduced by 1.25 pF. (Lower) Averaged results from nine cells. The voltage at peak capacitance (V_h) was found to vary among cells. To average the capacitance measures from different cells, all functions were shifted along the voltage axis so that V_h resided at 0 mV. Since the actual voltage at each step differed for each cell because of differences in the ratios of R_s to R_m , the data were binned into 10 mV ranges. Both voltages and capacitance values were averaged within bins. Symbols as above. The fit through the closed circles provided average parameters of $z = 0.98$, $Q_{max} = 1.7$ pC, and $C_{lin} = 27.7$ pF. The actual average voltage at peak capacitance (V_h) for the control condition was -15 mV and after trypsin effects were evident, -26 mV. The capacitance values after trypsin treatment (○) are similar (or slightly increased) to the control except at hyperpolarized voltage steps, where it appeared that membrane characteristics became unstable.

capacitance were also obtained by the tracking technique described in *Materials and Methods*. Fig. 4 provides an example of a cell that was monitored during trypsin treatment well beyond the point where it reached a fully spherical shape. Peak capacitance remained relatively constant throughout the recording period ($n = 7$).

Fig. 5 presents a low-power electron micrograph of an OHC after trypsin had caused the cell to become spherical. The striking feature of the trypsin treatment was a separation of the plasmalemma from subsurface cisternae and cortical cytoskeleton. Vast amounts of plasma membrane appeared free of any subsurface interactions. In higher magnification

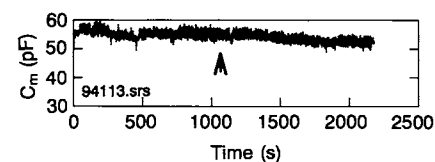


FIG. 4. Peak capacitance (C_m) of an OHC that was monitored with the tracking procedure during trypsin treatment (see text). The arrow indicates the point at which the cell became fully spherical. Note that peak capacitance remains nearly constant in this example.

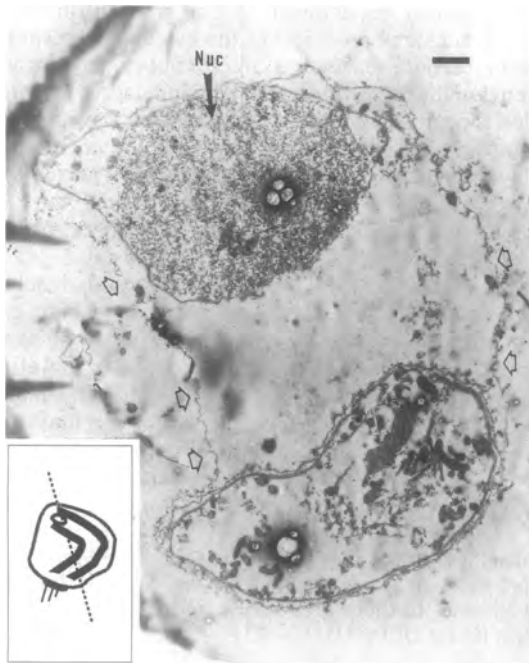


FIG. 5. Low-power electron micrograph of a trypsin-treated OHC within a microchamber. Five minutes after the initiation of recording the cell became spherical and was fixed. Arrows point to the plasmalemma, which is divorced from intracellular structures. (Inset) Schematic illustrating the section orientation through the spherical cell. Note, in the electron micrograph, on one side of the cell the nucleus (Nuc) is sectioned, and on the other side more apical regions are sectioned. (Bar = 1 μm .)

views (Fig. 6), it was apparent that the cytoskeletal attachments between the plasma membrane and subsurface cister-

nae were digested by the enzyme, allowing the cisternae to peel away from the plasma membrane. In five cells successfully recovered for electron microscopy, the bulk of plasma membrane was cleanly isolated, indicating that the capacitance measures reflected simply the intrinsic properties of plasma membrane components.

DISCUSSION

The OHC possesses a unique ability to alter its length in response to electrical stimulation (1). The driving force for this phenomenon is currently considered to be transmembrane voltage (3, 5), and in line with this hypothesis is the demonstration of a gating charge or nonlinear capacitance in the OHC that is associated with the mechanical event (9, 11). The charge displacement may reflect the movement of a proteinaceous motor's voltage sensor, just as voltage sensors of ionic channels demonstrate transient charge movements during channel gating. This contention is based upon similarities between some of the characteristics of the gating charge movement and the mechanical response in the OHC (12, 17). For example, the time course of gating charge movement and OHC motility are similar, and factors affecting the gating charge also are reflected in the motion of the cell. Another indication is that the extent of the charge movement along the length of the cell corresponds to those regions of the cell that are mechanically active (14). Furthermore, both motor activity and nonlinear charge movement are discretely distributed along the cell body and can be activated independently in different regions of the cell (13, 14).

Nevertheless, structural features exist in the OHC that could potentially account for a voltage-dependent charge movement that coincidentally occurs during the mechanical activity of the OHC. The OHC plasmalemma is intimately associated with an adjacent cortical cytoskeleton composed

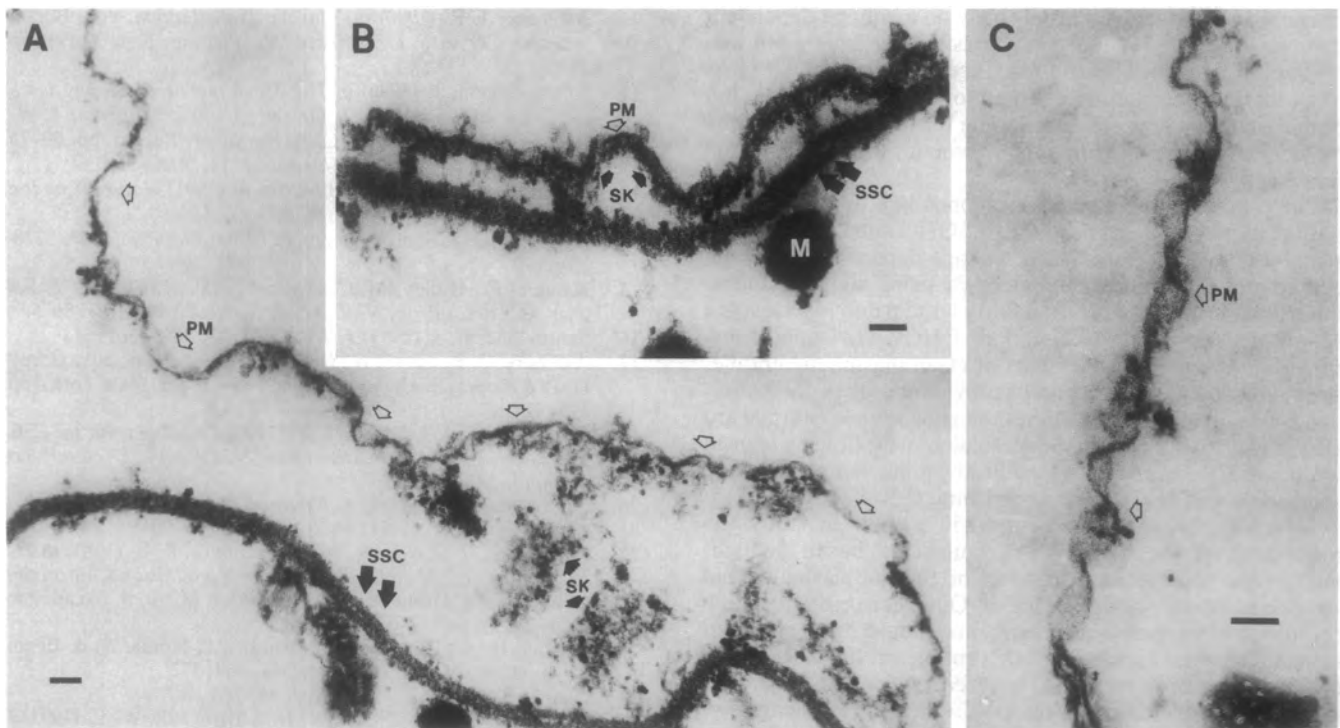


FIG. 6. Higher-magnification view of the same cell as in Fig. 5 at a different level. (A) Area in which the plasma membrane (PM) has peeled away from underlying structures. The subplasmalemmal cytoskeleton (SK) appears digested and has been freed from the intracellular aspect of the plasma membrane. As a result, the subsurface cisternae (SSC) are able to involute into the cell. In some cells there was evidence for cisternal vesiculation. (B) Area where the digestion process is in an early stage. Attachments between the plasma membrane and subsurface cisternae via the cytoskeleton are still visible. (C) At higher magnification, an area of plasma membrane fully clear of intracellular structures. (Bars = 100 nm.)

of circumferential actin filaments, cross-linked by spectrin (18). In addition, filamentous pillar processes extend from the plasma membrane to the circumferential filaments and subsurface cisternae (19), a membranous system whose surface area can be greater than that of the cell's plasma membrane. While the potential electrical interaction between subsurface cisternae and plasmalemma had been initially dismissed based on the observation that OHC capacitance could be accounted for by the linear dielectric properties of the OHC surface plasma membrane (2), subsequent experiments indicated that this was not the case (20). Clearly, it is now known that a portion of OHC capacitance is voltage dependent and can be of the same order of magnitude as the cell's linear capacitance (11, 12). Electrical interactions between two membranous systems could increase input capacitance, just as occurs during alterations of gap junctional communication in inner ear supporting cells (21). It is not inconceivable that the OHC plasma membrane could recruit cisternal membrane in a voltage-dependent manner, either through reversible membrane fusion or through some electrical interaction of the cisternae with the extracellular space, perhaps via the pillar processes spanning the region between plasma membrane and cisternal membrane.

Another potential generator of nonlinear charge movement might exist due to the restrictive subplasmalemma space, resulting in a series resistance between the OHC plasma membrane and axis core (9). For example, it has been suggested that the pillars or spectrin may be associated with the mechanical response in a charge-dependent manner (9, 18). Perhaps movement of these structures or transmembrane ionic flow into the restrictive subplasmalemma space can generate capacitive-like charge movements measurable across the intracellular series resistance. Indeed, a residual nonlinear ionic conductance exists in the OHC even after substantial efforts to block voltage-dependent currents (12, 14). Simple circuits of skeletal muscle membranous systems have been envisioned that theoretically could generate nonlinear charge movement based solely on a voltage-dependent conductance (22). While these possibilities have been dismissed for muscle, because evidence of the molecular basis of excitation-contraction charge movement exists (23), hypotheses of this type are appropriate for the OHC, where the molecular basis of the charge movement remains uncharacterized.

The present experiments were conducted in order to rule out these potential contributions of OHC subplasmalemma structures to the generation of voltage-dependent nonlinear charge movement or capacitance. By using high concentrations of trypsin (300 $\mu\text{g}/\text{ml}$) in fairly large patch pipettes, the subplasmalemma cytoskeleton of OHCs was rapidly disrupted, leaving expansive areas of clean plasma membrane, as evidenced by electron microscopy. Not only is the restrictive space no longer present but the subsurface cisternae are also physically remote to the plasmalemma following trypsin treatment. Despite such treatment, the nonlinear capacitance and motility of the cell remained intact. Kalinec *et al.* (15) used similar trypsin treatments (150 $\mu\text{g}/\text{ml}$) to study the robustness of the motility and concluded based on light microscopy that after disruption of the subplasmalemma structures motility remained intact. Our electron microscopic results confirm that their treatments should have provided isolated plasma membrane. Disruption of the subsurface cisternae has been shown to interfere with the normal longitudinal length changes of the OHC (24, 25). It is clear now, however, that the subplasmalemma structures, while providing structural and other support for the normal OHC, do not contribute directly to the generation of gating currents or the underlying mechanical response of the plasma membrane. The only logical explanation for the persistence of the

OHC's nonlinear capacitance is that it is intrinsic to the lateral plasma membrane, just as the mechanical response is. Furthermore, both sensor and effector appear to be protected from enzymatic digestion, possibly indicating that (i) the complex is proteinaceous and buried within the lipid bilayer, (ii) some sites of the proteinaceous complex are external to the bilayer but lack trypsin cleavage sites, (iii) portions of the complex external to the bilayer are digested but do not contribute significantly to sensor/motor activity, or (iv) the underlying mechanism is somehow lipid based.

Current theories of OHC motility envision molecular motors within the lateral plasma membrane, which change conformation upon sensing alterations in transmembrane voltage (15, 26, 27). The colocalization of sensor and effector, not only along the extent of the OHC's length (13, 14) but also within the plane of the OHC plasma membrane, may indicate that the densely packed intramembranous particles first observed nearly two decades ago (28) ultimately underlie the inner ear's remarkable sensitivity and frequency selectivity.

We thank Dr. Ilsa Schwartz, Patricia Eager, and Frank N. Tilley III. This research was supported by the National Institutes of Health-National Institute of Deafness and Other Communication Disorders (Grant DC00273).

1. Brownell, W. E., Bader, C. R., Bertrand, D. & de Ribaupierre, Y. (1985) *Science* **227**, 194-196.
2. Ashmore, J. F. (1987) *J. Physiol. (London)* **388**, 323-347.
3. Santos-Sacchi, J. & Dilger, J. P. (1988) *Hear. Res.* **35**, 143-150.
4. Santos-Sacchi, J. (1992) *J. Neurosci.* **12**, 1906-1916.
5. Iwasa, K. H. & Kachar, B. (1989) *Hear. Res.* **40**, 247-254.
6. Ruggero, M. A. (1992) *Curr. Opin. Neurobiol.* **2**, 449-456.
7. Kachar, B., Brownell, W. E., Altschuler, R. & Fex, J. (1986) *Nature (London)* **322**, 365-368.
8. Holley, M. C. & Ashmore, J. F. (1988) *Proc. R. Soc. London B* **232**, 413-429.
9. Ashmore, J. F. (1989) in *Mechanics of Hearing*, eds. Kemp, D. & Wilson, J. P. (Plenum, New York), pp. 107-113.
10. Ashmore, J. F. (1990) in *Sensory Transduction*, eds. Borsellino, A., Cervetto, L. & Torre, V. (Plenum, New York), pp. 25-50.
11. Santos-Sacchi, J. (1990) in *The Mechanics and Biophysics of Hearing*, eds. Dallos, P., Geisler, C. D., Mathews, J. W., Ruggero, M. A. & Steele, C. R. (Springer, Berlin), pp. 69-75.
12. Santos-Sacchi, J. (1991) *J. Neurosci.* **11**, 3096-3110.
13. Dallos, P., Evans, B. & Hallworth, R. (1991) *Nature (London)* **350**, 155-157.
14. Huang, G.-J. & Santos-Sacchi, J. (1993) *Biophys. J.* **65**, 2228-2236.
15. Kalinec, F., Holley, M. C., Iwasa, K. H., Lim, D. J. & Kachar, B. (1992) *Proc. Natl. Acad. Sci. USA* **89**, 8671-8675.
16. Santos-Sacchi, J. (1993) *J. Neurosci.* **13**, 3599-3611.
17. Ashmore, J. F. (1992) in *Sensory Transduction*, eds. Corey, D. P. & Roper, S. D. (Rockefeller Univ. Press, New York), pp. 395-412.
18. Holley, M. C. & Ashmore, J. F. (1990) *J. Cell Sci.* **96**, 283-291.
19. Flock, A., Flock, B. & Ulfendahl, M. (1986) *Arch. Otorhinolaryngol.* **243**, 83-90.
20. Santos-Sacchi, J. (1989) *J. Neurosci.* **9**, 2954-2962.
21. Santos-Sacchi, J. (1991) *Hear. Res.* **52**, 89-98.
22. Mathias, R. T., Levis, R. A. & Eisenberg, R. S. (1981) in *The Regulation of Muscle Contraction: Excitation-Contraction Coupling*, eds. Grinnell, A. D. & Brazier, M. A. B. (Academic, New York), pp. 39-52.
23. Adams, B. A., Tanabe, T., Mikami, A., Numa, S. & Beam, K. G. (1990) *Nature (London)* **346**, 569-572.
24. Evans, B. N. (1990) *Hear. Res.* **45**, 265-282.
25. Dieler, R., Shehata-Dieler, W. E. & Brownell, W. E. (1991) *J. Neurocytol.* **20**, 637-653.
26. Dallos, P., Hallworth, R. & Evans, B. N. (1993) *J. Neurophysiol.* **70**, 299-323.
27. Santos-Sacchi, J. (1993) *Biophys. J.* **65**, 2217-2227.
28. Gulley, R. L. & Reese, T. S. (1977) *Anat. Rec.* **189**, 109-124.

FIRING UP THE AMPLIFIER: TEMPERATURE, PRESSURE AND VOLTAGE JUMP STUDIES ON OHC MOTOR CAPACITANCE*

JOSEPH SANTOS-SACCHI, LEI SONG, XIANTAO LI

*Yale University School of Medicine
New Haven, Ct 06510, USA*

The outer hair cell (OHC) possesses molecular motors that drive electromotility and cochlear amplification. Here we look at the effects of fast perturbations of biophysical forces that affect the OHC, including voltage, temperature and pressure, on the electrical signature of motor activity, namely nonlinear capacitance (NLC). Under whole cell voltage clamp, we measure changes in NLC at fixed holding voltages following steps in voltage, jumps in temperature induced by ir laser, or jumps in intracellular turgor pressure. In each case we find time dependent changes in NLC resulting from induced shifts of the NLC function across the voltage axis. The time course of these shifts depends on the stimulus, with voltage jumps inducing shifts with fast exponential components less than a millisecond. Those induced by temperature and pressure are within the tens of millisecond ranges and may be limited by cellular and experimental constraints that voltage is able to overcome. The overall observation of time dependent changes to the electromotility function upon stimulation indicates a more complex mechanism than provided by a simple two-state Boltzmann model.

1 Introduction

The outer hair cell (OHC) drives cochlea amplification through a cellular mechanism that works at kilohertz rates [1,2,3,4]. Molecular motors that are housed within the OHC lateral membrane, comprising at least the molecule prestin [5], produce conformational changes in response to voltage which alter the somatic length of the cell [6,7,8]. The deformations of these cells within the organ of Corti feedback energy into the basilar membrane, thus amplifying the auditory stimulus that is delivered to IHC stereocilia [9]. The ultimate effect is a boost in our auditory sensations.

The OHC motor, or prestin transfected into non-auditory cells, produces a signature electrical response analogous to gating currents observed in other voltage dependent membrane bound proteins [2,10,11]. The gating currents, because they are restricted charge movements within the membrane dielectric, can also be measured as a nonlinear capacitance (NLC), bell-shaped as a function of voltage. This charge movement or NLC can be fit most simply by a two-state Boltzmann function, allowing extraction of Boltzmann parameters that provide information on voltage dependence, voltage sensor valence, and maximum charge moved. These steady state parameters do not provide dynamic information about the motor, but the time course of underlying gating charge movements or of shifts in the C-V function can provide hints on the motor's

* This work and the Plenary Lecture were supported by NIH grants DC000273, DC008130, DC008115 to JSS.

conformational kinetic properties. Here we report on the effects of fast perturbations of biophysical forces that affect the OHC, including voltage, temperature and pressure, on the electrical signature of motor activity, namely NLC. The occurrence of time dependent changes to the C-V (or equivalently, electromotility) function upon such stimulation indicates a more complex mechanism than provided by a simple two-state Boltzmann model.

2 Methods

Guinea pigs were decapitated following anesthetic overdose with halothane. OHCs were freshly isolated from the guinea pig cochlea using Dispase (1 mg/ml) followed by trituration, and were whole-cell voltage clamped at room temperature using an Axon 200B amplifier. Membrane voltages were corrected for the effects of residual series resistance, which ranged from 3-5 M Ω . Ionic blocking solutions were used to remove voltage-dependent ionic conductances so that capacitive currents could be analyzed in isolation [11]. Extracellular solution: 100mM NaCl, 20mM TEA, 20mM CsCl, 2mM CoCl₂, 1.48mM MgCl₂, 2 mM CaCl₂, 10 mM HEPES, and 5mM dextrose, adjusted to pH 7.2 with NaOH, and adjusted to 300mOsm with dextrose. Pipette solution: 140mM CsCl, 10mM EGTA, 2mM MgCl₂, and 10mM HEPES, adjusted to pH 7.2 with CsOH, and adjusted to 300mOsm with dextrose. In some cases, TEA, CsCl, CoCl₂, CaCl₂, and MgCl₂ were omitted. Also, in some experiments, the extracellular solution was used in patch electrodes. In a few experiments, 50 μ M GdCl₃ was included in the extracellular solution to decrease residual currents. At this concentration, gadolinium has an insignificant affect on OHC capacitance [12]. Additional solution modifications are noted in figure legends.

In order to deliver rapid changes in membrane tension, we used a pressure clamp system from ALA instruments. Pipette tip diameters were increased in size for these experiments (\sim 1 M Ω). In order to deliver rapid changes in temperature a Capella IR laser was used to deliver via fiber optic 5-20 ms light pulses (1850 nm).

OHC capacitance was measured with a continuous high-resolution two-sine voltage stimulus protocol (20mV peak at both f1 and f2; f2=2*f1; f1 ranging up to 3906.3 Hz), and subsequent FFT based admittance analysis [13,14]. These small, high frequency sinusoids were superimposed on voltage steps or ramps that spanned up to \pm 200 mV.

OHC C-V plots were fitted with the function $C_m = C_{lin} + C_v$, where C_{lin} is the voltage-independent (linear surface area component) capacitance of the lipid bilayer, and $C_v = dQ_{nonL}/dV$ is the voltage-dependent component of C_m originating from prestin's voltage-sensor activity. The first derivative with respect to V_m of a two-state Boltzmann function $Q = Q_{max}/(1 + \exp(-ze(V_m - V_{pkCm})/k_B T))$ was used to fit the C-V data [11]. Q_{max} is total charge moved. The measured apparent valence of prestin voltage-sensor (z) is defined as $z = q \cdot d$, where d is a normalized perpendicular projection of distance traveled by the voltage sensor charge (q) within the plasma membrane field. V_{pkCm} is the

membrane potential (V_m) at which prestin molecules are equally distributed between expanded and contracted states. It corresponds to the peak of the C_v function.

All data collection and most analyses were performed with an in-house developed Window's based whole-cell voltage clamp program, **jClamp** (www.scisoftco.com), utilizing a Digidata 1320 board (Axon, CA). Matlab (Natick, MA) or SigmaPlot was used for fitting the C_m data.

3 Results

3.1 Voltage jumps induce time dependent changes in NLC

When OHC voltage is stepped away from the holding potential, a nearly instantaneous change in C_m is observed because membrane capacitance is a bell shaped function of voltage (Fig. 1). However, unlike memory-less systems, the C-V function is not static but

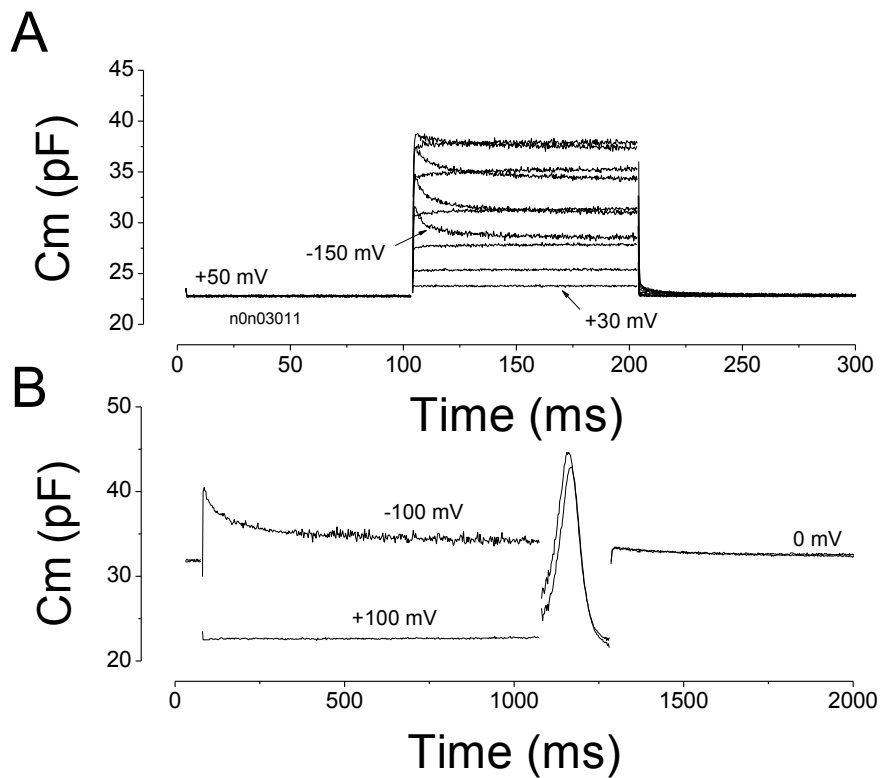


Figure 1 A) An OHC was held under voltage clamp at +50 mV and stepped to 30 (red),10,-10,-30,-50,-70,-90,-110,-130,-150 (blue) for 200 ms. The hyperpolarizing steps induced a time dependent change in C_m , increasing for steps approaching V_{pkcm} , and decreasing for steps beyond V_{pkcm} . B) Another OHC (held at 0 mV) showing that hyperpolarizing steps cause C_m relaxations (red line) due to depolarizing shifts in V_{pkcm} . A ramped voltage from -150 to +150 mV produced the bell shaped C_m response, indicating the rightward shift in V_{pkcm} .

shifts along the stimulus axis to alter C_m over time even though measures are made at a fixed voltage. The change in C_m is multi-exponential. With C_m sampling rates of about 4kHz, we find that the earliest exponential components are below one millisecond, with additional components at order of magnitude intervals.

3.2 Pressure jumps induce time dependent changes in NLC

Fig. 2 shows that rapid changes in membrane tension at a fixed voltage shifts V_{pkcm} in a time dependent manner, mimicking to some extent the C_m changes induced by step voltage changes. The pressure steps produced delayed onset responses because cellular material in the pipette tip obstructed flow. With increasing pressures it can be seen that the pipette unplugged at decreasingly shorter times following onset of the pressure steps (1: 0.8 kPa [fully obstructed], 2: 1.06kPa, 3: 1.33 kPa, and 4: 1.6 kPa). Lower pressures caused an increase in C_m over time, while the largest pressure pulse caused an immediate increase and subsequent relaxation. With this last pressure pulse the cell burst.

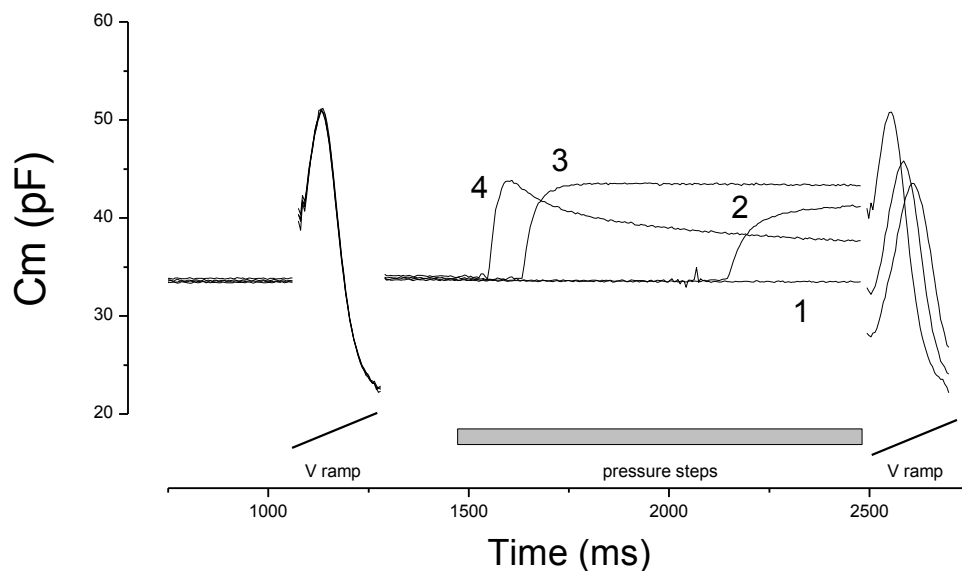


Figure 2 An OHC was held under voltage clamp at 0 mV. A voltage ramp (-100 to +100 mV, 200 ms) was delivered followed by incrementing pressure (1, 2, 3, 4) steps to the patch pipette, and the ramp was repeated (pressure was maintained during the final ramps). 3 sec intervals between traces were allowed for recovery from stimulation. Successful recovery is indicated by overlapping C-V functions. Increments in pressure cause time dependent changes in C_m at the fixed 0 mV holding potential, and occur due to shifts in V_{pkcm} , as the bell shaped C_m functions signify. The final pressure pulse caused the cell to burst; consequently, no C_m ramp data is plotted. In mM: 140 Cl in and out (NaCl 132, MgCl₂ 2, CaCl₂ 2, Hepes 10. Additional 10 EGTA for Intracellular solution)

3.32 Temperature jumps induce time dependent changes in NLC

We have previously shown that the C-V function of OHCs and prestin transfected HEK cells are very temperature sensitive, shifting about 20 mV to the right with a 10 °C increase in temperature [15,16]. Here we find that the effect of temperature jumps induced by IR laser is immediate in onset, followed by relaxation. Unlike steps in voltage and pressure, which could be maintained for unlimited durations, the Capella laser can only deliver up to 20 ms steps. Thus, the time course of C_m changes cannot be attributed to shifts in the C-V function during constant temperature, but could result from return to room temperature. Thus, the shifts in C-V we observed (Fig. 3B) likely correspond to expected changes in temperature as the bath cooled. However, we can glean from these experiments that temperature effects are very rapid, ruling out slow intracellular processes, such as phosphorylation, and likely indicating direct temperature effects on the conformational state of the motor protein prestin.

4 Discussion

By measuring OHC nonlinear membrane capacitance at sub-millisecond resolutions, we have examined the early time course of the OHC motor's dynamic response to jumps in membrane voltage, tension and temperature. We find that the time course of the voltage-induced response is multi-exponential, with the earliest detectable components residing

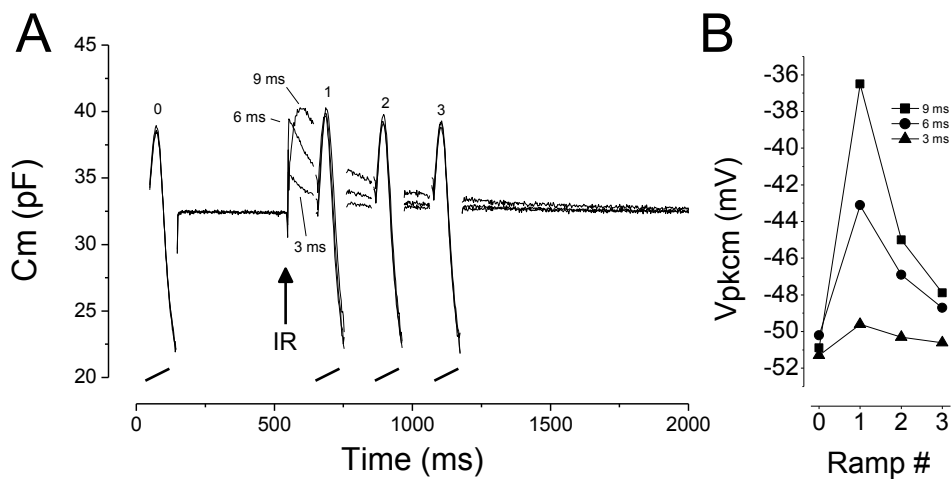


Figure 3 A) An OHC was held under voltage clamp at 0 mV. A voltage ramp (-100 to +100 mV, 200 ms) was delivered (denoted by 0) followed by incrementing temperature step durations to the cell, after which a series of voltage ramps (1, 2, 3) were delivered during the C_m relaxations. 10 sec intervals were used between traces to allow recovery from stimulation. Successful recovery is indicated by overlapping C-V functions. Increments in temperature duration (3, 6, 9 ms) cause time dependent changes in C_m at the fixed 0 mV holding potential, the shifts being plotted in B. Maximal temperature change is estimated to be about 10 °C. In this case the slow relaxations may be due to re-cooling to room temperature after laser stimulation.

in the kilohertz range, thereby establishing the phenomenon's potential significance in peripheral auditory processing of the mammal. These effects actually extend well into the low frequency range, as well; indeed, altering steady state resting potentials can stably set the operating point of electromotility to different points along the voltage axis.

Our data, though measuring whole cell capacitance, actually provide insight into the initial condition-dependent conformational states of the motor protein, prestin. That is, while capacitance may increase or decrease during incremental unidirectional steps in voltage or tension (**Figs. 1 and 2**), both correspond to a unidirectional change in motor state probability, as a conversion of capacitance to gating charge would reveal. Consequently, depolarizing voltages, in addition to causing a near instantaneous redistribution of motors to the compact state, will foster a supplemental recruitment of additional motors into that state, leading to an amplification of the initial response. The same amplification effect holds for hyperpolarizing voltages, where recruitment of motors will be into the expanded state. Tension effects appear to follow these rules, as well. However, because of equipment limitations on laser pulse duration we were unable to deliver long steps, and thus cannot confirm that temperature jumps mimic the effects of the other stimuli. We are attempting to modify the design to allow the further comparison.

Anions play a major role in NLC generation, and we were interested whether our results could reflect underlying interactions of chloride with the motor, since we have shown that V_{pkcm} shifts to the right when chloride is replaced with gluconate or other substitutes [17,18,19]. However, we find that modifying the driving force (changing extracellular chloride concentrations) for chloride movement across the OHC lateral membrane through G_{metL} [18] does not modify the extent or time course of the amplificatory shift (data not shown). It should be noted that although driving force for chloride did not significantly affect the motor's amplificatory shift, the interactions of anions with the motor may still play a role. In this regard, we have recently found that the state probability of prestin influences anion binding affinity (Song and Santos-Sacchi, ARO 2007), and that even if concentrations remain the same at the intracellular binding sites of prestin, changes in binding site affinity, as can occur with allosteric modulation, could alter energy profiles, resulting in V_{pkcm} shifts.

Since the initial observations of Iwasa [20], membrane tension effects on the OHC motor have provided important information on this protein's surprisingly efficient piezoelectric activity [21]. Because membrane tension can shift V_{pkcm} and, indeed, in extreme applications, restrict conformational activity [22], we had modeled the voltage-induced amplificatory shift as resulting from motor induced tension [14]. In the present report we attempted to directly test this by applying rapid changes in membrane tension and seeking C_m relaxations that mimic those induced by voltage steps. Though there are indications of C_m relaxations following rapid tension changes, the time courses of voltage-induced and tension-induced C_m relaxations differ, tension effects being slower. It is possible that during our attempts to alter membrane tension through global changes in OHC structure we may have been restricted by the viscoelastic properties of the whole

cell. For example, Dong and Iwasa [23] found that mechanical relaxations in the OHC have a time constant on the order of 40 s. However, because the fastest C_m relaxation time constants that we found with pressure steps were about 2 orders of magnitude faster than their measured time course, our pressure clamp driver appears to have been quite successful in overcoming this mechanical impediment. We suggest that tension induced by the molecular motors themselves can better bypass this viscoelastic constraint, thereby providing more rapid tensions to evoke fast amplificatory shifts. Thus, we still view motor-derived membrane tension, possibly through alterations of anion binding affinity, to underlie voltage-induced amplificatory shifts [14]. Nevertheless, as we have shown previously, the membrane environment of prestin can have profound effects on the magnitude and time course of the amplificatory shift [24].

In summary, we show remarkably fast changes in the Boltzmann distribution of prestin motor states induced by fast perturbations of the motor. The shifts along the voltage axis represent amplificatory supplementation to the near instantaneous voltage-induced mechanical response of the cell, and it is expected that this phenomenon will impact on high frequency peripheral auditory processing. Finally, it is expected that distortion in the mechanical response will arise, contributing to one of the hallmarks of mammalian cochlear amplification [25].

5 References

1. Santos-Sacchi, J. 1992. On the frequency limit and phase of outer hair cell motility: effects of the membrane filter. *J. Neurosci.* 12, 1906-1916.
2. Santos-Sacchi, J. *The Mechanics and Biophysics of Hearing*. Dallos, P., Geisler, C.D., Matthews, J.W., Ruggero, M.A. & Steele, C.R. (eds.), pp. 69-75 (Springer-Verlag, Berlin, 1990).
3. Dallos, P. & Evans, B.N. 1995. High-frequency motility of outer hair cells and the cochlear amplifier. *Science* 267, 2006-2009.
4. Frank, G., Hemmert, W. & Gummer, A.W. 1999. Limiting dynamics of high-frequency electromechanical transduction of outer hair cells. *Proc. Natl. Acad. Sci. U. S. A.* 96, 4420-4425.
5. Zheng, J. *et al.* 2000. Prestin is the motor protein of cochlear outer hair cells. *Nature* 405, 149-155.
6. Brownell, W.E., Bader, C.R., Bertrand, D. & de Ribaupierre, Y. 1985. Evoked mechanical responses of isolated cochlear outer hair cells. *Science* 227, 194-196.
7. Ashmore, J.F. 1987. A fast motile response in guinea-pig outer hair cells: the cellular basis of the cochlear amplifier. *J. Physiol* 388, 323-347.
8. Santos-Sacchi, J. & Dilger, J.P. 1988. Whole cell currents and mechanical responses of isolated outer hair cells. *Hear. Res.* 35, 143-150.
9. Ashmore, J. 2008. Cochlear outer hair cell motility. *Physiol Rev.* 88, 173-210.
10. Ashmore, J.F. 1990. Forward and reverse transduction in the mammalian cochlea. *Neurosci. Res. Suppl* 12, S39-S50.

11. Santos-Sacchi, J. 1991. Reversible inhibition of voltage-dependent outer hair cell motility and capacitance *J. Neurosci.* 11, 3096-3110.
12. Kakehata, S. & Santos-Sacchi, J. 1996. Effects of salicylate and lanthanides on outer hair cell motility and associated gating charge *J. Neurosci.* 16, 4881-4889.
13. Santos-Sacchi, J. 2004. Determination of cell capacitance using the exact empirical solution of dY/dC_m and its phase angle *Biophys. J.* 87, 714-727.
14. Santos-Sacchi, J., Kakehata, S. & Takahashi, S. 1998. Effects of membrane potential on the voltage dependence of motility-related charge in outer hair cells of the guinea-pig *J. Physiol* 510 (Pt 1), 225-235.
15. Meltzer, J. & Santos-Sacchi, J. 2001. Temperature dependence of non-linear capacitance in human embryonic kidney cells transfected with prestin, the outer hair cell motor protein *Neuroscience Letters* 313, 141-144.
16. Santos-Sacchi, J. & Huang, G. 1998. Temperature dependence of outer hair cell nonlinear capacitance *Hear. Res.* 116, 99-106.
17. Song, L., Seeger, A. & Santos-Sacchi, J. 2005. On membrane motor activity and chloride flux in the outer hair cell: lessons learned from the environmental toxin tributyltin *Biophys. J.* 88, 2350-2362.
18. Rybalchenko, V. & Santos-Sacchi, J. 2003. Cl⁻ flux through a non-selective, stretch-sensitive conductance influences the outer hair cell motor of the guinea-pig *J. Physiol* 547, 873-891.
19. Rybalchenko, V. & Santos-Sacchi, J. *Biophysics of the Cochlea: From Molecules to Models*. Gummer, A. (ed.), pp. 116-126 (World Scientific Publishing, Singapore, 2003).
20. Iwasa, K.H. 1993. Effect of stress on the membrane capacitance of the auditory outer hair cell *Biophys. J.* 65, 492-498.
21. Dong, X.X., Ospeck, M. & Iwasa, K.H. 2002. Piezoelectric reciprocal relationship of the membrane motor in the cochlear outer hair cell *Biophys. J.* 82, 1254-1259.
22. Adachi, M. & Iwasa, K.H. 1999. Electrically driven motor in the outer hair cell: effect of a mechanical constraint *Proc. Natl. Acad. Sci. U. S. A* 96, 7244-7249.
23. Ehrenstein, D. & Iwasa, K.H. 1996. Viscoelastic relaxation in the membrane of the auditory outer hair cell *Biophys. J.* 71, 1087-1094.
24. Santos-Sacchi, J. & Wu, M. 2004. Protein- and lipid-reactive agents alter outer hair cell lateral membrane motor charge movement *J. Membr. Biol.* 200, 83-92.
25. Takahashi, S. & Santos-Sacchi, J. 1999. Distortion component analysis of outer hair cell motility-related gating charge *Journal of Membrane Biology* 169, 199-207.

FIRING UP THE AMPLIFIER: TEMPERATURE, PRESSURE AND VOLTAGE JUMP STUDIES ON OHC MOTOR CAPACITANCE*

JOSEPH SANTOS-SACCHI, LEI SONG, XIANTAO LI

*Yale University School of Medicine
New Haven, Ct 06510, USA*

The outer hair cell (OHC) possesses molecular motors that drive electromotility and cochlear amplification. Here we look at the effects of fast perturbations of biophysical forces that affect the OHC, including voltage, temperature and pressure, on the electrical signature of motor activity, namely nonlinear capacitance (NLC). Under whole cell voltage clamp, we measure changes in NLC at fixed holding voltages following steps in voltage, jumps in temperature induced by ir laser, or jumps in intracellular turgor pressure. In each case we find time dependent changes in NLC resulting from induced shifts of the NLC function across the voltage axis. The time course of these shifts depends on the stimulus, with voltage jumps inducing shifts with fast exponential components less than a millisecond. Those induced by temperature and pressure are within the tens of millisecond ranges and may be limited by cellular and experimental constraints that voltage is able to overcome. The overall observation of time dependent changes to the electromotility function upon stimulation indicates a more complex mechanism than provided by a simple two-state Boltzmann model.

1 Introduction

The outer hair cell (OHC) drives cochlea amplification through a cellular mechanism that works at kilohertz rates [1,2,3,4]. Molecular motors that are housed within the OHC lateral membrane, comprising at least the molecule prestin [5], produce conformational changes in response to voltage which alter the somatic length of the cell [6,7,8]. The deformations of these cells within the organ of Corti feedback energy into the basilar membrane, thus amplifying the auditory stimulus that is delivered to IHC stereocilia [9]. The ultimate effect is a boost in our auditory sensations.

The OHC motor, or prestin transfected into non-auditory cells, produces a signature electrical response analogous to gating currents observed in other voltage dependent membrane bound proteins [2,10,11]. The gating currents, because they are restricted charge movements within the membrane dielectric, can also be measured as a nonlinear capacitance (NLC), bell-shaped as a function of voltage. This charge movement or NLC can be fit most simply by a two-state Boltzmann function, allowing extraction of Boltzmann parameters that provide information on voltage dependence, voltage sensor valence, and maximum charge moved. These steady state parameters do not provide dynamic information about the motor, but the time course of underlying gating charge movements or of shifts in the C-V function can provide hints on the motor's

* This work and the Plenary Lecture were supported by NIH grants DC000273, DC008130, DC008115 to JSS.

conformational kinetic properties. Here we report on the effects of fast perturbations of biophysical forces that affect the OHC, including voltage, temperature and pressure, on the electrical signature of motor activity, namely NLC. The occurrence of time dependent changes to the C-V (or equivalently, electromotility) function upon such stimulation indicates a more complex mechanism than provided by a simple two-state Boltzmann model.

2 Methods

Guinea pigs were decapitated following anesthetic overdose with halothane. OHCs were freshly isolated from the guinea pig cochlea using Dispase (1 mg/ml) followed by trituration, and were whole-cell voltage clamped at room temperature using an Axon 200B amplifier. Membrane voltages were corrected for the effects of residual series resistance, which ranged from 3-5 M Ω . Ionic blocking solutions were used to remove voltage-dependent ionic conductances so that capacitive currents could be analyzed in isolation [11]. Extracellular solution: 100mM NaCl, 20mM TEA, 20mM CsCl, 2mM CoCl₂, 1.48mM MgCl₂, 2 mM CaCl₂, 10 mM HEPES, and 5mM dextrose, adjusted to pH 7.2 with NaOH, and adjusted to 300mOsm with dextrose. Pipette solution: 140mM CsCl, 10mM EGTA, 2mM MgCl₂, and 10mM HEPES, adjusted to pH 7.2 with CsOH, and adjusted to 300mOsm with dextrose. In some cases, TEA, CsCl, CoCl₂, CaCl₂, and MgCl₂ were omitted. Also, in some experiments, the extracellular solution was used in patch electrodes. In a few experiments, 50 μ M GdCl₃ was included in the extracellular solution to decrease residual currents. At this concentration, gadolinium has an insignificant affect on OHC capacitance [12]. Additional solution modifications are noted in figure legends.

In order to deliver rapid changes in membrane tension, we used a pressure clamp system from ALA instruments. Pipette tip diameters were increased in size for these experiments (~1 M Ω). In order to deliver rapid changes in temperature a Capella IR laser was used to deliver via fiber optic 5-20 ms light pulses (1850 nm).

OHC capacitance was measured with a continuous high-resolution two-sine voltage stimulus protocol (20mV peak at both f1 and f2; f2=2*f1; f1 ranging up to 3906.3 Hz), and subsequent FFT based admittance analysis [13,14]. These small, high frequency sinusoids were superimposed on voltage steps or ramps that spanned up to +/- 200 mV.

OHC C-V plots were fitted with the function $C_m = C_{lin} + C_v$, where C_{lin} is the voltage-independent (linear surface area component) capacitance of the lipid bilayer, and $C_v = dQ_{nonL}/dV$ is the voltage-dependent component of C_m originating from prestin's voltage-sensor activity. The first derivative with respect to V_m of a two-state Boltzmann function $Q = Q_{max}/(1 + \exp(-ze(V_m - V_{pkCm})/k_B T))$ was used to fit the C-V data [11]. Q_{max} is total charge moved. The measured apparent valence of prestin voltage-sensor (z) is defined as $z = q \cdot d$, where d is a normalized perpendicular projection of distance traveled by the voltage sensor charge (q) within the plasma membrane field. V_{pkCm} is the

membrane potential (V_m) at which prestin molecules are equally distributed between expanded and contracted states. It corresponds to the peak of the C_v function.

All data collection and most analyses were performed with an in-house developed Window's based whole-cell voltage clamp program, **jClamp** (www.scisoftco.com), utilizing a Digidata 1320 board (Axon, CA). Matlab (Natick, MA) or SigmaPlot was used for fitting the C_m data.

3 Results

3.1 Voltage jumps induce time dependent changes in NLC

When OHC voltage is stepped away from the holding potential, a nearly instantaneous change in C_m is observed because membrane capacitance is a bell shaped function of voltage (Fig. 1). However, unlike memory-less systems, the C-V function is not static but

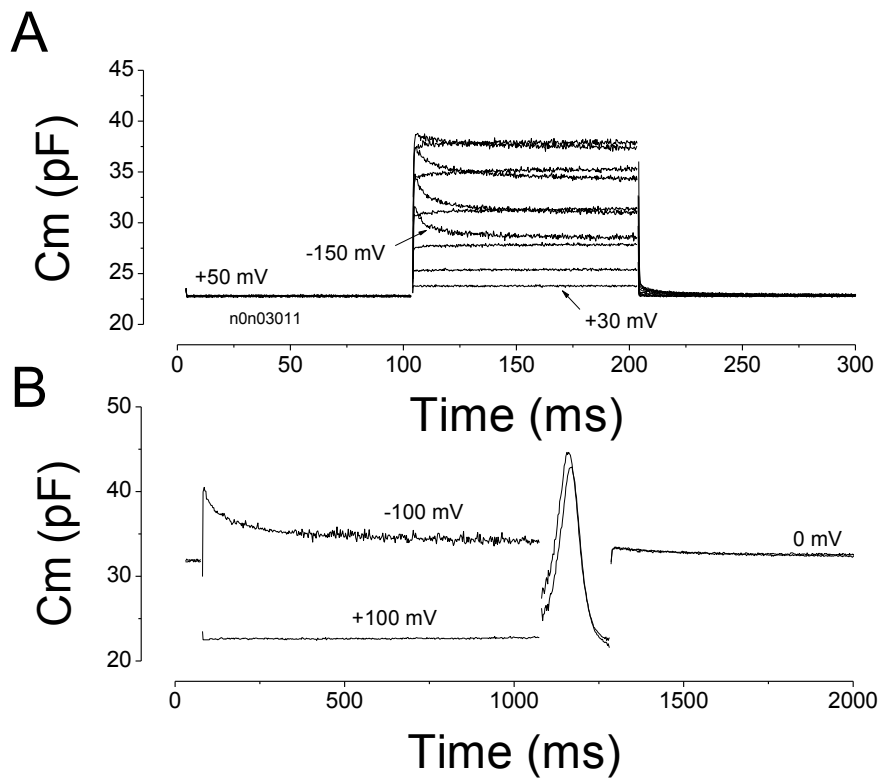


Figure 1 A) An OHC was held under voltage clamp at +50 mV and stepped to 30 (red),10,-10,-30,-50,-70,-90,-110,-130,-150 (blue) for 200 ms. The hyperpolarizing steps induced a time dependent change in C_m , increasing for steps approaching V_{pkcm} , and decreasing for steps beyond V_{pkcm} . B) Another OHC (held at 0 mV) showing that hyperpolarizing steps cause C_m relaxations (red line) due to depolarizing shifts in V_{pkcm} . A ramped voltage from -150 to +150 mV produced the bell shaped C_m response, indicating the rightward shift in V_{pkcm} .

shifts along the stimulus axis to alter C_m over time even though measures are made at a fixed voltage. The change in C_m is multi-exponential. With C_m sampling rates of about 4kHz, we find that the earliest exponential components are below one millisecond, with additional components at order of magnitude intervals.

3.2 Pressure jumps induce time dependent changes in NLC

Fig. 2 shows that rapid changes in membrane tension at a fixed voltage shifts V_{pkcm} in a time dependent manner, mimicking to some extent the C_m changes induced by step voltage changes. The pressure steps produced delayed onset responses because cellular material in the pipette tip obstructed flow. With increasing pressures it can be seen that the pipette unplugged at decreasingly shorter times following onset of the pressure steps (1: 0.8 kPa [fully obstructed], 2: 1.06kPa, 3: 1.33 kPa, and 4: 1.6 kPa). Lower pressures caused an increase in C_m over time, while the largest pressure pulse caused an immediate increase and subsequent relaxation. With this last pressure pulse the cell burst.

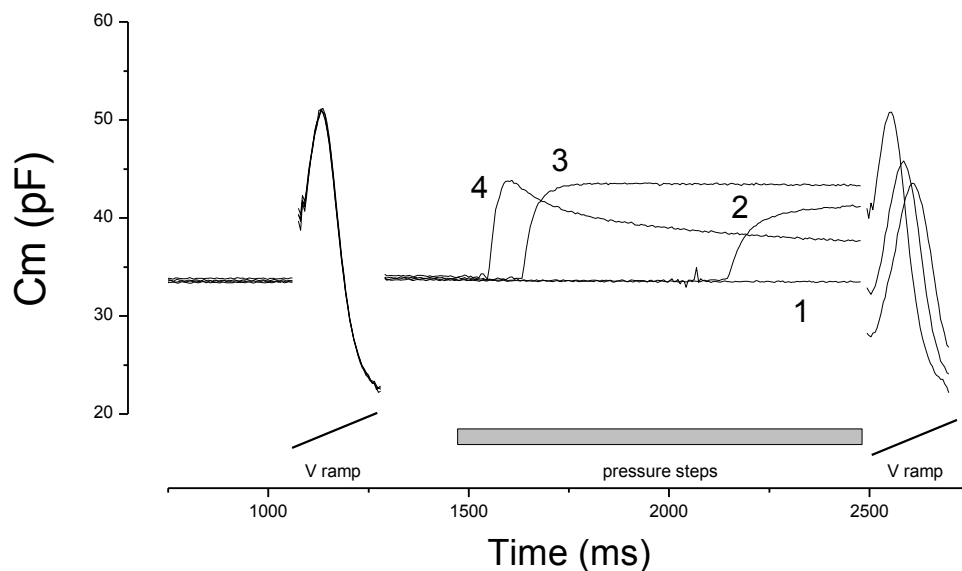


Figure 2 An OHC was held under voltage clamp at 0 mV. A voltage ramp (-100 to +100 mV, 200 ms) was delivered followed by incrementing pressure (1, 2, 3, 4) steps to the patch pipette, and the ramp was repeated (pressure was maintained during the final ramps). 3 sec intervals between traces were allowed for recovery from stimulation. Successful recovery is indicated by overlapping C-V functions. Increments in pressure cause time dependent changes in C_m at the fixed 0 mV holding potential, and occur due to shifts in V_{pkcm} , as the bell shaped C_m functions signify. The final pressure pulse caused the cell to burst; consequently, no C_m ramp data is plotted. In mM: 140 Cl in and out (NaCl 132, MgCl₂ 2, CaCl₂ 2, Hepes 10. Additional 10 EGTA for Intracellular solution)

3.32 Temperature jumps induce time dependent changes in NLC

We have previously shown that the C-V function of OHCs and prestin transfected HEK cells are very temperature sensitive, shifting about 20 mV to the right with a 10 °C increase in temperature [15,16]. Here we find that the effect of temperature jumps induced by IR laser is immediate in onset, followed by relaxation. Unlike steps in voltage and pressure, which could be maintained for unlimited durations, the Capella laser can only deliver up to 20 ms steps. Thus, the time course of C_m changes cannot be attributed to shifts in the C-V function during constant temperature, but could result from return to room temperature. Thus, the shifts in C-V we observed (Fig. 3B) likely correspond to expected changes in temperature as the bath cooled. However, we can glean from these experiments that temperature effects are very rapid, ruling out slow intracellular processes, such as phosphorylation, and likely indicating direct temperature effects on the conformational state of the motor protein prestin.

4 Discussion

By measuring OHC nonlinear membrane capacitance at sub-millisecond resolutions, we have examined the early time course of the OHC motor's dynamic response to jumps in membrane voltage, tension and temperature. We find that the time course of the voltage-induced response is multi-exponential, with the earliest detectable components residing

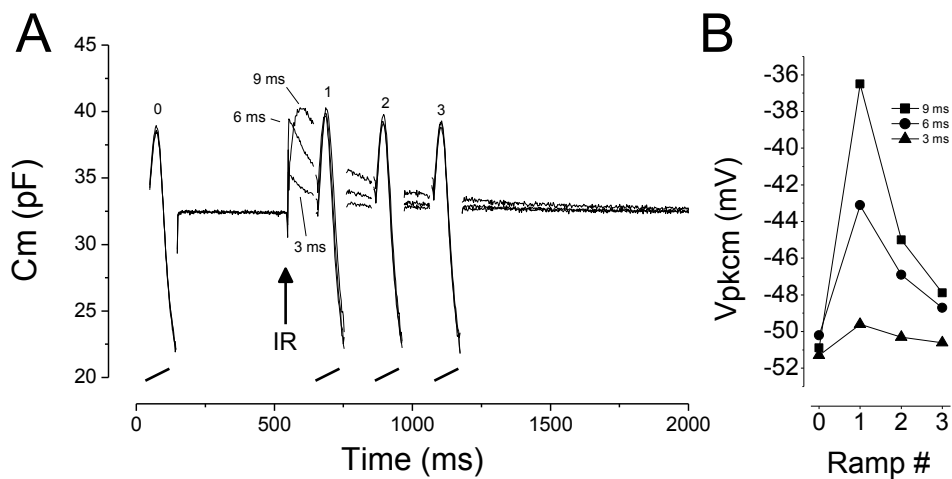


Figure 3 A) An OHC was held under voltage clamp at 0 mV. A voltage ramp (-100 to +100 mV, 200 ms) was delivered (denoted by 0) followed by incrementing temperature step durations to the cell, after which a series of voltage ramps (1, 2, 3) were delivered during the C_m relaxations. 10 sec intervals were used between traces to allow recovery from stimulation. Successful recovery is indicated by overlapping C-V functions. Increments in temperature duration (3, 6, 9 ms) cause time dependent changes in C_m at the fixed 0 mV holding potential, the shifts being plotted in B. Maximal temperature change is estimated to be about 10 °C. In this case the slow relaxations may be due to re-cooling to room temperature after laser stimulation.

in the kilohertz range, thereby establishing the phenomenon's potential significance in peripheral auditory processing of the mammal. These effects actually extend well into the low frequency range, as well; indeed, altering steady state resting potentials can stably set the operating point of electromotility to different points along the voltage axis.

Our data, though measuring whole cell capacitance, actually provide insight into the initial condition-dependent conformational states of the motor protein, prestin. That is, while capacitance may increase or decrease during incremental unidirectional steps in voltage or tension (**Figs. 1 and 2**), both correspond to a unidirectional change in motor state probability, as a conversion of capacitance to gating charge would reveal. Consequently, depolarizing voltages, in addition to causing a near instantaneous redistribution of motors to the compact state, will foster a supplemental recruitment of additional motors into that state, leading to an amplification of the initial response. The same amplification effect holds for hyperpolarizing voltages, where recruitment of motors will be into the expanded state. Tension effects appear to follow these rules, as well. However, because of equipment limitations on laser pulse duration we were unable to deliver long steps, and thus cannot confirm that temperature jumps mimic the effects of the other stimuli. We are attempting to modify the design to allow the further comparison.

Anions play a major role in NLC generation, and we were interested whether our results could reflect underlying interactions of chloride with the motor, since we have shown that V_{pkcm} shifts to the right when chloride is replaced with gluconate or other substitutes [17,18,19]. However, we find that modifying the driving force (changing extracellular chloride concentrations) for chloride movement across the OHC lateral membrane through G_{metL} [18] does not modify the extent or time course of the amplificatory shift (data not shown). It should be noted that although driving force for chloride did not significantly affect the motor's amplificatory shift, the interactions of anions with the motor may still play a role. In this regard, we have recently found that the state probability of prestin influences anion binding affinity (Song and Santos-Sacchi, ARO 2007), and that even if concentrations remain the same at the intracellular binding sites of prestin, changes in binding site affinity, as can occur with allosteric modulation, could alter energy profiles, resulting in V_{pkcm} shifts.

Since the initial observations of Iwasa [20], membrane tension effects on the OHC motor have provided important information on this protein's surprisingly efficient piezoelectric activity [21]. Because membrane tension can shift V_{pkcm} and, indeed, in extreme applications, restrict conformational activity [22], we had modeled the voltage-induced amplificatory shift as resulting from motor induced tension [14]. In the present report we attempted to directly test this by applying rapid changes in membrane tension and seeking C_m relaxations that mimic those induced by voltage steps. Though there are indications of C_m relaxations following rapid tension changes, the time courses of voltage-induced and tension-induced C_m relaxations differ, tension effects being slower. It is possible that during our attempts to alter membrane tension through global changes in OHC structure we may have been restricted by the viscoelastic properties of the whole

cell. For example, Dong and Iwasa [23] found that mechanical relaxations in the OHC have a time constant on the order of 40 s. However, because the fastest C_m relaxation time constants that we found with pressure steps were about 2 orders of magnitude faster than their measured time course, our pressure clamp driver appears to have been quite successful in overcoming this mechanical impediment. We suggest that tension induced by the molecular motors themselves can better bypass this viscoelastic constraint, thereby providing more rapid tensions to evoke fast amplificatory shifts. Thus, we still view motor-derived membrane tension, possibly through alterations of anion binding affinity, to underlie voltage-induced amplificatory shifts [14]. Nevertheless, as we have shown previously, the membrane environment of prestin can have profound effects on the magnitude and time course of the amplificatory shift [24].

In summary, we show remarkably fast changes in the Boltzmann distribution of prestin motor states induced by fast perturbations of the motor. The shifts along the voltage axis represent amplificatory supplementation to the near instantaneous voltage-induced mechanical response of the cell, and it is expected that this phenomenon will impact on high frequency peripheral auditory processing. Finally, it is expected that distortion in the mechanical response will arise, contributing to one of the hallmarks of mammalian cochlear amplification [25].

5 References

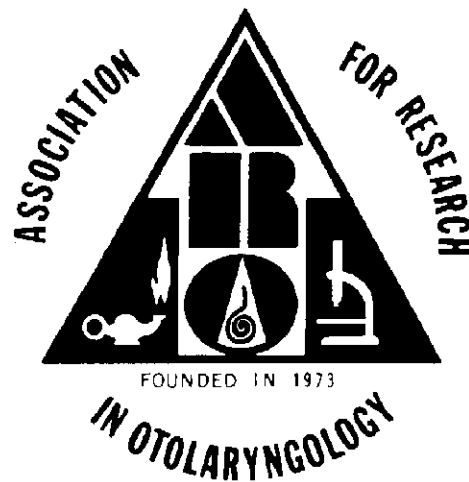
1. Santos-Sacchi, J. 1992. On the frequency limit and phase of outer hair cell motility: effects of the membrane filter. *J. Neurosci.* 12, 1906-1916.
2. Santos-Sacchi, J. *The Mechanics and Biophysics of Hearing*. Dallos, P., Geisler, C.D., Matthews, J.W., Ruggero, M.A. & Steele, C.R. (eds.), pp. 69-75 (Springer-Verlag, Berlin, 1990).
3. Dallos, P. & Evans, B.N. 1995. High-frequency motility of outer hair cells and the cochlear amplifier. *Science* 267, 2006-2009.
4. Frank, G., Hemmert, W. & Gummer, A.W. 1999. Limiting dynamics of high-frequency electromechanical transduction of outer hair cells. *Proc. Natl. Acad. Sci. U. S. A.* 96, 4420-4425.
5. Zheng, J. *et al.* 2000. Prestin is the motor protein of cochlear outer hair cells. *Nature* 405, 149-155.
6. Brownell, W.E., Bader, C.R., Bertrand, D. & de Ribaupierre, Y. 1985. Evoked mechanical responses of isolated cochlear outer hair cells. *Science* 227, 194-196.
7. Ashmore, J.F. 1987. A fast motile response in guinea-pig outer hair cells: the cellular basis of the cochlear amplifier. *J. Physiol* 388, 323-347.
8. Santos-Sacchi, J. & Dilger, J.P. 1988. Whole cell currents and mechanical responses of isolated outer hair cells. *Hear. Res.* 35, 143-150.
9. Ashmore, J. 2008. Cochlear outer hair cell motility. *Physiol Rev.* 88, 173-210.
10. Ashmore, J.F. 1990. Forward and reverse transduction in the mammalian cochlea. *Neurosci. Res. Suppl* 12, S39-S50.

11. Santos-Sacchi, J. 1991. Reversible inhibition of voltage-dependent outer hair cell motility and capacitance *J. Neurosci.* 11, 3096-3110.
12. Kakehata, S. & Santos-Sacchi, J. 1996. Effects of salicylate and lanthanides on outer hair cell motility and associated gating charge *J. Neurosci.* 16, 4881-4889.
13. Santos-Sacchi, J. 2004. Determination of cell capacitance using the exact empirical solution of dY/dC_m and its phase angle *Biophys. J.* 87, 714-727.
14. Santos-Sacchi, J., Kakehata, S. & Takahashi, S. 1998. Effects of membrane potential on the voltage dependence of motility-related charge in outer hair cells of the guinea-pig *J. Physiol* 510 (Pt 1), 225-235.
15. Meltzer, J. & Santos-Sacchi, J. 2001. Temperature dependence of non-linear capacitance in human embryonic kidney cells transfected with prestin, the outer hair cell motor protein *Neuroscience Letters* 313, 141-144.
16. Santos-Sacchi, J. & Huang, G. 1998. Temperature dependence of outer hair cell nonlinear capacitance *Hear. Res.* 116, 99-106.
17. Song, L., Seeger, A. & Santos-Sacchi, J. 2005. On membrane motor activity and chloride flux in the outer hair cell: lessons learned from the environmental toxin tributyltin *Biophys. J.* 88, 2350-2362.
18. Rybalchenko, V. & Santos-Sacchi, J. 2003. Cl⁻ flux through a non-selective, stretch-sensitive conductance influences the outer hair cell motor of the guinea-pig *J. Physiol* 547, 873-891.
19. Rybalchenko, V. & Santos-Sacchi, J. *Biophysics of the Cochlea: From Molecules to Models.* Gummer, A. (ed.), pp. 116-126 (World Scientific Publishing, Singapore, 2003).
20. Iwasa, K.H. 1993. Effect of stress on the membrane capacitance of the auditory outer hair cell *Biophys. J.* 65, 492-498.
21. Dong, X.X., Ospeck, M. & Iwasa, K.H. 2002. Piezoelectric reciprocal relationship of the membrane motor in the cochlear outer hair cell *Biophys. J.* 82, 1254-1259.
22. Adachi, M. & Iwasa, K.H. 1999. Electrically driven motor in the outer hair cell: effect of a mechanical constraint *Proc. Natl. Acad. Sci. U. S. A* 96, 7244-7249.
23. Ehrenstein, D. & Iwasa, K.H. 1996. Viscoelastic relaxation in the membrane of the auditory outer hair cell *Biophys. J.* 71, 1087-1094.
24. Santos-Sacchi, J. & Wu, M. 2004. Protein- and lipid-reactive agents alter outer hair cell lateral membrane motor charge movement *J. Membr. Biol.* 200, 83-92.
25. Takahashi, S. & Santos-Sacchi, J. 1999. Distortion component analysis of outer hair cell motility-related gating charge *Journal of Membrane Biology* 169, 199-207.

ISSN 0742-3152

ABSTRACTS
OF THE
SIXTEENTH MIDWINTER RESEARCH MEETING

**ASSOCIATION FOR RESEARCH
IN
OTOLARYNGOLOGY**



FEBRUARY 7-11, 1993

TRADEWINDS

ST. PETERSBURG BEACH, FLORIDA

464 METABOLIC CONTROL OF OHC FUNCTION: PHOSPHORYLATION AND DEPHOSPHORYLATION AGENTS SHIFT THE VOLTAGE DEPENDENCY OF MOTILITY RELATED CAPACITANCE. G-J Huang & J. Santos-Sacchi. Sections of Otolaryngology & Neurobiology, Yale University, School of Medicine, New Haven, CT 06510

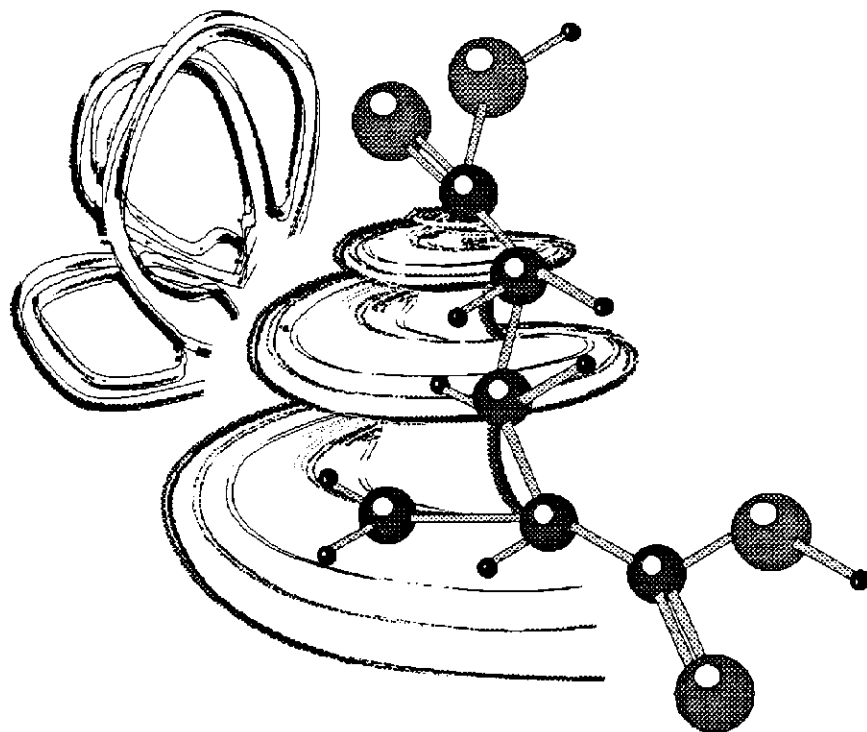
In the latter part of the last decade, it was shown that outer hair cells (OHCs) from the organ of Corti change their length as a function of voltage. Subsequently, a whole cell voltage-dependent capacitance (nonlinear charge movement) was measured in these cells (Ashmore, 1989), and such capacitance changes were shown to be closely co-related to cell length change (Santos-Sacchi, *J Neuroscience* 11:3096, 1991). Although the molecular basis of OHC length and capacitance changes remains to be determined, we explored the phosphorylation modulation on this OHC response.

Voltage-clamp whole cell recording was applied to freshly isolated guinea pig OHC cells. Ionic currents in the cells were blocked and the nonlinear capacitance was measured with transient analysis. Cells were held at -80 mV, and staired voltage steps from -160 to 60 mV were applied. The nonlinear capacitance was fit to the first derivative of a Boltzmann function and the voltage at half-maximal charge movement or peak capacitance (V_h) was calculated. Our preliminary data show that in 33 cells the V_h was -45.3 ± 5.3 mV (mean \pm SE) and the cell resting potential (RP, the zero current potential) was -23.9 ± 4.4 mV. There was a high correlation between V_h and RP ($r=0.838$). In our preparation calcium, sodium and potassium channels were blocked; the mechanism responsible for the RP is under further investigation.

Interestingly, when the cells were locally superfused for 3 minutes with 20 mM 2,3-butanedione monoxime (BDM), a non-specific phosphatase (Wilson & Ginsburg, *Biochem Biophys Acta* 18:168, 1955), the V_h was shifted leftward about -43.3 ± 17.9 mV ($N=6$, mean \pm SD) without changing RP. When these cells were further exposed to 10 mM 8-bromo-cAMP, a membrane permeable phosphorylation-inducing agent, V_h shifted back to the right about 40.8 ± 16.9 mV. If OHCs were pre-treated with 20 mM BDM in the bath for 15 minutes, the V_h of those cells ($n=3$) was around -80 mV, far more negative than non-treated cells; RP was between 0 and -10 mV. BDM does not alter the resting potential of skeletal muscle (Gage et al, *Bri J Pharmacol* 100:467, 1990). These data indicate that OHC nonlinear capacitance undergoes phosphorylation and dephosphorylation regulation, and imply that the auditory effects of metabolic insult in vivo could be due to a shift of the voltage-to-movement function along the voltage axis.

(Supported by NINDCD grant # DC00273)

Inner Ear Neuropharmacology
Neuropharmacologie de l'Oreille Interne



First International Symposium
1er Symposium International

PROGRAM AND ABSTRACTS
PROGRAMME ET RESUMES

Montpellier, France - September 14-15, 1994
Montpellier, France - 14-15 septembre 1994

EFFECTS OF PUTATIVE EFFERENT TRANSMITTERS ON THE OHC MOTILITY VOLTAGE SENSOR.

*J. Santos-Sacchi, S. Kakehata, and G. Huang

Yale Medical School, New Haven, CT 06510, USA

We have been evaluating the possible effects of phosphorylating agents, including efferent transmitters, on the voltage dependency of OHC nonlinear capacitance, an indicator of the motility voltage sensor. Evaluations of V_h (voltage at peak capacitance) under whole-cell voltage clamp with ionic blockers were made with a voltage stair step protocol, which has been previously described (Huang and Santos-Sacchi, 1993; Biophysical J.). Evaluations are limited to those cells which maintained a resting membrane resistance of at least 50 M Ω . Application of drugs was accomplished by gravity feed through a four barreled pipette or Y tube, and altered the media around the whole cell. Changes in V_h are relative to that obtained in the first couple of minutes after establishment of recording. Initial studies indicated that BDM (2,3-butandione monoxin), a chemical phosphatase, produces a shift of V_h to hyperpolarizing levels within 3 minutes of application. This agent (20 mM) produced a shift in V_h of -21 ± 4 mV in 10 out of 13 cells. This type of shift might be expected, since it has been shown that phosphorylation of K channels shifts the channel's voltage dependence in the positive direction (Perozo and Bezanilla, 1990). The shift in OHCs was reversible by wash with 10 mM 8-bromo cAMP; however, simply washing the cells also produced a reversal. 8-bromo cAMP (2 mM) alone produced essentially no change in V_h ($n=3$). However, in two cells, intracellular perfusion via the patch pipette with the catalytic subunit of PKA evidenced a shift in V_h greater than -20 mV, opposite that expected for electrostatic effects of phosphorylation. In 6 of 11 cells, carbachol (100 μ M) produced a shift to depolarizing levels of $+13 \pm 5$ mV; a smaller shift to negative potentials was observed in 4 of the remaining cells (-5 ± 3 mV). ACh (100 μ M), on the other hand, produced an initial slight shift to positive potentials ($+2.7$ mV \pm 1.3 mV; $n=4$) immediately after application, but then reversed direction at 2 minutes (-4.7 ± 0.8 mV) during application. This trend continued during a 3 minute wash with a total shift to negative potentials of -13.2 ± 2.3 mV. The data indicate that dephosphorylation tends to shift the nonlinear capacitance function to hyperpolarizing levels. However, efferent transmitters which presumably enhance phosphorylation via protein kinases produce inconsistent results. It is possible that mechanisms subsequent to protein phosphorylation are involved, i.e., perhaps the overall negative voltage shift observed with ACh is related to a positive charge screening potentially provided by an internal Ca^{+2} release working upon lateral plasma membrane voltage sensors. Further experiments are underway. (Supported by NIH grant NIDCD DC-00273).

outer hair cell, motility, voltage sensor, phosphorylation, efferent

Membrane Tension Directly Shifts Voltage Dependence of Outer Hair Cell Motility and Associated Gating Charge

Seiji Kakehata and Joseph Santos-Sacchi

Sections of Otolaryngology and Neurobiology, Yale University School of Medicine, New Haven, Connecticut 06510 USA

ABSTRACT The unique electromotility of the outer hair cell (OHC) is believed to promote sharpening of the passive mechanical vibration of the mammalian basilar membrane. The cell also presents a voltage-dependent capacitance, or equivalently, a nonlinear gating current, which correlates well with its mechanical activity, suggesting that membrane-bound voltage sensor-motor elements control OHC length. We report that the voltage dependence of the gating charge and motility are directly related to membrane stress induced by intracellular pressure. A tracking procedure was devised to continuously monitor the voltage at peak capacitance (V_{pkCm}) after obtaining whole cell voltage clamp configuration. In addition, nonlinear capacitance was more fully evaluated with a stair step voltage protocol. Upon whole cell configuration, V_{pkCm} was typically near -20 mV. Negative patch pipette pressure caused a negative shift in V_{pkCm} , which obtained a limiting value near the normal resting potential of the OHC (~ -70 mV) at the point of cell collapse. Positive pressure in the pipette caused a positive shift that could reach values greater than 0 mV. Measures of the mechanical activity of the OHC mirrored those of charge movement. Similar membrane-tension dependent peak shifts were observed after the cortical cytoskeletal network was disrupted by intracellular dialysis of trypsin from the patch pipette. We conclude that unlike stretch receptors, which may sense tension through elastic cytoskeletal elements, the OHC motor senses tension directly. Furthermore, since the voltage dependence of the OHC nonlinear capacitance and motility is directly regulated by intracellular turgor pressure, we speculate that modification of intracellular pressure in vivo provides a mechanism for controlling the gain of the mammalian “cochlear amplifier”.

INTRODUCTION

The term “cochlear amplifier” has been used to describe a physiologically vulnerable process that enhances near-threshold auditory sensitivity (Davis, 1983). In recent years, the outer hair cell (OHC) from the organ of Corti has been acknowledged to play a pivotal role in this process (see Dallos, 1992). The OHC is capable of voltage-dependent mechanical responses that appear to provide feedback into the basilar membrane, thereby sharpening the passive mechanical vibration of the cochlear partition (Brownell et al., 1985; Ashmore, 1987; Santos-Sacchi and Dilger, 1988; Ruggero, 1992). The cell also possesses a nonlinear gating charge movement or equivalently, a voltage-dependent capacitance, which correlates well with its mechanical activity (Ashmore, 1990; Santos-Sacchi, 1990, 1991). The similarity between characteristics of OHC nonlinear capacitance and OHC movement indicates that membrane-bound voltage sensor-motor elements control OHC length (Santos-Sacchi, 1990, 1991, 1993; Ashmore, 1992; Dallos et al., 1991; Iwasa, 1994). Indeed, estimates of the membrane-bound charge density of the OHC responsible for the nonlinear capacitance (7500 e⁻/mm²; Huang and Santos-Sacchi, 1993) coincide fairly well with estimates of the density of OHC intramem-

branous particles, the putative sensor-motor elements, observed electronmicroscopically ($6000/\text{mm}^2$; Forge, 1991).

We have been studying the voltage dependence of the nonlinear capacitance of the OHC and have found that the voltage at peak capacitance (V_{pkCm}), which corresponds to the voltage of maximal motile sensitivity or gain, varies among cells and within single cells during recording under whole cell voltage clamp (Santos-Sacchi et al., 1994). This voltage can range from 0 mV to potentials near the normal resting potential of the OHC in vivo, namely about -70 mV (Dallos et al., 1982). We report here that this variability of the nonlinear capacitance as well as the voltage dependence of OHC movement is directly related to intracellular turgor pressure. Notably, a reduction of turgor pressure induces graded increases in nonlinear capacitance and negative voltage shifts in sensor/motor function. Furthermore, the effects of turgor pressure are not directly mediated through cytoskeletal linkages with the membrane voltage sensor, since digestion of the cortical cytoskeleton with intracellular trypsin does not abolish the effects of turgor pressure-induced membrane tension. A preliminary account of this work has been presented (Santos-Sacchi and Kakehata, 1994).

MATERIALS AND METHODS

OHCs were freshly isolated from the organ of Corti of the guinea pig cochlea (Kakehata et al., 1993), and were whole cell voltage clamped using an Axon 200B amplifier with patch pipettes having initial resistances of $2\text{--}3$ M Ω , corresponding to tip sizes of $1\text{--}2$ μm (Hamill et al., 1981). Residual series resistance (after electronic compensation) ranged from 3 to 7 M Ω . The removal of nonlinear ionic conductances is crucial in evaluating nonlinear capacitive currents. In the presence of nonlinear ionic conductances, voltage-induced currents may possess ionic as well as capacitive components, thereby making extraction of gating charge difficult or impossible.

Received for publication 1 December 1994 and in final form 17 February 1995.

Address reprint requests to Dr. Joseph Santos-Sacchi, Dept. of Surgery (Otolaryngology), Yale University School of Medicine, BML 244, New Haven, CT 06510, Phone: 203-785-7566, Fax: 203-737-2245, E-mail: santos@biomed.med.yale.edu.

© 1995 by the Biophysical Society

0006-3495/95/05/2190/08 \$2.00

Therefore, ionic blocking solutions were used to remove voltage-dependent ionic conductances so that capacitive currents could be analyzed in isolation (Santos-Sacchi, 1991; Huang and Santos-Sacchi, 1993). The patch pipette solution contained (in mM): 140 CsCl, 2 MgCl₂, 10 EGTA, and 10 HEPES, with pH 7.2 and osmolarity (adjusted with dextrose) noted in figure legends. The external solution contained (in mM): 100 NaCl, 20 TEA, 20 CsCl, 2 CoCl₂, 1.52 MgCl₂, 10 HEPES, and 5 dextrose, pH 7.2, 300 mOsm. Drugs were applied using the "Y-tube" method (Murase et al., 1990), during simultaneous whole chamber perfusion. Experiments were performed at room temperature.

A tracking procedure was developed to continuously monitor V_{pkCm} after obtaining whole cell configuration. The procedure utilizes a voltage stimulus protocol where equal but opposite polarity voltage pulses are delivered to the cell and the generated currents summed to extract nonlinear gating currents, as originally developed to measure ionic channel gating currents, as originally developed to measure ionic channel gating currents ($\pm P$ protocol, ± 40 mV; Armstrong and Bezanilla, 1973; Keynes and Rojas, 1974). Averages of three to five paired pulses were used. While the term "gating current" is typically applied to nonlinear currents associated with voltage sensor activity during ionic channel gating, we use this term for the motility-related voltage sensor displacement currents to indicate a similar molecular transduction strategy (see Alkon et al., 1993). Fig. 1A is an electrical model simulation of OHC voltage-dependent capacitance showing gating current traces obtained with this protocol. When the holding potential is more hyperpolarized than V_{pkCm} , the gating current consists of an initial upward (outward) transient current followed by a downward (inward) transient at voltage step offset. The polarity of the current reverses when the holding potential is more depolarized than V_{pkCm} . To track V_{pkCm} , holding potential (V_{hold}) was automatically decreased in 2 mV steps until a reversal of gating current polarity was obtained, thereupon V_{hold} was increased in 2 mV steps until polarity reversed again. Thus, V_{hold} was varied to follow gating current reversals, namely, V_{pkCm} . Tracking was always initiated from a holding potential of 0 mV. Since initial voltage conditions do not appear

to alter the voltage dependence of the OHC gating currents and the charge moved demonstrates no immobilization (see Fig. 5; Santos-Sacchi, 1991), the tracking technique should not interfere with V_{pkCm} measures. Fig. 1B presents data from an OHC illustrating the procedure. The program Clampex (Axon Instruments, CA) was modified to perform the V_{pkCm} tracking procedure online, and holding potential was corrected for the effects of residual series resistance. Peak capacitance ($C_{m, pk}$) values were also monitored during the tracking procedure using transient analysis of capacitive currents induced by a -10 mV step. Detailed evaluation of total membrane capacitance was made at different potentials by transient analysis of currents induced by a voltage stair step stimulus, and the capacitance function was fit to the first derivative of a two state Boltzmann function relating nonlinear charge to membrane voltage ($\delta Q/\delta V$; Santos-Sacchi, 1991; Huang and Santos-Sacchi, 1993),

$$C_m = Q_{max} \frac{ze}{kT} \frac{b}{(1+b)^2} + C_{lin} \tag{1}$$

where

$$b = \exp\left(\frac{-ze(V - V_{pkCm})}{kT}\right) \tag{2}$$

Q_{max} is the maximum nonlinear charge moved, V_{pkCm} is voltage at peak capacitance or equivalently, at half-maximal nonlinear charge transfer, V_m is membrane potential, z is valence, C_{lin} is linear membrane capacitance, e is electron charge, k is Boltzmann's constant, and T is absolute temperature. Series resistance, R_s , was estimated from the decaying time constant and integrated charge of the voltage step-induced current, as fully described elsewhere (Santos-Sacchi, 1993; Huang and Santos-Sacchi, 1993). This technique is relatively insensitive to the effects of data filtering. Membrane resistance, R_m , was evaluated from steady state current. C_{lin} was estimated from the fit to above capacitance (C_m) equation, and indicates the intrinsic linear capacitance of the membrane upon which rides the bell-shaped voltage-dependent capacitance (C_v). All analysis techniques have been previously detailed in Huang and Santos-Sacchi (1993). Pipette pressure was modified with a syringe connected to the Teflon tubing attached to the patch pipette holder. Pressure was monitored via a T-connector to a pressure monitor (WPI, Sarasota, FL). Modifications of intracellular pressure have been shown to modulate OHC membrane tension (Iwasa and Chadwick, 1992; Iwasa, 1993), and as an indicator of pressure-induced membrane stress we present longitudinal strain measures (which are linearly related to membrane stress for small deformations (Iwasa and Chadwick, 1992). All experiments were videotaped using a Matrox (Montreal, Quebec, Canada) video overlay board which combines an enhanced graphics adaptor and video. Measures of voltage-induced (20 mV increments) mechanical responses were made off the video monitor with a differential optoresistor technique (Santos-Sacchi, 1989, 1991). Mechanical data were fit to a two state Boltzmann function to determine the voltage at maximum sensitivity ($V_{SL, max}$). All data analysis was performed with the software package MATLAB (Mathworks, Natick, MA).

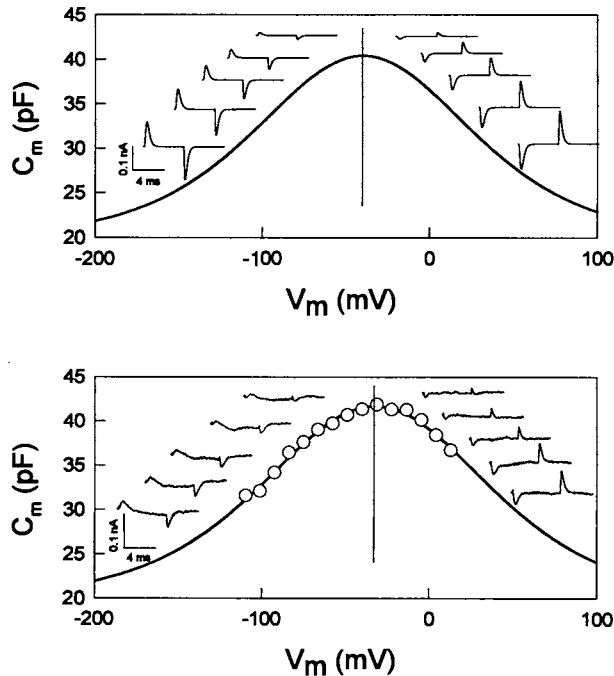


FIGURE 1 Illustration of underlying principle of V_{pkCm} tracking technique. (A) An electrical model simulation of OHC capacitance (that of Huang and Santos-Sacchi, 1993) showing traces obtained with the $\pm P$ protocol (2 mV holding potential alterations about V_{pkCm}). (B) Capacitance of an OHC (measured with the voltage stair step protocol; Huang and Santos-Sacchi, 1993) illustrating the same technique. Note the reversal of gating currents as the holding voltage passes through the region of peak capacitance. Osmolarity of the intracellular solution was 300 mOsm.

RESULTS

The isolated in vitro OHC possesses a positive intracellular turgor pressure of about 1 kPa (Ratnanather et al., 1993; Chertoff and Brownell, 1994). Thus, when a normally cylindrical OHC is under tight-seal whole cell recording, especially with large tipped pipettes, there exists a potential path through the pipette for the release of intracellular pressure, and the cell may depressurize. Fig. 2 illustrates the effect of reducing intracellular pressure during the course of whole cell recording on V_{pkCm} where depressurization of the OHC is assisted by an osmotic imbalance between pipette solution and extracellular media (Δ mOsm = -14). To indicate the effectiveness of pressure changes, longitudinal strain was calculated ($\delta z = (l - L)/L$, where L is initial

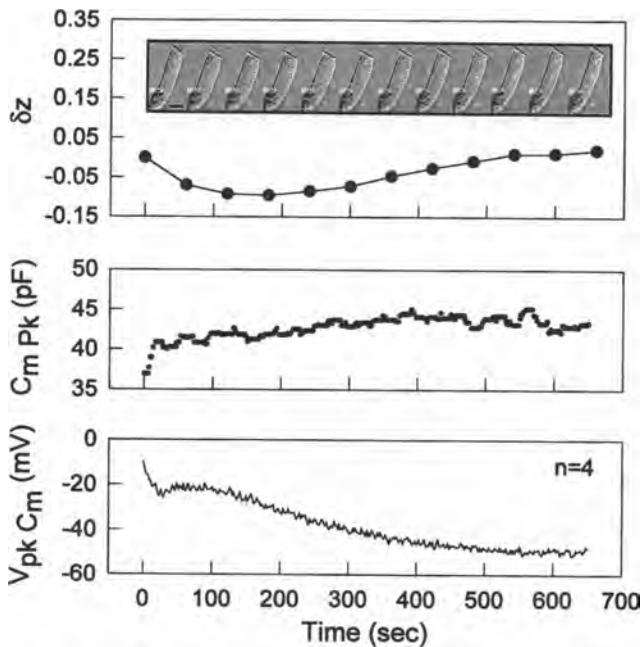


FIGURE 2 Effect of cell turgor reduction on OHC longitudinal strain, δz (top), peak capacitance (middle) and V_{pkCm} (bottom), utilizing the tracking technique, as a function of time after obtaining whole cell voltage clamp configuration (average of four cells; R_s : 7.2 M Ω ; R_m : 177 M Ω). Initial cell length was $55.5 \pm 4.1 \mu\text{m}$ (mean \pm SE). (Inset, top) Video images at 1-min intervals illustrate the shape changes of one of the OHCs. Scale bar 10 μm . Osmolarity of the intracellular and extracellular solutions in these cells was 286 and 300 mOsm, respectively. Whole cell configuration was obtained by electrical "zapping" (see Discussion). Cells did not collapse during the recording period.

length, and l is the length of the cell when deformed), and presented as well. The length of the OHC correlates well with turgor pressure (positive pressure reduces length and increases the radius; Chertoff and Brownell, 1994; Iwasa, 1993). The averaged time course of V_{pkCm} in four cells from the third cochlear turn indicates a shift from an initial value of -21.5 mV to a steady state value of -49.3 mV at 10 min. In addition, $C_{m\text{Pk}}$ increased from an initial value of 40.9 to 43.1 pF. Cell length was reduced immediately after entering the cells, but slowly recovered to initial levels, indicating that over the course of the 10 min recording turgor pressure decreased. During this time the cell did not collapse, and mechanical responses remained robust (however, see below). In four other cells, a more complete analysis of cell capacitance was performed using a voltage stair step protocol (see Materials and Methods). A fit to these capacitance data provided initial/steady state fitted parameters of (mean \pm SE), as follows. Q_{max} : $2.41 \pm 0.18/3.73 \pm 0.3$; V_{pkCm} : $-17.0 \pm 6/-54.5 \pm 3.5$; z : $0.73 \pm 0.04/0.71 \pm 0.02$; C_{lin} : $21.4 \pm 1.5/19.5 \pm 2.3$. Average electrode series resistance and membrane resistance were 4.0 and 315 M Ω , respectively. The slow negative shift in voltage dependence is not due to the dissipation of a diffusion potential at the pipette tip, for the following three reasons. 1) Whereas the time course for osmotic stress effects were on the order of 10 min, diffusion potentials are typically dissipated within 3 min, as the pipette

solution and cell solution equilibrate. Indeed, under current clamp with KCl solutions (140 mM), OHCs that initially have resting potentials greater than -20 mV attain potentials near -70 mV within 20–30 s after whole cell configuration. This is believed to reflect a restoration of intracellular potassium after depletion accompanying OHC isolation (Ashmore and Meech, 1986; Santos-Sacchi and Dilger, 1988). The immediate reduction of cell length noted upon entering whole cell configuration is probably due to clamping the cell at 0 mV at the onset of tracking, and the subsequent rapid exchange of pipette and cell solutions. 2) With small tipped pipettes (10 M Ω ; 0.5 μm tip) containing isoosmolar solutions, although the initial decrease in cell length occurred, no subsequent negative shifts of V_{pkCm} were observed over periods of 30 min or longer. 3) As shown below, pipette pressure changes were as effective as osmotic treatments. Thus, we find an increase in maximum nonlinear charge moved, and a slight decrease in linear capacitance as intracellular pressure and, correspondingly, membrane tension is dissipated. The decrease in linear capacitance might be expected because of a reduced stretch on the plasma membrane.

To investigate the effects of turgor pressure more directly, the intracellular pressure of OHCs was directly modified through the patch pipette. Fig. 3 illustrates the reversible effects of decreasing intracellular pressure on V_{pkCm} and cell capacitance. V_{pkCm} became more negative and the magnitude of peak capacitance grew as the pressure was decreased; subsequently, an increase of pressure reversed the effects. Stable values of V_{pkCm} could be attained with constant pipette pressure, although we do not claim that pipette pressure actually clamps the intracellular pressure. Indeed, during stable pipette pressure, modification of extracellular osmolarity produced results similar to those obtained with pipette pressure changes; namely, hyperosmotic media caused negative

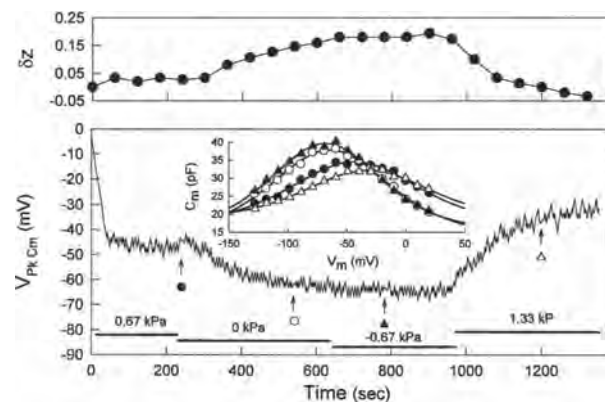


FIGURE 3 OHC longitudinal strain, δz (top), V_{pkCm} (bottom), and nonlinear capacitance (inset) at different pipette pressures. Initial cell length was 38.5 μm . This cell collapsed at -0.67 kPa , and longitudinal mechanical responses stopped. Responses returned upon delivery of positive pressure. R_s : 4.1 M Ω , R_m : 221 M Ω . Fits (insets, solid lines) for capacitance indicate V_{pkCm} , Q_{max} , z , and C_{lin} of -43.6 mV , 2.56 pC, 0.71, and 17.0 pF (@ 0.67 kPa); -64.28 mV , 3.18 pC, 0.76, and 14.2 pF (@ 0 kPa); -68.14 mV , 3.02 pC, 0.82, and 15.6 pF (@ -0.67 kPa); -32.4 mV , 1.95 pC, 0.72, and 18.57 pF (@ 1.33 kPa). Osmolarity of the intracellular solution was 286 mOsm.

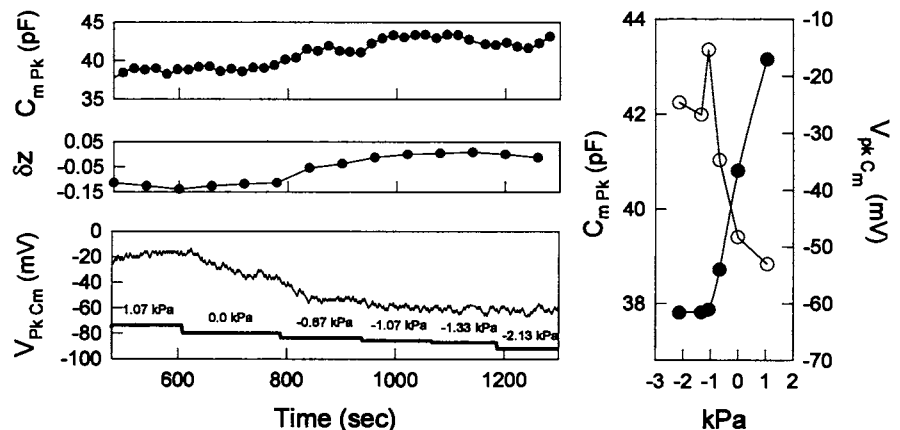
voltage shifts, and hypoosmotic media caused positive voltage shifts (data not shown). OHC δz changes mirrored those of V_{pkCm} . Fig. 4 illustrates, in another cell, that below a critical negative pipette pressure where the OHC just collapses, V_{pkCm} remains constant. This potential is likely to reflect the true voltage dependence of the motility voltage sensor/effector because there is no tension on the membrane motor at the point of cell collapse. In nine cells, this potential was -65.5 ± 1.2 mV (mean \pm SE), which is close to that of the resting potential of OHCs in vivo (Dallos et al., 1982). In some cases where the OHC not only lost its cylindrical shape, but flattened, the magnitude of peak capacitance decreased somewhat ($\sim 10\%$). This may have been due to resultant space clamp problems.

The cylindrical OHC has an elaborate cytoskeletal network linked to the plasma membrane (Holley and Ashmore, 1990; Forge, 1991), and it is conceivable that intracellular pressure works via this network to induce tension on the motility voltage sensors. To evaluate this possibility, we included trypsin (300 $\mu\text{g/ml}$) in the pipette solution (300 mOsm). This treatment is known to digest and/or disrupt the OHC cortical cytoskeleton, and produce a spherical cell whose plasma membrane is essentially free of cytoskeletal attachments, while leaving the voltage sensor fully functional (Huang and Santos-Sacchi, 1994). Fig. 5 illustrates the effect of intracellular pressure on V_{pkCm} and peak membrane capacitance of an OHC during the course of trypsin treatment. In more than 10 cells studied, V_{pkCm} initially shifted to negative potentials after whole cell configuration, but after about 10 min it shifted slowly to positive potentials. This positive shift coincided with the onset of trypsin-induced structural changes and is likely to reflect a growing tension on the membrane as the cell swelled into a sphere. Normally, C_{mPk} remains stable during trypsin treatment (Huang and Santos-Sacchi, 1994). However, in this case, at 14.5 min the electrode and cell were moved to position the cell so that pressure could be delivered without losing the seal. An immediate decrease in peak capacitance was noted, probably because of an induced membrane tension during the manipulation (Fig. 5, bottom). In this particular case, the cell became fully spherical at about 15 min, whereupon positive pipette pressure steps further shifted V_{pkCm} in the positive

direction and reduced peak capacitance, in a reversible manner. Subsequently, negative pressure restored peak capacitance to original levels, and only after the pipette was visibly clear of cellular debris could positive pipette pressure again shift V_{pkCm} to positive values. (In this case, and three others, although C_{mPk} increased with negative pipette pressure, V_{pkCm} did not change. We believe that this occurred because the magnitude of nonlinear charge movement is more susceptible to pressure effects than V_{pkCm} . In Fig. 5, the pipette became plugged with cellular debris upon delivery of negative pressure, and it is likely that the full negative pipette pressure was not delivered to the cell. Upon subsequent delivery of positive pipette pressure, which unplugged the tip, it can be seen that C_{mPk} decreased before a positive shift in V_{pkCm} ensued. Alternatively, it may be possible that the limiting voltage shift of V_{pkCm} became more positive with trypsin treatment. We are currently investigating this possibility.) Finally, the cell burst at a pipette pressure of about 1 kPa and V_{pkCm} of $+8$ mV. From these types of observations, in 10 cells out of 12, we conclude that membrane tension directly modulates the embedded motility voltage sensor.

A correspondence between OHC nonlinear capacitance and motility voltage dependence has been observed (Santos-Sacchi, 1991). Voltage at half maximal charge movement, V_h (or equivalently, V_{pkCm}), corresponds to the voltage where OHC mechanical responses are maximally voltage sensitive, $V_{\delta L, \max}$. We further demonstrate a close relationship between OHC membrane capacitance and movement under different pressure conditions within individual cells. The inset in the bottom panel of Fig. 6 depicts the structure of an OHC under two different pipette pressure conditions, $+0.54$ and -0.19 kPa. Positive pressure caused the cell to shorten, whereas negative pressure caused the cell to lengthen. Fig. 6 shows that the voltage dependence of OHC motility essentially mirrors that of the nonlinear capacitance of the cell. Both shifted to hyperpolarized levels as intracellular pressure was decreased. In three cells, $V_{\delta L, \max}$ was (mean \pm SE) -23.6 ± 2.9 mV and V_{pkCm} was -24.7 ± 4.2 mV for a high pipette pressure condition (0.49 ± 0.1 kPa); a reduced pipette pressure (-0.05 ± 0.07 kPa) shifted these values to -45.7 ± 2.2 mV and -56.5 ± 4.8 mV, respectively. Slight differences may be due to changes in intracellular pressure during the interval

FIGURE 4 Pipette pressure versus V_{pkCm} (bottom left), OHC longitudinal strain, δz (middle left), and peak capacitance (top left). R_s : 7.5 M Ω , R_m : 150 M Ω . Initial cell length was 69.7 μm . In this case, the cell collapsed at -1.33 kPa. Right plot of means of V_{pkCm} (●) and peak capacitance (○) obtained during the last 12 s of pressure durations. Osmolarity of the intracellular and extracellular solutions was 300 mOsm.



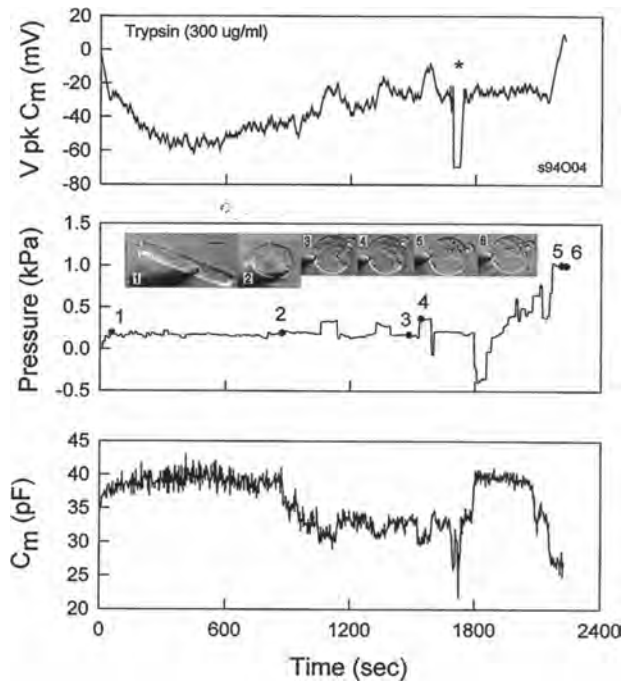


FIGURE 5 Effects of intracellular trypsin treatment on V_{pkCm} (top) and $C_{m, pk}$ (bottom). (middle) Pipette pressure delivered, sampled every 8 s. The numbered inset images are from selected time periods corresponding to the numbered solid circles on the pressure trace. Scale bar is $10 \mu\text{m}$. During constant pipette pressure, V_{pkCm} initially declines but shifts to hyperpolarized levels when cell structural changes ensue, around 10 min. After the OHC reached a spherical shape, positive pipette pressure induced positive voltage shifts and decreases in peak capacitance. At the point indicated by the asterisk, the holding potential was maintained at about ~ 70 mV to evaluate the effect of initial conditions on V_{pkCm} . After the release of holding potential, V_{pkCm} quickly shifted back to its previous value, indicating that holding potential does not influence V_{pkCm} . At 30 min, negative pressure is delivered and $C_{m, pk}$ increased to initial levels, but the electrode subsequently became plugged. Only after considerable attempts to unplug the pipette with positive pressure were we able to observe the release of cellular debris from the tip. At that point V_{pkCm} began to shift to depolarized levels and $C_{m, pk}$ decreased; the cell finally burst after reaching a steady state V_{pkCm} of $+8$ mV for about 20 s.

(~ 1 – 2 min) between nonlinear capacitance measurement (stair step protocol) and mechanical response measures (voltage pulse protocol). The correspondence between voltage dependencies indicates that motor and sensor are either tightly coupled or one entity. The singular identity of motor and sensor is further indicated by the co-localization of the two within a restricted region of the lateral plasma membrane (Dallos et al., 1991; Huang and Santos-Sacchi, 1993, 1994).

Fig. 6 also illustrates that negative pipette pressure reduces the maximum mechanical response of the OHC (Santos-Sacchi, 1991). Despite this reduction, however, the inset in the top panel of Fig. 6 illustrates that the maximum mechanical gain of the cell can remain essentially unaltered. That is, in this example, the maximum gain remained near 20 nm/mV under both pressure conditions.

Interestingly, lanthanides, which interfere with OHC osmotic pressure regulation (Crist et al., 1993; however, see Chertoff and Brownell, 1994), possibly via interaction with

OHC stretch receptors (Yang and Sachs, 1989; Iwasa et al., 1991; Ding et al., 1991) also shifted V_{pkCm} (Fig. 7). Lanthanides have been shown to reversibly block OHC motility and nonlinear gating charge (Santos-Sacchi, 1991). Extracellularly applied lutetium chloride ($100 \mu\text{M}$), one of the lanthanides tested, shifted V_{pkCm} to hyperpolarized levels and decreased peak capacitance only slightly. At a higher concentration (1 mM), however, it apparently shifted V_{pkCm} in the opposite direction but reduced the nonlinear capacitance markedly (Fig. 7, inset). Mechanical responses were fully blocked, as well, without cell collapse. Such a large drop in nonlinear capacitance may invalidate the tracking technique so that the shift to positive potentials is likely artifactual. In all cases of lanthanide treatment where nonlinear capacitance block was not complete, i.e., where V_{pkCm} could be evaluated unequivocally, tracking and full analysis with the voltage stair protocol indicated a V_{pkCm} shift to negative potentials, opposite that of potential charge screening effects. Lanthanides also increased cell length, similar to treatments that reduced turgor pressure. In three cells, 1 mM lutetium increased OHC length about 5% . It was of interest to determine whether lanthanides could interfere with the effects of membrane tension on nonlinear capacitance. Fig. 8 illustrates that turgor pressure changes remained capable of reversibly shifting V_{pkCm} and altering Q_{max} in cells that were treated with both

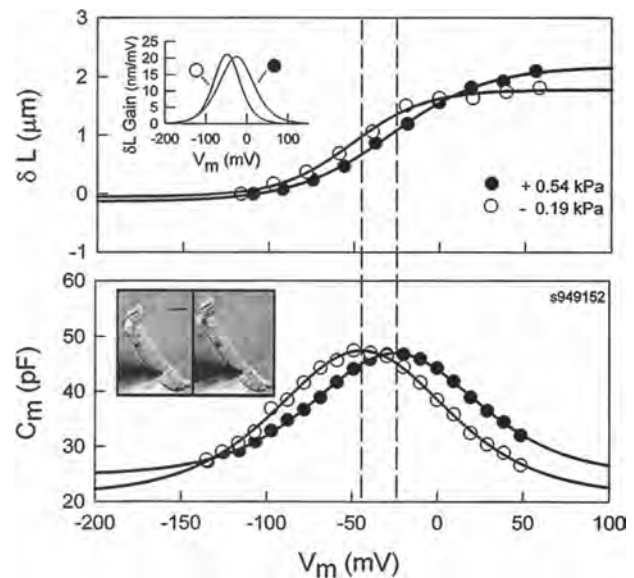


FIGURE 6 Membrane capacitance (bottom) and movement (top) of an OHC under different pressure conditions delivered through the pipette. Length changes induced by 20 mV steps from -140 to $+60$ mV (nominal), but corrected for series resistance effects in figure. R_s : 3.5 M Ω , R_m : 154 M Ω @ 0.54 kPa, and R_s : 2.0 M Ω , R_m : 88 M Ω @ -0.19 kPa. Fits (positive vs. negative pressure) for capacitance indicate V_{pkCm} , Q_{max} , z , and C_{lin} of -24.7 mV, 2.87 pC, 0.79 , and 24.8 pF versus -44.2 mV, 3.47 pC, 0.77 , and 21.3 pF. Fits (positive vs. negative pressure) for mechanical data indicate V_h (voltage midpoint) and z of -28.0 mV and 0.91 versus -51.1 mV and 1.2 . Dotted lines indicate V_{pkCm} under each condition. (Inset, top) First derivative of the fitted mechanical responses, indicating the gain of the mechanical response under the two pressure conditions. (Inset, bottom) Video images of OHC at high (left) and low (right) pressures. Scale bar: $10 \mu\text{m}$. Osmolarity of the intracellular and extracellular solutions was 300 mOsm.

trypsin and lutetium. This indicates that the activity of stretch receptors, which are blocked by low micromolar concentrations of lanthanides, is not responsible for stress-induced effects on OHC membrane capacitance.

DISCUSSION

Treatments that reduce OHC turgor are known to decrease the magnitude of electromotility (Brownell et al., 1989; Shehata et al., 1991). Indeed, we have previously shown that collapsing the OHC with negative pipette pressure produces a rapid and reversible loss of longitudinal motility, but the function of the motility voltage sensor remains intact (Santos-Sacchi, 1991). In fact, we reported that the magnitude of the nonlinear charge movement increased by about 10% under the negative pressure condition, corresponding to the increase in C_{mPK} that we now observe upon reduced cell turgor. Iwasa (1993) first systematically studied the effects of membrane tension on OHC capacitance, and found that increased turgor pressure decreased nonlinear capacitance measured at three fixed holding potentials. He correctly concluded, based on modeling the data, that membrane tension caused a positive shift in V_{pkCm} . More recently, Gale and Ashmore (1994a) showed that V_{pkCm} shifted to a depolarized level and peak capacitance decreased when positive pressure was applied via the patch pipette. However, they further reported that upon collapse of the cell with hyperosmotic extracellular media, V_{pkCm} remained unchanged (-36 ± 11 mV; mean \pm SD), but voltage-dependent capacitance decreased some 60–70%. Other differences are apparent between their results and ours. First, no change in linear capacitance was observed by them during pressure increases, and second, while we find either little change or a slight decrease in z during positive pressure conditions, perusal of their data indicates a marked increase. Notably, Gale and Ashmore (1994a) did not employ ionic channel blockers, and used a phase tracking technique that can be susceptible to changes in electrode and/or membrane resistance. Changes in OHC membrane resistance can be quite large under those conditions, where outward potassium currents can reach several nA.

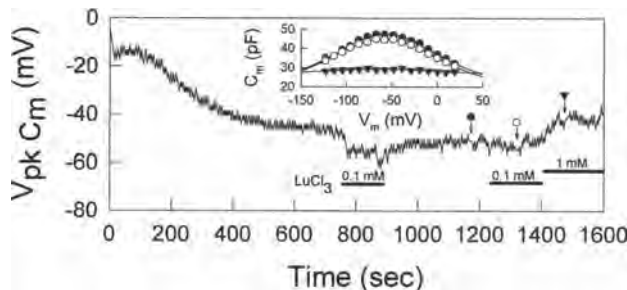


FIGURE 7 Effects of lanthanides on V_{pkCm} and nonlinear capacitance. After V_{pkCm} stabilized, lutetium chloride (1 mM) was applied extracellularly using a Y-tube delivery system. Inset shows voltage-dependent capacitance obtained by the voltage stair step technique (Huang and Santos-Sacchi, 1993). R_s : 6.5 M Ω , R_m : 145 M Ω . Fits (—) to the capacitance data indicate V_{pkCm} , Q_{max} , z , and C_{lin} of -56.9 mV, 4.1 pC, 0.67, and 20.9 pF (●) and -58.9 mV, 4.1 pC, 0.63, and 19.4 pF (○). Data obtained with 1 mM lutetium chloride (▼) could not be fit reliably.

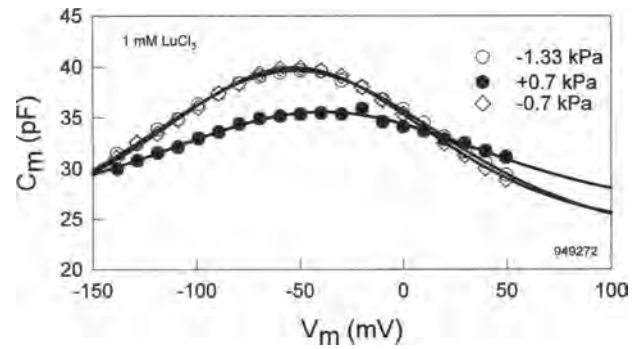


FIGURE 8 Effects of turgor pressure on nonlinear capacitance in a cell treated with intracellular trypsin and extracellular lutetium chloride (1 mM). Initial C_{mPK} was 47.5 pF, and in this cell only a partial block of nonlinear capacitance by lutetium was observed, enabling us to evaluate changes in V_{pkCm} . R_s : 2.5 M Ω , R_m : 300 M Ω . Reversible changes in cell capacitance induced by pressure modification are still observed. Fits (—) to the capacitance data indicate V_{pkCm} , Q_{max} , z , and C_{lin} of -52.0 mV, 3.4 pC, 0.52, and 22.5 pF (○): -1.33 kPa, and -38.6 mV, 2.2 pC, 0.47, and 25.3 pF (●): $+0.7$ kPa, and -52.8 mV, 2.9 pC, 0.57, and 23.6 pF (◇): -0.7 kPa.

Our work indicates that the variability of V_{pkCm} we initially noted (Santos-Sacchi et al., 1994) results from variability in OHC turgor pressure. Upon establishing whole cell configuration, OHC V_{pkCm} and $V_{\delta Lmax}$ are at a potential near -20 mV. Actually, this initial voltage depends on the method of obtaining whole cell configuration. Applying negative pressure to break the membrane patch can cause an immediate loss of cell turgor, whereas electrically breaking through the membrane patch (zapping) can prevent such a loss. The former technique produces a more negative initial V_{pkCm} . Subsequent to whole cell configuration, V_{pkCm} directly follows modifications of intracellular pressure, but shifts to a limiting negative voltage when depressurized. Before cell collapse, V_{pkCm} and correspondingly, $V_{\delta Lmax}$ can attain potentials close to that of the resting potential of OHCs in vivo (Dallos et al., 1982). At this point, mechanical responses are still robust and maximum voltage-dependent movement will exist near normal resting potentials. It should be emphasized that despite the fact that reduced turgor pressure decreases the overall magnitude of the mechanical response (Fig. 6; and see Santos-Sacchi, 1991, Fig. 11), maximum gain or sensitivity is little affected before cell collapse (Fig. 4, inset). Thus, for an OHC at a normal resting potential, reducing turgor pressure effectively increases the mechanical gain at that potential. In fact, another mechanism may aid in aligning the resting potential and $V_{\delta Lmax}$ under normal conditions. It is known that increased turgor can hyperpolarize, and reduced turgor can depolarize the OHC via the action of potassium selective stretch receptors (Iwasa et al., 1991; Harada et al., 1993). Correspondingly, sustained hyperpolarization can increase turgor and depolarization can reduce turgor pressure (Shehata et al., 1991). Thus, lowering turgor pressure may cause $V_{\delta Lmax}$ and membrane potential to approach each other, thereby maximizing the mechanical responsiveness of the OHC to receptor potentials, which presumably drive OHC motility in vivo (Evans and Dallos, 1993).

One problem with the potential role of OHC motility as the basis for the cochlear "amplifier" is that the magnitude of the AC mechanical response induced by receptor potentials in the high frequency region near threshold is calculated to be 20 dB smaller than basilar membrane motion (Santos-Sacchi, 1989, 1992). This is based on prior *in vitro* observations that the mechanical sensitivity of the OHC is not maximal near the normal *in vivo* resting potential of -70 mV. This dilemma has prompted suggestions that other hair cell mechanisms, e.g., stereociliar mechanics, might provide sensory gain (Santos-Sacchi, 1989; Hudspeth and Gillespie, 1994). However, the magnitude of turgor pressure *in vivo* is unknown. If it were close to 0, this might alleviate the apparent disparity between the magnitudes of basilar membrane motion and OHC motion, since the mechanical gain of the OHC would be maximal near the normal resting potential of the cell. It is possible that the high intracellular turgor pressure that is found in isolated OHCs (Ratnanather et al., 1993) is a consequence of the isolation procedures, since it is often noted that OHCs swell because of increased cytoplasmic osmolarity when they are maintained *in vitro* (Chertoff and Brownell, 1994).

Recently, Kalinec et al. (1992) have shown, using light microscopic evaluation, that treatment of the OHC with intracellular trypsin caused the cell to round up, presumably because of digestion of the cytoskeleton of the cell. Interestingly, voltage-dependent mechanical responses were still present. We confirmed by using electronmicroscopy that the cytoskeleton was digested; we also determined that the voltage sensor remained fully functional (Huang and Santos-Sacchi, 1994). In the present study we used trypsin treatment to show that cytoskeletal elements are not responsible for the susceptibility of the voltage sensor to modification of intracellular pressure. Thus, unlike stretch receptors that may sense tension through an elastic cytoskeleton (Sokabe et al., 1991), the OHC voltage sensor appears to respond to tension delivered directly to the plasma membrane. The role of the cortical cytoskeleton in the OHC has been proposed to provide structural constraints that funnel integral membrane motor protein area changes into anisotropic mechanical responses of the whole cell, namely predominant length changes (Kalinec et al., 1992; Santos-Sacchi, 1993). However, we have preliminary evidence that the sensitivity of the membrane motor to changes in turgor pressure increases after destruction of the cortical cytoskeleton. That is, smaller changes in pipette pressure are required to influence nonlinear capacitance after the cytoskeleton is destroyed. Thus, in addition to providing constraints on motility, the cytoskeleton may normally buffer the effects of turgor pressure alterations.

The underlying mechanism responsible for the effects of membrane tension on the nonlinear capacitance of the OHC has been theoretically evaluated by Iwasa (1993, 1994). By supplementing a simple two state Boltzmann model with an elastic energy term, shifts in V_{pkCm} were evidenced upon changes in the elastic energy. However, whereas the voltage shifts are predicted, the changes observed experimentally in

the magnitude of the voltage-dependent capacitance when tension is modified (Fig. 3; Gale and Ashmore, 1994a) are not. The increase in the amount of charge moved as membrane tension is dissipated may represent an increase in the number (N) of voltage sensors/motors capable of conformational change within the membrane. We find that the distance traversed by the sensor in the membrane electric field remains constant, evidenced by a fairly stable z during pressure modifications. Thus, in addition to Iwasa's elastic energy term, perhaps the number of functional sensors is tension-dependent. This possible change in the number of functional sensor/motors might indicate, in turn, that the maximum OHC length change would increase as turgor pressure is dissipated. However, the opposite is the case (Fig. 6; Santos-Sacchi, 1991). One possible explanation for this discrepancy is that coupling of the voltage sensor to the effector is less efficient under reduced tension, resulting in a smaller membrane area change. Alternatively, the membrane area changes thought to be responsible for the overall mechanical response of the cell (Kalinec et al., 1992; Iwasa and Chadwick, 1992; Iwasa, 1993; Santos-Sacchi, 1993) may actually be enhanced, but the translation mechanism funneling area changes into length changes may be compromised. It may be possible to explore this issue by measuring voltage-dependent changes in membrane patch area under conditions of variable tension.

Lanthanides have some effects similar to turgor pressure reductions, including negative shifts of V_{pkCm} and increases in cell length. We initially suggested that lanthanides shifted V_{pkCm} to positive potentials because of charge screening effects on the extracellular aspect of the OHC membrane (Santos-Sacchi, 1991). However, it is now clear that those initial studies were influenced by turgor pressure effects, since in those studies the pipette series resistance was kept low by delivering transient positive and negative pressures. Thus, it is likely that the effects of pipette pressure alterations on OHC turgor masked the true effects of lanthanides. Gale and Ashmore (1994b) have recently presented data indicating that extracellular gadolinium shifts V_{pkCm} in the negative direction, in agreement with our present results. They suggested that gadolinium charge screens from the inner aspect of the OHC membrane; however, it is unlikely that lanthanides enter the cell and charge screen on the intracellular aspect of the membrane, since intracellular EDTA-like calcium chelators, which both they and we used are far more effective (5–10 orders of magnitude) at buffering lanthanides (Kolthoff et al., 1969). While one mechanism of lanthanide action may involve interference with OHC osmo-regulation (Crist et al., 1993), clearly this cannot solely account for the reduction in nonlinear capacitance we observe, since induced turgor pressure changes continue to alter nonlinear capacitance in the presence of lanthanides. It is possible that lanthanides are capable of directly reducing tension on the membrane motors, perhaps via electrostatic effects. Further studies are required to resolve this issue.

In conclusion, our results indicate that OHC turgor pressure directly controls the voltage dependence of the nonlinear

capacitance and mechanical response of the cell, probably through direct induction of tension on the motility voltage sensor/effector. We speculate that modulation of turgor pressure *in vivo*, perhaps via OHC stretch receptor activity, may provide a unique mechanism for gain control of the cochlear “amplifier”.

We thank Sam Khalil for technical help and Dr. Guojie Huang for his comments throughout the study.

This work was supported by National Institute on Deafness and Other Communication Disorders NIDCD grant DC00273.

REFERENCES

- Alkon, D. L., R. Etcheberrigaray, and E. Rojas. 1993. Distribution of voltage sensors in mammalian outer hair cells. *Biophys. J.* 65:1755–1756.
- Armstrong, C. M., and F. Bezanilla. 1973. Currents related to movement of the gating particles of the sodium channels. *Nature.* 242:459–461.
- Ashmore, J. F. 1987. A fast motile response in guinea-pig outer hair cells: the cellular basis of the cochlear amplifier. *J. Physiol.* 388:323–347.
- Ashmore, J. F. 1990. Forward and reverse transduction in the mammalian cochlea. *Neurosci. Res. Suppl.* 12:S39–S50.
- Ashmore, J. F. 1992. Mammalian hearing and the cellular mechanism of the cochlear amplifier. In *Sensory Transduction*. D. P. Corey and S. D. Roper, editors. Rockefeller University Press, New York, 395–412.
- Ashmore, J. F., and R. W. Meech. 1986. Ionic basis of membrane potential in outer hair cells of guinea pig cochlea. *Nature.* 322:368–371.
- Brownell, W. E., C. R. Bader, D. Bertrand, and Y. de Ribaupierre. 1985. Evoked mechanical responses of isolated cochlear outer hair cells. *Science.* 227:194–196.
- Brownell, W. E., W. Shehata, and W. B. Imredy. 1989. Slow electrically and chemically evoked volume changes in guinea pig outer hair cells. In *Biomechanics of Active Movement and Deformation of Cells*. N. Akas, editor. Springer-Verlag, New York, 493–498.
- Chertoff, M. E., and W. E. Brownell. 1994. Characterization of cochlear outer hair cell turgor. *Am. J. Physiol.* 266:C467–C479.
- Crist, J. R., M. Fallon, and M. R. Bobbin. 1993. Volume regulation in cochlear outer hair cells. *Hearing Res.* 69:194–198.
- Dallos, P. 1992. The active cochlea. *J. Neurosci.* 12:4575–4585.
- Dallos, P., B. N. Evans, and R. Hallworth. 1991. On the nature of the motor element in cochlear outer hair cells. *Nature.* 350:155–157.
- Dallos, P., J. Santos-Sacchi, and A. Flock. 1982. Intracellular recordings from outer hair cells. *Science.* 218:582–584.
- Davis, H. 1983. An active process in cochlear mechanics. *Hearing Res.* 9:79–90.
- Ding, J. P., R. J. Salvi, and F. Sachs. 1991. Stretch-activated ion channels in guinea pig outer hair cells. *Hearing Res.* 56:19–28.
- Evans, B. N., and P. Dallos. 1993. Stereocilia displacement induced somatic motility of cochlear outer hair cells. *Proc. Natl. Acad. Sci. USA.* 90:8347–8351.
- Forge, A. 1991. Structural features of the lateral walls in mammalian cochlear outer hair cells. *Cell Tissue Res.* 265:473–483.
- Gale, J. E., and J. F. Ashmore. 1994a. Charge displacement induced by rapid stretch in the basolateral membrane of the guinea pig OHC. *Proc. R. Soc. Lond. B. Biol. Sci.* 255:243–249.
- Gale, J. E., and J. F. Ashmore. 1994b. An intracellular site for the inhibition of outer hair cell motility by gadolinium? Abstracts from the First International Symposium on Inner Ear Neuropharmacology, Montpellier, France, September 14–15.
- Hamill, O. P., A. Marty, E. Neher, B. Sakmann, and F. R. Sigworth. 1981. Improved patch clamp techniques for high resolution current recording from cells and cell-free membrane patches. *Pflugers Arch.* 391:85–105.
- Harada, N. A. Ernst, and H. P. Zenner. 1993. Hyposmotic activation hyperpolarizes outer hair cells of the guinea pig cochlea. *Brain Res.* 614:205–211.
- Holley, M. C., and J. F. Ashmore. 1990. Spectrin, actin and the structure of the cortical lattice in mammalian cochlear outer hair cells. *J. Cell Sci.* 96:283–291.
- Huang, G.-J., and J. Santos-Sacchi. 1993. Mapping the distribution of the outer hair cell motility voltage sensor by electrical amputation. *Biophys. J.* 65:2228–2236.
- Huang, G.-J., and J. Santos-Sacchi. 1994. Motility voltage sensor of the outer hair cell resides within the lateral plasma membrane. *Proc. Natl. Acad. Sci. USA.* 91:12268–12272.
- Hudspeth, A. J., and P. G. Gillespie. 1994. Pulling springs to tune transduction: adaptation by hair cells. *Neuron.* 12:1–9.
- Iwasa, K. H. 1993. Effect of stress on the membrane capacitance of the auditory outer hair cell. *Biophys. J.* 65:492–498.
- Iwasa, K. H. 1994. A membrane motor model for the fast motility of the OHC. *J. Acoust. Soc. Am.* 96:2216–2224.
- Iwasa, K. H., and R. S. Chadwick. 1992. Elasticity and active force generation of cochlear outer hair cells. *J. Acoust. Soc. Am.* 6:3169–3173.
- Iwasa, K. H., M. Li, M. Jia, and B. Kachar. 1991. Stretch sensitivity of the lateral wall of the auditory outer hair cell. *Neurosci. Lett.* 133:171–174.
- Kakehata, S., T. Nakagawa, T. Takasaka, and N. Akaïke. 1993. Cellular mechanism of Ach-induced response in dissociated OHCs of guinea pig cochlea. *J. Physiol.* 463:227–244.
- Kalínek, F., M. C. Holley, K. H. Iwasa, D. J. Lim, and B. Kachar. 1992. A membrane based force generation mechanism in auditory sensory cells. *Proc. Natl. Acad. Sci. USA.* 89:8671–8675.
- Keynes, R. D., and E. Rojas. 1974. Kinetics and steady state properties of the charged system controlling sodium conductance in the squid giant axon. *J. Physiol.* 239:393–434.
- Kolthoff, I. M., E. B. Sandell, E. J. Meeham, and S. Bruckenstein. 1969. *Quantitative Chemical Analysis*, 4th ed. The Macmillan Co., London.
- Murase, K., M. Randić, T. Shirasaki, T. Nakagawa, and N. Akaïke. 1990. Serotonin suppresses *N*-methyl-D-aspartate responses in acutely isolated rat spinal dorsal horn neurons. *Brain Res.* 525:84–91.
- Ratnanather, J. T., W. E. Brownell, and A. S. Popel. 1993. Mechanical properties of the outer hair cell. In *Biophysics of Hair Cell Sensory Systems*. H. Duifhuis, J. W. Horst, P. van Dijk, and S. M. van Netten, editors. World Scientific, Singapore, 199–206.
- Ruggero, M. A. 1992. Responses to sound of the basilar membrane of the mammalian cochlea. *Neurobiology.* 2:449–456.
- Santos-Sacchi, J. 1989. Asymmetry in voltage dependent movements of isolated outer hair cells from the organ of Corti. *J. Neurosci.* 9:2954–2962.
- Santos-Sacchi, J. 1990. Fast outer hair cell motility: how fast is fast? In *The Mechanics and Biophysics of Hearing*. P. Dallos, C. D. Geisler, J. W. Matthews, M. A. Ruggero, and C. R. Steele, editors. Springer-Verlag, Berlin, 69–75.
- Santos-Sacchi, J. 1991. Reversible inhibition of voltage dependent outer hair cell motility and capacitance. *J. Neurosci.* 11:3096–3110.
- Santos-Sacchi, J. 1992. On the frequency limit and phase of outer hair cell motility: effects of the membrane filter. *J. Neurosci.* 12:1906–1916.
- Santos-Sacchi, J. 1993. Harmonics of outer hair cell motility. *Biophys. J.* 65:2217–2227.
- Santos-Sacchi, J., and J. P. Dilger. 1988. Whole cell currents and mechanical responses of isolated outer hair cells. *Hearing Res.* 35:143–150.
- Santos-Sacchi, J., G.-J. Huang, and S. Kakehata. 1994. Variability of voltage dependency of the outer hair cell (OHC) motility voltage sensor. *J. Acoust. Soc. Am.* 95:2841.
- Santos-Sacchi, J., and S. Kakehata. 1994. Membrane tension directly shifts the voltage dependence of OHC gating charge and motility. Hot Poster Session, 1994 Meeting of the American Society for Cell Biology, San Francisco, December.
- Shehata, W., W. E. Brownell, and R. Dieler. 1991. Effects of salicylate on shape, electromotility and membrane characteristics of isolated hair cells from the guinea pig cochlea. *Acta Oto-Laryngol. (Stockholm).* 111:707–718.
- Sokabe, M., F. Sachs, and Z. Jing. 1991. Quantitative video microscopy of patch clamped membranes stress, strain, capacitance, and stretch channel activation. *Biophys. J.* 59:722–728.
- Yang, X. C., and F. Sachs. 1989. Block of stretch activated ion-channels in *Xenopus* oocytes by gadolinium and calcium ions. *Science.* 243:1068–1070.

Effects of Salicylate and Lanthanides on Outer Hair Cell Motility and Associated Gating Charge

Seiji Kakehata and Joseph Santos-Sacchi

Sections of Otolaryngology and Neurobiology, Yale University School of Medicine, New Haven, Connecticut 06510

Salicylate, one of the most widely used drugs, is known to induce reversible tinnitus and hearing loss. Salicylate interferes with outer hair cells (OHCs), which are believed to underlie normal auditory frequency selectivity and sensitivity. In the present experiments, the effects of salicylate and lanthanides on OHC motility and nonlinear capacitance were investigated by using isolated guinea-pig OHCs while attempting to avoid inadvertent intracellular pressure change, which itself can affect OHC motility and capacitance. Either extracellularly or intracellularly applied salicylate reduced nonlinear peak capacitance ($C_{m_{pk}}$) and shifted the voltage at peak capacitance to depolarized levels. Concentration–response curves for reduction in $C_{m_{pk}}$ by salicylate and $GdCl_3$ revealed a half-maximal concentration and Hill coefficient of 1.6 mM and 1.0, and 0.6 mM and 1.2, respectively. In comparable groups of OHCs, the normal $C_{m_{pk}}$ values of which were near 40 pF, average $C_{m_{pk}}$ de-

creased to 28 and 36 pF for intracellularly and extracellularly applied salicylate, respectively. Salicylate reduced, but did not completely block, the voltage-induced length change. Extracellularly, but not intracellularly, applied lanthanide blocked voltage-induced movement and capacitance almost completely. After intracellular trypsin treatment, salicylate reduced voltage-dependent capacitance reversibly, suggesting that salicylate directly acts on the sensor/motor and not via effects on intracellular structures, such as the subsurface cisternae. The results are consistent with the hypothesis that the dissociated, charged form of salicylate directly interacts with the sensor/motor on the inner aspect of the OHC plasma, whereas lanthanides interact on the outer aspect.

Key words: outer hair cell; salicylate; motility; nonlinear capacitance; gating currents; lanthanides

The outer hair cell (OHC), one of the two receptor cell types in the mammalian organ of Corti, is thought to play a crucial role in hearing by providing a local mechanical feedback into the basilar membrane via its unique voltage-dependent length changes (Brownell et al., 1985; Ashmore, 1987; Santos-Sacchi and Dilger, 1988; Dallos, 1992). This feedback sharpens the passive mechanical vibration of the cochlear partition. Recent studies demonstrate that the OHC has a nonlinear gating charge movement or, equivalently, a voltage-dependent capacitance that presents characteristics similar to those of OHC motility, indicating that membrane-bound voltage sensor/motor elements control OHC length (Ashmore, 1989, 1992; Dallos et al., 1991; Santos-Sacchi, 1991, 1993; Iwasa, 1994).

Salicylate, which is used as an analgesic and anticoagulant, is one of the most widely used drugs. Salicylate is known to produce reversible tinnitus and hearing loss (Myers and Bernstein, 1965; Mongan et al., 1973). Several lines of indirect evidence suggest that salicylate exerts these effects via the OHC (McFadden and Plattsmier, 1984; Long and Tubis, 1988; Puel et al., 1989; Kujawa et al., 1992; Carlyon and Butt, 1993). Indeed, direct studies on the OHC have shown that the nonlinear capacitance and/or motility of the cell can be modified by salicylate (Shehata et al., 1991; Tunstall et al., 1995). Shehata et al. (1991) reported that salicylate reduces OHC turgor pressure and motility. More recently, Tun-

stall et al. (1995) showed that salicylate reduces OHC membrane capacitance and concluded that salicylate is effective in the membrane-permeant uncharged form. Other treatments that are known to affect OHC motility and capacitance include lanthanides and altered turgor pressure, the latter acting via membrane stress (Santos-Sacchi, 1991; Iwasa, 1993; Gale and Ashmore, 1994b; Kakehata and Santos-Sacchi, 1995).

Because whole-cell patch-pipette recording inadvertently can permit changes in OHC turgor pressure (Kakehata and Santos-Sacchi, 1995), we examined the effect of salicylate and lanthanides on OHC nonlinear capacitance and voltage-induced mechanical responses while attempting to avoid such interference. The results suggest that each investigated agent seems to work via a different mechanism on the OHC sensor/motor and that the effects of both agents are independent of turgor pressure. Furthermore, the data indicate that the dissociated, charged form of salicylate interacts with the sensor/motor on the inner aspect of the plasma membrane, whereas lanthanides interact with the sensor/motor on the outer aspect.

MATERIALS AND METHODS

OHCs were freshly isolated from the organ of Corti of the guinea-pig cochlea (Kakehata et al., 1993) and were whole-cell voltage-clamped by an Axon 200 amplifier with patch pipettes having initial resistances of 2–3 M Ω or \sim 10 M Ω , corresponding to tip sizes of 1–2 μ m or \sim 0.5 μ m, respectively (Hamill et al., 1981). Residual series resistance (R_s ; after electronic compensation) ranged from 3 to 7 M Ω and from 20 to 30 M Ω , respectively. Ionic blocking solutions were used to remove voltage-dependent ionic conductances so that capacitive currents could be analyzed in isolation (Santos-Sacchi, 1991; Huang and Santos-Sacchi, 1993). The patch-pipette solution contained (in mM): 140 CsCl, 2 MgCl₂, 10 EGTA, and 10 HEPES, pH 7.2; osmolarity was adjusted with dextrose to 300 mOsm. The external solution contained (in mM): 100 NaCl, 20 TEA,

Received March 26, 1996; revised May 16, 1996; accepted May 21, 1996.

This work was supported by National Institutes of Health, National Institute on Deafness and Other Communication Disorders Grant DC00273 to J.S.S. We thank Bill Brownell for critical comments.

Correspondence should be addressed to Dr. Joseph Santos-Sacchi, Sections of Otolaryngology and Neurobiology, BML 244, 333 Cedar Street, New Haven, CT 06510.

Copyright © 1996 Society for Neuroscience 0270-6474/96/164881-09\$05.00/0

20 CsCl, 2 CoCl₂, 1.52 MgCl₂, 10 HEPES, and 5 dextrose, pH 7.2, at 300 mOsm. In some experiments, extracellular CaCl₂ (2 mM) was included, without any effect. Drugs were applied by using the Y-tube method (Murase et al., 1990) during simultaneous whole-chamber perfusion. Experiments were performed at room temperature.

A tracking procedure was used to monitor continuously the voltage at peak nonlinear capacitance (V_{pkCm}) after obtaining whole-cell configuration (Kakehata and Santos-Sacchi, 1995). The program Clampex (Axon Instruments, Foster City, CA) was modified to perform the V_{pkCm} tracking procedure on-line, and membrane potential was corrected for the effects of residual series resistance. Peak capacitance (Cm_{pk}) values also were monitored during the tracking procedure by using transient analysis of capacitive currents induced by a -10 mV step.

Detailed, corroborative evaluation of membrane capacitance was made at different potentials by transient analysis of currents induced by a voltage stair-step stimulus, and the capacitance function was fit to the first derivative of a two-state Boltzmann function relating nonlinear charge to membrane voltage (dQ/dV ; Santos-Sacchi, 1991; Huang and Santos-Sacchi, 1993):

$$C_m = Q_{max} \frac{ze}{kT} \frac{b}{(1+b)^2} + C_{lin},$$

in which

$$b = \exp\left(\frac{-ze(V - V_{pkCm})}{kT}\right).$$

Q_{max} is the maximum nonlinear charge moved, V_{pkCm} is voltage at peak capacitance or, equivalently, at half-maximal nonlinear charge transfer, V_m is membrane potential, z is valence, C_{lin} is linear membrane capacitance, e is electron charge, k is Boltzmann's constant, and T is absolute temperature. Pipette pressure was modified with a syringe connected to the Teflon tubing attached to the patch-pipette holder. Pressure was monitored via a T-connector to a pressure monitor (World Precision Instruments, Sarasota, FL). An in-house pipette pressure clamp was used to maintain constant pipette pressure when required. This device provided positive or negative pressure into the pipette via a motor-driven, gas-tight syringe by using feedback from the pressure monitor.

Previously, we have found that when recording with large-tipped patch pipettes (1.5–3 M Ω , 1.5 μ m tip) containing iso-osmolar solutions, V_{pkCm} shifts to hyperpolarized levels over the course of 10 min after patch membrane rupture (Kakehata and Santos-Sacchi, 1995). This occurs because of a decrease in OHC intracellular pressure. In the present set of experiments, three conditions were used to dismiss potential effects of uncontrolled, recording-induced intracellular pressure change during evaluation of salicylate and lanthanides on OHC capacitance and motility. First, the use of small-tipped pipettes provides for stable intracellular pressures, because no negative shifts of V_{pkCm} are observed over periods of 30 min or longer. Under this condition, the potential effects of exogenous agents on intracellular pressure are unhampered. Second, with large-tipped pipettes, maintenance of constant pipette pressure provides for stable intracellular pressures, because V_{pkCm} can be maintained constant. Third, with large-tipped pipettes after intracellular pressure dissipation (~ 10 min), intracellular pressure is stable, because V_{pkCm} remains constant. The drugs were evaluated under each condition.

All experiments were video taped with a Matrox (Montreal, Canada) video overlay board that combines EGA and video. Measures of voltage-induced (20 mV increments) mechanical responses were made from the video monitor with a differential optoresistor technique (Santos-Sacchi, 1989, 1991). Mechanical data were fit to a two-state Boltzmann function to determine the voltage at maximum sensitivity (V_{sLmax}).

Dose–response data were averaged and are given as mean \pm SE. A continuous theoretical curve was drawn according to a modified Michaelis–Menten equation with the use of a least-squares fitting routine after normalization of the response,

$$\Delta C = C_{max} \left(\frac{C^n}{C^n + K_D^n} \right),$$

in which ΔC is the observed reduction of capacitance, C is the drug concentration, K_D is the dissociation constant, and n is the Hill coefficient. All data analysis was performed with the software package MATLAB (Mathworks, Natick, MA).

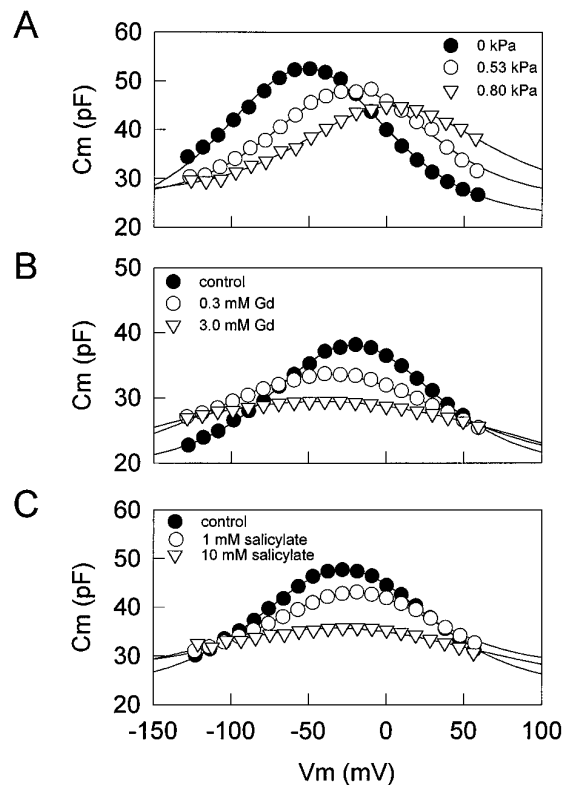


Figure 1. Effects of intracellular pressure (*A*), lanthanides (*B*), and salicylate (*C*) on C_m . Voltage-dependent capacitance was obtained by the voltage stair-step technique. *A*, After V_{pkCm} stabilized after intracellular pressure dissipation (~ 10 min), an increasing intracellular pressure caused a positive shift in the V_{pkCm} with decreasing peak capacitance (Cm_{pk}). R_s (series resistance), 1.9 M Ω (pipette tip, ~ 1.5 μ m); R_m (membrane resistance), 139 M Ω . The initial cell length was 75 μ m; the cell length was reduced to 73% when intracellular pressure was increased to 0.8 kPa. *B*, In another cell, after V_{pkCm} stabilized, GdCl₃ was applied extracellularly by a Y-tube delivery system. GdCl₃ caused a negative shift in V_{pkCm} with decreasing Cm_{pk} . R_s , 2.8 M Ω (pipette tip, ~ 1 μ m); R_m , 220 M Ω . The initial cell length was 50 μ m; the cell length elongated to 107%. *C*, In another cell, with the use of a small-tipped pipette to maintain initial intracellular turgor pressure, extracellularly applied salicylate caused a positive shift in V_{pkCm} with decreasing Cm_{pk} . R_s , 27.2 M Ω ; R_m , 350 M Ω . The initial cell length was 65 μ m; the cell length was reduced to 78%. All treatments were done after V_{pkCm} stabilized.

RESULTS

Effects of salicylate, lanthanides, and pressure on OHC nonlinear capacitance

Figures 1 and 2 illustrate the effects of intracellular pressure changes and extracellularly applied salicylate and lanthanides on OHC nonlinear capacitance. Positive changes in intracellular pressure consistently and reversibly shifted V_{pkCm} to depolarized levels and reduced Cm_{pk} (Figs. 1*A*, 2*A*). Lanthanides such as GdCl₃, LuCl₃, and CeCl₃ consistently, but not always reversibly, shifted V_{pkCm} to hyperpolarized levels and reduced Cm_{pk} (Figs. 1*B*, 2*B*). However, whereas salicylate consistently and reversibly shifted V_{pkCm} and reduced Cm_{pk} , the direction of the shift could be to either depolarized or hyperpolarized levels (Figs. 1*C*, 2*C,D*). About two-thirds of the cells tested exhibited a shift in the depolarized direction (Fig. 2*C*). Residual ionic conductance (leakage) remained unaffected by salicylate or intracellular pressure changes, but lanthanides suppressed it. These results suggest that lanthanides and salicylate do not exert their effects simply via a

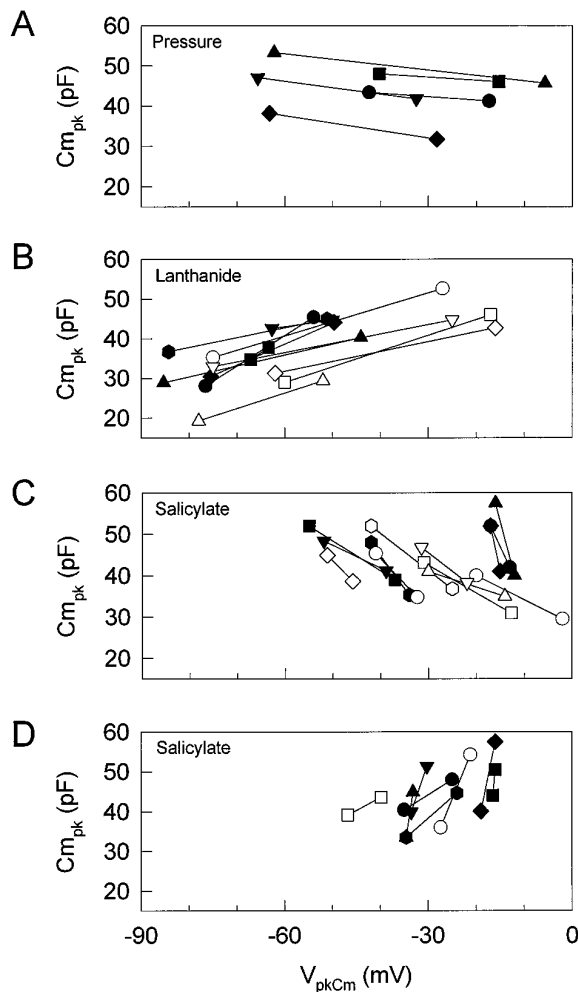


Figure 2. Effects of intracellular pressure (*A*), lanthanides (*B*), and salicylate (*C, D*) on the relationship between V_{pkCm} and Cm_{pk} . Each point shows the relationship between V_{pkCm} and Cm_{pk} . Increasing pressure, extracellularly applied lanthanides, or salicylate reduces Cm_{pk} . *A*, Cm_{pk} and V_{pkCm} under two pressure conditions, -0.41 ± 0.26 (mean \pm SE) and 0.64 ± 0.23 kPa. Increasing pressure caused a positive shift in V_{pkCm} . *B*, Cm_{pk} and V_{pkCm} before and during application of lanthanides (3 or 10 mM $GdCl_3$, $n = 7$; 1 mM $LuCl_3$, $n = 3$; 1 mM $CeCl_3$, $n = 1$). Extracellularly applied lanthanides caused a negative shift in V_{pkCm} with decreasing Cm_{pk} in all cells tested ($n = 11$). Reversibility was dependent on concentration. *C, D*, Cm_{pk} and V_{pkCm} before and during application of 10 mM salicylate. Extracellularly applied salicylate reduced Cm_{pk} , although the direction of the shift in V_{pkCm} was variable. The data are plotted in separate graphs for clarity. Of 21 cells tested, 13 showed a positive shift in V_{pkCm} (*C*), and 8 cells showed a negative shift (*D*). Each symbol indicates a different cell. All treatments were done after V_{pkCm} stabilized.

mechanism similar to that of turgor pressure change, which is believed to act via alterations in membrane stress (Iwasa, 1994; Kakehata and Santos-Sacchi, 1995).

The response time course of extracellularly applied salicylate was examined by using a tracking procedure to follow changes in V_{pkCm} and Cm_{pk} (Kakehata and Santos-Sacchi, 1995). One millimolar salicylate reversibly reduced Cm_{pk} and shifted V_{pkCm} to depolarized levels (Fig. 3*A*). These effects reached steady state in ~ 60 sec in this cell. An increase in the salicylate concentration accelerated the response (Fig. 3*B*). The reduction of Cm_{pk} was well fit with a single exponential. Tau of salicylate-induced reduction in Cm_{pk} was 19.2 ± 3.7 sec (mean \pm SE; $n = 5$) and $11.4 \pm$

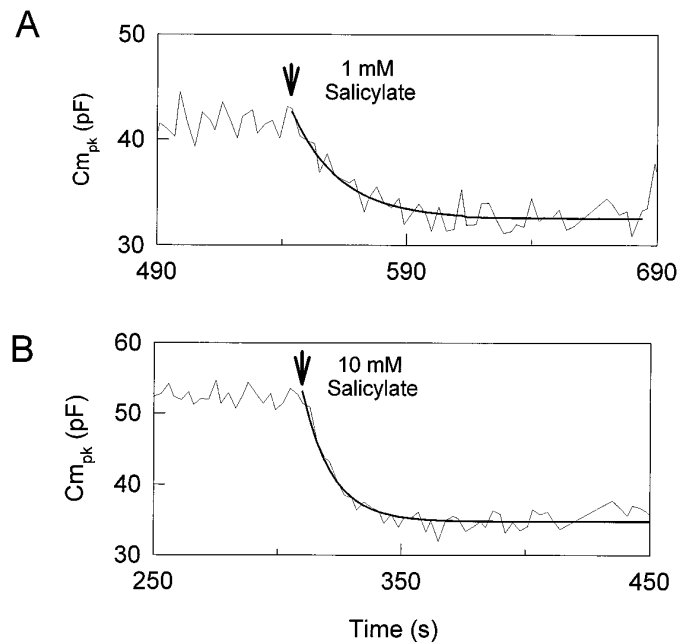


Figure 3. Effects of extracellularly applied salicylate on OHC capacitance. The effective time course of extracellularly applied salicylate was examined by using a tracking procedure. A small-tipped pipette was used to permit any turgor pressure change that salicylate may cause. Salicylate was applied after V_{pkCm} and Cm_{pk} reached steady state. *A*, Effects of 1 mM salicylate. Peak capacitance is shown as a function of time. The reduction of Cm_{pk} is well fit by using a single exponential curve fit. Tau is 19 sec. R_s , 27.1 M Ω ; R_m , 255 M Ω . *B*, Effects of 10 mM salicylate in a different cell. Tau is 12 sec. R_s , 26.6 M Ω ; R_m , 292 M Ω .

2.4 sec ($n = 8$) for 1 and 10 mM salicylate, respectively. With the use of fitted steady-state values, the average reduction of Cm_{pk} and average shift of V_{pkCm} (mean \pm SE) were 6.82 ± 1.48 pF and 4.6 ± 2.2 mV (1 mM; $n = 5$), and 10.63 ± 1.51 pF and 16.7 ± 2.2 mV (10 mM; $n = 7$). Nonlinear capacitance was evaluated more fully by using stair-step stimuli applied at least 120 sec after treatment. With this technique, average Cm_{pk} was 46.86 ± 1.25 ($n = 11$) and 36.75 ± 0.92 pF before and during application of 10 mM salicylate, respectively. The average reduction of Cm_{pk} was 10.11 ± 1.26 pF, which is comparable to the value of 10.63 ± 1.51 pF obtained by the tracking technique.

Concentration–response curves for salicylate and gadolinium

Concentration–response curves for reduction in Cm_{pk} by salicylate were obtained with the V_{pkCm} tracking technique. Salicylate was applied by Y-tube in increasing concentrations, without intermittent washing, until a steady-state response was achieved. Pipette pressure was kept slightly positive (up to approximately +0.07 kPa), to prevent turgor dissipation. Figure 4*A* shows a representative example. The effects of salicylate were just detectable at a concentration of $\sim 300 \mu M$. The reduction increased sigmoidally as the salicylate concentration increased to 10 mM, above which the response was saturated. The half-maximal concentration ($K_{1/2}$) and the Hill coefficient (n) were 1.6 mM and 1.0, respectively. V_{pkCm} shifted to depolarized levels at a concentration of >1 mM.

Concentration–response curves for $GdCl_3$ were obtained in a similar manner. Pipette pressure was kept positive (up to approximately +0.14 kPa) to prevent turgor dissipation. Compared with salicylate, longer perfusion times were required to reach steady-

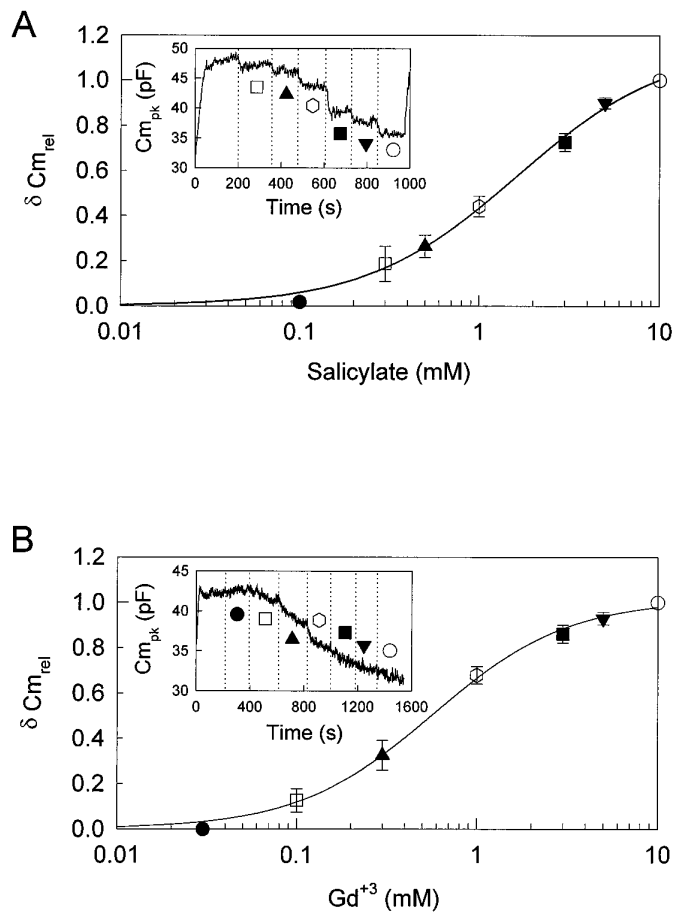


Figure 4. Concentration–response curve for reduction in Cm_{pk} by salicylate and $GdCl_3$. *A*, The concentration–response curve for salicylate. The inset shows the effect on the Cm_{pk} by various concentrations of salicylate in a representative example. R_s , 5.5 M Ω ; R_m , 450 M Ω . Pipette pressure was kept at 0 kPa. Reductions of Cm_{pk} induced by various concentrations were normalized to the reduction induced by 10 mM salicylate. Each point is the mean \pm SE of five cells. *B*, The concentration–response curve for $GdCl_3$. The inset shows the effect on the Cm_{pk} by various concentrations of $GdCl_3$ in a representative example. R_s , 6.5 M Ω ; R_m , 400 M Ω . Pipette pressure was kept at 0.11 kPa. Reductions of Cm_{pk} induced by various concentrations were normalized to the reduction induced by 10 mM $GdCl_3$. Each point is the mean \pm SE of five cells determined at the end of each perfusion.

state levels (Fig. 4*B*). The effects of $GdCl_3$ were detectable at a concentration of 100 μ M. $GdCl_3$ reduced Cm_{pk} in a concentration-dependent manner, and at 10 mM a near-maximal response was obtained. $K_{1/2}$ and n were 0.6 mM and 1.2, respectively. V_{pkCm} shifted to hyperpolarized levels and reached very negative potentials of -67.4 ± 3.9 mV ($n = 5$). Two of the treated cells collapsed during data collection.

Effects of intracellularly applied salicylate

Recent evidence indicates that salicylate is highly permeable through the OHC membrane (Tunstall et al., 1995; Zhi et al., 1996). However, the precise site in which salicylate acts on the OHC motility voltage sensor remains unknown. To investigate possible sites of salicylate effects, we applied salicylate intracellularly through patch pipettes and compared results with those obtained by extracellular application. Large-tipped pipettes were used, with pipette pressure clamped near zero. Tracking of Cm_{pk}

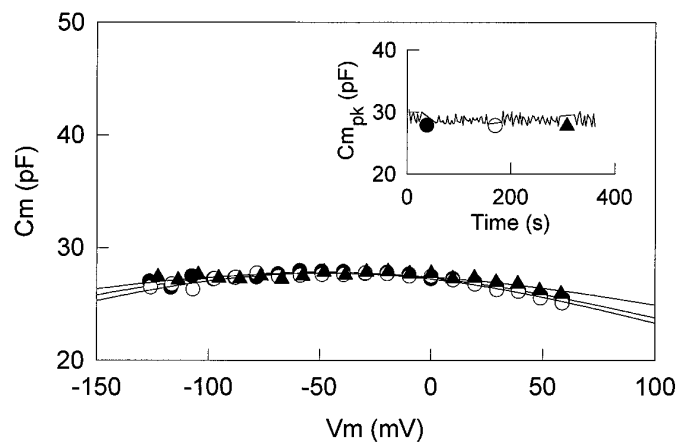


Figure 5. Effects of intracellularly applied salicylate on OHC capacitance. The OHC was dialyzed with a pipette solution containing 10 mM salicylate. The inset shows peak capacitance as a function of time, measured with the tracking procedure (solid line) or stair-step protocol (symbols) at 30, 160, and 300 sec. R_s , 6.01 M Ω ; R_m , 270 M Ω . Capacitance drops to low levels immediately after obtaining whole-cell configuration. This figure is representative of 20 cells tested.

and V_{pkCm} was started immediately after whole-cell configuration was obtained. In addition, stair-step stimuli in a wide voltage range (-150 to $+150$ mV) were applied periodically. Figure 5 shows the immediate effect of intracellularly applied salicylate on voltage-dependent capacitance. In OHCs dialyzed with 5 mM salicylate, stair-step analysis revealed that reduction of Cm_{pk} and the shift of V_{pkCm} were time-dependent (data not shown). In two cells, the exponential time constant of Cm_{pk} reduction was 11.25 and 6.89 sec. With 10 mM salicylate, Cm_{pk} was reduced to a steady level of <30 pF within, at most, 5 sec after whole-cell configuration was obtained (Fig. 5).

Because the effects of intracellularly applied salicylate are so rapid, it is impossible to obtain the initial normal capacitance value of the cell for comparison. Instead, we compared groups of intracellularly untreated and treated (10 mM) cells, the average cell length of which was 56.7 ± 3.1 ($n = 11$) and 58.5 ± 3.4 μ m ($n = 11$), respectively. OHC length correlates well with the membrane capacitance of the cell; thus, valid comparisons can be made between these groups. Average Cm_{pk} was 46.87 ± 1.25 and 28.20 ± 0.67 pF in untreated and treated groups, respectively. In those control OHCs subsequently treated with extracellular 10 mM salicylate, the average Cm_{pk} dropped to 36.75 ± 0.92 pF. This value differs significantly from the value of 28.20 ± 0.67 pF in the OHCs dialyzed with 10 mM salicylate (Student's t test < 0.001). These results indicate that salicylate works more effectively when applied intracellularly.

Voltage-induced OHC movement and voltage-dependent capacitance share many characteristics (Santos-Sacchi, 1991; Ashmore, 1992). OHC voltage-dependent movement as well as voltage-dependent capacitance were reduced in a concentration-dependent manner by intracellular salicylate treatment (Fig. 6). In the absence of salicylate, voltage-induced length changes saturate at positive voltages. The voltage in which saturation initiates depends on OHC turgor pressure, because $V_{\delta Lmax}$ shifts with turgor pressure (Kakehata and Santos-Sacchi, 1995). The maximum mechanical gain of the OHC, however, can remain fairly constant. Thus, to avoid the possible effect of turgor pressure on measures of OHC movement, we compared maximum mechanical

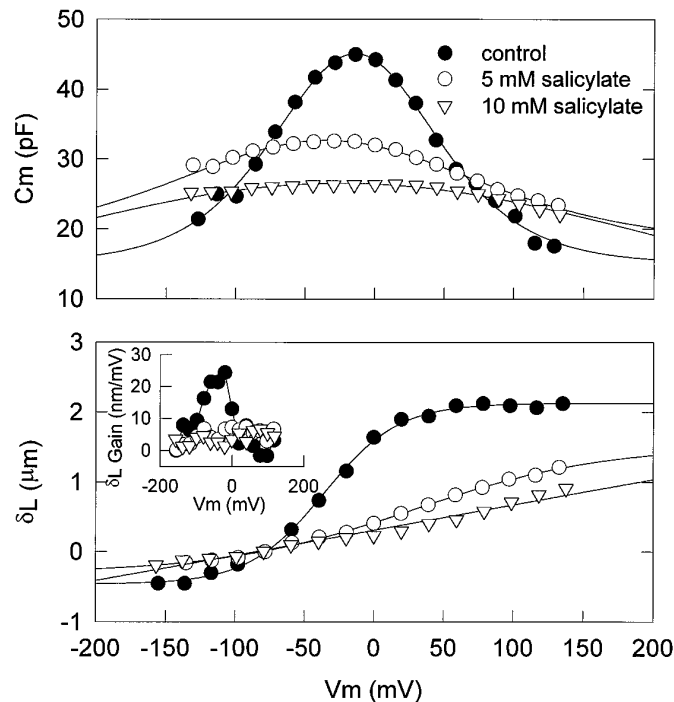


Figure 6. Effects of intracellularly applied salicylate on OHC capacitance and movement. Voltage-dependent capacitance and voltage-induced length change were measured 3–4 min after whole-cell configuration in three different cells. As the concentration of salicylate increased, voltage-dependent capacitance and nonlinearity of voltage-induced length change were reduced correspondingly. Length changes were induced by 20 mV steps from -150 to $+150$ mV at a V_{hold} of -80 mV. R_s , 3.38 M Ω and R_m , 66.5 M Ω (closed circles); R_s , 3.68 M Ω and R_m , 34.7 M Ω (open circles); R_s , 6.57 M Ω and R_m , 240 M Ω (open triangles). Fits (solid lines) for capacitance indicate V_{pkCm} , Q_{max} , and z of -14.3 mV, 4.74 pC, and 0.650 (open circles); -38.2 mV, 5.09 pC, and 0.317 (closed circles); -28.7 mV, 36.54 pC, and 0.111 (open triangles). Fits for the mechanical data indicate V_{hold} and z of -36.4 mV and 0.955 (closed circles), 2.89 mV and 0.376 (open circles), and 6.43 mV and 0.039 (open triangles). The inset shows the first derivative of the mechanical responses, indicating the gain of the mechanical response with different concentrations of salicylate. See text for details.

gain of OHCs in the absence and presence of intracellular salicylate. The average gain was 19.53 ± 1.98 nm/mV ($n = 3$) in the absence of salicylate, which is in line with previous measures (Ashmore, 1987; Santos-Sacchi and Dilger, 1988). In the presence of 10 mM salicylate, voltage-induced length change did not saturate, and the movement function appeared linear within the voltage range of -150 to 150 mV. The average cell-length change obtained by a voltage step from a holding potential of -80 to 150 mV was 1.03 ± 0.06 μm ($n = 7$). The average maximum mechanical gain was 5.17 ± 0.43 nm/mV ($n = 9$), which is about one-fourth of the average gain in the absence of salicylate.

Comparison of effects between salicylate and lanthanide on OHC capacitance and movement

The effect of salicylate on OHC nonlinear capacitance is similar to that of lanthanides, which are known to block voltage-dependent OHC movement and capacitance (Santos-Sacchi, 1991; Kakehata and Santos-Sacchi, 1995). However, significant differences exist between the effects of the two drugs and are revealed via dual-treatment experiments. In OHCs dialyzed with 10 mM salicylate, simultaneous measures of capacitance and voltage-dependent movements were made before and during extracellular applica-

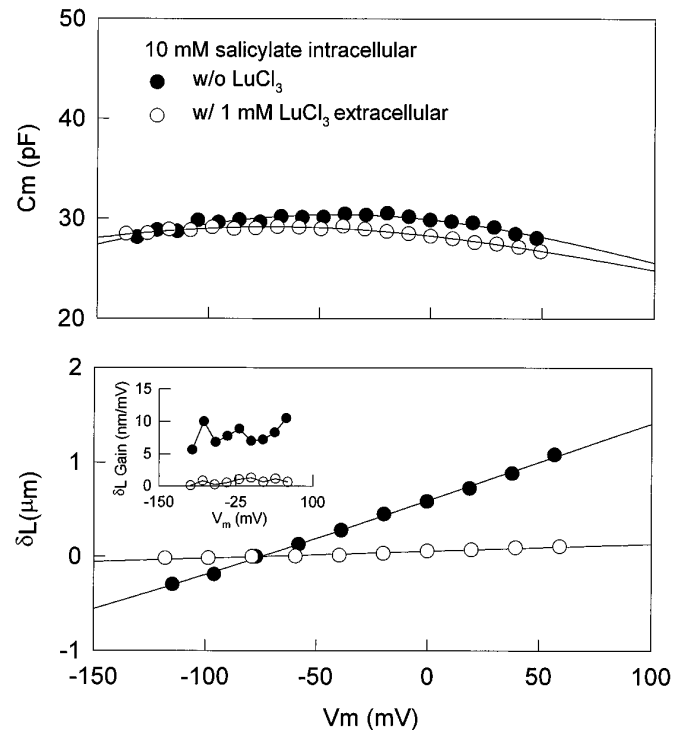


Figure 7. Comparison of effects between salicylate and lanthanide on OHC capacitance and movement. Voltage-dependent capacitance and voltage-induced length change were measured before and during extracellularly applied LuCl_3 (1 mM) in an OHC with intracellularly applied salicylate (10 mM). Length changes were induced by 20 mV steps from -20 to $+60$ mV at a V_{hold} of -80 mV. R_s , 4.75 M Ω and R_m , 89.2 M Ω (closed circles); R_s , 4.39 M Ω and R_m , 261 M Ω (open circles). Fits (solid lines) for capacitance indicate V_{pkCm} , Q_{max} , and z of -42.3 mV, 9.152 pC, and 0.205 (open circles); -71.3 mV, 7.35 pC, and 0.191 (closed circles). Fitting such depressed capacitance functions may not be reliable because of the limited voltage range that can be applied. The mechanical data could not be fit reliably with a two-state Boltzmann. Note that lanthanides, although changing the capacitance function minimally, effectively block mechanical responses. The inset shows mechanical gain of the cell under each condition.

tion of 1 mM LuCl_3 . An example is shown in Figure 7. At 4 min after whole-cell configuration, $C_{\text{m, pk}}$ was 30.4 pF, and z was 0.205 . Extracellularly applied LuCl_3 further reduced $C_{\text{m, pk}}$ and z to a small extent, namely, 29.2 pF and 0.191 , respectively. On the other hand, the effect elicited by LuCl_3 on the cell movement was significant. Voltage-induced movement was blocked almost completely; i.e., maximum mechanical gain was reduced from 8.04 to 0.70 nm/mV.

The effect of intracellularly applied lanthanide also was examined. Because EDTA-like calcium buffers are powerful lanthanide chelators, GdCl_3 (5 mM) was added to patch pipettes that did not include EGTA. Intracellularly applied GdCl_3 neither abolished the voltage-induced movement nor reduced nonlinear capacitance in all cells tested (data not shown; $n = 4$). This result suggests that lanthanides work exclusively from the extracellular side of the OHC membrane.

Effects of salicylate on the limiting value of V_{pkCm}

As OHC intracellular pressure is reduced, V_{pkCm} shifts in the negative direction until it reaches a limiting value that occurs when the cell collapses (Kakehata and Santos-Sacchi, 1995). Figure 8 illustrates the effects of salicylate on this limiting value.

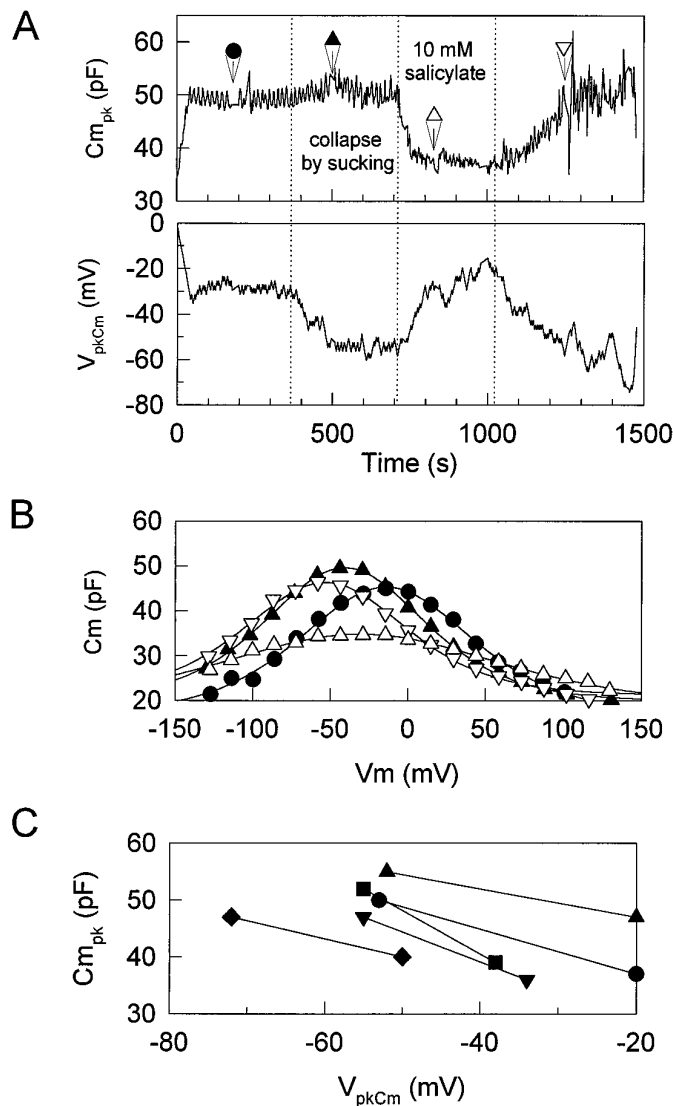


Figure 8. Effects of salicylate on the limited value of V_{pkCm} . Intracellular pressure of the OHC was reduced directly through the patch pipette to collapse the cell. *A*, The cell was maintained in collapse after the point indicated by the first dotted line. As expected, collapsing the cell caused Cm_{pk} to increase and V_{pkCm} to shift to a limiting negative value (Kakehata and Santos-Sacchi, 1995). At the second dotted line, 10 mM salicylate was applied extracellularly. V_{pkCm} shifted in the positive direction with a decrease in Cm_{pk} . Washout at the third dotted line caused recovery. *B*, Capacitance function determined by the stair-step protocol for the same cell. Fits (solid lines) to the capacitance data indicate V_{pkCm} , Q_{max} , and z of -14.3 mV, 4.74 pC, and 0.650 (closed circles, control); -41.0 mV, 4.09 pC, and 0.743 (closed triangles, after collapse); -32.3 mV, 3.86 pC, and 0.418 (open triangles, during application of salicylate); -53.6 mV, 3.54 pC, and 0.728 (closed triangles, after wash). *C*, Data from five cells showing consistent positive shift of V_{pkCm} and decrease in Cm_{pk} in collapsed cells after 10 mM salicylate treatment.

Intracellular pressure was reduced directly through the patch pipette. This treatment increased Cm_{pk} and shifted V_{pkCm} in the negative direction. In this case, V_{pkCm} reached a limiting value of -55 mV when the OHC collapsed. After treatment with 10 mM salicylate extracellularly, the limiting value consistently moved in the positive direction while the OHC remained collapsed ($n = 5$). The effect was reversible. This result further suggests that salicylate does not act via turgor pressure but affects the voltage

dependence of the voltage sensor directly. It also may indicate that the minority of cells in which salicylate shifted V_{pkCm} to negative potentials simultaneously may have experienced inadvertent changes in turgor pressure.

Effects of salicylate on V_{pkCm} and Cm_{pk} of trypsin-treated cells

It has been demonstrated that salicylate alters the structure of the OHC subsurface cisternae (Dieler et al., 1991). To investigate whether normal subsurface cisternae are required for the effects of salicylate on the voltage sensor, we disrupted subsurface cisternal architecture by destroying the cortical cytoskeleton of the cell with intracellular trypsin. This treatment causes the OHC to become spherical and the subsurface cisternae to vesiculate and peel away from the plasmalemma (Huang and Santos-Sacchi, 1994). Neither voltage-sensor gating charge movement nor the sensitivity of the sensor to intracellular pressure change is altered with this treatment (Kakehata and Santos-Sacchi, 1995). Figure 9 illustrates the persisting, reversible effects of salicylate on trypsin-treated OHCs. After the cell became fully spherical at ~ 13 min, 10 mM salicylate was applied extracellularly. Detailed measures of voltage-dependent capacitance also were made by using stair-step stimuli before, during, and after application of salicylate. Salicylate consistently and reversibly reduced voltage-dependent capacitance ($n = 3$), suggesting that salicylate acts directly on the membrane-bound motor/sensor and not via the subsurface cisternae.

DISCUSSION

Previously, we demonstrated that intracellular pressure directly shifts the voltage dependence of membrane capacitance and motility in OHCs (Kakehata and Santos-Sacchi, 1995). Increasing pressure shifts V_{pkCm} and $V_{\delta Lmax}$ to positive potentials while simultaneously suppressing Cm_{pk} ; decreasing pressure has the opposite effects. In addition, even with iso-osmolar intra- and extracellular solutions, V_{pkCm} slowly moves to more hyperpolarized voltages after whole-cell configuration is established. This phenomenon is believed to underlie the variability of V_{pkCm} in isolated OHCs. Thus, in evaluating OHC voltage-dependent movement and membrane capacitance, the effects of intracellular pressure have to be taken into account. In the present study, we used techniques to minimize or control for the effects of intracellular pressure. Under such conditions, it is clear that salicylate and lanthanides exert their effects independent of turgor pressure.

Two other reports have investigated the effects of salicylate on motility or membrane capacitance by the use of whole-cell voltage clamp (Shehata et al., 1991; Tunstall et al., 1995). Neither controlled for pipette-mediated intracellular pressure changes, because large-tipped pipettes were used ($2-5$ M Ω , $1.5-3$ μ m). Reduction of electromotility because of loss of turgidity by extracellularly applied salicylate was reported (Shehata et al., 1991), and disruption of subsurface cisternae was thought to be related to this phenomenon (Dieler et al., 1991). However, our data do not support their conclusions. First, salicylate suppresses Cm_{pk} and shifts V_{pkCm} to depolarized potentials—opposite the effects of decreasing turgor pressure. Second, extracellular salicylate application for up to 300 sec induced an apparent collapse of only one OHC ($n = 11$) in whole-cell configuration with clamped, positive pressure. No unpatched, isolated cells showed any detectable collapse when 10 mM salicylate was applied extracellularly for >10 min, which is in accord with previous findings (Shehata et al., 1991). In addition, only 2 of 11 OHCs tested with internal 10 mM

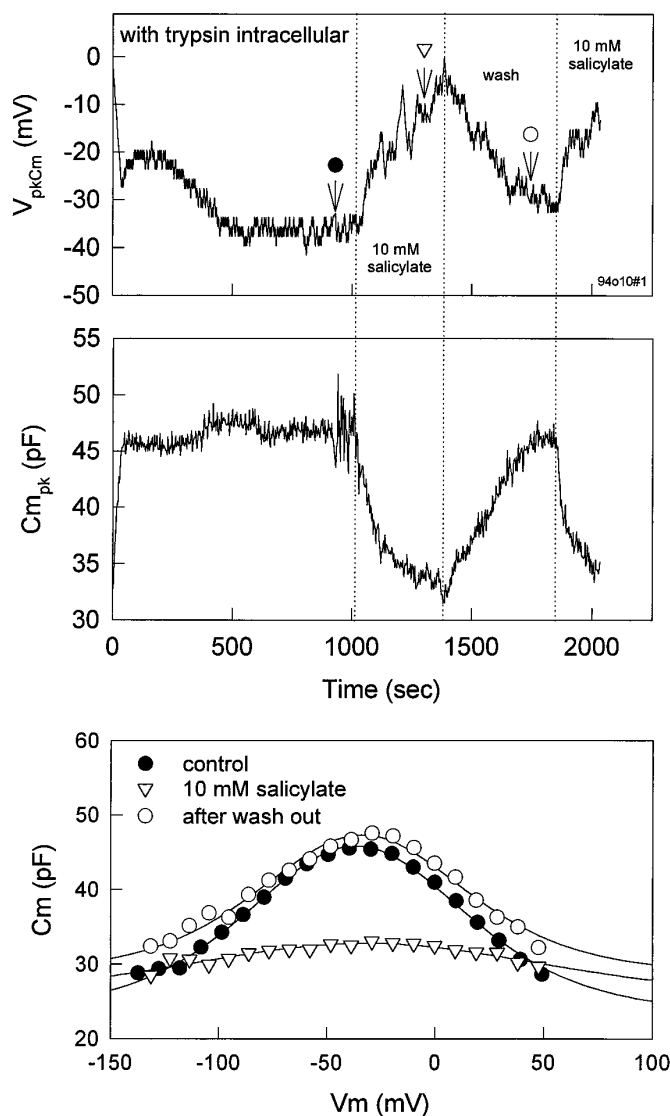


Figure 9. Effects of salicylate on V_{pkCm} and Cm_{pk} of a trypsin-treated cell. Trypsin (300 g/ml) was included in the patch pipette. After the cell became fully spherical at ~13 min, 10 mM salicylate was applied extracellularly. Voltage-dependent capacitance was measured before, during, and after application of salicylate. Salicylate reduced voltage-dependent capacitance reversibly, despite permanent disruption of the subsurface cisternae. Fits (solid lines) for capacitance indicate V_{pkCm} , Q_{max} , and z of -36.6 mV, 3.04 pC, and 0.757 (closed circles); -32.0 mV, 1.69 pC, and 0.450 (open triangles). The fit to open triangles is unreliable because of the shallowness of the function.

salicylate collapsed after 3 min. These time periods are far longer than necessary for the effects we observe on the sensor/motor. Third, in the OHCs treated with trypsin, in which the normal arrangement between membrane and subsurface cisternae is disrupted, effects of salicylate on the membrane voltage sensor remained. Thus, it is likely that the mechanisms of salicylate effects on the membrane sensor/motor and the subsurface cisternae are different and that the action of salicylate on the membrane sensor/motor is faster than that on the subsurface cisternae, which requires >10 min for detectable effects (Dieler et al., 1991).

Tunstall et al. (1995) reported values of the Hill coefficient (n) and half-maximal concentration ($K_{1/2}$) for salicylate of 3.40 and

3.95 mM, respectively. From these data they deduced that the sensor/motor within the OHC membrane is a tetramer, as originally suggested by Kalinec et al. (1992). Our results indicate an n of 1.0 and $K_{1/2}$ of 1.6 mM. These apparent differences can be accounted for. Tunstall et al. obtained their dose-response curve at a fixed voltage of -50 mV, but they did not attempt to keep intracellular pressure constant. Measured capacitance at a fixed voltage may be subject to fluctuation induced by inadvertent turgor pressure change. Nevertheless, one cell was evaluated at four different membrane potentials with similar results, and data collection was rapid, indicating that pressure changes in their cells may not have been significantly influential. More importantly, however, their dose-response curves were obtained with a perfusion technique (monitoring the drug concentration increase near the cell after the start of a continuous flow of 10 mM salicylate), which presented salicylate for too short a period of time at low concentrations to allow Cm levels to reach steady state. As we demonstrated in this paper, tau of salicylate-induced reduction in Cm_{pk} was 19.2 ± 3.7 and 11.4 ± 2.4 sec for 1 and 10 mM salicylate, respectively (see also Fig. 5 in Tunstall et al., 1995; tau of 5 mM salicylate-induced reduction in Cm is ~15 sec). Their Figure 8 indicates that exposure time at each measured concentration below 10 mM was no more than a few seconds, total perfusion time from 0 to 10 mM being 30 sec. Such short application times would make their dose-response curve steeper and $K_{1/2}$ larger than actual and also would account for the nonsymmetrical shape of their data.

In the present experiments, we obtained the concentration-response curve by measuring changes in the maximum capacitance of the cell (Cm_{pk}), and various concentrations of salicylate were applied for at least 120 sec, allowing steady levels to be reached. In addition, we attempted to control for the effects of inadvertent intracellular pressure change. Although the $K_{1/2}$ we observed was 1.6 mM, effects on the sensor/motor were observed in the hundred micromolar range. It has been shown that the perilymphatic salicylate concentration, which induces tinnitus and hearing loss in the rat, is near $400 \mu M$ (Jastreboff et al., 1986). Therefore, the data we obtain *in vitro* are in accord with *in vivo* results. The value of the Hill coefficient for salicylate obtained in this experiment is 1.0, which indicates that there is one binding site per sensor/motor molecule for salicylate. This type of information is not sufficient to speculate on the number of sensor/motor subunits but simply points to a lack of cooperativity.

Our data permit us to speculate on the site and mechanism of salicylate action. Salicylic acid, transported in the undissociated or unionized form, is highly permeable across lipid bilayers (Gutknecht and Tosteson, 1973) and human red cell membranes (Joy and Cutler, 1987). When salicylic acid enters a cell, dissociation to salicylate occurs, with the final concentration of the dissociated form being dependent on intracellular pH (pHi). Because pHi decreases on application of extracellular salicylate under whole-cell recording conditions (Tunstall et al., 1995), the resulting level of intracellular salicylate at equilibrium is less than that of extracellular salicylate. Given the pKa of salicylic acid (3.0), it can be calculated from the Henderson-Hasselbalch equation that $0.6 \mu M$ salicylic acid will exist as the undissociated form at a 10 mM extracellular concentration of salicylate anion. Assuming that extracellularly applied 10 mM salicylate causes pHi to shift from 7.2 to 6.9, then the concentration of salicylate inside the cell would be 5 mM at equilibrium. The actual pHi change would depend on the efficacy of the patch solution buffer. The relatively slow time

course of salicylate action by extracellular perfusion may correspond to the time taken for salicylate to form intracellularly. In fact, Tunstall et al. (1995) showed that pHi changed from 7.2 to 6.9 in 30 sec. This time course should reflect directly the dissociation of H⁺ from salicylic acid. Because they also showed that pHi itself is not the main cause of capacitance decrease, we conclude that the change in capacitance that we note with extracellular salicylate is attributable to the production of the dissociated form. On the other hand, when 10 mM sodium salicylate solution buffered to pH 7.2 is introduced intracellularly, the effect is almost immediate and more pronounced, presumably because the dissociated form is delivered directly and at higher concentrations. It should be emphasized that, for either intracellular or extracellular application, the concentration of salicylic acid would be the same (0.6 μ M). That is, the residence of the uncharged form within the membrane probably does not interfere with the sensor/motor. Thus, our data, which demonstrate that salicylate acts faster and to a greater extent when dialyzed into the OHC, suggest that salicylate works on the sensor/motor in the dissociated, charged form. The ability of the dissociated, charged form of salicylate to interact with the sensor/motor on the inner aspect of the plasma membrane may underlie the voltage dependence shifts that we observe in the capacitance functions. Although salicylate is effective on the intracellular aspect of the lateral plasma membrane, we show that lanthanides function exclusively on the outer aspect. These results are contrary to those reported by Gale and Ashmore (1994a).

The comparison between mechanical movements and charge movements in treated cells indicates that, whereas charge movement is suppressed to nearly the same extent by salicylate and lanthanides, motility is not. Mechanical responses remain substantial after salicylate treatment, but the motility function becomes linear between the range of -150 and $+150$ mV. It should be noted, however, that in both cases residual nonlinear capacitance remains. The difference between mechanical responses obtained with the two treatments may relate to differential changes in the axial stiffness of the cell under each condition. It has been found that extracellularly applied salicylate reversibly reduces axial stiffness of isolated OHCs of guinea pig (Russell et al., 1995), which may be related to the demonstration of a reversible decrease in OHC lateral wall stiffness (Lue et al., 1996). Under such conditions, the residual charge movement may correspond to conformational changes of the motor molecule that are capable of driving an unloaded cell with reduced axial stiffness. Lanthanide treatment, on the other hand, may increase axial stiffness. This may be indicated by the elongation and apparent stiffening of the OHC noted with lanthanide treatments (Santos-Sacchi, 1991; Kakehata and Santos-Sacchi, 1995). Under conditions of increased axial stiffness, the conformation change of the motor, indicated by the residual charge movement, may be unable to effect mechanical responses.

In conclusion, we show that salicylate and lanthanides do not work via mechanisms similar to changes in intracellular turgor pressure. The effects seem to be a result of direct action on the motility sensor/motor: lanthanides working on the external aspect of the lateral membrane and salicylates working on the intracellular aspect. It is interesting to note that simple modifications to the salicylate molecule, which would limit its entry into the OHC, are predicted to eliminate the attendant tinnitus and hearing loss associated with the ingestion of the drug.

REFERENCES

- Ashmore JF (1987) A fast motile response in guinea-pig outer hair cells: the cellular basis of the cochlear amplifier. *J Physiol (Lond)* 388:323-347.
- Ashmore JF (1989) Transducer motor coupling in cochlear outer hair cells. In: *Mechanics of hearing* (Kemp D, Wilson JP, eds), pp 107-113. New York: Plenum.
- Ashmore JF (1992) Mammalian hearing and the cellular mechanism of the cochlear amplifier. In: *Sensory transduction* (Corey DP, Roper SD, eds), pp 395-412. New York: Rockefeller UP.
- Brownell WE, Bader CR, Bertrand D, de Ribaupierre Y (1985) Evoked mechanical responses of isolated cochlear outer hair cells. *Science* 227:194-196.
- Carlyon RP, Butt M (1993) Effects of aspirin on human auditory filters. *Hear Res* 66:233-244.
- Dallos P (1992) The active cochlea. *J Neurosci* 12:4575-4585.
- Dallos P, Evans BN, Hallworth R (1991) Nature of the motor element in electrokinetic shape changes of cochlear outer hair cells. *Nature* 350:155-157.
- Dieler R, Shehata WE, Dieler W, Brownell WE (1991) Concomitant salicylate-induced alterations of outer hair cell subsurface cisternae and electromotility. *J Neurocytol* 20:637-653.
- Gale JE, Ashmore JF (1994a) An intracellular site for the inhibition of outer hair cell motility by gadolinium? *Soc Neurosci Abstr* 1:1.
- Gale JE, Ashmore JF (1994b) Charge displacement induced by rapid stretch in the basolateral membrane of the guinea-pig outer hair cell. *Proc R Soc Lond [Biol]* 255:243-249.
- Gutknecht J, Tosteson DC (1973) Diffusion of weak acids through lipid bilayer membranes: effect of chemical reactions in the aqueous unstirred layer. *Science* 182:1258-1261.
- Hamill OP, Marty A, Neher E, Sakmann B, Sigworth FR (1981) Improved patch-clamp techniques for high-resolution currents recording from cells and cell-free membrane patches. *Pflügers Arch* 391:85-100.
- Huang G-J, Santos-Sacchi J (1993) Mapping the distribution of the outer hair cell motility voltage sensor by electrical amputation. *Biophys J* 65:2228-2236.
- Huang G-J, Santos-Sacchi J (1994) Motility voltage sensor of the outer hair cell resides within the lateral plasma membrane. *Proc Natl Acad Sci USA* 91:12268-12272.
- Iwasa KH (1993) Effect of stress on the membrane capacitance of the auditory outer hair cell. *Biophys J* 65:492-498.
- Iwasa KH (1994) A membrane motor model for the fast motility of the outer hair cell. *J Acoust Soc Am* 96:2216-2224.
- Jastreboff PJ, Hansen R, Sasaki PG, Sasaki CT (1986) Differential uptake of salicylate in serum, cerebrospinal fluid, and perilymph. *Arch Otolaryngol Head Neck Surg* 112:1050-1053.
- Joy MM, Cutler DJ (1987) On the mechanism of transport of salicylate and p-hydroxybenzoic acid across human red cell membrane. *J Pharm Pharmacol* 39:266-271.
- Kakehata S, Santos-Sacchi J (1995) Membrane tension directly shifts voltage dependence of outer hair cell motility and associated gating charge. *Biophys J* 68:2190-2197.
- Kakehata S, Nakagawa T, Takasaka T, Akaike N (1993) Cellular mechanism of acetylcholine-induced response in dissociated outer hair cells of guinea-pig cochlea. *J Physiol (Lond)* 463:227-244.
- Kalinek F, Holley MC, Iwasa KH, Lim DJ, Kachar B (1992) A membrane-based force generation mechanism in auditory sensory cells. *Proc Natl Acad Sci USA* 89:8671-8675.
- Kujawa SG, Fallon M, Bobbin RP (1992) Intracochlear salicylate reduces low-intensity acoustic and cochlear microphonic distortion products. *Hear Res* 64:73-80.
- Long GR, Tubis A (1988) Modification of spontaneous and evoked otoacoustic emissions and associated psychoacoustic microstructure by aspirin consumption. *J Acoust Soc Am* 84:1343-1353.
- Lue AJ-C, Weng TX, Spector AA, Popel AS, Brownell WE (1996) Salicylate-induced changes of outer hair cell lateral wall stiffness. *Soc Neurosci Abstr* 2:2.
- McFadden D, Plattsmier HS (1984) Aspirin abolishes spontaneous otoacoustic emissions. *J Acoust Soc Am* 76:443-448.
- Mongan E, Kelly P, Nies K, Porter WW, Paulus HE (1973) Tinnitus as an indication of therapeutic serum salicylate levels. *JAMA* 226:142-145.

- Murase K, Randic M, Shirasaki T, Nakagawa T, Akaike N (1990) Serotonin suppresses *N*-methyl-D-aspartate responses in acutely isolated rat spinal dorsal horn neurons. *Brain Res* 525:84–91.
- Myers EN, Bernstein JM (1965) Salicylate ototoxicity: a clinical and experimental study. *Arch Otolaryngol Head Neck Surg* 82:483–493.
- Puel JL, Bledsoe SJ, Bobbin RP, Ceasar G, Fallon M (1989) Comparative actions of salicylate on the amphibian lateral line and guinea pig cochlea. *Comp Biochem Physiol* 93:73–80.
- Russell IJ, Murugasu E, Schauz C (1995) The effects of salicylate on the mechanics of the basilar membrane and isolated outer hair cells of the guinea pig cochlea. *Soc Neurosci Abstr* 3:3.
- Santos-Sacchi J (1989) Asymmetry in voltage-dependent movements of isolated outer hair cells from the organ of Corti. *J Neurosci* 9:2954–2962.
- Santos-Sacchi J (1991) Reversible inhibition of voltage-dependent outer hair cell motility and capacitance. *J Neurosci* 11:3096–3110.
- Santos-Sacchi J (1993) Harmonics of outer hair cell motility. *Biophys J* 65:2217–2227.
- Santos-Sacchi J, Dilger JP (1988) Whole-cell currents and mechanical responses of isolated outer hair cells. *Hear Res* 35:143–150.
- Shehata WE, Brownell WE, Dieler R (1991) Effects of salicylate on shape, electromotility, and membrane characteristics of isolated outer hair cells from guinea pig cochlea. *Acta Otolaryngol (Stockh)* 111:707–718.
- Tunstall MJ, Gale LE, Ashmore JF (1995) Action of salicylate on membrane capacitance of outer hair cells from the guinea-pig cochlea. *J Physiol (Lond)* 485:739–752.
- Zhi M, Phillips B, Brownell WE (1996) Alkaline cytoplasm and pH gradients in outer hair cell: evidence for a proton pump. *Soc Neurosci Abstr* 4:4.

Extracellular chloride regulation of Kv2.1, contributor to the major outward Kv current in mammalian outer hair cells

Xiantao Li, Alexei Surguchev, Shumin Bian, Dhasakumar Navaratnam and Joseph Santos-Sacchi

Am J Physiol Cell Physiol 302:C296-C306, 2012. First published 21 September 2011;
doi:10.1152/ajpcell.00177.2011

You might find this additional info useful...

This article cites 54 articles, 22 of which can be accessed free at:

<http://ajpcell.physiology.org/content/302/1/C296.full.html#ref-list-1>

Updated information and services including high resolution figures, can be found at:

<http://ajpcell.physiology.org/content/302/1/C296.full.html>

Additional material and information about *AJP - Cell Physiology* can be found at:

<http://www.the-aps.org/publications/ajpcell>

This information is current as of February 23, 2012.

Extracellular chloride regulation of Kv2.1, contributor to the major outward Kv current in mammalian outer hair cells

Xiantao Li,¹ Alexei Surguchev,¹ Shumin Bian,¹ Dhasakumar Navaratnam,^{2,3} and Joseph Santos-Sacchi^{1,2,4}

Departments of ¹Surgery (Otolaryngology), ²Neurobiology, ³Neurology, and ⁴Cellular and Molecular Physiology, Yale University School of Medicine, New Haven, Connecticut

Submitted 1 June 2011; accepted in final form 18 September 2011

Li X, Surguchev A, Bian S, Navaratnam D, Santos-Sacchi J. Extracellular chloride regulation of Kv2.1, contributor to the major outward Kv current in mammalian outer hair cells. *Am J Physiol Cell Physiol* 302: C296–C306, 2012. First published September 21, 2011; doi:10.1152/ajpcell.00177.2011.—Outer hair cells (OHC) function as both receptors and effectors in providing a boost to auditory reception. Amplification is driven by the motor protein prestin, which is under anionic control. Interestingly, we now find that the major, 4-AP-sensitive, outward K⁺ current of the OHC (I_K) is also sensitive to Cl⁻, although, in contrast to prestin, extracellularly. I_K is inhibited by reducing extracellular Cl⁻ levels, with a linear dependence of 0.4%/mM. Other voltage-dependent K⁺ (Kv) channel conductances in supporting cells, such as Hensen and Deiters' cells, are not affected by reduced extracellular Cl⁻. To elucidate the molecular basis of this Cl⁻-sensitive I_K , we looked at potential molecular candidates based on Cl⁻ sensitivity and/or similarities in kinetics. For I_K , we identified three different Ca²⁺-independent components of I_K based on the time constant of inactivation: a fast, transient outward current, a rapidly activating, slowly inactivating current (I_{K1}), and a slowly inactivating current (I_{K2}). Extracellular Cl⁻ differentially affects these components. Because the inactivation time constants of I_{K1} and I_{K2} are similar to those of Kv1.5 and Kv2.1, we transiently transfected these constructs into CHO cells and found that low extracellular Cl⁻ inhibited both channels with linear current reductions of 0.38%/mM and 0.49%/mM, respectively. We also tested heterologously expressed Slick and Slack conductances, two intracellularly Cl⁻-sensitive K⁺ channels, but found no extracellular Cl⁻ sensitivity. The Cl⁻ sensitivity of Kv2.1 and its robust expression within OHCs verified by single-cell RT-PCR indicate that these channels underlie the OHC's extracellular Cl⁻ sensitivity.

voltage-dependent potassium ion channels; chloride; outer hair cells

THE OUTER HAIR CELL (OHC) is both a receptor and an effector, possessing a distinct ensemble of membrane proteins, e.g., prestin (54), the α_9 - and α_{10} -nicotinic ACh receptor subunits (7, 8), and the unidentified transduction channel (5), which underlie these processes.

Concerning the effector role of OHCs, recent studies suggest that prestin activity is highly dependent on intracellular Cl⁻ anions (36, 38, 44, 46). Modulating intracellular Cl⁻ alters the motor's nonlinear charge movement (or nonlinear capacitance), thereby affecting the voltage sensitivity of OHC electromotility. The mechanism whereby anions work on prestin remains controversial; however, much evidence points to an allosteric mechanism (38, 45), similar to the way in which Ca²⁺ modulate the voltage sensitivity of large-conductance Ca²⁺-activated K⁺ (BK) channels (15, 53).

Address for reprint requests and other correspondence: J. Santos-Sacchi, Otolaryngology, Neurobiology, and Cellular and Molecular Physiology, Yale Univ. School of Medicine, BML 224, 333 Cedar St., New Haven, CT 06511 (e-mail: joseph.santos-sacchi@yale.edu).

Concerning the sensory role of the OHC, receptor potentials that drive neurotransmitter release and electromotility are subject to the shaping effects of the cell's basolateral voltage-dependent membrane conductances (17). The dominant conductances of the adult OHC are K⁺ conductances, with two types having been distinguished based on voltage dependence and pharmacological properties: a K⁺ current in OHC activated at negative potential ($I_{K,n}$) and the outward K⁺ current of the OHC (I_K) (16, 27, 42). $I_{K,n}$ is half-activated at -92 mV and likely helps to set the resting membrane potential of the OHC. I_K activates more positive to -40 mV. Because this voltage is depolarized sufficiently from the normal in vivo resting potential [approximately -70 mV (6)], it might be expected that only large suprathreshold receptor potentials could activate I_K to shape the cell's response (12).

Although the effects of Cl⁻ on prestin result from intracellular interactions with the protein, we have shown that extracellular Cl⁻ can modulate the motor via flux through a tension- and voltage-dependent Cl⁻ conductance, termed G_{metL} (38, 46). Indeed, manipulation of extracellular perilymphatic Cl⁻ was shown to reversibly and profoundly alter cochlear amplification in vivo (44).

In our quest to study the permeation characteristics of G_{metL} , we found that extracellular Cl⁻ has an unusual effect on I_K in OHCs. Reduction of extracellular Cl⁻ reduces the outward current in a concentration-dependent manner. We find that this effect is due, in part, to a selective action on the inactivation kinetics of the voltage-dependent K⁺ (Kv) conductance of the OHC alone, with Kv conductances of other inner ear cells being unaffected. The growing impact of anions in the auditory periphery is remarkable.

METHODS

Tissue preparation for electrophysiology. The experiments were performed in accordance with an approved protocol from Yale University's animal use and care committee. Hartley albino guinea pigs (150–200 g) were anesthetized with halothane, and temporal bones were excised rapidly. The top two turns of the organ of Corti were dissected and incubated for 10–12 min with neutral protease (0.5 mg/ml; Worthington) in a nominally Ca²⁺-free solution containing (in mM): 140 NaCl and 5 KCl. Subsequently, the tissue was triturated with a glass pipette for ~1 min with the above solution plus 2 mM Ca²⁺. Drops of the cell suspension were transferred into a small recording chamber mounted on the stage of a Nikon inverted microscope, and cells (OHCs, Hensen cells, and Deiters' cells) were allowed to settle onto the chamber bottom.

Electrophysiological recording. Patch-clamp experiments were performed in the whole cell configuration using pipettes pulled from borosilicate glass capillaries. The pipette resistance ranged between 1.5 and 3 M Ω and was <5–10 M Ω after whole cell establishment. Clamp tau values were <100–200 μ s, orders of magnitude less than measured current tau values. Pipette solution contained (in mM): 150

KCl, 2 MgCl₂, 5 EGTA, and 5 HEPES. The absence of Ca²⁺ intracellularly removes the influence of BK and small-conductance Ca²⁺-activated K⁺ (SK) channel conductances. We did not add ATP or other metabolites to the pipette solution so that currents dependent on these metabolites would be eliminated from our evaluations of Cl⁻ effects. The bath solution contained (in mM): 145 NaCl, 5 KCl, 1 MgCl₂, 2 CaCl₂, and 5 HEPES. The use of intra- and extracellular HEPES obviates the potential effect of pH alterations during changes in Cl⁻. Bath and pipette solutions were adjusted to ~300 mosmol/kg with dextrose and to pH 7.3. The liquid junction potential was around 1–3 mV with 3 M KCl salt bridges. Whole cell currents were recorded at room temperature using an Axon 200B amplifier (Axon Instruments), Digidata 1321 board (Axon Instruments), and the software program jClamp (Sciosoft).

Concentration-response curves were obtained by substituting gluconate for Cl⁻. Extracellular Cl⁻ concentrations of 5, 30, 70, 100, 125, and 150 mM were tested. Responses were plotted relative to the 150 mM Cl⁻ condition. Currents were averaged from the final 100 ms of a 200-ms test step to +50 mV from a holding potential of -40 mV. Attempts were made to fit the response function to the Hill equation, but fits were inadequate. Instead, data were fit to a linear equation to obtain slopes.

Isolation of individual OHCs for RT-PCR. Guinea pig temporal bones were dissected in PBS. Turns two to four of the cochleae were mechanically triturated separately in PBS and suspended in petri dishes to allow cells to settle. Silanized pipettes (trimethyl-chlorosilan; Fluka, St. Louis, MO) with a pore diameter of ~30 μm were used to pick up individual OHCs. Following capture of individual OHCs, the contents of the pipettes were expelled into Eppendorf tubes and stored at -80°C.

Single cell nested PCR from OHC. cDNAs from each isolated cell were synthesized as previously described (30). Nested PCR was performed in two steps. First, 35 cycles of PCR were run (94°C for 30 s, 55°C for 1 min, 68°C for 3 min) using 5 μl of each cDNA and corresponding Kv outer primers. Second, 5 μl of each reaction from the first step were used for another 35 cycles of amplification using Kv inner primers. Both steps used the Expand High Fidelity PCR System (Roche, Indianapolis, IN). Fragments were analyzed on 2% agarose resolute GPG gel (American Bioanalytical, Natick, MA). To confirm the presence of a correct Kv channel, the PCR products were purified from the gel using a gel purification kit (Qiagen, Valencia, CA) and sequenced using the corresponding amplification primers by Yale's Keck sequencing facility. The primers were designed to straddle an intron of at least 1,000 bp. The primers were as follows: Kv1.5 outer, Kv1.5FOT GACACTAGC-

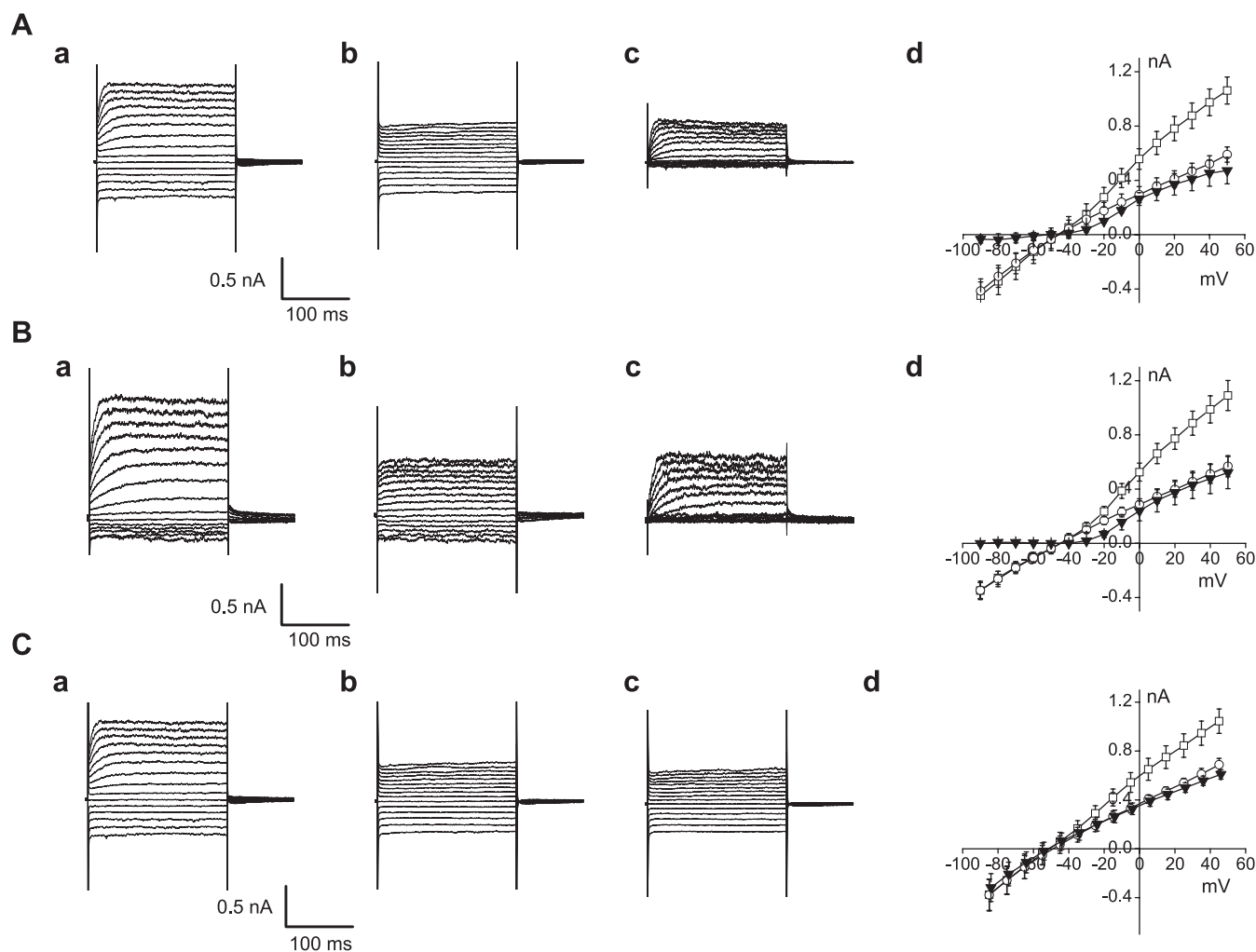


Fig. 1. Inhibition of outward K⁺ current of the outer hair cells (I_K) by 4-AP and low extracellular Cl⁻. Membrane current was recorded with 200-ms pulses to potentials between -90 and 50 mV from a holding potential of -40 mV. The waveforms of the 4-AP- and Cl⁻-sensitive currents were determined by subtraction of control currents. *A*: *a*, control; *b*, 100 μM 4-AP; *c*, 100 μM 4-AP-sensitive current; *d*, current-voltage relationship of I_K for control (□), 100 μM 4-AP (○), and 100 μM 4-AP-sensitive current (▼) ($n = 3$). *B*: *a*, control; *b*, 5 mM Cl⁻; *c*, 5 mM Cl⁻-sensitive current; *d*, current-voltage relationship of I_K for control (□), 5 mM Cl⁻ (○) and 5 mM Cl⁻-sensitive current (▼) ($n = 5$). *C*: *a*, control; *b*, 100 μM 4-AP; *c*, 100 μM 4-AP + 5 mM Cl⁻; *d*, current-voltage relationship of I_K for control (□), 100 μM 4-AP (◇), and 100 μM 4-AP + 5 mM Cl⁻ (▼) ($n = 3$).

CGGGAAACAGA and Kv1.5ROT GGTGACCCTGGTGTATGG; Kv1.5 inner, Kv1.5FIN TCAAGGCAGACTTGCAACAG and Kv1.5RIN GAAGTTAGAGGGCAGGAGGG; Kv2.1, Kv2.1FOT CAAAAGAAGGAGCAGATGAACGAG and Kv2.1ROT TTGAGTGACAGGGCAATGGTG; Kv4.2 outer, Kv4.2FOT: GCCTTCGTAGCAAATCTGG and Kv4.2ROT ACACATTGGCATTGGGATT; Kv4.2 inner, Kv4.2FIN TCACTGCCTGGAGAAAACC and Kv4.2RIN AGCAAGTGCTGGTGACTCCT; Kv4.3 outer, Kv4.3FOT GGCTACACCCTGAAGAGCTG and Kv4.3ROT AGTTGGTGACTATGACGGGG; and Kv4.3 inner, Kv4.3FIN CATGGCCATCATCTTTG and Kv4.3RIN GCCAAATATCTTCCAGCAA.

To investigate whether the pore residue 356 in Kv2.1 has an effect on extracellular Cl^- sensitivity (see RESULTS and DISCUSSION), K356G mutants were generated using QuickChange II or QuickChange Lightning site-directed mutagenesis kits (Stratagene, La Jolla, CA) with rat Kv2.1 as a template. Mutations were confirmed by DNA sequencing, including the entire coding region. The following primers were used: Kv2.1K356GF: GATGAGGACGACACCGGGTTCAAAGCATCCCC and Kv2.1K356GR GGGGATGCTTTGAACCCGGTGTCGCTCATC.

Analysis and statistics. For current-voltage (I - V) analysis, peak currents at each test potential were measured as the difference between the maximal outward current amplitudes and the zero current level. The waveforms of the 4-AP and Cl^- -sensitive currents were determined by subtraction of control currents (recorded in the absence of 4-AP and the presence of 150 mM Cl^-). The decay phases of the currents evoked during long (5.0 s) depolarizing voltage steps to test potentials from a holding potential of -80 mV were fitted by a single or the sum of two exponentials using one of the following expressions:

$$f(t) = A_1 \exp(-t/\tau_1) + A_{ss}$$

$$f(t) = A_1 \exp(-t/\tau_1) + A_2 \exp(-t/\tau_2) + A_{ss} \quad (1)$$

where t is time, τ_1 and τ_2 are the time constants of decay of the inactivating I_K currents, A_1 and A_2 are the amplitudes of the inactivating current components, and A_{ss} is the amplitude of the steady-state, noninactivating component of the total outward current. In the manuscript, control currents refer to those obtained in the presence of 150 mM extracellular Cl^- .

For the steady-state inactivation curve, the current amplitude during each test pulse was normalized to maximal current (I/I_{\max}) and plotted against the voltage during the conditioning prepulse. These data were fitted by a Boltzmann equation:

$$I/I_{\max} = 1/[1 + \exp(V_{1/2} - V_m)/k] \quad (2)$$

where $V_{1/2}$ is the conditioning potential that gives $I/I_{\max} = 0.5$, V_m is the conditioning potential, and k describes the steepness of the curve.

Data are reported as means \pm SE. Statistical significance was calculated using Student's t -test. All experiments were carried out at room temperature (22°C).

RESULTS

I_K in OHCs is sensitive to 4-AP and extracellular Cl^- . Outward currents were recorded routinely during depolarizing voltage steps to potentials more positive than the holding potential of -40 mV (Fig. 1). At this holding potential, $I_{K,n}$ is not further activated upon depolarization (16), thus allowing study of I_K in isolation following linear current subtractions (see DISCUSSION for details). These outward currents (I_K) did not decay appreciably during the 200-ms voltage steps, as previously observed (16, 27, 42). 4-AP ($100 \mu\text{M}$) strongly inhibits outward I_K in OHCs (Fig. 1A). Surprisingly, however, extracellular Cl^- can also modulate I_K of OHCs. Switching from a high- Cl^- solution to a 5 mM Cl^- solution strongly inhibits the

outward current (Fig. 1B). The effect was reversible ($68.5 \pm 16.7\%$ reversibility, $n = 3$). Comparison of the $100 \mu\text{M}$ 4-AP and Cl^- -sensitive currents indicates that they are similar in two ways: each has similar waveform and reversal potential (-70 mV). An initial perfusion of $100 \mu\text{M}$ 4-AP can abolish the subsequent effects of 5 mM Cl^- on I_K (Fig. 1C). These results suggest that Cl^- reduction inhibited the same I_K current that was specifically blocked by 4-AP. The average ($n = 6$) dose-response curve for extracellular Cl^- on I_K was not well fit by a sigmoidal Hill equation. Instead, the K^+ current appeared linear with Cl^- concentration, with a dependence of $0.4\%/m\text{M}$ (Fig. 2). This type of behavior may be related to actions on surface charges at the pore of channels (20) and is further explored below. Changes in intracellular Cl^- were ineffective (data not shown).

I_K of supporting cells is not sensitive to extracellular Cl^- . Prominent depolarization-activated outward K^+ currents (I_K) are recorded from supporting cells, such as Deiters' and Hensen cells (31, 40, 41, 47). We tested to determine whether these currents were also Cl^- sensitive. Figure 3A shows the macroscopic current from a Deiters' cell. Similar to the OHC, there is a rapid activation and slow inactivation elicited by depolarized potentials. For control Cl^- conditions, the peak amplitude was 2.47 ± 0.35 nA at $+50$ mV, and it was 2.33 ± 0.32 nA when extracellular Cl^- was reduced to 5 mM ($n = 3$, $P > 0.05$). The average I - V curve indicates no significant difference between the two conditions. A similar outward current was elicited from Hensen cells (Fig. 3B). The peak amplitude of the control was 1.41 ± 0.28 nA at $+50$ mV, and it was 1.32 ± 0.25 nA with 5 mM Cl^- ($n = 4$, $P > 0.05$). Again, the average I - V curve indicates no differences. We conclude that the I_K current of supporting cells is not sensitive to extracellular Cl^- changes.

Slick and slack channels are not sensitive to extracellular Cl^- . The molecular identity of outward I_K in the OHC is not clear. It is known that the sodium-activated K^+ channels Slick (Slo2.1) and Slack (Slo2.2), which are prominent in brain stem auditory pathways, are sensitive to intracellular Cl^- , but it is not known whether those channels are also sensitive to extracellular Cl^- (2) (Kaczmarek, personal communication). Whole

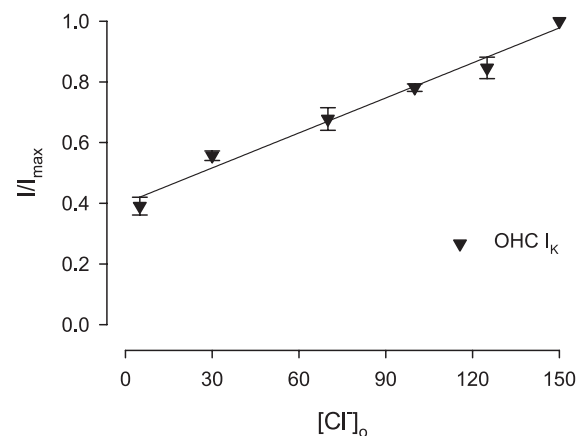


Fig. 2. Concentration-response curve of external Cl^- on magnitude of I_K . Functions were obtained by substituting gluconate for Cl^- . A linear fit (solid line) indicates an I_K change of $0.4\%/m\text{M}$ Cl^- . I/I_{\max} , the current amplitude during each test pulse normalized to maximal current; $[\text{Cl}^-]_o$, extracellular Cl^- concentration; OHC, outer hair cells.

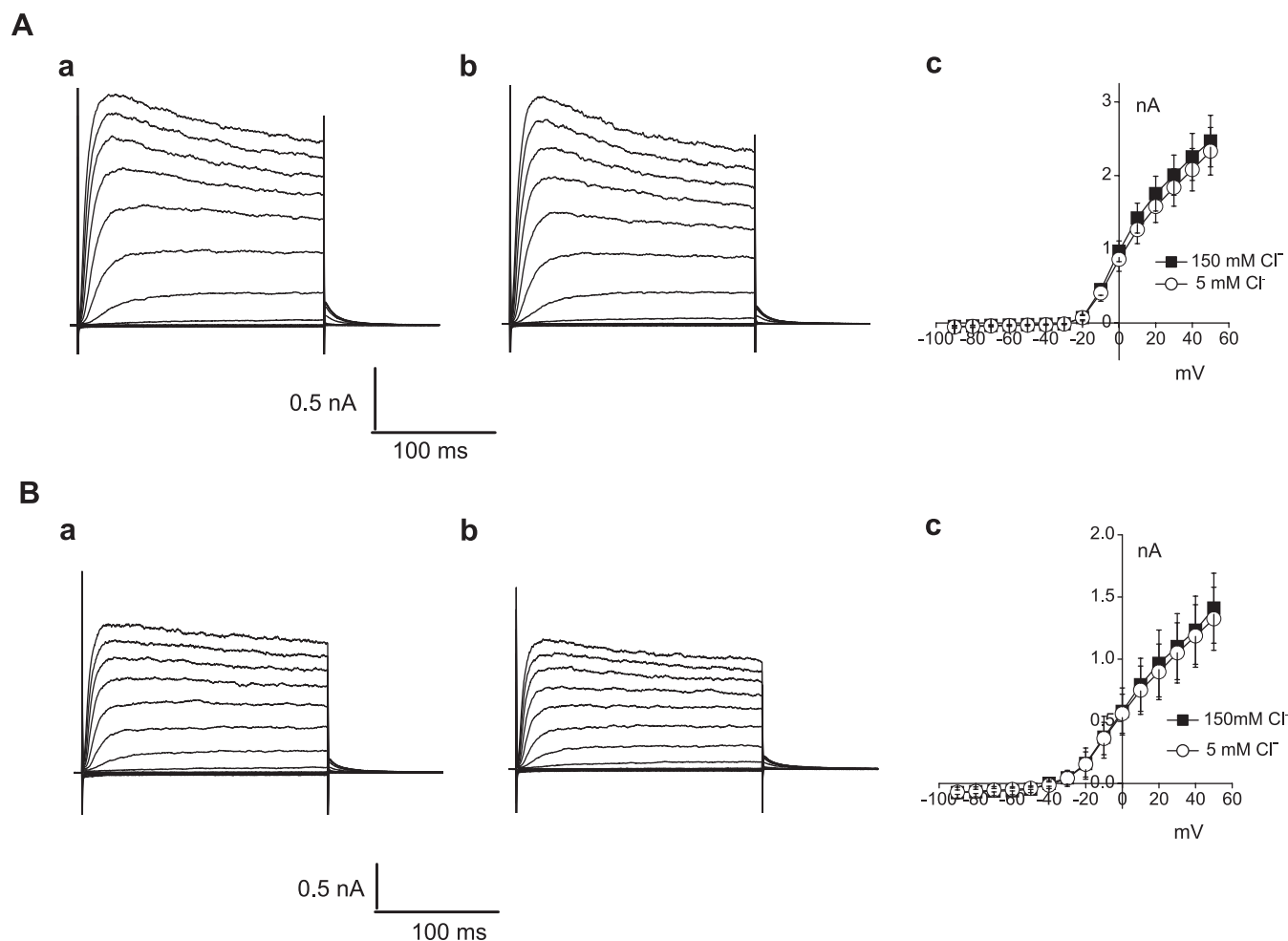


Fig. 3. Deiters' and Hensen cell K^+ currents are insensitive to extracellular Cl^- . Current traces obtained with 500-ms steps from -90 to 50 mV from a -40 -mV holding potential. *A*: *a*, 150 mM Cl^- control current of Deiters' cell; *b*, 5 mM Cl^- ; *c*, current-voltage relationship of I_K of Deiters' cell for control (\blacksquare) and 5 mM Cl^- (\circ). *B*: *a*, 150 mM Cl^- control current of Hensen cell; *b*, 5 mM Cl^- ; *c*, current-voltage relationship of I_K in Hensen cell for control (\blacksquare) and 5 mM Cl^- (\circ).

cell recording of transfected cells was employed to examine the sensitivity of Slick and Slack currents to extracellular Cl^- . Figure 4A shows Slack whole cell currents. The last 50-ms average current amplitude was 2.72 ± 0.79 nA at $+50$ mV (Fig. 4Aa). Upon changing extracellular Cl^- from 150 to 5 mM, the current amplitude was 2.76 ± 0.93 nA and was not different from control ($n = 4$, $P > 0.05$, Fig. 4Ab). The last 50-ms average current amplitude of Slick was 1.14 ± 0.11 nA at $+50$ mV (Fig. 4Ba). Upon changing extracellular Cl^- from 150 to 5 mM, the current amplitude was 1.17 ± 0.09 nA and was not different from control ($n = 4$, $P > 0.05$, Fig. 4Bb). These results show that Slick and Slack channels are not sensitive to extracellular Cl^- , indicating that they do not underlie OHC I_K .

Three components in outward I_K . Outward K^+ currents in other tissues have been characterized in terms of kinetic components (52). To further study the mechanism of inhibition by Cl^- on I_K of the OHC, we performed a similar analysis. Currents were elicited by a 5-s depolarizing step to a potential of $+40$ mV from a holding potential of -80 mV. Outward K^+ currents in all cells activated rapidly, and the decay phases of the currents were somewhat variable among cells (Table 1 and

Fig. 5). One group of cells exhibited only a single exponential decay phase, termed I_{to} (Fig. 5A). We used a dual exponential fit (see METHODS) for two additional populations of cells that each possessed the very fast component (I_{to}) and one of two additional slower second components, termed I_{K1} and I_{K2} (Fig. 5, B and C). Thus exponential fits revealed three inactivating components with decay time constants of 78.4 ± 6.3 ms ($n = 5$), 685.4 ± 61.3 ms ($n = 10$), and $1,504.4 \pm 104.6$ ms ($n = 10$), corresponding to I_{to} , I_{K1} , and I_{K2} , respectively. Of the cells studied, 14.3% had I_{to} alone, 48.6% had I_{to} and I_{K1} , and 37.1% had I_{to} and I_{K2} . The variance in the second term fits of each population was quite small and validates our initial separation into two second component populations. Figure 5D plots the relative distribution of the different current components, and Table 1 summarizes the data. Subsequent experiments were focused on characterizing the Cl^- sensitivity of these depolarization-activated K^+ current components.

Cl^- affects components of I_K in different ways. The voltage dependence of steady-state inactivation of I_{to} was examined using depolarizing voltage steps to $+40$ mV following 5-s conditioning prepulses to potentials between -100 and 0 mV (Fig. 6); the protocol is shown below the current records in Fig. 6C. Such

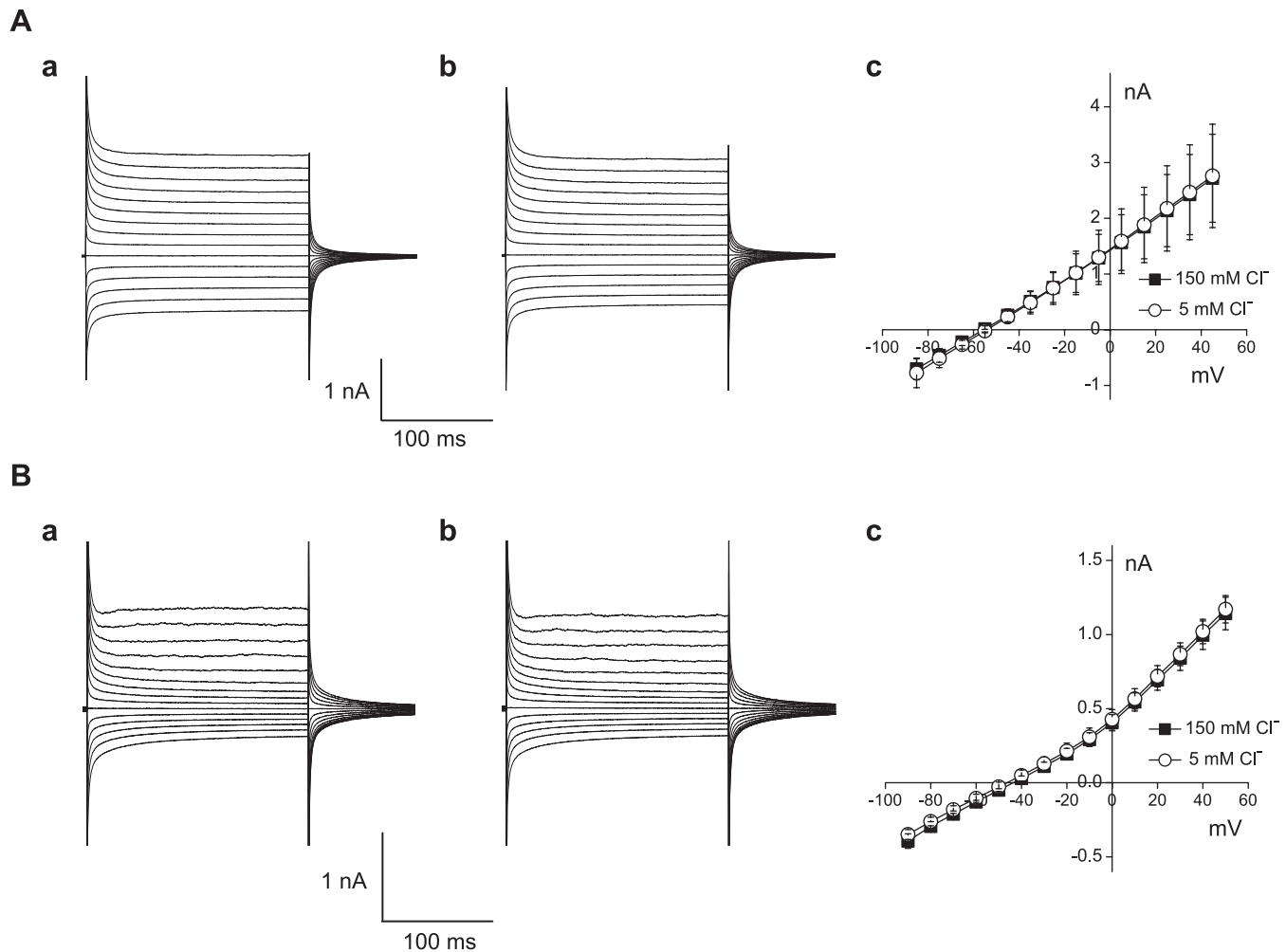


Fig. 4. Slack and Slick channel currents are insensitive to extracellular Cl^- . *A*: *a*, control current of Slack-transfected cell; *b*, 5 mM Cl^- ; *c*, current-voltage relationship of Slack for control (■) and 5 mM Cl^- (○). *B*: *a*, control current of Slick-transfected cell; *b*, 5 mM Cl^- ; *c*, current-voltage relationship of Slick for control (■) and 5 mM Cl^- (○).

robust inactivation of the outward I_K in OHCs has never been observed before, simply because such long-duration protocols have never been used. The amplitudes of I_{to} during each test pulse to +40 mV were measured as the difference between peak outward current and the current remaining at the end of

Table 1. Three distinct outward potassium currents in guinea pig outer hair cells

	I_{to}	I_{K1}	I_{K2}	I_{ss}
I_{to} ($n = 5$)				
τ_{decay} , ms	64.8 ± 12.7			
I_{peak} , %	49.3 ± 7.0			50.7 ± 7.0
$I_{to} + I_{K1}$ ($n = 10$)				
τ_{decay} , ms	78.4 ± 6.3	685.4 ± 61.3		
I_{peak} , %	36.5 ± 2.7	10.0 ± 1.1		53.4 ± 2.4
$I_{to} + I_{K2}$ ($n = 10$)				
τ_{decay} , ms	90.5 ± 5.4		1,504.4 ± 104.6	
I_{peak} , %	31.3 ± 2.2		12.0 ± 0.9	56.7 ± 2.7

All values are means ± SE; n , no. of experiments. I_{to} , transient outward K^+ currents; I_{K1} , K^+ currents of slow component 1; I_{K2} , K^+ currents of slow component 2; I_{ss} , steady-state currents. Currents were determined from analyses of records obtained on depolarization to +40 mV from a holding potential of -70 mV.

the depolarizing pulse [steady-state current (I_{ss})]. The amplitudes of I_{to} evoked from each conditioning potential were then normalized to maximal current amplitudes (in the same cell). For example, in the control condition (Fig. 6A), the amplitude of the peak current at the conditioning potential of -40 mV was 0.219 nA. When extracellular Cl^- was changed from 150 to 5 mM, the amplitude was reduced to 0.059 nA (Fig. 6B). The mean ± SE normalized I_{to} amplitudes are plotted as a function of conditioning potential in Fig. 6D; the continuous lines represent the best Boltzmann fits to the averaged data. The steady-state inactivation data for I_{to} in 150 mM Cl^- are well described by a single Boltzmann with a $V_{1/2}$ of -50 mV. Reducing extracellular Cl^- caused the inactivation curve of I_{to} to shift to the left (Fig. 6D), with 5 mM Cl^- producing an 8-mV hyperpolarizing shift.

Because we have no specific blockers for the identified kinetic components of I_{K1} , an analysis of the two additional components was performed by fitting two exponential functions to determine the amplitude and inactivation time constant of each component, I_{K1} and I_{K2} . The effects of Cl^- were analyzed with the simplified voltage protocol depicted in Figs. 7 and 8. In Figs. 7A and 8A, depolarization-induced outward currents are depicted

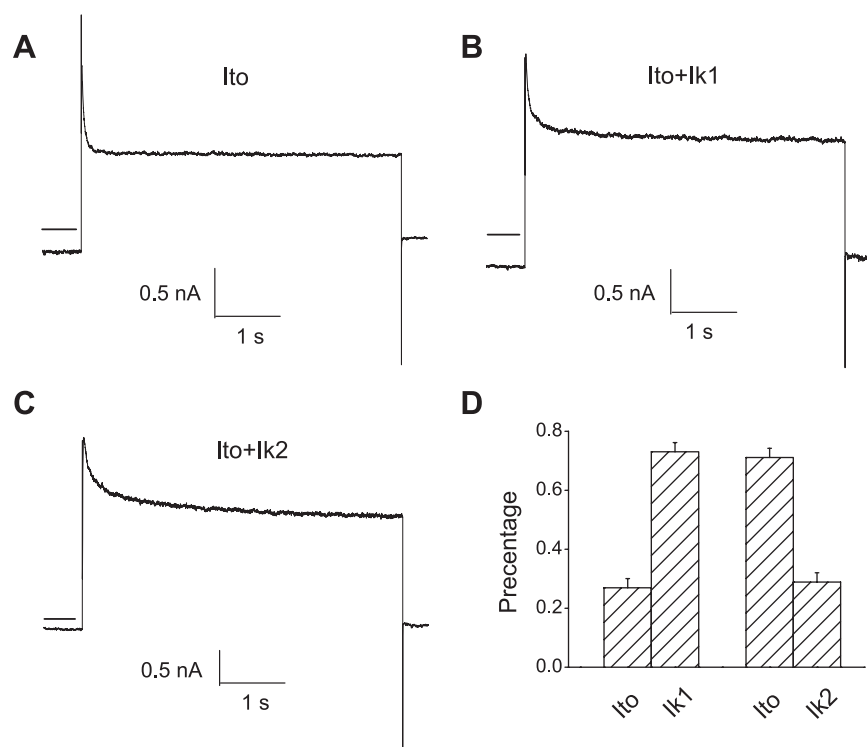


Fig. 5. Three kinetic components of outer hair cell (OHC) outward I_K are identified. Cells were held at -80 mV and stepped up to $+40$ mV for 5 s. *A*: only fast component, transient outward K^+ current (I_{to}). *B*: $I_{to} + I_{k1}$ (K^+ current of slow component 1) components. *C*: $I_{to} + I_{k2}$ (K^+ current of slow component 2) components. *D*: the ratio of different components of I_K . Horizontal solid lines on left of traces depict zero current levels.

before (traces on top) and after (traces on bottom) switching to 5 mM Cl^- . The bar plots in Figs. 7 and 8 show that, while the time constant of I_{to} remained unaffected, the magnitudes of all components decreased, and the inactivation time constants of I_{k1} and I_{k2} shortened. The inhibitory effect of Cl^- was time dependent on the scale of minutes. From these analyses, we conclude that lowering extracellular Cl^- inhibited I_K in OHCs by shifting the inactivation curve to the left and/or reducing the current amplitude.

Extracellular Cl^- inhibits Kv1.5 and Kv2.1 in CHO cells. The inactivation time constants of I_{k1} and I_{k2} are similar to those of the cardiac current in atrial myocytes that activates ultrarapidly but with no inactivation (I_{kur}) and the delayed-rectifier K^+ current in myocytes that slowly activates and deactivates, with a single channel conductance of 3–5 pS ($I_{k,slow}$), respectively (33, 34, 52). Kv1.5 and Kv2.1 contribute to I_{kur} and $I_{k,slow}$. To determine whether these subtypes contribute to OHC I_K , we transiently transfected Kv1.5 and Kv2.1

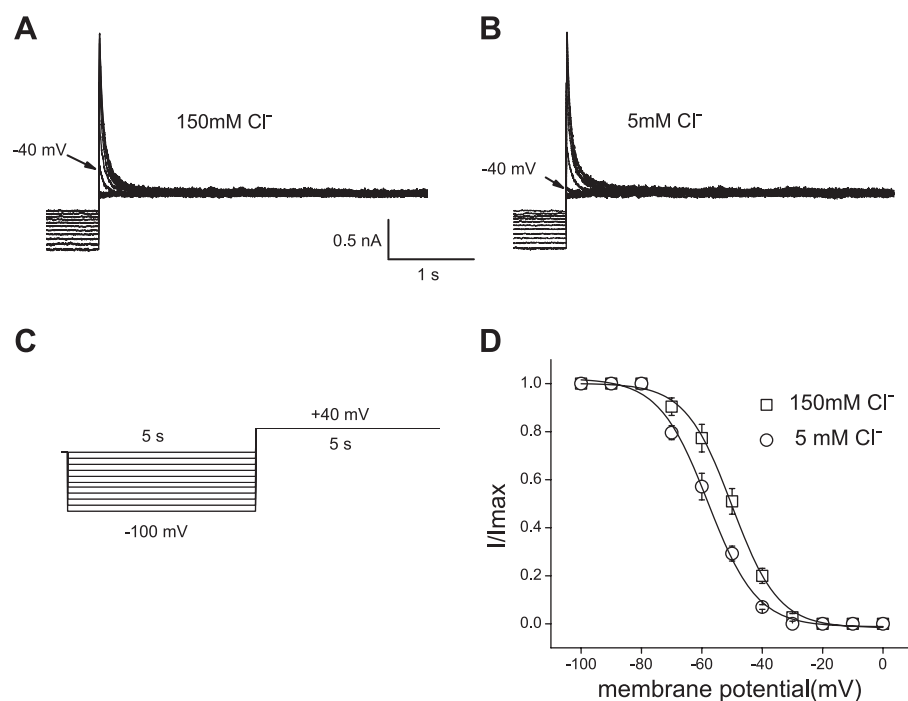


Fig. 6. Inhibition of I_{to} by external Cl^- . *A* and *B*: measurement of voltage dependence of inactivation. Superimposed current records during conditioning pulses and subsequent test pulses to $+40$ mV for control 150 mM Cl^- (*A*) and 5 mM Cl^- (*B*). Arrows indicate test current level at prepulse potential of -40 mV. *C*: protocol for inactivation curve: 5-s conditioning prepulses to various potentials (from -100 to 0 mV in 10-mV increments) were followed by a 5-s test pulse to $+40$ mV. Holding potential was -80 mV. *D*: mean \pm SE; $n = 4$. Steady-state inactivation curves of I_{to} . I_{to} during each test pulse was normalized to maximal I_{to} (I/I_{max}) and plotted against conditioning prepulse potential. Data are fitted with a Boltzmann equation.

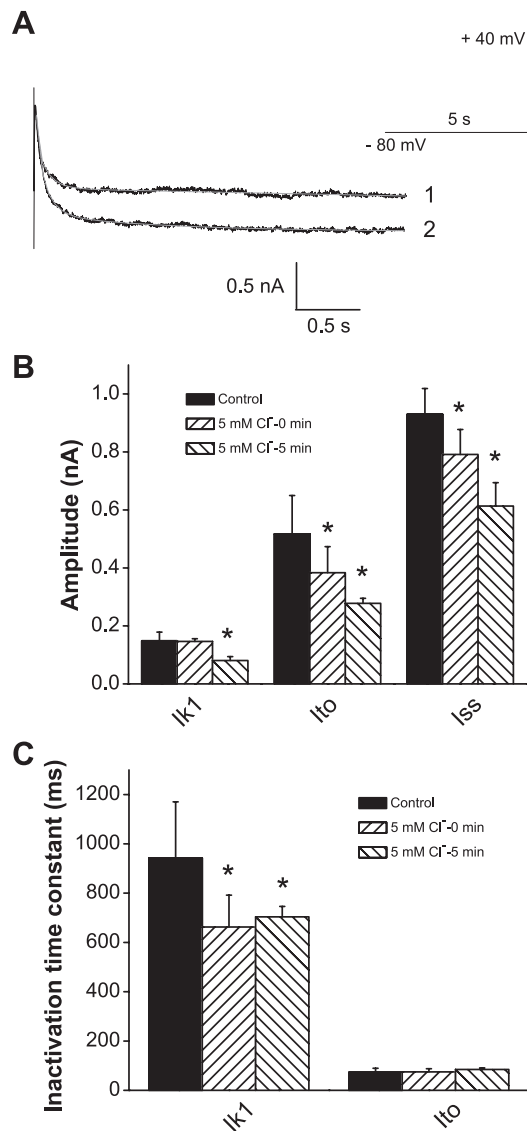


Fig. 7. Inhibition of I_{k1} by external Cl^- . A: superimposed pairs of currents at +40 mV recorded following conditioning pulses (-80 mV) for control 150 mM Cl^- (trace 1) and 5 mM Cl^- (trace 2). Red solid lines represent exponential fitting. Stimulation protocol is depicted at top right. B: time-dependent inhibition of current amplitude of I_{k1} , I_{to} , and steady-state current (I_{ss}). C: time-dependent inhibition of inactivation time constant of I_{k1} by external Cl^- . *Significance at the 0.05 level.

into CHO cells and tested the Cl^- sensitivity of the channels. Control macroscopic current of Kv1.5 is depicted in Fig. 9A, where peak amplitude at +50 mV is 3.65 ± 0.13 nA ($n = 4$). A switch to 5 mM extracellular Cl^- reduced the current amplitude to 2.00 ± 0.11 nA (Fig. 9B). Similar results were found with Kv2.1. In the control condition (Fig. 9C), the current amplitude is 8.52 ± 1.87 nA, and it is reduced to 6.15 ± 1.35 nA following the switch to 5 mM extracellular Cl^- ($n = 3$, Fig. 9D). Similar to OHC I_K , the dependence of Kv1.5 and Kv2.1 currents on extracellular Cl^- was not fit well by a sigmoidal Hill equation. Linear regression fits gave 0.38%/mM ($n = 6$) and 0.49%/mM ($n = 5$), respectively (Fig. 9E), similar to results in OHCs.

Kv2.1 and Kv1.5 as well as Kv4.2 and Kv4.3 are expressed in guinea pig OHCs. We sought to determine whether these Kv channels that have properties of the Cl^- -sensitive channel(s) in

the OHC are actually present in OHCs. We opted to use a single-cell RT-PCR strategy using primers that spanned introns to ascertain the presence of transcripts encoding Kv1.5 and Kv2.1 channels in the OHC. For comparison, we also tested for Kv4.2 and Kv4.3 transcripts. OHCs were isolated from different turns of the cochlea, and cDNA was made from these individual cells. Single-cell PCR amplifications were done, and the PCR products of the expected size were isolated and sequenced to confirm their identity. As shown in Fig. 10, Kv 2.1 was present in all nine OHCs and was detected after one round of amplification. In contrast, Kv1.5, Kv4.2, and Kv4.3 required two rounds of nested PCR amplification to be detected. Taken together, these data indicate that these channels are present in OHCs, with Kv2.1 predominating, and likely are responsible for its sensitivity to extracellular Cl^- .

Because the Cl^- dependence of these channels is linear, and such behavior may arise from charge screening effects at the mouth of channels (20), we investigated the mutation of residue K356G at the mouth of the Kv2.1 channel. This mutation has been shown to alter channel conductance by interfering with a K^+ -selective interaction with that site (4). We speculated that Cl^- might be modulating this interaction. However, no statistical difference was observed in the ability of low Cl^- to reduce K^+ currents [I_K 5/150 mM Cl^- : 0.521 ± 0.089 for WT ($n = 8$); 0.387 ± 0.059 for K356G ($n = 12$); $P > 0.05$].

DISCUSSION

There are two major voltage-dependent K^+ currents in OHC, $I_{K,n}$ and I_K , whose pharmacological sensitivities have been well studied (16, 27, 42). Both conductances are largely restricted to the basal pole of the OHC (43). Despite this wealth of knowledge, much remains to be learned about these channels; for example, we have recently shown that capsaicin can block OHC outward I_K and $I_{K,n}$ (51). The molecular entity underlying $I_{K,n}$ is believed to comprise KCNQ4 subunits (3, 14, 28). On the other hand, the molecular identity of I_K has not been suggested previously. In the present work, we identify I_K as a current sensitive to extracellular Cl^- and utilize this sensitivity and its kinetics to hone in on its molecular identity.

Sensitivity of OHC I_K to extracellular Cl^- and its significance. We found that OHC I_K , but neither I_K of Deiters nor Hensen cells, is decreased by reduction of extracellular Cl^- with a sensitivity of 0.4%/mM, indicating a significant sensitivity to Cl^- change over a wide range of extracellular levels. It is not known whether physiological fluctuations of Cl^- occur that could significantly modulate I_K . However, it may be possible that the restricted extracellular space between the Deiters cell and OHC base, where OHC voltage-dependent conductances reside (43), could support functionally significant fluctuations in ion concentrations, in the face of small transmembrane ion fluxes. Such a scenario is well established for intracellular compartmentalization (35).

To estimate the Cl^- concentration change made by a small flux of Cl^- ions at the base of the OHC, we assessed the volume within which Cl^- concentration may change from published electron microscopy descriptions (9, 22, 29, 39). As an example, we evaluate a typical mature OHC in the apical region, which has a diameter of ~ 7 μm . The distance from just above the nucleus to the bottom round end of the OHC, where

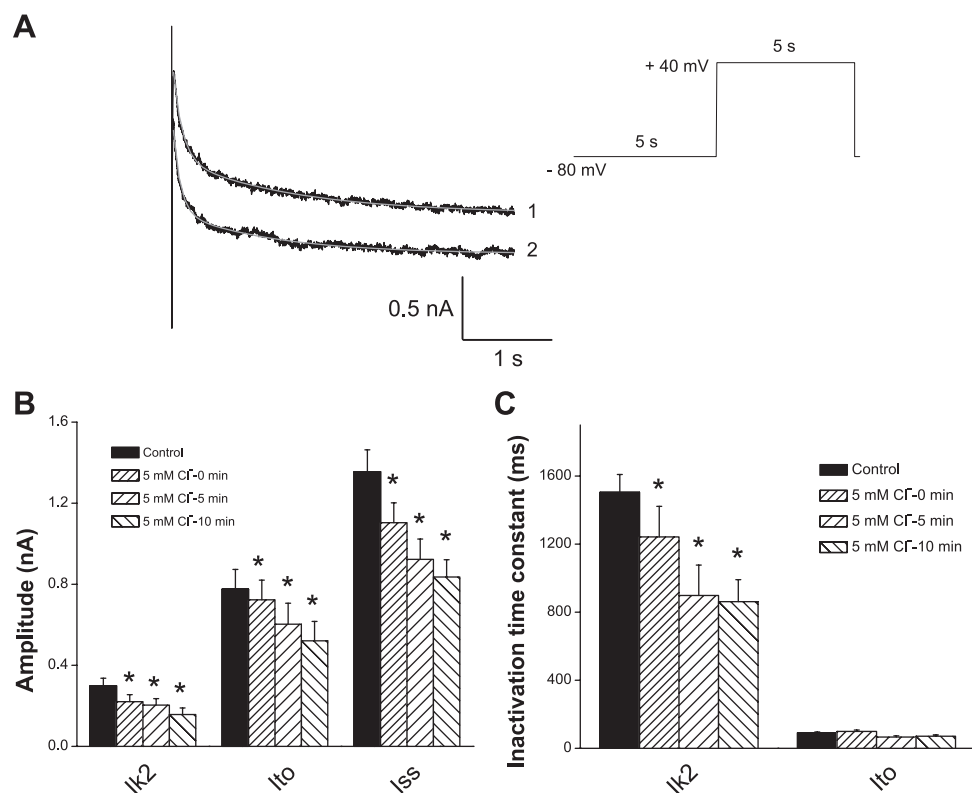


Fig. 8. Inhibition of I_{k2} by external Cl^- . **A**: superimposed pairs of currents at +40 mV recorded following conditioning pulses (−80 mV) for control 150 mM Cl^- (trace 1) and 5 mM Cl^- (trace 2). Red solid lines represent exponential fitting. Stimulation protocol is depicted at top right. **B**: time-dependent inhibition on current amplitude of I_{k2} , I_{to} , and I_{ss} . **C**: time-dependent inhibition of inactivation time constant of I_{k2} by external Cl^- . *Significance at the 0.05 level.

most of the Kv channels concentrate (43), is $\sim 13 \mu\text{m}$. This region resides in the cup formed by the Deiters' cell. An average of 15 afferent nerve terminals and 8 efferent terminals form close contact with the OHC (and with each other) through specialized synaptic structures, with a rather uniform gap of $0.04 \mu\text{m}$. This gap is similar to the reported intercellular space between the type I hair cell and its calyx ending in the vestibular system (10, 11). We assume a cylindrical OHC with hemispherical base and a Deiters' cell cup shaped like an inverted cone, whose height is $8.5 \mu\text{m}$ and base diameter the same as the OHCs. Next, the minimal volume in which the Kv channels can "see" a Cl^- fluctuation is the above-mentioned gap region, which is $\sim 11 \mu\text{m}^3$. If we assume the Kv channels have access to the whole cup region (no nerve ending present), then that volume is $\sim 27 \mu\text{m}^3$. Next, we estimate the Cl^- flux. One typical Cl^- channel with 25 pS conductance releases $\sim 10^6 \text{Cl}^-$ ions per second around resting potential (−60 mV). That translates into a 1.5 mM Cl^- concentration change in the minimal volume and 0.6 mM Cl^- concentration change in the maximal volume. If there are 10 Cl^- channels open simultaneously for 1 s, Kv channels will see anywhere between 6 and 15 mM Cl^- concentration change, which translates to 2.4–6% change in K^+ current magnitude. Specific ion accumulation in a very restricted space has been proposed to influence synaptic transmission, as reported recently in a very detailed work by Lim and colleagues (23) in their study of K^+ accumulation between type I hair cells and calyx terminals in mouse crista. They found that responses to a depolarizing voltage step in embedded, but not isolated, hair cells resulted in a >40-mV shift of the K^+ equilibrium potential and a rise in effective K^+ concentration of >50 mM in the intercellular space. These results strengthen our predictions for extracellular Cl^- fluctuation at the OHC/Deiters' cell interface.

The existence of the GABAergic efferent synapse at the basal pole, with associated conductances and transporters, could contribute to such fluctuations in local Cl^- levels (25). Although the demonstration of functional GABA effects on isolated OHCs has been variable (possibly because of inappropriate pipette Cl^- levels; see Ref. 44), recent knockout experiments clearly establish the efferent receptor's importance (26). Interestingly, an involvement of Cl^- in the efferent response of vestibular hair cells has been proposed, and one of the suggested mechanisms was a Cl^- dependence of the SK conductance known to be activated subsequent to ACh application (13). Perhaps efferent effects in the mammalian cochlea somehow involve Cl^- modulation of I_{K} ; in this case, the voltage activation range of the conductance would indicate that effects may only occur at suprathreshold acoustic levels where large receptor potentials could activate I_{K} (6, 12). Such suprathreshold GABAergic effects may not be observable by standard measures of efferent activity (26).

We have recently found that manipulations of perilymphatic Cl^- can impact on prestin-dependent cochlear amplification on the basilar membrane near threshold and concluded that intracellular Cl^- was being modified via the activity of G_{metL} , an OHC lateral membrane conductance for Cl^- (44). Could I_{K} modulation have played a role in those Cl^- effects? It is unlikely since, in that study, other agents, including salicylate and tributyltin (a Cl^- ionophore), were effective in the presence of normal, unperturbed extracellular Cl^- . Additionally, it has been shown that 4-AP, which blocks I_{K} , does not interfere with threshold cochlear function when perfused via perilymph (18).

Could BK or $I_{K,n}$ OHC conductances have contributed to the Cl^- -sensitive I_{K} that we identify? BK or Ca^{2+} -activated K^+ channel has been measured in OHCs (e.g., see Ref. 49) and

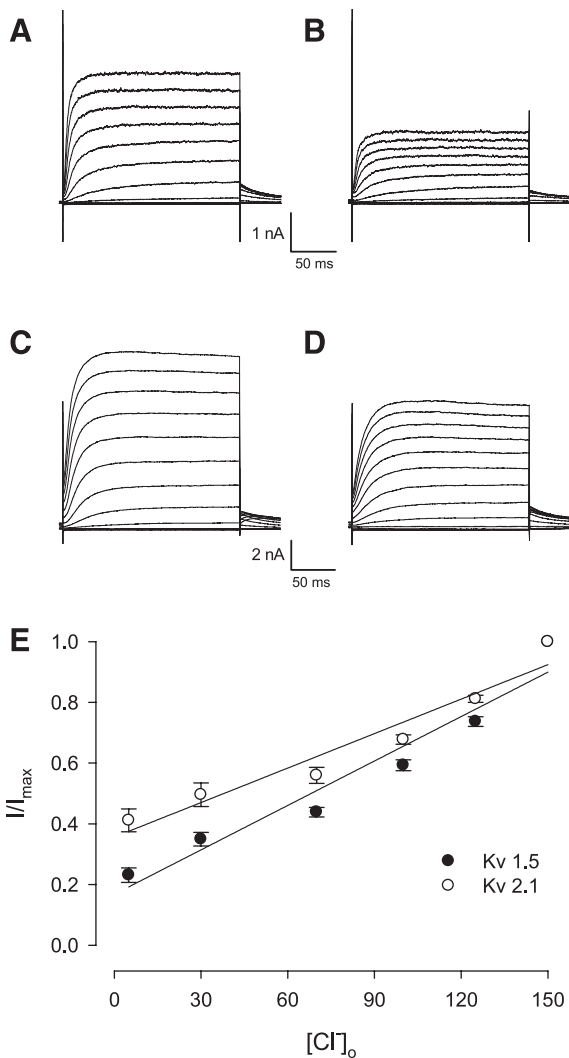


Fig. 9. Extracellular Cl⁻ inhibited voltage-dependent K⁺ (Kv) 1.5 and Kv2.1 in transfected CHO cells. *A*: whole cell current of Kv1.5 in 150 mM Cl⁻. *B*: 5 mM Cl⁻ inhibited the Kv1.5 current. *C*: whole cell current of Kv2.1 in 150 mM Cl⁻. *D*: 5 mM Cl⁻ inhibited the Kv2.1 current. *E*: concentration-response curve of external Cl⁻ on magnitude of Kv1.5 and Kv2.1.

potentially could contribute to the Cl⁻-sensitive K⁺ conductance that we identify. However, we think this is not the case, based on several observations. First, full rundown of Ca²⁺ current (*I*_{Ca}), which may supply Ca²⁺ for BK activation, likely has occurred in our cells, since this is known to happen in guinea pig OHCs whether or not ATP or GTP is included in the patch pipette (24). Thus, given the very low intracellular Ca²⁺ that we have intracellularly (estimated to be <1 nM) and the classic sensitivity of BK to Ca²⁺ (1), BK cannot significantly contribute to our measured *I*_K. Indeed, Wersinger et al. (49), even with a very high Ca²⁺ pipette solution, observed insignificant BK current (iberiotoxin sensitive) in apical OHC.

*I*_{K,n} is a major conductance near the resting potential of OHCs and potentially could have contributed to our measures. We think not, however, based on several observations. Housley and Ashmore (16) showed that resting OHC conductance varies with the length of the cell, decreasing dramatically with increases in length; consequently, *I*_{K,n} is expected to be quite small compared with *I*_K in our long OHC population from

low-frequency regions. Indeed, in this population, we previously found that *I*_{K,n} is not observable in about one-half of the cells (43). Nenov et al. (32) confirmed the above observations. Thus, we expect that relative contamination of the *I*_K we measure by *I*_{K,n} will be small. Interestingly, Wersinger et al. (49) found that linopirdine at 100–200 μM was able to substantially block outward K⁺ currents in apical OHCs and suggested that KCNQ4 channels underlie the major component of the outward *I*_K. It must be emphasized, however, that this drug will block both Kv2.1 [IC₃₀ ~100 μM (50)] and Kv4.3 [IC₅₀ 86 μM (48)], two channels we find transcripts for in OHCs.

Two other factors lead us to dismiss substantial KCNQ4 contributions to our measurements. Our holding protocol at

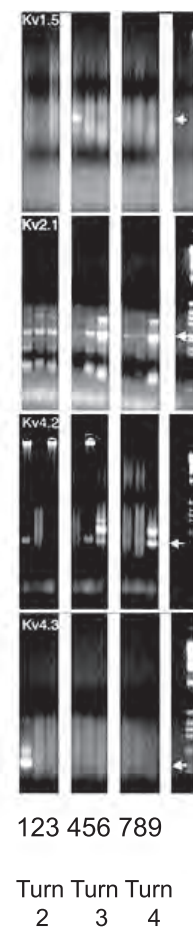


Fig. 10. Kv2.1, Kv1.5, Kv4.2, and Kv4.3 are present in guinea pig OHCs by single-cell RT-PCR. The figure shows single-cell PCR of individual Kv channels. Nine individual OHC were isolated as described in the METHODS, and cDNA was synthesized using Moloney murine leukemia virus reverse transcriptase (Superscript II). A fixed amount of cDNA from these cells was then used as template for amplifying Kv channels. The PCR products were separated on a 2% agarose gel, and the products were detected by ethidium bromide staining. Kv2.1 was present in all the cells and was detected after one round of amplification (35 cycles). In contrast, Kv1.5, Kv4.2, and Kv4.3 were present in only a fraction of cells and required two rounds of nested amplification. The amplification products of each Kv channel are shown in sequence (Kv1.5, Kv2.1, Kv4.2, and Kv4.3 from top to bottom). PCR products from individual cells from turns 2–4 are aligned. We analyzed three cells from each turn. The correct PCR product is indicated by an arrow and was confirmed by sequencing. Also shown are the negative controls and 1-kb markers (lanes 10 and 11, respectively).

−40 mV ensures that $I_{K,n}$ is fully activated, with no further activation upon depolarizations that we used to evoke I_K . Thus, similar to $I_{K,L}$ in vestibular type I hair cells [a conductance analogous to $I_{K,n}$ (37)], when depolarized from potentials where the conductance is fully activated, time-independent, instantaneous currents result and consequently are amenable to simple current subtractions that expose embedded voltage- and time-dependent currents. Thus, the time- and voltage-dependent Cl^- -sensitive current, I_K , is readily isolated from KCNQ4 contributions. Of course, we cannot dismiss that KCNQ4 channels are Cl^- sensitive, since our methods do not permit this evaluation. We would have to block I_K independently, and observe Cl^- effects on $I_{K,n}$. Such sensitivity, if it exists, would be very significant.

How might Cl^- alter I_K ? The linear dependence of I_K on extracellular Cl^- concentration may indicate that fixed charges at the mouth of the channel are screened, thereby altering the local concentration of K^+ available for permeation (20) or interfering with K^+ -specific interactions with the channel. It has been established that residue K356 at the extracellular mouth of Kv2.1 significantly controls K^+ permeation by interacting with K^+ (4), and we reasoned that this residue might be the target of Cl^- . However, we found that mutations of this residue were without effect on Cl^- sensitivity, possibly indicating that other charged residues underlie Cl^- sensitivity.

Molecular substrate of I_K . The K^+ channels Slick and Slack, which are highly expressed in central auditory neurons, are known to be sensitive to internal Cl^- (2) but had not been tested for extracellular Cl^- sensitivity. Here we show that they are unaffected by changes in extracellular Cl^- and therefore do not underlie OHC I_K .

To identify other molecular candidates of channels contributing to OHC I_K , we characterized the differing temporal components of I_K , as has been done previously (52). The distinct inactivation time constants of I_{K1} and I_{K2} are similar to those of $I_{K,cur}$ and $I_{K,slow}$ found in cardiac myocytes (33, 34, 52), and it is believed that Kv1.5 and Kv2.1 contribute to $I_{K,cur}$ and $I_{K,slow}$. Our experiments revealed that these two channels, when expressed in CHO cells, have extracellular Cl^- sensitivity similar to that in the native OHC. This result and similar channel blocker sensitivities between these channels and OHC I_K (24, 32, 42) led us to undertake verification of the channels' presence in OHCs. Our PCR amplification data suggest that Kv2.1 was the predominant form of Kv channel present in the OHC. Transcripts encoding this channel were present in all OHCs tested and moreover required only one round of amplification for detection. In contrast, Kv1.5 required two rounds of amplification and was present in only one cell of nine tested.

Extracellular Cl^- modulates the transient outward K^+ current (I_{to}) in rat ventricular myocytes (19, 21). Replacement of Cl^- with gluconate resulted in a leftward shift (−12 mV) of the steady-state inactivation curve (19), which was comparable to an OHC I_K shift of −8 mV. Interestingly, both Kv4.2 and Kv4.3 contribute to cardiac I_{to} , and, although we did not have these constructs available to us to test for Cl^- effects, we did detect transcripts for these channels in OHCs with RT-PCR, indicating that they may contribute to the Cl^- -sensitive I_K of OHCs.

Although expression level differences by PCR amplification in single cells may be difficult to quantify, the differences in detectability using PCR amplification between Kv2.1 and the

other channels were extreme. The presence of the Kv2.1 transcript in all single cells tested, its detection with only one round of amplification, and the channel's similar Cl^- sensitivity compared with that of OHC I_K strongly suggest that Kv2.1 is the dominant contributor to the Cl^- -dependent I_K in OHCs.

ACKNOWLEDGMENTS

We thank Dr. Len Kaczmarek for providing Kv channel plasmids and Dr. Lei Song for isolating OHCs for single cell PCR.

GRANTS

This work was supported by National Institute on Deafness and Other Communication Disorders Grant DC-00273 to J. Santos-Sacchi.

DISCLOSURES

No conflicts of interest are declared by the authors.

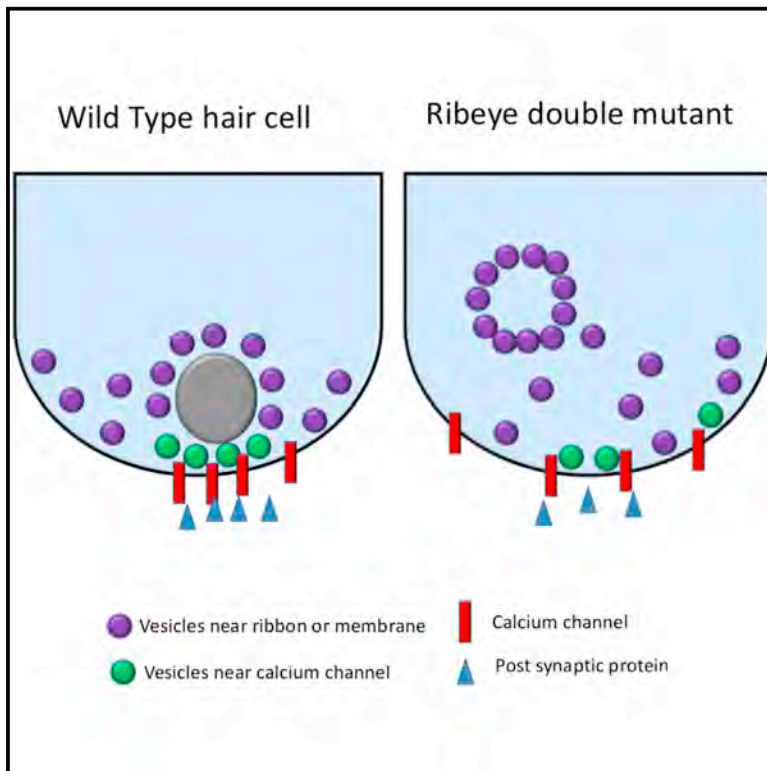
REFERENCES

- Ashmore JF, Meech RW. Ionic basis of membrane potential in outer hair cells of guinea pig cochlea. *Nature* 322: 368–371, 1986.
- Bhattacharjee A, Kaczmarek LK. For K^+ channels, Na^+ is the new Ca^{2+} . *Trends Neurosci* 28: 422–428, 2005.
- Chambard JM, Ashmore JF. Regulation of the voltage-gated potassium channel KCNQ4 in the auditory pathway. *Pflugers Arch* 450: 34–44, 2005.
- Consiglio JF, Andalib P, Korn SJ. Influence of pore residues on permeation properties in the Kv2.1 potassium channel Evidence for a selective functional interaction of K^+ with the outer vestibule. *J Gen Physiol* 121: 111–124, 2003.
- Corey DP. What is the hair cell transduction channel? *J Physiol* 576: 23–28, 2006.
- Dallos P, Santos-Sacchi J, Flock A. Intracellular recordings from cochlear outer hair cells. *Science* 218: 582–584, 1982.
- Elgoyhen AB, Johnson DS, Boulter J, Vetter DE, Heinemann S. Alpha 9: an acetylcholine receptor with novel pharmacological properties expressed in rat cochlear hair cells. *Cell* 79: 705–715, 1994.
- Elgoyhen AB, Vetter DE, Katz E, Rothlin CV, Heinemann SF, Boulter J. alpha10: a determinant of nicotinic cholinergic receptor function in mammalian vestibular and cochlear mechanosensory hair cells. *Proc Natl Acad Sci USA* 98: 3501–3506, 2001.
- Furness DN, Hulme JA, Lawton DM, Hackney CM. Distribution of the glutamate/aspartate transporter GLAST in relation to the afferent synapses of outer hair cells in the guinea pig cochlea. *J Assoc Res Otolaryngol* 3: 234–247, 2002.
- Goldberg JM. Theoretical analysis of intercellular communication between the vestibular type I hair cell and its calyx ending. *J Neurophysiol* 76: 1942–1957, 1996.
- Gulley RL, Bagger-Sjoberg D. Freeze-fracture studies on the synapse between the type I hair cell and the calyceal terminal in the guinea-pig vestibular system. *J Neurocytol* 8: 591–603, 1979.
- He DZZ, Jia SP, Dallos P. Mechano-electrical transduction of adult outer hair cells studied in a gerbil hemicochlea. *Nature* 429: 766–770, 2004.
- Holt JC, Pantoja AM, Athas GB, Guth PS. A role for chloride in the hyperpolarizing effect of acetylcholine in isolated frog vestibular hair cells. *Hear Res* 146: 17–27, 2000.
- Holt JR, Stauffer EA, Abraham D, Geleoc GS. Dominant-negative inhibition of M-like potassium conductances in hair cells of the mouse inner ear. *J Neurosci* 27: 8940–51, 2007.
- Horrigan FT, Aldrich RW. Coupling between voltage sensor activation, Ca^{2+} binding and channel opening in large conductance (BK) potassium channels. *J Gen Physiol* 120: 267–305, 2002.
- Housley GD, Ashmore JF. Ionic currents of outer hair cells isolated from the guinea-pig cochlea. *J Physiol (Lond)* 448: 73–98, 1992.
- Housley GD, Marcotti W, Navaratnam D, Yamoah EN. Hair cells—beyond the transducer. *J Membr Biol* 209: 89–118, 2006.
- Kirk DL. Effects of 4-aminopyridine on electrically evoked cochlear emissions and mechano-transduction in guinea pig outer hair cells. *Hear Res* 161: 99–112, 2001.
- Lai XG, Yang J, Zhou SS, Zhu J, Li GR, Wong TM. Involvement of anion channel(s) in the modulation of the transient outward K^+ channel in

- rat ventricular myocytes. *Am J Physiol Cell Physiol* 287: C163–C170, 2004.
20. **Latorre R, Labarca P, Naranjo D.** Surface charge effects on ion conduction in ion channels. *Methods Enzymol* 207: 471–501, 1992.
 21. **Lefevre T, Lefevre IA, Coulombe A, Coraboeuf E.** Effects of chloride ion substitutes and chloride channel blockers on the transient outward current in rat ventricular myocytes. *Biochim Biophys Acta* 1273: 31–43, 1996.
 22. **Lieberman MC, Dodds LW, Pierce S.** Afferent and efferent innervation of the cat cochlea: quantitative analysis with light and electron microscopy. *J Comp Neurol* 301: 443–460, 1990.
 23. **Lim R, Kindig AE, Donne SW, Callister RJ, Brichta AM.** Potassium accumulation between type I hair cells and calyx terminals in mouse crista. *Exp Brain Res* 210: 607–621, 2011.
 24. **Lin X, Hume RI, Nuttall AL.** Dihydropyridines and verapamil inhibit voltage-dependent K⁺ current in isolated outer hair cells of the guinea pig. *Hear Res* 88: 36–46, 1995.
 25. **Maison SF, Adams JC, Liberman MC.** Olivocochlear innervation in the mouse: immunocytochemical maps, crossed versus uncrossed contributions, and transmitter colocalization. *J Comp Neurol* 455: 406–416, 2003.
 26. **Maison SF, Rosahl TW, Homanics GE, Liberman MC.** Functional role of GABAergic innervation of the cochlea: phenotypic analysis of mice lacking GABA(A) receptor subunits alpha 1, alpha 2, alpha 5, alpha 6, beta 2, beta 3, or delta. *J Neurosci* 26: 10315–10326, 2006.
 27. **Mammano F, Ashmore JF.** Differential expression of outer hair cell potassium currents in the isolated cochlea of the guinea-pig. *J Physiol* 496: 639–646, 1996.
 28. **Marcotti W, Kros CJ.** Developmental expression of the potassium current IK,n contributes to maturation of mouse outer hair cells. *J Physiol* 520: 653–660, 1999.
 29. **Nadol JB Jr.** Synaptic morphology of inner and outer hair cells of the human organ of Corti. *J Electron Microscop Tech* 15: 187–196, 1990.
 30. **Navaratnam DS, Bell TJ, Tu TD, Cohen EL, Oberholtzer JC.** Differential distribution of Ca²⁺-activated K⁺ channel splice variants among hair cells along the tonotopic axis of the chick cochlea. *Neuron* 19: 1077–1085, 1997.
 31. **Nenov AP, Chen C, Bobbin RP.** Outward rectifying potassium currents are the dominant voltage activated currents present in Deiters' cells. *Hear Res* 123: 168–182, 1998.
 32. **Nenov AP, Norris C, Bobbin RP.** Outwardly rectifying currents in guinea pig outer hair cells. *Hear Res* 105: 146–158, 1997.
 33. **Nerbonne JM, Guo W.** Heterogeneous expression of voltage-gated potassium channels in the heart: roles in normal excitation and arrhythmias. *J Cardiovasc Electrophysiol* 13: 406–409, 2002.
 34. **Nerbonne JM, Nichols CG, Schwarz TL, Escande D.** Genetic manipulation of cardiac K(+) channel function in mice: what have we learned, and where do we go from here? *Circ Res* 89: 944–956, 2001.
 35. **Niggli E, Lipp P.** Subcellular restricted spaces: significance for cell signalling and excitation-contraction coupling. *J Muscle Res Cell Motil* 14: 288–291, 1993.
 36. **Oliver D, He DZ, Klocker N, Ludwig J, Schulte U, Waldegger S, Ruppersberg JP, Dallos P, Fakler B.** Intracellular anions as the voltage sensor of prestin, the outer hair cell motor protein. *Science* 292: 2340–2343, 2001.
 37. **Rusch A, Eatock RA.** A delayed rectifier conductance in type I hair cells of the mouse utricle. *J Neurophysiol* 76: 995–1004, 1996.
 38. **Rybalchenko V, Santos-Sacchi J.** Cl⁻ flux through a non-selective, stretch-sensitive conductance influences the outer hair cell motor of the guinea-pig. *J Physiol* 547: 873–891, 2003.
 39. **Saito K.** Freeze-fracture organization of hair cell synapses in the sensory epithelium of Guinea pig organ of Corti. *J Electron Microscopy Techniques* 15: 173–186, 1990.
 40. **Santos-Sacchi J.** Asymmetry in voltage-dependent movements of isolated outer hair cells from the organ of Corti. *J Neurosci* 9: 2954–2962, 1989.
 41. **Santos-Sacchi J.** Isolated supporting cells from the organ of Corti: some whole cell electrical characteristics and estimates of gap junctional conductance. *Hear Res* 52: 89–98, 1991.
 42. **Santos-Sacchi J, Dilger JP.** Whole cell currents and mechanical responses of isolated outer hair cells. *Hear Res* 35: 143–150, 1988.
 43. **Santos-Sacchi J, Huang GJ, Wu M.** Mapping the distribution of outer hair cell voltage-dependent conductances by electrical amputation. *Biophys J* 73: 1424–1429, 1997.
 44. **Santos-Sacchi J, Song L, Zheng J, Nuttall AL.** Control of mammalian cochlear amplification by chloride anions. *J Neurosci* 26: 3992–3998, 2006.
 45. **Song L, Santos-Sacchi J.** Conformational state-dependent anion binding in prestin: evidence for allosteric modulation. *Biophys J* 98: 371–376, 2010.
 46. **Song L, Seeger A, Santos-Sacchi J.** On membrane motor activity and chloride flux in the outer hair cell: lessons learned from the environmental toxin tributyltin. *Biophys J* 88: 2350–2362, 2005.
 47. **Szucs A, Somodi S, Batta TJ, Toth A, Szigeti GP, Csernoch L, Panyi G, Sziklai I.** Differential expression of potassium currents in Deiters cells of the guinea pig cochlea. *Pflugers Arch* 452: 332–341, 2006.
 48. **Wang HS, Pan Z, Shi W, Brown BS, Wymore RS, Cohen IS, Dixon JE, McKinnon D.** KCNQ2 and KCNQ3 potassium channel subunits: molecular correlates of the M-channel. *Science* 282: 1890–1893, 1998.
 49. **Wersinger E, McLean WJ, Fuchs PA, Pyott SJ.** BK channels mediate cholinergic inhibition of high frequency cochlear hair cells. *PLoS One* 5: e13836, 2010.
 50. **Wladyka CL, Kunze DL.** KCNQ/M-currents contribute to the resting membrane potential in rat visceral sensory neurons. *J Physiol* 575: 175–189, 2006.
 51. **Wu T, Song L, Shi X, Jiang Z, Santos-Sacchi J, Nuttall AL.** Effect of capsaicin on potassium conductance and electromotility of the guinea pig outer hair cell. *Hear Res* 272: 117–124, 2011.
 52. **Xu H, Guo W, Nerbonne JM.** Four kinetically distinct depolarization-activated K⁺ currents in adult mouse ventricular myocytes. *J Gen Physiol* 113: 661–678, 1999.
 53. **Zhang X, Solaro CR, Lingle CJ.** Allosteric regulation of BK channel gating by Ca(2+) and Mg(2+) through a nonselective, low affinity divalent cation site. *J Gen Physiol* 118: 607–636, 2001.
 54. **Zheng J, Shen W, He DZ, Long KB, Madison LD, Dallos P.** Prestin is the motor protein of cochlear outer hair cells. *Nature* 405: 149–155, 2000.

Synaptic Ribbons Require Ribeye for Electron Density, Proper Synaptic Localization, and Recruitment of Calcium Channels

Graphical Abstract



Authors

Caixia Lv, William J. Stewart, Otar Akanyeti, ..., Lavinia Sheets, James C. Liao, David Zenisek

Correspondence

david.zenisek@yale.edu

In Brief

Synaptic ribbons are features of the auditory, vestibular, and visual systems that hold vesicles close to release sites in sensory cells. Lv et al. now find that genetic reduction of Ribeye levels in zebrafish results in the disruption of synaptic ribbon localization and morphology with minor effects on kinetics or levels of vesicle exocytosis.

Highlights

- Ribeye is needed for electron density to form at hair cell synaptic ribbons
- Ribeye mutants have smaller synaptic vesicles and mislocalized ribbons
- Ribeye is required for synaptic ribbon association with calcium channels
- Continuous exocytosis is enhanced in ribeye mutants despite ribbon mislocalization



Synaptic Ribbons Require Ribeye for Electron Density, Proper Synaptic Localization, and Recruitment of Calcium Channels

Caixia Lv,¹ William J. Stewart,⁵ Otar Akanyeti,⁵ Courtney Frederick,¹ Jie Zhu,¹ Joseph Santos-Sacchi,^{1,3,4} Lavinia Sheets,^{6,7} James C. Liao,⁵ and David Zenisek^{1,2,*}

¹Department of Cellular and Molecular Physiology

²Department of Ophthalmology and Visual Sciences

³Department of Surgery (Otolaryngology)

⁴Department of Neuroscience

Yale University School of Medicine, New Haven, CT 06520-8066, USA

⁵The Whitney Laboratory for Marine Bioscience and Department of Biology, University of Florida, St. Augustine, FL 32080, USA

⁶Eaton-Peabody Laboratory, Massachusetts Eye and Ear Infirmary, Boston, MA 02114, USA

⁷Department of Otolaryngology, Harvard Medical School, Boston, MA 02114, USA

*Correspondence: david.zenisek@yale.edu

<http://dx.doi.org/10.1016/j.celrep.2016.05.045>

SUMMARY

Synaptic ribbons are structures made largely of the protein Ribeye that hold synaptic vesicles near release sites in non-spiking cells in some sensory systems. Here, we introduce frameshift mutations in the two zebrafish genes encoding for Ribeye and thus remove Ribeye protein from neuromast hair cells. Despite Ribeye depletion, vesicles collect around ribbon-like structures that lack electron density, which we term “ghost ribbons.” Ghost ribbons are smaller in size but possess a similar number of smaller vesicles and are poorly localized to synapses and calcium channels. These hair cells exhibit enhanced exocytosis, as measured by capacitance, and recordings from afferent neurons post-synaptic to hair cells show no significant difference in spike rates. Our results suggest that Ribeye makes up most of the synaptic ribbon density in neuromast hair cells and is necessary for proper localization of calcium channels and synaptic ribbons.

INTRODUCTION

Primary sensory cells of the auditory, vestibular, and visual systems encode sensory information as graded changes in voltage that lead to graded changes in glutamate release. These non-spiking cells use synaptic ribbons, which hold a dense array of synaptic vesicles in active zones near release sites. Because these cells exhibit tonic and graded signaling in response to sensory stimuli, it has largely been assumed that the synaptic ribbon is necessary to carry out this task (Matthews and Fuchs, 2010). Indeed, ribbon-synapse-containing cells have been demonstrated to exhibit a sustained phase of exocytosis in response to prolonged stimuli (Lagnado et al., 1996; Parsons et al.,

1994; Moser and Beutner, 2000; Edmonds et al., 2004; Bartoletti et al., 2010), and optical studies have revealed that vesicles are immobilized to and move along the ribbon in response to stimuli (Vaithianathan et al., 2016; Zenisek, 2008; Zenisek et al., 2000; Midorikawa et al., 2007).

The most abundant protein in the synaptic ribbon is Ribeye, a protein arising from an alternative start site at the gene encoding for the CtBP2 transcriptional co-repressor (Schmitz et al., 2000). Ribeye can be subdivided into two domains, a ribbon-specific A-domain and a B-domain, which is nearly identical to CtBP2 (Schmitz et al., 2000).

Genetic deletion of mouse Ribeye leads to a loss of synaptic ribbons in the retina, which is accompanied by a reduction in synaptic transmission from bipolar cells without observable changes in the kinetic features of release (Maxeiner et al., 2016), whereas morpholino-oligonucleotide (MO)-driven knock-down of Ribeye expression leads to the mislocalization of calcium channels (Sheets et al., 2011; Lv et al., 2012) and a reduction of spiking rates in afferent neurons postsynaptic to zebrafish hair cells (Sheets et al., 2011).

To better understand the function of Ribeye and the synaptic ribbon, we used genome editing to introduce frameshifting mutations in the A-domain of both zebrafish Ribeye-encoding genes and used light and electron microscopy (EM), whole-cell capacitance measurements, and recordings from afferent neurons to measure the effects on neuromast hair cells. The resultant double-homozygous mutant animals exhibited dramatically reduced Ribeye levels in hair cells, leading to a loss of electron density from hair cell ribbons, shrinkage of ribbon size, mislocalization of ribbon-like structures, and disruption in the association of calcium channels with the ribbon. Despite these changes, the continuous phase of exocytosis is enhanced, and we could not detect differences in afferent neuron response in mutant animals. These results indicate that Ribeye likely makes up the electron-dense portion of the ribbon and recruits calcium channels to release sites in zebrafish hair cells but is not required for vesicle binding, transport, or maintaining continuous release.

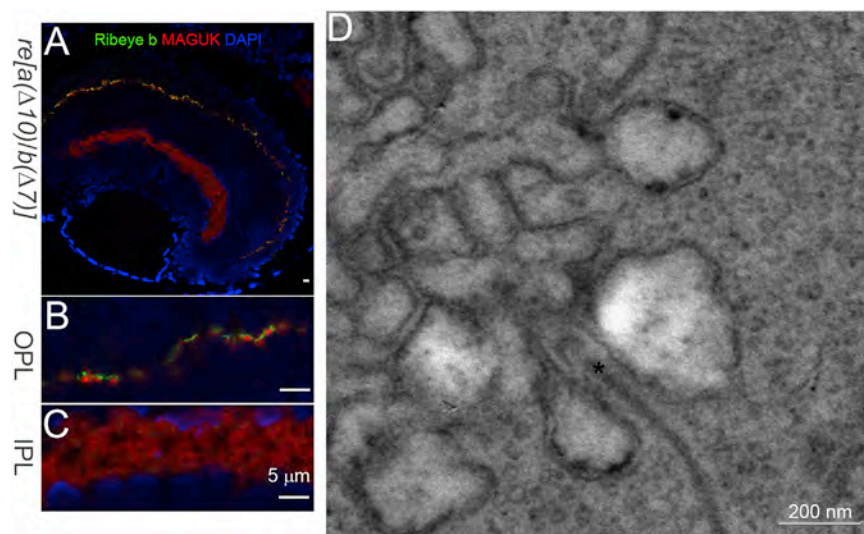


Figure 1. Ribeye and Synaptic Ribbons Remain in the Retina of *ribeye a(Δ10)/ribeye b(Δ7)* (*re[a(Δ10)/b(Δ7)]*) double homozygous mutants.

(A) Confocal image of Ribeye b (green) and post-synaptic marker MAGUK (red) staining in 5-dpf *re[a(Δ10)/b(Δ7)]* homozygous mutants. DAPI (blue) stains for the nucleus. Scale bar, 5 μ m.

(B) 3 \times magnification of outer plexiform layer staining in 5-dpf *re[a(Δ10)/b(Δ7)]* homozygous mutants retina. Scale bar, 5 μ m.

(C) 3 \times magnification of inner plexiform layer staining in 5-dpf *re[a(Δ10)/b(Δ7)]* homozygous mutants retina. Scale bar, 5 μ m.

(D) Electron micrograph of photoreceptor ribbon from 5-dpf *re[a(Δ10)/b(Δ7)]* homozygous mutant retina. Scale bar, 200 nm.

RESULTS

Generation of Targeted Zebrafish *ribeye* Mutants

To study Ribeye function, we first generated a line of zebrafish harboring mutations in the ribbon-synapse-specific A-domain of Ribeye a that leads to frameshifts resulting in a premature stop codon using zinc finger nucleases (ZFNs) (Supplemental Experimental Procedures; Figure S1). One such mutant that led to a 10-bp deletion (*ribeye a(Δ10)*) was bred to homozygosity for further experiments. Figure S2 shows immunostaining of retinal sections of wild-type (WT) and *ribeye a(Δ10)* homozygous fish with antibodies against Ribeye a or Ribeye b or with a CtBP antibody that labels CtBP1, CtBP2, and all isoforms of Ribeye. As expected, CtBP and Ribeye b staining was still evident in the *ribeye a(Δ10)* homozygous animals, due to expression of Ribeye b. Note that, while the CtBP expression level is greatly reduced in the inner plexiform layer (IPL), the CtBP staining in the outer plexiform layer (OPL) is similar in the *ribeye a(Δ10)* homozygous and WT animals, consistent with stronger expression of Ribeye b in photoreceptor terminals and higher expression of Ribeye a in bipolar cells. EM images revealed normal-appearing ribbons in both the retina and lateral line of *ribeye a(Δ10)* homozygous animals (data not shown). We found that animals homozygous for these mutations are viable and do not exert obvious sensory phenotypes.

Next, we targeted *ribeye b* using CRISPR/Cas9 (clustered regularly interspaced short palindromic repeats/CRISPR-associated protein 9)-based constructs. Using this strategy, we generated eight lines of fish harboring mutations in this region of *ribeye b*, which led to premature stop codons (Figure S1C). As with the ZFN-generated mutations of *ribeye a*, the mutations introduced into *ribeye b* are expected to cause a truncation of the sequence in the A-domain, with no effect on CtBP2 expression.

Characterization of *ribeye a(Δ10)/ribeye b(Δ7)* Homozygous Zebrafish

Next, we characterized the *ribeye a(Δ10)/ribeye b(Δ7)* (herein after termed *re[a(Δ10)/b(Δ7)]*) double-homozygous mutants at

the level of light and EM in the retina and in hair cells of the lateral line. Surprisingly, double-homozygous mutants were

immunopositive for CtBP and Ribeye b in the OPL of the retina, indicating that at least some Ribeye continues to be expressed, despite the mutations (Figure 1). Consistent with Ribeye expression, EM revealed that synaptic ribbons were also present in the OPL of *re[a(Δ10)/b(Δ7)]* fish (Figure 1D).

In contrast to the retina findings, Ribeye was found to be dramatically reduced in the hair cells of zebrafish neuromasts at 5 days postfertilization (dpf) (Figure 2). Figures 2A and 2B show results from neuromasts that are labeled for Ribeye a (Figure 2A) or Ribeye b (Figure 2B) with pan-MAGUK, a marker for post-synaptic densities that labels afferent post-synaptic structures in afferent fiber terminals (Sheets et al., 2011; Meyer et al., 2005). In WT animals, pan-MAGUK staining was found to colocalize near bright spots immunopositive for Ribeye a (Figure 2A, left) and Ribeye b (Figure 2B, left). By contrast, *re[a(Δ10)/b(Δ7)]* double homozygotes exhibit little staining for Ribeye a (Figure 2A, right) but continued to exhibit staining for pan-MAGUK (Figures 2A and 2B, right). Some residual fluorescent spots remained in double-homozygous mutant animals. The Ribeye a puncta were reduced in number from 2.5 ± 0.18 in WT fish to 1.5 ± 0.3 in double homozygotes (Figure 2D), and in intensity from $15,728 \pm 1,517$ to $6,369 \pm 1,021$ (Figure 2E). Ribeye b was not detectable (Figure 2B). Though the number of pan-MAGUK spots in double homozygotes was unchanged (Figure 2D), the puncta intensity was significantly reduced (Figure 2E).

Next, we tested whether overall CtBP levels were also reduced from synaptic sites by staining with an antibody that recognizes Ribeye a, Ribeye b, CtBP1, and CtBP2. As with the Ribeye a staining, we found fewer and dimmer CtBP puncta than in control animals. On average, puncta in double homozygotes had an integrated intensity of 17% of WT fish.

Lastly, to determine whether the Ribeye a immunofluorescent (IF) spots properly localized near post-synaptic structures, we measured the distance of the centroid of each Ribeye a spot to its nearest pan-MAGUK spot. Figure 2F plots the results as a cumulative histogram. As can be seen in the figure, spots in mutant animals were found further away from

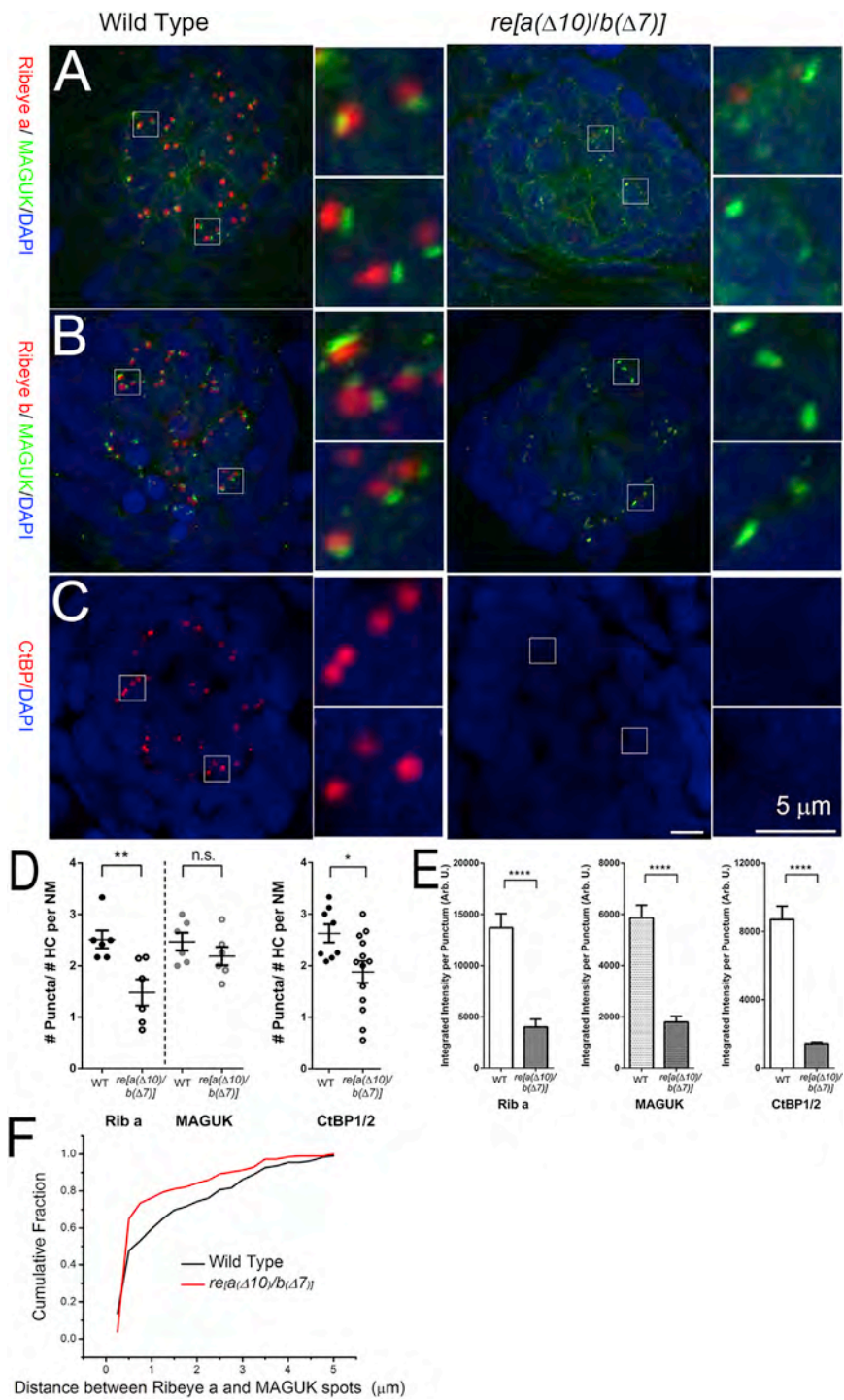


Figure 2. Ribeye Is Dramatically Reduced from Neuromast Hair Cells of *re[a(Δ10)/b(Δ7)]* Double Homozygous Mutants 5 dpf

(A) Confocal images of Ribeye A (red) and post-synaptic density marker pan-MAGUK (green) staining 5 dpf in WT (left) and *re[a(Δ10)/b(Δ7)]* homozygous mutant (right) neuromast. Insets show magnified images centered around synapses. Note the close apposition of Ribeye a and pan-MAGUK in WT animals, whereas little Ribeye a staining is found near pan-MAGUK in the *re[a(Δ10)/b(Δ7)]* double-homozygous mutants.

(B) Ribeye b (red) and pan-MAGUK (green) antibody staining in 5-dpf WT (left) and *re[a(Δ10)/b(Δ7)]* homozygous mutant (right) neuromast.

(C) CtBP antibody staining (green) in 5-dpf WT (left) and *re[a(Δ10)/b(Δ7)]* homozygous mutant (right) neuromast. DAPI (blue) stains nucleus. Scale bars, 5 μm.

(D) The number of Ribeye a, MAGUK, or CtBP1 immunolabeled puncta per hair cell in 5- to 6-dpf WT and *re[a(Δ10)/b(Δ7)]* mutants. Each circle represents an individual neuromast (NM) within a larva. The number of puncta per hair cell was approximated by dividing the number of Ribeye puncta within an NM by the number of hair cells in the NM. Error bars indicate SEM. Unpaired t test; **p = 0.0075; *p = 0.0226; n.s., not significant.

(E) Integrated intensities per punctum of Ribeye a, MAGUK, and CtBP1. Bars represent the means; error bars indicate SEM. Mann-Whitney U test; ***p < 0.0001, for both mutant alleles.

(F) Cumulative histogram of distances between Ribeye a spots to their nearest pan-MAGUK spot in confocal micrographs for WT (red) and *re[a(Δ10)/b(Δ7)]* double-homozygous mutants (black).

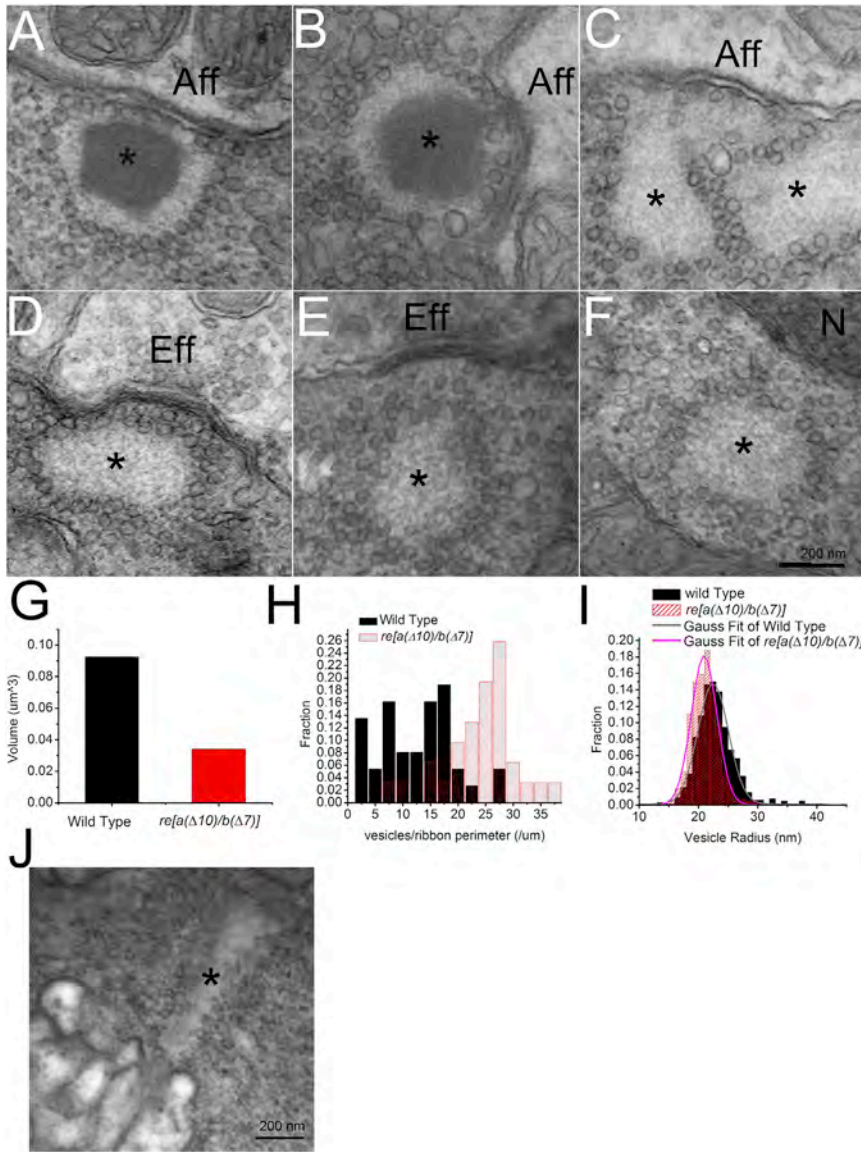
afferent fibers (Obholzer et al., 2008). Similarly, we found that EM sections of neuromasts in WT fish exhibited electron-dense synaptic ribbons (n > 20 fish). Figures 3A and 3B show typical electron micrographs of a synaptic ribbon from a WT hair cell, which were localized near afferent neurons separated by two cell membranes. Afferent neurons were identified in electron micrographs by their reduced density, lack of synaptic vesicles, and mitochondria. In WT fish, we found that 41 of 41 ribbons were localized within 70 nm of a visible plasma membrane opposite an afferent neuron. By contrast, we found no ribbons with typical electron-dense centers in *re[a(Δ10)/b(Δ7)]* double homozygotes. Instead, 5-dpf embryos of *re[a(Δ10)/b(Δ7)]* double homozygotes exhibited ribbon-like structures that lacked electron densities but maintained an organized collection of synaptic vesicles in a spherical array (Figures 3C–3F), which we have named “ghost ribbons.” While some ghost ribbons appeared to localize adjacent to afferent neurons (Figure 3C; n = 14 of 41 ghost ribbons), most were not found near

post-synaptic densities, suggesting defects in their ability to localize to synapses.

Morphology of Hair Cell Synaptic Ribbons in *re[a(Δ10)/b(Δ7)]* Homozygous Mutants

Neuromast hair cells of WT embryos at 5 dpf exhibit spherical synaptic ribbons that localize near the plasma membrane near

b(Δ7) double homozygotes. Instead, 5-dpf embryos of *re[a(Δ10)/b(Δ7)]* double homozygotes exhibited ribbon-like structures that lacked electron densities but maintained an organized collection of synaptic vesicles in a spherical array (Figures 3C–3F), which we have named “ghost ribbons.” While some ghost ribbons appeared to localize adjacent to afferent neurons (Figure 3C; n = 14 of 41 ghost ribbons), most were not found near



identifiable afferent fibers. Figure 3 shows examples of ghost ribbons near efferent neurons (Figure 3D), away from the cell membrane (Figure 3E), and in the center of cell (Figure 3F). By contrast, ribbons of the retina of *re[a(Δ10)/b(Δ7)]* double homozygotes were found to be largely normal; however, we found two examples of structures within photoreceptors of *re[a(Δ10)/b(Δ7)]* double homozygotes that resembled the hair cell ghost ribbons but took on the elongated shape of a photoreceptor ribbon (Figure 3J). These results indicate that Ribeye is necessary for the maintaining the electron density of the ribbon and plays a critical role in localizing ribbons to proper synaptic locations.

Next, we quantified and compared the morphological properties of ghost ribbons in *re[a(Δ10)/b(Δ7)]* double homozygotes to ribbons in WT animals. In WT hair cells ($n = 45$ ribbons, 18 fish), the area of the region beneath the vesicles, including both the electron density and the surrounding light space (e.g.,

Figures 3A and 3B), was, on average, $0.163 \mu\text{m}^2$. If we assume that the ribbons are roughly spherical and that each image represents a random cross-section of that sphere, WT ribbons would have a cross-section of $0.244 \mu\text{m}^2$ at their equator, which yields a spherical ribbon with a diameter of 560 nm and a volume of $0.091 \mu\text{m}^3$. The density occupied about 43% of WT ribbons. By contrast, ghost ribbons lacking the density were much smaller ($n = 32$ ribbons; ten fish), with an estimated cross-sectional area of $0.119 \mu\text{m}^2$, equivalent to a 390-nm diameter sphere and a volume of $0.031 \mu\text{m}^3$. Hence, when one does not factor in the vesicle volume, the volume of ghost ribbons is only 34% of the volume of WT ribbons, less than the 57% that one would predict if ribbons only lost the density but similar to a previous estimate of the contribution of Ribeye to ribbon volume in retinal bipolar cells using a ribbon-binding peptide (Zenisek et al., 2004).

To analyze the vesicles associated with ribbons and ghost ribbons, we counted the number of vesicles within one vesicle diameter of the ribbon. Despite the smaller area of the ghost ribbons, we observed more vesicles per section associated with ghost ribbons in mutant animals (21.8 ± 1.3) than with ribbons in WT cells (15.7 ± 2.0). To measure the density of vesicles on ribbons, we divided the number of vesicles by the length of the perimeter of the ribbon in each section. On average, we found

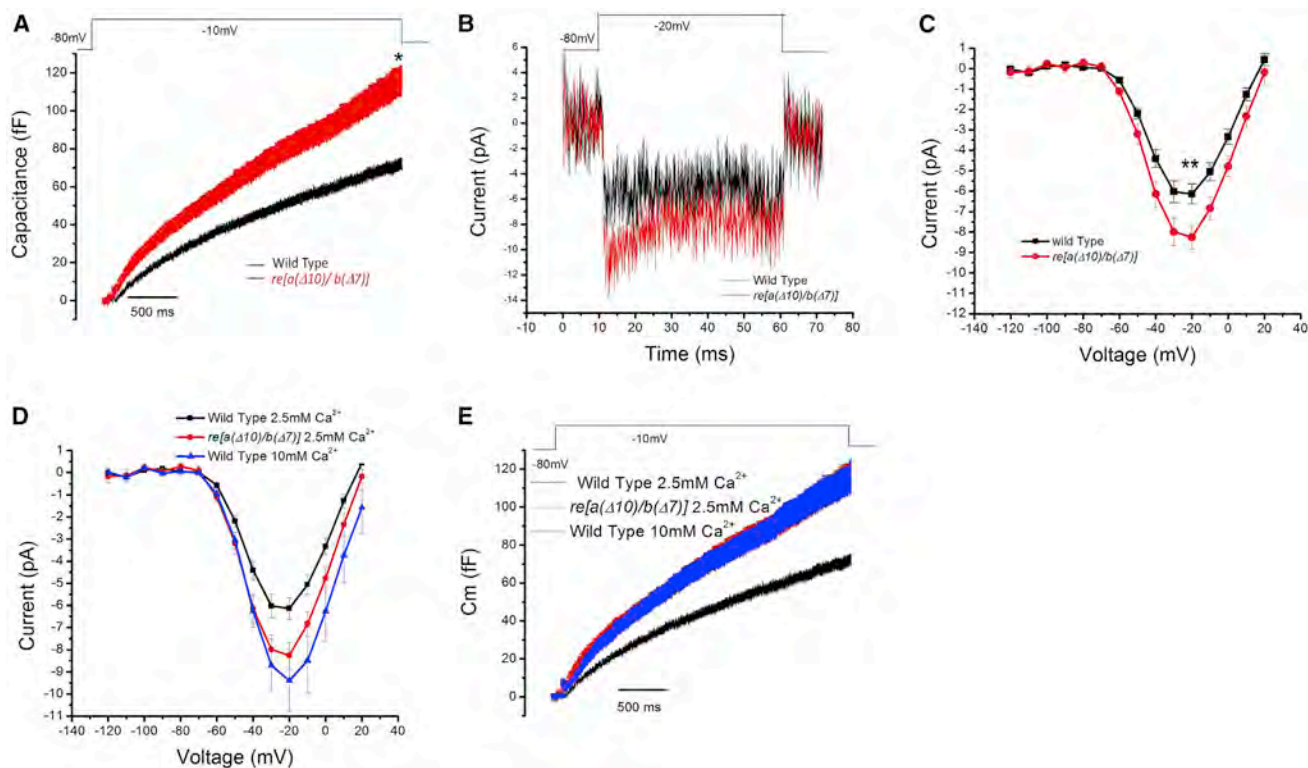


Figure 4. Results from Whole-Cell Voltage-Clamp Recordings from WT and *re[a(Δ10)/b(Δ7)]* Homozygous Mutant Neuromast Hair Cells
 (A) Average whole-cell capacitance measurements of WT (black, n = 11) and *re[a(Δ10)/b(Δ7)]* homozygous mutants (red, n = 12) neuromast hair cells in response to 3-s step-depolarizations. Note that all traces include error bars denoting SEM for each condition. The average capacitance increase at the end of the 3-s depolarization (averaged over 100 ms) was 67.8 ± 5.0 fF for the WT hair cells and was 106.1 ± 13.6 fF in the mutants. $p = 0.018$.
 (B) Averaged calcium current trace of WT (black) and *re[a(Δ10)/b(Δ7)]* homozygous (red) mutants in response to a -20 -mV step depolarization.
 (C) Plot of current-voltage relationship for WT fish NM hair cells (black, n = 15) and *re[a(Δ10)/b(Δ7)]* homozygous mutant neuromast hair cells (red, n = 17). At -20 mV, the average current in WT cells was -6.1 ± 0.5 pA, and mutant fish cells was -8.3 ± 0.6 pA. $p = 0.010$. The fish recorded were between 5 and 8 days old, and the neuromasts recorded were P3 and P4.
 (D) Capacitance recording of WT fish at 2.8 mM Ca^{2+} (black) and 10 mM Ca^{2+} (blue) external solution and double-mutant fish at 2.8 mM Ca^{2+} external solution (red) in response to a 3-s step depolarization. The average capacitance increase at the end of the 3-s depolarization (averaged over 100 ms) was 105.09 ± 13.74 fF for the WT hair cells at 10 mM Ca^{2+} solution. Capacitance increases in WT and double-mutant fish in 2.8 Ca^{2+} external solution are the same as in (A).
 (E) Plot of current-voltage relationship of WT fish at 2.8 mM Ca^{2+} (black) and 10 mM Ca^{2+} (blue) external solution, and double-mutant fish at 2.8 mM Ca^{2+} external solution (red). At -20 mV, the calcium current of WT fish in 10 mM Ca^{2+} external solution is -9.39 ± 1.40 pA, compared to double-mutant fish in 2.8 mM Ca^{2+} external solution is 8.26 ± 0.58 pA.

22.7 ± 1.0 vesicles per micrometer perimeter in mutant ghost ribbons and 11.1 ± 0.9 vesicles per millimeter in images of ribbons of WT animals. Even after the removal of a subset of WT ribbons that had very few vesicles (five or less), the vesicle density on ribbons remained lower in the WT cells ($13.0 \pm 0.8 \mu m^{-1}$). Figure 3H plots a histogram of these values for both genotypes. To estimate the effect on overall vesicle number, we estimated the area of ribbon assayed in each 80-nm section relative to the total ribbon surface area using our spherical assumption. Based on this method, we calculated an estimate of 133 ± 17 vesicles per ribbon in WT animals and 129 ± 8 associated with ghost ribbons in *re[a(Δ10)/b(Δ7)]* double-mutant animals.

Lastly, we measured the size of the vesicles associated with ribbons and ghosts. We measured the size of vesicles associated with ribbons (n = 671) and ghost ribbons (n = 627). On average, ribbon-associated vesicles in WT animals had an average area of $1,631 \pm 15$ nm², whereas vesicles in *re[a(Δ10)/*

b(Δ7)] were $1,437 \pm 12$ nm². Since the vesicles are round in the images, we converted the areas into vesicle radii and plotted the results as a histogram in Figure 3I. While the difference in vesicle size is small (21.4 ± 0.09 in double homozygotes versus 22.4 ± 0.1 nm in WT), the differences are highly significant ($p < 0.003$ when comparing averages across ribbons).

***re[a(Δ10)/b(Δ7)]* Double Mutants Exhibit Enhanced Exocytosis and Calcium Current**

Next, we tested the release properties of the *re[a(Δ10)/b(Δ7)]* double-homozygous animals and WT animals. To do so, we performed whole-cell membrane capacitance recordings in response to long step depolarizations in both WT and *re[a(Δ10)/b(Δ7)]* double-homozygous fish 5–8 dpf, using a two-sine approach that allows for measuring exocytosis during a depolarization (Ricci et al., 2013; Schnee et al., 2011). Figure 4A, shows the average responses of 11 WT hair cells and 12 *re*

Table 1. Best-Fit Values of Hair Cell Capacitance Measurements from WT and Mutant Zebrafish

	Linear Phase, β (fF/s)	Amplitude, A (fF)	Time Constant, τ (ms)
Wild type/1 EGTA/2.8 Ca ²⁺	17.6	18.9	501
Wild type/10 EGTA/2.8 Ca ²⁺	16.7	15.6	622
<i>re[a(Δ10)/b(Δ7)]/1 EGTA/2.8 Ca²⁺</i>	29.1	19.2	346
<i>re[a(Δ10)/b(Δ7)]/10 EGTA/2.8 Ca²⁺</i>	8.4	10.5	579
Wild type/1 EGTA/10 Ca ²⁺	28.8	22.7	481

[a(Δ 10)/b(Δ 7)] fish in response to 3-s voltage steps to -10 mV. WT hair cells exhibited a steady rise in whole-cell capacitance, which could be well fit by the sum of an exponentially asymptoting fast phase and a linear continuous phase, similar to what has been observed in mouse (Moser and Beutner, 2000) and chick (Eisen et al., 2004) cochlear hair cells. To fit the data, the latter half of the capacitance response was fit to a straight line, and a line with that slope was subtracted from the raw data. The residual was then fit by an exponential. Using this approach, the WT response was best fit by a linear phase of 17.6 fF/s and an exponential with an amplitude of 18.9 fF and with a time constant of 501 ms (see Table 1).

Surprisingly, the capacitance response from *re[a(Δ 10)/b(Δ 7)]* double-homozygous animals showed a larger increase in capacitance in response to step depolarization (Figure 4A; Table 1). The linear phase (65% greater than WT) was specifically enhanced in mutant animals, whereas the exponential amplitude was only minimally larger (1.6% greater than WT). The enhanced exocytosis in double-homozygous mutant zebrafish was accompanied by an increase in the calcium current in the hair cells measured at -20 mV (Figure 4B). Figure 4C shows the average current as a function of membrane potential from WT ($n = 15$) and *re[a(Δ 10)/b(Δ 7)]* double-homozygous ($n = 17$) fish. While the shape of the current-voltage (I-V) relationship appeared similar, the calcium currents were found to be larger in the cells lacking Ribeye. Increasing extracellular calcium to 10 mM in WT animals resulted in an increase in calcium current (Figure 4D) and exocytosis (Figure 4E) to levels that mimicked that of *re[a(Δ 10)/b(Δ 7)]* double-homozygous animals, suggesting that the enhanced exocytosis can largely be explained by the enhanced calcium current.

Calcium Channels Are Poorly Coupled to Release in *re[a(Δ 10)/b(Δ 7)]* Double-Homozygous Hair Cells

Next, we performed co-immunofluorescence staining with an antibody for the calcium channel CaV1.3 (Sheets et al., 2011, 2012) and a post-synaptic marker pan-MAGUK (Meyer et al., 2005). In WT animals, CaV1.3 staining revealed spots (Figure 5A, red), which were found localized near pan-MAGUK spots (Figure 5A, green). By contrast, CaV1.3 and pan-MAGUK spots were spatially segregated in *re[a(Δ 10)/b(Δ 7)]* double homozygotes (Figure 5B), suggesting improper localization.

As a second test for the proximity between calcium channels and active zones, we determined the effect of the slow calcium buffer EGTA on exocytosis in WT and *re[a(Δ 10)/b(Δ 7)]* double-homozygous mutant animals. High concentrations of EGTA have little effect on calcium concentrations in small nano-domains near the mouth of open calcium channels but efficiently reduce bulk calcium concentrations and calcium at other distal locations away from the channels. Hence, if sites of exocytosis are very near calcium channels, EGTA is expected to have little effect on release. Electrophysiological studies from various synapses have used this method to demonstrate tight proximity of calcium channels to release sites (Mennerick and Matthews, 1996; Adler et al., 1991; Roberts, 1994; Moser and Beutner, 2000; Mehta et al., 2014; Coggins and Zenisek, 2009; Wong et al., 2014). Similarly, WT hair cells showed little change in the amount of exocytosis when 10 mM EGTA was introduced into the cell via patch pipette and stepped to -10 mV, suggesting tight coupling between calcium channels and release sites in these cells (Figure 5C). On average, the capacitance response to a 3-s step depolarization from -80 mV to -10 mV was 67.8 ± 5.0 fF for cells loaded with 1 mM EGTA ($n = 11$) and 62.8 ± 4.9 fF for cells loaded with 10 mM EGTA ($n = 7$) with similar kinetics. By contrast, 10 mM EGTA had a dramatic effect on ΔC_m in *re[a(Δ 10)/b(Δ 7)]* double-homozygous hair cells, reducing release by 66% relative to 1 mM EGTA and only 55% of WT hair cells loaded with 10 mM EGTA (Figure 5D; Table 1). The effect of EGTA was more pronounced in the continuous phase (72% reduced) than the exponential phase (33%). These results suggest that Ribeye is required for proper formation of calcium channel/vesicle nanodomains and that the enhanced release observed in *re[a(Δ 10)/b(Δ 7)]* double homozygotes may arise primarily from vesicles residing outside of calcium channel nanodomains.

Recordings from Afferent Neurons

The aforementioned results indicate that hair cells from *re[a(Δ 10)/b(Δ 7)]* double homozygotes continue to exhibit robust exocytosis in response to depolarization, despite lacking ribbon densities, but the release is inefficiently coupled to calcium channels, and ribbons are mislocalized. Next, we tested whether ghost-ribbon-containing hair cells could efficiently drive post-synaptic spiking in afferent neurons. To do so, we recorded action potentials from primary afferent neurons of the posterior lateral line system using loose-patch extracellular recordings in response to piezo-electrically driven stimuli directed to the kinocilia of neuromast hair cells (Levi et al., 2015). For these experiments, cells were selected for analysis only if a stimulus was found to generate action potentials in the recorded afferent. Hence, these recordings represent cells that receive synaptic input from hair cells. We could find no differences between WT and mutant animals in their afferent responses. Figure 6 summarizes our results from these recordings in WT and *re[a(Δ 10)/b(Δ 7)]* double-homozygous animals. Figure 6A shows representative recordings taken from neuromast L1 from a WT animal and a mutant animal stimulated at 60 Hz. As can be observed from the recordings, both the WT and mutant animals showed robust spiking throughout a 10-s stimulus train. We found no difference in the spontaneous spike rate before stimulation for WT and *re[a(Δ 10)/b(Δ 7)]* double-homozygous fish (Figure 6B). Figure 6C

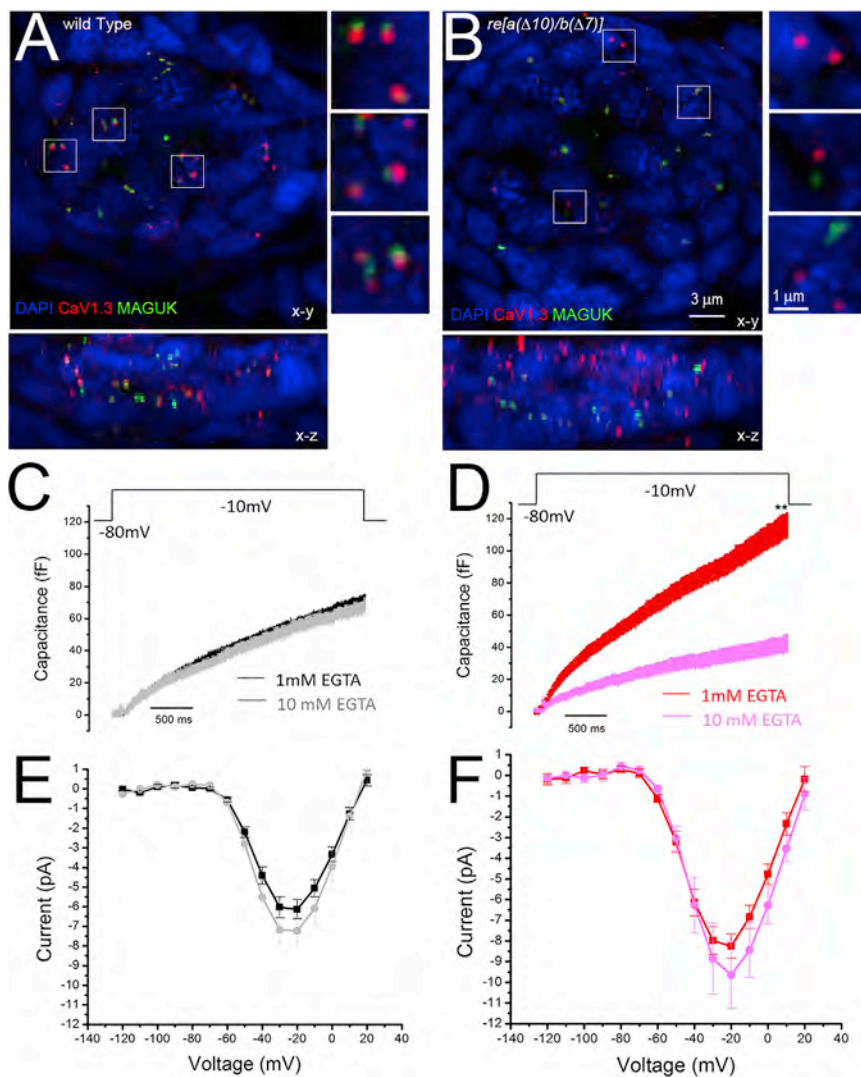


Figure 5. *re[a(Δ10)/b(Δ7)]* Homozygous Hair Cells Have Poorly Localized Calcium Channels and Exhibit Enhanced Sensitivity to 10 mM EGTA

(A and B) Immunolabel of CaV1.3a and MAGUK in 5-dpf WT (A) and *re[a(Δ10)/b(Δ7)]* (B). While Cav1.3 immunolabeled puncta generally localize to the presynapse adjacent to postsynaptic MAGUK immunolabel in WT (A; insets), CaV1.3a clusters fail to localize to the presynapse in *re[a(Δ10)/b(Δ7)]* mutants (B; inset).

(C and D) Capacitance increase of WT and double-mutant neuromast hair cells in response to a 3-s step depolarization with 1 mM EGTA or 10 mM EGTA (gray, n = 8) in the internal solution. The average capacitance increase at the end of the 3-s depolarization (averaged over 100 ms) of WT fish was 67.8 ± 5.0 fF at 1 mM EGTA (C; black, n = 11) and 62.8 ± 4.9 fF at 10 mM EGTA (C; gray, n = 7); p = 0.50. 10 mM EGTA blocks 7.4% of release, compared to 1 mM EGTA in WT fish. The average capacitance increase at the end of the 3-s depolarization (averaged over 100 ms) of double mutants was 106.1 ± 13.6 fF at 1 mM EGTA (D; red, n = 12), and 36.3 ± 8.7 fF at 10 mM EGTA (D; pink, n = 8), p = 0.01. 10 mM EGTA blocks 66.% of release compared to 1 mM EGTA.

(E and F), Plot of current-voltage relationship for WT fish NM hair cells (E) and *re[a(Δ10)/b(Δ7)]* homozygous mutant neuromast hair cells (F) at 1 mM EGTA and 10 mM EGTA internal solution. At -20 mV, the average current of WT cells was -6.1 ± 0.5 pA at 1 mM EGTA (E; red, n = 15) and 6.9 ± 0.9 pA (E; pink, n = 8). p = 0.46. The average current of mutant fish cells was -8.26 ± 0.58 pA at 1 mM EGTA solution (F; red, n = 17), and -9.9 ± 2.2 pA at 10 mM EGTA solution (F; pink, n = 6). p = 0.49. The fish recorded were between 5 and 8 days old, and the neuromasts recorded were P3 and P4.

plots the recorded spike frequency that has been time averaged over the 10-s stimulus train for three frequencies (2 Hz, 30 Hz, and 60 Hz). Figure 6F shows the spike rate over the entire 10 s of 60-Hz stimulation for all fish. As can be seen from the plots, *re[a(Δ10)/b(Δ7)]* double-homozygous fish exhibited spike rates similar to WT animals at all frequencies tested. We found no effect of genotype on the ability to phase lock to stimuli, as the vector strengths for both WT and mutant animals were similar across all stimulation frequencies (Figure 6D). Similarly, the measured preferred phase angles were indistinguishable among genotypes. Figure 6E shows that the latency to the first response was also unchanged in mutant animals.

DISCUSSION

Evidence for Ribeye Forming the Core of the Ribbon

In this study, we used genome editing techniques to introduce mutations into the coding regions of the synaptic ribbon-specific A-domain of both zebrafish *ribeye* genes. Mutant animals exhibit

greatly reduced levels of Ribeye, leading to striking morphological changes to the synaptic ribbons of hair cells. In particular, double-homozygous mutants have ribbons that lack the central electron density while maintaining a roughly spherical scaffold that harbors attached synaptic vesicles. Of note, the ghost ribbons were found to have lost 66% of their estimated volume, similar to the estimated contribution of Ribeye to ribbon volume in bipolar cells (Zenisek et al., 2004) but considerably more than the volume occupied by the density in micrographs. Previous studies have demonstrated that overexpressed Ribeye forms electron-dense aggregates in HEK and R28 cells (Schmitz et al., 2000; Magupalli et al., 2008) and leads to ectopic electron densities in neuromast hair cells (Sheets et al., 2011). In some systems, the A-domain alone is sufficient to form densities, whereas the B-domain alone forms a soluble protein (Schmitz et al., 2000). Summed together, it is reasonable to conclude that the core density observed in electron micrographs of synaptic ribbons is largely composed of the A-domain of Ribeye protein, whereas the surrounding halo of lighter material is made

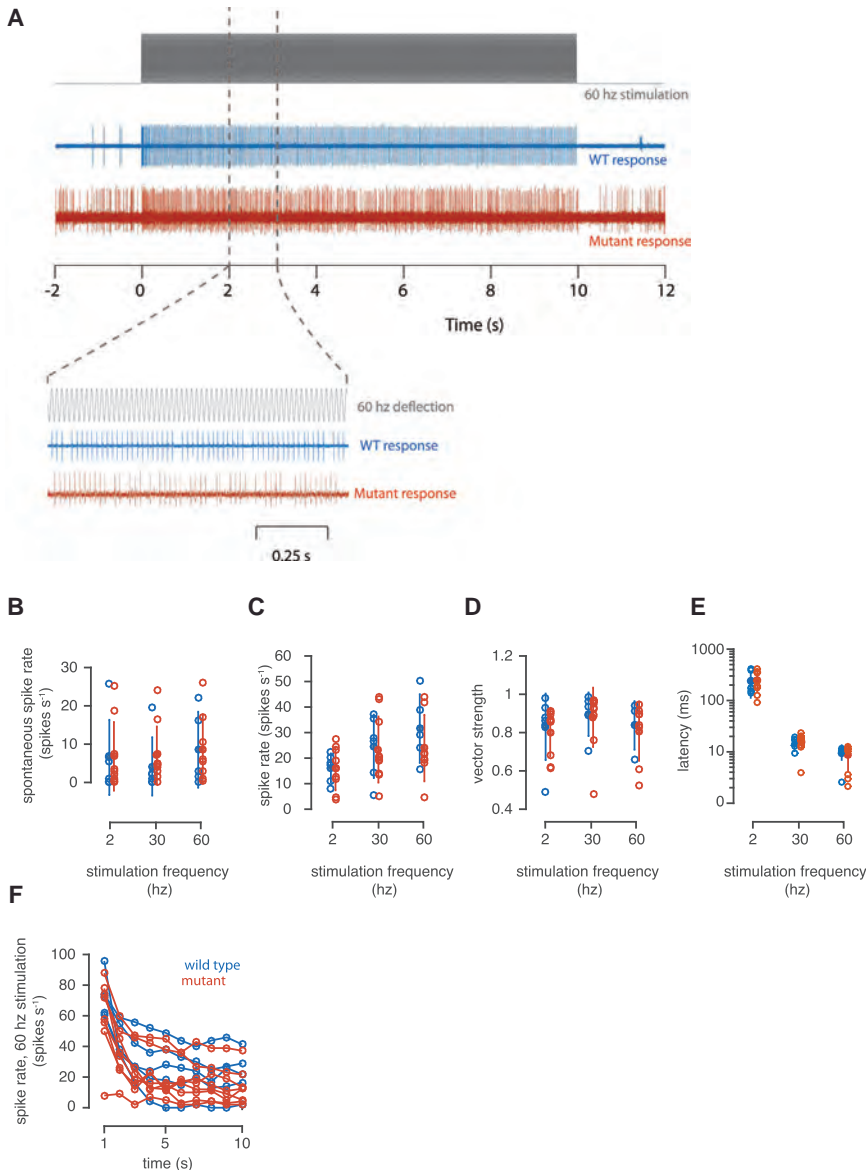


Figure 6. Electrophysiology Recordings from the Primary Afferent Neurons of Lateral Line Neuromasts

(A) Representative traces showing the spiking rates for the afferent neurons of WT (blue) and mutant (red) zebrafish in response to 10 s of 60-Hz sine wave stimulation.

(B) The spontaneous spike rate measured for WT and mutant animals before stimulation.

(C) The average spike rate calculated over the entire 10 s of stimulation for stimulation frequencies of 2, 30, and 60 Hz.

(D) The average vector strength calculated for the entire 10 s of stimulation.

(E) The latency between the onset of stimulation and the first spike.

(F) The spike rate as a function of time during 10 s of 60 Hz stimulation. Closed circles show the mean; error bars indicate SD.

Rim2, but each of these proteins is also found at conventional synapses, which lack the ribbon structure. Of note, a ribbon-specific isoform of Piccolo has been described in retina (Regus-Leidig et al., 2013, 2014b), suggesting that ribbon-specific splicing may underlie some of the diversity in ribbon shape and size.

It is noteworthy that some of the features we report here differ from those found in a recent report characterizing retinal ribbons in Ribeye knockout mice (Maxeiner et al., 2016). In that study, the authors found ribbons completely lacking from the retina and a general decrease in vesicles residing near active zones. Additionally, they found that synaptic transmission between rod bipolar cells and AII Amacrine cells was reduced by approximately 80%, whereas in our study, exocytosis, measured by capacitance, is slightly enhanced. As in our

study, the kinetics of the responses remained unchanged, suggesting that ribbons are not required to maintain continuous release from bipolar cells. Although the reasons for the differences in the two studies are unknown at this point, we hypothesize several possible explanations. (1) In our study, a small amount of Ribeye remains in hair cells, which may be sufficient to nucleate the ghost-ribbon structures and be sufficient to stabilize synaptic structures containing other ribbon proteins. (2) Occult ghost ribbons might account for 20% of release from mouse bipolar cells. Ghost ribbons lack the electron density and are smaller than WT ribbons and, thus, were initially difficult to find in electron micrographs in neuromast hair cells. Identifying such structures in mouse bipolar cells ribbons would be even more difficult, since bipolar cell ribbons are smaller and vesicles are found at high densities throughout the cytoplasm. Moreover, since release is reduced by 80%, ghost-ribbon

up of the B-domain of Ribeye along with other ribbon proteins that remain in place in our mutant animals. This idea is consistent with the original model put forth by Schmitz, Sudhof, and colleagues (Schmitz et al., 2000). We find that most “ghost ribbons,” while smaller, appear to take on a shape that is similar to that of normal ribbons (although see Figures 3C–3F) and still retain a scaffold capable of recruiting vesicles. Interestingly, we found two examples of ghost-ribbon-like structures in photoreceptors of mutant mice, which appeared more elongated than the hair cell ghost ribbons, mimicking the structure of photoreceptor ribbons. It remains possible that the sparse Ribeye remaining in these cells may maintain the structure but fail to form a density. Alternatively, numerous structural proteins have been shown to localize to the ribbon complex (Brandstätter et al., 1999), including Piccolo, Bassoon, Cast/ERC, Rim1, and

up of the B-domain of Ribeye along with other ribbon proteins that remain in place in our mutant animals. This idea is consistent with the original model put forth by Schmitz, Sudhof, and colleagues (Schmitz et al., 2000). We find that most “ghost ribbons,” while smaller, appear to take on a shape that is similar to that of normal ribbons (although see Figures 3C–3F) and still retain a scaffold capable of recruiting vesicles. Interestingly, we found two examples of ghost-ribbon-like structures in photoreceptors of mutant mice, which appeared more elongated than the hair cell ghost ribbons, mimicking the structure of photoreceptor ribbons. It remains possible that the sparse Ribeye remaining in these cells may maintain the structure but fail to form a density. Alternatively, numerous structural proteins have been shown to localize to the ribbon complex (Brandstätter et al., 1999), including Piccolo, Bassoon, Cast/ERC, Rim1, and

numbers may be similarly reduced. (3) The differences may reflect species- and/or tissue-specific roles for Ribeye.

Relationship between Ribeye and Vesicles

In this study, we find that ghost ribbons possess an estimated 50% of the surface area of WT ribbons, while maintaining near-normal vesicle numbers. Physical tethers linking the ribbon to synaptic vesicles are observable in some electron micrographs (e.g., Lenzi et al., 2002), but the molecular components of the tether remain obscure. Since vesicle numbers remain constant, despite dramatic reductions in Ribeye levels, we posit that a yet-to-be-identified protein may link vesicles to ribbons and that loss of ribbon volume results in an increase in concentration of this molecule on the ribbon. Our results here argue against Ribeye directly participating in the tethering of synaptic vesicles.

Synaptic vesicles associated with ghost ribbons were also found to be smaller than those associated with ribbons in WT animals. The reasons for this difference is currently unknown, but it is worth noting that Ribeye has been suggested to act as a lysophosphatidyl acyl transferase that adds an acyl group to lysolipids, thus converting lysophosphatidic acid (LPA) with one acyl chain to phosphatidic acid (PA) with two acyl chains (Schwarz et al., 2011). Since the LPA and PA have opposite effects on membrane curvature, the acyltransferase activity has the potential to influence membrane curvature and, by extension, vesicle size.

Ribeye, Synaptic Localization, and Calcium Channels

Prior to the present study, several lines of evidence have pointed toward a close relationship between Ribeye and calcium channels in ribbon synapses. Calcium channels have been shown to localize to clusters beneath the ribbon in ribbon synapses (Roberts et al., 1990; Zenisek et al., 2003; Frank et al., 2010). Moreover, the tight coupling of fast exocytosis to calcium channels appears to be a feature of many ribbon synapses (Singer and Diamond, 2003; Mennerick and Matthews, 1996; Moser and Beutner, 2000; Wong et al., 2014). A link between Ribeye and calcium channels has previously been inferred from overexpression and knockdown studies in zebrafish. MO-driven knockdown of ribeye leads to loss of calcium channel clusters in both retina (Lv et al., 2012) and neuromast hair cells (Sheets et al., 2012), whereas animals overexpressing Ribeye exhibit ectopic calcium channel clusters that colocalize with Ribeye protein aggregates (Sheets et al., 2012). More recently, knockout of Ribeye in mouse was found to cause a subtle change in the size of calcium channel clusters in photoreceptors (Maxeiner et al., 2016). Notably, in contrast to the previous MO results in retina (Lv et al., 2012), calcium channels remained clustered in discrete locations in the retina. Additionally, knockout mice were found to exhibit an increase in sensitivity of mEPSC frequency to high levels of the membrane-permeant analog of EGTA, EGTA-AM. Since mEPSC frequency is also reduced by calcium channel blockers (Mehta et al., 2013; Maxeiner et al., 2016), the results were suggestive of a loss of coupling between calcium channels and release sites.

Here, we show that genetic disruption of Ribeye expression leads to mislocalization and redistribution of calcium channels in neuromast hair cells, in line with the previous work using

MOs (Sheets et al., 2012). This redistribution of calcium channels is associated with a slight enhancement of calcium current. Although the reason for the increase in calcium current is unknown at present, we posit that homeostatic plasticity, in response to less neurotransmitter released on to afferent fibers, may trigger an upregulation of calcium current and exocytosis in these cells, similar to what has been described for other systems (Frank, 2014). Alternatively, Ribeye may act as a negative regulator of voltage-gated calcium channel expression or activity, with the latter being a distinct possibility, given that CtBP2 functions as a co-repressor. Further work will be necessary to determine the mechanisms behind the enhanced calcium current observed here. We also show here that the continuous phase of exocytosis in mutant animals exhibits an enhanced sensitivity to EGTA. Mutant hair cells retain an EGTA-insensitive component of release that retains similar exponential release kinetics, suggesting that some vesicles may still reside in nanodomains near calcium channels.

Of note, inner hair cells from mice harboring mutations to the synaptic ribbon protein Bassoon, which exhibit few ribbons that associate with the plasma-membrane exhibit a reduction in voltage-gated calcium current. Interestingly, a small subset of ribbons in Bsn mice associates with the plasma membrane at synapses, and these synapses exhibit more calcium channels than ribbon-less synapses (Frank et al., 2010). The opposite effect on calcium current in Bassoon mice, compared with *refa(Δ10)/b(Δ7)* double-homozygous fish, may indicate that the two proteins interact with and regulate calcium channels differently, with Bassoon influencing overall expression level or channel stability and Ribeye having an effect on channel localization.

Interestingly, several studies have demonstrated that mutations to calcium channel subunits have a reciprocal effect on synaptic ribbon morphology, although the magnitude and specific effects have varied between preparations. For example, a mutation in the zebrafish gene encoding for the alpha subunit of Cav 1.4 channels results in the disappearance of cone synaptic ribbons (Jia et al., 2014), whereas genetic or pharmacological removal of calcium conductance through Cav 1.3 channels increases the size of ribbons in lateral line hair cells (Sheets et al., 2012). In mouse, the genetic removal of Cav1.4 channels prevents the formation of mature synaptic ribbons (Liu et al., 2013; Regus-Leidig et al., 2014a), whereas Cav1.3 is not required for the generation or maturation of auditory hair cell ribbons but is required for proper maintenance of the synapses (Nemzou N et al., 2006).

Effects on Synaptic Transmission

Here, our results show an enhanced continuous phase of exocytosis in animals deficient in Ribeye. Given that there are fewer ghost ribbons than WT ribbons and that most ghost ribbons fail to localize to proper synaptic locations, we suggest that much of this continuous phase of release may arise from extra-ribbon locations. Our results are in line with several imaging and electrophysiological studies that have demonstrated that extra-ribbon release can occur in ribbon-bearing cells during prolonged stimulation (Mehta et al., 2014; Zenisek et al., 2000; Midorikawa et al., 2007; Pangršič et al., 2015; Chen et al.,

2013). We do not suggest, however, that synaptic transmission does not normally occur at ribbon locations in wild-type animals, since direct lines of evidence have firmly established exocytosis at ribbon sites (Vaithianathan et al., 2016; Zenisek, 2008; Chen et al., 2013; Midorikawa et al., 2007).

In contrast to our results here, acute inactivation of the synaptic ribbon using fluorophore-assisted light inactivation (FALI) of ribbon-targeted fluorescent peptides cause the loss of spontaneous and both fast and slow components of evoked release (Mehta et al., 2013; Snellman et al., 2011). Although the peptides used in those studies specifically target Ribeye, FALI generates a sphere of damage likely to also include local bystander proteins associated with the synaptic ribbon. The comparatively mild changes to release properties in cells missing Ribeye implicate these other nearby proteins in functions essential for maintaining focal neurotransmitter release in these cells. Indeed, ghost ribbons maintain a shape and vesicle clusters that resemble WT ribbons, suggesting that many ribbon-resident proteins inhabit these structures in mutant animals. Relatedly, inner hair cells from mice harboring mutations to Bassoon show decreases in both transient (Khimich et al., 2005) and sustained (Frank et al., 2010) components of exocytosis. This comparatively greater effect of Bassoon removal suggests that either Bassoon itself or proteins recruited by Bassoon to ribbons play a more fundamental role in determining release properties from ribbon synapses. Indeed, the genetic disruption of Bassoon causes a change in open probability, reduces channel number, and causes a redistribution of calcium channels in hair cells (Frank et al., 2010). The effect of Bassoon removal must overwhelm any homeostatic compensatory mechanisms that might normally return calcium current to normal levels. In addition to Bassoon, several other proteins already known to have critical functions in conventional synapses have been demonstrated to localize either to the ribbon or the plasma membrane beneath the ribbon (Regus-Leidig and Brandstatter, 2011; tom Dieck et al., 2005).

Surprisingly, despite the loss of efficient coupling between calcium channels and release sites in mutants and reduction in ribbon numbers, we could detect no differences in afferent responses. Spontaneous and evoked release rates at three different frequencies, the latency to first spike and the ability to phase lock were indistinguishable between genotypes. A key difference in capacitance measurements and afferent spike recordings is that afferent recordings are dependent upon exocytosis at specific locations, namely, on to receptors populating afferent fibers, whereas capacitance recordings have no such spatial requirements. As such capacitance measurements reflect both synaptic and extrasynaptic release. Similar to our results, hair cells in mice lacking endogenous calcium-binding proteins show enhanced continuous release, without an effect on afferent responses, consistent with extrasynaptic release contributing significantly to capacitance response (Pangršić et al., 2015). Given that, in the presence of 10 mM EGTA, some exocytosis persists with normal kinetics in mutant animals, we suggest that this EGTA-resistant component represents the subset of vesicles, which is properly localized near calcium channels, and could be sufficient to drive afferent neuron spiking to near normal levels for afferents that receive synaptic input. It

should be noted that, to perform afferent recordings, one first identifies and selects for synaptically connected neurons before performing experiments. Thus, recordings represent only those neurons, which generate spikes in response to mechanical stimuli to hair cells, and cannot account for cells that lack synaptic connections. These results suggest that when synapses with ghost ribbons are formed, they respond to stimuli normally under the conditions we tested. It should also be noted that while the stimulus frequencies we tested here are typical or slightly higher for neuromast hair cells, auditory hair cells of the inner ear respond to much higher frequencies and exhibit faster kinetics and greater demands on neurotransmitter release. Because of this, the faster hair cells of other systems may show greater defects in the absence of Ribeye.

EXPERIMENTAL PROCEDURES

Zebrafish Husbandry

Zebrafish were kept in accordance with the Yale University Animal Care and Use Committee guidelines.

Generation of *ribeye a* Mutant Fish

Ribeye a mutant fish were generated using zinc finger nucleases (ZFNs) targeting the A-domain of Ribeye a (ENSDARG00000044062) purchased from Sigma-Aldrich. mRNAs encoding the ZFNs were injected into one-cell-stage embryos, and progeny were screened for mutations. Mutants (Figure S1) were selected for breeding to generate homozygous mutants. Detailed experimental procedures are provided in the Supplemental Experimental Procedures.

Generation of *ribeye b* Mutant Fish

CRISPR/Cas9-induced mutagenesis procedures were adapted from previously published reports (Hruscha et al., 2013) and are detailed in the Supplemental Experimental Procedures. Single guide RNAs (sgRNAs) were designed to target to the Ribeye-specific A-domain of *ribeye b*. Several mutant lines were identified and selected for further study (Figure S2).

EM and Immunofluorescence

Procedures were adapted from standard previously published experimental protocols (Obholzer et al., 2008; Lv et al., 2012) and are detailed in the Supplemental Experimental Procedures.

Hair-Cell Voltage-Clamp Recordings

Whole-cell voltage-clamp recordings were carried out from neuromast hair cells in anesthetized live zebrafish (5–7 dpf), as previously described (Ricci et al., 2013). Details can be found in the Supplemental Experimental Procedures.

Afferent Neuron Recordings

Loose-patch recordings from soma of afferent neurons were made on anesthetized and paralyzed larval zebrafish as previously described and detailed in the Supplemental Experimental Procedures (Levi et al., 2015).

Statistical Analysis

Data are presented as mean \pm SEM. Statistical significance across datasets was determined using the unpaired two-tailed t test. Significance was considered $p < 0.05$; however, for most comparisons in the present study, $p < 0.01$.

SUPPLEMENTAL INFORMATION

Supplemental Information includes Supplemental Experimental Procedures and two figures and can be found with this article online at <http://dx.doi.org/10.1016/j.celrep.2016.05.045>.

AUTHOR CONTRIBUTIONS

C.L. designed and conducted experiments, analyzed data, and wrote the paper; W.J.S. performed experiments, analyzed data, and participated in the writing; O.A. analyzed data and participated in the writing; C.F. analyzed morphological data; J.Z. analyzed electrophysiological data; J.S.-S. analyzed data and provided technical expertise; L.S. performed experiments, analyzed data, and participated in writing; J.C.L. oversaw afferent recording experiments and interpreted and analyzed data; D.Z. designed experiments, analyzed data, and wrote the paper.

ACKNOWLEDGMENTS

This work was funded by NIH grants EY021195 (to D.Z.), DC008130 (to J.S.-S.), and DC010809 (to J.C.L.); the Amelia Peabody Charitable Fund (to L.S.); and National Science Foundation grant IOS1257150 (to J.C.L.).

Received: July 30, 2015

Revised: April 6, 2016

Accepted: May 10, 2016

Published: June 9, 2016

REFERENCES

- Adler, E.M., Augustine, G.J., Duffy, S.N., and Charlton, M.P. (1991). Alien intracellular calcium chelators attenuate neurotransmitter release at the squid giant synapse. *J. Neurosci.* *11*, 1496–1507.
- Bartoletti, T.M., Babai, N., and Thoreson, W.B. (2010). Vesicle pool size at the salamander cone ribbon synapse. *J. Neurophysiol.* *103*, 419–423.
- Brandstätter, J.H., Fletcher, E.L., Garner, C.C., Gundelfinger, E.D., and Wässle, H. (1999). Differential expression of the presynaptic cytomatrix protein bassoon among ribbon synapses in the mammalian retina. *Eur. J. Neurosci.* *11*, 3683–3693.
- Chen, M., Van Hook, M.J., Zenisek, D., and Thoreson, W.B. (2013). Properties of ribbon and non-ribbon release from rod photoreceptors revealed by visualizing individual synaptic vesicles. *J. Neurosci.* *33*, 2071–2086.
- Coggins, M., and Zenisek, D. (2009). Evidence that exocytosis is driven by calcium entry through multiple calcium channels in goldfish retinal bipolar cells. *J. Neurophysiol.* *101*, 2601–2619.
- Edmonds, B.W., Gregory, F.D., and Schweizer, F.E. (2004). Evidence that fast exocytosis can be predominantly mediated by vesicles not docked at active zones in frog saccular hair cells. *J. Physiol.* *560*, 439–450.
- Eisen, M.D., Spassova, M., and Parsons, T.D. (2004). Large releasable pool of synaptic vesicles in chick cochlear hair cells. *J. Neurophysiol.* *91*, 2422–2428.
- Frank, C.A. (2014). How voltage-gated calcium channels gate forms of homeostatic synaptic plasticity. *Front. Cell. Neurosci.* *8*, 40.
- Frank, T., Rutherford, M.A., Strenzke, N., Neef, A., Pangršič, T., Khimich, D., Fejtová, A., Gundelfinger, E.D., Liberman, M.C., Harke, B., et al. (2010). Bassoon and the synaptic ribbon organize Ca²⁺ channels and vesicles to add release sites and promote refilling. *Neuron* *68*, 724–738.
- Hruscha, A., Krawitz, P., Rechenberg, A., Heinrich, V., Hecht, J., Haass, C., and Schmid, B. (2013). Efficient CRISPR/Cas9 genome editing with low off-target effects in zebrafish. *Development* *140*, 4982–4987.
- Jia, S., Muto, A., Orisme, W., Henson, H.E., Parupalli, C., Ju, B., Baier, H., and Taylor, M.R. (2014). Zebrafish *Cacna1fa* is required for cone photoreceptor function and synaptic ribbon formation. *Hum. Mol. Genet.* *23*, 2981–2994.
- Khimich, D., Nouvian, R., Pujol, R., Tom Dieck, S., Egner, A., Gundelfinger, E.D., and Moser, T. (2005). Hair cell synaptic ribbons are essential for synchronous auditory signalling. *Nature* *434*, 889–894.
- Lagnado, L., Gomis, A., and Job, C. (1996). Continuous vesicle cycling in the synaptic terminal of retinal bipolar cells. *Neuron* *17*, 957–967.
- Lenzi, D., Crum, J., Ellisman, M.H., and Roberts, W.M. (2002). Depolarization redistributes synaptic membrane and creates a gradient of vesicles on the synaptic body at a ribbon synapse. *Neuron* *36*, 649–659.
- Levi, R., Akanyeti, O., Ballo, A., and Liao, J.C. (2015). Frequency response properties of primary afferent neurons in the posterior lateral line system of larval zebrafish. *J. Neurophysiol.* *113*, 657–668.
- Liu, X., Kerov, V., Haeseleer, F., Majumder, A., Artemyev, N., Baker, S.A., and Lee, A. (2013). Dysregulation of Ca(v)1.4 channels disrupts the maturation of photoreceptor synaptic ribbons in congenital stationary night blindness type 2. *Channels (Austin)* *7*, 514–523.
- Lv, C., Gould, T.J., Bewersdorf, J., and Zenisek, D. (2012). High-resolution optical imaging of zebrafish larval ribbon synapse protein RIBEYE, RIM2, and CaV 1.4 by stimulation emission depletion microscopy. *Microsc. Microanal.* *18*, 745–752.
- Magupalli, V.G., Schwarz, K., Alpadi, K., Natarajan, S., Seigel, G.M., and Schmitz, F. (2008). Multiple RIBEYE-RIBEYE interactions create a dynamic scaffold for the formation of synaptic ribbons. *J. Neurosci.* *28*, 7954–7967.
- Matthews, G., and Fuchs, P. (2010). The diverse roles of ribbon synapses in sensory neurotransmission. *Nat. Rev. Neurosci.* *11*, 812–822.
- Maxeiner, S., Luo, F., Tan, A., Schmitz, F., and Südhof, T.C. (2016). How to make a synaptic ribbon: RIBEYE deletion abolishes ribbons in retinal synapses and disrupts neurotransmitter release. *EMBO J.*, e201592701.
- Mehta, B., Snellman, J., Chen, S., Li, W., and Zenisek, D. (2013). Synaptic ribbons influence the size and frequency of miniature-like evoked postsynaptic currents. *Neuron* *77*, 516–527.
- Mehta, B., Ke, J.B., Zhang, L., Baden, A.D., Markowitz, A.L., Nayak, S., Briggman, K.L., Zenisek, D., and Singer, J.H. (2014). Global Ca²⁺ signaling drives ribbon-independent synaptic transmission at rod bipolar cell synapses. *J. Neurosci.* *34*, 6233–6244.
- Mennerick, S., and Matthews, G. (1996). Ultrafast exocytosis elicited by calcium current in synaptic terminals of retinal bipolar neurons. *Neuron* *17*, 1241–1249.
- Meyer, M.P., Trimmer, J.S., Gilthorpe, J.D., and Smith, S.J. (2005). Characterization of zebrafish PSD-95 gene family members. *J. Neurobiol.* *63*, 91–105.
- Midorikawa, M., Tsukamoto, Y., Berglund, K., Ishii, M., and Tachibana, M. (2007). Different roles of ribbon-associated and ribbon-free active zones in retinal bipolar cells. *Nat. Neurosci.* *10*, 1268–1276.
- Moser, T., and Beutner, D. (2000). Kinetics of exocytosis and endocytosis at the cochlear inner hair cell afferent synapse of the mouse. *Proc. Natl. Acad. Sci. USA* *97*, 883–888.
- Nemzou, N., Bulankina, A.V., Khimich, D., Giese, A., and Moser, T. (2006). Synaptic organization in cochlear inner hair cells deficient for the CaV1.3 (alpha1D) subunit of L-type Ca²⁺ channels. *Neuroscience* *141*, 1849–1860.
- Obholzer, N., Wolfson, S., Trapani, J.G., Mo, W., Nechiporuk, A., Busch-Nentwich, E., Seiler, C., Sidi, S., Söllner, C., Duncan, R.N., et al. (2008). Vesicular glutamate transporter 3 is required for synaptic transmission in zebrafish hair cells. *J. Neurosci.* *28*, 2110–2118.
- Pangršič, T., Gabrielaitis, M., Michanski, S., Schwaller, B., Wolf, F., Strenzke, N., and Moser, T. (2015). EF-hand protein Ca²⁺ buffers regulate Ca²⁺ influx and exocytosis in sensory hair cells. *Proc. Natl. Acad. Sci. USA* *112*, E1028–E1037.
- Parsons, T.D., Lenzi, D., Almers, W., and Roberts, W.M. (1994). Calcium-triggered exocytosis and endocytosis in an isolated presynaptic cell: capacitance measurements in saccular hair cells. *Neuron* *13*, 875–883.
- Regus-Leidig, H., and Brandstätter, J.H. (2011). Structure and function of a complex sensory synapse. *Acta Physiol. (Oxf.)* *204*, 479–486.
- Regus-Leidig, H., Ott, C., Löhner, M., Atorf, J., Fuchs, M., Sedmak, T., Kremers, J., Fejtová, A., Gundelfinger, E.D., and Brandstätter, J.H. (2013). Identification and immunocytochemical characterization of Piccolino, a novel Piccolo splice variant selectively expressed at sensory ribbon synapses of the eye and ear. *PLoS ONE* *8*, e70373.
- Regus-Leidig, H., Atorf, J., Feigenspan, A., Kremers, J., Maw, M.A., and Brandstätter, J.H. (2014a). Photoreceptor degeneration in two mouse models for congenital stationary night blindness type 2. *PLoS ONE* *9*, e86769.

- Regus-Leidig, H., Fuchs, M., Löhner, M., Leist, S.R., Leal-Ortiz, S., Chiodo, V.A., Hauswirth, W.W., Garner, C.C., and Brandstätter, J.H. (2014b). In vivo knockdown of Piccolino disrupts presynaptic ribbon morphology in mouse photoreceptor synapses. *Front. Cell. Neurosci.* **8**, 259.
- Ricci, A.J., Bai, J.P., Song, L., Lv, C., Zenisek, D., and Santos-Sacchi, J. (2013). Patch-clamp recordings from lateral line neuromast hair cells of the living zebrafish. *J. Neurosci.* **33**, 3131–3134.
- Roberts, W.M. (1994). Localization of calcium signals by a mobile calcium buffer in frog saccular hair cells. *J. Neurosci.* **14**, 3246–3262.
- Roberts, W.M., Jacobs, R.A., and Hudspeth, A.J. (1990). Colocalization of ion channels involved in frequency selectivity and synaptic transmission at presynaptic active zones of hair cells. *J. Neurosci.* **10**, 3664–3684.
- Schmitz, F., Königstorfer, A., and Südhof, T.C. (2000). RIBEYE, a component of synaptic ribbons: a protein's journey through evolution provides insight into synaptic ribbon function. *Neuron* **28**, 857–872.
- Schnee, M.E., Santos-Sacchi, J., Castellano-Muñoz, M., Kong, J.H., and Ricci, A.J. (2011). Calcium-dependent synaptic vesicle trafficking underlies indefatigable release at the hair cell afferent fiber synapse. *Neuron* **70**, 326–338.
- Schwarz, K., Natarajan, S., Kassas, N., Vitale, N., and Schmitz, F. (2011). The synaptic ribbon is a site of phosphatidic acid generation in ribbon synapses. *J. Neurosci.* **31**, 15996–16011.
- Sheets, L., Trapani, J.G., Mo, W., Obholzer, N., and Nicolson, T. (2011). Ribeye is required for presynaptic Ca_v1.3a channel localization and afferent innervation of sensory hair cells. *Development* **138**, 1309–1319.
- Sheets, L., Kindt, K.S., and Nicolson, T. (2012). Presynaptic Ca_v1.3 channels regulate synaptic ribbon size and are required for synaptic maintenance in sensory hair cells. *J. Neurosci.* **32**, 17273–17286.
- Singer, J.H., and Diamond, J.S. (2003). Sustained Ca²⁺ entry elicits transient postsynaptic currents at a retinal ribbon synapse. *J. Neurosci.* **23**, 10923–10933.
- Snellman, J., Mehta, B., Babai, N., Bartoletti, T.M., Akmentin, W., Francis, A., Matthews, G., Thoreson, W., and Zenisek, D. (2011). Acute destruction of the synaptic ribbon reveals a role for the ribbon in vesicle priming. *Nat. Neurosci.* **14**, 1135–1141.
- tom Dieck, S., Altmann, W.D., Kessels, M.M., Qualmann, B., Regus, H., Brauner, D., Fejtová, A., Bracko, O., Gundelfinger, E.D., and Brandstätter, J.H. (2005). Molecular dissection of the photoreceptor ribbon synapse: physical interaction of Bassoon and RIBEYE is essential for the assembly of the ribbon complex. *J. Cell Biol.* **168**, 825–836.
- Vaithianathan, T., Henry, D., Akmentin, W., and Matthews, G. (2016). Nano-scale dynamics of synaptic vesicle trafficking and fusion at the presynaptic active zone. *eLife* **5**, 13245.
- Wong, A.B., Rutherford, M.A., Gabrielaitis, M., Pangrsic, T., Göttfert, F., Frank, T., Michanski, S., Hell, S., Wolf, F., Wichmann, C., and Moser, T. (2014). Developmental refinement of hair cell synapses tightens the coupling of Ca²⁺ influx to exocytosis. *EMBO J.* **33**, 247–264.
- Zenisek, D. (2008). Vesicle association and exocytosis at ribbon and extraribbon sites in retinal bipolar cell presynaptic terminals. *Proc. Natl. Acad. Sci. USA* **105**, 4922–4927.
- Zenisek, D., Steyer, J.A., and Almers, W. (2000). Transport, capture and exocytosis of single synaptic vesicles at active zones. *Nature* **406**, 849–854.
- Zenisek, D., Davila, V., Wan, L., and Almers, W. (2003). Imaging calcium entry sites and ribbon structures in two presynaptic cells. *J. Neurosci.* **23**, 2538–2548.
- Zenisek, D., Horst, N.K., Merrifield, C., Sterling, P., and Matthews, G. (2004). Visualizing synaptic ribbons in the living cell. *J. Neurosci.* **24**, 9752–9759.

Cell Reports, Volume 15

Supplemental Information

**Synaptic Ribbons Require Ribeye for
Electron Density, Proper Synaptic Localization,
and Recruitment of Calcium Channels**

Caixia Lv, William J. Stewart, Otar Akanyeti, Courtney Frederick, Jie Zhu, Joseph Santos-Sacchi, Lavinia Sheets, James C. Liao, and David Zenisek

Supplemental Experimental Procedures:

Zebrafish husbandry

Zebrafish were kept in accordance with the Yale University Animal Care and Use Committee guidelines.

Generation of *ribeye a* mutant fish

ZFN pairs recognizing the target sequence:

ATCGGCCGATCCCAGAGCTTGGGACACGCTGGGTGGGAATGAG (underline

indicates the cut site), in the coding region of the A-domain of *ribeye a*. were designed by and purchased from Sigma Aldrich. Plasmids containing the DNA sequences encoding the ZFN left and right arrays were linearized by digestion with XbaI and purified using the Qiaquick PCR purification kit (Qiagen). mRNA encoding the left and right arrays was synthesized using the mMessage mMachine T7 Ultra kit (Ambion), according to the manufacturer's protocol, and purified using the RNeasy kit (Qiagen)

mRNA encoding left and right ZFN arrays (50-200 pg) was injected into zebrafish embryos at the one-cell stage. To evaluate the efficiency of ZFN, the Genomic DNA was isolated from 10 ZFN-injected embryos lacking severe developmental defects at 24 hpf and the ZFN target region was amplified by PCR (upstream primer:

TTCCTTACACCACTTGACATCAGC, downstream primer:

CTATTGGTGGTCGGTCATAATGGC) and subcloned into the TOPO-TA vector

(Invitrogen). A total of 100 colonies were selected and colony PCR followed by high-resolution fragment analysis of groups of 3 colonies was used to detect insertion-deletion mutations.

ZFN-injected fish were raised to adulthood and in-crossed. Founders (F0) were identified as in (Cifuentes et al. 2010) with some modifications. Briefly, genomic DNA was isolated from ~30 embryos from each cross. PCR of the ZFN target region followed by high-resolution fragment analysis of groups of 2 embryos was used to identify indels. 6 adults were screened and 5 founders carrying frameshift indels were identified. Sequences were confirmed by amplifying the target region, cloning the PCR product into the TOPO-TA vector (Invitrogen), and Sanger sequencing of plasmids using M13F/R primers. High-resolution fragment analysis results were analyzed using GeneMarker software (SoftGenetics).

Generation of *ribeye b* mutant fish

CRISPR introduced knockout procedures were adapted from previously published papers (Hruscha et al. 2013; Huang and Tan 2013; Hwang et al. 2013; Jao et al. 2013). Briefly, chimeric guide RNA Oligos (TAGGCCGGCTGACAGGACTCCA, AAAGTGGAGTCCTGTCAGCCGG) targeting at zebrafish *ribeye b* (PubMed: 15673675) (GGCCGGCTGACAGGACTCCA) were designed by ZiFit Target Website (<http://zifit.partners.org>) (Sander et al. 2010; Sander et al. 2007). Two oligos were annealed and cloned into T7cas9sgRNA2 vector (Addgene) (Jao et al. 2013). Plasmids containing the guide RNA sequences were linearized by digestion with BamHI and purified using the Qiaquick PCR purification kit (Qiagen). Short mRNA was synthesized using the MEGAshortscript T7 kit (Ambion/Invitrogen), according to the manufacturer's protocol, and purified using the *mir*Vana miRNA Isolation Kit (Ambion/Invitrogen).

Zebrafish optimized vector pCS2-nls-zCas9-nls (Addgene) was used to generate the Cas9 mRNA as previously described (Jao et al. 2013).

About 1 nl of 0.05% phenol red, 120 mM KCl, and 20 mM HEPES, pH 7.0, 150 ng/μl of *nls-zCas9-nls* RNA, and 75 ng/μl of gRNA were injected into the embryos at 1-cell-stage. The T7E1 assay and NgoMIV enzyme digestion were used to evaluate the efficiency. Fish were screened as described for ZFN introduced *ribeye a* mutant. The primers used for fragment analysis are: 5'CTATCCCGGTCACTCCATTC3' (upstream), and 5'GCATCCTTTGAGTCACCACA3' (downstream).

Electron Microscopy

Electron microscopy protocols were adapted from previously published protocols (Obholzer et al. 2008). Briefly, 4-6 dpf zebrafish larvae were fixed overnight in 3% glutaraldehyde and 1.5% paraformaldehyde in 0.1M phosphate buffer on ice for 10 minutes and then overnight at room temperature. After rinsing in 0.1M PBS, samples were stained with 1% osmium, dehydrated in serial washes of 50%, 80%, 95% and then 100% ethanol. Fish were embedded in EMbed-812 (EMS). Hair cells from arterial neuromasts were imaged on Tecnai Biotwin electron microscope.

Measurement of vesicle size

To measure the size of vesicles, a blinded observer drew a region of interest (ROI) using ImageJ around each vesicle associated judged to be associated with every ribbon or ghost-ribbon. The area for each ROI encompassing a vesicle was calculated. Since

vesicle profiles were nearly circular, an effective radius was calculated assuming a circular area for each vesicle.

Immuno-fluorescence

For retina slides staining, similar as previously published (Lv et al. 2012), 5 dpf zebrafish larval were anaesthetized and fixed in 4% paraformaldehyde in PBS and embedded in optimal cutting temperature compound (Sakura, Tokyo, Japan). Cryosections (12 μ m thick) on polylysine-coated slides were permeabilized in blocking buffer (BB) consisting of 1% bovine serum albumin (v), 3% normal goat serum (v/v), and 0.1% Triton X-100 in PBS at room temperature for 30 min, followed by overnight incubation with primary antibodies diluted in blocking buffer at 4°C, then 2 hours secondary antibodies incubation at room temperature. The primary antibodies used for CtBP (CtBP (H-440, Santa Cruz, USA) and MAGUK (Neuromab) were diluted 1:500. Ribeye A and Ribeye B antibodies (both generously provided by Teresa Nicolson, Oregon Health Sciences Center) were diluted 1:2000 (Sheets et al. 2011). The secondary antibodies (Alexa Fluor 488/568 goat anti mouse/rabbit IgG(H+L), Molecular Probes, USA) were diluted 1:200.

The whole mount staining for neuromast hair cells was carried out in a manner similar to a previously reported protocol (Sheets et al. 2011). 5dpf zebrafish larvae were fixed in 4% paraformaldehyde in phosphate buffer for 6 hours at 4°C, permeabilized using acetone for 5 minutes at -20°C, and blocked with blocking buffer containing 2% goat serum, 1% bovine serum albumin (BSA), and 1% dimethyl sulfoxide (DMSO). Samples were incubated in a solution containing primary antibodies overnight at 4°C. Primary antibodies CtBP (CtBP (H-440, Santa Cruz, USA) and MAGUK (Neuromab) were

diluted 1:500 in blocking buffer. Ribeye A and Ribeye B and CaV1.3a antibody was diluted 1:1000 (all donated by Dr. Teresa Nicolson, Vollum Institute, Portland, OR). The secondary antibodies (Alexa Fluor 488/568 goat anti mouse/rabbit IgG(H+L), Molecular Probes, USA) were diluted 1:500.

Confocal images were acquired with a Zeiss (Germany) LSM 780 laser-scanning confocal using Plan-Apochromat 63x/1.40 Oil DIC M27 objective and 0.6x, 3x or 3.5x digital zoom. Alexa Fluor 488 samples were imaged using a 488 nm Argon laser for excitation. DAPI fluorescence was excited using a 405 nm diode laser. Alex-568 samples were images using a laser DPSS 561 nm. The filter sets for DAPI are 405nm excitation and 420-500nm emission, Alexa Fluor 488 are 488nm excitation and 495-555nm emission, and Alex-568 are 561nm excitation and 580-680nm emission using the “best signal scanning” software feature to optimize image acquisition parameters. Images of 512x512 pixels were acquired at a plane scanning mode with 4 line averages. Images were stored as 8-bit RGB tif files for further analysis and processing. Neuromast hair cell images are taken by z-stack, with 0.5-1 μm interval over 9-12 μm . Digital images were processed by Image J and Photoshop software.

Quantitative image analysis was performed on raw images using Amira 3D Analysis software. Prior to analysis, 7 μm^2 region containing the highest level of background was selected from a max-intensity projection of each stack, and the average-fluorescence intensity of that region was subtracted from each pixel in the stack. To quantitatively measure immunolabel intensity, a user-defined inclusive threshold was applied to isolate pixels occupied by Ribeye, CtBP, or MAGUK immunolabeled punctae. The inclusive threshold values for each label were determined using 3D isosurface renderings, with the

minimum threshold value defined as the value above which the user could resolve two closely adjacent spheres or patches. The Material Statistics function was then used to measure the cumulative intensity of fluorescent pixels (sum of the grayscale values) within each individual sphere or patch as well as define the x,y,z coordinates of the center of each puncta within the stack.

Hair Cell voltage clamp recordings

Hair cell recordings were performed as previously described (Ricci et al. 2013). Briefly, zebrafish of either sex ranging in age from 5 to 8 days post-fertilization (dpf) were anesthetized in Tricaine and paralyzed using Tubocurarine, mounted in a recording chamber and tied down using dental floss. An upright Olympus microscopy was used for viewing, and recordings were made with an Axon 200B amplifier with an Axon DD1322 digitizer. To access hair cells for whole-cell recordings, supporting cells surrounding the hair cells were first removed and cleaned using a large bore pipette (3-5M Ω). All recordings were made with jClamp software (Scisoft (www.scisoftco.com), Ridgefield, CT). Cells were held at a membrane potential of -80 mV. Extracellular solution was as follows (in mM): 125 NaCl, 1.0 KCl, 2.2 MgCl₂, 2.8 CaCl₂, 10 HEPES, 6 D-glucose, 285 mOsm, pH 7.6. Pipette solution was (in mM): 90 CsCl, 20 TEA, 5Na₂ATP, 3.5 MgCl₂, 10 HEPES, 1 or 10 EGTA, pH 7.2. The osmolarity was adjusted to 260 mOsm by diluting with water or addition of CsCl. Pipette resistance was typically 9-10M Ω with Cs pipette solutions. Capacitance measures were made using the dual sine admittance technique (Santos-Sacchi 2004). Recordings were made at room temperature. Capacitance data were smoothed by averaging 10 adjacent points in time before

averaging across cells. To measure the current-voltage relationship, hair cells were subjected to 50 ms voltage steps from a holding potential of -80 mV to membrane potentials ranging from -120 mV up to +20 mV in 10 mV increments.

Afferent neuron recordings

Electrophysiological recordings of afferent neurons were conducted on 4-6 dpf larvae. Prior to experiments, larvae were paralyzed by immersion in 1 mg/ml α -bungarotoxin (Sigma) in 10% Hank's solution. Larvae were then placed in a Sylgard-bottom dish containing extracellular solution (134 mM NaCl, 2.9 mM KCl, 1.2 mM MgCl₂, 2.1 mM CaCl₂, 10 mM glucose, 10 mM HEPES buffer, adjusted to a pH of 7.8 with NaOH) and positioned on their side by pinning them through the notochord with four etched tungsten pins.

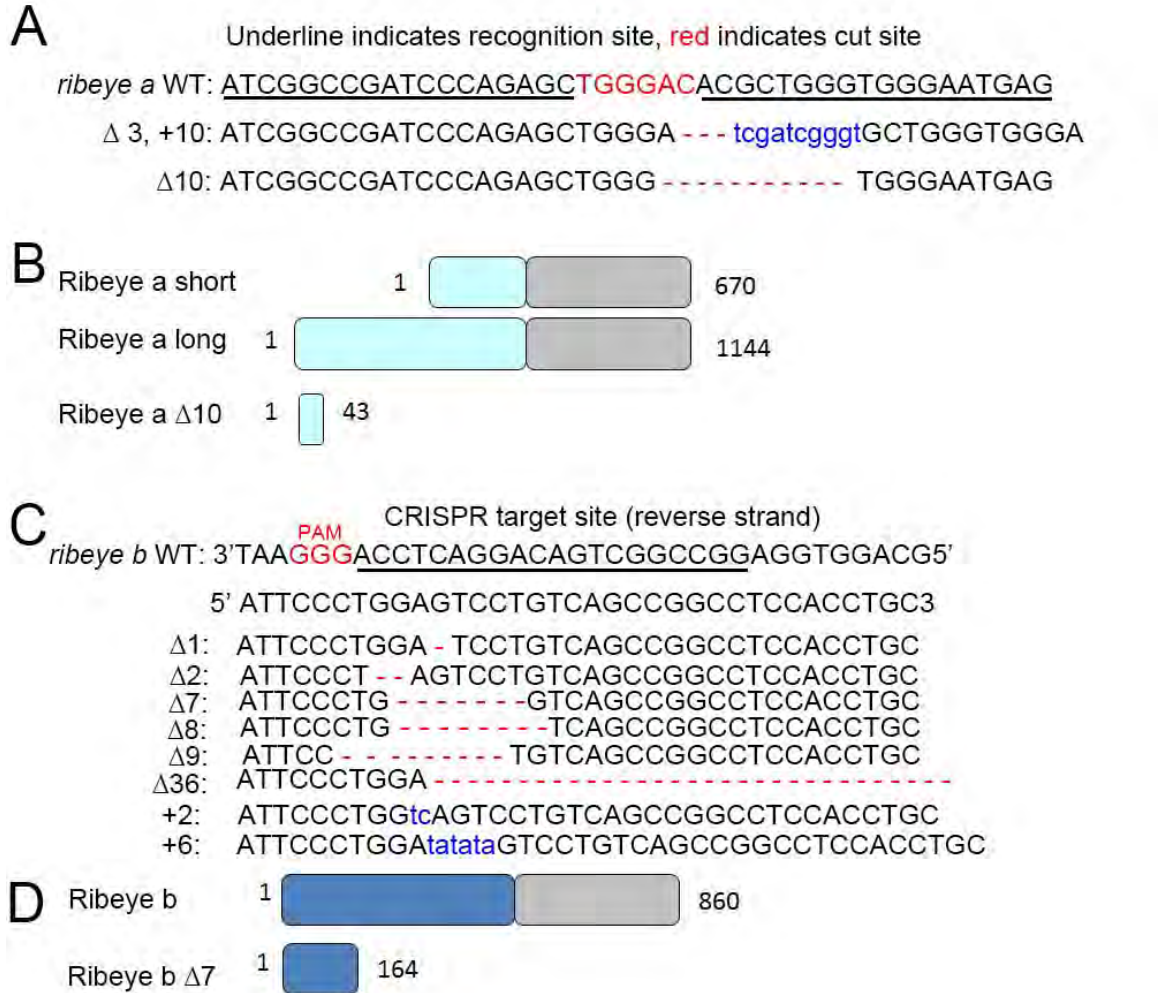
We deflected individual neuromasts of the posterior lateral line system in the zebrafish larvae. To stimulate a neuromast, the visible hair cell bundle (e.g., kinocilia) was deflected with a glass pipette attached to piezoelectric stimulator (30v300 model, Piezosystem, Jena, Germany; Figure 1A). The device was driven by an analog output from Digidata 1440A (Molecular Devices, Sunnyvale, CA). We deflected each neuromast for 10 seconds with sine wave stimuli at frequencies of 2, 30 and 60 Hz, which is within the frequency selectivity of superficial neuromasts (Levi et al., 2014). All stimulation protocols employed a constant amplitude of 50 μ m which was sufficient to evoke a reliable afferent response without visibly damaging the neuromast. The glass pipettes for stimulation were pulled from borosilicate glass (model G150-F-3; inner diameter, 0.86 mm; outer diameter, 1.5 mm; Warner Instruments) on a model P-97

Flaming/Brown micropipette puller (Sutter Instrument). The tip of the pipette was flame-polished to produce a spherical end that was approximately 75 μm in diameter.

Extracellular loose-patch recordings were made from the somata of single posterior lateral line afferent neurons. Patch electrodes were pulled from borosilicate glass (model G150-F-3; inner diameter, 0.86 mm; outer diameter, 1.5 mm; Warner Instruments) to 5–7 $\text{M}\Omega$ resistances on a model P-97 Flaming/Brown micropipette puller (Sutter Instrument). Neuronal activity was amplified with Axoclamp 770B (Molecular Devices, Sunnyvale, CA) at 10 kHz and gain of 1,000 in AC mode and then filtered between 300 Hz and 6 kHz. The signal was digitized with Digidata 1440A and saved with pClampv10 (Molecular Devices, Sunnyvale, CA). To find the neuromast that was connected to the recorded afferent neuron, we systematically stimulated neuromasts down the rostro-caudal axis of the body until we observed elicited spike responses. The afferent response to sine wave stimulation was quantified in terms of spike rate (number of spikes s^{-1}) and vector strength (phase locking between a periodic stimulus and a response) over the course of the 10 second stimulation, using the same procedure as in Levi et al, 2014. We calculated the latency of the afferent neuron's response as the delay in time between the onset of stimulation and the first spike. Recordings from 5 wt animals and 6 mutant animals were included for analysis.

Supplemental Figures:

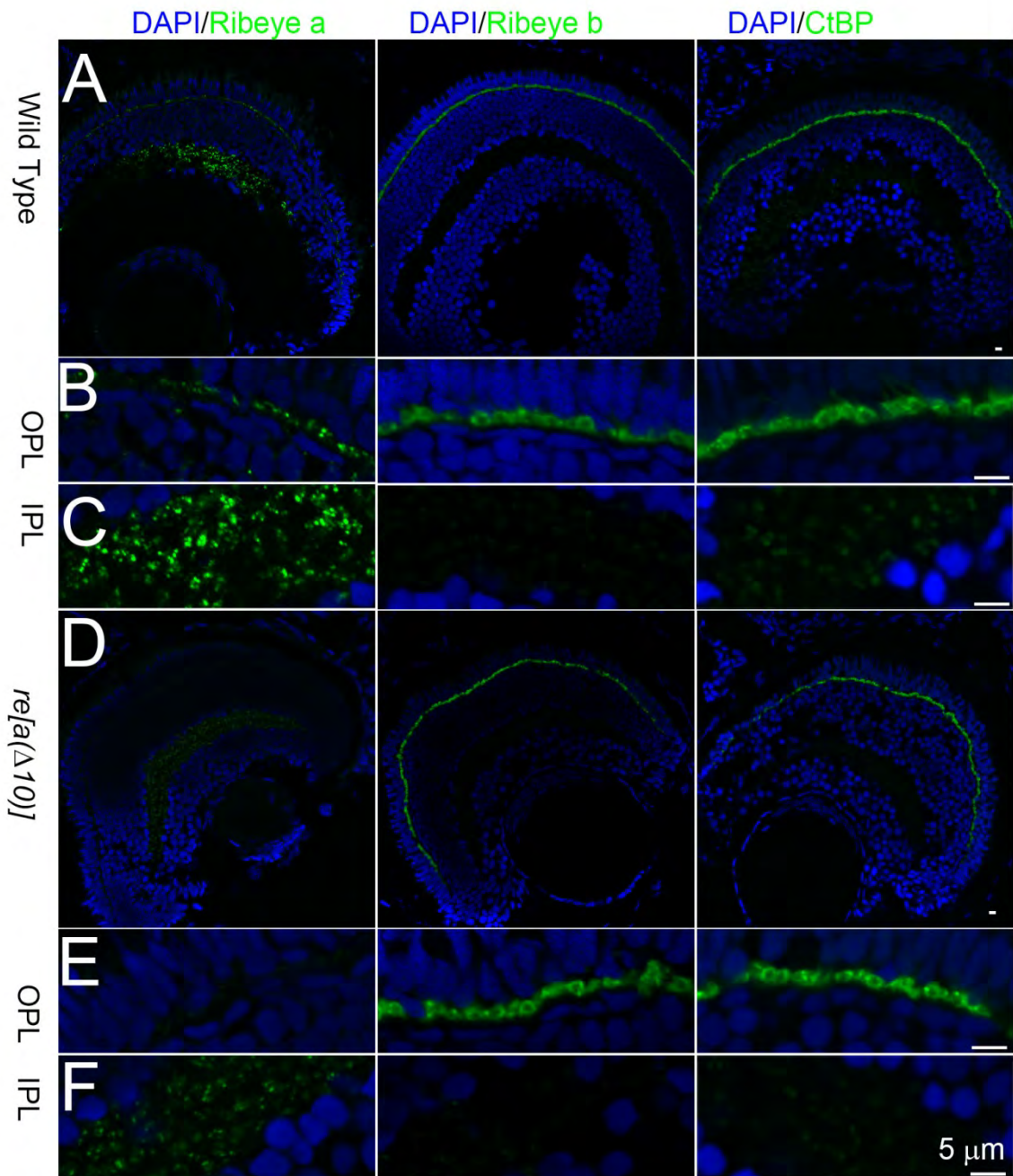
Supplemental Figure S1, related to Figure 1 and Experimental Procedures:



Supplemental Figure 1: Generation of Ribeye A and Ribeye B mutants. A, Alignment of wt and two mutant *ribeye a* genomic sequences showing the ZFN-induced mutations at the first exon. Underlines are ZFN recognition sites, and red letters are FokI enzyme cutting site. Red dashes are the nucleic tides missing, and blue letters are insertions. B, Schematic of Ribeye A and $\Delta 10$ mutation protein. Cyan indicates A domain, and grey indicates B domain. The deletion of 10 nucleic tides in $\Delta 10$ mutation cause a premature

stop codon, which make a very small protein with 43 amino acids. C, Alignment of wt and mutant *ribeye b* genomic sequences showing the CRISPR/Cas9-induced mutations at the first exon. Underlines are CRISPR guide RNA recognition site, and red letters show PAM. Red dashes are the nucleic tides missing, and blue letters are insertions. D, Schematic of Ribeye B and $\Delta 7$ mutation protein. Cyan indicates A domain, and grey indicates B domain. The deletion of 7 nucleic tides in $\Delta 7$ mutation cause a premature stop codon, which make a small protein with 164 amino acids.

Supplemental Figure 2, related to Figure 1 and Experimental Procedures



Supplemental Figure 2: Expression of Ribeye A, Ribeye B nor CtBP in 5dpf wt and ribeye a $\Delta 10$ retina. A, Confocal images of Ribeye A, Ribeye B, and CtBP staining (green) in 5dpf wt zebrafish retina. B, 3X magnification of outer plexiform layer staining

in wt 5dpf zebrafish retina. C, 3X magnification of inner plexiform layer staining in wt 5dpf zebrafish retina. D, Confocal images of Ribeye A, Ribeye B, and CtBP staining (green) in 5dpf *ribeye a* Δ 10 mutant fish retina. E, 3X amplification of outer plexiform layer staining in 5dpf *ribeye a* Δ 10 mutant fish retina. Notice the dramatic reduction of Ribeye A staining in *ribeye a* Δ 10 mutant fish. F, 3X magnification of inner plexiform layer staining in 5dpf *ribeye a* Δ 10 mutant fish retina. DAPI (blue) stains nucleus. WT and mutant fish were taken under the same settings for the same antibody. Scale bar is 5 μ m.

Cifuentes D, Xue H, Taylor DW, Patnode H, Mishima Y, Cheloufi S, Ma E, Mane S, Hannon GJ, Lawson N, Wolfe S, and Giraldez AJ. A Novel miRNA Processing Pathway Independent of Dicer Requires Argonaute2 Catalytic Activity. *Science* 2010.

Hruscha A, Krawitz P, Rechenberg A, Heinrich V, Hecht J, Haass C, and Schmid B. Efficient CRISPR/Cas9 genome editing with low off-target effects in zebrafish. *Development* 140: 4982-4987, 2013.

Huang J, and Tan S. Piccolo NuA4-catalyzed acetylation of nucleosomal histones: critical roles of an Esa1 Tudor/chromo barrel loop and an Epl1 enhancer of polycomb A (EPcA) basic region. *Mol Cell Biol* 33: 159-169, 2013.

Hwang WY, Fu Y, Reyon D, Maeder ML, Tsai SQ, Sander JD, Peterson RT, Yeh JR, and Joung JK. Efficient genome editing in zebrafish using a CRISPR-Cas system. *Nature biotechnology* 31: 227-229, 2013.

Jao LE, Wentz SR, and Chen W. Efficient multiplex biallelic zebrafish genome editing using a CRISPR nuclease system. *Proceedings of the National Academy of Sciences of the United States of America* 110: 13904-13909, 2013.

Lv C, Gould TJ, Bewersdorf J, and Zenisek D. High-resolution optical imaging of zebrafish larval ribbon synapse protein RIBEYE, RIM2, and CaV 1.4 by stimulation emission depletion microscopy. *Microsc Microanal* 18: 745-752, 2012.

Obholzer N, Wolfson S, Trapani JG, Mo W, Nechiporuk A, Busch-Nentwich E, Seiler C, Sidi S, Sollner C, Duncan RN, Boehland A, and Nicolson T. Vesicular glutamate transporter 3 is required for synaptic transmission in zebrafish hair cells. *The Journal of neuroscience : the official journal of the Society for Neuroscience* 28: 2110-2118, 2008.

Ricci AJ, Bai JP, Song L, Lv C, Zenisek D, and Santos-Sacchi J. Patch-clamp recordings from lateral line neuromast hair cells of the living zebrafish. *The Journal of neuroscience : the official journal of the Society for Neuroscience* 33: 3131-3134, 2013.

Sander JD, Maeder ML, Reyon D, Voytas DF, Joung JK, and Dobbs D. ZiFiT (Zinc Finger Targeter): an updated zinc finger engineering tool. *Nucleic Acids Res* 38: W462-468, 2010.

Sander JD, Zaback P, Joung JK, Voytas DF, and Dobbs D. Zinc Finger Targeter (ZiFiT): an engineered zinc finger/target site design tool. *Nucleic Acids Res* 35: W599-605, 2007.

Santos-Sacchi J. Determination of cell capacitance using the exact empirical solution of partial differential Y/partial differential Cm and its phase angle. *Biophys J* 87: 714-727, 2004.

Sheets L, Trapani JG, Mo W, Obholzer N, and Nicolson T. Ribeye is required for presynaptic Ca(V)1.3a channel localization and afferent innervation of sensory hair cells. *Development* 138: 1309-1319, 2011.

Immunocytochemical Demonstration of Astrocytes in the Eighth Cranial Nerve of the Red-Eared Turtle

DEBRA A. MARBEY AND JOSEPH SANTOS-SACCHI¹

Laboratory of Otolaryngology, University of Medicine and Dentistry of New Jersey—New Jersey Medical School, Newark, New Jersey 07103

Received March 17, 1986; revision received May 28, 1986

Coronal sections through the eighth cranial nerve and medulla of the red-eared turtle were immunocytochemically stained for the astrocytic intermediate filament protein, glial fibrillary acidic protein. Reaction product appeared in the medial one-third of the eighth cranial nerve fibers as they penetrated the medulla. The remaining two-thirds of the nerve did not show any staining for glial fibrillary acidic protein. The lateral aspect of the nerve corresponds with the extracranial portion of the nerve. When the eighth cranial nerve of the turtle has been transected extracranially it still regenerates into the cochlear nuclei. Results of the present study indicate that the eighth cranial nerve was transected in earlier studies in a region devoid of astrocytes. © 1986 Academic Press, Inc.

INTRODUCTION

The glial dome (transition zone) (4, 9, 18, 23, 25) is found at the boundary between the central and the peripheral portions of a nerve. It is composed of subpial astrocytes, their processes, and basal laminae (4, 9, 25). Some investigators (18, 21, 23, 26) believe that elongating axons are unable to penetrate the transition zone and that this prevents successful regeneration. The ability of the eighth cranial nerve of the red-eared turtle to regenerate into the cochlear nuclei following transection was recently demonstrated (14-17). In those experiments, the nerve was transected extracranially between the audi-

Abbreviations: GFAP—glial fibrillary acidic protein; PBS—phosphate-buffered saline.

¹ This work was supported by a Research Career Development Award (J.S.S.) from the National Institute of Neurological and Communicative Disorders and Stroke and grants from the Deafness Research Foundation, the Foundation of the UMDNJ, and the National Institutes of Health (NS 21380-01).

tory ganglion cells and the medulla. However, it is not known where the eighth cranial nerve was transected in relation to the glial dome.

Understanding the phenomenon of eighth nerve regeneration requires identifying the glial dome; the interaction between elongating axons and their microenvironment at the site of injury is important (2, 11, 13, 29). The position of the lesion site relative to the transition area has different implications. If the nerve was axotomized in its central nervous system extent, regenerating axons would have elongated through a microenvironment of astrocytes, as occurs in amphibia (5, 22, 23). If the eighth nerve was transected in its peripheral nervous system portion, regenerating fibers would have been led initially by Schwann cells and their basal laminae, as in other systems (1, 6, 10, 11, 13) to the glial dome. Here, regenerating axons would have projected through the transition zone to enter the central nervous system.

In the rat (9, 19, 24), the auditory nerve is separated into a long central nervous system segment and a relatively short peripheral nervous system segment by a glial dome situated at the base of the modiulus. The location of the transition zone of the eighth nerve of the red-eared turtle has not yet been characterized. By using astrocytes as markers for the central nervous system portion, the location of the transection site relative to the glial dome may be determined. The present study labeled astrocytes of turtles' eighth cranial nerves immunocytochemically for the cytoplasmic intermediate filament protein, glial fibrillary acidic protein (GFAP).

MATERIALS AND METHODS

Six turtles, *Chrysemys scripta elegans*, weighing 250 to 450 g were overdosed with an intrathoracic injection of sodium pentobarbital (Sigma). When a suitable areflexic state was obtained, the plastron was drilled open and the heart exposed. Turtles were perfused transcardially with reptilian Ringer's (28) followed by a fixative solution (20) of 2% paraformaldehyde, 0.3% glutaraldehyde, 0.2% picric acid in 0.1 M phosphate-buffered saline (PBS), pH 7.6. Brains with eighth nerves intact were removed and placed overnight in a postperfusion fixative solution (20) of 2% paraformaldehyde and 0.2% picric acid in PBS. Specimens were then washed 3 h in a 15% sucrose PBS solution. Brains were frozen-sectioned at 20- μ m intervals on a freezing stage (Baileys) at -40°C , mounted on a microtome (A O Reichart). The sections were washed in a solution (20) of 0.3% Triton X-100 (Fluka) for 3 days.

Turtle brain sections were reacted for GFAP according to the peroxidase-antiperoxidase technique of Sternberger *et al.* (27) as modified by Oteniente *et al.* (20). Sections through the turtle medulla and the eighth cranial nerve

were preincubated 1 h in normal swine serum (Dako Corp., 1:200). After rinsing three times in 1 h in a solution of 0.01% Triton X-100 (Fluka) in PBS, the sections were incubated 4 days at 4°C in rabbit antiserum to bovine GFAP (Dako Corp., 1:2000). Control sections were simultaneously incubated 4 days with nonimmune serum (Dako Corp., 1:2000) at 4°C. Specimens were rinsed three times in 1 h in a solution of 0.01% Triton X-100 (Fluka) in PBS and incubated 2 h in swine antiserum to rabbit immunoglobulin (Dako Corp., 1:200). Following three rinses during 1 h in a solution of 0.01% Triton X-100 (Fluka) in PBS, the sections were incubated 30 min in soluble horseradish peroxidase-rabbit anti-horseradish peroxidase complex (Dako Corp., 1:800). Brain sections were washed three times in 0.01% Triton X-100 (Fluka) in PBS and then placed 15 min in a reaction solution of 0.025% 3,3-diaminobenzidine with 0.005% hydrogen peroxide in 0.05 *M* Tris buffer (pH 7.6). Reacted specimens were washed 20 min in PBS and mounted on slides subbed with gelatin-chrome alum. After air drying 1 h, mounted sections were dehydrated in a graded series of ethanol and coverslipped with permount (Fisher Scientific Corp.)

RESULTS

Coronal sections of the eighth cranial nerve and the medulla of turtles were immunocytochemically reacted for GFAP. Positively stained astrocytic processes were present in the eighth cranial nerve as it penetrated the medulla and continued extending laterally (Fig. 1). Many long, slender (<1.0 μm in diameter) fibers paralleled the eighth cranial nerve axons (Fig. 2). Branching was evident (Fig. 2) among the stained processes. No GFAP reaction product was demonstrated in control sections stained with nonimmune serum (Fig. 3).

On closer examination, reaction product appeared in cell bodies of astrocytes among the axonal fibers of the eighth cranial nerve (Fig. 2). Cell bodies were round to oval and between 6 and 14 μm in length. Multiple processes projected either bipolarly or in any plane (Fig. 2) from the astrocytic cell bodies.

Glial fibrillary acidic protein-stained structures were present only in the medial one-third of the eighth cranial nerve (Fig. 1). Immunocytochemical reaction product disappeared at the lateral two-thirds of the length of the eighth cranial nerve (Fig. 1), the extracranial extent of the nerve (Fig. 1).

Coronal sections of the medulla and the eighth cranial nerve of mice were also stained for GFAP immunoreactivity (unpublished data). Positively stained astrocytic intermediate filaments were present along the mouse eighth cranial nerve to the base of the modiolus. These findings complement the electron microscopic observations (9, 19, 24) of the eighth cranial nerve of the rat.

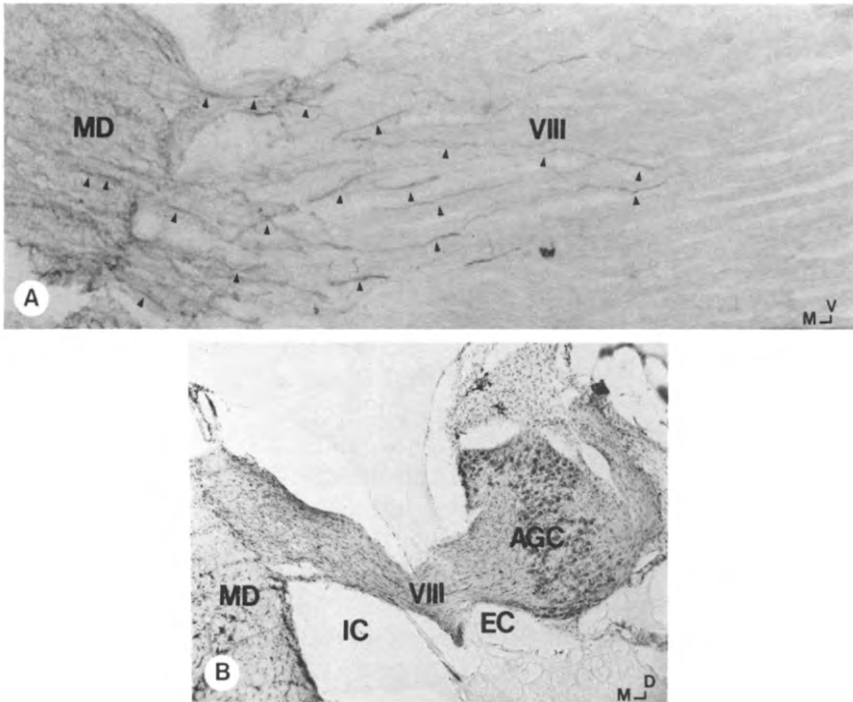


FIG. 1. A—glial fibrillary acidic protein (GFAP)-stained fibers (arrowheads) are evident in this coronal section through the eighth nerve (VIII) and the medulla (MD) of the red-eared turtle. Many positively stained processes parallel the VIII nerve axons. Immunocytochemical reaction product appears in the medial one-third of the nerve; this corresponds to a portion of the intracranial extent of the auditory nerve (VIII) (refer to B) $\times 195$; M, medial; V, ventral. B—the intra and extracranial (EC) portions of the VIII cranial nerve of the red-eared turtle are clearly delineated in this coronal section through the medulla (MD) and the nerve. Sections of turtle brain stained for GFAP (refer to A) contain reaction product in the medial one-third of the auditory nerve, i.e., intracranially (IC). Cresyl violet, $\times 60$; AGC, auditory ganglion cells; M, medial; D, dorsal.

DISCUSSION

Turtle astrocytes contain GFAP (7, 8, 20) similar in molecular weight and amino acid composition (7) to that of mammals. Although differences in peptide mapping (7) and immunological properties (7, 8) exist between turtle and mammalian GFAP, turtle astrocytic intermediate filament protein (7, 8) cross-reacts with antimammalian GFAP sera. Results of the present study confirm earlier reports (7, 20) of turtle astrocytic immunocytochemical staining with antimammalian GFAP sera. Biochemical (7) and many immu-

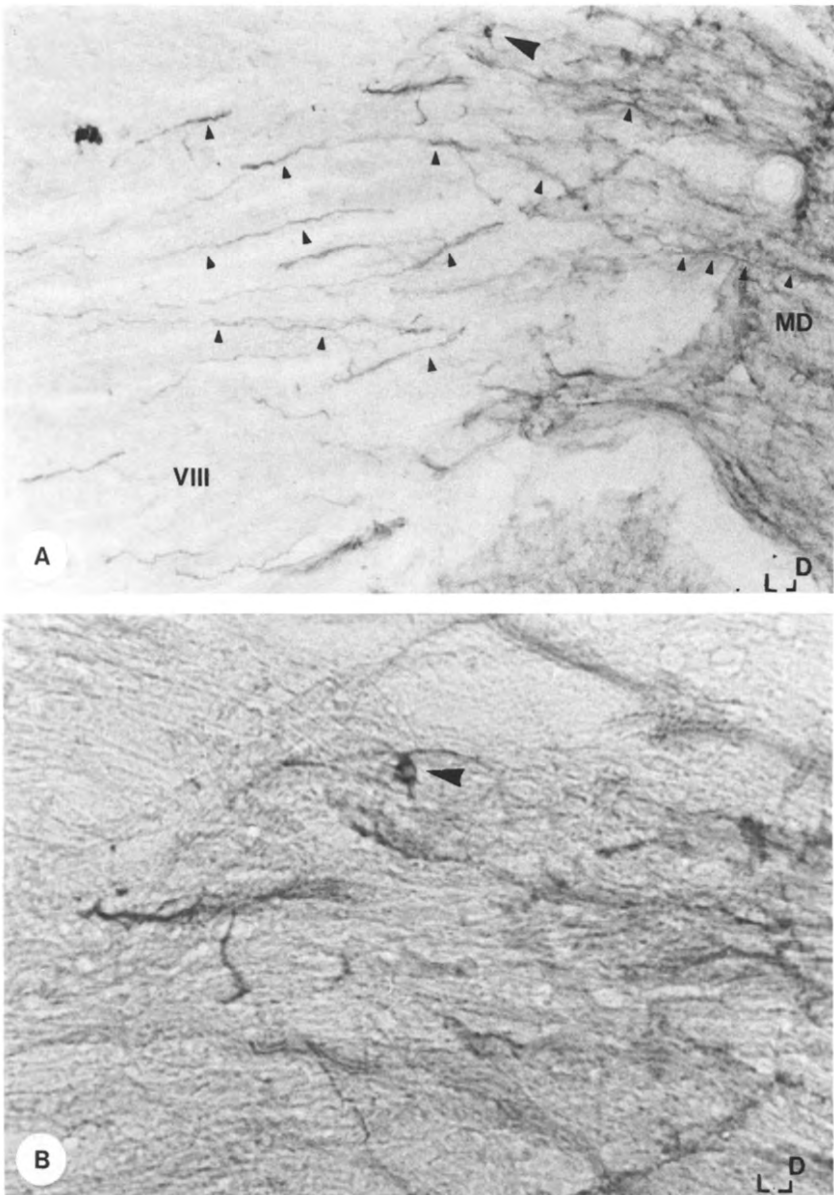


FIG. 2. A—GFAP stained processes are demonstrated in this coronal section through the VIII nerve and the medulla (MD) of the red-eared turtle. Branching is evident among the astrocytic fibers containing reaction product (small arrowheads). A stained astrocytic cell body (large arrowhead) lies among the axons of the VIII nerve $\times 160$; L, lateral; D, dorsal. B—at higher magnification ($\times 395$), the immunocytochemically stained astrocyte cell body (arrowhead) appeared round. Multiple processes appeared to be projecting from any plane of the glial cell. L, lateral; D, dorsal.

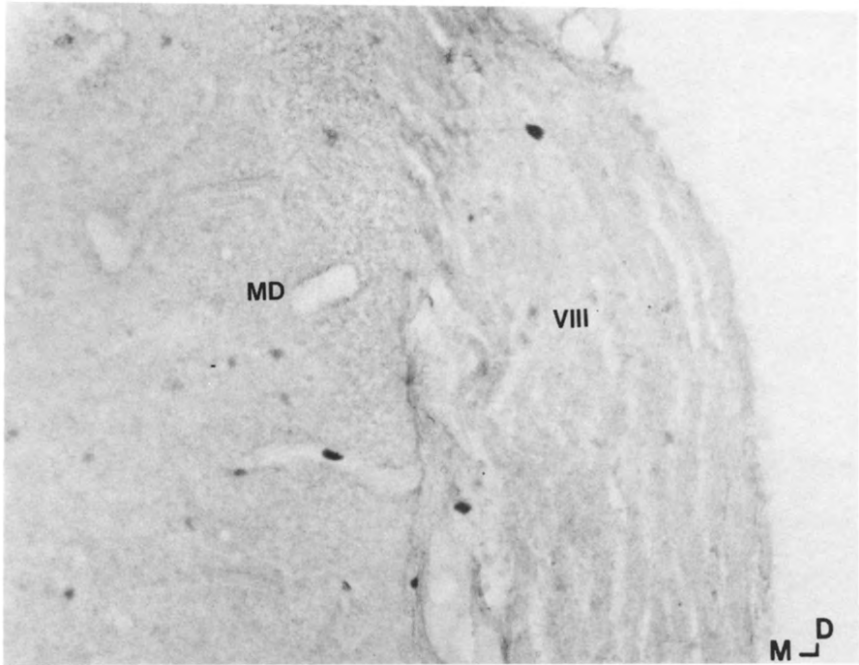


FIG. 3. No GFAP reaction product was demonstrated in this coronal section of turtle eighth nerve (VIII) and medulla (MD) incubated with nonimmune rabbit serum $\times 150$; M, medial; D, dorsal.

nological properties (7, 20) of GFAP have remained stable through the phylogenetic development from turtle to mammal.

Astrocytes are a major glial element of the reptilian central nervous system (12). The presence of astrocytes identifies a region of neural tissue as central. The extracranial portion of the turtle eighth cranial nerve lacks astrocytes and is therefore of peripheral nervous system origin. It is now clear that in earlier studies (14–17) the eighth cranial nerve was transected in its peripheral nervous system extent. It is significant that when the eighth cranial nerve of the turtle is axotomized extracranially (i.e., in its peripheral extent) it still regenerates into the cochlear nuclei in the medulla. Presumably regenerating eighth cranial nerve fibers were guided initially by Schwann cells and their basal laminae to the transition zone; regenerating axons then projected through the glial dome to enter the central nervous system.

The precise location of the glial dome in the eighth cranial nerve of the reared turtle was not identified in the present study; the intracranial astrocytic processes and scattered cell bodies indicate the general site of the transition

zone. Perhaps simultaneous immunocytochemical staining of the turtle eighth nerve with laminin and GFAP antisera (3) would demonstrate the glial dome more clearly, labeling peripheral and central nervous system elements. Electron microscopic examination of the intracranial extent of the turtle eighth cranial nerve also would determine the exact location of the glial dome and complement the data.

REFERENCES

1. AGUAYO, A., S. DAVID, P. RICHARDSON, AND G. BRAY. 1982. Axonal elongation in peripheral and central nervous system transplants. Pages 215-334 in S. FEDEROFF AND L. HURTZ, Eds., *Advances in Cellular Neurobiology*, Vol. 3, Academic Press, New York.
2. ANDERSON, H., T. RAPPORTEUR, A. AGUAYO, S. BLACKSHAW, D. BRAY, R. GILLIAT, A. GRINNELL, G. KREUTZBERG, I. PARNAS, D. PURRES, S. ROTJEMLER, S. SCHWAB, AND M. WILLARD. 1982. Early responses to neural injury. Pages 315-339 in J. G. NICHOLLS, Ed., *Repair and Regeneration of the Nervous System*. Springer-Verlag, New York.
3. BIGNAMI, A., N. H. CHI, AND D. DAHL. 1984. Regenerating dorsal roots and the nerve entry zone: an immunofluorescence study with neurofilament and laminin antisera. *Exp. Neurol.* **85**: 426-436.
4. BERTHOLD, C., AND T. CARLSTEDT. 1977. General organization of the transition between peripheral and central nervous system in the cat. *Acta Physiol. Scand. Suppl.* **446**: 23-42.
5. BOHN, R., P. J. REIER, AND E. SOURBEER. 1982. Axonal interactions with connective tissue and glial substrata during optic nerve regeneration in *Xenopus* larvae and adults. *Am. J. Anat.* **165**: 397-419.
6. BUNGE, R. 1981. Contribution of tissue culture studies to our understanding of the basic processes in peripheral nerve regeneration. Pages 105-113 in A. GORIO, H. MILLESI, AND S. MINGRINO, Eds., *Posttraumatic Peripheral Nerve Regeneration, Experimental Basis and Clinical Implications*. Raven Press, New York.
7. DAHL, D. 1976. Isolation and initial characterization of glial fibrillary acidic protein from chicken, turtle, frog, and fish central nervous systems. *Biochim. Biophys. Acta* **446**: 41-50.
8. DAHL, D., AND A. BIGNAMI. 1973. Immunochemical and immunofluorescence studies of the glial fibrillary acidic protein in vertebrates. *Brain Res.* **61**: 279-293.
9. GAMBLE, H. 1976. Spinal and cranial nerve roots. Pages 330-354 in D. H. LANDON, Ed., *The Peripheral Nerve*. Methuen, New York.
10. IDE, C., K. TOHYAMA, R. YOKATA, T. NITATORI, AND S. ONODURO. 1983. Schwann cell basal lamina and nerve regeneration. *Brain Res.* **288**: 61-75.
11. KIERNAN, J. 1979. An explanation of axonal regeneration in the mammalian nervous system. *Biol. Dev.* **54**: 155-197.
12. KRUGER, L., AND D. MAXWELL. 1967. Comparative fine structure of vertebrate teleosts and reptiles. *J. Comp. Neurol.* **129**: 115-142.
13. LUND, R. 1978. *Development and Plasticity of the Brain. An Introduction*. Oxford Univ. Press, New York.
14. MARBEY, D., AND R. BROWNER. 1984. Reconnection of the eighth nerve fibers after transection in the red-eared turtle. *Soc. Neurosci. Abstr.* **10**: 1024.
15. MARBEY, D., AND R. BROWNER. 1984. The reconnection of auditory posterior root fibers in the red-eared turtle, *Chrysemys scripta elegans*. *Hearing Res.* **15**: 88-94.

16. MARBEY, D., AND R. BROWNER. 1986. Regeneration of the eighth nerve fibers after transection in the red-eared turtle, *Chrysemys scripta elegans*. Submitted.
17. MARBEY, D., AND R. BROWNER. 1986. Regeneration of the eighth nerve fibers after transection in the red-eared turtle, *Chrysemys scripta elegans*. *Abstr. IXth Midwinter Res. Meet. Assoc. Res. Otolaryngol.* 24.
18. NATHANIEL, E., AND D. NATHANIEL. 1981. The reactive astrocyte. *Adv. Coll. Neurobiol.* 2: 249-301.
19. NEMECK, S., I. PARIZEK, I. SPACEK, AND J. NEMECKOVA. 1969. Histological histochemical and ultrastructural appearance of the transitional zone of the cranial and spinal nerve roots. *Folia Morphol. V. X. VII:* 171-181.
20. OTENIENTE, B., H. KIMURA, AND T. MAEDO. 1983. Comparative study of the glial fibrillary acidic protein in vertebrates by PAP immunohistochemistry. *J. Comp. Neurol.* 25: 427-436.
21. PERKINS, C. S., T. CARLSTEDT, K. MIZUNO, AND A. J. AGUAYO. 1980. Failure of regenerating dorsal root axons to regrow into the spinal cord. *Can. J. Neurol. Sci.* 7: 323.
22. REIER, P. J. 1979. Penetration of grafted astrocytic scars by regenerating optic nerve axons in *Xenopus* tadpoles. *Brain Res.* 154: 61-68.
23. REIER, P. J., L. J. STENSAAS, AND L. GUTH. 1983. The astrocytic scar as an impediment to regeneration in the central nervous system. Pages 163-195 in C. C. KAO, R. P. BUNGE, AND P. J. REIER, Eds., *Spinal Cord Reconstruction*. Raven Press, New York.
24. ROSS, M., AND W. BURKEL. 1971. Electron microscopic observations of the nucleus, glial dome, and the meninges of the rat acoustic nerve. *Am. J. Anat.* 130: 73-92.
25. STEER, J. 1971. Some observations of the fine structure of rat dorsal spinal nerve roots. *J. Anat.* 109: 467-485.
26. STENSAAS, L. J., P. R. BURGESS, AND K. W. HORSCH. 1979. Regenerating dorsal root axons are blocked by spinal cord astrocytes. *Soc. Neurosci. Abstr.* 5: 584.
27. STERNBERGER, L. A., P. H. HARDY, F. CUCULIS, AND H. G. MEYER. 1970. The unlabeled antibody enzyme method immunohistochemistry: preparation and properties of soluble antigen-antibody complex (horseradish peroxidase-antihorseradish peroxidase) and its use in identification of spirochetes. *J. Histochem. Cytochem.* 19: 315-333.
28. WEVER, E. 1978. The reptilian ear; its biological and evolutionary significance. Pages 967-984 in *The Reptilian Ear*. Princeton Univ. Press, Princeton, NJ.
29. WUJEK, J., AND P. J. REIER. 1984. Astrocytic membrane morphology: differences between mammalian and amphibian astrocytes after axotomy. *J. Comp. Neurol.* 222: 607-619.



ANIMAL MODELS

Auditory Pathology in a Transgenic mtTFB1 Mouse Model of Mitochondrial Deafness



Sharen E. McKay,^{*†} Wayne Yan,[‡] Jessica Nouws,^{*} Maximilian J. Thormann,^{*} Nuno Raimundo,[§] Abdul Khan,^{*} Joseph Santos-Sacchi,^{‡¶||} Lei Song,[‡] and Gerald S. Shadel^{*.***}

From the Departments of Pathology,^{*} Surgery,[‡] Cellular and Molecular Physiology,[¶] Neurobiology,^{||} and Genetics,^{**} Yale School of Medicine, New Haven, Connecticut; the Department of Psychology,[†] University of Bridgeport, Bridgeport, Connecticut; and the Institute of Cell Biology,[§] University Medical Center Göttingen, Göttingen, Germany

Accepted for publication
August 14, 2015.

Address correspondence to
Gerald S. Shadel, Ph.D.,
Department of Pathology, or to
Joseph Santos-Sacchi, Ph.D., or
Lei Song, Ph.D., Department of
Surgery, Yale School of
Medicine, New Haven,
CT 06437. E-mail: gerald.shadel@yale.edu, joseph.santos-sacchi@yale.edu, or lei.song@yale.edu.

The A1555G mutation in the 12S rRNA gene of human mitochondrial DNA causes maternally inherited, nonsyndromic deafness, an extreme case of tissue-specific mitochondrial pathology. A transgenic mouse strain that robustly overexpresses the mitochondrial 12S ribosomal RNA methyltransferase TFB1M (Tg-mtTFB1 mice) exhibits progressive hearing loss that we proposed models aspects of A1555G-related pathology in humans. Although our previous studies of Tg-mtTFB1 mice implicated apoptosis in the spiral ganglion and stria vascularis because of mitochondrial reactive oxygen species-mediated activation of AMP kinase (AMPK) and the nuclear transcription factor E2F1, detailed auditory pathology was not delineated. Herein, we show that Tg-mtTFB1 mice have reduced endocochlear potential, indicative of significant stria vascularis dysfunction, but without obvious signs of stria atrophy. We also observed decreased auditory brainstem response peak 1 amplitude and prolonged wave I latency, consistent with apoptosis of spiral ganglion neurons. Although no major loss of hair cells was observed, there was a mild impairment of voltage-dependent electromotility of outer hair cells. On the basis of these results, we propose that these events conspire to produce the progressive hearing loss phenotype in Tg-mtTFB1 mice. Finally, genetically reducing AMPK $\alpha 1$ rescues hearing loss in Tg-mtTFB1 mice, confirming that aberrant up-regulation of AMPK signaling promotes the observed auditory pathology. The relevance of these findings to human A1555G patients and the potential therapeutic value of reducing AMPK activity are discussed. (*Am J Pathol* 2015, 185: 3132–3140; <http://dx.doi.org/10.1016/j.ajpath.2015.08.014>)

Mitochondria are essential organelles that produce ATP via the process of oxidative phosphorylation, but are multifunctional, playing additional key roles in metabolism, as well as other cellular processes like apoptosis, inflammation, and signal transduction.^{1–4} Human mitochondria possess a 16,565-bp circular genome that is maternally inherited and present at hundreds to thousands of copies per cell in most tissues.⁵ In mammals, mitochondrial DNA (mtDNA) encodes 13 oxidative phosphorylation complex subunits and the two rRNAs and 22 tRNAs needed for translation of these by dedicated mitochondrial ribosomes.⁶ All other components of the estimated 1200-member mitochondrial proteome, including the remaining 70 to 75 oxidative phosphorylation subunits and all of the factors needed for mtDNA replication and expression, are encoded by nuclear genes and imported into the organelle.⁷ Thus, signaling pathways between mitochondria and the nucleus are

required to coordinate the biogenesis, composition, and activity of mitochondria and to trigger homeostatic nuclear gene expression responses to mitochondrial dysfunction. These responses can be beneficial or harmful, depending on the precise cellular context and, to date, remain poorly understood.

Mitochondrial dysfunction causes human diseases, with an estimated occurrence of 1 in 5000 to 10,000 live births.^{8–10} These can be inherited maternally, because of mutations in mtDNA, or in a Mendelian manner, because of mutations in

Supported by NIH grant AG047632 and a Yale Claude D. Pepper Older American Independence Center pilot grant (G.S.S.), an Ohse Research grant (L.S.), NIH National Institute on Deafness and Other Communication Disorders grants DC000273 and DC008130 (J.S.-S.), and European Molecular Biology Organisation (EMBO) postdoctoral fellowship EMBO ALTF 1328-2012 (J.N.).

Disclosures: None declared.

nuclear genes encoding mitochondrial components. Because mtDNA is present in multiple copies per cell, and different organs vary in their energy requirements, mitochondrial diseases are complicated and heterogeneous, characterized by cell- and tissue-specific responses and pathology.^{2,8–10} An extreme example of tissue specificity is the A1555G mtDNA mutation that causes maternally inherited deafness. This mutation causes a progressive, nonsyndromic hearing loss that can vary from mild to profound and has a variable age of onset.^{11,12} A1555G carriers can also be predisposed to aminoglycoside-induced deafness.¹³ Hearing loss induced by A1555G is incompletely penetrant, which has been attributed, at least in part, to multiple nuclear and mtDNA modifying loci.^{11,14,15} One such nuclear modifier is the *TFB1M* gene, which encodes an RNA methyltransferase that post-transcriptionally modifies the mtDNA-encoded 12S rRNA in mitochondrial ribosomes.¹⁶

The A1555G mutation is located near a highly conserved stem loop in the 12S rRNA that contains adjacent adenines that are dimethylated by TFB1M. We showed previously that patient-derived A1555G cybrid cell lines exhibit increased stem-loop dimethylation and/or increased amounts of 12S rRNA methylated at this site.^{17,18} These cells also exhibited enhanced apoptotic susceptibility in culture^{17,18} because of mitochondrial reactive oxygen species (ROS)–dependent activation of 5′-AMP–activated protein kinase (AMPK) that unmasks the pro-apoptotic function of the nuclear transcription factor E2F1. These phenotypes are recapitulated in cell lines that overexpress the TFB1M methyltransferase in the absence of the A1555G mutation. TFB1M binds to the mitochondrial RNA polymerase (POLRMT) in the context of mitochondrial ribosomes to promote proper 12S rRNA methylation and ribosome biogenesis.¹⁹ Thus, disruption of these interactions in the mature ribosome or during ribosome assembly may cause unique perturbations in mitochondrial homeostasis and increased ROS production that promote deafness. How this unique mitochondrial perturbation leads to tissue-specific pathology remains unknown.

Consistent with the above pathogenic mechanism, we showed that transgenic mice that globally overexpress TFB1M (Tg-mtTFB1) exhibit premature hearing loss in an E2F1-dependent manner.¹⁸ These mice have the increased 12S rRNA methylation signature and AMPK up-regulation in multiple tissues, as well as increased caspase 3 staining and E2F1 up-regulation in two tissues in the inner ear, the stria vascularis and spiral ganglion neurons. This suggested that deafness in Tg-mtTFB1 mice is induced by a pro-apoptotic, mROS-AMPK-E2F1 pathway similar to the one we delineated in the A1555G patient cybrids, making Tg-mtTFB1 mice an indirect, yet potentially useful, animal model for maternally inherited deafness caused by the A1555G mutation.¹⁸ Herein, we have characterized the mechanism of hearing loss in Tg-mtTFB1 mice and addressed directly the involvement of AMPK signaling in the pathogenic response *in vivo*.

Materials and Methods

Animals

The original mixed C57BL/6J × SJL/J transgenic Tg-mtTFB1 mice¹⁸ were extensively back-crossed to the C57BL/6J genetic background. F8 and F9 backcrossed animals were bred to generate the Tg-mtTFB1 and wild-type (WT) littermates used in electrophysiological and histological studies. F8 Tg-mtTFB1 mice were bred to C57BL/6J heterozygous knockouts of AMPK α 1^{+/-} (*Prkaa1*^{+/-}) obtained from Dr. Benoit Viollet (INSERM, Paris, France),^{20,21} and the resulting AMPK α 1^{+/-}/Tg-mtTFB1 mice were bred to AMPK α 1^{+/+} for studies of AMPK knockdown.

ABR Analysis

Animals were anesthetized with either 48 mg/kg pentobarbital or 480 mg/kg chloral hydrate (i.p.), and all recordings were conducted in a sound-attenuating chamber (Industrial Acoustics Corp., Bronx, NY). A customized TDT3 system (Tucker-Davis Technologies, Inc., Alachua, FL) was used for auditory brainstem response (ABR) recordings. Subdermal needle electrodes (Rochester Electro-Medical, Inc., Lutz, FL) were positioned at the vertex (active, noninverting), the infra-auricular mastoid region (reference, inverting), and the neck region (ground). Differentially recorded scalp potentials were bandpass filtered between 0.05 and 3 kHz over a 15-millisecond (ms) epoch. A total of 400 trials were averaged for each waveform for each stimulus condition.

Symmetrically shaped tone bursts were 3 ms long (1 ms raised cosine on/off ramps and 1 ms plateau). All acoustic stimuli were delivered free field via a speaker (Tucker Davis Technologies, Inc., Part FF1 2021) positioned 10 cm from the vertex. Stimulus levels were calibrated using a 0.5-in condenser microphone (model 4016; ACO Pacific, Belmont, CA) positioned at the approximate location of the animal's head during recording sessions and are reported in decibels sound pressure level (dB SPL; referenced to 20 μ Pa). Stimuli of alternating polarity were delivered at a rate of approximately 20 per second.

Tone burst responses were collected in half octave steps ranging from 32 to 2.0 kHz. The effects of level were determined by decreasing stimulus intensity in 5-dB steps. A maximum stimulus level of 90 dB SPL was used first to avoid overstimulation. If the thresholds exceed 90 dB SPL, gain was adjusted to 40 dB to deliver a maximum stimulus level of 110 dB SPL. ABR thresholds were determined visually by noting the response waveforms exceeding a 1:1 signal to noise ratio. A two-way analysis of variance was used to determine the overall effect of genotype on ABR thresholds at different frequencies. The uncorrected Fisher's least significant difference test was used to make post hoc comparisons for determining statistical significance at each frequency between WT and Tg-mtTFB1 mice.

Latencies of the initial four ABR peaks were measured from animals aged 3 to 6 months or 9 to 12 months by

setting time markers at maxima of the peaks and measuring the time from onset of stimulus to peaks. Measurements were made at 8 and 11 kHz on traces with visible peaks. Latencies of peak I and central conduction time (peak I to IV) were used in the analysis. Amplitudes of peak I were assessed by taking the mean of the ΔV of the upward and downward slopes of peak I.

EP Measurements

Tg-mtTFB1 and WT animals, aged 9 to 12 months, were anesthetized with sodium pentobarbital (48 mg/kg body weight as initial dose and supplement as needed at 24 mg/kg). Animals were then placed onto a stereotaxic mouse head holder (MA-6N; Narishige, Tokyo, Japan) mounted onto a ball-and-socket stage and a magnetic base (M-RN-56; Newport Corp.). The round window was exposed through a ventral approach by opening the bulla of the temporal bone. A sharp electrode (10 to 15 M Ω , 1B150F-4; World Precision Instruments, Sarasota, FL) with 3 mol/L KCl pipette solution was mounted onto a micromanipulator with a pulse motor driving unit (PF5-1; Narishige). Electrodes were first placed at the round window, with visualization under a surgical microscope. An Axon 200A patch clamp amplifier was used for current clamp recording with an Axon Digidata 1321A and jClamp software version 22.8.4 (Scisoft, Inc., Ridgefield, CT). When the electrode was inserted into the scala tympani, voltage was balanced to 0 mV and then the electrodes were advanced through the basilar membrane into the scala media to measure the endocochlear potential (EP). Pipettes were then withdrawn back to the scala tympani or advanced through the scala vestibuli for confirmation of EP. Data analyses were performed offline.

NLC Measurements

Whole cell patch clamp recordings were made from single isolated outer hair cells (OHCs) from the organ of Corti of Tg-mtTFB1 and WT mice. The temporal bones were excised, and the cochleae were dissected free. Enzyme treatment (1 mg/mL dispase I, 10 to 12 minutes) preceded gentle trituration, and isolated OHCs were placed in a glass-bottom recording chamber. An E600-FN microscope (Nikon, Tokyo, Japan) with a 40 \times water immersion objective was used to observe cells during voltage clamp. Experiments were performed at room temperature.

The base high chloride ionic blocking solution contained (in mmol/L) the following: NaCl, 100; TEA-Cl, 20; CsCl, 20; CoCl₂, 2; MgCl₂, 1; CaCl₂, 1; and HEPES, 10. Base intracellular solutions contained (in mmol/L) the following: CsCl, 140; MgCl₂, 2; HEPES, 10; and EGTA, 10. An Axon 200B amplifier was used for the whole-cell patch-clamping recording. Nonlinear capacitance (NLC) was measured using a continuous, high-resolution (2.56 ms sampling), two-sine stimulus protocol (10-mV peak at both 390.6 and 781.2 Hz) superimposed onto the voltage ramp range from

–200 to 200 mV.^{22,23} Capacitance data were fit to the first derivative of a two-state Boltzmann function.

$$C_m = Q_{\max} \frac{ze}{kT} \frac{b}{(1+b)^2} + C_{lin} \quad (1)$$

$$\text{where } b = \exp\left(\frac{-ze(V_m - V_{pkCm})}{kT}\right). \quad (2)$$

Q_{\max} is the maximum nonlinear charge moved, V_h is voltage at peak capacitance or equivalently, at half maximum charge transfer, V_m is membrane potential, z is valence, C_{lin} is linear membrane capacitance, e is electron charge, k is Boltzmann constant, and T is absolute temperature.

Hair Cell Counts

The temporal bones of 9- to 12-month-old WT ($n = 5$) were dissected, and cochlea removed and immersion fixed for 24 to 48 hours in 4% paraformaldehyde in phosphate-buffered saline (PBS). Bony capsules were partially dissected to enable fluid penetration, and the entire structure was then transferred to a blocking solution containing 10% normal goat serum and 0.1% Tween 20 in PBS. Mouse monoclonal Myo7a antibody (Developmental Hybridoma Studies Bank, University of Iowa, Iowa City, IA) was applied in blocking buffer at a 1:500 dilution overnight at 4°C and detected using an Alexa 546 donkey anti-mouse secondary antibody (Jackson Immunological, West Grove, PA). The bony capsule was then carefully removed, and the organ of Corti was detached from the modiolus as a single strip. Spiral ligaments were then dissected away to allow good exposure of the organ of Corti. The organ of Corti was then dissected and mounted. The apical region ranged from 57% to 64% from the base. This region has been described by Müller et al²⁴ as corresponding to frequencies between 13.5 and 16 kHz, which encompasses the range of frequencies showing elevated ABR thresholds in the Tg-mtTFB1 mice. Myo7a-labeled inner hair cells (IHCs) and OHCs in this region were visualized with an IX-71 inverted fluorescence microscope (Olympus, Center Valley, PA), and images were collected and analyzed with a Spot camera (Diagnostic Instruments, Inc, Sterling Heights, MI). The number of cells was normalized and expressed as hair cells per 100 μm .

Stria Vascularis Measurements

Temporal bones were dissected and fixed in 4% paraformaldehyde in PBS at 4°C for 24 to 48 hours, followed by decalcification in 10% EDTA in PBS for 96 hours. The cochleae were bisected in the midmodiolar plane, and the two halves were embedded in paraffin, divided into sections, and stained with hematoxylin and eosin (Yale Pathology Developmental Histology Service, New Haven, CT). The width and thickness of intact, cross-sectioned striae were measured at multiple points at apical-basal locations^{25,26} in each animal using an Olympus microscope and Spot camera software version 5.1 for analysis. Strial width was measured as the

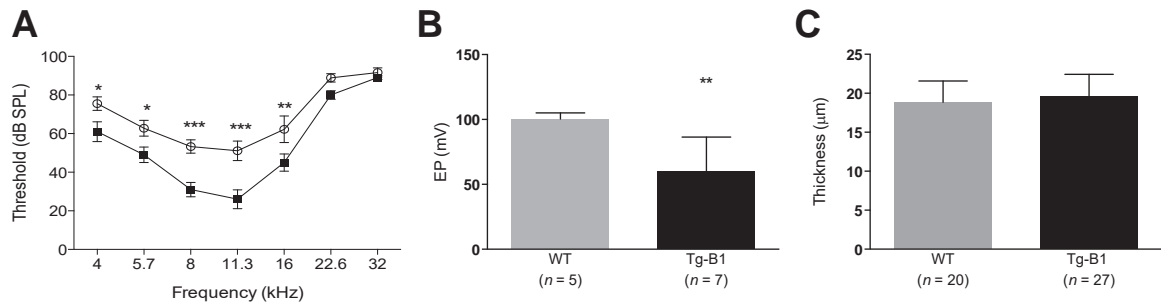


Figure 1 Hearing loss phenotype and stria vascularis dysfunction in a transgenic mouse strain that robustly overexpresses the mitochondrial 12S ribosomal RNA methyltransferase TFB1M (Tg-mtTFB1). **A:** Auditory brainstem response (ABR) results in wild-type (WT; closed squares) and Tg-mtTFB1 (Tg-B1; open circles) mice used in this study. Data were analyzed by two-way analysis of variance, and the main effect for genotype is $F_{(1,84)} = 38, P < 0.001$. Differences at each frequency were tested via post hoc Fisher’s least significant difference tests. **B:** Direct endocochlear potential (EP) measurements of the mice in **A**. There is a significant EP reduction in Tg-mtTFB1 (Tg-B1, black bars) mice compared with WT (gray bars) controls [Student’s $t_{(10)} = 3.3, **P < 0.01$]. **C:** Measurements of the thickness of the stria from hematoxylin and eosin–stained sections. No significant difference exists between WT and Tg-B1 mice [$t_{(45)} = 0.9$]. * $P < 0.05$, ** $P < 0.01$, and *** $P < 0.001$. dB SPL, decibels sound pressure level.

length of a curved line between the two end points of the stria in cross section, one near the insertion of Reissner’s membrane and the other near the spiral ligament. Thickness was measured by a straight line drawn through the midpoint of the section.

Results

Hearing Loss—Related Pathology in the Stria Vascularis

We previously characterized hearing loss in Tg-mtTFB1 mice as elevated ABR thresholds that progressed with age, accompanied by increased caspase 3 staining in the stria vascularis and spiral ganglia and reduced numbers of spiral ganglion neurons.¹⁸ Because defects in the stria vascularis, a three-layered epithelial organ lining the scala media and responsible for maintaining the requisite elevated extracellular potassium necessary for hair cell function, can also result in hearing loss characterized by increased ABR thresholds, we measured the EP to assess stria function directly. After confirming that ABR thresholds were prematurely elevated in a cohort of Tg-mtTFB1 mice now extensively backcrossed to the C57BL/6J background (Figure 1A), we recorded EP in a group of WT and Tg-mtTFB1 animals aged 9 to 12 months. We observed a 40% reduction in EP in Tg-mtTFB1 mice (mean_{Tg-mtTFB1} = 60 ± 10 mV) compared with WT controls, which was near 100 mV (mean_{WT} = 100.2 ± 2.1 mV) (Figure 1B). Hearing loss accompanied by stria dysfunction in aging humans is often accompanied by atrophy of the epithelium. To assess atrophy, the width and thickness of the stria were measured at multiple sites in cochlear cross sections of nine Tg-mtTFB1 and six WT animals. The widths, indicators of the cochlear spiral location of the stria, ranged from 131 to 387 µm in WT and from 98 to 358 µm in Tg-mtTFB1 animals. The thickness of the stria ranged from 13 to 22 µm in the WT and from 14 to 28 µm in the Tg-mtTFB1 animals. There was no significant correlation in either genotype between the width of the stria and the thickness (WT, $r^2 = -0.0049$; Tg-mtTFB1, $r^2 = 0.0077$). Because there was no difference in the

thickness as a function of apical-basal location, we combined all of the thickness measurements and compared the mean values by a *t*-test. There was no significant difference between WT and Tg-mtTFB1 mice (Figure 1C). These data suggest that the stria dysfunction in Tg-mtTFB1 mice is either distinct from presbycusis or we are sampling at a stage of progressive hearing loss that precedes gross stria atrophy.

To more precisely determine the source of auditory dysfunction, we analyzed details of the ABRs of WT and Tg-mtTFB1 mice with hearing loss. Mouse ABRs have five characteristic peaks, the first of which represents activity in nerve VIII. Changes in the latency or amplitude of peak I reflect dysfunctional cochlear and/or nerve VIII processing. By using two-way analysis of variance to assess the latency to peak I, we observed significant increases in 9- to 12-month-old Tg-mtTFB1 mice at both 8 kHz [$F_{(1,109)} = 34, P < 0.001$] (Figure 2A) and 11 kHz [$F_{(1,127)} = 28, P < 0.001$] (Figure 2B). When the same analysis was performed on 3- to 6-month-old animals, when only moderate ABR threshold shifts are observed in Tg-mtTFB1, the latencies were not significantly affected at 8 kHz [$F_{(1,128)} = 0.23$] (Figure 2C) or 11 kHz [$F_{(1,152)} = 0.04$] (Figure 2D). Thus, increased latency to peak I is only observed in older Tg-mtTFB1 animals with hearing loss. In contrast, central conduction time (elapsed time between peak I and peak IV), which reflects synaptic and nerve conduction timing after cochlear/nerve VIII processing, was unchanged in animals with severe hearing loss [$F_{(1,104)} = 1.2$ and $F_{(1,105)} = 1.0$] (Figure 2, E and F), respectively. These data suggest that hearing loss in Tg-mtTFB1 mice is induced by progressive pathological changes in the cochlea/nerve VIII, not central auditory system defects (ie, brainstem).

Hearing Loss—Related Pathology in OHCs

To determine whether hair cells are directly affected, we dissected the organ of Corti from cochleae of 9-month-old WT and Tg-mtTFB1 mice and labeled IHCs and OHCs with an antibody for Myo7a. Despite considerable ABR threshold

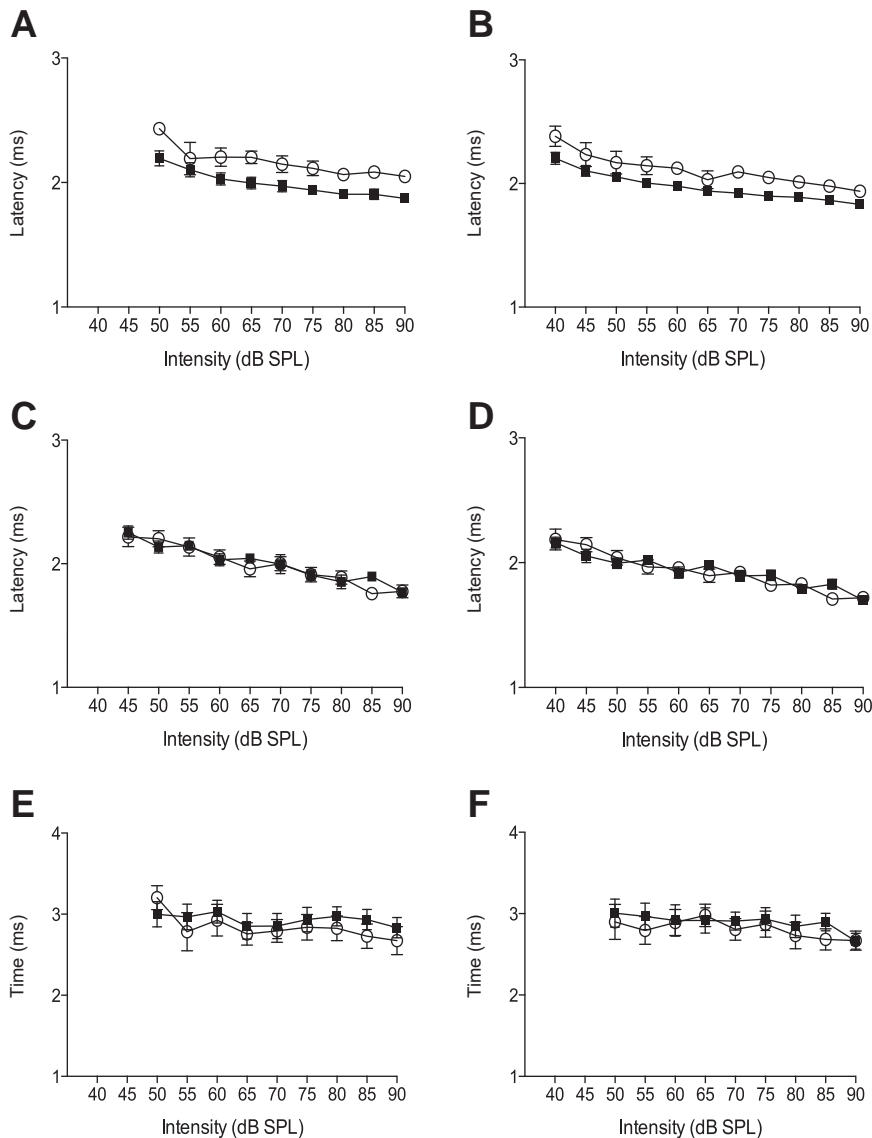


Figure 2 Changes in auditory brainstem response (ABR) latencies demonstrate progressive cochlear damage underlying deafness in a transgenic mouse strain that robustly overexpresses the mitochondrial 12S ribosomal RNA methyltransferase TFB1M (Tg-mtTFB1). The latency in milliseconds (ms) to ABR peak I is plotted as a function of the indicated suprathreshold decibels sound pressure level (dB SPL) for 9- to 12-month-old mice at 8 kHz (A), 9- to 12-month-old mice at 11 kHz (B), 3- to 6-month-old mice at 8 kHz (C), and 3- to 6-month-old mice at 11 kHz (D). The central conduction time was measured as the time from ABR peak I to peak IV and is shown for 9- to 12-month-old mice at 8 kHz (E) and 11 kHz (F). Closed squares indicate wild-type and open circles indicate Tg-mtTFB1 in all panels.

changes at frequencies from 4 to 16 kHz (Figure 1A), the hair cells in the apex of the cochlea, which detect frequencies in the range of hearing loss in Tg-mtTFB1 mice,²⁴ are largely intact, as evidenced by quantifying Myo7a-labeled IHCs and OHCs in the most apical 2.5 to 3.0 mm of the organ of Corti (Figure 3A). Although there might be a downward trend in the number of hair cells in Tg-mtTFB1 mice, a two-way analysis of variance shows that the counts do not differ significantly from WT [$F_{(1,10)} = 0.90$].

Next, to determine whether OHC function was altered, NLC, the electrical correlate of electromotility, was measured in OHCs isolated from WT and Tg-mtTFB1 mice between 9 and 12 months of age. NLC was measured by whole-cell patch clamp using symmetric chloride solutions (140 mmol/L Cl^- intracellular and extracellular). OHCs from Tg-mtTFB1 mice exhibited a positive shift of nearly 20 mV in the voltage at peak capacitance (V_h ; $\text{mean}_{\text{WT}} = -94 \pm 2.6$ mV; $\text{mean}_{\text{Tg-mtTFB1}} = -76 \pm 5$ mV) (Figure 3B), suggesting that

TFB1M overexpression in the cochlea induces a long-term change in OHC voltage responsiveness.

Functional Evidence for Spiral Ganglion Loss in Tg-mtTFB1 Mice

To determine whether the approximately 20% spiral ganglion neuronal loss we observe in Tg-mtTFB1 mice¹⁸ has an effect on hearing, we analyzed ABR peak I amplitude, which reflects the number of spiral ganglion neurons recruited for the generation of ABR and would be reduced in animals with neuronal death in the spiral ganglion. Consistent with spiral ganglion loss, peak I amplitudes were significantly reduced in 9- to 12-month-old Tg-mtTFB1 animals [$F_{(1,116)} = 57$, $P < 0.001$] (Figure 3C). In addition, as stimulus levels increase, the characteristics of the curves in Tg-mtTFB1 mice diverge from those of WT, which show a steeper upward slope (recruitment) >60 dB

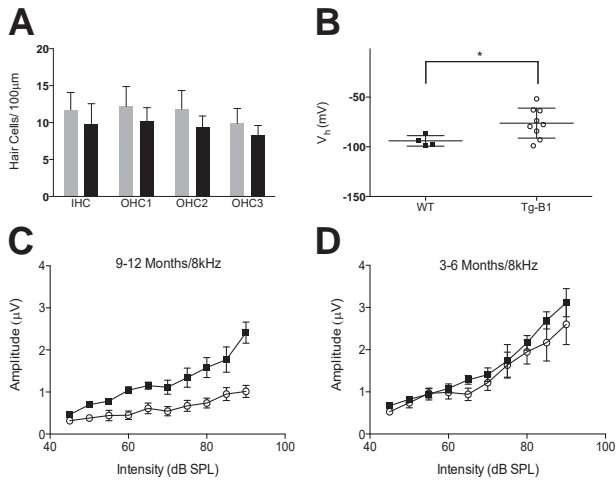


Figure 3 Outer hair cell dysfunction and reduced amplitude of auditory brainstem response (ABR) peak I in a transgenic mouse strain that robustly overexpresses the mitochondrial 12S ribosomal RNA methyltransferase TFB1M (Tg-mtTFB1). **A:** Hair cell counts in wild-type (WT; gray bars) and Tg-mtTFB1 (Tg-B1; black bars) mice. Cells counted are as indicated: inner hair cells (IHCs), outer hair cell rows 1 (OHC1), 2 (OHC2), and 3 (OHC3). **B:** Nonlinear capacitance (NLC) recordings from OHCs isolated from WT (closed squares) and Tg-B1 (open circles) mice. The voltage at peak capacitance (V_h) is plotted, and means were compared with a *t*-test. There is a statistically significant change in Tg-mtTFB1 [$t_{(11)} = 2.3$]. Other parameters of NLC were not different (means \pm SD): maximum nonlinear charge moved (pC), 0.54 ± 0.11 WT/ 0.42 ± 0.11 Tg-mtTFB1; *z*, 0.76 ± 0.05 WT/ 0.76 ± 0.07 Tg-mtTFB1; linear membrane capacitance (pF), 4.93 ± 0.47 WT/ 4.44 ± 0.72 Tg-mtTFB1. The amplitude of ABR peak I was measured at 8 kHz at the indicated intensities (decibels sound pressure level). Suprathreshold for 9- to 12-month-old mice (**C**) and 3- to 6-month-old mice (**D**). Suprathresholds at 9 to 12 months in Tg-mtTFB1 mice are significantly lower than WT controls by two-way analysis of variance. * $P < 0.05$.

(Figure 3C). This suggests that Tg-mtTFB1 animals have an impaired cochlear amplifier, consistent with the findings of EP decrease (Figure 1B) and OHC V_h shift (Figure 3B). Younger animals with only moderately elevated ABR thresholds (3 to 6 months) had no significant change in the peak I amplitude [$F_{(1,130)} = 3.1$, $P > 0.05$] (Figure 3D), consistent with a progressive nature to the hearing loss in Tg-mtTFB1 mice.

Rescue of Tg-mtTFB1 Hearing Loss by Genetically Reducing AMPK Signaling

We proposed previously that mitochondrial ribosomal disruptions in Tg-mtTFB1 mice resulted in increased mitochondrial ROS-mediated activation of AMPK that engages the pro-apoptotic function of E2F1.¹⁸ In Tg-mtTFB1 mice, there is also increased phosphorylation of AMPK in the spiral ligament, a tissue that supports the K-recirculation function of the stria vascularis.^{18,27} If up-regulation of AMPK in the stria (or other cochlear cells) activates E2F1 to initiate apoptosis or other deleterious signaling events, then reducing AMPK activity in Tg-mtTFB1 mice would be predicted to rescue hearing loss. We bred Tg-mtTFB1 mice with heterozygous AMPK $\alpha 1$ subunit knockout mice^{20,21} (AMPK $^{+/-}$) to

generate age-matched littermates of the following genotypes for ABR analysis: AMPK $^{+/+}$ WT (no transgene), AMPK $^{+/+}$ Tg-mtTFB1 (with mtTFB1 transgene), AMPK $^{+/-}$ WT (no transgene), and AMPK $^{+/-}$ Tg-mtTFB1 (with mtTFB1 transgene). At 9 to 12 months of age, we observed the typical increase in ABR threshold in Tg-mtTFB1 mice (Figure 4A). However, Tg-mtTFB1 mice with reduced AMPK signaling (AMPK $^{+/-}$) had an ABR threshold profile indistinguishable from WT littermate controls (Figure 4B). Thus, we conclude that reducing AMPK signaling has no effect on normal hearing at the ages tested, but rescues or delays premature hearing loss in Tg-mtTFB1 mitochondrial deafness model mice.

Discussion

In this study, we have characterized the pathological mechanisms of hearing loss in Tg-mtTFB1 mice that we speculate models, to some degree, the pathology underlying maternally inherited deafness in humans because of the common A1555G mtDNA mutation.¹⁸ Our results demonstrate that hearing loss in Tg-mtTFB1 mice is because of cochlear dysfunction rather than a central processing defect in the brainstem (Figure 2). In the cochlea, we observe multiple defects, including signs of reduced spiral ganglion output (Figure 3C) and direct evidence for dysfunction in the stria vascularis (Figure 1B). We did not observe significant atrophy in the stria (at the light microscopic level), suggesting the defects involve intrinsic functioning of the cells in the tissue (eg, an inability to maintain the proper ionic milieu of the endolymph and EP within the scala media). The mitochondrial dysfunction in these cells may affect the functioning of the many ion pumps and transporters that require high and sustained amounts of ATP to operate. Alternatively, or in addition, these cells may be

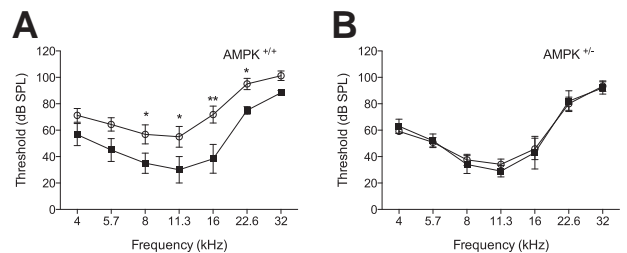


Figure 4 Reduced AMP kinase (AMPK) $\alpha 1$ signaling rescues hearing loss in a transgenic mouse strain that robustly overexpresses the mitochondrial 12S ribosomal RNA methyltransferase TFB1M (Tg-mtTFB1). Auditory brainstem response thresholds of littermates of the indicated genotypes were tested at 9 to 12 months of age. A two-way analysis of variance demonstrates that the overall effect for genotype was statistically significant [$F_{(3,126)} = 17$, $P < 0.001$]. **A:** All animals are AMPK $^{+/+}$ (wild-type for AMPK $\alpha 1$) and either wild-type (non-transgenic, closed squares) or transgenic for mtTFB1 (Tg-mtTFB1, open circles). **B:** All animals are AMPK $^{+/-}$ (heterozygous for AMPK $\alpha 1$) and either wild-type (non-transgenic) or transgenic for mtTFB1 (Tg-mtTFB1). Results of post hoc Fisher's least significant difference tests comparing the genotypes at individual frequencies. * $P < 0.05$, ** $P < 0.01$. db SPL, decibels sound pressure level.

more prone to oxidation reduction perturbations and oxidative stress driven by mitochondrial ROS. Also, Schmitz et al²⁶ observed reduced EP without morphological changes in the stria when hearing loss was induced with kanamycin and furosemide, which is similar to our results. We did not find evidence for major hair cell loss at ages when there is a clear ABR defect (Figure 3A), but there is some OHC dysfunction (Figure 3B). Interestingly, Niu et al²⁸ showed that mice with accumulated mtDNA mutations have hearing loss with pathological features in the spiral ganglion and stria vascularis, but do not display major effects on hair cells, suggesting this may be a common profile of mitochondrial dysfunction in the inner ear. The loss of spiral ganglion neurons we reported previously¹⁸ is consistent with the reduced ABR peak I amplitude (Figure 3C) caused by fewer nerve VIII fibers contributing to the compound action potential. We propose that this loss of spiral ganglion neurons is because of apoptosis on the basis of the heightened caspase 3 staining in this region we reported previously.¹⁸ Furthermore, we propose that the defects we observe in the stria, spiral ganglion neurons, and OHCs conspire to produce the observed progressive hearing loss profile in Tg-mtTFB1 mice. Whether different pathogenic mechanisms downstream of mitochondrial ribosome disruptions in Tg-mtTFB1 mice occur independently in the three cell types involved or defects in one tissue occur as the result of a primary dysfunction in another cannot be determined from our results.

One interesting issue raised by our findings is the functional changes in the OHCs. Tg-mtTFB1 OHCs show a shift in NLC *in vitro*, suggesting that some chronic change in their responsiveness had occurred *in vivo*. Shifts in NLC are expected to have detrimental effects on cochlear amplification.²⁹ It is possible that this shift is because of some intrinsic dysfunction. For example, the subsurface cisternae of the OHC that border the lateral membrane, which harbors the electromotile protein prestin,^{30,31} are lined by mitochondria,³² again suggesting that proper mitochondrial function may be necessary for normal OHC electromotility. Alternatively, stria dysfunction leading to altered composition of the endolymph (Figure 1B) may also produce some persistent cellular change in OHCs that we identified as a change in NLC. This could represent a new aspect of regulation of OHC activity.

Our previous study¹⁸ led to the formulation of a mitochondrial stress model that drives tissue-specific apoptotic signaling in the stria vascularis and spiral ganglion neurons. Specifically, altered mitochondrial ribosome activity and/or biogenesis because of premature or aberrant methylation of the 12S rRNA by TFB1M, or direct inhibition of ribosome assembly on the basis of our recent report of physical and functional interactions between TFB1M and POLRMT in the ribosome,¹⁹ is proposed to lead to ROS-dependent activation of AMPK kinase and unveiling of the pro-apoptotic function of the nuclear transcription factor E2F1.¹⁸ This model, based initially on *in vitro* results with

cultured human A1555G cybrids, was partially verified in our previous study¹⁸ by showing the following: i) hearing loss in Tg-mtTFB1 mice did not occur when E2F1 levels were reduced genetically, ii) there is increased E2F1 expression and caspase 3 activation in the strial epithelium, and iii) there is activation of AMPK in the associated spiral ligament. Herein, we provide additional direct evidence that the mitochondrial ROS-AMPK-E2F1 pathogenic signaling pathway is operational *in vivo* by showing that hearing loss in Tg-mtTFB1 is rescued by genetically reducing AMPK signaling. The AMPK α 1 form of the enzyme has been implicated in oxidative stress and ROS sensing,^{33–35} which is consistent with our results that hearing loss in Tg-mtTFB1 mice is rescued by inactivating one copy of the gene encoding AMPK α 1, which would presumably reduce signaling from mitochondrial ROS. Finally, thioredoxin regulates the oxidation reduction sensitivity of AMPK.³⁶ Thus, it will be interesting to determine whether this or other oxidation reduction-sensitive proteins are responsible for mediating mitochondrial ROS signals to AMPK in this pathogenic context and if antioxidants can also prove beneficial.

As a proposed animal model of the human deafness-associated A1555G mtDNA mutation, a comparison of our results in Tg-mtTFB1 mice to the human condition and how this might inform prophylactic or therapeutic strategies is warranted.^{37,38} In human A1555G patients, hearing loss is considered to be a progressive, sensorineural deafness. Two important audiological characteristics of A1555G patients compare favorably with Tg-mtTFB1. First, in A1555G carriers with normal hearing, there is a significant reduction in the distortion products of otoacoustic emissions³⁹ (DPOAEs). Reduced DPOAE is interpreted as OHC dysfunction, yet these patients have normal ABRs, indicating hair cells must be largely intact. In this case, the reduced DPOAE might suggest that it is the stria that is not functioning properly, leading to some dysfunction of the OHCs, but not enough to affect the ABR at the time of testing. Our observations of NLC may be relevant, and it is possible that the magnitude of OHC V_h shift in these patients is not sufficient to influence threshold. These asymptomatic carriers of the A1555G mutation may later lose their hearing either as part of the normal progression of the disease or in response to aminoglycosides or other cochlear stressors (eg, intense noise) that we predict might activate the mitochondrial ROS-AMPK-E2F1 pathway. The second relevant comparison between humans and the mouse model involves the peak I latency. In both cases, peak I takes significantly longer to reach maximum amplitude, suggesting that cochlear processing and activation of spiral ganglion neurons are impaired. Interestingly, central conduction time is not affected in this model or in A1555G carriers, thus eliminating any brainstem abnormalities from the pathogenic process.³⁹ One key difference between Tg-mtTFB1 mice and A1555G is the involvement of hair cells in humans with profound hearing loss who have no

measurable DPOAE, suggesting that they have no OHCs or they are seriously impaired. In contrast, Tg-mtTFB1 mice have intact OHCs and IHCs, as evidenced in this study both histologically and functionally. This may reflect a bona fide difference or a temporal difference in the progression of pathological events. Although future studies with older Tg-mtTFB1 mice might help clarify this, we acknowledge that studies of progressive hearing loss in the C57BL/6J background at older ages would become confounded by the age-related hearing loss locus in these mice that, on its own, causes premature deafness.^{40,41} Studies of Tg-mtTFB1 in other genetic backgrounds, that vary dramatically in their propensity for hearing loss,^{42,43} should help clarify the precise degree that our Tg-mtTFB1 mice model human deafness caused by the A1555G mutation.

Finally, it has recently been reported that lymphocytes and fibroblasts from A1555G patients do not exhibit increased 12S rRNA methylation like we observe in A1555G cybrid cells and Tg-mtTFB1 mice tissues.⁴⁴ Whether this reflects a difference in how methylation is assayed by our two groups or if increased methylation only occurs in the inner ear (or just during stress) in humans remains to be determined. It is also formally possible that increased 12S rRNA methylation of mature mitochondrial ribosomes is not the trigger of pathogenic responses in Tg-mtTFB1 mice or humans, as we proposed originally. For example, premature binding and/or methylation of 12S rRNA by TFB1M (eg, during transcription or before RNA processing is complete) might disrupt ribosome biogenesis. Alternatively, we have recently shown that TFB1M is in a complex with POLRMT in ribosomes¹⁹; thus, overexpression of TFB1M and/or the A1555G mutation may disrupt the function of this complex in ribosomes to initiate the mROS-AMPK-E2F1 pathway and hearing loss. These mechanistic details will be important to decipher to better understand deafness caused by the A1555G mutation in humans and the degree to which it can be modeled by our Tg-mtTFB1 mice.

Acknowledgments

We thank Drs. Benoit Viollet and Lawrence Young for providing the AMP kinase knockout mice for this study, Dr. Peter Santi for sharing data on stria morphology, and Dr. Reuben Shaw for helpful advice on AMP kinase.

References

- West AP, Shadel GS, Ghosh S: Mitochondria in innate immune responses. *Nat Rev Immunol* 2011, 11:389–402
- Kasahara A, Scorrano L: Mitochondria: from cell death executioners to regulators of cell differentiation. *Trends Cell Biol* 2014, 24:761–770
- Chandel NS: Mitochondria as signaling organelles. *BMC Biol* 2014, 12:34
- Hill S, Van Remmen H: Mitochondrial stress signaling in longevity: a new role for mitochondrial function in aging. *Redox Biol* 2014, 2: 936–944
- Shadel GS, Clayton DA: Mitochondrial DNA maintenance in vertebrates. *Annu Rev Biochem* 1997, 66:409–435
- Shutt T, Shadel G: A compendium of human mitochondrial gene expression machinery with links to disease. *Environ Mol Mutagen* 2010, 51:360–379
- Bestwick ML, Shadel GS: Accessorizing the human mitochondrial transcription machinery. *Trends Biochem Sci* 2013, 38:283–291
- Wallace DC: A mitochondrial paradigm of metabolic and degenerative diseases, aging, and cancer: a dawn for evolutionary medicine. *Annu Rev Genet* 2005, 39:359–407
- DiMauro S, Schon E: Mitochondrial respiratory-chain diseases. *N Engl J Med* 2003, 348:2656–2668
- Vafai SB, Mootha VK: Mitochondrial disorders as windows into an ancient organelle. *Nature* 2012, 491:374–383
- Guan MX, Fischel-Ghodsian N, Attardi G: Nuclear background determines biochemical phenotype in the deafness-associated mitochondrial 12S rRNA mutation. *Hum Mol Genet* 2001, 10:573–580
- Prezant TR, Shohat M, Jaber L, Pressman S, Fischel-Ghodsian N: Biochemical characterization of a pedigree with maternally inherited deafness. *Am J Med Genet* 1992, 44:465–472
- Prezant TR, Agopian JV, Bohlman MC, Bu X, Oztas S, Qiu WQ, Arnos KS, Cortopassi GA, Jaber L, Rotter JI: Mitochondrial ribosomal RNA mutation associated with both antibiotic-induced and non-syndromic deafness. *Nat Genet* 1993, 4:289–294
- Zhao H, Li R, Wang Q, Yan Q, Deng J-H, Han D, Bai Y, Young W-Y, Guan M-X: Maternally inherited aminoglycoside-induced and non-syndromic deafness is associated with the novel C1494T mutation in the mitochondrial 12S rRNA gene in a large Chinese family. *Am J Hum Genet* 2004, 74:139–152
- Dai P, Liu X, Han D, Qian Y, Huang D, Yuan H, Li W, Yu F, Zhang R, Lin H, He Y, Yu Y, Sun Q, Qin H, Li R, Zhang X, Kang D, Cao J, Young WY, Guan MX: Extremely low penetrance of deafness associated with the mitochondrial 12S rRNA mutation in 16 Chinese families: implication for early detection and prevention of deafness. *Biochem Biophys Res Commun* 2006, 340:194–199
- Bykhovskaya Y, Mengesha E, Wang D, Yang H, Estivill X, Shohat M, Fischel-Ghodsian N: Human mitochondrial transcription factor B1 as a modifier gene for hearing loss associated with the mitochondrial A1555G mutation. *Mol Genet Metab* 2004, 82:27–32
- Cotney J, McKay SE, Shadel GS: Elucidation of separate, but collaborative functions of the rRNA methyltransferase-related human mitochondrial transcription factors B1 and B2 in mitochondrial biogenesis reveals new insight into maternally inherited deafness. *Hum Mol Genet* 2009, 18:2670–2682
- Raimundo N, Song L, Shutt TE, McKay SE, Cotney J, Guan M-X, Gilliland TC, Hohuan D, Santos-Sacchi J, Shadel GS: Mitochondrial stress engages E2F1 apoptotic signaling to cause deafness. *Cell* 2012, 148:716–726
- Surovtseva YV, Shadel GS: Transcription-independent role for human mitochondrial RNA polymerase in mitochondrial ribosome biogenesis. *Nucleic Acids Res* 2013, 41:2479–2488
- Jørgensen SB, Wojtaszewski JFP, Viollet B, Andreelli F, Birk JB, Hellsten Y, Schjerling P, Vaulont S, Neuffer PD, Richter EA, Pilegaard H: Effects of alpha-AMPK knockout on exercise-induced gene activation in mouse skeletal muscle. *FASEB J* 2005, 19:1146–1148
- Faubert B, Boily G, Izreig S, Griss T, Samborska B, Dong Z, Dupuy F, Chambers C, Fuerth BJ, Viollet B, Mamer OA, Avizonis D, DeBerardinis RJ, Siegel PM, Jones RG: AMPK is a negative regulator of the Warburg effect and suppresses tumor growth in vivo. *Cell Metab* 2013, 17:113–124
- Santos-Sacchi J, Kakehata S, Takahashi S: Effects of membrane potential on the voltage dependence of motility-related charge in outer hair cells of the guinea-pig. *J Physiol* 1998, 510(Pt 1): 225–235
- Santos-Sacchi J: Determination of cell capacitance using the exact empirical solution of partial differential Y/partial differential Cm and its phase angle. *Biophys J* 2004, 87:714–727

24. Müller M, von Hünerbein K, Hoidis S, Smolders JWT: A physiological place-frequency map of the cochlea in the CBA/J mouse. *Hear Res* 2005, 202:63–73
25. Santi PA, Muchow DC: Morphometry of the chinchilla organ of Corti and stria vascularis. *J Histochem Cytochem* 1979, 27:1539–1542
26. Schmitz HM, Johnson SB, Santi PA: Kanamycin-furosemide ototoxicity in the mouse cochlea: a 3-dimensional analysis. *Otolaryngol Head Neck Surg* 2014, 150:666–672
27. Wangemann P: Supporting sensory transduction: cochlear fluid homeostasis and the endocochlear potential. *J Physiol* 2006, 1:11–21
28. Niu X, Trifunovic A, Larsson N-G, Canlon B: Somatic mtDNA mutations cause progressive hearing loss in the mouse. *Exp Cell Res* 2007, 313:3924–3934
29. Santos-Sacchi J, Song L, Zheng J, Nuttall AL: Control of mammalian cochlear amplification by chloride anions. *J Neurosci* 2006, 26:3992–3998
30. Yu N, Zhu M-L, Zhao H-B: Prestin is expressed on the whole outer hair cell basolateral surface. *Brain Res* 2006, 1095:51–58
31. He DZZ, Jia S, Dallos P: Prestin and the dynamic stiffness of cochlear outer hair cells. *J Neurosci* 2003, 23:9089–9096
32. Spicer SS, Thomopoulos GN, Schulte BA: Cytologic evidence for mechanisms of K⁺ transport and genesis of Hensen bodies and subsurface cisternae in outer hair cells. *Anat Rec* 1998, 251:97–113
33. Ju T-C, Chen H-M, Chen Y-C, Chang C-P, Chang C, Chern Y: AMPK- α 1 functions downstream of oxidative stress to mediate neuronal atrophy in Huntington's disease. *Biochim Biophys Acta* 2014, 1842:1668–1680
34. Choi SL, Kim SJ, Lee KT, Kim J, Mu J, Birnbaum MJ, Soo Kim S, Ha J: The regulation of AMP-activated protein kinase by H(2)O(2). *Biochem Biophys Res Commun* 2001, 287:92–97
35. Wang S, Dale GL, Song P, Viollet B, Zou M-H: AMPK α 1 deletion shortens erythrocyte life span in mice: role of oxidative stress. *J Biol Chem* 2010, 285:19976–19985
36. Shao D, Oka S-I, Liu T, Zhai P, Ago T, Sciarretta S, Li H, Sadoshima J: A redox-dependent mechanism for regulation of AMPK activation by Thioredoxin1 during energy starvation. *Cell Metab* 2014, 19:232–245
37. Tono T, Ushisako Y, Kiyomizu K, Usami S, Abe S, Shinkawa H, Komune S: Cochlear implantation in a patient with profound hearing loss with the A1555G mitochondrial mutation. *Am J Otol* 1998, 19:754–757
38. Sinnathuray AR, Raut V, Awa A, Magee A, Toner JG: A review of cochlear implantation in mitochondrial sensorineural hearing loss. *Otol Neurotol* 2003, 24:418–426
39. Bravo O, Ballana E, Estivill X: Cochlear alterations in deaf and unaffected subjects carrying the deafness-associated A1555G mutation in the mitochondrial 12S rRNA gene. *Biochem Biophys Res Commun* 2006, 344:511–516
40. Keithley EM, Canto C, Zheng QY, Fischel-Ghodsian N, Johnson KR: Age-related hearing loss and the ahl locus in mice. *Hear Res* 2004, 188:21–28
41. Johnson KR, Zheng QY, Erway LC: A major gene affecting age-related hearing loss is common to at least ten inbred strains of mice. *Genomics* 2000, 70:171–180
42. Johnson KR, Zheng QY, Noben-Trauth K: Strain background effects and genetic modifiers of hearing in mice. *Brain Res* 2006, 1091:79–88
43. Ohlemiller KK: Reduction in sharpness of frequency tuning but not endocochlear potential in aging and noise-exposed BALB/cJ mice. *J Assoc Res Otolaryngol* 2002, 3:444–456
44. O'Sullivan M, Rutland P, Lucas D, Ashton E, Hendricks S, Rahman S, Bitner-Glindzicz M: Mitochondrial m.1584A 12S m62A rRNA methylation in families with m.1555A>G associated hearing loss. *Hum Mol Genet* 2015, 24:1036–1044

Temperature dependence of non-linear capacitance in human embryonic kidney cells transfected with prestin, the outer hair cell motor protein

Jed Meltzer, Joseph Santos-Sacchi*

Sections of Otolaryngology and Neurobiology, Yale University School of Medicine, New Haven, CT 06510, USA

Received 19 July 2001; received in revised form 4 September 2001; accepted 4 September 2001

Abstract

The transmembrane motor protein prestin is thought to underlie outer hair cell (OHC) motility. Prestin expressed in non-auditory cells confers OHC-like electrical characteristics to the cell membrane, including the generation of gating-like currents (or non-linear capacitance), whose voltage dependence is susceptible to membrane tension and initial voltage conditions. Here we report that prestin's voltage sensitivity is, like that of the native motor, markedly temperature dependent. Prestin-transfected HEK cells were whole-cell voltage clamped while temperature was varied from 10–35°C. V_{pkcm} , the voltage at peak capacitance, reversibly and linearly shifted to depolarized levels with increasing temperatures, while peak capacitance also increased, but with significant hysteresis upon recooling. Mathematical modeling suggests that this increase may be due to a charged voltage sensor having a wider range of movement through or larger unit charge within the plasma membrane at higher temperatures. © 2001 Elsevier Science Ireland Ltd. All rights reserved.

Keywords: Prestin; Temperature; Capacitance; Cochlea; Membranes; Outer hair cell

The ability of outer hair cells (OHC) to generate mechanical responses to electrical stimulation is critical for the precise tonotopic tuning of the mammalian cochlea [2]. For several years it has been known that the mechanism underlying this motor activity is localized to the basolateral membrane of the OHC [5], and more recently a novel protein, prestin, has been identified as the putative motor protein [16]. Evidence for voltage-dependent mechanical activity of OHCs is easily detectable in whole-cell patch recording as a non-linear capacitance, or gating current, indicating the presence of a charged voltage-sensor participating in a conformational change [1,10]. Transfection of prestin into human embryonic kidney (HEK) cells confers non-linear capacitance with similar characteristics to that of the OHC lateral membrane [8,13,16]. Notably, transfected cells can exhibit electromotile responses in microchamber experiments [16], and excised patches from such cells have been shown to generate mechanical force in response to electrical stimulation [8]. These are necessary characteristics of the molecular mechanism for outer hair cell motility,

and the finding that expression of prestin is necessary and sufficient to invoke them in non-auditory cells is convincing evidence that prestin is the motor protein of OHCs.

It remains in question, however, whether or not prestin alone is responsible for the mechanical properties of OHCs, or if an interaction with other molecular species in the OHC basolateral membrane is required. Evidence is accumulating that prestin alone can indeed account for all of the electromechanical properties of OHCs. One interesting aspect of OHC non-linear capacitance is that its voltage dependence is subject to modulation by such fundamental conditions as membrane tension [6], resting potential [10], and temperature [11]. Specifically, the voltage at which half maximal charge movement occurs, or, correspondingly, the voltage at peak capacitance (V_{pkcm}), can be shifted in the positive direction by increased intracellular pressure, negatively shifted holding potential, or increased temperature. The replication of these findings in prestin-transfected cells is crucial evidence that OHC electromotility relies on a monomolecular mechanism requiring only prestin. Effects of membrane tension [8,13] and holding potential [13] in prestin-transfected cells have been reported, and here we report on the effects of varying temperature. V_{pkcm} in prestin-transfected cells is markedly dependent on temperature, in a manner no different from that of the OHC. Increasing

* Corresponding author. Department of Surgery (Otolaryngology), BML 244, Yale Medical School, 333 Cedar St., New Haven, CT 06510, USA. Tel.: +1-203-785-7566; fax: +1-203-737-2502.

E-mail address: joseph.santos-sacchi@yale.edu (J. Santos-Sacchi).

temperature shifts V_{pkC_m} in a positive direction, and the effect appears to be linear in the temperature range under investigation. In addition, increasing temperature was seen to increase the magnitude of peak capacitance, but with significant hysteresis in the temperature dependence, suggesting that the relationship of peak capacitance to temperature is more complex than that of V_{pkC_m} . Fitting of capacitance data to the first derivative of a two-state Boltzmann function [10] indicates that the temperature-dependent increase in capacitance is accounted for by an increase in the voltage-sensitivity of the OHC motor protein (z), but not an increase in the maximum charge moved (Q_{max}). These results suggest that movement of a voltage-sensor in the membrane is maximized at physiological temperature.

Transient transfection of HEK 293 cells was conducted as follows: Cells were cultured in MEME with 10% fetal calf serum. Cells were trypsinized and replated in 35 mm culture dishes 24 h prior to transfection with Lipofectamine 2000 (Life Technologies, MD). The transfection mixture consisted of OPTI-MEM media, Lipofectamine, the gPrestin-containing plasmid pcDNA3.1(-), and the GFP-containing plasmid pGreenLantern, used as a marker for successfully transfected cells. Generally, cells that successfully express one plasmid in a dual transfection will express both, and indeed, in the course of our recordings only one cell was found that exhibited green fluorescence (GFP) but not non-linear capacitance (prestin).

Twenty-four to 72 h after transfection, whole-cell patch clamp recordings were performed while varying bath temperature. The 35 mm culture dishes containing the cells were placed in a Peltier device (Dagan HCC-100A Heating/Cooling Bath Temperature Controller with HE-204 stage, Dagan Corp., MN). A temperature probe was inserted into the bath within 2 mm of the recorded cells. Cells were either patched at 10°C or cooled from room temperature after patching, after which the temperature was raised gradually up to 35°C and lowered back down to 10°C, and the cycle repeated as long as good recordings could be obtained from the cells. At 5-degree temperature intervals, we obtained full capacitance-voltage ($C-V$) functions as described below.

Round, isolated (non-coupled) cells exhibiting GFP-fluorescence were selected for electrophysiological recordings. Cells were whole-cell voltage clamped with an Axopatch 200A amplifier (Axon, CA) at a holding potential of 0 mV. The patch pipette solution contained (in mM): 130 CsCl, 10 EGTA, 2 MgCl₂, 10 HEPES, pH 7.2. The external bath solution contained (in mM): 99.2 NaCl, 20 TEA-Cl, 20 CsCl, 2 CoCl₂, 1.47 MgCl₂, 10 HEPES, 2 CaCl₂, pH 7.2. Osmolarity was adjusted to 300 mOsm with glucose. Gigohm seals were obtained and electrode capacitance was compensated. Current responses were filtered at 10 kHz. Data collection and analyses were performed with a Windows-based whole-cell voltage clamp program, jClamp (SciSoft, CT, USA), using a National Instruments PCI-6052 interface.

The magnitude of non-linear membrane capacitance was

evaluated using a continuous high-resolution (2.56 ms sampling) two-sine voltage stimulus protocol (10 mV peak at both 390.6 and 781.2 Hz), with subsequent FFT-based admittance analysis [12]. These high-frequency sinusoids were superimposed on a sinusoidal stimulus protocol sweeping from 0 to -175 mV, up to +175 mV, and back down to 0 mV. $C-V$ data were fit to the first derivative of a two-state Boltzmann function [10] where Q_{max} is the maximum non-linear charge moved, V_{pkC_m} is voltage at peak capacitance or half maximal non-linear charge transfer, V_m is membrane potential, C_{lin} is linear capacitance, z is valence, e is electron charge, k is Boltzmann's constant, and T is absolute temperature. Gating currents were obtained with a standard P/5 protocol, at a subtraction potential of +50 mV, as previously described [10]. In addition, in some experiments V_{pkC_m} was continuously tracked with 2 mV resolution by monitoring the reversal of gating current polarity as fully described previously [6]. This real-time tracking of V_{pkC_m} allowed a direct observation of the temperature dependence of non-linear capacitance, as V_{pkC_m} was observed to continuously follow changes in temperature in a reversible fashion.

Our results were very similar to those obtained from OHCs [11]. Fig. 1 plots non-linear capacitance vs. voltage for a cell at two temperatures. Two main effects of temperature can be seen - at the higher temperature, the magnitude of the capacitance is slightly greater, and the voltage at which the peak capacitance occurs is shifted to the right, to a more positive voltage. In all transfected cells exhibiting non-linear capacitance, V_{pkC_m} was seen to shift linearly in a positive direction with increasing temperature, at a rate of about 16.1 ± 6.8 mV/10°C ($n = 5$). This result agrees well with findings in OHC cells, which exhibited an average shift of 19.7 mV/10°C. Fig. 2a illustrates that these effects are continuous and fully reversible, using the continuous tracking of V_{pkC_m} as described above.

In order to calculate the average rate of shift in V_{pkC_m} in response to temperature changes from the data of five cells, it was necessary to verify that the effect is linear in the temperature range studied. Fig. 2b, *top panel* illustrates that this is the case. Cells that were continuously held through a wide temperature range yielded data that consistently fit a linear regression function of V_{pkC_m} vs. temperature ($r^2 \sim 0.93$). Peak C_m was also seen to increase with temperature (Fig. 2b, *bottom panel*), but there is a considerable amount of hysteresis in the response, rather than the simple linear temperature dependence of V_{pkC_m} . With cooling, peak C_m in all cells was relatively stable until temperatures well below physiological (<25°C) were reached.

The reason for this non-linearity is not entirely clear. As Fig. 2 illustrates, there was often a lag in the temperature dependent change in peak capacitance, compared with the change in V_{pkC_m} , which precisely followed temperature changes. The lag ranged up to three minutes, as seen in Fig. 2a. Fig. 2b *bottom panel* shows that peak C_m continued to increase for a short while after heating, even when the cell was cooling back down. Note that this lag cannot be

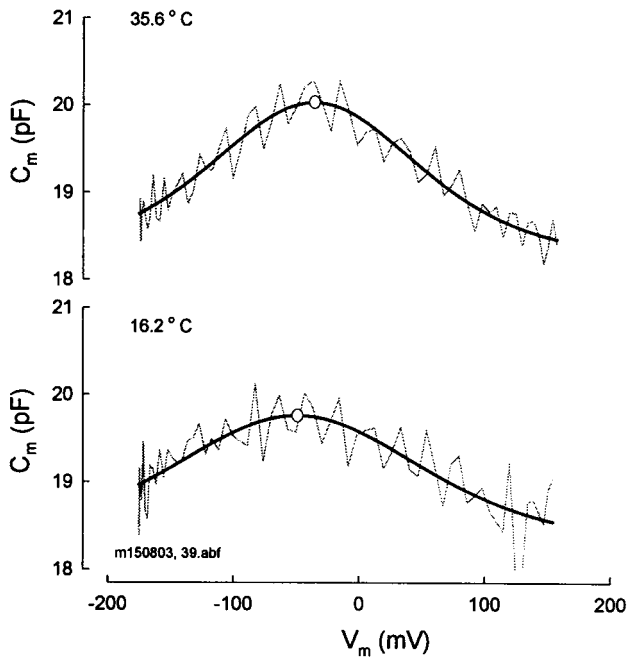


Fig. 1. Effect of temperature on non-linear capacitance of a prestin-transfected HEK cell. Capacitance was evaluated with a two-sine voltage stimulus protocol (see text) and the data were fit to the first derivative of a two-state Boltzmann function. Note two main effects of increasing temperature: a rightward (depolarizing) shift in the voltage at peak capacitance (V_{pkCm}), and an increase in peak capacitance. (35.6°C) V_{pkCm} : -32.2 mV, z : 0.49, Q_{max} : 0.37 pC, C_{lin} : 18.25 pF; (16.2°C) V_{pkCm} : -48.4 mV, z : 0.38, Q_{max} : 0.44 pC, C_{lin} : 18.17 pF.

explained by a discrepancy between the measured bath temperature and the actual temperature of the cell, since V_{pkCm} does not show any such delay. Such slow effects may be due to changes in metabolic processes, or state of motor protein phosphorylation [3,4]. It is significant that sensitivity to temperature change was minimal at physiological temperatures. Our results are comparable to those of Khvoles et al. [7], who found that the amplitude of otoacoustic emissions from rat cochleae is maximal and nearly temperature insensitive at temperatures approaching physiological, but is significantly and reversibly depressed at higher and lower temperatures. Otoacoustic emissions are a byproduct of the so-called ‘cochlear amplifier,’ which is thought to be dependent on the mechanical responses of OHCs. In related studies, Seifert et al. [14,15] found that the amplitude of otoacoustic emissions in humans and guinea pigs declines with decreasing temperature, and recovers with considerable hysteresis. Detectable emissions tended to return while rewarming at lower temperatures than those at which they disappeared during cooling. The authors hypothesize that hypothermia causes a hearing loss associated with a decline in function of the cochlear amplifier, due to a reduction in OHC motility subsequent to a depression of the endocochlear potential (EP). However, our results suggest that the effect is direct, a decrease in prestin’s non-linear capacitance being indicative of a decrease in its motor activity. Furthermore, the shift

in the voltage-dependence (indicated by V_{pkCm}) of the cochlear amplifier would affect its gain and influence emissions, even if EP were to remain constant.

To investigate further the nature of the temperature-dependent changes in prestin’s function, we fit voltage-dependent capacitance data to the first derivative of a two-state Boltzmann function, as described above and illustrated in Fig. 1. This fit allows for the derivation of the parameters Q_{max} , the total amount of non-linear charge moved, and z , the effective charge movement of a single voltage-sensor. An increase of either of these parameters would result in the increased capacitance seen at higher temperatures. Fig. 3 shows V_{pkCm} , Q_{max} , and z plotted at two temperatures for each of five cells. There was not a reliable trend in the variation of Q_{max} , which remains fairly stable, whereas z shows a consistent increase with increasing temperature. Similar findings were previously reported in OHCs [11]. z depends upon both the magnitude of charge and the distance it traverses within the membrane’s electric field. Thus, the increase in z may be caused by changes in either one of these factors. An increase in charge displacement may result from a decrease in plasma membrane viscosity at higher temperatures; the magnitude of charge may vary with phosphorylation and/or metabolism. Finally, it may be possible that some of the temperature-dependent effects that we observe could be due to a change in the availability of intracellular Cl^- , which is required for prestin activity [9]. These factors are expected to account for the non-linear effects of temperature on otoacoustic emissions [7,14,15], and their relative insensitivity to temperature changes in the physiological range. This insensitivity, reflecting properties of the motor protein prestin, would allow an animal to maintain

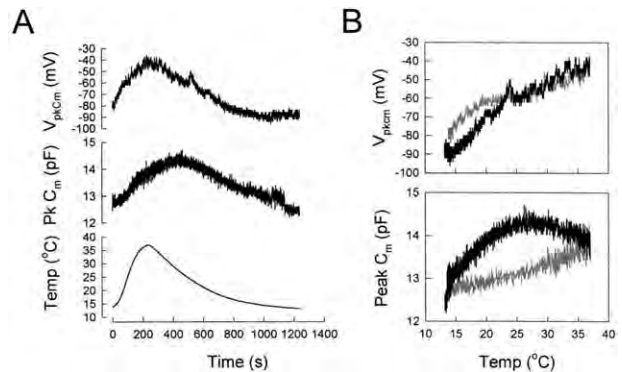


Fig. 2. (A) The voltage at peak capacitance (V_{pkCm}) and the peak capacitance (C_m) follow changes in temperature in a continuous and reversible manner. Here, a tracking procedure developed previously [6] was used to keep a cell voltage-clamped at V_{pkCm} during heating and cooling. (B) V_{pkCm} and peak C_m plotted as a function of temperature for the same cell. Data from the heating phase is shown in gray, while data obtained during subsequent cooling is plotted in black. V_{pkCm} increases nearly linearly with temperature (top panel), fitting a linear regression with $r^2 = 0.91$ (heating), $r^2 = 0.95$ (cooling). However, C_m shows considerable hysteresis in its response to changing temperature (bottom panel).

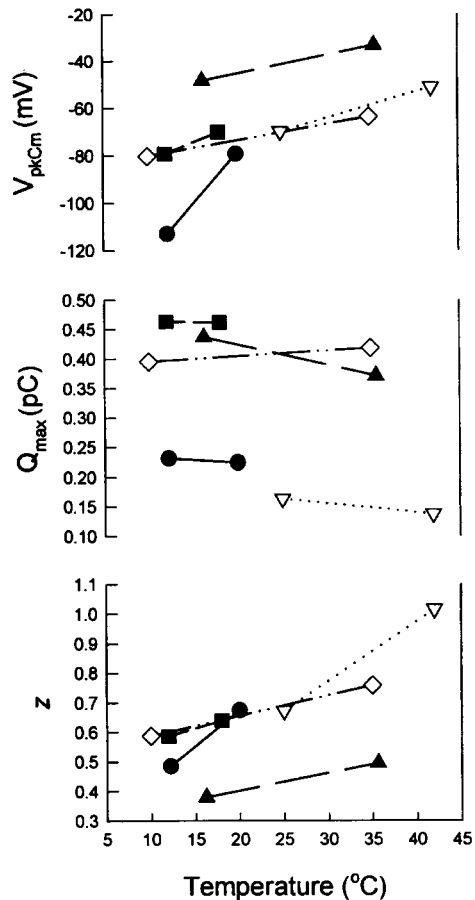


Fig. 3. The relationship between temperature and the parameters V_{pkCm} , Q_{max} , and z , derived from the fitting of capacitance data to a two-state Boltzmann function. Each of these quantities is plotted at two different temperatures for each of five cells. The increase in peak capacitance seen with increasing temperature cannot be due to an increased amount of total charge movement, because no clear increase is seen in Q_{max} . However, z shows a clear increasing trend.

optimal cochlear function across small fluctuations in environmental temperature.

This work was supported by grant NIDCD DC 00273 to JSS. We thank Daniel Folkinshteyn, Volodya Rybalchenko, Enrique Navarrate, and Margaret Mazzucco for technical assistance and discussion. Also, we are indebted to Douglas Sheridan, Thom Hughes, Laird Madison, and Peter Dallos for the generous provision of materials.

[1] Ashmore, J.F., Forward and reverse transduction in the mammalian cochlea, *Neurosci. Res. Suppl.*, 12 (1990) S39–S50.

- [2] Dallos, P., Overview: cochlear neurobiology, In P. Dallos, A.N. Popper and R.R. Fay (Eds.), *The Cochlea*, Springer-Verlag, New York, 1996, pp. 1–43.
- [3] Frolenkov, G.I., Mammano, F., Belyantseva, I.A., Coling, D. and Kachar, B., Two distinct Ca^{2+} -dependent signaling pathways regulate the motor output of cochlear outer hair cells, *J. Neurosci.*, 20 (2000) 5940–5948.
- [4] Huang, G.-J. and Santos-Sacchi, J., Metabolic control of OHC function: phosphorylation and dephosphorylation agents shift the voltage dependency of motility related capacitance, , Midwinter Meeting of the Association for Research in Otolaryngology, St. Petersburg, FL Fe.
- [5] Huang, G. and Santos-Sacchi, J., Motility voltage sensor of the outer hair cell resides within the lateral plasma membrane, *Proc. Natl. Acad. Sci. USA*, 91(25) (1994) 12268–12272.
- [6] Kakehata, S. and Santos-Sacchi, J., Membrane tension directly shifts voltage dependence of outer hair cell motility and associated gating charge, *Biophys. J.*, 68 (1995) 2190–2197.
- [7] Khvoles, R., Freeman, S. and Sohmer, H., Effect of temperature on the transient evoked and distortion product otoacoustic emissions in rats, *Audiol. Neurootol.*, 3 (6) (1998) 349–360.
- [8] Ludwig, J., Oliver, D., Frank, G., Klocker, N., Gummer, A.W. and Fakler, B., Reciprocal electromechanical properties of rat prestin: the motor molecule from rat outer hair cells, *Proc. Nat. Acad. Sci.*, 98 (7) (2001) 4178–4183.
- [9] Oliver, D., He, D.Z.Z., Klocker, N., Ludwig, J., Schulte, U., Waldegger, S., Ruppertsberg, J.P., Dallos, P. and Fakler, B., Intracellular anions as the voltage sensor of prestin, the outer hair cell motor protein, *Science*, 292 (2001) 2340–2343.
- [10] Santos-Sacchi, J., Reversible inhibition of voltage-dependent outer hair cell motility and capacitance, *J. Neurosci.*, (1991) 113096–113110.
- [11] Santos-Sacchi, J. and Huang, G., Temperature dependence of outer hair cell nonlinear capacitance, *Hearing Res.*, 116 (1998) 99–106.
- [12] Santos-Sacchi, J., Kakehata, S. and Takahashi, S., Effects of membrane potential on the voltage dependence of motility-related charge in outer hair cells of the guinea-pig, *J. Physiol.*, 510 (1) (1998) 225–235.
- [13] Santos-Sacchi, J., Shen, W., Zheng, J. and Dallos, P., Effects of membrane potential and tension on prestin, the outer hair cell lateral membrane motor protein, *J. Physiol.*, 531 (3) (2001) 661–666.
- [14] Seifert, E., Brand, K., van de Flierdt, K., Hahn, M., Rieband, M. and Lamprecht-Dinnesen, A., The influence of hypothermia on outer hair cells of the cochlea and its efferents, *Br. J. Audiol.*, 35 (2001) 87–98.
- [15] Seifert, E., Lamprecht-Dinnesen, A., Asfour, B., Rotering, H., Bone, H.G. and Scheld, H.H., The influence of body temperature on transient evoked otoacoustic emissions, *Br. J. Audiol.*, 32 (1998) 387–398.
- [16] Zheng, J., Shen, W., He, D.Z.Z., Long, K., Madison, L.D. and Dallos, P., Prestin is the motor protein of cochlear outer hair cells, *Nature*, 405 (2000) 149–155.

N-Terminal-Mediated Homomultimerization of Prestin, the Outer Hair Cell Motor Protein

Dhasakumar Navaratnam,* Jun-Ping Bai,[†] Haresha Samaranayake,* and Joseph Santos-Sacchi[†]

*Departments of Neurology and Neurobiology, and [†]Otolaryngology and Neurobiology, Yale University School of Medicine, New Haven, Connecticut

ABSTRACT The outer hair cell lateral membrane motor, prestin, drives the cell's mechanical response that underpins mammalian cochlear amplification. Little is known about the protein's structure-function relations. Here we provide evidence that prestin is a 10-transmembrane domain protein whose membrane topology differs from that of previous models. We also present evidence that both intracellular termini of prestin are required for normal voltage sensing, with short truncations of either terminal resulting in absent or modified activity despite quantitative findings of normal membrane targeting. Finally, we show with fluorescence resonance energy transfer that prestin-prestin interactions are dependent on an intact N-terminus, suggesting that this terminus is important for homo-oligomerization of prestin. These domains, which we have perturbed, likely contribute to allosteric modulation of prestin via interactions among prestin molecules or possibly between prestin and other proteins, as well.

INTRODUCTION

A key evolutionary step in the development of high-frequency acoustic sensitivity in mammals appears to have been the recruitment of an anion transporter family member, prestin (SLC26A5) (1), to enable amplification of passive basilar membrane motion by outer hair cells (OHCs) (2). When transfected into nonauditory cells, this voltage-dependent, integral membrane protein presents all of the known biophysical attributes expressed by the native OHC lateral membrane motor, including voltage and tension sensitivity (1,3–6). These preserved attributes confirm the identity of prestin as the prime component of the lateral membrane motor. Nevertheless, we and others have noted some differences in the electromechanical activity of transfected prestin compared to that of the native OHC motor, and suggested that subunit interactions might be required for amplification of prestin's activity (6,7).

The molecular conformation or state of prestin, which underpins OHC electromotility and drives cochlear amplification, can be deduced from “gating charge” measures, or measures of the cell's voltage-dependent, nonlinear capacitance (NLC). Using these measures, the control of prestin's voltage-dependent activity has recently been linked to prestin's affinity for anions, in particular chloride ions (9,10). It has been suggested that these ions function either as extrinsic voltage sensors (9), or as allosteric modulators that influence the protein's steady-state energy profile (10,11). In this series of experiments, we extend our concept of allosteric modulation of prestin to include modulation via protein-protein interactions.

METHODS

Preparing mutants and transient transfection

Truncations of the N-terminus were achieved by introducing start codons before the indicated amino acid positions by polymerase chain reaction (PCR) amplification. Similarly, C-terminal truncations were obtained by introducing stop codons after the indicated positions. Yellow (YFP) or cyan (CFP) fluorescent protein fusion proteins were made by introducing the fluorescent proteins at the C-terminus of the prestin. In the case of the C-terminal truncations the truncated protein was fused directly to the N-terminus of YFP without an intervening stop codon. Amplification by PCR was done using Hi-Fidelity DNA polymerase (Roche, Indianapolis, IN). The parameters were 10 cycles of 94°C for 40 s, 55°C for 2 min, and 68°C for 6 min; and 30 cycles of 94°C for 40 s, 55°C for 2 min, and 68°C for 6 min, with 20 s extension for every cycle. A clone of gerbil prestin served as the template. Amplified products were purified, ligated into pCDNA 3.1 topo TA (Invitrogen, Carlsbad, CA) or into eYFPN1 (Clontech, Palo Alto, CA). Each of the clones generated were sequenced to exclude the possibility of PCR-generated errors. Transient cotransfection into Chinese hamster ovary (CHO) cells was achieved with Lipofectamine (Invitrogen) in accordance with the manufacturer's recommendations.

Fluorescence resonance energy transfer

Fluorescence resonance energy transfer (FRET) was determined using a Zeiss 510 with a meta-analyzer. CHO cells transiently transfected with prestin-YFP and prestin-CFP constructs (at a 2:3 ratio, to counter a lower CFP quantum yield and CFP's more diffuse emission spectrum) were analyzed 24–48 h after transfection. Emission from 10 defined regions of interest of each cell, detected by the meta-analyzer (in 10-nm increments) while excited at 458 nm were recorded before and after photobleaching at 514 nm. Photobleaching at 514 nm was done with the 40W argon laser set at maximum for a period of 1 min. FRET efficiency was defined as $(E_a - E_b) \times 100/E_a$, where E_a was the CFP emission (473–494 windows) after photobleaching and E_b the CFP emission before photobleaching, and calculated as previously described (12). In determining FRET efficiency in unbleached controls, CFP emission values obtained 1 min after determining the initial CFP emission were defined as E_a (a period of 1 min was the interval of photobleaching). To minimize CFP photobleaching while determining its emission, the laser intensity was set at 5% while measuring CFP emission. Although there was some minimal CFP bleaching during photobleaching of YFP, the effect was the same across all the sample combinations tested

Submitted June 15, 2005, and accepted for publication August 8, 2005.

Address reprint requests to Joseph Santos-Sacchi, Sections of Otolaryngology and Neurobiology, Yale University School of Medicine, BML 246, 333 Cedar St., New Haven, CT 06510. Tel.: 203-785-5407; Fax: 203-737-2502; E-mail: joseph.santos-sacchi@yale.edu.

© 2005 by the Biophysical Society

0006-3495/05/11/3345/08 \$2.00

doi: 10.1529/biophysj.105.068759

where YFP photobleaching was performed. Thus, the increase in FRET efficiency observed in these bleaching experiments was found despite the slight decrease in CFP fluorescence after YFP bleaching. Thus, we cannot rule out that a relatively slight increase in FRET efficiency was masked in the observed decrease in efficiency found with start 21 prestin-YFP and prestin-CFP (see Fig. 5). Nevertheless, each group would be affected similarly.

Immunofluorescence staining

Affinity-purified rabbit polyclonal antibodies against two peptides corresponding to extracellular domains of prestin, GGKEFNERFKEKLPAPI (274–290) and KELANKHGYQVDGNQEL (359–375), respectively, were purchased from Genemed Synthesis (San Francisco, CA). Live OHCs or transfected CHO cells were incubated separately with these primary antibodies and then subsequently fixed. Primary antibody was detected using a fluorescent-labeled secondary antibody. Specificity of antibody labeling was established by preadsorption of the primary antibody with the corresponding peptide. Cells that were transfected with empty vector and stained in an identical fashion served as negative controls. Specific staining was not observed with either of these procedures.

Fluorescence-activated cell sorting analysis

CHO cells transfected with the different prestin-YFP constructs were labeled with affinity-purified anti-prestin antibodies. Live cells were dissociated and incubated with antibody in phosphate-buffered saline, 1% bovine serum albumin, and 0.5% fetal calf serum at 4°C. The primary antibody was detected using a biotinylated anti-rabbit antibody (Molecular Probes, Eugene, OR) followed by streptavidin conjugated to Alexa 647. The cells were fixed briefly in 1% paraformaldehyde before analysis. Fluorescence-activated cell sorting (FACS) analysis was carried out using FlowJo software. Stained cells were analyzed on a FACSCalibur TM (Becton Dickinson Immunocytometry Systems, Franklin Lakes, NJ). Forward and side scatter profiles were used to exclude dead cells. From 30,000 to 50,000 events were collected for analysis. Cells transfected with empty vector stained with the prestin antibodies and prestin-YFP stained with rabbit IgG served as negative controls for the primary and secondary antibodies, respectively.

Nonlinear capacitance

Cells were recorded by whole-cell patch-clamp configuration at room temperature using an Axon 200A amplifier (Axon Instruments, Foster City, CA), as described previously (13,14). The bath solution contained (in mM) TEA 20, CsCl 20, CoCl₂ 2, MgCl₂ 1.47, Hepes 10, NaCl 99.2, and CaCl₂·2H₂O 2, pH 7.2, and the pipette solution contained (in mM) CsCl 140, EGTA 10, MgCl₂ 2, and Hepes 10, pH 7.2. These conditions ensured that prestin-chloride interactions were maximal (9,10). Osmolarity was adjusted to 300 ± 2 mOsm with dextrose. Command delivery and data collections were carried out with a Windows-based whole-cell voltage-clamp program, jClamp (Scisoft, Ridgefield, CT), using an NI PCI 6052E interface (National Instruments, Austin, TX).

Capacitance was evaluated with a continuous high-resolution 2-sine wave technique fully described elsewhere (14,15). Capacitance data were fitted to the first derivative of a two-state Boltzmann function (13):

$$C_m = Q_{\max} \frac{ze}{kT} \frac{b}{(1+b)^2} + C_{\text{lin}}, \quad (1)$$

where

$$b = \exp\left(\frac{-ze(V_m - V_h)}{kT}\right), \quad (2)$$

Q_{\max} is the maximum nonlinear charge transfer, V_h is the voltage at peak capacitance or half-maximal nonlinear charge transfer, V_m is membrane potential, C_{lin} is linear capacitance, z is valence, e is electron charge, k is

Boltzmann's constant, and T is absolute temperature. Gating charge currents were obtained with a standard $P/-5$ procedure (13).

RESULTS

CHO cells transfected with the gene for normal prestin show large gating currents and NLC, similar to that in OHCs (see Fig. 2 *B*). This signature of prestin's electromechanical activity was quantified through estimates of V_h (the voltage at half-maximal motor charge transfer), z (the charge valance), and Q_{\max} (total charge moved) that were derived from fits with two-state Boltzmann functions (13). With our intracellular and extracellular solutions, average normal values for V_h , z , and Q_{\max} (mean ± SE) were -102.4 ± 1.8 mV, 0.67 ± 0.02 , and 130 ± 20 fC, respectively ($n = 30$). Nonlinear charge density (coulombs per pF of linear capacitance) averaged 4.8 ± 0.6 fC/pF. Additionally, we were able to measure NLC in prestin that had been fused with YFP at its C-terminus ($n = 20$). This fusion construct of prestin provides electrical properties statistically indistinguishable from normal prestin; fusion constructs of mutant prestin that we made (see below) similarly remained unaffected by the tag. The assessment of this YFP fusion construct permitted not only quantitative electrical evaluations, but both qualitative and quantitative evaluations of membrane targeting via confocal microscopy and FACS, respectively.

To better understand structure-function relationships of prestin, we sought to refine our working knowledge of prestin topology (Fig. 1). The current membrane topology model of prestin posits 12 transmembrane (TM) domains (9,16). This model is, in part, based on placing two potential N glycosylation sites on the extracellular surface of the protein (17). In our modeling of prestin's TM regions, we abandoned this constraint based on several pieces of information. First, potential N glycosylation sites are common and often non-specific, being present even in frank intracellular proteins, including two potential N glycosylation sites that are within prestin's intracellular C-terminus (603 and 736). Second, in contradistinction to the results of Matsuda et al. (17), we find no significant effects of glycosylation site mutations (N163Q + N166Q) or glycosidase F treatment on the voltage dependence of NLC in transfected CHO cells (control ($n = 28$)/mutant ($n = 10$)/enzyme ($n = 13$): $V_h = -100.2 \pm 1.76/-95.9 \pm 3.92/-100.1 \pm 3.61$; t -tests, $p = 0.26/0.98$). Furthermore, the molecular mass of both prestin and doubly mutated prestin (N163Q and N166Q) were indistinguishable at 80 kD (Fig. 2 *J*), this also being in contradistinction to the results of Matsuda et al. (17). In the absence of that constraint, we are left with the observation, supported by epitope tagging and/or antibody staining of live and permeabilized cells, that the N- and C-termini are likely intracellular (9,16), results that we too have since replicated. Consequently, the molecule has an even number of TM domains, and based on an analysis of prestin's structure with a number of topology prediction programs (TMPred, DAS, TMAP, TMHMM, and

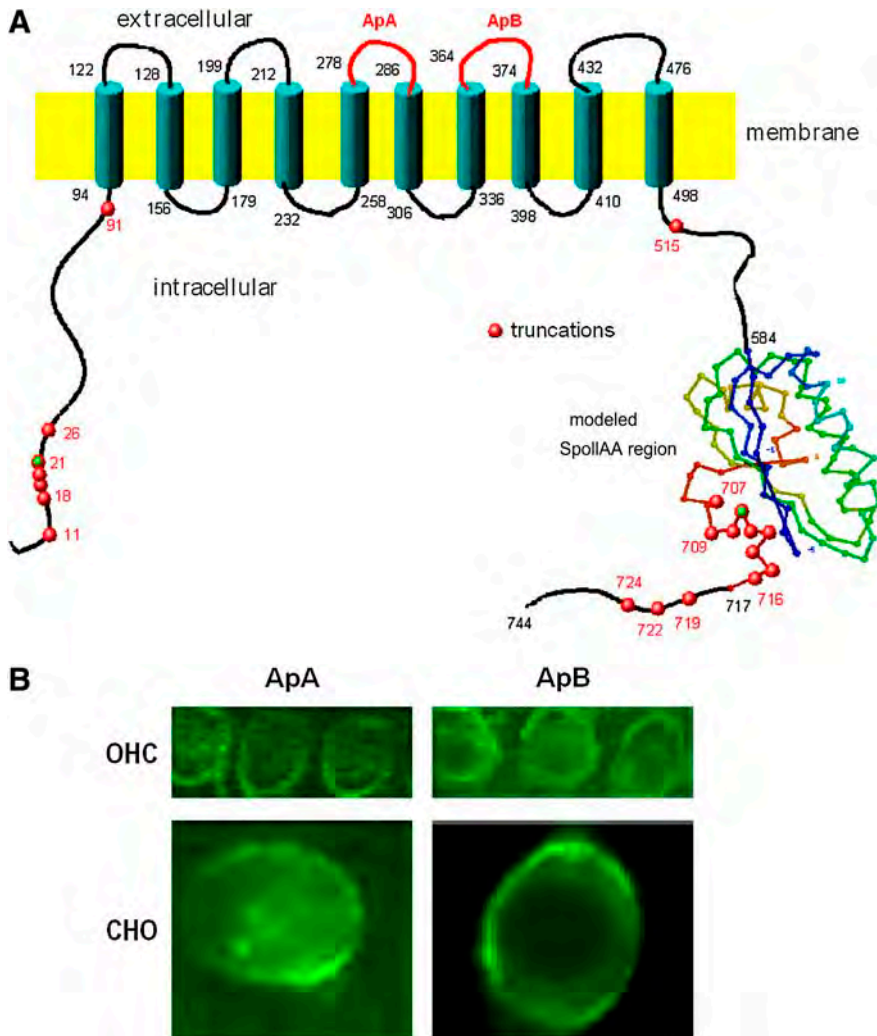


FIGURE 1 (A) Model of prestin's transmembrane topology that posits 10 transmembrane domains with intracellular amino and carboxy termini of the protein. Shown are the positions (red circles) of individual truncations of the protein that we tested. A cartoon of the crystal structure of the C-terminus of prestin modeled on the bacterial protein SpoIIAA, to which it shows strong homology, is shown. The positions of two peptides that would lie on the extracellular surface of the protein between transmembrane domains 4 and 5 (peptide A) and 6 and 7 (peptide B) are indicated. (B) Affinity-purified antibodies against these peptides (ApA and ApB) were used to stain both live guinea pig OHC (upper panel of confocal images) and live CHO cells transfected with prestin (lower panel). These results, together with other data (see text), confirm that these antigens lie on the extracellular surface, and support the 10-transmembrane model.

Predict Protein), we modeled prestin to contain 10 TM domains (Fig. 1 A). Our 10-TM model has a membrane topology the reverse of that previously proposed by Deak et al. (18); that is, segments on the intracellular surface in our model would lie on the extracellular surface of the cell in their model. We tested the model by immunostaining live outer hair cells and prestin-transfected CHO cells using antibodies raised to two peptides that are predicted, based on this model, to lie on the extracellular surface of the cell. The two peptides GGKEFNRFKEKLPAPI (274–290) and KE-LANKHGYQVDGNQEL (359–375) lie between TM domains 5 and 6, and 7 and 8 in our model (they would lie on the intracellular surface of the protein in the existing topology models (9,16,18)). We found live staining and fixed, nonpermeabilized staining of these cells with these two antibodies, confirming that the two peptides lie on the extracellular surface (Fig. 1 B). We also hemagglutinin (HA)-tagged prestin at residue 168, which proved functional, and were not able to find live staining by immunocytochemistry or FACS, but were able to immunocytochemically observe the tag after permeabilization (Fig. 2, A–F). HA tagging of residue 371

did not produce functional prestin (no NLC) and rarely showed membrane targeting; however, in those few rare cells live staining was observed (Fig. 2, G–I). We were unable to produce HA tagging of residue 281.

Our 10-TM model of prestin indicates that the amino and carboxy termini before residue 94 and after residue 498 reside intracellularly, that is, outside the lipid bilayer and beyond where a functional voltage sensor should reside. We used site-directed C-terminal and N-terminal truncations to evaluate the contribution of these intracellular moieties to prestin's voltage-dependent activity, as we did above with normal prestin. Successive truncations of the C- and N-terminus resulted in a graded decrease and eventual elimination of nonlinear charge movement (Fig. 2). In truncations that remained functional, voltage sensitivity (z) did not vary far from control values, indicating that the truncated protein's voltage sensor remained relatively unaltered. On the other hand, V_h varied among truncations, especially that of the N-terminal, and likely reflects structural influences on the steady-state energy profile that controls the voltage range over which the motors operate. Additionally, since the total

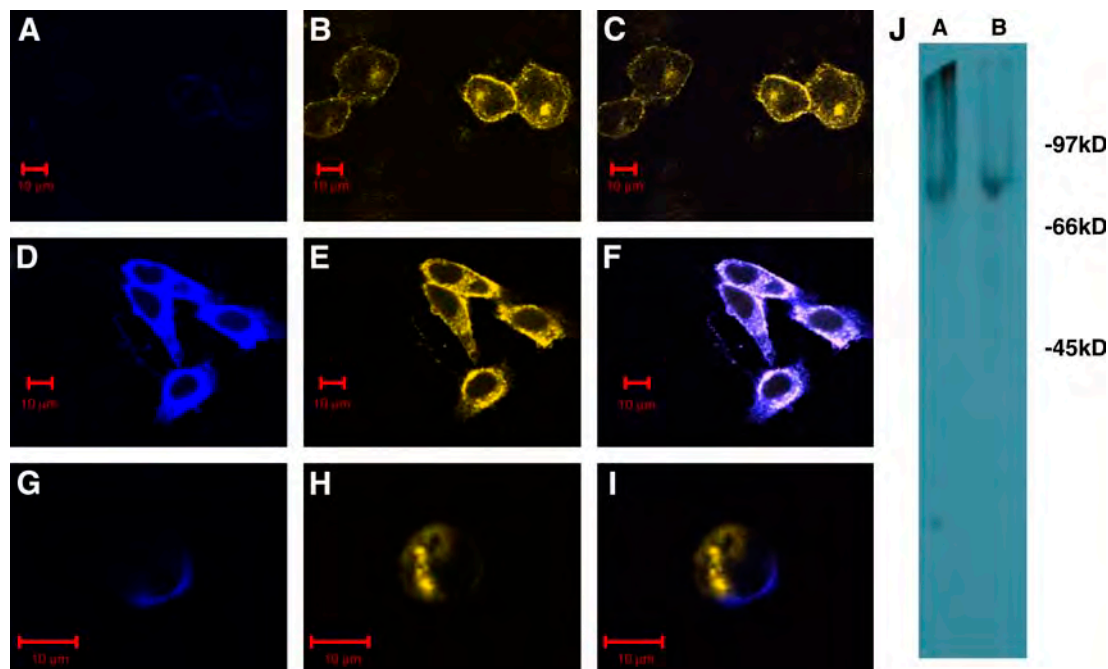


FIGURE 2 Confocal images show CHO cells transfected with prestin-YFP constructs into which the HA epitope was inserted into position 168 (A–F) and position 371 (G–I). The HA tags were detected with a mouse anti-HA epitope and Alexa 647-conjugated antimouse antibody (A, D, and G). (B, E, and H). YFP images. (C, F, and I) Merged images. Cells in A–C and G–I were stained live, and cells in D–F were fixed and permeabilized with detergent. As is evident, the detection of the HA epitope at position 168 required that the cells be permeabilized, whereas that at position 371 was detectable in live cells without permeabilization. These results suggest that position 168 of prestin in these constructs lies on the intracellular surface, whereas position 371 lies on the extracellular surface. (J) Substitution of the two potential N-glycosylation asparagine residues with glutamine residues does not result in a change in molecular weight, indicating that prestin is not glycosylated at these two residues. CHO cells were transfected with constructs of prestin fused to poly-His V5 epitope tag at its C-terminus (lane A) and prestin N163Q + N166Q double mutant fused to a poly-His V5 epitope tag at its C-terminus (lane B). Normal and mutated prestin were purified from lysed CHO cells on a Ni column and separated by PAGE (8%). The gel was blotted on to polyvinylidene difluoride and probed with an anti-V5 antibody/horseradish peroxidase-conjugated secondary antibody followed by enhanced chemiluminescence detection. As is evident, prestin migrates at its predicted molecular weight of 80 kD, as does the N163Q + N166Q double mutant.

charge movement Q_{\max} decreased, with z remaining normal, it appears that the number of functional proteins decreased. Stops N-terminal to residue 712 and starts C-terminal to residue 20 were functionally lethal, indicating catastrophic alterations in protein structure and/or absent or abnormal interactions with other potential intracellular subunits.

To rule out absent surface expression of these lethal truncations as a cause of a loss in NLC we confirmed proper targeting to the plasma membrane by live antibody staining of mutated prestin molecules in transfected cells. Similar patterns of antibody staining appear in both control and non-functional mutations. Additionally, several of the truncated mutations were evaluated with a YFP fusion construct. In each case, the results were the same as the ones we obtained with green fluorescent protein coexpression experiments, and each successfully targeted the plasma membrane (Fig. 3, E–G). The only exception was the full C-terminus truncation (stop 498), which was nonfunctional and confined intracellularly (Fig. 3 H). Full truncations of the C-terminus are not expected to properly target the membrane (D. Oliver, University of Freiburg, and J. Zheng, Northwestern University, personal communications, AOR meeting, 2004). Finally, to allay our concerns over the poor statistical power of confocal

microscopy, we used FACS in large populations of cells to confirm that membrane targeting was normal (Fig. 4). In these studies, the correspondence of fluorescence intensities in controls and mutants indicates that equal numbers of prestin molecules reach the plasma membrane in normal and mutant transfections. Thus, the proper targeting of functional and non-functional truncated mutations indicates that there is a decrease in the number of functional motors, not a decrease in the number of prestin molecules residing within the plasma membrane.

One possible mechanism for the reduction of functional motors is an interference with obligatory homomeric interactions among prestin molecules. To evaluate the possibility that prestin may function as multimers, we investigated whether individual prestin molecules could closely interact with each other using FRET. Fig. 5 shows that indeed close interactions (<100 Å) occur between fluorescently tagged neighboring C-terminals of prestin; additionally, controls with the fluorescently tagged Slo K channel do not show interactions with prestin. Restricting the area of interest to the plasma membrane produced the same FRET response, as larger cellular areas. Consistent with this data, chemical cross-linking of purified poly-his tagged prestin yielded a minimal molecular mass of 160 kD, suggesting that prestin formed dimers. To

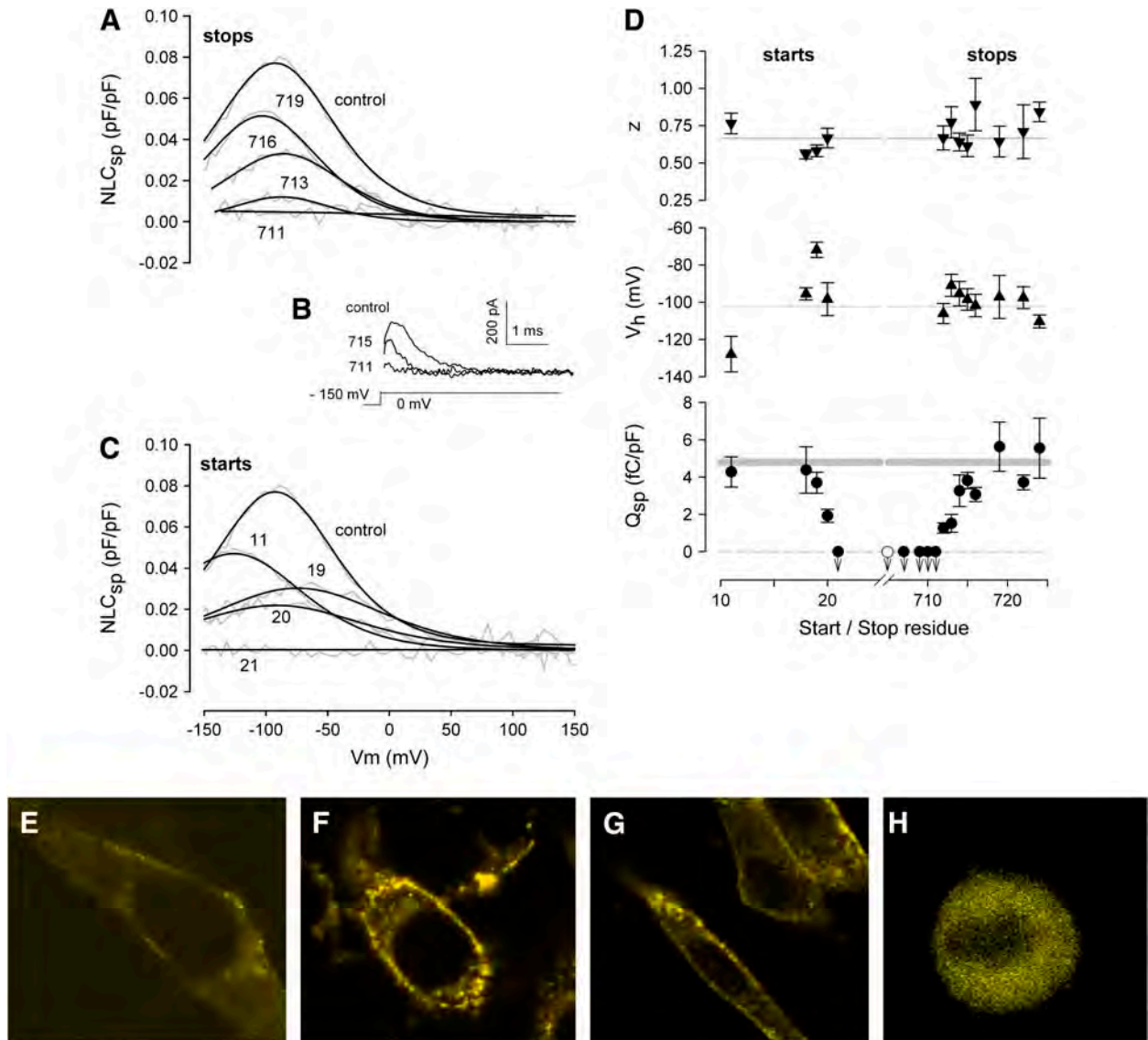


FIGURE 3 Serial truncations of the amino and carboxy termini of prestin result in a loss of NLC. (A) Nonlinear capacitance as a function of C-terminal truncations. A stop codon at 712 abolishes NLC. (B) Examples of gating currents induced by a voltage step showing a decrease in magnitude corresponding to reductions in NLC. (C) Nonlinear capacitance as a function of N-terminal truncations. A start codon at 21 abolishes NLC. (E–G) Confocal images of CHO cells transfected with prestin-YFP, start 21 prestin-YFP, and stop 709 prestin-YFP, respectively, showing plasma membrane targeting of these constructs. (H) A confocal image of a CHO cell transfected with stop 498 prestin-YFP that does not target the membrane (and corroborates work by other workers in the field; Jing Zheng, Northwestern University, and Dominik Oliver, University of Freiburg, personal communication, AOR meeting, 2004). These results confirm that the loss in NLC with these truncations is not due to absent targeting to the surface membrane.

determine whether the intracellular termini were required for these interactions, we used FRET to identify homomultimerization of two prestin truncations, start 21 prestin-YFP and stop 709 prestin-YFP, each of which was physiologically nonfunctional, but targeted the membrane successfully. In contrast to stop 709 prestin-YFP, which showed FRET when cotransfected with normal prestin-CFP, start 21 prestin-YFP did not show FRET when cotransfected with normal prestin-CFP. The differences in FRET efficiencies obtained before and after acceptor photobleaching were statistically significant (see Fig. 5), indicating that the N-terminus of prestin is

important for the formation of multimers, and the loss in NLC is possibly a result of an inability to form multimers. In contrast, since the C-terminal truncation that resulted in a loss of NLC was still able to form homomultimers, we speculate that the C-terminus interacts with other proteins that are important for generating NLC.

DISCUSSION

The discovery of prestin (19) identified a molecule that likely is the foundation of the mammalian auditory system’s

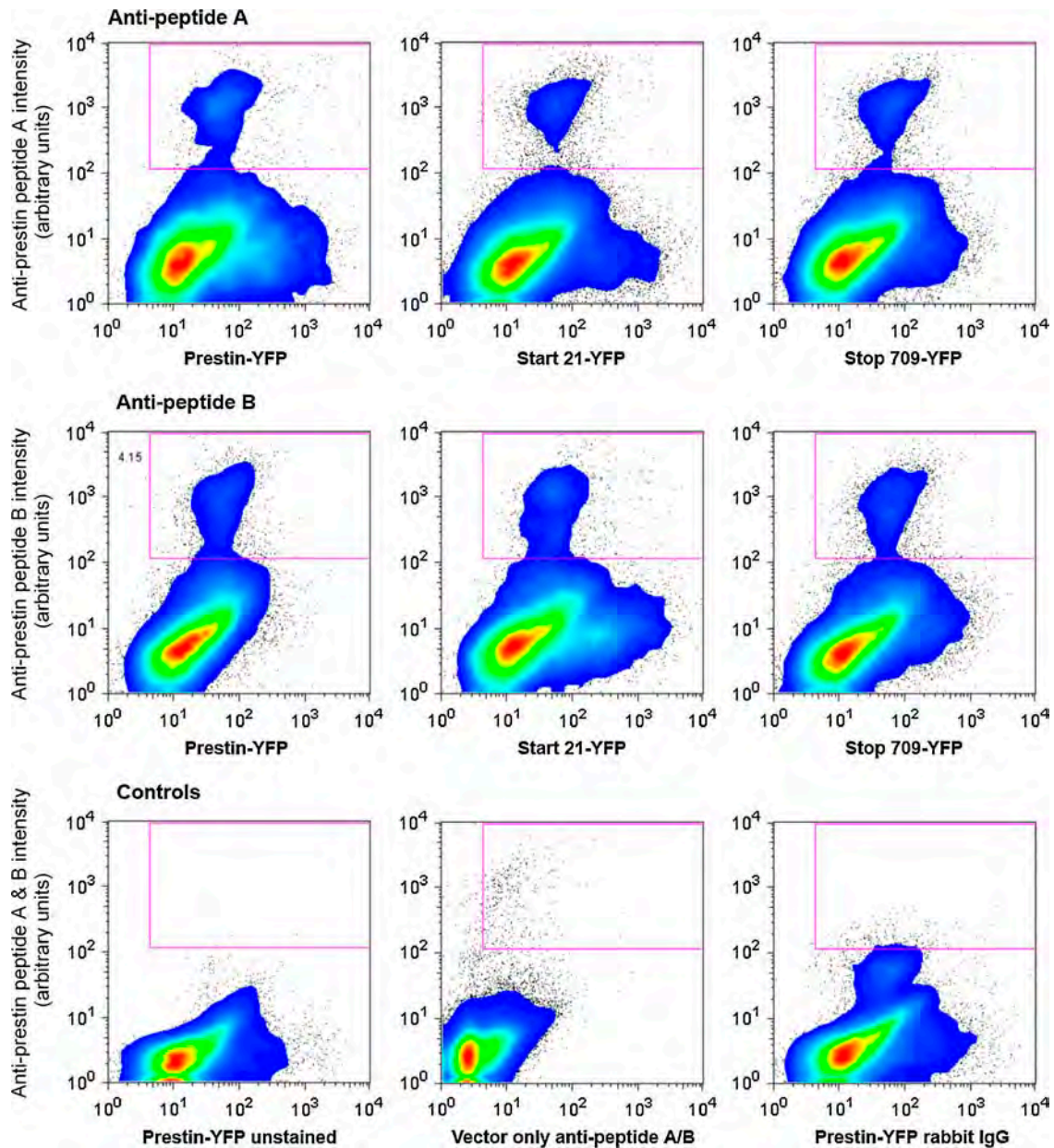


FIGURE 4 Quantification of prestin surface expression in transfected CHO cells by flow cytometry. CHO cells transfected with prestin-YFP fusion constructs (normal prestin, start 21, and stop 709) were dissociated and stained live with two affinity-purified rabbit polyclonal antibodies to two peptides expressed on the extracellular surface of the protein (*upper panels*: antibody to peptide A = GGKEFNRFKEKLPAPI (aa 274–290); *middle panels*: antibody to peptide B = KELANKHGYQVDGNQEL (aa 359–375)). The primary antibody was detected using a biotinylated anti-rabbit antibody (Molecular Probes) and streptavidin conjugated to Alexa 647. All antibody staining was done in phosphate-buffered saline and 0.5% bovine serum albumin at 4°C. The cells were then fixed in 4% paraformaldehyde before flow cytometric analysis. Shown are contour plots with outliers of YFP intensity (Phycocerythrin window) on the *x* axis and prestin intensity (Alexa 647) on the *y* axis of live stained cells (identified by forward and side scatter). As is evident, a subpopulation of YFP positive cells, recognized by both antibodies, is present in those cells transfected with the three prestin-YFP fusion constructs (normal prestin, start 21, and stop 709) and not in those cells transfected with empty vector alone stained with anti-prestin antibodies to peptides A and B, unstained prestin-YFP transfected cells, or prestin-YFP transfected cells stained with rabbit IgG (*lower panels*). Both the intensity of staining and the percentage of cells within the boxed area recognized by the antibodies are similar in cells transfected with full-length prestin (4.4% and 4.3% for anti-peptides A and B, respectively), start 21 (2.6% and 3.9%), and stop 709 (3.2% and 3.3%). The three control groups contained an insignificant number of cells labeled with the antibodies. Differences in number of cells indicate variability in expression efficiency among experiments hovering around 3–6%. These efficiencies are obtained by other workers in the field (Dominik Oliver, personal communication). These quantitative analyses are evidence that the absence in NLC in these two truncations is not due to aberrant surface expression.

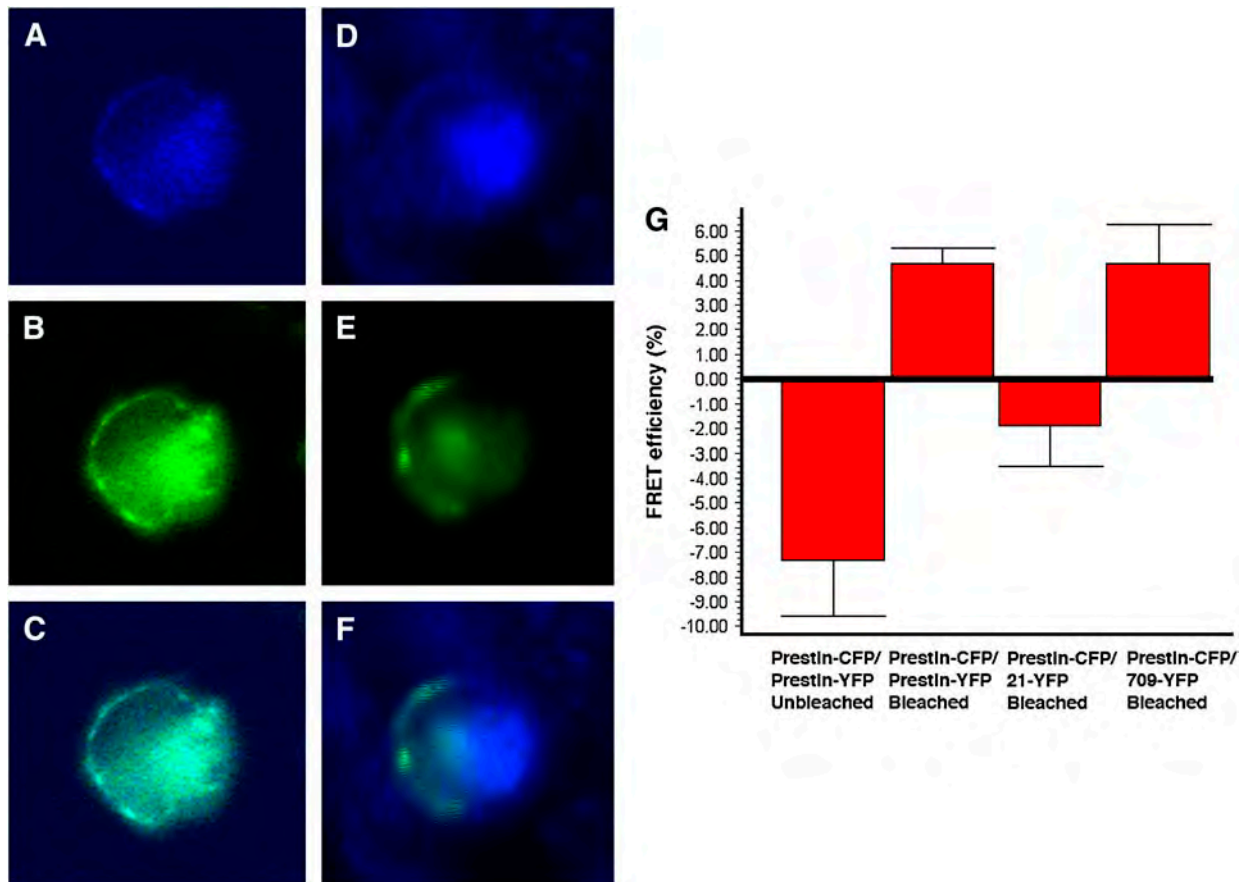


FIGURE 5 FRET demonstrated by acceptor (YFP) photobleaching confirms prestin-prestin interactions and suggests that the N-terminus is important in these interactions. The figure shows a CHO cell transfected with prestin-CFP (A and D) and prestin-YFP (B and E) before (A–C) and after (D–F) photobleaching YFP (514 line of the Argon laser) in the right half of the cell. (C and F) Merged images of A and B, and D and E, respectively. As is evident, there is an increase in CFP emission (D and F) concomitant with a decrease in YFP emission (E and F) in the right half of the cell. (G) The graph shows a quantitative estimate of FRET efficiencies after photobleaching (7). The efficiency of FRET is compared between CHO cells transfected with prestin-CFP together with prestin-YFP without (first bar) and with (second bar) acceptor photobleaching, prestin-CFP together with start 21 prestin-YFP (third bar), and prestin-CFP together with stop 709 prestin-YFP (fourth bar). A normal decrease in FRET efficiency in the absence of YFP photobleaching (-7.39 ± 2.189 (mean \pm SE), $n = 3$ cells) is converted to an increase in FRET efficiency with photobleaching in prestin-CFP and prestin-YFP (4.64 ± 0.63 , $n = 5$), and prestin-CFP and stop 709 prestin-YFP (4.67 ± 1.54 , $n = 4$), confirming interactions between normal prestin molecules, and C-terminally truncated prestin molecules and normal prestin. The absence of an increase in FRET efficiency with start 21 prestin-YFP and prestin-CFP (-1.94 ± 1.57 , $n = 4$ cells) confirms an absence of interaction between the N-terminally truncated prestin molecules and normal prestin. A one-way ANOVA between these groups demonstrated a significant difference between unbleached normal prestin and bleached normal prestin ($p < 0.002$) or stop 709 prestin ($p < 0.002$), but no difference between unbleached normal prestin and start 21 prestin. Similarly, there was a significant difference between FRET efficiencies in normal prestin and start 21 prestin ($p < 0.05$) transfected cells. Also noteworthy was that FRET efficiency at the membrane (6.5 ± 1.5 , $n = 3$) was not significantly different from elsewhere in the cell.

nonlinear amplificatory mechanism (20). How this protein works is key to understanding the remarkable ability of OHCs to respond mechanically to electrical stimuli, discovered some 20 years ago (21). Our observations on the functional consequences of short terminal truncations indicate that this protein does not work alone, but requires interacting partners to drive OHC motor activity. Though some molecular manipulations can interfere with proper membrane targeting (for example, full C-terminal truncations of prestin were not delivered to the plasma membrane), we combined techniques with low and high statistical power, namely confocal microscopy and FACS, respectively, to unambiguously confirm uncompromised membrane residence.

In previous work we demonstrated that intracellular chloride altered the operating voltage range of prestin, shifting V_h to more negative voltages (10). This observation was incongruent with a simple extrinsic voltage sensor scheme for anions previously proposed (9). Additionally, we showed that the valence of substituted anion did not, as expected, alter the valence of charge movement (11), further supporting our conclusion that anions serve as allosteric modulators rather than voltage sensors. However, although allosteric effects can be mediated by ion interactions with proteins, e.g., chloride with Cl channels (22) or Ca with K channels (23), conformational alterations can additionally arise from protein-protein/peptide/domain interactions (24).

Thus, our present data, which show a requirement for homomeric interactions among prestin's N-termini for normal charge movement, indicate that motor behavior is also allosterically controlled by these interactions. Indeed, we have previously interpreted the motors' sensitivity to prior voltage conditions as resulting from prestin-prestin interactions within the bilayer (6,14). Thus, we argued that prestin interactions may underlie the shift in the steady-state energy profile that results from prepulse perturbations, possibly through viscoelastic relaxations of prestin-induced membrane tension. Clearly, our new data open the possibility that these voltage-dependent viscoelastic effects could arise from interactions between homomeric components of prestin motor complexes, as well as among the complexes.

The topology of SLC26 transporter family members is not well delineated, with divergent models predicted possessing 10–14 TM domains (25). For prestin, a 12-TM domain model had been proposed, but our data do not support this model. Instead, we propose a 10-TM model, with the antibody-identified loops 5 (aa274–290) and 7 (aa359–375) residing extracellularly, as opposed to intracellularly as in previous models. Interestingly, Adler et al. (26), using antibody labeling, also placed region 274–290 on an extracellular loop. Additionally, the original 12-TM model of Zheng et al. (16,17) has recently been modified by that group with a reentrant loop to move a putative cGMP phosphorylation site at residue 238 onto the intracellular aspect of the protein (18)—a location already predicted by our model. Taken together, evidence for our 10-TM model is strong and dramatically changes our view of the landscape over which intracellular constituents can interact with prestin.

We thank Peter Dallos and colleagues for the gerbil prestin clone, and Margaret Mazzucco for technical help.

Financial support was provided by the National Institutes of Health's National Institute on Deafness and Other Communication Disorders grants DC 000273 (J.S.S.) and K08 DC05352 (D.N.).

REFERENCES

- Zheng, J., W. Shen, D. Z. He, K. B. Long, L. D. Madison, and P. Dallos. 2000. Prestin is the motor protein of cochlear outer hair cells. *Nature*. 405:149–155.
- Liberman, M. C., J. Gao, D. Z. He, X. Wu, S. Jia, and J. Zuo. 2002. Prestin is required for electromotility of the outer hair cell and for the cochlear amplifier. *Nature*. 419:300–304.
- Ludwig, J., D. Oliver, G. Frank, N. Klocker, A. W. Gummer, and B. Fakler. 2001. Reciprocal electromechanical properties of rat prestin: the motor molecule from rat outer hair cells. *Proc. Natl. Acad. Sci. USA*. 98:4178–4183.
- Meltzer, J., and J. Santos-Sacchi. 2001. Temperature dependence of nonlinear capacitance in human embryonic kidney cells transfected with prestin, the outer hair cell motor protein. *Neurosci. Lett.* 313:141–144.
- Santos-Sacchi, J., and E. Navarrete. 2002. Voltage-dependent changes in specific membrane capacitance caused by prestin, the outer hair cell lateral membrane motor. *Pflugers Arch.* 444:99–106.
- Santos-Sacchi, J., W. Shen, J. Zheng, and P. Dallos. 2001. Effects of membrane potential and tension on prestin, the outer hair cell lateral membrane motor protein. *J. Physiol.* 531:661–666.
- Dong, X. X., and K. H. Iwasa. 2004. Tension sensitivity of prestin: comparison with the membrane motor in outer hair cells. *Biophys. J.* 86:1201–1208.
- Reference deleted in proof.
- Oliver, D., D. Z. He, N. Klocker, J. Ludwig, U. Schulte, S. Waldegger, J. P. Ruppersberg, P. Dallos, and B. Fakler. 2001. Intracellular anions as the voltage sensor of prestin, the outer hair cell motor protein. *Science*. 292:2340–2343.
- Rybalchenko, V., and J. Santos-Sacchi. 2003. Cl⁻ flux through a non-selective, stretch-sensitive conductance influences the outer hair cell motor of the guinea-pig. *J. Physiol.* 547:873–891.
- Rybalchenko, V., and J. Santos-Sacchi. (2003). Allosteric modulation of the outer hair cell motor protein prestin by chloride. In *Biophysics of the Cochlea: From Molecules to Models*. A. Gummer, editor. World Scientific Publishing, Singapore. 116–126.
- Karpova, T. S., C. T. Baumann, L. He, X. Wu, A. Grammer, P. Lipsky, G. L. Hager, and J. G. McNally. 2003. Fluorescence resonance energy transfer from cyan to yellow fluorescent protein detected by acceptor photobleaching using confocal microscopy and a single laser. *J. Microsc.* 209:56–70.
- Santos-Sacchi, J. 1991. Reversible inhibition of voltage-dependent outer hair cell motility and capacitance. *J. Neurosci.* 11:3096–3110.
- Santos-Sacchi, J., S. Kakehata, and S. Takahashi. 1998. Effects of membrane potential on the voltage dependence of motility-related charge in outer hair cells of the guinea-pig. *J. Physiol. (Lond.)*. 510: 225–235.
- Santos-Sacchi, J. 2004. Determination of cell capacitance using the exact empirical solution of partial differential Y/partial differential Cm and its phase angle. *Biophys. J.* 87:714–727.
- Zheng, J., K. B. Long, W. Shen, L. D. Madison, and P. Dallos. 2001. Prestin topology: localization of protein epitopes in relation to the plasma membrane. *Neuroreport*. 12:1929–1935.
- Matsuda, K., J. Zheng, G. G. Du, N. Klocker, L. D. Madison, and P. Dallos. 2004. N-linked glycosylation sites of the motor protein prestin: effects on membrane targeting and electrophysiological function. *J. Neurochem.* 89:928–938.
- Deak, L., J. Zheng, A. Orem, G. G. Du, S. Aguinaga, K. Matsuda, and P. Dallos. 2005. Effects of cyclic nucleotides on the function of prestin. *J. Physiol.* 563:483–496.
- Zheng, J., L. D. Madison, D. Oliver, B. Fakler, and P. Dallos. 2002. Prestin, the motor protein of outer hair cells. *Audiol. Neurootol.* 7:9–12.
- Santos-Sacchi, J. 2003. New tunes from Corti's organ: the outer hair cell boogie rules. *Curr. Opin. Neurobiol.* 13:459–468.
- Brownell, W. E., C. R. Bader, D. Bertrand, and Y. de Ribaupierre. 1985. Evoked mechanical responses of isolated cochlear outer hair cells. *Science*. 227:194–196.
- Dutzler, R., E. B. Campbell, M. Cadene, B. T. Chait, and R. MacKinnon. 2002. X-ray structure of a CIC chloride channel at 3.0 Å reveals the molecular basis of anion selectivity. *Nature*. 415: 287–294.
- Johnson, J. P., Jr., J. R. Balsler, and P. B. Bennett. 2001. A novel extracellular calcium sensing mechanism in voltage-gated potassium ion channels. *J. Neurosci.* 21:4143–4153.
- Lim, W. A. 2002. The modular logic of signaling proteins: building allosteric switches from simple binding domains. *Curr. Opin. Struct. Biol.* 12:61–68.
- Mount, D. B., and M. F. Romero. 2004. The SLC26 gene family of multifunctional anion exchangers. *Pflugers Arch.* 447:710–721.
- Adler, H. J., I. A. Belyantseva, R. C. Merritt, G. I. Frolenkov, G. W. Dougherty, and B. Kachar. 2003. Expression of prestin, a membrane motor protein, in the mammalian auditory and vestibular periphery. *Hear. Res.* 184:27–40.

On the Effect of Prestin on the Electrical Breakdown of Cell Membranes

Enrique G. Navarrete* and Joseph Santos-Sacchi†

*Department of Cell and Molecular Biology, House Ear Institute, Los Angeles, California; and †Department of Surgery (Otolaryngology) and Neurobiology, Yale University School of Medicine, New Haven, Connecticut

ABSTRACT The voltage-dependent activity of prestin, the outer hair cell (OHC) motor protein essential for its electromotility, enhances the mammalian inner ear's auditory sensitivity. We investigated the effect of prestin's activity on the plasma membrane's (PM) susceptibility to electroporation (EP) via cell-attached patch-clamping. Guinea pig OHCs, TSA201 cells, and prestin-transfected TSA cells were subjected to incremental 50 μ s and/or 50 ms voltage pulse trains, or ramps, at rates from 10 V/s to 1 kV/s, to a maximum transmembrane potential of ± 1000 mV. EP was determined by an increase in capacitance to whole-cell levels. OHCs were probed at the prestin-rich lateral PM or prestin-devoid basal portion; TSA cells were patched at random points. OHCs were consistently electroporated with 50 ms pulses, with significant resistance to depolarizing pulses. Although EP rarely occurred with 50 μ s pulses, prior stimulation with this protocol had a significant effect on the sensitivity to EP with 50 ms pulses, regardless of polarity or PM domain. Consistent with these results, resistance to EP with depolarizing 10-V/s ramps was also found. Our findings with TSA cells were comparable, showing resistance to EP with both depolarizing 50-ms pulses and 10 V/s ramps. We conclude prestin significantly affects susceptibility to EP, possibly via known biophysical influences on specific membrane capacitance and/or membrane stiffness.

INTRODUCTION

In the mammalian cochlea, outer hair cells (OHC) enhance hearing sensitivity and frequency selectivity (1). This enhancement, known as the "cochlear amplifier" (2), results from OHC mechanical activity, as this unique neuroepithelial cell can undergo electrically induced rapid length changes (3–6) at acoustic rates (7–9). Prestin, the OHC motor protein (10), is fundamental for OHC electromotility (11). Mechanical, electrical, and morphological data indicate that these motors are distributed preferentially within the cell's lateral plasma membrane (PM) (12–17).

A variety of models for electromotility have been proposed, based on electro-osmosis (4), electrophoresis (18), membrane bending (19), stiffness changes (20), and via surface area modulation, designated the "area-motor" model (21–26). The latter three remain serious candidates. We have proposed, based on modeling the voltage dependent capacitance of the OHC, that prestin's conformational change alters tension within the lateral membrane (27).

It is well known that cell membranes break down when subjected to mechanical or electrical stress, and that these stimuli can interact (28,29). The vulnerability to electroporation (EP) can provide insight into the interaction between PM and cortical cytoskeleton (29–31); for instance, negative pressure has been found to be more effective in producing membrane breakdown, presumably due to the greater interaction with the cytoskeleton with positive pressure (29). In addition, the integrity of the cytoskeleton

is critical for resealing (32). The composition of the membrane is also highly influential; an increase in cholesterol, protein content, or certain surfactants can alter the susceptibility of the lipid bilayer to applied electrical tension (28,33). A variety of models have been proposed to explain the molecular mechanism of EP. It is generally accepted that a progression of membrane defects occurs as the energy threshold for their production is surpassed and maintained, resulting in increased permeability.

We have studied EP via cell-attached patch-clamping in OHCs to determine whether the electromechanical activity of prestin alters the biophysical properties of the PM. We also tested prestin-transfected TSA201 cells to divorce prestin's activity from modulation by the OHC's specialized cytoskeletal lattice. We find significant differences in susceptibility to EP between the lateral and basal membranes of OHCs, as well as between prestin-transfected and untransfected TSA cells, which we attribute to the residence of prestin.

MATERIALS AND METHODS

Cell preparation

Guinea pigs were overdosed with halothane, according to Yale University's Animal Use and Care Committee guidelines. Their temporal bones were dissected, isolating the top two turns of the organ of Corti. OHCs were dissociated with dispase in calcium-free medium for 10–15 min, followed by gentle pipetting. The cell-enriched solution was transferred to a 700- μ L perfusion chamber and allowed to settle on the coverglass bottom for 10–15 min.

TSA201 cells, clones of human embryonic kidney (HEK) 293 cells that express the simian virus 40 large T-antigen in a stable manner, were cultured in Dulbecco's modified Eagle's medium (Sigma Chemical, St. Louis, MO) with 5% fetal bovine serum, 100 U/ml of penicillin and 100 μ g/ml of

Submitted April 8, 2005, and accepted for publication October 25, 2005.

Address reprint requests to J. Santos-Sacchi, Dept. of Surgery (Otolaryngology) and Neurobiology, Yale University School of Medicine BML246, 333 Cedar St., New Haven, CT 06510. E-mail: joseph.santos-sacchi@yale.edu.

© 2006 by the Biophysical Society

0006-3495/06/02/967/08 \$2.00

doi: 10.1529/biophysj.105.064105

streptomycin. Cells were plated for 24 h before transfection using effectene (Qiagen). The transfection reaction mixture consisted of 1 $\mu\text{g}/\text{ml}$ of Pres cDNA plasmid added to 0.1 $\mu\text{g}/\text{ml}$ of green fluorescent protein (GFP) plasmid, as a transfection marker in the 3 ml of Dulbecco's modified Eagle's medium the TSA cells were cultured in. Experiments were carried out 24–48 h posttransfection in the same culture dish without any dissociating procedures to avoid trauma to the cells.

Experimental setup

The guinea pig OHC and TSA cell PMs were probed via cell-attached patch-clamp recording. All experiments were performed at room temperature ($\sim 23^\circ\text{C}$). A Nikon Diaphot (Melville, NY) inverted microscope with Hoffman optics (Aurora, IL) and a Sony VCR Model EV-C200 (Tokyo, Japan), were used to observe and tape record the experiments with OHCs. A Leica DM-IRB inverted microscope (McHenry, IL) with differential interference contrast optics was used for experiments with TSA cells.

OHC patches were clamped with an Axon Instruments Axopatch 200B amplifier (Foster City, CA) at a holding potential of -20 mV, the resting potential of dissociated OHCs (6), to zero the transmembrane voltage drop. Gigohm seals were obtained at the OHC lateral PM, where there is a high concentration of prestin, and at the basal area, which is devoid of these motors. TSA cells were also patch-clamped on random points of their PM that appeared smooth with an Axon Instruments Axopatch 200 amplifier holding them at their estimated average resting potential of -10 mV (E. G. Navarrete, unpublished observations). An ionic blocking solution was used in the bath and pipette, consisting of (in mM) 20 TEA, 20 CsCl, 2 CoCl_2 , 1.47 MgCl_2 , 10 Hepes, 99 NaCl, and 2 CaCl_2 . CsOH and glucose were used to adjust pH to 7.2 and osmolarity to 300 mOsm. Ion channel blockers were used to avoid increases in membrane conductance due to channel activity and to measure prestin's voltage-dependent capacitance. Pipettes had an average aperture of 1.43 ± 0.03 μm (mean \pm SE; $n = 78$ measurements) and initial resistances ranged from 1.5 to 3 $\text{M}\Omega$.

Pulse and ramp protocols

In all cells, EP was investigated using square voltage pulses and ramps. We used stimulus protocols based on Akinlaja and Sachs (31) in the case of the pulse trains, and O'Neill and Tung (36) in the case of the ramp stimuli. Initially, in OHCs two different pulse protocols were used, varying the duration of the voltage stimulus. The first protocol consisted of a series of 50- μs voltage pulses with sequential increments of 50 mV and an interpulse delay of 5 s to a transmembrane potential (TMP) of at least ± 1000 mV (-1020 mV, $+1030$ mV). The second protocol consisted of 50 ms voltage pulses with sequential increments of 20 mV and an interpulse delay of 7 s, to a TMP of ± 1000 mV. The 50-ms protocol was administered after the 50- μs pulse train in all cells that did not undergo EP and additionally to a set of cells in isolation to check for prior stimulation effects. Because OHCs were rarely permeabilized with 50- μs protocols, and to avoid loss of seal resistance or sensitization, TSA cells were only subjected to a 50-ms pulse train starting at 400 mV. During the interpulse interval, membrane capacitance (C_m) was measured every 120 ms, with transient analysis (14). EP was determined by a step increase in capacitance to whole-cell levels (Fig. 1). Occasionally, transient EP occurred (Fig. 2), which we defined as an increase in C_m to whole-cell levels for a minimum of two data points.

Ramps at speeds from 10 V/s to 1 kV/s were additionally used to study both cell types, also to a maximum voltage of ± 1000 mV. Membrane breakdown (MB) was defined, as it was previously (32), as a step increase in the conductance of the membrane patch indicated by a sudden and sharp rise in current (I). As with the pulse protocol, C_m was measured with transient analysis after administering the stimulus, occasionally revealing an intact, resealed patch. Thus, we defined the permanent increase in C_m to whole-cell levels as patch breakdown (PB).

Although membrane conductance will increase with EP, only the increase in charging time/capacitance irrefutably demonstrates EP; however, it is

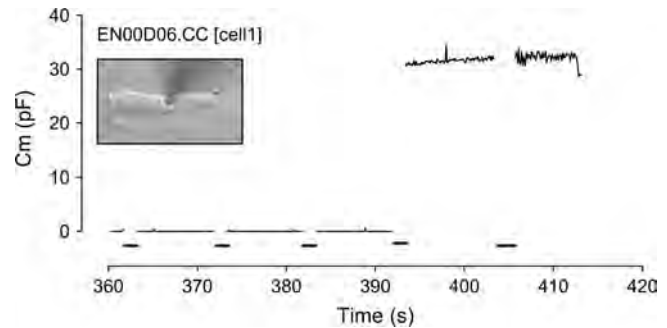


FIGURE 1 Increase in membrane capacitance (C_m) to whole-cell levels after a voltage pulse indicates electroporation (EP). Voltage pulses are indicated by the thick lines on the x axis.

possible that the plasma membrane was electroporated and quickly resealed. This would be unusual since cell membranes have relatively long sealing times, on the order of minutes; for example, in their study, O'Neill and Tung (34) found that conductance changes persisted when their cardiac myocytes were restimulated within a minute. Since the increase in capacitance may have been missed due to our sampling resolution, we proceeded to analyze the membrane instability (MI) and MB data.

Data analysis

Statistical analyses were performed with Excel (Microsoft) and Analyse-it (Analyse-it Software, Leeds, UK). To avoid obtaining a potentially misleading asymmetric polarity-dependent TMP at the onset of EP, the resting potential was subtracted/added to the applied voltage (35,36). For OHCs, absolute TMP at onset of EP was calculated taking into account the average resting potential of -20 mV (see above). With TSA we accounted for an average resting potential of -10 mV. Results were evaluated using parametric (t -tests, analysis of variance (ANOVA), and linear regression) and nonparametric (chi-square) statistical analyses when appropriate. After the electrical stimulation and establishment of whole-cell configuration, TSA cell capacitance was measured as fully described elsewhere (27,37) to confirm prestin's presence and functionality, and to measure the motor protein density. The density of prestin was assessed via charge density, a normalization metric measuring maximum charge moved per linear capacitance ($Q_{\text{max}}/C_{\text{lin}}$), since the linear capacitance will be proportional to cell surface area. To avoid sensitization, charge density in the cell-attached patch configuration was not measured before the EP protocols. It is assumed that the concentration of prestin would be very similar to the

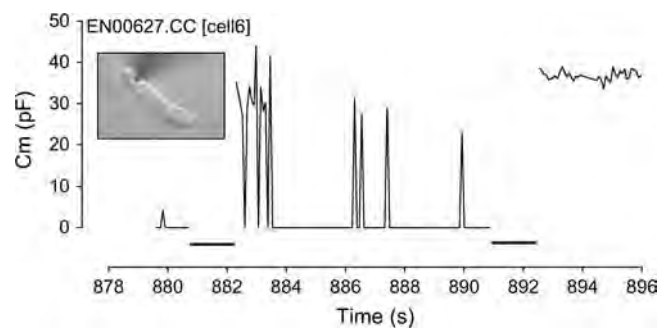


FIGURE 2 Episodes of transient membrane breakdown followed by fast resealing are indicated by the spikes in C_m on this data trace reaching whole-cell levels. Voltage pulses are indicated by the thick lines on the x axis. Electroporation is noted at the end of the trace by the sustained increase in C_m after a voltage pulse.

whole-cell value. We also assumed consistent patch geometry in TSA cells and OHCs based on images in the literature (13,31), although we did not control for this variable for each individual cell. A Windows-based software package, jClamp (SciSoft, Branford, CT), was used for acquisition and analysis. Igorpro (Wavemetrics; Lake Oswego, OR) was used to fit the capacitance data. All data are presented as mean ± SE.

RESULTS

Pulse protocols in outer hair cells

Susceptibility to EP with 50 μs pulse trains in our population of OHCs is very similar to that reported previously with HEK cells (29) and lipid bilayers (28). EP was rarely produced at voltages <1 V in the absence of extrinsic pressure (6.8%, *n* = 59). Nevertheless, the integrity of the membrane was undoubtedly compromised in the OHC by this prior stimulation. Sufficient current was injected through the patch to produce a change in the TMP and evoke the OHC's unique electromotile responses, as fast reversible movements in phase with the stimulus polarity were evident starting at an absolute average TMP of 765 mV. Furthermore, a consistent decrease in seal resistance was frequently revealed, which analyzed in isolation could have been mistaken for a loss of the seal were it not for our ability to monitor the electromotile responses and interpulse capacitance. Significant differences in the absolute average voltages at which mechanical responses occurred during 50 ms pulse trains were found depending on prior stimulation with the 50 μs protocol (71 ± 9 mV with prior stimulation versus 214 ± 12 mV with no prior stimulation, *p* < 0.001, *n* = 81, *t*-test). In addition, multiway analysis of variance demonstrated that prior stimulation with 50 μs pulses was a significant factor influencing the onset of EP in the OHC PM (*p* < 0.001, *n* = 85) during the subsequent 50 ms protocol.

EP occurred consistently between 240 and 580 mV, similar to the values reported previously for HEK cells (29). There was little difference in the average absolute TMP at onset of EP at the OHC basal area (see Table 1). At the lateral PM our results demonstrated a significant difference when polarity was varied (*p* < .05, *t*-test). Transient reversible EP with fast resealing (Fig. 2) on a timescale as short as 240 ms was observed in almost 20% (seven cells) of OHC patches subjected to depolarization (*n* = 40) at a TMP ranging be-

TABLE 1 Pulse protocols in OHCs: comparison of absolute TMP at onset of EP

Location	Stimulus polarity	Absolute TMP at onset of EP
Basal	Hyperpolarizing	388 ± 21 (<i>n</i> = 10)
	Depolarizing	382 ± 14 (<i>n</i> = 10)
Lateral	Hyperpolarizing	388 ± 13 (<i>n</i> = 10)
	Depolarizing	446 ± 20 (<i>n</i> = 10)

OHCs demonstrated a statistically significant difference in susceptibility to EP due to the effect of polarity at the lateral PM (*p* < .05, *t*-test). The incidence of EP was 100% in all categories. The charge density of the guinea pig OHCs lateral wall is estimated to be ~150–200 fC/pF.

tween 360 and 460 mV, regardless of location. Interestingly, this phenomenon was not observed with hyperpolarizing pulses, although its occurrence could have been possible at a timescale beyond the detection of our sampling frequency. Because of our 2-data-point minimum as criteria for determining transient reversible EP, it may also have been dismissed as noise.

Pulse protocols in prestin-transfected and nontransfected TSA cells

TSA cells transfected with gPres demonstrate significant resistance (*p* < .02, chi-square analysis) to EP with our depolarizing 50 ms pulse protocol, failing to be permeabilized in >50% of our sample (see Table 2). Untransfected TSA cells underwent EP in 90% of the cells tested at absolute TMPs between 400 and 580 mV, consistent with our OHC data. Regarding the average absolute TMP at onset of EP, no statistically significant trends were evident, although it is interesting that the average threshold TMPs required for EP were slightly higher in transfected cells, in addition to showing greater variance. Virtually every cell resealed within seconds of EP, regardless of transfection or stimulus polarity.

Ramp protocols in outer hair cells

Almost 100% of the OHCs displayed a period of MI before a rapid step increase in conductance attributed to MB (Fig. 3), as described in the literature (33), regardless of portion probed, polarity, or ramp speed. After the ramp stimulus, and despite evidence for MB during the ramp, *C_m* increase to whole-cell levels is not consistently observed at 1 kV/s (see Table 3). This resistance to EP was clearly a rate-dependent phenomenon as it occurred in almost 100% of the sample at 10 V/s (see Table 4). Significantly, the lateral PM was more resistant to PB with depolarizing 10 V/s ramps (*p* < .02, chi-square analysis). Although we find interesting polarity-dependent trends in both MI and MB, it is impossible to distinguish whether conductance increases were due to seal loss or EP without monitoring capacitance. Although it is plausible that the plasma membrane was electroporated and

TABLE 2 Pulse protocols in gPres transfected and nontransfected TSA cells: incidence of EP, absolute TMP at onset of EP

DNA	Stimulus polarity	EP incidence	Absolute TMP at onset of EP (mV)	Charge density
None	Hyperpolarizing	90% (<i>n</i> = 10)	464 ± 20	N/A
	Depolarizing	90% (<i>n</i> = 10)	495 ± 13	N/A
gPres	Hyperpolarizing	100% (<i>n</i> = 9)	549 ± 50	13.1 ± 3.1 fC/pF
	Depolarizing	44% (<i>n</i> = 9)	600 ± 122	14.5 ± 10.6 fC/pF

Transfected TSA cells demonstrate significantly reduced EP incidence with depolarizing 50 ms pulse trains (*p* < .02, chi-square analysis). No statistically significant differences are evident comparing absolute TMP at onset of EP.

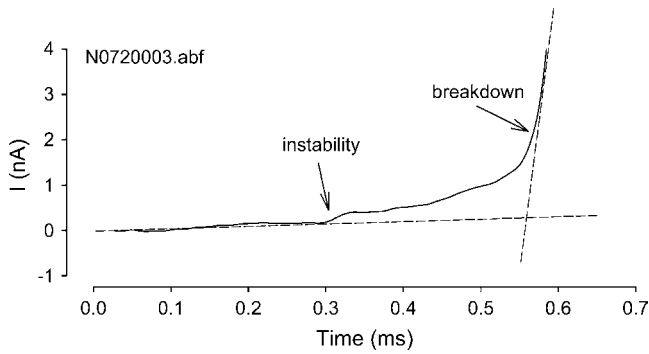


FIGURE 3 Response to a depolarizing voltage ramp at 1 kV/s in an OHC. Membrane instability is noted by the deviation from the preceding linear trace. Membrane breakdown is indicated by the rapid step increase in conductance.

quickly resealed, only the increase in capacitance indisputably demonstrates EP.

Since the increase in capacitance may have been missed due to our sampling resolution, we present our findings and analysis of the MI and MB data. Location did not have a significant effect on either MI or MB TMPs with the 1-kV/s ramps (see Table 3). The effect of polarity on the onset of MI is obvious at both ramp speeds, but more significant with 1 kV/s ramps ($p < .0001$, two-way ANOVA); there is more resistance to MI with depolarizing ramps. Interestingly, we find the opposite effect with 10 V/s ramps, an increased resistance to MI with hyperpolarizing ramps ($p < .05$, two-way ANOVA). We performed additional experiments using 100 mV/s ramps and found no polarity dependence in MI or MB at either region of the OHC (data not shown). Although there are no polarity-dependent differences with respect to MB at the lateral wall with 1 kV/s ramps, we find resistance to depolarizing ramps at the base. Regarding MB with 10 V/s ramps, we find significant effects due to polarity and resistance to depolarizing ramps ($p < .01$, two-way ANOVA), regardless of location.

Ramp protocols in prestin-transfected and nontransfected TSA cells

Both transfected and untransfected cells undergo MI somewhat consistently (100% at 1 kV/s, 77–93% at 10 V/s).

TABLE 3 Ramp protocols at 1 kV/s in OHCs: absolute TMP at onset of MI and MB and incidence of PB

Location	Polarity	MI (mV)	MB (mV)	PB
Basal	Hyperpolarizing	299 ± 4 ($n = 19$)	559 ± 9	16%
	Depolarizing	538 ± 12 ($n = 19$)	606 ± 11	37%
Lateral	Hyperpolarizing	290 ± 10 ($n = 18$)	590 ± 10	28%
	Depolarizing	527 ± 19 ($n = 13$)	582 ± 16	15%

PB did not occur consistently with this stimulus type. MI occurs at pronouncedly higher TMPs with depolarizing 1 kV/s ramps, demonstrating the significant effect of polarity ($p < .0001$, two-way ANOVA). MI and MB values are given as mean ± SE.

TABLE 4 Ramp protocols at 10 V/s in OHCs: absolute TMP at onset of MI and MB and incidence of PB

Location	Polarity	MI (mV)	MB (mV)	PB
Basal	Hyperpolarizing	314 ± 14 ($n = 12$)	445 ± 30	92%
	Depolarizing	273 ± 16 ($n = 13$)	374 ± 16	100%
Lateral	Hyperpolarizing	317 ± 12 ($n = 11$)	454 ± 31	91%
	Depolarizing	284 ± 10 ($n = 14$)	383 ± 15	57%

The incidence of PB is >90% at the basal area with 10 V/s ramps. Significantly, the lateral PM was more resistant to PB with depolarizing ramps ($p < .02$, chi-square analysis), although MI and MB are polarity-dependent regardless of region ($p < .05$ and $p < .01$, respectively, two-way ANOVA). In contrast to 1 kV/s responses, with 10 V/s ramps there is more resistance to MI with hyperpolarizing stimuli.

TMPs at onset of MI and MB were independent of transfection and polarity, although variance at 10 V/s in TSA cells was very large (see Tables 5 and 6).

After the ramp stimulus, PB was never observed after the 1 kV/s ramps. Interestingly, the incidence of PB at 10 V/s in the transfected TSA cell was virtually identical to that of the OHC lateral membrane, showing increased resistance to PB with depolarizing ramps ($p < .05$, chi-square analysis; see Table 6).

DISCUSSION

We have found that the OHC lateral membrane, as well as the prestin-transfected TSA cell membrane, exhibit polarity-dependent sensitivity to EP. Prestin's influence is to significantly increase resistance to EP and PB with depolarizing 50 ms pulse trains and with depolarizing 10 V/s ramps. These features appear to result from prestin's residence and/or activity within the PM. There are, however, clear differences in responses between OHCs and TSA cells that likely do not depend on prestin expression. First, in the TSA cell there was, in general, a greater resistance to EP, most notably with 50 ms pulse trains and 1 kV/s ramps. Also, unlike the OHC, MI in TSA cells was not affected by polarity when 1 kV/s ramps were used (see Tables 3 and 5) and we find higher TMPs at onset of MB with 10 V/s ramps (see Tables 4 and 6). Finally, in TSA cells, transient EP with fast resealing occurs much more frequently with pulse stimuli. It is conceivable that some of the divergence we find between responses of OHCs and transfected TSA cells may relate to peculiarities of each cell type. Probably most significant is the structural complexity of the OHC. In OHCs, prestin is uniformly concentrated within the lateral PM, which is closely associated with a well developed submembranous cortical cytoskeleton and subsurface cisternae. Additionally, the OHC has a cytoplasmic turgor pressure of up to 1–2 kPa (38), which contributes to cell shape and the tensile forces the OHC PM experiences. The TSA cell lacks these features, and prestin may be heterogeneously distributed throughout the entire PM, possibly providing patch densities that vary significantly. This disparity in prestin density is highlighted

TABLE 5 Ramp protocols at 1 kV/s in gPres transfected and nontransfected TSA cells: absolute TMP at onset of MI and MB

DNA	Polarity	MI (mV)	MB (mV)	Charge density
None	Hyperpolarizing	551 ± 27 (n = 9)	595 ± 35	N/A
	Depolarizing	526 ± 27 (n = 10)	601 ± 26	N/A
gPres	Hyperpolarizing	541 ± 36 (n = 10)	602 ± 36	30.3 ± 3.6 fC/pF
	Depolarizing	524 ± 20 (n = 10)	617 ± 23	20 ± 2 fC/pF

PB never occurred at this ramp speed.

by motor charge density estimates in OHCs (~150–200 fC/pF (14,25)) and our TSA cells (13–30 fC/pF). Despite these cell-specific contributing factors, our data clearly indicate that the presence of prestin within a membrane will alter the membrane's susceptibility to electrical breakdown.

Mechanistic considerations

Based on the mechanistic model of Needham and Hochmuth (28), derived from their investigation of lipid bilayers, membrane breakdown will occur when the average energy density, T , exceeds a critical value. T arises from mechanical and/or electrical loads applied to the membrane,

$$T = T_m + T_e, \quad (1)$$

where T_m is the mechanically induced tension and T_e is the electrically induced tension. The addition of mechanical tension to the PM will lower the voltage that is required for EP.

Though we did not subject the patches to extrinsic mechanical tension, mechanical forces must be taken into account due to the voltage-dependent conformational changes of prestin. As mentioned previously, we have evidence based on modeling of capacitance measures that depolarization, which drives the OHC into a compact state, produces tension in the lateral membrane (27). Consequently, depolarization might have been expected to be a more effective stimulus for EP in the lateral PM, but we found the opposite. It is possible that our data were influenced by the time dependence of interactions between electrical and mechanical tension, since we proposed that the tension generated by prestin dissipates in a multiexponential fashion (27). Time-dependent inter-

actions of electrical and mechanical tension have been observed previously. For example, though Akinlaja and Sachs (29) found that their results with HEK 293 cells probed with 50 μ s pulse trains were consistent with the simple Needham and Hochmuth model (see above), mechanical tension had no effect with longer 50 ms voltage pulses. There are probably other prestin-induced mechanical changes in the OHC PM that may influence EP. For example, lipid lateral diffusion in the OHC PM is a sigmoid function of voltage, depolarization reducing membrane fluidity by half (39). Voltage-dependent membrane folding could also explain the biophysical effects on the diffusion constant as well as on EP. In addition, a number of experiments suggest that the PM is a major contributor to the OHC's axial stiffness (40–43) and that this stiffness is also voltage-dependent secondary to the activity of prestin (44). These investigators have found that stiffness increases with hyperpolarized potentials and decreases with depolarization. Thus, prestin's effects on membrane fluidity and stiffness, as well as on electrically induced membrane bending, may significantly influence our results.

A role for prestin's voltage-dependent specific capacitance

We have previously noted polarity-dependent biophysical properties that prestin imparts to the PM in OHCs while studying capacitance changes at extreme voltages (25,45). In the OHC, we found that the linear capacitance is actually voltage-dependent and is greater in the hyperpolarized region. The capacitance increase, which averages 3.3 pF at voltages < -200 mV, is too great to be explained solely by the area motor model, and we concluded that the membrane dielectric and/or thickness is altered (see Fig. 4). The electrical tension is described by Needham and Hochmuth (28) as

$$T_e = \frac{1}{2} \epsilon \epsilon_0 (V/h_c)^2 h, \quad (2)$$

or, as simplified by Akinlaja and Sachs (31),

$$T_e = C_s V^2 / 2, \quad (3)$$

where ϵ_0 is the permittivity of free space, ϵ the dielectric constant of the membrane, V the transmembrane potential, h the membrane thickness, h_c the capacitive thickness of the membrane, and C_s the specific membrane capacitance.

TABLE 6 Ramp protocols at 10 V/s in gPres transfected and nontransfected TSA cells: absolute TMP at onset of MI and MB and incidence of PB

DNA	Polarity	MI (mV)	MB (mV)	PB	Charge density
None	Hyperpolarizing	321 ± 44 mV (n = 9)	514 ± 136 mV	100%	
	Depolarizing	331 ± 118 mV (n = 9)	579 ± 121 mV	88%	
gPres	Hyperpolarizing	338 ± 45 mV (n = 10)	592 ± 50 mV	90%	19.6 ± 4.2 fC/pF
	Depolarizing	364 ± 51 mV (n = 15)	564 ± 66 mV	53%	16.4 ± 3.2 fC/pF

Onset of MI and MB were independent of transfection and polarity. Increased resistance to PB with hyperpolarizing ramps ($p < .05$, chi-square analysis) in transfected TSA cells was consistent with the OHC lateral membrane results.

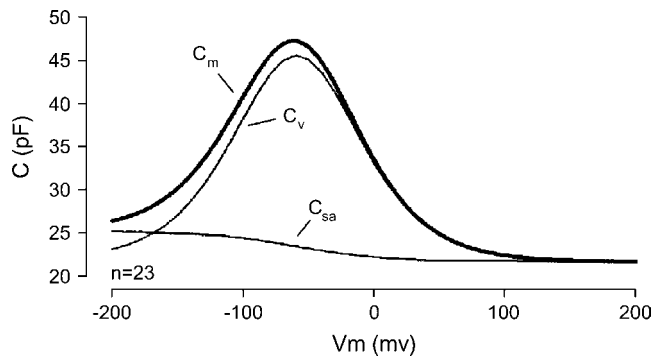


FIGURE 4 OHC capacitance derives from the sum of the parallel capacitance proportional to membrane surface area (C_{sa}) and the motor's voltage sensor-associated capacitance (C_v) to produce the total membrane capacitance (C_m).

It is clear that the effectiveness of a given voltage will depend directly on the specific capacitance of the membrane. If we assume that the specific capacitance of $0.5 \mu\text{F}/\text{cm}^2$ (48) characterizes the OHC PM at very positive voltage levels, then we estimate that the 3.3 pF increase at hyperpolarized extremes translates to an increased specific capacitance value of 0.61. Given this, we calculate for 50-ms pulse thresholds in the absence of prior stimulation:

$$T_{e\text{depol}} = 0.50 (0.446)^2 / 2 = 0.50 \text{ dynes/cm}$$

$$T_{e\text{hyperpol}} = 0.61 (0.388)^2 / 2 = 0.46 \text{ dynes/cm.}$$

To some extent, then, accounting for the voltage dependence of the OHC's specific membrane capacitance reconciles differences in breakdown voltage thresholds, since the membrane would require greater voltages in the depolarizing direction to reach breakdown threshold. Our values for pulse-induced breakdown are in line with those obtained by Akinlaja and Sachs (29), who found a T_e of 0.47 dynes/cm for hyperpolarizing pulses of 100 ms duration.

Time-dependent membrane breakdown and recovery

We find that the time integral of stimulation affects the membrane's susceptibility to EP; this is shown by the resistance to EP with 50 μs pulse trains compared to that with 50 ms pulse trains in the OHC. If the possibility of seal loss is eliminated, the short timescale of EP with 50 μs square voltage pulses would seem to have potential for gene transfer and drug delivery experiments in OHCs. Additionally, there is an increased susceptibility to PB with 10 V/s ramps, especially in TSA cells. After induced membrane instabilities, fast resealing was a common phenomenon in both cell types, although more frequent in TSA cells, probably due to prestin's reduced density, which likely results in faster lateral diffusion kinetics within the bilayer. Although fast resealing is commonly seen in pure lipid bilayers, such rapid resealing has never been documented in other biological

membranes (35,47,48) despite the vast amount of work done on HEK cell lines (34,49,50). Fast resealing may be impeded by the presence of proteins that limit the bilayer's lipid lateral diffusion (51). In the lateral OHC membrane, besides the high-density prestin known to be present, other protein species are present; these include AE2 (52), aquaporins (53,54), glut 5 (55,56), stretch-activated channels (57,58), and a nonselective stretch-sensitive conductance with significant chloride permeability (59). Although we can expect membrane composition to play an important role in fast resealing, we must also remain cognizant that within patches protein residence may be dramatically altered. In addition, the OHC's highly organized cytoskeleton, with its intimate relationship to the plasma membrane via the pillars, most likely plays a role in resealing, as it does in other cell types (31,32,47).

We should make one final point on resealing after apparent membrane breakdown during ramp stimuli in the prestin-containing membrane. The membrane breakdown (defined according to O'Neill and Tung (34)) during depolarizing ramp stimulation probably represents a lower energy state before PB, since subsequent C_m measures frequently do not show an increase to whole-cell levels. According to EP theory (60–63), progression from reversible unstable electropores to permanent stable electropores requires breaching a higher energy threshold. MB as defined by O'Neill and Tung (34) and the transient EP with fast resealing we encountered are likely a lower energy state with a predominance of unstable reversible electropores. Apparently the presence of prestin increases the energy requirement to achieve PB with depolarizing stimuli and fosters patch recovery after the electrical stimulus in the absence of a transmembrane potential. The fact that the thresholds for those patches that did undergo PB and those that did not were not significantly different in OHCs or TSA cells supports this conclusion. The differences between prestin's effects during ramp stimulation and during pulse stimulation, where breakdown thresholds were clearly altered during depolarization, again points to stimulus-type and rate influences on prestin's interaction with the lipid bilayer.

We thank Linda Bartoshuk and Adam Mendizabal for sharing their expertise in statistics in some of the analyses, Peter Dallos for his general support of this project, and the reviewers for their constructive and insightful comments.

This work was supported by the National Institutes of Health National Institute on Deafness and Other Communication Disorders grant DC000273.

REFERENCES

1. Dallos, P. 1992. The active cochlea. *J. Neurosci.* 12:4575–4585.
2. Davis, H. 1983. An active process in cochlear mechanics. *Hear. Res.* 9:79–90.
3. Brownell, W. E., C. R. Bader, D. Bertrand, and Y. de Ribaupierre. 1985. Evoked mechanical responses of isolated cochlear outer hair cells. *Science.* 227:194–196.

4. Kachar, B., W. E. Brownell, R. Altschuler, and J. Fex. 1986. Electrokinetic shape changes of cochlear outer hair cells. *Nature*. 322:365–368.
5. Ashmore, J. F. 1987. A fast motile response in guinea-pig outer hair cells: the cellular basis of the cochlear amplifier. *J. Physiol.* 388:323–347.
6. Santos-Sacchi, J., and J. P. Dilger. 1988. Whole cell currents and mechanical responses of isolated outer hair cells. *Hear. Res.* 35:143–150.
7. Santos-Sacchi, J. 1992. On the frequency limit and phase of outer hair cell motility: effects of the membrane filter. *J. Neurosci.* 12:1906–1916.
8. Dallos, P., and B. N. Evans. 1995. High-frequency motility of outer hair cells and the cochlear amplifier. *Science*. 267:2006–2009.
9. Frank, G., W. Hemmert, and A. W. Gummer. 1999. Limiting dynamics of high-frequency electromechanical transduction of outer hair cells. *Proc. Natl. Acad. Sci. USA*. 96:4420–4425.
10. Zheng, J., W. Shen, D. Z. He, K. B. Long, L. D. Madison, and P. Dallos. 2000. Prestin is the motor protein of cochlear outer hair cells. *Nature*. 405:149–155.
11. Liberman, M. C., J. Gao, D. Z. He, X. Wu, S. Jia, and J. Zuo. 2002. Prestin is required for electromotility of the outer hair cell and for the cochlear amplifier. *Nature*. 419:300–304.
12. Dallos, P., B. N. Evans, and R. Hallworth. 1991. Nature of the motor element in electrokinetic shape changes of cochlear outer hair cells. *Nature*. 350:155–157.
13. Kalinec, F., M. C. Holley, K. H. Iwasa, D. J. Lim, and B. Kachar. 1992. A membrane-based force generation mechanism in auditory sensory cells. *Proc. Natl. Acad. Sci. USA*. 89:8671–8675.
14. Huang, G., and J. Santos-Sacchi. 1993. Mapping the distribution of the outer hair cell motility voltage sensor by electrical amputation. *Biophys. J.* 65:2228–2236.
15. Huang, G., and J. Santos-Sacchi. 1994. Motility voltage sensor of the outer hair cell resides within the lateral plasma membrane. *Proc. Natl. Acad. Sci. USA*. 91:12268–12272.
16. Takahashi, S., and J. Santos-Sacchi. 2001. Non-uniform mapping of stress-induced, motility-related charge movement in the outer hair cell plasma membrane. *Pflugers Arch.* 441:506–513.
17. Belyantseva, I., H. J. Adler, R. Curi, G. I. Frolenkov, and B. Kachar. 2000. Expression and localization of Prestin and the sugar transporter GLUT-5 during development of electromotility in cochlear outer hair cells. *J. Neurosci.* 20:RC116.
18. Jen, D. H., and C. R. Steele. 1987. Electrokinetic model of cochlear hair cell motility. *J. Acoust. Soc. Am.* 82:1667–1678.
19. Raphael, R. M., A. S. Popel, and W. E. Brownell. 2000. A membrane bending model of outer hair cell electromotility. *Biophys. J.* 78:2844–2862.
20. Dallos, P., and D. Z. He. 2000. Two models of outer hair cell stiffness and motility. *J. Assoc. Res. Otolaryngol.* 1:283–291.
21. Dallos, P., R. Hallworth, and B. N. Evans. 1993. Theory of electrically driven shape changes of cochlear outer hair cells. *J. Neurophysiol.* 70:299–323.
22. Iwasa, K. H. 1993. Effect of stress on the membrane capacitance of the auditory outer hair cell. *Biophys. J.* 65:492–498.
23. Santos-Sacchi, J. 1993. Harmonics of outer hair cell motility. *Biophys. J.* 65:2217–2227.
24. Iwasa, K. H. 1994. A membrane motor model for the fast motility of the outer hair cell. *J. Acoust. Soc. Am.* 96:2216–2224.
25. Santos-Sacchi, J., and E. Navarrete. 2002. Voltage-dependent changes in specific membrane capacitance caused by prestin, the outer hair cell lateral membrane motor. *Pflugers Arch.* 444:99–106.
26. Dong, X. X., and K. H. Iwasa. 2004. Tension sensitivity of prestin: comparison with the membrane motor in outer hair cells. *Biophys. J.* 86:1201–1208.
27. Santos-Sacchi, J., S. Kakehata, and S. Takahashi. 1998. Effects of membrane potential on the voltage dependence of motility-related charge in outer hair cells of the guinea-pig. *J. Physiol.* 510:225–235.
28. Needham, D., and R. M. Hochmuth. 1989. Electro-mechanical permeabilization of lipid vesicles. Role of membrane tension and compressibility. *Biophys. J.* 55:1001–1009.
29. Akinlaja, J., and F. Sachs. 1998. The breakdown of cell membranes by electrical and mechanical stress. *Biophys. J.* 75:247–254.
30. Ko, K. S., and C. A. McCulloch. 2000. Partners in protection: interdependence of cytoskeleton and plasma membrane in adaptations to applied forces. *J. Membr. Biol.* 174:85–95.
31. Teissie, J., and M. P. Rols. 1994. Manipulation of cell cytoskeleton affects the lifetime of cell membrane electropermeabilization. *Ann. N. Y. Acad. Sci.* 720:98–110.
32. Rols, M. P., and J. Teissie. 1992. Experimental evidence for the involvement of the cytoskeleton in mammalian cell electropermeabilization. *Biochim. Biophys. Acta.* 1111:45–50.
33. Troiano, G. C., K. J. Stebe, R. M. Raphael, and L. Tung. 1999. The effects of gramicidin on electroporation of lipid bilayers. *Biophys. J.* 76:3150–3157.
34. O'Neill, R. J., and L. Tung. 1991. Cell-attached patch clamp study of the electropermeabilization of amphibian cardiac cells. *Biophys. J.* 59:1028–1039.
35. Teissie, J., M. Golzio, and M. P. Rols. 2005. Mechanisms of cell membrane electropermeabilization: A minireview of our present (lack of?) knowledge. *Biochim. Biophys. Acta.* 1724:270–280.
36. Barrau, C., J. Teissie, and B. Gabriel. 2004. Osmotically induced membrane tension facilitates the triggering of living cell electropermeabilization. *Bioelectrochemistry.* 63:327–332.
37. Santos-Sacchi, J. 2004. Determination of cell capacitance using the exact empirical solution of partial differential Y/partial differential Cm and its phase angle. *Biophys. J.* 87:714–727.
38. Ratnanather, J. T., M. Zhi, W. E. Brownell, and A. S. Popel. 1996. Measurements and a model of the outer hair cell hydraulic conductivity. *Hear. Res.* 96:33–40.
39. Oghalai, J. S., H. B. Zhao, J. W. Kutz, and W. E. Brownell. 2000. Voltage- and tension-dependent lipid mobility in the outer hair cell plasma membrane. *Science*. 287:658–661.
40. Holley, M. C., and J. F. Ashmore. 1988. A cytoskeletal spring in cochlear outer hair cells. *Nature*. 335:635–637.
41. Russell, I. J., and C. Schauz. 1996. Salicylate ototoxicity: effects on the stiffness and electromotility of outer hair cells isolated from the guinea pig cochlea. *Audit. Neurosci.* 1:309–320.
42. Tolomeo, J. A., C. R. Steele, and M. C. Holley. 1996. Mechanical properties of the lateral cortex of mammalian auditory outer hair cells. *Biophys. J.* 71:421–429.
43. He, D. Z. Z., S. P. Jia, and P. Dallos. 2004. Mechano-electrical transduction of adult outer hair cells studied in a gerbil hemicochlea. *Nature*. 429:766–770.
44. He, D. Z., and P. Dallos. 1999. Somatic stiffness of cochlear outer hair cells is voltage-dependent. *Proc. Natl. Acad. Sci. USA*. 96:8223–8228.
45. Navarrete, E., and J. Santos-Sacchi. 2001. Electropermeabilization and fast resealing in the cellular elements of the mammalian cochlea. *Assoc Res Otolaryngol Abs No.* 22058.
46. Solsona, C., B. Innocenti, and J. M. Fernandez. 1998. Regulation of exocytotic fusion by cell inflation. *Biophys. J.* 74:1061–1073.
47. Abidor, I. G., V. B. Arakelyan, L. V. Chernomordik, Y. A. Chizmadzhev, V. F. Pastushenko, and M. R. Tarasevich. 1979. Electric breakdown of bilayer lipid-membranes. 1. Main experimental facts and their qualitative discussion. *Bioelectrochem. Bioenerg.* 6:37–52.
48. Gehl, J. 2003. Electroporation: theory and methods, perspectives for drug delivery, gene therapy and research. *Acta Physiol. Scand.* 177:437–447.
49. Kinoshita, K., Jr., and T. Y. Tsong. 1977. Formation and resealing of pores of controlled sizes in human erythrocyte membrane. *Nature*. 268:438–441.
50. Zimmermann, U., and G. A. Neil. 1996. *Electromanipulation of Cells*. CRC Press, Boca Raton, FL.

51. Golan, D. E., M. R. Alecio, W. R. Veatch, and R. R. Rando. 1984. Lateral mobility of phospholipid and cholesterol in the human-erythrocyte membrane: effects of protein-lipid interactions. *Biochemistry*. 23:332–339.
52. Kalinec, F., G. Kalinec, C. Negrini, and B. Kachar. 1997. Immunolocalization of anion exchanger 2 alpha in auditory sensory hair cells. *Hear. Res.* 110:141–146.
53. Belyantseva, I. A., G. I. Frolenkov, J. B. Wade, F. Mammano, and B. Kachar. 2000. Water permeability of cochlear outer hair cells: characterization and relationship to electromotility. *J. Neurosci.* 20:8996–9003.
54. Orem, A. R., and J. Zheng. 2004. Investigating a Novel Aquaporin Mrna Expression in Organ of Corti. Assoc Res Otolaryngol Abs No. 1493.
55. Nakazawa, K., S. S. Spicer, and B. A. Schulte. 1995. Postnatal expression of the facilitated glucose transporter, GLUT 5, in gerbil outer hair cells. *Hear. Res.* 82:93–99.
56. Geleoc, G. S., S. O. Casalotti, A. Forge, and J. F. Ashmore. 1999. A sugar transporter as a candidate for the outer hair cell motor. *Nat. Neurosci.* 2:713–719.
57. Ding, J. P., R. J. Salvi, and F. Sachs. 1991. Stretch-activated ion channels in guinea pig outer hair cells. *Hear. Res.* 56:19–28.
58. Iwasa, K. H., M. X. Li, M. Jia, and B. Kachar. 1991. Stretch sensitivity of the lateral wall of the auditory outer hair cell from the guinea pig. *Neurosci. Lett.* 133:171–174.
59. Rybalchenko, V., and J. Santos-Sacchi. 2003. Cl⁻ flux through a non-selective, stretch-sensitive conductance influences the outer hair cell motor of the guinea-pig. *J. Physiol.* 547:873–891.
60. Benz, R., F. Beckers, and U. Zimmermann. 1979. Reversible electrical breakdown of lipid bilayer membranes: charge-pulse relaxation study. *J. Membr. Biol.* 48:181–204.
61. Weaver, J. C., and K. T. Powell. 1989. Theory of electroporation. In *Electroporation and Electrofusion in Cell Biology*. E. Neumann, A. E. Sowers, and C. A. Jordan, editors. Plenum Press, New York. 111–126.
62. Weaver, J. C., and A. Barnett. 1992. Progress toward a theoretical model for electroporation mechanism: membrane electrical behaviour and molecular transport. In *Guide to Electroporation and Electrofusion*. D. C. Chang, B. M. Chassy, J. A. Saunders, and A. E. Sowers, editors. Academic Press, San Diego. 91–118.
63. Ho, S. Y., and G. S. Mittal. 1996. Electroporation of cell membranes: a review. *Crit. Rev. Biotechnol.* 16:349–362.

IR Laser-Induced Perturbations of the Voltage-Dependent Solute Carrier Protein SLC26a5

Oluwarotimi Okunade[†] and Joseph Santos-Sacchi^{†‡§*}

[†]Department of Surgery (Otolaryngology), [‡]Department of Neurobiology, and [§]Department of Cellular and Molecular Physiology, Yale University School of Medicine, New Haven, Connecticut

ABSTRACT Alterations in membrane capacitance can arise from linear and nonlinear sources. For example, changes in membrane surface area or dielectric properties can modify capacitance linearly, whereas sensor residues of voltage-dependent proteins can modify capacitance nonlinearly. Here, we examined the effects of fast temperature jumps induced by an infrared (IR) laser in control and prestin (SLC26a5)-transfected human embryonic kidney (HEK) cells under whole-cell voltage clamp. Prestin's voltage sensor imparts a characteristic bell-shaped, voltage-dependent nonlinear capacitance (NLC). Temperature jumps in control HEK cells cause a monophasic increase in membrane capacitance (C_m) regardless of holding voltage due to double-layer effects. Prestin-transfected HEK cells, however, additionally show a biphasic increase/decrease in C_m with a reversal potential corresponding to the voltage at peak NLC of prestin (V_h), attributable to a rapid temperature-following shift in V_h , with shift rates up to 14 V/s over the course of a 5 ms IR pulse. Treatment with salicylate, a known inhibitor of NLC, reestablishes control cell behavior. A simple kinetic model recapitulates our biophysical observations. These results verify a voltage-dependent protein's ability to respond to fast temperature perturbations on a par with double-layer susceptibility. This likely arises from prestin's unique ability to move sensor charge at kilohertz rates, which is required for the outer hair cells' role as a cochlear amplifier.

INTRODUCTION

Outer hair cells (OHCs) are mechanically active components of the inner ear that underlie cochlear amplification (1). Cochlear amplification denotes a process whereby responses to low-level acoustic stimuli are enhanced, resulting in an increase in auditory sensitivity and frequency-resolving power. This is accomplished by OHCs feeding back mechanical energy into the vibrating sensory organ to boost stimulation to the inner hair cells, which are predominantly innervated by the auditory nerve. Prestin motor units (SLC26a5), proteins of the SLC26 anion transporter family (2), are localized to the OHC lateral membrane, drive rapid mechanical changes in OHCs, and are associated with nonlinear capacitance (NLC). NLC arises as the first derivative of a two-state Boltzmann function relating prestin voltage-sensor charge as a function of transmembrane voltage. It reflects the movement of charged residues within these motor units and peaks at a voltage (V_h) to which the OHCs' mechanical response is maximally sensitive. NLC is vulnerable to biophysical forces, including temperature and membrane tension (3–8).

Here, we examine the effects of fast temperature jumps induced by an infrared (IR) laser in control and prestin-transfected human embryonic kidney (HEK) cells under

whole-cell voltage clamp. We find effects on both linear and prestin-derived NLC. Whereas fast temperature jumps monotonically increase linear C_m in a voltage-independent manner, the Boltzmann distribution of motors along the voltage axis is rapidly and simultaneously altered in a reversible manner. Our observations clearly show that voltage-dependent proteins, given sufficiently fast kinetics (as with prestin), can contribute to rapid alterations of membrane capacitance.

MATERIALS AND METHODS

Cell culture and expression

We previously developed a tetracycline-inducible HEK293 cell line that highly expresses prestin (9). Here, we cultured HEK293 cells in Dulbecco's modified Eagle's high glucose base medium (DMEM) containing 50 U/ml each of penicillin, streptomycin, and L-glutamine, supplemented with 10% fetal bovine serum, 5 μ g/ml of blasticidin, and 130 μ g/ml of zeocin. The cells were maintained at 37°C in a humidified incubator gassed with 5% CO₂. The addition of 1 microgram/ml tetracycline to the growth medium induced prestin expression and trafficking to the cell membrane. Patch-clamp recordings of the cells were made 24–72 hr after induction at room temperature.

IR laser

Photonic stimulation with a Capella R-1850 laser was used to deliver rapid temperature jumps to cells in the recording chamber. The laser was coupled to a 600- μ m-diameter optical fiber that delivered an output wavelength of 1850 nm in pulses of variable duration. At a power setting of 100%, the optical pulse energy was 5 mJ/ms. Laser stimulation was computer-controlled via TTL and synchronized to voltage clamp commands using an Axon Instruments 1320 series A/D and D/A board. The laser fiber was mounted on a micromanipulator and the tip was placed within 0.5 mm of the recorded cell, ensuring that the whole cell was irradiated.

Submitted June 18, 2013, and accepted for publication September 10, 2013.

*Correspondence: joseph.santos-sacchi@yale.edu

This is an Open Access article distributed under the terms of the Creative Commons-Attribution Noncommercial License (<http://creativecommons.org/licenses/by-nc/2.0/>), which permits unrestricted noncommercial use, distribution, and reproduction in any medium, provided the original work is properly cited.

Editor: Joseph Mindell.

© 2013 The Authors

0006-3495/13/10/1822/7 \$2.00

<http://dx.doi.org/10.1016/j.bpj.2013.09.008>



We assume that our observations arise from temperature changes within the membrane fostered by temperature changes in bath solution water, in accord with conclusions made in previous studies (10,11). We calibrated the temperature change indirectly by monitoring changes in patch electrode resistance (R_s , i.e., changes in I_{R_s} with fixed voltage stimulation) as in the previous studies. Thus, in preliminary experiments, we correlated R_s versus changes in whole bath temperature. In the physiological experiments, our admittance analysis of currents allowed us to quantify R_s changes independently of C_m and R_m changes (12). We found that a 33% change in R_s indicated a temperature change of 17°C. In our experiment, peak R_s change averaged $31.2 \pm 0.02\%$ ($n = 5$) at 40% laser power. Our previous observation that a 20 mV shift in NLC V_h occurs per 10°C change in bath temperature corroborates these estimates (3,4).

Patch-clamp electrophysiology

Ionic blocking solutions were used to remove voltage-dependent ionic conductances so that capacitive currents could be analyzed in isolation. Extracellular bath solutions for whole-cell recording in HEK293 cells consisted of (mM) 20 TEA, 20 CsCl, 2 CoCl₂, 1 MgCl₂, 10 Hepes, 1 CaCl₂, 100 NaCl adjusted to pH 7.22 with NaOH, and 301 mOsm using D-glucose. An extracellular perfusion solution containing 132 NaCl, 2 CaCl₂, 2 MgCl₂, 10 Hepes, 10 Na salicylate (pH 7.20, 300 mOsm) was also used for experiments to block NLC. Electrodes were filled with (mM) 140 CsCl, 2 MgCl₂, 10 Hepes, 10 EGTA (pH 7.27, 302 mOsm). All chemicals used were purchased from Sigma.

Borosilicate glass pipettes were pulled using a P-2000 laser-heating pipette puller (Sutter Instruments) to initial resistances ranging between 3.5 and 5 MΩ. Pipette stray capacitance was compensated for before recordings were obtained, and voltages were corrected for effects of series resistance offline. A Nikon Eclipse TE300 inverted microscope with Hoffmann optics was used to observe the cells during electrical recording. Round, isolated cells growing on a glass coverslip were patched 24–72 hr after tetracycline induction.

Cells were clamped to a holding potential of 0 mV using an Axon 200B patch-clamp amplifier. During the temperature jump protocol, cells were held under voltage clamp at 0 mV and stepped in 30 mV increments (from hyperpolarizing values of –150 mV to 150 mV) for 1024 ms during which a brief IR laser pulse was delivered to the cells for each voltage step. Solution exchange (e.g., with salicylate) was performed using gravity flow. All recordings were made at room temperature. Local temperature measurements of the cells were calculated by measuring changes in electrode resistance and extrapolating from a resistance-temperature calibration curve (11). A resistance-temperature calibration curve was obtained by observing changes in pipette resistance in a hot bath solution (~55°C) that was allowed to cool passively.

Cell capacitance was measured under a whole-cell configuration using jClamp software (SciSoft, CT; www.SciSoftCo.com). Voltage records sampled at 10 μs were filtered at 10 kHz with an eight-pole Bessel filter and saved to disk for offline analysis. NLC was measured using a continuous high-resolution (2.56 ms sampling), two-sine stimulus protocol (10 mV peak at both 390.6 and 781.2 Hz) superimposed onto the voltage command (12,13). Capacitance data were fit to the first derivative of a two-state Boltzmann function (14):

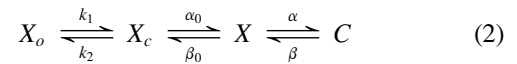
$$C_m = Q_{\max} \frac{ze}{kT} \frac{b}{(1+b)^2} + C_{lin}, \quad b = \exp\left(\frac{-ze(V_m - V_h)}{kT}\right) \quad (1)$$

where Q_{\max} is the maximum nonlinear charge moved; V_h is voltage at peak capacitance or, equivalently, at half-maximum charge transfer; V_m is membrane potential; z is valence; C_{lin} is linear membrane capacitance; e is electron charge; k is Boltzmann's constant; and T is absolute temperature. Our justification for using steady-state fits of prestin's charge movement at the

2.56 ms C_m measurement sampling rate is that the parameters are largely stable (z , Q_{\max}), except for V_h , across time samples. ΔC_m is defined as the difference between pre-IR and post-IR maximal capacitance. Results are reported as the mean \pm standard error (SE).

Model

To understand the biophysical data, we used a kinetic model of SLC26a5 that we previously developed (15). The model was developed to account for a chloride-dependent disparity between NLC and electromotility V_h , requiring intermediate transitions much slower than either chloride- or voltage-dependent transitions. A model cartoon is shown in Fig. 5 A of Song and Santos-Sacchi (15).



State X_o is SLC26a5 in the absence of bound anion; state X_c is with bound anion; state X is voltage-enabled after anion binding, with its residence being favored by hyperpolarization (expanded state); and state C results from depolarization (contracted state). The model has very fast anion (chloride) binding and unbinding transitions ($X_o \leftrightarrow X_c$) and very fast voltage-dependent conformational transitions ($X \leftrightarrow C$). The transition to state C carries a unit charge, q ; Q_{\max} , the total charge moved, will reflect the maximal accumulation of motors in that state. Nestled between the anion-binding and voltage-dependent transitions resides a nonvoltage-dependent transition ($X_c \leftrightarrow X$), which is very much slower than the other two transitions.

We assessed the kinetic model using MATLAB (The MathWorks, Natick, MA) Simulink via an automation link with jClamp (www.scisoftco.com). The kinetic model was interfaced to jClamp via a model of the patch-clamp amplifier and cell. The linear component of the patch-cell model possessed an R_s of 5 MΩ, R_m of 500 MΩ, and C_{lin} of 10 pF. The nonlinear component, NLC, derived from charge movement of the SLC26a5 model, with the following parameters: $k_1 = 10^7 * [Cl]_{in}$, $k_2 = 10^7 * k_d$, $\alpha_0 = 75 * \exp(t_m)$, $\beta_0 = 95$, $\alpha = 10^6 * \exp(zFV_m/2RT)$, $\beta = 583 * 10^9 * \exp(-zFV_m/2RT + t_m/2 - E_a/RT)$, $k_d c_1 = 0.001$, $T = 296$ kelvin, $E_a = 45$ kJ/mol, $F = 9.648 * 10^4$ C/mol, $R = 8.315$ J/Kmol, $k = 1.381 * 10^{-23}$ VC/K.

The rates α_0 and β are tension sensitive because tension is known to increase prestin residence in the expanded (X) state (5,6), t_m in units kT (eRT/F); the rate β is temperature sensitive, with Arrhenius activation energy, E_a . α and β are voltage dependent, with sensor valence $z = 0.7$. At $T = 296$ K, $V_m = 0$ mV, $T_m = 0$ kT, and $[Cl]_{in} = 0.14$ M, initial rates are $k_1 = 1.4e6$, $k_2 = 1e4$, $\alpha_0 = 75$, $\beta_0 = 95$, $\alpha = 1e6$, and $\beta = 1e5$. Chloride concentrations and K_d are in molar; rates are $1/t$, with time (t) being 1 s. Voltage is in volts.

RESULTS

Capacitance

The rapid temperature change associated with an IR laser pulse delivered directly to a cell via optical fiber alters membrane capacitance. Control HEK cells and cells of our uninduced SLC26a5 HEK cell line increase their linear membrane capacitance in a voltage-independent fashion. Fig. 1 A shows C_m measures of a voltage-clamped, uninduced SLC26a5 HEK cell for a wide range of holding potentials. The delivery of a 20 ms IR pulse (40% of maximal laser power) induces a linearly ramped increase in C_m coinciding with the duration of the pulse. To better visualize the overlapped traces and indicate holding voltage, we offset the

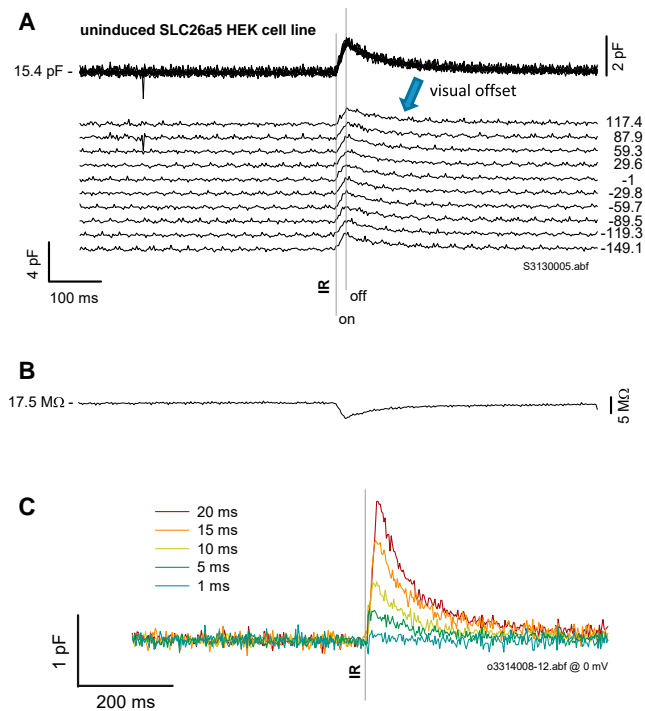


FIGURE 1 IR laser-induced temperature jump alters linear capacitance. (A) Under whole-cell voltage clamp, an uninduced SLC26a5 HEK cell was nominally stepped to the membrane potentials indicated. During the voltage step, an IR laser pulse of 20 ms duration (nominally 40% Capella laser power) was delivered via optical fiber. Regardless of the holding potential, the laser pulse induced a fixed maximal increase in C_m , $\sim 10\%$ of resting C_m . Averages are given in Results section. (B) Simultaneously measured series resistance indicates a linear increase in temperature during the pulse and an exponential cooling of bath media after the pulse. (C) An increase in duration of the pulse results in a greater C_m change. The holding potential is 0 mV.

traces by an arbitrary constant, allowing clearer observation of the voltage independence. The increase in C_m is $10.8\% \pm 2.5\%$ ($n = 5$) of whole-cell capacitance for a 20 ms pulse. In Fig. 1 A, at laser offset, a single exponential decrease in C_m occurs with a time constant of 70 ms at 0 holding potential (81.5 ± 3.2 ms; $n = 5$). These linear and exponential phases of C_m change correspond, respectively, to a linear increase in temperature during the pulse and an exponential cooling of the bath solution/cytoplasm after the pulse, both of which are reflected in simultaneous changes in the series resistance of the pipette electrode (Fig. 1 B). Our admittance analysis allows us to quantify R_s changes, which are known to correspond to temperature manipulations (11). Fig. 1 C shows that increases in pulse durations induce increasing temperature changes that evoke larger C_m responses. Within our exposure range, we do not see any threshold effect for cell damage that is not associated with loss of cell recording.

In our SLC26a5 HEK cell line after tetracycline induction, cells possess a voltage-dependent NLC atop their linear capacitance (16). This arises from the voltage sensor activity underlying the protein's role in OHC electromotility (3,4).

Fig. 2 illustrates the voltage-dependent nature of the induced HEK cell's C_m , and the influence of temperature jumps on NLC and linear C_m . Again, we offset the overlapped traces by an arbitrary constant, allowing clearer observation of the effects of IR pulse on C_m ; obvious differences are found in comparison with uninduced HEK cells (see Fig. 1). Indeed, a voltage-dependent effect is now observed. In Fig. 2 B, C_m - V_m functions are plotted at various time points relative to the start of the IR pulse. The laser pulse induced a shift of the C_m - V_m relation in the depolarizing direction. After correction of voltages for R_s effects, Boltzmann fits to the data (see Materials and Methods) allow a high-resolution (2.56 ms) inspection of dynamic changes in NLC and linear capacitance during and after the IR pulse (Fig. 2 C). In this example, NLC V_h shifted 40 mV in 20 ms at a linear rate of 2.03 V/s (average is 2.32 ± 0.21 V/s; $n = 6$) during the heating phase, and recovers (with temperature) exponentially with a time constant of 73 ms (average is 65.4 ± 10.8 ms; $n = 6$) during the cooling phase. The shift in V_h represents a redistribution of prestin motors into the

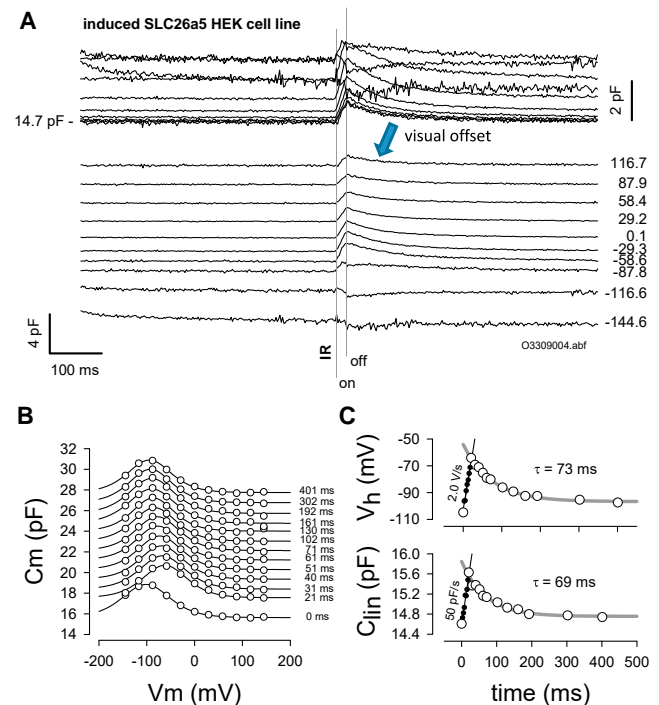


FIGURE 2 IR laser-induced temperature jump alters SLC26a5-generated NLC and linear capacitance. (A) Under whole-cell voltage clamp, an induced SLC26a5 HEK cell was nominally stepped to the membrane potentials indicated. During the voltage step, an IR laser pulse of 20 ms duration (nominally 40% Capella laser power) was delivered via optical fiber. The laser pulse induced a maximal change in C_m that depended on the holding potential. The change could be either an increase or decrease. (B) C_m - V_m plots of NLC as a function of time after pulse onset. Note the effect on the voltage dependence of NLC, namely, a shift to the right. (C) Changes in V_h and C_{lin} follow temperature. Rapid shifts and increases in C_{lin} occur during laser heating and return back to initial levels during bath cooling. Averages are given in the Results section. To see this figure in color, go online.

expanded conformation during heating. We previously observed this shift over the course of minutes using Peltier control of the bath solution temperature, with the shift averaging ~ 20 mV/10°C (3,4). In two additional cells, we were able to determine the V_h shift with 5 ms pulses at 90% laser power. The shift was 67 and 70 mV in 5 ms or 13.4 and 14 V/s, indicating that heating rates and corresponding V_h shift rates increase with greater laser power. The increase in rates with laser power indicates that we have yet to observe the fastest response and are limited by the laser power (for technical reasons, we avoid $>90\%$ power usage). Linear capacitance also changes simultaneously, with a time course similar to that of NLC V_h . In this case, there is a linear change of 50 pF/s during heating and a recovery due to cooling with a time constant of 69 ms (average is 78.9 ± 7.7 ms; $n = 6$). The changes due to cooling in linear capacitance are similar to those observed in control HEK cells. These rapid rates of change during heating and cooling mirror the changes in temperature as gauged from R_s inspection or predicted from previous observations on temperature-dependent shifts of V_h during slow bath changes in temperature (3,4), i.e., they correspond to a temperature-induced change of 20 mV/10°C.

The difference in susceptibility of NLC and linear C_m to temperature jump is readily illustrated by the behavior of ΔC_m , defined as the maximal difference between pre-IR and post-IR capacitance. Examples from two cells are shown in Fig. 3, A and B. Whereas IR pulse-induced linear C_m changes occur at the same magnitude and direction (increase) regardless of the holding potential (Fig. 1), NLC changes vary depending on the holding potential, and reverse in direction near voltages (average is -96.8 ± 6.4 mV; $n = 5$) around NLC V_h (average is $-94.7 \pm$

6.2 mV; $n = 5$), with an R^2 value of 0.9943 (Fig. 3, A and B). Thus, it is possible, depending on the magnitude of NLC and its V_h (relative to holding potential), to induce a decrease in C_m by IR laser pulse. Salicylate (10 mM) not only reduces NLC, as expected (18,19), but also eliminates the characteristic reversal of ΔC_m normally afforded by SLC26a5 expression, essentially returning the induced HEK cell back to its preinduced condition ($n = 2$). That is, only an increase in C_m is observed, regardless of the holding potential (Fig. 3 A).

To understand the data, we evaluated the temperature-dependent behavior of a recently developed kinetic model of SLC26a5 (15). In this model (see Materials and Methods), only the backward, voltage-dependent transition, β , is temperature sensitive, indicating that only movements into the hyperpolarized (expanded) state of SCL26a5 are affected by temperature. In the simulation, we simply modeled the temperature change as that revealed by our experimental measures of R_s (in this case, with a 23°C maximum change; Fig. 4 A). Similar to the biophysical data, a rapid temperature change followed by cooling induced characteristic changes in C_m , which derived from NLC magnitude and induced V_h shifts (Fig. 4, B and C). As we deduced from the biophysical data, NLC V_h shifts directly mirror temperature changes. To match the average biophysical data of 2.3V/s (~ 20 mV/10°C), an Arrhenius activation energy of 45 kJ/mol was required. The model also recapitulates the reversal of ΔC_m near V_h (Fig. 4 D). Also note that ΔC_m recovers with temperature back to zero at voltages away from V_h , in contrast to the biophysical data (Fig. 3), because the original model had no temperature-sensitive linear C_m (Fig. 4, solid circles). However, when a linearly temperature-dependent C_m is introduced, ΔC_m appears more similar to the biophysical data (Fig. 4 D, open circles). The original implementation of the kinetic model (15) had temperature dependence of both the backward intermediate rate, β_0 , and the backward voltage-dependent rate, β . Here, however, we obtained better correspondence to the biophysical data by setting temperature dependence only in β .

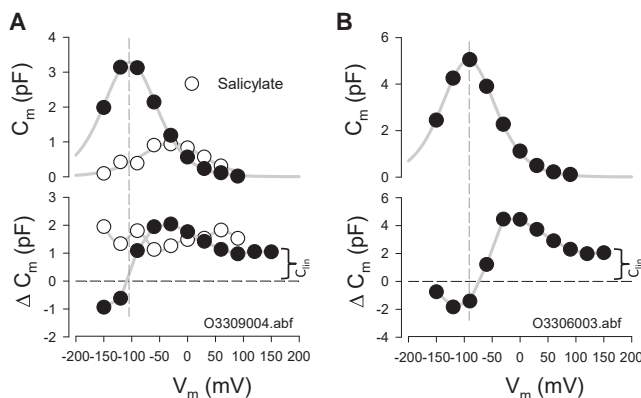


FIGURE 3 IR laser-induced temperature jump alters NLC showing increases and decreases that reverse near V_h of NLC. The NLC plotted is the one before the temperature jump. (A and B) Shown are data from two cells. ΔC_m at positive voltages remains offset from zero due to the temperature-dependent increase in linear C_m (curly brackets). In the first case (A), after data collection, salicylate (10 mM) was perfused onto the cell and collection was repeated. Salicylate removes the ΔC_m reversal as a result of NLC block, leaving intact a constant linear C_m increase across holding voltage. Averages are given in Results.

Currents

We found two components of currents associated with fast temperature jump (Fig. 5). The first component coincided with the IR heating phase and its magnitude was related to the rate of heating (or correspondingly to the rate of linear C_m change; Fig. 5, A and B). This current appeared to reverse at positive voltages, as found by Shapiro et al. (10) (Fig. 5 C). We agree with their discussion on the matter, especially their interpretation that this may arise from asymmetrical fixed charges on the membrane leaflets. The second, slower component, which reversed near 0 mV, peaked at maximal temperature and then decayed during the cooling phase (Fig. 5, C and D). We interpret this as

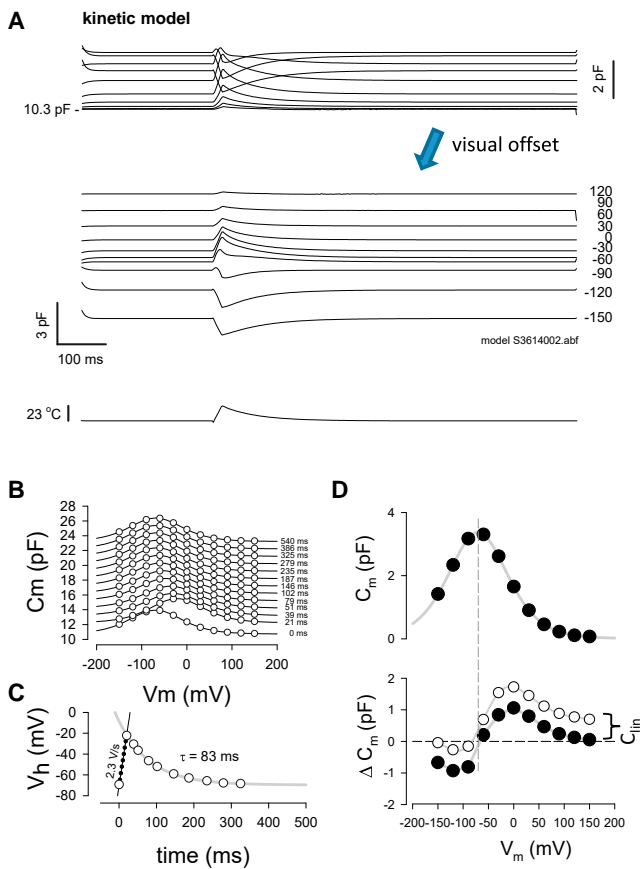


FIGURE 4 A kinetic model recapitulates biophysical data. (A) Stimulation with the experimentally observed temperature change induced by an IR laser pulse induces C_m behavior similar to the biophysical results. Here, the model transition rates are set to give a V_h of -71 mV. (B) Plots of NLC show rightward shifts along the voltage axis as a result of temperature increase. (C) Rates of V_h shift are comparable to biophysical data and directly follow temperature alterations. (D) Voltage at reversal of ΔC_m is related to V_h . Note that ΔC_m goes back to zero, in contrast to the biophysical data, when C_{in} is not temperature sensitive (closed circles). Including temperature dependence for C_{in} results in an offset similar to the biophysical data (open circles, curly brackets). To see this figure in color, go online.

an ionic current that is nonspecific with a reversal potential near zero. Sometimes we found that the second, slower component obscured the first component as described in Shapiro et al. (10). Nevertheless, the rapid component is clearly observable in the traces near zero potential (Fig. 5 C). The second, slow-decaying membrane current displays nonlinear features (Fig. 5 D) reminiscent of G_{metL} , a conductance found in OHCs with marked temperature dependence (20,21). The current increase due to IR stimulation is likewise nonlinear, and therefore is unlikely due to linear decreases in R_s with temperature.

DISCUSSION

Control HEK cells and HEK cells expressing the voltage-dependent protein SLC26a5 show very fast changes in membrane capacitance when rapid temperature jumps are

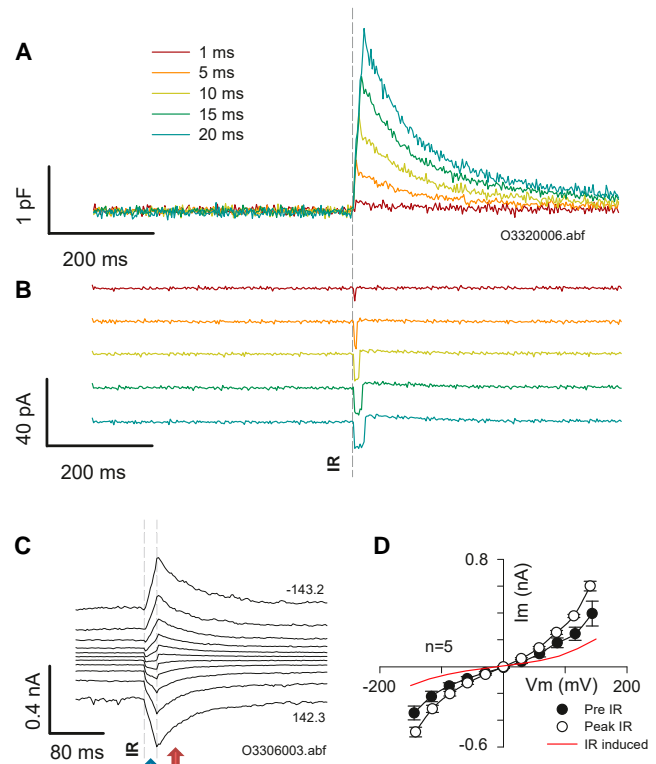


FIGURE 5 Two components of current induced during temperature jump. (A and B) Capacitance increases during temporally incremental IR laser pulses (A) and corresponding currents arise (B). Current magnitude depends on rate of C_m change and duration depends on pulse duration. For all traces, pulses were delivered at a holding potential of 0 mV. (C) Current responses for a 20 ms duration pulse within the holding potential extremes indicated, stepped nominally at 30 mV. Note the fast inward current response during the laser pulse, with a reversal potential predicted to be at positive potentials. Simultaneously, a slow-decaying current with reversal near 0 mV is observed. The red arrow shows the sum of the two components (note step behavior around zero potential that rides on the slower current ramp) and the blue arrow shows the slow component after the fast component ends after the laser pulse. (D) IV plot of average cell currents before and at termination of the IR pulse (mean \pm SE; $n = 5$). The red line is IR-induced current. Note that current voltage dependence is unaffected by temperature, unlike that of NLC.

delivered to the cells by IR laser. For control cells, rapid alterations in linear C_m directly follow changes in temperature, as observed by Shapiro et al. (10). With the pulse energies we used, the rates of change were up to 50 pF/s and magnitudes peaked near 10% of the cell's resting membrane capacitance. Effects were reversible upon heat dissipation through the bathing solution. HEK cells expressing prestin showed additional effects on the Boltzmann characteristics of voltage sensor-related NLC. With 20 ms IR pulse durations, V_h was shifted in the positive direction at an average rate of 2.3 V/s, corresponding to 20 mV/ $^{\circ}$ C, and subsequently returned to prior conditions as the heat dissipated. In two cells, delivery of near-maximum laser power produced V_h shift rates of 13–14 V/s. The rates of recovery of linear C_m and V_h with cooling were indistinguishable,

indicating that each is directly coupled to thermal energy. A simple kinetic model of prestin (15) that possesses temperature-sensitive, voltage-dependent transitions that move prestin into the expanded state can mimic our biophysical observations. Thus, we conclude that temperature-induced alteration of transition rates between voltage-dependent conformations of prestin can alter NLC as fast as thermal influences on the membrane double layer (10).

Capacitance

It is well established that capacitance is temperature sensitive; for example, Taylor (22) reported that squid axon capacitance increased 1% per degree centigrade. Others have reported that the kinetics of voltage-dependent channels is temperature sensitive, consequently influencing gating currents (23,24) and necessarily altering their equivalent voltage-dependent capacitance. It is therefore not surprising that prestin NLC is temperature dependent, as we previously showed with slow alterations in bath temperature (3,4). Prestin's NLC V_h shifts ~ 20 mV per 10°C . What may appear surprising is that prestin can redistribute between expanded and contracted states so rapidly upon IR stimulation, showing V_h shift rates up to 14 V/s. Of course, by nature, prestin is poised to transition between states at kilohertz rates, and apparently is capable of rapidly responding to a variety of energy forms, including mechanical, electrical, and thermal forms (7,8,25,26). Nevertheless, our observations are not simply related to the ability of prestin to rapidly transition between states; more importantly, they reflect the efficacy of realigning the protein's operating voltage range by external influences, namely, adjusting the gain of cochlear amplification.

Our modeling of temperature effects on prestin's voltage-dependent backward rate is similar to that employed to understand TRP channel heat sensitivity (27). In this regard, we recently found that prestin is sensitive to capsaicin (28), an agent that mimics heat activation of TRP channels. However, in prestin, the mechanism of action must be different from that of temperature since it causes negative shifts in V_h , pointing toward action on forward rates. Thus, it will be of interest to evaluate the simultaneous effects of capsaicin and temperature on prestin NLC. Of course, other proposed mechanisms in TRP channels that may also contribute to temperature sensing by prestin include allosteric mechanisms (29) and changes in specific heat capacity (30). Nevertheless, the simplest scheme is likely that of temperature-sensitive transition rates as modeled here, which show excellent agreement with the biophysical data. This is not to say that the sensitivities of the other transitions in the model, i.e., those displaying tension and chloride sensitivity, cannot influence the temperature-sensitive, voltage-dependent transition, as it is well known that a voltage-independent transition can affect the characteristics of a linked voltage-dependent one (31–33).

Currents

In this study, we used blockers to reduce ionic conductances so that we could effectively measure capacitance. We identified two components of residual current: one that is fast, coinciding with the duration of laser heating, and one that follows the temperature of the bath as it cooled. This observation is similar to that of Parker (24), who suggested that the fast component represents gating currents of oocyte ion channels. This was suggested because in the absence of the slow component (i.e., at its reversal potential), transient capacitive-like currents were revealed. Although we do expect that sensor charge movement (i.e., gating-like currents) should arise when prestin's V_h suddenly shifts, we find no evidence of transient-like currents near the reversal potential of our slow component, around 0 mV. We should note that when the cell is held at 0 mV, we are interrogating a linear region of C_m , since NLC V_h is very negative. Our laser-induced currents at 0 mV resemble those found by Shapiro et al. (10), and we conclude that they represent currents generated by rapid changes in linear C_m . The second component of current, which reverses near zero, has some nonlinear features of a conductance, G_{metL} , found in OHCs (20,21). Notably, increases in temperature augment the nonlinear current and are not simply leakage currents.

In summary, we find that SLC26a5 (prestin) is remarkably responsive to fast temperature jumps, rapidly moving its operating point along the voltage axis. This susceptibility to thermal perturbations likely arises from the protein's natural ability to follow voltage changes at acoustic frequencies, but it also has implications for manipulation of cochlear amplifier gain control. Thus, we predict that we may be able to drive auditory sensation by stimulating OHCs with a high-frequency gated IR laser, and manipulate cochlear amplification in vivo.

The authors thank Lei Song and Jun-Ping Bai for their technical assistance and discussions. This research was supported by NIH NIDCD grant DC00273 to J.S.S. and an HHHMI Medical Research Fellowship to O.O.

REFERENCES

1. Ashmore, J., P. Avan, ..., B. Canlon. 2010. The remarkable cochlear amplifier. *Hear. Res.* 266:1–17.
2. Zheng, J., W. Shen, ..., P. Dallos. 2000. Prestin is the motor protein of cochlear outer hair cells. *Nature.* 405:149–155.
3. Meltzer, J., and J. Santos-Sacchi. 2001. Temperature dependence of non-linear capacitance in human embryonic kidney cells transfected with prestin, the outer hair cell motor protein. *Neurosci. Lett.* 313:141–144.
4. Santos-Sacchi, J., and G. Huang. 1998. Temperature dependence of outer hair cell nonlinear capacitance. *Hear. Res.* 116:99–106.
5. Takehata, S., and J. Santos-Sacchi. 1995. Membrane tension directly shifts voltage dependence of outer hair cell motility and associated gating charge. *Biophys. J.* 68:2190–2197.
6. Iwasa, K. H. 1993. Effect of stress on the membrane capacitance of the auditory outer hair cell. *Biophys. J.* 65:492–498.

7. Gale, J. E., and J. F. Ashmore. 1994. Charge displacement induced by rapid stretch in the basolateral membrane of the guinea-pig outer hair cell. *Proc. Biol. Sci.* 255:243–249.
8. Santos-Sacchi, J., L. Song, and X. T. Li. 2009. Firing up the amplifier: temperature, pressure and voltage jump studies on Ohc motor capacitance. Concepts and challenges in the biophysics of hearing. Proc. Int. Workshop Mechan. Hearing, 10th, Staffordshire, UK. 363–370.
9. Bian, S., B. W. Koo, ..., D. S. Navaratnam. 2010. A highly expressing Tet-inducible cell line recapitulates in situ developmental changes in prestin's Boltzmann characteristics and reveals early maturational events. *Am. J. Physiol. Cell Physiol.* 299:C828–C835.
10. Shapiro, M. G., K. Homma, S. Villarreal, C. P. Richter, and F. Bezanilla. 2012. Infrared light excites cells by changing their electrical capacitance. *Nat. Commun.* 3:736.
11. Yao, J., B. Liu, and F. Qin. 2009. Rapid temperature jump by infrared diode laser irradiation for patch-clamp studies. *Biophys. J.* 96:3611–3619.
12. Santos-Sacchi, J. 2004. Determination of cell capacitance using the exact empirical solution of differential Y/partial differential Cm and its phase angle. *Biophys. J.* 87:714–727.
13. Santos-Sacchi, J., S. Kakehata, and S. Takahashi. 1998. Effects of membrane potential on the voltage dependence of motility-related charge in outer hair cells of the guinea-pig. *J. Physiol.* 510:225–235.
14. Santos-Sacchi, J. 1991. Reversible inhibition of voltage-dependent outer hair cell motility and capacitance. *J. Neurosci.* 11:3096–3110.
15. Song, L., and J. Santos-Sacchi. 2013. Disparities in voltage-sensor charge and electromotility imply slow chloride-driven state transitions in the solute carrier SLC26a5. *Proc. Natl. Acad. Sci. USA.* 110:3883–3888.
16. Bian, S. M., B. W. Koo, ..., D. Navaratnam. 2011. Evaluating prestin's changing biophysical attributes in development using a Tet-induced cell line. *AIP Conf. Proc.* 1403:143–147.
17. Reference deleted in proof.
18. Kakehata, S., and J. Santos-Sacchi. 1996. Effects of salicylate and lanthanides on outer hair cell motility and associated gating charge. *J. Neurosci.* 16:4881–4889.
19. Tunstall, M. J., J. E. Gale, and J. F. Ashmore. 1995. Action of salicylate on membrane capacitance of outer hair cells from the guinea-pig cochlea. *J. Physiol.* 485:739–752.
20. Santos-Sacchi, J., V. Rybalchenko, ..., D. Navaratnam. 2006. On the temperature and tension dependence of the outer hair cell lateral membrane conductance GmetL and its relation to prestin. *Pflugers Arch.* 452:283–289.
21. Rybalchenko, V., and J. Santos-Sacchi. 2003. Cl⁻ flux through a non-selective, stretch-sensitive conductance influences the outer hair cell motor of the guinea-pig. *J. Physiol.* 547:873–891.
22. Taylor, R. E. 1965. Impedance of the squid axon membrane. *J. Cell. Comp. Physiol.* 66:21–25.
23. Collins, C. A., and E. Rojas. 1982. Temperature dependence of the sodium channel gating kinetics in the node of Ranvier. *Q. J. Exp. Physiol.* 67:41–55.
24. Parker, I. 1989. Ionic and charge-displacement currents evoked by temperature jumps in *Xenopus* oocytes. *Proc. R. Soc. Lond. B Biol. Sci.* 237:379–387.
25. Santos-Sacchi, J. 1992. On the frequency limit and phase of outer hair cell motility: effects of the membrane filter. *J. Neurosci.* 12:1906–1916.
26. Frank, G., W. Hemmert, and A. W. Gummer. 1999. Limiting dynamics of high-frequency electromechanical transduction of outer hair cells. *Proc. Natl. Acad. Sci. USA.* 96:4420–4425.
27. Voets, T., G. Droogmans, ..., B. Nilius. 2004. The principle of temperature-dependent gating in cold- and heat-sensitive TRP channels. *Nature.* 430:748–754.
28. Wu, T., L. Song, ..., A. L. Nuttall. 2011. Effect of capsaicin on potassium conductance and electromotility of the guinea pig outer hair cell. *Hear. Res.* 272:117–124.
29. Jara-Oseguera, A., and L. D. Islas. 2013. The role of allosteric coupling on thermal activation of thermo-TRP channels. *Biophys. J.* 104:2160–2169.
30. Clapham, D. E., and C. Miller. 2011. A thermodynamic framework for understanding temperature sensing by transient receptor potential (TRP) channels. *Proc. Natl. Acad. Sci. USA.* 108:19492–19497.
31. Lacroix, J. J., A. J. Labro, and F. Bezanilla. 2011. Properties of deactivation gating currents in Shaker channels. *Biophys. J.* 100:L28–L30.
32. Colquhoun, D. 1998. Binding, gating, affinity and efficacy: the interpretation of structure-activity relationships for agonists and of the effects of mutating receptors. *Br. J. Pharmacol.* 125:924–947.
33. Shirokov, R. 2011. What's in gating currents? Going beyond the voltage sensor movement. *Biophys. J.* 101:512–514, discussion 515–516.



Mitochondrial Stress Engages E2F1 Apoptotic Signaling to Cause Deafness

Nuno Raimundo,¹ Lei Song,² Timothy E. Shutt,¹ Sharen E. McKay,¹ Justin Cotney,³ Min-Xin Guan,⁴ Thomas C. Gilliland,¹ David Hohuan,² Joseph Santos-Sacchi,² and Gerald S. Shadel^{1,3,*}

¹Department of Pathology

²Department of Surgery (Otolaryngology), Department of Cellular and Molecular Physiology, and Department of Neurobiology

³Department of Genetics

Yale University School of Medicine, New Haven, CT 06520, USA

⁴Institute of Genetics, Zhejiang University, Hangzhou, Zhejiang, China 310058

*Correspondence: gerald.shadel@yale.edu

DOI 10.1016/j.cell.2011.12.027

SUMMARY

Mitochondrial dysfunction causes poorly understood tissue-specific pathology stemming from primary defects in respiration, coupled with altered reactive oxygen species (ROS), metabolic signaling, and apoptosis. The A1555G mtDNA mutation that causes maternally inherited deafness disrupts mitochondrial ribosome function, in part, via increased methylation of the mitochondrial 12S rRNA by the methyltransferase mtTFB1. In patient-derived A1555G cells, we show that 12S rRNA hypermethylation causes ROS-dependent activation of AMP kinase and the proapoptotic nuclear transcription factor E2F1. This retrograde mitochondrial-stress relay is operative *in vivo*, as transgenic-mtTFB1 mice exhibit enhanced 12S rRNA methylation in multiple tissues, increased E2F1 and apoptosis in the stria vascularis and spiral ganglion neurons of the inner ear, and progressive E2F1-dependent hearing loss. This mouse mitochondrial disease model provides a robust platform for deciphering the complex tissue specificity of human mitochondrial-based disorders, as well as the precise pathogenic mechanism of maternally inherited deafness and its exacerbation by environmental factors.

INTRODUCTION

Mitochondria are multi-functional cellular organelles involved in oxidative metabolism, ion homeostasis, signal transduction, and apoptosis and hence contribute to human disease by a variety of mechanisms. Mitochondrial pathogenesis is complex and involves maternally inherited diseases due to mutations in mtDNA, as well as Mendelian-inherited disease due to mutations in nuclear genes required for mitochondrial function (DiMauro and Schon, 2003). Furthermore, mitochondrial dysfunction is implicated in more common disorders such as diabetes, heart

disease, cancer, neurodegeneration, and aging (Wallace, 2005; Shadel, 2008), making efforts to better understand how mitochondria cause and exacerbate human disease pathology imperative and of broad significance.

A major hurdle in understanding mitochondrial disease pathogenesis is the current lack of understanding of the often-extreme tissue specificity involved (DiMauro and Schon, 2003). Because defective oxidative phosphorylation (OXPHOS) *per se* can be pathogenic, this is often attributed to variable energetic thresholds in different cell types. However, defective OXPHOS is also frequently associated with increased mitochondrial reactive oxygen species (ROS) that are a major cause of pathology because they promote molecular damage, oxidative stress, and cell death. Finally, mitochondria and ROS are involved in signal transduction pathways (Hamanaka and Chandel, 2010) that are likely an underappreciated downstream cause of pathology due to mitochondrial dysfunction. For example, a major signaling node that reacts to mitochondrial dysfunction is the AMP-dependent protein kinase (AMPK) pathway, which responds to cellular energy decline that can occur when OXPHOS is disrupted (Hardie, 2007) and is regulated by ROS (Emerling et al., 2009; Quintero et al., 2006).

A hallmark case of tissue-specific mitochondrial disease pathology is maternally inherited deafness caused by the A1555G mutation in human mtDNA (Prezant et al., 1993). This relatively common mutation (Vandebona et al., 2009) causes nonsyndromic and/or aminoglycoside-induced deafness and occurs in the 12S rRNA gene, encoding the RNA component of the small (28S) mitochondrial ribosome subunit. It is also in close proximity to an evolutionarily conserved stem-loop that contains two tandem adenine residues that are methylated by the site-specific rRNA adenine N6-di-methyltransferase, h-mtTFB1/TFB1M (McCulloch et al., 2002; Seidel-Rogol et al., 2003). This methylation occurs during ribosome biogenesis in bacteria (Pulicherla et al., 2009) and is essential in mice, the lack of which disrupts mitochondrial 28S ribosome subunit assembly (Metodieva et al., 2009).

Hearing loss caused by the A1555G mutation is irreversible (Prezant et al., 1993), implying death of critical, irreplaceable cells in the inner ear by an unknown pathogenic cell-death pathway. The A1555G mutation alters mitochondrial ribosome

function and translation (Cotney et al., 2009; Guan et al., 1996, 2000; Hobbie et al., 2008), which in turn causes OXPHOS defects that are thought to contribute to deafness pathology. However, mitochondrial translation and OXPHOS defects observed in patient-derived primary and cytoplasmic hybrid (cybrid) cell lines are mild and highly dependent on the nuclear genetic background (Guan et al., 1996, 2000), suggesting that other aspects of mitochondrial dysfunction may also be operative. Finally, polymorphisms near the *TFB1M* gene encoding h-mtTFB1 are nuclear modifiers of the A1555G deafness phenotype (Bykhovskaya et al., 2004), suggesting a connection between 12S rRNA methylation and hearing loss (Shadel, 2004b).

We recently showed that patient-derived A1555G cybrids are hypermethylated at the 12S rRNA stem-loop methylated by h-mtTFB1 (Cotney et al., 2009). These A1555G cybrids exhibit defective mitochondrial biogenesis and membrane potential and heightened sensitivity to stress-induced apoptosis (Cotney et al., 2009), apparently due to disrupted coordination of overall mitochondrial biogenesis with the assembly of mitochondrial ribosomes (Cotney et al., 2007). Remarkably, these phenotypes are shared by HeLa cells with wild-type mtDNA that instead have hypermethylated 12S rRNA due to overexpression of h-mtTFB1, leading us to conclude that hypermethylation of mitochondrial ribosomes per se is a key molecular defect driving the apoptotic phenotype (Cotney et al., 2009).

In the current study, we tested the hypothesis that this hypermethylation of mitochondrial ribosomes instigates a unique form of mitochondrial stress signaling involved in the deafness pathology of the A1555G mutation. We show that increased mitochondrial ROS generated in A1555G cybrids activate the proapoptotic nuclear transcription factor E2F1 in an AMPK-dependent manner, and that overexpression of mtTFB1 in mice (to model pathogenesis due to increased mitochondrial 12S rRNA methylation) is sufficient to cause progressive hearing loss associated with tissue-specific upregulation of E2F1 and apoptosis of critical cells of the inner ear.

RESULTS

A Mitochondrial Stress-Response Pathway Activates Nuclear Transcription Factor E2F1

We hypothesized that mitochondrial defects due to 12S rRNA hypermethylation elicit a mitochondrial retrograde stress signal (Butow and Avadhani, 2004) that explains the apoptotic susceptibility we documented previously in A1555G and h-mtTFB1 methyltransferase overexpression cell lines (Cotney et al., 2009). Therefore, we performed microarray analysis on these cell lines, which exhibit 12S hypermethylation for different reasons (i.e., due to the A1555G point mutation or overexpression of the h-mtTFB1), reasoning that this would define a common transcriptional signature, which, in turn, would allow elements of this mitochondrial stress-response pathway to be deciphered.

Expression microarrays were performed on A1555G cybrids, using analogous 143B cybrids containing the corresponding wild-type mtDNA ("A" at position 1555) as the negative control, and on HeLa cells overexpressing h-mtTFB1 compared to

those expressing a methyltransferase-deficient G65A mutant of h-mtTFB1 as a negative control (Figure 1A). We identified genes that were significantly upregulated or downregulated in the hypermethylation cell lines (Table S1 available online), which we reasoned would include genes that were responding specifically to 12S hypermethylation. We then analyzed the promoters of this set of hypermethylation-responsive genes (Figure 1B) for transcription factor binding sites and found that E2F1 sites were the most frequently overrepresented in genes upregulated in 12S hypermethylation (Table 1). We next crossed our microarray dataset with a published dataset identifying E2F1-responsive genes and found significant overlap (Table S2), again supporting E2F1 induction in our experimental system. We also prepared a list of E2F1 targets by selecting human genes whose promoter is predicted to contain *cis*-elements for E2F1, and found that there is a significant enrichment of E2F1 targets in the transcripts induced by 12S rRNA hypermethylation (Table S2), again suggesting an increase in E2F1 transcriptional activity.

E2F1 Mediates Proapoptotic Signaling in Cells Containing the Human Deafness-Associated A1555G Mutation

E2F1 is one of a family of eight E2F transcription factors that are involved in cell cycle regulation through their cyclin-dependent interactions with pocket proteins, including the tumor suppressor Rb (DeGregori and Johnson, 2006). Of particular significance, E2F1 is involved in proapoptotic signaling (Field et al., 1996; Hou et al., 2000; Polager and Ginsberg, 2009). This connection to cell death, in conjunction with our microarray results, made E2F1 a likely candidate for a stress-responsive protein that is responding to mitochondrial dysfunction caused by the A1555G mutation and perhaps also the causative factor in the observed apoptosis susceptibility in the 12S hypermethylation cell lines (Cotney et al., 2009). Entirely consistent with this concept, we confirmed *E2F1* transcriptional induction in cells with 12S rRNA hypermethylation by q-PCR (Figure S1A), and found that the steady-state level of E2F1 protein was increased in A1555G cybrids and in HeLa cells that overexpress h-mtTFB1 compared to appropriate control lines (Figure 2A; Figure S1B). In addition, we observed a decrease in the steady-state amount of Rb (Figure 2A; Figure S1B) and/or its increased phosphorylation (Figure 2A; Figure S1B), either of which is consistent with increased E2F1 activity in the 12S hypermethylated cell lines.

Given the association of active E2F1 with apoptosis, we next tested whether the upregulation of E2F1 per se in A1555G cybrids is involved in their heightened sensitivity to apoptotic cell death. In strong support of this concept, we found that suppressing the hypermethylation of the 12S rRNA via knockdown of h-mtTFB1 abolished E2F1 induction (Figure 2B; Figure S1C) and reduced the susceptibility of A1555G cybrids to apoptosis (Figure 2C). Furthermore, reduction of E2F1 to near wild-type levels by shRNA in the A1555G cybrids abrogated the increase in apoptosis susceptibility, as measured by caspase 3/7 activity (Figure 2D) and accumulation of the cleaved form of PARP (Figure 2E; Figure S1D). Altogether, these results indicate that the Rb-E2F1 apoptotic pathway responds to

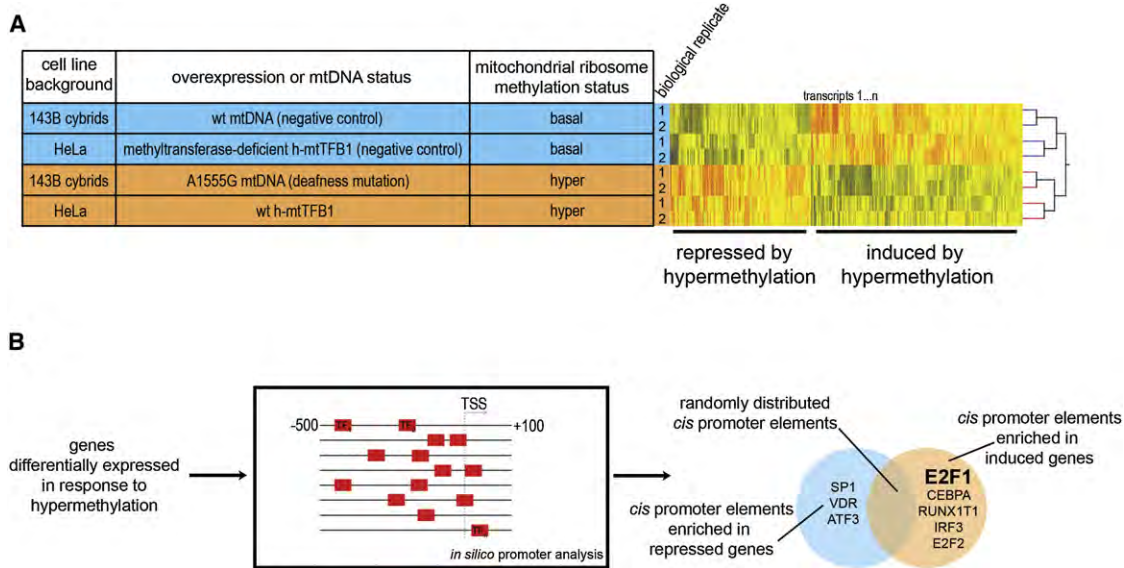


Figure 1. Integrative Genomic Analysis Reveals Upregulation of Nuclear Transcription Factor E2F1 in Response to Mitochondrial Stress Induced by Mitochondrial Ribosome Hypermethylation

(A) Table showing the four cell lines on which we performed microarray analysis to develop a signature of the gene expression response to mitochondrial 12S hypermethylation: two control lines with “basal” mitochondrial 12S hypermethylation (blue) and two experimental cell lines with 12S hypermethylation (orange), with the number of biological replicates indicated. To the right of the table is the representative heat map of all replicates of the cell lines analyzed, with transcripts that are induced or repressed depending on 12S hypermethylation status delineated. “wt” indicates wild-type with regard to either mtDNA or h-mtTFB1. Transcripts whose expression was significantly different (t test p value < 0.05) between the two groups (“basal” versus “hyper”-methylated) represented a 12S hypermethylation signature list that was analyzed further (total of 4,333 transcripts, 2,492 induced, and 1,841 repressed).

(B) The promoter regions (–500 to +100 bp of the predicted transcription start site, TSS) of the genes that were differentially expressed were analyzed for known transcription factor binding sites. The Venn diagram indicates the top transcription factors identified in the repressed (blue) and induced (orange) genes. Since E2F1 was the most overrepresented binding site in the genes induced by 12S rRNA hypermethylation, it became a focus of this study.

mitochondrial stress induced by hypermethylation of 12S rRNA in mitochondrial ribosomes.

ROS-Dependent AMPK Activation Underlies E2F1 Induction in A1555G Cells

To determine the proximal signal leading to E2F1 activation we examined respiratory function in A1555G and corresponding wild-type cybrids and found that the former have decreased basal and maximal mitochondrial O₂ consumption rates (Figure 3A). Furthermore, the respiratory chain in the A1555G cells

is reduced (Figure 3B), a condition conducive to increased ROS production (e.g., superoxide) (Jones et al., 2005). Accordingly, we found that A1555G cells have increased mitochondrial superoxide, as measured by MitoSox (Figure 3C). To determine if this increased superoxide was underlying proapoptotic signaling to E2F1 in A1555G cybrids, we overexpressed mitochondrial superoxide dismutase 2 (SOD2) and found that this eliminated E2F1 induction, increased the total amount of Rb, decreased Rb hyperphosphorylation and eliminated the apoptosis susceptibility in A1555G cells (Figures 3D and 3E).

We next sought to determine how mitochondrial superoxide is sensed and promotes E2F1 activation. AMPK is an established sensor of mitochondrial dysfunction. Furthermore, its activity is activated by superoxide (Quintero et al., 2006) and regulates E2F1 by phosphorylating Rb (Dasgupta and Milbrandt, 2009) making it a potential candidate in the stress pathway we have elucidated. Accordingly, we found that A1555G cybrids have increased active AMPK α (phospho-AMPK α) compared to wild-type controls, and that AMPK α activity was restored close to normal upon overexpression of SOD2 (Figure 3D). To determine if the increased AMPK activity was linked to E2F1 induction in A1555G cells, we treated A1555G cells with AMPK inhibitor compound C, which was confirmed by reduced phosphorylation of AMPK target acetyl-CoA carboxylase (ACC) (Figure 3F). Pharmacological inactivation of AMPK in A1555G cybrids reduced

Table 1. Transcription Factors Whose cis-Elements Are Detected in the Promoters of Transcripts Upregulated in Response to 12S rRNA Hypermethylation, but Not in the Promoters of the Downregulated Transcripts

Transcription Factor	Upregulated Target Genes	Downregulated Target Genes	p Value
E2F1	50	0	0.00010
CEBPA	43	0	0.00012
RUNX1T1	15	0	0.0010
IRF3	13	0	0.0018
E2F2	9	0	0.0128

The p value was calculated using Fisher’s exact test.

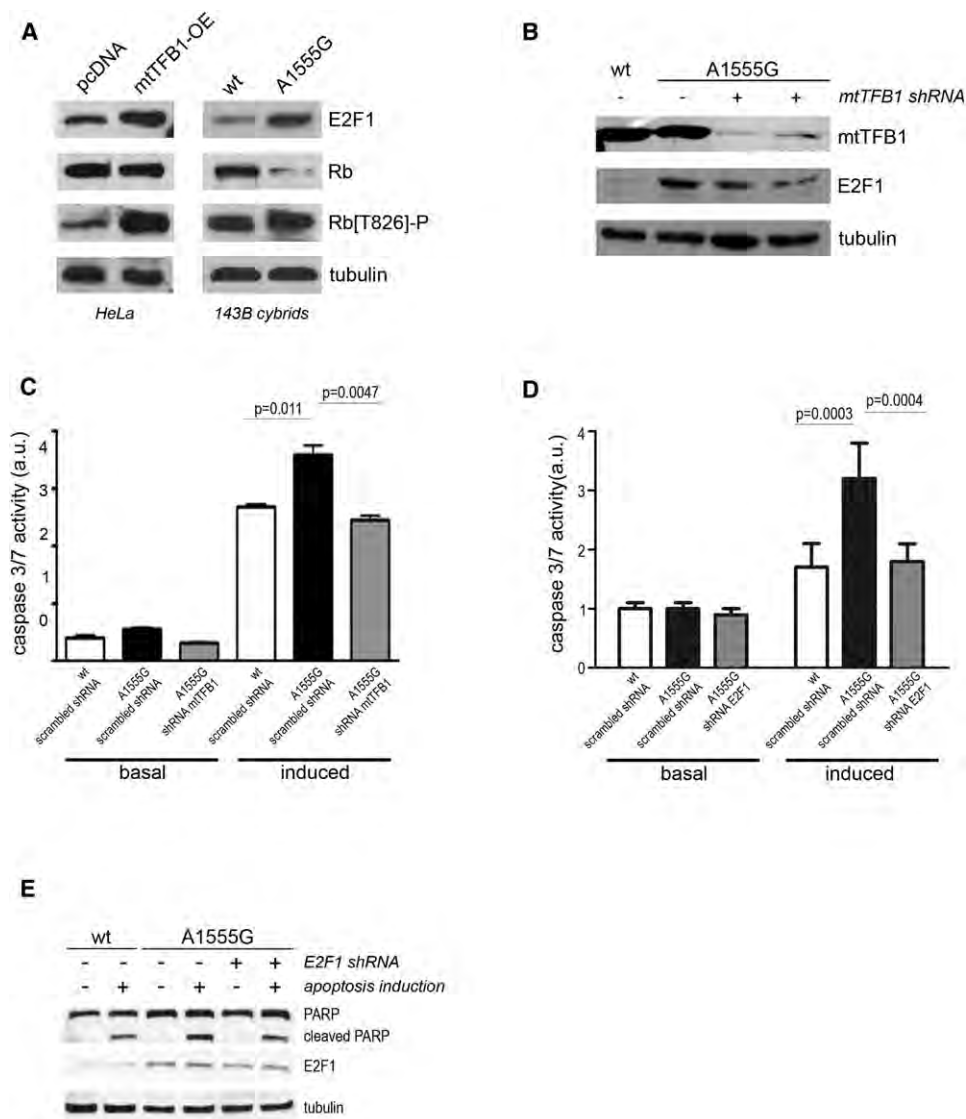


Figure 2. Hypermethylation of Mitochondrial 12S rRNA Leads to Activation of E2F1- and E2F1-Dependent Apoptosis

(A) Western blot analysis of whole-cell extracts for E2F1, Rb and phosphorylated-Rb, (Rb[T826]-P) in HeLa cells that overexpress h-mtTFB1 (mtTFB1-OE) compared to cell containing an empty-vector negative control (pcDNA), and in human 143B cybrids containing wild-type (wt) or A1555G mtDNA. Tubulin was probed as a loading control. Quantification is shown in Figure S1B.

(B) Effect of mtTFB1 knockdown (to reduce 12S hypermethylation) on E2F1 levels in A1555G cybrids by Western blot using tubulin as a loading control. Two independent knockdown constructs were used (+), and a scrambled shRNA was used as a negative control (-). 143B cybrids with wild-type (wt) mtDNA treated with the negative control shRNA are shown in lane 1. Quantification is shown in Figure S1C.

(C) Quantitation of apoptosis (caspase 3/7 activity) in 143B cybrids containing wild-type (wt) or A1555G mtDNA without (-) or with (+) mtTFB1 knocked down by shRNA. Basal and induced apoptosis refer to the presence and absence of staurosporine. The values plotted represent mean \pm standard deviation (n = 12), with t test p values indicated.

(D) Quantitation of apoptosis (caspase 3/7 activity) in 143B cybrids containing wild-type (wt) or A1555G mtDNA without (-) or with (+) E2F1 knocked down by shRNA. Basal and induced apoptosis refer to the presence and absence of staurosporine. The values plotted represent mean \pm standard deviation (n = 12), with t test p values indicated.

(E) Western blot analysis of full-length and cleaved PARP and of E2F1 in wild-type (wt) and A1555G treated with scrambled (-) or E2F1 (+) shRNA without (-) or with (+) induction of apoptosis by staurosporine. E2F1, full-length (PARP) and caspase-3-cleaved forms of PARP are shown, with tubulin probed as a loading control. Quantification is shown in Figure S1D.

Rb phosphorylation and E2F1 levels (Figure 3F), and lowered apoptosis susceptibility of the A1555G cells (Figure 3G). Taken together, these results strongly implicate AMPK as a ROS-sensi-

tive component of the mitochondrial stress-response pathway that leads to proapoptotic E2F1 signaling in cells containing the deafness-causing A1555G mutation.

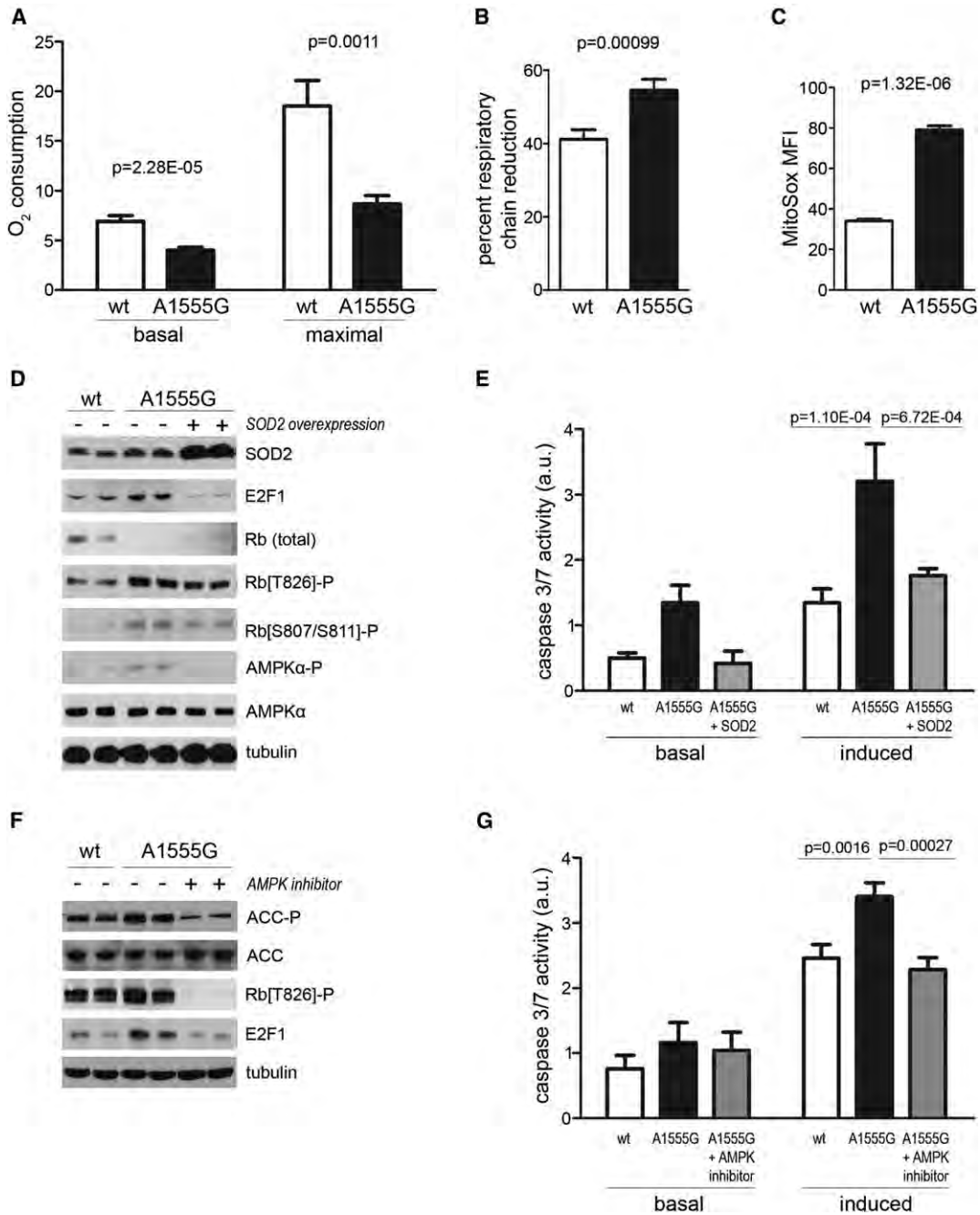


Figure 3. A Proapoptotic Mitochondrial Stress-Signaling Pathway that Involves Mitochondrial ROS-Dependent Activation of E2F1 by AMPK

(A) Basal and maximal (+ FCCP uncoupler) mitochondrial O₂ consumption rates in 143B cybrids containing wild-type (wt) or A1555G mtDNA are shown. The mean ± standard deviation (n = 24) is plotted, with t test p values indicated.

(B) Degree of respiratory chain reduction in the same cells as in (A). This is the ratio of basal to maximal respiration, the latter of which was considered 100% reduction (i.e., the chain handling the maximal amount of electrons). The mean ± standard deviation (n = 12) is plotted, with t test p values indicated.

(C) Mitochondrial ROS in 143B cybrids containing wild-type (wt) or A1555G mtDNA as measured by FACS analysis of MitoSox staining. The mean fluorescence intensity ± standard deviation is plotted (n = 3), with t test p values indicated.

(D) Western blot analysis of A1555G cybrids that overexpress SOD2. Immunoblotting of E2F1, Rb, phospho-Rb T826 and S807/811, AMPK α , and phospho-AMPK α T172 are shown in A1555G cybrids transfected with the SOD2 overexpression vector (lanes 5 and 6), and in control cybrids with wild-type mtDNA (“wt,” lanes 1 and 2) and A1555G mtDNA (lanes 3 and 4) transfected with empty vector. Lanes 1 and 2, 3 and 4, and 5 and 6 represent independent biological replicates. Tubulin was probed as a loading control.

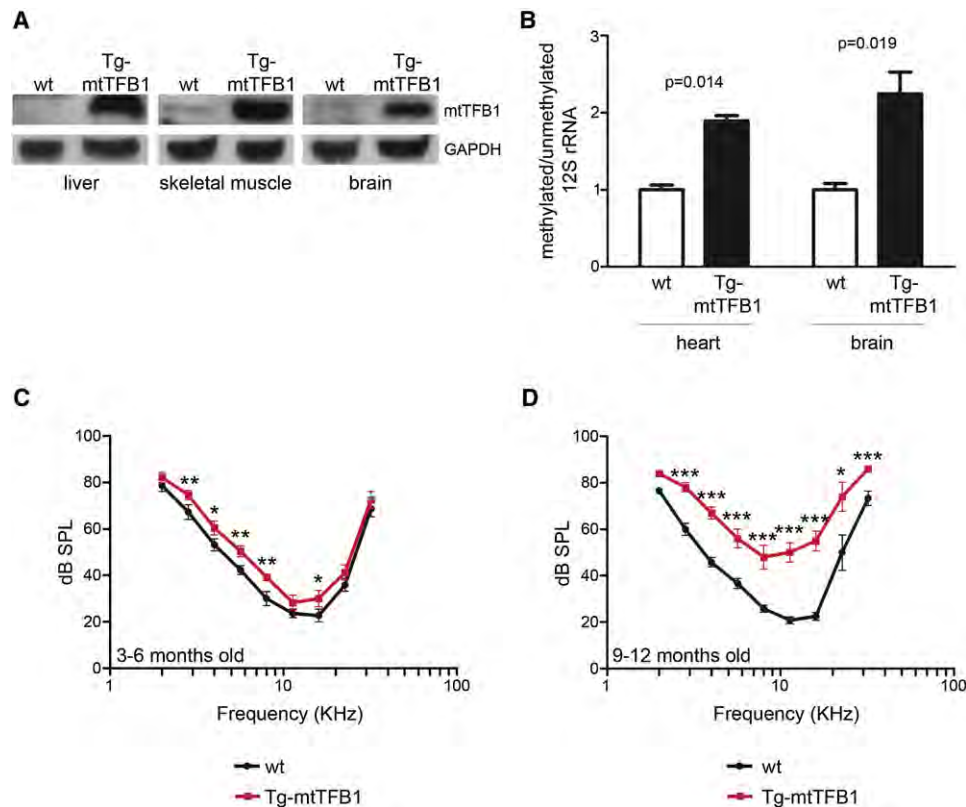


Figure 4. Transgenic Mice that Overexpress the mtTFB1 rRNA Methyltransferase Exhibit 12S Hypermethylation and Progressive Hearing Loss

(A) Western blot of mtTFB1 in wild-type (wt) and transgenic mtTFB1 (Tg-mtTFB1) mouse tissues using GAPDH as loading control.

(B) Quantification of the degree of 12S rRNA methylation in Tg-mtTFB1 mouse heart and brain tissues using a methylation-sensitive mitochondrial 12S rRNA primer-extension assay (Cotney et al., 2009). The values plotted represent mean of methylated/unmethylated \pm standard deviation ($n = 3$), with t test p values indicated.

(C) Hearing thresholds determined by ABR analysis of Tg-mtTFB1 (red points) and control wild-type (wt), nontransgenic littermate control mice (black points) are shown in the audiogram (frequency versus threshold curve). The threshold (in sound pressure level, dB SPL) was tested with 5 dB resolution and frequencies in half octave steps from 32 to 2 kHz. The values plotted represent mean \pm SEM, with t test p values indicated (* $p < 0.05$; ** $p < 0.01$; *** $p < 0.001$). Mice were tested at ages 3–6 months (9 wt mice and 12 Tg-mtTFB1 mice were used).

(D) Same as in (C) except mice were tested at ages 9–12 months (5 wild-type mice and 6 Tg-mtTFB1 mice were used).

Transgenic Mice that Overexpress the Mitochondrial rRNA Methyltransferase mtTFB1 Exhibit Increased Mitochondrial 12S rRNA Methylation in Multiple Tissues and Progressive Hearing Loss

The cell culture studies above strongly implicate an E2F1-dependent, proapoptotic mitochondrial stress signaling pathway downstream of mitochondrial 12S hypermethylation as a potential pathogenic component of deafness caused by the A1555G mtDNA mutation. To test this hypothesis directly, we generated

transgenic mice that globally overexpress the mouse mtTFB1 rRNA methyltransferase (Tg-mtTFB1) responsible for the specific mitochondrial 12S methylation event implicated (Seidel-Rogol et al., 2003). These animals are viable and fertile, and have increased mtTFB1 protein in multiple tissues (Figure 4A) that corresponds with increased 12S rRNA methylation (Figure 4B). When we measured hearing function in Tg-mtTFB1 mice by the auditory brainstem response (ABR) and compared them to age-matched, nontransgenic littermate controls, we found that

(E) Quantitation of apoptosis (caspase 3/7 activity) in 143B cybrids containing wild-type (wt) mtDNA (white bars) or A1555G mtDNA without (black bars) or with SOD2 overexpression (gray bars). Basal and induced apoptosis refer to the presence and absence of staurosporine. The values plotted represent mean \pm standard deviation ($n = 12$), with t test p values indicated.

(F) Effect of pharmacological AMPK inhibition on the levels of acetyl-CoA carboxylase (ACC), phospho-ACC S79 (ACC-P), phospho-Rb T826, and E2F1 in A1555G cybrids (lanes 5 and 6), determined by western blot of whole-cell extracts using tubulin as a loading control. Lanes 1 and 2 (wild-type cybrids) and 3 and 4 (A1555G cybrids) are the vehicle controls (–). Lanes 1 and 2, 3 and 4, and 5 and 6 represent independent biological replicates.

(G) Quantitation of apoptosis (caspase 3/7 activity) in 143B cybrids containing wild-type (wt) mtDNA (white bars), or A1555G mtDNA without (black bars) or with AMPK inhibition (gray bars). Basal and induced apoptosis refer to the presence and absence of staurosporine. The values plotted represent mean \pm standard deviation ($n = 12$), with t test p values indicated.

at 3–6 months of age Tg-mtTFB1 mice have higher ABR thresholds across the entire range of frequencies, indicating significant hearing loss (Figure 4C). Similar hearing-threshold defects are observed in patients with the A1555G mutation (Noguchi et al., 2004). This hearing loss in the Tg-mtTFB1 animals progresses dramatically with age, with a much greater difference in ABR thresholds in animals aged to 9–12 months (Figure 4D). It is important to note that, even though the C57BL/6 genetic background used here exhibits premature age-related hearing loss (Someya et al., 2009), significant decreases in ABR in these mice are not observed until 12–15 months of age, which is beyond the time frame we analyzed in this study.

E2F1 Induction and Apoptosis in Critical Inner Ear Cells of Tg-mtTFB1 Mice

The cochlea of the Tg-mtTFB1 mice display a largely normal structure, with no obvious loss of the hair cells in the organ of Corti (Figure 5A, upper panel) or obvious disruption of the spiral ganglion (Figure 5B, upper panel). Not observing significant hair cell dysfunction or apoptosis even in 1-year-old animals with severe hearing loss, we turned our attention to other critical inner ear cell types. We found that E2F1 protein was increased in the stria vascularis (Figure 5A, middle panel) and in the spiral ganglion neurons (Figure 5B, middle panel) of Tg-mtTFB1 mice, but not in the organ of Corti. This tissue-specific upregulation of E2F1 correlated with increased caspase 3/7 staining in the stria vascularis (Figure 5A, bottom panel) and spiral ganglion neurons (Figure 5B, bottom panel), consistent with E2F1 enacting a proapoptotic signal in critical cells involved in inner ear homeostasis and hearing. To confirm the caspase-3 activation in the spiral ganglion of Tg-mtTFB1 mice, we measured the number of spiral ganglion neurons and the number of caspase-3-positive neurons, and found that Tg-mtTFB1 mice have ~30% fewer spiral ganglion neurons and a 3-fold increase in the number of caspase-3-positive cells (Figure 5C). Consequently, the percentage of caspase-3-positive cells is 4-fold higher in Tg-mtTFB1 spiral ganglion (Figure 5D).

In support of the cell-type specificity of the mitochondrial-stress pathway to E2F1 *in vivo*, we found that E2F1 is not induced in other tissues of Tg-mtTFB1 mice (Figure S2A). Interestingly, activation of AMPK, measured by phosphorylation of both AMPK α and ACC, is detectable in some tissues (skeletal muscle and heart) but not in the liver (Figure S2A). To further confirm the tissue specificity of E2F1 activation, we measured the transcript levels of *E2F1*, and found an increase in the stria vascularis, but not in the organ of Corti or in the brain (Figure S2B). Furthermore, there is increased phospho-AMPK in the stria vascularis of Tg-mtTFB1 mice (Figure S2C). Finally, analysis of available microarray datasets from the mtDNA-mutator mouse (Trifunovic et al., 2004), which exhibits age-related pathology including deafness (Someya et al., 2008), revealed that E2F1 transcripts and its targets are upregulated in the cochlea, but not in skeletal muscle (Figure S2D; Table S3), further supporting the role of E2F1 in cell death in the inner ear.

E2F1 Mediates Hearing Loss in Tg-mtTFB1 Mice

In order to determine if E2F1 induction *per se* has a causal role in the observed hearing loss in this new mouse model of deafness,

we crossed the Tg-mtTFB1 mice with E2F1 knockout mice, to generate mice heterozygous for E2F1 that either overexpress Tg-mtTFB1 (E2F1^{+/-},Tg-mtTFB1) or not (E2F1^{+/-}). Evaluation of hearing function in these animals by ABR revealed that overexpression of mtTFB1 no longer promoted significant hearing loss in the E2F1^{+/-} genetic background (Figure 5E), which has reduced expression of E2F1. These results confirm a causal role for activation of E2F1 above a certain threshold level in the hearing loss observed in Tg-mtTFB1 mice.

DISCUSSION

In this study, we endeavored to gain new insight into the complexity and tissue specificity of mitochondrial-based diseases by studying the common human mtDNA mutation A1555G that has one primary outcome, deafness, and modeling its pathogenic mechanism in mice. Based on our results, we conclude that a major pathogenic driving force is cell death due to activation of the proapoptotic nuclear transcription factor E2F1 by a cell-type-specific mitochondrial stress pathway. Below we will discuss the results that led us to this conclusion and the potential broader implications of this study with regard to the documented environmental exacerbation of this form of deafness (Warchol, 2010), age-related hearing loss (presbycusis), and other diseases where mitochondria are implicated in pathogenesis.

We propose that mitochondrial stress due the hypermethylation of the mtDNA-encoded 12S rRNA is a critical component of the inner ear pathology associated with deafness caused by the human mtDNA A1555G mutation. This is perhaps best demonstrated by our results in the Tg-mtTFB1 transgenic mice, which exhibit 12S rRNA hypermethylation in multiple tissues and activation of the proapoptotic transcription factor E2F1 that causes progressive hearing loss similar to that observed in human A1555G patients. Deafness is the primary effect of the A1555G mutation even though most patients are homoplasmic (i.e., have 100% mutant mtDNA) in all cells and tissues (Fischel-Ghodsian, 1999; Prezant et al., 1993). This implies a cell-type specific response to mitochondrial dysfunction is at play. Our results showing that upregulation of E2F1 and increased cell death occur in the stria vascularis and in the spiral ganglion neurons, but not in the organ of Corti, are consistent with activation of E2F1 by mitochondrial stress occurring only in certain critical cells in the inner ear and their subsequent apoptosis via this pathway.

E2F1-dependent cell death in the stria vascularis and spiral ganglion neurons is consistent with the pattern of hearing loss across all frequencies that we observe in the Tg-mtTFB1 mice. With regard to the irreversible nature of the deafness, neurodegeneration in spiral ganglion itself could itself be responsible, as has been proposed for age-related hearing loss (Someya et al., 2009). Alternatively, or in addition, dysfunction of the stria vascularis and spiral ganglion neurons could ultimately result in a higher susceptibility of irreplaceable inner hair cells to undergo cell death (Fetoni et al., 2011). Furthermore, since activation of the cell cycle in post-mitotic neuronal cells is an established trigger for apoptosis (Chen et al., 2003; Hou et al., 2000; Shadel, 2004a) the mitochondrial stress pathway to E2F1 identified

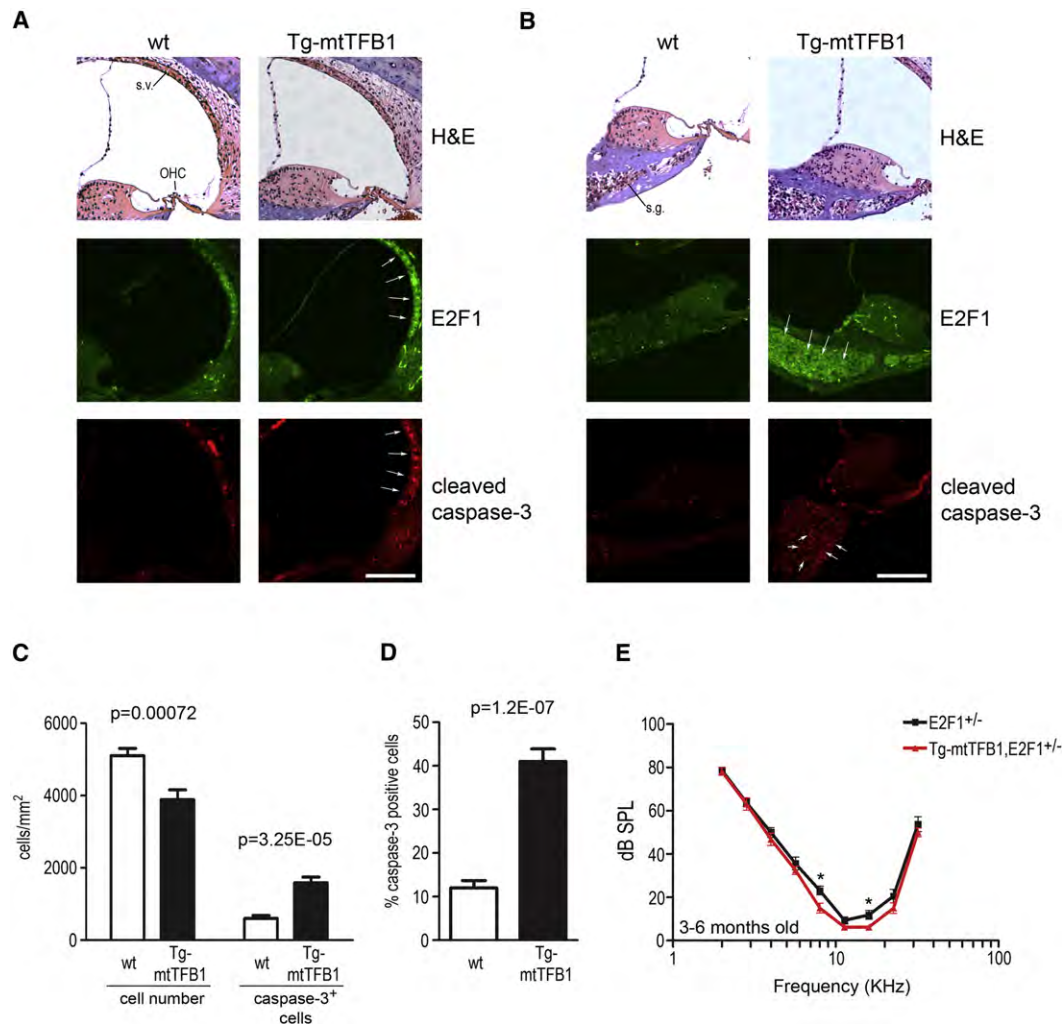


Figure 5. Deafness Pathology in Tg-mtTFB1 Mice Involves Upregulation of E2F1 and Apoptosis in the Stria Vascularis and Spiral Ganglion Neurons of the Inner Ear

(A) H&E staining of the organ of Corti and stria vascularis (top panels) from representative 1-year-old wild-type (wt, left column) and Tg-mtTFB1 mice (right column). The middle panels show immunohistochemistry staining for E2F1 and the lower panels show immunohistochemistry for cleaved caspase-3 in similar representative sections. White arrows indicate areas where significant changes in signal are observed. Stria vascularis (s.v.), outer hair cells (OHC), scale bar, 100 μ m. See also Figure S2.

(B) Same as in (A) but sections that highlight staining in the spiral ganglion neurons are shown. Spiral ganglion (s.g.), scale bar, 100 μ m.

(C) Quantification of cellular density in the spiral ganglion (the left side of the plot) and of caspase-3-positive spiral ganglion neurons (right side). The sections were obtained from three wild-type and three Tg-mtTFB1 mice at 1 year of age, and six independent sections were counted for each animal. The values plotted represent mean \pm standard deviation, with t test p values indicated.

(D) Same as in (C), but expressing the percentage of caspase-3-positive cells in the spiral ganglion. The values plotted represent mean \pm standard deviation, with t test p values indicated.

(E) ABR analysis of E2F1^{+/-} mice (black points) and E2F1^{+/-}/Tg-mtTFB1 mice (red points) performed as described in Figure 4C. Mice were tested at ages 3–6 months (eight E2F1^{+/-} mice and ten E2F1^{+/-}/Tg-mtTFB1 mice were used). The values plotted represent mean \pm SEM, with t test p values indicated (*p < 0.05).

herein may also make some cells of the inner ear inherently more susceptible to cell death due to being forced into the cell cycle, as opposed to activation the E2F1 apoptosis pathway per se. Based on these considerations, we propose that A155G patients would likewise be more prone to eventual loss of critical inner ear cells via this mitochondrial stress pathway to E2F1, explaining their irreversible hearing loss either spontaneously, as a function of age, or in response to environ-

mental stimuli such as noise or aminoglycosides. Even though our results strongly implicate 12S hypermethylation per se in the deafness phenotype in mice, it is likely that defects in mitochondrial translation caused by the A155G mutation, such as infidelity (Hobbie et al., 2008), conspire with hypermethylation to produce the precise deafness pathology in humans and/or mediate its exacerbation by aminoglycoside antibiotics. Therefore, it remains important to determine precisely which

mechanisms and cell types within the inner ear instigate deafness pathology in this new mouse model and in human A1555G patients. A full understanding of these events may be therapeutic in this regard and could help advance efforts to regenerate hearing function.

Our results in A1555G cybrids also provide key insight into the nature of the pathogenic mitochondrial stress-signaling pathway. Specifically, hypermethylation of mitochondrial ribosomes, which are needed for translational and assembly of the respiratory chain (Bonawitz et al., 2006), disrupts mitochondrial respiration in a manner that increases ROS production (Figure 3). We propose that increased mitochondrial superoxide is sensed by AMPK (Emerling et al., 2009; Quintero et al., 2006), activation of which relays the stress signal to E2F1. Since E2F1 activity is associated with proapoptotic signaling and is necessary for the enhanced cell death on A1555G cybrids (Figure 2D) and hearing loss in Tg-mtTFB1 mice (Figure 5E), we speculate ROS- and AMPK-dependent activation of E2F1 is the major mitochondrial stress-signaling pathway involved under these circumstances. Going forward, it will be important to determine precisely how E2F1 is regulated by ROS and AMPK.

The marked tissue specificity of E2F1 induction and, to a lesser degree, of AMPK activation (Figure S2A), provides insight into the complex mechanisms underlying tissue specificity of mitochondrial diseases. The requirement for multiple sequential steps to fully activate the mitochondrial ROS-AMPK-E2F1 apoptotic pathway provides a variety of opportunities for different tissues to suppress a pathogenic mechanism. For example, tissues with lower OXPHOS activity or better redox buffering could prevent initial activation of the pathogenic mechanism. Alternatively, in other tissues, AMPK may not respond to ROS, E2F1 may not be activated by AMPK, or E2F1 may not be a potent trigger of apoptosis, any of which would presumably prevent a pathogenic outcome. These observations may be generalizable, in that other pathogenic mitochondrial retrograde signaling pathways likely exist with their differential activation or readout in tissues contributing to the complex tissue specificity observed in mitochondrial diseases.

Finally, the induction of E2F1 in response to a mitochondrial malfunction may represent a paradigm in mitochondrial pathogenesis where the cause of the disease is not the immediate OXPHOS dysfunction, but instead the misinterpretation of resulting retrograde signals generated by mitochondria. The pivotal role of AMPK as a sensor of energy charge and now as a ROS-dependent regulator of E2F1 activity highlights the complexity of mitochondrial stress responses and the need for additional research to uncover other such pathways. Finally, it is tempting to speculate that aberrant mitochondrial stress signaling may also be of general significance in diseases and circumstances where mitochondrial dysfunction and apoptosis are implicated, such as heart disease, cancer, neurodegenerative diseases and aging.

EXPERIMENTAL PROCEDURES

Cell Culture, shRNA-Mediated Gene Knockdown, FACS Analysis, and 12S Methylation Assays

143B osteosarcoma cybrids containing either wild-type (A1555A) or mutant (A1555G) mtDNA (Guan et al., 2001) were grown in DMEM high glucose (Sigma

D5648) plus 10% fetal calf serum at 37°C and 5% CO₂. Prior to all experiments, cells were plated at 5,000 cells/cm² and grown for 96 hr to 70%–80% confluence. When puromycin was used for selection, it was removed at least 24 hr prior to harvesting cells. HeLa cells that overexpress h-mtTFB1 have been described (Cotney et al., 2007, 2009).

Retroviral-mediated shRNA knockdown of mtTFB1 and E2F1 by was carried as described (Cotney et al., 2009) with the following modifications. Wild-type or mutant 143B cybrids were transfected and plated at 5,000/cm² in DMEM with 10% fetal calf serum and 600 ng/ml puromycin and used for experiments at 70%–80% confluence. Puromycin was removed 48 hr prior to analysis. Target sequences ligated into the pSiren-RetroQ vector (Clontech) for mtTFB1 and E2F1 knockdown, as well the scrambled negative-control shRNA used were described previously (Cotney et al., 2009; Goto et al., 2006). To overexpress SOD2, cybrids were transfected with pCMV-SPORT6-SOD2 (Open Biosystems MMM4769-99609684) or pcDNA3.0 as a negative control as described (Cotney et al., 2009). To inhibit AMPK, cybrids were treated for 16 hr with 10 μM of compound C (Calbiochem) and then used immediately for experiments.

To analyze mitochondrial superoxide by FACS, wild-type and A1555G cybrids were treated with 50 nM MitoSOX (Invitrogen) for 20 min at 37°C, rinsed, and detached with trypsin. Fluorescence was measured using a FACScan (BD Biotechnology) and analyzed using FlowJo software. Primer-extension analysis of mitochondrial 12S rRNA adenine dimethylation was performed on 1–5 μg of total cellular or tissue RNA prepared using the RNEasy Kit (QIAGEN) as described (Cotney et al., 2007; Seidel-Rogol et al., 2003), except 2 μM each of dATP, dCTP, and dTTP and 0.5 μM ddGTP were used.

Western Blotting

Whole-cell extracts of cultured human cells were prepared in 1.5% n-dodecyl-maltoside in PBS as described (Raimundo et al., 2009). Gels were loaded with 50 μg of total protein per well, and the following antibodies were used for immunoblotting: E2F1 (Santa Cruz, sc193), mtTFB1/TFBM1 (McCulloch and Shadel, 2003) or that provided by Dr. Craig Cameron, tubulin (Thermo, DM1A), Rb (BD PharMingen, 554136), phospho-Rb (T826) (Abcam, ab4779-50), phospho-Rb (S807/811) (Cell Signaling, 9308S), AMPKα (Cell Signaling, 2603), phospho-AMPKα (T172) (Cell Signaling, 2535S), acetyl-CoA carboxylase (ACC) (Cell Signaling, 3676), phospho-ACC (S79) (Cell Signaling, 3661), SOD2 (Assay Designs, SOD-111), PARP (Cell Signaling, 9542), and GAPDH (Ambion, AM4300). Western blots were performed on three to four biological replicates and at least three technical replicates.

Apoptosis Assays

To induce E2F1-dependent apoptosis, cybrids were treated with 200 nM staurosporine for 3 hr in the presence of 10 mM wortmannin as described (Hallstrom et al., 2008). Cells were then rinsed and used for two different apoptosis assays. Caspase 3/7 activity was determined using a plate reader 1 hr after treatment with Caspase-Glo reagent (Promega) as described by the manufacturer, and full-length and cleaved PARP were assayed by western blot.

Oxygen Consumption Analysis

Cells were plated in XF96 plates (SeaHorse Biosciences) at 10,000 cells/well and the next day cellular O₂ consumption was determined in a SeaHorse Bioscience XF96 extracellular flux analyzer according to manufacturer instructions. Cells were maintained at 37°C in normal growth medium without serum. In some wells 8 μM of the mitochondrial uncoupler FCCP was added.

Microarrays and Data Analysis

Total cellular RNA from the cultured cells was prepared using an RNeasy mini RNA extraction kit (QIAGEN GmbH, Hilden, Germany) and used for the expression microarray procedure in conjunction with the Yale University W.M. Keck Foundation Biotechnology Resource Laboratory. RNA integrity was first verified by an Agilent Bioanalyzer and then amplified, labeled and hybridized onto GeneChip HG-U133 Plus 2.0 arrays (Affymetrix, Agilent, Santa Clara, CA) using standard protocols recommended by the manufacturer, starting from 5 μg of total RNA. Data were normalized by the RMA method (Irizarry et al., 2003), using commercial software (GeneSpring, Agilent, Santa Clara, California, CA). For each biological sample, two RNA samples were prepared

from two independently collected cell pellets. To analyze the expression data, samples were grouped according to their 12S rRNA methylation status (Figure 1A). The four samples in the hypermethylation group were compared to the four samples with basal methylation to control for nonspecific effects of overexpression of mtTFB1 independent of increased 12S rRNA methylation and in an attempt to subtract effects due to cell nuclear genetic background. Transcripts whose expression was significantly changed between the two groups formed the 12S rRNA hypermethylation list (4333 transcripts; Table S1). The student's t test was used to determine statistically significant changes in expression, with a cutoff p value of 0.05 (Raimundo et al., 2009). The false-positive rate was determined to be 3.8% as described (Hovatta et al., 2005). The correlation of the Q-PCR with the microarray results for six genes tested was $R^2 = 0.77$ (Raimundo et al., 2009).

To determine which *cis*-elements were present in the promoters of the genes up- or downregulated in 12S rRNA hypermethylated samples, we used the Biblosphere software (Genomatix Software GmbH, Munich, Germany). To minimize false positives, a cutoff of at least two *cis* element-gene cocitations was implemented. Enrichment in *cis*-elements of the genes up- or downregulated was determined by Fisher's exact test.

Generation and Analysis of Transgenic Mice that Overexpress mtTFB1

A mouse mtTFB1 cDNA was amplified with primers containing EcoR1 and EcoRV restriction sites and ligated into the vector pCAGGS that contains a CMV immediate early-enhancer/chicken β -actin/rabbit β -globin promoter (Niwa et al., 1991) and confirmed by sequencing. Purified pCAGGS/mtTFB1 plasmid was digested with Sall and PstI, to liberate a fragment containing the enhancer, promoter, *TFB1M* ORF, and poly-A tail. This linear DNA fragment was then used by the Yale Animal Genomic Services to microinject pronuclear, C57BL/6J X SJL/J embryos. Seventy-four animals were born from the six foster mothers. After genotyping, one female (F1) founder was identified that contained the transgene. This female was then mated with a wild-type C57BL/6J male to generate the second generation (F2) and then serially to create subsequent generations. Female F3 to F5 transgenics and control nontransgenic littermates were used for all of the experiments. All procedures were IACUC-approved as determined by the Yale University Animal Care and Use Committee.

For analysis of mouse samples, tissues from 9-month-old mice were harvested, immediately frozen in liquid nitrogen, and stored at -80°C . The tissues were ground using a mortar and pestle previously frozen at -80°C , kept on dry ice during the procedure. Whole-tissue homogenates were prepared as described (Cotney et al., 2009). Primer extension analysis and q-PCR were performed on RNA purified from these same mouse tissues using the RNeasy kit using the method already described for human cells, but with the following mouse 12S-specific primer: 5'-ATTATTCGAAGC-3'. To generate Tg-mtTFB1/E2F1^{+/-} mice, a C57BL/6J male E2F1^{-/-} was obtained from the Jackson Laboratory (Bar Harbor, ME) and mated with F4 Tg-mtTFB1 females, yielding E2F1^{+/-} progeny with and without the mtTFB1 transgene.

Auditory Brainstem Response and Cochlear Histology

Detailed methods for the ABR analysis can be found in the *Extended Experimental Procedures*. A total of 21 animals (9 Tg-mtTFB1 and 12 wild-type littermates) between the ages of 3 and 6 months, and 11 animals between 9 and 12 months (5 wild-type, 6 Tg-mtTFB1), were used for auditory brainstem response (ABR) testing. The E2F1^{+/-} animals were tested at 3–6 months of age (total of 20, 8 wild-type and 12 Tg-mtTFB1). In all experiments, age-matched littermates were compared directly on the same day and by the same experienced specialist blinded to the genotype of the mice. The mice were subsequently combined into 3–6 and 9–12 groups for data presentation and statistical analysis. Animals were anesthetized with chloral hydrate (480 mg/kg IP) and all recordings were conducted in a sound-attenuating chamber (Industrial Acoustics Corp) using a customized TDT3 system (Tucker-Davis Technologies, Inc.). A t test was used to determine the statistical significance of the threshold difference at each frequency.

The inner ear was prepared for histology by removing the temporal bone and exposing and rupturing the bulla. The cochlea was perfused with 4% paraformaldehyde (in PBS) using a syringe outfitted with small diameter tubing

through the oval and round windows. The tissue was incubated overnight, decalcified in 10% EDTA in PBS for 3 days, and then paraffin embedded, sectioned in 5 mm samples and mounted onto glass slides by the Yale Histology section. Following deparaffinization and rehydration, sections were used for immunohistochemistry and hematoxylin staining. Images were obtained using an Olympus IX71 microscope and Metamorph image analysis software. Nine independent cochlear sections were analyzed from three 1-year-old wild-type and three Tg-mtTFB1 mice. Spiral ganglion cells were counted using the DAPI counterstain in an area of 100 × 100 pixels and normalized to area (mm²). Cells displaying cytoplasmic foci of caspase-3 were considered caspase-3⁺.

ACCESSION NUMBERS

The raw data were deposited in the Gene Expression Omnibus repository (accession #GSE33780).

SUPPLEMENTAL INFORMATION

Supplemental Information includes Extended Experimental Procedures, three tables, and two figures and can be found with this article online at doi:10.1016/j.cell.2011.12.027.

ACKNOWLEDGMENTS

This study was supported by grants R01 HL-059655 to G.S.S. and R01 DC000273 to J.S.-S. from the U.S. NIH and a UMDf fellowship to T.E.S. The authors thank Zimei Zhang for animal husbandry, Yale Animal Genomic Services for help in generating the Tg-mtTFB1 mice, and Dr. Susan Kaech for comments on the manuscript, helpful discussions and access to the SeaHorse instrument.

Received: September 6, 2011

Revised: October 31, 2011

Accepted: December 15, 2011

Published: February 16, 2012

REFERENCES

- Bonawitz, N.D., Clayton, D.A., and Shadel, G.S. (2006). Initiation and beyond: multiple functions of the human mitochondrial transcription machinery. *Mol. Cell* 24, 813–825.
- Butow, R.A., and Avadhani, N.G. (2004). Mitochondrial signaling: the retrograde response. *Mol. Cell* 14, 1–15.
- Bykhovskaya, Y., Mengesha, E., Wang, D., Yang, H., Estivill, X., Shohat, M., and Fischel-Ghodsian, N. (2004). Human mitochondrial transcription factor B1 as a modifier gene for hearing loss associated with the mitochondrial A1555G mutation. *Mol. Genet. Metab.* 82, 27–32.
- Chen, P., Zindy, F., Abdala, C., Liu, F., Li, X., Roussel, M.F., and Segil, N. (2003). Progressive hearing loss in mice lacking the cyclin-dependent kinase inhibitor Ink4d. *Nat. Cell Biol.* 5, 422–426.
- Cotney, J., Wang, Z., and Shadel, G.S. (2007). Relative abundance of the human mitochondrial transcription system and distinct roles for h-mtTFB1 and h-mtTFB2 in mitochondrial biogenesis and gene expression. *Nucleic Acids Res.* 35, 4042–4054.
- Cotney, J., McKay, S.E., and Shadel, G.S. (2009). Elucidation of separate, but collaborative functions of the rRNA methyltransferase-related human mitochondrial transcription factors B1 and B2 in mitochondrial biogenesis reveals new insight into maternally inherited deafness. *Hum. Mol. Genet.* 18, 2670–2682.
- Dasgupta, B., and Milbrandt, J. (2009). AMP-activated protein kinase phosphorylates retinoblastoma protein to control mammalian brain development. *Dev. Cell* 16, 256–270.

- DeGregori, J., and Johnson, D.G. (2006). Distinct and Overlapping Roles for E2F Family Members in Transcription, Proliferation and Apoptosis. *Curr. Mol. Med.* 6, 739–748.
- DiMauro, S., and Schon, E.A. (2003). Mitochondrial respiratory-chain diseases. *N. Engl. J. Med.* 348, 2656–2668.
- Emerling, B.M., Weinberg, F., Snyder, C., Burgess, Z., Mutlu, G.M., Violet, B., Budinger, G.R., and Chandel, N.S. (2009). Hypoxic activation of AMPK is dependent on mitochondrial ROS but independent of an increase in AMP/ATP ratio. *Free Radic. Biol. Med.* 46, 1386–1391.
- Fetoni, A.R., Picciotti, P.M., Paludetti, G., and Troiani, D. (2011). Pathogenesis of presbycusis in animal models: a review. *Exp. Gerontol.* 46, 413–425.
- Field, S.J., Tsai, F.Y., Kuo, F., Zubiaga, A.M., Kaelin, W.G., Jr., Livingston, D.M., Orkin, S.H., and Greenberg, M.E. (1996). E2F-1 functions in mice to promote apoptosis and suppress proliferation. *Cell* 85, 549–561.
- Fischel-Ghodsian, N. (1999). Mitochondrial deafness mutations reviewed. *Hum. Mutat.* 13, 261–270.
- Goto, Y., Hayashi, R., Kang, D., and Yoshida, K. (2006). Acute loss of transcription factor E2F1 induces mitochondrial biogenesis in HeLa cells. *J. Cell. Physiol.* 209, 923–934.
- Guan, M.X., Fischel-Ghodsian, N., and Attardi, G. (1996). Biochemical evidence for nuclear gene involvement in phenotype of non-syndromic deafness associated with mitochondrial 12S rRNA mutation. *Hum. Mol. Genet.* 5, 963–971.
- Guan, M.X., Fischel-Ghodsian, N., and Attardi, G. (2000). A biochemical basis for the inherited susceptibility to aminoglycoside ototoxicity. *Hum. Mol. Genet.* 9, 1787–1793.
- Guan, M.X., Fischel-Ghodsian, N., and Attardi, G. (2001). Nuclear background determines biochemical phenotype in the deafness-associated mitochondrial 12S rRNA mutation. *Hum. Mol. Genet.* 10, 573–580.
- Hallstrom, T.C., Mori, S., and Nevins, J.R. (2008). An E2F1-dependent gene expression program that determines the balance between proliferation and cell death. *Cancer Cell* 13, 11–22.
- Hamanaka, R.B., and Chandel, N.S. (2010). Mitochondrial reactive oxygen species regulate cellular signaling and dictate biological outcomes. *Trends Biochem. Sci.* 35, 505–513.
- Hardie, D.G. (2007). AMP-activated/SNF1 protein kinases: conserved guardians of cellular energy. *Nat. Rev. Mol. Cell Biol.* 8, 774–785.
- Hobbie, S.N., Bruell, C.M., Akshay, S., Kalapala, S.K., Shcherbakov, D., and Böttger, E.C. (2008). Mitochondrial deafness alleles confer misreading of the genetic code. *Proc. Natl. Acad. Sci. USA* 105, 3244–3249.
- Hou, S.T., Callaghan, D., Fournier, M.C., Hill, I., Kang, L., Massie, B., Morley, P., Murray, C., Rasquinha, I., Slack, R., and MacManus, J.P. (2000). The transcription factor E2F1 modulates apoptosis of neurons. *J. Neurochem.* 75, 91–100.
- Hovatta, I., Tennant, R.S., Helton, R., Marr, R.A., Singer, O., Redwine, J.M., Ellison, J.A., Schadt, E.E., Verma, I.M., Lockhart, D.J., and Barlow, C. (2005). Glyoxalase 1 and glutathione reductase 1 regulate anxiety in mice. *Nature* 438, 662–666.
- Irizarry, R.A., Bolstad, B.M., Collin, F., Cope, L.M., Hobbs, B., and Speed, T.P. (2003). Summaries of Affymetrix GeneChip probe level data. *Nucleic Acids Res.* 31, e15.
- Jones, R.G., Plas, D.R., Kubek, S., Buzzai, M., Mu, J., Xu, Y., Birnbaum, M.J., and Thompson, C.B. (2005). AMP-activated protein kinase induces a p53-dependent metabolic checkpoint. *Mol. Cell* 18, 283–293.
- McCulloch, V., Seidel-Rogol, B.L., and Shadel, G.S. (2002). A human mitochondrial transcription factor is related to RNA adenine methyltransferases and binds S-adenosylmethionine. *Mol. Cell. Biol.* 22, 1116–1125.
- McCulloch, V., and Shadel, G.S. (2003). Human mitochondrial transcription factor B1 interacts with the C-terminal activation region of h-mtTFA and stimulates transcription independently of its RNA methyltransferase activity. *Mol. Cell. Biol.* 23, 5816–5824.
- Metodiev, M.D., Lesko, N., Park, C.B., Cámara, Y., Shi, Y., Wibom, R., Hulthenby, K., Gustafsson, C.M., and Larsson, N.G. (2009). Methylation of 12S rRNA is necessary for in vivo stability of the small subunit of the mammalian mitochondrial ribosome. *Cell Metab.* 9, 386–397.
- Niwa, H., Yamamura, K., and Miyazaki, J. (1991). Efficient selection for high-expression transfectants with a novel eukaryotic vector. *Gene* 108, 193–199.
- Noguchi, Y., Yashima, T., Ito, T., Sumi, T., Tsuzuku, T., and Kitamura, K. (2004). Audiovestibular findings in patients with mitochondrial A1555G mutation. *Laryngoscope* 114, 344–348.
- Polager, S., and Ginsberg, D. (2009). p53 and E2f: partners in life and death. *Nat. Rev. Cancer* 9, 738–748.
- Prezant, T.R., Agopian, J.V., Bohlman, M.C., Bu, X., Oztas, S., Qiu, W.Q., Arnos, K.S., Cortopassi, G.A., Jaber, L., Rotter, J.I., et al. (1993). Mitochondrial ribosomal RNA mutation associated with both antibiotic-induced and non-syndromic deafness. *Nat. Genet.* 4, 289–294.
- Pulicherla, N., Pogorzala, L.A., Xu, Z., O Farrell, H.C., Musayev, F.N., Scarsdale, J.N., Sia, E.A., Culver, G.M., and Rife, J.P. (2009). Structural and functional divergence within the Dim1/KsgA family of rRNA methyltransferases. *J. Mol. Biol.* 391, 884–893.
- Quintero, M., Colombo, S.L., Godfrey, A., and Moncada, S. (2006). Mitochondria as signaling organelles in the vascular endothelium. *Proc. Natl. Acad. Sci. USA* 103, 5379–5384.
- Raimundo, N., Vanharanta, S., Aaltonen, L.A., Hovatta, I., and Suomalainen, A. (2009). Downregulation of SRF-FOS-JUNB pathway in fumarate hydratase deficiency and in uterine leiomyomas. *Oncogene* 28, 1261–1273.
- Seidel-Rogol, B.L., McCulloch, V., and Shadel, G.S. (2003). Human mitochondrial transcription factor B1 methylates ribosomal RNA at a conserved stem-loop. *Nat. Genet.* 33, 23–24.
- Shadel, G.S. (2004a). Coupling the mitochondrial transcription machinery to human disease. *Trends Genet.* 20, 513–519.
- Shadel, G.S. (2004b). A dual-function mitochondrial transcription factor tunes out deafness. *Mol. Genet. Metab.* 82, 1–3.
- Shadel, G.S. (2008). Expression and maintenance of mitochondrial DNA: new insights into human disease pathology. *Am. J. Pathol.* 172, 1445–1456.
- Someya, S., Yamasoba, T., Kujoth, G.C., Pugh, T.D., Weindruch, R., Tanokura, M., and Prolla, T.A. (2008). The role of mtDNA mutations in the pathogenesis of age-related hearing loss in mice carrying a mutator DNA polymerase gamma. *Neurobiol. Aging* 29, 1080–1092.
- Someya, S., Xu, J., Kondo, K., Ding, D., Salvi, R.J., Yamasoba, T., Rabinovitch, P.S., Weindruch, R., Leeuwenburgh, C., Tanokura, M., and Prolla, T.A. (2009). Age-related hearing loss in C57BL/6J mice is mediated by Bak-dependent mitochondrial apoptosis. *Proc. Natl. Acad. Sci. USA* 106, 19432–19437.
- Trifunovic, A., Wredenberg, A., Falkenberg, M., Spelbrink, J.N., Rovio, A.T., Bruder, C.E., Bohlooly-Y, M., Gidlöf, S., Oldfors, A., Wibom, R., et al. (2004). Premature ageing in mice expressing defective mitochondrial DNA polymerase. *Nature* 429, 417–423.
- Vandebona, H., Mitchell, P., Manwaring, N., Griffiths, K., Gopinath, B., Wang, J.J., and Sue, C.M. (2009). Prevalence of mitochondrial 1555A→G mutation in adults of European descent. *N. Engl. J. Med.* 360, 642–644.
- Wallace, D.C. (2005). A mitochondrial paradigm of metabolic and degenerative diseases, aging, and cancer: a dawn for evolutionary medicine. *Annu. Rev. Genet.* 39, 359–407.
- Warchol, M.E. (2010). Cellular mechanisms of aminoglycoside ototoxicity. *Curr. Opin. Otolaryngol. Head Neck Surg.* 18, 454–458.

Patch-Clamp Recordings from Lateral Line Neuromast Hair Cells of the Living Zebrafish

Anthony J. Ricci,¹ Jun-Ping Bai,⁴ Lei Song,² Caixia Lv,³ David Zenisek,³ and Joseph Santos-Sacchi^{2,3,5}

¹Departments of Otolaryngology and Molecular and Cellular Physiology, Stanford University School of Medicine, Stanford, California 94305, and Departments of ²Surgery (Otolaryngology), ³Cellular and Molecular Physiology, ⁴Neurology, and ⁵Neurobiology, Yale University School of Medicine, New Haven, Connecticut 06510

Zebrafish are popular models for biological discovery. For investigators of the auditory and vestibular periphery, manipulations of hair cell and synaptic mechanisms have relied on inferences from extracellular recordings of physiological activity. We now provide data showing that hair cells and supporting cells of the lateral line can be directly patch-clamped, providing the first recordings of ionic channel activity, synaptic vesicle release, and gap junctional coupling in the neuromasts of living fish. Such capabilities will allow more detailed understanding of mechano-sensation of the zebrafish.

Introduction

Zebrafish hold promise for uncovering physiological mechanisms that are difficult to realize in other model species, because of the benefits of rapid reproductive rate and reduced organismal complexity (Rinkwitz et al., 2011). Indeed, progress has been enormous with this species, even in the auditory/vestibular arena, a field that usually prides itself on understanding human mechanisms with mammalian models. For example, great strides have been made in hair cell mechano-transduction and synaptic mechanisms (Nicolson, 2005). However, an obstacle to truly capitalizing on zebrafish for hair cell mechanism discovery is the heretofore inability to obtain patch-clamp recordings from neuromast sensory hair cells. We now report that this impediment has been overcome. We show preliminary data of whole-cell recordings from cells within lateral line neuromasts of living zebrafish, demonstrating ionic channel activity and synaptic vesicle release in hair cells. Additionally, we identify voltage-dependent gap junctional coupling in neuromast supporting cells. Our approach should help investigators obtain cellular data crucial to understanding the powerful genetic manipulations already available in zebrafish.

Materials and Methods

Zebrafish of either sex ranging in age from 3 to 14 days postfertilization (dpf) were anesthetized in Tricane and mounted in a recording chamber using dental floss tie downs (see Ricci and Fettiplace, 1997). Viability was monitored by visually monitoring heart rate and blood flow. An upright Nikon Eclipse was used for viewing, and recordings were made with an

Axon 200B amplifier with an Axon DD1322 digitizer. Images were enhanced with a Hamamatsu CCD camera. All recordings and image capture were made with jClamp software (Scisoft). Cells were held at -80 mV. Extracellular solution was as follows (in mM): 125 NaCl, 1.0 KCl, 2.2 MgCl₂, 2.8 CaCl₂, 10 HEPES, 6 D-glucose, 285 mOsm, pH 7.6. Pipette solution was (in mM): 90 CsCl, 20 TEA, 5 Na₂ATP, 3.5 MgCl₂, 10 HEPES, 1 EGTA, 260 mOsm, pH 7.2. Intracellular KCl (110 mM) solution lacked TEA. P/-5 protocols were made at a subtraction holding potential of -80 mV. Pipette resistance was typically 6.5 M Ω with Cs pipette solutions. Pipettes used to clean a pathway toward hair cells were ~ 1 –2 M Ω . For patch pipettes, 1.5-mm-thick-walled borosilicate glass was used without any coating. Capacitance measures were made with a dual sine admittance technique (Santos-Sacchi, 2004; Schnee et al., 2011a,b). Recordings were made at room temperature. Data are reported as mean \pm SE.

Results

Zebrafish lateral line neuromasts are peripherally located on each side of the zebrafish. Before scale formation, the organ is accessible via micropipette. Figure 1 shows a series of Hoffman optics images at different levels through the neuromast, starting apically where the hair cell kinocilia insert into the gelatinous cupola (A,B). Each kinocilium arises from one hair cell, and can be used to count the number of hair cells in the neuromast. In this example, 17 hair cells are present. Further medial, the outlines of the supporting cell boundaries (C,D; arrows) are visible. In the center of the neuromast, the tear drop-shaped hair cells are visible (E; arrows). To prepare for patch clamping, the supporting cells at the neuromast periphery must be breached by suction from a large-tipped pipette, whereupon entry into the neuromast is confirmed by positive pressure expanding the neuromast extracellular volume (F–H; arrows depict fluid-filled space). By maneuvering a patch pipette under positive pressure through the path previously made, a hair cell can be patched (I). This approach has been used to record from hair cells in a variety of hair cell organs (Ricci and Fettiplace, 1997; Ricci et al., 2005). We have recorded from >10 neuromasts on several fish. Gigohm seals were readily obtained. With Cs pipette solutions, average membrane capacitance (C_m) of hair cells determined from transient analysis at -80 mV at the

Received Sept. 6, 2012; revised Dec. 12, 2012; accepted Dec. 21, 2012.

Author contributions: A.J.R., D.Z., and J.S.-S. designed research; A.J.R., J.-P.B., L.S., C.L., and J.S.-S. performed research; A.J.R. and J.S.-S. analyzed data; A.J.R. and J.S.-S. wrote the paper.

This work was supported by NIH Grants EY021195 to D.Z., DC009913 to A.J.R. and J.S.-S., P30 44992 to A.J.R., and DC000273 to J.S.-S.

Correspondence should be addressed to Joseph Santos-Sacchi, Surgery (Otolaryngology), Yale University School of Medicine, BML 224, 333 Cedar Street, New Haven, CT 06510. E-mail: joseph.santos-sacchi@yale.edu.

DOI:10.1523/JNEUROSCI.4265-12.2013

Copyright © 2013 the authors 0270-6474/13/333131-04\$15.00/0

beginning of recording was 1.6 ± 0.09 pF ($n = 5$). Usually, 1–2 hair cells were recorded during a day's work.

Figure 2 shows K currents recorded from a patched hair cell with a K-based intracellular solution. Raw currents were evoked with voltage steps (C) following a prepulse to -120 mV from a holding potential of -80 mV. The outward currents were composed of at least two components, a fast decaying one and a slower noninactivating one (A). The fast-inactivating (A-type) current was removed with a prepulse to -40 mV (B), and by subtraction (traces A minus B), the transient current was isolated (D). Figure 2E shows an average $I-V$ curve of unsubtracted currents collected from a -80 mV holding potential, illustrating outward rectification averaging 0.25 ± 0.07 nA at $+10$ mV ($n = 3$). Slope resistance between -120 and -60 mV was ~ 2 G Ω . Using Cs solutions and P/N leakage subtraction, we also identified an inward Ca^{2+} current (Fig. 2F). The current was small and noninactivating during voltage steps. At -10 mV the Ca current averaged 0.018 ± 0.003 nA ($n = 5$). Ca influx is expected to release synaptic vesicles at the basal pole of hair cells. Figure 2G illustrates the release of vesicles, measured as a membrane capacitance increase. In this case, during the course of a 3 s depolarization to -10 mV, C_m increased ~ 40 fF. Open circles depict average responses. The average increase in C_m at 3 s under these conditions was 52 ± 23 fF ($n = 3$; initial C_m was 1.37 ± 0.15 pF). Assuming a vesicle capacitance of 38–50 aF (Schnee et al., 2005; Graydon et al., 2011), the C_m increase equates to a surface area equivalent to 1040–1370 vesicles. This release is greater than estimates of vesicles associated with synaptic ribbons (2–5 ribbons possessing ~ 120 vesicles each; Obholzer et al., 2008; Trapani and Nicolson, 2011), which predicts 12–30 fF for vesicles of 50 aF size. The larger measured values indicate recruitment of non-ribbon-associated vesicles, though not nearly at the rate observed in turtle or rat (Schnee et al., 2011a,b). We also tested for transduction currents during whole-cell voltage clamp by displacing the cupola sinusoidally with a fluid jet delivered by a puff pipette ($n = 4$) (Fig. 3). Currents of ~ 100 pA were evoked in this cell of ~ 1.3 G Ω input impedance. A decrease in amplitude during the extent of stimulation resembles adaptation. It should be noted that the Tricane anesthetic that we used is expected to reduce MET function (Farris et al., 2004).

Finally, we observed cells that had larger than the average 1.6 pF capacitance of hair cells, which we identify as supporting cells ($n = 4$). Auditory support cells are known to be joined into a

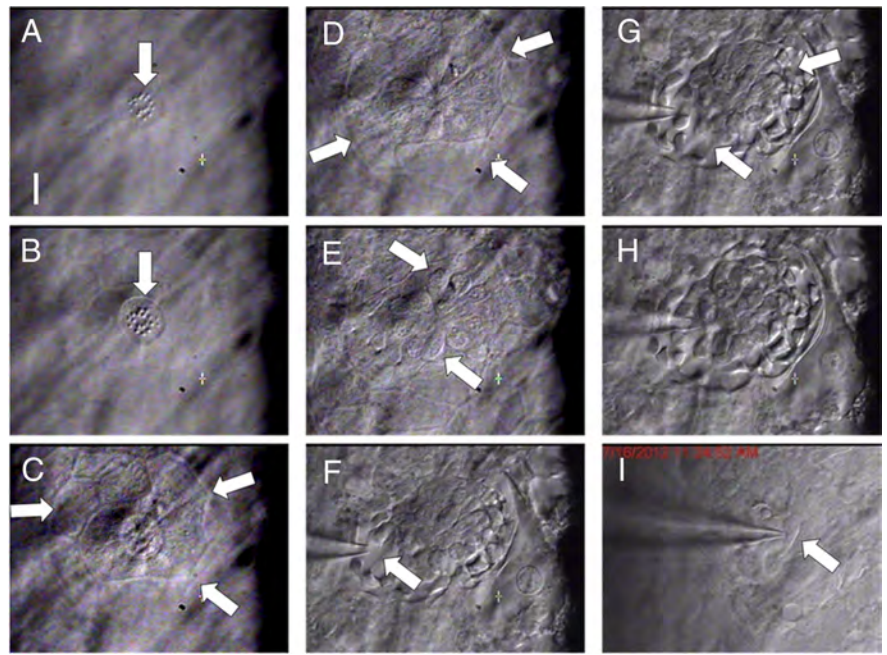


Figure 1. Electrode approach for patch clamping zebrafish hair cells. Zebrafish were anesthetized and fixed laterally onto a recording chamber. **A–E**, Images show neuromast structure from cupola/kinocilia top (**A**) to location of hair cell soma (**E**). See Results for details. **F–I**, Outer supporting cell ring is breached with large suction electrode, providing a path for patch electrode to seal on hair cell. See Results for details. Scale bar (**A**), 8 μm . Images from 7 dpf.

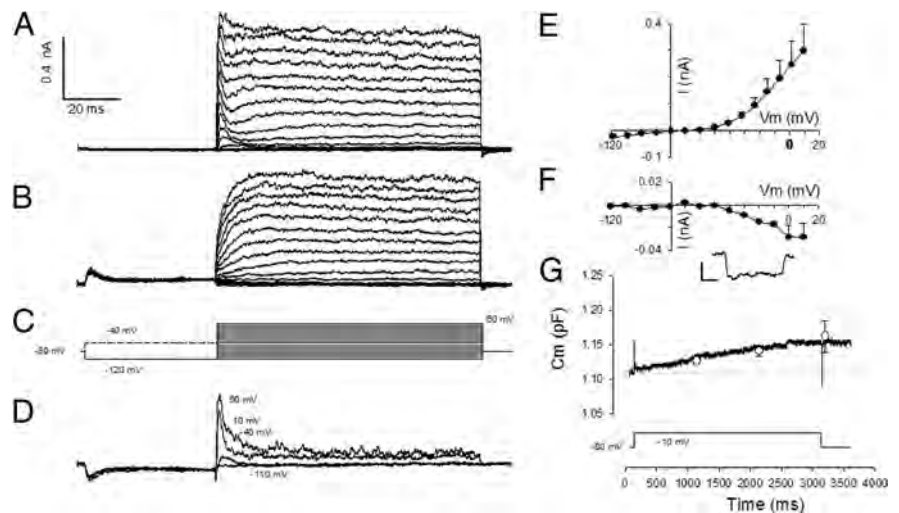


Figure 2. K, Ca currents and synaptic vesicle release from hair cells in living zebrafish. **A**, Outward K currents induced by voltage steps from prepulse level (-120 mV) to a range of voltages depicted in **C**. **B**, K currents generated following prepulse to -40 mV. **D**, Subtraction of traces (**A** minus **B**) reveals A-type inactivating current. **E**, Outward currents without leakage subtraction. Average $I-V$ ($+SE$; $n = 3$) of last 20 ms of 100 ms current traces. **F**, Inward Ca current is revealed by P/N leakage subtraction protocol collected with Cs pipette solution. Average $I-V$ ($+SE$; $n = 5$) of last 10 ms of 50 ms current traces. Inset, Noninactivating Ca current trace, generated in response to -30 mV step from -80 mV holding potential. Scale is 6 pA/10 ms. **G**, Hair cell synaptic vesicle release was determined with membrane capacitance measures. The cell was held at -80 mV and stepped to -10 mV for 3 s; vesicle release is evident from increase in C_m ; δC_m is ~ 40 fF (dark traces). Endocytosis was not observed in our experimental time frame. Dotted lines show initial capacitance level. Open circles indicate average ($\pm SE$) responses at 1 ($n = 5$), 2 ($n = 3$), and 3 ($n = 3$) s following the onset of depolarization. Data were obtained at 7–12 dpf.

syncytium and display large capacitances (Santos-Sacchi, 1991). Figure 4 illustrates supporting cell recordings where voltage was ramped to voltage extremes of $\sim \pm 90$ mV. Capacitance, in this case calculated from transient current response to step voltages, varied according to holding potential (Fig. 4A). In fact, there is the expected reciprocal relationship between input resistance and

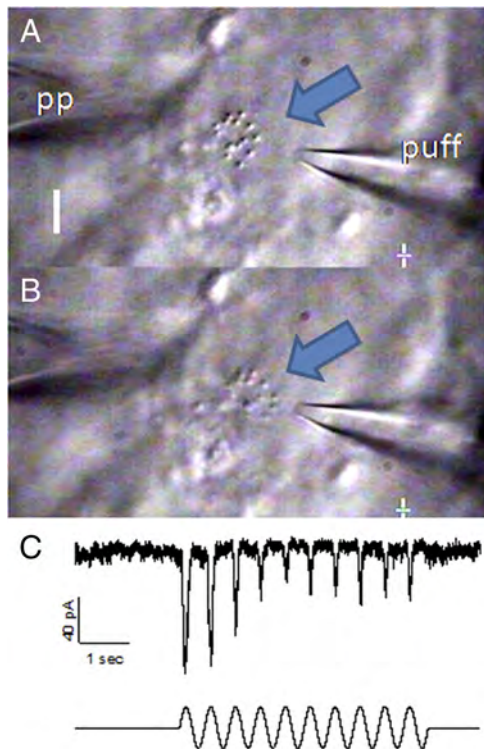


Figure 3. MET current activity during cupola deflection. *A*, A patch pipette (pp) voltage-clamped one hair cell in the neuromast, while a puff pipette (puff) was used to stimulate the kinocilia-embedded cupola. *B*, Suction phase of cupola stimulation showing kinocilia displaced closer to puff pipette. *C*, Receptor currents generated by sinusoidal fluid jet activity. Stimulus voltage driving the water jet is shown beneath currents. With the solutions we used, rectification of the response is expected (Farris et al., 2004). Scale bar, 6 μm . Data were obtained at dpf 7. Stimulus frequency was 2.0 Hz.

capacitance as gap junctions uncouple and recouple during depolarization and hyperpolarization, respectively (Fig. 4*B*). Auditory supporting cells possess voltage-dependent gap junctions (Zhao and Santos-Sacchi, 2000) and exhibit this type of behavior, as well.

Discussion

The zebrafish is a powerful model for auditory/vestibular research. Here we provide data demonstrating the feasibility of patch recording hair cells and supporting cells in lateral line neuromasts from the living zebrafish. The approach is similar to the one we have used to record from a variety of auditory/vestibular end organs (Ricci et al., 2005; Schnee et al., 2011a), and should allow direct assessment of hair cell function in the multitude of existing genetic manipulations available in the zebrafish.

Zebrafish hair cells possess outward K currents, and inward Ca currents similarly found in other auditory/vestibular-like organs. For example, the component K currents presented here are similar to those in the frog vestibular hair cell, where depolarizing prepulse was found to dissociate A-type and delayed rectifier-type contributions (Norris et al., 1992). Indeed, the basolateral electrical properties measured in the zebrafish hair cells are quite similar to those measured in bird (Lang and Correia, 1989; Ricci and Correia, 1999), frog (Norris et al., 1992; Masetto et al., 1994), turtle (Brichta et al., 2002), and mammal (Eatock and Hutzler, 1992). Though the zebrafish hair cell Ca current is small, its properties are similar to those of CaV(1.3) identified in zebrafish (Sidi et al., 2004) and its magnitude is similar to that of other vestibular hair cell types including those of frog (Prigioni et al., 1992;

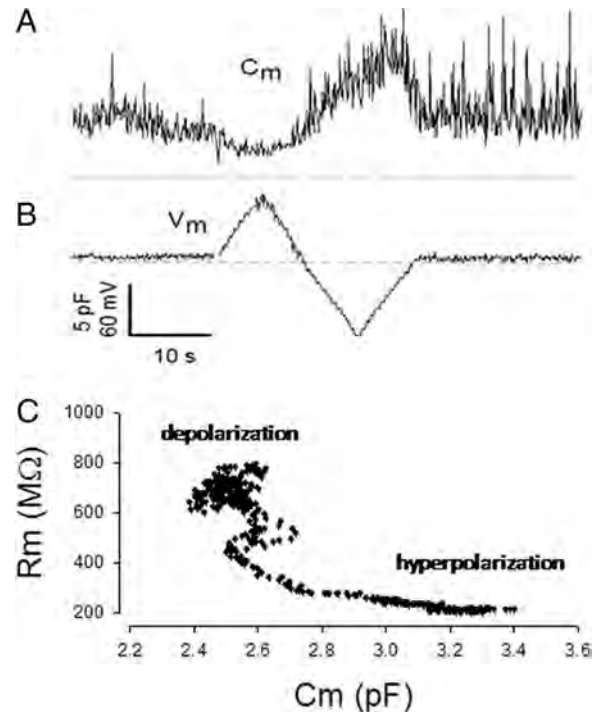


Figure 4. Input capacitance and resistance of supporting cell syncytium. *A*, *B*, An individual supporting cell was patch-clamped (*A*) and the membrane voltage modulated with a slow ramp to $\sim \pm 90$ mV (*B*). Note slow changes in input capacitance corresponding to membrane voltage, indicative of voltage-dependent gap junctional coupling found in the organ of Corti. Input capacitance indicates that several cells contribute to membrane surface area. Dotted lines indicate zero levels. Data were obtained at 12 dpf. *C*, In another cell, the reciprocal relationship between input resistance and capacitance as gap junctions uncouple and recouple during depolarization and hyperpolarization, respectively, is shown. Data were obtained at 3 dpf.

Martini et al., 2000), chick (Ohmori, 1984), and rat (Bao et al., 2003). Very recently, dissociated inner ear hair cells of the zebrafish were successfully recorded, and the reported K current was similar to that reported here (Einarsson et al., 2012).

The calcium current elicited was sufficient to evoke substantial transmitter release, indicative of vesicle replenishment from pools remote to the synaptic ribbon. The apparent absence of a superlinear vesicular release component that is found in auditory hair cells of turtle, mouse, and rat (Schnee et al., 2011a,b), and which may be associated with a release of intracellular stored Ca, might underscore differences in functional requirements for vesicle recruitment mechanisms in zebrafish hair cells. Perhaps this difference relates to auditory versus vestibular hair cell properties, although calcium-induced calcium release has been observed in frog vestibular hair cells (Lelli et al., 2003); alternatively, the very small volume of zebrafish hair cells may not require elaborate vesicle recruitment mechanisms, or the small volume may make a kinetic separation between release components more difficult to observe. Finally, in contrast to observations in some other species (Schnee et al., 2005; Graydon et al., 2011), the substantial vesicle release arising from such small Ca currents may indicate efficient synaptic mechanisms. Of course, the preliminary data we report here require further investigation. Nevertheless, one of the main benefits of recordings in the zebrafish hair cell will be to capitalize on the wealth of tools and genetic manipulations available for the ribbon synapse (Nicolson, 2005; Francis et al., 2011) in a preparation that we now show to be readily accessible.

Aside from direct investigations on sensory hair cell mechanisms, the neuromast provides an opportunity to understand supporting cell roles in sensory transduction. In the organ of

Corti, electrical coupling has been proposed to sink K away from active hair cells, thereby preserving indefatigable hair cell function (Santos-Sacchi, 1985, 2000). Our observation of similar voltage-dependent gap junctional coupling in zebrafish neuro-masts indicates a corresponding role in this simple organ, with the preparation offering model benefits similar to those for hair cell study.

References

- Bao H, Wong WH, Goldberg JM, Eatock RA (2003) Voltage-gated calcium channel currents in type I and type II hair cells isolated from the rat crista. *J Neurophysiol* 90:155–164. [CrossRef Medline](#)
- Brichta AM, Aubert A, Eatock RA, Goldberg JM (2002) Regional analysis of whole cell currents from hair cells of the turtle posterior crista. *J Neurophysiol* 88:3259–3278. [CrossRef Medline](#)
- Eatock RA, Hutzler MJ (1992) Ionic currents of mammalian vestibular hair cells. *Ann N Y Acad Sci* 656:58–74. [CrossRef Medline](#)
- Einarsson R, Haden M, Dicioli G, Lim A, Mah-Ginn K, Aguilar K, Yazejian L, Yazejian B (2012) Patch clamp recordings in inner ear hair cells isolated from zebrafish. *J Vis Exp* 68:e4281.
- Farris HE, LeBlanc CL, Goswami J, Ricci AJ (2004) Probing the pore of the auditory hair cell mechanotransducer channel in turtle. *J Physiol* 558:769–792. [CrossRef Medline](#)
- Francis AA, Mehta B, Zenisek D (2011) Development of new peptide-based tools for studying synaptic ribbon function. *J Neurophysiol* 106:1028–1037. [CrossRef Medline](#)
- Graydon CW, Cho S, Li GL, Kachar B, von Gersdorff H (2011) Sharp Ca^{2+} nanodomains beneath the ribbon promote highly synchronous multivesicular release at hair cell synapses. *J Neurosci* 31:16637–16650. [CrossRef Medline](#)
- Lang DG, Correia MJ (1989) Studies of solitary semicircular canal hair cells in the adult pigeon. II. Voltage-dependent ionic conductances. *J Neurophysiol* 62:935–945. [Medline](#)
- Lelli A, Perin P, Martini M, Ciubotaru CD, Prigioni I, Valli P, Rossi ML, Mammano F (2003) Presynaptic calcium stores modulate afferent release in vestibular hair cells. *J Neurosci* 23:6894–6903. [Medline](#)
- Martini M, Rossi ML, Rubbini G, Rispoli G (2000) Calcium currents in hair cells isolated from semicircular canals of the frog. *Biophys J* 78:1240–1254. [CrossRef Medline](#)
- Masetto S, Russo G, Prigioni I (1994) Differential expression of potassium currents by hair cells in thin slices of frog crista ampullaris. *J Neurophysiol* 72:443–455. [Medline](#)
- Nicolson T (2005) The genetics of hearing and balance in zebrafish. *Annu Rev Genet* 39:9–22. [CrossRef Medline](#)
- Norris CH, Ricci AJ, Housley GD, Guth PS (1992) The inactivating potassium currents of hair cells isolated from the crista ampullaris of the frog. *J Neurophysiol* 68:1642–1653. [Medline](#)
- Obholzer N, Wolfson S, Trapani JG, Mo W, Nechiporuk A, Busch-Nentwich E, Seiler C, Sidi S, Söllner C, Duncan RN, Boehland A, Nicolson T (2008) Vesicular glutamate transporter 3 is required for synaptic transmission in zebrafish hair cells. *J Neurosci* 28:2110–2118. [CrossRef Medline](#)
- Ohmori H (1984) Studies of ionic currents in the isolated vestibular hair cell of the chick. *J Physiol* 350:561–581. [Medline](#)
- Prigioni I, Masetto S, Russo G, Taglietti V (1992) Calcium currents in solitary hair cells isolated from frog crista ampullaris. *J Vestib Res* 2:31–39. [Medline](#)
- Ricci AJ, Correia MJ (1999) Electrical response properties of avian lagena type II hair cells: a model system for vestibular filtering. *Am J Physiol* 276:R943–R953. [Medline](#)
- Ricci AJ, Fettiplace R (1997) The effects of calcium buffering and cyclic AMP on mechano-electrical transduction in turtle auditory hair cells. *J Physiol* 501:111–124. [CrossRef Medline](#)
- Ricci AJ, Kennedy HJ, Crawford AC, Fettiplace R (2005) The transduction channel filter in auditory hair cells. *J Neurosci* 25:7831–7839. [CrossRef Medline](#)
- Rinkwitz S, Mourrain P, Becker TS (2011) Zebrafish: an integrative system for neurogenomics and neurosciences. *Prog Neurobiol* 93:231–243. [CrossRef Medline](#)
- Santos-Sacchi J (1985) The effects of cytoplasmic acidification upon electrical coupling in the organ of Corti. *Hear Res* 19:207–215. [CrossRef Medline](#)
- Santos-Sacchi J (1991) Isolated supporting cells from the organ of Corti: some whole cell electrical characteristics and estimates of gap junctional conductance. *Hear Res* 52:89–98. [CrossRef Medline](#)
- Santos-Sacchi J (2000) Cell coupling in Corti's organ. *Brain Res Brain Res Rev* 32:167–171. [Medline](#)
- Santos-Sacchi J (2004) Determination of cell capacitance using the exact empirical solution of dY/dCm and its phase angle. *Biophys J* 87:714–727. [CrossRef Medline](#)
- Schnee ME, Lawton DM, Furness DN, Benke TA, Ricci AJ (2005) Auditory hair cell-afferent fiber synapses are specialized to operate at their best frequencies. *Neuron* 47:243–254. [CrossRef Medline](#)
- Schnee ME, Santos-Sacchi J, Castellano-Muñoz M, Kong JH, Ricci AJ (2011a) Calcium-dependent synaptic vesicle trafficking underlies indefatigable release at the hair cell afferent fiber synapse. *Neuron* 70:326–338. [CrossRef Medline](#)
- Schnee ME, Castellano-Muñoz M, Kong JH, Santos-Sacchi J, Ricci AJ (2011b) Tracking vesicle fusion from hair cell ribbon synapses using a high frequency, dual sine wave stimulus paradigm. *Commun Integr Biol* 4:785–787. [Medline](#)
- Sidi S, Busch-Nentwich E, Friedrich R, Schoenberger U, Nicolson T (2004) gemini encodes a zebrafish L-type calcium channel that localizes at sensory hair cell ribbon synapses. *J Neurosci* 24:4213–4223. [CrossRef Medline](#)
- Trapani JG, Nicolson T (2011) Mechanism of spontaneous activity in afferent neurons of the zebrafish lateral-line organ. *J Neurosci* 31:1614–1623. [CrossRef Medline](#)
- Zhao HB, Santos-Sacchi J (2000) Voltage gating of gap junctions in cochlear supporting cells: evidence for nonhomotypic channels. *J Membr Biol* 175:17–24. [CrossRef Medline](#)

Cl⁻ flux through a non-selective, stretch-sensitive conductance influences the outer hair cell motor of the guinea-pig

Volodymyr Rybalchenko and Joseph Santos-Sacchi

Departments of Surgery (Otolaryngology) and Neurobiology, Yale University School of Medicine, 333 Cedar Street, New Haven, CT 06510, USA

Outer hair cells underlie high frequency cochlear amplification in mammals. Fast somatic motility can be driven by voltage-dependent conformational changes in the motor protein, prestin, which resides exclusively within lateral plasma membrane of the cell. Yet, how a voltage-driven motor could contribute to high frequency amplification, despite the low-pass membrane filter of the cell, remains an enigma. The recent identification of prestin's Cl⁻ sensitivity revealed an alternative mechanism in which intracellular Cl⁻ fluctuations near prestin could influence the motor. We report the existence of a stretch-sensitive conductance within the lateral membrane that passes anions and cations and is gated at acoustic rates. The resultant intracellular Cl⁻ oscillations near prestin may drive motor protein transitions, as evidenced by pronounced shifts in prestin's state-probability function along the voltage axis. The sensitivity of prestin's state probability to intracellular Cl⁻ levels betokens a more complicated role for Cl⁻ than a simple extrinsic voltage sensor. Instead, we suggest an allosteric modulation of prestin by Cl⁻ and other anions. Finally, we hypothesize that prestin sensitivity to anion flux through the mechanically activated lateral membrane can provide a driving force that circumvents the membrane's low-pass filter, thus permitting amplification at high acoustic frequencies.

(Resubmitted 22 November 2002; accepted after revision 18 December 2002; first published online 31 January 2003)

Corresponding author J. Santos-Sacchi: Department of Surgery (Otolaryngology), BML 244, Yale University School of Medicine, 333 Cedar Street, New Haven, CT 06510, USA. Email: joseph.santos-sacchi@yale.edu

The mammalian outer hair cell (OHC) evolved from more primitive hair cells, such as its counterpart, the inner hair cell (IHC), to enhance detection and discrimination of high frequency sounds (Dallos, 1992). A key evolutionary step appears to have been the recruitment of an anion transporter family member, prestin (Zheng *et al.* 2000), to transform the cell into an effector as well as sensor, capable of boosting passive basilar membrane motion (Liberman *et al.* 2002). Electrical stimulation evokes rapid length changes in OHCs (Brownell *et al.* 1985; Kachar *et al.* 1986), which possibly result from membrane surface area changes caused by conformational transitions in the integral membrane motor protein (Kalinec *et al.* 1992; Santos-Sacchi, 1993; Iwasa, 1994; Santos-Sacchi & Navarrete, 2002). The mechanism displays a sigmoidal voltage dependence (Ashmore, 1987; Santos-Sacchi & Dilger, 1988), resides exclusively in the OHC lateral plasma membrane (Dallos *et al.* 1991; Huang & Santos-Sacchi, 1993; Takahashi & Santos-Sacchi, 2001) and shows reciprocal sensitivity to membrane voltage and tension (Iwasa, 1993; Gale & Ashmore, 1994; Kakehata & Santos-Sacchi, 1995; Ludwig *et al.* 2001; Santos-Sacchi *et al.* 2001). The electrical signature of the motor protein is its displacement current, or an

equivalent bell-shaped, voltage-dependent capacitance owing to its voltage sensor's charge movement within and normal to the plane of the lateral plasma membrane (Ashmore, 1990; Santos-Sacchi, 1991*b*). The probability of the motor being in a contracted or expanded state (referred to as state probability hereafter) can be determined from capacitance *vs.* voltage (*C-V*) functions.

Initial work on electromotility indicated that it was driven by transmembrane potassium current (Ashmore, 1986; Ashmore & Meech, 1986). Subsequently, evidence accumulated showing that the phenomenon was voltage dependent (Santos-Sacchi & Dilger, 1988; Ashmore, 1989; Iwasa & Kachar, 1989; Santos-Sacchi, 1992). This observation coupled to the finding that the gain of the mechanical response is less than maximal near the OHC's normal resting potential, led to the realization that the resistance-capacitance (RC) membrane filter would seriously limit the driving force for electromotility at high frequencies (Santos-Sacchi, 1989, 1992). But, in fact, the high frequency region is where the cochlear amplifier is most effective (Ruggero & Rich, 1991). Thus, although the prestin-based motor mechanism can be driven by experimentally

applied voltage sources at very high frequencies (> 70 kHz (Frank *et al.* 1999)), the problem remains that receptor potentials in the OHC are attenuated at 6 db octave⁻¹ above the cell's RC cut-off frequency (Dallos & Santos-Sacchi, 1983). The recent discovery of the intracellular Cl⁻ sensitivity of prestin (Oliver *et al.* 2001) revealed a possible alternative mechanism where a hypothetical transmembrane Cl⁻ current could affect prestin activity. We report here the existence of an OHC conductance that is Cl⁻ permeable, and mechanically gated at high frequencies. Spatially co-located with prestin to the lateral plasma membrane, this conductance results in changes in intracellular Cl⁻ concentration near prestin that drive motor protein transitions and, consequently, OHC mechanical activity. Thus, we hypothesize that a mechanically gated ionic current, which is intrinsically unaffected by the membrane time constant τ , could provide the driving force for the cochlear amplifier.

METHODS

General

Guinea-pigs were killed with halothane inhalation overdose in accordance with an approved protocol from Yale University's animal use and care committee. OHCs were freshly isolated from the adult guinea-pig organ of Corti by sequential enzymatic (dispase 0.5 mg ml⁻¹) and mechanical treatment in Ca²⁺-free medium. Currents from voltage-clamped cells were recorded at room temperature using an Axon 200B amplifier, Digidata 1231A board (Axon Instruments, CA, USA) and the software program jCLAMP (Scisoft, CT, USA). The major intracellular and extracellular solutions are listed in Tables 1 and 2. At the ion concentrations listed, pH was 7.25–7.30; the osmolality was ~ 325 mosmol kg⁻¹ for extracellular solutions, and ~ 5 mosmol kg⁻¹ lower for intracellular solutions to prevent swelling.

In some cases we added CdSO₄ (1 mM) to block Ca²⁺ currents. When evaluating K⁺ ions, 4-aminopyridine (4-AP; 1 mM) and linopirdine (200 μ M) were used to block K⁺ channels. Solutions were delivered to individual cells by Y tube, during continuous whole-bath perfusion with Tris-Hepes solution. Series resistance (before correction off-line) was ~ 7 –20 M Ω in Tris-Hepes solution. A combined Ag–AgCl–KCl–K₂SO₄-agar ground electrode maintained liquid junction potentials in the range ± 1 –2 mV during solution exchanges. Up to 1% DMSO used in extracellular solutions for dissolution of tested pharmacological agents had no influence on the membrane resistance, capacitance or ionic currents. All chemicals were from Sigma (MO, USA) or Fluka (Switzerland). Data are presented as means \pm S.E.M.

Measurement of non-linear capacitance

Non-linear membrane capacitance was evaluated using a continuous high resolution (2.56 ms sampling) two-sine voltage stimulus protocol (10 mV peak at both 390.6 and 781.2 Hz), with subsequent fast Fourier transform-based admittance analysis as fully described by Santos-Sacchi *et al.* (1998b). These high frequency sinusoids were superimposed on voltage ramps. Peak non-linear capacitance was determined by subtracting linear capacitance. C–V data were fitted with the first derivative of a two-state

Boltzmann function and a constant representing the linear capacitance (Santos-Sacchi, 1991b):

$$C_m = Q_{\max} \frac{ze}{kT} \frac{b}{(1+b)^2} + C_{\text{lin}}, \quad (1)$$

and

$$b = \exp\left(\frac{-ze(V_m - V_{\text{pkcm}})}{kT}\right),$$

where Q_{\max} is the maximum non-linear charge moved, V_{pkcm} is voltage at peak capacitance or half-maximal non-linear charge transfer, V_m is membrane potential, C_{lin} is linear capacitance, z is apparent valence, e is electron charge, k is Boltzmann's constant and T is absolute temperature.

Mechanical stimulation of the lateral membrane

Three methods were used to mechanically stimulate the lateral membrane while recording whole-cell currents. In order to induce steady-state changes in membrane tension, positive or negative pressure into the cells was applied through the patch pipette and was monitored with an electronic pressure monitor. For step and low frequency stimulation, a piezoelectrically driven stiff glass probe was used to deform the cell near the mid region of the lateral membrane. The device was the same as that used previously to calibrate a photodiode displacement measurement technique (see Santos-Sacchi, 1992). The long axis of the probe was positioned parallel to the perfusion chamber bottom and normal to the longitudinal axis of the cell (see Fig. 11). OHCs were compressed statically and vertical DC or AC displacements of the probe (± 2 μ m) were superimposed. For high frequency stimulation, a closely positioned (15–20 μ m) piezoelectric-driven fluid-jet pipette (5–10 μ m tip diameter) was used as previously described (Takahashi & Santos-Sacchi, 2001). The pipette contained bath solution and was pointed perpendicular to the surface of the lateral membrane. The latter system is similar to that used previously (Brundin & Russell, 1994), although we used it simply to stimulate the lateral membrane and measure whole-cell currents. That is, we did not replicate their study. Care was taken to drive the piezoelectric only within its linear range, and use filters to limit driver resonances. Following dissociation of OHCs in Ca²⁺-free medium, stereocilia were either fully absent or very badly damaged; thus there was no contribution from stereocilia to the mechanically generated currents we observed.

RESULTS

Intracellular dialysis of Cl⁻-free solution shifts prestin's voltage dependence with little effect on motor charge movement

In order to study the effects of Cl⁻ removal on the OHC motor, we used intracellular solutions that were either Tris-sulfate or Tris-Hepes based (Tables 1 and 2), as these solutes are expected to be neutral with respect to prestin activity (Oliver *et al.* 2001). The OHC presents a bell-shaped C–V function whose voltage at peak capacitance (V_{pkcm}) is highly susceptible to intracellular Cl⁻ washout following the establishment of whole-cell configuration, shifting in the depolarizing direction (Fig. 1). The degree of voltage shift and modulation of peak non-linear capacitance depends upon the species of control anion.

Figure 1A and B shows that, in the presence of 140 mM extracellular Cl⁻, and after washout of intracellular Cl⁻ during whole-cell dialysis with Cl⁻-free patch pipette solutions, peak non-linear capacitance remained stable when the major intracellular anion was sulfate (steady state: 96.5 ± 5 % of initial value of 20.63 ± 1.12 pF; mean ± S.E.M.; n = 5). However, V_{pkcm} showed a very large positive shift from an initial value of -4.9 ± 2.7 to +97.4 ± 7.6 mV, reflecting a change in motor-state probability. On the other hand, washout with Tris-Hepes based, Cl⁻-free intracellular solutions decreased peak C_m to 75.3 ± 3.7 % at steady state (initial value: 19.53 ± 2.64 pF; n = 4), with a smaller V_{pkcm} shift from -24.4 ± 0.6 to +8.2 ± 3.5 mV.

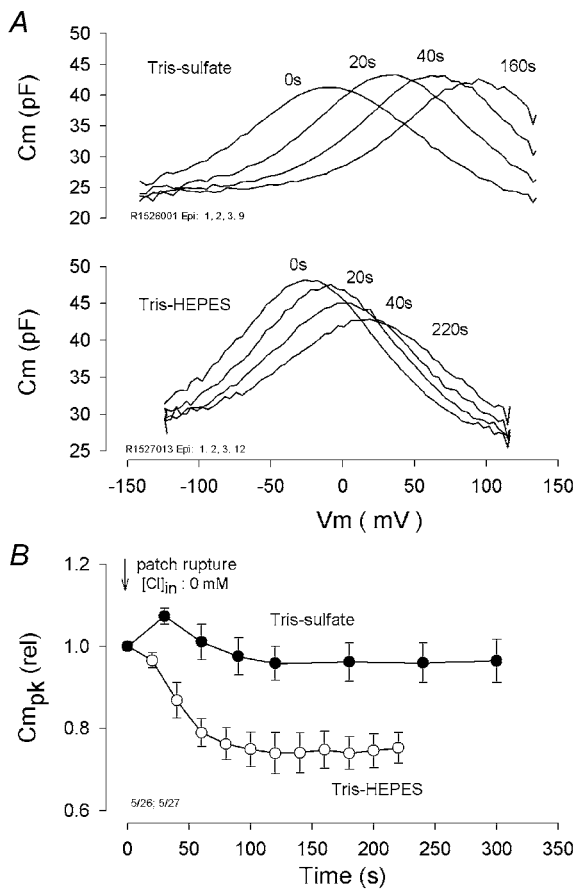


Figure 1. Effects of intracellular Cl⁻ on prestin-generated non-linear capacitance in outer hair cells (OHCs)

A, top, C-V functions of an OHC during washout of Cl⁻ with Tris-sulfate patch-pipette solution, in the presence of 140 mM Tris-Cl extracellular solution. Bottom, same as above except with Tris-Hepes pipette solution. B, relative peak non-linear capacitance (C_{mpk} (rel)) as a function of time after patch rupture with either Tris-sulfate (n = 4; mean ± S.E.M.) or Tris-Hepes (n = 5) Cl⁻-free intracellular solutions and Tris-Cl 140 mM (140 Cl) extracellular solution. Recordings began at the moment of patch rupture at a holding potential of 0 mV. Data were obtained from full C-V functions, and peak non-linear membrane capacitance C_m was obtained by subtracting linear capacitance determined by fits (see Methods) to the data. [Cl]_{in}, intracellular Cl⁻ concentration.

Since peak non-linear capacitance (C_{mpk} = Q_{max}ze/4kT) depends on slope (z) and Q_{max} of the charge-voltage (Q-V) relationship, the parameters describing the motor's charge movement were obtained by fitting (see Methods) OHC non-linear capacitance with the first derivative of a two-state Boltzmann function (Fig. 2). In addition to the large shifts in the operating voltage range, both the voltage sensitivity (z) and the maximum charge moved (Q_{max}) of the motor were affected by intracellular Cl⁻ removal; however, even in the steady state presence of Cl⁻-free intracellular solutions, Q_{max} remained greater than 80 % of initial values. Following the removal of extracellular Cl⁻, Q_{max} remained robust, but its magnitude, as well as that of z, depended on the species of intracellular anion (SO₄²⁻ vs. Hepes; see Fig. 2). In order to assure ourselves that sub-membranous, intracellular Cl⁻ and other active anions, e.g. bicarbonate (Oliver *et al.* 2001), were depleted, we pretreated cells in a continuous wash of Tris-Hepes Cl⁻-free extracellular solutions for over 4 h prior to recording with Cl⁻-free patch-pipette solutions, a procedure that has been shown to rapidly deplete intracellular stores of Cl⁻ (Aickin & Brading, 1984; Thoreson *et al.* 2000). Even under these conditions, non-linear charge movement remained considerable (Tris-sulfate intracellular: Q_{max}, 0.99 ± 0.27 pC; z, 0.62 ± 0.07; V_{pkcm}, 141 ± 9 mV; C_{lin}, 22.9 ± 1.7 pF; n = 5; Tris-Hepes intracellular: Q_{max}, 1.45 ± 0.19 pC; z, 0.66 ± 0.02; V_{pkcm}, 57 ± 4 mV; C_{lin}, 24.6 ± 2.0 pF; n = 5).

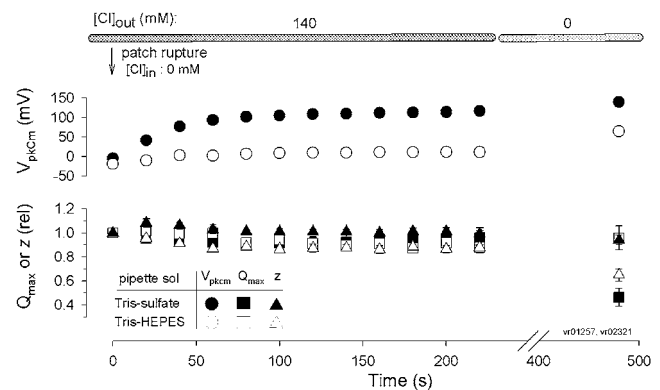


Figure 2. Boltzmann parameters of motor charge movement determined from capacitance functions during washout of intracellular Cl⁻

Horizontal bar at top represents extracellular Cl⁻ concentrations ([Cl]_{out}) during whole-cell recording. Pipette contained either Tris-sulfate or Tris-Hepes solutions (n = 5 for each condition; mean ± S.E.M.). The dominant effect of Cl⁻ washout is a shift in V_{pkcm}, with small changes in Q_{max} and z. Error bars are within symbol dimensions for most data points. After removal of extracellular Cl⁻, steady-state levels of parameters show changes that depend upon species of the intracellular substitute anion. Recordings began at the moment of patch rupture at a holding potential of 0 mV.

Our results differ from those of Oliver *et al.* (2001) since they found that non-linear capacitance was not affected by extracellular Cl^- manipulations and was abolished when intracellular Cl^- was removed. Figure 3A shows the relationship between extracellular Cl^- concentration and the magnitude of non-linear capacitance in OHCs. In this case, the extracellular Cl^- manipulations were made after the cells were allowed to equilibrate (> 5 min) with intracellular Tris-sulfate Cl^- -free solutions. For comparison, Fig. 3A also shows the relationship between intracellular Cl^- concentration and Q_{max} (derived from non-linear capacitance) determined by Oliver *et al.* (2001). At concentrations above 5 mM, manipulation of Cl^- concentration on the extracellular aspect of the OHC membrane mirrored the effects obtained by Oliver *et al.* (2001) that relate to manipulation of intracellular Cl^- ; however, we were unable to extinguish non-linear capacitance after total removal of extracellular (and intracellular) Cl^- . Another major difference between our results

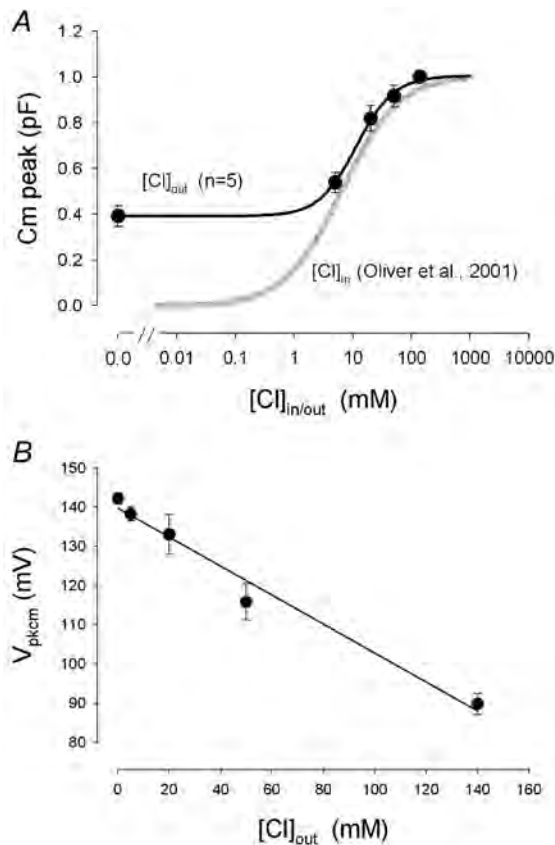


Figure 3. Dependence of peak C_m and V_{pkcm} on extracellular Cl^- concentration

A, continuous line is sigmoidal fit to data points (mean \pm S.E.M.; $n = 5$). Intracellular solution was Tris-sulfate (Table 1) and initial extracellular solution was 140 Cl (Table 2). Extracellular Cl^- ($[\text{Cl}]_{\text{out}}$) reductions were made by replacement with Hepes. For comparison, we show relative Q_{max} (determined from capacitance measures) vs. intracellular Cl^- ($[\text{Cl}]_{\text{in}}$) concentration published by Oliver *et al.* (2001). B, same procedures as above. Line is linear regression ($r^2 = 0.98$) with a slope of 0.37 mV mM^{-1} .

and theirs is our finding that very large shifts in V_{pkcm} occur not only as a function of intracellular- (see above) but also extracellular- Cl^- concentration (Fig. 3B). An increase in Cl^- concentration shifted V_{pkcm} to more negative potentials. The linear regression in Fig. 3B indicates a shift in V_{pkcm} of 0.37 mV mM^{-1} of extracellular Cl^- when Tris-sulfate Cl^- -free intracellular solutions were used. In the presence of Tris-Hepes intracellular solutions, the shift was about 0.1 mV mM^{-1} . Thus, the magnitude of the shift was dependent upon the identity of the intracellular anion.

In order to determine if differences in intracellular control solutions were responsible for some of the discrepancies between our results and those of Oliver *et al.* (2001), we tested their major control anion, pentane sulfonate, and found that intracellular dialysis of such Cl^- -free preparations (Table 1) had several atypical effects on OHC motor charge movement, compared with our other control anions. First, the initial peak C_m value ($11.5 \pm 1.1 \text{ pF}$; $n = 4$; collected within a few seconds after patch rupture) was about half that obtained with Tris-Hepes or Tris-sulfate solutions, indicating that the reduction following patch rupture was more rapid than the typical time course of ion washout (Pusch & Neher, 1988); the block is too fast to result from Cl^- removal during patch-pipette solution exchange. It is, however, typical of intracellular application of high affinity motor blockers, such as the charged form of salicylate, which blocks non-linear capacitance within seconds of patch rupture (Kakehata & Santos-Sacchi, 1996). As with salicylate, we still observed significant, though reduced, electromotility in all OHCs studied with

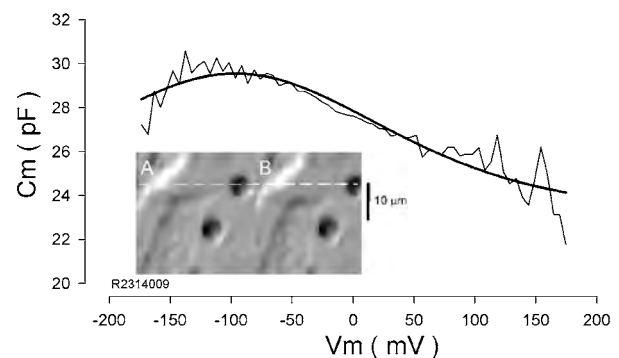


Figure 4. OHC non-linear capacitance and mechanical response with sodium pentane sulfonate patch-pipette solutions

In the presence of 140 Cl extracellular solution, and after steady-state intracellular perfusion of Cl^- -free pentane sulfonate solution, non-linear capacitance remains significant, and mechanical responses during voltage stimulation are prominent. Smooth line is fit to eqn (1) (V_{pkcm} , -96 mV ; z , 0.31; Q_{max} , 2.1 pC and C_{lin} , 23.2 pF, respectively). Inset: image of OHC at negative (A) and positive (B) extremes of voltage ramp. Note displacement of cuticular plate.

Table 1. Intracellular solutions

Solution name	Hepes (mM)	Tris ₂ SO ₄ (mM)	Sodium pentane sulfonate (mM)	MgSO ₄ (mM)	EGTA (mM)	Tris(OH) (mM), approx
Tris-Hepes	190	—	—	2	10	120
Tris-sulfate	10	110	—	2	10	35
Sodium pentane sulfonate	10	—	140	2	10	30

Cl⁻-free, pentane sulfonate solutions ($n = 5$; Fig. 4). At steady state (>3 min), intracellular pentane sulfonate solutions decreased peak C_m to $78.1 \pm 8.8\%$ of the initial value. Second, unlike the results with Hepes⁻ or SO₄²⁻ intracellular anions, the subsequent removal of extracellular Cl⁻ had no effect on the substantial remaining non-linear capacitance ($78.5 \pm 4.6\%$ of initial value). Last, shifts in V_{pkcm} were in the hyperpolarizing direction during washout, as opposed to the other control anion solutions we used. Boltzmann fits of these data showed that voltage sensitivity (z) was substantially reduced, while total charge moved was minimally affected (sodium pentane sulfonate intracellular; Cl⁻-free Tris-Hepes extracellular: Q_{max} , 1.71 ± 0.20 pC; z , 0.33 ± 0.02 ; V_{pkcm} , -99 ± 12 mV; C_{lin} , 21.9 ± 0.7 pF; $n = 5$). These data clearly show that the effect of pentane sulfonate is not due to manipulation of intracellular Cl⁻, but instead results from its direct action on the OHC motor.

Cl⁻ flux through a lateral membrane conductance influences prestin activity

Our data may indicate that in native, intact OHCs, extracellular Cl⁻ can influence the lateral membrane motor. Alternatively, Cl⁻ ions might be entering the OHC to work on the inner aspect of the lateral membrane. We evaluated this possibility by monitoring OHC currents and capacitance during whole-cell recording with Cl⁻-free intracellular solutions while manipulating extracellular Cl⁻ concentrations. Figure 5 shows results for a typical OHC held at 0 mV. As noted above, intracellular washout with Tris-Hepes solution causes an initial decrease in peak C_m , and a positive shift in V_{pkcm} , demonstrating the dependence of motor charge transfer on intracellular Cl⁻. Subsequently, in the face of continuous intracellular washout, the removal of extracellular Cl⁻ betrayed an outward current (Cl⁻ influx) that sustained a substantial component of non-linear capacitance; in the absence of current, owing to the removal of extracellular Cl⁻, capacitance again fell and V_{pkcm} shifted as intracellular Cl⁻ levels dropped. Steady-state levels were reached within minutes, which is typical for washout times under whole-cell voltage clamp (Pusch & Neher, 1988). Replenishment of extracellular Cl⁻ restored the Cl⁻ influx, thereby increasing the non-linear capacitance of the cell and shifting V_{pkcm} back to hyperpolarized levels. These effects were

repeatable. These experiments demonstrate that in the absence of Cl⁻ in the patch pipette, the source of intracellular Cl⁻ that modulates prestin derives from the extracellular solution.

In order to localize the Cl⁻ conductance, we directly mapped the increase in non-linear capacitance and Cl⁻ current as a restricted source of Cl⁻ roved along the length of OHCs whose intracellular Cl⁻ was depleted (Fig. 6). The largest responses were obtained along the lateral region of the OHC, in the same region where prestin is localised (Belyantseva *et al.* 2000a), and the reciprocal electro-mechanical sensitivity of the motor is found (Takahashi & Santos-Sacchi, 2001). Further confirmation of this conductance site is provided by reversal potential measurements during application of extracellular Cl⁻ solutions (see supporting data below). The site of this Cl⁻ conductance is ideally poised to affect the activity of prestin rapidly.

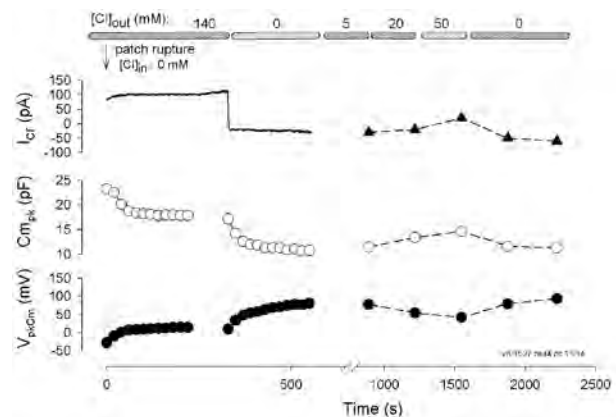


Figure 5. Correspondence among Cl⁻ current, peak non-linear C_m and V_{pkcm}

Horizontal bars at top represent extracellular Cl⁻ concentrations ($[Cl]_{out}$) during whole-cell recording. Recordings began at the moment of patch rupture with Tris-Hepes Cl⁻-free pipette solution at a holding potential of 0 mV. Despite a large sustained inward Cl⁻ flux (outward current; I_{Cl} , top), non-linear C_{mpk} decreases (middle), and V_{pkcm} shifts to depolarized levels (bottom) during Cl⁻ washout through the patch pipette. Subsequent removal of extracellular Cl⁻ shifts C_{mpk} and V_{pkcm} values further, showing their dependence on Cl⁻ influx into the cell. The treatments are reversible and responses are graded with magnitude of Cl⁻ current. ($[Cl]_{in}$, intracellular $[Cl^-]$).

Table 2. Extracellular solutions

Solution name	Hepes (mM)	HCl (mM)	NaOH (mM)	KOH (mM)	Tris(OH) (mM), approx	MgSO ₄ (mM)	CaSO ₄ (mM)
Tris-Hepes	210	—	—	—	110	5	0.2
140 Cl	10	140	—	—	155	5	0.2
80 Cl	108	80	—	—	30	5	0.2
80 Na	220	—	80	—	—	5	0.2
80 K	220	—	—	80	—	5	0.2

Cl⁻ channels do not underlie the lateral membrane conductance

Guinea-pig OHCs typically have a relatively low membrane resistance (< 300 MΩ) even in the presence of K⁺ and Ca²⁺ channel blockers (Santos-Sacchi, 1991b; Santos-Sacchi & Navarrete, 2002). However, when OHCs were perfused with solutions containing mainly large, poorly permeable ions (Tris-Hepes, see Tables 1 and 2), input resistances ranged from 1–3 GΩ. Under these conditions, with approximately equal amounts of Tris⁺ and Hepes⁻ as major charge carriers intra- and extracellularly, whole-cell steady-state currents revealed non-linear current-to-voltage characteristics (*I*-*V*s) reversing near 0 mV ($V_{rev,TH} = +1 \pm 1$ mV, range: -3 to +6 mV, $n = 20$); moderate inward and outward rectification was evident at hyperpolarizing and depolarizing potentials (Fig. 7Aa,b and B). The activation phase of currents at any voltage was faster than our clamp-time constant, typically less than 1 ms. These control currents were not influenced by the stereocilia transducer channel blocker streptomycin (500 μM) and were not due to an imperfect seal between patch pipette and OHC membrane, since their *I*-*V*s showed clearly reproducible non-linear, sigmoidal shapes. Preconditioning hyper-

polarizing steps did not influence the current at +60 mV (Fig. 7Aa and B). Additionally, a pre-depolarizing step to +60 mV did not influence the subsequently evoked currents at a variety of membrane potentials (Fig. 7 Ab and B), indicating that no slow-type inactivation of these currents (5 ms < τ < ~100 ms) exists at any physiological membrane potential.

To study the Cl⁻ permeability of the conductance responsible for the sigmoidal currents observed in Tris-Hepes solutions, we substituted the bulk of extracellular Hepes with 140 mM TrisCl. This substitution significantly and reversibly increased both inward and outward currents, whose kinetics, absence of slow gating and sigmoidal shape of *I*-*V*s were the same as for Tris-Hepes currents (Fig. 7Ac,d and B). The reversal potentials in 140 mM TrisCl extracellular solution ($V_{rev,140Cl}$) were smaller in magnitude than expected, but appropriate in polarity ($V_{rev,140Cl} = -12 \pm 2$ mV, range: -33 to -1 mV; $n = 20$). This deviation presumably derives from rapid equilibration of ions into the restricted space (~33 nm) between the lateral plasma membrane and subsurface cisternae (Pollice & Brownell, 1993). It is well known that such ion accumulation under whole-cell voltage clamp can affect reversal potentials and provide apparent changes in ion selectivity (Frazier *et al.* 2000). Accordingly, then, Cl⁻ applied extracellularly was the major carrier for outward currents (Cl⁻ influx), and its intracellular accumulation provided for the inward current component (Cl⁻ efflux).

In addition to Cl⁻, we tested whether the major monovalent cations, K⁺ and Na⁺, could carry measurable currents through this lateral membrane conductance. In the same cells, 80 mM K⁺, Na⁺ and Cl⁻ were sequentially substituted in the external solution for the equivalent amount of poorly permeable ions (K⁺ and Na⁺ for Tris⁺, Cl⁻ for Hepes⁻). In these experiments, 1 mM 4AP and 200 μM linopirdine were added to all solutions to block voltage-dependent potassium channels described earlier in OHCs (Santos-Sacchi & Dilger, 1988; Marcotti & Kros, 1999). All three substitutions increased both inward and outward components of the currents above controls (Fig. 7C). In fact, the resulting currents showed kinetics and rectification resembling those observed in reference Tris-Hepes solutions (Fig. 7C and E).

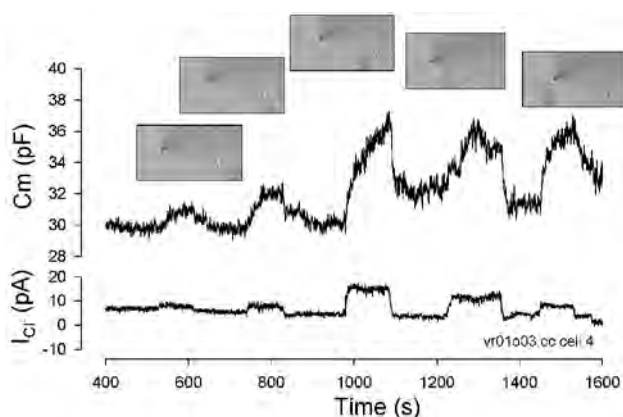


Figure 6. Localization of the Cl⁻ conductance to the lateral membrane

A 1 M Cl⁻ point-diffusion source (high impedance pipette), briefly positioned close to different OHC regions (image insets), revealed a maximum increase in *I*_{Cl} and *C*_m in the mid region of the cell. After each placement, the pipette was moved away from the cell and is indicated as a return of current and capacitance to near baseline.

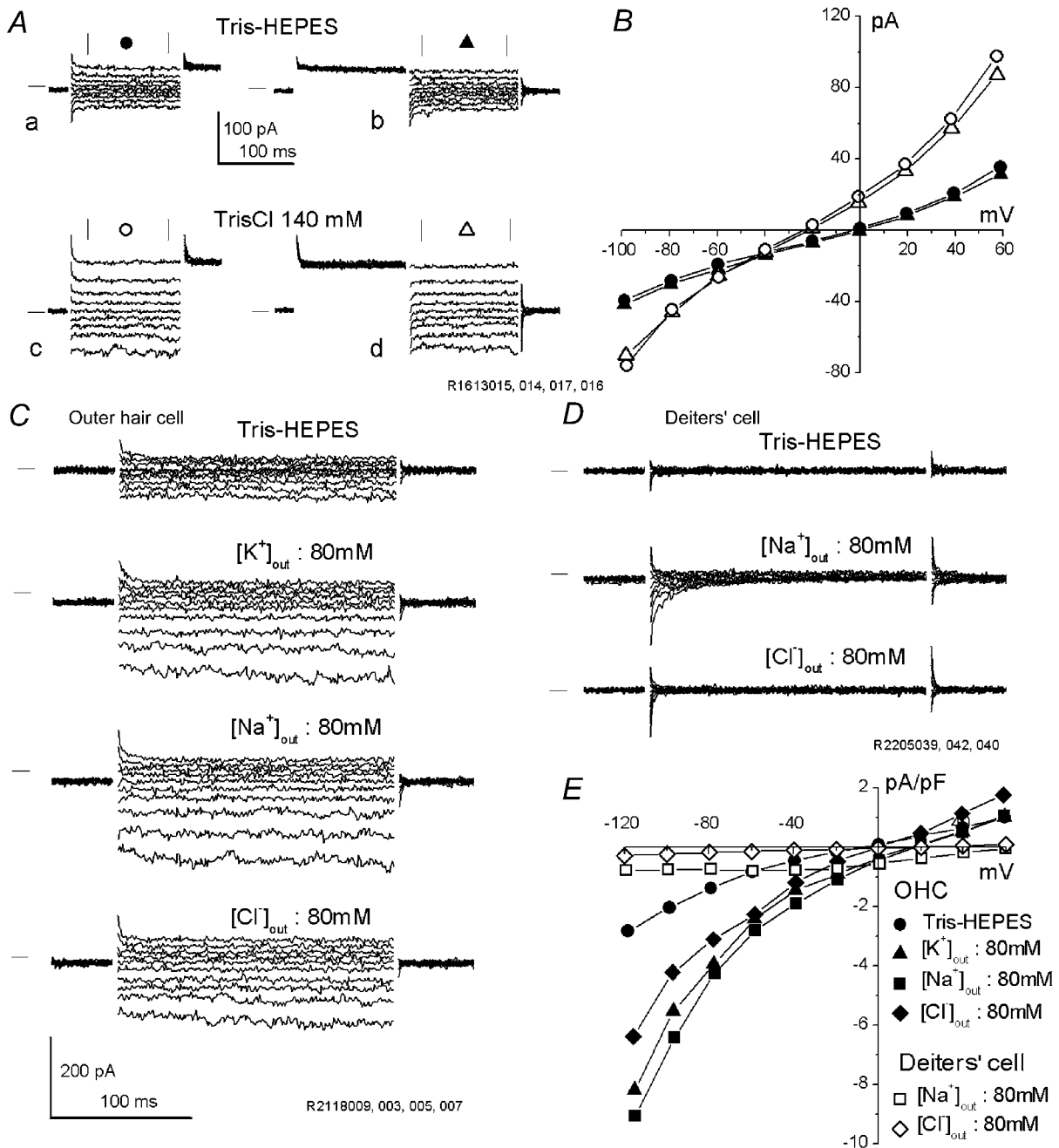


Figure 7. OHCs possess a voltage-dependent, cation-anion non-selective conductance

All recordings were made with Tris-Hepes intracellular solution (Table 1). *A*, currents recorded in the same OHC subjected to voltage pre-conditioning step protocol (*a,c*: holding potential, $V_{\text{hold}} = -20$ mV, 150 ms conditioning steps from -100 to $+60$ mV ($\Delta V = 20$ mV), 150 ms test step to $+60$ mV) and pre-depolarizing step protocol (*b,d*: $V_{\text{hold}} = -20$ mV, 150 ms conditioning step to $+60$ mV, 150 ms test steps from -100 to $+60$ mV ($\Delta V = 20$ mV)) in Tris-Hepes reference extracellular solution (*a,b*) or 140 mM TrisCl-based (140 Cl) extracellular solution (*c,d*). Horizontal lines at left of traces indicate zero-current level. *B*, series-resistance corrected I - V curves from currents in *A*, trace averaged between vertical marks. *C*, OHC currents recorded in (top to bottom) Tris-Hepes, 80 K, 80 Na and 80 Cl extracellular solutions (Table 2) in the presence of 1 mM 4AP + 200 μ M linopirdine, evoked by voltage steps from $+60$ to -120 mV ($\Delta V = -20$ mV) from $V_{\text{hold}} = -20$ mV. Records are from the same OHC. *D*, Deiters' cell currents recorded in (top to bottom) Tris-Hepes, 80 Na and 80 Cl extracellular solutions, evoked by the same voltage protocol as in *C*. Scale is same as in *C*. *E*, relative currents for OHC and Deiters' cell from *C* and *D* above, normalized by their membrane capacitance (24.7 pF linear capacitance for OHC and 21.8 pF linear capacitance for Deiters' cell).

In order to study further the accumulation of ions into the restricted sub-plasmalemmal space, we compared the reversal potentials of currents obtained in 80 mM $[\text{Na}^+]_{\text{out}}$ and 80 mM $[\text{Cl}^-]_{\text{out}}$ -containing extracellular solutions and found that although they were appropriate in polarity, they were smaller in magnitude than expected ($V_{\text{rev},80\text{Na}} = +29 \pm 2$ mV, range: 17 to 39 mV, $n = 12$; $V_{\text{rev},80\text{Cl}} = -16 \pm 3$ mV, range: -33 to $+3$ mV, $n = 14$). These results clearly indicate that both extracellular cations and anions can accumulate in the sub-plasmalemmal space of the OHC at our holding potential of 0 mV. For Cl^- , the Nernst equation shows that an intracellular concentration of ~ 40 mM was achieved at steady state with 80 mM Cl^- extracellularly. The same calculations for Na^+ show an intracellular concentration of ~ 30 mM. No indication of a similar

conductance was found under the same experimental conditions in isolated supporting Deiters' cells, which lack prestin but have approximately the same size and passive membrane capacitance as OHCs (Fig. 7D and E). Normalized conductance of Deiters' cells in Tris-Hepes and 80 mM $[\text{Cl}^-]_{\text{out}}$ (80 Cl) extracellular solutions was ($n = 5$) 1.0 ± 0.05 and 2.28 ± 0.73 pS pF^{-1} , respectively. For comparison, OHC conductance was 15.6 ± 5.5 and 56.6 ± 18.9 pS pF^{-1} , respectively.

We found that steady-state Cl^- current levels remain stable for several seconds at membrane potentials from -80 to $+40$ mV (Fig. 8A). However, during prolonged hyperpolarizations more negative to -100 mV, a slowly developing increase in current was often observed. Because such behaviour might be characteristic of ClC-2 chloride channels,

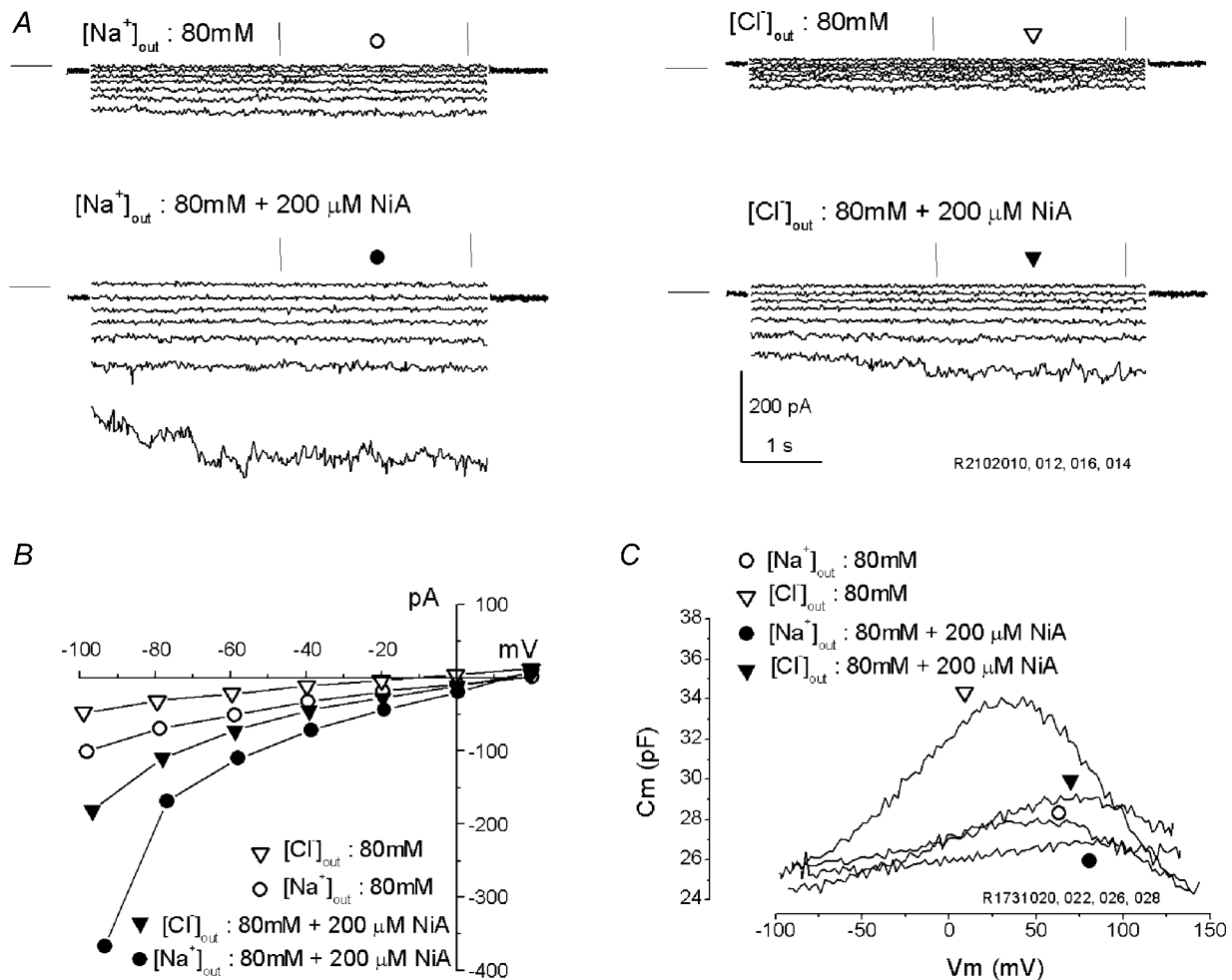


Figure 8. Cl^- channel blockers increase the lateral membrane conductance but block non-linear capacitance

A, currents were evoked by prolonged (5 s) pulses from $+20$ to -100 mV (step = -20 mV) from $V_{\text{hold}} = 0$ mV. Data were collected from the same OHC in 80 Na (left) or 80 Cl (right) extracellular solutions (Table 2), in the absence (top) or in the presence (bottom) of $200 \mu\text{M}$ niflumic acid (NiA). Horizontal lines at left of traces indicate zero-current level. Note the identical kinetics, voltage dependence and increase by NiA for Na^+ and Cl^- currents. B, $I-V$ plots obtained from trace averages (between vertical marks) in A above. C, C_m-V functions obtained from another OHC after treatments as in A above. Note potent block of niflumic acid of prestin-related non-linear capacitance, despite enhanced inward-outward Cl^- currents.

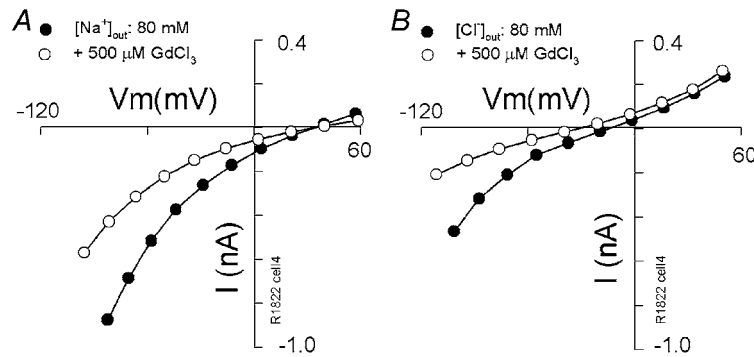


Figure 9. Partial block of the lateral membrane conductance by gadolinium

OHC I - V plots with extracellular solutions 80 Na (A) or 80 Cl (B) without (●) and with (○) the stretch-channel blocker gadolinium (500 μ M) obtained in the same cell.

we compared the currents at long hyperpolarizing potentials in 80 mM $[\text{Na}^+]_{\text{out}}$ and 80 mM $[\text{Cl}^-]_{\text{out}}$ extracellular solutions. Cl^- channels are not expected to pass cations. In either solution the slowly developing component was observed. Additionally, well-known Cl^- channel blockers (niflumic acid 200–400 μ M, DIDS 0.5–2.5 mM, furosemide 200 μ M, NPPB 10–500 μ M, 9-AC 1–2 mM; (Jentsch *et al.* 2002)) did not decrease the currents. Instead, Cl^- and Na^+ currents, including the slow component, were reversibly increased. For example, niflumic acid at 200 μ M increased the Cl^- current by a factor of 3.4 at -75 mV, while the Na^+ current was increased by a factor of 2.2 ($n = 3$). Figure 8B and C illustrates the effect of niflumic acid (200 μ M) on currents and capacitance. While currents were increased, non-

linear capacitance was reduced; in fact, niflumic acid was a potent blocker of non-linear capacitance, working in the micromolar range. Additionally, a slowly developing outward component, never observed in CIC-type channels, could also be observed at large depolarizing potentials (more positive to $+60$ mV), but could not be studied in detail because of irreversible damage to the OHC at prolonged depolarizations. Taken together, these observations clearly indicate that CIC channels, whose messenger RNA is found in OHCs (Kawasaki *et al.* 1999), or other clearly characterized types of Cl^- pathways (cystic fibrosis transmembrane conductance regulator (CFTR), transporters), do not underlie the non-selective conductance of the lateral membrane.

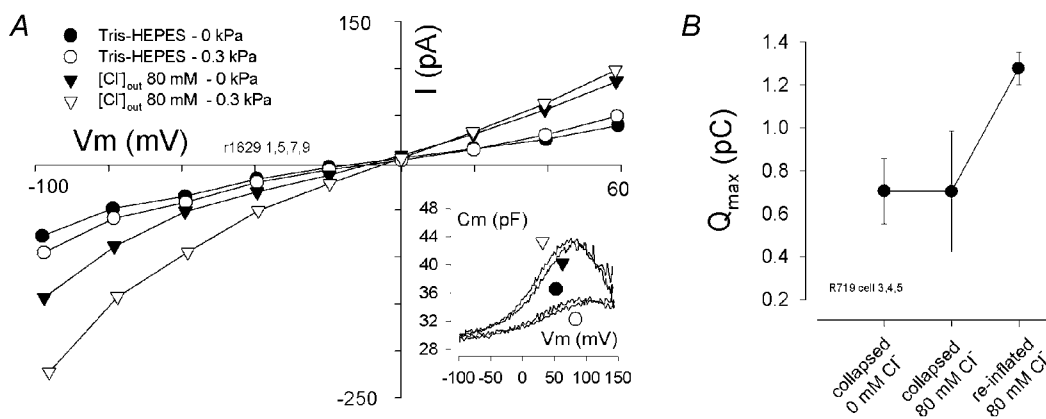


Figure 10. Membrane tension dependence of the Cl^- current

A, sigmoidal I - V curves were derived from trace-averaged currents recorded with Cl^- -free Tris-Hepes patch pipette in the presence of Tris-Hepes (circles) and 80 Cl (triangles) extracellular solutions before (filled symbols) and after (open symbols) turgor pressure increases in the initially cylindrical OHC ($V_{\text{hold}} = 0$ mV, step from $+60$ to -100 mV). Currents are substantially increased and pressure sensitive in Cl^- -containing solution. Inset: C - V functions, corresponding to the treatments in A, reflect a significant increase in membrane displacement charge and are shifted in the hyperpolarizing direction in Cl^- -containing solution. The additional charge increase and C_m shift in the pressurized state (∇) is due to increased Cl^- flux, because in Cl^- -free solutions (\circ), as well as in Cl^- -saturated solutions (Kakehata & Santos-Sacchi, 1995), the C_m functions are shifted to depolarizing potentials with positive pressure. B, non-linear charge (Q_{max}), determined from C - V function fits ($n = 3$) does not increase in initially collapsed cells in Cl^- -containing extracellular solution (140 Cl) until Cl^- flux is restored by cell re-inflation.

The lateral membrane current is partly reduced by blockers of stretch-activated conductances

Thus far we have ruled out the contribution of Cl^- and stereocilia transducer channels to the conductance we observe. In addition, we have evaluated other blockers of channels that conceivably could support components of the lateral membrane current. Blockers of aquaporin (HgCl_2 0.4–2 mM; (Belyantseva *et al.* 2000b)), gap junction hemichannels (carbenoxolone 200 μM , octanol 2 mM; (Santos-Sacchi, 1991a; Draguhn *et al.* 1998)) and cation-selective vanilloid receptor channels (Ruthenium Red; (Gunthorpe *et al.* 2002)) were without success. Additionally, the absence or presence of intra/extracellular Ca^{2+} , or the presence of intracellular ATP and GTP did not affect the currents.

Finally, we evaluated agents known to block swelling-activated conductances. Stretch-activated channels have been found in the lateral membrane of OHCs; however, they are selective for cations (Ding *et al.* 1991; Iwasa *et al.* 1991). Several blockers were partly effective. Gadolinium (Gd^{3+} ; 500 μM , $n = 5$; Fig. 9), tamoxifen (50 μM , $n = 4$ –7) and quinine (1 mM, $n = 4$) were from 10 to 40% effective at -60 mV in blocking Na^+ (relative I , Gd^{3+} : 0.59 ± 0.07 , quinine: 0.74 ± 0.05 , tamoxifen: 0.77 ± 0.04) and Cl^- currents (Gd^{3+} : 0.72 ± 0.2 , quinine: 0.76 ± 0.16 , tamoxifen:

0.91 ± 0.16). Whereas Gd^{3+} effectively blocked OHC capacitance and motility, even in the presence of high Cl^- levels (Santos-Sacchi, 1991b), tamoxifen and quinine did not. These blockers are non-specific, inasmuch as they have been shown to block a variety of anionic and cationic channels, some involved in cell swelling (Yang & Sachs, 1989; Allen *et al.* 1998; Welsh *et al.* 2000). Interestingly, tamoxifen and quinine are known to block swelling of OHCs in cochlear explants (Siegel *et al.* 2001), and Gd^{3+} interferes with volume regulation in isolated OHCs (Crist *et al.* 1993).

One other agent, poly-lysine (4 μM , molecular weight 70 000–150 000), which has been shown to block stretch-induced mechanical responses in OHCs (Brundin *et al.* 1989), had a small blocking effect on both Na^+ (relative I : 0.90 ± 0.2 ; $n = 3$) and Cl^- (relative I : 0.84 ± 0.13 ; $n = 3$) currents at -60 mV. Poly-lysine, which might be considered a potent charge-screening agent, had virtually no effect on the reversal potentials of the currents.

The Cl^- conductance is stretch sensitive and gated at acoustic rates

Since the lateral membrane ionic current was susceptible to stretch-activated channel blockers, we evaluated its response to membrane stress with a variety of means

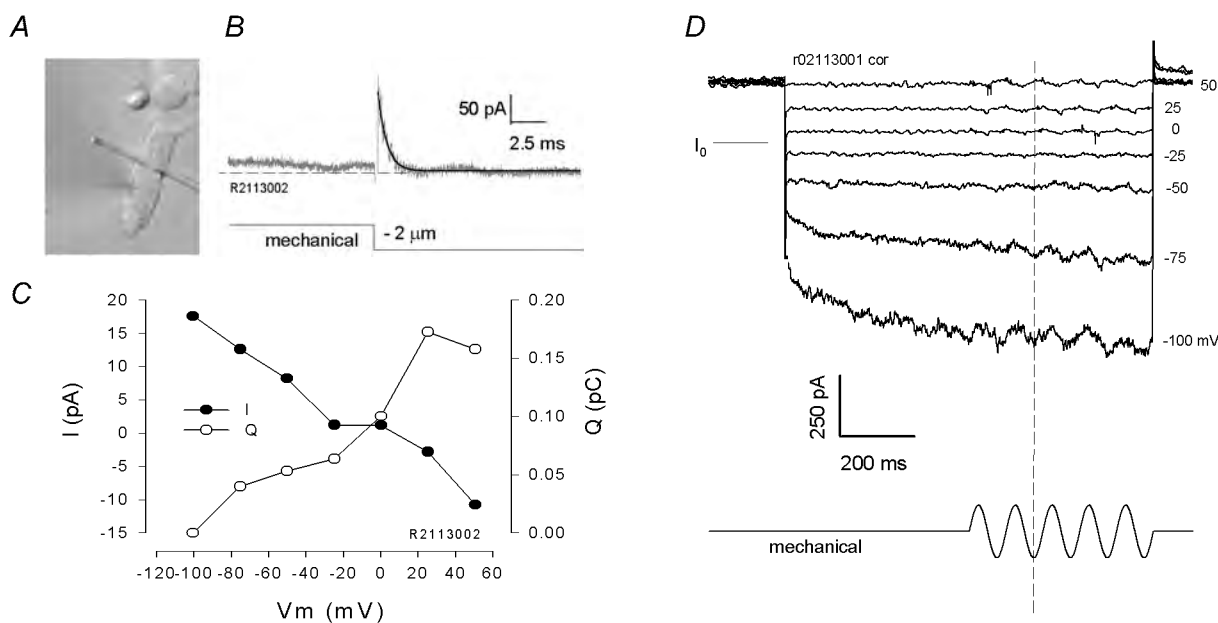


Figure 11. Whole-cell current responses evoked by stiff probe deformations of the lateral membrane

A, digitized image of OHC under whole-cell voltage clamp with stiff probe placed across the middle of the cell. B, step mechanical deformation of the lateral membrane evokes a transient gating current and a DC ionic current at the fixed potential of 50 mV. C, relationship of motor gating charge (integrated transient current, Q) and ionic current magnitude (I , difference between steady-state levels before and after membrane stress) with membrane voltage. Motor charge peaks at V_{pkcm} , whereas I reverses at the potential (-10.5 mV) where total current reverses. D, sinusoidal mechanical stimulation at various potentials produces a corresponding current whose phase reverses at the cell's steady ionic current reversal potential. Extracellular solution was 140 Cl and intracellular was Tris-Hepes + 1 mM Tris- Cl^- .

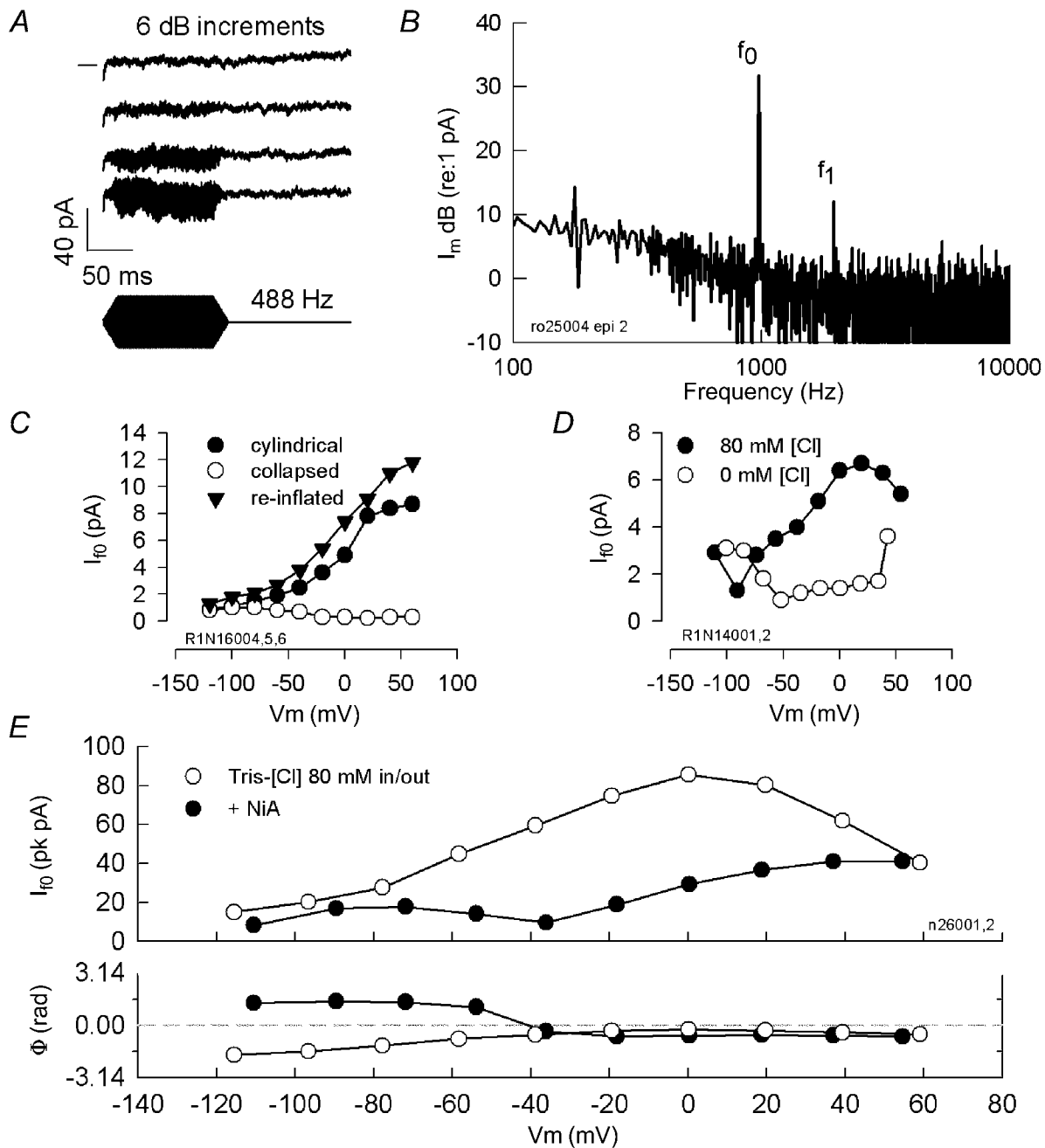


Figure 12. Whole-cell current responses evoked by fluid-jet stimulation of the lateral membrane

A, traces depict an intensity series (6 dB increments in the voltage that drives the piezoelectric fluid-jet) at 488 Hz. Note AC and DC components. DC components grow with stimulus level indicating that they do not arise from bottoming out of the piezoelectric driver. Zero current level is indicated by horizontal line on left of top trace. Traces are separated vertically for clarity. Tris-Hepes intracellular vs. 80 Cl extracellular. B, fundamental (f_0) and first harmonic (f_1) are present in FFT transform from whole-cell currents generated by OHC in response to 1 kHz fluid-jet mechanical stimulation against the lateral wall of the cell. I_m , membrane current plotted on a decibel scale. C, I_{f_0} is blocked by collapsing the OHC with negative pipette pressure; re-inflation restores the current. Niflumic acid (250 μ M)-treated OHC. D, removal of extracellular Cl⁻, in the absence of intracellular Cl⁻ reduces the fluid-jet evoked current. E, the reduction of non-linear peak capacitance after 250 μ M niflumic acid (NiA) treatment (16.6 pF (V_{pkcm} : -12.7 mV) vs. 8.63 pF (V_{pkcm} : 20.3 mV) derived from C-V functions) produced a reduction of the capacitive component and shift in the current's voltage dependence to the depolarized levels. Consequently, characteristics of the ionic component are revealed as I_{f_0} magnitude displays a minimum where an abrupt phase reversal occurs. Tris-Hepes-based intracellular solution (10 mM [Cl⁻]); extracellular solution 80 Cl.

including turgor pressure modulation, and localized membrane deformation with stiff probe and fluid jet. In the presence of only poorly permeable ions inside and outside the OHC, increasing intracellular pressure had only a slight effect on the resting conductance of the cell; subsequent to the addition of extracellular Cl^- the effect was much more pronounced (Fig. 10A). For example, at -60 mV the Cl^- current was nearly doubled. Simultaneous with the increase in Cl^- flux, the non-linear capacitance was augmented. In this example, the OHC was cylindrically shaped throughout the experiment, that is, there was tension on the membrane even when no positive pipette pressure was administered (0 kPa). The effect of the stretch sensitivity of the current on non-linear capacitance was more clearly appreciated when re-inflating initially collapsed OHCs, where the initial tension on the lateral membrane was minimal or absent (Fig. 10B). Indeed, the augmentation

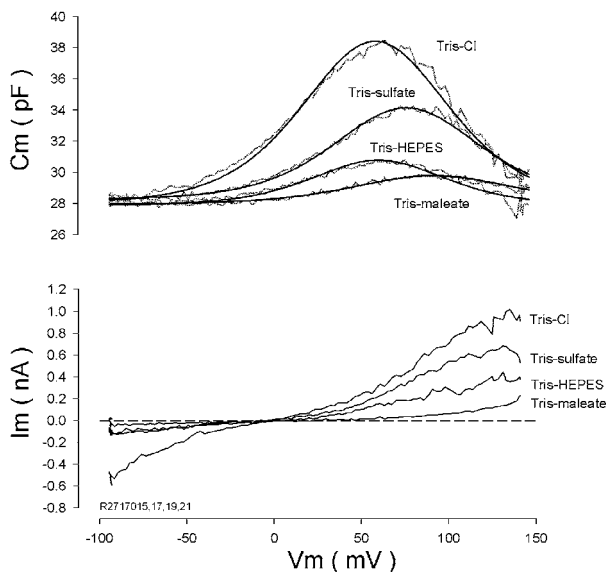


Figure 13. Effects of control anions on OHC non-linear capacitance and current

A, the OHC was perfused with solutions of minimal composition in order to evaluate the effects of control anions. The intracellular solution was maleate-based (mM: 120 maleate, 250 Tris, 2 EGTA). The initial extracellular maleate-based solution (mM: 120 maleate, 250 Tris) was sequentially substituted by Tris-Hepes (mM: 220 Hepes, 60 Tris), Tris-sulfate (mM: 120 SO_4^{2-} , 250 Tris) and Tris-Cl (mM: 155 Cl^- , 165 Tris) solutions. Capacitance measures and corresponding fits (smooth lines) to eqn (1) provide Boltzmann parameters for the tested anions: (maleate: V_{pkcm} , 91 mV; z , 0.82; Q_{max} , 0.23 pC; C_{lin} , 27.96 pF; Hepes: V_{pkcm} , 60 mV; z , 0.99; Q_{max} , 0.30 pC; C_{lin} , 27.89 pF; sulfate: V_{pkcm} , 75 mV; z , 0.92; Q_{max} , 0.65 pC; C_{lin} , 28.28 pF; Cl^- : V_{pkcm} , 58 mV; z , 0.91; Q_{max} , 1.16 pC; C_{lin} , 28.0 pF. B, corresponding ionic currents generated by downward voltage ramps (+150 to -100 mV, 125 ms; corrected for ramp-induced passive capacitive offset current component -52 pA for this cell). Note increasing outward (inward anionic) currents associated with the different anions, and the corresponding increases in non-linear capacitance.

of non-linear capacitance or charge movement by restoring extracellular Cl^- did not occur in OHCs that had been collapsed with negative pressure prior to the restoration, but ensued when the cells were returned to a cylindrical shape by positive intracellular pressure. The resulting increase in membrane tension caused an influx of Cl^- ions, and an augmentation of prestin-generated charge movement.

The stretch sensitivity of the Cl^- current was further tested by mechanically stimulating the lateral membrane with stiff glass probes (Fig. 11A). A step change in membrane deformation evoked an initial transient current due to motor charge movement, followed by a shift in steady-state current (Fig. 11B). As expected, the magnitude of the charge moved was dependent on holding potential and reached a maximum at positive potentials where V_{pkcm} resides under these ionic conditions (Gale & Ashmore, 1994; Zhao & Santos-Sacchi, 1999) (Fig. 11C). On the other hand, the polarity of the mechanically induced component of the ionic current reversed near the reversal potential (-10.5 mV) of the total ionic current. Low frequency AC stimulation with the probe generated corresponding AC currents whose phase reversed at the reversal potential of the current. The reversals in total current polarity are not exactly 180 deg since only a pure ionic current is expected to show this behaviour. These data are consistent with a dual-component current, one capacitive (motor-based) and one ionic.

Finally, in order to assess the physiological significance of the conductance better, we studied its gating by deformation of the lateral membrane at acoustic rates. We used stimulus frequencies that were physiologically appropriate for the OHCs that we isolated, namely for cells whose characteristic frequency ranged up to about 1 kHz (Dallos *et al.* 1982). Figure 12 illustrates that mechanical perturbation of the lateral membrane with micropipette-based, fluid-jet stimulation delivered at frequencies up to 1 kHz. The mechanical perturbation generated high frequency whole-cell currents that display distortion, including harmonic (I_{fl}) and DC components (Fig. 12A and B). This type of stimulation had been used previously to generate, poly-lysine-sensitive, tuned AC and DC mechanical responses from isolated OHCs (Brundin *et al.* 1989; Brundin & Russell, 1994); however, we did not measure the mechanical response of the cell under these conditions, which in any case would not be readily observable with our video sampling rate. We found strong evidence that the evoked current results from direct mechanical perturbation of the lateral cell membrane and is Cl^- dependent. First, it was generated only in OHCs possessing positive turgor pressure, and was reversibly abolished when the cells were collapsed (Fig. 12C). This dependence is similar to that of the mechanical sensitivity of prestin in the lateral membrane (Takahashi & Santos-Sacchi, 2001). Second, in the absence of intracellular Cl^- ,

removal of extracellular Cl⁻ abolished or reduced the current (Fig. 12D).

Since it is known that mechanical stimulation of the lateral membrane can generate non-linear capacitive currents (Gale & Ashmore, 1994; Zhao & Santos-Sacchi, 1999; Takahashi & Santos-Sacchi, 2001), we performed experiments to dissociate capacitive and ionic components of the high frequency current. As with our stiff probe experiments, several pieces of evidence indicate that it is composed of capacitive as well as ionic components. First, while DC current components (Fig. 12A) are not expected for mechanically driven capacitive currents, they can arise from the rectified ionic conductance we described above. Second, in cells that were treated with niflumic acid to decrease non-linear capacitance and increase ionic (Cl⁻) currents, I_{f0} showed two maxima: one near V_{pkcm} , where the non-linear capacitive component is largest (Gale & Ashmore, 1994; Zhao & Santos-Sacchi, 1999), and another at hyperpolarized potentials, where the ionic component is largest (Fig. 12E). Third, magnitude minima corresponded to abrupt phase changes, as expected for an ionic, but not for a mechanically driven capacitive current. The phase change in current polarity is not exactly 180 deg since only a purely ionic current is expected to show this behaviour. Based on results from all three methods of mechanical stimulation, we conclude that the mechanically evoked currents arise from two sources – the ionic conductance we described above, and the intrinsic displacement currents of the voltage sensor of prestin.

A role for sulfonic moieties in prestin activation

Since our observations and those of Oliver *et al.* (2001) suggest that variations in the cationic composition of solutions do not produce substantial effects on the non-linear capacitance of prestin, it is possible that our major control anions, Hepes⁻ and SO₄²⁻, could play a role as co-factors supporting the charge translocation of prestin. The common structural feature between these two anions is the presence of a negatively charged sulfonic group, SO₃. To explore the possible active role of sulfonate-containing molecules in prestin functioning further, we performed one last set of experiments using maleate (divalent, sulfonic-free) as control anion, in place of Hepes⁻ and SO₄²⁻ (Fig. 13). Under symmetrical maleate solutions intra- and extracellularly, a small non-linear capacitance still remained. However, the exchange of extracellular solutions with Tris-Hepes, Tris-sulfate, or Tris-Cl produced an increase in non-linear capacitance and a further shift in V_{pkcm} . Thus, each of these anions is able to permeate the lateral membrane through the non-selective conductance we describe above, and activate prestin. We conclude that in the intact OHC, maleate, which lacks a sulfonic group, is barely active, while Hepes⁻ and SO₄²⁻, which possess sulfonic groups, partially support prestin activity similar to Cl⁻.

DISCUSSION

We report several new observations. (1) Motor charge movement remains substantial in the absence of Cl⁻ and other known active anions inside and outside the intact OHC. (2) Cl⁻ ions significantly affect the state probability of prestin. (3) A Cl⁻ current through a non-selective lateral membrane conductance modulates prestin activity thereby making the OHC responsive to extracellular Cl⁻, and (4) the Cl⁻ current is stretch sensitive and gated at acoustic rates. Taken together, these observations have substantial impact on our understanding of OHC function.

How does Cl⁻ work on prestin?

The current state. Recently, Oliver *et al.* (2001) proposed that prestin possesses an extrinsic voltage sensor where charge movement arises due to the binding and subsequent translocation of Cl⁻ or other anions from the intracellular to the extracellular aspect of the plasma membrane of the cell; simultaneous with this translocation, prestin is driven to the expanded state producing cell elongation. Intracellular SO₄²⁻ ions were ineffective in promoting charge movement, as were extracellular Cl⁻ ions. This was observed in native OHC membrane patches and whole-cell recorded prestin-transfected CHO cells.

Evidence for a new state. One of the main differences that we have with the the data of Oliver *et al.* (2001) is our observation of large shifts in the operating voltage of the motor (V_{pkcm}) during intracellular Cl⁻ removal. Since we first presented evidence for this phenomenon (Rybalchenko & Santos-Sacchi, 2001), we realized that the simple voltage sensor scheme of Oliver *et al.* (2001) was incomplete. A shift in V_{pkcm} suggests significant changes in the energy profile for voltage-dependent motor transitions regardless of whether extrinsic or intrinsic voltage sensors control prestin. Supporting this contention, we previously showed that salicylate, working on the inner aspect of the lateral plasma membrane, not only reduces the voltage sensitivity of the motor (z), but shifts V_{pkcm} in the positive direction (Kakehata & Santos-Sacchi, 1996), indicating a more complex interaction than simple competition for an extrinsic sensor's binding site as suggested by Oliver *et al.* (2001).

Another major difference between our data and that of Oliver *et al.* (2001) is that we find that extracellular Cl⁻ can enter the cell through a lateral membrane stretch-activated conductance to influence prestin activity. Since they studied excised membrane patches, it is possible that in the absence of applied tension to the patch, the conductance was inactive. Additionally, in transfected cells the conductance may not have been expressed. In their motility studies on intact OHCs, the use of intracellular pentane sulfonate solutions confounded the evaluation of Cl⁻ effects.

Finally, the most controversial difference between our data and theirs is our observation that SO₄²⁻ and other

sulfonate-containing anions can support significant voltage sensitivity of prestin. The active role of SO_4^{2-} may not seem unreasonable since protein database comparisons indicate that prestin shows homology to sulfate transporters (Zheng *et al.* 2001). Nevertheless, we performed tests to rule out possible contamination of our solutions with other known active anions, namely the halides and nitrate. Independent laboratory (Galbraith Labs, TN, USA) tests indicate that these anions were less than 100–200 μM in our solutions. Additionally, we confirmed even lower Cl^- levels by measuring junction potentials at the Ag–AgCl pipette solution interface. Furthermore, bicarbonate, whose K_d for prestin effects is 44 mM (Oliver *et al.* 2001), is unlikely to be influential for several reasons. First, carbonic anhydrase is not located at the lateral wall but at the apical and basal ends of the OHC (Okamura *et al.* 1996); thus, under our conditions, the little bicarbonate that might be produced in the absence of energy substrates (i.e. in the absence of robust CO_2 generation) would be readily washed out from the cell's cytosol during pipette perfusion. Second, a control series of experiments in the presence of acetazolamide, a carbonic anhydrase inhibitor, performed in the absence of atmospheric CO_2 (using lithium hydroxide absorption), left our results unchanged (data not shown). Thus we are sure that contaminants are not responsible for our results, since, according to Oliver *et al.* (2001), at these levels of active anions non-linear capacitance should be miniscule.

Apart from differences in animal species, the membrane preparations used could be responsible for discrepancies between our data and those of Oliver *et al.* (2001) on the sulfate sensitivity of prestin. While it is certainly true that the isolated patch technique as used by Oliver *et al.* (2001) is a good method to control solutions delivered to the inner aspect of the membrane, potential problems may arise. For example, removal of a patch from a cell, or measurement of an attached patch in a transfected cell will drastically alter membrane structure, not to mention the intracellular environment that a transmembrane protein normally experiences (Milton & Caldwell, 1990). How this affects an integral membrane protein is difficult to assess. For example, both cell-attached and excised patches of oocyte-expressed Shaker-IR channels display anomalous mechanical sensitivity because normal cellular mechano-control mechanisms are absent (Gu *et al.* 2001). We have chosen to use the native, whole-cell approach because we are trying to understand how the intact cell functions. We conclude that we do have control over solutes delivered to the intracellular aspect of the lateral sub-plasmalemmal space (LSpS), at least at steady state. This, we are sure of because we find washout rates of Cl^- (based on prestin activity) typical for whole-cell washout (~ 1 – 3 min; (Pusch & Neher, 1988)); indeed, we have perfused for longer than 4 h and our results remain consistent. So, in the presence of the lateral membrane conductance that we find, the

continuous perfusion of Cl^- -free intracellular and extracellular solutions will eventually deplete Cl^- in the LSpS. Reversal potentials also indicate that we can effectively change LSpS Cl^- concentrations.

Allosteric effects on motor state. Oliver *et al.* (2001) suggested that extrinsic anions serve as the voltage sensor for prestin. Our data lead us to a differing view. The major effect of Cl^- is to shift the voltage operating range or state probability function of prestin along the voltage axis. The sensitivity of the operating range to Cl^- is remarkably similar to that of the CIC-0 channel (Pusch *et al.* 1995; Chen & Miller, 1996). State probability of that Cl^- channel is highly Cl^- dependent, showing a 40–50 mV change in the open probability function per 10-fold change in Cl^- concentration. We find a similar sensitivity to Cl^- concentration for prestin. In the case of CIC-0, this Cl^- sensitivity and the Cl^- ion requirement for gating have led to a consensus that the extrinsic ion serves as the voltage sensor of the channel; the channel maintains only slight residual voltage dependence under Cl^- -free conditions. Our data do not support a similar conclusion for prestin, since we find substantial voltage dependence under Cl^- -free conditions, with voltage sensitivity (z) and charge movement (Q_{max}) only partially affected, and dependent upon control anion species. Additionally, if prestin required an external anionic voltage sensor, the charge movement characteristics in the presence of SO_4^{2-} and absence of Cl^- should differ significantly, with z and Q_{max} doubling owing to the change in sensor valence from -1 to -2 . Thus, we conclude that the effect of Cl^- is probably due to an allosteric action on the motor protein, prestin. That is, as is typical of indirect allosteric interactions (Monod *et al.* 1963; Changeux & Edelstein, 1998), a modulator, in this case Cl^- , binds to a site (sites) that is distinct from the active site (sites) responsible for the main function of the protein, namely the intrinsically charged voltage-sensing moiety. The binding produces a reversible conformational change in prestin that changes the free energy minima of the steady-state energy profile. This we measure as a shift in the motor charge's Boltzmann function along the voltage axis. Allosteric modulation such as this is not unusual. For example, allosteric modulation of the HERG potassium channel by Ca^{2+} induces voltage shifts in the activation curve of the channel (Johnson *et al.* 2001).

Effect of Cl^- on area state of prestin. We showed that pentane sulfonate has direct effects on the OHC motor, depressing the motor's voltage sensitivity (z) much as salicylate does (Kakehata & Santos-Sacchi, 1996), while maintaining near normal Q_{max} . Indeed, as with salicylate, we still observe reduced electromotility, in contrast to the results of Oliver *et al.* (2001). Additionally, the shift of V_{pkcm} with pentane sulfonate solutions is opposite to that of our other control anions, sulfate or Hepes. We suspect that the lipophilic pentane side chain allows this organic

anion to work on normally inaccessible sites within the lipid environment of the motor, and its use does not allow an adequate evaluation of the effect of chloride on the charge or mechanical activity of prestin.

Oliver *et al.* (2001) concluded that removal of intracellular Cl⁻ causes the lateral membrane motor to reside in the contracted state, and consequently modelled prestin as expanding following the binding and translocation of intracellular Cl⁻ to the outer aspect of the membrane. However, this is unlikely because the state probability of the motor at a fixed holding voltage depends directly on the relative position of V_{pkcm} . Since we clearly show that the effects of pentane sulfate are unrelated to intracellular Cl⁻ concentration, their results probably reflect not the removal of Cl⁻, but the negative shift of V_{pkcm} produced by pentane sulfonate, which they exclusively used in their motility studies. We find that with sulfate- or HEPES-based solutions, where the effects we observe actually correspond to the removal of Cl⁻, the motors tend to reside in the expanded state with Cl⁻ removal, i.e. the OHC elongates at a fixed holding potential, as V_{pkcm} shifts in the positive direction. Thus, we conclude that the binding of Cl⁻ to prestin actually increases the probability that the protein resides in the contracted state and it is unlikely that binding and movement of the negatively charged Cl⁻ ion towards the outer membrane leaflet would increase prestin surface area as Oliver *et al.* (2001) modelled. We suggest that upon Cl⁻ binding, prestin activity is shifted into the physiological range of voltages where intrinsic charge may sense voltage perturbation. Contraction of prestin would be caused by a moiety of net positive charge moving outward, or one of net negative charge moving inward as the electrophysiological data suggests (Ashmore, 1990; Santos-Sacchi, 1991b).

How many prestin binding sites are there for anions? We find differential changes in V_{pkcm} , z and Q_{max} that depend on the control anions (sulfate or HEPES) that we use to replace Cl⁻. This observation indicates that multiple populations of anion-bound prestin may exist simultaneously, and we hypothesize that there are multiple binding sites that can bind not only Cl⁻ but other anions with different affinities, each having differential effects on the Boltzmann parameters. For the whole cell, and large patches, we must also be cognisant that still other restricted populations of motors (with different Boltzmann characteristics) may also exist as a result of local forces other than Cl⁻, e.g. tension, phosphorylation (Santos-Sacchi, 2002). Consequently, owing to distributed populations, the resulting single Boltzmann distributions that we observe do not demonstrate any apparent discontinuities.

Flux of Cl⁻ through the lateral membrane

Identity of the lateral membrane conductance. In this report we directly measured voltage- and stretch-activated anionic and cationic currents that arise from a lateral membrane conductance, and confirmed Cl⁻ movements

by monitoring non-linear capacitance. Several lines of evidence indicate that these non-selective currents, hereafter referred to as I_{metL} (mechano-electrical transducer, lateral membrane), pass through the same conductance: (1) the anionic and cationic currents co-vary in magnitude among OHCs, and never exist separately; each of the magnitudes proportionately fluctuates among and within cells; (2) all modulating agents (drugs, turgor pressure) affect each current in the same direction, and with approximately equal effects; (3) each shows identical rapid kinetics and sigmoidal voltage dependence; and (4) the currents localize to the lateral plasma membrane, being absent in plasma membrane lacking prestin, namely, at the OHC base and in supporting cells.

The number of ionic conductances that are known to exist in the OHC is growing. Some have been molecularly identified and physiologically characterized, e.g. the KCNQ channel subunits responsible for the $I_{k,n}$ current (Kubisch *et al.* 1999; Marcotti & Kros, 1999), or functionally linked to a particularly well characterized channel type, e.g. the L-type Ca²⁺ channel (Santos-Sacchi & Dilger, 1988; Nakagawa *et al.* 1991). Others have been identified through the detection of messenger RNA, e.g. ClC family members (Kawasaki *et al.* 1999), but lack corresponding physiological confirmation of expression. There are still others that have been highly characterized but whose molecular identity remains elusive after decades of study, e.g. the stereocilia transduction channel (Russell *et al.* 1989; Kros *et al.* 1992). Although the molecular identity of the conductance responsible for I_{metL} is unknown, its unusual characteristics are not unprecedented. Indeed, a poorly charge-selective, stretch-sensitive conductance that passes Na⁺, K⁺ and Cl⁻ has been characterized at the single channel level in opossum kidney cells (Uhl *et al.* 1988).

The major voltage-dependent ionic conductances of the OHC, including outward K⁺ and inward Ca²⁺, are restricted to the basal pole of the cell (Santos-Sacchi *et al.* 1997). Though it is generally accepted that the predominant constituent of the lateral membrane is the motor protein, prestin, ionic conductances other than the one we have characterized are localized to this region. Notably, stretch-activated channels have been found in the lateral membrane of OHCs, though they are selective for cations (Ding *et al.* 1991; Iwasa *et al.* 1991), and clearly could not account for the anionic currents that we observed. Brownell and colleagues have observed stretch-induced pore formation up to 4 nm in size in the OHC membrane, which is inhibited by chlorpromazine (Morimoto *et al.* 2002). They found that the pores passed mono and disaccharides, though the ionic permeability of these pores has not been elucidated. Interestingly, there are some reports that may have observed the effects of I_{metL} on OHC shape. Notably, tamoxifen and quinine have been shown to block swelling of OHCs in cochlear explants (Siegel *et al.* 2001), and Gd³⁺

was found to interfere with volume regulation in isolated OHCs (Crist *et al.* 1993). It was suggested that tamoxifen had its effect on ClC-3 channels in OHCs (Siegel *et al.* 2001). Our data do not support this.

Finally, we note that I_{metL} shares some properties of prestin, namely, its location, tension dependence, and modulation by Cl⁻ channel blockers. In this regard, it is well established that some transporters underlie ionic conductances, including CFTR (Hasegawa *et al.* 1992) and the sodium/bicarbonate co-transporter, NBCn1 (Choi *et al.* 2000). In fact, the Na⁺ current associated with NBCn1 expression shows an increase in response to DIDS (Choi *et al.* 2000), similar to the activity of this blocker on I_{metL} . It is conceivable that I_{metL} could result from the expression of prestin. Nevertheless, regardless of the conductance's molecular identity, it is clear that it has a major impact on the activity of prestin and the OHC.

Sub-membranous Cl⁻. I_{metL} is localized to the lateral plasma membrane of the OHC. The lateral membrane and subsurface cisternae form membranous barriers of a restricted compartment (LSpS) whose diffusional access to and from the cytosol is limited owing to its ~30 nm width (Pollice & Brownell, 1993). The LSpS may have distinctive properties (Halter *et al.* 1997; Ratnanather *et al.* 2000). As the cistern nearest the plasma membrane is continuous, ion diffusion must predominantly occur at the apical and basal extremes of the OHC, where the cisternae terminate. For the isolated cells we used in the present study, with lengths from 50 to 80 μm , the volume of the LSpS is about 47–66 fl. If washout from the bulk cytosol under whole-cell voltage clamp were completely absent, the magnitude of I_{metL} we observed, for example ~100 pA at -60 mV (see Fig. 10A), would change LSpS Cl⁻ levels at a rate of 20 mM s⁻¹. Actually, the concentration change just beneath the plasma membrane and at high frequencies (owing to diffusion-rate limitations), especially in the middle of the cell, could be substantially larger. This may explain to some extent our observation of non-uniform stretch-activated gating currents along the length of the OHCs, as non-linear capacitance magnitude will vary with Cl⁻ concentration (Takahashi & Santos-Sacchi, 2001). Since we find that intracellular dialysis with Cl⁻-free solutions affects prestin activity with a time course typical for whole-cell washout (Pusch & Neher, 1988), it is clear that LSpS is not absolutely isolated, and thus, Cl⁻ levels in that space are under our experimental control, at least at steady state (> 3 min). Nevertheless, reversal potential measures indicate substantial gradients in concentration between core cytosol and LSpS. Under whole-cell voltage clamp, the concentration of Cl⁻ in the LSpS is a balance between intracellular/LSpS diffusion and flux across the lateral plasma membrane. Clearly, then, in the absence of Cl⁻-containing solutions inside and outside the cell for more

than several minutes we are assured that Cl⁻ is depleted in the LSpS, and the conclusions that we reached based on this result, e.g. that Q_{max} is resistant to Cl⁻ depletion, are valid.

Under normal physiological conditions, other homeostatic mechanisms to control Cl⁻ levels may come into play, for example, pumps, transporters and sequestration mechanisms (see Frings *et al.* 2000), just as they do in calcium metabolism. Most cells maintain an intracellular Cl⁻ concentration that is substantially below the typical extracellular concentration of 140 mM, as in perilymph. Nevertheless, in many cell types Cl⁻ is maintained at levels higher than the predicted electrochemical equilibrium levels. This is usually achieved by Na⁺-K⁺-2Cl⁻ cotransport (Russell, 2000). However, there is an apparent absence of NKCC1 transporter in OHCs (Crouch *et al.* 1997; Goto *et al.* 1997); this may indicate that levels in the OHC are close to equilibrium levels, namely, for a resting potential < -70 mV (Dallos *et al.* 1982), Cl⁻ would be < 9 mM. Furthermore, efficient mechanisms for the control of Cl⁻ must exist within the very localized region of the LSpS, since an incessant flux of Cl⁻ across the lateral membrane is predicted to accompany acoustically induced (or basilar membrane vibration-induced) mechanical deformations of the cell. As noted above, changes in Cl⁻ levels in the LSpS will have a strong impact on OHC mechanical function. We speculate that the subsurface cisternae and associated mitochondria aid in controlling LSpS Cl⁻ levels. Indeed, it may be that interference with Cl⁻ homeostatic mechanisms underlies the susceptibility of the cochlear amplifier to trauma, or that modulation of these mechanisms accounts for normal phenomenon such as the shift in V_{pkcm} observed during OHC development (Oliver & Fakler, 1999).

Physiological implications of a fast stretch-activated lateral membrane Cl⁻ current – a hypothesis

The observation that OHC somatic motility is driven by voltage quickly led to the suggestion that the low-pass filter of the membrane would seriously limit high frequency electromotility (Santos-Sacchi, 1989). This problem only arises when one considers that owing to the non-linear nature of the mechanical response function, the mechanical gain of the OHC is about one tenth of its maximum (max: ~30 nm mV⁻¹) at the normal resting potential of -70 mV (Santos-Sacchi, 1989). Since that observation, a few solutions for the apparent RC filter problem have been suggested. Dallos & Evans (1995) suggested a mechanism that may work in the intact cochlea; during stimulation with high acoustic frequencies, extracellular voltages (which have a wider bandwidth than intracellular potentials) deriving from excited OHCs could induce a voltage drop across unexcited OHCs at basilar membrane regions basal to the excited cell region. Alternatively, we have suggested two cellular-based mechanisms whereby the problem could be alleviated. First, we found that the mechanical

gain of the cell at its resting potential could be increased via reductions in turgor pressure (Kakehata & Santos-Sacchi, 1995). Second, since we found that motor charge density is greater in higher frequency OHCs, we reasoned that the resultant electrical energy ($Q \times V$) delivered to the lateral membrane of high frequency OHCs could render the filter-induced drop in receptor potentials less detrimental (Santos-Sacchi *et al.* 1998a). All these arguments presuppose the existence of an RC filter problem due to voltage dependence of prestin. Our new data identify a potential mechanism for the operation of the cochlear amplifier without RC filter problems.

The identification of a stretch-activated conductance (G_{metL}) in the lateral membrane may indicate that the OHC motor can react to currents evoked by mechanical perturbations that accompany acoustic stimulation *in vivo*. This scenario had been envisioned following the discovery of stretch-activated cationic channels in the lateral membrane (Ding *et al.* 1991; Iwasa *et al.* 1991). Under that scheme, voltage perturbations accompanying the flux of cations were suggested to drive the OHC motor. However, in that case the RC filter problem remained. In our hypothetical view, however, Cl⁻ oscillations near prestin, driven by the stretch-activated AC and/or DC Cl⁻ current component of I_{metL} , would directly drive prestin transitions. This mechanism naturally follows from the substantial influence of Cl⁻ on the state probability of prestin. As the current or its integral, not the resultant voltage, would directly modulate prestin, the mechanism would be unencumbered by the RC membrane filter. Thus, we hypothesise that the OHC soma has adopted a mechanism similar to that which stereocilia may use to provide cochlear amplification in lower vertebrates (Choe *et al.* 1998; Ricci *et al.* 2000). In that case, Ca²⁺ ion entry through the mechanically gated transduction channels modulates the channels themselves and thus stereocilia bundle mechanics (Choe *et al.* 1998; Ricci *et al.* 2000). In an analogous manner, we view the lateral membrane as a forward and reverse transducer, where local changes in intracellular Cl⁻ levels lead to a cyclical binding of Cl⁻ to prestin, with resultant changes in OHC mechanical properties. Obviously, to be functional, the lateral membrane model must meet many of the requirements laid out for models of stereocilia amplification (Choe *et al.* 1998), including the need for rapid association and dissociation rate constants and mechanisms for Cl⁻ removal.

If this hypothesis has merit, then extracellular perilymphatic Cl⁻ levels should be important for normal auditory function. Manipulations of perilymphatic Cl⁻ levels have been made, but the results are not clear cut (Desmedt & Robertson, 1975). Regarding the interpretation of perilymphatic perfusion of any type, we must remain cognisant of the possibility that preparation for these kinds

of experiments can sometimes reduce response levels significantly such that threshold (active) effects can be missed. Indeed, Desmedt & Robertson (1975) described their preparations as 'fairly intact', and found variations of up to 20% in cochlear microphonic (CM) and eighth nerve compound action potential (N1) thresholds during control perfusions. Nevertheless, when low Cl⁻ perilymphatic-perfusion rates were increased so as to drop Cl⁻ levels down to 5 mM, N1 threshold levels did deteriorate, as we would predict.

REFERENCES

- Aickin CC & Brading AF (1984). The role of chloride–bicarbonate exchange in the regulation of intracellular chloride in guinea-pig *vas deferens*. *J Physiol* **349**, 587–606.
- Allen MC, Newland C, Valverde MA & Hardy SP (1998). Inhibition of ligand-gated cation-selective channels by tamoxifen. *Eur J Pharmacol* **354**, 261–269.
- Ashmore JF (1986). The cellular physiology of isolated outer hair cells: implications for cochlear frequency selectivity. In *Auditory Frequency Selectivity*, ed. Moore BC & Patterson RD, pp. 103–108. Plenum Press, New York.
- Ashmore JF (1987). A fast motile response in guinea-pig outer hair cells: the cellular basis of the cochlear amplifier. *J Physiol* **388**, 323–347.
- Ashmore JF (1989). Transducer motor coupling in cochlear outer hair cells. In *Mechanics of Hearing*, ed. Kemp D & Wilson JP, pp. 107–113. Plenum Press, New York.
- Ashmore JF (1990). Forward and reverse transduction in the mammalian cochlea. *Neurosci Res Suppl* **12**, S39–50.
- Ashmore JF & Meech RW (1986). Ionic basis of membrane potential in outer hair cells of guinea pig cochlea. *Nature* **322**, 368–371.
- Belyantseva I, Adler HJ, Curi R, Frolenkov GI & Kachar B (2000a). Expression and localization of prestin and the sugar transporter GLUT-5 during development of electromotility in cochlear outer hair cells. *J Neurosci* **20**, RC116.
- Belyantseva IA, Frolenkov GI, Wade JB, Mammano F & Kachar B (2000b). Water permeability of cochlear outer hair cells: characterization and relationship to electromotility. *J Neurosci* **20**, 8996–9003.
- Brownell WE, Bader CR, Bertrand D & de Ribaupierre Y (1985). Evoked mechanical responses of isolated cochlear outer hair cells. *Science* **227**, 194–196.
- Brundin L, Flock A & Canlon B (1989). Sound-induced motility of isolated cochlear outer hair cells is frequency-specific. *Nature* **342**, 814–816.
- Brundin L & Russell I (1994). Tuned phasic and tonic motile responses of isolated outer hair cells to direct mechanical stimulation of the cell body. *Hear Res* **73**, 35–45.
- Changeux JP & Edelman SJ (1998). Allosteric receptors after 30 years. *Neuron* **21**, 959–980.
- Chen TY & Miller C (1996). Nonequilibrium gating and voltage dependence of the ClC-0 Cl⁻ channel. *J Gen Physiol* **108**, 237–250.
- Choe Y, Magnasco MO & Hudspeth AJ (1998). A model for amplification of hair-bundle motion by cyclical binding of Ca²⁺ to mechano-electrical-transduction channels. *Proc Natl Acad Sci U S A* **95**, 15321–15326.
- Choi I, Aalkjaer C, Boulpaep EL & Boron WF (2000). An electroneutral sodium/bicarbonate cotransporter NBCn1 and associated sodium channel. *Nature* **405**, 571–575.

- Crist JR, Fallon M & Bobbin RP (1993). Volume regulation in cochlear outer hair cells. *Hear Res* **69**, 194–198.
- Crouch JJ, Sakaguchi N, Lytle C & Schulte BA (1997). Immunohistochemical localization of the Na–K–Cl co-transporter (NKCC1) in the gerbil inner ear. *J Histochem Cytochem* **45**, 773–778.
- Dallos P (1992). The active cochlea. *J Neurosci* **12**, 4575–4585.
- Dallos P & Evans BN (1995). High-frequency outer hair cell motility: corrections and addendum. *Science* **268**, 1420–1421.
- Dallos P, Evans BN & Hallworth R (1991). Nature of the motor element in electrokinetic shape changes of cochlear outer hair cells. *Nature* **350**, 155–157.
- Dallos P & Santos-Sacchi J (1983). AC receptor potentials from hair cells in the low frequency region of the guinea pig cochlea. In *Mechanisms of Hearing*, ed. Webster WR & Aitkin LM, pp. 11–16. Monash University Press, Clayton, Australia.
- Dallos P, Santos-Sacchi J & Flock A (1982). Intracellular recordings from cochlear outer hair cells. *Science* **218**, 582–584.
- Desmedt JE & Robertson D (1975). Ionic mechanism of the efferent olivo-cochlear inhibition studied by cochlear perfusion in the cat. *J Physiol* **247**, 407–428.
- Ding JP, Salvi RJ & Sachs F (1991). Stretch-activated ion channels in guinea pig outer hair cells. *Hear Res* **56**, 19–28.
- Draguhn A, Traub RD, Schmitz D & Jefferys JG (1998). Electrical coupling underlies high-frequency oscillations in the hippocampus *in vitro*. *Nature* **394**, 189–192.
- Frank G, Hemmert W & Gummer AW (1999). Limiting dynamics of high-frequency electromechanical transduction of outer hair cells. *Proc Natl Acad Sci U S A* **96**, 4420–4425.
- Frazier CJ, George EG & Jones SW (2000). Apparent change in ion selectivity caused by changes in intracellular K(+) during whole-cell recording. *Biophys J* **78**, 1872–1880.
- Frings S, Reuter D & Kleene SJ (2000). Neuronal Ca²⁺-activated Cl⁻ channels – homing in on an elusive channel species. *Prog Neurobiol* **60**, 247–289.
- Gale JE & Ashmore JF (1994). Charge displacement induced by rapid stretch in the basolateral membrane of the guinea-pig outer hair cell. *Proc R Soc Lond B Biol Sci* **255**, 243–249.
- Goto S, Oshima T, Ikeda K, Ueda N & Takasaka T (1997). Expression and localization of the Na–K–2Cl cotransporter in the rat cochlea. *Brain Res* **765**, 324–326.
- Gu CX, Juranka PF & Morris CE (2001). Stretch-activation and stretch-inactivation of Shaker-IR, a voltage-gated K⁺ channel. *Biophys J* **80**, 2678–2693.
- Gunthorpe MJ, Benham CD, Randall A & Davis JB (2002). The diversity in the vanilloid (TRPV) receptor family of ion channels. *Trends Pharmacol Sci* **23**, 183–191.
- Halter JA, Kruger RP, Yium MJ & Brownell WE (1997). The influence of the subsurface cisterna on the electrical properties of the outer hair cell. *NeuroReport* **8**, 2517–2521.
- Hasegawa H, Skach W, Baker O, Calayag MC, Lingappa V & Verkman AS (1992). A multifunctional aqueous channel formed by CFTR. *Science* **258**, 1477–1479.
- Huang G & Santos-Sacchi J (1993). Mapping the distribution of the outer hair cell motility voltage sensor by electrical amputation. *Biophys J* **65**, 2228–2236.
- Iwasa KH (1993). Effect of stress on the membrane capacitance of the auditory outer hair cell. *Biophys J* **65**, 492–498.
- Iwasa KH (1994). A membrane motor model for the fast motility of the outer hair cell. *J Acoust Soc Am* **96**, 2216–2224.
- Iwasa KH & Kachar B (1989). Fast *in vitro* movement of outer hair cells in an external electric field: effect of digitonin, a membrane permeabilizing agent. *Hear Res* **40**, 247–254.
- Iwasa KH, Li MX, Jia M & Kachar B (1991). Stretch sensitivity of the lateral wall of the auditory outer hair cell from the guinea pig. *Neurosci Lett* **133**, 171–174.
- Jentsch TJ, Stein V, Weinreich F & Zdebek AA (2002). Molecular structure and physiological function of chloride channels. *Physiol Rev* **82**, 503–568.
- Johnson JP Jr, Balser JR & Bennett PB (2001). A novel extracellular calcium sensing mechanism in voltage-gated potassium ion channels. *J Neurosci* **21**, 4143–4153.
- Kachar B, Brownell WE, Altschuler R & Fex J (1986). Electrokinetic shape changes of cochlear outer hair cells. *Nature* **322**, 365–368.
- Takehata S & Santos-Sacchi J (1995). Membrane tension directly shifts voltage dependence of outer hair cell motility and associated gating charge. *Biophys J* **68**, 2190–2197.
- Takehata S & Santos-Sacchi J (1996). Effects of salicylate and lanthanides on outer hair cell motility and associated gating charge. *J Neurosci* **16**, 4881–4889.
- Kalinek F, Holley MC, Iwasa KH, Lim DJ & Kachar B (1992). A membrane-based force generation mechanism in auditory sensory cells. *Proc Natl Acad Sci U S A* **89**, 8671–8675.
- Kawasaki E, Hattori N, Miyamoto E, Yamashita T & Inagaki C (1999). Single-cell RT-PCR demonstrates expression of voltage-dependent chloride channels (ClC-1, ClC-2 and ClC-3) in outer hair cells of rat cochlea. *Brain Res* **838**, 166–170.
- Kros CJ, Rusch A & Richardson GP (1992). Mechano-electrical transducer currents in hair cells of the cultured neonatal mouse cochlea. *Proc R Soc Lond B Biol Sci* **249**, 185–193.
- Kubisch C, Schroeder BC, Friedrich T, Lutjohann B, El Amraoui A, Marlin S, Petit C & Jentsch TJ (1999). KCNQ4, a novel potassium channel expressed in sensory outer hair cells, is mutated in dominant deafness. *Cell* **96**, 437–446.
- Lieberman MC, Gao J, He DZZ, Wu XD, Jia SP & Zuo J (2002). Prestin is required for electromotility of the outer hair cell and for the cochlea amplifier. *Nature* **419**, 300–304.
- Ludwig J, Oliver D, Frank G, Klocker N, Gummer AW & Fakler B (2001). Reciprocal electromechanical properties of rat prestin: The motor molecule from rat outer hair cells. *Proc Natl Acad Sci U S A* **98**, 4178–4183.
- Marcotti W & Kros CJ (1999). Developmental expression of the potassium current $I_{K,n}$ contributes to maturation of mouse outer hair cells. *J Physiol* **520**, 653–660.
- Milton RL & Caldwell JH (1990). How do patch clamp seals form? A lipid bleb model. *Pflugers Arch* **416**, 758–762.
- Monod J, Changeux JP & Jacob F (1963). Allosteric proteins and cellular control systems. *J Mol Biol* **6**, 306–329.
- Morimoto N, Raphael RM, Nygren A & Brownell WE (2002). Excess plasma membrane and effects of ionic amphipaths on mechanics of outer hair cell lateral wall. *Am J Physiol Cell Physiol* **282**, C1076–1086.
- Nakagawa T, Takehata S, Akaike N, Komune S, Takasaka T & Uemura T (1991). Calcium channel in isolated outer hair cells of guinea pig cochlea. *Neurosci Lett* **125**, 81–84.
- Okamura HO, Sugai N, Suzuki K & Ohtani I (1996). Enzyme-histochemical localization of carbonic anhydrase in the inner ear of the guinea pig and several improvements of the technique. *Histochem Cell Biol* **106**, 425–430.
- Oliver D & Fakler B (1999). Expression density and functional characteristics of the outer hair cell motor protein are regulated during postnatal development in rat. *J Physiol* **519**, 791–800.
- Oliver D, He DZ, Klocker N, Ludwig J, Schulte U, Waldegger S, Ruppertsberg JP, Dallos P & Fakler B (2001). Intracellular anions as the voltage sensor of prestin, the outer hair cell motor protein. *Science* **292**, 2340–2343.

- Pollice PA & Brownell WE (1993). Characterization of the outer hair cell's lateral wall membranes. *Hear Res* **70**, 187–196.
- Pusch M, Ludewig U, Rehfeldt A & Jentsch TJ (1995). Gating of the voltage-dependent chloride channel CIC-0 by the permeant anion. *Nature* **373**, 527–531.
- Pusch M & Neher E (1988). Rates of diffusional exchange between small cells and a measuring patch pipette. *Pflugers Arch* **411**, 204–211.
- Ratnanather JT, Popel AS & Brownell WE (2000). An analysis of the hydraulic conductivity of the extracisternal space of the cochlear outer hair cell. *J Math Biol* **40**, 372–382.
- Ricci AJ, Crawford AC & Fettiplace R (2000). Active hair bundle motion linked to fast transducer adaptation in auditory hair cells. *J Neurosci* **20**, 7131–7142.
- Ruggero MA & Rich NC (1991). Furosemide alters organ of corti mechanics: evidence for feedback of outer hair cells upon the basilar membrane. *J Neurosci* **11**, 1057–1067.
- Russell IJ, Richardson GP & Kossel M (1989). The responses of cochlear hair cells to tonic displacements of the sensory hair bundle. *Hear Res* **43**, 55–69.
- Russell JM (2000). Sodium–potassium–chloride cotransport. *Physiol Rev* **80**, 211–276.
- Rybalchenko & Santos-Sacchi (2001) Modulation of outer hair cell capacitance by chloride ions. *Inner Ear Biology Meeting Abstracts*, Rome, Italy, September 2001. http://ieb.unife.it/ieb2001/abstracts/cell_signalling.html
- Santos-Sacchi J (1989). Asymmetry in voltage-dependent movements of isolated outer hair cells from the organ of Corti. *J Neurosci* **9**, 2954–2962.
- Santos-Sacchi J (1991a). Isolated supporting cells from the organ of Corti: some whole cell electrical characteristics and estimates of gap junctional conductance. *Hear Res* **52**, 89–98.
- Santos-Sacchi J (1991b). Reversible inhibition of voltage-dependent outer hair cell motility and capacitance. *J Neurosci* **11**, 3096–3110.
- Santos-Sacchi J (1992). On the frequency limit and phase of outer hair cell motility: effects of the membrane filter. *J Neurosci* **12**, 1906–1916.
- Santos-Sacchi J (1993). Harmonics of outer hair cell motility. *Biophys J* **65**, 2217–2227.
- Santos-Sacchi J (2002). Functional motor microdomains of the outer hair cell lateral membrane. *Pflugers Arch* **445**, 331–336.
- Santos-Sacchi J & Dilger JP (1988). Whole cell currents and mechanical responses of isolated outer hair cells. *Hear Res* **35**, 143–150.
- Santos-Sacchi J, Huang GJ & Wu M (1997). Mapping the distribution of outer hair cell voltage-dependent conductances by electrical amputation. *Biophys J* **73**, 1424–1429.
- Santos-Sacchi J, Kakehata S, Kikuchi T, Katori Y & Takasaka T (1998a). Density of motility-related charge in the outer hair cell of the guinea pig is inversely related to best frequency. *Neurosci Lett* **256**, 155–158.
- Santos-Sacchi J, Kakehata S & Takahashi S (1998b). Effects of membrane potential on the voltage dependence of motility-related charge in outer hair cells of the guinea-pig. *J Physiol* **510**, 225–235.
- Santos-Sacchi J & Navarrete E (2002). Voltage-dependent changes in specific membrane capacitance caused by prestin, the outer hair cell lateral membrane motor. *Pflugers Arch* **444**, 99–106.
- Santos-Sacchi J, Shen W, Zheng J & Dallos P (2001). Effects of membrane potential and tension on prestin, the outer hair cell lateral membrane motor protein. *J Physiol* **531**, 661–666.
- Siegel J, Sikka R, Zeddies DG & Dong Q (2001). Intact explanted adult gerbil cochleae maintained at body temperature. *Assoc Res Otolaryngol Abs*, p. 240.
- Takahashi S & Santos-Sacchi J (2001). Non-uniform mapping of stress-induced, motility-related charge movement in the outer hair cell plasma membrane. *Pflugers Arch* **441**, 506–513.
- Thoreson WB, Nitzan R & Miller RF (2000). Chloride efflux inhibits single calcium channel open probability in vertebrate photoreceptors: chloride imaging and cell-attached patch-clamp recordings. *Vis Neurosci* **17**, 197–206.
- Uhl J, Murer H & Kolb HA (1988). Ion channels activated by osmotic and mechanical stress in membranes of opossum kidney cells. *J Membr Biol* **104**, 223–232.
- Welsh DG, Nelson MT, Eckman DM & Brayden JE (2000). Swelling-activated cation channels mediate depolarization of rat cerebrovascular smooth muscle by hyposmolarity and intravascular pressure. *J Physiol* **527**, 139–148.
- Yang XC & Sachs F (1989). Block of stretch-activated ion channels in *Xenopus* oocytes by gadolinium and calcium ions. *Science* **243**, 1068–1071.
- Zhao HB & Santos-Sacchi J (1999). Auditory collusion and a coupled couple of outer hair cells. *Nature* **399**, 359–362.
- Zheng J, Long KB, Shen W, Madison LD & Dallos P (2001). Prestin topology: localization of protein epitopes in relation to the plasma membrane. *NeuroReport* **12**, 1929–1935.
- Zheng J, Shen W, He D, Long K, Madison L & Dallos P (2000). Prestin is the motor protein of cochlear outer hair cells. *Nature* **405**, 149–155.

Acknowledgements

We thank Chris Miller and Fred Sachs for helpful discussions and Margaret Mazzucco for technical help. This study was supported by NIH NIDCD DC00273.

Anion Control of Voltage Sensing by the Motor Protein Prestin in Outer Hair Cells

Volodymyr Rybalchenko*[†] and Joseph Santos-Sacchi*^{†§}

*Department of Surgery (Otolaryngology), Yale University School of Medicine, New Haven Connecticut; [†]Department of Pharmacology and Neuroscience, University of North Texas Health Science Center, Fort Worth, Texas; and [‡]Department of Neurobiology and [§]Department of Cellular and Molecular Physiology, Yale University School of Medicine, New Haven Connecticut

ABSTRACT The outer hair cell from Corti's organ possesses voltage-dependent intramembranous molecular motors evolved from the SLC26 anion transporter family. The motor, identified as prestin (SLC26a5), is responsible for electromotility of outer hair cells and mammalian cochlear amplification, a process that heightens our auditory responsiveness. Here, we describe experiments designed to evaluate the effects of anions on the motor's voltage-sensor charge movement, focusing on prestin's voltage-dependent Boltzmann characteristics. We find that the nature of the anion, including species, valence, and structure, regulates characteristics of the charge movement, signifying that anions play a more complicated role than simple voltage sensing in cochlear amplification.

INTRODUCTION

The mammalian cochlea possesses unique cellular structures evolutionarily designed for active amplification, providing enhanced detection and discrimination of acoustic frequencies beyond 70 kHz (1,2). Despite much progress, our understanding of the molecular mechanisms responsible for this active amplification within the organ of Corti remains incomplete. Nevertheless, there is a growing consensus that it is the electrically evoked mechanical activity of the outer hair cells (OHCs) that boosts auditory performance (3–6). These OHCs possess a fast electromotility arising from the recently cloned voltage-sensitive protein prestin (SLC26a5) (7,8), which is densely expressed in the OHC lateral membrane (9,10). The electrical signature of conformational changes in prestin is a displacement current or nonlinear capacitance (NLC) (11–13). The estimated millions of motor molecules (14,15) that reside within each OHC power plasma membrane surface area fluctuations (16–18), thereby predominantly producing longitudinal movements of the cylindrically shaped cells on a submillisecond timescale.

The discovery of a fundamental role for intracellular anions (Cl⁻ in particular) in promoting prestin's voltage sensitivity (19) gave rise to a model in which anions serve as extrinsic voltage sensors whose intramembrane movement directly alters the conformational state of prestin. The model, which we refer to as the partial anion transporter (PAT) model, is encapsulated by an animated cartoon (www.sciencemag.org/content/vol292/issue5525/images/data/2340/DC1/Prestin_movie.mov). It purports that the voltage-driven movement of a bound anion from the intracellular aspect of prestin toward the extracellular

aspect (resulting from a truncated transport cycle) gates prestin from the contracted to the expanded state. Thus, apparent gating charge (z) would derive from the distance (d) that the anion/sensor charge ($q = \text{ion valence} \times e$) moves perpendicular to the membrane field; that is, two-state Boltzmann fits of gating charge or NLC would provide an apparent gating charge of $z = d \times q$. Thus, in this model, z is expected to scale with either d or anion valence. However, the model (19) posits only monovalent anion sensors.

This initial observation was complimented by our recent observations that certain intracellular anions, which were initially considered, according to the PAT model (19), to be unable to serve as prestin's voltage sensor (e.g., SO₄²⁻), can support NLC and shift prestin's voltage operational range (V_{op} , defined in Methods) (20). These observations led to a model for prestin voltage sensing in which anions allosterically modulate the voltage-sensing activity of intrinsic charged residues. In this model, apparent z is still obtained from fits to a two-state Boltzmann function, but it describes, instead, an equivalent charge, q , the sum of an unknown number of partial charges, through a trajectory perpendicular to the membrane field. In this model, z does not necessarily scale with anion valence. We also found that anions pass through a lateral membrane conductance, under the control of membrane stretch and voltage (20). These findings led to a hypothesis that prestin state transitions can occur at constant membrane potential (V_m), being driven by anion flux resulting from acoustically evoked OHC lateral membrane deformations (3,4,20,21). These conformational transitions would primarily result from binding and unbinding of anions, a process that could be unencumbered by the OHC's membrane RC filter (22,23). Here, we expand on our initial observation that intracellular anions significantly shift prestin's V_{op} , and we provide further data that the nature of the anion, including species, valence, and structure, regulates Boltzmann characteristics of the charge movement, indicating a more compli-

Submitted March 27, 2008, and accepted for publication July 18, 2008.

Address reprint requests to Joseph Santos-Sacchi, PhD, Depts. of Surgery (Otolaryngology), Neurobiology, and Cellular and Molecular Physiology, Yale University School of Medicine, BML 244, 333 Cedar St., New Haven, CT 06510. Tel.: 203-785-7566 (office); 203-785-5407 (lab); E-mail: joseph.santos-sacchi@yale.edu.

Editor: Richard W. Aldrich.

© 2008 by the Biophysical Society
0006-3495/08/11/4439/09 \$2.00

doi: 10.1529/biophysj.108.134197

cated picture of anion interactions with prestin than a simple extrinsic voltage sensor model (19) can yield.

METHODS

Adult guinea pigs were euthanized with a halothane inhalation overdose protocol approved by the Yale University animal use and care committee. OHCs were freshly isolated from the organ of Corti after enzymatic (dispase 0.5 mg/ml) and mechanical treatment in Ca^{2+} -free medium. Cells of approximately the same size (50–70 μm) were used. Electrical recordings from voltage-clamped OHCs were done at room temperature, as described in our previous work (20). Combined leakage-free liquid bridges (Ag-ACI-TrisCl-TrisMalate-agar) were used in grounding and patch pipette circuits to minimize liquid junction potentials that were kept within ± 4 mV while Cl^- -free and Cl^- -containing solutions were exchanged during the experiment. These values were obtained in control test conditions with solution exchanges around an open pipette. The solution buildup within the bridge was not observed during the relatively short time of the exposure (~ 2 – 5 min) of one particular solution. The solutions were either low- Ca^{2+} or Ca^{2+} -free and K^+ -free (listed in Table 1) to prevent OHC K^+ and Ca^{2+} currents. At the ion concentrations listed, the osmolarity for extracellular solutions was ~ 325 mOsm, whereas solutions 5 mOsm lower were used intracellularly to prevent OHC swelling and effects of altered membrane tension on prestin's functional parameters (24–26). The pH of solutions was adjusted to ~ 7.25 – 7.30 with TrisOH. No difference in osmolarity for equimolar solutions of short- and long-tail sulfonic anions was noticed, indicating that no micelles were formed by any of the alkyl-sulfonates tested. All chemicals were from Sigma (St. Louis, MO) and Fluka (Buchs, Switzerland).

Extracellular solutions were locally applied to the individual cells by Y tube while a bath was continuously perfused with Tris-Hepes_(o) solution. When evaluating the effects of extracellularly applied anions on the intracellular aspect of prestin (see Figs. 3 and 4), at least a 2-min interval was allowed from

the moment of extracellular solution application to the time the membrane capacitance was recorded, to allow the extracellular anions to permeate the membrane and equilibrate with the intracellular solution. Where appropriate, as noted in the text, the patch pipette solutions were exchanged during continuous recording from the cell, using the intrapipette perfusion system 2PK+ (ALA Scientific Instruments, Westbury, NY). In most experiments, 200 μM streptomycin + 400 μM acetazolamide (OHC stereocilia channels and hemichannel blockers) were added to all extracellular solutions to rule out possible influence on the data from unaccounted currents.

OHC membrane capacitance measurements

The OHC voltage-dependent membrane capacitance (C_m), i.e., the capacitance-voltage (C-V) plot, was measured by applying a command voltage protocol (ramp + superimposed two-sine (10 mV peak at 390.6 and 781.2 Hz) from holding potential $V_{\text{hold}} = 0$ mV) that allowed us to sample at 2.56 ms resolution. Subsequently, off-line extraction of C-V plots was performed using a fast-Fourier-transform-based admittance analysis (27,28) incorporated into jClamp software (SciSoft, Branford, CT).

Prestin molecular parameters

Experimentally measured OHC C-V plots were fitted with the function $C_m = C_{\text{lin}} + C_v$, where C_{lin} is the voltage-independent (linear surface area component) capacitance of the lipid bilayer, and $C_v = dQ_{\text{nonl}}/dV$ is the voltage-dependent component of C_m originating from prestin's intramembrane voltage-sensor translocation evoked by external voltage, described with a two-state Boltzmann function, $Q = Q_{\text{max}}/(1 + \exp(-ze(V - V_{\text{pkCm}})/k_B T))$. The total nonlinear fitting function for C_m (13), $C_m = C_{\text{lin}} + \{Q_{\text{max}}ze/k_B T\} \times \exp(-ze(V - V_{\text{pkCm}})/k_B T)/(1 + \exp(-ze(V - V_{\text{pkCm}})/k_B T))^2$ represents a bell-shaped C-V plot (Fig. 1, middle) from which the parameters of Q_{max} , z , V_{pkCm} , and C_{lin} were obtained using a nonlinear curve-fitting procedure. Q_{max} is the total charge translocated if all active prestin molecules underwent conformational transition to the alternative state. $Q_{\text{max}} = q \times N$, where q is

TABLE 1 Composition of intracellular and extracellular solutions

Solution name	Special notes	MgSO ₄	Mg(OH) ₂	EGTA	Malate	TrisOH	HCl
Tris-Mal _(i)	Malate ²⁻ , 115	—	2	2	—	~260	—
Tris-Cl _(i)	—	2	2	~180	—	150	—
Tris - Mal _(i) ^{10Cl}	Malate ²⁻ , 107	—	2	2	—	~245	10
Tris-Hepes _(i) * ^{10Cl}	Hepes ⁽⁻⁾ , 190	2	—	10	—	~120	—
Tris-SO _{4(i)}	SO ₄ ²⁻ , 110; Hepes ⁽⁻⁾ , 10	2	—	10	—	~265	—
Na-SO _{4(i)}	Na ₂ SO ₄ , 110; Hepes ⁽⁻⁾ , 30	2	—	10	—	—	—
Na-PnSO _{3(i)} * ^{10Cl}	NaPentSO ₃ , 140; Hepes ⁽⁻⁾ , 10	2	—	10	—	~30	—
Tris-PO _{4(i)}	PO ₄ ³⁻ , 120	—	2	10	—	~290	—
Tris-Hepes _(o)	Hepes ⁽⁻⁾ , 210; CaSO ₄ , 0.2	5	—	—	—	~110	—
Tris-Cl _(o)	Hepes ⁽⁻⁾ , 10; CaSO ₄ , 0.2	5	—	—	—	~155	140
Na-Cl _(o)	NaCl, 150	—	5	—	17	~26	—
Na-SO _{4(o)}	Na ₂ SO ₄ , 125	—	5	—	15	~21	—
Na-Mal _(o)	Na ₂ Malate, 125	—	5	—	5	~20	—
Na-MeSO _{3(o)}	NaMethaneSO ₃ , 150	—	5	—	13	~18	—
Na-EtSO _{3(o)}	NaEthaneSO ₃ , 150	—	5	—	11	~13	—
Na-PrSO _{3(o)}	NaPropaneSO ₃ , 150	—	5	—	12	~15	—
Na-PnSO _{3(o)}	Na-1-PentaneSO ₃ , 150	—	5	—	12	~15	—
Na - SO _{4(o)} ^{10Cl}	Na ₂ SO ₄ , 117; NaOH, 10	—	5	—	15	~21	10
Na - Mal _(o) ^{10Cl}	Na ₂ Malate, 117; NaOH, 10	—	5	—	5	~20	10
Na - MeSO _{3(o)} ^{10Cl}	NaMethaneSO ₃ , 140; NaOH, 10	—	5	—	13	~18	10
Na - EtSO _{3(o)} ^{10Cl}	NaEthaneSO ₃ , 140; NaOH, 10	—	5	—	11	~13	10
Na - PrSO _{3(o)} ^{10Cl}	NaPropaneSO ₃ , 140; NaOH, 10	—	5	—	12	~15	10
Na - PnSO _{3(o)} ^{10Cl}	Na-1-PentSO ₃ , 140; NaOH, 10	—	5	—	12	~15	10

Subscripts (i) and (o) are used to denote intracellular and extracellular solutions, respectively. All values are given in mM.

*The presence of 2 mM of SO_{4(i)}²⁻ in this solution did not influence the effect of the major anion.

prestin's voltage-sensor elementary charge and N is a number of prestin molecules. The measured "apparent valence" of prestin voltage sensor (z) is defined as $z = q \times d$, where d ($0 < d < 1$) is a normalized perpendicular projection of distance traveled by the voltage sensor within the plasma membrane field (Fig. 1). V_{pkCm} is the membrane potential (V_m) at which prestin molecules are equally distributed between expanded and contracted states. It corresponds to the peak of the C_v function. Another parameter, prestin's voltage operation range, was defined as $V_{op} = \{V_{10}, V_{90}\}$, within which the probability for prestin to switch from the expanded to the contracted state varies between 10% and 90%. Within the V_{op} , prestin molecules are sensitive to V_m variations, whereas at more negative potentials the prestin population is virtually locked in the expanded state, and at more positive potentials in the contracted state. As follows trivially from the above equation for Q , the $V_{op} = V_{pkCm} \pm 2.2k_B T/ze = V_{pkCm} \pm z^{-1} \times 56.2$ mV.

Experimental C-V curves were corrected off-line for the effects of series resistance, R_s , using a jClamp built-in algorithm. The nonlinear fitting of C-V curves was performed using the least-square algorithms incorporated in

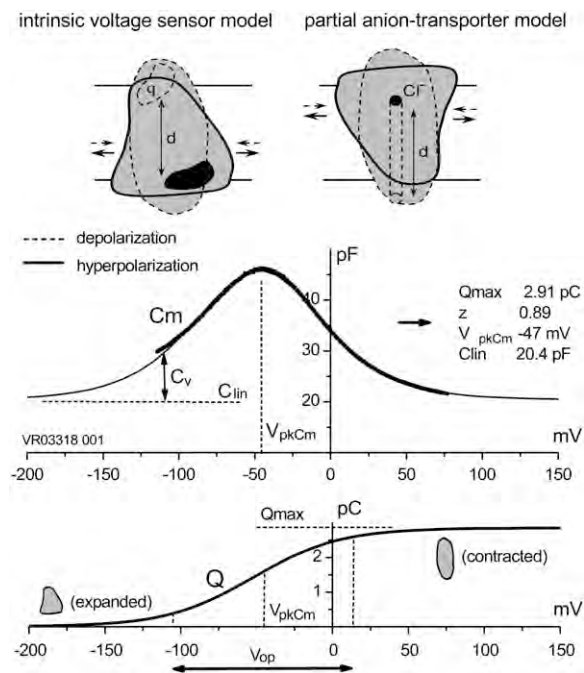


FIGURE 1 Schematic representation of the IVS and PAT models for prestin, and definitions of prestin molecular parameters. (Upper) Conformational transitions between prestin expanded (solid lines) and contracted (dashed lines) states after membrane hyper/depolarization cycles, result from intramembrane translocation of either 1), prestin's charged moiety q (IVS model, left); or 2), Cl^- /bicarbonate-binding moiety (PAT model, right). (Middle) Experimentally measured (in OHCs) bell-shaped C-V curve (heavy line) is composed of a passive capacitance of a membrane lipid bilayer (C_{lin}) and a bell-shaped voltage-dependent component of membrane capacitance (C_v) originating from intramembrane translocation of prestin's charged voltage sensor at membrane voltages within the prestin operation range (V_{op} , indicated in lower panel). The thin line is a two-state Boltzmann function first-derivative fit (see Methods) to a C-V component, from which the parameters characterizing prestin conformational transitions (Q_{max} , z , and V_{pkCm} (inset)) are obtained. Intracellular and extracellular solutions were Tris- $Cl_{(i)}$ and Tris- $Cl_{(o)}$, respectively. (Lower) Integration of the C_v component from the middle panel reproduces a Boltzmann function that characterizes prestin voltage-dependent transitions between expanded (hyperpolarization) and contracted (depolarization) states. The range of membrane potentials between 10% and 90% of prestin molecules residing in the contracted state is defined as prestin's voltage operation range (V_{op} ; see Methods).

jClamp and Origin (Microcal, Northampton, MA) software ($\Delta\chi^2 < 0.05$). Data are presented as mean \pm SD. The statistical significance of difference obtained for the parameters V_{pkCm} , Q_{max} , and z was calculated using one-way analysis of variance ($^o p < 0.1$, $*p < 0.05$, $**p < 0.01$, and $***p < 0.001$). For Figs. 3 and 5, statistics are relative to those characteristics for Cl^- . For Fig. 4, statistics are for the extracellular anions (2–6) relative to those characteristics for control conditions with basal extracellular solution Na-Mal(o)10Cl (1). The number of cells tested for each anion is presented in parentheses for V_{pkCm} , and at the bottom of columns for Q_{max} and z .

RESULTS

Recently, we reported that substitution of sulfate (SO_4^{2-}) for intracellular chloride ($Cl_{(i)}^-$) in guinea pig OHC cells supports NLC and shifts prestin's V_{op} to very positive membrane potentials without substantial change in electromechanical activity (20,29). We posited an intrinsic voltage sensor (IVS) model (20,29), wherein the existence of intracellular anion binding sites on prestin (binding both $Cl_{(i)}^-$ and SO_4^{2-}) influences the free energy profile for prestin's voltage-dependent transitions, thereby establishing V_{op} . According to the PAT model, however, the divalent sulfate is ineffective in supporting prestin charge movement, and the positive shift in V_{op} results from decreasing chloride levels (30). Clearly, if $Cl_{(i)}^-$ removal were the sole reason for the positive V_{op} shift during the $SO_4^{2-} \rightarrow Cl_{(i)}^-$ substitution, the shift should be in the same (positive) direction and of similar amplitude irrespective of the nature of the anion that substitutes for $Cl_{(i)}^-$. To address this issue, we monitored the changes in C-V functions during patch pipette solution washin using three different anion substitutes (SO_4^{2-} , HEPES $^{(-)}$, and 1-pentanesulfonate $^-$ ($PnSO_3^-$) (Fig. 2)). With SO_4^{2-} in the pipette, V_{pkCm} progressively shifted to high depolarizing potentials ($\sim +140$ mV) upon $Cl_{(i)}^-$ washout. The nonlinear C_v component of C-V function remained robust, in accordance with our earlier reports (20,29), but contrary to observations made on excised patches (30). With HEPES $^{(-)}$ anions in lieu of $Cl_{(i)}^-$, the rightward V_{pkCm} shift was less pronounced. Finally, with $PnSO_3^-$ in the pipette, the C-V curve shift was in the opposite (negative) direction, with V_{pkCm} stabilized at extremely hyperpolarized potentials (-150 to -180 mV). The experiments depicted in Fig. 2 clearly indicate that the direction and amplitude of the shift of prestin-generated C-V functions depend on the nature of the intracellular anion and not solely on $Cl_{(i)}^-$ washout.

From our data above, it is clear that the structurally different intracellular anions SO_4^{2-} , HEPES $^{(-)}$, and $PnSO_3^-$, which can be considered sulfonate (SO_3^-)-containing anions, shift prestin's C-V function over a wide range of membrane potentials. To better understand the structure-function aspects of prestin interaction with (SO_3^-)-containing anions, we examined C-V functions of prestin in the presence of alkylsulfonic anions with increasing hydrocarbon tail lengths. Because of technical difficulties with the intrapipette exchange of multiple solutions, the four sulfonic anions: methane SO_3^- ($MeSO_3^-$), ethane SO_3^- ($EtSO_3^-$), propane SO_3^- ($PrSO_3^-$), and $PnSO_3^-$, as well as SO_4^{2-} and Cl^- , were consecutively applied extracellularly to the same

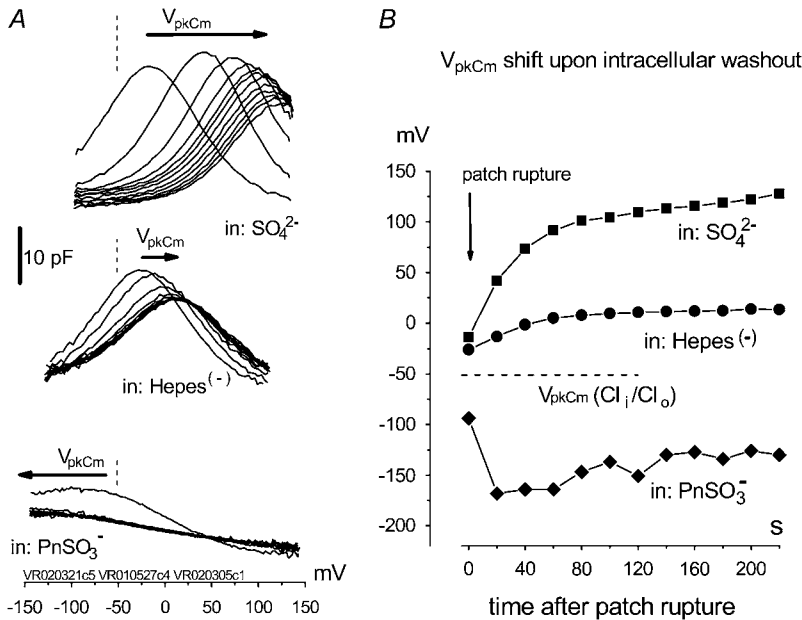


FIGURE 2 Removal of $\text{Cl}^-_{(i)}$ does not determine the direction of the shift of prestin's voltage operation range. (A) Three different OHCs were equilibrated with $\text{Cl}^-_{(i)}$ in Tris- $\text{Cl}_{(o)}$ extracellular solution and then were voltage-clamped using patch pipettes containing intracellular Tris- $\text{SO}_{4(i)}$ (upper), Tris-Hepes $_{(i)}$ (middle), and Na-Pn $\text{SO}_{3(i)}$ (lower) solutions. C-V curves were recorded at 20-s intervals starting at the moment of patch rupture. Upon $\text{Cl}^-_{(i)}$ substitution with intrapipette anions, the C-V characteristics exhibit a voltage shift of different amplitude and direction from $V_{\text{pkCm}}(\text{Cl}^-_{(i)}/\text{Cl}^-_{(o)}) = -51 \pm 11$ mV ($n = 9$, dashed line) recorded at the initial "all Cl^- conditions" (Tris- $\text{Cl}_{(i)}/\text{Tris-Cl}_{(o)}$). The shift depends on the nature of the substitute anion and is not a result of a reduction in $[\text{Cl}^-]_{(i)}$. The 10 pF scale is common for all panels. The horizontal axis is the scale for V_m . (B) V_{pkCm} values obtained from fits (not shown) to the experimental curves for three cells from A were plotted against time, starting from the moment of patch rupture. The irregular time course of the $V_{\text{pkCm}}(\text{PnSO}_{3(i)}/\text{Cl}^-_{(o)})$ curve is due to the difficulties in fitting C-V curves with V_{pkCm} values close to, or beyond, the limit of mechanical stability of the cell.

OHC during the experiment. In addition, we had to limit our voltage excursions to ± 100 mV to limit cell loss during the six perfusions and data collections. We have recently shown that extracellularly applied ions can pass through a nonselective OHC lateral membrane conductance (G_{metL}) to interact with prestin intracellularly (29). Intracellular malate²⁻ was used as a reference anion, since it supported the lowest Q_{max} in our previous experiments, allowing us to monitor increases in NLC due to supplemental anions. The C-V curves with fits from representative OHCs and statistics on V_{pkCm} values obtained from 10 cells ($n > 5$ for each particular anion) are presented in Fig. 3 A. In symmetric $\text{Mal}_{(i)}/\text{Mal}_{(o)}$ conditions, the reference values for $V_{\text{pkCm}}(\text{Mal}_{(i)}/\text{Mal}_{(o)}) = +99 \pm 22$ mV were at very positive membrane potentials, similar to the earlier measured $V_{\text{pkCm}}(\text{SO}_4^{2-})$. With extracellular MeSO_3^- and EtSO_3^- , V_{pkCm} was progressively shifted to more negative potentials: $V_{\text{pkCm}}(\text{Mal}_{(i)}/\text{MeSO}_3^-_{(o)}) = +79 \pm 28$ mV and $V_{\text{pkCm}}(\text{Mal}_{(i)}/\text{EtSO}_3^-_{(o)}) = +59 \pm 27$ mV. The appearance of the third alkyl-carbonate in the anion PrSO_3^- produced a dramatic shift of V_{pkCm} to negative membrane potentials: $V_{\text{pkCm}}(\text{Mal}_{(i)}/\text{PrSO}_3^-_{(o)}) = -68 \pm 54$ mV. Further elongation of the hydrocarbon chain for PnSO_3^- showed only moderate additional V_{pkCm} shift to more negative potentials: $V_{\text{pkCm}}(\text{Mal}_{(i)}/\text{PnSO}_3^-_{(o)}) = -97 \pm 21$ mV. The final control applications of Na- $\text{SO}_{4(o)}$ and Na- $\text{Cl}_{(o)}$ solutions produced $V_{\text{pkCm}}(\text{Mal}_{(i)}/\text{SO}_4^{2-}_{(o)}) = +96 \pm 23$ mV and $V_{\text{pkCm}}(\text{Mal}_{(i)}/\text{Cl}^-_{(o)}) = +36 \pm 13$ mV, in agreement with expected values. Statistics on Q_{max} and z values obtained in this series of experiments are presented in Fig. 3, B and C. $Q_{\text{max}}(\text{Mal}_{(i)}/\text{Mal}_{(o)}) = 0.63 \pm 0.15$ pC, $Q_{\text{max}}(\text{Mal}_{(i)}/\text{MeSO}_3^-_{(o)}) = 1.16 \pm 0.33$ pC, $Q_{\text{max}}(\text{Mal}_{(i)}/\text{EtSO}_3^-_{(o)}) = 1.42 \pm 0.47$ pC, $Q_{\text{max}}(\text{Mal}_{(i)}/\text{PrSO}_3^-_{(o)}) = 2.44 \pm 0.45$ pC, $Q_{\text{max}}(\text{Mal}_{(i)}/\text{PnSO}_3^-_{(o)}) = 2.70 \pm 0.68$ pC, $Q_{\text{max}}(\text{Mal}_{(i)}/\text{SO}_4^{2-}_{(o)}) =$

1.60 ± 0.35 pC, and $Q_{\text{max}}(\text{Mal}_{(i)}/\text{Cl}^-_{(o)}) = 2.59 \pm 0.73$ pC; and $z(\text{Mal}_{(i)}/\text{Mal}_{(o)}) = 0.71 \pm 0.10$, $z(\text{Mal}_{(i)}/\text{MeSO}_3^-_{(o)}) = 0.57 \pm 0.08$, $z(\text{Mal}_{(i)}/\text{EtSO}_3^-_{(o)}) = 0.51 \pm 0.08$, $z(\text{Mal}_{(i)}/\text{PrSO}_3^-_{(o)}) = 0.38 \pm 0.04$, $z(\text{Mal}_{(i)}/\text{PnSO}_3^-_{(o)}) = 0.30 \pm 0.05$, $z(\text{Mal}_{(i)}/\text{SO}_4^{2-}_{(o)}) = 0.58 \pm 0.07$, and $z(\text{Mal}_{(i)}/\text{Cl}^-_{(o)}) = 0.75 \pm 0.07$.

It should be noted that V_{pkCm} , Q_{max} , and z values obtained in these experiments simply serve to illustrate the general effects of these anions on NLC, since the accumulated intracellular concentration of tested anions is not known. Nevertheless, the relatively high Q_{max} values obtained for all tested anions, compared to the reference $Q_{\text{max}}(\text{Mal}_{(i)}/\text{Mal}_{(o)})$ value, indicated that accumulated concentrations of test anions were sufficient to substitute for malate²⁻ on prestin's intracellular anion-binding site(s) that modulates prestin's voltage sensor function. This issue is revisited in the experiments described in Fig. 4. It should also be noted that SO_4^{2-} and PnSO_3^- anions shift prestin C-V curves consistently in one direction (positive and negative, respectively) regardless of their intra- or extracellular application. This observation rules out the origin of V_{op} shifts from membrane charge screening effects and/or from liquid junction potential artifacts. The same observation ruled out electrogenic transport of those anions by prestin, since V_{pkCm} would be expected to shift in opposite directions upon switching the side of the membrane where the transported anions are applied.

Since different anion species can bind to prestin regulatory anion binding sites, it might be expected that various anions would compete for binding to these sites under normal conditions. At present, intracellular $\text{Cl}^-_{(i)}$ anions are strong candidates to be the major anions regulating prestin Q_{max} and V_{op} in OHCs. To verify whether the sulfonic anions can compete with $\text{Cl}^-_{(i)}$ for prestin regulatory binding sites, we repeated the previous experiment represented in Fig. 3 in the presence of 10 mM Cl^- in the intra- and extracellular solutions. The test

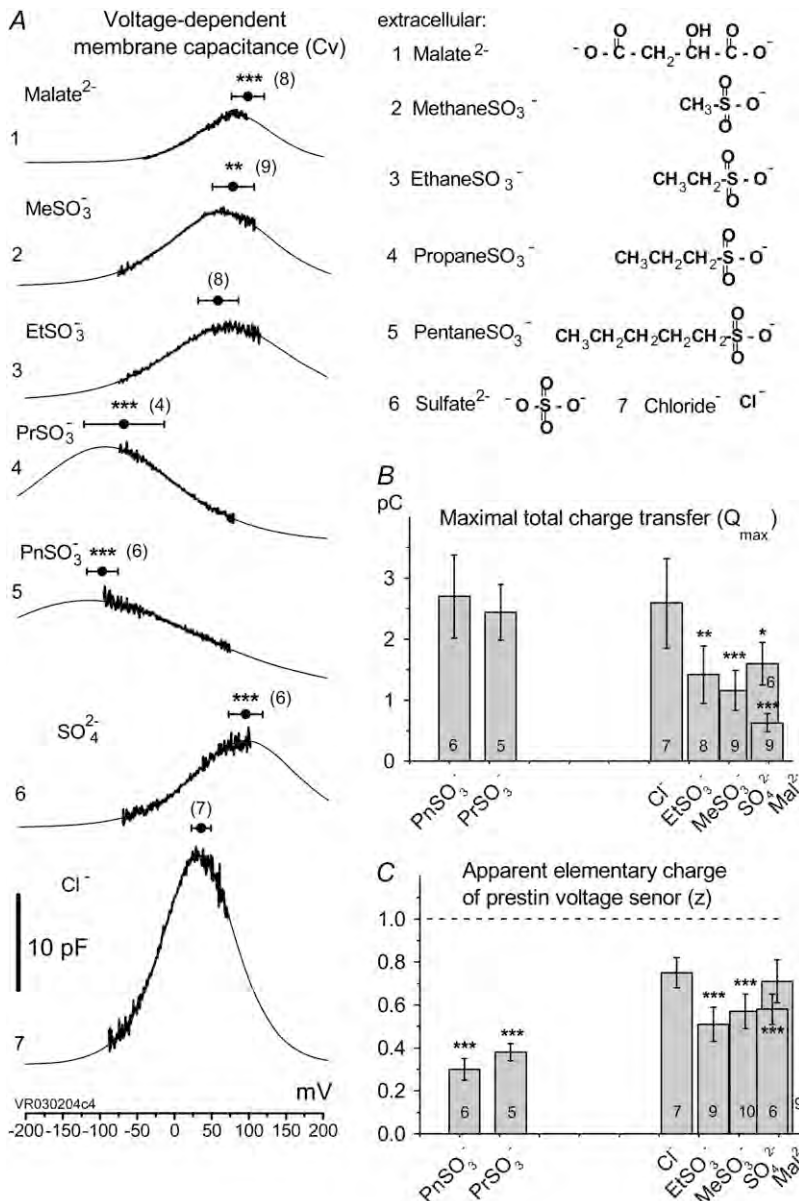


FIGURE 3 Alkylsulfonic anions shift prestin's V_{op} over a wide range (from depolarizing to hyperpolarizing) of membrane potentials as a function of hydrocarbon chain length. (A) C_v - V curves (thick line) and their fits (thin line) obtained from the same OHC perfused with Na-Mal_(i) intracellular solution while control anions and sulfonic anions with increasing hydrocarbon chain length were applied extracellularly in the order (of solutions) (1) Na-Mal_(o), (2) Na-MeSO_{3(o)}, (3) Na-EtSO_{3(o)}, (4) Na-PrSO_{3(o)}, (5) Na-PnSO_{3(o)}, (6) Na-SO_{4(o)}, and (7) Na-Cl_(o). Circles and horizontal error bars above traces represent mean \pm SD for prestin V_{pkCm} values obtained in 10 cells. (B and C) Columns and vertical error bars represent statistics (mean \pm SD) for Q_{max} (B) and z (C) values obtained from the same fits that were used to obtain V_{pkCm} parameters in A. Columns for the appropriate anions are placed in the order and relative position of their V_{pkCm} values on the scale of membrane potentials.

sulfonic anions were again applied extracellularly in order of their V_{pkCm} positive shift demonstrated in the previous experiment. The C-V curves and fits for representative OHCs and statistics on V_{pkCm} values obtained in five cells are presented in Fig. 4 A. In the present condition, where 10 mM $[Cl]_{(i)}$ is fixed, the reference value of $V_{pkCm}(Mal_{(i)}^{10Cl}/Mal_{(o)}^{10Cl}) = +2 \pm 7$ mV (Fig. 4 A I) was shifted to more negative potentials than the value of $V_{pkCm}(Mal_{(i)}/Cl_{(o)}) = +36$ mV obtained in the previous experiment for conditions with all Cl^- extracellular ($Mal_{(i)}/Cl_{(o)}$) (Figs. 3 A 7 and 4 A I (vertical dashed line)). The fact that the $V_{pkCm}(Mal_{(i)}/Cl_{(o)})$ value is more positive than the $V_{pkCm}(Mal_{(i)}^{10Cl}/Mal_{(o)}^{10Cl})$ value indicates that the averaged accumulated $[Cl^-]_{(i)}$ in the previous experiment (Fig. 3) for conditions of $Mal_{(i)}/Cl_{(o)}$ was <10 mM, since lower $[Cl^-]_{(i)}$ would shift the prestin V_{pkCm} to more positive potentials. Thus, we estimated that accumulated intracellular sub-

plasmalemmal concentrations of sulfonic anions applied extracellularly in this and the previous experiment did not reach (and were probably significantly lower than) 10 mM.

The following values of V_{pkCm} were obtained for conditions with fixed 10 mM $[Cl]_{(i)}$ and test anions applied extracellularly (Fig. 4 A): $V_{pkCm}(Mal_{(i)}^{10Cl}/SO_4^{2-(o)10Cl}) = +16 \pm 6$ mV, $V_{pkCm}(Mal_{(i)}^{10Cl}/MeSO_3^{-(o)10Cl}) = +38 \pm 7$ mV, $V_{pkCm}(Mal_{(i)}^{10Cl}/EtSO_3^{-(o)10Cl}) = +31 \pm 9$ mV, $V_{pkCm}(Mal_{(i)}^{10Cl}/PrSO_3^{-(o)10Cl}) = +8 \pm 37$ mV, $V_{pkCm}(Mal_{(i)}^{10Cl}/PnSO_3^{-(o)10Cl}) = -5 \pm 27$ mV. Using the relative shift of V_{pkCm} by SO_3^- -containing anions from reference $V_{pkCm}(Mal_{(i)}^{10Cl}/Mal_{(o)}^{10Cl}) = +2$ mV as a measure of their efficacy to alter V_{op} , the following rank was obtained: $MeSO_3^- > EtSO_3^- > SO_4^{2-}$. The displacement ability by $PrSO_3^-$ and $PnSO_3^-$ could not be ranked in these experiments

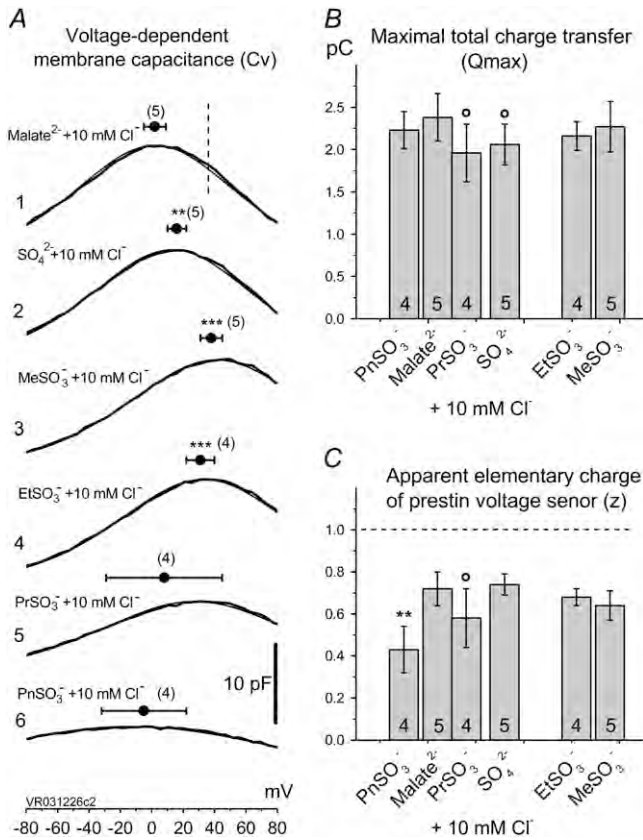


FIGURE 4 Sulfonic anions compete with Cl⁻ for prestin's regulatory anion-binding sites. (A) Select regions of C_v-V curves (thick lines) and their fits (thin lines, indistinguishable due to the close match) obtained from the same OHC examined at 10 mM intra- and extracellular [Cl⁻] "clamped" conditions with Na - Mal^{10Cl}_(i) intracellular and reference anion and SO₃⁻-containing extracellular solutions applied in the order (1), Na - Mal^{10Cl}_(o), (2), Na - SO₄^{10Cl}_(o), (3), Na - MeSO₃^{10Cl}_(o), (4), Na - EtSO₃^{10Cl}_(o), (5), Na - PrSO₃^{10Cl}_(o), and (6), Na - PnSO₃^{10Cl}_(o). Circles and horizontal error bars above traces represent mean ± SD for prestin V_{pkCm} values obtained in five cells. The vertical dashed line is drawn in the position of the V_{pkCm}(Mal_(i)/Cl_(o)) value from Fig. 3 A 7. (Note the different V_m scales in A of this figure and Fig. 3 A.) (B and C) Columns and vertical error bars represent statistics (mean ± SD) on Q_{max} (B) and z (C) values obtained from the same fits that were used to obtain V_{pkCm} parameters in A. Columns for the appropriate anions are placed in the order and relative position of their V_{pkCm} values on the scale of membrane potentials.

due to the high error margins. However, a visual inspection of C-V curves by those anions in most of the experiments (e.g., Fig. 4 A, 5 and 6) indicated their ability to modify the V_{pkCm} and z of prestin, regardless of the presence of Cl_(i)⁻. This is clear from the analysis of z values obtained through this series of experiments (Fig. 4 C): z(Mal_(i)^{10Cl}/Mal_(o)^{10Cl}) = 0.72 ± 0.08, z(Mal_(i)^{10Cl}/SO₄^{2-10Cl}) = 0.74 ± 0.05, z(Mal_(i)^{10Cl}/MeSO₃^{10Cl}) = 0.64 ± 0.07, z(Mal_(i)^{10Cl}/EtSO₃^{10Cl}) = 0.68 ± 0.04, z(Mal_(i)^{10Cl}/PrSO₃^{10Cl}) = 0.58 ± 0.14, and z(Mal_(i)^{10Cl}/PnSO₃^{10Cl}) = 0.43 ± 0.11. The ability of anions to decrease the parameter z (in the presence of 10 mM [Cl_(i)⁻]) seemed to be stronger for long-tail anions: PnSO₃⁻ > PrSO₃⁻ >

MeSO₃⁻ ≈ EtSO₃⁻ > SO₄²⁻. The Q_{max} values in these experiments (shown in Fig. 4 B) did not vary significantly from reference conditions: Q_{max}(Mal_(i)^{10Cl}/Mal_(o)^{10Cl}) = 2.38 ± 0.28 pC, Q_{max}(Mal_(i)^{10Cl}/SO₄^{2-10Cl}) = 2.06 ± 0.24 pC, Q_{max}(Mal_(i)^{10Cl}/MeSO₃^{10Cl}) = 2.27 ± 0.30 pC, Q_{max}(Mal_(i)^{10Cl}/EtSO₃^{10Cl}) = 2.16 ± 0.17 pC, Q_{max}(Mal_(i)^{10Cl}/PrSO₃^{10Cl}) = 1.96 ± 0.34 pC, Q_{max}(Mal_(i)^{10Cl}/PnSO₃^{10Cl}) = 2.23 ± 0.22 pC. For SO₄²⁻, MeSO₃⁻, and EtSO₃⁻ anions with relatively low intrinsic Q_{max} (Fig. 3 B), this result might indicate an overriding control of motor function by chloride. PrSO₃⁻ and PnSO₃⁻ anions appear to support high Q_{max} (comparable to that for Cl⁻) on their own (Fig. 3).

The series of experiments in Figs. 3 and 4 demonstrates that SO₃⁻-containing anions (including SO₄²⁻) control prestin's voltage sensitivity via shifts in V_{pkCm} and alteration of the V_{op} range, or, equivalently, z. Our data can be explained by reasoning that anions applied both intracellularly and extracellularly bind to putative intracellular regulatory binding sites on prestin, thereby producing an allosteric or electrostatic influence on prestin's intrinsic voltage sensor to alter its free energy profile. There is a host of evidence that anions work on prestin intracellularly (4,19,31,32). The possibility remains that some of the alkyl anion effects on V_{op} result from the hydrophobic nature of the anions, since we and others have found that membrane lipid reactive agents can alter NLC (33–38). However, we note that in our previous experiments (32), ethanol had minimal effects below concentrations of 1%, above which V_{op} shifted to the right, in a direction opposite to the effects of ethane sulfonate. Furthermore, the inability of these alkyl anions, in the presence of 10 mM [Cl_(i)⁻], to shift V_{op} to the extreme voltages observed in the absence of chloride indicates that they are not working via membrane perturbation alone, but somehow are competing with chloride to establish V_{op}. Perhaps alkyl anion lipid permeability enables access to anion interaction sites of prestin not normally accessible to lipid-insoluble anions.

In its current state, the PAT model does not explain the shift of prestin's V_{op} in both negative and positive directions upon intracellular Cl_(i)⁻ substitution by the various nonhalide anions (Figs. 2–4), even supposing that these anions are working as voltage-sensor substitutes.

Thus far, we have shown that anions other than Cl⁻ can support NLC. The capability of an alternative anion to serve as prestin's voltage sensor, as envisioned in the PAT model, can be tested knowing that the apparent valence, z, of the voltage sensor can be obtained from two-state Boltzmann function fits to C-V functions (see Methods). For di- and trivalent anions serving as voltage sensors, instead of Cl_(i)⁻, the experimentally measured z parameter should double or triple relative to the values obtained with monovalent Cl_(i)⁻, if the distance traveled by the replacement voltage sensor within the membrane (Fig. 1, d) remains approximately the same as for Cl_(i)⁻. In Fig. 5, we present experimental C-V curves and extracted values of z and Q_{max} obtained with patch pipettes filled

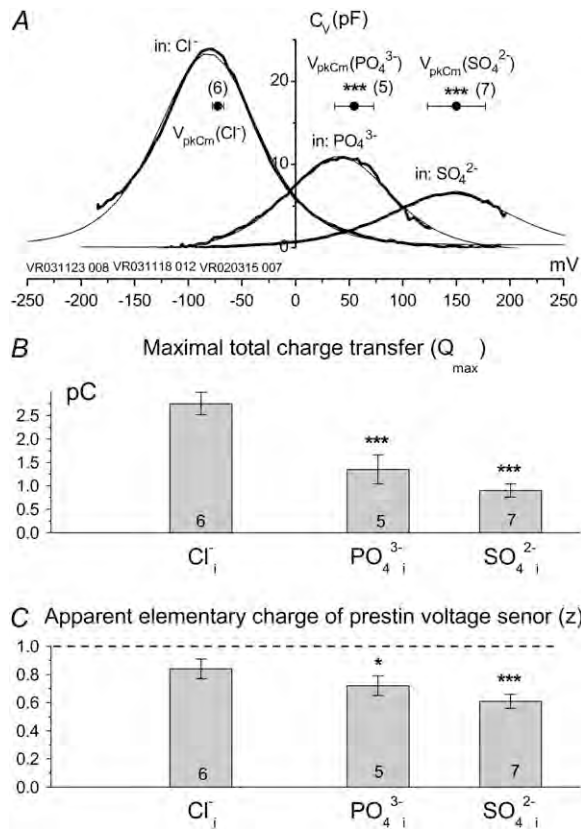


FIGURE 5 Experimentally measured apparent prestin voltage sensor elementary charge (z) is not proportional to the ionic valence of tested intracellular anions. (A) Voltage-dependent components (C_v) of C-V curves (thick line) and their theoretical fits (thin line) obtained from typical cells patch-clamped with pipettes filled with Tris-Cl_(i), Tris-SO_{4(i)}, and Tris-PO_{4(i)} solutions. The horizontal axis is the scale of membrane potentials. The solution was Tris-Hepes_(o). Solid circles with horizontal error bars represent statistics (mean ± SD) for V_{pkCm} values obtained from fits to the C_v-V curves (see Results). (B) and (C) Columns and vertical error bars represent statistics (mean ± SD) for Q_{max} (B) and z (C) values obtained from the same fits that were used to obtain V_{pkCm} parameters in A. Columns for the appropriate anions are placed at the relative position of their V_{pkCm} values on the scale of membrane potentials.

with intracellular solutions based on monovalent Cl⁻, and multivalent SO₄²⁻ and phosphate (HPO₄²⁻/PO₄³⁻) anions, whereas the extracellular solution contained Cl⁻-free Hepes⁻-based solution. C-V curves were recorded 8–10 min after the patch rupture and cell equilibration. With Tris-Cl_(i), the values of $Q_{max}(Cl^-) = 2.75 \pm 0.24$ pC and $z(Cl^-) = 0.84 \pm 0.07$ were obtained at $V_{pkCm}(Cl^-) = -72 \pm 5$ mV, resulting in prestin $V_{op}(Cl^-) = \{-139, -5\}$ mV ($n = 6$). With Tris-SO_{4(i)}, the values of $Q_{max}(SO_4^{2-}) = 0.90 \pm 0.14$ pC, $z(SO_4^{2-}) = 0.61 \pm 0.05$, and $V_{pkCm}(SO_4^{2-}) = +150 \pm 27$ mV resulted in $V_{op}(SO_4^{2-}) = \{+58, +242\}$ mV ($n = 7$). With Tris-PO_{4(i)}, the values of $Q_{max}(HPO_4^{2-}/PO_4^{3-}) = 1.35 \pm 0.31$ pC, $z(HPO_4^{2-}/PO_4^{3-}) = 0.72 \pm 0.07$, and $V_{pkCm}(HPO_4^{2-}/PO_4^{3-}) = +55 \pm 18$ mV resulted in $V_{op}\{HPO_4^{2-}/PO_4^{3-}\} = \{-23, +133\}$ mV ($n = 5$). Results obtained for z (Fig. 5 C) revealed that the values of z for multivalent anions decreased,

showing no correlation between the measured apparent elementary charge of prestin's voltage sensor and the ionic charge of the tested intracellular anions (Fig. 5 C). The observed motility of OHCs with SO₄²⁻ and HPO₄²⁻/PO₄³⁻ intracellular anions remained robust, confirming the proper function of prestin's voltage sensor/effector. Reduced Q_{max} values (Fig. 5 B) could indicate that either the number of active prestin molecules (N) or the elementary charge of prestin's voltage sensor (q) was reduced with SO₄²⁻ and HPO₄²⁻/PO₄³⁻ relative to conditions with Cl_(i)⁻. The latter suggestion is more likely, given the decreased values of z . Thus, the data in Fig. 5 appear to be incompatible with the PAT model.

DISCUSSION

The prevailing concept of OHC somatic electromotility is based on voltage-dependent conformational transitions between expanded and contracted states of millions of prestin molecules residing within the lateral OHC plasma membrane. Though the primary amino acid sequence of prestin was defined several years ago (7), controversy reigns in defining prestin membrane topology (5). To sustain significant size and shape rearrangements at high frequencies (up to 70 kHz), unique thermodynamic characteristics must have evolved to set prestin close to mechanical instability, having very shallow energy minima. Therefore, conventional protein structure analysis techniques that rely on energy minima resolution could easily fail or produce ambiguous results.

An analogous controversy exists over defining the structural part of the prestin molecule that grants it voltage sensitivity. Based on an apparent disappearance of prestin voltage sensitivity and OHC electromotility upon removal of halides and other monovalent anions from the cytoplasmic side of the membrane, the initial PAT model (19) postulated that intracellular monovalent anions are prestin's extrinsic voltage sensors. The other cornerstone of the PAT model was the absence in prestin's primary sequence (relative to other SLC26 family members that lack C_v) of a clearly identifiable cluster of charged residues that might serve as prestin's voltage sensor: selective point mutations of certain scattered charged amino acids could not alter prestin's apparent unitary charge, z . An additional attraction of the PAT model was provided by an analogy with the CIC-type chloride channel model, where mixed [Cl⁻]/voltage dependence of CIC-0 channel gating led to the suggestion that Cl⁻ anions serve as extrinsic voltage sensors (39).

Despite a logical background, the PAT model generated some immediate concerns (40): 1), single charged-residue mutations in prestin/pendrin (SLC26a5/SLC26a6) nonconsensus regions might be an insufficient test, since voltage sensitivity of prestin might be conferred by a number of small movements of distributed partial charges rather than movement of a single point charge; and 2), nonspecific anion binding might distort the local electrostatic field influencing prestin's properties. Recent findings on CIC channel structure also preclude a direct analogy between prestin PAT and CIC

channel models by reducing the voltage-sensing role of Cl^- anions in CIC channels to a mere competition with a Glu residue carboxyl group obstructing the CIC channel's ion pore. The conformational change associated with gating of the CIC channel was limited to a small and local swing of a single amino acid side chain (41,42). Quite a different role would be expected from the Cl^- anion in the prestin PAT model: to serve as prestin's voltage sensor, it must be trapped by a cytoplasmic mobile domain to drive this domain at hyperpolarizing potentials to the extracellular side of the membrane. The mobile domain must be large enough to account for significant changes in prestin's molecular shape during conformational transitions. Specifically, simple propulsion of the Cl^- anion inside prestin would not produce significant prestin resizing due to the small atomic size of the anion itself, $\sim 3 \text{ \AA}$. Structural rearrangements ranging up to 8 nm^2 are estimated to occur in prestin (17,24,25,43,44).

Soon after the development of the PAT model, we provided data that prompted rethinking of the PAT model, including observations that anion substitutes cause shifts in V_{pkcm} , and that the nonhalides SO_4^{2-} and PnSO_3^- are capable of supporting prestin's voltage sensitivity (20). In this work, we address in depth further issues of the PAT model. First, we emphasize that shifts of prestin's V_{op} are not a function of $[\text{Cl}^-]$ per se, but are determined by the nature of alternative intracellular anions (Figs. 2–4). Indeed, the wide variation in direction and amplitude of prestin's V_{op} shift by mono- and polyvalent organic and inorganic anions does not support the idea that monovalent Cl^- and HCO_3^- are the only natural chemical modulators of prestin's voltage sensitivity. In fact, all anions tested in our experiments are capable of interacting with prestin to modify its electromotive properties. Second, we obtained statistical data demonstrating that the experimentally measured apparent valence, z , of prestin's voltage sensor does not correspond to the molecular valence of intracellular polyvalent anions, as might be expected for the PAT model (Fig. 4).

Two mechanisms could serve to reconcile this latter observation with the PAT model: 1), protonation to achieve monovalency of polyvalent anions, and 2), an inversely proportional adjustment of distance (d) traveled within the membrane field based on the size of the anion or the magnitude of the anion charge. We believe it unlikely that the relatively small differences in anion size hinder a putative hemicycle movement within the prestin core, since the anions, according to the PAT model, must drive estimated conformational changes (see above) that are orders of magnitude larger. It is also difficult to conceive how the charge magnitude (valence of the anion) could be influential in reducing the ability of the anion to pass through the membrane field. Indeed, the electrical energy to work against the load on the OHC would be amplified by the increase in valence ($E = Q \times V$), so that higher-valence anions would likely move more efficiently through the membrane for a given voltage change. Finally, although protonation during the transport cycle is conceivable, the pH effects on the motor that would be expected in such a scenario are not found (45).

The most economical explanation of our data is that although polyvalent anions support charge movement by prestin, they work not as voltage sensors but as allosteric modulators.

A conventional model would consider prestin to be a voltage-dependent protein that possesses mobile charged residues forming an IVS. Due to prestin's unique functional properties (i.e., piezoelectric operability), its voltage-dependent transitions should be accompanied by significant rearrangement of the shape of the molecule, involving movements of multiple charged amino acid residues back and forth within the membrane. Indeed, as noted above, large surface area changes in the motor have been predicted. As a result, we have considered that even intracellular charged clusters at the C-terminus of prestin might be temporarily immersed in the membrane, participating in voltage-sensing events. However, our data do not support such a role for the C-terminus charges (46). At this time, it is difficult to predict which amino acids are more and which are less important in forming the voltage sensor, because the entire molecule might contain nonuniformly distributed elements of the voltage sensor.

The discovery of prestin's Cl^- sensitivity (19) was of fundamental importance, regardless of the mechanism whereby anions influence prestin's voltage sensitivity. Indeed, we have recently shown that manipulations of Cl^- within the living animal's cochlea can drastically alter cochlear amplification in a reversible manner (4). Nevertheless, we consider the mechanism of anionic control of prestin voltage sensitivity key to understanding how the motor molecule drives cochlear amplification. In this report, we highlight two observations that are not easily reconciled with the current embodiment of the PAT model, and we reason that anions may additionally, or only allosterically, modulate prestin by binding to intracellular target sites on the protein (5,20,29). Such allosteric effects of anions have been reported before, for example, for the yeast enzyme Fet3p (47). We expect that identification of anion binding sites and of residues that contribute to prestin's apparent charge will lead to a better understanding of how this remarkable protein boosts hearing.

This work was supported by National Institutes of Health grant NIH NIDCD 000273 to J.S.S.

REFERENCES

1. Brownell, W. E., C. R. Bader, D. Bertrand, and Y. de Ribaupierre. 1985. Evoked mechanical responses of isolated cochlear outer hair cells. *Science*. 227:194–196.
2. Frank, G., W. Hemmert, and A. W. Gummer. 1999. Limiting dynamics of high-frequency electromechanical transduction of outer hair cells. *Proc. Natl. Acad. Sci. USA*. 96:4420–4425.
3. Santos-Sacchi, J. 2003. New tunes from Corti's organ: the outer hair cell boogie rules. *Curr. Opin. Neurobiol.* 13:459–468.
4. Santos-Sacchi, J., L. Song, J. Zheng, and A. L. Nuttall. 2006. Control of mammalian cochlear amplification by chloride anions. *J. Neurosci.* 26:3992–3998.
5. He, D. Z., J. Zheng, F. Kalinec, S. Kakehata, and J. Santos-Sacchi. 2006. Tuning in to the amazing outer hair cell: membrane wizardry with a twist and shout. *J. Membr. Biol.* 209:119–134.

6. Ashmore, J. 2008. Cochlear outer hair cell motility. *Physiol. Rev.* 88:173–210.
7. Zheng, J., W. Shen, D. He, K. Long, L. Madison, and P. Dallos. 2000. Prestin is the motor protein of cochlear outer hair cells. *Nature.* 405:149–155.
8. Liberman, M. C., J. Gao, D. Z. He, X. Wu, S. Jia, and J. Zuo. 2002. Prestin is required for electromotility of the outer hair cell and for the cochlear amplifier. *Nature.* 419:300–304.
9. Huang, G., and J. Santos-Sacchi. 1994. Motility voltage sensor of the outer hair cell resides within the lateral plasma membrane. *Proc. Natl. Acad. Sci. USA.* 91:12268–12272.
10. Belyantseva, I. A., H. J. Adler, R. Curi, G. I. Frolenkov, and B. Kachar. 2000. Expression and localization of prestin and the sugar transporter GLUT-5 during development of electromotility in cochlear outer hair cells. *J. Neurosci.* 20:RC116.
11. Ashmore, J. F. 1989. Transducer motor coupling in cochlear outer hair cells. In *Mechanics of Hearing*. D. Kemp and J. P. Wilson, editors. Plenum Press, New York. 107–113
12. Santos-Sacchi, J. 1990. Fast outer hair cell motility: how fast is fast? In *The Mechanics and Biophysics of Hearing*. P. Dallos, C. D. Geisler, J. W. Matthews, M. A. Ruggero, and C. R. Steele, editors. Springer-Verlag, Berlin. 69–75.
13. Santos-Sacchi, J. 1991. Reversible inhibition of voltage-dependent outer hair cell motility and capacitance. *J. Neurosci.* 11:3096–3110.
14. Huang, G., and J. Santos-Sacchi. 1993. Mapping the distribution of the outer hair cell motility voltage sensor by electrical amputation. *Biophys. J.* 65:2228–2236.
15. Gale, J. E., and J. F. Ashmore. 1997. The outer hair cell motor in membrane patches. *Pflugers Arch.* 434:267–271.
16. Kalinec, F., M. C. Holley, K. H. Iwasa, D. J. Lim, and B. Kachar. 1992. A membrane-based force generation mechanism in auditory sensory cells. *Proc. Natl. Acad. Sci. USA.* 89:8671–8675.
17. Iwasa, K. H. 1994. A membrane motor model for the fast motility of the outer hair cell. *J. Acoust. Soc. Am.* 96:2216–2224.
18. Santos-Sacchi, J., and E. Navarrete. 2002. Voltage-dependent changes in specific membrane capacitance caused by prestin, the outer hair cell lateral membrane motor. *Pflugers Arch.* 444:99–106.
19. Oliver, D., D. Z. He, N. Klocker, J. Ludwig, U. Schulte, S. Waldegger, J. P. Ruppersberg, P. Dallos, and B. Fakler. 2001. Intracellular anions as the voltage sensor of prestin, the outer hair cell motor protein. *Science.* 292:2340–2343.
20. Rybalchenko, V., and J. Santos-Sacchi. 2003. Cl⁻ flux through a non-selective, stretch-sensitive conductance influences the outer hair cell motor of the guinea-pig. *J. Physiol.* 547:873–891.
21. Fridberger, A., and J. B. De Monvel. 2003. Sound-induced differential motion within the hearing organ. *Nat. Neurosci.* 6:446–448.
22. Santos-Sacchi, J. 1989. Asymmetry in voltage-dependent movements of isolated outer hair cells from the organ of Corti. *J. Neurosci.* 9:2954–2962.
23. Santos-Sacchi, J. 1992. On the frequency limit and phase of outer hair cell motility: effects of the membrane filter. *J. Neurosci.* 12:1906–1916.
24. Iwasa, K. H. 1993. Effect of stress on the membrane capacitance of the auditory outer hair cell. *Biophys. J.* 65:492–498.
25. Gale, J. E., and J. F. Ashmore. 1994. Charge displacement induced by rapid stretch in the basolateral membrane of the guinea-pig outer hair cell. *Proc. R. Soc. Lond. B. Biol. Sci.* 255:243–249.
26. Kakehata, S., and J. Santos-Sacchi. 1995. Membrane tension directly shifts voltage dependence of outer hair cell motility and associated gating charge. *Biophys. J.* 68:2190–2197.
27. Santos-Sacchi, J. 2004. Determination of cell capacitance using the exact empirical solution of partial differential Y/partial differential C_m and its phase angle. *Biophys. J.* 87:714–727.
28. Santos-Sacchi, J., S. Kakehata, and S. Takahashi. 1998. Effects of membrane potential on the voltage dependence of motility-related charge in outer hair cells of the guinea-pig. *J. Physiol.* 510:225–235.
29. Rybalchenko, V., and J. Santos-Sacchi. 2003. Allosteric modulation of the outer hair cell motor protein prestin by chloride. In *Biophysics of the Cochlea: From Molecules to Models*. A. Gummer, editor. World Scientific Publishing, Singapore. 116–126.
30. Fakler, B., and D. Oliver. 2003. Functional properties of prestin: how the motor molecule works. In *Biophysics of the Cochlea: From Molecules to Models*. A. Gummer, editor. World Scientific Publishing, Singapore. 110–115.
31. Kakehata, S., and J. Santos-Sacchi. 1996. Effects of salicylate and lanthanides on outer hair cell motility and associated gating charge. *J. Neurosci.* 16:4881–4889.
32. Song, L., A. Seeger, and J. Santos-Sacchi. 2005. On membrane motor activity and chloride flux in the outer hair cell: lessons learned from the environmental toxin tributyltin. *Biophys. J.* 88:2350–2362.
33. Fang, J., and K. H. Iwasa. 2007. Effects of chlorpromazine and trinitrophenol on the membrane motor of outer hair cells. *Biophys. J.* 93:1809–1817.
34. Rajagopalan, L., J. N. Greeson, A. Xia, H. Liu, A. Sturm, R. M. Raphael, A. L. Davidson, J. S. Oghalai, F. A. Pereira, and W. E. Brownell. 2007. Tuning of the outer hair cell motor by membrane cholesterol. *J. Biol. Chem.* 282:36659–36670.
35. Spector, A. A., N. Deo, K. Grosh, J. T. Ratnanather, and R. M. Raphael. 2006. Electromechanical models of the outer hair cell composite membrane. *J. Membr. Biol.* 209:135–152.
36. Santos-Sacchi, J., and M. Wu. 2004. Protein- and lipid-reactive agents alter outer hair cell lateral membrane motor charge movement. *J. Membr. Biol.* 200:83–92.
37. Brownell, W. E., A. A. Spector, R. M. Raphael, and A. S. Popel. 2001. Micro- and nanomechanics of the cochlear outer hair cell. *Annu. Rev. Biomed. Eng.* 3:169–194.
38. Raphael, R. M., A. S. Popel, and W. E. Brownell. 2000. A membrane bending model of outer hair cell electromotility. *Biophys. J.* 78:2844–2862.
39. Pusch, M., U. Ludewig, A. Rehfeldt, and T. J. Jentsch. 1995. Gating of the voltage-dependent chloride channel ClC-0 by the permeant anion. *Nature.* 373:527–531.
40. Meech, R., and M. Holley. 2001. Ion-age molecular motors. *Nat. Neurosci.* 4:771–773.
41. Dutzler, R., E. B. Campbell, and R. MacKinnon. 2003. Gating the selectivity filter in ClC chloride channels. *Science.* 300:108–112.
42. Dutzler, R., E. B. Campbell, M. Cadene, B. T. Chait, and R. MacKinnon. 2002. X-ray structure of a ClC chloride channel at 3.0 Å reveals the molecular basis of anion selectivity. *Nature.* 415:287–294.
43. Adachi, M., and K. H. Iwasa. 1999. Electrically driven motor in the outer hair cell: effect of a mechanical constraint. *Proc. Natl. Acad. Sci. USA.* 96:7244–7249.
44. Santos-Sacchi, J. 1993. Harmonics of outer hair cell motility. *Biophys. J.* 65:2217–2227.
45. Tunstall, M. J., J. E. Gale, and J. F. Ashmore. 1995. Action of salicylate on membrane capacitance of outer hair cells from the guinea-pig cochlea. *J. Physiol.* 485:739–752.
46. Bai, J. P., D. Navaratnam, H. Samaranayake, and J. Santos-Sacchi. 2006. En block C-terminal charge cluster reversals in prestin (SLC26A5): effects on voltage-dependent electromechanical activity. *Neurosci. Lett.* 404:270–275.
47. Davis-Kaplan, S. R., C. C. Askwith, A. C. Bengtzen, D. Radisky, and J. Kaplan. 1998. Chloride is an allosteric effector of copper assembly for the yeast multicopper oxidase Fet3p: an unexpected role for intracellular chloride channels. *Proc. Natl. Acad. Sci. USA.* 95:13641–13645.

Chapter 5

Prestin: Molecular Mechanisms Underlying Outer Hair Cell Electromotility

**Joseph Santos-Sacchi, Dhasakumar Navaratnam, Rob Raphael,
and Dominik Oliver**

Abstract Prestin is a member of the SLC26 family of anion transporters that has evolved to serve as a molecular motor in outer hair cells (OHCs) of the mammalian inner ear. The protein is piezoelectric-like, exhibiting voltage and tension sensitivity, with significant modulation by anions, chiefly intracellular chloride. Receptor potentials of OHCs drive molecular conformational changes in prestin, as evidenced by voltage sensor charge movements, that evoke robust length changes in OHCs, thereby contributing to a mechanical feedback mechanism and, therefore, to cochlear amplification, which enhances our auditory sensitivity. Current research has been focused on tertiary structural determinations, prestin interactions with other proteins and membrane lipids, trafficking, and the mechanism of anion effects. One of the key remaining questions is the determination of structural changes induced by membrane voltage perturbations and how those changes result in forces exerted by the OHCs. Indeed, much remains to be understood about this extraordinary molecule.

J. Santos-Sacchi (✉)

Departments of Surgery (Otolaryngology), Neuroscience, and Cellular
and Molecular Physiology, Yale University School of Medicine, 333 Cedar Street,
New Haven, CT 06520-8018, USA
e-mail: joseph.santos-sacchi@yale.edu

D. Navaratnam

Departments of Neurology and Neuroscience, Yale University School of Medicine,
333 Cedar Street, New Haven, CT 06520-8018, USA
e-mail: dhasakumar.navaratnam@yale.edu

R. Raphael

Department of Biomedical Engineering, Rice University, 6100 Main Street,
Houston, TX 77521, USA
e-mail: rraphael@rice.edu

D. Oliver

Department of Neurophysiology, Philipps-Universität Marburg,
Deutschhausstrasse 2, 35037 Marburg, Germany
e-mail: oliverd@staff.uni-marburg.de

© Springer International Publishing AG 2017

G.A. Manley et al. (eds.), *Understanding the Cochlea*, Springer Handbook
of Auditory Research 62, DOI 10.1007/978-3-319-52073-5_5

113

Keywords Chloride · Cochlea · Cochlear amplifier · Hearing · Membrane · Membrane curvature · Motor protein · Nonlinear capacitance · Nonsteroidal anti-inflammatory drug · Protein interactions · Protein structure · SCL26A5 · Voltage sensor

5.1 Introduction

Prestin is a remarkable protein that underlies our keen sense of hearing. It is a member of an anion transporter family (SLC26) that has role changed into a fast molecular motor that drives outer hair cell (OHC) somatic electromechanical activity, the transduction of the receptor potential of the cell (see Corey, Ó Maoiléidigh, and Ashmore, Chap. 4) into pronounced cell length changes at acoustic rates, thereby boosting perceptual thresholds by 40–60 dB. In this chapter, three broad areas focus on how this protein works. They include an overview of the protein's biophysical traits, the structural features of the protein that will lead to detailed structure–function relationships, and the role of accessory protein/lipid partners in helping this protein to carry out its important work. Much is to be learned. Pertinent reviews on the subjects of this chapter are available in the literature (He et al. 2006; Ashmore 2008; Ashmore et al. 2010).

5.2 Known Biophysical Properties of Prestin

5.2.1 *The OHC Sensor/Motor: Preprestin*

An intense investigation of this somatic motility began soon after its discovery by Bill Brownell and colleagues (Brownell et al. 1985; Kachar et al. 1986). Surprisingly, when OHCs are stimulated electrically by a current injection within or across the cell, their length changes as a function of stimulus intensity and waveform. It soon became clear that OHC somatic motility [also known as electromotility (eM)] was driven by voltage and not any particular ionic current (Ashmore 1987; Santos-Sacchi and Dilger 1988), evidencing movements of 15 nm/mV on average (Santos-Sacchi 1989). One of the most powerful pieces of evidence that eM was driven by voltage was the observation of displacement currents, capacitive-like currents, similar in some respects to the gating currents of ion channels (Bezanilla 2000), which are evoked by membrane voltage steps under whole cell voltage clamp (Ashmore 1989; Santos-Sacchi 1990). These displacement currents, or, equivalently, a voltage-dependent or nonlinear membrane capacitance (NLC), arise from the movements of a voltage sensor charge across the electric field of the membrane. The identification of such a charge movement immediately led to the notion of a sensorimotor unit residing in the OHC plasma membrane that obeyed

two-state Boltzmann statistics (Ashmore 1990; Santos-Sacchi 1991), where characterization of the charge-voltage (Q-V) or, equivalently, the capacitance-voltage (C-V) relationship provides estimates of the unitary sensor charge (z ; assuming full passage of the sensor charge through the field of the membrane), the maximum charge transferred (Q_{\max}), and, the voltage where charge is equally distributed across the membrane (V_h ; Fig. 5.1). The Boltzmann characterization of motor charge movement also provided the impetus for the development of “molecular” models of motor action that incorporated Boltzmann statistics, including area and conformational state models (Kalinec et al. 1992; Dallos et al. 1993; Iwasa 1994). Given the Q_{\max} and an elementary sensor charge estimate, the number of motors residing in the membrane can be estimated, giving a density in OHCs of about $10,000/\mu\text{m}^2$ (Huang and Santos-Sacchi 1993; Gale and Ashmore 1997a; Mahendrasingam et al. 2010), although this number may need to be reevaluated (Santos-Sacchi and Song 2016). V_h and z have been used to define the voltage operating range of the motor, with V_h localizing the eM-V function relative to the resting membrane potential of the cell and z defining the extent over which the motor is voltage sensitive. With z being less than unity, the motor has a quite shallow voltage dependence compared with ion channels. The two-state formalism also imposes strict correspondence between charge movement and eM, where according to a now widely accepted area-state model (Iwasa 1994; Santos-Sacchi and Song 2014a), motors will fluctuate between a compact and expanded surface area state, with unitary motor area change estimates varying between 0.37 and 8 nm^2 (Iwasa 1993; Santos-Sacchi 1993; Gale and Ashmore 1994; Adachi and

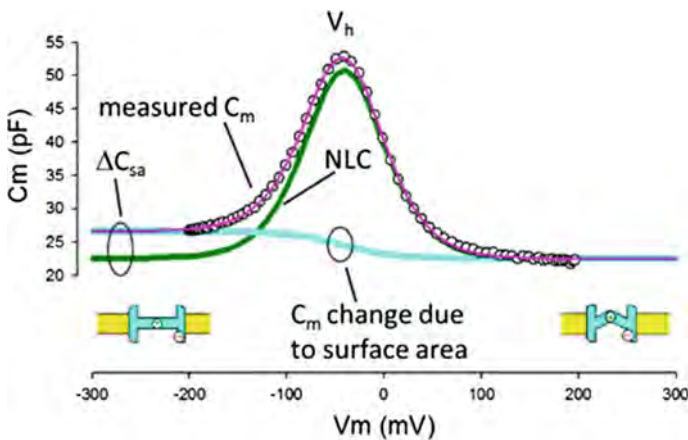


Fig. 5.1 Outer hair cell (OHC) nonlinear membrane capacitance (NLC). OHC voltage-dependent capacitance (*circles*) is composed of two components, both riding atop a linear capacitance corresponding to the cell’s surface area. One is associated with the voltage sensor charge of prestin (NLC; *green*), and the other is associated with motor state occupancy (*blue*). Cartoon depicts prestin in either state, expanded or contracted. V_h , voltage where charge is equally distributed across the membrane; C_m , membrane capacitance; ΔC_{sa} , state-dependent capacitance; V_m , membrane voltage. See text for further details. Modified from Santos-Sacchi and Navarrete (2002)

Iwasa 1999). As indicated in Fig. 5.1, voltage-dependent C_m possesses an additional component, state-dependent capacitance (ΔC_{sa}), that has been attributed to area/membrane thickness changes associated with motor state occupancy, each motor contributing an additional 17 aF when residing in the expanded state (Santos-Sacchi and Navarrete 2002). The high variance of area estimates highlights the need for structural observations at the molecular level.

During the ensuing years, a host of biophysical attributes of the OHC plasma membrane motor were characterized, and these traits, together with its NLC, would be crucial in identifying the molecular nature of the motor. One of the most important discoveries was the piezoelectric nature of the motor (Iwasa 1993). On introducing tension into the OHC membrane, NLC shifts along the voltage axis. The shift in V_h effects the charge movement in the membrane, and this phenomenon is intrinsic to the membrane (Gale and Ashmore 1994; Kakehata and Santos-Sacchi 1995). These data are fully consistent with a direct voltage-to-mechanical (and vice versa) transduction process that does not directly require any intermediate steps (e.g., second messengers) or biochemical energy sources (except, of course, those sources required to maintain the membrane voltage). Other early observations that defined the nature of the motor and set the stage for its molecular identification included the simultaneous block of the NLC and motor activity by intracellularly acting salicylate and extracellularly acting gadolinium (Santos-Sacchi 1991; Tunstall et al. 1995; Kakehata and Santos-Sacchi 1996), the influence of altered membrane potential (prepulse effect) on V_h (Santos-Sacchi et al. 1998), the tension and turgor pressure effects (piezoelectric-like) on the NLC (Iwasa 1993; Gale and Ashmore 1994; Kakehata and Santos-Sacchi 1995), and the temperature susceptibility of the NLC (Santos-Sacchi and Huang 1998; Meltzer and Santos-Sacchi 2001).

5.2.2 *Enter Prestin*

Zheng et al. (2000) identified the OHC motor protein as prestin (SLC26A5), a member of an anion transporter family. Key to this identification was the localization of the protein to the OHC lateral membrane where electromechanical activity is restricted (Dallos et al. 1991; Huang and Santos-Sacchi 1994) and biophysical demonstrations of OHC motor-like activity in heterologously transfected cells, including the NLC, the voltage-driven membrane movement, and a block by salicylate. Subsequently, prestin was shown to exhibit membrane tension (Ludwig et al. 2001; Santos-Sacchi et al. 2001), prepulse (Santos-Sacchi et al. 2001), and temperature sensitivities similar to those in the native OHCs (Meltzer and Santos-Sacchi 2001). It was clear at that point that all known biophysical traits of prestin matched those that had been identified before its discovery. Another fundamental observation that indisputably linked prestin to OHC eM was the absence of eM in the prestin-knockout mouse (Lieberman et al. 2002).

5.2.3 Importance of Prestin for Cochlear Amplification

Interestingly, while the knockout implicated the importance of prestin in cochlear amplification, issues were quickly identified that dampened such a conclusion, including the obvious mechanical impedance changes in the OHCs (and consequently the cochlear partition) that result from removal of the abundant protein content within the OHC lateral membrane, which substantially shortened OHCs. Subsequently, persuasive evidence that prestin predominantly underlies cochlear amplification was obtained from a knockin of mutated prestin (499 mutant) that has its voltage operating range (assessed by NLC V_h) shifted far out of the physiological range while maintaining other features of normal OHC function, structure, and mechanics (Dallos et al. 2008). That mutation also altered the kinetics of prestin (Homma et al. 2013). Another important observation linking prestin to cochlear amplification was that manipulations of chloride, previously shown to control the electromechanical activity of prestin (Oliver et al. 2001), reversibly altered the basilar membrane tuning in vivo (Santos-Sacchi et al. 2006). Salicylate, which competes with chloride for the anion binding site of prestin and reduces the NLC (Oliver et al. 2001), also adversely affects basilar membrane motion (Santos-Sacchi et al. 2006; Fisher et al. 2012). Finally, there is evidence for prestin mutations causing deafness (Mutai et al. 2013).

5.2.4 How Does Prestin Sense Voltage?

The voltage-dependent nature of eM naturally begs the question, What makes the protein sensitive to voltage? It is clear that prestin must possess a charged voltage sensor that is moved by voltage drops across the plasma membrane. In other well-studied voltage-dependent membrane proteins, charged amino acid residues serve this function. For example, the S4 segment in the voltage sensor domain of all classical voltage-gated ion channels comprises the voltage sensor domain (Bezanilla 2000). In a fundamental study investigating this issue, Oliver et al. (2001) found that neutralization of candidate electrically charged amino acid residues had little effect on voltage sensitivity of prestin, whereas removal of monovalent intracellular anions, namely intracellular chloride or bicarbonate, abolished charge movement and hence voltage sensitivity. Recently, careful examination of this phenomenon indicated that the OHC eM magnitude (Song and Santos-Sacchi 2013) and the total Q_{\max} (Santos-Sacchi and Song 2016) do not decrease with intracellular chloride level, but rather chloride levels influence the rate of prestin transitions (Santos-Sacchi and Song 2016), resulting in an apparent reduction of NLC when the membrane potential is changed at rates exceeding the Cl^- -dependent kinetics of prestin. Based on the observation of anion sensitivity, Oliver et al (2001) concluded that the voltage sensor of prestin is not made up from intrinsic residues in prestin, but instead, monovalent anions serve as extrinsic voltage sensors, i.e., that

charge movements (NLC) arise directly from the translocation of the anion across the electrical field along some hypothetical access channel in the protein. This anion translocation, in turn, would then drive simultaneous conformational changes between the expanded and contracted states, thus producing eM. In fact, the voltage dependence of prestin varied with the size of the monovalent anion present, as if bulkier anions can travel a smaller fraction of the electrical field (Oliver et al. 2001). However, other findings are difficult to reconcile with this simple external voltage sensor model. First, a shift of the voltage dependence (V_h) toward depolarized potentials observed when the anion concentration is lowered is contrary to the prediction of the model (Rybalchenko and Santos-Sacchi 2003a). Interestingly, a variety of anion substitutes can markedly shift V_h in either the depolarizing or hyperpolarizing direction to varying degrees (Oliver et al. 2001; Rybalchenko and Santos-Sacchi 2008). Second, if other than monovalent anions can maintain prestin function, the charge number z moved per prestin molecule should correspond to the valence of the anion serving as voltage sensor (assuming that the electrical distance traveled remains the same). However, an increase in z has not been observed when monovalent anions are substituted with di- or trivalent anions (Rybalchenko and Santos-Sacchi 2008). Third, hyperpolarization, which drives prestin into the expanded state, should move the anion toward a more extracellular position, but in the expanded state, the apparent affinity for the anions is reduced, suggesting the release toward the cytosol (Song and Santos-Sacchi 2010). Observations such as these have led to a counter theory that anions serve as allosteric-like modulators of prestin charge movement, anion binding conformationally transitioning the protein into a voltage-enabled state, with sensor charge contributed by a wide-ranging distribution of charged residues within the protein (Bai et al. 2009). A current structural view of anion interaction with prestin is provided in Sects. 5.3.4 and 5.3.5.

5.2.5 How Many States/Transitions Does Prestin Have?

Simply based on standard fits of the NLC, it was not possible to differentiate between two-state and multistate behavior in the motor protein prestin (Huang and Santos-Sacchi 1993; Scherer and Gummer 2005). For example, fits with two-state Boltzmann or infinite state Langevin equations each adequately fit the NLC because of measurement uncertainty at the extreme voltages needed to interrogate the very shallow voltage dependence of the protein. The NLC has been used routinely as a surrogate for eM under the assumption that sensor charge movement exhibits fast two-state behavior directly linked to eM. It was natural to assume such fast kinetics because eM had been measured in the acoustic frequency range (Ashmore 1987; Santos-Sacchi 1992; Dallos and Evans 1995), even out to about 80 kHz (Frank et al. 1999) at room temperature. Interestingly, the NLC cutoff frequency was near 10 kHz at room temperature (Gale and Ashmore 1997b). The recent observation that characteristics of the NLC and eM can diverge as a function of reduced anion

concentration revealed that prestin activity is not governed by a simple two-state process but is instead multistate (Song and Santos-Sacchi 2013). A basis for disparity between the two measures may be related to slow, chloride-controlled intermediate transitions between chloride-binding and voltage-enabled states (Song and Santos-Sacchi 2013; Santos-Sacchi and Song 2014a). Essentially, steady-state (or low-frequency) evaluations of eM do not correspond to sensor charge movement that is measured at higher frequencies because each will only be equal when measured at the same frequency. Although the simple model developed in that work (*meno presto* model) can recapitulate features of the behavior of prestin, thus revealing its multistate nature with attendant time/phase delays (Santos-Sacchi and Song 2014b), it is likely that models incorporating transporter characteristics expected from the SLC heritage of prestin will offer greater insight (Muallem and Ashmore 2006; Schaechinger et al. 2011), provided they can account for all known biophysical properties exhibited by prestin.

Clearly, a lack of consensus on the structure of prestin based on software prediction algorithms, as indicated by the wide range of secondary topologies attributed to the membrane protein such as the 12 transmembrane domain (TMD) model (Oliver et al. 2001; Deak et al. 2005; Rajagopalan et al. 2006), the 10 TMD model (Navaratnam et al. 2005), and the 8 TMD model (Lovas et al. 2015), has led to difficulties in understanding the biophysical basis of the NLC and eM. Additionally, the limited information on the interacting partners of prestin and the influence of its membrane environment has contributed to these difficulties. Fortunately, significant progress is currently being made on these fronts.

5.3 Structure and Function of Prestin

5.3.1 *Molecular and Functional Features of Prestin*

Prestin is the fifth member of the SLC26 family of anion exchangers (hence SLC26A5; Zheng et al. 2000), a group of 10 mammalian proteins (Mount and Romero 2004; Alper and Sharma 2013). SLC26 proteins belong to a large, ubiquitous, and evolutionarily ancient “sulfate permease” (SulP) family of anion transporters present in animals, plants, fungi, and bacteria. Although the SLC26 nomenclature was originally used for the mammalian SulP proteins (Mount and Romero 2004), the SulP and SLC26 nomenclature may be used interchangeably (Dorwart et al. 2008; Geertsma et al. 2015). These evolutionary and molecular relationships are of particular relevance because structural information on mammalian prestin has emerged only very recently and is entirely based on crystallographic data for close (i.e., within the SLC26/SulP family) or remotely homologous relatives of mammalian SLC26 proteins.

The mammalian SLC26 proteins are diverse in terms of both their transport substrates and the transport modes. Thus, SLC26 transport activities include

electrogenic or electroneutral exchange of monovalent (e.g., chloride, iodide) and divalent anions (e.g., sulfate, oxalate). Two members, SLC26A7 and SLC26A11, mediate uncoupled flux of chloride at high rates, which may indicate that these members function as anion channels. Detailed reviews on SLC26 transport function and roles in physiology and pathophysiology are available (Mount and Romero 2004; Dorwart et al. 2008; Alper and Sharma 2013).

The closest prestin relatives of mammalian prestin, nonmammalian orthologs of SLC26A5 (e.g., chicken and zebrafish prestin), are highly active anion transporters that mediate the stoichiometric exchange of monovalent anions such as chloride against divalent anions (either sulfate or oxalate; Schaechinger and Oliver 2007; Schaechinger et al. 2011). Because this transport mode is electrogenic, i.e., one electrical charge is transferred per transport cycle, nonmammalian prestins generate robust transport currents in the presence of divalent transport substrates (Schaechinger and Oliver 2007). In contrast, transport currents were not observed with mammalian prestin in the presence of divalents (Schaechinger and Oliver 2007; Schaechinger et al. 2011), indicating that prestin has no transport activity, that it acts in an electroneutral mode that does not generate electrical current, or that transport rates are much lower than in its nonmammalian orthologs. In fact, by using fluorescent pH sensors and electrophysiology, Mristik et al. (2012) showed that prestin may function as a $\text{Cl}^- / 2\text{HCO}_3^-$ exchanger, however with a low transport rate. Recently, prestin has been shown to allow ion currents through a pathway distinct from its transporter pathway (Bai et al. 2017). Moreover, based on a tracer-flux assay, one study suggested transport capability for formate and chloride (Bai et al. 2009), although another group could not reproduce this finding while confirming transport in nonmammalian orthologs (Tan et al. 2011). Interestingly, prestin, as well as other SLC26 proteins, mediates uncoupled permeation of thiocyanate (SCN^-) at appreciable rates (Schanzler and Fahlke 2012). Although the permeation of this anion has no obvious physiological relevance, this finding underscores the high degree of mechanistic and structural similarity between prestin and other SLC26 transporters and may turn out as helpful in deciphering potential common molecular mechanisms of transport and eM.

Mammalian prestin is a 744-amino acid protein with a high degree of sequence conservation across mammalian species (Zheng et al. 2000). As with other SLC26 proteins, prestin consists of a large TMD containing numerous hydrophobic stretches indicative of multiple transmembrane segments. This TMD is flanked by hydrophilic intracellular N- and C-termini (Ludwig et al. 2001; Zheng et al. 2001). The detailed topology of the TMD had long remained enigmatic, but it is now clear that it contains 14 membrane-spanning domains (Gorbunov et al. 2014; Geertsma et al. 2015). Within this TMD, two regions have been recognized for their particularly high sequence conservation across the SLC26/SulP family. One is located more N-terminally and is designated as the “SulP consensus signature” (Prosite PS01130); the other one located in the C-terminal half of the TMD is known as the Saier motif (Saier et al. 1999; Mount and Romero 2004). The high degree of conservation suggested that these protein regions are of particular importance for SLC26 function and may be critically involved in anion transport and possibly in eM. This is supported by the finding that transplantation of protein regions, including these motifs from mammalian prestin into

the prestin ortholog from zebrafish, is sufficient to confer mammalian-like function (i.e., fast charge transfer and eM) onto the nonmammalian prestin, which otherwise functions as a transporter (Schaechinger et al. 2011).

Another well-conserved domain of all mammalian and most bacterial SLC26/SuIP proteins is the sulfate transporter and anti-sigma factor antagonist (STAS) domain, which occupies most of the cytoplasmic C-terminus (Sharma et al. 2011). The name refers to sequence and structural similarity with bacterial anti-sigma factor antagonist (ASA) proteins. In prestin from rats, the STAS domain approximately comprises amino acids 505–714 (Pasqualetto et al. 2010). Although the TMD mediates and determines the eM and transport function of SLC26 members as shown by transplantation of domains between mammalian and transport-active nonmammalian prestin (Schaechinger et al. 2011), mutagenesis studies indicated that the STAS domain is indispensable both for proper membrane targeting (Navaratnam et al. 2005; Zheng et al. 2005) and for protein function (Bai et al. 2006) in prestin and in other SLC26 transporters (Sharma et al. 2011). How the cytosolic domain affects eM or transport function is yet unknown. Nevertheless, as also found with other SLC26 transporters (Ko et al. 2004), the STAS domain is implicated in the interaction of prestin with other proteins including MAP1S (Bai et al. 2010) and calmodulin (Keller et al. 2014; see Sect. 5.4.2).

Although the prestin sequence is generally highly conserved across mammalian species, parallel or convergent evolution of the prestin gene has been discovered in echolocating bats and whales (Li et al. 2010; Liu et al. 2010). Thus, the same amino acid substitutions are found specifically in these phylogenetically unrelated lineages of echolocating mammals. Most of these sites cluster in the cytoplasmic C-terminus including the STAS domain (Li et al. 2010; Liu et al. 2010). Some of these residue replacements were found to modulate the voltage dependence of prestin (Liu et al. 2014), but the physiological consequences of these specific molecular traits are unknown. Given the parallel occurrence in echolocating species that use particularly high frequencies, it has been speculated that these amino acid changes may support the function of prestin in ultrasonic hearing (Li et al. 2010; Liu et al. 2010).

5.3.2 *Molecular Structure of Prestin*

Two papers in 2014 and 2015 revealed the molecular structure of SLC26/SuIP transporters and of prestin in particular. Gorbunov et al. (2014) used a homology modeling approach based on the X-ray crystal structure of the bacterial uracil transporter UraA (Lu et al. 2011), which belongs to the NCS2 family of nucleobase/cation symporters, as the template. Although direct sequence conservation between UraA and prestin (or other mammalian SLC26 members) is low, advanced remote homology detection methods indicate that SLC26/SuIP and NCS transporters are directly related, arguing that they share a common molecular architecture (Hoglund et al. 2011; Wong et al. 2012; Vastermark and Saier 2014). Homology models of mammalian and chicken prestin were scrutinized and refined

by molecular dynamics (MD) simulations (Gorburnov et al. 2014), which supported the validity of this conclusion. Soon afterward, this homology model was confirmed by the first experimental atomic structure of a SLC26/SuIP transporter, the bacterial fumarate transporter SLC26Dg from *Deinococcus geothermalis* (Geertsma et al. 2015).

Modeling and X-ray crystallography consistently revealed a 7 + 7 inverted-repeat architecture for the TMD of SLC26 transporters and thus prestin (Gorburnov et al. 2014; Geertsma et al. 2015). As illustrated in Fig. 5.2, the central domain (TMD) of prestin is made up of 14 mostly helical transmembrane (TM) segments of variable length. The two halves (or repeats) of the TMD, each containing seven TM segments, are related to each other by a twofold pseudosymmetry such that they are inversely oriented with respect to the intracellular side. TMs from both repeats are interdigitated with their counterparts from the other repeat (Fig. 5.3a), forming the inverted-repeat organization that is characteristic of many different transporters (Forrest and Rudnick 2009). The topology of prestin was further probed by examining the intra- and extracellular accessibility of

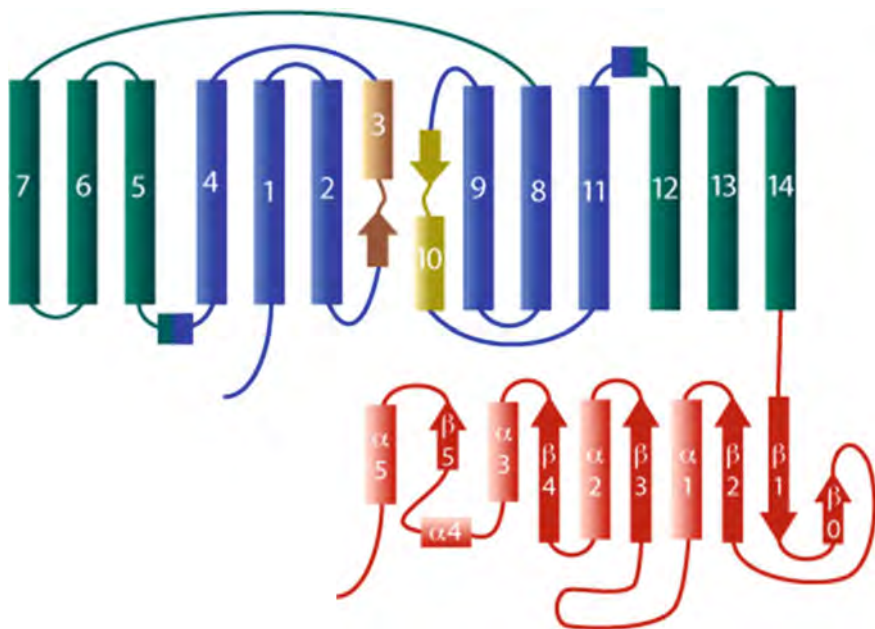


Fig. 5.2 Topology of prestin. The transmembrane domain (TMD) contains 14 largely helical membrane-spanning domains, forming two inverted repeats (TMs 1–7 and TMs 8–14). Colors indicate the three-dimensional structural organization into two main helix bundles, the “core” domain (blue) and the “gate” domain (green). Two central, partially helical and antiparallel TMs within the core domain are highlighted in brown (TM3) and yellow (TM10). Arrows: short β -strand segments. The cytoplasmic C-terminus (red) is mostly folded into a sulfate transporter and anti-sigma factor antagonist (STAS) domain consisting of several α -helical and β -strand segments

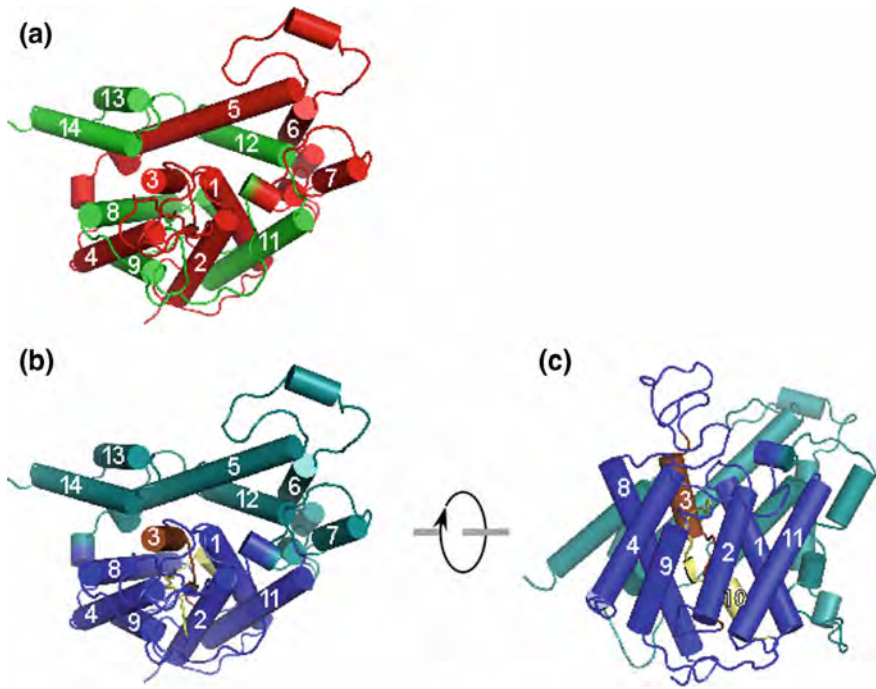


Fig. 5.3 Three-dimensional structure of prestin. **a** Extracellular surface view of overall TMD structure of prestin as derived from homology modeling with the experimental structure of SLC26Dg (Geertsma et al. 2015) as the template. *Red*: inverted repeat I; *green*: inverted repeat II. Transmembrane segments are labeled as in Fig. 5.2; helical part of TM10 is largely hidden by TM1. **b** Same structure colored according to structural organization in core and gate domain. Color code as in Fig. 5.2. **c** Side view

mutationally inserted cysteine residues to cysteine-reactive, membrane-impermeant reagents (Gorbunov et al. 2014). These experiments unequivocally showed that the topology of mammalian prestin is fully consistent with the architecture of the bacterial homolog and the homology model based on UraA.

The TMD is organized into two structural units, each consisting of a bundle of TM helices containing segments from both inverted repeats (Figs. 5.2, 5.3b, c). TMs 1–4 and the pseudosymmetry-related counterpart TMs 8–11 form a compact bundle that has been designated the core domain. TMs 5–7 and 12–14 fold into a more planar (extended) bundle of helices termed the gate domain, which aligns with one side of the core domain, forming an extensive interface between both domains (Fig. 5.3b).

Attempts were also made to address the molecular structure of SLC26A6 and prestin by homology modeling based on the crystal structures of a bacterial chloride transporter, CLC-ec1 (Ohana et al. 2011), or the bacterial amino acid transporter Glt_{PH} (Lovas et al. 2015) as the templates, respectively. However, these approaches produced structures that can now be excluded given the lack of similarity with the

SLC26 crystal structure (Geertsma et al. 2015), disagreement with the experimentally determined topology (Gorbunov et al. 2014), and the lack of a sufficiently close evolutionary relationship between the respective transporter families and the SLC26/SulP family (Hoglund et al. 2011; Vastermark and Saier 2014).

The structure of the cytosolic STAS domain of prestin was solved at atomic resolution both for mammalian prestin (from the rat; Pasqualetto et al. 2010) and nonmammalian prestin (from the chicken; Lolli et al. 2015), revealing an ovoid domain assembled from a central β -sheet surrounded by five α -helices (Fig. 5.2). The core of the domain is structurally similar to STAS domains of bacterial SulP/LC26 proteins and to bacterial ASA proteins, but there are significant differences at the N- and C-termini, most notably an N-terminal extension including some rigid turns and an extra β -strand. Interestingly, the mammalian, but not the chicken, STAS domain harbors an anion binding site, the function of which is yet unknown (Lolli et al. 2015). Given its impact on prestin function, a close structural interaction with the TMD would seem likely. Although Pasqualetto et al. (2010) identified a molecular surface that may interact with either the lipid bilayer or the intracellular face of the TMD, the STAS orientation relative to the TMD remains unknown in the vertebrate SLC26 proteins. In the bacterial SLC26Dg full-length structure, the domain is facing away from the TMD and occupies a position corresponding to the inner lipid bilayer, which is apparently an artifact from cocrystallization with a nanobody (Geertsma et al. 2015). Low-resolution structural data from additional prokaryotic SLC26 homologs suggested that the STAS domain may project away from the TMD (Compton et al. 2014).

5.3.3 *Oligomerization*

Biochemical and low-resolution structural findings indicated that eukaryotic and bacterial SLC26 transporters share a conserved dimeric architecture (Detro-Dassen et al. 2008; Compton et al. 2011, 2014). However, some studies suggest that prestin forms tetramers (Zheng et al. 2006; Hallworth and Nichols 2012). Tetramers might be expected because particles in the lateral membrane of OHCs that are observed by freeze-fracture electron microscopy (EM) and believed to represent native prestin molecules, showed estimated diameters somewhat above 10 nm (Forge 1991; Kalinec et al. 1992). Given the dimensions of an SLC26 monomer of about 4.5×6 nm in the membrane plane (Gorbunov et al. 2014; Geertsma et al. 2015), these EM-resolved particles may correspond to tetrameric prestin assemblies. Also, a low-resolution structure of recombinant prestin, as obtained by a three-dimensional reconstruction based on single-particle EM images, exhibited four-fold symmetry consistent with tetrameric stoichiometry (Mio et al. 2008). It remains to be shown if these observations are due to the formation of higher order oligomers (i.e., dimers of dimers) and, if so, whether tetrameric assembly is important for functional or cell biological behavior.

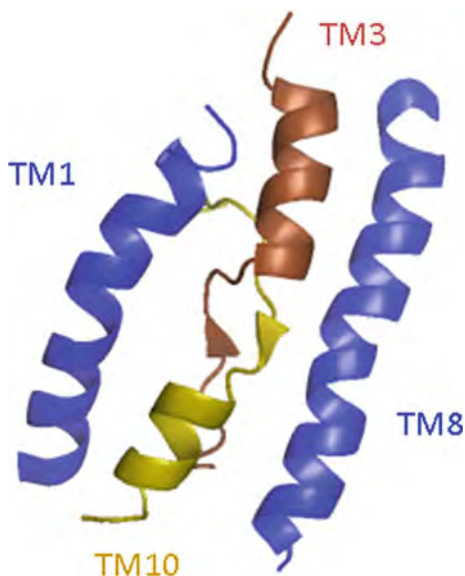
The recent crystal structure of the bacterial SLC26Dg as well as the prestin homology structure provided no direct clues to the structural nature of dimerization. However, Geertsma et al. (2015) noted that the surface of the gate domain (opposite to the interface with the core domain) stood out due to high sequence conservation, which suggested that it may mediate dimerization. Interestingly, a recent crystal structure of the human anion exchanger AE1 (SLC4A1; also known as erythrocyte band 3 protein) showed that SLC4 transporters also share the 7 + 7 inverted-repeat architecture with SLC26 transporters, including an essentially superimposable arrangement of core and gate domains (Arakawa et al. 2015). This is consistent with the fact that together with the NCS2 family, the SLC4 family of bicarbonate transporters is one of the closest SulP/SLC26 relatives as indicated, e.g., by the Pfam database of protein families (Finn et al. 2014). This AE1 structure revealed a dimeric structure mediated by dimerization of the gate domains, lending support to a similar dimeric assembly of SLC26 proteins through the gate domains as proposed for SLC26 by Geertsma et al. (2015).

Although the mechanistic role of oligomerization in the transport or motor function of SLC26 proteins is unknown, for prestin it has been shown that subunits interact functionally, likely by an allosteric mechanism (Detro-Dassen et al. 2008). However, the atomic structure revealed the complete anion binding site and putative translocation pathway within the monomeric subunit (see Sect. 5.3.4), indicating that each subunit is basically functioning as an independent unit rather than forming an oligomeric common transport or motor domain with the other subunit.

5.3.4 Anion Binding Site

The SLC26/prestin structures provided a fresh mechanistic view into the anion dependence of the electromotile activity of prestin and the relationship to the transport function of related SLC26 proteins. Thus, the SLC26 structures feature a central cavity in the TMD, located halfway through the membrane and close to the interface between the core and gate domains. In both computational and X-ray structures, this cavity is accessible to solutes from the cytoplasm but is occluded from the extracellular space. Structural considerations and experimental evidence indicate that this central cavity is the principal binding site for the transport substrate in SLC26 transporters and specifically for the anion that enables eM in mammalian prestin. The pocket is formed largely by the two complementary pseudosymmetry-related, partially helical TMs 3 and 10 and by two complementary TM helices 1 and 8 (Fig. 5.4). Notably, these regions overlap with the Saier motif comprising TMs 9 and 10 (Saier et al. 1999; Mount and Romero 2004; Gorbunov et al. 2014), consistent with the high functional importance of this protein region as suggested by sequence conservation. Moreover, two protein regions previously recognized as molecular determinants of electromotile capability in prestin (Schaechinger et al. 2011) largely coincide with the domains forming the central pocket, further emphasizing the functional importance of these domains.

Fig. 5.4 Anion binding site. Main structural elements that contribute to the proposed central anion binding site. Anions are thought to bind at a central binding site with contributions from the nonhelical segments and the inward-pointing (N-terminal) ends of the partial helices of TMDs 3 and 10



In the crystal structure of the (non-SLC26) transporter UraA, a substrate molecule, uracil, occupies the structurally equivalent central site (Lu et al. 2011). Although the SLC26Dg crystal structure lacked bound substrate, the high similarity to UraA and structural details support the identity of the binding site. The dimensions of the cavity in computational and experimental SLC26 structures are compatible with the range of the substrate anions accepted by SLC26Dg and prestin, respectively (Gorbunov et al. 2014; Geertsma et al. 2015). Furthermore, the N-terminal ends of the partial helices from TM segments 3 and 10 point toward the binding site from opposite directions, providing likely hydrogen-bond partners for the substrate (Geertsma et al. 2015; Fig. 5.4). In UraA, a similar arrangement has been observed, with additional coordination of the substrate by side-chain interactions (Lu et al. 2011). For prestin, Gorbunov et al. (2014) directly tested the role of the structurally corresponding positions by introducing point mutations. Such mutations either altered the anion selectivity of prestin, affected the efficacy of the competitive inhibitory anion salicylate, or abolished function. Similarly, mutations at the homologous positions in transport-competent prestin orthologs from non-mammals (chicken; cPres) altered anion selectivity or abolished transport function (Gorbunov et al. 2014). Altogether, as expected for a transporter, a substrate binding site is located centrally in SLC26 proteins, including prestin. Importantly, the mutational analysis suggested that this same binding site not only mediates transport in SLC26 transporters (including nonmammalian prestin) but also is responsible for the anion-dependence of eM and NLC mediated by mammalian prestin.

How can these structural findings be reconciled with the functional knowledge on prestin? Kinetic analysis of the charge movement and motility of prestin indicated that rapid initial binding of a monovalent anion (chloride) is followed by a

slower transition and, subsequently, by the fast voltage-dependent rearrangement that generates both molecular motion and charge movement (Song and Santos-Sacchi 2013). Given that mutating the binding site disrupts prestin function, a plausible conclusion is that the first fast binding step corresponds to the binding of chloride into the SLC26 substrate binding site.

5.3.5 Electromotile Molecular Transitions

Here we consider the prestin structure in the context of the prevailing area-motor model that postulates (at least) two major states with different cross-sectional dimensions. Although this issue awaits its elucidation, some considerations can be made on the basis of the current knowledge.

Functionally, binding of an anion and a subsequent slower conformational transition appear to precede the mechanically productive fast structural rearrangement in mammalian prestin (Oliver et al. 2001; Song and Santos-Sacchi 2013). The concept of molecular rearrangements following binding of an anion into the central substrate binding site shared with other SLC26 homologs (Gorbunov et al. 2014) has been taken to indicate that the mechanical activity of prestin is mechanistically related to the anion transport cycle (Schaechinger et al. 2011; Gorbunov et al. 2014; Geertsma et al. 2015).

In many secondary transporters, substrate translocation occurs via an alternate access mechanism. Thus, a central binding site is alternately exposed to the extra- and intracellular environment, thereby allowing binding of a substrate on one site and dissociation/release at the opposite site of the membrane (Rudnick 2013). Such a mechanism involves at least one major conformational rearrangement and may additionally involve an intermediate occluded state (Fig. 5.5). For some

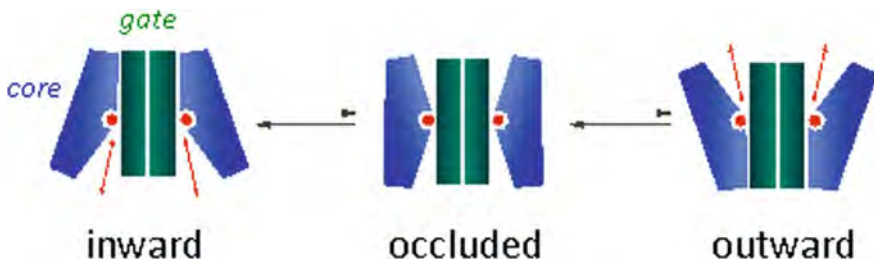


Fig. 5.5 Structural model for anion transport by SLC26. Alternating access of the central anion binding site may result from rotational movement of the core domains against the dimerized gate domains acting as a central scaffold. Experimental crystal structure of SLC26Dg and computational structures of prestin have an inward-facing conformation, but the experimental structure of the structurally homologous exchanger, AE1, revealed an outward-facing conformation (Arakawa et al. 2015). The conformational repertoire of mammalian prestin may be restricted to inward-open and hypothetical occluded states. Modified from Geertsma et al. (2015)

transporters, the conformational change mediating alternate access transport has been structurally resolved. Notably, these transporters also conform to the principle of inverted-repeat architecture, although they are not directly related to SLC26 transporters (Vastermark and Saier 2014). It was shown that there, the conformational switch between inward and outward orientation occurs by a tilting motion between rigid TM bundles (Forrest and Rudnick 2009; Rudnick 2013). For SLC26 transporters, the available structure of SLC26Dg and the UraA-based homology model (as well as the UraA structure itself) describe essentially the same inward-open conformation; therefore, the nature of the molecular rearrangements could not be inferred directly from the structural data (Lu et al. 2011; Gorbunov et al. 2014; Geertsma et al. 2015). However, it has been suggested that a relative motion between core and gate domains mediates transport in SLC26 transporters and UraA (Lu et al. 2011; Gorbunov et al. 2014; Geertsma et al. 2015). Indeed, this idea is strongly supported by the AE1 structure, which revealed an (inhibitor-bound) outside-out state. This structure superposes closely with the UraA and SLC26 structures, with the exception of altered relative positions of core and gate domains (Arakawa et al. 2015). The AE1 structure thus supports the idea of rotation between core and gate domain as the conformational mechanism mediating substrate transport as previously suggested by Gorbunov et al. (2014) and Geertsma et al. (2015; Fig. 5.5). Additional experimental support comes from the finding that a cysteine residue introduced into the central binding site of the transport-active prestin ortholog from chicken is accessible to nonpermeable cysteine-modifying reagents both from the intra- and extracellular sites, consistent with the alternate exposure of this site to both faces of the membrane (Gorbunov et al. 2014).

Given that anion binding into the central binding site in prestin enables eM, it is tempting to speculate that (voltage-dependent) motor activity arises from subsequent conformational transitions equivalent to those mediating anion translocation in other SLC26 transporters (Schaechinger et al. 2011; Gorbunov et al. 2014; Geertsma et al. 2015). In fact, a chimeric SLC26A5 construct based on the zebrafish prestin ortholog (“synthetic prestin”) has both electromechanical and transport activity, consistent with the idea that the transport cycle may accommodate transitions that produce eM (Schaechinger et al. 2011). Also, observations on native chicken hair cells suggested that even nonmammalian, i.e., transport-competent, prestin orthologs may be able to generate forces sufficient for motions at the cellular scale (Beurg et al. 2013). However, in contrast to the transport-active prestin orthologs, the central binding of mammalian prestin is exclusively exposed to the intracellular side (Gorbunov et al. 2014), which is consistent with its interaction with anions selectively at the intracellular, cytoplasmic side (Oliver et al. 2001; Rybalchenko and Santos-Sacchi 2003b, 2008). In structural terms, this indicated that mammalian prestin is unable to reach a state where the binding site is fully exposed to the extracellular medium (Schaechinger et al. 2011; Gorbunov et al. 2014). Therefore, if eM arises from structural rearrangements similar to those that mediate anion transport, these states should be equivalent to a segment of the transport cycle from the fully inward-open conformation to a state preceding full exposure to the extracellular face (Schaechinger et al. 2011; Gorbunov et al. 2014).

Another open issue is the molecular nature of the voltage sensitivity of prestin. The steepness of the voltage-induced motility or charge movement suggests that roughly one elementary electrical charge is moved across the electrical field of the membrane to drive electromechanical activity (Santos-Sacchi 1991). Either exchanging the prevalent intracellular monovalent anion (Oliver et al. 2001) or neutralizing the charged amino acids by mutation (Bai et al. 2009) affects the steepness of the voltage dependence of prestin. Accordingly, anions or polar protein domains have been postulated as extrinsic or intrinsic voltage sensors, respectively. Structural identification of the mechanically effective conformational rearrangements should help to identify the molecular nature of the voltage sensor. Understanding the dynamic electromechanical behavior on this structural level will be one of the most fascinating challenges for future work on prestin.

5.4 Interaction of Prestin with Its Cellular Environment

5.4.1 *Localization of Prestin Along the Basolateral Wall*

After the identification of prestin (Zheng et al. 2000), immunolocalization studies showed the protein along the basolateral surface of OHCs (Belyantseva et al. 2000; Yu et al. 2006). These observations were presaged by electrophysiological localization of motor activity along the lateral membrane (Kalinec et al. 1992; Dallos et al. 1993; Huang and Santos-Sacchi 1993). This localization pattern has important physiological significance because the electromotile force generated by prestin is directed along the longitudinal axis of these elongated cells (Holley and Ashmore 1990; Holley et al. 1992; Matsumoto et al. 2010). It is believed that the unusual structure of the lateral wall of the OHCs, encompassing a prestin-containing plasma membrane, the underlying cortical cytoskeleton, and subsurface cisternae, plays a critical role in eM. The plasma membrane is connected to the underlying cytoskeleton by “pillars,” ultrastructurally identified electron-dense entities (Holley and Ashmore 1990; Forge 1991). Nonetheless, the molecular links of prestin to the underlying cytoskeleton are unknown.

The delivery of prestin to the basolateral wall of OHCs has several potential confounding mechanisms. Protein sorting has been best studied in polarized epithelial cells, where work has established a dichotomy of targeting to the apical or basolateral surface. Although hair cells are polarized epithelial cells, they also show properties of neurons, with an apical-receptive area housing the mechanosensitive channels corresponding to a dendritic end and a basal pole housing the synaptic machinery that corresponds to a neuronal axonal end. A long-standing hypothesis first proposed by Dotti and Simons (1990) posited the dendritic end of a neuron to be equivalent to the basolateral surface and the axonal end to correspond to the apical end of polarized epithelial cells. Hair cells, however, confound this neat

division. Thus, hair cells have to be categorized in terms of protein sorting as either epithelial cell-like or neuronal-like.

It has long been established that classic basolateral markers such as β -catenin and Na^+/K^+ -ATPase are localized along the basolateral surface of hair cells (Schneider et al. 1987; Leonova and Raphael 1997; Zhang et al. 2015). Zheng et al. (2010) demonstrated that stereociliary proteins, including harmonin and cadherin 23, are targeted to the apical surface of the CL4 cell, a model polarized epithelial cell. The authors also established that prestin was targeted to the basolateral surface of CL4 cells. These data confirm that, at least for these proteins, hair cell protein-sorting mechanisms are akin to those of polarized epithelial cells. Interestingly, using the apically targeted pendrin as a vehicle, Zheng et al. (2010) showed that basolateral targeting of prestin is determined by the C-terminus of prestin. Using site-directed mutagenesis, Zhang et al. (2015) established that two tyrosine residues, Y520 and Y667, are important for targeting prestin to the basolateral surface of polarized MDCK cells. Moreover, these authors demonstrated that this targeting is also dependent on AP μ 1-B, which is present in hair cells (and epithelial cells) but absent in neuronal cells (Zhang et al. 2015).

5.4.2 *Prestin's Interactome*

As alluded to in Sect. 5.2, the identity of prestin as the protein responsible for OHC eM has been well established. Recent efforts have also focused on identifying the role of ancillary proteins in the function of prestin. Because prestin has all the molecular features of the motor responsible for eM, this raises the question, Why look for other associated proteins? The response to this lies in three parts. First, in parallel with other systems, in particular ion channels, ancillary proteins modify the biophysical properties of the protein while establishing its localization and transport between different vesicular compartments as well as modifying its rates of turnover. Thus, protein partners may play a similar role with prestin. Second, although many of the biophysical attributes of prestin in OHCs are comparable to those of prestin expressed in heterologous cells, important discrepancies exist (for instance, the V_h of prestin in OHCs lies between -40 and -80 mV, whereas prestin in heterologous cells consistently shows more negative V_h values). Third, although prestin is clearly responsible for eM, there is evidence that links to the underlying cytoskeleton are important for harnessing forces generated by prestin along the longitudinal axis of the cell (Holley and Ashmore 1990; Holley et al. 1992; Matsumoto et al. 2010). How this is brought about is still unknown.

5.4.2.1 **Vesicle-Associated Membrane Protein**

To date, many proteins that interact with prestin have been identified, although definitive interactions and a clear physiological role have yet to be defined for the

vast majority of these proteins. An initial membrane yeast two-hybrid screen identified several proteins as potential prestin interactors (Zheng et al. 2009). Chief among these interacting proteins were those known for transport between different vesicular compartments. These include vesicle-associated membrane protein, vesicle-associated protein A (VAPA), and Yip1 domain family member 6 (Yipf6; Zheng et al. 2009). Association with VAPA, important for integrity of the endoplasmic reticulum (ER), was found to increase the surface expression of prestin. Interestingly, the effect seemed reciprocal, with decreased amounts of VAPA in prestin-knockout OHCs (Zheng et al. 2009). Although a role for Yipf6 in prestin transport has not been demonstrated, its closest yeast homolog, Yip1p, has been demonstrated to be important for Rab-mediated transport from the ER to the Golgi apparatus (Matern et al. 2000; Barrowman et al. 2003; Spang 2004). Yipf6 mutants have intestinal inflammatory disease, although a clear mechanism has yet to be identified and a hearing phenotype has not yet been defined (Brandl et al. 2012). A second group of proteins (38%) identified by the membrane yeast two-hybrid screen included several mitochondrial membrane proteins (cytochrome *b*, subunits of NADH-ubiquinone oxidoreductase, and ATP synthase 6; Zheng et al. 2009). Mitochondrial proteins are known to be nonspecific interactors in yeast two-hybrid screens. In their screens, mitochondrial proteins were a dominant fraction, and they saw no interactions between mitochondrial proteins and the tip-link protein cadherin 23, arguing against a nonspecific interaction. OHCs from prestin knockouts and knock-in mice with altered voltage sensitivity showed early cell death. Actual measures of mitochondrial dysfunction in prestin knockouts have, however, yet to be demonstrated.

5.4.2.2 Cystic Fibrosis Transmembrane Conductance Regulator

The cystic fibrosis transmembrane conductance regulator (CFTR) was identified by Homma et al. (2010) as interacting with prestin. Interest in the CFTR was piqued because a lateral wall conductance that carries Cl^- has been identified in OHCs (Rybalchenko and Santos-Sacchi 2003b) and because Cl^- is a critical modulator of prestin activity (see Sect. 5.2.5). Like the lateral wall Cl^- conductance, the CFTR also shows mechanosensitivity (Zhang et al. 2010). The CFTR has been shown to interact with a number of other SLC26 family members through their STAS domain (Ko et al. 2004). Although many of these interactions are dependent on PKA phosphorylation of the CFTR R domain, the interactions also result in a mutual activation of CFTR and SLC26 transporter activity (Ko et al. 2004). Homma et al. (2010) convincingly showed interactions between prestin and the CFTR (although the interaction is not dependent on PKA phosphorylation). They also showed that the presence of prestin results in the localization of CFTR from its exclusively apical location to a partial basolateral location in OHCs. Unexpectedly, however, there was little reciprocal functional effect on prestin or the CFTR in OHCs; no effects on NLC or CFTR conductance were observed. In contrast, the interaction in heterologous cells results in enhanced prestin charge movement in response to PKA

activation; a reciprocal enhanced effect on CFTR conductance was not demonstrable in the presence of prestin. Although the findings of the CFTR in the lateral membrane of OHCs in the presence of prestin is intriguing, a physiological role for the CFTR in OHCs has yet to be established. Blockers of CFTR had no effect on OHC lateral wall Cl^- conductance (Rybalchenko and Santos-Sacchi 2003b). Furthermore, mutations of CFTR that causes cystic fibrosis are not associated with hearing defects. Hearing phenotypes in these patients have been well studied, and sensorineural hearing loss was described only in the context of toxic levels of gentamicin that is used for treating repeated pulmonary infections in these patients (Homma et al. 2010).

5.4.2.3 Calmodulin

A recent paper by Keller et al. (2014) identified calmodulin as an interactor of prestin. The identity of calmodulin as an interactor was determined after initial assessments showed intrinsically disordered regions in the C-terminus of prestin in proximity to its STAS domain (Keller et al. 2014). Intrinsically disordered regions have been shown to interact with calmodulin, and Keller et al. (2014) go on to show that prestin binds to calmodulin using these regions in a Ca^{2+} -dependent manner. Importantly, they show a 35-mV shift in V_h with increasing Ca^{2+} , an effect that was reversed by the calmodulin inhibitor trifluoperazine (Keller et al. 2014). The authors then speculate that the Ca^{2+} -induced changes in V_h could have physiological importance, with efferent modulation from the olivocochlear bundle effecting changes in OHC stiffness through increases in Ca^{2+} . These interpretations may not be complete, with changes in V_h induced by Ca^{2+} perfusion being secondary to the effects on turgor pressure and not entirely due to the effects on V_h by a direct effect from calmodulin binding to prestin. Thus, the changes in V_h were not evident when the cells were collapsed before Ca^{2+} perfusion (Song and Santos-Sacchi 2015).

5.4.2.4 Microtubule-Associated Proteins

Microtubule-associated protein 1S (MAP1S) is a protein that was identified as interacting with prestin using a conventional Gal4-based yeast two-hybrid assay (Surguchev et al. 2012). In this assay, the C-terminus of prestin was used as bait. MAP1S is a member of the microtubule-associated protein family. MAP1S coexpression enhanced the surface expression of prestin as established by both biochemical and electrophysiological measures (Surguchev et al. 2012). These findings are paralleled by a gradient of MAP1S mRNA expression along the tonotopic axis, suggesting that MAP1S may bring about the higher amounts of prestin in the plasma membrane of high-frequency hair cells. Interestingly, MAP1S has also been shown to interact with actin, and its concentration in proximity to the lateral wall of OHCs raises the possibility that it serves as the link between prestin and the underlying cytoskeleton. As previously referred to, the lateral wall of OHCs

includes a cortical cytoskeleton sandwiched between subsurface cisternae and the lateral plasma membrane. The cortical cytoskeleton consists of circumferentially arranged actin filaments linked to longitudinally arranged spectrin ($\alpha 2$, $\beta 5$) filaments (Forge 1991; Kalinec et al. 1992; Legendre et al. 2008). Previous work identified pillars that are electron-dense entities linking OHC lateral membranes to circumferentially arranged actin filaments (Holley and Ashmore 1990; Forge 1991; Kalinec et al. 1992). The molecular composition of pillars is unknown. Because MAP1S also forms a complex with a host of other actin-binding proteins (Liu et al. 2002; Liu and McKeehan 2002), these data raise the possibility that MAP1S is one component of a complex of proteins that form pillar structures.

5.4.2.5 Spectrin and Spectrin-Interacting Proteins

Although prior reports have shown a concentration of two spectrin-interacting proteins (ankyrin or protein 4.1) along the periphery of OHCs (Knipper et al. 1995; Zine and Schweitzer 1997), the wide gap (50 nm) between the cytoskeleton and the lateral membrane makes it unclear whether these proteins have a physiological role or not (Legendre et al. 2008). Moreover, there are no data showing a direct interaction between prestin and ankyrin or protein 4.1. Interestingly, a paper identifying $\beta 5$ spectrin as a component of the OHC cytoskeleton showed no interaction between prestin and this spectrin isoform (Legendre et al. 2008). However, these authors found an unknown component in OHC lysates that enabled such an interaction. A key area of research in the future will be exploring the interactions between prestin and other components of the lateral wall.

5.4.2.6 Calcium/Calmodulin-Dependent Serine Protein Kinase

A subsequent study using yeast two-hybrid screens identified calcium/calmodulin-dependent serine protein kinase (CASK) as an interacting partner of prestin (Cimerman et al. 2013). CASK is a membrane-associated guanylate kinase (MAGUK). Members of this family have been shown in other systems to bind membrane proteins linking them to actin through protein 4.1 (Zhu et al. 2016). The subcellular distribution of CASK showed a developmental change that correlated with prestin and was affected by thyroid hormone levels. Normally, by postnatal day (P) 18, both NLC and eM reach mature levels. In hypothyroid animals, there is a delay in the expression of prestin, with NLC levels taking until P28 to reach normal levels. Prestin is normally expressed along the entire basolateral surface early in development and is then localized predominantly along the lateral wall while being largely excluded from the basal pole. In contrast, CASK is found predominantly at the basal pole where OHCs contact Deiters cells. In hypothyroid animals, CASK is expressed at low levels, with prestin expressed over the entire basolateral surface at P28. Coincidentally, although NLC levels were normal, eM responses were markedly reduced. Zhu et al. (2016) reasoned that the interactions

with CASK may be involved in the redistribution of prestin to the lateral wall and in generating force, possibly through the cytoskeleton or OHC interactions with Deiter's cells.

5.4.3 Prestin in the Membrane Environment

It is becoming increasingly appreciated that an interplay of membrane structure, organization, and mechanics regulates the function of membrane proteins. It is thus important to understand how the membrane environment affects the function of prestin. From a thermodynamic point of view, the lipid environment is the “solvent” in which prestin operates, just as water is the solvent for biochemical reactions. Thus, changes in the composition, fluidity, and mechanical properties of the membrane can all affect the molecular function of prestin. At the same time, prestin has a large C-terminus that contains a STAS domain possessing a number of potential protein-protein interaction motifs. It is reasonable to postulate that the STAS domain connects prestin to the cytoskeleton of the cell and places constraints on its mobility. Understanding these supramolecular interactions of prestin is necessary to ultimately understand how the molecular nanoscale events that occur in the prestin protein proper result in the mesoscale rearrangements that must ultimately be responsible for OHC eM.

5.4.3.1 Prestin as a Mechanosensitive Protein

After the original discovery that the membrane capacitance of the OHC was sensitive to membrane stress (Iwasa 1993), the tension sensitivity of prestin was further characterized in both OHCs and HEK cells expressing prestin (Kakehata and Santos-Sacchi 1995; Ludwig et al. 2001; Santos-Sacchi et al. 2001). These studies implied that the application of mechanical force results in a geometric rearrangement in prestin that, in turn, affects its ability to move charge in response to voltage changes, establishing prestin as similar to mechanosensitive channels such as MscL, Piezo1, and TREK1 (Sukharev et al. 1996; Coste et al. 2010; Brohawn et al. 2014). Given that the OHC is under turgor pressure, this mechanical sensitivity is likely to be physiologically important.

The question may be raised as to how prestin senses membrane mechanical forces. Membranes are thin structures that have a large resistance to changes in surface area but a very small resistance to changes in curvature. Curvature stress can be induced by differential partitioning of molecules into the two leaflets of the membrane, corresponding to the classic “bilayer couple” explanation of red blood cell shape changes (Singer and Oster 1992). It has become increasingly appreciated that many mechanosensitive membrane proteins sense mechanical force through the lipid bilayer in accordance with the “force from lipid” principle (Anishkin et al. 2014). Forces may be applied to the lipid bilayer by stretching the area or through

the direct or indirect application of membrane curvature stress. Indeed, many reagents that affect prestin function are also known to change membrane curvature (Oghalai et al. 2000; Brownell et al. 2001). It has been postulated that in the intact OHC, turgor pressure would supply a force leading to nanoscale bending of the membrane between the pillar proteins (Raphael et al. 2000; Spector et al. 2006). Although this is difficult to directly measure in living cells with current technology, measurements using fluorescence polarization microscopy (Greeson and Raphael 2009) are consistent with both the existence of nanoscale curvature and pharmacological-induced changes in this curvature. Specifically, reagents that changed the curvature in opposite directions were found to be consistent with the corresponding changes in the function of prestin as measured by the Boltzmann parameter (V_h) of the NLC (Fang et al. 2007; Greeson and Raphael 2009). Other studies have obtained evidence that prestin is also sensitive to the thickness of the membrane (Fang et al. 2010).

One of the challenges in prestin research has been the lack of pharmacological compounds that inhibit its function. This is an also issue for other mechanosensitive proteins such as MscL (Hamill 2006). The most utilized inhibitor of prestin function is salicylate, an active metabolite of aspirin related to nonsteroidal anti-inflammatory drugs (NSAIDs). NSAIDs and analgesics are associated with ototoxicity, hearing loss, and tinnitus (ringing in the ears). In other membrane proteins, NSAID effects have been attributed to both indirect effects on membrane properties and direct binding to functional regions of proteins (Lichtenberger et al. 2006; Manrique-Moreno et al. 2009). Additional research is needed to identify specific inhibitors of prestin function.

5.4.3.2 Prestin as a Confined Protein

The original fluid-mosaic membrane model proposed that proteins diffuse freely in a sea of lipids (Singer and Nicolson 1972). This picture has been refined by the discovery that different proteins have varying degrees of confinement in the membrane. In the membrane biophysics community, many concepts such as “membrane microdomains” and “lipid rafts” have been espoused to characterize the restricted mobility of membrane proteins. Here, the important questions are, Can prestin diffuse freely or is it constrained? If it is constrained, does this occur through interactions with the cytoskeleton?

The lateral diffusion of prestin was first directly measured using fluorescence recovery after photobleaching (FRAP) in HEK cells expressing prestin (Organ and Raphael 2007). These studies revealed that the diffusion of prestin is relatively slow when compared with proteins of similar molecular weight. In addition, using a dual-bleach protocol, these studies suggested that prestin was transiently confined. To confirm transient confinement and better understand the membrane dynamics of prestin, single-molecule imaging studies were performed (Kamar et al. 2012). Individual molecules of prestin labeled with a highly stable fluorophore were expressed in HEK cells and tracked using total internal fluorescence microscopy.

These studies confirmed that prestin is indeed confined in the membrane and undergoes anomalous diffusion (Kamar et al. 2012). The results could be fit to a “hop-diffusion” model in which prestin molecules diffuse within a limited area, then “hop” to a different area of the membrane. In this model, there is a timescale associated with confinement that corresponds to the strength of the intermolecular interactions restricting free diffusion of the protein. These studies raised the question of how prestin diffuses in the native OHCs. Later studies in knock-in mice expressing prestin fused to yellow fluorescent protein (YFP) obtained results consistent with the minimal diffusion of prestin in OHCs as measured with traditional FRAP (Yamashita et al. 2015). When compared with the HEK cell single-molecule results, it appears that OHCs contain additional mechanisms that further confine prestin (Yamashita et al. 2015). This raises the question whether robust electromechanical activity seen in OHCs as opposed to HEK cells could be related to the presence of additional interactions that limit the membrane lateral mobility of prestin, i.e., whether membrane confinement has implications for prestin function. One of the key ways to alter the confinement of membrane proteins is to manipulate membrane cholesterol, which changes the structure of membrane microdomains. Depletion of membrane cholesterol with MBCD was shown to have a dramatic impact on prestin confinement (Kamar et al. 2012). Taking into account an earlier study that indicated that cholesterol affects the Boltzmann parameter (V_h) of the NLC in OHCs (Rajagopalan et al. 2007), it suggests that alterations in prestin confinement affect at least the operating voltage range of prestin. Similar cholesterol depletion experiments were also carried out in the knock-in mouse model (Yamashita et al. 2015), but here the addition of salicylate was also required to enable prestin to undergo free membrane diffusion. Identifying the molecular mechanisms responsible for prestin confinement and understanding whether they affect prestin function is an important priority for future research.

5.5 Conclusions and Open Questions

Gaining a molecular and cellular understanding of eM function has been the major driving force for the research summarized above. Considering the major advances achieved over the last decade, a mechanistic framework for prestin function is finally emerging.

Only recently have experimental and computational data on the structure of prestin and its relatives been obtained. Yet, these findings already provide unprecedented insights and show remarkable agreement between structure and the wealth of biophysical data assembled since the discovery of eM. This initial structural picture of prestin should now provide a productive ground for well-directed structural and functional approaches toward understanding how molecular conformational dynamics generate eM. Given this goal, it should be kept in mind that the present structural data provide only a snapshot of one particular state, that many structural details are still missing, and, importantly, that the structure of prestin itself

has not been determined experimentally. Thus, much remains to be explored. Additionally, such work may also provide important insights into the inner workings of other SLC26 transporters, including pendrin, another SLC26 member with high relevance for cochlear homeostasis and pathophysiology.

Structure-function results are consistent with the idea that prestin works as a conformationally constrained alternate access transporter (see Fig. 5.5). In such a model, eM would arise from the transition between distinct states within an anion transport cycle that differ mechanically and electrostatically, in turn rendering prestin mechanosensitive. The conformational transition may result in a change of cross-sectional area as proposed by the prevailing area motor model (Iwasa 1994); alternatively, the tilting motion between helical bundles suggested by the available structural data may also indicate the generation of differential stresses between the two leaflets of the membrane bilayer, consistent with a previously proposed membrane bending model of eM based on flexoelectricity (Raphael et al. 2000).

Beyond these molecular mechanisms, many observations suggest that integration of prestin into a complex cellular structure, i.e., the highly specialized trilaminar lateral wall of OHCs, is important for effectively channeling the molecular movements into the generation of macroscopic cellular eM. Yet, components of this cortical structure as well as how it is assembled and whether prestin is part of it remain unknown. Despite identification of various potential interaction partners of prestin described in this chapter, their involvement in the OHC lateral wall and thus their relevance for eM remain unknown. Other important interaction partners likely await identification. Future work on the function of prestin-associated proteins will not only require elucidation of their ultrastructural localization and molecular interactions within the supramolecular OHC cortex but should also include selective manipulation of these proteins and disruption of their interactions in living OHCs.

It can be anticipated that the molecular and supramolecular characterization of prestin will lead to new approaches for selective alteration of eM that can, in turn, increase our overall understanding of the role of eM in cochlear mechanics (i.e., amplification). Ultimately, research along these avenues will increase our understanding of this unique protein that is so important for our sense of hearing.

Compliance with Ethics Requirements Joseph Santos-Sacchi declares that he has no conflict of interest. Dhasakumar Navaratnam declares that he has no conflict of interest. Robert Raphael declares that he has no conflict of interest. Dominik Oliver declares that he has no conflict of interest.

References

- Adachi, M., & Iwasa, K. H. (1999). Electrically driven motor in the outer hair cell: Effect of a mechanical constraint. *Proceedings of the National Academy of Sciences of the United States of America*, 96(13), 7244–7249.
- Alper, S. L., & Sharma, A. K. (2013). The SLC26 gene family of anion transporters and channels. *Molecular Aspects of Medicine*, 34(2–3), 494–515.

- Anishkin, A., Loukin, S. H., Teng, J., & Kung, C. (2014). Feeling the hidden mechanical forces in lipid bilayer is an original sense. *Proceedings of the National Academy of Sciences of the United States of America*, 111(22), 7898–7905.
- Arakawa, T., Kobayashi-Yurugi, T., Alguel, Y., Iwanari, H., Hatae, H., Iwata, M., Abe, Y., Hino, T., Ikeda-Suno, C., Kuma, H., Kang, D., Murata, T., Hamakubo, T., Cameron, A. D., Kobayashi, T., Hamasaki, N., & Iwata, S. (2015). Crystal structure of the anion exchanger domain of human erythrocyte band 3. *Science*, 350(6261), 680–684.
- Ashmore, J. (2008). Cochlear outer hair cell motility. *Physiological Reviews*, 88(1), 173–210.
- Ashmore, J., Avan, P., Brownell, W. E., Dallos, P., Dierkes, K., Fettiplace, R., Grosh, K., Hackney, C. M., Hudspeth, A. J., Juelicher, F., Lindner, B., Martin, P., Meaud, J., Petit, C., Santos-Sacchi, J. R., & Canlon, B. (2010). The remarkable cochlear amplifier. *Hearing Research*, 266(1–2), 1–17. Corrigendum. *Hearing Research*, 280(1–2), 245.
- Ashmore, J. F. (1987). A fast motile response in guinea-pig outer hair cells: The cellular basis of the cochlear amplifier. *The Journal of Physiology*, 388, 323–347.
- Ashmore, J. F. (1989). Transducer motor coupling in cochlear outer hair cells. In D. Kemp & J. P. Wilson (Eds.), *Mechanics of Hearing* (pp. 107–113). New York: Plenum Press.
- Ashmore, J. F. (1990). Forward and reverse transduction in the mammalian cochlea. *Neuroscience Research Supplement*, 12, S39–S50.
- Bai, J. P., Navaratnam, D., Samaranyake, H., & Santos-Sacchi, J. (2006). En block C-terminal charge cluster reversals in prestin (SLC26A5): Effects on voltage-dependent electromechanical activity. *Neuroscience Letters*, 404(3), 270–275.
- Bai, J. P., Surguchev, A., Montoya, S., Aronson, P. S., Santos-Sacchi, J., & Navaratnam, D. (2009). Prestin's anion transport and voltage-sensing capabilities are independent. *Biophysical Journal*, 96(8), 3179–3186.
- Bai, J. P., Surguchev, A., Ogando, Y., Song, L., Bian, S., Santos-Sacchi, J., & Navaratnam, D. (2010). Prestin surface expression and activity are augmented by interaction with MAP1S, a microtubule-associated protein. *Journal of Biological Chemistry*, 285(27), 20834–20843.
- Bai, J.P., Moeini-Naghani, I., Zhong, S., Li, F.Y., Bian, S., Sigworth, F.J., Santos-Sacchi, J., & Navaratnam, D. (2017). Current carried by the Slc26 family member prestin does not flow through the transporter pathway. *Scientific Reports*, 7:46619.
- Barrowman, J., Wang, W., Zhang, Y., & Ferro-Novick, S. (2003). The Yip1p•Yif1p complex is required for the fusion competence of endoplasmic reticulum-derived vesicles. *Journal of Biological Chemistry*, 278(22), 19878–19884.
- Belyantseva, I. A., Adler, H. J., Curi, R., Frolenkov, G. I., & Kachar, B. (2000). Expression and localization of prestin and the sugar transporter GLUT-5 during development of electromotility in cochlear outer hair cells. *The Journal of Neuroscience*, 20(24), RC116.
- Beurg, M., Tan, X., & Fettiplace, R. (2013). A prestin motor in chicken auditory hair cells: Active force generation in a nonmammalian species. *Neuron*, 79(1), 69–81.
- Bezannilla, F. (2000). The voltage sensor in voltage-dependent ion channels. *Physiological Reviews*, 80(2), 555–592.
- Brandl, K., Tomisato, W., Li, X., Nepl, C., Pirie, E., Falk, W., Xia, Y., Moresco, E. M., Baccala, R., Theofilopoulos, A. N., Schnabl, B., & Beutler, B. (2012). Yip1 domain family, member 6 (Yipf6) mutation induces spontaneous intestinal inflammation in mice. *Proceedings of the National Academy of Sciences of the United States of America*, 109(31), 12650–12655.
- Brohawn, S. G., Su, Z., & MacKinnon, R. (2014). Mechanosensitivity is mediated directly by the lipid membrane in TRAAK and TREK1 K⁺ channels. *Proceedings of the National Academy of Sciences of the United States of America*, 111(9), 3614–3619.
- Brownell, W. E., Bader, C. R., Bertrand, D., & de Ribaupierre, Y. (1985). Evoked mechanical responses of isolated cochlear outer hair cells. *Science*, 227(4683), 194–196.
- Brownell, W. E., Spector, A. A., Raphael, R. M., & Popel, A. S. (2001). Micro- and nanomechanics of the cochlear outer hair cell. *Annual Review of Biomedical Engineering*, 3, 169–194.
- Cimerman, J., Waldhaus, J., Harasztosi, C., Duncker, S. V., Dettling, J., Heidrych, P., Bress, A., Gampe-Braig, C., Frank, G., Gummer, A. W., Oliver, D., Knipper, M., & Zimmermann, U.

- (2013). Generation of somatic electromechanical force by outer hair cells may be influenced by prestin-CASK interaction at the basal junction with the Deiter's cell. *Histochemistry and Cell Biology*, 140(2), 119–135.
- Compton, E. L., Karinou, E., Naismith, J. H., Gabel, F., & Javelle, A. (2011). Low resolution structure of a bacterial SLC26 transporter reveals dimeric stoichiometry and mobile intracellular domains. *Journal of Biological Chemistry*, 286(30), 27058–27067.
- Compton, E. L., Page, K., Findlay, H. E., Haertlein, M., Moulin, M., Zachariae, U., Norman, D. G., Gabel, F., & Javelle, A. (2014). Conserved structure and domain organization among bacterial SLC26 transporters. *Biochemical Journal*, 463(2), 297–307.
- Coste, B., Mathur, J., Schmidt, M., Earley, T. J., Ranade, S., Petrus, M. J., Dubin, A. E., & Patapoutian, A. (2010). Piezo1 and Piezo2 are essential components of distinct mechanically activated cation channels. *Science*, 330(6000), 55–60.
- Dallos, P., & Evans, B. N. (1995). High-frequency motility of outer hair cells and the cochlear amplifier. *Science*, 267(5206), 2006–2009.
- Dallos, P., Evans, B. N., & Hallworth, R. (1991). Nature of the motor element in electrokinetic shape changes of cochlear outer hair cells. *Nature*, 350(6314), 155–157.
- Dallos, P., Hallworth, R., & Evans, B. N. (1993). Theory of electrically driven shape changes of cochlear outer hair cells. *Journal of Neurophysiology*, 70(1), 299–323.
- Dallos, P., Wu, X., Cheatham, M. A., Gao, J., Zheng, J., Anderson, C. T., Jia, S., Wang, X., Cheng, W. H., Sengupta, S., He, D. Z., & Zuo, J. (2008). Prestin-based outer hair cell motility is necessary for mammalian cochlear amplification. *Neuron*, 58(3), 333–339.
- Deak, L., Zheng, J., Orem, A., Du, G. G., Aguinaga, S., Matsuda, K., & Dallos, P. (2005). Effects of cyclic nucleotides on the function of prestin. *The Journal of Physiology*, 563(2), 483–496.
- Detro-Dassen, S., Schanzler, M., Lauks, H., Martin, I., zu Berstenhorst, S. M., Nothmann, D., Torres-Salazar, D., Hidalgo, P., Schmalzing, G., & Fahlke, C. (2008). Conserved dimeric subunit stoichiometry of SLC26 multifunctional anion exchangers. *Journal of Biological Chemistry*, 283(7), 4177–4188.
- Dorwart, M. R., Shcheynikov, N., Yang, D., & Muallem, S. (2008). The solute carrier 26 family of proteins in epithelial ion transport. *Physiology*, 23, 104–114.
- Dotti, C. G., & Simons, K. (1990). Polarized sorting of viral glycoproteins to the axon and dendrites of hippocampal neurons in culture. *Cell*, 62(1), 63–72.
- Fang, J., & K. H. Iwasa. (2007). Effects of chlorpromazine and trinitrophenol on the membrane motor of outer hair cells. *Biophysical journal*, 93:1809–1817.
- Fang, J., Izumi, C., & Iwasa, K. H. (2010). Sensitivity of prestin-based membrane motor to membrane thickness. *Biophysical Journal*, 98(12), 2831–2838.
- Finn, R. D., Bateman, A., Clements, J., Coggill, P., Eberhardt, R. Y., Eddy, S. R., Heger, A., Hetherington, K., Holm, L., Mistry, J., Sonnhammer, E. L., Tate, J., & Punta, M. (2014). Pfam: The protein families database. *Nucleic Acids Research*, 42, D222–D230.
- Fisher, J. A., Nin, F., Reichenbach, T., Uthaiyah, R. C., & Hudspeth, A. J. (2012). The spatial pattern of cochlear amplification. *Neuron*, 76(5), 989–997.
- Forge, A. (1991). Structural features of the lateral walls in mammalian cochlear outer hair cells. *Cell and Tissue Research*, 265(3), 473–483.
- Forrest, L. R., & Rudnick, G. (2009). The rocking bundle: A mechanism for ion-coupled solute flux by symmetrical transporters. *Physiology*, 24, 377–386.
- Frank, G., Hemmert, W., & Gummer, A. W. (1999). Limiting dynamics of high-frequency electromechanical transduction of outer hair cells. *Proceedings of the National Academy of Sciences of the United States of America*, 96(8), 4420–4425.
- Gale, J. E., & Ashmore, J. F. (1994). Charge displacement induced by rapid stretch in the basolateral membrane of the guinea-pig outer hair cell. *Proceedings of the Royal Society of London B: Biological Sciences*, 255(1344), 243–249.
- Gale, J. E., & Ashmore, J. F. (1997a). The outer hair cell motor in membrane patches. *Pflügers Archiv - European Journal of Physiology*, 434(3), 267–271.
- Gale, J. E., & Ashmore, J. F. (1997b). An intrinsic frequency limit to the cochlear amplifier. *Nature*, 389(6646), 63–66.

- Geertsma, E. R., Chang, Y. N., Shaik, F. R., Neldner, Y., Pardon, E., Steyaert, J., & Dutzler, R. (2015). Structure of a prokaryotic fumarate transporter reveals the architecture of the SLC26 family. *Nature Structural & Molecular Biology*, 22, 803–808.
- Gorbunov, D., Sturlese, M., Nies, F., Kluge, M., Bellanda, M., Battistutta, R., & Oliver, D. (2014). Molecular architecture and the structural basis for anion interaction in prestin and SLC26 transporters. *Nature Communications*, 5, 3622.
- Greeson, J. N., & Raphael, R. M. (2009). Amphipath-induced nanoscale changes in outer hair cell plasma membrane curvature. *Biophysical Journal*, 96(2), 510–520.
- Hallworth, R., & Nichols, M. G. (2012). Prestin in HEK cells is an obligate tetramer. *Journal of Neurophysiology*, 107(1), 5–11.
- Hamill, O. P. (2006). Twenty odd years of stretch-sensitive channels. *Pflügers Archiv - European Journal of Physiology*, 453(3), 333–351.
- He, D. Z., Zheng, J., Kalinec, F., Kakehata, S., & Santos-Sacchi, J. (2006). Tuning into the amazing outer hair cell: Membrane wizardry with a twist and shout. *Journal of Membrane Biology*, 209(2–3), 119–134.
- Hoglund, P. J., Nordstrom, K. J., Schioth, H. B., & Fredriksson, R. (2011). The solute carrier families have a remarkably long evolutionary history with the majority of the human families present before divergence of bilaterian species. *Molecular Biology and Evolution*, 28(4), 1531–1541.
- Holley, M. C., & Ashmore, J. F. (1990). Spectrin, actin and the structure of the cortical lattice in mammalian cochlear outer hair cells. *Journal of Cell Science*, 96(2), 283–291.
- Holley, M. C., Kalinec, F., & Kachar, B. (1992). Structure of the cortical cytoskeleton in mammalian outer hair cells. *Journal of Cell Science*, 102(3), 569–580.
- Homma, K., Miller, K. K., Anderson, C. T., Sengupta, S., Du, G. G., Aguinaga, S., Cheatham, M., Dallos, P., & Zheng, J. (2010). Interaction between CFTR and prestin (SLC26A5). *Biochimica et Biophysica Acta*, 1798(6), 1029–1040.
- Homma, K., Duan, C., Zheng, J., Cheatham, M. A., & Dallos, P. (2013). The V499G/Y501H mutation impairs fast motor kinetics of prestin and has significance for defining functional independence of individual prestin subunits. *Journal of Biological Chemistry*, 288(4), 2452–2463.
- Huang, G., & Santos-Sacchi, J. (1993). Mapping the distribution of the outer hair cell motility voltage sensor by electrical amputation. *Biophysical Journal*, 65(5), 2228–2236.
- Huang, G. J., & Santos-Sacchi, J. (1994). Motility voltage sensor of the outer hair cell resides within the lateral plasma-membrane. *Proceedings of the National Academy of Sciences of the United States of America*, 91(25), 12268–12272.
- Iwasa, K. H. (1993). Effect of stress on the membrane capacitance of the auditory outer hair cell. *Biophysical Journal*, 65(1), 492–498.
- Iwasa, K. H. (1994). A membrane motor model for the fast motility of the outer hair cell. *The Journal of the Acoustical Society of America*, 96(4), 2216–2224.
- Kachar, B., Brownell, W. E., Altschuler, R., & Fex, J. (1986). Electrokinetic shape changes of cochlear outer hair cells. *Nature*, 322(6077), 365–368.
- Kakehata, S., & Santos-Sacchi, J. (1995). Membrane tension directly shifts voltage dependence of outer hair cell motility and associated gating charge. *Biophysical Journal*, 68(5), 2190–2197.
- Kakehata, S., & Santos-Sacchi, J. (1996). Effects of salicylate and lanthanides on outer hair cell motility and associated gating charge. *The Journal of Neuroscience*, 16(16), 4881–4889.
- Kalinec, F., Holley, M. C., Iwasa, K. H., Lim, D. J., & Kachar, B. (1992). A membrane-based force generation mechanism in auditory sensory cells. *Proceedings of the National Academy of Sciences of the United States of America*, 89(18), 8671–8675.
- Kamar, R. I., Organ-Darling, L. E., & Raphael, R. M. (2012). Membrane cholesterol strongly influences confined diffusion of prestin. *Biophysical Journal*, 103(8), 1627–1636.
- Keller, J. P., Homma, K., Duan, C., Zheng, J., Cheatham, M. A., & Dallos, P. (2014). Functional regulation of the SLC26-family protein prestin by calcium/calmodulin. *The Journal of Neuroscience*, 34(4), 1325–1332.

- Knipper, M., Zimmermann, U., Kopschall, I., Rohbock, K., Jungling, S., & Zenner, H. P. (1995). Immunological identification of candidate proteins involved in regulating active shape changes of outer hair cells. *Hearing Research*, 86(1–2), 100–110.
- Ko, S. B., Zeng, W., Dorwart, M. R., Luo, X., Kim, K. H., Millen, L., Goto, H., Naruse, S., Soyombo, A., Thomas, P. J., & Muallem, S. (2004). Gating of CFTR by the STAS domain of SLC26 transporters. *Nature Cell Biology*, 6(4), 343–350.
- Legendre, K., Safieddine, S., Kussel-Andermann, P., Petit, C., & El-Amraoui, A. (2008). α II- β V spectrin bridges the plasma membrane and cortical lattice in the lateral wall of the auditory outer hair cells. *Journal of Cell Science*, 121(20), 3347–3356.
- Leonova, E. V., & Raphael, Y. (1997). Organization of cell junctions and cytoskeleton in the reticular lamina in normal and ototoxically damaged organ of Corti. *Hearing Research*, 113(1–2), 14–28.
- Li, Y., Liu, Z., Shi, P., & Zhang, J. (2010). The hearing gene prestin unites echolocating bats and whales. *Current Biology*, 20(2), R55–R56.
- Liberman, M. C., Gao, J., He, D. Z., Wu, X., Jia, S., & Zuo, J. (2002). Prestin is required for electromotility of the outer hair cell and for the cochlear amplifier. *Nature*, 419(6904), 300–304.
- Lichtenberger, L. M., Zhou, Y., Dial, E. J., & Raphael, R. M. (2006). NSAID injury to the gastrointestinal tract: Evidence that NSAIDs interact with phospholipids to weaken the hydrophobic surface barrier and induce the formation of unstable pores in membranes. *Journal of Pharmacy and Pharmacology*, 58(11), 1421–1428.
- Liu, L., & McKeehan, W. L. (2002). Sequence analysis of LRPPRC and its SEC1 domain interaction partners suggests roles in cytoskeletal organization, vesicular trafficking, nucleocytoplasmic shuttling, and chromosome activity. *Genomics*, 79(1), 124–136.
- Liu, L., Amy, V., Liu, G., & McKeehan, W. L. (2002). Novel complex integrating mitochondria and the microtubular cytoskeleton with chromosome remodeling and tumor suppressor RASSF1 deduced by in silico homology analysis, interaction cloning in yeast, and colocalization in cultured cells. *In Vitro Cellular & Developmental Biology - Animal*, 38(10), 582–594.
- Liu, Y., Cotton, J. A., Shen, B., Han, X., Rossiter, S. J., & Zhang, S. (2010). Convergent sequence evolution between echolocating bats and dolphins. *Current Biology*, 20(2), R53–R54.
- Liu, Z., Qi, F. Y., Zhou, X., Ren, H. Q., & Shi, P. (2014). Parallel sites implicate functional convergence of the hearing gene prestin among echolocating mammals. *Molecular Biology and Evolution*, 31(9), 2415–2424.
- Lolli, G., Pasqualetto, E., Costanzi, E., Bonetto, G., & Battistutta, R. (2015). The STAS domain of mammalian SLC26A5 prestin harbors an anion-binding site. *Biochemical Journal*, 473(4), 365–370.
- Lovas, S., He, D. Z., Liu, H., Tang, J., Pecka, J. L., Hatfield, M. P., & Beisel, K. W. (2015). Glutamate transporter homolog-based model predicts that anion- π interaction is the mechanism for the voltage-dependent response of prestin. *Journal of Biological Chemistry*, 290(40), 24326–24339.
- Lu, F., Li, S., Jiang, Y., Jiang, J., Fan, H., Lu, G., Deng, D., Dang, S., Zhang, X., Wang, J., & Yan, N. (2011). Structure and mechanism of the uracil transporter UraA. *Nature*, 472(7342), 243–246.
- Ludwig, J., Oliver, D., Frank, G., Klöcker, N., Gummer, A. W., & Fakler, B. (2001). Reciprocal electromechanical properties of rat prestin: The motor molecule from rat outer hair cells. *Proceedings of the National Academy of Sciences of the United States of America*, 98(7), 4178–4183.
- Mahendrasingam, S., Beurg, M., Fettiplace, R., & Hackney, C. M. (2010). The ultrastructural distribution of prestin in outer hair cells: A post-embedding immunogold investigation of low-frequency and high-frequency regions of the rat cochlea. *European Journal of Neuroscience*, 31(9), 1595–1605.

- Manrique-Moreno, M., Garidel, P., Suwalsky, M., Howe, J., & Brandenburg, K. (2009). The membrane-activity of ibuprofen, diclofenac, and naproxen: A physico-chemical study with lecithin phospholipids. *Biochimica et Biophysica Acta*, 1788(6), 1296–1303.
- Matern, H., Yang, X., Andrusis, E., Sternglanz, R., Trepte, H. H., & Gallwitz, D. (2000). A novel Golgi membrane protein is part of a GTPase-binding protein complex involved in vesicle targeting. *The EMBO Journal*, 19(17), 4485–4492.
- Matsumoto, N., Kitani, R., Maricle, A., Mueller, M., & Kalinec, F. (2010). Pivotal role of actin depolymerization in the regulation of cochlear outer hair cell motility. *Biophysical Journal*, 99(7), 2067–2076.
- Meltzer, J., & Santos-Sacchi, J. (2001). Temperature dependence of non-linear capacitance in human embryonic kidney cells transfected with prestin, the outer hair cell motor protein. *Neuroscience Letters*, 313(3), 141–144.
- Mio, K., Kubo, Y., Ogura, T., Yamamoto, T., Arisaka, F., & Sato, C. (2008). The motor protein prestin is a bullet-shaped molecule with inner cavities. *Journal of Biological Chemistry*, 283(2), 1137–1145.
- Mistrik, P., Daudet, N., Morandell, K., & Ashmore, J. F. (2012). Mammalian prestin is a weak $\text{Cl}^-/\text{HCO}_3^-$ electrogenic antiporter. *The Journal of Physiology*, 590(22), 5597–5610.
- Mount, D. B., & Romero, M. F. (2004). The SLC26 gene family of multifunctional anion exchangers. *Pflügers Archiv - European Journal of Physiology*, 447(5), 710–721.
- Muallem, D., & Ashmore, J. (2006). An anion antiporter model of prestin, the outer hair cell motor protein. *Biophysical Journal*, 90(11), 4035–4045.
- Mutai, H., Suzuki, N., Shimizu, A., Torii, C., Namba, K., Morimoto, N., Kudoh, J., Kaga, K., Kosaki, K., & Matsunaga, T. (2013). Diverse spectrum of rare deafness genes underlies early-childhood hearing loss in Japanese patients: A cross-sectional, multi-center next-generation sequencing study. *Orphanet Journal of Rare Diseases*, 8, 172.
- Navaratnam, D., Bai, J. P., Samaranyake, H., & Santos-Sacchi, J. (2005). N-terminal-mediated homomultimerization of prestin, the outer hair cell motor protein. *Biophysical Journal*, 89(5), 3345–3352.
- Oghalai, J. S., Zhao, H. B., Kutz, J. W., & Brownell, W. E. (2000). Voltage- and tension-dependent lipid mobility in the outer hair cell plasma membrane. *Science*, 287(5453), 658–661.
- Ohana, E., Shcheynikov, N., Yang, D., So, I., & Muallem, S. (2011). Determinants of coupled transport and uncoupled current by the electrogenic SLC26 transporters. *The Journal of General Physiology*, 137(2), 239–251.
- Oliver, D., He, D. Z., Klocker, N., Ludwig, J., Schulte, U., Waldegger, S., Ruppertsberg, J. P., Dallos, P., & Fakler, B. (2001). Intracellular anions as the voltage sensor of prestin, the outer hair cell motor protein. *Science*, 292(5525), 2340–2343.
- Organ, L. E., & Raphael, R. M. (2007). Application of fluorescence recovery after photobleaching to study prestin lateral mobility in the human embryonic kidney cell. *Journal of Biomedical Optics*, 12(2), 021003.
- Pasqualetto, E., Aiello, R., Gesiot, L., Bonetto, G., Bellanda, M., & Battistutta, R. (2010). Structure of the cytosolic portion of the motor protein prestin and functional role of the STAS domain in SLC26/SulP anion transporters. *Journal of Molecular Biology*, 400(3), 448–462.
- Rajagopalan, L., Patel, N., Madabushi, S., Goddard, J. A., Anjan, V., Lin, F., Shope, C., Farrell, B., Lichtarge, O., Davidson, A. L., Brownell, W. E., & Pereira, F. A. (2006). Essential helix interactions in the anion transporter domain of prestin revealed by evolutionary trace analysis. *The Journal of Neuroscience*, 26(49), 12727–12734.
- Rajagopalan, L., Greeson, J. N., Xia, A., Liu, H., Sturm, A., Raphael, R. M., Davidson, A. L., Oghalai, J. S., Pereira, F. A., & Brownell, W. E. (2007). Tuning of the outer hair cell motor by membrane cholesterol. *Journal of Biological Chemistry*, 282(50), 36659–36670.
- Raphael, R. M., Popel, A. S., & Brownell, W. E. (2000). A membrane bending model of outer hair cell electromotility. *Biophysical Journal*, 78(6), 2844–2862.
- Rudnick, G. (2013). How do transporters couple solute movements? *Molecular Membrane Biology*, 30(7), 355–359.

- Rybalchenko, V., & Santos-Sacchi, J. (2003a). Allosteric modulation of the outer hair cell motor protein prestin by chloride. In A. Gummer (Ed.), *Biophysics of the Cochlea: From Molecules to Models* (pp. 116–126). Singapore: World Scientific Publishing.
- Rybalchenko, V., & Santos-Sacchi, J. (2003b). Cl^- flux through a non-selective, stretch-sensitive conductance influences the outer hair cell motor of the guinea-pig. *The Journal of Physiology*, 547(3), 873–891.
- Rybalchenko, V., & Santos-Sacchi, J. (2008). Anion control of voltage sensing by the motor protein prestin in outer hair cells. *Biophysical Journal*, 95(9), 4439–4447.
- Saier, M. H., Jr., Eng, B. H., Fard, S., Garg, J., Haggerty, D. A., Hutchinson, W. J., Jack, D. L., Lai, E. C., Liu, H. J., Nusinew, D. P., Omar, A. M., Pao, S. S., Paulsen, I. T., Quan, J. A., Sliwinski, M., Tseng, T. T., Wachi, S., & Young, G. B. (1999). Phylogenetic characterization of novel transport protein families revealed by genome analyses. *Biochimica et Biophysica Acta*, 1422(1), 1–56.
- Santos-Sacchi, J. (1989). Asymmetry in voltage-dependent movements of isolated outer hair cells from the organ of Corti. *The Journal of Neuroscience*, 9(8), 2954–2962.
- Santos-Sacchi, J. (1990). Fast outer hair cell motility: How fast is fast? In P. Dallos, C. D. Geisler, J. W. Matthews, M. A. Ruggero, & C. R. Steele (Eds.), *The Mechanics and Biophysics of Hearing* (pp. 69–75). Berlin: Springer-Verlag.
- Santos-Sacchi, J. (1991). Reversible inhibition of voltage-dependent outer hair cell motility and capacitance. *The Journal of Neuroscience*, 11(10), 3096–3110.
- Santos-Sacchi, J. (1992). On the frequency limit and phase of outer hair cell motility: Effects of the membrane filter. *The Journal of Neuroscience*, 12(5), 1906–1916.
- Santos-Sacchi, J. (1993). Harmonics of outer hair cell motility. *Biophysical Journal*, 65(5), 2217–2227.
- Santos-Sacchi, J., & Dilger, J. P. (1988). Whole cell currents and mechanical responses of isolated outer hair cells. *Hearing Research*, 35(2–3), 143–150.
- Santos-Sacchi, J., & Huang, G. J. (1998). Temperature dependence of outer hair cell nonlinear capacitance. *Hearing Research*, 116(1–2), 99–106.
- Santos-Sacchi, J., & Navarrete, E. (2002). Voltage-dependent changes in specific membrane capacitance caused by prestin, the outer hair cell lateral membrane motor. *Pflügers Archiv - European Journal of Physiology*, 444(1–2), 99–106.
- Santos-Sacchi, J., & Song, L. (2014a). Chloride and salicylate influence prestin-dependent specific membrane capacitance. *Journal of Biological Chemistry*, 289(15), 10823–10830.
- Santos-Sacchi, J., & Song, L. (2014b). Chloride-driven electromechanical phase lags at acoustic frequencies are generated by SLC26a5, the outer hair cell motor protein. *Biophysical Journal*, 107(1), 126–133.
- Santos-Sacchi, J., & Song, L. (2016). Chloride anions regulate kinetics but not voltage-sensor Q_{max} of the solute carrier SLC26a5. *Biophysical Journal*, 110, 1–11.
- Santos-Sacchi, J., Kakehata, S., & Takahashi, S. (1998). Effects of membrane potential on the voltage dependence of motility-related charge in outer hair cells of the guinea-pig. *The Journal of Physiology*, 510(1), 225–235.
- Santos-Sacchi, J., Shen, W., Zheng, J., & Dallos, P. (2001). Effects of membrane potential and tension on prestin, the outer hair cell lateral membrane motor protein. *The Journal of Physiology*, 531(3), 661–666.
- Santos-Sacchi, J., Song, L., Zheng, J. F., & Nuttall, A. L. (2006). Control of mammalian cochlear amplification by chloride anions. *The Journal of Neuroscience*, 26(15), 3992–3998.
- Schaechinger, T. J., & Oliver, D. (2007). Nonmammalian orthologs of prestin (SLC26A5) are electrogenic divalent/chloride anion exchangers. *Proceedings of the National Academy of Sciences of the United States of America*, 104(18), 7693–7698.
- Schaechinger, T. J., Gorbunov, D., Halaszovich, C. R., Moser, T., Kugler, S., Fakler, B., & Oliver, D. (2011). A synthetic prestin reveals protein domains and molecular operation of outer hair cell piezoelectricity. *The EMBO Journal*, 30(14), 2793–2804.
- Schanzler, M., & Fahlke, C. (2012). Anion transport by the cochlear motor protein prestin. *The Journal of Physiology*, 590(2), 259–272.

- Scherer, M. P., & Gummer, A. W. (2005). How many states can the motor molecule, prestin, assume in an electric field? *Biophysical Journal: Biophysical Letters*, 88(5), L27–L29.
- Schneider, M. E., Cotanche, D. A., Fambrough, D. M., Saunders, J. C., & Matschinsky, F. M. (1987). Immunocytochemical and quantitative studies of Na⁺,K⁺-ATPase distribution in the developing chick cochlea. *Hearing Research*, 31(1), 39–53.
- Sharma, A. K., Rigby, A. C., & Alper, S. L. (2011). STAS domain structure and function. *Cellular Physiology and Biochemistry*, 28(3), 407–422.
- Singer, S. J., & Nicolson, G. L. (1972). The fluid mosaic model of the structure of cell membranes. *Science*, 175(4023), 720–731.
- Singer, S. J., & Oster, G. F. (1992). The bilayer couple hypothesis. *Trends in Cell Biology*, 2(3), 69–70.
- Song, L., & Santos-Sacchi, J. (2010). Conformational state-dependent anion binding in prestin: Evidence for allosteric modulation. *Biophysical Journal*, 98(3), 371–376.
- Song, L., & Santos-Sacchi, J. (2013). Disparities in voltage-sensor charge and electromotility imply slow chloride-driven state transitions in the solute carrier SLC26a5. *Proceedings of the National Academy of Sciences of the United States of America*, 110(10), 3883–3888.
- Song, L., & Santos-Sacchi, J. (2015). Intracellular calcium affects prestin's voltage operating point indirectly via turgor-induced membrane tension. In K. D. Karavitaki & D. P. Corey (Eds.), *Mechanics of Hearing: Protein to Perception: Proceedings of the 12th International Workshop on the Mechanics of Hearing*, Cape Sounio, Greece, June 23–29, 2014. Melville, NY: American Institute of Physics Conference Proceedings 1703, 030009.
- Spang, A. (2004). Vesicle transport: A close collaboration of Rabs and effectors. *Current Biology*, 14(1), R33–R34.
- Spector, A. A., Deo, N., Grosh, K., Ratnanather, J. T., & Raphael, R. M. (2006). Electromechanical models of the outer hair cell composite membrane. *Journal of Membrane Biology*, 209(2–3), 135–152.
- Sukharev, S. I., Blount, P., Martinac, B., Guy, H. R., & Kung, C. (1996). MscL: A mechanosensitive channel in *Escherichia coli*. *Society of General Physiologists Series*, 51, 133–141.
- Surguchev, A., Bai, J. P., Joshi, P., & Navaratnam, D. (2012). Hair cell BK channels interact with RACK1, and PKC increases its expression on the cell surface by indirect phosphorylation. *American Journal of Physiology - Cell Physiology*, 303(2), C143–C150.
- Tan, X., Pecka, J. L., Tang, J., Okoruwa, O. E., Zhang, Q., Beisel, K. W., & He, D. Z. (2011). From zebrafish to mammal: Functional evolution of prestin, the motor protein of cochlear outer hair cells. *Journal of Neurophysiology*, 105(1), 36–44.
- Tunstall, M. J., Gale, J. E., & Ashmore, J. F. (1995). Action of salicylate on membrane capacitance of outer hair cells from the guinea-pig cochlea. *The Journal of Physiology*, 485(3), 739–752.
- Vastermark, A., & Saier, M. H. (2014). Evolutionary relationship between 5 + 5 and 7 + 7 inverted repeat folds within the amino acid-polyamine-organocation superfamily. *Proteins: Structure, Function, and Bioinformatics*, 82(2), 336–346.
- Wong, F. H., Chen, J. S., Reddy, V., Day, J. L., Shlykov, M. A., Wakabayashi, S. T., & Saier, M. H., Jr. (2012). The amino acid-polyamine-organocation superfamily. *Journal of Molecular Microbiology and Biotechnology*, 22(2), 105–113.
- Yamashita, T., Hakizimana, P., Wu, S., Hassan, A., Jacob, S., Temirov, J., Fang, J., Mellado-Lagarde, M., Gursky, R., Horner, L., Leibiger, B., Leijon, S., Centonze, V. E., Berggren, P. O., Frase, S., Auer, M., Brownell, W. E., Fridberger, A., & Zuo, J. (2015). Outer hair cell lateral wall structure constrains the mobility of plasma membrane proteins. *PLoS Genetics*, 11(9), e1005500.
- Yu, N., Zhu, M. L., & Zhao, H. B. (2006). Prestin is expressed on the whole outer hair cell basolateral surface. *Brain Research*, 1095(1), 51–58.
- Zhang, W. K., Wang, D., Duan, Y., Loy, M. M., Chan, H. C., & Huang, P. (2010). Mechanosensitive gating of CFTR. *Nature Cell Biology*, 12(5), 507–512.
- Zhang, Y., Moeini-Naghani, I., Bai, J., Santos-Sacchi, J., & Navaratnam, D. S. (2015). Tyrosine motifs are required for prestin basolateral membrane targeting. *Biology Open*, 4(2), 197–205.

- Zheng, J., Shen, W., He, D. Z., Long, K. B., Madison, L. D., & Dallos, P. (2000). Prestin is the motor protein of cochlear outer hair cells. *Nature*, 405(6783), 149–155.
- Zheng, J., Long, K. B., Shen, W., Madison, L. D., & Dallos, P. (2001). Prestin topology: Localization of protein epitopes in relation to the plasma membrane. *NeuroReport*, 12(9), 1929–1935.
- Zheng, J., Du, G. G., Matsuda, K., Orem, A., Aguinaga, S., Deak, L., Navarrete, E., Madison, L. D., & Dallos, P. (2005). The C-terminus of prestin influences nonlinear capacitance and plasma membrane targeting. *Journal of Cell Science*, 118(13), 2987–2996.
- Zheng, J., Du, G. G., Anderson, C. T., Keller, J. P., Orem, A., Dallos, P., & Cheatham, M. (2006). Analysis of the oligomeric structure of the motor protein prestin. *Journal of Biological Chemistry*, 281(29), 19916–19924.
- Zheng, J., Anderson, C. T., Miller, K. K., Cheatham, M., & Dallos, P. (2009). Identifying components of the hair cell interactome involved in cochlear amplification. *BMC Genomics*, 10, 127.
- Zheng, L., Zheng, J., Whitlon, D. S., Garcia-Añoveros, J., & Bartles, J. R. (2010). Targeting of the hair cell proteins cadherin 23, harmonin, myosin XVa, espin, and prestin in an epithelial cell model. *The Journal of Neuroscience*, 30(21), 7187–7201.
- Zhu, J., Shang, Y., & Zhang, M. (2016). Mechanistic basis of MAGUK-organized complexes in synaptic development and signalling. *Nature Reviews Neuroscience*, 17(4), 209–223.
- Zine, A., & Schweitzer, L. (1997). Localization of proteins associated with the outer hair cell plasma membrane in the gerbil cochlea. *Neuroscience*, 80(4), 1247–1254.

An electronmicroscopic study of microtubules in the development of marginal cells of the mouse stria vascularis *

J. Santos-Sacchi

*Auditory Physiology Laboratory, Frances Searle Bldg., Northwestern University, 2299 Sheridan Rd.,
Evanston, IL 60201, U.S.A.*

(Received 22 January 1981; accepted 26 June 1981)

This study provides an ultrastructural evaluation of cytoplasmic microtubules during the maturation of marginal cells of the mouse stria vascularis. Postnatal marginal cells are cuboidal in structure and over a period of days develop the numerous cellular processes typical of transporting epithelia. Immediately after birth, marginal cells contain numerous microtubules randomly oriented throughout the cytoplasm. Golgi bodies and vesicles are also abundant. The initiation of cellular extension is characterized by the presence of sheet-like extensions of plasma membrane about areas of the cell periphery. Subsequently, large organelle-containing processes form, whose plasmalemma appear pleated due to the presence of the above mentioned sheet-like extensions. Typically, these processes contain microtubules oriented parallel to the direction of their extension. Within these processes, microtubules are closely associated with organelles, such as mitochondria, and may function to displace and stratify these organelles within the processes. The number and length of microtubules increase as the processes grow larger. In the adult mouse, the stria marginal cell processes are attenuated and contain almost exclusively microtubules and mitochondria. The membrane pleats unfold, apparently to provide plasma membrane for cellular extension. The data strongly implicate microtubules in stria development. Furthermore, it is suggested that the depolymerization of microtubules in the adult may underlie stria atrophy.

Key words: stria marginal cells; microtubules; development.

Introduction

Cell surface folding is the single common anatomic feature of transporting epithelia [1]. Such folding greatly expands the cell membrane surface area, thereby providing an enhanced ability for membrane transport. The stria vascularis displays numerous interdigitations among its cell components [7,15]. The establishment of this adult stria architecture is prerequisite for the development of the endolymph's ionic composition and electrical potential and, in turn, for normal cochlear function [2,5,8]. Kikuchi and Hilding [9] have shown that the adult stria evolves from a single

* Portions of this work were completed at Mt. Sinai School of Medicine, Department of Anatomy and Otolaryngology, and School for Biomedical Education, City College, City University of New York.

layer of cuboidal marginal cells separated from underlying fibroblasts by a basement membrane. After varying periods of time, depending upon the position along the length of the cochlear duct, the numerous interdigitations characteristic of the adult stria are formed. However, the basement membrane is absent from beneath the marginal cells. The fully differentiated form of the stria vascularis is dependent upon a process of cellular extension.

Recently, Santos-Sacchi [13] noted the abundance of microtubules within the cytoplasm of adult mouse marginal cells and suggested a possible role for microtubules in strial maturation. Microtubules have been shown to be involved in cell shape development. For example, Heywood et al. [6] provided morphologic evidence that microtubules influence cell shape during *in vitro* development of vestibular hair cells. The present study offers a morphologic evaluation of marginal cell cytoplasmic microtubules during the development of strial architecture.

Methods

The preservation of microtubules necessitates the use of aldehyde fixatives; unfortunately, glutaraldehyde fixation of strial tissue induces artifacts such as mitochondrial vacuolation [10,14].

Mice (Balb/cJ) at varying stages from newborn (0, 2, 4, 6, 8, 10 days postnatal) to adult were decapitated, the cochleae dissected out, fractured open and immersed in either 2% or 6% glutaraldehyde buffered with cacodylate (0.1 M), pH 7.4, at room temperature. After 2 h primary fixation, strial tissue from various cochlear turns was microdissected free and post-fixed in cacodylate-buffered 1% osmium tetroxide, pH 7.4, at 0–4°C for 2 h. Samples were rinsed with buffer, rapidly dehydrated in a graded series of acetone, and embedded in Epon at 60°C overnight. Thick sections were cut and stained with toluidine blue for orientation purposes. Gray-silver sections (50–80 nm) were cut with a diamond knife on an LKB Ultratome, stained with lead citrate, and examined with a Zeiss 9S-2 or Philips 300 electron microscope.

Results

Although the onset of marginal cell development proceeds from base to apex over an extended period of time [9], the cellular mechanisms involved are the same regardless of location along the cochlear duct. Areas of transition between developing and immature marginal cells along the duct were chosen for study. As such, marginal cells are characterized by the degree of maturation and not by their location along the duct or by the age of the particular animal.

Prior to the evolution of adult strial structure, marginal cells can be distinguished within the cochlear duct by virtue of their dark cytoplasm. Whereas future intermediate and basal cells generally contain few organelles at this time, marginal cells possess numerous structural elements. Particularly prominent are the Golgi bodies (Fig 1). Microtubules are present in immature cuboidal marginal cells at birth. They

are randomly distributed within the cytoplasm (Fig. 1). This random orientation is preserved in the apical cytoplasm through adulthood, although occasionally microtubules are found perpendicular to the apical plasma membrane in the adult [13].

The initiation of marginal cell development is characterized by the production of small cellular extensions, about 60 nm in width, within which microfilaments may sometimes be distinguished. These extensions occur laterally as well as basally (Figs. 2, 3). Serial sectioning demonstrates that they are sheet-like. Subsequently, large organelle-containing cell processes extend basally (Figs. 2, 3). The plasmalemma of these large processes often appears pleated due to the presence of the smaller sheet-like extensions which decorate the perimeter of the large processes (Fig. 3). Within the processes microtubules are invariably found, frequently oriented parallel to the longitudinal axes of the processes. As the processes increase in size, the number and length of microtubules increase. In fact, microtubules can often be observed coursing for several micrometers within developing cell elongations.

The basement membrane which is present between the cuboidal marginal cells

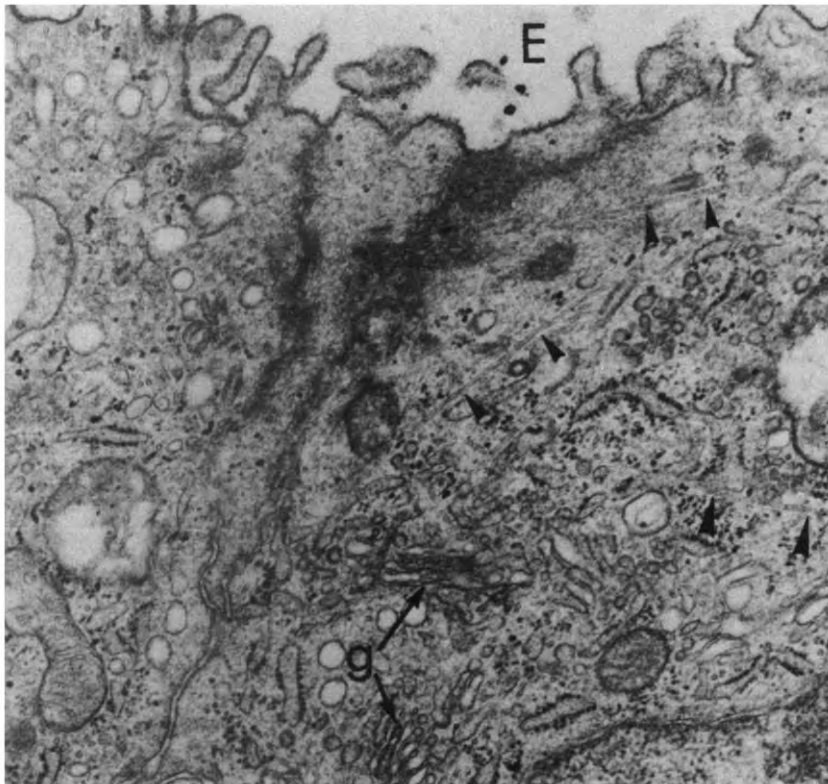


Fig. 1. Cytoplasm of immature marginal cells displaying numerous Golgi bodies (g), vesicles and endoplasmic reticulum. Arrows indicate randomly oriented microtubules. E, endolymphatic space. $\times 20000$.

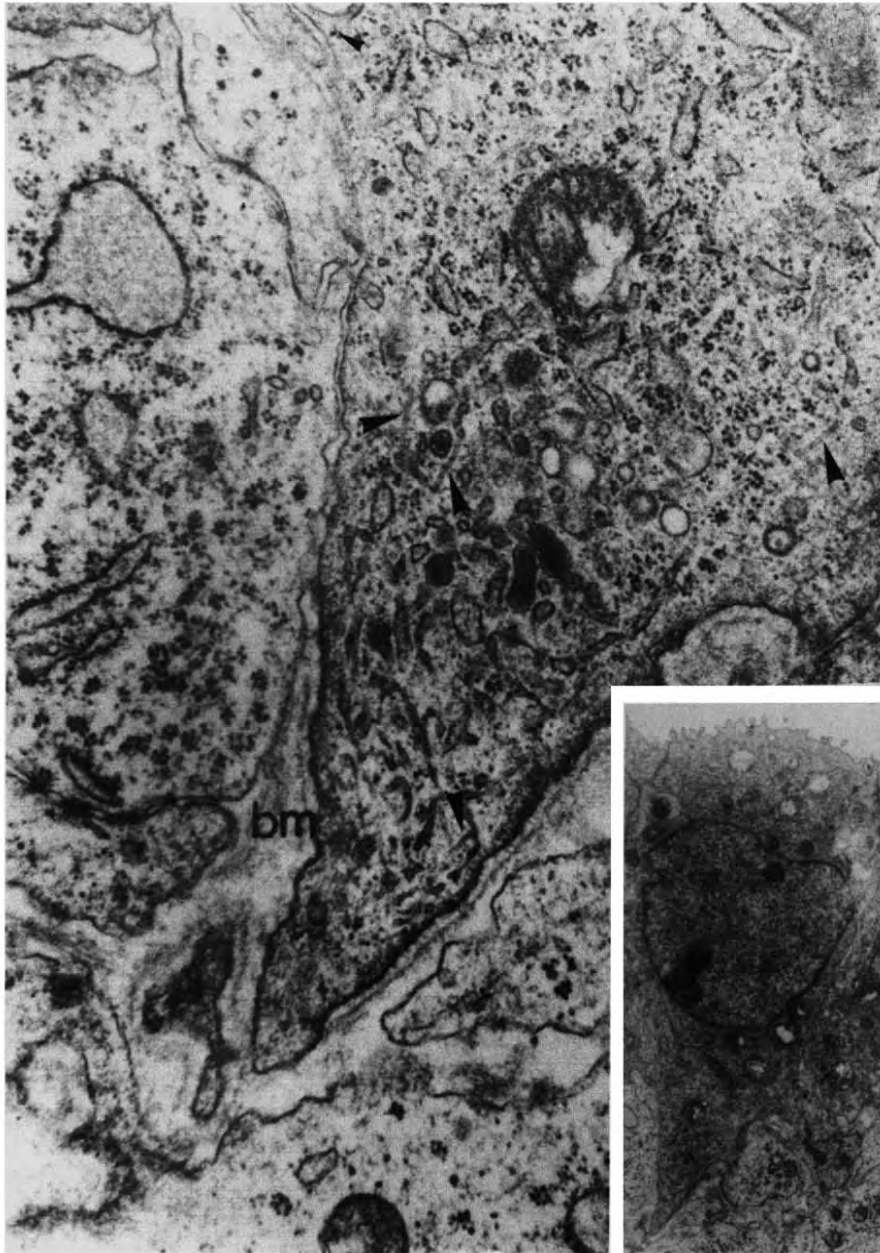


Fig. 2. Early developing cell process of marginal cell. Large arrows indicate microtubules. Small arrow indicates lateral sheet-like extension. bm, basement membrane. $\times 32,000$. Insert: Low-power electron-micrograph of same marginal cell. $\times 4,200$.

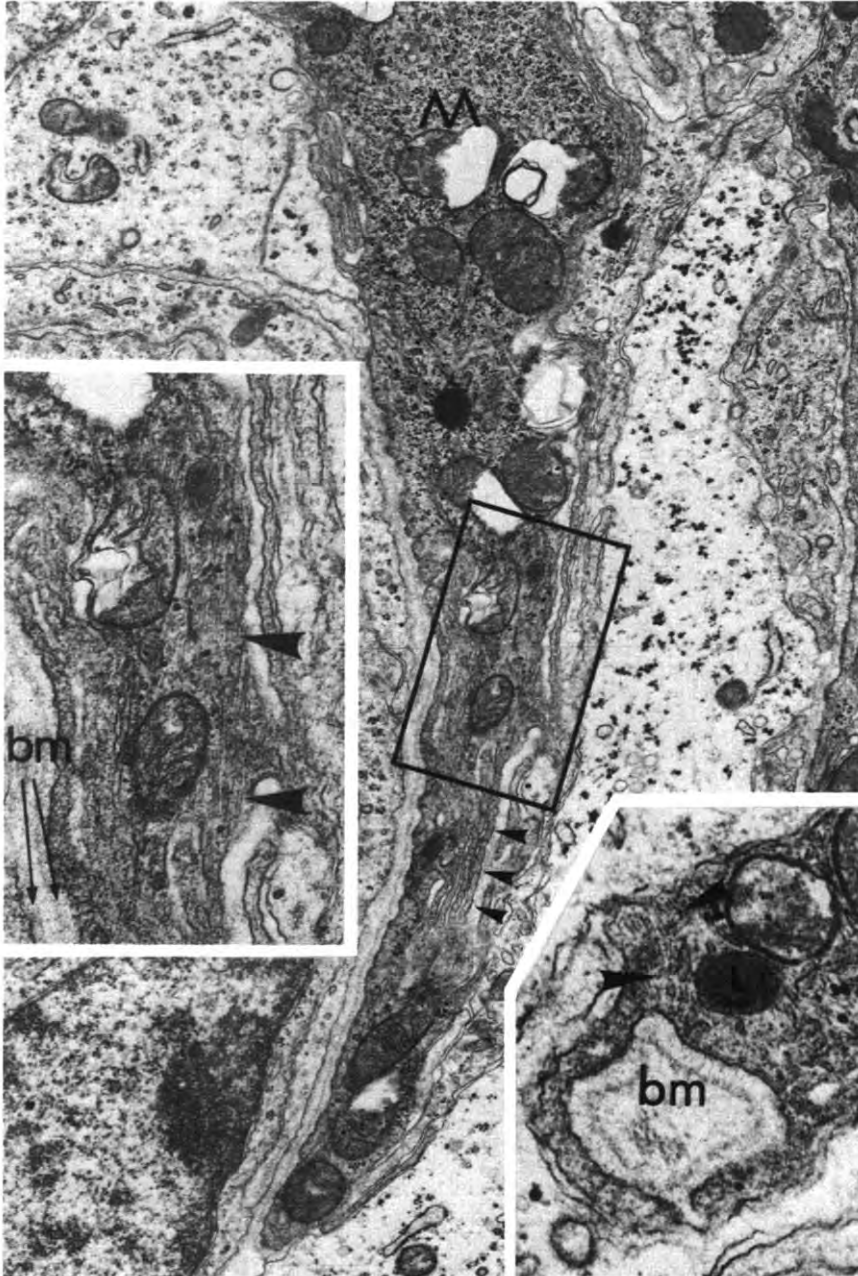


Fig. 3. Cell process (M) of maturing marginal cell abutting strial capillary. Small arrows indicate plicating of plasmalemma of large process by small sheet-like extensions. Insert at left: enlargement of boxed-in area. Note longitudinally oriented microtubules (arrows) and double basement membrane (bm) adjacent to capillary. Insert at lower right shows tip of a different maturing marginal cell process engulfing basement membrane. Note microtubules and lysosome (L). $\times 17000$. Left insert: $\times 34000$. Right insert: $\times 40000$.

and deeper cell layers of the immature stria disappears during maturation. Initially, the basement membrane extends with the developing marginal cell processes (Figs. 2, 3), and occasionally it can be observed within marginal cell invaginations, as if being phagocytized (Fig. 3, insert lower right). Despite this, the absence of a basement membrane in the adult is probably largely due to dispersion and thinning of this structure as a result of the expansive increase of plasma membrane surface area.

Discussion

Numerous researchers have presented evidence that microtubules are important for cellular elongation [3,12]. In addition, microtubules have been implicated in the process of organelle displacement. For example, Raine et al. [11] reported close lateral associations between mitochondria and microtubules within mammalian axons and suggested that microtubules may provide a mechanism for mitochondrial displacement. The close proximity of microtubules to organelles, especially mitochondria, in marginal cell processes may be indicative of such a function. Indeed, such associations apparently promote the stratification of mitochondria within the cell processes, thereby providing the spatial arrangement of energy production sites requisite for fluid transport.

The dramatic increase in cell surface area which accompanies cellular extension necessitates the manufacture and incorporation of new plasma membrane. Accordingly, immature cuboidal marginal cells often contain large amounts of smooth endoplasmic reticulum, Golgi bodies, and vesicles. It is interesting to note that in the adult mouse the typical marginal cell process is extremely attenuated, contains almost exclusively mitochondria and microtubules, and the membrane pleats characteristic of immature cell processes are largely absent [13]. Apparently, as processes extend, membrane pleats unfold. In addition, the number of apical microvilli is drastically reduced in the adult marginal cell, and this process may provide another source of plasma membrane for the rapidly expanding cell surface.

The data presented here indicate an important role for microtubules in strial development. Microtubular integrity may also be required for the morphologic stability of the adult stria. It is known that disruption of microtubules by anti-tubulins can induce the retraction of cell processes [16]. The strial atrophy induced by a number of experimental manipulations, including intermixing of endolymph and perilymph [4] may be related to microtubule effects. Although microtubules have not been studied under such circumstances, electron micrographs of atrophied striae show extensive loss of cellular processes. The study of microtubular integrity under conditions of advancing strial atrophy is certainly warranted.

References

- [1] Berridge, M.J. and Ochman, J.L. (1972): *Transporting Epithelia*. Academic Press, New York.
- [2] Boshier, S. and Warren, R. (1971): *A study of electrochemistry and osmotic relationships of the*

- cochlear fluids in the neonatal rat at the time of development of the endocochlear potential. *J. Physiol. (London)* 212, 739–761.
- [3] Byers, B. and Porter, K.R. (1964): Oriented microtubules in elongating cells of the developing lens rudiment after induction. *Proc. Natl. Acad. Sci. U.S.A.* 52, 1091–1099.
 - [4] Duvall, A.J. (1968): Ultrastructure of the lateral cochlear wall following intermixing of fluids. *Ann. Otol.* 77, 317–331.
 - [5] Fernandez, C. and Hinojosa, R. (1974): Postnatal development of the endocochlear potential and stria vascularis in the cat. *Acta Otolaryngol.* 78, 173–186.
 - [6] Heywood, P., Van De Water, T.R., Hilding, D.A. and Ruben, R.J. (1975): Distribution of microtubules and microfilaments in developing vestibular sensory epithelium of mouse otocysts grown in vitro. *J. Cell Sci.* 17, 171–179.
 - [7] Hinojosa, R. and Rodriguez-Echandia, E.L. (1966): The fine structure of the stria vascularis of the cat inner ear. *Am. J. Anat.* 118, 631–664.
 - [8] Honrubia, V. and Ward, P. (1969): Dependence of the cochlear microphonic and summing potential on the endocochlear potential. *J. Acoust. Soc. Am.* 46, 388–392.
 - [9] Kikuchi, K. and Hilding, D. (1966): The development of the stria vascularis in the mouse. *Acta Otolaryngol.* 62, 277–291.
 - [10] Merck, W., Sparwald, E. and Curten, I. (1974): Über den Einfluss verschiedener Fixationsmethoden und Fixationsmittel auf die electronenmikroskopische Struktur der Stria vascularis, Prominentia spiralis und des Ligamentum spirale beim Meerschweinchen. *Arch. Oto-Rhino-Laryngol.* 206, 299–310.
 - [11] Raine, C., Ghetti, B. and Shelanski, M. (1971): On the association between microtubules and mitochondria within axons. *Brain Res.* 34, 389–393.
 - [12] Reiser, G., Lautenshlager, E. and Hamprecht, B. (1975): Effects of colcemid and lithium ions on the processes of cultured cells derived from the nervous system. In: *Microtubules and Microtubule Inhibitors*, pp. 259–268. Editors: M. Borgers and M. De Brabander. North-Holland Publishing Co., Amsterdam.
 - [13] Santos-Sacchi, J. (1978): Cytoplasmic microtubules in strial marginal cells. *Arch. Oto-Rhino-Laryngol.* 218, 297–300.
 - [14] Santos-Sacchi, J. (1978): Differential effects of primary fixation with glutaraldehyde and osmium upon the membranous systems of the strial and external sulcus cells. *Acta Otolaryngol.* 86, 56–63.
 - [15] Smith, C. (1957): Structure of the stria vascularis and spiral prominence. *Ann. Otol. Rhinol. Laryngol.* 66, 521–537.
 - [16] Tilney, L.G. (1968): The effect of colchicine on the formation and maintenance of the axodopia and redevelopment of pattern in *Actinosphaerium nucleofilum*. *J. Cell Sci.* 3, 549–562.

HRR 00492

Short Communication

A re-evaluation of cell coupling in the organ of Corti

J. Santos-Sacchi *

Laboratory of Neurobiology and Department of Anatomy, University of Puerto Rico Medical School, Rio Piedras, PR 00931, U.S.A.

(Received 17 January 1984; accepted 8 March 1984)

Intercellular electrical coupling was assessed in an in vitro organ of Corti preparation using separate electrodes to inject current and record voltage drops in Hensen's cells. The results demonstrate much better coupling among these supporting cells than previously thought. Coupling ratios between adjacent Hensen's cells are greater than 0.6.

electrical coupling, organ of Corti, gap junction

All the supporting cells of the organ of Corti are structurally joined to each other by communicating or gap junctions [2,3,4]. Recently, Santos-Sacchi and Dallos [5], demonstrated that these junctions permit the passage of electrical currents between Hensen's cells. In that study, the degree of electrical coupling between cells was difficult to assess accurately since a single electrode-bridge balance system was used to inject current and record voltage simultaneously. The coupling ratio is defined as the voltage drop in one cell (V_2) divided by the voltage drop due to current injections in a neighboring cell (V_1). Thus, if an inaccurate measure of the voltage drop, V_1 , is obtained due to bridge unbalancing as a result of electrode resistance change, the degree of coupling between cells is misjudged. A decrease of the electrode resistance occurring upon entry into a cell will produce overestimates of coupling ratios; an increase in resistance will produce underestimates. There is evidence that electrode resistance increases intracellularly [6]. This possibility led us to speculate from indirect measures (spatial spread of current studies) that the coupling between supporting cells was greater than that suggested by the

data (see footnote in [5]). This report corroborates that initial speculation.

Cochleas were removed after decapitation of anesthetized guinea pigs. The apical and third turns of the cochlea, lateral wall removed, were placed in one piece into a microscope perfusion chamber. The organ was perfused at a rate of 0.8 ml/min with artificial perilymph, bubbled with O_2 (tissue culture medium M199 with Hank's salts (1.26 mM $CaCl_2$, 1.7 μM $Fe(NO_3)_3$, 5.36 mM KCl, 0.44 mM KH_2PO_4 , 0.81 mM $MgSO_4$, 137 mM NaCl, 4.16 mM $NaHCO_3$, 0.33 mM Na_2HPO_4), pH 7.2, Gibco, Grand Island, N.Y.) and the temperature was maintained near 37°C. Membrane potentials and coupling responses were measured with high-input impedance devices using KCl (3 M) electrodes. Coupling measures were performed by injecting current pulses into one cell through one barrel of a double-barreled electrode, while measuring voltage drops in that same cell with the other barrel and in a neighboring cell with a single electrode.

Immediately after dissection, membrane potentials of the Hensen's cells are low (ca. -20 mV); however, over the next 2–3 h the potentials gradually recover and reach levels which are recorded in vivo (-60 to -80 mV [1,5]). Cell-to-cell coupling occurs throughout this recovery period. Fig. 1 demonstrates electrical coupling between two adjacent Hensen's cells, both with good membrane

* Present address: Dept. of Surgery, Section of Otolaryngology, New Jersey Medical School, Medical Sciences Building H586, 100 Bergen St., Newark, NJ 07103, U.S.A.

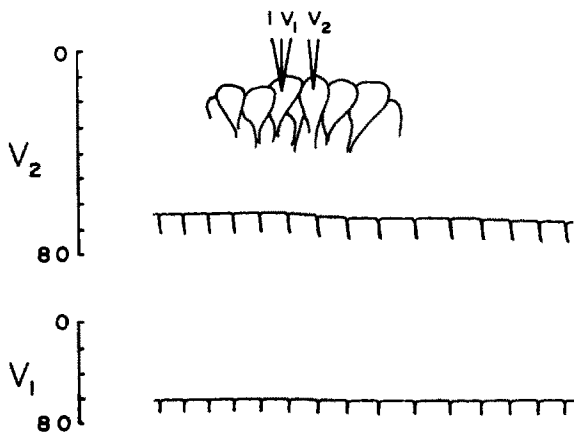


Fig. 1. Under visual control, adjacent Hensen's cells were impaled with 3 M KCl glass microelectrodes. Constant current pulses (-11 nA, 0.5 s) were delivered every 5 s through one barrel of the double-barreled microelectrode. Voltage drops in that same cell and the adjacent cell were measured with voltage recording electrodes. The coupling ratio (V_2/V_1) for this preparation was 0.77 . The organ had been in culture for 2 h when the measure was taken.

potentials. The coupling ratio in this case is 0.77 . Although coupling can be variable, it is usually greater than 0.6 for adjacent cells (5 animals) and is much greater than the estimates previously obtained with the single electrode technique [5]. Input resistance of Hensen's cells in this in vitro preparation is $1-3$ M Ω , one order of magnitude less than previous measures using the single electrode technique.

These results clearly show that electrical coupling among the supporting cells of the organ of Corti is much better than previously thought. It is not clear, however, whether these results are indicative of the in vivo situation. Considering the harsh treatment to the organ necessitated by the in vitro setup, if a difference in coupling did exist, one might expect coupling to be poorer in vitro than in vivo (M.V.L. Bennett, pers. commun.). The fact that membrane potentials are similar in both preparations lends credence to the notion that coupling is also similar. Nevertheless, other factors (e.g. EP, endolymph-perilymph compartmentalization) may be influential in affecting in vivo coupling. In vivo re-evaluations are planned.

The fact that coupling (and space constant) is now known to be substantial provides impetus to

re-evaluate the absence of dye coupling previously reported [5]. It had been suggested then that dye coupling might exist, but that because of slow transfer between cells and dilution within the cytoplasm the dye was impossible to visualize with the experimental setup available. Image enhancement techniques may be necessary to fully evaluate this issue.

The role that such electrical communication may play in an organ whose electrical activity is of paramount functional importance remains unclear. There can be no doubt, however, that supporting cells play a crucial role in inner ear function – perhaps even in sensory transduction. That is, it is inconceivable that the supporting cells do not influence cochlear micromechanics. Supporting cells, as do hair cells, contain contractile and structural proteins [7], which may be modified by ionic conditions. Substantial electrical/ionic communication might provide a means to effectively influence organ of Corti structure and function.

Acknowledgement

This work was supported by the Deafness Research Foundation and PHS grants NS 20221-01 and NS 07464.

References

- 1 Dallos, P., Santos-Sacchi, J. and Flock, Å. (1982): Intracellular recordings from outer hair cells. *Science* **218**, 582–584.
- 2 Gulley, R.S. and Reese, T.S. (1976): Intercellular junctions in the reticular lamina of the organ of Corti. *J. Neurocytol.* **5**, 479–507.
- 3 Iurato, S., Franke, K., Luciano, L., Werbter, G., Pannese, E. and Reale, E. (1976): Intercellular junctions in the organ of Corti as revealed by freeze fracturing. *Acta Otolaryngol.* **82**, 57–69.
- 4 Jahnke, K. (1975): The fine structure of freeze-fractured intercellular junctions in the guinea pig inner ear. *Acta Otolaryngol. Suppl.* **336**.
- 5 Santos-Sacchi, J. and Dallos, P. (1983): Intercellular communication in the supporting cells of the organ of Corti. *Hearing Res.* **9**, 317–326.
- 6 Schanne, O., Kawata, H., Schafer, B. and Lavalley, M. (1966): A study on the electrical resistance of the frog sartorius muscle. *J. Gen. Physiol.* **49**, 897–912.
- 7 Slepecky, N. and Chamberlain, S.C. (1983): Distribution and polarity of actin in inner ear supporting cells. *Hearing Res.* **10**, 359–370.

HRR 00639

The effects of cytoplasmic acidification upon electrical coupling in the organ of Corti

J. Santos-Sacchi

Department of Surgery, Section of Otolaryngology, MSB 11518, UMDNJ – New Jersey Medical School, Newark, NJ 07103, U.S.A.

(Received 18 February 1985; accepted 8 July 1985)

The supporting cells of the organ of Corti are joined to one another by gap junctions, and electrical coupling among them is known to be good. It is demonstrated here, using an in vitro preparation, that electrical communication between Hensen's cells can be modified by treatments which are known to cause cytoplasmic acidification. Treatment of the preparation with 100% CO₂-saturated medium causes a drop in membrane potential, increase in input resistance, and decrease in steady-state coupling ratio. These measures return to pretreatment levels upon washout of the CO₂ medium. Also, direct injection of H⁺ into a Hensen's cell uncouples that cell from the supporting cell network. An increase in coupling ratio is sometimes observed immediately before and after uncoupling due to CO₂ treatment. In fact, in some cases it is possible to solely increase coupling ratios with limited CO₂ treatments, although prolonged treatment with CO₂ invariably produces uncoupling. This phenomenon may be due to an increase in cell resistance without a change in junctional conductance. A few possible roles for gap junctions in the inner ear are suggested, and the significance of the present results discussed.

carbon dioxide, organ of Corti, cell coupling, gap junction, pH

Introduction

In the latter part of the last decade various groups demonstrated by electronmicroscopy the presence of gap junctions between all the supporting cells of the mammalian organ of Corti [13,17,18]. These results suggested that the supporting cells form a functional syncytium interconnected via low-resistance pathways. This concept was recently confirmed by studies which demonstrated electrical coupling in the supporting cells both in vivo and in vitro [24,25,26]. The supporting cells of the organ of Corti supply physical support for the receptor cells (inner and outer hair cells); and although current concepts of cochlear function rest heavily upon micromechanical interactions between receptor cells [20,35], it is difficult to ignore a possible influence of supporting cells on cochlear micromechanics. In addition, because of the avascular nature of the organ proper, metabolic cooperation between supporting cells may be important in meeting the metabolic de-

mands of the organ of Corti.

Cell-to-cell communication can be modulated experimentally by treatments (e.g. CO₂ treatment) which alter intracellular hydrogen ion activity [31,33]. For example, Turin and Warner [37,38] have shown that cytoplasmic acidification of coupled *Xenopus* blastomeres produces a reversible electrical uncoupling. Subsequently, uncoupling (electrical or dye) due to cytoplasmic acidification has been demonstrated in many cell types [6,7,12,19,22,27].

The pH of the cochlear fluids is near 7.2–7.4 [34], and may be influenced by the very high carbonic anhydrase activity of the inner ear [10]. The pH of the endolymph can be markedly reduced within minutes after the onset of anoxia [4]. Because of the possible importance of hydrogen ion control in the normal and pathologic functioning of the inner ear, the present studies were designed to evaluate the effects of cytoplasmic acidification upon electrical coupling in an in vitro preparation of the organ of Corti.

Methods

Guinea pigs were anesthetized with pentobarbital and killed by decapitation. The cochleas were quickly removed, and the apical and third turn in one piece was microdissected free after removing the spiral ligament and stria vascularis. The preparation was transferred to a perfusion chamber on a Nikon Diaphot inverted microscope. Alternately, the whole temporal bone was placed in a perfusion chamber on a Zeiss ACM microscope, and the bony capsule around the two most apical turns chipped away. The stria vascularis and spiral ligament were removed. In some instances membrane potentials of the Hensen's cells were measured before and after the removal of the stria vascularis and spiral ligament. Both chambers were maintained near 37°C with Peltier devices (Bailey Instruments, NJ). Medium 199 (with Hanks' salts (1.26 mM CaCl₂, 1.7 μM Fe(NO₃)₃, 5.36 mM KCl, 0.44 mM KH₂PO₄, 0.81 mM MgSO₄, 137 mM NaCl, 4.16 mM NaHCO₃, 0.33 mM Na₂HPO₄; for HEPES-buffered media (25 mM) and high K⁺ media, NaCl was adjusted to maintain tonicity), pH 7.2–7.4, Gibco, NY; in some experiments gassed with 100% oxygen) was perfused at a rate of 0.8–1.5 ml/min. Electrodes were pulled on a Narishige puller.

Coupling measurements were made with high input impedance devices (WPI KS-700, Dagan 8100-1) capable of constant current injection. Coupling was assessed by injecting negative current pulses of varying magnitudes into one cell and noting the voltage drop in the same and an adjacent cell. Under visual control, Hensen's cells were impaled with electrodes; four electrode techniques were used to record from Hensen's cells. (1) Single-barreled electrodes were inserted into adjacent or neighboring cells. Using bridge balance techniques, the voltage drops in the two cells (V_1 , V_2) were measured in response to current injection in one (I_1). Alternately, a sampling technique using the switched current clamp mode of the Dagan 8100-1 was used to obtain the voltage drop in the current injected cell (V_1). Using this sampling technique, measurement of V_1 was obtained without contamination from electrode voltage drop. (2) Double-barreled electrodes or theta glass electrodes were used to separately inject current

(I_1) and record voltage drops (V_1) in one cell, while a neighboring cell was impaled with a single-barreled voltage recording electrode (V_2). (3) Patch-type electrodes (140 mM KCl, 2 mM MgCl₂, 5 mM EGTA, 10 mM HEPES, pH 7.2) were used to suck into adjacent Hensen's cells. These electrodes permit the rapid exchange of electrode fluids within the cell interior. The switched current clamp was used in these cases. (4) Three separate electrodes were used: one for current injection (I) in one cell, one for voltage recording (V_1) in a cell nearby, and another for voltage recording in a cell more distal (V_2).

Coupling responses, membrane potentials, and current magnitude were recorded on a Gould four channel recorder. In some experiments extracellular pH was measured and recorded as well. Current pulses were generated by an A/D converter controlled by an IBM PC/XT. Coupling ratios were either determined offline, by visual inspection of the records, or online using a Data 6000 waveform analyzer (Data Precision, MA) in conjunction with the IBM. Individual coupling responses were digitally stored within the Data 6000 and saved to disk.

Coupling ratio is defined as the voltage drop in cell 2 divided by the voltage drop in cell 1 in response to current injection in cell 1 (V_2/V_1) [2]*. CO₂ effects were evaluated by measuring the changes in steady state coupling after introducing various amounts of 100% CO₂-saturated medium into the perfusion system, followed by a return to normal medium. Control perfusions of media buffered to low pH levels were performed to evaluate the effects of extracellular acidification. HCl- (0.1M) filled electrodes were used to evaluate the effects of intracellular ionophoretic injection of hydrogen ions. High K⁺ solutions (70 mM) were perfused through the cell chamber in order to evaluate the effects of depolarization on coupling.

* In a two cell system, coupling ratio is determined by $R_{m2}/(R_j + R_{m2})$, where R_{m2} is the membrane resistance of cell 2 and R_j is the junctional resistance between cells 1 and 2. Thus, changes in coupling ratio may occur due to changes in membrane and/or junctional resistance. Whereas it is possible to calculate membrane resistance and junctional conductance in a two cell system, from experimentally determined input and transfer resistances, it is not possible to do the same for a cellular syncytium (see [2]).

Results

Electrical coupling in the supporting cells of the organ of Corti, utilizing Hensen's cells as a model, is very good. Frequently, coupling ratios greater than 0.8 are found between adjacent Hensen's cells (Fig. 1). It was previously reported that the membrane potentials of Hensen's cells in vitro (-63 ± 10 mV; $n = 111$; [26]) are very close to those obtained in vivo when in vitro recordings are made by passing electrodes through Reissner's membrane in the intact cochlear duct. After removal of the stria vascularis and spiral ligament, however, membrane potentials are dramatically reduced, but subsequently recover during the next few hours of incubation. For example, in a series of 9 preparations the membrane potential was -32 ± 10.9 mV ($n = 27$) at the beginning of the experiment, and within a few hours the membrane potential recovered to -58.96 ± 8.99 mV. Despite low membrane potentials at the outset, coupling is present.

Treatment with CO₂-saturated medium disrupts electrical communication between Hensen's cells. Fig. 2a demonstrates the effects of a 45 s bolus of

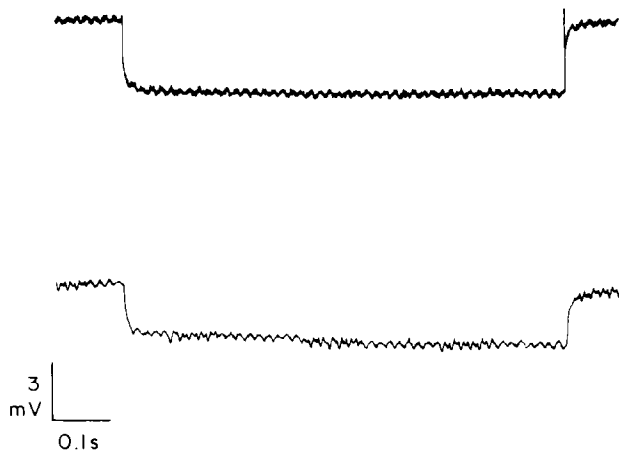


Fig. 1. Neighboring Hensen's cells, separated by one intervening cell, were impaled with electrodes. The traces were digitally stored and plotted. The top trace is of a cell with a membrane potential of -62 mV into which a 0.8 s current pulse of -10 nA was injected through one barrel of a theta glass electrode. The resulting voltage drop measured through the other barrel indicates an input resistance of 0.7 M Ω . The membrane potential of the neighboring cell depicted in the bottom trace is -60 mV and the coupling response measured indicates a coupling ratio of about 0.8.

CO₂-saturated medium injected into the perfusion system. Coupling ratio in this example is initially greater than 0.6. When the CO₂ medium enters the cell chamber, indicated by the drop in extracellular pH, several changes in steady-state conditions are noted. Initially, cell membrane potentials depolarize, in this case 25–30 mV, relative to resting potentials. The voltage drop due to -5 nA current pulses in cell 1 indicates that cell input resistance increases, and concurrently, electrical communication between the two cells decreases, as indicated by the coupling ratio. As the extracellular CO₂ is washed away, and presumably intracellular pH returns to normal, membrane potentials, input resistance and coupling ratio return to pretreatment levels. This uncoupling procedure is repeatable upon further exposures to CO₂-saturated medium. Fig. 2b presents individual coupling responses during a similar uncoupling event. The top two traces show the voltage drops in cell 1 and 2 in response to a -10 nA pulse in cell 1. The coupling ratio is 0.66. The bottom measures were taken at the maximum point of uncoupling after a 40 s bolus of CO₂ medium. The coupling ratio at this point is 0.22. Equivalent perfusions of the organ with low pH-buffered media produced neither depolarizations nor uncoupling, although in one case of prolonged exposure a slight increase in coupling ratio occurred.

Direct acidification of Hensen's cell cytoplasm can be accomplished by intracellular ionophoretic injection of H⁺ ions. Injection into one cell of a neighboring pair uncouples only the injected cell; other neighboring cells in the tissue network remain coupled. Fig. 3 demonstrates the uncoupling effect of H⁺ injection. It can be seen that in response to injection of H⁺ the coupling response in the adjacent cell decreases, followed by recovery. Associated with the increase in intracellular hydrogen ion activity is a drop in membrane potential. On many occasions injection of H⁺ caused complete irreversible uncoupling, associated with lasting depolarization of the injected cell. Suction into Hensen's cells with patch pipets containing acidic solutions also demonstrated a drop in coupling associated with depolarization.

Fig. 4 again shows uncoupling, accompanied by membrane depolarization and increased input resistance following treatment with CO₂-saturated

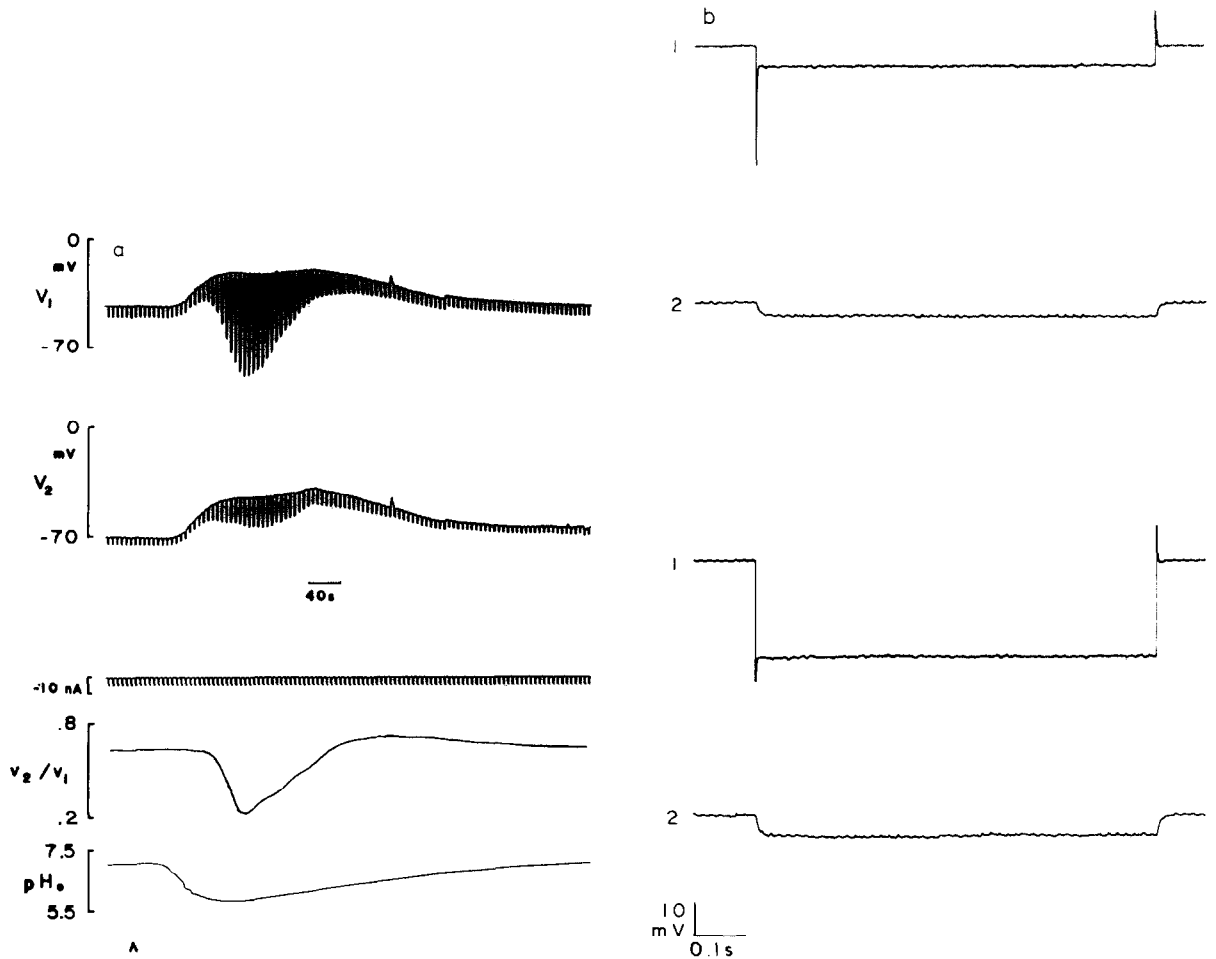


Fig. 2. (a) Impaled Hensen's cells are separated by two intervening cells in this case. A double-barreled electrode was used in cell 1. Steady-state coupling ratio is about 0.64. The arrow indicates the end of a 45 s injection of CO_2 -saturated medium into the perfusion system, whereupon perfusion of normal medium is reinstated. The CO_2 medium reaches the chamber at the time indicated by the drop in extracellular pH (bottom trace). Associated with the CO_2 treatment is a drop in the membrane potentials, an increase in input resistance, and a decrease in coupling ratio. Upon washout of the CO_2 medium, these measures return to pretreatment levels. (b) Conditions were the same in (a); however, individual coupling responses were digitally stored during steady-state coupling (top two traces, cell 1 and cell 2; coupling ratio 0.66) and during maximum uncoupling (bottom two traces; coupling ratio 0.22) in response to a 40 s treatment with CO_2 medium. Capacitive coupling of the double-barreled glass is apparent.

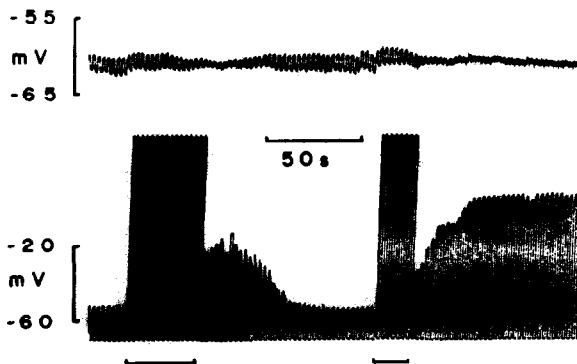


Fig. 3. Neighboring Hensen's cells were impaled with single-barreled electrodes, one containing 0.1 M HCl and the other 3 M KCl. Constant current pulses of -10 nA were injected into one cell through the HCl electrode (bottom trace) and the coupling response in the other cell was recorded (top trace). It was impossible to balance out the voltage drop in the high resistance HCl electrode. At the first bar indicator, a positive steady current of 3.1 nA was superimposed on the pulsed negative current in order to eject H^+ from the electrode into the cell. Consequently, the coupling response decreased (top trace) along with the membrane potential of the injected cell (bottom trace). Both measures recovered, whereupon another positive current injection produced irreversible uncoupling and depolarization in the injected cell.

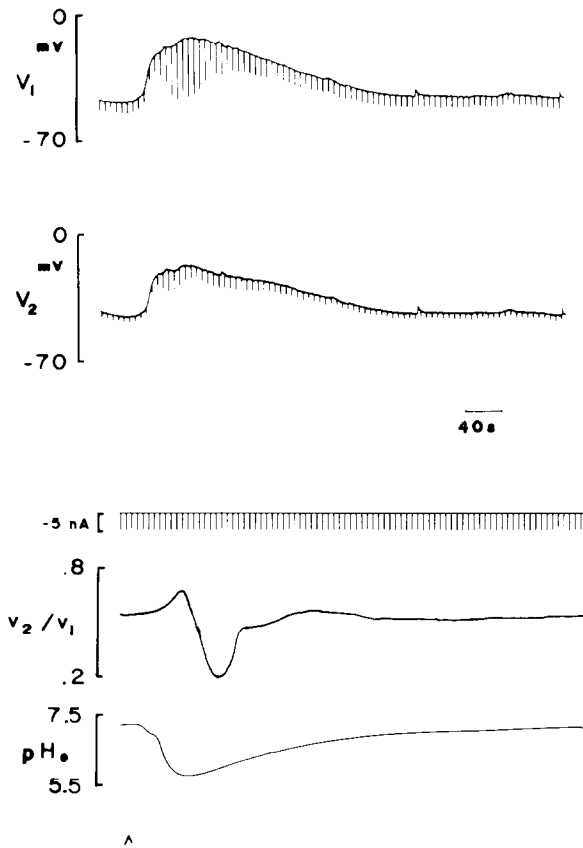


Fig. 4. Adjacent Hensen's cells were impaled with single-barreled electrodes. Current was injected into the cell depicted in the top trace by means of the switched current clamp mode of the Dagan 8100-1. The first arrow indicates the end of a 30 s injection of CO_2 -saturated medium into the perfusion system. An increase in coupling ratio can be observed prior to the uncoupling effects of intracellular acidification. After washout of the CO_2 medium, measures return to steady state.

medium. In this instance, however, there is a transient increase in coupling ratio preceding the drop in coupling ratio. After return to normal medium there is recovery of the cells. Preliminary experiments indicate that high potassium medium causes the membrane potentials to depolarize, and the input resistance to decrease slightly. There is no dramatic uncoupling as occurs with CO_2 treatment.

The increase in coupling ratio noted in Fig. 4 is often seen prior to and sometimes following uncoupling due to CO_2 treatment. It is possible, however, to observe instances where only an in-

crease in coupling ratio occurs in response to CO_2 treatments. Fig. 5 demonstrates this phenomenon. In response to CO_2 treatment, the membrane potentials depolarize, and input resistance increases; however, there is a dramatic increase in coupling ratio from a steady state level of just over 0.6 to nearly 1. The electrical measures return to pretreatment levels following washout of the CO_2 medium. This phenomenon is further demonstrated in Fig. 6 where three separate electrodes are used to gauge current spread through the organ's supporting cells. The ratio of voltage drops between these two Hensen's cells, one more distal than the other to the current injected cell, increases in response to CO_2 treatment. However, it is always possible to inevitably produce uncoupling with prolonged CO_2 treatments.

Discussion

The drop in membrane potentials of the Hensen's cells in response to removal of the lateral wall of the cochlear duct may be accounted for by the presence of gap junctions between the Claudius' cells and the Hensen's cells. The removal of the lateral wall is accomplished by tearing at the interface of these two cell types and consequently the intracellular space of the torn cells is exposed to the extracellular medium. Damage to coupled cardiac muscle fibers also results in a drop in membrane potential of coupled cells [8], and in damaged lens fibers there is a leakage of K^+ ions into the extracellular medium [3]. Over time, as the cytoplasmic faces of the gap junctions in the injured cells close off, the membrane potentials of the undamaged cells recover, and the K^+ leakage subsides. This process is known as healing over.

The supporting cells of the organ of Corti can be reversibly uncoupled by treatments which acidify their cell cytoplasm. H^+ injection directly acidifies the cell interior. CO_2 treatment is known to acidify cytoplasm by crossing the cell membrane and becoming hydrated by the action of carbonic anhydrase. It then dissociates to H^+ and HCO_3^- intracellularly. The process is reversible upon washout of extracellular CO_2 . The extent of cytoplasmic acidification is determined by the amount of H^+ released or injected intracellularly and the cell's buffering capacity. In the present

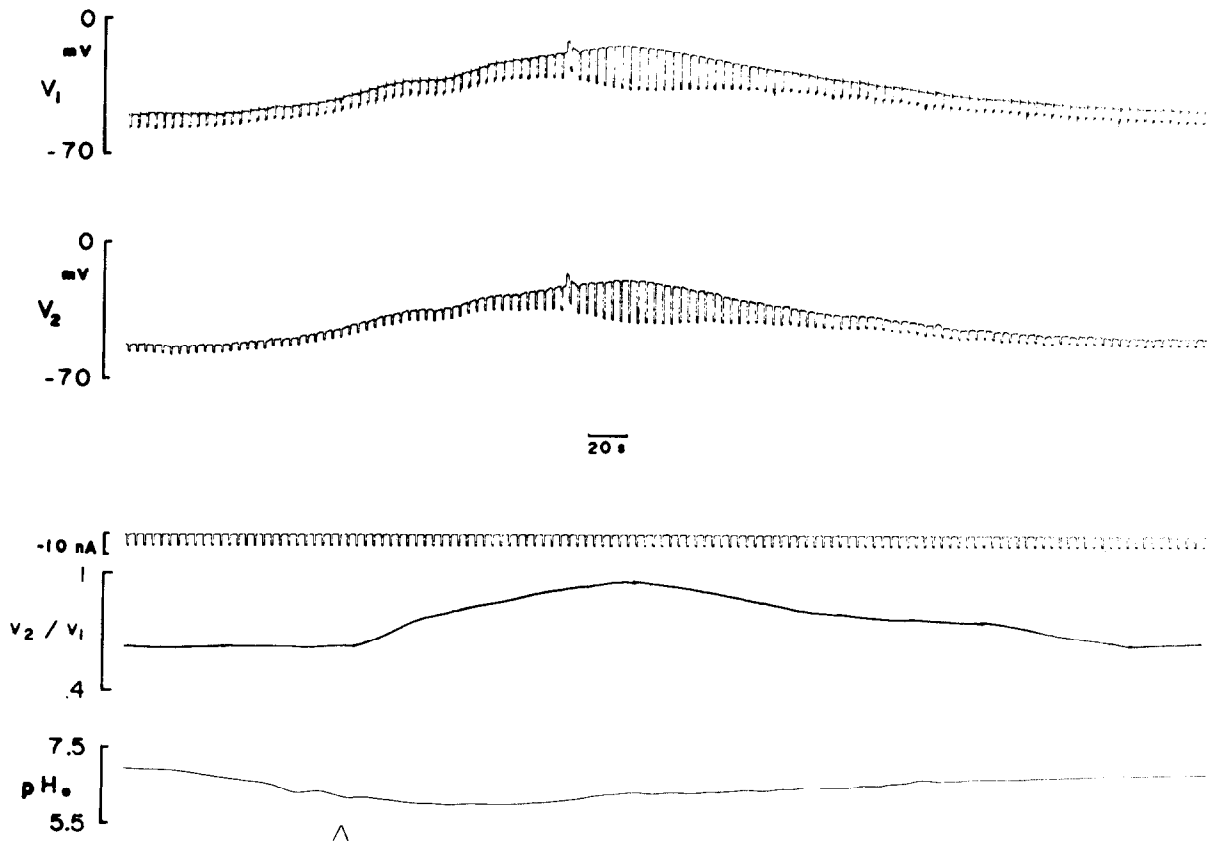


Fig. 5. Adjacent Hensen's cells were impaled, the one depicted in the top trace with a theta glass electrode and the other with a single-barreled electrode. In this case the organ was perfused with HEPES-buffered medium. The arrow indicates the end of a 3 min injection of CO_2 -saturated medium into the perfusion system. Membrane potentials drop but there is a dramatic increase in coupling ratio from about 0.62 to about 0.96. Measures return to pretreatment levels after washout of CO_2 medium.

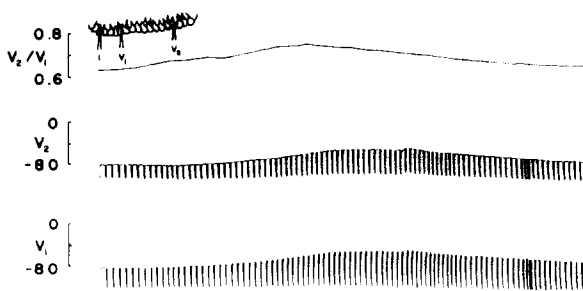


Fig. 6. Three separate Hensen's cells were impaled, one with a current injecting electrode, another with a voltage recording electrode and a more distal one with another voltage recording electrode. The beginning of the traces marks the end of a 25 s injection of CO_2 medium into the perfusion system. Current pulses of -40 nA were delivered about every 2.5 s. The ratio of voltage drops between the two distal cells increases concurrently with membrane depolarization, indicating an increase in the space constant. Measures return to pretreatment levels as the CO_2 medium is washed out.

experiments it is not known to what extent the intracellular pH declined. It is known that the slope of junctional conductance vs. intracellular pH varies among cell types [22,29]. The susceptibility to uncoupling depends upon the steepness of this slope, and the position of the normal resting intracellular pH relative to the pK_H ; thus a similar acidification in two different cell types may have different effects. Intracellular pH measurements are required to determine the precise relationship between coupling and pH in the supporting cells.

Uncoupling of the supporting cells can also be accomplished by intracellular Ca^{2+} injection [23]. There are known to be intracellular interactions between H^+ and Ca^{2+} , such that increases in one ion's activity can increase the activity of the other. However, Spray et al. [33,30], at least in their

model system, have demonstrated a far greater effect of H^+ than Ca^{2+} upon junctional communication. This is still a controversial issue and indeed membrane potential (inside–outside and trans-junctional) may play an important role in the control of junctional conductance [21,32]. Although preliminary studies indicate that membrane potential appears not to play a critical role in cell coupling in the supporting cells *in vitro*, further studies, perhaps using isolated supporting cells and voltage clamp techniques, may be required to fully evaluate the issue. Such studies performed in other cell systems have demonstrated uncoupling due to cytoplasmic acidification under voltage clamp conditions; still there appears to be interactions between membrane potential, H^+ , and Ca^{2+} in the control of junctional conductance [21,32].

The increase in coupling ratio that is occasionally observed upon treatment with CO_2 medium was an unexpected result. It is, however, important because it demonstrates that the intracellular spread of current between supporting cells can be increased under certain conditions. This may have important consequences as discussed below. Three explanations of this phenomenon can be presented. First, it may be possible that the effect is actually due to an increase in junctional conductance caused by an *increase* in intracellular pH. Reber and Weingart [22] have found a decrease in the longitudinal resistance of Purkinje fibers in response to an increase in intracellular pH above resting levels. Perhaps the effect of sub-uncoupling levels of CO_2 primes the supporting cells to enhance their H^+ pumping and buffering capabilities, thus raising intracellular pH. It should be stated, however, that in one preliminary attempt to raise Hensen's cell pH by NH_4Cl treatment, no effects were noted upon supporting cell coupling. This must be investigated further, however. Second, there may be a decrease in the intracellular Ca^{2+} activity due to cell acidification. This has been shown to occur in sheep cardiac Purkinje fibers [15]. A decrease in Ca^{2+} activity might increase junctional conductance. Third, and probably the simplest explanation may be that the membrane resistance of the supporting cells increases without a concomitant decrease in junctional conductance. Such an effect would produce

a greater flow of ions through gap junctions relative to the flow to ground (extracellular medium). Thus the space constant would increase. These possibilities are being evaluated.

Previous studies have suggested that all the supporting cells of the organ of Corti are coupled via gap junctions [13,17,18]. However, it is difficult to quantify the exact distribution of gap junctions by electron microscopy. Light microscopic visualization by the fluorescent antibody (against gap junction protein [14]) technique may provide a more comprehensive demonstration of gap junction distribution in the organ of Corti. Still, the demonstration of gap junctions cannot provide information as to the extent of electrical coupling; nor can the demonstration of electrical communication necessarily indicate that larger molecules (dyes, metabolites) are able to pass through gap junctions. The previously reported lack of dye spread between Hensen's cells illustrates this problem [26]. Others have found this to be the case in other electrically coupled cells [1,36]. Recent efforts to reinvestigate this issue, have revealed that injection of Lucifer Yellow into Hensen's cells causes depolarization, which raises the possibility that the dye is toxic to these cells and may uncouple them. In any case, the existence of electrical communication and the possibility of metabolic communication in the supporting cells may indicate roles in the inner ear similar to those proposed in other tissues. They are discussed below.

(1) The supporting cells may provide a K^+ buffering system whereby increases in local extracellular K^+ in response to hair cell and neuronal activity are reduced by active uptake of K^+ by supporting cells, as is thought to occur in the CNS by astrocytes [28,11]. The syncytial nature of the supporting cells might then allow shunting of K^+ from the tunnel and spaces of Nuel through the supporting cells to areas of lower K^+ concentration (nonactive regions of the duct) or perhaps through metabolic means into the scala media. Supporting cells are known to have microvilli on the endolymphatic surface which are ATPase positive [16]. Thus high K^+ concentrations would be reduced in regions where the ion might interfere with hair cell and neural activity.

(2) Metabolically, the supporting cells may provide for the rapid dissemination of energy sub-

strates in areas of the cochlea duct requiring these molecules. Perhaps the external sulcus cells whose projections are intertwined with spiral ligament capillaries [9] initiate a transfer of metabolites through the Claudius cells to the Hensen's cells and then on to the other supporting cells. The fact that there is a drop in supporting cell membrane potentials, with a subsequent healing over, when the spiral ligament and stria vascularis are removed by means of a tear in the Claudius cell-Hensen's cell interface, indicates that electrical communication occurs between this interface. Thus the possibility of a metabolic route also exists.

(3) Finally, the syncytial nature of the supporting cells may permit pervasive modifications of supporting cell tonus which could affect organ of Corti micromechanics. If ionic conditions arose in a localized area due to local receptor-neuronal activity, and these in some manner effected alterations in local supporting cell structural-contraction proteins, gap junctional communication might permit the spread of these ionically mediated alterations to areas beyond the area of local activity. It is interesting to note that Brownell et al. [5] detected structural changes in response to current only in outer hair cells and not in inner hair cells or supporting cells. However, they noted that changes in supporting cell shape may have been below their limit of resolution. It is difficult to imagine that even slight changes in supporting cell tonus would not affect organ of Corti function, based on numbers of supporting cells and their structural role.

If indeed any of these above mentioned roles exist, the results presented here demonstrate that they could be modified by certain changes in the organ of Corti's microenvironment. Thus in cases where the supporting cell length constant may increase, a possible increase in K^+ buffering and shunting capacity may occur. On the other hand, uncoupling of supporting cell gap junctions might compromise K^+ shunting and metabolic cooperation which could detrimentally affect the organ.

Acknowledgements

Portions of this work were performed at the Laboratory of Neurobiology, University of Puerto

Rico. This work was supported by an RCDA from NINCDS and grants from the Deafness Research Foundation, the Foundation of the UMDNJ, and the NIH (NS 21380-01 and NS 07464). Thanks are due to Barbara Fate for her technical assistance.

References

- 1 Audesirk, G., Audesirk, T. and Bowsher, P. (1982): Variability and frequent failure of Lucifer yellow to pass between two electrically coupled neurons in *Lymnaea stagnalis*. *J. Neurobiol.* 13, 369-375.
- 1 Bennett, M.V.L. (1966): Physiology of electrotonic junctions. *Ann. N.Y. Acad. Sci.* 137, 509-539.
- 3 Bernardini, G., Peracchia, C. and Venosa, R.A. (1981): Healing-over in rat crystalline lens. *J. Physiol. (London)* 320, 187-192.
- 4 Boshier, S.K. (1979): The nature of the negative endocochlear potentials produced by anoxia and ethacrynic acid in the rat and guinea pig. *J. Physiol. (London)* 293, 329-345.
- 5 Brownell, W.E., Bader, C.R., Bertrand, D. and de Ribaupierre, Y. (1985): Evoked mechanical responses of isolated cochlear outer hair cells. *Science* 227, 194-196.
- 6 Connors, B.W., Benardo, L.S. and Prince, D.A. (1984): Carbon dioxide sensitivity of dye coupling among glia and neurons of the neocortex. *J. Neurosci.* 4, 1324-1330.
- 7 De Mello, W.C. (1980): Influence of intracellular injection of H^+ on the electrical coupling in cardiac Purkinje fibres. *Cell Biol. Int. Rep.* 4, 51-57.
- 8 De Mello, W.C. (1983): The influence of pH on the healing-over of mammalian cardiac muscle. *J. Physiol. (London)* 339, 299-307.
- 9 Duvall, A.J. and Sutherland, C.R. (1970): The ultrastructure of the extrasensory cells in the cochlear duct. In: *Biochemical Mechanisms in Hearing and Deafness*, pp. 149-170. Editor: M. Paparella. C. Thomas, Springfield, IL.
- 10 Erulkar, S.D. and Maren, T.H. (1961): Carbonic anhydrase in the inner ear. *Nature (London)* 189, 459-460.
- 11 Gardner-Medwin, A.R. (1982): Analysis of potassium dynamics in mammalian brain tissue. *J. Physiol. (London)* 335, 393-426.
- 12 Giaume, C., Spira, M.E. and Korn, H. (1980): Uncoupling of invertebrate electrotonic synapses by carbon dioxide. *Neurosci. Lett.* 17, 197-202.
- 13 Gulley, R.S. and Reese, T.S. (1976): Intercellular junctions in the reticular lamina of the organ of Corti. *J. Neurocytol.* 5, 479-507.
- 14 Hertzberg, E.L., Spray, D.C. and Bennett, M.V.L. (1984): An antibody to gap junctions blocks junctional conductance. *J. Cell Biol.* 99, 343a.
- 15 Hess, P. and Weingart, R. (1980): Intracellular free calcium modified by pH in sheep cardiac Purkinje fibres. *J. Physiol. (London)* 307, 60-61P.
- 16 Hilding, D.A. and Sugiura, A. (1970): Electronmicroscopic histochemistry of the cochlea. In: *Biochemical Mechanisms in Hearing and Deafness*, pp. 137-147. Editor: M. Paparella. C. Thomas, Springfield, IL.

- 17 Iurato, S., Franke, K., Luciano, L., Wermbter, G., Pannese, E. and Reale, E. (1976): Intercellular junctions in the organ of Corti as revealed by freeze fracturing. *Acta Otolaryngol.* 82, 57–69.
- 18 Jahnke, K. (1975): The fine structure of freeze-fractured intercellular junctions in the guinea pig inner ear. *Acta Otolaryngol.* 82, 57–69.
- 19 Jarrell, J.A. (1983): Reversible carbon dioxide-induced inhibition of dye coupling in *Necturus* gallbladder. *Am. J. Physiol.* 244, C419–C421.
- 20 Mountain, D.C. (1980): Changes in endolymphatic potential and crossed olivo-cochlear bundle stimulation alter cochlear mechanics. *Science* 210, 71–72.
- 21 Obaid, A.L., Socolar, S.J. and Rose, B. (1983): Cell-to-cell channels with two independent regulated gates in series: analysis of junctional channel modulation by membrane potential, calcium and pH. *J. Membr. Biol.* 73, 69–89.
- 22 Reber, W.R. and Weingart, R. (1982): Ungulate cardiac purkinje fibres: the influence of intracellular pH on the electrical cell-to-cell coupling. *J. Physiol. (London)* 328, 87–104.
- 23 Santos-Sacchi, J. (1984): An increase in the intracellular activities of H^+ and Ca^{++} uncouples the supporting cells of Corti's organ. In: *Midwinter Meeting of the Association for Research in Otolaryngology*, St. Petersburg, FL.
- 24 Santos-Sacchi, J. (1984): A re-evaluation of cell coupling in the organ of Corti. *Hearing Res.* 14, 203–204.
- 25 Santos-Sacchi, J. and Dallos, P. (1982): Intercellular coupling in the supporting cells of the guinea pig organ of Corti. In: *Midwinter Meeting of the Association for Research in Otolaryngology*, St. Petersburg, FL.
- 26 Santos-Sacchi, J. and Dallos, P. (1983): Intercellular communication in the supporting cells of the organ of Corti. *Hearing Res.* 9, 317–326.
- 27 Schuetze, S.M. and Goodenough, D.A. (1982): Dye transfer between cells of the embryonic chick lens becomes less sensitive to CO_2 treatment with development. *J. Cell Biol.* 92, 694–705.
- 28 Somjen, G.G. (1979): Extracellular potassium in the mammalian central nervous system. *Annu. Rev. Physiol.* 41, 159–177.
- 29 Spray, D.C., Harris, A.L. and Bennett, M.V.L. (1979): Voltage dependence of junctional conductance in early amphibian embryos. *Science* 204, 432–434.
- 30 Spray, D.C., Harris, A.L. and Bennett, M.V.L. (1981): Gap junctional conductance is a simple and sensitive function of intracellular pH. *Science* 211, 712–715.
- 31 Spray, D.C., Stern, J.H., Harris, A.L. and Bennett, M.V.L. (1982): Gap junctional conductance: Comparison of sensitivities to H and Ca ions. *Proc. Natl. Acad. Sci. U.S.A.* 79, 441–445. Editors: R. Nuccitelli and D.W. Deamer. Alan R. Liss, New York.
- 32 Spray, D.C., Harris, A.L. and Bennett, M.V.L. (1982): Comparison of pH and calcium dependence of gap junctional conductance. In: *Intracellular pH: Its Measurement, Regulation, and Utilization in Cellular Functions*, pp. 445–461.
- 33 Spray, D.C., White, R.L., Campos de Carvalho, A., Harris, A.L. and Bennett, M.V.L. (1984): Gating of gap junction channels. *Biophys. J.* 45, 219–223.
- 34 Sterkers, O., Saumon, G., Tran Ba Huy, P. and Amiel, C. (1983): pH of endolymph and perilymph of the rat: effect of acetazolamide. In: *Midwinter Meeting of the Association for Research in Otolaryngology*, St. Petersburg, FL.
- 35 Strelieff, D. and Flock, A. (1984): Stiffness of sensory-cell bundles in the isolated guinea pig cochlea. *Hearing Res.* 15, 19–28.
- 36 Tajkato, M. and Goldring, S. (1979): Intracellular marking with lucifer yellow CH and horseradish peroxidase of cells electrophysiologically characterized as glia in the cerebral cortex of the cat. *J. Comp. Neurol.* 186, 173–188.
- 37 Turin, L. and Warner, A.E. (1977): Carbon dioxide reversibly abolishes ionic communication between cells of early amphibian embryo. *Nature (London)* 270, 56–57.
- 38 Turin, L. and Warner, A.E. (1980): Intracellular pH in early *Xenopus* embryos: its effect on current flow between blastomeres. *J. Physiol. (London)* 300, 489–504.

HRR 00691

The temperature dependence of electrical coupling in the organ of Corti

J. Santos-Sacchi

Laboratory of Otolaryngology, Dept. of Surgery, Sect. of Otolaryngology, MSB H518, UMDNJ-New Jersey Medical School, Newark, NJ 07103, U.S.A.

(Received 27 August 1985; accepted 8 December 1985)

Electrical coupling in an in vitro preparation of the organ of Corti was evaluated during changes in temperature of the bathing media. The effect of cooling the organ from $35 \pm 2^\circ\text{C}$ to $17 \pm 3^\circ\text{C}$ is to reduce membrane potentials, increase input resistance and decrease coupling ratios. Decreases in coupling ratios ranging from 15 to 75% have been observed. The effects are reversible upon warming. Membrane potentials are very susceptible to depolarization caused by cooling. The reduction in coupling is not due to depolarization nor is it dependent upon extracellular Ca^{2+} . It is conceivable, however, that intracellular stores of Ca^{2+} are released or that intracellular pH is altered.

electrical coupling, gap junctions, organ of Corti, temperature effects, DNP, membrane potentials

Introduction

Gap junctions are thought to mediate intercellular communication between a variety of cell types (Bennett and Goodenough, 1978). These channels permit the direct cellular exchange of materials (ions, dyes and metabolites) up to molecular masses of approximately 1000 daltons in mammalian cell types (Flagg-Newton et al., 1979). Over the past 20 years a variety of treatments has been shown to influence the conductance of these junctions (Spray and Bennett, 1985). In the supporting cells of the organ of Corti, electrical coupling via gap junctions is present (Santos-Sacchi and Dallos, 1982, 1983; Santos-Sacchi, 1984a) and can be modified by treatments which alter the intracellular activities of Ca^{2+} and H^+ (Santos-Sacchi, 1984b, 1985). Gap junctional communication in the organ of Corti may be important for normal cochlear function (Santos-Sacchi, 1985), and may (1) underlie metabolic cooperation among the supporting cells, (2) provide a means to buffer K^+ in the extracellular spaces of the organ of Corti, as occurs in the CNS by ionically coupled astrocytes, and (3) influence cochlear micromechanics by permitting the spread of ionically mediated tonus alterations throughout the supporting cells.

Many studies have shown that cochlear electrophysiology is quite sensitive to cochlear temperature (Butler et al., 1960; Coats, 1965; Manley and Johnstone, 1974; Brown et al., 1983). Temperature is also known to influence gap junctional communication (Politoff et al., 1967; Payton et al., 1969). The present study evaluates the effects of cooling upon electrical coupling between supporting cells in vitro.

Methods

Guinea pigs were anesthetized with pentobarbitol and killed by decapitation. The whole temporal bone was placed in a perfusion chamber on a Zeiss ACM microscope, and the bony capsule around the two most apical turns was chipped away. The stria vascularis and spiral ligament were removed. Medium 199 (with Hanks salts [1.26 mM CaCl_2 , 1.7 μM $\text{Fe}(\text{NO}_3)_3$, 5.36 mM KCl , 0.44 mM KH_2PO_4 , 0.81 mM MgSO_4 , 137 mM NaCl , 4.16 mM NaHCO_3 , 0.33 mM Na_2HPO_4 ; for high K^+ media, NaCl was adjusted to maintain tonicity, pH 7.2–7.4, Gibco, NY) was perfused at a rate of 0.8–1.5 ml/min under an air atmosphere. High K^+ solutions (140 mM) were perfused through the cell chamber in order to evaluate the effects of depolarization on coupling.

2,4-Dinitrophenol (2,4-DNP) (1 mM) was used to evaluate the effect of this metabolic inhibitor on membrane potential. Ca^{2+} -free medium was used to evaluate the effects of extracellular Ca^{2+} upon changes which occur with temperature manipulations. The temperature of the preparation was controlled by Peltier devices utilizing a Bailey Instruments (NJ) controller unit. Electrodes were pulled on a Narishige puller.

Coupling measurements were made with high input impedance devices (WPI KS-700, Dagan 8100-1) capable of constant current injection. Coupling was assessed by injecting negative current pulses of varying magnitudes into one cell and noting the voltage drop in the same and an adjacent cell. Under visual control, Hensen's cells were impaled with electrodes; double-barreled theta glass electrodes were used to inject separately current (I_1) and record voltage drops (V_1) in one cell, while a neighboring cell was impaled with a single-barreled voltage recording electrode (V_2).

Coupling ratio is defined as the voltage drop in cell 2 divided by the voltage drop in cell 1 in response to current injection in cell 1 (V_2/V_1) (Bennett, 1966). Current pulses were generated by a D/A converter controlled by an IBM PC/XT.

Coupling ratios were determined online using a Data 6000 waveform analyzer (Data Precision, MA) in conjunction with the IBM. Coupling responses, membrane potentials, coupling ratios and temperature were recorded on a Gould four-channel recorder. Individual coupling responses were digitally stored within the Data 6000 and saved to disk.

Results

The supporting cells of the organ of Corti are very susceptible to cold-induced depolarization. Fig. 1 illustrates the effects of a reduction in temperature from 35 to 15°C upon membrane potential. The Hensen's cell depolarizes coincident with the temperature drop, and repolarizes as the temperature rises. A lack of precise temporal correspondence between the measured temperature change and membrane potential change is possibly due to the inability to place the temperature probe directly on the specimen. In 7 preparations (35 cells), a 10°C drop in temperature caused an average drop in membrane potential of 13.98 ± 4.44 mV, with the original membrane potentials being 40 ± 10 mV. The magnitude of the depolarization associated with the temperature decrease

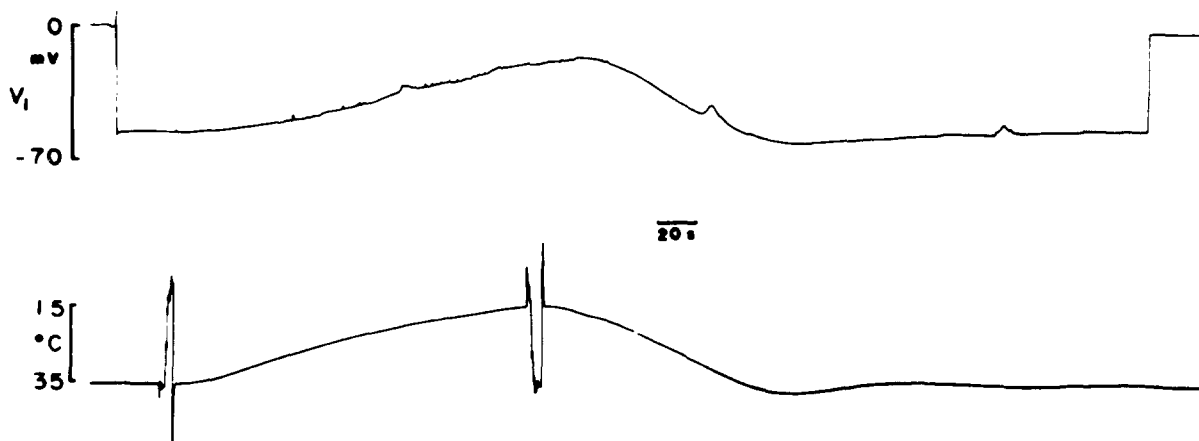


Fig. 1. The effect of cooling upon supporting cell membrane potential. The top trace is a strip chart recording of the membrane potential of a Hensen's cell. The bottom trace indicates the temperature of the perfused media which bathes the cell. As the temperature is reduced from about 36 to 15°C there is a corresponding drop in the membrane potential of the Hensen's cells. Return of the temperature to pretreatment levels causes a repolarization of the membrane potential. Note that the temperature overshoots the initial level during rewarming, and the membrane potential follows this overshoot.

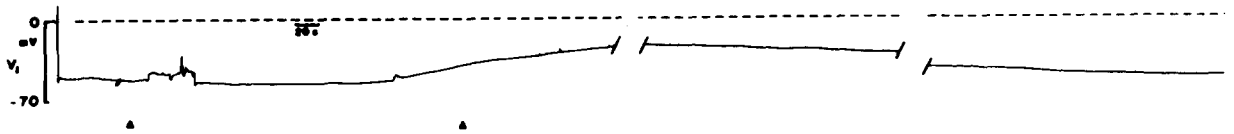


Fig. 2. The effect of 2,4-DNP on membrane potential. A Hensen's cell was recorded from during perfusion of the bath with 1 mM DNP. The first arrow indicates the start of the DNP perfusion and the second arrow indicates the return to normal medium. Membrane potential undergoes a gradual depolarization which is reversible upon washout of the poison. Portions of the trace were removed and accounted for 150 and 340 s, respectively.

was positively correlated with the initial membrane potential of cell ($r = +0.573$, $p < 0.01$, two-tailed). Since a reduction in temperature is known to affect metabolic rate, it was of interest to determine if a metabolic poison would also produce depolarization of Hensen's cells. This might help differentiate between a direct effect upon the cell membrane and an intermediate ef-

fect upon metabolism. As is demonstrated in Fig. 2, the metabolic inhibitor 2,4-DNP also depolarizes cells in a reversible manner although the time course is longer because of the time required to wash out the poison.

Electrical coupling between Hensen's cells is dependent upon temperature as well. However, the uncoupling due to cold is variable in extent

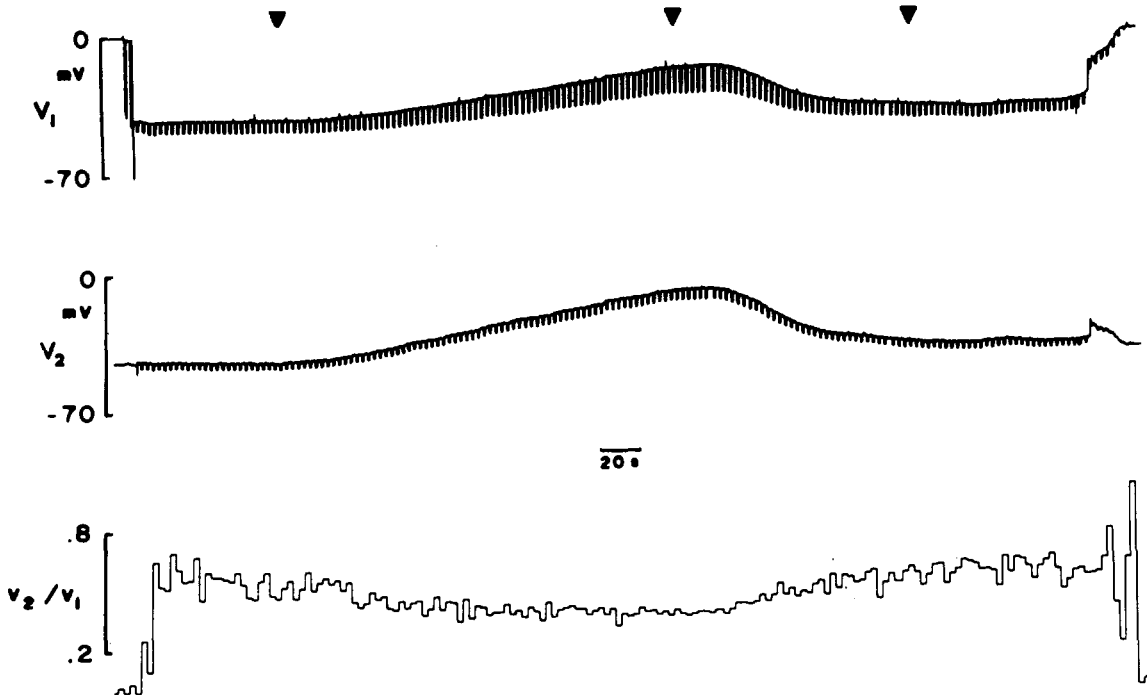


Fig. 3. The effect of cooling upon electrical coupling between supporting cells. Two neighboring Hensen's cells were penetrated with 3 M KCl electrodes. Cell 1 received current pulses of -15 nA through one barrel of a theta glass electrode and the resulting voltage drop was recorded with the other barrel. The coupling response in the other cell was measured with a single barreled electrode. Coupling ratio (bottom trace) was computed on-line and plotted out simultaneously. Temperature of the bath was 37°C initially, and cooling began at the first arrow. A temperature of 15°C was reached at the second arrow, whereupon rewarming began. 37°C was reached at the third arrow. The result of cooling is to reduce membrane potentials, increase input resistance, and decrease coupling ratio. These measures return to pretreatment levels upon rewarming.

despite the fact that depolarization is always substantial. Fig. 3 depicts the effects of lowering the temperature from 37 to 15°C upon electrically coupled supporting cells. In response to cooling, membrane potentials drop, input resistance increases and coupling ratios decrease; upon warming, the measures recover. Reductions in initial coupling ratios ranged from 15 to 75% for temperature changes from 37 ± 2 to $17 \pm 3^\circ\text{C}$. Mean coupling ratios for these temperature extremes are 0.58 ± 0.17 and 0.34 ± 0.11 , respectively ($n = 17$, 9 preparations).

Note in Fig. 3 that near the end of the trace there is a sudden drop in the membrane potentials of the cells. This apparently indicates some sort of injury to cell 1, since its membrane potential continues to decline while cell 2's membrane potential recovers. That is, because the cells are electrically

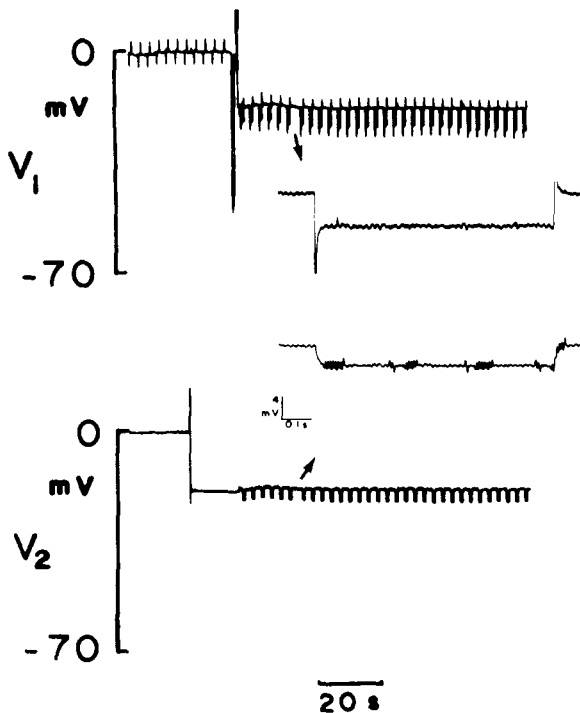


Fig. 4. Good coupling is demonstrable despite low membrane potentials of Hensen's cells. Immediately after removal of the lateral wall of the cochlear duct, membrane potentials drop, but recover over time. This example illustrates that coupling between supporting cells is substantial during periods of reduced membrane potential. Current pulses of -10 nA into cell 1 produces voltage drops in both cells which calculate to a coupling ratio of about 0.7. Inserts are plots of the digitally saved voltage drops in each cell.

coupled, the membrane potential of cell 2 initially follows that of cell 1. The subsequent recovery of cell 2 indicates that uncoupling of the cells is occurring. It is interesting to note that the ratio of initial membrane potential drop in cells 1 and 2 in response to cell 1 injury is, in fact, equivalent to the coupling ratio.

Since uncoupling due to reduced temperature and other treatments (e.g., lowered pH (Santos-Sacchi, 1985)) is accompanied by depolarization, it is of interest to determine if depolarization, per se, is causal. It is known that supporting cells initially have low membrane potentials following removal of the stria vascularis and spiral ligament which recover over time (Santos-Sacchi, 1984a, 1985). Yet, even prior to the recovery of the supporting cell membrane potentials, good coupling is demonstrable (Fig. 4). Furthermore, treatment of Hensen's cells with high potassium solutions, while causing depolarization, neither results in an increase in input resistance nor a concomitant reduction of coupling ratio (Fig. 5). Fig 6 presents a scatter plot of the magnitude of decrease in coupling ratio versus the magnitude (cell

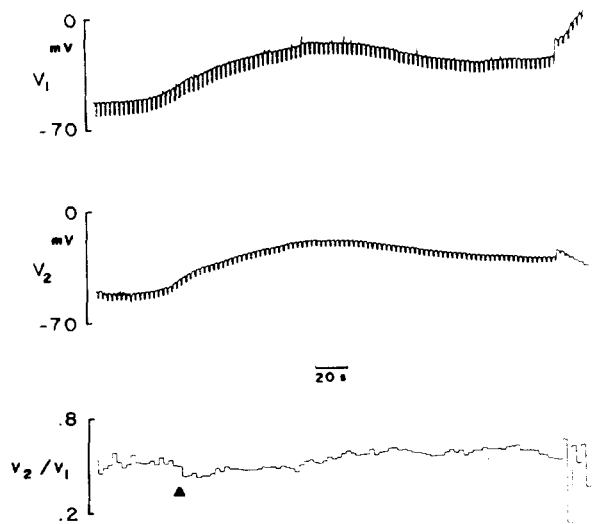


Fig. 5. Effect of depolarization upon coupling in supporting cells. High K^+ media (140 mM) was perfused into the organ chamber for 130 s, and normal medium perfusion was reinstated at the arrow. In response to the high extracellular K^+ , a rapid fall in membrane potential is seen. Input resistance decreases slightly, and no uncoupling trend is correlated with the pronounced depolarization. Upon washout of the K^+ , membrane potentials repolarize.

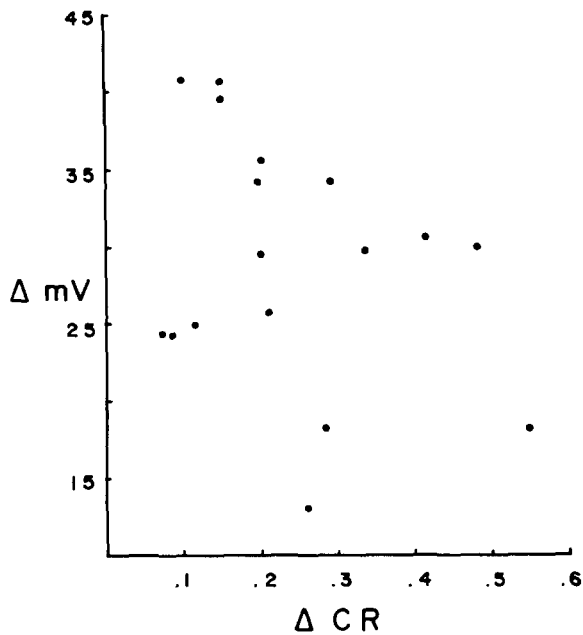


Fig. 6. Scatter plot of the magnitude of depolarization (Δ mV) vs. magnitude of coupling ratio change (Δ CR) in response to cooling the preparation from $37 \pm 2^\circ\text{C}$ to $17 \pm 3^\circ\text{C}$. Correlation coefficient is -0.29 , but is not significant at the 0.1 level.

pair average) of concomitant membrane depolarization in response to cooling. Correlation between the two is not significant ($r = -0.29$, $p > 0.1$, two-tailed). Thus, depolarization of the cell membrane is probably not related to the uncoupling action of reduced temperature.

The recovery of supporting cell membrane potentials following removal of the lateral well is probably similar to the 'healing over' process observed following injury to cardiac purkinje fibers (DeMello, 1983). Extracellular Ca^{2+} is known to be required for this 'healing over'. This is also the case for the supporting cells, since incubation of the organ of Corti in calcium-free media prevents the recovery of membrane potentials. Fig. 7 demonstrates that coupling during this type of incubation is good, and that reduced temperature still promotes uncoupling. Influx of extracellular calcium is therefore not required for the uncoupling effect.

Discussion

The present results indicate that temperature is an important factor which influences both membrane potentials and coupling ratios of supporting cells of the organ of Corti.

Temperature and metabolic inhibitors have been shown to influence membrane potentials of some cells in other systems, but not of others. For example, Creed and McDonald (1975) found no temperature effect (20 – 40°C) upon resting potentials of submandibular acinar cells but did find a 50% drop in membrane potentials with prolonged exposure to DNP, *in vivo*. Similarly, Payton et al. (1969) found only small depolarizations in crayfish giant axons upon cooling to 5°C , which they attributed to alteration of the electrode tip potential. In the present study, only very small (< 5 mV) changes in electrode tip potential were associated with temperature reductions capable of near total depolarization of the supporting cells. Al-

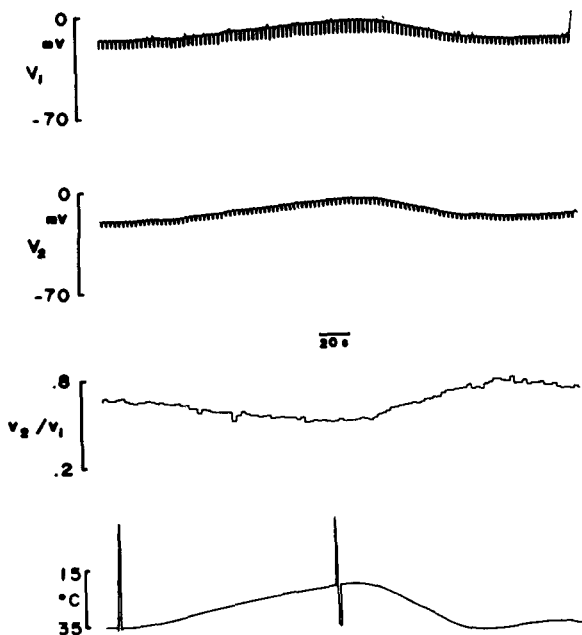


Fig. 7. Effect of cooling on coupling in Ca^{2+} -free media. In this example, it is demonstrated that coupling ratios are decreased upon cooling despite the absence of Ca^{2+} in the external medium, thus indicating that Ca^{2+} influx is not required for uncoupling. Current pulses into cell 1 are -20 nA. Note the close correspondence between coupling ratio and temperature.

though no alterations in membrane potential were noted by Payton et al. (1969), cooling had a profound effect upon junctional communication between crayfish axons. Junctional conductance was found to follow rapidly alterations in temperature, similar to the effects reported here on supporting cell coupling ratios. It is interesting that slow cooling of the crayfish axon apparently does not alter junctional conductance (Ramon and Zampighi, 1980).

Politoff et al. (1967) did find a reduction of membrane potential associated with cooling of salivary glands of *Chironomus thummi* larvae from 20 to 5°C. However, uncoupling of cells from this tissue, which was observed, initially required prolonged cooling. These authors speculated that some change in a metabolically dependent concentration of a cellular constituent (e.g., Ca^{2+}) occurs which is responsible for the uncoupling. Subsequently, they showed that depolarization of these cells by outward currents caused uncoupling, and again they speculated that it was possibly due to an increase in intracellular Ca^{2+} . It is currently known that Ca^{2+} can uncouple cells although H^+ is apparently a more potent uncoupler (Spray et al., 1982). Supporting cells of the organ of Corti can be uncoupled by treatments which increase the intracellular concentrations of either ion (Santos-Sacchi, 1984b, 1985). Whereas membrane potential (both inside-out and transjunctional) may be important factors in junctional conductance of non-mammalian cells, it appears not to be for mammalian cells (Spray and Bennett, 1985). It is demonstrated here that depolarization, per se, of Hensen's cells does not interfere with cellular communication. In addition, an influx of extracellular Ca^{2+} is not responsible for the uncoupling observed; however, the release of an intracellular store of Ca^{2+} or a decrease in intracellular pH is a possibility. Intracellular pH and Ca^{2+} measurements are required to evaluate this issue. Finally, a direct effect of cooling upon membrane structure cannot be ruled out (Payton et al., 1969).

The fact that 2,4-DNP produces a drop in membrane potential may indicate that temperature reductions produce depolarizations via metabolic interference. Nuttall and Lawrence (1978) found minimal changes in the in vivo recorded membrane potentials of supporting cells

during anoxia. In fact, membrane potentials remain stable for some time after death of the animal (J.S.S., unpublished observations). These apparent differences between in vivo and in vitro susceptibility to metabolic insult warrants investigation, especially since there is currently widespread use of in vitro preparations to study organ of Corti function.

As indicated in the introduction, cell coupling in the organ of Corti may be very important for the normal functioning of the inner ear. Interference with cell coupling by temperature reductions or metabolic insults may possibly contribute to the altered functioning of the ear which occurs during such manipulations. For example, if the supporting cells act as a buffer to maintain low potassium levels in the spaces of Nuel, uncoupling these cells might compromise this function and ultimately interfere with hair cell and neuronal electrical activity. Experiments which measure extracellular potassium in the organ of Corti during temperature manipulations may shed light on this issue.

Acknowledgements

This work was supported by an RCDA from NINCDS and grants from the Deafness Research Foundation, the Foundation of the UMDNJ, and the NIH (NS 21380-01). I thank Barbara Fate for her technical assistance.

References

- Bennett, M.V.L. (1966) Physiology of electrotonic junctions. *Ann. N.Y. Acad. Sci.* 137, 509–539.
- Bennett, M.V.L. and Goodenough, D.M. (1978) Gap junctions, electrotonic coupling and intercellular communication. *Neurosci. Res. Program Bull.* 16, 373–486.
- Brown, M.C., Smith, D.I. and Nuttall, A.L. (1983) The temperature dependency of neural and hair cell responses evoked by high frequencies. *J. Acoust. Soc. Am.* 73, 1662–1670.
- Butler, R.A., Konishi, T. and Fernandez, C. (1960) Temperature coefficients of cochlear potentials. *Am. J. Physiol.* 199, 688–692.
- Coats, A.C. (1965) Temperature effects on the peripheral auditory apparatus. *Science* 150, 1481–1483.
- Creed, J.E. and McDonald, I.R. (1975) The effects of temperature and 2,4-dinitrophenol on transmembrane potentials of submandibular acinar cells. *J. Physiol.* 247, 521–535.
- DeMello, W.C. (1983) The influence of pH on the healing-over of mammalian cardiac muscle. *J. Physiol.* 339, 299–307.

- Flag-Newton, J., Simpson, I. and Loewenstein, W. (1979) Permeability of the cell-to-cell membrane channels in mammalian cell junction. *Science* 205, 404-407.
- Manley, J.A. and Johnstone, B.M. (1974) A comparison of cochlear summing potentials in the bat and guinea pig, including temperature effects. *J. Comp. Physiol.* 88, 43-66.
- Nuttall, A.L. and Lawrence, M. (1978) Hypoxia independence of organ of Corti cell transmembrane potentials. *Otolaryngology* 86, 623-624.
- Payton, B.W., Bennett, M.V.L. and Pappas, G.D. (1969) Temperature dependence of resistance at an electrotonic junction. *Science* 165, 594-597.
- Politoff, A., Socolar, S.J. and Loewenstein, W.R. (1967) Metabolism and the permeability of cell membrane junctions. *Biochim. Biophys. Acta.* 135, 791-793.
- Ramon, F. and Zampighi, G. (1980) On the electronic coupling mechanism of crayfish segmented axons: temperature dependence of junctional conductance. *J. Membrane Biol.* 54, 165-171.
- Santos-Sacchi, J. (1984) A re-evaluation of cell coupling in the organ of Corti. *Hearing Res.* 14, 203-204.
- Santos-Sacchi, J. (1984) An increase in the intracellular activities of H^+ and Ca^{++} uncouples the supporting cells of Corti's organ. Midwinter meeting of the Association for Research in Otolaryngology, St. Petersburg, FL.
- Santos-Sacchi, J. (1985) The effects of cytoplasmic acidification upon electrical coupling in the organ of Corti. *Hearing Res.* 19, 207-215.
- Santos-Sacchi, J. and Dallos, P. (1982) Intercellular coupling in the supporting cells of the guinea pig organ of Corti. Midwinter Meeting of the Association for Research in Otolaryngology, St. Petersburg, FL.
- Santos-Sacchi, J. and Dallos, P. (1983) Intercellular communication in the supporting cells of the organ of Corti. *Hearing Res.* 9, 317-326.
- Spray, D.C. and Bennett, M.V.L. (1985) Physiology and pharmacology of gap junctions. *Annu. Rev. Physiol.* 47, 281-303.
- Spray, D.C., Harris, A.L. and Bennett, M.V.L. (1982) Comparison of pH and calcium dependence of gap junctional conductance. In: *Intracellular pH: Its Measurement, Regulation, and Utilization in Cellular Functions*, pp. 445-461. Editors: R. Nuccitelli and D. Deamer. Alan R. Liss, Inc., New York.

HRR 00853

Electrical coupling differs in the in vitro and in vivo organ of Corti

J. Santos-Sacchi

Laboratory of Otolaryngology, Dept. of Surgery, Sect. of Otolaryngology, MSB H518, UMDNJ-New Jersey Medical School, Newark, NJ 07103, U.S.A.

(Received 16 March 1986; accepted 17 August 1986)

Electrical communication between the supporting cells of the guinea pig organ of Corti was studied. For in vitro experiments, the inner ear was rapidly removed and placed in a heated perfusion chamber. Medium 199 was used. The bony cochlea and the lateral wall (spiral ligament and stria vascularis) were removed to expose the top two coils of the organ of Corti. In vivo experiments were performed upon anesthetized animals whose cochleas were exposed surgically. A tiny fenestra was made in the bony cochlea which permitted the passage of electrodes through the lateral wall and into the organ of Corti of the third turn. Coupling was assessed by impaling neighboring cells with 3 M KCl electrodes, and noting the spread of intracellularly injected current. Coupling ratios in the in vitro preparation were consistently greater than those obtained in vivo (0.58 ± 0.17 vs. 0.104 ± 0.064). Differences exist between the in vitro and in vivo preparations which might account for these results. In vivo the supporting cells are bathed in two different media, endolymph apically, and perilymph basally. Consequently, on their apical side the supporting cells are exposed to fluid high in K^+ , low in Ca^{2+} and at a potential of 80 mV, the endolymphatic potential. In vitro the cells are bathed on all sides in fluid similar to perilymph. Intermixing the fluids in an in vivo preparation, by tearing away the stria vascularis and Reissner's membrane, increases the magnitude of the coupling ratio (0.455 ± 0.209). Thus the unique microenvironment of the inner ear maintains lower coupling ratios, and smaller space constants for the supporting cells.

organ of Corti, supporting cell, electrical coupling, in vivo, in vitro, gap junction

Introduction

The organ of Corti, the sensory epithelium of the mammalian inner ear, is composed of hair cells and supporting cells. The extracellular fluid environments facing the epithelium's apical and basal surfaces are markedly different in composition. For example, the apical environment, the endolymphatic space, has concentrations of K^+ , Na^+ , and Ca^{2+} of about 140 mM, 1 mM and 25 μ M, respectively (Bosher and Warren, 1968, 1978); all are maintained by metabolic processes. In addition, the electrical potential of this apical compartment is about 80 mV relative to the basal compartment, a perilymphatic space, whose ionic composition is more typical of extracellular fluid. This unique compartmentalization is required for normal auditory function.

Adjacent supporting cells in vitro (wholly incubated in perilymph-like culture media) can have coupling ratios greater than 0.8 (Santos-Sacchi,

1984, 1985). This implies that supporting cells directly interact over a wide area of the organ, potentially permitting ionically mediated changes in supporting cell tonus to spread along the organ. If coupling in vivo is comparable, then such interactions may influence cochlear micromechanics. It is important, therefore, to determine if electrical coupling among supporting cells is as good under in vivo conditions as is indicated by the in vitro studies.

Methods

In vitro

Guinea pigs were anesthetized with pentobarbital and killed by decapitation. The whole temporal bone was placed in a perfusion chamber on a Zeiss ACM microscope, and the bony capsule around the two most apical turns was chipped away. The stria vascularis and spiral ligament were removed. Medium 199 (with Hanks salts

[1.26 mM CaCl_2 , 1.7 μM $\text{Fe}(\text{NO}_3)_3$, 5.36 mM KCl , 0.44 mM KH_2PO_4 , 0.81 mM MgSO_4 , 137 mM NaCl , 4.16 mM NaHCO_3 , 0.33 mM Na_2HPO_4], pH 7.2–7.4, Gibco, NY) was perfused at a rate of 0.8 to 1.5 ml/min under an air atmosphere. The temperature of the preparation was controlled by Peltier devices utilizing a Bailey Instruments (NJ) controller unit.

In vivo

A ventrolateral approach was used to expose the right cochlea of anesthetized guinea pigs. The animals were artificially respirated during surgery and experimentation. A small fenestra (0.3×0.5 mm) was made in the bony cochlea overlying the lateral wall (stria vascularis and spiral ligament) of the third turn. Through this fenestra electrode penetrations were made into the organ of Corti with the aid of fiber optic backlight transillumination. In order to intermix cochlear fluids the lateral wall was torn away.

Coupling measurements were made with high input impedance devices (WPI KS-700, Dagan 8100-1) capable of constant current injection. Coupling was assessed by injecting negative current pulses of varying magnitudes into one cell and noting the voltage drop in the same and an adjacent cell. Electrodes (10–15 $\text{M}\Omega$) were pulled on a Narashige puller; double-barreled theta glass electrodes were used to separately inject current (I_1) and record voltage drops (V_1) in one cell, while a neighboring cell was impaled with a single-barreled voltage recording electrode (V_2). For *in vitro* experiments, electrodes were separately impaled into neighboring cells under visual observation. For *in vivo* experiments, a single barreled electrode was bent according to the method of Hudspeth and Corey (1979) so that it and a theta electrode could be epoxied together with the shanks parallel and tips separated by 25–40 μm . Because the Hensen's cells are 15–25 μm in diameter, this design permits the penetration of adjacent Hensen's cells despite the inability to view the organ of Corti beyond the lateral wall.

Coupling ratio is defined as the voltage drop in cell 2 divided by the voltage drop in cell 1 in response to current injection in cell 1 (V_2/V_1) (Bennett, 1966). Current pulses were generated by

a D/A convertor controlled by an IBM PC/XT. Coupling ratios were determined online using a Data 6000 waveform analyzer (Data Precision, MA) in conjunction with the IBM. Membrane potentials, coupling responses, and coupling ratios were recorded on a Gould four channel recorder. Individual coupling responses were digitally stored within the Data 6000 and saved to disk.

Results

Adjacent Hensen's cells *in vitro* are very well coupled electrically. Fig. 1c illustrates electrical coupling in a pair of cells. Current injection of a -5 nA 0.8 s pulse into one cell produces a voltage drop in that same cell and in an adjacent one. The coupling ratio in this case is 0.6. Coupling ratios averaged 0.58 ± 0.17 ($n = 17$ cell pairs, 9 preparations). The input resistance of these cells *in vitro* is 0.47 ± 0.15 $\text{M}\Omega$ ($n = 47$, 5 preparations).

Unlike the *in vitro* preparation, the *in vivo* preparation consistently demonstrates poor coupling. Fig. 2c illustrates this point. Current pulses of -25 nA were injected into one Hensen's cell and the voltage drops in that cell and an adjacent cell indicate a coupling ratio of 0.12. After pulling out of the cells the endolymphatic potential is encountered; a potential of zero is obtained upon further withdrawal of the electrodes outside the scala media. Coupling ratios obtained *in vivo* averaged 0.104 ± 0.064 ($n = 40$ cell pairs, 9 preparations). The input resistance under these circumstances is 0.43 ± 0.23 $\text{M}\Omega$ ($n = 47$, 7 preparations).

One obvious difference between these two experimental conditions is the lack of physiologic compartmentalization *in vitro*. That is, the cells of the organ of Corti are bathed on both sides by perilymph-like media, unlike *in vivo* where the fluids bathing the apical and basal compartments differ drastically in ionic composition and electrical potential. In order to evaluate whether this may be the cause for the difference in coupling ratios, the normal compartmentalization of the *in vivo* preparation was disrupted by tearing away the lateral wall of the cochlear duct as illustrated in Fig. 3. By doing so the fluids of the three scalae are intermixed and the endolymphatic potential is abolished. Since there is a greater volume of per-

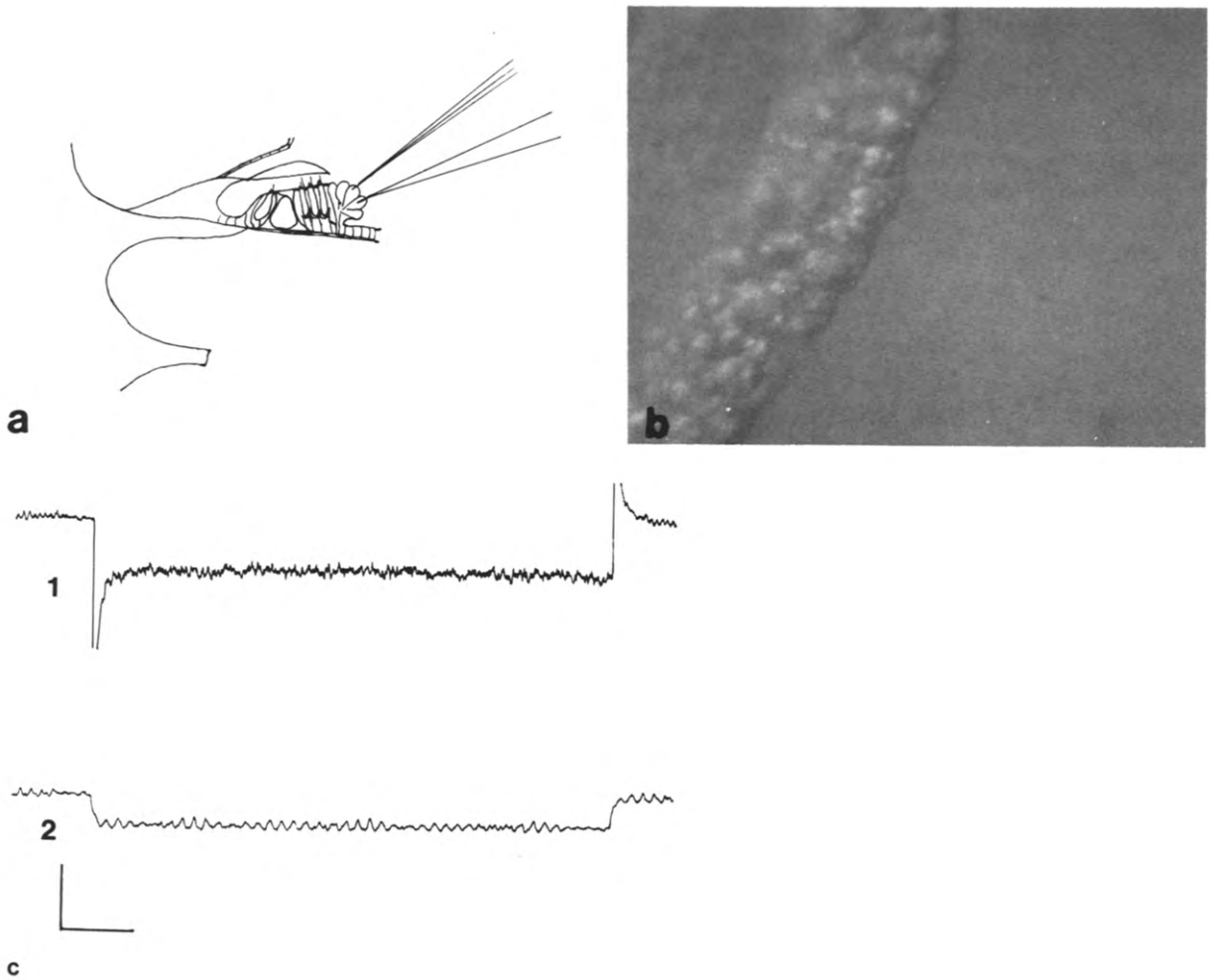


Fig. 1. (a) A schematic drawing showing the in vitro experimental setup. (b) A photomicrograph of the Hensen's cells within the perfusion chamber. (c) A trace of the voltage drop in cell 1 and the coupling response in cell 2, in response to a current pulse (0.8 s) of -5 nA in cell 1. The coupling ratio in this example is 0.6. Horizontal scale, 0.1 s; vertical scale, 6 mV.

ilymph, this fluid, albeit diluted somewhat with endolymph, will surround the organ of Corti. Under such conditions it is demonstrated that coupling ratios between Hensen's cell are increased in magnitude. Fig. 3 illustrates a case where -20 nA current pulses were delivered intracellularly into one Hensen's cell. The voltage drops in that cell and an adjacent one indicate a coupling ratio of 0.69. Upon pulling out of the cells, the potential drops to zero because the stria had been torn away. Coupling ratios under these conditions averaged 0.455 ± 0.209 ($n = 42$ cell pairs, 7 pre-

parations). The input resistance was 0.50 ± 0.21 M Ω ($n = 29$, 5 preparations).

It is interesting to note that the membrane potentials of the Hensen's cells in vitro are reduced initially after stripping away the lateral wall, but that these potentials recover over time close to those recorded under normal in vivo conditions (Santos-Sacchi, 1985). This is also the case for the membrane potentials recorded in the in vivo condition after removal of the lateral wall. For example, the membrane potentials of the preparation illustrated in Fig. 3 initially measured

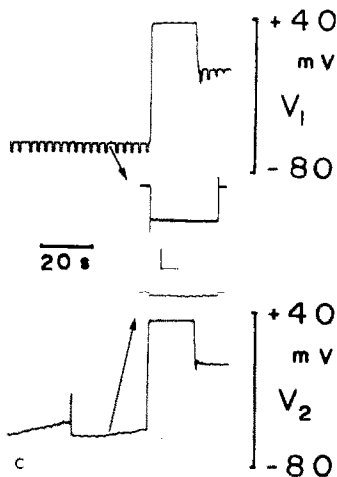
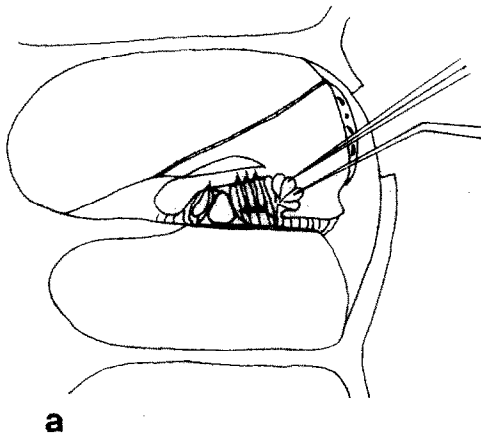


Fig. 2. (a) A schematic drawing showing the in vivo experimental setup. (b) A photo through the operating microscope showing the cochlea backlit with a fiber optic light source. The electrodes can be seen penetrating through a fenestra made in the bone overlying the third turn of the cochlear duct. (c) Traces depicting electrical coupling in vivo. Cell 1 received current pulses of -25 nA. After recording coupling ratios, the electrodes were withdrawn into the scala media where the resting potential is positive. Upon withdrawal from the cochlea the potential drops to zero. The arrows indicate that region of the traces from which the expanded insets are taken. The coupling ratio in this case is 0.12. Inset horizontal scale, 0.2 s; vertical scale, 6 mV.

around -20 mV following removal of the lateral wall; after a few hours they had returned to normal levels. This possibly signifies a process similar to the "healing over" which occurs in cardiac muscle and lens following injury to these tissues (De Mello, 1983; Bernardini et al., 1981). As with the in vitro inner ear preparation, coupling ratios in vivo are good throughout the recovery of membrane potentials.

Discussion

The results demonstrate that coupling ratios in the in vitro and in vivo preparation of the organ of Corti differ in magnitude. In vivo electrical coupling is substantially poorer than in vitro. Fur-

thermore, this poor coupling appears to be due to the physiologic compartmentalization which characterizes the intact cochlea, since disruption of the organ's normal architecture (with concomitant intermixing of cochlear fluids) increases electrical coupling in vivo.

Recently, it has become clear that micromechanical interactions between outer and inner hair cells may underlie the inner ear's exquisite frequency resolving power (see Dallos, 1985). These interactions are thought to be mediated by hair cell cytoskeletal characteristics. It is also known, however, that supporting cells possess cytoskeletal elements (Slepecky and Chamberlain, 1983), which conceivably could influence organ of Corti micromechanics. Since the frequency resolv-

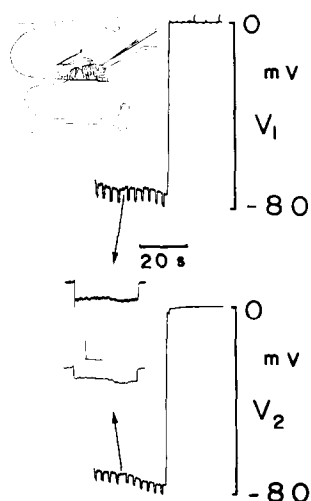


Fig. 3. After recording from the intact cochlea, the lateral wall of the cochlear duct was torn away. In the upper left portion of the figure is a schematic drawing showing the experimental setup. The traces depict electrical coupling *in vivo* after intermixing the cochlear fluids. Cell 1 received -20 nA current pulses. After recording coupling ratios, the electrodes were withdrawn into the scala media. The positive resting potential of the scala media is abolished by the experimental treatment. The arrows indicate that region of the traces from which the expanded insets are taken. The coupling ratio in this case is 0.69. Inset horizontal scale, 0.2 s; vertical scale, 6 mV.

ing power of the inner ear is dependent upon the ability to physically perturb small, discrete portions of the basilar membrane, upon which the organ of Corti lies, it would appear non-advantageous that supporting cells ionically and electrically communicate over long distances. Thus it may be requisite for normal function that the inner ear's unique compartmentalization maintains low coupling ratios and space constants for the supporting cells.

Electrical coupling can be modified by alterations of cellular ionic environment. For example, acidification of cell cytoplasm can decrease coupling (Spray et al., 1981). This is also true for *in vitro* preparations of the organ of Corti (Santos-Sacchi, 1985). Although it is demonstrated here that the unique compartmentalization of the inner ear maintains low coupling ratios and space constants *in vivo*, it is not known what particular aspect of the physiological compartmentalization is responsible for this observation. We have preliminary evidence (Santos-Sacchi and Marbey, un-

publ.), however, that the endolymphatic potential is not a contributing factor. In addition, it is known that high K^+ solutions do not decrease the coupling ratio *in vitro* (Santos-Sacchi, 1986b). Experimental modifications of the endolymph composition *in vivo* may provide a means to determine possible contributions.

Interestingly, Chuang et al. (1985) have found differences between electrical coupling in explanted vs. intact newt embryo epithelium. They suggested that the extraepithelial environment in the intact system promoted coupling as compared to the explant system. It is known that hormones and second messengers can influence the production and the conduction of gap junctions in sensitive tissues, such as the myometrium and sympathetic neurons (MacKenzie and Garfield, 1985; Wolinsky et al., 1985). It is conceivable that in the present experiments something similar is occurring. That is, perhaps the lateral wall produces some factor which acts via the endolymph to inhibit coupling, or the *in vitro* and *in vivo* stria removed condition provides some factor to enhance coupling. In the myometrium (MacKenzie and Garfield, 1985), estradiol treatment can actually increase the frequency of gap junctions between smooth muscle cells. It would be worthwhile evaluating, ultrastructurally, the frequency of occurrence and structure of gap junctions in the inner ear under high and low coupling conditions.

In contrast to our initial concepts (Santos-Sacchi and Dallos, 1983), it is now established that dye coupling is present in the *in vitro* preparation of the organ of Corti (Santos-Sacchi, 1986a). This suggests that metabolic cooperation may occur between the supporting cells of the organ. However, the present finding that electrical coupling in the normal *in vivo* preparation is poor could indicate that dye coupling *in vivo* is likewise poor. This may not be the case, however, depending on the reason for the poor electrical coupling *in vivo*. Coupling ratios are dependent not only upon the junctional resistance between cells but also upon the non-junctional membrane resistance. Thus coupling ratios may increase or decrease due to an increase or decrease in the non-junctional membrane resistance, without a concomitant alteration of junctional conductance. If the poor coupling *in vivo* is simply due to a lower membrane resistance

than is present *in vitro*, dye coupling may not be compromised. Yet, if the difference in coupling ratios is due to junctional conductance differences, then the degree of dye coupling may correspond with the degree of electrical coupling. Since the organ is an electrical syncytium, only input resistance can be measured directly and this measure is a function of both membrane and junctional resistances. Dye coupling studies performed *in vivo* will help determine whether junctional conductance is similar to that measured *in vitro*.

Acknowledgements

This work was supported by an RCDA from NINCDS and grants from the Deafness Research Foundation, the Foundation of the UMDNJ, and NIH (NS 21380-01). I thank Barbara Fate for her technical assistance.

References

- Bennett, M.V.L. (1966) Physiology of electrotonic junctions. *Ann. NY Acad. Sci.* 137, 509–539.
- Bernardini, G., Peracchia, C. and Venosa, R.A. (1981) Healing over in rat crystalline lens. *J. Physiol.* 320, 187–192.
- Bosher, S. and Warren, R. (1968) Observations on the electrochemistry of the cochlear endolymph of the rat, a quantitative study of its electrical potential and ionic composition as determined by means of flame spectrophotometry. *Proc. R. Soc. B*171, 227.
- Bosher, S.K. and Warren, R.L. (1978) Very low calcium content of cochlear endolymph, an extracellular fluid. *Nature* 273, 377–378.
- Chuang, H.H., Chuang-Tseng, M.P., Wu, W.L., Sandri, C. and Akert, K. (1985) Coupling of gap junctions by induction of impulse conductivity in cultured epithelium of newt embryo (*Cynops orientalis*). *Cell Tissue Res.* 241, 25–29.
- Dallos, P. (1985) The Role of Outer Hair Cells in Cochlear Function. In: *Contemporary Sensory Neurobiology*, pp. 207–230. Editors: M.J. Correia and A.A. Perachio. Alan R. Liss, New York.
- De Mello, W.C. (1983) The influence of pH on the healing-over of mammalian cardiac muscle. *J. Physiol.* 339, 299–307.
- Hudspeth, A.J. and Corey, D.P. (1979) Controlled bending of high input resistance electrodes. *Am. J. Physiol.* 234, C56–C57.
- MacKenzie, L.W. and Garfield, R.E. (1985) Hormonal control of gap junctions in the myometrium. *Am. J. Physiol.* 248, C296–C308.
- Santos-Sacchi, J. (1984) A re-evaluation of cell coupling in the organ of Corti. *Hear. Res.* 14, 203–204.
- Santos-Sacchi, J. (1985) The effects of cytoplasmic acidification upon electrical coupling in the organ of Corti. *Hear. Res.* 19, 207–215.
- Santos-Sacchi, J. (1986a) Dye coupling in the organ of Corti. *Cell Tissue Res.* 245, 525–529.
- Santos-Sacchi, J. (1986b) The temperature dependence of electrical coupling in the organ of Corti. *Hear. Res.* 21, 205–211.
- Santos-Sacchi, J. and Dallos, P. (1983) Intercellular communication in the supporting cells of the organ of Corti. *Hear. Res.* 9, 317–326.
- Slepecky, N. and Chamberlain, S.C. (1983) Distribution and polarity of actin in inner ear supporting cells. *Hear. Res.* 10, 359–370.
- Spray, D.C., Harris, A.L. and Bennett, M.V.L. (1981) Gap junctional conductance is a simple and sensitive function of intracellular pH. *Science* 211, 712–715.
- Wolinsky, E.J., Patterson, P.H. and Willard, A.L. (1985) Insulin promotes electrical coupling between cultured sympathetic neurons. *J. Neurosci.* 5, 1675–1679.

Asymmetry in Voltage-Dependent Movements of Isolated Outer Hair Cells from the Organ of Corti

J. Santos-Sacchi

Laboratory of Otolaryngology, UMDNJ–New Jersey Medical School, Newark, New Jersey 07103

The electrically induced movements of outer hair cells (OHC) were studied using the whole-cell voltage-clamp technique and video analysis. Cell shortening occurs during depolarization and elongation occurs during hyperpolarization from holding potentials near -70 mV. However, a marked asymmetry in response magnitude exists such that depolarization produces larger cell length changes than do comparable levels of hyperpolarization. The response is such that at normal resting potentials *in vivo*, displacements are about 2 nm/mV, but increase to about 15 nm/mV as the cell is depolarized. This mechanical rectification in the depolarizing direction manifests itself during symmetrical sinusoidal voltage stimulation as a “DC” reduction in cell length superimposed upon “AC” length changes. The observed OHC mechanical rectification may be involved in the reported production of “DC” basilar membrane displacements during suprathreshold acoustic stimulation (LePage, 1987). Estimates of the magnitude of OHC movements at acoustic threshold levels induced by receptor potentials in the high-frequency region of the cochlea indicate a disparity between basilar membrane and OHC movements on the order of 21 dB. Thus, it appears questionable whether OHC mechanical movements solely underlie the “active process” thought to be responsible for the high degree of neural tuning at sound pressures near 0 dB.

The organ of Corti is composed of a variety of cell types, including supporting and receptor cells. Two populations of receptor cells exist in the organ, inner (IHC) and outer hair cells (OHC). Each type of hair cell produces receptor potentials in response to acoustic stimulation (Dallos et al., 1982; Russell and Sellick, 1983). However, IHCs receive the majority of afferent innervation from the eighth nerve (Spoendlin, 1969), indicating the IHC's predominant role in information transfer to the CNS. It is becoming increasingly clear that OHCs influence, possibly through mechanical means, the electrical activity of IHCs (Mountain, 1980; Siegal and Kim, 1982; Brown et al., 1983; Nuttall, 1985). The net result of this interaction is the exquisite tuning characteristics and sensitivity of eighth nerve fibers.

Direct electrical stimulation of isolated OHCs induces reversible cell length changes on the order of micrometers which

are not based upon an actin–myosin system (Brownell et al., 1985; Ashmore, 1986; Brownell, 1986; Kachar et al., 1986). These fast mechanical responses, measured up to 8 kHz (Ashmore and Brownell, 1986; Ashmore, 1987), conceivably underlie the mechanical interactions alluded to above and appear to depend upon transmembrane potential since blocking the known ionic conductances of these cells during voltage clamp does not interfere with the mechanical response due to depolarization (Santos-Sacchi and Dilger, 1988a, b). Thus, the OHC may function as both receptor and effector, generating receptor potentials that modify cell length and, in turn, influence organ of Corti micromechanics.

Brownell (1983, 1984) first demonstrated the polarity dependence of electrically induced OHC movements—hyperpolarizing currents elongate and depolarizing currents shorten the OHC. Studies on the displacement magnitude due to electrical stimulation in the hyperpolarizing and depolarizing directions have provided conflicting results. Ashmore (1987) determined that the responses are largely symmetrical, whereas Evans (1988) found them to be asymmetrical. The asymmetry noted by Evans indicates that for a given stimulus magnitude, elongation of the OHC is as much as 50% greater than shortening. Considering the recent finding of LePage (1987) that basilar membrane “DC” displacements occur in response to tone bursts and that OHC movements may be implicated, it is important to determine the existence and extent of mechanical rectification in the OHC.

Preliminary reports of some of the results have been presented (Santos-Sacchi, 1988a, b).

Materials and Methods

Sensory and supporting cells were isolated from guinea pig cochleas by gentle pipetting of the isolated top 2 turns of the organ of Corti. No enzymatic digestion was employed for hair cell isolation. The cell-enriched supernatant was then transferred to a 700 μ l perfusion chamber, and cells were permitted to settle onto the coverglass bottom. A Nikon Diaphot inverted microscope with Hoffmann optics was used to observe the cells during electrical recording. A modified Leibovitz medium (NaCl, 142.2 mM; KCl, 5.37 mM; CaCl_2 , 1.25 mM; MgCl_2 , 1.48 mM; HEPES, 5.0 mM; dextrose, 5.0 mM; pH 7.0–7.2) was used as the perfusate. Patch electrodes (flint glass) had initial resistances of 3–5 M Ω . The series resistance, i.e., the actual electrode resistance obtained upon establishment of whole-cell configuration, typically ranged from 8 to 15 M Ω . These values were estimated from current transients initiated at the onset of voltage pulses and were corrected during analysis (Marty and Neher, 1983). Pipette solutions were composed of 140 mM KCl, 1, 5, or 10 mM EGTA, 2 mM MgCl_2 , and 5 mM HEPES buffered to pH 7.0–7.2. Giga-ohm seals were obtained at the nuclear level of the OHC membrane prior to whole-cell recording.

Single cells were clamped to holding potentials near -70 mV using a Dagan patch-clamp amplifier. Under computer control, hyperpolarizing and depolarizing voltage steps, 200 msec long, nominally ranging from -170 to $+30$ or $+50$ mV, in 10 or 20 mV steps, were used to elicit membrane currents and mechanical movements. Current records, filtered at 2 kHz with an 8-pole Bessel filter, were digitized and stored

Received Sept. 29, 1988; revised Jan. 13, 1989; accepted Jan. 30, 1989.

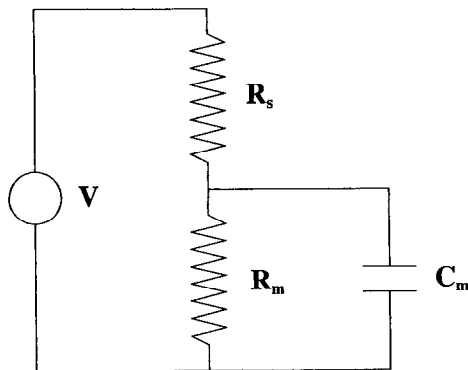
Supported by an NINCDS Research Career Development Award and NIH grant NS21380. I thank C. Witzmann and J. Nolan for technical assistance, and Jont Allen and Bill Brownell for many helpful discussions.

Correspondence should be addressed to J. Santos-Sacchi, Laboratory of Otolaryngology, UMDNJ–New Jersey Medical School, MSB H518, 185 S. Orange Ave., Newark, New Jersey 07103.

Copyright © 1989 Society for Neuroscience 0270-6474/89/082954-09\$02.00/0

on a Data 6000 waveform analyzer and saved to disk for off-line analysis. All OHC movements were taped with a Panasonic AG6300 video recorder. Movements of the cuticular plate region were analyzed off the video monitor during playback using differential optoresistors (output filtered at 30 Hz) placed across the image of the cuticular plate at a monitor magnification of $2800\times$. The linearity of the optoresistor method was confirmed by measuring the video taped movement of the tip of a microelectrode driven by a piezoelectric bimorph element (Fig. 2C). Absolute values were determined by measuring off the video monitor the cell movement in response to the largest depolarizing voltage step. The error in absolute measures was estimated to be less than 20%. Apical and basal ends of the OHC move towards and away from the electrode insertion point during depolarization and hyperpolarization, respectively (Santos-Sacchi and Dilger, 1988a, b). Because the movement of the cuticular plate is relative to the stationary insertion point of the electrode, which was typically near the nuclear region, total cell length change was determined by multiplying the measured movements of the cuticular region by the ratio of total cell length to electrode-cuticular plate distance.

OHC capacitance measures were determined by 2 methods. Electrode shanks were coated with M-coat D (M-Line Accessories, Raleigh, NC) in order to reduce electrode capacitance, and during gigaseal establishment and prior to cell entry, electrode capacitance was compensated fully. For these procedures the current records were filtered at 7 or 10 kHz. The first method involved a determination of the time constant of the initial current transient of the whole-cell voltage-clamp circuit in response to a voltage step of 10 mV from the holding potential. The time constant was estimated by a computerized exponential fitting procedure. The electrode series resistance was estimated from the fitted onset current, and the cell resistance, corrected for the series resistance, was measured from the steady-state current. The capacitance and time constant of the cell were determined as follows (Lecar and Smith, 1985; Ogden and Stanfield, 1987):



Clamp - cell model

$$\tau_{\text{clamp}} = C_m R_{\parallel}, \text{ where } R_{\parallel} = \left[\frac{R_m R_s}{R_m + R_s} \right] \quad (1)$$

$$C_m = \frac{\tau_{\text{clamp}}}{R_{\parallel}} \quad (2)$$

$$\tau_{\text{cell}} = R_m C_m \quad (3)$$

where τ_{clamp} is the voltage-clamp time constant, C_m is the capacitance of the cell, R_m is the resistance of the cell, R_s is the series resistance of the electrode, R_{\parallel} is the parallel resistance of R_m and R_s , and τ_{cell} is the time constant of the cell.

The other method involved an AC analysis of the whole-cell voltage-clamp circuit, using a DSP-16 digital signal-processing unit with associated software (sys16; Ariel Corp., NY). After establishing whole-cell configuration, periodic swept frequency bursts (0.005–8 kHz) of a constant voltage (5–20 mV peak) were delivered through the electrode at a holding potential near -70 mV. The frequency response of the clamp amplifier was 10 kHz. Current responses were time-averaged a minimum of 20 times. The resultant average was fast-Fourier-transformed and stored for subsequent analysis. An analysis of the current magnitude responses provides the necessary information for cell-capacitance determination.

The input impedance of the whole-cell voltage-clamp model is given as follows (Lakshminarayanaiah, 1984), where $s = j\omega$, $\omega = 2\pi f$, and $j = \sqrt{-1}$:

$$Z_{\text{in}} = (R_s + R_m) \left[\frac{1 + R_m C_m s}{1 + R_m C_m s} \right] \quad (4)$$

Substituting the time constant terms τ_{\parallel} for $R_m C_m$ and τ_m for $R_m C_m$

$$Z_{\text{in}} = (R_s + R_m) \left[\frac{1 + \tau_{\parallel} s}{1 + \tau_m s} \right] \quad (5)$$

The resulting magnitude function for $I = V/Z_{\text{in}}$ is a high-pass response (see Fig. 6B) with a high-frequency asymptote whose magnitude is dependent upon R_s and whose 3 dB break frequency (f_{high}) is related to τ_{\parallel} . The low-frequency asymptote is dependent upon $R_s + R_m$, and its break frequency is related to τ_m . Thus, the capacitance can be calculated by

$$C_m = \frac{1}{2\pi R_{\parallel} f_{\text{high}}} \quad (6)$$

Results

A variety of cell types can be viably isolated from the mammalian organ of Corti. These include outer and inner hair cells, Deiter cells, and Hensen cells. Although OHCs and Deiter cells are easily isolated mechanically without the use of enzymatic treatment, Hensen cells require additional trypsinization to obtain single cells. IHCs are seen in short rows of cells.

Figure 1 illustrates $I-V$ plots of these cell types with their associated current traces. All cells demonstrate an outward rectification upon depolarization from a holding potential near -70 mV. In Hensen cells and OHCs these outward currents have been shown to be K^+ currents (Santos-Sacchi and Dilger, 1986, 1988a, b; Santos-Sacchi, 1988a, b). The magnitude and voltage dependence of outward rectification varies among cell type, with the IHC demonstrating the largest currents. The time dependence of outward currents also differs, although OHCs and Deiter cells are similar. Despite some electrical similarities among these cells, only OHCs respond to voltage steps from the holding potential by altering their cell length (Fig. 2). The length changes are not dependent upon specific or total transmembrane current but appear to be voltage dependent (Santos-Sacchi and Dilger, 1988a, b).

The direction of the OHC length changes depends upon the polarity of the step; however, the magnitude of length change is not equal for symmetrical voltage displacements of opposite polarity. Depolarizations elicit larger mechanical responses than do hyperpolarizations. Figure 2, A, B illustrates whole-cell currents and mechanical responses for an isolated OHC in response to voltage steps above and below the holding potential of -67 mV. Time- and voltage-dependent outward currents are generated in response to depolarization; inward currents generated upon hyperpolarization probably represent currents of the anomalous inward rectifier, as described by Ohmori (1984) in vestibular hair cells. The voltage-dependent displacements of the OHC are linear with voltage steps in the depolarizing direction (up to $+20$ mV, above which the response begins to saturate; Santos-Sacchi and Dilger, 1988a, b). However, mechanical responses saturate rapidly at step levels more negative than the holding potential. This phenomenon is demonstrated for 9 cells in Figure 3. In each case, the mechanical response is rectified in the depolarizing direction. The average response in the depolarizing direction is about 15 nm/mV; in the hyper-

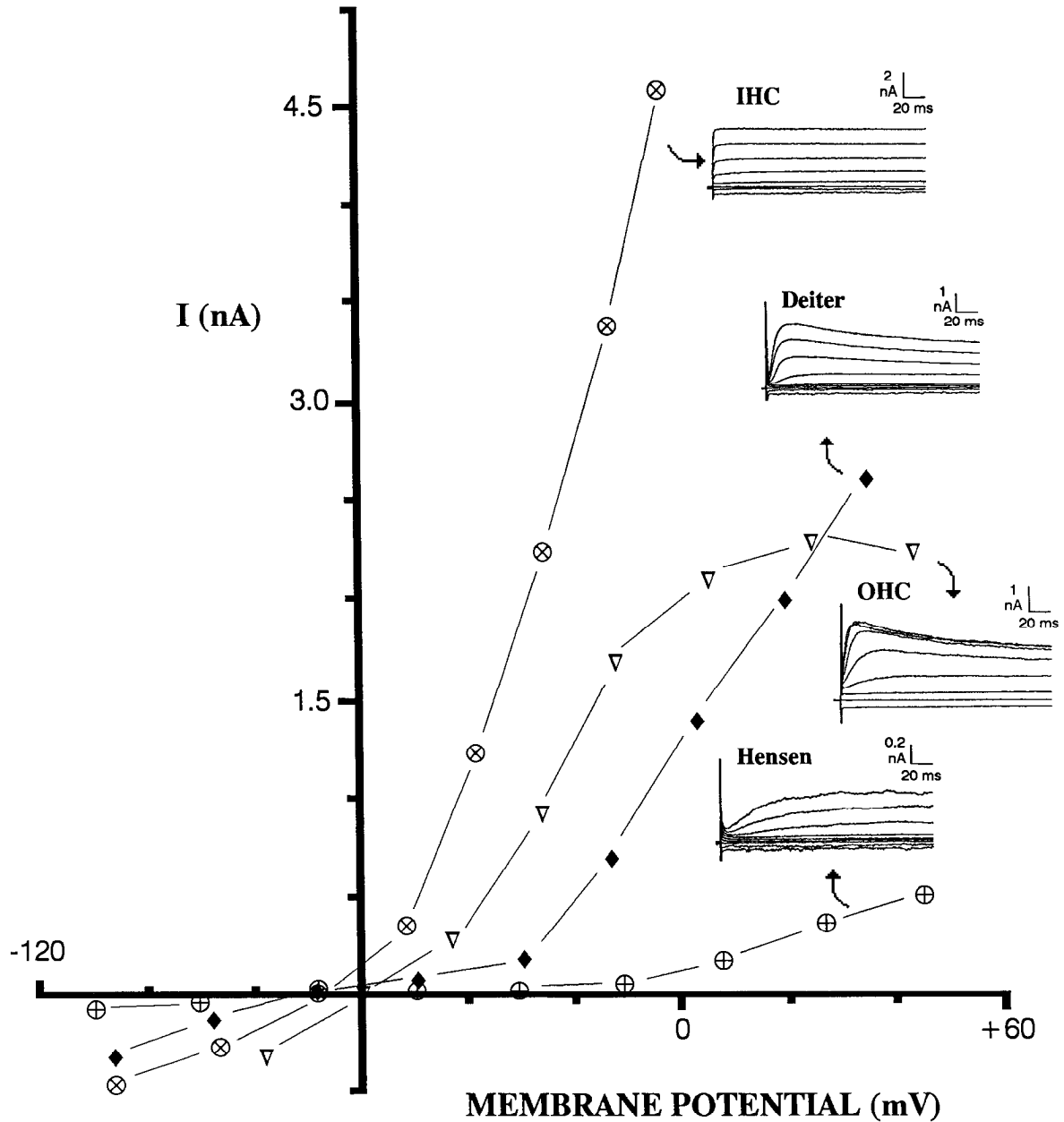


Figure 1. Examples of current recordings from isolated cells from the organ of Corti under whole-cell voltage clamp. Electrode solution contained 140 mM K⁺, 2 mM MgCl₂, 1 mM EGTA, 5 mM HEPES, pH 7.0. Traces and plots are not leakage-subtracted. Note differences in current-magnitude scales beside each trace. Holding potentials and input resistances corrected for series resistance: Hensen cell, -69.6 mV, 687 M Ω ; Deiter cell, -68.3 mV, 127 M Ω ; OHC, -59.7 mV, 69 M Ω ; IHC, -67.4 mV, 92 M Ω .

polarizing direction, it is about 2 nm/mV. It was of interest to determine whether the rectified mechanical response is dependent upon rectified currents generated during voltage steps (Santos-Sacchi and Dilger, 1988a, b). Treatments that block the various ionic conductances of OHCs (e.g., intracellular Cs⁺, extracellular Cd²⁺, Ba²⁺, TEA) also do not affect the mechanical rectification. Figure 4 demonstrates the Ca²⁺ independence of the mechanical rectification. In this case, the electrode solution contained 5 mM EGTA and no added calcium, and the extracellular medium contained 1 mM EGTA with no added calcium.

This mechanical rectification indicates that sinusoidal voltage stimulation should produce a sustained shortening of the OHC during an AC voltage stimulus. This, in fact, occurs. Figure 5A

demonstrates the mechanical rectification of an OHC in response to 400 msec bursts of a 10 Hz command voltage of about 90 mV peak to peak, at a holding potential near -70 mV. The "AC" mechanical response is superimposed upon a "DC" shift (reduction) in the length of the cell. The trace in Figure 5B is the response of a glass probe driven at 10 Hz by a piezoelectric bimorph, which displays symmetrical movements, indicating that rectification under these conditions is not due to the measuring technique. Higher frequency stimulation of OHCs also produced a "DC" shift, but the "AC" response appeared as a blurring of the image on the video monitor. Because the linear portion of the OHC mechanical response function lies roughly between -60 and $+20$ mV, the value of the holding potential

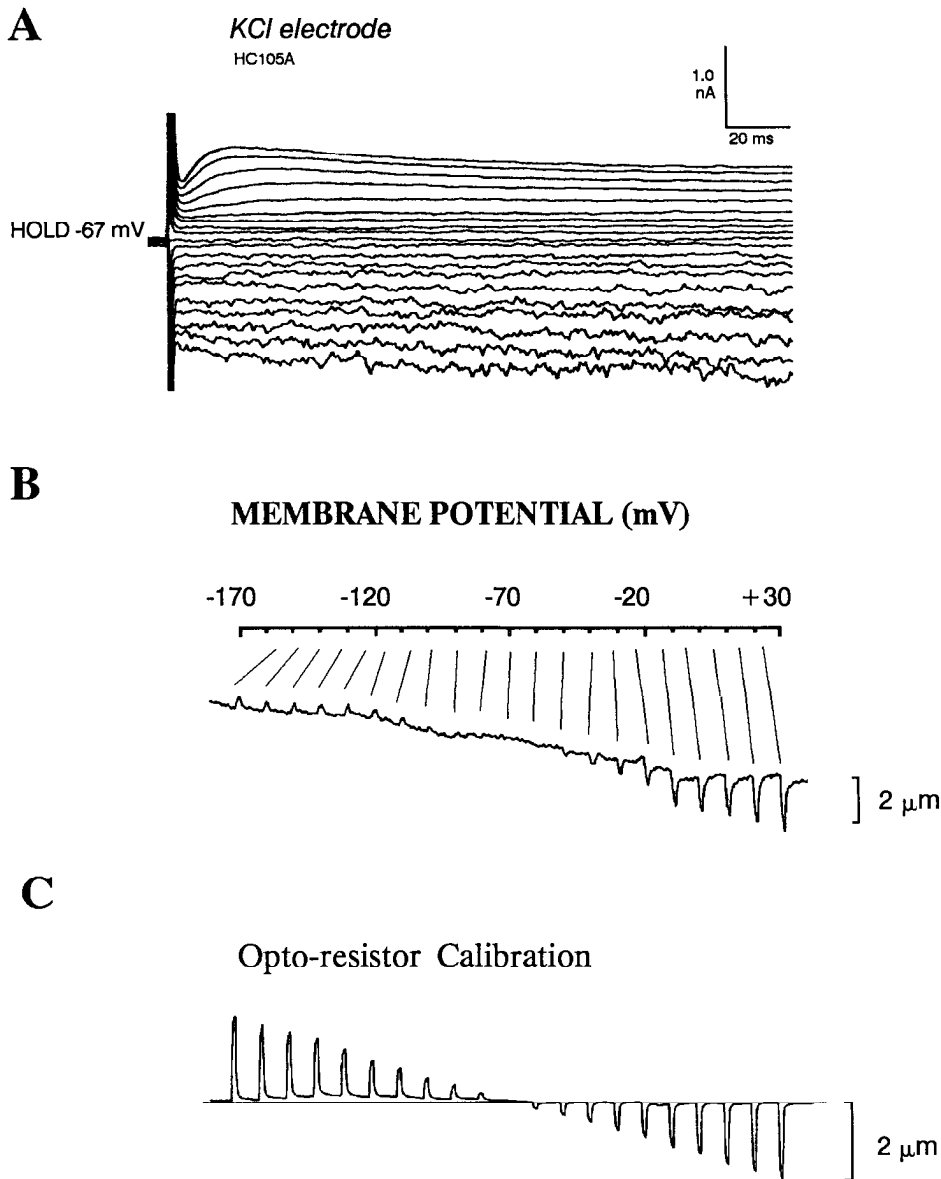


Figure 2. *A*, An isolated OHC was whole-cell voltage-clamped at a holding potential of -67 mV and stepped to various membrane potentials for periods of 200 msec. The traces depict currents generated during depolarizations (upward) and during hyperpolarizations (downward). The membrane potentials during each step are illustrated in *B*. *B*, Record of the output from the differential optoresistor indicating the magnitude of the cell's displacement (downward deflections represent cell shortening). The lines point to the membrane potential of the cell, corrected for series resistance, during each displacement. Note that cell elongations associated with hyperpolarizing voltage steps saturate rapidly above the holding potential, whereas cell contractions associated with depolarizations do not saturate in the range of voltages studied here. *C*, A glass probe driven by a piezoelectric bimorph was displaced for 200 msec and then returned to baseline. Twenty displacements, in linearly graded steps, were produced such that an absolute maximum displacement of about ± 2 μm about the resting baseline was video recorded. The displacements were measured during playback with differential optoresistors placed on the video screen over the image of probe, perpendicular to the displacement axis. The linearity of the measuring device is evident in the recorded output.

should influence the direction of mechanical rectification due to sinusoidal stimulation. Figure 5C illustrates this effect. When the holding potential is changed from -70 to 0 mV, the direction of the "DC" length shift appears to reverse. This occurs because the hyperpolarizing phase of the stimulus now resides in the linear portion of the mechanical response function, whereas at a holding potential of -70 mV the depolarizing phase of the stimulus resided in the linear portion of the function.

Capacitance of the OHC was estimated for a total of 15 cells using 2 methods described in Materials and Methods. Figure 6 illustrates examples for each method. The current transient method ($n = 8$) yielded an average (\pm SD) capacitance of 38.6 ± 4.7 pF, with an average clamp time constant (τ_{clamp}) equal to 0.34 ± 0.072 msec and an average cell resistance equal to 96 ± 91 M Ω . The AC analysis method ($n = 7$) yielded a capacitance of 39.5 ± 5.7 pF, with an average τ_{clamp} equal to 0.38 ± 0.15 msec and an average cell resistance equal to 80 ± 34 M Ω . These measurements indicate an average OHC membrane time constant of about 3.5 msec.

The average cell surface area of these cells, using a cylindrical cell body model and not including stereocilia, was $2.32 \pm 0.45 \times 10^{-5}$ cm 2 for the transient analysis group and $2.50 \pm 0.38 \times 10^{-5}$ cm 2 for the AC analysis group. Stereocilia measures were not included because most cells lose their stereocilia during the isolation procedure. If actual basolateral surface area is 133% of that estimated from light microscopy (due to lateral membrane ruffling; Dallos, 1983), then the specific capacitance of the OHC membrane is roughly 1.2 $\mu\text{F}/\text{cm}^2$.

Discussion

Of all the cells studied that rest upon the basilar membrane, only the OHCs appear to respond to voltage alterations by modifying their cell length. These cells are truly unique in that they may function as both receptor and effector. The mechanical responses of OHCs are large in the depolarizing direction, attaining length reductions up to a few micrometers; however, the responses are rectified such that at typical *in vivo* resting potentials of -70 to -90 mV, responses are much smaller. Thus, at

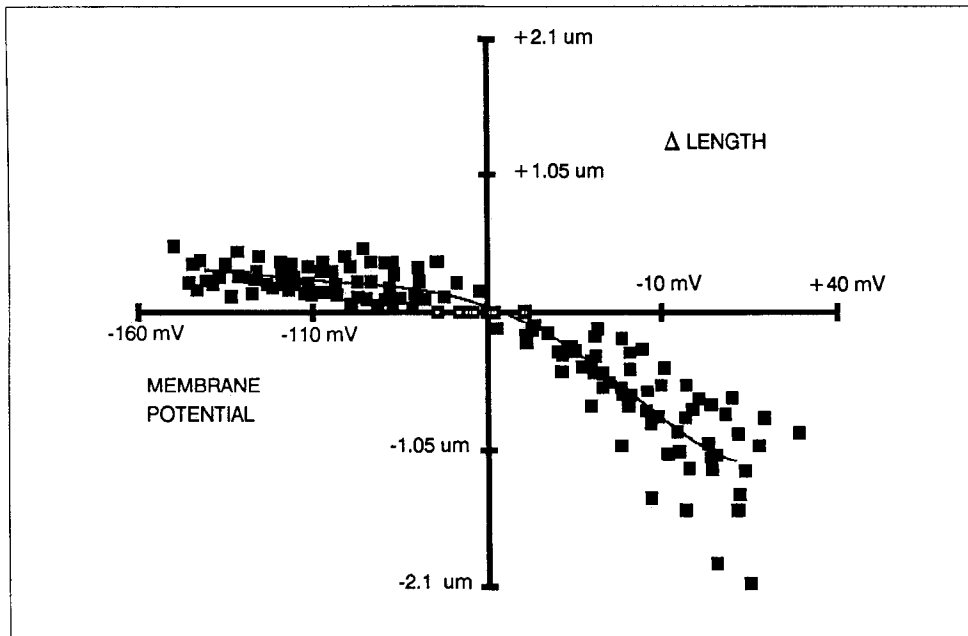
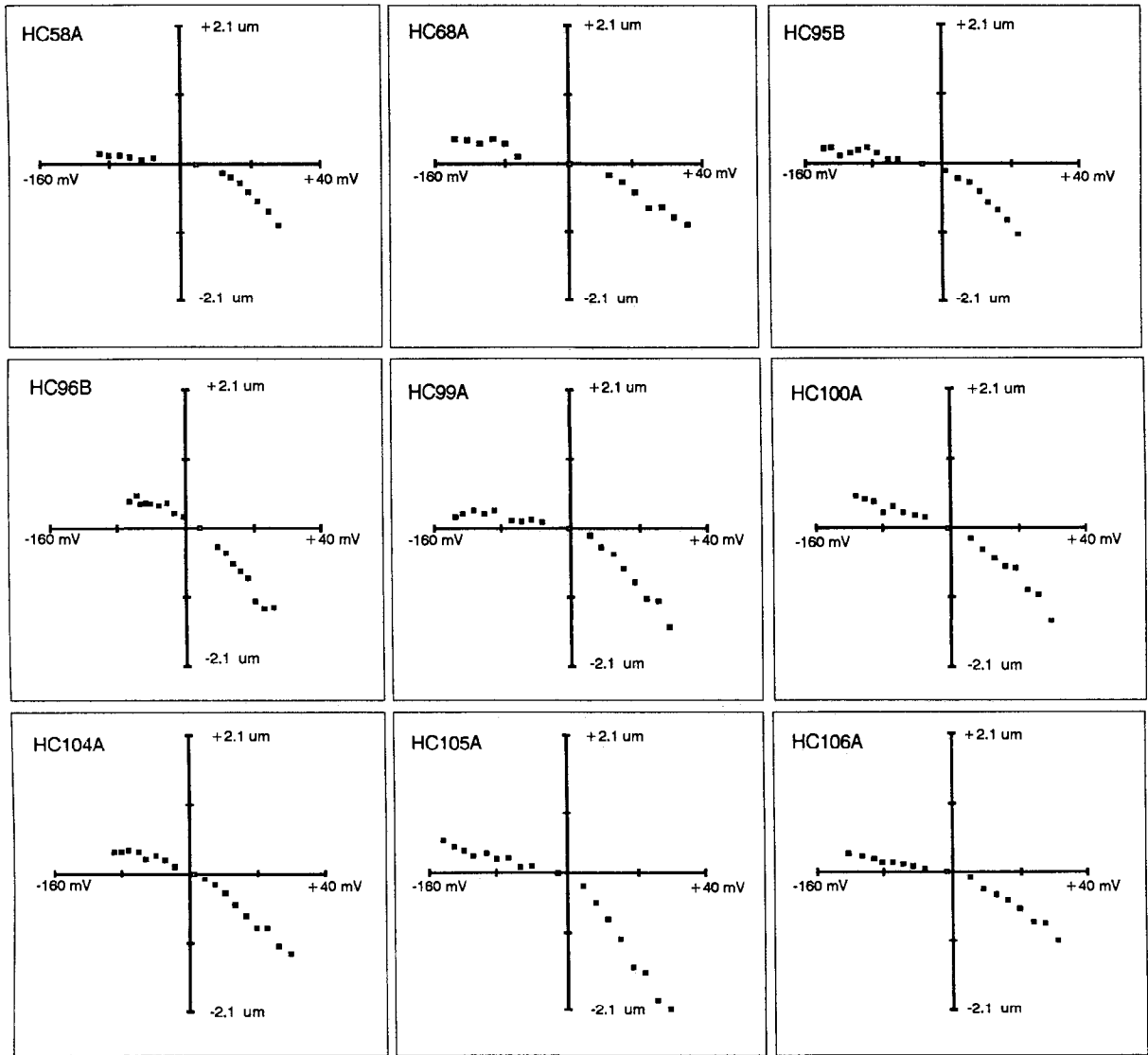
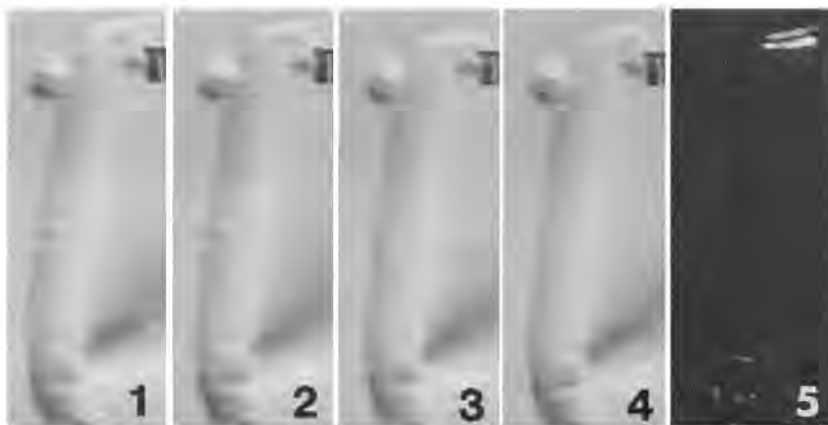
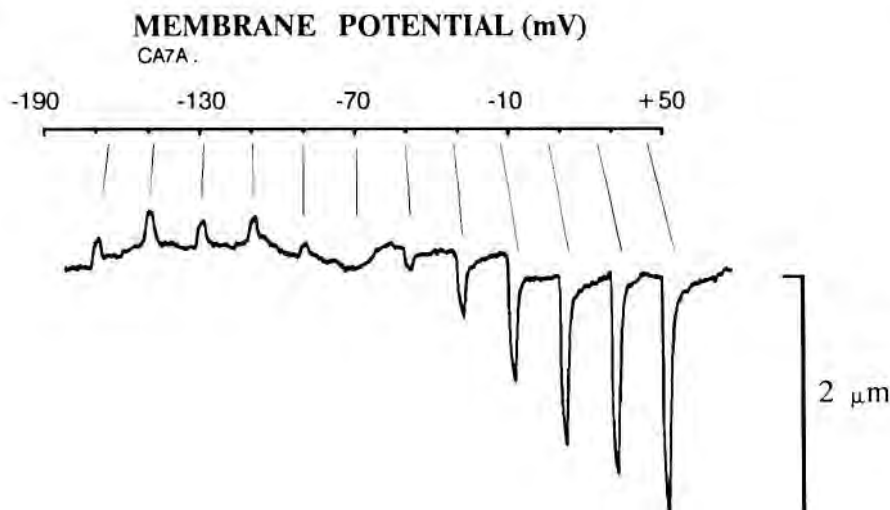


Figure 3. Voltage-displacement functions for 9 OHCs. Open boxes on the abscissa indicate the holding potential. Each function was measured as in Figure 2. In each case, mechanical responses to depolarizations are larger than equivalent amplitude hyperpolarizations. Pooled data in the bottom plot clearly indicate the mechanical rectification in the depolarizing direction. The average slope in the depolarizing direction is about 15 nm/mV, and in the hyperpolarizing direction < 2 nm/mV.

A**B**

the cell's normal resting potential it is capable of shortening to a greater extent than lengthening. Evans (1988) reported that mechanical responses are asymmetrical but that elongation is greater than shortening for a given stimulus strength. In that study, cells were stimulated with transmembrane current via an extracellular electrode, and membrane potential was not measured. Because isolated OHCs can have depolarized membrane potentials, and cell movement is not dependent upon absolute transmembrane current (Santos-Sacchi and Dilger, 1988a, b), it is difficult to interpret these data. It is possible, however, that the results represent responses under depolarized conditions, where hyperpolarization would be a more effective stimulus because of the mechanical response saturation in the depolarizing direction.¹

Ashmore (1987) reported on mechanical responses of OHCs under whole-cell voltage clamp. Near the holding potentials

¹ Recently, Evans et al. (1989) have demonstrated that asymmetry in the OHC mechanical response due to extracellular AC current stimulation is biphasic. At low current magnitudes, the "DC" component of the response is toward contraction. However, as the current magnitude is increased, the "DC" component eventually changes towards elongation.

used in that study, the mechanical responses were fairly symmetrical but saturated at reported voltage levels far removed from the holding potential (see figure 7, Ashmore, 1987). The rate of saturation in the hyperpolarizing direction was much less than reported here. However, in his study, the estimation of absolute voltage levels was confounded by the very high series resistance of the patch electrodes. The average value of the series resistance can be determined from the data presented in that report and calculates to about 83 M Ω .² The voltage divider effect

² Ashmore (1987) reported that the average time constant of his clamp (τ_{clamp}) was 1.29 msec, which, incidentally, was erroneously reported to be the OHC's membrane time constant. Cell capacitance (C_m) was reported to be 27.3 pF, and from his data on 7 cells that the OHC mechanical movements were 2.11 nm/pA, or correspondingly, 19.8 nm/mV (p. 331), an average input resistance (R_{in}) of 106 M Ω can be deduced. Although this value of input resistance is very similar to our results (Santos-Sacchi and Dilger, 1988a, b), the actual value in his report may be less since series resistance compensation, when performed, was not complete (as indicated in his figure legends). Using this value, however, the average series resistance can be calculated as

$$R_s = \frac{R_{\text{in}} \tau_{\text{clamp}}}{(R_{\text{in}} C_m) - \tau_{\text{clamp}}} = 83.4 \text{ M}\Omega$$

Figure 4. Rectification of OHC mechanical response in Ca^{2+} -free, 1 mM EGTA extracellular media. Electrode solution contained 140 mM KCl, 2 mM MgCl_2 , 5 mM EGTA, 5 mM HEPES, pH 7.0. **A:** 1, Video print of digitally captured image of the OHC induced to elongate by stepping cell membrane potential from -69 to -165 mV. 2, After return to holding potential of -69 mV. 3, During voltage step to $+43$ mV. 4, After return to holding potential of -69 mV. 5, Digital subtraction of 3 and 4 indicating distance moved of cuticular plate. Note the obvious shortening of cell during depolarization but the difficulty in observing elongation due to hyperpolarization. Height of black mark in upper-right corner is 6 μm . **B,** Mechanical response measured with optoresistors indicating mechanical rectification as cell is stepped for 200 msec to various potentials from the holding potential of -69 mV.

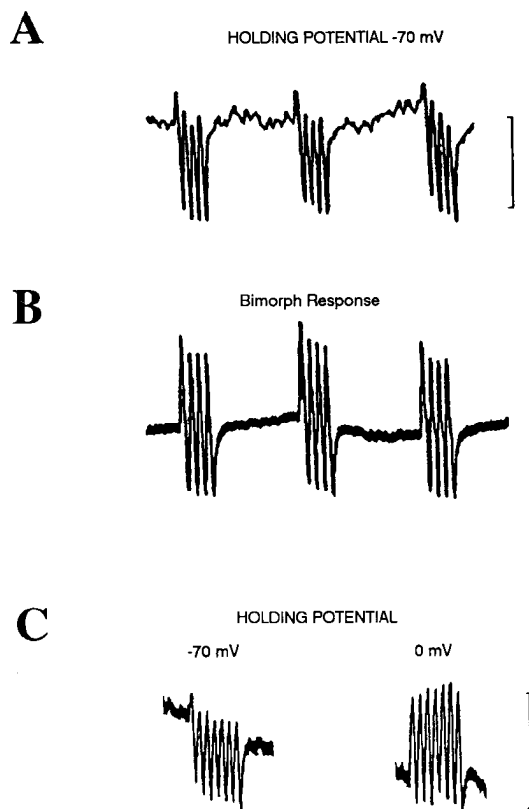


Figure 5. *A*, This trace depicts the movement of an OHC in response to 400 msec bursts of a 10 Hz voltage sinusoid at a level of 90 mV peak to peak. Downward deflections represent cell contractions. Note, in addition to an “AC” displacement at the stimulus frequency, a “DC” shift, indicating a sustained reduction in length during the stimulus. The frequency response of the optoresistor is considerably low-pass, such that the scale for the “AC” component whose magnitude was measured off the video monitor is $0.7 \mu\text{m}$ and that estimated for the “DC” component is about $0.23 \mu\text{m}$. *B*, This trace illustrates the symmetrical response from a bimorph probe at 10 Hz, indicating that the “DC” offset is not due to the measuring procedure. *C*, Both traces illustrate movements of a different cell in response to stimuli as in *A*, except at bursts of 700 msec, and at the holding potentials indicated. Note that at the holding potential of -70 mV the “DC” displacement is in the downward direction (contraction), but at the holding potential of 0 mV the “DC” displacement is in the upward direction (elongation). Scale values are as in *A*.

of such a high series resistance will drastically compromise the amplifier’s ability to clamp the potential of OHCs whose membrane resistances are of the same magnitude. Even if series resistance is compensated somewhat, large overestimates of the membrane voltage will exist unless voltages are subsequently corrected for residual series resistance effects, which was not performed in that study. In the present study, patch electrode resistance was initially low and series resistance was corrected for during analysis. A correction for series resistance in Ashmore’s data would tend to reconcile some of the differences between our data.

We have previously studied the mechanical responses of OHCs in response to depolarizing voltage steps and determined that responses as large as 29 nm/mV occur (Santos-Sacchi and Dilger, 1988a, b). In the present study, the average response in the depolarizing direction was about 15 nm/mV . Ashmore (1987) obtained similar response magnitudes (19.8 nm/mV) in the lin-

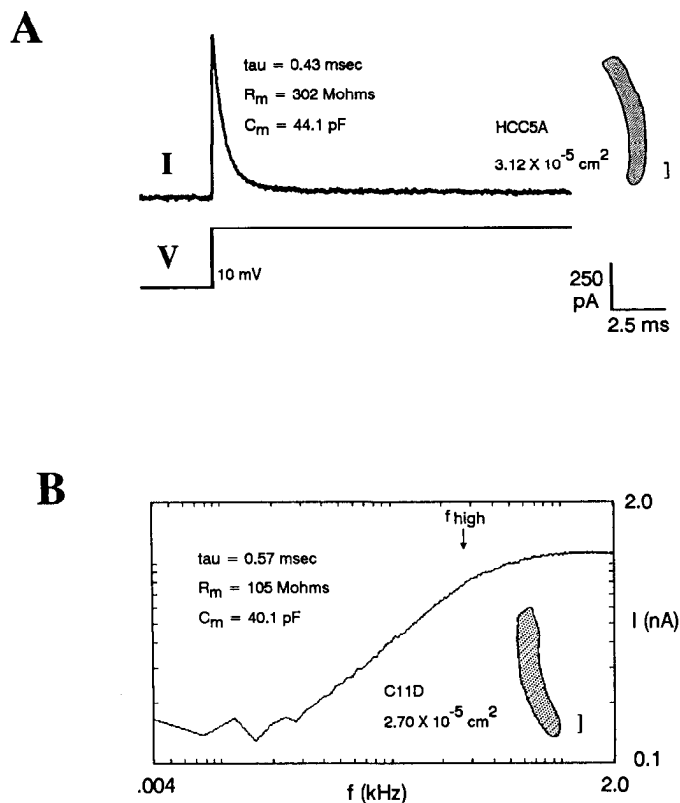


Figure 6. Examples of capacitance determination utilizing transient and AC analyses. *A*, OHC was voltage-clamped at a holding potential near -70 mV and a voltage step of 10 mV elicited a current response that was analyzed to determine the values indicated. See Materials and Methods for details. Cell outline is shown as drawn from the video monitor. Surface area was estimated as in Materials and Methods. Small scale bar, $10 \mu\text{m}$. *B*, OHC was voltage-clamped at a holding potential near -70 mV and the response to a periodic swept frequency burst (20 mV peak) was time-averaged 20 times. The FFT of this average is shown and was used to determine the values indicated. The high-frequency cutoff (f_{high}) is 286 Hz . See Materials and Methods for details. Cell outline is shown as drawn from the video monitor. Surface area was estimated as in Materials and Methods. Small scale bar, $10 \mu\text{m}$.

ear portion of OHC mechanical responses. The findings of the present study, however, indicate that at the normal resting potential of OHCs *in vivo* (-70 to -90 mV ; Dallos et al., 1982), mechanical responses are about an order of magnitude smaller, near 2 nm/mV . Thus, at low sound pressures, where receptor potentials are small and symmetrical, mechanical responses will be small and symmetrical.

Receptor potentials from OHCs in the apical and basal regions of the cochlea have been recorded *in vivo*, and the tuning of these cells is as fine as basilar membrane or neural tuning (Dallos et al., 1982; Khanna and Leonard, 1982; Patuzzi and Sellick, 1983; Robles et al., 1986; Russell et al., 1986). Clearly, if basilar membrane tuning is dependent upon an “active” mechanism (Neely and Kim, 1986) and the active mechanism is indeed the mechanical response of OHCs, then the effect should be present at threshold, near sound pressure levels of 0 dB , where the sharpest tuning occurs. At present, the data, especially for the high-frequency region of the organ, are not persuasive. The problem stems from the observation that the mechanical responses of the OHCs are voltage dependent. This dependency places constraints upon the physiological relevance of the phe-

nomenon at frequencies where hair cell receptor potentials, the presumed stimuli for OHC mechanical responses, are attenuated by the membrane time constant, τ_{cell} . The scenario is somewhat more complex; since the mechanical response is dependent upon transmembrane potential, the effects of extracellular potentials, the cochlear microphonic and summing potential, must be accounted for in determining actual transmembrane potential.

The specific capacitance of the OHC membrane was calculated in the present study to be about $1.2 \mu\text{F}/\text{cm}^2$. For the large low-frequency OHCs (60–80 μm in length) utilized in this study, the calculated membrane time constant, τ_{cell} , was about 3.5 msec. Calculations using data in Ashmore (1987) give a time constant of about 3 msec. These figures indicate a cutoff frequency for OHCs in the low-frequency area of the cochlea of about 46 Hz. This is markedly different from the time constants obtained *in vivo* from receptor potential measures, where corner frequencies near 1200 Hz are obtained from OHCs (Dallos and Santos-Sacchi, 1983). These measures indicate a time constant of 0.13 msec. Of course, input resistance measures of OHCs *in vivo* are low, averaging 30 M Ω or less. This may be due to the poor sealing properties of the high-resistance microelectrodes used and may account for the small time constants observed. Alternatively, the input resistance of hair cells under *in vivo* conditions may be less than measured *in vitro*. Ohmori (1985) obtained time constants for vestibular hair cells *in vitro* that ranged from 4.5 to 50 msec. He speculated that activation of membrane conductances at physiologically depolarized membrane potentials may reduce the cell's time constant. For OHCs in the high-frequency region of the cochlea where cell length is about one-third, the time constant should not be too different from that of the low-frequency OHC, considering that, as capacitance of the cell decreases due to less membrane surface area, input resistance will likely increase.

Response magnitudes near auditory threshold for OHCs in the apical and basal regions are quite small. Electrical measurements made in the low-frequency area of the cochlea are not hampered by the roll-off associated with high-impedance electrode filter characteristics, but in the high-frequency region corrections are required. After such corrections (Russell et al., 1986), threshold measures from OHCs in the 14 kHz region indicate AC responses near $15 \mu\text{V}$. In the 0.8 kHz region, AC responses in OHCs at 0 dB SPL have been measured, and magnitudes up to $100 \mu\text{V}$ occur (Dallos and Santos-Sacchi, 1983; Dallos, personal communication). Using this information from low-frequency OHCs, a corroboration of the OHC response at 14 kHz can be made, considering a 6 dB/octave roll-off above 1200 Hz for *in vivo* OHCs (Dallos and Santos-Sacchi, 1983; Russell et al., 1986). The calculated value of about $9 \mu\text{V}$ is in agreement with that calculated from Russell et al. (1986). Thus, estimates of OHC mechanical responses (assuming a 2 nm/mV movement at resting potentials near -70 mV) generated by

receptor potentials near threshold are probably less than 0.03 nm in magnitude. Corresponding basilar membrane displacement at the high-frequency region is 0.35 nm (Sellick et al., 1982), which indicates a disparity of about 21 dB between basilar membrane displacement and OHC movements.

These calculations indicate that a possible influence of OHC mechanical responses at threshold is questionable, especially at high frequencies where active mechanisms are most expected. At higher suprathreshold levels, however, 2 mechanisms will affect the mechanical movements of the OHCs—first, the inherent nonlinear mechanical response magnitude function described here (i.e., a shift from 2 nm/nV towards 15 nm/mV at increasing depolarization levels) and, second, the inherent rectification present in the receptor potential generator mechanism (Dallos et al., 1982; Russell et al., 1986). Theoretically, these 2 mechanisms should jointly promote an increased OHC shortening at progressively higher sound pressure levels, thereby raising the likelihood of OHC-basilar membrane interactions. In fact, at suprathreshold levels, rectified mechanical responses of OHCs may underlie some of the rapid “DC” basilar membrane displacements noted by LePage (1987) in response to tone bursts of 55–75 dB SPL. On the other hand, the cumulative displacements he also noted are not likely to reflect the fast mechanical motion of the OHCs but conceivably may be due to osmotic- or K^+ -induced OHC morphologic alterations (Zenner et al., 1985), which have a longer time course than the electrically induced movements. *In vivo* the time course of these slower movements may further reflect an ability of electrically communicating supporting cells to buffer K^+ released into the spaces of Nuel during hair and nerve cell excitation (Santos-Sacchi, 1986).

The demonstration by Kemp (1978) of otoacoustic emissions initiated the growing consensus that passive basilar membrane tuning is fine-tuned by an “active process” that somehow involves the OHC. A body of data confirms the OHC's role (Mountain, 1980; Siegal and Kim, 1982; Brown et al., 1983; Nuttall, 1985); and with the discovery of Brownell (1983), the source of this “active process” was assumed to be the ability of the OHC to alter its length (Geisler, 1986). The voltage dependence of these OHC mechanical responses (Santos-Sacchi and Dilger, 1988a, b) and the results presented here place constraints upon this assumption and suggest that other mechanisms may be involved. Indeed, it may be that a variety of factors supplementary to OHC mechanical responses, such as stereociliar and tectorial membrane micromechanics (Allen, 1980, 1988; Zwislocki and Kletsky, 1980; Crawford and Fettiplace, 1985; Zwislocki, 1986; Howard and Hudspeth, 1987) mutually effect sharp tuning at auditory threshold.

References

- Allen, J. B. (1980) Cochlear micromechanics—A physical model of transduction. *J. Acoust. Soc. Am.* 68: 1660–1670.
- Allen, J. B. (1988) Cochlear signal processing. In *Physiology of the Ear*, A. F. Jahn and J. Santos-Sacchi, eds., pp. 243–270, Raven, New York.

³ The symmetrical AC receptor potentials noted in high-frequency OHCs (Russell et al., 1986) may lead some to infer that these OHCs function in the linear region of their $I-V$ function and hence to infer that these cells normally function in the linear (15–29 nm/mV) range of the voltage-cell displacement function described here. The $I-V$ functions described for OHCs by various investigators are essentially DC evaluations and therefore cannot be used to predict high-frequency response characteristics. The current traces depicted here (Figs. 1, 2) and in previous reports (Santos-Sacchi and Dilger, 1988a, b) clearly show that the outward rectification is time dependent, with a time constant of several milliseconds. At increasingly smaller time intervals following voltage stimulation, the traces clearly show that the $I-V$ response becomes more and more linear, and more accurately reflects basolateral conductance effects upon high-frequency receptor potentials. Clearly, the OHC can produce symmetrical AC receptor poten-

tials at resting potentials ranging from -70 to -100 mV , if rectifying basolateral conductances are not activated by these potentials either because of their speed or small amplitude. Thus, symmetrical AC receptor potentials do not require that the cell function in the linear portion of the $I-V$ curve, and likewise do not indicate that the OHC is functioning in the 15–29 nm/mV range of the voltage-cell displacement function. The important factor determining whether the cell functions in the 2 or the 15–29 nm/mV range is the resting potential. OHCs whose normal resting potential is from -70 to -100 mV should function in the 2 nm/mV range, unless the cell is sufficiently depolarized.

- Ashmore, J. F. (1986) The cellular physiology of isolated outer hair cells: Implications for cochlear frequency selectivity. In *Auditory Frequency Selectivity*, B. C. J. Moore and R. D. Patterson, eds., pp. 103–108, Plenum, New York.
- Ashmore, J. F. (1987) A fast motile response in guinea-pig outer hair cells: The cellular basis of the cochlear amplifier. *J. Physiol. (Lond.)* 388: 323–347.
- Ashmore, J. F., and W. E. Brownell (1986) Kiloherz movements induced by electrical stimulation in outer hair cells isolated from the guinea-pig cochlea. *J. Physiol. (Lond.)* 377: 41P.
- Brown, M. C., A. L. Nuttall, and R. I. Masta (1983) Intracellular recordings from cochlear inner hair cells: Effects of stimulation of the crossed olivocochlear efferents. *Science* 222: 69–72.
- Brownell, W. E. (1983) Observations on a motile response in isolated outer hair cells. In *Mechanisms of Hearing*, W. R. Webster and L. M. Aitken, eds., pp. 5–10, Monash University Press, Clayton, Australia.
- Brownell, W. E. (1984) Microscopic observation of cochlear hair cell motility. *Scanning Electron Microsc. 1984/III*: 1401–1406.
- Brownell, W. E. (1986) Outer hair cell motility and cochlear frequency selectivity. In *Auditory Frequency Selectivity*, B. C. J. Moore and R. D. Patterson, eds., pp. 109–116, Plenum, New York.
- Brownell, W. E., C. R. Bader, D. Bertrand, and Y. de Ribaupierre (1985) Evoked mechanical responses of isolated cochlear outer hair cells. *Science* 227: 194–196.
- Crawford, A. C., and R. Fettiplace (1985) The mechanical properties of ciliary bundles of turtle cochlear hair cells. *J. Physiol. (Lond.)* 364: 359–379.
- Dallos, P. (1983) Some electrical circuit properties of the organ of Corti. I. Analysis without reactive elements. *Hear. Res.* 12: 89–119.
- Dallos, P., and J. Santos-Sacchi (1983) AC receptor potentials from hair cells in the low frequency region of the guinea pig cochlea. In *Mechanisms of Hearing*, W. R. Webster and L. M. Aitken, eds., pp. 11–16, Monash University Press, Clayton, Australia.
- Dallos, P., J. Santos-Sacchi, and A. Flock (1982) Intracellular recordings from cochlear outer hair cells. *Science* 218: 582–584.
- Evans, B. (1988) Asymmetries in outer hair cell electro-mechanical responses. In *Association for Research in Otolaryngology Abstracts of the Eleventh Midwinter Research Meeting*, p. 29, Clearwater Beach, FL.
- Evans, B., P. Dallos, and R. Hallworth (1989) Asymmetries in motile responses of outer hair cells in simulated in vivo conditions. In *Mechanics of Hearing*, J. P. Wilson and D. T. Kemp, eds. (in press).
- Geisler, C. D. (1986) A model of the effect of outer hair cell motility on cochlear vibrations. *Hear. Res.* 24: 125–131.
- Howard, J., and A. J. Hudspeth (1987) Mechanical relaxation of hair bundle mediates adaptation in mechano-electrical transduction by the bullfrog's saccular hair cell. *Neuron* 1: 189–199.
- Kachar, B., W. E. Brownell, R. Altschuler, and J. Fex (1986) Electrokinetic shape changes of cochlear outer hair cells. *Nature* 322: 365–368.
- Kemp, D. T. (1978) Stimulated acoustic emissions from within the human auditory system. *J. Acoust. Soc. Am.* 64: 1386–1391.
- Khanna, S. M., and D. G. B. Leonard (1982) Basilar membrane tuning in the cat cochlea. *Science* 215: 305–306.
- Lakshminarayanaiah, N. (1984) *Equations of Membrane Biophysics*, Academic, Orlando, FL.
- Lecar, H., and T. G. Smith, Jr. (1985) Voltage clamping small cells. In *Voltage and Patch Clamping with Microelectrodes*, T. G. Smith, Jr., H. Lecar, S. J. Redman, and P. W. Cagle, eds., pp. 231–256, American Physiological Society, Bethesda, MD.
- LePage, E. L. (1987) Frequency-dependent self-induced bias of the basilar membrane and its potential for controlling sensitivity and tuning in the mammalian cochlea. *J. Acoust. Soc. Am.* 82: 139–154.
- Marty, A., and E. Neher (1983) Tight-seal whole-cell recording. In *Single-Channel Recording*, B. Sakmann and E. Neher, eds., pp. 107–122, Plenum, New York.
- Mountain, D. C. (1980) Changes in endolymphatic potential and crossed olivocochlear bundle stimulations alter cochlear mechanics. *Science* 210: 71–72.
- Necly, S. T., and D. O. Kim (1986) A model for active elements in cochlear biomechanics. *J. Acoust. Soc. Am.* 79: 1472–1480.
- Nuttall, A. L. (1985) Influence of direct current on dc receptor potentials from the cochlear inner hair cells in the guinea pig. *J. Acoust. Soc. Am.* 77: 165–175.
- Ogden, D. C., and P. R. Stanfield (1987) Introduction to single channel recording. In *Microelectrode Techniques: The Plymouth Workshop Handbook*, N. B. Standen, P. T. A. Gray, and M. J. Whitaker, eds., pp. 63–81, The Company of Biologists, Ltd., Cambridge, U.K.
- Ohmori, H. (1984) Studies of ionic currents in the isolated vestibular hair cell of the chick. *J. Physiol. (Lond.)* 350: 561–581.
- Ohmori, H. (1985) Mechano-electrical transduction currents in isolated vestibular hair cells of the chick. *J. Physiol. (Lond.)* 359: 189–217.
- Patuzzi, R. B., and P. Sellick (1983) A comparison between basilar membrane and inner hair cell receptor potential input-output functions in the guinea pig cochlea. *J. Acoust. Soc. Am.* 74: 1731–1741.
- Robles, L., M. A. Ruggero, and N. C. Rich (1986) Basilar membrane mechanics at the base of the chinchilla cochlea. I. Input-output functions, tuning curves, and response phases. *J. Acoust. Soc. Am.* 80: 1364–1374.
- Russell, I. J., and P. M. Sellick (1983) Low frequency characteristics of intracellularly recorded receptor potentials in mammalian hair cells. *J. Physiol. (Lond.)* 338: 179–206.
- Russell, I. J., A. R. Cody, and G. P. Richardson (1986) The responses of inner and outer hair cells in the basal turn of the guinea-pig cochlea and in the mouse cochlea grown in vitro. *Hear. Res.* 22: 199–216.
- Santos-Sacchi, J. (1986) Dye coupling in the organ of Corti. *Cell Tissue Res.* 245: 525–529.
- Santos-Sacchi, J. (1988a) Whole cell voltage clamp studies on isolated outer hair cells. *Current Concepts of Hair Cell Function: A Consensus Meeting*, Kresge Hearing Research Institute, University of Michigan, June 1988, Ann Arbor, MI.
- Santos-Sacchi, J. (1988b) Rectified mechanical responses in outer hair cells from the mammalian organ of Corti. In *Abstracts Fourth International Congress of Cell Biology*, p. 155, Montreal, Québec, Canada.
- Santos-Sacchi, J., and J. P. Dilger (1986) Patch clamp studies on isolated outer hair cells. In *Advances in Auditory Neuroscience*, p. 23, The IUPS Satellite Symposium on Hearing, University of California, San Francisco, CA.
- Santos-Sacchi, J., and J. P. Dilger (1988a) Whole cell currents and mechanical responses in outer hair cells. In *Association for Research in Otolaryngology Abstracts of the Eleventh Midwinter Meeting*, p. 171, Clearwater Beach, FL.
- Santos-Sacchi, J., and J. P. Dilger (1988b) Whole cell currents and mechanical responses of isolated outer hair cells. *Hear. Res.* 35: 143–150.
- Sellick, P. M., R. Patuzzi, and B. M. Johnstone (1982) Measurement of basilar membrane motion in the guinea pig using the Mossbauer technique. *J. Acoust. Soc. Am.* 72: 131–141.
- Siegal, J. H., and D. O. Kim (1982) Efferent neural control of cochlear mechanics? Olivocochlear bundle stimulation affects cochlear biomechanical nonlinearity. *Hear. Res.* 6: 171–182.
- Spoendlin, H. (1969) Innervation patterns in the organ of Corti of the cat. *Acta Otolaryngol. (Stockh.)* 67: 239–254.
- Zenner, H. P., U. Zimmermann, and U. Schmitt (1985) Reversible contraction of isolated mammalian cochlear hair cells. *Hear. Res.* 18: 127–133.
- Zwislocki, J. J. (1986) Analysis of cochlear mechanics. *Hear. Res.* 22: 155–169.
- Zwislocki, J. J., and E. J. Kletsky (1980) Micromechanics in the theory of cochlear mechanics. *Hear. Res.* 2: 505–512.

HEARES 01514

Isolated supporting cells from the organ of Corti: Some whole cell electrical characteristics and estimates of gap junctional conductance

J. Santos-Sacchi

Laboratory of Otolaryngology, New Jersey Medical School, Newark, New Jersey, U.S.A.

(Received 12 July 1989; accepted 12 September 1990)

Whole cell voltage clamp studies were performed upon isolated and small groups of supporting cells from the guinea pig organ of Corti in order to evaluate junctional and non-junctional membrane characteristics. Single Hensen cells have an average input resistance and capacitance of 1.03 G Ω and 24.9 pF, respectively. I-V functions indicate an outward K⁺ rectification, which is blocked by external TEA, intracellular Cs, or photo-irradiation of intracellularly injected fluorescent dye. Voltage clamping of pairs or small groups of cells indicates that supporting cells 'share' K⁺ channels within the syncytium. The input impedance of coupled cells was studied during uncoupling with CO₂ or octanol media. As expected, coupled cells showed an increase in input capacitance and a decrease in input resistance over single cell values. Input capacitance is a more sensitive indicator of cell coupling than dc input resistance. During uncoupling, input capacitance values drop to single cell levels prior to an increase of dc input resistance to single cell levels. Modeling the results indicates that Hensen cells are well-coupled under normal conditions and may have junctional resistances with values less than 0.1% of the non-junctional resistance. The sensitivity of the supporting cell syncytium's input impedance to small changes in junctional resistance markedly influences the syncytium's RC filter characteristics, and thus may control the frequency response of sound evoked electrical activity measurable in supporting cells *in vivo*.

Voltage clamp; Organ of Corti; Supporting cells; Gap junctions; Cell coupling

Introduction

The mammalian organ of Corti is comprised of sensory (inner and outer hair cells) and supporting cells (e.g., Hensen, Deiter, Pillar cells). Ultrastructural studies established that the various supporting cells are joined to one another by gap junctions (Iurato et al., 1976; Jahnke, 1975; Gulley and Reese, 1976; Hama and Saito, 1977). Subsequently, it was demonstrated that these supporting cells are dye and electrically coupled, presumably via gap junctions (Santos-Sacchi and Dallos, 1983; Santos-Sacchi, 1984b; 1986a). Electrical coupling among these cells can be modulated by a variety of treatments, including alteration of intracellular pH, Ca²⁺ and temperature

(Santos-Sacchi, 1984a; 1985; 1986a). A possible physiological role for such coupling may involve K⁺ uptake and buffering in areas of the organ where hair cell and neuronal activity is high. Although electrical coupling between sensory and supporting cells may occur in the lower vertebrate inner ear (Weiss et al., 1975), ultrastructural studies (cited above) as well as indirect electrophysiological evidence (Oesterle and Dallos, 1988; 1989) indicate an absence of electrical communication between supporting and sensory cells in the mammal.

Previous measures of electrical coupling in the supporting cells have relied upon coupling ratio measurements (the ratio of voltage drops in adjacent cells due to current injection in one cell; Bennett, 1966) in the intact organ of Corti, both *in vitro* and *in vivo* (Santos-Sacchi, 1987). Because these measures were made in a coupled syncytium, no estimates of junctional conductance could be made. The present report relies upon the analysis

Correspondence to: J. Santos-Sacchi, Laboratory of Otolaryngology, New Jersey Medical School, MSB H518, Newark, NJ 07103, U.S.A.

of input impedance measures from isolated and small groups of supporting cells using whole cell voltage clamp to provide estimates of junctional and non-junctional conductances. Preliminary accounts of this work have been reported (Santos-Sacchi, 1988a, b).

Methods

Isolated Hensen cells or cell aggregates were obtained from the excised guinea pig organ of Corti by agitation for 15 min in Ca^{2+} -free Leibovitz medium containing 1 mg/ml of trypsin. The cell enriched supernatant was then transferred to a 700 μl perfusion chamber, and cells were allowed to settle and attach to the untreated glass bottom of the chamber at room temperature. A modified Leibovitz medium (NaCl 136.9 mM, KCl 5.37 mM, CaCl_2 1.25 mM, MgSO_4 0.81 mM, MgCl_2 , 0.98 mM, KH_2PO_4 0.44 mM, NaHPO_4 1.54, Dextrose 5.00 mM, pH 7.0) was used as the normal perfusate. In some experiments, 10 mM TEA was added to the culture media (NaCl adjusted) to block K^+ currents. The cells were washed with medium to remove the enzyme and cell debris (≈ 15 min) prior to recording, and were continuously perfused for the duration of each experiment. Pipette solutions were composed of 140 mM KCl or CsCl, 1 mM EGTA, 2 mM MgCl_2 , and 5 mM HEPES, pH 7.0. Patch electrodes (flint glass) had initial resistances of 3–5 $\text{M}\Omega$. Subsequent to the formation of gigohm seals, cells were whole cell voltage clamped at a holding potential near -70 mV and pulsed to various potentials for 200 ms at 1 s intervals, under computer control. Current traces sampled at 25–30 μs and filtered at 3 kHz with an eight pole bessel filter were observed on a D6000 waveform analyzer (Analogic, MA) and stored to disk for subsequent analysis. Actual voltages were obtained by correcting for the electrode series resistance (10–15 $\text{M}\Omega$) which was estimated from the capacitative current transient at the onset of the voltage pulse (Marty and Neher, 1983). Current values for I-V plots were obtained by averaging the final 20 ms of each current trace. Chord conductance [$g_{\kappa} = I/(V_m - V_{\text{eq}})$] for outwardly rectifying K^+ currents between -30 and 50 mV was calculated using a K equilibrium potential (V_{eq}) of -81 mV. Linear

leakage current was subtracted for these calculations.

Specific membrane capacity of biologic membrane is a fairly robust quality, which according to Cole (1971) is 'largely independent of cell physiology, pathology and pharmacology, and probably life itself.' Measurements of membrane capacitance have been used extensively during this cen-



Fig. 1. Video prints of isolated Hensen cells viewed with Hoffman optics. (a) single cell; (b) cell pair; (c) three cell group. Note lipid inclusions. Scale bar: 10 μm .

tury to estimate the amount of electrically contiguous membrane surface area of cells, a technique which has its origins in the classical experiments of Fricke (1925). In the present report, membrane capacitance measures are used in conjunction with input resistance measures to estimate changes in electrical coupling between and among supporting cells, since by definition, membranes of coupled cells are electrically contiguous.

In order to evaluate the changes of input capacitance and resistance during Hensen cell uncoupling, the cells were treated with the known uncoupling agents, CO_2 and octanol (Turin and Warner, 1977; Johnston et al., 1980). CO_2 saturated media was perfused through the chamber. Saturated octanol media was perfused directly on the cells via a separate small tipped pipette. At the holding potential, input capacitance and resistance were determined using 10 mV pulses of 25–30 ms duration, by integration of the capacitative current transient and measuring steady state current, respectively (Marty and Neher, 1983; Ogden and Stanfield, 1987). These measures were performed online every 3.5–4.5 s, and the results saved to disk. Data were smoothed using a three point running average, and for presentation purposes, sigmoidal fits were made.

Fluorescein was delivered through patch pipettes which contained 1–5% dye. Epi-illumination was provided by a Nikon Diaphot filter system with a 50 watt high pressure mercury lamp. All experiments were video taped with a Panasonic AG6300 recorder, and photographs were made with an Hitachi video printer.

Results

Hensen cells isolated from the apical turns of the guinea pig cochlea are readily identified by light microscopy due to their lipid inclusions (Fig. 1). Groups of any number of cells can be obtained, although with larger groups it is difficult to determine exact numbers. The size of the cells is quite variable as is indicated by input resistance and capacitance measures. Isolated cells have input resistances much higher than those determined from the intact organ of Corti ($1.03 \pm 0.585 \text{ G}\Omega$ [$N = 9$] vs. $0.5 \text{ M}\Omega$ [Santos-Sacchi, 1987a]), indicating the high degree of electrical coupling pre-

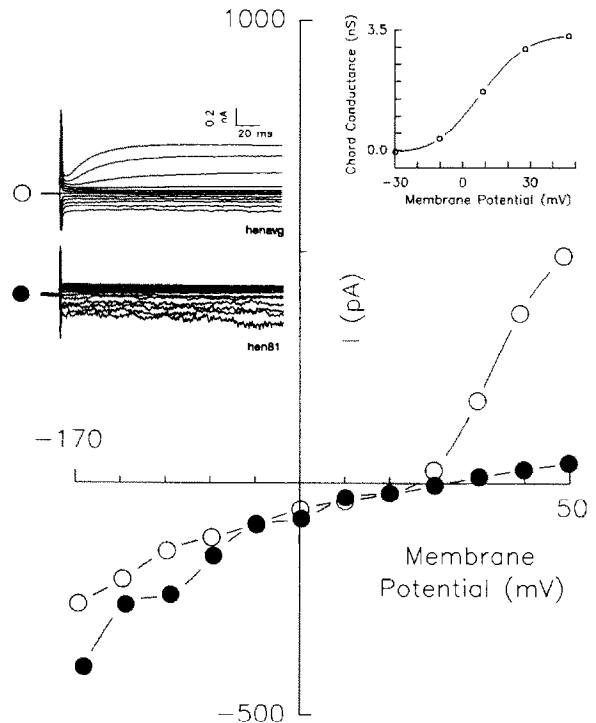


Fig. 2. Seven single isolated Hensen cells were individually whole cell voltage clamped at a holding potential of -70 mV , with normal perfusion media and KCl electrode solutions. The averaged traces (open circles) depict currents generated by pulsing the membrane potential to potentials nominally ranging from -170 to 50 mV , in steps of 20 mV . Outward current is upward. Linear leakage currents have not been subtracted in any of the figures. The I-V plot represents the averaged currents obtained during the last 20 ms of the traces, corrected for residual series resistance. Note the delayed outward rectification at potentials greater than -30 mV . Average resting potential estimated from zero current is -20 mV . Traces and I-V plot labeled with closed circles represent responses from a single isolated Hensen cell as above, except that CsCl replaced KCl in the patch pipette. Note the absence of outward rectification, indicating that K^+ ions are the charge carriers. Resting potential estimated from zero current is $+2 \text{ mV}$. Insert: Average K chord conductance after subtraction of linear leakage currents for the seven Hensen cells exhibiting outward rectification above (see Methods). Probability of K channel activation is very low at potentials more hyperpolarized than -30 mV and reaches a maximum value near $+50 \text{ mV}$.

sent in the intact in vitro syncytium. The average capacitance of these isolated cells was $24.9 \pm 9.19 \text{ pF}$. Fig. 2 shows averaged current traces and an I-V plot (open circles) obtained from 7 isolated Hensen cells in response to a series of voltage steps. Delayed outward currents were measured

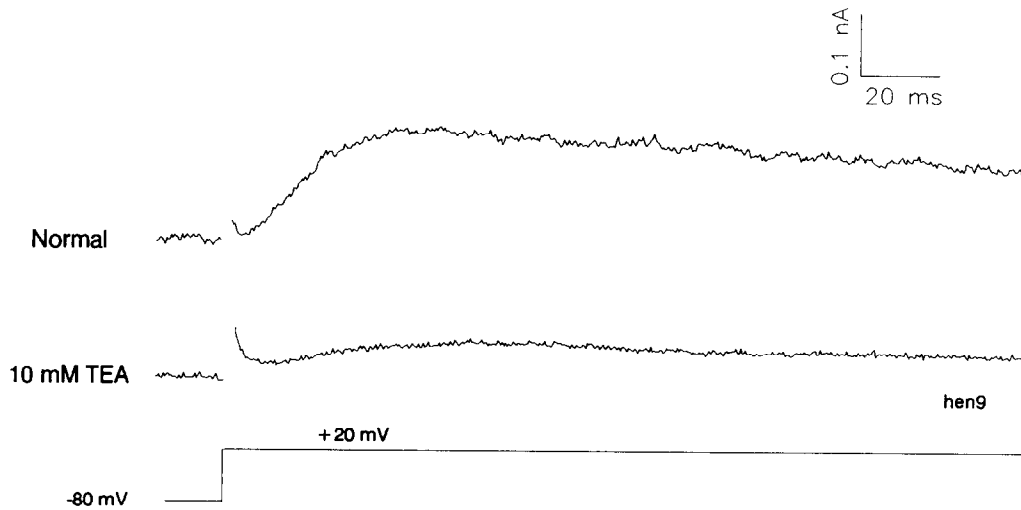


Fig. 3. Outward K^+ current trace obtained from a single Hensen cell before and after perfusion of the cell with 10 mM TEA solution. Note marked reduction of outward current in response to treatment with the K^+ channel blocker. Outward currents returned following washout of TEA. Zero current potentials before, during and after TEA treatment were -24 , -8 , -17 mV, respectively.

upon depolarizations greater than -30 mV, and were blocked by intracellular CsCl (closed circles), indicating that they are K^+ currents. Reversible block of these outward currents by 10 mM TEA provides further evidence that these currents are carried by K^+ (Fig. 3). Zero current levels for isolated cells recorded with the KCl intracellular solution indicate a resting potential of -20 mV. After subtraction of linear leakage currents, the average chord conductance for the outwardly rectifying K^+ currents increased sigmoidally from very low levels at -30 mV to a near maximum value of 3.3 nS at a potential of -47.3 mV (Fig. 2, insert). The inward currents noted upon hyperpolarization probably represent K^+ currents through the inward rectifier as has been demonstrated in the vestibular hair cell (Ohmori, 1985).

Interestingly, the outward K^+ currents were also blocked by photo-irradiating cells which had been perfused intracellularly with fluorescein (Fig. 4), a procedure which is known to electrically uncouple Hensen cells (Santos-Sacchi, 1986b). TEA, intracellular cesium, and photo-irradiation also produced a depolarization of isolated Hensen cells, as estimated from zero current levels (Figs. 2, 3 and 4); in the case of TEA blockade, repolarization follows washout.

Cell coupling in isolated cell aggregates was studied by noting cell input resistance and capacitance changes during uncoupling with CO_2 saturated media. Fig. 5 demonstrates uncoupling-induced changes in the I-V characteristics of a large group (≈ 10) of Hensen cells, one of which was whole cell recorded. The tremendous outward current depicted in Fig. 5 prior to uncoupling (note scales) indicates the summation of outward K^+ currents from the electrically coupled cells. Also note the summation of hyperpolarization-induced inward currents, and the large capacitive transients, indicating a large membrane surface area. Due to the large cytoplasmic volume resulting from coupling, and the attenuating effects of the junctional resistances, it is unlikely that all cells were voltage clamped equally; despite this, however, elicited currents indicate substantial voltage alterations in adjacent cells. After perfusion of the cells with CO_2 saturated medium, the cells uncouple from each other and the current traces approach those of a single cell. Fig. 6 depicts similar results obtained with a group of four Hensen cells. As expected, the currents and capacitive transients are smaller in magnitude than the 10 cell group; after CO_2 treatment, values approach that of a single Hensen cell. These data

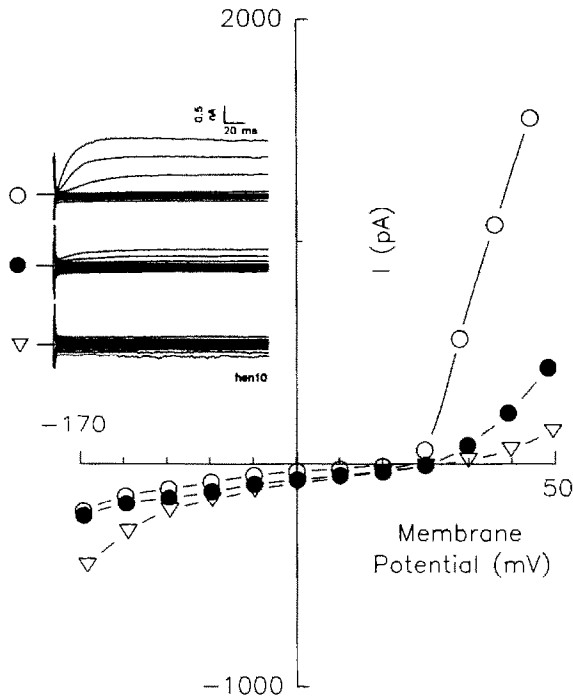


Fig. 4. Single isolated Hensen cell with KCl pipette solution, except that 5% fluorescein was added. I-V plot of steady state current vs. membrane potential corrected for series resistance. Open circles represent currents obtained after fluorescein had entered the cell, but prior to epi-illumination. Note outward rectification similar to cells not containing fluorescein. After 12 s of epi-illumination, the outward K^+ current is partially reduced (closed circles). After a total of 28s exposure, the K^+ current is markedly reduced, probably due to release of free radicals during fluorescence of the dye (open triangles). Membrane potential of the cell, estimated from zero current levels, decreased during the channel inactivation [0 s, -27 mV; 12 s, -8 mV; 28 s, -2 mV], indicating that K^+ permeability is involved in the maintenance of membrane potential in isolated cells.

suggest that coupled supporting cells 'share' K^+ channels via functional gap junctions. To provide clearer proof of this phenomenon, Fig. 7a shows the results of a similar treatment on a group of three Hensen cells; however, in this case, the K^+ channels of the recorded cell were blocked by the use of a CsCl electrode solution. Note that prior to uncoupling, outward K^+ currents are present, and represent only the currents generated in the adjacent coupled cells, since upon uncoupling by CO_2 treatment, the current response is solely from

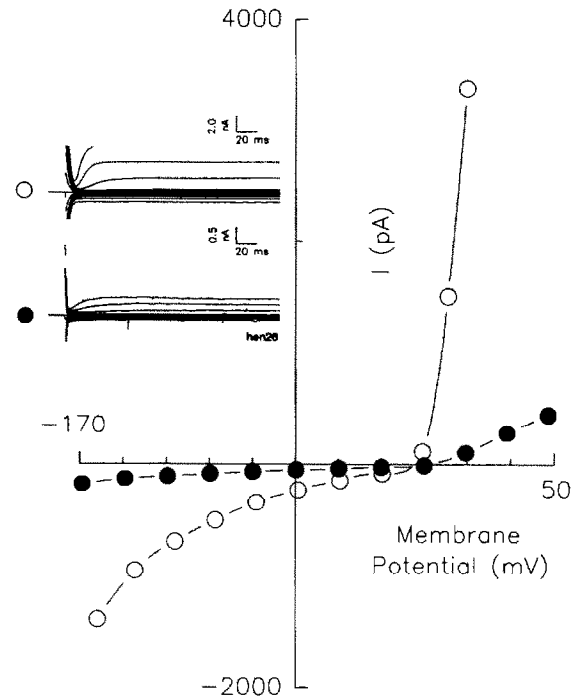


Fig. 5. Voltage clamp of single Hensen cell within a large group (≈ 10) of cells. I-V plot of steady state current vs. membrane potential corrected for series resistance. The tremendous outward current indicates the summation of outward currents from electrically coupled cells (open circles). Due to the large cytoplasmic volume resulting from coupling, it is unlikely that all cells were voltage clamped equally. After perfusion of the cells with CO_2 saturated medium, the cells uncouple from each other and the I-V response approaches that of a single cell (closed circles).

the recorded cell, and lacks outward currents due to the cesium block. Apparently, sufficient amounts of Cs^+ did not diffuse into the adjacent cells through gap junctions during the 5 min period required to collect the data. Fig. 7b shows the time course of input resistance and capacitance changes which accompany uncoupling. During CO_2 perfusion, input capacitance decreases and input resistance increases, until single cell values are attained.

Fig. 8a demonstrates the effect of octanol perfusion on a coupled Hensen cell pair. Octanol rapidly abolishes cell communication. During the process of uncoupling, it is typically found that input capacitance decreases to single cell values

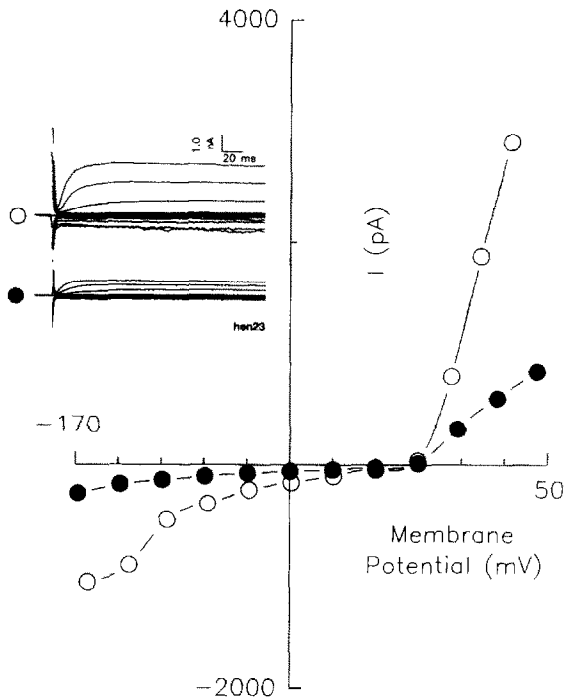


Fig. 6. Single Hensen cell within a group of four cells voltage clamped as in Fig. 5. Currents are smaller than that of the 10 cell group in Fig. 5, but larger than that of single cells, indicating that these cells are electrically coupled (open circles). After perfusion of CO_2 saturated medium, the I-V response is reduced to that of a single cell, confirming that the cells were coupled and that channel 'sharing' among the cells occurs (closed circles).

before dc input resistance reaches single cell values. The reversibility of octanol uncoupling is readily demonstrated by monitoring input capacitance during treatment and washout (Fig. 8b).

Discussion

Hensen cells display an outward rectification upon depolarization, which is mediated by K^+ channels. For individual Hensen cells, this current is small and is activated at potentials far removed from the normal *in vivo* resting potential. Deiter cells, supporting cells which are closely apposed to outer hair cells and are also coupled to Hensen cells (Santos-Sacchi, 1986b), exhibit larger outward currents (Santos-Sacchi, 1989). Supporting cells within the organ of Corti typically have resting potentials ranging from -60 to -100 mV, and are dependent upon extracellular K^+ con-

centration, since high extracellular potassium solutions produce reversible depolarizations in the *in vitro* organ (Santos-Sacchi, 1986a). The membrane potential of isolated supporting cells as determined from zero current levels is depolarized compared to normal resting levels, being on average about -20 mV. It has been demonstrated that the potential of Hensen cells in the intact (stria removed) *in vitro* organ of Corti is about -32 mV immediately upon removal from the animal, but increases to *in vivo* levels (-59 mV) over the course of a few hours only when the temperature is maintained at 37°C (Santos-Sacchi, 1985a). In that study, it was also shown that metabolic inhibitors can induce depolarization. Interestingly, whole cell recordings from isolated OHCs indicate that their membrane potentials are depolarized compared to *in vivo* values (Santos-Sacchi and Dilger, 1988; Dallos et al., 1982); but in many OHCs the potential approaches *in vivo* levels as the KCl patch pipette solution enters the cell over the course of a few minutes. This has not been observed with isolated Hensen cells. A variety of factors may be responsible for the depolarized state of isolated Hensen cells in this study, including temperature, use of simple salt solutions as opposed to culture media, and isolation procedure. Nevertheless, it has been shown that uncoupling agents will produce a depolarization in the Hensen cell syncytium (Santos-Sacchi, 1985; 1986a, b), and obviously, isolated cells and small groups of cells are uncoupled from the very large number of supporting cells normally forming the intact syncytium. It is demonstrated here that membrane potentials of isolated supporting cells are decreased by treatments (TEA, intracellular cesium, photoirradiation of intracellularly inject dye) which block K^+ conductance, indicating the dependence of membrane potential in these isolated cells upon a susceptible K^+ conductance. Conceivably, photoirradiation may produce free radicals which destroy K^+ channel function; Hensen cells have been shown to be uncoupled by the same treatment (Santos-Sacchi, 1986b). Clearly, the present results indicate that the supporting cells can 'share' ionic channels with neighboring cells, and for a cell type whose membrane potential is to some degree K^+ dependent, this may play an important role in maintaining the stable

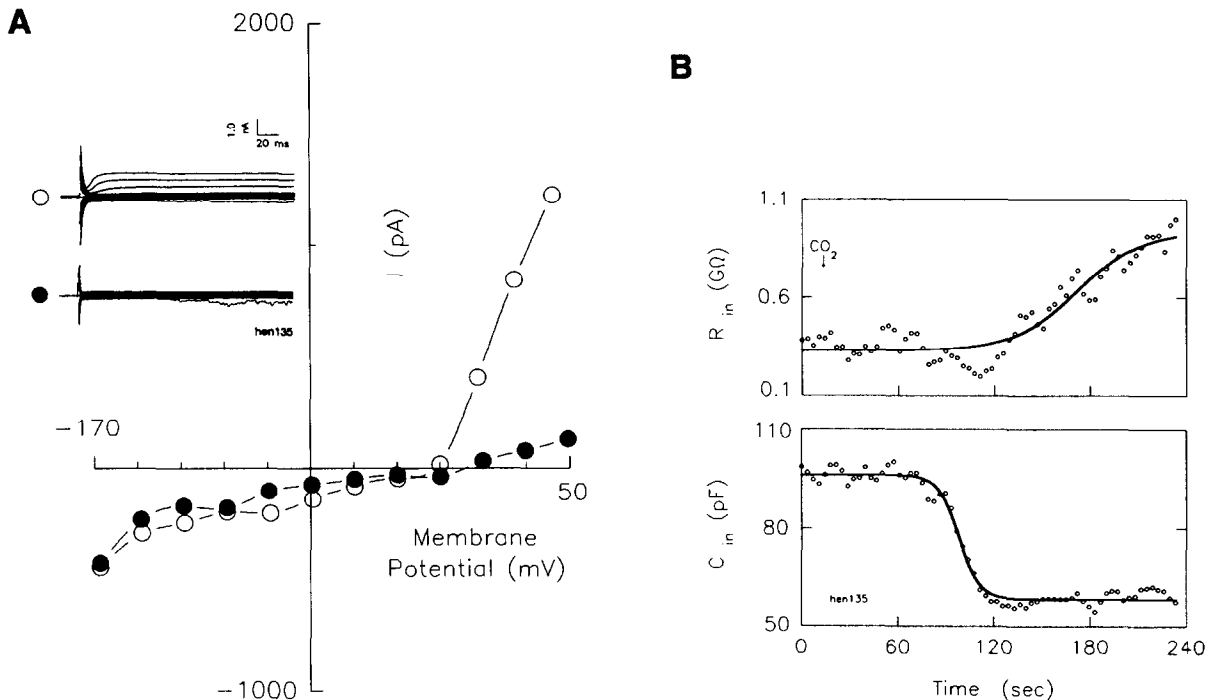


Fig. 7. (A) Single Hensen cell in a group of 3 Hensen cells was voltage clamped with a patch electrode containing the K^+ channel blocker CsCl. Normally, the CsCl patch solution will replace intracellular fluid and block the K^+ channels, thus eliminating outward rectification as in Fig. 2. In this case, however, outward rectification is present (open circles), because the pipette solution has not replaced the intracellular fluid of the other two coupled cells. Thus, the cell which is recorded from is utilizing the K^+ channels of its neighbors. After perfusion of CO_2 saturated medium, the cells uncouple and the cell recorded from appears as a single cell whose K^+ channels are blocked by Cs^+ (closed circles). (B) Time course of CO_2 uncoupling as indicated by changes in input resistance and capacitance. At onset of recording, R_{in} is low relative to isolated single cells and C_{in} is high relative to isolated single cells (see Results). During CO_2 medium perfusion, there is a dramatic change in these values, such that they approach the values of single cells, as would be expected in the uncoupled state. Note that capacitance values reach a minimum before resistance values reach a maximum.

resting potentials found *in vivo*. Maruyama et al. (1983) have estimated that isolated salivary acinar cells have few potassium channels per cell, numbering about 50. Open channel probability is very low at normal resting potentials, and since the possibility exists that no K^+ channels will be open at a given point in time, it was speculated that the stability of the K^+ -dependent resting potentials noted in the intact acinar syncytium is due to the sharing of these channels among coupled cells. The input conductance of isolated Hensen cells is less than 1 nS at the holding potential of -70 mV, and it appears that a major component of this may be due to linear leakage current. Conceivably, a non-specific leakage current may dominate any potential generating effects of a small K^+ conductance at normal resting potentials. Thus, it is

possible that the highly coupled nature of the supporting cells of the organ of Corti, with the attendant 'sharing' of K^+ channels, contributes to the stable, highly negative, K^+ -dependent resting potentials encountered in the intact syncytium. This would indicate that the drop in membrane potential noted upon uncoupling of Hensen cells (Santos-Sacchi, 1985; 1986a) may have been due to the reduction of utilizable neighboring cell K^+ channels.

The change in input resistance and capacitance which occurs upon uncoupling of cell groups or pairs is interesting in that the increase in input resistance is preceded by a reduction of input capacitance values to single cell levels. This type of behavior may not appear intuitive since one might expect both input capacitance and input

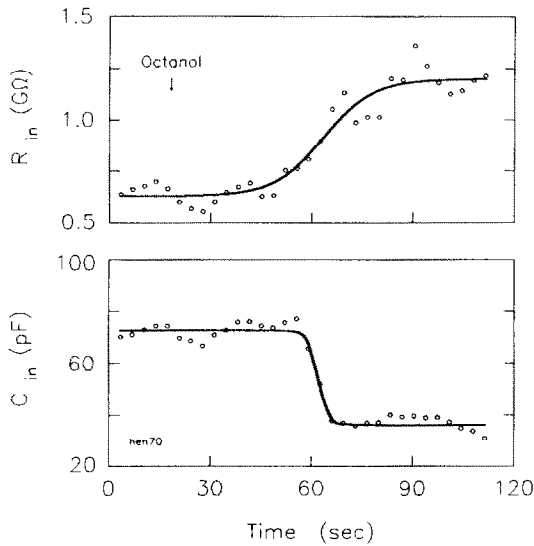
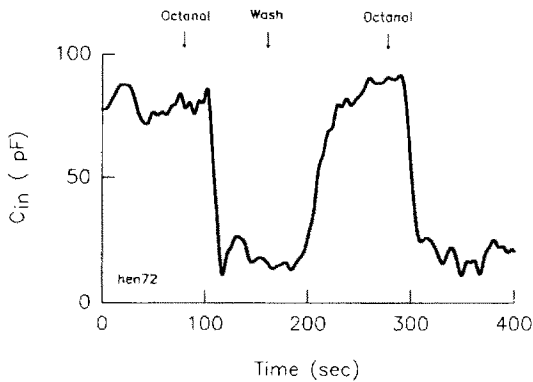
A**B**

Fig. 8. (a) Demonstration that octanol is capable of uncoupling a pair of Hensen cells. Note similarities with CO_2 uncoupling, i.e., the capacitance decreases to single cell values before resistance change is complete. Fig. 9 presents an electrical model based on these data. (b) Reversibility of uncoupling by octanol in a group of 4 Hensen cells. C_{in} decreases to single cell levels during perfusion with octanol, and returns to coupled state levels during washout. Further treatment with octanol uncouples the cells again.

resistance to change reciprocally. The results, however, are not aberrant, as is demonstrated by an analysis of cell models comprised solely of resistive and capacitive elements. In fact, these alterations of input impedance provide information which allows the estimation of gap junctional conductance between the Hensen cells. Fig. 9 de-

picts a circuit model and a voltage step analysis of a cell pair, with single cell component values of $1.1 \text{ G}\Omega$ and 35 pF , and a series resistance of $10 \text{ M}\Omega$, similar to the values obtained from the cell pair of Fig. 8a, after uncoupling.

Fig. 9 indicates the results of a computer simulation where the junctional resistance, R_j , is varied over ten orders of magnitude, and the input capacitance and dc resistance are plotted. It can be seen that the resultant changes in impedance are similar to those of the actual cells, and corroborates the observation that input capacitance is a more sensitive indicator of the state of coupling at low R_j values than dc input resistance. Analyses such as these indicate that junctional conductance in the supporting cells of the organ of Corti can be 3 orders of magnitude larger than non-junctional resting conductance, in this case about $1 \mu\text{S}$ vs. 900pS , respectively. Freeze fracture studies have indicated expansive areas of gap junctional mem-

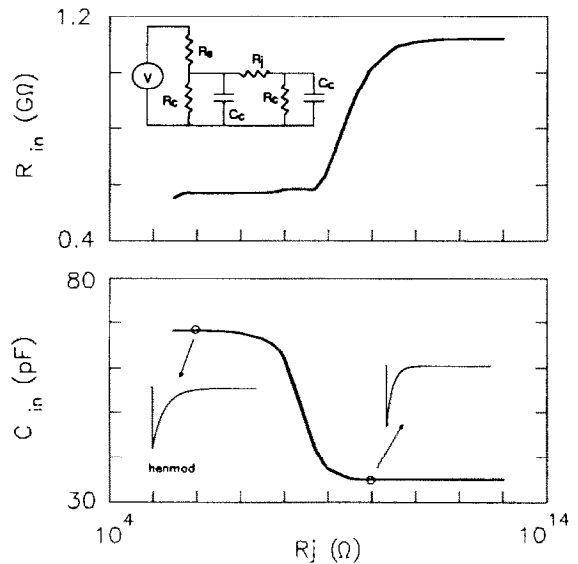


Fig. 9. Two cell model of uncoupling based on data from Fig. 8a. Values for individual cell resistance (R_c) and capacitance (C_c) are $1.1 \text{ G}\Omega$ and 35 pF , respectively. Electrode series resistance (R_s) is $10 \text{ M}\Omega$. Uncoupling was simulated by varying the junctional resistance (R_j) and a voltage step analysis of the network R_{in} and C_{in} was performed. The resulting plots are similar to actual data in that values approach single cell levels as junctional conductance is decreased. For these cells, R_j in the normal coupled state appears to be less than $1 \times 10^6 \Omega$. Capacitive current traces are shown for R_j values of $1 \times 10^6 \Omega$ and $1 \times 10^{10} \Omega$.

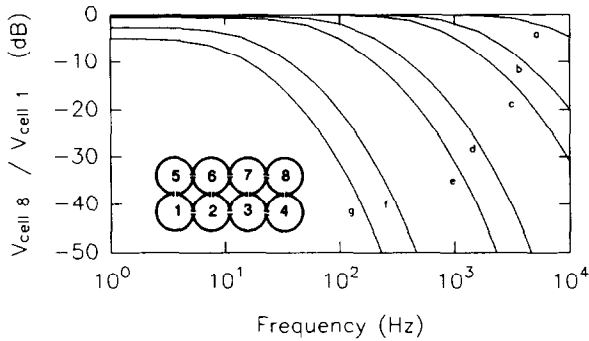


Fig. 10. Simulated ac response in cell 8 in response to a constant voltage injection into cell 1, in a coupled eight cell model (insert). Individual cell capacitances and resistances were 35 pF and 1 G Ω , respectively. Junctional resistances were varied: a, 0.1 M Ω ; b, 0.5 M Ω ; c, 1.0 M Ω ; d, 5.0 M Ω ; e, 10 M Ω ; f, 50 M Ω ; g, 100 M Ω . Note the dramatic drop in cutoff frequency as the junctional conductance is reduced, whereas very low frequency coupling is little affected.

brane which may account for such high junctional conductance (Jahnke, 1975; Gulley and Reese, 1976; Iurato et al., 1976).

Various investigators have recorded sound evoked electrical activity from mammalian supporting cells (Dallos et al., 1982; Goodman et al., 1982; Russell and Sellick, 1978; Oesterle and Dallos, 1986; 1989). In the mammal, this activity is thought to be passively picked up from hair cells (Russell and Sellick, 1978; Oesterle and Dallos, 1988, 1989). Regardless of the mechanism whereby acoustically evoked potentials are established in the supporting cells, it is important to understand the effects of junctional conduction upon such measures. The presently reported sensitivity of supporting cell input impedance to small changes in junctional conductance may indicate that the spectral content of evoked ac activity in supporting cells is sensitive to modifications of gap junctional communication. That is, small fluctuations in gap junctional conductance may alter the low pass RC filter effect of the coupled syncytium. This is examined in Fig. 10 where the ac frequency response is simulated in a model of eight coupled supporting cells. The ratio of the response measured in cell 8 to a constant voltage input into the system via cell 1 is plotted against frequency. The family of curves (a–g) represents the result of a decreasing junctional conductance (non-junctional

membrane conductance and capacitance kept constant, see figure legend for values), and indicates that the frequency response of a coupled cell in the syncytium falls dramatically with relatively small changes in junctional conductance. For example, a change in junctional conductance from 10 μ S (response a) to 0.1 μ S (response e) results in a two octave shift (reduction) in the high frequency cut-off, but only results in about a one dB drop in the dc (0.001 kHz) response. Clearly, good dc coupling can remain during dramatic changes in ac coupling. Since supporting cell coupling can be perturbed by a variety of micro-environmental influences (Santos-Sacchi, 1984a; 1985; 1986a) it is conceivable that fluctuations in organ of Corti homeostasis are more readily expressed as changes in ac coupling rather than dc coupling. This observation may prove useful in future evaluations of coupling in the organ of Corti. For example, in vivo studies of electrical coupling using a dc paradigm to measure cell-to-cell communication alterations during manipulation of the endolymphatic potential have demonstrated little effect upon coupling (Santos-Sacchi and Marbey, 1987). Perhaps an ac analysis would provide the required sensitivity to detect changes in junctional communication during such manipulations.

Finally, the sharing of K⁺ channels of the inwardly rectifying type may help buffer K⁺ levels in the extracellular spaces of the organ of Corti, where K⁺ levels may increase over perilymphatic levels due to sensory and neural activity. Increased K⁺ in the spaces of Nuel may induce slow length changes of outer hair cells (Goldstein and Mizukoshi, 1967; Zenner et al., 1985) and affect the rapid motility characteristics of these cells by its depolarizing effects (Santos-Sacchi, 1989). Obviously, extracellular K⁺ levels must be controlled. It is conceivable that the high resting membrane potentials of the supporting cells (up to –100 mV) may induce a steady state activation of the inward rectifier, thereby promoting K⁺ uptake; gap junctions may contribute to the overall buffering as is speculated in the CNS (Smojen, 1979).

Acknowledgments

Supported by an NINCDS Research Career Development Award and NIH grant NS21380. I

thank C. Witzmann, and Janet Santos for technical assistance.

References

- Bennett, M.V.L. (1966) Physiology of electrotonic junctions. *Ann. N.Y. Acad. Sci.* 137, 509–539.
- Cole, K.S. (1971) Some aspects of electrical studies of the squid giant axon membrane. In: W.J. Adelman (Ed.), *Biophysics and Physiology of Excitable Membranes*, Van Nostrand Reinhold, New York.
- Dallos, P., Santos-Sacchi, J. and Flock, Å. (1982) Intracellular recordings from cochlear outer hair cells. *Science* 218, 582–584.
- Fricke, H. (1925) The electric capacity of suspensions with special reference to blood. *J. Gen. Physiol.* 9, 137–152.
- Goldstein, A.J. and Mizukoshi, O. (1967) Separation of the organ of Corti into its component cells. *Ann. Otol. Rhinol. Laryngol.* 76, 414–426.
- Goodman, D.A., Smith, R.L. and Chamberlain, S.C. (1982) Intracellular and extracellular responses in the organ of Corti of the gerbil. *Hear. Res.* 7, 161–179.
- Gulley, R.S. and Reese, T.S. (1976) Intercellular junctions in the reticular lamina of the organ of Corti. *J. Neurocytol.* 5, 479–507.
- Hama, K. and Saito, K. (1977) Gap junctions between the supporting cells in some acousticovestibular receptors. *J. Neurocytol.* 6, 1–12.
- Iurato, S., Franke, K., Luciano, L., Werbter, G., Pannese, E. and Reale, E. (1976) Intercellular junctions in the organ of Corti as revealed by freeze fracturing. *Acta Otolaryngol.* 82, 57–69.
- Jahnke, K. (1975) The fine structure of freeze-fractured intercellular junctions in the guinea pig inner ear. *Acta Otolaryngol.* [Suppl.] 336.
- Johnston, M., Simon, S. and Ramon, F. Interaction of anesthetics with electrical synapses. *Nature* 286, 498–500.
- Marty, A. and Neher, E. (1983) Tight-seal whole-cell recording. In: B. Sakmann and E. Neher (Ed.), *Single-Channel Recording*. Plenum Press, N.Y., pp. 107–122.
- Maruyama, Y., Petersen, O.H., Flanagan, P. and Pearson, G.T. (1983) Quantification of Ca^{2+} -activated K^+ channels under hormonal control in pig pancreatic acinar cells. *Nature* 305, 228–232.
- Oesterle, E. and Dallos, P. (1989) Intracellular recordings from supporting cells in the guinea pig cochlea: AC potentials. *J. Acoust. Soc. Am.* 86, 1013–1032.
- Oesterle, E. and Dallos, P. (1988) Indirect evidence for the absence of electrotonic coupling between hair and support cells in the mammalian cochlea. 115th Meeting, Acoustical Society of America, May. *J. Acoust. Soc. Am.* 83 Supp. 1, p. S97.
- Oesterle, E. and Dallos, P. (1986) Intracellular recordings from supporting cells in the organ of Corti. *Hear. Res.* 22, 229–232.
- Ogden, D.C. and Stanfield, P.R. (1987) Introduction to single channel recording. In: N.B. Standen, P.T.A. Gray and M.J. Whitaker (Ed.), *Microelectrode Techniques: The Plymouth-Workshop Handbook*. The Company of Biologists, Ltd., Cambridge, U.K., pp. 63–81.
- Ohmori, H. (1984) Studies of ionic currents in the isolated vestibular hair cell of the chick. *J. Physiol. (Lond.)* 350, 561–581.
- Petersen, O.H. (1985) Importance of electrical cell-cell communication in secretory epithelia. In: M.V.L. Bennett and D.C. Spray (Ed.), *Gap Junctions*. Cold Spring Harbor Laboratory, N.Y., pp. 315–324.
- Russell, I.J. and Sellick, P.M. (1978) Intracellular studies of hair cells in the mammalian cochlea. *J. Physiol. (Lond.)* 284, 261–290.
- Santos-Sacchi, J. (1989) Asymmetry in voltage dependent movements of isolated outer hair cells from the organ of Corti. *J. Neurosci.* 9, 2954–2962.
- Santos-Sacchi, J. (1988a) Gap junctional communication in isolated supporting cells of the organ of Corti. Fourth Intl. Cong. of Cell Biol., Montreal, Quebec, Canada, August.
- Santos-Sacchi, J. (1988b) Whole cell studies of gap junctional communication in supporting cells of the organ of Corti. *Abstr. Assoc. Res. Otolaryngol.*, Clearwater, FL, February.
- Santos-Sacchi, J. (1987) Cell coupling differs in the in vitro and in vivo organ of Corti. *Hear. Res.* 25, 227–232.
- Santos-Sacchi, J. (1986a) The temperature dependence of electrical coupling in the organ of Corti. *Hear. Res.* 21, 205–211.
- Santos-Sacchi, J. (1986b) Dye coupling in the organ of Corti. *Cell Tissue Res.* 245, 525–529.
- Santos-Sacchi, J. (1985) The effects of cytoplasmic acidification upon electrical coupling in the organ of Corti. *Hear. Res.* 19, 207–215.
- Santos-Sacchi, J. (1984a) Increased intracellular H^+ and Ca^{++} uncouples the cells of Corti's organ. *Abstr. Assoc. Res. Otolaryngol.*, Clearwater, FL, February.
- Santos-Sacchi, J. (1984b) A reevaluation of cell coupling in the organ of Corti. *Hear. Res.* 14, 203–204.
- Santos-Sacchi, J. and Dallos, P. (1983) Intercellular communication in the supporting cells of the organ of Corti. *Hear. Res.* 9, 317–326.
- Santos-Sacchi, J. and Marbey, D. (1987) The effects of endolymphatic potential alterations on gap junctional communication in the organ of Corti. *Abstr. Assoc. Res. Otolaryngol.*, Clearwater, FL.
- Somjen, G.G. (1979) Extracellular potassium in the mammalian central nervous system. *Ann. Rev. Physiol.* 41, 151–177.
- Turin, L. and Warner, A. (1977) Carbon dioxide reversibly abolishes ionic communication between cells of the amphibian embryo. *Nature*, 270, 56–57.
- Zenner, H.P., Zimmermann, U. and Schmitt, U. (1985) Reversible contraction of isolated mammalian cochlear hair cells. *Hear. Res.* 18, 127–133.

Reversible Inhibition of Voltage-dependent Outer Hair Cell Motility and Capacitance

J. Santos-Sacchi^a

Laboratory of Otolaryngology, UMDNJ–New Jersey Medical School, Newark, New Jersey 07103

Outer hair cells (OHC) from the organ of Corti are capable of fast voltage-induced length changes (Santos-Sacchi and Dilger, 1988), suggesting that an associated voltage sensor should reside in the OHC plasma membrane. Voltage-dependent mechanical responses and nonlinear charge movement of isolated OHCs from the guinea pig were analyzed using the whole-cell voltage-clamp technique. Ionic currents in the cells were blocked. Nonlinear voltage-dependent charge movement or, correspondingly, voltage-dependent capacitance was measured with step or AC analysis. OHC movements were measured either from video or using a differential photodiode technique. Maximum charge movements up to 2.5 pC were measured in OHCs from the low-frequency region of the cochlea. Both AC and step analyses indicated a peak nonlinear capacitance of 16–17 pF. The voltage dependence was fit to a Boltzmann relation with the step analysis indicating a maximum nonlinear capacitance at –23 mV step potential from a holding potential of about –120 mV, and AC analysis indicating a maximum at a holding potential near –40 mV. AC analysis probably provides a more accurate evaluation of voltage dependence. Measures of OHC motility magnitude versus voltage follow the nonlinear capacitance–voltage function obtained from AC measures. Treatment of the cells with gadolinium ions (0.5–1 mM) blocked OHC motility. This treatment also produced a shift of the nonlinear capacitance function along the voltage axis in the depolarizing direction, which can be explained by membrane surface charge screening. However, maximum capacitance was reduced as well and may correspond to the reduction or abolition of OHC motility in response to gadolinium treatment. Gadolinium effects were reversible. Nonlinear capacitance is not a function of membrane deformation due to length changes, since removal of OHC cytosol via the patch pipette abolished longitudinal movement but did not reduce nonlinear charge movement. It is interesting to note that the nonlinear capacitance will dynamically influence the time constant of the OHC during acoustically evoked receptor potential generation.

Both types of hair cells within the organ of Corti, inner (IHC) and outer (OHC), transduce mechanical movements of the basilar membrane into electrical responses. However, even though OHCs are capable of generating receptor potentials (Dallos et al., 1982) and have recently been shown to possess depolarization induced inward calcium currents (a requisite for vesicular transmitter release; Katz and Miledi, 1967; Santos-Sacchi and Dilger, 1988; Santos-Sacchi, 1989b; Lin et al., 1990), it is not certain whether OHCs participate in the direct transfer of neurally coded information to the CNS. It is certainly clear, however, that OHCs participate in the shaping of acoustical information that reaches the CNS. A variety of experiments have established this, including OHC lesion experiments (Dallos and Harris, 1978; Harrison and Evans, 1979) and crossed olivocochlear bundle (COCB) stimulation experiments (Brown and Nuttall, 1984). The participation appears to be at the level of OHC–IHC interaction. However, neither morphologic data (Iurato et al., 1976) nor indirect physiologic data (Oesterle and Dallos, 1988) indicate the existence of direct electrical interactions. The early work of Kemp (1978) on otoacoustic emissions indicated that some sort of active process occurs within the cochlea. This concept was strengthened by studies demonstrating electrically evoked acoustic emissions (Hubbard and Mountain, 1983). With the discovery of Brownell et al. (1985) that isolated OHCs are capable of electrically induced rapid length changes, an exciting new concept arose regarding OHC function—one that envisions a mechanical feedback of OHCs upon basilar membrane motion, which in turn determines the input to the inner hair cell stereocilia (Mountain et al., 1983; Patuzzi et al., 1989). Indeed, evidence suggesting a role of OHCs in controlling basilar membrane motion has been recently obtained (Ruggero and Rich, 1991).

Several lines of evidence indicate that the fast mechanical response of the OHC is voltage dependent (Santos-Sacchi and Dilger, 1988; Iwasa and Kachar, 1989). At the systems level, this voltage dependency is important for understanding the role of OHC motility in frequency selectivity and sensitivity in the mammalian inner ear, since the AC receptor potential generated in these cells *in vivo*, that is, the presumed driving force for OHC motility, will be attenuated above the cells' RC cutoff frequency; thus, the magnitude of mechanical response will necessarily depend upon the frequency of acoustic stimulation (see Santos-Sacchi, 1989c). At the cellular level, a voltage dependence of OHC motility suggests that a charged voltage-sensing particle should reside in the OHC membrane. This concept was first postulated for voltage-dependent ionic channels (Hodgkin and Huxley, 1952), and indeed, nonlinear charge movement, which implies the existence of channel-gating particle movement, is

Received Mar. 8, 1991; revised Apr. 24, 1991; accepted May 2, 1991.

This work was supported by an NIDCD Research Career Development Award and NIH Grant DC00273. I thank Jack Callahan and Janet Santos for technical assistance, and Jont Allen, Francisco Bezanilla, and Bill Brownell for many helpful discussions. I also thank the reviewers for their constructive criticism.

Correspondence should be addressed to J. Santos-Sacchi, Ph.D., Department of Surgery, Section of Otolaryngology, Yale University School of Medicine, 333 Cedar St., New Haven, CT 06510.

^a Present address: Sections of Otolaryngology and Neurobiology, Yale University School of Medicine, New Haven, CT 06510.

Copyright © 1991 Society for Neuroscience 0270-6474/91/113096-15\$05.00/0

now known to occur during activation of a variety of ionic channels (Armstrong and Bezanilla, 1973; Bezanilla et al., 1982a; Adams et al., 1990). Recently, nonlinear charge movement (which presents itself as a voltage-dependent capacitance) has been detected in the OHC (Ashmore, 1989).

The voltage-dependent movement of the OHC cannot be blocked by a variety of treatments, including ionic channel blockers, metabolic inhibitors, Ca^{2+} -free media, and anti-cytoskeletal agents (Kachar et al., 1986; Holley and Ashmore, 1988; Santos-Sacchi and Dilger, 1988). While these data indicate that the rapid movements are not based upon a muscle-like system, they have created a sense that fast voltage-dependent OHC movement is unstoppable, except by irreversible means. The ability to reversibly inhibit a phenomenon is an important step in understanding its underlying mechanism. I report here two methods that rapidly and reversibly diminish or abolish longitudinal OHC mechanical responses induced under voltage clamp. The first is treatment of OHCs with gadolinium (Gd^{3+}) ions, and the second is the removal of OHC cytosol via a patch pipette. These two treatments appear to interfere with the mechanical response at distinct cellular levels, since only Gd^{3+} treatment reversibly reduces the voltage-dependent capacitance of the OHC membrane.

Preliminary accounts of this work have been reported (Santos-Sacchi, 1989a, 1990a,b).

Materials and Methods

General. Guinea pigs were anesthetized with pentobarbital and decapitated. The temporal bones were removed, and the sensory and supporting cells were isolated from the cochleas by gentle pipetting of the isolated top two turns of the organ of Corti. No enzymatic digestion was employed for isolation of OHCs or Deiters cells; however, Hensen cells were isolated using trypsin (Santos-Sacchi, 1991). The cell-enriched supernatant was then transferred to a 700 μl perfusion chamber, and cells were permitted to settle onto the coverglass bottom. All experiments were performed at room temperature ($\sim 23^\circ\text{C}$). A Nikon Diaphot inverted microscope with Hoffmann optics was used to observe the cells during electrical recording. All experiments were taped with a Panasonic AG6300 video recorder. A modified Leibovitz medium (NaCl , 142.2 mM; KCl , 5.37 mM; CaCl_2 , 1.25 mM; MgCl_2 , 1.48 mM; HEPES, 5.0 mM; dextrose, 5.0 mM; pH 7.2) was used as the normal perfusate. Modifications to the extracellular medium are noted in figure captions, with NaCl adjusted to maintain osmolarity (300 mOsm). Extracellular solutions were changed via two methods. The chamber perfusion system permits the fluid in the whole chamber to be constantly exchanged with fresh medium (0.1–1 ml/min) and can be used to change to solutions of different ionic makeup. A more rapid and direct perfusion system was used to perfuse single cells selectively under voltage clamp, during continuous exchange of bulk medium via chamber perfusion. The device is a two- or four-barreled glass pipette tapered to about 100 μm and fitted with a polyethylene sleeve at the tip to permit fluid flow from a single port with a small dead volume. Solutions are fed to the pipette under gravity control and are rapidly switched with solenoid valves. The tip of the pipette is brought to within 50 μm of the cell being studied, and the flow of solution is adjusted so as not to perturb the cell physically.

Voltage step studies were performed with an Axolab 1100 A/D and D/A board (Axon Instruments, Foster City, CA) with associated software (pCLAMP). AC studies were performed using a digital signal processing board with custom-written software (DSP-16; Ariel Corp., Highland Park, NJ) capable of delivering and analyzing pure tone or swept frequency stimuli. Filtered current records were saved to disk for offline analysis.

Patch electrodes (flint or borosilicate glass) had initial resistances of 3–6 M Ω . The series resistance, that is, the actual electrode resistance obtained upon establishment of whole-cell configuration, typically ranged from 6 to 14 M Ω ; for the collection of gating currents and short-duration mechanical events, care was taken to maintain low series resistance values during recording by delivering transient positive or negative pressure into the electrode to maintain an unobstructed orifice. The resistance values were estimated from current transients initiated at the

onset of voltage pulses and were corrected for during analysis, so that actual voltages imposed upon the cell are known (Marty and Neher, 1983). The program CLAMPX (Axon Instruments) was modified to provide a continuous display of clamp time constant, cell capacitance (C_m) and resistance (R_m), and series resistance (R_s) between data collections. Pipette solutions were composed of 140 mM KCl or CsCl , 5 or 10 mM EGTA, 2 mM MgCl_2 , and 5 mM HEPES buffered to pH 7.2. In some cases, EGTA was not used. Gigohm seals were obtained at the nuclear level of the cell membrane, and electrode capacitance was compensated prior to whole-cell recording. Generally, single cells were clamped to holding potentials near -70 to -80 mV using a Dagan patch-clamp amplifier. Hyperpolarizing and depolarizing voltage steps, 5–500 msec in length, were used to elicit membrane currents (filtered at 10 kHz) and, in the case of OHCs, mechanical movements.

Measurement of OHC voltage-dependent capacitance. In response to membrane potential perturbations induced by voltage-clamp stimuli, ionic and capacitive membrane currents are normally generated. In order to permit the study of capacitive currents in isolation, OHC ionic currents were blocked. Typically, patch electrodes contained 140 mM CsCl , and extracellular solutions contained 20 mM tetraethylammonium (TEA), 20 mM CsCl , and 2 mM CoCl_2 (see figure captions for modifications). These ionic substitutions were used to block outward and inward K^+ currents and Ca^{2+} currents. Although hair cells possess no fast inward sodium currents (however, see Evans and Fuchs, 1987), in some experiments TTX was used in an attempt to reduce residual leakage currents. No apparent effects were noted in those cases.

Step analysis. The aim of the following voltage step protocols was to extract nonlinear charge movement from total charge movement by subtracting out that component due to the linear dielectric properties of the membrane. OHC gating currents (nonlinear capacitive currents) were measured by averaging current responses elicited by voltage pulses (5 msec) of alternating polarity (40 mV magnitude) about the holding potential of -80 mV ($\pm P$ technique; Armstrong and Bezanilla, 1973). Under certain conditions, this technique may not adequately measure nonlinear charge movement. That is, the amount of charge movement produced for opposite-polarity pulses depends upon where the holding potential lies along the actual nonlinear Q - V function. Thus, at holding potentials well within this function, the capacitive current induced by a hyperpolarizing pulse is not solely linear, and this technique will result in measurement inaccuracies (see Bezanilla and Armstrong, 1977). In the present study, this technique was only used to evaluate relative changes in nonlinear charge movement at a fixed holding potential. In order to evaluate the voltage dependency of nonlinear charge movement, the following protocols were used to overcome the problems inherent in the $\pm P$ technique.

Detailed measures of voltage versus charge movement were obtained by using a $P/-4$ protocol (Bezanilla and Armstrong, 1977) at a holding and subtraction potential of -120 mV. This technique derives nonlinear charge movement from total charge movement by subtracting estimates of linear charge movement obtained at a membrane potential where nonlinear components are small or absent. The procedure entails the presentation of four subpulses of a magnitude equal to $P/-4$; the generated capacitive currents of these subpulses are summed and added to those generated by the depolarizing pulse, P . The highly negative holding potential should provide subtraction currents that will more accurately permit measures of nonlinear charge movement for a range of step potentials. Alternatively, linear charge movement was estimated with 5 mV hyperpolarizing pulses at a holding potential of -120 mV, scaled, and subtracted from total charge movement measured in response to a range of depolarizing voltage steps. Voltage-dependent nonlinear charge [$Q_{(v)}$] was fit to a Boltzmann function (see Fig. 6A and top of Fig. 10A,B):

$$Q_{(v)} = \left(\frac{Q_{\text{max}}}{1 + \exp[-ze(V - V_h)/kT]} \right) + Q_{\text{min}} \quad (1)$$

where V is the potential of the step corrected for series resistance using non-leakage-subtracted steady state current levels at the end of the step, V_h is voltage at half-maximal charge movement, e is electron charge, k

¹ For a nonlinear voltage-dependent charge movement that occurs only upon depolarization from a given holding potential, the summation of capacitive currents induced by opposite polarity steps about the holding potential will result in the extraction of nonlinear capacitive currents. That is, the linear capacitive current produced by the hyperpolarizing step is used to subtract out the linear component induced by the depolarizing step, and only the nonlinear charge movement remains.

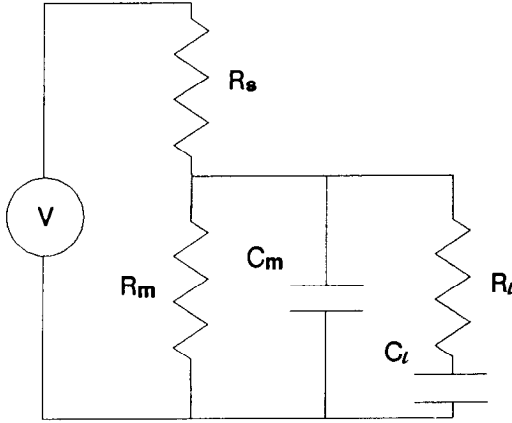


Figure 1. Cell-electrode model. See Materials and Methods for description.

is Boltzmann's constant, T is absolute temperature, z is the valence, Q_{\max} is maximum charge transfer, and Q_{\min} is minimum charge transfer (an offset included to account for possible nonlinear charge movement at levels more hyperpolarized than the subtraction holding potential). Since capacitance, in this case voltage-dependent [$C_{(v)}$], is defined as the first derivative of charge with respect to voltage,

$$C_{(v)} = \frac{dQ_{(v)}}{dv} \quad (2)$$

estimates of voltage-dependent capacitance were obtained by differentiation of the Boltzmann fits of nonlinear charge movement (see Fig. 6B).

AC analysis. AC analyses of the voltage-dependent capacitance were also made using the Ariel DSP board, with sampling at 12 kHz. OHCs were ramped to hyperpolarized and depolarized potentials from a holding potential of -80 mV, and after 0.2 sec, continuous swept frequency stimuli of constant voltage (3.53 mV RMS) were delivered; filtered current responses and input voltage (6 kHz, eight pole Bessel; averaged $20\times$) were saved to disk. The first two collections were discarded prior to averaging. Cell capacitance was evaluated using impedance data similar to techniques used by others (Fishman et al., 1977; Takashima, 1978; Fernández et al., 1982); however, estimates were made using measures of capacitive reactance (X_c) obtained from the impedance calculations. The real and imaginary components of the impedance were obtained by Fast Fourier transform (FFT) using the software package MATLAB (Mathworks, Natick, MA).

A model often used to analyze whole-cell voltage-clamp data is composed of an electrode resistance (series resistance, R_s) in series with a parallel combination of a membrane resistance (R_m) and a membrane capacitance (C_m) (Ogden and Stanfield, 1987; see model schematic in Santos-Sacchi, 1989c). The capacitive reactance (X_c) of such an RC-dominated system can be described as a bell-shaped function of frequency (using a linear-log plot), whose characteristic frequency is dependent upon the cell membrane's RC time constant (see Schanne and Ruiz P.-Ceretti, 1978, their Appendix 2). It is a function in which the effects of R_s are absent:

$$X_c = \frac{\omega C_m R_m^2}{1 + \omega^2 C_m^2 R_m^2}, \quad \omega = 2\pi f. \quad (3)$$

It is useful to avoid the effects of series resistance during the fitting of the experimental data to the model, because series resistance is difficult to measure precisely and can influence the analysis of impedance data (Fernández et al., 1982; Salzberg and Bezanilla, 1983). Unfortunately, the simple model of Equation 3 cannot account for the frequency-dependent nature of membrane capacitance observed in cells possessing nonlinear charge movement. For example, in the squid axon, Fernández et al. (1982) required an additional single or double time constant factor, modeled as lossy capacitors in parallel with the membrane capacitance.²

² The physical correlates of this model are not easily made. However, the lossy capacitance (series combination of resistance and capacitance) may be viewed as

In the present study, fits of experimentally measured X_c to that of clamp-cell models were made using the Nelder-Mead simplex algorithm for frequencies between 0.1 and 3 kHz, across a range of holding potentials. The characteristic frequency of the OHC's X_c is well below 100 Hz because the cell's time constant under the experimental conditions is quite large; for example, Santos-Sacchi (1989c) determined the OHC time constant at -70 mV to be about 3.5 msec (45 Hz). Actually, the characteristic frequency will change as a function of holding potential and ultimately depends upon changes of input capacitance (due to voltage-dependent capacitance) and input resistance (due to unblocked nonlinear leakage currents). Fits of the measured X_c at various holding potentials were made to determine the model's component values. Goodness of fit was estimated from the square root of the sum of squared residuals: the smaller the value, the better the fit. Fits of OHC X_c with the simple RC model of Equation 3 (illustrated in Santos-Sacchi, 1989c) did demonstrate voltage-dependent capacitance, but the goodness of fit was poorer than that obtained with the model of Figure 1, which incorporates an additional lossy capacitance (described below). For an example, see the caption of Figure 7 where the results of fitting the data to both models are presented. While at very negative potentials (e.g., -136 mV) both models yield similarly good fits, at depolarized potentials, where voltage-dependent capacitance is substantial, the model of Figure 1 fits the data points more accurately. Therefore, for the analysis of the AC data, the input impedance of the OHC in series with the electrode resistance (R_s) was modeled as a membrane resistance (R_m) and capacitance (C_m) in parallel with a lossy dielectric consisting of a series combination of another capacitance (C_l) and resistance (R_l):

$$Z_{in} = (R_s + R_{ren}) - jX_c \quad (4)$$

$$= R_s + \frac{R_m(R_l + 1/sC_l)}{(1 + sC_m R_m)(R_l + 1/sC_l + R_m/(1 + sC_m R_m))}, \quad (5)$$

where $s = j\omega$ and $j = \sqrt{-1}$. The model's capacitive reactance (X_c) is given as

$$X_c = -\text{imag}(Z_{in}) \quad (6)$$

$$= \frac{R_m \omega (\tau_m + \tau_{im} + \tau_m \tau_l^2 \omega^2)}{1 + \omega^2 (\tau_m^2 + \tau_l^2 + 2\tau_m \tau_{im} + 2\tau_l \tau_{im} + \tau_{im}^2) + \tau_m^2 \tau_l^2 \omega^4}, \quad (7)$$

where $\tau_l = R_l C_l$, $\tau_{im} = R_m C_l$, and $\tau_m = R_m C_m$.

Although the capacitive reactance is independent of R_s , all other components (R_m , C_m , R_l , and C_l) contribute. Thus, by fitting OHC X_c with the parameters of the model, an estimate of the cell's total capacitance can be obtained ($C_{tot} = C_m || C_l$, the parallel combination of the component capacitances; Chandler et al., 1976).

The total capacitance of the OHC ($C_{(v)}$) at any given holding potential is the sum of the linear, non-voltage-dependent, capacitance (C_{lin}) and voltage-dependent capacitance ($C_{(v)}$):

$$C_{tot} = C_{(v)} + C_{lin} \quad (8)$$

Estimates of linear and voltage-dependent capacitance were made by fitting C_{tot} to Equation 8, with $C_{(v)}$ defined as the first derivative of a Boltzmann function relating charge movement and voltage (see Fig. 8 and bottom of Fig. 10A,B):

$$C_{(v)} = \left\{ \frac{(Q_{\max} z e / k T)}{\exp[(z e / k T)\{V - V_h\}][1 + \exp[-(z e / k T)\{V - V_h\}]]^2} \right\}. \quad (9)$$

Measurement of OHC movement. Movements of the OHCs were analyzed by three methods. For steady state movements (voltage steps > 100 msec), length changes were analyzed off the video monitor during playback either by direct measurement off the video monitor using single still frames (Santos-Sacchi and Dilger, 1988) or by placing differential optoresistors or a position-sensitive detector (PSD; Hamamatsu Corp., Bridgewater, NJ) (output filtered at 30 Hz) across the image of the cuticular plate at a monitor magnification of $2800\times$. The linearity of

the voltage-dependent capacitive component, and the frequency dependence it imparts to the model may correspond to the time-dependent nature of nonlinear charge movement within the membrane (see Fernández et al., 1982).

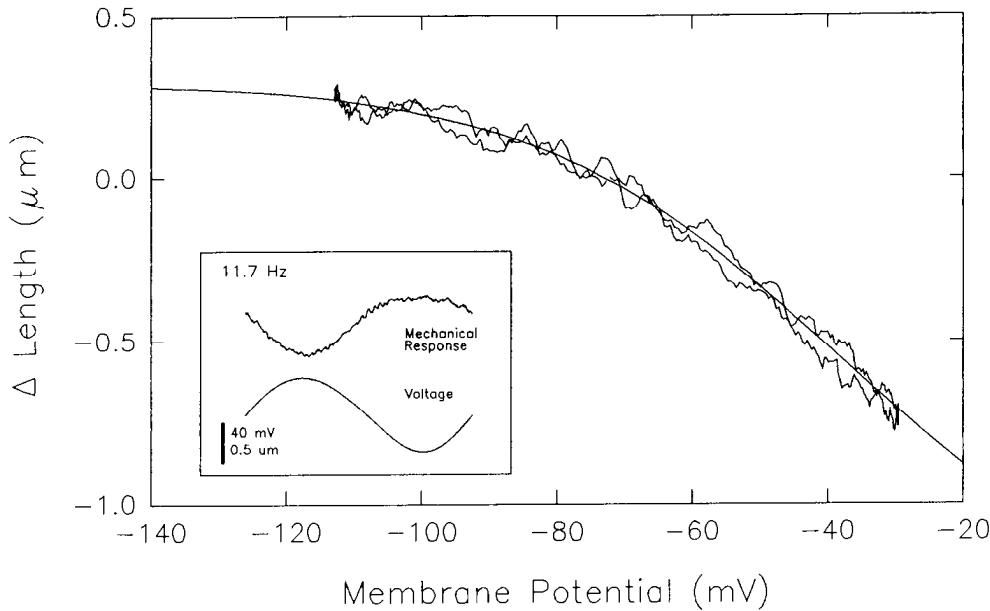


Figure 2. The voltage–displacement response of an OHC to an 11.7 Hz sinusoidal voltage stimulus superimposed upon a holding potential of about -74 mV, as measured with the differential photodiode technique. *Solid smooth line* is fit to a Boltzmann function with V_h at -38 mV and $z = 1.14$. *Inset*, Movement and voltage waveforms. Series resistance–corrected voltage trace was derived from the simultaneously recorded whole-cell current record by modeling the cell-clamp setup as a simple $R_m C_m$ cell circuit in series with the electrode's series resistance (Santos-Sacchi, 1989c), the values of which were estimated from responses to voltage steps. Current was transformed into the frequency domain by FFT and the voltage was calculated using the component values and converted into the time domain by reverse Fourier transform. Extracellular medium contained 20 mM TEA, 300 nM TTX, and no added Ca^{2+} . CsCl pipette solution.

the optoresistor method was confirmed by measuring the videotaped movement of the tip of a microelectrode driven by a piezoelectric bimorph element (Santos-Sacchi, 1989c). Fast OHC movements elicited by voltage clamp with short-duration stimuli (below video detection) were measured with a differential photodiode onto which the image of the cuticular plate from the microscope was projected. The placement and manipulation of the photodiode was accomplished by a computer controlled micromanipulator. The photodiode was backlit by two fiber optic beams projected through the microscope's camera port onto a 30% mirrored glass coverslip base of the perfusion chamber, and reflected back to a charge coupled device (CCD) video camera via a 90° prism to allow photodiode placement during simultaneous cell visualization on a mixed video–computer monitor (Matrox Corp., Canada). Backlighting was not required after calibration of the photodiode's position on the monitor. The frequency response of the differential photodiode was flat out to 2 kHz (measured with a light-emitting diode or piezoelectric bimorph). Measures of OHC movements by the photodiode method were performed by averaging the simultaneously recorded current and photodiode output 200 times, in response to step or pure tone voltage stimuli. Absolute calibration of cell movements was determined by measuring off the video monitor the cell movement in response to a large steady state depolarizing voltage stimulus. The error in absolute measures was estimated to be less than 20%.

Results

Under voltage clamp, OHCs respond to voltage alterations by changing their length. Figure 2 illustrates the voltage dependence of the magnitude of OHC cell length changes. At a holding potential near -75 mV, an 11.7 Hz sinusoidal voltage stimulation of the OHC induces contraction during the depolarizing phase and elongation during the hyperpolarizing phase. The response is greater in the depolarization direction and corroborates the voltage–mechanical response function obtained by voltage step analysis (Santos-Sacchi, 1989c). The maximum excursion for these mechanical responses, at voltage step extremes, can be up to about 3–4 μm , with slopes in the midregion as great as 30 nm/mV. The voltage–mechanical response function indicates that at potentials near the resting potential measured *in vivo*, -70 mV (Dallos et al., 1982), sinusoidal stimulation will produce asymmetrical mechanical responses, that is, DC mechanical responses in addition to sinusoidal responses (Santos-Sacchi, 1989c). These DC responses are in the depolar-

ization–contraction direction and have been observed up to frequencies as high as 3.2 kHz (J. Santos-Sacchi, unpublished observations).

Depolarization of the OHC elicits outward K^+ currents, which are blocked to varying degrees by a host of treatments, including intracellular Cs, or extracellular TEA, Cd^{2+} , Ba^{2+} , charybdotoxin (ChTX), 4-aminopyridine (4-AP), octanol, and Gd^{3+} . Figure 3A illustrates an I – V function and associated current traces for a cell voltage clamped with a pipette containing KCl solution, before and after treatment with 500 μM Gd^{3+} . Outward K^+ currents are blocked by Gd^{3+} ; however, unlike other ionic blockers, Gd^{3+} treatment reduces or abolishes the OHC mechanical responses elicited by depolarizations. This can be seen in the simultaneously measured mechanical responses of this cell; mechanical responses were undetectable after Gd^{3+} treatment (Fig. 3A).

OHC mechanical responses are rapid in onset following a voltage stimulus, with the onset time constant principally determined by the speed of the voltage clamp (Santos-Sacchi, 1990a). Figure 3B depicts the response of an OHC to voltage steps of 5 msec duration. Treatment of this cell with 1 mM Gd^{3+} caused a developing block of motility (traces a–d). In this case, about 5 min after the start of Gd^{3+} perfusion, the cell contractions stopped. Recovery followed washout. Traces labeled f represent steps from -80 mV to -30 , 0, and $+30$ mV and illustrate the saturating nonlinearity in the magnitude of response occurring at highly depolarized levels (Santos-Sacchi and Dilger, 1988). The time constant of mechanical response onset changed during the development of Gd^{3+} block. Since this time constant is critically dependent upon the time constant of the clamp amplifier (Santos-Sacchi, 1990a), it is necessary to determine whether the clamp time constant was altered during the data collections. Simultaneously recorded currents revealed that the clamp time constant actually shortened (from 0.21 to 0.18 msec) during the collections and thus could not account for the increases of the time constant for mechanical responses (0.26, 0.44, and 0.57 msec for traces a–c, respectively).

The reversibility of the Gd^{3+} effects upon the OHC mechan-

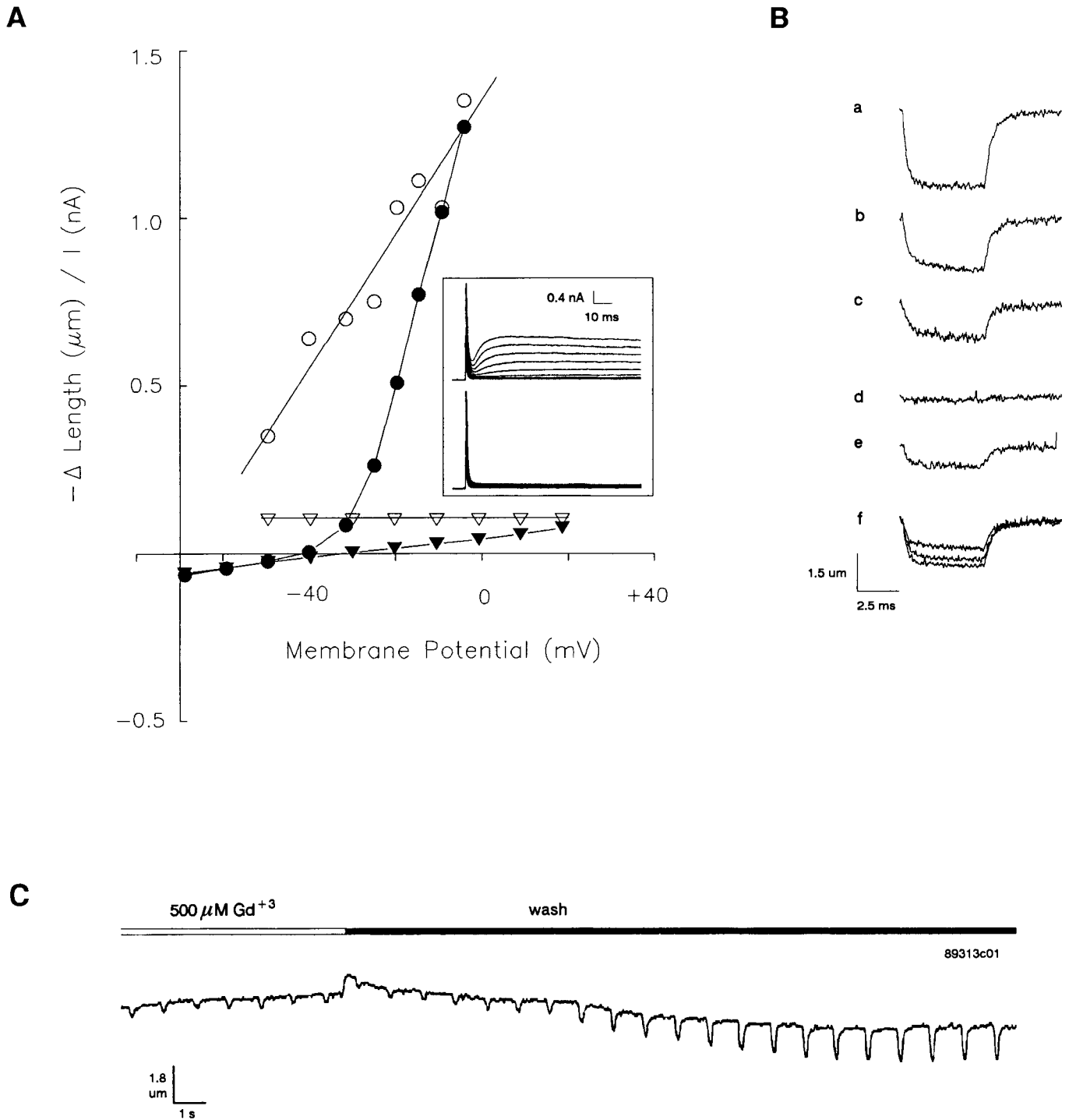
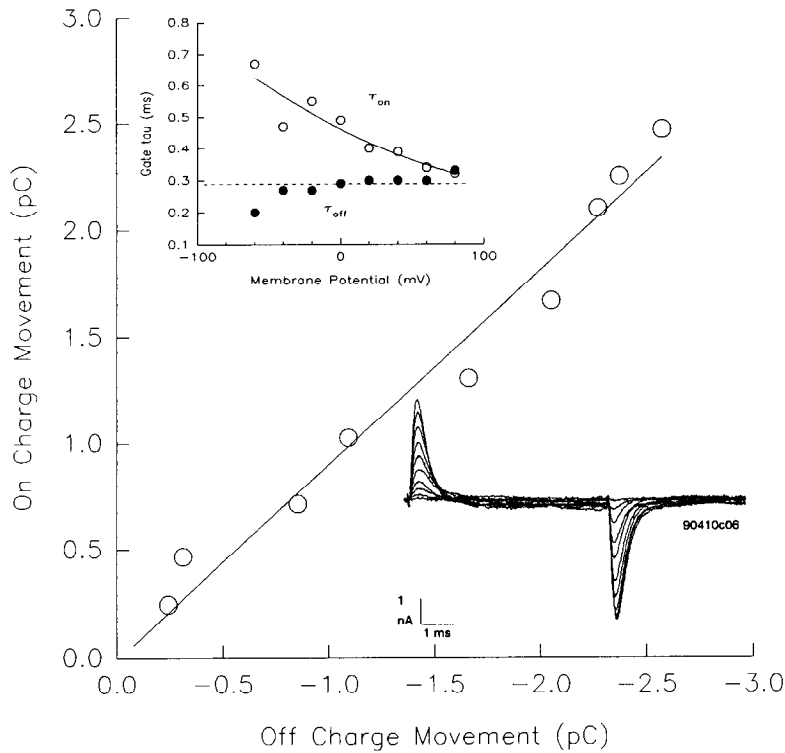
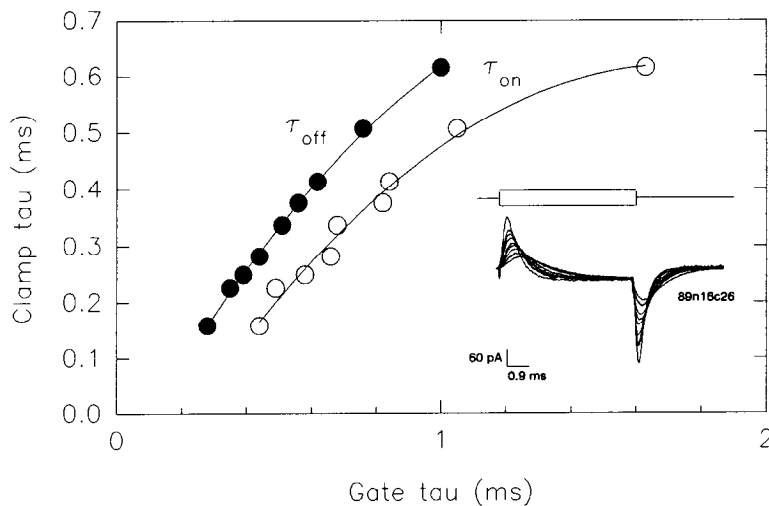


Figure 3. *A*, Simultaneously recorded whole-cell currents and mechanical responses of an OHC before and after treatment with 500 μM Gd^{3+} . Medium was Leibovitz without added Ca^{2+} . Electrode contained KCl solution. *Solid circles*, Currents before Gd^{3+} treatment; *open circles*, movements before Gd^{3+} treatment measured with differential optoresistor from video monitor. *Solid triangles*, Currents after addition of Gd^{3+} ; *open triangles*, movements undetectable after Gd^{3+} . Vertical scale corresponds to nA or μm of contraction. Series resistance corrected, no leakage current subtraction. *Inset*, Current traces before and after Gd^{3+} treatment. *B*, Mechanical responses of an OHC to short duration voltage steps from a holding potential of -80 to 40 mV (nominal; *a–e*) before (*a*), during [*b* (1 min), *c* (2 min), *d* (5 min)], and after [*e* (2 min wash)] perfusion with 1 mM Gd^{3+} . Traces labeled *f* (7 min wash) depict mechanical responses to voltages of -30 , 0 , and $+30$ mV. Extracellular medium contained 20 mM TEA, 20 mM CsCl, and no added Ca^{2+} . CsCl pipette solution. *C*, Reversibility of Gd^{3+} effects upon mechanical response. OHC was directly perfused with 500 μM Gd^{3+} in Ca-free Leibovitz, as indicated. Upon washout of the trivalent cation, the mechanical response increases over time. Contraction of the cell is indicated by the downward deflections of the trace measured with differential optoresistor from video monitor.

A



B



ical response is more clearly demonstrated in Figure 3C. This cell was continuously stepped to a voltage of 0 mV from a holding potential near -80 mV. While the cell was in the presence of $500 \mu\text{M}$ Gd^{3+} , mechanical responses were barely detectable; however, changeover to wash medium quickly initiated a recovery from the trivalent cation's effects. The block of ionic conductances is also rapidly reversible. Interestingly, washout with medium containing $500 \mu\text{M}$ Cd^{2+} did not restore motility. It is important to note that the block of OHC longitudinal motility by gadolinium ions was not due to or associated with a loss of cell turgor (see below). However, gadolinium produced a lengthening of the OHC, sometimes up to several micrometers.

The shapes of supporting cells were not affected by similar treatments. Typically, concentrations of about $500 \mu\text{M}$ were required to interfere with the magnitude of mechanical response. On the other hand, OHC outward currents were readily blocked, and under current clamp, membrane potentials were reversibly depolarized at concentrations as low as $50 \mu\text{M}$. Low concentrations of Gd^{3+} similarly affected ionic currents of supporting Deiters cells.

OHCs exhibit a nonlinear capacitive (gating) current that is directed outward at the onset of a voltage depolarization and inward during the repolarization. Such gating currents are readily observed after blocking ionic currents (Fig. 4A, trace inset).

Figure 4. *A*, OHC on-charge versus off-charge measured by integrating on- and off-gating currents over time as a function of voltage step size. *Trace inset* depicts nonlinear capacitive currents obtained by $P/4$ procedure at a holding and subtracting potential of -120 mV. Step depolarizations were in 20 mV increments up to 80 mV. *Line* is least-squares linear fit, indicating roughly equal nonlinear charge movements at onset and offset of voltage pulses. *Inset*, Single exponential time constant of current decay for on and off currents as a function of step potential. *Broken line* indicates clamp time constant. *Open circles*, τ_{on} ; *solid circles*, τ_{off} . Cell perfused with Leibovitz containing 20 mM TEA, 20 mM CsCl, and 2 mM CoCl_2 . CsCl electrode. *B*, Dependence of OHC gating current time constants upon clamp time constant. Procedure was $\pm P$ (40 mV) at a holding potential of -80 mV. *Traces* depict nine individual collections (averaged $200\times$) with different clamp time constants. The time constant of the clamp is dependent upon the series resistance of the patch electrode (Ogden and Stanfield, 1987) and was modified by electronically compensating the series resistance through feedback controls on the amplifier. *Open circles*, τ_{on} ; *solid circles*, τ_{off} . Cell perfused with 20 mM TEA Leibovitz. CsCl electrode.

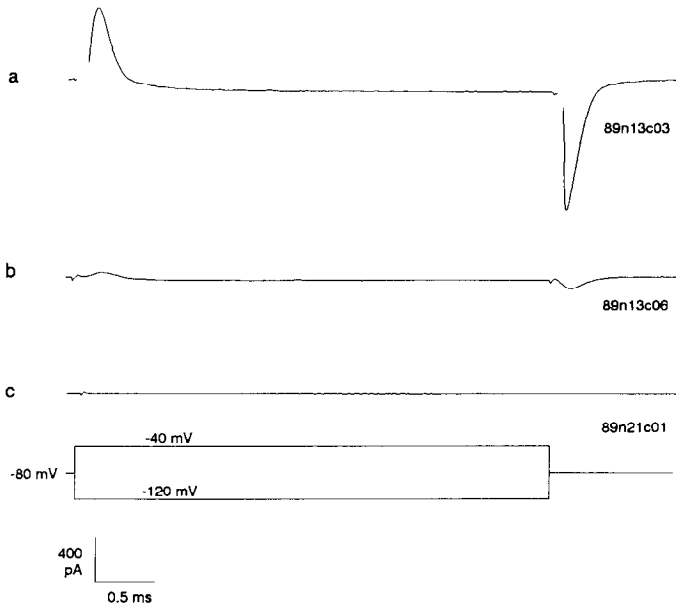


Figure 5. Block of OHC nonlinear charge movement by gadolinium ions. *Bottom trace* indicates voltage protocol of the $\pm P$ technique used to obtain the current traces (see Materials and Methods). *a*, Gating currents of OHC measured with the $\pm P$ technique; 10 mM TEA, 300 nM TTX Leibovitz. CsCl electrode. *b*, Same cell after treatment with same medium containing 500 μM Gd^{3+} . Gating current returned after washout. *c*, Absence of gating currents in Deiters cell; 20 mM TEA Leibovitz. CsCl electrode.

Charge transfer at voltage step onset and offset is essentially equal (Fig. 4). In cells where nonlinear leakage currents were small it was possible to look at the time constant of decay of the on-gate current. Whereas the time constant for the off-gate current was not voltage dependent, that of the on-gate was voltage dependent, decreasing with increasing depolarization step size until it approached both off-gate and clamp time constant values (Fig. 4*A*, inset); however, it was impossible to study this relationship validly because both gate time constants were dependent upon the time constant of the voltage clamp. Figure 4*B* clearly demonstrates this dependence and indicates that charge movement across the membrane is redistributed in time as a function of clamp time constant.

Figure 5 illustrates the effect of Gd^{3+} treatment on OHC gating current measured at -80 mV with the $\pm P$ technique. In this case, 500 μM Gd^{3+} nearly abolishes the current (Fig. 5*b*); the current can recover during washout of Gd^{3+} . Supporting cells do not demonstrate a nonlinear capacitive current under the same conditions (Fig. 5*c*). A more detailed analysis of the effects of Gd^{3+} on OHC nonlinear charge movement follows.

OHC nonlinear charge movement displays a saturating magnitude–voltage relation (Fig. 6*A*, solid circles). A Boltzmann fit to the data (solid line) indicates that the voltage (V_h) for half-maximal charge movement is -23.8 mV, with a valence (z) of 0.87. Maximum charge transfer up to about 2.5 pC has been observed in OHCs from the apical portion of the cochlea using the $P/-4$ technique at a holding and subtraction potential of -120 mV. Differentiating the Boltzmann fit (Fig. 6*B*, solid line marked with solid circle) indicates a peak nonlinear voltage-dependent capacitance of about 17 pF. Gadolinium ions shift

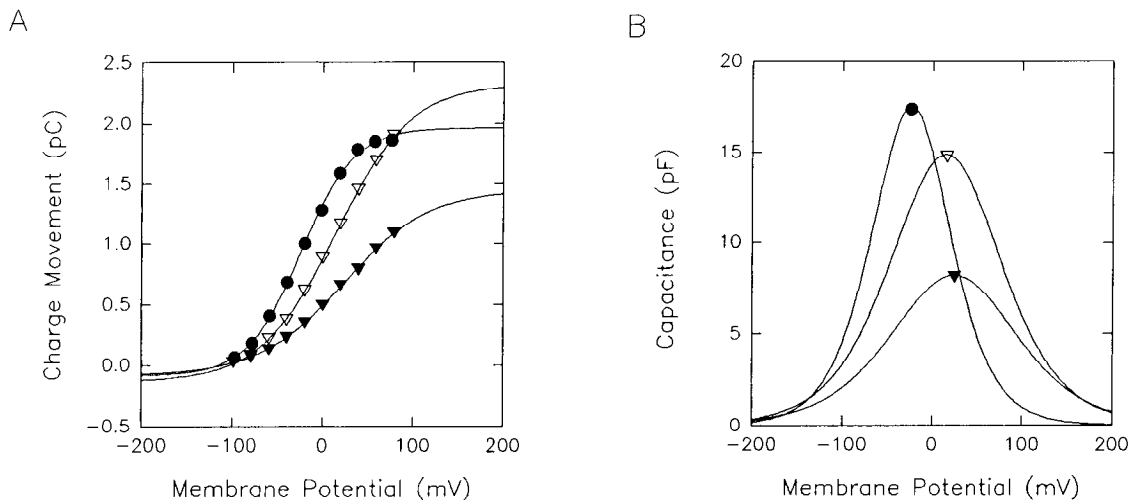
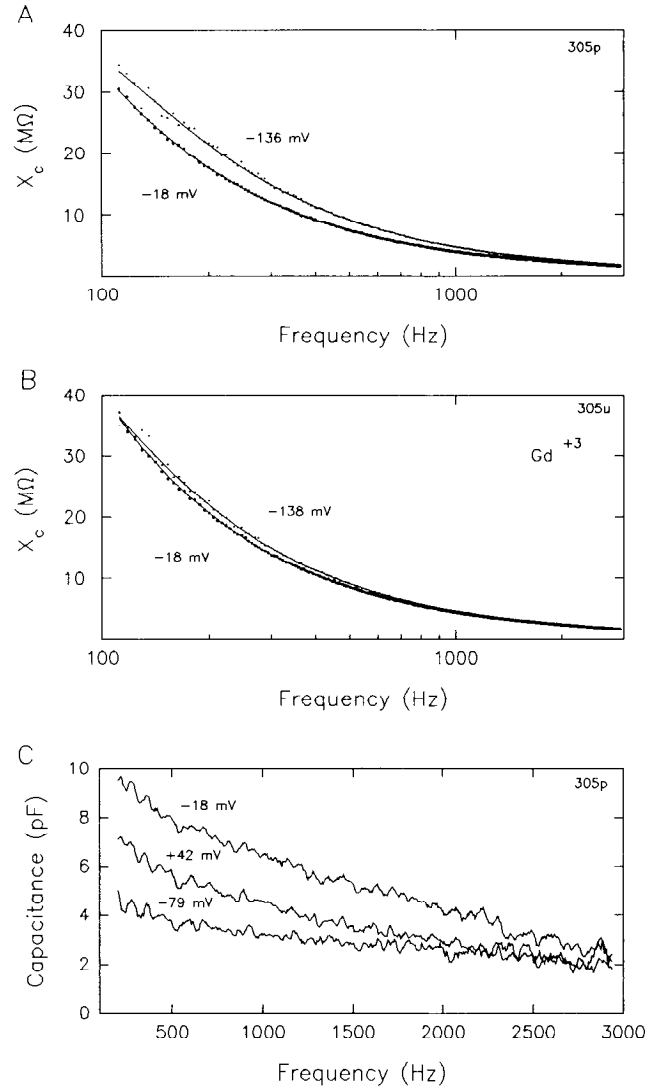


Figure 6. Average nonlinear charge movement and capacitance versus step potential corrected for series resistance determined using the $P/-4$ technique. On-charge and off-charge were averaged. Cells were held at -120 mV and stepped in 20 mV increments to a maximum of 80 mV (nominal voltages; see Materials and Methods). *A*, *Solid circles*, Average of four cells. *Solid line* is the fit to Equation 1. V_h and z : -23.8 mV and 0.87, respectively. Bath perfusion contained 20 mM TEA, 20 mM CsCl, 2 mM CoCl_2 , and no added Ca^{2+} . No direct cell perfusion. CsCl electrode, no EGTA. *Open triangles*, Average of four different cells. *Solid line* is the fit to Equation 1. V_h and z : 14.8 mV and 0.62, respectively. Cells were individually perfused with 20 mM TEA, 20 mM CsCl, 2 mM CoCl_2 , and no added Ca^{2+} medium from one barrel of a double-barreled pipette whose other barrel contained an additional 1 mM GdCl_3 . Bath perfusion as above. CsCl electrode, no EGTA. *Solid triangles*, Average of same four cells as depicted by *open triangles*. *Solid line* is the fit to Equation 1. V_h and z : 24.1 mV and 0.55, respectively. Cells were individually perfused from barrel containing 20 mM TEA, 20 mM CsCl, 2 mM CoCl_2 , 1 mM GdCl_3 , and no added Ca^{2+} medium. Bath perfusion as above. CsCl electrode, no EGTA. *B*, Voltage-dependent capacitance of cells in *A* as determined from first derivative of fitted charge movement with respect to voltage. *Symbol-marked curves* correspond to fits in *A*. Note, in addition to apparent charge screening by gadolinium, the reduction of voltage-dependent capacitance.

the voltage dependence and reduce the amount of OHC nonlinear charge movement. Charge movements represented by the open triangles in Figure 6A were obtained while perfusing an ionic blocking solution (see figure caption) via a double-barreled pipette, the other barrel containing an additional 1 mM Gd^{3+} . The voltage shift relative to the data represented by the solid circles suggests that charge screening³ had occurred due to diffusion of Gd^{3+} from the gadolinium-containing barrel. A Boltzmann fit to these data (solid line) indicates a V_h of 14.8 mV and z of 0.62. Figure 6B indicates that the peak capacitance is about 14 pF (solid line marked with open triangle). Upon perfusion with the 1 mM Gd^{3+} -containing solution, an additional voltage shift is noted and a marked decrease in the charge displacement is observed (solid triangles). The Boltzmann fit (solid line) gives a V_h of 24.2 mV and z of 0.55. Corresponding peak capacitance is about 7.5 pF (Fig. 6B, solid line marked with solid triangle).

Analysis of the nonlinear charge movement in the frequency domain for the same cells corroborates the time domain analysis. The capacitive reactance of the cells was determined at various holding potentials for frequencies up to 3 kHz. These measures were fit with the model of Figure 1 to obtain estimates of linear and nonlinear membrane capacitance. Figure 7A demonstrates that the capacitive reactance (X_c) of the OHC changes when the holding potential of the cell is changed from -136 to -18 mV. In this case, fitting the data (solid lines; see Materials and Methods) reveals an increase of about 10 pF upon depolarization of the cell to -18 mV. Perfusion of the cell with 1 mM Gd^{3+} reduces the nonlinear voltage-dependent capacitance (Fig. 7B). Since measures of X_c reflect the contribution of resistive as well as capacitive elements, frequency-dependent changes in cell capacitance cannot be obtained simply by taking the difference between X_c measures obtained at different holding levels. In order to evaluate the frequency dependence of the membrane capacitance, it is necessary to process the impedance data according to the techniques of Fernández et al. (1982).⁴ Figure 7C illustrates the results of such an analysis. The traces depict the voltage-dependent capacitance at selected holding potentials (-79 , -18 , and $+42$ mV; corrected for series resis-



³ Membrane surface potentials can arise from fixed surface charges. Charge screening refers to the alteration of this surface potential by the application of counterions. Since the voltage that a membrane-bound voltage sensor detects will be influenced by the membrane surface potential, the alteration of surface potential by charge screening can shift voltage-dependent membrane processes along the voltage axis (for review, see Hille, 1984).

⁴ The technique involves manipulation of the impedance data, after removal of series resistance effects. Briefly, after subtracting estimates of the series resistance from the input impedance measures and calculating the susceptance (B_m) from the admittance transform ($1/Z_{in}$), a measure of cell capacitance as a function of frequency (B_m/ω) can be obtained (for more detailed information, see Fernández et al., 1982).

Figure 7. Capacitive reactance of OHC as determined with AC analysis (see Materials and Methods). *A*, Capacitive reactance (points) prior to gadolinium treatment determined at a holding potential of -136 and -18 mV as indicated in figure. Fitted curves were obtained with Equation 7. Fitted parameters for -136 mV collection were R_m , 87.2 $M\Omega$; C_m , 29 pF; R_s , 13.4 $M\Omega$; C_s , 5.5 pF. C_{tot} ($C_m \parallel C_s$), 34.5 pF. Goodness of fit (see Materials and Methods), 4.5 $M\Omega$. Fitted parameters for -18 mV collection were R_m , 132 $M\Omega$; C_m , 32.4 pF; R_s , 11.4 $M\Omega$; C_s , 11.6 pF. C_{tot} ($C_m \parallel C_s$), 44 pF. Goodness of fit, 1.1 $M\Omega$. Voltage-dependent change in capacitance, 9.5 pF. Data were also fitted (not shown) to the simple RC model (Eq. 3) described in Materials and Methods. Fitted parameters for -136 mV collection were R_m , 82.5 $M\Omega$; C_m , 34.2 pF. Goodness of fit, 5.2 $M\Omega$. Fitted parameters for -18 mV collection were R_m , 86.6

$M\Omega$; C_m , 42.1 pF. Goodness of fit, 5.9 $M\Omega$. Voltage-dependent change in capacitance, 7.9 pF. Cell was individually perfused with 20 mM TEA, 20 mM CsCl, 2 mM $CoCl_2$, and no added Ca^{2+} medium from one barrel of a double-barreled pipette whose other barrel contained an additional 1 mM $GdCl_3$. Bath perfusion as in Figure 6. CsCl electrode, no EGTA. *B*, Capacitive reactance (points) of same cell after gadolinium treatment determined at a holding potential of -138 and -18 mV as indicated in figure. Fitted curves were obtained with Equation 7. Fitted parameters for -138 mV collection were R_m , 120 $M\Omega$; C_m , 29 pF; R_s , 12.1 $M\Omega$; C_s , 5.95 pF. C_{tot} ($C_m \parallel C_s$), 34.95 pF. Goodness of fit, 3.9 $M\Omega$. Fitted parameters for -18 mV collection were R_m , 236 $M\Omega$; C_m , 31.7 pF; R_s , 21.5 $M\Omega$; C_s , 6.6 pF. C_{tot} ($C_m \parallel C_s$), 38.3 pF. Goodness of fit, 1.8 $M\Omega$. Voltage-dependent change in capacitance, 3.3 pF. Data were also fitted (not shown) to the simple RC model (Eq. 3) described in Materials and Methods. Fitted parameters for -136 mV collection were R_m , 109 $M\Omega$; C_m , 34.5 pF. Goodness of fit, 5.2 $M\Omega$. Fitted parameters for -18 mV collection were R_m , 130 $M\Omega$; C_m , 37 pF. Goodness of fit, 5.9 $M\Omega$. Voltage-dependent change in capacitance, 2.5 pF. Cell was individually perfused from barrel containing 20 mM TEA, 20 mM CsCl, 2 mM $CoCl_2$, 1 mM $GdCl_3$, and no added Ca^{2+} medium. Bath perfusion as in Figure 6. CsCl electrode, no EGTA. *C*, Membrane capacitance of the OHC in *A*. The frequency dependence of OHC membrane capacitance was estimated using the technique of Fernández et al. (1982) (see footnote 4) and plotted using linear axes. Data are plotted after subtraction of the response obtained at -136 mV, and were smoothed using a five-point running average. These plots are a true measure of the real part of the membrane's voltage-dependent complex capacitance, provided that the value used for series resistance subtraction is correct and that minimal voltage-dependent capacitance is present at the subtraction holding potential of -136 mV.

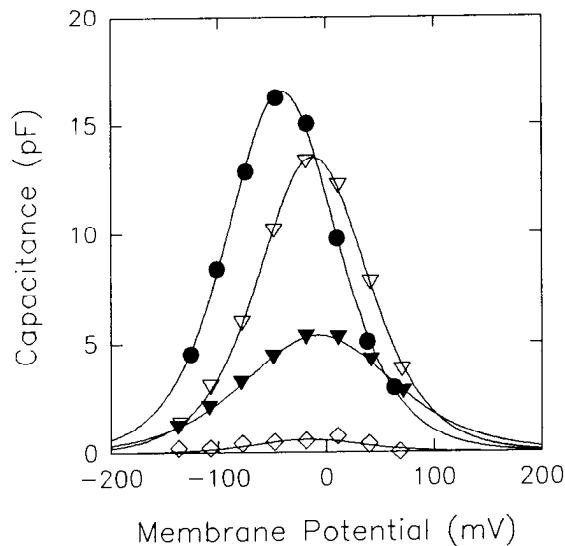


Figure 8. Average voltage-dependent capacitance determined from AC analysis for same cells as in Figure 6. Total capacitance was determined as a function of holding potential as in Figure 7 (see Materials and Methods). Symbols correspond to those of Figure 6. In addition, *open diamonds* represent average of data obtained from two Deiters cells and two Hensen cells, treated the same as those cells depicted by *solid circles* (see Fig. 6). Data were fit to Equation 8 to obtain voltage-dependent ($C_{(v)}$) and non-voltage-dependent ($C_{(in)}$) capacitance and were plotted after subtracting $C_{(in)}$. $C_{(in)}$, V_{h_2} , and z : *solid circles*, 23.2 pF, -40.7 mV, 0.76; *open triangles*, 29.9 pF, -11.8 mV, 0.76; *solid triangles*, 30.3 pF, -7 mV, 0.55; *open diamonds*, 30 pF, -16.3 mV, 0.76.

tance effects) as a function of frequency. The data demonstrate the voltage- and frequency-dependent nature of OHC membrane capacitance and are similar to the results obtained by Fernández et al. (1982) in the squid giant axon. Unfortunately, the usefulness of this type of analysis depends upon precise measurement of series resistance, since small inaccuracies in the measurement will provide incorrect estimates of the capacitance's frequency dependence. It should be reemphasized that estimating model parameters from reactance measures avoids problems imposed by series resistance effects, since these measures are not influenced by series resistance (see Materials and Methods).

Figure 8 shows the average input capacitance obtained, using AC analysis, from the same cells as in Figure 6, as a function of holding potential, before and after gadolinium treatment (symbols correspond to those in Fig. 6). A significant nonlinear capacitance is present at potentials near the normal resting potential *in vivo*, -70 mV. As was evident in the time domain analysis (Fig. 6B), AC measures indicate that treatment with gadolinium ions reduces the magnitude of the voltage-dependent capacitance and does not merely shift its voltage dependence. Supporting cells (Deiters and Hensen) demonstrate no or very little nonlinear capacitance when analyzed in the frequency domain (Fig. 8, open diamonds). OHC peak nonlinear capacitance occurs at potentials that are shifted about 17 mV in the hyperpolarizing direction compared to step analyses. Since holding potentials were different for the AC and time domain analyses, it is conceivable that initial conditions may be responsible for the shift. Such effects have been found for Na

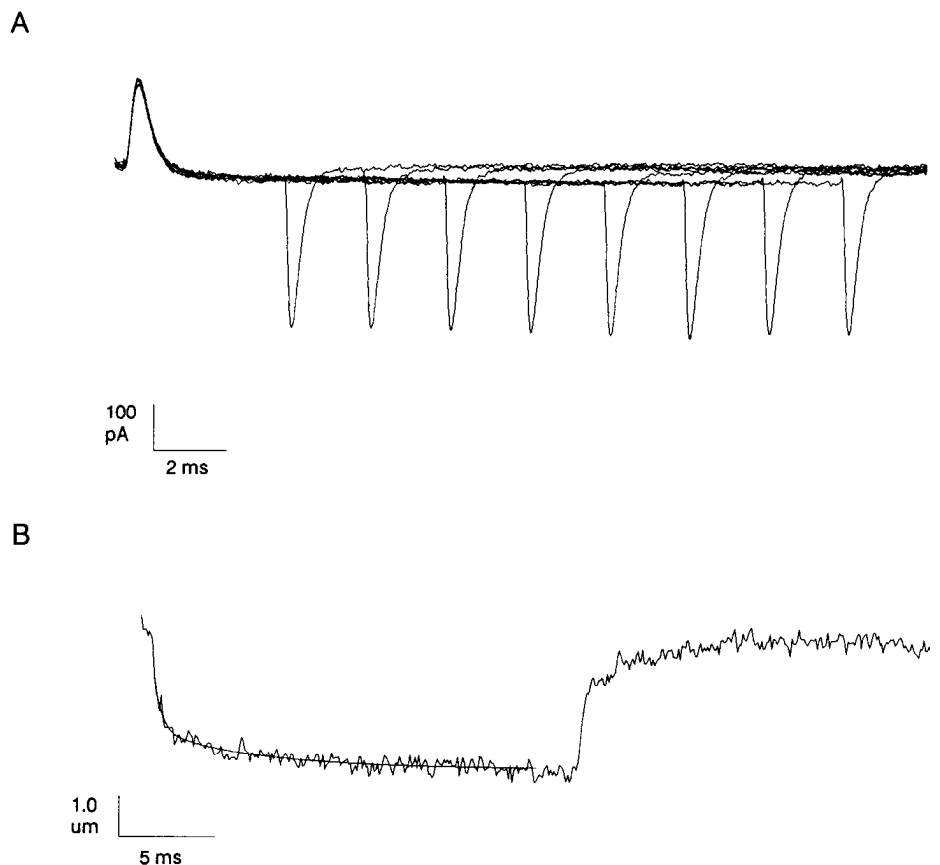


Figure 9. Demonstration of absence of gating charge immobilization or mechanical response decay. *A*, An OHC was held at -80 mV, and gating currents were obtained with the $\pm P$ method for a range of voltage step durations. Traces are overlaid, and the occurrence of equivalent off-charge movement at differing pulse widths indicates absence of charge immobilization in this time frame. Charge immobilization would have been indicated by a decreasing off-charge movement as a function of increasing pulse duration. *B*, An OHC was stepped to $+40$ mV from a holding potential of -80 mV for about 20 msec, and the mechanical response was measured with the differential photodiode technique. Downward deflection is contraction. Note absence of decay in the mechanical response during depolarization.

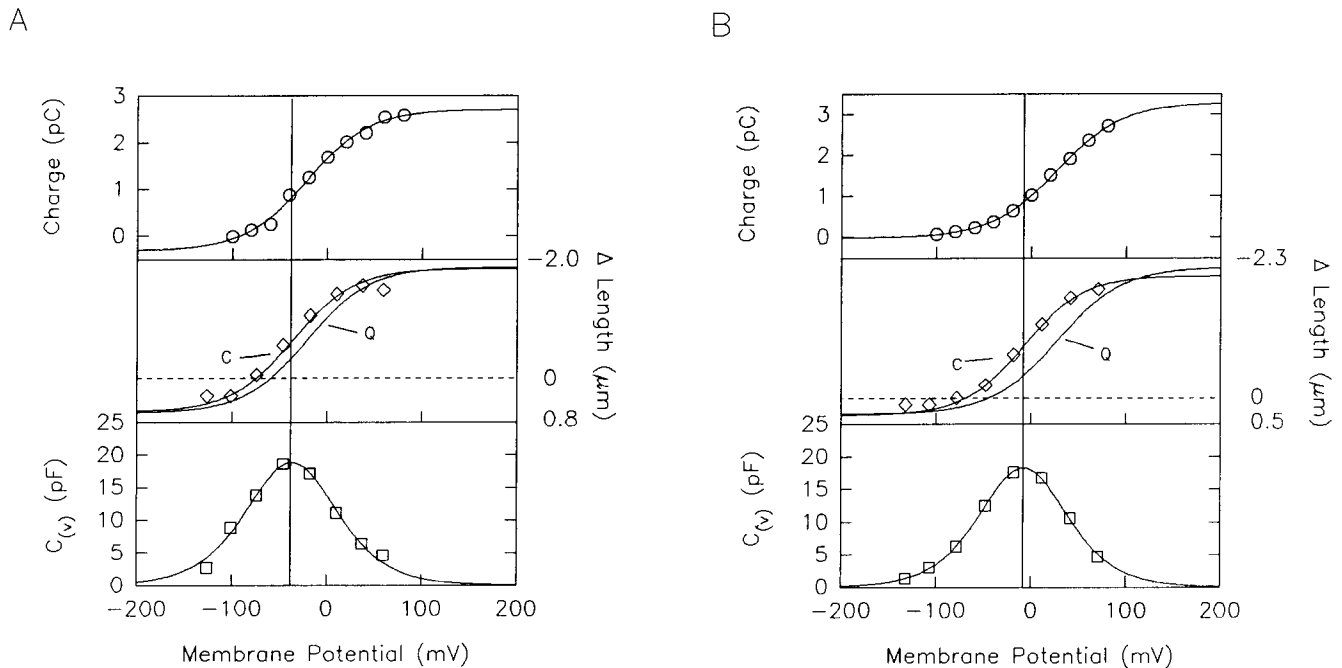


Figure 10. Comparison of AC-determined capacitance (*open squares*), step-determined charge movement (*open circles*), and mechanical response (*open diamonds*) for two OHCs demonstrating differing V_h . Comparison indicates that voltage dependence of mechanical response more closely corresponds to voltage dependence of capacitance derived from AC analysis (V_h of AC measures indicated by vertical lines through plots) than to voltage dependence derived from step analysis. OHC mechanical responses were measured off the video monitor with the differential optoresistor. *A*, Parameters determined from charge movement measures (*open circles*): V_h , -21 mV; z , 0.78 . Parameters determined from AC capacitance measures (*open squares*): V_h , -37 mV; z , 0.79 . Mechanical response (*open diamonds*) is plotted along with scaled Boltzmann functions using V_h and z values obtained from charge data (Q) or capacitance data (C). Note the closer correspondence of the mechanical data points with the function obtained from the capacitance fit (C). No direct cell perfusion. CsCl electrode, no EGTA. Bath perfusion contained 20 mM TEA, 20 mM CsCl, 2 mM CoCl₂, and no added Ca²⁺. *B*, Parameters determined from charge movement measures (*open circles*): V_h , 26.7 mV; z , 0.75 . Parameters determined from AC capacitance measures (*open squares*): V_h , -8 mV; z , 0.82 . Mechanical response (*open diamonds*) is plotted along with scaled Boltzmann functions using V_h and z values obtained from charge data (Q) or capacitance data (C). Note the closer correspondence of the mechanical data points with the function obtained from the capacitance fit (C). Cell individually perfused with 20 mM TEA, 20 mM CsCl, 2 mM CoCl₂, and no added Ca²⁺ medium from one barrel of a double-barreled pipette whose other barrel contained an additional 1 mM GdCl₃. Bath perfusion as above. CsCl electrode, no EGTA.

channel nonlinear charge movement (Bezanilla et al., 1982b; Fernández et al., 1982). In that case, charge immobilization⁵ as well as long-term inactivation may contribute to apparent voltage shifts. However, in the OHC charge immobilization is absent, since off-gating charge magnitude is not time dependent (Fig. 9A). In addition, unlike Na currents, OHC mechanical responses demonstrate no decay during prolonged depolarizations (Fig. 9B, see Fig. 11).

The differing voltage dependencies of OHC nonlinear capacitance obtained with the two measurement techniques used here may be due to problems that are associated with the step analysis technique (see Discussion). It is suggested that the AC analysis result more accurately reflects the voltage dependency of nonlinear capacitance. It is of interest, therefore, to make comparisons between the voltage dependence of OHC motility and the voltage dependence of nonlinear capacitance obtained by AC or step analysis. Figure 10 demonstrates for two OHCs that the voltage dependence of OHC motility corresponds more closely to the voltage dependence of nonlinear capacitance obtained by

the AC method, rather than that obtained by step analysis. This result may be due to an inaccurate estimate of the voltage dependency of OHC nonlinear capacitance by step analysis.

It is conceivable that voltage-induced length changes may cause deformation of the OHC membrane (stretching and contracting), leading to changes in the specific membrane capacitance. Therefore, it is necessary to determine the possible contribution of such a phenomenon to the measured nonlinear capacitance. This issue was directly evaluated by taking advantage of the observations of Brownell et al. (1989a,b) that cell turgor governs the robustness of electrically induced OHC motility. That is, experiments were performed to determine whether gating currents are abolished when OHC longitudinal motility is inhibited due to loss of cell turgor. Utilizing fairly large-tipped patch pipettes (~ 2 μ m), it is possible to induce reversible cytosolic volume changes rapidly by applying slight suction or pressure to the pipette. Such was the case for the cell depicted in Figure 11. Length changes induced by depolarizing the cell from -80 to $+40$ mV were absent when the cell's cytosol was removed. Immediately upon refilling the cell, the length changes were robust. The effect can be reversibly repeated as long as the whole-cell configuration is maintained. Gating currents (Fig. 11E) were not blocked by the cytosolic volume reduction. These results indicate that nonlinear capacitance is not a function of membrane deformations induced by longitudinal length changes.

⁵ Charge immobilization refers to magnitude inequalities of on- and off-gating charge generated by a voltage step. These measures are thought to reflect processes involved in fast inactivation and long-term depolarization-induced slow inactivation of Na currents. That is, there is a decrease in off-gating charge relative to on charge that is time dependent; the time course is correlated with the time course of Na current inactivation (for review, see Hille, 1984).

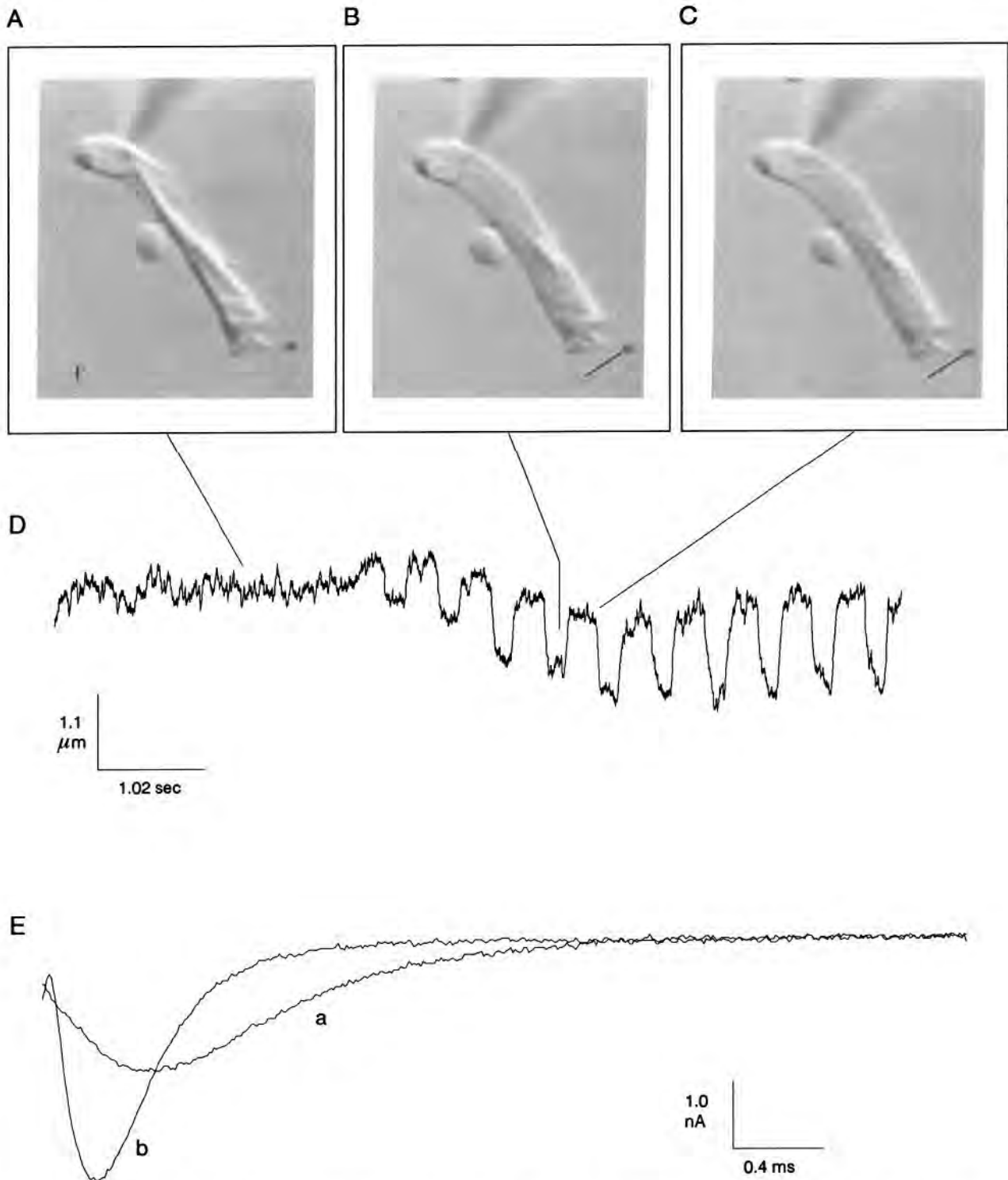


Figure 11. Effect of cytosolic volume alterations on voltage-induced OHC movements: video prints of an OHC that was induced to collapse by gentle suction on the patch electrode located at the nuclear pole of the cell (*A*) and after restoring normal cell volume by gentle pressure into the pipette (*B*, during depolarization of the cell to 40 mV; and *C*, at the holding potential of -80 mV). Scale bar in *A*, $3\ \mu\text{m}$. Simultaneously collected trace of cuticular plate movements (*D*) indicates that movement was abolished during volume reduction but returned immediately upon volume replacement. Downward deflections indicate contraction. Traces in *E* were obtained from a different cell and depict off-gate currents obtained with the $P/-4$ technique at a step potential of $+80$ mV from a holding potential of -120 mV (nominal). Trace *a* was collected when the cell was flattened due to loss of turgor, and trace *b* was obtained immediately after reinflating the cell. Integration indicates that the nonlinear charge movements were roughly equivalent, differing by about 10%, with the deflated condition being larger. This difference may be due to the change in the series resistance before ($11.4\ \text{M}\Omega$) and after ($6.4\ \text{M}\Omega$) reinflation. Series resistance consistently decreases when cells are reinflated by applying pressure to the patch electrode, and this is reflected in the redistribution of charge in time (difference between trace time constants) for conditions *a* and *b*.

Under the deflated conditions, slight dimpling of the OHC's lateral membrane coincident with voltage steps was noted. Gadolinium ions can reduce or abolish this voltage-dependent dimpling.

Discussion

Nonlinear capacitance of the OHC membrane

AC and step analyses presented here demonstrate that OHC membranes possess a capacitance that is voltage dependent. Previous measures of OHC membrane capacitance (Santos-Sacchi, 1988, 1989c) demonstrated that these cells possess input capacitance values, at holding potentials near *in vivo* levels, exceeding the typical $1 \mu\text{F}/\text{cm}^2$ found in biological membranes. In that study, input capacitance of OHCs from the apical turns of the cochlea averaged near 38 pF (at a holding potential of -70 mV), with a specific capacitance of about $1.2 \mu\text{F}/\text{cm}^2$. Clearly, the present findings indicate that such large values were due to the significant nonlinear capacitance present at typical *in vivo* potentials. Ashmore (1987) had also measured OHC membrane capacitance from cells dissociated from the apical turns, reporting an average value of 27 pF, which corresponded to estimates based upon a specific capacity of $1 \mu\text{F}/\text{cm}^2$. This is surprising since measures were made at holding potentials where the nonlinear capacitance should have been substantial. Subsequently, Ashmore (1989, 1990) demonstrated the existence of nonlinear charge movement in OHCs and estimated maximum charge movements of 350 fC for OHCs from the low-frequency region of the cochlea; it was stated that 5% of the cell's capacitance is membrane potential sensitive. In the present study, average maximum nonlinear charge transfer was shown to be about 2 pC, and step or AC analysis provided roughly equivalent estimates of peak nonlinear capacitance of about 17 pF; that is, about 40% of the cell's maximum capacitance is membrane potential sensitive. It is not clear why such large differences exist between the present results and those of Ashmore (1989, 1990), although the $\pm P$ technique was exclusively used in that study.

The magnitude of nonlinear capacitance relative to membrane potential follows a bell-shaped function, whereby it increases upon depolarization from highly negative membrane potentials, reaches a maximum, and then declines upon further depolarization. However, the step and AC analyses utilized in this study give differing voltage dependencies, with the AC voltage technique indicating a peak capacitance at about -40 mV and the step technique indicating a peak at about -23 mV . Bezanilla et al. (1982b) have demonstrated that the voltage dependence of nonlinear charge movement due to Na channel gating is dependent upon holding potential, that is, the initial conditions prior to charge movement measurement. This dependence is thought to be related to processes underlying the inactivation of sodium currents. Although the holding potentials were different for the two measuring techniques used in this study, it is unlikely that a voltage shift due to initial conditions as occurs for the Na channel is responsible for the present results. That is, it was shown that charge immobilization is absent in the OHC, at least during the time window reported here. Correspondingly, the OHC mechanical response does not inactivate, even for durations up to 500 msec (Fig. 11). Furthermore, prolonged depolarization (up to 2 min at 0 mV , followed by return to -80 mV) also has no apparent effect on gating currents or mechanical responses. Still, initial condition effects should be evaluated more systematically.

There are several problems with the step analysis technique that are not encountered with the AC technique. First, because of series resistance, a true voltage step is not delivered to the cell because of the large capacitive currents generated, and consequently the voltage applied across the cell membrane is significantly less depolarized during step depolarizations than is commanded, even at steady state. In addition, due to the voltage-dependent capacitance, the clamp time constant, and consequently the time course of membrane potential change, will vary at different levels of step depolarizations, as it depends upon cell capacitance and series resistance. Nevertheless, the total charge movement should be independent of the time it takes to reach steady state, and correcting voltages for series resistance effects using steady state, non-leak-subtracted current levels should prove sufficient. Unfortunately, the on-line subtraction protocol to extract nonlinear charge movement ($P/-4$) is based on the assumption that series resistance effects are absent. That is, the protocol simply measures linear charge movement at a selected potential and scales that charge movement prior to subtraction based on nominal voltages, without taking into account nonlinear leakage current, which can often be a confounding factor in time domain analysis (Fernández et al., 1982). Thus, scaling inaccuracies may arise and may depend upon the value of the series resistance. Furthermore, in the present experiments the subtraction potential (-120 mV) used for removal of linear charge displacement still falls within the region where some nonlinear charge contributes, as is evident in the AC data. Thus, subtraction values include linear as well as nonlinear components, and this may further contribute to an apparent voltage shift between step and AC data. Other problems associated with comparisons between time and frequency domain measures of nonlinear capacitance have been discussed by Fernández et al. (1982). While holding the OHC at very hyperpolarized subtraction levels would permit a more accurate step analysis, such potentials are difficult to use because the cell-electrode setup becomes unstable. Despite these problems and the differing voltage dependencies⁶ derived from the AC and step techniques, both methods indicate similar estimates of peak nonlinear capacitance in the OHC.

Measures of the gating currents associated with ionic channel activation have been useful in estimating the number of channels within a membrane (see Hille, 1984). Estimates are achieved by comparing the voltage-dependent characteristics of charge movement to those characteristics of the processes that are controlled by such charge movements (e.g., ion conductance). For example, Nonner et al. (1975) determined that two particles with an effective charge of $-1.65e^-$ move within the membrane to activate the sodium channel in frog node of Ranvier. This was determined by computing the ratio of effective valence (z) of the sodium conductance-voltage ($g_{\text{Na}}-V$) function to that of the $Q-V$ function associated with channel activation. Since total nonlinear charge was $17,200 e^-/\mu\text{m}^2$ in their preparation, the number of channels was estimated to be $5212/\mu\text{m}^2$ [i.e., $17,200/(2 \times 1.65)$]. In a similar manner, the number of voltage sensors within the OHC membrane can be estimated. The average total nonlinear charge (Q_{max}) of about 2 pC per OHC observed in the

⁶ It should be reemphasized that voltage-dependent processes are susceptible to the ionic makeup (charge screening ability) of the medium that bathes the plasmalemma. Thus, the *in vitro* voltage dependence of nonlinear capacitance and motility shown here may not reflect *in vivo* conditions.

present study translates to about $3850 e^-/\mu\text{m}^2$. Assuming that this charge movement is associated with the motility of the cell, the similarity of the valences of OHC length changes and charge movement indicates the existence of a single voltage-sensing particle with an absolute charge magnitude close to $1 e^-$. Thus, the number of voltage-sensing particles within the OHC membrane approaches $4000/\mu\text{m}^2$. These particles presumably represent the voltage sensors of independent, membrane-bound motor elements. In fact, Dallos et al. (1991) have elegantly shown that, indeed, OHC motility is driven by independent motor elements distributed in the basolateral region of the cell. They extend from nuclear to cuticular regions, that is, roughly paralleling the extent of the subsurface cisternae. Interestingly, the number of motor elements inferred from charge movement data reported here is of the same order of magnitude as the number of tightly packed 10 nm intramembranous particles recently observed by Kalinec et al. (1991). These investigators have speculated that the intramembranous particles represent the OHC motor units.

Initial observations that OHC motility and gating currents were blocked by gadolinium ions (Santos-Sacchi, 1989a) raised the possibility that voltage-dependent stretch-activated channels may underlie the observed gating and mechanical events through some sort of reverse process, since it had been shown that gadolinium is a potent blocker of stretch-activated channels (Yang and Sachs, 1989). In fact, voltage-dependent stretch-activated channels have been found in the lateral membrane of the OHC (Ding et al., 1989, 1991), but the channel number is probably too low to account for the observed charge displacement.

Interestingly, Ashmore (1987) ruled out any interaction between plasma membrane and the extensive intracellular subsurface cisternal membrane system of the OHC because his calculations indicated that OHC capacitance can be accounted for by linear dielectric plasmalemmal properties. Since it is now clear that OHC capacitance is not simply due to linear membrane properties, possible voltage-dependent electrical interactions between these two membranous systems should be considered. However, similar considerations concerning a possible voltage-dependent recruitment of a hypothetically unavailable portion of transverse tubular membrane capacitance in striated muscle have proved untenable (Chandler et al., 1976). Indeed, there is rather good evidence now that the bulk of nonlinear charge displacement in striated muscle is afforded by dihydropyridine-sensitive calcium channels (Adams et al., 1990). It may be that most of the nonlinear charge movement in OHCs is associated with intramembranous voltage sensors responsible for OHC motility, but certainly the issue of a subsurface cisternal contribution is not yet resolved. However, it is unlikely that the nonlinear capacitance is a function of membrane deformations caused by length changes since charge movement is still measured during loss of cell turgor, which abolishes longitudinal movement. Also, changes in membrane dielectric properties due to electrostriction can be ruled out based on the arguments of Chandler et al. (1976). It should also be pointed out that a possible contribution may come from gating currents associated with ionic channels within the OHC membrane. Regardless of the underlying mechanisms that contribute to the voltage-dependent capacitance, its existence will alter the RC time constant of the OHC in a voltage-dependent manner, thereby dynamically modifying the receptor potential waveform generated *in vivo*. This leads to the conclusion that sensing of the stimulus

for OHC motility effectively modifies the stimulus for OHC motility.

Relation between nonlinear capacitance and cell motility

As discussed above, the voltage dependence of OHC fast motility suggests the existence of a corresponding gating current. In other systems, correlation between gating current characteristics and the processes they presumably control provides evidence linking the two. In squid axon, for example, treatments that modify gating current characteristics typically are reflected in measures of Na currents (Bezanilla and Armstrong, 1974; Armstrong, 1981; although see Tanguy and Yeh, 1988). It is shown here that gadolinium ions are capable of simultaneously reducing or abolishing OHC motility and gating currents (or nonlinear capacitance). This blockade and the reversibility of gadolinium's effects upon washout may indicate that the two phenomena are dependent. Further evidence linking the two includes their similar voltage dependencies and their similar susceptibility to charge screening. Based on these results, a more detailed study of the concentration-dependent effects of gadolinium is warranted and may lead to quantitative estimates of OHC membrane surface charge.

It is interesting to note that the time course of gating current is a function of clamp time constant, indicating that charge movement is redistributed in time depending upon the speed of transmembrane voltage change. The speed limitations imposed by electrode series resistance prevent an accurate measure of the actual gating time constant, which is probably much faster than can be measured. However, the dependence of gating time constant upon clamp time constant can be used to characterize further the relationship between charge movement and OHC motility. Thus, it has been shown that the speed or frequency response of OHC motility increases in parallel with clamp time constant or correspondingly with gate time constant (Santos-Sacchi, 1990a).

Cell turgor requirement for fast motility

Brownell et al. (1989a,b) have demonstrated that prolonged depolarization of the OHC under voltage clamp or treatments with salicylates causes a decrease in OHC cytoplasmic turgor. The process is slow and reversible (on the order of tens of minutes) and is accompanied by a reduction or abolition of longitudinal OHC motility, which also recovers upon restoration of cell turgor. The results presented here demonstrate directly that the reduction of cytosolic volume is one factor responsible for the reduction in OHC motility, since holding potential was held constant and no exogenous treatments were involved. This clearly confirms the hypothesis of Brownell and colleagues that cell turgor is directly involved in the robustness of electrically evoked OHC motility. Cell turgor may underlie the translation of voltage-dependent membrane phenomena to longitudinal force generation. Indeed, gating currents remain intact during cell turgor alterations. The observation of depolarization-induced membrane dimpling, which was susceptible to gadolinium treatment, during loss of cell turgor further suggests that the membrane-associated portion of the OHC motility mechanism remained intact and was simply uncoupled from a longitudinal translation process. It is conceivable that loss of cell volume disrupts elements linking a motility voltage sensor and subsurface structures; however, clearly, such a disruption must be reversible on a time scale of tens of minutes, at least (Brownell et al., 1989a,b). The study of the intricate subplas-

mammalian cytoskeleton and cisterns of the OHC may provide clues needed to understand the translational process (Bannister et al., 1988; Slepecky, 1989; Evans, 1990; Holley and Ashmore, 1990; Dieler et al., 1991).

For some time, anecdotal observations of isolated OHCs have led to the idea that the intracellular pressure of the OHC is greater than extracellular pressure. For example, OHCs often burst when impaled with microelectrodes, ejecting cytoplasm and intracellular organelles (Brownell, 1983). Kaufman and Brownell (1991) have recently provided indirect evidence confirming this notion. Considering the dependence of longitudinal motility upon cell turgor, it is now clear that estimates of the magnitude of OHC motility may require reinspection. That is, measures of the voltage versus length function of OHCs have been made with the use of the whole-cell voltage-clamp configuration, where inherently the cells' internal turgor pressure is compromised by establishing contiguity between cell and pipette interiors (Ashmore, 1987; Santos-Sacchi and Dilger, 1988; Santos-Sacchi, 1989c). For example, Santos-Sacchi (1989c) estimated that near the normal *in vivo* resting potential, -70 mV, the response of the OHC is about 2 nm/mV; at that holding potential the cells reside near the hyperpolarizing saturation area of the response function. Based on these observations and on evidence indicating the voltage dependence of OHC motility (Santos-Sacchi and Dilger, 1988), a calculated disparity of 21 dB exists between threshold basilar membrane motion and OHC motion at high frequencies (see Santos-Sacchi, 1989c). Obviously, this leads to difficulties in assigning the role of "cochlear amplifier" solely to OHCs. It is now clear that these measures of OHC movement may be underestimates, though certainly not approaching an order of magnitude. Nevertheless, nonintracellular techniques, such as that used by Evans et al. (1989), may provide more accurate estimates of movement magnitude since cell turgor is not directly compromised. Still, these techniques pose other problems; notably, membrane potential must be estimated and cannot be directly measured or controlled with the precision of the whole-cell voltage-clamp technique.

The evidence linking basilar membrane mechanics to OHC function is growing (Ruggero and Rich, 1991). Currently, the most likely candidate responsible for this interaction is the motility of the OHC, which has recently been shown to have a much wider frequency response than previously thought, the 3 dB break frequency of which approaches 1 kHz (Santos-Sacchi, 1990a). Although many basic properties of the OHC and its motility have been detailed, the molecular basis of this motility remains to be determined and no doubt promises to be a novel cellular adaptation designed to meet the mammals' high frequency communicative requirements.

Note added in proof. Ashmore presented data on the nonlinear capacitance of OHCs in the published proceedings of the Taniguchi International Symposium on Visual Science [Neurosci Res, Suppl 12 (1990) S39-S50], which indicate larger values of nonlinear capacitance than his other reports. Experimental methods were not detailed, but estimates of capacitance were obtained at different holding potentials by integration of the charging transient presumably induced by a small voltage step. His data appear to be in general agreement with the capacitance data reported here.

References

Adams BA, Tanabe T, Mikami A, Numa S, Beam KG (1990) Intramembrane charge movement restored in dysgenic skeletal muscle by

- injection of dihydropyridine receptor cDNAs. *Nature* 346:569-572.
- Armstrong CM (1981) Sodium channels and gating currents. *Physiol Rev* 61:644-683.
- Armstrong CM, Bezanilla F (1973) Currents related to movement of the gating particles of the sodium channels. *Nature* 242:459-461.
- Ashmore JF (1987) A fast motile response in guinea-pig outer hair cells: the cellular basis of the cochlear amplifier. *J Physiol (Lond)* 388:323-347.
- Ashmore JF (1989) Transducer motor coupling in cochlear outer hair cells. In: *Mechanics of hearing* (Kemp D, Wilson JP, eds), pp 107-113. New York: Plenum.
- Ashmore JF (1990) Mechanoreception. In: *Sensory transduction* (Borsellino A, Cervetto L, Torre V, eds), pp 25-50. New York: Plenum.
- Bannister LH, Dodson HC, Astbury AF, Douek EE (1988) The cortical lattice: a highly ordered system of subsurface filaments in guinea pig cochlear outer hair cells. *Prog Brain Res* 74:213-219.
- Bezanilla F, Armstrong CM (1974) Gating currents of the sodium channel: three ways to block them. *Science* 183:753-754.
- Bezanilla F, Armstrong CM (1977) Inactivation of the sodium channel. I. Sodium current experiments. *J Gen Physiol* 70:549-566.
- Bezanilla F, White MM, Taylor RE (1982a) Gating currents associated with potassium channel activation. *Nature* 296:657-659.
- Bezanilla F, Taylor RE, Fernández JM (1982b) Distribution and kinetics of membrane dielectric polarization. I. Long-term inactivation of gating currents. *J Gen Physiol* 79:21-40.
- Brown MC, Nuttall AL (1984) Efferent control of cochlear inner hair cell responses in the guinea-pig. *J Physiol (Lond)* 354:625-646.
- Brownell WE (1983) Observations on a motile response in isolated outer hair cells. In: *Mechanisms of hearing* (Webster WR, Aitken LM, eds), pp 5-10. Clayton, Australia: Monash UP.
- Brownell WE, Bader CR, Bertrand D, de Ribaupierre Y (1985) Evoked mechanical responses of isolated cochlear outer hair cells. *Science* 227:194-196.
- Brownell WE, Imredy JB, Shehata W (1989a) Stimulated volume changes in mammalian outer hair cells. *Proc Annu Int Cong IEEE-Eng Med Biol Soc* 11:1344-1345.
- Brownell WE, Shehata W, Imredy JB (1989b) Slow electrically and chemically evoked volume changes in guinea pig outer hair cells. In: *Biomechanics of active movement and deformation of cells* (Akas N, ed), pp 493-498. New York: Springer.
- Chandler WK, Rakowski RF, Schneider MF (1976) A non-linear voltage dependent charge movement in frog skeletal muscle. *J Physiol (Lond)* 254:245-283.
- Dallos P, Harris D (1978) Properties of auditory nerve responses in absence of outer hair cells. *J Neurophysiol* 41:365-383.
- Dallos P, Santos-Sacchi J, Flock Å (1982) Intracellular recordings from outer hair cells. *Science* 218:582-584.
- Dallos P, Evans BN, Hallworth R (1991) On the nature of the motor element in cochlear outer hair cells. *Nature* 350:155-157.
- Dieler R, Shehata-Dieler WE, Brownell WE (1991) Concomitant salicylate-induced alterations of outer hair cell subsurface cisternae and electromotility. *J Neurocytol*, in press.
- Ding JP, Salvi RJ, Sachs F (1989) Stretch activated ion channels in outer hair cells from the guinea pig cochlea. Paper presented at the midwinter meeting of the Association for Research in Otolaryngology, St. Petersburg, FL, February.
- Ding JP, Salvi RJ, Sachs F (1991) Stretch-activated ion channels in guinea pig outer hair cells. *Hear Res*, in press.
- Evans B, Dallos P, Hallworth R (1989) Asymmetries in motile responses of outer hair cells in simulated *in vivo* conditions. In: *Mechanics of hearing* (Kemp D, Wilson JP, eds), pp 205-206. New York: Plenum.
- Evans BN (1990) Fatal contractions: ultrastructural and electromechanical changes in outer hair cells following transmembranous electrical stimulation. *Hear Res* 45:265-282.
- Evans MG, Fuchs PA (1987) Tetrodotoxin-sensitive, voltage-dependent sodium currents in hair cells from the alligator cochlea. *Biophys J* 52:649-652.
- Fernández JM, Bezanilla F, Taylor RE (1982) Distribution and kinetics of membrane dielectric polarization. II. Frequency domain studies of gating currents. *J Gen Physiol* 79:41-67.
- Fishman HM, Moore LE, Poussart D (1977) Asymmetry currents and admittance in squid axons. *Biophys J* 19:177-183.
- Harrison RV, Evans EF (1979) Cochlear fiber responses in guinea pigs with well defined cochlear lesions. *Scand Audiol Suppl* 9:83-92.

- Hille B (1984) Ionic channels of excitable membranes. Sunderland, MA: Sinauer.
- Hodgkin AL, Huxley AF (1952) A quantitative description of membrane current and its application to conduction and excitation in nerve. *J Physiol (Lond)* 117:500–544.
- Holley MC, Ashmore JF (1988) On the mechanism of a high frequency force generator in outer hair cells isolated from the guinea pig cochlea. *Proc R Soc Lond [Biol]* 232:413–429.
- Holley MC, Ashmore JF (1990) Spectrin, actin and the structure of the cortical lattice in mammalian cochlear outer hair cells. *J Cell Sci* 96:283–291.
- Hubbard AE, Mountain DC (1983) Alternating current delivered into the scala media alters sound pressure at the eardrum. *Science* 222:510–512.
- Iurato S, Franke K, Luciano L, Wermbter G, Pannese E, Reale E (1976) Intercellular junctions in the organ of Corti as revealed by freeze fracturing. *Acta Otolaryngol (Stockh)* 82:57–69.
- Iwasa KH, Kachar B (1989) Fast *in vitro* movement of outer hair cells in an external electric field: effect of digitonin, a membrane permeabilizing agent. *Hear Res* 40:247–254.
- Kachar B, Brownell WE, Altschuler R, Fex J (1986) Electrokinetic shape changes of cochlear outer hair cells. *Nature* 322:365–368.
- Kalinec F, Iwasa K, Lim DJ, Kachar B (1991) Dynamic and structural characterization of a voltage dependent motor in the lateral wall of outer hair cells. Paper presented at the midwinter meeting of the Association for Research in Otolaryngology, St. Petersburg, FL, February.
- Katz B, Miledi R (1967) A study of synaptic transmission in the absence of nerve impulses. *J Physiol (Lond)* 192:407–436.
- Kaufman G, Brownell WE (1991) Determination of the cytoplasmic pressure of the cochlear outer hair cell. Paper presented at the midwinter meeting of the Association for Research in Otolaryngology, St. Petersburg, FL, February.
- Kemp DT (1978) Stimulated acoustic emissions from within the human auditory system. *J Acoust Soc Am* 64:1386–1391.
- Lin X, Hume RL, Nuttall AL (1990) Voltage-gated Ca^{2+} currents recorded *in vitro* from outer hair cells of the guinea pig. Paper presented at the 20th annual meeting of the Society for Neuroscience, St. Louis, MO, October.
- Marty A, Neher E (1983) Tight-seal whole-cell recording. In: Single-channel recording (Sakmann B, Neher E, eds), pp 107–122. New York: Plenum.
- Mountain DC, Hubbard AE, McMullen TA (1983) Electromechanical processes in the cochlea. In: Mechanics of hearing (de Boer E, Viergever MA, eds), pp 119–126. Delft, The Netherlands: Delft UP.
- Nonner W, Rojas E, Stampfli R (1975) Displacement currents in the node of Ranvier: voltage and time dependence. *Pflugers Arch* 354:1–18.
- Oesterle E, Dallos P (1988) Indirect evidence for the absence of electrotonic coupling between hair and support cells in the mammalian cochlea. *J Acoust Soc Am [Suppl 1]* 83:S97.
- Ogden DC, Stanfield PR (1987) Introduction to single channel recording. In: Microelectrode techniques (Standen NB, Gray PTA, Whittaker MJ, eds), pp 63–81. Cambridge: Company of Biologists.
- Patuzzi RB, Yates GK, Johnstone BM (1989) Outer hair cell receptor currents and sensorineural hearing loss. *Hear Res* 42:47–72.
- Ruggero MA, Rich NC (1991) Furosemide alters organ of Corti mechanics: evidence for feedback of outer hair cells upon the basilar membrane. *J Neurosci* 11:1057–1067.
- Salzberg BM, Bezanilla F (1983) An optical determination of the series resistance in *Logigo*. *J Gen Physiol* 82:807–817.
- Santos-Sacchi J (1988) Whole cell voltage clamp studies on isolated outer hair cells. Paper presented at symposium, Current concepts of hair cell function: a consensus meeting. Kresge Hearing Research Institute, University of Michigan, Ann Arbor, MI, June.
- Santos-Sacchi J (1989a) Gadolinium ions reversibly block voltage dependent movements of isolated outer hair cells. Paper presented at the 19th annual meeting of the Society for Neuroscience, Phoenix, AZ, October.
- Santos-Sacchi J (1989b) Calcium currents, potassium currents and the resting potential in isolated outer hair cells. Paper presented at the midwinter meeting of the Association for Research in Otolaryngology, St. Petersburg, FL, February.
- Santos-Sacchi J (1989c) Asymmetry in voltage dependent movements of isolated outer hair cells from the organ of Corti. *J Neurosci* 9:2954–2962.
- Santos-Sacchi J (1990a) Fast outer hair cell motility: how fast is fast? In: The mechanics and biophysics of hearing (Dallos P, Geisler CD, Matthews JW, Ruggero MA, Steele CR, eds). Berlin: Springer.
- Santos-Sacchi J (1990b) Nonlinear voltage dependent capacitance of the outer hair cell (OHC) membrane. Paper presented at the 120th meeting of the Acoustical Society of America, San Diego, CA, November.
- Santos-Sacchi J (1991) Isolated supporting cells from the organ of Corti: some whole cell electrical characteristics and estimates of gap junctional conductance. *Hear Res* 52:89–98.
- Santos-Sacchi J, Dilger JP (1988) Whole cell currents and mechanical responses of isolated outer hair cells. *Hear Res* 35:143–150.
- Schanne OF, Ruiz P, Ceretti E (1978) Impedance measures in biological cells. New York: Wiley.
- Slepecky N (1989) Cytoplasmic actin and cochlear outer hair motility. *Cell Tissue Res* 257:69–75.
- Takashima S (1978) Frequency domain analysis of asymmetry current in squid axon membrane. *Biophys J* 22:115–119.
- Tanguy J, Yeh JZ (1988) Batrachotoxin uncouples gating charge immobilization from fast Na inactivation in squid giant axons. *Biophys J* 54:719–730.
- Yang XC, Sachs F (1989) Block of stretch-activated ion channels in *Xenopus* oocytes by gadolinium and calcium ions. *Science* 243:1068–1070.

On the Frequency Limit and Phase of Outer Hair Cell Motility: Effects of the Membrane Filter

J. Santos-Sacchi

Sections of Otolaryngology and Neurobiology, Yale University School of Medicine, New Haven, Connecticut 06510

Whole-cell voltage clamp and displacement-measuring photodiode techniques were used to study electrophysiological and mechanical properties of the guinea pig outer hair cell (OHC). OHCs demonstrate a voltage–mechanical response (V-M) function that can be fit by a two state Boltzmann relation, where the cell normally rests near the hyperpolarizing saturation region (–70 to –90 mV). The voltage at half-maximal length change (V_h) is depolarized relative to the resting potential, and this ensures that for symmetrical sinusoidal voltage stimulation about the resting potential, AC and DC mechanical responses will be generated. Analysis of OHC motility using pure tone voltage bursts from 11 to 3200 Hz demonstrates both AC and DC mechanical responses. By exploiting the frequency-dependent current–voltage phase separation that is characteristic of an RC-dominated system under voltage clamp, it is demonstrated that OHC motility follows the phase of AC transmembrane voltage and not that of current. For voltage stimulation across frequencies in the acoustic range, the motility cutoff frequency corresponds to the cutoff frequency of the imposed transmembrane voltage. Frequency cutoffs approaching 1 kHz have been measured but are clamp time constant limited. These observations are congruent with the voltage dependency hypothesis of OHC motility. In addition, the DC component of the mechanical response is shown to be frequency independent, but to decrease in magnitude disproportionately compared to the AC component as the magnitude of the driving voltage decreases. This is predicted from the form of the V-M function, whose level dependent DC nonlinearity is a consequence of the resting potential being displaced from V_h . The net effect is that the mechanical DC:AC ratio approaches zero for small AC voltages. Taken together, these findings question the ability of the OHC mechanical response to influence organ of Corti micromechanics at high acoustic frequencies where a tuned amplification of basilar membrane motion is hypothesized.

Hair cells transduce mechanical stimuli into electrical signals by modulating a standing transduction current in response to stereocilia displacement; this current induces a receptor poten-

tial across the basolateral membrane of the cell, the depolarizing phase of which may promote the release of neurotransmitter (Hudspeth, 1989). Although evidence had accumulated that some type of interaction between outer (OHCs) and inner hair cells (IHCs) of the organ of Corti promoted the highly selective and sensitive responses of the mammalian auditory system to high-frequency acoustic stimulation (Dallos and Harris, 1978; Harrison and Evans, 1979; Brown and Nuttall, 1984), a potential mechanism for such an interaction remained obscure until recently. Following the discovery that the OHC is capable of electrically evoked mechanical responses (Brownell et al., 1985), a reevaluation of the classical concepts of mammalian hearing has been underway. Current theories concerning the basis of a cochlear amplifier envision an acoustically evoked cycle by cycle feedback process between OHC and basilar membrane (Geisler and Shan, 1990; Robles et al., 1991; Ruggero and Rich, 1991). That is, *in vivo*, the acoustically evoked electrical responses of the OHC should effect rapid length changes of these cells that modify the mechanical input to the IHC—the receptor cell that receives up to 95% of the afferent innervation (Spoendlin, 1988).

We have previously shown that under whole-cell voltage clamp, blocking the known ionic conductances of the OHC does not interfere with the cell's mechanical response, and we proposed that transmembrane potential was the driving force responsible for OHC motility (Santos-Sacchi and Dilger, 1988). Although the molecular basis of OHC motility remains to be determined, the physiological consequences of its voltage dependence are readily discernible. For example, the voltage dependence suggests that AC motility magnitude and phase characteristics should be governed by the attenuation effects of the OHC membrane (RC) filter. Any feedback contribution of the OHC to basilar membrane mechanics will be dependent upon these magnitude and phase characteristics. I report here that an analysis of OHC motility in response to step and AC voltage stimuli confirms the voltage dependency hypothesis, since the frequency extent and phase of motility are dependent upon the extent and phase of the imposed transmembrane voltage. Furthermore, while the effects of the membrane filter influence the AC mechanical component directly, the DC component is indirectly susceptible. Indeed, the DC component is far more susceptible than the AC component. These results are important for understanding the possible contribution of OHC motility in peripheral auditory processing.

Preliminary reports of this work have been presented previously (Santos-Sacchi, 1990, 1991a).

Materials and Methods

General. Guinea pigs were overdosed with pentobarbital. The temporal bones were removed, and OHCs were isolated nonenzymatically from

Received Oct. 1, 1991; revised Dec. 13, 1991; accepted Dec. 18, 1991.

This work was supported by an NIDCD Research Career Development Award and NIH Grant DC00273. I thank Jack Callahan and Janet Santos for technical assistance, and Dr. Jont Allen for many helpful discussions. I also thank Drs. Yukihiro Sato, Lisa Olson, Paul Manis, and Mike Zidanic for comments on early versions of the manuscript. Portions of this work were completed at NJ Medical School.

Correspondence should be addressed to Joseph Santos-Sacchi, Ph.D., Department of Surgery, Section of Otolaryngology, Yale University School of Medicine, BML 244, 333 Cedar Street, New Haven, CT 06510.

Copyright © 1992 Society for Neuroscience 0270-6474/92/121906-11\$05.00/0

the cochleas by gentle pipetting of the isolated top two turns of the organ of Corti. The cell enriched supernatant was then transferred to a 700 μ l perfusion chamber, and cells were permitted to settle onto the cover glass bottom. All experiments were performed at room temperature ($\sim 23^\circ\text{C}$). A Nikon Diaphot inverted microscope with Hoffmann optics was used to observe the cells during electrical recording. All experiments were taped with a Panasonic AG6300 video recorder. A modified Leibovitz medium (NaCl, 142.2 mM; KCl, 5.37 mM; CaCl_2 , 1.25 mM; MgCl_2 , 1.48 mM; HEPES, 5.0 mM; dextrose, 5.0 mM; pH 7.2) was used as the normal perfusate. Modifications to the extracellular medium are noted in figure captions, with NaCl adjusted to maintain osmolarity (300 mOsm). Extracellular solutions were changed via two methods. A chamber perfusion system permitted the fluid in the whole chamber to be constantly exchanged with fresh medium (0.1–1 ml/min). A more rapid and direct perfusion system was used to perfuse single cells selectively under voltage clamp, during continuous exchange of bulk medium via chamber perfusion. The device is a four-barreled glass pipette tapered to about 100 μ m and fitted with a polyethylene sleeve at the tip to permit fluid flow from a single port with a small dead volume. Solutions were fed to the pipette under gravity control and rapidly switched with solenoid valves. The tip of the pipette was brought to within 50 μ m of the cell being studied, and the flow of solution was adjusted so as not to perturb the cell physically.

Electrical recording. OHCs were whole-cell voltage clamped with a Dagan patch-clamp amplifier at holding potentials between -70 and -80 mV, similar to potentials recorded *in vivo* (Dallos et al., 1982). Pipette solutions were composed of 140 mM KCl or CsCl, 5 or 10 mM EGTA, 2 mM MgCl_2 , and 5 mM HEPES buffered to pH 7.2. Gigohm seals were obtained at the nuclear level of the cell membrane, and electrode capacitance was compensated prior to whole-cell recording. Voltage step studies were performed with an Axolab 1100 A/D and D/A board (Axon Instruments, Foster City, CA) with associated software (PCLAMP). AC studies were performed using a digital signal processing board with custom-written software (DSP-16; Ariel Corp., Highland Park, NJ) capable of delivering and analyzing pure tone or swept frequency stimuli. Data were saved to disk for off-line analysis.

For most experiments, ionic conductances were blocked. Under these conditions, the cell clamp can be modeled most simply as an electrode resistance (R_e) in series with a parallel combination of the membrane resistance (R_m) and capacitance (C_m). These component values were estimated at the holding potential from current records in response to -10 mV voltage steps, and were accounted for during analysis, so that actual voltages imposed upon the cell are known (Marty and Neher, 1983). Care was taken to maintain low series resistance values during recording by delivering transient positive or negative pressure into the electrode to maintain an unobstructed orifice; electronic series resistance compensation was employed as well. The program CLAMPX (Axon Instruments, Foster City, CA) was modified to provide a continuous display of clamp time constant, cell capacitance and resistance, and series resistance between data collections. The magnitude and phase of the transmembrane voltage (V_m), predicted from the command voltage (V_c), were obtained using the estimated component values by modeling the impedance (Z_{in}) of the cell clamp with the software package MATLAB (Mathworks, Natick, MA):

$$Z_{in} = R_s + Z_m, \quad (1)$$

where

$$Z_m = \frac{R_m}{1 + sC_m R_m}, \quad s = j\omega, \quad j = \sqrt{-1}, \quad \omega = 2\pi f; \quad (2)$$

$$I = V_c / Z_{in}; \quad (2)$$

$$V_m = I Z_m. \quad (3)$$

In some cases, an absolute delay ($I = I \cdot e^{-st}$, where t is the delay in seconds) was included in the model so that the predicted phase plots coincided (as determined by eye) with those of the measured current and mechanical response plots. Typically, this was required when series resistance compensation was used, and may be the result of delays introduced as a result of the compensation feedback.

OHC motility measures. OHC mechanical responses and currents were simultaneously measured in response to step or sinusoidal voltage stimuli. For steady state movements (voltage steps > 100 msec), length changes were analyzed off the video monitor during playback by placing differential optoresistors or a position-sensitive detector (Hamamatsu

Corp., NJ; output filtered at 30 Hz) across the image of the cuticular plate (apical end of the cell) at a monitor magnification of $2800\times$ (Santos-Sacchi, 1989). Fast OHC movements elicited by voltage clamp with short-duration stimuli (below video detection) were measured with a differential photodiode (PD) onto which the image of the cuticular plate from the microscope was projected. Placement of the PD was accomplished remotely by a computer-controlled micromanipulator, so as not to perturb whole-cell recording. The PD was backlit by two fiber optic beams projected through the microscope's camera port onto a 30% mirrored glass coverslip base of the perfusion chamber, and reflected back to a CCD video camera via a 90° prism to allow PD placement during simultaneous cell visualization on a mixed video-computer monitor (Matrox Corp., Dorval, Quebec, Canada). Backlighting was not required after calibration of the PD's position on the monitor. The frequency response of the PD system was measured by driving an on-biased light-emitting diode (LED) and had a 3 dB rolloff at 6 kHz (Fig. 1). The validity of the PD system was verified by measuring the movements of a glass probe driven by a piezoelectric bimorph (Fig. 1, insets). Sinusoidal voltage bursts (onset and offset linearly ramped) of frequencies ranging from 11.7 to 3201 Hz were delivered to OHCs under voltage clamp. PD output and whole-cell currents were filtered at 10 kHz (12 dB/octave) and collected simultaneously using a sampling rate of 20 kHz for AC analysis or up to 50 kHz for step analysis. Responses were averaged 200 times. Fundamental magnitude and phase of the mechanical responses were measured by fast Fourier transformation (FFT) of the central portion of the digitized waveforms using the software package MATLAB. Mechanical responses were corrected for the phase and magnitude characteristics of the PD system. Absolute calibration of cell movements was determined by measuring off the video monitor the cell movement in response to a large steady state depolarizing voltage stimulus (Santos-Sacchi, 1989).

Motility estimates using a photodiode technique rely upon intensity measures of the projected image of the OHC's cuticular plate. The problems with such a technique have been addressed by Clark et al. (1990). In the present study, care was taken to maintain the position of the cells within the bounds of the differential photodiode; in order to check this, cells were visualized on a video monitor during data collection. While magnitude measures may be affected by changes in image intensity, phase measures should not. Similar cutoff frequencies of the mechanical responses were obtained from phase and magnitude data, indicating that the image intensity did not change during the data collection period, typically about 5 min.

The mechanical response $\Delta L(v)$ was fit with a Boltzmann function:

$$\Delta L(v) = \left[\frac{\Delta L_{\max}}{1 + e^{(V_m - V_h)/b}} \right] + \Delta L_{\min}, \quad (4)$$

where ΔL_{\max} and ΔL_{\min} are the fitted maximum and minimum length changes from the resting state, b is the voltage slope factor, and V_h is the voltage at half-maximal length change.

Results

The OHC changes length when its transmembrane potential is altered. Figure 2A demonstrates the V-M function for an isolated OHC using step voltage commands from a holding potential of -68.4 mV. The function follows a saturating Boltzmann relation, such that the mechanical response is larger in the depolarizing (shortening) direction near the cell's normal resting potential. This is a consequence of the holding potential being displaced from V_h . For this cell, a maximum slope of about 21 nm/mV at -26 mV is calculated (Fig. 2B). Responses as large as 30 nm/mV have been observed (Santos-Sacchi and Dilger, 1988).

The OHC membrane possesses a nonlinear charge movement that is correlated in time and voltage dependence with induced length changes (Ashmore, 1989; Santos-Sacchi, 1990, 1991b); this nonlinear charge probably represents the movement of membrane-bound voltage sensors responsible for the cell's voltage-dependent mechanical response. Figure 3 demonstrates that the kinetics of the charge movement are such that the time

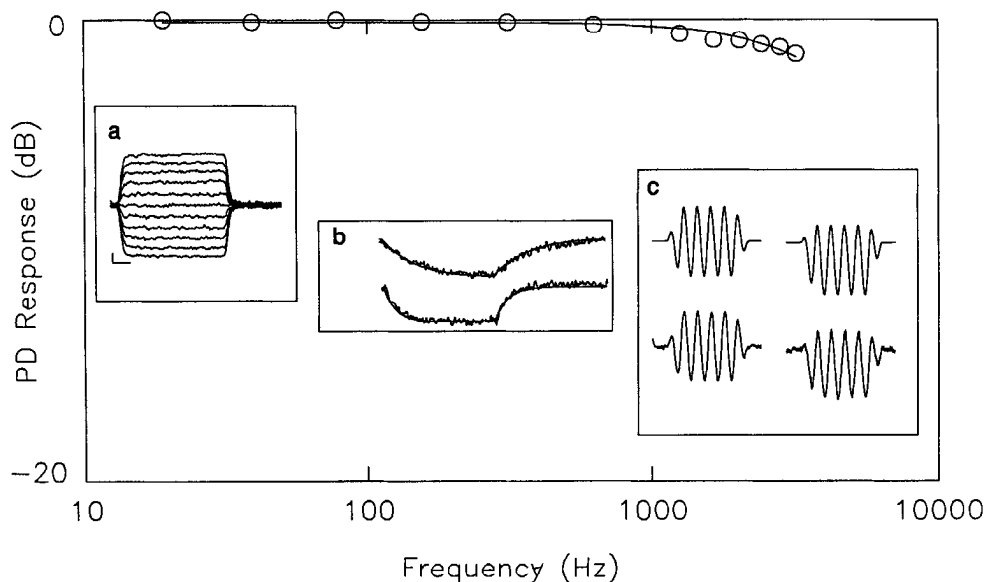


Figure 1. Characteristics of the movement measurement system. Frequency response of differential PD output (*open circles*, averaged 200 \times) in response to off-centered LED emission elicited by sine wave bursts. Cutoff frequency was 6 kHz. *Insets*, Outputs from PD in response to simulated cell movement. The tip of a glass microelectrode shank was melted to a sphere of about 15 μm ; transmitted light produced a bright area in the sphere's center, which was used to mimic the bright OHC cuticular plate observed under Hoffmann optics. The artificial cell was attached to a piezoelectric bimorph and moved using various voltage waveform inputs to test the linearity and frequency following capability of the PD measurement system. *a*, PD output measured in response to bimorph movements produced by fixed incremental voltage steps (filtered to avoid bimorph resonance at 2 kHz). Linearity is good. Response filtered at 800 Hz. Calibration *vertical*, 0.1 μm ; *horizontal*, 2 msec. *b*, PD output (*noisy traces*) in response to bimorph voltage stepped through a filter of 100 Hz (*top trace*) and 300 Hz (*bottom trace*). Simultaneously recorded voltage (*solid traces*) corresponds faithfully to the PD output. Maximum excursion is about 1 μm . Pulse width is 5 msec. *c*, Bimorph was stimulated with sinusoidal voltage bursts (156 Hz). *Two traces on top* are measured voltage; corresponding *two traces on bottom* are PD output (filtered at 800 Hz). Excellent frequency following is apparent. Stimulus and response traces on *right* demonstrate that the measurement system is capable of detecting DC offsets.

constant of the voltage-clamp amplifier limits their study under whole-cell configuration. That is, the time constant of nonlinear capacitive current decay follows changes in the time constant of the clamp amplifier, indicating that the kinetics are faster than the fastest clamp speed presently attainable. Measures of OHC mechanical response induced by voltage steps indicate a similar trend (Fig. 4A). In this case, an OHC was stepped from a holding potential near -70 mV to about 40 mV, while the clamp time constant was modified between 0.8 and 0.52 msec with series resistance feedback compensation. Both movement onset and offset are directly correlated with clamp time constant. Note that fitted single exponentials of the movement onset appear faster than the clamp time constant. This is due to the fact that the voltage steps are saturating, and is consistent with model simulations based on the OHC's V-M function (see Discussion). It was noted by Ashmore (1987) that delays in mechanical response onset occurred following voltage step onset. The insets in Figure 4A illustrate that clamp time constant modifications do not appear to influence the mechanical response onset, which occurred within 40 μsec of stimulus onset in this case. In other cells, however, delays were observed up to about 100 μsec (Fig. 4B). It is conceivable that alterations of cell turgor that occur during whole-cell voltage clamp may underlie this delay phenomenon (Santos-Sacchi, 1991b). Figure 4C illustrates the mechanical response of an OHC driven by a voltage step depolarization of about 5 msec in duration, with one of the fastest clamp time constants attained, 0.14 msec. The onset of the mechanical response is rapid (onset τ of a double exponential fit, 0.240 msec); a maximum velocity of 6.5 mm/sec is calcu-

lated, which is about 3.5 times faster than previous estimates of OHC velocity (Ashmore, 1987).

The form of the V-M function (Fig. 2A) indicates that the mechanical response will include both AC and DC components when a sinusoidal voltage command is delivered about the holding potential. Such mechanical rectification has been demonstrated with low-frequency sinusoidal stimuli (Evans et al., 1989; Santos-Sacchi, 1989). Figure 5 illustrates this phenomenon as a function of stimulus frequency. Sinusoidal voltage command stimuli of frequencies ranging from 11.7 to 3201 Hz elicit AC and DC mechanical responses. Figure 5A documents the rectified nature of the V-M function of this cell based on the response from an 11.7 Hz transmembrane voltage stimulus. Mechanical rectification is also apparent at higher stimulus frequencies, as reflected in the DC mechanical components present in the raw data (Fig. 5B). The measured reduction in magnitude of the mechanical response as frequency increases is *not* inherent in the OHC, but is due to limitations of the voltage-clamp amplifier. That is, command voltage magnitude decreases with increasing frequency because of the voltage clamp's limited frequency response;¹ therefore, voltage dependent AC mechanical responses roll off as well (see below).

As command voltage magnitude decreases (due to the clamp time constant), there is a disproportionate decrease in the mag-

¹ The effectiveness of the whole-cell voltage clamp technique is limited by the patch electrode's series resistance and the cell's impedance. The speed at which a voltage can be imposed across the membrane of a cell depends upon the clamp time constant ($\tau = R_s \parallel R_m C_m$). This time constant corresponds to the effective bandwidth of AC stimulation ($f_{\text{cutoff}} = 1/2\pi\tau$).

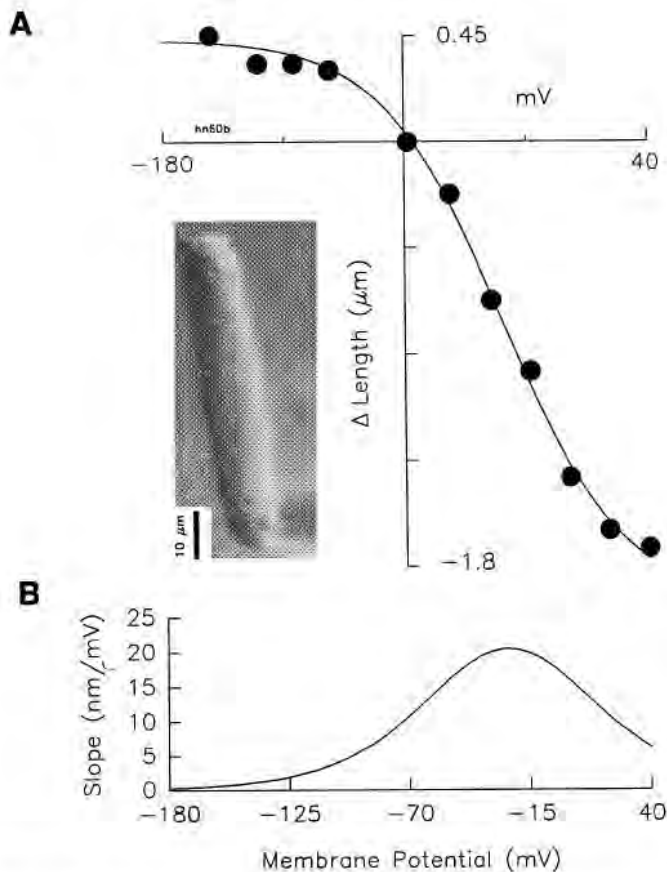


Figure 2. *A*, Change in length of an isolated OHC in response to voltage steps delivered from a holding potential of -68.4 mV. The residual series resistance has been corrected. Hyperpolarizing steps from the holding potential induce elongations whose magnitudes saturate more rapidly with step potential than do contractions due to depolarizing steps. The mechanical response $\Delta L(v)$ was fit with a Boltzmann function (Eq. 1; solid line). The least squares fit gives $V_h = -25.7$ mV and $b = 27$ mV. Normal extracellular solution, and KCl-containing patch pipette. Cell length measures were made off the video monitor. *Inset*, Digitally captured video image of the whole-cell voltage-clamped OHC. *B*, Slope of the Boltzmann fit above, indicating the voltage sensitivity of the mechanical response across voltage. The sensitivity at the holding potential of -68.4 mV is smaller than the maximum.

nitude of the DC mechanical component relative to the decrease of the AC mechanical component. This phenomenon is an inherent property of the V-M function of the OHC; as the AC voltage excursion about the holding potential is reduced, the input-output function within the limited stimulus region approaches linearity. Although Evans et al. (1990) obtain similar V-M functions (see Fig. 5*A*, solid triangles), they report a linear correspondence between AC and DC mechanical responses as voltage magnitude is altered. However, Figure 5*C* exemplifies the nonlinear correspondence inherent in the V-M function by plotting the ratio of DC to AC mechanical response as a function of AC voltage magnitude. The measured ratio (open circles) decreases as the stimulating voltage magnitude decreases, and is well predicted (solid line) from the V-M function of this cell (Fig. 5*A*). This observation indicates that the form of the V-M function measured at 11.7 Hz is preserved at higher frequencies; that is, the nature of the function is *frequency independent*.

The top panels of Figure 6, *A* and *B*, examine the magnitude of the mechanical response fundamental (obtained by FFT) and

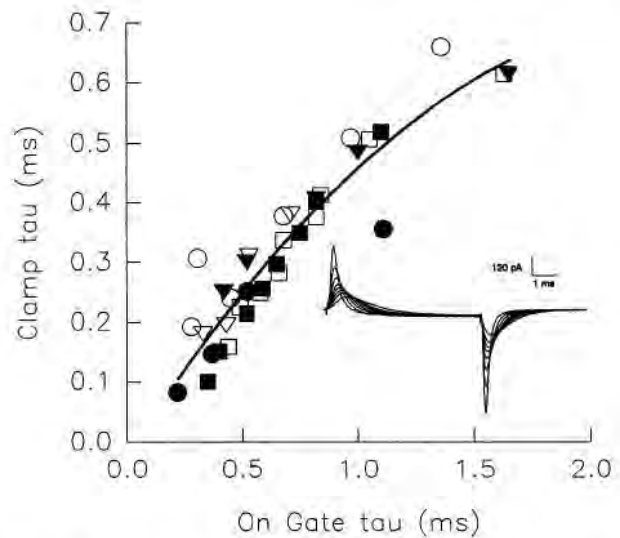


Figure 3. Dependence of on-gate current time constant upon time constant of clamp amplifier. Six cells (different symbols) were held at a potential of -80 mV and alternately pulsed to 40 mV above and below the holding potential. Nonlinear capacitive currents were unmasked by averaging the resultant currents 200 times ($\pm P$ technique; Armstrong and Bezanilla, 1973). Clamp time constants were determined by fitting single exponentials to the decaying current transient in response to a -10 mV step. Time constants of on-gate currents were also single exponential fits of current decay. Clamp time constant was modified by adjusting the electronic compensation for the series resistance. Reduction of clamp time constant caused reduction of gate time constant. *Inset*, A series of nonlinear capacitive current traces from a single OHC under different clamp time constant conditions. Note the shift in the speed of current response. Both on-gate and off-gate time constants are directly influenced by clamp time constant. CsCl electrode solution. Extracellular solution was Leibovitz with 10 mM tetraethylammonium (TEA) and 300 nM TTX.

compare it to the voltage delivered to the cell as predicted from the clamp time constant, before (top panel, Fig. 6*A*) and after (top panel, Fig. 6*B*) series resistance compensation. The cutoff frequency of the cell's mechanical response increased following compensation of the series resistance. The mechanical response rolloff roughly follows the rolloff of the transmembrane voltage, demonstrating that the mechanical response can follow rapid voltage fluctuations quite faithfully ($f_{\text{cutoff}} \sim 1$ kHz). This is in marked contrast to the limited frequency response ($f_{\text{cutoff}} \sim 60$ Hz) reported by Ashmore (1987; see thick line in top panels of Fig. 6*A,B*). The analysis of phase data presents a more robust test of the voltage dependence hypothesis. In an RC-dominated system, such as the OHC under voltage clamp, as voltage command frequency is increased, an asymptotic phase separation of 1.57 radians (90°) will develop between injected current and voltage. Voltage phase will lag that of current. The clamp time constant, $R_s \parallel R_m C_m$, dictates the resultant frequency dependence of the separation. The bottom panels in Figure 6, indeed, demonstrate that the mechanical response follows the phase of the induced transmembrane voltage and not that of the transmembrane current. Similar data on the magnitude and phase of current, voltage, and motility obtained from four additional cells, each with a different clamp time constant, are presented in Figure 7. In all, an asymptotic phase separation between motility and injected transmembrane current is reached [1.66 ± 0.18 radians at 625 Hz (mean \pm SD; $n = 6$ cells)], as would be

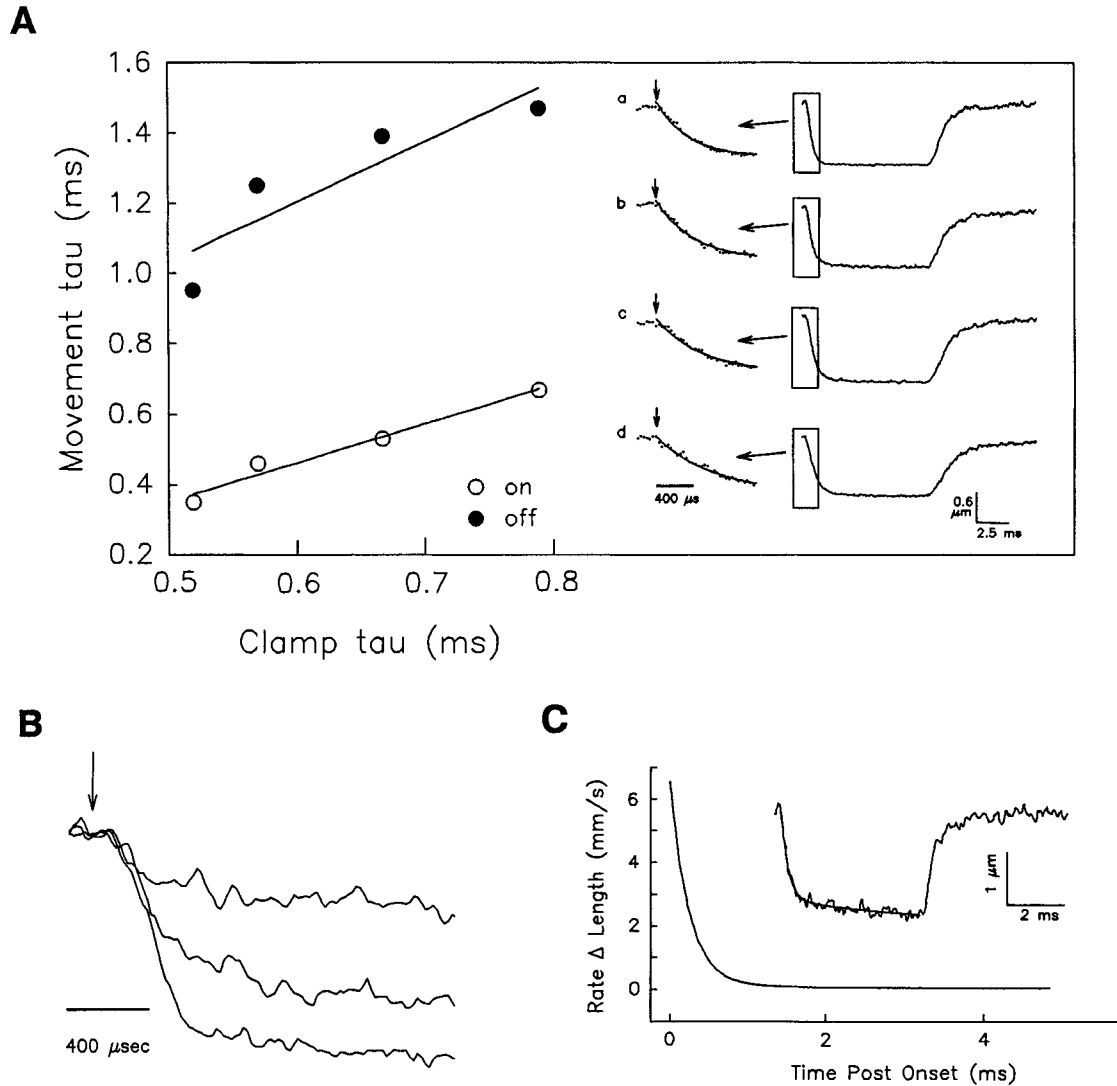


Figure 4. *A*, Effect of clamp time constant upon speed of OHC movement induced by voltage steps. An OHC was nominally held at -80 mV and stepped to $+40$ mV for 10 msec. *Traces a–d* represent the contraction of the OHC (photodiode output) as the clamp time constant is modified. Responses were averaged $200\times$. Single exponentials were fit to the onset (expanded fits shown) and offset of cell movement. It is clear that movement time constants are dependent upon clamp time constants. *Downward arrows* of expanded onset traces indicate voltage step onset. Holding potential and steady state potential (corrected for series resistance) were *a*, -73.5 mV, 36.8 mV; *b*, -72.8 mV, 36.6 mV; *c*, -71.1 mV, 35.8 mV; *d*, -69.2 mV, 35 mV. *B*, *Traces* represent mechanical responses of an OHC stepped nominally to -30 , 0 , and $+30$ mV from a holding potential of -80 mV. *Downward arrow* indicates voltage step onset. Note the delay in onset of the mechanical responses. Also note the saturation of the response at the most depolarized potential, and the resultant apparent decrease in the onset time constant compared to the other responses. *C*, Rate of length change of an OHC to a depolarizing step from -78 mV to $+29$ mV (residual series resistance corrected). Rate was obtained from the first derivative of the fitted mechanical response to *inset*. *Inset*, Mechanical response filtered at 3.184 kHz and fit with a double exponential (*smooth line*). The time constants were 0.24 msec and 5 msec, with an amplitude ratio of $4:1$. Clamp time constant was 0.14 msec.

expected for a voltage driven process. This is strong evidence favoring the voltage dependence hypothesis of OHC motility.²

The relationship of the mechanical response time constant (i.e., cutoff frequency) to that of the voltage clamp is summarized for five cells in Figure 8. The frequency response of OHC motility is positively correlated with the speed of the voltage clamp.

² It should be noted that the measured current phase consists of both a resistive and capacitive component, and that at high frequencies the capacitive component dominates. However, the current through membrane-resistive elements is always in phase with transmembrane voltage. Nevertheless, alterations of the resistive currents by means of various ionic blocking agents do not interfere with voltage-induced mechanical responses (Santos-Sacchi and Dilger, 1988; Santos-Sacchi, 1989, 1991b).

For two OHCs (circles and diamonds), mechanical responses were obtained before and after series resistance compensation; mechanical response cutoff frequency paralleled the resulting changes in clamp speed. There is, however, a trend for the mechanical response fundamental to roll off at lower frequencies than the applied transmembrane voltage. This phenomenon may be a consequence of the nonlinear V-M function, as a similar trend is also found with model simulations (solid line, Fig. 8).

Discussion

The data presented here provide insight into the mechanism and potential significance of OHC motility. The observation

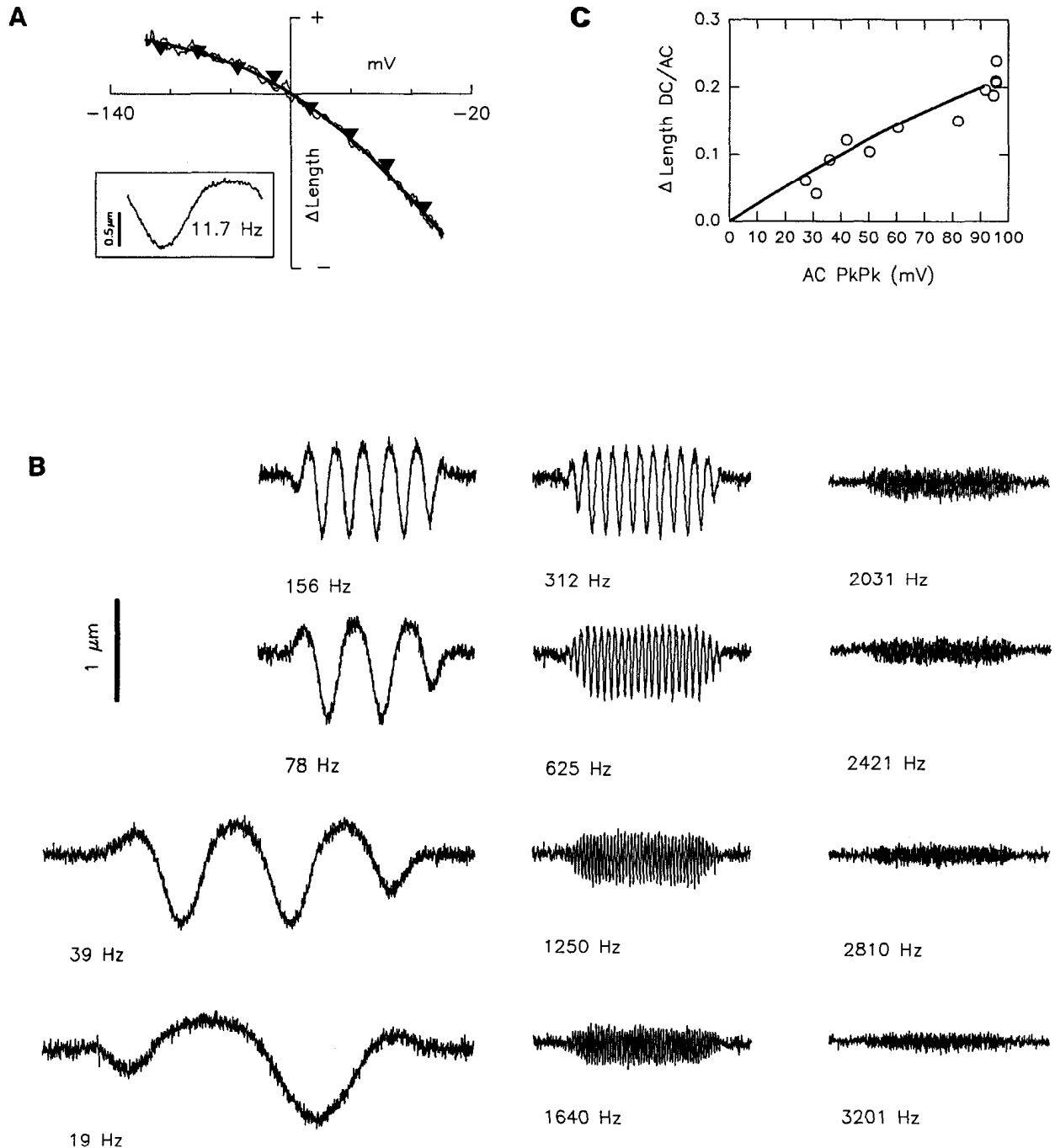


Figure 5. OHC AC and DC mechanical responses elicited by AC voltage stimulation. *A*, Voltage versus movement for an 11.7 Hz voltage stimulus. Voltage is the estimated intracellular potential obtained from the command potential corrected for series resistance and phase shifted to minimize phase differences between it and movement response. The *solid line* is a fit to a portion of a Boltzmann function with $V_h = -30.5$ mV and $b = 31$ mV. For comparison, the data (*solid triangles*) of Evans et al. (1990) based on step commands about the authors' estimated resting potential of -60 mV were scaled and superimposed (see Results and Discussion). *Inset*, Movement response waveform smoothed with five point running average. Peak-to-peak (PkPk) response is about $1 \mu\text{m}$. *B*, Photodiode output indicating the movement of the OHC in response to voltage sine wave bursts of varying frequency. The movement consists of an AC and DC response, both of which decrease as a function of frequency; this results from the decrease of the magnitude of voltage stimulation due to the voltage-clamp time constant. DC responses can be observed above 3 kHz but decrease in magnitude disproportionately compared to AC response magnitude. *C*, Ratio of DC movement to AC PkPk movement versus PkPk voltage stimulus corrected for the frequency-dependent attenuating effects of series resistance. Measures are from the raw data shown in *B*. Data were obtained by visually determining PkPk movement response and DC movement response (difference between baseline and half-PkPk response). The *solid line* is the predicted ratio based upon the movement versus voltage response for 11.7 Hz as in *A*. Note the greater susceptibility of the DC response to reduction of driving voltage magnitude. That is, the DC:AC ratio is *not* constant as a function of driving voltage magnitude.

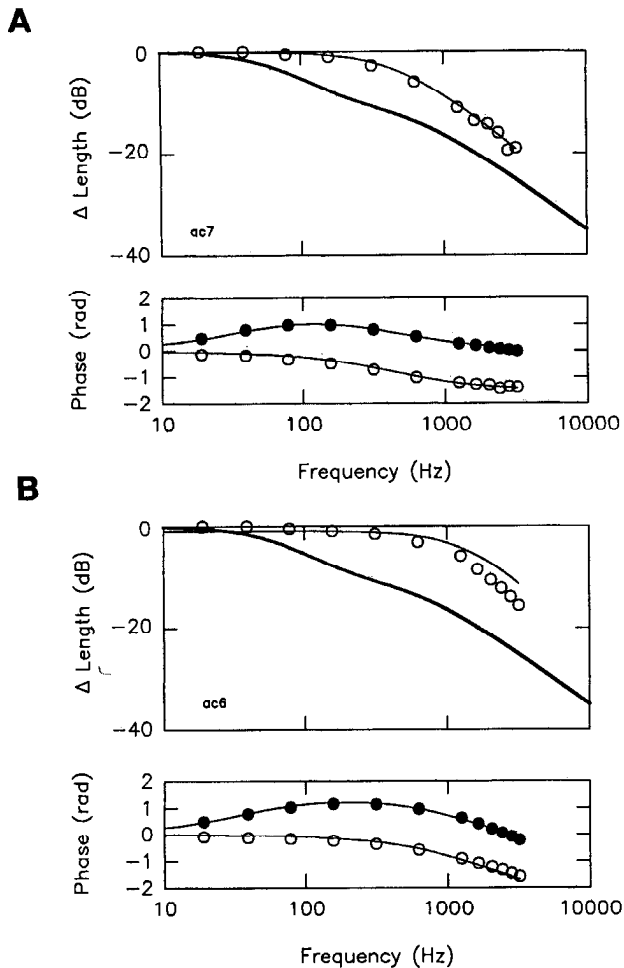


Figure 6. Frequency response (magnitude and phase) of OHC motility for the cell of Figure 5 with a clamp time constant of 0.38 msec (*A*; no series resistance compensation) or 0.125 msec (*B*; series resistance maximally compensated). Nominal peak voltage was 50 mV. CsCl electrode. Extracellular medium was Ca-free Leibovitz with 20 mM TEA and 20 mM CsCl. *A*: Top, Magnitude. Open circles represent the fundamental magnitude of length change obtained by FFT (see Materials and Methods). The line through the data points is the predicted cell voltage using a voltage clamp-cell model (see Materials and Methods), with the electrical characteristics of the clamp-cell setup determined from the current response to a 5 mV step ($R_m = 139.5$ M Ω ; $C_m = 33.3$ pF; clamp $\tau = 0.38$ msec). For comparison, the thick line is Ashmore's fit to his data (1987, Fig. 7). Bottom, Phase. The solid circles represent the phase of the fundamental component of the simultaneously recorded current, after equipment phase correction. The open circles represent the phase of the length change fundamental. The solid lines are the predicted phase for the current and voltage using the voltage clamp-cell model component values. No absolute phase delay is included in the phase predictions. *B*, As in *A*, except clamp-cell electrical characteristics at this time were $R_m = 125.5$ M Ω , $C_m = 35.4$ pF, and clamp $\tau = 0.125$ msec. An absolute phase delay of 25 μ sec is included in current and voltage predictions.

that OHC motility does indeed follow the time course and phase of transmembrane voltage stimuli provides the strongest evidence thus far that the motility mechanism is voltage dependent.³ The presence of voltage-dependent nonlinear charge

³ While the results of Dallos et al. (1991a) clearly demonstrate the elemental nature of the OHC motor, their data do not unequivocally support the voltage dependency hypothesis. Neither transmembrane current nor transmembrane voltage could be measured with the microchamber technique, and either would have been in phase opposition at the opposite poles of the cell, just as the mechanical responses were.

movement within the membrane of the OHC (indicative of membrane-bound voltage sensors) corroborates this concept (Ashmore, 1989; Santos-Sacchi, 1990, 1991b). Similarities between characteristics of the nonlinear charge movement and motility, including voltage dependence (V_h , b), susceptibility to charge screening, and reversible block by gadolinium ions, indicate that the estimated 4000 voltage sensors/ μm^2 control OHC length through an equal number of associated elemental motors (Santos-Sacchi, 1991b). Assuming that the motors are equally distributed within the membrane along the extent of the sub-surface cisternae, it is calculated that each elemental motor would contribute an effective unit displacement of about 1 nm in the longitudinal direction. The actual displacement vector may not be purely longitudinal (Dallos et al., 1991b). Ultimately, the dependence of OHC motility on transmembrane voltage and the form of the V-M function will determine the physiological significance of OHC motility.

Velocity and frequency response of OHC motility

An important indicator for evaluating the significance of OHC motility in inner ear function is its frequency response. Certainly, there will be a point at which the OHC will be unable physically to follow an imposed transmembrane AC voltage, and a determination of this cutoff frequency will permit a more realistic assessment of the OHC's mechanical influence in the high-frequency region of the cochlea. Unfortunately, the maximum velocity and the frequency extent of OHC motility are as yet undetermined, due to the speed limitations imposed by the voltage-clamp amplifier. Thus, the current maximum OHC velocity measured during a step response (6.5 mm/sec; Fig. 4C), or estimated from the AC data [Fig. 6B; ($\Delta L/\omega$) 4 mm/sec at 1250 Hz] is likely to be an underestimate. Indeed, the OHC mechanical response probably extends beyond the widest frequency response measured, which approached a 1 kHz cutoff.

It is interesting to note that although the speed of the mechanical response follows changes in the speed of the imposed voltage, the time constants of each are not necessarily equal. In fact, in Figure 4 it was illustrated that the mechanical on-response can have an apparent time constant faster than that of the imposed voltage; contrarily, the off-response can be slower than the imposed voltage. This is not unusual for a nonlinear system, and the same effects are simulated for a model V-M function in Figure 9. It is clear that despite a constant membrane potential time course, level-dependent changes in the apparent time constant of the mechanical response arise. Mechanical response saturation at the extremes of the V-M function accounts for much of these effects. The tendency for the mechanical frequency response to roll off sooner than the imposed voltage frequency response (Fig. 8) may also reflect the effects of the nonlinear V-M function. If the resting potential (holding potential) were equal to V_h and the stimulus amplitude were very small, the time course of the mechanical response would more closely mirror that of the driving voltage.

Despite their limitations, the measurements of velocity and frequency response reported here more closely reflect OHC mechanical response capabilities than previous measures (Ashmore, 1987), and are useful in evaluating some timely issues. For example, electrically evoked otoacoustic emissions recorded from the ear canal, presumably due to the activity of OHCs, have been measured in pass bands up to several kHz (Hubbard and Mountain, 1990). These investigators have suggested, based on Ashmore's (1987) mechanical frequency response data, that

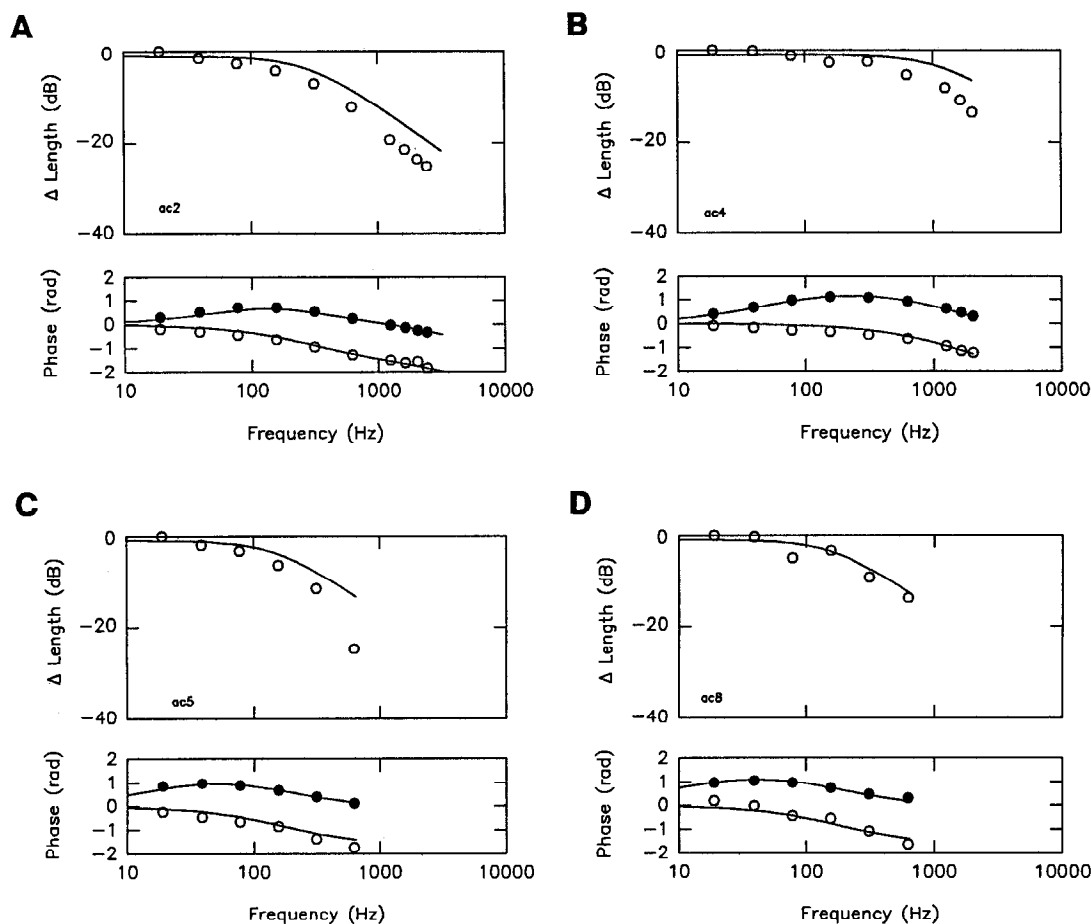


Figure 7. Frequency response for four additional cells (magnitude and phase) with varying clamp time constants. See Figure 6 for details. Clamp-cell electrical characteristics are as follows: *A*, $R_m = 96 \text{ M}\Omega$, $C_m = 24.73 \text{ pF}$, clamp $\tau = 0.553 \text{ msec}$. Absolute phase delay, $25 \text{ }\mu\text{sec}$. Nominal peak voltage was 60 mV . CsCl electrode. Extracellular medium was Leibovitz with 20 mM TEA . *B*, $R_m = 79 \text{ M}\Omega$, $C_m = 41.89 \text{ pF}$, clamp $\tau = 0.128 \text{ msec}$. Absolute delay, $20 \text{ }\mu\text{sec}$. Nominal peak voltage was 40 mV . CsCl electrode. Extracellular medium was Leibovitz with 20 mM TEA , 300 nM TTX , and 1 mM CdCl_2 . *C*, $R_m = 346 \text{ M}\Omega$, $C_m = 27.35 \text{ pF}$, clamp $\tau = 1.00 \text{ msec}$. Absolute delay, $20 \text{ }\mu\text{sec}$. Nominal peak voltage was 40 mV . CsCl electrode. Extracellular medium was Leibovitz with 20 mM TEA and 300 nM TTX . *D*, $R_m = 490 \text{ M}\Omega$, $C_m = 33.0 \text{ pF}$, clamp $\tau = 0.934 \text{ msec}$. Absolute delay, $20 \text{ }\mu\text{sec}$. Nominal peak voltage was 100 mV . CsCl electrode. Extracellular medium was Leibovitz with 10 mM TEA and 300 nM TTX .

the OHC length changes are too low pass to account for such high-frequency phenomena. Clearly, the data presented here suggest that OHC length changes may be significant at those acoustic frequencies where electrically evoked otoacoustic emissions occur. Ashmore's (1987) observation that OHC motility was extremely low pass was probably due to the very slow clamp time constants achieved in that study (see footnote 3 of Santos-Sacchi, 1989).

Since the *in vivo* receptor potential will provide the OHC motility driving force, the effectiveness of evoked AC mechanical events in influencing organ of Corti micromechanics at high frequencies can be evaluated to a first approximation by an assessment of OHC receptor potential characteristics. Thus, it is known that OHC AC receptor potentials for cells with high characteristic frequencies ($> 15 \text{ kHz}$) are quite small due to the cell's RC time constant ($f_{\text{cutoff}} \sim 1.2 \text{ kHz}$); AC potentials of about $15 \text{ }\mu\text{V}$ have been recorded in these cells near auditory threshold (Russell et al., 1986). Consequently, it has been argued that evoked AC movements of an OHC with a resting potential of 70 mV are much smaller ($\sim 20 \text{ dB}$) than basilar membrane movements near auditory threshold (Santos-Sacchi, 1989; but see Santos-Sacchi, 1991b).

The present velocity estimates, though clamp limited, appear incompatible with the electro-osmotic theory of OHC motility proposed by Brownell and Kachar (1986). The rate of movement is far greater than that attributable to an electro-osmotic mechanism; experiments on a variety of preparations indicate the maximum velocity achievable is $1 \text{ }\mu\text{m/sec}$ per V/cm (McLaughlin and Mathias, 1985). The steady state voltage drop across the membrane of the OHC in Figure 4C was 107 mV . The maximum field strength along a cell of $70 \text{ }\mu\text{m}$, assuming that the total imposed voltage drops across the length of the cell (which is unlikely, since space-clamp estimates indicate little longitudinal decay) would be 15.3 V/cm . Thus, an electro-osmotic based velocity of $15.3 \text{ }\mu\text{m/sec}$ is predicted, over 2 orders of magnitude smaller than the observed maximum velocity. Iwasa and Kachar (1989) employed the same argument against an electro-osmotic mechanism, although the disparity between their velocity measures and electro-osmotic estimates were not as great as those reported here. Furthermore, an electro-osmotic mechanism would predict that the velocity, not the displacement, of OHC motility would be in phase with voltage. This is in conflict with the phase data reported here. It should be noted that velocities associated with electro-osmosis are derived for

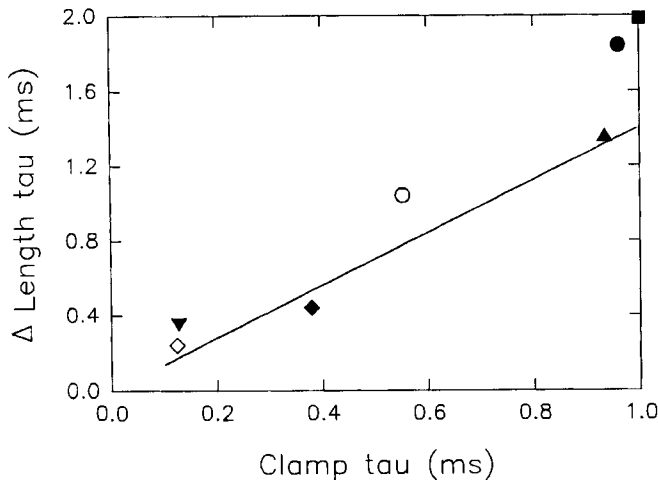


Figure 8. Clamp time constant versus measured time constant of movement. Time constants of movement were from linear interpolation of 3 dB breakpoint of measured magnitude response as in Figure 2. Data from a total of five cells (different symbols) are presented, with two cells (circles and diamonds) being measured at two different clamp time constants (open and solid symbols). Clamp time constant dictates frequency response of OHC motility. However, the mechanical response has a slower time constant (lower cutoff frequency) than the voltage command. This may be a function of the nonlinear V-M function since model simulations predict this type of behavior. For example, the solid line was obtained by performing the same type of analysis on a model V-M function with Boltzmann parameters of $b = 26$ mV and $V_h = -30$ mV, at a holding potential of -70 mV, with a peak AC voltage stimulation of 50 mV.

steady state conditions, and the preceding arguments may not be absolutely appropriate. Nevertheless, in the absence of a more complete electro-osmotic model of OHC motility, it remains questionable whether electro-osmosis can account for the maximum velocity and phase of OHC motility presently found. Dallos et al. (1991a) also dismissed an electro-osmotic mechanism based on other arguments.

DC mechanical response

Voltage-dependent OHC motility, analyzed under whole-cell voltage clamp, is well characterized by a two-state Boltzmann function, whose V_h is offset in the depolarizing direction relative to the normal resting potential of the cell. A mechanical DC nonlinearity is not inherent in the V-M function but is expressed only due to this voltage offset. This concept differs from the contention of Dallos et al. (1991b), who suggest, based on DC responses measured at very small stimulus levels, that the DC component is the result of an essential nonlinearity of the OHC's stochastic motor. Clearly, however, should the cell's resting potential and V_h superimpose, then no DC mechanical component would arise.

The normal resting potential *in vivo* is near -70 mV (Dallos et al., 1982; Russell and Sellick, 1983). V_h of the V-M function ranged from about -40 mV to -20 mV, which to a large extent is dependent upon membrane surface charge and agents that affect the resultant surface potential (Santos-Sacchi, 1991b). Thus, a DC mechanical response appears ensured under normal *in vivo* conditions⁴ and is dependent on the many factors governing

OHC resting membrane potential and membrane surface potential. The effects of resting potential on the sum of elemental motor contributions, that is, on the observable OHC mechanical response, can be complex. For example, whereas shifts of the normal resting potential toward V_h will reduce the DC component, the peak-to-peak component can grow. It is interesting to note that noise-induced threshold shift, which produces a depolarization of the OHC (Cody and Russell, 1985), should affect both AC and DC mechanical response production.

It is demonstrated here that the OHC DC mechanical response is a frequency-independent consequence of the V-M function. The persistence of the DC mechanical response above 3 kHz is the first demonstration that the mechanical rectification extends to physiologically important frequencies. Previous studies have reported DC responses at frequencies between 10 and 200 Hz (Evans et al., 1989; Santos-Sacchi, 1989). It is conceivable that DC mechanical responses of OHCs could provide a bias that may change mechanical characteristics (e.g., stiffness) of the organ of Corti–basilar membrane complex, leading in some manner to enhanced tuning. At first thought, this may appear to alleviate some of the problems associated with the membrane filtering effects on the high-frequency AC mechanical response. However, the DC nonlinearity is highly stimulus level dependent, greatly diminishing with level. Consequently, as the AC voltage stimulus is reduced (e.g., due to the membrane filter), the DC mechanical response magnitude declines much more precipitously than the AC mechanical response. Figure 10 demonstrates this inherent outcome of such a V-M function in a model AC simulation. DC mechanical components are vanishingly small at low stimulus levels.

Evans et al. (1990, 1991) have reported significant DC mechanical responses at low AC stimulation levels. The superposition of their data (from Evans et al., 1990, their Fig. 2) onto the AC data in Figure 2A indicates that the form of their V-M function in the voltage range shown is remarkably similar to the form obtained in the present study under voltage clamp. This is of interest since their stimulus delivery technique (a partitioning microchamber) differs from the whole-cell technique used here. However, while they may have control over the voltage imposed across the membrane of the OHC, their technique permits neither the control of the resting membrane potential nor the control of the intracellular environment (e.g., pH). Calculation of the DC:AC ratio predicted by their V-M function presents essentially the same result as that calculated for the voltage-clamp data reported here. It is surprising, therefore, that they detect a linear modification in both the AC and DC mechanical components as stimulus magnitude is changed. The inability to control resting potential and/or intracellular environment with the microchamber technique may underlie their observation; for example, the resting potential along the V-M function or V_h may be changing as a function of stimulus level. DC responses necessarily change when resting voltage shifts relative to V_h . Relatedly, Evans et al. (1991) presented data that they interpreted to indicate that the DC component was vulnerable to repeated voltage stimulations. These data may

⁴ Actually, V_h is not known for the *in vivo* situation. Unfortunately, the traditional *in vitro* whole-cell technique modifies both intra- and extracellular environments, so that biochemical conditions (e.g., membrane surface charge screening, phosphorylations, etc.) existing *in vitro* may not represent those *in vivo*. Thus, it is very difficult extrapolating to *in vivo* conditions. It should be noted, however, that DC mechanical responses of the basilar membrane *in vivo*, presumably due to the effects of OHCs, have been measured at high sound pressure levels (LePage, 1987). Obviously, it is important to obtain V_h estimates *in vivo*. Since the voltage dependence of nonlinear capacitance in the OHC is similar to that of the cell's mechanical response (Santos-Sacchi, 1991b), inferences concerning the mechanical response V_h may be made from *in vivo* estimates of voltage-dependent capacitance.

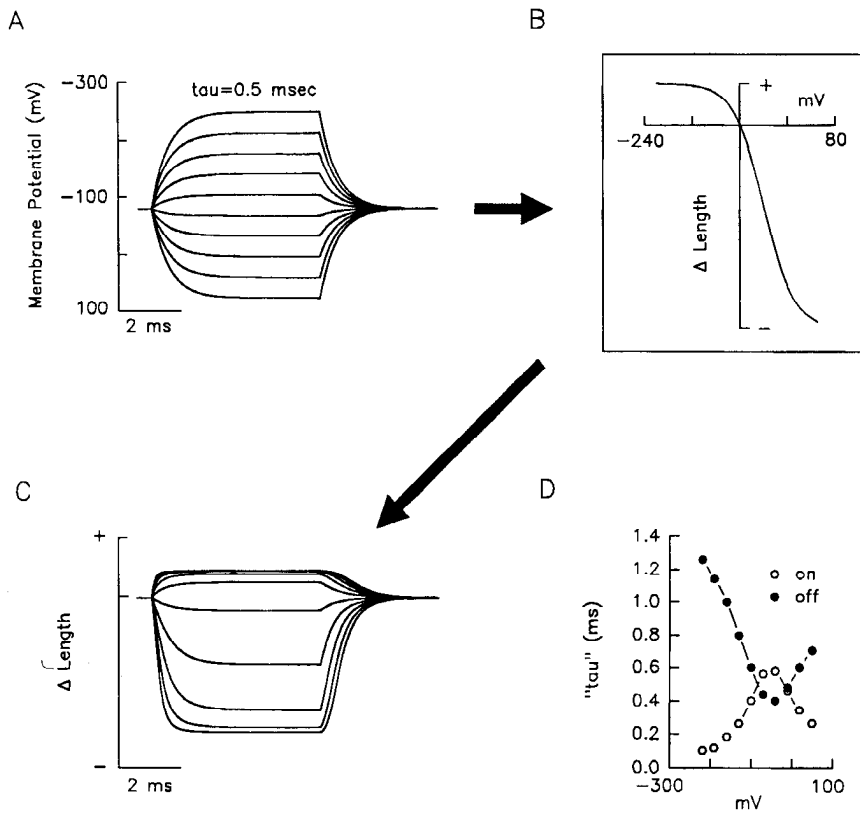


Figure 9. Simulation of voltage step induction of mechanical response in an OHC based on a model input-output V-M function. Filtered voltage steps ($\tau = 0.5$ msec) of various magnitudes (A) about the holding potential of -80 mV were passed through the model OHC V-M function (B) of $V_h = -40$ and $b = 25$ mV. The resultant motility responses (C) are governed by the form of the V-M function, and the value of the holding potential. The saturating nonlinearity of the V-M function produces apparent level-dependent (step potential) changes in the "time constant" of the mechanical response (D). Time constants (" τ ") for on and off responses were determined by noting the time to rise to 63% or fall to 37% of the steady state values, respectively.

also reflect the effects of a drift of the resting potential or V_h of the OHC, and not an induced linearization of the V-M function. No induced linearization of a given V-M function is observed under whole-cell voltage clamp, where the holding potential is readily maintained and the intracellular environment is highly buffered, even with prolonged saturating voltage stimuli.

The physiological consequence of a level-dependent DC mechanical component is clear. *In vivo*, for a $15 \mu\text{V}$ AC receptor potential near auditory threshold, it is calculated that the mechanical DC:AC ratio will be less than 0.0004. Even if the OHC mechanical response were as great as the largest response we have observed in the midregion of the V-M function (~ 30 nm/

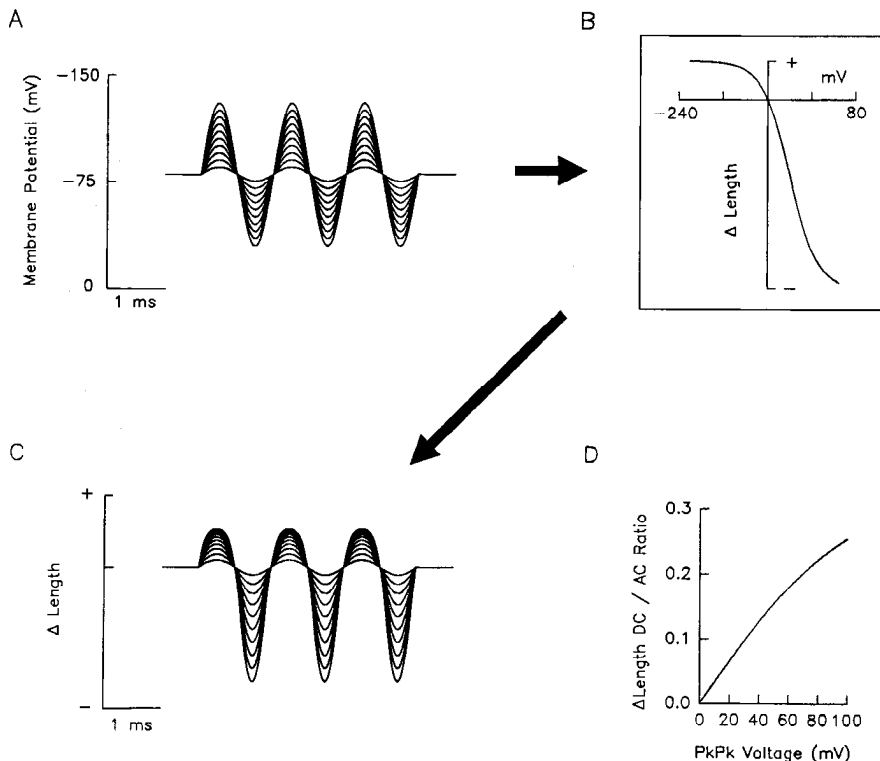


Figure 10. Simulation of voltage sine wave burst induction of AC and DC mechanical responses in an OHC based on a model input-output V-M function. Voltage sine wave bursts of various magnitudes (A) about the holding potential of -80 mV were passed through the model OHC V-M function (B) of $V_h = -40$ and $b = 25$ mV. The resultant motility responses (C) are governed by the form of the V-M function, and the value of the holding potential. The offset of V_h from the holding potential ensures the production of DC responses (difference between baseline and half-PkPk response). A decrease in the amplitude of the driving voltage affects the magnitudes of the AC and DC responses differently. The DC:AC ratio (D) clearly indicates that the DC response is more susceptible to voltage magnitude alterations.

mV),⁵ the DC mechanical response would be 18 fm. Clearly, it is difficult to imagine the significance of such DC displacements when basilar membrane motions at threshold are estimated to be near 350 pm in the guinea pig (Sellick et al., 1982) and 2000 pm in the chinchilla (Robles et al., 1986).⁶ It is important to note, however, that hair cells are capable of generating DC receptor potentials that are not susceptible to the attenuation effects of the cell's RC time constant (Dallos et al., 1982; Russell and Sellick, 1983). Such DC potentials generated at high acoustic frequencies should induce movements of the OHC. However, whereas IHCs produce significant DC potentials at the characteristic frequency threshold in the high-frequency region of the cochlea, OHCs do not (Russell et al., 1986). Thus, the occurrence of rapid, stimulus related DC mechanical responses that are physiologically significant at auditory threshold is not readily envisioned.

In summary, this report demonstrates the widest mechanical frequency response of the OHC measured to date, and shows that the mechanical rectification due to the V-M function extends well into the kilohertz range. These results attest to the unique nature of the OHC's motility mechanism among known cellular mechanisms of movement. Nevertheless, the results confirm the voltage dependency hypothesis of OHC motility, and the limitations that this dependency imposes *in vivo* remain to be reconciled with current concepts of OHC performance in the high-frequency region of the mammalian inner ear.

References

- Ashmore JF (1987) A fast motile response in guinea-pig outer hair cells: the cellular basis of the cochlear amplifier. *J Physiol (Lond)* 388:323–347.
- Ashmore JF (1989) Transducer motor coupling in cochlear outer hair cells. In: *Mechanics of hearing* (Kemp D, Wilson JP, eds), pp 107–113. New York: Plenum.
- Armstrong CM, Bezanilla F (1973) Currents related to movement of the gating particles of the sodium channels. *Nature* 242:459–461.
- Brown MC, Nuttall AL (1984) Efferent control of cochlear inner hair cell responses in the guinea-pig. *J Physiol (Lond)* 354:625–646.
- Brownell WE, Kachar B (1986) Outer hair cell motility: a possible electro-kinetic mechanism. In: *Peripheral auditory mechanisms* (Allen JB, Hall JL, Hubbard AE, Neely ST, Tubis A, eds), pp 369–376. New York: Springer.
- Brownell WE, Bader CR, Bertrand D, de Ribaupierre Y (1985) Evoked mechanical responses of isolated cochlear outer hair cells. *Science* 227:194–196.
- Clark BA, Hallworth R, Evans BN (1990) Calibration of photodiode measurements of cell motion by a transmission optical lever method. *Pfluegers Arch* 415:490–493.
- Cody AR, Russell IJ (1985) Outer hair cells in mammalian cochlea and noise-induced hearing loss. *Nature* 315:662–665.
- Dallos P, Harris D (1978) Properties of auditory nerve responses in absence of outer hair cells. *J Neurophysiol* 41:365–383.
- Dallos P, Santos-Sacchi J, Flock Å (1982) Intracellular recordings from outer hair cells. *Science* 218:582–584.
- Dallos P, Evans BN, Hallworth R (1991a) On the nature of the motor element in cochlear outer hair cells. *Nature* 350:155–157.
- Dallos P, Hallworth R, Evans BN (1991b) Stochastic theory of outer hair cell electromotility. In: *Auditory physiology and perception. Proceedings of the 9th International Symposium on Hearing*, Carcans, France, June 9–14, 1991.
- Evans BN, Dallos P, Hallworth R (1989) Asymmetries in motile responses of outer hair cells in simulated *in vivo* conditions. In: *Mechanics of hearing* (Kemp D, Wilson JP, eds), pp 205–206. New York: Plenum.
- Evans BN, Hallworth R, Dallos P (1990) The nonlinearity of outer hair cell motility: implications for cochlear physiology and pathology. In: *The mechanics and biophysics of hearing* (Dallos P, Geisler CD, Matthews JW, Ruggero MA, Steele CR, eds), pp 61–68. Berlin: Springer.
- Evans BN, Hallworth R, Dallos P (1991) Outer hair cell electromotility: the sensitivity and vulnerability of the DC component. *Hearing Res* 52:288–304.
- Geisler CD, Shan X (1990) A model for cochlear vibrations based on feedback from motile outer hair cells. In: *The mechanics and biophysics of hearing* (Dallos P, Geisler CD, Matthews JW, Ruggero MA, Steele CR, eds), pp 86–95. Berlin: Springer.
- Harrison RV, Evans EF (1979) Cochlear fiber responses in guinea pigs with well defined cochlear lesions. *Scand Audiol [Suppl]* 9:83–92.
- Hubbard AE, Mountain DC (1990) Hair cell forward and reverse transduction: differential suppression and enhancement. *Hear Res* 43:269–272.
- Hudspeth AJ (1989) How the ear's works work. *Nature* 341:397–404.
- Iwasa KH, Kachar B (1989) Fast *in vitro* movement of outer hair cells in an external electric field: effect of digitonin, a membrane permeabilizing agent. *Hear Res* 40:247–254.
- LePage EL (1987) Frequency-dependent self-induced bias of the basilar membrane and its potential for controlling sensitivity and tuning in the mammalian cochlea. *J Acoust Soc Am* 82:139–154.
- Marty A, Neher E (1983) Tight-seal whole-cell recording. In: *Single-channel recording* (Sakmann B, Neher E, eds), pp 107–122. New York: Plenum.
- McLaughlin S, Mathias RT (1985) Electro-osmosis and the reabsorption of fluid in renal proximal tubules. *J Gen Physiol* 85:699–728.
- Robles L, Ruggero MA, Rich NC (1986) Basilar membrane mechanics at the base of the chinchilla cochlea. I. Input-output functions, tuning curves, and response phases. *J Acoust Soc Am* 80:1364–1374.
- Robles L, Ruggero MA, Rich NC (1991) Two-tone distortion in the basilar membrane of the cochlea. *Nature* 349:413–414.
- Ruggero MA, Rich NC (1991) Furosemide alters organ of Corti mechanics: evidence for feedback of outer hair cells upon the basilar membrane. *J Neurosci* 11:1057–1067.
- Russell IJ, Sellick PM (1983) Low frequency characteristics of intracellularly recorded receptor potentials in mammalian hair cells. *J Physiol (Lond)* 338:179–206.
- Russell IJ, Cody AR, Richardson GP (1986) The responses of inner and outer hair cells in the basal turn of the guinea-pig cochlea and in the mouse cochlea grown *in vitro*. *Hear Res* 22:199–216.
- Spoendlin H (1988) Neural anatomy of the inner ear. In: *Physiology of the ear* (Jahn A, Santos-Sacchi J, eds), pp 201–219. New York: Raven.
- Santos-Sacchi J (1989) Asymmetry in voltage dependent movements of isolated outer hair cells from the organ of Corti. *J Neurosci* 9:2954–2962.
- Santos-Sacchi J (1990) Fast outer hair cell motility: how fast is fast? In: *The mechanics and biophysics of hearing* (Dallos P, Geisler CD, Matthews JW, Ruggero MA, Steele CR, eds), pp 69–75. Berlin: Springer.
- Santos-Sacchi J (1991a) Relations between DC and AC mechanical responses of the outer hair cell. Paper presented at the 121st meeting of the Acoustical Society of America, Houston, TX, November.
- Santos-Sacchi J (1991b) Reversible inhibition of voltage-dependent outer hair cell motility and capacitance. *J Neurosci* 11:3096–3110.
- Santos-Sacchi J, Dilger JP (1988) Whole cell currents and mechanical responses of isolated outer hair cells. *Hearing Res* 35:143–150.
- Sellick PM, Patuzzi R, Johnstone BM (1982) Measurement of basilar membrane motion in the guinea pig using the Mossbauer technique. *J Acoust Soc Am* 72:131–141.

⁵ The use of the ~30 nm/mV figure (from Santos-Sacchi and Dilger, 1988) is unrealistic since the OHC normally rests at a potential of about -70 mV and the mechanical response slope at this region of the V-M function is far smaller than the maximum slope (see Fig. 2B).

⁶ The inherent linearization of the OHC mechanical response at low stimulation levels was alluded to previously (Santos-Sacchi, 1989) but was deemed incorrect by Evans et al. (1991) based on their measures of large DC mechanical components at low stimulus levels. They suggested, based on their measures, that the nonlinearity of OHC motility may be an important source of cochlear nonlinearity. However, considering the present findings, it remains questionable whether their suggestion is valid at threshold in the high-frequency regions of the cochlea.

Harmonics of Outer Hair Cell Motility

J. Santos-Sacchi

Sections of Otolaryngology and Neurobiology, Yale University School of Medicine, New Haven, Connecticut 06510 USA

ABSTRACT The voltage-dependent mechanical activity of outer hair cells (OHC) from the organ of Corti is considered responsible for the peripheral auditory system's enhanced ability to detect and analyze sound. Nonlinear processes within the inner ear are presumed to be characteristic of this enhancement process. Harmonic distortion in the OHC mechanical response was analyzed under whole-cell voltage clamp. It is shown that the OHC produces DC, fundamental and second harmonic length changes in response to sinusoidal transmembrane voltage stimulation. Mechanical second harmonic distortion decreases with frequency, whereas the predicted transmembrane second harmonic voltage increases with frequency. Furthermore, the phase of the second harmonic distortion does not correspond to the phase of the predicted transmembrane voltage. In contradistinction, it has been previously shown (Santos-Sacchi, J. 1992. *Neuroscience*. 12:1906–1916) that fundamental voltage and evoked mechanical responses share magnitude and phase characteristics. OHC length changes are modeled as resulting from voltage-dependent cell surface area changes. The model suggests that the observed harmonic responses in the mechanical response are consistent with the nonlinearity of the voltage-to-length change ($V\text{-}\delta L$) function. While these conclusions hold for the data obtained with the present voltage clamp protocol and help to understand the mechanism of OHC motility, modeling the electromechanical system of the OHC in the *in vivo* state indicates that the mechanical nonlinearity of the OHC contributes minimally to mechanical distortion. That is, *in vivo*, at moderate sound pressure levels and below, the dominant factor which contributes to nonlinearities of the OHC mechanical response resides within the nonlinear, voltage-generating, stereociliar transduction process.

INTRODUCTION

The organ of Corti, the mammalian auditory sensory epithelium, possesses two types of sensory cells, the inner (IHC) and outer (OHC) hair cells. The OHC has received a tremendous amount of attention in the last decade, primarily because it appears to function as both receptor and effector (Brownell, 1992; Dallos, 1992). The OHC produces receptor potentials in response to acoustic stimulation (Dallos et al., 1982; Russell et al., 1986), and rapidly alters its length as a function of transmembrane voltage (Ashmore, 1987; Santos-Sacchi and Dilger, 1988; Santos-Sacchi, 1992). Currently, the OHC is presumed to modify basilar membrane motion through a mechanical feedback mechanism (Ruggero, 1992). This feedback is ultimately considered to enhance the tuning and sensitivity characteristics of the inner hair cell, the cell type which is innervated by the majority of eighth nerve fibers.

Factors which influence the voltages generated in the OHC are therefore crucial in understanding the impact of the postulated OHC mechanical feedback within the organ of Corti. There are a variety of intrinsic nonlinear processes which may shape the voltages controlling OHC mechanical activity. Included are asymmetrical transduction processes (Russell et al., 1986; Dallos, 1986), and voltage-dependent basolateral membrane conductances (Santos-Sacchi and Dilger, 1988; Ashmore and Meech, 1986; Nakagawa et al., 1991; Housley and Ashmore, 1992) and capacitance (Ashmore, 1989; Santos-Sacchi, 1990, 1991). These nonlinearities

will be expected to generate distortions (DC and harmonic components) in AC membrane voltages, which should be reflected in the voltage-dependent mechanical activity of the OHC. In this report, I evaluate the OHC mechanical response with the whole cell voltage clamp, under conditions where the nonlinear basolateral and transducer conductances contribute minimally. It is demonstrated that fundamental and harmonic mechanical responses are generated upon sinusoidal transmembrane voltage stimulation. Furthermore, it is shown that the phase of the second mechanical harmonic does not correspond to the phase of the second voltage harmonic. Thus, while the phase and magnitude of the fundamental mechanical component mirror that of the fundamental membrane voltage (Santos-Sacchi, 1992), the nonlinearity of the voltage-to-length change ($V\text{-}\delta L$) function dominates the production of higher mechanical harmonics under voltage clamp at the voltage magnitudes studied. Nevertheless, through modeling, it is shown that mechanical nonlinearities in the *in vivo* situation will be a dominant function of voltage nonlinearities effected by the stereociliar transducer mechanism.

MATERIALS AND METHODS

General

Guinea pigs were overdosed with pentobarbital. The temporal bones were removed, and OHCs were isolated nonenzymatically from the cochleas by gentle pipetting of the isolated top two turns of the organ of Corti in Ca^{2+} -free medium. OHC stereocilia are damaged or lost during this treatment. The cell-enriched supernatant was then transferred to a 700-ml perfusion chamber, and the cells permitted to settle onto the cover glass bottom. All experiments were performed at room temperature ($\sim 23^\circ\text{C}$). A Nikon Diaphot inverted microscope with Hoffmann optics was used to observe the cells during electrical and mechanical recording. All experiments were taped with

Received for publication 29 March 1993 and in final form 25 June 1993.

Address reprint requests to Joseph Santos-Sacchi.

© 1993 by the Biophysical Society

0006-3495/93/11/2217/11 \$2.00

a Panasonic AG6300 video recorder. A modified Leibovitz medium (142.2 mM NaCl, 5.37 mM KCl, 1.25 mM CaCl₂, 1.48 mM MgCl₂, 5.0 mM 4-(2-hydroxyethyl)-1-piperazineethanesulfonic acid, 5.0 mM dextrose, pH 7.2) was used as the normal perfusate. Modifications made to the extracellular medium in order to block ionic conductances are noted in figure legends. NaCl was adjusted to maintain osmolarity (300 mOsm).

Electrical recording

OHCs were whole cell voltage-clamped with a Dagan patch clamp amplifier at holding potentials between -70 and -80 mV, similar to potentials recorded *in vivo* (Dallos et al., 1982). Pipette solutions were composed of 140 mM CsCl, 5 or 10 mM EGTA, 2 mM MgCl₂, and 5 mM 4-(2-hydroxyethyl)-1-piperazineethanesulfonic acid buffered to pH 7.2. Gigohm seals were obtained at the nuclear level of the cell membrane and electrode capacitance was compensated prior to whole cell recording. AC studies were performed using a digital signal-processing board with custom written software (DSP-16; Ariel Corp., Highland Park, NJ), capable of delivering and analyzing pure tone or swept frequency stimuli. Data were saved to disk for off-line analysis.

Electrode resistance (R_s), membrane resistance (R_m), and capacitance (C_m) were estimated from current transients evoked by small voltage steps (Santos-Sacchi, 1992). Care was taken to maintain low series resistance values during recording by delivering transient positive or negative pressure into the electrode to maintain an unobstructed orifice; electronic series resistance compensation was employed as well. Measurements were made on a physical R-C cell model to rule out potential artifacts generated within the voltage clamp system.

OHC Motility Measures

OHC mechanical responses and currents were simultaneously measured in response to sinusoidal voltage stimuli. Fast OHC movements were measured

with a differential photodiode (PD) onto which the image of the cuticular plate (apical end of cell) from the microscope was projected (Santos-Sacchi, 1992). Placement of the PD was accomplished remotely by a computer-controlled micromanipulator, so as not to perturb whole cell recording. The frequency response of the PD system, measured with an LED, had a 3-dB rolloff at 6 kHz. Sinusoidal voltage bursts (onset and offset linearly ramped) were delivered to OHCs under voltage clamp. PD output and whole cell currents were filtered at 10 kHz (12 dB/octave) and collected simultaneously using a sampling rate of 20 kHz. Responses were averaged 200 times. Magnitude and phase of the current and mechanical responses were measured by fast Fourier transform of the central portion of the digitized waveforms using the software package Matlab (Mathworks, Natick, MA). Numerical solutions to model equations were also performed with this package. Mechanical responses were corrected for the phase and magnitude characteristics of the PD system. The pertinent response characteristics of the system were evaluated by measuring the movements of a glass probe driven by a piezoelectric bimorph (Fig. 1). Since the measured quantities in these experiments are the change in cell length (δL) and the current through the resistance of the patch electrode (I_R), all phase relations (data and model) are conveniently referenced to that of current (I_R). That is, fundamental movement phase [$\phi(\delta L_{f_0})$] is referenced to fundamental current phase [$\phi(I_{Rf_0})$], and harmonic movement phase [$\phi(\delta L_{fn})$] is referenced to harmonic current phase [$\phi(I_{Rfn})$]. Absolute calibration of cell movements was determined by measuring off the video monitor the cell movement in response to a large steady state depolarizing voltage stimulus (Santos-Sacchi, 1989).

RESULTS

Sinusoidal voltage stimulation of the OHC produces sinusoidal alterations in the cell's length. Fig. 2 illustrates, for three cells, the waveforms, magnitudes, and phases of the

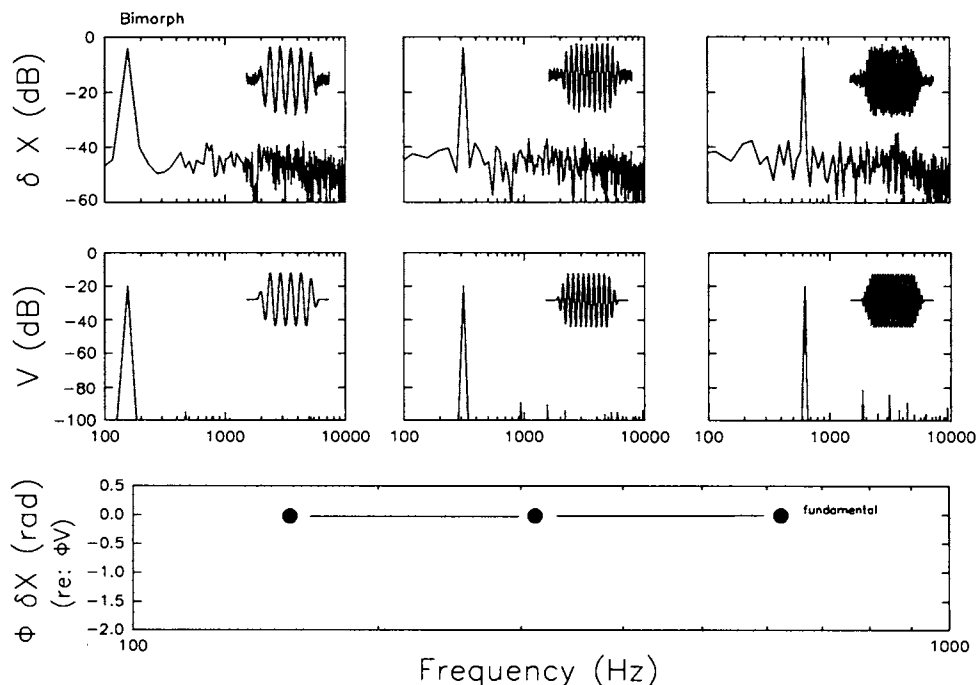


FIGURE 1 Characteristics of the mechanical measurement system. Outputs from PD in response to simulated cell movement. The tip of a glass microelectrode shank was melted to a sphere of about $15 \mu\text{m}$; transmitted light produced a bright area in the sphere's center which was used to mimic the bright OHC cuticular plate observed under Hoffmann optics. The artificial cell was attached to a piezoelectric bimorph and moved using the same voltage waveforms that were used to collect OHC movement data. Upper panel depicts the movement waveforms and magnitude responses obtained by FFT for the stimulus frequencies of 156, 313, and 625 Hz. Peak to peak movements were about $1 \mu\text{m}$. Middle panel depicts the voltage stimulus waveforms and magnitude responses. Note that only fundamental components are observed, indicating the linearity of the measurement system. Lower panel shows the phase of the mechanical response fundamental relative to the driving voltage. As expected for the voltage-dependent piezoelectric response, the phase difference is zero.

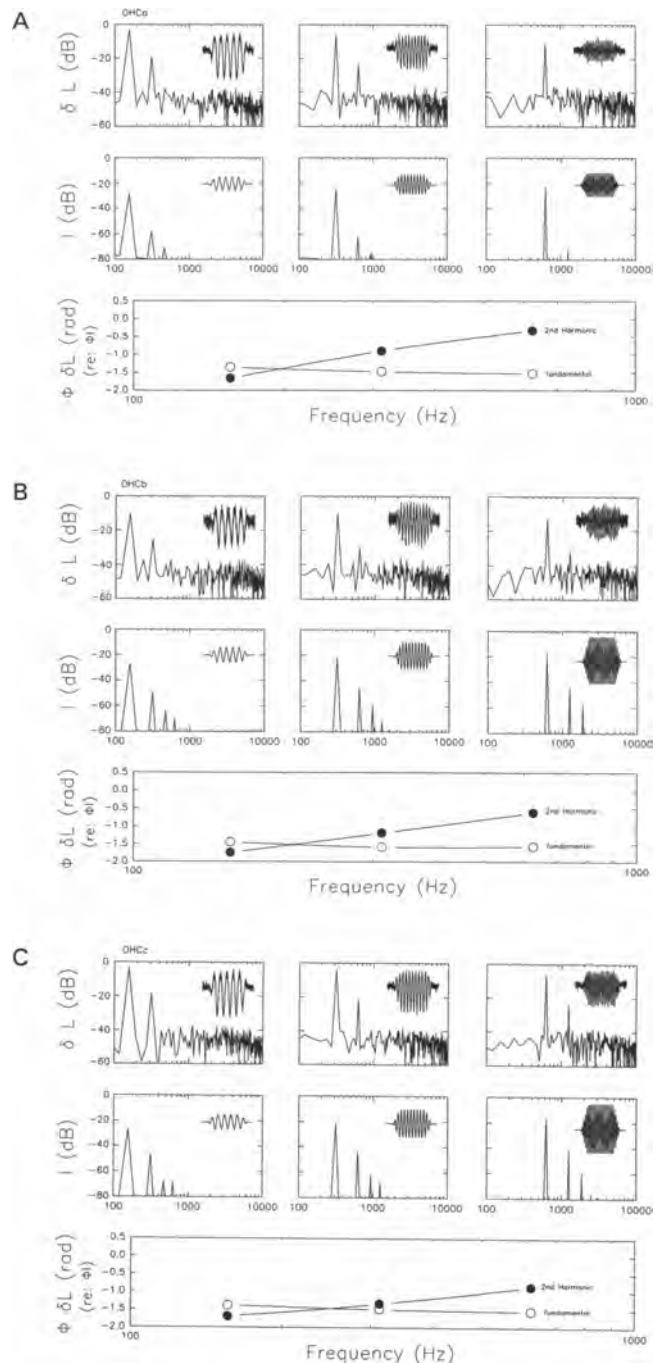
FIGURE 2 OHC mechanical responses induced by sinusoidal voltage clamp stimulation. Results from three different cells are presented in *A*, *B*, and *C*. Upper panels depict the movement waveforms and magnitude responses obtained by FFT for the stimulus frequencies of 156, 313, and 625 Hz. Middle panels depict the measured current waveforms and magnitude responses. Peak-to-peak movements at low frequency were about 1 μm . Lower panel shows the phase of the mechanical response fundamental and second harmonic relative to the measured current phase. Phase is plotted versus fundamental frequency. Note in each case that the mechanical response consists of a DC, fundamental, and second harmonic response. The phase of the fundamental component asymptotes near -1.57 rad, while that of the second harmonic presents an initial phase lag of greater than -1.57 rad which decreases as frequency increases. Clamp-cell electrical characteristics: (*A*) $R_m = 96 \text{ M}\Omega$; $C_m = 24.73 \text{ pF}$; clamp tau = 0.553 ms. Nominal peak voltage was 60 mV. CsCl electrode. Extracellular medium was Leibovitz with 20 mM TEA. (*B*) $R_m = 79 \text{ M}\Omega$; $C_m = 41.89 \text{ pF}$; clamp tau = 0.128 ms. Nominal peak voltage was 40 mV. CsCl electrode. Extracellular medium was Leibovitz with 20 mM TEA, 300 nM TTX, and 1 mM CdCl₂. (*C*) Nominal peak voltage: 50 mV. CsCl electrode. Extracellular medium was Ca²⁺-free Leibovitz with 20 mM TEA and 20 mM CsCl. $R_m = 125 \text{ M}\Omega$; $C_m = 35.4 \text{ pF}$; and clamp tau = 0.125 ms.

measured mechanical and current responses at three frequencies, 156, 313, and 625 Hz. In addition to the fundamental component, the mechanical responses exhibit nonlinear characteristics, including a DC component and a second harmonic (higher harmonics may lie below the noise floor). In all cells successfully recorded from ($n = 9$), harmonics were observed. The DC component is clearly due to the nonlinear form of the V - δL function, and the position of the holding potential along this function (Santos-Sacchi, 1989; Evans et al., 1989). The phase of the mechanical fundamental relative to the current fundamental differs by some 1.5 rad at these frequencies; this has been observed to be characteristic of a voltage-driven mechanical process (Santos-Sacchi, 1992). Note, however, that the phase of the mechanical second harmonic relative to the current second harmonic demonstrates a phase lag which decreases as frequency increases. This, as will be demonstrated below, is not characteristic of a directly driven voltage-induced mechanical response.

As a first step toward evaluating the data, the OHC is modeled to determine the currents and voltages generated under whole cell voltage clamp. The electrical characteristics of the OHC when ionic conductances are blocked can be modeled most simply as an electrode resistance (access resistance, R_s) in series with a parallel combination of a membrane resistance (R_m), a linear membrane capacitance (C_{lin}), and a voltage-dependent membrane capacitance (C_v) (Fig. 3 *a*).¹ The total membrane capacitance (C_m) at any given voltage is the sum of the linear and nonlinear capacitances,

$$C_m = C_v + C_{lin}, \quad (1)$$

¹ A residual resistive nonlinearity remains in OHCs despite considerable attempts to block ionic conductances (Santos-Sacchi, 1991). However, while this nonlinearity varies markedly in magnitude (essentially absent in some cells), the nonlinear capacitance is robust. Modeling the OHC with a resistive nonlinearity indicates that the capacitive nonlinearity dominates. Thus, any residual resistive nonlinearity is ignored in the model.



where C_v is defined as the first derivative of the Boltzmann function relating OHC nonlinear charge movement and voltage (see Santos-Sacchi, 1991). Thus,

$$C_v = \frac{(Q_{\max}(ze/kT))}{\exp\left(\frac{ze}{kT}\{V_m - V_h\}\right)\left[1 + \exp\left(\frac{-ze}{kT}\{V_m - V_h\}\right)\right]^2}, \quad (2)$$

where V_m is the membrane potential, V_h is voltage at half-maximal nonlinear charge transfer, e is electron charge, k is Boltzmann's constant, T is absolute temperature, z is the valence, and Q_{\max} is maximum charge transfer.

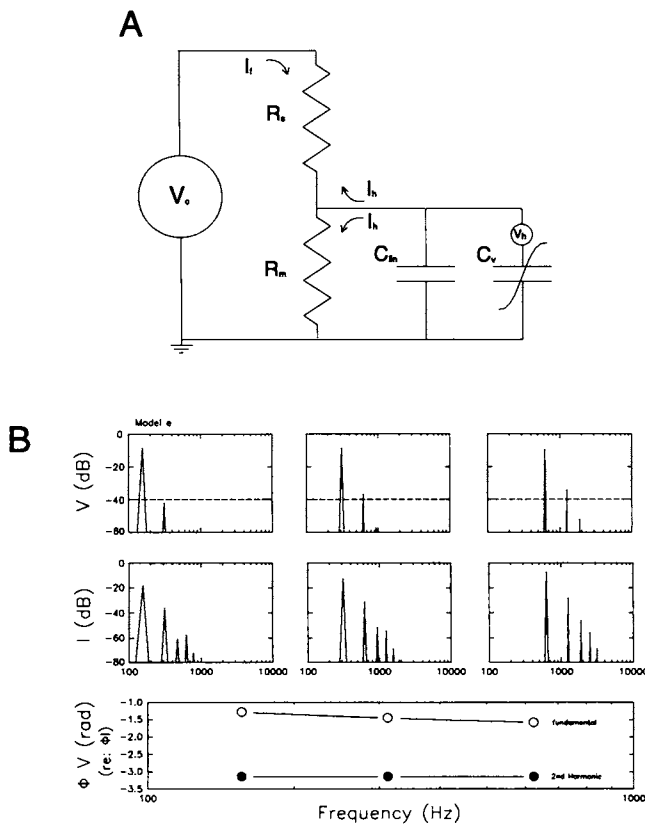


FIGURE 3 (A) OHC-clamp model used to determine the currents and voltages generated under whole cell voltage clamp. The model consists of an electrode resistance (access resistance, R_s) in series with a parallel combination of a membrane resistance (R_m), a linear membrane capacitance (C_{lin}), and a voltage-dependent membrane capacitance (C_v). V_c is the voltage clamp source and V_h is the source of the harmonic voltages within the voltage-dependent capacitance. I_i denotes the direction of fundamental currents through R_s elicited by the voltage clamp source. I_h denotes the direction of harmonic currents through R_s and R_m . (B) Solution of the model utilizing the parameter value (see Results): V_h , -30 mV; z , -1; Q_{max} , 2 pC; R_m , 100 M Ω ; R_s , 5 M Ω ; C_{lin} , 20 pF; T , 298K; V_{hold} , -80 mV; and V_c , 40 mV Pk. Upper panel depicts the membrane voltage (V_m) magnitude responses obtained by FFT for the stimulus frequencies of 156, 313, and 625 Hz. Middle panel depicts the current (I_{R_s}) magnitude responses. Note that fundamental and harmonic components are observed, as is expected in a nonlinear system under nonideal voltage clamp. Lower panel shows the phase of the voltage response fundamental relative to the driving current. As expected the phase of the fundamental voltage asymptotes near -1.57 rad, and the phase of the second harmonic voltage is 180° out of phase (-3.12 rad) with the phase of I_{R_s} .

Given an AC command voltage of V_c which is offset by a holding potential of V_{hold} , the current measurable under whole cell voltage clamp, I_{R_s} , is given as

$$I_{R_s} = I_{R_m} + I_{C_m} \quad (3)$$

or

$$\frac{([V_c + V_{hold}] - V_m)}{R_s} = \frac{V_m}{R_m} + C_m \frac{\delta V_m}{\delta t} \quad (4)$$

Numerical solutions were obtained with typical empirically determined parameter values (Santos-Sacchi (1991): V_h , -30 mV; z , -1; Q_{max} , 2 pC; R_m , 100 M Ω ; R_s , 5 M Ω ; C_{lin} , 20 pF; T , 298K; V_{hold} , -80 mV; and V_c , 40 mV Pk).

Fig. 3 b demonstrates, in the nonlinear electrical model of the OHC under voltage clamp, the current (I_{R_s}) and membrane voltage (V_m) responses due to sinusoidal voltage clamp stimulation. The model generates both fundamental and harmonic responses. Under whole cell voltage clamp, sinusoidal stimulation will elicit voltage harmonics across the nonlinear cell membrane since, due to the finite value of the series resistance, R_s , the clamp is less than ideal (if R_s were equal to zero then the voltage across the membrane would be solely the undistorted sinusoidal clamp voltage). As expected at these frequencies with the chosen typical component values, the phase of the fundamental of V_m lags that of I_{R_s} by about 1.57 rad or 90°. Note, however, that the phase of the second harmonic of V_m lags that of I_{R_s} by 3.14 rad. This derives from the fact that the input voltage clamp stimulus contains no harmonics, and the source of the second harmonic is within the voltage-dependent capacitance, C_v . Thus, at the second harmonic, current flows through R_s and R_m to ground. Keeping the current sign convention through R_s constant (see Fig. 3 a), it is apparent why the phase of I_{R_s} at the second harmonic is -3.14 rad relative to that of V_m (i.e., current lags voltage by 3.14 rad). Why, then, if OHC motility is voltage-dependent do the phase characteristics of the motility at the second harmonic differ from those of the voltage predicted by the model?

In order to explore this dilemma, an extension of the simple electrical model is generated whereby the voltage change across the OHC membrane is translated to changes in cell length and cell radius. This mechanical component of the model revolves around the assumption that the voltage-dependent charge movement measured in the OHC (Santos-Sacchi, 1991) corresponds to a conformational change induced by the movement of charged moieties within 10-nm particles known to reside within the OHC plasmalemma (Gulley and Reese, 1977; Saito, 1983; Forge, 1991). The conformational change is assumed to alter the surface area occupied by such particles within the membrane (Fig. 4). Kalinec et al. (1992) have observed depolarization-induced reductions in surface area of OHC lateral membrane patches. Given the constraints of constant cell volume (likely because the OHC mechanical frequency response probably extends beyond a 1-kHz cutoff (Santos-Sacchi, 1992)), and a fixed cell architecture, a change in length and radius will ensue following a change in cell surface area.

The diameter (d_p) of the membrane particle when the cell is fully elongate is taken as 10 nm. The particle area within the membrane is then,

$$A_p = \pi \left(\frac{d_p}{2} \right)^2, \quad (5)$$

and the change in diameter (δd_p) due to voltage-dependent conformation change results in a single particle area change of

$$\delta A_p = \pi \left(\frac{d_p + \delta d_p}{2} \right)^2 - \pi \left(\frac{d_p}{2} \right)^2. \quad (6)$$

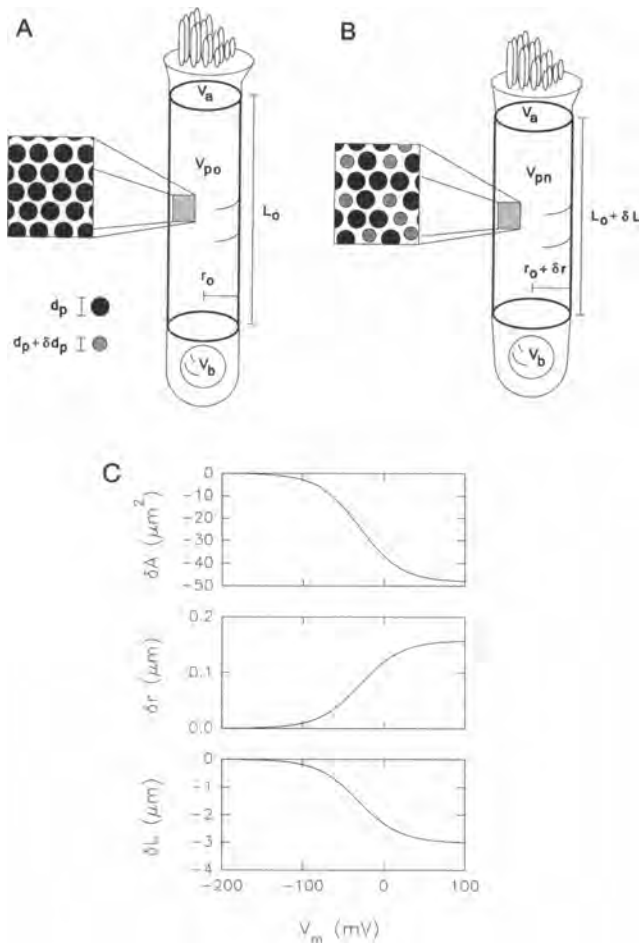


FIGURE 4 OHC mechanical model (see Results). (A) Hyperpolarized OHC in fully elongate state where all membrane particles (blow up) are in maximum surface area state. (B) Partially depolarized OHC where some particles are in minimum surface area state. Note that when cell is depolarized length is decreased and radius is increased. Drawing is not to scale. V_{po} , volume of portion of fully elongate cell which is bounded by active, particle containing region; r_o , radius of cell in fully elongate state; V_a , volume of apical region of cell not containing membrane particles; V_b , volume of basal region of cell not containing membrane particles; L_o , length of cell in fully elongate state; V_{pn} , volume of portion of partially contracted cell which is bounded by active, particle containing region; δr , change in radius due to depolarization; δL , change in length of cell due to depolarization; d_p , particle diameter in maximum surface area state; δd_p , change in particle surface area in minimum surface area state. (C) Predicted change in model OHC surface area, radius, and length as a function of transmembrane voltage. Changes in length and radius are similar to experimental observations under voltage clamp. Ratio of length to radial change is about 18.

The maximum change in cell surface area (δA_{\max}) depends upon the number of particles (N_i) in the membrane,

$$\delta A_{\max} = \delta A_p N_i. \quad (7)$$

The aggregate membrane surface area change ($\delta A(V_m)$) will be voltage-dependent and will display the same Boltzmann characteristics of the voltage-dependent charge movement alluded to above (Santos-Sacchi, 1991).

$$\delta A(V_m) = \frac{\delta A_{\max}}{1 + \exp\left(\frac{-ze}{kT}\{V_m - V_h\}\right)} \quad (8)$$

The architecture of an OHC is normally close to cylindrical,

and the following analysis adheres to that form; however, since it is known that length changes occur even when the cell has swelled into a spherical form (Holley and Ashmore, 1988a), an analysis assuming the form of a prolate spheroid was performed and similar results were obtained. Forces need not be considered directly, but are simply acknowledged to promote the maintenance of the cylindrical shape (or, in the case of a spheroid model, the spheroid shape). The existence of a cytoskeletal spring beneath the OHC plasmalemma (Holley and Ashmore, 1988b), in conjunction with intracellular pressure is taken to provide these forces. The force providing the change in surface area derives from the imposed transmembrane voltage.

For the cylindrical cell model (Fig. 4), the volumes of the particle containing region of the cell before (V_{po}) and after (V_{pn}) a change in length (δL) and radius (δr) are

$$V_{po} = \pi r_o^2 L_o, \quad (9)$$

and

$$V_{pn} = \pi (r_o + \delta r)^2 (L_o + \delta L), \quad (10)$$

where L_o and r_o are the cell length and radius in the fully elongate state.

The total cell volumes before (V_o) and after (V_n) are

$$V_o = V_{po} + V_{ab}, \quad (11)$$

and

$$V_n = V_{pn} + V_{ab}, \quad (12)$$

where V_{ab} is the sum of the volumes of the apical (V_a) and basal (V_b) regions of the cell which are devoid of the presumed membrane motor particles. To simplify matters, an assumption is made that V_{ab} remains constant. This assumption may be taken to indicate that the apical and basal compartments are either rigid or deformable to the extent that the sum of the volumes remains constant. Because total cell volume is constant for each condition,

$$\delta L = -\delta r L_o \frac{2r_o + \delta r}{r_o^2 + 2r_o \delta r + \delta r^2}. \quad (13)$$

The surface areas of the active, particle-containing regions under each condition are

$$A_o = 2\pi r_o L_o \quad (14)$$

$$A_n = 2\pi (r_o + \delta r)(L_o + \delta L), \quad (15)$$

The change in cell surface area, $\delta A(V_m)$, is then

$$\delta A(V_m) = A_n - A_o = \frac{\delta A_{\max}}{1 + \exp\left(\frac{-ze}{kT}\{V_m - V_h\}\right)}. \quad (16)$$

Given the Boltzmann dependence of $\delta A(V_m)$, the cell volume constraint, and the further constraint that $|\delta r| < |r_o|$, physically realizable values of δL and δr are obtained. Fig. 4c plots the solution to the equations as voltage is varied between -200 and 100 mV. The parameters used were: L_o , 50 μm ; r_o , 5 μm ; δd_p , -0.5 nm; and N_i , 4000/ μm^2 . The

number of particles derives not only from estimates based on the relation between charge movement and length changes in OHCs (Santos-Sacchi, 1991), but also from ultrastructural studies (Kalinec et al., 1992). The outcome of this model (Fig. 4 c) displays characteristics which are comparable to actual results obtained under whole cell voltage clamp (Ashmore, 1987; Santos-Sacchi and Dilger, 1988; Santos-Sacchi, 1989, 1991, 1992). For example, maximal length changes are about 20 times greater than radial changes, and while depolarization decreases cell length, cell radius is increased. More importantly for the present analysis, the model can be used to simulate the nonlinear effects evoked by sinusoidal voltage stimulation.

Fig. 5 illustrates the fundamental and harmonic structure of δL and V_m for the complete model (electrical and mechanical) when excited by those same frequencies used to collect the biophysical data. Several characteristics of the model output should be noted. First, it is obvious that phase relations are similar between model and data (Fig. 2). Second, the relative magnitudes of the fundamental and second harmonic mechanical responses resemble those of the actual mechanical data. Clearly, the relative magnitude of the second harmonic mechanical response is greater than would be predicted from the corresponding predicted voltage. Finally, note that while the magnitude of the voltage second harmonic increases with frequency, the magnitude of the mechanical second harmonic decreases with frequency. Overall, the

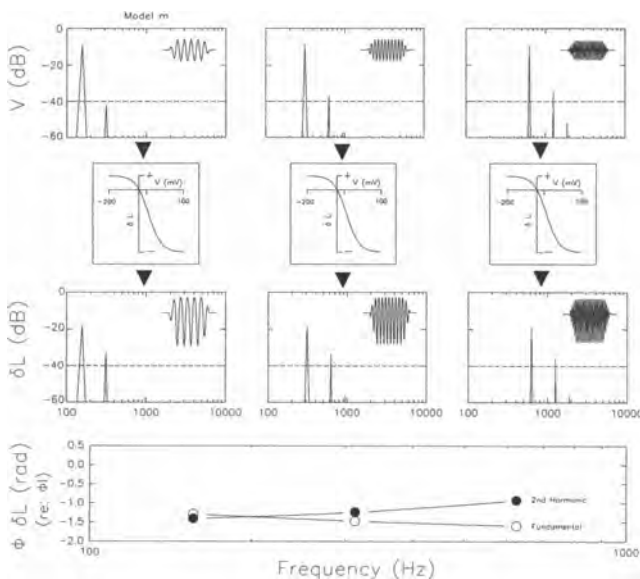


FIGURE 5 Combined electrical and mechanical model of OHC mechanical response under voltage clamp. Parameters as in Figs. 3 and 4. Upper panels depict the membrane voltage waveforms and magnitude responses obtained by FFT for the stimulus frequencies of 156, 313, and 625 Hz. Panels between arrowheads represent the V - δL function with parameters as in Results. Middle panels depict the mechanical waveforms and magnitude responses. Lower panel shows the phase of the mechanical response fundamental and second harmonic relative to the current phase. Phase is plotted versus fundamental frequency. Note that the mechanical second harmonic decreases with frequency unlike the voltage second harmonic. The phase response is similar to the actual biophysical data (Fig. 2).

model results are similar to the actual data in that they suggest that the second harmonic mechanical response is due to forces other than the second harmonic voltage.

Certainly, however, the voltage harmonics should induce mechanical responses at their respective frequencies. A model simulation was performed where the voltage from the nonlinear electrical cell model was stripped of its fundamental prior to evoking changes in membrane surface area. This was accomplished mathematically by zeroing the fundamental component of the voltage fast Fourier transform, followed by reverse transformation. Obviously, the fundamental component is absent in the mechanical response. Informatively, however, the voltage-dependent mechanical response at the second harmonic is unmasked. It mirrors the increase in magnitude which the second harmonic voltage displays. More importantly for this analysis, the phase of the mechanical response lags that of I_R by 3.14 rad, just as voltage does (Fig. 3).

It is shown in Fig. 6 that the fundamental component of the voltage, i.e., the voltage stripped of its harmonics (an ideal voltage clamp), induces a mechanical response which presents both fundamental and second harmonic structure. The magnitude of the second harmonic decreases with frequency less so than for the complete model (Fig. 5), and it appears to follow the similar slight decrease of the fundamental magnitude. The phase of the second harmonic relative to the current is somewhat similar to the complete model (Fig. 5), however, the phase lag is decreased at all frequencies. The apparent frequency dependence of the mechanical second harmonic phase is not real, but only reflects the frequency dependence of the I_R phase to which the mechanical

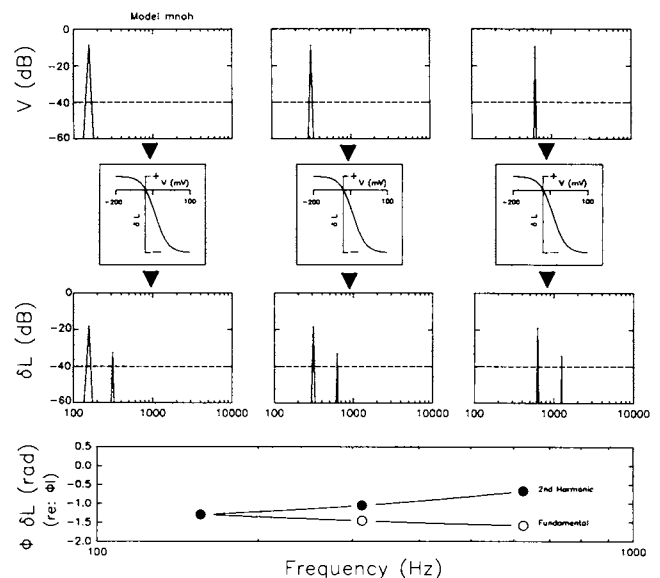


FIGURE 6 As in Fig. 5 except that the second harmonic voltage has been removed prior to generating the mechanical response. This is equivalent to an ideal voltage clamp, without the effects of series resistance. Note that mechanical second harmonics are generated due to the nonlinearity of the V - δL function. The phase is somewhat similar to the complete model (Fig. 5), but the second harmonic lag is slightly decreased at all frequencies (see Fig. 7).

phase is referenced. The phase of the mechanical second harmonic actually mirrors that of the fundamental, i.e., $\phi(\delta L_{f_2}) = \phi(\delta L_{f_1})/2$. The frequency independence of the mechanical second harmonic phase is demonstrated in Fig. 7, where the phase of the mechanical second harmonic of the fundamental-only model is plotted relative to that of the complete model (essentially, the phase reference to current is removed). Note, however, that a slight residual frequency dependence in this phase plot is revealed, showing a lag accumulating with frequency. This is totally attributable to the mechanical effects of the frequency-dependent increase in the magnitude of the voltage second harmonic of the complete model, given its phase lag of 3.14 rad. That is, in the complete model, and presumably in the actual data, although the second harmonic mechanical response is dominated by distortion in the mechanical transformation, voltage distortion plays a minor role.

DISCUSSION

In the present report, the higher harmonic components of the OHC voltage-dependent mechanical response were measured, and deduced through modeling to arise primarily from nonlinearities in the V - δL process. Voltage nonlinearities generated due to the OHC nonlinear capacitance (see Footnote 1), under nonideal voltage clamp, account for little of the mechanical harmonic distortion. Thus, while mechanical distortion can be induced by nonlinearities in the voltages of the OHC, the nonlinear nature of the mechanical transformation ensures distortion product generation under the present experimental conditions.

Effects of the V - δL function on evoked mechanical nonlinearities of the OHC

The form of the OHC V - δL function under voltage clamp can be fit by a two-state Boltzmann relation (Santos-Sacchi, 1991, 1992) and consequently the mechanical sensitivity of the cell, the slope of the V - δL function, varies depending upon resting potential. Because the normal resting potential

lies at the hyperpolarizing saturation knee of the V - δL function, sinusoidal voltage excitation elicits both DC and harmonic mechanical distortion. The production of DC mechanical components has been documented (Santos-Sacchi, 1989; Evans et al., 1989), and the polarity of this component has been shown to reverse, as expected, when the holding potential is shifted to values more positive than V_h (the voltage (~ -30 mV) at half-maximal length change (Santos-Sacchi, 1989, 1992)). Indeed, under voltage clamp, the DC component has been measured at stimulus frequencies as high as 3.2 kHz (Santos-Sacchi, 1992). Nevertheless, it was shown that the magnitude of the DC component is highly level-dependent, decreasing in size much more precipitously than the fundamental component as voltage level decreases (see Figs. 5 *c* and 10 *d* in Santos-Sacchi (1992)). This is a consequence of the inherent linearization of the V - δL function as stimulus amplitude is decreased. Modeling indicates that the same level dependence characterizes the mechanical harmonic components as well. In the intact, normal organ of Corti, these level-dependent effects will be expressed as auditory threshold is approached; that is, near auditory threshold, mechanically generated distortion will be several orders of magnitude smaller than the fundamental component, given a pure sinusoidal voltage stimulus.

In addition to level-dependent effects, mechanisms which alter the relationship between resting potential (operating point along the V - δL function) and V_h of the V - δL function will also influence the generation of nonlinearities. That is, shifts in either resting potential or V_h will modify the characteristics of mechanical distortion. For a two state Boltzmann process (namely, the V - δL function) which is symmetrical about its midpoint, V_h , the DC mechanical component theoretically will be abolished by superposition of the resting potential and V_h . Nonetheless, harmonic distortion will remain, and under these conditions predominantly odd harmonics will be generated. In the absence of superposition, level-dependent DC, odd and even harmonics are always expected. In the present study, harmonics above the second were probably below the noise floor.

Modeling the mechanism of OHC motility

The similarity between characteristics of OHC nonlinear charge movement (indicative of membrane-bound voltage sensors) and OHC motility has been suggested to indicate that an estimated $4000/\mu\text{m}^2$ membrane-bound voltage sensor-motor elements control OHC length (Santos-Sacchi, 1991, 1992). In the present report, the mechanism responsible for OHC motility was modeled as a modification of membrane surface area due to a two state voltage-dependent conformational change of an intrinsic membrane particle, representing the sensor-motor element. Intrinsic membrane particles, presumably membrane proteins, have been observed in the OHC lateral plasmalemma (Gulley and Reese, 1977; Saito, 1983; Forge, 1991; Kalinec et al., 1992). The density of particles is similar to estimates based on nonlinear charge data.

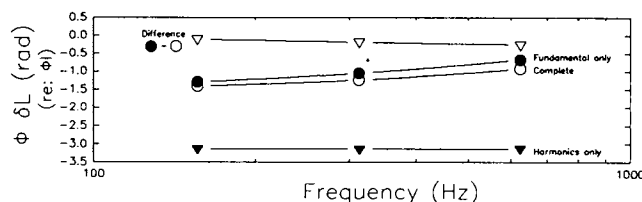


FIGURE 7 Relations between second harmonic mechanical phase data for the three model conditions: complete (fundamental and harmonic voltages, open circles), fundamental voltage only (closed circles), and harmonic voltage only (closed triangles). The difference between fundamental only and complete model (open triangles) essentially removes the reference to current and demonstrates the minimal frequency dependence of the mechanical phase. The remaining slight frequency dependence (increasing lag with frequency) is due to the effects of the mechanical response induced by second harmonic voltage, since this voltage driven response increases in magnitude with frequency, and has a phase lag of -3.12 rad.

Kalinec et al. (1992) have provided evidence that voltage-dependent OHC length changes continue to occur after subplasmalemmal cytoskeletal elements are disrupted with intracellular trypsin. In fact, they report that membrane patches change surface area when hyperpolarized or depolarized—hyperpolarization increases the membrane patch area, while depolarization decreases it. They have suggested that a rearrangement of membrane particles within the plasmalemma induces a change in membrane surface area, and a concomitant change in OHC length. Furthermore, these same investigators (Kalinec et al., 1993) have speculated that tetrameric anion exchangers in the lateral OHC membrane underlie OHC motility. However, according to their model, it is not clear how two-state tetrameric rearrangements of the observed membrane particles within the OHC membrane can account for the one-to-one correspondence between voltage sensor and motor element derived from nonlinear charge movement and motility data (Santos-Sacchi, 1991, 1992; Ashmore, 1992); that is, the reduced number of discrete motor elements (four per element rather than one per element; hence, one quarter the density of membrane particles) might predict results contrary to experimental observations relating nonlinear charge movement and motility.

Dallos et al. (1991a) have presented a model of OHC motility based on a “motor unit” of circumferentially arranged discrete sensor-motor elements which acts in series along the length of the OHC. The model accurately predicts motility data obtained with the partitioning microchamber technique (Dallos et al., 1991b). The motor elements are predicted to be anisotropic, providing a greater displacement in the longitudinal direction than in the radial direction. The putative alignment of the individual motor’s displacement vector ($\sim 20^\circ$) roughly corresponds to an early estimate of the angle of the circumferential filaments described by Holley and Ashmore (1988b). Newer estimates of the filament angle are closer to 9° , although the range is substantial (-55° to 74°) (Holley et al., 1992). It should be noted that recently Iwasa and Chadwick (1992) presented evidence that the active tension within the OHC plasma membrane is likely to be isotropic. Furthermore, they suggested that the presumed motors are not aligned within the plasmalemma.

The simple model developed in the present report is fundamentally isotropic, but evokes anisotropic shape changes in the OHC due to the geometric constraints of the cell architecture (see Results). The modifications in cell surface area are simply governed by changes in particle (protein) conformation and attendant reductions in the area of the particle within the lipid bilayer. The lipid bilayer is assumed to instantaneously occupy the potential void created by the particle’s reduced area; the particle need not be spherical as depicted. It is the simplest model available to fit the whole-cell voltage-clamped OHC, and its usefulness is evident from the similarity between model predictions and data.

Voltage nonlinearities of the OHC

As was demonstrated through modeling, nonlinear voltages will evoke voltage-induced mechanical responses. The de-

gree to which these voltage nonlinearities contribute to the measured mechanical nonlinearities will depend upon their magnitudes. Voltage nonlinearities will arise from several processes known to exist within distinct domains of the OHC plasmalemma. The very process that translates acoustically driven stereociliar movements into OHC receptor currents is nonlinear (Russell et al., 1986; Dallos, 1986). That is, opposite but equal displacements of the hair bundle from the resting position generate asymmetrical conductance changes, resulting in asymmetrical voltage responses. Whereas it is probable that the only channel in the apical membrane of hair cells is the stereociliary transduction channel, a variety of ionic channel types is found in the basolateral membrane, including voltage-dependent K^+ , and Ca^{2+} channels (Santos-Sacchi and Dilger, 1988; Ashmore and Meech, 1986; Nakagawa et al., 1991; Housley and Ashmore, 1992), as well as ligand gated channels (e.g., Housley and Ashmore, 1991). In addition to these nonlinearities, there exists the unique motility-related voltage-dependent capacitance of the OHC (Ashmore, 1989; Santos-Sacchi, 1990, 1992; Iwasa, 1993). Thus, the intrinsically nonlinear receptor potential registered in the OHC cell may be further affected by the nonlinear RC properties of the basolateral membrane.

It would be useful to have an estimate of the contribution of these basolateral membrane nonlinearities to the mechanical response in the *in vivo* state. Because the membrane nonlinearities which can potentially affect OHC motility on a cycle-by-cycle basis² are voltage and time-dependent, hence stimulus level and frequency-dependent, it is possible to rule out specific contributions based on stimulus parameters. That is, considering stimulus frequencies above 200 Hz and sound pressure levels below that required to generate 5-mV Pk AC receptor potentials,³ certain basolateral characteristics can be ignored. This is not an unreasonable approach, since the feedback effects of OHC motility are presumed to be most important at low stimulus magnitudes, where tuning is greatest. In order to evaluate whether a basolateral membrane characteristic can be ignored given these stimulus constraints, the time- and voltage-dependent nature of that characteristic must be considered. It becomes readily apparent, then, that the contribution of many of the basolateral conductances can be ignored in a model analysis at the typical *in vivo* resting potential of -70 mV (Dallos et al. (1982); see Footnote 3 in Santos-Sacchi (1989)). For example, the outward K^+ conductance, which dominates the basolateral membrane conductance, can be ignored because the activation time constant is on the order of tens of milliseconds at potentials near its activation voltage of about -50 mV (Santos-Sacchi and Dilger, 1988; Housley and Ashmore, 1992). The same rea-

² Ligand gated channels typically are slower in their action than voltage or mechanically gated channels, and may be considered to have mainly steady state effects on membrane potential and or V_h . For example, the effects of efferent transmitters on the OHC may produce hyperpolarization (Housley and Ashmore, 1991) or shifts of V_h (Huang and Santos-Sacchi, 1993).

³ A 5-mV Pk response from the OHC is obtained with moderate intensities at the cell’s characteristic frequency (Dallos, Santos-Sacchi and Flock, 1982).

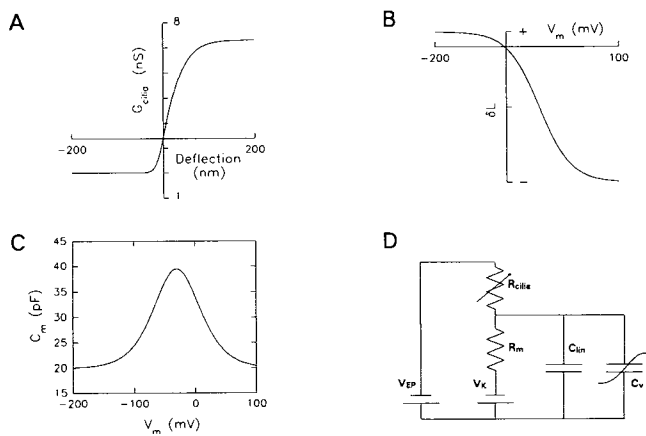
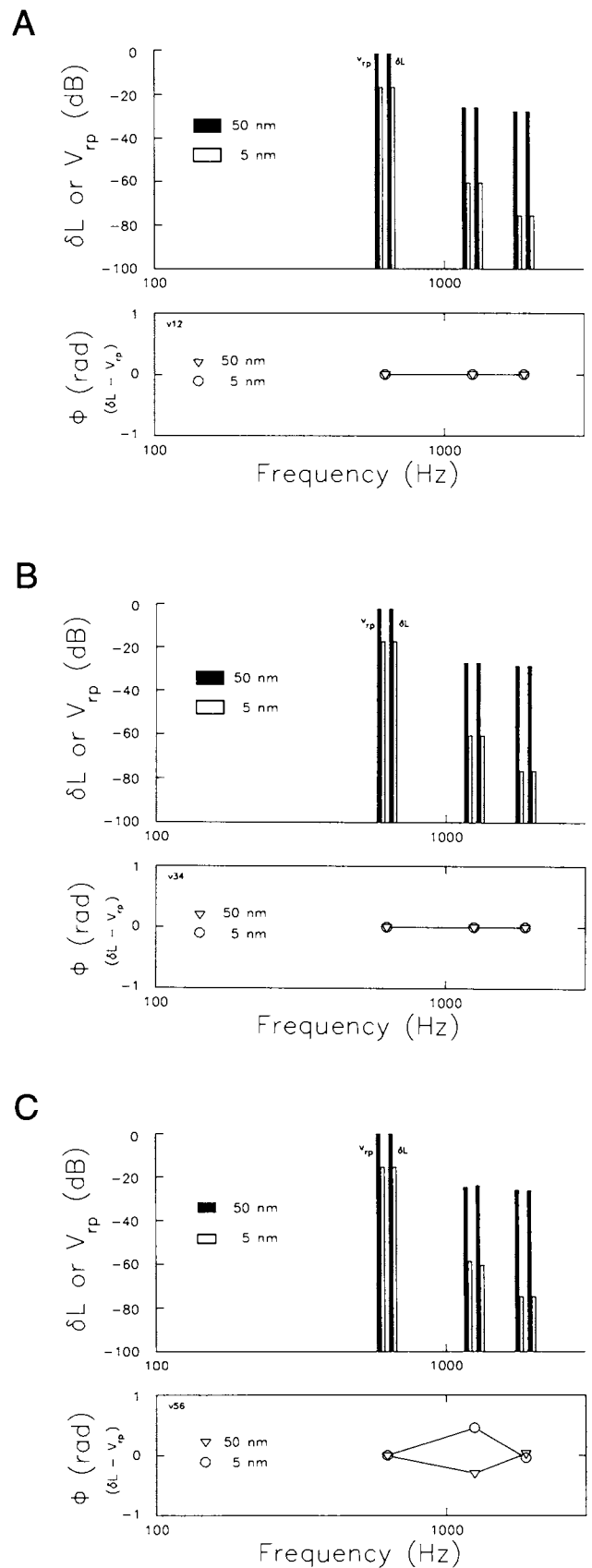


FIGURE 8 Nonlinearities of the in vivo model. (A) Conductance of the apical membrane of the OHC, including transducer conductance (max 5.3 nS) and leakage conductance (2 nS). The form is that observed by Kros et al. (1992). However, the resting conductance is shifted to the right so that about 25% of the transducer conductance is active. Under these conditions the model generates voltage responses which are similar to those obtained in OHCs from the 3rd turn of the guinea pig cochlea (Dallos, 1986). (B) V - δL function with parameters as in Results. (C) Voltage-dependent capacitance function with parameters as in Results. (D) In vivo electrical model. R_{cilia} , resistance of apical OHC membrane whose conductance is depicted in A; R_m , basolateral membrane resistance of 40 M Ω ; V_{ep} , endolymphatic potential of +90 mV; V_k , potassium reversal potential of -90 mV; C_{lin} , linear membrane capacitance of 20 pF; C_v , voltage-dependent membrane capacitance depicted in C. Stimulation of the model is via transducer conductance changes induced by sinusoidal deflection of the stereociliar bundle as in A. Resting potential under these conditions is near -67 mV.

soning holds for the basolateral Ca^{2+} conductance (Santos-Sacchi and Dilger, 1988; Nakagawa et al., 1991). While it is known that a nonlinear leakage conductance remains even after considerable attempts to block the OHC voltage-dependent conductances (Santos-Sacchi, 1991; Huang and Santos-Sacchi, 1993), the slope conductance near resting potential is fairly linear. In fact, Housley and Ashmore (1992), have shown that even with “normal” intra- and extracellular solutions the slope conductance between -50 and -85 mV is nearly constant for a given cell under voltage clamp, although it varies as a function of cell length. Thus, with the given stimulus parameter constraints, it seems acceptable to model the OHC as an electromechanical system comprised of only three nonlinearities—the transducer conductance, the voltage-dependent capacitance, and the V - δL function.

FIGURE 9 (A) Magnitudes and phases of receptor potentials (V_{rp}) and mechanical responses (δL) generated by sinusoidal stereociliar deflections of 5- and 50-nm PK in the in vivo model with only the transducer nonlinearity. A fixed membrane capacitance of 30 pF and a linear V - δL function were employed. Note the generation of fundamental, second, and third harmonics in the voltage and consequently in the mechanical response. Magnitudes (responses were scaled to set fundamentals equal) and phases are the same for voltage and mechanical response. (B) As above, except that the nonlinear capacitance has been introduced. At the voltages generated, little or no effect of the nonlinear capacitance is observed. (C) As above, except that the nonlinear V - δL function is added. Only slight changes in the magnitudes and phases of the harmonics are evident, indicating that the dominant nonlinearity which influences distortion in the mechanical response is due to the transducer function.



The forms of these nonlinearities and the *in vivo* electrical model are displayed in Fig. 8. The form of the transducer conductance of the OHC is that determined by Kros et al. (1992). However, the resting point has been shifted to the right to correspond more closely with *in vivo* measures (Fig. 8 in Dallos (1986)). Fig. 9 *a* presents a comparison between receptor potential (at 625 Hz) and induced mechanical responses when the voltage-dependent capacitance and $V\text{-}\delta L$ function are linearized. It is clear that harmonic distortion (evident as a second and third harmonic) is present in the receptor potential, and that mechanical response distortion simply mirrors this voltage distortion. In Fig. 9 *b*, the nonlinear capacitance is introduced. At the magnitudes of the receptor potential generated by the 50- and 5-nm Pk stereociliar displacements (~ 7 and ~ 1 mV peak-to-peak, respectively), the voltage-dependent capacitance induces minimal additional distortion in the voltages and mechanical responses (compare Figs. 9 *a* and 9 *b*). Finally, when the nonlinear $V\text{-}\delta L$ function is added (Fig. 9 *c*), it is observed that the mechanical response displays only slight differences in the magnitudes and phases of the mechanical response harmonics viz a viz the voltage. It is clear from this modeling effort that the dominant factor contributing to distortion production in the mechanical response *in vivo* will be the transduction process nonlinearity.

Patuzzi et al. (1989) have previously argued that the transducer mechanism nonlinearity of the OHC dominates in the *in vivo* cochlea. While this is in accord with the present modeling effort, it cannot be dismissed that the magnitude and/or effectiveness of the mechanical nonlinearity may be different *in vivo*. For example, it is clear that the position of the $V\text{-}\delta L$ function is not static—it can be shifted along the voltage axis (Santos-Sacchi, 1991; Huang and Santos-Sacchi, 1993; Evans et al., 1991). That is, the operating point can be placed in a more or less linear portion of the function. Clearly, *in vivo* estimates of this nonlinearity are necessary.

SUMMARY

The voltage-induced mechanical properties are believed to provide the means whereby the auditory system enhances its frequency sensitivity and selectivity (Dallos, 1992). Nonlinearity in the peripheral auditory system is believed to be the hallmark of the enhancement mechanism. It is demonstrated here that under voltage clamp, OHC mechanical responses possess nonlinear attributes. The mechanical harmonic components observed are effected by the nonlinear nature of the $V\text{-}\delta L$ function, since through modeling it is shown that the voltage harmonic distortion generated under nonideal voltage clamp of the OHC contributes minimally. While these conclusions hold for the data obtained with large voltage clamp stimuli, modeling efforts indicate that *in vivo*, at moderate sound pressure levels and below, the dominant factor which contributes to nonlinearities of the OHC mechanical response resides within the process that translates stereociliar movement into receptor potentials.

This work was supported by a National Institute of Deafness and other Communication Disorders Research Career Development Award and National Institutes of Health grant DC00273.

REFERENCES

- Ashmore, J. F., and R. W. Meech. 1986. Ionic basis of the resting potential in outer hair cells isolated from the guinea pig cochlea. *Nature (Lond.)* 322:368–371.
- Ashmore, J. F. 1987. A fast motile response in guinea-pig outer hair cells: the cellular basis of the cochlear amplifier. *J Physiol (Lond.)* 388:323–347.
- Ashmore, J. F. 1989. Transducer motor coupling in cochlear outer hair cells. *In Mechanics of Hearing*. D. Kemp and J. P. Wilson, editors. Plenum Press, New York. 107–113.
- Ashmore, J. F. 1992. Mammalian hearing and the cellular mechanisms of the cochlear amplifier. *In Sensory Transduction*. D. P. Corey, and S. D. Roper, editors. Rockefeller University Press, New York.
- Brownell, W. E. 1992. Outer hair cell electromotility and otoacoustic emissions. *Ear Hear.* 11:82–92.
- Dallos, P., J. Santos-Sacchi, and Å. Flock. 1982. Intracellular recordings from outer hair cells. *Science (Wash. DC)* 218:582–584.
- Dallos, P. 1986. Neurobiology of cochlear inner and outer hair cells: intracellular recordings. *Hear. Res.* 22:185–198.
- Dallos, P., R. Hallworth, and B. N. Evans. 1991a. Stochastic theory of outer hair cell electromotility. *In Auditory Physiology and Perception*. Y. Cazals, K. Horner, and L. Demany, editors. Pergamon Press, Oxford, England. 35–43.
- Dallos P, B. N. Evans, and R. Hallworth. 1991b. On the nature of the motor element in cochlear outer hair cells. *Nature (Lond.)* 350:155–157.
- Dallos, P. 1992. The active cochlea. *J. Neurosci.* 12:4575–4585.
- Evans, B. N., P. Dallos, and R. Hallworth. 1989. Asymmetries in motile responses of outer hair cells in simulated *in vivo* conditions. *In Mechanics of Hearing*. D. Kemp, and J. P. Wilson, editors. Plenum Press, New York. 205–206.
- Evans, B. N., R. Hallworth, and P. Dallos. 1991. Outer hair cell electromotility: the sensitivity and vulnerability of the DC component. *Hear. Res.* 52:288–304.
- Forge, A. 1991. Structural features of the lateral walls in mammalian cochlear outer hair cells. *Cell Tissue Res.* 265:473–483.
- Gulley, R. L., and T. S. Reese. 1977. Regional specialization of the hair cell plasmalemma in the organ of Corti. *Anat. Rec.* 189:109–124.
- Holley, M. C., and J. F. Ashmore. 1988a. On the mechanism of a high-frequency force generator in outer hair cells isolated from the guinea pig cochlea. *Proc. R. Soc. Lond. Ser. B Biol. Sci.* 232:413–429.
- Holley, M. C., and J. F. Ashmore. 1988b. A cytoskeletal spring in cochlear outer hair cells. *Nature (Lond.)* 335:635–637.
- Holley, M. C., F. Kalinec, and B. Kachar. 1992. Structure of the cortical cytoskeleton in mammalian outer hair cells. *J. Cell Sci.* 102:569–580.
- Housley, G. D., and J. F. Ashmore. 1991. Direct measurement of the action of acetylcholine in outer hair cells of the guinea pig cochlea. *Proc. R. Soc. Lond. Ser. B Biol. Sci.* 244:161–267.
- Housley, G. D., and J. F. Ashmore. 1992. Ionic currents of outer hair cells isolated from the guinea-pig cochlea. *J. Physiol. (Lond.)* 448:73–98.
- Huang, G.-J., and J. Santos-Sacchi. Metabolic control of OHC function: phosphorylation and dephosphorylation agents shift the voltage dependency of motility related capacitance. Midwinter meeting of the Association for Research in Otolaryngology, St. Petersburg, FL, February 1993.
- Iwasa, K. H., and R. S. Chadwick. 1992. Elasticity and active force generation of cochlear outer hair cells. *J. Acoust. Soc. Am.* 6:3169–73.
- Iwasa, K. H. 1993. Effect of stress on the membrane capacitance of the auditory outer hair cell. *Biophysical J.* 65:492–498.
- Kalinec, F., M. C. Holley, K. H. Iwasa, D. J. Lim, and B. Kachar. 1992. A membrane-based force generation mechanism in auditory sensory cells. *J. Proc. Natl. Acad. Sci. USA.* 89:8671–8675.
- Kalinec, F., R. A. Urrutia, R. G. Jaeger, D. J. Lim, and B. Kachar. Membrane channel proteins and the force generator mechanism in the lateral wall of

- cochlear outer hair cells. Midwinter meeting of the Association for Research in Otolaryngology, St. Petersburg, FL, February, 1993.
- Kros, C. J., A. Rusch, and G. P. Richardson. 1992. Mechano-electrical transducer currents in hair cells of the cultured neonatal mouse cochlea. *Proc. R. Soc. Lond. Ser. B Biol. Sci.* 249:185–193.
- Nakagawa, T., S. Kakehata, N. Akaïke, S. Komune, T. Takasaka, and T. Uemura. 1991. Calcium channel in isolated outer hair cells of guinea pig cochlea. *Neurosci. Lett.* 125:81–84.
- Patuzzi, R. B., G. K. Yates, and B. M. Johnstone. 1989. Outer hair cell receptor current and sensorineural hearing loss. *Hear. Res.* 42:47–72.
- Ruggero, M. A. 1992. Responses to sound of the basilar membrane of the mammalian cochlea. *Curr. Opin. Neurobiol.* 2:449–456.
- Russell, I. J., A. R. Cody, and G. P. Richardson. 1986. The responses of inner and outer hair cells in the basal turn of the guinea-pig cochlea and in the mouse cochlea grown in vitro. *Hear. Res.* 22:199–216
- Saito, K. 1983. Fine structure of the sensory epithelium of guinea pig organ of Corti: subsurface cisternae and lamellar bodies in the outer hair cells. *Cell Tissue Res.* 229:467–481.
- Santos-Sacchi, J., and J. P. Dilger. 1988. Whole cell currents and mechanical responses of isolated outer hair cells. *Hear. Res.* 35:143–150.
- Santos-Sacchi, J. 1989. Asymmetry in voltage dependent movements of isolated outer hair cells from the organ of Corti. *J. Neurosci.* 9:2954–2962.
- Santos-Sacchi, J. 1990. Fast outer hair cell motility: how fast is fast? *In The Mechanics and Biophysics of Hearing.* P. Dallos, C. D. Geisler, J. W. Matthews, M. A. Ruggero, and C. R. Steele, editors. Springer-Verlag, Berlin. 69–75.
- Santos-Sacchi, J. 1991. Reversible inhibition of voltage-dependent outer hair cell motility and capacitance. *J. Neurosci.* 11:3096–3110.
- Santos-Sacchi, J. 1992. On the frequency limit and phase of outer hair cell motility: effects of the membrane filter. *J. Neurosci.* 12:1906–1916.

Voltage-dependent Ionic Conductances of Type I Spiral Ganglion Cells from the Guinea Pig Inner Ear

J. Santos-Sacchi

Sections of Otolaryngology and Neurobiology, Yale University School of Medicine, New Haven, Connecticut 06510

Type I spiral ganglion cells provide the afferent innervation to the inner hair cells of the mammalian organ of Corti and project centrally to the cochlear nucleus. While single-unit studies conducted over the past several decades have provided a wealth of information concerning the response characteristics of these neurons and, to some extent, their receptor targets, little is known about the neuron's intrinsic electrical properties. These properties undeniably will contribute to the firing patterns induced by acoustic stimuli. Type I spiral ganglion cell somata from the guinea pig inner ear were acutely isolated and the voltage-dependent conductances were analyzed with the whole-cell voltage clamp. Under conditions that mimic the normal intra- and extracellular ionic environments, type I spiral ganglion cells demonstrate fast inward TTX-sensitive Na currents (whose current density varied markedly among cells) and somewhat more slowly developing outward K currents. Resting potentials averaged -67.3 mV. Under current clamp, no spontaneous spike activity was noted, but short current injections produced graded action potentials with after hyperpolarizations lasting several milliseconds. The nondecaying outward K current activated at potentials near rest and was characterized by a pronounced rectification. The kinetics of the Na and K currents were rapid. Maximum peak inward Na currents occurred within 400 μ sec, between a voltage range of -10 and 0 mV, and inactivated within 4 msec. Recovery from inactivation was also rapid. At a holding potential of -80 mV, the time constant for recovery from an inactivating voltage step to -10 mV was 2.16 msec. Above -50 mV outward K currents reach half-maximal amplitude within 1.5 msec. In addition to these currents, a slow noninactivating TTX-sensitive inward current was observed that was blockable with Cd^{2+} or Gd^{3+} . Problems encountered with blocking the tremendous outward K current hampered the characterization of this inward current. Similarities between the kinetics of ganglion cell currents and some of the rapid temporal characteristics of eighth nerve single-unit activity confirm the notion that intrinsic membrane properties help shape auditory neuron responses to sound.

[Key words: spiral ganglion cell, inner ear, voltage clamp, organ of Corti, eighth nerve, ionic currents]

Received Nov. 12, 1992; revised Jan. 25, 1993; accepted Mar. 2, 1993.

This work was supported by an NIDCD Research Career Development Award and NIH Grant DC00273. I thank Drs. G. Huang, L. Kaczmarek, and H. Sontheimer for comments on the manuscript, and M. Scott Herness for sharing unpublished data.

Correspondence should be addressed to Joseph Santos-Sacchi, Ph.D., Department of Surgery, Section of Otolaryngology, Yale School of Medicine, BML 244, 333 Cedar Street, New Haven, CT 06510.

Copyright © 1993 Society for Neuroscience 0270-6474/93/133599-13\$05.00/0

A tremendous amount of information has been gathered on eighth nerve single-fiber activity (for reviews, see Javel, 1986; Ruggero, 1992), and this information has aided in understanding much of what is known about mammalian inner ear function. The afferent innervation pattern of the organ of Corti provides an anatomical clue to the receptor dichotomy present in this sensory organ (see Dallos, 1988). Nearly all afferent fibers (up to 95%) innervate the inner hair cells; these fibers arise from type I spiral ganglion cells (Spoendlin, 1988). The remaining type II fibers contact outer hair cells. Because of the small number and diameter of type II eighth nerve fibers, the preponderance, if not all, of eighth nerve single-unit studies have necessarily focused upon type I cells. Consequently, early studies on type I units were often used to provide insights into the physiology of the inner hair cell. Subsequent, direct intracellular recordings from inner hair cells have corroborated some single-unit findings; for example, inner hair cells are as finely tuned as eighth nerve fibers (Russell and Sellick, 1978; Dallos et al., 1982). Unfortunately, the interpretation of some single-unit data is difficult because synaptic and neuronal influences are uncharacterized. Few recordings from inner hair cell afferent synapses have been made (Palmer and Russell, 1986; Siegel and Dallos, 1986; Siegel, 1992), and only preliminary information concerning mammalian type I spiral ganglion cell voltage-dependent ionic conductances is available (Santos-Sacchi, 1989a, 1990). I report here on some of the voltage-dependent ionic conductances of type I spiral ganglion cells that may underlie the generation of single-fiber activity.

Materials and Methods

General. Guinea pigs were anesthetized with halothane and killed by cervical dislocation. The temporal bones were removed, and spiral ganglion cells were obtained nonenzymatically by crushing the cochlear modiolus and bony spiral lamina, followed by trituration in nominally calcium-free medium. The supernatant was transferred to a 700 μ l perfusion chamber, and the cells allowed to settle onto a glass coverslip bottom. A modified Leibovitz medium (NaCl, 142.2 mM; KCl, 5.37 mM; $CaCl_2$, 1.25 mM; $MgCl_2$, 1.48 mM; HEPES, 5.0 mM; dextrose, 5.0 mM; pH 7.2) was used as the normal perfusate. Modifications to the extracellular medium are noted in figure captions, with NaCl adjusted to maintain osmolarity (300 mOsm). Extracellular solutions were changed via two methods. A chamber perfusion system was used to exchange fresh medium constantly (0.1 – 1 ml/min). A more rapid and direct pipette perfusion system was used to perfuse selectively single cells under voltage clamp during continuous exchange of bulk medium via chamber perfusion (Santos-Sacchi, 1991a). All experiments were performed at room temperature ($\sim 23^\circ C$). Cell diameter was determined for each cell by averaging three measures at different axes. A Nikon Diaphot inverted microscope with Hoffmann optics was used to observe the cells during electrical recording, and all experiments were taped with a Panasonic AG6300 video recorder.

Electrical recording. Type I spiral ganglion cell somata were whole-cell voltage clamped with a Dagan patch-clamp amplifier typically at holding potentials between -70 and -80 mV, unless otherwise noted.

Pipette solutions were composed of 140 mM KCl or CsCl, 5 or 10 mM EGTA or BAPTA, 2 mM MgCl₂, and 5 mM HEPES buffered to pH 7.2. Cell somata are normally myelinated, but over the course of the *in vitro* incubation the myelin is shed. The type I spiral ganglion cell outnumbered the type II cell by about 20:1, and type I spiral ganglion cells are about 20 μm in diameter while type II cells are about 15 μm. The average cell size in this study was about 19 μm (see Results). Given these facts and the fact that most recorded cells had residual myelin figures associated with the cell somata (only type I are myelinated), it is concluded that most, if not all, of the cells studied were type I.

Gigohm seals were made on the neuronal plasmalemma and electrode capacitance was compensated prior to whole-cell recording. Voltage-step studies were performed with an Axolab 1100 A/D and D/A board (Axon Instruments, Foster City, CA) with associated software (pCLAMP). The software was modified to provide a continuous display of clamp time constant (τ), cell capacitance (C_m), and resistance (R_m), and series resistance (R_s) between data collections. Leakage subtraction was performed with the P/−4 technique at holding potentials noted in figure captions. Currents were filtered with an 8-pole Bessel filter at 7 kHz.

Series resistance and cell capacitance were determined from capacitive transients induced by small voltage steps. The membrane resistance (200–800 MΩ) of spiral ganglion cells is not great enough to permit the use of a simple method (Marty and Neher, 1983) of determining series resistance and membrane capacitance under whole-cell voltage clamp. This problem of estimating series resistance was encountered by Yamaguchi and Ohmori (1990) while studying chick cochlear ganglion cells. The method employed here for these determinations is robust despite filter settings, and accurately takes into account the effects of series resistance on capacitance measures. It is based on the simple circuit model of the voltage-clamped cell, that is, an access resistance (R_s) in series with a parallel combination of a membrane capacitance (C_m) and resistance (R_m).

For the model, the steady state (I_∞) and instantaneous (I₀) current responses to a voltage step are defined as

$$I_{\infty} = \frac{V_c}{R_s + R_m}, \quad (1)$$

$$I_0 = \frac{V_c}{R_s}, \quad (2)$$

with the exponentially decaying capacitive current given as

$$I_{C_m} = (I_0 - I_{\infty})e^{-t/\tau}, \quad (3)$$

where

$$\tau = R_{\parallel} C_m, \quad (4)$$

$$R_{\parallel} = R_m R_s / R_{in}, \quad (5)$$

and

$$R_{in} = R_m + R_s, \quad (6)$$

the input resistance readily obtained at steady state.

The charge moved is then obtained by integration

$$\int_0^{\infty} I_{C_m} dt = Q = \frac{C_m R_m^2 V_c}{R_{in}^2}. \quad (7)$$

Solving for C_m,

$$C_m = \frac{R_{in}^2 Q}{R_m^2 V_c}, \quad (8)$$

and utilizing Equations 4 and 8, we obtain

$$R_s = \frac{R_{in} \tau V_c}{Q R_{in} + \tau V_c}. \quad (9)$$

The time constant (τ) of the exponentially decaying current, and the charge moved (Q) are little affected by filter settings as low as 2 kHz (8-pole Bessel). Equation 8 had been identified and used by Mathias et al. (1981) to evaluate alternative explanations of nonlinear gating charge movement, and it is, in fact, the proper evaluation of cell capacitance for the cell model when the ratio of R_s and R_m does not approach zero. In this article, series resistance was compensated electronically, and voltages were corrected for residual series resistance effects.

Steady state inactivation of Na currents was fit with a Boltzmann

function,

$$I_{\text{relative}} = \left[\frac{I_{\text{max}} - I_{\text{min}}}{1 + \exp[-ze(V - V_h)/kT]} \right] + I_{\text{min}}, \quad (10)$$

where V is the potential of an inactivating prepulse, V_h is voltage at half-maximal inactivation, e is electron charge, k is Boltzmann's constant, T is absolute temperature, z is the valence, I_{max} is maximum Na current induced by a fixed depolarization step, and I_{min} is minimum current.

Results

Type I spiral ganglion cells, including cell somata, are normally enveloped by a myelin sheath. Immediately after isolation by trituration, cell somata remain myelinated; however, over the course of tens of minutes many cells shed this coating (Fig. 1), making the neuronal plasmalemma accessible to patch pipettes. After whole-cell configuration is attained, and following a few minutes to allow equilibration of the normal KCl-containing pipette solution into the cells, resting potentials averaged −67.3 ± 5.7 mV (mean ± SD; n = 11). The capacitance of the cells averaged 10.14 ± 1.68 pF (n = 32) and agreed well with corresponding estimates (11.3 pF) based on surface area calculated from the average cell diameter of 19.01 ± 1.66 μm (n = 59).

Under conditions that mimic the normal intra- and extracellular environments, type I spiral ganglion cells demonstrate fast inward Na currents and more slowly developing outward K currents. Figure 2A illustrates the whole-cell currents under these conditions. Under current clamp, no spontaneous activity was noted, and brief current injections only produced graded spikes (Fig. 2B). Afterhyperpolarizations lasting several milliseconds followed the current induced depolarizations. Longer current injections did not produce repetitive spiking.

The magnitude of the fast inward Na currents varied greatly across cells, some cells demonstrating none. Figure 3 illustrates outward K currents in a cell in which no inward Na currents were evoked from the holding potential of −70 mV (a few cells were found that required holding potentials more negative than −80 mV to reveal Na currents). The outward K currents in spiral ganglion somata are blockable by extracellular tetraethylammonium (TEA), or Gd³⁺, or intracellular Cs (but see below) and display fairly rapid onset kinetics, with little or no inactivation. Raising extracellular K levels above 100 mM reverses the current polarity. Figure 4 illustrates responses from another KCl-loaded cell in which the fast inward Na currents were blocked with TTX. Outward rectification is pronounced and initiates near the resting potential. At −43 mV activation ensues within 360 μsec after step onset (Fig. 4D). The voltage dependence of current onset kinetics was estimated by measuring the time required to reach half-maximal current amplitude (Fig. 4C). Above −50 mV outward currents reach half-maximal amplitude within 1.5 msec.

Reduction of extracellular Ca had profound effects upon the neural membrane; an extreme example, where Ca-free extracellular medium containing 2 mM EGTA was perfused onto the cell, is illustrated in Figure 5A. Removal of Ca caused a reversible reduction of the K currents, a depolarizing shift in the zero current potential (opposite in sign to a potential charge screening effect), and an increase in the leakage conductance. [Armstrong and Miller (1990) showed that voltage-dependent K channels are adversely affected by removal of extracellular Ca, causing the cell to become leaky and the channels to become nonselective. However, they determined that in the presence of 1 mM extracellular K, this effect was absent. In the present

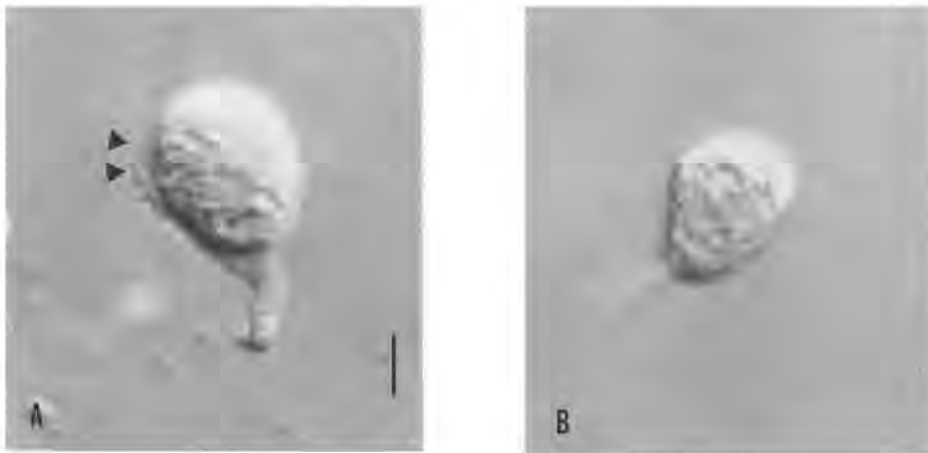


Figure 1. *A*, Spiral ganglion cell immediately after isolation. Myelin sheath can be observed enveloping the somata (arrowheads). *B*, Spiral ganglion cell that has lost its myelin sheath after incubation and whose neuronal plasmalemma is accessible to patch pipettes. Scale bar, 7 μm .

experiments, 5 mM K was present in the extracellular medium, and the type of effect noted by Armstrong and Miller probably does not occur. Indeed, outward rectification is still robust.] Gd^{3+} (50 μM) substantially blocked outward currents in ganglion cells (Fig. 5*B,C*).

Fast inward Na currents were readily isolated when outward currents were blocked, and the Na currents could be totally blocked with TTX (100–300 nM). Figure 6 illustrates the current–voltage relation for a spiral ganglion cell before and during

TTX perfusion. In addition, the fast inward current was abolished by replacement of extracellular Na by Tris or TEA. Maximum peak inward Na currents occurred within 400 μsec , between a voltage range of -10 and 0 mV, and inactivated within 4 msec. Single exponential fits to the decaying Na currents indicate a voltage-dependent inactivation (Fig. 7*A*). Averaged inactivation time constants for a group of spiral ganglion cells ranged from 0.8 msec at -23 mV to 0.3 msec at $+25$ mV. The time required for Na currents to reach half-peak levels was also

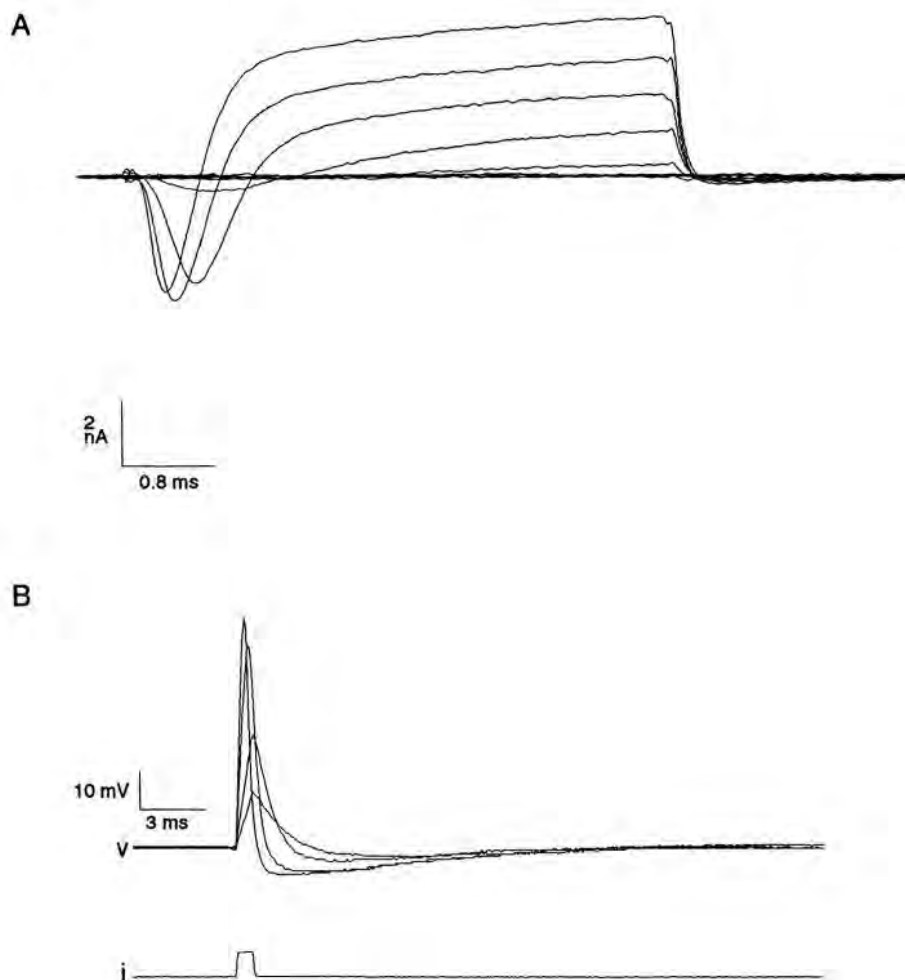


Figure 2. *A*, Isolated spiral ganglion cell under whole-cell voltage clamp. Pipette solution was normal KCl solution. Extracellular solution was modified Leibovitz. Cell was held at -80 mV and nominally stepped in 10 mV increments from -100 mV to -10 mV. Note fast inward Na currents followed by outward K^+ currents. Leakage subtracted. Clamp τ , 69 μsec ; series resistance, 6.1 $\text{M}\Omega$; holding current, -62 pA. *B*, Same cell under current clamp. Current pulse injection (*i*; 0.8 msec at 0.5, 1, 2.5, and 4 nA) initiated a depolarization (*v*) from the resting potential that was graded with step size. Respective times to peak depolarization were 0.72, 0.72, 0.56, and 0.40 msec. Note the increasingly rapid repolarization and afterhyperpolarization as a function of spike amplitude due to the inactivation of Na conductance and activation of K conductance. Membrane potential returned to baseline within about 18 msec. Voltage drop across electrode, based on the instantaneous step in voltage, was subtracted during pulse width. Resting potential was -64.4 mV.

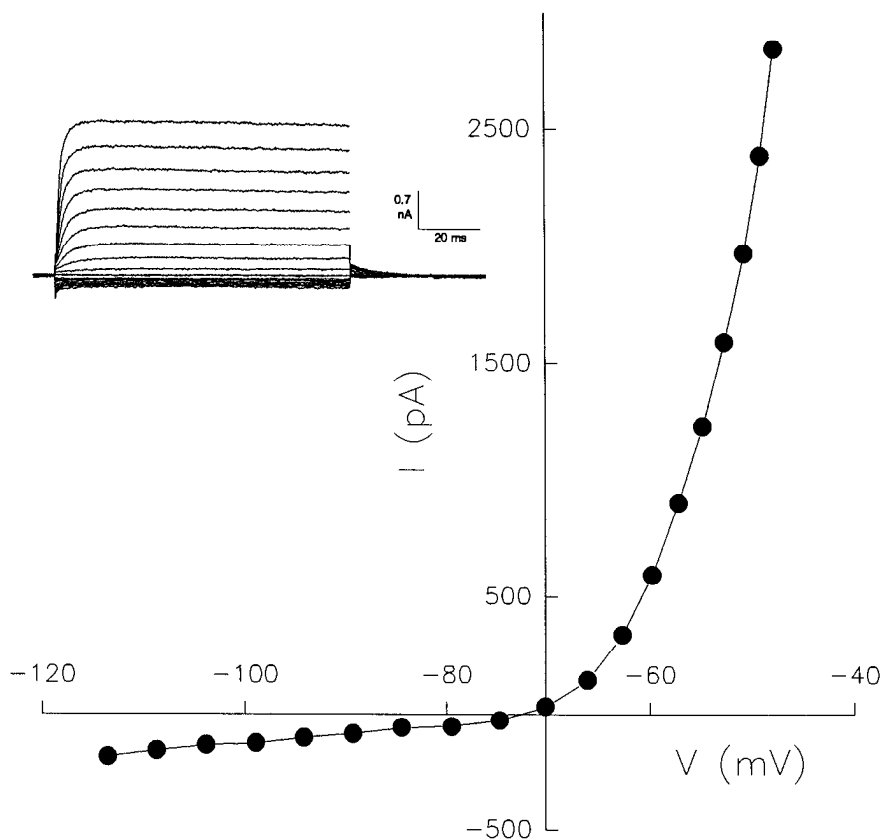


Figure 3. Isolated spiral ganglion cell under whole-cell voltage clamp. Cell was held at -70 mV and nominally stepped in 5 mV increments through the voltage range of -115 to -25 mV. Plotted outward K^+ currents were determined from the final 10 msec average of each trace (inset, upper left). KCl pipette, Leibovitz medium. Na currents were absent in this cell and may have been due partly to steady state inactivation at this holding potential (see Results). No leakage subtraction. Corrected for an uncompensated series resistance of 8 M Ω . Holding current, 37 pA.

voltage dependent (Fig. 7A), decreasing from 0.43 msec at -23 mV to 0.26 msec at $+25$ mV. The recovery of Na channels from inactivation due to a fixed depolarization was evaluated with the two-step protocol (Fig. 7B). At a holding potential of -80 mV, the time constant for recovery from an inactivating voltage step to -10 mV was 2.16 msec.

Figure 8 exemplifies the effects of holding potential on the Na current-voltage relation. Changing the holding potential from -80 to -60 mV inactivates nearly all Na channels. As mentioned, the maximum peak Na currents varied markedly among cells, and this variation conceivably may be related to differing degrees of steady state inactivation at the holding potential of the cells. For example, actual holding potentials may vary from the imposed voltage, depending upon series resistance values. This possibility was examined in cells that were particularly well voltage clamped (Fig. 9A). Despite fine voltage control, Na current densities show great variability. In addition, Figure 9B illustrates that voltage-dependent inactivation curves (h_{inf}) are similar for cells possessing large and small Na current densities. It is likely that current density differences arise from differing Na channel densities.

Another voltage-dependent inward current with slower onset kinetics was observed in CsCl-loaded spiral ganglion cells perfused with Leibovitz solutions, either with or without 10 mM TEA. The current had an activation time constant of several milliseconds, activated at potentials near -70 mV, did not inactivate during sustained depolarizations, and, surprisingly, reversed near -20 mV (Fig. 10). The reversal potential indicates that it is carried by multiple ionic species. Nearly identical $I-V$ curves were obtained with cells perfused with Na-free Tris/ 10 mM TEA solutions or in CsF-loaded cells. It seems likely that the tremendous outward K current was not completely blocked

under these conditions (see Discussion). This sustained inward current and associated tail current are shown in Figure 11 to be somewhat reduced in magnitude by 50 μ M Cd^{2+} and totally blocked by 50 μ M Gd^{3+} . Cobalt (2 mM) in the absence of extracellular Ca^{2+} also abolishes this current. These data provide evidence for a component calcium conductance that is activated near the resting potential. Interestingly, an increased intracellular Ca concentration prolongs the decay of the associated tail currents (which are TEA blockable) and reduced extracellular Ca speeds the decay, possibly indicating that K(Ca) channels may be involved in generating the tail currents.

It was observed that not only did TTX block fast inward Na currents but it reduced the magnitude of the slow inward currents in a reversible manner as well (Fig. 12a,b). The reduction was not due to a decrease in a noninactivating Na current, since replacement of extracellular Na by Tris abolished the fast inward Na current, but did not affect the sustained inward currents (Fig. 12c).

Discussion

Firing patterns and firing rates are considered important aspects of auditory frequency and intensity coding (Ruggero, 1992). The mammalian auditory nerve encodes very high-frequency information. Auditory sensitivity of the guinea pig extends above 40 kHz, and that of the bat above 100 kHz. Indeed, Javel (1986) has commented that within a few milliseconds after the initiation of an acoustic stimulus firing rates can approach 2000 spikes/sec in the cat. Average steady rates have been measured up to about 400 spikes/sec. Necessarily, eighth-nerve fibers must detect and process inner hair cell activity at a tremendous pace to faithfully transmit receptor potential information centrally. In this study, it is demonstrated that type I spiral ganglion cells

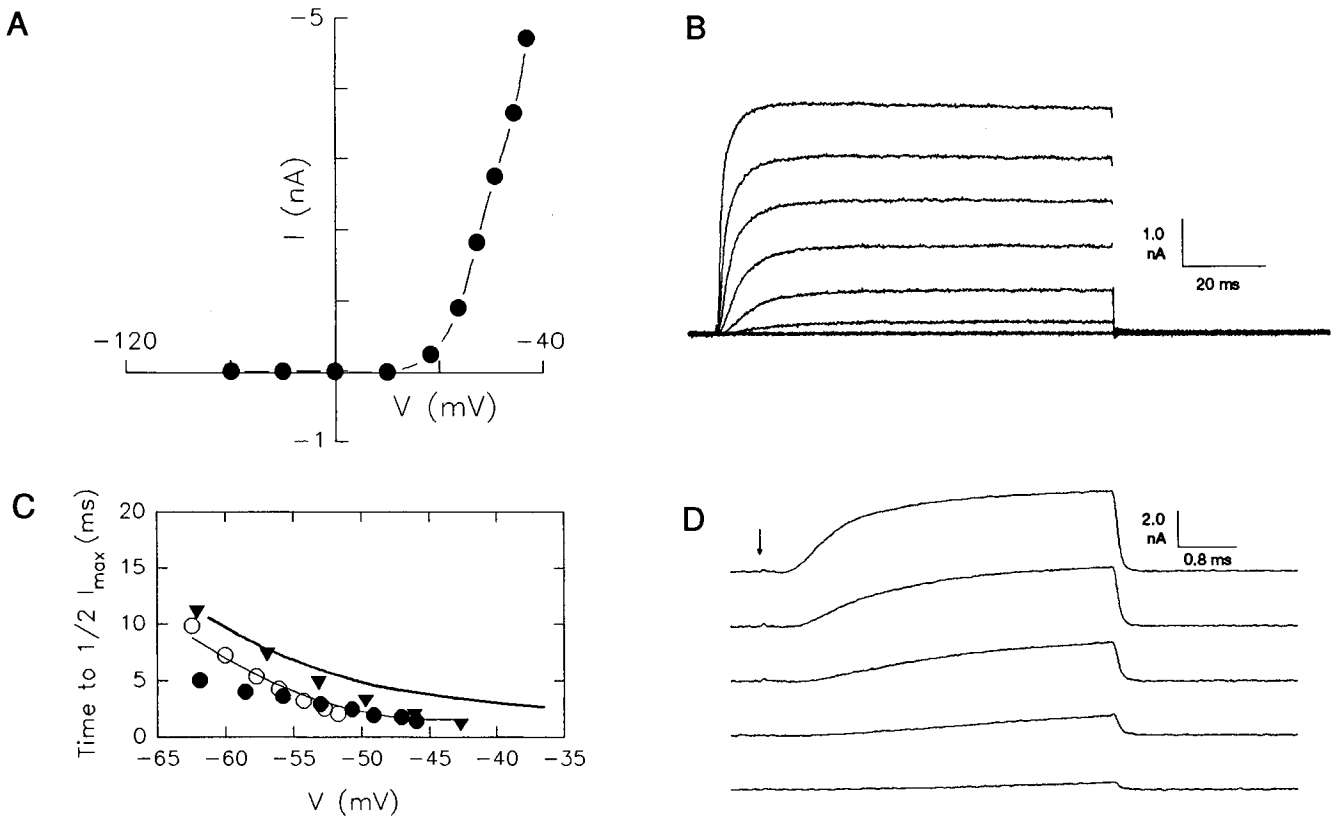


Figure 4. Isolated spiral ganglion cell under whole-cell voltage clamp. Cell was held at -80 mV and nominally stepped in 10 mV increments through the voltage range of -110 to -10 mV. I - V curve (*A*) is corrected for series resistance effects, and plotted outward K^+ currents were determined from the final 10 msec average of each trace (*B*). The times to reach half-maximal K current levels (*C*, plotted against corrected steady state voltage) were obtained from the traces in Figures 3-5 (symbols with thin fitted line). Marked voltage dependence is evident. The thick line represents data obtained from Yamaguchi and Ohmori (1990, their Fig. 3). Data collection at a higher sampling rate (*D*) illustrates delay in onset of outward currents. KCl pipette, Leibovitz medium with 100 nM TTX. Leakage subtraction. Corrected for an uncompensated series resistance of 7 M Ω . Clamp τ , 62 μ sec; holding current, 40 pA.

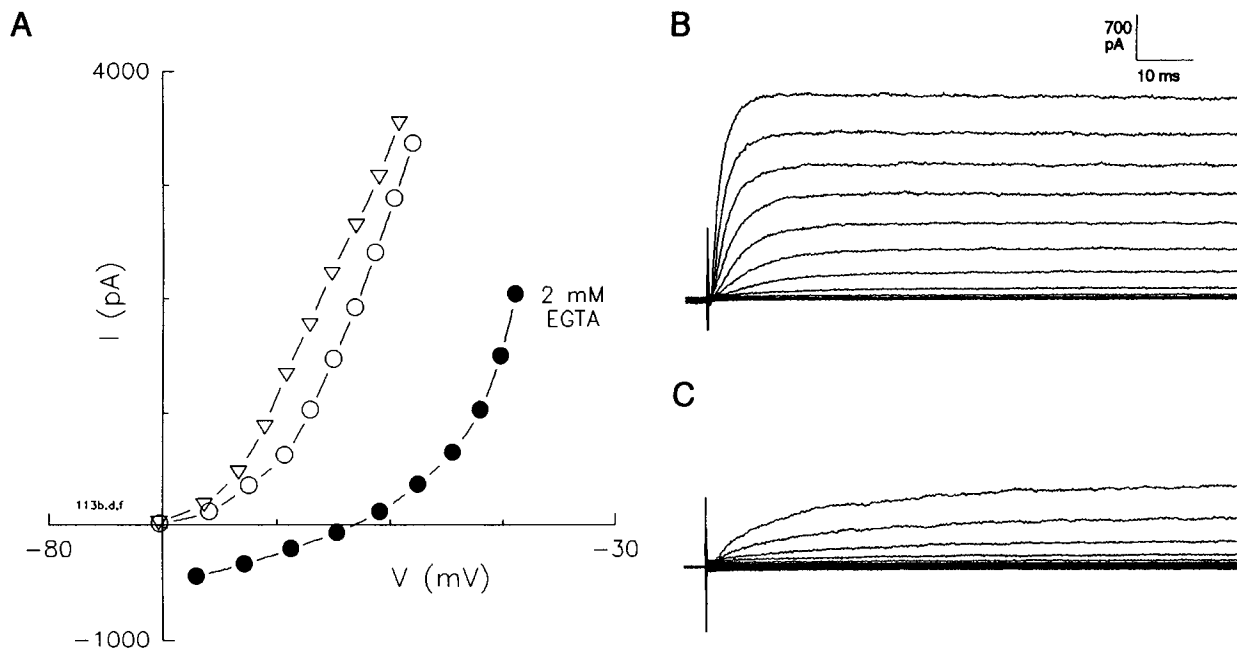


Figure 5. *A*, Isolated spiral ganglion cell under whole-cell voltage clamp. I - V plots of outward K^+ currents were determined before (open circles) and after (triangles) removal of extracellular Ca (solid circles; no added Ca and 2 mM EGTA), at a holding potential of -70 mV. Plotted outward K currents were determined from the final 10 msec average of each 100 msec trace. Note reversible drop in zero current potential and input resistance. No leakage subtraction. Corrected for an uncompensated series resistance of 6.8 M Ω . *B* and *C*, Traces depicting outward K currents in another ganglion cell after recovery from (*B*) and during (*C*) perfusion of normal extracellular medium supplemented with 50 μ M Gd^{3+} . Holding potential was -70 mV, and steps were from -100 to -30 mV (nominal). Holding current: *B*, -81.7 pA; *C*, -66.4 pA.

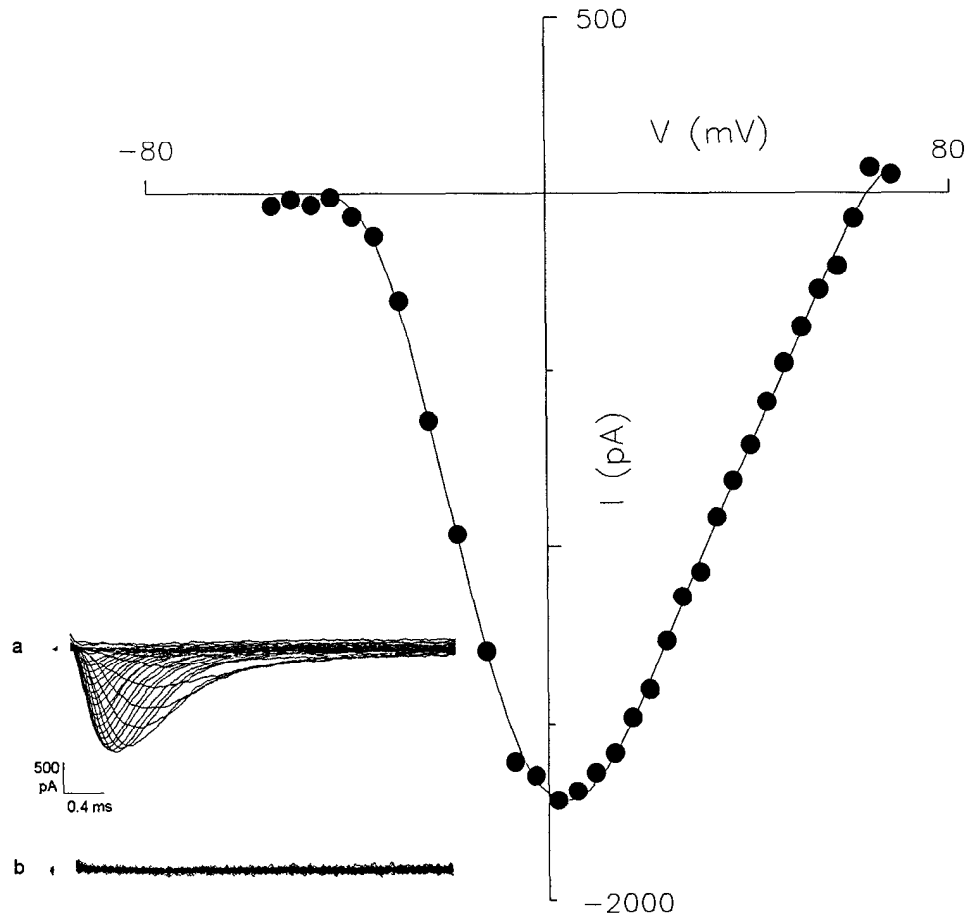


Figure 6. Fast Na currents from a spiral ganglion cell whose outward currents had been blocked. Intracellular solution contained 140 mM CsCl, supplemented with 5 mM NaCl. Extracellular solution contained 20 mM TEA, 20 mM CsCl, 2 CoCl₂, with no added Ca and NaCl appropriately adjusted. Peak inward currents occurred near 0 mV. Leakage subtracted. Corrected for an uncompensated series resistance of 4.98 M Ω ; voltage corrections were made based on nonleakage subtracted peak current magnitudes. Holding current was -43 pA; clamp τ was 29 μ sec. *Insets:* *a*, Na currents prior to block; *b*, block of Na currents by 300 nM TTX. Traces were digitally filtered for presentation at 3.2 kHz.

possess the required conductances and kinetics to account for such high-frequency phenomena.

Resting potential of spiral ganglion cells

Type I spiral ganglion cell somata have resting potentials near -70 mV when loaded with 140 mM KCl. Palmer and Russell (1986) measured membrane potentials in type I afferent terminals in the guinea pig, which ranged from -40 to -60 mV. The activation of K currents near these potentials and the observation that removal of extracellular Ca shifts zero current levels suggest that the resting potential may be maintained partly by a Ca-activated K conductance. The likelihood of the existence of a Ca-activated K conductance is strengthened by the observation of prolongation of TEA-blockable tail currents associated with increased levels of intracellular Ca. Single-channel Ca-activated K currents have been measured in cultured goldfish auditory ganglia (Davis et al., 1989). The effect of calcium removal on the ganglion cell is in marked contrast to the effects of extracellular calcium removal on outer hair cell outward K currents and zero current levels, where little or no effect is seen (Santos-Sacchi, 1989c). However, the block of ganglion cell outward K currents by Gd³⁺ is similar to the trivalent cation's effects on outer hair cells and Deiters cells from the organ of Corti (Santos-Sacchi, 1991a).

Na channels in spiral ganglion cell somata

The bipolar spiral ganglion somata have input resistances around 500 M Ω , and capacitances around 10 pF, giving a membrane

time constant of about 5 msec near -80 mV. This is similar to that observed in chick cochlear ganglion cells (Yamaguchi and Ohmori, 1990). This time constant is fairly slow, and might interfere with spike transmission through ganglion cell somata. Means must exist to permit the unobstructed transmission of spike activity containing timing information across the 20 μ m somata of the eighth-nerve fiber, as temporal coding is important for many aspects of auditory function, including sound localization. If resting potentials are more depolarized than -70 mV *in vivo* (see above), then the activation of the K conductance will dramatically reduce the membrane time constant and increase timing resolution. More notably, Na conductances are present in cell somata, indicating that the somata are excitable. Thus, while Na channels are usually restricted to neuronal nodal regions (Waxman and Ritchie, 1985; Black et al., 1990; Gilley et al., 1990), it is possible that Na channels are normally present in spiral ganglion cell somata and are required for fast throughput with little attenuation. Fast Na currents are also observed in chick cochlear ganglion cells (Yamaguchi and Ohmori, 1990) and acutely isolated cells of the cochlear nucleus (Manis and Marx, 1991).

It cannot be ruled out, however, that cell somata actually have few Na channels, and during isolation cellular processes are retracted into the somata with differing amounts of nodal membrane. The variability of Na channel density in cell somata is great, and differing degrees of nodal resorption may account for it. Another possibility is that Na channels destined for remote sites are incorporated into somata plasmalemma during isola-

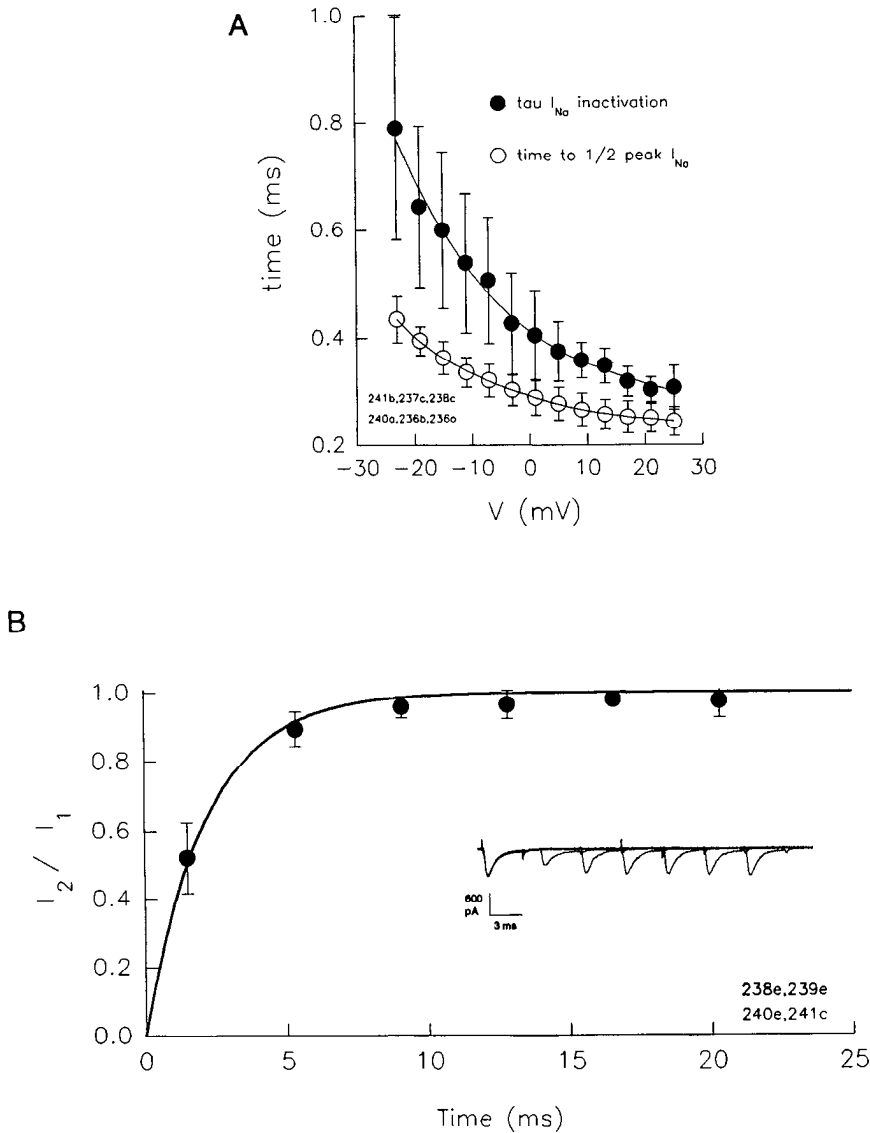


Figure 7. *A*, Averages and standard deviations ($n = 6$) of Na current inactivation (single exponential fit to decaying phase; *filled circles*) and time to half-peak inward Na current (*circles*) versus nominal step voltage. Intracellular solution contained 140 mM CsCl. Extracellular solution contained 20 mM TEA, 20 mM CsCl, 2 CoCl₂, with no added Ca and NaCl appropriately adjusted. Clamp τ was 0.033 ± 0.006 msec. Holding potential was -80 mV. *B*, Recovery of Na currents from inactivation. An initial 3.5 msec voltage step to -10 mV was followed at increasing time intervals by the same stimulus. Peak inward current magnitude evoked by the second pulse is plotted relative to the first response. Rest periods of 4 sec were given between each trial. Average and standard deviations are plotted ($n = 4$). Time constant of recovery was 2.16 msec. Holding potential was -80 mV. Solutions were as in Figure 7*A*. *Inset*, Example of current traces; six trials are superimposed.

tion. Variation in Na channel density may reflect differing degrees of Na channel production in the course of normal turnover, since spiral ganglion cells vary markedly in length.

Is the spiral ganglion cell soma simply another internode?

Because the type I cell soma of the guinea pig spiral ganglion is enveloped by a myelin sheath, one may conceive of it as an internode inserted along the course of the myelinated eighth-nerve fiber. The myelin sheath of the spiral ganglion cell is not characteristic of all mammalian species. For example, in the human there is typically no sheath (Ota and Kimura, 1980) and in the monkey it is very poorly developed (Kimura et al., 1987). In fact, the number of lamellae in those species having sheaths is considerably lower than that surrounding adjacent internodes (Kellerhals et al., 1967; Spöndlin, 1971; Robertson, 1976). These are not trivial observations. That is, since the number of lamellae is inversely proportional to internode capacity and directly proportional to internode resistance, it is not known how a partially myelinated soma (~ 20 μ m in diameter) affects conduction in auditory nerve fibers. Nevertheless, the concept that type I somata function as internodes should be considered

in understanding the ability of the fiber to transmit impulse trains across a potential somal filter. The distribution of ionic channels within mammalian myelinated fibers is not random—specific ionic conductances are restricted to distinct neurolemmal domains (Waxman and Ritchie, 1985). Whereas in mammals nodal regions possess only Na channels, myelinated internodal regions possess voltage-dependent K and possibly Na channels (Chiu and Schwartz, 1987). What effects might the voltage and kinetic characteristics of the spiral ganglion soma conductances have on somal impulse throughput? Indeed, if the conductances are representative of other internodal regions along the eighth-nerve fiber, what general consequences might their characteristics have for auditory neural transmission?

It has been speculated that the K conductance in the internodal region of the mammalian nerve fiber maintains the internodal and nodal resting membrane potential, especially if the conductance is active near rest (Chiu and Ritchie, 1984). The activation potential (near -70 mV) of the spiral ganglion cell K conductance is consistent with this scheme. A consequence of K channel activation near rest is a reduced membrane time constant, that is, a reduction of the filtering capacity of the

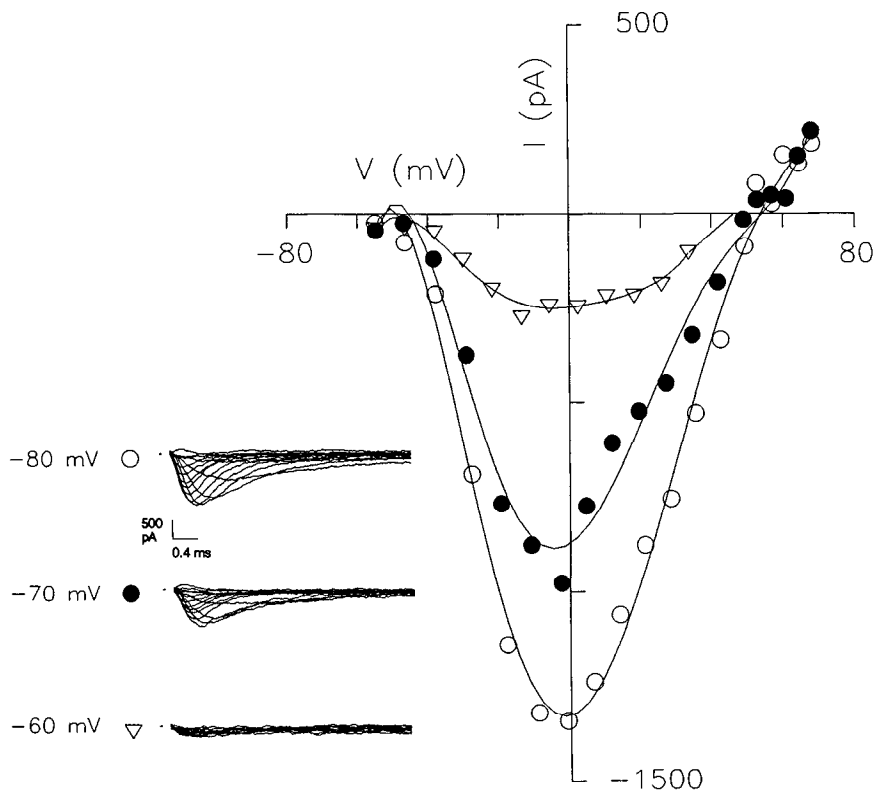


Figure 8. The effect of holding potential on Na current magnitude. Reducing holding potential from -80 mV to -60 mV inactivates nearly all Na channels in spiral ganglion cells. Voltage dependence remains constant. Holding current at -80 mV was -124.5 pA. Corrected for an uncompensated series resistance of 4.79 M Ω . Clamp τ was 0.031 msec. *Inset*, Current traces digitally filtered at 3.2 kHz for presentation.

internode. However, this resting conductance will also limit electrotonic spread between nodes, which is requisite for saltatory conduction.

A more important issue raised by Chiu and Ritchie (1984) is the contribution of internodal K conductances to the repolarization of nodal membrane. Following an action potential, the nodal membrane must repolarize to permit recovery from Na channel inactivation and restoration of excitability. These authors convincingly argue that electrotonic spread of depolarization from nodal to internodal membrane can activate voltage-dependent internodal K conductances that effectively repolarize nodal membrane. The characteristics of this conductance may help limit the duration of action potentials and reduce the possibility of repetitive afterspiking (Baker et al., 1987; Black et al., 1990). Currently, it is thought that discharge of capacitive current through leakage pathways between the myelin sheath and axonal membrane promotes an afterdepolarization following the action potential (Barrett and Barrett, 1982; Baker et al., 1987). This afterdepolarization is believed to promote repetitive spiking, as it will lower spike threshold. In fact, Black et al. (1990) have demonstrated that blockade of internodal K conductances elicits repetitive afterspiking, and David et al. (1992) have shown that action potentials can activate internodal K conductances. By evaluating the myelinated axon model of Barrett and Barrett (1982) it is clear that an increased conductance of internodal axonal membrane will limit the duration of this afterdepolarization. In fact, the more rapidly the conductances are activated, the more quickly the afterdepolarization is dissipated. For fibers that conduct information in the precise timing of action potentials, it is reasonable that K conductances should possess rapid activation kinetics, or else slow repolarization will distort the timing of later signals. In the eighth nerve, fibers are known to phase lock to acoustic frequencies as high as 4 kHz,

indicating that the temporal resolution must be great. Phase locking is known to be important for one mechanism of frequency discrimination (see Javel, 1986). The kinetics of spiral ganglion cell K conductances are faster than those of internodal membrane of rabbit myelinated sciatic nerve fibers, whose firing rates do not approach that of eighth-nerve fibers [e.g., at -25 mV, time to half-peak K current is about 5 msec in the sciatic nerve (Chiu and Ritchie, 1984), whereas at -43 mV the value is 1 msec for the spiral ganglion cell; temperatures are comparable]. The fast recovery of Na channel inactivation in the spiral ganglion cell also indicates that the effects of rapid K channel activation will be registered quickly. It appears, then, that even with the spiral ganglion cell soma viewed as an internode among other internodes, the voltage dependence and kinetics of the intrinsic membrane conductances contribute to the temporal characteristics of auditory nerve performance.

Comparison of spiral ganglion cell kinetics with those of other primary sensory neurons

The kinetics of ionic channels are temperature dependent (Hodgkin and Huxley, 1952; Frankenhaeuser and Moore, 1963). Thus, the results presented in the present report at room temperature ($\sim 23^\circ\text{C}$) should be interpreted accordingly. The temperature dependence of channel kinetics typically has a temperature coefficient (Q_{10}) of about 3 (Frankenhaeuser and Moore, 1963; Huguenard et al., 1991). Measures at higher, *in vivo*, temperatures will be faster by a factor of 3 for each 10°C increase. Keeping temperature effects in mind, it is illuminating to compare the kinetics of Na and K conductances of the guinea pig spiral ganglion cell to comparable results obtained from other mammalian primary sensory systems. In addition, a comparison is made to data obtained from a nonmammalian cochlear ganglion cell, that of the chick (Yamaguchi and Ohmori, 1990).

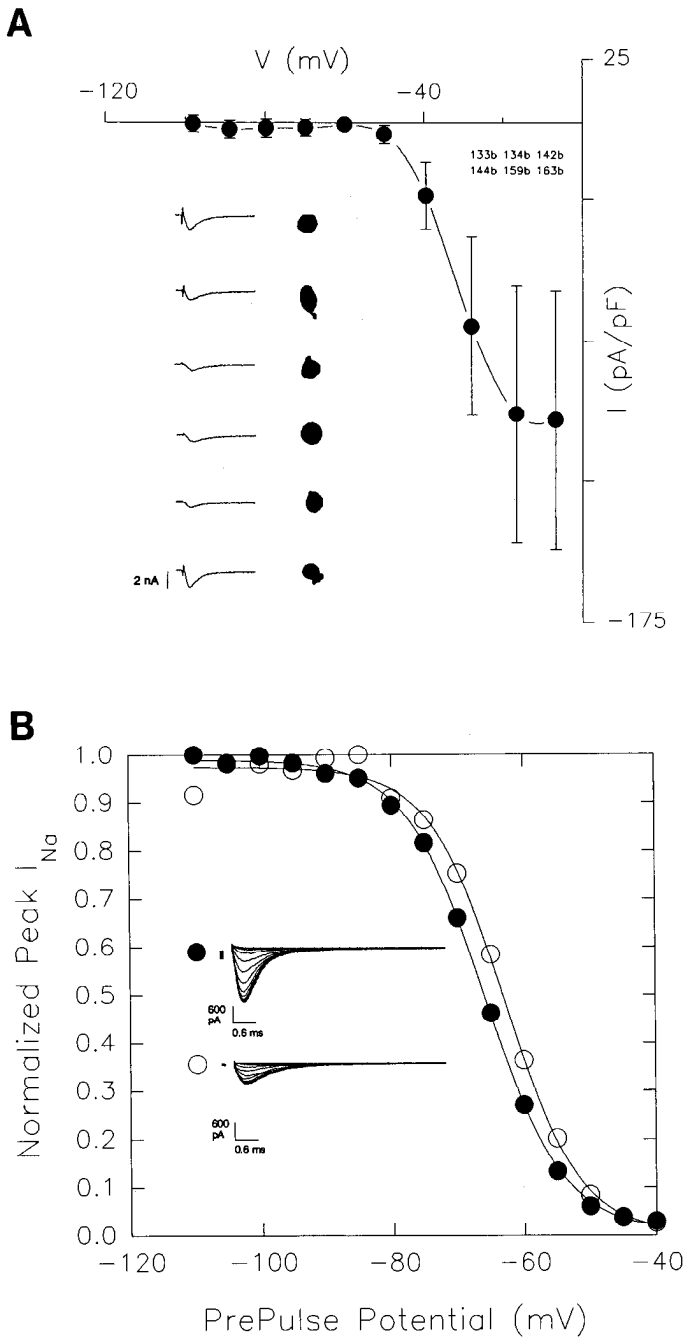


Figure 9. *A*, Variability of Na current magnitudes: averages and standard deviations of Na current densities versus voltage, for a group of cells ($n = 6$) that were particularly well voltage clamped. Intracellular solution contained 140 mM CsCl. Extracellular solution was modified Leibovitz with 10 mM TEA. Corrected for an uncompensated series resistance of $3.69 \pm 1.75 \text{ M}\Omega$; clamp τ , $38.73 \pm 25 \text{ }\mu\text{sec}$; C_m , $11.8 \pm 1.6 \text{ pF}$; R_{in} , $480 \pm 100 \text{ M}\Omega$. Voltage variations are within the symbol widths. Holding potential was -80 mV ; holding current was $-38 \pm 31 \text{ pA}$. *Inset*, Current traces in response to -10 mV steps, and outlines of associated cell somata. Scale is 2 nA or $15 \text{ }\mu\text{m}$. *B*, Steady state inactivation of Na currents. Two cells of high and low current densities are compared. Cells were held at -100 mV and prepulsed to various potentials (nominal) for 200 msec prior to step to -10 mV . Fits were made to a Boltzmann function. Inactivation characteristics are similar for both cells. *Open circles*: z , -4.55 ; V_h , -62.9 mV ; clamp τ , $24 \text{ }\mu\text{sec}$; R_s , $6.76 \text{ M}\Omega$. *Solid circles*: z , -4.34 ; V_h , -66 mV ; clamp τ , $24 \text{ }\mu\text{sec}$; R_s , $3.26 \text{ M}\Omega$. Intracellular solution contained 140 CsCl. Extracellular was modified Leibovitz with 10 mM TEA and 0.1 mM CdCl. *Inset*, Current traces for each cell.

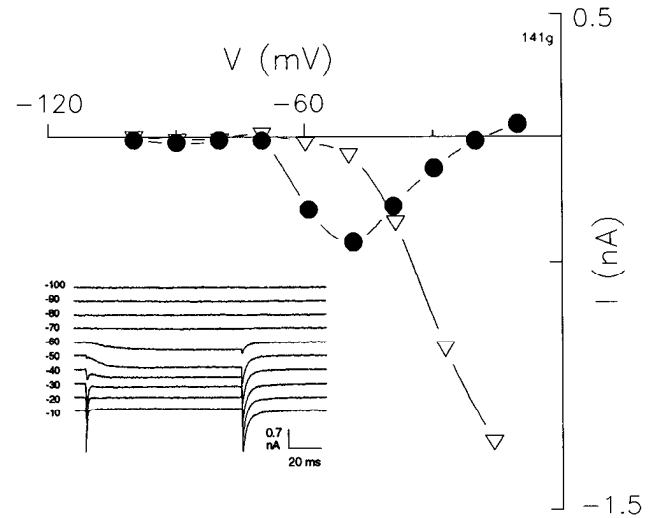


Figure 10. Simultaneous measurement of slow inward current (circles) and fast inward Na current (triangles) of spiral ganglion cell loaded with 140 mM CsCl, and perfused with 10 mM TEA Leibovitz solution. The slow inward current activates at a potential more negative than the Na current. Note the unusual reversal potential of the slow current (-20 mV), indicative of charge being carried by multiple ionic species. Also note the tail currents activated during return to the holding potential. Holding potential was -80 mV for each trace, and the cell was stepped to the potential noted on the left of the traces. Corrected for an uncompensated series resistance of $3.3 \text{ M}\Omega$.

In rat retinal ganglion cells at $\sim 23^\circ\text{C}$, peak Na currents reach half-maximal magnitude in about $500 \text{ }\mu\text{sec}$, and the inactivation time constant at -20 mV , for example, is 1.3 msec (Barres et al., 1989). These values are somewhat slower than those of the spiral ganglion cell (see Fig. 7A). Interestingly, these authors found that the kinetics of glial cells were considerably slower than retinal ganglion cells. While the K currents of spiral ganglion cells reach half-peak amplitude in 1 msec at -43 mV at room temperature, the whole-cell K currents in cat retinal ganglion cells required about 1.5 msec to reach half-peak values at -20 mV at 33°C (Lipton and Tauck, 1987). The time constant of recovery of Na currents from voltage-induced inactivation differs depending upon specific type of rat retinal ganglion cell, being less than or equal to 1 sec for X-cells and greater than 1 sec for W-cells (Kaneda and Kaneko, 1990). The average time constant of recovery for spiral ganglion cells is 2.16 msec .

Lynch and Barry (1991a) found in rat olfactory neurons that the major outward K conductance is a transient type that reaches half-maximal peak values within about 4 msec at $+20 \text{ mV}$ ($\sim 21^\circ\text{C}$). These same authors also found a smaller, more slowly activating K current (Lynch and Barry, 1991b). In a study by Trombley and Westbrook (1991), however, only a noninactivating K current was found that reached half-peak amplitude at 3.75 msec at a step potential of $+40 \text{ mV}$ (room temperature). These same authors measured fast inward Na currents that reached half-maximal peak magnitude at about $160 \text{ }\mu\text{sec}$. This is extremely fast and may indicate that the scale in their figure was mislabeled. In fact, the value is between 400 and $500 \text{ }\mu\text{sec}$ (P. Trombley, personal communication).

To my knowledge, there are no published voltage-clamp data on the conductances of mammalian taste cell primary afferents. However, in rat taste cells, some of which possess fast Na currents, half-maximal peak Na current is reached in about $450 \text{ }\mu\text{sec}$ (room temperature; S. M. Herness, personal communica-

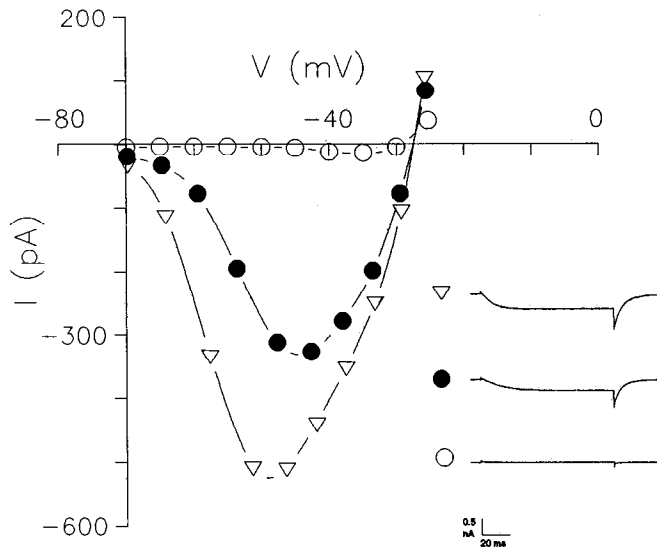


Figure 11. Reduction of slow inward currents by inorganic ions. Triangles and associated trace depict voltage dependence of sustained inward currents. Following perfusion with an additional $50 \mu\text{M Cd}^{2+}$ (solid circles) the current magnitudes were decreased and the peak current shifted in the depolarizing direction. Treatment with Gd^{3+} ($50 \mu\text{M}$; open circles) totally abolishes the inward currents. Cell was perfused with normal Leibovitz medium; note that reversal potential is near -30 mV , and does not change with Cd treatment. Inset. Traces depict current responses to voltage steps at -50 mV (nominal). Corrected for an uncompensated series resistance of $7 \text{ M}\Omega$. Holding potential -80 mV . CsCl pipette.

tion). Interestingly, recovery of Na currents from voltage inactivation is quite slow, having a time constant of about 56 msec. Delayed-rectifier outward K currents reach half-maximal levels at 12.5 msec at 0 mV.

It is clear from comparisons with spiral ganglion cell data that the channel kinetics of the cells from the mammalian visual, olfactory, and taste systems are comparatively slow. Kinetic differences probably relate to the type of stimulus each sensory system is required to detect, and the molecular method of detection (see Hille, 1992).

Yamaguchi and Ohmori (1990) studied the conductances of chick cochlear ganglion cells and observed outward K currents whose voltage dependence (if voltage corrections for series resistance are made for their data) is somewhat similar to the K conductance of the guinea pig. However, at temperatures comparable to that used in the present study, the onset kinetics of the chick's K currents are appreciably slower (see Fig. 4C). For example, voltage steps to levels above -50 mV require about twice as long to reach half-maximal current levels in the chick as compared to the guinea pig. While the extent of frequency sensitivity differs markedly in the guinea pig and the chick, the observed differences in the kinetics of outward K currents between mammalian and nonmammalian species may further reflect differences in maturity of the cells. Yamaguchi and Ohmori obtained ganglion cells from chicks between embryonic days 15 and 19, and it is possible that conductances may not exhibit adult characteristics. For example, Fuchs and Sokolowski (1990) have shown that chick cochlear hair cells do not acquire a Ca-activated K conductance until after embryonic day 19. Thus, beyond species differences, it may be difficult to make direct comparisons between potentially immature cells of the chick and acutely dissociated adult cells of the guinea pig. Neverthe-

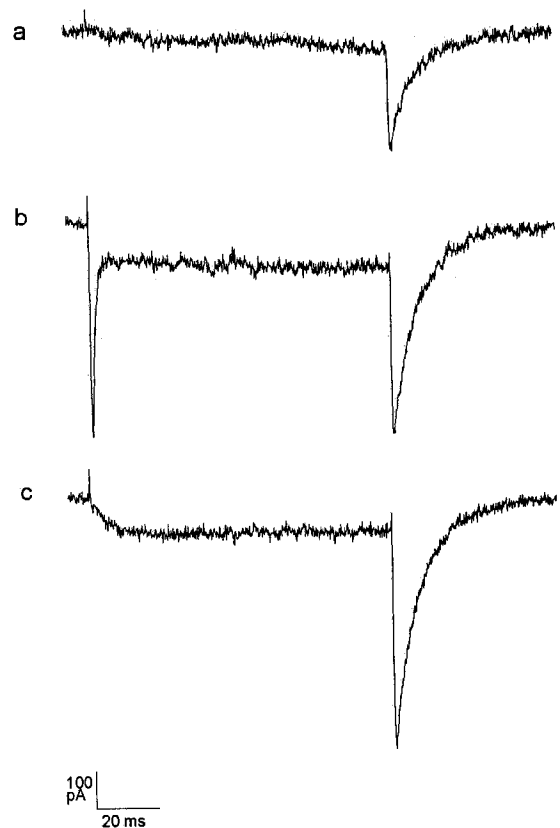


Figure 12. Effect of TTX and Na removal on fast and slow inward currents of a spiral ganglion cell. Cell was held at -80 mV and stepped to -40 mV (nominal). Trace *a* shows response during perfusion of $10 \text{ mM TEA Leibovitz}$ supplemented with 200 nM TTX . Trace *b* shows response with $10 \text{ mM TEA Leibovitz}$. Trace *c* shows response when Tris replaced all external Na. Digitally filtered at 0.1 msec . Note changes in magnitudes of tail currents. R_s , $2.26 \text{ M}\Omega$.

less, some characteristics of the studied currents appear similar, including voltage dependence of Na and K conductances and kinetics of the Na conductance. For example, Yamaguchi and Ohmori found that the time to half-peak Na current ranged from 0.57 to 0.26 msec within the voltage range of -23 to $+13 \text{ mV}$, and the present data ranged from 0.43 to 0.26 msec.

Relevance of spiral ganglion cell conductances to eighth-nerve activity

The electrical properties of auditory neurons help shape their response characteristics (Manis and Marx, 1991; Oertel, 1991). Indeed, the voltage dependence and kinetics of spiral ganglion cells conductances are probably highly influential. The rapidly activating K conductances of guinea pig spiral ganglion cells, occurring near the resting potential, will limit the duration of action potentials, and promote the rapid recovery of Na channels from inactivation, thereby potentially permitting higher average rates, and precise timing—traits that are requisite for auditory coding mechanisms such as phase locking.

Siegel (1992) has recorded spontaneous activity from guinea pig afferent terminals at the base of inner hair cells and speculated that possible relative refractory effects due to rapidly activated K conductances might account for the reduced EPSP size immediately following prior neural activity. [No spontaneous activity was found in isolated ganglion cells. Although spontaneous activity in eighth-nerve fibers can approach 140

spikes/sec in the absence of sound, it is likely that this activity is transmitter activated, since damage to inner hair cells or treatments designed to reduce receptor current decrease or abolish spontaneous activity (Kiang et al., 1976; Sewell, 1984.) Indeed, Siegel found that spike initiation and amplitude were also reduced. Under current clamp, in the present study, the occurrence of graded depolarizing spikes with increasing current pulse magnitude reflects the rapid onset and tremendous magnitude of the outward K currents generated in guinea pig spiral ganglion cells—the effect of Na conductance activation is rapidly curtailed, and afterhyperpolarizations lasting several milliseconds ensue. Clearly, such rapid activation of K conductances is congruent with Siegel's findings.

Investigations of acoustically evoked eighth-nerve adaptation also reveal temporal processes that may directly relate to some of the intrinsic refractory properties of spiral ganglion cells (Westerman and Smith, 1984; Yates et al., 1985; Lutkenhoner and Smith, 1986). Peristimulus time histograms (PSTHs) of eighth-nerve activity typically show a very high probability of spiking within the first few hundred microseconds following the onset of an acoustic stimulus. This is followed by a very short period of inactivity, probably reflecting the nerve's absolute refractory period. Interspike intervals in auditory nerve fibers can be as short as 0.7 msec (Kiang et al., 1965). In the gerbil, Westerman and Smith (1984) found two additional temporal components of activity decline during sustained acoustic stimulation. The rapid component had a time constant of 1–10 msec that was level dependent (decreasing with intensity), and the slower component, which was not level dependent, had a time constant of 60 msec. Similarly, Yates et al. (1985) found two temporal processes in the guinea pig, one ranging from about 2–25 msec that was sound-level dependent and another that had a time course greater than 100 msec. The fast form of adaptation may correspond to relative refractory periods of the spiral ganglion cell, that is, the kinetics of voltage-dependent inactivation and recovery of the Na conductance and K conductance-induced afterhyperpolarization. Another auditory neural phenomenon, forward masking, a paradigm where the response to a second tone is diminished by a prior tone, may also reflect the temporal characteristics of spiral ganglion cell ionic channel activation and inactivation. Harris and Dallos (1979) have shown that for short masking tones (2 msec) complete recovery of firing rate occurs within 20 msec. This process is also level dependent. While it is tempting to make comparisons between these fast level-dependent processes and the voltage-dependent characteristics of Na and K conductances in ganglion cells, the more slowly developing decline in fiber rate probably reflects synaptic events (transmitter rundown, hair cell calcium current kinetics) or discharge history effects (Smith and Brachman, 1982; Lutkenhoner and Smith, 1986; Kidd and Weiss, 1990). For example, it is conceivable that prior neural activity may increase extracellular K, thereby inactivating Na channels through depolarizing effects. Perhaps some of the longer adaptation time constants reflect the time constants of ionic recovery mechanisms, for example, pump activities and K sinking through supporting cells (Santos-Sacchi, 1991b).

Slow inward currents

The slow inward current observed in Cs-loaded cells may partially consist of a Ca component, since Cd^{2+} , Gd^{3+} , and Co^{2+} in the absence of Ca^{2+} are blockers. Gd^{3+} has been shown to block both sustained and transient Ca currents in cerebellar

granule cells (Slesinger and Lansman, 1991) but only transient Ca currents in NG108-15 cells (Docherty, 1988). Nonetheless, the sustained inward current displays many puzzling features, including its voltage dependence and reversal potential. One difficulty encountered in this study was the incomplete block of outward currents by Cs loading, even with the addition of 10 mM TEA extracellularly. While it is known that Cs can permeate Ca channels (Fenwick et al., 1982), and while this may be occurring to some extent in spiral ganglion cells, it appears that the use of Cs does not lead to complete isolation of Ca currents, as it does in some cell types (e.g., Kinnamon et al., 1989; Fuchs et al., 1990). Indeed, Dryer et al. (1991) have documented that Ca currents are not adequately isolated in chick ciliary ganglion cells when using intracellular Cs and extracellular K channel blockers. Ca conductances in the spiral ganglion cell of the guinea pig require further in-depth characterization, utilizing more aggressive current isolation techniques.

It is interesting to note that Wilson et al. (1991) have described a TTX-blockable voltage-dependent inward current in bag cell neurons of *Aplysia* that is activated by venom from *Conus textile*. It is carried mainly by Na, activates near -60 mV, and reverses near zero potential. This current appears to have some similarities with other Ca-activated nonspecific cation currents (Partridge and Swandulla, 1988). Despite the observation that the slow inward current in spiral ganglion cells is not Na dependent, it is noteworthy that it shares some of the characteristics of the bag cell neuron current; namely, it shares a similar TTX sensitivity, activation potential, and reversal potential, which indicates permeation by multiple ionic species.

Summary

It is becoming increasingly clear that the ability of the auditory system to process high-frequency acoustic events reflects the underlying rapid kinetics of the system's constituent cells. Within the sensory epithelium, mechanical events are remarkable. The mechanical transduction mechanism in hair cells utilizes one of the fastest gating processes known (Corey and Hudspeth, 1983), and outer hair cell voltage-dependent mechanical responses are measurable in the kilohertz range (Santos-Sacchi, 1992). The K conductance in inner hair cells is appropriately very rapid in onset (Santos-Sacchi, 1989b; Kros and Crawford, 1990), as are those in cells of the cochlear nucleus (Manis and Marx, 1991). It is no wonder that the observed membrane properties of the spiral ganglion cells that join peripheral receptors to central targets are also fast.

References

- Armstrong CM, Miller C (1990) Do voltage-dependent K^+ channels require Ca^{2+} ? A critical test employing a heterologous expression system. *Proc Natl Acad Sci USA* 87:7579–7582.
- Baker M, Bostock H, Grafe P, Martius P (1987) Function and distribution of three types of rectifying channel in rat spinal root myelinated axons. *J Physiol (Lond)* 383:45–67.
- Barres BA, Chun LLY, Corep DP (1989) Glial and neuronal forms of the voltage-dependent sodium channel: characteristics and cell-type distribution. *Neuron* 2:1375–1388.
- Barrett EF, Barrett JN (1982) Intracellular recording from vertebrate myelinated axons: mechanism of the depolarizing afterpotential. *J Physiol (Lond)* 323:117–144.
- Black JA, Kocsis JD, Waxman SG (1990) Ion channel organization of the myelinated fiber. *Trends Neurosci* 13:48–54.
- Chiu SY, Ritchie JM (1984) On the physiological role of internodal potassium channels and the security of conduction in myelinated nerve fibers. *Proc R Soc Lond [Biol]* 220:415–422.
- Chiu SY, Schwartz W (1987) Sodium and potassium currents in acute-

- ly demyelinated internodes of rabbit sciatic nerves. *J Physiol (Lond)* 391:631–649.
- Corey DP, Hudspeth AJ (1983) Kinetics of the receptor current in bullfrog saccular hair cells. *J Neurosci* 3:962–976.
- Dallos P (1988) Cochlear neurobiology. In: *Auditory function: neurobiological bases of hearing*, pp 153–188. New York: Wiley.
- Dallos P, Santos-Sacchi J, Flock A (1982) Intracellular recordings from outer hair cells. *Science* 218:582–584.
- David G, Barrett JN, Barrett EF (1992) Evidence that action potentials activate an internodal potassium conductance in lizard myelinated axons. *J Physiol (Lond)* 445:277–301.
- Davis RL, Mroz EA, Sewell WF (1989) Properties of single channels under the myelin sheath in goldfish auditory neurons. Paper presented at midwinter meeting of the Association for Research in Otolaryngology, St. Petersburg, FL, February.
- Docherty RJ (1988) Gadolinium selectively blocks a component of calcium current in rodent neuroblastoma × glioma hybrid (NG108-15) cells. *J Physiol (Lond)* 398:33–47.
- Dryer SE, Dourado MM, Wisgirda ME (1991) Properties of Ca²⁺ currents in acutely dissociated neurons of the chick ciliary ganglion: inhibition by somatostatin-14 and somatostatin-28. *Neuroscience* 44:663–672.
- Fenwick EM, Marty A, Neher E (1982) Sodium and calcium channels in bovine chromaffin cells. *J Physiol (Lond)* 331:599–635.
- Frankenhaeuser B, Moore LE (1963) The effect of temperature on the sodium and potassium permeability changes in myelinated nerve fibers of *Xenopus laevis*. *J Physiol (Lond)* 169:431–437.
- Fuchs PA, Sokolowski BH (1990) The acquisition during development of Ca-activated potassium currents by cochlear hair cells of the chick. *Proc R Soc Lond [Biol]* 241:122–126.
- Fuchs PA, Evans MG, Murrow BW (1990) Calcium currents in hair cells isolated from the cochlea of the chick. *J Physiol (Lond)* 429:553–568.
- Gilley WF, Lucero MT, Horrigan FT (1990) Control of the spatial distribution of sodium channels in giant fiber lobe neurons of the squid. *Neuron* 5:663–674.
- Harris D, Dallos P (1979) Forward masking of auditory nerve fiber responses. *J Neurophysiol* 42:1083–1107.
- Hille B (1992) *Ionic channels of excitable membranes*. Sunderland, MA: Sinauer.
- Hodgkin AL, Huxley AF (1952) A quantitative description of membrane current and its application to conduction and excitation in nerve. *J Physiol (Lond)* 117:500–544.
- Huguenard JR, Coulter DA, Prince DA (1991) A fast transient potassium current in thalamic relay neurons: kinetics of activation and inactivation. *J Neurophysiol* 66:1304–1315.
- Javel E (1986) Basic response properties of auditory nerve fibers. In: *Neurobiology of hearing: the cochlea* (Altschuler RA, Hoffman DW, Bobbin RP, eds). New York: Raven.
- Kaneda M, Kaneko A (1990) I_{Na} of cat ganglion cells: the time course of recovery from inactivation is related to soma size. *Jap J Physiol Suppl* 40:S177.
- Kellerhals B, Engstrom H, Ades HW (1967) Die Morphologie des Ganglion Spirale Cochlea. *Acta Otolaryngol [Suppl]* 226:1–78.
- Kiang NY-S, Watanabe T, Thomas C, Clark LF (1965) *Discharge patterns of single fibers in the cats auditory nerve*. Cambridge, MA: MIT Press.
- Kiang NY-S, Liberman MC, Levine RA (1976) Auditory-nerve activity in cats exposed to ototoxic drugs and high intensity sounds. *Ann Otol Rhinol Laryngol* 85:752–768.
- Kidd RC, Weiss TF (1990) Mechanisms that degrade timing information in the cochlea. *Hear Res* 49:181–208.
- Kimura RS, Bongiorno CL, Iverson NA (1987) Synapses and ephapses in the spiral ganglion. *Acta Otolaryngol [Suppl]* 438:1–18.
- Kinnamon SC, Cummings TA, Roper SD, Beam KG (1989) Calcium currents in isolated taste receptor cells of the mudpuppy. *Ann NY Acad Sci* 560:112–115.
- Kros CJ, Crawford AC (1990) Potassium currents in inner hair cells isolated from the guinea pig. *J Physiol (Lond)* 421:263–291.
- Lipton SA, Tauck DL (1987) Voltage-dependent conductances of solitary ganglion cells dissociated from the rat. *J Physiol (Lond)* 385:361–391.
- Lutkenhoner B, Smith RL (1986) Rapid adaptation of auditory-nerve fibers: fine structure at high intensities. *Hear Res* 24:289–294.
- Lynch JW, Barry PH (1991a) Properties of transient K⁺ currents and underlying single K⁺ channels in rat olfactory receptor neurons. *J Gen Physiol* 97:1043–1072.
- Lynch JW, Barry PH (1991b) Slowly activating K⁺ channels in rat olfactory receptor neurons. *Proc R Soc Lond [Biol]* 244:219–225.
- Manis PB, Marx SO (1991) Outward currents in isolated ventral cochlear nucleus neurons. *J Neurosci* 11:2865–2880.
- Marty A, Neher E (1983) Tight-seal whole-cell recording. In: *Single-channel recording* (Sakmann B, Neher E, eds), pp 107–122. New York: Plenum.
- Mathias RT, Levis RA, Eisenberg RS (1981) An alternative interpretation of charge movement in muscle. In: *The regulation of muscle contraction: excitation-contraction coupling*. New York: Academic.
- Oertel D (1991) The role of intrinsic neuronal properties in encoding of auditory information in the cochlear nuclei. *Curr Opin Neurobiol* 1:221–228.
- Ota CY, Kinura RS (1980) Ultrastructural study of the human spiral ganglion. *Acta Otolaryngol* 89:53–62.
- Palmer AR, Russell IJ (1986) Phase-locking in the cochlear nerve of the guinea pig and its relation to the receptor potential of inner hair-cells. *Hear Res* 24:1–15.
- Partridge LD, Swandulla D (1988) Calcium-activated non-specific cation channels. *Trends Neurosci* 11:69–72.
- Robertson D (1976) Possible relation between structure and spike shapes of neurones in the guinea pig cochlear ganglion. *Brain Res* 109:487–496.
- Ruggero MA (1992) Physiology of the auditory nerve. In: *The mammalian auditory pathway: neurophysiology* (Popper AN, Fay RR, eds), pp 34–93. New York: Springer.
- Russell IJ, Sellick PM (1978) Intracellular studies of hair cells in the mammalian cochlea. *J Physiol (Lond)* 284:261–290.
- Santos-Sacchi J (1989a) Whole-cell voltage clamping of spiral ganglion and outer hair cells. Paper presented at Hearing and Chemical Senses Seminars, Kresge Hearing Research Institute, University of Michigan, Ann Arbor, MI, April.
- Santos-Sacchi J (1989b) Asymmetry in voltage dependent movements of isolated outer hair cells from the organ of Corti. *J Neurosci* 9:2954–2962.
- Santos-Sacchi J (1989c) Calcium currents, potassium currents and the resting potential in isolated outer hair cells. Paper presented at the midwinter meeting of the Association for Research in Otolaryngology, St. Petersburg, FL, February.
- Santos-Sacchi J (1990) Studies on the fast inward Na⁺ current in isolated type I spiral ganglion cells. Paper presented at midwinter meeting of the Association for Research in Otolaryngology, St. Petersburg, FL, February.
- Santos-Sacchi J (1991a) Reversible inhibition of voltage dependent outer hair cell motility and capacitance. *J Neurosci* 11:3096–3110.
- Santos-Sacchi J (1991b) Isolated supporting cells from the organ of Corti: some whole cell electrical characteristics and estimates of gap junctional conductance. *Hearing Res* 52:89–98.
- Santos-Sacchi J (1992) On the frequency limit and phase of outer hair cell motility: effects of the membrane filter. *J Neurosci* 12:1906–1916.
- Sewell (1984) The relation between the endocochlear potential and spontaneous activity in auditory nerve fibers of the cat. *J Physiol (Lond)* 347:685–696.
- Siegel JH (1992) Spontaneous synaptic potentials from afferent terminals in the guinea pig cochlea. *Hear Res* 59:85–92.
- Siegel JH, Dallos P (1986) Spike activity recorded from the organ of Corti. *Hear Res* 22:245–248.
- Slesinger PA, Lansman JB (1991) Inactivation of calcium currents in granule cells cultured from mouse cerebellum. *J Physiol (Lond)* 435:101–121.
- Smith RL, Brachman ML (1982) Adaptation in auditory nerve fibers: a revised model. *Biol Cybern* 44:107–120.
- Spoendlin H (1971) Degeneration behavior of the cochlear nerve. *Arch Klin Exp Ohrennasen Kehlkopfheilkd* 200:275–291.
- Spoendlin H (1988) Neural anatomy of the inner ear. In: *Physiology of the ear* (Jahn A, Santos-Sacchi J, eds), pp 201–219. New York: Raven.
- Trombley PQ, Westbrook GL (1991) Voltage-gated currents in identified rat olfactory receptor neurons. *J Neurosci* 11:435–444.
- Waxman SG, Ritchie JM (1985) Organization of ion channels in the mammalian nerve fiber. *Science* 228:1502–1507.
- Westerman LA, Smith RL (1984) Rapid and short-term adaptation in auditory nerve responses. *Hear Res* 15:249–260.

Wilson GF, Fisher TE, Joiner WJ, Olivera BM, Kaczmarek LK (1991)
Venom from *Conus textile* activates a tetrodotoxin-sensitive inward
current in bag cell neurons of *Aplysia*. Soc Neurosci Abstr 17:955.
Yamaguchi K, Ohmori H (1990) Voltage-gated and chemically gated

ionic channels in the cultured cochlear ganglion neurone of the chick.
J Physiol (Lond) 420:185-206.
Yates GK, Robertson D, Johnstone BM (1985) Very rapid adaptation
in the guinea pig auditory nerve. Hear Res 17:1-12.

Short review

Cell coupling in Corti's organ

J. Santos-Sacchi *

Surgery (Otolaryngology) and Neurobiology, Yale University School of Medicine, BML 244, 333 Cedar St., New Haven, CT 06510, USA

Abstract

The mammalian organ of Corti is responsible for the initial analysis of sound; injury leads to hearing loss. During the last two decades, the characteristics of cellular coupling in this specialized epithelium have been studied. In this review, data on both electrical and mechanical coupling are covered. While electrical coupling likely contributes to homeostasis in the organ, this concept is far from proven. © 2000 Elsevier Science B.V. All rights reserved.

Keywords: Coupling; Corti's organ; Cell

Contents

1. Introduction	167
2. How the organ works	168
3. Coupling between supporting cells	168
4. Coupling between hair cells	170
5. What does it all mean?	170
Acknowledgements.	170
References	170

1. Introduction

The organ of Corti is a specialized, avascular sensory epithelium that rests on the basilar membrane of mammals.

Within this organ, mechanical energy is transduced into electrical activity. A variety of cell types populate the organ along the whole spiral length of the basilar membrane. The cells can be categorized into two major classes — hair cells and supporting cells. In order to appreciate the consequences of cell coupling in the organ, a brief account of our current concept of mammalian peripheral

* Corresponding author. Fax: +1-203-737-2502; e-mail: joseph.santos-sacchi@yale.edu

auditory physiology is presented (for additional information, see Ruggero and Santos-Sacchi [23]).

2. How the organ works

There are two types of auditory hair cells in mammals — inner hair cells (IHCs) and outer hair cells (OHCs). Each cell type generates receptor potentials when its stereociliar bundle is deflected by sound-induced basilar membrane vibration [5,24]. While OHCs outnumber IHCs by about four to one, it is the IHC type that receives up to 95% of the afferent innervation of the eighth nerve [38]. OHCs are mechanical effectors as well as receptors [1], and are capable of voltage-driven length changes in the acoustic frequency range [3,31,33]. Through their mechanical activity, OHCs provide a boost to basilar membrane motion that ultimately results in enhanced sensitivity and frequency selectivity in the output of IHCs. This physiologically labile enhancement has been termed the “cochlear amplifier” [6].

Hair cells are enveloped by supporting cells. IHCs have closely opposed supporting cells that provide a restricted interstitial fluid space. OHCs, on the other hand, lose close appositions with supporting cells during development; in the adult, the OHCs' lateral membranes are exposed to the large fluid spaces of Nuel. However, the supporting Deiters' cells retain close apposition at the apical and basal poles of the OHC.

The mechanism by which hair cells are excited is well characterized (see Pickles and Corey [22]). Bundle deflection modulates a standing cationic current through mechano-sensitive channels located in apical stereocilia tips. The current is predominantly carried by K^+ since the endolymphatic fluid which bathes the bundle is high in potassium (~ 140 mM; Ref. [25]). The driving force for transduction current derives from the voltage drop across the hair cell's apical membrane, i.e., the difference between the positive endolymphatic potential (+80 mV) and the cell's negative resting potential. An accessory epithelium, the stria vascularis, is responsible for the ionic content and potential of the endolymphatic space. The perilymphatic fluid that bathes the basolateral membranes of hair cells is similar to CSF. As a consequence of incessant hair cell and synaptic activity, potassium is continuously released into the extracellular spaces. In the case of the IHC, whose extracellular space is small, even slight increases in potassium may seriously impair hair cell and neural activity. Even though the OHC lateral membrane is exposed to the fluid spaces of Nuel, this membrane lacks voltage-dependent conductances that could contribute to potassium efflux [34]. Instead, voltage-dependent potassium conductances are restricted to the basal pole of the cell — where tight apposition of Deiters' cell cups provide a restricted fluid space with the potential for potassium accumulation. In either hair cell type, potassium-induced

depolarization will interfere with sound transduction since the driving force for transducer current will be reduced. Furthermore, normal transmitter release and afferent activity will be disrupted. In the OHC, however, additionally the mechanism responsible for cellular motility is directly susceptible to membrane potential [35]. Thus, the cochlear amplifier may be compromised.

3. Coupling between supporting cells

In the mid-1970's, a few groups characterized the ultrastructural extent of gap junctional contacts in the organ of Corti [11,12,14]. Based on structure, all supporting cells were found to potentially contribute to a syncytium of coupled cells. In 1983, Santos-Sacchi and Dallos [32] electrophysiologically confirmed that functional coupling was present in the organ of Corti. Using high impedance electrodes, they determined, both *in vitro* and *in vivo*, that current injection into one supporting cell produced voltage drops in adjacent cells (Fig. 1). Subsequently, it was shown that coupling ratios as high as 0.8 occur between adjacent Hensen cells [26]. Supporting cell coupling is sensitive to the effects of intracellular H^+ and Ca^{2+} , temperature, membrane tension and other uncoupling agents, such as octanol [27,28,31,41]. The sensitivity to intracellular pH is greater than that to intracellular calcium; calcium levels in the millimolar range are required to uncouple Hensen cells [36].

Supporting cells, as evidenced through Hensen cell studies, are so well coupled that voltage-dependent ionic conductances are effectively shared among coupled cells [31]. Outward K currents and inward rectifier currents from adjacent coupled cells are measurable under whole cell voltage clamp in one cell of a cell pair or group (Fig. 2). Uncoupling treatments reduce current magnitudes to single cell levels. This recruitment is believed to be important for the maintenance of the stable supporting cell

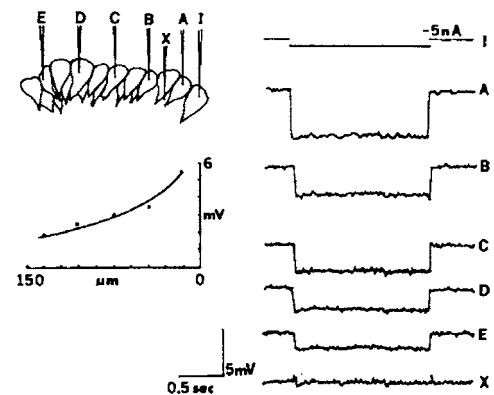


Fig. 1. Voltage responses in the Hensen cells of the isolated organ of Corti as a function of distance from a fixed intracellular current injection electrode. From Ref. [32].

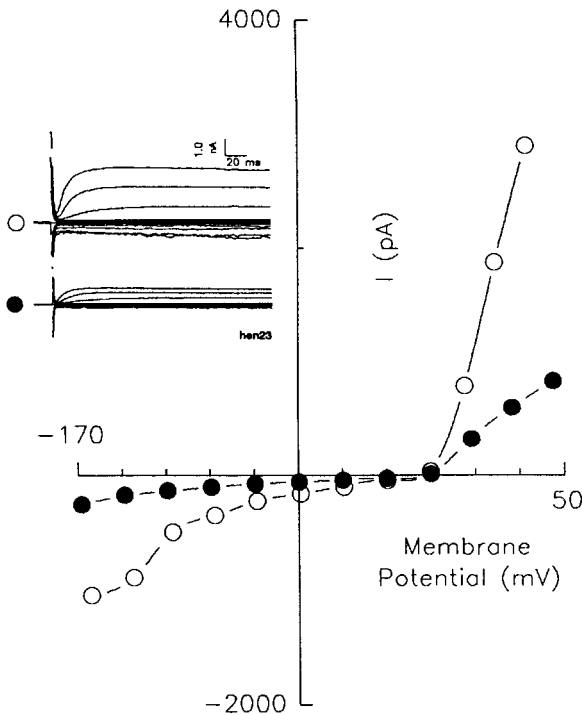


Fig. 2. Whole cell currents obtained under voltage clamp of one cell in a coupled triplet of Hensen cells. Before (open symbols) and after (filled symbols) uncoupling with CO₂ saturated medium. Note the reduction of currents to single cell levels after uncoupling. From Ref. [31].

membrane potentials (~ -100 mV), since uncoupled single cells, which possess few K channels, are depolarized.

Cell coupling in Hensen and Deiters' cells has been studied with input capacitance measures and the double voltage clamp technique [31,36,41]. Because the supporting cells are so well coupled, input capacitance reflects the parallel combination of the coupled cells' capacitance. For example, visually confirmed single cells, pairs and triplets have average input capacitances of 31.0, 64.8 and 104 pF, respectively [41]. Using capacitance measures, junctional conductance was estimated to be nearly three orders of magnitude greater than single Hensen cell resting nonjunctional conductance [33]. Indeed, direct measurement under double voltage clamp provides an average conductance of about 50 nS, with some pairs exhibiting values above 500 nS (Fig. 3; Ref. [41]).

Although it was found in early studies that low temperature and CO₂ reversibly uncouple the supporting cell syncytium, reversible depolarization invariably accompanied such effects [27,28]. The direct effects of depolarization could not be fully evaluated in that type of preparation since neither the voltage nor the activities of H⁺ and Ca²⁺ could be adequately controlled. It is now known that gap junctional conductance in supporting cells is voltage dependent [40,41,43]. In fact, most cell pairs studied with the double voltage clamp technique exhibit transjunctional voltage dependence and/or nonjunctional membrane volt-

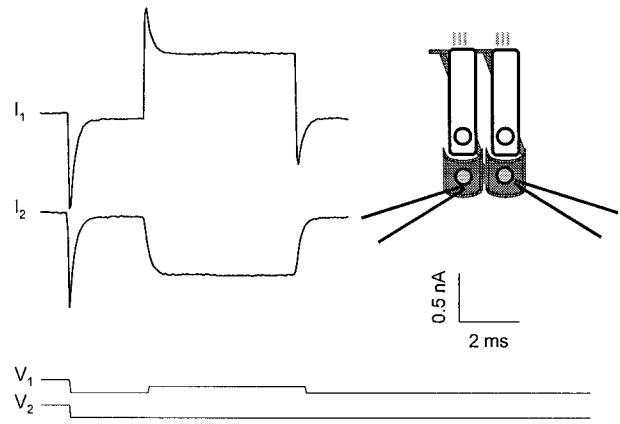


Fig. 3. Double voltage clamp of Deiters' cell pair. Ten millivolts test pulse delivered to cell 1. Junctional currents indicate a conductance, G_j , of about 75 nS. From Ref. [40].

age dependence. This dependence is observable through capacitance measures as well.

One of the most striking features of the voltage dependence in supporting cell pairs is its diversity. Fig. 4 illustrates two cases of Hensen cell pairs where G_j rectifies to opposite polarities as V_j is altered. In fact, cases are also found that exhibit symmetrical V_j dependence or an absence of voltage dependence [43]. Nonjunctional voltage dependence is just as variable. We have speculated that this variability is due to heterotypic or heteromeric junctional channels [43], since a variety of connexin subtypes, including Cx26, Cx30, Cx43, are localized to the organ of Corti [9,17,18]. Such combinatorial effects may give rise to directional intracellular pathways along the supporting cell syncytium.

Initial studies on dye coupling in supporting cells showed little or no spread of intracellularly injected dyes [32]. Subsequently, it was determined that junctional communication in supporting cells is highly sensitive to photoinactivation occurring during real time viewing of fluorescent dye injections. By using low light level viewing technology, it was possible to demonstrate pronounced

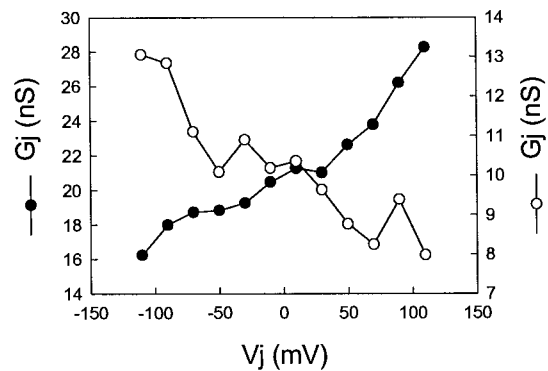


Fig. 4. Double voltage clamp of Hensen cell pairs indicating variability of transjunctional voltage dependence. In one case (open symbols), positive V_j in the voltage-stepped cell, caused a decrease in G_j , whereas in another cell pair (filled symbols) the opposite was found. From Ref. [43].

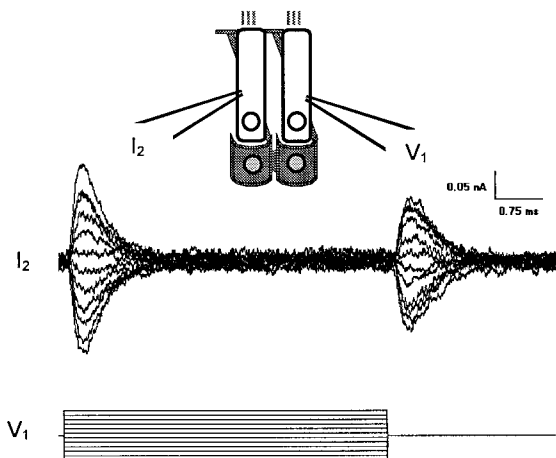


Fig. 5. Double voltage clamp of adjacent OHCs. Voltage steps in one OHC induced transient gating current in the adjacent cell. From Ref. [42].

dye coupling [29]. Recently, very interesting patterns of dye spread have been observed in the living animal, indicating that dye passage may be limited to preferential pathways [19].

4. Coupling between hair cells

In the mammal, there is no morphological evidence for gap junctional communication between hair cells or between supporting cells and hair cells. It is also clear from electrophysiological measures of sound-evoked hair cell activity that coupling is absent *in vivo*. Dallos and Santos-Sacchi [4] found that intracellularly recorded receptor potential cutoff frequencies for IHCs and OHCs were 340 and 1250 Hz, respectively. These equate to time constants of 0.47 and 0.13 ms, respectively. Considering that the membrane resistance obtained *in vivo* for either cell type is greater than 10 M Ω , membrane capacitances can be computed to be roughly in the low tens of picofarad range — single cell values. As we have shown before, a coupled cellular syncytium would be predicted to have much greater input capacitance. Additionally, as expected in the absence of hair cell to supporting cell coupling, receptor potentials in the guinea pig are larger in the hair cells and extracellular fluid spaces of the cochlea than in the supporting cells [2,5,20,21]. Contrary results have been obtained in the gerbil [44].

While gap junction-mediated coupling is absent between hair cells, we have recently found a mechano-electrical coupling between adjacent OHCs [42]. Because of the voltage-dependent mechanical activity of OHCs, voltage drops across the lateral membrane of an OHC will additionally cause deformation of physically adjacent cells. Since the motility voltage sensor in OHCs is sensitive not only to voltage but to membrane tension, gating currents are evoked in the adjacent cell (Fig. 5). The gating currents in adjacent OHCs result from a tension-induced shift in the

voltage dependence of gating charge movement [10,13,15]. Interestingly, the resulting charge-induced transient polarization of the adjacent OHC is opposite in polarity to that of the voltage in the stimulated cell — indicative of lateral inhibition. Furthermore, since the voltage dependence of the charge movement and the mechanical response are equivalent, the mechanical activity of any one OHC is directly influenced by that of its neighbors. We believe that sharpening of the basilar membrane response beyond that of Bekeasy's passive tuning results from this mechanical coupling.

5. What does it all mean?

Cell coupling in the organ of Corti is pronounced and diverse. It is likely that both the mechanical and electrical interactions reviewed here are important for the organ.

As far as gap junction-mediated coupling is concerned, the truth is that we have no direct indications what function it plays. Since the discovery of junctional coupling in the organ of Corti, we have contended that junctional coupling must be crucial for normal cochlear function [26,33]; however, only recently has this been shown. The occurrence of nonsyndromic deafness associated with connexin gene mutations, such as in Cx26, indicates the physiological requirement for these channels [7,8,16,39]. Yet, while we have argued for a role of coupling in K sinking and metabolic cooperation within the organ [27,29,31,41], there is no reason to believe that sensorineural deafness results solely from the disruption of these homeostatic mechanisms. For example, it is possible that the stria vascularis may be an important target [37]. These answers will only be obtained through further *in vivo* analysis of junctional coupling within the cochlea [30].

Acknowledgements

We thank the following people whose work has contributed to this review: H.-B. Zhao, Y. Sato, S. Kakehata, M. Wu, S. Takahashi, and M. Mazzucco. This work was supported by NIH-NIDCD grant DC00273.

References

- [1] W.E. Brownell, C.R. Bader, D. Bertrand, Y. de Ribaupierre, Evoked mechanical responses of isolated cochlear outer hair cells, *Science* 227 (1985) 194–196.
- [2] P. Dallos, Response characteristics of mammalian cochlear hair cells, *J. Neurosci.* 5 (6) (1985) 1591–1608.
- [3] P. Dallos, B.N. Evans, High-frequency motility of outer hair cells and the cochlear amplifier, *Science* 267 (1995) 2006–2009.
- [4] P. Dallos, J. Santos-Sacchi, AC receptor potentials from hair cell in the low frequency region of the guinea pig cochlea, in: W.R.

- Webster, L.M. Aitkin (Eds.), *Mechanisms of Hearing*, Monash Univ. Press, Clayton, Australia, 1983, pp. 11–16.
- [5] P. Dallos, J. Santos-Sacchi, Å. Flock, Intracellular recordings from cochlear outer hair cells, *Science* 218 (1982) 582–584.
- [6] H. Davis, An active process in cochlear mechanics, *Hear. Res.* 9 (1983) 79–90.
- [7] F. Denoyelle, G. Lina-Granade, H. Plauchu, R. Bruzzone, H. Chaïb, F. Lévi-Acobas, D. Weil, C. Petit, Connexin26 gene linked to a dominant deafness, *Nature* 393 (1998) 319–320.
- [8] X. Estivill, P. Fortina, S. Surrey, R. Rabionet, S. Melchionda, L. D'Agruma, E. Mansfield, E. Rappaport, N. Govea, M. Milà, L. Zelante, P. Gasparini, Connexin-26 mutations in sporadic and inherited sensorineural deafness, *Lancet* 351 (1998) 394–398.
- [9] A. Forge, D. Becker, W.H. Evans, Gap junction connexin isoforms in the inner ear of gerbils and guinea pigs, *Br. J. Audiol.* 31 (1997) 76–77.
- [10] J.E. Gale, J.F. Ashmore, Charge displacement induced by rapid stretch in the basolateral membrane of the guinea pig OHC, *Proc. R. Soc. London, Ser. B* 255 (1994) 243–249.
- [11] R.S. Gulley, T.S. Reese, Intercellular junctions in the reticular lamina of the organ of Corti, *J. Neurocytol.* 5 (1976) 479–507.
- [12] S. Iurato, K. Franke, L. Luciano, G. Wermber, E. Pannese, E. Reale, Intercellular junctions in the organ of Corti as revealed by freeze fracturing, *Acta Oto-Laryngol.* 82 (1976) 57–69.
- [13] K.H. Iwasa, Effect of stress on the membrane capacitance of the auditory outer hair cell, *Biophys. J.* 65 (1993) 492–498.
- [14] K. Jahnke, The fine structure of freeze-fractured intercellular junctions in the guinea pig inner ear, *Acta Oto-Laryngol. (Suppl.)* (1975) 336.
- [15] S. Kakehata, J. Santos-Sacchi, Membrane tension directly shifts voltage dependence of outer hair cell motility and associated gating charge, *Biophys. J.* 68 (1995) 2190–2197.
- [16] D.P. Kelsell, J. Dunlop, H.P. Stevens, N.J. Lench, J.N. Liang, G. Parry, R.F. Mueller, I.M. Leigh, Connexin 26 mutations in hereditary non-syndromic sensorineural deafness, *Nature* 387 (1997) 80–83.
- [17] T. Kikuchi, R.S. Kimura, D.L. Paul, J.C. Adams, Gap junctions in the rat cochlea: immunohistochemical and ultrastructural analysis, *Anat. Embryol.* 191 (1995) 101–118.
- [18] J. Lautermann, W.J.F. ten Cate, P. Altenhoff, R. Grümmer, O. Traub, H.G. Frank, K. Jahnke, E. Winterhager, Expression of the gap-junction connexins 26 and 30 in the rat cochlea, *Cell Tissue Res.* 294 (1998) 415–420.
- [19] P. Oberoi, J.C. Adams, In vivo measurements of dye-coupling among non-sensory cells in the organ of Corti. Mid-winter Meeting of the Association for Research in Otolaryngology, St. Petersburg, FL, February, 1998.
- [20] E.C. Oesterle, P. Dallos, Intracellular recordings from supporting cells in the guinea-pig cochlea: AC potentials, *J. Acoust. Soc. Am.* 86 (3) (1989) 1013–1032.
- [21] E.C. Oesterle, P. Dallos, Intracellular recordings from supporting cells in the guinea pig cochlea: DC potentials, *J. Neurophys.* 64 (2) (1990) 617–636.
- [22] J.O. Pickles, D.P. Corey, Mechano-electrical transduction by hair cells, *Trends Neurosci.* 15 (7) (1992) 254–259.
- [23] M.A. Ruggero, J. Santos-Sacchi, Cochlear mechanics and biophysics, in: M.J. Croker (Ed.), *Handbook of Acoustics*, Wiley, 1997.
- [24] I.J. Russell, P.M. Sellick, Intracellular studies of hair cells in the mammalian cochlea, *J. Physiol.* 284 (1978) 261–290.
- [25] A. Salt, R. Thalmann, Cochlear fluid dynamics, in: A. Jahn, J. Santos-Sacchi (Eds.), *Physiology of the Ear*, Raven Press, NY, 1988.
- [26] J. Santos-Sacchi, A reevaluation of cell coupling in the organ of Corti, *Hear. Res.* 14 (1984) 203–204.
- [27] J. Santos-Sacchi, The effects of cytoplasmic acidification upon electrical coupling in the organ of Corti, *Hear. Res.* 19 (1985) 207–215.
- [28] J. Santos-Sacchi, The temperature dependence of electrical coupling in the organ of Corti, *Hear. Res.* 21 (1986) 205–211.
- [29] J. Santos-Sacchi, Dye coupling in the organ of Corti, *Cell Tissue Res.* 245 (1986) 525–529.
- [30] J. Santos-Sacchi, Cell coupling differs in the in vitro and in vivo organ of Corti, *Hear. Res.* 25 (1987) 227–232.
- [31] J. Santos-Sacchi, Isolated supporting cells from the organ of Corti: some whole cell electrical characteristics and estimates of gap junction conductance, *Hear. Res.* 52 (1991) 89–98.
- [32] J. Santos-Sacchi, P. Dallos, Intercellular communication in the supporting cells of the organ of Corti, *Hear. Res.* 9 (1983) 317–326.
- [33] J. Santos-Sacchi, J.P. Dilger, Whole cell currents and mechanical responses of isolated outer hair cells, *Hear. Res.* 35 (1988) 143–150.
- [34] J. Santos-Sacchi, G.-J. Huang, M. Wu, Mapping the distribution of outer hair cell voltage-dependent conductances by electrical amputation, *Biophys. J.* 73 (1997) 1424–1429.
- [35] J. Santos-Sacchi, S. Kakehata, S. Takahashi, Effects of membrane potential on the voltage-dependence of motility — related in outer hair cells of the guinea pig, *J. Physiol. (London)* 510 (1998) 225–235.
- [36] Y. Sato, J. Santos-Sacchi, Cell coupling in the supporting cells of Corti's organ: sensitivity to intracellular H^+ and Ca^{2+} , *Hear. Res.* 80 (1994) 21–24.
- [37] M. Souter, A. Forge, Intercellular junctional maturation in the stria vascularis — possible association with onset and rise of endocochlear potential, *Hear. Res.* 119 (1–2) (1998) 81–95.
- [38] H. Spoendlin, Neural anatomy of the inner ear, in: A. Jahn, J. Santos-Sacchi (Eds.), *Physiology of the Ear*, Raven Press, NY, 1988.
- [39] J.H. Xia, C.Y. Liu, B.S. Tang, Q. Pan, L. Huang, H.P. Dai, B.R. Zhang, W. Xie, D.X. Hu, D. Zheng, X.L. Shi, D.A. Wang, K. Xia, K.P. Yu, X.D. Liao, Y. Feng, Y.F. Yang, J.Y. Xiao, D.H. Xie, J.Z. Huang, Mutations in the gene encoding gap junction protein β -3 associated with autosomal dominant hearing impairment, *Nature Genet.* 20 (1998) 370–373.
- [40] H.B. Zhao, J. Santos-Sacchi, Fast voltage dependence of gap junctions in cochlear supporting cells, Society for Neuroscience, 27th Annual Meeting, New Orleans, LA, 1997, p. 461.
- [41] H.B. Zhao, J. Santos-Sacchi, Effect of membrane tension on gap junctional conductance of supporting cells in Corti's organ, *J. Gen. Physiol.* 112 (1998) 447–455.
- [42] H. Zhao, J. Santos-Sacchi, Auditory collusion and a coupled couple of outer hair cells, *Nature* 399 (1999) 359–362.
- [43] H. Zhao, J. Santos-Sacchi, Multiple types of asymmetric voltage gating in gap junctions of cochlear supporting cells: evidence for heterotypic and heteromeric-like channels, 1999b, submitted.
- [44] J.J. Zwislocki, N.B. Slepceky, L.K. Cefaratti, R.L. Smith, Ionic coupling among cells in the organ of Corti, *Hear. Res.* 57 (1992) 175–194.

Joseph Santos-Sacchi

Functional motor microdomains of the outer hair cell lateral membrane

Received: 8 July 2002 / Accepted: 13 August 2002 / Published online: 6 September 2002
© Springer-Verlag 2002

Abstract The outer hair cell (OHC) of the mammalian inner ear is a highly partitioned neuroepithelial cell whose lateral membrane is devoted to electromotility, a fast mechanical length change owing to the motor protein, prestin. Spatially restricted measures of prestin-derived nonlinear capacitance or gating charge, using either electrical amputation or discrete membrane mechanical deformation, were used to determine that functional variation exists within the extensive lateral membrane of the cell. This was evidenced by variation in the motor's operating voltage range and sensitivity among microdomains within the lateral membrane. That is, localized regions of the membrane evidenced Boltzmann distributions of motor charge whose midpoint voltage and slope differed from those obtained for the whole cell. These data highlight the functional independence of microdomains and imply that measured whole cell characteristics may differ from the microscopic characteristics of elementary motors.

Keywords Motility · Gating charge · Membrane capacitance

Introduction

The outer hair cell (OHC) underlies the mammal's enhanced auditory abilities [5]. It is a cell that is functionally partitioned [10, 23], possessing regions of its plasma membrane that are predominantly devoted to the tasks of forward transduction (apical membrane), reverse transduction (lateral membrane) and neurotransmission (basal membrane). The lateral membrane houses the motors of the OHC, recently identified as prestin [16,

25, 30], which are responsible for the cell's electromotility [4]. The mechanical response of the cell is mirrored by a motor-associated gating charge movement (or nonlinear capacitance) [3, 20]; the voltage dependence of the nonlinear capacitance is the same as that of electromotility [14], allowing the former to be used to assess some aspects of the cell's mechanical activity.

While the OHC lateral membrane harbors an enormous number of identical prestin molecules (approx. $7,500/\mu\text{m}^2$ based on charge estimates [10]), the lateral membrane itself is composed of structural microdomains [15, 28]. This heterogeneity may underlie similar variability in the mechanical activity of the lateral membrane. For example, Kalinec and Kachar [15] observed local variation in the direction that microbeads moved along the surface of the electrically excited OHC. We hypothesize that the direction of forces arising from electrical stimulation of the lateral membrane results not only from cellular structural and mechanical constraints but also from intrinsic motor properties as well. Utilizing techniques to gauge motor characteristics from restricted regions (which we refer to as microdomains) of the OHC lateral membrane, we show that microdomains of molecular motors possess voltage characteristics that differ substantially from those obtained through whole cell measures.

Materials and methods

General preparation

Guinea pigs were overdosed with pentobarbital. The temporal bones were removed and OHCs were isolated from cochleas by gentle pipetting of the isolated top two turns of organ of Corti in Ca-free medium with collagenase (0.3 mg/ml). The cell-enriched supernatant was then transferred to a 700- μl perfusion chamber, and the cells were permitted to settle onto the coverglass bottom. All experiments were performed at room temperature ($\sim 23^\circ\text{C}$). A Nikon Diaphot inverted microscope with Hoffmann optics was used to observe the cells during electrical recording. A modified Lebovitz medium (NaCl, 142.2 mM; KCl, 5.37 mM; CaCl_2 , 1.25 mM; MgCl_2 , 1.48 mM; HEPES, 10 mM; dextrose, 5 mM;

J. Santos-Sacchi (✉)

Department of Surgery (Otolaryngology) and Section of Neurobiology, BML 244, Yale University School of Medicine, 333 Cedar St, New Haven, CT 06510, USA

e-mail: joseph.santos-sacchi@yale.edu

Tel.: +1-203-7857566

Fax: +1-203-7372502

adjusted to pH 7.2 with NaOH, and adjusted to 300 mosmol with dextrose) was used as the standard perfusion solution.

Electrical recordings

Cells were whole cell voltage-clamped with a Dagan 3900 (Dagan Corp., Minnesota) or Axopatch 200B amplifier (Axon Instruments, California). Gigohm seals were obtained at the supranuclear region of the OHC membrane prior to whole cell recording. Pipette solutions were composed of 140 mM CsCl, 10 mM EGTA, 2 mM MgCl₂, and 10 mM HEPES (buffered to pH 7.2 with CsOH, and adjusted to 300 mosmol with dextrose). In order to evaluate nonlinear capacitive gating currents in the absence of confounding ionic currents, the standard perfusion solution was replaced with an ionic blocking solution following seal formation (NaCl, 100 mM; tetraethylammonium, 20 mM; CsCl, 20 mM; CoCl₂, 2 mM; MgCl₂, 1.48 mM; HEPES, 10 mM; dextrose, 5 mM; adjusted to pH 7.2 with NaOH, and adjusted to 300 mosmol with dextrose [10, 20]). Data collection and analysis were performed with a Window's based whole cell voltage-clamp program, jClamp (Scisoft, Connecticut), utilizing a Digidata 1200 board (Axon Instruments). Series resistance effects on membrane voltage were corrected offline. All experiments were video taped.

Whole cell membrane capacitance was measured with two techniques: transient and AC. The former technique entailed the delivery of a stair-step voltage ranging from -160 to 120 mV, in 14 mV increments. Capacitive transients were integrated to obtain cell capacitance (C_m) measures as previously described [10]. The latter technique utilized a continuous high-resolution (2.56 ms sampling) two-sine voltage stimulus protocol (10 mV peak at both 390.6 and 781.2 Hz), with subsequent fast Fourier transform-based admittance analysis [24]. These high frequency sinusoids were superimposed on voltage ramp, step or sinusoidal stimuli. Capacitance data were fitted to the first derivative of a two-state Boltzmann function [20].

$$C_m = Q_{\max} \frac{ze b}{kT(1-b)^2} + C_{\text{lin}} \quad (1)$$

$$b = \exp\left(\frac{-ze(V_m - V_{\text{pkcm}})}{kT}\right)$$

where Q_{\max} is the maximum nonlinear charge moved, V_{pkcm} is voltage at peak capacitance or half-maximal nonlinear charge transfer, V_m is membrane potential, C_{lin} is linear capacitance, z is valence, e is electron charge, k is Boltzmann's constant, and T is absolute temperature.

Two methods to measure motor characteristics in restricted regions of the OHC

A double voltage-clamp technique, fully described elsewhere [10, 23], was used to electrically amputate portions of the OHC membrane. Briefly, the OHC was placed in a tight-fitting glass microchamber and simultaneously whole cell voltage-clamped (see Fig. 1, inset). The voltages within the microchamber were either the same as those delivered to the whole cell or set to ground. When set to ground, the system functions as a simple whole cell voltage clamp, where the entire cell membrane's voltage-dependent activity is evaluated. However, when the microchamber voltage command is the same as that delivered to the whole cell, only that portion of the OHC membrane outside the microchamber experiences a voltage drop, thus permitting the inspection of a restricted region of the OHC. Changing between configurations was performed instantaneously by manually switching the microchamber to ground or to the whole cell command voltage. During these experiments C - V functions were obtained with the transient capacitance measurement technique.

A micropipette aspiration technique was used to stress restricted regions of the OHC lateral membrane, as fully described elsewhere [26]. Briefly, patches of lateral membrane were deformed with a

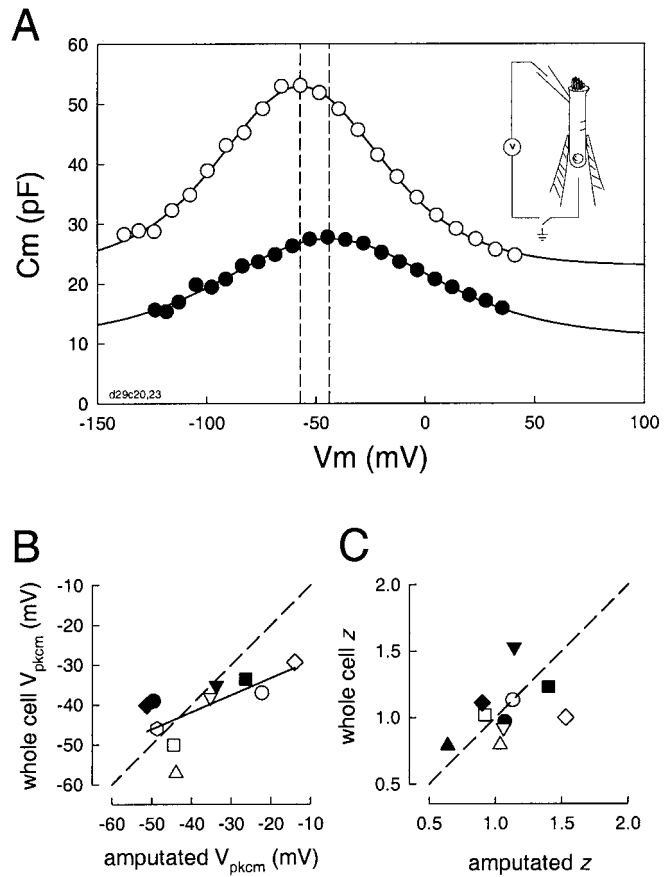


Fig. 1 A Membrane capacitance of outer hair cells (OHCs) before (*open circles*) and after (*closed circles*) electrical amputation in a microchamber. *Parallel dashed lines* indicate V_{pkcm} for each trace. **B** Comparison of V_{pkcm} for whole cell and amputated regions for 10 cells. *Dashed diagonal line* indicates equality. *Solid line* is linear fit to data. **C** z values for the same 10 cells. Note variability in whole cell z value

solution-filled glass pipette (2.5 μm diameter) fitted to a computer controlled piezoelectric driver (PZL, Burleigh Instruments, N.Y., USA). Membrane deformation near the middle of the cell was induced by movements of the driver's piston stepped in the negative direction (producing suction) of about 800 nm, controlled by the voltage magnitude delivered to the piezoelectric. Step stimuli produced motor-evoked currents that were measured as an rms response. Whole cell holding voltage was varied to obtain the current's voltage dependence. The data were fitted to Eq. 1 only to determine the voltage at peak current (V_{pkig}). During these experiments C - V functions were obtained with the AC capacitance measurement technique.

Results

For the double voltage-clamp technique, the nonlinear capacitance measured when the micro-chamber is grounded to the bath derives from all motor containing regions of the cell, since the voltage drop is impressed across the entire membrane of the cell. The capacitance measures are thus typical of whole cell conditions (Fig. 1A) and have characteristics similar to those of past reports [20].

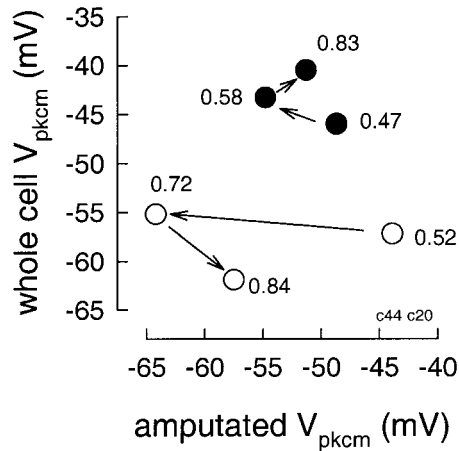


Fig. 2 Same as Fig. 1 except for two OHCs where three successive amputations were made (in the sequence of the *arrows*) following repositioning of the cell in the microchamber. Note that even though V_{pkcm} of the whole cell has shifted following repositioning, the region after amputation does not shift in parallel (neither in magnitude nor polarity), indicating its independence. The numbers indicate the degree of amputation at each measurement

Upon switching to amputation mode, the measured capacitance derives only from that portion of the cell that is outside the microchamber. The magnitude of linear as well as nonlinear capacitance is reduced (Fig. 1A), and there is an apparent shift in the V_{pkcm} to depolarized levels relative to whole cell V_{pkcm} . Figure 1B and C present V_{pkcm} data from ten cells. V_{pkcm} , which is the midpoint of the voltage range over which the motors work, differs between whole cell and the amputated region. The difference may be in the hyperpolarizing or depolarizing direction (Fig. 1B). Additionally, z , an indicator of voltage sensitivity, differs from whole cell estimates and z values can be greater or less than whole cell measures, as expected since they will sum to produce intermediate whole cell values (Fig. 1C). Pre- and post-amputation recordings were made within a few seconds of each other, in order to ensure both stationary conditions and that any experimentally induced forces, such as membrane tension imposed by the microchamber, would remain constant under each condition. Accordingly, the correlation between absolute ΔV_{pkcm} and degree of amputation was poor ($r^2=0.015$).

For the data just presented, the OHCs were inserted into the microchamber and remained unperturbed during the collection of pre- and post-amputation data. However, it is possible to reposition the OHC within the microchamber to obtain progressive amputations. In two cells where three successive amputations of differing magnitude were made, it was clear that whole cell V_{pkcm} changed during the repositioning (possibly due to changes in membrane tension or intracellular chloride), but that of the amputated portion tracked neither the amplitude nor the polarity of those changes (Fig. 2). For example, in one cell the initial pair of values (whole cell vs amputation) was -57.2 , -43.9 mV; after repositioning for the next

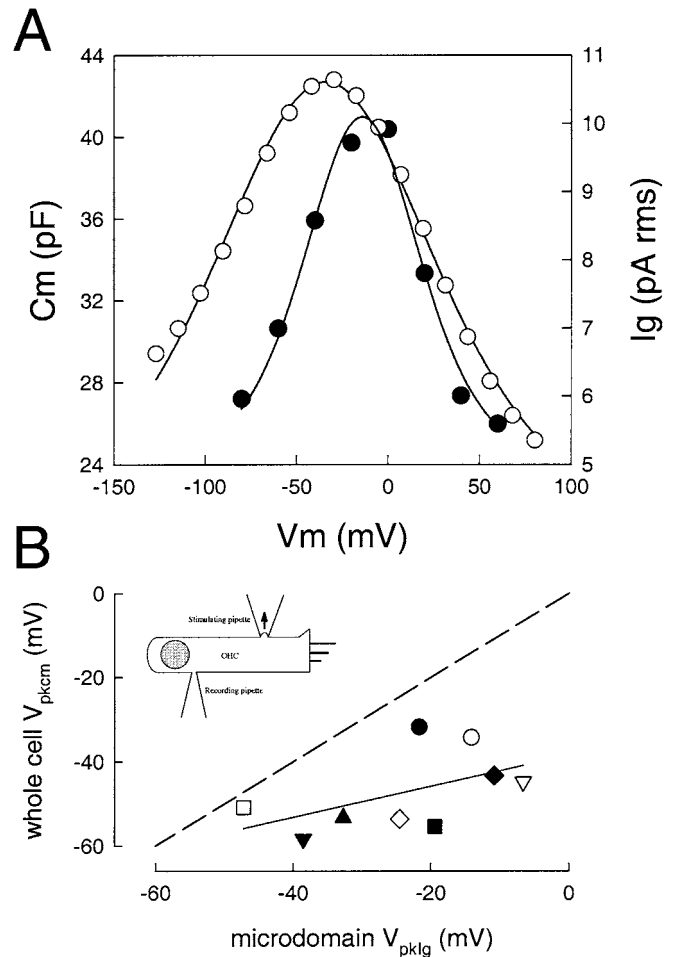


Fig. 3 **A** Whole cell capacitance (*open circles*) and microdomain stretch-induced gating currents. Note difference in voltage at peak response. **B** Comparison of voltage at peak response for 9 cells. *Dashed diagonal line* indicates equality. *Solid line* is linear fit to data. Note wide variability of V_{pkig} relative to V_{pkcm}

amputation the pair was -55.2 , -64.2 mV; and after repositioning for the final amputation, the pair was -61.9 , -57.5 mV. This is very strong evidence for the independent nature of OHC motor domains.

Mechanical stress of the lateral plasma membrane evokes a motor-generated displacement current (I_g) whose voltage dependence is bell-shaped like that of the cell's nonlinear capacitance (Fig. 3A). V_{pkig} is expected to be shifted to the right (in the depolarizing direction) of V_{pkcm} , since membrane stress shifts the underlying charge-voltage ($Q-V$) function to the right. That is, the evoked $I-V$ function results from the difference between the shifted $Q-V$ functions under the stressed and nonstressed conditions [9,29]. Figure 3B shows for nine cells that this expectation is met, as the data points fall to the right of the plot's dashed line of equivalence. However, the V_{pkig} of individually stressed microdomains varies widely relative to their respective whole cell V_{pkcm} . If the V_{pkcm} of the microdomains were the same as whole cell values then the two should be strictly correlated as V_{pkig} is

predicted to be midway between pre- and post-tension V_{pkcm} . Additionally, the variability is not due to differences in the degree of shift caused by the stimulus, since the correlation between peak I_g and shift magnitude was poor ($r^2 = 0.05$). This same poor correlation also indicates that any possible variability of d.c. tension introduced by sealing the loose pipette to the membrane was not influential, since we have previously shown that steady-state tension is directly related to the magnitude of I_g [26]. If steady-state membrane tension were responsible for the variability in the shift, we might have expected a good correlation between I_g and shift. The simplest explanation is that such wide variability reflects an underlying V_{pkcm} of the stressed microdomains that differs from that of the whole cell.

Discussion

The data presented here indicate that the mechanically active lateral membrane is functionally heterogeneous, showing variability in the voltage dependence of nonlinear capacitance or motor charge movement. The gain of the OHC's electrically evoked mechanical response depends on the position of its sigmoidal displacement voltage (or corresponding bell-shaped capacitance voltage) function along the voltage axis vis-à-vis the cell's resting potential [19]. V_{pkcm} , which defines the midpoint of these functions, and therefore the OHC's voltage of maximum piezoelectric-like sensitivity, is susceptible to a variety of agents including membrane tension [9, 12, 14], resting membrane potential [24], temperature [21], phosphorylation [8, 11] and intracellular [18, 22] or extracellular [22] chloride concentration. In many cases, it has been demonstrated that these effects arise from direct action on the OHC motor protein, prestin [16, 17, 18, 25]. It should be noted that efforts were made to avoid experimentally induced changes in the parameters that describe OHC charge movement; for example, measurements of whole cell V_{pkcm} and microdomain V_{pkcm} or V_{pkig} were obtained without perturbation of the preparation and within seconds of each other, thus ensuring stationary conditions. Additionally, unequivocal evidence of microdomain independence was found when multiple amputations were made; that is, in the face of whole cell V_{pkcm} changes during repositioning cells within the microchamber, nonparallel changes (in magnitude and polarity) of microdomain V_{pkcm} were found. This could not occur if the forces that changed whole cell measures during repositioning, e.g., membrane tension or chloride concentration, were acting on a uniform population of lateral membrane motors. We conclude that while molecular sensor/motors are restricted to the expansive lateral plasma membrane, this membrane actually harbors populations of sensor/motor microdomains whose characteristics are set by local forces. Independent microdomain characteristics sum to contribute to whole cell characterizations of OHC mechanical and electrical activity.

The existence of functionally distinct microdomains, whose voltage- and tension-dependent characteristics are locally set, may have important consequences for understanding the mechanism of OHC motility. Such diversity could promote differential activation of OHC motor elements resulting in mechanical forces other than in a predominantly axial direction. For example, at a given resting membrane potential, adjacent microdomains may be contracted to different extents because mechanical gains may be different; bending or twisting movements of the OHC might be expected. Indeed, Frolenkov et al. [7] have observed bending of the OHC in an external field, but provided an explanation based on differential stimulus distributions. Whether the causes of those nonaxial motions were due to motor or stimulus characteristics is arguable; however, the likelihood that even in the face of uniform lateral membrane stimulation nonaxial forces will be evoked is strengthened by evidence from these same authors who showed lateral membrane substructure and function [15]. In addition to observing local variation in the direction that microbeads moved on the surface of the OHC, they showed by freeze etch electron microscopy that the lateral membrane presented a mosaic of microdomains with differing orientations. The mechanism that produces this mosaic is unknown, but it is possible that forces derived from the variable motor characteristics that we observed result in structural correlates. It is well known that extrinsic, local membrane forces can initiate substantial rearrangement of membrane and submembrane structure over extended time periods [27]. Alternatively, the structural differences themselves could affect motor characteristics, for example, by inducing local membrane tensions.

Our data may also relate to theories on OHC motor function, since until now it has been tacitly assumed that elementary characteristics derived from whole cell measures of motility and/or gating charge apply to all motors in the lateral membrane. Under this assumption, it has been difficult to explain the observation that a decrease in membrane tension under whole cell conditions causes a negative shift in V_{pkcm} accompanied by an increase in peak C_m [9, 14]. It has been argued that changes in peak C_m arise from membrane tension working through an anisotropic cytoskeleton or working on an anisotropic motor [9, 13]; indeed, isolated patch recordings, where tension can be applied isotropically, show only a shift in V_{pkcm} [9, 16]. Nevertheless, even in OHCs that have become spherical due to intracellular trypsin treatment, and where applied tension should be isotropic, peak C_m is altered by turgor pressure [1, 14]. We noted that motor sensitivity to membrane stress appeared greater after cortical cytoskeleton destruction with trypsin [14]. Adachi and Iwasa [1] quantified this sensitivity change by degree of V_{pkcm} shift, and found that sensitivity was about six times greater than normal, i.e., 155 mV/kPa compared to normal whole cell values of 25 mV/kPa [2, 14], which may account for their observed step-like C_m decrease [1]. Our present data may provide an alternative explanation for the effects of stress on the whole cell as opposed to

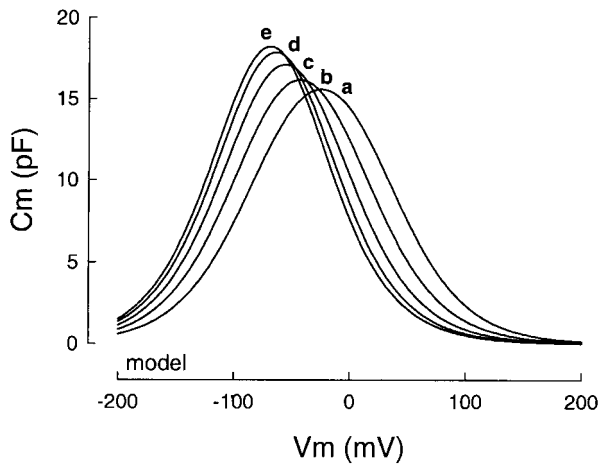


Fig. 4 Model of microdomain contributions to whole cell capacitance. In the model, each of 10 hypothetical microdomains experiences local tensions such that each V_{pkcm} is shifted 10 mV offset from each other, all of them to the right of -70 mV. The sum of these individual capacitances produces the whole cell capacitance trace *a*, and the other four traces are the result of graded decreases in tension under whole cell conditions. When tension is reduced, each microdomain V_{pkcm} shifts left towards -70 mV, the limiting V_{pkcm} [14]. As each microdomain tension is dissipated, its V_{pkcm} halts at -70 mV, and accumulates with other microdomain V_{pkcm} s producing larger peak whole cell capacitances (traces *b–d*). When all microdomain tensions are dissipated, all V_{pkcm} s reside at -70 mV and the peak capacitance is maximal (trace *e*). Q_{max} (0.25 pC) and z (0.75) were fixed and the same for each microdomain

patch nonlinear capacitance. First, we note that the negative shift of V_{pkcm} and increase in peak C_m during reduction of turgor pressure is asymptotic, each reaching fixed values when the OHC begins to collapse, despite continued reduction of turgor pressure [14]. The limiting negative potential is near -70 mV, close to the OHC's normal resting potential [6]. Because of this brick-wall effect, we suggest that microdomains that may have unchanging peak capacitance but variable V_{pkcm} will all shift to a single common V_{pkcm} as turgor pressure is reduced. As a result, at positive turgor pressure peak C_m will be depressed compared to negative pressure, but with increasingly negative pressures peak C_m will increase asymptotically as summation of the parallel microdomain capacitances occurs (Fig. 4). In this model we used a constant z of 0.66 across microdomains, yet fits of these model data to a single Boltzmann function indicate that apparent z is less than 0.66 initially, but increases to this level as turgor pressure is reduced. We have observed this behavior experimentally [14]. Nevertheless, the present observation that V_{pkcm} and z of microdomains are variable about whole cell values (Fig. 1 c) emphasizes that other forces besides tension influence the distribution of these parameters. Consequently, tension-induced changes in the form of the whole cell capacitance function may not necessarily provide insight into the microscopic characteristics of motor function. Spatially restricted patch capacitance measures, on the other hand, may provide a better sampling of microdomain characteristics.

Acknowledgements This work was supported by NIH-NIDCD grant DC00273 to J.S.S. I thank Guojie Huang, Shin Takahashi, and Margaret Mazzucco.

References

- Adachi M, Iwasa KH (1999) Electrically driven motor in the outer hair cell: effect of a mechanical constraint. *Proc Natl Acad Sci USA* 96:7244–7249
- Adachi M, Sugawara M, Iwasa KH (2000) Effect of turgor pressure on outer hair cell motility. *J Acoust Soc Am* 108:2299–2306
- Ashmore JF (1990) Forward and reverse transduction in the mammalian cochlea. *Neurosci Res [Suppl]* 12:S39–S50
- Brownell WE, Bader CR, Bertrand D, de Ribaupierre Y (1985) Evoked mechanical responses of isolated cochlear outer hair cells. *Science* 227:194–196
- Dallos P (1992) The active cochlea. *J Neurosci* 12:4575–4585
- Dallos P, Santos-Sacchi J, Flock A (1982) Intracellular recordings from cochlear outer hair cells. *Science* 218:582–584
- Frolenkov GI, Kalinec F, Tavartkiladze GA, Kachar B (1997) Cochlear outer hair cell bending in an external electric field. *Biophys J* 73:1665–1672
- Frolenkov GI, Mammano F, Belyantseva IA, Coling D, Kachar B (2000) Two distinct Ca(2+)-dependent signaling pathways regulate the motor output of cochlear outer hair cells. *J Neurosci* 20:5940–5948
- Gale JE, Ashmore JF (1994) Charge displacement induced by rapid stretch in the basolateral membrane of the guinea-pig outer hair cell. *Proc R Soc Lond B Biol Sci* 255:243–249
- Huang G, Santos-Sacchi J (1993) Mapping the distribution of the outer hair cell motility voltage sensor by electrical amputation. *Biophys J* 65:2228–2236
- Huang G-J, Santos-Sacchi J (1993) Metabolic control of OHC function: phosphorylation and dephosphorylation agents shift the voltage dependence of motility related capacitance. *ARO Midwinter Meeting Abstr* 16:464
- Iwasa KH (1993) Effect of stress on the membrane capacitance of the auditory outer hair cell. *Biophys J* 65:492–498
- Iwasa KH (1996) Membrane motor in the outer hair cell of the mammalian ear. *Comments. Theor Biol* 4:93–114
- Takehata S, Santos-Sacchi J (1995) Membrane tension directly shifts voltage dependence of outer hair cell motility and associated gating charge. *Biophys J* 68:2190–2197
- Kalinec F, Kachar B (1995) Structure of the electromechanical transduction mechanism in mammalian outer hair cells. In: Flock Å, Ottoson D, Ulfendahl M (eds) *Active hearing*. Elsevier, Oxford, pp179–191
- Ludwig J, Oliver D, Frank G, Klocker N, Gummer AW, Fakler B (2001) Reciprocal electromechanical properties of rat prestin: the motor molecule from rat outer hair cells. *Proc Natl Acad Sci USA* 98:4178–4183
- Meltzer J, Santos-Sacchi J (2001) Temperature dependence of non-linear capacitance in human embryonic kidney cells transfected with prestin, the outer hair cell motor protein. *Neurosci Lett* 313:141–144
- Oliver D, He DZ, Klocker N, Ludwig J, Schulte U, Waldegger S, Ruppertsberg JP, Dallos P, Fakler B (2001) Intracellular anions as the voltage sensor of prestin, the outer hair cell motor protein. *Science* 292:2340–2343
- Santos-Sacchi J (1989) Asymmetry in voltage-dependent movements of isolated outer hair cells from the organ of Corti. *J Neurosci* 9:2954–2962
- Santos-Sacchi J (1991) Reversible inhibition of voltage-dependent outer hair cell motility and capacitance. *J Neurosci* 11:3096–3110
- Santos-Sacchi J, Huang G (1998) Temperature dependence of outer hair cell nonlinear capacitance. *Hear Res* 116:99–106

22. Santos-Sacchi J, Rybalchenko V (2002) Tension-dependent chloride current affects OHC capacitance. ARO Midwinter Meeting Abstr 25:255
23. Santos-Sacchi J, Huang GJ, Wu M (1997) Mapping the distribution of outer hair cell voltage-dependent conductances by electrical amputation. *Biophys J* 73:1424–1429
24. Santos-Sacchi J, Kakehata S, Takahashi S (1998) Effects of membrane potential on the voltage dependence of motility-related charge in outer hair cells of the guinea-pig. *J Physiol (Lond)* 510 (Pt 1):225–235
25. Santos-Sacchi J, Shen W, Zheng J, Dallos P (2001) Effects of membrane potential and tension on prestin, the outer hair cell lateral membrane motor protein. *J Physiol (Lond)* 531:661–666
26. Takahashi S, Santos-Sacchi J (2001) Non-uniform mapping of stress-induced, motility-related charge movement in the outer hair cell plasma membrane. *Pflügers Arch* 441:506–513
27. Veselska R, Janisch R (2001) Reaction of the skin fibroblast cytoskeleton to micromanipulation interventions. *J Struct Biol* 136:110–118
28. Zhang M, Kalinec F (2002) Structural microdomains in the lateral plasma membrane of cochlear outer hair cells. *JARO* DOI: 10.1007/s101620020016
29. Zhao HB, Santos-Sacchi J (1999) Auditory collusion and a coupled couple of outer hair cells. *Nature* 399:359–362
30. Zheng J, Shen W, He D, Long K, Madison L, Dallos P (2000) Prestin is the motor protein of cochlear outer hair cells. *Nature* 405:149–155



ELSEVIER

New tunes from Corti's organ: the outer hair cell boogie rules

Joseph Santos-Sacchi

The amplification of acoustic stimuli is a feature of hair cells that evolved early on in vertebrates. Though standard stereocilia mechanisms to promote such amplification may persist in the mammal, an additional mechanism evolved to enhance high frequency sensation. Only in mammals, a special cell type, the outer hair cell, arose that possesses a remarkably fast somatic mechanical response, which probably endows the passive cochlea with a boost in sensitivity by a factor of 100 (40 dB), at least. Experiments conducted over the past few years have shed light on many aspects of outer hair cell electromotility, including the molecular identification of the motor, the effects of a knockout, and underlying mechanisms of action. A review of this remarkable progress is attempted.

Addresses

Yale University School of Medicine, Otolaryngology and Neurobiology,
BML 244 333 Cedar Street, New Haven, CT 06510, USA
e-mail: joseph.santos-sacchi@yale.edu

Current Opinion in Neurobiology 2003, 13:1–10

This review comes from a themed issue on
Sensory systems
Edited by Clay Reid and King-Wai Yau

0959-4388/\$ – see front matter
© 2003 Elsevier Ltd. All rights reserved.

DOI 10.1016/S0959-4388(03)00100-4

Abbreviations

BM basilar membrane
IHC inner hair cell
NLC non-linear capacitance
OHC outer hair cell
RC resistor x capacitor
TH thyroid hormone
TM tectorial membrane

Introduction

The organ of Corti, the auditory sensory epithelium of the mammal, houses two types of hair cells, the inner (IHC) and outer (OHC) hair cell. Both cell types transduce mechanical stimuli into electrical signals by modulating a standing cationic current in response to stereocilia displacement (forward transduction). This current induces a receptor potential across the basolateral membrane of the cell, the depolarizing phase of which may promote the release of neurotransmitter [1,2]. Evidence accumulated that an interaction between OHCs and IHCs promoted the highly selective and sensitive responses of the mammalian auditory system to high frequency acoustic stimulation [3–5]. However, a potential mechanism for such an interaction remained obscure until Brownell [6]

observed the twitching of outer hair cells in response to electrical stimulation. Following his discovery of reverse transduction [6], a re-evaluation of the classical concepts of mammalian hearing has been underway. Current theories that are concerned with the basis of the cochlear amplifier envision an acoustically evoked cycle by cycle feedback process between the OHCs and the basilar membrane (BM) [7–10]. That is, *in vivo*, the acoustically evoked electrical responses of the OHCs (receptor potentials) are assumed to effect rapid mechanical responses (length changes) by these cells, which boost the mechanical input to the IHC — the receptor cell that receives up to 95% of the afferent innervation [11].

Just three years ago, Dallos and colleagues identified the OHC lateral membrane motor, a protein of 744 amino acid residues that they called prestin, its primary structure classifying it as one of the newer anion transporter family members (SLC26A5) [12]. Subsequently, a flurry of manuscripts have appeared (most of which are review articles! — mea culpa) attesting to prestin's significant role in cochlear physiology. So many questions remain regarding the protein's workings; however, the recent production of a prestin knockout and the demonstration of a human non-syndromic deafness that is linked to a prestin mutation demonstrate the protein's requirement for OHC electromotility, and the devastating effects of its absence on the cochlea amplifier [13^{••},14[•]]. The knockout work also raised several more questions, including what proportional contribution does the cellular collection of motors make to the overall cochlea amplifier, and what other cellular and acellular structures direct its force into the organ? For example, in homozygotes, in which prestin was absent, threshold elevations ranged from 40 to 60 dB, but in heterozygotes, roughly a halving of the cellular motor number and activity (3.4 versus 2.3% cell length change) resulted in an apparent proportional (around 6 dB) decline in auditory performance. How might half the motor complement in the OHCs provide only for linear response (e.g. 8th nerve spike rate, BM displacement) growth near threshold, yet the full complement promote non-linear amplificatory growth above that? There are hints in the data that something more than a reduction in the motor number may be occurring. For example, the voltage-displacement function, which can be derived from their figure 3a [13^{••}], seems to show, in addition to the decrease in magnitude, a change in the voltage dependence between wild type and heterozygote. Such a shift denotes an adjustment in the gain of the remaining motor activity, that is, an alteration in the sensitivity of the remaining motors to voltage change. Additionally, could

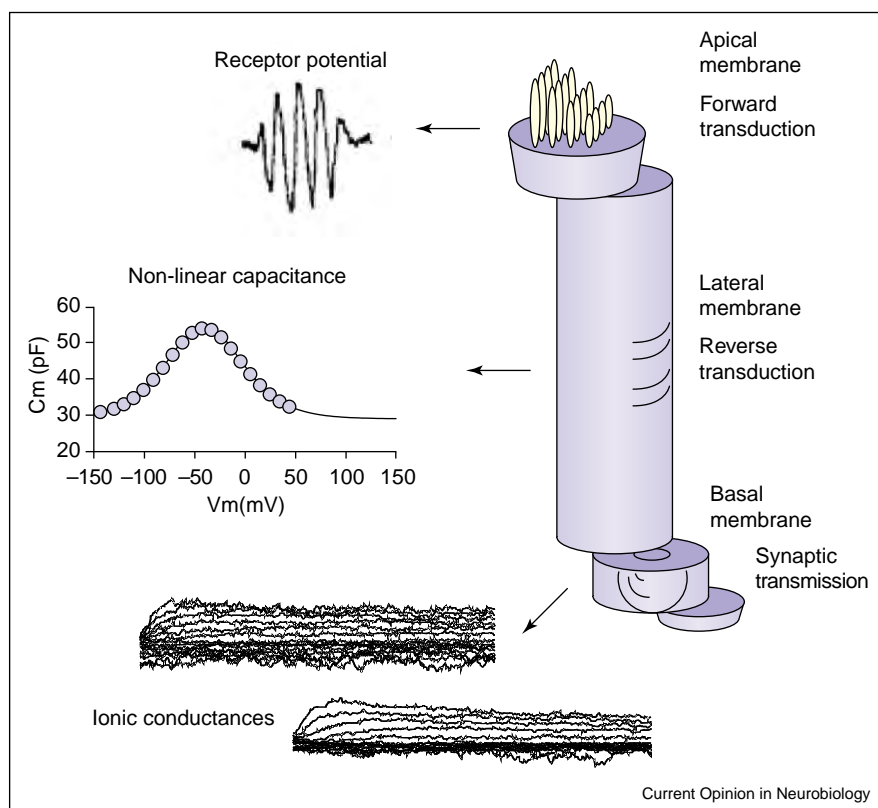
the change in cell length that accompanied the knockout have compromised normal interactions of OHCs with themselves [15] or the tectorial membrane (TM) superstructure [16]? Indeed, a knockout of a major TM protein, α -tectorin, which resulted in disruption of such interactions, proved detrimental to cochlea amplification [16]. Certainly, a molecular biological trick that could turn on and off prestin, or diminish its activity in a graded way, rather than removing it outright, could help to clarify matters. There is no doubt, however, that understanding the molecular aspects of the cells which form the basis of the cochlea amplifier will be far easier than putting together the whole picture. Here, I first review some basic properties of the OHC lateral membrane motor, and then look at some recent data that relate to the mechanism of OHC electromotility and its effects on cochlear performance.

Biophysical characterization of the outer hair cell lateral membrane motor

The steady-state behavior of the OHC lateral membrane motor is routinely evaluated by fitting a two state

Boltzmann function, a sigmoidal function typically used to relate charge displacement and voltage across a membrane, to measures of OHC length change (you can see a video of this length change evoked by a charming voltage stimulus delivered through a patch pipette at the Yale Ear lab website [17]) or non-linear charge movement of the motor's voltage sensor [18,19]. Alternatively, the charge movement is evaluated by fitting the cell's voltage-dependent or non-linear capacitance (NLC; Figure 1) with the first derivative of the same Boltzmann function. In each case, the parameters obtained are V_h (or V_{pkcm} , the voltage at half maximal charge transfer or peak capacitance), z (the unitary charge moved through some portion of the membrane field; otherwise interpreted as the motor's voltage sensitivity) and Q_{max} (the total charge moved across the membrane, indicative of the number of motors possessing unitary charge within the membrane). Typical values for an OHC isolated from the low frequency region of the cochlea are -40 mV, 0.75 , and 2.5 pC, respectively. Motor density, derived from non-linear charge density within the cell's lateral membrane has been estimated to be near $8000/\mu m^2$ [20,21]. Although

Figure 1



The OHC has a highly compartmentalized membrane. Apical, lateral and basal membranes possess characteristic integral membrane constituents with measurable electrical correlates. Of interest for the present review is the non-linear capacitance (NLC) that characterizes the lateral membrane motor. The voltage-dependent capacitance, which rides atop the linear (membrane surface area-dependent) capacitance, peaks at a voltage (V_h) near -40 mV that is modulated by a variety of biophysical forces. In addition to information on the state probability of the motor (contracted versus expanded) provided by V_h , measures of NLC also provide estimates of the motor's unitary charge or voltage sensitivity (z), and the total charge moved across the membrane (Q_{max}).

there is a consensus that non-linear charge movement and OHC mechanical activity are inextricably related, contrary to some claims [22], we do not know if charge movements or displacement currents mirror mechanical responses in time, as simultaneous mechanical and charge measures have not yet been made with sufficient time resolution [23–25]. Such measures could provide valuable information on the link between charge movement and OHC mechanical activity, the latter having been measured beyond 70 kHz [26].

Prior to the identification of prestin as the OHC motor [12], several biophysical attributes of the motor had been characterized. These included the effects of membrane tension (turgor pressure), preconditioning voltage, and temperature [27–34]. The main action of these biophysical forces is to set the steady state energy profile of the motor, perturbation effectively and reversibly shifting the operating voltage range over which the motors work in a time-dependent manner. Each of the following perturbations induces a 20–25 mV rightward (depolarizing) shift in V_h : an increase in OHC turgor pressure of 1 kPa (or circumferential membrane tension of 1 mN/m), a step in resting potential from +40 to –120 mV, and a 10°C increase in temperature. The sensitivity of the motor to these biophysical forces is likely to reflect as yet unraveled mysteries of the motor and underscores the susceptibility to insult of the cochlear amplifier. Recently, these same biophysical attributes have been identified in non-auditory cells transfected with prestin [35,36,37], confirming the identity of the lateral membrane motor. However, we did note that the effects were smaller in magnitude than those found in the native OHC [36], and thus, it is possible that prestin requires additional subunit interactions to achieve the desired amplification. Indeed, estimates of the unit magnitude of the motor stroke (area change) are also smaller in prestin transfected cells [38]. One possible interacting species is GLUT-5, an initial motor protein candidate [39].

A motor complex?

Although GLUT-5, a fructose transporter, presented some characteristics that indicated its similarity to the OHC motor [39], this hexose transporter took a back seat following the identification of prestin. GLUT-5 has a different time course of developmental expression than that of electromotility, whereas prestin expression correlates well [40]; indeed, the co-expression of GLUT-5 with prestin apparently has no effect on the activity of prestin [37]. Whether these observations mean that GLUT-5 is out of the picture or not is debatable, as preliminary indications are that in prestin knockout mice GLUT-5 is absent [41], and expression of prestin may promote fructose transport [42]. Could GLUT-5 and prestin expression be under some common control mechanism? Are they members of a motor complex?

At present we do not know if prestin functions alone or as multimers, or whether additional subunits are required for its activity or not. The initial subtractive screen between IHCs and OHCs that was used to identify prestin produced a large number of unique OHC proteins [12,43]. Presumably, some of these may interact with prestin. There has been one preliminary report of an interacting protein (termed couplin), which links prestin to structural members (pillars) of the OHC sub-membranous cytoskeleton [44]. However, on the basis of estimates of prestin density in the OHC, there are far too few pillars to suggest a one-to-one interaction of couplin with prestin. Couplin's function is unknown, but it is similar to the calponin homology (CH) domain, a superfamily of actin-binding domains. Interestingly, couplin is expressed in several tissues, indicating that potential interacting proteins of prestin may extend well beyond the number of unique OHC proteins identified in the initial differential screen. Indeed, interacting proteins may naturally exist in cell lines used for prestin transfections, possibly confounding our supposed view of prestin in isolation.

Prestin structure

The primary structure of prestin places it in a newly identified anion transporter family, SLC26. Prestin is the fifth identified member, SCL26A5. The nine members identified thus far [45] possess good sequence homology within the probable transmembrane region, but poor homology in the extreme carboxy and amino termini. Most of the SCL26 family members have a clear anion transport function [45–48], but prestin has yet to be fully evaluated, although preliminary evidence indicates that it may transport Cl^- and bicarbonate [42]. The topology of prestin, that is, the number of transmembrane regions and the location of carboxy and amino termini, has received some attention. The carboxy and amino termini are both located intracellularly as determined by antibody staining [37,49], indicating that the number of transmembrane domains is even. More detailed topology mapping is lacking, and the results of topology prediction programs are divided among 10 to 12 transmembrane domains. Nevertheless, the favored opinion is that prestin and SCL26A6, arguably prestin's closest relative [46], have 12 transmembrane domains [49]. This opinion is formed on the basis of the placement of conserved potential N-glycosylation sites within a putative second extracellular loop. The confirmation of prestin topology is important as site directed mutation studies have already been conducted that have observed effects on prestin activity.

Playing with prestin

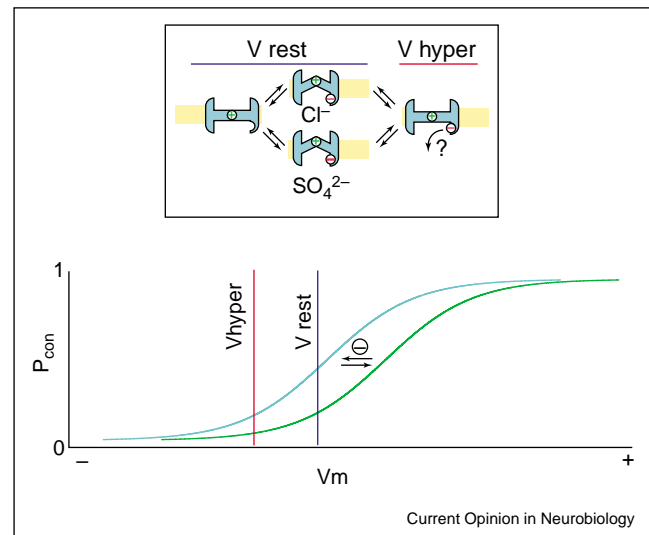
The first structural manipulations of prestin were designed to modify the polarity of non-conserved (among SLC26 members) charged amino acid residues that presumably reside within the voltage sensing transmembrane domain [50]. Such manipulation failed to

abolish non-linear charge movement under voltage stimulation, but shifted the value of V_h . Subsequently, it was found that full truncation of the carboxy terminus, distal to residue 590, results in absent voltage sensitivity, that is, immeasurable NLC [51]. However, in the absence of a functional protein it is difficult to prove correct plasma membrane targeting and/or folding; thus, it is imperative to also identify similar, yet active truncations. Recently, we [52] were able to produce highly restricted truncations of both carboxy and amino termini at their extreme ends (within 20 residues) that abolished NLC in a graded manner. Additionally, charge reversals of carboxy-terminal charged clusters produced marked shifts in V_h . Therefore, it is clear that the non-conserved (among SLC26 members) carboxy and amino termini of prestin, which are unable to sense the membrane field, are nevertheless important for its sensor function. This importance may relate to allosteric actions that these termini could have on prestin's voltage sensor through prestin–protein or prestin–anion interactions (see below). One other observation that is of interest in light of these data is the resistance of the motor to proteolytic destruction despite the presence of many potential cleavage sites [31,53,54]. Evidently, in the native OHC, the carboxy and amino termini are protected by either their own structural features or interactions with other proteins (or lipids).

Anion effects on prestin's voltage sensor

Two years ago, Oliver *et al.* [50^{••}] made the key discovery that prestin requires anions to function, notably Cl^- and bicarbonate, but not sulfate. They used membrane patches from prestin-transfected chinese hamster ovary (CHO) cells and rat OHCs to determine that NLC requires either of these physiologically abundant anions. The $K_{1/2}$ (concentration at half maximal response) for chloride and bicarbonate's ability to generate NLC was 6 and 44 mM, respectively. Additionally, they found that salicylate, a known ototoxic agent that modulates NLC on the inner aspect of the OHC plasma membrane [55,56], increased chloride's $K_{1/2}$. It was suggested that these anions function as prestin's extrinsic voltage sensor, in which an incomplete anion transport cycle moves negative charge through the membrane field, causing prestin to reside in the expanded state. Some of these data are consistent with previous work showing that only negatively charged lipophilic ions influenced motility and NLC in intact OHCs [57], and that furosemide, a chloride transporter antagonist, interfered with NLC [58]. Nevertheless, the outcome of more recent studies on the effects of mono and divalent anions on intact OHCs [59^{••}] offers an alternative to the extrinsic voltage sensor hypothesis. Notably, in intact OHCs, sulfate and other sulfonate-containing anions can promote significant non-linear charge movement in the absence of bicarbonate and chloride. Moreover, if sulfates were simply able to substitute for monovalent anions as prestin's extrinsic voltage sensor, the unit charge of the motor and Q_{max} would have

Figure 2



Effect of anions on OHC motor. Boltzmann functions describe the voltage-dependent probability of the motor being in the contracted state (P_{con}). At the fixed resting voltage (V_{rest} , blue line) and in the absence of bound anions (green Boltzmann), a small proportion of motors are in the contracted state. With the delivery and possible binding of Cl^- to a site (or sites) on the intracellular aspect of the membrane motor, the steady state energy profile is altered, resulting in a leftward shift in the probability function along the voltage axis (cyan Boltzmann). Consequently, at V_{rest} , an increased number of motors reside in the contracted state (inset, motors in cyan, membrane in yellow). A hyperpolarizing step to V_{hyper} (red line) restores the original distribution of motor states. Whether chloride or sulfate is bound, the slope (z), which is indicative of the voltage sensor's unit charge, remains the same, showing that the extrinsic anion does not serve as the voltage sensor [60].

doubled, as sulfate is divalent. However, the motor's valence, z , remained the same. Another issue that complicated the simple voltage sensor scheme of Oliver *et al.* [50^{••}] was the identification of large shifts in V_h as a function of chloride concentration, that is, an increase in intracellular chloride shifting V_h to negative potentials [59^{••},60]. Thus, chloride strongly influences the probability that prestin will reside in the compact or expanded state. In view of these observations, we proposed [59^{••}] that anions serve not as extrinsic voltage sensors but as allosteric modulators of prestin that upon binding shift prestin's voltage dependence into the physiological range, where intrinsic charge senses voltage perturbation (Figure 2). Thus, at any given voltage, the binding of chloride to prestin increases the likelihood of the motor being in the contracted state, which corresponds to cell shortening. Recently, chloride's effect on prestin's operational voltage range has been confirmed [61].

Targeting the lateral plasma membrane

The OHC motor is clearly restricted to the cell's lateral plasma membrane, which possesses a surface area of

greater than $2,000 \mu\text{m}^2$ in low frequency OHCs. This layout has been revealed through physiological tests of the motor's electro-mechanical activity [53,54,62] as well as its mechano-electrical activity [31]. Indeed, prestin has been mapped exactly to the location identified by those physiological measures by antibody labeling [40]. However, the lateral membrane is not uniform, but instead composed of structural and functional microdomains, in which local forces may impose on motor activity [63,64]. That is, the voltage range over which the motors work, and the sensitivity of the motors may not be uniform along the cell surface [64]. These microdomains can have an impact on the overall mechanical activity of the OHC. For example, movements of the cell along an axis other than the longitudinal one, as has been observed *in vitro* [65] and *in vivo (in situ)* [66], could arise from local characteristics of motor microdomains that provide for anisotropic (on the level of the whole cell) electromechanical properties. Thus, the evolving concept that the organ of Corti or parts of it deform in a non-rigid manner [66,67,68*,69] may be substantially derived from the mosaicism of the OHC lateral membrane.

The distribution of prestin along the lateral membrane, spanning from nuclear to sub-cuticular regions of the cylindrical cell, is apparently under thyroid hormone (TH) control. In TH deficient rats, prestin expression is delayed and the protein is distributed along the whole basolateral extent of the cell, never attaining restricted membrane targeting to the lateral membrane [70**]. Motor function, however, appears unaffected, as the absence of TH in *in vitro* explants of Corti's organ is not required for the development of electromotility [71]. The correct localization may not only depend upon targeting per se, possibly with helper proteins, but also on the limitation of lateral diffusion. In the normal OHC, the diffusion of lateral membrane motors into adjacent basal regions of the OHC membrane, in which ion channels are restricted [72], does not occur, even after cytoskeletal destruction with proteolytic enzymes [31]. The membrane-based barriers to diffusion across these membrane domains are unknown. However, within the lateral membrane proper, lateral diffusion of motors appears to occur at rates typical for untethered integral membrane proteins, namely at around $0.08 \mu\text{m}^2/\text{s}$ [73]. The diffusion coefficient of the lipid permeable dye di-8-ANNEPS within the OHC lateral membrane is faster, as expected for lipids, but interestingly, it is voltage-dependent and tension-dependent [74,75]. This may relate to the voltage and tension-dependence of the major protein prestin that is located in that membrane. However, another lipid soluble dye, SP-DiIC18, is relatively immobile but can redistribute within the membrane in a voltage-dependent manner, and this redistribution probably depends on prestin activity [63]. In light of these data, it is possible that the diffusion of prestin itself depends on the protein's voltage-dependent area state, an area that has yet to be explored.

Molecular motions

The whole cell mechanical response of the OHC (which can be seen at the Yale ear lab website [17]) is truly amazing. Movements as large as $30 \text{ nm}/\text{mV}$ have been measured [76]. One of the perplexing questions about prestin or its complex is how the voltage dependent conformational change, which we are able to observe microscopically through displacement current measures, results in cell movements? A variety of hypotheses have been tested, but two putative mechanisms remain entertained in the field. Following the observation that OHC membrane patches change surface area in response to membrane voltage change [53], molecular motor models incorporating two-state area changes appeared. These mechanical models naturally arose from the two-state Boltzmann models of non-linear charge transfer that preceded them [18,19], and suggested that unitary motors fluctuate among area states with an area difference ranging from 0.4 to 8 nm^2 [27,28,34,77–79]. Given the constraints imposed by a cylindrical shape, caused by the cortical cytoskeleton [80] and the fixed volume (especially expected at high acoustic frequencies), surface area changes are predicted to alter OHC length and diameter in line with physiological observations [77]. Of course, an alteration in surface area should cause a change in the cell's linear (specific) capacitance, which correlates with the number of motors that occupy each state, hyperpolarization favoring an increase in specific capacitance (expanded state). Indeed, such a phenomenon appears to occur [81].

The other motor mechanism currently favored is formed on the basis of membrane curvature and interfacial tension. Proponents of this mechanism maintain that prestin functions not as a motor but simply as an entity that provides the membrane with an enhanced capacitance (charge), which in turn amplifies a basic biophysical process that drives membrane motion [82*]. It has been argued that this flexoelectric property of membranes accounts for such phenomena as salicylate and chlorpromazine's (both amphipaths, which affect membrane curvature) actions on the magnitude and voltage dependence of OHC motility and NLC [83–86]. The theory appears solid, but there is disparity between the 'area motor' and 'membrane bending motor' camps over magnitude effects, polarity, and the precise requirements for helper charge that may point to the superiority of one hypothesis over the other. It is likely that each camp will fight until an experiment unequivocally reveals the truth [22,86]! We should not hold our breath, however, as it took nearly a decade to dissuade supporters of an electro-osmotic mechanism for OHC motility [87].

Another property of the OHC that may account for mechanical responses or help to modify them is its voltage dependent stiffness [88]. Two models have been proposed whereby mechanical activity could accompany a

stiffness change [89]; one invokes intrinsic and simultaneous changes in stiffness and the conformation of a motor unit, whereas the other derives from the consequences of a pure stiffness change under constant cellular preload (steady state application of cellular deformation). The results of preload effect (induced by turgor pressure) on OHC motility are contradictory [19,33]. Nevertheless, the conformational changes embodied in the area model of motility are predicted to evoke a voltage dependent compliance that peaks at V_h (corresponding to the voltage at maximal electrical compliance [capacitance], or mechanical voltage sensitivity), much as the stereociliar transduction channels sponsor a maximum bundle compliance when half the channels are open [90]. Iwasa [91] modeled this molecular inevitability and confirmed that motor activity should affect global OHC stiffness. However, as expected, at V_h stiffness is at a minimum, whereas neither the stiffness data nor the models of He and Dallos [88,89] show a minimum at V_h , but instead, a simple (sigmoidal) correspondence between stiffness and motility magnitude. In light of this, it is likely that the modulation of OHC stiffness additionally arises from mechanisms other than direct motor activity. Indeed, it is understandable that global OHC stiffness should derive from the combined structure of the OHC lateral wall (plasma membrane, cortical cytoskeleton, and subsurface cisternae) [92]. Thus, another means to alter global OHC stiffness would be through cytoskeletal effects of second messengers (e.g. cGMP [93], or calcium ions [94–97]) and other signaling pathways (e.g. those employing the small GTPases [98,99]). Neural efferent effects on cochlea mechanics may be mediated partly by modulation of OHC stiffness [100].

The consequences of direct motor effects (viewed through NLC measures) of chemical modifiers (e.g. phosphorylation) have been considered for some time [94,101]. Indeed, there are several sites identified within prestin that could be important targets for functional modification [12,49], including N-glycosylation and phosphorylation sites. There are some preliminary data of interest with regards to these sites. Mutation of two N-glycosylation sites at residues 163 and 166 produced no changes in NLC [102]. On the other hand, the PKC inhibitors, RO31-8220 and bisindolylmaleimide (BIM), shifted V_h in the depolarizing direction in prestin-transfected cells [103], although the PKC activator phorbol 12-myristate 13-acetate (PMA) had previously been shown to lack effect on OHC motility [93]. The compelling story of prestin's modulation by second messengers and the like is not yet available.

Hop or Hopf?

One of the raging controversies that concerns mammalian cochlea function is the relative importance of stereocilia versus somatic mechanics, each viewed as potential powerhouses for amplification [10,104,105]. The stereo-

cilia bundle may very well sit at or near a point of instability, at a Hopf bifurcation, where oscillation and amplification struggle to prevail [106]; but whether or not it rules in the mammalian system is difficult to reconcile with the obvious need for such a momentous evolutionary stride as the OHC lateral membrane. Certainly, the prestin knockout mouse has strengthened the case for the dominating role of OHC electromotility [13**]. Yet reasonable issues with this experiment remain, as noted above. To highlight one concern, could the structural changes (e.g. shortening) in the OHC that result from a reduction in prestin numbers have modified the interaction of the stereocilia with the TM, ultimately interfering with stereocilia feedback into the organ? That is, could stereocilia mechanics have been altered because, for example, of bundle biasing? Could this possible biasing have also altered their resting potentials? In addition, what is the consequence of missing GLUT-5? In any case, whether or not a Hopf bifurcation underlies the sensitivity, tuning and non-linearity of the mammalian auditory system may not necessarily point to one mechanism over another, as such an instability could conceivably reside within the soma, as well as the stereocilia (see annotation to Julicher *et al.* [107]). As far as the bifurcation concept itself goes, there is some quite heated debate [108**]! However, beyond the underlying principles of amplification, questions of speed persist and may ultimately help to decide which amplificatory mechanism will win. Clearly, stereocilia work at frequencies across the mammalian acoustic spectrum, indicating that the bundle's driving force for amplification is truly wideband; however, can the effector arm follow the input? Using realistic parameters, bundle amplificatory abilities have been modeled up to 5 kHz [105], still far short of mammalian needs. Unfortunately, the lateral membrane mechanism also faces difficulty.

How fast can fast be?

There is no doubt that the OHC motor is fast; as already noted, mechanical activity is measurable above 70 kHz [26], and in some mammals, such as bats, in which the cochlear amplifier presumably works, frequency sensation can extend well beyond 100 kHz. However, in all evaluations of the motor's frequency response, external voltage commands under the frequency and level control of the experimenter were used, thus avoiding one of the enigmatic problems facing the realization of voltage-driven cochlear amplification at high frequencies, the RC (resistor \times capacitor) membrane filter [24,109]. The OHC membrane's low pass filter is expected to seriously limit high frequency electromotility, and this difficulty is one of the key arguments employed by proponents of stereocilia-based cochlea amplification in the mammal [105]. The problem arises when one considers that because of the non-linear nature of the OHC electromotility function, the mechanical gain of the OHC is about one-tenth of its maximum (max: around 20 nm/mV) at the

cell's normal resting potential of -70 mV [109]. At this gain, receptor potentials near threshold would result in mechanical responses that fall short of threshold BM movements, making it unlikely that BM motion can be boosted. Since its identification, a few solutions for the apparent RC filter problem have been proposed. Dallos and Evans [110] suggested a mechanism that relies on stimulation of motor activity by wide-band extracellular voltages evoked by remote OHCs within the organ of Corti. Alternatively, we have suggested two cellular-based mechanisms whereby the problem could be alleviated. First, we found that the mechanical gain of the cell at its resting potential could be increased through reductions in turgor pressure [29]. Second, as we found that motor charge density is greater in higher frequency OHCs, we reasoned that the resultant electrical energy ($Q \cdot V$) delivered to the lateral membrane of high frequency OHCs could render the filter-induced drop in receptor potentials less detrimental [111]. The latest suggestions are based on modeling, one positing that the piezoelectric-like properties, that is, reciprocal electro-mechanical properties, of the OHC lateral membrane can provide for an enhanced receptor potential in high frequency OHCs [112], whereas the other suggests that the apparent inductance of ionic channels may enhance the cell's frequency response [113]. All of these arguments presuppose the existence of an RC filter problem due to prestin's voltage dependence. What if prestin were driven by something other than voltage?

The recent identification of a stretch-activated chloride conductance (termed G_{metL} ; [59^{••}]) in the OHC lateral membrane may indicate that the motor can react to currents evoked by mechanical perturbations of the lateral membrane accompanying acoustic stimulation *in vivo*. Indeed, sound induced deformations of the OHC have been observed in the intact cochlea [68[•]]. In this model, intracellular Cl^- oscillations located near prestin, driven by stretch-activated ac and/or dc Cl^- currents, would directly drive prestin transitions. Because the current or its integral, not the resultant voltage, directly modulates prestin, the mechanism is unencumbered by the RC membrane filter. If this model proves true, then the OHC soma has adopted a mechanism similar to that which stereocilia use to provide cochlea amplification in lower vertebrates. In that case, calcium ion entry through the mechanically-gated forward transduction channels modulates the channels themselves and thus stereocilia bundle mechanics, leading to amplification [104,105]. Nature's capitalization on such a primitive yet well-designed system may possibly have usurped the stereocilia's rule by elevating the OHC lateral membrane to function as both a forward and a reverse transducer.

Conclusions

Despite the advances made in understanding OHC function and its role in cochlear amplification, so many more

unknowns remain. In a way, OHC aficionados are faced with the excitement that ion channel biophysicists felt when molecular identifications of their sweetheart proteins were first made. A host of investigations that employ the now well-developed fields of molecular biology, protein biophysics, and the like, which have been successfully employed in other fields, are beginning to surface in our small field. This can be clearly observed when perusing the abstracts of international meetings, some of which have been highlighted here. Although the information gleaned in the past few years has truly been remarkable, I would bet that the next timely review of OHC electromotility will be astonishing by comparison.

Update

Two manuscripts of significant interest have appeared since this review was completed. In a follow-up to the published abstract [42] on sugar transport by prestin, Chambard and Ashmore [114] provide evidence that prestin and another SLC26 family member, Pendrin, can transport fructose. The ability to transport fructose was not assessed in other family members but conceivably could be a general trait. The full significance of the transport is not clear, but certainly it could influence turgor pressure regulation in OHCs.

Weber *et al.* [115] identify a few new SLC26 family members that are homologous to prestin in species that are distant from mammals, namely fish and insects. Nevertheless, the best homology is around 50% (or less) with prestin. It would not be considered unusual to find solute transporters in these species. Furthermore, it is unlikely that motor activity would arise from such homologues, as other members of the SLC26 family that have substantial homology to prestin lack this capacity. Nevertheless, investigation of motor activity (e.g. NLC) is certainly warranted.

Acknowledgements

This work was supported by the National Institutes of Health, National Institutes for Deafness and Communication Disorders grant DC00273.

References and recommended reading

Papers of particular interest, published within the annual period of review, have been highlighted as:

- of special interest
 - of outstanding interest
1. Flock A: **Transducing mechanisms in the lateral line canal organ receptors.** *Cold Spring Harb Symp Quant Biol* 1965, **30**:133-145.
 2. Hudspeth AJ: **The cellular basis of hearing: the biophysics of hair cells.** *Science* 1985, **230**:745-752.
 3. Brown MC, Nuttall AL, Masta RI, Lawrence M: **Cochlear inner hair cells: effects of transient asphyxia on intracellular potentials.** *Hear Res* 1983, **9**:131-144.
 4. Dallos P, Harris D: **Properties of auditory nerve responses in absence of outer hair cells.** *J Neurophysiol* 1978, **41**:365-383.
 5. Harrison RV, Evans EF: **Cochlear fiber responses in guinea pigs with well defined cochlear lesions.** *Scand Audiol* 1979, **9**:83-92.

8 Sensory systems

6. Brownell WE, Bader CR, Bertrand D, de Ribaupierre Y: **Evoked mechanical responses of isolated cochlear outer hair cells.** *Science* 1985, **227**:194-196.
 7. Geisler CD: **A cochlear model using feedback from motile outer hair cells.** *Hear Res* 1991, **54**:105-117.
 8. Geisler CD, Sang C: **A cochlear model using feed-forward outer-hair-cell forces.** *Hear Res* 1995, **86**:132-146.
 9. Ruggero MA, Rich NC: **Furosemide alters organ of corti mechanics: evidence for feedback of outer hair cells upon the basilar membrane.** *J Neurosci* 1991, **11**:1057-1067.
 10. Dallos P: **The active cochlea.** *J Neurosci* 1992, **12**:4575-4585.
 11. Spoendlin H: **Neural anatomy of the inner ear.** In *Physiology of the Ear*. Edited by Jahn AF, Santos-Sacchi J. New York: Raven Press; 1988.
 12. Zheng J, Shen W, He DZ, Long KB, Madison LD, Dallos P: **Prestin is the motor protein of cochlear outer hair cells.** *Nature* 2000, **405**:149-155.
 13. Liberman MC, Gao J, He DZ, Wu X, Jia S, Zuo J: **Prestin is required for electromotility of the outer hair cell and for the cochlear amplifier.** *Nature* 2002, **419**:300-304.
- The authors used a mouse knockout of prestin to evaluate cochlear function *in vivo* and isolated OHC mechanical activity *in vitro*. In homozygotes auditory function was severely compromised, whereas in heterozygotes minimal dysfunction was realized. OHC mechanical activity was absent in homozygotes, and reduced to about half magnitude in heterozygotes. Cell length decreases resulted from the absence or reduction of prestin in the lateral membrane of OHCs. It remains to be clarified whether the absence of prestin function or the consequences of the removal of a major (structural) lateral membrane protein contributed to the results.
14. Liu XZ, Ouyang XM, Xia XJ, Zheng J, Pandya A, Li F, Du LL, Welch KO, Petit C, Smith RJ *et al.*: **Prestin, a cochlear motor protein, is defective in non-syndromic hearing loss.** *Hum Mol Genet* 2003, **12**:1155-1162.
- As might have been expected from knockout work, a mutation in the gene for prestin was found by the authors to underlie hearing loss in two families. Similar to the situation in the knockout, it is not certain whether the loss of prestin function or other sequelae were causal.
15. Zhao HB, Santos-Sacchi J: **Auditory collusion and a coupled couple of outer hair cells.** *Nature* 1999, **399**:359-362.
 16. Legan PK, Lukashkina VA, Goodyear RJ, Kossi M, Russell IJ, Richardson GP: **A targeted deletion in alpha-tectorin reveals that the tectorial membrane is required for the gain and timing of cochlear feedback.** *Neuron* 2000, **28**:273-285.
 17. Santos-Sacchi J: **Yale Ear Lab** URL: www.YaleEarLab.org
 18. Ashmore JF: **Forward and reverse transduction in the mammalian cochlea.** *Neurosci Res Suppl* 1990, **12**:S39-S50.
 19. Santos-Sacchi J: **Reversible inhibition of voltage-dependent outer hair cell motility and capacitance.** *J Neurosci* 1991, **11**:3096-3110.
 20. Huang G, Santos-Sacchi J: **Mapping the distribution of the outer hair cell motility voltage sensor by electrical amputation.** *Biophys J* 1993, **65**:2228-2236.
 21. Gale JE, Ashmore JF: **The outer hair cell motor in membrane patches.** *Pflugers Arch* 1997, **434**:267-271.
 22. Dallos P, Fakler B: **Prestin, a new type of motor protein.** *Nat Rev Mol Cell Biol* 2002, **3**:104-111.
 23. Santos-Sacchi J: **Fast outer hair cell motility: how fast is fast?** In *The Mechanics and Biophysics of Hearing*. Edited by Dallos P, Geisler CD, Matthews JW, Ruggero MA, Steele CR. Berlin: Springer-Verlag; 1990:69-75.
 24. Santos-Sacchi J: **On the frequency limit and phase of outer hair cell motility: effects of the membrane filter.** *J Neurosci* 1992, **12**:1906-1916.
 25. Gale JE, Ashmore JF: **An intrinsic frequency limit to the cochlear amplifier.** *Nature* 1997, **389**:63-66.
 26. Frank G, Hemmert W, Gummer AW: **Limiting dynamics of high-frequency electromechanical transduction of outer hair cells.** *Proc Natl Acad Sci USA* 1999, **96**:4420-4425.
 27. Iwasa KH: **Effect of stress on the membrane capacitance of the auditory outer hair cell.** *Biophys J* 1993, **65**:492-498.
 28. Gale JE, Ashmore JF: **Charge displacement induced by rapid stretch in the basolateral membrane of the guinea-pig outer hair cell.** *Proc R Soc Lond B Biol Sci* 1994, **255**:243-249.
 29. Kakehata S, Santos-Sacchi J: **Membrane tension directly shifts voltage dependence of outer hair cell motility and associated gating charge.** *Biophys J* 1995, **68**:2190-2197.
 30. Santos-Sacchi J, Kakehata S, Takahashi S: **Effects of membrane potential on the voltage dependence of motility-related charge in outer hair cells of the guinea-pig.** *J Physiol* 1998, **510**:225-235.
 31. Takahashi S, Santos-Sacchi J: **Non-uniform mapping of stress-induced, motility-related charge movement in the outer hair cell plasma membrane.** *Pflugers Arch* 2001, **441**:506-513.
 32. Santos-Sacchi J, Huang G: **Temperature dependence of outer hair cell nonlinear capacitance.** *Hear Res* 1998, **116**:99-106.
 33. Adachi M, Sugawara M, Iwasa KH: **Effect of turgor pressure on outer hair cell motility.** *J Acoust Soc Am* 2000, **108**:2299-2306.
 34. Dong XX, Ospeck M, Iwasa KH: **Piezoelectric reciprocal relationship of the membrane motor in the cochlear outer hair cell.** *Biophys J* 2002, **82**:1254-1259.
 35. Meltzer J, Santos-Sacchi J: **Temperature dependence of non-linear capacitance in human embryonic kidney cells transfected with prestin, the outer hair cell motor protein.** *Neurosci Lett* 2001, **313**:141-144.
 36. Santos-Sacchi J, Shen W, Zheng J, Dallos P: **Effects of membrane potential and tension on prestin, the outer hair cell lateral membrane motor protein.** *J Physiol* 2001, **531**:661-666.
- We transfected gerbil prestin into non-auditory cells and found that it presented additional biophysical attributes of the native OHC motor, including membrane tension and prior voltage dependence. These data confirm the identity of prestin as one of the important players in OHC motility. Possible subunit interactions were suggested to amplify prestin's response.
37. Ludwig J, Oliver D, Frank G, Klocker N, Gummer AW, Fakler B: **Reciprocal electromechanical properties of rat prestin: the motor molecule from rat outer hair cells.** *Proc Natl Acad Sci USA* 2001, **98**:4178-4183.
- The authors identified the rat ortholog of prestin, and were able to show that it possessed tension dependence. Antibodies were used against the carboxy and amino termini to localize these moieties to the cytoplasmic face of the membrane. Additionally, co-expression with GLUT-5 did not influence prestin's characterization.
38. Dong X, Iwasa K: **Tension sensitivity of prestin.** *Assoc Res Otolaryngol Abs* 2003, 103.
 39. Geleoc GS, Casalotti SO, Forge A, Ashmore JF: **A sugar transporter as a candidate for the outer hair cell motor.** *Nat Neurosci* 1999, **2**:713-719.
 40. Belyantseva IA, Adler HJ, Curi R, Frolenkov GI, Kachar B: **Expression and localization of prestin and the sugar transporter GLUT-5 during development of electromotility in cochlear outer hair cells.** *J Neurosci* 2000, **20**:5940-5948.
 41. Gao J, Zuo J: **Apoptotic cell death in the organ of Corti and absence of Glut5 in outer hair cells in prestin knock-out mice.** *Assoc Res Otolaryngol Abs* 2003, 105.
 42. Chambard J-M, Harding I, Ashmore J: **What prestin transports.** *Assoc Res Otolaryngol Abs* 2003, 104.
 43. Zheng J, Long KB, Robison DE, He DZ, Cheng J, Dallos P, Madison LD: **Identification of differentially expressed cDNA clones from gerbil cochlear outer hair cells.** *Audiol Neurootol* 2002, **7**:277-288.
 44. Dougherty G, Adler HJ, Merritt R, Rzdzinska A, de Azevedo R, Frolenkov G, Belyantseva I, Pompeia C, Kachar B: **Couplin, a novel 27 kDa Pprotein, links prestin to the actin-spectrin cytoskeleton in auditory outer hair cells.** *Assoc Res Otolaryngol Abs* 2003, 208.
 45. Lohi H, Kujala M, Makela S, Lehtonen E, Kestila M, Saarialho-Kere U, Markovich D, Kere J: **Functional characterization of three**

- novel tissue-specific anion exchangers SLC26A7, -A8, and -A9.** *J Biol Chem* 2002, **277**:14246-14254.
46. Lohi H, Kujala M, Kerkela E, Saarialho-Kere U, Kestila M, Kere J: **Mapping of five new putative anion transporter genes in human and characterization of SLC26A6, a candidate gene for pancreatic anion exchanger.** *Genomics* 2000, **70**:102-112.
47. Lohi H, Lamprecht G, Markovich D, Heil A, Kujala M, Seidler U, Kere J: **Isoforms of SLC26A6 mediate anion transport and have functional PDZ interaction domains.** *Am J Physiol Cell Physiol* 2003, **284**:C769-C779.
48. Jiang Z, Grichtchenko II, Boron WF, Aronson PS: **Specificity of anion exchange mediated by mouse Slc26a6.** *J Biol Chem* 2002, **277**:33963-33967.
49. Zheng J, Long KB, Shen W, Madison LD, Dallos P: **Prestin topology: localization of protein epitopes in relation to the plasma membrane.** *Neuroreport* 2001, **12**:1929-1935.
- The authors present a model of prestin topology formed on the basis of antibody localization of the carboxy and amino termini intracellularly, and placement of conserved sites (among SLC26 family members). Twelve transmembrane domains are suggested, but this topology has yet to be confirmed.
50. Oliver D, He DZ, Klocker N, Ludwig J, Schulte U, Waldegger S, Ruppertsberg JP, Dallos P, Fakler B: **Intracellular anions as the voltage sensor of prestin, the outer hair cell motor protein.** *Science* 2001, **292**:2340-2343.
- The authors present one of the first attempts to identify the voltage sensor region of prestin. Select charge neutralizations within presumed transmembrane domains failed to abolish NLC in transfected cells. This result led to the investigation of an extrinsic source as the carrier of sensor charge. Anions, including Cl⁻ and bicarbonate, but not sulfate, were found to promote charge movement. A model of prestin possessing an incomplete transport cycle was presented to account for its motor activity.
51. Navarrete E, Matsuda K, Zheng J, Long K, Madison L, Dallos P: **C-terminus deletion mutants of the prestin molecule.** *Assoc Res Otolaryngol Abs* 2002, **254**.
52. Bai J-P, Samaranyake H, Navaratnam D, Santos-Sacchi J: **Carboxy-terminal truncations and mutations of Prestin; affects on NLC.** *Assoc Res Otolaryngol Abs* 2003, **208**.
53. Kalinec F, Holley MC, Iwasa KH, Lim DJ, Kachar B: **A membrane-based force generation mechanism in auditory sensory cells.** *Proc Natl Acad Sci USA* 1992, **89**:8671-8675.
54. Huang G, Santos-Sacchi J: **Motility voltage sensor of the outer hair cell resides within the lateral plasma membrane.** *Proc Natl Acad Sci USA* 1994, **91**:12268-12272.
55. Tunstall MJ, Gale JE, Ashmore JF: **Action of salicylate on membrane capacitance of outer hair cells from the guinea-pig cochlea.** *J Physiol* 1995, **485**:739-752.
56. Kakehata S, Santos-Sacchi J: **Effects of salicylate and lanthanides on outer hair cell motility and associated gating charge.** *J Neurosci* 1996, **16**:4881-4889.
57. Wu M, Santos-Sacchi J: **Effects of lipophilic ions on outer hair cell membrane capacitance and motility.** *J Membr Biol* 1998, **166**:111-118.
58. Santos-Sacchi J, Wu M, Kakehata S: **Furosemide alters nonlinear capacitance in isolated outer hair cells.** *Hear Res* 2001, **159**:69-73.
59. Rybalchenko V, Santos-Sacchi J: **Cl⁻ flux through a non-selective, stretch-sensitive conductance influences the outer hair cell motor of the guinea-pig.** *J Physiol* 2003, **547**:873-891.
- We studied the effects of anions in intact OHCs, and presented evidence, such as the positive effects of sulfate on NLC and Cl⁻-induced shifts in the motor's working voltage range, which counters the extrinsic voltage sensor hypothesis. In addition, we found that a lateral membrane conductance allows Cl⁻ to flow at acoustic rates, possibly allowing prestin's area state to be gated directly by Cl⁻ through stretch rather than voltage.
60. Rybalchenko V, Santos-Sacchi J: **Allosteric modulation of the outer hair cell motor protein prestin by chloride.** In *Biophysics of the Cochlea: from Molecules to Models*. Edited by Gummer A. Singapore: World Scientific Publishing; 2003:116-126.
61. Fakler B, Oliver D: **Functional properties of prestin - how the motor-molecule works work.** In *Biophysics of the Cochlea: from Molecules to Models*. Edited by Gummer A. Singapore: World Scientific Publishing; 2003:110-115.
62. Hallworth R, Evans BN, Dallos P: **The location and mechanism of electromotility in guinea pig outer hair cells.** *J Neurophysiol* 1993, **70**:549-558.
63. Zhang M, Kalinec F: **Structural microdomains in the lateral plasma membrane of cochlear outer hair cells.** *J Assoc Res Otolaryngol* 2002, **3**:289-301.
64. Santos-Sacchi J: **Functional motor microdomains of the outer hair cell lateral membrane.** *Pflugers Arch* 2002, **445**:331-336.
65. Frolenkov GI, Kalinec F, Tavartkiladze GA, Kachar B: **Cochlear outer hair cell bending in an external electric field.** *Biophys J* 1997, **73**:1665-1672.
66. Fridberger A, Boutet M, Ulfendahl M: **Internal shearing within the hearing organ evoked by basilar membrane motion.** *J Neurosci* 2002, **22**:9850-9857.
67. Nuttall AL, Guo M, Ren T: **The radial pattern of basilar membrane motion evoked by electric stimulation of the cochlea.** *Hear Res* 1999, **131**:39-46.
68. Fridberger A, De Monvel JB: **Sound-induced differential motion within the hearing organ.** *Nat Neurosci* 2003, **6**:446-448.
- The authors analyzed images of the organ of Corti within an intact cochlea explant during sound stimulation at high levels. Differential motion of the two surfaces of the organ (reticular lamina and basilar membrane) showed that OHCs sandwiched between them are deformed. Such deformation could gate a chloride conductance in the lateral membrane.
69. Richter C-P, Dallos P: **Micromechanics in the gerbil hemicochlea.** In *Biophysics of the Cochlea: from Molecules to Models*. Edited by Gummer A. Singapore: World Scientific Publishing; 2003:127-134.
70. Weber T, Zimmermann U, Winter H, Mack A, Kopschall I, Rohbock K, Zenner HP, Knipper M: **Thyroid hormone is a critical determinant for the regulation of the cochlear motor protein prestin.** *Proc Natl Acad Sci USA* 2002, **99**:2901-2906.
- The authors present a very interesting finding that the absence of TH delays the expression of prestin in OHCs, but more importantly, even after the attainment of adult expression levels, the final localization of prestin to the lateral membrane proper is hindered. Prestin remains restricted to the basolateral extent of the cell.
71. He DZ, Jia S, Feng F: **Thyroid hormone is not necessary for the development of outer hair cell electromotility.** *Hear Res* 2003, **175**:183-189.
72. Santos-Sacchi J, Huang GJ, Wu M: **Mapping the distribution of outer hair cell voltage-dependent conductances by electrical amputation.** *Biophys J* 1997, **73**:1424-1429.
73. Santos-Sacchi J, Zhao HB: **Excitation of fluorescent dyes inactivates the outer hair cell integral membrane motor protein prestin and betrays its lateral mobility.** *Pflugers Arch* 2003, PMID:12783229.
74. Oghalai JS, Zhao HB, Kutz JW, Brownell WE: **Voltage- and tension-dependent lipid mobility in the outer hair cell plasma membrane.** *Science* 2000, **287**:658-661.
75. Oghalai JS, Tran TD, Raphael RM, Nakagawa T, Brownell WE: **Transverse and lateral mobility in outer hair cell lateral wall membranes.** *Hear Res* 1999, **135**:19-28.
76. Santos-Sacchi J, Dilger JP: **Whole cell currents and mechanical responses of isolated outer hair cells.** *Hear Res* 1988, **35**:143-150.
77. Santos-Sacchi J: **Harmonics of outer hair cell motility.** *Biophys J* 1993, **65**:2217-2227.
78. Adachi M, Iwasa KH: **Electrically driven motor in the outer hair cell: effect of a mechanical constraint.** *Proc Natl Acad Sci USA* 1999, **96**:7244-7249.
79. Iwasa KH: **A membrane motor model for the fast motility of the outer hair cell.** *J Acoust Soc Am* 1994, **96**:2216-2224.
80. Holley MC, Ashmore JF: **A cytoskeletal spring in cochlear outer hair cells.** *Nature* 1988, **335**:635-637.

10 Sensory systems

81. Santos-Sacchi J, Navarrete E: **Voltage-dependent changes in specific membrane capacitance caused by prestin, the outer hair cell lateral membrane motor.** *Pflugers Arch* 2002, **444**:99-106.
82. Zhang PC, Keleshian AM, Sachs F: **Voltage-induced membrane movement.** *Nature* 2001, **413**:428-432.
This report provides confirmation that membrane movement (measured by AFM [atomic force microscopy]) should result from interfacial forces working on the surface charge of a curved membrane during voltage stimulation. This manuscript instigated a heated debate as to whether prestin functions as a motor or as a passive contributor of charge to enhance the flexoelectric effect.
83. Raphael RM, Popel AS, Brownell WE: **A membrane bending model of outer hair cell electromotility.** *Biophys J* 2000, **78**:2844-2862.
84. Lue AJ, Zhao HB, Brownell WE: **Chlorpromazine alters outer hair cell electromotility.** *Otolaryngol Head Neck Surg* 2001, **125**:71-76.
85. Brownell WE, Spector AA, Raphael RM, Popel AS: **Micro- and nanomechanics of the cochlear outer hair cell.** *Annu Rev Biomed Eng* 2001, **3**:169-194.
86. Morimoto N, Raphael RM, Nygren A, Brownell WE: **Excess plasma membrane and effects of ionic amphipaths on mechanics of outer hair cell lateral wall.** *Am J Physiol Cell Physiol* 2002, **282**:C1076-C1086.
87. Jerry RA, Popel AS, Brownell WE: **Outer hair cell length changes in an external electric field. I. The role of intracellular electroosmotically generated pressure gradients.** *J Acoust Soc Am* 1995, **98**:2000-2010.
88. He DZ, Dallos P: **Somatic stiffness of cochlear outer hair cells is voltage-dependent.** *Proc Natl Acad Sci USA* 1999, **96**:8223-8228.
89. Dallos P, He DZ: **Two models of outer hair cell stiffness and motility.** *J Assoc Res Otolaryngol* 2000, **1**:283-291.
90. Howard J, Hudspeth AJ: **Compliance of the hair bundle associated with gating of mechano-electrical transduction channels in the bullfrog's saccular hair cell.** *Neuron* 1988, **1**:189-199.
91. Iwasa KH: **Effect of membrane motor on the axial stiffness of the cochlear outer hair cell.** *J Acoust Soc Am* 2000, **107**:2764-2766.
92. Li Z, Anvari B, Takashima M, Brecht P, Torres JH, Brownell WE: **Membrane tether formation from outer hair cells with optical tweezers.** *Biophys J* 2002, **82**:1386-1395.
93. Szonyi M, He DZ, Ribari O, Sziklai I, Dallos P: **Cyclic GMP and outer hair cell electromotility.** *Hear Res* 1999, **137**:29-42.
94. Frolenkov GI, Mammano F, Belyantseva IA, Coling D, Kachar B: **Two distinct Ca²⁺-dependent signaling pathways regulate the motor output of cochlear outer hair cells.** *J Neurosci* 2000, **20**:5940-5948.
95. Frolenkov GI, Mammano F, Kachar B: **Regulation of outer hair cell cytoskeletal stiffness by intracellular Ca²⁺: underlying mechanism and implications for cochlear mechanics.** *Cell Calcium* 2003, **33**:185-195.
96. Sziklai I, Szonyi M, Dallos P: **Phosphorylation mediates the influence of acetylcholine upon outer hair cell electromotility.** *Acta Otolaryngol* 2001, **121**:153-156.
97. Beurg M, Bouleau Y, Dulon D: **The voltage-sensitive motor protein and the Ca²⁺-sensitive cytoskeleton in developing rat cochlear outer hair cells.** *Eur J Neurosci* 2001, **14**:1947-1952.
98. Kalinec F, Zhang M, Urrutia R, Kalinec G: **Rho GTPases mediate the regulation of cochlear outer hair cell motility by acetylcholine.** *J Biol Chem* 2000, **275**:28000-28005.
99. Zhang M, Kalinec G, Kalinec F: **Rock 'N' Rho in outer hair cell motility.** In *Biophysics of the Cochlea: from Molecules to Models*. Edited by Gummer A. Singapore: World Scientific Publishing; 2003:278-284.
100. Cooper NP, Jr JJ: **Separate mechanical processes underlie fast and slow effects of medial olivocochlear efferent activity.** *J Physiol* 2003, **548**:307-312.
101. Huang G-J, Santos-Sacchi J: **Metabolic control of OHC function: phosphorylation and dephosphorylation agents shift the voltage dependence of motility related capacitance.** *Assoc Res Otolaryngol Abs* 1993.
102. Zheng J, Matsuda K, Navarrete E, Du G, Long K, Madison L, Dallos P: **The effects of prestin's N-glycosylation sites on prestin protein distribution and function.** *Assoc Res Otolaryngol Abs* 2002, **163**.
103. Matsuda K, Zheng J, Du G-G, Deak L, Navarrete E, Dallos P: **Protein kinase C and voltage-dependent capacitance in prestin-transfected TSA cells.** *Assoc Res Otolaryngol Abs* 2003, **105**.
104. Ricci AJ, Crawford AC, Fettiplace R: **Active hair bundle motion linked to fast transducer adaptation in auditory hair cells.** *J Neurosci* 2000, **20**:7131-7142.
105. Choe Y, Magnasco MO, Hudspeth AJ: **A model for amplification of hair-bundle motion by cyclical binding of Ca²⁺ to mechano-electrical-transduction channels.** *Proc Natl Acad Sci USA* 1998, **95**:15321-15326.
106. Martin P, Julicher F, Hudspeth A: **The contribution of transduction channels and adaptation motors to the hair cell's active process.** In *Biophysics of the Cochlea: from Molecules to Models*. Edited by Gummer A. Singapore: World Scientific Publishing; 2003:3-15.
107. Julicher F, Camalet S, Prost J, Duke T: **Active amplification by critical oscillations.** In *Biophysics of the Cochlea: from Molecules to Models*. Edited by Gummer A. Singapore: World Scientific Publishing; 2003:16-27.
108. Allen J: **Meeting discussion session.** In *Biophysics of the Cochlea: from Molecules to Models*. Edited by Gummer A. Singapore: World Scientific Publishing; 2003:563-592.
This paper is one of the highlights of the meeting in Titisee, Germany where a host of topics relating to the OHC were discussed. Among the heated debates (concerning chapters appearing in the book) were the stereocilia versus the lateral membrane for mammalian amplification, the anion effects on OHCs, the relevance of a Hopf bifurcation, and the modeling of the amplification process. A book you must read!
109. Santos-Sacchi J: **Asymmetry in voltage-dependent movements of isolated outer hair cells from the organ of Corti.** *J Neurosci* 1989, **9**:2954-2962.
110. Dallos P, Evans BN: **High-frequency motility of outer hair cells and the cochlear amplifier.** *Science* 1995, **267**:2006-2009.
111. Santos-Sacchi J, Kakehata S, Kikuchi T, Katori Y, Takasaka T: **Density of motility-related charge in the outer hair cell of the guinea pig is inversely related to best frequency.** *Neurosci Lett* 1998, **256**:155-158.
112. Spector AA, Brownell WE, Popel AS: **Effect of outer hair cell piezoelectricity on high-frequency receptor potentials.** *J Acoust Soc Am* 2003, **113**:453-461.
113. Dong X-X, Ospeck M, Iwasa K: **Fast nonlinear currents in outer hair cells from the basal turn of the cochlea.** In *Biophysics of the Cochlea: from Molecules to Models*. Edited by Gummer A. Singapore: World Scientific Publishing; 2003:161-168.
114. Chambard JM, Ashmore JF: **Sugar transport by members of the SLC26 superfamily of anion-bicarbonate exchangers.** *J Physiol* 2003, PMID:12777445.
115. Weber T, Gopfert MC, Winter H, Zimmerman U, Kohler H, Meier A, Hendrich O, Rohbock K, Robert D, Knipper M: **Expression of prestin homologous solute carrier (SLC26) in auditory organs of non-mammalian vertebrates and insects.** *Proc Natl Acad Sci USA* 2003, **100**:7690-7695.

Determination of Cell Capacitance Using the Exact Empirical Solution of $\partial Y/\partial C_m$ and Its Phase Angle

Joseph Santos-Sacchi

Otolaryngology and Neurobiology, Yale University School of Medicine, New Haven, Connecticut 06510

ABSTRACT Measures of membrane capacitance offer insight into a variety of cellular processes. Unfortunately, popular methodologies rely on model simplifications that sensitize them to interference from inevitable changes in resistive components of the traditional cell-clamp model. Here I report on a novel method to measure membrane capacitance that disposes of the usual simplifications and assumptions, yet is immune to such interference and works on the millisecond timescale. It is based on the exact empirical determination of the elusive partial derivative, $\partial Y/\partial C_m$, which heretofore had been approximated. Furthermore, I illustrate how this method extends to the vesicle fusion problem by permitting the determination of $\partial Y_v/\partial C_v$, thereby providing estimates of fusion pore conductance and vesicle capacitance. Finally, I provide simulation examples and physiological examples of how the method can be used to study processes that are routinely interrogated by measures of membrane capacitance.

INTRODUCTION

Biological cells are typically modeled as simple parallel combinations of an electrical resistance and capacitance. Measures of membrane capacitance (C_m) based on this model under voltage clamp provide an informative view of such varied processes as fertilization (Jaffe and Schlichter, 1985), ionic channel gating (Fernandez et al., 1982), synaptic vesicle fusion (Neher and Marty, 1982), gap junctional coupling (Santos-Sacchi, 1991a), and receptor cell activity (Zhao and Santos-Sacchi, 1999).

A powerful feature of capacitance measures is the ability to monitor interactions between membrane-bound compartments, e.g., fusion of vesicles with the plasma membrane or cell coupling via gap junctions (Neher and Marty, 1982; Joshi and Fernandez, 1988; Santos-Sacchi, 1991a; Zhao and Santos-Sacchi, 1998), because these measures provide an estimate of membrane surface area (Fricke, 1925; Cole, 1971). Indeed, electrical measures of vesicular fusion (Alvarez De Toledo et al., 1993) have played a significant role in the development of one of the most controversial issues facing neurobiology today, namely, the occurrence of kiss-and-run synaptic vesicle transmitter release (Gandhi and Stevens, 2003; Aravanis et al., 2003). Single-frequency admittance analysis of membrane fusion, pioneered by Neher and Marty (1982), has been used by a number of investigators to gauge the time course of vesicular membrane fusion by monitoring the changes in the conductance of the fusion pore that initiates membrane fusion (Breckenridge and Almers, 1987; Alvarez De Toledo et al., 1993; Debus and Lindau, 2000; Klyachko and Jackson, 2002). Estimates of the pore's initial conductance hover near single-channel

conductance values (Breckenridge and Almers, 1987; Lollike et al., 1995).

Arguably the most widely used method to measure membrane capacitance (C_m) is the phase-angle method, variously termed, but all employing approaches to extract the current at a particular phase angle arising from small changes in C_m (Neher and Marty, 1982; Gillis, 1995). Such AC methods ostensibly provide excellent time resolution and sensitivity. Multifrequency approaches, which we and others have used (Fernandez et al., 1982; Santos-Sacchi, 1989; Zhao and Santos-Sacchi, 1999), are less in vogue, but offer potential protection from changes in admittance that can plague single-sine methods. Implementations of step, single-, and dual-sine techniques are available in a few software packages (jClamp, www.SciSoftCo.com; pClamp, www.Axon.com; Pulse Control, www.Instrutech.com, chroma.med.miami.edu/cap).

One of the key problems that challenges the validity of C_m measures, and thus our understanding of those cellular processes that are interrogated by C_m measurements, is the interference of those measures by changes in either patch electrode resistance (R_s) or cell membrane resistance (R_m), the latter often a natural corollary of those cellular processes (Gillis, 1995; Debus et al., 1995). An extensively discussed topic of the single-sine camp concerns the determination of the proper phase angle to utilize in measuring small changes in membrane capacitance. There are various mechanisms to determine an appropriate phase angle, but all estimates of capacitance employ simplifying assumptions and requirements, usually devised to limit the effects of uncontrollable R_s and R_m changes on C_m measures. Indeed, the traditional methodology of single-sine admittance analysis suffers from a number of assumptions and simplifications, especially those methods used to extract vesicle capacitance and conductance, and the fusion pore conductance. These

Submitted August 29, 2003, and accepted for publication March 8, 2004.

Address reprint requests to Joseph Santos-Sacchi, E-mail: joseph.santos-sacchi@yale.edu.

© 2004 by the Biophysical Society

0006-3495/04/07/714/14 \$2.00

doi: 10.1529/biophysj.103.033993

assumptions cannot be met in all cases, and this quandary is clearly indicated by the posthoc manipulations of data that are often required (Lindau, 1991; Ratnov et al., 1998). In detailing these assumptions, I refer to the traditional electrical circuit models that are used to evaluate admittance data (Fig. 1). A nearly universal assumption is that $R_m \gg R_s$; additionally, for fusion vesicle analysis, $R_v \gg R_p$, and in some cases $R_v = \infty$. Below I illustrate through circuit analysis and modeling how these assumptions can lead to errors, and provide a method, based on the exact empirical identification of the partial derivatives $\partial Y/\partial C_m$ and $\partial Y_v/\partial C_v$, that offers solutions without compromising assumptions. The approach is referred to as the *eCm* method.

Theory

The phase of the capacitive current components evoked by a sinusoidal command voltage (V) across the simple models presented in Fig. 1 can be used to arrive at measures of the capacitive components themselves. Once the capacitive component values are obtained, the resistive component values are easily deduced. This can be appreciated from the

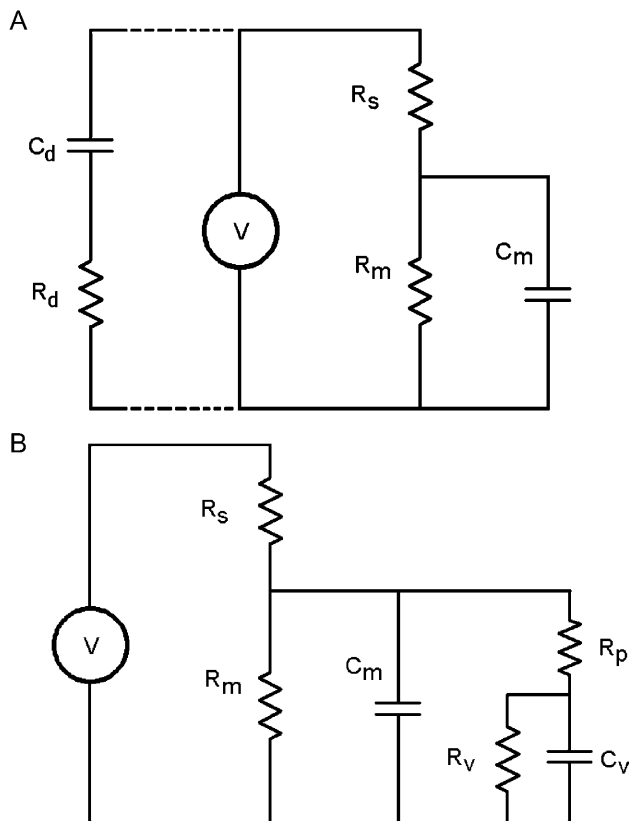


FIGURE 1 Circuit models. (A) The standard patch-clamp-cell model. Voltage (V) is set across the electrode (R_s) and cell membrane resistance (R_m)—capacitance (C_m). The series components between headstage and ground, R_d and C_d , model the whole-cell capacitance compensation circuitry when connected. (B) A vesicle is fused with the plasma membrane. C_v is vesicle capacitance, R_p is fusion pore resistance, and R_v is vesicle resistance.

following evaluation, which first deals with the model without a fusion vesicle and without capacitance compensation components (Fig. 1 A).

Two standard conditions must be met for successful use of the methods detailed here: 1), the patch-clamp system transfer function (which derives from all equipment that contributes to shaping the output current) must be corrected for. This is a trivial matter, where a pure resistor, say $1\text{ M}\Omega$, is used at the input of the headstage to determine the correction phase and magnitude at each frequency (see Gillis, 1995 for details); and 2), the pipette stray capacitance must be neutralized before establishing whole-cell configuration.

Absent vesicle fusion

The current measurable under voltage clamp (Fig. 1) is that through R_s , namely, I_{R_s} . According to Ohm's law, I_{R_s} is defined as the product of the clamp voltage (V) and input admittance (Y) of the circuit,

$$I_{R_s} = YV = (A_Y + jB_Y)V, \quad (1)$$

where A_Y and B_Y are the real and imaginary components of the admittance. Closer inspection of the circuit reveals that I_{R_s} is the sum of a resistive and a capacitive component induced by only that portion (V_m) of the clamp voltage (V), which drops across the cell membrane ($R_m \parallel C_m$),

$$I_{R_s} = I_{R_m} + I_{C_m} = \frac{V_m}{R_m} + j\omega C_m V_m. \quad (2)$$

These equations show that I_{R_s} can be represented as a frequency ($\omega = 2\pi f$) dependent complex number,

$$Y_m = \frac{(A_{I_{R_s}} + jB_{I_{R_s}})}{V_m}, \quad (3)$$

where Y_m is the membrane admittance, $A_{I_{R_s}}$ is the real component, and $B_{I_{R_s}}$ is the imaginary component of I_{R_s} . Plainly, this signifies that the phase relationship between capacitive (I_{C_m}) and resistive (I_{R_m}) membrane current components is 90° . It is important to realize that the magnitude of the series resistance (R_s), or its existence (i.e., $R_s = 0$), is irrelevant, and will not affect the phase relationship between I_{C_m} and I_{R_m} . Of course, for $R_s > 0$, the phase of I_{R_s} , relative to that of V , will vary as a result of any circuit parameter change, because the phase of I_{R_s} is dependent on that of V_m ,

$$\angle V_m = -\tan^{-1}(\omega\tau_{\text{clamp}}), \quad (4)$$

where τ_{clamp} , the actual clamp time constant, is

$$\tau_{\text{clamp}} = R_{\parallel}C_m = \frac{R_s R_m}{R_s + R_m} C_m = \frac{R_s R_m}{R_m} C_m. \quad (5)$$

Viewed relative to the phase of the command voltage (V), the capacitive current phase angle, Φ , will always reside at

$$\begin{aligned}\Phi &= \angle V_m + 90^\circ = \angle I_{R_m} + 90^\circ \\ &= -\tan^{-1}(\omega\tau_{\text{clamp}}) + 90^\circ.\end{aligned}\quad (6)$$

Thus, in the absence of R_s ($R_s = 0$), the angles of V_m and V are identical, and Φ will be orthogonal to the angle of V . However, as pointed out by Neher and Marty (1982), the introduction of R_s causes Φ to shift away from orthogonality with respect to the applied command voltage (V). The phase shift, θ , in the angle of I_{R_s} that accompanies changes in the circuit parameters is defined as

$$\begin{aligned}\theta &= \angle V_m - \angle I_{R_s} = \angle I_{R_m} - \angle I_{R_s} \\ &= -\tan^{-1}(\omega R_m C_m),\end{aligned}\quad (7)$$

and thus

$$\Phi = \angle I_{R_s} + \theta + 90^\circ.\quad (8)$$

Although it is apparent from Eq. 2 that the magnitude of the current at Φ , namely, I_{C_m} , can be used to extract C_m

$$|I_{C_m}| = \text{Re}(I_{R_s} e^{-j\Phi})\quad (9)$$

$$C_m = \frac{I_{C_m}}{j\omega V_m} = \frac{|I_{C_m}|}{\omega |V_m|},\quad (10)$$

neither absolute angle, θ nor Φ , can be determined from direct manipulation of the empirically obtained input admittance at any one frequency. Thus, in the face of changing circuit parameters, estimating C_m by directly measuring raw current at Φ appears unfeasible. Nevertheless, inspection of the current at Φ can be achieved by operating on the imaginary component of I_{R_s} , whose phase follows those phase shifts that result from parameter changes.

$$I_{C_m} = \text{conj} \left[\frac{\mathbf{B}_{I_{R_s}} V}{j V_m} \right].\quad (11)$$

Thus, the imaginary component of \mathbf{Y} (or I_{R_s}) can be used to find C_m . To obtain direct estimates of C_m from \mathbf{B}_Y , one needs to correct \mathbf{B}_Y with a noncomplex gain factor (H_c) that accounts for the relationship between inevitable changes in R_s , R_m , and C_m that occur during the course of an experiment.

$$C_m = H_c \mathbf{B}_Y,\quad (12)$$

where, after substitution and rearrangement,

$$H_c = \frac{(1 + \omega^2 \tau_{\text{clamp}}^2)}{\omega \left[1 - \frac{\tau_{\text{clamp}}}{\tau_{\text{cell}}} \right]^2},\quad (13)$$

and

$$\tau_{\text{cell}} = R_m C_m.\quad (14)$$

Note that τ_{cell} is the membrane time constant, and most importantly,

$$H_c^{-1} = \text{abs}(\partial \mathbf{Y} / \partial C_m).\quad (15)$$

Thus, to extract C_m from \mathbf{B}_Y , we must precisely evaluate the partial derivative, $\partial \mathbf{Y} / \partial C_m$. This is one of the enigmas facing cell capacitance aficionados.

There are two methods that are routinely used to provide estimates of $\partial \mathbf{Y} / \partial C_m$ and its phase angle; both involve dithering of circuit parameters, and typically require hardware modifications and/or manipulations (Fidler and Fernandez, 1989; Joshi and Fernandez, 1988; Neher and Marty, 1982). Series resistance dithering and capacitance compensation dithering each have shortcomings that have been discussed in detail (Joshi and Fernandez, 1988). Ultimately, these shortcomings stem from the untoward effects of series resistance, because as $R_m / R_{in} \rightarrow 1$, the circuit of Fig. 1 A approaches a simple parallel $R_m C_m$ configuration, and the estimates ultimately provide precise solutions. Regrettably, we are rarely so lucky during our experimental manipulations of cells to guarantee such relationships (Debus et al., 1995). Can this problem be resolved? That is, can the true magnitude and phase angle of $\partial \mathbf{Y} / \partial C_m$ be obtained, so that estimates of C_m are impervious to cell and clamp parameter changes? Furthermore, can this be accomplished without hardware additions and manipulations? Actually, it is a simple task, requiring, in addition to measures of \mathbf{B}_Y , the determination of the partial derivative, $\partial \mathbf{Y} / \partial \omega$ or correspondingly, $\partial I_{R_s} / \partial \omega$. As we shall see, such a determination ensures accurate measures of membrane capacitance.

$$\partial \mathbf{Y} / \partial \omega = \alpha_\omega e^{j\beta_\omega},\quad (16)$$

where the magnitude (α_ω) and phase (β_ω) are

$$\alpha_\omega = \frac{\mathbf{B}_Y}{\omega}\quad (17)$$

$$\beta_\omega = -\tan^{-1} \left[\frac{\omega^2 \tau_{\text{clamp}}^2 - 1}{2\omega \tau_{\text{clamp}}} \right].\quad (18)$$

Significantly, β_ω , the phase angle of $\partial I_{R_s} / \partial \omega$ and $\partial \mathbf{Y} / \partial \omega$, is identical to that of $\partial \mathbf{Y} / \partial C_m$, and also to the angle of

$\partial\mathbf{Y}/\partial R_m + 90^\circ$. This can be appreciated immediately by inspection of the partial derivatives.

$$\partial\mathbf{Y}/\partial\omega = \frac{\mathbf{Y}^2}{\mathbf{Y}_m^2} jC_m \quad (19)$$

$$\partial\mathbf{Y}/\partial C_m = \frac{\mathbf{Y}^2}{\mathbf{Y}_m^2} j\omega \quad (20)$$

$$\partial\mathbf{Y}/\partial R_m = -\frac{\mathbf{Y}^2}{\mathbf{Y}_m^2} \frac{1}{R_m^2}, \quad (21)$$

where

$$\frac{1}{\mathbf{Y}_m} = \frac{1}{\mathbf{Y}} - \frac{1}{G_s} = \frac{1}{\mathbf{Y}} - R_s, \quad (22)$$

It is this equivalence between the angles of $\partial\mathbf{Y}/\partial\omega$ and $\partial\mathbf{Y}/\partial C_m$ that forms the basis of the new *eCm* method of capacitance measurement that I report here. Given the angle, β_ω , and the real and imaginary components of \mathbf{Y} , the two time constants, τ_{clamp} and τ_{cell} , can be found. Each has two solutions, one of which will be realizable (positive) depending on the circuit parameters. For subsequent calculations the positive values must be used.

$$\tau_{\text{clamp}} = \left[-\tan(\beta_\omega) \pm \sqrt{1 + \tan(\beta_\omega)^2} \right] \omega^{-1} \quad (23)$$

$$\tau_{\text{cell}} = \frac{1 - \omega^2 \tau_{\text{clamp}}^2 - 2\eta\omega\tau_{\text{clamp}} \pm c}{\omega(-\eta + \eta\omega^2\tau_{\text{clamp}}^2 - 2\omega\tau_{\text{clamp}})} \quad (24)$$

where

$$c = \left[\sqrt{1 + \eta^2} + \sqrt{1 + \eta^2\omega^2\tau_{\text{clamp}}^2} \right] \quad (25a)$$

$$\eta = \tan \left[2 \tan^{-1} \left(\frac{\mathbf{B}_Y}{\mathbf{A}_Y} \right) \right] = \tan(\angle \partial\mathbf{Y}/\partial G_s). \quad (25b)$$

Finally, with τ_{clamp} and τ_{cell} in hand, H_c (Eqs. 13 and 15) can be obtained, thus revealing the exact solution for all clamp parameters, R_s , R_m , and C_m .

$$C_m = \mathbf{B}_Y H_c = \frac{\mathbf{B}_Y}{|\partial\mathbf{Y}/\partial C_m|} = \mathbf{B}_Y \frac{(1 + \omega^2 \tau_{\text{clamp}}^2)}{\omega \left[1 - \frac{\tau_{\text{clamp}}}{\tau_{\text{cell}}} \right]^2} \quad (26)$$

$$R_m = \frac{\tau_{\text{cell}}}{C_m} \quad (27)$$

$$R_s = \frac{-\tau_{\text{clamp}}\tau_{\text{cell}}}{C_m(\tau_{\text{clamp}} - \tau_{\text{cell}})}. \quad (28)$$

For completeness, the pertinent partial derivatives are provided in polar form (all parameters obtainable through a combination of measurement (that of \mathbf{Y} and β_ω ; see following) and calculation (as above)),

$$\partial\mathbf{Y}/\partial C_m = H_c^{-1} e^{j\beta_\omega} = \frac{\omega \left[1 - \frac{\tau_{\text{clamp}}}{\tau_{\text{cell}}} \right]^2}{(1 + \omega^2 \tau_{\text{clamp}}^2)} e^{j\beta_\omega}. \quad (29)$$

$$\partial\mathbf{Y}/\partial\omega = \frac{\mathbf{B}_Y}{\omega} e^{j\beta_\omega}. \quad (30)$$

The exact determination of β_ω

Several practical approaches to obtain β_ω via frequency manipulations are available. Ordinarily, the empirical determination of an angle of a partial derivative with respect to angular frequency, such as β_ω , is found by introducing a second voltage sinusoid (ω_1), in addition to the primary, ω_0 , at an infinitesimal interval of $d\omega$, which must be approximated with $\Delta\omega$. The angle of the resulting difference current will closely approximate β_ω . However, the determination of β_ω using digital techniques necessitates that the two frequencies be no closer than the minimum frequency interval, ω_{min} . This interval is determined by the number of points (*npts*) of the stimulus ($\omega_{\text{min}} = 1/(dt \text{ npts})$, where $dt = \text{sample clock}$) (see Oppenheim and Schaffer, 1975). Unfortunately, the rather large size of ω_{min} offered by a stimulus composed of, say, 128 points at 4 μs clock, will provide for a poor approximation of $d\omega$ by $\Delta\omega$ (f_{min} would be 1953.1 Hz). Of course, *npts* can be increased such that ω_{min} would be very small and permit a reasonable approximation of β_ω , but time resolution suffers. If high time resolution is not an issue, or if discrete determinations (as in ‘‘pause and dither’’ approaches) are acceptable, then determining the angle of the difference current at the primary frequency (ω_0) and secondary frequency (ω_1) at a very small interval will give β_ω .

Alternatively, a nondiscrete hardware implementation of this technique could easily allow $d\omega$ to be approached; furthermore, the magnitude of the second frequency could be quite small, because only the phase would be required. In fact, the stimulus could very well resemble a single sinusoid, thus limiting the cell’s stimulus exposure.

Notwithstanding these approaches to the determination of β_ω , our overriding intent is to obtain a method for C_m measurement without additional hardware or hardware manipulations, and to correct for parameter changes on a point-by-point (real time) basis. To this end, it is fortuitous that the need for an infinitesimal interval, $d\omega$, can be circumvented by acknowledging that for the linear component

model of Fig. 1 *a*, R_s or R_m may be considered frequency independent. That is, we may use either of the derivations of R_s or R_m provided by Pusch and Neher, 1988 (their Eqs. 5 and 6 reproduced below); also see Lindau and Neher (1988) to obtain an exact solution of β_ω at ω_0 .

$$R_s = \frac{\mathbf{A}_{\omega n} - b}{\mathbf{A}_{\omega n}^2 + \mathbf{B}_{\omega n}^2 - \mathbf{A}_{\omega n}b} \quad (31)$$

$$R_m = \frac{1}{b} \frac{(\mathbf{A}_{\omega n} - b)^2 + \mathbf{B}_{\omega n}^2}{\mathbf{A}_{\omega n}^2 + \mathbf{B}_{\omega n}^2 - \mathbf{A}_{\omega n}b}, \quad (32)$$

where $b = 1 / (R_s + R_m)$ and $n = 0, 1$.

Equating R_s (or R_m , either of which produce the exact same result) determined at two angular frequencies, ω_0 and ω_1 , provides two solutions for b (b_0, b_1 ; solutions not shown), and therefore two solutions for τ_{clamp} at ω_0 (obtained by utilizing Pusch and Neher's (1988) solution for C_m ; their Eq. 7),

$$\tau_{\text{clamp}_n} = \frac{\mathbf{A}_0 - b_n}{\mathbf{B}_0 \omega_0}. \quad (33)$$

Notably, however, either solution of τ_{clamp} , τ_{clamp_0} , or τ_{clamp_1} , when used to derive the angle of $\partial \mathbf{Y} / \partial \omega$, i.e., $\beta_{\omega 0}$, from Eq. 18 produces only one, unique result, namely

$$\beta_{\omega 0} = \tan^{-1} \left[\frac{1}{2} \frac{\mathbf{A}_1^2 - 2\mathbf{A}_1\mathbf{A}_0 + \mathbf{A}_0^2 - \mathbf{B}_0^2 + \mathbf{B}_1^2}{\mathbf{B}_0(\mathbf{A}_1 - \mathbf{A}_0)} \right], \quad (34)$$

where the subscripts denote the real (\mathbf{A}) and imaginary (\mathbf{B}) admittance components at any two angular frequencies, ω_0 and ω_1 . It should be pointed out that whereas two frequencies are required to obtain β_ω , the value itself is derived from $\partial \mathbf{Y} / \partial \omega_0$, whose location is exactly at ω_0 .

$$d_\omega \mathbf{Y} / d\omega_0 = \lim_{\Delta\omega \rightarrow 0} \mathbf{Y}_{\omega_0 + \Delta\omega} - \mathbf{Y}_{\omega_0} \quad (35)$$

$$\partial \mathbf{Y} / \partial \omega_0 \triangleq d_\omega \mathbf{Y} / d\omega_0, \quad (36)$$

that is, all three pieces of information, \mathbf{B}_Y , \mathbf{A}_Y , and β_ω that are used to measure C_m theoretically derive from single (ω_0), not dual, frequency inspection.

Present vesicle fusion

The fusion of independent membrane-bound compartments (vesicle to the plasma membrane or gap junctional coupling between two cells) can be evaluated with input capacitance measures, and modeled to obtain component values of the

applicable circuit (Fig. 1 *B*) (Zhao and Santos-Sacchi, 1998; Bigiani and Roper, 1995; Santos-Sacchi, 1991a). Below, I focus on vesicular fusion. If experiments are performed using the cell-attached mode it must be determined that the cell's input admittance is far greater than the patch admittance. Additionally, data must be corrected posthoc after determination of stray pipette capacitance (perhaps using the Sylgard bead-sealing technique (Sakmann and Neher, 1995)), which may be greater than patch capacitance. Thus, the application of this method under cell-attached mode is not straightforward. Nevertheless, in that case, or if vesicle fusion is monitored under whole-cell mode, the following applies; the subscript m denotes either patch or whole-cell characteristics. The input admittance before (\mathbf{Y}_b) and after (\mathbf{Y}_a) vesicle fusion differs.

$$\mathbf{Y}_b = [\mathbf{R}_s + \mathbf{Y}_m^{-1}]^{-1} \quad (37)$$

$$\mathbf{Y}_a = [\mathbf{R}_s + (\mathbf{Y}_m + \mathbf{Y}_v)^{-1}]^{-1}, \quad (38)$$

where

$$\mathbf{Y}_v = \left[R_p + \frac{R_v}{1 + j\omega R_v C_v} \right]^{-1}. \quad (39)$$

Typically, access to the circuit parameters defining the vesicle admittance (\mathbf{Y}_v : R_p , R_v , and C_v ; see Fig. 1 *B*) is obtained experimentally by making an inescapable assumption – that at the onset of fusion R_s , R_m , and C_m remain unchanged. Given the model, without this assumption estimates cannot be obtained with confidence.

The original and still common method to calculate vesicle parameters, including fusion pore conductance, employs capacitance compensation to estimate vesicle admittance (Breckenridge and Almers, 1987; Lindau, 1991; Ales et al., 1999). In this case, membrane admittance before fusion is removed by subtracting the \mathbf{Y}_m baseline determined by capacitance compensation dithering (Neher and Marty, 1982); the subsequent change in admittance after vesicle fusion is used to calculate vesicle components based on a simplified vesicle circuit model of C_v in series with R_p (Breckenridge and Almers, 1987). We can employ the *eCm* method to arrive at \mathbf{Y}_v , in a similar manner. First, \mathbf{Y}_m is extracted from \mathbf{Y}_b , the exact value of R_s having been obtained by analysis (see above) before fusion.

$$\mathbf{Y}_m = - \left[\frac{\mathbf{Y}_b}{\mathbf{Y}_b R_s - 1} \right]. \quad (40)$$

Consequently, the vesicle admittance, \mathbf{Y}_v , which includes the fusion pore, can be calculated (by substitution of Eq. 40 into Eq. 38) as a function of admittances measured before and after fusion,

$$\mathbf{Y}_v = \frac{R_s^{-2}(\mathbf{Y}_b - \mathbf{Y}_a)}{(R_s^{-1} - \mathbf{Y}_b)(R_s^{-1} - \mathbf{Y}_a)}. \quad (41)$$

From inspection of the vesicle circuit (Fig. 1 B), it is clear that

$$I_{Rp} = I_{Rv} + I_{Cv}, \quad (42)$$

that is, we have the analogous circuit conditions that we analyzed above in the absence of fusion. The parameters R_p , R_v , and C_v simply and, respectively, replace R_s , R_m , and C_m . Using the same analysis logic as above, the magnitude and angle of $\partial\mathbf{Y}_v/\partial C_v$ is obtained, thus enabling the solution of all vesicle circuit parameters. The following equations detail fusion event analysis.

$$C_v = H_{cv}\mathbf{B}_{Yv} = \frac{\mathbf{B}_{Yv}}{|\partial\mathbf{Y}_v/\partial C_v|} = \mathbf{B}_{Yv} \frac{(1 + \omega^2\tau_f^2)}{\omega \left[1 - \frac{\tau_f}{\tau_v}\right]^2} \quad (43)$$

$$R_v = \frac{\tau_v}{C_v} \quad (44)$$

$$R_p = \frac{-\tau_f\tau_v}{C_v(\tau_f - \tau_v)}, \quad (45)$$

where

$$\tau_f = [-\tan(\beta_{\omega v}) \pm \sqrt{1 + \tan(\beta_{\omega v})^2}] \omega^{-1} \quad (46)$$

$$\tau_v = \frac{1 - \omega^2\tau_f^2 - 2\eta\omega\tau_f \pm \left[\sqrt{1 + \eta^2} + \sqrt{1 + \eta^2\omega^2\tau_f^2} \right]}{\omega(-\eta + \eta\omega^2\tau_f^2 - 2\omega\tau_f)}, \quad (47)$$

and

$$\eta = \tan \left[2 \tan^{-1} \left(\frac{\mathbf{B}_{Yv}}{\mathbf{A}_{Yv}} \right) \right]. \quad (48)$$

Simulations and biological cell examples

I provide several approaches to evaluate the *eCm* method of parameter estimation, including mathematical modeling, physical modeling, and tests on biological cells. It is important to realize that tests on biological cells may provide important information on real-world capabilities, but cannot be used to truly verify the validity of an approach. For example, it is impossible to know if a certain time course of C_m change is truly occurring in cells, unless, of course, confirmation is obtained through other measures. However,

physical and mathematical model evaluations can confirm validity of an approach, and do provide confidence that the results from biological cells are sound. In the first set of evaluations, MatLab (Natick, MA) was used to model the circuit admittance and implement *eCm* strictly in the frequency domain. In the following mathematical and physical simulations, measures were made at an f_0 of 390.6 Hz and f_1 of twice that, delivered simultaneously, unless otherwise noted. Amplitudes at each frequency were set equal, at 10–20 mV peak. Fig. 2 presents a simple whole-cell mathematical model simulation where the circuit parameters are stepped to evaluate component interactions on C_m measures; comparisons are made of calculated component values using either the *eCm* method or other approaches that contain approximations. Clearly, *eCm* is superior, and is impervious to fluctuations in circuit component values. Fig. 3 presents another mathematical simulation in Matlab where vesicle fusion under whole-cell mode is evaluated, and compared with the standard methodology (Breckenridge and Almers, 1987; Lollike et al., 1995). Both methods are excellent even in the face of substantial R_s changes, but even with changes in vesicle resistance the *eCm* method produces an exact reconstruction of the model parameter changes. Although these model data highlight the exact nature of the *eCm* method, more demanding modeling efforts show the method's strengths. For the tests that follow, capacitance measures were obtained with *eCm* as implemented in the software package jClamp using a time resolution of 2.56 ms (i.e., f_0 of 390.6 Hz), unless otherwise noted.

Fig. 4 shows the results of a physical implementation of the simple model in Fig. 1 A under voltage clamp during a large step in capacitance, that was evoked by physically dislodging an additional capacitor that was placed parallel with C_m . Simultaneous measures of R_s and R_m remain essentially unperturbed. To evaluate large changes in R_m , this parallel approach did not work because of associated parasitic capacitances of the large resistances involved. Instead, Fig. 5 shows two separate measures where all circuit and measurement details remained exactly the same except that either a 50-M Ω or 800-M Ω R_m resistor was soldered into place. Again, there are minimal changes in C_m measures. Fig. 6 shows the effects of maladjustments of the amplifier's fast capacitive compensation on parameter estimates. The model cell was measured over 10 seconds at a resolution of 2.56 ms while changes in compensation were made. Stray R_s capacitance of ± 0.15 pF had little effect on C_m ($\pm 0.4\%$) or R_m ($< \pm 0.01\%$) parameter estimation. R_s estimates varied $\pm 1.8\%$.

Finally, in Figs. 7 and 8 biological cells are investigated. Fig. 7 shows measures of outer hair cell (OHC) capacitance obtained with jClamp using a time resolution of 512 μ s. Detrending of data before analysis was performed (Santos-Sacchi, 2002). The rapid relaxation in capacitance during a step voltage change is due to the shift of the cell's nonlinear Q - V function along the voltage axis (Santos-Sacchi et al.,

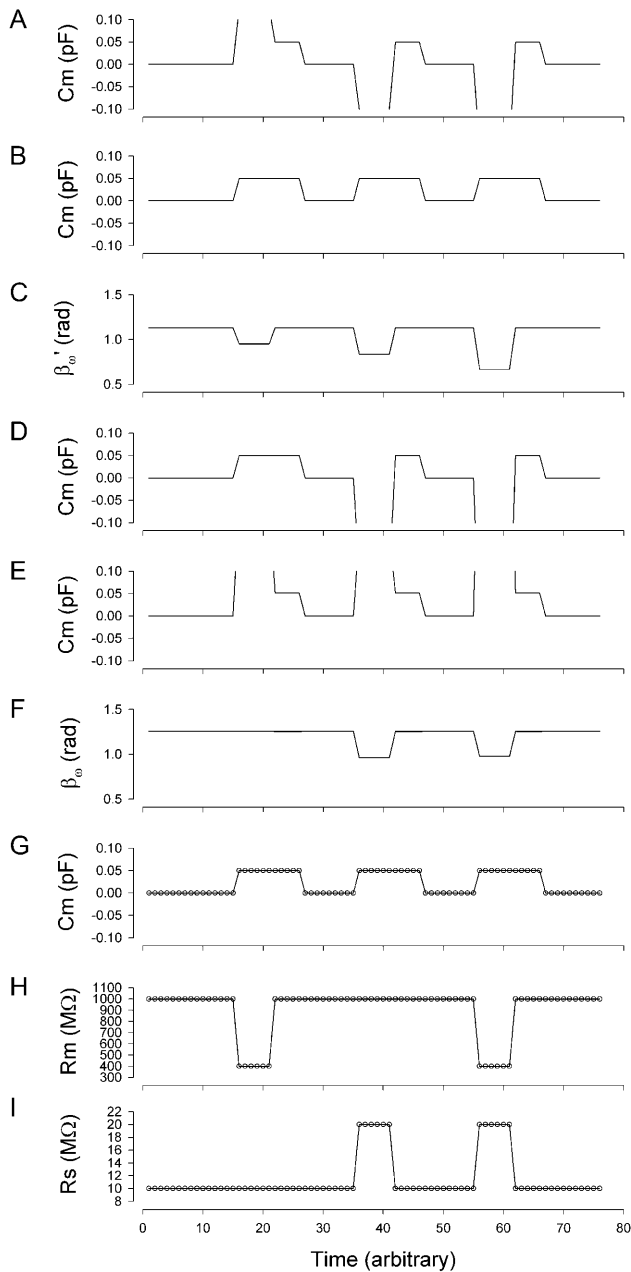


FIGURE 2 Simulation of capacitance changes in whole-cell mode. The component values of the model (R_s : 10 M Ω , R_m : 1 G Ω , and C_m : 6.5 pF) in Fig. 1 A were modulated out of phase with each other, with a C_m jump of 0.05 pF accompanied by either a 600-M Ω drop in R_m , or a 10-M Ω increase in R_s or all changes occurring simultaneously (see panels G–I). The stimulating frequency f_0 was the same for single-sine and eCm methods, with f_0 at 390.6 Hz and f_1 at twice that. In panels A–C, calculations are based on setting the PSD angle to an estimate (denoted by the prime) of β_ω , the angle of $\partial\mathbf{Y}/\partial G_s - 90^\circ$, $\beta'_\omega = (2 \tan^{-1}(\mathbf{B}_Y/\mathbf{A}_Y) - 90^\circ)$, to mimic R_s dithering. (A) A true piecewise linear approach was employed using this angle β'_ω in place of β_ω in Eq. 52. Whole-cell capacitance compensation was modeled by connecting and supplying the circuit components R_d and C_d (Fig. 1) with corresponding values of R_s and C_m , but with an overall negative admittance. PSD angle and gain corrections ($1/|\text{abs}(\partial\mathbf{Y}/\partial C_m)|$) were determined from whole-cell conditions at the zero time point and remained fixed throughout. It can be seen that when cell components are changed (G–I) the phase angle changes causing errors in C_m estimation (A). Even

1998). In that article, we confirmed through alternative measures that the time course of C_m relaxation corresponded to the shift. The shift signifies the very rapid change in the gain of OHC electromotility, a process that likely drives the mammalian cochlear amplifier (Santos-Sacchi, 2003). The solid shaded line is a triple exponential fit to the data. The three time constants are 1.04, 5.96, and 36 ms. This time course is over an order of magnitude faster than has been previously reported (Santos-Sacchi et al., 1998). The substantial noise levels in this trace derive from the huge nonlinear capacitance (>20 pF) and low input resistance (<300 M Ω) of the OHC. For comparison, Fig. 8 shows capacitance measures in a HEK cell transfected with prestin (Meltzer and Santos-Sacchi, 2001), where C_m noise was 5.5 fF (rms; 0.256 ms time resolution (f_0 : 390.6 Hz); see discussion on noise effects below). This cell possesses a nonlinear Q_{max} (by fitting the Q - V curve with a two-state Boltzmann function (Santos-Sacchi, 1991b)) of 63.7 fC, giving rise to a peak voltage-dependent capacitance at -101 mV of 420 fF. The figure shows a 30-fF step in capacitance when voltage was stepped from $+50$ mV to $+30$ mV. These data indicate that the sensitivity of the eCm method is well within the range required for fusion event analysis.

though the PSD angle is set to guard against R_s changes, a change from 10 to 20 M Ω (I) is too large to counter; such overpowering effects of parameter changes are well known (Lindau, 1991). However, if capacitance compensation is not employed and point-by-point resetting of new angle and gain factors are made and applied, absolute C_m is obtained without any errors (B). To make point-by-point corrections experimentally, the raw admittance (\mathbf{Y}) at each point was taken and the angle of β'_ω was calculated according to Zierler (1992), namely, $\beta'_\omega = (2 \tan^{-1}(\mathbf{B}_Y/\mathbf{A}_Y) - 90^\circ)$. The true gain factor, H_c , at each data point was calculated as $1/|\text{abs}(\partial\mathbf{Y}/\partial C_m)|$. With each new gain and angle, circuit parameters were calculated as in Eq. 52, by extracting the component of \mathbf{Y} at that phase angle and multiplying by that gain factor. Each admittance point was so treated to obtain circuit parameters. The reason this procedure works so well is that the value returned by this modified PSD analysis is the imaginary component of \mathbf{Y} ; thus, this method produces the same results as the eCm method as shown in panel G. This useful single-sine approach, employing the estimate of H_c provided by Gillis (1995), $H'_c = \omega/1 + \tan(\pi/2 - \mathbf{B}_Y)^2$, is implemented in jClamp. However, because this is an estimate of the true gain, $1/|\text{abs}(\partial\mathbf{Y}/\partial C_m)|$, relying on circuit approximations, C_m estimates are not fully immune from circuit parameter changes. In panels D–F, calculations are based on setting the PSD angle to the angle of $\partial\mathbf{Y}/\partial C_m$, namely β_ω , to mimic capacitance compensation dithering. (D) The true piecewise linear approach was employed as above in panel A. In this case, using β_ω , the large change in R_m does not affect the phase angle substantially (F), so C_m estimates are accurate and robust. However, R_s changes do interfere with angle and estimate, as expected (Joshi and Fernandez, 1988). Unlike the treatment above (B), panel E shows that applying a point-by-point correction as detailed above to the uncompensated admittance fails to provide error free C_m estimation, because the imaginary component of \mathbf{Y} is not returned in this case. Panels G–I show the results of the eCm method, where the calculated absolute values are depicted by the circles. Note an exact correspondence between actual parameter values (solid lines) and calculated estimates (\circ), with no parameter interactions. Simulation in MatLab.

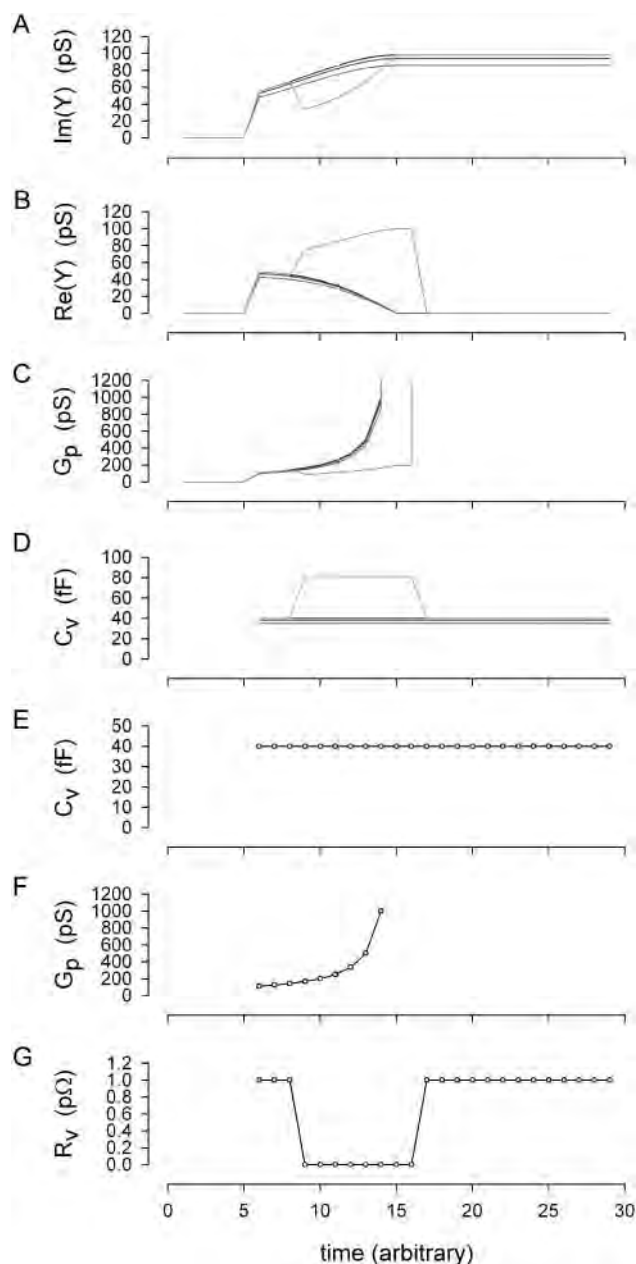


FIGURE 3 Simulation and analysis of vesicle fusion event. Whole-cell conditions remained constant throughout simulation at R_m : 1 G Ω , and C_m : 6.5 pF, with R_s : 1, 10, and 20 M Ω for dark traces (vesicle resistance, R_v , held constant at 1 p Ω (1e15 Ω)). For the shaded trace, R_s was 1 M Ω and vesicle resistance, R_v , was stepped transiently from 1 p Ω to 10 G Ω as shown in panel G. (A, B) Imaginary and real components of admittance determined according to Breckenridge and Almers (1987). (C, D) Vesicle pore conductance and capacitance extracted from admittance using standard methodology (Breckenridge and Almers, 1987; Lollike et al., 1995). Note very good correspondence between components of model even when R_s changes substantially (solid lines in panels E, F), but not when R_v is altered (shaded line). This discrepancy is not unanticipated because the standard methodology sets R_v as infinite (Breckenridge and Almers, 1987; Lollike et al., 1995). (E, F) Vesicle model parameters (solid lines) and estimates made with the *eCm* method (\circ). Correspondence is exact under all conditions. At time >5, vesicular fusion was simulated by linearly ramping the fusion pore resistance (R_p ; initially infinite) from 9 G Ω (111 pS) to 1 G Ω

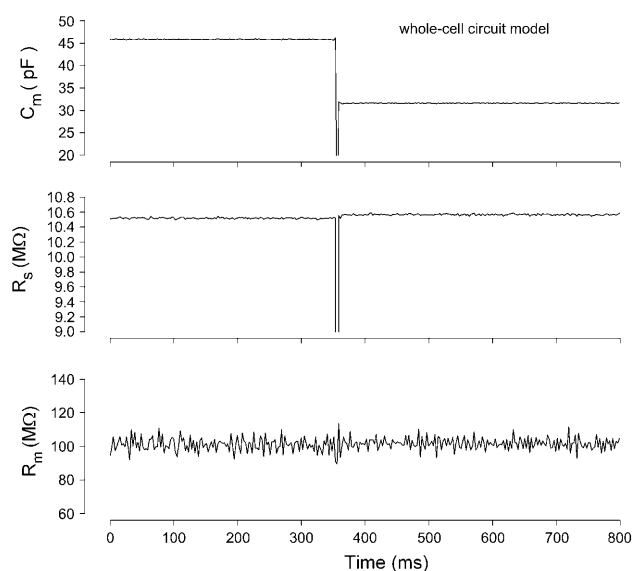


FIGURE 4 Effects of large C_m changes on parameter estimates with the *eCm* method. Nominal initial component values of R_s : 10 M Ω , R_m : 100 M Ω , and C_m : 33 pF \parallel 15 pF. A step decrease in capacitance was accomplished by suddenly removing the parallel 15 pF component. The three panels show the calculated values of the parameters using the *eCm* method at a sampling rate of 2.56 ms. Note large abrupt drop in capacitance (top) with virtually no effect on measures of R_s and R_m (middle and bottom). Model was voltage clamped with a PC clone, Axon 200 amplifier (Union City, CA) in resistive feedback mode ($\beta = 0.1$), 10-kHz Bessel filter, and Axon 1322A A/D D/A board.

DISCUSSION

Three pieces of information are required to determine the circuit parameters, R_s , R_m , and C_m of the traditional patch-clamp-cell model circuit (Fig. 1 A). The typical information obtained in a one-frequency (ω_0) measurement, namely, the real and imaginary components of the admittance, is insufficient. A third piece of information is required, and is usually obtained by exploring beyond ω_0 , that is, by utilizing information obtained at frequencies other than ω_0 . One popular solution is the “sine + dc” method (Pusch and Neher, 1988; Gillis, 2000), where a third piece of information, the input resistance ($R_{in} = R_s + R_m$), is extracted based on a priori knowledge of membrane reversal potential. This is basically a measurement at $\omega_1 = 0$. Alternatively, another non-dc piece of information, the admittance at $\omega_1 > 0$ ($\omega_1 \neq \omega_0$) can be used to extract R_{in} (Santos-Sacchi et al., 1998; Santos-Sacchi, 2002). The latter approach benefits from statistical modeling to obtain an optimal result (Barnett and Mislser, 1997). In this report, I have uncovered an additional piece of information at ω_0 , namely, β_{ω} , which can be used to determine all circuit parameters. Despite the location of β_{ω} precisely at ω_0 , the method does require two-frequency stimulation, and therefore analogous to the standard dual-sine method, it is

(1000 pS); the resulting pore conductance is shown in panel F (solid line). Fusion event analysis was implemented at that time.

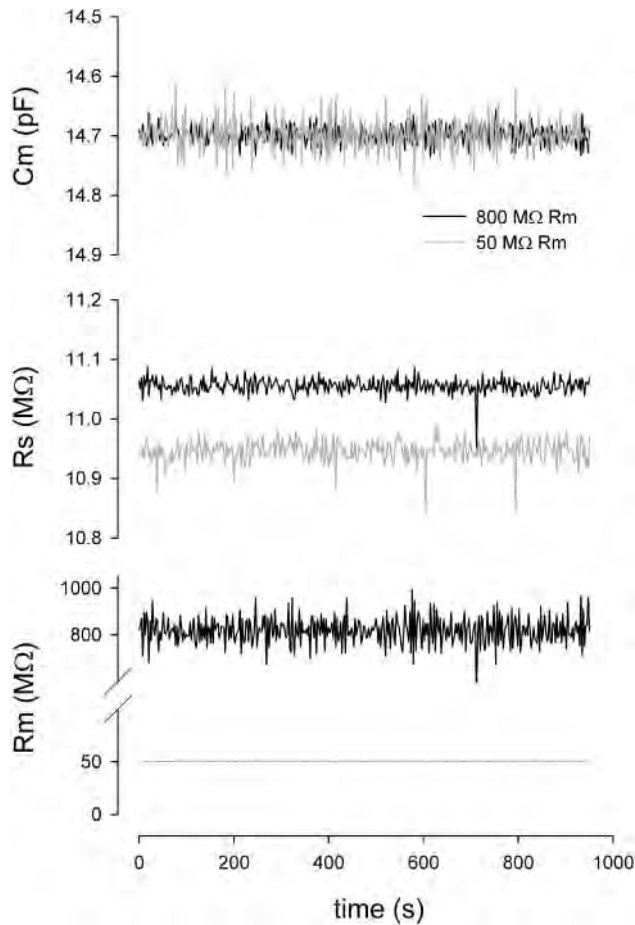


FIGURE 5 Effects of large R_m changes on parameter estimates with the eCm method. Nominal component values of R_s : 10 M Ω , R_m : 50 or 800 M Ω , and C_m : 15 pF. Note minimal interference with C_m and R_s estimates when a 50-M Ω resistor replaced the 800-M Ω resistor, other than changes in noise levels. PC clone, Axon 200 amplifier in capacitive feedback mode, 10-kHz Bessel filter, and Axon 1322A A/D D/A board were used.

reasonable to expect that optimal results could arise from further refinement (Barnett and Mislner, 1997). I should also note that because β_ω depends on τ_{clamp} , an alternative approach would be fitting of current transients induced by step voltage commands. Of course, any method that does not measure β_ω synchronously with the primary frequency component will be unable to correct for changes in cell parameters on a point-by-point basis. This will limit the utility of the technique, and this limitation is inherent in all “pause and dither” techniques. The eCm method benefits from point-by-point correction because gain and angle are redetermined and applied point-by-point at the f_0 rate.

Relation of the eCm method to traditional phase-tracking methods

The eCm method that I have developed here simply estimates absolute C_m by dividing the imaginary component of the input admittance (\mathbf{B}_Y) at a single frequency by the

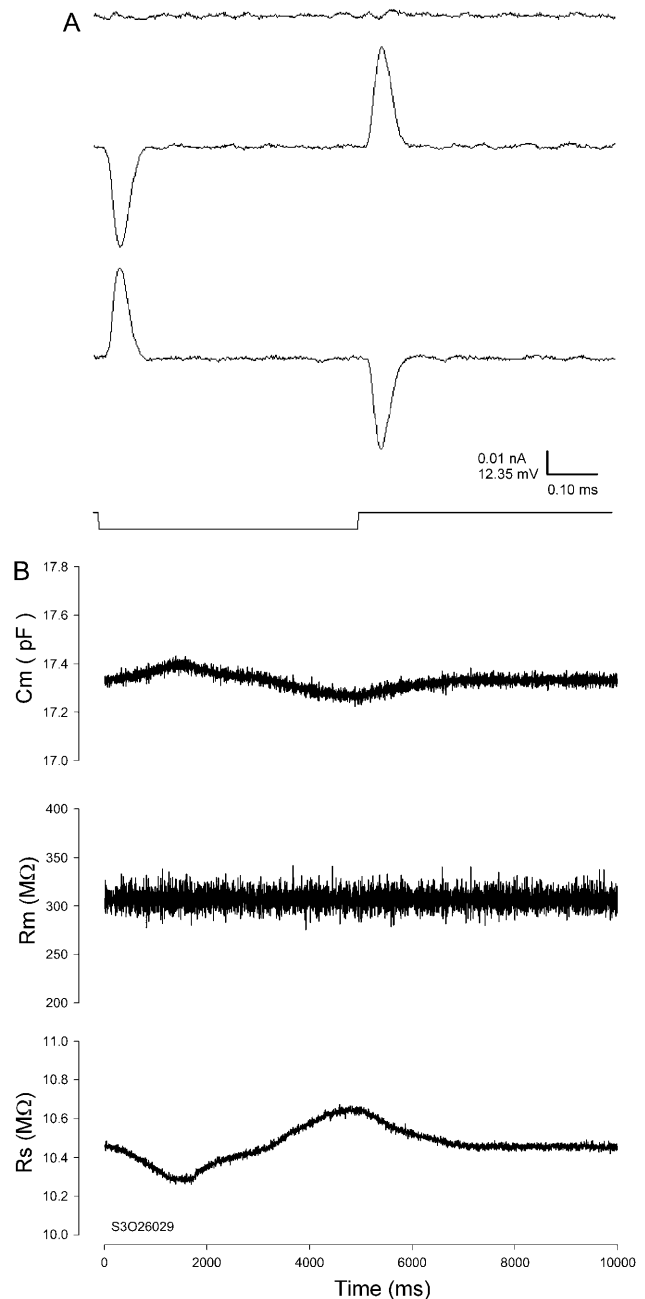


FIGURE 6 Effects of uncompensated stray capacitance on C_m measures with the eCm method. (A) Capacitive currents evoked by voltage step. Model R_s was in headstage but ungrounded. (Top) Fully compensated, (middle) undercompensated, and (bottom) overcompensated. The effect of these extremes was evaluated during parameter estimations after reassembly of the model circuit. (B) The three panels show model cell parameter estimates during manual under- and overcompensation of fast capacitance compensation. C_m was modulated $\pm 0.3\%$; R_s , $\pm 1.8\%$; and R_m , $< \pm 0.01\%$. The increase in C_m occurred during undercompensation. Nominal component values of R_s : 10 M Ω , R_m : 300 M Ω , and C_m : 18 pF. C_m noise: 14.6 fF rms; system noise with model 3.75 pA rms, 10-kHz Bessel filter, PC clone, Axon 200 amplifier in capacitive feedback mode, and Axon 1322A A/D D/A board.

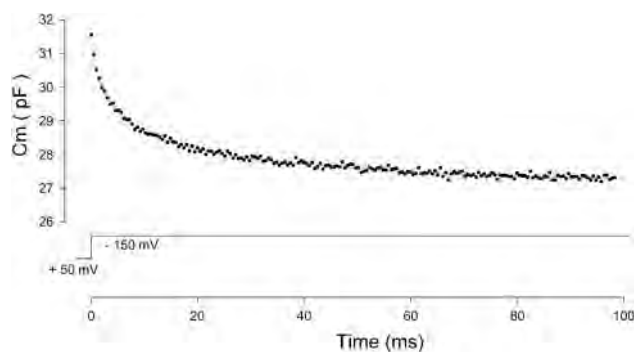


FIGURE 7 Measurement of outer hair cell nonlinear capacitance with the eC_m method. The rapid relaxation in capacitance during a step voltage change is due to the shift of the cell's nonlinear Q - V function along the voltage axis (Santos-Sacchi et al., 1998), and was confirmed through alternative measures. Cell was clamped with a PC clone, Axon 200B amplifier, 10-kHz Bessel filter, and Axon 1321A A/D D/A board with conditions described previously (Santos-Sacchi et al., 1998). See text for further details.

absolute value of the partial derivative $\partial \mathbf{Y} / \partial C_m$ at that same frequency. This method has an unforeseen relation to traditional phase-tracking techniques. The original phase-tracking method was devised to account for and limit the effects of resistive components on C_m measures (Neher and Marty, 1982; Joshi and Fernandez, 1988). It is a method that theoretically strives to determine C_m changes through measurement of changes in input admittance ($\Delta \mathbf{Y}$) as a function of changes in the circuit parameter, C_m .

$$\Delta I_{C_m} \approx \partial \mathbf{Y} / \partial C_m \Delta C_m V \quad (49)$$

$$\Delta C_m \approx \frac{1}{\partial \mathbf{Y} / \partial C_m} \frac{\Delta I_{C_m}}{V} \quad (50)$$

$$\Delta C_m \approx \frac{1}{|\partial \mathbf{Y} / \partial C_m|} \operatorname{Re} \left[\frac{\Delta \mathbf{Y}}{e^{j\beta_\omega}} \right] \quad (51)$$

$$\Delta C_m \approx H_c \operatorname{Re}(\Delta \mathbf{Y} e^{-j\beta_\omega}). \quad (52)$$

The latter equation is related to the nonsimplified form of Eq. 43 in Gillis (1995) and is addressed in a subsequent article of his (Gillis, 2000). However, heretofore, approximations of both β_ω and H_c have only been possible. The benefits and drawbacks of using particular parameter approximations have been discussed in detail (Joshi and Fernandez, 1988). Thus, phase-tracking paradigms that use estimates of the magnitude and angle of $\partial \mathbf{Y} / \partial C_m$ are recognized as better suited to systems where R_s is stable and R_m may fluctuate (Joshi and Fernandez, 1988). However, where the resistive components have the converse behavior, the angle of $\partial \mathbf{Y} / \partial G_s - 90^\circ$, namely, $2 \tan^{-1} (\mathbf{B}_Y /$

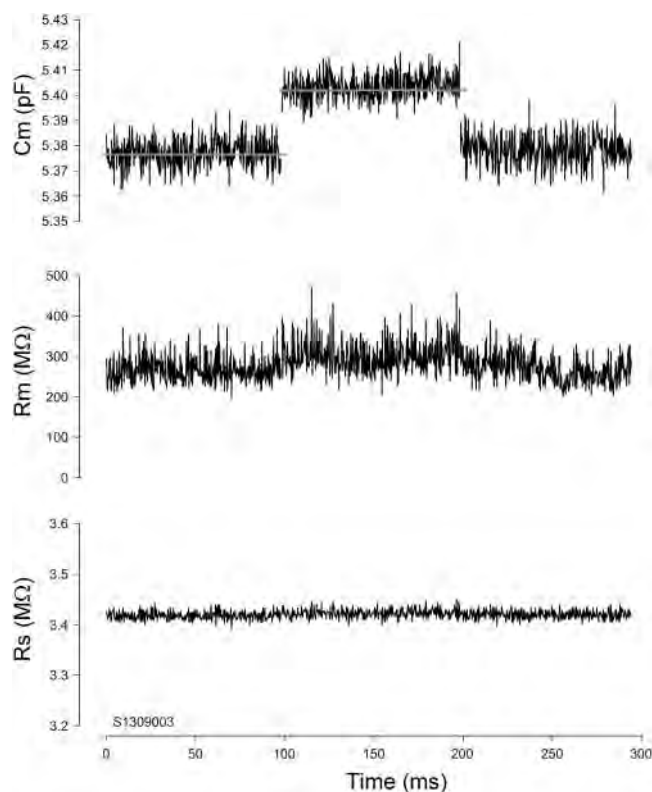


FIGURE 8 Measurement of capacitance step in prestin transfected HEK cell. Under voltage clamp a step voltage from +50 mV to +30 mV evoked a step increase in capacitance of 30 fF. C_m noise: 5.5 fF rms. PC clone, Axon 200B amplifier in resistive feedback mode, 10-kHz Bessel filter, and National Instruments (Austin, TX) PCI-6052E A/D D/A board were used.

$\mathbf{A}_Y) - 90^\circ$ as nicely provided by Zierler (1992), may be a better choice (Joshi and Fernandez, 1988). Unfortunately, where both resistive components simultaneously fluctuate, phase tracking is problematic. Despite these caveats, and even with the correct quantities I now provide, implementation of the phase tracking either by feeding the raw current output of the patch clamp into a hardware lock-in amplifier or a software phase detector (PSD) appears to be an inappropriate implementation of the phase analysis concept (Joshi and Fernandez, 1988; Neher and Marty, 1982; Fidler and Fernandez, 1989). That is, if the analyzed signal is \mathbf{Y} , then in contradistinction to Eq. 52,

$$\Delta C_m \neq H_c \operatorname{Re}(\mathbf{Y} e^{-j\beta_\omega}). \quad (53)$$

Consequently, the result of evaluating \mathbf{Y} (or I_{R_s}) directly should not provide an accurate picture of changes in C_m (i.e., ΔC_m).

The surprising fact is, however, that implementations using direct evaluations of \mathbf{Y} can, under certain conditions, provide very good estimates of absolute C_m .

It should be noted that applying capacitance and series resistance compensation at the onset of an experiment cannot be construed as providing a ΔI_{R_s} (i.e., $\Delta \mathbf{Y} V$) output from the

amplifier. This is simply a one-time subtraction that would have to be repeated, along with a new angle determination, every time a data point is collected. Additionally, only a two-element model is used by amplifiers for such compensation.

One reason for success with this direct approach would be if R_s were very small, i.e., as R_s approaches zero, $\beta_\omega \approx \Phi = 90^\circ$, and absolute values of I_{C_m} will be evaluated. Unfortunately, it is unlikely that R_s will be so low (and maintained so low) so as to approach this condition. Notwithstanding this apparent quandary, it is possible to implement phase-tracking paradigms with direct evaluations of \mathbf{Y} and still obtain excellent estimates of C_m in the face of very large changes in R_s and R_m . Surprising, the angle returned by series resistance dithering works better than that returned by capacitance compensation dithering.

Series resistance dithering

Dithering of the series resistance, championed by Joshi and Fernandez (1988), is used to return a close approximation of β_ω , namely $\angle \partial \mathbf{Y} / \partial G_s - 90^\circ$. This approximation, however, when used with a direct analysis of \mathbf{Y} , rather than $\Delta \mathbf{Y}$, and point-by-point (i.e., real time) gain and angle correction is surprisingly exact (see the simulations in Fig. 2 B). The outcome of such an implementation does not suffer from the caveats normally expected with the phase-tracking approach (Joshi and Fernandez, 1988)—namely, large changes in R_m (or R_s) have no effect on the measure of C_m . The reason for this is because the angle of $\partial \mathbf{Y} / \partial G_s$ is twice the angle of \mathbf{Y} (Zierler, 1992), and the PSD measurements are simply returning \mathbf{B}_Y ,

$$\mathbf{B}_Y = \text{Im}(\mathbf{Y}) \quad (54)$$

$$\mathbf{B}_Y = \text{Re}[\mathbf{Y} e^{-j(\angle \partial \mathbf{Y} / \partial G_s - \pi/2)}] = \text{Re}[\mathbf{Y} e^{-j(2\angle \mathbf{Y} - \pi/2)}]. \quad (55)$$

Thus, whereas Eq. 53 fails to provide ΔC_m estimates, simply replacing the angle $\angle \partial \mathbf{Y} / \partial C_m$ with $\angle \partial \mathbf{Y} / \partial G_s - 90^\circ$ results in an exact solution for absolute C_m , as shown previously in Eq. 26,

$$C_m = H_c \mathbf{B}_Y = H_c \text{Re}[\mathbf{Y} e^{-j(\angle \partial \mathbf{Y} / \partial G_s - \pi/2)}]. \quad (56)$$

Any complex number can be evaluated at twice its angle to return its real component and at twice its angle -90° to return its imaginary component. Thus, in this case, it turns out that the eCm method is simply being employed.

Capacitance compensation dithering

The initial work of Neher and Marty (1982) utilized capacitance compensation dithering to obtain an angle at which to evaluate, via PSD, changes in C_m . The angle provides an excellent approximation of β_ω when capacitance

compensation is in effect. This is shown by inspection of $\partial \mathbf{Y} / \partial C_d$ and its angle, based on the model of Fig. 1 A, now including the capacitance compensation components C_d and R_d (in series with each other, from headstage to ground).

$$\partial \mathbf{Y} / \partial C_d = \frac{-j\omega}{(R_d C_d \omega - j)^2} \quad (57)$$

$$\angle \partial \mathbf{Y} / \partial C_d = -\tan^{-1} \left[\frac{\omega^2 \tau_d^2 - 1}{2\omega \tau_d} \right], \quad (58)$$

where $\tau_d = R_d C_d$.

β_ω , the angle of $\partial \mathbf{Y} / \partial C_m$, remains unaffected by the addition of the capacitance compensation circuitry,

$$\beta_\omega = -\tan^{-1} \left[\frac{\omega^2 \tau_{\text{clamp}}^2 - 1}{2\omega \tau_{\text{clamp}}} \right], \quad (59)$$

thus indicating that when the clamp time constant (τ_{clamp}) and compensation time constant (τ_d) are equal, i.e., when compensation is in effect, the angle returned by dithering equals β_ω . Unlike the use of the angle returned by series resistance dithering, the use of this angle to measure C_m with direct evaluations of \mathbf{Y} is not as accurate (Fig. 2 E). It should be noted that these analyses only apply to direct measures of \mathbf{Y} that are corrected on a point-by-point basis for phase and gain changes, and not necessarily to the traditional use of the angle (Neher and Marty, 1982).

Validity, accuracy, and sensitivity of C_m measurement methods

There are several factors, including model validity, approximations, and noise that contribute to errors in the measurement of capacitance with sinusoidal analysis. Obviously, approximations lead to errors only if they fail; however, because approximations often remove a particular component, e.g., R_s or R_v , from the system of equations, it is impossible to gauge failure during an experiment. Thus, it is prudent to make as few simplifications and approximations as possible. The mathematical and physical modeling that I have presented clearly indicate that the eCm method benefits from this rule.

Noise, on the other hand, is an issue that affects all electrical measures of cell activity regardless of the method's validity. Even for a method that provides a valid measure of some electrical quantity in the absence of noise, the introduction of noise can prove devastating, or at least render it useless for a given task. Not surprisingly, some methods may be able to deal with system noise better than others.

The design of sinusoidal stimulus protocols has enormous impact on C_m measurement sensitivity in the face of real-world noise. Important issues such as stimulus frequency,

stimulus magnitude, stray capacitance, and unexpected conductance changes have been discussed in detail (Gillis, 1995; Barnett and Mislner, 1997; Thompson et al., 2001; Debus et al., 1995). Careful attention to these issues can lead to incredible sensitivity; for example, with very high-frequency stimulation and very large voltages, very good signal/noise ratios can be obtained, providing noise floors well below 1 fF (Klyachko and Jackson, 2002). One of the consequences of the equivalency between the *eCm* method and the phase-tracking method as typically employed, is that effects of noise on performance might be expected to be similar for each method. To evaluate issues like this, comparisons were made under varying noise conditions in model simulations.

In Fig. 9, a modeling approach is used to compare the effects of Gaussian noise levels on C_m estimate noise among a few common methods of C_m estimation. In this approach, the simple circuit of Fig. 1 A was modeled in the time domain using the RK4 method hardcoded in C within jClamp; the results were then independently analyzed by transient step analysis, single-sine analysis, dual-sine analysis, or the *eCm* method. Step analysis follows the method outlined in a prior publication (see appendix in Huang and Santos-Sacchi,

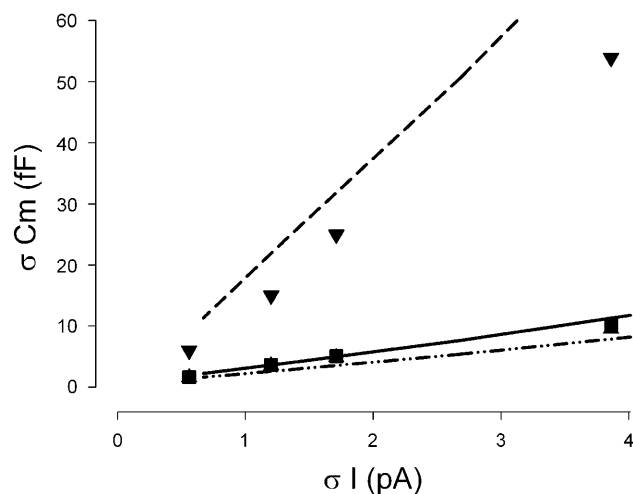


FIGURE 9 Effect of system noise on C_m estimate noise. Results from either mathematical modeling (lines) or physical modeling (symbols). Three methodologies, step (dashed line, ▼), *eCm* (dash-dotted line, ▲), and single-sine phase tracking (solid line, ■) are presented. For the software model, forced Gaussian noise levels were imposed, and the noise of C_m estimates calculated. For the physical model, system noise levels were 3.8 pA rms when the model was attached to the headstage. To obtain lower system noise levels, averaging was performed to produce the plotted noise levels. For the electrical model, a 10-kHz Bessel filter was used, and the frequency components of the remaining noise were likely different from the wideband noise used for the math model. This likely accounts for differences in math and electrical model results. In any case, the data from each model indicate that as system noise decreases, all of the methods become comparable. Nominal component values of R_s: 10 MΩ, R_m: 300 MΩ, and C_m: 18 pF. IBM T40 laptop in battery mode (Armonk, NY), Axon 200 amplifier in capacitive feedback mode, 10-kHz Bessel filter, and Quatech (Hudson, OH) DAQP 308 PCMCIA PC card A/D D/A board were used.

1993). Such an analysis is multifrequency, providing extended information similar to that obtained from “chirp” stimuli (Santos-Sacchi, 1991b; Santos-Sacchi, 1989), and wideband noise stimuli (Fernandez et al., 1982). Features of our step method included automatic clocking to reach steady state and utilization of exponential fitting after the initial onset transient, methodology recently reemphasized as important for the robust use of transient analysis for C_m measurement (Thompson et al., 2001). In our original implementation and in jClamp, a correction for errors introduced by the R_s/R_m voltage divider on Q, namely that C_m = (R_m + R_s)²/R_m² Q/V_m, is employed (Huang and Santos-Sacchi, 1993). To my knowledge, no other implementation accounts for this potential error. Single-sine analysis follows the approximation (for β_ω and H_c) method outlined in the Fig. 2 legend. The dual-sine method (Santos-Sacchi, 1992; Santos-Sacchi et al., 1998), follows the same fast Fourier transform-based determination of the real and imaginary components employed by the *eCm* method. In both cases estimates derived from both ω₀ and ω₁ are averaged (f₀: 390.6 Hz; f₁: 781.2 Hz). This averaging benefit must be kept in mind when comparing single-sine estimates. All methodologies are standard features in jClamp. In Fig. 9 the relation between measured C_m noise and imposed current noise is examined for each of the methodologies with either a 100-MΩ or 500-MΩ R_m. All methods work well under low-noise conditions, and this simply indicates that the true limitation for C_m estimation is the noise of the system at those frequencies used by the method. Indeed, under real-world conditions where system noise levels are well minimized, step, single-sine and dual-sine techniques can provide roughly equivalent C_m estimate noise levels (within ±10–30%) close to theoretical limits (Gillis, 1995; Barnett and Mislner, 1997; Thompson et al., 2001). However, under forced noise levels as in Fig. 9 the *eCm* and single-sine techniques appear better able to deal with higher noise levels than this step implementation. Because of the exact same implementation of frequency analysis and the absence of approximations for *eCm* and dual-sine approaches, sensitivities turn out to be essentially equivalent. Had β_ω been determined in another manner, e.g., by the dω approach, the results may have differed. Given the relation between the single-sine phase-tracking approach and the *eCm* method detailed above, it is not surprising that these two methods are roughly equivalent in handling noise. For each method, slightly better noise levels are achieved when β_ω is fixed during analysis to simulate a “pause and dither” approach; thus, recalculating β_ω for each sample introduces additional noise in the analysis that must be balanced with the increased validity afforded by point-by-point correction. The step analysis is particularly prone to high noise levels; this is especially obvious when low frequency (e.g., 60 Hz) interference is included, and is in marked contrast to sinusoidal approaches that can avoid extraneous spectral interference. The conclusions based on this mathematical

modeling effort were essentially confirmed with a physical implementation (see Fig. 9). From these results, it is clear that given a sufficiently low system noise or actually a sufficiently high signal/noise level, the *eCm* method will have the sensitivity to analyze fusion events, as clearly suggested by the physiological results shown in Fig. 8.

SUMMARY

The new *eCm* method that I outlined here provides another tool for analysis of cellular processes that can be interrogated by C_m measures. It is a method that works in the absence of usual simplifying assumptions and approximations of the traditional patch-clamp-cell model circuit. In detailing the approach, several new observations have been made. They include: 1), the imaginary component of the input admittance \mathbf{Y} , namely, \mathbf{B}_Y , can be worked on by $\partial\mathbf{Y}/\partial C_m$ to obtain absolute values of C_m ; 2), the angle of $\partial\mathbf{Y}/\partial C_m$, namely, β_ω , is the same as that of $\partial\mathbf{Y}/\partial\omega$ and therefore can be obtained from frequency manipulation alone; 3), given β_ω , the absolute value of $\partial\mathbf{Y}/\partial C_m$ can be determined; 4), frequency manipulation need not require an infinitesimal $d\omega$ to extract β_ω ; and 5), the traditional phase-tracking technique that evaluates raw amplifier currents, rather than difference currents, at the angle provided by series resistance dithering, works similar to the *eCm* method by simply returning estimates of \mathbf{B}_Y , not ΔI_{C_m} , and ultimately provides absolute, not delta, C_m estimates. Finally, it might be expected that enhancements of the *eCm* technique may arise from future implementations in hardware and by statistical optimizations.

I thank Peter Dallos, Fred Sigworth, and Alan Segal for looking at early drafts. I especially thank Peter Dallos for confirming some of the concepts presented in the manuscript, and identifying others that needed rethinking. Finally, I thank the reviewers for many helpful suggestions.

This work was supported in part by the National Institutes of Health (National Institute on Deafness and Other Communication Disorders grant no. DC00273).

REFERENCES

- Ales, E., L. Tabares, J. M. Poyato, V. Valero, M. Lindau, and D. T. Alvarez. 1999. High calcium concentrations shift the mode of exocytosis to the kiss-and-run mechanism. *Nat. Cell Biol.* 1:40–44.
- Alvarez De Toledo, G. A., R. Fernandez-Chacon, and J. M. Fernandez. 1993. Release of secretory products during transient vesicle fusion. *Nature.* 363:554–558.
- Aravanis, A. M., J. L. Pyle, and R. W. Tsien. 2003. Single synaptic vesicles fusing transiently and successively without loss of identity. *Nature.* 423:643–647.
- Barnett, D. W., and S. Misler. 1997. An optimized approach to membrane capacitance estimation using dual-frequency excitation. *Biophys. J.* 72:1641–1658.
- Bigiani, A., and S. D. Roper. 1995. Estimation of the junctional resistance between electrically coupled receptor cells in *Necturus* taste buds. *J. Gen. Physiol.* 106:705–725.
- Breckenridge, L. J., and W. Almers. 1987. Currents through the fusion pore that forms during exocytosis of a secretory vesicle. *Nature.* 328:814–817.
- Cole, K. S. 1971. Some aspects of electrical studies of the squid giant axon membrane. In *Biophysics and Physiology of Excitable Membranes*. W. J. Adelman, editor. Van Nostrand Reinhold Co., New York. 125–42.
- Debus, K., J. Hartmann, G. Kilic, and M. Lindau. 1995. Influence of conductance changes on patch clamp capacitance measurements using a lock-in amplifier and limitations of the phase tracking technique. *Biophys. J.* 69:2808–2822.
- Debus, K., and M. Lindau. 2000. Resolution of patch capacitance recordings and of fusion pore conductances in small vesicles. *Biophys. J.* 78:2983–2997.
- Fernandez, J. M., F. Bezanilla, and R. E. Taylor. 1982. Distribution and kinetics of membrane dielectric polarization. II. Frequency domain studies of gating currents. *J. Gen. Physiol.* 79:41–67.
- Fidler, N., and J. M. Fernandez. 1989. Phase tracking: an improved phase detection technique for cell membrane capacitance measurements. *Biophys. J.* 56:1153–1162.
- Fricke, H. 1925. The electric capacity of suspensions with special reference to blood. *J. Gen. Physiol.* 9:137–152.
- Gandhi, S. P., and C. F. Stevens. 2003. Three modes of synaptic vesicular recycling revealed by single-vesicle imaging. *Nature.* 423:607–613.
- Gillis, K. D. 1995. Techniques for membrane capacitance measurements. In *Single-Channel Recording*. B. Sakmann and E. Neher, editors. Plenum Press, New York. 155–98.
- Gillis, K. D. 2000. Admittance-based measurement of membrane capacitance using the EPC-9 patch-clamp amplifier. *Pflugers Arch.* 439:655–664.
- Huang, G., and J. Santos-Sacchi. 1993. Mapping the distribution of the outer hair cell motility voltage sensor by electrical amputation. *Biophys. J.* 65:2228–2236.
- Jaffe, L. A., and L. C. Schlichter. 1985. Fertilization-induced ionic conductances in eggs of the frog, *Rana pipiens*. *J. Physiol.* 358:299–319.
- Joshi, C., and J. M. Fernandez. 1988. Capacitance measurements. An analysis of the phase detector technique used to study exocytosis and endocytosis. *Biophys. J.* 53:885–892.
- Klyachko, V. A., and M. B. Jackson. 2002. Capacitance steps and fusion pores of small and large-dense-core vesicles in nerve terminals. *Nature.* 418:89–92.
- Lindau, M. 1991. Time-resolved capacitance measurements: monitoring exocytosis in single cells. *Q. Rev. Biophys.* 24:75–101.
- Lindau, M., and E. Neher. 1988. Patch-clamp techniques for time-resolved capacitance measurements in single cells. *Pflugers Arch.* 411:137–146.
- Lollike, K., N. Borregaard, and M. Lindau. 1995. The exocytotic fusion pore of small granules has a conductance similar to an ion channel. *J. Cell Biol.* 129:99–104.
- Meltzer, J., and J. Santos-Sacchi. 2001. Temperature dependence of non-linear capacitance in human embryonic kidney cells transfected with prestin, the outer hair cell motor protein. *Neurosci. Lett.* 313:141–144.
- Neher, E., and A. Marty. 1982. Discrete changes of cell membrane capacitance observed under conditions of enhanced secretion in bovine adrenal chromaffin cells. *Proc. Natl. Acad. Sci. USA.* 79:6712–6716.
- Oppenheim, A., and R. Schaffer. 1975. *Digital Signal Processing*. Prentice-Hall, Englewood Cliffs, NJ.
- Pusch, M., and E. Neher. 1988. Rates of diffusional exchange between small cells and a measuring patch pipette. *Pflugers Arch.* 411:204–211.
- Ratinov, V., I. Plonsky, and J. Zimmerberg. 1998. Fusion pore conductance: experimental approaches and theoretical algorithms. *Biophys. J.* 74:2374–2387.
- Sakmann, B., and E. Neher. 1995. Geometric parameters of pipettes and membrane patches. In *Single-Channel Recording*. B. Sakmann and E. Neher, editors. Plenum Press, New York. 637–50.
- Santos-Sacchi, J. 1989. Asymmetry in voltage-dependent movements of isolated outer hair cells from the organ of Corti. *J. Neurosci.* 9:2954–2962.
- Santos-Sacchi, J. 1991a. Isolated supporting cells from the organ of Corti: some whole cell electrical characteristics and estimates of gap junctional conductance. *Hear. Res.* 52:89–98.

- Santos-Sacchi, J. 1991b. Reversible inhibition of voltage-dependent outer hair cell motility and capacitance. *J. Neurosci.* 11:3096–3110.
- Santos-Sacchi, J. 1992. On calculating series resistance: step and two-sine approaches. Poster presentation at the Yale Neuroscience Retreat, February 21–23. Marine Biological Laboratory, Woods Hole, MA.
- Santos-Sacchi, J. 2002. Scisoft Technical Note. http://www.scisoftco.com/detrending_for_2_sine_cm_measures.pdf.
- Santos-Sacchi, J. 2003. New tunes from Corti's organ: the outer hair cell boogie rules! *Curr. Opin. Neurobiol.* 13:459–468.
- Santos-Sacchi, J., S. Kakehata, and S. Takahashi. 1998. Effects of membrane potential on the voltage dependence of motility-related charge in outer hair cells of the guinea-pig. *J. Physiol.* 510:225–235.
- Thompson, R. E., M. Lindau, and W. W. Webb. 2001. Robust, high-resolution, whole cell patch-clamp capacitance measurements using square wave stimulation. *Biophys. J.* 81:937–948.
- Zhao, H. B., and J. Santos-Sacchi. 1998. Effect of membrane tension on gap junctional conductance of supporting cells in Corti's organ. *J. Gen. Physiol.* 112:447–455.
- Zhao, H. B., and J. Santos-Sacchi. 1999. Auditory collusion and a coupled couple of outer hair cells. *Nature.* 399:359–362.
- Zierler, K. 1992. Simplified method for setting the phase angle used in capacitance measurements in studies of exocytosis. *Biophys. J.* 63: 854–856.

Thematic Issue

Membranes and Their Interacting Partners in Peripheral Auditory Function

J. Santos-Sacchi, Guest Editor

Foreword: Let's Hear It for the Membranes!

Joseph Santos-Sacchi

Otolaryngology, Neurobiology and Cellular and Molecular Physiology, Yale University School of Medicine, 333 Cedar St., New Haven, CT 06510, USA

Received: 20 February 2006

Membranes have always held a special place in my heart, having been entranced by their magic when I was a freshman at Columbia College in New York City in 1969. Of course not much was known about them then, and even less was known about how these organelles help us hear. During the next 35 years, auditory researchers worked hard to elucidate the role of membranes in inner ear function. Indeed, during that time, scores of (now) senior auditory biophysicists have shaped our knowledge of how the inner ear works. In this special issue of the *Journal of Membrane Biology*, I have broken from tradition, and chosen to enlist a large group of young (except for me, of course) independent investigators to collaborate in telling us about the importance of membranes and associated molecules in a variety of cell types within the auditory periphery. Seven review articles are presented which span the molecular workings of cells ranging from hair cells to primary afferents. We begin by looking at the first step in auditory processing, the stereocilia transduction apparatus housed in the apical stereocilia of hair cells. This unique organelle not only can convert sound-evoked mechanical stimuli into electrical signals (receptor potentials) that permit us to perceive sound, but, as well, may play an important role in a feedback mechanism that can amplify those incoming stimuli. Drs. Ricci, Kachar, Gale, and Van Netten provide us with a detailed description of these events. The hair cell does not simply cable the resultant receptor potentials to afferents, but instead shapes its

own responsiveness with the multitude of channel types within its apical and basolateral membranes. The next article in our special issue by Drs. Housley, Marcotti, Navaratnam, and Yamoah details what we know about these membrane constituents. In mammals, two hair cell types have evolved to aid in high-frequency discrimination, the inner and outer hair cells. The outer hair cell is both sensory receptor and mechanical effector, working to augment the mechanical responsiveness of the cochlea partition – cochlear amplification, as it is commonly called. Two reviews are devoted to this marvelous outer hair cell. In the first, Drs. He, Zheng, Kalinec, Kakehata, and Santos-Sacchi tell us about the experimental approaches which have led to understanding the so called electromotility of this cell and the electromechanical characteristics of the cell's lateral membrane, which houses the unique voltage-dependent motor protein, prestin (SLC26A5). The following review of OHC models by Drs. Spector, Deo, Grosh, Ratnanather and Raphael explains to the physiologists what their experiments mean! In fact, by modeling the OHC's electromechanical activity we can also glean things which experimentalists cannot yet appraise. Inner hair cells provide up to 95% of the afferent input to the CNS. The cell type that begins the transit of acoustic information to the CNS, the spiral ganglion cell, must reliably capture the activity of inner hair cells, and the synaptic events that lead to AP generation are of prime import in this process. Drs. Nouvian, Beutner, Parsons and Moser provide us with our current understanding of synaptic transmission between hair cells and eighth nerve. Of course, it is the spiral ganglion cell soma and processes that ultimately must pass this information

Correspondence to: J. Santos-Sacchi; email: joseph.santos-sacchi@yale.edu

centrally, and their membrane plays the most critical role in determining timing characteristics required for high frequency transmission. Drs. Dulon, Jagger, Lin, and Davis detail the unique characteristics of these important links to the CNS. Finally, the hair cells and nerve fibers that reside within the organ of Corti cannot stand alone. A variety of supporting-cells provide structural and metabolic support for the organ, and without them our mechanoreceptors would be useless. One of the most important aspects of supporting-cell physiology is the syncytial network provided by gap junctional communication. Muta-

tions of gap junctions account for a leading cause of deafness. Drs. Zhao, Kikuchi, Ngezahayo, and White review what we know about the role of gap junctions in cochlear homeostasis and pathology.

I think that this compilation of reviews underscores why membranes are important for peripheral auditory function. The wealth of information that these young investigators display in their reviews and the energy that these scientists bring to our field indicate that understanding membranes will remain an important goal for our community — for many years to come. Let's hear it for the membranes!

translocating from the ER to CpG DNA in the lysosome. *Nat. Immunol.* 5, 190–198.

11. Brint, E.K., Xu, D., Liu, H., Dunne, A., McKenzie, A.N., O'Neill, L.A., and Liew, F.Y. (2004). ST2 is an inhibitor of interleukin 1 receptor and Toll-like receptor 4 signaling and

maintains endotoxin tolerance. *Nat. Immunol.* 5, 373–379.

12. DeYoung, B.J., and Innes, R.W. (2006). Plant NBS-LRR proteins in pathogen sensing and host defense. *Nat. Immunol.* 7, 1243–1249.

School of Biochemistry and Immunology, Trinity College Dublin, Ireland.
E-mail: laoneill@tcd.ie

DOI: 10.1016/j.cub.2008.02.021

Cochlear Mechanics: No Shout but a Twist in the Absence of Prestin

Mammalian hearing is boosted by mechanically active auditory receptor cells, the outer hair cells which amplify the actions of incoming sounds. Recent evidence indicates that the molecular motor that drives this amplification, prestin, may do more than boogie.

Joseph Santos-Sacchi

About a half century ago, in experiments on the mammalian inner ear, Bekesy [1] observed acoustically driven, frequency-tuned responses of the basilar membrane, the cochlear structure which bears the sound-detecting organ of Corti. These tuned responses underlie tonotopicity, the mapping of characteristic frequency onto anatomical space throughout the auditory system. Modern measurements have shown that the peripheral auditory system response — involving sequentially the basilar membrane, hair cell and eighth nerve fiber — is nonlinear with intensity, at least at low intensities. Measures of basilar membrane motion near threshold are thus several orders of magnitude larger than Bekesy's atomic scale estimates [2]. This nonlinear response is the hallmark of cochlear amplification, and is vulnerable to metabolic insult. Metabolic lability issues from the fragile outer hair cell, one of two receptor cell types in the inner ear.

The outer hair cell employs, as Gold's 'negative resistance' hypothesis predicted [3], voltage-driven mechanical activity which helps counter cochlear fluid viscosity, thus enabling sharply tuned mechanical responses [4–6]. The identification of a unique motor protein [7], termed prestin, which is found exclusively in the outer hair cell, shed light on the molecular basis of this amplificatory process (Figure 1). As expected, elimination of prestin by knocking out its gene produced mice that were deaf, despite having normal stereociliar mechanisms [8,9], attesting to the

dominant role of prestin in mammalian cochlear amplification.

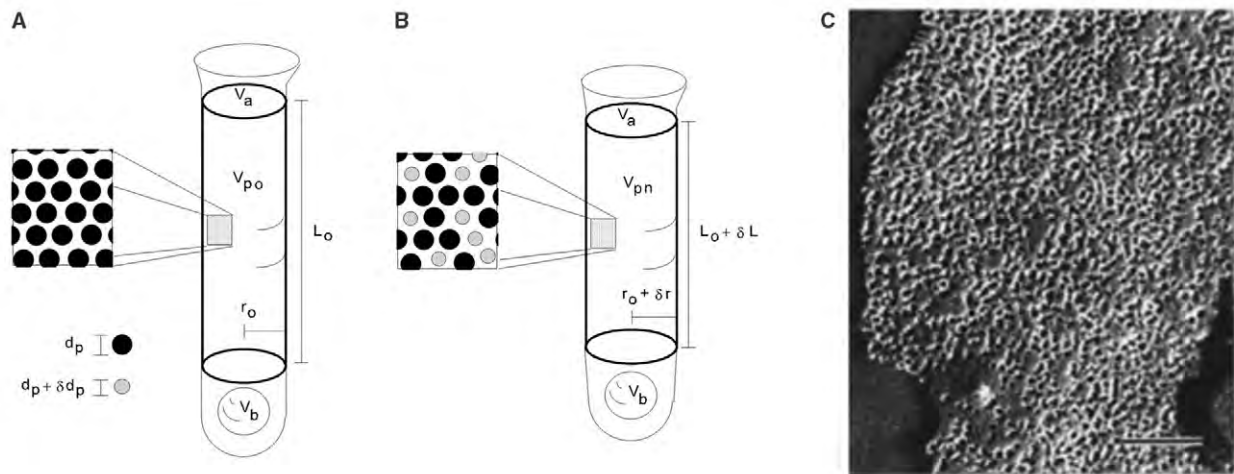
In all experiments to date in which normal outer hair cell function or specifically prestin function has been compromised, physiological measures have shown broadened frequency tuning, shifts in characteristic frequency to lower frequencies, and loss in auditory sensitivity. These experiments include studies that have also measured basilar membrane motion [10–12]. But the first measurements of basilar membrane tuning in prestin knockout mice, reported recently in *Current Biology* [13], have shown the story is more complex than suspected.

Mellado Lagarde *et al.* [13] observed that the effect on the peripheral auditory system was different when prestin was silenced by interfering with its function, for example with salicylate or anoxia, compared to when it was molecularly absent from the outer hair cell, as in the knockout mouse. In the former case, the sensitivity of both basilar membrane motion and eighth nerve activity are compromised, whereas in the latter case basilar membrane sensitivity is maintained, albeit at a shifted characteristic frequency with poor tuning, but eighth nerve activity is devastated. This is an interesting finding, as basilar membrane motions and eighth nerve fiber activity are expected to show a tight correspondence, at least in the characteristic frequency region [14]. The authors rightly point out that the dichotomy in response sensitivities between nerve and basilar membrane in the knockout mouse highlights the critical link between basilar membrane motion and inner hair cell stereociliar

shear, the drive for forward transduction and auditory sensation [15]. The inner hair cell is the other purely sensory cell that synapses with the majority of eighth nerve afferents. The paper [13] thus presents two interesting findings on the knockout mouse: first, that basilar membrane responses appear as acoustically sensitive as normal; and second, that despite the high sensitivity, coupling between basilar membrane and inner hair cell is lost. How can the absence of prestin do this?

We must revisit the effects of the prestin knockout on the outer hair cell itself. It is well known that prestin influences the static and dynamic mechanical properties of the outer hair cell [5,16–18]. There are several million prestin molecules within an outer hair cell membrane [19], and the absence of molecules reduces the membrane surface area and produces shorter cells [9]. This, in turn, affects the cell's mechanical properties. Cell stiffness also relies directly on the activity of prestin in the membrane ([17], but see [20]), possibly through cytoskeletal interactions. Collectively, these changes could alter cochlear partition impedance and account for the observed shifts in best frequency in the passive basilar membrane of the knockout mice; but can they account for the apparent increase in basilar membrane motion over that found in anoxic animals with normal prestin? Can a simple change in basilar membrane impedance and resonance overcome viscous damping effects? Or perhaps prestin did not evolve to overcome viscous damping.

Consider this evolutionary scenario that might help us understand the data. A passive cochlear with outer hair cells lacking prestin will have basilar membrane motion that we consider sensitive, but really it is just how things work in the presence of normal viscous damping. In this case, tuning at the passive characteristic frequency and coupling between basilar membrane



Current Biology

Figure 1. Prestin and outer hair cell function.

The outer hair cell soma is schematized in the fully elongated (A) and partially contracted (B) condition, corresponding to hyperpolarization and depolarization, respectively. (The abbreviations refer to a popular Boltzmann model of motility where motors fluctuate between two states: d_p , diameter of motor; δd_p , change in diameter when motor contracts; L_o , normal length of the lateral membrane; δL , change in length when motors contract; r_o , normal radius of the cylindrical cell; δr , change when motors contract; V_a and V_b , constant volume of apex and base, respectively; V_{po} and V_{pn} , volumes of motor-containing cell region during elongation and contraction, respectively.) The outer hair cell motor, prestin, is embedded within the lateral membrane of the cell, forming a dense array. Motors (dark and light circles in the blowup) are depicted in compact or expanded states, corresponding to the two-state model of their activity. Electrical measures of the motor's voltage sensor provide estimates of millions of motor molecules per cell. The lateral membrane (C) when viewed with freeze fracture electron microscopy, displays a dense array of 10 nm particles, which are believed to represent multimers of prestin. The dense packing must have substantial structural consequences beyond the dynamic activity of the protein. (Reproduced with permission from [19].)

and inner hair cell stereociliar shear are normally poor. Now, for mammals, there was a need for auditory sensitivity at higher frequencies. Prestin evolved to improve the coupling of basilar membrane motion to inner hair cell stereociliar shear and simultaneously shift characteristic frequency to higher frequencies, but in the process, the tightened mechanical coupling caused a reduction in the sensitivity of basilar membrane motion, thus necessitating an amplificatory mechanism to reestablish high sensitivity at the new higher characteristic frequency. In this scenario the passive presence of prestin enhances coupling, but is detrimental to basilar membrane motion, and the electrical activity of prestin amplifies the movements of the well coupled basilar membrane.

How could a protein within the lateral membrane of the outer hair cell work to couple basilar membrane motion into inner hair cell stereociliar shear? The organ of Corti is a mass of supporting cells and hair cells bounded apically by the reticular lamina/tectorial membrane and basally by the basilar membrane. Displacements of the

basilar membrane, induced acoustically, must be sensed at the apical region where stereocilia of inner hair cells and outer hair cells reside. It is possible that the increase in stiffness provided to the outer hair cells by the immense numbers of prestin protein in the lateral membrane reinforces or stiffens the cellular link between basilar membrane and reticular lamina.

If this is true, we might predict that a knock-in of a nonfunctional prestin into the knock-out mouse would produce a basilar membrane response at lower characteristic frequency, as we see in the knock-out, but with a reduced sensitivity that would reflect an enhanced coupling between basilar membrane and inner hair cell stereocilia. We know how long it takes to get a new mutant mouse. So it may be a while before we get at the deeper significance of the new data reported by Mellado Lagarde *et al.* [13].

References

1. von Bekesy, G. (1960). Experiments in Hearing (New York: McGraw-Hill Book Company).
2. Rhode, W.S. (1971). Observations of the vibration of the basilar membrane in squirrel

- monkeys using the Mossbauer technique. *J. Acoust. Soc. Am. Suppl.* 49, 1218–1231.
3. Gold, T. (1948). Hearing. II. The physical basis of the action of the cochlea. *Proc. R. Soc. Lond. B* 135, 492–498.
4. Brownell, W.E., Bader, C.R., Bertrand, D., and de Ribaupierre, Y. (1985). Evoked mechanical responses of isolated cochlear outer hair cells. *Science* 227, 194–196.
5. He, D.Z., Zheng, J., Kalinec, F., Kakehata, S., and Santos-Sacchi, J. (2006). Tuning in to the amazing outer hair cell: membrane wizardry with a twist and shout. *J. Membr. Biol.* 209, 119–134.
6. Ashmore, J. (2008). Cochlear outer hair cell motility. *Physiol. Rev.* 88, 173–210.
7. Zheng, J., Shen, W., He, D.Z., Long, K.B., Madison, L.D., and Dallos, P. (2000). Prestin is the motor protein of cochlear outer hair cells. *Nature* 405, 149–155.
8. Cheatham, M.A., Huynh, K.H., Gao, J., Zuo, J., and Dallos, P. (2004). Cochlear function in Prestin knockout mice. *J. Physiol.* 560, 821–830.
9. Liberman, M.C., Gao, J., He, D.Z., Wu, X., Jia, S., and Zuo, J. (2002). Prestin is required for electromotility of the outer hair cell and for the cochlear amplifier. *Nature* 419, 300–304.
10. Ruggero, M.A., and Rich, N.C. (1991). Furosemide alters organ of corti mechanics: evidence for feedback of outer hair cells upon the basilar membrane. *J. Neurosci.* 11, 1057–1067.
11. Murugasu, E., and Russell, I.J. (1995). Salicylate ototoxicity: the effects on basilar membrane displacement, cochlear microphonics, and neural responses in the basal turn of the guinea pig cochlea. *Auditory Neurosci.* 1, 139–150.
12. Santos-Sacchi, J., Song, L., Zheng, J., and Nuttall, A.L. (2006). Control of mammalian cochlear amplification by chloride anions. *J. Neurosci.* 26, 3992–3998.

13. Mellado Lagarde, M.M., Drexler, M., Lukashkin, A.N., Zuo, J., and Russell, I.J. (2008). Prestin's role in cochlear frequency tuning and transmission of mechanical responses to neural excitation. *Curr. Biol.* **18**, 200–202.
14. Narayan, S.S., Temchin, A.N., Recio, A., and Ruggero, M.A. (1998). Frequency tuning of basilar membrane and auditory nerve fibers in the same cochleae. *Science* **282**, 1882–1884.
15. Nowotny, M., and Gummer, A.W. (2006). Nanomechanics of the subreticular space caused by electromechanics of cochlear outer hair cells. *Proc. Natl. Acad. Sci. USA* **103**, 2120–2125.
16. Spector, A.A., Deo, N., Grosh, K., Ratnanather, J.T., and Raphael, R.M. (2006). Electromechanical models of the outer hair cell composite membrane. *J. Membr. Biol.* **209**, 135–152.
17. He, D.Z., Jia, S., and Dallos, P. (2003). Prestin and the dynamic stiffness of cochlear outer hair cells. *J. Neurosci.* **23**, 9089–9096.
18. Jensen-Smith, H., and Hallworth, R. (2007). Lateral wall protein content mediates alterations in cochlear outer hair cell mechanics before and after hearing onset. *Cell Motil. Cytoskel.* **64**, 705–717.
19. Santos-Sacchi, J., Kakehata, S., Kikuchi, T., Katori, Y., and Takasaka, T. (1998). Density of motility-related charge in the outer hair cell of the guinea pig is inversely related to best frequency. *Neurosci. Lett.* **256**, 155–158.
20. Hallworth, R. (2007). Absence of voltage-dependent compliance in high-frequency cochlear outer hair cells. *J. Assoc. Res. Otolaryngol.* **8**, 464–473.

Department of Surgery (Otolaryngology), Cellular and Molecular Physiology, and Neurobiology, Yale University School of Medicine, BML 244, 333 Cedar Street, New Haven, Connecticut 06510, USA.
E-mail: joseph.santos-sacchi@yale.edu

DOI: 10.1016/j.cub.2008.02.019

Chemical Coevolution: Host–Parasite Arms Race Runs Hot and Cold

Coevolution is a major process operating across biological communities at a range of spatial scales. Rapid ecological change makes it vital that we understand how coevolution proceeds if we are to conserve genetic diversity, combat disease and predict the effects of species invasions.

Duncan E. Jackson

Coevolution is a reciprocal evolutionary change in the genetic composition of one species in response to change in another interacting species. We can only invoke coevolution as an explanation when the observed traits of two species have evolved through ongoing interaction between the two species. Research has shown that coevolution is a dynamic process that can continually change the nature of inter-specific interactions over broad geographic ranges [1]. The current rapid environmental change makes it essential that we understand coevolutionary processes if we are to predict the changing dynamics of biological communities, conserve biodiversity and combat disease [2]. Some of the best examples of coevolution are found in mutualisms, especially flowers and their pollinators, but several ‘coevolutionary arms races’ are well-documented in the context of predator–prey and host–parasite relationships. Nash *et al.* [3] have recently shed fresh light on dynamic coevolutionary processes with a long-term study of the relationship between the parasitic Alcon blue butterfly (*Maculinea alcon*) and its *Myrmica* ant host. They have shown that Alcon blue caterpillars adopt a chemical disguise, matching that of ant larvae, to

mediate their ‘adoption’ into *Myrmica* nests, and that local variations in ant chemistry are closely matched by their caterpillar parasites.

Unlike the familiar examples of mutualistic coevolution seen in flowering plants and their pollinators, coevolving parasites and their hosts are engaged in an antagonistic process. The most important property of a parasite that is attributed to coevolution is its virulence. A more virulent parasite will reduce a host's fitness more quickly, relative to an unparasitised host. Clearly selection must favour highly virulent parasites, those which more quickly exploit host resources, but this process might lead to the death of all potential hosts. However, if a parasite is so virulent that it kills its host before transmission of the parasite's offspring then this will select for a reduction in parasitic virulence, as well as more resistant hosts. The best-cited example of how parasitic virulence can decline is that of myxomatosis among European and Australian rabbits during the 1950s. An initially maximally virulent myxoma virus (100% kill) declined rapidly, accompanied by sharp increases in host resistance, such that the disease was seldom seen after less than 20 years. The myxoma virus still persists in populations in an attenuated form, although on occasions more

virulent strains appear causing short-lived, localised outbreaks.

Antagonistic coevolution can lead to static equilibria where an optimal situation is reached, such as may be the case with the myxoma virus, but also dynamic equilibria where adaptive improvement is always possible. Dynamic equilibria are known as the ‘Red Queen hypothesis’ because, as



Figure 1. An Alcon blue butterfly (*Maculinea alcon*) lays her eggs on marsh gentian (*Gentiana pneumonanthe*) flower heads.

After 2–3 weeks of feeding on flower heads the caterpillar lowers itself to the ground using a silken thread and awaits discovery by foraging *Myrmica* ants. Alcon blue caterpillars are chemical mimics of *Myrmica* ant larvae, an attribute which tricks ants into carrying caterpillars back to their nest (‘adoption’) where they become social parasites. (Photo: David Nash.)

The speed limit of outer hair cell electromechanical activity

J. Santos-Sacchi

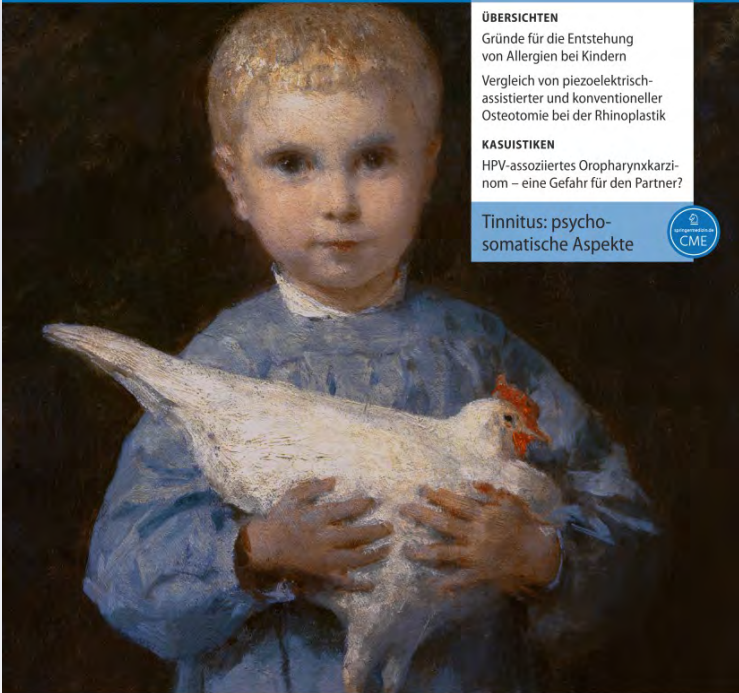
HNO

Deutsche Gesellschaft für Hals-Nasen-Ohren-Heilkunde, Kopf- und Hals-Chirurgie

ISSN 0017-6192

HNO

DOI 10.1007/s00106-019-0615-9



HNO

Deutsche Gesellschaft für Hals-Nasen-Ohren-Heilkunde, Kopf- und Hals-Chirurgie
Deutsche Akademie für Hals-Nasen-Ohren-Heilkunde, Kopf- und Hals-Chirurgie

ONLINE FIRST

ÜBERSICHTEN
Gründe für die Entstehung von Allergien bei Kindern
Vergleich von piezoelektrisch-assistierter und konventioneller Osteotomie bei der Rhinoplastik

KASUISTIKEN
HPV-assoziiertes Oropharynxkarzinom – eine Gefahr für den Partner?

Tinnitus: psychosomatische Aspekte 

www.springermedizin.de 

HNO

<https://doi.org/10.1007/s00106-019-0615-9>

© Springer Medizin Verlag GmbH, ein Teil von Springer Nature 2019



J. Santos-Sacchi

Surgery (Otolaryngology), Neuroscience, and Cellular and Molecular Physiology, Yale University School of Medicine, New Haven, USA

The speed limit of outer hair cell electromechanical activity

Introduction

The outer hair cell (OHC) is one of two receptor cell types within the organ of Corti, the other being the inner hair cell (IHC). Since Corti's description of the cellular components of the mammalian inner ear in 1851 ([5]; **Fig. 1**), the role of the cylindrical OHCs he observed has been debated. For example, why are there three times as many OHCs as IHCs? We now know that the IHC functions as the primary sensor of acoustic stimulation, centrally relaying its activity via 95% of the eight nerve fibers [30]. The OHC is supportive, in a sense, in that it basically modulates gain of cochlear output via the IHCs. That modulation, however, is quite significant and amounts to a sensitivity gain of 40–60 dB ($\times 100$ –1000). Of course, in their absence this translates to a hearing loss of equal magnitude. These cells, thus, provide cochlear amplification that arises from their electromechanical activity, the OHC being electromotile [4, 14], and the mechanics driven by receptor voltages across the OHC lateral membrane [12, 22].

» Prestin is the molecular motor of OHCs

Given their role, it is likely that OHCs outnumber IHCs in order to provide a more powerful feedback into the cochlear partition. The voltage-dependence of this mechanical activity necessarily involves gating charge movements (or nonlinear capacitance [NLC]) that arise during displacement of charged voltage sensors of the OHC lateral membrane molecular motors [2, 19, 21]. NLC is a bell-shaped

function of voltage, with its peak occurring at a characteristic voltage (V_h). The molecular motor has been identified as prestin [31]. One of the early issues that captivated auditory scientists following the discovery of electromotility was its frequency cut-off; since mammals have very high frequency hearing, it was expected that cochlear amplification would require OHCs to work at equivalent high speeds. This short review (readers are expected to seek original referenced articles for more detail, or email me with questions!) will focus on the historical quest to determine the OHC *Geschwindigkeitsbegrenzung* (speed limit).

Early history

The early observation on OHC electromotility by Brownell [3] was merely descriptive, and subject to initial skepticism from the research community. Only when the alternating length changes induced by sinusoidal currents were

captured on video and analyzed was it clear that these cells were remarkably mechanically active for electrical stimulation frequencies of 1–30 Hz [14]. Of course, those early video studies were made at very low frequency video frame rates (~ 60 Hz), so that no estimate of the cell's frequency response could be made (**Fig. 2**). The earlier demonstration of otoacoustic emissions at acoustic frequencies [15] foretold that the OHC would move much faster.

In 1987, Ashmore measured the frequency response of OHC electromotility under whole-cell voltage clamp using a photodiode technique allowing for high-frequency observations [1]. As shown in **Fig. 3**, the measured frequency response was low pass with dual Lorentzian cut-offs of 67 and 664 Hz; nevertheless, the cell response could be measured into the kilohertz range, albeit at low magnitudes. It was likely that the voltage clamp time constant was a limiting factor, since it will impose

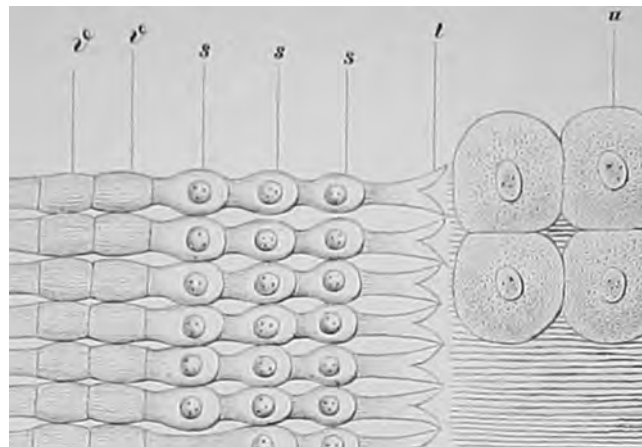


Fig. 1 ◀ Corti's original drawing of the three rows (s) of outer hair cells in surface mount view. Cat and dog used as specimens. (From original Fig. 5)

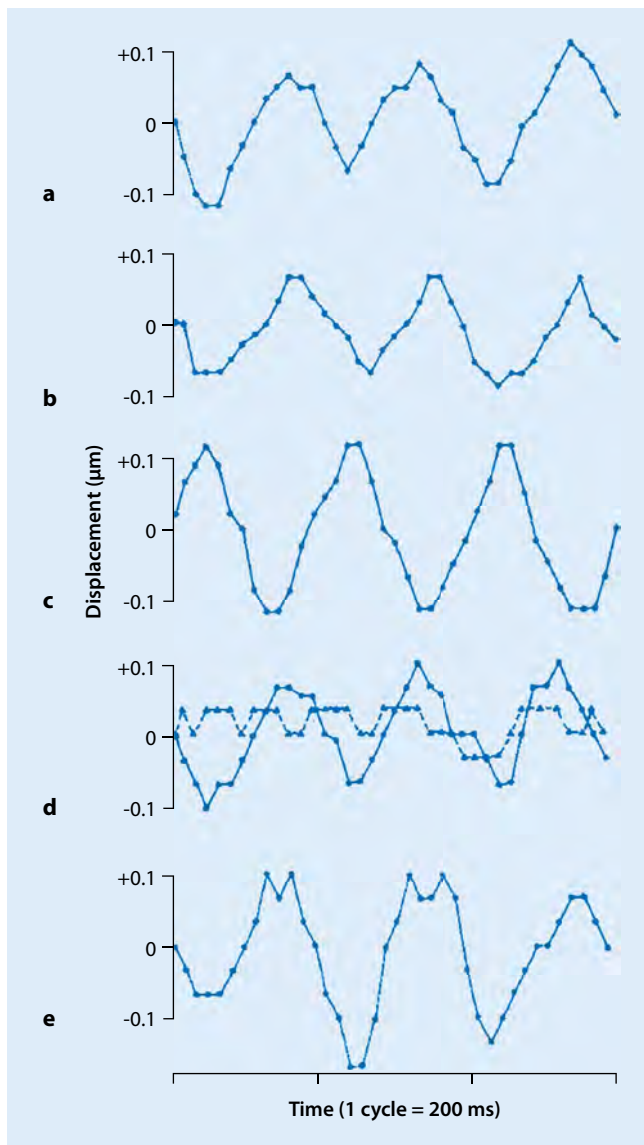


Fig. 2 ▲ Outer hair cell electromotility evoked by transcellular electrical stimulation at 5 Hz illustrating an apparent synchronization with the phase of the electrical stimulus. **a** OHC apical end movements, **b** basal end movements, **c** unusual reverse response found in some cells, **d** enhanced response of cell when ionic strength was reduced, **e** organelle movements. See original paper for detailed description. (Adapted from [14])

limitations to the delivery of voltages to the OHC at high frequencies.

Into the 1990s

In 1992, also using the whole-cell voltage clamp and a photodiode approach, Santos-Sacchi [20] was able to overcome to some extent the clamp time constant and extend the frequency response of voltage delivery to the cell. Given a wider stimulation bandwidth, OHC electromotility frequency cut-offs near 1 kHz

were obtained (■ Fig. 4). Still, the voltage clamp time constant was a limiting factor. In 1993, Zenner and colleagues [18] extended the study of electromotility by utilizing stroboscopic techniques to enhance video analysis of movements evoked by high-frequency transcellular current stimulations across the organ of Corti in situ. They showed reticular laminar movements into the kilohertz range, with reported roll-offs of 40 dB at 15 kHz, not unlike Ashmore's results in the voltage-clamped single cell [1]. Of

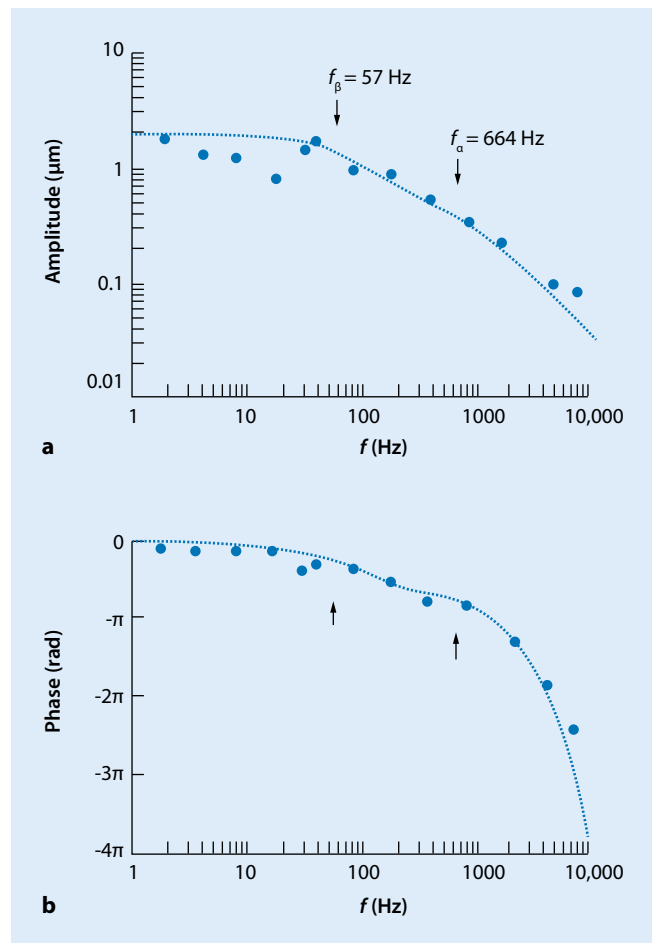


Fig. 3 ▲ Outer hair cell electromotility evoked under whole-cell voltage clamp. The response exhibited a dual Lorentzian roll-off at 57 and 664 Hz. See original paper for detailed description. **a** Magnitude response of OHC, **b** Phase response. (Adapted from [1])

course, current stimulation will involve substantial voltage stimulation roll-off across the OHC membranes owing to the membrane resistor \times capacitor (RC) filter. In any case, at this point in time, it was clear that the OHC responded to electric stimuli well into the audio-frequency range, but better estimates of the isolated OHC cut-off frequency were essential.

With a technical advancement designed to extend the frequency response of voltage delivery to the OHC, Dallos and Evans [6] measured the OHC frequency response out to at least 10 kHz (■ Fig. 5). They utilized a large microchamber glass pipette into which an OHC was inserted to deliver currents across the cell; this approach provides a capacitive divider that limits the negative effect of the OHC capacitance on

Abstract · Zusammenfassung

voltage delivery. Nevertheless, even this approach has limitations that arise from the series resistance of the microchamber, which in combination with the cell capacitance controls frequency delivery bandwidth just as in the whole-cell voltage clamp technique. Furthermore, in that study a voltage clamp configuration was not used, but instead the cell was driven by a low-output impedance waveform generator. With that configuration, it was impossible to monitor membrane currents to directly estimate the fidelity of voltage delivery, as can be done under voltage clamp. In 1999, Frank et al. [8] used the microchamber technique under voltage clamp to obtain a ground-breaking result. Outer hair cell electromotility was measured using an interferometer and found to be flat to beyond 50 kHz for short portions ($\leq 25 \mu\text{m}$) of the OHC that extruded from the microchamber! Of course, this was the frequency response following corrections for the estimated frequency roll-off of voltage delivery (■ Fig. 6). In their in-house-developed voltage clamp, no capacitance compensation circuitry was included to remove stray capacitance (e. g., from the amplifier, electrode holder, and glass microchamber), so that this stray capacitance *may have* interfered with estimates, based on measured currents, of voltage delivery across the OHC membranes. That is, stray capacitance does not influence the bandwidth of voltage delivery under voltage clamp, but it will interfere with measures of membrane currents that are used to estimate voltage delivery. For nearly two decades, these data have driven our concepts of cochlear amplification.

Present day

In 2018, Santos-Sacchi and Tan [28] revisited this issue. This was instigated by a series of previous studies showing that prestin possesses slow kinetics that were influenced by chloride anions [24–26, 29]. These data led to a kinetic model—the *meno presto* model—of prestin that includes slow intermediary transitions between chloride binding and a voltage-enabled configuration. What this meant was that sensor charge move-

HNO <https://doi.org/10.1007/s00106-019-0615-9>
© Springer Medizin Verlag GmbH, ein Teil von Springer Nature 2019

J. Santos-Sacchi

The speed limit of outer hair cell electromechanical activity

Abstract

The outer hair cell of Corti's organ provides mechanical feedback into the organ to boost auditory perception. The fidelity of voltage-dependent motility has been estimated to extend beyond 50 kHz, where its force generation is deemed a requirement for sensitive high-frequency mammalian hearing. Recent investigations have shown, however, that the frequency response is substantially more low pass at physiological membrane

potentials where the kinetics of prestin impose their speed limit. Nevertheless, it is likely that the reduced magnitude of electromotility is sufficient to drive cochlear amplification at high frequencies.

Keywords

Organ of Corti · Auditory perception · Cochlea · Membrane potentials · Feedback

Geschwindigkeitsbegrenzung der elektromechanischen Aktivität der äußeren Haarzellen

Zusammenfassung

Von der äußeren Haarzelle des Corti-Organs gibt es zur Verstärkung der Hörwahrnehmung eine mechanische Rückkopplung. Die Genauigkeit der spannungsabhängigen Motilität wurde auf über 50 kHz geschätzt, wobei ihre Krafterzeugung als Voraussetzung für das empfindliche Hochfrequenzhören der Säugetiere angesehen wird. Neuere Untersuchungen haben jedoch gezeigt, dass die Frequenzantwort bei physiologischen Membranpotenzialen, bei denen sich die

Geschwindigkeitsgrenze der Kinetik von Prestin auswirkt, wesentlich niedriger ist. Es ist jedoch wahrscheinlich, dass das verringerte Ausmaß der Elektromotilität ausreicht, um die Cochleaverstärkung bei hohen Frequenzen zu steuern.

Schlüsselwörter

Corti-Organ · Auditorische Wahrnehmung · Cochlea · Membranpotenziale · Rückkopplung

ments were low pass in nature. Since sensor charge movements correspond to conformational changes in prestin, it was expected that electromotility would likewise demonstrate this low-pass behavior.

» Sensor charge movements are low pass in nature

The study by Santos-Sacchi and Tan [28] confirmed this. In their experiments, electromotility was measured using a microchamber under voltage clamp with high-speed video at frame rates of 50 kHz (■ Fig. 7). The Phantom camera (Vision Research, Berwyn, PA, USA) can actually record at frame rates exceeding 400 kHz (with its smallest pixel resolution), but because electromotility was measured out to 12.5 kHz, that frame rate was sufficient. Stray capacitance was removed with amplifier compensation circuitry, so that

measured membrane current relaxations could be used to estimate the clamp time constant. It was found, after corrections for voltage delivery roll-off, that electromotility frequency response depends on OHC resting membrane potential relative to $NLC V_h$. When the OHC resting membrane potential is held at V_h , electromotility shows dual Lorentzian behavior with a large roll-off at frequencies below 1 kHz. Away from V_h , the response is relatively flat, but quite reduced in magnitude. The frequency cut-off of the fastest Lorentzian component was about 8.7 kHz. This compares with a 33-kHz cut-off obtained by Frank et al. [8] with a similar experimental configuration, namely, degree of OHC extrusion. Thus, it is likely that differences between the work of Frank et al. [8] and Santos-Sacchi and Tan [28] arise from experimental differences, possibly including how stray capacitance is dealt with, and certainly the OHC holding volt-

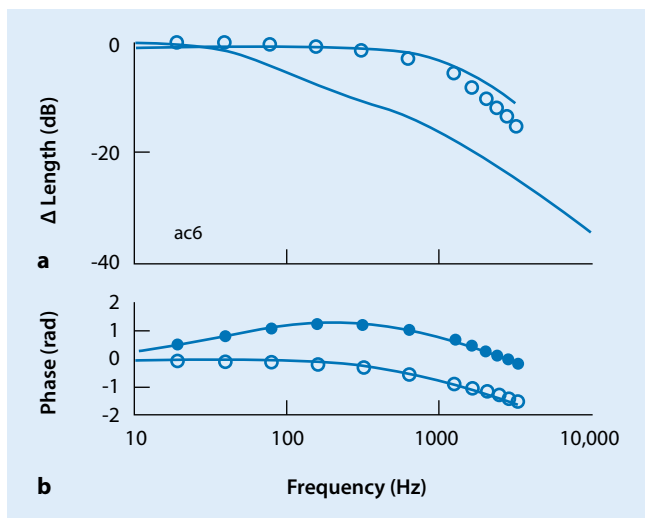


Fig. 4 ▲ Outer hair cell (OHC) electromotility evoked under whole-cell voltage clamp. For this OHC, the response exhibited a roll-off near 1 kHz. The mechanical response (*circles*) was lower pass than the predicted membrane voltage (*solid line*). **a** Magnitude response of OHC, **b** phase response. See original paper for detailed description. *ac6* label that identifies the particular cell studied. (Adapted from [20])

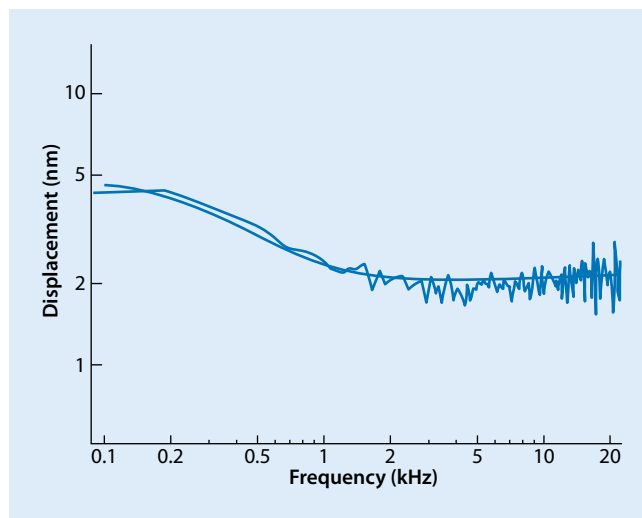


Fig. 5 ▲ Outer hair cell (OHC) electromotility evoked with the microchamber technique. For this OHC, the response exhibited an initial roll-off near 300 Hz, but stabilized past 10 kHz. See original paper for detailed description. (Adapted from [6])

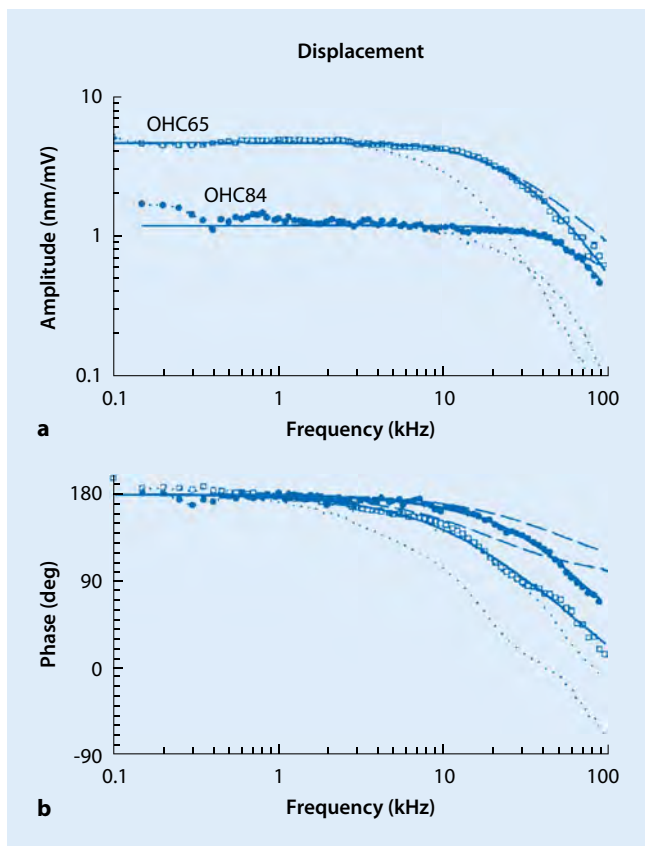


Fig. 6 ▲ Outer hair cell (OHC) electromotility evoked with the microchamber technique. Data from two OHCs are shown. In **a** the *dotted lines* depict electromotility magnitude *prior* to corrections for system voltage roll-off, and the *other symbols* show the same after corrections for voltage roll-off. In **b** the phase response of the cells is shown. See original paper for detailed description. (Adapted from [8])

age at which electromotility measures are made—both Frank et al. [8] and Dallos and Evans [6] had OHC holding voltage set far away from V_h (we estimate about 68 mV away from $NLC V_h$). After correcting for effects of experimental temperature (from 25 to 37 °C), the fastest cut-off component of electromotility from Santos-Sacchi and Tan [28] was about 20 kHz, and interestingly is similar to the temperature-corrected NLC cut-off of Gale and Ashmore [10]. That the two should correspond makes sense since NLC defines the speed of prestin conformational change, the basis of electromotility.

Summary

The remarkable ability of the OHC to respond mechanically to voltage (i.e., sound-induced receptor potentials), relying on prestin and in a manner distinct from usual mechanisms of cellular motility, forms the basis of cochlear amplification [7, 27]. Consequently, the frequency response of electromotility is pertinent, and over the years its assessment has benefitted from technological refinements, providing estimates of cut-off frequencies that have incrementally grown. However, prior to the work of Santos-Sacchi and Tan [28], these assessments had not taken into account the possible influence of prestin's voltage-

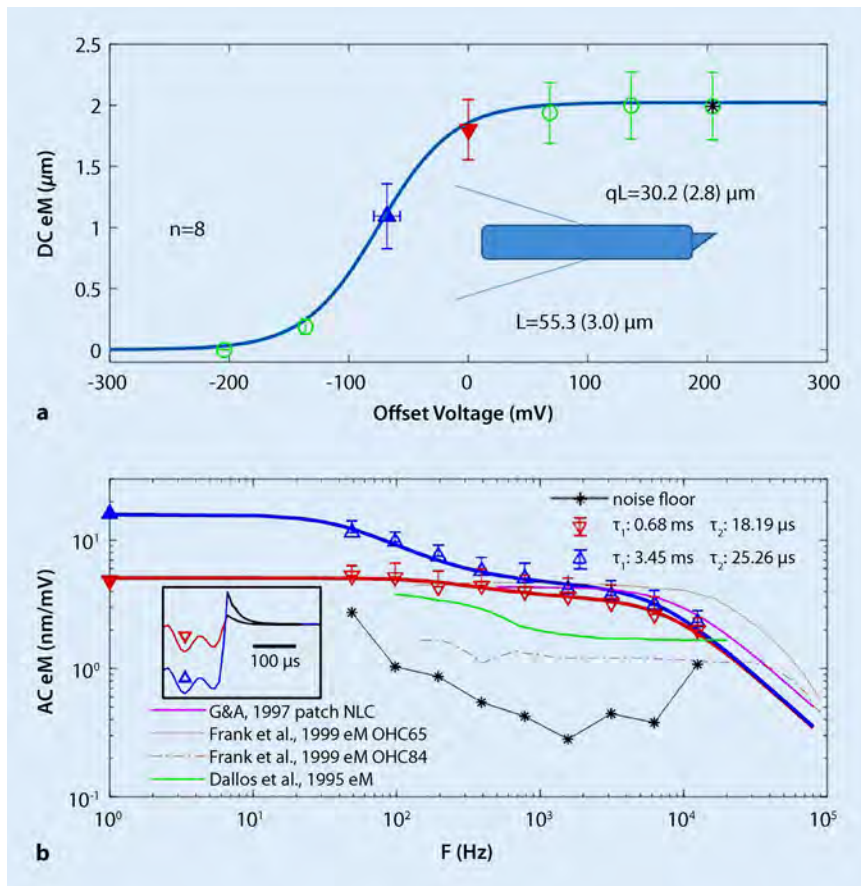


Fig. 7 ▲ Outer hair cell (OHC) electromotility evoked with the microchamber technique. Average data from eight OHCs positioned midway in the microchamber are shown. In **a** the DC movements are shown for different offset holding voltages. In **b** the frequency response at V_h (blue line) shows low- and high-pass behavior, but away from V_h (red line) the response is faster with a flatter frequency response. See original paper for detailed description. (Adapted from [28])

dependent kinetics on the frequency response. Thus, at a resting membrane potential near V_h (which itself is susceptible to a variety of biophysical influences [9, 11, 13, 16, 17, 23, 26]), electromotility is predominantly low pass, with a faster component extending to about 20 kHz. Clearly, the magnitude of electromotility will be a fraction of its response at very low frequencies. Nevertheless, it is obvious that this is sufficient to provide amplification in the high-frequency regions of mammalian audition. How this might be accomplished requires new cochlear models incorporating these new observations.

Practical conclusion

- The outer hair cells of Corti's organ provide mechanical feedback to the organ to boost auditory perception.

- Voltage-dependent motility has been measured beyond 50 kHz, where its force generation is needed for sensitive high-frequency mammalian hearing.
- Recent studies report that the frequency response is substantially more low pass at physiological membrane potentials where the kinetics of prestin enforce their speed limit.
- The reduced magnitude of electromotility is likely sufficient to drive cochlear amplification at high frequencies.

Corresponding address

Prof. Dr. J. Santos-Sacchi

Surgery (Otolaryngology), Neuroscience, and Cellular and Molecular Physiology, Yale University School of Medicine
BML 224, 333 Cedar Street, CT 06510 New Haven, USA
joseph.santos-sacchi@yale.edu

Acknowledgements. This work was supported by National Institutes of Health-National Institute on Deafness and Other Communication Disorders Grants R01 DC000273, R01 DC016318, and R01.

Compliance with ethical guidelines

Conflict of interest. J. Santos-Sacchi declares that he has no competing interests.

This article does not contain any studies with human participants or animals performed by any of the authors.

References

- Ashmore JF (1987) A fast motile response in guinea-pig outer hair cells: the cellular basis of the cochlear amplifier. *J Physiol* 388:323–347
- Ashmore JF (1990) Forward and reverse transduction in the mammalian cochlea. *Neurosci Res Suppl* 12:S39–S50
- Brownell WE (1984) Microscopic observation of cochlear hair cell motility. *Scan Electron Microsc* 1984(Pt 3):1401–1406
- Brownell WE, Bader CR, Bertrand D et al (1985) Evoked mechanical responses of isolated cochlear outer hair cells. *Science* 227:194–196
- Corti A (1851) Recherches sur l'organe de l'ouïe des mammifères. Première partie: Limaçon. *Z Wiss Zool* 3:109–169
- Dallos P, Evans BN (1995) High-frequency motility of outer hair cells and the cochlear amplifier. *Science* 267:2006–2009
- Dallos P, Wu X, Cheatham MA et al (2008) Prestin-based outer hair cell motility is necessary for mammalian cochlear amplification. *Neuron* 58:333–339
- Frank G, Hemmert W, Gummer AW (1999) Limiting dynamics of high-frequency electromechanical transduction of outer hair cells. *Proc Natl Acad Sci USA* 96:4420–4425
- Gale JE, Ashmore JF (1994) Charge displacement induced by rapid stretch in the basolateral membrane of the guinea-pig outer hair cell. *Proc R Soc Lond B Biol Sci* 255:243–249
- Gale JE, Ashmore JF (1997) An intrinsic frequency limit to the cochlear amplifier. *Nature* 389:63–66
- Iwasa KH (1993) Effect of stress on the membrane capacitance of the auditory outer hair cell. *Biophys J* 65:492–498
- Iwasa KH, Kachar B (1989) Fast in vitro movement of outer hair cells in an external electric field: effect of digitonin, a membrane permeabilizing agent. *Hear Res* 40:247–254

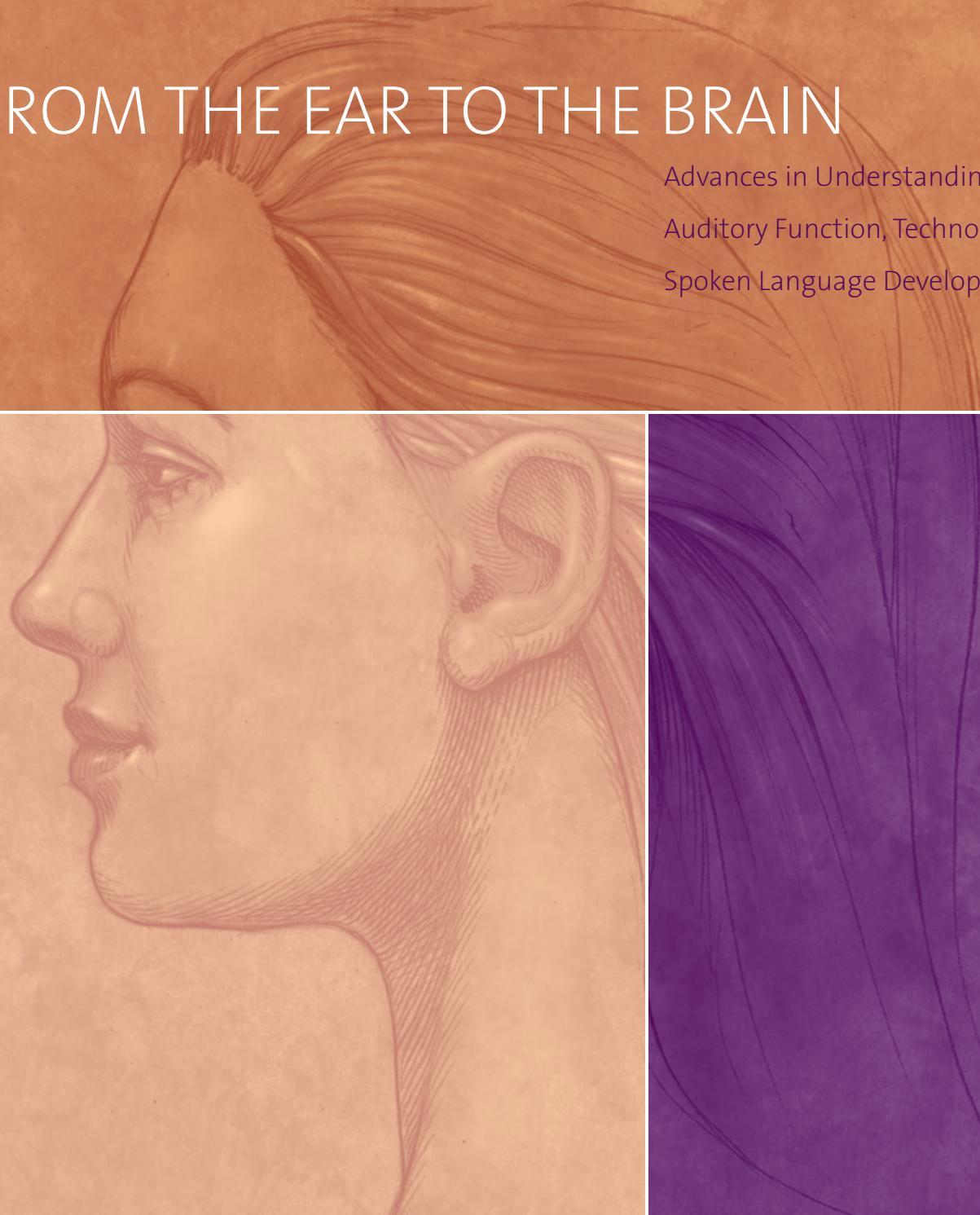
13. Izumi C, Bird JE, Iwasa KH (2011) Membrane thickness sensitivity of prestin orthologs: the evolution of a piezoelectric protein. *Biophys J* 100:2614–2622
14. Kachar B, Brownell WE, Altschuler R et al (1986) Electrokinetic shape changes of cochlear outer hair cells. *Nature* 322:365–368
15. Kemp DT (1978) Stimulated acoustic emissions from within the human auditory system. *J Acoust Soc Am* 64:1386–1391
16. Meltzer J, Santos-Sacchi J (2001) Temperature dependence of non-linear capacitance in human embryonic kidney cells transfected with prestin, the outer hair cell motor protein. *Neurosci Lett* 313:141–144
17. Oliver D, He DZ, Klocker N et al (2001) Intracellular anions as the voltage sensor of prestin, the outer hair cell motor protein. *Science* 292:2340–2343
18. Reuter G, Gitter AH, Thurm U et al (1992) High frequency radial movements of the reticular lamina induced by outer hair cell motility. *Hear Res* 60:236–246
19. Santos-Sacchi J (1990) Fast outer hair cell motility: how fast is fast? In: Dallos P, Geisler CD, Matthews JW, Ruggero MA, Steele CR (eds) *The mechanics and biophysics of hearing*. Springer, Berlin, pp 69–75
20. Santos-Sacchi J (1992) On the frequency limit and phase of outer hair cell motility: effects of the membrane filter. *J Neurosci* 12:1906–1916
21. Santos-Sacchi J (1991) Reversible inhibition of voltage-dependent outer hair cell motility and capacitance. *J Neurosci* 11:3096–3110
22. Santos-Sacchi J, Dilger JP (1988) Whole cell currents and mechanical responses of isolated outer hair cells. *Hear Res* 35:143–150
23. Santos-Sacchi J, Shen W, Zheng J et al (2001) Effects of membrane potential and tension on prestin, the outer hair cell lateral membrane motor protein. *J Physiol* 531:661–666
24. Santos-Sacchi J, Song L (2014) Chloride-driven electromechanical phase lags at acoustic frequencies are generated by SLC26a5, the outer hair cell motor protein. *Biophys J* 107:126–133
25. Santos-Sacchi J, Song L (2014) Chloride and Salicylate influence Prestin-dependent specific membrane capacitance: support for the area motor model. *J Biol Chem* 289:10823. <https://doi.org/10.1074/jbc.m114.549329>
26. Santos-Sacchi J, Song L (2016) Chloride anions regulate kinetics but not voltage-sensor Q_{max} of the solute carrier SLC26a5. *Biophys J* 110:1–11
27. Santos-Sacchi J, Song L, Zheng J et al (2006) Control of mammalian cochlear amplification by chloride anions. *J Neurosci* 26:3992–3998
28. Santos-Sacchi J, Tan W (2018) The frequency response of outer hair cell voltage-dependent motility is limited by kinetics of prestin. *J Neurosci* 38:5495–5506
29. Song L, Santos-Sacchi J (2013) Disparities in voltage-sensor charge and electromotility imply slow chloride-driven state transitions in the solute carrier SLC26a5. *Proc Natl Acad Sci U S A* 110:3883. <https://doi.org/10.1073/pnas.1218341110>
30. Spoendlin H (1988) Neural anatomy of the inner ear. In: Jahn AF, Santos-Sacchi J (eds) *Physiology of the ear*. Raven Press, New York
31. Zheng J, Shen W, He DZ et al (2000) Prestin is the motor protein of cochlear outer hair cells. *Nature* 405:149–155

Sunday, July 1
8:00 a.m. – 11:30 a.m.
Westin Kierland Resort
Scottsdale, Ariz.

2012 RESEARCH SYMPOSIUM

FROM THE EAR TO THE BRAIN

Advances in Understanding
Auditory Function, Technology, and
Spoken Language Development



Alexander Graham Bell
ALEXANDER GRAHAM BELL
ASSOCIATION FOR THE DEAF AND HARD OF HEARING



Hearing Health Foundation
Prevention | Research | Cure

- 2** THE QUEENS OF AUDITION
Joseph Santos-Sacchi, Ph.D., Yale School of Medicine

- 5** SPEECH PERCEPTION AND HEARING LOSS
Jont B. Allen, Ph.D., University of Illinois

- 9** THE RESTORATION OF SPEECH UNDERSTANDING BY ELECTRICAL STIMULATION OF THE AUDITORY SYSTEM
Michael Dorman, Ph.D., Arizona State University

- 13** SPOKEN LANGUAGE DEVELOPMENT IN INFANTS WHO ARE DEAF OR HARD OF HEARING: THE ROLE OF MATERNAL INFANT-DIRECTED SPEECH
Tonya Bergeson-Dana, Ph.D., Indiana University



MODERATOR

Tamala S. Bradham, Ph.D., CCC-A, is an assistant professor at the Vanderbilt Bill Wilkerson Center in Nashville, Tenn., and the associate director of quality, protocols, and risk management. She is the coordinator for the Steering Committee of the American Speech-Language-Hearing Association (ASHA) Special Interest Group 9: Hearing and Hearing Disorders in Childhood. She is also the former director of the MUSC Cochlear Implant Center in Charleston, S.C., and the past president of the South Carolina Academy of Audiology and the AG Bell South Carolina Chapter. Bradham has published in the areas of cochlear implants, newborn hearing screening, and early intervention. She received her doctorate in Speech and Hearing Sciences and her master's degree in Audiology at the University of South Carolina.

This guide is provided as an information piece only. The contents are presented with no warranty expressed or implied by AG Bell, the presenters or the person(s) making it available as a resource. No legal responsibility is assumed for the accuracy of the information contained herein or for the outcome of decisions, contracts, commitments, or obligations made on the basis of this information.

This document may not be produced without permission. For additional copies of this publication, contact AG Bell at editor@agbell.org.



This symposium was funded by the National Institute on Deafness and Other Communicative Disorders, National Institutes of Health, and the Hearing Health Foundation.

© 2012 Alexander Graham Bell Association for the Deaf and Hard of Hearing

Alexander Graham Bell Association for the Deaf and Hard of Hearing
3417 Volta Place NW
Washington, DC 20007
(202) 337-5220 (202) 337-8314 (fax)
www.listeningandspokenlanguage.org

THE QUEENS OF AUDITION

BY JOSEPH SANTOS-SACCHI, PH.D., YALE SCHOOL OF MEDICINE

Alexander Graham Bell would have been amazed to find out how the ear uses the outer hair cell (OHC) to boost our sensitivity to sounds. The OHC does this by providing mechanical feedback into the organ of Corti, thus enhancing the input to the inner hair cells, which predominantly send information to the central nervous system. Prestin is the protein that drives the OHC mechanical response, and we have learned much since its discovery in the year 2000. Notably, we now know that the cochlear amplifier is controlled by anions interacting with prestin. The upshot is that the OHC evolved to use very primitive constituents to do exquisite things. There is still more to learn.

When I was a teenager I damaged my right ear by standing too close to fireworks on the 4th of July. Tinnitus and hearing loss persist to this day, only enhanced by an additional 45 years of auditory abuse. The culprit of my problem is the hair cell, probably the outer hair cell (OHC). Hair cells that enable us to perceive sound are fragile, and when lost do not regenerate, causing permanent hearing loss (and sometimes ringing in the ear). They are amazing machines, and the whole of the ear—outer ear, middle ear, inner ear and the auditory brain—is devastated without their sustenance. They are the Queens of Audition!

PRE-AMPLIFICATION

My Ph.D. thesis was concerned with blood capillary function in the inner ear, an attempt to understand how, at the electron microscopic level, blood-borne molecules enter the inner ear (Santos-Sacchi & Marovitz, 1980). The inner ear is a privileged site that blocks most molecular entry, just as the brain does. I convinced myself (and my doctoral committee) that this was good for the inner ear—namely that the ear protects its hair cells.

Two years later I pursued a postdoc in Peter Dallos' lab at Northwest-

ern University. I was able to directly investigate what the OHCs were doing by recording electrical activity from them through microelectrodes in living guinea pigs. Research at that time showed that OHCs are sharply tuned to particular frequencies based on the location along the cochlea (Dallos, 1985; Dallos, Santos-Sacchi, & Flock, 1982; Russell & Sellick, 1983). Hair cells in the basal part of the cochlea respond best to high frequency sounds and those in the apex of the cochlea respond best to low frequency sounds. The frequency selectivity and sensitivity of hair cells along the cochlea were predicted based on basilar membrane and eighth nerve fiber measurements (Ruggero & Santos-Sacchi, 1997).

Also during my postdoc research, Dallos and I showed that the supporting cells were electrically coupled by gap junctions (Santos-Sacchi & Dallos, 1983), presaging subsequent independent studies that suggested connexon-based communication among supporting cells was important for potassium sinking and metabolic maintenance within the organ of Corti—two phenomenon that are required for hair cell survival and proper functioning (Santos-Sacchi, 1985). Not surprisingly, connexon mutations are now known to underlie

a major proportion of genetically based hearing loss (Kelsell et al., 1997).

POST-AMPLIFICATION

Something special happens in the inner ear to provide such fine frequency tuning and sensitivity. The momentous identification of otoacoustic emissions (OAE; emissions of sound from the ear canal) by Kemp (1978) did not subdue Brownell's amazing discovery of OHC electromotility (Brownell, Bader, Bertrand, & de Ribaupierre, 1985). Indeed, the observation that OHCs are not only receptors of sound, but can respond mechanically, and the identification of OAEs prompted a paradigm change in auditory research. I joined the electromotility club early on, providing evidence that electromotility was driven by the voltage across the OHC membrane (Santos-Sacchi & Dilger, 1988). Since then I have focused on the biophysical and molecular aspects of OHC motility.

THE AMAZING OHC

The OHC is more specialized than its neighbor, the inner hair cell (IHC). Similar to the IHC, however, OHCs have an apical region of the cell that houses the sound transduction apparatus, a collection of yet-to-be-identified mechanically activated (MET) channels that

reside in the membrane tips of stereocilia. Stereocilia are tall membrane extrusions that are stiff because they contain a tightly packed core of actin filaments. Movement of the stereociliar bundle permits MET channels to allow potassium to enter the cell, and the resulting receptor potential depolarizes the cell's membrane. For the IHC, the main purpose of this depolarization is to evoke neurotransmitter release at the bottom part of the cell where auditory eighth nerve fibers synapse. OHCs also have synapses with the eighth

nerve but are dwarfed in number by those of the IHC. Thus, the main job of sending acoustic information to the brain centrally falls to the IHC.

It's the middle part of the OHC, which IHCs do not have, that piqued my interest. Research has shown that the membrane in this region houses the molecular motors responsible for electromotility (Figure 1). One of the ways to study the activity of the motors is to measure its conformational change (shape change) within the membrane

when voltage across the membrane is altered, as might occur when receptor potentials are generated. The conformational change is associated with the restricted movement of motor-bound charges within the membrane that can be measured as a nonlinear capacitance (NLC).

Capacitance is the ability to store charge, and normally a membrane will have a capacitance proportional to its area, just like an electrical capacitor component. The membrane capacitance, defined as the change in charge divided by the change in membrane voltage (dQ/dV_m), is the same at any membrane potential in IHCs, i.e., it is linear because this cell lacks the charged molecular motors found in the OHC. The OHCs, however, have a voltage-dependent capacitance that is bell-shaped riding atop a flat linear capacitance (Figure 2). The peak of the NLC occurs at a membrane voltage where the voltage sensitivity of motor conformational activity, and consequently, electromotility, is greatest (called V_p). The range over which NLC extends across V_m is the operational range of the motor. Research in the previous two decades has established that NLC and electromotility share such common characteristics.

In 2000, Dallos and colleagues discovered the motor protein responsible for electromotility (Zheng et al., 2000). They called it prestin because it is fast. When artificially expressed in non-auditory cells, it displays all the characteristics that the native OHC displays, including a NLC with a voltage dependent mechanical response of the membrane. Prestin has been shown to display additional qualities that were previously identified in the native OHC (reviewed in Santos-Sacchi, 2003). Shared qualities include 1) a piezo-electric-like phenomenon, where not

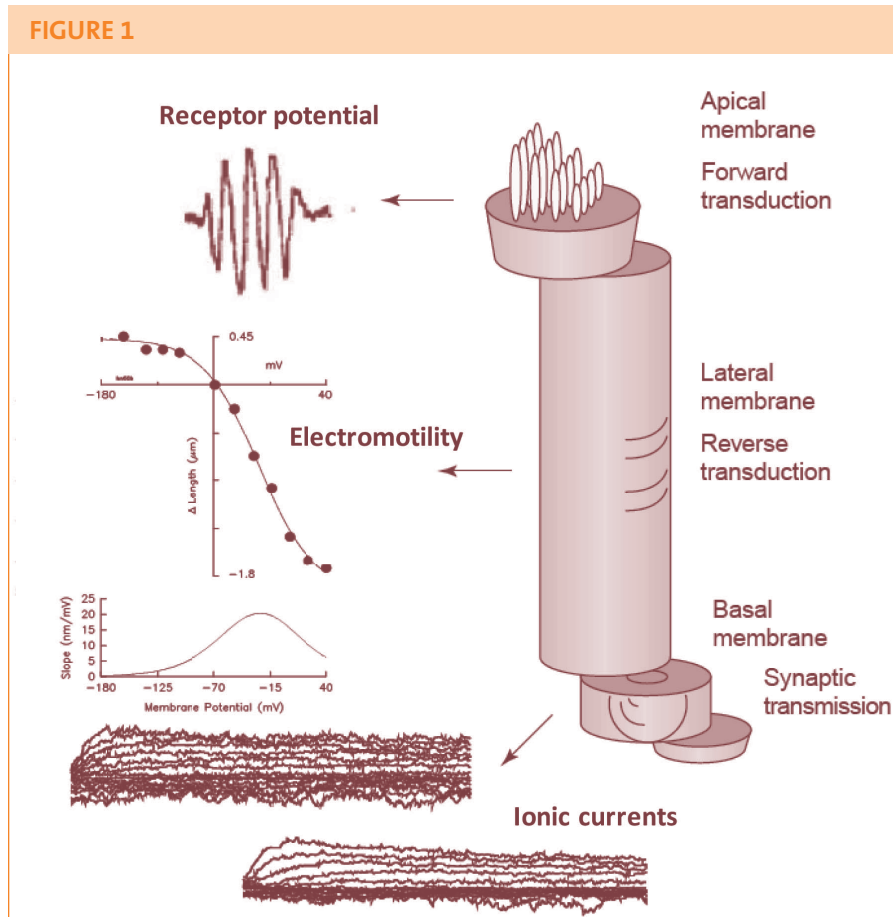


Figure 1. The OHC is a highly partitioned cell. The apical portion houses the stereocilia where receptor potentials are generated, and the base houses synaptic machinery and voltage-dependent ionic channels that allow information to be sent to the brain. The middle of the cell is the most interesting part! Here there are molecular motors embedded in the lateral membrane that underlie electromotility, a voltage dependent length change that can occur at acoustic rates. The mechanical response is sigmoidal versus voltage, and its maximum sensitivity is at voltage V_p , which is at the mid-point of the sigmoid or at its maximum first derivative with voltage. Notice that the sensitivity curve looks like the NLC curve in Figure 2.

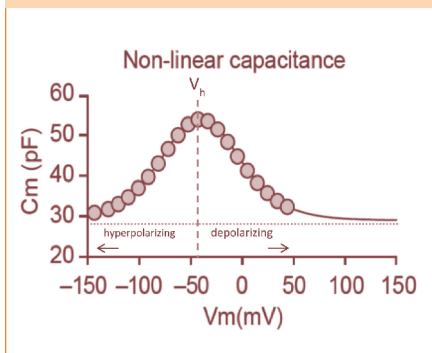
FIGURE 2

Figure 2. The molecular motors in the OHC lateral membrane produce a restricted charge movement in the membrane that can be measured as a NLC. The curve can shift along the voltage axis in the hyperpolarizing or depolarizing direction in response to a variety of biophysical forces, indicating that the operational voltage range is not stable for electromotility. V_h of NLC generally coincides with V_h of electromotility; however, see text for new observations

only does voltage induce a mechanical response, but reciprocally membrane deformation induces an electrical response; 2) marked temperature sensitivity; 3) a dependence of the protein's operational voltage ranges on resting potential; and 4) a dependence on intracellular chloride.

The latter characteristic, chloride dependence of the motor, has been a topic of focus for 12 years now. The anion appears to work by binding to prestin and affecting the protein's ability to change conformation within the membrane when voltage is modulated. This chloride sensitivity is not totally unexpected since prestin is part of a family of proteins that transports anions across the membrane. What is surprising is that the protein, unlike its family members, has evolved to aid in cochlear amplification. This was very apparent when, in collaboration with Fred Nuttall's research group, we were able to reversibly reduce basilar membrane motion in the guinea pig by manipulat-

ing chloride levels bathing the OHCs (Santos-Sacchi, Song, Zheng, & Nuttall, 2006). The defeat of cochlear amplification was reversible upon restoring normal chloride levels (Figure 3).

One of the characteristic properties of chloride on prestin is to shift the motor's operating voltage range; should intracellular chloride levels decrease from normal, a shift of the electromotility function in the depolarizing direction will follow, effectively making the receptor potential incapable of generating mechanical responses. In another demonstration of the importance of prestin's operating voltage range, Dallos and colleagues (Dallos et al., 2008) were able to knock-in genetically modified prestin molecules into the OHCs of the living mouse. The new prestin was engineered to have its op-

erating range shifted in the depolarizing direction, thus preventing the OHC receptor potential from evoking mechanical responses. Of course, in this case, the hearing loss was irreversible. Experiments such as these support the notion that, in mammals, cochlear amplification results from prestin activity, and not other mechanisms.

While we know the effects of anions on the NLC of OHCs and predict their effects on electromotility in vivo, little work has been done on OHC mechanics directly. Our predictions assume that NLC exactly characterizes electromotility. Could chloride be working in ways other than changing the OHC operating range? Lately, we have been re-investigating the coupling between prestin motor conformational change and electromotility. It turns out that the

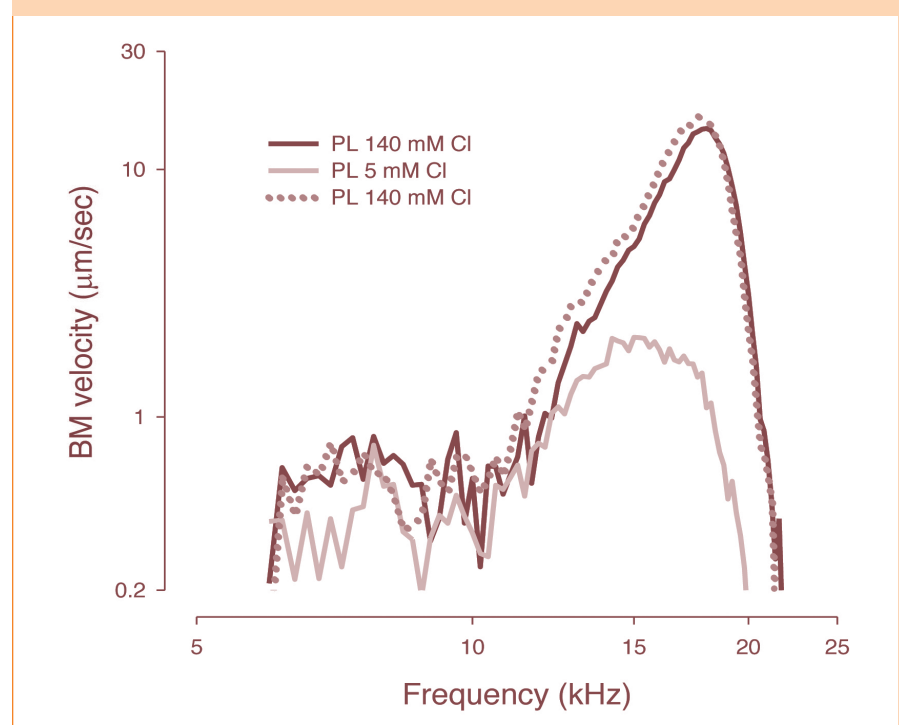
FIGURE 3

Figure 3. Basilar membrane measures are considered the classic assessment of cochlear amplification. Here we show that sharp tuning (dark solid line) under normal 140 mM chloride bathing solution is severely reduced by replacement with 5 mM chloride solution (light solid line). Return to 140 mM chloride solution restores hearing and basilar membrane motion in the guinea pig by manipulat-

two are variably uncoupled depending on concentration of intracellular chloride; that is, the operating voltage ranges appear to be separately modifiable (Song & Santos-Sacchi, 2012).

To further explain, within the organ of Corti, in order for OHCs to effectively promote enhanced basilar membrane motion, they must exert their forces at the proper moment during sound induced basilar membrane vibration. This is akin to pushing with your child's movements on a swing, not against her. That is, the timing, or phase of, energy injection must be appropriate. In the past, cochlear modelers have resorted to various strategies to generate enough phase delay between receptor potentials and OHC forces for their models to reasonably describe experimental data. The physiological basis for such delays was always removed from the OHC. We think that the variable couplings between conformational changes of prestin (NLC) and electromotility results from a time delay between the two, and we suggest that the mechanical forces of the OHC can be tuned to the requirements of the cochlea by chloride homeostasis. Thus, we believe that anions have a preeminent role in how we hear.

SUMMARY

Over the years that I have been working on the mechanics of hearing, I have learned about many things that the supporting cells and hair cells do right. Unfortunately, these are the same things that can be disturbed and have, I'm sure, contributed to my own hearing problems. But I am convinced that with a better understanding of how things work, we will ultimately know what and how to repair. So tell me more Queens of Audition, I'm listening!

REFERENCE LIST

- Brownell, W. E., Bader, C. R., Bertrand, D., & de Ribaupierre, Y. (1985). Evoked mechanical responses of isolated cochlear outer hair cells. *Science*, 227, 194-196.
- Dallos, P. (1985). Response characteristics of mammalian cochlear hair cells. *Journal of Neuroscience*, 5, 1591-1608.
- Dallos, P., Santos-Sacchi, J., & Flock, A. (1982). Intracellular recordings from cochlear outer hair cells. *Science*, 218, 582-584.
- Dallos, P., Wu, X., Cheatham, M. A., Gao, J., Zheng, J., Anderson, C. T., et al. (2008). Prestin-based outer hair cell motility is necessary for mammalian cochlear amplification. *Neuron*, 58, 333-339.
- Kelsell, D. P., Dunlop, J., Stevens, H. P., Lench, N. J., Liang, J. N., Parry, G., et al. (1997). Connexin 26 mutations in hereditary non-syndromic sensorineural deafness [see comments]. *Nature*, 387, 80-83.
- Kemp, D. T. (1978). Stimulated acoustic emissions from within the human auditory system. *Journal of the Acoustical Society of America*, 64, 1386-1391.
- Ruggero, M. A., & Santos-Sacchi, J. (1997). Cochlear mechanics and biophysics. In M.J.Crocker (Ed.), *Handbook of Acoustics*, ch. 108. Hoboken, NJ: John Wiley & Sons.
- Russell, I. J., & Sellick, P. M. (1983). Low-frequency characteristics of intracellularly recorded receptor potentials in guinea-pig cochlear hair cells. *The Journal of Physiology*, 338, 179-206.
- Santos-Sacchi, J. (1985). The effects of cytoplasmic acidification upon electrical coupling in the organ of Corti. *Hearing Research*, 19, 207-215.
- Santos-Sacchi, J. (2003). New tunes from Corti's organ: The outer hair cell boogie rules. *Current Opinion in Neurobiology*, 13, 459-468.
- Santos-Sacchi, J., & Dallos, P. (1983). Intercellular communication in the supporting cells of the organ of Corti. *Hearing Research*, 9, 317-326.
- Santos-Sacchi, J., & Dilger, J. P. (1988). Whole cell currents and mechanical responses of isolated outer hair cells. *Hearing Research*, 35, 143-150.
- Santos-Sacchi, J., & Marovitz, W. F. (1980). An evaluation of normal strial capillary transport using the electron-opaque tracers ferritin and iron dextran. *Acta Otolaryngologica*, 89, 12-26.
- Santos-Sacchi, J., Song, L., Zheng, J., & Nuttall, A. L. (2006). Control of mammalian cochlear amplification by chloride anions. *Journal of Neuroscience*, 26, 3992-3998.
- Song, L., & Santos-Sacchi, J. (2012). Chloride dependent coupling of molecular to cellular mechanics in the outer hair cell of corti's organ. *AIP Conference Proceedings*, 1403, 179-184.
- Zheng, J., Shen, W., He, D. Z., Long, K. B., Madison, L. D., & Dallos, P. (2000). Prestin is the motor protein of cochlear outer hair cells. *Nature*, 405, 149-155.



ABOUT THE AUTHOR

Joseph Santos-Sacchi, Ph.D., is a professor in the Department of Otolaryngology at Yale School of Medicine. He has an undergraduate degree in psychology from Columbia College and a Ph.D. in audiology from Columbia University. He joined Yale University in 1991. Prior to that, Santos-Sacchi worked in labs at the City College of New York, Northwestern University and the University of Puerto Rico. He has been funded continuously by NIH/NINCDS/NIDCD since 1984 to study hair cell and supporting cell physiology. More information can be found on his website www.YaleEarLab.org.

SPEECH PERCEPTION AND HEARING LOSS

BY JONT B. ALLEN, PH.D., ANDREA TREVINO, AND WOOJAE HAN, PH.D.,
UNIVERSITY OF ILLINOIS, URBANA-CHAMPAIGN

Over 150 years after the early research of Alexander Graham Bell, it remains unclear how the auditory system decodes speech, both in individuals who have “normal ears” and those who have “non-normal ears.” Recent research has shown that normal ears can decode isolated consonants without error. However, when the inner ear is damaged, such as with sensorineural hearing loss where hair cells and synaptic connections are not properly functioning, speech can be heard but not understood. In these cases, two seemingly-normal articulated utterances of the same consonant can result in totally different responses. Such specific and consistent confusions uniquely depend on the auditory system’s function and the utterance. This presentation will discuss the differences between how the auditory systems of normal ears and non-normal ears receive and decode speech.

INTRODUCTION

Existing clinical methods for diagnosing speech disorders in individuals with damaged inner ears seem fundamentally broken. Today when patients go to an audiology clinic, their pure-tone hearing thresholds are first measured. Based on the degree of tonal hearing loss, a hearing aid may be prescribed, which is subsequently adjusted to partially compensate for the pure-tone loss. This may or may not improve the ear’s speech loss (Walden & Montgomery, 1975). But since the speech loss is infrequently measured (or worse, the method of measurement is ineffective), the change is not quantified.

Based on the evidence available, it has been shown that speech testing has not been successful in fitting hearing aids (Walden & Montgomery, 1975). This seems counterintuitive since the main purpose of wearing a hearing aid is to improve speech understanding. Due to historically poor understanding

of the fundamentals of speech perception, it has proven difficult to resolve this inconsistency. First, researchers may not understand the process of learning speech, which typically takes place in the first one to two years of life. Second, due to middle ear infections, young children can temporarily lose their hearing, which can interfere with learning spoken language. It is not until the first year of school when the child is learning how to read that the child’s ability to hear consonants is first fully tested.

Children who cannot accurately decode consonants may have increased difficulty with orthography. For example, if an ear cannot hear the distinction between /b/ and /d/ or between /t/ and /f/, the child is likely to misunderstand the importance of the shape of the letter [loop at bottom, closing to the left (d) or right (b), and curl at top (f) or bottom (t)]. The classroom teacher assumes that if a child’s hearing is normal, then the child can hear the consonant distinctions.

However, this assumption can be wrong and if so, the child’s consonant decoding deficiency will go undetected (it will not show up in a pure-tone hearing test). When the child passes a hearing screen it is assumed, incorrectly, that they can decode syllables. What is needed is a targeted consonant discrimination test to predict these reading disorders.

Clinical audiologists can also make the same assumptions about adult speech perception, and research has shown that many of these assumptions can be wrong. The most serious assumption has been that consonants are homogeneous. Research has shown that for “normal ears,” confusions systematically depend on the consonant (Phatak & Allen, 2007; Phatak, Lovitt, & Allen, 2008; Singh & Allen, 2012). For “non-normal ears,” the errors dramatically increase, again depending on the ear, the noise-level, and, most significantly, the utterance.

If consonants were homogeneous, the

confusions, as a function of the noise level, would be the same from one consonant to the next. This is not the case, since consonant confusions are highly dependent on the utterance (Han, 2011; Singh & Allen, 2012). While normal ears give similar confusions for a given utterance as a function of the noise, non-normal ears are idiosyncratic in their error patterns. The idiosyncratic nature of the speech scores implies that they may not be averaged. It is this inappropriate averaging that has led clinicians to believe that speech is not a reliable measure for fitting hearing aids.

In the last few years, the Human Speech Research (HSR) group at the Beckman Institute for Advanced Science and Technology at the University of Illinois, Urbana-Champaign, has determined some key elements in this chain that seem to enlighten responses from both normal and non-normal ears. For our purposes, “normal ears” are defined as those with pure-tone thresholds less than 20 dB-SPL, and “non-normal ears” are defined as having pure-tone thresholds greater than 20 dB-SPL.

Until very recently, it was not understood that the normal ear can detect speech with essentially zero error, down to -10 dB SNR (three times more speech-shaped noise than speech) (Phatak et al., 2008). As the noise increases, the error goes from zero to chance performance over a small signal-to-noise ratio (SNR) range. These new results totally change the understanding of what is happening in normal ears because it means consonant perception is binary (Singh & Allen, 2012).

The focus of this presentation is to describe this difference in performance between the normal and non-normal

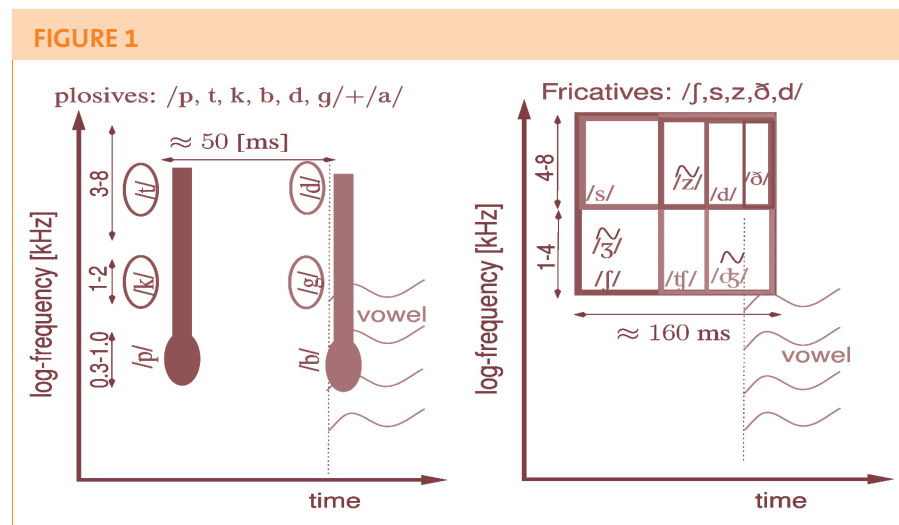


Figure 1. Time-frequency allocation of the plosives and the fricatives. Mapping these regions into perceptual cues required extensive perceptual experiments (Li et al., 2010). Once the sounds have been evaluated, it is possible to prove how the key noise-robust perceptual cues map to acoustic features. In the cases of the three voiced consonants indicated with a tilde (/z, ʒ, dʒ/), the frication noise is modulated at the pitch frequency.

ear at the utterance level. The paper will explain what the HSR group has found, and then predict where this research will go in the next few years. In addition, we will discuss a speech test that teases out such natural occurring idiosyncratic speech confusions, which we argue will eventually be useful for fitting hearing aids.

HOW DOES SPEECH PERCEPTION FAIL?

The challenge remains to understand the auditory processing strategy of the auditory cortex, which is wired to non-normal ears. To understand how normal ears decode consonants, the HSR group repeated the classic consonant perception experiments of Fletcher (1922) and Miller and Nicely (1955), among others. This gave us access to important new data and the ability to reassess many widely held assumptions. The first lesson of this research is the “sin of averaging”—while audiology is built on averaging measures, most of the interesting information is lost in these averages. We have shown, for example, that averaging across consonants distorts the measure as does averaging across

talkers for a given consonant. We have also found that entropy (a probabilistic measure of consistency) is more robust than the average error.

In 1970-80, a number of studies explored the role of the transitional and burst cues in a consonant-vowel (CV) context. In a review of the literature, Cole and Scott (1974) argued that the burst must play at least a partial role in perception, along with transition and speech energy envelope cues. Explicitly responding to Cole and Scott (1974), Dorman and colleagues (1977) executed an extensive experiment using natural speech made up from nine vowels preceded by /b, d, g/. The experimental procedure consisted of truncating the consonant burst and the devoiced transition (following the burst) of a CVC, and then splicing these onto a second VC sound, presumably with no transition component (since it had no initial consonant). Their results were presented as a complex set of interactions between the initial consonant (burst and devoiced cue) and the following vowel (i.e., coarticulations).

FIGURE 2

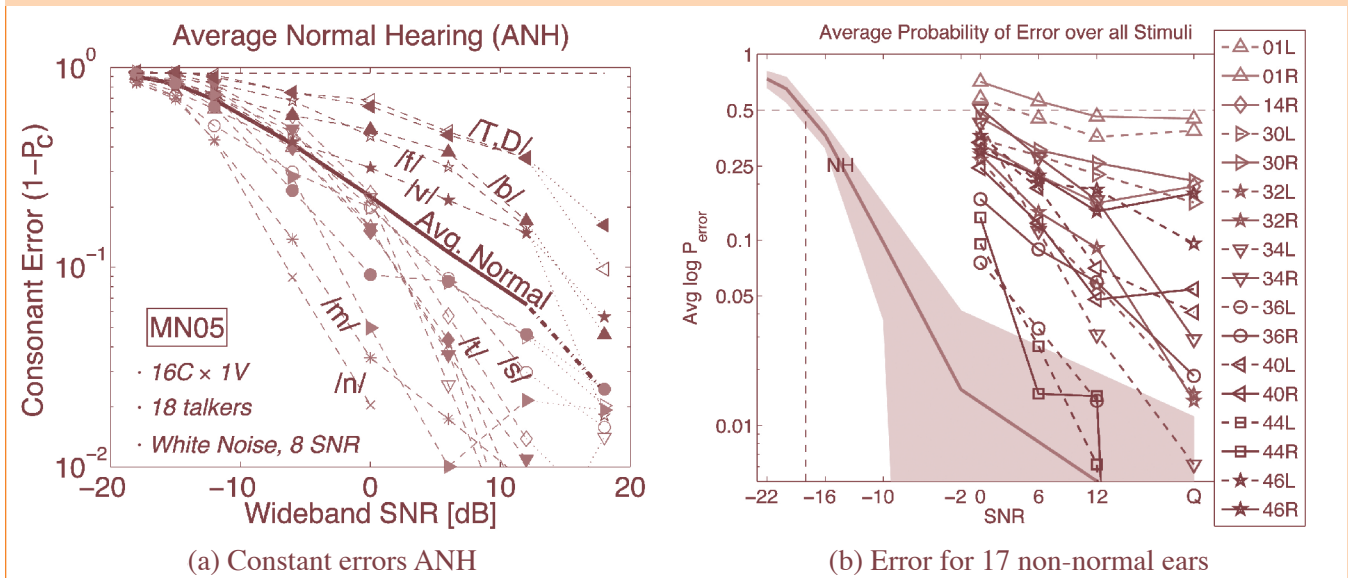


Figure 2. LEFT: Shown here is the average error (log scale) for 16 CV consonants as a function of the relative intensity of constant-spectrum-level masking noise (Phatak et al., 2009). The solid black curve labeled “Avg. Normal” shows the average across all the consonants. Note the large variation in error. RIGHT: This family of curves compares the average consonant error for 14 normal and 17 non-normal ears in speech shaped masking noise. For the non-normal ears, there is a large spread in scores due to the variation in hearing loss as compared to listeners with normal hearing (gray region), all of whom are similar in their average performance.

The same year Blumstein and colleagues (1977) published a related /b, d, g/ study using synthetic speech that also presented a look at the burst and a host of transition cues. They explored the possibility that the acoustic cues were *integrated* (acted as a whole). This study was looking to distinguish the *necessary* from the *sufficient* cues, and first introduced the concept of *conflicting cues* in an attempt to pit one type (burst cues) against the other (transition cues).

While these three key studies highlighted the relative importance of the two main types of acoustic cue, burst and transition, they left unresolved the identity and relative roles of these cues. No masking noise was used in the studies, ruling out any form of information analysis. Masking is key to an information theoretic analysis of any communication channel (Allen, 1994, 1996; Fletcher, 1922; Shannon, 1948). As discussed by Allen (2005), based on

the earlier work of Fletcher and Galt (1950), Miller and Nicely (1955), and inspired by Shannon’s source-channel model of communication, the HSR group repeated many of the classic experiments (Li & Allen, 2009; Phatak & Allen, 2007; Phatak et al., 2008). The data resulting from our several experiments will be discussed in the remainder of the paper.

IDENTIFYING PERCEPTUAL CUES

Li and colleagues (2010) first described a method to robustly identify speech cues for a variety of naturally produced CV speech sounds. This method uses a 3-dimensional psychophysical approach using a variety of noise levels, time-truncation, and high and low pass filtering. These experiments made it possible, for the first time, to reliably locate the subset of perceptually relevant cues in time and frequency, while the noise-masking data characterizes the cue’s masked threshold (i.e., its strength).

Figure 1 describes the resulting consonant maps. Not surprisingly, the perceptual cues associated with fricative sounds are quite different from the plosives. Timing and bandwidth remain important variables. For the fricative sounds, the lower edge of the swath of frication noise is the perceptual cue.

Briefly summarized in Figure 1, the CV sounds /ta, da/ are defined by a burst at high frequencies, /ka, ga/ are defined by a similar burst in the mid frequencies, and /ba, pa/ were traced back to a wide-band burst. As noise is added, the wide-band burst frequently degenerates into a low frequency burst, resulting in low-level confusions. The recognition of burst-consonants further depends on the delay between the burst and the sonorant onset, defined as the voice onset time (VOT). Consonants /t, k, p/ are voiceless sounds, occurring about 50 [ms] before the onset of F0 voicing while /d, g/ have a VOT <20 [ms]. Plosive /b/ may have a negative VOT.

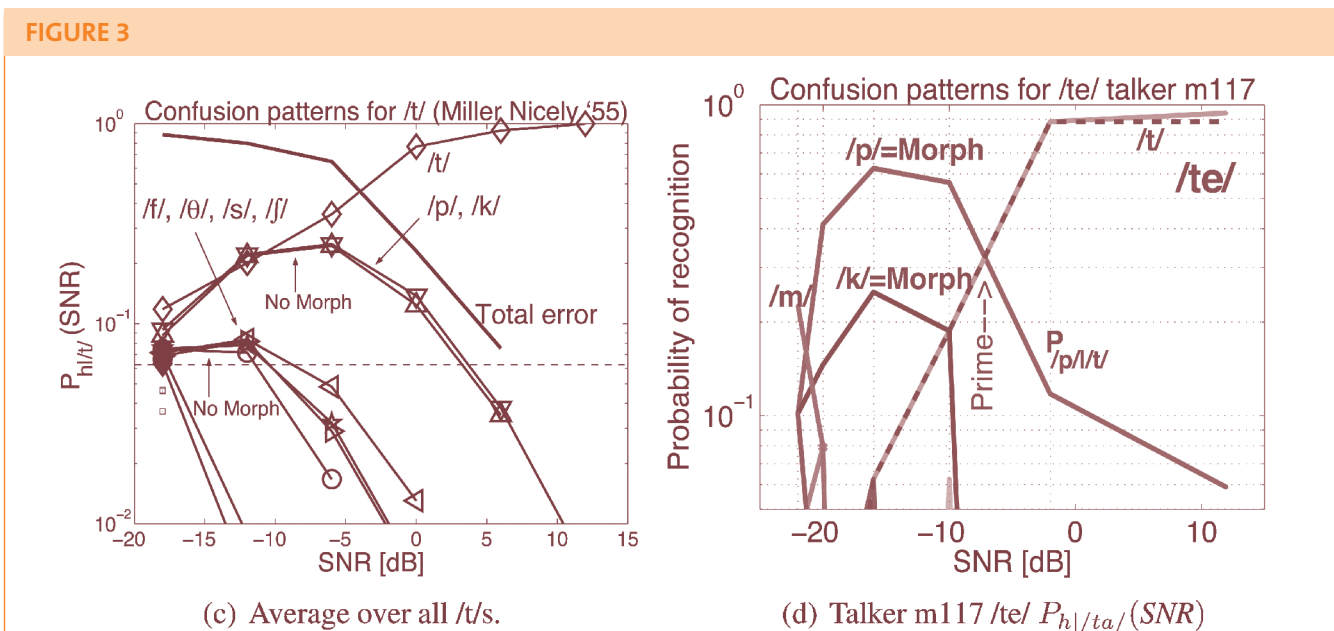


Figure 3: The “sin of averaging” extends to the utterance level. On the left (a) we see confusion patterns for the average score for /ta/ from Miller and Nicely (1955) (white masking noise). On the right (b) we show the confusion patterns for male talker 117 saying /te/ (speech shaped noise). Based on data with the same masking conditions, and as concluded in Figure 2, averaging across utterances removes critical information from the ANH scores. The confusion error is a function of the SNR in dB. As we shall see, this “sin” is much worse for non-normal ears at the utterance level. The arrow at -8 dB and 30% shows the priming point, defined as where a listener reports one of a small set of sounds (Li & Allen, 2011).

Based on the results of Li and colleagues (2010), this study, along with a host of verification experiments on the ~100 CV utterances in the HSR database (Kapoor & Allen, 2012; Li & Allen, 2011; Régnier & Allen, 2008), we have conclusively demonstrated that these features uniquely label the indicated consonant.

METHODS

Isolated CVs were taken from naturally produced speech from 18 talkers. Noise was added to the speech with a range from -26 dB to quiet (Q). Both uniform and speech weighted spectrum level noise was added to the speech. The listener corpus consisted of more than 200 normal and 45 non-normal ears, with 9-16 consonant and 8 vowel sounds. To assure the estimates of the error are reliable, a minimum of 10 trials per utterance and SNR are required (Han, 2011; Phatak, Yoon, Gooler, & Allen, 2009; Singh & Allen, 2012). The difference between these new experi-

ments and their classic counterparts is that the utterances of each consonant are not averaged.

RESULTS

In Figure 2, the average probability of the error $P_e(SNR)$ is shown (for speech-weighted noise the SNR is the same as the articulation index). On the left (a), the “average normal hearing” (ANH) score $P_e(SNR)$ (black line), along with the score for each heard consonant /h/, given spoken consonant /s/ as a function of the SNR for flat-spectrum masking noise (Phatak et al., 2009). There is a huge variation in scores across the consonants: the SNR corresponding to the 50% point ranges from -12 dB [m, n/] to +8 dB [θ, ð/] [shown as /T/ and /D/ in Figure 2)]. Such a large range of scores is not captured by an average. Not shown here, each utterance in the HSR database has a wide range of scores, varying in error from zero to chance depending on the masking

noise intensity (Singh & Allen, 2012). The right panel (b) shows the average scores for the 17 non-normal ears as compared to the average scores of the participants with normal hearing in speech-shaped masking noise. One of the best ears in terms of average error is 36R. Not shown is that his error for /ba/ reaches 100%, while the remaining 13 consonants tested had zero error. Thus, the reported performance is highly distorted, again due to the “sin of averaging.”

A second major conclusion is that when characterizing a listener with hearing loss, one must look at the individual confusions. In Figure 3, confusion patterns (CPs) are compared to SNR. The CP is a graphical display of the confusion probabilities as a function of the intensity of the masking noise relative to the speech. To estimate a CP requires a totally different clinical measure than is being applied today. CPs allow one to

visualize the confusions of each sound as a function of the SNR. From the CP it is easy to identify a sound that primes, meaning that it can be heard as one of several sounds with equal probability by changing one's mental bias. In this case the CPs show subject responses that are equal (the curves cross each other), similar to the CP of Figure 3(b) at -8 dB where one naturally primes /p/, /t/, and, to a lesser extent, /k/ (at -10 dB).

When asked, most clinicians report that they do not have the time to make detailed measures. In our opinion, this is more a reflection of old habits than actual time constraints. The confusion sets, and their dependence on the noise, are not predictable without such tests. Utterance confusions and their masked dependence are important because they reveal the mix of underlying perceptual cues being confused with the target sound.

When using an utterance confusion measure, each non-normal ear consistently makes large errors on a small subset of utterances. Furthermore, for a given utterance, there are patterns in these errors across listeners with hearing loss. In other words, normally spoken utterances are heard idiosyncratically by non-normal ears, yet with correlated error patterns.

CONFUSIONS IN NON-NORMAL EARS

As a direct extension of earlier studies (e.g., Phatak et al., 2009), four experiments were performed (Han 2011), two of which will be reported on here. In Experiment 1 (Exp-1), full-rank confusion matrices for the 16 Miller-Nicely CV sounds were determined at 6 SNR [Q, 12, 6, 0, -6, and -12 dB] for 46 non-normal ears (25 subjects). In Experiment 2 (Exp-2), a subset of 17 ears were remeasured, but with the total number of trials per SNR per consonant raised from 2–8 (Exp-1) to as high as

FIGURE 4

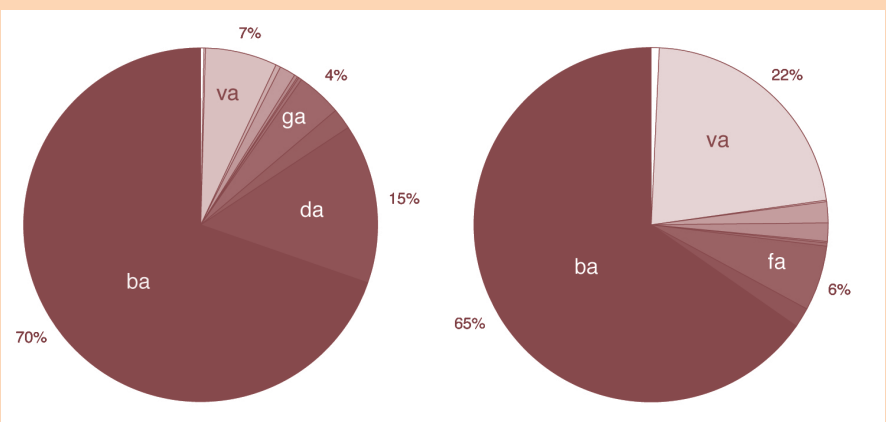


Figure 4: These pie charts show the proportion of confusions for two different /ba/ utterances, as reported by all of the 17 non-normal ears. The most common error for the /ba/ on the left is /da/ and then /va/, while the one on the right is most frequently heard as /va/ and then /fa/. The one on the left is almost never heard as /fa/ and the one on the right almost never as /da/. These two /ba/ sounds are reported correctly by normal ears.

20 (Exp-2) to statistically verify the reliability of the subjects' responses in doing the task.

Figure 4 shows that listeners with hearing loss are using a common strategy that depends systematically on the utterance. Clearly, if such very different scores for the two /ba/ sounds were to be averaged together (i.e., present clinical practice), the idiosyncratic (i.e., the most important) information about the ears would be lost. As discussed earlier, the average score is a distorted metric due to its high variance a) across consonants, b) across utterances for each consonant, and c) across subjects with hearing loss. Entropy gives a direct measure of consistency and is insensitive to mislabeling errors (e.g., consistently across a voicing error, as in reporting /d/ given /t/). Given the observed increased mislabeling of sounds in non-normal ears, a high-consistency measure (i.e., entropy) seems to be a better measure.

SUMMARY

This article has reviewed some of what the HSR group has recently learned about speech perception of consonants, and how this knowledge might im-

pact understanding of nonlinear (NL) cochlear speech processing. However, the role of outer hair cell (OHC) processing of speech is still poorly understood (Allen, 2008; Allen & Li, 2009). It is now widely accepted that OHCs provide dynamic range and are responsible for much of the NL cochlear speech signal processing, thus the common element that links all the NL data (Allen, Régnier, Phatak, & Li, 2009). OHC dynamics must be understood before any model can hope to succeed in predicting basilar membrane, hair cell, neural tuning, and NL compression. Understanding the OHC's two-way mechanical transduction may be the key to solving the problem of the cochlea's dynamic range and dynamic response (Allen, 2003).

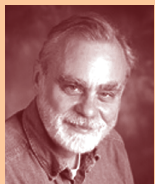
However, the perception of speech by the non-normal ear does not seem to be consistent with the above commonly held view. For example, the large individual differences seem inconsistent with the OHC as the tying link, and seem more likely related to synaptic dead regions (Kujawa & Liberman, 2009). Continued analysis of these confusions will hopefully provide further insights into this important question.

The detailed study of how a complex system fails can give deep insights into how the normal system works.

The key open problem here is, “How does the auditory system (e.g., the NL cochlea and the auditory cortex) process human speech?” There are many applications of these results including speech coding, speech recognition in noise, hearing aids, and cochlear implants as well as language acquisition and reading disorders in children. If we can solve the *robust phone decoding problem*, we will fundamentally change the effectiveness of human-machine interactions. For example, the ultimate hearing aid is the hearing aid with built in robust speech feature detection and phone recognition. While researchers have no idea when speech-aware hearing aids will come to be, and the time is undoubtedly many years off, when it happens, it will be a technological revolution of some magnitude.

ACKNOWLEDGMENTS

We gratefully acknowledge Phonak and Research in Motion for their generous support of this research. Much of the work was also supported by NIH grant # RDC009277A.



ABOUT THE AUTHORS

Jont Allen, Ph.D., is an associate professor in the Department of Electrical and Computer Engineering at the University of Illinois. Allen received a B.S. in electrical engineering from the University of Illinois, Urbana-Champaign, and an M.S. and Ph.D. from the University of Pennsylvania. Upon graduation in 1970, Allen joined Bell Laboratories in Murray Hill N.J. From 1997-2002 he was a member of the newly created Research Division of AT&T (formerly Bell) Labs. In 2003, Allen retired from AT&T and joined the Department of Electrical and Computer Engineering at the University of Illinois.

Andrea Trevino is a Ph.D. student in Human Speech Recognition group of the Department of Electrical and Computer Engineering at the University of Illinois, Urbana-Champaign.

Woojae Han, Ph.D., is a recent graduate of the Department of Electrical and Computer Engineering at the University of Illinois, Urbana-Champaign and current assistant professor at Hallym University in Korea.

REFERENCES

- Allen, J. B. (1994). How do humans process and recognize speech? *IEEE Transactions on Speech and Audio*, 2, 567–577.
- Allen, J. B. (1996). Harvey Fletcher’s role in the creation of communication acoustics. *Journal of the Acoustical Society of America*, 99, 1825–1839.
- Allen, J. B. (2003). Amplitude compression in hearing aids. In *MIT Encyclopedia of Communication Disorders*, R. Kent (ed.), p. 413–423. Boston: MIT Press.
- Allen, J. B. (2005). *Articulation and intelligibility*. LaPorte, CO: Morgan and Claypool.
- Allen, J. B. (2008). Nonlinear cochlear signal processing and masking in speech perception. In *Springer Handbook on speech processing and speech communication*, J. Benesty & M. Sondhi (eds.), p. 1–36. Heidelberg, Germany: Springer.
- Allen, J. B. & Li, F. (2009). Speech perception and cochlear signal processing. *IEEE Signal Processing Magazine*, 26, 73–77.
- Allen, J. B., Régnier, M., Phatak, S., & Li, F. (2009). Nonlinear cochlear signal processing and phoneme perception. In *Proceedings of the 10th mechanics of hearing workshop*, y N. P. Cooper & D. T. Kemp (eds.), p. 93–105. Singapore: World Scientific Publishing Co.
- Blumstein, S. E., Stevens, K. N., & Nigro, G. N. (1977). Property detectors for bursts and transitions in speech perceptions. *Journal of the Acoustical Society of America*, 61, 1301–1313.
- Cole, R., & Scott, B. (1974). Toward a theory of speech perception. *Psychological Review*, 81, 348–74.
- Dorman, M., Studdert-Kennedy, M., & Raphael, L. (1977). Stop-consonant recognition: Release bursts and formant transitions as functionally equivalent, context-dependent cues. *Perception and Psychophysics*, 22, 109–22.
- Fletcher, H. (1922). The nature of speech and its interpretation. *Journal of the Franklin Institute*, 193, 729–747.
- Fletcher, H., & Galt, R. (1950). Perception of speech and its relation to telephony. *Journal of the Acoustical Society of America*, 22, 89–151.
- Han, W. (2011). Methods for robust characterization of consonant perception in hearing-impaired listeners. Ph.D. thesis, University of Illinois at Urbana-Champaign.
- Kapoor, A., & Allen, J. B. (2012). “Perceptual effects of plosive feature modification.” *Journal of the Acoustical Society of America*, 131, 478–491.
- Kujawa, S., & Liberman, M. (2009). Adding insult to injury: Cochlear nerve degeneration after “temporary” noise-induced hearing loss. *Journal of Neuroscience*, 29, 14077–14085.
- Li, F., & Allen, J. B. (2009). Additivity law of frequency integration for consonant identification in white noise. *Journal of the Acoustical Society of America*, 126, 347–353.
- Li, F., & Allen, J. B. (2011). Manipulation of consonants in natural speech. *IEEE Transactions on Audio, Speech, and Language Processing*, 19, 496–504.
- Li, F., Menon, A., & Allen, J. B. (2010). A psychoacoustic method to find the perceptual cues of stop consonants in natural speech. *Journal of the Acoustical Society of America*, 127, 2599–2610.
- Miller, G. A., & Nicely, P. E. (1955). An analysis of perceptual confusions among some English consonants. *Journal of the Acoustical Society of America*, 27, 338–352.
- Phatak, S., & Allen, J. B. (2007). Consonant and vowel confusions in speech-weighted noise. *Journal of the Acoustical Society of America*, 121, 2312–2326.
- Phatak, S., Lovitt, A., & Allen, J. B. (2008). Consonant confusions in white noise. *Journal of the Acoustical Society of America*, 124, 1220–1233.
- Phatak, S., Yoon, Y., Gooler, D. M., & Allen, J. B. (2009). Consonant loss profiles in hearing impaired listeners. *Journal of the Acoustical Society of America*, 126, 2683–2694.
- Régnier, M. S., & Allen, J. B. (2008). A method to identify noise-robust perceptual features: Application for consonant /t/. *Journal of the Acoustical Society of America*, 123, 2801–2814.
- Shannon, C. E. (1948). The mathematical theory of communication. *Bell System Technical Journal*, 27, 379–423 (parts I, II), 623–656 (part III).
- Singh, R., & Allen, J. B. (2012). Sources of stop consonant errors in low-noise environments. *Journal of the Acoustical Society of America*, 131, in press.
- Walden, B. F., & Montgomery, A. A. (1975). Dimensions of consonant perception in normal and hearing-impaired listeners. *Journal of Speech and Hearing Research*, 18, 444–455.

THE RESTORATION OF SPEECH UNDERSTANDING BY ELECTRICAL STIMULATION OF THE AUDITORY SYSTEM

BY MICHAEL DORMAN, PH.D., ARIZONA STATE UNIVERSITY

The first cochlear implant surgery was performed over 50 years ago and allowed a patient to hear “sounds.” Today, professionals expect high levels of speech understanding for adults who are post-lingually deaf and who receive a cochlear implant, and for children who are congenitally deaf—if the children receive a cochlear implant early and if they receive intensive listening and spoken language intervention. This presentation will provide a broad view of the technology underlying cochlear implants and describe possible next steps in the evolution of these devices.

Over 50 years ago, William House, M.D., performed the first cochlear implant surgery. The results were modest—the patient reported hearing “sounds.” Today, professionals expect that the majority of adult patients who are late-deafened, when fit with a cochlear implant, will achieve 80–100% correct scores on tests of sentence understanding in quiet (Wilson & Dorman, 2008). Professionals expect that many children who are congenitally deaf, if fitted with a cochlear implant before the age of 3 and if given extensive (re)habilitation, will perform near the level of their age-matched peers who have typical hearing on tests of speech understanding when in elementary school. These results, for adults and children, underlie the claim that cochlear implants are one of the miracles of modern medicine.

After 50 years of effort, cochlear implantation is now a mature discipline—professionals expect good results for most patients. Nonetheless, researchers continue their work and new developments extend the promise of even higher levels of speech understanding for individuals with hearing loss.

BETTER HEARING BY “HYBRID” STIMULATION

One innovation, a relatively simple one at that, is combining electric stimulation

with acoustic stimulation. The majority of patients who qualify for a cochlear implant in one ear have some low-frequency acoustic hearing in the other. Researchers at Arizona State University have found that patients with hearing only at 125 Hz and 250 Hz, i.e., at very low frequencies, can use the information carried by these frequencies to improve speech understanding via their implant. This low-frequency information is especially useful in noise, which is fortunate because cochlear implants alone do not provide high levels of speech understanding when speech is presented against a background of noise.

A recent surgical innovation, hearing preservation surgery, allows surgeons to implant an electrode array and to preserve low-frequency hearing. This provides much better speech understanding via the implanted ear and provides the listener with two partially hearing ears—the ear opposite the implant and the ear with the implant. Having two partially hearing ears is of benefit in listening environments where noise surrounds the listener.

Hearing preservation surgery allows patients with substantial low-frequency hearing and speech understanding to receive a cochlear implant and to benefit from “hybrid” hearing. Research-

ers working on this technique expect to see, in the near future, patients with up to 60% word scores by hearing alone to qualify for a cochlear implant. The logical extension of this idea is cochlear implantation for the “common variety” of high-frequency hearing loss. Of course, the greater the amount of hearing and speech understanding, the greater the consequences of losing both, if hearing is not preserved. The calculation for or against cochlear implant surgery for these individuals will not be simple.

Hearing preservation surgery will also create patients with a cochlear implant in each ear and low-frequency hearing in each ear. Researchers have tested several patients like this and, when tested in complex listening situations, find that they benefit from having two implants versus one and having two partially hearing ears versus one.

BETTER HEARING THROUGH CHEMISTRY

The odds of retaining low-frequency hearing following cochlear implant surgery can be improved by the administration of protective drugs during the surgical procedure. Studies have shown that some drugs, such as dexamethasone, can prevent inner-ear cell damage from exposure to very loud noises, similar to the noise produced by surgical

drilling for cochlear implants. The same drug can rescue cells 24 hours after exposure to loud noises or other drugs that destroy hearing. These results have stimulated researchers to create electrode arrays that both deliver a drug and provide electrical stimulation to the cochlea. The delivery of drugs during cochlear implant surgery and in the weeks and months post-surgery via the electrode array will allow for the maximum conservation of residual hearing in the implanted ear.

This same technology of combined drug delivery and electrical stimulation holds tremendous promise for young children receiving cochlear implants. Research has shown that administration of a class of drugs called neurotropic drugs can stimulate the growth of neurons (Sinohara et al., 2002) and could even promote the growth of neural fibers up the chemical gradient to the electrode that is releasing the drug. If this can be achieved in very young children, then professionals will have a method of preserving the neural elements in the child's cochlea and a method of getting neural elements very close to the electrode array. The latter would allow very low levels of current to be used for stimulation and should result in much better frequency resolution. Better frequency resolution would lead to better speech understanding and, perhaps, better appreciation of music.

BETTER HEARING FROM EARLY STIMULATION

Brain wiring is determined by both intrinsic factors of biology and by environmental stimulation. In the absence of auditory stimulation early in development, the auditory brain will not develop typically and will not have the usual connections to other areas of the brain that process speech and language (Kral & O'Donoghue, 2010). Indeed, in the absence of auditory stimulation,

some auditory areas can be usurped by other sensory modalities, such as vision or touch. Thus, early stimulation of the auditory pathways is critical to driving a developing brain into the configuration shown by infants with typical hearing. At issue for parents is, how early is "early" and how late is "late?" If a child has had no auditory stimulation for the first seven years of life, then the odds of achieving reasonable levels of speech understanding via a cochlear implant are poor. A child who receives a cochlear implant by age 2-3 years will have better odds of a good outcome (Svirsky et al., 2007), and age 1 year is now a standard for most children who receive cochlear implants. There is some evidence that receiving a cochlear implant under the age of 1 provides some advantages (Houston & Miyamoto, 2010), but very early implantation must be weighed against surgical risks and other factors (Cosetti & Roland, 2010).

The need for early stimulation to shape connections within and among different areas of the auditory brain puts parents, who wish to wait for something better than a cochlear implant for their child, in a difficult position. Imagine a therapy, for example, based on stem cells that could regenerate the cell bodies and related structures in the cochlea that are absent in a child who has a profound hearing loss. And imagine that this therapy is still 10 years away. What would

speech understanding be like for a child with regenerated cells in the cochlea but who had been without stimulation for 10 years? Because the brain would not have developed typical connections within and between brain areas that subserve hearing and language, the value of having new cells in the cochlea could be very small. Early restoration of function should be the hope of parents who wish their child to experience typical or near typical development of speech and language skills.

REFERENCES

- Cosetti, M., & Roland, J. T. (2010). Cochlear implantation in the very young child: Issues Unique to the under-1 population. *Trends in Amplification, 14*, 46-57.
- Houston, D., & Miyamoto, R. (2010). Effects of early auditory experience on word learning and speech perception in deaf children with cochlear implants: Implications for sensitive periods of language development. *Otology and Neurotology, 31*(8), 1248-1253.
- Kral, A., & O'Donoghue, G. (2010). Profound deafness in childhood. *The New England Journal of Medicine, 363*, 1438-50.
- Shinohara, T., Bredberg, G., Ulfendahl, M., Pyykko, I., Olivius, N. P., Kaksonen, R., et al. (2002). Neurotrophic factor intervention restores auditory function in deafened animals. *Proceedings of the National Academy of Sciences, U. S. A., 99*, 1657-60.
- Svirsky, M., Chin, S., & Jester, A. (2007). The effects of age at implantation on speech intelligibility in pediatric cochlear implant users: Clinical outcomes and sensitive periods. *Audiological Medicine, 5*, 293-306.
- Wilson, B., & Dorman, M. (2008) Cochlear implants: A remarkable past and a brilliant future. , 1-19.



ABOUT THE AUTHOR

Michael Dorman, Ph.D., is a professor in the Department of Speech and Hearing Sciences at Arizona State University. He received his Ph.D. in experimental child and developmental psychology (with a linguistics minor) from the University of Connecticut in 1971. He is a Fellow of the Acoustical Society of America and the author of over 150 publications in areas including speech perception by infants, adults, listeners with hearing loss and listeners fit with cochlear implants; cortical lateralization of function; and neural plasticity. His work on cochlear implants has been supported continuously by the National Institutes of Health since 1989.

SPOKEN LANGUAGE DEVELOPMENT IN INFANTS WHO ARE DEAF OR HARD OF HEARING: THE ROLE OF MATERNAL INFANT-DIRECTED SPEECH

BY TONYA R. BERGESON-DANA, PH.D., INDIANA UNIVERSITY

How do children learn spoken language? Most children with typical hearing learn from infancy the sound of their mother's voice, a type of speech researchers call infant-directed speech. Mothers, fathers and most adults speak to infants in a sing-song manner, exaggerating the melody and rhythm of their speech. But what happens when this connection is broken, such as with a child who has hearing loss? This article will discuss the importance of infant-directed speech, and how infants with hearing loss respond to such talk in comparison to infants with typical hearing.

How do children learn spoken language? In children who are developing typically, this feat is accomplished more or less naturally through active experiences with caregivers and the child's environment. Parents don't enroll infants and toddlers in spoken language classes; instead, they model, encourage, and stimulate their speech and language attempts by responding to the cries and coos of infants and holding simple conversations with toddlers. In fact, caregivers across the world actually speak to their infants and young children using a special style of speech commonly known as "babytalk" or "motherese." Researchers and scholars call this *infant-directed speech*. Mothers, fathers, and even strangers off the streets speak to infants in a sing-song manner, exaggerating the melody and rhythm of their speech (e.g., Ferguson, 1964; Fernald, 1989). Caregivers are flexible with this speech style, adjusting the levels of exaggeration according to the social context and their infant's age (e.g., Kitamura, Thanavishuth, Burnham, & Luksaneeyanawin, 2002; Stern, Spieker, Barnett, & MacKain, 1983). This speech style is now known to contribute in many ways not only to

infants' social-emotional development, but also to their speech, language, and cognitive development (e.g., Liu, Kuhl, & Tsao, 2003).

Sometimes that natural connection between caregivers and infants can be disrupted. For example, caregivers who suffer from depression have difficulty connecting with their children, speaking to them in monotones with flat affect. Researchers have shown that infants of mothers who are depressed have a difficult time learning new associations from such speech (Kaplan, Bachorowski, Smoski, & Hudenko, 2002), which likely has cascading effects on the development of spoken language and cognition. Moreover, children in families with low socioeconomic status are at a serious disadvantage compared to children in families with high socioeconomic status in terms of both spoken language input quantity and quality. Researchers have found that caregivers with fewer financial and educational resources use fewer words in their infant- and child-directed speech than caregivers with greater financial and educational resources (Hart & Risley, 1995). This effect later translates to

language abilities, with children from low income homes exhibiting much worse language skills compared to children from high income homes (Hart & Risely, 1995). These studies, among others, highlight the importance of caregivers' speech to infants as they develop spoken language.

What happens, then, if infants have a hard time hearing their caregivers? How do children who are deaf or hard of hearing learn spoken language? With the advent of new technologies, such as cochlear implants and state-of-the-art hearing aids, children with hearing loss now have the most access to sound and spoken language in their environment than ever before. Because of this, we would expect caregivers to speak to their infants and children with hearing loss just the same as those with typical hearing. And children with hearing loss who use hearing aids or cochlear implants should demonstrate similar spoken language development as children with typical hearing. Children who are deaf or hard of hearing *can* achieve speech and spoken language abilities on par with their typically developing peers with the use

of such assistive devices (e.g., Peterson, Pisoni, & Miyamoto, 2010). However, there are large individual differences among these children; not all children with hearing loss benefit to the same degree from cochlear implants or hearing aids (Pisoni, Cleary, Geers, & Tobey, 1999; Pisoni et al., 2008). As recently as 10 years ago, researchers could only guess at why this is the case because there were no pre-amplification predictors of outcome and benefit. However, recent studies have shown potential predictors of children who will succeed with hearing aids or cochlear implants that are related to early auditory experience (e.g., Bergeson & Pisoni, 2004).

CHILD PERCEPTION OF INFANT-DIRECTED SPEECH

The focus of this paper is one of the most important factors that can determine infants' benefit and success in spoken language development via amplification: early auditory experiences from infants' interactions with their caregivers, or infant-directed speech. The first question addressed is, do infants who have hearing loss for the first part of their life pay the same kind of attention to infant-directed speech as infants with typical hearing do? This is one way to determine if infants with hearing loss are reinforcing caregivers' use of infant-directed speech.

To answer this question, let's first review what is known about infant attention to maternal speech in typical development. At least two types of infant behaviors have been established by researchers. First, infants with typical hearing, from birth to 12 months old, prefer to listen to infant-directed speech over adult-directed speech (Fernald & Simon, 1984; Fernald et al., 1989; Grieser & Kuhl, 1988; Kitamura et al., 2002; Kuhl et al., 1997). Infants are especially responsive to the melodic quality of infant-directed speech

(Fernald & Kuhl, 1987). Infants' increased attention to infant-directed speech might actually help them process and understand speech and language. For example, infants find it easier to pick out new words from a spoken passage when listening to infant-directed speech rather than adult-directed speech (Thiessen, Hill, & Saffran, 2005). Mothers tend to highlight new words when speaking to infants much more so than when speaking to adults.

Second, infants with typical hearing recognize and prefer to listen to their own mothers' voice (DeCasper & Fifer, 1980). Amazingly, preference for maternal voices seems to develop even before infants are born. One study found that infants in the womb have different heart rate patterns in response to their mother's voice as compared to a stranger's voice (Kisilevsky et al., 2003). These findings also highlight the important effects of very early auditory experience on infants' speech perception abilities.

But what about infants and toddlers who have congenital hearing loss and receive hearing aids or cochlear implants? Do they pay the same type of attention to speech as infants with typical hearing? Research from the Babytalk Research Laboratory has been addressing this very question. One of the difficulties of assessing attention in this population is that the research participants are preverbal. That is, we cannot simply ask the infants and toddlers, "What do you think about this speech? Do you like this type of speech better than the other?" Instead, we use tried-and-true methods taken from the field of developmental psychology. Infants sit on their caregivers' laps inside a large sound-proof booth. We draw their attention to a TV monitor in front of them, and then present various

audio-visual stimuli. Previous research has shown that infants will naturally look longer towards a visual display near a sound source if they're interested in what they're hearing.

In one particular study, we measured infants' looking time to a red-and-white checkerboard pattern on the TV monitor while listening to four different mothers speaking in either an infant-directed or adult-directed style of speech. The study also included silent trials to determine how much infants prefer speech in general to silence. Infants with typical hearing attended much longer to speech trials than silent trials, and generally preferred infant-directed to adult-directed speech. Infants with mild-to-moderate hearing loss who use hearing aids showed similar patterns, but it took a little longer for them to develop their preferences than infants with typical hearing. Finally, infants with cochlear implants did not show a preference for infant-directed speech over adult-directed speech until approximately 9-12 months post-implantation. And even then, they did not attend any longer to the adult-directed speech than to silence! These findings have major implications for child-caregiver interactions and spoken language development.

There are some studies about recognition of voices in children who are deaf or hard of hearing. Several studies have shown that cochlear implant users find it difficult to distinguish the voices of different talkers, particularly if the talkers are the same sex (Cleary & Pisoni, 2002; Cleary, Pisoni, & Kirk, 2005; Fu, Chinchilla, & Galvin, 2004). However, one recent study showed that children ages 5-15 years old who use cochlear implants can tell apart their own mother's voice from other men, children, and even other women, although

their performance is not as good as that of children with typical hearing (Vongpaisal, Trehub, Schellenberg, van Lieshout, & Papsin, 2010).

The Babytalk Research Laboratory is in the midst of conducting another study to determine whether infants with congenital hearing loss can distinguish their own mother's voice from a stranger's voice. This study uses a habituation paradigm, in which a series of different women reciting passages in an infant-directed speech style is presented to infants who have about one year of hearing aid or cochlear implant experience. The idea is that infants will again pay attention to a checkerboard pattern on the TV monitor directly ahead of them when they are interested in the speech sounds. In a habituation paradigm, it is also expected that infants will start off with a high amount of interest and gradually become bored as the same category of sound (i.e., women's infant-directed speech) is repeated. Two test trials are presented once they reach a criterion point of boredom: one is their own mother's voice and the other is a stranger's voice. If they recognize their mother's voice, infants should theoretically pay more attention than to the last habituation trial and the test trial with the stranger's voice. If they do not recognize their mother's voice, then they should pay equal attention to all three trials. Data have been collected from a handful of infants and toddlers who are deaf or hard of hearing who have used a hearing aid or cochlear implant for approximately one year. These children have not yet shown recognition of their own mother's voice from that of a strange woman. Future studies will likely be needed to determine how infants and toddlers learn to recognize their mother's voice with additional hearing aid or cochlear implant use.

CAREGIVER PRODUCTION OF INFANT-DIRECTED SPEECH

Thus far, research has shown that infants and young children who are deaf or hard of hearing do not pay attention to infant-directed speech, or even speech in general, in the same way as children with typical hearing until they've had at least 9-12 months of auditory experience. Imagine now parents interacting with infants who are deaf or hard of hearing. If their infants are not paying active attention to their attempts to entertain or soothe using infant-directed speech, how must this affect caregivers' further use of this special speech style? That is, do caregivers speak in the same or different ways to young children with and without hearing loss?

To date there has been very little research on caregiver speech to infants with hearing loss who use hearing aids and cochlear implants. One reason is that, prior to state-mandated universal newborn hearing screening programs, infants were typically not diagnosed with hearing loss until 2-3 years of age (Meadow-Orlans, Spencer, & Koester, 2004). The existing literature suggests that an infant's hearing status may affect the way in which caregivers speak to their infants. One study of speech to infants with hearing loss showed that mothers with typical hearing tend to increase their use of vocal exaggeration when they first discover their infant's hearing loss, but gradually decrease the amount of vocal exaggeration over time (Wedell-Monnig & Lumley, 1980). Other studies of mother-child interactions have revealed that mothers tend to be more controlling, more repetitive, and less responsive in their interactions with children who are deaf or hard of hearing than with children who have typical hearing (Cheskin, 1981; Goss, 1970; Henggeler & Cooper, 1983). Mothers also produce fewer and less complex

verbal utterances but more nonverbal attention-getting behaviors when interacting with children with hearing loss than children with typical hearing (Goldin-Meadow & Saltzman, 2000; Koester, Brooks, & Karkowski, 1998; Koester, Karkowski, & Traci, 1998). Some researchers have shown, however, more similarities in mothers' speech styles to both sets of children when the children were matched by linguistic age rather than chronological age (Cross, Nienhuys, & Kirkman, 1985; Nienhuys, Cross, & Horsborough, 1984).

The Babytalk Research Laboratory recently investigated the effects of infant age and hearing loss on several prosodic characteristics of mothers' speech to infants with typical hearing and infants with hearing loss who use cochlear implants (Bergeson, Miller, & McCune, 2006; Kondaurova, Bergeson, & Xu, 2012). The results of these studies revealed that mothers do use infant-directed speech when interacting with their infants with cochlear implants, and that their vocal styles are more similar to mothers of infants with typical hearing when infants are matched by hearing experience rather than chronological age. Thus, these mothers adapt their prosodic speech style to the hearing experience and linguistic abilities of their infants who are deaf or hard of hearing.

Researchers have proposed that one of the functions of infant-directed speech is to help infants learn about language (e.g., Fernald, 1992). For example, infant-directed speech actually exaggerates certain cues to sentence structure. Caregivers will change the pitch of their voice from the end of one sentence to the beginning of another when speaking to an infant. They will also tend to linger on the last syllable of a sentence and take an exaggerated pause before starting a new sentence. In a recent

analysis of maternal speech, we found that mothers use similar sentence boundary cues when interacting with their infants who are profoundly deaf and use cochlear implants (Kondaurova & Bergeson, 2011).

Infant-directed speech might also help infants learn about the sound structure of their language. One study found that mothers potentially help their infants with typical hearing and infants with hearing loss discriminate among vowel categories (e.g., “ah,” “ee,” and “oo”) by exaggerating the differences among them (Dilley & Bergeson, 2010). Another study measured mothers’ exaggeration of cues that commonly distinguish tense vowels (e.g., “sheep”) and lax vowels (e.g., “ship”) in their speech to infants with profound hearing loss. There are two cues to this vowel contrast, one of which should be easily encoded with cochlear implant technology (duration of the vowel) and the other which is more problematic for cochlear implant users (spectrum of the vowel). Results showed that mothers exaggerated duration but not spectrum cues in speech to infants with hearing loss compared to speech to adults (Kondaurova, Bergeson, & Dilley, in press).

Taken together, these studies suggest that mothers’ speech is sensitive to their young children’s linguistic and hearing levels. In other words, mothers seem to be providing their infants and toddlers who are deaf or hard of hearing with speech cues tailored to their individual abilities. These findings are important given previous research that shows that the features of infant-directed speech have significant effects on language and cognitive development (Hart & Risley, 1995; Kaplan et al., 2002; Liu et al., 2003; Meadow-Orlans & Spencer, 1996; Pressman, Pipp-Siegel, Yoshinaga-Itano, & Deas, 1999; Spencer & Meadow-Orlans, 1996).

Nevertheless, there are still several unanswered questions regarding the acquisition of speech and language skills in both populations. Which aspects of infant-directed speech make it particularly beneficial for language acquisition? It could be that infant-directed speech is most beneficial because the vowel/consonant categories are clearer or more exaggerated. Or it could be the case that more general exaggeration (e.g., higher pitch or slower speaking rate) in mothers’ speech to infants elicits and maintains infants’ attention, which then allows the infants to pay attention to particular sounds or sentence structures. Moreover, infants with hearing loss may benefit from different features of infant-directed speech than infants with typical hearing. What is the best way for a mother (or a speech-language pathologist) to speak to an infant, and is this the same for infants who use a hearing aid or a cochlear implant? Preliminary data in the Babytalk Research Laboratory shows that some features of mothers’ speech to infants with hearing loss, such as use of repetition, is associated with their infants’ ability to learn new words and other speech and language outcomes. Answers to these questions will provide valuable new information to parents and clinicians of infants who are deaf or hard of hearing and use hearing aids and cochlear implants.

REFERENCES

- Bergeson, T. R., Miller, R. J., & McCune, K. (2006). Mothers’ speech to hearing-impaired infants with cochlear implants. *Infancy, 10*, 221-240.
- Bergeson, T. R., & Pisoni, D. B. (2004). Audiovisual speech perception in deaf adults and children following cochlear implantation. In G. A. Calvert, C. Spence, & B. E. Stein (Eds.), *The Handbook of Multisensory Processes* (pp. 749-772). Cambridge, MA: MIT Press.
- Cheskin, A. (1981). The verbal environment provided by hearing mothers for their young deaf children. *Journal of Communication Disorders, 14*(6), 485-496.
- Cleary, M., & Pisoni, D. B. (2002). Talker discrimination by prelingually deaf children with cochlear implants: Preliminary results. *Annals of Otology, Rhinology, and Laryngology, 119*, 113-118.
- Cleary, M., Pisoni, D. B., & Kirk, K. I. (2005). Influence of voice similarity on talker discrimination in children with normal hearing and children with cochlear implants. *Journal of Speech, Language, and Hearing Research, 48*, 204-223.
- Cross, T. G., Nienhuys, T. G., & Kirkman, M. (1985). Parent-child interaction with receptively disabled children: Some determinants of maternal speech style. In K. E. Nelson (Ed.), *Child Language* (Vol. 5, pp. 247-290). Hillsdale, NJ: Lawrence Erlbaum Associates.
- DeCasper, A. J., & Fifer, W. P. (1980). Of human bonding: Newborns prefer their mother’s voices. *Science, 208*, 1174-1176.
- Dilley, L., & Bergeson, T. R. (2010). *Mothers’ use of exaggerated vowel space in speech to hearing-impaired infants with hearing aids or cochlear implants*. Paper presented at the 11th International Conference on Cochlear Implants and Other Implantable Auditory Technologies, Stockholm, Sweden.
- Ferguson, C. A. (1964). Baby talk in six languages. *American Anthropologist, 66*, 103-114.
- Fernald, A. (1989). Intonation and communicative intent in mothers’ speech to infants: Is the melody the message? *Child Development, 60*, 1497-1510.
- Fernald, A. (1992). Meaningful melodies in mothers’ speech to infants. In H. Papoušek, U. Juergens & M. Papoušek (Eds.), *Nonverbal vocal communication: Comparative and developmental approaches* (pp. 262-282). Cambridge, United Kingdom: Cambridge University Press.
- Fernald, A., & Kuhl, P. (1987). Acoustic determinants of infant preference for motherese speech. *Infant Behavior and Development, 10*, 279-293.
- Fernald, A., & Simon, T. (1984). Expanded intonation contours in mothers’ speech to newborns. *Developmental Psychology, 20*(1), 104-113.

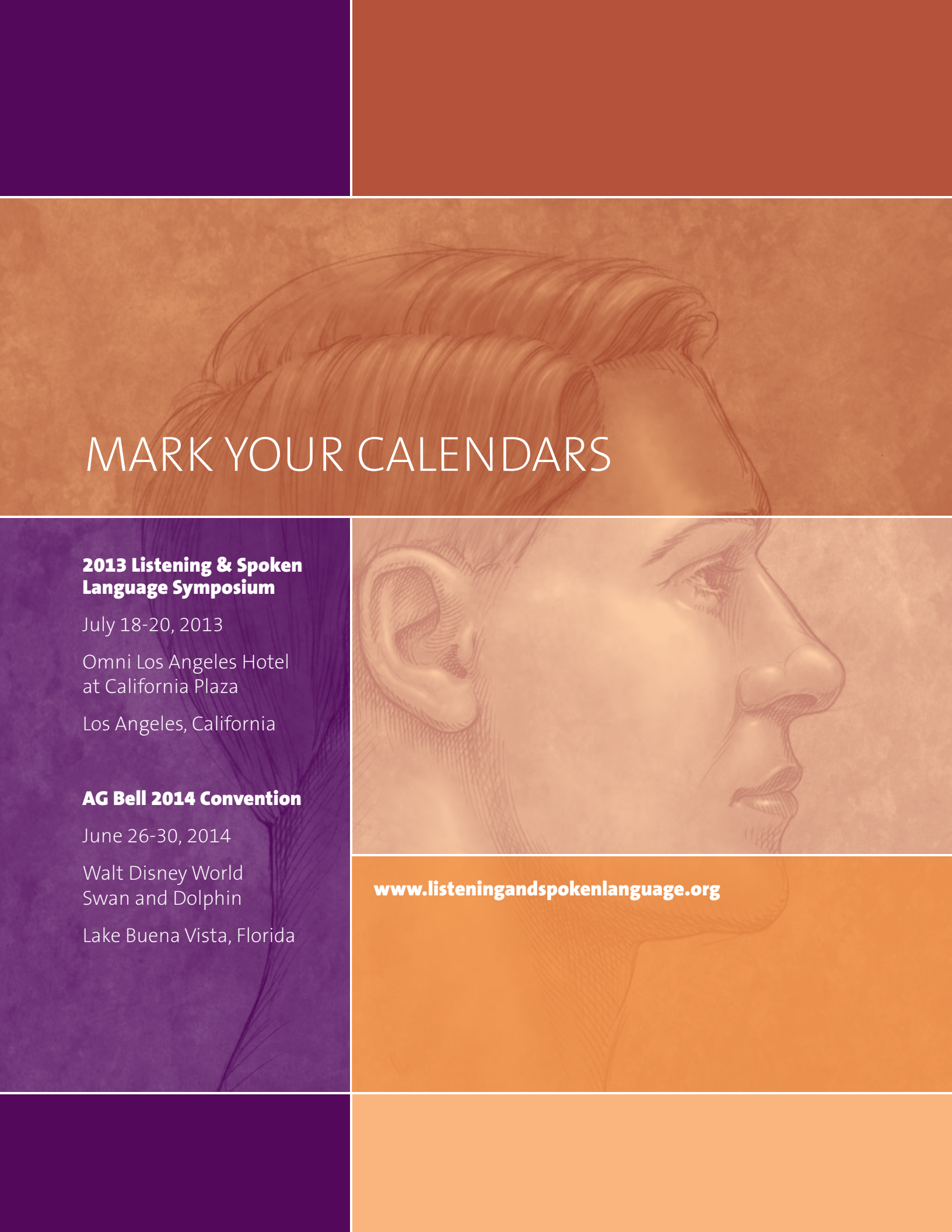
- Fernald, A., Taeschner, T., Dunn, J., Papoušek, M., Boysson-Bardies, B. D., & Fukui, I. (1989). A cross-language study of prosodic modifications in mothers' and fathers' speech to preverbal infants. *Child Language, 16*, 477-501.
- Fu, Q. J., Chinchilla, S., & Galvin, J. J. (2004). The role of spectral and temporal cues in voice gender discrimination by normal-hearing listeners and cochlear implant users. *Journal of the Association for Research on Otolaryngology, 5*, 253-260.
- Goldin-Meadow, S., & Saltzman, J. (2000). The cultural bounds of maternal accommodation: How Chinese and American mothers communicate with deaf and hearing children. *Psychological Science, 11*(4), 307-314.
- Goss, R. N. (1970). Language used by mothers of deaf children and mothers of hearing children. *American Annals of the Deaf, 115*(2), 93-96.
- Grieser, D. L., & Kuhl, P. K. (1988). Maternal speech to infants in a tonal language: Support for universal prosodic features in motherese. *Developmental Psychology, 24*(1), 14-20.
- Hart, B., & Risley, T. R. (1995). *Meaningful differences in the everyday experience of young American children*. Baltimore, MD: Paul H. Brookes.
- Henggeler, S. W., & Cooper, P. F. (1983). Deaf child-hearing mother interaction: Extensiveness and reciprocity. *Journal of Pediatric Psychology, 8*(1), 83-95.
- Kaplan, P. S., Bachorowski, J. A., Smoski, M. J., & Hudenko, W. J. (2002). Infants of depressed mothers, although competent learners, fail to learn in response to their own mothers' infant-directed speech. *Psychological Science, 13*(3), 268-271.
- Kisilevsky, B. S., Hains, S. M. J., Lee, K., Xie, X., Huang, H., Ye, H. H., et al. (2003). Effects of experience on fetal voice recognition. *Psychological Science, 14*(3), 220-224.
- Kitamura, C., Thanavishuth, C., Burnham, D., & Luksaneeyanawin, S. (2002). Universality and specificity in infant-directed speech: Pitch modifications as a function of infant age and sex in a tonal and non-tonal language. *Infant Behavior and Development, 24*, 372-392.
- Koester, L. S., Brooks, L. R., & Karkowski, A. M. (1998). A comparison of the vocal patterns of deaf and hearing mother-infant dyads during face-to-face interactions. *Journal of Deaf Studies and Deaf Education, 3*(4), 290-301.
- Koester, L. S., Karkowski, A. M., & Traci, M. A. (1998). How do deaf and hearing mothers regain eye contact when their infants look away? *American Annals of the Deaf, 143*(1), 5-13.
- Kondaurova, M. V., & Bergeson, T. R. (2011). The effects of age and infant hearing status on maternal use of prosodic cues for clause boundaries in speech. *Journal of Speech, Language, and Hearing Research, 54*(3), 740-754.
- Kondaurova, M. V., Bergeson, T. R., & Dilley, L. (in press). Effects of deafness on acoustic characteristics of American English tense/lax vowels in maternal speech to infants. *Journal of the Acoustic Society of America*.
- Kondaurova, M. V., Bergeson, T. R., & Xu, H. (2012). *Age-related changes in prosodic features of maternal speech to prelingually deaf infants with cochlear implants*. Paper presented at the International Conference on Infant Studies, Minneapolis, MN.
- Kuhl, P. K., Andruski, J. E., Chistovich, I. A., Chistovich, L. A., Kozhevnikova, E. V., Ryskina, V. L., et al. (1997). Cross-language analysis of phonetic units in language addressed to infants. *Science, 277*(5626), 684-686.
- Liu, H.-M., Kuhl, P. K., & Tsao, F.-M. (2003). An association between mothers' speech clarity and infants' speech discrimination skills. *Developmental Science, 6*(3), F1-F10.
- Meadow-Orlans, K. P., & Spencer, P. E. (1996). Maternal sensitivity and the visual attentiveness of children who are deaf. *Early Development and Parenting, 5*, 213-223.
- Meadow-Orlans, K. P., Spencer, P. E., & Koester, L. S. (2004). *The world of deaf infants: A longitudinal study*. New York: Oxford University Press, Inc.
- Nienhuys, T. G., Cross, T. G., & Horsborough, K. M. (1984). Child variables influencing maternal speech style: Deaf and hearing children. *Journal of Communication Disorders, 17*(3), 189-207.
- Peterson, N. R., Pisoni, D. B., & Miyamoto, R. T. (2010). Cochlear implants and spoken language processing abilities: Review and assessment of the literature. *Restorative Neurology and Neuroscience, 28*(2), 237-250.
- Pisoni, D. B., Cleary, M., Geers, A. E., & Tobey, E. A. (1999). Individual differences in effectiveness of cochlear implants in children who are prelingually deaf: New process measures of performance. *The Volta Review, 101*(3), 111-164.
- Pisoni, D. B., Conway, C. M., Kronenberger, W. G., Horn, D. L., Karpicke, J., & Henning, S. C. (2008). Efficacy and effectiveness of cochlear implants in deaf children. In M. Marschark & P. C. Hauser (Eds.), *Deaf cognition: Foundations and outcomes* (pp. 52-101). New York: Oxford University Press.
- Pressman, L. J., Pipp-Siegel, S., Yoshinaga-Itano, C., & Deas, A. (1999). Maternal sensitivity predicts language gain in preschool children who are deaf and hard of hearing. *Journal of Deaf Studies and Deaf Education, 4*(4), 294-304.
- Spencer, P. E., & Meadow-Orlans, K. P. (1996). Play, language, and maternal responsiveness: A longitudinal study of deaf and hearing impaired infants. *Child Development, 67*, 3176-3191.
- Stern, D. N., Spieker, S., Barnett, R. K., & MacKain, K. (1983). The prosody of maternal speech: Infant age and context related changes. *Journal of Child Language, 10*, 1-15.
- Thiessen, E. D., Hill, E. A., & Saffran, J. R. (2005). Infant-directed speech facilitates word segmentation. *Infancy, 7*(1), 53-71.
- Vongpaisal, T., Trehub, S. E., Schellenberg, E. G., van Lieshout, P., & Papsin, B. (2010). Children with cochlear implants recognize their mother's voice. *Ear & Hearing, 31*, 555-566.
- Wedell-Monnig, J., & Lumley, J. M. (1980). Child deafness and mother-child interaction. *Child Development, 51*, 766-774.



ABOUT THE AUTHOR

Tonya R. Bergeson-Dana, Ph.D., is an associate professor, Philip F. Holton Investigator, and co-director of the Babytalk Research Laboratory in the Department of Otolaryngology-Head & Neck Surgery at the Indiana University School of Medicine in Indianapolis, Ind. She received undergraduate degrees in music

theory and psychology from Northwestern University, and an M.A. and Ph.D. in cognitive psychology from the University of Toronto. Bergeson is currently interested in three areas of research: the effects of hearing loss and subsequent amplification via hearing aids or cochlear implants on mothers' speech to infants with mild to profound hearing loss; the development of multimodal perception skills in infants who are deaf following amplification; and the effects of cochlear implantation and hearing experience on music perception and production in infants, children, and adults. She is particularly interested in the effects of early experience on developing language and auditory perception.



MARK YOUR CALENDARS

2013 Listening & Spoken Language Symposium

July 18-20, 2013

Omni Los Angeles Hotel
at California Plaza

Los Angeles, California

AG Bell 2014 Convention

June 26-30, 2014

Walt Disney World
Swan and Dolphin

Lake Buena Vista, Florida

www.listeningandspokenlanguage.org

High frequency measures of OHC nonlinear capacitance (NLC) and their significance: Why measures stray away from predictions

Joseph Santos-Sacchi

Citation: [AIP Conference Proceedings](#) **1965**, 060004 (2018); doi: 10.1063/1.5038477

View online: <https://doi.org/10.1063/1.5038477>

View Table of Contents: <http://aip.scitation.org/toc/apc/1965/1>

Published by the [American Institute of Physics](#)

Corrigendum: “High Frequency Measures of OHC Nonlinear Capacitance (NLC) and their Significance: Why Measures Stray Away from Predictions,” Joseph Santos-Sacchi, AIP Conference Proceedings **1965**, 060004 (2018)

At the request of the author and the conference editor an updated version of this article was published on 29 June 2018. Due to a processing error, the original editorial version supplied to AIP Publishing excluded Figure 2. This error has been corrected in the updated and re-published article.

High Frequency Measures of OHC Nonlinear Capacitance (NLC) and their Significance: Why Measures Stray Away from Predictions

Joseph Santos-Sacchi

Departments of Surgery, Neuroscience, and Cellular and Molecular Physiology
Yale University School of Medicine
333 Cedar St., BML 244
New Haven, Ct 06510

joseph.santos-sacchi@yale.edu

Abstract Measures of membrane capacitance (C_m) can be used to assess important characteristics of voltage-dependent membrane proteins (e.g., channels and transporters). In particular, a protein's time-dependent voltage-sensor charge movement is equivalently represented as a frequency-dependent component of C_m , telling much about the kinetics of the protein's conformational behavior. Recently, we have explored the frequency dependence of OHC voltage-dependent capacitance (aka nonlinear capacitance, NLC) to query rates of conformational switching within prestin (SLC26a5), the cell's lateral membrane molecular motor¹. Following removal of confounding stray capacitance effects, high frequency C_m measures using wide-band stimuli accurately reveal unexpected low pass behavior in prestin's molecular motions.

INTRODUCTION

The outer hair cell (OHC) powers a feedback process within the cochlea that augments hearing sensitivity by 40 to 60 decibels, termed cochlear amplification². The molecular basis of this process resides within the lateral plasma membrane of that cell, where millions of unusual motor proteins, known as prestin (SLC26a5)³, contribute to force generation. Activation of the motor protein by voltage (*in vivo*, the receptor potential) evokes two characteristic, measurable responses; these are a mechanical response called electromotility (eM)⁴⁻⁷, and a corresponding electrical response. The latter is commonly called NonLinear Capacitance (NLC), and results from the restricted charge movement of the motility voltage sensor within the plasma membrane, normal to membrane's electric field^{8,9}. This phenomenon is similar to gating/sensor charge movements driving opening/closing of voltage dependent ion channels¹⁰. NLC has been used as a surrogate of OHC mechanical activity because of its relative ease of measurement; since eM has been measured beyond 80 kHz¹¹, sensor movement effecting eM is expected to be extremely rapid.

Though the usefulness of membrane capacitance (C_m) measurement dates from the time of Frick¹², its general applicability has grown tremendously since patch clamp technology blossomed¹³. Because of the widespread interest in neurotransmitter release, techniques were developed to assess vesicle membrane fusion by monitoring the surface area of the membrane during fusion. Because the plasma membrane acts as a linear capacitor (C_{lin}) proportional to

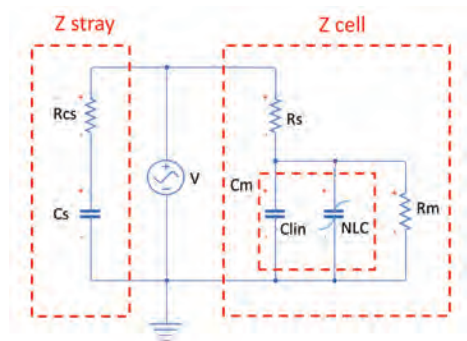


FIGURE 1. Electrical model of patch-clamped OHC. Electrode resistance (R_s), membrane resistance (R_m), membrane capacitance (C_m), composed of linear (C_{lin}) and nonlinear capacitance (NLC). Stray capacitance is modeled as series of R_{cs} and C_s . Model is stimulated with sinusoidal voltage, V .

surface area, synaptic vesicle fusion can be monitored by focusing on changes in linear membrane capacitance^{14, 15}. C_m measures have also been useful for estimating electrical coupling of cells through gap junctions^{16, 17}.

Linear C_m Measurement Approaches

Figure 1 shows the standard simple schematic of a voltage-clamped biological cell, in the case of an OHC, with an additional parallel voltage-dependent capacitance (NLC). The electrode resistance (R_s) limits the voltage (V) imposed across the cell membrane in time and magnitude. Roughly, the speed with which a voltage command can be delivered to the membrane is limited in time by $R_s * C_m$, the clamp time constant (τ_{clamp}), with a step voltage command slowly rising to a maximum of $R_m / (R_s + R_m) * V$. The actual τ_{clamp} is $C_m * (R_s * R_m / (R_s + R_m))$, but since R_s is usually much less than R_m the approximation may hold. Thus, in evaluating the effectiveness of the voltage command, τ_{clamp} and attenuation by the voltage divider effect must be considered. Additionally, stray capacitance (e.g., from the pipette and holder, and residual within the patch clamp amplifier), modelled in **Fig. 1** as a series combination of R_{cs} and C_s , needs to be cancelled by patch amplifier compensation circuitry. With just R_s , R_m and C_m , the circuit is simple, and assuming linear components (no NLC), C_m can be estimated accurately.

One method to estimate surface area under voltage clamp relies on monitoring the capacitive currents that arise from changes in membrane capacitance, namely, the AC voltage-evoked currents measurable at the phase angle of the partial derivative $\delta Y / \delta C_m$. Since the introduction of admittance analysis of C_m , the phase angle of $\delta Y / \delta C_m$ had been estimated by techniques requiring dithering of either patch clamp capacitance compensation circuitry (effectively altering C_s) or by dithering an R_s increment to arrive at estimates of the proper phase angle¹⁸. These methods provide measuring angles that are only estimates, and consequently changes in resistive currents (i.e., resulting from changes in membrane or electrode resistances) may influence attempts to measure capacitive currents. In 2004¹⁹, a simple method not relying on dithering and providing the exact identification of $\delta Y / \delta C_m$ and its angle was developed. This was based on the identity between the angles of $\delta Y / \delta C_m$ and $\delta Y / \delta \omega$. Thus, using two simultaneous voltage frequencies to measure membrane currents, the angle of $\delta Y / \delta C_m$ at one of those frequencies can be obtained and used to measure capacitive currents directly and accurately. However, a calibration during experiments is required to get at absolute C_m values.

Another method, which I developed in 1991, also used dual frequency stimulation²⁰. The method arose in a proposal to measure OHC C_m *in vivo*, and the following description is taken from my funded NIH grant proposal (R01 DC02003, submitted in 1992).

.... In the present experiment, a discrete frequency analysis will be attempted. Pusch and Neher (1988) have used a single "tone" (sine wave, actually) technique to determine cell characteristics under whole cell voltage clamp. By injecting a sinusoidal voltage into a cell, and measuring the current response, they calculated from the system's impedance, the cell capacitance, resistance and electrode resistance.

.... with the use of one "tone" (ω), it is necessary to obtain an independent estimate of the input resistance (b). However, the utilization of a "two tone" (ω_1 and ω_2) stimulus allows one to determine all parameters, given the signal and response. That is, b need not be determined independently, and can be solved for, since, for example, R_s is the same at any two frequencies. The evaluations should work under voltage clamp or current clamp ...

The component solutions at the harmonic angular frequencies ω_n , $n=0, 1$ are

$$R_{sn} = \frac{a_n - \beta}{a_n^2 + b_n^2 - a_n \beta} \quad (1)$$

$$R_{mn} = \frac{1((a_n - \beta)^2 + b_n^2)}{b(a_n^2 + b_n^2 - a_n \beta)} \quad (2)$$

$$C_{mn} = \frac{1}{(\omega_n b_n)} \frac{(a_n^2 + b_n^2 - a_n \beta)^2}{((a_n - \beta)^2 + b_n^2)} \quad (3)$$

where from the measured input admittance Y_{in} we obtain

$$Y_{cell\omega_n} = Y_{in\omega_n} - Y_{stray\omega_n}, n = 0,1 \quad (4)$$

$$a_n = Re(Y_{cell\omega_n}) \quad (5)$$

$$b_n = Im(Y_{cell\omega_n}) \quad (6)$$

$$c_n = a_n^2 + b_n^2 \quad (7)$$

$$\beta = -0.5 \times \frac{-c_1 + c_0 + \sqrt{c_1^2 - 2c_1c_0 + c_0^2 - 4a_1a_0c_1 + 4a_1^2c_0 + 4a_0^2c_1 - 4a_0a_1c_0}}{a_1 - a_0} \quad (8)$$

Thus, membrane currents evoked by two voltage frequencies can be used to solve for R_s , R_m and C_m , even in the face of resistive changes, but only in the absence of stray capacitance. Nevertheless, it is prudent, if not imperative under many circumstances, that ionic conductances be blocked when actually measuring C_m .

In 2006, Farrell, Do Shope and Brownell²¹ devalued this electrical dual-sine admittance approach²⁰ for estimation of C_m at high frequencies given the standard model of the patch-clamped cell, without stray capacitance (**Fig.1**). This devaluation has hindered the application of such admittance measures to high frequencies. They reasoned that as angular frequency (ω) increases, estimates of C_m derived from the imaginary component of circuit admittance, $Im(Y)$, namely $Im(Y)/\omega$, provides inaccurate estimates of C_m . Only when $R_m \gg R_s$ and $\omega \rightarrow 0$ does *this* calculation provide reasonable values, as expected. But, this estimate of model C_m across stimulating frequency is inappropriate. We previously showed¹⁹ that, with no circuit simplifications, $Im(Y)$ must be divided by the absolute value of the partial derivative $\delta Y / \delta C_m$ to obtain correct values of C_m , regardless of model component values and interrogating frequency.

Figure 2A illustrates the interrogating frequency dependence of these measurement techniques in a model cell (R_s : 10 M Ω ; R_m : 100 M Ω ; C_m : 30 pF) without stray capacitance; only $Im(Y)/\omega$ provides incorrect estimates. **Figure 2B** shows the effects of stray capacitance on dual-sine estimates. In fact, not only is C_m erroneously estimated but R_s is, as well. Thus, in order to evaluate frequency-dependent effects on linear and nonlinear components of C_m , we must remove stray capacitance at each of our interrogating frequencies, else our estimates are wrong. The linear component of C_m , i.e., C_{lin} , as well as R_s , should be frequency invariant.

OHCs and Models with NLC

Using small signal analysis where the sinusoidal voltage perturbation is small relative to inherent nonlinearities, C_m , including C_{lin} and NLC, at any given holding voltage can be measured. Subsequent Boltzmann fits of C_m vs. holding voltage can then accurately assess the voltage dependence of NLC⁹, which rides atop the linear (surface-area dependent) C_{lin} . In order to glean frequency dependent behavior, wideband stimuli (e.g., voltage chirps) are delivered to the cell and the real and imaginary components of the current response extracted by FFT. Harmonic components across frequency are analyzed with the dual-sine approach. **Figure 3** shows NLC extracted across stimulating frequency in an OHC, using sums of

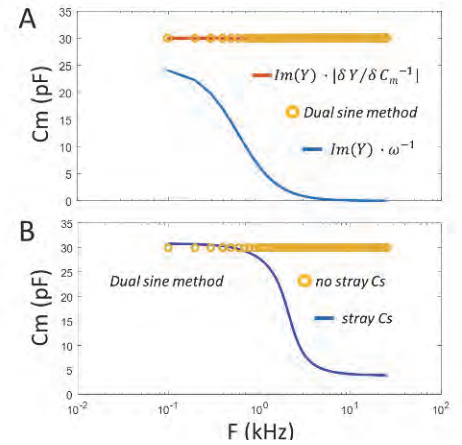


FIGURE 2. Robust frequency measures of model C_m . A) $Im(Y)/\omega$ is inappropriate to extract C_m across stimulation frequency for a model lacking stray capacitance. B) Stray capacitance must be removed to accurately measure C_m with dual-sine approach.

discrete sinusoidal (A) or chirp (B) stimuli. We balance out stray capacitance with patch clamp capacitance compensation controls to ensure that linear capacitance at depolarized holding potentials, where NLC is minimal, is linear across frequency, as required. Note that contrary to prevailing dogma, the results indicate that prestin sensor charge movements has low pass behavior. Indeed, we have developed a kinetic model that very nicely accounts for these data, and incorporates an essential chloride binding step preceding voltage dependent transitions in prestin¹ that underlies its low pass characteristics.

OHCs are fragile, and extreme voltage excursions during experiments (± 200 mV) required for full characterization of prestin's shallow voltage dependence can cause loss of recordings. Indeed, the requirement to balance out stray capacitance prior to frequency interrogation involves holding the cell at very depolarized levels where C_{lin} dominates. Cells are often compromised by such procedures. Fortunately, corrections for stray capacitance can be done post-hoc. To illustrate, we present such an approach in a MATLAB Simulink model that incorporates both NLC and stray capacitance.

Figure 4 illustrates model C_m magnitude versus voltage across frequency obtained by chirp analysis, as above. In **Fig. 4A**, NLC capacitance is modeled as the first derivative of a 2-state Boltzmann Q-V function, with no inherent frequency dependence. While prestin NLC involves molecular kinetics that engender frequency dependence, the present electrical model (**Fig. 4B**) provides frequency dependence of NLC by an additional series resistance, R_f . This electrical modelling approach has been used previously to characterize frequency dependence of Na channel voltage sensor charge movement²² and OHC NLC⁹. Consequently, C_m shows a low pass characteristic. In **Fig. 4C**, stray capacitance is introduced and this seriously distorts the measurements deriving from

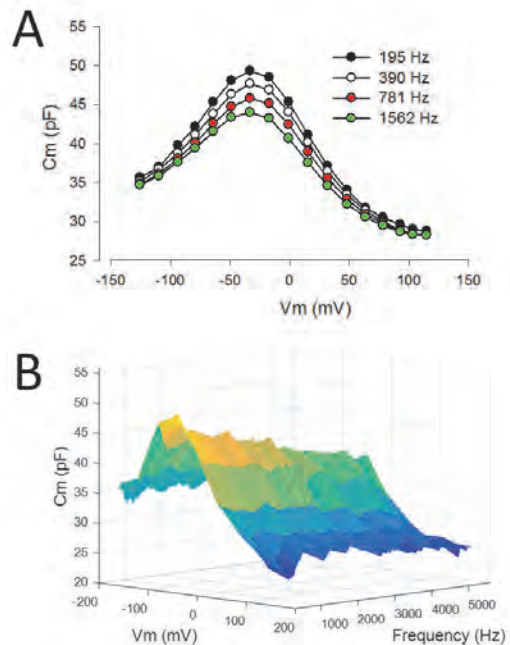


FIGURE 3. Frequency dependence of OHC NLC is revealed using the dual-sine measurement approach. A) Discrete sinusoidal stimulation shows reduction of peak NLC while C_{lin} remains constant. B) Chirp analysis provides better frequency resolution and limits stimulation times, which preserve cellular health during an experiment. No averaging.

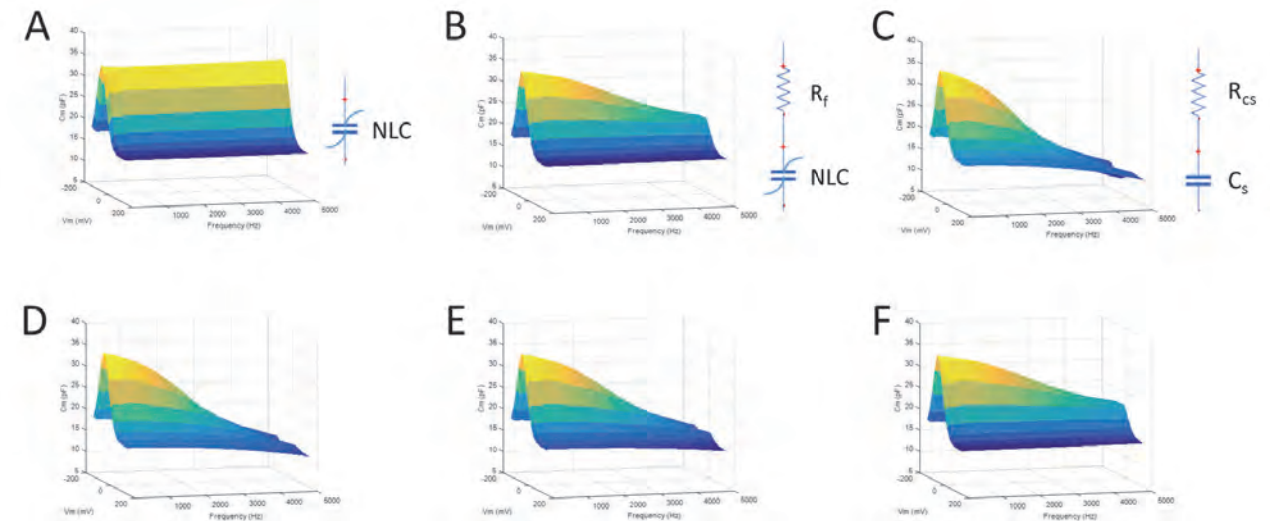


FIGURE 4. Model C_m frequency dependence can be extracted by correcting for stray capacitance post-hoc. See text for details.

dual-sine measures. In order to remove the effects of stray capacitance, and restore dual-sine measurement accuracy, estimates of stray capacitance are subtracted from the input admittance until the slopes of both R_s and C_m vs. frequency at the most depolarizing holding potential are zero. An automated fitting process accomplishes this. In **Figs. 4D** and **4E**, plots are shown depicting improvements in correction until in **Fig. 4F**, successful compensation for stray capacitance is achieved, as indicated by favorable comparisons between plots **Figs. 4B** and **4F**.

SUMMARY

Contrary to prevailing thought²¹, NLC can be measured accurately across stimulating frequency to extract the molecular kinetics of prestin. The ability to do so enables us to directly compare voltage-sensor charge movement, eM and force generation within a single OHC across frequency. Such studies are underway.

ACKNOWLEDGEMENTS

Support provided by NIH DC000273 and DC008130.

REFERENCES

1. J. Santos-Sacchi and L. Song, *Biophys. J.* **110**, 1-11 (2016).
2. J. Ashmore, P. Avan, W. E. Brownell, P. Dallos, K. Dierkes, R. Fettiplace, K. Grosh, C. M. Hackney, A. J. Hudspeth, F. Julicher, B. Lindner, P. Martin, J. Meaud, C. Petit, J. Santos-Sacchi and B. Canlon, *Hear. Res.* **266** (1-2), 1-17 (2010).
3. J. Zheng, W. Shen, D. Z. He, K. B. Long, L. D. Madison and P. Dallos, *Nature* **405** (6783), 149-155 (2000).
4. W. E. Brownell, C. R. Bader, D. Bertrand and Y. de Ribaupierre, *Science* **227** (4683), 194-196 (1985).
5. B. Kachar, W. E. Brownell, R. Altschuler and J. Fex, *Nature* **322** (6077), 365-368 (1986).
6. J. F. Ashmore, *J. Physiol.* **388**, 323-347 (1987).
7. J. Santos-Sacchi and J. P. Dilger, *Hear. Res.* **35** (2-3), 143-150 (1988).
8. J. F. Ashmore, *Neurosci. Res. Suppl.* **12**, S39-S50 (1990).
9. J. Santos-Sacchi, *J. Neurosci.* **11** (10), 3096-3110 (1991).
10. F. Bezanilla, *Nat.Rev.Mol.Cell Biol.* **9** (4), 323-332 (2008).
11. G. Frank, W. Hemmert and A. W. Gummer, *Proc. Natl. Acad. Sci. U. S. A.* **96** (8), 4420-4425 (1999).
12. H. Frick, *J.Gen.Physiol* **9**, 137-152 (1925).
13. E. Neher and A. Marty, *Proc. Natl. Acad. Sci. U. S. A.* **79** (21), 6712-6716 (1982).
14. M. E. Schnee, J. Santos-Sacchi, M. Castellano-Munoz, J. H. Kong and A. J. Ricci, *Commun. Integr. Biol.* **4** (6), 785-787 (2011).
15. M. E. Schnee, J. Santos-Sacchi, M. Castellano-Munoz, J.-H. Kong and A. J. Ricci, *Neuron* **70** (2), 326-338 (2011).
16. J. Santos-Sacchi, *Hear. Res.* **52** (1), 89-98 (1991).
17. H. B. Zhao and J. Santos-Sacchi, *J.Gen.Physiol* **112** (4), 447-455 (1998).
18. K. D. Gillis, in *Single Channel Recording*, edited by B. Sakmann and E. Neher (Plenum Press, New York, 1995), pp. 155-198.
19. J. Santos-Sacchi, *Biophys. J.* **87** (1), 714-727 (2004).
20. J. Santos-Sacchi, S. Kakehata and S. Takahashi, *J. Physiol.* **510** (Pt 1), 225-235 (1998).
21. B. Farrell, S. C. Do and W. E. Brownell, *Phys.Rev.E.Stat.Nonlin.Soft.Matter Phys.* **73** (4 Pt 1), 041930 (2006).
22. J. M. Fernandez, F. Bezanilla and R. E. Taylor, *J.Gen.Physiol* **79** (1), 41-67 (1982).

Intercellular communication in the supporting cells of the organ of Corti

Joseph Santos-Sacchi * and Peter Dallos

Auditory Physiology Laboratory (Audiology) and Department of Neurobiology and Physiology, Northwestern University, Evanston, Ill., U.S.A.

(Received 28 June 1982; accepted 25 October 1982)

We have directly tested the concept that the supporting cells of the organ of Corti are functionally coupled through gap junctions. *In vitro* and *in vivo* preparations were evaluated. Electrical measurements clearly show that the cells are coupled ionically. Voltage drops measured in neighboring cells in response to intracellular current injections indicate that current spread decays rapidly. Despite the existence of electrical coupling, fluorescent dye injection studies revealed no dye spread into adjacent cells, other than a few instances which were clearly artifactual. However, it is possible that dye spread is very slow and that dye in adjacent cells is diluted below visual detectability. In any case, dye coupling is remarkably poor compared to other electrically coupled tissues. The role of coupling in the supporting cells may be nutritive, considering the avascular nature of Corti's organ.

Key words: electrical coupling; dye coupling; organ of Corti.

Introduction

Over twenty years have passed since Furshpan and Potter [10] demonstrated that cytoplasmic communication can occur between individual cells. Subsequently, numerous studies have elucidated various details governing direct intercellular communication (for summaries see [17,22,14]). Indeed, in a variety of cell systems the existence of electrical as well as metabolic coupling has been established.

The cellular organelle thought to be responsible for such information transfer is the gap junction [11]. Its ultrastructure has been extensively studied by means of specific electronmicroscopic techniques, including freeze fracture and interstitial lanthanum infiltration [24,23,19]. However, despite the good correlation between intercellular coupling and the presence of gap junctions, the existence of gap junctional structures is not proof of electrical and/or metabolic coupling. For example, it is known that gap junctional structure is maintained following certain

* Present address and reprint requests: Department of Anatomy, Neurobiology Laboratory, Medical School, University of Puerto Rico, Old San Juan, PR 00901, U.S.A.

treatments which electrically uncoupled cells (e.g. glutaraldehyde, DNP, Li) ([25]; however, see [21]). Furthermore, Gulley and Reese [12], using freeze-fracture techniques, were able to find structures normally associated with gap junctions on the lateral walls of outer hair cells, which were exposed to the fluid filled spaces of Nuel. Clearly, as has been cautioned by Detwiler and Hodgkin [7], the electronmicroscopic demonstration of gap junctions is not sufficient to establish the existence or degree of intercellular coupling.

Several studies have indicated the presence of gap junctions in the adult mammalian inner ear [16,15,12]. An extensive array of gap junctions was demonstrated between all the supporting cells of the chinchilla and guinea pig organ of Corti. Freeze fracture revealed typical plaque-like structures and expansive areas of intramembranous particles. These results led to the conclusion that the supporting cells of the organ of Corti are electrically and metabolically coupled – a significant concept considering the metabolic demands and electrical activity of the organ. However, a direct evaluation of this proposal has never been attempted. We report here the results of experiments designed to evaluate such presumed intercellular coupling.

Materials and Methods

Animal preparations

In vivo. Young adult albino guinea pigs were used. This preparation has been previously described [5]. Briefly, after induction with urethane anesthesia, the animals were tracheotomized and the cochleas exposed through a ventrolateral approach. A fenestra was made in the bone over the stria vascularis in the third turn of the cochlea. Microelectrodes were inserted through the stria vascularis and the endolymphatic space into the supporting cells of the organ of Corti.

In vitro. Animals were decapitated after anesthetic induction and their cochleas removed. Two methods were employed to obtain specimens. Individual turns of the cochlea (stria vascularis removed) were microdissected out for study. Alternatively, only the bony capsule from the two apical most turns was removed. In this case the cochlea in toto, endolymphatic duct intact, was incubated in a microscope perfusion chamber. Electrode penetrations were made through Reissner's membrane into the supporting cells of the organ of Corti under visual control.

Electrophysiology

Electrodes were fabricated with a Brown–Flaming puller. Resistance of electrodes when filled with 3 M KCl ranged from 50 to 225 M Ω , with the mode around 120 M Ω . Lucifer Yellow, Procion Yellow, Niagara Sky Blue and 6'-carboxyfluorescein-filled electrodes were used for dye injection studies. Current pulses (–0.25 to –4 nA) were used to inject the fluorescent dyes.

For in vivo electrical coupling studies, double-barreled electrodes were made with tip-to-tip distances of 15–30 μ m. One electrode was bent according to the method of Hudspeth and Corey [13] so that the two electrode shanks could be placed parallel to

each other and epoxied together. This enabled us to penetrate adjacent Hensen's cells (diameter 15–25 μm) despite the inability to directly visualize the cells hidden beyond the stria vascularis. A stepping motor drive (Transvertex AB., Sweden) was used to advance the electrode assembly through the stria vascularis and into the organ of Corti's supporting cells.

For *in vitro* electrical coupling studies, separate micromanipulators were used to place the electrodes into neighboring supporting cells. Tissue was perfused with M199 culture medium (Gibco, Long Island, N.Y., U.S.A.) with modified Hank's salts (1.3 mg/100 ml Na_2HCO_3 , 10 mM Hepes, adjusted to pH 7.4 after equilibration with 5% CO_2 /95% O_2). The microscope perfusion chamber was maintained at $37 \pm 1^\circ\text{C}$. The cells were visualized and photographed with a Zeiss Standard microscope, equipped for epifluorescence.

Recordings and dye injections were made with either a commercial high-input impedance, capacitance-compensated amplifier (Mentor) or a dual-channel device constructed according to Fein [8] utilizing AD545 operational amplifiers (Analog Devices, Mass., U.S.A.). Both devices are capable of recording during current injection. Data were plotted on a strip chart recorder and in some instances electrical coupling was analyzed using a signal averager (Nicolet).

Cell input resistance was measured by injecting small negative currents (-0.25 to -1 nA) through the recording electrode and measuring the voltage drop across the cell membrane. Electrode resistance was linear in this current range. Current pulses from -1 to -10 nA were used to evaluate cell coupling. Coupling indices include coupling ratio (voltage drop in cell 2/voltage drop in cell 1, in response to current injected into cell 1; [1]) and mutual resistance (voltage drop in cell 2/current injected into cell 1; [7]).

Hensen's cells remained in good condition for up to several hours *in vitro*, as evidenced by interference optics and resting potentials. Experiments were completed before swelling and autolysis occurred, and they typically lasted from 1 to 2 h.

Light microscopy

For *in vivo* experiments, cochleas were fixed from 1 to 2 h after dye injection. Fixative was either 4% paraformaldehyde in 0.1 M phosphate buffer, pH 7.4, or 2% glutaraldehyde in 0.1 M cacodylate buffer, pH 7.2. Desired portions of the cochlea were dissected out in buffer and either examined in surface mount or dehydrated in alcohols, embedded in Spurr and serially sectioned at about 12 μm . Injected cells were visualized with epifluorescence, using a BP450-490 nm exciting filter with a high-pressure mercury lamp. Photographs were taken with Kodak Ektachrome (ASA 200) and developed with the E-6 process (Unicolor). *In vitro* dye injection was monitored during experiments with brightfield and epifluorescence.

Results

In vivo

Upon passage through the stria vascularis in the *in vivo* preparation, the positive

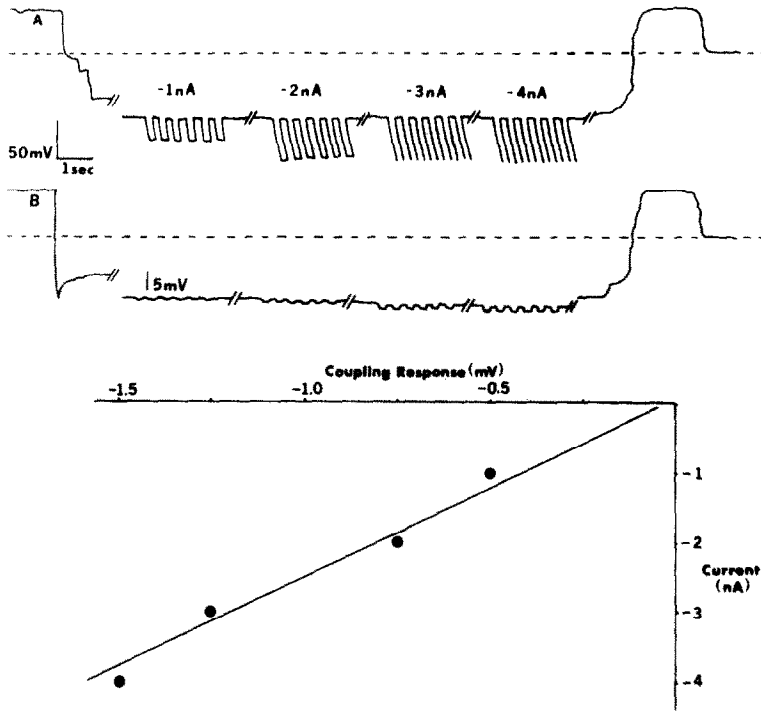


Fig. 1. Record of in vivo electrical coupling between adjacent Hensen's cells. Trace begins with electrode in endolymphatic space where the potential is near +70 mV. The sudden reversal of sign indicates that Hensen's cells are penetrated. Negative current pulses were injected in cell A at magnitudes of 1, 2, 3 and 4 nA. Bridge unbalancing in trace A indicates that cell A has an input resistance of 35 M Ω . Responses in cell B are linearly dependent upon current injection magnitude. Mutual resistance of these cells is 0.5 M Ω . The endolymphatic potential is again observed upon removal of electrodes from the cells, and after removal from the cochlear duct the potential drops to zero.

endocochlear potential is encountered (Fig. 1). After advancing the electrodes about 100–150 μ m further, the Hensen's cells are contacted. The stable membrane potentials averaged -70 ± 13 mV ($n = 87$). Input resistances are on the order of 35 ± 24 M Ω ($n = 37$). *

Fig. 1 illustrates the measurement of electrical coupling between adjacent Hensen's

* There is some evidence that the use of the single electrode technique to measure input resistance may overestimate the actual value by a factor of eight [27]. Apparently, the problem is that the resistance of the electrode must be taken into account in the calculations. Electrode resistance may increase preferentially inside the cell, thereby providing incorrect estimates of cell resistance. It would appear that if the electrode resistance does change preferentially inside the cell, the value of that change might be dependent upon the initial resistance of the electrode. A positive correlation between electrode resistance and Hensen's cell resistance might than be expected if the electrode were influencing the measurements. However, no such correlation was found in our measurements (Pearson $r = 0.013$).

cells. Membrane potentials of the cells are near -80 mV. Negative current pulses in cell A produce a voltage drop in that cell, proportional to its input resistance. Simultaneously, a voltage drop is noted in cell B. In this instance the voltage drop in cell B is considerably smaller than that in cell A, indicating a small but measurable coupling. The mutual resistance (see Materials and Methods) here is about 0.5 M Ω . Mutual resistances of up to about 1 M Ω have been found in the *in vivo* preparation. Mutual resistances with the current injecting electrode intracellular and the recording electrode immediately extracellular are typically less than 0.2 M Ω , indicating that spread is not through extracellular pathways. Fig. 1 also demonstrates that increasing the magnitude of the current injection produces a corresponding and proportional increase in cell B's response.

Despite the existence of electrical coupling, dye studies have failed to show spread into adjacent cells (Fig. 3a, b). Over 75 cells have been marked. Dye spread has occurred only on rare occasions when obvious mechanical trauma, i.e. from microdissecting prior to fixation, had been causal. Perhaps artifactual cytoplasmic bridges had formed between cells [4].

In vitro

An *in vitro* preparation was considered important in order to evaluate dye coupling fully. The direct visualization of dye injection under fluorescence microscopy eliminates the uncertainty associated with the processing required after *in vivo* injections. Initially, preparations for *in vitro* studies were obtained by microdissecting free the apical or third turn of the cochlea, after removing the stria vascularis. An

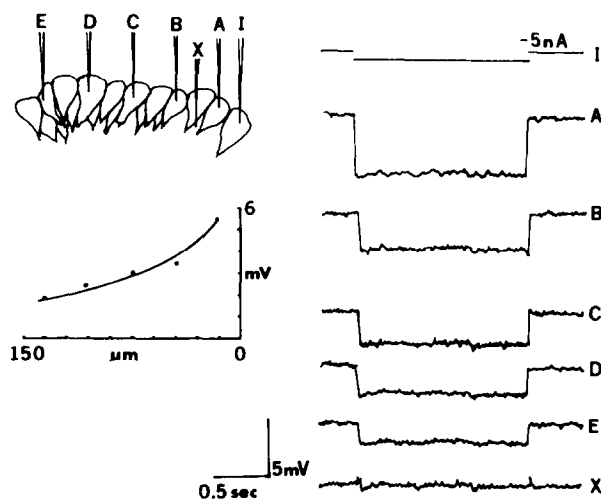


Fig. 2. Spatial analysis of electrical coupling in Hensen's cells *in vitro*. Current electrode *I* remained stationary while a roving electrode sampled intracellular responses to -5 nA current pulses at various inter-electrode distances. Responses were signal averaged. Response magnitudes indicate a fairly rapid decay as a function of inter-electrode distance, with a decay to one-third the adjacent cell response at about 130 μ m in this instance.

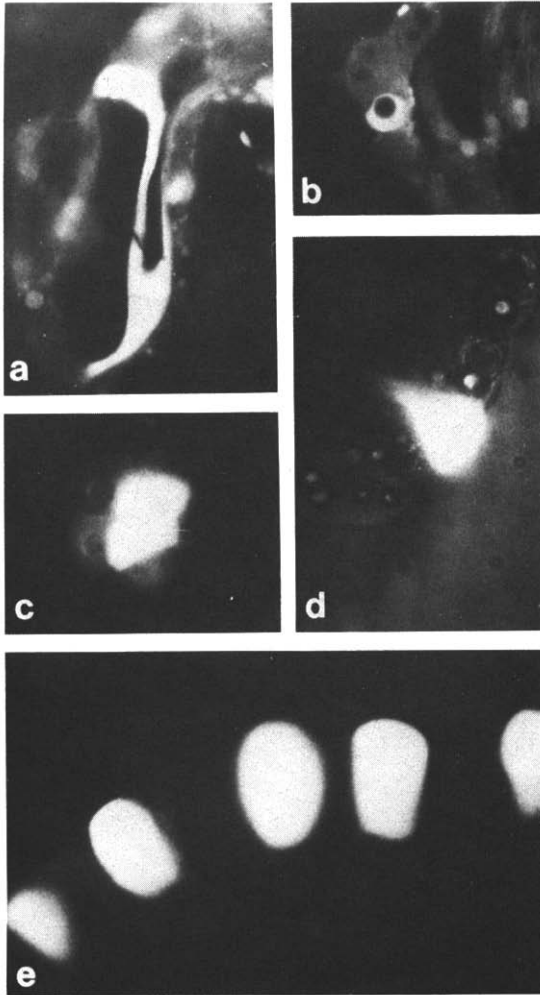


Fig. 3. (a) In vivo Procion Yellow injected outer pillar cell. Adjacent supporting cells above, below and in the plane of section were not stained. $800\times$. (b) In vivo Procion Yellow injected Hensen's cell. Note lipid vacuole is unstained. Adjacent cells demonstrate no detectable dye fluorescence. $470\times$. (c) In vitro Hensen's cells exhibiting Lucifer Yellow spread from a single injected cell. Five cells are stained. No spread was noted during dye injection (ca. 5 min). However, upon rebound of cells after difficult electrode removal, dye spread occurred within seconds. No further equilibration of dye occurred. $600\times$. (d) In vitro Lucifer Yellow injected Hensen's cell. Note lack of dye spread. This was typical of such experiments. Brightfield and epifluorescence. $600\times$. (e) In vitro preparation of Hensen's cells individually injected over a period of about 30 min. Each Lucifer Yellow injected cell is separated by an uninjected cell. $1000\times$.

analysis of these preparations revealed that cell potentials were depolarized as compared to in vivo preparations. Dye injections in these cells never demonstrated spread, except when physical trauma, e.g. difficult electrode removal, caused dye to enter adjacent cells (Fig. 3c).

By using a whole cochlea preparation, it is possible to maintain the functional integrity of the supporting cells of the inner ear. With endolymphatic duct intact, penetrations into Hensen's cells through Riessner's membrane permitted recordings of resting potentials (-63 ± 10 mV; $n = 111$) that were similar although statistically significantly different in magnitude to those measured in vivo (Student's *t*-test: $P < 0.001$). Electrical coupling was also similar to that in the in vivo preparation. Fig. 2 demonstrates coupling between Hensen's cells, as a function of inter-electrode distance. These data represent one of the better examples of spatial current spread. Current injecting electrode I remained stationary while the recording electrode sampled responses from cells at about 40 μm steps distal. The magnitude of the voltage drop in neighboring cells (Fig. 2A–E) in response to current injections (-5 nA, 1.5 s on–off) is dependent upon the distance from the current injected cell; the coupling response decays fairly rapidly as a function of increasing distance. The mutual resistance of the immediately adjacent coupled cells is about 1.0 $\text{M}\Omega$. Mutual resistances up to 2.0 $\text{M}\Omega$ have been found in this type of preparation. Note that the voltage drop in the extracellular space is miniscule (Fig. 2, X). Input resistance of these cells was also similar to that of cells in vivo.

Dye injections of Lucifer Yellow and 6'-carboxyfluorescein in over 75 cells demonstrated no dye spread into adjacent cells (Fig. 3d). The cells were observed for over an hour after injection. It was often possible to inject a row of single cells separated by uninjected cells (Fig. 3e).

Discussion

Electrical measurements clearly indicate that ionic coupling in the supporting cells of the organ of Corti is present both in vivo and in well maintained in vitro preparations. Coupling characteristics are similar for both preparations, showing mutual resistances around 1–2 $\text{M}\Omega$ for immediately adjacent Hensen's cells. Difficulty arises when attempts are made to determine coupling ratios because a single electrode was used to deliver current and measure voltage drops simultaneously. If the single electrode resistance measures were correct, this would mean that coupling ratios are poor. A comparison of mutual resistances of Hensen's cells and turtle retinal cones, for example [7], would seem to substantiate this contention. In these experiments, mutual resistances in better penetrations of neighboring cones averaged about 29 $\text{M}\Omega$ at a mean separation of 20 μm ; input resistance of cones were reported to be 24 $\text{M}\Omega$. Thus, turtle cones are much better coupled than Hensen's cells, if indeed measures of Hensen's cell input resistance are valid. *

* It is possible to obtain information on coupling ratios by comparing coupling responses in neighboring cells distal to the current electrode. That is, with a stationary current electrode and a roving measuring

Another indication of coupling efficiency is the analysis of spatial characteristics of intercellular current spread. At distances ranging from 2 to 9 Hensen's cell diameters ($\approx 45\text{--}130\ \mu\text{m}$) from the current injecting electrode, the coupling response is already about $1/3$ the response in the immediately adjacent cell. Sachs et al. [26] found a 50% reduction in coupling response magnitude from 3 to 5 cells distal in isolated gastric tubules. In contrast, Shueteze and Goodenough [29] demonstrated in the embryonic chick lens that the magnitude of the coupling response remained the same up to $80\ \mu\text{m}$ removed from the current injecting electrode. Furthermore, dye spread of intracellularly injected Lucifer Yellow is rapid and pervasive; it was reported that the whole chick lens can be stained given a sufficient length of time. Similar strong coupling has been found in other cell systems, e.g. insect gland epithelium and rat liver [18,20]. In rat liver, fluorescent dye spread occurs rapidly in over a dozen cells. This is in marked distinction from our dye studies.

About a decade ago it was thought that embryonic cells during certain developmental stages could maintain electrical coupling despite the inability to permit dye transfer [28,2,30]. A careful re-evaluation of this phenomenon has led Bennett et al. [4] to conclude that dye transfer does occur if cells are electrically coupled. The inability to observe dye spread, despite the presence of electrical coupling, in the supporting cells of the organ of Corti may represent a very slow passage of dye. However, it should be emphasized that observations were made up to several hours after dye injection. Yet it cannot be ruled out that such a slow spread would allow for dye dilution below visual detectability. Dye was observed in cells other than the injected ones only in those cases where supporting cells were physically traumatized, i.e. roughly manipulated. Spread in these instances was very rapid (less than 1 min) and may have been due to the artifactual formation of cytoplasmic bridges, although pathways through gap junctions cannot be dismissed. Nevertheless, dye coupling in the inner ear is clearly not at all like that in other well coupled cell systems, i.e. liver or lens.

Recently, Fraser and Bode [9] have shown that previous studies which demonstrated a lack of dye coupling in epithelial cells of *Hydra* [6] were due to dye injections into cellular vacuoles. It is important to note that this was not the case in our Hensen's cell studies. Although Hensen's cells in the apical and third turn of the guinea pig cochlea do contain large lipid vacuoles, cell penetrations always showed high negative resting potentials, and furthermore, after injection of dyes whole cells were filled but vacuoles were unstained.

The significance of electrical coupling in the supporting cells of the mammalian organ of Corti is obscure. Weiss et al. [31] have presented indirect evidence that hair

electrode, it has been found (e.g. Fig. 2) that voltage attenuation between Hensen's cells can be relatively low. Coupling ratios can be determined from this information and are found to average greater than 0.6. This indicates that input resistance of Hensen's cells may be *lower* than that measured directly with a single electrode. Attempts to measure input resistance with two electrodes have been difficult, but in a few presumably successful cases, measures have shown resistances below $10\ \text{M}\Omega$. In these cases adjacent cells have coupling ratios of about 0.5. Of course, it is possible that the penetration of cells the size of Hensen's cells with two electrodes may be injurious and reduce input resistance.

cells and supporting cells in the alligator lizard cochlea are electrically coupled. Thus, lateral hair cell interactions may be mediated through supporting cells in this case. However, in mammalia effects upon sensory transduction are apparently non-existent; no gap junctions are present between hair cells and supporting cells in the adult [16,15,12]. Furthermore, we have shown [5] that the magnitudes of receptor potentials of mammalian hair cells (inner and outer) are much larger than potentials recorded in any supporting cell type. Indeed, responses in intercellular spaces are also larger than in supporting cells, indicating that responses to sound in the latter are picked up from the extracellular space. The fact that spatial spread of current through supporting cells is not great further limits possible interactions.

A more likely role for intercellular communication in the organ is nutritive or metabolic. Such cooperation among the supporting cells may be requisite considering the avascular nature of Corti's organ proper. In fact, this may account for the continued survival of supporting cells under adverse conditions which destroy uncommunicating hair cells. A difficulty with this nutritive hypothesis is the consistent finding that dye spread is absent. The molecular weights of the fluorescent dyes used in this study are similar to those of many metabolites. Again, the inability to find dye spread may be due to very slow dye passage and dilution of dye below visual detectability. Further investigations are required to resolve this issue.

References

- 1 Bennett, M.V.L. (1966): Physiology of electronic junctions. *Ann. N.Y. Acad. Sci.* 137, 509–539.
- 2 Bennett, M.V.L. (1978): Junction formation and experimental modification. In: *Intercellular Junctions and Synapses*. Editors: J. Feldman, N.B. Gilula, and J.D. Pitts. Chapman and Hall, London.
- 3 Bennett, M.V.L., Spira, M.E. and Pappas, G.D. (1972): Properties of electrotonic junctions between embryonic cells of *Fundulus*. *Dev. Biol.* 29, 419–435.
- 4 Bennett, M.V.L., Spira, M.E. and Spray, D.C. (1978): Permeability of gap junctions between embryonic cells of *Fundulus*. A reevaluation. *Dev. Biol.* 65, 114–125.
- 5 Dallos, P., Santos-Sacchi, J. and Flock, A. (1982): Outer hair cells: Intracellular recordings. *Science* 218, 582–584.
- 6 De Latt, S.W., Tertoolen, L.G.J. and Grimmelikhuijzen, C.J.P. (1980): No junctional communication between epithelial cells in *Hydra*. *Nature (London)* 288, 711–713.
- 7 Detwiler, P.B. and Hodgkin, A.L. (1979): Electrical coupling between cones in turtle retina. *J. Physiol. (London)* 291, 75–100.
- 8 Fein, H. (1966): Passing current through recording glass micropipette electrodes. *IEEE Trans. BME-13*, 211–212.
- 9 Fraser, S.E. and Bode, H.R. (1981): Epithelial cells of *Hydra* are coupled. *Nature (London)* 294, 356–358.
- 10 Furshpan, E.J. and Potter, D.D. (1959): Transmission at the giant motor synapses of the crayfish. *J. Physiol. (London)* 143, 289–325.
- 11 Gilula, N.B., Reeves, O.R. and Steinbach, A. (1972): Metabolic coupling, ionic coupling and cell contacts. *Nature (London)* 235, 262–265.
- 12 Gulley, R.S. and Reese, T.S. (1976): Intercellular junctions in the reticular lamina of the organ of Corti. *J. Neurocytol.* 5, 479–507.
- 13 Hudspeth, A.J. and Corey, D.P. (1979): Controlled bending of high input resistance electrodes. *Am. J. Physiol.* 234, C56–C57.
- 14 Hertzberg, E.L., Lawrence, T.S. and Gilula, N.B. (1981): Gap junctional communication. *Annu. Rev. Physiol.* 43, 479–491.

- 15 Iurato, S., Franke, K., Luciano, L., Werbter, G., Pannese, E. and Reale, E. (1976): Intercellular junctions in the organ of Corti as revealed by freeze fracturing. *Acta Otolaryngol.* 82, 57–69.
- 16 Jahnke, K. (1975): The fine structure of freeze-fractured intercellular junctions in the guinea pig inner ear. *Acta Otolaryngol. Suppl.* 336.
- 17 Loewenstein, W.R. (1966): Permeability of membrane junctions. *Ann. N.Y. Acad. Sci.* 137, 441–472.
- 18 Loewenstein, W.R. and Kanno, Y. (1966): Studies on an epithelial (gland) cell junction. I. Modifications of surface membrane permeability. *J. Cell Biol.* 22, 565–586.
- 19 McNutt, N.S. and Weinstein, R.S. (1973): Membrane ultrastructure at mammalian intercellular junctions. *Prog. Biophys. Mol. Biol.* 26, 45–101.
- 20 Meyer, D.J., Yancey, S.B. and Revel, J.-P. (1981): Intercellular communication in normal and regenerating rat liver: A quantitative analysis. *J. Cell Biol.* 91, 505–523.
- 21 Perrachia, C. (1977): Gap junctions. Structural changes after uncoupling procedures. *J. Cell Biol.* 72, 628–641.
- 22 Pitts, J.D. (1978): Junctional communication and cellular growth control. In: *Intercellular Junctions and Synapses*. Editors: J. Feldman, N.P. Gilula, and J.D. Pitts. Chapman and Hall, London.
- 23 Revel, J.-P. and Karnovsky, M.J. (1967): Hexagonal array of subunits in intercellular junctions of mouse heart and liver. *J. Cell Biol.* 33, C7–C12.
- 24 Robertson, J.D. (1963): The occurrence of a subunit pattern in the unit membranes of club endings in Mauthner cell synapses in goldfish brains. *J. Cell Biol.* 19, 201–221.
- 25 Rose, B. (1971): Intercellular communication and some structural aspects of membrane junctions in a simple cell system. *J. Membrane Biol.* 5, 1–19.
- 26 Sachs, G., Shoemaker, R.L., Blum, A.L., Heflander, H.L., Makhlof, G.M. and Hirschowitz, B.I. (1971): Microelectrode studies of gastric mucosa and isolated gastric cells. In: *Electrophysiology of Epithelial Cells*. F.K. Schattauer Verlag, Stuttgart.
- 27 Schanne, O., Kawata, H., Schafer, B. and Lavalley, M. (1966): A study on the electrical resistance of the frog sartorius muscle. *J. Gen. Physiol.* 49, 897–912.
- 28 Slack, C. and Palmer, J.F. (1969): The permeability of intercellular junctions in the early embryo of *Xenopus laevis* studied with a fluorescent tracer. *Exp. Cell Res.* 55, 416–419.
- 29 Schuetze, S.M. and Goodenough, D.A. (1982): Dye transfer between cells of the embryonic chick lens becomes less sensitive to CO₂ treatment with development. *J. Cell Biol.* 92, 694–705.
- 30 Tupper, J.T. and Saunders, J.W. Jr. (1972): Intercellular permeability in the early *Asterias* embryo. *Dev. Biol.* 27, 546–554.
- 31 Weiss, T.F., Mulroy, M.J. and Altemann, D.W. (1974): Intracellular responses to acoustic clicks in the inner ear of the alligator lizard. *J. Acoust. Soc. Am.* 55, 606–619.

HRR 01107

Whole cell currents and mechanical responses of isolated outer hair cells

J. Santos-Sacchi and J.P. Dilger

Laboratory of Otolaryngology, UMDNJ, New Jersey Medical School, Newark, New Jersey, U.S.A. and Departments of Anesthesiology and Physiology and Biophysics, Health Sciences Center, State University of New York Stony Brook, New York, U.S.A.

(Received 8 March 1988; accepted 8 May 1988)

Outer hair cells (OHCs) exhibit electrically induced cell movements which are considered to enhance the frequency selectivity and sensitivity of basilar membrane vibration. Using simultaneous whole cell voltage clamp and video analysis, we demonstrate that the mechanical response of OHCs is not altered by agents which alter membrane currents under voltage clamp. Thus the underlying mechanism of OHC movements appears to be dependent upon membrane potential, rather than transmembrane currents.

Outer hair cell; Whole cell voltage clamp; Membrane current; OHC mechanical movements

Introduction

Major differences are known to exist between the two types of hair cells which populate the organ of Corti (see Dallos, 1985a). Whereas *in vivo* intracellular recordings have clearly shown that both inner and outer hair cells (OHCs) are capable of generating receptor potentials in response to acoustic stimulation (Dallos et al., 1982; Russell and Sellick, 1983), it is becoming increasingly clear that OHCs additionally function as effectors. The electrical activity of the OHCs is thought to modify the mechanical properties of these same cells and in turn influence organ of Corti micromechanics (Mountain, 1980; Siegal and Kim, 1982; Brown et al., 1983; Nuttall, 1985). Thus, an indirect micromechanical interaction between outer and inner hair cells may account for the exquisite tuning characteristics and sensitivity of the eighth nerve fibers, which predominantly innervate inner hair cells. It has been established that OHCs are capable of slow K^+ induced length changes (Zenner et al., 1985), and fast electrically induced, reversible cell movements on the order of micrometers (Brownell, 1983, 1984; Brownell et

al., 1985; Ashmore, 1986). Studies using isolated OHCs have shown that cell elongation or contraction begins within 200 μs of an applied voltage clamp stimulus, and that the direction of movement is polarity dependent (Brownell, 1983, 1984; Brownell and Kachar; Ashmore, 1986). Time- and voltage-dependent currents have been identified in OHCs using whole cell voltage clamp recording (Ashmore, 1986, Ashmore and Meech, 1986a, b; Santos-Sacchi and Dilger, 1986, 1988). It has been suggested that transmembrane currents are coupled to the fast mechanical responses of OHCs (Ashmore, 1986; Ashmore and Meech, 1986). We have directly tested this hypothesis by recording OHC whole cell currents under voltage clamp while simultaneously monitoring cell movement. We report here that manipulations which drastically reduce or reverse transmembrane current during voltage clamp, do not interfere with the OHC mechanical response, which remains a nearly linear function of applied voltage over much of its dynamic range.

Methods

OHCs were non-enzymatically isolated from guinea pig cochleas by gentle pipetting of the isolated top two turns of the organ of Corti. The cells were then transferred to a 700 μL perfusion chamber with a cover glass bottom. A Nikon

Correspondence to: J. Santos-Sacchi, Laboratory of Otolaryngology, UMDNJ-New Jersey Medical School, Newark, NJ 07103, U.S.A.

Diaphot inverted microscope, with Hoffmann optics, was used to observe the cells during electrical recording. Tissue culture Medium 199 with Hanks salts (GIBCO, NY; major ions: NaCl 137 mM, KCl 5.4 mM, CaCl₂ 1.3 mM, MgSO₄ 0.8 mM, with HEPES or bicarbonate buffer, pH 7.2) was used as the control perfusate. The same ion concentrations were used in test solutions except that NaCl was reduced to maintain osmolarity. Patch electrodes had initial resistances of 3–5 MΩ. Series resistance was typically between 10 and 15 MΩ, and was partially compensated during recording. Residual series resistance was estimated from current transients at the onset of voltage pulses and was corrected for during analysis (Marty and Neher, 1983). Pipette solutions were composed of 140 mM KCl or CsCl, 1 mM or 5 mM EGTA, 2 mM MgCl₂, and 5 mM HEPES buffered to pH 7.0–7.2. Both borosilicate and flint glass electrodes were used; flint glass provided better sealing. Giga-ohm seals were obtained at a location slightly above the nuclear level of the OHC membrane prior to whole cell recording.

OHCs were clamped to holding potentials near –60 mV, using a Dagan patch clamp amplifier. Under computer control, hyperpolarizing and depolarizing voltage pulses (50–500 ms), ranging from –100 to +100 mV, were used to elicit membrane currents and mechanical movements. Current records, filtered at 2 kHz with an 8 pole Bessel filter, were digitized and stored on a Data 6000 waveform analyzer, and saved to disk for off-line analysis. Simultaneously, cell movements were taped with a Panasonic AG6300 video recorder for later evaluation. OHC displacement reaches steady state several milliseconds after a voltage clamp step (Ashmore, 1986). Displacements of the cuticular plate region were measured from the video monitor after they had reached steady state. Two methods were employed, either manual measurement from digital still frames using a Toshiba digital VHS (14800 × monitor magnification) or measurement during playback using differential optoresistors (output filtered at 50 Hz) placed across the image of the cuticular plate on the monitor (2800 × monitor magnification). Still frame measurements were repeated at least five times and averaged. Standard deviations of these repeated measurements were about 0.16 μm. The

position of the cuticular plate was measured before, during, and after each voltage step. The linearity of the optoresistor method was confirmed by measuring the video taped movement of the tip of a microelectrode driven by a piezoelectric bimorph element. For the optoresistor method, absolute values were determined from manual measurements of cell displacements in response to the largest depolarizing voltage pulse. The movement of the cuticular plate is relative to the stationary insertion point of the electrode, which was typically near the nuclear region. However, upon depolarization, both the apical and basal ends of the OHC move towards the electrode insertion point. Thus, in order to account for total cell length change, the measured displacements of the cuticular region were multiplied by the ratio of total cell length to the electrode-cuticular plate distance, under the assumption that movement is linearly related to length of the cell.

Results

The resting membrane potential of isolated OHCs ranged from –10 to –68 mV with a mean

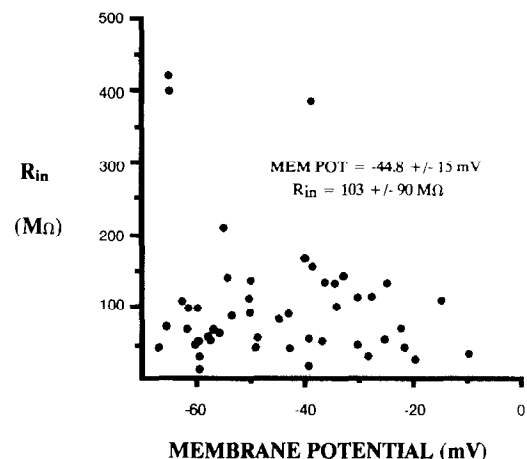


Fig. 1. Input resistance and membrane potential (+/- S.D.) for isolated OHCs whole cell recorded using pipettes containing 140 mM KCl solution. Input resistance was determined at a holding potential near –60 mV using –10 mV voltage steps. Membrane potential was determined by finding zero current level under voltage clamp or alternatively by directly measuring under current clamp. Measures were made a few minutes after the establishment of whole cell recording, i.e., following exchange of pipette and intracellular fluids.

A

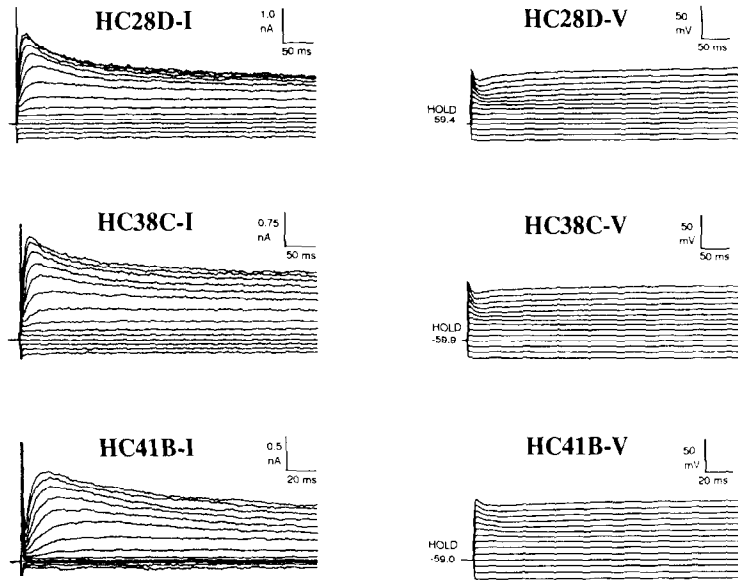


Fig. 2a. Examples of whole cell voltage clamp recordings from three isolated OHCs. Patch electrode contained 140 mM KCl solution. On the left are current traces in response to voltage steps from a holding potential near -60 mV (actual voltage listed in figure). Outward current is upward. On the right are the voltage step magnitudes corrected for estimates of residual series resistance. Depolarization is upward. Upon depolarization above -40 mV, a delayed outward current develops, the magnitude of which is voltage- and time-dependent. Current peaks within 20 ms after the onset of the voltage step, and inactivates slowly over hundreds of milliseconds. Note differences in time and current scales. Membrane potential (determined at zero current level) and input resistance (determined at the holding potential) of each cell: HC28D: -57 mV, 70 m Ω ; HC38C: -60 mV, 100 m Ω ; HC41C: -38 mV, 380 m Ω .

B

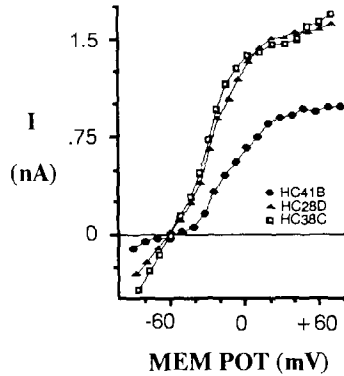


Fig. 2b. I-V plot for the three cells in Fig. 1a. Total transmembrane currents (no leak subtraction) measured at 200 ms. Note the outward rectification upon depolarization from the holding potential. The I-V curves begin to saturate above -10 mV.

C

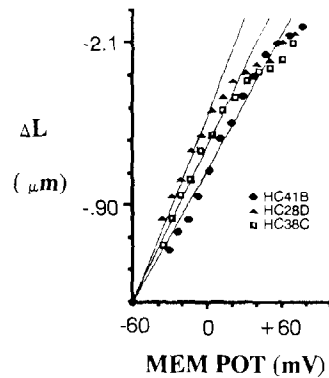


Fig. 2c. Mechanical responses (contractions) of the same three OHCs in response to depolarizing pulses from the holding potential. Mechanical responses from the three cells essentially overlap. Individual cell lengths and percent maximal contraction: HC41C: 64 μm , 3.8% , HC28D: 74 μm , 3.2% , HC38C: 83 μm , 2.7% .

value of -45 mV (Fig. 1). This is similar to the membrane potentials obtained in vivo for apical OHCs (Dallos et al., 1982). Upon establishment of whole cell recordings, membrane potentials often

increased over the course of a few minutes. This type of behavior has occasionally been observed from OHCs recorded in vivo using high resistance

electrodes (Dallos, 1985b). With whole cell recording this behavior may arise from the exchange of pipette and cytoplasmic solutions, possibly indicating that isolated OHCs have a reduced internal K^+ concentration. This phenomenon suggests that the membrane potential is dependent upon K^+ conductance. However, we have recorded from OHCs having membrane potentials near -60 mV from the onset of whole cell recording. The conductance of these cells at the holding potential of about -60 mV was also variable (2.4 to 62 nS), having a mean of 9.2 nS.

Under voltage clamp, OHCs exhibit time- and voltage-dependent outward currents upon depolarization from -60 mV (Fig. 2). These currents rise sigmoidally to peak values within 10 to 20 ms (with a voltage-dependent time constant) and partially inactivate on a somewhat longer time scale. Leak-subtracted peak outward currents typically show saturation at pulse potentials above

$+40$ mV, and begin to roll over about $+60$ mV. Steady state current (no leak subtraction, measured at 200 ms, Fig. 2b) begins to saturate above $+10$ mV.

OHCs, but not supporting cells, clearly exhibit mechanical movements in response to step changes in holding potential (Fig. 2c). The magnitude of cell concentrations induced by depolarization increases as the size of the voltage step is increased, and in most cells studied the linear relationship between voltage and contraction is lost at high voltage step levels, where the mechanical response falls off. Our largest calculated mechanical response about the -60 mV holding potential was 29 nm/mV. The electrically induced contraction of cells is not limited to any region of the cell; both basal and apical regions contract towards the point of electrode insertion in the supranuclear region. Hyperpolarization causes elongation of the cell, but quantitative measurements of these move-

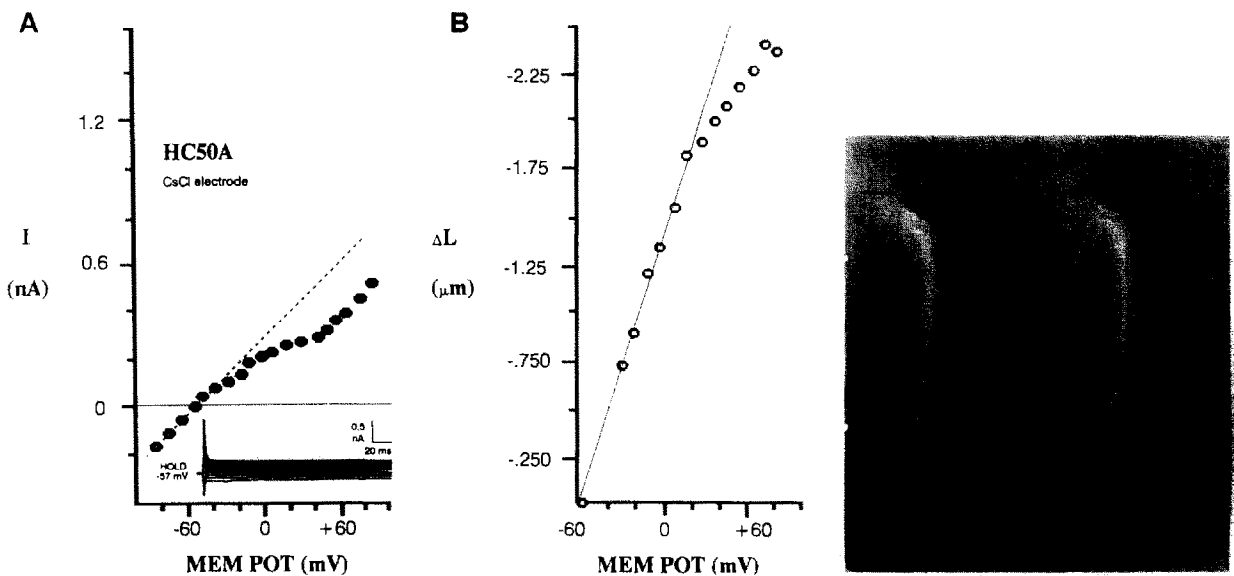


Fig. 3a. I-V curve measured at 200 ms after voltage step for an OHC in which the outward currents were blocked by using a patch pipette containing 140 mM CsCl isolation. Dotted line indicates leakage current. Leakage current subtraction (not shown) revealed inward currents at depolarizations greater than -30 mV, probably indicative of Ca^{2+} influx. Inset shows current traces associated with voltage steps from a holding potential of -57 mV.

Fig. 3b. Mechanical responses of the same OHC in response to step depolarizations from a holding potential of -57 mV. Despite the reduction in outward current the voltage induced mechanical response of the cell is as robust as those exhibiting normal I-V characteristics (see Fig. 1c). In this case, the mechanical response about the holding potential is 23 nm/mV.

Fig. 3c and d. Photographs of video images of same OHC. (c) during the 200 ms pulse of $+81$ mV, and (d) upon return to the holding potential of -57 mV. Vertical scale: $4.8 \mu\text{m}$.

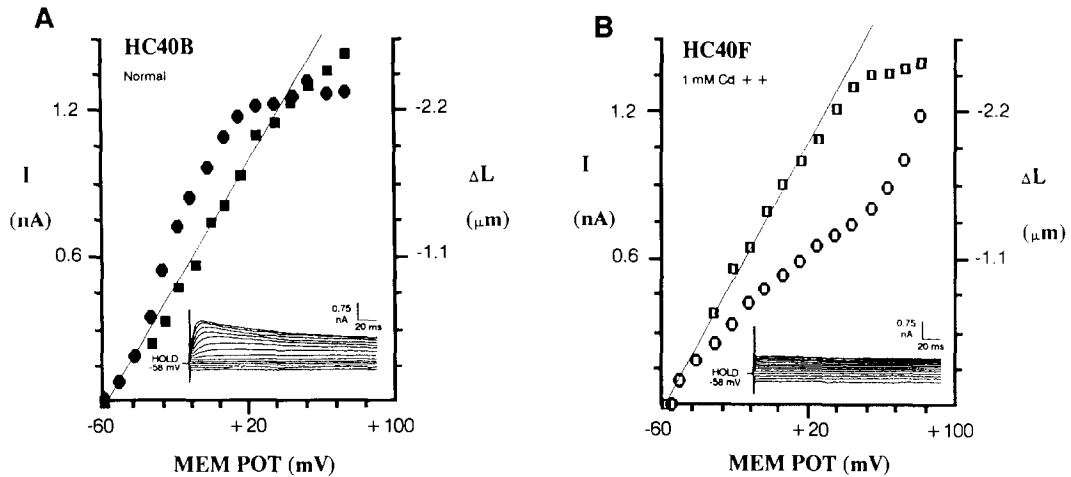


Fig. 4. Steady state current (measured at 200 ms), and mechanical response of an isolated OHC before and after addition of 1 mM CdCl_2 to the extracellular perfusate. Pipette contained 140 mM KCl. No leakage current subtraction. Despite reduction of outward current, mechanical responses remain unaltered. (a) Normal extracellular medium. Steady state current: closed circles; mechanical response: closed squares. Mechanical response is 23 nm/mV about the holding potential. Inset: Current traces associated with voltage steps from the holding potential. (b) Normal extracellular medium + 1 mM CdCl_2 . Steady state current: open circles; mechanical response: open squares. Mechanical response is 25 nm/mV about the holding potential. Inset: current traces associated with voltage steps from the holding potential.

ments were not possible for the small range of hyperpolarizations examined in this study.

Outward currents in OHCs are blocked by various manipulations which are generally considered to suppress K^+ currents in cells. Replacing intracellular K^+ with Cs^+ (Fig. 3a) eliminates most of the outward current. However, mechanical responses are robust despite the reduction of outward current (Fig. 3b). Other treatments which block the outward current including extracellular additions of 25 mM TEA, 10 or 50 mM Ba^{2+} , or 1 mM Cd^{2+} do not interfere with the electrically induced OHC movements. Figs. 4a and b illustrate the effects of 1 mM extracellular Cd^{2+} on OHC currents and mechanical movements. Although the time- and voltage-dependent outward current is reduced by this treatment, the mechanical response is left intact. One mechanism by which Cd^{2+} may suppress outward current is by blocking Ca^{2+} entry through voltage gated Ca^{2+} channels, thus preventing the opening of Ca^{2+} -activated K^+ channels. A voltage-dependent inward current can, in fact, be measured when outward currents are reduced (see Fig. 3). This inward current is Cd^{2+} sensitive and its magnitude is increased when the bath contains 50 mM Ba^{2+} and no Ca^{2+} (Fig. 5). Thus, a link between Ca^{2+}

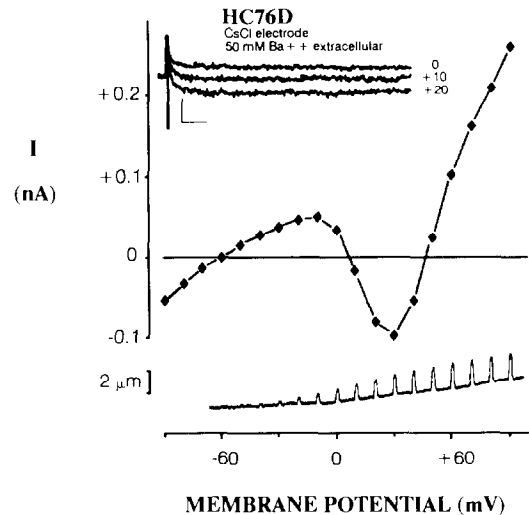


Fig. 5. I-V curve of an isolated OHC, obtained with a pipette solution of 140 mM CsCl, and extracellular solution in which 50 mM Ba^{2+} replaced Ca^{2+} . Note the reversal of net current as the cell is depolarized to levels between +10 and +40 mV. At the top, current traces are depicted at depolarizations of 0, 10, and 20 mV, from a holding potential of -60 mV (insert: horizontal scale 20 ms, vertical scale 0.1 nA). Note the absence of inactivation during the 200 ms pulses. At the bottom, the magnitude of cellular contractions is presented for depolarizing pulses. In this case the responses were recorded with the use of differential optoresistors to measure apical cell movements directly off a video monitor. Note that the cell continues to contract in a graded fashion during net current reversal.

influx and OHC movements can be ruled out. In addition to the inability of extracellular Cd^{2+} or Ba^{2+} to inhibit cell movements, OHC movements persist when the extracellular Ca^{2+} is reduced to zero (either due to omission of Ca^{2+} or chelation with EGTA).

Finally, in the presence of high extracellular Ba^{2+} concentrations there is a net inward current during depolarizing voltage clamp steps to +10 through +40 mV (Fig. 5); yet, the cells still contract rather than elongate, as might have been expected if the direction of movement were dependent upon the direction of current across the membrane.

Discussion

The mechanical response of OHCs has been postulated to be coupled to the magnitude and direction of transmembrane current in the cell (Ashmore, 1986; Ashmore and Meech, 1986). Ashmore (1986) initially reported that replacing intracellular K^+ with Na^+ under whole cell voltage clamp blocked outward K^+ currents and altered OHC mechanical responses, suggesting that outward K^+ current is important for OHC movements. Subsequently, it was postulated that the sensory stimulus to the outer hair cell is directly coupled to the cell mechanical response via these large basolateral outward currents (Ashmore and Meech, 1986). Indeed, this concept prompted others (Gitter et al., 1987) to analyze single K^+ channel kinetics of OHCs in an effort to account for the speed of OHC movements. The data presented here clearly demonstrate that OHC movements are not dependent upon outward K^+ currents, since blocking them with a variety of treatments does not affect movements. Recently, Ashmore (1987) reported that, in fact, replacing intracellular K^+ with Na^+ does not affect OHC movements, and suggested that his initial reports to the contrary were due to the small range of voltages studied and pipette series resistance changes.

While outer hair cells *in vivo* have resting potentials near -70 mV (Dallos, et al., 1982; Russell et al., 1986), and values of up to -68 mV were observed in this and other studies (Ashmore and Meech, 1986; Zenner et al., 1985), it is clear that potentials *in vitro* are variable and often

poorer than *in vivo*. Many studies have evaluated mechanical responses of OHCs under current clamp or by means of extracellular current stimulation without simultaneously accounting for changes in cell membrane potential (Brownell et al., 1985; Kachar et al., 1986; Evans, 1988). Under these conditions, the variability of membrane potential and input resistance *in vitro* may place limitations upon the interpretation of certain aspects of the measured mechanical responses, since we show that mechanical responses are not dependent upon total transmembrane current.

We demonstrate here that OHCs possess a voltage dependent Ca^{2+} current, but that this inward current is not required for mechanical responses. OHCs continue to contract in response to depolarizations when inward Ca^{2+} currents are blocked by Cd^{2+} or when extracellular Ca^{2+} is absent. This result indicates that fast electrically induced OHC movements are not dependent upon an actin-myosin system, as has been suggested for the slow movements of OHCs (Zenner, 1986). This notion is strengthened by the fact that OHCs continue to respond mechanically when intracellular Ca^{2+} is buffered to below 10 nM (Ashmore, 1987), and when metabolic inhibitors are present (Kachar et al., 1986). Furthermore, the frequency response of OHC movements, measured up to 8 kHz, is unlikely to be accounted for by a muscle-like system (Ashmore and Brownell, 1986; Ashmore, 1987).

The average input conductance of OHCs in this study was 9.2 nS (108 M Ω). This contrasts with the range of conductances (25–50 nS; 40–20 M Ω) reported by Ashmore and Meech (1986) for OHCs isolated using trypsin. These authors have suggested that inclusion of the Ca^{2+} chelator BAPTA in the patch pipette solution is necessary to obtain cells with high resistances and membrane potentials. It is difficult to understand how a reduction in internal calcium levels would increase the cell's membrane potential when such measures would be expected to reduce the cell's Ca^{2+} -activated K^+ conductance. In a cell whose membrane potential is dependent upon K^+ conductance, a reduction in the conductance would cause depolarization. We find that with our non-enzymatic isolation technique, cells with high resistances and membrane potentials are obtained with or without Ca^{2+} che-

lators in the pipette solution. Furthermore, the presence of time- and voltage-dependent outward currents was not dependent upon the inclusion of a Ca^{2+} chelator in the pipette solution.

The resting input resistance of OHCs is low compared to hair cells from other systems, where values can be an order of magnitude greater (Ohmori, 1984; Corey and Hudspeth, 1979). This difference is not due to the methods employed in this study since similar measures on isolated Hensen cells (having comparable membrane surface area) demonstrate an average input resistance of 1.1 G Ω (Santos-Sacchi, 1988). The OHC leakage conductance is probably not due to transduction channel activity in the stereocilia since many of the cells studied lacked stereocilia as a result of the isolation procedure. Induced mechanical movements in these cells were indistinguishable from movements of cells with stereocilia. Still, the average input resistance reported here is higher than that determined *in vivo* (30–50 M Ω , Dallos, et al., 1982; Russell et al., 1986). These *in vivo* measures probably underestimate true values because they were made with high impedance micro-electrodes whose electrode-to-membrane seal resistance is considerably less than that obtained with the patch electrode technique.

Currently, a major effort is being made to elucidate the roles played by inner and outer hair cells in the organ of Corti. The discovery that OHCs can rapidly alter their cell length in response to electrical stimulation (Brownell et al., 1985) fits well with models incorporating active bi-directional transduction processes (mechanical to electrical and vice versa) to account for the high sensitivity and sharp tuning of basilar membrane vibration (Kim, 1986; Geisler, 1986; Mountain, 1986; Jen and Steele, 1987). The elucidation of the mechanism of OHC movements will aid in the understanding of OHC-IHC interactions and pathologies which compromise these interactions. At present, the mechanism of this mechanical response is unknown. The data presented demonstrate that the mechanical response is not dependent upon either the specific ionic currents blocked here or the direction and magnitude of total transmembrane current. Furthermore, studies using the Cl^- channel blocker SITS indicate that a Cl^- current is not involved (Santos-Sacchi, unpub-

lished). While it is possible that movements are dependent upon some unidentified current which is masked by the residual leakage conductance, we believe that a membrane potential dependence is more likely. This may not conflict with Brownell's electro-osmotic theory (Brownell, 1986) of OHC movement if an axial potential gradient is present along the cell. Axial potential gradients are conceivable under physiologic conditions. Under voltage clamp, however, the existence of such a gradient is dependent upon the ability to adequately space clamp the cell. Ashmore has estimated (see comments after Brownell, 1986) that under voltage clamp, the cell is isopotential to within 1%. Of course, this value will depend upon the cable properties of the cell during stimulation, i.e., the magnitude and spatial distribution of basolateral conductances during depolarization. Presumably, in the present study, cells whose basolateral conductances were blocked would have been better space clamped than those under normal conditions. Yet, no differences in mechanical responses were observed. In preliminary experiments (Santos-Sacchi and Brownell, unpublished), voltage clamping OHCs with two patch electrodes, one at the cell apex and one at the cell base, in order to reduce axial potential gradients did not abolish the mechanical movements due to depolarization. Further studies of this sort are necessary.

Whatever underlying mechanism is responsible for the OHC's mechanical response, the results presented here indicate that it is associated with the magnitude of transmembrane potential, and potential differences less than a millivolt produce mechanical responses on the same scale as basilar membrane movements near threshold. It is conceivable that the effects of OHCs on the mechanical properties of the cochlear partition may be influenced by both intracellular and extracellular voltage responses associated with acoustic stimulation.

Acknowledgments

JS-S supported by an NINCDS Research Career Development Award and NIH grant NS21380. JPD supported by NIH grant R23 NS21581. We thank C. Witzmann, K. Dilger, and J. Nolan for technical assistance.

References

- Ashmore, J.F. (1986) The cellular physiology of isolated outer hair cells: implications for cochlear frequency selectivity. In: B.C.J. Moore and R.D. Patterson, (Eds.), *Auditory Frequency Selectivity*, Plenum Press, New York, pp. 103–108.
- Ashmore, J.F. (1987) A fast motile response in guinea-pig outer hair cells: the cellular basis of the cochlear amplifier. *J. Physiol. (London)*, 388, 323–347.
- Ashmore, J.F. and Brownell, W.E. (1986) Kilohertz movements induced by electrical stimulation in outer hair cells isolated from the guinea-pig cochlea. *J. Physiol. (Lond.)* 377, 41P.
- Ashmore, J.F. and Meech, R.W. (1986) Ionic basis of membrane potential in outer hair cells of guinea pig cochlea. *Nature* 322, 368–371.
- Brown, M.C., Nutall, A.L. and Masta, R.I. (1983) Intracellular recordings from cochlear inner hair cells: effects of stimulation of the crossed olivocochlear efferents. *Science* 222, 69–72.
- Brownell, W.E. (1983) Observations on a motile response in isolated outer hair cells. In: W.R. Webster and L.M. Aitken (Eds.), *Mechanisms of Hearing*, Monash University Press, Melbourne, pp. 5–10.
- Brownell, W.E. (1984) Microscopic observation of cochlear hair cell motility. *Scanning Electron Microscopy*, 1984/III, 1401–1406.
- Brownell, W.E. (1986) Outer hair cell motility and cochlear frequency selectivity. In: B.C.J. Moore and R.D. Patterson, (Eds.), *Auditory Frequency Selectivity*, Plenum Press, New York, pp. 109–116.
- Brownell, W.E. and Kachar, B. (1986) Outer hair cell motility: A possible electro-kinetic mechanism. In: J.B. Allen, J.L. Hall, A.E. Hubbard, S.T. Neely and A. Tubis (Eds.), *Peripheral Auditory Mechanisms*, Springer-Verlag, Berlin, Heidelberg, New York, pp. 369–376.
- Brownell, W.E., Bader, C.R., Bertrand, D. and de Ribaupierre, Y. (1985) Evoked mechanical responses of isolated cochlear outer hair cells. *Science* 227, 194–196.
- Corey, D.P. and Hudspeth, A.J. (1979) Ionic basis of the receptor potential in a vertebrate hair cell. *Nature* 281, 675–677.
- Dallos, P. (1985a) The role of outer hair cells in the cochlea. In: M.J. Correia and A.A. Perachio, (Eds.), *Contemporary Sensory Neurobiology*, Alan R. Liss, Inc., New York, pp. 207–230.
- Dallos, P. (1985b) Membrane potential and response changes in mammalian cochlear hair cells during intracellular recording. *J. Neuroscience* 5, 1609–1615.
- Dallos, P., Santos-Sacchi, J. and Flock, A. (1982) Intracellular recordings from cochlear outer hair cells. *Science* 218, 582–584.
- Evans, B.N. (1988) Sensitivity measurements of isolated outer hair cell electro-mechanical responses. In: *Abstr. Assoc. Res. Otolaryngol. Clearwater Beach, FL. USA.*
- Geisler, C.D. (1986) A model of the effect of outer hair cell motility on cochlear vibrations. *Hear. Res.* 24, 125–131.
- Gitter, A.H., Fromter, E. and Zenner, H.P. (1987) Kinetic properties and physiologic implications of the high-conductive potassium channel in the lateral membrane of mammalian outer hair cells. In: *Abstr. Assoc. Res. Otolaryngol. Clearwater Beach, FL. USA.*
- Jen, D.H. and Steele, C.R. (1987) Electrokinetic model of cochlear hair cell motility. *J. Acoust. Soc. Am.* 82, 1667–1678.
- Kachar, B., Brownell, W.E., Altschuler, R. and Fex, J. (1986) Electrokinetic shape changes of cochlear outer hair cells. *Nature* 322, 365–368.
- Kim, D.O. (1986) Active and nonlinear cochlear biomechanics and the role of the outer hair cell subsystem in the mammalian auditory system. *Hear. Res.* 22, 105–14.
- Marty, A. and Neher, E. (1983) Tight-seal whole-cell recording. In: B. Sakmann and E. Neher, (Eds.), *Single-Channel Recording*, Plenum Press, New York, pp. 107–122.
- Mountain, D.C. (1980) Changes in endolymphatic potential and crossed olivocochlear bundle stimulation alter cochlear mechanics. *Science* 210, 71–72.
- Mountain, D.C. (1986) Active filtering by hair cells. In: J.B. Allen, J.L. Hall, A.E. Hubbard, S.T. Neely and A. Tubis (Eds.), *Peripheral Auditory Mechanisms*, Springer-Verlag, Berlin, Heidelberg, New York, pp. 179–188.
- Nuttall, A.L. (1985) Influence of direct current on dc receptor potentials from the cochlear inner hair cells in the guinea pig. *J. Acoust. Soc. Am.* 77, 165–175.
- Ohmori, H. (1984) Studies of ionic currents in the isolated vestibular hair cell of the chick. *J. Physiol. (London)* 350, 561–581.
- Russell, I.J. and Sellick, P.M. (1983) Low frequency characteristics of intracellularly recorded receptor potentials in mammalian hair cells. *J. Physiol. (Lond.)* 338, 179–206.
- Russell, I.J., Cody, A.R. and Richardson (1986) The responses of inner and outer hair cells in the basal turn of the guinea-pig cochlea and in the mouse cochlea grown in vitro. *Hear. Res.* 22, 199–216.
- Santos-Sacchi, J. (1988) Whole cell studies of gap junctional communication in isolated supported cells of the organ of Corti. In: *Abstr. Assoc. Res. Otolaryngol. Clearwater Beach, FL. USA.*
- Santos-Sacchi, J., and Dilger, J.P. (1986) Patch clamp studies on isolated outer hair cells. *Advances in Auditory Neuroscience, The IUPS Satellite Symposium on Hearing, University of California, San Francisco, CA. USA*, p. 23.
- Santos-Sacchi, J. and Dilger, J.P. (1988) Whole cell currents and mechanical responses in outer hair cells. In: *Abstr. Assoc. Res. Otolaryngol. Clearwater Beach, FL. USA.*
- Siegal, J.H. and Kim, D.O. (1982) Efferent neural control of cochlear mechanics? Olivocochlear bundle stimulation affects cochlear biomechanical nonlinearity. *Hear. Res.* 6, 171–182.
- Zenner, H.P. (1986) Motile responses in outer hair cells. *Hear. Res.* 22, 83–90.
- Zenner, H.P., Zimmermann, U. and Schmitt, U. (1985) Reversible contraction of isolated mammalian cochlear hair cells. *Hear. Res.* 18, 127–133.
- Zenner, H.P., Gitter, A., Zimmermann, U., Schmitt, U. and Fromter, E. (1985) Die isolierte, lebende Haarzelle. *Laryng. Rhinol. Otol.* 64, 642–648.

INDUCTION OF THE ACROSOME REACTION IN GUINEA PIG SPERMATOZOA BY cGMP ANALOGUES

J. SANTOS-SACCHI and MILDRED GORDON

From the School for Biomedical Education, The City College, New York 10031

ABSTRACT

The effect of cyclic nucleotide analogues upon the immediate induction of the guinea pig acrosome reaction (AR) was studied. Dibutyryl (dB) cGMP and 8-bromo-cGMP, when added to sperm suspensions after varying periods of preincubation in glucose-free BWW medium (NaCl 94.59 mM, KCl 4.7 mM, CaCl₂ 1.71 mM, KH₂PO₄ 1.19 mM, MgSO₄ 1.19 mM, NaHCO₃ 25.07 mM, pyruvate 0.25 mM, lactate 21.58 mM, and bovine serum albumen 1 g/liter), induced the AR in a large proportion of spermatozoa relative to controls. The proportion of ARs induced upon the addition of dB cGMP or 8-bromo-cGMP (10 mM) at 1 h was equivalent to that obtained after a 5-h incubation in glucose-free BWW alone. The effect of cGMP analogues was concentration dependent over the tested range of 2–12 mM (<1–20%). The simultaneous addition of imidazole (10 mM), a cAMP phosphodiesterase stimulator, potentiated the effect (imidazole + 12 mM 8-bromo-cGMP: 73%). cAMP analogues were without effect. The presence of extracellular Ca⁺⁺ was required, and it is suggested that a rise in the cGMP/cAMP ratio triggers Ca⁺⁺ influx and the AR.

The acrosome reaction (AR) is a massive exocytosis of the acrosome vesicle which occurs in capacitated sperm before fertilization. Early studies claimed that pretreatment of spermatozoa with exogenous cAMP analogues enhanced capacitation as evidenced by increased rates of egg penetration (2, 15, 18). Recently, however, Garcia and Rogers (3, 12) determined that the incubation of guinea pig spermatozoa for 4 h within a capacitating medium, Minimum Culture Medium (MCM), containing dibutyryl (dB) cAMP (10 mM) or phosphodiesterase inhibitors reduced the acrosome reaction percentage as compared to controls (10 vs. 50%). On the other hand, the presence of imidazole, a cAMP phosphodiesterase stimulator, increased the numbers of ARs over controls (90 vs. 50%). The effects of these agents were concentration dependent over the tested range of 1–10 mM.

The data reviewed thus far suggest that capacitation may involve a rise in intracellular cAMP levels, but the subsequent AR may be associated with a reduction in cAMP levels.

In accord with this hypothesis are the results of cAMP effects upon other secretory systems. For example, incubation of neutrophils, basophils, and mast cells in media containing agents that promote a rise in cAMP levels inhibits the release of secretory granule contents (for reviews, see references 10 and 11). On the other hand, an increase in cGMP levels promotes the release of secretory granule contents in these same cells. Calcium ion influx is requisite for such secretory activity, and apparently plays a significant role in modulating intracellular levels of cGMP (5). One interpretation of such data is that cGMP and cAMP control opposing cellular function (Yin-Yang hypothesis,

reference 6). The fact that extracellular Ca^{++} is required for the AR and that its influx parallels or precedes the occurrence of the AR (16, 19) may be related to cyclic nucleotide flux. Indeed, cAMP and cGMP may control opposing cellular functions in sperm as they apparently do in other secretory systems. It may be possible, then, that a rise in the intracellular cGMP/cAMP ratio is associated with the mammalian AR. Accordingly, in this report, the effects of cyclic nucleotide analogues on the AR of guinea pig spermatozoa were investigated.

MATERIALS AND METHODS

Guinea pig epididymal spermatozoa were extruded into 0.9% NaCl in H_2O , disaggregated by pipetting, and washed two times by centrifugation (1,000 g, 4 min each). Spermatozoa were then suspended in glucose-free BWB medium (NaCl 94.59 mM, KCl 4.7 mM, CaCl_2 1.71 mM, KH_2PO_4 1.19 mM, MgSO_4 1.19 mM, NaHCO_3 25.07 mM, pyruvate 0.25 mM, lactate 21.58 mM, and bovine serum albumen 1 g/liter) at a final concentration of $1-1.5 \times 10^7$ spermatozoa/ml and were incubated at 37°C for 5 h in screw-capped tubes under an air atmosphere. Calcium ion-free medium was also employed. Media were prepared daily, immediately before use. The initial pH was adjusted to 7.55, and throughout the experiments it remained <8.00 .

At 0 and 1 h after the suspension of spermatozoa, db cAMP, 8-bromo-cAMP (0.001–10 mM), dB cGMP, 8-bromo-cGMP (0.001–10 mM), AMP, 8-bromo-AMP (10 mM), GMP, or bromo-GMP (10 mM) was added to sperm samples. Butyrate (0.1 and 10 mM) was also tested as a control for possible butyrate contamination of the dibutyl cyclic nucleotides. After a 20-min incubation with these agents, ARs were assessed. In this report, direct counts of acrosome-reacted spermatozoa were made by hemocytometer,¹ six to eight chambers (0.5 mm^3 each) being counted for each condition. ARs were not induced artifactually by the use of the counting apparatus. Counting was rapid and was facilitated because activated, acrosome-reacted spermatozoa tend to remain within confined areas. Care was taken, however, to

¹ We have chosen not to use the method of Rogers and Yanagimachi (14) to assess the percentage of ARs. Their technique involves placing an aliquot of sperm upon a slide and counting the number of ARs in a sample of 100 motile sperm. The validity of such a sampling technique is directly dependent upon a random distribution of sperm in which each sperm has an equal likelihood of being chosen. Because guinea pig sperm autoagglutinate spontaneously in physiologic media (16, 1) and because these agglutinated sperm, although motile, are non-acrosome reacted, there exists a nonrandom distribution of sperm. Thus, if a sperm is sampled from an aggregate, a priori, it will be unreacted. On the other hand, the chances of sampling an acrosome-reacted sperm from the freely motile pool are very high, because the majority of non-acrosome-reacted sperm are agglutinated. Whenever we have attempted to use this technique, we obtained spuriously high AR scores, with high variability as compared to the hemocytometer technique.

focus through the 0.1-mm counting chamber depth so as not to overlook cells. Standard errors of the mean averaged $<20\%$. The results are reported as a percentage of AR in the total motile sperm population ($\%AR^{\text{tot}} = [\text{concn of AR spermatozoa}/\text{concn of total spermatozoa} - \text{concn of immotile spermatozoa}] \times 100$). Sperm samples were also qualitatively evaluated in wet mounts without coverslips by light and differential interference microscopy. The speed of onset of ARs as well as the incidence of autoagglutination over time was determined. For electron microscopy, spermatozoa were prepared as described previously (7) and examined with a Philips 300 electron microscope at 80 kV.

cAMP levels were determined by the protein binding technique (cAMP Assay Kit, Amersham Corp., Arlington Heights, Ill.) and were corroborated by the antibody technique (cAMP Assay Kit, New England Nuclear, Boston, Mass.). After rapid centrifugation for 30 s, cell pellets were sonicated in 2 ml of absolute ethyl alcohol. After centrifugation, the supernate was evaporated to dryness at 75°C with a stream of air, and the residue was resuspended in buffer for assay. Counts were made with a Beckman LS-250 Liquid Scintillation System (Beckman Instruments, Inc., Fullerton, Calif.) or Nuclear-Chicago gamma counter (Nuclear-Chicago Corp., Des Plaines, Ill.). Recovery of cAMP was $\sim 59\%$.

RESULTS

Suspension of washed guinea pig spermatozoa in either Ca^{++} -deficient or Ca^{++} -containing, glucose-free BWB resulted in head-to-head agglutination within a matter of minutes (Fig. 1). Incubation in glucose-free BWB from 0 to 5 h (Fig. 2) resulted in a gradual increase in the absolute number of activated, acrosome-reacted spermatozoa, although a large proportion of aggregated, non-acrosome-reacted spermatozoa remained throughout incubation. All agents were without pronounced effect upon AR induction when added at 0 h (Table I). Whereas dB cAMP, 8-bromo-cAMP, AMP, 8-bromo-AMP, GMP, 8-bromo-GMP, and butyrate remained ineffective upon addition at 1 h, dB cGMP or 8-bromo-cGMP (10 mM) was able to induce a large proportion of ARs, being roughly equivalent to the $\%AR^{\text{tot}}$ score obtained after a 5-h incubation in glucose-free BWB alone.

Dose-response data were collected to determine the relationship between analogue concentration and $\%AR^{\text{tot}}$ scores (Fig. 3). Incremental increases from 2 to 12 mM 8-bromo-cGMP produced increasingly higher numbers of ARs, reaching 20.46% for the highest concentration tested (12 mM). In addition, the simultaneous addition of 10 mM imidazole, a cAMP phosphodiesterase stimulator, caused a dramatic potentiation of the 8-bromo-cGMP effects (Fig. 3). For example, the addition at 1 h of imidazole with 12 mM 8-bromo-cGMP produced a phenomenal 73.94% AR^{tot} score, nearly fourfold greater than 8-bromo-cGMP alone and 112-fold greater than the no-addition

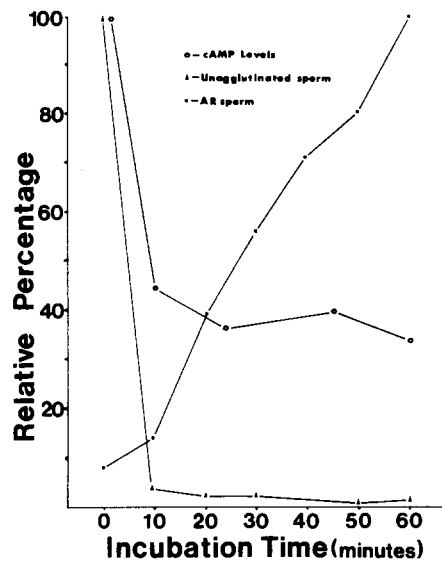


FIGURE 1 The relationship among db cGMP-induced AR, sperm agglutination, and cAMP levels over a 1-h incubation period in glucose-free BWW. Intracellular cAMP levels were assayed 0, 10, 25, 45, and 60 min after suspension of sperm in glucose-free BWW at 37°C. The number of unagglutinated sperm was determined by hemocytometer over the 1-h incubation. Sperm were induced to acrosome react by the addition of 10 mM dB cGMP at 0, 10, 20, 30, 40, 50, or 60 min, and counts were made after a 20-min incubation with the cyclic nucleotide. AR are reported relative to the 60-min score. Sperm concn: 1.5×10^7 /ml; cAMP at 0 h: 17 pmol/ 10^7 sperm; %AR^{tot} score at 1 h: 12.71.

control. Imidazole alone was ineffective.

The addition of 10 mM dB cGMP but not dB cAMP at 0 h appeared to inhibit agglutination of spermatozoa and did not elicit ARs. If, however, 10 mM dB cGMP was added after agglutination had begun, ARs were induced. This suggested a correlation between agglutination and the ability of spermatozoa to acrosome react. To further evaluate the time dependence of dB cGMP effects, additions of dB cGMP (10 mM) to sperm samples were made at 10-min intervals over a 1-h incubation period and ARs were assessed as described previously (Fig. 1). Results show a time-dependent increase in the ability of dB cGMP to induce ARs. In addition, it was found that, over the 1-h incubation period, sperm cAMP levels decreased from 17 pmol/ 10^7 sperm to nearly 30% of the initial level and that this decrease was accompanied by a rapid rise in the number of autoagglutinated spermatozoa (Fig. 1).

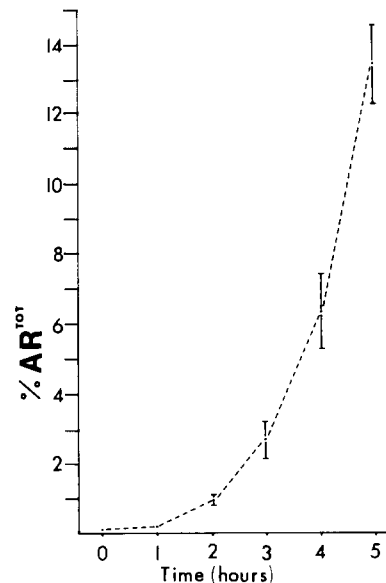


FIGURE 2 The percentage (mean \pm SEM) of guinea pig AR occurring during incubation for 5 h in glucose-free BWW.

TABLE I
%AR^{tot} Score Induced by Addition of Agents after 0- or 1-h Incubation in Glucose-free BWW

Addition	Time	
	0 h	1 h
dB cGMP		
10 mM	0.48 \pm 0.14	12.96 \pm 1.46
1 mM	0.44 \pm 0.07	0.67 \pm 0.13
8-bromo-cGMP		
10 mM	0.81 \pm 0.20	13.79 \pm 1.79
1 mM	0.10 \pm 0.02	0.28 \pm 0.04
dBc AMP		
10 mM	0.43 \pm 0.09	0.95 \pm 0.09
1 mM	0.47 \pm 0.17	0.58 \pm 0.08
8-bromo-cAMP		
10 mM	0.08 \pm 0.02	0.28 \pm 0.06
1 mM	0.36 \pm 0.09	0.23 \pm 0.04
AMP		
10 mM	0.05 \pm 0.01	0.84 \pm 0.06
8-bromo-AMP		
10 mM	0.28 \pm 0.07	0.11 \pm 0.02
GMP		
10 mM	0.07 \pm 0.02	0.95 \pm 0.07
8-bromo-GMP		
10 mM	0.02 \pm 0.01	0.05 \pm 0.01
Butyrate		
10 mM	0.17 \pm 0.03	0.69 \pm 0.08
0.1 mM	0.11 \pm 0.02	0.49 \pm 0.11
No addition	0.08 \pm 0.03	0.69 \pm 0.10

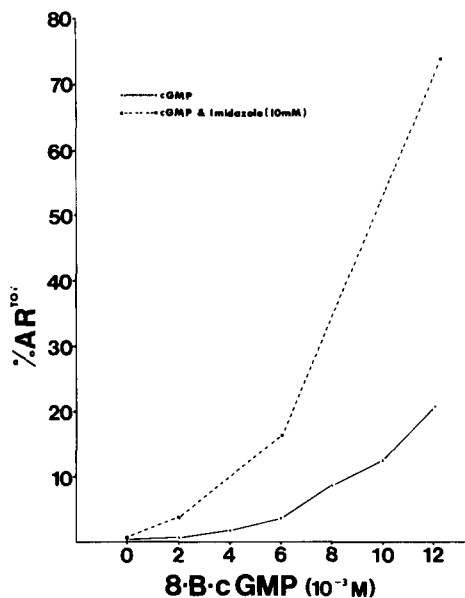


FIGURE 3 Dose-response curves for the induction of ARs by 8-bromo-cGMP or 8-bromo-cGMP + 10 mM imidazole, a cAMP phosphodiesterase stimulator. Sperm were incubated for 1 h at 37°C in glucose-free BWB before addition of drugs. ARs were assessed after an additional 20-min incubation at 37°C in medium containing drugs as indicated.

Typically, within a matter of minutes after the addition of cGMP analogues, vigorous flagellar activity of aggregated spermatozoa ensued. After 5–10 min, freely motile acrosome-reacted spermatozoa were observed attended by an activated pattern of motility (19), and by 15–25 min, a maximum was reached. Activated, acrosome-reacted spermatozoa remained motile for periods up to 2 h, after which an increasingly large number became immotile. ARs were judged physiological as evidenced by differential interference and electron microscopy (Fig. 4).

ARs could not be induced in Ca^{++} -deficient media. In addition, EGTA (2 mM) and nucleotide 5'-triphosphates (ATP, GTP, ITP, UTP; 10 mM) when previously added to Ca^{++} -containing media inhibited AR induction by dB cGMP, and this inhibition could be reversed by a subsequent and sufficient increase in Ca^{++} concentration.

DISCUSSION

A role for cGMP as an effector of the mammalian AR has not been previously considered. Perhaps this is because of the proposal of Gray et al. (9) that guanylate cyclase activity is absent in dog and

human spermatozoa. However, their results may have been caused by limitations of their assay procedure, because others (4) have shown that bovine sperm cGMP levels increase more than cAMP levels in the presence of pyruvate and the phosphodiesterase inhibitor, caffeine. Furthermore, cGMP has been localized immunocytochemically within rat spermatids (17). It seems probable that mammalian spermatozoa do possess an active guanylate cyclase.

In a given population, spermatozoa are not in maturational synchrony (8). This is also borne out by the observation that under in vitro conditions known to promote the AR, only a small percentage of the total sperm population will undergo the acrosome reaction at any point in time (Fig. 2). Because sperm nucleotide levels probably fluctuate on an individual basis, the high levels of analogues employed herein were considered necessary to compensate for this individual variability and to produce a large-scale synchronous AR. In addition, there is the possibility of poor membrane permeability of these analogues.

The facts that exogenous cGMP analogues but not cAMP analogues produced an almost immediate AR in a large proportion of spermatozoa and that these spermatozoa were motile for at least 2 h thereafter, lend credence to the idea that an increase, or perhaps a relative increase over cAMP in the levels of intracellular cGMP, promotes the AR. This is further substantiated by the potentiating effect of the cAMP phosphodiesterase stimulator, imidazole. These cyclic nucleotide fluctuations probably initiate Ca^{++} influx, because the absence of Ca^{++} or the presence of agents that chelate calcium ions (EGTA, nucleotide 5'-triphosphates) inhibits the induction of ARs by cGMP analogues. In this regard, the reduction of sperm ATP levels as sperm capacitate (13) may be functionally important, because this reduction may increase the availability of calcium ions, which are requisite for the AR.

The time-dependent effects of dB cGMP upon AR induction indicate that physiologic preparation for the AR, such as capacitation, is occurring. Furthermore, the results reported here suggest that the basis of dB cGMP's increased effectiveness over time may be related to a concomitant decrease in sperm cAMP levels. In effect, then, the cGMP/cAMP ratio increased over time, although the amount of added dB cGMP remained constant at 10 mM. Whether sperm autoagglutination is truly related to the decrease in cAMP levels, as is

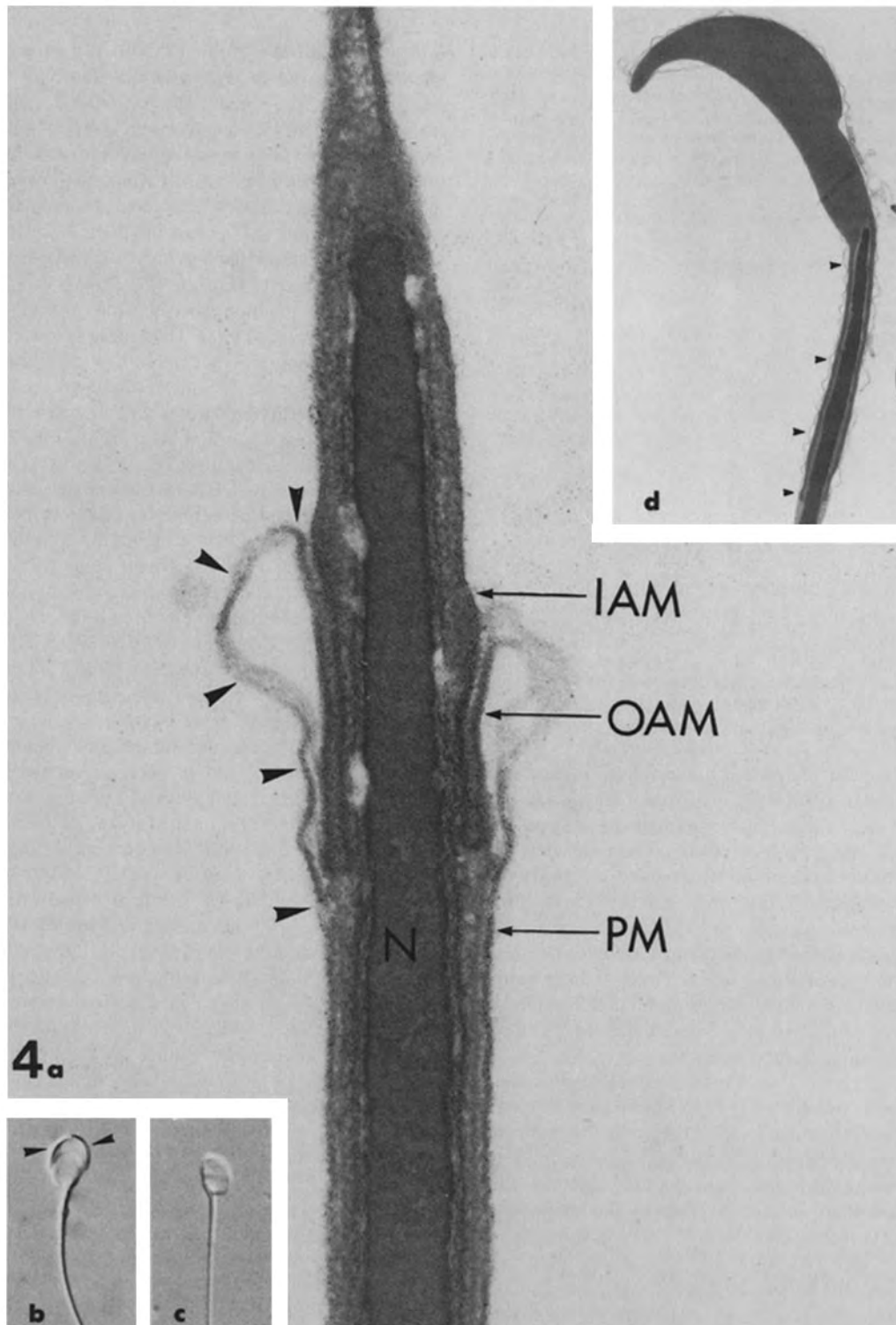


FIGURE 4 (a) Electron micrograph of acrosome-reacted guinea pig sperm fixed 20 min after the addition of 10 mM dB cGMP. Note fusion (arrows) of plasmalemma (*PM*) with outer acrosomal membrane (*OAM*) which is typical of physiological AR. Inner acrosomal membrane, *IAM*, nucleus, *N*. $\times 90,000$. (b) Differential interference micrograph of fixed non-acrosome-reacted sperm. Arrows indicate bulbous acrosome. (c) Differential interference micrograph of fixed guinea pig sperm induced to acrosome react by dB cGMP. Note absence of acrosome. (d) Electron micrograph of non-acrosome-reacted sperm. Note presence of large acrosome and continuity of plasmalemma (arrows). $\times 16,000$.

suggested by their inverse correlation, remains to be proven. However, it is plausible that sperm agglutination indicates surface modifications concomitant with capacitation (8).

In sum, the previously reported results that dB cAMP inhibits the AR (3, 12) and those reported here seem to suggest that an increase in the cGMP/cAMP ratio promotes the guinea pig AR.

Thanks to Celeste Conway and Barbara Cooper for help in the preparation of this manuscript.

This work was supported by the National Institutes of Health grant HD 13163.

Received for publication 15 November 1979, and in revised form 15 January 1980.

REFERENCES

1. BARROS, C. 1974. Capacitation of mammalian spermatozoa. In *Physiology & Genetics of Reproduction*. Part A. E. M. Continho and F. Fuchs, editors. Plenum Press, New York. 3-24.
2. BRACKETT, B., G. JEITLES, and Y. OH. 1975. Fertilization by sperm treated with high ionic strength and N⁶,O²-dibutyryl adenosine 3':5'-cyclic monophosphoric acid. *Fed. Proc. Fed. Am. Soc. Exp. Biol.* **34**:256 (Abstr.).
3. GARCIA, L., and B. J. ROGERS. 1978. Effect of cyclic-AMP on capacitation and fertilization. *Soc. Study Reprod. 11th Meeting Biol. Reprod. Suppl. 1*: 79A.
4. GARBERS, D., W. LUST, N. FIRST, and H. LARDY. 1971. Effects of phosphodiesterase inhibitors and cyclic nucleotides on sperm respiration and motility. *Biochemistry*. **10**:1825-1831.
5. GOLDBERG, N., and M. HADDOX. 1977. Cyclic GMP metabolism and involvement in biological regulation. *Annu. Rev. Biochem.* **46**:823-896.
6. GOLDBERG, N., M. HADDOX, E. DUNHAM, C. LOPEZ, and J. HADDEN. 1974. The Yin Yang hypothesis of cyclic GMP and cyclic AMP in the regulation of cell proliferation and other biological processes. In *Control of Proliferation in Animal Cells*. B. Clarkson and R. Boserga, editors. Cold Spring Harbor Laboratory, Cold Spring Harbor, New York. 609-626.
7. GORDON, M. 1973. Localization of phosphatase activity on the membranes of the mammalian sperm head. *J. Exp. Zool.* **185**:11-120.
8. GORDON, M. 1977. Cytochemical analysis of the membranes of the mammalian sperm head. In *Male Reproductive System*. R. Yates and M. Gordon, editors. Masson Publishing, Inc., New York. 15-33.
9. GRAY, J. P., G. DRUMMOND, W. LUK, J. HARDMAN, and E. SUTHERLAND. 1976. Enzymes of cyclic nucleotide metabolism in invertebrate and vertebrate sperm. *Arch. Biochem. Biophys.* **172**:20-30.
10. IGNARRO, L. 1977. Cyclic nucleotides and lysosomal enzyme secretion. In *Cyclic 3',5'-Nucleotides: Mechanisms of Action*. H. Cramer and J. Schultz, editors. John Wiley & Sons, New York. 189-206.
11. RASMUSSEN, H., and D. GOODMAN. 1977. Relationships between calcium and cyclic nucleotides in cell activation. *Physiol. Rev.* **57**:422-494.
12. ROGERS, B. J., and L. GARCIA. 1979. Effect of cAMP on acrosome reaction and fertilization. *Biol. Reprod.* **21**:365-372.
13. ROGERS, B. J., and B. MORTON. 1973. ATP levels in hamster spermatozoa during capacitation in vitro. *Biol. Reprod.* **9**:361-369.
14. ROGERS, B. J., and R. YANAGIMACHI. 1975. Retardation of guinea pig sperm acrosome reaction by glucose: the possible importance of pyruvate and lactate metabolism in capacitation and the acrosome reaction. *Biol. Reprod.* **13**:568-575.
15. ROSADO, A., J. HICKS, A. REYES, and I. BLANCO. 1974. Capacitation in vitro of rabbit spermatozoa with cyclic adenosine monophosphate and human follicular fluid. *Fertil. Steril.* **25**:821-824.
16. SINGH, J., D. BABCOCK, and H. LARDY. 1978. Increased calcium-ion influx is a component of capacitation of spermatozoa. *Biochem. J.* **172**:549-556.
17. STEINER, A. L., S. H. ONG, and H. J. WEDNER. 1976. Cyclic nucleotide immunocytochemistry. *Adv. Cyclic Nucleotide Res.* **7**:115-155.
18. TOYODA, Y., and M. CHANG. 1974. Capacitation of epididymal spermatozoa in a medium with high K/Na ratio and cyclic AMP for the fertilization of rat eggs in vitro. *J. Reprod. Fertil.* **36**:125-134.
19. YANAGIMACHI, R., and N. USUI. 1974. Calcium dependence of the acrosome reaction and activation of guinea pig spermatozoa. *Exp. Cell Res.* **89**:161-174.

The Effect of ATP Depletion upon the Acrosome Reaction in Guinea Pig Sperm

J. SANTOS-SACCHI* AND MILDRED GORDON

From the School for Biomedical Education, The City College, New York, New York

The suspension of guinea pig spermatozoa in substrate-free medium results in the cessation of sperm motility and a 94% reduction in adenosine triphosphate (ATP) levels within minutes. ATP depletion was not deleterious to spermatozoa since motility was fully restored by the addition of pyruvate. In addition, sperm were able to synthesize ATP by metabolizing pyruvate. Following incubation for 0, 30, and 60 minutes in medium without substrate, acrosome reactions were measured before and after motility restoration. ATP depletion induced a large percentage of acrosome reactions relative to controls ($32.29 \pm 1.22\%$ compared with $0.63 \pm 0.02\%$ at 60 minutes). Ca^{2+} was required for the effect. It is suggested that ATP depletion inactivates a Ca^{2+} -dependent ATPase expulsion mechanism for Ca^{2+} , thereby permitting Ca^{2+} influx and the acrosome reaction.

Key words: sperm motility, ATP depletion, acrosome.

Calcium was originally implicated in fertilization mechanisms in invertebrates (Dan, 1956). The demonstration of a Ca^{2+} -dependent ATPase on the outer acrosomal membrane of rabbits, humans (Gordon, 1973), guinea pigs (Gordon et al, 1974), mice, and rats (Gordon, unpublished observations) implicated Ca^{2+} as a potent factor in the mammalian acrosome reaction. Calcium was invoked both as a prerequisite for membrane fusion (Gordon, 1973) and as an activator of acrosomal enzymes which are necessary for sperm passage through egg investments (Williams et al, 1974). Subsequently, it was established that the mammalian acrosome reaction is dependent upon the

presence of external Ca^{2+} (Yanagimachi and Usui, 1974) and that Ca^{2+} influx precedes or parallels its occurrence (Singh et al, 1978).

Mechanisms of Ca^{2+} entry into the sperm head are still not definitely known. However, based on observations of the activity of plasmalemmal and acrosomal membrane transport enzymes, Gordon (1973) considered that a Ca^{2+} -dependent ATPase on the outer acrosome membrane is inactive until the plasmalemma is modified during capacitation (Gordon et al, 1974), when Ca^{2+} levels rise in the periacrosomal fluid. At this point, Ca^{2+} is transported into the acrosome.

Most cells maintain low Ca^{2+} levels by active extrusion and mitochondrial sequestration (Kretzinger, 1979). It is clear that sperm Ca^{2+} must be kept low to prevent premature acrosome reactions. Since intracellular Ca^{2+} levels are dependent upon passive membrane permeability and an active Ca^{2+} -dependent ATPase, an alteration in either processes will result in altered Ca^{2+} flux. Oleate, lysolecithin, and Cd^{2+} , agents that increase Ca^{2+} membrane permeability (Hasselbach, 1972; Hurwitz et al, 1977), can induce the acrosome reaction in the presence of external Ca^{2+} (Gordon, unpublished observation). In the present study, the authors have examined the effect of depletion of ATP, and thus decreased activity of the Ca^{2+} -dependent ATPase expulsion mechanism, upon the guinea pig acrosome reaction.

Materials and Methods

Guinea pig spermatozoa were extruded from the cauda epididymidis into 0.9% NaCl in H_2O . After

This work was supported by NIH grant HD 13163.

Reprint requests: Dr. M. Gordon, School for Biomedical Education, City College, 138th Street and Convent Avenue, New York, New York 10031.

* Present Address: Northwestern University, Auditory Research Laboratory, Frances Searle Building, 2299 Sheridan Road, Evanston, Illinois 60201.

Submitted for publication January 15, 1981; revised version received June 18, 1981; accepted for publication August 18, 1981.

washing three times by centrifugation (1000 g; 4 minutes each) spermatozoa were suspended in substrate-free BWB medium (NaCl 94.6 mM, KCl 4.7 mM, CaCl₂ 1.71 mM, KH₂PO₄ 1.19 mM, MgSO₄ 1.19 mM, NaHCO₃ 25.07 mM, and bovine serum albumin 1 g/l), pH 7.55, at a final concentration of 1×10^7 sperm/ml. Pyruvate-containing medium (10 mM) and Ca²⁺-free medium were also employed. Spermatozoa were incubated at 37 C under air.

After suspension of spermatozoa in the substrate-free BWB, ATP was assayed at 0, 15, 30, 45, and 60 minutes. At 60 minutes, either glucose (8 mM) or pyruvate (8 mM) was added and ATP was assayed 15 minutes later. Assays were performed on two occasions. The caudae of three guinea pigs were pooled to perform each assay. According to the method of Cole et al (1967), ATP was extracted from aliquots of spermatozoa with perchloric acid and was measured by the luciferase assay as described by Stanley and Williams (1969).

Acrosome reactions were assessed by use of a hemocytometer (four chambers, 0.1 mm³ each) after 0-, 30-, and 60-minute incubations (Santos-Sacchi and Gordon, 1980). For spermatozoa incubated in the absence of energy substrates, acrosome reactions were counted before and after motility restoration by 10 mM pyruvate. Acrosome reaction indices for spermatozoa incubated in medium with pyruvate from 0 time were based upon motile spermatozoa only. Spermatozoa were examined by light and phase contrast microscopy. Motile sperm are sperm with an active flagellar beat, including those freely swimming and those whose heads have attached

to the slide during the counting procedure. The following formulae were used to calculate acrosome reaction (AR) responses: %AR = (AR spermatozoa/total spermatozoa) × 100; %AR^{tot} = [(AR spermatozoa/(total spermatozoa - immotile spermatozoa))] × 100 (Santos-Sacchi and Gordon, 1980).

Results

Within 15 minutes after suspension in substrate-free BWB, over 95% of the spermatozoa become immotile. Figure 1 demonstrates the concomitant rapid decrease in sperm ATP levels, which dropped to about 6% of initial values (2.14 μg/10⁸ cells) within 15 minutes. Pyruvate restores motility to a large proportion of spermatozoa (Fig. 2, insert), but glucose does not. A difference in the ability of ATP-depleted spermatozoa to utilize these substrates was also observed (Fig. 1). Whereas pyruvate increases sperm ATP levels to nearly half their initial levels within 15 minutes, glucose is essentially ineffective. The inability of pyruvate to restore motility to all spermatozoa was not the result of damage to spermatozoa by the absence of substrate, since approximately the same percentage of motile spermatozoa were present in controls where pyruvate had been present from 0 time (Fig. 2, insert).

Figures 2 and 3 show the effect of incubation

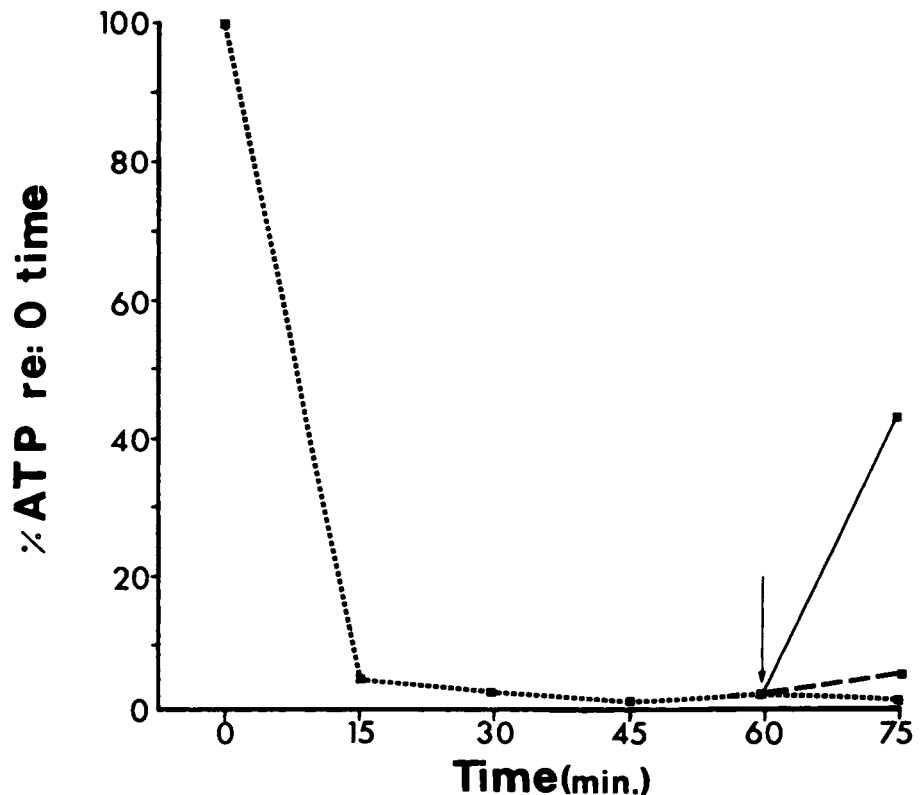


Fig. 1. Sperm samples were assayed for ATP at 15-minute intervals after suspension in substrate-free BWB (-----). At 60 minutes pyruvate or glucose (8 mM) was added (arrow) to samples, and ATP was assayed 15 minutes later (pyruvate —; glucose ---). The ATP levels determined at 0 time for the first and second assay were 2.22 μm/10⁸ sperm and 2.14 μm/10⁸ sperm, respectively. The 15-minute levels were reduced to 2.95% and 6.4% of initial values, respectively. The average of the two assays is reported here as a percentage of the 0 time value.

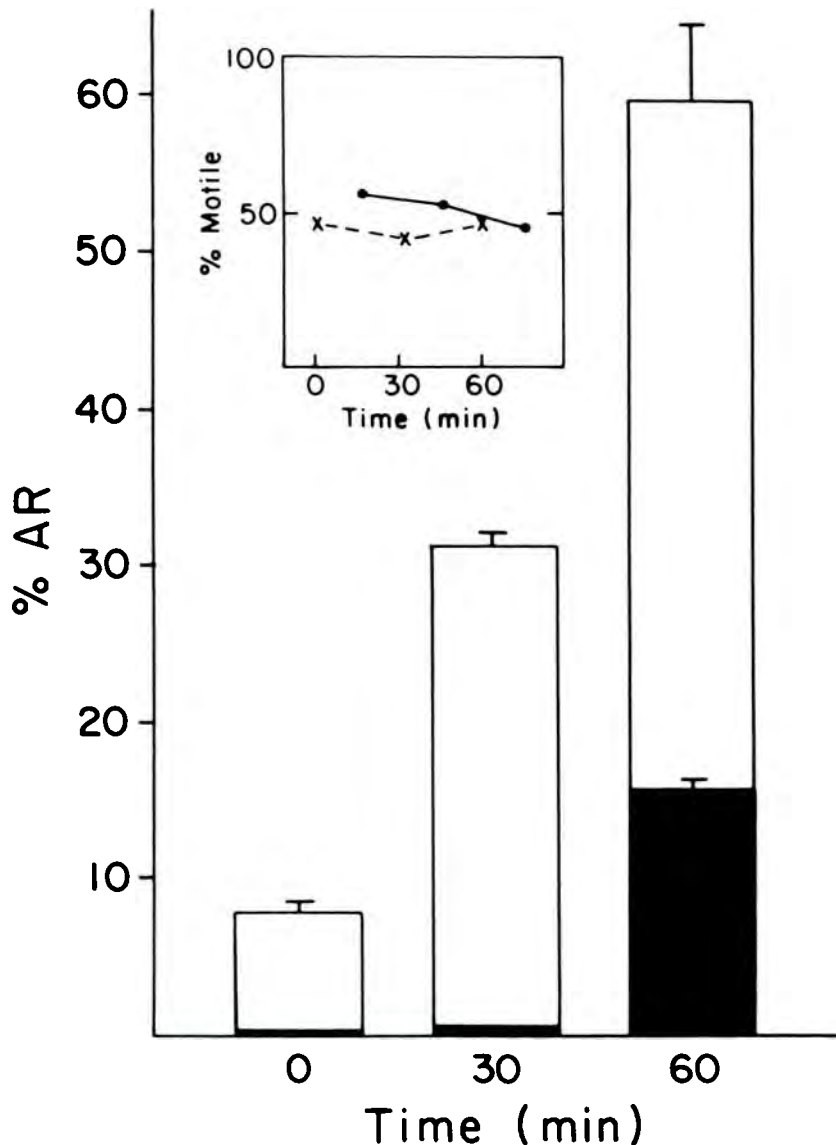


Fig. 2. Sperm were incubated in substrate-free BWW medium, and the percentages of acrosome reactions were determined prior to restoration of motility (light bars). The dark bars show the percentages of acrosome-reacted sperm whose motility was restored by pyruvate addition (10 mM). Insert: the percentages of sperm that remained motile during incubation in the presence of pyruvate from 0 time (—) and the percentages of sperm incubated in substrate-free BWW whose motility was restored by the addition of pyruvate (10 mM) at 0, 30, and 60 minutes (---).

time upon the induction of acrosome reactions. In the presence of Ca^{2+} , a time-dependent increase in the $\%AR^{\text{tot}}$ score is observed for spermatozoa incubated with or without an energy substrate. However, the $\%AR^{\text{tot}}$ scores for those spermatozoa incubated without substrate are dramatically higher than for those incubated in the presence of pyruvate (1 hour: $32.29 \pm 1.22\%$ vs. $0.63 \pm 0.02\%$) (Fig. 3). The number of immotile acrosome-reacted spermatozoa that became motile upon the addition of pyruvate also increases over time (Fig. 2). Because pyruvate was added to restore sperm motility prior to determining the $\%AR^{\text{tot}}$ scores, it was necessary to establish whether pyruvate induced the acrosome reaction. The pyruvate effect

on motility is not related to the acrosome reaction, because an increase in the number of *immotile acrosome-reacted spermatozoa* is found prior to pyruvate addition (Fig. 2). Furthermore, microscopic examination showed that acrosome-reacted and non-acrosome-reacted spermatozoa regain motility immediately (within 2 minutes) after pyruvate addition, with the acrosome-reacted spermatozoa exhibiting an "activated" pattern of motility (Yanagimachi and Usui, 1974).

In the absence of Ca^{2+} , the $\%AR$ score is very low relative to that in the presence of Ca^{2+} . After a 2-hour incubation in Ca^{2+} -free medium, only $27 \pm 4\%$ immotile acrosome-reacted spermatozoa are found. Pyruvate *did not* restore motility of

acrosome-reacted spermatozoa but did restore the motility of non-acrosome-reacted spermatozoa, indicating that acrosome degeneration occurred after the death of these sperm. The 2-hour %AR^{tot} score for spermatozoa incubated from 0 time with pyruvate in Ca²⁺-free medium was also very low, equivalent to that obtained after 30 minutes in the Ca²⁺-containing control.

Osmolality differences between substrate and substrate-free conditions were not responsible for the observed results, since glucose (5 mM) could replace pyruvate if added at the initiation of incubation. Under such circumstances, osmolality differences between substrate and substrate-free conditions were insignificant (5 mOsmol).

Discussion

Gordon (1973) originally suggested that an outer acrosome membrane Ca²⁺-dependent ATPase initiates the acrosome reaction by actively increasing acrosomal Ca²⁺ concentration. Green (1978), however, suggested that influx of calcium during the acrosome reaction is a result of passive diffusion. The induction of the acrosome reaction after ATP depletion suggests passive Ca²⁺ influx. Thus, rather than activity of the ATPase, the entry of Ca²⁺ for initiation of membrane fusion and exocytosis may be due to inhibition of an active Ca²⁺-dependent ATPase expulsion mechanism for calcium. The consistent demonstration of an active Ca²⁺-dependent ATPase on the outer acrosome membrane in epididymal and seminal spermatozoa (Gordon, 1973) lends support to this idea. The demonstration that plasmalemmal glycoproteins (Gordon et al, 1974) and enzymes (Gordon and Dandekar, 1977) are modified during capacitation of rabbit sperm may now be interpreted as a prerequisite to inactivation of the acrosomal membrane Ca²⁺-dependent ATPase. Thus loss of plasmalemmal integrity may affect the functional properties of the outer acrosomal membrane. In fact, Gordon et al (1978) demonstrated that the loss of Ca²⁺-dependent ATPase on the acrosome surface was correlated with destabilization of the plasma membrane of guinea pig sperm.

It is interesting to note that ATP levels decrease during capacitation (Rogers and Morton, 1973). A decrease in acrosomal membrane ATPase activity could be due to a decrease in substrate availability as well as to a decline in enzyme activity. Stores of ATP could be depleted within cellular compartments located near the acrosome independently of

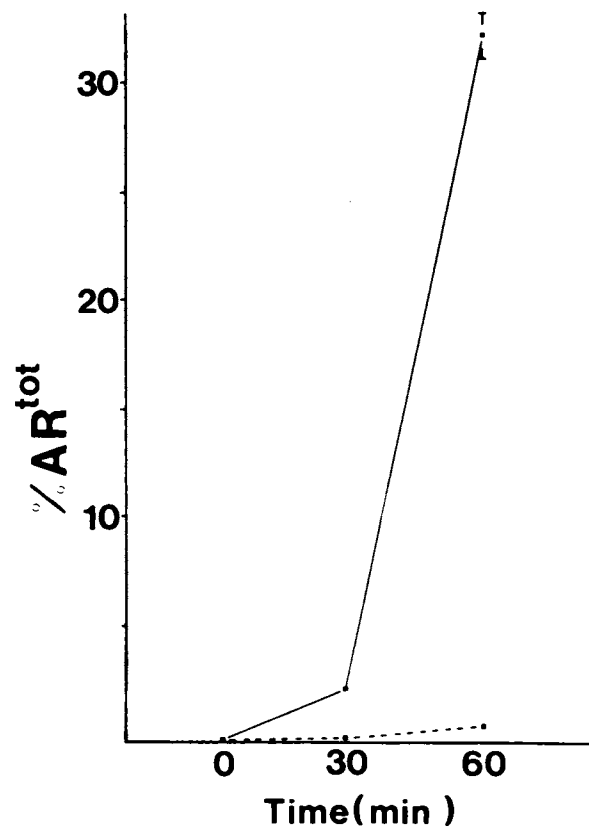


Fig. 3. The percentages of motile acrosome-reacted sperm as a function of incubation time. The motility of sperm incubated in substrate-free BWB (—) was restored by pyruvate addition (10 mM) at 0, 30, and 60 minutes, whereupon acrosome reactions were assessed. Sperm incubated in the presence of pyruvate from 0 time were assessed as well (---).

axonemal ATP. The sperm head is effectively isolated from the flagellum by a tight membrane junction (Fawcett, 1975). Therefore, the acrosome reaction may occur as a result of localized ATP depletion, despite intense flagellar "activation." In this study, ATP depletion produced immotility. Since pyruvate fully restored motility, ATP depletion does not damage the flagellar-mitochondrial system. The inability of glucose to restore motility is probably due to the ATP requirement for glucose utilization, since glucose alone can maintain motility if present at onset of incubation, ie, when ATP levels are high.

The consequences of ATP depletion on cAMP production may be significant. If cAMP generation is reduced or abolished, this may affect Ca²⁺ flux and the acrosome reaction. It has been shown that exogenous cAMP inhibits (Garcia and Rogers, 1978; Rogers and Garcia, 1979) and exogenous cGMP in the presence of Ca²⁺ induces the guinea

pig acrosome reaction (Santos-Sacchi and Gordon, 1980; Santos-Sacchi et al, 1980).

The rate of induction of acrosome reactions by ATP depletion is slower than that induced by changes in membrane Ca^{2+} permeability. For example, after a 1-hour incubation in glucose-free BWW, the addition of $4.5 \mu\text{g}$ oleate/ 10^7 spermatozoa induces a high percent acrosome reaction within a few minutes (Gordon, unpublished observations). This difference in induction time can be explained by the intrinsically poor Ca^{2+} permeability of plasma membrane (Lee and Shin, 1979). It appears that inhibition of Ca^{2+} -dependent ATPase in an otherwise intact membrane will not increase the rate of passive Ca^{2+} permeation but will permit a slow equilibration due to the inability to extrude Ca^{2+} . Agents that increase the passive Ca^{2+} permeability, on the other hand, result in a rapid influx of Ca^{2+} , despite the presence of an active Ca^{2+} -dependent ATPase (Hasselbach, 1972). Hence the rapidity of onset of Ca^{2+} -dependent events is related to the particular mechanism disrupted, whether passive or active.

The spermatozoon is a terminal cell. Irreversible changes in the sperm surface during capacitation prepare the sperm for the acrosome reaction. Thus the breakdown of a Ca^{2+} expulsion mechanism associated with the external acrosome membrane would follow the breakdown of the sperm surface membrane barrier. The fluid compartment between the plasma membrane and acrosome would facilitate such a sequence of membrane changes.

Although the exact mechanism of acrosome reaction induction needs further study, the present findings suggest that Ca^{2+} concentration can increase in the acrosome as a result of ATP depletion. Decreased activity of a Ca^{2+} expulsion mechanism may therefore be the cellular mechanism that initiates the acrosome reaction and prepares the sperm for fertilization.

Acknowledgments

The authors wish to thank Dr. A Guffanti, Department of Biochemistry, Mt. Sinai School of Medicine, for his help with the ATP assays and Barbara Cooper for her assistance in the preparation of the manuscript.

References

- Cole H, Wimpenny JWT, Hughes DE. The ATP pool in *Escherichia coli*. I. Measurement of the pool using modified luciferase assay. *Biochem Biophys Acta* 1967; 143:445-453.
- Dan JC. The acrosome reaction. *Intl Rev Cytol* 1956; 5:356-393.
- Fawcett DW. The mammalian spermatozoon. *Dev Biol* 1975; 44:394-436.
- Garcia L, Rogers BJ. Effect of cyclic-AMP on capacitation and fertilization. Society for the Study of Reproduction, 11th Meeting. *Biol Reprod* 1978; 18(Suppl 1): 79A.
- Gordon M. Localization of phosphatase activity on the membranes of the mammalian sperm head. *J Exp Zool* 1973; 185:11-120.
- Gordon M, Dandekar, PV. Fine structural localization of phosphatase activities on the plasma membrane of the rabbit sperm head. *J Reprod Fert* 1977; 49:155-156.
- Gordon M, Dandekar PV, Bartoszewicz W. The surface coat of epididymal, ejaculated and capacitated sperm. *J Ultrastr Res* 1974; 50:199-207.
- Gordon M, Dandekar PV, Eager PR. Identification of phosphatases on the membranes of guinea pig sperm. *Anat Rec* 1978; 191:123-133.
- Green, DPL. The induction of the acrosome reaction in guinea-pig sperm by the divalent metal cation ionophore A23187. *J Cell Sci* 1978; 32:137-151.
- Hasselbach W. The sarcoplasmic calcium pump. In: Weber HH, eds. *Molecular bioenergetics and macromolecular biochemistry*. Berlin: Springer-Verlag, 1972; 149-171.
- Hurwitz L, Debbas G, Little, S. Effects of temperature and inorganic ions on calcium uptake microsomes. In: Stephens NL, ed. *The biochemistry of smooth muscle*. Baltimore: University Park Press, 1977; 595-615.
- Kretsinger RH. The informational role of calcium in the cytosol. *Adv Cyclic Nucleotide Res* 1979; 11:1-26.
- Lee KS and Shin BC. Studies on the active transport of calcium in human red cells. *J Gen Physiol* 1979; 54:713-729.
- Rogers BJ and Garcia L. Effect of cAMP on acrosome reaction and fertilization. *Biol Reprod* 1979; 21:365-372.
- Rogers BJ, Morton B. ATP levels in hamster spermatozoa during capacitation in vitro. *Biol Reprod* 1973; 9:361-369.
- Santos-Sacchi J, Gordon M. The induction of the acrosome reaction in guinea pig spermatozoa by cyclic guanosine monophosphate analogues. *J Cell Biol* 1980; 85:798-803.
- Santos-Sacchi J, Gordon M, Williams WL. Potentiation of the cGMP-induced guinea acrosome reaction by zinc. *J Exp Zool* 1980; 213:289-291.
- Singh J, Babcock D, Lardy H. Increased calcium-ion influx is a component of capacitation of spermatozoa. *Biochem J* 1978; 172:549-556.
- Stanley PE, Williams SG. Use of the liquid scintillation spectrometer for determining adenosine triphosphate by the luciferase enzyme. *Anal Biochem* 1969; 29:381-392.
- Williams WL, Srivastava PN, Dudkiewicz AB. Membrane and enzyme events in penetration of the mammalian ovum by sperm. In: *Regulation of growth and differentiated function in eukaryote cells*. New York: Raven Press, 1974; 491-497.
- Yanagimachi R, Usui N. Calcium dependence of the acrosome reaction and activation of guinea pig spermatozoa. *Exp Cell Res* 1974; 89:161-174.

Temperature dependence of outer hair cell nonlinear capacitance

J. Santos-Sacchi^{a,b,*}, Guojie Huang^a

^a Section of Otolaryngology, BML 244, Yale University School of Medicine, 333 Cedar St., New Haven, CT 06510, USA

^b Section of Neurobiology, Yale University School of Medicine, New Haven, CT 06510, USA

Received 22 July 1997; revised 25 October 1997; accepted 28 October 1997

Abstract

The temperature dependence of outer hair cell motility-related gating current and capacitance was evaluated under whole-cell voltage clamp. Temperature change caused a shift of these voltage-dependent functions along the voltage axis, with a decrease in temperature causing a negative shift in the voltage at peak capacitance (V_{pkcm}) of 19.2 mV per 10°C. Gating current kinetics showed only mild temperature dependence, the Q_{10} being about 1.5. Temperature is speculated to affect outer hair cell (OHC) mechanical gain and frequency response by alterations in lateral membrane viscoelastic properties. Such temperature-dependent effects on the OHC may mediate known temperature effects on in vivo cochlear physiology. © 1998 Published by Elsevier Science B.V.

Key words: Outer hair cell; Motility; Capacitance; Temperature; Patch clamp

1. Introduction

The discovery that outer hair cells (OHC) can change their length in response to electrical stimuli profoundly influenced the study of cochlear physiology (Brownell et al., 1985). OHC motility is dependent upon transmembrane voltage (Santos-Sacchi and Dilger, 1988; Iwasa and Kachar, 1989); hyperpolarization elongates and depolarization shortens the cylindrically shaped cell. The mechanism underlying this shape change which occurs at acoustic frequencies is unknown. However, it is not based on typical cellular mechanisms of motility (Kachar et al., 1986; Santos-Sacchi and Dilger, 1988; Holley and Ashmore, 1988). In fact, current indications are that the force generating mechanism resides solely within the lateral plasma membrane (Kaliniec et al., 1992; Huang and Santos-Sacchi, 1993, 1994), possibly corresponding to the 8–10 nm intramembranous particles observed ultrastructurally (Gulley and Reese, 1977; Forge, 1991).

The mechanical activity of the OHC is mirrored by an electrical signature, a voltage-dependent capacitance

or, equivalently, a gating charge movement (Ashmore, 1989; Santos-Sacchi, 1990, 1991; Iwasa, 1993), which indicates that membrane-bound voltage sensor-motor elements control OHC length (Santos-Sacchi, 1990, 1991, 1993; Ashmore, 1989, 1992; Dallos et al., 1991; Iwasa, 1994). In this report we measure the effects of temperature on the OHC motility-related gating currents and nonlinear capacitance. We report that both the kinetics and voltage dependence of nonlinear charge movement are affected. Preliminary accounts of this work have been presented (Santos-Sacchi, 1990; Santos-Sacchi et al., 1995).

2. Materials and methods

Guinea pigs were overdosed with halothane. The temporal bones were removed, the apical two turns of the organ of Corti micro-dissected free, and OHCs isolated enzymatically with collagenase (0.3 mg/ml for 10 min followed by gentle reflux through a tapered polyethylene pipette tip) in medium 199 with Hanks' salts (Gibco). The cell enriched supernatant was then transferred to a 700 μ l perfusion chamber, and the cells permitted to settle onto the cover glass bottom. A Ni-

* Corresponding author.

Tel.: +1 (203) 785-7566 (office); +1 (203) 785-5407 (lab);

Fax: +1 (203) 737-2245; E-mail: joseph.santos-sacchi@yale.edu

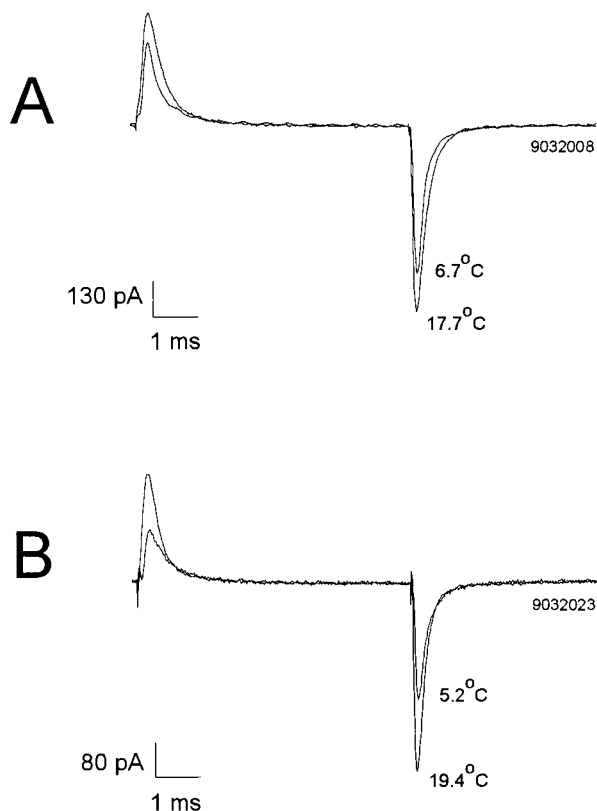


Fig. 1. Two OHCs were clamped to -80 mV and gating currents were extracted with the $\pm P$ protocol (40 mV about the holding potential). A drop in temperature decreased both the gating charge moved and the exponential time constant of the current decay. A: Larger amplitude trace: 17.7°C ; Q_{off} : 240 fC; τ_{off} : 0.21 ms. Smaller amplitude trace: 6.7°C ; Q_{off} : 162 fC; τ_{off} : 0.24 ms. B: Larger amplitude trace: 19.4°C ; Q_{off} : 144 fC; τ_{off} : 0.18 ms. Smaller amplitude trace: 5.2°C ; Q_{off} : 98 fC; τ_{off} : 0.26 ms. The effects were reversible.

kon Diaphot inverted microscope with Hoffmann optics was used to observe the cells during electrical recording. A modified Leibovitz medium (NaCl 100 mM, KCl 5.37 mM, CoCl_2 2.0 mM, MgCl_2 1.48 mM, 20 mM TEA, 2 μM TTX, 20 mM CsCl, HEPES 5.0 mM, dextrose 5.0 mM, pH 7.2) was used in order to block ionic conductances which might otherwise interfere with capacitive current measures. OHCs maintained normal appearance in this solution for up to 1 h. Osmolarity was adjusted to 300 mOsm with dextrose.

OHCs were whole-cell voltage clamped with a Dagan 8900 patch clamp amplifier at a holding potential of -80 mV, similar to the resting potential recorded in vivo (Dallos et al., 1982). Pipette solutions were composed of 140 mM CsCl, 10 mM EGTA, 5 mM TEA, 2 mM MgCl_2 , and 5 mM HEPES buffered to pH 7.2. Osmolarity was adjusted to 300 mOsm with dextrose. Gigohm seals were obtained at the nuclear level of the cell membrane; electrode capacitance and series resistance were compensated. A modified version of Clampex (Axon Instruments, CA) utilizing the Labmaster board (Axon) was used to collect data which were saved to

disk for off-line analysis. Current was filtered at 5 kHz with an 8-pole Bessel filter. Temperature was controlled with a custom-built Peltier recording chamber, and measured with a micro temperature probe (Sensortek, NJ) placed within 0.5 mm of the recorded cells. In addition, data were confirmed using pre-cooled or pre-warmed solutions in the absence of the Peltier device.

Detailed evaluation of the bell-shaped OHC membrane capacitance function was made at different potentials by transient analysis of currents induced by a voltage stair step stimulus. Step duration was adjusted on-line to $15\times$ the time constant of the capacitive transient to ensure steady-state conditions. The capacitance function was fit to the first derivative of a two-state Boltzmann function relating nonlinear charge to membrane voltage ($\delta Q/\delta V$; Santos-Sacchi, 1991; Huang and Santos-Sacchi, 1993),

$$C_m = Q_{\text{max}} \frac{ze}{kT} \frac{b}{(1+b)^2} + C_{\text{lin}} \quad (1a)$$

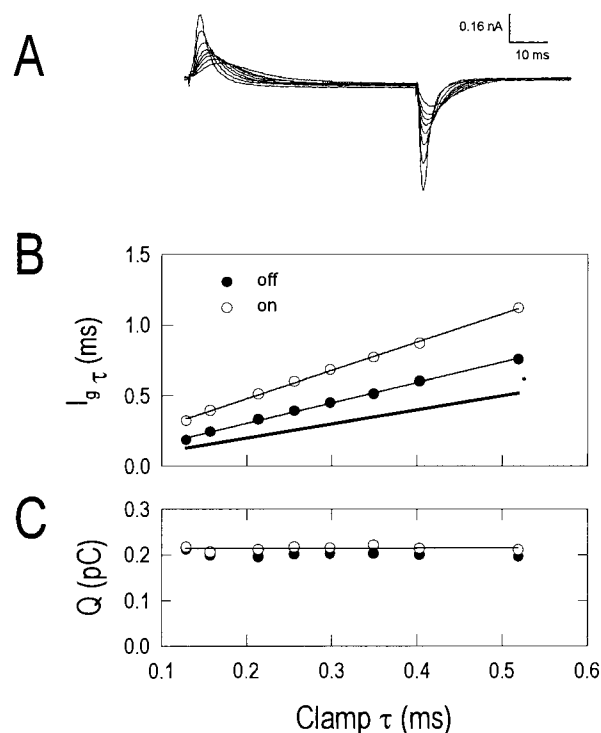


Fig. 2. A: The time constant of OHC gating current decay was modified by altering the speed of the voltage clamp via series resistance compensation. Gating currents were obtained as in Fig. 1. B: Gating charge time constant followed that of the voltage clamp. The thick solid line represents a one-to-one correspondence between clamp τ and gate τ . C: However, changing the gating time constant does not modify total charge moved. The charge is simply redistributed over time. The change in charge moved as a function of temperature (Fig. 1) is therefore not due to a simple effect on the time constant of the clamp amplifier.

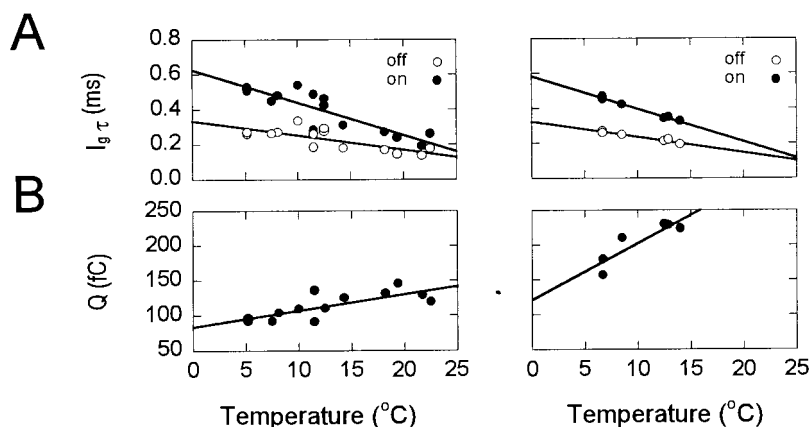


Fig. 3. The effects of temperature on gating currents are presented in detail for two OHCs (left and right panel). A: The time constant of on and off gating current relaxation as a function of temperature. Note the differences between on and off time constants. Left panel: $\tau^{-1} Q_{10}$ on: 1.55; off: 1.4. Right panel: $\tau^{-1} Q_{10}$ on: 1.62; off: 1.45. B: The average of on and off charge moved as a function of temperature. On and off charge were essentially equivalent.

where

$$b = \exp \frac{-ze(V - V_{\text{pkcm}})}{kT} \quad (1b)$$

Q_{max} is the maximum nonlinear charge moved, V_{pkcm} is voltage at peak capacitance or equivalently, at half maximal nonlinear charge transfer, V_m is membrane potential, z is valence, C_{lin} is linear membrane capacitance, e is electron charge, k is Boltzmann's constant, and T is absolute temperature. Gating currents were extracted online with the $\pm P$ procedure (± 40 mV; Armstrong and Bezanilla, 1973) about a holding potential of -80 mV, or with the $P/-5$ protocol, at a subtraction potential of -160 mV (Armstrong and Bezanilla, 1977). All data analysis was performed with the software package MATLAB (Mathworks, MA). In some experiments, V_{pkcm} was monitored during temperature changes using a previously developed tracking procedure (Kakehata and Santos-Sacchi, 1995). Cell turgor pressure was either maintained constant by pipette pressure, or cells were collapsed so that pressure-induced shift in V_{pkcm} did not interfere with analysis of temperature effects (Kakehata and Santos-Sacchi, 1995). Q_{10} was determined as in Kimura and Meves (1979). The use and treatment of animals was approved by the Yale University animal care committee.

3. Results

Nonlinear gating currents associated with the mechanical responses of OHCs are induced at the onset and offset of voltage steps. Fig. 1 illustrates these currents in two cells obtained at a holding potential of -80 mV, each at two different temperatures. The effect of temperature change is to alter the total amount of

charge moved and the time constant (τ_{on} and τ_{off}) of the current decay. Both the rate and quantity of charge moved are decreased as temperature is decreased. Note also that τ_{on} and τ_{off} differ, with τ_{on} being slower. It has been previously shown that the clamp time constant affects the speed of OHC charge movement (Santos-Sacchi, 1990, 1992). However, changing the clamp time constant does not alter the amount of charge moved (Fig. 2). Thus, any affects of temperature upon clamp time constant (Santos-Sacchi, 1990) would not be

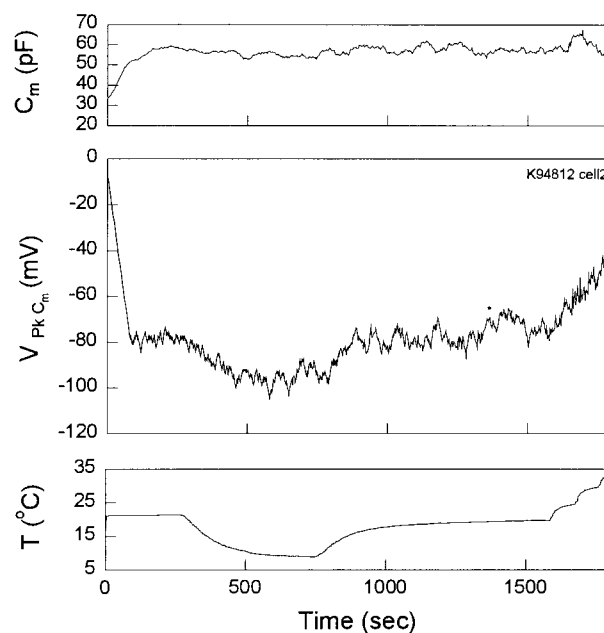


Fig. 4. The voltage at peak capacitance (V_{pkcm}) follows changes in temperature. A tracking procedure developed previously (Kakehata and Santos-Sacchi, 1995) was used to follow changes in C_{mpk} and V_{pkcm} as temperature was reversibly modified over the course of minutes. Tracking initiated at 0 mV. Note close correspondence between changes in temperature and V_{pkcm} .

expected to modify the total charge moved. In Fig. 3, a detailed analysis of the temperature effects is presented for two cells. It can be seen that the gating current time constants (τ_{on} and τ_{off}) and charge movement (Q) are proportional to temperature. The τ_{off} appears less affected by temperature than does τ_{on} . In each cell, the Q_{10} for τ_{on}^{-1} and τ_{off}^{-1} was about 1.6 and 1.4, respectively.

The OHC possesses a bell-shaped voltage-dependent capacitance function as a consequence of its membrane-bound nonlinear charge movement. The voltage where capacitance is maximal (V_{pkcm}) corresponds to the voltage where half maximal charge movement occurs, and where OHC motility is most sensitive to voltage fluctuations. Fig. 4 illustrates with a real time tracking technique that V_{pkcm} closely follows changes in temperature. Decreasing temperature causes a negative shift in V_{pkcm} and visa versa. Detailed capacitance evaluations support these tracking observations. Fig. 5A illustrates a family of capacitance functions obtained from a single OHC during temperature plateaus at 25, 21, 14, 8 and 6°C. V_{pkcm} shifted 26.8 mV between temperature extremes. Peak capacitance also decreased in this case, accompanied by a decrease in valence, z . Average results ($n=6$) are depicted in Fig. 5B. Q_{max} showed little significant systematic change. The valence, z , showed a change of 0.12 per 10°C, and V_{pkcm} changed 19.2 mV per 10°C.

Gating currents were also evaluated using the P/−5 protocol, which more effectively extracts gating currents (Armstrong and Bezanilla, 1977). Fig. 6 provides examples of gating currents from the same OHC evaluated in Fig. 5A. Fig. 6A,B show currents elicited by stepping from −120 mV to −30 and −60 mV, respectively. In both cases, decreasing temperature causes a decrease in the rate and quantity of charge moved. The average ($n=4$) $\tau_{\text{on}}^{-1} Q_{10}$ was 1.50 ± 0.06 (mean \pm S.E.M.). The $\tau_{\text{off}}^{-1} Q_{10}$ was 1.55 ± 0.08 . These results are in accord with the magnitudes obtained with the \pm P technique used above; differences between on and off time constant Q_{10} are not significant.

Finally, an attempt was made to obtain gating currents from giant patches of OHC membrane (Hilgemann, 1989). Unfortunately, patch pipettes with tip diameters near 5 μm consistently broke through the membrane to yield whole-cell configurations with poor seals. Nevertheless, recordings under these conditions were sometimes capable of garnering gating current information. Fig. 7 presents such an example, where the cell was held at 0 mV and gating currents extracted with the \pm P technique. The very fast time constant of the clamp amplifier under these conditions permitted recording of gating current time constants down to about 50 μs . Deiters cells under the same configuration showed no gating current. As in regular whole-cell configuration, decreases in temperature caused a reduction

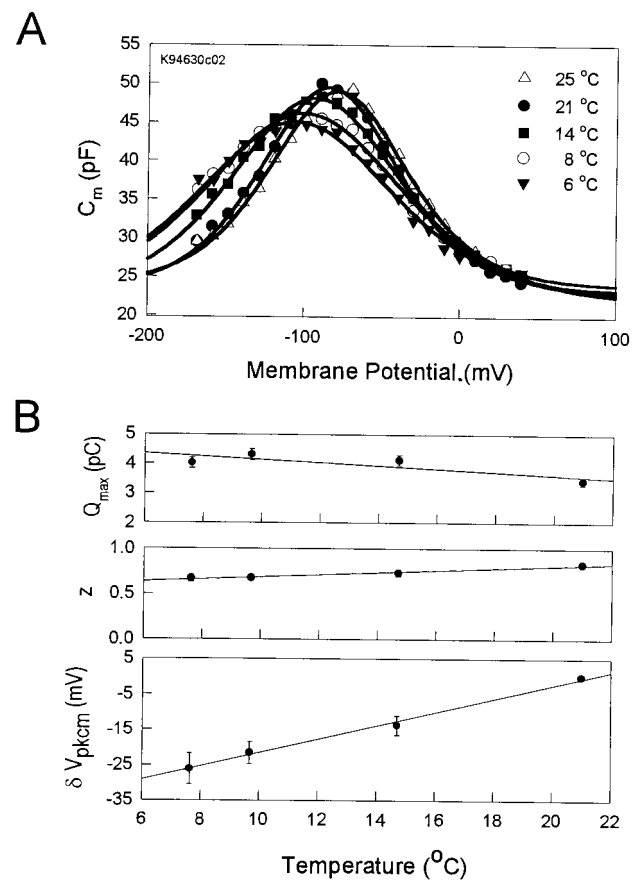


Fig. 5. Effect of temperature on OHC nonlinear capacitance. A: Capacitance was evaluated with the stair step protocol. As temperature is decreased from 25°C to 6°C, the functions shift in the hyperpolarizing direction. Solid lines are fits to Eq. 1. 25°C: V_{pkcm} : −78.8 mV; z : 0.87; Q_{max} : 2.99 pC; C_{lin} : 23.75 pF; 21°C: V_{pkcm} : −84.3 mV; z : 0.87; Q_{max} : 3.1 pC; C_{lin} : 23.12 pF; 14°C: V_{pkcm} : −93.1 mV; z : 0.71; Q_{max} : 3.74 pC; C_{lin} : 22.3 pF; 8°C: V_{pkcm} : −100.5 mV; z : 0.61; Q_{max} : 4.14 pC; C_{lin} : 21.7 pF; 6°C: V_{pkcm} : −105.6 mV; z : 0.62; Q_{max} : 3.77 pC; C_{lin} : 22.4 pF. B: Average results from six OHCs showing changes in parameters Q_{max} , z and V_{pkcm} . Error bars are \pm S.E.M. Q_{max} remains fairly stable with temperature, although a slight increase below 21°C may be significant. z changes slightly with temperature. V_{pkcm} is significantly susceptible to temperature, showing a 1.9 mV change per degree centigrade.

of OHC nonlinear charge moved, but had little effect on rate of charge movement.

4. Discussion

The OHC voltage-dependent charge movement or capacitance is sensitive to alterations in temperature. The most prominent effect appears to be on the position of these functions along the voltage axis, with a decrease in temperature causing a reversible negative shift in V_{pkcm} of 19.2 mV per 10°C. At a fixed holding and step potential, such a shift would be expected to result in a change in magnitude of charge moved. This is illustrated through modeling in Fig. 8. A small com-

ponent of the decrease in charge movement noted in gating current records as temperature is decreased may also be due to a redistribution in time beyond the experimental recording period, since steady-state indications from capacitance measures show little change in total charge moved (Q_{\max}). The whole-cell capacitance determinations from stair step stimuli were robust since integrations were made over intervals greater than 15 times the capacitive current time constants (Huang and Santos-Sacchi, 1993). Gating current kinetics are sensitive to temperature, as well, but show only a mild temperature dependence, the Q_{10} being about 1.5. The Q_{10} of ion channel gating current kinetics, on the other hand, is typically between 2 and 3 (Bezánilla and Taylor, 1978; Kimura and Meves, 1979; Adams and Gage, 1979; Schauf and Bullock, 1979; Collins and Rojas, 1982). It should be emphasized, however, that OHC motility-related gating current kinetics are faster than clamp time constants obtainable under whole-cell configuration (Santos-Sacchi, 1990, 1992), and are thus constrained by clamp characteristics. Nevertheless, at least for ion channels, a temperature-dependent shift in the voltage dependence of conformational state often accompanies a temperature dependence of the underlying molecular kinetics. For example, in batrachotoxin treated Na channels, a 7 mV per 10°C shift in the open probability function accompanied a Q_{10} of about 2.3 for mean open times

(Correa et al., 1992). For a two-state model, while a shift in steady-state probability reflects a change in the difference between open and closed steady-state energy levels, changes in kinetics are governed by alterations of the activation energy barrier height relative to those steady-state energy levels. Thus, changes in steady-state energy levels which effect shifts in the two-state probability function may also lead to changes in the relative height of the activation energy barrier, thereby affecting gating kinetics. Under the assumption that ionic channel and OHC molecular motor characteristics are similar, it is best to cautiously acknowledge that the large shift in OHC V_{pkcm} may be accompanied by a Q_{10} for the underlying kinetics which is greater than the measured value of 1.5, and that this value is a limitation of clamp speed. Temperature effects on OHC mechanical responses are also probably constrained by clamp speed (Holley and Ashmore, 1988). Recently, Ashmore and Gale (1997) found that gating current kinetics in OHC membrane patches, while remarkably fast (down to 7 μs τ), still evidenced Q_{10} s below 1.5. This is similar to results obtained with very fast clamp characteristics as in Fig. 7. However, they found no change in gating charge magnitude vs. temperature. This may indicate that, unlike our whole-cell results, V_{pkcm} did not shift in their membrane patch recording configuration, or just like our whole-cell results, clamp speed remained limiting.

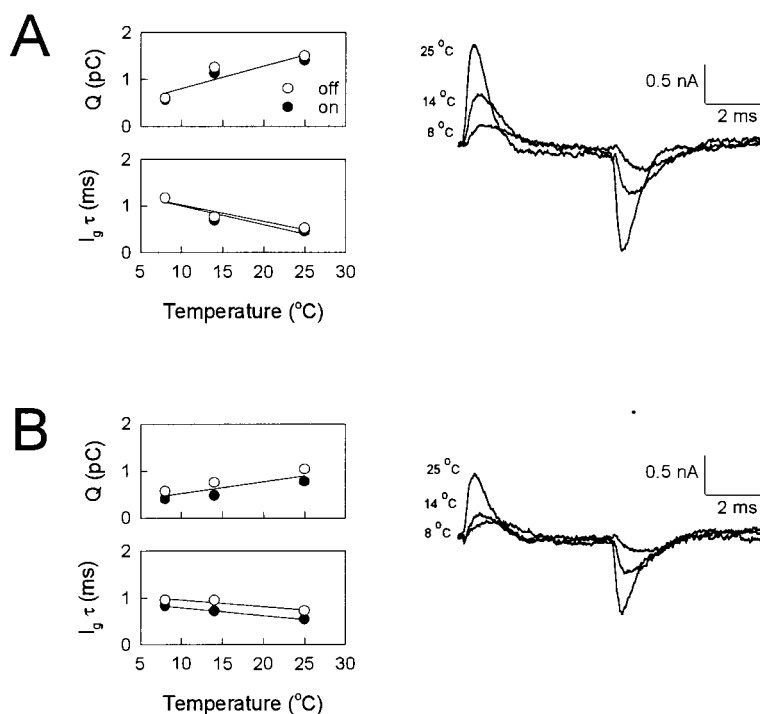


Fig. 6. Effect of temperature on gating currents obtained with the P/–5 protocol. Same cell as in Fig. 5A. A: Step voltage from –120 to –30 mV. A decrease in temperature from 25°C to 8°C decreases both charge moved and rate of movement. Q_{10} determined from the line fits for on and off gate τ was 1.61 and 1.49, respectively. B: Step voltage from –120 to –60 mV. Similar decreases were obtained. Q_{10} for on and off gate τ was 1.26 and 1.18, respectively.

A likely factor which might underlie the effects of temperature upon the kinetics of OHC lateral membrane motors, is a temperature dependence of OHC membrane viscosity. Membrane particle kinetics are governed by frictional forces within the medium, which are proportional to the medium's viscosity and particle size (see Rojas and Keynes, 1975). Interestingly, membrane viscosity may also underlie a component of the double exponential time course in voltage-induced V_{pkcm} shifts that we have recently found (Santos-Sacchi et al., 1996, 1997). It should be the case, then, that factors in addition to temperature, e.g. lipid composition, which influence OHC membrane viscosity or fluidity will have profound effects on OHC function.

OHC voltage-dependent capacitance is known to mirror characteristics of the OHC's mechanical activity (Ashmore, 1989, 1992; Santos-Sacchi, 1990, 1991, 1992; Kakehata and Santos-Sacchi, 1995). Given this relationship, temperature is expected to modify OHC motility and its physiological consequences, namely its contribution to the 'cochlear amplifier'. In this regard it is known that decreases in temperature are able to adversely affect *in vivo* cochlear frequency selectivity and sensitivity (e.g. Brown et al., 1983). Temperature change will alter the frequency response of OHC motility. In addition, a temperature-dependent shift in the OHC motility function along the voltage axis, which is indicated by the observed shift in V_{pkcm} , will alter the gain of OHC motility. Such effects may be sufficient to explain the *in vivo* results. However, it has also been shown that temperature modifies the resting length of isolated OHCs, which conceivably could modify basilar

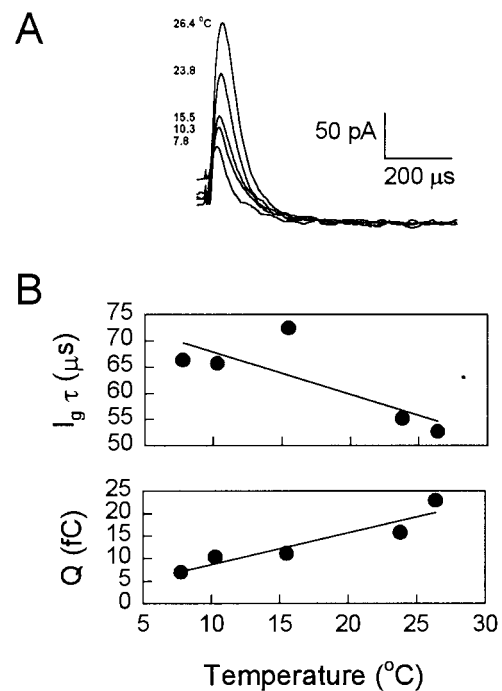


Fig. 7. A: Effect of temperature on gating currents obtained with very fast clamp time constant. During an attempt at giant patch formation with a 5 μm patch electrode tip, whole cell configuration was established. The trace shows off gating currents extracted with the $\pm P$ technique at 0 mV holding potential. The actual order of temperature change was 26.4, 10.3, 7.8, 15.5, and 23.8°C. B: Gate time constant and charge movement as a function of temperature. Charge moved decreases with temperature. Gating time constant is little effected by temperature; the fitted line represents a Q_{10} of about 1.2.

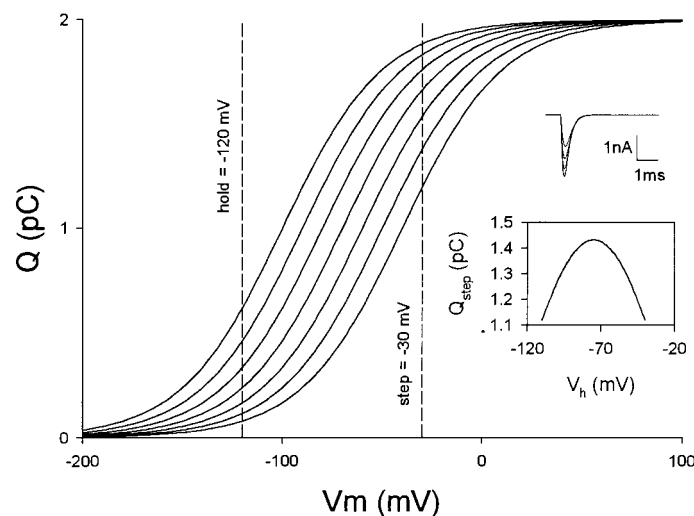


Fig. 8. Model illustrating the expected change in charge moved as a function of V_{pkcm} (V_h) shift. Cell model was as in Santos-Sacchi (1992), with R_s : 5 $\text{M}\Omega$, R_m : 100 $\text{M}\Omega$, C_m : 29 pF, Q_{max} : 2 pC, z : 1, V_{pkcm} (V_h): -40 to -100, in steps of 10 mV. Charge is plotted vs. membrane potential for each value of V_{pkcm} . The dotted lines indicate the holding potential and step potential used to obtain the off gating currents in the inset, which were obtained with the P/5 technique as for the biophysical data. The traces are plots only from V_{pkcm} of -70 to -100 mV, charge decreasing as V_{pkcm} shifts negatively. Scale: 1 ms, 1 nA. The inserted figure plots charge at the -30 mV step vs. V_{pkcm} (V_h), and illustrates that increases and decreases in charge moved can be obtained depending upon the relationship between holding, step and V_{pkcm} potential.

membrane tension in vivo (Gitter, 1992; LeCates et al., 1995). In addition to affecting the gain of OHC motility, a change in resting length at a fixed resting potential is expected from a shift in V_{pkcm} . This occurs because a displacement of the length vs. voltage function along the voltage axis (i.e. shift in V_{pkcm}) while holding the membrane potential constant will change the degree of contraction of the OHC. Given an OHC mechanical response of 20–30 nm/mV (Santos-Sacchi and Dilger, 1988), the temperature dependence of V_{pkcm} will provide for a resting length change of 0.04–0.06 $\mu\text{m}/^\circ\text{C}$. However, both Gitter (1992) and LeCates et al. (1995) found values nearly an order of magnitude larger, which indicates that something other than a direct effect on the membrane motor was responsible for their observations.

In sum, we provide additional evidence that physical modification of the environment which harbors the molecular motors for OHC motility can profoundly modify the cell's electromechanical behavior. Previously, it had been shown that membrane tension, either externally applied (Iwasa, 1993; Gale and Ashmore, 1994; Kakehata and Santos-Sacchi, 1995) or intrinsically generated by the molecular motors themselves (Santos-Sacchi et al., 1996, 1997), can alter the voltage dependence of OHC capacitance/motility. Taken together, these data attest to the OHC's, and, indeed, the cochlea's, exceptional susceptibility to functional perturbation.

Acknowledgments

We thank Margaret Mazzucco for technical support, and Dr. Knox Chandler for helpful discussions. This work was supported by NIH-NIDCD Grant DC00273 to J.S.S.

References

- Adams, D.J., Gage, P.W., 1979. Sodium and calcium gating currents in an aplysia neurone. *J. Physiol. (Lond.)* 291, 467–481.
- Armstrong, C.M., Bezanilla, F., 1973. Currents related to movement of the gating particles of the sodium channels. *Nature* 242, 459–461.
- Armstrong, C.M., Bezanilla, F., 1977. Inactivation of the sodium channel. II. Gating current experiments. *J. Gen. Physiol.* 70, 567–590.
- Ashmore, J.F., 1989. Transducer motor coupling in cochlear outer hair cells. In: Kemp, D., Wilson, J.P. (Eds.), *Mechanics of Hearing*, Plenum Press, New York, pp. 107–113.
- Ashmore, J.F., 1992. Mammalian hearing and the cellular mechanism of the cochlear amplifier. In: Corey, D.P., Roper, S.D. (Eds.), *Sensory Transduction*, Rockefeller University Press, New York, pp. 395–412.
- Ashmore, J.F., Gale, J.E., 1997. An intrinsic frequency limit to the cochlea amplifier. *Nature* (in press).
- Bezanilla, F., Taylor, R.E., 1978. Temperature effects on gating currents in the squid giant axon. *Biophys. J.* 23, 479–484.
- Brown, M.C., Smith, D.I., Nuttall, A.L., 1983. The temperature dependency of neural and hair cell responses evoked by high frequencies. *J. Acoust. Soc. Am.* 73, 1662–1670.
- Brownell, W.E., Bader, C.R., Bertrand, D., de Ribaupierre, Y., 1985. Evoked mechanical responses of isolated cochlear outer hair cells. *Science* 227, 194–196.
- Collins, C.A., Rojas, E., 1982. Temperature dependence of the sodium channel gating kinetics in the node of Ranvier. *Q. J. Exp. Physiol.* 67, 41–55.
- Correa, A.M., Bezanilla, F., Latorre, R., 1992. Gating kinetics of batrachotoxin-modified Na^+ channels in the squid giant axon. Voltage and temperature effects. *Biophys. J.* 61, 1332–1352.
- Dallos, P., Santos-Sacchi, J., Flock, A., 1982. Intracellular recordings from outer hair cells. *Science* 218, 582–584.
- Dallos, P., Evans, B.N., Hallworth, R., 1991. On the nature of the motor element in cochlear outer hair cells. *Nature* 350, 155–157.
- Forge, A., 1991. Structural features of the lateral walls in mammalian cochlear outer hair cells. *Cell Tissue Res.* 265, 473–483.
- Gale, J.E., Ashmore, J.F., 1994. Charge displacement induced by rapid stretch in the basolateral membrane of the guinea pig OHC. *Proc. R. Soc. Lond. B Biol. Sci.* 255, 243–249.
- Gitter, A.H., 1992. The length of isolated outer hair cells is temperature dependent. *ORL J. Oto-Rhino-Laryngol. Relat. Spec.* 54, 121–123.
- Gulley, R.L., Reese, T.S., 1977. Regional specialization of the hair cell plasmalemma in the organ of Corti. *Anat. Rec.* 189, 109–124.
- Hilgemann, D.W., 1989. Giant excised cardiac sarcolemmal membrane patches: sodium and sodium-calcium exchange currents. *Pflugers Arch.* 415, 247–249.
- Holley, M.C., Ashmore, J.F., 1988. On the mechanism of a high-frequency force generator in outer hair cells isolated from the guinea pig cochlea. *Proc. R. Soc. Lond. B* 232, 413–429.
- Huang, G.-J., Santos-Sacchi, J., 1993. Mapping the distribution of the outer hair cell motility voltage sensor by electrical amputation. *Biophys. J.* 65, 2228–2236.
- Huang, G.-J., Santos-Sacchi, J., 1994. Motility voltage sensor of the outer hair cell resides within the lateral plasma membrane. *Proc. Natl. Acad. Sci. USA* 91, 12268–12272.
- Iwasa, K.H., 1993. Effect of stress on the membrane capacitance of the auditory outer hair cell. *Biophys. J.* 65, 492–498.
- Iwasa, K.H., 1994. A membrane motor model for the fast motility of the OHC. *J. Acoust. Soc. Am.* 96, 2216–2224.
- Iwasa, K.H., Kachar, B., 1989. Fast in vitro movement of outer hair cells in an external electric field: effect of digitonin, a membrane permeabilizing agent. *Hear. Res.* 40, 247–254.
- Kachar, B., Brownell, W.E., Altschuler, R., Fex, J., 1986. Electrokinetic shape changes of cochlear outer hair cells. *Nature* 322 (6077), 365–368.
- Kakehata, S., Santos-Sacchi, J., 1995. Membrane tension directly shifts voltage dependence of outer hair cell motility and associated gating charge. *Biophys. J.* 68, 2190–2197.
- Kalincic, F., Holley, M.C., Iwasa, K.H., Lim, D.J., Kachar, B., 1992. A membrane-based force generation mechanism in auditory sensory cells. *Proc. Natl. Acad. Sci. USA* 89, 8671–8675.
- Kimura, J.E., Meves, H., 1979. The effect of temperature on the asymmetrical charge movement in squid giant axons. *J. Physiol. (Lond.)* 289, 479–500.
- LeCates, W.W., Kuo, S.C., Brownell, W.E., 1995. Temperature dependent length changes of the outer hair cell. Mid-winter Meeting of the Association for Research in Otolaryngology, St. Petersburg, FL, February.
- Rojas, E., Keynes, R.D., 1975. On the relation between displacement currents and activation of the sodium conductance in the squid giant axon. *Phil. Trans. R. Soc. Lond. Ser. B Biol. Sci.* 270, 459–482.
- Santos-Sacchi, J., 1990. Fast outer hair cell motility: how fast is fast? In: Dallos, P., Geisler, C.D., Matthews, J.W., Ruggero, M.A.,

- Steele, C.R. (Eds.) *The Mechanics and Biophysics of Hearing*, Springer-Verlag, Berlin, pp. 69–75.
- Santos-Sacchi, J., 1991. Reversible inhibition of voltage-dependent outer hair cell motility and capacitance. *J. Neurosci.* 11, 3096–3110.
- Santos-Sacchi, J., 1992. On the frequency limit and phase of outer hair cell motility: effects of the membrane filter. *J. Neurosci.* 12, 1906–1916.
- Santos-Sacchi, J., 1993. Harmonics of outer hair cell motility. *Biophys. J.* 65, 2217–2227.
- Santos-Sacchi, J., Dilger, J.P., 1988. Whole cell currents and mechanical responses of isolated outer hair cells. *Hear. Res.* 35, 143–150.
- Santos-Sacchi, J., Huang, G.-J., Kakehata, S., 1995. Physical modulators of OHC nonlinear capacitance. Mid-winter Meeting of the Association for Research in Otolaryngology, St. Petersburg, FL, February.
- Santos-Sacchi, J., Kakehata, S., Takahashi, S., 1996. The voltage-dependent capacitance function of the outer hair cell has memory. *Soc. Neurosci.* 26th Annual Meeting.
- Santos-Sacchi, J., Kakehata, S., Takahashi, S., 1997. Voltages past: The outer hair cell has memory. Mid-winter Meeting of the Association for Research in Otolaryngology, St. Petersburg, FL, February.
- Schauf, C.L., Bullock, J.O., 1979. Modifications of sodium channel gating in *Myxicola* giant axons by deuterium oxide, temperature, and internal cations. *Biophys. J.* 27, 193–208.

AN EVALUATION OF NORMAL STRIAL CAPILLARY TRANSPORT
USING THE ELECTRON-OPAQUE TRACERS
FERRITIN AND IRON DEXTRAN

J. Santos-Sacchi¹ and William F. Marovitz²

From the ¹Center for Biomedical Education and ²Dept. of Otolaryngology,
Mount Sinai School of Medicine, City University of New York, New York

(Received March 14, 1979)

Abstract. Enzymatic tracer techniques to study normal and pathologic stria capillary transport pose various problems. The use of electron opaque tracers can circumvent many of these problems. Iron dextran (mol. diam 20–70 Å) and ferritin (mol. diam 110 Å) were injected intravenously and the mice sacrificed at intervals of $\frac{1}{2}$, 1, 2, 5, and 24 h. The iron dextran results were unusual in that from $\frac{1}{2}$ to 5 h after administration the tracer was present within the cytoplasmic matrix of endothelia, but by 24 h it had been cleared out. No transendothelial exchange was noted. The ferritin results were in conflict with previous results using horse-radish peroxidase. Transport of ferritin was minimal regardless of time sacrificed. No more than a few molecules were scattered about the capillary basal lamina. Those molecules transported across capillaries were apparently delivered by means of the micropinocytotic system. The results suggest a blood-stria barrier similar to the blood-thymic and blood-myenteric barriers. Experimental as well as control animals exhibited stria light cells which contained ferritin-like particles within their cytoplasmic matrices. These light cells are probably reticulo-endothelial type cells. Ferritin may be useful to gauge stria capillary transport alterations associated with auditory pathologies.

The functional role of the stria vascularis, which includes the production of the endocochlear DC potential and ionic composition of the endolymph, is important for normal inner ear function (Honrubia & Ward, 1969; Konishi et al., 1966). The stria vascularis lines the lateral wall of the cochlear duct and is composed of three cell layers, termed marginal, intermediate and basal (Smith, 1957). The tissue is effectively a separate compartment sealed off from the endolymphatic space and spiral ligament by zonulae occludens which occur between the cell membranes of abutting marginal cells and abutting basal cells

(Jahnke, 1976). This tight junctional seal around the stria limits the nutrient inflow from neighboring sources; therefore, the high stria metabolic requirements (Chou & Rodgers, 1962) must be met essentially by intrinsic capillary networks (Reale et al., 1975). Thus the permeability functions of the stria capillaries are paramount when considering the survival and function of the stria cells; accordingly, stria capillary permeability is important for normal cochlear function.

Tracer molecules have been used to map the transport of materials through stria capillaries (Yamamoto & Nakai, 1964; Duvall et al., 1971; Winther, 1971; Gorgas & Jahnke, 1974). Tight junctions have been found to exist between stria endothelial cells as have been found to exist between capillary endothelia of most CNS tissue (Duvall et al., 1971; Gorgas & Jahnke, 1974; Reese & Karnovsky, 1967). Tight junctional seals are known to prevent the passage of lipid insoluble materials through intercellular clefts. Therefore, passage of lipid insoluble materials through the capillaries of the stria vascularis appears to be limited to the micropinocytotic vesicular system (Duvall et al., 1971; Gorgas & Jahnke, 1974). By means of the vesicular system, transport of the tracer molecule horseradish peroxidase (HRP, mol. wt. 43 000, mol. diam 55 Å) is very rapid. As early as 1–2 min following HRP injection, Duvall et al. (1971) observed the HRP reaction product distributed through stria capillary basal lamina. In muscle, however, more than

5 min following HRP injection were required before Karnovsky (1967) found capillary basal lamina densely stained. Although transport of HRP in muscle capillaries was primarily by means of pinocytosis, intercellular cleft transport also occurred.

In contrast with other permeability studies, Osako & Hilding (1971) have reported that HRP is transported across strial capillaries by a route between endothelial cells and that micropinocytotic vesicles are absent within strial endothelia of both Ames Waltzer mice and normal Swiss strain mice.

Yamamoto & Nakai (1964) studied strial capillary transport in the Guinea pig using iron dextran. At no time point after injection (10 min to 72 h) was the tracer observed in capillary basal lamina, although membrane bound accumulations were frequently found within endothelia. While these authors determined the size of iron dextran to be 100 Å in diameter, others have shown that the diameter of this tracer ranges from 20–70 Å (Muir & Goldberg, 1961; Richter, 1959). Molecules this size should be transported across strial endothelia if indeed the HRP results are sound. In fact, if one considers that the transport rate of HRP (mol. diam 55 Å) is more rapid through strial than muscle capillaries and that transport in both cases primarily involves pinocytosis, then it is difficult to account for the iron dextran results in light of the successful transport of molecules as large as ferritin (mol. diam 110 Å) across muscle endothelia (Bruns & Palade, 1968). Clearly, the literature on strial capillary permeability is in conflict.

It should be noted that the use of HRP as a tracer to study strial capillary permeability has certain drawbacks. For example, the enzyme HRP was noted by Duvall et al. (1971) to cause strial capillary alterations, consisting of intraluminal protrusions of endothelial cell membranes and pores within capillary walls. Cell protrusions have been known to occur in injured cells (Trump & Arstila, 1974). The artifactual production of pores in strial capillaries could have resulted in the release of HRP

to the basal lamina. Such changes do not occur in adjacent spiral ligament vessels, where no HRP exists. Whether strial capillary alteration is a manifestation of HRP toxicity to select portions of the inner ear is not clear; however, it has been found that perilymphatic perfusion of HRP in vivo is acutely ototoxic (Ross et al., 1977).

Other problems of HRP use include: (1) the enzyme must retain its catalytic activity until and throughout incubation; (2) quantitative analysis of transported tracer substance cannot be performed since a) the HRP itself is not directly visualized and b) the quantity and quality of the reaction product is dependent upon the quality of both the enzyme preparation and incubation medium, the penetration of the medium into the tissue and the duration of the incubation; (3) histamine, which affects vessel permeability and strial capillary blood flow, is released in some species in response to HRP injection; (4) an endogenous peroxidase reaction exists which may interfere with the interpretation of experimental findings.

These problems are especially troublesome when evaluating capillary permeability changes in experimentally induced pathologies. For example, Duvall et al. (1974) used the tracer substance HRP to evaluate strial capillary permeability after intense noise exposure. They suggested that some of their unusual experimental results may have been due to the degradation of the protein HRP by lysosomal enzymes. Of course, if HRP is inactivated by lysosomal hydrolases, then the electron dense HRP reaction product, which indicates the presence of HRP, will not be produced. Therefore, the transport of the tracer cannot be determined.

Certainly, then, HRP and similar enzymatic tracers pose serious problems when used as a means to gage strial capillary transport during pathologic as well as normal conditions. A reliable method of evaluating the function of strial capillaries without the limitations imposed by the use of an enzymatic tracer would be beneficial.

Table I. Number of mice per experimental condition

Tracer	Post injection sacrifice time (h)				
	1/2	1	2	5	24
Ferritin	6	4	3	4	7
Iron dextran	2	2	2	2	2

Many non-enzymatic, electron-opaque tracers have been used to study capillary transport at the ultrastructural level. In particular, ferritin has been successfully used to delineate certain aspects of transendothelial exchange in a variety of tissues (Farquhar et al., 1961; Bruns & Palade, 1968; Clementi & Palade, 1969). There are many reasons why ferritin may be considered an ideal tracer (Bruns & Palade, 1968) especially for strial capillaries. They include: (1) ferritin (mol. wt. 460 000; mol. diam 110 Å) is the size required for a probe molecule of the large pore transport system, which is reportedly the only system in strial capillaries; (2) it is a biological substance, similar in nature and in size to most plasma proteins; (3) high blood concentrations are well tolerated by experimental animals; (4) individual molecules can be identified within ultrathin sections and therefore a direct measure of transport is possible; (5) ferritin is resistant to lysosomal hydrolases (Drysdale & Munro, 1966; Coffey & DeDuve, 1968) and therefore may be useful in pathologic conditions.

The advantage which the electron opaque tracer molecule ferritin may provide over enzymatic tracers warranted its evaluation. In addition, because the iron dextran results reported by Yamamoto & Nakai (1964) are in conflict with other strial capillary permeability studies, a reevaluation was judged necessary. Therefore, it was the purpose of this study to evaluate strial capillary permeability with the electron-opaque tracer molecules ferritin and iron dextran.

MATERIALS AND METHODS

Tracer substances

Iron dextran (Imferon, Lakeside Labs, Milwaukee, Wis.) was dispersed in physiological saline with 0.5% phenol as a preservative, and contained the equivalent of 50 mg elemental iron per ml.

A 10 ml stock solution of 100 mg of cadmium crystallized ferritin per ml of physiological saline was obtained (Nutritional Biochemicals, Cleveland, Ohio). To remove the cadmium, the solution was dialysed against 3.7% ethylenediamine tetraacetic acid (EDTA) in 0.2 M phosphate buffer, pH 7.0, at 0–4°C for two changes (48 h each). Following two additional changes in buffer alone (24 h each), the ferritin solution was dialysed against physiological saline (24 h) and then passed through a 0.45 micrometer millipore filter into a sterile 10 ml injection vial.

Animals

Young adult male mice, BALB c/J (Jackson Labs, Bar Harbor, Maine) ranging in weight from 15 to 20 g and showing positive Preyer reflexes to finger snaps were used. The animals were screened for middle ear infection by direct examination during temporal bone removal.

Methods

All animals received subcutaneous injections of sodium pentobarbital 2 mg/20 g body weight, prior to injection of tracer. Anesthesia was reached within 15 min, and lasted for 2–3 h for those animals allowed to recover. Under anesthesia, either the jugular vein or the inferior vena cava was exposed and was injected with 1 ml per 100 g body weight of ferritin or iron dextran solution. The injection was delivered through a 30 gauge needle over a period of 1–2 min. Animals were sacrificed by decapitation 1/2, 1, 2, 5, or 24 h after injection. Twelve control animals received anesthetic injection only and were sacrificed immediately after induction. The number of

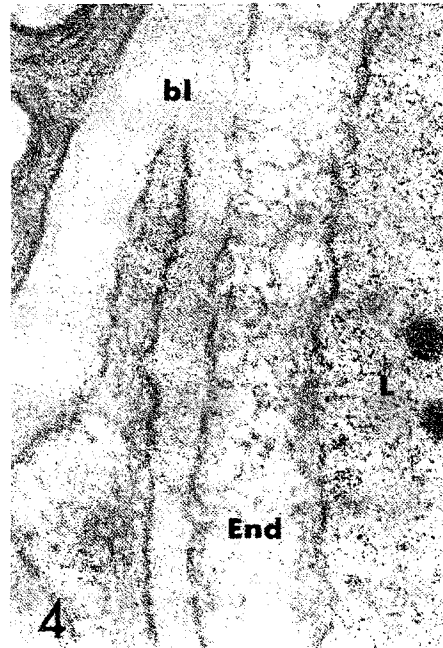
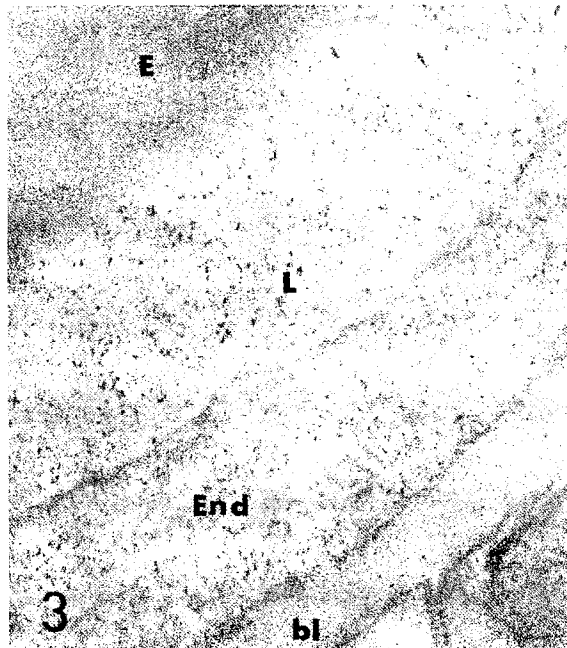
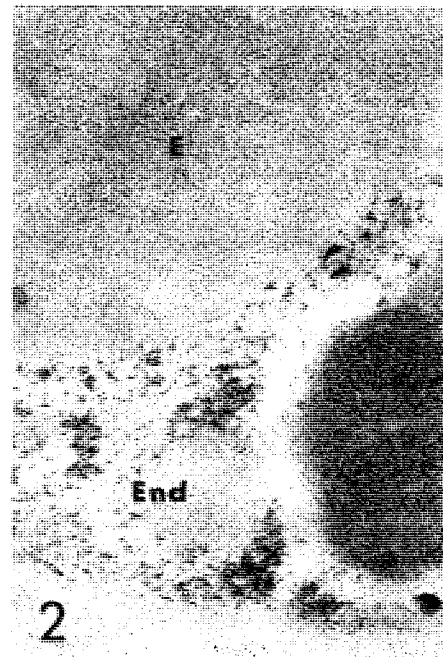
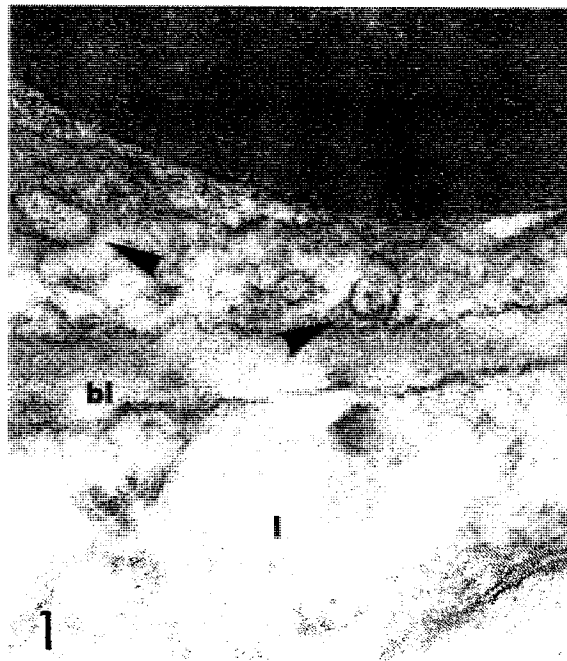


Fig. 1. Arrows indicate iron dextran within pinocytotic vesicles only of endothelial cell. $\frac{1}{2}$ h post injection. Glutaraldehyde and osmium fixed. Unstained. $\times 78\,380$.

Fig. 2. Iron dextran within cytoplasm of endothelial cell. 1 h post injection. Glutaraldehyde fixation only. Unstained. $\times 69\,215$.

Fig. 3. Iron dextran within vesicles and free in cytoplasm of endothelial cell. 5 h post injection. Glutaraldehyde and

osmium fixed. Unstained. $\times 80\,000$.

Fig. 4. Note absence of iron dextran in endothelial cytoplasm. 24 h post injection. Glutaraldehyde and osmium fixed. Unstained. $\times 83\,300$.

bl, basal lamina; *E*, erythrocyte; *End*, endothelial cell; *I*, intermediate cell; *L*, capillary lumen; *R*, reticuloendothelial type cell.

animals per experimental condition is noted in Table 1.

Cochleae were fixed either in 1% osmium tetroxide or 2% glutaraldehyde in 0.2 M Cacodylate buffer, pH 7.4. Within 1 min after decapitation, the right temporal bone of each animal was excised, fractured open and immersed in about 5 ml of primary fixative. After 2 h of primary fixation at 0–4°C, all cochleae were briefly washed in buffer. Those ears fixed in glutaraldehyde were then osmicated for an additional 2 h. However, from each cochlea of those animals injected with iron dextran, pieces of stria were removed while in buffer and were not osmicated. At the completion of osmication, the specimens were again briefly washed in buffer. In ferritin injected animals, specimens were selected from basal, mid and apical portions of the cochlear duct. After the striae were microdissected free from the cochleae in 70% acetone, dehydration was completed in graded acetone, and the tissue embedded in Epon at 60°C for 24 h.

Ultra-thin sections were cut on glass and diamond knives using either the Sorvall MT 1 ultramicrotome or an LKB Ultratome. Section interference colors ranged around silver. Sections were picked up on copper grids and most were examined unstained so that electron dense tracer particles could be unequivocally identified. Some sections were stained with lead citrate (Reynolds, 1963). Contrast was significantly enhanced by the use of projector field diaphragms with the Zeiss 9S-2 EM.

RESULTS

Those animals allowed to recover from anaesthesia had positive Preyer reflexes. None of the experimental ears showed evidence of middle ear infection upon direct examination using a dissecting microscope.

The ultrastructural appearance of the stria vascularis was typical of the fixation procedure employed (Merck et al., 1974; Santos-Sacchi, 1978*a* and *b*). One noteworthy difference between the two fixation procedures

was the decreased concentration of tracer particles within capillary lumina in primary osmium fixed specimens as compared to primary glutaraldehyde fixed tissues.

Iron dextran

The plasma concentration of iron dextran decreased over time. In the 1/2 h specimens, capillaries were observed which contained iron dextran only within endothelial pinocytotic vesicles (Fig. 1). However, more frequently, and in all animals beyond 1/2 h up to 5 h, the iron dextran appeared free as well as in vesicles within the cytoplasm of endothelia (Figs. 2 and 3). In fact, the tracer was occasionally observed within the nucleoplasm of some endothelia. By 24 h after injection, however, the iron dextran was absent from endothelia (Fig. 4). The passage of the tracer to the basal lamina was found to be almost nil, since rarely were any electron dense particles found in the basal lamina at any time point after injection. No tracer was observed within stria cells.

Ferritin

The appearance of ferritin within various spaces of the tissues studied was indicative of its passage from the circulatory system into the stria vascularis. The results are reported in terms of compartments within which ferritin was observed.

Capillary lumen

From 1/2 to 24 h following injection, ferritin was present within the capillary lumina of the stria in all areas studied. However, the concentration of ferritin within the blood plasma varied with time. By 24 h after ferritin administration the plasma concentration was considerably lower than its initial level. Ferritin was never present within capillary lumina of control animals.

Endothelial tunic

From the earliest to the latest time points after administration, ferritin labeled pinocytotic

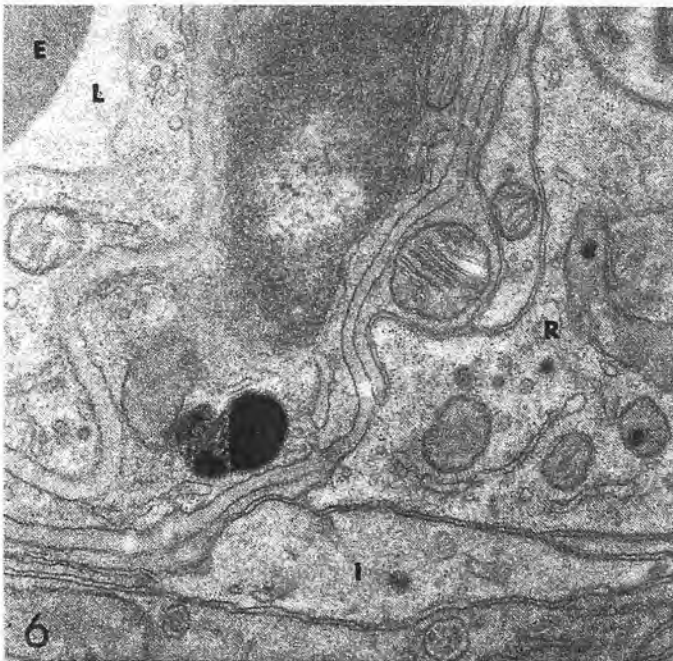
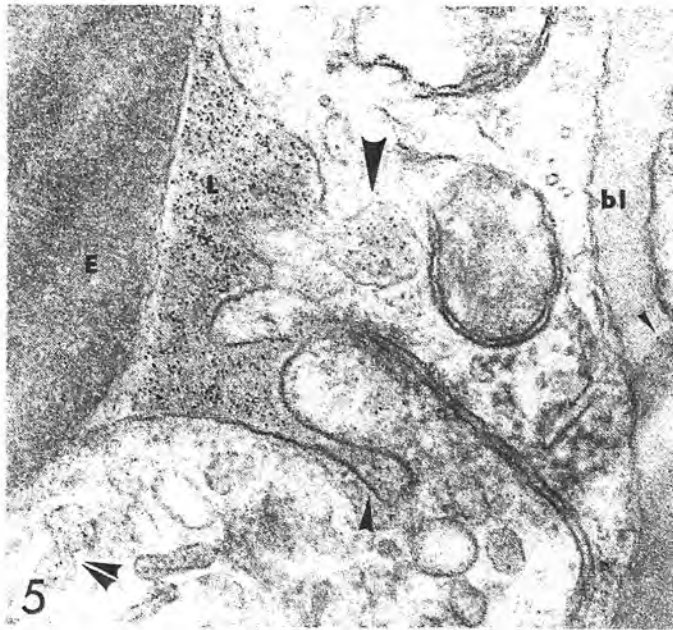


Fig. 5. Large arrow indicates open-mouthed vacuole containing large amount of ferritin on luminal front. Medium arrow indicates luminal tubular invagination containing ferritin. Double arrow indicates fusion of two labeled pinocytotic vesicles. Ferritin molecule can be seen in basal lamina (small arrow). $\frac{1}{2}$ h post injection. Glutaraldehyde and osmium fixed. Unstained. Mid portion of cochlear duct. $\times 90\,025$.

Fig. 6. Control animal (uninjected) showing light cell (R) with abundant supply of endogenous ferritin-like granules. Osmium fixed. Unstained. $\times 39\,600$.

vesicles were observed within endothelial cells (Figs. 5, 7, 8 and 9). Labeling of any pinocytotic vesicles was limited to no more than a few molecules of ferritin. In any section, the number of such labeled vesicles per endo-

thelial cell varied from none to a few, with no discernible relation to time after injection or area of cochlear duct. At times, the number of unlabeled vesicles was great. Although endothelial vesicles opening to the tissue front were

often empty, on occasion ferritin could be visualized within the basal lamina either just in front of the opening or not far away (Fig. 9). Nevertheless, there were direct observations of ferritin within vesicles opened upon the luminal and tissue fronts (Figs. 7, 8 and 9), as well as in those within the endothelial cytoplasm. Labeled vesicles within the endothelial cytoplasm were encountered more frequently. It cannot be ruled out that ferritin within open-mouthed vesicles diffused out during fixation.

Another occasional phenomenon was the appearance of tubular invaginations from luminal and tissue surface membranes of endothelial cells (Fig. 5). These structures were only encountered in thick portions of endothelia. Ferritin was found within some luminal invaginations, but direct connections from luminal to tissue fronts were never observed.

There appeared to be a relation between the time after injection and the accumulation of ferritin within vacuoles of endothelia. At the earlier time points, vacuoles containing ferritin in fairly large amounts were occasionally observed (Fig. 8). Rarely large vesicles with high concentrations of ferritin were seen open to the plasma front as if in the process of loading (Fig. 5). With increasing time, larger and denser cytoplasmic vacuoles were noted within which individual ferritin granules could be observed (Fig. 11). Pinocytotic vesicles labeled with ferritin were seen fused with large ferritin containing vacuoles (Fig. 8) or with each other (Fig. 5). Multi-vesicular bodies were also seen, that is, single membrane vacuoles within which were found labeled as well as unlabeled pinocytotic-like vesicles (Fig. 10).

Ferritin was neither seen in pinocytotic or other structures within endothelia of control animals, nor was it observed free in the endothelial cytoplasm of experimental or control animals.

Basal lamina and intercellular spaces

The basal lamina was not heavily infiltrated with ferritin molecules at any time point after

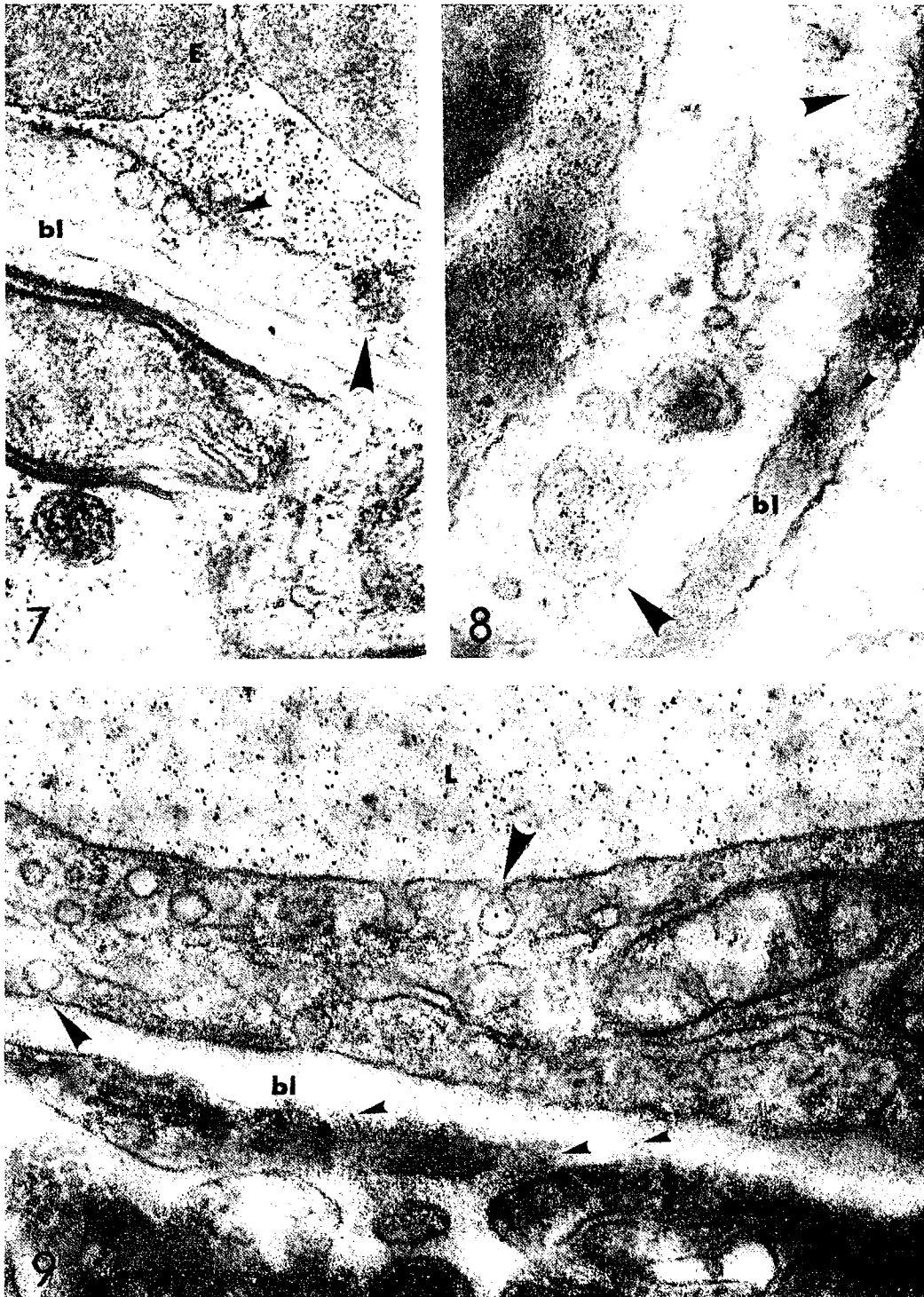
injection. In the earlier specimens observed, molecules were either absent, or present at extremely low concentrations, singly scattered about the perimeter of the capillary (Figs. 5 and 8). No accumulation of ferritin within the basal lamina at particular points around the capillary was noted, save one instance. This occurred in a capillary of an animal sacrificed 1/2 h after injection (Fig. 12). An apparent leak within a discrete portion of a single capillary allowed a relatively large quantity of ferritin to escape into the basal lamina. This was the only occurrence of this kind in all specimens studied, and adjacent strial capillaries within the same section did not exhibit this profuse transendothelial passage of ferritin. This phenomenon was clearly not typical of normal strial capillary function.

In the 5 and 24 h specimens, accumulation of ferritin appeared slightly greater around some capillaries than in earlier specimens. However this was not the rule since other capillaries at the same time periods showed little or no ferritin present within the basal lamina. The overall picture revealed that ferritin labeling of the basal lamina was variable at all time points studied and that labeling even at its greatest was scant.

Fig. 7. Large arrow indicates numerous labeled pinocytotic vesicles within endothelium. Smaller arrow indicates open-mouthed vesicle upon luminal front which appears to have ferritin molecules within neck portion of vesicle. 1 h post injection. Osmium fixed. Stained with lead citrate. Mid portion of cochlear duct. $\times 92\,325$.

Fig. 8. Note numerous open-mouthed pinocytotic vesicles upon tissue front. Medium arrow indicates a ferritin labeled one. A ferritin molecule can be seen in the basal lamina (small arrow). Within the endothelial cell a pinocytotic vesicle can be seen fused with a large vacuole containing numerous ferritin molecules (large arrow). 5 h post injection. Glutaraldehyde and osmium fixed. Unstained. Basal portion of cochlear duct. $\times 88\,635$.

Fig. 9. Large arrow indicates open-mouthed pinocytotic vesicle containing two ferritin molecules on luminal front. A ferritin molecule can be seen at the opening of a pinocytotic vesicle at the tissue front (medium arrow). Small arrows indicate ferritin molecules within basal lamina. 2 h after injection. Osmium fixed. Unstained. Mid portion of cochlear duct. $\times 92\,470$.



Ferritin molecules within the intercellular spaces of the stria vascularis were not observed, and presumably the size of the molecule limited its penetration into such spaces. Ferritin was not seen within the basal lamina of control animals.

Strial cells

Ferritin was not seen within the marginal cells. However, large accumulations of electron dense particles closely resembling ferritin in size and shape were often found in specific cell processes of light cells (Fig. 6). In fact, the particles within these cells and the injected ferritin molecules appeared indistinguishable. The particles were found in high concentration free in the cytoplasm often accompanied by lysosomes containing the same particles. This phenomenon was found throughout all time periods studied, and *in control animals as well*. Further description and analysis of these cells will be the subject of another report (Santos-Sacchi and Marowitz, in preparation). No pinocytotic uptake of injected ferritin by these light cells was seen, although light cells occasionally possessed open-mouthed vesicles on the basal lamina. Also, no spectacular accumulation of ferritin within vacuoles was ever observed in these cells. There were no apparent differences in cytoplasmic ferritin-like concentration between experimental and control animals.

DISCUSSION

Iron dextran

The iron dextran results were perplexing. Iron dextran was present within strial endothelial cytoplasm from 1/2 to at least 5 h, but was apparently absent by 24 h. This did not seem to be a fixation artifact. It was concluded that the tracer initially entered the endothelia by means of pinocytotic uptake, since in some 1/2 h specimens and in the endothelia of a control animal (killed immediately after injection) iron dextran was present within vesicles and

absent within the cytoplasmic matrix. The occurrence of iron dextran within the cytoplasmic matrix of endothelia is difficult to explain, since it is generally acknowledged that macromolecules have no route by which to enter the "membrane protected" cytoplasm. Although molecules the size of iron dextran are unable to pass through intact membranes, similar observations of free intracytoplasmic iron dextran following administration have been reported. Richter (1959), after injecting iron dextran intraperitoneally, studied the fate of that substance within liver and spleen. After 1 h he found accumulations of iron dextran within macrophages and sinusoidal endothelia of both organs. There were non-membrane bound aggregates of iron dextran within the cytoplasmic matrices, as well as numerous free particles. This is similar to the results of the present study. However, in Richter's study, by the fourth hour following injection, aggregates were enclosed by limiting membranes. Further, iron dextran was discernible within the cells up to 6 days after administration. In this regard, Richter's results differ from the present study, because iron dextran was absent from 24 h. However, it should be recalled that in the only previous study of iron dextran permeability in strial capillaries (Yamamoto & Nakai, 1964) the molecules remained within endothelia, reportedly within vacuoles, for 5 h, but by 24 h and beyond iron dextran was absent from endothelia. It seems that strial endothelia have an ability to remove or possibly metabolize iron dextran, so that by 24 h very little or none remains observable. Yamamoto and Nakai reported no transendothelial passage of iron dextran into the stria. Although this appears to be the case for the present study as well, the possibility exists that passage of some degraded form of the original molecule occurred which could not be visualized electronmicroscopically. Richter's experiment suggests that mouse cells may be able to metabolize the partially depolymerized dextran sufficiently to abolish the colloidal stability of the iron dextran preparation.

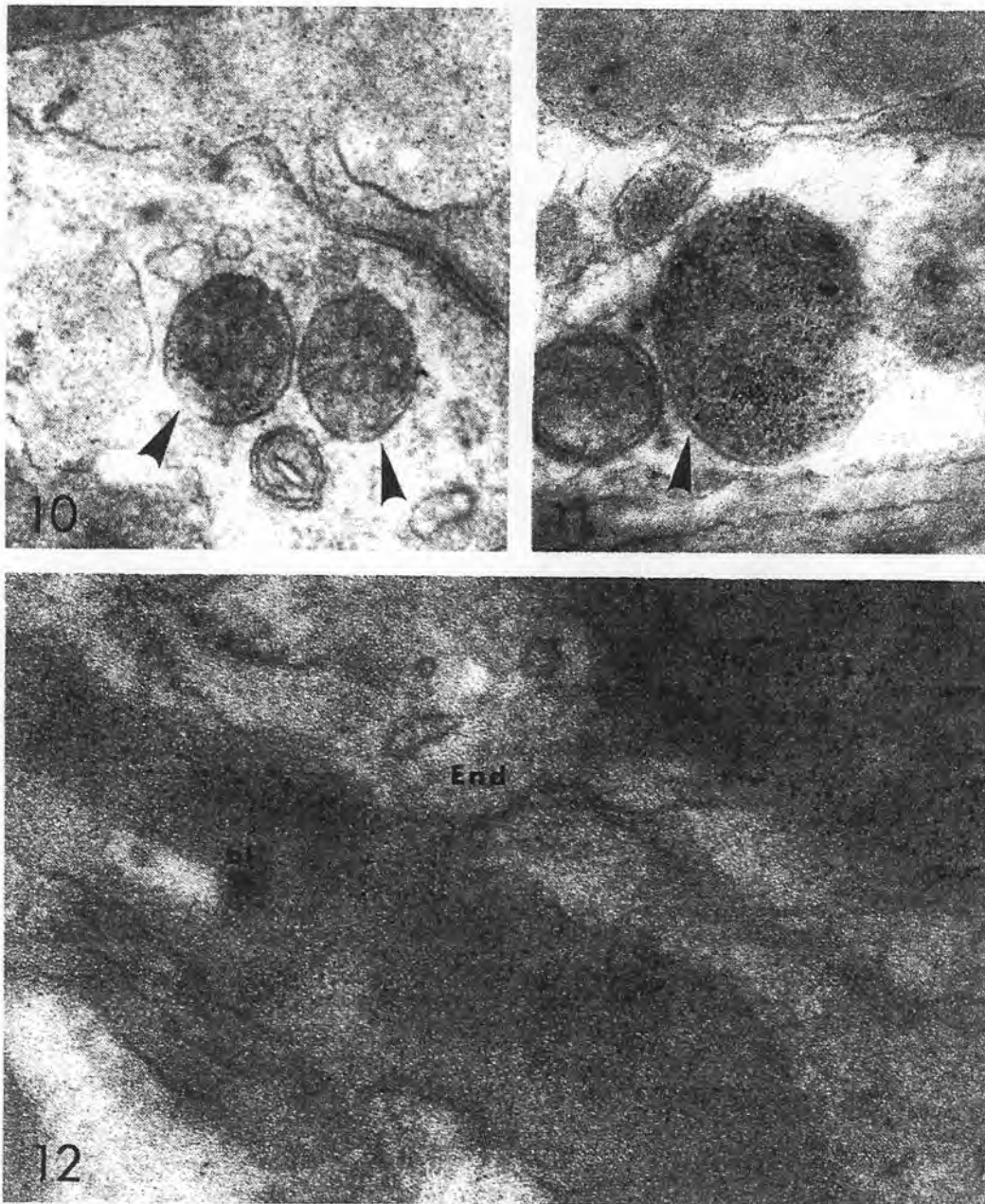


Fig. 10. Arrows indicate multivesicular bodies of labeled and unlabeled pinocytotic-like vesicles within endothelial cell. 24 h post injection. Glutaraldehyde and osmium fixed. Unstained. Apical portion of cochlear duct. $\times 85\,500$.

Fig. 11. Large lysosome containing ferritin within an endothelial cell (arrow). 5 h post injection. Glutaraldehyde and osmium fixed. Unstained. Basal portion of cochlear duct. $\times 88\,065$.

Fig. 12. Note large accumulation of ferritin within basal lamina. This was the only occurrence of its kind throughout all specimens. It is not typical of normal strial capillary transport, but highlights the possibility of such leakage. $\frac{1}{2}$ h post injection. Glutaraldehyde and osmium fixed. Unstained. Basal portion of cochlear duct. $\times 118\,000$.

Of course, diffuse iron in ionic form or bound in low concentrations to carrier substances cannot be seen (Muir & Goldberg, 1961).

Clearly then, the use of iron dextran as an electron opaque tracer molecule for strial capillary transport is obviated by the possibly unique treatment it receives by strial endothelia which apparently results in the intracytoplasmic sequestration and eventual removal of iron dextran.

Ferritin

Although ferritin transport across strial capillaries had not been evaluated prior to the present study, HRP transport had been examined. The transport of the enzyme through strial vessels is very rapid. Within a few min after HRP injection, the basal lamina and intercellular spaces are densely stained with reaction product (Duvall et al., 1971; Winther, 1971). These results are more similar to those obtained with muscle capillaries than to those obtained with CNS capillaries, except that intercellular cleft transport of HRP is reportedly absent in strial capillaries. However, the results of the present study, which suggest minimal capillary transport, indicate that the permeability function of the strial capillaries is more similar to that of the CNS vessels. Thus, even by 24 h post injection, transport of ferritin across endothelia is scanty as determined by basal lamina labeling. Although transport of lipid insoluble substances certainly increases as molecular weight decreases, the evidence evaluated by Renkin (1964) suggests that transport rates of molecules in excess of about 60 000 Daltons remains constant. If the micro-pinocytotic transport system is the sole means of transendothelial passage of lipid-insoluble material within the stria, then the passage of HRP (whose molecular weight is close to Renkin's cut off size) should not be drastically different from that of ferritin. This may especially be true if, as some researchers believe (Balint & Nagy, 1971), HRP binds to B-globulin and IgG within plasma, thereby increasing

the particle size and bringing it closer to the size of ferritin. Thus by size comparison it is difficult to explain the similarity of HRP results and the dissimilarity of ferritin results between strial and muscle capillaries. Certainly, the very small number of labeled strial capillary pinocytotic vesicles could account for the smaller amount of ferritin transport in strial as compared to muscle capillaries. Moreover, the dissimilarity of transport suggests that some other factor may play an important role in the rapid transport of HRP across strial endothelia. It is here that the established ototoxicity of HRP may come to bear (Ross et al., 1977). Perhaps the transport of HRP is rapid in strial capillaries because the HRP *itself* alters strial capillary permeability. Such a hypothesis would explain the similarity of HRP results in muscle and strial capillaries, and would not conflict with the ferritin results.

Research on the permeability of continuous type capillaries in other tissues also leads to the conclusion that the strial HRP results are unusual, i.e. in the light of this study's findings with ferritin. Raviola & Karnovsky (1972) evaluated thymic capillary transport using a variety of enzymatic tracers, including HRP. They also used the tracer molecule ferritin, so that it is possible to compare the permeabilities of both HRP and ferritin in the same capillary system. One must note however that the thymus contains both continuous and fenestrated capillaries. For the present purpose, only the continuous capillaries' permeability functions are of significance, since these capillaries, are structurally comparable to strial capillaries. Interestingly, these continuous capillaries, located within the cortical areas of the thymus, present a blood-thymic barrier. As in the stria and CNS, circumferential tight junctions halt extravascular leakage through endothelial intercellular clefts. At all time periods, from 1–24 h after ferritin injection, minimal amounts of the electron opaque tracer had traversed the thymic capillary endothelia. Labeling of pinocytotic vesicles was variable, but represented a very

small fraction of the whole vesicle population. Within the basal lamina only isolated or small groups of 2-3 ferritin molecules were scattered along the circumference of the capillaries. These findings are surprisingly similar to those of the present study. However, despite the similarities in capillary structure and ferritin transport, the transendothelial passage of HRP is vastly different between strial and cortical thymic capillaries. Raviola and Karnovsky (1972) demonstrated that the amount of HRP transport across cortical thymic capillaries is comparable to that of ferritin. That is, from 2-20 min post injection only limited vesicular transport of the enzymatic tracer occurred through endothelia; vascular adventitia was free of peroxidase reaction product. Apparently then, the transport of both ferritin and HRP is similar for a given capillary bed, provided that the micropinocytotic transport system is the sole means of transendothelial passage. The similar transport characteristics of HRP and ferritin agree well with the conclusions of Renkin (1964).

Another blood-tissue barrier has been reported which is similar to the thymic one (Gershon & Bursztajn, 1978). The myenteric plexus is supplied with continuous-type capillaries. Using HRP, Gershon & Bursztajn (1978) demonstrated minimal transport of the tracer, presumably by the pinocytotic pathway, since intercellular cleft transport was impossible due to tight junctional seals. Extravascular accumulation of the HRP reaction product in the myenteric plexus was undetectable, as Raviola and Karnovsky reported for cortical thymic tissue. However, in both tissues—thymus and myenteric plexus—it was concluded that some transport has occurred because perivascular phagocytes contained vacuolated tracer substance.

In the present study, the ferritin results appear to indicate the existence of a blood-strial barrier which is closer in nature to the blood-thymic and blood-myenteric plexus barriers than to the blood-brain barrier.

Another phenomenon which might account

for the observed minimal transport of ferritin across strial capillaries is the phagocytotic activity of strial endothelial cells. Within these cells were observed large vacuoles and multivesicular bodies containing ferritin similar to those reported by Raviola & Karnovsky (1972). Apparently, one means of such vacuole formation was by pinocytotic vesicular fusion, since with increasing time, larger and denser ferritin containing bodies (presumably lysosomes) were present. It appeared that once ferritin conglomerates formed, the ferritin was immobilized within endothelia until degraded. In essence then, the phagocytotic activities of strial endothelia in conjunction with minimal pinocytotic transport and endothelial tight junctions contribute to the formation of a blood-strial barrier at least for molecules the size of ferritin.

Previous studies have suggested that intermediate cells may serve as macrophages within the stria. Such cells have been found to have open-mouthed pinocytotic vesicles and intracytoplasmic vacuoles labeled with HRP reaction product after a sufficient interval of time following HRP administration (Duvall et al., 1971; Winther, 1971). Also at the light microscopic level, Nomura (1961) found that intravenously injected trypan blue was phagocytized by certain strial cells scattered about the capillaries. Similarly, transported tracer substances within cortical thymic and myenteric plexus blood-tissue barrier systems were incorporated within perivascular phagocytic cells (Raviola & Karnovsky, 1972; Gershon & Bursztajn, 1978). The possibility exists that in this study some ferritin-like particles within the light cells of experimental animals may be exogenous ferritin; that is, perhaps the cytoplasm of these cells serves as a sink for transported exogenous ferritin. However, the fact that such particles were located, for the most part, free within the light cell cytoplasmic matrix argues against an exogenous source, since macromolecules of this size are not able to enter free cytoplasm. Further, it should be noted that there were no obvious differences

between control and experimental animals in regard to concentration of intracytoplasmic ferritin-like particles. Nevertheless within the cytoplasm of liver cells there is *de novo* apoferritin production within a few h following administration; subsequently, iron sequestration by apoferritin occurs, producing ferritin (Drysdale & Munro, 1966). In the present study, since the injected tracer contains iron, the *de novo* production of endogenous ferritin by experimental strial light cells might occur if indeed they phagocytized transported exogenous ferritin. The problem is made more difficult because the horse spleen ferritin tracer is very resistant to lysosomal breakdown (Coffey & DeDuve, 1968). Thus, although ferritin may accumulate within lysosomes, elemental iron may not be able to enter the cytoplasm because of the hydrolytic resistance of the protein. On the other hand, there is some evidence that the iron may enter and leave the apoferritin shell without protein disintegration (Mazur & Carleton, 1963). In this regard, it is noteworthy that in other permeability studies using ferritin as a tracer (Bruns & Palade, 1968; Raviola & Karnovsky, 1972), after 24 h, perivascular macrophages did exhibit intracytoplasmic ferritin granules. Presumably, they were endogenously produced, after the phagocytes accumulated the ferritin tracer within lysosomes. In the present study, since numerous lysosomes containing ferritin were found in control animals, a normal turnover mechanism may be deduced. However, it cannot be totally dismissed that the select light cells in experimental animals also contain exogenously injected ferritin within lysosomes. Finally, it should be noted that although light cells often exhibited open-mouthed vesicles upon the basal lamina, no ferritin labeling of these vesicles in experimental animals was found. Certainly, the scanty accumulation of ferritin within the basal lamina offered little probability of finding ferritin within such open-mouthed vesicles.

The central nervous system of mammals appears to require an unusually stable internal

environment in order to function effectively (Katzman, 1972). Clearly, the blood-brain barrier affords such an environment. In a like manner, thymic and myenteric plexus blood-tissue barriers serve their own physiologic purposes. The finding that the transport of ferritin across strial endothelia is scanty may indicate that the internal milieu of the stria must be carefully regulated. The probable existence of strial phagocytic cells may also be important in this regard. Normal strial function may very well depend upon an intact blood-strial barrier.

The ferritin labeling technique used in this study of normal animals may be useful in determining altered strial capillary transport possibly associated with various auditory pathologies. It is known that under pathologic conditions of inflammation, extravascular leakage of high protein content fluid occurs (Florey, 1964). Indeed, this is known to occur in brain tissue, and involve a breakdown of the blood-brain barrier (Katzman, 1972). Certainly, under some deleterious influences, strial tissue becomes edematous, e.g. in response to ethacrynic acid or noise exposure. In the present study, only one instance of abundant ferritin accumulation within the basal lamina was observed. Since adjacent capillaries within the same section, and all other capillaries did not exhibit such abundant transport, the phenomenon was judged atypical of strial capillary transport. However, this occurrence indicates that the tracer molecule ferritin may be useful in determining altered strial transport. Ferritin is highly resistant to lysosomal hydrolases (Coffey & DeDuve, 1968). Therefore, if large amounts did traverse the endothelial tunic they would no doubt be detected within some "compartment" of strial tissue, assuming, of course, that the tight junctional seal delimiting the stria vascularis remains intact. However, the possibility of light cell incorporation of exogenous tracer, and the difficulty in differentiating between endogenous and exogenous electron dense particles should be kept cognizant.

ZUSAMMENFASSUNG

Enzymatische Tracermethoden für die Erforschung normales und pathologisches Kapillartransports der Stria stellen verschiedene Probleme vor. Die Verwendung opaker Elektronentracer kann viele von diesen Problemen verhüten. Eisendextran (mol. Dm. 20–70 Å) und Ferritin (mol. Dm. 110 Å) wurden intravenös eingespritzt, und die Mäuse wurden nach Zwischenzeiten von $\frac{1}{2}$, 1, 2, 5 und 24 Stunden geopfert. Die Eisendextran-Ergebnisse waren ungewöhnlich, weil der Tracer von $\frac{1}{2}$ bis 5 Stunden nach der Einspritzung in der zytoplasmatischen Matrize der Endothelen zugegen war, aber gegen die 24. Stunde war er ausgeräumt worden. Kein transendothelialer Austausch wurde bemerkt. Die Ferritin-Ergebnisse widersprachen vorhergehenden Ergebnissen, die Meerrettichperoxidase benutzten. Der Transport von Ferritin war ungeachtet der verstrichenen Zeit minimal. Nur ein paar Molekeln wurden um die Basalkapillarlamina bestreut. Die quer durch Kapillaren übergeführten Molekeln wurden anscheinend mittels des mikropinozytotischen Systems überbracht. Die Ergebnisse deuten eine Blut-Stria-Sperre an, die den Blut-Thymus- und Blut-Myenterus-Sperren ähnlich ist. Versuchs- sowie auch Kontrolltiere wiesen Lichtzellen der Stria auf, die Ferritin-ähnliche Partikeln in ihren zytoplasmatischen Matrizen enthielten. Diese Lichtzellen sind wahrscheinlich Zellen des reticuloendothelialen Types. Ferritin könnte nutzbar sein, um die auf Gehörpathologien bezogenen Änderungen des Kapillartransports der Stria abzuschätzen.

ACKNOWLEDGEMENTS

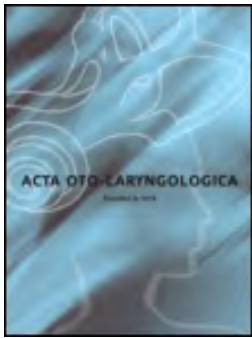
The authors wish to thank Prof. I. M. Ventry and Prof. O. R. Anderson, Teachers College, Columbia University, for their support of this work. Portions of this work were taken from the dissertation submitted by J. S.-S. in partial fulfillment of the requirements of the Ph.D. degree, Columbia University, 1978. This work was supported in part by a Grant-in-Aid of Research from Sigma Xi, The Scientific Research Society of North America and by a grant from the Deafness Research Foundation. Thanks to Celeste Conway for help in the preparation of this manuscript.

REFERENCES

- Balint, A. & Nagy, Z. 1971. Permeability tracers and serum proteins. *Experientia* 27, 175.
- Bruns, R. & Palade, G. 1968. Studies on blood capillaries. II. Transport of ferritin molecules across the wall of muscle capillaries. *J Cell Biol* 37, 277.
- Chou, J. & Rodgers, K. 1962. Respiration of tissues lining the mammalian membranous labyrinth. *J Laryngol* 76, 341.
- Coffey, J. & DeDuve, C. 1968. Digestive activity of lysosomes. *J Biol Chem* 243, 3255.
- Clementi, F. & Palade, G. 1969. Intestinal capillaries. I. Permeability to peroxidase and ferritin. *J Cell Biol* 41, 33.
- Drysdale, J. & Munro, H. 1966. Regulation of synthesis and turnover of ferritin in rat liver. *J Biol Chem* 241, 3630.
- Duvall, A., Quick, C. & Sutherland, C. 1971. Horseradish peroxidase in the lateral cochlear wall: An electron microscopic study of transport. *Arch Otolaryngol* 92, 304.
- Duvall, S., Ward, W. & Lauhala, K. 1974. Stria ultrastructure and vessel transport in acoustic trauma. *An Otol* 83, 498.
- Farquhar, M. G., Wissig, S. L. & Palade, G. E. 1966. Glomerular permeability. I. Ferritin transfer across the normal glomerular capillary wall. *J Exp Med* 113, 4.
- Florey, H. 1964. The transport of materials across the capillary wall. *Quart J Exp Physiol* 49, 117.
- Gershon, M. D. & Bursztajn, S. 1978. Properties of the enteric nervous system: A blood-myenteric plexus barrier. Submitted for publication.
- Gorgas, K. & Jahnke, K. 1974. The permeability of blood vessels in the Guinea pig cochlea. II. Vessels in the spiral ligament and the stria vascularis. *Anat Embryol* 146, 33.
- Honrubia, V. & Ward, P. 1969. Dependence of the cochlear microphonic and summating potential on the endocochlear potential. *JASA* 46, 388.
- Jahnke, K. 1976. The fine structure of freeze-fracture intercellular junctions in the Guinea pig inner ear. *Acta Otolaryngol* (Stockh), Suppl. 336.
- Karnovsky, M. 1967. The ultrastructural basis of capillary permeability studied with peroxidase as a tracer. *J Cell Biol* 35, 213.
- Katzman, R. 1972. Blood-brain-CSF barriers. In *Basal neurochemistry* (ed. Albers, Siegel, Katzman, Agronoff). Little, Brown and Co., Boston.
- Konishi, T., Kelsey, E. & Singleton, G. 1966. Effects of chemical alteration in the endolymph on the cochlear potentials. *Acta Otolaryngol* (Stockh) 62, 393.
- Mazur, A. & Carleton, A. 1963. Relation of ferritin iron heme synthesis in marrow and reticulocytes. *J Biol Chem* 238, 1817.
- Merck, W., Sparwald, E., & Curten, I. 1974. Über den Einfluß verschiedener Fixationsmethoden und Fixationsmittel auf die elektronenmikroskopische Struktur der Stria vascularis, Prominentia spiralis und des Ligamentum spirale beim Meerschweinchen. *Arch Otolaryngol* 206, 299.
- Muir, A. & Goldberg, L. 1961. Observations on subcutaneous macrophages. Phagocytosis of iron-dextran and synthesis of ferritin. *Quart J Exp Physiol* 46, 28.
- Nomura, Y. 1961. Capillary permeability of the cochlea. *Ann Otol* 70, 81.
- Osako, S. & Hilding, D. 1971. Electron microscopic studies of capillary permeability in normal and Am Waltzer deaf mice. *Acta Otolaryngol* (Stockh) 71, 36.
- Raviola, E. & Karnovsky, M. 1972. Evidence for a blood-thymus barrier using electronopaque tracers. *J Exp Med* 136, 466.
- Reale, E., Luciano, L., Franke, E., Pannese, E., Wermter, G. & Iurato, S. 1975. Intercellular junctions in the vascular stria and spiral ligament. *J Ultrastruct Res* 53, 284.
- Reese, T. & Karnovsky, M. 1967. Fine structural localization of ferritin in the stria vascularis of the Guinea pig cochlea. *J Cell Biol* 1, 1.

- of a blood-brain barrier to exogenous peroxidase. *J Cell Biol* 34, 207.
- Renkin, E. 1964. Transport of large molecules across capillary walls. *Physiologist* 7, 13.
- Reynolds, E. 1963. The use of lead citrate at high pH as an electron-opaque stain in electron microscopy. *J Cell Biol* 17, 208.
- Richter, G. 1959. The cellular transformation of injected colloidal iron complexes into ferritin and hemosiderin in experimental animals. *J Exp Med* 109, 197.
- Ross, M., Nuttall, A. & Wright, Ch. 1977. HRP acute ototoxicity and the uptake and movement of the peroxidase in the auditory system of the Guinea pig. *Acta Otolaryngol* (Stockh) 84, 187.
- Santos-Sacchi, J. 1978a. Cytoplasmic microtubules in strial marginal cells. *Arch Oto-Rhino-Laryngol* 218, 297.
- Santos-Sacchi, J. 1978b. Differential effects of primary fixation with glutaraldehyde and osmium upon the membranous systems of the strial and external sulc cells. *Acta Otolaryngol* (Stockh) 86, 56.
- Smith, C. 1957. Structure of the stria vascularis and spiral prominence. *Ann Otol Rhinol Laryngol* 66, 521.
- Trump, B. & Arstila, A. 1974. Cell injury and cell death. In *Principles of pathobiology* (ed. La Via and Hill) pp. 9-95. Oxford University Press, New York.
- Winther, F. 1971. The permeability of the Guinea pig cochlear capillaries to HRP. *Z Zellforsch* 114, 193.
- Yamamoto, K. & Nakai, Y. 1964. Electronmicroscopic studies on the functions of the stria vascularis and the spiral ligament in the inner ear. *Ann Otol* 73, 332.

J. Santos-Sacchi, Ph.D.
Center for Biomedical Education
City College, Science Bldg. Rm. 915
The City University of New York
New York, NY 10031
USA



A Ferritin-containing Cell Type in the Stria Vascularis of the Mouse Inner Ear

J. Santos-Sacchi & William F. Marovitz

To cite this article: J. Santos-Sacchi & William F. Marovitz (1985) A Ferritin-containing Cell Type in the Stria Vascularis of the Mouse Inner Ear, *Acta Oto-Laryngologica*, 100:1-2, 26-32

To link to this article: <http://dx.doi.org/10.3109/00016488509108583>



Published online: 08 Jul 2009.



Submit your article to this journal [↗](#)



Article views: 1



View related articles [↗](#)

A Ferritin-containing Cell Type in the Stria Vascularis of the Mouse Inner Ear

J. SANTOS-SACCHI¹ and WILLIAM F. MAROVITZ²

From the ¹Department of Surgery, Section of Otolaryngology, UMDNJ-New Jersey Medical School and the ²Department of Anatomy and Otolaryngology, Mt. Sinai School of Medicine, City University of New York, New York, USA

Santos-Sacchi J, Marovitz W. F. A ferritin-containing cell type in the stria vascularis of the mouse inner ear. *Acta Otolaryngol (Stockh)* 1985; 100: 26-32.

This report describes a new cell type within the stria vascularis of the mouse inner ear. The cell is similar ultrastructurally to the classically described intermediate cell. However, it can be distinguished by the presence of dense vacuoles, presumably lysosomes, within which can be visualized electron dense particles resembling ferritin molecules. In addition, the ferritin-like particles are present throughout the cytoplasm and occasionally within the endoplasmic reticulum. These cells characteristically abut capillary basal lamina. Electron probe analysis of the dense vacuoles revealed the presence of iron. It is suggested that these cells may sequester iron released from dying erythrocytes in the strial capillary system, whereupon the iron is conserved through ferritin synthesis.

J. Santos-Sacchi, Department of Surgery, Section of Otolaryngology, UMDNJ-New Jersey Medical School, 100 Bergen St., Newark, NJ 07103, USA.

The stria vascularis, located on the lateral wall of the cochlear duct, is classically described as a three-cell layered tissue—marginal, intermediate, and basal (Smith, 1957). The marginal cell layer, which is ectodermal in origin, lines the lateral endolymphatic space and interdigitates laterally with the two other fibroblastic-like cell layers. The stria is important for normal cochlear function, and is unique in that capillaries (continuous type) maintain intimate contact with this epithelium; that is, in the adult there is no epithelial basal lamina. Various studies have noted the phagocytic activity of pericapillary strial light cells (Ruedi, 1951; Nomura, 1961; Duvall et al., 1971; Winther, 1971).

The monocyte-phagocyte system is considered crucial in iron metabolism (MacSween & MacDonald, 1969). The chief storage form of iron is ferritin, a protein which may be found in high concentrations in the cytoplasm of liver and spleen phagocytic cells. Intracellular iron storage as ferritin can be induced by the administration of exogenous iron compounds (Richter, 1959; Muir & Goldberg, 1961; Drysdale & Munro, 1966). Within hours of iron administration, ferritin molecules can be visualized electronmicroscopically within phagocytic cells which have incorporated the exogenous iron compound. Such induced phagocytic sequestration and ferritin synthesis mimics the normal mechanism of iron conservation. Considering the high capillary density and hematocrit of strial tissue, it might be expected that phagocytotic light cells would incorporate iron released from dying erythrocytes.

Recently, in a report on strial capillary permeability, we commented on the presence of a strial cell type which contains endogenous intracytoplasmic ferritin-like granules (Santos-Sacchi & Marovitz, 1980). This report presents a detailed analysis of these cells.

METHODS

Twelve young adult male mice, BALB/cJ (Jackson Labs, Barr Harbor, Maine) showing positive preyer reflexes were killed by decapitation. Within one minute of death, the right

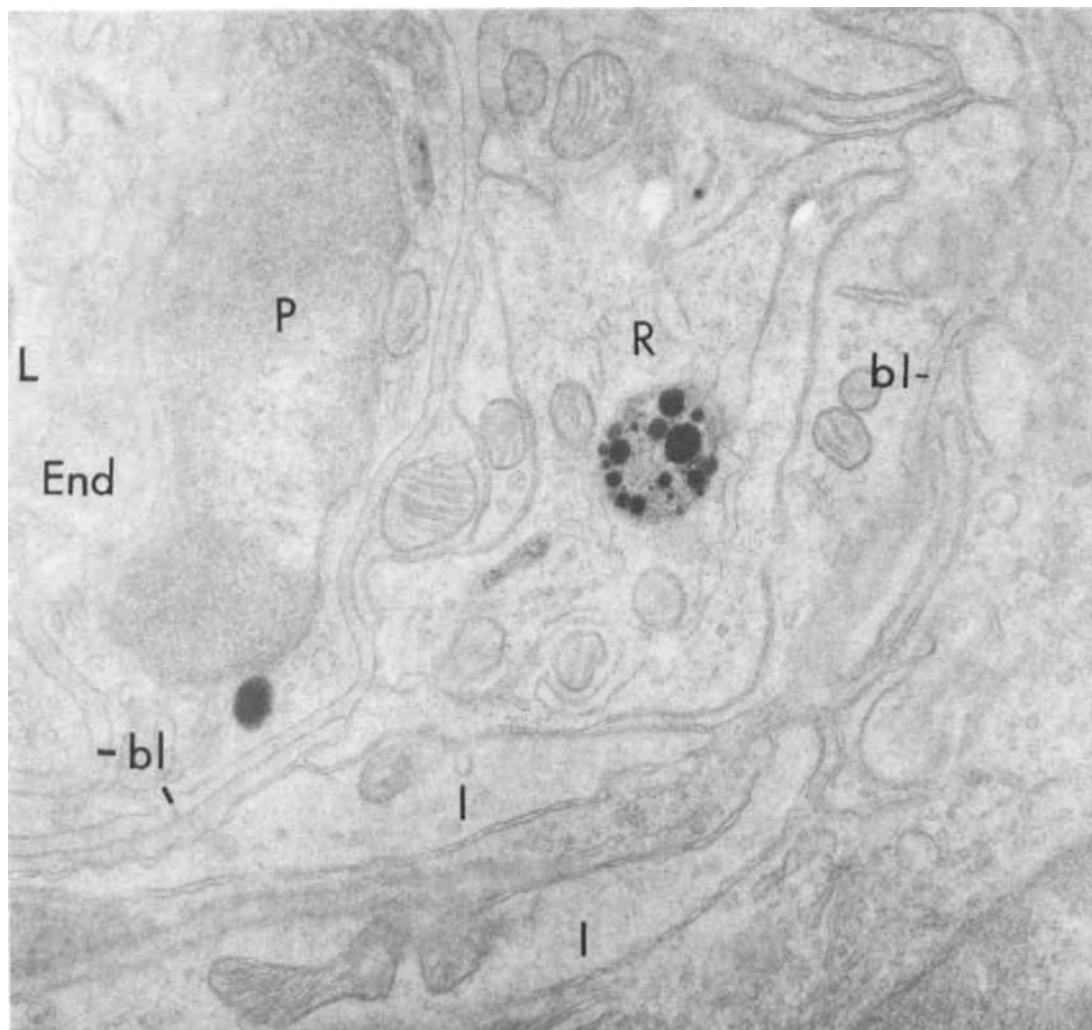


Fig. 1. Light cell abutting basal lamina near strial capillary. Note abundant supply of intracytoplasmic electron-dense granules and dense cored lysosomes. Adjacent intermediate cells lack granules. Osmium fixed. Unstained. $\times 30\,500$. *L*, capillary lumen; *End*, endothelial cell; *P*, pericyte; *I*, intermediate cell; *bl*, basal lamina; *R*, ferritin-containing cell; *M*, marginal cell; *Ly*, lysosome; *ER*, endoplasmic reticulum.

temporal bone was excised, fractured open and immersed in a primary fixative of either 2% glutaraldehyde or 1% osmium tetroxide, buffered with 0.2 M cacodylate, pH 7.4 (4°C for two hours). After a brief rinse in 0.2 M cacodylate buffer, those cochleas fixed in glutaraldehyde were post-fixed with osmium. The cochleas were again washed in buffer and dehydrated in a graded series of acetone. While in 70% acetone the striae were microdissected from surrounding tissue and after dehydration was complete, embedded in Epon 812 at 60°C. Grey-silver sections (50–80 nm) were cut with an LKB Ultratome, picked up on copper grids and examined with a Zeiss 9S-2 EM or Phillips 300 EM. Sections were examined unstained or lightly stained by lead citrate.

Because certain monocyte-phagocyte cells show endogenous peroxidase activity, this enzyme was assessed by the diaminobenzidine (DAB) technique, according to the modifi-

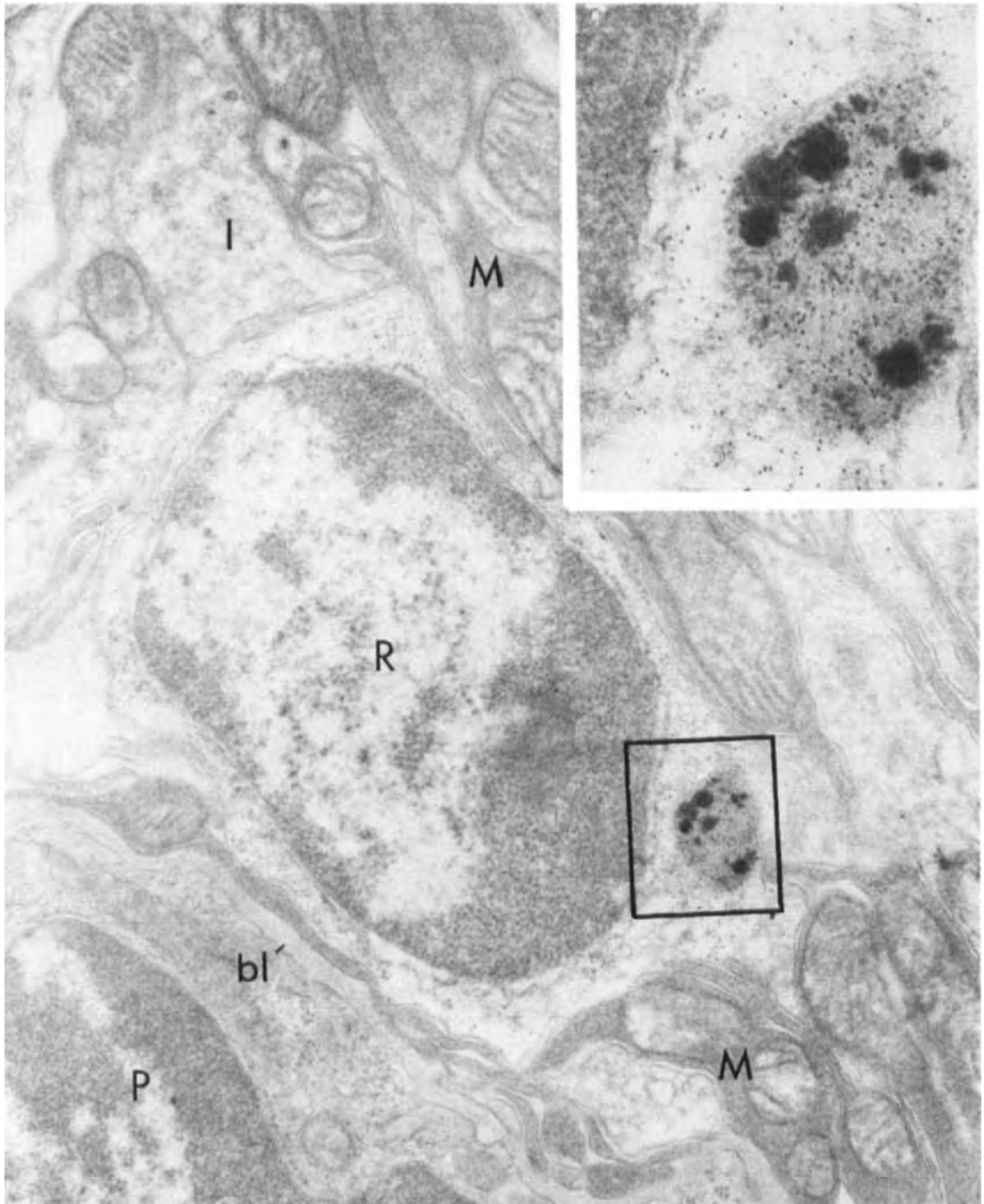


Fig. 2. Ferritin-containing light cell showing ovoid nucleus with peripheral heterochromatin. Marginal and typical intermediate cells surround the cell which lies on the basal lamina of a stria capillary pericyte. Note uniform accumulation of electron dense particles throughout cytoplasm and the presence of a lysosome. $\times 34\,800$. *Inset:* Enlargement of lysosome showing intralysosomal ferritin-like granules and large electron densities. $\times 120\,000$. Glutaraldehyde and osmium fixed. Unstained. Abbreviations, see Fig. 1.

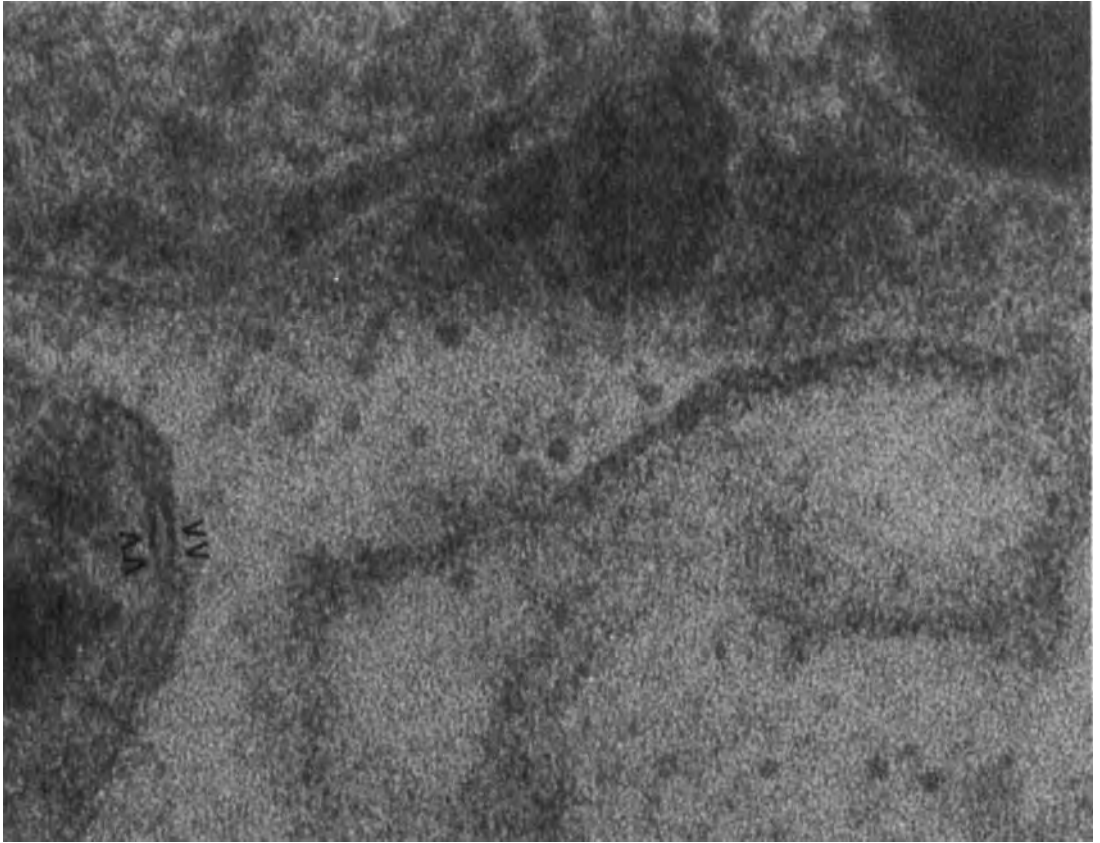


Fig. 3. High magnification of light cell cytoplasm showing lysosome and ferritin-like granules in cytoplasm and endoplasmic reticulum. Note size of granules relative to size of unit membrane (arrows). Osmium fixed. Lightly stained with lead citrate. $\times 368\,000$.

cation of Widmann et al. (1972). Electron probe elemental analyses were performed upon thin sectioned material using a JEOL JEM 100CX EM. Iron determinations were performed using a window of 6.190–6.550 KeV.

RESULTS

At low magnifications and in spite of the absence of normal staining the three known strial cell types were distinguished: marginal, intermediate and basal. However, at higher magnification, careful analysis of unstained strial tissues reveals the presence of ferritin-like particles within the cytoplasm of certain light cells (Figs. 1, 2, 3). At very high magnifications, the electron dense particles presented the characteristic appearance of ferritin (Fig. 3). The dimension of the electron dense ferritin core is slightly less than the thickness of the unit membrane, or approximately 50–60 Å.

These presumptive ferritin containing cells characteristically abut the basal lamina of strial capillaries, and possess electron dense vacuoles consistent with ferritin containing monocyte-phagocyte cells (Figs. 1, 2, 4). The electron density of these vacuoles is not dependent upon heavy metal staining as demonstrated in Fig. 4: tissues fixed only in glutaraldehyde and viewed with the electronmicroscope possess electron opaque va-

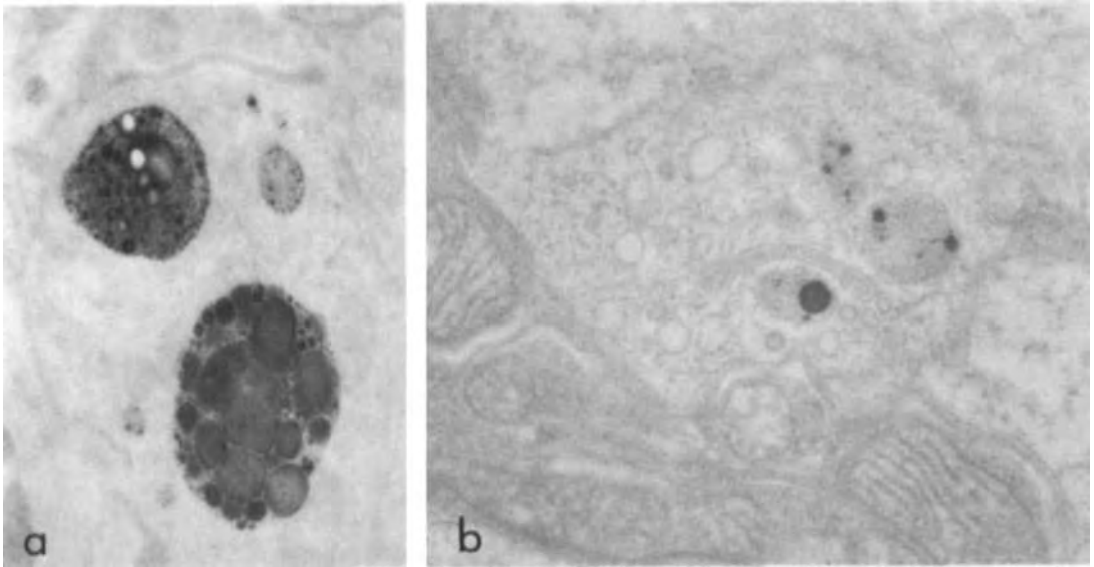


Fig. 4. (a) Note electron opacity of strial light cell vacuoles despite absence of postossification or heavy metal stains. Glutaraldehyde fixation only. $\times 17\,400$. (b) Process of strial light cell containing abundant supply of ferritin-like granules, lysosomes and membranous structures. Glutaraldehyde and osmium fixed. Unstained $\times 30\,500$.

cuoles. Electron probe elemental analysis of these vacuoles revealed iron in roughly equivalent concentration to that measured in a nearby erythrocyte, and significantly higher than in intermediate cell cytoplasm or Epon alone (Fig. 5). Interestingly, the chloride content of the lysosome and red cell was similar indicating a chloride shift within the lysosome.

Although ferritin granules are observed free within the cytoplasm as well as within certain membrane bound structures, i.e. endoplasmic reticulum and lysosomes (Figs. 1, 2, 4), they were never observed within mitochondria or nuclei. The cytoplasmic concentration of ferritin was variable; some cell processes exhibited sparsely scattered molecules while others, particularly when accompanied by lysosomes, contained an abundant supply. Except for the presence of ferritin, electron dense lysosomes and substantial amounts of membranous structures, including Golgi bodies, the ultrastructural detail of these cells is very similar to the typical intermediate cell. Strial capillary pericytes typically showed no accumulation of ferritin.

Light and electron microscopic cytochemical analysis of endogenous peroxidase activity within the stria vascularis failed to demonstrate reaction product within ferritin-containing cells. Strial capillary erythrocytes were the only structures which demonstrated positive staining with this technique.

DISCUSSION

Ferritin-containing strial light cells do not demonstrate endogenous peroxidase activity as do Kupffer cells (Widmann et al., 1972). However, species differences may be involved here. Whereas macrophagic cells in the rat and guinea pig are peroxidase positive (Fahimi et al., 1970; Widmann et al., 1972; Wisse, 1974), mature macrophages in the mouse are not (van Furth et al., 1970).

The stria's high capillary density and hematocrit provide an environment rich in iron.

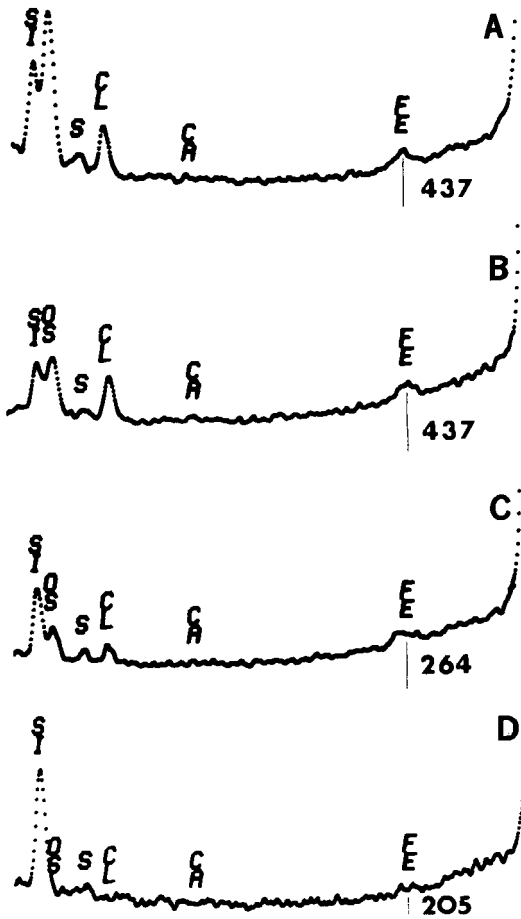


Fig. 5. Electron probe analyses of selected areas of a single thin section. Iron content measured with a window of 6.190–6550 KEV over a 658 sec period. (A) Dense core of light cell lysosome. Net count: 437. Also note high chloride content. (B) Adjacent red cell cytoplasm. Net count: 437. Note high chloride content. (c) Intermediate cell cytoplasm. Net count: 264. (d) Epon alone. Net count: 205. Silicon due to silicious probe element.

Possibly hemoglobin from dying erythrocytes is transported across strial capillaries and taken up preferentially by the light cells described herein. Lysosomal degradation coupled to ferritin synthesis would then ensue. The process of acquiring ferritin stores by this means would appear to be a slow one, considering the slow transendothelial passage of electron-dense tracers (Santos-Sacchi & Marovitz, 1980). This is confirmed by preliminary results which indicate the absence of intracellular light cell ferritin in the postnatal mouse.

Nomura (1961) demonstrated at the light microscopic level the uptake of trypan blue from guinea pig strial capillaries by sparsely scattered cells which rested near the capillaries. It was necessary for him to induce capillary leakage with intravenous injection of histamine and acetic acid. We have been unable to correlate the uptake of trypan blue and the presence of ferritin in mouse strial cells due to the inability to induce trypan blue extravascular leakage, even after acetic acid treatment. Horseradish peroxidase which has been shown to leak through strial capillaries has been demonstrated within pinocytotic and phagocytic vacuoles of strial intermediate cells (Duvall et al., 1971; Winther, 1971).¹

¹ Recently, Duvall (ARO Midwinter Meeting, 1981) reported that the HRP capillary transport in the normal preparation may have been due to dissection artifact. Thus the supposed phagocytic incorporation of HRP by light cells may actually have been staining of these cells by reaction product after the cells were killed by fixation.

However, these investigators suggest that the ability to phagocytize HRP is general among intermediate cells. Thus the ability to produce and store ferritin may be differentiated from simple phagocytotic functions, since only very few intermediate type cells exhibit detectable amounts of intracellular ferritin.

The storage of iron in the stria vascularis may have functional significance; e.g., it may be utilized by metalloenzymes within the stria or inner ear. Alternately, the storage may simply be a general response to high local levels of iron. Studies are planned to evaluate this issue.

ACKNOWLEDGEMENTS

This work was supported by the Deafness Research Foundation and NIH Grant NS 21380-1.

REFERENCES

- Drysdale, J. & Munro, H. 1966. Regulation of synthesis and turnover of ferritin in the rat liver. *J Biol Chem* 241, 3630.
- Duvall, A., Quick, C. & Sutherland, C. 1971. Horseradish peroxidase in the later cochlear wall: An electronmicroscopic study of transport. *Arch Otolaryngol* 93, 304.
- Fahimi, H. D., Cotran, R. S. & Litt, M. 1970. Localization of endogenous and exogenous peroxidase activity in Kupffer and peritoneal macrophages. *Fed Proc* 29, 493.
- MacSween, R. N. M. & MacDonald, R. A. 1969. Iron metabolism by reticuloendothelial cells. *Lab Investigation* 21, 230.
- Muir, A. & Goldberg, L. 1961. Observations on subcutaneous macrophages. Phagocytosis of iron-dextran and synthesis of ferritin. *Quart J Exp Physiol* 46, 289.
- Nomura, Y. 1961. Capillary permeability of the cochlea. *Ann Otol* 70, 81.
- Richter, G. 1959. The cellular transformation of injected colloidal iron complexes into ferritin and hemosiderin in experimental animals. *J Exp Med* 109, 197.
- Rüedi, L. 1951. Some animal experimental findings on the functions of the inner ear. *Ann Otol* 60, 993.
- Santos-Sacchi, J. & Marovitz, W. F. 1980. An evaluation of normal strial capillary transport using the electron-opaque tracers ferritin and iron dextran. *Acta Otolaryngol (Stockh)* 89, 12.
- Smith, C. 1957. Structure of the stria vascularis and spiral prominence. *Ann Otol* 66, 521.
- Van Furth, R., Hirsch, J. G. & Fedorko, M. E. 1970. Morphology and peroxidase cytochemistry of mouse promonocytes, monocytes, and macrophages. *J Exp Med* 132, 794.
- Widmann, J. J., Cotran, R. S. & Fahimi, H. D. 1972. Mononuclear phagocytes (Kupffer cells) and endothelial cells. *J Cell Biol* 52, 1959.
- Winther, F. 1971. The permeability of guinea pig cochlear capillaries to HRP. *Z Zellforsch* 114, 193.
- Wisse, E. 1974. Observations on the fine structure and peroxidase cytochemistry of normal rat liver Kupffer cells. *J Ultrastruct Res* 46, 393.

Joseph Santos-Sacchi · Enrique Navarrete

Voltage-dependent changes in specific membrane capacitance caused by prestin, the outer hair cell lateral membrane motor

Received: 4 December 2001 / Revised: 23 January 2002 / Accepted: 23 January 2002 / Published online: 20 February 2002
© Springer-Verlag 2002

Abstract In the outer hair cell (OHC), membrane capacitance principally derives from two components – that associated with lateral membrane sensor/motor charge movement, and that proportional to the membrane surface area (C_{sa}). We used measures of membrane capacitance to test a model hypothesis that OHC lateral membrane molecular motors, recently identified as the protein prestin, fluctuate between two area states. By measuring membrane capacitance in native OHCs or prestin-transfected HEK cells at extreme voltages (± 200 mV) where motor-derived charge movement is small or absent, we observed that C_{sa} depends on the state of the motors, or correspondingly on membrane voltage. Deiters cells or control HEK cells, which lack motors, do not show this dependence. We modeled the voltage-dependent change in C_{sa} as a Boltzmann process with the same parameters that describe the charge movement of the motors' voltage sensors. C_{sa} is 3.28 ± 0.75 pF (mean \pm SD; $n=23$) larger during extreme hyperpolarization, and the number of motors in OHCs and prestin-transfected HEK cells correlates with the magnitude of ΔC_{sa} ($r=0.78$). Although these data are consistent with the area motor model, the corresponding area change, assuming $0.5 \mu\text{F}/\text{cm}^2$ under constant membrane thickness, is unphysiologically large, and indicates that the capacitance change must result from changes not only in lateral membrane area but also specific capacitance. Thus, we conclude that a conformational change in the lateral membrane motor, prestin, additionally alters the dielectric constant and/or thickness of the lateral plasma membrane.

Keywords Gating charge · Membrane capacitance · Motility

Introduction

The capacitance per unit area of plasma membrane, i.e., specific capacitance (C_{sp}), is determined by the membrane's dielectric constant and thickness. It is a robust quantity that Cole [5] described as “largely independent of cell physiology, pathology and pharmacology, and probably life itself”. Based on this property, the magnitude of an individual cell's membrane capacitance ($C_m = \text{surface area} \times C_{sp}$) may be considered fixed, invariant with changes in membrane voltage. In that same essay, however, Cole realized that his view could be modified by future investigations; it is now known that deviations from the expected invariant behavior provide information on such varied processes as ionic channel gating [10], synaptic vesicle fusion [29], gap junctional coupling [36], and, in the case of the outer hair cell (OHC), its lateral membrane motor's activity [2, 37]. In the OHC, such deviation arises from restricted charge movement during conformational change in a membrane motor protein [2, 37], the recently identified lateral membrane protein, prestin [26, 41, 48]. Consequently, membrane capacitance (C_m) in the OHC is characterized as a bell-shaped, voltage-dependent capacitance (C_v) that rides atop a parallel capacitance (C_{sa}) whose magnitude is proportional to cell surface area [2, 16, 37]. Peak motor-associated capacitance can range up to nearly twice that of the cell's C_{sa} [39].

One of the model mechanisms whereby the lateral membrane motor can effect whole-cell mechanical responses is by changing the surface area that it occupies within the lateral plasma membrane [17, 18, 38], although other models have been proposed [7, 14, 22, 33]. We reasoned that if the integral lateral membrane motors fluctuate in area between two states, as the model suggests, we should be able to observe whole-cell changes in C_{sa} due to changes in the cell's surface area. Indeed, one of the major criticisms of the area-motor model has been the apparent absence of effects on C_{sa} [33]. According to the model, depolarization, which is predicted to drive the motors into the compact state and reduce the

J. Santos-Sacchi (✉) · E. Navarrete
Sections of Otolaryngology and Neurobiology, Yale University
School of Medicine, 333 Cedar St., New Haven, CT 06510 USA
e-mail: joseph.santos-sacchi@yale.edu
Tel.: +1-203-7857566 office, Fax: +1-203-7372502

area occupied by them within the bilayer, should in turn reduce total membrane surface area and C_{sa} , whereas hyperpolarization should do the opposite. In order to test this prediction, we measured capacitance over an extreme voltage range in isolated OHCs and prestin-transfected human embryonic kidney cells under whole-cell voltage-clamp conditions. At extreme voltage polarities where motor-derived charge movement is small or absent, we find that C_{sa} depends on the state of the motors, or correspondingly on membrane voltage. During extreme hyperpolarization, when the motors cause the cylindrical OHC to elongate, C_{sa} is increased – a prediction of the area motor model of OHC motility [17, 18, 38]. Nevertheless, the predicted area change based on typical, fixed values of specific membrane capacitance is unphysiologically large, and must be accounted for by additional mechanisms such as membrane thinning or alterations in the membrane's dielectric properties.

Materials and methods

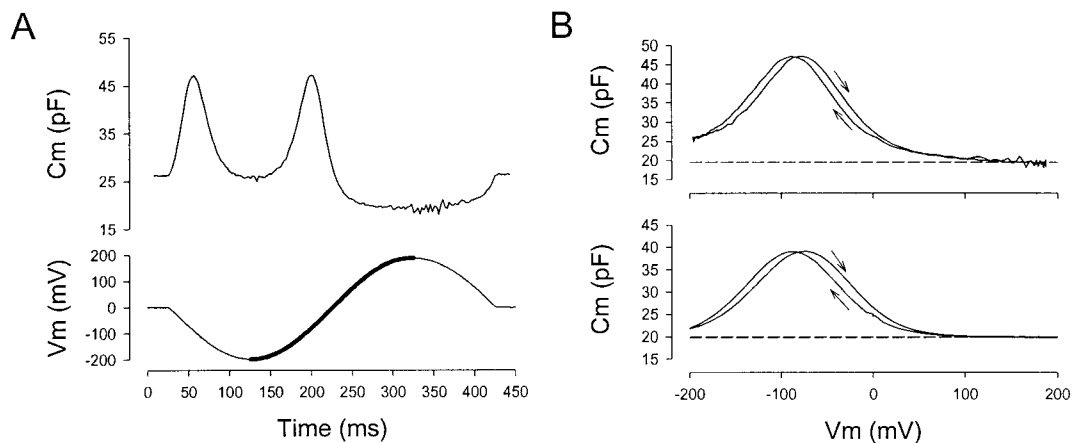
Guinea pigs were decapitated following anesthetic overdose with halothane, in accordance with the guidelines of Yale University's Animal Care and Use Committee. OHCs were freshly isolated from the guinea pig cochlea using dispase (1 mg/ml) followed by trituration. Transient transfection of human embryonic kidney (TSA201) cells with gerbil prestin was performed as previously described [48]. Co-expression of green fluorescent protein (GFP) provided visual identification of transfected cells. Only isolated, single HEK cells were studied. Cells were whole-cell voltage clamped at room temperature using an Axon 200B amplifier. Membrane voltages were corrected for the effects of residual series resistance, which ranged from 3–5 M Ω . Ionic blocking solutions were used with all cell types to remove voltage-dependent ionic conductances so that capacitive currents could be analyzed in isolation [37]. Extracellular solution: 100 mM NaCl, 20 mM TEA, 20 mM CsCl, 2 mM CoCl₂, 1.48 mM MgCl₂, 2 mM CaCl₂, 10 mM HEPES, and 5 mM dextrose, adjusted to pH 7.2 with NaOH, and adjusted to 300 mosmol/l with dextrose; in some cases CaCl₂ and MgCl₂ were omitted. Pipette solution: 140 mM CsCl, 10 mM EGTA, 2 mM MgCl₂, and 10 mM HEPES, adjusted to pH 7.2 with CsOH, and adjusted to 300 mosmol/l with dextrose. In some experiments, the extracellular solution was also used in patch electrodes. For experiments with 10 mM sodium salicylate, NaCl was reduced to maintain osmolarity. In a few experiments, 50 μ M GdCl₃ was included in the extracellular solution to decrease residual currents. At this concentration, gadolinium has an insignificant effect on OHC capacitance [21]. Capacitance was

measured with a continuous high-resolution (2.56 ms) two-sine voltage stimulus protocol (20 mV peak at both 390.6 and 781.2 Hz), and subsequent FFT-based admittance analysis [40], utilizing the parameter derivations provided by Pusch and Neher [32]. These small, high-frequency sinusoids were superimposed on voltage sinusoids that spanned ± 200 mV. OHCs that showed evidence of instability at the extremes were not included (see Results). All data collection and most analyses were performed with an in-house-developed Windows-based whole-cell voltage-clamp program, jClamp (SciSoft, CT), utilizing either an Axon Instruments Digidata 1320 board or a National Instruments PCI-6052E board. Matlab (Natick, Mass., USA) was used for fitting the capacitance data. Fits were made with the Nelder-Mead algorithm, and the minimization metric employed was $s = \sum \sqrt{(C_m - \text{fit})^2}$. In some cases, we used Sigmaplot (Jandel Scientific, California, USA) to fit model data, and determine standard errors.

Results

Under whole-cell voltage-clamp, OHCs do not tolerate extreme voltages that are abrupt in onset. We have only been able to record consistently from cells using a low-frequency sinusoidal stimulus whose range was limited to ± 200 mV (not including the superimposed high frequency two-sine stimuli – see Materials and methods). Whole-cell voltages more extreme than that usually resulted in loss of recordings. In a separate study we determined that breakdown in the membranes of the OHC oc-

Fig. 1A, B Outer hair cell (OHC) capacitance shows hysteresis and asymmetry at voltage polarity extremes. **A** Stimulation with a wide-ranging voltage sinusoid reveals a voltage-dependent capacitance. The highlighted portion of the voltage stimulus and associated capacitance are used in subsequent fits of the membrane capacitance (C_m) data as in Fig. 3. **B** *Top panel*: C_m versus voltage function from **A**. Note hysteresis. Direction of voltage change is shown by *arrows*. Additionally, note that the function is asymmetrical, with C_m at the hyperpolarized extreme never approaching the value of membrane surface area (C_{sa}) found at depolarized potentials. This is more rigorously shown in the fits of Fig. 3. *Dashed line* shows minimum capacitance at depolarized levels. *Lower panel*: model results using the wide-ranging voltage sinusoid (based on model fully described in Santos-Sacchi et al. [40]). *Dashed line* shows minimum capacitance at depolarized levels. The result indicates that the hysteresis is due to dependency on prior voltage, but the asymmetry is not, since model C_{sa} at hyperpolarized levels eventually reaches the same minimum magnitude as at depolarized levels



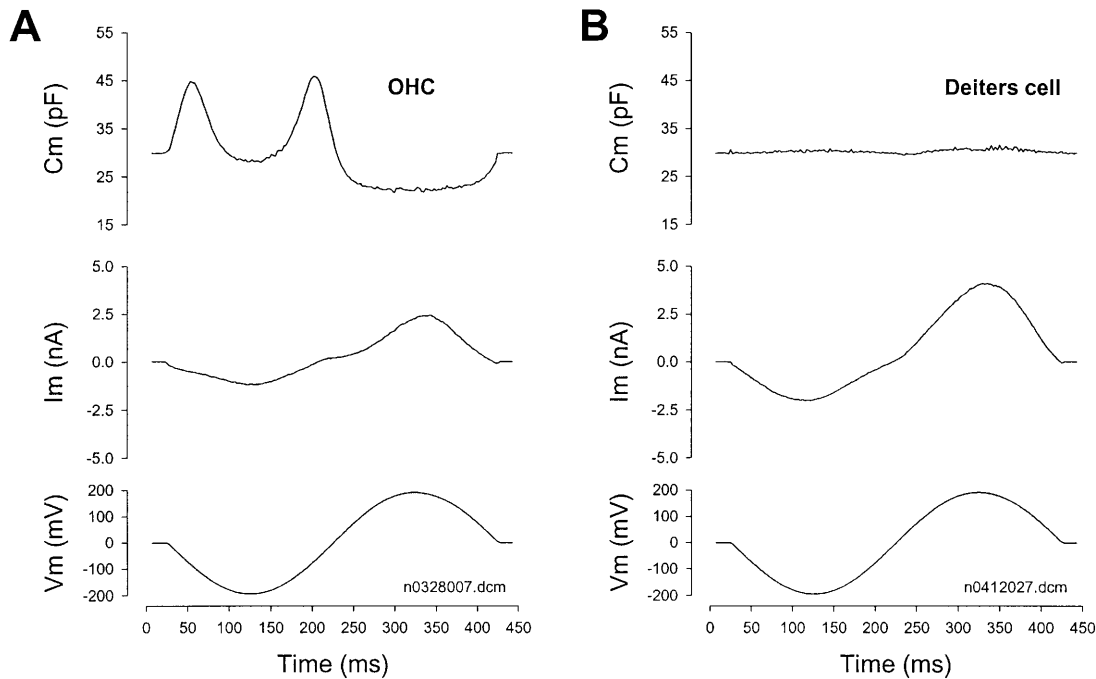


Fig. 2A, B Residual nonlinear current does not influence capacitance measures. **A** Residual nonlinear currents are evoked in the OHC despite our attempts to block membrane conductances. Note that this does not influence the measurement of capacitance, since similar though larger current nonlinearities generated in Deiters' cells (**B**) do not compromise the measurement of its voltage-independent capacitance

cur at absolute membrane potentials greater than 380 mV [27], far greater than the voltage extremes used here; thus, the loss of cells that we experienced with voltages above 200 mV under whole-cell conditions was probably due to compromised pipette-membrane seals resulting from robust mechanical activity of the OHC. We found that deflating the OHC by applying negative pipette pressure, which is known to abolish OHC motility [37], decreased the chances of loss. The results we report here were not affected by reducing OHC turgor pressure. Figure 1A illustrates the membrane capacitance changes that occur with our type of stimulation. During the hyperpolarizing phase of the stimulus, membrane capacitance presents as a double peaked response, and during the depolarizing phase a monophasic minimum is reached. A plot of membrane capacitance (C_m) versus membrane voltage (Fig. 1B, upper panel) shows the bell-shaped capacitance function characteristic of OHCs. However, in this case, two previously unobserved features are found. First, C_m shows hysteresis; namely, C_m magnitude depends on the prior voltage value and, thus, on the direction of voltage change. Second, the bell-shaped C_m function is asymmetrical, indicating that C_{sa} at extreme hyperpolarizations is larger than at extreme depolarizations. The hysteresis is fully predictable since it is known that there is a voltage-dependent shift in the capacitance function that is adequately modeled as a voltage-dependent, motor-induced change in membrane

tension [40, 41]. Membrane tension effectively shifts the capacitance function along the voltage axis [11, 17, 20, 47]. Fig. 1B (lower panel) shows the result of that model simulation using our extreme sinusoidal voltage stimulus. The hysteresis is similar to the biophysical data. However, whereas the model output indicates that hysteresis results from voltage-induced shifts in the C_v function, it cannot produce and therefore cannot account for the asymmetry in the C_m function. Additionally, the asymmetry was not related to the initial direction of voltage change, i.e., it did not matter whether the large sinusoid's phase was initially hyperpolarizing (as presented in the figures) or depolarizing. Rate of voltage change was also not influential, as sinusoids from 200 to 800 ms in duration produced the same asymmetry.

Despite the use of ionic blocking solutions, substantial currents are evoked by our extreme voltage protocol (Fig. 2). In order to assure ourselves that large currents or residual current nonlinearities did not confound our measurements, we compared OHC responses to those of supporting Deiters' cells, which lack membrane motors. In Fig. 2 we plot C_m , I_m , and V_m of a typical OHC and typical Deiters' cell. In each case, nonlinear currents are evidenced, notably larger in the Deiters' cell. Yet, Deiters' cells present a linear capacitance largely independent of variations in membrane voltage and current. These control experiments show that unblocked currents do not influence our capacitance measurements. Additionally, we have preliminary data [35] indicating that even in the presence of intracellular and extracellular solutions containing only large impermeant ions, where residual currents are less than 100 pA, capacitance remains asymmetrical. Furthermore, prestin-transfected HEK cells, which display small linear currents, show similar capacitance functions as OHCs (see below). Thus, residual currents and corresponding changes in membrane resistance can-

not account for our C_m data. We also ruled out potential increases of membrane surface area via incorporation of intracellular membrane by recording with high-BAPTA (10–20 mM) or pronase-containing (500 $\mu\text{g}/\text{ml}$) intracellular solutions, treatments known to block membrane fusion [16, 43]. Under these conditions C_{sa} asymmetry is still observed. As an additional check on our admittance technique, we used a standard stair step, transient analysis protocol to confirm the admittance measures within individual OHCs [16]. Although we were unable to provide such extreme voltages as the sinusoidal stimulus because of cell loss, capacitance values measured within the fairly wide range of -160 to 100 mV overlaid the admittance-based values (data not shown). We conclude that the asymmetry evidenced in the OHC C_m is real. This asymmetry is illustrated more rigorously through fits of the C_m data.

In order to gauge the asymmetry in our C_m data, we fit the data to the first derivative of a two-state Boltzmann function that has been used routinely to fit OHC C_m data [12, 17, 37].

$$C_m = C_v + C_{sa}$$

$$C_m = Q_{max} \frac{ze}{kT} \frac{b}{(1+b)^2} + C_{sa}$$

$$b = \exp\left(\frac{-ze(V_m - V_{pkcm})}{kT}\right) \quad (1)$$

where C_v is the motor's voltage sensor-associated capacitance, C_{sa} is parallel capacitance proportional to membrane surface area, Q_{max} is the maximum nonlinear charge moved, V_{pkcm} is voltage at peak capacitance or half-maximal nonlinear charge transfer, V_m is membrane potential, z is valence, e is electron charge, k is Boltzmann's constant, and T is absolute temperature. Figure 3A, B show, for two different cells, that this symmetrical function does not adequately describe our C_m data, although the equation had proven sufficient previously [12, 17, 37]. In those previous studies, voltage stimulation was substantially more restricted than employed here, typically not extending beyond ± 125 mV, and fits were understandably less constrained. In order to obtain a better understanding of our data, a modified equation was developed, where the state of lateral membrane motors contributes to the magnitude of C_{sa} . We reasoned that the contribution of a putative motor area change would be voltage dependent, and that the relationship should follow a sigmoidal two-state Boltzmann function identical to that of the sensor motor's nonlinear charge movement or the cell's mechanical response [37]. Depolarization, which drives the motor into its compact state, should decrease membrane surface area and C_{sa} . Thus, C_{sa} is described as a sigmoidal function

$$C_{sa} = \frac{\Delta C_{sa}}{(1+b^{-1})} + C_0 \quad (2)$$

where C_0 is defined as the capacitance of the membrane when all motors are in their compact state, the minimum

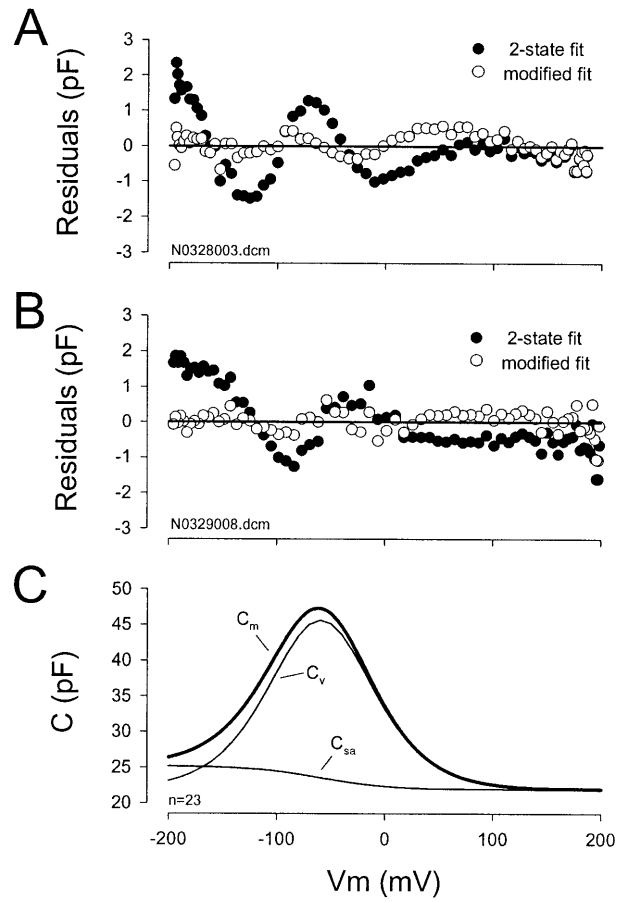


Fig. 3A–C OHCs present two types of voltage-dependent capacitance. **A, B** Plots show residuals of fits to capacitance of two OHCs as a function of membrane voltage. In each case, the C_m data were fit either with an equation based on a simple two-state Boltzmann function (*filled circles*, Eq. 1) or with an additional voltage-dependent C_{sa} component (*open circles*; modified by Eq. 2). Note the poor fit with the simple equation (**A**, *filled circles*: $s=8.11$ pF; **B**, *filled circles*: $s=8.62$ pF), and the good fit with the modified one (**A**, *open circles*: $s=2.81$ pF; **B**, *open circles*: $s=2.69$ pF), especially at negative voltages. **C** OHC capacitance derives from the sum of C_{sa} and C_v to produce C_m . Plots are from fitted parameters of the modified equation for 23 cells (averaged $s=3.96$ pF). Fitted parameters: Q_{max} : 3.09 ± 0.53 pC; V_{pkcm} : -59.4 ± 17.8 mV; z : 0.79 ± 0.10 ; C_0 : 21.9 ± 1.6 pF; ΔC_{sa} : 3.28 ± 0.75 pF. Average residuals for the two-state fit was $s=8.13$ pF

membrane capacitance, ΔC_{sa} is the maximum increase in capacitance that occurs when all motors change from compact to expanded state, and b is as above. The residuals in Fig. 3A, B illustrate the goodness of fit of this modified equation to the C_m data; the average sum of the residuals was halved with the fit to the modified equation ($s=8.13$ pF for the two-state fit; $s=3.96$ pF for the modified fit). The significantly better fit substantiates our contention that C_{sa} increases during hyperpolarization, and aids in quantifying the magnitude of change. In Fig. 3C, we plot capacitance functions based on averages of the fitted parameters for 23 cells. The difference in C_{sa} between conditions where all motors exist in either the compact or expanded states is 3.28 ± 0.75 pF (mean \pm SD;

see Fig. 3C legend for other fitted parameters and statistical comparisons). The plot further illustrates how this voltage-dependent change in C_{sa} results in an asymmetrical C_m function.

Capacitance asymmetry may arise from multi-state models of motor activity; however, Iwasa [19], using realistic values for OHC charge parameters found little evidence of asymmetry in model capacitance functions (his Fig. 3). We also fit our data to the sum of two bell-shaped Boltzmann derivatives, each providing distinct parameters for z , V_{pkcm} , and Q_{max} . In this case however, the fitted parameters of the second underlying Boltzmann are unrealistic; for example, V_{pkcm} is unphysiologically negative in magnitude, showing values as great as -780 mV, with Q_{max} up to 15 pC. Of course, this type of fit describes a function that mimics that of Eq. 2 within the voltage range that we studied.

What evidence is there that ΔC_{sa} results from the activity of OHC lateral membrane motors? This is an important point since recently, Kilic and Lindau [24] have found an asymmetrical bell-shaped membrane capacitance, similar in form to the one we observe here, that they attribute to Na channel gating charge in nerve terminals. In fact, they find voltage-dependent changes in their control C_m recordings (in the absence of Na channel activity) that mimic the form of our Eq. 2. In order to determine whether the activity of the lateral membrane motor accounts for ΔC_{sa} , we measured capacitance in Deiters' cells and HEK cells that were either successfully or unsuccessfully (based on the generation of nonlinear capacitance) transfected with the gene for prestin. Prestin has recently been identified as the OHC motor protein, since when expressed in HEK cells it displays the electro-mechanical signature of the OHC motor [41, 48]. We do not observe voltage-dependent C_m in control cells that lack the motor. Figure 4A shows that Deiters' cells, which lack lateral membrane motors, or human embryonic kidney cells *unsuccessfully* transfected with prestin do not evidence C_m differences at voltage extremes. More telling, those non-auditory cells *successfully* transfected with prestin present asymmetrical capacitance functions matching those of OHCs (Fig. 4B). Additional evidence arises from the direct correlation between the number of membrane motors based on charge estimates ($N=Q_{max}/ze$) and the magnitude of ΔC_{sa} (unconstrained fit, solid line; $r=0.78$; Fig. 4C). A unit capacitance change of 0.11 aF per motor is obtained. With the fit constrained to the origin (Fig. 4C, dashed line), 0.13 aF per motor is obtained. These data were derived from mature OHCs of different lengths ($n=23$), from prestin-transfected cells with differing expression efficiencies ($n=6$), and from published data on developing OHCs ($n=2$) [30]. Finally, we note that the generation of nonlinear capacitance, in and of itself, is not responsible for the asymmetry we find. That is, treatment with lipophilic ions is able to induce a bell-shaped capacitance in Deiters cells and an augmented capacitance in OHCs. However, we found no evidence that this additional gating charge either produced or augmented the asymmetry

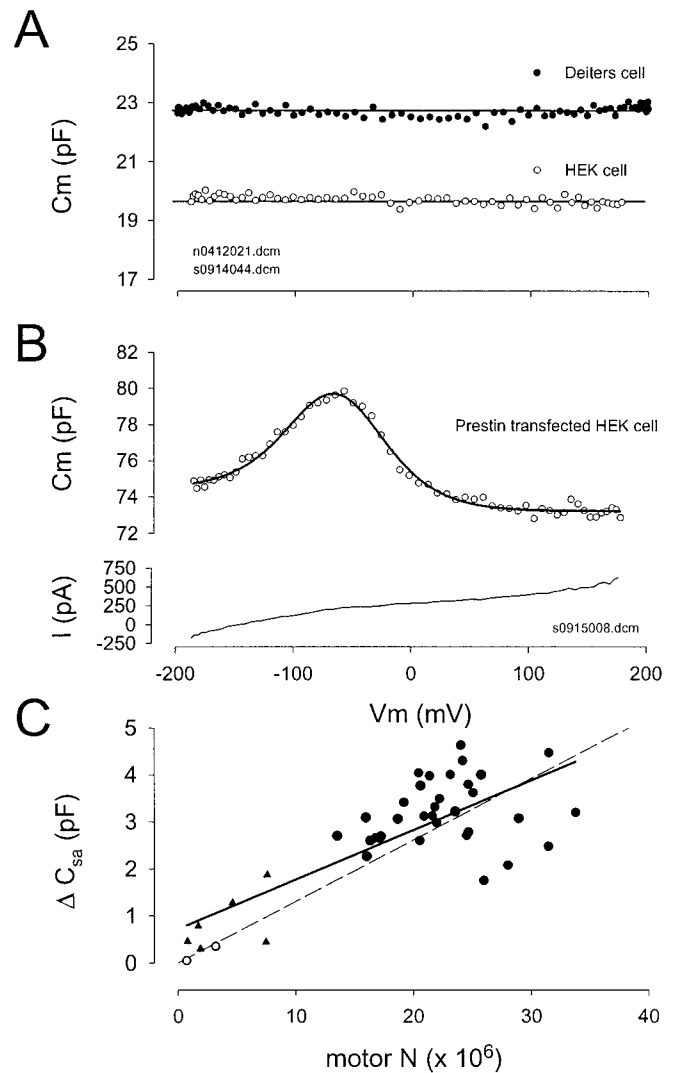


Fig. 4A–C The increase in C_{sa} at hyperpolarized potentials arises from the lateral membrane motor protein, prestin. **A** Neither Deiters' cells (*filled circles*), which do not express prestin, nor human embryonic kidney cell unsuccessfully transfected with prestin (*open circles*) give evidence of an increase in C_{sa} with hyperpolarization. *Lines* are straight horizontals. **B** Prestin-transfected human embryonic kidney cells show the same asymmetrical C_m function as OHCs. *Fitted solid line*: Q_{max} : 0.90 pC; V_{pkcm} : -65.0 mV; z : 0.66 ; C_0 : 73.2 pF; ΔC_{sa} : 1.25 pF. **C** The maximum change in C_{sa} (ΔC_{sa}) is correlated with the estimated number of motors ($N=Q_{max}/ze$). The *filled circles* are adult OHCs, the *filled triangles* are prestin-transfected cells, and the *open circles* are obtained from fits to the developmental OHC data of Oliver and Fakler (their Fig. 1, P6, P11; limited voltage range but low noise traces) [30]. The *dotted line* is a linear regression through the origin (slope of 0.13 aF/motor), whereas the *solid line* is an unconstrained regression, with a slope of 0.11 aF/motor and an r of 0.78

in OHC capacitance [46]. All these data strongly suggest that ΔC_{sa} arises from the activity of lateral membrane motors.

Finally, we explored the effect of the widely used drug, salicylate, on OHC C_{sa} . Salicylate, which can cause temporary hearing loss and tinnitus, has been found to reduce OHC motor-derived capacitance and

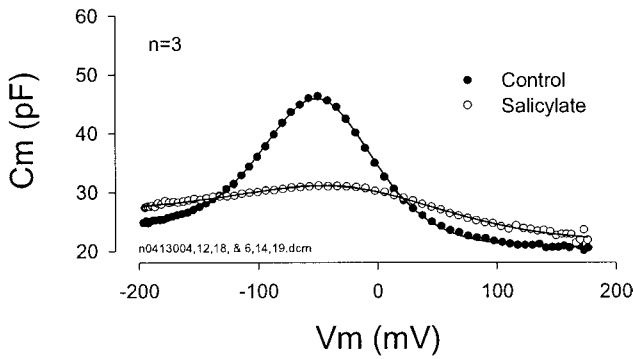


Fig. 5 Salicylate reduces C_v but increases C_{sa} . Averaged responses from three cells before and after extracellular salicylate treatment (10 mM). Three minutes after obtaining the whole-cell configuration control measures were made; following an additional 3 min of superfusion with salicylate the measures were repeated. Note the reduction in motor-derived capacitance, but an increase in C_{sa} . Fitted parameters for control: Q_{max} : 2.93 pC; V_{pkcm} : -48.9 mV; z : 0.83; C_0 : 20.5 pF; C_{sa} : 3.6 pF. Fitted parameters for salicylate: Q_{max} : 1.6 pC; V_{pkcm} : -23.2 mV; z : 0.44; C_0 : 21.2 pF; C_{sa} : 5.4 pF

motility [21, 42, 44]. Deiters' cell capacitance, on the other hand, is unaltered by salicylate treatments (data not shown). However, the effect on the OHC is not simply to reduce capacitance uniformly across voltage. The averaged data ($n=3$) in Fig. 5 shows that whereas peak capacitance is substantially reduced, capacitance on either side of the peak actually increases, and this is partially owing to a reduction in the steepness of the voltage dependence, as indicated by the fits to the C_m data (see Fig. 5 legend). Interestingly, the fit with our new model demonstrates that C_{sa} in the hyperpolarized region increases by about 2 pF above controls. Since salicylate has no effect on the capacitance of cells that lack the lateral membrane motor, and since there is a simultaneous effect on C_v and C_{sa} , this result additionally identifies ΔC_{sa} as arising from the activity of lateral membrane motors.

Discussion

In the OHC, membrane capacitance (C_m) arises from two superimposed components; one component (C_v) derives from gating charge movement owing to voltage-dependent activity of motor proteins within the lateral plasma membrane, while the other component (C_{sa}) derives from the intrinsic dielectric properties of all segments of its plasma membrane [2, 8, 37]. The latter component, often termed “linear” membrane capacitance, though typically considered independent of voltage, may co-vary with mechanisms, including voltage-dependent ones, that alter the underlying characteristics which define whole-cell capacitance, namely the membrane's surface area, dielectric constant, or thickness. We find that the activity of the lateral membrane motor, prestin, either in native OHCs or expressed in nonauditory cells influences the magnitude of the plasma membrane's C_{sa} , providing a clue to the motor's mechanism of action.

What fraction of ΔC_{sa} may arise from voltage-induced, OHC lateral membrane area change?

The change in C_{sa} that we observe resulting from fluctuations in the state of lateral membrane motors may arise from corresponding fluctuations in the area occupied by the motors within the lipid bilayer. Direct modifications of membrane surface area by integral proteins can be accomplished by a variety of molecular mechanisms. For example, reversible insertion of proteins or protein regions within the plasma membrane could serve to change membrane surface area [25]. The insertion of the bactericidal colicin protein into the lipid bilayer is voltage dependent, with at least 68 amino acid residues reversibly inserting into the bilayer [23]. Obviously, such a phenomenon will displace lipid, and alter membrane surface area. Alternatively, integral membrane proteins could change surface area by rearrangement of subunits, as may occur in gap junctions [45].

Based on our set of measures, the average number of motors [$N=Q_{max}/(ze)$] per cell is 25.7 ± 4.3 million. Thus, we estimate that each motor contributes ≈ 0.13 aF to C_{sa} as the motor changes from the compact to the expanded state. We previously determined the OHC-specific membrane capacitance to be $8 \text{ fF}/\mu\text{m}^2$, accounting for additional membrane area ($\approx 30\%$; see [6]) due to rippling that is unobservable at the light microscopic level [16]. More recent and rigorous attempts to account for membrane folding provide estimates in other cell types of $5 \text{ fF}/\mu\text{m}^2$ [43]. Using the latter value, we arrive at a motor area change of $\approx 26 \text{ nm}^2$. Based on our estimates of C_0 (21.9 pF), the area of the lateral membrane can be estimated to be $3134 \mu\text{m}^2$, after correcting for the capacitance of those membrane regions devoid of motors (6.23 pF; [16]). The density of motors within the lateral membrane is then $8168/\mu\text{m}^2$, similar to our previous estimates obtained from low-frequency OHCs [16, 39]. Given these values, the estimated area change in the lateral membrane, if ΔC_{sa} fully reflects area changes, would be about 21%. This large area change is in contrast with results of modeling. We had previously determined that the OHC area motor model could account for physiological length and diameter changes by a lateral membrane surface area modification of about 3%. Indeed, even the unit motor area change that we now obtain, 26 nm^2 , is much larger than estimates previously made ($\approx 8 \text{ nm}^2$ [38]; $2\text{--}7 \text{ nm}^2$ [1, 17, 18]; 0.37 nm^2 [11]). We conclude that ΔC_{sa} does not simply reflect changes in the membrane surface area.

Kalinec et al. [22] found voltage-induced surface area changes up to 8% in lateral membrane patches utilizing voltage pulses between ± 80 mV. Since this voltage excursion is less than the motor's range of voltage sensitivity, it might be expected that their measured area changes were sub-maximal. Considering the Boltzmann characteristics of the mechanical response [37], their data are reconcilable with a maximal area change of 10.9%. While our capacitance data may be viewed as arising from changes in membrane characteristics other than ar-

ea, the direct measures of Kalinec et al. [22] must be taken at face value and supersede model predictions. It should be noted that the OHC plasma membrane area is not increased by stretch but instead by supplementation; consequently, an area increase above that typically considered to cause membrane breakdown by stretching ($\approx 4\%$; [9]) is not unrealistic. Thus, we consider that a portion of ΔC_{sa} arises from a 10.9% change in lateral membrane surface area, amounting to 1.7 pF, and the remainder (1.6 pF) reflects changes in either the membrane's dielectric constant or thickness. That is, the specific membrane capacitance changes from 5.0 to 5.37 fF/ μm^2 when all prestin motors change from the compact to the extended state.

How might an integral membrane protein, such as prestin, alter specific membrane capacitance?

Membrane dielectric

The dielectric constant of the lipid bilayer is about 2. Proteins possess a higher dielectric constant, and thus they may be expected to alter the overall dielectric properties of the membrane when inserted within the bilayer. Indeed, many investigators have found changes in capacitance upon insertions of proteins into lipid bilayers, although in some cases the changes were transient [4], or may have been attributed to channel gating capacitance [34]. A direct test with exogenously expressed glycine receptors in HEK cells did not alter the specific membrane capacitance [13], although only about 20,000 receptors were expressed per cell. In the adult OHC from the low-frequency region of the cochlea, 25 million motors are expressed, increasing the likelihood of the protein's effect on the membrane dielectric. Voltage-dependent movement of charged regions of the protein prestin into or out of the hydrophobic membrane domain could affect the membrane dielectric. Alternatively, binding of anions to prestin could change the protein's dielectric [31].

Membrane thickness

Transmembrane voltage may affect membrane thickness directly. Indeed, one of the mechanisms whereby voltage-induced membrane breakdown is thought to occur is via electro-compressive forces [28]. Regardless, it is unlikely that the magnitude of voltages we employed here is capable of inducing sufficient changes in membrane thickness to significantly alter its capacitance, since in control Deiters' and HEK cells, membrane capacitance was not affected by voltage. Interestingly, in pure lipid bilayers, membrane capacitance was shown to be voltage dependent, presumably as a result of membrane compression [3]. Voltage-induced increases in capacitance up to 100% were found. However, those results were attributable to the solvent content of the bilayer. More ger-

mane to our data, the action of membrane proteins may also affect bilayer thickness. For example, the anti-microbial peptide, proegrin-1, resides as a membrane surface adsorbed structure (residing within the polar head group region) or as a transmembrane spanning structure [15], depending on the concentration. In the former state, the peptide thins the membrane, whereas in the latter state the membrane is thickened. Little is known about the secondary and tertiary structure of the integral membrane protein prestin, and it may be that some voltage-dependent mechanism akin to the concentration-dependent activity of proegrin-1 is occurring. The possibility cannot be dismissed that the presence of the highly hydrophobic prestin molecule within the lateral membrane provides for an effect similar to the solvent effects observed by Benz and Janko [3]; for example, by altering lipid packing at the protein-lipid interface. In these scenarios, voltage-dependent, prestin-induced perturbations of the bilayer could permit fluctuations of membrane thickness either as a result of the direct compressive action of voltage on a susceptible bilayer or through voltage-induced protein conformational changes. In this regard, salicylate, a drug capable of modifying lipid packing and bilayer mechanics [33], may function to increase the effectiveness of prestin in altering membrane thickness. It should be noted that in either scenario membrane surface area would also change as a function of thickness.

Acknowledgements We thank Margaret Mazzucco for technical help, and Peter Dallos and Fred Sigworth for reading and discussing an early version of the manuscript. This work was supported by NIH-NIDCD grant DC00273 to J.S.S.

References

1. Adachi M, Iwasa KH (1999) Electrically driven motor in the outer hair cell: effect of a mechanical constraint. *Proc Natl Acad Sci USA* 96:7244–7249
2. Ashmore JF (1990) Forward and reverse transduction in the mammalian cochlea. *Neurosci Res Suppl* 12:S39–S50
3. Benz R, Janko K (1976) Voltage-induced capacitance relaxation of lipid bilayer membranes. Effects of membrane composition. *Biochim Biophys Acta* 455:721–738
4. Chanturiya AN (1990) Detection of transient capacitance increase associated with channel formation in lipid bilayers. *Biochim Biophys Acta* 1026:248–250
5. Cole KS (1971) Some aspects of electrical studies of the squid giant axon membrane. In: Adelman WJ (ed) *Biophysics and physiology of excitable membranes*. Van Nostrand Reinhold, New York, pp 125–142
6. Dallos P (1983) Some electrical circuit properties of the organ of Corti. I. Analysis without reactive elements. *Hear Res* 12:89–119
7. Dallos P, Hallworth R, Evans BN (1993) Theory of electrically driven shape changes of cochlear outer hair cells. *J Neurophysiol* 70:299–323
8. Dong X, Ehrenstein D, Iwasa KH (2000) Fluctuation of motor charge in the lateral membrane of the cochlear outer hair cell. *Biophys J* 79:1876–1882
9. Evans EA, Waugh R, Melnik L (1976) Elastic area compressibility modulus of red cell membrane. *Biophys J* 16:585–595
10. Fernandez JM, Bezanilla F, Taylor RE (1982) Distribution and kinetics of membrane dielectric polarization. II. Frequency domain studies of gating currents. *J Gen Physiol* 79:41–67

11. Gale JE, Ashmore JF (1994) Charge displacement induced by rapid stretch in the basolateral membrane of the guinea-pig outer hair cell. *Proc R Soc Lond B Biol Sci* 255:243–249
12. Gale JE, Ashmore JF (1997) An intrinsic frequency limit to the cochlear amplifier. *Nature* 389:63–66
13. Gentet LJ, Stuart GJ, Clements JD (2000) Direct measurement of specific membrane capacitance in neurons. *Biophys J* 79:314–320
14. He DZ, Dallos P (1999) Somatic stiffness of cochlear outer hair cells is voltage-dependent. *Proc Natl Acad Sci USA* 96:8223–8228
15. Heller WT, Waring AJ, Lehrer RI, Harroun TA, Weiss TM, Yang L, Huang HW (2000) Membrane thinning effect of the beta-sheet antimicrobial protegrin. *Biochemistry* 39:139–145
16. Huang G, Santos-Sacchi J (1993) Mapping the distribution of the outer hair cell motility voltage sensor by electrical amputation. *Biophys J* 65:2228–2236
17. Iwasa KH (1993) Effect of stress on the membrane capacitance of the auditory outer hair cell. *Biophys J* 65:492–498
18. Iwasa KH (1994) A membrane motor model for the fast motility of the outer hair cell. *J Acoust Soc Am* 96:2216–2224
19. Iwasa KH (1997) Current noise spectrum and capacitance due to the membrane motor of the outer hair cell: theory. *Biophys J* 73:2965–2971
20. Kakehata S, Santos-Sacchi J (1995) Membrane tension directly shifts voltage dependence of outer hair cell motility and associated gating charge. *Biophys J* 68:2190–2197
21. Kakehata S, Santos-Sacchi J (1996) Effects of salicylate and lanthanides on outer hair cell motility and associated gating charge. *J Neurosci* 16:4881–4889
22. Kalinec F, Holley MC, Iwasa KH, Lim DJ, Kachar B (1992) A membrane-based force generation mechanism in auditory sensory cells. *Proc Natl Acad Sci USA* 89:8671–8675
23. Kienker PK, Qiu X, Slatin SL, Finkelstein A, Jakes KS (1997) Transmembrane insertion of the colicin Ia hydrophobic hairpin. *J Membr Biol* 157:27–37
24. Kilic G, Lindau M (2001) Voltage-dependent membrane capacitance in rat pituitary nerve terminals due to gating currents. *Biophys J* 80:1220–1229
25. Lesieur C, Vecsey-Semjen B, Abrami L, Fivaz M, Gisou vdG (1997) Membrane insertion: the strategies of toxins [review]. *Mol Membr Biol* 14:45–64
26. Ludwig J, Oliver D, Frank G, Klocker N, Gummer AW, Fakler B (2001) Reciprocal electromechanical properties of rat prestin: the motor molecule from rat outer hair cells. *Proc Natl Acad Sci USA* 98:4178–4183
27. Navarrete E, Santos-Sacchi J (2001) Electroporabilization and fast resealing in the cellular elements of the mammalian cochlea. *Santi, Peter*. 24, 72. 2001. St. Petersburg, FL. *Assoc Res Otolaryngol Abstract* 2-4-2001
28. Needham D, Hochmuth RM (1989) Electro-mechanical permeabilization of lipid vesicles. Role of membrane tension and compressibility. *Biophys J* 55:1001–1009
29. Neher E, Marty A (1982) Discrete changes of cell membrane capacitance observed under conditions of enhanced secretion in bovine adrenal chromaffin cells. *Proc Natl Acad Sci USA* 79:6712–6716
30. Oliver D, Fakler B (1999) Expression density and functional characteristics of the outer hair cell motor protein are regulated during postnatal development in rat. *J Physiol (Lond)* 519:791–800
31. Oliver D, He DZ, Klocker N, Ludwig J, Schulte U, Waldegger S, Ruppertsberg JP, Dallos P, Fakler B (2001) Intracellular anions as the voltage sensor of prestin, the outer hair cell motor protein. *Science* 292:2340–2343
32. Pusch M, Neher E (1988) Rates of diffusional exchange between small cells and a measuring patch pipette. *Pflugers Arch* 411:204–211
33. Raphael RM, Popel AS, Brownell WE (2000) A membrane bending model of outer hair cell electromotility. *Biophys J* 78:2844–2862
34. Rojas E, Pollard HB (1987) Membrane capacity measurements suggest a calcium-dependent insertion of synexin into phosphatidylserine bilayers. *FEBS Lett* 217:25–31
35. Rybalchenko V, Santos-Sacchi J (2001) Modulation of OHC capacitance by Cl⁻ ions. XXXVIII Workshop on Inner Ear Biology, Rome, Italy. http://ieb.unife.it/ieb2001/roma_index.html
36. Santos-Sacchi J (1991) Isolated supporting cells from the organ of Corti: some whole cell electrical characteristics and estimates of gap junctional conductance. *Hear Res* 52:89–98
37. Santos-Sacchi J (1991) Reversible inhibition of voltage-dependent outer hair cell motility and capacitance. *J Neurosci* 11:3096–3110
38. Santos-Sacchi J (1993) Harmonics of outer hair cell motility. *Biophys J* 65:2217–2227
39. Santos-Sacchi J, Kakehata S, Kikuchi T, Katori Y, Takasaka T (1998) Density of motility-related charge in the outer hair cell of the guinea pig is inversely related to best frequency. *Neurosci Lett* 256:155–158
40. Santos-Sacchi J, Kakehata S, Takahashi S (1998) Effects of membrane potential on the voltage dependence of motility-related charge in outer hair cells of the guinea-pig. *J Physiol (Lond)* 510:225–235
41. Santos-Sacchi J, Shen W, Zheng J, Dallos P (2001) Effects of membrane potential and tension on prestin, the outer hair cell lateral membrane motor protein. *J Physiol (Lond)* 531:661–666
42. Shehata WE, Brownell WE, Dieler R (1991) Effects of salicylate on shape, electromotility and membrane characteristics of isolated outer hair cells from guinea pig cochlea. *Acta Otolaryngol (Stockh)* 111:707–718
43. Solsona C, Innocenti B, Fernandez JM (1998) Regulation of exocytotic fusion by cell inflation. *Biophys J* 74:1061–1073
44. Tunstall MJ, Gale JE, Ashmore JF (1995) Action of salicylate on membrane capacitance of outer hair cells from the guinea-pig cochlea. *J Physiol (Lond)* 485:739–752
45. Unwin N (1989) The structure of ion channels in membranes of excitable cells. *Neuron* 3:665–676
46. Wu M, Santos-Sacchi J (1998) Effects of lipophilic ions on outer hair cell membrane capacitance and motility. *J Membr Biol* 166:111–118
47. Zhao HB, Santos-Sacchi J (1999) Auditory collusion and a coupled couple of outer hair cells. *Nature* 399:359–362
48. Zheng J, Shen W, He DZ, Long KB, Madison LD, Dallos P (2000) Prestin is the motor protein of cochlear outer hair cells. *Nature* 405:149–155

Chloride Anions Regulate Kinetics but Not Voltage-Sensor Q_{\max} of the Solute Carrier SLC26a5

Joseph Santos-Sacchi^{1,2,3,*} and Lei Song¹

¹Department of Surgery (Otolaryngology), ²Department of Neuroscience, and ³Department of Cellular and Molecular Physiology, Yale University School of Medicine, New Haven, Connecticut

ABSTRACT In general, SLC26 solute carriers serve to transport a variety of anions across biological membranes. However, prestin (SLC26a5) has evolved, now serving as a motor protein in outer hair cells (OHCs) of the mammalian inner ear and is required for cochlear amplification, a mechanical feedback mechanism to boost auditory performance. The mechanical activity of the OHC imparted by prestin is driven by voltage and controlled by anions, chiefly intracellular chloride. Current opinion is that chloride anions control the Boltzmann characteristics of the voltage sensor responsible for prestin activity, including Q_{\max} , the total sensor charge moved within the membrane, and V_h , a measure of prestin's operating voltage range. Here, we show that standard narrow-band, high-frequency admittance measures of nonlinear capacitance (NLC), an alternate representation of the sensor's charge-voltage (Q - V) relationship, is inadequate for assessment of Q_{\max} , an estimate of the sum of unitary charges contributed by all voltage sensors within the membrane. Prestin's slow transition rates and chloride-binding kinetics adversely influence these estimates, contributing to the prevalent concept that intracellular chloride level controls the quantity of sensor charge moved. By monitoring charge movement across frequency, using measures of multifrequency admittance, expanded displacement current integration, and OHC electromotility, we find that chloride influences prestin kinetics, thereby controlling charge magnitude at any particular frequency of interrogation. Importantly, however, this chloride dependence vanishes as frequency decreases, with Q_{\max} asymptoting at a level irrespective of the chloride level. These data indicate that prestin activity is significantly low-pass in the frequency domain, with important implications for cochlear amplification. We also note that the occurrence of voltage-dependent charge movements in other SLC26 family members may be hidden by inadequate interrogation timescales, and that revelation of such activity could highlight an evolutionary means for kinetic modifications within the family to address hearing requirements in mammals.

INTRODUCTION

Typically, voltage-sensor charge movement in membrane proteins rapidly follows voltage perturbations, producing capacitive-like gating/displacement currents (1,2). However, intrinsic properties of the protein or interactions of the protein with other membrane constituents (protein or lipid) can influence the movement's time course (3). In essence, gating currents may be low-pass filtered relative to the actual driving voltage, often exhibiting multiexponential behavior that depends on the timing of intramolecular and/or intermolecular interactions. Thus, interrogation of charge at other than infinite timescales (or zero frequency) may produce inaccurate quantification of the total charge

moved (Q_{\max}) across a given cell membrane's electric field where the protein's voltage sensor resides. This issue was recently highlighted by the discovery that previously unidentified slow charge movements, revealed by utilizing longer integration times of 300 ms, account for an apparent charge immobilization in *Shaker* ion channels (4). Importantly, cellular events that result from charge movements may correspondingly be inaccurately assessed.

The family of SLC26 solute carriers functions to maintain gradients of anions across the membranes of a variety of cells (5). However, SLC26a5 (prestin) has been recruited by the outer hair cell (OHC) in Corti's organ to function as a motor protein that underlies cochlear amplification, a mechanical feedback process that boosts auditory sensitivity by 100- to 1000-fold (6,7). OHCs have been shown to produce voltage-dependent length changes (electromotility (eM)) in the audio frequency range (8–10), extending out at least to 80 kHz at room temperature (11). On the other hand, prestin's sensor charge movement, measured as a voltage-dependent or nonlinear capacitance (NLC), displays

Submitted January 26, 2016, and accepted for publication May 4, 2016.

*Correspondence: joseph.santos-sacchi@yale.edu

Lei Song's present address is Department of Otolaryngology Head & Neck Surgery, Shanghai 9th People's Hospital, School of Medicine, Shanghai Jiao Tong University, Shanghai Key Laboratory of Translational Medicine on Ear and Nose Diseases, Shanghai, China.

Editor: Miriam Goodman.

<http://dx.doi.org/10.1016/j.bpj.2016.05.002>

© 2016 Biophysical Society.



a limiting frequency, with a cutoff of ~ 10 kHz at room temperature (12). Thus, the frequency response of the motor protein prestin has differed depending on whether sensor charge or mechanical activity of the protein is evaluated. The expectation that each metric (NLC or eM) should be equivalently fast is based on the assumption that prestin's electromechanical responsiveness to voltage is governed by a direct ultrafast two-state process, switching molecular conformations between compact and expanded states. Thus, technical issues affecting each of these measures could have contributed to the mismatch.

The activity of prestin and its effects on cochlear amplification are strongly dependent on chloride (13–17); it has been shown that alteration of perilymphatic chloride reversibly abolishes cochlear amplification (16). Recently, we observed a dissociation between the eM and NLC magnitude and voltage operating range that we attributed to slow intermediate transitions between prestin's chloride-binding and voltage-enabled states (18). This discrepancy arose because each was evaluated within different frequency regimes (eM at near steady state and NLC at high frequency), under the assumption that the two should have been equivalent. Here, we simultaneously evaluate prestin's charge movement with measures of high-frequency alternating-current (AC) capacitance and step-induced charge integration. We find that quantification of charge is highly dependent on frequency of interrogation, pointing to behavior in prestin that is inconsistent with a simple ultrafast two-state process. Consequently, prestin charge distribution, the rate of which we show to be chloride-dependent, has been wrongly estimated by standard high-frequency AC admittance measures. Voltage-evoked, frequency-dependent eM measurements within the same bandwidth used for NLC measurements confirm these observations. These data reveal that prestin activity is low pass in this frequency domain, and that chloride does not influence Q_{\max} , the total prestin charge within the membrane. Our results have significant implications for our current understanding of prestin behavior and cochlear amplification.

MATERIALS AND METHODS

Whole-cell patch-clamp recordings were made from single isolated OHCs from the organs of Corti of Hartley albino guinea pigs. After animals were overdosed with isoflurane, the temporal bones were excised and the top turns of the cochleae dissected free. Enzyme treatment (1 mg/mL Dispase I for 10 min) preceded trituration, and isolated OHCs were placed in a glass-bottom recording chamber. An inverted Nikon (Tokyo, Japan) Eclipse TI-2000 microscope with a $40\times$ lens was used to observe cells during voltage clamping. Experiments were performed at room temperature. Direct-current (DC) voltages were corrected for series-resistance (R_s) effects, and AC currents were corrected for system roll-off, as previously described (19,20). Series and membrane resistance determined from step analysis were similar for the two chloride groups. For the 140 mM Cl group, $R_s = 9.37 \pm 0.31$ M Ω and $R_m = 337 \pm 45.9$ M Ω for $n = 21$ OHCs; for the 1 mM Cl group, $R_s = 8.39 \pm 0.47$ M Ω and $R_m = 365 \pm 40.5$ M Ω for $n = 6$ OHCs. Fig. 5, G and H, shows that our measurement system, after corrections for R_s effects, is flat out to 5 kHz, within which bandwidth our data arise (see the Appendix

in the Supporting Material). All data collection and analysis was done with the software program jClamp (<http://www.scisoftco.com>).

Solutions

Intracellular chloride levels were set to either 140 or 1 mM, levels that bracket the intracellular concentration found in intact OHCs, namely, ~ 10 mM (16). An ionic blocking solution was used to remove ionic currents to ensure valid measures of membrane capacitance. The extracellular-base high-Cl solution contained 100 mM NaCl, 20 mM TEA-Cl, 20 mM CsCl, 2 mM CoCl₂, 1 mM MgCl₂, 1 mM CaCl₂, and 10 mM Hepes. In some cases, 1 μ M Gd³⁺ was included in the bath solution to block stretch channels and assist in gigohm seal formation. We had previously shown that Gd³⁺ three orders of magnitude greater can block NLC. At the concentration used, no effects on NLC were observed. The intracellular-base solution contained 140 mM CsCl, 2 mM MgCl₂, 10 mM Hepes, and 10 mM EGTA. Lower chloride concentrations were set by substituting chloride with gluconate. Intracellular chloride levels in the subplasmalemmal space of the OHC, where prestin's chloride-binding site resides, were guaranteed by setting both intracellular and extracellular chloride concentrations equal. All chemicals used were purchased from Sigma (St. Louis, MO).

Cell capacitance

An Axon Instruments (Foster City, CA) 200B amplifier was used for whole-cell recording. To measure both AC capacitance and integrated charge movement, a simple voltage protocol was designed that included both step stimulation and dual sine stimulation at a range of dual-sine interrogation frequencies (Fig. 1, A and B). For AC admittance analysis, real and imaginary components of currents were corrected for the recording-system frequency response (19). No averaging was used with this protocol.

Membrane capacitance (C_m) was measured using a continuous dual-frequency (discrete sinusoidal frequencies at f_1 and f_2 , where $f_2 = 2 \times f_1$) voltage-stimulus protocol (19,21). Simultaneous AC C_m sampling resolutions (5.12, 2.56, 1.28, and 0.064 ms) were achieved by stimulating with a summed multisine voltage (the multi-dual-sine approach) whose phases were the same. Primary frequencies (f_1) were 195.3, 390.6, 781.3, and 1562.5 Hz; all frequencies (10 mV peak) were superimposed onto steps from -160 to $+100$ mV for a duration of 700 ms at a clock sample period of 10 μ s. We limited our voltage delivery to -160 to 100 mV because with this protocol, larger voltages caused cell recordings to be lost or unstable. On return from each step to a sinusoidal-free holding potential of 0 mV for at least 40 ms (see Fig. 1, where only a portion of the protocol is plotted), voltage-sensor displacement currents are extractable. Thus, this approach provided both multifrequency AC capacitance and step-induced charge movement measures within one protocol, an important approach that ensures that the preparation is quasistationary in time.

After gigohm seal formation, stray capacitance was cancelled with amplifier compensation controls, as is usually done. Since stray capacitance is frequency dependent, it is important to ensure that it is cancelled out at each recording frequency. The existence of stray capacitance causes an apparent frequency dependence of linear capacitance, which should *not* be frequency dependent. Measures of R_s are similarly affected. Consequently, in the whole-cell configuration, residual stray capacitance at each of the recording frequencies was cancelled with further manipulations of amplifier compensation by ensuring that cell linear capacitance (or, equivalently, R_s) was constant across frequency. This was done at very positive voltages, where OHC capacitance is dominated by linear capacitance. Removal of stray capacitance is necessary to meet C_m estimation algorithm requirements (19). We have used this compensation approach to ensure accurate measures of hair cell synaptic vesicle release at high interrogating dual-sine frequencies (20,22). The Supporting Material Appendix expands on our approach.

For each cell, capacitance data were fit to the first derivative of a two-state Boltzmann function with an additional component describing the

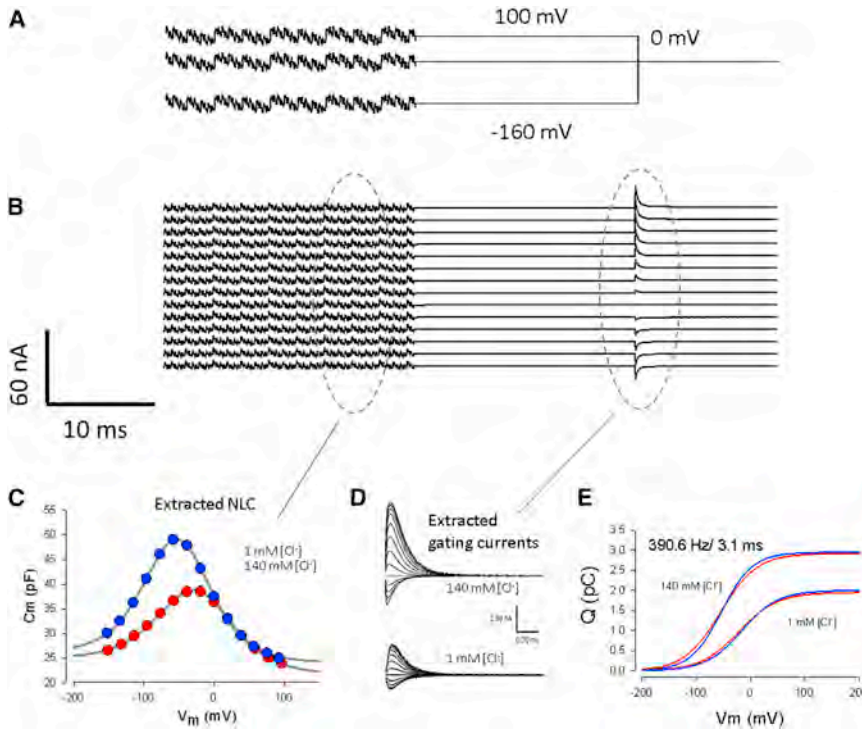


FIGURE 1 Stimulus and analysis paradigms. (A) Traces of voltage protocol. Step voltages (-160 mV to $+100$ mV by 20 mV increments) were delivered for 700 ms followed by a return to a holding potential of 0 mV for 40 ms. Superimposed on the steps were summed discrete dual-sine frequencies 655 ms in duration (see [Materials and Methods](#)). (B) Elicited currents (offset for easy visualization), AC and step-induced, were used to extract capacitance and integrated charge movements (dashed ovals), respectively. (C) Averaged NLC traces of OHCs with intracellular chloride clamped to 1 or 140 mM chloride. NLC was estimated from the latter half of the dual-sine stimulation duration. (D and E) Corresponding displacement currents extracted by linear capacitive current subtraction (D) and extracted Q - V curves (E) at 1 mM and 140 mM chloride conditions for an equivalent interrogation time based on fits of NLC with Eq. 1 (blue traces) or on fits of integrated off charge with Eq. 2 (red traces) give comparable results, as expected (see [Materials and Methods](#) for details). To see this figure in color, go online.

changes in specific membrane capacitance generated by prestin state transitions (23). The occupancy of prestin in the expanded state contributes ~ 140 zeptofarads/motor (δC_{sa}) to the linear capacitance, producing an apparent voltage-dependent change in linear capacitance at hyperpolarized levels (23,24). This equation is called the two-state- C_{sa} equation.

$$C_m = Q_{\max} \frac{ze}{kT} \frac{b}{(1+b)^2} + \frac{\Delta C_{sa}}{(1+b^{-1})} + C_{lin}, \quad (1)$$

where

$$b = \exp\left(\frac{ze}{kT} U\right) \text{ and } U = V_h - V_m.$$

Q_{\max} is the maximum nonlinear charge moved, V_h is the voltage at peak capacitance or, equivalently, at half-maximum sensor charge transfer, V_m is the membrane potential, z is valence, e is the electron charge, k is Boltzmann's constant, and T is absolute temperature. C_{lin} is defined as the linear capacitance of the membrane when all prestin motors are in their compact state, the minimum membrane capacitance evident at depolarized voltages; ΔC_{sa} is the maximum increase in capacitance that occurs when all prestin motors change from the compact to the expanded state, each motor contributing a unit response of δC_{sa} . From such fits, voltage-dependent NLC (C_v) is calculated from estimates of Q_{\max} , i.e., $C_v = Q_{\max}/(4 kT/ze)$ (25).

To confirm AC admittance estimates of sensor Q_{\max} , we integrated capacitive currents evoked at the end of voltage steps (exponentially decaying currents of each trace, with the baseline set to current relaxations at 20 ms). Residual ionic currents that remained after our ionic blocking conditions are time independent and thus were excluded for the most part from integrations of the exponentially decaying currents. The integration time window, starting at voltage offset, was varied from 3 to 20 ms. Previously, we and others used a similar approach that we developed to extract NLC during stair-step protocols by integrating total capacitive current at each step and fitting the resulting C_m - V_m data to a two-state Boltzmann deriva-

tive plus a linear capacitance (26,27). Here, Q - V curves were fit to the integral of Eq. 1 with respect to V_m , yielding

$$Q_{\text{tot}} = \left[\frac{Q_{\max} \times b + C_{lin} \times (U + U \times b)}{b + 1} + \frac{\Delta C_{sa} \times \log(b + 1)}{ze/kT} \right] + \text{off}. \quad (2)$$

The constant of integration (off) depends on the return holding voltage and accounts for a vertical offset in the Q_{tot} - V_m function. For fitting, we fixed linear capacitance to the average value obtained from AC admittance measures for each chloride group, since these measures provided robust, constant estimates across all frequencies (see [Fig. 3](#)). Additionally, we only report measures of integrated charge after 3 ms (10 times our clamp time constant), since earlier charge distribution at the voltage-pulse offset would be influenced by our clamp time constants of $< 300 \mu\text{s}$ ($\sim R_s \times C_m$). With this approach we essentially removed linear capacitive charge contamination from the total integrated charge. [Fig. 1 E](#) illustrates the equivalence of AC and time-domain estimates of Q_{\max} .

Higher resolution of prestin's frequency-dependent behavior was obtained by stimulating OHCs with voltage chirps (linear increasing frequency), with a frequency resolution of 24.41 Hz, and analyzing dual-frequency admittance, obtained by fast Fourier transform, at each component dual frequency (f_1 and $2 \times f_1$). The stimulus consisted of voltage steps (-160 to 160 mV by 40 mV increments) superimposed with voltage chirps of 10 mV peak (4096 points at a $10 \mu\text{s}$ sampling rate, giving an F_{\max} of 50 kHz). One benefit of the chirp signal is that it is a multifrequency stimulus whose individual frequency components are equal in amplitude, this being accomplished by varying the phase of each frequency. Another benefit is that duration of the chirp can be easily changed (although the duration used here was only 40.96 ms). Admittance at one frequency and its harmonic were analyzed in exactly the same way as the dual-sine approach, above (see the [Supporting Material Appendix](#)). We do that at all frequencies within the chirp at a primary frequency increment of 24.41 Hz. With this

protocol, filtered responses (10 kHz four-pole Bessel) were averaged three times for each cell to reduce noise. The first chirp response during a step was discarded, since it contains a transient response. We were able to balance out stray capacitance up to a frequency of ~5 kHz. This approach enabled us to construct 3D images of NLC across frequency using averages of all individual cell responses, thereby confirming and expanding on the resolution of the multi-dual-sine approach detailed above.

eM measures

OHC eM data derive from our recent study on the phase relationships of eM and membrane voltage (28). Here, we present the magnitude data transformed into mechanical gain (nm/mV) so that they can be compared to sensor charge movements, i.e., NLC. Briefly, cells were whole-cell voltage clamped and eM was elicited with voltage bursts of frequency ranging from 0.024 to 6 kHz. A photodiode technique was used to measure movements of the apex of the cell, with the cell bound at its basal pole by the patch electrode. Full details can be found in (28).

Kinetic model

A full description of the *meno presto* model of prestin activity is provided in our recent publications (24,28). Briefly, the model is multistate; after chloride binding, a slow intermediate transition leads to a voltage-enabled state, which generates sensor charge movement. The delays afforded by its multistate nature underlie the model's frequency dependence. The only parameter that was modified to fit (by eye) the data in Fig. 4 was the model's forward transition rate constant, k_1 , for Cl^- binding. The kinetic diagram and description are reproduced in Fig. 2 (reproduced from our previous work (24)).

RESULTS

Fig. 1 C shows the group-averaged NLC determined from admittance measures (5.12 ms sampling rate) for OHCs recorded under 140 mM and 1 mM intracellular chloride conditions. NLC fits for the 1 mM Cl group yield $V_h = -26.3$ mV, $Q_{\max} = 2.2$ pC, $C_{\text{lin}} = 21.84$ pF, $z = 0.71$, and $\Delta C_{\text{sa}} = 3.2$ pF; those for the 140 mM Cl group yield

$V_h = -52.3$ mV, $Q_{\max} = 3.1$ pC, $C_{\text{lin}} = 24.24$ pF, $z = 0.80$, and $\Delta C_{\text{sa}} = 2.1$ pF. Fig. 1 D shows voltage-sensor displacement currents after the offset of voltage steps extracted by subtraction of scaled difference currents evoked between the potential of +80 and +100 mV, in an attempt to remove linear capacitive currents, as is required for gating/displacement current extraction (29). Clear chloride differences exist, consistent with expectations. However, because C_m plots show that substantial NLC resides at these subtraction voltages, these displacement currents are inaccurate. We and others have studied OHC/prestin displacement currents for decades (12,30–33); however, because of the shallow voltage dependence of prestin ($z \sim 0.75$), extracted waveforms and estimates of Q_{\max} using P/N subtraction holding potentials, typically 40–50 mV, were adversely affected in those studies. Extraction of the sensor charge using Eq. 2 (see Materials and Methods) overcomes this problem in determining Q_{\max} . Fig. 1 E shows that determining Q_{\max} with either AC analysis or this time-domain approach produces equivalent results.

Fig. 3, A and B, shows group averages of both peak NLC (C_v) and linear capacitance as a function of interrogation frequency. Our success at stray capacitance compensation is borne out by the frequency independence of OHC linear capacitance provided by fits to the C_m data (Fig. 3 B). Interestingly, however, NLC shows a marked frequency dependence, with larger magnitudes as interrogating frequency decreases (Fig. 3 A). In fact, the frequency-dependent trend in C_m data suggests that NLC at frequencies lower than our lowest primary interrogating frequency of 195.3 Hz would be larger. The Boltzmann parameters V_h and z are stable across frequency (Fig. 3, C and D).

To better compare our measures across cells within the two chloride conditions, we converted our measures to specific nonlinear charge (Q_{sp} in pC/pF), thereby normalizing for surface area and prestin content. In Fig. 4 A, we plot AC-derived (Eq. 1) and integration-derived (Eq. 2) sensor charge over a range of interrogation times. Admittance interrogation time refers to the geometric mean of sampling periods of both primary and secondary sinusoids, whereas for integration estimates of sensor displacement charge, interrogation time refers to an integration window increasing up to 20 ms. It can be seen, as predicted from admittance measures alone, that as interrogation time increases, Q_{sp} continuously increases. Integration times >20 ms suffered from excess low-frequency noise, since no averaging could be performed during data collections. Electrode seals were routinely lost after the demanding protocol, since the OHC is quite mechanically active, with responses up to ~30 nm/mV (34) and on average 15 nm/mV (35). To extend our estimates of sensor charge beyond 20 ms, we resorted to measures of averaged electromotility (28), which were analyzed by fast Fourier transform, providing much better signal/noise ratios. Since it is established that eM is voltage-dependent (8,34), sensor charge

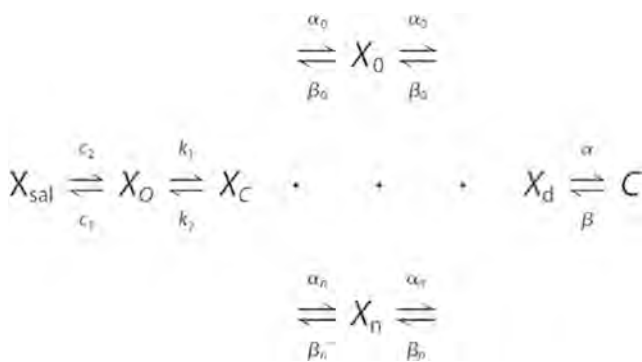


FIGURE 2 Kinetic model of the *meno presto* model. The X_{sal} state is bound by salicylate, but in this manuscript, salicylate is absent. The X_o state is unbound by an anion. The X_c state is bound by chloride, but the intrinsic voltage-sensor charge is not responsive to the membrane electric field. A slow, multiexponential conformational transition to the X_d state via X_n states enables voltage sensing within the electric field. Depolarization moves the positive sensor charge outward, simultaneously resulting in the compact state, C , which corresponds to cell contraction. Parameters and differential equations are provided in (24).

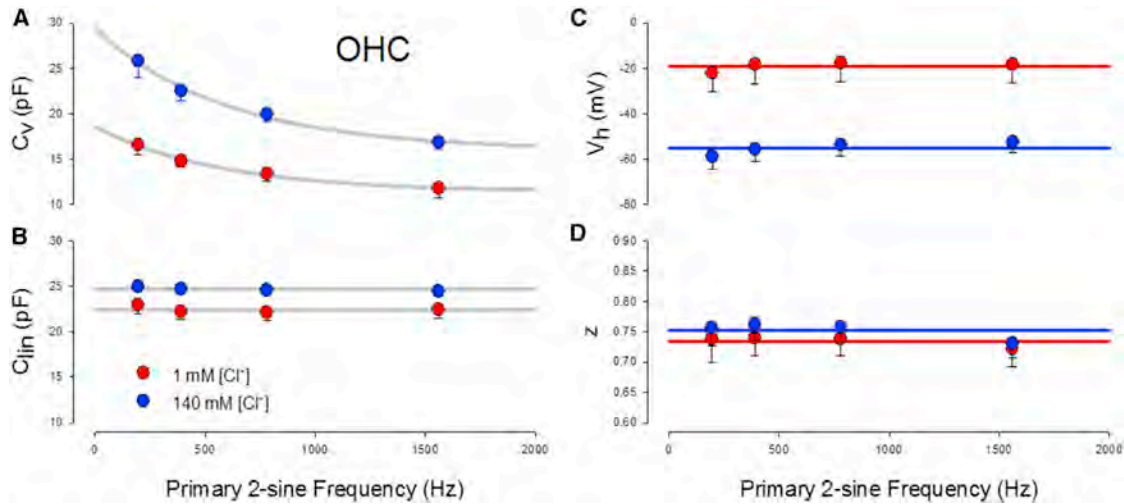


FIGURE 3 Voltage-dependent (C_v) and linear (C_{lin}) components of OHC capacitance simultaneously measured with the multi-dual-sine approach. (A) C_v displays a low-pass frequency dependence, which is unexpected for a fast two-state Boltzmann process. Differences between 1 mM (red circles, $n = 6$) and 140 mM (blue circles, $n = 17$) chloride conditions also show chloride-dependent frequency effects. (B) C_{lin} is flat across frequency, as expected. The frequency independence of C_{lin} demonstrates that calibration of system responsiveness was accurately performed. (C and D) V_h and z are also stable across frequency. Error bars depict the mean \pm SE, which in some cases is obscured by symbols. The solid lines in (A) are exponential, and those in (B)–(D) are linear fits for presentation. To see this figure in color, go online.

must correspond to eM magnitude. In Fig. 4 B, we plot eM gain as a function of the stimulating-frequency period and show that it corresponds to measures of AC-determined sensor charge. Indeed, eM magnitude continues to grow substantially as interrogation time increases, clearly indicating that sensor charge for both the 140 and 1 mM conditions trends toward equivalence with longer interrogations. These data indicate that total sensor charge movement, Q_{max} , is not directly linked to chloride concentration; rather, only a frequency-dependent, *apparent* Q_{max} is linked, depending on the kinetics of prestin's conformational transitions. It is not necessary to model these data to draw these conclusions.

To understand molecular mechanisms that may underlie this phenomenon, we simulated the *meno presto* model (initially developed in (18) and expanded with full details in (24)) with the same protocol (Fig. 4 B, gray lines). As

with the biophysical data, charge magnitude is dependent on interrogation time and chloride level. The model fits the data quite well, with increasing integration times (up to 200 ms in the model) incrementally increasing the charge measured. Importantly, for the model, estimated charge at either chloride level asymptotes at the actual set Q_{max} , with the time course depending on prestin's transition rates. Modification of our model parameters (24) was limited to one parameter, namely, a reduction of the model's forward transition rate constant, k_1 , for Cl^- binding (from $1e5$ to $0.7e4$). These results derive from the multiexponential kinetics of sensor charge movement in the *meno presto* model, some slowly moving charge contributions being missed due to shorter interrogation times, and the fact that only an *apparent* Q_{max} was provided. Such behavior corresponds to our biophysical observations of OHCs and complements the biophysical data, which show that total sensor charge

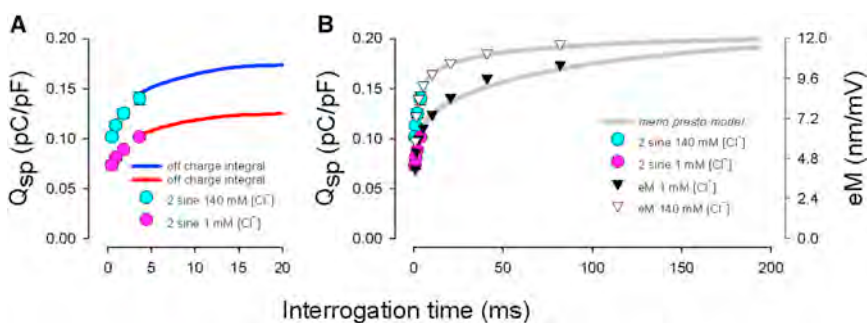


FIGURE 4 Sensor charge movements estimated from two-sine admittance analysis, off-current integration, or eM show low-pass frequency characteristics. (A) The AC measured specific sensor charge (Q_{sp}) corresponds to the integrated off-charge and shows that discrete measures of charge movement by AC admittance provide underestimates of the total prestin charge. (B) Q_{sp} (circles) and eM (triangles), which is known to be driven by voltage, display magnitudes that correspond to the predictions of the *meno presto* model (gray lines). Interrogation time is the geometric average

of periods of the dual-sine protocol, the integration time of sensor charge, or the eM fundamental frequency period (see Results). The biophysical data and model indicate that regardless of chloride concentration (but at above-zero concentrations), positive voltage will move prestin into the compact state, asymptoting at the maximum sensor charge dictated by prestin membrane content. Data are derived from averages of multi-dual-sine currents (circles) and eM (triangles) from $n = 5$ –8 OHCs. To see this figure in color, go online.

movement is not directly linked to chloride concentration, but rather is misestimated due to prestin kinetics, in contradistinction to long-held concepts.

Finally, to measure prestin's frequency-dependent behavior in finer detail and expand on our data set, we measured NLC using chirp stimuli. Fig. 5 shows averaged results from another group of cells under each of the two chloride conditions (five to six cells per condition). NLC increases with a reduction of interrogating frequency, approaching that expected from zero-frequency or infinite-integration estimates of sensor charge (Fig. 5, A and B). The meno presto model produces similar results (Fig. 5, C

and D), whereas a fast two-state Boltzmann model and a linear electrical resistor-capacitor (RC) model show no indication of frequency- or voltage/frequency-dependent capacitance, respectively (Fig. 5, E, G, and H). Appropriately setting the rate constants in a two-state model (forward/backward rate constants of $0.5e3\text{ s}^{-1}$) can produce a frequency-dependent roll-off within the measured bandwidth (Fig. 5 F); however, the resulting single-exponential transitions produce a different form of frequency dependence as compared to either the biophysical data or the meno presto model. These data confirm the validity of multi-dual-sine analysis of both linear electrical models and OHC NLC,

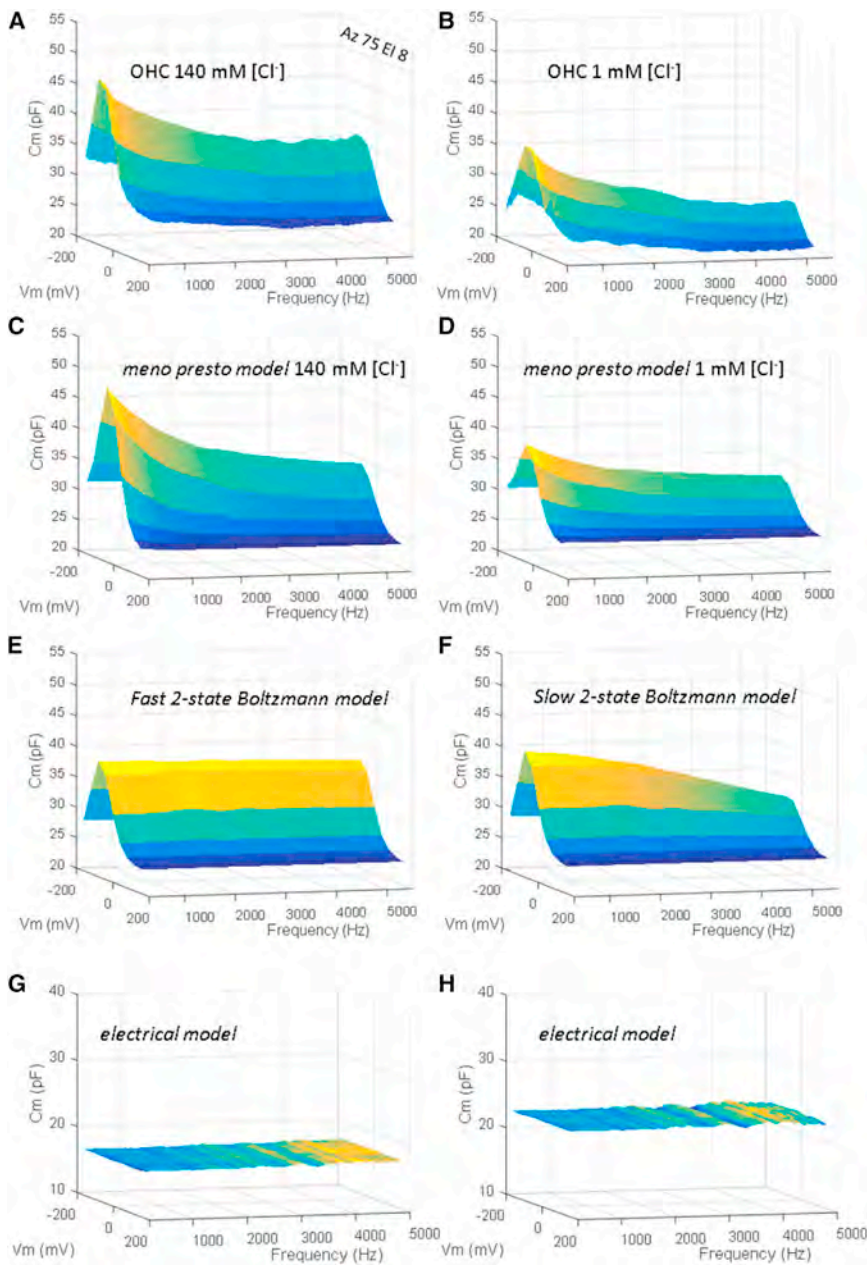


FIGURE 5 Membrane capacitance versus frequency measured by high-resolution frequency-dependent NLC of OHCs, the meno presto model, the fast two-state model, and the electrical model. (A) Averaged OHC NLC ($n = 5$) measured using the chirp protocol between 300 and 5000 Hz with 140 mM intracellular chloride. Note the rapid decline of peak capacitance. (B) Another group average of OHCs with 1 mM intracellular chloride ($n = 6$). The peak NLC decline is also evident in this condition. (C and D) C_m versus frequency as measured by the meno presto model at 140 mM and 1 mM chloride, respectively. The stimulus protocol and analysis were the same as the biophysical measures. Note the similarity to the biophysical data. (E) C_m versus frequency as measured by the fast two-state Boltzmann model (forward/backward rate constants of $1.5e5\text{ s}^{-1}$). Note the absence of NLC decline across frequency. (F) C_m versus frequency as measured by the slower two-state Boltzmann model (forward/backward rate constants of $0.5e4\text{ s}^{-1}$). Note the gradual roll-off due to reduced single-exponential transitions. (G) C_m versus frequency as measured by the electrical cell model with $R_s = 10\text{ M}\Omega$, $R_m = 300\text{ M}\Omega$, $C_m = 17\text{ pF}$, all nominal. Note the flat C_m response across frequency and voltage. (H) C_m versus frequency as measured by the same electrical model, with an additional 5 pF C_m switched in using a magnetically activated reed relay with minimal additional stray capacitance. To see this figure in color, go online.

highlighting, in the case of the OHC, the need to consider interrogation frequency effects when assessing prestin's voltage-sensor Q_{\max} , namely, total sensor charge in a given cell.

DISCUSSION

Characterizing sensor-charge movement in voltage-sensitive proteins provides a host of important information on protein function, including operating voltage range and maximum charge moved (Q_{\max}). The latter metric aids in quantifying protein content within the membrane, and our data indicate that prestin may be present at densities higher than the long-held estimates (26,36). For over a decade, chloride has been believed to be a key player in prestin function (13–16), influencing the quantity of measured sensor charge. However, our new data point to a role of chloride in controlling prestin kinetics and not in limiting the quantity of charge movement. Indeed, we previously showed that the maximum OHC eM magnitude, which is expected to correspond to the charge moved, since eM is voltage-driven, is little affected by chloride (18).

Does chloride underlie prestin's voltage-driven charge movement?

Zheng et al. (7) identified the OHC molecular motor as the fifth member of the mammalian SLC26 family of anion exchangers, of which 10 members have been identified (5,37). These anion exchangers facilitate the transmembrane movements of monovalent and divalent anions; however, prestin's transport capabilities are controversial, with some studies showing transport capabilities and others not (38–43). It is interesting to note that the influence of anions on NLC had been observed before the identification of prestin. For example, lipophilic anions, but not cations, were shown to influence OHC eM and NLC (44), and it has been known since the mid 1990s that the anion salicylate blocks NLC and eM, working on the intracellular aspect of the OHC (45,46). Notwithstanding the controversy of anion transport, the existence of voltage-dependent displacement currents, or NLC, has been taken to indicate an evolutionary change that enables eM, since SLC26a5's closest mammalian homolog, SLC26a6, lacks this capability, as assessed by standard high-frequency admittance techniques (13). Whether other SLC26 family members actually possess NLC is a subject for future investigation, since our data indicate that we must now consider the occurrence of charge movements that are slower than typically expected. Should other family members possess slow voltage-sensor charge movements, a scenario wherein kinetic modifications within the family underlie prestin's change to a molecular motor would be compelling. Interestingly, zebra fish prestin shows a lower-pass frequency response than rat prestin (33).

In 2001, Oliver et al. (13) identified the chloride anion as a key element in prestin activation by voltage. They speculated that extrinsic anions serve as prestin's voltage sensor (17), moving only partially through the membrane. Our observations and those of others over the ensuing years have challenged this concept, and we have suggested that chloride works as an allosteric-like modulator of prestin. These observations are as follows. 1) Monovalent, divalent, and trivalent anions, which support NLC, show no expected changes in z or Q_{\max} (47). 2) A variety of sulfonic anions shift V_h in widely varying magnitudes and directions along the voltage axis (47). 3) The apparent anion affinity changes depending on the state of prestin, with anions being released from prestin upon hyperpolarization, opposite to the extrinsic sensor hypothesis (48). 4) Mutations of charged residues alter z , our best estimate of unitary sensor charge (41). 5) Prestin shows transport properties ((40,41,43); however, see (39,42)). Despite these challenges, the extrinsic voltage-sensor hypothesis is still entertained. For example, Geertsma et al. (49) used their recently determined crystal structure of SLC26Dg, a prokaryotic fumarate transporter, to speculate on how prestin's extrinsic voltage sensor might work. They reasoned that a switch to an outward-facing state could move a bound anion a small distance within the membrane. Unfortunately, there are no data showing an outward-facing state, only an inward-facing one. Indeed, if prestin did bind chloride but was incapable of reaching the outward-facing state (a defunct transporter), no chloride movements would occur upon voltage perturbation. Furthermore, the fact that the anion-binding pocket is in the center of the protein would mean that if an outward-facing state were achieved with no release of chloride, the monovalent anion would move a very small distance through the electric field of the membrane. However, z , from Boltzmann fits, indicates that the anion moves three-quarters of the distance through the electric field. Unless the electric field is inordinately concentrated only at the binding site, it is difficult to envisage this scenario. The data presented here clearly indicate that no direct relation between chloride level and Q_{\max} exists, further suggesting that chloride does not serve as an extrinsic voltage sensor for prestin. Nevertheless, our recent work and *meno presto* model indicate that chloride binding to prestin is fundamental to the activation of this unusual motor. The model and data indicate that a stretched exponential intermediate transition between the chloride binding and the voltage-enabled state imposes lags that are expressed in whole-cell mechanical responses (28). This intermediate transition also accounts for our frequency- and chloride-dependent effects on measures of total charge movement, Q_{\max} . Indeed, based on site-directed mutations of charged residues, we favor intrinsic charges serving as prestin's voltage sensors (41).

Recently, Gorbunov et al. (50), used cysteine accessibility scanning and molecular modeling to suggest structural homology of prestin to UraA. Notably, the crystal structure

of SLC26Dg (49) supports Gorbunov et al.'s structural interpretations of prestin. Given the deduced structure, Gorbunov et al. identified possible chloride-binding residues within prestin's central permeation pathway. When those residues were mutated, the protein became anion-insensitive, yet maintained NLC. For example, in the rPres mutation, R399S, which maintains NLC, salicylate inhibition of NLC was abolished. These data are in line with our observations that truncated Cl^- movements are not responsible for voltage sensing, namely, the generation of NLC.

We suggest, instead, that various anions differentially modulate the transition rates of prestin, likely as a consequence of their different binding affinities, thereby influencing V_h (i.e., the distribution of compact and expanded states of prestin) and the *apparent* Q_{max} obtained via discrete frequency admittance measures. This concept may explain the wide variability in prestin's Boltzmann parameters that we and others have found with various anions (13,47).

Some of prestin's voltage-dependent characteristics are inadequately assessed using admittance analysis

The prevailing concept of prestin activity has been that of an ultrafast two-state Boltzmann process. This is not surprising, since the OHC can change its length at acoustic rates up to 80 kHz (8–11). Consequently, this reasoning has guided our assessment method of prestin activity, where AC NLC measures have usurped the more tedious gating-current methods that were utilized early on (32,35,51). Nevertheless, even gating-charge evaluations have suffered from problems associated with inadequate integration times and the shallow voltage dependence of prestin, which makes adequate linear leakage subtraction nearly impossible. Our data now show that AC capacitance measures do not correspond to full motor capability (18). The inaccuracies that fast single or dual AC measurements provide needn't preclude their use, however, now that we have uncovered their limitations. Thus, by measuring C_m with a range of frequencies, with proper calibration for stray capacitance effects and including long interrogation times, valid measures of Q_{max} can be obtained.

We previously noted that Boltzmann fits to the Q - V function of prestin cannot reliably predict unitary motor charge, Q_m , since even Langevin fits are reasonable, which would place Q_m values 3 times higher relative to two-state fits (26). This has been clearly emphasized by the Gummer group (52). One outcome of our study indicates that regardless of unitary charge magnitude (which remains stable across frequency, as indicated by invariant z values), the larger Q_{max} estimates from long interrogation times point to a higher density of prestin within the OHC lateral membrane. Consequently, the changes in prestin charge density observed in previous studies by narrow-band admittance

techniques may have been due to the effects of altered kinetics rather than prestin membrane content.

Frequency dependence of OHC charge movement

The frequency dependence of OHC charge movement has been investigated previously (12,31). Using the methodology of Fernandez et al. (53), we showed that capacitive reactance of the OHC with 140 mM intracellular solution in the whole-cell voltage-clamp configuration was voltage- and frequency-dependent, rising as zero frequency was approached (31). Subsequently, Gale and Ashmore (12) measured NLC in OHC membrane patches, where clamp time constants were better suited to high-frequency assessment. They found flat responses out to ~10 kHz at room temperature. Importantly, the direct effects of temperature on OHC displacement currents and NLC have been evaluated and shown to substantially affect NLC V_h (indicative of transition-rate effects) of both OHC and prestin-transfected cells when the bath temperature is altered (30,54,55). Shifts of ~20 mV/°C were found. Additionally, temperature jumps using an infrared laser on prestin-transfected cells (56) induced C_m changes attributable to NLC as well as linear C_m , as originally described by Shapiro et al. (57). NLC V_h shifted with rates up to 14 V/s over the course of a 5 ms infrared pulse. Thus, it is clear that temperature will influence the frequency dependence of OHC NLC. Consequently, after correcting for temperature, Gale and Ashmore (12) arrived at a 25 kHz cutoff for NLC, still far below the eM cutoff observed at room temperature (11). We suggest that these incompatible measures arise from technical issues. Considering the characteristics of our recently espoused *meno presto* model (24,28), we further suggest that sufficiently long stimulations of the OHC will drive substantial numbers of prestins into the chloride-bound, voltage-enabled state where they may rapidly respond to voltage perturbations with cutoff frequencies possibly unencumbered by the chloride-binding step. Thus, the performance of the OHC may modulate between two frequency regimes, high and low; the latter likely related to a slow transport function of the protein (40,41,43).

Recently, Homma et al. (58) have measured the frequency dependence of OHC NLC using our dual-sine approach, but only with discrete dual-sine frequencies and without presentation of linear capacitance data. Interestingly, they found that NLC in control mouse OHCs was frequency *independent* with high intracellular iodide solutions, but frequency *dependent* with high intracellular chloride conditions. The latter results are similar to our results under high-chloride conditions. Thus, we concur that anions are influential in controlling prestin kinetics, and we now must consider the effects of chloride substitutes on prestin kinetics. Here, we used gluconate—previously confirmed to be similar to aspartate substitution (18)—to lower chloride to near

physiological levels (16). Whether any of the effects of iodide were due to chloride reductions remains to be investigated.

Interestingly, Albert et al. (33) also presented data showing low-pass NLC activity in rat prestin using single-sine measurements (see their Fig. 3 E), which they attributed to their recording equipment. Yet they note very fast clamp speeds, and furthermore, they do not claim any untoward influences on the low-pass nature of zebra fish prestin in that same study.

How can low-pass prestin sensor charge movement that directly drives eM underlie cochlear amplification?

Cochlear amplification provides a boost to auditory sensitivity ranging from 100- to 1000-fold. It is thought to be maximal at high acoustic frequencies, in the tens of kilohertz range. There is ample evidence that prestin-driven OHC electromechanical activity underlies cochlear amplification, yet how can a voltage-dependent process that relies on a low-pass voltage sensor to drive mechanical activity work? We have previously estimated that mechanical responses at high acoustic frequencies would be markedly smaller than basilar motion, based on the cell's RC time constant. This problem has been addressed by many investigators, and many ostensible resolutions to the RC time-constant problem have been proposed (15,25,59–62). However, we must now consider the slow kinetics of prestin at physiological chloride levels that we have uncovered. This can only make matters worse. To be sure, we have recently found that eM magnitude rolls off faster than membrane voltage (28), and now we show that this roll-off corresponds to sensor charge activity (Fig. 4 B). It is possible that eM is not the main player and that OHC voltage-dependent stiffness, for which there is a wealth of evidence (63–65), is important.

On the other hand, we have found that the low-pass kinetic features of prestin can have high-frequency effects that could influence its ability to interact with basilar membrane/cochlear partition mechanics. Notably, we recently found a frequency-dependent phase lag in eM (re voltage) that is chloride dependent and is attributable to prestin's multistate kinetic features (28). Interestingly, phase lags are also predicted based on an electrodiffusion model of prestin (66), although the group that made that prediction suggested through additional modeling that power-law viscoelastic properties of the membrane could counter the effects of such lags (67). Whether such unusual viscoelastic properties characterize prestin's membrane environment is not known; however, our measured eM phase behavior in OHCs suggests no countering effects of viscoelasticity in the frequency range we studied. We propose that an accumulating phase lag at the molecular level could have a significant influence on the OHC's ability to inject power into

the cochlear partition, despite an associated magnitude roll-off dictated by low-pass sensor charge movement.

SUPPORTING MATERIAL

Supporting Materials and Methods and three figures are available at [http://www.biophysj.org/biophysj/supplemental/S0006-3495\(16\)30278-8](http://www.biophysj.org/biophysj/supplemental/S0006-3495(16)30278-8).

AUTHOR CONTRIBUTIONS

J.S.S. designed and performed experiments, analyzed data, and wrote the article. LS performed experiments.

ACKNOWLEDGMENTS

This research was supported by National Institutes of Health National Institute on Deafness and Other Communication Disorders grants DC00273 and DC008130 to J.S.S.

REFERENCES

1. Armstrong, C. M., and F. Bezanilla. 1973. Currents related to movement of the gating particles of the sodium channels. *Nature*. 242:459–461.
2. Schneider, M. F., and W. K. Chandler. 1973. Voltage dependent charge movement of skeletal muscle: a possible step in excitation-contraction coupling. *Nature*. 242:244–246.
3. Bezanilla, F. 2008. How membrane proteins sense voltage. *Nat. Rev. Mol. Cell Biol.* 9:323–332.
4. Lacroix, J. J., A. J. Labro, and F. Bezanilla. 2011. Properties of deactivation gating currents in *Shaker* channels. *Biophys. J.* 100:L28–L30.
5. Alper, S. L., and A. K. Sharma. 2013. The SLC26 gene family of anion transporters and channels. *Mol. Aspects Med.* 34:494–515.
6. Ruggero, M. A., and N. C. Rich. 1991. Furosemide alters organ of Corti mechanics: evidence for feedback of outer hair cells upon the basilar membrane. *J. Neurosci.* 11:1057–1067.
7. Zheng, J., W. Shen, ..., P. Dallos. 2000. Prestin is the motor protein of cochlear outer hair cells. *Nature*. 405:149–155.
8. Ashmore, J. F. 1987. A fast motile response in guinea-pig outer hair cells: the cellular basis of the cochlear amplifier. *J. Physiol.* 388:323–347.
9. Santos-Sacchi, J. 1992. On the frequency limit and phase of outer hair cell motility: effects of the membrane filter. *J. Neurosci.* 12:1906–1916.
10. Dallos, P., and B. N. Evans. 1995. High-frequency motility of outer hair cells and the cochlear amplifier. *Science*. 267:2006–2009.
11. Frank, G., W. Hemmert, and A. W. Gummer. 1999. Limiting dynamics of high-frequency electromechanical transduction of outer hair cells. *Proc. Natl. Acad. Sci. USA*. 96:4420–4425.
12. Gale, J. E., and J. F. Ashmore. 1997. An intrinsic frequency limit to the cochlear amplifier. *Nature*. 389:63–66.
13. Oliver, D., D. Z. He, ..., B. Fakler. 2001. Intracellular anions as the voltage sensor of prestin, the outer hair cell motor protein. *Science*. 292:2340–2343.
14. Song, L., A. Seeger, and J. Santos-Sacchi. 2005. On membrane motor activity and chloride flux in the outer hair cell: lessons learned from the environmental toxin tributyltin. *Biophys. J.* 88:2350–2362.
15. Rybalchenko, V., and J. Santos-Sacchi. 2003. Cl⁻ flux through a non-selective, stretch-sensitive conductance influences the outer hair cell motor of the guinea-pig. *J. Physiol.* 547:873–891.

16. Santos-Sacchi, J., L. Song, ..., A. L. Nuttall. 2006. Control of mammalian cochlear amplification by chloride anions. *J. Neurosci.* 26:3992–3998.
17. Oliver, D., T. Schächinger, and B. Fakler. 2006. Interaction of prestin (SLC26A5) with monovalent intracellular anions. *Novartis Found. Symp.* 273:244–253, discussion 253–260, 261–264.
18. Song, L., and J. Santos-Sacchi. 2013. Disparities in voltage-sensor charge and electromotility imply slow chloride-driven state transitions in the solute carrier SLC26a5. *Proc. Natl. Acad. Sci. USA.* 110:3883–3888.
19. Santos-Sacchi, J. 2004. Determination of cell capacitance using the exact empirical solution of $\partial Y/\partial C_m$ and its phase angle. *Biophys. J.* 87:714–727.
20. Schnee, M. E., J. Santos-Sacchi, ..., A. J. Ricci. 2011. Calcium-dependent synaptic vesicle trafficking underlies indefatigable release at the hair cell afferent fiber synapse. *Neuron.* 70:326–338.
21. Santos-Sacchi, J., S. Kakehata, and S. Takahashi. 1998. Effects of membrane potential on the voltage dependence of motility-related charge in outer hair cells of the guinea-pig. *J. Physiol.* 510:225–235.
22. Schnee, M. E., M. Castellano-Muñoz, ..., A. J. Ricci. 2011. Tracking vesicle fusion from hair cell ribbon synapses using a high frequency, dual sine wave stimulus paradigm. *Commun. Integr. Biol.* 4:785–787.
23. Santos-Sacchi, J., and E. Navarrete. 2002. Voltage-dependent changes in specific membrane capacitance caused by prestin, the outer hair cell lateral membrane motor. *Pflugers Arch.* 444:99–106.
24. Santos-Sacchi, J., and L. Song. 2014. Chloride and salicylate influence prestin-dependent specific membrane capacitance: support for the area motor model. *J. Biol. Chem.* 289:10823–10830.
25. Santos-Sacchi, J., S. Kakehata, ..., T. Takasaka. 1998. Density of motility-related charge in the outer hair cell of the guinea pig is inversely related to best frequency. *Neurosci. Lett.* 256:155–158.
26. Huang, G., and J. Santos-Sacchi. 1993. Mapping the distribution of the outer hair cell motility voltage sensor by electrical amputation. *Biophys. J.* 65:2228–2236.
27. Oliver, D., and B. Fakler. 1999. Expression density and functional characteristics of the outer hair cell motor protein are regulated during postnatal development in rat. *J. Physiol.* 519:791–800, (In Process Citation).
28. Santos-Sacchi, J., and L. Song. 2014. Chloride-driven electromechanical phase lags at acoustic frequencies are generated by SLC26a5, the outer hair cell motor protein. *Biophys. J.* 107:126–133.
29. Bezanilla, F., and C. M. Armstrong. 1977. Inactivation of the sodium channel. I. Sodium current experiments. *J. Gen. Physiol.* 70:549–566.
30. Santos-Sacchi, J., and G. Huang. 1998. Temperature dependence of outer hair cell nonlinear capacitance. *Hear. Res.* 116:99–106.
31. Santos-Sacchi, J. 1991. Reversible inhibition of voltage-dependent outer hair cell motility and capacitance. *J. Neurosci.* 11:3096–3110.
32. Ashmore, J. F. 1989. Transducer motor coupling in cochlear outer hair cells. In *Mechanics of Hearing*. D. Kemp and J. P. Wilson, editors. Plenum Press, New York, pp. 107–113.
33. Albert, J. T., H. Winter, ..., D. Oliver. 2007. Voltage-sensitive prestin orthologue expressed in zebrafish hair cells. *J. Physiol.* 580:451–461.
34. Santos-Sacchi, J., and J. P. Dilger. 1988. Whole cell currents and mechanical responses of isolated outer hair cells. *Hear. Res.* 35:143–150.
35. Santos-Sacchi, J. 1989. Asymmetry in voltage-dependent movements of isolated outer hair cells from the organ of Corti. *J. Neurosci.* 9:2954–2962.
36. Gale, J. E., and J. F. Ashmore. 1997. The outer hair cell motor in membrane patches. *Pflugers Arch.* 434:267–271.
37. Mount, D. B., and M. F. Romero. 2004. The SLC26 gene family of multifunctional anion exchangers. *Pflugers Arch.* 447:710–721.
38. Schaechinger, T. J., D. Gorbunov, ..., D. Oliver. 2011. A synthetic prestin reveals protein domains and molecular operation of outer hair cell piezoelectricity. *EMBO J.* 30:2793–2804.
39. Schaechinger, T. J., and D. Oliver. 2007. Nonmammalian orthologs of prestin (SLC26A5) are electrogenic divalent/chloride anion exchangers. *Proc. Natl. Acad. Sci. USA.* 104:7693–7698.
40. Mistrik, P., N. Daudet, ..., J. F. Ashmore. 2012. Mammalian prestin is a weak $\text{Cl}^-/\text{HCO}_3^-$ electrogenic antiporter. *J. Physiol.* 590:5597–5610.
41. Bai, J. P., A. Surguchev, ..., D. Navaratnam. 2009. Prestin's anion transport and voltage-sensing capabilities are independent. *Biophys. J.* 96:3179–3186.
42. Tan, X., J. L. Pecka, ..., D. Z. He. 2011. From zebrafish to mammal: functional evolution of prestin, the motor protein of cochlear outer hair cells. *J. Neurophysiol.* 105:36–44.
43. Schänzler, M., and C. Fahlke. 2012. Anion transport by the cochlear motor protein prestin. *J. Physiol.* 590:259–272.
44. Wu, M., and J. Santos-Sacchi. 1998. Effects of lipophilic ions on outer hair cell membrane capacitance and motility. *J. Membr. Biol.* 166:111–118.
45. Kakehata, S., and J. Santos-Sacchi. 1996. Effects of salicylate and lanthanides on outer hair cell motility and associated gating charge. *J. Neurosci.* 16:4881–4889.
46. Tunstall, M. J., J. E. Gale, and J. F. Ashmore. 1995. Action of salicylate on membrane capacitance of outer hair cells from the guinea-pig cochlea. *J. Physiol.* 485:739–752.
47. Rybalchenko, V., and J. Santos-Sacchi. 2008. Anion control of voltage sensing by the motor protein prestin in outer hair cells. *Biophys. J.* 95:4439–4447.
48. Song, L., and J. Santos-Sacchi. 2010. Conformational state-dependent anion binding in prestin: evidence for allosteric modulation. *Biophys. J.* 98:371–376.
49. Geertsma, E. R., Y. N. Chang, ..., R. Dutzler. 2015. Structure of a prokaryotic fumarate transporter reveals the architecture of the SLC26 family. *Nat. Struct. Mol. Biol.* 22:803–808.
50. Gorbunov, D., M. Sturlese, ..., D. Oliver. 2014. Molecular architecture and the structural basis for anion interaction in prestin and SLC26 transporters. *Nat. Commun.* 5:3622.
51. Santos-Sacchi, J. 1990. Fast outer hair cell motility: how fast is fast? In *The Mechanics and Biophysics of Hearing*. P. Dallos, C. D. Geisler, J. W. Matthews, M. A. Ruggero, and C. R. Steele, editors. Springer-Verlag, Berlin, pp. 69–75.
52. Scherer, M. P., and A. W. Gummer. 2005. How many states can the motor molecule, prestin, assume in an electric field? *Biophys. J.* 88:L27–L29.
53. Fernández, J. M., F. Bezanilla, and R. E. Taylor. 1982. Distribution and kinetics of membrane dielectric polarization. II. Frequency domain studies of gating currents. *J. Gen. Physiol.* 79:41–67.
54. Santos-Sacchi, J., L. Song, and X. T. Li. 2009. Firing up the amplifier: temperature, pressure and voltage jump studies on ohc motor capacitance. In *Proceedings of the International Workshop on the Mechanics of Hearing* (Keele University): 363–370.
55. Meltzer, J., and J. Santos-Sacchi. 2001. Temperature dependence of non-linear capacitance in human embryonic kidney cells transfected with prestin, the outer hair cell motor protein. *Neurosci. Lett.* 313:141–144.
56. Okunade, O., and J. Santos-Sacchi. 2013. IR laser-induced perturbations of the voltage-dependent solute carrier protein SLC26a5. *Biophys. J.* 105:1822–1828.
57. Shapiro, M. G., M. F. Priest, ..., F. Bezanilla. 2013. Thermal mechanisms of millimeter wave stimulation of excitable cells. *Biophys. J.* 104:2622–2628.
58. Homma, K., C. Duan, ..., P. Dallos. 2013. The V499G/Y501H mutation impairs fast motor kinetics of prestin and has significance for defining functional independence of individual prestin subunits. *J. Biol. Chem.* 288:2452–2463.
59. Ospeck, M., X. X. Dong, ..., K. H. Iwasa. 2006. Electromotility in outer hair cells: a supporting role for fast potassium conductance. *ORL J. Otorhinolaryngol. Relat. Spec.* 68:373–377.

60. Spector, A. A., W. E. Brownell, and A. S. Popel. 2003. Effect of outer hair cell piezoelectricity on high-frequency receptor potentials. *J. Acoust. Soc. Am.* 113:453–461.
61. Johnson, S. L., M. Beurg, ..., R. Fettiplace. 2011. Prestin-driven cochlear amplification is not limited by the outer hair cell membrane time constant. *Neuron*. 70:1143–1154.
62. Corbitt, C., F. Farinelli, ..., B. Farrell. 2012. Tonotopic relationships reveal the charge density varies along the lateral wall of outer hair cells. *Biophys. J.* 102:2715–2724.
63. He, D. Z., S. Jia, and P. Dallos. 2003. Prestin and the dynamic stiffness of cochlear outer hair cells. *J. Neurosci.* 23:9089–9096.
64. He, D. Z., and P. Dallos. 2000. Properties of voltage-dependent somatic stiffness of cochlear outer hair cells. *J. Assoc. Res. Otolaryngol.* 1:64–81.
65. He, D. Z., and P. Dallos. 1999. Somatic stiffness of cochlear outer hair cells is voltage-dependent. *Proc. Natl. Acad. Sci. USA.* 96:8223–8228.
66. Sun, S. X., B. Farrell, ..., A. A. Spector. 2009. Voltage and frequency dependence of prestin-associated charge transfer. *J. Theor. Biol.* 260:137–144.
67. Roy, S., W. E. Brownell, and A. A. Spector. 2012. Modeling electrically active viscoelastic membranes. *PLoS One.* 7:e37667.

Biophysical Journal, Volume 110

Supplemental Information

**Chloride Anions Regulate Kinetics but Not Voltage-Sensor Q_{\max} of the
Solute Carrier SLC26a5**

Joseph Santos-Sacchi and Lei Song

Supporting material

Removal of stray capacitance at C_m measuring frequencies

We use an Axon 200B patch clamp amplifier to measure OHC capacitance. Methodology was coded in jClamp and utilizes admittance measures at 2 frequencies to measure capacitance (1, 2). A linear cell model is depicted below, where R_s , R_m and C_m at each frequency (ω_0 , ω_1) are derived from the following equations.

$$\begin{aligned} a_0 &= \text{real}(Y) @ w_0 \\ a_1 &= \text{real}(Y) @ w_1 \\ b_0 &= \text{imag}(Y) @ w_0 \\ b_1 &= \text{imag}(Y) @ w_1 \end{aligned}$$

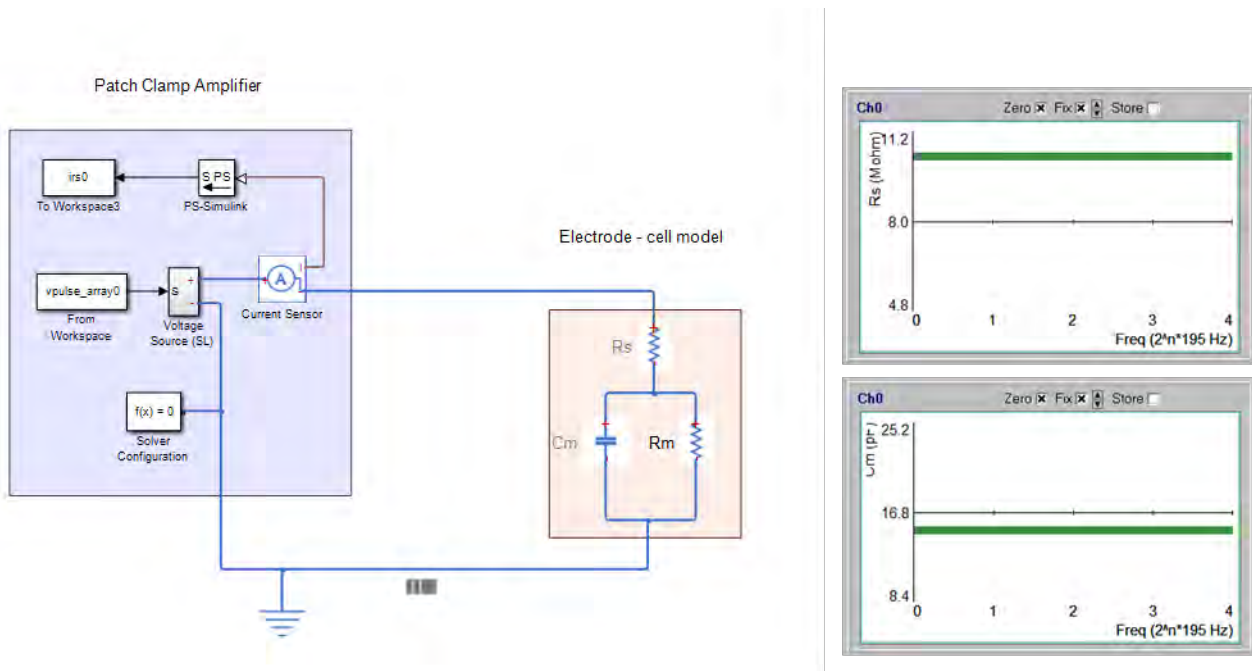
$$\begin{aligned} c_0 &= a_0^2 + b_0^2; \\ c_1 &= a_1^2 + b_1^2; \end{aligned}$$

$$b = (-0.5) * (-c_1 + c_0 + \sqrt{c_1^2 - 2 * c_1 * c_0 + c_0^2 - 4 * a_1 * a_0 * c_1 + 4 * a_1^2 * c_0 + 4 * a_0^2 * c_1 - 4 * a_0 * a_1 * c_0}) / (a_1 - a_0);$$

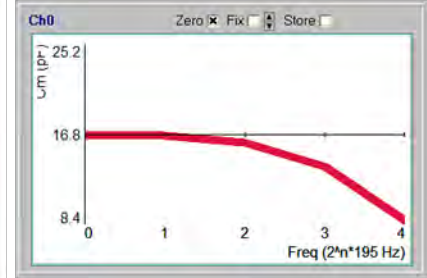
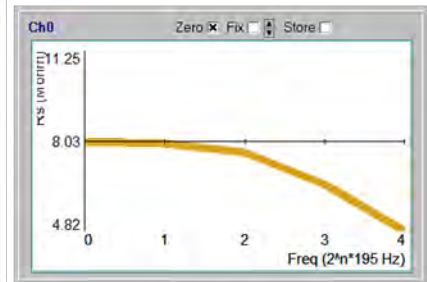
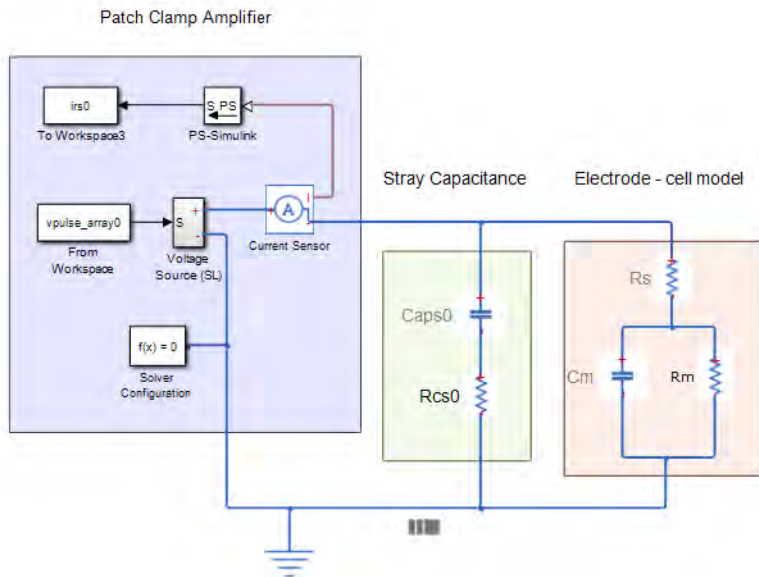
$$\begin{aligned} R_{s0} &= (a_0 - b) ./ (a_0.^2 + b_0.^2 - a_0 * b); \\ R_{m0} &= 1/b * ((a_0 - b).^2 + b_0.^2) ./ (a_0.^2 + b_0.^2 - a_0 * b); \\ C_{m0} &= (1 ./ (w_0 * b_0)) .* ((a_0.^2 + b_0.^2 - a_0 * b).^2) ./ ((a_0 - b).^2 + b_0.^2); \end{aligned}$$

$$\begin{aligned} R_{s1} &= (a_1 - b) ./ (a_1.^2 + b_1.^2 - a_1 * b); \\ R_{m1} &= 1/b * ((a_1 - b).^2 + b_1.^2) ./ (a_1.^2 + b_1.^2 - a_1 * b); \\ C_{m1} &= (1 ./ (w_1 * b_1)) .* ((a_1.^2 + b_1.^2 - a_1 * b).^2) ./ ((a_1 - b).^2 + b_1.^2); \end{aligned}$$

An example of our approach to remove stray capacitance is shown below using jClamp interfaced to a MatLab Simulink model. First, the model is evaluated without stray capacitance, where $R_s = 10$ Mohm, $R_m = 200$ Mohm, $C_m = 15$ pF.



Note that the solutions (R_s and C_m plotted) provide exact parameter estimates regardless of frequency of stimulation (or, in fact, regardless of component values). However, real world recording includes parasitic capacitances, termed stray capacitance, the inclusion of which is modeled below.

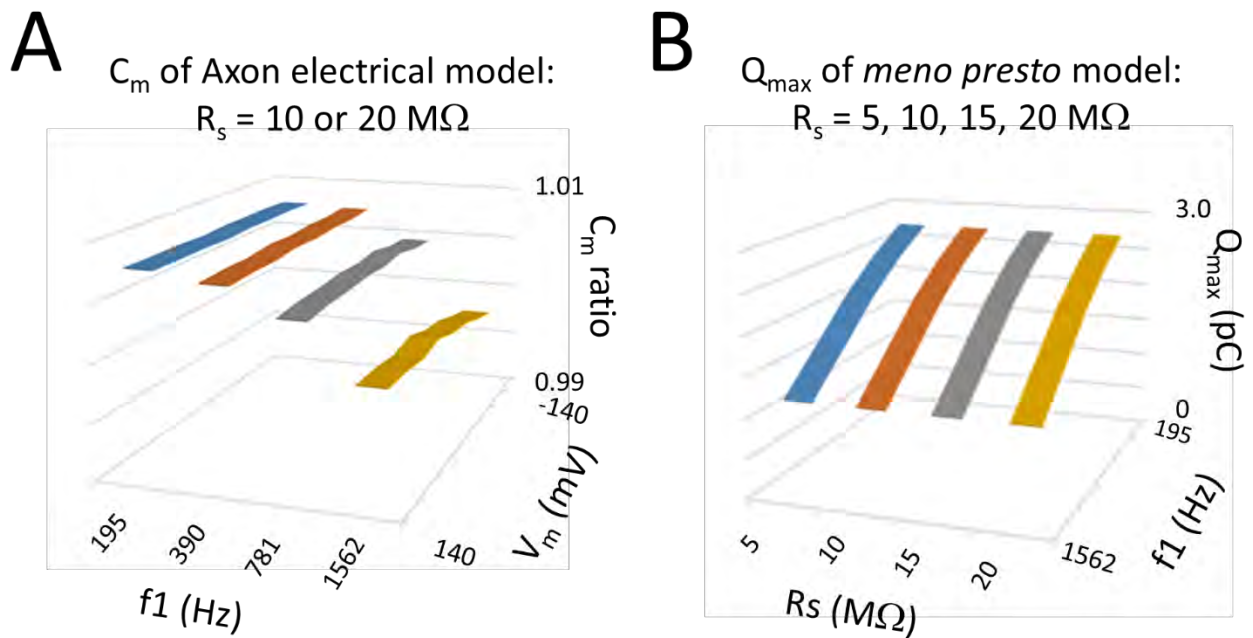


Here, utilization of the exact solutions above provides inaccurate measures, showing both R_s and C_m decreasing with increasing frequency. Both R_s and C_m are linear, and as defined are neither frequency nor voltage dependent. It behooves us then to remove stray capacitance effects during our recordings, since only without stray capacitance are our equations valid. Typically, stray capacitance effects (e.g., due to pipette holder and pipette – we use thick wall borosilicate glass pipettes coated with M-coat to reduce stray capacitance) are cancelled following gigohm seal formation during patch clamp recording by utilizing Axon 200B amplifier capacitance compensation controls. Unfortunately, this balancing procedure (using voltage steps in the time domain to cancel capacitive spikes) often is imperfect and stray capacitance effects can remain at our measurement frequencies. We attempt to overcome this problem after establishing whole cell configuration by stimulating in the frequency domain with a multi-frequency protocol that defines our interrogating frequencies. We then further fine balance with amplifier controls until calculated linear C_m and R_s are flat across frequency, as they should be. Any change in stray capacitance during the course of a recording session can be cancelled in this manner, e.g., if bath fluid levels changes. For our studies on synaptic activity (3-5), we can remove stray capacitance at any holding potential since the membranes of cells we study have no large intrinsic voltage dependent capacitance. However, in order to balance out stray capacitance for OHCs we hold the cell at positive potentials where linear capacitance dominates. Having succeeded in minimizing confounding effects of stray capacitance on linear membrane capacitance measurements across frequency, we then can investigate the frequency dependence of **NLC**. As detailed in the *Methods* section of our manuscript, C_m is measured at a range of holding potentials to generate a C_m - V_m plot that is fit with eq. 1, enabling extraction of Boltzmann characteristics, Q_{max} , V_h , and z . When sensor charge (Q_{max}) is plotted versus frequency of interrogation, we find that **NLC** is frequency dependent but linear capacitance is frequency independent (Fig. 2), confirming stray capacitance cancellation at our measuring frequencies. Our modelling indicates that the frequency dependence of **NLC** relates to the transition rates between conformational states of prestin.

R_s effects on membrane voltage drop and clamp time constant are removed with our methodology

Equipment frequency response (magnitude and phase of amplifier and associated equipment in the recording path) is corrected for by generating a calibration table across measurement frequencies, which is applied post-hoc to correct data for system response characteristics. This is a standard approach in all areas of system identification, including patch clamp assessment of C_m (6).

Our dual-sine analysis fundamentally corrects for effects of R_s , since it works by finding the parameter solutions of the total admittance of the patch clamp-cell circuit (as modelled above), given a known voltage across the total admittance. Thus, C_m derivation by this method takes into account the voltage drop across R_s at any frequency, providing true measures of C_m across frequency. Fits to C_m - V_m (or Q - V_m , in the case of current integrations) are made using corrected V_m values based on measured R_s , namely, $V_m = V_{com} - I_{rs} * R_s$, where the cell has been held sufficiently long to reach steady state voltage levels (in our case, for hundreds of ms before C_m analysis). Below, we show with electrical and mathematical models that R_s effects do not interfere with our C_m measures.



- A) An electrical model cell was used to measure C_m , following stray capacitance cancellation as above. Model parameters were $R_s=10$ or $20 \text{ M}\Omega$, $R_m = 500 \text{ M}\Omega$, $C_m = 33 \text{ pF}$. The plot shows that the ratios of $C_m@20 \text{ M}\Omega / C_m@10 \text{ M}\Omega$ measured at a range of holding potentials and frequencies (primary f_1 frequency of dual-sine stimulus shown) are essentially identical (ratio ~ 1), regardless of R_s value. This indicates that R_s (with its influence on clamp time constant) does not affect our C_m frequency response measures in the absence of stray capacitance. Average C_m across voltages at 195 Hz was 33.0 pF for $10 \text{ M}\Omega R_s$ and 33.2 pF for $20 \text{ M}\Omega R_s$. At 1562 Hz values were 33.1 pF for $10 \text{ M}\Omega R_s$ and 33.0 pF for $20 \text{ M}\Omega R_s$. Differences arise from variability in stray capacitance cancellation, as is evident from model evaluations in B) in the absence of stray capacitance.
- B) The *meno presto* model (7) was used to measure C_m - V_m functions that were fit to extract Q_{max} . R_s ranging from 5 - $20 \text{ M}\Omega$ has no effect on the magnitude or frequency response of NLC (Q_{max}), which is frequency-dependent due to model transition rates. Frequency is (plotted on a linear scale). Chloride set to 140 mM . $R_m=200 \text{ M}\Omega$, $C_{lin}=20 \text{ pF}$.

References

1. Santos-Sacchi, J. 2004. Determination of cell capacitance using the exact empirical solution of dY/dC_m and its phase angle. *Biophys J* 87:714-727.
2. Santos-Sacchi, J., S. Kakehata, and S. Takahashi. 1998. Effects of membrane potential on the voltage dependence of motility-related charge in outer hair cells of the guinea-pig. *J. Physiol* 510 (Pt 1):225-235.
3. Ricci, A. J., J.-P. Bai, L. Song, C. Lv, D. Zenisek, and J. Santos-Sacchi. 2013. Patch-Clamp Recordings from Lateral Line Neuromast Hair Cells of the Living Zebrafish. *Journal of Neuroscience* 33:3131-3134.
4. Schnee, M. E., J. Santos-Sacchi, M. Castellano-Munoz, J. H. Kong, and A. J. Ricci. 2011. Calcium-dependent synaptic vesicle trafficking underlies indefatigable release at the hair cell afferent fiber synapse. *Neuron* 70:326-338.
5. Schnee, M. E., J. Santos-Sacchi, M. Castellano-Munoz, J. H. Kong, and A. J. Ricci. 2011. Tracking vesicle fusion from hair cell ribbon synapses using a high frequency, dual sine wave stimulus paradigm. *Communicative & Integrative Biology* 4:785-787.
6. Gillis, K. D. 1995. Techniques for Membrane Capacitance Measurements. In *Single Channel Recording*. B. Sakmann, and E. Neher, editors. Plenum Press, New York. 155-198.
7. Santos-Sacchi, J., and L. Song. 2014. Chloride and Salicylate Influence Prestin-dependent Specific Membrane Capacitance. *Journal of Biological Chemistry* 289:10823-10830.

Article

Chloride-driven Electromechanical Phase Lags at Acoustic Frequencies Are Generated by SLC26a5, the Outer Hair Cell Motor Protein

Joseph Santos-Sacchi^{1,2,3,*} and Lei Song¹¹Surgery (Otolaryngology), ²Neurobiology, and ³Cellular and Molecular Physiology, Yale University School of Medicine, New Haven, Connecticut

ABSTRACT Outer hair cells (OHC) possess voltage-dependent membrane bound molecular motors, identified as the solute carrier protein SLC26a5, that drive somatic motility at acoustic frequencies. The electromotility (eM) of OHCs provides for cochlear amplification, a process that enhances auditory sensitivity by up to three orders of magnitude. In this study, using whole cell voltage clamp and mechanical measurement techniques, we identify disparities between voltage sensing and eM that result from stretched exponential electromechanical behavior of SLC26a5, also known as prestin, for its fast responsiveness. This stretched exponential behavior, which we accurately recapitulate with a new kinetic model, the *meno presto* model of prestin, influences the protein's responsiveness to chloride binding and provides for delays in eM relative to membrane voltage driving force. The model predicts that in the frequency domain, these delays would result in eM phase lags that we confirm by measuring OHC eM at acoustic frequencies. These lags may contribute to canceling viscous drag, a requirement for many models of cochlear amplification.

The outer hair cell (OHC) is one of two receptor cell types in the organ of Corti, but unlike the inner hair cell it displays electromotile behavior distinct from any other form of cellular motility (1–4). OHC electromotility (eM) arises from the concerted action of millions of molecular motors embedded in the lateral membrane of the cell. They respond directly to membrane voltage and evidence reciprocal activity; namely, they are piezoelectric-like (5–7). Indeed, there is clear evidence that surface area changes accompany state transitions in the motor [see (8)]. The identification of these motors as members of the anion transporter family SLC26 (9), of which prestin is the 5th member (a5), underscores an interesting molecular evolution designed to boost the performance of auditory sensitivity and selectivity. This enhancement is known as cochlear amplification (10).

A class of cochlear models requires an electromechanical phase disparity for effective cochlear amplification (11–13), OHC eM lagging receptor potentials. Traditionally, these models assign the mechanism to processes other than the OHC itself. The phase lag provides for the properly timed injection of mechanical force into the cochlear partition to counter viscous detriment. Most molecular models of prestin behavior envision tightly coupled interactions between membrane voltage and eM, arising from sensor charge movements obeying Boltzmann statistics (14–20). Thus, Boltzmann characteristics of sensor charge and eM, namely Q_{\max} / eM_{\max} and $Q / V_h / eM / V_h$, are commonly believed to tightly correspond. However, we recently showed significant uncoupling of these character-

istics depending on rate and polarity of voltage stimulation and on intracellular chloride level (21). We showed that a slow intermediate transition placed between prestin's chloride binding transition and the voltage dependent transition responsible for eM could qualitatively account for the data, and we surmised that a molecularly based phase lag should arise. In this study we test this hypothesis by measuring eM at acoustic frequencies and find that indeed substantial frequency dependent phase lags are produced between membrane voltage and eM, showing chloride dependence. An enhanced stretched-exponential kinetic model, termed the *meno presto* model of prestin, nicely fits the data, whereas a model lacking the intermediate transitions fails.

METHODS

Whole cell recordings were made from single isolated OHCs from the organ of Corti. Hartley albino guinea pigs were overdosed with isoflurane, the temporal bones excised and the top turns of the cochleae dissected free. Enzyme treatment (1 mg/ml Dispase I, 10 min) preceded gentle trituration, and isolated OHCs were placed in a glass-bottom recording chamber. Either a Nikon E600-FN microscope with 40× water immersion lens or an inverted Nikon Eclipse TI-2000 microscope with 40× lens was used to observe cells during voltage clamp. Experiments were performed at room temperature.

Solutions

Chloride levels were set to surround the 10 mM intracellular level in intact OHCs (22). Valid measures of membrane capacitance required an ionic blocking solution to remove ionic currents. The base high Cl solution contained (in mM): NaCl 100, TEA-Cl 20, CsCl 20, CoCl₂ 2, MgCl₂ 1, CaCl₂ 1, and Hepes 10. Lower chloride concentrations (10, 1, and 0.1 mM) were achieved by substituting chloride with gluconate. Base intracellular solutions contains (in mM): CsCl 140, MgCl₂ 2, Hepes 10, and EGTA 10.

Submitted December 19, 2013, and accepted for publication May 9, 2014.

*Correspondence: joseph.santos-sacchi@yale.edu

Editor: Andreas Engel

© 2014 by the Biophysical Society
0006-3495/14/07/0126/8 \$2.00

<http://dx.doi.org/10.1016/j.bpj.2014.05.018>



To unequivocally set intracellular chloride levels in the subplasmalemmal space of the OHC, both intracellular and extracellular chloride concentrations were set equal. All chemicals used were purchased from Sigma (Sigma-Aldrich, St. Louis, MO).

Cell capacitance and mechanical response

An Axon (Molecular Devices, Sunnyvale, CA) 200B amplifier was used for whole cell recording. Coupled voltage ramps (depolarizing followed immediately by hyperpolarizing ramp) of 100 and 500 ms were delivered to the cells from a holding potential of 0 mV. No averaging was done.

Nonlinear capacitance was measured using a continuous high resolution (2.56 ms sampling) two-sine stimulus protocol (10 to 20 mV peak at a primary frequency of 390.6 and harmonic of 781.2 Hz) superimposed onto the voltage ramps (23,24). It is mandatory that ionic conductances be blocked to insure accurate results, and imperative that system calibration be performed, as specified in our software design, jClamp (Sciosoft, Ridgefield, CT). Capacitance data were fit to the first derivative of a two-state Boltzmann function (15) as follows:

$$C_m = Q_{max} \frac{ze}{kT} \frac{b}{(1+b)^2} + C_{lin},$$

$$b = \exp\left(\frac{-ze(V_m - V_h)}{kT}\right)$$

providing Q_{max} , the maximum nonlinear charge moved; V_h , the voltage at peak capacitance or equivalently, at half maximum charge transfer; z , the valence; and C_{lin} , the linear membrane capacitance.

Simultaneous eM measurements were made either with fast video recording or photo diode. A Prosilica GE680 camera (Allied Vision Technologies, Exton, PA) was used for video measures, and details can be found in a previous publication (21). For photodiode measures, the image of the OHC apical region was projected onto a photodiode to measure cell movement, in a similar fashion to the method of Clark et al. (25). Two aligned, same optical axis, microscope cameras (Logitech webcam C650, Newark CA) were used: one to image the cell during patch recording and the other to ensure proper image placement. The inner camera (Fig. 1 A, 1) sensor area (white bordered quadrangles), upon which a 1.1×2.67 mm photodiode (SD076-11-31-211, Advanced Photonics, Ann Arbor, MI) was mounted (yellow boxed area), monitored only the OHC apex, whereas the other camera (Fig. 1 A, 2) sensor region (which actually viewed the whole cell) was used for patch electrode placement and monitoring image rotation and x-y shifts utilizing a dove prism and gimbaled mirror, respectively. Video capture was made with the wide field camera to determine actual cell displacement magnitude. With either the Prosilica camera or the photo diode approach, the edge of the cuticular plate was used to track OHC length change, the patch electrode providing a fixed point at the basal end of the cell. For photodiode measures, calibration was additionally made by movements of the OHC image via gimbaled mirror tilt (see Fig. 5). Sigmoidal fits (four parameters) provided estimates of V_h , maximal movement, and slope factor, b . Shift of motility against NLC (NonLinear Capacitance) is calculated by subtracting NLC V_h from eM V_h .

AC analysis of membrane currents (I_m) and eM were made by stimulating cells with voltage bursts at harmonic frequencies from 12.207 to 6250 Hz, with a $10 \mu s$ sample clock. Voltage bursts were ramped on and off to avoid transients. Magnitude and phase of responses were computed by FFT (fast Fourier transform) in jClamp. Fits in Matlab were made using least squares simultaneously on the transformed real and imaginary components of all spectral components of both eM and I_m . The effects of turgor pressure and magnitude of voltage stimulation on eM phase were also investigated. Turgor pressure was modified by applying pressure to the patch pipette using an ALA's High Speed Pressure Clamp, HSPC-1 (Westbury, NY).

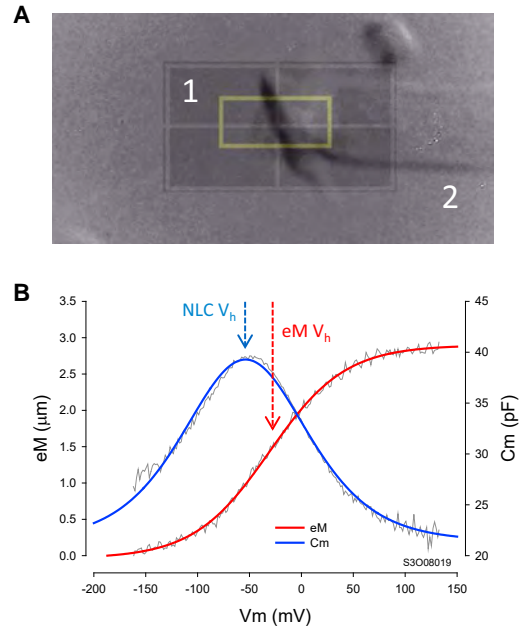
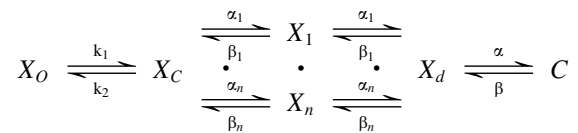


FIGURE 1 Electromechanical measures of prestin activity. (A) Image of OHC apical region was projected onto a photodiode to measure cell movement. (B) Simultaneous measures of OHC NLC and eM, measured via photodiode. No averaging. Note that NLC V_h and eM V_h differ (arrows) with that of eM shifted rightward. Chloride level was 1 mM. To see this figure in color, go online.

Model assessment

A kinetic model, termed the *meno presto* model of prestin, was used to fit the eM data. The *meno presto* model (Fig. 3) was assessed using Matlab Simulink in conjunction with jClamp. It is an extension of the simple model in Song and Santos-Sacchi (2013) that now introduces stretched exponential behavior in the intermediate transition between chloride binding and voltage dependency.



X_o state is unbound by anion. X_c state is bound by anion but intrinsic voltage sensor charge is not responsive to membrane electric field. A slow, multi-exponential conformational transition to X_d state via X_n states enables voltage sensing within the electric field. Depolarization moves positive sensor charge outward, simultaneously resulting in compact state C, which corresponds to cell contraction. The differential equations are as follows:

$$\frac{dX_o}{dt} = X_c \cdot k_2 - X_o \cdot [Cl^-]k_1$$

$$\frac{dX_c}{dt} = X_o \cdot [Cl^-]k_1 + \sum_{n=1}^{27} X_n \cdot \beta_n - X_c \cdot k_2 - \sum_{n=1}^{27} X_c \cdot \alpha_n$$

$$\frac{dX_n}{dt} = X_c \cdot \alpha_n + X_d \cdot \beta_n - X_n \cdot \alpha_n - X_n \cdot \beta_n$$

$$\frac{dX_d}{dt} = C \cdot \beta + \sum_{n=1}^{27} X_n \cdot \alpha_n - X_d \cdot \alpha - \sum_{n=1}^{27} X_d \cdot \beta_n$$

$$\frac{dC}{dt} = X_d \cdot \alpha - C \cdot \beta$$

where $\alpha_n = A \cdot (\exp(-(n-1)))^w$, $\beta_n = \alpha_n$, $w = 0.6$, $A = 2.5e4$ for $n = 0.25$, $k_1 = 1.5e5$, $k_2 = k_1 \cdot k_d$, $k_d = .012$, $z = 0.7$, $nPres = 25e6$, $\alpha = 1.3e6 \cdot \exp((z \cdot F \cdot V_m / (2 \cdot R \cdot T)))$, $\beta = 7.7e4 \cdot \exp((-z \cdot F \cdot V_m / (2 \cdot R \cdot T)))$. Equivalence of α_n and β_n transition rates assures detailed balance of the reaction scheme (26). Parameters were varied until a good approximation of the data was obtained. We used 27 intermediate transitions to get as many exponential components such that a range of frequencies could be fit by the model. A single exponential intermediate transition will only influence one small frequency range, as we showed in our PNAS paper (21). Basically the prestin model is frequency sensitive, showing effects across our measured frequency range.

jClamp provides an automation link to Matlab that allows voltage stimuli to be delivered to and current responses to be obtained from Simulink models. Solutions were obtained with the ode45 (Dormand-Prince) solver at a fixed absolute tolerance of 10^{-6} . The *meno presto* model was interfaced to jClamp via a model of the patch clamp amplifier and OHC. The linear component of the patch-cell model was composed of R_s (pipette resistance) in series with a parallel combination of R_m (membrane resistance) and C_{lin} (linear capacitance). For the AC data fits, an additional uncompensated stray pipette capacitance modeled as a series combination of resistance (R_p) and capacitance (C_p) was included (24). Given the above *meno presto*

model parameters, fits of AC data were made with patch clamp parameters of $R_s = 6.1 \text{ M}\Omega$, $R_m = 275 \text{ M}\Omega$, $C_{lin} = 23 \text{ pF}$, $R_p = 15 \text{ M}\Omega$, $C_p = 0.4 \text{ pF}$ for the 140 mM chloride condition, and $R_s = 6.6 \text{ M}\Omega$, $R_m = 265 \text{ M}\Omega$, $C_{lin} = 26.5 \text{ pF}$, $R_p = 10 \text{ M}\Omega$, and $C_p = 0.4 \text{ pF}$ for the 1 mM chloride condition. The exact same voltage stimuli and exact same analysis of model data were performed as with the biophysical data. For comparison purposes, a model emulating a fast two-state Boltzmann, with the intermediate transitions removed and k_1 rate constant set to $1.5e10$, was evaluated, as well. Mechanical contraction data of the model, namely eM, was taken as the accumulated residence in the C state (see Fig. 3).

RESULTS

Under whole cell voltage clamp, OHCs change length when membrane voltage is altered. Fig. 1 B shows an example of an OHC mechanical response (eM) measured with photodiode during a voltage ramp. Simultaneously, a bell-shaped nonlinear capacitance (NLC) is measured, an estimate of prestin's voltage sensor charge movement. Note that the arrows depicting NLC V_h and eM V_h are separated, with eM shifted rightward along the voltage axis. This disparity underscores an uncoupling between voltage sensor and eM.

The magnitude of this V_h disparity is dependent both on the polarity of the voltage ramp that is used to obtain C_m - V_m functions and on intracellular chloride level. Hyperpolarizing ramps (Fig. 2 A) produce a maximal disparity

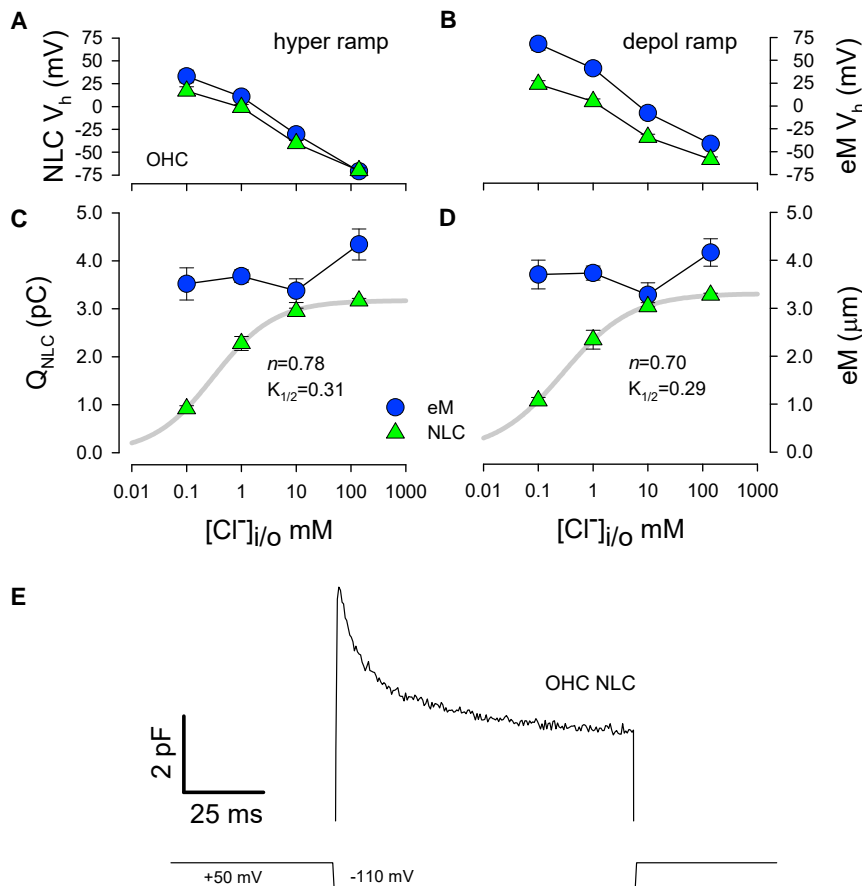


FIGURE 2 Chloride dependence of Boltzmann characteristics of eM and NLC as a function of depolarizing and hyperpolarizing ramps. (A) NLC V_h disparities arise as chloride levels are decreased, with effects being larger on eM, and larger disparities being observed with depolarizing ramps (B). (C) Q_{max} , determined from NLC fits, decreases as chloride levels are lowered. Hill coefficient (n) and $K_{1/2}$ are shown. Contrarily, eM magnitude is little affected. Similar results are obtained with depolarizing ramps (D). Plots are of average (\pm se) results from combined responses to 100 ms and 500 ms ramps. ($n = 5$ to 15). (E) Stretched exponential changes in OHC NLC occur during a constant voltage step from +50 mV to -110 mV. 4 μsec clock, C_m inspection resolution 0.512 ms. To see this figure in color, go online.

appreciably less than depolarizing ramps (Fig. 2 B), each polarity, however, showing larger disparities as chloride levels are reduced. Plots show means and se (5 to 15 cells per point) of the average responses to 100 and 500 ms ramps. At the 0.1 mM chloride level, eM V_h was 32.9 ± 6.9 mV and NLC V_h was 16.9 ± 4.8 mV for hyperpolarizing ramps, whereas for depolarizing ramps eM V_h was 67.8 ± 6.6 mV and NLC V_h was 23.8 ± 3.9 mV ($n = 5$). In individual cells with faster ramps, we have observed such disparities greater than 60 mV. Similarly, disparities in Q estimates and eM measures are found as chloride levels are lowered (Fig. 2 C and D). Whereas estimates of Q from NLC are highly chloride dependent, showing a $K_{1/2}$ of 0.3 mM from Hill fits, eM changes very little across chloride levels. These data indicate an uncoupling between sensor charge movement determined from NLC and OHC mechanical activity. In simple two-state models of electromotility, no disparities are expected.

Thus, we believe that this uncoupling results from an additional slow molecular transition in prestin that derives from a more complicated molecular scheme (21); this slow process is readily evidenced as a stretched exponential component of OHC C_m when membrane voltage is stepped. Fig. 2 E illustrates the resulting complex behavior in C_m during a fixed step from +50 mV to -100 mV, showing an initial rapid rise in C_m followed by a multi-exponential decay with tau components ranging from millisecond to seconds (27). Unfortunately, our recently developed model (21), which introduces an intermediate transition between chloride binding and voltage-dependent mechanical activity, cannot account for the observations shown in Fig. 2 because it provides only a single exponential transition. To more accurately account for our experimental findings, we expanded on this model to give stretched exponential behavior. A cartoon of the new *meno presto* model is shown in Fig. 3 and is described in detail in the Methods section. As can be seen in Fig. 4, the model results show marked simi-

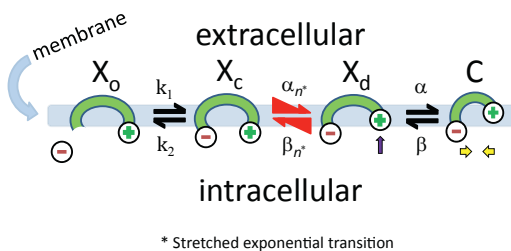


FIGURE 3 Stretched kinetic model of prestin activity within the plasma membrane. X_o state is unbound by anion. X_c state is bound by anion but intrinsic voltage sensor charge is not responsive to membrane electric field. Slow, multi-exponential conformational transition to X_d state via X_n state enables voltage sensing of electric field. Depolarization moves positive sensor charge outward, simultaneously resulting in compact state C, which corresponds to cell contraction. Equivalence of α_n and β_n transition rates assures detailed balance of the reaction scheme. To see this figure in color, go online.

larities to the biophysical data, with V_h disparities showing chloride dependence and depolarizing ramps producing larger disparities (Fig. 4 A and B). $K_{1/2}$ values for NLC-derived Q are quantitatively similar to those in OHCs (Fig. 4 C and D), and importantly, stretched exponential behavior of C_m arises during step voltages (Fig. 4 E). To reiterate, these results are not observed with our previous single exponential model (21). Thus, we believe that an intermediate transition with stretched exponential kinetics is required to recapitulate the biophysical data.

To appreciate the impact of prestin's complex behavior on audition, we measured the magnitude and phase of OHC eM at acoustic frequencies. We stimulated cells with a nominal 50 mV peak AC voltage command under whole cell voltage clamp. Such magnitudes allowed us to generate eM magnitudes easily measurable via photodiode with fairly low number of averages to ensure maintenance of patch recording and limit cell damage. Because we were especially interested in phase behavior of the OHC eM, we ensured that phase behavior was not stimulus magnitude dependent (Fig. 5 A). We also determined that phase behavior was not dependent on steady-state turgor pressure, because this may vary among cells (Fig. 5 B). Though turgor pressure did not affect phase, magnitude of eM increased with pressure. Thus, cell magnitudes are reported as relative to lowest frequency response. Fig. 6 shows the average (\pm se; $n = 5$ to 8) magnitude and phase of both measured membrane current (I_m , blue symbols) and eM (red symbols) for two groups of cells under (A) 140 mM chloride and (B) 1 mM chloride conditions. The correspondingly colored solid lines are fits with the *meno presto* model, quantitatively falling within the standard errors for each condition at every frequency. Model parameters are reported in the Methods section. The thick solid green lines depict the membrane voltage magnitudes and phases. The striking observation is that there is a frequency dependent phase lag between V_m and eM, for both low and high chloride conditions, with the lag being significantly larger at several frequencies in the low chloride condition (asterisks in Fig. 7). Furthermore, the eM magnitude roll-off is greater than that of V_m , showing some chloride level dependence. For comparison, the V_m and eM magnitude and phase of a simple fast kinetic model (see Methods) is plotted (eM, red square symbols; V_m , dark green dashed line) and demonstrates neither phase lags nor magnitude disparities between the two. Indeed, the phase and magnitude of biophysical data cannot be fit by such simple models. We conclude that a slow, stretched exponential behavior of prestin generates the disparities between membrane voltage/sensor charge movement and electromotility.

DISCUSSION

Our data show marked uncoupling of OHC eM, voltage sensor charge movement and membrane voltage. The

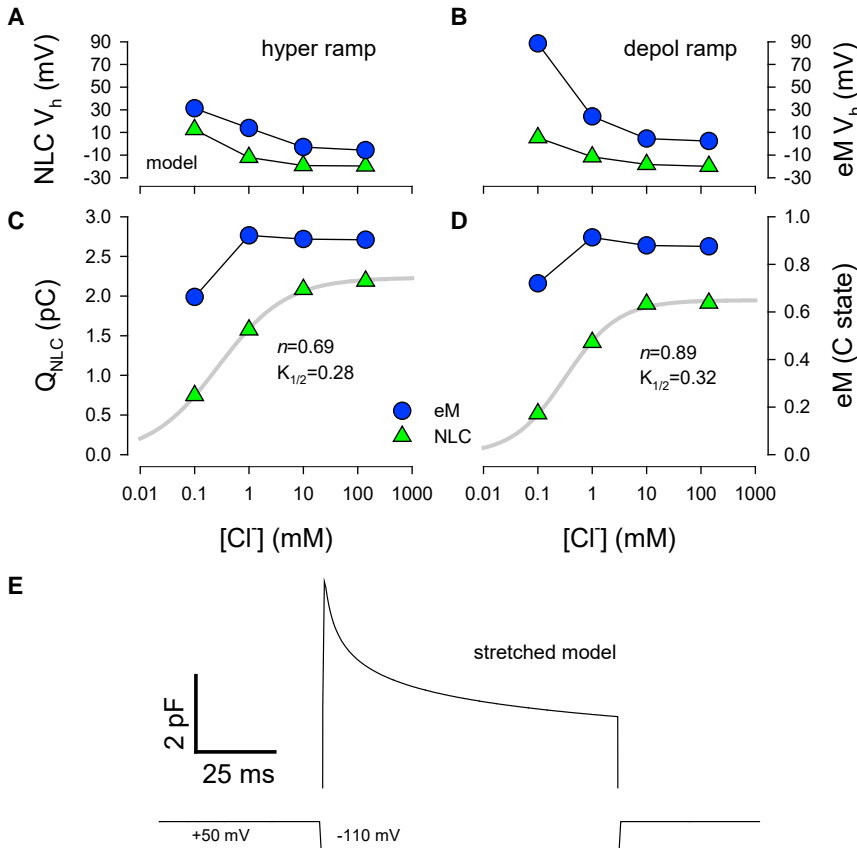


FIGURE 4 Stretched kinetic model recapitulates Boltzmann characteristics of eM and NLC. (A) In the model, NLC V_h disparities arise as chloride levels are decreased, with effects being larger on eM, and larger disparities being observed with depolarizing ramps (B). (C) Q_{NLC} , determined from NLC fits, decreases as chloride levels are lowered. Hill coefficient (n) and $K_{1/2}$ are shown. Contrarily, eM magnitude is little affected. Similar results are obtained with depolarizing ramps (D). (E) Stretched exponential changes in model NLC occur during a constant voltage step from +50 mV to -110 mV. 4 μs clock, C_m inspection resolution 0.512 ms. To see this figure in color, go online.

ensuing disparities in those measures are chloride dependent, with lower chloride levels producing greater uncoupling. In the frequency domain, these disparities display as a differential roll-off in magnitude and a phase lag between membrane voltage and electromotility. The *meno presto* kinetic model that we developed fits the data quantitatively, and illustrates how molecular delays introduced by multi-exponential transitions can influence OHC electro-me-

chanics. A simple model without a stretched-exponential intermediate transition cannot account for our data.

Chloride and the OHC

Prestin is a member of the SLC26 solute carrier family and as such is expected to bear archetypal interactions with anions. Indeed, early experiments on OHC NLC pointed in this

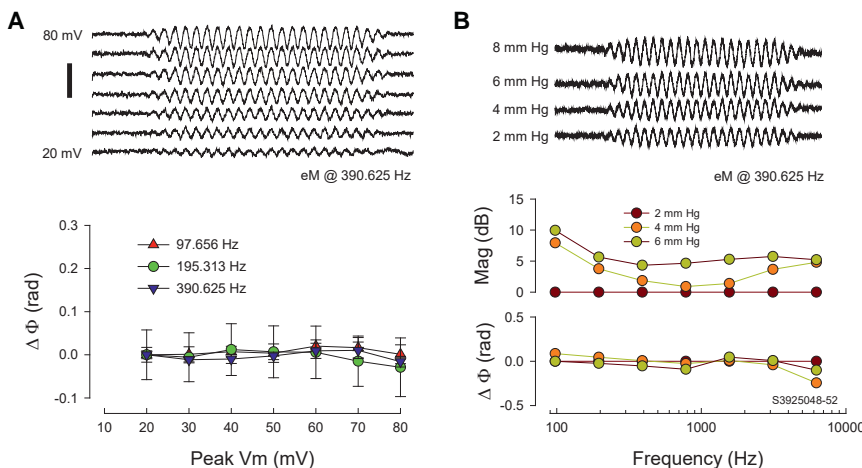


FIGURE 5 Effects of V_m magnitude and turgor pressure on eM phase. (A) Command magnitude was varied from 20 to 80 mV peak at 98, 195, and 391 Hz. Example traces are in top panel; average (\pm se) phase (re: 20 mV response) is plotted in bottom panel. No differences in phase were found. (B) Turgor pressure was varied from 0 to 8 mm Hg via the patch pipette. Though magnitude increased with pressure, phase remains unaffected. Example traces are in top panel (low frequency responses to left of eM response were calibration movements of the image). Note that smart averaging (see Methods) was performed for each trace, hence the different noise levels. An example of frequency dependence is in bottom panel. No changes were observed. Average results for three cells at 390 Hz (mean \pm se @ 4, 6, and 8 re: 2 mm Hg condition) are -0.063 ± 0.02 , -0.055 ± 0.04 , and -0.019 ± 0.06 , respectively. All phase analysis was via FFT. Scale bar: 3 μm . Chloride is 140 mM. To see this figure in color, go online.

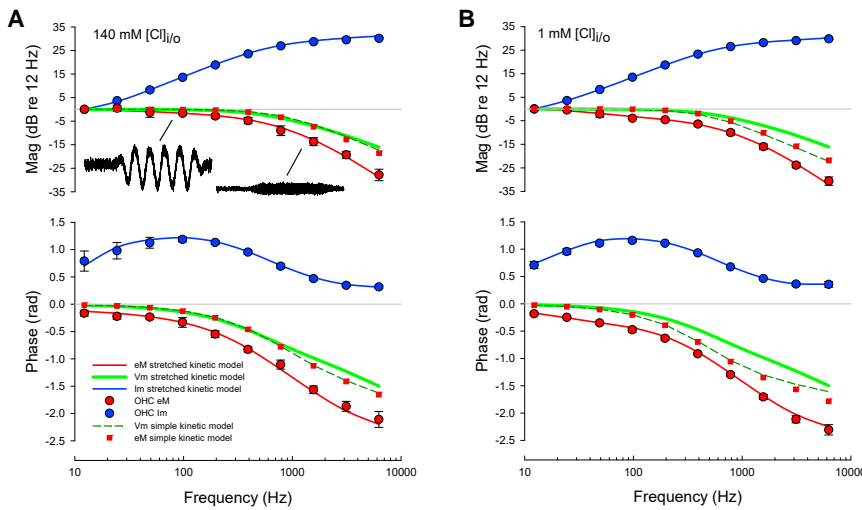


FIGURE 6 Chloride effects on magnitude and phase of simultaneously measured membrane current and eM. High frequency mechanical responses were measured with a photodiode under whole cell voltage clamp. eM waveforms shown are averaged responses to sinusoidal voltage bursts of 98 (1.9 μm pk-pk response) and 1563 Hz. Frequency response was measured up to 6.25 kHz and subsequently analyzed by FFT. Smart averaging in jClamp (see Methods) assured that a minimum number of averages was performed to establish a given signal-to-noise ratio, thereby limiting cell stimulation. Because of robust mechanical response, repeated stimulation can cause loss of cell recording. In these examples, the 98 Hz response was averaged eight times, and the 1563 Hz response was averaged 64 times. (A) 140 mM condition. Fundamental magnitude and phase of OHC I_m (blue) and eM (red) are plotted. Standard errors are given and mostly fall within

symbol size. Solid red and blue lines are model fits (see Methods). The solid green line is the membrane voltage of the patch clamp-kinetic model. Note frequency dependent phase lag between membrane voltage and eM, and faster roll of eM magnitude than membrane voltage. For comparison, a fast simple kinetic model without intermediate transitions is plotted. V_m and eM of that simple model show neither phase nor magnitude differences, as expected for a simple 2-state model of prestin activity. (B) 1 mM chloride condition. Notable differences from (A) include a greater magnitude roll-off in eM vs. V_m and a greater frequency dependent phase lag. The simple model again shows no differences between V_m and eM magnitude and phase. To see this figure in color, go online.

direction. In the mid-1990s, the anion salicylate was shown to interfere with NLC and eM, working intracellularly with a Hill coefficient of 1 (28,29). Additionally, the anionic, lipophilic molecule tetraphenylborate (TPB⁻), unlike its cationic counterpart tetraphenylphosphonium (TPP⁺), modulates NLC (30). Thus it was not totally unexpected that normally residing intracellular anions, including chloride and bicarbonate, were found to influence prestin activity (31). We have amassed evidence that chloride ions modulate prestin in an allosteric-like manner, where intrinsic residue

charge provides for voltage sensing (21,32–37). In some ways, the *meno presto* model, which fashions chloride as an enabler of voltage sensitivity, possesses qualities of an allosteric process whereby binding of a ligand to a remote site (or in response to other biophysical forces) induces a conformation state change that promotes the primary function of the protein (38,39), in our case electromotility. Though the occurrence of anion transport in prestin is a controversial issue (33,40–43), we believe that the slow intermediate transition that we have identified is related to prestin's ancestral transporter legacy.

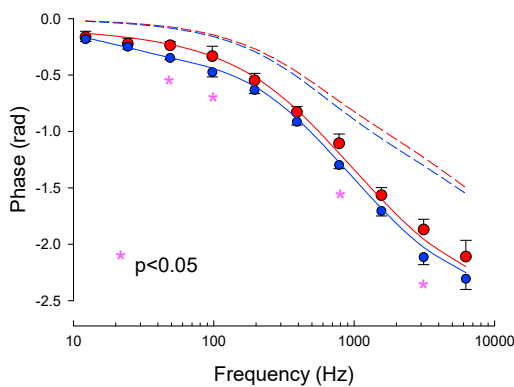


FIGURE 7 Expanded, overlapped plot of phase from high and low chloride conditions. Red symbols are from OHCs with 140 mM Cl intracellular pipette solutions, and blue symbols with 1 mM Cl solutions. Asterisks denote significantly different phases ($p < 0.05$, t -test, 2-tailed). Red dashed line is estimated membrane voltage phase under high chloride condition, and the blue dashed line under the 1 mM Cl condition. Regardless of chloride condition, the stretched exponential behavior of prestin results in phase lags in eM versus membrane voltage. Data from Fig. 6. To see this figure in color, go online.

Coupling between charge movement and electromotility

Our data show an apparent dissociation between voltage sensor charge movement and electromotility. For example, V_h of the two during depolarizing ramps under 0.1 mM chloride conditions can differ by greater than 60 mV, and NLC Q_{max} is reduced by one-third with little effect on eM. The reason for the disparity is the existence of an intermediate transition between chloride binding and mechanical response. The delays afforded by the stretched exponential transition may appear to separate sense and effect, but do not indicate that the two are unrelated. An analogy between voltage-dependent ion channels can be made where the current onset after a step voltage is delayed (44). The greater the number of intermediate states before pore opening, the greater is the delay in current onset. In our case, we observe the mechanical response delayed relative to sensing; however, according to our *meno presto* kinetic model the delay

need not be imposed between charge movements per se and eM (C state occupancy). In fact, in a linked reaction scheme, all transitions (including voltage-independent ones) influence each other (45–47). Thus, what appears to be an event before voltage sensing (chloride binding and an exponential evolution into voltage dependence) does in fact alter the balance of transition rates between states X_d and C, thereby altering V_h during fast ramps. Indeed, the hysteresis and charge immobilization that we initially observed in the Q - V_m response of OHCs (23) and in prestin expressing cells (48) must arise from a process that is not expected of simple fast two-state Boltzmanns, such as previous models of prestin (14–20). Consequently, because of the real complexity of prestin kinetics phase lags between V_m and eM will ensue.

Phase behavior of OHC electromotility

The phase of OHC eM has been studied previously. In 1992, in an effort to confirm voltage vs. current dependence of eM, we measured magnitude and phase in a similar manner to our experiments here (49). We concluded that the phase of eM followed predicted V_m under whole cell voltage clamp. This complemented our previous work showing eM voltage dependence (4). However, whereas there was apparent correspondence between V_m and eM phase, perusal of the phase data in our previous manuscript clearly indicates a significant phase lag in all cells studied. In fact, we had corrected for some phase discrepancies by introducing delays in the fits, and in low frequency data by shifting V_m and eM to overlap (see Fig. 5 A in (49)). Our current work indicates that those delays were actually correcting for the kinetic behavior of prestin. Indeed, our present eM phase data can be approximated by a delay that is inversely proportional to frequency. In this study, unlike our previous work, we did not use series resistance compensation, which can introduce lags in measured phase. Frank et al. (50) measured magnitude and phase of OHC eM using an extracellular microchamber technique, which although allowing for extended frequency perturbation, provides for neither direct membrane voltage control nor measures of membrane current (51). They provided corrected zero lag phase plots that were flat out to tens of kilohertz. Still, to fully account for the frequency response they needed to model the response with an electrical and mechanical component, showing second-order resonant effects to fit their data. Though the microchamber effectively produces a simple capacitive divider for the linear-membrane capacitance, any effects on a frequency-dependent, voltage-dependent and polarity dependent capacitance such as that resulting from OHC sensor charge movement is presently unresolved. Thus, they may have been inadvertently correcting for prestin-based phase characteristics. It will be interesting to see how simulations of the *meno presto* model compare with their data when inserted into a microchamber model. Regardless, the ability to simultaneously fit both actual I_m

magnitude and phase, and eM magnitude and phase, as we have done in this study (and cannot be done with the microchamber approach), is important for accurately modeling eM data. We are confident that the correspondence of our *meno presto* model responses to the measured frequency response of eM, to the measured stretched exponential behavior of NLC, and to the measured chloride dependence of NLC and eM indicate a successful understanding of prestin behavior on OHC electromechanical behavior.

Our identification of substantial eM phase lag leads us to concur with early modelers on its role in cochlear amplification. A preponderance of cochlea models find that a phase lag between receptor potential and eM is required for effective cancellation of viscous drag expected from the cochlea environment (11–13). Indeed, the dependence of phase on prestin's stretched exponential behavior that we find must also be significant, because it augments the phase lag toward the 90 degree requirement of cochlear modelers. We have previously shown that altering perilymphatic chloride levels, which effectively alters intracellular chloride concentration via the lateral membrane chloride conductance, G_{metL} (36), can reversibly modify cochlear amplification (22). Because we have shown here that the magnitude of eM is little affected by chloride level, we conclude that phase characteristics provided by the evolution of chloride-bound prestin into a voltage-enabled state predominantly underlie the OHC's role in contributing to hearing sensitivity and selectivity by cochlear amplification. Furthermore, contrary to all cochlear models, we place a significant component of the phase lag not on cochlear partition super structures, but within the OHC motor itself. Finally, we note that implications of our in vitro observations for in vivo performance, where additional loads may impinge on the OHC requires further exploration. In fact, any biophysical study of hair cells in isolated or explant conditions in the absence of in vivo structures, such as those evaluating electro-mechanics or stereociliary transduction mechanisms, require cochlear modeling to assess physiological impact.

This research was supported by NIH NIDCD grant DC00273 to JSS.

REFERENCES

1. Brownell, W. E., C. R. Bader, ..., Y. de Ribaupierre. 1985. Evoked mechanical responses of isolated cochlear outer hair cells. *Science*. 227:194–196.
2. Kachar, B., W. E. Brownell, ..., J. Fex. 1986. Electrokinetic shape changes of cochlear outer hair cells. *Nature*. 322:365–368.
3. Ashmore, J. F. 1987. A fast motile response in guinea-pig outer hair cells: the cellular basis of the cochlear amplifier. *J. Physiol.* 388:323–347.
4. Santos-Sacchi, J., and J. P. Dilger. 1988. Whole cell currents and mechanical responses of isolated outer hair cells. *Hear. Res.* 35:143–150.
5. Iwasa, K. H. 1993. Effect of stress on the membrane capacitance of the auditory outer hair cell. *Biophys. J.* 65:492–498.

6. Gale, J. E., and J. F. Ashmore. 1994. Charge displacement induced by rapid stretch in the basolateral membrane of the guinea-pig outer hair cell. *Proc. Biol. Sci.* 255:243–249.
7. Kakehata, S., and J. Santos-Sacchi. 1995. Membrane tension directly shifts voltage dependence of outer hair cell motility and associated gating charge. *Biophys. J.* 68:2190–2197.
8. Santos-Sacchi, J., and L. Song. 2014. Chloride and salicylate influence prestin-dependent specific membrane capacitance: support for the area motor model. *J. Biol. Chem.* 289:10823–10830.
9. Zheng, J., W. Shen, ..., P. Dallos. 2000. Prestin is the motor protein of cochlear outer hair cells. *Nature.* 405:149–155.
10. Ashmore, J., P. Avan, ..., B. Canlon. 2010. The remarkable cochlear amplifier. *Hear. Res.* 266:1–17.
11. Geisler, C. D. 1993. A realizable cochlear model using feedback from motile outer hair cells. *Hear. Res.* 68:253–262.
12. Neely, S. T. 1993. A model of cochlear mechanics with outer hair cell motility. *J. Acoust. Soc. Am.* 94:137–146.
13. Markin, V. S., and A. J. Hudspeth. 1995. Modeling the active process of the cochlea: phase relations, amplification, and spontaneous oscillation. *Biophys. J.* 69:138–147.
14. Ashmore, J. F. 1989. Transducer motor coupling in cochlear outer hair cells. In *Mechanics of Hearing*. D. Kemp and J. P. Wilson, editors. Plenum Press, New York, pp. 107–113.
15. Santos-Sacchi, J. 1991. Reversible inhibition of voltage-dependent outer hair cell motility and capacitance. *J. Neurosci.* 11:3096–3110.
16. Homma, K., and P. Dallos. 2011. Evidence that prestin has at least two voltage-dependent steps. *J. Biol. Chem.* 286:2297–2307.
17. Iwasa, K. H. 1994. A membrane motor model for the fast motility of the outer hair cell. *J. Acoust. Soc. Am.* 96:2216–2224.
18. Wang, X., S. Yang, ..., D. Z. He. 2010. Prestin forms oligomer with four mechanically independent subunits. *Brain Res.* 1333:28–35.
19. Dallos, P., R. Hallworth, and B. N. Evans. 1993. Theory of electrically driven shape changes of cochlear outer hair cells. *J. Neurophysiol.* 70:299–323.
20. Santos-Sacchi, J. 1993. Harmonics of outer hair cell motility. *Biophys. J.* 65:2217–2227.
21. Song, L., and J. Santos-Sacchi. 2013. Disparities in voltage-sensor charge and electromotility imply slow chloride-driven state transitions in the solute carrier SLC26a5. *Proc. Natl. Acad. Sci. USA.* 110:3883–3888.
22. Santos-Sacchi, J., L. Song, ..., A. L. Nuttall. 2006. Control of mammalian cochlear amplification by chloride anions. *J. Neurosci.* 26:3992–3998.
23. Santos-Sacchi, J., S. Kakehata, and S. Takahashi. 1998. Effects of membrane potential on the voltage dependence of motility-related charge in outer hair cells of the guinea-pig. *J. Physiol.* 510:225–235.
24. Santos-Sacchi, J. 2004. Determination of cell capacitance using the exact empirical solution of dY/dC_m and its phase angle. *Biophys. J.* 87:714–727.
25. Clark, B. A., R. Hallworth, and B. N. Evans. 1990. Calibration of photodiode measurements of cell motion by a transmission optical lever method. *Pflugers Arch.* 415:490–493.
26. Colquhoun, D., K. A. Dowsland, ..., A. J. Plested. 2004. How to impose microscopic reversibility in complex reaction mechanisms. *Biophys. J.* 86:3510–3518.
27. Santos-Sacchi, J., E. Navarrete, and L. Song. 2009. Fast electromechanical amplification in the lateral membrane of the outer hair cell. *Biophys. J.* 96:739–747.
28. Kakehata, S., and J. Santos-Sacchi. 1996. Effects of salicylate and lanthanides on outer hair cell motility and associated gating charge. *J. Neurosci.* 16:4881–4889.
29. Tunstall, M. J., J. E. Gale, and J. F. Ashmore. 1995. Action of salicylate on membrane capacitance of outer hair cells from the guinea-pig cochlea. *J. Physiol.* 485:739–752.
30. Wu, M., and J. Santos-Sacchi. 1998. Effects of lipophilic ions on outer hair cell membrane capacitance and motility. *J. Membr. Biol.* 166:111–118.
31. Oliver, D., D. Z. He, ..., B. Fakler. 2001. Intracellular anions as the voltage sensor of prestin, the outer hair cell motor protein. *Science.* 292:2340–2343.
32. Song, L., and J. Santos-Sacchi. 2010. Conformational state-dependent anion binding in prestin: evidence for allosteric modulation. *Biophys. J.* 98:371–376.
33. Bai, J. P., A. Surguchev, ..., D. Navaratnam. 2009. Prestin's anion transport and voltage-sensing capabilities are independent. *Biophys. J.* 96:3179–3186.
34. Rybalchenko, V., and J. Santos-Sacchi. 2008. Anion control of voltage sensing by the motor protein prestin in outer hair cells. *Biophys. J.* 95:4439–4447.
35. Song, L., A. Seeger, and J. Santos-Sacchi. 2005. On membrane motor activity and chloride flux in the outer hair cell: lessons learned from the environmental toxin tributyltin. *Biophys. J.* 88:2350–2362.
36. Rybalchenko, V., and J. Santos-Sacchi. 2003. Cl⁻ flux through a non-selective, stretch-sensitive conductance influences the outer hair cell motor of the guinea-pig. *J. Physiol.* 547:873–891.
37. Rybalchenko, V., and J. Santos-Sacchi. 2003. Allosteric modulation of the outer hair cell motor protein prestin by chloride. In *Biophysics of the Cochlea: From Molecules to Models*. A. Gummer, editor. World Scientific Publishing, Singapore, pp. 116–126.
38. Horrigan, F. T., J. Cui, and R. W. Aldrich. 1999. Allosteric voltage gating of potassium channels I. Mslo ionic currents in the absence of Ca²⁺. *J. Gen. Physiol.* 114:277–304.
39. Monod, J., J. Wyman, and J.-P. Changeux. 1965. On the nature of allosteric transitions: a plausible model. *J. Mol. Biol.* 12:88–118.
40. Schaechinger, T. J., and D. Oliver. 2007. Nonmammalian orthologs of prestin (SLC26A5) are electrogenic divalent/chloride anion exchangers. *Proc. Natl. Acad. Sci. USA.* 104:7693–7698.
41. Tang, J., J. L. Pecka, ..., D. Z. He. 2011. Engineered pendrin protein, an anion transporter and molecular motor. *J. Biol. Chem.* 286:31014–31021.
42. Schänzler, M., and C. Fahlke. 2012. Anion transport by the cochlear motor protein prestin. *J. Physiol.* 590:259–272.
43. Mistrik, P., N. Daudet, ..., J. F. Ashmore. 2012. Mammalian prestin is a weak Cl⁻/HCO₃⁻ electrogenic antiporter. *J. Physiol.* 590:5597–5610.
44. Zagotta, W. N., and R. W. Aldrich. 1990. Voltage-dependent gating of Shaker A-type potassium channels in *Drosophila* muscle. *J. Gen. Physiol.* 95:29–60.
45. Colquhoun, D. 1998. Binding, gating, affinity and efficacy: the interpretation of structure-activity relationships for agonists and of the effects of mutating receptors. *Br. J. Pharmacol.* 125:924–947.
46. Lacroix, J. J., A. J. Labro, and F. Bezanilla. 2011. Properties of deactivation gating currents in Shaker channels. *Biophys. J.* 100:L28–L30.
47. Shirokov, R. 2011. What's in gating currents? Going beyond the voltage sensor movement. *Biophys. J.* 101:512–514, discussion 515–516.
48. Santos-Sacchi, J., W. Shen, ..., P. Dallos. 2001. Effects of membrane potential and tension on prestin, the outer hair cell lateral membrane motor protein. *J. Physiol.* 531:661–666.
49. Santos-Sacchi, J. 1992. On the frequency limit and phase of outer hair cell motility: effects of the membrane filter. *J. Neurosci.* 12:1906–1916.
50. Frank, G., W. Hemmert, and A. W. Gummer. 1999. Limiting dynamics of high-frequency electromechanical transduction of outer hair cells. *Proc. Natl. Acad. Sci. USA.* 96:4420–4425.
51. Dallos, P., and B. N. Evans. 1995. High-frequency motility of outer hair cells and the cochlear amplifier. *Science.* 267:2006–2009.

Molecular Biophysics:
Chloride and Salicylate Influence
Prestin-dependent Specific Membrane
Capacitance: SUPPORT FOR THE AREA
MOTOR MODEL

MOLECULAR
BIOPHYSICS



Joseph Santos-Sacchi and Lei Song
J. Biol. Chem. 2014, 289:10823-10830.
doi: 10.1074/jbc.M114.549329 originally published online February 19, 2014

Access the most updated version of this article at doi: [10.1074/jbc.M114.549329](https://doi.org/10.1074/jbc.M114.549329)

Find articles, minireviews, Reflections and Classics on similar topics on the [JBC Affinity Sites](http://www.jbc.org/).

Alerts:

- [When this article is cited](#)
- [When a correction for this article is posted](#)

[Click here](#) to choose from all of JBC's e-mail alerts

This article cites 39 references, 16 of which can be accessed free at
<http://www.jbc.org/content/289/15/10823.full.html#ref-list-1>

Chloride and Salicylate Influence Prestin-dependent Specific Membrane Capacitance

SUPPORT FOR THE AREA MOTOR MODEL*

Received for publication, January 10, 2014, and in revised form, February 9, 2014. Published, JBC Papers in Press, February 19, 2014, DOI 10.1074/jbc.M114.549329

Joseph Santos-Sacchi^{‡§¶1} and Lei Song[‡]

From the Departments of [‡]Surgery (Otolaryngology), [§]Neurobiology, and [¶]Cellular and Molecular Physiology, Yale University School of Medicine, New Haven, Connecticut 06510

Background: The SLC26a5 outer hair cell motor drives electromechanical behavior of this sensory/effector cell.

Results: A kinetic model fits the combined effects of salicylate and chloride on prestin-associated membrane capacitance.

Conclusion: Data support a theory whereby prestin differentially changes area state upon binding of chloride and salicylate.

Significance: The model of prestin activity points to the molecular underpinnings of electromotility in outer hair cells.

The outer hair cell is electromotile, its membrane motor identified as the protein SLC26a5 (prestin). An area motor model, based on two-state Boltzmann statistics, was developed about two decades ago and derives from the observation that outer hair cell surface area is voltage-dependent. Indeed, aside from the nonlinear capacitance imparted by the voltage sensor charge movement of prestin, linear capacitance (C_{lin}) also displays voltage dependence as motors move between expanded and compact states. Naturally, motor surface area changes alter membrane capacitance. Unit linear motor capacitance fluctuation (δC_{sa}) is on the order of 140 zeptofarads. A recent three-state model of prestin provides an alternative view, suggesting that voltage-dependent linear capacitance changes are not real but only apparent because the two component Boltzmann functions shift their midpoint voltages (V_H) in opposite directions during treatment with salicylate, a known competitor of required chloride binding. We show here using manipulations of nonlinear capacitance with both salicylate and chloride that an enhanced area motor model, including augmented δC_{sa} by salicylate, can accurately account for our novel findings. We also show that although the three-state model implicitly avoids measuring voltage-dependent motor capacitance, it registers δC_{sa} effects as a byproduct of its assessment of C_{lin} , which increases during salicylate treatment as motors are locked in the expanded state. The area motor model, in contrast, captures the characteristics of the voltage dependence of δC_{sa} , leading to a better understanding of prestin.

The piezoelectric-like motor molecule SLC26a5 (prestin) underlies the ability of OHC² to enhance hearing (1–3). This boost in performance is driven by a voltage-dependent mechanical response, termed somatic electromotility (4–6).

* This work was supported, in whole or in part, by National Institutes of Health Grant NIDCD DC00273 (to J. S. S.).

¹ To whom correspondence should be addressed: Dept. of Surgery (Otolaryngology), Yale University School of Medicine, BML 224, 333 Cedar St., New Haven, CT 06510. Tel.: 203-785-5407; Fax: 203-737-2502; E-mail: joseph.santos-sacchi@yale.edu.

² The abbreviations used are: OHC, outer hair cell; NLC, nonlinear capacitance; F, farads.

Associated with the mechanical response is a bell-shaped nonlinear capacitance (NLC), which results from the voltage sensor activity of the motor (7, 8). Long before the molecular identification of the motor, two-state Boltzmann models of the motor incorporating state-dependent surface areas were developed (9–12). These were founded on experimental evidence that surface area in the OHC is voltage-dependent (13). In support of these models, we measured changes in specific membrane capacitance that corresponded to the distribution of motors, evidencing an increase in linear capacitance as more motors were driven into the expanded state by hyperpolarization (14). Membrane capacitance necessarily depends on membrane surface area and/or associated changes in membrane thickness. A derived equation based on that observation, termed the two-state C_{sa} model equation, is far superior in fitting NLC data than is a simple two-state one. Recently, Homma and Dallos (15) proposed a three-state Boltzmann model that rivals the two-state C_{sa} model in the data-fitting precision of salicylate-treated OHCs, but that additionally challenges the existence of a voltage-dependent area change accompanying the conformational transitions of prestin. Here we provide further evidence that an area motor model better describes the biophysical behavior of the motor. Through modeling, we show how salicylate competition with chloride may result in state-dependent modification of specific membrane capacitance.

EXPERIMENTAL PROCEDURES

The methods for single hair cell recordings were the same as described previously in detail (16). Hartley albino guinea pigs were sacrificed with halothane. Temporal bones were excised, and the top three turns of the cochleae were dissected for enzyme treatment (0.5 mg/ml dispase I, 10–12 min). Individual outer hair cells were isolated by gentle trituration. Isolated single outer hair cells were then studied under whole cell voltage clamp and were held at 0 mV to eliminate the electrical drive for chloride across the lateral membrane. A custom made Y-tube perfusion system was used to deliver experimental solutions to isolated OHCs. The base extracellular solution contained, in mM, 140 NaCl, 2 CaSO₄, 1.2 MgSO₄ and 10 Hepes. Chloride concentration was adjusted from 1 to 140 mM by substituting chloride with gluconate. Final solutions were adjusted to ~300

Active Surface Area of SLC26a5

mOSM with D-glucose and adjusted to pH 7.2–7.3 with NaOH. Pipette solutions (same as extracellular solution except with the addition of 10 mM EGTA) contained chloride ranging from 1 to 140 mM. The extracellular perfusion solution (1–140 mM chloride) also contained graded concentrations of salicylate (1 μ M to 10 mM).

Nonlinear capacitance was measured using a continuous high resolution (2.56-ms sampling) two-sine stimulus protocol (10-mV peak at both 390.6 Hz and 781.2 Hz) superimposed onto a voltage ramp from –150 to +140 mV at a clock sample period of 10 μ s (17, 18). Capacitance data were fit to the first derivative of a two-state Boltzmann function with an additional component describing the changes in specific membrane capacitance generated by motor state transitions (14). This equation is termed the two-state C_{sa} model equation.

$$C_m = Q_{\max} \frac{ze}{kT} \frac{b}{(1+b)^2} + \frac{\Delta C_{sa}}{(1+b^{-1})} + C_0 \quad (\text{Eq. 1})$$

where

$$b = \exp\left(\frac{-ze(V_m - V_h)}{kT}\right) \quad (\text{Eq. 2})$$

Q_{\max} is the maximum nonlinear charge moved, V_h is voltage at peak capacitance or equivalently, at half-maximum charge transfer, V_m is membrane potential, z is valence, e is electron charge, k is Boltzmann's constant, and T is absolute temperature. C_0 is defined as the capacitance of the membrane when all motors are in their compact state, the minimum membrane capacitance; ΔC_{sa} is the maximum increase in capacitance that occurs when all motors change from compact to expanded state, each motor contributing a unit response of δC_{sa} . Voltage-dependent NLC was calculated from estimates of Q_{\max} , namely $NLC = Q_{\max}/(4kT/ze)$. The number of motors is: $N = Q_{\max}/ze$.

Alternatively, NLC was fit with the three-state model equation, possessing two sets of Boltzmann parameters ($z_1, V_{h1}, z_2, V_{h2}, N = N_1 + N_2$) of Homma and Dallos (15).

$$C_m = NkT \times \frac{\alpha_1^2 K_{12} + (\alpha_1 + \alpha_2)^2 K_{12} K_{23} + \alpha_2^2 K_{12}^2 K_{23}}{(1 + K_{12} + K_{12} K_{23})^2} + C_0 \quad (\text{Eq. 3})$$

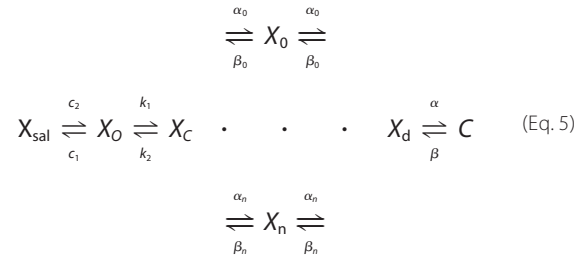
where

$$\alpha_1 = \frac{z_1 e}{kT}, \alpha_2 = \frac{z_2 e}{kT}, K_{12} = \exp(V_m - V_{h1}), K_{23} = \exp(V_m - V_{h2}) \quad (\text{Eq. 4})$$

Fits and plots were made in SigmaPlot. Data points from published plots were extracted using Plot Digitizer version 2.0 (University of South Alabama).

A kinetic model describing prestin activity, which we used previously to explain chloride-dependent coupling between prestin charge movement and electromotility (19) and the effects of thermal jumps on prestin voltage dependence (20), was extended to provide competitive binding of salicylate to the chloride binding site of the protein. The model was assessed using MATLAB Simulink in conjunction with jClamp. The new

model, which includes a stretched exponential transition that accounts for stretched exponential behavior of NLC (21) and accurately reproduces magnitude and phase behavior of the electromotility frequency response,³ is presented below with the new salicylate binding component.



X_{sal} state is bound by salicylate. X_o state is unbound by anion. X_c state is bound by chloride, but intrinsic voltage sensor charge is not responsive to the membrane electric field. A slow, multiexponential conformational transition to X_d state via X_n states enables voltage sensing within the electric field. Depolarization moves positive sensor charge outward, simultaneously resulting in compact state C , which corresponds to cell contraction. The differential equations are

$$\frac{dX_{\text{sal}}}{dt} = X_o \times [\text{Sal}]c_1 - X_{\text{sal}} \times c_2 \quad (\text{Eq. 6})$$

$$\frac{dX_o}{dt} = X_c \times k_2 + X_{\text{sal}} \times c_2 - X_o \times [\text{Cl}^-]k_1 - X_o \times [\text{Sal}]c_1 \quad (\text{Eq. 7})$$

$$\frac{dX_c}{dt} = X_o \times [\text{Cl}^-]k_1 + \sum_{n=0}^{25} X_n \times \beta_n - X_c \times k_2 - \sum_{n=0}^{25} X_c \times \alpha_n \quad (\text{Eq. 8})$$

$$\frac{dX_n}{dt} = X_c \times \alpha_n + X_d \times \beta_n - X_n \times \alpha_n - X_n \times \beta_n \quad (\text{Eq. 9})$$

$$\frac{dX_d}{dt} = C \times \beta + \sum_{n=0}^{25} X_n \times \alpha_n - X_d \times \alpha - \sum_{n=0}^{25} X_d \times \beta_n \quad (\text{Eq. 10})$$

$$\frac{dC}{dt} = X_d \times \alpha - C \times \beta \quad (\text{Eq. 11})$$

where $\alpha_n = A \times (\exp(-n))^w$, $w = 0.6$, $A = 2.5 \times 10^4$ for $N = 0.25$, $\beta_n = \alpha_n$, $k_1 = 1.5 \times 10^5$, $k_2 = k_1 \times \text{Clk}_{d^*}$, $\text{Clk}_d = 0.012$, $c_1 = 3 \times 10^8$, $c_2 = c_1 \times \text{Salk}_{d^*}$, $\text{Salk}_d = 30 \times 10^{-7}$, $\alpha = 1.3 \times 10^6 \times \exp((z \times F \times V_m)/(2 \times R \times T))$, $\beta = 7.7 \times 10^4 \times \exp((-z \times F \times V_m)/(2 \times R \times T))$, $z = 0.7$, $n_{\text{Pres}} = 25 \times 10^6$, or in the case of Fig. 5, N determined from fits to the biophysical data. The

³ Santos-Sacchi, J. and Song, L. *Abstracts of the Association for Research in Otolaryngology*, 2014.

equivalence of α_n and β_n transition rates assures detailed balance of the reaction scheme (22).

jClamp provides an automation link to MATLAB, which allows voltage stimuli to be delivered to and current responses to be obtained from Simulink models. Thus, biophysical and model data are analyzed exactly the same. Solutions were obtained with the ode45 (Dormand-Prince) solver at a fixed absolute tolerance of 10^{-6} . The *meno presto* model was interfaced to jClamp via a model of the patch clamp amplifier and OHC. The linear component of the patch-cell model was composed of R_s in series with a parallel combination of R_m and C_{lin} . Given the above *meno presto* model parameters, model results were obtained with patch clamp parameters of $R_s = 6.1$ megohms, $R_m = 275$ megohms, and $C_0 = 23$ pF. To reiterate, the exact same voltage stimuli and exact same analysis of model data were performed as with the biophysical data. Model responses were allowed to reach steady state prior to ramp perturbations.

RESULTS

We previously showed that the effectiveness of salicylate inhibition of NLC is chloride-dependent (3). Fig. 1A shows NLC traces of an OHC with 140 mM intracellular chloride. Increasing concentrations (0.001, 0.01, 0.1, 1, 10 mM) of salicylate reduce the magnitude of NLC and shift its voltage dependence in the depolarizing direction. The traces were fit to the two-state C_{sa} model equation (Equation 1) and the three-state model equation (Equation 3) (see "Experimental Procedures"). Note that each fit is indistinguishable without statistical analysis. In fact, Homma and Dallos (15) found that Equation 1 gave a $4\times$ better fit. Nevertheless, it is not the quality of the fit that is of concern here; it is the underlying mechanism. In Fig. 1B, the 0.1, 1, and 10 mM traces are replotted with the subcomponents of the two equations shown. In the *left panels*, two *independent* Boltzmann functions underlie the full fit. In the *right panels*, a single Boltzmann function and a *coupled* sigmoidal function, sharing the same V_n and number of motors, contribute to the full fit. Within the data region, each fit is quite reasonable. However, whereas the two-state C_{sa} fit shows an increasing membrane surface area/reduced membrane thickness, reflected in C_m , as the motors redistribute to the extended state, the three-state fit indicates no such changes. Similar results are found when intracellular chloride is set to 5 mM (Fig. 1, C and D). Note, however, that with reduced chloride there is a different dose-dependent effect of salicylate on ΔC_{sa} as compared with the 140 mM chloride condition. As with the 140 mM chloride data, the three-state model shows no differences in linear capacitance at voltage polarity extremes. A more telling evaluation of the two models is shown in Fig. 2, where both equations are used to fit the data of Santos-Sacchi and Navarrete (14) who utilized extreme voltages of ± 200 mV to measure NLC. Those fits indicate that one Boltzmann component of the three-state model may actually serve as a surrogate for the sigmoidal component of the two-state C_{sa} model equation. Below we evaluate the interaction of salicylate and chloride effects on prestin to explore the appropriateness of the two models.

To help understand the effects of salicylate, we extended a kinetic model of prestin we are currently working on, termed

the *meno presto* model because it includes a slow, stretched exponential intermediate transition between chloride binding and the voltage-enabled state (Fig. 3). We have used this model previously to explain chloride-dependent uncoupling between prestin charge movement and electromotility (19) and the effects of thermal jumps on prestin voltage dependence (20). Because we will use this model to evaluate the interaction of salicylate and chloride on ΔC_{sa} , we first confirm its ability to reproduce known chloride-dependent salicylate effects on NLC (3). Fig. 4A shows the model results illustrating that the IC_{50sal} reduces when intracellular chloride is reduced. Five publications report on salicylate effects on NLC (all reporting at least the 140 mM chloride condition), and from those we estimate IC_{50sal} by fitting Hill functions with the coefficient n set to 1 (Fig. 4B), as experimentally determined (23). Three values arise from studies on guinea pigs (3, 23, 24), being 1.67, 1, and 1.42 mM; a value of 0.64 mM comes from rat prestin-transfected cells (25), and a value of 0.22 mM comes from mouse OHCs (15). These values are plotted in Fig. 4C along with the extended measures of IC_{50sal} reported in Santos-Sacchi *et al.* (3). The model IC_{50sal} data (*open white triangles*) from Fig. 4A shows chloride dependence similar to our previous biophysical data (*filled black circles*) (3), indicating that our model may be useful in characterizing any chloride-dependent behavior of ΔC_{sa} .

Homma and Dallos (15) uncovered behavior of ΔC_{sa} that they believed was incompatible with our two-state C_{sa} area motor model (see their Fig. 2H). They found that ΔC_{sa} increases with salicylate concentration before it decreases. Because we determined that the conformational switch of the motor from compact to expanded state results in a 130 zF/motor (δC_{sa}) increase in C_m (23), they reasoned that as salicylate removed motors from the active pool there should only be a decrease in ΔC_{sa} with increasing salicylate concentration. This reasoning disregards our published observation that salicylate increases ΔC_{sa} above that measured in its absence. Thus, we contend that when salicylate binds to a motor, either its surface area is greater than an unbound expanded motor and/or the membrane thickness is reduced when bound. We and others have shown that salicylate in the absence of prestin has no measurable effects on membrane capacitance (23, 24). Homma and Dallos (15) also show this. Clearly, then, the salicylate effect results from interaction with prestin. Fig. 5A shows the effects of salicylate with 140 mM intracellular chloride on ΔC_{sa} . The data have been normalized by motor number, N , in the absence of salicylate for comparisons ($\Delta C_{sa}/N_{sal=0}$). A non-monotonic increase followed by a decrease is similar to the Homma and Dallos data (15). At this chloride concentration, in the absence of salicylate, a unit δC_{sa} per motor is calculated to be 141 zF, similar to our previous estimates (14). In our model, to account for the salicylate dose-response function, each salicylate-bound motor unit δC_{sa} had to be factored by 1.9 (*solid line*), in line with our previous observations (14). We also observed similar behavior when chloride levels were reduced; however, the salicylate dose-response function shifted leftward along the concentration axis with reduced chloride. With a fixed unit δC_{sa} scale factor of 1.9 for salicylate-bound motors, the model response also shifted when chloride was reduced, and exhibited appropriate response magnitude.

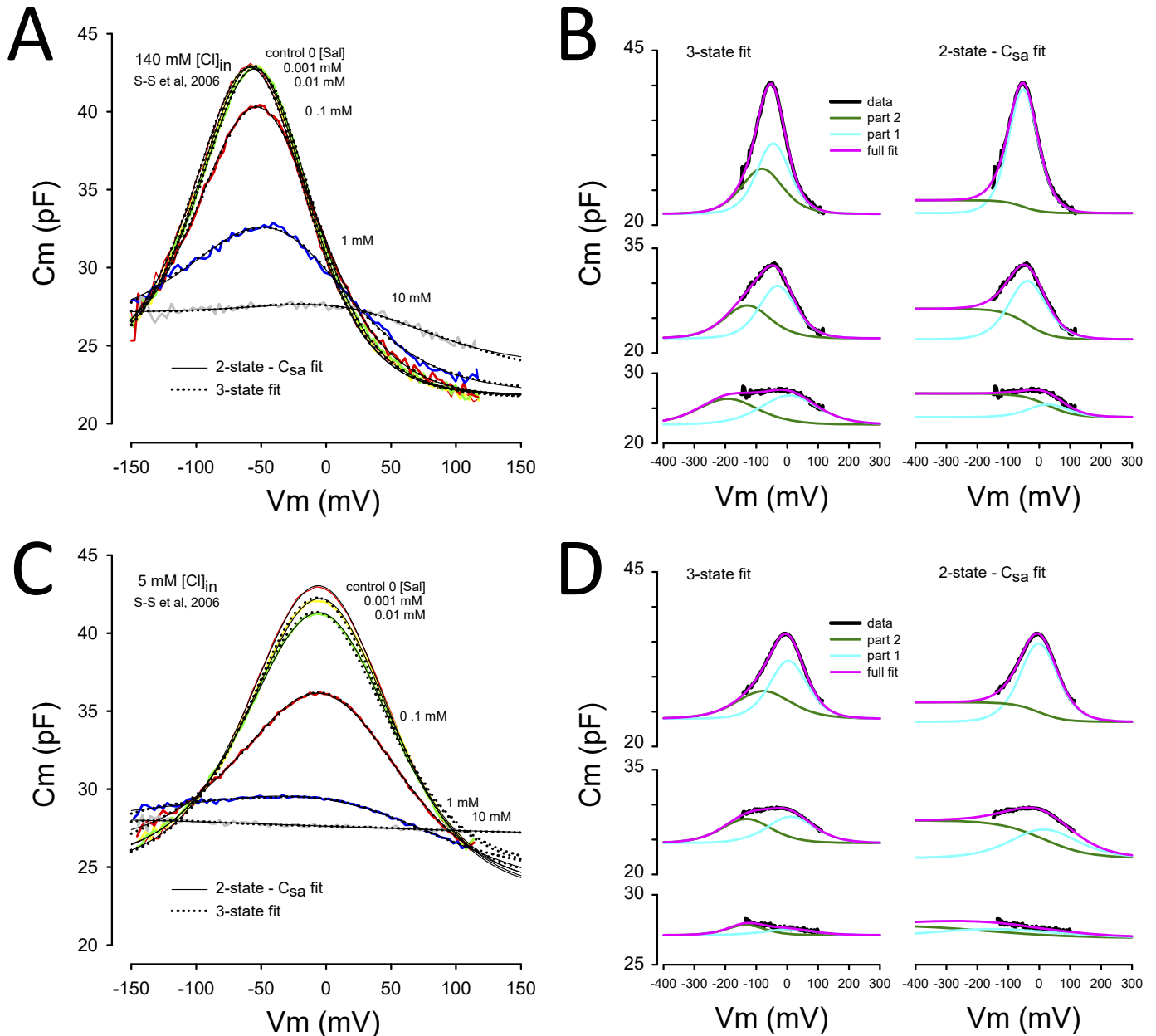


FIGURE 1. Model-dependent differences in salicylate effects on the NLC of prestin. Contributions of area fluctuations in prestin differ with the three-state model of Homma and Dallos (15) or the two-state C_{sa} model of Santos-Sacchi and Navarrete (14). **A**, data from Fig. 1B of Santos-Sacchi *et al.* (3) (S-S *et al.*, 2006) showing effects of different salicylate concentrations on NLC at an intracellular chloride level of 140 mM. Each trace was fit with both models, each providing near equivalent fit quality. **B**, details of fits by each model for the 0.1, 1, and 10 mM salicylate conditions, *top*, *middle*, and *bottom* panels, respectively. Each model is composed of two components, labeled *part 1* and *part 2*. Essentially, the sum of each component produces the full fit. Although the two-state model gives an offset in C_m at hyperpolarized levels, the three-state model does not. **C**, data from Fig. 1A of Santos-Sacchi *et al.* (3) with an intracellular chloride level of 5 mM showing an enhanced effect of salicylate. As above, fits of both models were made, both showing good correspondence. Some small differences are noted at depolarized levels. **D**, fit components of both models. Again, an offset in C_m arises at hyperpolarized levels for the two-state model, but not the three-state model. Note that for each chloride condition, the offset in C_m (ΔC_{sa}) increases and then decreases with increasing chloride concentration.

We previously showed that the effects of externally applied salicylate (1 mM) on NLC required about 60 s to reach steady state (23). Because Homma and Dallos (15) used a 1-min perfusion to change salicylate from 0 to 1.5 mM, during which time they evaluated NLC, steady state effects were only achieved before and after perfusion. For this reason, we evaluate the data from their supplemental Fig. S3A (140 mM chloride, intracellular) where salicylate concentration was set definitively. Interestingly, those data (Fig. 5B) required that the salicylate K_d

($Salk_d$) or equivalently the rate constant c_2 of our model be reduced by an order of magnitude, in line with their more sensitive estimated IC_{50sal} (Fig. 4B). Additionally, the δC_{sa} scale factor had to be increased to 3. It must be emphasized that the $Salk_d$ and Clk_d in our model do not necessarily correspond in magnitude to IC_{50} values of NLC effects that we and others have measured, because through our experiments on NLC we neither inspect these directly, nor should IC_{50} values necessarily agree with K_d values in other than a simple two-state system.

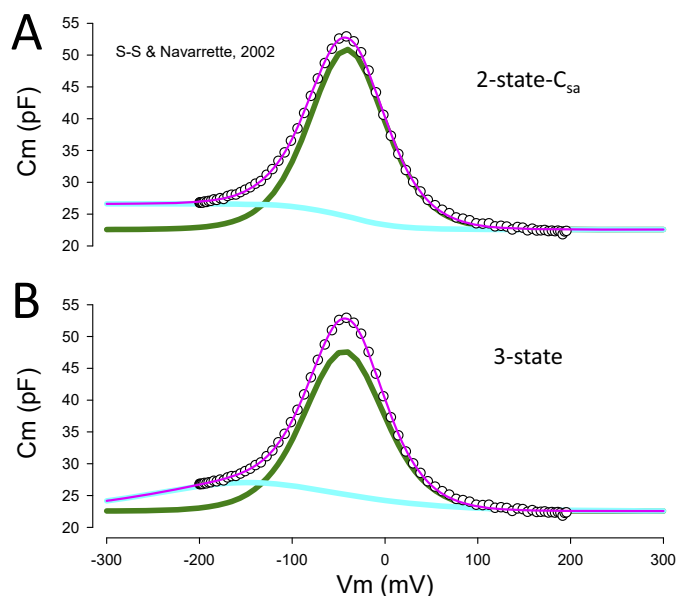


FIGURE 2. **Two-state C_{sa} and three-state fits of NLC determined over a very wide voltage range.** *A*, two-state C_{sa} fit, showing underlying components. *B*, three-state fit with underlying components. Note that the unconstrained fit of the three-state equation found one component V_h that effectively placed a sigmoidal-like C_m function at the hyperpolarized extreme, mimicking the two-state C_{sa} model's constrained fit of its single V_h . Data are from Santos-Sacchi and Navarrete (14) (S-S. & Navarrete, 2002).

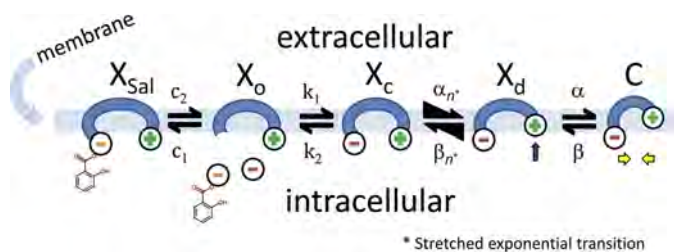


FIGURE 3. **Extension of the stretched kinetic model of prestin activity to provide salicylate competition with chloride.** X_{sal} state is bound by salicylate. X_o state is unbound by anion. X_c state is bound by chloride, but intrinsic voltage sensor charge is not responsive to membrane electric field. Slow, multiexponential conformational transition to X_d state via X_n states enables voltage sensing of electric field. The α_n and β_n transitions are multiexponential (see "Experimental Procedures"). Depolarization moves positive sensor charge outward, simultaneously resulting in compact state C, which corresponds to cell contraction. Equivalence of α_n and β_n transition rate constants assures detailed balance of the reaction scheme.

The utilized k_d values, however, produce IC_{50} values for NLC that are consistent with our experimental observations.

Finally, we investigated the behavior of C_{lin} . For the two-state C_{sa} model equation, C_{lin} is the linear capacitance, which is the minimum capacitance at extreme depolarized voltages where all motors are in the compact state. For the three-state model equation, C_{lin} is equivalently the capacitance at either hyperpolarized or depolarized extremes. Similar to Homma and Dallos (15), we find a monotonic increase in C_{lin} in our data when fit with the two-state C_{sa} equation (Fig. 5C). It reaches an asymptote when ΔC_{sa} vanishes, that is, when salicylate binds to all motors and locks them in the expanded state. Thus, C_{lin} tells about the state residence of motors, just as ΔC_{sa} does; the measures are reciprocal. Importantly, just as ΔC_{sa} is dependent on the interaction of salicylate and chloride (Fig. 5A), so too is C_{lin} (Fig. 5C). In Fig. 5D, we plot C_{lin} that arises from three-state fits

of our model data that explicitly incorporate motor-generated δC_{sa} . As expected, and in agreement with Homma and Dallos (15), C_{lin} rises monotonically to an asymptote, until all motors are in the salicylate-bound extended state. Unfortunately, Homma and Dallos (15) only report on salicylate effects on C_{lin} using a 1-min perfusion of extracellular salicylate, so we cannot unequivocally determine intermediate concentrations of salicylate from their data (see their Fig. 2C) except at the onset of perfusion (zero salicylate) and at the steady state end of perfusion (1.5 mM salicylate). Thus, we only plot those two points, and they lie on our model prediction curve. Thus, although the three-state model cannot identify the voltage-dependent nature of prestin-associated capacitance change, it nevertheless reports on it as C_{lin} .

DISCUSSION

The area motor model of OHC motor activity was based on biophysical evidence that OHC surface area increases upon hyperpolarization (13). Given the constraints of a cylindrically shaped cell and a constant cytoplasmic volume, alterations in surface area result in cell length changes that correspond to measured characteristics of OHC electromotility (9, 11). Although various models of OHC electromechanical activity have arisen, including electro-osmosis (26, 27) and membrane flexo-electricity (28), several arguments against them have been made (29–31), chief among them the identification of the voltage-dependent motor protein prestin (1). Considering the vast number of prestin motors embedded in the OHC lateral membrane, whose membrane residence contributes markedly to OHC surface area (32, 33), unit area changes, ranging from 0.4 to 8 nm² (9, 11, 12, 34, 35), will have substantial effects on membrane surface area. Linear membrane capacitance is expected to change when either membrane surface area or associated changes in membrane thickness occur.

Recently, Homma and Dallos (15) have developed a three-state model of prestin activity, which challenges those earlier area motor models. In their model, no changes occur in linear capacitance at extreme hyperpolarizations or depolarizations despite very nice fits of NLC data within a restricted voltage range. In contrast, fits with the two-state C_{sa} model equation (14) predict that linear capacitance increases when motors redistribute into the expanded state, reaching an asymptote, ΔC_{sa} , at extreme hyperpolarizations where all motors reside in the expanded state. There are two reasons why Homma and Dallos (15) championed their new model over the area model, despite a better fit by the latter model. First, they observed that when fitting with the two-state C_{sa} model equation there is a non-monotonic change in ΔC_{sa} as salicylate concentration rises, an increase followed by a decrease. It was assumed that salicylate simply removes motors from the active pool, and thus motor contribution to area changes should monotonically decrease. However, we previously showed that salicylate increases ΔC_{sa} above that measured in its absence (14), implying that salicylate-bound motors are augmented in surface area and/or decrease membrane thickness. To be sure, we and others have shown that salicylate in the absence of prestin has no measurable effects on membrane capacitance (15, 23, 24). Consequently, when we use our new *meno presto* model incorpo-

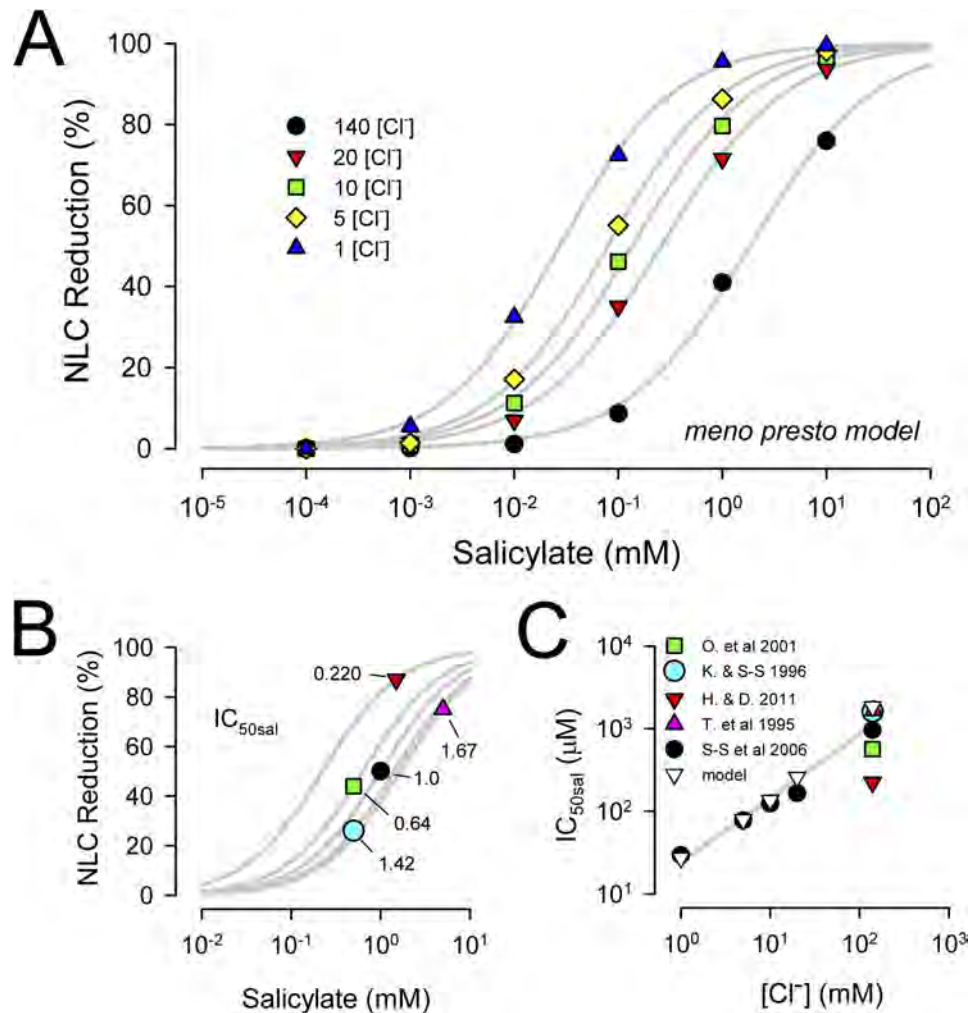


FIGURE 4. Model results of salicylate effect on NLC correspond to biophysical data. *A*, model predicts chloride dependence of salicylate effects, showing that reduced IC_{50sal} as chloride is lowered, as determined experimentally by Santos-Sacchi *et al.* (3) (see their Fig. 2). *B*, comparison of IC_{50sal} from different studies. Because only one study fully evaluated the chloride dependence of IC_{50sal} , IC_{50sal} was estimated by fitting a Hill function through the single data points obtained at 140 mM chloride with the Hill slope, n , fixed at 1, as experimentally determined (3). Biophysical data points were from guinea pig OHCs (Tunstall *et al.* (24), extracted from their Fig. 5C; Kakehata and Santos-Sacchi ((24)), extracted from their Fig. 1C; Santos-Sacchi *et al.* (3), extracted from their Fig. 2); rat prestin transfected HEK cells (Oliver *et al.* (25), extracted from their Fig. 5b); and mouse OHCs (Homma and Dallos (15), extracted from their Fig. 2). *C*, comparison between model and biophysical data shows that the model recapitulates biophysical data. Straight line fit is through model points. Legend: O. *et al.* 2001, Oliver *et al.* (25); K. & S-S 1996, Kakehata and Santos-Sacchi ((24)); H. & D. 2001, Homma and Dallos (15); T. *et al.* 1995, Tunstall *et al.* (24); S-S *et al.* 2006, Santos-Sacchi *et al.* (3).

rating salicylate effects on the motor, we satisfactorily fit the non-monotonic ΔC_{sa} behavior caused by salicylate. Furthermore, we show that this non-monotonic biophysical behavior varies with chloride level, with the model capable of describing the chloride dependence. Curiously, the three-state model accurately identifies a biophysical change in linear capacitance that is salicylate-dependent, which is precisely expected of that model should surface area increase due to increasing residence of prestin in the expanded state. Thus, although that model is built to ignore the voltage-dependent surface area changes due to prestin, it unavoidably detects that surface area change as a voltage-independent one.

The other reason why Homma and Dallos (15) favor their three-state model is that the coupling between sensor charge movement and electromotility is not tight, with zero charge extrapolations giving non-zero mechanical responses, regardless of the model equation. We previously observed uncoupling between sensor charge and electromotility (23, 36, 37). Indeed,

we had shown that salicylate even at 10 mM, whereas nearly abolishing NLC, had much less of an effect on electromotility (23). Recently, we determined that the discrepancy between charge movement, measured with the dual sine admittance approach (17, 18) (also coded into jClamp), and electromotility is chloride-dependent (19), and thus, considering its competition with chloride, salicylate-dependent. Furthermore, we showed that a model incorporating slow intermediate kinetics between chloride binding and a two-state Boltzmann process substantially predicted disparities between sensor charge and electromotility (19). The *meno presto* model presented here, which integrates characteristics of the two-state C_{sa} model, possesses this capability as well. It should be noted that the three-state model, as is, can neither reproduce this result nor generate stretched exponential kinetics that is evident in OHC NLC (18, 21, 39) and prestin-transfected cell NLC (40). The *meno presto* model exhibits stretched exponential kinetics in capacitance measures similar to biophysical observations. One

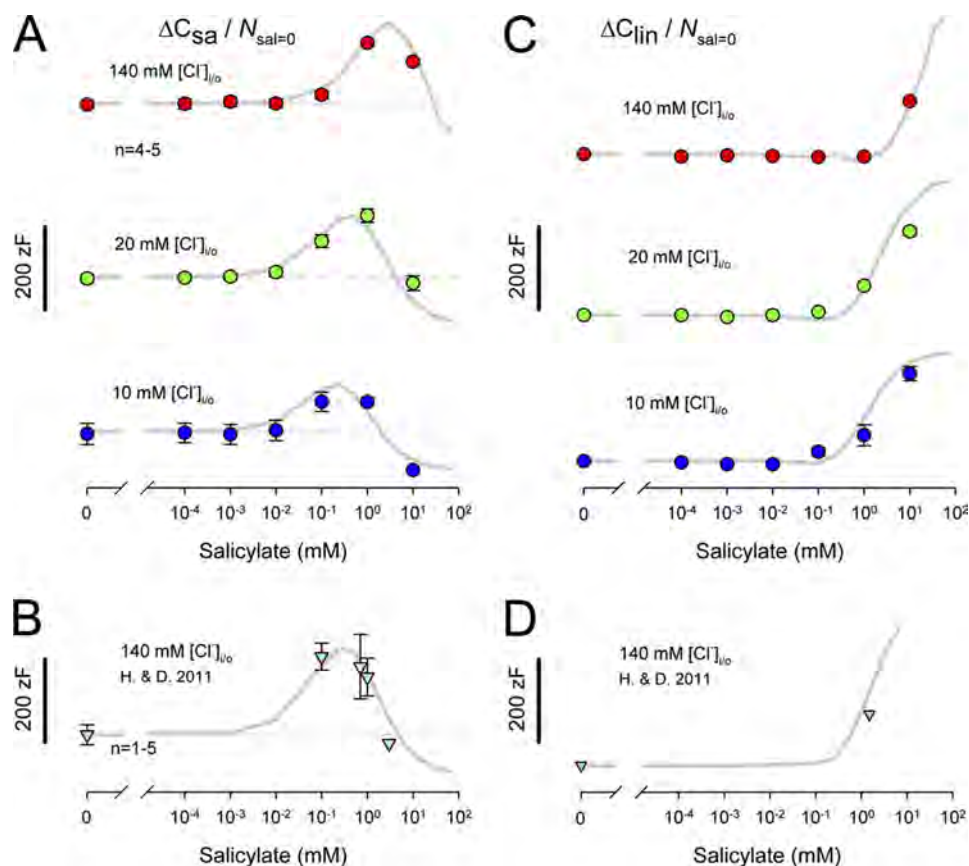


FIGURE 5. Chloride and salicylate dependence of specific membrane capacitance. ΔC_{sa} is normalized by dividing by $N(Q_{max}/ze)$ at 0 salicylate conditions. *A*, dashed lines show initial ΔC_{sa} for each chloride condition in the absence of salicylate: upper panel, 140 mM chloride, 141 zF; middle panel, 20 mM chloride, 110 zF; lower panel, 10 mM chloride, 88 zF. Note that in each case ΔC_{sa} is stable until a particular concentration of salicylate induces an increase in ΔC_{sa} followed by a decrease. The onset of salicylate effects is chloride-dependent, arising at lower salicylate levels as chloride is reduced. The *meno presto* model, which incorporates prestin-dependent changes in C_m arising from changes in motor surface area/membrane thickness, follows this pattern. *B*, data from Homma and Dallos (15) (*H. & D. 2011*); see their supplemental Fig. S3A (140 mM [chlorine] internal). The dashed line shows an initial ΔC_{sa} of 96 zF. A similar pattern of ΔC_{sa} change is observed when salicylate concentration is changed. Both the salicylate K_d and the ΔC_{sa} scaling factor for salicylate bound motors required adjustment to fit their data and are related to the higher salicylate sensitivity of mouse prestin (see “Results” for details). *C*, Clin also depends on the interaction between salicylate and chloride, showing a leftward shift along the salicylate concentration axis as chloride is reduced. The area motor model (gray lines) recapitulates this behavior. *D*, Homma and Dallos (15) Clin data are well described by the area motor model (see “Results”).

other point should be mentioned about the three-state model. Although the two-state C_{sa} model derives from biophysical evidence showing voltage-dependent surface area changes, the rationale for two independent Boltzmann processes in the three-state model is curiously lacking a rationale, other than its ability to fit NLC data within a restricted voltage region. In this regard, it is not at all clear why the V_h of each Boltzmann process should shift in an opposite direction during salicylate treatment (15). Even if salicylate could charge screen the membrane (41), voltage-dependent processes should shift in the same direction. The mechanism whereby the three-state model works is especially clear in the absence of salicylate when extended voltage ranges are used to measure NLC as in Fig. 2. One underlying Boltzmann process is simply shifted such that it mimics the sigmoidal nature of ΔC_{sa} generation that is revealed by the two-state C_{sa} model.

Interestingly, inspection of the literature on salicylate inhibition of prestin shows that mouse prestin appears more susceptible to inhibition than guinea pig prestin, with the guinea pig IC_{50sal} being ~ 1 – 1.5 mM and mouse IC_{50sal} being ~ 0.2 mM. Consequently, our new *meno presto* model was able to fit the mouse data of Homma and Dallos (15) by the reducing the

forward rate constant, c_2 (see “Experimental Procedures”), by an order of magnitude. Although homology is high between the two species, perhaps some key residue differences could account for this. Alternatively, chloride and/or salicylate concentration may differ within the minute space between plasma membrane and subsurface cisternae among species. This femtoliter compartment is exactly where interactions between anions and prestin occur. Thus, it may be interesting to compare salicylate sensitivity among OHCs from a wide range of species.

In summary, we find that an area motor model, such as our *meno presto* model, accurately accounts for interactions between salicylate and chloride on the OHC motor, and that models that do not explicitly incorporate a motor-dependent area change will nevertheless detect one as an increase in linear capacitance. To be sure, it is crucial that a model be appropriate to understand the elementary nature of a voltage-dependent molecule (38).

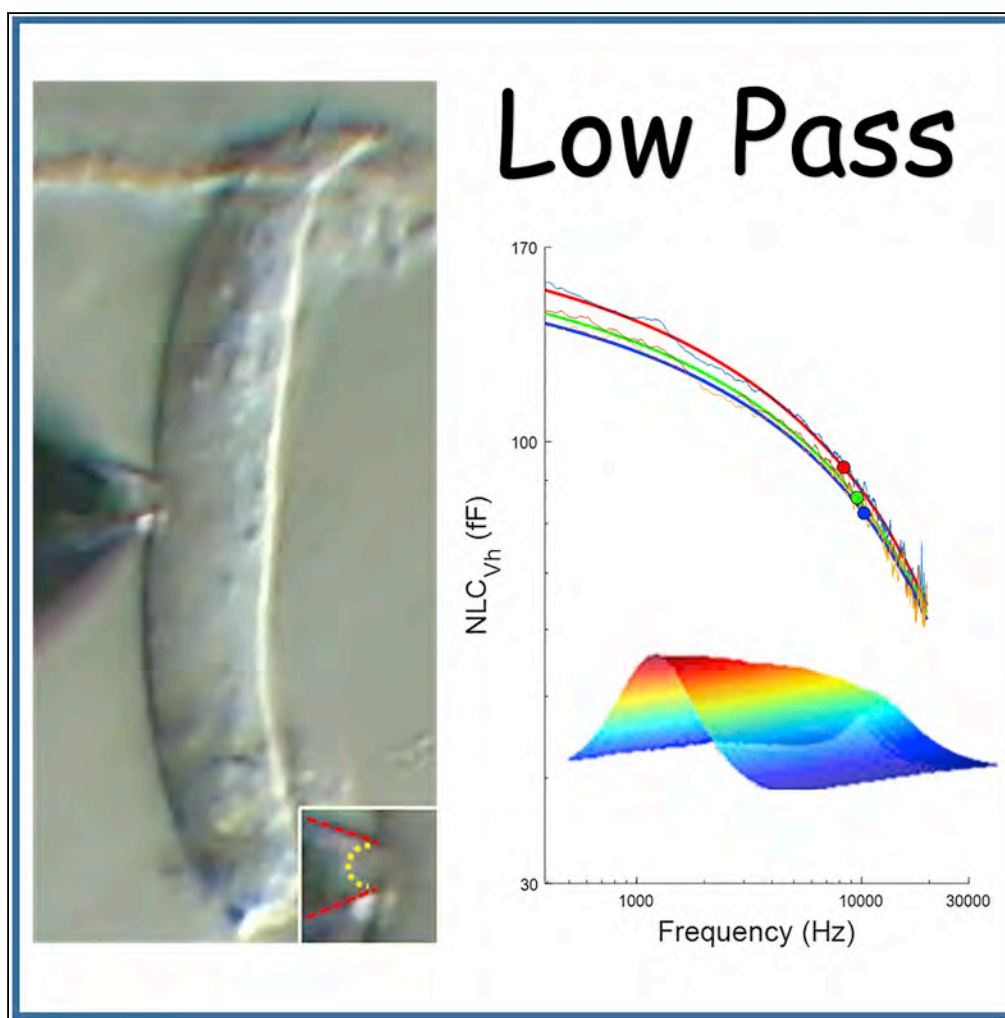
Acknowledgment—We thank Fred Sigworth for discussions on the salicylate and chloride microscopic binding efficiencies of the model relative to the observed effects on nonlinear capacitance.

REFERENCES

- Zheng, J., Shen, W., He, D. Z., Long, K. B., Madison, L. D., and Dallos, P. (2000) Prestin is the motor protein of cochlear outer hair cells. *Nature* **405**, 149–155
- Dallos, P., Wu, X., Cheatham, M. A., Gao, J., Zheng, J., Anderson, C. T., Jia, S., Wang, X., Cheng, W. H., Sengupta, S., He, D. Z., and Zuo, J. (2008) Prestin-based outer hair cell motility is necessary for mammalian cochlear amplification. *Neuron* **58**, 333–339
- Santos-Sacchi, J., Song, L., Zheng, J., and Nuttall, A. L. (2006) Control of mammalian cochlear amplification by chloride anions. *J. Neurosci.* **26**, 3992–3998
- Brownell, W. E., Bader, C. R., Bertrand, D., and de Ribaupierre, Y. (1985) Evoked mechanical responses of isolated cochlear outer hair cells. *Science* **227**, 194–196
- Ashmore, J. F. (1987) A fast motile response in guinea-pig outer hair cells: the cellular basis of the cochlear amplifier. *J. Physiol* **388**, 323–347
- Santos-Sacchi, J., and Dilger, J. P. (1988) Whole cell currents and mechanical responses of isolated outer hair cells. *Hear. Res.* **35**, 143–150
- Ashmore, J. F. (1990) Forward and reverse transduction in the mammalian cochlea. *Neurosci. Res. Suppl* **12**, S39–S50
- Santos-Sacchi, J. (1991) Reversible inhibition of voltage-dependent outer hair cell motility and capacitance. *J. Neurosci.* **11**, 3096–3110
- Santos-Sacchi, J. (1993) Harmonics of outer hair cell motility. *Biophys. J.* **65**, 2217–2227
- Iwasa, K. H. (2001) A two-state piezoelectric model for outer hair cell motility. *Biophys. J.* **81**, 2495–2506
- Iwasa, K. H. (1994) A membrane motor model for the fast motility of the outer hair cell. *J. Acoust. Soc. Am.* **96**, 2216–2224
- Iwasa, K. H. (1993) Effect of stress on the membrane capacitance of the auditory outer hair cell. *Biophys. J.* **65**, 492–498
- Kalinec, F., Holley, M. C., Iwasa, K. H., Lim, D. J., and Kachar, B. (1992) A membrane-based force generation mechanism in auditory sensory cells. *Proc. Natl. Acad. Sci. U.S.A.* **89**, 8671–8675
- Santos-Sacchi, J., and Navarrete, E. (2002) Voltage-dependent changes in specific membrane capacitance caused by prestin, the outer hair cell lateral membrane motor. *Pflugers Arch.* **444**, 99–106
- Homma, K., and Dallos, P. (2011) Evidence that prestin has at least two voltage-dependent steps. *J. Biol. Chem.* **286**, 2297–2307
- Song, L., Seeger, A., and Santos-Sacchi, J. (2005) On membrane motor activity and chloride flux in the outer hair cell: lessons learned from the environmental toxin tributyltin. *Biophys. J.* **88**, 2350–2362
- Santos-Sacchi, J. (2004) Determination of cell capacitance using the exact empirical solution of $\delta Y/\delta C_m$ and its phase angle. *Biophys. J.* **87**, 714–727
- Santos-Sacchi, J., Kakehata, S., and Takahashi, S. (1998) Effects of membrane potential on the voltage dependence of motility-related charge in outer hair cells of the guinea-pig. *J. Physiol.* **510**, 225–235
- Song, L., and Santos-Sacchi, J. (2013) Disparities in voltage-sensor charge and electromotility imply slow chloride-driven state transitions in the solute carrier SLC26a5. *Proc. Natl. Acad. Sci. U.S.A.* **110**, 3883–3888
- Okunade, O., and Santos-Sacchi, J. (2013) IR laser-induced perturbations of the voltage-dependent solute carrier protein SLC26a5. *Biophys. J.* **105**, 1822–1828
- Santos-Sacchi, J., Navarrete, E., and Song, L. (2009) Fast electromechanical amplification in the lateral membrane of the outer hair cell. *Biophys. J.* **96**, 739–747
- Colquhoun, D., Dowsland, K. A., Beato, M., and Plested, A. J. (2004) How to impose microscopic reversibility in complex reaction mechanisms. *Biophys. J.* **86**, 3510–3518
- Kakehata, S., and Santos-Sacchi, J. (1996) Effects of salicylate and lanthanides on outer hair cell motility and associated gating charge. *J. Neurosci.* **16**, 4881–4889
- Tunstall, M. J., Gale, J. E., and Ashmore, J. F. (1995) Action of salicylate on membrane capacitance of outer hair cells from the guinea-pig cochlea. *J. Physiol.* **485**, 739–752
- Oliver, D., He, D. Z., Klöcker, N., Ludwig, J., Schulte, U., Waldegger, S., Ruppertsberg, J. P., Dallos, P., and Fakler, B. (2001) Intracellular anions as the voltage sensor of prestin, the outer hair cell motor protein. *Science* **292**, 2340–2343
- Jerry, R. A., Popel, A. S., and Brownell, W. E. (1995) Outer hair cell length changes in an external electric field. I. The role of intracellular electro-osmotically generated pressure gradients. *J. Acoust. Soc. Am.* **98**, 2000–2010
- Kachar, B., Brownell, W. E., Altschuler, R., and Fex, J. (1986) Electrokinetic shape changes of cochlear outer hair cells. *Nature* **322**, 365–368
- Raphael, R. M., Popel, A. S., and Brownell, W. E. (2000) A membrane bending model of outer hair cell electromotility. *Biophys. J.* **78**, 2844–2862
- Santos-Sacchi, J. (1992) On the frequency limit and phase of outer hair cell motility: effects of the membrane filter. *J. Neurosci.* **12**, 1906–1916
- Iwasa, K. H., and Kachar, B. (1989) Fast *in vitro* movement of outer hair cells in an external electric field: effect of digitonin, a membrane permeabilizing agent. *Hear. Res.* **40**, 247–254
- Santos-Sacchi, J. (2003) New tunes from Corti's organ: the outer hair cell boogie rules. *Curr. Opin. Neurobiol.* **13**, 459–468
- Lieberman, M. C., Gao, J., He, D. Z., Wu, X., Jia, S., and Zuo, J. (2002) Prestin is required for electromotility of the outer hair cell and for the cochlear amplifier. *Nature* **419**, 300–304
- Abe, T., Kakehata, S., Kitani, R., Maruya, S., Navaratnam, D., Santos-Sacchi, J., and Shinkawa, H. (2007) Developmental expression of the outer hair cell motor prestin in the mouse. *J. Membr. Biol.* **215**, 49–56
- Adachi, M., and Iwasa, K. H. (1999) Electrically driven motor in the outer hair cell: effect of a mechanical constraint. *Proc. Natl. Acad. Sci. U.S.A.* **96**, 7244–7249
- Gale, J. E., and Ashmore, J. F. (1994) Charge displacement induced by rapid stretch in the basolateral membrane of the guinea-pig outer hair cell. *Proc. Biol. Sci.* **255**, 243–249
- Song, L., and Santos-Sacchi, J. (2011) Chloride and OHC electromotility: Another hurdle for prestin to overcome. in *Abstracts of the Association for Research in Otolaryngology*, Association for Research in Otolaryngology, Mt. Royal, NJ
- Song, L., and Santos-Sacchi, J. (2012) Chloride dependent coupling of molecular to cellular mechanics in the outer hair cell of Corti's organ. in *Proceedings of the 11th International Mechanics of Hearing Workshop. AIP Conference Proceedings*, Vol. 1403, pp. 179–184, American Institute of Physics, College Park, MD
- Bezanilla, F., and Villalba-Galea, C. A. (2013) The gating charge should not be estimated by fitting a two-state model to a Q-V curve. *J. Gen. Physiol.* **142**, 575–578
- Santos-Sacchi, J., and Wu, M. (2004) Protein- and lipid-reactive agents alter outer hair cell lateral membrane motor charge movement. *J. Membr. Biol.* **200**, 83–92
- Santos-Sacchi, J., Shen, W., Zheng, J., and Dallos, P. (2001) Effects of membrane potential and tension on prestin, the outer hair cell lateral membrane motor protein. *J. Physiol* **531**, 661–666
- Homma, K., and Dallos, P. (2011) Dissecting the electromechanical coupling mechanism of the motor-protein prestin. *Commun. Integr. Biol.* **4**, 450–453

Article

Voltage Does Not Drive Prestin (SLC26a5) Electro-Mechanical Activity at High Frequencies Where Cochlear Amplification Is Best



Joseph Santos-Sacchi, Winston Tan

joseph.santos-sacchi@yale.edu

HIGHLIGHTS

Outer hair cells (OHC) boost auditory sensation for very high acoustic frequencies

We studied the frequency response of OHC's electromechanical nonlinear capacitance

The response is incommensurate with cycle-by-cycle feedback at very high frequencies

OHCs likely use another mechanism to drive cochlear amplification at high frequencies

Santos-Sacchi & Tan, iScience
22, 392–399
December 20, 2019 © 2019
The Author(s).
<https://doi.org/10.1016/j.isci.2019.11.036>

Article

Voltage Does Not Drive Prestin (SLC26a5) Electro-Mechanical Activity at High Frequencies Where Cochlear Amplification Is Best

Joseph Santos-Sacchi^{1,2,3,4,*} and Winston Tan¹

SUMMARY

Cochlear amplification denotes a boost to auditory sensitivity and selectivity that is dependent on outer hair cells from Corti's organ. Voltage-driven electromotility of the cell is believed to feed energy back into the cochlear partition via a cycle-by-cycle mechanism at very high acoustic frequencies. Here we show using wide-band macro-patch voltage-clamp to drive prestin, the molecular motor underlying electromotility, that its voltage-sensor charge movement is unusually low pass in nature, being incapable of following high-frequency voltage changes. Our data are incompatible with a cycle-by-cycle mechanism responsible for high-frequency tuning in mammals.

INTRODUCTION

In some mammalian species, hearing capabilities can extend out to 60–160 kHz (Heffner and Masterton, 1980; Castellote et al., 2014; Szymanski et al., 1999; Heffner et al., 2001). Indeed, tuned hair cell receptor potential-derived cochlear microphonic potentials have been measured beyond 60 kHz in the bat (Pollak et al., 1972). Underlying this electrical behavior are sharp frequency tuning and enhanced cochlear partition vibration, which are susceptible to outer hair cell (OHC) damage; studies in laboratory rodents provide such evidence, e.g., in the mouse sharp basilar membrane tuning is measurable beyond 60 kHz (MelladoLagarde et al., 2008). This enhancement over Bekesy's passive partition vibration (von Bekesy, 1960) is termed cochlear amplification (CA) (Davis, 1983) and amounts to an apparent gain of 100–1000 at best frequency locations along the cochlear duct. DC and AC trans-membrane voltages are sensed by the membrane protein prestin (SLC26a5) (Santos-Sacchi and Dilger, 1988; Iwasa and Kachar, 1989), a special member of the SLC26 family of anion transporters (Zheng et al., 2000), that populates the OHC lateral membrane at molecular densities up to 8,000/ μm^2 (Santos-Sacchi et al., 1997; Gale and Ashmore, 1997b). Voltage is thought to faithfully govern prestin's conformational state, evoking rapid switching between expanded and contracted molecular conformations that leads to rapid length changes (termed electromotility; eM) (Ashmore et al., 2010). Current dogma has it that evoked OHCeM provides mechanical feedback into the organ of Corti on a cycle-by-cycle basis to power CA. In fact, Frank et al. measured high-fidelity OHC AC eM responses beyond 80 kHz (Frank et al., 1999). During the last few years, however, the kinetics or frequency dependence of prestin's electromechanical capabilities have been reassessed in OHCs (Santos-Sacchi and Song, 2014; Santos-Sacchi, 2019). Both the frequency of prestin charge movement (measured as a nonlinear capacitance [NLC]) and that of its associated eM were found to be low-pass, precipitously rolling off within the bandwidth of human speech (200–8000 Hz) (Santos-Sacchi and Tan, 2018; Santos-Sacchi et al., 2019). However, those data must be viewed cautiously because measures were made in whole cell mode. In fact, being a piezoelectric-like protein (Iwasa, 1993; Gale and Ashmore, 1994; Kakehata and Santos-Sacchi, 1995), where reciprocal influences of mechanical load and voltage are at play, whole cell measures of OHC electromechanical activity may fail to establish the actual frequency capabilities of prestin. Here we address this issue by measuring the frequency response of prestin's NLC with on-cell and excised macro-patches from the cell's lateral membrane where isolation from external whole cell loads can be achieved. The macro-patch is the preferred methodology to gauge fast charge movement in voltage sensitive membrane proteins (Lu et al., 1995). Our patch data in mouse and guinea pig show low pass, voltage-driven electromechanical behavior of the protein, whose frequency response alters over time but still falls far short of its expected influence on cochlear amplification at very high frequencies, leading us to question prestin's role in this process.

RESULTS

Our recording system response (Figures S1A and S1B), and results on an electrical model of a membrane patch (Figures S1C–S1F), confirming our capability to measure capacitance flat out to 20 kHz, is provided

¹Surgery (Otolaryngology), Yale University School of Medicine, BML 224, 333 Cedar Street, New Haven, CT 06510, USA

²Neuroscience, Yale University School of Medicine, 333 Cedar Street, New Haven, CT 06510, USA

³Cellular and Molecular Physiology, Yale University School of Medicine, 333 Cedar Street, New Haven, CT 06510, USA

⁴Lead Contact

*Correspondence: joseph.santos-sacchi@yale.edu

<https://doi.org/10.1016/j.isci.2019.11.036>



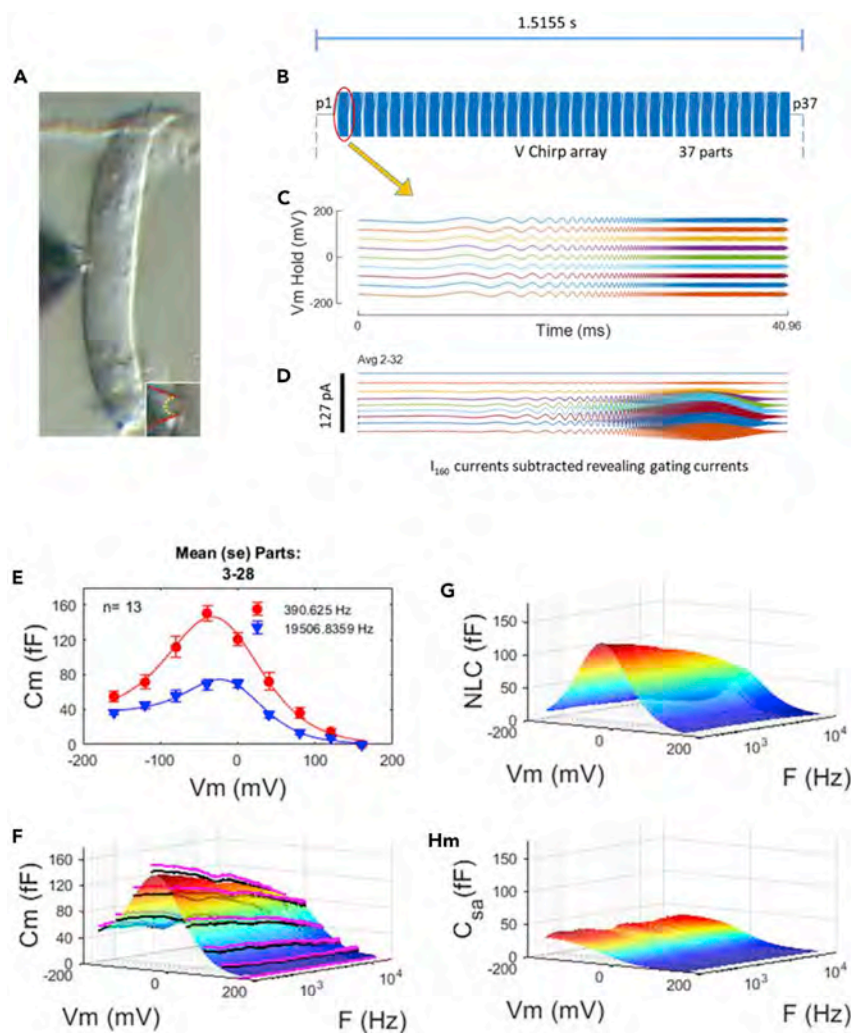


Figure 1. Measures of NLC in Macro-Patches from Outer Hair Cells (OHC)

(A) An image of an OHC (10 μm wide) showing a patch pipette sealed to the lateral membrane. Inset: enlarged view of patch. Red lines outline pipette, dotted yellow line outlines membrane patch.

(B) Section of command voltage stimulus, composed of 35 repeats of a chimp stimulus of 10 mV peak.

(C) Expanded view of individual chimp stimuli at the range of holding potential delivered to the patch (–160 to 160 mV).

(D) Extracted AC displacement (“gating”) currents, representative of voltage sensor charge movements during conformational changes in prestin. Evoked raw currents at each holding potential were averaged from parts 2–32, then the averaged current at 160 mV, where prestin activity is absent, was subtracted from all raw currents at each holding potential, revealing prestin displacement currents. Here, for illustration, we plot the average of currents from all cells, but for subsequent data analysis each cell was individually analyzed to provide statistics. The magnitude of AC currents peaks near V_h , where prestin charge movement vs. voltage is maximal. The displacement currents were used to analyze for nonlinear capacitance (NLC).

(E) Extracted membrane capacitance at two stimulating frequencies, (390 Hz [red circles]) and 19,500 Hz [blue triangles]). Mean \pm SE. Solid lines are fits based on Equation 1 (see [Methods](#)).

(F) Membrane capacitance as a function of voltage and frequency. Black lines are averages from 13 patches, and pink lines show mean \pm SE. Smooth multicolored surface is fit to averaged data.

(G) Extracted NLC. Note the roll-off in peak NLC magnitude as frequency of stimulation increases from 390 to 20,000 Hz.

(H) C_{sa} component of fit. Note frequency independence.

in the [Transparent Methods](#) section of the supplement. [Figures 1A–1D](#) illustrate our basic experimental strategy. Macro-patches (3.5–4 μm inner diameter) were made on the lateral membrane of OHCs ([Figure 1A](#)) and a voltage chimp array delivered to the patch superimposed on stepped holding voltages (–160 to 160 mV) to

extract prestin displacement currents (Figure 1D), following subtraction of currents at +160 mV where NLC is absent (Santos-Sacchi and Navarrete, 2002). Single-sine or dual-sine admittance analysis of the displacement currents provides estimates of NLC. Figure 1E shows average (\pm SE) cell capacitance data fitted with Equation 1 (see Methods) at 2 frequencies (390 and 19,500 Hz). Note the substantial drop in peak membrane capacitance at the higher frequency. Figure 1F displays in a 3D rendition all frequencies studied across holding voltage. Black lines are average data and pink lines are mean +SE, whereas the multicolored plot shows fits. The extracted NLC is shown in Figure 1G and illustrates the continuous roll-off of NLC with increasing frequency. Figure 1H shows the largely frequency independent component of membrane capacitance (C_{sa}) at negative holding potentials that we previously attributed to membrane surface area/thickness changes during prestin's conformational changes between compact and expanded states (Santos-Sacchi and Navarrete, 2002). The clear roll-off differences between NLC and this C_{sa} response (Figures 1G and 1H) indicate that our previous interpretation of the C_{sa} component may need reevaluation.

NLC at V_h reflects the charge distribution where an equal amount of voltage sensor charge resides on either side of the plasma membrane. Furthermore, that characteristic voltage (V_h) is a reflection of the ratio of forward and backward rates of prestin transitions, providing a voltage at which to measure the characteristic rate or frequency of sensor charge movement. The coupling of charge movement and eM (Santos-Sacchi and Tan, 2018) also indicates that at this voltage OHCeM gain (cell length change/membrane potential) is maximal. In Figure 2A, we plot the frequency response of NLC at V_h (mean: blue line; mean +SE: light blue dotted line). The roll-off is precipitous commencing at the lowest measured frequency. It is clear that our data, collected at 24.4 Hz resolution, requires a multi-Lorentzian (double in this case), or a power function fit (Figure 2B). The double Lorentzian fit indicates a slow and fast component with frequency cut-offs (F_c) at about 1.5 and 16.2 kHz, respectively. For the power fit, we estimate a cut-off at one-half magnitude of 11.3 kHz. Figure 2C indicates that the frequency response of NLC is the same with on-cell or immediately excised macro-patches in the guinea pig. In Figure 2D, we show that the frequency response of NLC in mouse patches is similar to that of the guinea pig. Half-magnitude cut-off of the power fit is at 10.5 kHz. For comparison, we plot the chloride dependent capacitance frequency response of GAT1 (triangles) (Lu et al., 1995), and its power function fit (green line), indicating that it is somewhat faster than the frequency response of prestin. The guinea pig response (pink line) is replotted in the figure along with scaled eM data (OHC 65: magenta solid line; OHC84: dashed magenta line) from Frank et al. (1999) (Figure 2A), showing that the speed of prestin conformational transitions falls far below OHC mechanical responses. In other words, the drive for eM (voltage-dependent conformational changes in prestin) does not correspond to their measured eM. Can NLC frequency response be augmented?

We have previously shown that NLC is not stationary in time (Santos-Sacchi et al., 2009). Step changes in voltage evoke initial rapid changes in NLC, which immediately alter in magnitude in a stretched exponential fashion, accompanied by shifts in V_h . In Figure 3, we explore the frequency response of NLC along the duration of our holding potential steps. Figure 3A shows the regions of chirp currents that were averaged for comparison. The extracted NLC from the three regions are shown in Figure 3B, and for the first region (p3-8) a red line is plotted along the slope of NLC at V_h across frequency. That same red line is recast onto the two other plots of regions p13-18 and p23-28, showing alterations in the frequency response of NLC as duration of the step increases. A quantification of the frequency responses is made in Figure 3C. Power fits indicate that low frequency components are reduced over time such that the frequency cut-off effectively increases over time. Figures 3D-3G plot the fitted parameters of the power fit across holding potential duration, showing reductions in NLC_0 , and time-dependent changes in the power parameters that control frequency dependence, with frequency cut-offs increasing over time.

It has been observed that patch size can change during the course of experiments (Sokabe et al., 1991). It is unlikely that patch size alterations across the duration of our voltage protocol account for the changes in frequency responses that we find because such changes would likely alter the size of NLC across the full frequency range (e.g., see Figure 2D, where smaller mouse patches simply shift all components of NLC downward relative to guinea pig patches). Indeed, Figures 3H and 3I illustrate that NLC across holding potential duration exhibits shifts in V_h that correspond to the nonstationary behavior of NLC that we previously found (Santos-Sacchi et al., 2009), rather than changes in patch area.

Salicylate is a known intracellular blocker of NLC (Kakehata and Santos-Sacchi, 1996; Tunstall et al., 1995), working in a competitive fashion on chloride binding (Oliver et al., 2001). Chloride anions are *not* extrinsic

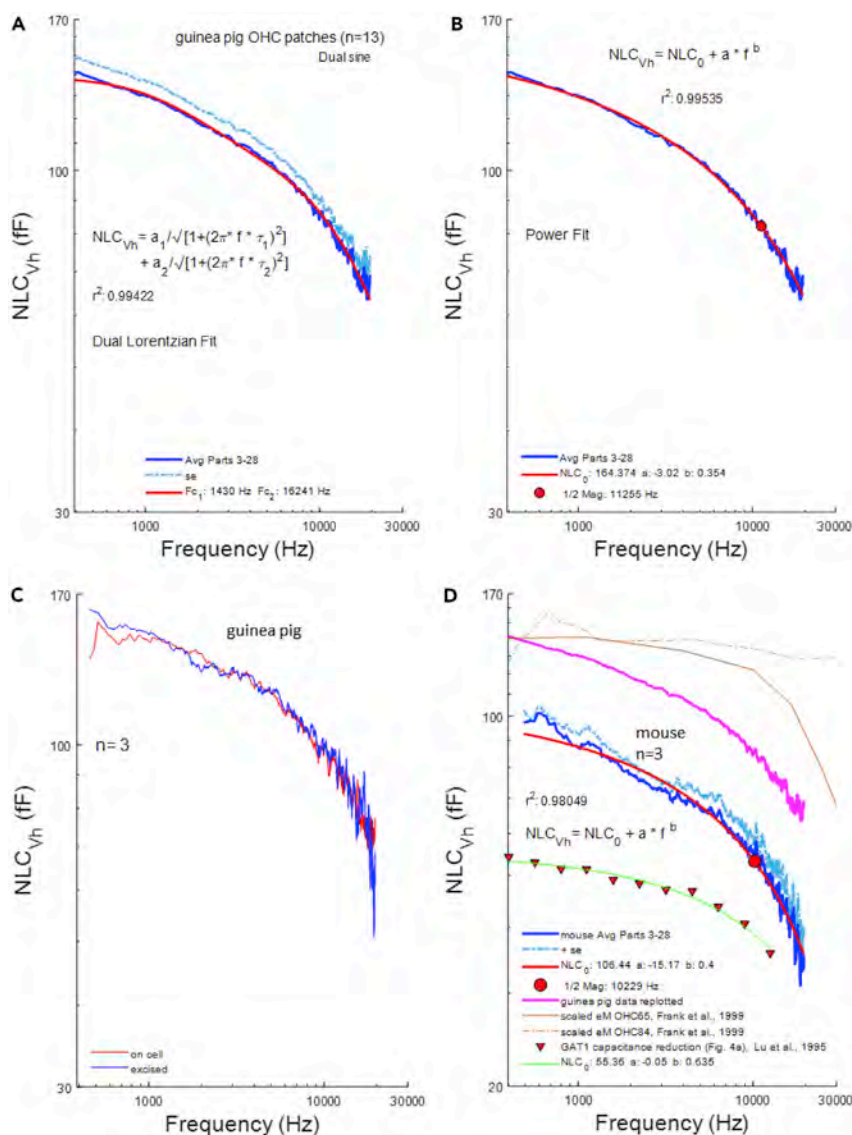


Figure 2. Frequency Response of NLC at V_h

(A) Blue line indicates mean NLC, dotted light blue line shows mean +SE. We require at least a double Lorentzian fit that indicates low and high pass components.

(B) Power fit of our data illustrating the continuous roll-off of NLC across frequency. One-half magnitude (red circle) is near 10.5 kHz.

(C) Average of three patches before and after inside-out patch excision, illustrating similar frequency response for each.

(D) Mouse NLC frequency response (mean, mean +SE, blue line, dotted light blue line, respectively) is similarly low pass compared with guinea pig response (pink line). Red circle shows one-half magnitude at 10.5 kHz. For comparison, we plot the capacitance function of Lu et al. (1995) (Figure 4A) for GAT1, fitted with a power function (solid green line). Also, for comparison, the scaled electromotility for the two presented cells from Frank et al. (1999) (Figure 2A) is shown. Note prestin's voltage-driven charge movements are remarkably lower-pass than eM.

voltage sensors for prestin but instead likely work allosterically (Song and Santos-Sacchi, 2010; Rybalchenko and Santos-Sacchi, 2003) (also see our comment #1 on Walter et al. [2019]—<https://elifsciences.org/articles/46986>). In Figure 4, we explore the effects of salicylate on NLC frequency response. Blue symbols denote responses after salicylate treatment, and red symbols denote response before treatment. Extracellular perfusion of high concentrations of salicylate (10 mM) substantially reduces NLC but not completely (Figure 4A). The effect results from intracellular loading of the ionized form of the molecule, working in the micromolar range (Kakehata and Santos-Sacchi, 1996). In order to gauge salicylate effects

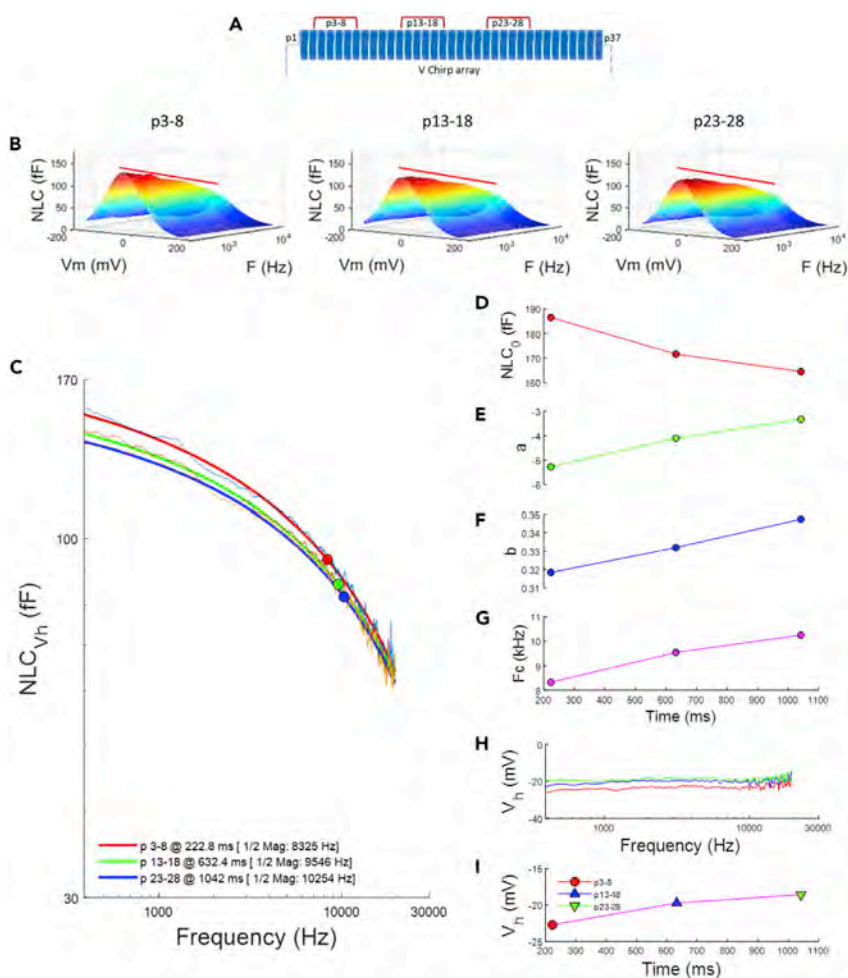


Figure 3. NLC Frequency Response Alters Over Time

(A) Currents were averaged at three time regions, six chirp responses each, over the duration of holding potential, p3-8, p13-18, and p23-28, and NLC was extracted for each region.

(B) NLC for the three durations is shown. The red line demarks the slope of NLC at V_h for the first region (p3-8) and is recast on the others. Note the change in NLC as duration of holding voltage increases.

(C) The frequency response of NLC at V_h is fit with a power function and shows that low-frequency regions of the response decreases over time. Circles depict one-half magnitude, which increases over time.

(D–G) Plots show the parameters of the power fits ([D] NLC_0 , [E] a , [F] b , and [G] F_c) that alter over time.

(H and I) V_h shifts over the duration of holding voltage steps. (H) V_h across frequency (colors correspond to those in [C]).

(I) Mean V_h across frequency corresponding to data and colors in (H).

on NLC frequency response, we utilized lower concentrations (10 μ M), assessing the response before (Figure 4B, top panel) and after (Figure 4B, bottom panel) treatment. Figure 4C shows that low-frequency components of NLC were reduced by 10 μ M salicylate, effectively increasing the frequency cut-off. None of the NLC frequency modulations we observed, due to time dependence or salicylate interference with chloride binding, sufficiently increased the response to promote very high frequency electromechanical activity.

DISCUSSION

The identification of AC electromotile responses of the OHC (Kachar et al., 1986) offered a clue to the OHCs' ability to promote high-frequency enhancement of hearing in mammals (Dallos, 2008). The subsequent identification of the response's voltage dependence and associated voltage-sensor activity (Santos-Sacchi, 1990, 1991; Santos-Sacchi and Dilger, 1988; Ashmore, 1990) suggested that OHC receptor potentials, evoked by acoustic stimulation, drive feedback of mechanical energy into the cochlear partition. It is current dogma that this feedback is cycle-by-cycle, working best at high frequencies, where tonotopic

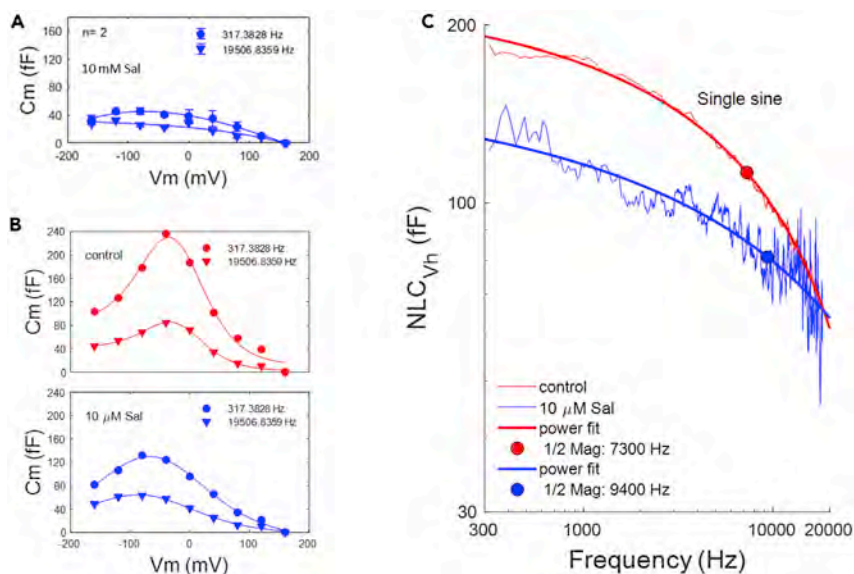


Figure 4. Salicylate Blocks NLC by Reducing Low Frequency Components

Blue color denotes responses after salicylate treatments. Red color denotes control prior to treatment.

(A) NLC is substantially reduced by 10 mM salicylate.

(B) *Top panel*: control before and *bottom panel*: after application of 10 μ M salicylate to a single patch to provide partial block of NLC.

(C) The resultant partial inhibition of fit extracted NLC illustrates a low-frequency block, which effectively increases NLC frequency response.

frequency tuning is best (Ashmore et al., 2010). Indeed, OHC eM had been measured in a whole-cell micro-chamber configuration to work without attenuation beyond 80 kHz at room temperature (Frank et al., 1999), this in spite of initial studies showing more limited charge movement (Gale and Ashmore, 1997a). More recent investigations on whole cells have challenged the concept of OHC high-frequency electromechanical activity, with both NLC and eM exhibiting significant low-pass behavior below 10 kHz (Santos-Sacchi, 2019; Santos-Sacchi et al., 2019; Bai et al., 2019). Our current data on excised and on-cell macro-patch measures of NLC, where whole-cell mechanical loads on the piezoelectric-like protein prestin are absent, directly show continuous roll-off of prestin's conformational activity and indicate that attenuation of sensor-charge movement in both mouse and guinea pig is not single Lorentzian in nature, but instead fit well by a power function of frequency. This frequency response is not very different from that of capacitance measures in the GAT1GABA transporter (Lu et al., 1995). Mechanisms that we find to enhance the frequency response of prestin, namely, time-dependence or motor block with salicylate, do not increase its high-frequency behavior, but simply work by reducing the magnitude of low-frequency components. These observations place a severe restraint on the effectiveness of voltage (i.e., receptor potentials) to drive electromechanical responses of the OHC at very high acoustic frequencies where several mammals possess hearing in the 60–160 kHz range. That is, there can be little or no OHC mechanical feedback in the absence of prestin sensor charge movement at high frequencies, assuming that prestin works as an AC motor driven by AC voltage. Interestingly, *in vivo* indications of OHC electromechanical activity in the gerbil obtained with OCT show low pass behavior, as well (Vavakou et al., 2019). Those authors considered the RC filter problem (Santos-Sacchi, 1989), where OHC receptor potentials are expected to be attenuated at very high frequencies by more than 20 dB relative to partition movements, and thus not be able to drive prestin. Our data show that the RC filter problem is inconsequential, in as much as the ability of prestin to follow wide-band voltage perturbations is insufficient in and of itself.

There is no doubt that normal prestin activity is involved in the process that enhances hearing capabilities (Dallos et al., 2008; Santos-Sacchi et al., 2006). Knock-in of prestin mutations that alter its voltage operating range (i.e. V_h) or manipulations of OHC chloride, known to influence prestin activity, are catastrophic to cochlear amplification in the mouse, the latter in a reversible manner. How can a slow motor protein work to enhance high-frequency hearing? Could low pass eM actually be countering low-frequency acoustic responses in order to “highlight” high-frequency input to the cochlea? Intriguing results on basilar

membrane tuning have been obtained in prestin knock-out/in mice that may point to possible mechanisms of OHC action (MelladoLagarde et al., 2008). Alternatively, a rectified DC component of prestin activity (Evans et al., 1991; Santos-Sacchi, 1989) could contribute to effects on high-frequency tuning, as Vavakou et al. (Vavakou et al., 2019) have intimated. Finally, global hydromechanical influences of the OHC may be at play (He et al., 2018). In any case, the long-held cycle-by-cycle hypothesis of cochlear amplification at very high frequencies is directly countered by our present observations.

Limitations of the Study

Ion concentrations in pipette and cell over the timescale of recording are likely fixed; however, conceivably, as in any macro-patch experiment, ion depletion or accumulation on the patched membrane could influence electrical measures.

METHODS

All methods can be found in the accompanying [Transparent Methods supplemental file](#).

SUPPLEMENTAL INFORMATION

Supplemental Information can be found online at <https://doi.org/10.1016/j.isci.2019.11.036>.

ACKNOWLEDGMENTS

This research was supported by NIH-NIDCD R01DC000273, R01DC016318, and R01DC008130 to J.S.-S.

AUTHOR CONTRIBUTIONS

J.S.-S. designed and performed experiments, analyzed data and wrote the paper. W.T. performed experiments, analyzed data, and edited paper.

DECLARATION OF INTERESTS

The authors declare no conflict of interest.

Received: October 7, 2019

Revised: November 13, 2019

Accepted: November 18, 2019

Published: December 20, 2019

REFERENCES

- Ashmore, J., Avan, P., Brownell, W.E., Dallos, P., Dierkes, K., Fettiplace, R., Grosh, K., Hackney, C.M., Hudspeth, A.J., Juelicher, F., et al. (2010). The remarkable cochlear amplifier. *Hear. Res.* *266*, 1–17.
- Ashmore, J.F. (1990). Forward and reverse transduction in the mammalian cochlea. *Neurosci. Res. Suppl.* *12*, S39–S50.
- Bai, J.P., Navaratnam, D., and Santos-Sacchi, J. (2019). Prestin kinetics and corresponding frequency dependence augment during early development of the outer hair cell within the mouse organ of Corti. *Sci. Rep.* *9*, 16460.
- Castellote, M., Mooney, T.A., Quakenbush, L., Hobbs, R., Goertz, C., and Gaglione, E. (2014). Baseline hearing abilities and variability in wild beluga whales (*Delphinapterus leucas*). *J. Exp. Biol.* *217*, 1682–1691.
- Dallos, P. (2008). Cochlear amplification, outer hair cells and prestin. *Curr. Opin. Neurobiol.* *18*, 370–376.
- Dallos, P., Wu, X., Cheatham, M.A., Gao, J., Zheng, J., Anderson, C.T., Jia, S., Wang, X., Cheng, W.H., Sengupta, S., et al. (2008). Prestin-based outer hair cell motility is necessary for mammalian cochlear amplification. *Neuron* *58*, 333–339.
- Davis, H. (1983). An active process in cochlear mechanics. *Hear. Res.* *9*, 79–90.
- Evans, B.N., Hallworth, R., and Dallos, P. (1991). Outer hair cell electromotility: the sensitivity and vulnerability of the DC component. *Hear. Res.* *52*, 288–304.
- Frank, G., Hemmert, W., and Gummer, A.W. (1999). Limiting dynamics of high-frequency electromechanical transduction of outer hair cells. *Proc. Natl. Acad. Sci. U S A* *96*, 4420–4425.
- Gale, J.E., and Ashmore, J.F. (1994). Charge displacement induced by rapid stretch in the basolateral membrane of the Guinea-pig outer hair cell. *Proc. R. Soc. Lond. B Biol. Sci.* *255*, 243–249.
- Gale, J.E., and Ashmore, J.F. (1997a). An intrinsic frequency limit to the cochlear amplifier. *Nature* *389*, 63–66.
- Gale, J.E., and Ashmore, J.F. (1997b). The outer hair cell motor in membrane patches. *Pflugers Arch.* *434*, 267–271.
- Heffner, H., and Masterton, B. (1980). Hearing in Glires: domestic rabbit, cotton rat, feral house mouse, and kangaroo rat. *J. Acoust. Soc. Am.* *68*, 1584–1599.
- He, W., Kemp, D., and Ren, T. (2018). Timing of the reticular lamina and basilar membrane vibration in living gerbil cochleae. *Elife* *7*, e37625.
- Heffner, R.S., Koay, G., and Heffner, H.E. (2001). Audiograms of five species of rodents: implications for the evolution of hearing and the perception of pitch. *Hear. Res.* *157*, 138–152.
- Iwasa, K.H. (1993). Effect of stress on the membrane capacitance of the auditory outer hair cell. *Biophys. J.* *65*, 492–498.
- Iwasa, K.H., and Kachar, B. (1989). Fast in vitro movement of outer hair cells in an external electric field: effect of digitonin, a membrane permeabilizing agent. *Hear. Res.* *40*, 247–254.

- Kachar, B., Brownell, W.E., Altschuler, R., and Fex, J. (1986). Electrokinetic shape changes of cochlear outer hair cells. *Nature* 322, 365–368.
- Takehata, S., and Santos-Sacchi, J. (1995). Membrane tension directly shifts voltage dependence of outer hair cell motility and associated gating charge. *Biophys. J.* 68, 2190–2197.
- Takehata, S., and Santos-Sacchi, J. (1996). Effects of salicylate and lanthanides on outer hair cell motility and associated gating charge. *J. Neurosci.* 16, 4881–4889.
- Lu, C.C., Kabakov, A., Markin, V.S., Mager, S., Frazier, G.A., and Hilgemann, D.W. (1995). Membrane transport mechanisms probed by capacitance measurements with megahertz voltage clamp. *Proc. Natl. Acad. Sci. U S A* 92, 11220–11224.
- MelladoLagarde, M.M., Drexler, M., Lukashkin, A.N., Zuo, J., and Russell, I.J. (2008). Prestin's role in cochlear frequency tuning and transmission of mechanical responses to neural excitation. *Curr. Biol.* 18, 200–202.
- Oliver, D., He, D.Z., Klocker, N., Ludwig, J., Schulte, U., Waldegger, S., Ruppertsberg, J.P., Dallos, P., and Fakler, B. (2001). Intracellular anions as the voltage sensor of prestin, the outer hair cell motor protein. *Science* 292, 2340–2343.
- Pollak, G., Henson, O.W., Jr., and Novick, A. (1972). Cochlear microphonic audiograms in the "pure tone" bat *Chilonycterisparnelliiiparnellii*. *Science* 176, 66–68.
- Rybalchenko, V., and Santos-Sacchi, J. (2003). Allosteric modulation of the outer hair cell motor protein prestin by chloride. In *Biophysics of the Cochlea: From Molecules to Models*, A. Gummer, ed. (World Scientific Publishing), pp. 116–126.
- Santos-Sacchi, J. (1989). Asymmetry in voltage-dependent movements of isolated outer hair cells from the organ of Corti. *J. Neurosci.* 9, 2954–2962.
- Santos-Sacchi, J. (1990). Fast outer hair cell motility: how fast is fast? In *The Mechanics and Biophysics of Hearing*, P. Dallos, C.D. Geisler, J.W. Matthews, M.A. Ruggero, and C.R. Steele, eds. (Springer-Verlag), pp. 69–75.
- Santos-Sacchi, J. (1991). Reversible inhibition of voltage-dependent outer hair cell motility and capacitance. *J. Neurosci.* 11, 3096–3110.
- Santos-Sacchi, J. (2019). The speed limit of outer hair cell electromechanical activity. *HNO* 67, 159–164.
- Santos-Sacchi, J., and Dilger, J.P. (1988). Whole cell currents and mechanical responses of isolated outer hair cells. *Hear. Res.* 35, 143–150.
- Santos-Sacchi, J., Huang, G.J., and Wu, M. (1997). Mapping the distribution of outer hair cell voltage-dependent conductances by electrical amputation. *Biophys. J.* 73, 1424–1429.
- Santos-Sacchi, J., Iwasa, K.H., and Tan, W. (2019). Outer hair cell electromotility is low-pass filtered relative to the molecular conformational changes that produce nonlinear capacitance. *J. Gen. Physiol.* <https://doi.org/10.1085/jgp.201812280>.
- Santos-Sacchi, J., and Navarrete, E. (2002). Voltage-dependent changes in specific membrane capacitance caused by prestin, the outer hair cell lateral membrane motor. *Pflügers Arch.* 444, 99–106.
- Santos-Sacchi, J., Navarrete, E., and Song, L. (2009). Fast electromechanical amplification in the lateral membrane of the outer hair cell. *Biophys. J.* 96, 739–747.
- Santos-Sacchi, J., and Song, L. (2014). Chloride-driven electromechanical phase lags at acoustic frequencies are generated by SLC26a5, the outer hair cell motor protein. *Biophys. J.* 107, 126–133.
- Santos-Sacchi, J., Song, L., Zheng, J., and Nuttall, A.L. (2006). Control of mammalian cochlear amplification by chloride anions. *J. Neurosci.* 26, 3992–3998.
- Santos-Sacchi, J., and Tan, W. (2018). The frequency response of outer hair cell voltage-dependent motility is limited by kinetics of prestin. *J. Neurosci.* 38, 5495–5506.
- Sokabe, M., Sachs, F., and Jing, Z.Q. (1991). Quantitative video microscopy of patch clamped membranes stress, strain, capacitance, and stretch channel activation. *Biophys. J.* 59, 722–728.
- Song, L., and Santos-Sacchi, J. (2010). Conformational state-dependent anion binding in prestin: evidence for allosteric modulation. *Biophys. J.* 98, 371–376.
- Szymanski, M.D., Bain, D.E., Kiehl, K., Pennington, S., Wong, S., and Henry, K.R. (1999). Killer whale (*Orcinus orca*) hearing: auditory brainstem response and behavioral audiograms. *J. Acoust. Soc. Am.* 106, 1134–1141.
- Tunstall, M.J., Gale, J.E., and Ashmore, J.F. (1995). Action of salicylate on membrane capacitance of outer hair cells from the Guinea-pig cochlea. *J. Physiol.* 485 (Pt 3), 739–752.
- Vavakou, A., Cooper, N.P., and van der Heijden, M. (2019). The frequency limit of outer hair cell motility measured in vivo. *Elife* 8, e47667.
- von Békésy, G. (1960). *Experiments in Hearing* (McGraw-Hill).
- Walter, J.D., Sawicka, M., and Dutzler, R. (2019). Cryo-EM structures and functional characterization of murine SLC26a9 reveal mechanism of uncoupled chloride transport. *Elife* 8, <https://doi.org/10.7554/eLife.46986>.
- Zheng, J., Shen, W., He, D.Z., Long, K.B., Madison, L.D., and Dallos, P. (2000). Prestin is the motor protein of cochlear outer hair cells. *Nature* 405, 149–155.

ISCI, Volume 22

Supplemental Information

Voltage Does Not Drive Prestin (SLC26a5)

Electro-Mechanical Activity at High Frequencies

Where Cochlear Amplification Is Best

Joseph Santos-Sacchi and Winston Tan

Transparent Methods

OHCs were isolated from guinea pig and mouse as described previously (Santos-Sacchi et al., 2019; Santos-Sacchi and Tan, 2018). Briefly, animals were killed by anesthetic overdose, the cochleas removed and the organ of Corti of the top two coils dissected out. Following 5 minutes of enzymatic digestion with trypsin (0.5mg/ml), the OHCs were isolated by gentle trituration and placed in a petri dish on a Nikon Eclipse TI-2000 microscope for recording. Extracellular solution was (in mM): NaCl 100, TEA-Cl 20, CsCl 20, CoCl₂ 2, MgCl₂ 1, CaCl₂ 1, Hepes 10, pH 7.2. Extracellular solution was in the patch pipette. Macro-patches on the OHC lateral membrane were made near the middle of the cylindrical cell; since prestin density/activity is uniform within the lateral membrane (Dallos et al., 1991; Huang and Santos-Sacchi, 1993), they provide representative information. For the guinea pig on-cell macro-patch approach we used pipette inner diameters of 3.38 +/- 0.20 μm (electrode resistance in bath 1.46 +/- 0.06 M Ω , n=13), with M-coat applied within about 20 μm of the tip to minimize pipette capacitance. Hemispheric estimate of patch surface area was 179 fF. Mouse pipette tip size was smaller at 2.29 +/- 0.024 μm (n=3). In order to establish Gohm seals (5.54 +/- 0.59 G Ω , n=13) we supplemented extracellular solution with 5-7.5 μM Gd⁺³; we have shown previously that these low concentrations help to form seals without affecting NLC (Santos-Sacchi and Song, 2016; Santos-Sacchi et al., 2019). **Fig. 1A-D** illustrates our protocol to measure high frequency NLC. Voltage steps from -160 mV to 160 mV were superimposed with an array of voltage chirps. We have previously shown that breakdown of prestin expressing membrane occurs at voltages greater than 300 mV (Navarrete and Santos-Sacchi, 2006). Nevertheless, patches where instabilities of the membrane produced erratic currents at the largest potentials were removed from our data set. An Axon 200B amplifier was used with jClamp software (www.scisoftco.com). An Axon Digidata 1440 was used for digitizing at 10 μs (Nyquist frequency of 50 kHz). Currents were filtered at 10 kHz with a 4-pole Bessel filter. The voltage chirps were generated in the software program jClamp (www.scisoftco.com) using the Matlab logarithmic “chirp” function (10 mV pk; pts=4096; F0=24.4141 Hz; F1=50 kHz; t1=0.04095 s). Subtraction of currents at very depolarized potentials (160 mV) where NLC is absent (Santos-Sacchi and Navarrete, 2002), provided prestin-associated nonlinear currents, absent stray capacitive currents. Subsequently, these subtracted nonlinear membrane currents were used

for dual-sine or single-sine based capacitance estimation by evaluating real and imaginary components of the differential input admittance (Y_{diff}) derived from the subtracted currents (Santos-Sacchi, 2004; Santos-Sacchi et al., 1998). The removal of stray capacitance is required for the application of membrane capacitance algorithms (see below). Briefly, real and imaginary components of the nonlinear membrane admittance at all chirp frequencies were determined by FFT in jClamp, and corrected for the roll-off of recording system admittance (Gillis, 1995). That is, the frequency response of the system, including all components (AD/DA, amplifier and filter) was assessed by placing a small shielded resistor, 10 M Ω , into the head stage input. Stray capacitance was balanced out with amplifier circuitry prior to grounding the resistor. Then, following grounding, voltage chirps (frequency span from 3.05 to 50 kHz, 32768 points at 10 μ s clock) were delivered, and currents recorded to provide system admittance. The magnitude and phase of our system response is shown in **Figure S1 A and B**. That system admittance is used to correct experimental data admittance. The necessity for such corrections are shown in **Figure S1 C-D**, where an electrical cell model (R_s : 10 M Ω , R_m : 2 G Ω , and C_m : 1 pF) was analyzed similar to macro-patches, after stray capacitance compensation with amplifier circuitry. It can be seen, for both the dual sine and single sine analysis, that uncorrected responses are aberrant, but following correction for system magnitude and phase (i.e., dividing the complex response admittance by system admittance at each stimulus frequency), the subsequently estimated capacitance is flat at about 1 pF across frequency, regardless of holding potential. Thus, our methodology permits us to measure capacitance with high fidelity out to 20 kHz across holding potentials. We and others have previously used such an approach, though at lower interrogating frequencies, to measure NLC, as well as capacitance associated with synaptic vesicle release (Santos-Sacchi, 2018; Schnee et al., 2011b; Schnee et al., 2011a; Santos-Sacchi et al., 1998).

For the dual sine method, the solution of the standard electrode-cell model is obtained from the admittances at 2 interrogating frequencies (Santos-Sacchi et al., 1998; Santos-Sacchi, 2018), based on the original single sine solution of Pusch and Neher (Pusch and Neher, 1988). The component solutions at harmonic angular frequencies ω_n , where $n=0, 1$ and $\omega_n=2\pi f_n$, are

$$R_{s_n} = \frac{a_n - \beta}{a_n^2 + b_n^2 - a_n \beta}$$

$$R_{m_n} = \frac{1((a_n - \beta)^2 + b_n^2)}{b(a_n^2 + b_n^2 - a_n\beta)}$$

$$C_{m_n} = \frac{1}{(\omega_n b_n)} \frac{(a_n^2 + b_n^2 - a_n\beta)^2}{((a_n - \beta)^2 + b_n^2)}$$

where from the measured input admittance Y_{in} we obtain

$$Y_{cell\omega_n} = Y_{in\omega_n} - Y_{stray\omega_n}, n = 0,1$$

$$a_n = Re(Y_{cell\omega_n})$$

$$b_n = Im(Y_{cell\omega_n})$$

$$c_n = a_n^2 + b_n^2$$

$$\beta = -0.5 \times \frac{-c_1 + c_0 + \sqrt{c_1^2 - 2c_1c_0 + c_0^2 - 4a_1a_0c_1 + 4a_1^2c_0 + 4a_0^2c_1 - 4a_0a_1c_0}}{a_1 - a_0}$$

Thus, membrane currents evoked by two voltage frequencies can be used to solve for R_s , R_m and C_m , even in the face of resistive changes, *but only in the absence of stray capacitance*. This applies to measures of patch capacitance, as well. We report on C_m measures derived from f_n , where $n=0$.

For single sine analysis, capacitance was estimated from the imaginary component of the admittance, $C_m = Im(Y_{diff}) / \omega$, where $\omega = 2\pi f$, after minimizing the real component of admittance by rotating the phase angle of the complex admittance. Single and dual sine frequency response estimates were essentially the same (for example, see **Figure S1 D and F**).

To extract NLC at each frequency, we fit V_m - C_m data to the following *eq. 1* (Santos-Sacchi and Navarrete, 2002). This equation extracts NLC based on a 2-state charge movement (Boltzmann) model, which predicts symmetrical NLC on either side of V_h . In fact, measured membrane capacitance in OHCs or prestin-expressing heterologous cells is greater at hyperpolarized potentials than at depolarized potentials. This voltage-dependent sigmoidal offset is removed by the fit (see **Fig. 1H**). The equation has been routinely used to evaluate NLC (Santos-Sacchi and Song, 2014; Homma and Dallos, 2011; Duret et al., 2017; Chessum et al., 2018; Harasztosi and Gummer, 2016).

eq. 1

$$C_m = Q_{max} \frac{ze}{kT} \frac{b}{(1+b)^2} + \frac{\Delta C_{sa}}{(1+b^{-1})} + C_0$$

where

$$b = \exp\left(\frac{-ze(V_m - V_h)}{kT}\right)$$

Q_{max} is the maximum nonlinear charge moved, V_h is voltage at peak capacitance or equivalently, at half maximum charge transfer, V_m is membrane potential, z is valence, e is electron charge, k is Boltzmann's constant, and T is absolute temperature. C_0 is defined as the capacitance of the membrane when all motors are in their compact state, the minimum membrane capacitance; ΔC_{sa} is the maximum increase in capacitance that occurs when all motors change from compact to expanded state, each motor contributing a unit response of δC_{sa} .

Data are presented as mean +/- standard error (SE). Data points from previous publications were extracted from plots using the application Grabit (written by Jiro Doke) in Matlab.

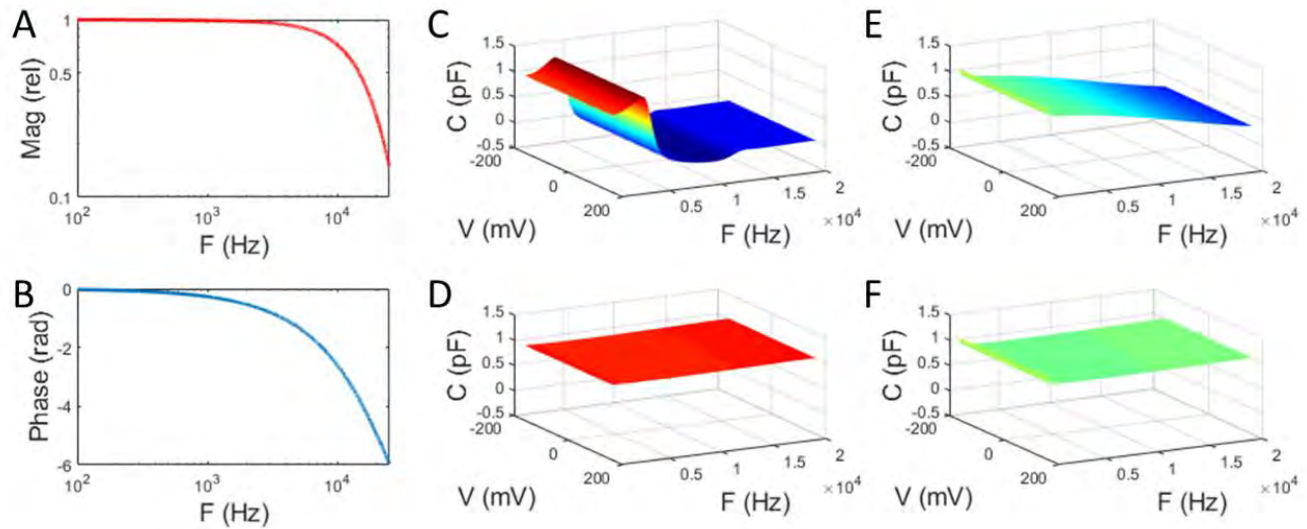


Figure S1 Requirement to correct for the frequency response of the patch clamp system prior to capacitance estimation, Related to Figure 1 and 2. A) Magnitude and B) phase of the system. Determination is detailed in the Methods. In C-D, a model electrical patch (R_s : 10 M Ω , R_m : 2G Ω , C_m : 1 pF) is used to confirm proper system performance. C,D) illustrate capacitance measures utilizing dual sine analysis and E,F) using single sine analysis as detailed in Methods. In C) and E) capacitance measures are not corrected for system frequency response. Responses are aberrant. In D) and F) corrections are made to the measured model patch admittance based on measured system admittance. Following corrections, capacitance measures are flat out to 20 kHz, across holding potentials of -160 to 160 mV.

References

Chessum, L., Matern, M. S., Kelly, M. C., Johnson, S. L., Ogawa, Y., Milon, B., McMurray, M., Driver, E. C., Parker, A., Song, Y., Codner, G., Esapa, C. T., Prescott, J., Trent, G., Wells, S., Dragich, A. K., Frolenkov, G. I., Kelley, M. W., Marcotti, W., Brown, S. D. M., Elkon, R., Bowl, M. R. & Hertzano, R. 2018. Helios is a key transcriptional regulator of outer hair cell maturation. *Nature*, 563(7733), pp 696-700.

Dallos, P., Evans, B. N. & Hallworth, R. 1991. Nature of the motor element in electrokinetic shape changes of cochlear outer hair cells. *Nature*, 350(6314), pp 155-157.

- Duret, G., Pereira, F. A. & Raphael, R. M. 2017. Diflunisal inhibits prestin by chloride-dependent mechanism. *PLoS One*, 12(8), pp e0183046.
- Gillis, K. D. 1995. Techniques for Membrane Capacitance Measurements. *In: Sakmann, B. & Neher, E. (eds.) Single Channel Recording*. New York: Plenum Press.
- Harasztosi, C. & Gummer, A. W. 2016. The chloride-channel blocker 9-anthracenecarboxylic acid reduces the nonlinear capacitance of prestin-associated charge movement. *Eur J Neurosci*, 43(8), pp 1062-74.
- Homma, K. & Dallos, P. 2011. Evidence that prestin has at least two voltage-dependent steps. *J.Biol.Chem.*, 286(3), pp 2297-2307.
- Huang, G. & Santos-Sacchi, J. 1993. Mapping the distribution of the outer hair cell motility voltage sensor by electrical amputation. *Biophys.J.*, 65(5), pp 2228-2236.
- Navarrete, E. G. & Santos-Sacchi, J. 2006. On the effect of prestin on the electrical breakdown of cell membranes. *Biophys.J.*, 90(3), pp 967-974.
- Pusch, M. & Neher, E. 1988. Rates of diffusional exchange between small cells and a measuring patch pipette. *Pflugers Arch.*, 411(2), pp 204-211.
- Santos-Sacchi, J. 2004. Determination of cell capacitance using the exact empirical solution of dY/dC_m and its phase angle. *Biophys.J.*, 87(1), pp 714-727.
- Santos-Sacchi, J. 2018. High frequency measures of OHC nonlinear capacitance (NLC) and their significance: Why measures stray away from predictions. *AIP Conference Proceedings*, 1965(1), pp 060004-1–060004-5.
- Santos-Sacchi, J., Iwasa, K. H. & Tan, W. 2019. Outer hair cell electromotility is low-pass filtered relative to the molecular conformational changes that produce nonlinear capacitance. *J Gen Physiol*, jgp.201812280. doi: 10.1085/jgp.201812280(
- Santos-Sacchi, J., Kakehata, S. & Takahashi, S. 1998. Effects of membrane potential on the voltage dependence of motility-related charge in outer hair cells of the guinea-pig. *J.Physiol*, 510 (Pt 1)(225-235.
- Santos-Sacchi, J. & Navarrete, E. 2002. Voltage-dependent changes in specific membrane capacitance caused by prestin, the outer hair cell lateral membrane motor. *Pflugers Arch.*, 444(1-2), pp 99-106.

- Santos-Sacchi, J. & Song, L. 2014. Chloride and Salicylate Influence Prestin-dependent Specific Membrane Capacitance. *Journal of Biological Chemistry*, 289(15), pp 10823-10830.
- Santos-Sacchi, J. & Song, L. 2016. Chloride anions regulate kinetics but not voltage-sensor Qmax of the solute carrier SLC26a5. *Biophysical Journal*, 110(1-11).
- Santos-Sacchi, J. & Tan, W. 2018. The Frequency Response of Outer Hair Cell Voltage-Dependent Motility Is Limited by Kinetics of Prestin. *J Neurosci*, 38(24), pp 5495-5506.
- Schnee, M. E., Santos-Sacchi, J., Castellano-Munoz, M., Kong, J.-H. & Ricci, A. J. 2011a. Calcium-Dependent Synaptic Vesicle Trafficking Underlies Indefatigable Release at the Hair Cell Afferent Fiber Synapse. *Neuron*, 70(2), pp 326-338.
- Schnee, M. E., Santos-Sacchi, J., Castellano-Munoz, M., Kong, J. H. & Ricci, A. J. 2011b. Tracking vesicle fusion from hair cell ribbon synapses using a high frequency, dual sine wave stimulus paradigm. *Communicative & Integrative Biology*, 4(6), pp 785-787.

The Frequency Response of Outer Hair Cell Voltage-Dependent Motility Is Limited by Kinetics of Prestin

Joseph Santos-Sacchi^{1,2,3} and Winston Tan¹

¹Department of Surgery (Otolaryngology), ²Department of Neuroscience, and ³Department of Cellular and Molecular Physiology, Yale University School of Medicine, New Haven, Connecticut 06510

The voltage-dependent protein SLC26a5 (prestin) underlies outer hair cell electromotility (eM), which is responsible for cochlear amplification in mammals. The electrical signature of eM is a bell-shaped nonlinear capacitance (NLC), deriving from prestin sensor-charge (Q_p) movements, which peaks at the membrane voltage, V_h , where charge is distributed equally on either side of the membrane. Voltage dependencies of NLC and eM differ depending on interrogation frequency and intracellular chloride, revealing slow intermediate conformational transitions between anion binding and voltage-driven Q_p movements. Consequently, NLC exhibits low-pass characteristics, substantially below prevailing estimates of eM frequency response. Here we study in guinea pig and mouse of either sex synchronous prestin electrical (NLC, Q_p) and mechanical (eM) activity across frequencies under voltage clamp (whole cell and microchamber). We find that eM and Q_p magnitude and phase correspond, indicating tight piezoelectric coupling. Electromechanical measures (both NLC and eM) show dual-Lorentzian, low-pass behavior, with a limiting (τ_2) time constant at V_h of 32.6 and 24.8 μ s, respectively. As expected for voltage-dependent kinetics, voltage excitation away from V_h has a faster, flatter frequency response, with our fastest measured τ_2 for eM of 18.2 μ s. Previous observations of ultrafast eM ($\tau \approx 2 \mu$ s) were obtained at offsets far removed from V_h . We hypothesize that trade-offs in eM gain-bandwidth arising from voltage excitation at membrane potentials offset from V_h influence the effectiveness of cochlear amplification across frequencies.

Key words: capacitance; cochlear amplification; electromotility; membrane proteins; outer hair cell; sensor charge

Significance Statement

Of two types of hair cells within the organ of Corti, inner hair cells and outer hair cells, the latter evolved to boost sensitivity to sounds. Damage results in hearing loss of 40–60 dB, revealing amplification gains of 100–1000 \times that arise from voltage-dependent mechanical responses [electromotility (eM)]. eM, driven by the membrane protein prestin, may work beyond 70 kHz. However, this speed exceeds, by over an order of magnitude, kinetics of typical voltage-dependent membrane proteins. We find eM is actually low pass in nature, indicating that prestin bears kinetics typical of other membrane proteins. These observations highlight potential difficulties in providing sufficient amplification beyond a cutoff frequency near 20 kHz. Nevertheless, observed trade-offs in eM gain-bandwidth may sustain cochlear amplification across frequency.

Introduction

The voltage-dependent protein SLC26a5 (prestin) underlies outer hair cell (OHC) electromotility (eM; Zheng et al., 2000; Liberman et al., 2002), considered to be responsible for cochlear amplifica-

tion in mammals (Santos-Sacchi et al., 2006; Dallos et al., 2008). This mechanism provides 40–60 dB gain in our perceptions of sound. eM has been characterized biologically as ultrafast, exhibiting no attenuation beyond 70 kHz (Frank et al., 1999), and such uniform mechanical activity across frequencies is assumed to be required for cochlear amplification by some mammalian species that have hearing capabilities well beyond the range of human frequency detection.

While cochlear amplification clearly results from the voltage-dependent mechanical activity of the OHC, it behooves us to understand frequency-response characteristics of eM, since amplification may extend to very high frequencies in some mammals. There are at least two independent influences on eM frequency response. The first is the ability of the cell to provide

Received Feb. 16, 2018; revised May 14, 2018; accepted May 16, 2018.

Author contributions: J.S.-S. designed research; J.S.-S. and W.T. performed research; J.S.-S. analyzed data; J.S.-S. wrote the paper.

This work was supported by National Institutes of Health—National Institute on Deafness and Other Communication Disorders Grants R01 DC000273, R01 DC016318, and R01 DC008130 to J.S.-S. We appreciate thoughtful discussions with Fred Sigworth, and help with statistics from Fangyong Li.

Correspondence should be addressed to Joseph Santos-Sacchi, Surgery (Otolaryngology), Neuroscience, and Cellular and Molecular Physiology, Yale University School of Medicine, BML 224, 333 Cedar Street, New Haven, CT 06510. E-mail: joseph.santos-sacchi@yale.edu.

DOI:10.1523/JNEUROSCI.0425-18.2018

Copyright © 2018 the authors 0270-6474/18/385495-12\$15.00/0

the drive for eM, namely, the attenuating influence of the membrane resistive–capacitive (RC) time constant on receptor potentials at high frequency; the second is the ability of the prestin motor protein to follow voltage changes at high frequencies. It is this second issue, the focus of the pioneering work of Dallos and Evans (1995) and Frank et al. (1999), that we explore here.

The electrical correlate of eM is a bell-shaped nonlinear capacitance (NLC; Ashmore, 1990; Santos-Sacchi, 1991), which peaks at the membrane voltage (V_h) where the prestin voltage-sensor charge (Q_p) is equally distributed across the OHC membrane field in a way that is analogous to voltage-dependent ion channel capacitance/gating behavior (Armstrong and Bezanilla, 1974; Kilic and Lindau, 2001). We recently determined that the apparent, simultaneously evaluated, voltage dependence of NLC and eM differs depending on intracellular chloride level and interrogation frequency, revealing slow (multiexponential) intermediate conformational transitions between required anion binding and Q_p movements (Song and Santos-Sacchi, 2013). Consequently, analysis of NLC across frequency has revealed significant low-frequency roll-off (Santos-Sacchi and Song, 2014, 2016) that is incompatible with the demonstration of ultrafast eM lacking any evidence of low-pass components (Frank et al., 1999). Additionally, disparities that we and others have reported between electrical and mechanical properties (Gale and Ashmore, 1997) of the OHC motor appear to challenge the concept of tight electromechanical coupling in OHCs, namely, its piezoelectric-like behavior (Iwasa, 1993; Gale and Ashmore, 1994; Mountain and Hubbard, 1994; Kakehata and Santos-Sacchi, 1995; Dong et al., 2002).

Here we study simultaneously evoked prestin electrical (both NLC and Q_p) and mechanical (eM) responses, synchronously measured across frequencies to quantify electromechanical coupling in OHCs. We find that while Q_p and eM are indeed tightly coupled, NLC reports not on the frequency response of eM, but only on the limiting kinetics of eM. Finally, we identify two frequency components of NLC and eM (one slow, one fast), and show that trade-offs between frequency response and gain of eM, similar to the gain–bandwidth product optimization used in operational amplifiers, may be obtained by excitation of the OHC at a resting voltage offset from V_h . We conclude that voltage-dependent eM is intrinsically low-pass, in line with behavior of most voltage-dependent proteins, relative to the highest frequencies perceivable by certain mammals. However, we hypothesize that mechanisms that provide stimulus offsets from V_h , either shifts in resting potential or prestin's voltage dependence, may actually work to enhance the bandwidth of cochlea amplification.

Materials and Methods

Whole-cell recordings were made from single isolated OHCs from the apical turns of organ of Corti of guinea pigs and mice of either sex. Since prestin's identification in 2000 (Zheng et al., 2000), there is no evidence that prestin itself or its behavior differs in long or short OHCs from different regions of the cochlea (Santos-Sacchi et al., 2017). An inverted Nikon Eclipse TI-2000 microscope with a 40× lens was used to observe cells during voltage clamp. Experiments were performed at room temperature. Blocking solutions were used to remove ionic currents, thus limiting confounding effects on NLC determination and voltage delivery under voltage clamp (Santos-Sacchi, 1991; Santos-Sacchi and Song, 2016). Extracellular solution was as follows (in mM): 100 NaCl, 20 tetraethylammonium-Cl, 20 CsCl, 2 CoCl₂, 1 MgCl₂, 1 CaCl₂, 10 HEPES. Intracellular solution was as follows (in mM): 140 CsCl, 2 MgCl₂, 10 HEPES, and 10 EGTA. Contamination of prestin NLC by ion channel gating current is negligible since channel charge movement is orders of magnitude smaller than the OHC charge due to prestin (2–4 pC; Santos-Sacchi, 1991). All chemicals were purchased from Sigma-Aldrich.

Cell capacitance, prestin charge, and mechanical response. An Axon 200B amplifier was used for whole-cell (head stage $\beta = 1$) and microchamber (head stage $\beta = 0.1$) recording with jClamp software (www.scisoftco.com). A National Instruments 6550 AD/DA or Axon Digidata 1440 was used for digitizing. To avoid time-dependent influences on our measures, no averaging was done, except where noted. AC analysis of membrane currents (I_m) and eM were made by stimulating cells with individually delivered or summed voltages at harmonic frequencies from 48.8 to 12,500 Hz (depending on recording configuration) with a 10 μ s sample clock. Magnitude and phase of responses were computed by FFT in Matlab. Integration of AC currents to extract charge was performed in the frequency domain ($Q_p = I_m/j\omega$; $\omega = 2\pi f$; $j = \sqrt{-1}$). Since prestin charge movement has very shallow voltage dependence ($z \approx 0.85$), charge at very positive voltages where NLC is minimized (+50 or +130 mV) was subtracted following scaling to estimated values at 300 mV ($\times 0.875$ – 0.9), based on two-state Boltzmann fits, thereby removing charge generated by linear capacitance. Capacitance was measured using dual-sine analysis at harmonic frequencies (Santos-Sacchi et al., 1998; Santos-Sacchi, 2004). To extract Boltzmann parameters, capacitance-voltage data were fit to the first derivative of a two-state Boltzmann function as follows:

$$C_m = Q_{max} \frac{ze}{kT} \frac{b}{(1+b)^2} + C_{lin} \text{ where } b = \exp\left(\frac{-ze(V_m - V_{pkCm})}{kT}\right)$$

Q_{max} is the maximum nonlinear charge moved, V_{pkCm} or V_h is voltage at peak capacitance or equivalently, at half-maximum charge transfer, V_m is membrane potential, z is valence, C_{lin} is linear membrane capacitance, e is electron charge, k is Boltzmann's constant, and T is absolute temperature.

NLC determination requires stray capacitance removal due to analysis constraints (viz, admittance solutions assume no stray capacitance; Santos-Sacchi et al., 1998; Santos-Sacchi and Song, 2016). NLC was not measured following changes in series resistance compensation circuitry because phase lags introduced by compensation circuitry invalidate the system calibration used to correct for the system's frequency response. The system response is required for NLC measures. Patch pipettes were coated with M-coat (Micro Measurements) to reduce stray capacitance. Remaining stray capacitance was removed by amplifier compensation circuitry before whole-cell configuration. If necessary, additional compensation was applied under whole-cell conditions (Schnee et al., 2011a,b) and/or through a software algorithm to ensure expected frequency-independent linear capacitance (Santos-Sacchi, 2018).

Simultaneous eM measures were made with fast video recording or a photo diode system. The photo diode measurement details have been published (Santos-Sacchi and Song, 2014). Briefly, we stimulated with 50 mV peak discrete AC bursts across harmonic frequencies (12.2–6250 Hz) to explicitly excite the OHC eM nonlinearity and generate fundamental and harmonic responses. For video analyses, a Phantom 110 camera (Vision Research) was used for video measures at frame rates of 25 kHz (whole cell) or 50 kHz (microchamber). For whole cell, stimuli were the sum of nine 15 mV peak harmonic frequencies (48.8–12,500 Hz). Additional magnification was set to provide 176 nm/pixel. The bright edge of the cuticular plate was used to track OHC length change by fitting a Gaussian to the peak of the image, providing subpixel resolution of movements (see Fig. 2A). The fitted line (five pixels wide) was drawn to encompass the cuticular plate at right angles, the number of points (pixels) depending on the image thickness of the plate, which can vary from cell to cell. Only a single peak was chosen for tracking.

The patch electrode or microchamber provided a fixed point at the basal end or middle of the cell, respectively. For cells studied with video analysis under whole-cell mode, charge-movement magnitude was corrected for the magnitude roll-off of the 10 kHz Bessel filter. Series resistance (R_s) was determined from voltage step-induced whole-cell currents (Huang and Santos-Sacchi, 1993, their appendix). For the microchamber, a 30 kHz filter (external Frequency Devices 9002 filter with 200B open filter) was used to collect current data, but because of the complexity of charge movements (moving in opposite directions in each part of the partitioned cells), no analysis was performed. Resultant movements

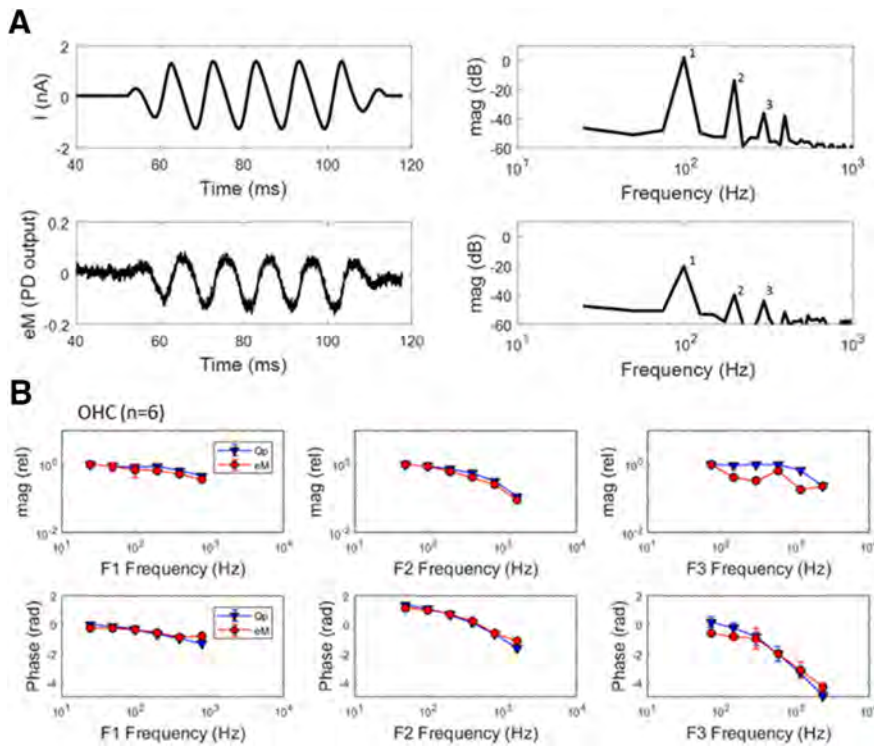


Figure 1. Gating charge and eM are coupled. **A**, Example of currents and eM at 97.7 Hz. Harmonics (1, 2, 3) are generated by nonlinearities in the process generating mechanical responses. **B**, Comparison of average ($n = 6$) relative magnitude and phase of eM and prestin sensor charge (Q_p) for harmonics 1, 2, and 3, illustrating tight coupling between the two measures of prestin activity across frequencies. Responses were time averaged 8–64 times to achieve an equal signal-to-noise ratio across frequencies. Fifty millivolt peak discrete AC bursts across harmonic frequencies were delivered to explicitly excite the OHC eM nonlinearity and generate fundamental and harmonic responses.

were analyzed by FFT in Matlab. The colors in surface plots were generated in the Matlab plotting routine `surf` with shading set to `<interp>`. This procedure allows contours to be readily observable. No relation to 3 dB breakpoint is intended.

For the microchamber, voltage across the membrane of the extruded length of the cell, qL , is estimated as the imposed microchamber voltage, V , factored by $1 - q$, q being extent (0–1) of extrusion (Dallos et al., 1993; Frank et al., 1999). The calculated correction is 0.4539, since our average $q = 0.546$. Shunt resistance could also be influential (Dallos et al., 1991; Huang and Santos-Sacchi, 1993); our average was $4.97 \pm 0.8 \text{ M}\Omega$ ($n = 8$), approximately estimated from voltage steps. With this shunt resistance, the calculated correction is quite accurate as shown by near equivalence of the Boltzmann z parameter for both eM and NLC (see Fig. 10). For the microchamber, AC stimuli were the sum of nine 30 mV peak harmonic frequencies (48.8–12,500 Hz), and given the correction factor above 0.4539, 13.62 mV was delivered to the extruded cell membrane, similar to whole-cell conditions. Microchamber eM responses were corrected for extrusion factor to equate to whole-cell measures (eM/q ; Frank et al., 1999).

At other than DC, the frequency cutoff [f_c , 3 dB down point, or time constant τ ($1/2\pi f_c$)] of voltage delivery will be determined, as in whole-cell voltage clamp, by R_s and predominantly cell capacitance, since for the OHC, cell capacitance dominates any stray capacitance of the macropipette. Additional lumped stray capacitance of the amplifier, pipette holder, etc., will not influence clamp τ since it only influences the circuit as a current divider (see Fig. 9). It is typically compensated electronically (e.g., in whole-cell mode) only to limit amplifier saturation, not to extend voltage-clamp frequency response. Thus, given a voltage-clamp amplifier that can provide sufficient current to the microchamber, voltage delivery across R_s in series with cell impedance will be immune to this stray capacitance. Thus, f_c will chiefly depend on q , where at $q = 0.5$, a balanced capacitance divider can be achieved (assuming inserted and extruded membrane τ 's are equal), and provide a maximally flat fre-

quency response for voltage delivery. The f_c will increase in a U-shaped manner on either side of $q = 0.5$, but will depend critically on R_s (see Fig. 11). We compensated stray capacitance with our amplifier (Axon 200B) compensation circuitry before recording to limit amplifier saturation. eM was corrected for microchamber clamp time constant effects based on voltage-induced transient responses of measured currents following AC stimulation (see Figs. 9, 10). Measurement noise floor was estimated from the saturated AC eM responses at +200 mV offset. Cells displaying maximum steady-state (DC) microchamber eM responses $< 1.0 \mu\text{m}$ were discarded, since such small responses may be a sign of reduced turgor pressure, which can reduce eM (Santos-Sacchi, 1991). Models were implemented in Matlab Simulink and Simscape, as detailed previously (Song and Santos-Sacchi, 2013; Santos-Sacchi and Song, 2014). Data points from previous publications were extracted from plots using the application Grabit (written by Jiro Doke) in Matlab.

Statistics. R_s -corrected V_m versus NLC, Q_p , and eM data were fit with the first derivative of a two-state Boltzmann function to provide comparable Boltzmann parameters z and V_h for each measure (Santos-Sacchi, 1991). Data are presented as mean \pm SE. Regressions were performed in Matlab. Using SAS 9.4 (SAS Institute), the mean phase data in Figure 9C were tested for significance from zero. A one-group t test was used to test the null hypothesis. The results are reported in the figure.

Results

In whole-cell mode, we simultaneously measured the first (fundamental), second, and third harmonic of both eM and membrane current I_m using single sinusoidal bursts of voltage (Fig. 1A). For the OHC under voltage clamp, the following equations apply:

$$I_m = i_{R_s} = i_{R_m} + i_{C_{lin}} + i_{NLC}$$

$$I_m = \frac{V_m}{R_m} + C_{lin} \frac{dV_m}{dt} + NLC \frac{dV_m}{dt}$$

$$i_{NLC} = \frac{dQ_p}{dt}$$

where Q_p is prestin charge. In our experiments, NLC is the dominant nonlinearity, since nonlinear ionic membrane currents are blocked. Nonlinear harmonic currents thus predominantly represent voltage-driven displacement currents arising from prestin sensor charge movements normal to the membrane field. Prestin charge at these harmonic frequencies, Q_p , is obtainable by integration of current, signifying that the phases of harmonic charge components will lag current phase by 90° .

While the nonlinear harmonic currents arise from prestin charge movements alone, those of the fundamental have additional contributions from linear components (C_{lin} , R_m) of the cell. To remove those linear components, so we can additionally compare electrical and mechanical responses at the fundamental, we note that the relationship between second harmonic eM and second harmonic nonlinear current should hold for the fundamental re-

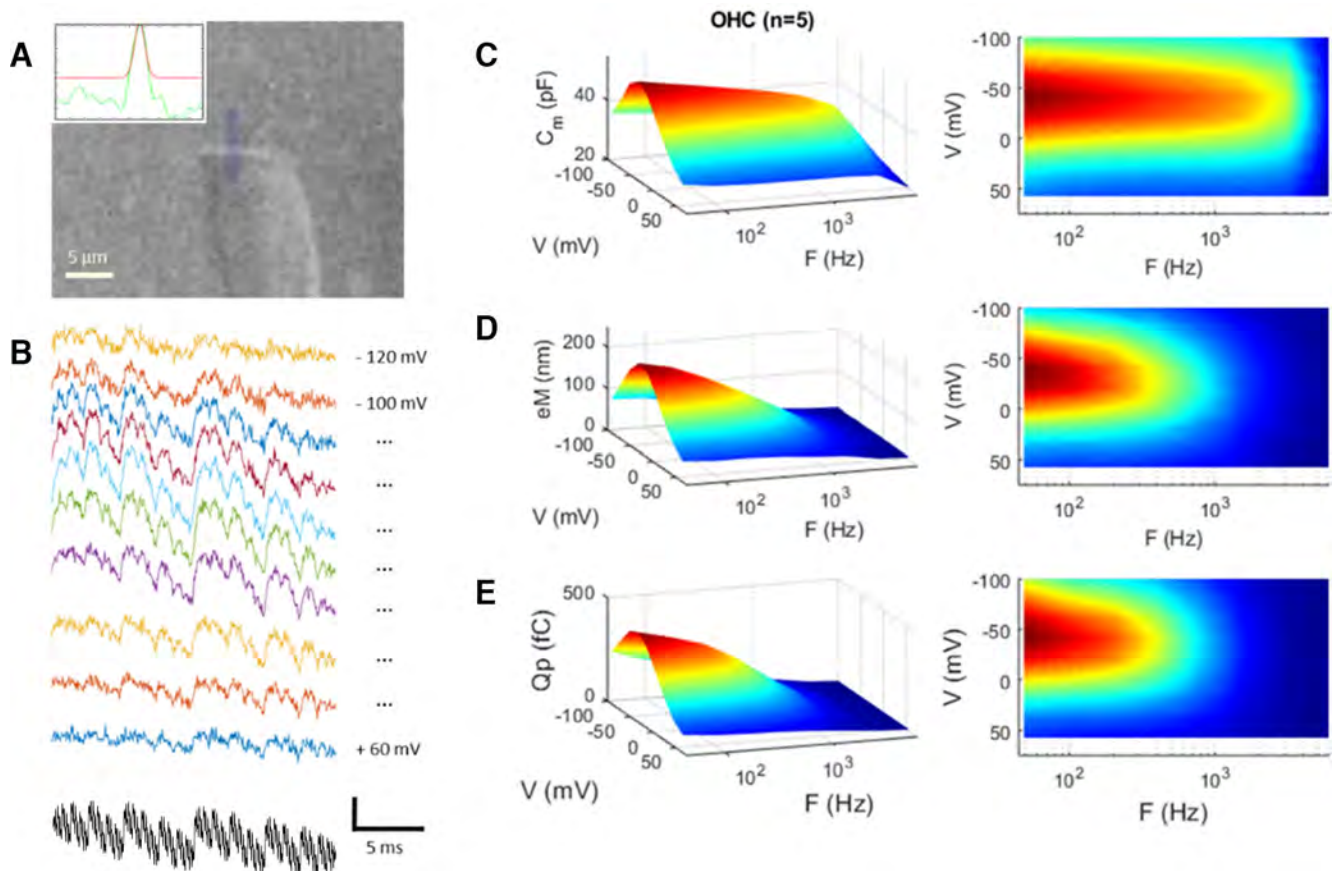


Figure 2. Low-pass electromechanical behavior of the OHC under whole-cell voltage clamp. **A**, Video frame of an OHC whose eM was measured by tracking the edge of its cuticular plate. Inset, Bright edge (green line) is fitted with a Gaussian (red line) and tracked across frames (25,000 fps). **B**, Raw eM responses (colored traces) generated by the multifrequency voltage stimulus (black trace) summed to differing holding potentials. eM responses are arbitrarily offset and colored for easy visualization. Vertical scale bar is 0.45 μm for eM and 50 mV for voltage (sum of 9 15 mV peak harmonic frequencies starting at 48.8 Hz). **C**, NLC, in contrast to linear capacitance, is frequency dependent, showing low-pass behavior. Rightmost panels show alternative view of surface plots to appreciate frequency response. **D**, eM shows lower-pass behavior compared with NLC. **E**, Prestin sensor charge (Q_p) shows behavior similar to eM. eM and Q_p frequency-response time constants at V_h are statistically indistinguishable by t test ($p = 0.134$). Average responses from five cells.

sponses (confirmed through modeling). Thus, the complex ratio of eM and current at the second harmonic will approximate that at the first harmonic (fundamental), expressed as follows:

$$\frac{eM_{f_2}}{Im_{f_2}} \approx \frac{eM_{f_1}}{Im_{f_1} - Im_{f_1lin}}$$

The linear component of Im_{f_1} , namely, Im_{f_1lin} , was solved for and subtracted from Im_{f_1} . These manipulations only affect fundamental frequency comparisons. The underlying premise to be confirmed is that the electromechanical activity of the OHC is piezoelectric-like, and that prestin sensor charge movements (Q_p) correspond to eM, despite recently identified phase differences between V_m and eM (Santos-Sacchi and Song, 2014), and previously identified timing disparities between Q_p and eM (Gale and Ashmore, 1997; Santos-Sacchi and Song, 2014). In our kinetic models, we assume eM corre-

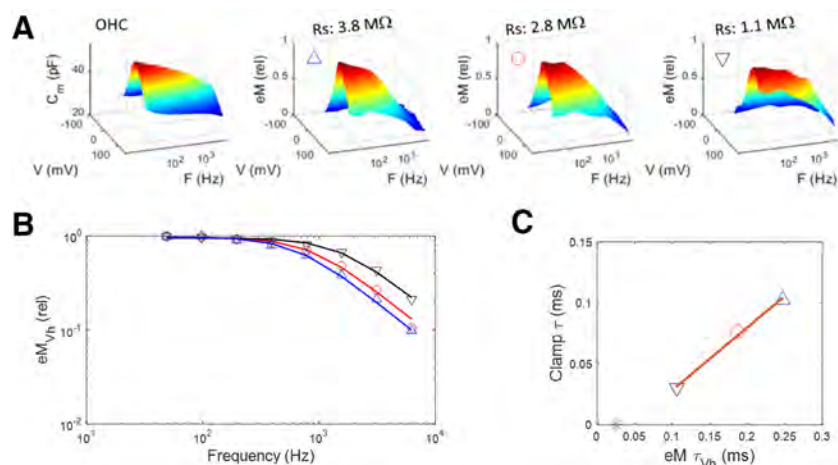


Figure 3. Whole-cell clamp time constant limits eM frequency response. **A**, Left panel shows NLC in an OHC, whose eM was measured at three different values of R_s (achieved through amplifier R_s compensation circuitry). As clamp time constant is decrementally reduced (clamp $\tau \approx R_s * C_m$), eM frequency response approaches that of NLC. Symbols correspond to all plots. **B**, Magnitude–frequency plot illustrating enhanced frequency response of eM at V_h . **C**, Linear relationship between eM and clamp time constants. eM τ_{Vh} approaches this cell’s NLC τ_{Vh} , determined from a single exponential fit (blue asterisk). Stimulus was 15 mV peak at each frequency.

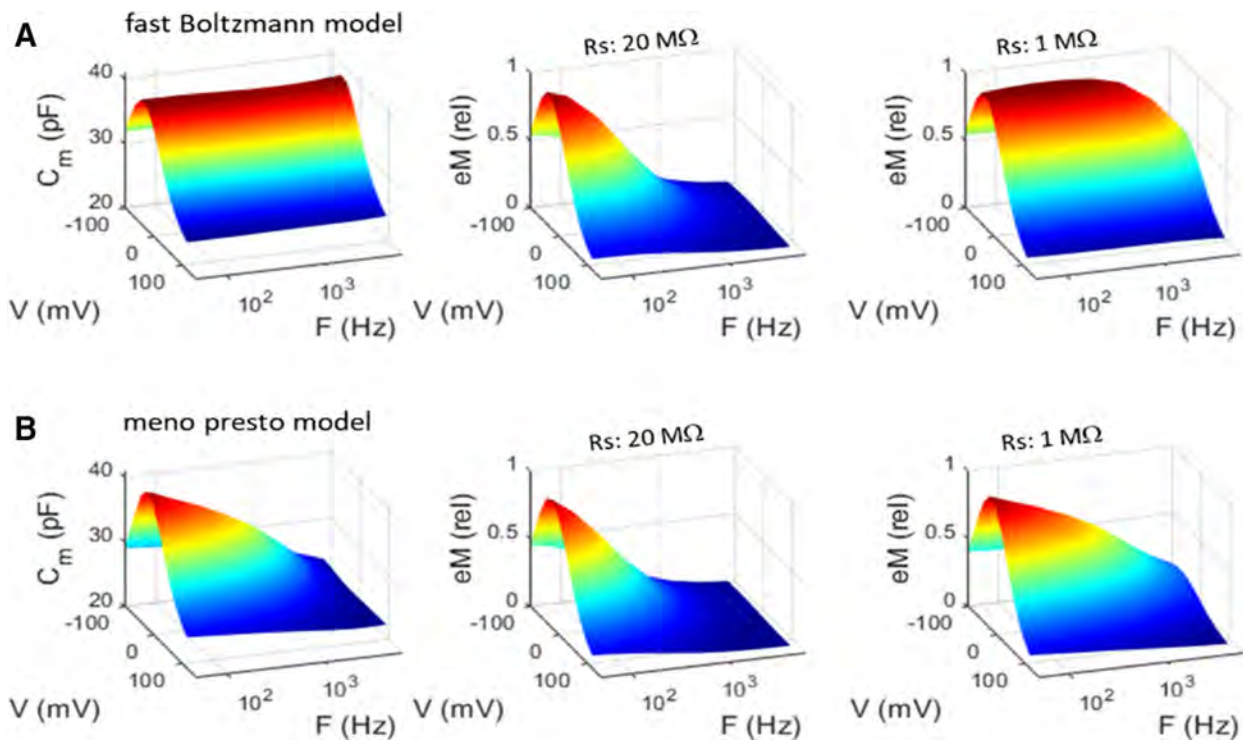


Figure 4. Models show that kinetics underlying NLC frequency response restrain frequency response of eM (Q_p). **A**, NLC of a two-state Boltzmann model is frequency independent. However, eM (Q_p ; right) faithfully follows clamp time constant. **B**, NLC of *meno presto* model incorporating slow multiexponential kinetics is low-pass. Note that eM (Q_p) frequency response is also increased by reducing clamp time constant, but is limited by kinetics that define NLC response. AC stimulus was 15 mV peak at each frequency.

sponds to the occupancy of the protein in the contracted state where positive sensor charge accumulates during depolarization/cell shortening. Thus, the validity of our model and of other similar (e.g., two state) models depends on tight coupling.

In Figure 1B, average (\pm SE; $n = 6$) magnitude and phase of first, second, and third harmonics of Q_p and eM are shown. The eM and Q_p data compare favorably, indicating that eM is tightly coupled in magnitude and time (phase) to prestin charge, as expected for a piezoelectric process. Considering the phase lag between OHC V_m and eM (Santos-Sacchi and Song, 2014), our observation of tight coupling between Q_p and eM identifies the piezoelectric nature of the OHC as being one with hysteresis. Namely, there is a delay between voltage drive and charge motion, but no delay between charge motion and OHC motion. We previously observed V_m – eM hysteresis in OHC electromechanical behavior (Santos-Sacchi et al., 1998, 2001).

Recently, NLC has been shown to present low-pass frequency-dependent behavior that we attributed to a slow, multiexponential kinetic process within prestin state transitions (Santos-Sacchi and Song, 2016). How does the frequency response of OHC NLC relate to eM ? To answer this question, we measured eM , NLC, and Q_p simultaneously across stimulation frequency. Figure 2A,B presents an example of an OHC whose eM was measured with video analysis at 25,000 fps during multifrequency voltage stimulation. In Figure 2C–E, average responses ($n = 5$) are depicted for NLC, eM , and Q_p , respectively. NLC shows low-pass behavior as we reported on previously (Santos-Sacchi and Song, 2016), but Q_p and eM show even lower pass behaviors. The latter two measures are remarkably similar, in line with our Q_p/eM data of Figure 1. The underlying mechanism for the differences between NLC and eM/Q_p is explored in the next couple of figures, where the influence of the whole-cell voltage-clamp time constant is considered. In Figure 3, an example of clamp τ effects on eM is

shown. As clamp speed is increased via amplifier R_s compensation circuitry, the frequency response of eM is similarly increased; $eM \tau_{vh}$ approaches this cell's NLC τ_{vh} , determined from a single exponential fit (Fig. 3C, blue asterisk), where prestin's kinetics are limiting. We had previously shown this effect for both AC and step eM responses (Santos-Sacchi, 1992), and this result derives from the voltage-dependent nature of eM (Ashmore, 1987; Santos-Sacchi and Dilger, 1988; Iwasa and Kachar, 1989).

Whereas eM (and Q_p ; see below) measures mirror clamp speed, NLC frequency-dependent behavior is independent of clamp speed. NLC estimates derive from the solution of the cell's admittance (Santos-Sacchi et al., 1998; Santos-Sacchi, 2004), essentially providing the ratio dQ_p/dV_m . Thus, in the face of V_m roll-off due to clamp time constant, the ratio of changes in V_m -driven Q_p and the driving force V_m remains unaffected by clamp τ , and therefore reports simply on the limiting kinetics of prestin transitions. This is confirmed through modeling (Fig. 4). Here clamp τ is altered by changes in R_s (clamp $\tau \approx R_s * C_m$). In Figure 4A, a model of an OHC possessing an NLC with frequency-independent Boltzmann characteristics shows an unencumbered increase in eM (i.e., Q_p) frequency response as R_s is lowered. However, the OHC possessing a multistate kinetic (*meno presto*) model of NLC (Santos-Sacchi and Song, 2016; Fig. 4B) shows that the frequency response of eM is governed by the kinetics revealed by NLC. That is, NLC specifies limits to the frequency behavior of eM or Q_p .

Figure 5 shows average ($n = 21$) guinea pig OHC NLC frequency dependence, and corresponding Q_p measures. For the NLC Lorentzian fit, we use the geometric mean of the dual stimulating frequencies, as we have done previously (Santos-Sacchi and Song, 2016). Only AC NLC was estimated with dual sine, but neither eM nor Q_p , so that eM and Q_p data correspond to the

primary frequencies directly. To estimate peak NLC at DC (33.5 pF, plotted leftmost on *x*-axis), measures were derived from voltage step-induced transients (Huang and Santos-Sacchi, 1993), namely, during changes in command holding potential. The mean (SE) Boltzmann characteristics of NLC at the lowest primary frequency of 48.8 Hz (geometric mean, 69.1 Hz) are NLC_{pk} : 32.03 (0.76) pF; V_h : -52.8 (4.1) mV; *z*: 0.86 (.016); and Q_{max} : 3.875 (0.17) pC. C_{lin} for this group of cells was 22.57 (0.46) pF. For comparison, our standard estimates of NLC at 390.6 Hz (geometric mean, 552.4 Hz) gives V_h : -53.3; *z*: 0.86; and Q_{max} : 3.24 pC. Note here that Q_{max} is larger at the lower frequency. At 97 Hz (near that of the NLC geometric mean of 69.1 Hz), Q_p fits provide V_h : -56.3 (2.6) mV; *z*: 0.836 (0.021); and Q_p : 127.9 (6.8) fC. AC voltage stimulation was 5 mV.

Normalized NLC (Fig. 5A) is characterized by two distinct kinetic components, one slow component ($\tau_1 = 1.12$ ms) and one fast component ($\tau_2 = 32.6 \mu s$). The latter component's amplitude is only a couple of decibels down from the former. Thus, the limiting frequency response of eM, dictated by the NLC frequency response, will derive from the second, faster component. The speed of Q_p (determined from single Lorentzian fits above 100 Hz stimulation), in agreement with eM measures, is dictated by whole-cell clamp speed (Fig. 5C,E). Here, we increased clamp speed (reduced clamp τ) to the point just before amplifier oscillation and correlated with Q_p speed, in an effort to predict prestin's cutoff τ at V_h . A linear extrapolation to zero clamp time constant (which works reasonably well for two-state kinetic models of differing kinetics; Fig. 5B) provides a limiting τ of 49 μs , compared with the fast NLC component τ of 32.6 μs . Notably, the apparent speed of Q_p increases when interrogated at voltages offset from V_h . At an offset of 30 mV from V_h , τ_{Qp} reduces to 13.3 μs , in a tradeoff between gain and bandwidth.

Figure 6 explores this gain–bandwidth trade-off in our eM data. We replot (Fig. 6A) the average data and Boltzmann fits from Figure 2, and construct eM–frequency plots at different offset voltages from V_h (Fig. 6B). The frequency responses further away from V_h are flatter and have faster time constants. These were single Lorentzian fits, and clearly even the fastest time constant (198 μs) is constrained by a slow whole-cell clamp τ .

To obtain faster clamp time constants, we recorded from mouse OHCs, where the reduced magnitude of both linear and nonlinear capacitances will enhance the speed of voltage delivery under whole-cell conditions (clamp τ down to ~15 μs). In Figure 7, we show kinetic behavior similar to that of guinea pig OHCs, with Q_p frequency response being clamp-speed dependent. Linear extrapolation provides a limiting τ_{Qp} of 27 μs .

Clearly, despite reductions in clamp time constant, the frequency responses of eM and Q_p are limited in whole-cell mode, to a limiting rate being, at best, approximate. Thus, to avoid whole-cell clamp τ effects, we measured Q_p frequency response in membrane patches, where speed of voltage delivery is unquestionably

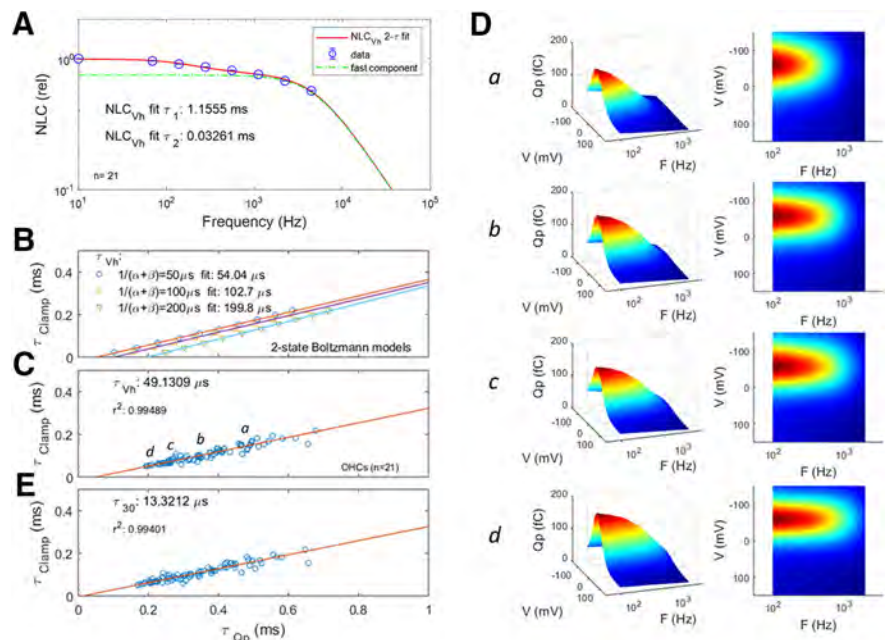


Figure 5. NLC has two frequency components whose kinetics limits Q_p frequency response. Average responses from 21 cells. **A**, Magnitude–frequency plot of average NLC at V_h . A dual-Lorentzian fit reveals slow and fast components (A_1 : 0.2453; τ_1 : 1.12 ms; A_2 : 0.7469; τ_2 : 32.6 μs). NLC is plotted relative to values at lowest frequency, which is NLC determined from step-induced (DC) transients (Huang and Santos-Sacchi, 1993) during changes in command holding potential. Error bars indicate SE. Dotted green line is plot of faster component. **B**, Relationship between clamp τ and $Q_p \tau$ for three two-state models of differing rate constants, illustrating that regressions to zero clamp τ can identify each model's characteristic time constant. **C**, Similarly, regressions on OHC Q_p provide a limiting time constant approaching the fast τ component of NLC. **D**, **a–d**, Five cell-binned averages computed and plotted, illustrating the enhanced frequency response as clamp τ decreases (**a**: $153.0 \pm 1.75 \mu s$; **b**: $100.9 \pm 1.2 \mu s$; **c**: $70.9 \pm 1.4 \mu s$; **d**: $55.7 \pm 1.9 \mu s$. Q_p Lorentzian fits data and model are from 100 to 3200 Hz. **E**, Plot of Q_p at an offset voltage of 30 mV from V_h , showing that τ_{Qp} decreases at voltages away from V_h (with gain–bandwidth tradeoffs). Five millivolt peak AC stimulation. See text for Boltzmann mean (SE).

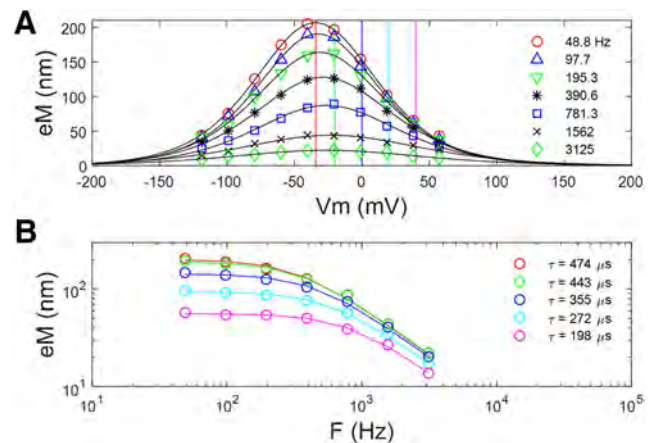


Figure 6. Similar to Q_p results, eM τ decreases at voltages offset from V_h . **A**, eM and Boltzmann fits from cells depicted in Figure 2 at the various recorded frequencies. **B**, Frequency plots derived from data at vertical lines in **A**. The further away from V_h , the faster is the frequency response, with a trade-off between gain and bandwidth.

fast. Figure 8 shows average responses ($n = 10$) of Q_p from on-cell patch recordings before establishment of whole-cell configuration. Patches (Fig. 8A,B) show frequency responses that are slower than whole-cell responses. This likely arises from physical constraints on patch membrane movements, as previously suggested by Gale and Ashmore (1997). That is, because eM is mirrored in Q_p , since each are tightly coupled, our measures of patch Q_p will show evidence of physical constraints in patch move-

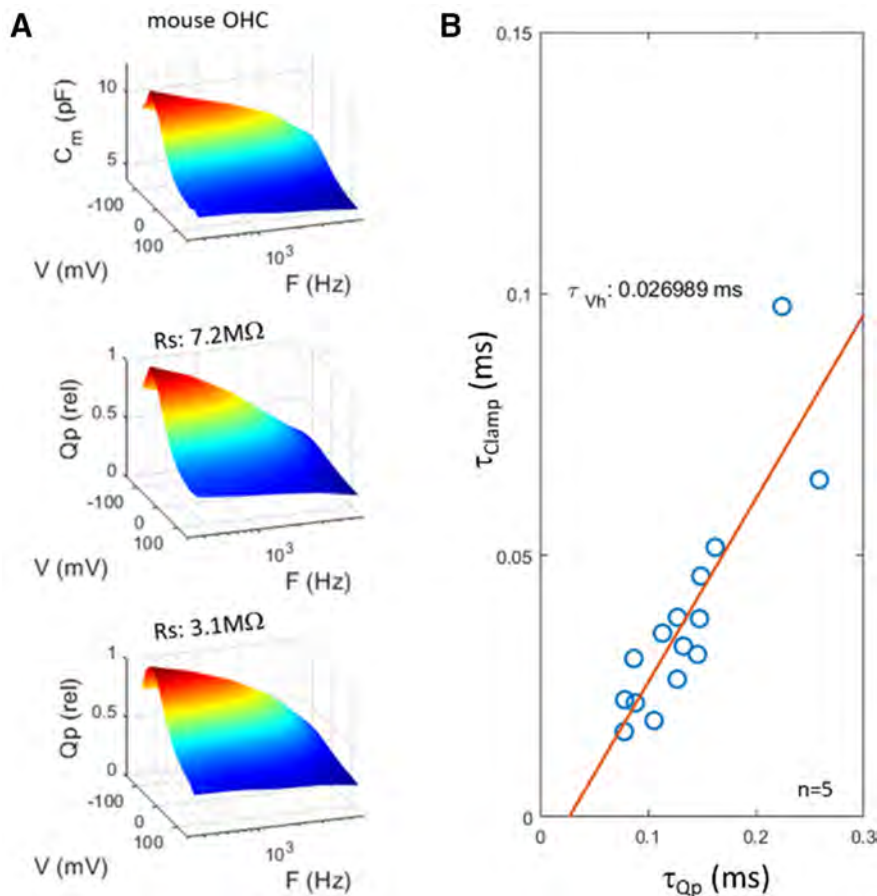


Figure 7. Mouse OHC recordings have reduced clamp time constants, but show low-pass frequency-response behavior similar to guinea pig OHCs. **A, B**, NLC is low pass at V_h (**A**) and clamp τ influences Q_p frequency response (**B**). Extrapolation estimate of τ_{Op} is 27 μ s. Five millivolt peak AC stimulation.

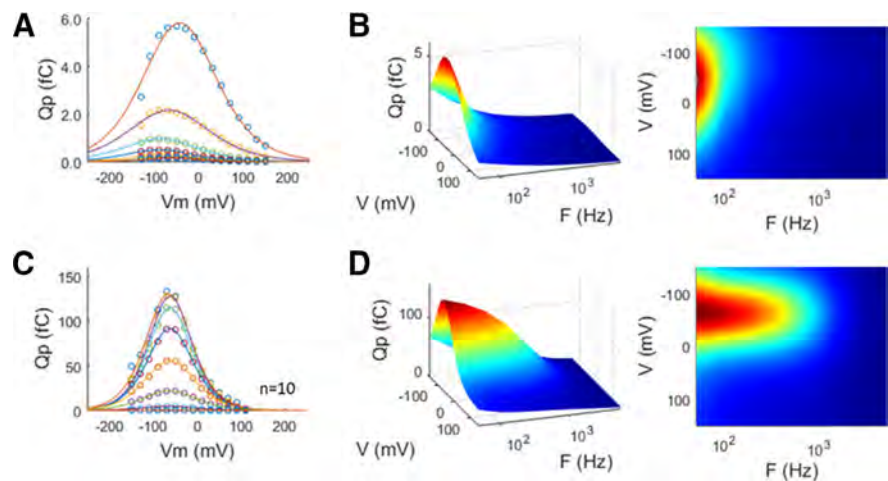


Figure 8. Average Q_p frequency response for on-cell patches compared with subsequent whole-cell measures. **A**, On-cell Q_p with Boltzmann fits to data from individual frequencies. **B**, Frequency response in patches is low pass. **C, D**, Following patch rupture, Q_p increases (**C**) and frequency response extends (**D**). These data possibly signify that patch movements are constrained compared with whole-cell conditions, as previously suggested (Gale and Ashmore, 1997). Five millivolt peak AC stimulation. Patch responses were averaged 32 times.

ments. Indeed, Adachi and Iwasa (1999) have shown that NLC can be blocked by physical constraints on the membrane. On the other hand, following whole-cell establishment (Fig. 8C,D), conformational changes in prestin are freely expressible, and an increase in bandwidth is found.

Finally, we directly studied eM frequency response using the microchamber technique, which theoretically has enormous wideband voltage delivery (Dallos and Evans, 1995; Frank et al., 1999) and, similar to whole-cell configuration, allows for unencumbered conformational changes in prestin.

It is well known that the relaxation time course of measured currents induced by voltage perturbation in whole-cell voltage clamp mirrors the time course (frequency response) of the voltage imposed across the cell membrane (Sigworth, 1995). We discussed some electrical characteristics of the microchamber in Materials and Methods. In Figure 9C–E, we additionally emphasize that the frequency response of the currents measured in the microchamber configuration also characterizes the frequency response of the voltages delivered to the membranes inside and outside the chamber. In this figure, we show results from a Matlab Simscape model of the microchamber using our stimulus protocol (see Fig. 11, model parameters in legend). The time constants of current in Figure 9C (fitted black lines; $\tau_{ta} = 19.5 \mu$ s; $\tau_{tb} = 16.2 \mu$ s) are the same for membrane voltage inside (Fig. 9D; $\tau_{ta} = 19.4 \mu$ s; $\tau_{tb} = 15.9 \mu$ s) and outside (Fig. 9E; $\tau_{ta} = 19.5 \mu$ s; $\tau_{tb} = 16.5 \mu$ s) the microchamber. A Lorentzian function $A = 1/[1 + (2\pi f\tau)^2]^{1/2}$ is used to generate a normalized magnitude frequency response that can be used to correct the frequency roll-off of voltage-dependent processes driven by the clamp, which we do below for our microchamber eM data. It is important to have frequency response estimates coincident with protocol stimulation, as drifts in the resistive components of the microchamber can have dramatic effects on the speed of voltage excitation (see Fig. 11).

Figure 10 shows microchamber measures of OHC eM at DC and across frequencies. Maximum DC eM gain (peak of the Boltzmann fit derivative) is 16.8 nm/mV in excellent agreement with earlier reports (Ashmore, 1987; Santos-Sacchi, 1989; Fig. 10A). The z parameter of the microchamber eM Boltzmann fit (0.83) also compares favorably to that of NLC (0.86) and Q_p (0.84), detailed above (Fig. 5). Based on our microchamber clamp τ (Fig. 10B), eM data were corrected for a cutoff frequency of 6.17–6.64 kHz. The microchamber approach reveals a second exponential component (τ_2) of eM that was unseen in the whole-cell data because of clamp τ limitations. Fitted sums of two Lorentzians were made at two microchamber offset voltages. At zero microchamber offset, A_1 : 1.63 nm/mV; A_2 : 3.45 nm/mV; τ_1 : 0.68 ms; τ_2 : 18.19 μ s. At -68 mV microchamber

At zero microchamber offset, A_1 : 1.63 nm/mV; A_2 : 3.45 nm/mV; τ_1 : 0.68 ms; τ_2 : 18.19 μ s. At -68 mV microchamber

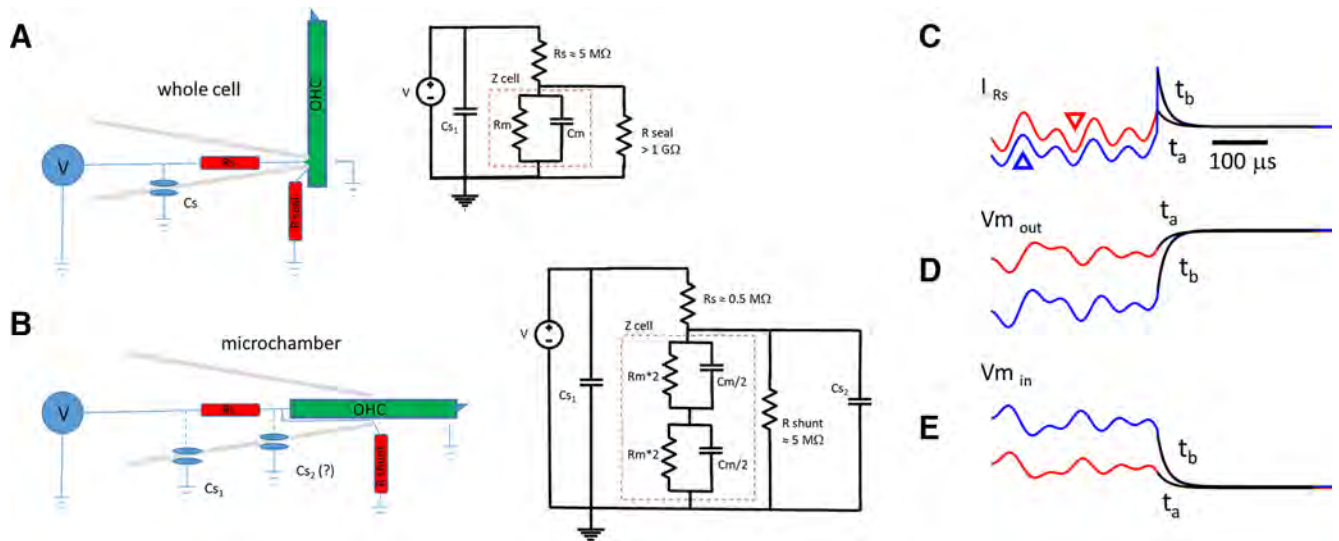


Figure 9. Electrical configuration of whole-cell and microchamber voltage clamp. **A**, Whole-cell clamp speed is limited by $\tau \approx R_s * C_m$. Stray capacitance (amplifier, pipette holder, and pipette) is typically modeled in a position that does not interfere with voltage-clamp speed, but can influence measured high-frequency currents if not compensated. **B**, The microchamber partitions the cell partway within the orifice of the macropipette. Stray C_{s1} is as with whole-cell mode. The frequency response of voltage clamp also depends on R_s and C_m , since stray C_{s2} , if it contributes at all, is dominated by C_m . The configuration in the figure is for a cell midway in the microchamber, membrane C_m equally divided. At high frequencies, the input capacitance will be the series combination of $C_m/2$ and $C_m/2$, giving a value of $C_m/4$. Thus, $\tau \approx R_s * C_m/4$ provides a faster clamp than whole cell, but the configuration suffers from lack of DC voltage-clamp control across the membranes. With partitioning of the cell more or less within the chamber, the series combination of the nonequal partitioned cell C_m will provide an input C_m less than the smaller of the two partitioned capacitances, regardless of its location inside or outside the microchamber. Thus, clamp τ for both inserted and extruded membranes will have the same U-shaped speed function, being slowest at the half-inserted condition, as depicted. **C**, Displayed are two current traces (t_a and t_b) generated by a Matlab Simscape microchamber model using a voltage protocol similar to our DC off-set AC voltage protocol (Fig. 10B, inset). The red trace (also marked with a downward red triangle) is at zero offset, and the blue trace (also marked with an upward blue triangle) is at an offset of -65 mV. Black lines are single exponential fits. Under voltage clamp, the time course of capacitive currents mirrors the time course of the voltage delivered to the cell membrane, as shown in **D** and **E**. See text for more details.

offset, near V_h , A_1 : 11.52 nm/mV; A_2 : 4.32 nm/mV; τ_1 : 3.45 ms; τ_2 : 25.26 μ s. Both slow and fast exponential component magnitudes and time constants were influenced by offsets from V_h , in a similar fashion to whole-cell data (Fig. 7). This indicates that the kinetics of the second component takes on increasingly greater dominance as excitation moves away from V_h , and that prestin follows the kinetic rules governing voltage-dependent proteins.

Discussion

NLC reflects the restricted movement of sensor charge (or gating charge) in response to transmembrane voltage perturbations, and is a characteristic of membrane-bound, voltage-dependent proteins, such as ion channels and some transporter family members, including prestin. The time constant of charge movement in voltage-dependent proteins is typically within the 100–1000 μ s range. For example, Lu et al. (1995), using very wideband capacitance measures, have shown that the GAT1 cotransporter and the cardiac Na, K pump present capacitance frequency responses over an order of magnitude slower than that produced by voltage-induced translocations of the small hydrophobic ion dipicrylamine across the membrane field: a rate of 9500 s^{-1} ($\tau = 105$ μ s, $f_c = 1.5$ kHz). Similar time constant estimates of ion channel gating currents are also within this range, and differences in kinetics among voltage-sensitive proteins likely arise from molecular variation within the protein (even within a single residue), leading to alterations in energy barriers between conformational states (Lacroix and Bezanilla, 2012). In the case of prestin, displacement currents represent charge movements that drive conformational changes in the protein, and effect voltage-dependent mechanical responses in OHCs, so-called electromotility. Since the initial identification and characterization of NLC/gating cur-

rents in OHCs (Ashmore, 1989, 1990; Santos-Sacchi, 1990, 1991), it has been viewed as a frequency-independent, fast two-state Boltzmann process. In fact, the frequency extent of NLC and eM has been documented out to progressively higher limits over the years (Ashmore, 1987; Santos-Sacchi, 1990, 1992; Dallos and Evans, 1995; Frank et al., 1999). Indeed, electrically evoked eM presents well above the auditory frequency requirements of species that have been studied (Frank et al., 1999; Grosh et al., 2004). In the present study, we provide evidence that counters the prevailing concept of ultrafast, voltage-driven eM.

By analyzing simultaneous and synchronous measures of eM, NLC, and sensor charge (Q_p) at voltage-stimulating frequencies from DC to 12.5 kHz, we show that within this bandwidth NLC displays a low-pass nature that reveals the limiting kinetics acting on eM and Q_p . Both eM and NLC display slow and fast components, the eM components near V_h [$\tau_1 = 3.45$ ms (33.8 Hz); $\tau_2 = 25.26$ μ s (6.25 kHz)] being similar to our current estimate of NLC cutoff frequency at V_h [$\tau_1 = 1.16$ ms (137.2 Hz); $\tau_2 = 32.6$ μ s (4.88 kHz)] at room temperature. At zero microchamber offset, eM time constants are faster [$\tau_1 = 0.68$ ms (234 Hz); $\tau_2 = 18.2$ μ s (8.74 kHz)]. Earlier, Gale and Ashmore (1997) found a time constant of 16 μ s (9.94 kHz) for NLC. Corrections for *in vivo* temperatures could extend the bandwidth. Indeed, we have found significant effects of temperature on NLC (Santos-Sacchi and Huang, 1998; Meltzer and Santos-Sacchi, 2001; Santos-Sacchi et al., 2009; Okunade and Santos-Sacchi, 2013), giving approximately a Q_{10} of 2. A previous Q_{10} estimate was 1.33 (Ashmore and Holley, 1988). Assuming a Q_{10} of 2, Gale and Ashmore's f_c for NLC is 22.8 kHz. Our fastest eM response would indicate an f_c of 20 kHz at 37°C. Thus, even correcting voltage-dependent NLC kinetics to body temperature would not match the widest eM

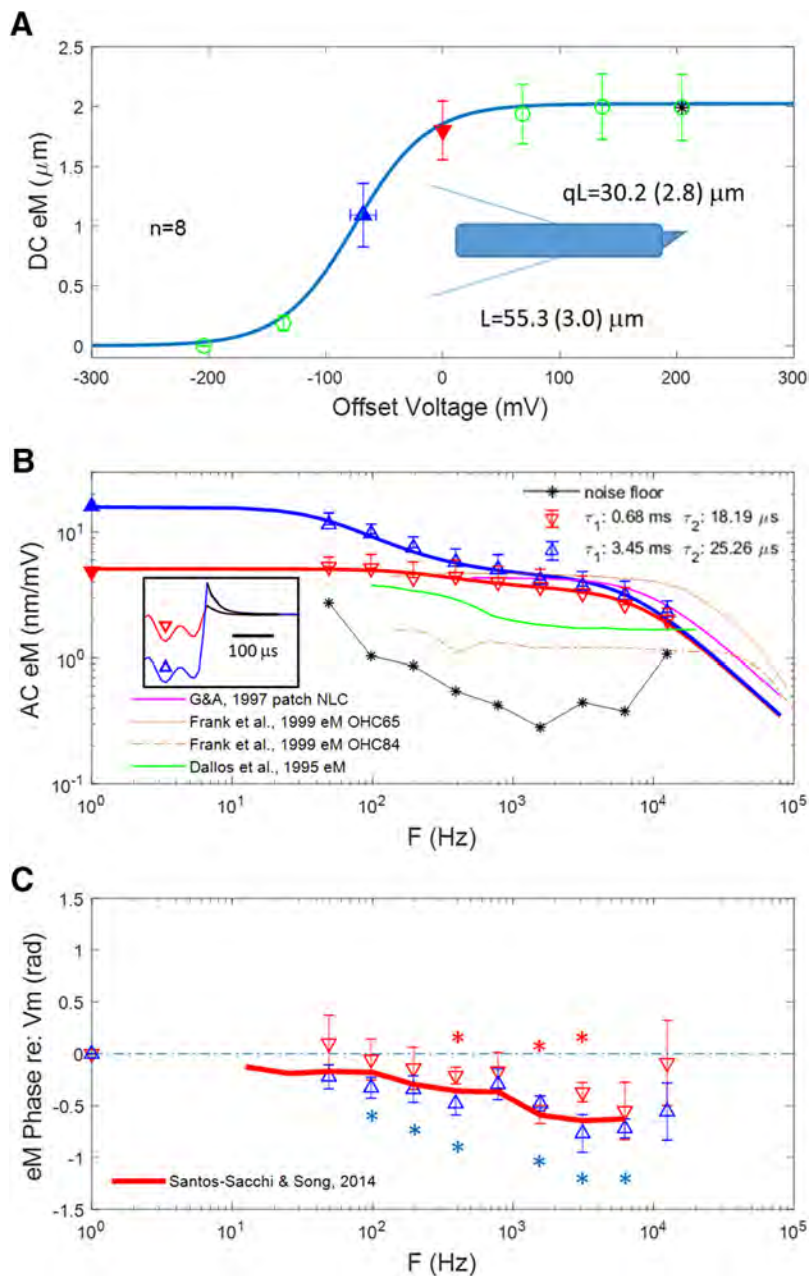


Figure 10. eM evoked with the microChamber wide-band stimulus delivery system and video captured at 50,000 fps. No frame averaging. Two components are evident, whose frequency response is dependent on offset from V_h . **A**, DC eM magnitude versus offset voltage. Cells were partitioned near midway along cell length (schematic), with average length (L) being $55.3 \pm 3.0 \mu\text{m}$, and the average portion outside the chamber (qL) being $30.2 \pm 2.8 \mu\text{m}$. The Boltzmann fit provides a z parameter of 0.83, in good agreement with our estimates from NLC and Q_p . Our eM gain of 16.8 nm/mV is typical of reported whole-cell responses. In the absence of a voltage offset, stimulation is substantially removed from V_h , the location of maximal gain. **B**, Magnitude–frequency plot of average eM from two regions of the DC plot (denoted by solid triangles). DC average gains derived from **A** are replotted on left gain (nm/mV) axis. The boxed inset shows the current relaxations after return to zero voltage (red and blue), fit with a single exponential (black lines), and used to correct for voltage frequency roll-off. Clamp τ at zero offset: $25.8 \mu\text{s}$; near V_h : $23.96 \mu\text{s}$. Colors and symbols correspond to offsets and match those of the model of Figure 9C–E. See text for more details. Responses obtained from an offset close to V_h (upward blue triangles) show a large low-pass component, whereas responses without an offset (downward red triangles) show a reduced low-pass component. Each has faster components away from V_h . Thin, black asterisk line is noise floor estimated from $+200 \text{ mV}$ offset in **A**, where AC responses are saturated. For comparison, magenta lines depict patch NLC from Gale and Ashmore. Brown lines show microchamber eM gain functions for two cells from Frank et al. Green line from Dallos et al. shows microchamber eM gain derived from their reported excitation voltage of $\pm 0.6 \text{ mV}$. Clearly, these eM data were collected at offset from V_h . See text for discussion. **C**, eM phase shows differences depending on voltage offset that may be due to differing eM gain. While a clear frequency-dependent lag relative to voltage occurs near V_h , it is less clear for responses away from V_h . Statistical significance ($p < 0.05$) from zero is indicated by correspondingly colored asterisks. The red line depicts the eM phase found by us previously under whole-cell conditions (Santos-Sacchi and Song, 2014). AC voltage stimulation at each frequency was $\sim 14 \text{ mV}$ (see Materials and Methods).

bandwidth estimate (80 kHz or $2 \mu\text{s}$ τ_c , being given by $1/2\pi\tau$) of Frank et al. (1999) found at room temperature.

Our observation of low-pass electro-mechanical behavior within our investigated bandwidth is clearly related to offset position along the eM– V_m Boltzmann relation where measures were made (Fig. 10). Frequency response measures arising from voltage perturbations away from V_h provide enhanced V_m following fidelity, i.e., a faster and flatter frequency response. It is well known that two-state, voltage-dependent transition kinetics between conformations is slowest at V_h (where the peak energy barrier resides), and speeds up on either side of V_h (Hodgkin and Huxley, 1952; Hille, 1992; Destexhe and Huguenard, 2000). The replotted eM gain data of Frank et al. and Dallos et al. (Fig. 10) clearly show that their measures were taken at significant offsets from V_h , where we also find flatter frequency responses. This likely explains the missing slower component in their data. However, what about the high-frequency limit derived from our eM/NLC and Gale and Ashmore's NLC measures? Why would the Frank et al. eM response extend beyond the limits indicated by NLC kinetics? That is, why is there an apparent uncoupling between prestin charge movement and OHC motility, which we have demonstrated should exist (Figs. 1, 2)? Possible explanations for these kinetic disparities between charge movement and eM may be due to experimental differences among studies.

In voltage-clamp experiments, including the microchamber method, corrections for voltage delivery roll-off must be made since the fidelity of voltage clamp across frequencies suffers from the effects of electrode resistance and membrane capacitance. Accounting for these effects is simply a matter of correcting for the time course of relaxation of measured capacitive currents, as we did. This is a valid and standard approach. Only in the unattainable absence of electrode resistance would no correction be necessary. In Frank et al. (1999), voltage corrections for microchamber frequency response were based on assumed stray capacitance influences, which they explicitly identified, in the absence of compensation circuitry, as limiting their microchamber voltage delivery. However, the microchamber voltage clamp behaves exactly as that of the whole-cell voltage clamp where the bulk of stray capacitance (amplifier, pipette holder, and pipette) does not diminish clamp speed. Indeed, in simulations of models shown in Figure 9, stray capacitance C_s has no

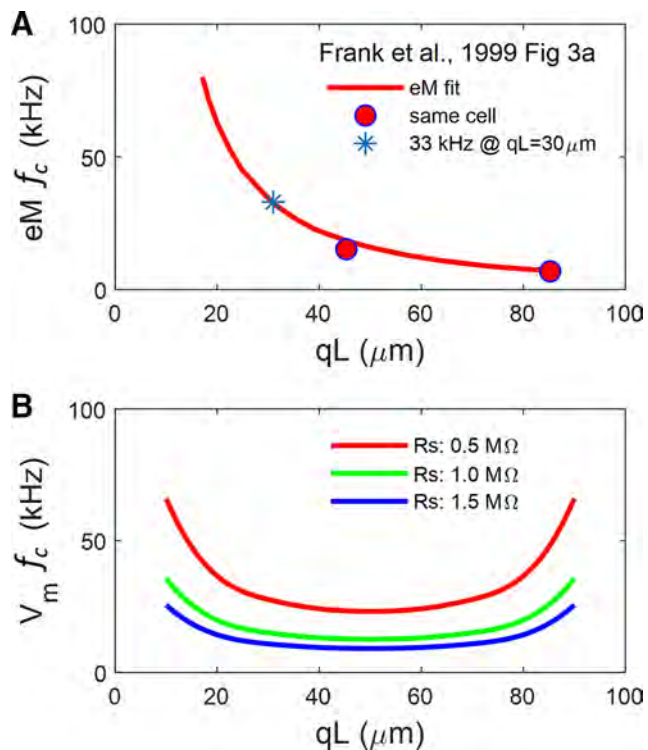


Figure 11. Apparent disparity between microchamber voltage and eM. **A**, Fit of eM f_c for 57 cells from Frank et al. Figure 3A, and response of same cell with differing cell extrusion, qL . Asterisk denotes f_c at a qL similar to our present average. **B**, V_m cutoffs for a cell model possessing NLC (capacitor with 2-state Boltzmann characteristics), indicating marked dependence of f_c on R_s . Cell parameters are C_{lin} : 22 pF; R_m : 300 M Ω ; R_s : 0.5 (red), 1.0 (green), or 1.5 (blue) M Ω ; R_{sh} : 5 M Ω ; NLC parameters are z : 0.85; Q_{max} : 3.8 pC; V_h : 0 mV. f_c is a U-shaped function of qL .

effect on clamp frequency response, and Cs_2 , which might arise at the extreme tip of the pipette, would be extremely small with negligible influence on clamp speed. Thus, correction for an assumed effect of voltage roll-off due to stray capacitance could likely have resulted in voltage overcorrections. On the other hand, we agree with Frank et al. that mechanical responses may be impeded by physical constraints, and this is potentially borne out by our very low pass Q_p behavior in patches, compared with subsequent whole-cell measures (Fig. 8). Indeed, Gale and Ashmore found a time constant for patch movements $\sim 84 \mu\text{s}$, compared with 16 μs for NLC. So, we might surmise for our measures, that the fast time constant of eM, even in whole-cell mode, could have been physically constrained. It is noteworthy that Frank et al. found a wide range of cutoffs depending on OHC qL , and that for our average qL of 30 μm , their roll-off was at 33 kHz, still substantially faster than our measure at 8.74 kHz.

This possibility of eM physical constraints is highlighted by Frank et al.'s Figure 3A, where eM f_c continuously increases as qL decreases, showing an apparent length-dependent cutoff (Fig. 11A). In Figure 11B, we show that this behavior is not expected for an ultrafast process that relies upon and can faithfully follow voltage excitation within the microchamber (see Fig. 9B, legend). That is, the efficacy of AC voltage delivery (f_c) in the microchamber should follow a U-shaped function of cell extrusion, with $qL = 0.5$ providing the slowest voltage-dependent frequency response. That is, the f_c of microchamber voltage delivery is symmetrical on either side of $qL = 0.5$, since the reduced capacitance of the smaller pole, regardless of whether it is the included or excluded pole, will present to the voltage clamp a series combination of the partitioned capacitances. The observation that for

$qL > 0.5$ mechanical f_c does not follow voltage f_c indicates that the response is not strictly voltage-dependent or that the movement of that excluded pole is mechanically impeded. Interestingly, Frank et al. required an additional overdamped resonance to fit their ultrafast eM data, which they attribute to an inertial contribution ($\sim 6\%$ of the cell's mass).

The relation between resting membrane potential and NLC V_h will determine where along the eM gain function the OHC works. Receptor potentials driving eM at a location away from V_h will provide reduced gain, but enhanced frequency response. Which characteristic is more important for cochlear amplification is difficult to assess; however, it is known that mouse mutants showing one-third of prestin expression and Q_p hear normally at low and middle frequencies (Yamashita et al., 2012), indicating that full gain may not be required. Currently, we do not know V_h *in vivo*. Even the value of resting potential of the OHC *in vivo* is contested (Dallos et al., 1982; Russell and Sellick, 1983; Johnson et al., 2011). To complicate matters, there is a plethora of biophysical forces that can alter V_h , including intracellular Cl^- level, membrane tension, and even membrane potential itself (Iwasa, 1993; Gale and Ashmore, 1994; Kakehata and Santos-Sacchi, 1995; Santos-Sacchi et al., 1998, 2017; Oliver et al., 2001; Rybalchenko and Santos-Sacchi, 2003, 2008). We hypothesize that feedback mechanisms that influence these biophysical forces, and efferent feedback (Brown et al., 1983) that alters resting membrane potential, contribute to a mechanism where eM gain–bandwidth trade-offs influence the effectiveness of cochlear amplification, similar to the tuning performed on operational amplifiers.

A note should be made about the implications of isolated OHC studies to the cell's role *in vivo*. Currently, it is impossible to monitor, across acoustic frequencies, the length changes in individual OHCs within the organ of Corti. However, tremendous strides have been made using optical coherence tomography to visualize movements within the intact living organ. Thus, unexpected observations of low-frequency mechanical behavior of supporting cells in the cochlear apex (Gao et al., 2014), and intriguing observations of motions at the OHC–Deiters cell interface deep within the organ (Cooper and van der Heijden, 2017) are changing the way we view OHC mechanical influences in the cochlea that underlie cochlear amplification. However, until more precise measures evolve, single-cell studies, which are required to determine intrinsic capabilities of the OHC that may influence cochlear mechanics, remain important for cochlear modelers.

In summary, we find that OHC eM and associated electrical correlates (NLC, Q_p) are low pass in nature, presenting behavior that is not very different from other voltage-dependent proteins, including characteristic changes in kinetics with voltage. We establish that eM and sensor charge are coupled in magnitude and time (phase), and confirm, with the microchamber technique, that driving voltage and eM phase differs, as we have shown under whole-cell voltage clamp (Santos-Sacchi and Song, 2014). eM phase lags voltage, similar to a piezoelectric with hysteresis. We speculate that the identification by some ultrafast eM *in vivo* (Grosh et al., 2004) simply reflects the effects of eM at very low gain levels, which are sufficient to influence structures within the cochlear partition. In other words, cochlear amplification does not require the full magnitude of eM observed at very low frequencies. Finally, it should be noted that intriguing indications exist that within the organ of Corti, mechanical loads on the OHC could alter the cell's frequency response (Iwasa, 2017).

References

- Adachi M, Iwasa KH (1999) Electrically driven motor in the outer hair cell: effect of a mechanical constraint. *Proc Natl Acad Sci U S A* 96:7244–7249. [CrossRef Medline](#)
- Armstrong CM, Bezanilla F (1974) Charge movement associated with the opening and closing of the activation gates of the Na channels. *J Gen Physiol* 63:533–552. [CrossRef Medline](#)
- Ashmore JF (1987) A fast motile response in guinea-pig outer hair cells: the cellular basis of the cochlear amplifier. *J Physiol* 388:323–347. [CrossRef Medline](#)
- Ashmore JF (1989) Transducer motor coupling in cochlear outer hair cells. In: *Mechanics of hearing* (Kemp D, Wilson JP, eds), pp 107–113. New York, NY: Plenum.
- Ashmore JF (1990) Forward and reverse transduction in the mammalian cochlea. *Neurosci Res Suppl* 12:S39–S50. [CrossRef Medline](#)
- Ashmore JF, Holley MC (1988) Temperature-dependence of a fast motile response in isolated outer hair cells of the guinea-pig cochlea. *Q J Exp Physiol* 73:143–145. [Medline](#)
- Brown MC, Nuttall AL, Masta RI (1983) Intracellular recordings from cochlear inner hair cells: effects of stimulation of the crossed olivocochlear efferents. *Science* 222:69–72. [CrossRef Medline](#)
- Cooper N, van der Heijden M (2017) Spatial profiles of sound-evoked vibration in the gerbil cochlea. In: *Mechanics of hearing conference*. St. Catherines, ON, Canada, June.
- Dallos P, Evans BN (1995) High-frequency motility of outer hair cells and the cochlear amplifier. *Science* 267:2006–2009. [CrossRef Medline](#)
- Dallos P, Santos-Sacchi J, Flock A (1982) Intracellular recordings from cochlear outer hair cells. *Science* 218:582–584. [CrossRef Medline](#)
- Dallos P, Evans BN, Hallworth R (1991) Nature of the motor element in electrokinetic shape changes of cochlear outer hair cells. *Nature* 350:155–157. [CrossRef Medline](#)
- Dallos P, Hallworth R, Evans BN (1993) Theory of electrically driven shape changes of cochlear outer hair cells. *J Neurophysiol* 70:299–323. [CrossRef Medline](#)
- Dallos P, Wu X, Cheatham MA, Gao J, Zheng J, Anderson CT, Jia S, Wang X, Cheng WH, Sengupta S, He DZ, Zuo J (2008) Prestin-based outer hair cell motility is necessary for mammalian cochlear amplification. *Neuron* 58:333–339. [CrossRef Medline](#)
- Destexhe A, Huguenard JR (2000) Nonlinear thermodynamic models of voltage-dependent currents. *J Comput Neurosci* 9:259–270. [CrossRef Medline](#)
- Dong XX, Ospeck M, Iwasa KH (2002) Piezoelectric reciprocal relationship of the membrane motor in the cochlear outer hair cell. *Biophys J* 82:1254–1259. [CrossRef Medline](#)
- Frank G, Hemmert W, Gummer AW (1999) Limiting dynamics of high-frequency electromechanical transduction of outer hair cells. *Proc Natl Acad Sci U S A* 96:4420–4425. [CrossRef Medline](#)
- Gale JE, Ashmore JF (1994) Charge displacement induced by rapid stretch in the basolateral membrane of the guinea-pig outer hair cell. *Proc Biol Sci* 255:243–249. [CrossRef Medline](#)
- Gale JE, Ashmore JF (1997) An intrinsic frequency limit to the cochlear amplifier. *Nature* 389:63–66. [CrossRef Medline](#)
- Gao SS, Wang R, Raphael PD, Moayed Y, Groves AK, Zuo J, Applegate BE, Oghalai JS (2014) Vibration of the organ of Corti within the cochlear apex in mice. *J Neurophysiol* 112:1192–1204. [CrossRef Medline](#)
- Grosh K, Zheng J, Zou Y, de Boer E, Nuttall AL (2004) High-frequency electromotile responses in the cochlea. *J Acoust Soc Am* 115:2178–2184. [Medline](#)
- Hille B (1992) *Ionic channels of excitable membranes*, 2nd edition. Sunderland, MA: Sinauer Associates.
- Hodgkin AL, Huxley AF (1952) A quantitative description of membrane current and its application to conduction and excitation in nerve. *J Physiol* 117:500–544. [CrossRef Medline](#)
- Huang G, Santos-Sacchi J (1993) Mapping the distribution of the outer hair cell motility voltage sensor by electrical amputation. *Biophys J* 65:2228–2236. [CrossRef Medline](#)
- Iwasa KH (1993) Effect of stress on the membrane capacitance of the auditory outer hair cell. *Biophys J* 65:492–498. [CrossRef Medline](#)
- Iwasa KH (2017) Negative membrane capacitance of outer hair cells: electromechanical coupling near resonance. *Sci Rep* 7:12118. [CrossRef Medline](#)
- Iwasa KH, Kachar B (1989) Fast in vitro movement of outer hair cells in an external electric field: effect of digitonin, a membrane permeabilizing agent. *Hear Res* 40:247–254. [CrossRef Medline](#)
- Johnson SL, Beurq M, Marcotti W, Fettiplace R (2011) Prestin-driven cochlear amplification is not limited by the outer hair cell membrane time constant. *Neuron* 70:1143–1154. [CrossRef Medline](#)
- Kakehata S, Santos-Sacchi J (1995) Membrane tension directly shifts voltage dependence of outer hair cell motility and associated gating charge. *Biophys J* 68:2190–2197. [CrossRef Medline](#)
- Kilic G, Lindau M (2001) Voltage-dependent membrane capacitance in rat pituitary nerve terminals due to gating currents. *Biophys J* 80:1220–1229. [CrossRef Medline](#)
- Lacroix JJ, Bezanilla F (2012) Tuning the voltage-sensor motion with a single residue. *Biophys J* 103:L23–25. [CrossRef Medline](#)
- Liberman MC, Gao J, He DZ, Wu X, Jia S, Zuo J (2002) Prestin is required for electromotility of the outer hair cell and for the cochlear amplifier. *Nature* 419:300–304. [CrossRef Medline](#)
- Lu CC, Kabakov A, Markin VS, Mager S, Frazier GA, Hilgemann DW (1995) Membrane transport mechanisms probed by capacitance measurements with megahertz voltage clamp. *Proc Natl Acad Sci U S A* 92:11220–11224. [CrossRef Medline](#)
- Meltzer J, Santos-Sacchi J (2001) Temperature dependence of non-linear capacitance in human embryonic kidney cells transfected with prestin, the outer hair cell motor protein. *Neurosci Lett* 313:141–144. [CrossRef Medline](#)
- Mountain DC, Hubbard AE (1994) A piezoelectric model of outer hair cell function. *J Acoust Soc Am* 95:350–354. [CrossRef Medline](#)
- Okunade O, Santos-Sacchi J (2013) IR laser-induced perturbations of the voltage-dependent solute carrier protein SLC26a5. *Biophys J* 105:1822–1828. [CrossRef Medline](#)
- Oliver D, He DZ, Klöcker N, Ludwig J, Schulte U, Waldegger S, Ruppersberg JP, Dallos P, Fakler B (2001) Intracellular anions as the voltage sensor of prestin, the outer hair cell motor protein. *Science* 292:2340–2343. [CrossRef Medline](#)
- Russell IJ, Sellick PM (1983) Low-frequency characteristics of intracellularly recorded receptor potentials in guinea-pig cochlear hair cells. *J Physiol* 338:179–206. [CrossRef Medline](#)
- Rybalchenko V, Santos-Sacchi J (2003) Cl⁻ flux through a non-selective, stretch-sensitive conductance influences the outer hair cell motor of the guinea-pig. *J Physiol* 547:873–891. [CrossRef Medline](#)
- Rybalchenko V, Santos-Sacchi J (2008) Anion control of voltage sensing by the motor protein prestin in outer hair cells. *Biophys J* 95:4439–4447. [CrossRef Medline](#)
- Santos-Sacchi J (1989) Asymmetry in voltage-dependent movements of isolated outer hair cells from the organ of corti. *J Neurosci* 9:2954–2962. [CrossRef Medline](#)
- Santos-Sacchi J (1990) Fast outer hair cell motility: how fast is fast? In: *The mechanics and biophysics of hearing* (Dallos P, Geisler CD, Matthews JW, Ruggero MA, Steele CR, eds), pp 69–75. Berlin, Germany: Springer.
- Santos-Sacchi J (1991) Reversible inhibition of voltage-dependent outer hair cell motility and capacitance. *J Neurosci* 11:3096–3110. [CrossRef Medline](#)
- Santos-Sacchi J (1992) On the frequency limit and phase of outer hair cell motility: effects of the membrane filter. *J Neurosci* 12:1906–1916. [CrossRef Medline](#)
- Santos-Sacchi J (2004) Determination of cell capacitance using the exact empirical solution of dY/dCm and its phase angle. *Biophys J* 87:714–727. [CrossRef Medline](#)
- Santos-Sacchi J (2018) High frequency measures of OHC nonlinear capacitance (NLC) and their significance: why measures stray away from predictions. In: *To Ear and Back Again—Advances in Auditory Biophysics* (Proceedings of the 13th Mechanics of Hearing Workshop) (Bergevin C, Puria S, eds). Melville, NY: AIP, in press.
- Santos-Sacchi J, Dilger JP (1988) Whole cell currents and mechanical responses of isolated outer hair cells. *Hear Res* 35:143–150. [CrossRef Medline](#)
- Santos-Sacchi J, Huang G (1998) Temperature dependence of outer hair cell nonlinear capacitance. *Hear Res* 116:99–106. [CrossRef Medline](#)
- Santos-Sacchi J, Song L (2014) Chloride-driven electromechanical phase lags at acoustic frequencies are generated by SLC26a5, the outer hair cell motor protein. *Biophys J* 107:126–133. [CrossRef Medline](#)
- Santos-Sacchi J, Song L (2016) Chloride anions regulate kinetics but not voltage-sensor Q_{max} of the solute carrier SLC26a5. *Biophys J* 110:2551–2561. [CrossRef Medline](#)

- Santos-Sacchi J, Kakehata S, Takahashi S (1998) Effects of membrane potential on the voltage dependence of motility-related charge in outer hair cells of the guinea-pig. *J Physiol* 510:225–235. [CrossRef Medline](#)
- Santos-Sacchi J, Shen WX, Zheng J, Dallos P (2001) The outer hair cell lateral membrane motor, prestin, shows hysteresis. *Biophys J* 80:346A.
- Santos-Sacchi J, Song L, Zheng J, Nuttall AL (2006) Control of mammalian cochlear amplification by chloride anions. *J Neurosci* 26:3992–3998. [CrossRef Medline](#)
- Santos-Sacchi J, Song L, Li XT (2009) Firing up the amplifier: temperature, pressure and voltage jump studies on OHC motor capacitance. In: *Concepts and challenges in the biophysics of hearing*. Singapore: World Scientific. [CrossRef](#)
- Santos-Sacchi J, Navaratnam D, Raphael R, Oliver D (2017) The cochlea, chapter 5: prestin—molecular mechanisms underlying outer hair cell electromotility. In: *Springer handbook of auditory research*. New York, NY: Springer.
- Schnee ME, Santos-Sacchi J, Castellano-Muñoz M, Kong JH, Ricci AJ (2011a) Calcium-dependent synaptic vesicle trafficking underlies indelible release at the hair cell afferent fiber synapse. *Neuron* 70:326–338. [CrossRef Medline](#)
- Schnee ME, Castellano-Muñoz M, Kong JH, Santos-Sacchi J, Ricci AJ (2011b) Tracking vesicle fusion from hair cell ribbon synapses using a high frequency, dual sine wave stimulus paradigm. *Commun Integr Biol* 4:785–787. [CrossRef Medline](#)
- Sigworth FJ (1995) Electronic design of the patch clamp. In: *Single-channel recording* (Sakmann B, Neher E, eds), pp 95–127. Boston, MA: Springer US.
- Song L, Santos-Sacchi J (2013) Disparities in voltage-sensor charge and electromotility imply slow chloride-driven state transitions in the solute carrier SLC26a5. *Proc Natl Acad Sci U S A* 110:3883–3888. [CrossRef Medline](#)
- Yamashita T, Fang J, Gao J, Yu Y, Lagarde MM, Zuo J (2012) Normal hearing sensitivity at low-to-middle frequencies with 34% prestin-charge density. *PLoS One* 7:e45453. [CrossRef Medline](#)
- Zheng J, Shen W, He DZ, Long KB, Madison LD, Dallos P (2000) Prestin is the motor protein of cochlear outer hair cells. *Nature* 405:149–155. [CrossRef Medline](#)

Protein- and Lipid-Reactive Agents Alter Outer Hair Cell Lateral Membrane Motor Charge Movement

J. Santos-Sacchi and M. Wu

Sections of Otolaryngology and Neurobiology, Yale University School of Medicine, New Haven, CT 06510, USA

Received: 4 May 2004/Revised: 7 July 2004

Abstract. Outer hair cells from the mammalian cochlea are mechanically active cells that rely on charged voltage sensors within their lateral plasma membrane to gate the integral membrane motor protein, prestin, into one of two area states. Here we use protein and lipid reactive reagents to probe the influence of these bilayer components on motor-induced nonlinear membrane capacitance. Of the protein-reactive reagents tested, cross-linking and sulfhydryl reagents were most effective in altering steady state and time-varying motor activity. Of the lipid-altering agents, chloroform and HePC were most effective. Chloroform, in particular, drastically modified the susceptibility of the motor to prior voltage (initial conditions). Our data suggest that outer hair cell motor activity derives substantially from interactions with its lipid environment.

Key words: Motility — Gating charge — Membrane capacitance — Protein — Lipid

Introduction

Mechanical activity of the outer hair cell (OHC) underlies the enhanced sensitivity and frequency-resolving power of the mammalian cochlea (Dallos, 1992). The molecular motors that drive this activity harness electrical energy in a manner similar to other integral membrane proteins that generate gating currents upon voltage-induced conformational change (Armstrong & Bezanilla, 1974; Hilgemann, Nicoll & Philipson, 1991; Alkon, Etcheberrigaray, & Rojas, 1993; Bezanilla, 2002), namely, a motor-related displacement current or equivalently, a nonlinear capacitance (NLC) has been identified within

the OHC's lateral membrane, which reflects conformational fluctuations of the motor (Ashmore, 1990; Santos-Sacchi, 1991; Huang & Santos-Sacchi, 1993; Wu & Santos-Sacchi 1998). Recently, Dallos and colleagues have identified the OHC motor protein as prestin, a member of the SLC26 transporter family (Zheng et al., 2000). Thus far, when expressed in non-auditory cells, this integral membrane protein displays all the known biophysical characteristics of the OHC lateral membrane motor (Zheng et al., 2000; Ludwig et al., 2001; Meltzer & Santos-Sacchi, 2001; Santos-Sacchi et al., 2001; Santos-Sacchi & Navarrate, 2002).

Integral membrane proteins, such as ionic channels and transporters, are influenced by their lipid bilayer environment (Goulian et al., 1998). Predictably, then, both protein-and lipid-reactive reagents would be capable of modulating prestin's function. We report here on the modulation of OHC NLC, including the effects of prior voltage on OHC NLC (Santos-Sacchi, Kakehata & Takahashi, 1998), by such agents and find that OHC motor protein functional characteristics likely arise from interactions with the lipid environment. Preliminary accounts of some portions of this work have been presented in abstract form (Santos-Sacchi & Wu, 1998).

Materials and Methods

CELL PREPARATION

Guinea pigs were anesthetized with halothane and killed by cervical dislocation. OHCs and supporting cells were isolated enzymatically with dispase I (0.5mg/ml for 10 min followed by gentle trituration through a polyethylene pipette) in a modified Leibovitz medium that contained (in mM): NaCl 142, KCl 5.37, MgCl₂ 1.47, HEPES 5, CaCl₂ 2 and dextrose 5; 300 mOsm, pH7.2. The cells were then transferred to a 700- μ l perfusion chamber. Most experiments were conducted at room temperature (~23°C). Temperature for a subset of experiments was set by a Peltier device. A

Nikon Diaphot inverted microscope with Hoffmann optics was used to observe the cells during electrical recording.

VOLTAGE CLAMP

Single OHCs were studied under whole-cell voltage-clamp conditions using an Axon 200A amplifier at a holding potential of -80mV . Initial resistances of patch pipettes were 2–3 M Ω , corresponding to tip sizes of 1–2 μm . Residual series resistance ranged from 3 to 7 M Ω . All data collection and analysis were performed with a Windows-based program, jClamp (SciSoft, CT). Ionic blocking solutions were used to remove voltage-dependent ionic conductances so that capacitive currents could be analyzed in isolation (Santos-Sacchi, 1991; Huang & Santos-Sacchi, 1993). The patch-pipette solution contained (in mM): CsCl 140, MgCl₂ 2, EGTA 10, HEPES 5, with pH 7.2 and osmolarity 300 mOsm (adjusted with dextrose). The external ionic blocking solution contained (in mM): BaCl₂ 10, CoCl₂ 2, MgCl₂ 1.47, NaCl 100, CaCl₂ 2, HEPES 5, with pH 7.2 and osmolarity 300 mOsm (adjusted with dextrose). Whole-chamber perfusion was continuous. Protein- and lipid-reactive reagents were perfused via a Y-tube directly onto the cell under study for short periods of time (1.5–10 min).

REAGENTS

Several protein-reactive reagents were tested, including glutaraldehyde (0.3%), N-ethylmaleimide (NEM; 2 mM), p-chloromercuriphenylsulfonate (pCMPS; 2 mM), dithiothreitol (DTT; 2 mM) and diamide (2–5 mM). Glutaraldehyde is a dialdehyde fixative that works by crosslinking peptide chains; NEM, pCMPS and diamide are sulfhydryl reagents that react with cysteine groups; DTT is a reducing agent that breaks disulfide bonds [(Stirling, 1975); see also Lundblad (1995) and references therein]. Lipid-reactive reagents included saturated chloroform, hexadecylphosphocholine (HePC; 2–10 mM), filipin (0.75 mg/ml), phospholipase A2 (PLA2; 1 ng/ml), and triton (0.01%). Triton is a commonly used laboratory detergent. Chloroform is a commonly used lipid solvent. Filipin binds to cholesterol in membranes (Stetson & Wade, 1983). PLA2 cleaves fatty acyl chains from phospholipids (Danthi, Enyeart & Enyeart, 2003). HePC is a lysophospholipid analogue that can intercalate within plasma membrane (Rakotomanga, Loiseau & Saint-Pierre-Chazalet, 2004). The effects of these agents on the membrane likely ranges from altering its viscosity to changing its curvature and thickness, with subsequent effects on integral proteins.

CAPACITANCE MEASUREMENTS

Continuous high-resolution capacitance measures were acquired through admittance (Y) analysis at time resolutions of 5.12 or 2.56 ms, utilizing a two-sine-wave voltage-stimulus protocol (Santos-Sacchi et al., 1998). The stimulus consisted of the sum of two voltage sine waves (390.625 and 781.25 Hz), each at a magnitude (V) of 10 mV peak. This AC stimulus was superimposed on voltage-ramp or step stimuli. Capacitance-voltage functions were fit to the first derivative of a two-state Boltzmann function relating nonlinear charge to membrane voltage (dQ/dV ; (Santos-Sacchi, 1991; Huang & Santos-Sacchi, 1993))

$$C_m = Q_{\max} \frac{ze}{kT} \frac{b}{(1+b)^2} + C_{\text{lin}}$$

Where

$$b = \exp\left(\frac{-ze(V - V_{\text{pkcm}})}{kT}\right)$$

Q_{\max} is the maximum nonlinear charge moved, V_{pkcm} is voltage at peak capacitance or equivalently, at half-maximal nonlinear charge transfer, V_m is membrane potential, z is valence, C_{lin} is linear membrane capacitance, e is electron charge, k is Boltzmann's constant, and T is absolute temperature. All results are reported as mean \pm SE. Gating currents were measured with the P/-5 technique at a subtraction holding potential of +50 mV (Armstrong & Bezanilla, 1977).

Pipette pressure was monitored via a T-connector to a pressure monitor (WPI, Sarasota, FL), and modified when required with a syringe connected to the Teflon tubing attached to the patch-pipette holder (Kakehata & Santos-Sacchi, 1995). The cylindrical shape of OHCs was maintained with slight positive pressure during data collection.

There are two potential, non-specific problems that must be considered when treating cell membranes with reactive agents. The membrane resistance (leakage) and/or the linear capacitance (e.g., membrane thickness) might be altered. With our dual-sine measurement technique, however, capacitance measures are resistant to membrane resistance changes. Also, linear as well as nonlinear capacitance are simultaneously measured. Changes in linear capacitance will simply shift the baseline of the NLC function, and should not interfere with the Boltzmann fit. Other than correcting steady-state voltages for series-resistance errors, which we do, we cannot correct for space-clamp changes. Nevertheless, estimates of delayed electrotonic spread in the OHC, about 70 μm for a cell of 70 μm (Ashmore 1986), indicate that our measures, which use frequencies below 800 Hz, should be reliable. Additionally, since the voltage-dependent conductances in the OHC are located in the basal pole of the cell (Santos-Sacchi, Huang & Wu 1997), the voltage drop along the lateral membrane where the motors are should be close to isopotential.

Results

PROTEIN-REACTIVE REAGENTS

OHCs present a voltage-dependent C_m that arises from restricted charge movement within the lateral plasma membrane and this electrical measure of motor activity is modifiable by protein-reactive reagents (Fig. 1A, B). Low concentrations of the cross-linking fixative, glutaraldehyde (0.3%), caused a reduction in charge movement that probably indicates an abridged conformational change of the motor protein. Simultaneously, in all tested cells ($n = 5$) V_{pkcm} shifted in the hyperpolarizing direction. The effects were cumulative over the perfusion period (10 min in this case), indicating progressive inactivation of motors. In the control condition, prior to glutaraldehyde treatment, dc steps in voltage resulted in an immediate change in OHC C_m (Fig. 1C, top trace), followed by an exponential decay that obtains from a voltage- and time-dependent shift in the voltage operating range (i.e., V_{pkcm}) of motor charge movement. This phenomenon is referred to hereafter as an amplifactory shift, since at a fixed voltage it represents a time-dependent recruitment of motors into the same conformational state evoked by the eliciting voltage step (Santos-Sacchi et al., 1998). Glutaraldehyde treatment prevented this time-dependent change

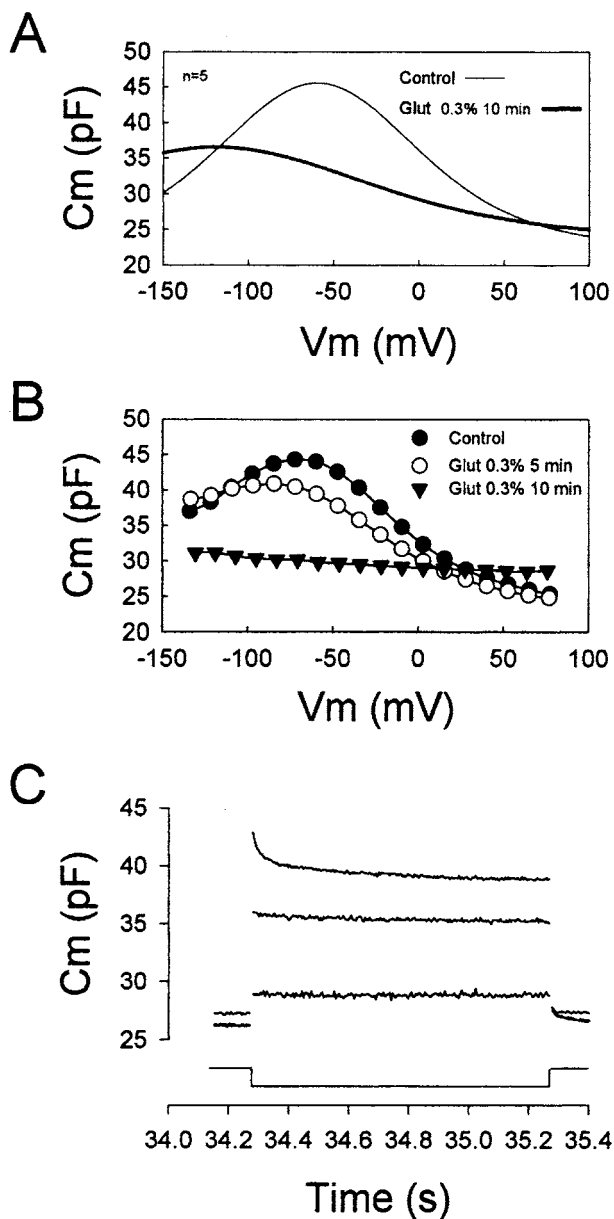


Fig. 1. Effect of low concentration (0.3%) of glutaraldehyde on OHC nonlinear capacitance. (A) C - V functions were obtained in five OHCs before and after 4.5 ± 1.1 min exposure to 0.3% glutaraldehyde. Fits with Eq. 1 were made and the estimated parameters were averaged. The resultant average fits (before and after treatment) are plotted. Control: Q_{\max} , 3.60 ± 0.13 pC; V_{pkcm} , -59.6 ± 6.8 mV; z , 0.67 ± 0.06 ; C_{lin} , 22.6 ± 0.68 ; glutaraldehyde: Q_{\max} , 3.1 ± 0.56 pC; V_{pkcm} , -119 ± 12.4 mV; z , 0.43 ± 0.04 ; C_{lin} , 23.7 ± 1.42 . (B) Nonlinear capacitance of an individual OHC is shown over time (0, 5, 10 min) following glutaraldehyde treatment. Note progressive shift in voltage dependence and decrease in capacitance. (C) Voltage step from a holding potential of +50 mV to -100 mV induces an instantaneous jump in capacitance followed by an exponential decrease in capacitance (top trace, control). Following glutaraldehyde treatment, this decay is abolished (middle trace, 5 min; bottom trace, 10 min). Same cell as in (B).

in capacitance (Fig. 1C, bottom traces), even at post-treatment times where substantial charge movement or NLC was evidenced.

Other protein-reactive agents altered OHC NLC to varying extents. Average results are presented for N-ethylmaleimide (NEM; 2 mM; $n = 4$), *p*-chloromercuriphenylsulfonate (pCMPS; 2 mM; $n = 7$), dithiothreitol (DTT; 2 mM; $n = 7$) and diamide (2–5 mM; $n = 7$) (Fig. 2; see fit statistics in legend). Though the average NEM results showed little effect on V_{pkcm} , actually, of the four cells tested, two showed shifts to the left (-12.1 ± 2.9 mV), while the other two shifted to the right (20.9 ± 3.5 mV). Similarly, DTT caused a positive shift in 3 of 7 cells (10.7 ± 4.2 mV), while the remaining cells showed a negative shift (-11.1 ± 2.8 mV). pCMPS, like glutaraldehyde, was effective in substantially reducing nonlinear capacitance, but on average shifted V_{pkcm} in the positive direction. In 5 of 7 cells, pCMPS caused V_{pkcm} to shift in the positive direction (25 ± 4.5 mV); the 2 remaining cells showed a negative shift (-10.1 ± 1.4 mV). However, Fig. 3 illustrates, in the same OHC, that while nonlinear capacitance was reduced by pCMPS, the amplificatory shift in V_{pkcm} remained essentially intact. This result is the same for DTT effects on the amplificatory shift, where comparing the C_m traces relative to pre- and post-treatment steady-state V_{pkcm} indicates similar relaxation phenomena (see Fig. 6 as well).

LIPID-REACTIVE REAGENTS

Chloroform moderately reduced NLC and shifted V_{pkcm} to the left in all cells tested ($n = 6$) (Fig. 4A). The effects on the amplificatory shift, however, were profound (Fig. 4B). Compared to controls, the magnitude and time course of the voltage step-induced change in C_m were markedly decreased. Gating currents were only slightly affected by chloroform treatment, other than showing the expected effects of a shift in V_{pkcm} (V_h), namely, changes in the magnitude of charge movement at a given voltage (Fig. 4C). Additionally, a slight reduction (~ 20 – 30%) in gating time constants was found. The effects of hexadecylphosphocholine (HePC; 2–10 mM, $n = 10$), filipin (0.75 mg/ml, $n = 3$), phospholipase A2 (PLA2; 1 ng/ml, $n = 4$), and triton (0.01%, $n = 2$) are illustrated in Fig. 5. Triton concentrations above 0.01 caused rapid and severe cell damage with loss of recordings. Only HePC significantly affected NLC, shifting V_{pkcm} in all cells tested to the right and decreasing peak capacitance slightly. Slight effects of HePC on the amplificatory shift were found, but in this case, it appears that the effects arose, as it did from DTT and pCMPS (see above), from the shift in steady-state V_{pkcm} , since realigning the traces relative to V_{pkcm} results in corresponding traces whose characteristics

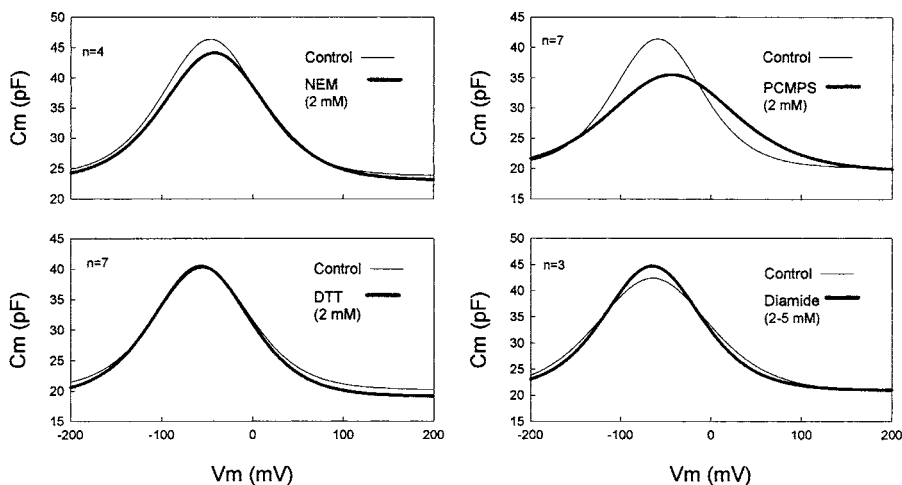


Fig. 2. Average OHC capacitance functions before and following treatments with NEM, pCMPS, DTT, and diamide. Data analyzed and presented as in Fig. 1A. pCMPS showed the greatest average effect. *NEM Control*: Q_{\max} , 3.13 ± 0.59 pC; V_{pkcm} , -46.9 ± 11.5 mV; z , 0.74 ± 0.05 ; C_{lin} , 23.8 ± 1.6 . *NEM* (3.12 ± 1.0 minutes): Q_{\max} , 3.1 ± 0.3 pC; V_{pkcm} , -42.2 ± 6.1 mV; z , 0.69 ± 0.03 ; C_{lin} , 23.0 ± 0.8 . *DTT Control*: Q_{\max} , 2.82 ± 0.06 pC; V_{pkcm} , -55.2 ± 4.3 mV; z , 0.73 ± 0.02 ; C_{lin} , 20.2 ± 0.35 ; *DTT* (2.85 ± 0.3 minutes): Q_{\max} , 3.03 ± 0.43 pC; V_{pkcm} , -56.9 ± 2.2

mV; z , 0.73 ± 0.02 ; C_{lin} , 19.13 ± 0.5 . *pCMPS Control*: Q_{\max} , 2.81 ± 0.18 pC; V_{pkcm} , -59.0 ± 6.8 mV; z , 0.77 ± 0.03 ; C_{lin} , 20.1 ± 0.66 ; *pCMPS* (3.05 ± 0.44 minutes): Q_{\max} , 2.95 ± 0.25 pC; V_{pkcm} , -43.4 ± 8.5 mV; z , 0.55 ± 0.02 ; C_{lin} , 19.6 ± 1.23 . *Diamide Control*: Q_{\max} , 3.64 ± 0.09 pC; V_{pkcm} , -64.4 ± 6.4 mV; z , 0.61 ± 0.03 ; C_{lin} , 20.6 ± 0.02 ; *Diamide* (5.43 ± 0.23 minutes): Q_{\max} , 3.38 ± 1.58 pC; V_{pkcm} , -64.9 ± 4.6 mV; z , 0.72 ± 0.02 ; C_{lin} , 21.0 ± 0.6 .

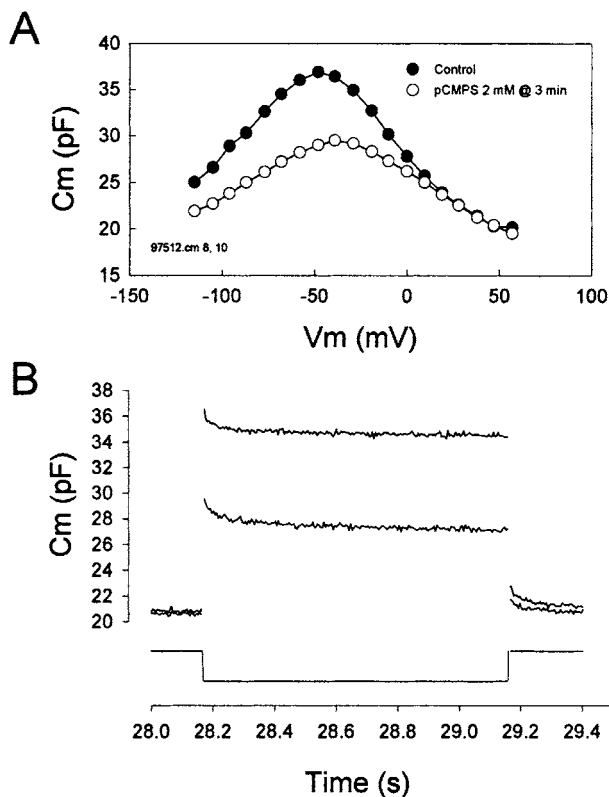


Fig. 3. Nonlinear capacitance of a single OHC before and after treatment with 2 mM pCMPS. (A) Following treatment, NLC is markedly reduced and right-shifted. (B) Voltage step from +50 to -100 mV induces an instantaneous jump in capacitance followed by an exponential decrease in capacitance. Little difference in the traces is observed except for the absolute offset magnitude.

are similar (Fig. 6; compare similarity in traces correspondingly labeled 1, 2, and 3).

TEMPERATURE AND OSMOTIC SWELLING

Finally, we looked at the effects of temperature and membrane tension (osmotic cell swelling) on OHC capacitance. As we found previously, V_{pkcm} shifted to negative potentials and the magnitude of capacitance decreased with cooling (Santos-Sacchi & Huang, 1998). Interestingly, cooling also caused a decreased amplificatory shift (Fig. 7). On the other hand, membrane tension produced little effect on the amplificatory shift, despite showing the characteristic shift of V_{pkcm} to positive potentials (Kakehata & Santos-Sacchi, 1995) (Fig. 8).

Discussion

The OHC motor is an integral membrane protein that can be viewed as fluctuating between conformational states under the control of membrane voltage and chloride concentration (Santos-Sacchi & Dilger, 1988; Oliver et al., 2001; Rybalchenko & Santos-Sacchi, 2003). One model that can accurately account for mechanical and electrical activity of the OHC posits that the motor occupies two area states, contracted and expanded (Santos-Sacchi, 1993; Iwasa, 1994; Santos-Sacchi & Navarrete, 2002). Measures of NLC provide estimates of motor-state probability, and have been used to characterize the effects of a

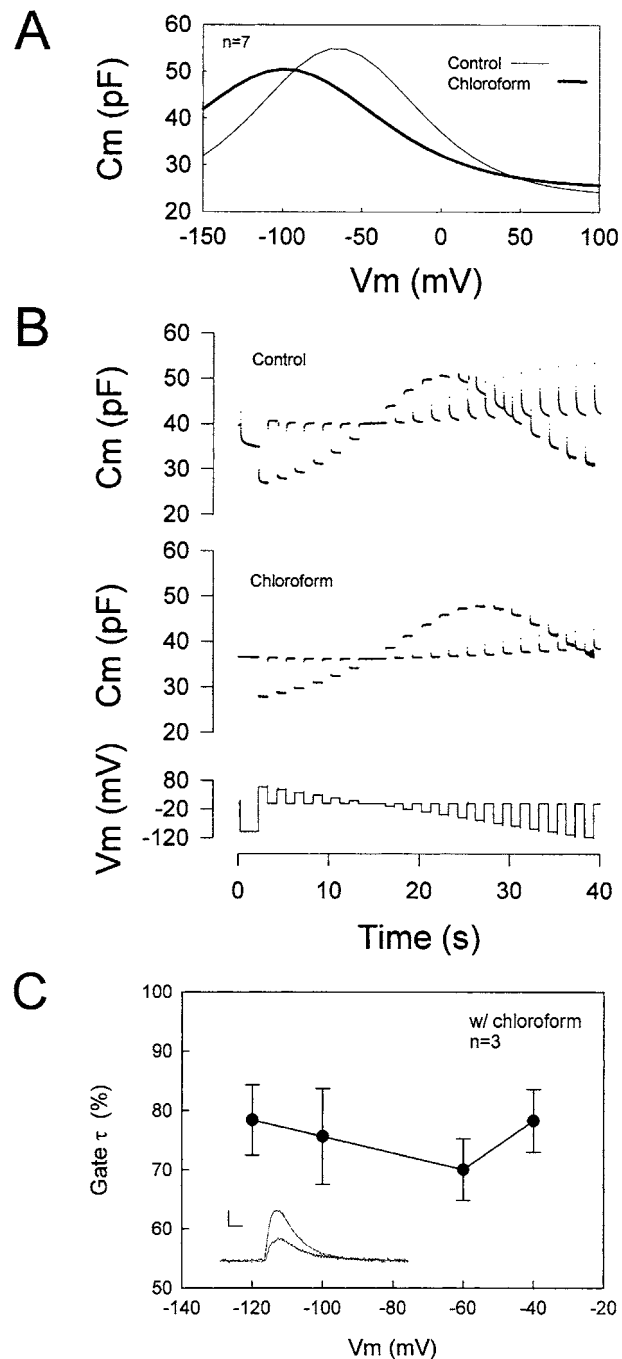


Fig. 4. Effect of chloroform on OHC nonlinear capacitance. **(A)** $C-V$ functions were obtained in seven OHCs before and after exposure to a saturated chloroform solution. Fits with Eq. 1 were made and the estimated parameters were averaged. The resultant average fits (before and after treatment) are plotted. *Control:* Q_{\max} , 4.21 ± 0.26 pC; V_{pkcm} , -65.4 ± 4.4 mV; z , 0.77 ± 0.09 ; C_{lin} , 23.3 ± 0.74 ; *Chloroform* (5.58 \pm 0.39 minutes): Q_{\max} , 4.0 ± 0.21 pC; V_{pkcm} , -98.5 ± 7.1 mV; z , 0.66 ± 0.02 ; C_{lin} , 25.0 ± 0.8 . **(B)** Nonlinear capacitance of an individual OHC is shown during steps to a range of voltages (*lower panel*). Note large capacitance relaxations in control (*upper panel*) condition, and markedly attenuated response at all voltages in chloroform-treated condition (*middle panel*). **(C)** Average gating current time course (single exponential fits to the decaying current component) is slightly speeded up ($\sim 80\%$ of control tau) after chloroform treatment. *Inset:* gating current traces from a single OHC obtained by P/-5 technique. Step from -120 to -80 mV. Larger trace is before treatment, but differences in magnitude largely result from the shift in V_h . Scale: 0.53 nA, 0.2 ms.

time- and voltage-dependent (Santos-Sacchi et al., 1998). That is, membrane voltage change, while instantaneously altering the probability of the motors' occupying either the² contracted or expanded state, also influences future motor-state probability. Since a given polarity of voltage stimulation recruits additional motors into the same conformational state evoked by that eliciting voltage step, this dynamic shift in V_{pkcm} can be viewed as an amplificatory shift (Santos-Sacchi et al., 1998). This amplificatory event is an intrinsic characteristic of prestin, since this susceptibility to initial voltage is observed in non-auditory cells expressing prestin (Santos-Sacchi et al., 2001).

Our new data indicate that membrane-reactive agents can alter OHC electro-mechanical activity. Specifically, both lipid- and protein-altering drugs are capable of influencing the energy profile of the motor protein, prestin, as evidenced by shifts in the voltage at half-maximal charge movement (V_{pkcm}). Additionally, some of these agents have significant effects on the exponential amplificatory shift of V_{pkcm} .

EFFECTS OF PROTEIN-REACTIVE REAGENTS ON THE MOTOR

Low concentrations of glutaraldehyde blocked nonlinear charge movement presumably by interfering with conformational changes normally evoked by voltage. Yet, during the development of its effects, in the face of substantial nonlinear charge movement, the time-dependent change in capacitance during steady-state voltage step, namely the amplificatory shift, was abolished. This may indicate that the mechanism or molecular structure responsible for the amplificatory shift differs from the one underlying voltage sensing. Since we previously modeled the amplificatory shift as resulting from interactions

variety of biophysical forces on the motor including membrane tension and temperature (Iwasa, 1993; Gale & Ashmore, 1994; Santos-Sacchi & Huang, 1998; Santos-Sacchi & Navarrete, 2002). These forces are capable of shifting steady-state V_{pkcm} , the voltage where the population of motors is equally distributed between the two area states. Additionally, sensitivity to initial or prior voltage conditions manifests itself as a dynamic shift in the gating charge-voltage relation ($Q-V$; or correspondingly, the capacitance-voltage relation, $C-V$) along the voltage axis, which is

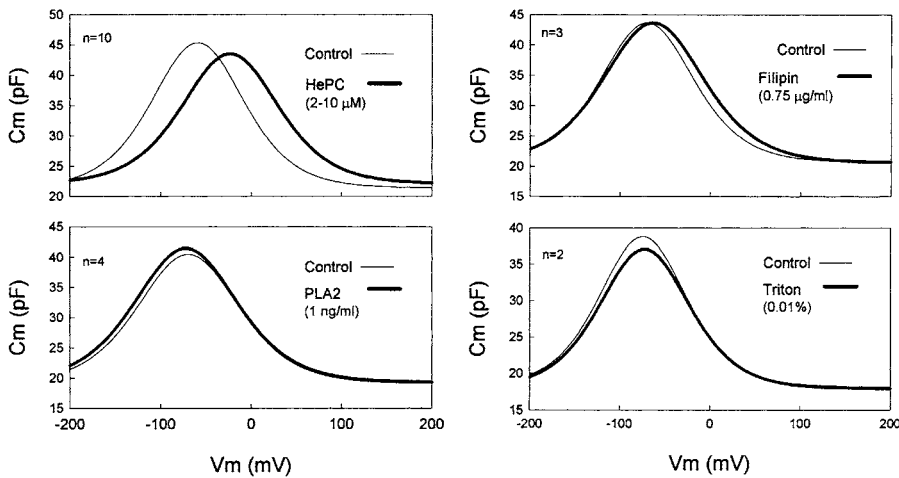


Fig. 5. Average OHC capacitance functions before and following treatments with HePC, Filipin, PLA2 and Triton. Data analyzed and presented as in Fig. 1A. HePC showed the greatest average effect. *HePC Control*: Q_{\max} , 3.26 ± 0.24 pC; V_{pkcm} , -59.2 ± 4.4 mV; z , 0.76 ± 0.01 ; C_{lin} , 21.4 ± 1.6 ; *HePC* (4.89 \pm 0.8 minutes): Q_{\max} , 3.0 ± 0.1 pC; V_{pkcm} , -23.6 ± 9.3 mV; z , 0.72 ± 0.03 ; C_{lin} , 22.0 ± 0.9 . *PLA2 Control*: Q_{\max} , 3.19 ± 0.22 pC; V_{pkcm} , -69.8 ± 8.6 mV; z , 0.69 ± 0.04 ; C_{lin} , 19.0 ± 0.7 ; *PLA2* (10.5 \pm 3.2

minutes): Q_{\max} , 3.36 ± 0.22 pC; V_{pkcm} , 72.2 ± 7.7 mV; z , 0.68 ± 0.02 ; C_{lin} , 19.2 ± 0.7 . *Filipin Control*: Q_{\max} , 3.18 ± 0.47 pC; V_{pkcm} , -69.9 ± 3.4 mV; z , 0.75 ± 0.03 ; C_{lin} , 20.6 ± 1.7 ; *Filipin* (3.0 \pm 0.3 minutes): Q_{\max} , 3.45 ± 0.3 pC; V_{pkcm} , -63.0 ± 12.7 mV; z , 0.69 ± 0.06 ; C_{lin} , 20.6 ± 2.2 . *Triton Control*: Q_{\max} , 2.69 ± 0.33 pC; V_{pkcm} , -74.2 ± 14.6 mV; z , 0.79 ± 0.13 ; C_{lin} , 18.1 ± 1.6 ; *Triton* (5.0 \pm 1.0 minutes): Q_{\max} , 2.56 ± 0.63 pC; V_{pkcm} , -72.3 ± 22 mV; z , 0.77 ± 0.08 ; C_{lin} , 17.9 ± 0.6 .

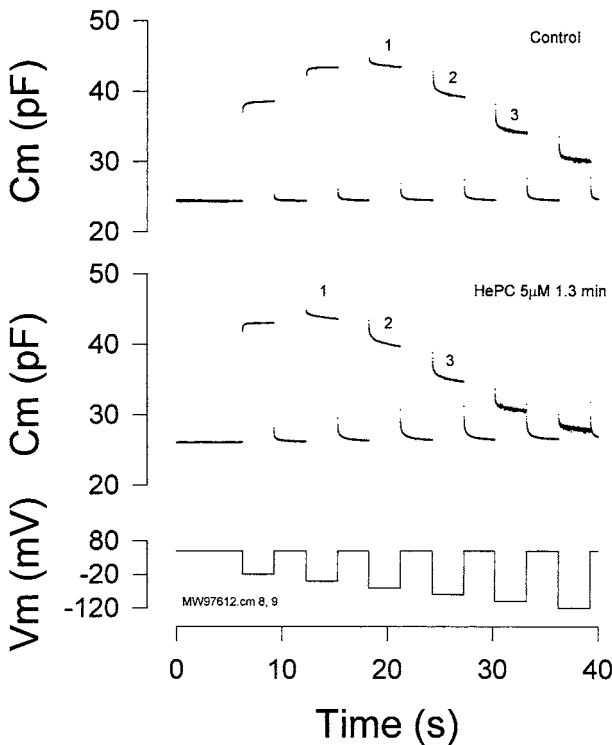


Fig. 6. Nonlinear capacitance of a single OHC during steps to a range of voltages before (*upper panel*) and after (*lower panel*) treatment with HePC. Following treatment, NLC is reduced and shifted in the depolarizing direction. Note large capacitance relaxations in control (*upper panel*) condition, which at any particular step voltage is modified by HePC. However, the similarity of relaxations at voltage step magnitudes relative to V_{pkcm} , i.e., comparing, for example, corresponding traces 1, 2 and 3 in each panel, indicates that changes in relaxations may have resulted from the shift in V_{pkcm} .

among motors via motor-induced tension (Santos-Sacchi et al., 1998), it may be that glutaraldehyde can interfere with motor-generated tension within the bilayer.

Kalinec and Kachar (1993) studied the effects of sulfhydryl reagents on voltage-dependent OHC mechanical activity. Our complementary data on the lateral membrane's voltage-sensor mechanism confirm and extend their findings. Thus, they showed that pCMPS significantly reduced the percentage of mechanically active OHCs after 60 minutes incubation, but neither NEM nor diamide were significantly effective (Kalinec & Kachar, 1993). Similarly, we found that the sulfhydryl reagent pCMPS had the most potent effect on NLC, decreasing peak capacitance and shifting V_{pkcm} to depolarized levels. Whereas, in our hands, the effects of pCMPS were fairly rapid in onset, clearly occurring within 2–3 minutes of direct cell perfusion, Kalinec and Kachar (1993) found that significant effects on motor activity required greater than 20 minutes incubation. It is likely that their population measures, based on percent of motile cells, were not as sensitive as our single-cell gating-charge measures in determining the time course of effects. Consequently, our data may indicate that affected cysteine residues may reside at exposed sites within prestin. Based on current topology models (Zheng et al., 2001; Oliver et al., 2001; Adler et al., 2003; Navaratnam et al., 2004), three cysteine residues are predicted to lie external to the bilayer. In most models, only residue C415 resides extracellularly (Oliver et al., 2001; Zheng et al., 2001; Adler et al., 2003). However, the 10 transmembrane domain topology model of Navaratnam et al. (2004), predicts

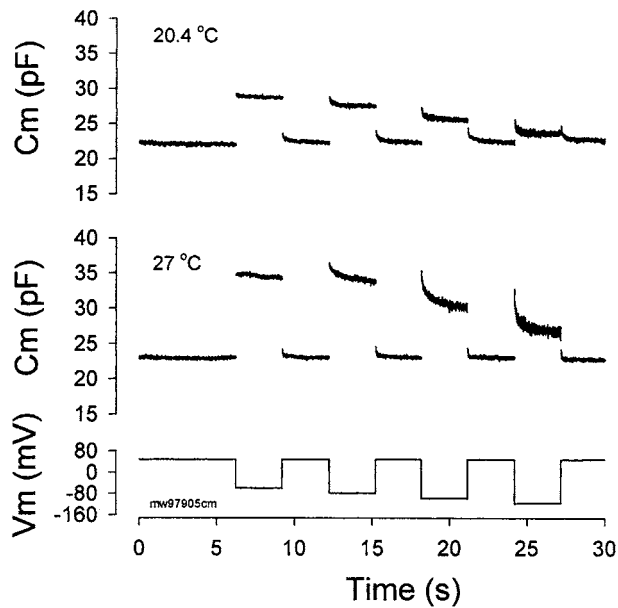


Fig. 7. Nonlinear capacitance of a single OHC during steps to a range of voltages at two different temperatures (*upper panel*: 20.4°C and *lower panel*: 27°C). Upon cooling, NLC is reduced but, in this case, there is little change in V_{pkcm} . However, C_m relaxations are markedly attenuated.

that C124, and not C415, resides extracellularly. Thus it may be that pCMPS works mainly on only one extracellularly exposed cysteine residue in prestin. Nevertheless, supplementing any effects on these putative extracellularly exposed residues, it may be that pCMPS quickly enters the OHC, possibly via large aqueous channels in the lateral membrane (Morimoto et al., 2002; Rybalchenko & Santos-Sacchi, 2003), thereby working on intracellular cysteine residues. In all models, the two other cysteine residues are found within the N and C termini, which reside within the intracellular aqueous phase (C52, C679), and though their co-location may indicate that these residues could interact, the absence of a significant effect of the membrane-permeable monothiol stabilizing agent, DTT, on NLC indicates that such potential interactions are not required for normal function.

Diamide has a dramatic effect on OHC mechanical characteristics (Adachi & Iwasa, 1997). We found little effect on NLC with our short perfusions. However, since the effects of diamide on the OHC cytoskeleton (spectrin, in particular) may require prolonged incubations, we tested an additional 5 OHCs at incubation times of 1–1.5 h at 5 mM; neither overall charge movement nor amplificatory shift was significantly affected, indicating that the diamide-sensitive subsurface cytoskeleton has little impact on intrinsic motor activity, though it can have effects on whole-cell mechanical performance (Adachi & Iwasa, 1997). Similarly, it had been previously reported that

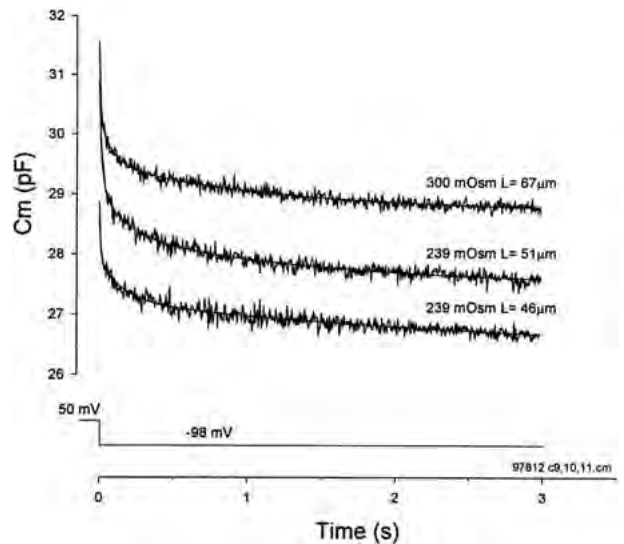


Fig. 8. Capacitance relaxations in a single OHC in response to a step voltage at increasing turgor levels. A switch from 300 mOsm to 239 mOsm caused a slow cell swelling, evidenced as cell shortening (length changed from 67 to 46 μm over a 5 min interval). Despite the increasing turgor pressure and marked shift of V_{pkcm} to hyperpolarizing levels (evidenced here as a reduction in baseline C_m magnitude) the C_m relaxation remains relatively unaltered.

digestion of the OHC cytoskeleton by intracellular enzymes did not adversely affect NLC (Huang & Santos-Sacchi, 1994; Santos-Sacchi et al., 1998) or mechanical activity (Kalinec et al., 1992).

EFFECTS OF LIPID-REACTIVE REAGENTS ON THE MOTOR

Prestin is a protein predicted by topology mapping programs to reside substantially within the lipid bilayer (Zheng et al., 2001). Consequently, it is not surprising that we find significant effects of drugs that are known to modify the lipid bilayer. Notably, chloroform has marked effects on OHC charge movement, reducing peak capacitance and shifting the motor's operating range in the negative direction; its major effect, however, was on the amplificatory shift, reducing its magnitude while increasing its speed. This was observed across a wide voltage range, and cannot be accounted for by a simple steady-state shift in V_{pkcm} . OHC gating-current speed was little affected by chloroform, and this substantially derives from the limiting effect of the whole-cell-clamp time constant (Santos-Sacchi & Huang 1998).

The effects of chloroform on other integral membrane proteins have been studied. Chloroform reduces the magnitude of Na channel gating currents but does not affect their kinetics or their operating voltage (Fernandez, Bezanilla & Taylor, 1982). On the other hand, the kinetics of Shaker K channels were speeded up, though the operating voltage remained stable (Correa, 1998). In both cases ionic

currents were blocked. Interestingly, chloroform has been found to enhance K currents through two-pore-domain K channels (Patel et al., 1999). The effects on these ion channels and other integral membrane proteins have been suggested to arise from direct actions on the proteins themselves (Franks & Lieb, 1994). However, despite this possibility it is clear that chloroform does have substantial effects on the lipid bilayer since, for example, Fernandez et al. (1982) also showed by measuring displacement currents that the hydrophobic anion, dipicrylamine, more rapidly traverses the bilayer in the presence of chloroform. Thus, although it cannot be ruled out that the OHC motor is directly affected by chloroform, the lipid-altering capabilities of this agent, especially at the saturating concentrations used in this and the previously noted studies (Correa, 1998; Fernandez et al., 1982), indicate a likely lipid-based mechanism of action.

The only other lipid-reactive agent tested that significantly affected NLC was HePC, though the absence of major effects from some of the other treatments may have been due in part to the short exposure times that we employed. HePC is a phospholipid analog that can insert into lipid monolayers and interact with cholesterol (Rakotomanga et al., 2004). Although the operating range of the OHC motor is susceptible to HePC, the amplificatory shift was minimally affected, showing behavior that apparently resulted indirectly from the steady-state shift in V_{pkcm} . It should be noted, however, that regardless of the underlying reason for alterations in the amplificatory shift, such a change at a fixed resting potential can be physiologically important. Thus, it may be possible that lipids can modulate the time course of OHC mechanical activity, just as they are able to modulate the time course of ionic currents (Oliver et al., 2004). It should also be stressed that a simple steady-state shift in V_{pkcm} does not necessarily result in changes to the amplificatory shift. For example, membrane tension produces marked changes in steady-state V_{pkcm} but has little effect on the amplificatory shift at a fixed voltage.

TEMPERATURE EFFECTS ON THE MOTOR

We have previously shown that OHC NLC is highly temperature sensitive, shifting steady-state V_{pkcm} to the left and reducing peak capacitance as temperature is decreased (Santos-Sacchi & Huang, 1998; Meltzer & Santos-Sacchi, 2001). However, we were unable to evaluate any changes in the speed of gating currents because the clamp time constant, even at 50 μ s, under whole-cell mode was limiting. Effects of temperature on the amplificatory shift are clearly observed and a decrease in temperature markedly reduces the shift. Since temperature is known to affect both membrane

proteins and lipids, it is possible that effects on motor activity may be dual.

MECHANISMS OF ACTION ON V_{pkcm}

The amplificatory shift has been modeled to result from interactions among motors via induced membrane tension (Santos-Sacchi et al., 1998). Whether the shift derives from motor interactions directly or via intervening lipid is an important issue, which can impact on OHC function. Thus, we have recently shown that functional motor microdomains may exist within the OHC, where local biophysical forces foster independent, local motor activity (Santos-Sacchi et al., 2001). The efficiency of coupling such forces, e.g., membrane tension, among motors could depend heavily upon the physical types of interactions responsible for motor coupling. For example, interactions via bilayer lipids may limit the distance over which motors could interact, whereas direct protein interactions could provide longer-range interactions. While our data may indicate that both lipid and protein moieties can influence the amplificatory shift, the high density of motor protein expression within the lateral membrane, estimated to be near 8000/ μ m² (Huang & Santos-Sacchi 1993; Gale and Ashmore 1997), may significantly promote direct motor-motor interactions. In this regard, it would be interesting to test the effect of motor expression density on the amplificatory shift. Expression density is known to influence integral membrane protein function; for example, the fraction of non-inactivating CLC-0 channels is directly related to expression level (Pusch, Ludewig & Jentsch, 1997).

Regarding the steady-state shifts in V_{pkcm} , these modulations can not be due to changes in membrane viscosity, since forward and backward transition rates between protein conformations should be affected equally by changes in viscosity (Lee, 1991). Thus, based on a two-state model, temperature, chloroform and other lipid-modifying agents known to shift V_{pkcm} must instead alter the relative energy level of each motor state. Perhaps these manipulations act via perturbation of membrane tension or membrane bending, resulting in changes in conformational stability. Each of these phenomena has been implicated in motor activity (Iwasa, 1993; Gale & Ashmore 1994; Kakehata & Santos-Sacchi, 1995; Raphael, Popel & Brownell, 2000; Lue, Zhao & Brownell, 2001; Morimoto et al., 2002; Spector & Jean 2004). However, while viscosity is not likely to be involved in steady-state shifts, the rate of amplificatory shift induced by voltage steps might be expected to be affected. We suggest that chloroform may be working to reduce membrane viscosity, thereby speeding up the amplificatory shift.

Finally, we note that while prestin is considered to be essential for motor activity (Zheng et al., 2000;

Liberman et al., 2002), and the manipulations that we have made here may, in fact, alter prestin or its interactions with the lipid bilayer, it is not certain whether homo- or heteromeric configurations comprise the intact OHC motor (Santos-Sacchi, 2003). Thus, our manipulations may actually be working on players besides prestin. Indeed, we must remain cognizant that unexpected effects of the tested agents on mechanisms other than those we have highlighted may come into play, for example, altered anion binding. We are currently working on these issues (Navaratnam et al., 2004).

This work was supported by NIH-NIDCD grant DC00273 to JSS.

References

- Adachi, M., Iwasa, K.H. 1997. Effect of diamide on force generation and axial stiffness of the cochlear outer hair cell. *Biophys. J.* **73**:2809–2818
- Adler, H.J., Belyantseva, I.A., Merritt, R.C. Jr., Frolenkov, G.I., Dougherty, G.W., Kachar, B. 2003. Expression of prestin, a membrane motor protein, in the mammalian auditory and vestibular periphery. *Hear. Res.* **184**:27–40
- Alkon, D.L., Etcheberrigaray, R., Rojas, E. 1993. Distribution of voltage sensors in mammalian outer hair cells. *Biophys. J.* **65**:1755–1756
- Armstrong, C.M., Bezanilla, F. 1974. Charge movement associated with the opening and closing of the activation gates of the Na channels. *J. Gen. Physiol.* **63**:533–552
- Armstrong, C.M., Bezanilla, F. 1977. Inactivation of the sodium channel. II. Gating current experiments. *J. Gen. Physiol.* **70**:567–590
- Ashmore, J.F. 1986. The cellular physiology of isolated outer hair cells: implications for cochlear frequency selectivity. In: Moore, B.C.J, Patterson, R.D., (eds) *Auditory Frequency Selectivity*. pp 103–108, Plenum Press, New York
- Ashmore, J.F. 1990. Forward and reverse transduction in the mammalian cochlea. *Neurosci. Res. Suppl.* **12**:S39–S50
- Bezanilla, F. 2002. Voltage sensor movements. *J. Gen. Physiol.* **120**:465–473
- Correa, A.M. 1998. Gating kinetics of Shaker K⁺ channels are differentially modified by general anesthetics. *Am. J. Physiol.* **275**:C1009–C1021
- Dallos, P. 1992. The active cochlea. *J. Neurosci.* **12**:4575–4585
- Danthi, S., Enyeart, J.A., Enyeart, J.J. 2003. Modulation of native TREK-1 and KV1.4 K⁺ channels by polyunsaturated fatty acids and lysophospholipids. *J. Membrane Biol.* **195**:147–164
- Fernandez, J.M., Bezanilla, F., Taylor, R.E. 1982. Effect of chloroform on charge movement in the nerve membrane. *Nature* **297**:150–152
- Franks, N.P., Lieb, W.R. 1994. Molecular and cellular mechanisms of general anaesthesia. *Nature* **367**:607–614
- Gale, J.E., Ashmore, J.F. 1994. Charge displacement induced by rapid stretch in the basolateral membrane of the guinea-pig outer hair cell. *Proc. R. Soc. Lond. B Biol. Sci.* **255**:243–249
- Gale, J.E., Ashmore, J.F. 1997. The outer hair cell motor in membrane patches. *Pfluegers Arch.* **434**:267–271
- Goulian, M., Mesquita, O.N., Fygenon, D.K., Nielsen, C., Andersen, O.S., Libchaber, A. 1998. Gramicidin channel kinetics under tension. *Biophys. J.* **74**:328–337
- Hilgemann, D.W., Nicoll, D.A., Philipson, K.D. 1991. Charge movement during Na⁺ translocation by native and cloned cardiac Na⁺/Ca²⁺ exchanger. *Nature* **352**:715–718
- Huang, G., Santos-Sacchi, J. 1993. Mapping the distribution of the outer hair cell motility voltage sensor by electrical amputation. *Biophys. J.* **65**:2228–2236
- Huang, G., Santos-Sacchi, J. 1994. Motility voltage sensor of the outer hair cell resides within the lateral plasma membrane. *Proc. Natl. Acad. Sci. USA* **91**:12268–12272
- Iwasa, K.H. 1993. Effect of stress on the membrane capacitance of the auditory outer hair cell. *Biophys. J.* **65**:492–498
- Iwasa, K.H. 1994. A membrane motor model for the fast motility of the outer hair cell. *J. Acoust. Soc. Am.* **96**:2216–2224
- Kakehata, S., Santos-Sacchi, J. 1995. Membrane tension directly shifts voltage dependence of outer hair cell motility and associated gating charge. *Biophys. J.* **68**:2190–2197
- Kalincic, F., Holley, M.C., Iwasa, K.H., Lim, D.J., Kachar, B. 1992. A membrane-based force generation mechanism in auditory sensory cells. *Proc. Natl. Acad. Sci. USA* **89**:8671–8675
- Kalincic, F., Kachar, B. 1993. Inhibition of outer hair cell electromotility by sulfhydryl specific reagents. *Neurosci. Lett.* **157**:231–234
- Lee, A.G. 1991. Lipids and their effects on membrane proteins: evidence against a role for fluidity. *Prog. Lipid Res.* **30**:323–348
- Liberman, M.C., Gao, J., He, D.Z.Z., Wu, X.D., Jia, S.P., Zuo, J. 2002. Prestin is required for electromotility of the outer hair cell and for the cochlea amplifier. *Nature* doi:10.1038/nature01059
- Ludwig, J., Oliver, D., Frank, G., Klocker, N., Gummer, A.W., Fakler, B. 2001. Reciprocal electromechanical properties of rat prestin: The motor molecule from rat outer hair cells. *Proc. Natl. Acad. Sci. USA* **98**:4178–4183
- Lue, A.J., Zhao, H.B., Brownell, W.E. 2001. Chlorpromazine alters outer hair cell electromotility. *Otolaryngol. Head Neck Surg.* **125**:71–76
- Lundblad, R.L. 1995. *Techniques in Protein Modification*. CRC, Boca Raton,
- Meltzer, J., Santos-Sacchi, J. 2001. Temperature dependence of non-linear capacitance in human embryonic kidney cells transfected with prestin, the outer hair cell motor protein. *Neurosci. Lett.* **313**:141–144
- Morimoto, N., Raphael, R.M., Nygren, A., Brownell, W.E. 2002. Excess plasma membrane and effects of ionic amphipaths on mechanics of outer hair cell lateral wall. *Am. J. Physiol.* **282**:C1076–C1086
- Navaratnam, D.S., Bai, J.-P., Samaranyake, H., Santos-Sacchi, J. 2004. Structure-function studies of prestin, the OHC lateral membrane motor. *Assoc. Res. Otolaryngol. Abs.* 270
- Oliver, D., He, D.Z., Klocker, N., Ludwig, J., Schulte, U., Waldegger, S., Ruppertsberg, J.P., Dallos, P., Fakler, B. 2001. Intracellular anions as the voltage sensor of prestin, the outer hair cell motor protein. *Science* **292**:2340–2343
- Oliver, D., Lien, C.C., Soom, M., Baukowitz, T., Jonas, P., Fakler, B. 2004. Functional conversion between A-type and delayed rectifier K⁺ channels by membrane lipids. *Science* **304**:265–270
- Patel, A.J., Honore, E., Lesage, F., Fink, M., Romey, G., Lazdunski, M. 1999. Inhalational anesthetics activate two-pore-domain background K⁺ channels. *Nat. Neurosci.* **2**:422–426
- Pusch, M., Ludewig, U., Jentsch, T.J. 1997. Temperature dependence of fast and slow gating relaxations of CIC-0 chloride channels. *J. Gen. Physiol.* **109**:105–116
- Rakotomanga, M., Loiseau, P.M., Saint-Pierre-Chazalet, M. 2004. Hexadecylphosphocholine interaction with lipid monolayers. *Biochim. Biophys. Acta* **1661**:212–218

- Raphael, R.M., Popel, A.S., Brownell, W.E. 2000. A membrane bending model of outer hair cell electromotility. *Biophys. J.* **78**:2844–2862
- Rybalchenko, V., Santos-Sacchi, J. 2003. Cl^- flux through a non-selective, stretch-sensitive conductance influences the outer hair cell motor of the guinea-pig. *J. Physiol.* **547**:873–891
- Santos-Sacchi, J. 1991. Reversible inhibition of voltage-dependent outer hair cell motility and capacitance. *J. Neurosci.* **11**:3096–3110
- Santos-Sacchi, J. 1993. Harmonics of outer hair cell motility. *Biophys. J.* **65**:2217–2227
- Santos-Sacchi, J. 2003. New tunes from Corti's organ: the outer hair cell boogie rules. *Curr. Opin. Neurobiol.* **13**:459–468
- Santos-Sacchi, J., Dilger, J.P. 1988. Whole cell currents and mechanical responses of isolated outer hair cells. *Hear. Res.* **35**:143–150
- Santos-Sacchi, J., Huang, G. 1998. Temperature dependence of outer hair cell nonlinear capacitance. *Hear. Res.* **116**:99–106
- Santos-Sacchi, J., Huang, G.J., Wu, M. 1997. Mapping the distribution of outer hair cell voltage-dependent conductances by electrical amputation. *Biophys. J.* **73**:1424–1429
- Santos-Sacchi, J., Kakehata, S., Takahashi, S. 1998. Effects of membrane potential on the voltage dependence of motility-related charge in outer hair cells of the guinea-pig. *J. Physiol.* **510**:225–235
- Santos-Sacchi, J., Navarrete, E. 2002. Voltage-dependent changes in specific membrane capacitance caused by prestin, the outer hair cell lateral membrane motor. *Pfluegers Arch.* **444**:99–106
- Santos-Sacchi, J., Shen, W., Zheng, J., Dallos, P. 2001. Effects of membrane potential and tension on prestin, the outer hair cell lateral membrane motor protein. *J. Physiol.* **531**:661–666
- Santos-Sacchi, J., Wu, M. 1998. Electrical correlates of OHC viscoelastic behavior—evidence for voltage-induced membrane tension. Mtg. Assoc. Res. Otolaryng. St. Petersburg, FL
- Spector, A.A., Jean, R.P. 2004. Modes and balance of energy in the piezoelectric cochlear outer hair cell wall. *J. Biomech. Eng.* **126**:17–25
- Stetson, D.L., Wade, J.B. 1983. Ultrastructural characterization of cholesterol distribution in toad bladder using filipin. *J. Membrane Biol.* **74**:131–138
- Stirling, C.E. 1975. Mercurial perturbation of brush border membrane permeability in rabbit ileum. *J. Membrane Biol.* **23**:33–56
- Wu, M., Santos-Sacchi, J. 1998. Effects of lipophilic ions on outer hair cell membrane capacitance and motility. *J. Membrane Biol.* **166**:111–118
- Zheng, J., Shen, W., He, D., Long, K., Madison, L., Dallos, P. 2000. Prestin is the motor protein of cochlear outer hair cells. *Nature* **405**:149–155
- Zheng, J., Long, K.B., Shen, W., Madison, L.D., Dallos, P. 2001. Prestin topology: localization of protein epitopes in relation to the plasma membrane. *Neuroreport* **12**:1929–1935

Joseph Santos-Sacchi · Hong-Bo Zhao

Excitation of fluorescent dyes inactivates the outer hair cell integral membrane motor protein prestin and betrays its lateral mobility

Received: 18 November 2002 / Accepted: 6 March 2003 / Published online: 29 May 2003
© Springer-Verlag 2003

Abstract The outer hair cell motor protein, prestin, which resides exclusively in the cell's lateral membrane, underlies the mammal's exquisite sense of hearing. Here we show that photoexposure of the commonly used dyes Lucifer yellow, 6-carboxy-fluorescein, and 4-{2-[6-(dioctylamino)-2-naphthalenyl]ethenyl}-1-(3-sulfo-propyl)-pyridinium (di-8-ANEPPS), that are in contact with the cell's lateral membrane can photo-inactivate the motor irreversibly, as evidenced by reduction in prestin's gating charge displacement or non-linear capacitance. Furthermore, utilizing restricted fiber optic illumination of the lateral membrane, we show that whole-cell, non-linear capacitance is depleted beyond that expected for an immobile population in the exposed area. These data indicate that lateral diffusion of prestin occurs within the cell's lateral plasma membrane.

Keywords Lucifer yellow · Fluorescein · di-8-ANEPPS · Outer hair cell · FRAP · Gating charge · Membrane capacitance

Introduction

The molecular motors of the outer hair cell (OHC) drive a somatic mechanical response that underlies the enhanced sensitivity and frequency resolving power of the mammalian cochlea [2, 5, 12, 23]. Electrical measures indicate that these motors reside within the lateral plasma membrane of the OHC, and probably resemble other integral membrane proteins that are capable of generating

gating currents upon voltage-induced conformational changes [3, 10, 11, 22]. In fact, Dallos and coworkers have cloned the gene for a protein, prestin, that, when expressed in non-auditory cells, presents electrical and mechanical signatures that match those of the OHC lateral membrane motor [25, 31]. Prestin is expressed in exactly that location, namely, the lateral plasma membrane [4], predicted by the electrophysiological evidence [10].

Integral membrane proteins are capable of diffusing through the plasma membrane [7]. To study the constraints that maintain prestin's residence in the lateral membrane, we have mapped recently the extent of prestin along the OHC lateral membrane using discrete mechanical stimulation [27], and evaluated the effect of cytoskeletal destruction on motor diffusion to areas normally devoid of motor molecules, namely, the basal region of the cylindrical cell. Surprisingly, the motors did not migrate to the basal region, indicating some type of integral membrane barrier. Here we use a technique to photo-inactivate motors while monitoring their gating charge movement so that their ability to diffuse within the lateral membrane can be assessed. We provide evidence that prestin, in intact OHCs, is capable of diffusing within the lateral plasma membrane.

Materials and methods

Guinea pigs were euthanized with halothane. OHCs and supporting cells were isolated enzymatically with dispase I (0.5 mg/ml for 10 min followed by gentle trituration through a polyethylene pipette) in a modified Leibovitz medium containing (in mM): NaCl 142, KCl 5.37, MgCl₂ 1.47, HEPES 5, CaCl₂ 2 and dextrose 5; 300 mOsm, pH7.2. The cells were then transferred to a 700- μ l perfusion chamber. All experiments were conducted at room temperature (~23 °C). A Nikon Diaphot inverted microscope with Hoffmann optics was used to observe the cells during electrical recording. All experiments were video-taped.

Single OHCs were studied under whole-cell voltage-clamp conditions using a patch clamp amplifier (200A, Axon Instruments, Union City, Calif., USA) at a holding potential of -80 mV. Initial resistances of patch pipettes were 2–3 M Ω , corresponding to tip sizes of 1–2 μ m. Residual series resistance was 3–7 M Ω . Data were collected and analyzed using a Windows-based program (jClamp,

J. Santos-Sacchi (✉) · H.-B. Zhao
Surgery (Otolaryngology) and Neurobiology, BML 244,
Yale University School of Medicine,
333 Cedar St., New Haven, CT 06510, USA
e-mail: joseph.santos-sacchi@yale.edu
Tel.: +1-203-7857566

Present address:

H.-B. Zhao, Div. of Otolaryngology, Dept. of Surgery,
University of Kentucky Medical Center,
Lexington, KY 40536, USA

SciSoft, New Haven, Conn., USA). Ionic blocking solutions were used to remove voltage-dependent ionic conductances so that capacitive currents could be analyzed in isolation [10, 22]. The patch pipette solution contained (in mM): CsCl 140, MgCl₂ 2, EGTA 10, HEPES 5, with pH 7.2 and osmolarity 300 mOsm (adjusted with dextrose). The extracellular ionic blocking solution contained (in mM): 100 NaCl, 20 TEA, 20 CsCl, 1.25 CoCl₂, 1.48 MgCl₂, 10 HEPES, pH 7.2 and osmolarity 300 mOsm (adjusted with dextrose). Whole chamber perfusion was continuous.

OHC capacitance was monitored using transient analysis [10]. Additionally, continuous, high-resolution capacitance measurements were acquired through admittance analysis at time resolutions of 5.12 or 2.56 ms utilizing a two-sine wave voltage stimulus protocol fully described elsewhere [24]. The stimulus consisted of the sum of two voltage sine waves (390.625 and 781.25 Hz), each at a magnitude of 10 mV peak. In some cases, this AC stimulus was superimposed on voltage ramp or step stimuli. Capacitance-voltage (*C-V*) functions were fit to the first derivative of a two-state Boltzmann function relating non-linear charge to membrane voltage (dQ/dV ; [10, 22]):

$$C_m = Q_{max} \frac{ze}{kT} \frac{b}{(1+b)^2} + C_{lin}$$

where

$$b = \exp\left[\frac{-ze(V - V_{pkCm})}{kT}\right]$$

and Q_{max} is the maximum nonlinear charge moved, V_{pkCm} the voltage at peak capacitance or, equivalently, at half-maximal non-linear charge transfer, V_m is the membrane potential, z valence, C_{lin} linear membrane capacitance, e electron charge, k Boltzmann's constant, and T absolute temperature.

Patch pipettes were filled with either Lucifer Yellow (5%) or 6-carboxyfluorescein (5%) to load OHCs with the dye. The lipophilic dye 4-[2-[6-(dioctylamino)-2-naphthalenyl]ethenyl]-1-(3-sulfo-propyl)-pyridinium (di-8-ANEPPS) was delivered to the OHC plasma membrane as previously described [14, 15]. Briefly, cells were incubated with 1% dye in extracellular solution for 15 min prior to washing and recording. For whole-cell exposure, the dyes were excited with blue light (450–490 nm filter; Nikon 100-W high-pressure mercury lamp). For discrete excitation, a pulled quartz fiber optic (tip size ~2 μm) was fed directly from a Zeiss 75-W high-pressure mercury lamp, without filters. Whole cells were exposed by opening/closing the microscope light barrier manually. Fiber optic exposures were controlled via a computer-driven shutter.

Results

Prestin can be photo-inactivated

OHC membrane capacitance derives from two components: that associated with lateral membrane sensor/motor charge movement, and that proportional to membrane surface area. Figure 1 illustrates through measurements of capacitance that prestin can be irreversibly photo-inactivated. Figure 1a shows the exponential decrease in motor-associated capacitance following whole-cell photoexposure of a cell perfused intracellularly with 5% Lucifer Yellow via the patch pipette. The time constant for inactivation was 14.2 s (mean 26.4 ± 10.2 s, $n=6$). To accomplish this inactivation, the photosensitive dye must be in contact with the cell's plasma membrane (Fig. 1b). In the absence of dye, photoexposure of OHCs did not reduce whole-cell capacitance; following perfusion of the

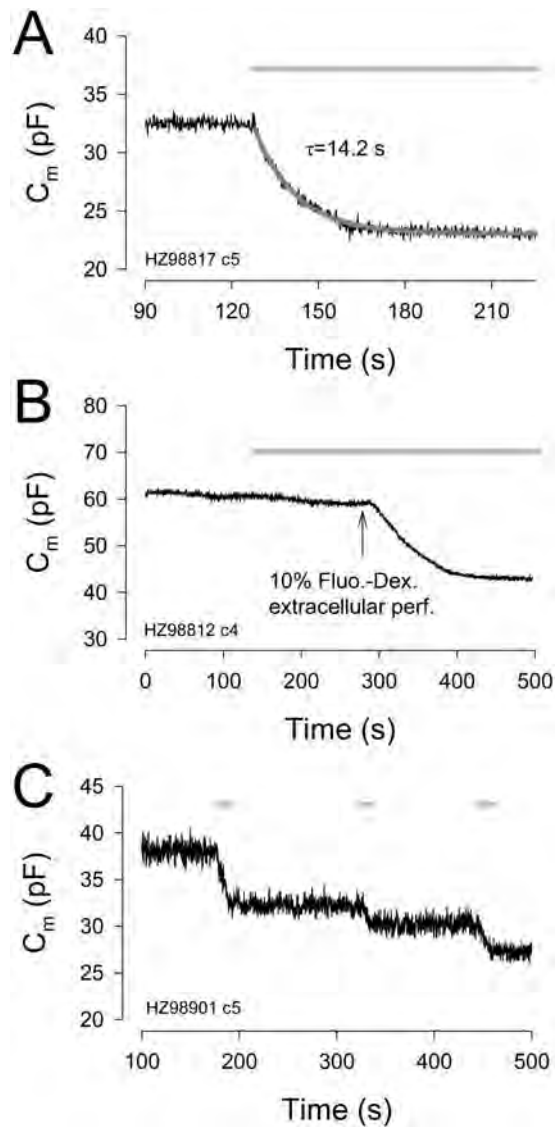
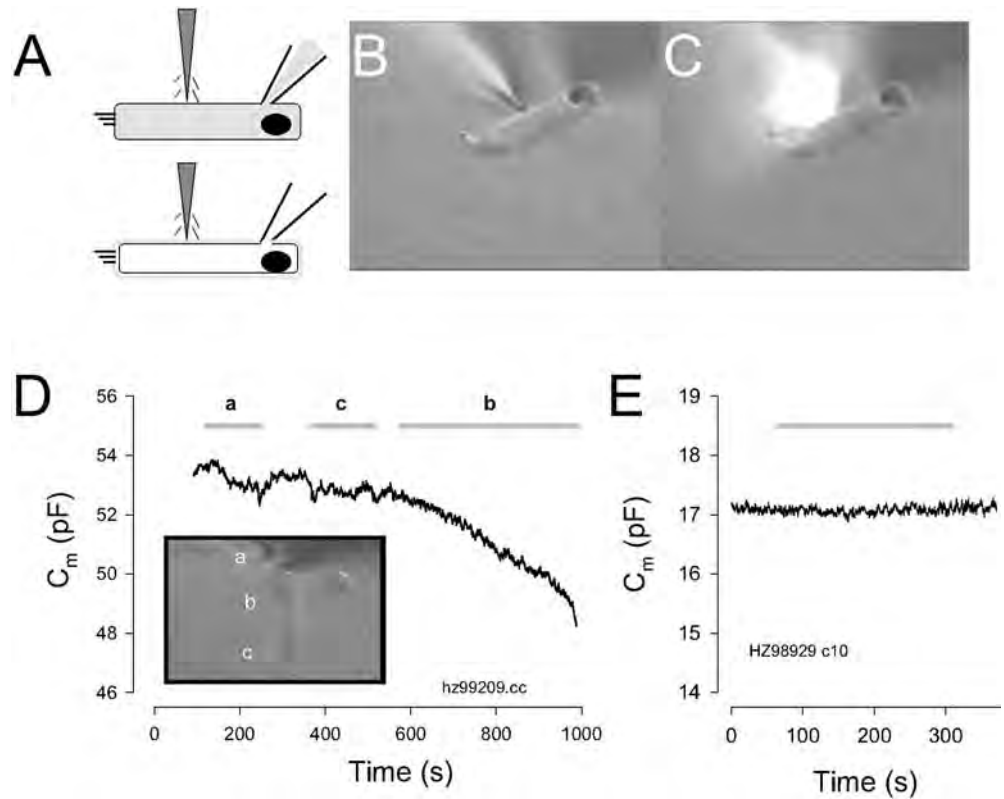


Fig. 1A–C Outer hair cell (OHC) motors can be irreversibly photo-inactivated. **A** OHC with intracellular Lucifer Yellow. Light was turned on for the period indicated by the *gray bar*. Note exponential decay of non-linear component of membrane capacitance (C_m , ordinate). Fit (*solid line*) indicates a time constant of 14.2 s. **B** Non-linear capacitance (NLC) was resistant to photoexposure in the absence of sensitizing dye. After the addition of the membrane impermeant dye fluorescein-dextran, NLC exponentially decreased. **C** OHC with 6-carboxyfluorescein intracellular. NLC decreased only during photoexposure (*bars*)

cells with extracellular solutions containing fluorescent dye the motors became susceptible. The inactivation of lateral membrane motors was rapid and only occurred during the duration of the light exposure. This is shown in Fig. 1c where the light was switched on for only short periods; between exposures the reduced capacitance remained stable.

Fig. 2A–E Restricted exposure with fiber optic light probe. **A** Cells were whole-cell patch clamped and the fiber placed adjacent to the plasma membrane of cells with either intracellular dye (*top figure*, Lucifer Yellow) or intra-membrane [*bottom figure*, 4-{2-[6-(dioctylamino)-2-naphthalenyl]ethenyl}-1-(3-sulfo-propyl)-pyridinium (di-8-ANEPPS) dye, see Methods]. **B**, **C** Digitally captured image of an OHC before and during exposure to the lateral membrane. **D** An OHC treated with di-8-ANEPPS was exposed at the basal (*a*), middle (*b*) and apical (*c*) regions of the cell. Only the lateral region exposure produced marked capacitance decreases. **E** A Deiters' cell treated with di-8-ANEPPS showed no reduction of linear capacitance during exposure



Photoexposure of restricted regions of the OHC

By delivering light through a tapered fiber optic light guide (tip size: $\sim 2 \mu\text{m}$; rough estimate of diffusive exposure: $80 \mu\text{m}^2$), photo-exposure can be directed to selected regions of the OHC (Fig. 2). In Fig. 2d, exposure of the basal and apical region of the OHC produced little decrease in capacitance, whereas exposure of the lateral membrane caused a substantial drop in capacitance. This is expected, since the motors are restricted to the lateral membrane [4, 10]. In Deiters' cells, which lack prestin, membrane capacitance remained stable during photo exposure (Fig. 2e).

We used this restricted fiber optic exposure to evaluate the possibility of motor diffusion in the lateral membrane. Figure 3 illustrates that repeated or continuous restricted exposure of the OHC lateral membrane to the light source produced accumulating capacitance decreases not expected for an immobilized, finite population of motors. Repeated fiber optic exposure to fixed portions of the OHC sensitized with either intracellular 6-carboxy fluorescein (Fig. 3a), or with the membrane-soluble dye di-8-ANEPPS (Fig. 3b), resulted in an apparent linear (i.e. non-exponential) decrease in capacitance during exposure, and stabilization in the absence of exposure. The slope of the capacitance decrease with restricted exposures ($12.3 \pm 1.8 \text{ fF/s}$; $n=6$) was substantially less than the initial slope ($312 \pm 33 \text{ fF/s}$; $n=6$) following whole-cell exposure, though the ultimate magnitude of decrease could be quite large (Fig. 3c). We interpret these

observations to result from the continuous movement of functional motors into the small region of photoexposure. That is, the rate of inactivation is limited by diffusion rate of the motor into the restricted region of exposure. Figure 4 shows whole-cell C - V functions for an OHC in which the lateral membrane was exposed for 8 min via fiber optic. In addition to a reduction in total charge moved (Q_{max}), indicating the removal of functional motors from the whole cell population, z and V_{pkCm} were altered.

Discussion

A number of studies have shown that integral membrane proteins are modified either directly by light at particular wavelengths [8, 9, 17] or by sensitizers following light activation [1, 17, 28]. Our data indicate that the OHC motor protein prestin can be rapidly photo-inactivated. Whole-cell C - V functions result from the combined characteristics of the photo-inactivated population of motors and the remaining normal populations of motors, and confirm the destruction of motors since Q_{max} was reduced. Motors are not directly susceptible to the light sources that we used but to some product that is released following the excitation of commonly used fluorescent dyes near or within the membrane. We have shown previously that gap junctions and K^+ channels within supporting Hensen's cells can be similarly photo-inactivated [20, 21]. It should be stressed that the decrease in

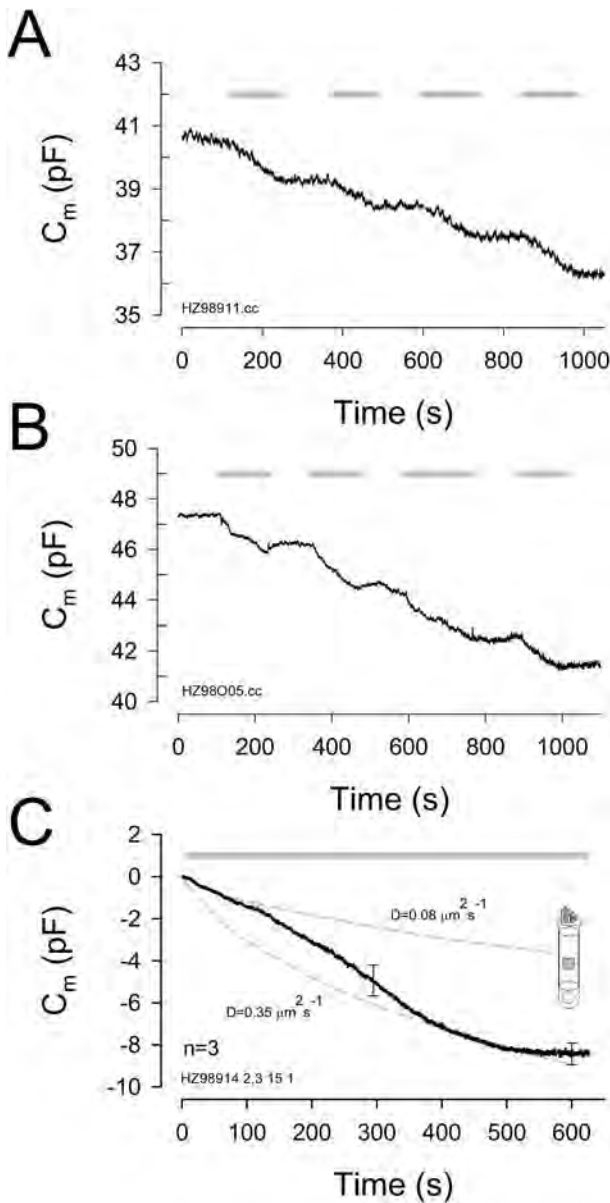


Fig. 3A–C Repeated or continuous exposure of restricted regions of the lateral membrane. **A** OHC filled with Lucifer Yellow showed accumulating decreases in NLC during repeated exposures. The slope of decrease appears linear. **B** OHC treated with di-8-ANEPPS showed similar behavior during exposures. **C** Continuous exposure of restricted region (gray area in OHC schematic) produced an initial linear segment of NLC decrease followed by a decaying rate. The trace is the mean \pm SEM of three OHC responses. The dotted lines indicate the result of model simulations with the indicated diffusion coefficients (see Discussion for details)

capacitance or conductance is not likely to be due to diffusion of reactive species far from areas of exposure, since inactivation stops immediately after the light is turned off. This is expected since photo-sensitizers probably act after binding to the membrane, and the estimated lifetime and diffusion of the evolved reactive species, e.g., singlet oxygen, are of the order of a few microseconds, and a hundred nanometers, respectively

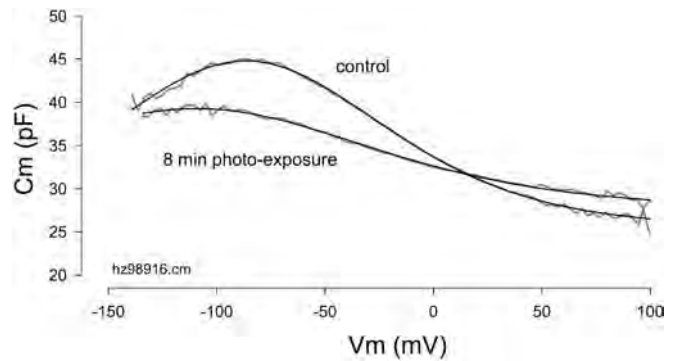


Fig. 4 Functions relating C_m to membrane potential (V_m) before and after an 8-min fiber optic exposure of an OHC treated with di-8-ANEPPS. Fitted parameters: control (V_{pkC_m} , z , Q_{max} , C_{lin} , respectively): -86.5 , 0.59 , 3.36 , 25.5 , exposed: -109.4 , 0.47 , 2.55 , 27.7

(see [19] for discussion and references). Thus, the fiber optic exposures that we made probably resulted in highly restricted lesions. Since motors can be inactivated by hydrophilic dyes (Lucifer yellow, 6-carboxyfluorescein, fluorescein-dextran) delivered to the membrane via intracellular or extracellular routes, and by the lipophilic dye (di-8-ANEPPS), susceptible targets are possibly present at intracellular, extracellular and intramembrane domains. The amino acids histidine, methionine, tryptophan and cysteine are most sensitive to reactive oxygen species [13], and these residues are found in all three domains of prestin [32] (J. Zheng, personal communication).

The inactivation of sensitized lateral membrane motors by light may be viewed as a simple irreversible reaction:



For whole cell exposure, where M_+^* is the sensitized active motor pool, M_- is the inactivated motor pool, and k_{kill} is the inactivation rate constant, the time course of inactivation is a simple exponential, with a time constant of $1/k_{kill}$. For our whole-cell data the rate constant was 0.0384 s^{-1} . If we consider that in this case the non-linear capacitance (NLC) decrease arises from destruction of all motors in the cell (~ 10 million for a low-frequency OHC [10]), we can derive an estimate of motor inactivation rate, namely, about 384,000/s. This high sensitivity to inactivation is mirrored by the inner ear's sensitivity to a variety of insults, including agents that generate reactive oxygen species [6, 16].

The description of the inactivation process in a partially exposed cell is more complicated, as the sensitized active motor pool may be supplied by the unexposed active motor pool, M_+ .



The rate constants k and $k-1$ will influence the time course of motor inactivation, and actually represent more complex diffusion processes. Thus, the forward rate constant k may be influenced by motor density, motor interactions with other integral membrane proteins and sub-membranous cytoskeleton, and diffusion distances from the irradiated area. The backward rate $k-1$ will also reflect similar influences, but additionally may suffer from the untoward effects of photo-irradiation, for example, molecular cross-linking.

Peters et al. [18] have performed a conceptually similar study to ours using continuous fluorescence recovery after photobleaching (FRAP) of the dye 3,3'-diiodoacetylcarboxyanine perchlorate (DiO) within a restricted membrane region. They pointed out that in the case where the diffusion time constant ($\tau_d = \text{irradiated radius}^2/D$; where D is the diffusion coefficient) is very much greater than the photo-inactivation time constant ($\tau_k = 1/k_{\text{kill}}$), the time course of fluorescence decay (or in our case capacitance decay) would follow the exponential time course characteristic of photo-inactivation alone. This behavior essentially accounts for the characteristic time of capacitance decrease that we observe under whole-cell photo irradiation. However, in the case where the photo-inactivation process is very much faster than the delivery of motors to the irradiated area, the time course of capacitance decrease would be dominated by the factors that govern the diffusion process. With fiber optic illumination, the time course of capacitance decrease was not a simple exponential (Fig. 3c), as we might have expected for an immobile population of motors, and as we observed with whole-cell irradiation; instead, there was a prolonged linear-like segment followed by an exponentially decaying termination. Furthermore, the magnitude of NLC decrease is far greater than that expected for the estimated exposed area. We conclude from these data that there is, in fact, lateral diffusion of motors into the irradiated area, and that the photo-inactivation process is faster than that of diffusion. This contrasts with observations on Na^+ channels in skeletal muscle that were photo-inactivated under a loose patch pipette; currents did not return for more than 60 min, indicating a diffusion coefficient of less than $0.0001 \mu\text{m}^2/\text{s}$ [26, 29].

The diffusion coefficient of untethered proteins within lipid bilayers typically ranges around $0.01 \mu\text{m}^2/\text{s}$ [7]. That of lipid molecules within the membrane is larger, ranging around $1.0 \mu\text{m}^2/\text{s}$. The diffusion of the lipid permeable dye di-8-ANEPPS within the OHC lateral membrane is within that range, but interestingly, it is voltage dependent to some extent [14, 15]. This may relate to the voltage dependence of the major protein, prestin, located in that membrane. Another lipid soluble dye, SP-DiIC18, is relatively immobile, but can redistribute within the membrane in a voltage dependent manner and probably depends on prestin activity [30]. In light of these data, it may be possible that the diffusion of prestin itself may depend on the protein's voltage-dependent area state. In the present study, we held the OHCs at a constant

membrane voltage, but it will be interesting to evaluate the effects of various holding potentials in future studies.

Given our data, the diffusion coefficient of prestin may be roughly estimated by considering that the problem is basically one of modeling a molecular sink. As a first approximation, we consider an uncapped cylindrical bilayer possessing the surface area (source) of the lateral membrane of a $65\text{-}\mu\text{m}$ -long OHC, $1,288 \mu\text{m}^2$, within which reside motors at a density of $7,500/\mu\text{m}^2$ (equated to a NLC of $0.01 \text{ pF}/\mu\text{m}^2$) [10]. The motors are considered freely diffusible, but exit the system upon entering a central region (sink) of $\sim 1/20$ ($81 \mu\text{m}^2$) the full surface area. The question is what diffusion coefficient must the molecules possess to produce a decrease in numbers at a rate of $10,000/\text{s}$ ($\sim 10 \text{ fF}/\text{s}$ in the OHC), as we estimate during fiber optic irradiation of the OHC? The problem was modeled in Berkeley Madonna using $1\text{-}\mu\text{m}$ square cells, with a square sink ($9 \mu\text{m}$ edge) in the middle of the OHC (Fig. 3c inset). The dotted lines in Fig. 3c show the time course of reductions in NLC for two diffusion coefficients that bracket the averaged data. A D of $0.08 \mu\text{m}^2/\text{s}$ can account for the initial segment of the data; however, the subsequent segments require larger coefficients. The divergence from a simple and fixed course of diffusion indicates that something more complicated is occurring, perhaps cross-linking of proteins or lipid peroxidation. We must also be aware that the diffusion of the dyes (which themselves may be rendered ineffective in the exposed area) may also influence our measures. We suggest that the earlier segments of the data, where membrane damage may be less, may better represent the diffusion characteristics of prestin and indicate that prestin is untethered. The ability to diffuse may be important for the redistribution of motors after insertion into the plasma membrane during normal motor turnover. Additionally, the absence of tethering may indicate that the proteins freely rotate within the plane of the membrane, and are unlikely to acquire any anisotropic characteristics owing to diffusional constraints.

In sum, we have shown that the OHC membrane motor is susceptible to photo-inactivation, and that this sensitivity can be exploited to reveal the protein's ability to diffuse within the lateral membrane. With the recent molecular identification of the motor [25, 31] we can expect more detailed examinations of the protein's activities in the lateral membrane.

Acknowledgements This work was supported by NIH-NIDCD grant DC00273 to JSS. We thank Paul Fahey, Michael Edidin, and Robert Phair for helpful discussions, and Margaret Mazzucco for technical help.

References

1. Arriaga E, Frolov A, Tarr M, Valenzano DP (1994) Membrane ionic current photomodification by rose bengal and menadione: role of singlet oxygen. *Photochem Photobiol* 59:637-642

2. Ashmore JF (1987) A fast motile response in guinea-pig outer hair cells: the cellular basis of the cochlear amplifier. *J Physiol (Lond)* 388:323–347
3. Ashmore JF (1990) Forward and reverse transduction in the mammalian cochlea. *Neurosci Res Suppl* 12:S39–S50
4. Belyantseva I, Adler HJ, Curi R, Frolenkov GI, Kachar B (2000) Expression and localization of Prestin and the sugar transporter GLUT-5 during development of electromotility in cochlear outer hair cells. *J Neurosci* 20:RC116:1–5
5. Brownell WE, Bader CR, Bertrand D, Ribaupierre Y de (1985) Evoked mechanical responses of isolated cochlear outer hair cells. *Science* 227:194–196
6. Clerici WJ, Hensley K, DiMartino DL, Butterfield DA (1996) Direct detection of ototoxicant-induced reactive oxygen species generation in cochlear explants. *Hear Res* 98:116–124
7. Edidin M (1987) Rotational and lateral diffusion of membrane proteins and lipids: phenomena and function. *Curr Top Membr Transp* 29:91–127
8. Fox JM, Stampfli R (1971) Modification of ionic membrane currents of Ranvier nodes by UV-radiation under voltage clamp conditions. *Experientia* 27:1289–1290
9. Fox JM, Neumcke B, Nonner W, Stampfli R (1976) Block of gating currents by ultraviolet radiation in the membrane of myelinated nerve. *Pflugers Arch* 364:143–145
10. Huang G, Santos-Sacchi J (1993) Mapping the distribution of the outer hair cell motility voltage sensor by electrical amputation. *Biophys J* 65:2228–2236
11. Huang G, Santos-Sacchi J (1994) Motility voltage sensor of the outer hair cell resides within the lateral plasma membrane. *Proc Natl Acad Sci USA* 91:12268–12272
12. Liberman MC, Gao J, He DZ, Wu X, Jia S, Zuo J (2002) Prestin is required for electromotility of the outer hair cell and for the cochlear amplifier. *Nature* 419:300–304
13. Lundblad RL (1995) *Techniques in protein modification*. CRC Press, Boca Raton
14. Oghalai JS, Tran TD, Raphael RM, Nakagawa T, Brownell WE (1999) Transverse and lateral mobility in outer hair cell lateral wall membranes. *Hear Res* 135:19–28
15. Oghalai JS, Zhao HB, Kutz JW, Brownell WE (2000) Voltage- and tension-dependent lipid mobility in the outer hair cell plasma membrane. *Science* 287:658–661
16. Ohlemiller KK, Dugan LL (2002) Elevation of reactive oxygen species following ischemia-reperfusion in mouse cochlea observed in vivo. *Audiol Neurootol* 4:219–228
17. Oxford GS, Pooler JP (1975) Ultraviolet photoalteration of ion channels in voltage-clamped lobster giant axons. *J Membr Biol* 20:13–30
18. Peters R, Brunger A, Schulten K (1981) Continuous fluorescence microphotolysis—a sensitive method for study of diffusion-processes in single cells. *Proc Natl Acad Sci USA* 78:962–966
19. Rokitskaya TI, Block M, Antonenko YN, Kotova EA, Pohl P (2000) Photosensitizer binding to lipid bilayers as a precondition for the photoinactivation of membrane channels. *Biophys J* 78:2572–2580
20. Santos-Sacchi J (1986) Dye coupling in the organ of Corti. *Cell Tissue Res* 245:525–529
21. Santos-Sacchi J (1991) Isolated supporting cells from the organ of Corti: some whole cell electrical characteristics and estimates of gap junctional conductance. *Hear Res* 52:89–98
22. Santos-Sacchi J (1991) Reversible inhibition of voltage-dependent outer hair cell motility and capacitance. *J Neurosci* 11:3096–3110
23. Santos-Sacchi J, Dilger JP (1988) Whole cell currents and mechanical responses of isolated outer hair cells. *Hear Res* 35:143–150
24. Santos-Sacchi J, Kakehata S, Takahashi S (1998) Effects of membrane potential on the voltage dependence of motility-related charge in outer hair cells of the guinea-pig. *J Physiol (Lond)* 510:225–235
25. Santos-Sacchi J, Shen W, Zheng J, Dallos P (2001) Effects of membrane potential and tension on prestin, the outer hair cell lateral membrane motor protein. *J Physiol (Lond)* 531:661–666
26. Stuhmer W, Almers W (1982) Photobleaching through glass micropipettes: sodium channels without lateral mobility in the sarcolemma of frog skeletal muscle. *Proc Natl Acad Sci USA* 79:946–950
27. Takahashi S, Santos-Sacchi J (2001) Non-uniform mapping of stress-induced, motility-related charge movement in the outer hair cell plasma membrane. *Pflugers Arch* 441:506–513
28. Valenzano DP, Arriaga E, Trank J, Tarr M (1993) Membrane potential can influence the rate of membrane photomodification. *Photochem Photobiol* 57:996–999
29. Weiss RE, Roberts WM, Stuhmer W, Almers W (1986) Mobility of voltage-dependent ion channels and lectin receptors in the sarcolemma of frog skeletal muscle. *J Gen Physiol* 87:955–983
30. Zhang M, Kalinec F (2002) Structural microdomains in the lateral plasma membrane of cochlear outer hair cells. *J Assoc Res Otolaryngol* 3:289–301
31. Zheng J, Shen W, He D, Long K, Madison L, Dallos P (2000) Prestin is the motor protein of cochlear outer hair cells. *Nature* 405:149–155
32. Zheng J, Long KB, Shen W, Madison LD, Dallos P (2001) Prestin topology: localization of protein epitopes in relation to the plasma membrane. *Neuroreport* 12:1929–1935

33. Grushka, M., Epstein, J., and Mott, A., An open-label, dose escalation pilot study of the effect of clonazepam in burning mouth syndrome, *Oral Surg. Oral Med. Oral Pathol. Oral Radiol. Endod.*, 86, 557, 1998.
34. Bartoshuk, L.M., Kveton, J., Yanagisawa, K., and Catalanotto, F. (1994). Taste loss and taste phantoms: a role of inhibition in taste, in Kurihara, K., Suzuki, N., and Ogawa, H., Eds., *Olfaction and Taste XI*, Springer-Verlag, New York, 1994, 557.

PART IV: ANIMAL RESEARCH IN PERIPHERAL AUDITORY PHYSIOLOGY

Joseph Santos-Sacchi

BACKGROUND

Cataloging the microanatomy of the auditory end organ provided an important start for understanding the physiology of the peripheral auditory system. These anatomical studies, conducted on a variety of species, began in earnest following the development of the compound light microscope in the 1700s. The detail in some of the original work of such pioneers as Alfonso Corti is remarkable (see Hawkins¹ and references within), but alas the microscopic structures were necessarily altered by the decay following extirpation and dissection. As we shall see, this decay had a major impact on our understanding of cochlear physiology as well. Whereas the development of fixatives proved a boon for anatomists, physiologists would not benefit directly but would belatedly profit from histologists' appreciation of the need to preserve the natural state.

The cochlea, we now know, is a remarkable electromechanical device. Prior to the discovery of animal electricity and means to measure it, only the mechanical components of cochlea function could be investigated. Thus, the microscopic structures in the inner ear were used to deduce the mechanical foundation of cochlea function; for example, Helmholtz postulated his resonance theory based on the changing length (hence mechanical properties) of radial basilar membrane fibers. Clearly, in mammals, the basilar membrane with its varying dimensions and stiffness would be a prime candidate for the basis of hearing. Indeed, von Bekesy's studies² confirmed the importance of the basilar membrane's mechanical qualities by demonstrating tuned traveling waves evoked by basilar membrane disturbances. von Bekesy used a variety of animal models, mainly the human temporal bone, but also mouse to elephant, to assess the sharpness of tuning in the cochlea, and while the data he obtained contributed immensely to our understanding of cochlea mechanics and won him the Nobel prize in 1961, unforeseen factors worked to stymie an understanding of the true sensitivity and tuning of the mammalian cochlea. These factors were the same that stymied early anatomists, namely the difficult-to-avoid decay of normal cellular structure and function after death. These problems, though acknowledged by von Bekesy, were argued away, so that for many years auditory aficionados were led to believe that his data were gold. In fact, there were serious problems with his experiments, which when ultimately realized and solved would help elucidate the roles of the two types of hair cells, the inner and outer hair cells, that the early anatomists identified with the aid of improved fixation techniques. To improve on the work of von Bekesy, models other than the human would be required.

WHY DO WE STUDY ANIMAL MODELS?

There are two main reasons for the study of peripheral auditory physiology, namely, the quest to understand and cure auditory dysfunction, and simply to understand how our and other animals'

ears work. Clearly, study based on the former rationale would benefit from direct investigations on humans. Unfortunately, though, immense difficulties are associated with human experimentation on the auditory periphery. These problems include limited number of specimens, inability to control for pathological effects, and the inevitable problem of tissue destruction caused by delays in the access to the cochlea (caused by dissection difficulties due to the dense temporal bone and delays in acquisition following death). Thus, for many reasons and regardless of the clinical vs. scientific rationales, animal models are best for studies on cochlear physiology. The major hurdle in rationalizing a particular animal model is its validity and generality. As far as providing insight to the human condition, most investigators believe that a range of small mammals, including cat, chinchilla, guinea pig, rat, and mouse, are appropriate. Of course, one or another species may prove better for particular experimental questions. In general, however, these small animals are particularly well suited since very nice access to the cochlea structures can be had. This enhanced accessibility (and heightened concern for better physiological status) has led directly to enhancements of the findings of von Bekesy.

BASILAR MEMBRANE TUNING

The data on basilar membrane movement that von Bekesy obtained indicated that the response of the basilar membrane was linear, i.e., the magnitude of the displacement response grew linearly with the stimulus level. By extrapolating down to threshold levels, it was argued that basilar membrane movements at the threshold of hearing were a fraction of an atom's width. Tuning of the basilar membrane was also observed to be not as good as psychophysical measures, and von Bekesy sought reasons beyond the basilar membrane to explain how we hear so well. With the aid of animal models, these notions would dramatically change.

Using the squirrel monkey, Rhode and colleagues^{3,4} first noticed that in some animals a nonlinear growth in basilar membrane motions occurred as stimulation levels were changed. Importantly, this compressive nonlinearity of the basilar membrane response was vulnerable to the animal's status. Only when extreme care was used to maintain a healthy preparation did the response remain nonlinear, otherwise it resembled the data of von Bekesy. We know now that tuning on the basilar membrane is far sharper than the data of von Bekesy showed, indicating that his human temporal bone preparation and his animal preparations were working in a passive, damaged mode. Of course, the new Mossbauer measurement tool that Rhode and colleagues used helped to record at lower stimulus levels than von Bekesy could using stroboscopic illumination. Today, it is clear that the sharp tuning found in the eighth nerve has its direct counterpart in basilar membrane motion.⁵ This turnaround in the description of basilar membrane tuning highlights the caveat that while animal models have the potential to provide valid data, care must be exercised in order to attain validity.

THE COCHLEA IS ELECTRIC

In the 1700s, electricians (as serious students of electricity were then called) often relied on themselves or acquaintances to serve as subjects. Indeed, Volta perceived a deafening blast as a result of self-inflicted aural electrocution.⁶ Despite this early indication, it would be nearly two centuries after the controversial discovery of animal electricity that the electrical nature of audition would be confirmed. The discovery had to wait for the invention of the vacuum tube and oscilloscope, but once in hand Wever and Bray⁷ demonstrated the "cochlear microphonic," an electrical response of the hair cells (which they mistakenly took as eighth nerve firings) measured from electrodes placed on a decerebrate cat's eighth nerve. The response mimicked the acoustic stimulus, and they confirmed this finding in a number of animal species, including turtles and insects.

The study of the electrical activity of the cochlea took off, and small mammals were perfect models since their cochleae were easily exposed for electrode implantations. Extracellular (from scala media and the perilymphatic scalae) electrical recordings were made of the resting (e.g., endolymphatic potential) and sound-evoked potentials (cochlea microphonic, summing potential, and even action potentials; see Dallos⁸), but eventually these were usurped by intracellular recording directly from hair cells^{9,10} after the high impedance electrode was devised. The clear correspondence of electrical activity within the auditory periphery with hearing capabilities would place this measure above that of histopathologic determination of auditory insult and recovery.

ANIMAL MODELS OF CLINICAL IMPORTANCE

The anatomical identification and characterization of cochlear dysfunction is time-consuming. The classic histological work on otopathology (see Schuknecht¹¹), while quite informative, could not be used with high efficiency, simply because the animal or human temporal bone had to be removed and processed after death. The use of electrical measures to determine auditory sensitivity, especially those that were noninvasive (e.g., auditory brainstem response [ABR], compound action potential [CAP]) permitted ongoing and quantitative studies on the effects of noise exposure, ototoxic drug exposure, and hazardous chemicals (e.g., see Henderson and coworkers¹²). As a direct result of animal experimentation, we would no longer have to experience devastation such as that caused by the first uses of the ototoxic antibiotic dihydrostreptomycin.¹³ Nevertheless, while animal models have immensely contributed towards our understanding of pathologies that afflict humans, we must remain cognizant of species-specific differences.

One of the hottest areas of current research is that of hair cell regeneration (see Warchol¹⁴). Mammalian hair cells do not regenerate following destruction, as do those of some lower vertebrates. Thus, unlike some tissues that can be interrogated via cell culture, mammalian inner ears must be harvested for each new experiment. Perhaps some day, if the key that controls hair cell production is found, hair cell cultures may reduce the need for animal sacrifice.

In the heyday of electron microscopy, transport of electron-dense markers into various compartments of the inner ear was studied. These studies included, for example, movements of molecules out of the vasculature and into cochlea scalae, thus identifying the blood-labyrinthine barriers¹⁵⁻¹⁷ and movements of molecules across the round window membrane into the scala tympani.¹⁸ The latter experiments contributed to the scientific basis for the currently popular clinical approach of intratympanic drug delivery, notably used to deliver gentamycin for control of intolerable vertigo. This type of approach heralds a new era where the otologist will successfully treat previously inaccessible structures of the inner ear and will ultimately do so with the new tools of molecular biology.

FROM MOLECULES TO EAR

Some very important advances in auditory physiology have been made in recent years using the techniques of molecular biology. Two of them are especially dear to my heart, namely, the determination that mutations of the connexon 26 gene result in nonsyndromic deafness¹⁹ and the identification of the protein responsible for the mechanical activity of the outer hair cell.²⁰

Connexons are proteins that form gap junction channels between adjacent cells, in the ear's case, allowing ionic and metabolic communication between supporting cells.²¹ These channels were proposed to aid in the removal of harmful extracellular potassium away from active hair cells,²² and this is a likely reason for the mutation's devastation of hearing.

The mammalian outer hair cell has long been known to dance wildly in response to electrical stimulation;²³⁻²⁵ this mechanical activity is believed to promote the sharp tuning and nonlinearity

that Rhode and colleagues found in the basilar membrane. Finally, after nearly two decades, the motor responsible for the outer hair cell (OHC) boogie was molecularly identified as the protein prestin.²⁰ The story is a continuing one that is full of twists,²⁶ but most recently a knockout of the prestin gene in the mouse seriously interfered with normal auditory function,²⁷ and a mutation of the gene was shown to cause deafness in humans.²⁸ In the end, it will likely be the mouse model that holds the key to our interests in the ear, as this small prolific rodent is a perfect molecular biology laboratory. But let us not forget the guinea pig, which is a classic model in auditory research; indeed, this animal has just helped show that gene transfection (of Math1 transcription factor) into the intact cochlea can induce new hair cell growth.²⁹ Imagine, the future otologist growing some new hair cells for us hard-of-hearing baby boomers — thanks to animal research.

REFERENCES

1. Hawkins, J.E., Auditory physiological history: a surface view, in *Physiology of the Ear*, Jahn, A.F. and Santos-Sacchi, J., Eds., Raven Press, New York, 2001.
2. von Bekesy, G., *Experiments in Hearing*, McGraw-Hill, New York, 1960.
3. Rhode, W.S., Measurement of vibration of the basilar membrane in the squirrel monkey, *Ann. Otol. Rhinol. Laryngol.*, 83, 619, 1974.
4. Rhode, W.S. and Robles, L., Evidence from Mossbauer experiments for nonlinear vibration in the cochlea, *J. Acoust. Soc. Am.*, 55, 588, 1974.
5. Narayan, S.S., Temchin, A.N., Recio, A., and Ruggero, M.A., Frequency tuning of basilar membrane and auditory nerve fibers in the same cochleae, *Science*, 282, 1882, 1998.
6. Piccolino, M., The bicentennial of the Voltaic battery (1800–2000): the artificial electric organ, *Trends Neurosci.*, 23, 147, 2000.
7. Wever, E.G. and Bray, C., Action currents in the auditory nerve in response to acoustic stimulation, *PNAS*, 16, 344, 1930.
8. Dallos, P., *The Auditory Periphery*, Academic Press, New York, 1973.
9. Dallos, P., Santos-Sacchi, J., and Flock, A., Intracellular recordings from cochlear outer hair cells, *Science*, 218, 582, 1982.
10. Russell, I.J. and Sellick, P.M., Intracellular studies of hair cells in the mammalian cochlea, *J. Physiol.*, 284, 261, 1978.
11. Schuknecht, H.F., *Pathology of the Ear*, Harvard University Press, Cambridge, MA, 1974.
12. Henderson, D., Salvi, R.J., Quaranta, A., McFadden, S.L., and Burkard, R.F., *Ototoxicity: Basic Science and Clinical Applications*, New York Academy of Sciences, New York, 1999.
13. Shambaugh, G.E., Jr., Derlacki, E.I., Harrison, W.H., House, H., House, W., Hildyard, V., Schuknecht, H., and Shea, J.J., Dihydrostreptomycin deafness, *J. Am. Med. Assoc.*, 170, 1657, 1959.
14. Warchol, M.E., Regeneration of cochlear hair cells, in *Physiology of the Ear*, Jahn, A.F. and Santos-Sacchi, J., Eds., Raven Press, New York, 2001.
15. Duvall, A.J., III and Klinkner, A., Macromolecular tracers in the mammalian cochlea, *Am. J. Otolaryngol.*, 4, 400, 1983.
16. Hukee, M.J. and Duvall, A.J., III, Cochlear vessel permeability to horseradish peroxidase in the normal and acoustically traumatized chinchilla: a reevaluation, *Ann. Otol. Rhinol. Laryngol.*, 94, 297, 1985.
17. Santos-Sacchi, J. and Marovitz, W.F., An evaluation of normal stria capillary transport using the electron-opaque tracers ferritin and iron dextran, *Acta Otolaryngol.*, 89, 12, 1980.
18. Schachern, P.A., Paparella, M.M., Goycoolea, M.V., Duvall, A.J., III and Choo, Y.B., The permeability of the round window membrane during otitis media, *Arch. Otolaryngol. Head Neck Surg.*, 113, 625, 1987.
19. Kelsell, D.P., Dunlop, J., Stevens, H.P., Lench, N.J., Liang, J.N., Parry, G., Mueller, R.F., and Leigh, I.M., Connexin 26 mutations in hereditary nonsyndromic sensorineural deafness, *Nature*, 387, 80, 1997.
20. Zheng, J., Shen, W., He, D.Z., Long, K.B., Madison, L.D., and Dallos, P., Prestin is the motor protein of cochlear outer hair cells, *Nature*, 405, 149, 2000.

21. Santos-Sacchi, J. and Dallos, P., Intercellular communication in the supporting cells of the organ of Corti, *Hear. Res.*, 9, 317, 1983.
22. Santos-Sacchi, J., Cell coupling in Corti's organ, *Brain Res. Brain Res. Rev.*, 32, 167, 2000.
23. Brownell, W.E., Bader, C.R., Bertrand, D., and de Ribaupierre, Y., Evoked mechanical responses of isolated cochlear outer hair cells, *Science*, 227, 194, 1985.
24. Ashmore, J.F., A fast motile response in guinea-pig outer hair cells: the cellular basis of the cochlear amplifier, *J. Physiol. (Lond.)*, 388, 323, 1987.
25. Santos-Sacchi, J. and Dilger, J.P., Whole cell currents and mechanical responses of isolated outer hair cells, *Hear. Res.*, 35, 143, 1988.
26. Santos-Sacchi, J., New tunes from Corti's organ: the outer hair cell boogie rules, *Curr. Opin. Neurobiol.*, 13, 459, 2003.
27. Liberman, M.C., Gao, J., He, D.Z., Wu, X., Jia, S., and Zuo, J., Prestin is required for electromotility of the outer hair cell and for the cochlear amplifier, *Nature*, 419, 300, 2002.
28. Liu, X.Z., Ouyang, X.M., Xia, X.J., Zheng, J., Pandya, A., Li, F., Du, L.L., Welch, K.O., Petit, C., Smith, R. J., Webb, B.T., Yan, D., Arnos, K.S., Corey, D., Dallos, P., Nance, W.E., and Chen, Z.Y., Prestin, a cochlear motor protein, is defective in nonsyndromic hearing loss, *Hum. Mol. Genet.*, 12, 1155, 2003.
29. Kawamoto, K., Ishimoto, S., Minoda, R., Brough, D.E., and Raphael, Y., Math 1 gene transfer generates new cochlear hair cells in mature guinea pigs *in vivo*, *J. Neurosci.*, 23, 4395, 2003.

Dye coupling in the organ of Corti

Joseph Santos-Sacchi

Laboratory of Otolaryngology, New Jersey Medical School, Newark, USA

Summary. Dye-coupling in an in vitro preparation of the supporting cells of the guinea-pig organ of Corti was evaluated by use of the fluorescent dyes, Lucifer Yellow, fluorescein and 6 carboxyfluorescein. Despite the presence of good electrical coupling in Hensen cells (coupling ratios >0.6) the spread of Lucifer yellow was inconsistent. Hensen cells are very susceptible to photoinactivation, i.e., cell injury upon illumination of intracellular dye; and this in conjunction with Lucifer Yellow's charge and K^+ -induced precipitability may account for its variability of spread. Fluorescein and 6 carboxyfluorescein, on the other hand, spread more readily and to a greater extent than Lucifer Yellow, often spreading to cell types other than those of Hensen. Dye spread is rapid, occurring within a few minutes. These results suggest that molecules of metabolic importance also may be shared by the supporting cells of the organ of Corti.

Key words: Organ of Corti – Supporting cells – Dye coupling – Gap junctions – Photoinactivation – Guinea pig

The supporting cells of the mammalian organ of Corti are joined together by gap junctions (Jahnke 1975; Gulley and Reese 1976; Iurato et al. 1976). In a previous study, electrical coupling among these cells was shown to be present, although it was thought to be poor (Santos-Sacchi and Dallos 1983). At that time, dye spreading studies with the fluorescent dye Lucifer Yellow did not reveal dye-coupling in the supporting cells, except on very rare occasions. In recent studies on electrical coupling of Hensen cells with more precise electrophysiological techniques, coupling has been shown to be very good in vitro (Santos-Sacchi 1984, 1985). This result prompted a reinvestigation of dye coupling in the supporting cells of the mammalian inner ear.

Methods

Guinea pigs were anesthetized with pentobarbital and killed by decapitation. The cochleas were quickly removed, and

Send offprint requests to: J. Santos-Sacchi, Laboratory of Otolaryngology, Section of Otolaryngology, Department of Surgery, MSB H518, UMDNJ – New Jersey Medical School, Newark, NJ 07103, USA

Acknowledgements. This work was supported by an RCDA from NINCDS and grants from the Deafness Research Foundation, the Foundation of the UMDNJ, and the NIH (NS 21380-01). I thank Barbara Fate for technical assistance

the apical and third turn was microdissected in one piece after removing the spiral ligament and stria vascularis. The preparation was transferred to a perfusion chamber. Alternately, the whole temporal bone was placed in a perfusion chamber on a Zeiss ACM microscope, and the bony capsule around the two most apical turns chipped away. The stria vascularis and spiral ligament were removed. Both chambers were maintained near $37^\circ C$ with Peltier devices (Bailey Instruments, N.J.). Medium 199 (with Hanka salts [1.26 mM $CaCl_2$, 1.7 μM $Fe(NO_3)_3$, 5.36 mM KCl , 0.44 mM KH_2PO_4 , 0.81 mM $MgSO_4$, 137 mM $NaCl$, 4.16 mM $NaHCO_3$, 0.33 mM Na_2HPO_4]; pH 7.2–7.4, GIBCO, NY) was perfused at a rate of 0.8 to 1.5 ml/min. Electrodes were pulled on a Narishige puller.

Coupling measurements were made with high input impedance devices (WPI KS-700, Dagan 8100-1) capable of constant current injection. Coupling was assessed by injecting negative current pulses of varying magnitudes into one cell and noting the voltage drop in the same and an adjacent cell. Under visual control, Hensen cells were impaled with electrodes. Double-barreled electrodes or theta glass electrodes were used to separately inject current (I1) and record voltage drops (V1) in one cell, while a neighboring cell was impaled with a single-barreled voltage recording electrode (V2).

Coupling responses and membrane potentials were recorded on a Gould strip chart recorder. Individual coupling responses were digitally stored within a Data 6000 waveform analyzer (Data Precision, MA) and saved to floppy disk. Coupling ratio is defined as the voltage drop in cell 2 divided by the voltage drop in cell 1 in response to current injection in cell 1 (V_2/V_1) (Bennett 1966).

Dye injections were made iontophoretically into individual supporting cells through single barreled electrodes. One to five percent solutions of Lucifer Yellow CH (Sigma), 6 carboxy fluorescein (Calbiochem) and fluorescein (sodium salt, Sigma) in H_2O were used. Epifluorescence observations were made with Zeiss filters (G436, FT510, LP520), with a 50 watt high pressure mercury illumination system. A Zeiss F10/0.25 objective lens was used. Photographs were taken with Polaroid type 667 black and white film. Dye spread was also evaluated under reduced epi-illumination with neutral density filters. For these studies video analyses were made with an ISIT video camera (Dage-MTI) and high resolution monitor (Ikagami). Photographs of video images were made with a Kodak Instagaphic CRT camera.

Results

Electrical coupling among the supporting cells is good; adjacent cells usually have coupling ratios around 0.6, under favorable culture conditions (Fig. 1 a). Despite the fact that Hensen cells are well coupled electrically, spread of the injected dye Lucifer Yellow occurs inconsistently. Observations have been made in which dye spread did not occur with Lucifer Yellow, although simultaneous measurements indicated the existence of electrical coupling between the injected Hensen cell and adjacent cells.

It was noted that frequently cell membrane potentials drop upon injection of Lucifer Yellow. In fact, the Hensen cells are very susceptible to photoinactivation. Photoinactivation (Miller and Selverston 1979; Cohan et al. 1983) denotes the selective killing of cells or parts of cells by irradiating intracellularly injected dyes. Apparently, during absorption of light, heat is generated which deleteriously affects cells, causing drops in membrane potential and electrical

activity. Membrane potentials of supporting cells are normally very stable; however, blue light irradiation causes an immediate and coincident drop in membrane potential of dye filled cells (Fig. 1 c). Membrane potential declines when the light is turned on and stabilizes when the light is turned off. Usually, spread of Lucifer Yellow did not occur during simultaneous epifluorescent observation. However, sometimes dye spread was observable when cells were injected prior to fluorescence observation (Fig. 1 b). Spread of Lucifer Yellow, when it occurs, is typically rapid (within one to a few min) and is limited to no more than several neighboring cells. In addition to reducing membrane potentials, blue light exposure causes coupling responses to decrease in coupled Hensen cells (Fig. 2).

Unlike Lucifer Yellow, fluorescein spreads more consistently to neighboring cells (Fig. 3 a-c), and is often observed during epi-illumination, although photoinactivation can occur with this dye. As with Lucifer Yellow, the spread of dye is almost immediate. However, a greater number

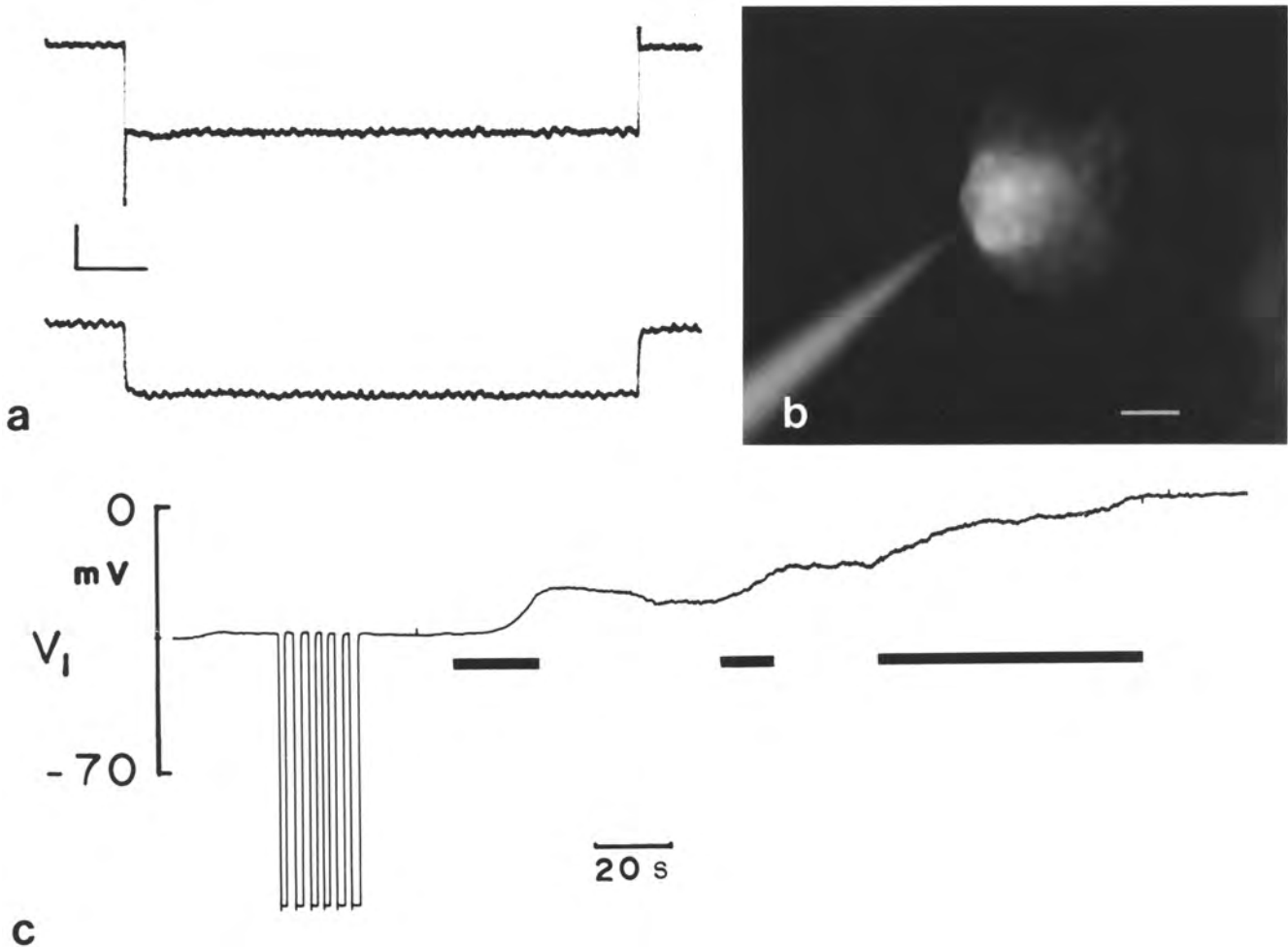


Fig. 1. **a** Two adjacent Hensen cells impaled under visual observation with 3M KCl glass electrodes. In one cell current pulses (-10 nA) were injected down one barrel of a theta glass pipet and the voltage drop was measured with the other barrel. Coupling responses were measured in the other cell with a single barreled electrode. One event was digitally stored and displayed. Calculated coupling ratio 0.8. Vertical scale: 4 mV. Horizontal scale: 0.2 sec. **b** Hensen cell injected with Lucifer Yellow without epi-illumination 45 sec prior to fluorescence observation as indicated in the trace from this cell (Fig. 1c). Dye spread had occurred. Scale: 15 μ m. **c** Hensen cell impaled with single barreled electrode containing Lucifer Yellow. A stable membrane potential was recorded for a few min whereupon dye was injected into cell with negative current pulses (-1 nA; negative deflections). Membrane potential remained stable after dye injection until blue light illumination was turned on (first black bar). Consequently cell depolarized but stabilized after light was turned off. Photoinactivation process continued upon reinstatement of epi-illumination (second black bar). Finally, light source was left on until total depolarization had occurred (third black bar)

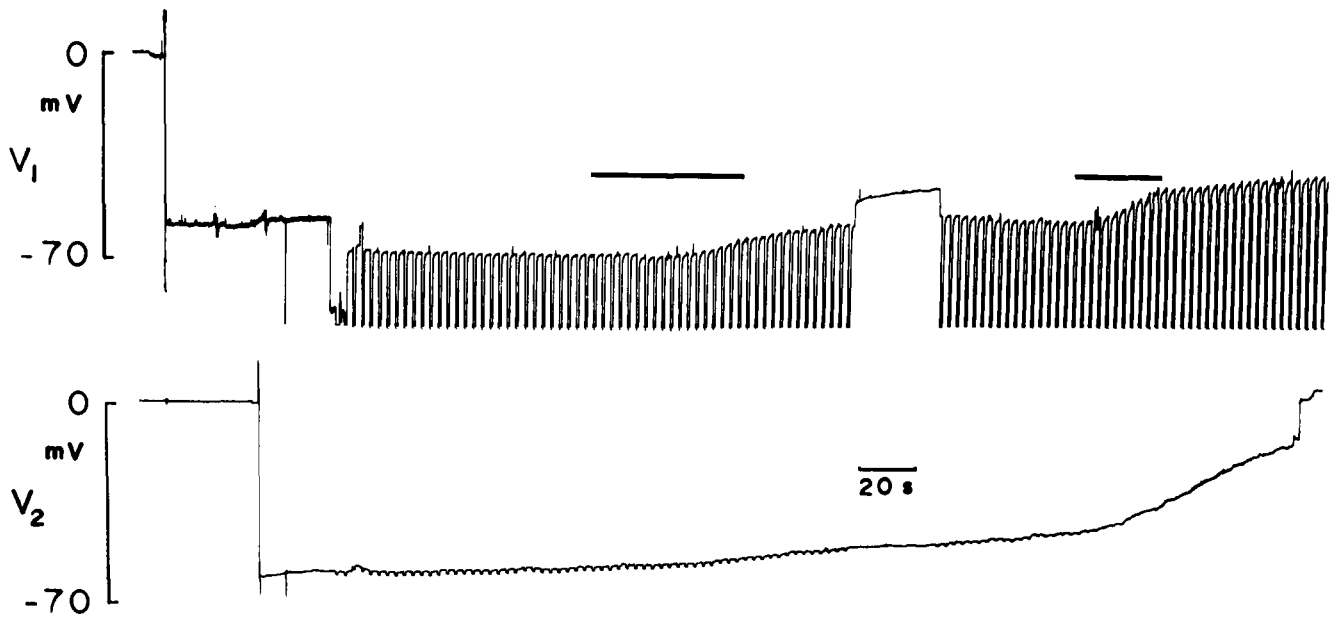


Fig. 2. Neighboring Hensen cells impaled with single barreled electrodes, one containing KCl, the other Lucifer Yellow. Current pulses (-5 nA) injected into Lucifer electrode and coupling responses measured in the other cell. Voltage drop across Lucifer electrode unbalanceable and thus off scale; however, since input resistance of Hensen cells is about 0.4 megaohms initial calculated coupling ratio is 0.7. Dye spread occurred in this example. Upon illumination of cells with blue light (*first black bar*), membrane potentials begin to fall. Subsequently, coupling response in other cell decreases. Further exposure to blue light depolarizes cells further (*second black bar*)

of cells are usually stained, and supporting cells other than Hensen cells are involved. These other cells include Deiters cells and possibly outer pillar cells. Fluorescein is somewhat membrane permeable; yet, the spread does not appear to be due to non-junctional membrane passage from one cell to another because 1) several attempts to observe dye passage through plasma membranes by directly iontophoresing fluorescein onto the external aspect of Hensen cell membranes failed to reveal cytoplasmic uptake; 2) extended soaking (up to 20 min) of Hensen cells with external solutions of fluorescein revealed much poorer staining of Hensen cell cytoplasm after washout than that of cells previously stained by intracellular spread of the dye; 3) on a few occasions fluorescein injection did not result in spread of the dye to adjacent cells, probably indicating that these cells were uncoupled; and 4) extracellular spaces between stained Hensen cells showed less fluorescence than intracellular spaces.

The dye 6 carboxyfluorescein, which is less membrane permeant than fluorescein, shows similar dye spread patterns and also spreads more consistently than Lucifer Yellow. Nevertheless, there were cases where the dye did not spread. The kinetics of dye movement were interesting for 6 carboxyfluorescein and fluorescein. Often, during the first min or two following injection of dye into a particular cell, spread was absent or was limited to closely neighboring cells. Subsequently, a sudden and rapid movement of the dye into a more extensive group of cells occurred. This is demonstrated in Fig. 3d-e, which illustrates the time course of dye spread for an injection of 6 carboxyfluorescein into a Hensen cell. After one min, spread of dye is barely detectable in the two immediately adjacent cells. At 1.5 min, the dye has begun to spread rapidly and by 3 min has spread to a large portion of the organ of Corti, including areas occupied by supporting cells other than those of Hensen, i.e., Deiters and pillar cells.

Discussion

Lucifer Yellow is a highly fluorescent molecule which has been used to demonstrate dye coupling in many cell systems (Stewart 1981; Kaneko and Stewart 1984). Presumably, electrically coupled cells permit the spread of dye through gap junctions. Yet, there is a growing number of observations of electrically coupled cells which do not demonstrate dye coupling or demonstrate dye coupling inconsistently by use of Lucifer Yellow (Takato and Goldring 1979; Audesirk et al. 1982; Kater and Hadley 1982).

In our previous study of dye coupling in the *in vitro* organ of Corti, fluorescence observations were made during injections of Lucifer Yellow and spread of the dye was observed only occasionally (Santos-Sacchi and Dallos 1983). Possibly the cells were killed by photoirradiation during observations. It would appear that Lucifer Yellow does not spread as easily to coupled cells as does fluorescein and 6 carboxyfluorescein. Perhaps the difference in molecular weights (LY 457, F 330) is responsible for this disparity. Yet, Flagg-Newton et al. (1979) have shown that the molecular cut-off for mammalian junctional spread is around 1000 Daltons. Furthermore, molecular models of the two dyes do not reveal sufficient size differences to account for dye spread differences, so that other factors, e.g., charge and precipitability, may be influential (D.C. Spray, personal communication). Lucifer Yellow readily precipitates as the potassium salt, and thus may do so intracellularly. Fluorescein is somewhat membrane permeable, and care must be taken in dye spread studies to exclude possible spread across non-junctional membranes. Several facts suggest that dye spread is through junctions, most notably the speed of dye spread and the observation that some fluorescein injections did not result in spread. 6 carboxyfluorescein spreads as well and because of its charge it is likely that the route of passage is through the aqueous channels of gap junctions.

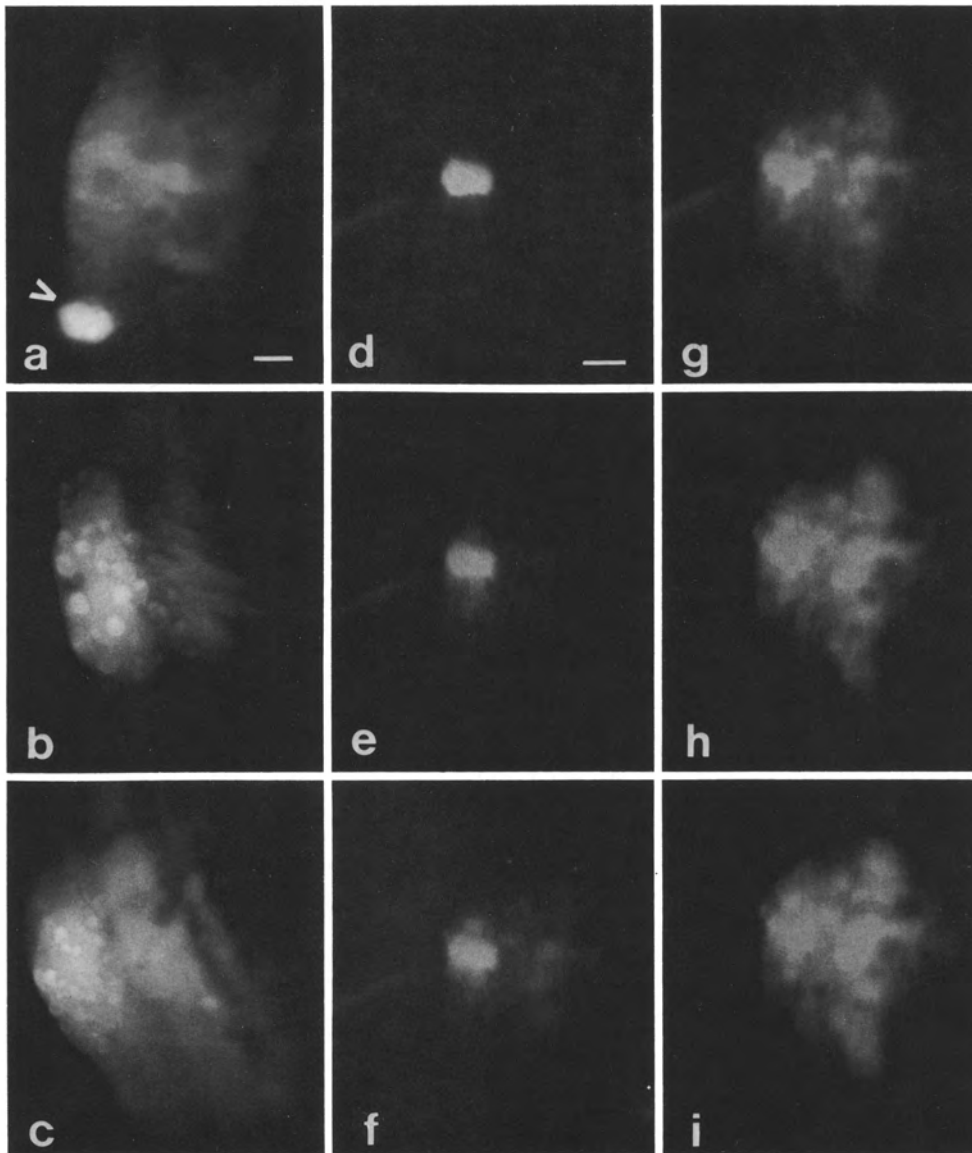


Fig. 3. **a** Organ of Corti spirals around bony modiolus through which eighth nerve courses. Hensen cells are most distal to modiolus which is located to right in all photographs. *Arrow* depicts Hensen cell injected with Lucifer Yellow. No dye spread occurred. Subsequently, fluorescein was injected about four cells away, and dye did spread to adjacent Hensen cells as well as other supporting cells closer to modiolus. Scale: 15 μm . **b** Fluorescein injected into single Hensen cell, spread of dye occurred rapidly to adjacent Hensen cells and to presumed processes of Deiters cells. Bright spherical structures in Hensen cells are lipid droplets. Scale: same as in **Fig. 3a**. **c** Fluorescein observed to spread from Hensen cells to other supporting cell types of organ of Corti. All injections depicted thus far made during epi-illumination. Scale: same as in **Fig. 3a**. **d-i** Series of photographs depicting time course of spread of 6 carboxyfluorescein through supporting cells. Epi-illumination present during whole process; however, neutral density filters were used to reduce intensity. Spread of dye video taped with low light level Dage MTI camera and individual photographs taken of monitor screen. **d** 1 min after start of injection. Barely detectable spread in immediately adjacent Hensen cells. Scale: 15 μm for this and subsequent photographs. **e** 1 min 30 sec. Dye now seen clearly in spirally adjacent Hensen cells and in cells nearer modiolus. **f** 1 min 40 sec. Cell staining more clearly seen near modiolus, **g** 2 min. Spread of dye continues spirally. **h** 2 min 30 sec. Intensity of dye in adjacent cells approaching that of injected cell. **i** 3 min. Dye more uniformly distributed in group of supporting cells of different types.

It is clear that the presence of electrical or ionic coupling cannot necessarily indicate that dye coupling exists. This has been directly demonstrated by Kettenmann and Orkand (1983), who showed that in electrically and dye coupled cells, dye coupling can be abolished without uncoupling ionic communication between the cells. It is probably true, however, that dye coupling indicates the presence of electrical coupling. Thus the observation that fluorescent dyes spread from Hensen cells to other supporting cells, includ-

ing Deiter and pillar cells, indicates that electrical communication occurs among supporting cells of different types. This may have important consequences for the organ of Corti.

The supporting cells of the organ of Corti provide structural support for the sensory hair cells. Other roles that they may play are speculative at present, yet the presence of electrical and dye coupling between them may provide clues. For example, metabolic cooperation between the sup-

porting cells may be required for normal cochlear function under conditions of high sound stimulation. Perhaps metabolites diffuse intracellularly through the supporting cells from areas of high metabolic activity, e.g., from the lateral wall of the cochlear duct. In addition, the supporting syncytium may provide a K⁺ sink as is thought to occur in astrocytes of the CNS (Somjen 1979). Potassium levels may be kept low in those areas of the organ (e.g., spaces of Nuel) where its presence would interfere with electrical activity. This may be specially important considering the recently identified outer hair cell contracture associated with potassium induced hair cell depolarization (Brownell et al. 1985; Zenner et al. 1985). Finally, the possibility exists that supporting cells may influence cochlear mechanics. The fact that Hensen cells are dye coupled and can be photoinactivated (killed) may permit an evaluation of the role supporting cells play in cochlear mechanics. That is, selective destruction of dye-injected supporting cells by photoirradiation may alter electrical responses to sound.

References

- Audesirk G, Audesirk T, Bowsher P (1982) Variability and frequent failure of lucifer yellow to pass between two electrically coupled neurons in *lymnaea stagnalis*. *J Neurobiol* 13:369–375
- Bennett MVL (1966) Physiology of electrotonic junctions. *Ann N Y Acad Sci* 137:509–539
- Brownell WE, Bader CR, Bertrand D, de Ribaupierre (1985) Evoked mechanical responses of isolated cochlear outer hair cells. *Science* 227:194–196
- Cohan CS, Hadley RD, Kater SB (1983) Zap axotomy: localized fluorescent excitation of single dye-filled neurons induces growth by selective axotomy. *Brain Res* 270:93–101
- Flagg-Newton J, Simpson I, Loewenstein W (1979) Permeability of the cell-to-cell membrane channels in mammalian cell junction. *Science* 205:404–407
- Gulley RS, Reese TS (1976) Intercellular junctions in the reticular lamina of the organ of Corti. *J Neurocytol* 5:479–507
- Iurato S, Franke K, Luciano L, Werbter G, Pannese E, Reale E (1976) Intercellular junctions in the organ of Corti as revealed by freeze fracturing. *Acta Otolaryngol* 82:57–69
- Jahnke K (1975) The fine structure of freeze-fractured intercellular junctions in the guinea pig inner ear. *Acta Otolaryngol [Suppl]* 336
- Kaneko A, Stuart AE (1984) Coupling between horizontal cells in the carp retina revealed by diffusion of lucifer yellow. *Neurosci Lett* 47:1–7
- Kater SB, Hadley RD (1982) Intracellular staining combined with video fluorescence microscopy for viewing living identified neurons. In: Liss AR (ed): *Cytochemical methods in neuroanatomy*. New York, pp 441–459
- Kettenmann H, Orkand RK (1983) Intracellular SITS injection dye uncouples mammalian oligodendrocytes in culture. *Neurosci Lett* 39:21–26
- Miller JP, Selverston AI (1979) Rapid killing of single neurons by irradiation of intracellularly injected dye. *Science* 206:702–704
- Santos-Sacchi J (1984) A re-evaluation of cell coupling in the organ of Corti. *Hear Res* 14:203–204
- Santos-Sacchi J (1985) The effects of cytoplasmic acidification upon electrical coupling in the organ of Corti. *Hear Res* 19:207–215
- Santos-Sacchi J, Dallos P (1983) Intercellular communication in the supporting cells of the organ of Corti. *Hear Res* 9:317–326
- Somjen GG (1979) Extracellular potassium in the mammalian central nervous system. *Ann Rev Physiol* 41:159–177
- Stewart WW (1981) Lucifer dyes – highly fluorescent dyes for biological tracing. *Nature* 292:17–21
- Takato M, Goldring S (1979) Intracellular marking with lucifer yellow CH and horseradish peroxidase of cells electrophysiologically characterized as glia in the cerebral cortex of the cat. *J Comp Neurol* 186:173–188
- Zenner HP, Zimmermann U, Schmitt U (1985) Reversible contraction of isolated mammalian cochlear hair cells. *Hear Res* 18:127–133

Accepted February 20, 1986

THE ORGAN TRANSPLANT MYTH

Discover

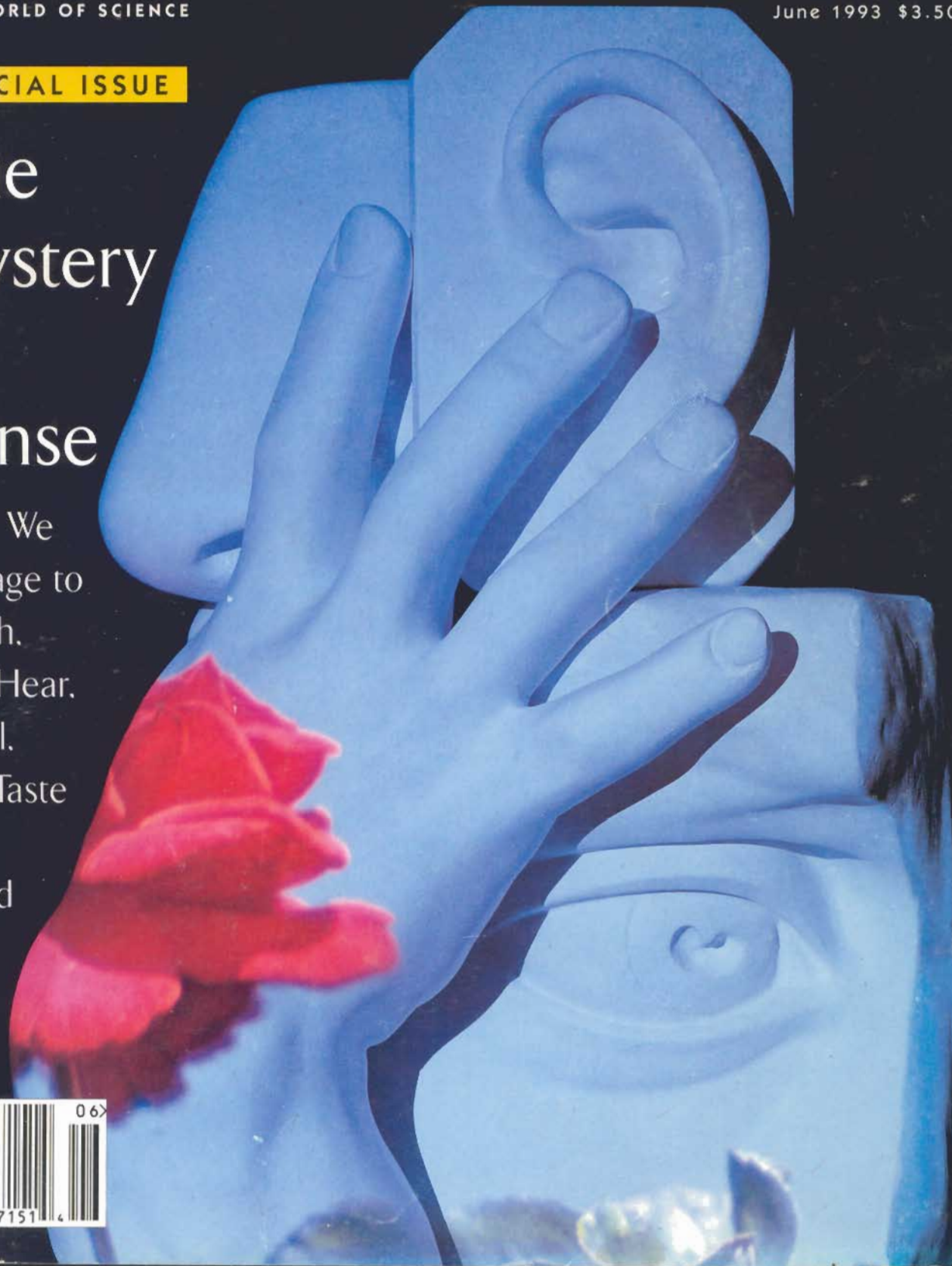
THE WORLD OF SCIENCE

June 1993 \$3.50

SPECIAL ISSUE

The Mystery of Sense

How We
Manage to
Touch,
See, Hear,
Smell,
and Taste
the
World





teenager in the black T-shirt was stunned.

GOOD

We were both standing in the damp twilight

outside San Francisco's Cow Palace, waiting for

the doors to the Megadeth concert to open, and I had asked him a patently insane question.

"Wear earplugs during the concert?" he echoed,

blankly. "Why would I do that? Earplugs are,

like, *condoms* for your ears." ■ His nonchalance

about strafing his ears with 115 decibels of heavy

VIBRATIONS

WE'RE UNDER SIEGE

*from age, drugs, and rock and roll,
and all that stands between
us and utter silence is 32,000
dancing hearing receptors.*

metal is sad but understandable: hearing has always been the Cinderella of the senses. Helen Keller thought its absence was more painful and isolating than blindness, yet most people say they'd rather lose hearing than sight. Such second-class status has had a predictable effect on research funding (low), the number of scientists attracted to the field (few), and the rate of progress (slow). As recently as the early 1980s auditory researchers were still laying the foundations for the microscopic and biochemical basis of hearing while their counterparts in vision research were, so to speak, putting up the drywall. As for the numbers, sniffed one biophysicist, "Go to the vision meetings and it's like the Super Bowl or something." He estimates that serious auditory researchers might, worldwide, number 200.

RATHER THAN PASSIVELY VIBRATING IN SYNC WITH THE MEMBRANE, THE HAIR CELLS WERE BOUNCING LIKE MANIC KIDS ON A TRAMPOLINE.

But Cinderella had her moments in the limelight, and it looks as though the Cinderella sense is about to do the same. Technological advances in laboratory techniques, coupled with an aging population—and perhaps a few influential government boomers who put in some hours listening to “Stairway to Heaven” at top volume—portend a bright future for the field. There is already a whisper of a hint, in fact, that scientists may someday be able to restore some of the hearing receptors my young friend was so casually sacrificing.

Those hearing receptors are called hair cells, specialized sensory cells that are among the most remarkable structures in the body. Only 32,000 strong (compared with, say, the eyes’ 300 million light-sensitive cells), under constant siege from age, drugs, and a world that includes snowmobiles and jet planes as well as Megadeth, they are all that stand between us and silence. Like princesses turning straw into gold, the inner hair cells transform the mechanical forces of sound into the electrical impulses of hearing.

The neurological phenomenon called hearing begins when the ear collects wave-like air-pressure disturbances—sound—produced by any physical force: a vibrating A string, a tree falling in the forest. The outer ear, which includes the fleshy pinna and the auditory canal, picks up and funnels these waves toward the tympanic membrane, or eardrum. The eardrum vibrates and jiggles the three articulated bones of the middle ear; in turn, the last of these three bones, the stapes (or “stirrup”), flexes the membrane of a small oval “window” in the fluid-filled, coiled cochlea.

Evolution has been called the great tinkerer, assembling new structures from bits and pieces of old ones, and the ear is certainly one of its most protracted projects. Natural selection has been remodeling and redecorating the ear for hundreds of millions of years, as the latest model of vertebrate moved from the ocean to the shore to dry land. Yet the hair cells at its core have hardly been touched; their structure is virtually identical in the hearing and balance systems of all animals with backbones. As it happens, this is a very good thing, since the

cochlea has made mammalian hair cells nearly impossible to study.

The cochlea is one of those structures, like black holes or the Hoover Dam, that tend to provoke awe in observers. “It’s a jewel box of an organ, isn’t it?” sighed one smitten researcher, interrupting himself in midequation. Said another, “It’s such an incredible structure! When I finish a session on the microscope, I feel disoriented, like I’ve been cave diving.” The cochlea is indeed amazing: a pea-size, spiral-shaped bony fortress buried in the thickest part of the skull, containing a mechanism of mind-boggling complexity. But like most fortresses, it imprisons as much as it protects. There’s no way to get to the hair cells when an organism is alive, since all the works are barricaded in bone, and the inner ear stops functioning seconds after death. And until recently it was impossible to keep hair cells alive outside the body.

Ironically, though the security system fashioned for the inner ear has discouraged invasions by armies of researchers, it hasn’t worked particularly well at preserving its inhabitants: we begin losing hair cells as soon as we’re born. They simply wear out from use, particularly the cells that process high-frequency sounds. Over time, exposure to loud noise makes them stiffen. No one understands the sequence of cellular events causing the stiffness, but it is known that when hair cells hold this rigid pose too long they just keel over and die.

So it goes: a firecracker too close to the ear here, a jackhammer outside the window there, perhaps even a couple of football seasons in the high-school marching band alongside the tuba and we damage a few or a hundred. By middle age the attrition has become an avalanche: studies have shown that at 65, the average male has lost more than 40 percent of his hair-cell birthright. And, in a phenomenon that might on a bad day strike you as evidence of a malign force in the universe, our hair cells are not able to regrow. Reptiles and amphibians, who have very modest hearing abilities and

nonsocial life-styles, replenish their store of hair cells throughout life. We mammals, on the other hand, with our high-fidelity ears, are organisms that depend on hearing to survive both physically and—in the case of humans and other primates—emotionally. Yet we’re the group stuck with a relatively paltry and nonrenewable allotment.

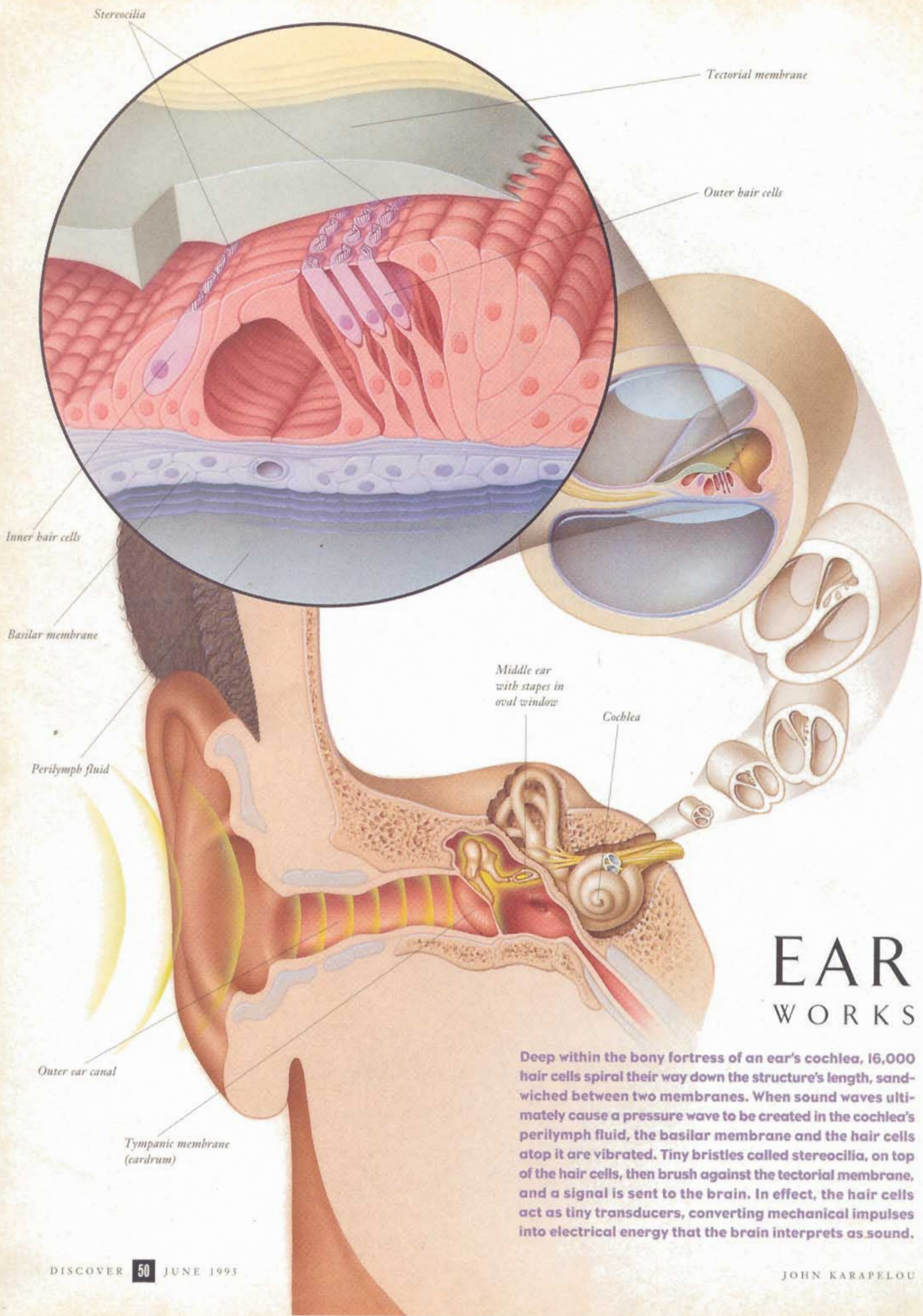
WITHIN THE cochlea, the architecture of the hair cells is supremely functional. The 16,000 cells are arranged in four parallel rows, one inner and three outer rows (relative to their distance from the cochlea’s central pole); they are sandwiched between two membranes, the basilar below and the tectorial above. Together these two membranes form a partition that spirals down the length of the cochlea. When the stapes pushes on the cochlea’s oval window, it sends a wave of pressure through the perilymph, a fluid in the inner ear, which begins a chain of events: the wave sets the basilar membrane vibrating, which vibrates the hair cells, which cause a set of bristles atop the hair cells to brush against the tectorial membrane. There are about 100 of these bristles, or stereocilia, on each human hair cell, and they are arranged in rows according to their height, as if posing for a class photo. When inactive, they lean together in a bundle in the shape of a cone. But when they are active, their movement against the tectorial membrane ultimately results in a signal being sent along the auditory

NEUROSCIENTIST Jim Hudspeth holds a model of a human hair cell's stereocilia. His question: How do the stereocilia move, and what happens when you move them?

nerve. Thus the hair cells as a whole act as tiny transducers, converting the mechanical impulses they pick up from the cochlear fluid into the electrical energy that the brain interprets as sound.

There’s an undeniably Rube Goldbergian aspect to this chain of events, and elucidating the final mechanical link in the





EAR WORKS

Deep within the bony fortress of an ear's cochlea, 16,000 hair cells spiral their way down the structure's length, sandwiched between two membranes. When sound waves ultimately cause a pressure wave to be created in the cochlea's perilymph fluid, the basilar membrane and the hair cells atop it are vibrated. Tiny bristles called stereocilia, on top of the hair cells, then brush against the tectorial membrane, and a signal is sent to the brain. In effect, the hair cells act as tiny transducers, converting mechanical impulses into electrical energy that the brain interprets as sound.

TOP: P. Motta/University "La Sapienza," Rome/Photo Researchers; BOTTOM: courtesy Ed Rubel/University of Washington

chain (the place where, if the ear were one of Goldberg's fanciful contraptions for, say, making doughnuts, the dough would hit the fat) has occupied neuroscientist Jim Hudspeth for most of his career. Hudspeth, who is now director of the Center for Basic Neuroscience Research at the University of Texas Southwestern Medical Center, recalls his initial aim: "What I saw as important was getting from a macroscopic system—the whole cochlea—to a microscopic and cellular system." That involved ignoring some tantalizing questions; it forced him, he says, to "throw away the complicated and interesting mechanics and hydrodynamics of the ear." He also resigned himself to ignoring "the complicated and interesting stuff" that happens on the way to the brain. "I just wanted to deal with one step on an intimate basis." That step was the mechanical input to the hair cells.

THE QUESTION he and his group of researchers set out to answer was, How do a hair cell's stereocilia move, and what happens when you move them? In the late 1970s, using a frog as their experimental animal, they found that prodding a stereociliary bundle with an extremely fine quartz fiber—which, given the mere millionths-of-an-inch size of the stereocilia, became known as "the telephone pole approach"—sent a current through the cells. (This current produces the chemical that excites the nerve going to the brain.) They discovered two surprising things: the direction of this nudge was critical, and the magnitude of the nudge needed to get the stereocilia to respond was infinitesimal.

Hudspeth found that only a push from front or back produced the current; side-to-side nudging did nothing, for reasons that didn't become clear to the researchers until later. Furthermore, Hudspeth calculated that if the cells were deflected by an amount of prodding equivalent to that produced by a sound at the threshold of hearing, the cilia would move the hair bundle about three-thousandths of a degree. (Just for scale, several atoms in a row add up to a full degree.) In essence, then, the whole jury-rigged mechanism—ear drum to middle-ear bones, middle-ear bones to oval window, oval window to pressure wave in the perilymph, pressure wave in the perilymph to basilar membrane vibration—is distilled to this: a

movement measured in fractions of atomic diameters. Observes Hudspeth, "It's as if the Eiffel Tower were to move a thumb's breadth."

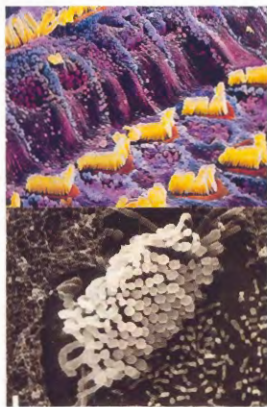
At the time Hudspeth was doing his first work, biologists understood the basic mechanism of cell signaling: a stimulus caused tiny pores—ion channels—to open in the cell membrane, and the movement of charged particles from outside to inside the cell registered as a tiny current change. Vision, for example, had been established as a process in which light hitting the eye's photoreceptors caused chemical reactions that opened ion channels and excited nerve fibers.

Hudspeth and his group assumed, then, that ion channels must be opening and closing in the hair cells when they prodded the stereocilia. What troubled them was how these relatively sluggish biochemical events could occur in the ear, which is built for speed. You can, after all, trick the eye into believing it has seen movement at 30 images a second, a phenomenon the first animators understood intuitively. But that speed is glacial to the ear: 30 cycles per second (or 30 hertz) is so low in frequency we can barely hear it. A young human ear can, however, process the highest overtone on a violin, a frequency of 20,000 vibrations a second. And our ears can discern the delay when a sound is presented to one ear six to ten millionths of a second after it's presented to the other. A biochemical cascade takes thousandths of a second—three orders of magnitude slower—and couldn't possibly do the trick.

To get around the time problem, Hudspeth's group hypothesized that there might be some kind of mechanical gate to the ion channels in the ear, a device that could open them as briskly—near instantaneously, actually—as the ear's acuity demanded. Such a device, if it existed, would be unique to the auditory system, but it would at least have the virtue of fitting the ear's design specs.

There were, Hudspeth makes clear, theoretical reasons and indirect evidence for a mechanical gate. All the same, he says, "it was kind of miraculous" when the structures began to appear in scanning electron micrographs. They were first recognized for what they were by a British lab, which, recalls Hudspeth, "was slightly embarrassing. We'd seen some of them ourselves, but we didn't know what to make of them." The strandlike structures, dubbed tip links, joined each stereocilium to its tallest neighbor, rather like wires connecting a regiment of telephone poles running over a mountain.

The front-to-back route of the tip links was the reason a side-to-side prodding of the stereocilia did not produce a current. Hudspeth likens the links to pieces of elastic tied to the handle of a door that's kept shut by one of those "noisemaking door-closers at the top of it. That's the intrinsic elasticity of the transduction channel; it keeps the door closed unless you do



TOP: Highly magnified and colorized scanning electron micrograph of human stereocilia (yellow). Above: Regenerating hair cells from the cochlea of a chick, just five days after it was exposed to an ototoxic drug.

something about it. If you pull on the elastic—that's deflection of the hair bundle—that tension is communicated to the door. As the hair bundle moves, you're literally pulling the channels ajar." When the door closes, silence reigns.

The micron-size gadgetry sported by the hair-cell bristles is only part of the unfolding story of how the ear hears. What goes on inside the cell bodies—particularly the bodies of the three outer rows of hair cells—is equally intriguing.

Auditory physiologist Joseph Santos-Sacchi of the Yale University School of Medicine is one of those intrigued. He shares with many of his colleagues an almost paternal affection for the outer hair cells and their antics: "This is a fun system to work with," he says. To show how hair cells move and to illustrate just how much fun it is, he made a videotape of a hair cell

THE AUDITORY SYSTEM IS ELABORATE, SENSITIVE BEFORE ITS OWNERS DO, PARTICULARLY IF THE

bopping along to rap star Hammer's "Can't Touch This."

The outer hair cells that captivate Santos-Sacchi are a mammalian refinement of the more primitive hair cells found in lower animals. Though the outer hair cells are differentiated from the inner hair cells by their position in the cochlea, much more than geography marks their distinction—the real difference lies in the realm of neuroanatomy.

A nerve is a one-way street: it goes either toward the brain or away from it. Most of the nerves between the inner hair cells and the brain go from the outside in, just as you might expect; after all, our ears are supposed to get information about external events to our brains. Oddly, though, most of the nerves between the outer hair cells and the brain go the other way, from brain to ear. What could the brain be telling the outer hair cells?

In the early 1980s the outer hair cell story got stranger still. Researchers found that the outer hair cells were not only wired oddly, they behaved oddly. Rather than passively vibrating in sync with the basilar membrane, which is more or less what the inner hair cells do, they were bouncing up and down like manic kids on a trampoline. Indeed, they stretched

and contracted at a speed that was orders of magnitude greater than any other cell in the body could muster.

This unexpected display of personality by the outer hair cells—called fast motility—is now one of the hottest areas of auditory research. (Santos-Sacchi has graphed the number of publications since 1985 on a time axis and says that the resulting curve can be described as "exponential, going to infinity.") Whatever its research trajectory, fast motility is hot because it poses two intriguing questions: How are the outer cells doing this? And why?

"Why" may turn out to be the easier question to answer. It's beginning to look as though one reason the outer hair cells boogie is to accelerate the motion of the basilar membrane.

The 3.2-centimeter-long membrane (about 1.25 inches) spiraling inside the cochlea is essentially an acoustical decoder. It processes the tangled mass of auditory frequencies that make up a sound like speech, sorting them into individual frequency bands. For example, in response to high-frequency sounds, the basilar membrane will vibrate more strongly at the base of the cochlea's spiral than it will at its apex. Conversely,

low-frequency sounds vibrate the membrane more strongly at the apex than at the base. (Like a tiny helical keyboard upended on its highest note, the basilar membrane processes about one-third of an octave per millimeter.)

But—and here's the mystery—the basilar membrane vibrates at frequencies a hundred times faster than any movement it could conceivably pick up merely by riding the sound wave that travels through the perilymph fluid in the inner ear. Might the outer hair cells be dancing in order to modify the movement of the basilar membrane? Might the connections between brain and outer hair cells be there so the brain can tell the hair cells how fast to dance?

Santos-Sacchi frames the problem thus: "Can outer hair cell motility function in the living animal as we all hope it might? That is, can the cells wiggle and modify the mechanics of the inner ear" at the high frequencies at which the ear works? There are reasons to think they can; after all, they must be moving for a reason. And drugs that were used experimentally to knock out the hair cells definitely altered the mechanics of the basilar membrane.

That's the why; the how of fast motility may be a little trickier to answer. In the

Merlin D. Turtle/Bat Conservation International

A LITTLE NIGHT MUSIC

EACH NIGHT, under cover of darkness, a life-and-death struggle is played out.

Night is when the bats take wing—after their avian competitors have returned to their nests, and after the nocturnal insects, their prey, have begun to show themselves. Bats glide through the night, emitting ultrasonic clicks and cries that bounce off the insects (as well as off branches and houses and trees) and return to tell the bats where to swoop down for their dinner (or where to turn left to avoid bumping into a mighty oak). But the bats are not the only ones listening to the echoes in the night. Many insects have developed the ability to eavesdrop on the sonar signals, to give themselves a fighting chance to evade their onrushing enemy.

Researchers have known since the late 1950s that some insects can hear ultrasound. That was discovered by physiologist Kenneth Roeder of Tufts University and entomologist Asher Treat of the City University of New York when they put elec-



trodes on the auditory nerves of moths and played sounds at different frequencies; only at ultrasound levels did the auditory nerves fire. Later experiments, in which some moths with ears and some without were thrown into a chamber with bats, showed that moths without the ability to hear ultrasound were captured almost 100 percent of the time while ultrasound-hearing moths had a 90 percent chance of getting away.

Obviously, for moths, ultrasound detection is a good thing.

It's good for lots of other insects too. The ability to hear ultrasound has since been uncovered in green lacewings, tiger beetles, praying mantises, katydids, crickets, and locusts. With the moths, these keen-eared insects represent five different insect orders: the Lepidoptera, Neuroptera, Coleoptera, Dictyoptera, and Orthoptera. "We really expect this to be a pattern," says Ron Hoy, a Cornell neuroethologist who has been studying the different ways

TIVE. AND INGENIOUS. BUT IT BREAKS DOWN THEY'RE PARTIAL TO NOISY ENVIRONMENTS.

laboratory, hair cells can't be coaxed to move any faster than a few thousand cycles a second, not nearly the frequencies that must be attained in living animals. Santos-Sacchi suspects his laboratory apparatus may be preventing the cells from really cutting loose, wigglywise. He thinks the limiting factor is the electrical resistance of the electrode he's using to deliver stimulus to the cell: "It's as if I were trying to measure how fast a car could actually go, but my broken ankle prevented me from pushing down on the accelerator."

However, another problem is not so easily explained away. At the base of the basilar membrane, where high-frequency sounds are decoded, hair cells don't seem to have the juice to alter the basilar membrane vibration. What researchers are left with, then, is two remarkable phenomena—the highly tuned basilar membrane and the rapidly moving cells—and no obvious bridge to connect them. "There is something missing here," Santos-Sacchi admits. "Things don't quite jibe yet." But he's sure the connection is there. "Think about it," he asks rhetorically. "Would evolution go to all this trouble for nothing?"

Of course, the average heavy-metal fan could argue that evolution didn't go to quite enough trouble. The auditory

system is elaborate, sensitive, and ingenious, but it does break down before its owners do, particularly if they're partial to noisy environments. Yet even this flaw may eventually yield to research.

IN THE MID-1980s researchers made a remarkable discovery about birds that may have important implications for us. Everyone had assumed that our feathered friends, who have relatively acute hearing, were in the same boat as mammals vis-à-vis hair cells: when you abuse 'em you lose 'em. But in 1985 both Doug Cotanche, then at the University of South Carolina, and Ed Rubel, at the University of Washington, found that in young chicks hair cells could regrow.

In Rubel's case, it was a classic story of scientific serendipity. His lab was using the chicks as their experimental animal to study the ototoxic properties of a class of antibiotics—that is, they wanted to see to what degree the drugs damaged hearing organs. "Raul Cruz, the medical resident running the study, found that the number of damaged hair cells was greatest just after we administered the drug," recalls

Rubel. But when a little time had passed, there seemed to be more and more healthy cells. "He brought me the results and I, like anybody who has completely bought into the dogma of his field, said, 'Raul, you must have counted the hair cells wrong. Go back and do it again.'"

Well, as anyone familiar with Hollywood movies or checkout-stand science fiction could have told Rubel, the counting was fine but the dogma was wrong. There really *were* more hair cells because new ones were growing. Meanwhile, in South Carolina, Cotanche and his colleagues were seeing what looked like embryonic hair cells on the noise-damaged cochleas of adult birds, leading them also to suspect that the hearing organ might be repairing itself. A collective "Aha!" ensued, followed by experiments designed to isolate hair cell regeneration. These have confirmed that hair cells in birds do grow back.

And the new hair cells work. The researchers have trained starlings to peck at a key in response to a given tone by rewarding the maneuver with a food pellet. Immediately after they're dosed with ototoxic drugs, trained birds will fail the tone test, but they gradually regain the skill as hair cells regrow.

animals hear for some 20 years. "I would not be surprised if many insects that fly at night can hear ultrasound."

Indeed, Hoy thinks he has just uncovered the sixth order of ultrasound-hearing insects: the Diptera, or flies. He and his colleagues were studying a type of parasitic fly that flits through the night listening for the chirping of crickets and then lays its larvae on them. But when the researchers analyzed the fly's hearing ability, they found that not only could it pick up the cricket's song, it could pick up ultrasound as well. "Since they fly around at night," Hoy speculates, "they probably have a bat problem. And while we haven't proved that that's what their ultrasonic hearing is for, it sure is circumstantial evidence."

That many insects have developed ultrasonic hearing is in itself an intriguing finding—in fact, for moths, green lacewings, tiger beetles, and most species of praying mantis, ultrasound is all they can hear. But researchers are now focusing their attention on the organs they developed to do it. "They all have a common structural plan," Hoy explains. "If you're going to hear bats, you need certain things. You need a sensory organ contained within an air-filled chamber, where one wall of the chamber is a tympanic membrane that, when set into vibration, is going to set the whole organ into vibra-

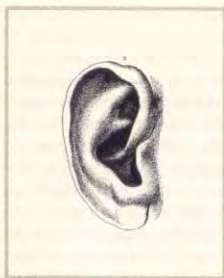
tion. And you need receptor cells to pick up those vibrations."

Interestingly, this complex solution to the bat problem, he notes, was arrived at not once but a number of times. "Insects have ears all over the place," Hoy says. "Some stick them on their waist, some on their abdomen, some on their thorax. And what that says is there was independent evolution of the ear. In other words, not all insect ears, not even all moth ears, came from one ancestral source. Independently, in each group, there's been pressure to evolve ears."

So which came first, the bat or the insect ear? Hoy says it depends on which insect you're talking about. For the moths, probably the bats came first; for crickets and grasshoppers, it was the ears. "Insects like crickets have wings that look as if they were capable of producing sounds way before bats came on the scene. And you don't sing unless somebody's around to hear. So when bats came along, the crickets just extended their hearing range."

But he admits it's all just a matter of opinion. "It would be nice if there were a fossil record to tell us. Unfortunately, though, insect ears are very small and probably don't fossilize very well. And not an awful lot of fossil hunters give a damn about insect ears, so they don't look very hard." —Lori Oliwenstein

PINNA TO THE FORE



FORGET THE EARDRUM and those three weird-shaped bones; forget the cochlea with its showy hair cells and fancy frequency sorting. Focus instead on the most visible part of our ear, the pinna—that long-ignored fleshy appendage that hugs closely (or not so closely) to the side of our head. With a few flicks of his quill pen, Darwin shrugged off the pinna in *The Descent of Man*, citing a study of a sailor who'd had one pinna cut off in a scuffle but could still hear just as well with that ear. "Darwin noted that our pinnae are small and we can't move them about as many animals can," explains psychologist Robert Butler of the University of Chicago. "He

argued that our pinnae may have had a function earlier on in our evolutionary history, but that now they're vestiges. That thinking simply carried the day."

Not that the pinna's been *totally* ignored over the years; flip through the right medical text and you'll see plenty of squirm-inducing pictures of deformed ears labeled "cup ear," "lop ear," and so on. And each swirl and swivel of the pinna has its distinguished Latin title: Rufus of Ephesus, first-century Roman anatomist, named them all one rainy day, so we have *concha*, *meatus*, *antitragus*, *scaphoid fossa*, and more. But none of this descriptive stuff answers the central, burning question: Why do we have an outer ear at all? The answer, thanks to scientists like Butler, a pinna veteran of 25 years' standing, is now known: we need the pinna to locate precisely the origin of a sound.

A few pioneering experiments led the way to our deeper pinna knowledge. In the 1950s, for example, when glass tubes were stuck into people's ear canals so that sound bypassed the pinna entirely, researchers found that the subjects couldn't tell whether sounds were coming from front or behind—until, that is, a fake ear was added to the end of the tube. Other experiments have since shown that the pinna provides not only front-back clues but clues to the horizontal and vertical position of a sound's source as well. The horizontal contribution of the pinna isn't crucial as long as we can hear through both ears—since a sound coming from the right, for example, will reach the right ear before the left ear and will also be louder in the right ear. Combined, these time and intensity differences give us enough horizontal information to make do. But with a pair of pinnae we do a better job.

For height information, however, the pinna stands alone. "Think about a sound to your right, maybe at 45 degrees and a little above eye level," says Butler. "Make it a complex sound, like that of snapping fingers—one that's a whole mix of frequencies. If you record from a microphone in your ear canal"—that is, from somewhere past the pinna—"you'll discover that a certain frequency band is amplified. Snap your fingers from another position and a *different* frequency band gets amplified. Well, that's what the pinna does; it somehow amplifies different frequencies depending on where the sound is coming from."

It's not magic, says Butler, just physics. Sound travels through the air as waves of air compression—the higher the frequency, the closer the waves are to each other. When those waves hit the pinna, they pile up on each other like ocean waves against a rock, interacting in complicated ways that diminish some of the frequencies while amplifying others. Since the contours of the ear determine which sounds are amplified and which diminished, and since the contours encountered depend on the angle at which the waves hit the ear, it's reasonable to suppose that noises from one place will be tweaked differently from those from another.

The mysterious next step is how our brains change "enrichment at 6,000 hertz" into "Oh, it came from in front of me," and "a tad more than 8,000 hertz" into "Gee, it came from above." "The sound has to be complex so you can compare frequencies," says Butler. "If the sound is pure, then we're unable to localize that pure tone. When the frequency's high, we'll point up. If it's low, we'll point below—no matter where that sound is coming from." —Rosie Mestel

Furthermore, the birds' ears *sound* as if they're up and running. Although no one yet understands why, it turns out that a click or other soft tone made in a functioning ear will echo microseconds later. If the hair cells are damaged, the echo is absent. These "otoacoustic emissions" are the best tool yet for diagnosing deafness in infants, which is what Susan Norton, a researcher-clinician who works with Rubel, usually does. Recently, however, she has been using the emissions to track the recovery of hearing in Rubel's avian subjects. Norton finds no emission right after the hair cells are damaged; with time, as the hair cells regenerate, the emissions return, first to high-intensity sounds and then to low.

The big question, of course, is what this work means for human hearing. "Very little work has been done on mammals," Rubel cautions. His group has looked at the cochleas of gerbils and seen a small increase in cell growth, although they saw no new hair cells developing. Other labs have found small rates of hair-cell regeneration, but only in the segment of the inner ear that controls equilibrium. In March, Andrew Forge of University College in London and Jeffrey Corwin and his colleagues at the University of Virginia School of Medicine announced that they had observed hair-cell regeneration in guinea pigs. The Virginia researchers also found, in culture, signs of human hair-cell regeneration by using human tissue taken from the area of the cochlea (called the utricle) responsible for balance. Even though these are balance hair cells, the researchers are excited about the implications this raises for regenerating hearing hair cells.

But first things first: the current task is to isolate the molecule that stimulates hair-cell proliferation in birds. (Or, if a molecule inhibits proliferation in mammals, to find that.) Several labs are now working on the problem, aided by biotech companies eager to be part of research that might, over the long haul, produce a drug useful to some of the 28 million Americans with hearing loss.

Rubel is expansive about the possibilities: "We're at an absolutely wonderful time in the history of biology to have discovered this," he says happily. "We are learning so much, and we have so many powerful techniques we couldn't imagine when we were in grad school." It's early yet, he takes pains to point out. "You've got to remember, this whole field of hair-cell regeneration is only four years old. But we're doing great! And in my opinion," he adds, "when you talk about actually restoring hearing, hair-cell regeneration is the only game in town." □

RESEARCH ARTICLE

Outer hair cell electromotility is low-pass filtered relative to the molecular conformational changes that produce nonlinear capacitance

 Joseph Santos-Sacchi^{1,2,3} , Kuni H. Iwasa⁴ , and Winston Tan¹ 

The outer hair cell (OHC) of the organ of Corti underlies a process that enhances hearing, termed cochlear amplification. The cell possesses a unique voltage-sensing protein, prestin, that changes conformation to cause cell length changes, a process termed electromotility (eM). The prestin voltage sensor generates a capacitance that is both voltage- and frequency-dependent, peaking at a characteristic membrane voltage (V_h), which can be greater than the linear capacitance of the OHC. Accordingly, the OHC membrane time constant depends upon resting potential and the frequency of AC stimulation. The confounding influence of this multifarious time constant on eM frequency response has never been addressed. After correcting for this influence on the whole-cell voltage clamp time constant, we find that both guinea pig and mouse OHC eM is low pass, substantially attenuating in magnitude within the frequency bandwidth of human speech. The frequency response is slowest at V_h , with a cut-off, approximated by single Lorentzian fits within that bandwidth, near 1.5 kHz for the guinea pig OHC and near 4.3 kHz for the mouse OHC, each increasing in a U-shaped manner as holding voltage deviates from V_h . Nonlinear capacitance (NLC) measurements follow this pattern, with cut-offs about double that for eM. Macro-patch experiments on OHC lateral membranes, where voltage delivery has high fidelity, confirms low pass roll-off for NLC. The U-shaped voltage dependence of the eM roll-off frequency is consistent with prestin's voltage-dependent transition rates. Modeling indicates that the disparity in frequency cut-offs between eM and NLC may be attributed to viscoelastic coupling between prestin's molecular conformations and nanoscale movements of the cell, possibly via the cytoskeleton, indicating that eM is limited by the OHC's internal environment, as well as the external environment. Our data suggest that the influence of OHC eM on cochlear amplification at higher frequencies needs reassessment.

Introduction

Outer hair cell (OHC) electromotility (eM) underlies cochlear amplification in mammals, where in its absence, hearing deficits amount to 40–60 dB (Dallos et al., 2008; Ashmore et al., 2010). The molecular basis of OHC eM is the membrane-bound protein prestin (SLC26a5), an anion transporter family member that has evolved to work as a voltage-dependent motor protein in these cells (Zheng et al., 2000). The protein's voltage-sensor activity presents as a voltage-dependent (or nonlinear) capacitance (NLC), obeying Boltzmann statistics (Ashmore, 1990; Santos-Sacchi, 1991), and whose peak magnitude corresponds to the voltage (V_h) where sensor charge is equally displaced to either side of the membrane. Voltage-dependent conformational change in prestin is believed to form the basis of precise phase differences between OHC activity and basilar membrane motion

that leads to amplification, indicative of local cycle-by-cycle feedback (Dallos et al., 2008). Recent measurements of OHC extracellular voltage and basilar membrane motion have observed the predicted amplifying phase differences (Dong and Olson, 2013). However, other recent measurements did not find appropriate phase or timing differences in the motions within the organ of Corti, and have challenged the standard view of amplification (Ren et al., 2016; He et al., 2018). Additionally, it is commonly accepted that unconstrained (load-free) OHC eM magnitude is invariant across stimulating frequency, having been measured out beyond 70 kHz (Frank et al., 1999); the flat frequency response is another important element in cycle-by-cycle feedback theory. However, these data were obtained at voltage offsets far removed from V_h , which has questionable

¹Department of Surgery (Otolaryngology), Yale University School of Medicine, New Haven, CT; ²Department of Neuroscience, Yale University School of Medicine, New Haven, CT; ³Department of Cellular and Molecular Physiology, Yale University School of Medicine, New Haven, CT; ⁴National Institute on Deafness and Other Communication Disorders, National Institutes of Health, Bethesda, MD.

Correspondence to Joseph Santos-Sacchi: joseph.santos-sacchi@yale.edu.

© 2019 Santos-Sacchi et al. This article is distributed under the terms of an Attribution–Noncommercial–Share Alike–No Mirror Sites license for the first six months after the publication date (see <http://www.rupress.org/terms/>). After six months it is available under a Creative Commons License (Attribution–Noncommercial–Share Alike 4.0 International license, as described at <https://creativecommons.org/licenses/by-nc-sa/4.0/>).

physiological significance. Based on our measures (Santos-Sacchi and Tan, 2018), we estimate that their depolarized offset from V_h would have been ~ 65 mV. Indeed, by exploring at an offset potential near V_h , we recently demonstrated that eM measured with the microchamber displays significant low-pass behavior (Santos-Sacchi and Tan, 2018). Here we further explore the low-pass nature of eM under whole-cell voltage clamp out to 6.25 kHz in the guinea pig and mouse with ramped changes in holding potential that provide shorter, more stationary-in-time measures compared with our previous experiments. Furthermore, whole-cell voltage clamp provides far better voltage control than the microchamber, but patch electrode series resistance effects must be considered. Following precise corrections for NLC-induced, voltage- and frequency-dependent voltage roll-off under whole-cell voltage clamp, never previously done, we find that eM and NLC show similarities in their nonlinear voltage and frequency dependence, both frequency cut-offs being U-shaped functions of holding voltage, with minima near V_h . Macro-patch experiments on the OHC lateral membrane, which provide robust voltage control, confirm our low-pass whole-cell measures of NLC within the speech frequency range. We further find that the frequency cut-offs of eM and NLC are disparate. Modeling suggests that both internal (e.g., cytoskeletal interactions, membrane lipid interactions) and external (e.g., viscous environment of the cell) loads are influential in effecting this disparity.

Materials and methods

Whole-cell recordings were made from single isolated OHCs from the apical two turns of organ of Corti of guinea pigs. An inverted Nikon Eclipse TI-2000 microscope with a 40 \times lens was used to observe cells during voltage clamp. Experiments were performed at room temperature. Blocking solutions were used to remove ionic currents, limiting confounding effects on NLC determination and voltage delivery under voltage clamp (Santos-Sacchi, 1991; Santos-Sacchi and Song, 2016). Extracellular solution was (in mM): NaCl 100, TEA-Cl 20, CsCl 20, CoCl₂ 2, MgCl₂ 1, CaCl₂ 1, and HEPES 10. Intracellular solution was (in mM): CsCl 140, MgCl₂ 2, HEPES 10, and EGTA 10. All chemicals were purchased from Sigma-Aldrich.

An Axon 200B amplifier was used for whole-cell recording with jClamp software (<http://www.scisoftco.com>). An Axon Digidata 1440 was used for digitizing. AC (frequency) analysis of membrane currents (I_m) and eM were made by stimulating cells with a voltage ramp from 100 to -110 mV (nominal), superimposed with summed AC voltages at harmonically related frequencies of 195.3, 390.6, 781.3, 1,562.5, 3,125, and 6,250 Hz, with a 10- μ s sample clock. Currents were filtered at 10 kHz with a four-pole Bessel filter. Corrections for series resistance were made during analysis. Capacitance was measured using dual-sine analysis at harmonic frequencies (Santos-Sacchi et al., 1998; Santos-Sacchi, 2004). Briefly, real and imaginary components of membrane current at harmonic frequencies were determined by Fast Fourier Transform (FFT) in jClamp, corrected for the roll-off of recording system admittance (Gillis, 1995) and stray capacitance (Santos-Sacchi, 2018). Series resistance (R_s),

membrane resistance (R_m), and membrane capacitance (C_m) were extracted using the dual-sine, three-parameter solution of the standard patch clamp model (Santos-Sacchi et al., 1998; Santos-Sacchi, 2004), based on the original single sine solution (Pusch and Neher, 1988). To extract Boltzmann parameters, capacitance-voltage data were fit to the first derivative of a two-state Boltzmann function.

$$C_m = NLC + C_{lin} = Q_{max} \frac{ze}{k_B T} \frac{b}{(1+b)^2} + C_{lin}, \quad (1)$$

where

$$b = \exp\left(-ze \frac{V_m - V_h}{k_B T}\right).$$

Q_{max} is the maximum nonlinear charge moved, V_h is voltage at peak capacitance or equivalently, at half-maximum charge transfer, V_m is membrane potential, z is valence, C_{lin} is linear membrane capacitance, e is electron charge, k_B is Boltzmann's constant, and T is absolute temperature.

As noted above, whole-cell NLC determination was made following stray capacitance removal (Santos-Sacchi et al., 1998; Santos-Sacchi and Song, 2016; Santos-Sacchi, 2018; Santos-Sacchi and Tan, 2018). Patch pipettes were coated with M-coat (Micro Measurements) to reduce stray capacitance. Remaining stray capacitance was removed by amplifier compensation circuitry before establishing whole-cell configuration, and if necessary, additional compensation was applied under whole-cell voltage-clamp conditions (Schnee et al., 2011a,b) and/or through a software algorithm within jClamp software to ensure expected frequency-independent linear capacitance (Santos-Sacchi and Song, 2016; Santos-Sacchi, 2018). The latter approach simply performs single tau capacitance compensation mathematically on collected data, analogous to the electronic compensation with the amplifier. R_s was determined from voltage step-induced whole-cell currents before AC measures, the derivation provided in the appendix of (Huang and Santos-Sacchi, 1993). $R_m(v)$ across ramp voltage was determined from R_s -corrected ramp voltage and generated ramp currents with AC components removed, $\Delta V_m / (\Delta I_{R_s})$.

Simultaneous and synchronous eM measures were made with fast video recording. A Phantom 110 or 310 camera (Vision Research) was used for video measures at a frame rate of 25 kHz. Magnification was set to provide 176 or 106 nm/pixel. A method was developed to track the apical image of the OHC, providing subpixel resolution of movements (see Fig. 1). Video frames were filtered with a Gaussian Blur filter (<http://www.gimp.org>) before measurement. The patch electrode provided a fixed point near the basal end of the cell. Since movements were measured at the apical pole of the cell and the cell was held physically at the point of electrode insertion, estimates of full whole-cell movements were obtained from the ratio of apical/basal partitioning at the point of electrode insertion as in microchamber experiments (Frank et al., 1999; Santos-Sacchi and Tan, 2018). Resultant movements were analyzed by FFT in MATLAB. The colors in surface plots were generated in the MATLAB plotting routine *surf* with shading set to <interp>. This procedure allows contours to be readily observable. Although eM was measured at all

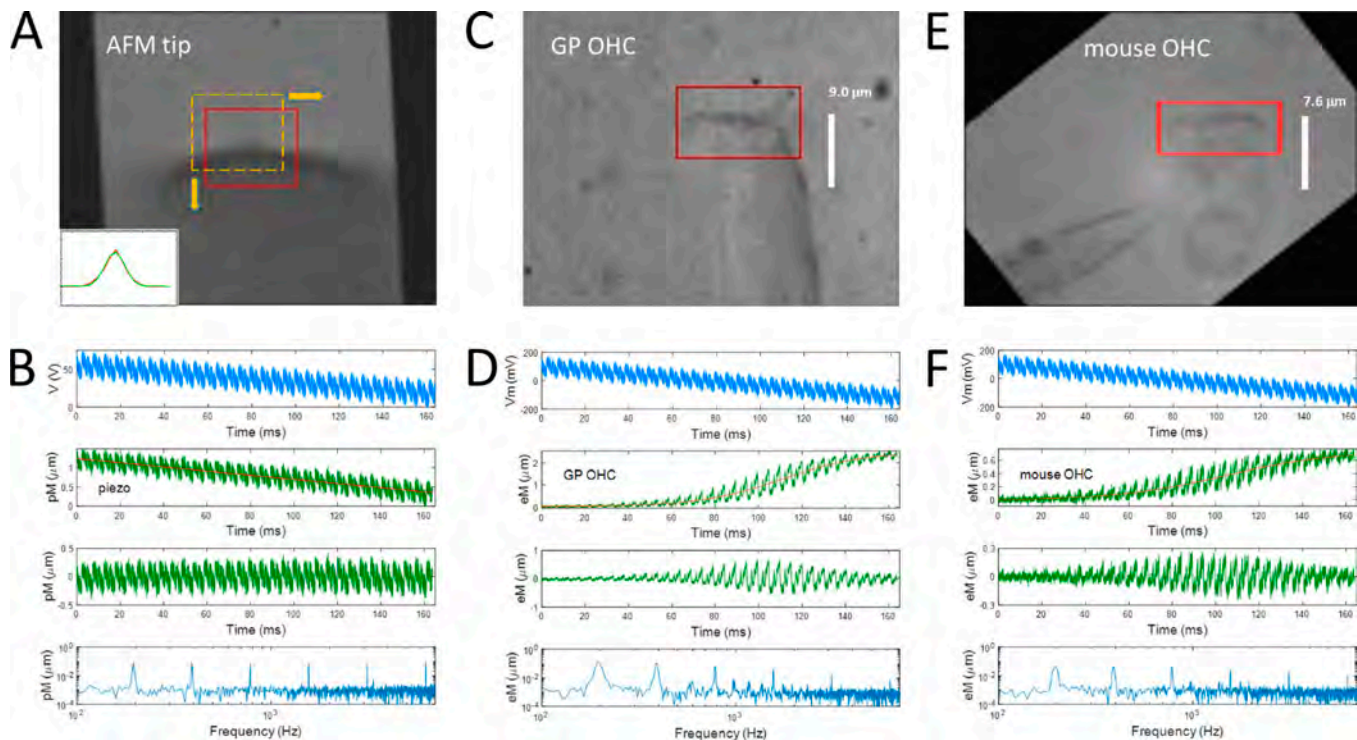


Figure 1. **Motion measures from fast video using a shape tracking algorithm implemented in the program jClamp.** (A) Frame of an AFM probe tip with a fiducial red box delimiting a region of the image to track. For each frame in the video stream, the image was sampled at single pixel offsets of ± 10 pixels in both the vertical and horizontal dimensions (yellow dotted box) relative to the fiducial image. Rotation of the image was possible to maximize displacements to a single dimension. A pixel comparison was made (subtraction of sampled image pixels from fiducial pixels and summed). The resulting distribution along the x and y axis was fit with a Gaussian function to obtain subpixel image movements. (B) Panel 1 shows the voltage command to the piezo stack. Panel 2 shows the piezo movements (pM) induced by the voltage command. The red line is a linear fit used to detrend the data (Panel 3), before FFT of the whole duration response (Panel 4). The magnitude plot shows high fidelity in capturing tip movements across frequency. (C) The apical portion of a guinea pig OHC under whole-cell voltage clamp was similarly tracked. (D) Panel 1 shows voltage clamp command. Panel 2 shows OHC eM. The red line is a sigmoidal fit used to detrend the data (Panel 3), before FFT of the whole duration response (Panel 4). (E and F) Similar results for a mouse OHC. Unlike the piezo response, eM falls precipitously across frequency. The frequency response arises from τ_{clamp} and the intrinsic low-pass nature of eM. The removal of τ_{clamp} contribution is easily accomplished (see Results). GP, guinea pig.

six AC frequencies, only five estimates of NLC were possible using the dual-sine approach. To obtain τ_{clamp} estimates at 6.25 kHz, the magnitude of NLC at 3.125 kHz was used, factored by 0.748, in line with the slope of its decrease across frequency.

Models were implemented in MATLAB Simulink and Simscape, as detailed previously (Song and Santos-Sacchi, 2013; Santos-Sacchi and Song, 2014b). Model R_s and R_m were from the averages of guinea pig and mouse OHC parameters obtained (see below). R_s -corrected V_m vs. eM data were fit with the first derivative of a two-state Boltzmann function (Santos-Sacchi, 1991). We processed biophysical data as either group-averaged (whole-cell currents and eM averaged before analysis) or individual cell analysis followed by averaging, thus providing statistics (mean \pm SEM).

Under voltage clamp, the voltage delivered across the cell membrane depends on the electrode R_s . In the absence of R_s , the command voltage is delivered faithfully to the cell membrane in magnitude and time (phase). Otherwise, the voltage delivered to the membrane will suffer from voltage drops across R_s , depending on the magnitude and time (phase) of evoked currents. In any analysis of voltage-dependent cellular processes, such as eM (Santos-Sacchi and Dilger, 1988; Iwasa and Kachar, 1989), it

is important to accurately assess membrane voltage. Actual membrane potential under voltage clamp can be exactly determined by subtraction of the voltage drop across R_s , i.e., $I_{R_s} * R_s$, with I_{R_s} being the sum of resistive and capacitive components of the cell membrane current. For sinusoidal stimulation across the voltage ramp, the AC command voltage V_c and evoked currents I_{R_s} are evaluated as complex values at each excitation frequency and ramp offset voltage, $(A + jB)$, where A and B are the real and imaginary components, obtained by FFT, thereby supplying $V_c(f, v)$ and $I_{R_s}(f, v)$. Our goal is to accurately determine the frequency response of eM, given a nonzero series resistance that imposes its own influence on the frequency response of voltage-driven eM data. The method essentially seeks to identify the true excitation voltage, $V_m(f, v)$, i.e., the drive for eM, supplied to the plasma membrane.

Before we present an analysis of averaged eM data, we illustrate the approaches available for R_s correction in a MATLAB Simulink model. In the model, we are able to directly measure imposed membrane voltage so we can compare results from these approaches to actual values. The generated charge in the model is taken as the equivalent of eM, since we have shown that OHC eM and prestin charge movement are

directly coupled (Santos-Sacchi and Tan, 2018). The model we use to confirm our voltage corrections has been fully described before (Santos-Sacchi and Song, 2014a), and includes a slow, stretched exponential intermediary transition between chloride binding transitions and voltage-dependent charge transitions, the latter corresponding to eM. Modifications of the model were made to correspond to the biophysical data. Chloride was 140 mM. For the model, the number of prestin particles was set to 25.92e6, and $z = 0.92$ for the guinea pig, and correspondingly 5.62e6, and 1 for the mouse. The forward (α) and backward (β) voltage-dependent transition rate constants for the electromechanical component of the model were 1.2947e6 and 1.1558e4, respectively. Both forward (α_m) and backward (β_m) parallel intermediary transition rate constants (which are equal to each other, but separately labeled to distinguish direction—incidentally, the equivalence is the basis of detailed balance in the model) were defined as

$$\alpha_m, \beta_m = A \cdot \exp(b \cdot m), \text{ for } m = 0.. 26, \quad (2)$$

where $b = -0.4663$ and $A = 3.0398e4$ for the guinea pig data comparisons, or $A = 15.199$ for the mouse data comparisons to account for the difference in NLC and eM frequency response of the species that we find. Units for rate constants and A are in s^{-1} ; b is unitless.

For the model, there are three ways to correct the frequency response of eM magnitude for the confounding effects of R_s -induced membrane voltage roll-off.

Method 1

The complex ratio of AC command voltage (located at differing ramp voltage offsets [v]) to the directly measured membrane voltage within the model at each excitation frequency can be used to correct eM magnitude frequency response, eM being both a function of frequency and holding voltage (Santos-Sacchi and Tan, 2018), namely, eM (f, v), akin to NLC (f, v) (Santos-Sacchi and Song, 2016). Parallel bars indicate absolute values:

$$V_m(f, v) = V_m(f, v)_{\text{model}} \quad (3)$$

$$|eM(f, v)_{\text{actual}}| = \left| eM(f, v)_{\text{measured}} \cdot \frac{V_c(f, v)}{V_m(f, v)} \right| \quad (4)$$

Method 2

The complex ratio of command voltage to calculated $V_m(f, v)$, namely, $I_{R_s}(f, v) \cdot R_s$, can be used for correction.

$$V_m(f, v) = V_c(f, v) - I_{R_s}(f, v) \cdot R_s \quad (5)$$

$$|eM(f, v)_{\text{actual}}| = \left| eM(f, v)_{\text{measured}} \cdot \frac{V_c(f, v)}{V_m(f, v)} \right| \quad (6)$$

Method 3

Finally, the multifarious clamp time constant, $\tau_{\text{clamp}}(f, v)$, determined at each excitation frequency and ramp voltage offset, can be used to correct, via a Lorentzian function ($A=1/[1+(2\pi f\tau)^2]^{1/2}$), the magnitude of eM, scaled to DC (steady state) levels $[1 - R_s/R_m(f_0, v)]$, $f_0 = 0 \approx$ ramp frequency.

$$\tau_{\text{clamp}}(f, v) = [C_{\text{lin}} + \text{NLC}(f, v)] \cdot R_{\parallel}(f_0, v), \quad (7)$$

where

$$R_{\parallel}(f_0, v) = \frac{R_s \cdot R_m(f_0, v)}{R_s + R_m(f_0, v)} \quad (8)$$

$$V_m(f, v) = V_c(f, v) \cdot \frac{[1 - \frac{R_s}{R_m(f_0, v)}]}{[1 + (2\pi f \cdot \tau_{\text{clamp}}(f, v))^2]^{1/2}} \quad (9)$$

$$|eM(f, v)_{\text{actual}}| = \left| eM(f, v)_{\text{measured}} \cdot \frac{V_c(f, v)}{V_m(f, v)} \right| \quad (9)$$

For the model, Fig. S1 (guinea pig parameters) and Fig. S2 (mouse parameters) show that each method of R_s correction gives the same results, revealing the intrinsic low pass eM response of the meno presto model that derives from its stretched-exponential intermediary transition kinetics (Song and Santos-Sacchi, 2013; Santos-Sacchi and Tan, 2018).

Because R_s was measured before running the ramp protocols, there is always a possibility that it changed during recording. The possibility of slight changes in R_s is well established in the literature. Fortunately, the currents generated simultaneously with eM must also report on R_s . Thus, we plot frequency cut-offs of eM based on Methods 2 and 3, each showing overlap (see Fig. 6), and indicating that our estimates of R_s are indeed accurate, with only minor corrections of the initial estimates ($0.95\text{--}1.05 \times$ initial estimates).

For the on-cell macro-patch approach, we used pipette inner diameters of $3.31 \pm 0.24 \mu\text{m}$ (electrode resistance in bath $1.49 \pm 0.04 \text{ M}\Omega$, $n = 10$), with M-coat applied within $\sim 20 \mu\text{m}$ of the tip. Extracellular solution was in the pipette. To establish Gohm seals ($2.7 \pm 0.24 \text{ G}\Omega$, $n = 10$) we supplemented extracellular solution with $5\text{--}7.5 \mu\text{M Gd}^{+3}$; we have shown previously that these low concentrations help to form seals without affecting NLC (Santos-Sacchi and Song, 2016). Ramps with superimposed sinusoids were used, as above. Subtraction of currents at very depolarized potentials, where predominantly linear membrane capacitance and stray capacitance contribute, provided prestin-associated nonlinear currents (see Fig. 7). Subsequently, these nonlinear capacitive currents were used for dual-sine capacitance estimation.

Data points from previous publications were extracted from plots using the application Grabit (written by Jiro Doke) in MATLAB.

Online supplemental material

Figs. S1 and S2 depict model data of the meno presto model for guinea pig and mouse. Each illustrates that voltage corrections used on the collected cell data are accurate and appropriate.

Results

Fig. 1 depicts the method used to measure eM. Movement of a piezo-driven AFM tip (0.2 N/m) confirmed the fidelity of the measuring technique out to 6,250 Hz (Fig. 1 B, panel 4). To obtain accurate FFT results, the ramp-induced movement was detrended by subtracting a linear fit for the AFM tip measures or a sigmoidal fit for the guinea pig or mouse OHC eM measures (Fig. 1, B panel 3; D, panel 3; and F, panel 3). Subsequent analyses followed this detrending approach. In Fig. 1, D and F, panel 4, an

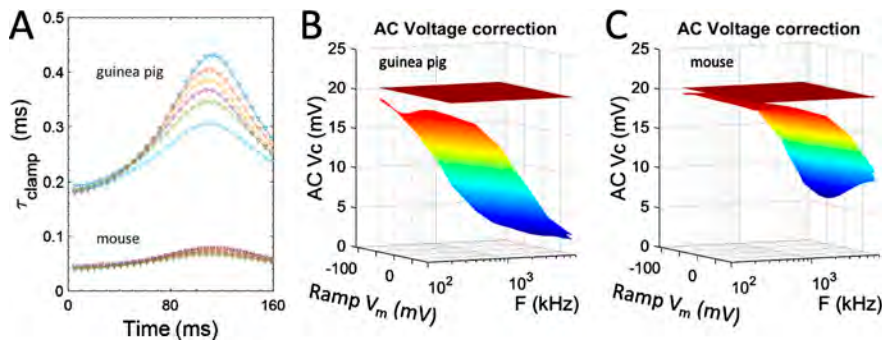


Figure 2. Voltage roll-off corrections. (A) Guinea pig and mouse OHC NLC is voltage-dependent and, as such, will influence the voltage clamp time constant, which is commonly calculated for whole-cell voltage clamp as $\tau_{\text{clamp}} = R_s * C_m$, or in our case, $\tau_{\text{clamp}} = R_s * (C_{\text{lin}} + \text{NLC})$ (precisely, $R_{ij} * [C_{\text{lin}} + \text{NLC}]$; see Materials and methods). The time constant is multifarious, and depends on holding voltage and frequency of stimulation. The voltage (or voltage-dependent eM) correction for the clamp time constant must be done at each stimulating frequency and holding voltage. (B and C) Complex whole-cell currents or calculated multifarious clamp time

constants were used to predict the roll-off in AC command voltage that actually excites the membrane (multicolored surface plots; see equations in Materials and methods). Each approach gives equivalent results. Note that because of the small size of mouse OHCs, τ_{clamp} is faster than the guinea pig OHCs, and introduces better voltage delivery. Nevertheless, each must be corrected (brown flat surface plot, equivalent to command voltage) to ensure removal of voltage roll-off issues when analyzing eM data. F, frequency.

FFT of the whole ramped eM response was made, and shows that unlike the piezo-driven response (Fig. 1 B, panel 4), the magnitude of both guinea pig and mouse OHC eM falls precipitously with frequency. This roll-off arises from both the voltage-filtering effects of R_s and the kinetics of prestin and/or mechanical impediments to cell movements. In the following analysis, we restrict FFT inspection to defined integral segments (see the red and blue highlighted example regions in Fig. S1, Fig. S2, Fig. 3, and Fig. 4) of the eM ramp response to assess voltage dependence of the frequency response. Furthermore, we detail methods (see Materials and methods) to remove the effects of series resistance interference, thus revealing true eM frequency response as a function of true membrane voltage.

For the OHC under voltage clamp, we do not have direct access to the membrane voltage as in the model (see Materials and methods), so only two methods for eM correction are available—that using estimates of R_s and NLC to gauge τ_{clamp} , and that using direct measures of whole-cell currents. In Fig. 2, complex whole-cell currents or calculated multifarious clamp time constants were used to predict the roll-off in AC command voltage (see equations in Materials and methods). Corrections will precisely account for the frequency-dependent roll-off in AC voltages and subsequently, the same corrections are applied to voltage-dependent eM measures.

We analyzed eight guinea pig OHCs. eM was commensurate with previously reported average eM gains of 15–19 nm/mV (Ashmore, 1987; Santos-Sacchi, 1989). Average (\pm SEM) Boltzmann parameters of NLC at the lowest frequency of 195 Hz are Q_{max} : 3.18 ± 0.06 pC, V_h : -46.1 ± 1.1 mV, z : 0.92 ± 0.02 , and C_{lin} : 22.58 ± 0.51 pF. R_s was 9.1 ± 0.8 M Ω . R_m at zero holding potential was 401 ± 75 M Ω . Average eM gain evoked by the ramp protocol (Fig. 3 B) was 22.8 ± 2.8 nm/mV. Maximum eM was 2.54 ± 0.32 μ m; equivalent z was 0.94 ± 0.02 . Fig. 3, E–G, surface and two-dimensional (2-D) plots, show average guinea pig OHC eM before and after correcting for R_s -induced voltage errors.

We also analyzed four mouse OHCs. Average (\pm SEM) Boltzmann parameters of NLC at the lowest frequency of 195 Hz are Q_{max} : 0.74 ± 0.02 pC, V_h : -47.2 ± 3.3 mV, z : 0.82 ± 0.01 , and C_{lin} : 7.60 ± 0.13 pF. R_s was 5.7 ± 0.1 M Ω . R_m at zero holding potential was 239 ± 53 M Ω . Average eM gain evoked by the ramp protocol

(Fig. 4 B) was 7.0 ± 0.6 nm/mV. Maximum eM was 1.06 ± 0.08 μ m; equivalent z was 0.70 ± 0.03 . Fig. 4, E–G, surface and 2-D plots, show average mouse OHC eM before and after correcting for R_s -induced voltage errors.

Fig. 3, E–G, and Fig. 4, E–G, illustrate that using either of the two possible correction approaches (Method 2 and Method 3) produces essentially the same results (in line with modeling in the figures in the Online supplemental material) and confirming the low pass nature of both guinea pig and mouse eM. Notably, the equivalence of the two methods also confirms the validity of the dual sine approach to measure high frequency capacitance, whose multifarious influence on clamp time constant must be considered in order to properly evaluate eM frequency response under voltage clamp.

In Fig. 5, A and B, we plot, at all interrogated frequencies, the voltage dependence of group-averaged eM gain and NLC for mouse and guinea pig OHCs. Guinea pig responses are lower pass than mouse responses. We additionally analyzed OHC response data individually, followed by averaging. Fig. 5, C and D, show mean and SEM of eM at V_h , and Boltzmann parameters of fits based on single cell analysis at frequencies spanning 195 to 3,125 Hz (mouse eM was additionally measured at 6,250 Hz). It is clear that the guinea pig eM frequency response is lower pass than the mouse response (quantification is shown in Fig. 6). It is noteworthy that guinea pig OHCs show a disparity between eM and NLC V_h that is not found in the mouse. Such disparity has been observed previously for guinea pig OHCs (Song and Santos-Sacchi, 2013; Duret et al., 2017), and we previously found that the disparity is diminished with increased turgor pressure for the guinea pig. For our mouse OHCs, we note that the cells appear substantially turgid (see Fig. 1 E), so this may be the reason for the absence in disparity in the mouse.

Fig. 6 shows eM and NLC cut-off frequencies (F_c) for guinea pig and mouse. To approximate differences in frequency responses between NLC and eM for the mouse and guinea pig, we apply single Lorentzian fits to group-averaged eM and NLC within a restricted bandwidth (195–3,125 Hz) at each incremental holding potential of the ramped AC response. The cut-off frequencies display U-shaped dependencies on holding potential, AC voltage stimulation at V_h providing the slowest response.

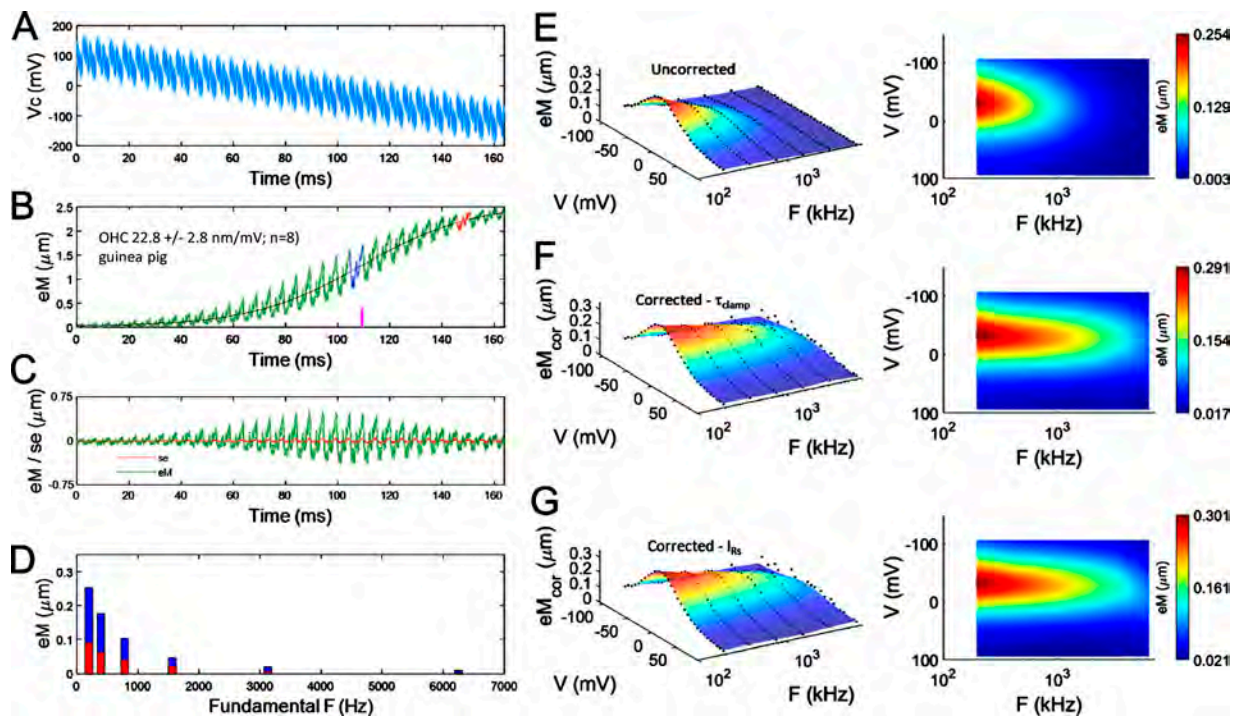


Figure 3. **Group-averaged guinea pig OHC eM frequency response corrected by two methods.** Data presented in A–E are pre-correction, and in F and G are after correction. (A) The hyperpolarizing ramp voltage stimulus (100 to –120 mV) with superimposed sum of 20 mV AC harmonic frequencies (195.3–6,250 Hz). A pedestal of 100 mV (81.32 ms) preceded the ramp. (B) Raw averaged eM. Two selected integral regions are highlighted. Blue is near V_h (magenta bar beneath shows position of V_h). Red highlights a hyperpolarized region. (C) The eM data detrended (green) and the standard error (red). (D) Magnitude responses at the six interrogated frequencies of the two highlighted regions (colors correspond to those in B). Data were detrended as in C before FFT. The surface plots on the right provide a full analysis across ramp voltage at all integral regions of the eM data. (E) Uncorrected eM; the 2-D voltage frequency plots permit clearer visualization of the frequency responses. Black dots are data points. (F) eM adjusted with Method 3 based on corrections to multifarious τ_{clamp} (see Materials and methods). (G) eM adjusted with Method 2 based on membrane current corrections, namely, $V_m = V_c - I_{R_s} * R_{ij}$. Note tight correspondence between the two approaches. These data indicate that OHC eM is low pass in nature. eM_{cor} , corrected eM.

eM corrections based on Methods 2 and 3 are overlapped, indicating accurate estimates of R_s . Individually analyzed cell averages (filled symbols with SEM, using Method 2) show good agreement with the group-averaged data. The F_c at V_h for guinea pig OHC eM is 1.47 ± 0.065 kHz, and that for mouse OHC eM is 4.26 ± 0.74 kHz. NLC measures follow this pattern, with cut-offs faster than that for eM. The F_c at V_h for guinea pig OHC NLC is 2.47 ± 0.091 kHz, and that for mouse OHC NLC is 6.83 ± 0.46 kHz.

To assess the frequency response of NLC under near ideal voltage clamp, we employed macro-patches of the guinea pig OHC lateral membrane. NLC measures were made using the ramp protocol, as above. Our video analysis setup was insufficient to measure patch movements induced by our ramped 20 mV AC stimuli. However, as with voltage-corrected whole-cell measures, patch NLC shows low-pass behavior (Fig. 7). At the lowest frequency of 195 Hz, fitted Boltzmann parameters of NLC are Q_{max} : 38.6 ± 6.1 fC, V_h : -38.1 ± 4.4 mV, and z : 0.67 ± 0.03 . No correction for resting potential was made for on-cell patch V_h . z is lower than whole-cell measures. For comparison, Gale and Ashmore (1997b), using a lock-in amplifier to measure NLC with 1 kHz sinusoids, found z to be 0.65 (slope factor $\beta = 0.04$). Given our z and a hemispherical patch surface area (diameter equal to 3.5–4 μm), we calculate 3,851–5,030/ μm^2 elementary prestin motor units, in line with previous estimates.

Fig. 8 compares peak NLC from on-cell macro-patches with scaled values of whole-cell eM, NLC, and data from Gale and Ashmore (1997a). For frequency roll-off comparison, values were scaled to coincide with our macro-patch NLC values at 390.6 Hz. The roll-off of whole-cell eM and that of the patch movements measured by Gale and Ashmore are similar. The measures of peak NLC of whole-cell, macro-patch, and Gale and Ashmore’s patch NLC (points within our recording bandwidth are shown) are similar. The cut-off frequencies obtained with Lorentzian fits (either whole-cell or macro-patch data) show that eM and NLC frequency responses differ, with eM being slower, as noted above. We emphasize that the single Lorentzian fits here do not describe the full frequency response of NLC, but only that within our recording bandwidth. These measures are intended to make comparisons with our eM measures within the same recorded bandwidth. Thus, we conclude that the degree of coupling between prestin conformational changes (i.e., NLC) and eM must underlie differences between their frequency responses.

Finally, we observe that fits of the square root of eM provide cut-offs comparable to those for NLC for both mouse and guinea pig OHCs. The F_c at V_h for guinea pig OHC $eM^{1/2}$ is 2.77 ± 0.11 kHz, and that for mouse OHC $eM^{1/2}$ is 7.69 ± 0.81 kHz. t test comparisons to the cut-offs of NLC (2.47 ± 0.091 and 6.83 ± 0.46 ,

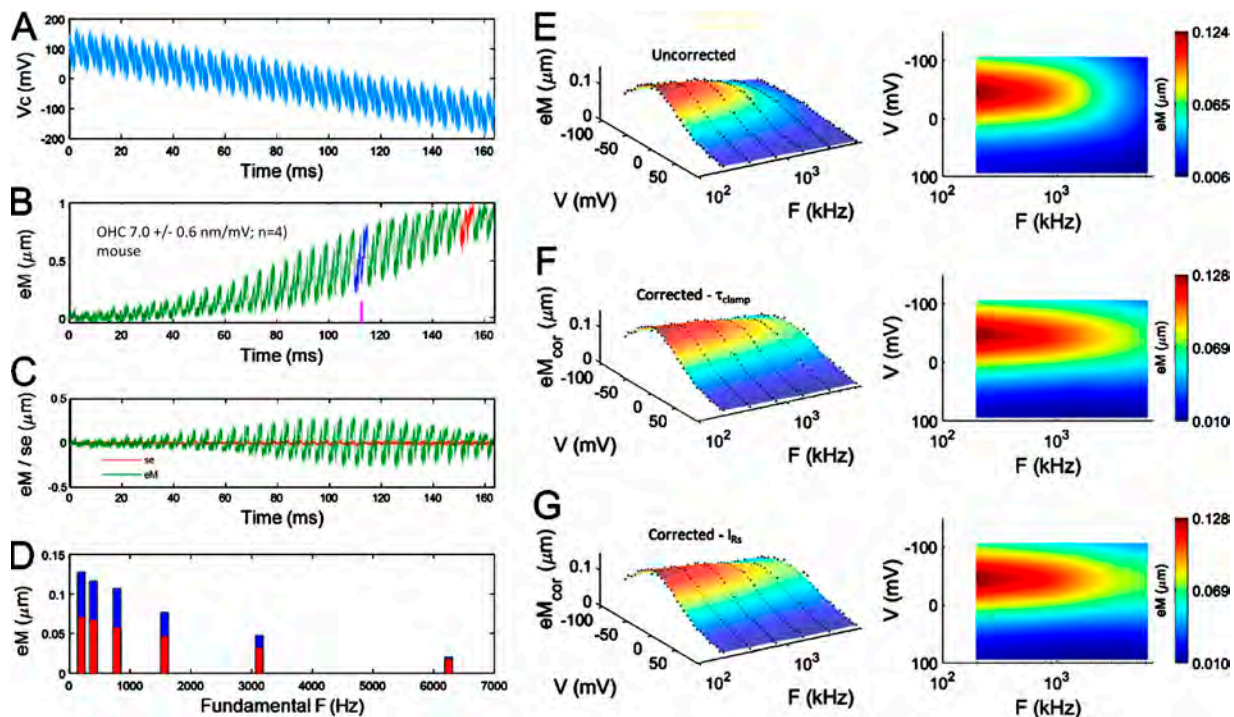


Figure 4. **Group-averaged mouse OHC eM frequency response corrected by two methods.** The caption of Fig. 3 directly applies to this figure. Note that the frequency extent of eM for the mouse is wider band than the guinea pig, before and after voltage corrections.

respectively) show no statistically significant differences ($P = 0.1092$ and $P = 0.4948$, respectively). Below we consider the basis of such disparity.

Discussion

Prestin works by sensing voltage with consequent alterations in its conformational state, leading to contractions and elongations of the cylindrical cell that provides enhancement of auditory threshold (Ashmore, 2008; Santos-Sacchi et al., 2017). Because of the large restricted prestin-generated charge movements evoked by voltage (Ashmore, 1990; Santos-Sacchi, 1991), a substantial alteration in membrane capacitance ensues, paradoxically altering the very voltage that the sensor senses. This is even expected to occur during normal acoustic stimulation, where the receptor potential will suffer from a multifarious membrane resistor-capacitor (RC) filter. For example, the receptor potential cut-off frequencies estimated using linear capacitance alone (Johnson et al., 2011) would be greatly reduced at V_h , where NLC can be as great as linear capacitance. In our study under voltage clamp, series resistance and membrane capacitance conspire to limit the imposition of voltage across the membrane, interfering in both time and magnitude. To evaluate effects of membrane potential across frequency, it is required to alleviate this interference. Here we have compensated for the multifarious time constants induced by R_s and NLC(v, f) in order to reveal the true voltage-induced frequency response of both guinea pig and mouse OHC eM across an array of holding potentials. Before proceeding, we review the literature on measures of eM frequency response.

eM bandwidth studies

A review of OHC eM bandwidth studies has been published recently (Santos-Sacchi, 2019). Here we briefly review those studies with the aid of Table 1. Over the years, better techniques that have extended voltage delivery capabilities have provided increasingly higher estimates for eM cut-off frequencies. Of course, R_s of the patch pipette or the microchamber pipette, in combination with OHC capacitance, ultimately controls frequency delivery bandwidth under voltage clamp. Typically, the time course of the clamp can be garnered from exponential decays of current induced by voltage steps, but AC currents can also be used as we have done in our present work. Prior to Frank et al. (1999), eM cut-offs were typically below 10 kHz. Interestingly, Gale and Ashmore (1997a) measured both patch NLC and membrane movements, and found a NLC cut-off near 10 kHz, but a patch movement cut-off significantly lower (see Fig. 8). The reduced cut-off was attributed to mechanical impediments to patch movements, despite the expected coupling between charge movement and mechanical response. The introduction of the partitioning microchamber by Dallos and Evans essentially reduced membrane capacitance by delivering the voltage stimulus across the reduced series combination of the partitioned cell membrane capacitance (Dallos and Evans, 1995). Given membrane time constants that are equal for each partition, each will experience a flat delivery of a command voltage across the cell. However, the command voltage frequency response itself will be attenuated by the $R_s * C_{in}$ filter, C_{in} being the input capacitance resulting from the series combination of partitioned capacitances (see microchamber

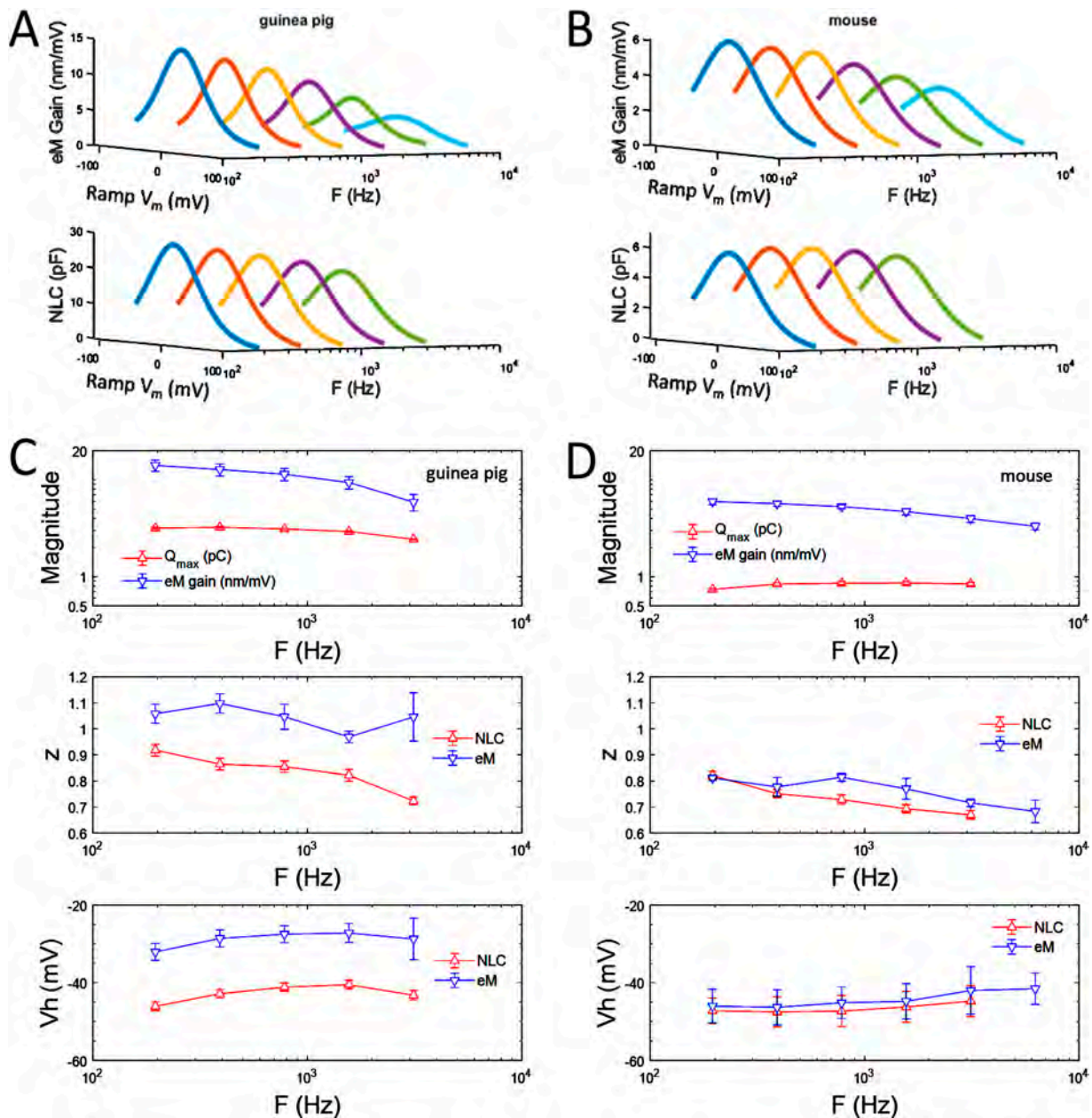


Figure 5. **Comparison of AC measured group-averaged guinea pig (A) and mouse (B) OHC NLC and associated eM frequency response as a function of holding voltage at each of the interrogated frequencies.** Neither mouse OHC NLC nor eM frequency response is as low pass as that of guinea pig OHC. These data were derived from cell averages of raw eM and membrane currents, as in Figs. 3 and 4. (C and D) Mean and SEM of eM at V_h and Boltzmann parameters of fits based on single-cell analysis. Note disparity of eM and NLC V_h and z for guinea pig as previously observed (Song and Santos-Sacchi, 2013). Mouse OHC eM and NLC V_h , on the other hand, are comparable.

schematic in Fig. 9 of Santos-Sacchi and Tan, 2018). Thus, Dallos and Evans, even though they did not monitor membrane currents to determine actual voltage roll-off, did estimate, given published OHC characteristics, the voltage delivery cut-off to be ~30 kHz in their experiments. This cut-off, as noted above, depended on their microchamber R_s and the input membrane capacitance. Of note for the studies by both Dallos and Evans and Frank et al., their zero microchamber offsets interrogated eM at holding membrane potentials far removed from V_h ; this is apparent from the small

eM gains reported compared with established eM gains between 15–19 nm/mV. Santos-Sacchi and Tan (2018) measured eM frequency response at two microchamber offsets, one near V_h and the other well offset from V_h (we estimate ~65 mV away). By measuring clamp tau from exponential decays at those two offsets, they found that eM is lower pass at V_h . Unfortunately, none of the previous studies have actually accounted for the voltage- and frequency-dependent roll-off of voltage delivery to the OHC, and without that correction, the true voltage-dependent eM frequency response remained unclear.

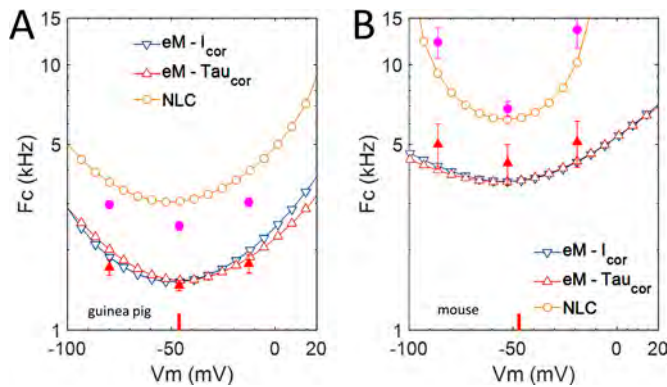


Figure 6. **Frequency cut-offs (F_c) for NLC and eM.** (A and B) Single Lorentzian fits of NLC and associated eM data in Fig. 5, A and B. The plots show that the F_c of NLC and eM increases as ramp voltage deviates from V_h . The open symbols are from fits to averaged data. The cut-off frequency for each is a U shaped function of holding voltage, with NLC measures showing frequency cut-offs faster than that for eM. Using either of the two eM correction methods gives equivalent results (see Materials and methods section). The filled symbols with SEM are obtained from individually analyzed OHC data. The F_c at V_h for guinea pig OHC eM is 1.47 ± 0.065 kHz, and that for mouse OHC eM is 4.26 ± 0.74 kHz. The F_c at V_h for guinea pig OHC NLC is 2.47 ± 0.091 kHz, and that for mouse OHC NLC is 6.83 ± 0.46 kHz. The red bar on the voltage axis indicates NLC V_h .

Similarities and differences between voltage-sensor movement (NLC) and eM

The electromechanical results we report on now explore the component of eM within 0.195–6.3 kHz, corresponding to human speech frequencies, and are made under whole-cell voltage clamp where, unlike the microchamber, precise DC and AC voltage delivery to the membrane is possible and predictable. Thus, we find with whole-cell recording, following voltage corrections due to the multifarious clamp time constant, that prestin’s eM and NLC frequency response, in both mouse and guinea pig, exhibits low-pass electromechanical behavior within our measurement bandwidth. The frequency response is slowest at V_h , with a cut-off, approximated by single Lorentzian fits within that bandwidth, near 1.5 kHz for the guinea pig OHC and near 4.3 kHz for the mouse OHC, each increasing in a U-shaped manner away from V_h . NLC measures follow this U-shaped pattern.

By using macro-patch measurements, where voltage control is near ideal, we find that NLC frequency response is similar in roll-off to corresponding whole-cell measures within the speech frequency bandwidth, indicating our whole-cell voltage corrections were effective. Nevertheless, eM frequency cut-offs differ from those of NLC, which are faster. In OHC patches, Gale and Ashmore found that patch movement F_c was only 0.19 times that of NLC F_c (using the ratio of their reported corresponding tau values of 16 and 83.5 μ s for NLC and movements, respectively), which they attributed to interactions of prestin with cytoskeletal elements and viscous damping (Gale and Ashmore 1997a). That is, factors that influence prestin electromechanical behavior are present within the on-cell patch, i.e., intrinsic to the local environment of prestin within the membrane. Indeed, we have found physical and functional interactions of MAP1S, a small actin-binding protein, with prestin (Bai et al., 2010). However,

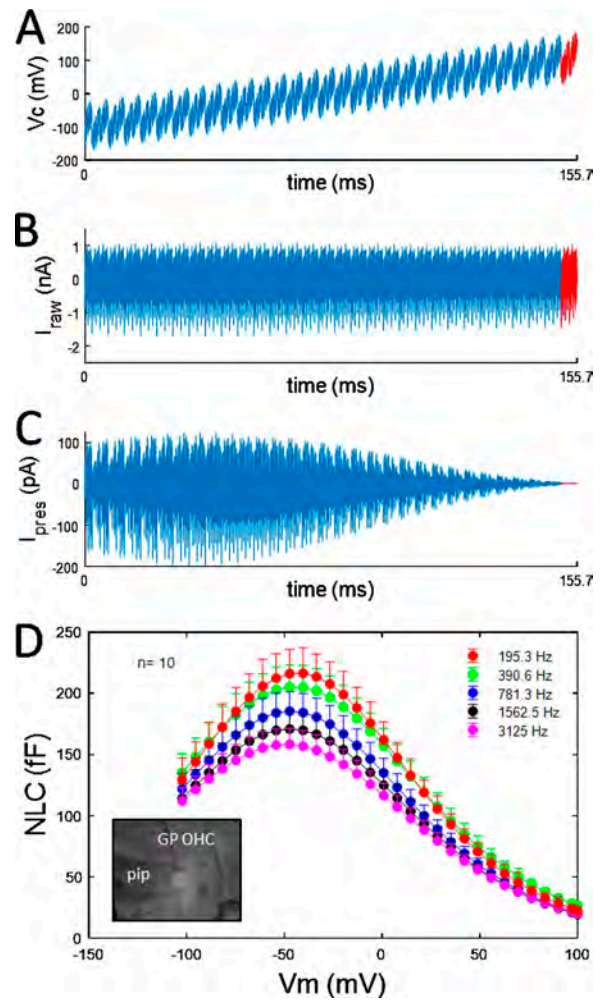


Figure 7. **Macro patches were made on the GP OHC lateral membrane to verify low pass behavior found in whole-cell measures of NLC.** (A) Command voltage; red highlighted regions used for stray and linear current subtractions; see Materials and methods). (B) Group-averaged currents recorded from on-cell macro-patches. Currents with AC components removed were used for detrending AC responses before highlighted region subtraction and FFT. (C) Resulting prestin-associated nonlinear currents. (D) Patches were individually analyzed to obtain NLC derived from nonlinear currents. Inset shows a patched OHC lateral membrane. Diameter of the OHC is 10 μ m. Mean \pm SEM. Pip, patch pipette; I_{raw} , raw current; fF, femtofarads; I_{pres} , prestin currents.

such influential effects on eM might be expected to work on both eM and NLC, since charge movement and mechanics are coupled (Dong and Iwasa, 2004; Santos-Sacchi and Tan, 2018). Consequently, the discrepancy between eM and NLC frequency response that is observed must point to variability of coupling charge movement to eM. Of course, uncoupling is clearly observable by deflating the OHC, which preserves NLC while abolishing whole-cell eM (Santos-Sacchi, 1991). Thus, we suggest that a variable coupling between whole-cell mechanics and prestin activity limits OHC influences on cochlear amplification at high frequencies. To this point, Vavakou et al., 2019 have recently observed limited, low-pass estimates of OHC eM frequency response using optical coherence microscopy vibrometry in the high-frequency region of the living gerbil.

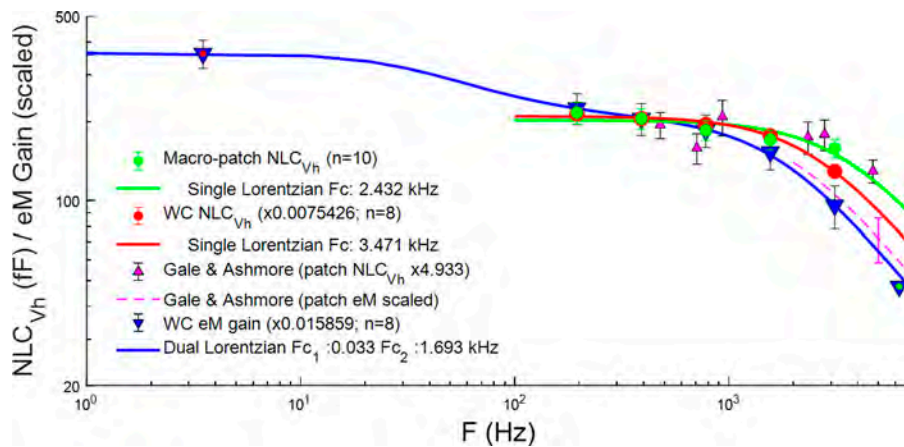


Figure 8. **Comparison of macro-patch peak NLC frequency response with whole-cell responses and published data (eM and NLC).** Data are scaled to macro-patch NLC at 390.6 Hz to compare frequency roll-off. Whole-cell NLC and macro-patch NLC both show low pass behavior. A single Lorentzian fit of the macro-patch (green) and whole-cell (red) NLC, indicates low pass behavior for each that is faster than whole-cell eM cut-off. For comparison, the roll-off of patch movement measures of Gale and Ashmore (1997a; purple dashed line being the equivalent Lorentzian of their movement tau and the purple SEM error bar depicting the equivalent mean \pm SEM response at 5 kHz; scaled in magnitude to over lie our eM roll-off) are plotted, and roll-off appears similar to that of our whole-cell eM. Gale and Ashmore’s patch NLC data (their points

within our measurement bandwidth) are comparable to our macro-patch measures. The downward blue triangle with a red dot is derived from the ramp eM gain (Fig. 3 B), and that with the light blue dot is from group-averaged responses (Fig. 5 A). Overall, the figure shows the discrepancy between eM and NLC roll-off, with NLC presenting a higher frequency cut-off. Mean \pm SEM. WC, whole cell.

What factors may influence OHC eM frequency response?

Within our interrogation bandwidth, NLC and eM are low pass. Since we accurately corrected for voltage delivery roll-off, the differential eM roll-off must result from other factors intrinsic and/or extrinsic to the cell. Two features require exploration not previously considered. One is the mechanism for voltage dependence of the cut-off frequency, F_c (Fig. 6). The other is a discrepancy in F_c for NLC and eM. The values of F_c for NLC are higher than those of eM. That is, eM appears to be low-pass filtered.

There are two factors that contribute to the frequency dependence that we measure. One is due to the intrinsic transition rates between prestin’s conformational states (Iwasa, 1997). Another factor, which is extrinsic to the motile element itself, is due to mechanical loads imposed on both the cell and the motile element. In the absence of mass, the characteristic frequency is determined by viscoelastic relaxation.

Mechanical factors could lead to a voltage dependence of F_c if the axial stiffness of the cell is itself voltage dependent, because the characteristic frequency of viscoelastic relaxation is determined by k/η , where k is the axial stiffness and η the drag coefficient. Indeed, it has been reported that the axial stiffness significantly decreases on deep depolarization (He and Dallos, 1999, 2000). Such a reduction in stiffness leads to a lower viscoelastic frequency as holding voltage is moved away from V_h , and is inconsistent with our observations. On the other hand, an alteration of axial stiffness has been theoretically predicted as an analogue of “gating compliance,” in which conformational transitions contribute to length changes of the cell (Iwasa, 2000). The predicted voltage dependence of the compliance, the inverse of stiffness, is bell-shaped, similar to NLC and qualitatively similar to our observed F_c values. Nevertheless, this effect is much too small to account for our observations. Actually, the magnitude of the “gating compliance” is quantitatively consistent with a report that voltage dependence of axial OHC stiffness is absent (Hallworth, 2007). Indeed, a previous treatment of a viscoelastic process involving the OHC does not lead to voltage dependence of the viscoelastic frequency for a

voltage driven stimulus, while it does for a force stimulus (Iwasa, 2016).

A stochastic transition model, even the simplest two-state model, inherently predicts voltage dependence because the characteristic frequency is expressed as a sum of transition rates in opposite directions from the distribution’s midpoint (Iwasa, 1997). In one direction, the rates increase exponentially with larger depolarizations, and in the other direction with larger hyperpolarizations, similar to the F_c values in Fig. 6.

Disparate frequency dependence for NLC and eM is a new observation, and there is no previous theoretical prediction or explanation. This is because it has been assumed that the cell undergoes the same mode of motion as the motile element. For a model in which eM is the low-pass filtered output of the motile element, it is possible to obtain different values of F_c for NLC and eM.

To capture the essential features of the observed high-frequency behavior of NLC and that of eM, we examined various mechanical loads assuming two conformations for the motile element (see Appendix). Virtually all kinetic models of prestin thus far reported, including the meno presto model (Santos-Sacchi and Song, 2014a), use this two-state formalism for eM and NLC generation.

We found that our experimentally observed eM and NLC frequency dependence can be explained by assuming that the motile element, which undergoes stochastic transitions, drives a mechanical system with two modes of motion. More specifically, cell displacement is the low-pass filtered output of the motile element displacement (see Appendix). The schematic configuration of the mechanical model is shown in Fig. 9. The model is constructed based on likely mechanical interactions within and external to the OHC. Thus, we view the elements k_2 , η_2 , and k_1 as representing the local environment, consisting of the lateral plasma membrane and cytoskeletal structures, surrounding the motile element (P). The elements k_0 and η_0 represent parts of the cell distant from the given motile element, primarily involved in energy dissipation due to the drag against the external medium. The existence of the elastic element k_0 may indicate

Table 1. History table of OHC eM frequency measurements

Publication	Method to evoke and measure load-free eM	Frequency response cut-off	Voltage delivery and/or eM measurement limitations	Notes
(Kachar et al., 1986)	Transcellular AC current; standard video	No estimate of roll-off; 1–30 Hz frame rates.	$R_m * C_m$ time constant; limited to 60 frames/s	
(Ashmore, 1987)	Whole-cell voltage clamp; photodiode	Dual Lorentzian cut-offs at 67 and 664 Hz	Voltage clamp $R_s * C_m$ time constant	
(Santos-Sacchi, 1992)	Whole-cell voltage clamp; photodiode	Single Lorentzian cut-off at 1 kHz	Voltage clamp $R_s * C_m$ time constant	
(Reuter et al., 1992)	Transcellular AC current stimulation in organ explants; stroboscopic video	40 dB down at 15 kHz	Membrane $R_m * C_m$ time constant	
(Dallos and Evans, 1995)	Microchamber cell partitioning, AC voltage from low-impedance waveform generator; photodiode	No estimate of roll-off, as shape of frequency response is a function of apical to basal impedances; eM detection above 10 kHz; zero microchamber V offset	$R_s * C_{in}$ (input capacitance of partitioned cell) for command voltage; ratio of partitioned impedance modifies roll-off shape	Low frequency eM gain: ~5 nm/mV indicative of offset away from V_h ; no estimation of V delivery roll-off based on generated currents
(Gale and Ashmore 1997b)	On-cell and excised membrane patch under voltage clamp	Patch movements (\approx eM) measured with step voltages; 10 kHz cut-off for patch NLC; 0.19 \times lower cut-off for movements	Near ideal voltage clamp	First indication that eM and NLC frequency response may differ
(Frank et al., 1999)	Microchamber cell partitioning; voltage clamp; laser Doppler vibrometer	Variable cut-off; for 30 μ m cell extrusion 33 kHz; smaller extrusions > 70 kHz; zero microchamber V offset	$R_s * C_{in}$ for command voltage; ratio of partitioned impedance modifies roll-off shape	Low frequency eM gain: ~5 nm/mV indicative of offset away from V_h ; voltage corrections based on $R_s * C_{in}$ (stray membrane capacitance)
(Kitani et al., 2011)	Transcellular AC current; video analysis at 18 kHz	Responses measured up to 4 kHz	$R_m * C_m$ time constant	Time dependent changes in eM magnitude may be attributed to mechanisms other than prestin
(Santos-Sacchi and Tan, 2018)	Microchamber cell partitioning; voltage clamp; video analysis at 50 KHz frame rate	At microchamber V offset to V_h , dual Lorentzian cut-offs of 33 Hz and 6.3 kHz; at zero microchamber V offset, dual Lorentzian cut-offs of 234 Hz and 8.7 kHz	$R_s * C_{in}$ for command voltage; ratio of partitioned impedance modifies roll-off shape	Low frequency eM gain (at V_h): 16.8 nm/mV; voltage corrections based on exponential current decays during V stimulation at two microchamber offsets; eM measures made under whole cell voltage clamp were not corrected for delivery roll-off

that the drag is not concentrated at a single location, but it is distributed along the cellular axis.

Small mechanical displacements, x and y , elicited by small sinusoidal voltages with frequency f applied on the motile element, can be expressed as (see derivation in Appendix),

$$x(f) = \frac{k_{12} \gamma(f)}{k_{02} + k_{12} + i f / f_1}, \quad (10a)$$

$$\gamma(f) = \frac{\beta \bar{P}_{\pm} a q N}{1 + f / f_g} \cdot \frac{\nu}{k_{12}^2 (k_{01} + k_{12} + i f / f_1) - (k_{12} + i f / f_2)}, \quad (10b)$$

where f_g is the gating frequency, $k_{02} = k_0/k_2$, $k_{12} = k_1/k_2$, $2\pi f_0 = \eta_0/k_2$, and $2\pi f_2 = \eta_0/k_2$. Here, $i = \sqrt{-1}$. The voltage dependence of the magnitude of these quantities is determined by \bar{P}_{\pm} , which is proportional to NLC at low frequencies (see Appendix). Notice here that NLC is associated with x , and eM with γ . Eq. 10a indeed shows that x is a low-pass filtered output of γ .

Importantly, the model captures two features of our experimental observations. One is the voltage dependence of F_c due to

gating frequency f_g . The other is that the roll-off of eM takes place at lower frequency than that of NLC.

Fig. 10 shows model fits of experimentally determined eM and NLC frequency responses at three holding potentials, passing through V_h . The parameter values obtained by simultaneous data fit at each holding voltage appear reasonable. However, standard errors are large, mainly due to the dependency between the substantial number of parameters. Such an example is shown in Fig. 10 A, which shows plots using two sets of parameter values, where the stiffness ratios of one set are larger than the other by about fivefold. For this reason, it is unlikely that the present analysis can provide definitive information regarding the axial stiffness of OHCs. Nevertheless, Fig. 10 indicates that the gating frequency f_g obtained at each holding voltage is consistent with the stochastic model with the lowest value, namely near V_h (at -45.8 mV). That is, the values of f_g distinctly characterize the plots at each holding voltage, while the values for the remaining parameters remain essentially the same.

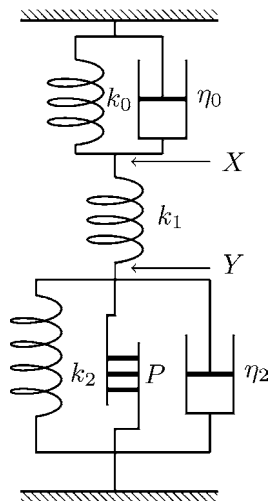


Figure 9. **Schematic diagram of mechanical load on the motile element.** Mechanical load consists of three elastic elements k_0 , k_1 , and k_2 , and two dashpots η_0 and η_2 . X represents the displacement of the cell, and Y indicates the displacement of the motile element, labeled as P.

Summary

The relationship between OHC resting potential and NLC V_h will govern the frequency response of eM. We previously proposed that a mismatch between resting potential and NLC V_h could enhance the frequency response of eM through a gain-bandwidth adjustment (Santos-Sacchi and Tan, 2018). Our new data are in line with this proposal and provide a detailed description of the OHC’s electromechanical cut-off frequency across voltage in both guinea pig and mouse OHCs. This cut-off frequency is U-shaped about V_h , and increases as holding voltage deviates from V_h . Importantly, the eM voltage dependence is mirrored by that of NLC, though frequency cut-offs differ. The cut-off disparity likely results from the influences of internal and external loads upon the motile mechanism. In this regard, we should comment on the observed differences in F_c values for mouse and guinea pig. Do differences in intrinsic prestin

kinetics exist between mouse and guinea pig, as the viscoelastic model might suggest? While preliminary, we have macro-patch measures out to 20 kHz that indicate similar prestin kinetics in the two species. That is, we explored the frequency response of NLC in patches from mouse and guinea pig OHC lateral membranes, each showing low-pass, stretched exponential behavior with roll-offs at half magnitude near 10–12 kHz at room temperature (unpublished data). In this light, we expect that the structural differences between the two species’ cells (e.g., length, diameter) may have provided differing loads on prestin with consequential differences in eM and NLC, given that the piezoelectric nature of prestin will be affected by load. In sum, all of our observations indicate that the influence of OHC activity on cochlear amplification is more complicated than has been envisioned.

Finally, we note that the kinetics of prestin are readily monitored through shifts in V_h , a reflection of the ratio of forward to backward transition rates. These kinetics, a determining factor in eM frequency response, depend on a host of other factors, including intracellular chloride, membrane tension and thickness, and temperature (Iwasa, 1993; Gale and Ashmore, 1994; Meltzer and Santos-Sacchi, 2001; Oliver et al., 2001; Santos-Sacchi et al., 2001; Izumi et al., 2011; Santos-Sacchi and Song, 2016). Indeed, alterations in prestin kinetics have been found in mutations in prestin (Homma et al., 2013). We suspect that eM frequency response is not a static feature in vivo.

Appendix

Rate equations for membrane molecules with mechanoelectric coupling: Introduction

There are two kinds of theories for describing the frequency dependence of cells with motile elements based on mechano-electric coupling. One of them is based on kinetic equations with intrinsic transition rates, which have been used to describe conformational changes of proteins, such as ion transporters (Kolb and Läuger, 1978), ignoring the effect of mechanical load imposed on those cells (Iwasa, 1997).

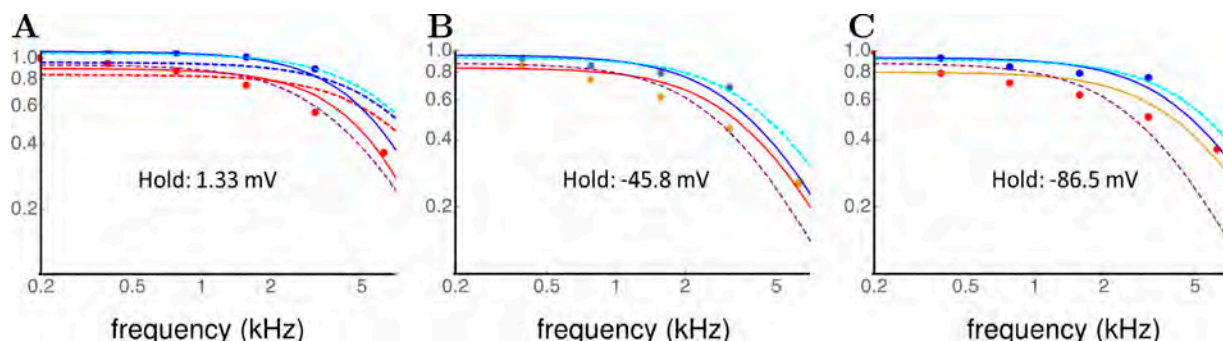


Figure 10. **Frequency dependence of NLC and eM.** Comparison with model predictions. Blue data points represent NLC and red data points eM. Solid lines indicate simultaneous fit for NLC and eM with the model at each holding potential. The color coding is the same as for the data points. Dashed lines in cyan and purple represent Lorentzian fit, respectively, for NLC and eM data. **(A)** Holding potential 1.33 mV; fit parameters are $f_g = 7.86$ kHz, $f_1 = 23.4$ kHz, $f_2 = 69.9$ kHz, $k_0/k_2 = 0.58$, and $k_1/k_2 = 0.26$. **(B)** Holding potential -45.8 mV, $f_g = 3.97$ kHz, $f_1 = 29.5$ kHz, $f_2 = 80.6$ kHz, $k_0/k_2 = 3.82$, and $k_1/k_2 = 1.31$. **(C)** Holding potential -86.5 mV, $f_g = 5.14$ kHz, $f_1 = 38.1$ kHz, $f_2 = 74.3$ kHz, $k_0/k_2 = 4.37$, and $k_1/k_2 = 1.60$. At 1.33 mV (in A), the best fit stiffness ratios are different from at other voltages. To examine the effect of difference in the stiffness ratios, additional dashed lines are drawn in blue and red, respectively, for NLC and eM, where the parameter values for B are used, except for the gating frequency f_g , which is set at 7.86 kHz.

Another kind of treatment assumes that intrinsic conformational transitions are infinitely fast. Conformational transitions are determined by the equation of motion for these cells, on which mechanical load is imposed (Iwasa, 2016). The resulting frequency responses of these cells are characterized by mechanical factors, such as the resonance frequency and the frequency for viscoelastic relaxation.

The present treatment introduces the dependence on mechanical load into the conformational transition rates, enabling description of the general case, where the intrinsic transition rates are finite. Two previous theories are recovered as special cases. In addition, we examine how mechanical complexity of the system can give rise to discrepancy in the frequency dependence of nonlinear capacitance NLC and that of motile response. For simplicity, we assume that the motile molecule has two discrete conformational states. The terms “motile molecules” and “motile element” are used interchangeably.

Motile element with two states

Consider a membrane molecule with two discrete conformational states, C_0 and C_1 , and let the transition rates k_+ and k_- between them be schematically expressed as



Let P_1 be the probability that the molecule is in state C_1 . Then, the probability P_1 can be expressed by the transition rates

$$\frac{P_1}{1 - P_1} = \frac{k_+}{k_-} = \exp[-\beta q(V - V_0)], \quad (A1)$$

where q is the charge transferred across the membrane during conformational changes, V the membrane potential, V_0 a constant, and $\beta = 1/k_B T$ with the Boltzmann constant and T the temperature.

If q is positive, the energy level of the state C_1 is higher, reducing P_1 as the membrane potential V rises. For prestin in outer hair cells, which shorten on depolarization, if we choose C_1 as the shortened state, the unit length change a on conformational change is negative, and then we have $q < 0$. Notice that the quantity a does not appear in Eq. A1.

The transition rates that satisfy Eq. A1 can be given by

$$k_+ = \exp[-\alpha\beta q(V - V_0)], \quad (A2)$$

$$k_- = \exp[(1 - \alpha)\beta q(V - V_0)], \quad (A3)$$

where α is an arbitrary constant.

The time dependence of P_1 can be expressed by the rate equation

$$\frac{d}{dt}P_1 = k_+ - (k_+ + k_-)P_1. \quad (A4)$$

Now we introduce sinusoidal voltage changes of small amplitude v on top of constant voltage \bar{V} , i.e., $V = \bar{V} + v \exp[i\omega t]$, where ω is the angular frequency and $i = \sqrt{-1}$. Then the transition rates are time-dependent due to the voltage dependence Eq. A1. They satisfy

$$\frac{k_+}{k_-} = \frac{\bar{k}_+}{\bar{k}_-} (1 - \beta q v \exp[i\omega t]). \quad (A5)$$

Notice \bar{k}_+ and \bar{k}_- are time independent, and we assume that v is small so that $\beta q v \ll 1$. A set of k_+ and k_- that satisfies Eq. A5 can be expressed

$$k_+ = \bar{k}_+ (1 - \alpha\beta q v \exp[i\omega t]), \quad (A6)$$

$$k_- = \bar{k}_- \{1 - (1 - \alpha)\beta q v \exp[i\omega t]\}. \quad (A7)$$

If we express $P_1 = \bar{P}_1 + p_1 \exp[i\omega t]$, we have respectively for the 0th and first order terms (Iwasa, 1997)

$$\bar{P}_1 = \frac{\bar{k}_+}{\bar{k}_+ + \bar{k}_-}, \quad (A8)$$

$$p_1 = -\frac{\bar{k}_+ \bar{k}_-}{\bar{k}_+ + \bar{k}_-} \cdot \frac{\beta q v}{i\omega + \bar{k}_+ + \bar{k}_-}. \quad (A9)$$

Notice that p_1 does not depend on the factor α .

Eq. A9 leads to voltage-driven mechanical displacement $ap_1 \exp[i\omega t]$ with

$$ap_1 = -\bar{P}_1 \cdot \frac{\beta a q v}{1 + i\omega/\omega_g}, \quad (A10)$$

where $\bar{P}_\pm = \bar{P}_1(1 - \bar{P}_1)$. The amplitude $|x|$ of the motile response is given by

$$|x|^2 = \frac{(\beta a q \bar{P}_\pm)^2}{1 + (\omega/\omega_g)^2} \cdot v^2. \quad (A11)$$

Charge displacement is expressed by qp_1 and the contribution to complex admittance $Y(\omega)$ is given by $(q/v)(d/dt)p_1 \exp[i\omega t]$ (Iwasa, 1997). The contribution to the membrane capacitance is $C_{nl}(\omega) = \text{Im}[Y(\omega)]/\omega$ and therefore

$$C_{nl}(\omega) = \frac{\beta q^2 \bar{P}_1(1 - \bar{P}_1)}{1 + (\omega/\omega_g)^2}. \quad (A12)$$

This contribution to the membrane capacitance is commonly referred to as NLC because it shows marked voltage dependence. Notice also that the above derivation evaluates the contribution of a single unit of motile element. For a cell that contains N motile units, both $|x|$ and C_{nl} need to be multiplied by N .

The roll-off frequency ω_g due to gating is expressed by $\omega_g = \bar{k}_+ + \bar{k}_-$, which is voltage dependent. Using Eqs. A2 and A3, we obtain

$$\omega_g = \exp[-\alpha\beta q(\bar{V} - V_0)] + \exp[(1 - \alpha)\beta q(\bar{V} - V_0)]. \quad (A13)$$

This means that $1/\omega_g$ rises at both ends of the membrane potential because α can take any value between 0 and 1. That means ω_r can be asymmetric unless $\alpha = 1/2$.

In the special case of $\alpha = 1/2$, $k_+ = 1/k_-$. If we define $b(V) = \exp[-\beta q(\bar{V} - V_0)/2]$, then

$$1/\omega_g = 1/[b(V) + 1/b(V)], \quad (A14)$$

which resembles the bell-shaped voltage dependence of nonlinear capacitance at low frequencies ($\omega \rightarrow 0$).

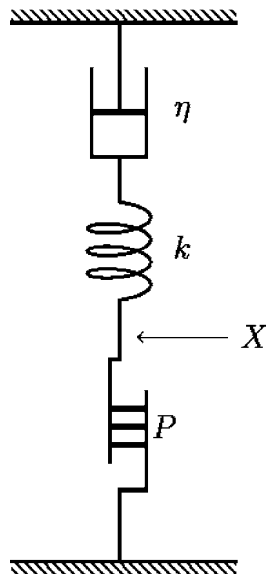


Figure A1. **Schematic representation of a cell with viscous drag.** The stiffness of the cell is k , and drag coefficient is η . The motile element is labeled P . The mechanical displacement of the cell is represented by X .

Mechanoelastic coupling

For motile membrane proteins based on mechanoelectric coupling, charge transfer is affected by mechanical factors. Here, we assume the cell is cylindrical as in the case of cochlear outer hair cells and approximate it as a one-dimensional object (Fig. A1).

Supposing charge transfer q is associated with a change a in the length of the cell, Eq. A1 should be replaced by

$$\frac{P_1}{1 - P_1} = \frac{k_+}{k_-} = \exp[-\beta[q(V - V_0) + aF]], \tag{A15}$$

where F is the axial force on the cell. The revised transition rates k_+ and k_- also depend on the mechanical factor

$$K_+ = \exp\left[-\alpha \frac{\beta}{2}[q(V - V_0) + aF]\right], \tag{A16}$$

$$k_- = \exp\left[(1 - \alpha) \frac{\beta}{2}[q(V - V_0) + aF]\right]. \tag{A17}$$

For the rest of the present paper, the dependence on the value of the parameter α does not appear except for ω_g .

With a shorthand notation $\bar{P}_\pm (= \bar{P}_1(1 - \bar{P}_1))$, the change of the conformational probability p_1 can be driven either by changes in the voltage as well force:

$$p_1 = -\beta \bar{P}_\pm \frac{qv + af}{1 + i\omega/\omega_g}. \tag{A18}$$

If the motile element is driven by voltage changes, p_1 is proportional to v and mechanical displacement is given by ap_1 .

Effect of viscous drag

Movement is driven by a deviation from Boltzmann distribution. When voltage changes with amplitude v imposed, p_1 as expressed by Eq. A18 is the goal of the drive. Since this force is countered by viscous drag (with drag coefficient η), the equation of motion in the frequency domain can be expressed by

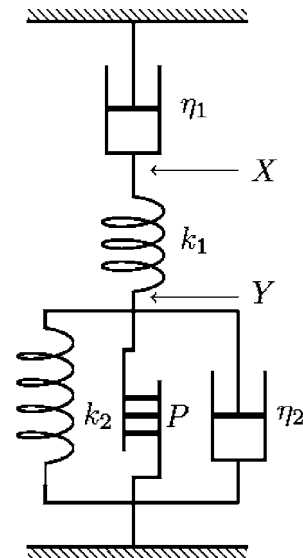


Figure A2. **Schematic representation of a cell with complex mechanical relaxation.** The local relaxation process associated with the motile element P is characterized by a spring with stiffness k_2 and a dashpot with drag coefficient η_2 . The local displacement is expressed by Y . The global relaxation process is characterized by a spring k_1 and a dashpot with drag coefficient η_1 . The cellular displacement is expressed by X .

$$i\eta\omega ap = ka(p_1 - p). \tag{A19}$$

Notice here that the equilibrium transition rates here depend not only on \bar{V} but also on \bar{F} because the motile element based on piezoelectricity is sensitive to mechanical force as well as the membrane potential.

Eq. A19 leads to

$$(1 + i\omega/\omega_\eta)p = -\frac{\beta \bar{P}_\pm}{1 + i\omega/\omega_g} \cdot qv, \tag{A20}$$

similar to the previous treatment for the special case without inertial loading (Iwasa, 2016). Here, the viscoelastic relaxation frequency is defined by $\omega_\eta = k/\eta$. It is essentially an equation for viscoelastic relaxation, adding a low pass filter to the motile mechanism. It is consistent with previous expressions in both extremes, i.e., $\omega_g \rightarrow \infty$ and $\omega_\eta \rightarrow \infty$.

The voltage dependence of NLC and that of motile response are identical. In the following, we show that mechanical load with complex relaxation can lead to discrepancy in their frequency dependences.

Complex mechanical relaxation

Let X represent the point that links a spring k_1 with a dashpot η_1 . Let Y represent the point that joins the spring k_1 with the rest, which includes a spring k_2 , a dashpot η_2 , and a driver (Fig. A2). The equations of motion of this system driven by force F generated at the location P can be expressed

$$\eta_1 \frac{dX}{dt} = -k_1(X - Y), \tag{A21}$$

$$F + k_2Y + \eta_2 \frac{dY}{dt} = k_1(X - Y). \tag{A22}$$

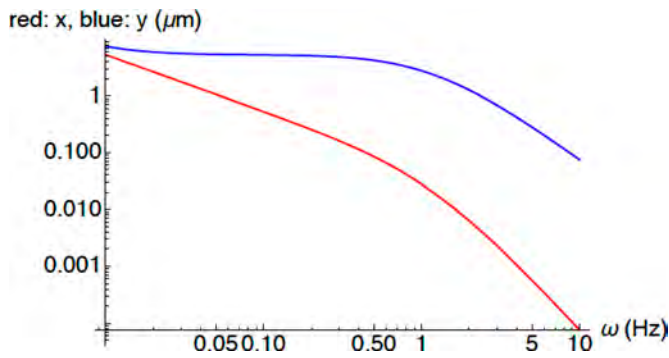


Figure A3. An example of the frequency dependence of x (red) and y (blue). Parameter values: $\omega_g = 2$, $\omega_1 = 0.01$, $\omega_2 = 5.12$, and $\frac{k_1}{k_2} = 0.16$.

If the force generator operates at a frequency ω with small amplitude on top of its steady value \bar{F} , $F = \bar{F} + f \exp[i\omega t]$. By letting the small amplitude components of X and Y with frequency ω be represented by x and y , Eqs. A21 and A22 turn into

$$i\omega\eta_1 x = -k_1(x - y), \tag{A23}$$

$$f + (k_2 + i\omega\eta_2)y = k_1(x - y). \tag{A24}$$

Eq. A23 can be rewritten as

$$x = \frac{y}{1 + i\omega/\omega_1}, \tag{A25}$$

which indicates that the quantity x is obtained by low-pass filtering Y with roll-off frequency of $\omega_1 (= k_1/\eta_1)$.

By introducing a characteristic frequency, $\omega_2 (= (k_1 + k_2)/\eta_2)$, Eq. A24 can be transformed into

$$f + (k_1 + k_2)[1 + i\omega/\omega_2]y = k_1x. \tag{A26}$$

Elimination of x from Eq. A26 with the aid of Eq. A25 leads to

$$y = f/G_1(\omega), \tag{A27}$$

$$G_1(\omega) = \frac{k_1}{1 + i\omega/\omega_1} - (k_1 + k_2)(1 + i\omega/\omega_2). \tag{A28}$$

An approach analogous to those in the previous sections lead to an equation

$$G_1(\omega)ap = ak_2(p - p). \tag{A29}$$

Since we have $y = ap$, this equation leads to

$$[G_1(\omega) + k_2]y = \frac{\beta\bar{P}_\pm k_2 a q v}{1 + i\omega/\omega_g}. \tag{A30}$$

Eqs. A25 and A30 show that the relationship between y and v has three adjustable parameters, ω_1 , ω_2 , and $k_r (= k_1/k_2)$. For an example of the frequency dependence of y , see Fig. A3.

The frequency dependence of NLC is the same as that of y . Motile response x is obtained by low-pass filtering y . The roll-off frequency of y is voltage-dependent due to the voltage dependence of ω_g .

With the connectivity of Fig. A2, it is difficult to make high frequency roll off of both quantities as similar as the experimental data. For y to roll off at relatively high frequency, ω_1 has to be small and ω_2 has to be large because G_1

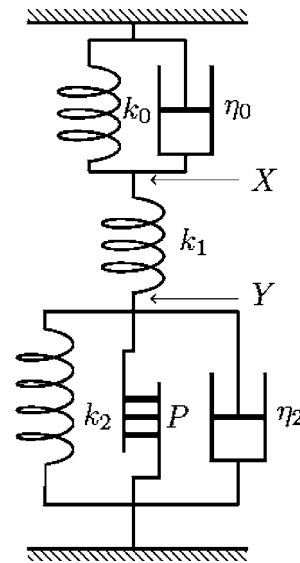


Figure A4. Schematic diagram of a cell with an alternative complex mechanical relaxation. The top dashpot η_1 in Fig. A2 is replaced by a combination of a dashpot η_0 and an elastic element k_0 .

must be small as required by Eq. A30. This requirement makes x roll off at a frequency much lower than y does (Fig. A3).

Modified complex mechanical relaxation

The model described above predicts a difference between x and y much larger than the experimentally observed frequency dependence. Let us add a spring across the upper dashpot (Fig. A4).

The set of equations that describe this configuration are

$$\left(\eta_0 \frac{d}{dt} + k_0\right)X = k_1(Y - X), \tag{A31}$$

$$F + \left(\eta_2 \frac{d}{dt} + k_2\right)Y = -k_1(Y - X). \tag{A32}$$

If force F is driven at angular frequency ω with amplitude f , the equation is transformed into

$$(i\omega\eta_0 + k_0)x = k_1(y - x), \tag{A33}$$

$$f + (i\omega\eta_2 + k_2)y = -k_1(y - x), \tag{A34}$$

where variables in the lower case x and y are the complex amplitude of frequency ω .

Eqs. A33 and A34 can be rewritten as

$$x = \frac{k_1}{k_0 + k_1 + i\omega\eta_0} \cdot y, \tag{A35}$$

$$f = k_1x - (k_1 + k_2 + i\omega\eta_2)y. \tag{A36}$$

In the manner similar to Eqs. A27 and A28 in the previous case, these equations can be expressed as

$$y = f/G_2(\omega), \tag{A37}$$

$$G_2(\omega) = \frac{k_1}{k_0 + k_1 + i\omega\eta_0} - (k_1 + k_2 + i\omega\eta_2), \tag{A38}$$

which corresponds to $G_1(\omega)$ in the previous case.

Since force generation is associated with spring k_2 in the manner similar to the previous case, we obtain

$$[G_2(\omega) + k_2]y = \frac{\beta a q k_2 \bar{P}_\pm}{1 + i\omega/\omega_g} \cdot v, \quad (\text{A39})$$

and x is obtained with Eq. A35.

If the cell contains N motile units, a should be replaced by aN . For numerical analysis, the number of parameters can be reduced by introducing the ratios $k_{02} (= k_0/k_2)$, $k_{12} (= k_1/k_2)$, $\omega_0 (= k_2/\eta_0)$, and $\omega_2 (= k_2/\eta_2)$ and x and y are expressed by

$$x = \frac{k_{12}}{k_{02} + k_{12} + i\omega/\omega_0} \cdot y, \quad (\text{A40})$$

$$y = \frac{\beta a q N \bar{P}_\pm}{1 + i\omega/\omega_g} \cdot \frac{1}{k_{12}^2 / (k_{01} + k_{12} + i\omega/\omega_0) - (k_{12} + i\omega/\omega_2)} \cdot v. \quad (\text{A41})$$

The corresponding equations (Eq. 10) in the main text are expressed with linear frequency f instead of angular frequency ω . Because these equations depend only on frequency ratios, no extra factor appears.

Acknowledgments

Richard W. Aldrich served as editor.

This research was supported by National Institute on Deafness and Other Communication Disorders, National Institutes of Health grants R01 DC000273, R01 DC016318, and R01 DC008130 to J. Santos-Sacchi.

The authors declare no competing financial interests.

Author contributions: J. Santos-Sacchi conceived and performed experiments and wrote paper. W. Tan performed experiments. K.H. Iwasa did the modeling for the Appendix and wrote the Appendix and parts of the paper concerning this modeling.

Submitted: 23 October 2018

Revised: 24 August 2019

Accepted: 30 September 2019

References

Ashmore, J.F. 1987. A fast motile response in guinea-pig outer hair cells: the cellular basis of the cochlear amplifier. *J. Physiol.* 388:323–347. <https://doi.org/10.1113/jphysiol.1987.sp016617>

Ashmore, J.F. 1990. Forward and reverse transduction in the mammalian cochlea. *Neurosci. Res. Suppl.* 12:S39–S50. [https://doi.org/10.1016/0921-8696\(90\)90007-P](https://doi.org/10.1016/0921-8696(90)90007-P)

Ashmore, J. 2008. Cochlear outer hair cell motility. *Physiol. Rev.* 88:173–210. <https://doi.org/10.1152/physrev.00044.2006>

Ashmore, J., P. Avan, W.E. Brownell, P. Dallos, K. Dierkes, R. Fettiplace, K. Grosh, C.M. Hackney, A.J. Hudspeth, F. Jülicher, et al. 2010. The remarkable cochlear amplifier. *Hear. Res.* 266:1–17. <https://doi.org/10.1016/j.heares.2010.05.001>

Bai, J.P., A. Surguchev, Y. Ogando, L. Song, S. Bian, J. Santos-Sacchi, and D. Navaratnam. 2010. Prestin surface expression and activity are augmented by interaction with MAP1S, a microtubule-associated protein. *J. Biol. Chem.* 285:20834–20843. <https://doi.org/10.1074/jbc.M110.117853>

Dallos, P., and B.N. Evans. 1995. High-frequency motility of outer hair cells and the cochlear amplifier. *Science.* 267(5206):2006–2009. <https://doi.org/10.1126/science.7701325>

Dallos, P., X. Wu, M.A. Cheatham, J. Gao, J. Zheng, C.T. Anderson, S. Jia, X. Wang, W.H. Cheng, S. Sengupta, et al. 2008. Prestin-based outer hair cell motility is necessary for mammalian cochlear amplification. *Neuron.* 58:333–339. <https://doi.org/10.1016/j.neuron.2008.02.028>

Dong, X.X., and K.H. Iwasa. 2004. Tension sensitivity of prestin: comparison with the membrane motor in outer hair cells. *Biophys. J.* 86:1201–1208. [https://doi.org/10.1016/S0006-3495\(04\)74194-6](https://doi.org/10.1016/S0006-3495(04)74194-6)

Dong, W., and E.S. Olson. 2013. Detection of cochlear amplification and its activation. *Biophys. J.* 105:1067–1078. <https://doi.org/10.1016/j.bpj.2013.06.049>

Duret, G., F.A. Pereira, and R.M. Raphael. 2017. Difflunilal inhibits prestin by chloride-dependent mechanism. *PLoS One.* 12:e0183046. <https://doi.org/10.1371/journal.pone.0183046>

Frank, G., W. Hemmert, and A.W. Gummer. 1999. Limiting dynamics of high-frequency electromechanical transduction of outer hair cells. *Proc. Natl. Acad. Sci. USA.* 96:4420–4425. <https://doi.org/10.1073/pnas.96.8.4420>

Gale, J.E., and J.F. Ashmore. 1994. Charge displacement induced by rapid stretch in the basolateral membrane of the guinea-pig outer hair cell. *Proc. Biol. Sci.* 255:243–249. <https://doi.org/10.1098/rspb.1994.0035>

Gale, J.E., and J.F. Ashmore. 1997a. An intrinsic frequency limit to the cochlear amplifier. *Nature.* 389:63–66. <https://doi.org/10.1038/37968>

Gale, J.E., and J.F. Ashmore. 1997b. The outer hair cell motor in membrane patches. *Pflügers Arch.* 434:267–271. <https://doi.org/10.1007/s004240050395>

Gillis, K.D. 1995. Techniques for Membrane Capacitance Measurements. In *Single Channel Recording*. B. Sakmann, and E. Neher, editors. Plenum Press, New York. 155–198. https://doi.org/10.1007/978-1-4419-1229-9_7

Hallworth, R. 2007. Absence of voltage-dependent compliance in high-frequency cochlear outer hair cells. *J. Assoc. Res. Otolaryngol.* 8(4): 464–473. <https://doi.org/10.1007/s10162-007-0097-4>

He, D.Z., and P. Dallos. 1999. Somatic stiffness of cochlear outer hair cells is voltage-dependent. *Proc. Natl. Acad. Sci. U.S.A.* 96(14):8223–8228. <https://doi.org/10.1073/pnas.96.14.8223>

He, D.Z., and P. Dallos. 2000. Properties of voltage-dependent somatic stiffness of cochlear outer hair cells. *J. Assoc. Res. Otolaryngol.* 1(1):64–81. <https://doi.org/10.1007/s101620010006>

He, W., D. Kemp, and T. Ren. 2018. Timing of the reticular lamina and basilar membrane vibration in living gerbil cochlea. *eLife.* 7:e37625. <https://doi.org/10.7554/eLife.37625>

Homma, K., C. Duan, J. Zheng, M.A. Cheatham, and P. Dallos. 2013. The V499G/Y501H mutation impairs fast motor kinetics of prestin and has significance for defining functional independence of individual prestin subunits. *J. Biol. Chem.* 288:2452–2463. <https://doi.org/10.1074/jbc.M112.411579>

Huang, G., and J. Santos-Sacchi. 1993. Mapping the distribution of the outer hair cell motility voltage sensor by electrical amputation. *Biophys. J.* 65: 2228–2236. [https://doi.org/10.1016/S0006-3495\(93\)81248-7](https://doi.org/10.1016/S0006-3495(93)81248-7)

Iwasa, K.H. 1993. Effect of stress on the membrane capacitance of the auditory outer hair cell. *Biophys. J.* 65:492–498. [https://doi.org/10.1016/S0006-3495\(93\)81053-1](https://doi.org/10.1016/S0006-3495(93)81053-1)

Iwasa, K.H. 1997. Current noise spectrum and capacitance due to the membrane motor of the outer hair cell: theory. *Biophys. J.* 73:2965–2971. [https://doi.org/10.1016/S0006-3495\(97\)78325-5](https://doi.org/10.1016/S0006-3495(97)78325-5)

Iwasa, K.H.. 2000. Effect of membrane motor on the axial stiffness of the cochlear outer hair cell. *J. Acoust. Soc. Am.* 107(5 Pt 1):2764–2766. <https://doi.org/10.1121/1.428663>

Iwasa, K.H. 2016. Energy Output from a Single Outer Hair Cell. *Biophys. J.* 111: 2500–2511. <https://doi.org/10.1016/j.bpj.2016.10.021>

Iwasa, K.H., and B. Kachar. 1989. Fast in vitro movement of outer hair cells in an external electric field: effect of digitonin, a membrane permeabilizing agent. *Hear. Res.* 40:247–254. [https://doi.org/10.1016/0378-5955\(89\)90165-2](https://doi.org/10.1016/0378-5955(89)90165-2)

Izumi, C., J.E. Bird, and K.H. Iwasa. 2011. Membrane thickness sensitivity of prestin orthologs: the evolution of a piezoelectric protein. *Biophys. J.* 100:2614–2622. <https://doi.org/10.1016/j.bpj.2011.04.032>

Johnson, S.L., M. Beurg, W. Marcotti, and R. Fettiplace. 2011. Prestin-driven cochlear amplification is not limited by the outer hair cell membrane time constant. *Neuron.* 70:1143–1154. <https://doi.org/10.1016/j.neuron.2011.04.024>

Kachar, B., W.E. Brownell, R. Altschuler, and J. Fex. 1986. Electrokinetic shape changes of cochlear outer hair cells. *Nature.* 322(6077):365–368.

Kitani, R., S. Kakehata, and F. Kalinec. 2011. Motile responses of cochlear outer hair cells stimulated with an alternating electrical field. *Hear. Res.* 280(1–2):209–218. <https://doi.org/10.1016/j.heares.2011.05.013>

- Kolb, H.A., and P. Luger. 1978. Spectral analysis of current noise generated by carrier-mediated ion transport. *J. Membr. Biol.* 41:167–187. <https://doi.org/10.1007/BF01972631>
- Meltzer, J., and J. Santos-Sacchi. 2001. Temperature dependence of nonlinear capacitance in human embryonic kidney cells transfected with prestin, the outer hair cell motor protein. *Neurosci. Lett.* 313:141–144. [https://doi.org/10.1016/S0304-3940\(01\)02266-2](https://doi.org/10.1016/S0304-3940(01)02266-2)
- Oliver, D., D.Z. He, N. Klocker, J. Ludwig, U. Schulte, S. Waldegger, J.P. Ruppersberg, P. Dallos, and B. Fakler. 2001. Intracellular anions as the voltage sensor of prestin, the outer hair cell motor protein. *Science*. 292: 2340–2343. <https://doi.org/10.1126/science.1060939>
- Pusch, M., and E. Neher. 1988. Rates of diffusional exchange between small cells and a measuring patch pipette. *Pflügers Arch.* 411:204–211. <https://doi.org/10.1007/BF00582316>
- Ren, T., W. He, and D. Kemp. 2016. Reticular lamina and basilar membrane vibrations in living mouse cochleae. *Proc. Natl. Acad. Sci. USA.* 113: 9910–9915. <https://doi.org/10.1073/pnas.1607428113>
- Reuter, G., A.H. Gitter, U. Thurm, and H.P. Zenner. 1992. High frequency radial movements of the reticular lamina induced by outer hair cell motility. *Hear. Res.* 60(2):236–246. [https://doi.org/10.1016/0378-5955\(92\)90025-i](https://doi.org/10.1016/0378-5955(92)90025-i)
- Santos-Sacchi, J. 1989. Asymmetry in voltage-dependent movements of isolated outer hair cells from the organ of Corti. *J. Neurosci.* 9:2954–2962. <https://doi.org/10.1523/JNEUROSCI.09-08-02954.1989>
- Santos-Sacchi, J. 1991. Reversible inhibition of voltage-dependent outer hair cell motility and capacitance. *J. Neurosci.* 11:3096–3110. <https://doi.org/10.1523/JNEUROSCI.11-10-03096.1991>
- Santos-Sacchi, J.. 1992. On the frequency limit and phase of outer hair cell motility: effects of the membrane filter. *J. Neurosci.* 12(5):1906–1916. .
- Santos-Sacchi, J. 2004. Determination of cell capacitance using the exact empirical solution of dY/dCm and its phase angle. *Biophys. J.* 87:714–727. <https://doi.org/10.1529/biophysj.103.033993>
- Santos-Sacchi, J. 2018. High frequency measures of OHC nonlinear capacitance (NLC) and their significance: Why measures stray away from predictions. AIP Conference Proceedings 1965:060004–060001–060004–060005.
- Santos-Sacchi, J. 2019. The speed limit of outer hair cell electromechanical activity. *HNO.* 67:159–164. <https://doi.org/10.1007/s00106-019-0615-9>
- Santos-Sacchi, J., and J.P. Dilger. 1988. Whole cell currents and mechanical responses of isolated outer hair cells. *Hear. Res.* 35:143–150. [https://doi.org/10.1016/0378-5955\(88\)90113-X](https://doi.org/10.1016/0378-5955(88)90113-X)
- Santos-Sacchi, J., and L. Song. 2014a. Chloride and salicylate influence prestin-dependent specific membrane capacitance: support for the area motor model. *J. Biol. Chem.* 289:10823–10830. <https://doi.org/10.1074/jbc.M114.549329>
- Santos-Sacchi, J., and L. Song. 2014b. Chloride-driven electromechanical phase lags at acoustic frequencies are generated by SLC26a5, the outer hair cell motor protein. *Biophys. J.* 107:126–133. <https://doi.org/10.1016/j.bpj.2014.05.018>
- Santos-Sacchi, J., and L. Song. 2016. Chloride anions regulate kinetics but not voltage-sensor Qmax of the solute carrier SLC26a5. *Biophys. J.* 110: 2551–2561. <https://doi.org/10.1016/j.bpj.2016.05.002>
- Santos-Sacchi, J., and W. Tan. 2018. The Frequency Response of Outer Hair Cell Voltage-Dependent Motility Is Limited by Kinetics of Prestin. *J. Neurosci.* 38:5495–5506. <https://doi.org/10.1523/JNEUROSCI.0425-18.2018>
- Santos-Sacchi, J., S. Kakehata, and S. Takahashi. 1998. Effects of membrane potential on the voltage dependence of motility-related charge in outer hair cells of the guinea-pig. *J. Physiol.* 510:225–235. <https://doi.org/10.1111/j.1469-7793.1998.225bz.x>
- Santos-Sacchi, J., W. Shen, J. Zheng, and P. Dallos. 2001. Effects of membrane potential and tension on prestin, the outer hair cell lateral membrane motor protein. *J. Physiol.* 531:661–666. <https://doi.org/10.1111/j.1469-7793.2001.0661h.x>
- Santos-Sacchi, J., D. Navaratnam, R. Raphael, and D. Oliver. 2017. The Cochlea Chapter 5: Prestin - molecular mechanisms underlying outer hair cell electromotility. In *Springer Handbook Of Auditory Research*. Springer, New York.
- Schnee, M.E., J. Santos-Sacchi, M. Castellano-Muñoz, J.H. Kong, and A.J. Ricci. 2011a. Calcium-dependent synaptic vesicle trafficking underlies indefatigable release at the hair cell afferent fiber synapse. *Neuron.* 70: 326–338. <https://doi.org/10.1016/j.neuron.2011.01.031>
- Schnee, M.E., M. Castellano-Muñoz, J.H. Kong, J. Santos-Sacchi, and A.J. Ricci. 2011b. Tracking vesicle fusion from hair cell ribbon synapses using a high frequency, dual sine wave stimulus paradigm. *Commun. Integr. Biol.* 4:785–787. <https://doi.org/10.4161/cib.17822>
- Song, L., and J. Santos-Sacchi. 2013. Disparities in voltage-sensor charge and electromotility imply slow chloride-driven state transitions in the solute carrier SLC26a5. *Proc. Natl. Acad. Sci. USA.* 110:3883–3888. <https://doi.org/10.1073/pnas.1218341110>
- Vavakou, A., N.P. Cooper, and M. van der Heijden. 2019. The frequency limit of outer hair cell motility measured in vivo. *Elife.* 8. <https://doi.org/10.7554/eLife.47667>
- Zheng, J., W. Shen, D.Z. He, K.B. Long, L.D. Madison, and P. Dallos. 2000. Prestin is the motor protein of cochlear outer hair cells. *Nature.* 405: 149–155. <https://doi.org/10.1038/35012009>

Supplemental material

Santos-Sacchi et al., <https://doi.org/10.1085/jgp.201812280>

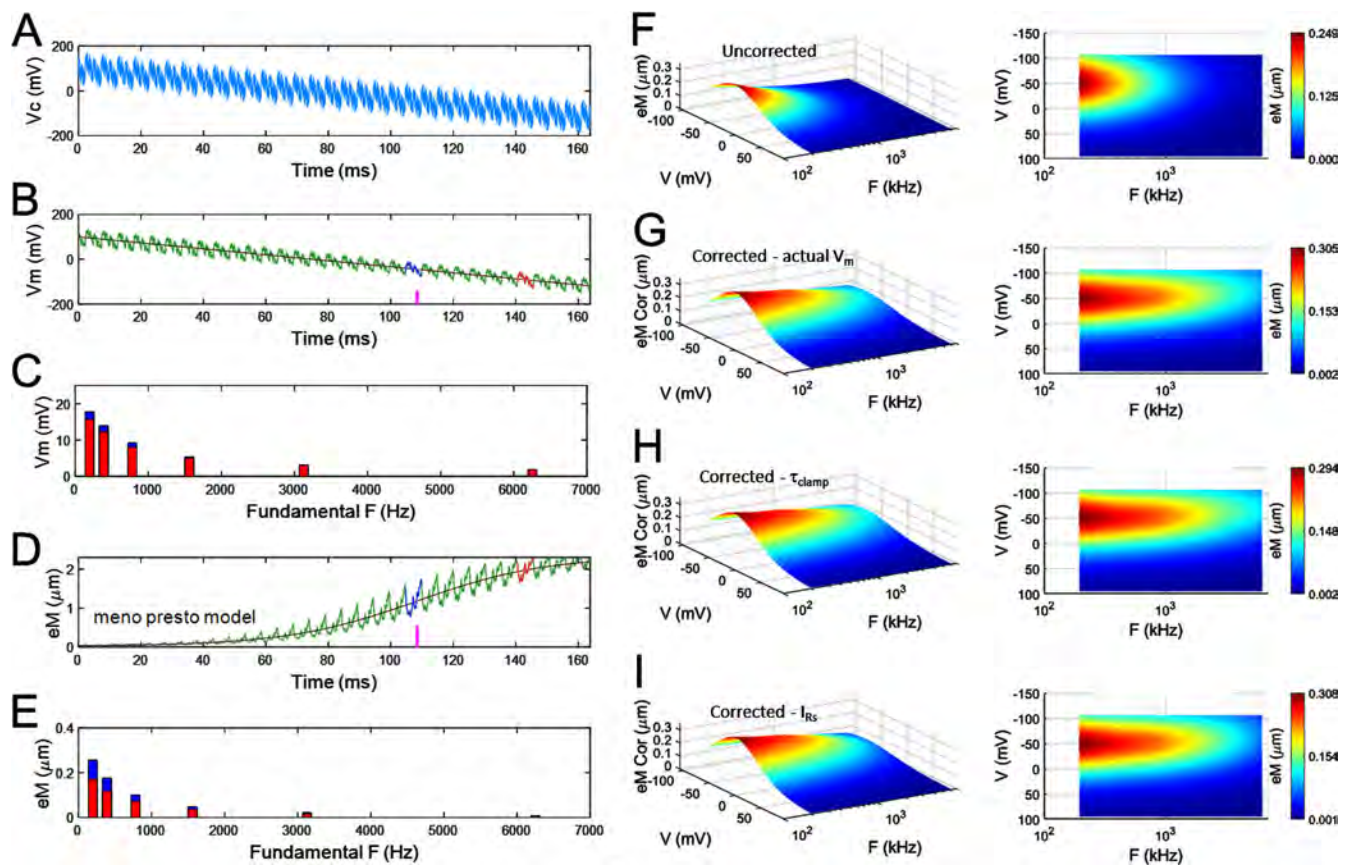


Figure S1. **Meno presto model (based on guinea pig [Fig. 3] and mouse [Fig. 4] averaged experimental parameters) of OHC under voltage clamp illustrating three methods for eM correction.** (A) The hyperpolarizing ramp voltage stimulus (100 to -120 mV) with superimposed sum of 20 mV AC harmonically related frequencies (195.3–6,250 Hz). A pedestal of 100 mV (81.32 ms) preceded the ramp. (B) Membrane voltage. Two selected integral regions are highlighted. Blue is near V_h (magenta bar beneath shows position of V_h). Red highlights a hyperpolarized region. In C, these regions were analyzed by FFT and magnitude results shown. (D) Raw eM (scaled charge from model) also depicting selected regions to analyze. (E) Magnitude responses at the six interrogated frequencies. Data were detrended as in Fig. 1 before FFT. The surface plots on the right provide a full analysis across ramp voltage at all integral regions of the eM model data. The adjacent 2-D plots present the frequency response that can more easily be compared among plots. eM- V_m data at each frequency were fit with the first derivative of a two-state Boltzmann before plotting. (F) Uncorrected eM. (G) Corrected eM using Method 1 based on actual V_m measures within MATLAB model. (H) eM adjusted with Method 3 based on corrections to multifarious τ_{clamp} (see Materials and methods). (I) eM adjusted with Method 2 based on membrane current corrections, namely, $V_m = V_c - I_{rs} * R_{ij}$. Each method provides comparable results. Note also that the frequency response of eM resulting from the guinea pig kinetic parameters is more low pass than those of the mouse (corresponding to the different imposed stretched intermediary rates), and the frequency responses are similar to the experimental data.

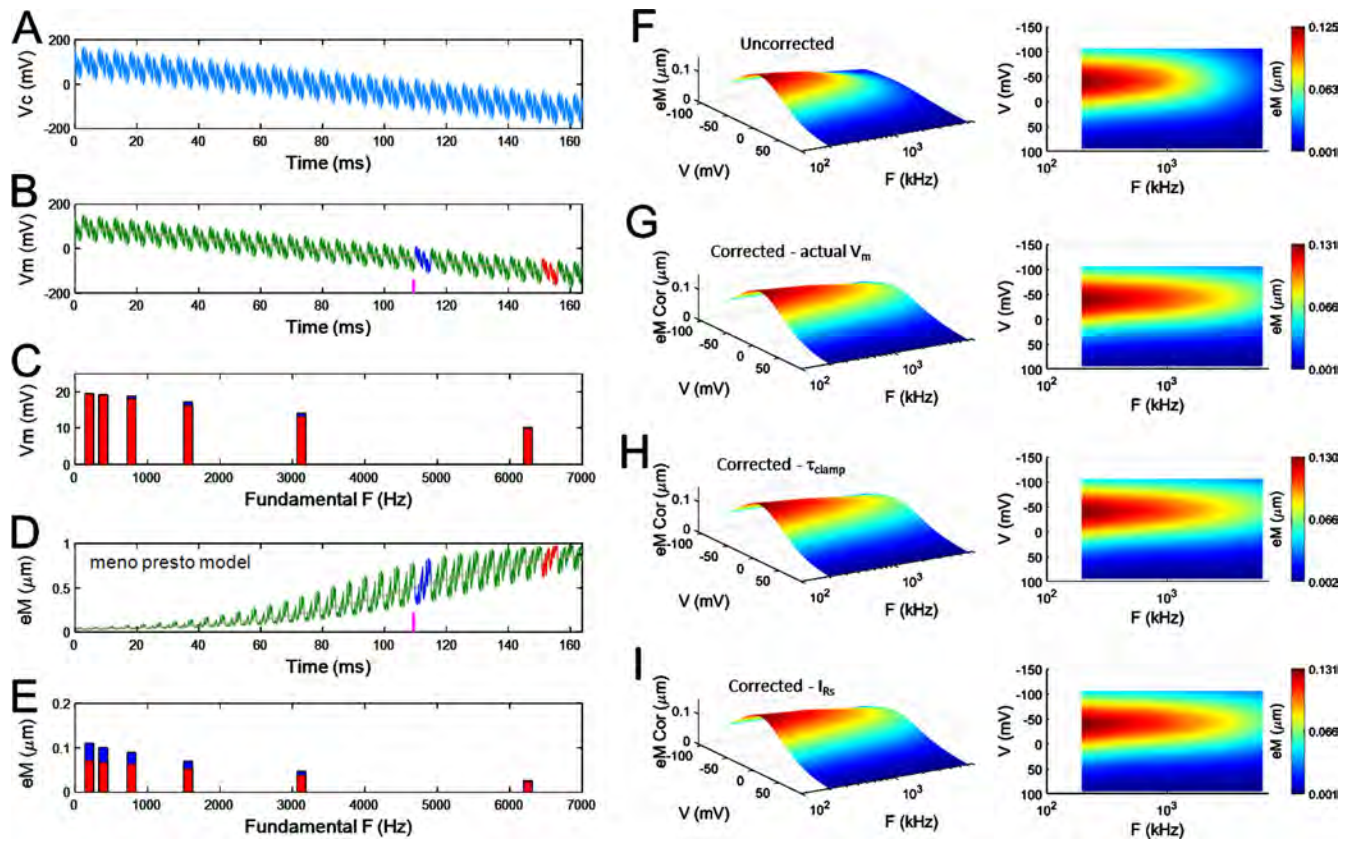


Figure S2. Meno presto model (based on guinea pig [Fig. 3] and mouse [Fig. 4] averaged experimental parameters) of OHC under voltage clamp illustrating three methods for eM correction. See legend of Fig. S1.

OPEN

Complex nonlinear capacitance in outer hair cell macro-patches: effects of membrane tension

Joseph Santos-Sacchi^{1,2,3*} & Winston Tan¹

Outer hair cell (OHC) nonlinear capacitance (NLC) represents voltage sensor charge movements of prestin (SLC26a5), the protein responsible for OHC electromotility. Previous measures of NLC frequency response have employed methods which did not assess the influence of dielectric loss (sensor charge movements out of phase with voltage) that may occur, and such loss conceivably may influence prestin's frequency dependent activity. Here we evaluate prestin's complex capacitance out to 30 kHz and find that prestin's frequency response determined using this approach coincides with all previous estimates. We also show that membrane tension has no effect on prestin's frequency response, despite substantial shifts in its voltage operating range, indicating that prestin transition rate alterations do not account for the shifts. The magnitude roll-off of prestin activity across frequency surpasses the reductions of NLC caused by salicylate treatments that are known to abolish cochlear amplification. Such roll-off likely limits the effectiveness of prestin in contributing to cochlear amplification at the very high acoustic frequencies processed by some mammals.

Prestin (SLC26a5) underlies outer hair cell (OHC) mechanical activity¹, whereby voltage-dependent conformational transitions couple into length changes of the cell (electromotility; eM)^{2–4}. Sensor charge movements associated with these conformational changes are measurable as an electrical correlate of eM, i.e., nonlinear capacitance (NLC)^{5–7}, which is maximal at V_h , the voltage where prestin charge is distributed equally across the OHC membrane and where eM gain is greatest.

The study of OHC NLC by admittance techniques in whole cell voltage clamp is compromised by contributions from stray capacitance, membrane conductances, and electrode series resistance (R_s), the latter altering over time due to plugging of the patch pipette tip with intracellular constituents. Because of this, it is virtually impossible to measure complex membrane capacitance in whole cell mode. We avoid these issues by measuring membrane admittance from macro-patches of the OHC lateral membrane. The lateral membrane of the cylindrical OHC is dominantly populated by prestin (>8000 functional units/ $\mu\text{m}^{2,8-10}$), whereas voltage-dependent membrane conductances are housed in the basal pole membrane¹¹. Consequently, macro-patch admittance, following removal of stray capacitance by subtraction of admittance at very depolarized levels where NLC is absent¹², can be used to study complex sensor-charge movements arising from voltage-induced conformational changes in prestin.

Here, we evaluate patch admittance to provide estimates of complex capacitance representing charge movements both in phase and 90° out of phase with AC voltage excitation. We compare such data to previously obtained measures of OHC NLC frequency response^{13,14}, and additionally report on the effects of membrane tension^{15–17} on the frequency response of complex NLC. Will an assessment of NLC based on measures of complex NLC alter our current view, as suggested¹⁸, and can turgor pressure, normally present in the OHC¹⁹, with its effect on membrane tension be influential? Our observations indicate that the bulk of sensor charge movement is in phase with voltage, while the resistive component (dielectric loss) is relatively small. Furthermore, membrane tension, though altering prestin's operating voltage point, has no effect on its frequency response. Thus, magnitude estimates of complex NLC are comparable to those measured with other methods^{13,14}, being unusually low pass in nature (non-Lorentzian) and indicating that the absolute movement of prestin charge that drives electromotility (eM)^{20,21} is unlikely to extend with high fidelity to the very high acoustic frequencies (60–160 kHz) detected by some mammals.

¹Surgery (Otolaryngology), Yale University School of Medicine, 333 Cedar Street, New Haven, CT, 06510, USA.

²Neuroscience, Yale University School of Medicine, 333 Cedar Street, New Haven, CT, 06510, USA. ³Cellular and Molecular Physiology, Yale University School of Medicine, 333 Cedar Street, New Haven, CT, 06510, USA. *email: joseph.santos-sacchi@yale.edu

Methods

All experimental protocols were approved by the Yale Animal Care and Use Committee, and were in accordance with relevant guidelines and regulations. Methods, including details of our voltage chirp stimulus protocol, are detailed in¹³. Briefly, extracellular solution was (in mM): NaCl 100, TEA-Cl 20, CsCl 20, CoCl₂ 2, MgCl₂ 1, CaCl₂ 1, Hepes 10, pH 7.2. Experiments were performed at room temperature. Extracellular solution was in the patch pipette. On-cell macro-patches on the guinea pig OHC lateral membrane were made near the middle of the cylindrical cell, since prestin density/activity is uniform within the lateral membrane^{8,22}. We have previously shown that capacitance frequency response in the OHC patch remains the same after excision of the patch, indicating that on-cell recording is applicable for our purposes¹³. Borosilicate pipettes of inner tip diameters between 3–4 μm were used, with M-coat applied within about 20 μm of the tip to minimize pipette capacitance. In order to establish gigohm seals we supplemented extracellular solution with 5 μM Gd³⁺; we have shown previously that these low concentrations help to form seals without affecting NLC^{13,23}. In 2 on-cell patches, we have omitted Gd³⁺ in the pipette solution and NLC frequency response is not significantly different than in its presence. An Axon 200B amplifier was used with jClamp software (www.scisoftco.com). An Axon Digidata 1440 was used for digitizing at 10 μs (Nyquist frequency of 50 kHz), with a 4-pole Bessel filter of 10 kHz. Membrane admittance was determined using a series of voltage chirps (4096 points each, resolution 24.4 Hz) superimposed onto holding potentials ranging from –160 to 160 mV, in 40 mV increments. 100 ms after each step to a new holding potential, 26 contiguous chirp-induced current responses at each holding potential were time-averaged. Real and imaginary components of the membrane admittance at all chirp frequencies were determined by FFT in jClamp, and corrected for the roll-off of recording system admittance^{13,24}. This correction controls for all attenuation and phase characteristics of the system, including the filter, as we have shown previously¹³, providing valid estimates of capacitance beyond the filter cut-off. Our dual-sine methodology permitted us to measure capacitance with high fidelity out to 20 kHz across holding potentials¹³. Here using single sine analysis we extend that to 30 kHz.

Our patch pipette inner tip diameters (see Results) were used to estimate the linear capacitance of membrane patches. We estimate a linear membrane patch capacitance of 187.8 ± 15.4 fF (n = 25). This was determined by estimating membrane patch hemispheric surface area using the standard value of 1 μF/cm²²⁵. In our presentation below, we provide absolute estimates of NLC, and specific estimates of NLC by dividing patch admittance with linear capacitance for each patch, thereby accounting for different patch size. Patch experiment data were accepted for inclusion if maximum NLC within our recording bandwidth was >150 fF. Complex values were first averaged for all average-based analyses. Plot traces are smoothed with a 6 point (150 Hz bandwidth) running average in Matlab.

In order to extract Boltzmann parameters, capacitance-voltage data were fit to the first derivative of a two-state Boltzmann function.

$$C_m = NLC + C_{sa} + C_{lin} = Q_{max} \frac{ze}{k_B T} \frac{b}{(1+b)^2} + C_{sa} + C_{lin} \quad (m1)$$

where

$$b = \exp\left(-ze \frac{V_m - V_h}{k_B T}\right), \quad C_{sa} = \frac{\Delta C_{sa}}{(1+b^{-1})}$$

Q_{max} is the maximum nonlinear charge moved, V_h is voltage at peak capacitance or equivalently, at half-maximum charge transfer, V_m is R_s -corrected membrane potential, z is valence, C_{lin} is linear membrane capacitance, e is electron charge, k_B is Boltzmann's constant, and T is absolute temperature. C_{sa} is a component of capacitance that characterizes sigmoidal changes in specific membrane capacitance^{12,26}. Functional prestin density in the membrane is based on quantity of sensor charge.

$$Q_{max} = \left[\frac{4 \cdot k_B \cdot T}{z \cdot e} \right] \cdot NLC_{Vh} \quad (m2)$$

$$Prestin \text{ density} = \frac{Q_{max}}{\text{patch surface area}} \quad (m3)$$

A power fit of NLC across frequency (f) was performed^{13,27}.

$$NLC(f) = NLC_0 + a * f^b \quad (m4)$$

where NLC_0 is the zero frequency component, and a and b control the frequency response.

Results

In our present study, we successfully recorded from 25 macro-patches on the OHC lateral membrane, where membrane breakdown did not occur; breakdown might be expected beyond our voltage protocol voltages²⁸. Our pipette inner tip diameter was 3.45 ± 0.15 μm. R_s of pipettes (under slight positive pressure) in bath prior to patching, determined by step voltages, was 1.34 ± 0.04 MΩ. However, this may not reflect series resistance following patch configuration. We therefore calculated R_s given a typical resistivity for pipette solutions of 100 ohm-cm²⁹, and our pipette taper angle of 0.2 rad; we calculate an R_s of about 920 kΩ. Since the patch membrane extends into the pipette where pipette diameter is larger, we further estimate a reduction of R_s to 735 kΩ. The difference in NLC frequency response provided between measured and calculated R_s were minimal, showing

a -2.2 dB reduction in NLC at 30 kHz for the directly measured values. Below we utilize the calculated value response.

The lateral membrane of the OHC is virtually devoid of voltage-dependent conductances¹¹, and we additionally use channel blockers to insure this. Our seal resistance, determined by linear fit of step induced currents within a linear region of the I-V between -40 and $+40$ mV, was 5.39 ± 0.65 G Ω .

Consequently, the macro-patch membrane, unlike the membrane in whole cell conditions, may be considered an isolated capacitor under voltage clamp, and thus amenable to determination of complex capacitance. In the following analysis of complex capacitance, we follow the methodology of Fernandez *et al.*³⁰, applied to each patch individually, based on its characteristics. The OHC patch capacitance presents as a parallel combination of linear (C_{lin}) and prestin-generated (NLC) capacitance. Conceivably, prestin's voltage-sensor may work as an imperfect, lossy capacitor that possesses both resistive (due to dielectric loss) and capacitive components (e.g., modelled as a combination of capacitor and resistor); that imperfection may influence estimates of NLC¹⁸. In addition to biophysical capacitance, system-generated stray capacitance (C_{stray}) will contribute to our measures. C_{stray} , though voltage-independent, may also possess resistive and capacitive components, its admittance being $Y_{stray}^*(\omega)$. Under voltage clamp, an AC voltage across the patch membrane (V_m) induces an AC current (I_m), where the admittance ($Y_m = I_m/V_m$) is a complex function of angular frequency, $\omega = 2\pi f$ and $i = \sqrt{-1}$

$$Y_m(\omega) = G_m(\omega) + iB_m(\omega) \quad (1)$$

with G_m representing membrane conductance, B_m representing membrane susceptance. Before continuing, we remove the effects of series resistance (R_s) by subtracting it from the real component of membrane impedance $Z_m(\omega)(1/Y_m(\omega))$, and then converting back to admittance³⁰. $Y_m(\omega)$ can be described in more detail,

$$Y_m(\omega) = G_m(\omega) + G_{leak} + Y_{stray}^*(\omega) + i\omega C_m(\omega) \quad (2)$$

where $C_m(\omega) = C_{lin} + \text{NLC}$.

G_{leak} represents a DC leakage conductance. C_{lin} is taken as frequency independent and via small signal analysis we seek to determine the frequency dependence of NLC, after removing $Y_{stray}^*(\omega)$. To our benefit, admittance at $+160$ mV lacks NLC¹²

$$Y_m^{160}(\omega) = G_m(\omega) + G_{leak} + Y_{stray}^*(\omega) + i\omega C_{lin} \quad (3)$$

Thus, subtraction of membrane admittance at $+160$ mV from those corresponding measures at all other holding potentials provides a differential admittance, $Y_m^*(\omega)$, devoid of stray capacitance effects.

$$Y_m^*(\omega) = Y_m(\omega) - Y_m^{160}(\omega) = G_m^*(\omega) + iB_m^*(\omega) \quad (4)$$

Actually, after subtraction, there remains a small differential residual nonlinear, voltage-dependent DC leakage conductance (G_{leak}), which we remove from $G_m^*(\omega)$ by subtraction of the real part of $Y_m^*(\omega)$ at zero frequency. We determine this value to subtract by extrapolating to zero frequency with a linear fit of $\text{Re}(Y_m^*(\omega))$ between 24.41 and 463.86 Hz at each of the stepped holding potentials. This is akin to removing leakage conductance determined by prior DC step estimates, but has the further advantage of being determined during the actual chirp stimulation period.

Complex membrane capacitance, a function of angular frequency, is defined as (see Fernandez *et al.*³⁰)

$$C_m^*(\omega) = \frac{Y_m^*(\omega)}{i\omega} = \frac{B_m^*(\omega)}{\omega} - i \frac{G_m^*(\omega)}{\omega} = C_m^*(\omega) - i C_m^{*''}(\omega) \quad (5)$$

In Fig. 1A, we plot the average capacitive (real, $C_m^*(\omega)$) and apparent conductance (imaginary, $C_m^{*''}(\omega)$) components of the complex capacitance for holding potentials of 40, 0, -40 and -80 mV. The values are voltage dependent. While the capacitive component is large and frequency dependent, the conductance component is smaller and less frequency dependent, differing from a larger component predicted from diffusion-based charge translocation¹⁸.

The absolute magnitude of the complex capacitance can be used to glean an estimate of membrane capacitance ($C_m^1(\omega)$),

$$C_m^1(\omega) = |C_m^*(\omega)| \quad (6)$$

In Fig. 1B, the absolute magnitude, $|C_m^*(\omega)|$, of the complex capacitance is plotted. The lower panel plots the phase angle. The magnitude rolls off continuously across frequency at each holding potential. In Fig. 1C, the data are plotted as a specific complex capacitance, i.e., per linear capacitance of the patches. As found in whole cell recordings, peak NLC can be larger than linear capacitance^{5,6}.

It is also possible to estimate capacitance of the macro-patch membrane by a "phase tracking" approach. That is, the phase angle of the complex admittance $Y_m^*(\omega)$ can be rotated to minimize its real component ($G_m^*(\omega)$), providing a new value (Y_m^{**}), whose imaginary component reflects the capacitive component (susceptance) of the admittance in the absence of conductance interference. Another estimate of membrane capacitance, $C_m^2(\omega)$, can then be obtained.

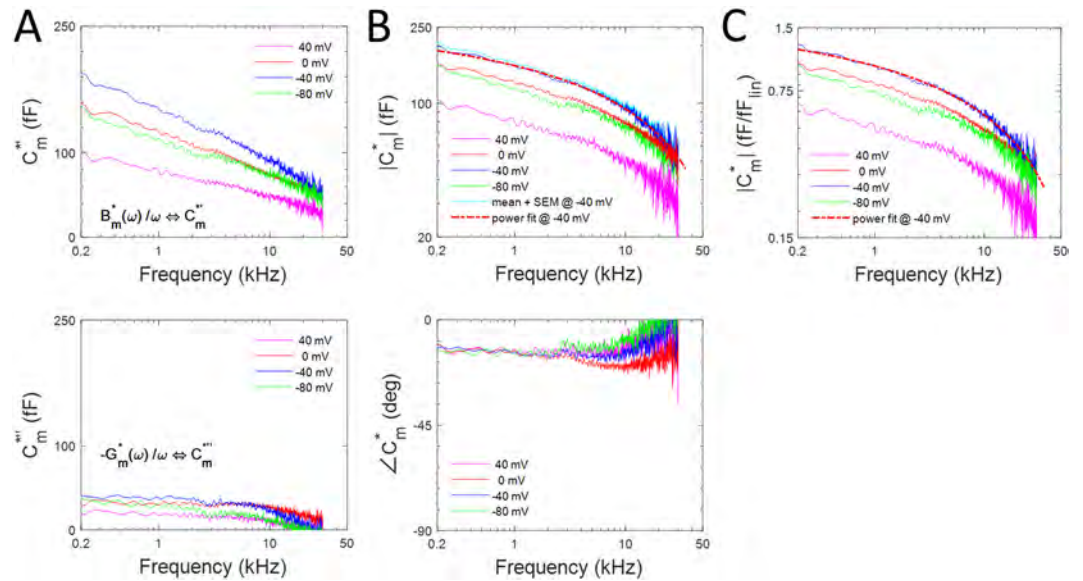


Figure 1. Complex capacitance of OHC lateral membrane macro-patches. (A) Top panel shows the mean real components of complex capacitance at selected holding potentials; bottom panel shows corresponding imaginary parts. (B) Top panel plots mean magnitudes of complex capacitance at different holding potentials. A power function fit of the magnitude at the -40 mV holding potential is shown by the dotted line (red) overlying the mean (dark blue line). The light blue line is the mean + SEM at that same holding potential data. Fit parameters: NLC_0 : 279.17 fF, a: -34.35 , b: 0.18. Bottom panel show the phase of complex capacitance. (C) Plot of the means of complex capacitance magnitude per estimated linear patch capacitance (see Methods). Fit parameters: NLC_0 : 1.71 fF, a: -0.19 , b: 0.19. Note low-pass behavior of magnitude functions.

$$\angle(Y_m^*(\omega)) = \text{atan}\left(\frac{B_m^*(\omega)}{G_m^*(\omega)}\right) \quad (7)$$

$$Y_m^{**} = Y_m^*(\omega) \cdot e^{-i\left(\angle(Y_m^*(\omega)) - \frac{\pi}{2}\right)} \quad (8)$$

$$C_m^2(\omega) = \frac{\text{Im}(Y_m^{**})}{\omega} \quad (9)$$

This approach is similar to traditional real time capacitance phase tracking under voltage clamp³¹, where the capacitive component at the angle of $\delta Y/\delta C_m$ ³² is obtained by adjusting the lock-in recording angle until the conductance component is minimized and the capacitive component is maximized. In that approach, calibration with a known capacitance provides membrane capacitance estimates at the measurement frequency. This approach to measure OHC patch NLC was used by Gale and Ashmore¹⁴.

In Fig. 2A, we plot the two estimates of OHC NLC [$C_m^1(\omega)$, and $C_m^2(\omega)$], corresponding to methods utilizing the complex capacitance magnitude, and the phase tracking approach, respectively – both at -40 mV holding potential (near V_h). The measures overlap, indicating that Eqs. 6 and 9 return the same result. In Fig. 2B, the voltage dependence of the complex capacitance magnitude at selected frequencies, presents a bell-shaped function typical of OHC NLC^{5,6}, whose peak precipitously decreases with frequency, but whose voltage at peak (V_h) remains similar across frequency. These data are fit (Eq. m1) to extract the Boltzmann parameters given in the legend. Prestin density based on fits to capacitance at 1 kHz is $1133/\mu\text{m}^2$, similar to previous estimates at a similar frequency^{8–10}.

Having arrived at practical approaches to estimate OHC patch NLC, we now look at the influence of membrane tension. Several studies under whole cell voltage clamp have found that as membrane tension is increased, NLC V_h shifts in the depolarizing direction, and decreases in peak magnitude^{15–17}. However, utilizing lock-in estimates of lateral membrane patch capacitance instead of the whole cell technique, Gale and Ashmore⁹ found no evidence for a reduction in peak capacitance despite shifts in the depolarizing direction.

In Fig. 3, we explore the effects of membrane tension on the magnitude, $|C_m^*(\omega)|$, of complex NLC across frequency, as it is a robust measure of NLC, equivalent to that obtained with the phase tracking approach. Results at 0, -4 , -8 and -10 mm Hg (i.e., 0, 0.53, 1.06 and 1.33 kPa) pipette pressure are shown in Fig. 3A–D, left panels. Membrane tension shifts V_h , as indicated by the rearrangement of the capacitance magnitude traces as negative pressure alters. For example, in left panel A, the trace at -80 mV (green) is above the trace at 0 mV (red), whereas in left panel D, the positions are reversed. In the right panels, plots of C-V functions of complex capacitance magnitude at the four different pipette pressures are shown (mean \pm SEM, $n = 8$). The depolarizing shift in V_h is

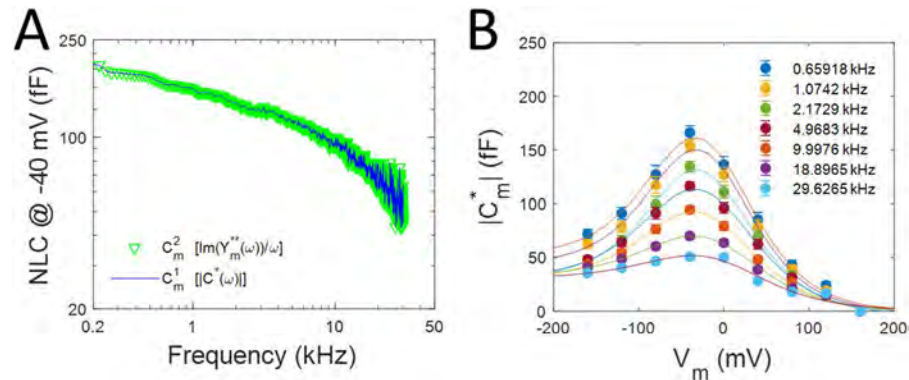


Figure 2. Comparison of two estimates of NLC frequency response at -40 mV holding potential. (A) Each estimate provides equivalent results. (B) C-V plot of complex capacitance magnitude of OHC lateral membrane macro-patches at selected frequencies (mean \pm SEM). Data are fit (Eq. m1) to extract Boltzmann parameters (see Methods). -40 mV is close to V_h . From lowest to highest frequency fit values are (peak NLC, V_h , z): 133.60, 127.61, 115.42, 98.81, 76.81, 52.60, 34.35 fF; -25.2 , -25.3 , -26.0 , -26.4 , -26.9 , -20.6 , -16.4 mV; 0.61, 0.62, 0.62, 0.57, 0.59, 0.56, 0.54. Prior to averaging patch responses ($n = 25$), capacitance values from each patch were obtained by averaging over a bandwidth of about 200 Hz about the listed frequency value.

readily apparent as negative pressure increases (red bars). There is little change in peak capacitance, however. ΔC_{sa} is mainly unaffected by tension.

For comparison of frequency dependence as a function of membrane tension, Fig. 4A replots the peak magnitude traces (-40 mV) from Fig. 3 at the different pipette pressures. The frequency response of complex capacitance magnitude is unaffected by membrane tension, indicated by the overlap of traces. The sensitivity of patch V_h shift to tension was 24.1 mV/kPa based on our fits (Fig. 4B).

We previously measured OHC NLC in macro-patches using a dual-sinusoidal methodology¹³. In Fig. 5, we replot selected NLC_{v_h} data points from that study (yellow circles) alongside NLC_{v_h} data (green circles) from Gale and Ashmore¹⁴. We also plot whole cell data on NLC_{v_h} (rat, mouse and guinea pig) from previous studies that used either the phase-tracking approach or 2-sine methodology. These scaled whole cell data interrogated a frequency bandwidth extending to 5 kHz, and closely follow the attenuation of patch NLC within that bandwidth. The Gale and Ashmore data (green circles, SEM, and fit from their Fig. 3B; in green) are also scaled ($\times 3.5$) to overlie our data. Their measures were made with a lock-in amplifier using a 100 fF calibration at each frequency. Scaling to our data was necessary because our average patch size/capacitance was greater than theirs. As is evident, our previous data intersects their data points, indicating an acceptable correspondence. Finally, extraction of NLC_{v_h} from our new measures (red circles) of patch absolute complex capacitance (from Fig. 3, scaled $\times 1.05$) corresponds well to our previous observations and theirs. We emphasize that the absolute magnitude of complex capacitance ($C_m^1(\omega)$) is equivalent to our phase tracking approach ($C_m^2(\omega)$) to estimate capacitance (Fig. 2), each corresponding to the estimates provided by the traditional phase tracking method³³ employed by Gale and Ashmore¹⁴. In the discussion, despite their assertions, we detail how Gale and Ashmore's data points above their 60 kHz amplifier cut-off are actually valid data points depicting NLC_{v_h}. Capitalizing on the validity of their high frequency data, we combine all three patch data sets in the plot to arrive at a unified power function fit ($r^2 = 0.97$) of NLC_{v_h} across frequency (solid magenta line), which shows precipitous roll-off of sensor charge movement relative to voltage drive. Fitted parameters are NLC₀: 185.2 fF, a : -7.22 , and b : 0.28. At 77 kHz, NLC_{v_h} is 40 dB down from NLC₀. Furthermore, since each method takes into account the dielectric loss in prestin, we conclude that this dielectric loss does not significantly account for the low-pass nature of prestin charge movement. To further substantiate this claim, we make another estimate of membrane capacitance, $C_m^3(\omega)$, one that does not take into account dielectric loss, but is appropriate for a loss-less capacitor.

$$C_m^3(\omega) = \frac{\text{Im}(Y_m^*(\omega))}{\omega} = \frac{B_m^*(\omega)}{\omega} \quad (10)$$

Figure 6 shows the results for our three estimates of prestin capacitance [$C_m^1(\omega)$, $C_m^2(\omega)$ and $C_m^3(\omega)$], all reasonably overlying each other, and exhibiting low-pass behavior. Thus, all results available to date show an unusually low-pass behavior of prestin voltage-sensor performance, with little influence of dielectric loss.

Discussion

We previously evaluated OHC macro-patch NLC frequency dependence utilizing a dual-sine methodology that worked on extracted prestin displacement currents¹³. That approach did not allow separation of real and imaginary components of NLC. Here we provide an analysis of OHC NLC in membrane macro-patches utilizing single sine methods that have been used to characterize gating charge movements in other voltage-dependent proteins³⁰, where real (capacitive) and imaginary ("resistive", representing dielectric loss) components of sensor charge are separated. We explored these alternative approaches in order to determine whether new estimates of NLC frequency response incorporating the influence of dielectric loss would substantially alter our previous estimates,

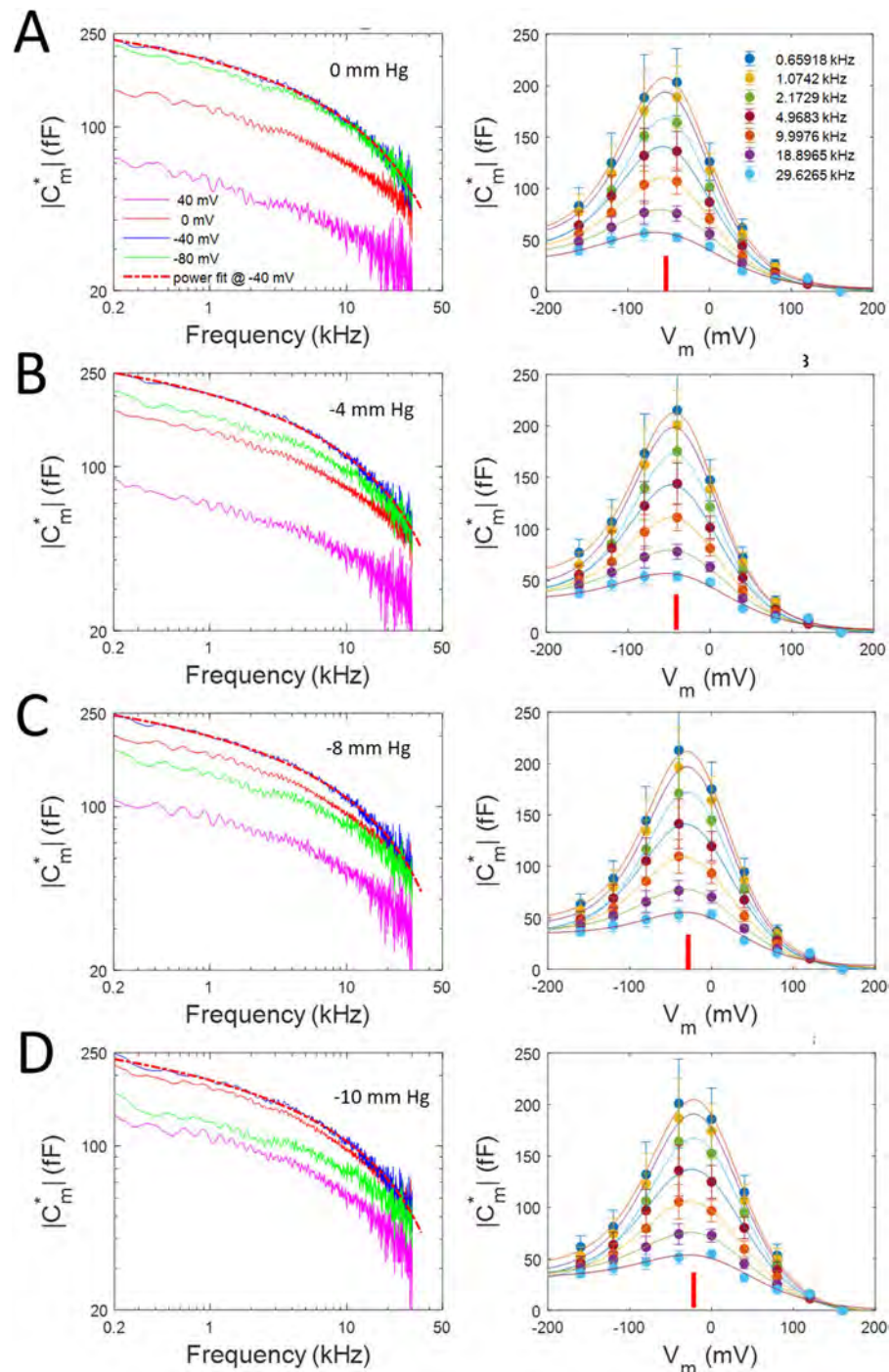


Figure 3. Effect of membrane tension on magnitude of complex capacitance voltage and frequency dependence. Panels (A–D) depict results at 0, –4, –8 and –10 mm Hg pipette pressure. The effect of membrane tension is to shift V_h , as indicated by the change in voltage at maximal capacitance as negative pressure increases, without appreciably altering frequency response (dotted lines are fits to a power function). On the right, C–V plots of complex capacitance magnitude at the four different pipette pressures are shown. Red bars indicate voltage at peak capacitance. The depolarizing shift in V_h is readily apparent as pressure increases. Peak magnitudes do not appreciably alter. ΔC_{ss} is tension and frequency independent. Mean \pm SEM ($n=8$). From lowest to highest frequency fit values from Eq. m1 are (peak NLC, V_h , z): Panel A, 179.15, 166.45, 146.43, 120.30, 88.90, 62.62, 41.51 fF; –49.4, –49.0, –49.0, –50.9, –49.0, –48.2, –51.2 mV; 0.70, 0.71, 0.71, 0.66, 0.70, 0.58, 0.53; Panel B, 182.80, 175.62, 153.91, 124.40, 91.56, 60.38, 39.08 fF; –38.5, –40.0, –39.4, –40.7, –39.4, –36.4, 35.8 mV; 0.74, 0.72, 0.72, 0.67, 0.66, 0.60, 0.57. Panel C, 187.73, 175.16, 155.35, 124.08, 90.68, 57.97, 34.77 fF; –25.9, –25.7, –25.7, –26.2, –26.0, –20.6, –14.5 mV; 0.73, 0.73, 0.72, 0.67, 0.66, 0.62, 0.65. Panel D, 185.03, 175.67, 156.00, 124.51, 91.22, 58.39, 36.32, fF; –17.2, –17.7, –18.0, –18.1, –8.8, –12.3, –8.0 mV; 0.67, 0.66, 0.66, 0.61, 0.60, 0.58, 0.55.

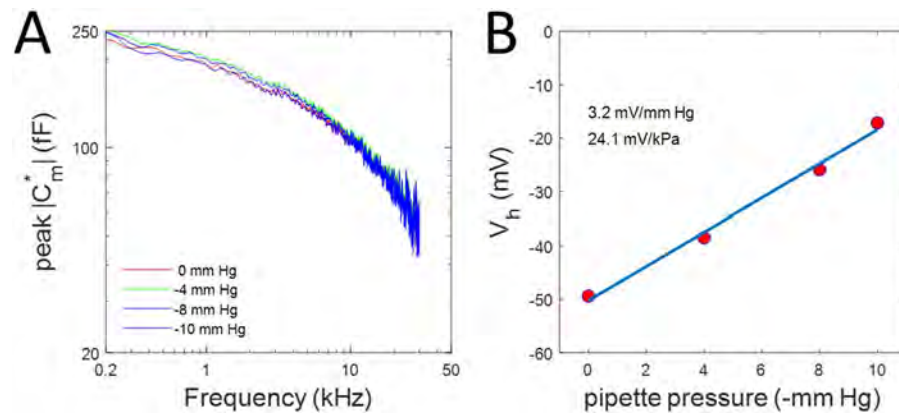


Figure 4. Effects of membrane tension on NLC frequency response and operating voltage. **(A)** Comparison of NLC frequency response at -40 mV at four pipette pressures. Roll-off is equivalent as indicated by overlap of traces. **(B)** V_h of NLC at the lowest frequency in Fig. 3 is plotted versus pipette pressure. A linear fit (blue line) indicates a sensitivity of 24.1 mV/kPa.

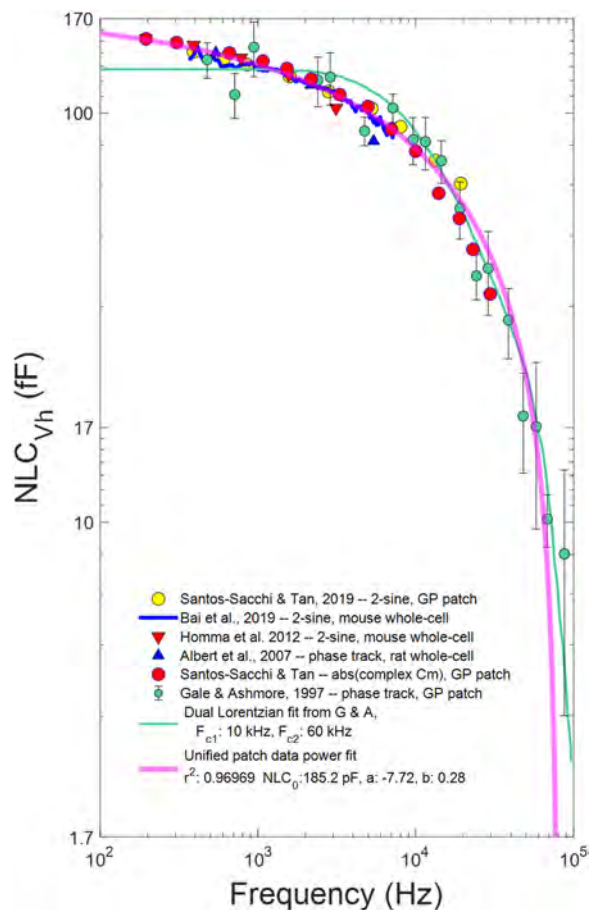


Figure 5. Replot of some whole-cell NLC data^{27,45,46}, and NLC patch data from Santos-Sacchi and Tan¹³ with those of Gale and Ashmore¹⁴. Using a dual-sine capacitance estimation algorithm, NLC of OHC patches (yellow circles) overlie the data of Gale and Ashmore, collected with a traditional phase tracking approach using a lock-in amplifier (data: green circles; their fit green solid line). Whole cell data, both 2-sine and phase-tracking, show a similar frequency response within their interrogation bandwidth. Finally, NLC_{Vh} (red symbols) obtained from Eq. m1 fits of our complex capacitance data (obtained as in Fig. 2B) are also commensurate with previous observations, giving a unified power fit for the patch data (magenta line; see Discussion) with parameters NLC_0 : 185.2 fF, a : -7.22 , b : 0.28.

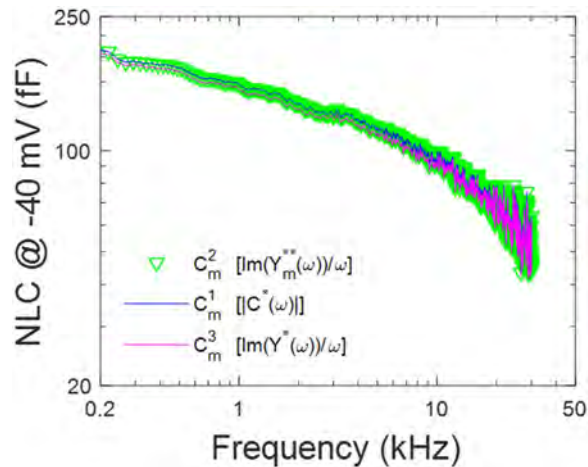


Figure 6. Three estimates of the frequency response of NLC at -40 mV holding potential. Estimates from raw admittance data (pink line) reasonably compare with the other estimates despite the fact that the real component is not taken into account.

as was predicted through modelling¹⁸. This is not the case, however. Thus, the bulk of prestin charge movement appears to move in phase with voltage, and the small dielectric loss that we find does not significantly influence measures of OHC NLC frequency response.

It was previously noted that low frequency determined OHC NLC (C-V) measures are unable to identify whether prestin charge movement is multistate/diffusional in nature^{8,34}. However, wide-band frequency interrogation of prestin NLC may provide clues. In this regard, the large bell-shaped (across frequency) resistive component of complex capacitance, which is associated with DPA^- voltage-driven translocation through bulk membrane lipid³⁵, and which Sun *et al.*¹⁸ predicted for prestin modelled as a simple diffusion process of charge translocation is not found here. The resistive component we measure is relatively small and flat across frequency (Fig. 1A, lower panel). This is likely because prestin charge movement is not a diffusional process, but instead similar to gating charge movement in other membrane proteins. Thus, Fernandez *et al.*³⁶ found that whereas chloroform, which alters membrane viscosity, can influence the speed of DPA^- charge translocation within the membrane, Na channel voltage-sensor charge translocation speed is not affected. Similarly, sensor charge in prestin is likely constrained to charged protein residues that move during protein conformational change³⁷. Indeed, Sun *et al.*'s model included membrane diffusion of chloride ions as voltage sensors in prestin. However, chloride anions do not solely function as extrinsic voltage sensors for prestin, nor do they move through bulk lipid; instead they likely influence prestin kinetics^{13,38,39} (also see our comment #1 on Walter *et al.* eLife 8, 2019 - <https://elifesciences.org/articles/46986>)⁴⁰.

Prestin's voltage operating range, whose midpoint is at V_h , is very sensitive to membrane tension¹⁵. Here, we measured the effect of membrane tension on prestin performance by changing patch pipette pressure to study its influence on NLC frequency response. The average sensitivity of patch V_h shift to tension was 24.1 mV/kPa, which corresponds well to our previous measures¹⁷ in whole cell mode of 21.6 mV/kPa. Adachi *et al.*⁴¹ found similar sensitivity in whole cell mode (27.5 mV/kPa). Gale and Ashmore⁹, in their patches, found a somewhat smaller sensitivity of 11.1 mV/kPa. In prestin transfected cells, values of near 4 mV/kPa were found^{42,43}. One mechanism whereby shifts in V_h might occur would be due to changes in the ratio of transition rates between its conformational states. Naturally, if this were occurring then changes in NLC frequency response might arise. We found no change in NLC magnitude, similar to results of Gale and Ashmore⁹, or frequency response during alterations in membrane tension, and conclude that tension is not altering transition rates. Indeed, we previously found that membrane tension in whole cell mode did not significantly alter the phase or frequency response of electromotility⁴⁴. This is in contrast to salicylate which likely alters transition rates since NLC frequency response is affected¹³.

Lastly, we revisited the seminal patch data of Gale and Ashmore¹⁴, along with those whole-cell NLC measures of others^{27,45,46}, and recast our current and previous patch data¹³ with those prior results on OHC NLC. The small variability within our current and previous patch NLC data set allowed us to identify a power dependence of frequency, whereas Gale and Ashmore originally applied a Lorentzian fit. Their interpretation of NLC frequency response requires re-examination. They asserted that their capacitance measures made above their amplifier's 60 kHz cut-off frequency were inaccurate, being unduly reduced by this cut-off. However, the amplifier's transfer function effect on the phase tracking approach^{24,31,33} is inconsequential, since the lock-in phase is adjusted to maximize the imaginary (capacitive) component and minimize the real (resistive) component of the recorded signal. That is, the phase shift due to the amplifier was eliminated, and amplifier attenuation was corrected by their 100 pF calibration. Thus, their small-signal capacitance measurement was truly that of the patch membrane (and possibly non-voltage dependent stray capacitance), but when fitted by a Boltzmann derivative across voltage, provided valid, *not invalid*, estimates of voltage-dependent OHC NLC *above the amplifier cut-off*. Consequently, their fit to OHC NLC data at V_h , which included the amplifier roll-off component, actually provided a dual-Lorentzian evaluation of OHC NLC, and their conclusion that only the lower frequency Lorentzian component of the fit

fully characterized the behavior of OHC NLC (10 kHz cut-off) was misplaced. Furthermore, their interpretation suggested that OHC NLC roll-off is 6 dB/octave, when, in fact, roll-off is more than double that at high frequencies and is actually frequency dependent. Finally, the proposed inaccuracies in their high frequency estimates provided leeway to dismiss low-pass NLC indications of electromechanical behavior in favor of eM measures that were flat beyond 80 kHz⁴⁷, the latter driving our concept of OHC eM's wideband influence on cochlear amplification over the last couple of decades. In addition to all of our frequency evaluations of OHC NLC, past^{13,20,23,48,49} and present, recent eM measures, *in vitro* and *in vivo*, have challenged that concept^{20,44,48,50}.

In summary, Fig. 5 shows that a power function fit to all patch data to-date reasonably describes the roll-off in NLC_{V_h} . This unifying observation highlights an inability of voltage to sufficiently drive prestin electromechanical activity at very high frequencies (60–160 kHz), where CA (cochlear amplification) is known or expected to exist. The additional low pass influence of external loads on the whole cell eM frequency response and the frequency-dependent RC membrane time constant that we characterized recently⁴⁸, also lessens the effectiveness of voltage-dependent eM in influencing organ of Corti motion at very high frequencies. This point is further emphasized by experiments showing that perilymphatic perfusion of 5 mM salicylate or its congener is devastating to CA^{51,52}. Considering the 1.6 mM $K_{1/2}$ of salicylate action, the effect of the perilymphatic treatment is not a full block of NLC, but rather about 75% (12 dB) reduction⁵³. Thus, the reduction in NLC resulting from its power frequency dependence (12 dB down at 25 kHz, 20 dB down at 53 kHz, and 40 dB down at 77 kHz; Fig. 5) likely has biological impact across the full auditory frequency spectrum of mammals, and indicates a continuously diminishing influence of voltage alone to drive prestin electromechanical activity and CA via a cycle-by-cycle means. As a caveat, it may be possible that at any given frequency the measured NLC/eM amplitude is sufficient to drive CA, as we implied previously^{20,54}, and that a reduction in CA that might occur with salicylate could be working on the existent magnitude at that particular frequency.

Two additional issues need to be addressed. They are temperature dependence, and species dependence of NLC frequency response. It is likely that temperature dependence of NLC frequency response is not so great (Q_{10} of 1.33), as Gale and Ashmore (1997) have directly attested to in membrane patches. We had previously argued that because V_h is highly temperature sensitive^{55,56}, the kinetics of prestin should be, as well – we estimated a Q_{10} of 2 based on modelling of V_h shifts observed in IR temperature jump experiments⁵⁷. But, since we now find that membrane tension does not influence prestin kinetics, in spite of shifts in V_h , it is possible that temperature-induced shifts, likewise, work not through kinetics, but by some other means. Given that one-half magnitude NLC is at 7 kHz (from the power fit, Fig. 5), a Q_{10} of 1.33 would increase the cut-off to only about 10 kHz. Concerning species specificity, the data so far do not support such differences, since rat, mouse and guinea pig show similar frequency responses (see Fig. 5). Whether genetic variations in prestin that have been observed in mammals that capitalize on very high frequency detection^{58,59} could change this view remains possible, and we need to test these species. Currently, however, how CA is driven by OHCs in the basal high frequency turn of mammals that enjoy perception of sound above 60 kHz is an enigma.

Received: 6 February 2020; Accepted: 26 March 2020;

Published online: 10 April 2020

References

- Zheng, J. *et al.* Prestin is the motor protein of cochlear outer hair cells. *Nature* **405**, 149–155 (2000).
- Santos-Sacchi, J. & Dilger, J. P. Whole cell currents and mechanical responses of isolated outer hair cells. *Hear. Res.* **35**, 143–150 (1988).
- Kachar, B., Brownell, W. E., Altschuler, R. & Fex, J. Electrokinetic shape changes of cochlear outer hair cells. *Nature* **322**, 365–368 (1986).
- Liberman, M. C. *et al.* Prestin is required for electromotility of the outer hair cell and for the cochlear amplifier. *Nature* **419**, 300–304 (2002).
- Santos-Sacchi, J. Reversible inhibition of voltage-dependent outer hair cell motility and capacitance. *J. Neurosci.* **11**, 3096–3110 (1991).
- Ashmore, J. F. Forward and reverse transduction in the mammalian cochlea. *Neurosci. Res. Suppl.* **12**, S39–S50 (1990).
- Santos-Sacchi, J. Fast outer hair cell motility: how fast is fast? in *The Mechanics and Biophysics of Hearing* (eds Dallos, P. *et al.*) 69–75 (Springer-Verlag, 1990).
- Huang, G. & Santos-Sacchi, J. Mapping the distribution of the outer hair cell motility voltage sensor by electrical amputation. *Biophys. J.* **65**, 2228–2236 (1993).
- Gale, J. E. & Ashmore, J. F. The outer hair cell motor in membrane patches. *Pflugers Arch.* **434**, 267–271 (1997).
- Mahendrasingam, S., Beurg, M., Fettiplace, R. & Hackney, C. M. The ultrastructural distribution of prestin in outer hair cells: a post-embedding immunogold investigation of low-frequency and high-frequency regions of the rat cochlea. *Eur. J. Neurosci.* **31**, 1595–1605, doi:EJN7182 [pii];10.1111/j.1460-9568.2010.07182.x [doi] (2010).
- Santos-Sacchi, J., Huang, G. J. & Wu, M. Mapping the distribution of outer hair cell voltage-dependent conductances by electrical amputation. *Biophys. J.* **73**, 1424–1429 (1997).
- Santos-Sacchi, J. & Navarrete, E. Voltage-dependent changes in specific membrane capacitance caused by prestin, the outer hair cell lateral membrane motor. *Pflugers Arch.* **444**, 99–106 (2002).
- Santos-Sacchi, J. & Tan, W. Voltage Does Not Drive Prestin (SLC26a5) Electro-Mechanical Activity at High Frequencies Where Cochlear Amplification Is Best. *iScience* **22**, 392–399, <https://doi.org/10.1016/j.isci.2019.11.036> (2019).
- Gale, J. E. & Ashmore, J. F. An intrinsic frequency limit to the cochlear amplifier. *Nature* **389**, 63–66 (1997).
- Iwasa, K. H. Effect of stress on the membrane capacitance of the auditory outer hair cell. *Biophys. J.* **65**, 492–498 (1993).
- Gale, J. E. & Ashmore, J. F. Charge displacement induced by rapid stretch in the basolateral membrane of the guinea-pig outer hair cell. *Proc. R. Soc. Lond. B. Biol. Sci.* **255**, 243–249 (1994).
- Kakehata, S. & Santos-Sacchi, J. Membrane tension directly shifts voltage dependence of outer hair cell motility and associated gating charge. *Biophys. J.* **68**, 2190–2197 (1995).
- Sun, S. X. *et al.* Voltage and frequency dependence of prestin-associated charge transfer. *J. Theor. Biol.* **260**, 137–144, doi:S0022-5193(09)00231-8 [pii];10.1016/j.jtbi.2009.05.019 [doi] (2009).
- Ratnanather, J., Brownell, W. & Popel, A. Mechanical properties of the outer hair cell. *Biophysics of hair cell sensory systems*, 199–206 (1993).

20. Santos-Sacchi, J. & Tan, W. The Frequency Response of Outer Hair Cell Voltage-Dependent Motility Is Limited by Kinetics of Prestin. *J. Neurosci.* **38**, 5495–5506, <https://doi.org/10.1523/JNEUROSCI.0425-18.2018> (2018).
21. Wu, M. & Santos-Sacchi, J. Effects of lipophilic ions on outer hair cell membrane capacitance and motility. *J. Membr. Biol.* **166**, 111–118 (1998).
22. Dallos, P., Evans, B. N. & Hallworth, R. Nature of the motor element in electrokinetic shape changes of cochlear outer hair cells. *Nature* **350**, 155–157 (1991).
23. Santos-Sacchi, J. & Song, L. Chloride anions regulate kinetics but not voltage-sensor Qmax of the solute carrier SLC26a5. *Biophys. J.* **110**, 1–11 (2016).
24. Gillis, K. D. Techniques for Membrane Capacitance Measurements In *Single Channel Recording* (eds. Sakmann, B. & Neher, E.) Ch. 7, 155–198 (Plenum Press, 1995).
25. Hille, B. *Ionic channels of excitable membranes*. 2nd edn, (Sinauer Associates, 1992).
26. Santos-Sacchi, J. & Song, L. Chloride and Salicylate Influence Prestin-Dependent Specific Membrane Capacitance: Support for the Area Motor Model. *J Biol Chem*, <https://doi.org/10.1074/jbc.M114.549329> (2014).
27. Bai, J. P., Navaratnam, D. & Santos-Sacchi, J. Prestin kinetics and corresponding frequency dependence augment during early development of the outer hair cell within the mouse organ of Corti. *Sci. Rep* **9**, 16460, <https://doi.org/10.1038/s41598-019-52965-1> (2019).
28. Navarrete, E. G. & Santos-Sacchi, J. On the effect of prestin on the electrical breakdown of cell membranes. *Biophys. J.* **90**, 967–974 (2006).
29. Mathias, R. T., Cohen, I. S. & Oliva, C. Limitations of the whole cell patch clamp technique in the control of intracellular concentrations. *Biophys. J.* **58**, 759–770, [https://doi.org/10.1016/S0006-3495\(90\)82418-8](https://doi.org/10.1016/S0006-3495(90)82418-8) (1990).
30. Fernandez, J. M., Bezanilla, F. & Taylor, R. E. Distribution and kinetics of membrane dielectric polarization. II. Frequency domain studies of gating currents. *J. Gen. Physiol* **79**, 41–67 (1982).
31. Fidler, N. & Fernandez, J. M. Phase tracking: an improved phase detection technique for cell membrane capacitance measurements. *Biophys. J.* **56**, 1153–1162, [https://doi.org/10.1016/S0006-3495\(89\)82762-6](https://doi.org/10.1016/S0006-3495(89)82762-6) (1989).
32. Santos-Sacchi, J. Determination of cell capacitance using the exact empirical solution of dY/dCm and its phase angle. *Biophys. J.* **87**, 714–727 (2004).
33. Neher, E. & Marty, A. Discrete changes of cell membrane capacitance observed under conditions of enhanced secretion in bovine adrenal chromaffin cells. *Proc. Natl. Acad. Sci. USA.* **79**, 6712–6716 (1982).
34. Scherer, M. P. & Gummer, A. W. How many states can the motor molecule, prestin, assume in an electric field? *Biophys. J.* (2005).
35. Lu, C. C. *et al.* Membrane transport mechanisms probed by capacitance measurements with megahertz voltage clamp. *Proc. Natl. Acad. Sci. USA.* **92**, 11220–11224 (1995).
36. Fernandez, J. M., Bezanilla, F. & Taylor, R. E. Effect of chloroform on charge movement in the nerve membrane. *Nature* **297**, 150–152, <https://doi.org/10.1038/297150a0> (1982).
37. Bai, J. P. *et al.* Prestin's anion transport and voltage-sensing capabilities are independent. *Biophys. J.* **96**, 3179–3186, doi:S0006-3495(09)00470-6 [pii];10.1016/j.bpj.2008.12.3948 [doi] (2009).
38. Song, L. & Santos-Sacchi, J. Conformational state-dependent anion binding in prestin: evidence for allosteric modulation. *Biophys. J.* **98**, 371–376, doi:S0006-3495(09)01669-5 [pii];10.1016/j.bpj.2009.10.027 [doi] (2010).
39. Rybalchenko, V. & Santos-Sacchi, J. Allosteric modulation of the outer hair cell motor protein prestin by chloride. In *Biophysics of the Cochlea: From Molecules to Models* (ed. Gummer, A.) 116–126 (World Scientific Publishing, 2003).
40. Walter, J. D., Sawicka, M. & Dutzler, R. Cryo-EM structures and functional characterization of murine Slc26a9 reveal mechanism of uncoupled chloride transport. *Elife* **8**, <https://doi.org/10.7554/eLife.46986> (2019).
41. Adachi, M., Sugawara, M. & Iwasa, K. H. Effect of turgor pressure on outer hair cell motility. *J. Acoust. Soc. Am.* **108**, 2299–2306 (2000).
42. Ludwig, J. *et al.* Reciprocal electromechanical properties of rat prestin: The motor molecule from rat outer hair cells. *Proc. Natl. Acad. Sci. U. S. A.* **98**, 4178–4183 (2001).
43. Santos-Sacchi, J., Shen, W., Zheng, J. & Dallos, P. Effects of membrane potential and tension on prestin, the outer hair cell lateral membrane motor protein. *J. Physiol* **531**, 661–666 (2001).
44. Santos-Sacchi, J. & Song, L. Chloride-driven Electromechanical Phase Lags at Acoustic Frequencies Are Generated by SLC26a5, the Outer Hair Cell Motor Protein. *Biophys. J.* **107**, 126–133, <https://doi.org/10.1016/j.bpj.2014.05.018> (2014).
45. Homma, K., Duan, C., Zheng, J., Cheatham, M. A. & Dallos, P. The V499G/Y501H mutation impairs fast motor kinetics of prestin and has significance for defining functional independence of individual prestin subunits. *J Biol Chem* **288**, 2452–2463, <https://doi.org/10.1074/jbc.M112.411579> (2013).
46. Albert, J. T. *et al.* Voltage-sensitive prestin orthologue expressed in zebrafish hair cells. *J. Physiol* **580**, 451–461 (2007).
47. Frank, G., Hemmert, W. & Gummer, A. W. Limiting dynamics of high-frequency electromechanical transduction of outer hair cells. *Proc. Natl. Acad. Sci. U. S. A.* **96**, 4420–4425 (1999).
48. Santos-Sacchi, J., Iwasa, K. H. & Tan, W. Outer hair cell electromotility is low-pass filtered relative to the molecular conformational changes that produce nonlinear capacitance. *J. Gen. Physiol.* **151**, 1369–1385, <https://doi.org/10.1085/jgp.201812280> (2019).
49. Santos-Sacchi, J. High frequency measures of OHC nonlinear capacitance (NLC) and their significance: Why measures stray away from predictions. *AIP Conference Proceedings* 1965, 060004–060001–060004–060005, <https://doi.org/10.1063/1.5038477> (2018).
50. Vavakou, A., Cooper, N. P. & van der Heijden, M. The frequency limit of outer hair cell motility measured *in vivo*. *Elife* **8**, <https://doi.org/10.7554/eLife.47667> (2019).
51. Santos-Sacchi, J., Song, L., Zheng, J. F. & Nuttall, A. L. Control of mammalian cochlear amplification by chloride anions. *J. Neurosci.* **26**, 3992–3998, <https://doi.org/10.1523/jneurosci.4548-05.2006> (2006).
52. Fisher, J. A., Nin, F., Reichenbach, T., Uthaiha, R. C. & Hudspeth, A. J. The spatial pattern of cochlear amplification. *Neuron* **76**, 989–997, doi:S0896-6273(12)00885-9 [pii];10.1016/j.neuron.2012.09.031 [doi] (2012).
53. Kakehata, S. & Santos-Sacchi, J. Effects of salicylate and lanthanides on outer hair cell motility and associated gating charge. *J. Neurosci.* **16**, 4881–4889 (1996).
54. Santos-Sacchi, J. The speed limit of outer hair cell electromechanical activity. *HNO* **67**, 159–164, <https://doi.org/10.1007/s00106-019-0615-9> (2019).
55. Santos-Sacchi, J., Meltzer, J. & Folkinshteyn, D. Temperature dependence of prestin's nonlinear capacitance. *Society for Neuroscience Abstracts* **27**, 1053–1053 (2001).
56. Santos-Sacchi, J. & Huang, G. Temperature dependence of outer hair cell nonlinear capacitance. *Hear. Res.* **116**, 99–106 (1998).
57. Okunade, O. & Santos-Sacchi, J. IR laser-induced perturbations of the voltage-dependent solute carrier protein SLC26a5. *Biophys. J.* **105**, 1822–1828, <https://doi.org/10.1016/j.bpj.2013.09.008> (2013).
58. Liu, Z., Qi, F. Y., Zhou, X., Ren, H. Q. & Shi, P. Parallel sites implicate functional convergence of the hearing gene prestin among echolocating mammals. *Mol. Biol. Evol.* **31**, 2415–2424, <https://doi.org/10.1093/molbev/msu194> (2014).
59. Davies, K. T., Cotton, J. A., Kirwan, J. D., Teeling, E. C. & Rossiter, S. J. Parallel signatures of sequence evolution among hearing genes in echolocating mammals: an emerging model of genetic convergence. *Heredity (Edinb.)* **108**, 480–489, doi:hdy2011119 [pii];10.1038/hdy.2011.119 [doi] (2012).

Acknowledgements

This research was supported by NIH-NIDCD R01 DC000273, R01 DC016318 and R01 DC008130 to J.S.-S. We thank Fred Sigworth for confirming our conclusions that the phase tracking approach to capacitance measurement is insensitive to patch clamp amplifier roll-off.

Author contributions

J.S.S. wrote the paper, designed and performed experiments and analyzed data. W.T. edited manuscript, performed experiments and analyzed data.

Competing interests

The authors declare no competing interests.

Additional information

Correspondence and requests for materials should be addressed to J.S.-S.

Reprints and permissions information is available at www.nature.com/reprints.

Publisher's note Springer Nature remains neutral with regard to jurisdictional claims in published maps and institutional affiliations.



Open Access This article is licensed under a Creative Commons Attribution 4.0 International License, which permits use, sharing, adaptation, distribution and reproduction in any medium or format, as long as you give appropriate credit to the original author(s) and the source, provide a link to the Creative Commons license, and indicate if changes were made. The images or other third party material in this article are included in the article's Creative Commons license, unless indicated otherwise in a credit line to the material. If material is not included in the article's Creative Commons license and your intended use is not permitted by statutory regulation or exceeds the permitted use, you will need to obtain permission directly from the copyright holder. To view a copy of this license, visit <http://creativecommons.org/licenses/by/4.0/>.

© The Author(s) 2020

RAPID COMMUNICATION

Potentialiation of the cGMP-Induced Guinea Pig Acrosome Reaction by Zinc

JOSEPH SANTOS-SACCHI, MILDRED GORDON, AND WILLIAM L. WILLIAMS
School for Biomedical Education, The City College, New York, NY 10031 (J.S.-S., M.G.), and Population Council, Center for Biomedical Research, Rockefeller University, New York, NY 10021 (W.L.W.)

ABSTRACT The addition of 8 bromo cGMP (10 mM) immediately (~2 min) upon suspension of Guinea pig sperm in glucose-free BWW medium induces a significant number of acrosome reactions within minutes. The simultaneous addition of micromolar concentrations of $ZnCl_2$ (25–1000 μM) potentiates the cGMP effects. Mid-micromolar concentrations were able to dramatically increase the percentage of acrosome reactions by a factor of 6.5 over 8 bromo cGMP alone. The induction of acrosome reactions was dependent upon external Ca^{++} , and it is suggested that in this species Zn^{++} functions by affecting cyclic nucleotide metabolism and/or Ca^{++} flux.

Considerable attention has been focused upon the role of Zn^{++} in sperm metabolism. For example, it has been shown that removal of bound Zn^{++} from human sperm increases both oxygen uptake and motility (Huacuja et al., '73), whereas incubation of sperm with Zn^{++} reduces motility (Holland et al., '76). Johnsen and Eliasson ('78) have demonstrated that a reduction of membrane-associated Zn^{++} promotes membrane destabilization in human sperm, as indicated by an increased susceptibility to lipid peroxidation. Results such as these have led some workers to speculate that spermatozoal Zn^{++} depletion may be involved in the capacitation process (Johnsen and Eliasson, '76, '78) and, indeed, some evidence exists in support of this. Aonuma et al. ('78) have shown that mouse sperm preincubated with zinc (250 μM) are unable to fertilize eggs, and by experimental manipulation they related the zinc effects to an inhibition of capacitation. Williams and Lenz ('79) showed that zinc salts were effective vaginal contraceptives in the rabbit. Meizel and Lui ('76) determined that incubation of hamster sperm with zinc (250 μM) as well as synthetic trypsin inhibitors, (Lui and Meizel, '79) dramatically inhibited the acrosome reaction (AR). Thus, zinc may well influence the critical events necessary for egg penetration.

Recently, Santos-Sacchi and Gordon ('80) have demonstrated that the Guinea pig sperm acrosome reaction can be induced by exoge-

nous cyclic guanosine monophosphate (cGMP) analogues, and they suggested that a rise in the cGMP/cAMP ratio is the critical effector of the AR. Because Zn^{++} has been shown to inhibit adenylate cyclase in human sperm (Haesungcharern and Chulavatnatol, '78), it seemed worthwhile to study the effects of zinc upon the cGMP-induced Guinea pig acrosome reaction.

MATERIALS AND METHODS

Guinea pig cauda epididymal spermatozoa were extruded into 0.9% NaCl in H_2O , disaggregated by pipetting, and washed two times by centrifugation (1,000 g, 4 min each). Spermatozoa were then suspended in glucose-free BWW medium (NaCl 94.59 mM, KCl 4.7 mM, $CaCl_2$ 1.71 mM, KH_2PO_4 1.19 mM, $MgSO_4$ 1.19 mM, $NaHCO_3$ 25.07 mM, pyruvate 0.25 mM, lactate 21.58 mM, and bovine serum albumin 1 gm/L) at a final concentration of 2×10^7 spermatozoa/ml and were incubated at 37°C in capped tubes under an air atmosphere. Calcium-free medium was also employed. Media were prepared immediately prior to use.

Address reprint requests to Mildred Gordon, School for Biomedical Education, the City College, 138th St. and Convent Ave., New York, NY 10031.

After October 1, 1980, William L. Williams will be at the following address: Reproduction Research Labs, Dept. of Biochemistry, University of Georgia, Athens, GA. 30602.

The initial pH was adjusted to 7.55 and throughout experiments remained less than 8.20.

Immediately (~2 min) after suspension of sperm in glucose-free BWW, various combinations of the following agents were added to sperm samples: 8 bromo cGMP, 8 bromo cAMP, 8 bromo GMP and ZnCl₂ (Table 1). The bromo analogues were chosen because they proved to be more efficacious than dibutyryl cyclic nucleotides (Santos-Sacchi and Gordon, '80). After 20 min incubation with these agents, acrosome reactions were assessed by hemocytometer. At least five chambers (0.5 mm³ each) were counted for each condition. Care was taken to count all cells through the 0.1 mm counting chamber depth. Standard errors of the mean averaged less than 15%. Results are reported as percentage of acrosome reactions in the total motile sperm population (%AR^{tot} = [conc. of AR spermatozoa/conc. of total spermatozoa - conc. of immotile spermatozoa] × 100) (Santos-Sacchi and Gordon, '80). The onset of the AR and activated motility were qualitatively evaluated over time by light and differential interference microscopy. Spermatozoa were processed for electron microscopy (Gordon, '73) and examined with a Philips 300EM at 80kV.

RESULTS

Table 1 presents the percentages of acrosome reactions induced by various agents. Whereas 8 bromo cGMP alone was able to induce a significant number of acrosome reactions, the simultaneous addition of micromolar concentrations of Zn⁺⁺ enhanced its effect, and this effect was concentration-dependent. The highest potentiating effects of Zn⁺⁺ were observed at mid-micromolar concentrations, where a 6.5-fold increase in the percent of acrosome reactions was obtained over 8 bromo cGMP alone. The presence of Ca⁺⁺ was nec-

essary for the induction of acrosome reactions. Zinc ions alone (250 μM) or in combination with 8 bromo cAMP or 8 bromo GMP were essentially an ineffective inducer of the acrosome reaction. In addition, zinc ions (250 μM) added at 0 time had no effect upon the percent of acrosome reactions present after 5 hr incubation in glucose-free BWW (Zn⁺⁺: 5.94 ± 0.91% vs. no Zn⁺⁺: 5.92 ± 0.61%).

Upon the addition of 8 bromo cGMP alone or in combination with Zn⁺⁺, sperm become extremely active within minutes. By 5-10 min activated, acrosome-reacted sperm were observed, and by 15-25 min a maximum was reached. Acrosome-reacted sperm remained motile for at least 2 hr, after which increasing numbers became immotile. Differential interference and electron microscopy indicate that the induced reactions are physiological, as previously determined for the cGMP-induced AR (Santos-Sacchi and Gordon, '80).

DISCUSSION

Cyclic GMP analogues are able to induce acrosome reactions in Guinea pig sperm, and this ability was found to be dependent upon the time of addition after initial suspension in media (Santos-Sacchi and Gordon, '80). That is, a dramatic increase in the ability of 8 bromo or dibutyryl cGMP (10 mM) to induce acrosome reactions was observed over a 1 hr period (0 hr: < 1% vs. 1 hr: ≥ 13%). This increased ability was correlated with a decrease in sperm cyclic AMP levels during 1-hr incubation. The present finding that Zn⁺⁺ in micromolar concentrations can potentiate the action of cGMP analogues may be explained by its ability to inhibit adenylate cyclase (Haesungcharern and Chulavatnatol, '78). Thus, the addition of Zn⁺⁺ may further increase the cGMP/cAMP ratio, thereby promoting Ca⁺⁺ influx and the acrosome reaction. Spermatozoa will not acrosome-react in cal-

TABLE 1. %AR^{tot} score induced by addition of agents immediately after suspension of sperm in glucose-free BWW

		%AR ^{tot} ($\bar{X} \pm \text{SEM}$)
8 bromo cGMP(10 mM)	ZnCl ₂ (1 mM)	5.64 ± 0.84%
8 bromo cGMP(10 mM)	ZnCl ₂ (750 μM)	21.54 ± 2.04%
8 bromo cGMP(10 mM)	ZnCl ₂ (250 μM)	23.46 ± 1.92%
8 bromo cGMP(10 mM)	ZnCl ₂ (25 μM)	7.55 ± 1.36%
8 bromo cGMP(10 mM)	—	3.64 ± 0.82%
8 bromo cAMP(10 mM)	ZnCl ₂ (250 μM)	1.31 ± 0.02%
8 bromo GMP(10 mM)	ZnCl ₂ (250 μM)	1.80 ± 0.77%
—	ZnCl ₂ (250 μM)	0.19 ± 0.02%
—	—	0.09 ± 0.03%

cium-free media (Yanagimachi and Usui, '74) nor in calcium-free media containing micromolar concentrations of Zn^{++} and 8 bromo cGMP. Furthermore, the addition of Zn^{++} alone had no effect upon acrosome reaction induction. These data suggest that while Zn^{++} cannot substitute for Ca^{++} , it is possible that optimal concentrations of Zn^{++} affect intracellular Ca^{++} availability and distribution, perhaps by promoting release of bound Ca^{++} , thereby potentiating the effect of a cGMP-induced Ca^{++} influx.

Data from several sources indicate that Zn^{++} profoundly affects sperm function. For example, vaginal inserts of several zinc salts result in the reduction or absence of fertilized ova in mated does (Williams and Lenz, '79). Interestingly, *in vitro* experiments with hamster sperm gave results that are opposite from those with the Guinea pig. Whereas Zn^{++} (250 μ M) in the present study was unable to inhibit acrosome reactions in Guinea pig sperm, it has been reported to inhibit hamster sperm acrosome reactions (Meizel and Lui, '76). Furthermore, it was recently reported that TLCK (a synthetic trypsin inhibitor) actually increased the number of acrosome reactions in Guinea pig sperm as compared to controls (Vitug et al., '79), while the same compound was found to inhibit hamster acrosome reactions (Meizel and Lui, '76; Lui and Meizel, '79). We have observed a potentiation of cGMP-induced Guinea pig acrosome reactions by TLCK (unpublished results). Species differences may be the underlying reason for such disparities.

ACKNOWLEDGMENTS

This paper was supported by NIH Grant HD13163 and Ford Foundation Grant 680-0805B. We appreciate the help of Celeste Conway in the preparation of this manuscript.

Dr. Williams is indebted to Dr. C. Wayne Bardin of the Population Council for making it possible to conduct research for one year in New York City.

LITERATURE CITED

- Aonuma, S., M. Okabe, and M. Kawaguchi (1978) The effect of zinc ions on fertilization of mouse ova *in vitro*. *J. Reprod. Fert.*, **53**:179-183.
- Gordon, M. (1973) Localization of phosphatase activity on the membranes of the mammalian sperm head. *J. Exp. Zool.*, **185**:111-119.
- Haesungcharern, A., and M. Chulavattnatol (1978) Inhibitors of adenylate cyclase from ejaculated human spermatozoa. *J. Reprod. Fert.*, **53**:59-61.
- Holland, M.K., D.A.I. Suter, and I.G. White (1976) Possible mechanisms involved in the reduction in motility of human spermatozoa by copper, zinc and silver. *J. Reprod. Fert.*, **46**:507-508.
- Huacuja, L., A. Sosa, N.M. Delgado, and A. Rosado (1973) A kinetic study of the participation of zinc in human spermatozoa metabolism. *Life Sciences*, **13**:1383-1394.
- Johnsen, O., and R. Eliasson (1978) Destabilization of human sperm membranes by albumin, EDTA and Histidine. *Int. J. Androl.*, **1**:485-488.
- Johnsen O., and R. Eliasson (1976) Studies on the succinate induced respiration of human spermatozoa in relation to zinc ions. *Int. J. Androl.*, **1**:Suppl. 1.
- Lui C.W., and S. Meizel (1979) Further evidence in support of a role for hamster sperm hydrolytic enzymes in the acrosome reaction. *J. Exp. Zool.*, **207**:173-185.
- Meizel, S., and C. Lui (1976) Evidence for the role of a trypsin-like enzyme in the hamster sperm acrosome reaction. *J. Exp. Zool.*, **195**:137-144.
- Santos-Sacchi, J., and M. Gordon (1980) The induction of the acrosome reaction in guinea pig spermatozoa by cyclic guanosine monophosphate analogues. (in press, *J. Cell Biol.*).
- Vitug, L., S. Perreault, and B.J. Rogers (1979) Effects of trypsin inhibitors on acrosome reaction of guinea pig spermatozoa. *Soc. Study Reprod. XII Annual Meeting. Biol. Reprod.*, **20**:Suppl. 1, 78A.
- Williams, W.L., and R.W. Lenz (1979) Prevention of mammalian fertilization with sperm enzyme inhibitors. *XIth Int. Congress of Biochem.*, Toronto, Canada, p. 708.
- Yanagimachi, R., and N. Usui (1974) Calcium dependence of the acrosome reaction and activation of guinea pig spermatozoa. *Exp. Cell Res.*, **89**:161-174.

Mapping the Distribution of Outer Hair Cell Voltage-Dependent Conductances by Electrical Amputation

J. Santos-Sacchi, G.-J. Huang, and M. Wu

Sections of Otolaryngology and Neurobiology, Yale University School of Medicine, New Haven, Connecticut 06510 USA

ABSTRACT The mammalian outer hair cell (OHC) functions not only as sensory receptor, but also as mechanical effector; this unique union is believed to enhance our ability to discriminate among acoustic frequencies, especially in the kilohertz range. An electrical technique designed to isolate restricted portions of the plasma membrane was used to map the distribution of voltage-dependent conductances along the cylindrical extent of the cell. We show that three voltage-dependent currents, outward K, $I_{K,n}$, and I_{Ca} are localized to the basal, synaptic pole of the OHC. Previously we showed that the lateral membrane of the OHC harbors a dense population of voltage sensor-motor elements responsible for OHC motility. This segregation of membrane molecules may have important implications for auditory function. The distribution of OHC conductances will influence the cable properties of the cell, thereby potentially controlling the voltage magnitudes experienced by the motility voltage sensors in the lateral membrane, and thus the output of the “cochlear amplifier.”

INTRODUCTION

The outer hair cell (OHC) plays a pivotal role in mammalian auditory perception (see Dallos, 1992). In addition to being one of the two sensory type cells in the organ of Corti, the OHC is capable of voltage-dependent mechanical responses that appear to provide feedback into the basilar membrane, thereby enhancing the passive mechanical vibration of the cochlear partition (Brownell et al., 1985; Ashmore, 1987; Santos-Sacchi and Dilger, 1988; Ruggero, 1992). Electrophysiological and ultrastructural evidence indicates that membrane-bound voltage sensor-motor elements control OHC length (Santos-Sacchi, 1990, 1991, 1992; Ashmore, 1990, 1992; Kalinec et al., 1992; Forge, 1991; Iwasa, 1993). These molecular motors reside predominantly within the lateral plasma membrane of the OHC (Dallos et al., 1991; Huang and Santos-Sacchi, 1993, 1994).

The voltage-dependent nature of OHC motility necessarily indicates that factors which influence the voltages generated in the cell are capable of having an impact on the cell's role in hearing. Although the driving force for OHC motility is the voltage generated by the gating of transduction channels in the stereocilia of the apical membrane (Evans and Dallos, 1993), ultimately, receptor potentials may be modulated by ionic conductances located in the basolateral membrane. A variety of ionic channel types is found in the basolateral membrane (see Ashmore, 1994), including voltage-dependent K and Ca channels (Santos-Sacchi and Dilger, 1988; Ashmore and Meech, 1986; Nakagawa et al., 1991; Housley and Ashmore, 1992). We focus here on the distribution of these voltage-dependent conductances in the cylindrical OHC, because the arrange-

ment of such conductances within the membrane will affect the cell's cable properties and the corresponding driving force imposed on the distributed system of OHC molecular motors. We demonstrate through an electrical isolation technique that voltage-dependent ionic conductances are restricted to the basal pole of the OHC. These results augment our concept of the highly partitioned nature of the OHC membrane, i.e., that mechano-electrical transduction (sensory) resides within the apical membrane, electromechanical transduction (motor) resides within the lateral membrane, and voltage-gated channels (and synaptic machinery) reside within the basal membrane.

Preliminary presentations of these data have been made (Santos-Sacchi, 1995; Santos-Sacchi and Huang, 1996).

METHODS

Guinea pigs were overdosed with pentobarbital. The temporal bones were removed and OHCs were isolated from the cochleas by gentle pipetting of the isolated top two turns of the organ of Corti in Ca-free medium with collagenase (0.3 mg/ml). The cell-enriched supernatant was then transferred to a 700- μ l perfusion chamber, and the cells were permitted to settle onto the coverglass bottom. All experiments were performed at room temperature ($\sim 23^\circ\text{C}$). A Nikon Diaphot inverted microscope with Hoffmann optics was used to observe the cells during electrical recording. Cell lengths ranged from $\sim 60\ \mu\text{m}$ to $80\ \mu\text{m}$.

We have developed a technique for electrically amputating portions of the OHC so that characteristics of restricted areas of the plasma membrane can be analyzed in isolation (Huang and Santos-Sacchi, 1993). The technique involves a double voltage-clamp protocol with two independent clamp amplifiers. Utilizing the partitioning microchamber of Evans et al. (1991) in combination with whole-cell voltage clamp, we are able to electrically amputate that portion of the OHC housed within the chamber (see Fig. 1 A). That is, when identical voltage clamp stimuli are simultaneously delivered to the microchamber and the cell interior, only that portion of the membrane outside the chamber is excited. The efficiency of this amputation technique is dependent upon the seal (shunt resistance) that the microchamber makes with the OHC, and we have determined that a seal of $>5\text{--}10\ \text{M}\Omega$ is sufficient and obtainable (Huang and Santos-Sacchi, 1993). By grounding the microchamber interior, the cell is put equivalently and simply under the whole-cell voltage-clamp condition. Incremental amputations were made by moving the cell into or out of the chamber with

Received for publication 24 March 1997 and in final form 28 May 1997.

Address reprint requests to Dr. Joseph Santos-Sacchi, Surgery (Otolaryngology), BML 244, Yale University School of Medicine, 333 Cedar St., New Haven, CT 06510. Tel.: 203-785-7566 (office), 203-785-5407 (lab); Fax: 203-737-2245; E-mail: joseph.santos-sacchi@yale.edu.

© 1997 by the Biophysical Society

0006-3495/97/09/1424/06 \$2.00

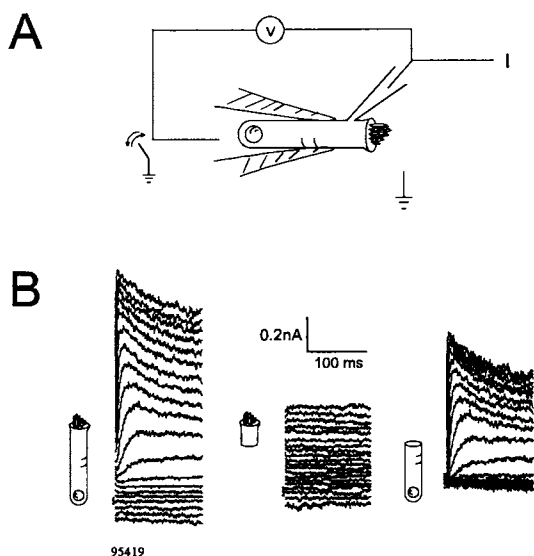


FIGURE 1 (A) Schematic of an outer hair cell, two-thirds of which is inserted into a microchamber and whole-cell voltage-clamped via a patch pipette. The microchamber and perfusion dish contain extracellular solution (see Methods). Identical voltage protocols are delivered to both microchamber and patch pipette to electrically isolate properties of the extruded portion of the cell. Grounding the microchamber (or clamping to zero) provides whole-cell measures. Membrane current is measured via the patch pipette. (B) OHC is held at -80 mV and nominally stepped from -120 to $+90$ mV in 10 -mV increments. Series resistance corrected traces depict currents from -110 to $+80$ mV in 10 -mV increments. Residual series resistance: 5.6 M Ω . OHC figures indicate the portion of the cell from which associated currents arise. (Left) Whole-cell condition. (Middle) Currents obtained by amputating the basal two-thirds of the cell, that is, deriving from the apical one-third of the OHC. (Right) Subtraction of currents resulting in those attributable to the basal two-thirds of the cell. Note that time- and voltage-dependent outward K currents are restricted to this region of the cell.

slight suction or pressure, while simultaneously moving the whole-cell patch pipette via a motorized manipulator. Fortunately, the membrane is somewhat giving, so that sometimes seals are maintained during the motion. Because the microchamber orifice diameter was smaller than initial OHC diameter and during the course of recording under whole-cell mode OHCs typically swell somewhat (cells were monitored with video), we are confident that shunt resistances remained adequate. Transmembrane currents were measured via the patch pipette. Patch pipette series resistance was estimated after the establishment of whole-cell configuration from the transient current response induced by a 10 -mV step (Huang and Santos-Sacchi, 1993).

To study voltage-dependent K currents, the cells were bathed in a modified Leibovitz medium containing (in mM): NaCl 142.2, KCl 5.37, CaCl₂ 2, MgCl₂ 1.48, HEPES 5, with 300 mOsm osmolarity (adjusted with dextrose) and pH 7.2. The intracellular solution was (in mM): KCl 140, EGTA 10, MgCl₂ 2, and HEPES 5, with 300 mOsm and pH 7.2. The K currents were studied at holding potentials of either -80 mV or -60 mV. The latter holding potential was used to observe $I_{K,n}$, a K current that is active at rest but deactivates at hyperpolarized potentials (Housley and Ashmore, 1992). To study the inward Ca conductance, Ba was used as the charge carrier. After the formation of whole-cell configuration in normal bath solution, barium solution (in mM: BaCl₂ 100, MgCl₂ 2, tetraethylammonium 35, 4-amino pyridine 5, CsCl 5, HEPES 10) was perfused. Intracellular solution was (in mM): CsCl 140, EGTA 10, MgCl₂ 2, HEPES 5. Osmolarity and pH were adjusted as above. Typically, OHCs were stepped from the holding potential in nominal increments of 10 mV to a range of potentials. For the identification of inward Ca currents, leakage subtraction was performed with the $P/4$ technique.

Although averaging and subtraction of ionic currents are routinely performed to evaluate the effects of a variety of treatments, problems may arise because of residual series resistance. Essentially, current traces may not have been obtained at constant voltage. Because the OHC has a relatively low resting membrane resistance and large voltage-dependent conductances, this problem may be intensified. To overcome this problem and allow averaging and subtraction of current traces, point-by-point I - V curves were constructed, and each nominal voltage was corrected by subtracting the voltage drop across the series resistance. Currents at fixed voltage increments were then obtained through interpolation, so that generated current traces represented true currents at 10 -mV increments. Because only interpolation was used, the complete range of corrected trace voltages was sometimes less than the nominal voltage range. Valid manipulations of current traces were then feasible. It should be noted that these corrections did not alter the experimental conclusions, because analyses without series resistance correction produced qualitatively similar results. Data collection was performed with either pClamp (Axon Instruments, CA) or a Windows-based voltage-clamp program, jClamp, both utilizing an Axon AD1200 A/D board. Analyses were performed with the software program MATLAB (Mathworks, MA) or jClamp.

RESULTS

The OHC possess a prominent voltage-dependent outward K current (Fig. 1 B, left; Ashmore and Meech, 1986; Santos-Sacchi and Dilger, 1988; Santos-Sacchi, 1989). Fig. 1 B (middle) illustrates the effects of electrically amputating the basal two-thirds of the OHC plasma membrane on the currents measured through the patch pipette; the remaining currents are attributable to the apical third of the cell. Note that activation of time- and voltage-dependent K conductances is absent. An essentially linear response is observed. The right panel demonstrates, by subtracting the apical currents from the whole-cell currents, the response of the basal two-thirds of the cell. It is clear that K currents are restricted to this area, and that little leakage current is present.

It is possible, although not at all easy, to progressively amputate smaller and smaller portions of an OHC body so that a more precise distribution of the K conductances can be obtained. Fig. 2 A illustrates average results ($n = 3$) from such successful single-cell amputations, where, in each case, four successive amputations were accomplished. The left panel depicts the whole-cell current before each partitioning condition. Slight changes in what appears to be leakage conductance are probably produced by the inescapable trauma of cell manipulation. Nevertheless, these relatively small effects are essentially eliminated by the resultant current subtractions that follow. The middle panel shows the currents generated by the apical portions of the cells as the amputation is restricted to more basal regions. Note that voltage-dependent conductances are progressively uncovered as the amputation is lessened. The right panel reveals, through subtraction as in Fig. 1, the decrease in K current magnitude as measures are restricted to smaller and smaller regions of the basal pole. In Fig. 2 B, the I - V plot obtained from the right panel emphasizes that reductions in K current are not observed until amputation falls below the supranuclear region; this, of course, indicates that the voltage-dependent K conductance of the OHC resides below the

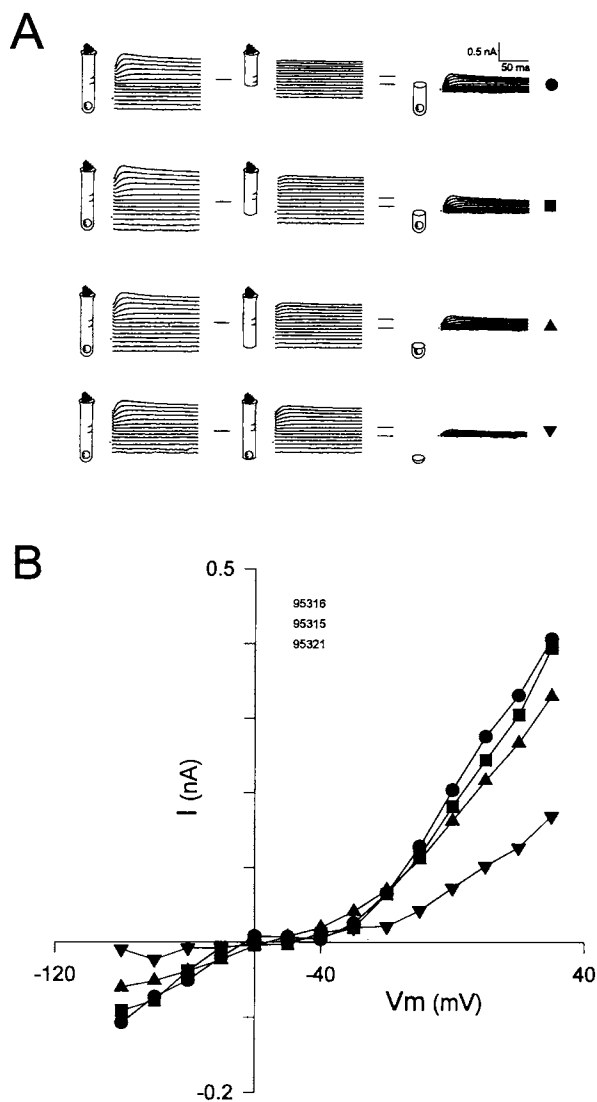


FIGURE 2 (A) Series resistance corrected and averaged current traces from three cells, each of which was successfully amputated at four positions. Each OHC was held at -80 mV and nominally stepped from -120 to $+90$ mV in 10 -mV increments. Corrected traces depict currents from -100 to $+30$ mV in 10 -mV increments. Average residual series resistance: 8.38 M Ω . OHC figures indicate portion of cell from which associated currents arise. (Left) Whole-cell condition obtained before amputation. (Middle) Apically restricted currents obtained by amputating four incrementally larger portions of the OHC's base. (Right) Subtraction of currents resulting in those attributable to the basal portions of the cell. (B) Peak current versus step potential obtained from the traces in A, right panel.

supranuclear region. Fig. 3 summarizes the results of electrical amputation by further subtracting the current traces to provide discrete localization of K currents along the basal extent of the cell. A total of 13 additional cells, where at least two incremental amputations were made, provided similar results.

Another prominent OHC K current that is active near rest and is believed to govern the cell's resting potential (Housley and Ashmore, 1992) is that of $I_{K,n}$. The current is characterized by a nearly instantaneous onset upon step

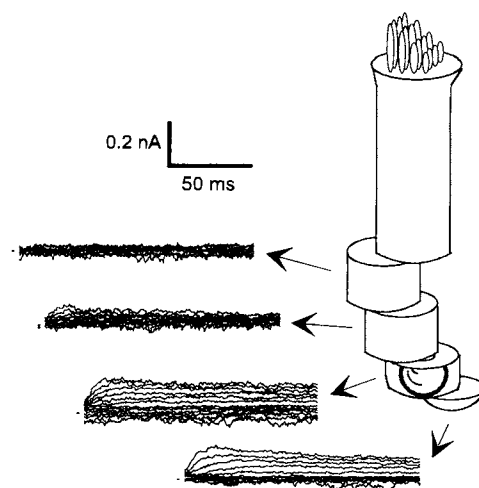


FIGURE 3 Localization of outward K currents along the basal extent of the OHC. Currents from the illustrated sections of the OHC were obtained by subtraction of currents in Fig. 2 A, right panel. From apical to basal, the currents correspond to (symbols in Fig. 2 A): circle-square, square-upward triangle, upward triangle-downward triangle, and simply downward triangle. The bulk of K conductances are restricted to the basal, nuclear region of the OHC.

hyperpolarizations from somewhat positive holding potentials (> -60 mV). The current deactivates upon hyperpolarization with a fairly long time constant that is variable among cells. Thus, while $I_{K,n}$ contributed to those currents studied above at the holding potential of -80 mV it was considerably deactivated. Fig. 4 exemplifies the effect of electrical amputation on OHCs whose $I_{K,n}$ is robust, because for these experiments holding potential was -60 mV. In this case, amputation was made slightly above the nucleus, and it is clear that the principal location of $I_{K,n}$ is within the basally amputated region, corresponding to the location of outward K currents. Six additional cells, with varying extents of $I_{K,n}$, were successfully amputated at the same level and provided similar results.

The OHC possesses a small, noninactivating Ca conductance that is revealed by leakage subtraction (Fig. 5) (Santos-Sacchi and Dilger, 1988; Nakagawa et al., 1991). Fig. 5 presents the averaged results ($n = 4$) of amputation experiments designed to localize Ca conductances. In these experiments, amputation of the basal pole of the cell successfully and reversibly removed the inward Ba currents, indicating that the Ca conductance colocalizes with K conductances.

DISCUSSION

Hair cells, like other nonsensory epithelial cells, are polarized morphologically and functionally. The apical and basolateral membranes of hair cells are specialized for mechanoreception and synaptic transmission, respectively (Hudspeth, 1989). Stereocilia, which are modified microvilli, are confined to the hair cell's apical region, where they serve to gate mechanically sensitive ion channels.

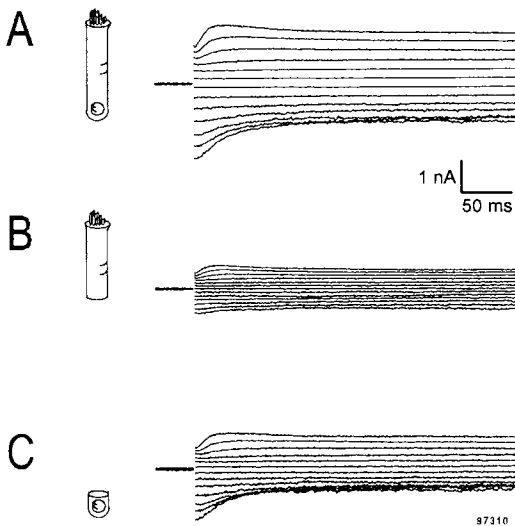


FIGURE 4 OHC held at -60 mV and nominally stepped from -140 to $+10$ mV in 10 -mV increments. Series resistance-corrected traces depict currents from -125 to $+5$ mV in 10 -mV increments. Residual series resistance: 6.5 M Ω . OHC figures indicate portion of cell from which associated currents arise. (A) $I_{K,n}$ is observed upon hyperpolarization with an instantaneous onset and slow deactivation. Outward K currents are also observed upon depolarization. (B) Amputation of the basal, nuclear pole of the OHC results in a nearly complete removal of $I_{K,n}$ and outward K currents. (C) Subtraction of apical currents (B) from whole cell currents (A) reveals those currents attributable to the basal, nuclear pole of the OHC. It is clear that $I_{K,n}$ resides in the same location as the outward K currents.

Gating of these channels generates receptor potentials and ultimately leads to calcium-dependent neurotransmitter release onto eighth nerve afferents. Furthermore, the outer hair cell's lateral membrane serves an electromechanical function. OHCs generate voltage-dependent mechanical responses, the frequency limit (> 20 kHz) of which is currently imposed by measurement techniques (Santos-Sacchi, 1992; Dallos and Evans, 1995). Membrane-bound sensor-motor elements responsible for this unique motility have been localized to the central extent of the OHC's cylindrical soma, namely between apical cuticular plate and basal, nuclear region (Dallos et al., 1991; Huang and Santos-Sacchi, 1993). Gating current studies indicate that the density of molecular motors within the OHC lateral membrane is $\sim 7500/\mu\text{m}^2$ (Huang and Santos-Sacchi, 1993); this is in line with morphological evidence showing similar densities of 10 -nm intramembranous particles, the putative molecular motors (Forge, 1991). It is clear that the lateral membrane of the OHC, unlike that of other types of hair cells, is uniquely specialized.

It is demonstrated here that the voltage-dependent K and Ca conductances of the OHC are not distributed within the plasmalemma along the entire length of the cell, but instead are restricted to the basal, synaptic pole. The cellular mechanisms that direct and maintain the segregation of molecular motors to the lateral membrane and ionic channels to the basal membrane possibly involve the extensive cortical cytoskeleton found in OHCs (Holley and Ashmore, 1988).

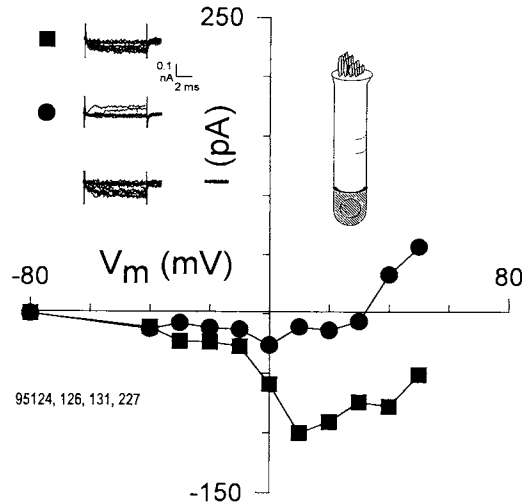


FIGURE 5 Localization of voltage-dependent Ca conductance. Average results from four cells. OHCs were held at -80 mV and stepped nominally from -40 to $+40$ mV in 10 -mV increments. Leakage subtraction was performed with the $P/4$ protocol to reveal inward Ba currents. Because the currents were so small, no correction for residual series resistance was made. Average residual series resistance: 8.25 M Ω . The I - V plot was obtained from the top two averaged sets of traces in the upper left; data points were averages of the final 4 ms of the current traces. Squares indicate currents obtained before amputation, and circles indicate currents obtained after amputation of the basal, nuclear pole, as indicated in the figure of the OHC. The bottom set of traces was obtained after return to whole-cell conditions. These data indicate that the OHC Ca conductance resides in the same region as the voltage-dependent K conductances.

Disruption of the cytoskeleton might promote intermixing of the molecules, which could be identified electrophysiologically. It is important to note that the K conductances were not amputated, because of a simultaneous removal of a required Ca influx. Although a component of the outward K current may be Ca-dependent, the bulk of this current is not (Santos-Sacchi, 1989). Recently this independence from Ca was confirmed and, in addition, it was shown that $I_{K,n}$ is little affected by the removal of extracellular calcium (Mammano and Ashmore, 1996; Nenov et al., 1997). Thus, electrical amputation of the K as well as Ca currents in this study is due almost exclusively to direct removal of the voltage stimulus to the channels' voltage sensors.

After the identification of a noninactivating L-type Ca current in OHCs (Santos-Sacchi and Dilger, 1988; Santos-Sacchi, 1989), other detailed examinations, including a localization study, of the conductance were made (Nakagawa et al., 1991, 1992). Focal Ca channel blocker application demonstrated that Ca current blockade occurred primarily during application to the basal pole of the OHC. This is in line with the results of the present experiments. Similar $I_{K,n}$ localization studies by these investigators, using focal application of the blocker Ba, indicated that $I_{K,n}$ is distributed along the length of the OHC (Nakagawa et al., 1994). Our data, however, present a more restricted localization of $I_{K,n}$ at the basal pole of the OHC. Focal application ("puffer") studies may sometimes suffer from diffusion of drugs away

from sites of presumed application. Earlier studies in lower-vertebrate hair cells, using unequivocal localization methods, demonstrated that Ca-activated K and Ca conductances are colocalized to synaptic sites along the full extent of the basolateral membrane of these cells (Issa and Hudspeth, 1994; Roberts et al., 1990). In addition to a role in synaptic function, the clustering of these conductances may be required for the electrical tuning found in these nonmammalian hair cells. Electrical resonance is not found in mammalian auditory hair cells, and in the case of the OHC it has been suggested that the Ca-independence of the outward K current might preclude such oscillatory behavior (Santos-Sacchi, 1989). Also unlike lower vertebrate hair cells, OHC synaptic sites are restricted to the basal, nuclear region of the plasma membrane—the same region where voltage-dependent K and Ca conductances reside. Thus it is conceivable that the K and Ca conductances of the OHC, as in lower-vertebrate hair cells, are associated with afferent and/or efferent synaptic sites. Whereas it is clear that efferent synaptic functionality is robust based on a host of indirect physiological studies (e.g., Brown et al., 1983), the functionality of the meager afferent supply to the OHC, which most likely has never been recorded from, remains questionable (Lieberman, 1982; Robertson, 1985). The contribution of K and Ca conductances to synaptic activity of the OHC must await direct studies of this issue.

Many characteristics of OHCs are correlated with cell length. Although we did not study the effects of cell length on conductance distribution, it is likely that the basic compartmentalization of the OHC remains the same, regardless of length. Indeed, regardless of length, it is clear, for example, that mechanically gated transduction channels are restricted to the cell apex, synapses are restricted to the basal pole, and subsurface cisternae line the lateral membrane. One of the characteristics that does depend on cell length is the occurrence of $I_{K,n}$ (Housley and Ashmore, 1992), with the whole-cell conductance being greater in shorter cells. All of our cells were between $\sim 60 \mu\text{m}$ and $80 \mu\text{m}$, but the occurrence of $I_{K,n}$ in cells of this length range is not clearly dependent on cell length. In 83 cells studied, 43 were found to have observable $I_{K,n}$ (length: $68.26 \pm 1.2 \mu\text{m}$ [mean \pm SE]; zero current potential [after pipette-cell solution equilibration]: $-57.5 \pm 1.4 \text{ mV}$). The remaining cells lacked observable $I_{K,n}$ (length: $64.1 \pm 0.8 \mu\text{m}$; zero current potential: $-39.8 \pm 1.5 \text{ mV}$). Thus, in this length range there appears to be little dependence of $I_{K,n}$ on cell length. Note, however, that this is not in disagreement with the data of Housley and Ashmore (1992), where clear dependence of OHC conductance on length is not obvious in this restricted range of length.

Given the conductance localization pattern in the OHC, it is possible to draw some conclusions about ionic channel density. The length, unlike the constant width ($10 \mu\text{m}$), of OHCs is inversely related to its characteristic frequency, ranging in the guinea pig from $\sim 80 \mu\text{m}$ ($\sim 200 \text{ Hz}$) to $20 \mu\text{m}$ ($\sim 40,000 \text{ Hz}$). Whereas the surface area of the lateral membrane is directly related to the cell's length, the surface

area of the basal, synaptic pole remains roughly constant. As noted above, the K current density of OHCs has been shown to increase as cell length decreases (Housley and Ashmore, 1992). Clearly, then, K channel density must increase, not as a consequence of reduced surface area, but as a consequence of an increased channel population. Interestingly, we have recently shown that motility gating current density and intramembranous particle density in the lateral membrane increase as length decreases (Kakehata et al., 1997). The higher density of these molecules (channels and molecular motors) in high-frequency OHCs probably corresponds to the enhanced frequency tuning afforded by these cells in the high-frequency region of the cochlea.

Finally, the voltage-dependent ionic channel distribution determined here necessarily limits the conductances' influence on local voltage drops across the lateral membrane, where the motility voltage sensors reside. The OHC lateral wall (subsurface cisternae, cortical cytoskeleton, and plasma membrane) is a complex structure with electrical properties that are equally complex (Pollice and Brownell, 1993; Kruger et al., 1997). Nevertheless, the absence of current shunting in the lateral membrane may ensure that voltages generated there (viz., the driving force for the "cochlea amplifier") will be largely unaffected by remote conductance changes in the basal pole of the cell.

We thank Margaret Mazzucco for technical help.

This work was supported by National Institutes of Health-NIDCD grant DC00273 to JSS.

REFERENCES

- Ashmore, J. F. 1987. A fast motile response in guinea-pig outer hair cells: the cellular basis of the cochlear amplifier. *J. Physiol. (Lond.)* 388: 323–347.
- Ashmore, J. F. 1990. Forward and reverse transduction in the mammalian cochlea. *Neurosci. Res. Suppl.* 12:S39–S50.
- Ashmore, J. F. 1992. Mammalian hearing and the cellular mechanism of the cochlear amplifier. In *Sensory Transduction*. D. P. Corey and S. D. Roper, editors. Rockefeller University Press, New York. 395–412.
- Ashmore, J. F. 1994. The G. L. Brown Prize Lecture. The cellular machinery of the cochlea. *Exp. Physiol.* 79:113–134.
- Ashmore, J. F., and R. W. Meech. 1986. Ionic basis of membrane potential in outer hair cells of guinea pig cochlea. *Nature*. 322:368–371.
- Brown, M. C., A. L. Nuttall, and R. I. Masta. 1983. Intracellular recordings from cochlear inner hair cells: effects of stimulation of the crossed olivocochlear efferents. *Science*. 222:69–72.
- Brownell, W. E., C. R. Bader, D. Bertrand, and Y. de Ribaupierre. 1985. Evoked mechanical responses of isolated cochlear outer hair cells. *Science*. 227:194–196.
- Dallos, P. 1992. The active cochlea. *J. Neurosci.* 12:4575–4585.
- Dallos, P., and B. N. Evans. 1995. High-frequency motility of outer hair cells and the cochlear amplifier. *Science*. 267:2006–2009.
- Dallos, P., B. N. Evans, and R. Hallworth. 1991. On the nature of the motor element in cochlear outer hair cells. *Nature*. 350:155–157.
- Evans, B. N., and P. Dallos. 1993. Stereocilia displacement induced somatic motility of cochlear outer hair cells. *Proc. Natl. Acad. Sci. USA*. 90:8347–8351.
- Evans, B. N., R. Hallworth, and P. Dallos. 1991. Outer hair cell electromotility: the sensitivity and vulnerability of the DC component. *Hear. Res.* 52:288–304.

- Forge, A. 1991. Structural features of the lateral walls in mammalian cochlear outer hair cells. *Cell Tissue Res.* 265:473–483.
- Holley, M. C., and J. F. Ashmore. 1988. Spectrin, actin and the structure of the cortical lattice in mammalian cochlear outer hair cells. *J. Cell Sci.* 96:283–291.
- Housley, G. D., and J. F. Ashmore. 1992. Ionic currents of outer hair cells isolated from the guinea-pig cochlea. *J. Physiol. (Lond.)* 448:73–98.
- Hudspeth, A. J., 1989. How the ear's works work. *Nature.* 341:397–404.
- Huang, G.-J., and J. Santos-Sacchi. 1993. Mapping the distribution of the outer hair cell motility voltage sensor by electrical amputation. *Biophys. J.* 65:2228–2236.
- Huang, G.-J., and J. Santos-Sacchi. 1994. Motility voltage sensor of the outer hair cell resides within the lateral plasma membrane. *Proc. Natl. Acad. Sci. USA.* 91:12268–12272.
- Issa, N. P., and A. J. Hudspeth. 1994. Clustering of Ca^{2+} channels and Ca^{2+} -activated K^{+} channels at fluorescently labeled presynaptic active zones of hair cells. *Proc. Natl. Acad. Sci. USA.* 91:7578–7582.
- Iwasa, K. H. 1993. Effect of stress on the membrane capacitance of the auditory outer hair cell. *Biophys. J.* 65:492–498.
- Kakehata, S., J. Santos-Sacchi, T. Kikuchi, and Y. Katori. 1997. Higher frequency outer hair cells have a greater specific voltage-dependent capacitance. Midwinter Meeting of the Association for Research in Otolaryngology, St. Petersburg, FL, February 1997.
- Kalinec, F., M. C. Holley, K. H. Iwasa, D. J. Lim, and B. Kachar. 1992. A membrane based force generation mechanism in auditory sensory cells. *Proc. Natl. Acad. Sci. USA.* 89:8671–8675.
- Kruger, R. P., M. J. Yium, J. A. Halter, and W. E. Brownell. 1997. Outer hair cell electrophysiology: modeling the electrical properties of the subsurface cisterna. Midwinter Meeting of the Association for Research in Otolaryngology, St. Petersburg, FL, February 1997.
- Liberman, M. C. 1982. Single neuron labeling in the cat auditory nerve. *Science.* 216:1239–1241.
- Mammano, F., and J. F. Ashmore. 1996. Differential expression of outer hair cell potassium currents in the isolated cochlea of the guinea pig. *J. Physiol. (Lond.)* 496.3:639–646.
- Nakagawa, T., S. Kakehata, N. Akaike, S. Komune, T. Takasaka, and T. Uemura. 1991. Calcium channel in isolated outer hair cells of guinea pig cochlea. *Neurosci. Lett.* 125:81–84.
- Nakagawa, T., S. Kakehata, N. Akaike, S. Komune, T. Takasaka, and T. Uemura. 1992. Effects of Ca^{2+} antagonists and aminoglycoside antibiotics on Ca^{2+} current in isolated outer hair cells of guinea pig cochlea. *Brain Res.* 580:345–347.
- Nakagawa, T., S. Kakehata, T. Yamamoto, N. Akaike, S. Komune, and T. Uemura. 1994. Ionic properties of $I_{\text{K,n}}$ in outer hair cells of guinea pig cochlea. *Brain Res.* 661:293–297.
- Nenov, A. P., C. Norris, and R. P. Bobbin. 1997. Outwardly rectifying currents in guinea pig outer hair cells. *Hear. Res.* 105:146–158.
- Pollice, P. A., and W. E. Brownell. 1993. Characterization of the outer hair cell's lateral wall membranes. *Hear. Res.* 70:187–196.
- Roberts, W. M., R. A. Jacobs, and A. J. Hudspeth. 1990. Colocalization of ion channels involved in frequency selectivity and synaptic transmission at presynaptic active zones of hair cells. *J. Neurosci.* 10:3664–3684.
- Robertson, D. 1985. Brainstem location of efferent neurons projecting to the guinea pig cochlea. *Hear. Res.* 20:79–84.
- Ruggero, M. A. 1992. Responses to sound of the basilar membrane of the mammalian cochlea. *Neurobiology.* 2:449–456.
- Santos-Sacchi, J. 1989. Calcium currents, potassium currents, and the resting potential in isolated outer hair cells. Midwinter Meeting of the Association for Research in Otolaryngology, St. Petersburg, FL, February 1989.
- Santos-Sacchi, J. 1990. Fast outer hair cell motility: how fast is fast? In *The Mechanics and Biophysics of Hearing*. P. Dallos, C. D. Geisler, J. W. Matthews, M. A. Ruggero, and C. R. Steele, editors. Springer-Verlag, Berlin. 69–75.
- Santos-Sacchi, J. 1991. Reversible inhibition of voltage dependent outer hair cell motility and capacitance. *J. Neurosci.* 11:3096–3110.
- Santos-Sacchi, J. 1992. On the frequency limit and phase of outer hair cell motility: effects of the membrane filter. *J. Neurosci.* 12:1906–1916.
- Santos-Sacchi, J. 1995. Electrical dissection of ionic conductances in the outer hair cell. Symposium on the Molecular Biology of Hearing and Deafness, Bethesda, MD, October 6–8, 1995. 125.
- Santos-Sacchi, J., and J. P. Dilger. 1988. Whole cell currents and mechanical responses of isolated outer hair cells. *Hear. Res.* 35:143–150.
- Santos-Sacchi, J., and G.-J. Huang. 1996. Electrical dissection of ionic conductances in the outer hair cell. Midwinter Meeting of the Association for Research in Otolaryngology, St. Petersburg, FL, February 1996.

Density of motility-related charge in the outer hair cell of the guinea pig is inversely related to best frequency

Joseph Santos-Sacchi^{a,*}, Seiji Kakehata^{a,b}, Toshihiko Kikuchi^b,
Yukio Katori^b, Tomonori Takasaka^b

^aSection of Otolaryngology and Neurobiology, BML 244, Yale University School of Medicine, 333 Cedar Street, New Haven, CT 06510, USA

^bDepartment of Otolaryngology, Tohoku University School of Medicine, Sendai, Japan

Received 24 August 1998; received in revised form 22 September 1998; accepted 22 September 1998

Abstract

Whole cell voltage clamp and freeze fracture were used to study the electrophysiological and ultrastructural correlates of the outer hair cell (OHC) lateral membrane molecular motors. We find that specific voltage-dependent capacitance, which derives from motility-related charge movement, increases as cell length decreases. This increasing non-linear charge density predicts a corresponding increase in sensor-motor density. However, while OHC lateral membrane particle density increases, a quantitative correspondence is absent. Thus, the presumed equivalence of particle and motor is questionable. The data more importantly indicate that whereas the voltage driving OHC motility, i.e. the receptor potential, may decrease with frequency due to the OHC's low-pass membrane filter, the electrical energy ($Q \times V$) supplied to the lateral membrane will tend to remain stable. This conservation of energy delivery is likely crucial for the function of the cochlear amplifier at high frequencies. © 1998 Elsevier Science Ireland Ltd. All rights reserved

Keywords: Outer hair cell; Motility; Gating charge; Capacitance; Cochlea; Membranes

The outer hair cell (OHC) lateral membrane possesses voltage-dependent molecular motors that work at acoustic frequencies to enhance basilar membrane motion [10]. The motors are believed to be proteins represented by ultrastructurally observable intramembranous particles [5,13], which based on electrophysiological determinations of associated voltage-sensor charge movement, possess about 1 equivalent electron charge for each 10 nm particle [1,10,17]. The voltage-dependent nature of OHC motility is predicted to limit the cochlear amplifier's effectiveness at high acoustic frequencies, where the cell's receptor potential is attenuated by the RC properties of the plasma membrane; receptor potentials at threshold levels may provide insufficient drive to evoke enhancement of basilar membrane motion [16,18]. In fact, however, it is the high frequency region that appears to benefit most from the activity of OHCs [14]. In an attempt to reconcile this dilemma, we have analyzed the

voltage-dependent capacitance of OHCs isolated from different best-frequency locations along the cochlea spiral. A variety of evidence indicates that the OHC's robust non-linear charge movement is inextricably related to the cell's mechanical activity [6,11,20].

OHCs were freshly isolated from the organ of Corti of the guinea-pig cochlea, and were whole-cell voltage clamped at room temperature using an Axon 200B (see [9] for details). Recordings were made within 3 min after whole cell establishment to limit any confounding effects of gradual turgor pressure change [12]. Membrane capacitance was evaluated at different potentials by transient analysis of currents induced by a voltage stair step stimulus (–150–100 mV, 10 mV steps), and the capacitance function was fit to the first derivative of a two state Boltzmann function relating non-linear charge to membrane voltage (dQ/dV [9]),

$$c_m = Q_{\max} \frac{ze}{kT} \frac{b}{(1+b)^2} + c_{\text{lin}} \quad b = \exp\left(\frac{-ze(V - V_{pkCm})}{kT}\right)$$

Q_{\max} is maximum nonlinear charge, V_{pkCm} is voltage at peak

* Corresponding author. Tel.: +1 203 7857566/7855407, fax: +1 203 7372245; e-mail: joseph.santos-sacchi@yale.edu

capacitance or equivalently, at half maximal non-linear charge transfer, V_m is membrane potential, z is valence, C_{lin} is linear membrane capacitance, e is electron charge, k is Boltzmann's constant, and T is absolute temperature. C_{lin} was estimated from the fit to the above capacitance (C_m) equation, and indicates the membrane's intrinsic linear capacitance. Cell length (L) was measured in 20 cells before whole-cell configuration was obtained. The fitted linear function, $L = 2.9 \times C_{lin} - 0.24$ ($r^2 = 0.89$), was used to obtain length from C_{lin} in all cells ($n = 245$; cochleae > 100). Data collection and analysis was performed with a Windows-based patch clamp program jClamp (<http://www.med.yale.edu/surgery/otolar/santos/jclamp.html>).

For ultrastructural studies, guinea pigs ($n = 15$) were deeply anesthetized, and the cochleae fixed by intra-labyrinthine perfusion of 2.5% glutaraldehyde in 0.1 M sodium cacodylate buffer (pH 7.4). Following dissection, the cochleae were kept in the same fixative overnight at 4°C. Specimens were infiltrated with 30% glycerol for 1–4 h, and frozen in liquid nitrogen slush (-210°C). Fracturing was carried out at 10^{-7} Torr, at -130°C , and rotary shadowing

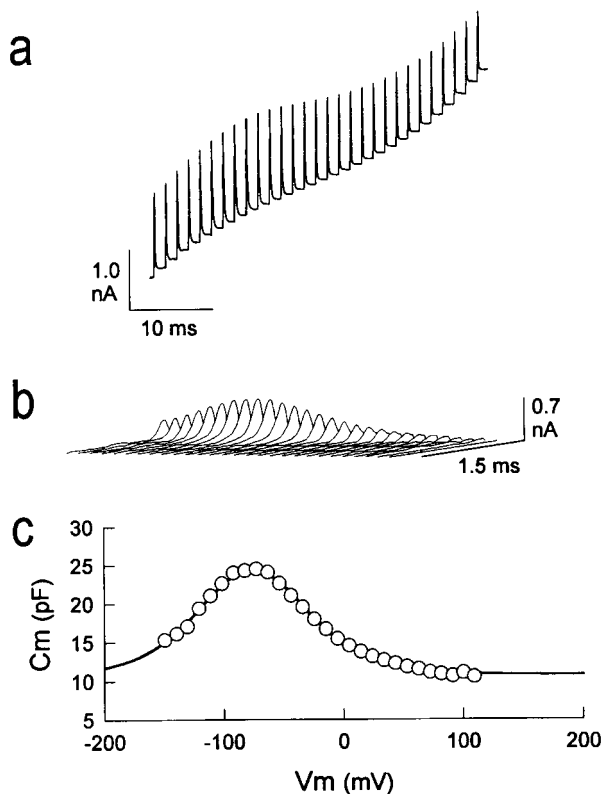


Fig. 1. Non-linear capacitance of an OHC isolated from the basal, high frequency region of the cochlea. (a) Capacitive currents induced by a stair step voltage protocol. (b) Gating currents extracted by subtracting the linear capacitive current obtained at the largest depolarization. (c) Capacitance of the cell (oc), comprised of a bell shaped voltage dependent capacitance riding atop a linear capacitance. The solid line is a fit (see text) indicating V_{pkC_m} , -76 mV; Q_{max} , 1.7 pC; C_{lin} , 10.8 pF; z , 0.83 . Length is 30.3 μm . Electrode series resistance was 3.7 M Ω .

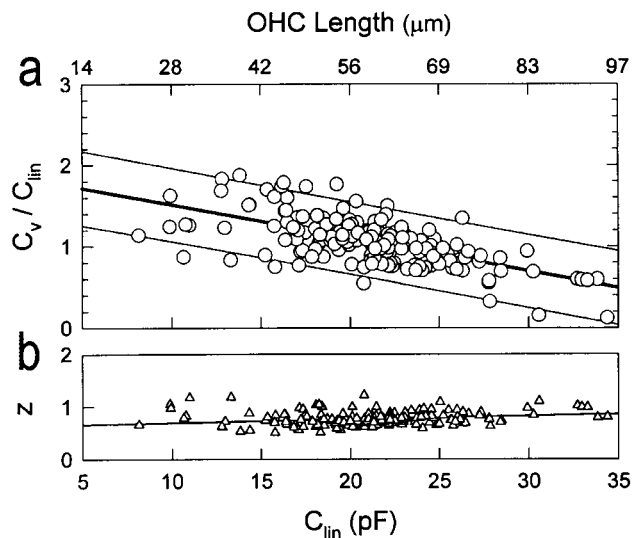


Fig. 2. (a) The ratio of maximum voltage dependent capacitance (C_v) to linear capacitance (C_{lin}) increases as OHC length (or equivalently, C_{lin}) decreases. Total capacitance was determined directly from capacitive currents. C_v is the peak capacitance minus C_{lin} , the latter being determined from Boltzmann fits to the data. (b) The valence z changes little with cell length or C_{lin} . The slight decrease in z may indicate a decreased charge for the voltage sensor and/or a decrease in the electrical distance displaced within the plane of the lateral membrane.

with platinum and carbon backing were made with a vacuum evaporator JEOL JFD-7000. Replicas were examined with a JEOL 1010 or JEOL JEM-100S transmission electron microscope at 100 kV. The protoplasmic fracture face of the OHC lateral membrane was examined at final photographic magnifications of 120 000. Images were divided into 2 cm^2 samples, and the total number of particles was used to obtain densities.

OHC length is inversely related to best frequency; as best frequency decreases from about 40 kHz to 100 Hz in the guinea pig, cell length increases from about 20 to 90 μm . Short, high frequency, OHCs possess a non-linear capacitance whose peak value can be greater than the cell's linear capacitance (Fig. 1). This is markedly different from cells residing in the low frequency region where the magnitude of non-linear capacitance is typically equivalent to or less than the cell's linear capacitance [1,17]. Moreover, as OHC length decreases (indicated by decreasing linear capacitance, C_{lin}), the relative magnitude of maximum voltage dependent capacitance (C_v) increases, as indicated by the ratio of the two (Fig. 2). Boltzmann fits show that the valence, z , changes little with cell length indicating that the parameter responsible for the relative increase in capacitance is the maximum charge, Q_{max} ($Q_{max} = 4kT/ze \times C_v$). The specific non-linear charge (Q_{sp}), based on whole cell surface area, changes with a slope of -413 $\text{e}^-/\mu\text{m}^2$ per pF of linear capacitance (Fig. 3a). This change, however, is an underestimate and does not reflect the highly compartmentalized nature of the OHC plasma membrane. While mechano-electrical transduction channels are restricted to

the OHC apical membrane [15], and voltage-dependent ionic channels are restricted to the basal membrane [19], mechanical responses and associated non-linear capacitance are restricted to the central extent of the cell, the lateral membrane [2,9,13]. Accordingly, a constant 6.2 pF (from [9]) of linear capacitance or correspondingly, 620 μm^2 , representing the constant apical and basal membrane should be excluded from calculations of Q_{sp} . When only the sensor-motor area is considered, the change in Q_{sp} as a function of cell length is striking, showing an increasing non-linear growth as cell length decreases (Fig. 3b). Q_{sp} 's up to 46 000 $e^-/\mu\text{m}^2$ are observed.

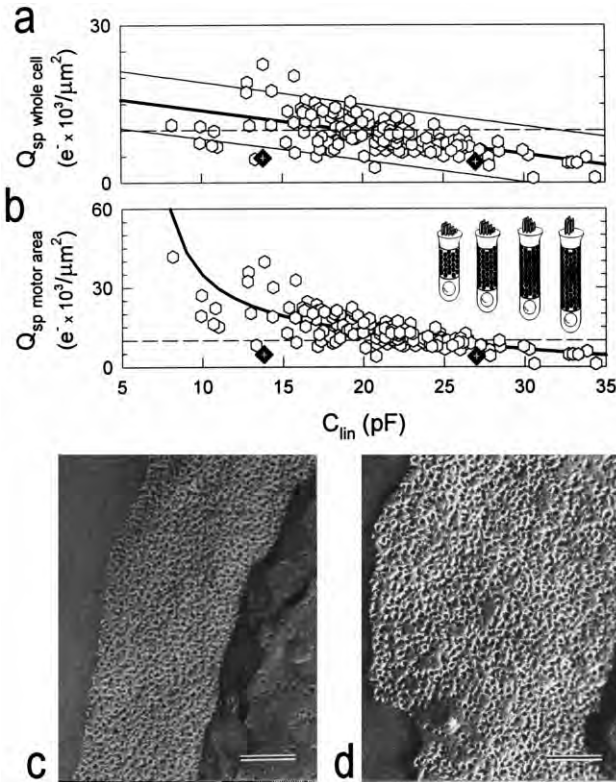


Fig. 3. (a) Non-linear charge density determined from whole cell surface area. Surface area was determined from the equivalence of linear capacitance and membrane surface area ($0.01\text{pF} = 1 \mu\text{m}^2$; [9]). Charge density increases as cell length or C_{lin} decreases. The slope, indicated by the solid line fit is $-413/pF$, and the thin parallel lines are 95% prediction limits. The two diamonds indicate the particle densities within the OHC lateral plasma membrane at two disparate frequencies. For values see text. The dashed line is the theoretical maximum density of particles based on 10 nm diameter. (b) Charge density obtained after correction of whole cell surface area for area devoid of sensor-motors. A constant $620 \mu\text{m}^2$ was subtracted from whole cell surface area. The solid line is simply the linear fit as above similarly corrected. The OHC schematics illustrate the relative change in sensor-motor containing lateral membrane area as cell length decreases. Other symbols as in (b). (c) Freeze-fracture replica showing the protoplasmic fracture face of the lateral plasma membrane of an OHC from a high frequency region of the cochlea. Densely packed intramembranous particles are characteristically found. Scale bar, 100 nm. (d) Same view obtained from cell in a low frequency region of the cochlea. Density is less than in (c). Scale bar, 100 nm.

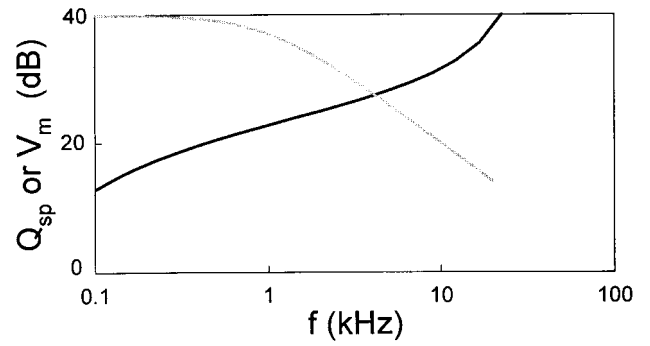


Fig. 4. Relationship between roll-off of receptor potential of a hypothetical OHC and increase of non-linear charge density as a function of frequency. The receptor potential falls at 20 dB per decade above about 1 kHz (gray line), whereas the charge density increases by a similar amount over frequency (black line obtained from b). OHC data were converted to frequency based on the map of Dannhof et al. [4].

A two state Boltzmann model has been successfully employed by several groups to characterize the OHC sensor-motor [1,10,17]. If this model is appropriate for the analysis of OHC charge movement, then the Boltzmann characteristics indicate that the density of independent sensor-motors should increase in correspondence with the specific charge density. A frequency-associated increase in the density of membrane protein is not unusual for the OHC. One K channel current, IK_n , is known to increase as characteristic frequency increases [8], and since this current is limited to the fixed area of the cell's basal pole, channel density must increase [19] (see [7] for an alternative explanation). Using freeze fracture, we measured the density of the putative ultrastructural correlate of the sensor-motor in the lateral membrane from areas of disparate characteristic frequencies (Fig. 3c,d). In a low frequency region (~ 200 Hz) where cell length averaged $76.3 \pm 2.2 \mu\text{m}$, particle density was $4033 (\pm 90; 35 \text{ samples})/\mu\text{m}^2$. In a high frequency region (~ 4 kHz) where cell length averaged $38.8 \pm 0.4 \mu\text{m}$, particle density was $4745 (\pm 155; 38 \text{ samples})/\mu\text{m}^2$. While the densities are significantly different (t -test, $P < .001$), they do not correspond to the densities predicted by Q_{sp} . Indeed, even the theoretical maximum density of 10 nm intramembranous particles, namely about $10\,000/\mu\text{m}^2$, does not approach electrophysiological estimates. Two possibilities may account for the disparity. First, the particles may not represent the sensor-motor molecules. Second, the two-state Boltzmann model inappropriately characterizes the sensor-motor as an independent entity possessing close to one electron charge. However, even if each intramembranous particle possessed more than one charge, the measured growth in particle density still requires that particle (voltage sensor) charge not remain fixed along the cochlea spiral. While a variably charged voltage sensor may not be unrealizable, the simplest explanation is the first.

Finally, the charge density data may help to explain how the OHC is able to overcome the effects of its membrane filter. In vivo measures of OHC receptor potentials show

that above about 1 kHz, AC voltages decrease at a rate 6 dB/octave [3,15]. Thus, the driving force for OHC motility is attenuated at high frequencies. However, our data indicate that, across frequency, motility-related charge increases to nearly the same extent as the decrease in receptor potential magnitude (Fig. 4). Thus, the electrical energy ($Q \times V$) delivered to the OHC lateral plasma membrane remains stable across frequency. It is likely that this frequency-independent energy delivery sustains the wide-band nature of the cochlear amplifier.

This work was supported by the National Institutes of Health, National Institute for Deafness and other Communication Disorders (DC00273). We thank Margaret Mazzucco for technical help. We also thank Dr. Akira Tonosaki and Dr. Hiroshi Washioka for EM equipment use and technical support.

- [1] Ashmore, J.F., Forward and reverse transduction in the mammalian cochlea, *Neurosci. Res.*, 11 (Suppl.) (1990) 39–50.
- [2] Dallos, P., Evans, B.N. and Hallworth, R., On the nature of the motor element in cochlear outer hair cells, *Nature*, 350 (1991) 155–157.
- [3] Dallos, P. and Santos-Sacchi, J., AC receptor potentials from hair cell in the low frequency region of the guinea pig cochlea. In W.R. Webster and L.M. Aitkin (Eds.), *Mechanisms of Hearing*, Monash University Press, Clayton, Australia, 1983, pp. 11–16.
- [4] Dannhof, B.J., Roth, B. and Bruns, V., Length of hair cells as a measure of frequency representation in the mammalian inner ear?, *Naturwissenschaften*, 78 (1991) 570–573.
- [5] Forge, A., Structural features of the lateral walls in mammalian cochlear outer hair cells, *Cell Tiss. Res.*, 265 (1991) 473–483.
- [6] Gale, J.E. and Ashmore, J.F., Charge displacement induced by rapid stretch in the basolateral membrane of the guinea pig OHC, *Proc. R. Soc. Lond. B*, 255 (1994) 243–249.
- [7] Halter, J.A., Kruger, R.P., Yium, M.J. and Brownell, W.E., The influence of the subsurface cisternae on the electrical properties of the outer hair cell, *NeuroReport*, 8 (1997) 2517–2521.
- [8] Housley, G.D. and Ashmore, J.F., Ionic currents of outer hair cells isolated from the guinea-pig cochlea, *J. Physiol. (Lond.)*, 448 (1992) 73–98.
- [9] Huang, G.-J. and Santos-Sacchi, J., Mapping the distribution of the outer hair cell motility voltage sensor by electrical amputation, *Biophys. J.*, 65 (1993) 2228–2236.
- [10] Iwasa, K.H., A membrane motor model for the fast motility of the outer hair cell, *J. Acoust. Soc. Am.*, 96 (1994) 2216–2224.
- [11] Kakehata, S. and Santos-Sacchi, J., Effects of lanthanides and salicylate on outer hair cell motility and associated gating charge, *J. Neurosci.*, 16 (1996) 4881–4891.
- [12] Kakehata, S. and Santos-Sacchi, J., Membrane tension directly shifts voltage dependence of outer hair cell motility and associated gating charge, *Biophys. J.*, 68 (1995) 2190–2197.
- [13] Kalinec, F., Holley, M.C., Iwasa, K.H., Lim, D.J. and Kachar, B., A membrane-based force generation in auditory sensory cells, *Proc. Natl. Acad. Sci. USA*, 89 (1992) 8671–8675.
- [14] Ruggero, M.A. and Santos-Sacchi, J., Cochlear mechanics and biophysics. In M.J. Croker (Ed.), *Handbook of Acoustics*, Wiley, New York, 1997, pp. 1357–1369.
- [15] Russell, I.J., Cody, A.R. and Richardson, G.P., The responses of inner and outer hair cells in the basal turn of the guinea-pig cochlea and in the mouse cochlea grown in vitro, *Hearing Res.*, 22 (1986) 199–216.
- [16] Santos-Sacchi, J., Asymmetry in voltage dependent movements of isolated outer hair cells from the organ of Corti, *J. Neurosci.*, 9 (1989) 2954–2962.
- [17] Santos-Sacchi, J., Reversible inhibition of voltage dependent outer hair cell motility and capacitance, *J. Neurosci.*, 11 (1991) 3096–3110.
- [18] Santos-Sacchi, J., On the frequency limit and phase of outer hair cell motility: the effects of membrane filter, *J. Neurosci.*, 12 (1992) 1906–1916.
- [19] Santos-Sacchi, J., Huang, G.-J. and Wu, M., Mapping the distribution of outer hair cell voltage-dependent conductance's by electrical amputation, *Biophysical J.*, 73 (1997) 1424–1429.
- [20] Takahashi, S. and Santos-Sacchi, J., Tension-induced OHC gating currents are restricted to the cell's mid-region, Mid-winter Meeting Abstracts of the Association for Research in Otolaryngology, St. Petersburg, FL, February, 1998.

Effects of membrane potential on the voltage dependence of motility-related charge in outer hair cells of the guinea-pig

J. Santos-Sacchi, S. Kakehata and S. Takahashi

*Sections of Otolaryngology and Neurobiology, Yale University School of Medicine,
New Haven, CT 06510, USA*

(Received 24 November 1997; accepted after revision 11 March 1998)

1. Isolated outer hair cells (OHCs) from the guinea-pig were whole-cell voltage clamped to study the influence of initial voltage on the voltage dependence of motility-related gating current or, equivalently, on the voltage dependence of membrane capacitance.
2. Prepulse delivery caused changes in the magnitude of motility-related gating currents, which are due predominantly to shifts in the voltage at peak capacitance (V_{pkC_m}). Depolarization shifts V_{pkC_m} in the hyperpolarizing direction, and hyperpolarization does the opposite. The mean shift between -120 and $+40$ mV prepulse states with long-term holding potentials (> 2 min) at -80 mV was 14.67 ± 0.95 mV ($n = 10$; mean \pm s.e.m.).
3. The effect of initial membrane potential is sigmoidal, with a voltage dependence of 23 mV per e-fold change in V_{pkC_m} , and maximum slope within the physiological range of OHC resting potentials. This indicates that the cell is poised to respond maximally to changes in resting potential.
4. The kinetics of prepulse effects are slow compared with motility-related gating current kinetics. High-resolution measurement of membrane capacitance (C_m) using two voltage sinusoids indicates that shifts in V_{pkC_m} induce C_m changes with time courses fitted by two exponentials (τ_0 , 0.070 ± 0.003 s; τ_1 , 1.28 ± 0.07 s; A_0 , 1.54 ± 0.13 pF; A_1 , 1.51 ± 0.13 pF; means \pm s.e.m.; $n = 22$; step from $+50$ to -80 mV). Recovery of prepulse effects exhibits a similar time course.
5. Prepulse effects are resistant to intracellular enzymatic digestion, to fast intracellular calcium buffers, and to intracellular pressure. Through modelling, we indicate how the effect may be explained by an intrinsic voltage-induced tension generated by the molecular motors residing in the lateral membrane.

The outer hair cell (OHC) is one of two receptor cell types within the organ of Corti, and plays a critical role in mammalian hearing. The OHC sharpens the passive mechanical vibration of the cochlear partition through a mechanical feedback mechanism (Ruggero, 1992). The basis of this high-frequency feedback mechanism is believed to be the unique voltage-dependent mechanical activity of the cell (Brownell, Bader, Bertrand & de Ribaupierre, 1985; Ashmore, 1987; Santos-Sacchi & Dilger, 1988). This electro-mechanical transduction is mirrored by an electrical signature, a voltage-dependent capacitance or, correspondingly, a gating charge movement (Ashmore, 1989; Santos-Sacchi, 1990, 1991), which may indicate that membrane-bound voltage sensor-motor elements control OHC length (Santos-Sacchi, 1990, 1991, 1993; Ashmore, 1992; Iwasa, 1993). Indeed, estimates of the OHC membrane-bound charge density responsible for the non-linear capacitance ($7500 e^- \mu m^{-2}$; Huang & Santos-Sacchi, 1993) coincide fairly well with estimates of the density of OHC intramembranous particles, the putative

sensor-motor elements, observed with electronmicroscopy ($6000 \mu m^{-2}$; Forge, 1991). One currently held hypothesis is that these membrane motors control OHC length via membrane areal changes induced by voltage-dependent, two-state conformational changes (Santos-Sacchi, 1993; Iwasa, 1994).

The voltage-dependent mechanical response may be dynamically modulated by a variety of physiologically important factors that can modify the mechanical gain of the cell. One of the most effective means of influencing the motility function is by exerting tension on the plasma membrane (Iwasa, 1993). Reducing membrane tension effectively increases the mechanical gain at the normal resting potential, by shifting the most sensitive region of the motility function along the voltage axis towards the resting potential value (Kakehata & Santos-Sacchi, 1995). Ligand-gated ion channels which can alter the resting membrane potential (Ashmore & Ohmori, 1990; Housley & Ashmore, 1993) may also influence the mechanical gain of the cell by moving the cell operating point, i.e. resting

potential, closer or further away from the most sensitive region of the motility function. Thus, either shifts in resting potential or shifts in the voltage dependence of OHC motility can alter the gain of the cochlear amplifier. We report here that these two mechanisms are not independent. That is, a change in resting potential affects the voltage dependence of OHC capacitance and motility. Furthermore, through modelling, we indicate that the effect can be explained by motor-driven tension on viscoelastic elements within the lateral plasma membrane.

METHODS

OHCs were freshly isolated from the organ of Corti of the guinea-pig cochlea following anaesthetic overdose (halothane inhalant; Halocarbon Labs, NJ, USA) and decapitation (Kakehata & Santos-Sacchi, 1995). The cells were whole-cell voltage clamped at -80 mV (unless otherwise noted) using an Axon 200B amplifier with patch pipettes having initial resistances of 2–3 M Ω , corresponding to tip sizes of 1–2 μ m. No series resistance compensation was performed. Residual series resistance (R_s) ranged from 3–7 M Ω . Ionic blocking solutions were used to remove voltage-dependent ionic conductances so that capacitive currents could be analysed in isolation (Santos-Sacchi, 1991; Huang & Santos-Sacchi, 1993). The patch pipette solution contained (mM): 140 CsCl, 2 MgCl₂, 10 EGTA and 10 Hepes, pH 7.2 and 300 mosmol l⁻¹ (adjusted with dextrose). The external solution contained (mM): 100 NaCl, 20 TEA, 20 CsCl, 2 CoCl₂, 1.52 MgCl₂, 10 Hepes and 5 dextrose, pH 7.2, 300 mosmol l⁻¹. In some experiments, modifications to the standard solutions were made: pipette solution, replacement of 10 mM EGTA with 10 or 20 mM BAPTA, or inclusion of pronase or trypsin (500 μ g ml⁻¹); extracellular solution, inclusion of neomycin (1 mM), or sodium salicylate (5 mM). Drugs were obtained from Sigma, and were selectively applied to individual cells by local perfusion, during simultaneous whole-chamber perfusion with control solution. Experiments were performed at room temperature (21–23 °C).

Three methods were used to analyse OHC motility-related gating charge movement and the corresponding non-linear membrane capacitance. Gating currents were extracted with the $P/-5$ leakage subtraction procedure (Bezanilla & Armstrong, 1977) using a subtraction holding potential of +60 mV. This procedure permits isolation of non-linear capacitive currents by subtracting out the intrinsic linear membrane capacitive currents obtained at a potential where non-linear currents do not contribute significantly. Fits of charge movement were made with a two-state Boltzmann function.

Detailed evaluation of membrane capacitance was made at different potentials by transient analysis of currents induced by a voltage stair-step stimulus (10 mV stair steps from a holding potential of -150 mV to $+40$ mV). The full stair-step duration was variable and depended upon the time constant of the clamp amplifier; the duration of each individual step was automatically adjusted to 15 times the clamp time constant determined immediately before presentation of the stair-step protocol. This was done to ensure a steady-state current response at each progressive step. Since our clamp time constant was typically less than 0.15 ms, each step was about 2.25 ms in duration. Given twenty, 10 mV incrementing steps in the stair-step, the total duration of the protocol was about 45 ms. The time between prepulse and stair-step was 10 ms and was spent at the prior long-term (> 2 min) holding potential, which was either 0 mV (Fig. 2) or -80 mV (Fig. 3). Thus, a full capacitance function can be obtained within 45 ms with this technique. The

capacitance function was fitted to the first derivative of a two-state Boltzmann function relating non-linear charge to membrane voltage (dQ/dV ; Santos-Sacchi, 1991; Huang & Santos-Sacchi, 1993),

$$C_m = Q_{\max} \frac{ze}{kT} \frac{b}{(1+b)^2} + C_{\text{lin}}, \quad (1a)$$

where

$$b = \exp\left(\frac{-ze(V - V_{\text{pk}C_m})}{kT}\right), \quad (1b)$$

Q_{\max} is the maximum non-linear charge moved, $V_{\text{pk}C_m}$ is voltage at peak capacitance or, equivalently, at half-maximal non-linear charge transfer, V_m is membrane potential, z is valency, C_{lin} is linear membrane capacitance, e is electron charge, k is the Boltzmann constant, and T is absolute temperature.

Continuous high-resolution capacitance measures were acquired through admittance (Y) analysis at time resolutions of 5.12 or 2.56 ms, utilizing a two-sine wave voltage-stimulus protocol. The stimulus consisted of the sum of two voltage sine waves (390.625 and 781.25 Hz), each at a magnitude (V) of 10 mV peak. Two (one) full cycles of the low-frequency signal and four (two) full cycles of the high-frequency signal (512 (256) points at 10 μ s sampling rate) were continuously delivered every 5.12 (2.56) ms, and the real and imaginary components of the current responses were obtained through Fast Fourier Transform every 5.12 (2.56) ms. The analysis, which was performed in real time and saved to disk, is model dependent; the OHC clamp was modelled as a pipette resistance (R_p) in series with a parallel combination of membrane resistance (R_m) and capacitance (C_m) (Santos-Sacchi, 1993). Given an independent measure of input resistance of such a model and the real and imaginary components of the current response to single sinusoidal stimulation, Pusch & Neher (1988) provide solutions for C_m , R_s and R_m :

$$R_s = (A - b)/(A^2 + B^2 - Ab), \quad (2)$$

$$R_m = (1/b)[(A - b)^2 + B^2]/(A^2 + B^2 - Ab), \quad (3)$$

$$C_m = [1/(\omega B)][(A^2 + B^2 - Ab)^2]/[(A - b)^2 + B^2], \quad (4)$$

where,

$$b = 1/(R_s + R_m) = 1/R_{\text{in}},$$

$$Y = I/V,$$

$$A = \text{Re}(Y),$$

$$B = \text{Im}(Y),$$

$$\omega = 2\pi f,$$

and Re is real, Im is imaginary, and f is frequency. Since R_s remains the same at each of the two stimulating frequencies, the input resistance, R_{in} , can be obtained without an independent measure, as is required by the Pusch & Neher technique.

In some experiments, OHCs were collapsed and re-inflated by pipette pressure. Pipette pressure was modified with a syringe connected to the Teflon tubing attached to the patch pipette holder, and was monitored via a T-connector to a pressure monitor (WPI, FL, USA). Voltages were corrected for the effects of residual series resistance. All experiments were video taped. Data collection and analysis were performed with an in-house developed Windows-based whole-cell voltage clamp program, jClamp (www.med.yale.edu/surgery/otolar/santos/jclamp.html), utilizing a Digidata 1200 board (Axon Instruments). Fits were made with the Levenberg–Marquardt least-squares algorithm. Data are presented as means \pm standard error of the mean.

RESULTS

The OHC generates gating-like currents when the membrane potential is stepped away from the holding potential (Fig. 1). The decay time constant of the current is very fast (in this example, $\sim 110 \mu\text{s}$ for the current at voltage offset), and essentially follows the speed of the voltage-clamp stimulus (Santos-Sacchi, 1992; however, see Gale & Ashmore, 1997). Charge movement induced by a step from 0 to -60 mV was increased by prepulsing the OHC to negative voltages. Prepulse effects were clearly evident for durations greater than 30 ms and appeared to plateau at values greater than 1 s (Fig. 1C). A single-exponential fit to the charge increase induced by -120 mV prepulses at increasing durations (Fig. 1C, inset) gave a time constant of 200 ms.

Figures 2A and B indicate that voltage prepulse can cause a shift in the voltage dependence of the charge movement or, correspondingly, the capacitance of the cell. In this example, a 1 s prepulse to $+40 \text{ mV}$ produced a voltage at peak capacitance ($V_{\text{pk}C_m}$) or voltage at half-maximal charge movement (V_h) of -76.5 and -83.4 mV , respectively. A 1 s prepulse to -120 mV shifted the values to -56.8 and -56.7 mV . The differences in the magnitude of the fitted shift may have arisen from the inherent difference in prepulse delivery for each data collection protocol. In the case of stair-step analysis, a single prepulse preceded the entire stair-step stimulus, while in the $P/-5$ procedure, a prepulse preceded each step potential. The shift of these functions along the voltage axis was opposite to that of the prepulse direction. Furthermore, the shift in the voltage dependence of OHC capacitance (viz. $\delta V_{\text{pk}C_m}$) was non-linearly related to initial voltage. Figure 2C shows that the relation was sigmoidal and, significantly, the greatest sensitivity to prepulse was within the physiological voltage range. OHCs normally have resting potentials near -70 mV

(Dallos, Santos-Sacchi & Flock, 1982). The maximum mean shift due to a 1 s prepulse was 14.8 mV , with a voltage slope factor of 22.2 mV , and a mid-point voltage of -54.4 mV ($n = 4$).

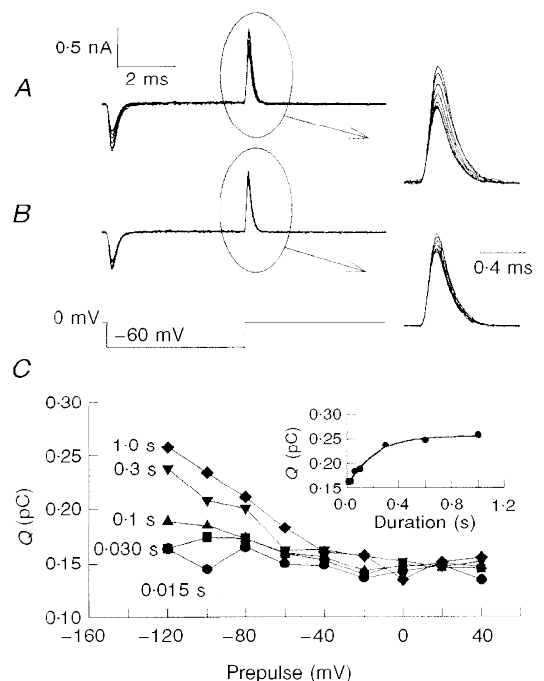
The effects of prepulse were reversible on the same time scale as onset. Figure 2D depicts the mean ($n = 22$) recovery from a 1 s prepulse to 50 mV . After a 1 s recovery at -150 mV , $V_{\text{pk}C_m}$ has nearly recovered to steady state from the prepulse-induced shift. A single-exponential fit to $V_{\text{pk}C_m}$ (Fig. 2D, inset) gave a time constant of 330 ms. Under these conditions, the mean $V_{\text{pk}C_m}$ shift was about 10 mV .

The data of Figs 1 and 2 were obtained with the cells held at a long-term holding potential of 0 mV , because whole-cell recording stability was better at this potential; in order to demonstrate the physiological relevance of the observed prepulse phenomenon, additional experiments were conducted at long-term holding potentials of -80 mV prior to the evaluation of prepulse effects. Figure 3 illustrates that the phenomenon remains qualitatively and quantitatively the same under such conditions. The mean shift between -120 mV and $+40 \text{ mV}$ prepulse states with long-term holding potentials ($> 2 \text{ min}$) at -80 mV was $14.67 \pm 0.95 \text{ mV}$ ($n = 10$).

The time course of prepulse effects is slow compared with the gating current time constants. In order to confirm the stair-step and P/N kinetic data, we utilized another technique to garner high-resolution information on the time course of prepulse effects. Since the shift in $V_{\text{pk}C_m}$ will necessarily cause the capacitance measured at a fixed potential to change, the time course of the capacitance change can be used to study prepulse effect kinetics. This is illustrated in Fig. 4, where OHC capacitance was monitored as the cell was stepped from a holding potential of $+50 \text{ mV}$

Figure 1. Motility-related charge movement is affected by initial voltage conditions

At a fixed membrane potential, an increase in charge is induced by a negative prepulse. The charge increase is due to the shift in the voltage dependence of charge movement, and the response is time dependent. An OHC was stepped to -60 mV from a holding potential of 0 mV . The command which generated each current trace was preceded by a prepulse of either 1 s (A) or 60 ms (B), with a magnitude ranging from -120 to $+40 \text{ mV}$ (20 mV increments). Leakage subtraction ($P/-5$; subtraction hold, 60 mV) revealed gating-like currents associated with OHC motility. As the length of prepulse increased, charge increased. C, under these conditions, prepulse effects were clearly present at potentials more negative than -50 mV and at durations greater than 30 ms. Inset shows time course of charge increase induced by prepulse to -120 mV . Fit indicates a single-exponential time constant of 0.2 s .



to -89 mV for 4 s. At the onset, C_m was about 39.8 pF, but decreased during the maintained voltage step to about 35.5 pF (Fig. 4B). The time course of this decrease was composed of fast and slow components, which was well fitted by a double exponential (t_0 , 0.058 s; t_1 , 1.34 s; A_0 , 2.2 pF; A_1 , 1.48 pF). (It might be expected that the time course would deviate somewhat from a true double exponential, even if the underlying mechanism followed a double-exponential time course, since the change in C_m is not linear, but follows the bell-shaped capacitance function.) The change in C_m was accounted for by a shift in V_{pkC_m} of about $+25$ mV. This was determined from responses to 25 ms voltage ramps delivered during the course of a maintained voltage step (Fig. 4A; arrows indicate ramp presentations). V_{pkC_m} , determined by fits of the resultant capacitance functions, corresponded in time to the relaxation in membrane capacitance (Fig. 4B). All cells studied with this high-resolution C_m measurement technique showed a double-exponential time course (τ_0 , 0.070 ± 0.003 s; τ_1 , 1.28 ± 0.07 s; A_0 , 1.54 ± 0.13 pF; A_1 , 1.51 ± 0.13 pF; $n = 22$; nominal step from $+50$ to -80 mV). In order to show that the time course of C_m change is not due to recovery from membrane breakdown at very depolarized potentials, we measured more physiological membrane potential pertur-

bations. Voltage steps from -80 to -40 mV, where membrane stability is unquestionable, produced changes in C_m with similar time courses. Figure 4C presents such an example.

The apparent difference in the time course observed with standard transient analysis techniques used in Figs 2 and 3 and the admittance measuring technique is explained by the higher time resolution and measurement density afforded by the latter method. A single-exponential fit to double-exponential data obtained with the admittance method also generates time constants in the tenths of seconds range when the extent is limited to 1 s, and few data points are sampled. It should also be noted that the duration of the stair-step protocol, typically around 50 ms, is close to τ_0 , and, as such, some V_{pkC_m} shift may have accumulated during that ramped measurement.

The actual direction and magnitude of C_m change during a shift in V_{pkC_m} depended on the initial holding potential and the step potential *vis-à-vis* the initial V_{pkC_m} . This is illustrated in Fig. 5A where the OHC membrane potential was stepped through V_{pkC_m} in 10 mV increments. Steps in potential induced essentially instantaneous jumps in C_m followed by slower changes. Small voltage steps from the initial holding level produced small time-dependent changes

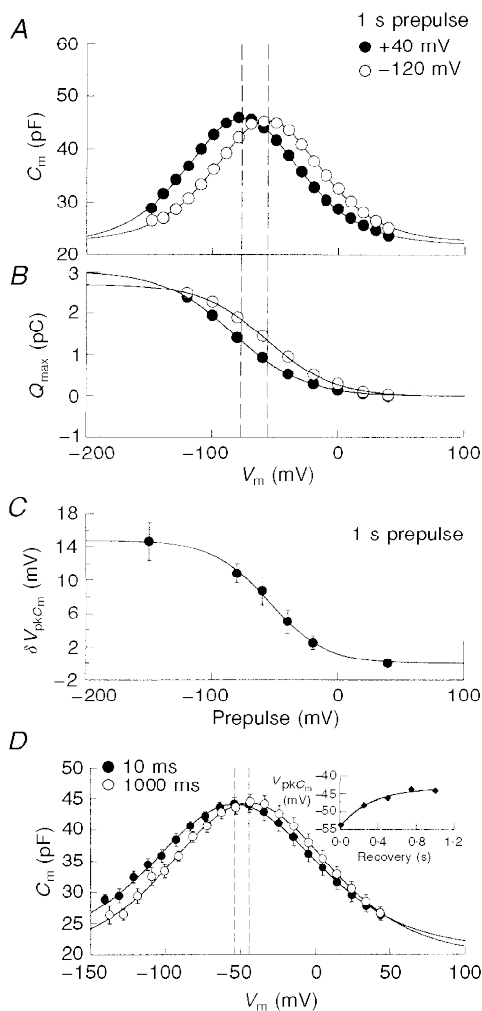


Figure 2. Voltage prepulse causes a shift in the voltage dependence of charge movement and non-linear capacitance

Long-term holding potential was 0 mV. Voltage-dependent capacitance was evaluated with the stair-step technique (A), and corresponding gating charge movement was evaluated with the $P/5$ technique at a subtraction holding potential of $+60$ mV (B). With either technique, voltage dependence was evidenced by a shift in the positive direction for negative prepulses (1 s duration). The shift is about 20 mV for a 40 mV prepulse (V_{pkC_m} is indicated by the dashed lines). Continuous line fit in A for -120 mV prepulse: V_{pkC_m} , -56.8 mV; z , 0.9 ; Q_{max} , 2.6 pC; C_{lin} , 22.5 pF; peak C_m ($C_{m,pk}$), 45.4 pF. For $+40$ mV prepulse: V_{pkC_m} , -76.5 mV; z , 0.86 ; Q_{max} , 2.86 pC; C_{lin} , 22.0 pF; $C_{m,pk}$, 45.9 pF. Continuous line fit in B for -120 mV prepulse: V_h , -56.7 mV; z , 0.96 ; Q_{max} , 2.7 pC. For $+40$ mV prepulse: V_h , -83.4 mV; z , 0.90 ; Q_{max} , 3.0 pC. C, the shift in voltage dependence is sigmoidal. The plot illustrates for 4 cells the mean (\pm s.e.m.) shift in the voltage at peak capacitance, obtained with the stair-step technique. The sigmoidal continuous line fit ($\delta V_{pkC_m} = a/[1 + \exp((V_{prepulse} - V_h)/b)]$) indicates a maximum mean shift, a , of 14.8 mV, a slope factor, b , of 22.2 mV, and a mid-point voltage, V_h , of -54.4 mV. Data are normalized to $+40$ mV response. D, recovery from prepulse effects has a similar time course to onset. Mean (\pm s.e.m.) from 22 cells. V_{pkC_m} was evaluated with the stair-step protocol from a holding potential of -150 mV. A 1 s prepulse to 50 mV preceded recovery durations of 10, 250, 500, 750 and 1000 ms at -150 mV. Only the 10 ms and 1000 ms recovery functions are shown. Inset shows time course of V_{pkC_m} recovery. Fit indicates a single-exponential time constant of 0.33 s. Recovery from prepulse appears nearly complete at 1 s. Continuous line fit for 10 ms recovery: V_{pkC_m} , -53.7 mV; z , 0.7 ; Q_{max} , 3.39 ; C_{lin} , 20.9 pF. Continuous line fit for 1000 ms recovery: V_{pkC_m} , -44.2 mV; z , 0.73 ; Q_{max} , 3.45 pC; C_{lin} , 19.8 pF. Parallel dashed lines indicate the V_{pkC_m} of each function.

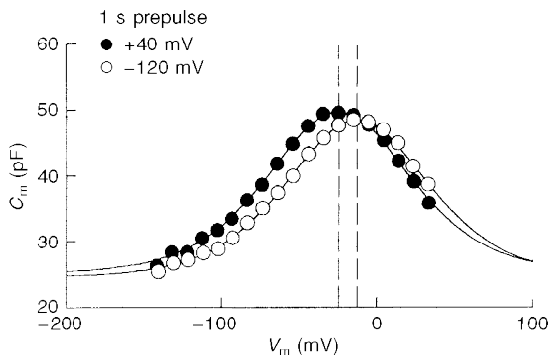


Figure 3. Prepulse-induced shifts occur at physiological holding potentials

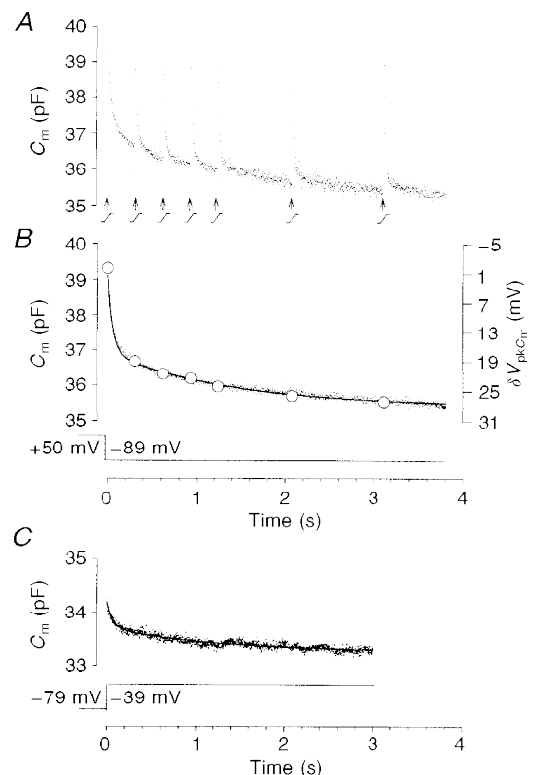
Prepulse-induced shift of capacitance function after an OHC was held at a long-term holding potential of -79 mV. As with depolarized long-term holding potentials, prepulses from physiological holding potentials caused a shift in the positive direction for negative prepulses (1 s duration). The shift in this case is 11.8 mV for a 40 mV prepulse. Continuous line fit for -120 mV prepulse: V_{pkC_m} , -12.5 mV; z , 0.84 ; Q_{max} , 2.9 pC; C_{lin} , 24.7 pF; $C_{m,pk}$, 48.5 pF. For $+40$ mV prepulse: V_{pkC_m} , -24.3 mV; z , 0.84 ; Q_{max} , 3.0 pC; C_{lin} , 25.2 pF, $C_{m,pk}$, 49.8 pF.

in C_m because the magnitude of V_{pkC_m} shift was small. Progressively larger voltage steps produced larger V_{pkC_m} shifts and, thus, larger changes in C_m at each fixed step potential. The direction of capacitance change was increasing for voltage steps positive to V_{pkC_m} , and decreasing for voltage steps negative to V_{pkC_m} . Also note for this protocol that C_m at the holding potential accumulated somewhat over time because full C_m relaxation was not reached during the interstep recovery period. Figure 5B shows the effect of voltage-step duration on the non-linear capacitance function. Determination of C_m at zero time (5 ms; the initial data point measured during a voltage step is contaminated by the transient response) or after 1 s provided differing functions, with the 1 s determination showing a relative compression of the function in the depolarizing direction; indeed, C_m overlap occurred at very depolarized levels. This is expected since the magnitude of prepulse effect is a function of step potential.

There are several possible mechanisms which may account for the observed prepulse effects, including intracellular pressure change. OHC voltage-dependent motility occurs under a constant cell volume constraint (Santos-Sacchi, 1993; Dallos, Hallworth & Evans, 1993). Thus, during whole-cell voltage stimulation, intracellular pressure may change, despite continuity with pipette volume. Since modification of intracellular pressure is known to shift V_{pkC_m} via tension applied to the plasma membrane (Iwasa, 1993; Gale & Ashmore, 1994; Kakehata & Santos-Sacchi, 1995), it is of interest to determine whether prepulse effects are simply related to a motility-induced intracellular pressure change. Figure 6A illustrates that when OHCs ($n=6$) were collapsed with negative pipette pressure, causing a limiting negative shift in V_{pkC_m} (Kakehata & Santos-Sacchi, 1995), prepulse effects were still observed. Collapsed OHCs cannot generate an intracellular pressure change (nor the consequent pressure-induced membrane tension) since the usual voltage-

Figure 4. The time course of prepulse effects has a fast and a slow component

A, an OHC was stepped to -89 mV from a holding potential of $+50$ mV, and the C_m at the new step potential was monitored every 2.5 ms using the admittance technique (see Methods). At the time points indicated, voltage ramps (25 ms in duration) were delivered in order to determine V_{pkC_m} from the voltage-capacitance function. In B, the step stimulus was delivered without ramps, and the continuous line (which is difficult to see, since it is obscured by the many data points) is a double-exponential fit to the resultant capacitance data (t_0 , 0.058 s; t_1 , 1.34 s; A_0 , 2.2 pF; A_1 , 1.48 pF). The close correspondence of the overlying open symbols, which denote the change in V_{pkC_m} relative to the first ramp measurement (i.e. δV_{pkC_m}), indicates that the shift of the OHC capacitance function along the voltage axis accounts for the relaxation of capacitance during step potentials. C, a voltage step from a long-term holding potential (> 2 min) of -79 mV to -39 mV, induces a change in C_m over a similar time course to that in 4B. The fitted line (t_0 , 0.067 s; t_1 , 1.18 s; A_0 , 0.46 pF; A_1 , 0.44 pF) is obscured by the data points.



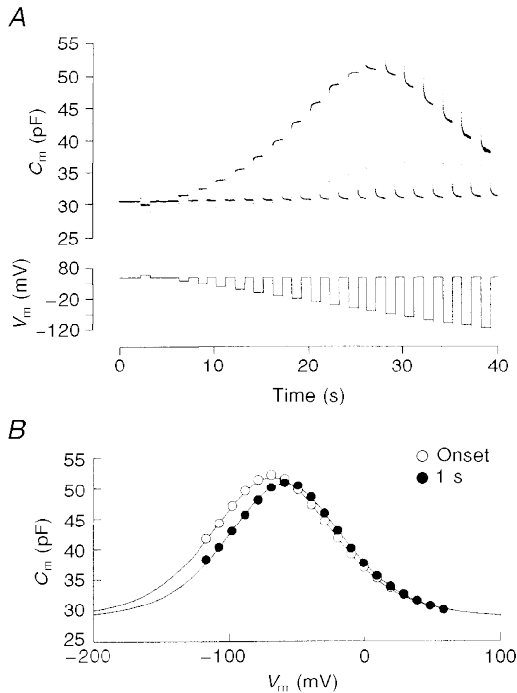


Figure 5. The direction and magnitude of C_m change depends on initial holding potential and step potential relative to V_{pkC_m}

A, an OHC was stepped (-10 mV increments) from a holding potential of $+48$ mV through V_{pkC_m} . Step durations were 1 s, with equal recovery intervals at the holding potential. A total of 40 s of data were collected at 5 ms resolution. The top panel shows C_m measured with the admittance technique. The bottom panel shows the DC voltage stimulus, corrected for residual series resistance. Note that steps to voltages more depolarized than V_{pkC_m} induce C_m changes which increase over time, while steps to potentials more hyperpolarized than V_{pkC_m} induce C_m changes which decrease over time. The magnitude of C_m change corresponds to step size. *B*, the C_m functions derived from the measurements at onset (5 ms point; the initial data point measured by Fast Fourier Transform during a voltage step is invalid since it is contaminated by the transient response – these aberrant points are visible at the transitions between voltage steps) or 1000 ms are plotted, along with fitted functions. The plots indicate differences in the instantaneous and steady-state C_m functions; notably a shift and compression in the steady-state function in the depolarizing direction. Continuous line fits for onset: Q_{max} , 2.81 pC; z , 0.85; C_{lim} , 28.7 pF; V_{pkC_m} , -68 mV. For steady-state: Q_{max} , 2.54 pC; z , 0.9; C_{lim} , 28.7 pF; V_{pkC_m} , -58.7 mV.

dependent whole-cell mechanical response (but not gating current) is abolished. Prepulse-induced voltage shifts merely superimposed upon the negative pressure-induced steady-state voltage shift. These data suggest that voltage-induced motility induces little or no intracellular pressure changes, in line with modelling efforts (Tolomeo & Steele, 1995).

Other possible prepulse mechanisms might involve intracellular Ca^{2+} increases, and cytoskeletal–motor interactions. These can be excluded since we have found no alterations of prepulse effects upon using the fast Ca^{2+} chelator BAPTA (10 mM ($n = 4$) or 20 mM ($n = 4$)) intracellularly, or after intracellular digestion with pronase ($n = 5$) or trypsin

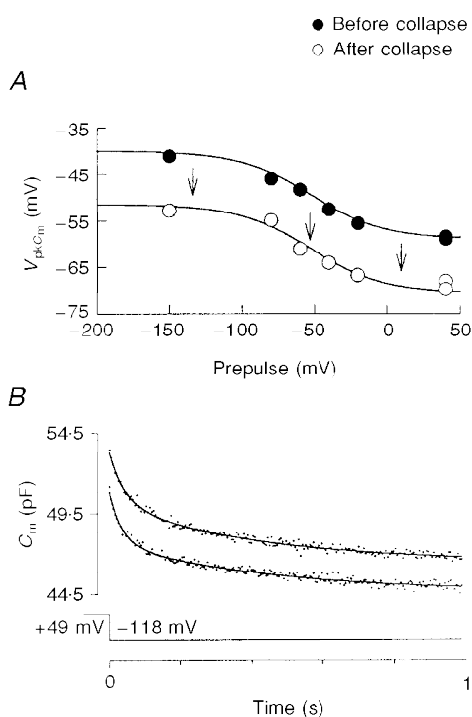


Figure 6. The mechanism responsible for prepulse effects appears intrinsic to the lateral membrane

A, intracellular pressure does not alter prepulse effects. Before (●) and after (○) collapse of OHC by reduction of intracellular pressure via patch pipette. Note the parallel negative shift in V_{pkC_m} with negative pressure. Prepulse at each potential was 1 s in duration. The sigmoidal lines were generated with the electro-mechanical model described in the Discussion. Parameter values are the same as set out in the Discussion, except that for the continuous line corresponding to data before collapse: μ_1 , 4 mN m $^{-1}$; η_1 , 0.24 mN s m $^{-1}$; μ_2 , 4 mN m $^{-1}$; and η_2 , 4.8 mN s m $^{-1}$. The continuous line corresponding to data after cell collapse was generated with the same parameters except that a constant of 1 kTorr was subtracted from the mechanical energy, E_m , to account for the resultant decrease in membrane tension (see Discussion for model details). *B*, C_m measurements made before (zero time after whole-cell configuration, bottom trace) and after (10 min after whole-cell configuration, top trace) intracellular pronase treatment (500 μ g ml $^{-1}$, delivered via the patch pipette). After 10 min, the cell had lost its cylindrical shape and formed a sphere. The cell was held at $+49$ mV and stepped to -118 mV for 1 s. In each case the onset C_m relaxed with a double-exponential time course. The difference in absolute magnitude (DC) is due to a steady-state shift in V_{pkC_m} , from -90.7 to -97.6 mV, possibly induced by osmotic effects or a release in tension on the membrane after cytoskeletal disruption. Such shifts during intracellular enzymatic treatments have been noted previously (Huang & Santos-Sacchi, 1994). The relaxations are quite similar, indicating that the treatment had little effect on the molecular structures responsible for voltage-induced V_{pkC_m} shift. The continuous lines indicate the sum of two exponentials – zero time: τ_0 , 0.034 s; τ_1 , 0.447 s; 10 min: τ_0 , 0.042 s; τ_1 , 0.417 s.

($n = 4$; 500 mg ml^{-1}). Intracellular proteolytic treatment has been shown to abolish normal OHC cyto-architecture by disrupting the cortical cytoskeleton and subsurface cisternae (Huang & Santos-Sacchi, 1994). An example of the negligible effect of intracellular pronase treatment on voltage-dependent $V_{\text{pk}C_m}$ shift is provided in Fig. 6B. Another indication that the $V_{\text{pk}C_m}$ shift was unrelated to intracellular structures is the poor correlation between the fitted C_m exponential parameters and precise estimates of cell length, viz. linear capacitance (r^2 of τ_0 vs. C_{lin} , 0.23; r^2 of τ_1 vs. C_{lin} , 0.15; r^2 of A_0 vs. C_{lin} , 0.004; r^2 of A_1 vs. C_{lin} , 0.033; $n = 22$; step from +50 mV to -80 mV). It should be noted that the pronase and trypsin experiments also exclude a host of biochemical processes which would rely on enzymes susceptible to proteolytic destruction, for example protein kinases. Other treatments which did not interfere with prepulse effects were salicylate (sub-maximal dose, 5 mM; $n = 5$), and neomycin (1 mM; $n = 3$).

DISCUSSION

The OHC possesses a voltage-dependent capacitance or gating charge movement with a $V_{\text{pk}C_m}$ or mid-point voltage, V_h , that is variable (Santos-Sacchi, Huang & Kakehata, 1994). The present data indicate that one of the factors contributing to this variability is a dependence on initial voltage conditions. More importantly, since motility-related gating charge characteristics are known to mirror characteristics of the mechanical activity of the OHC (Ashmore, 1989, 1992; Santos-Sacchi, 1991, 1992; Kakehata & Santos-Sacchi, 1995), the present experiments demonstrate a link between the two factors, membrane potential and $V_{\text{pk}C_m}$, that control the gain of OHC motility.

Some superficial characteristics of prepulse effects on OHC motility-related gating currents are reminiscent of the Cole-Moore effect on K^+ channel gating currents (Cole & Moore, 1960; Stefani, Toro, Perozo & Bezanilla, 1994); however, no shift in voltage dependence is associated with the Cole-Moore effect. On the other hand, a shift in voltage dependence is responsible for depolarization-induced fast (complete within 50 ms) and slow (occurring over seconds to minutes) inactivation of Na^+ channel gating (Bezanilla, Taylor & Fernandez, 1982). Inactivation of Na^+ channels is characterized by charge immobilization (Armstrong & Bezanilla, 1977; Bezanilla & Armstrong, 1977). We had previously noted an absence of OHC charge immobilization on very short time scales (within a window of 26 ms; Fig. 9 in Santos-Sacchi, 1991), where Na^+ channel gating charge immobilization is clearly observed. Given the present results, this is understandable since in the OHC the fast prepulse effect has a mean time constant of 70 ms; additionally, since the voltage dependence of OHC charge movement is significantly less steep than Na^+ channel gating charge movement, a given shift in voltage dependencies will present a smaller charge immobilization for the OHC. In preliminary experiments, an extended observation window

permits the observation of charge immobilization in the OHC, with a time course similar to the capacitance data. To a limited extent, then, Na^+ channel gating behaviour is comparable to that of the OHC lateral membrane motor. Simple kinetic schemes to account for prepulse effects on the Na^+ channel were discussed by Bezanilla *et al.* (1982), and may possibly apply to the OHC. These abstract schemes do not, however, provide insight into the physical correlates of prepulse effects in the OHC.

The present data suggest that voltage prepulse appears to work directly on the lateral membrane and/or the embedded molecular motors, and not via extrinsic tension delivered by intracellular pressure or delivered by some other means, e.g. Ca^{2+} -dependent cytoskeletal interactions or enzyme-based second messengers. While an extrinsic source of tension can probably be ruled out, an intrinsic source of tension can be envisioned. In this regard, it is notable that the magnitude of voltage prepulse effects presents characteristics similar to those of OHC motility itself. Namely, the sigmoidal voltage dependence is similar between the two. It is, therefore, conceivable that the activity (conformational changes) of the molecular motors themselves produces a force within the lateral membrane which dynamically modifies $V_{\text{pk}C_m}$. Thus, while the electrical energy supplied by the membrane potential will drive lateral molecular motors into a preferred state, leading to an overall change in membrane area, the force induced by this strain within the viscoelastic membrane will influence the state of adjacent motors, but will decay over time. In order to account for the kinetics of $V_{\text{pk}C_m}$ shift, the induced membrane tension must dissipate following the time course observed in the OHC C_m measurements (Figs 4 and 5). Iwasa (1994) evaluated the effects of an externally applied tension on the OHC membrane by redefining eqn (1) to include an additional energy term (E_m) in the description of OHC C_m :

$$b = \exp\left(\frac{-ze(V - V_{\text{pk}C_m}) + E_m}{kT}\right), \quad (5)$$

where E_m , the mechanical energy per motor unit, was calculated from the product of a , the unit areal change in the lateral membrane motor, and T_m , the mean membrane tension in the axial and circumferential directions, determined from the law of Laplace. From Iwasa (Fig. 4, 1993) and Kakehata & Santos-Sacchi (Fig. 4, 1995), it is known that 1 kPa intracellular pressure induces an OHC longitudinal strain ($\Delta L/L$) of 0.07. Such a longitudinal strain corresponds to a shift in $V_{\text{pk}C_m}$ of 22.5 mV (Kakehata & Santos-Sacchi, 1995), and can be accounted for by an induced membrane mechanical energy of $1.2 kT$ according to eqns (1a) and (5).

We model E_m as being additionally voltage and time dependent. The voltage-dependent characteristics match those of OHC motility, and the time-dependent characteristics accord with the time constants of OHC C_m measurements. Depolarization, which drives the motors into

a compact state, induces tension in the membrane. The electro-mechanical model is implemented as follows.

The patch-clamped OHC is modelled electrically as an electrode resistance (R_s) in series with a parallel combination of a membrane resistance (R_m), linear capacitance (C_{lin}) and voltage-dependent capacitance (C_v) as defined above (see Santos-Sacchi, 1993, for details). The electrical model parameters are: R_s , 5 M Ω ; R_m , 100 M Ω ; C_{lin} , 29 pF; Q_{max} , 2.3 pC; V_{pkC_m} , -50 mV; and z , 1. Voltage-dependent OHC contraction, δL , is described by a two-state Boltzmann function (Santos-Sacchi, 1991):

$$\delta L = \frac{\delta L_{max}}{1 + \exp\left(\frac{-ze(V - V_{pkC_m}) + E_m}{kT}\right)}, \quad (6)$$

now including the additional mechanical energy term E_m , which is derived from the deformation-induced membrane force (F).

$$E_m = F_m \times \delta d_m, \quad (7)$$

$$F_m = F/N_{cir}, \quad (8)$$

where F_m is the force per motor unit, determined by dividing whole-cell membrane force (F) by N_{cir} , the number of parallel motors along the circumferential dimension of the OHC. δd_m is the diameter change of the lateral membrane motor.

The OHC lateral membrane is modelled as a parallel combination of Maxwell (series combination of spring and dash-pot) elements (standard 4-parameter Maxwell model; Tschoegl, 1989) (inset in Fig. 7A). The equations describing the mechanical model are:

$$\frac{dx}{dt} = \frac{\dot{F}_1}{\mu_1} + \frac{F_1}{\eta_1} = \frac{\dot{F}_2}{\mu_2} + \frac{F_2}{\eta_2}, \quad (9)$$

$$F = F_1 + F_2, \quad (10)$$

where the dot, e.g. in \dot{F}_1 , indicates differentiation with respect to time, μ_1 and μ_2 are the spring stiffness coefficients, and η_1 and η_2 are the dash-pot coefficients of viscosity.

The force induced by step deformation is a decaying double-exponential function of time:

$$F = x[\mu_1 \exp(-t/\tau_1) + \mu_2 \exp(-t/\tau_2)], \quad (11)$$

where:

$$\tau_1 = \eta_1/\mu_1,$$

$$\tau_2 = \eta_2/\mu_2,$$

$$x = 0, t \leq 0,$$

$$x = 1, t > 0,$$

and the deformation of the model, x , is obtained from the motility function $\delta L(V)$. Maximum contraction, δL_{max} , is set at 3 μm (Santos-Sacchi & Dilger, 1988). The parameter values of the mechanical elements are chosen to produce

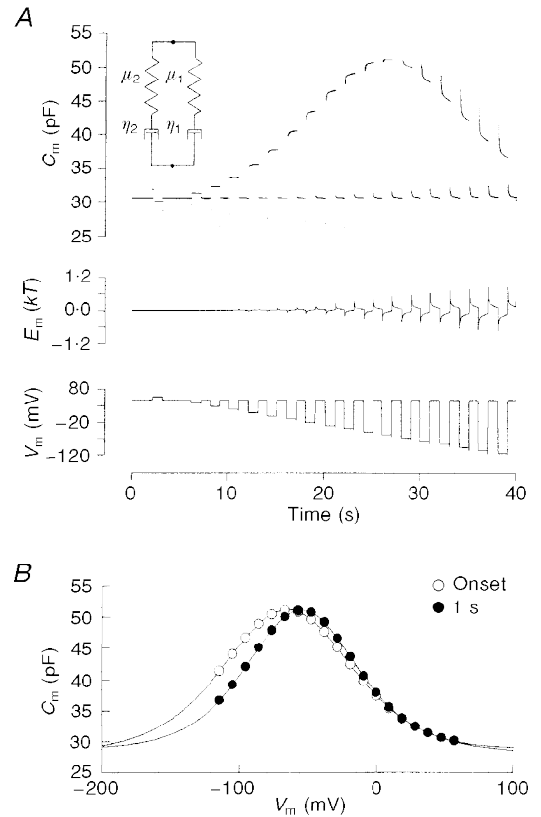
maximal instantaneous voltage-dependent mechanical energy (E_m) of 1.2 kT , and to provide a double-exponential time course for the relaxation of that energy which matches the time course empirically determined in Fig. 5. The mechanical parameter values which satisfy these conditions are: μ_1 , 5.8 mN m $^{-1}$; η_1 , 0.35 mN s m $^{-1}$; μ_2 , 4.2 mN m $^{-1}$; and η_2 , 5 mN s m $^{-1}$. δd_m is set to 0.5 nm and N_{cir} is 3000 (Santos-Sacchi, 1993). Notably, our model is of the plasma membrane, since contributions by intracellular structures have been dismissed. In this regard, our model differs from classical treatments of the red cell membrane (e.g. Chien, Sinu, Skalak, Usami & Tozeren, 1978) and a recent treatment of OHC viscoelastic behaviour (see below; Ehrenstein & Iwasa, 1996), since, in those analyses, cytoskeletal element contributions were not ruled out. The model was evaluated with the software package Simulink (Mathworks, MA, USA) or hard-coded in C. Maximum force (F) generated with the model is about 30 nN. This compares favourably with the force determined from whole-cell stiffness measurements (10 mN m $^{-1}$ \times 3 μm = 30 nN; Hallworth, 1996; Iwasa & Adachi, 1997), or voltage-dependent force estimates (0.1 nN mV $^{-1}$ \times 200 mV = 20 nN; Hallworth, 1996; Iwasa & Adachi, 1997). The stiffness coefficients for the membrane spring components are also in good agreement with the OHC membrane stiffness estimate (1 mN m $^{-1}$) of Tolomeo, Steele & Holley (1996); the values are greater than red blood cell plasma membrane stiffness (10 $\mu\text{N m}^{-1}$; Skalak, Tozeren, Zarda & Chein, 1973).

Figure 7 illustrates the results obtained from the model when it is stimulated with the same voltage protocol used in Fig. 5. The voltage-dependent mechanical energy which develops is shown in the middle panel of Fig. 7A, and at large voltage steps approaches instantaneous values of 1 kT , followed by relaxations towards zero. The model was also used to account for the data in Fig. 6A, indicating its usefulness in describing prepulse effects. The similarity between the capacitance of the model and OHC indicates that tension developed by the voltage-driven molecular motors residing within the lateral membrane can account for the biophysical data.

Because of the correspondence between OHC capacitance and motility, the length of the OHC is expected to mirror the intrinsic tension-dependent changes in C_m . However, the physiological significance of the link between membrane potential and the voltage dependence of OHC capacitance and motility is dependent on the magnitude and time course of the phenomenon. The magnitude of V_{pkC_m} shift is maximal in the physiological voltage range, showing a voltage dependence of about 22 mV per e-fold change in V_{pkC_m} . A step in membrane potential will produce not only a very rapid change in cell length, but, in addition, a slow length change as V_{pkC_m} shifts. Given the model parameters used above, the ratio of slow length change to rapid length change following a voltage step from the resting potential of -70 mV is a bell-shaped function of step voltage, with a maximum of about 0.2 at a voltage near the resting

Figure 7. Model results incorporating a voltage-induced mechanical energy within the plasma membrane

A, the top panel shows the whole-cell capacitance induced by the voltage stimulus in the bottom panel. Same voltage protocol as used in Fig. 5. The middle panel shows the generated mechanical energy, E_m . Model C_m results are quite similar to the OHC C_m data of Fig. 5. Inset, viscoelastic model of membrane, consisting of a parallel combination of two Maxwell elements (series combination of spring and dash-pot). The symbols μ_1 and μ_2 indicate the spring stiffness coefficients, and the symbols η_1 and η_2 indicate the dash-pot coefficients of viscosity. B, onset (5 ms) and steady-state (1 s) C_m function as in Fig. 5B. Continuous line fits for onset: Q_{max} , 2.94 pC; z , 0.81; C_{lin} , 28.1 pF; V_{pkC_m} , -65.1 mV. For steady state: Q_{max} , 2.42 pC; z , 0.95; C_{lin} , 28.7 pF; V_{pkC_m} , -54.8 mV.



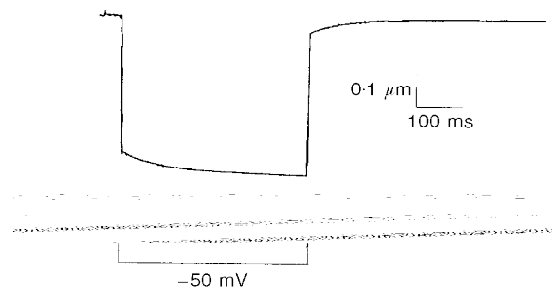
potential. An example of the mechanical response of the model is shown in Fig. 8. This is a significant component of the length change, and such a slow length change is observable in records of OHC mechanical responses obtained under whole-cell voltage clamp (Ashmore, 1987; Santos-Sacchi, 1990, 1992).

The physical basis of the time course of V_{pkC_m} shift observed here probably derives from viscoelastic elements within the motor itself and/or within the lipid bilayer. Alterations in the mechanical properties of these structures may, therefore, control the time course of the phenomenon. Nevertheless, the double-exponential time course indicates that the mechanism may only be significant at frequencies below about 3 Hz. Even correcting for temperature effects (e.g. Q_{10} for OHC gating charge kinetics is 1.5; Santos-Sacchi, 1990) will not significantly increase the frequency response. However, such slow effects may be utilized by the OHC medial efferent

system. The effects of the medial efferent system on the peripheral auditory system encompass the time scales reported here (Sridhar, Liberman, Brown & Sewell, 1995). It is also to be expected that pathological states which cause membrane potential alterations in the OHC, e.g. acoustic overexposure (Cody & Russell, 1985), may evoke V_{pkC_m} shifts with attendant changes in the gain of OHC motility. Since, normally, V_{pkC_m} is more depolarized than the OHC resting membrane potential (Dallos *et al.* 1982; Santos-Sacchi, 1991; Ashmore, 1992; Kakehata & Santos-Sacchi, 1995), a depolarizing shift in resting potential augmented by a hyperpolarizing shift in the motility function should increase mechanical gain, but reduce motor-generated non-linearities; namely, DC and harmonic mechanical components (Santos-Sacchi, 1993). In the peripheral auditory system, where non-linearities are the hallmark of normal activity, such interference with motility-based non-linearities may be significant.

Figure 8. Predicted mechanical responses of the OHC to voltage steps

Model results indicating the slow DC component attributable to motor-induced membrane tension. Step voltage from -70 mV to -50 mV.



Interestingly, Ehrenstein & Iwasa (1996) have observed external, osmotically induced viscoelastic behaviour in the intact OHC with a single time constant of about 40 s. Within this time scale, tension induced by steady-state membrane strain relaxes exponentially. This very slow time course may suggest that the underlying mechanical elements responsible for their observed viscoelastic behaviour are distinct from those responsible for the V_{pkC_m} shifts observed here. However, it should be noted that the apparent viscosity of a medium may depend upon rate, duration and magnitude of deformation (see Hochmuth, 1993). For example, Chien *et al.* (1978) found that an increase in duration of erythrocyte deformation from 2 to 20 s, caused an increase in the time constant of recovery from about 110 to 260 ms. In this regard, the fast rate and small magnitude of deformation induced by membrane voltage markedly differ from those of the osmotic treatments of Ehrenstein & Iwasa (1996).

Finally, it is noted that the V_{pkC_m} shift which is induced by voltage-dependent motor activity underlies the existence of both an instantaneous and a steady-state electro-mechanical transduction function, as exemplified through capacitance measurements (Fig. 5). This is somewhat analogous to the instantaneous and steady-state stereociliar mechano-electrical transducer functions which derive from displacement-induced adaptation (Shepherd & Corey, 1994). In each case, a time-dependent relaxation in a tension produced by the appropriate physiological stimulus on a membrane component (stereociliar channel or OHC motor) will effectively result in a repositioning of the cell operating point along the corresponding transduction function.

- ARMSTRONG, C. M. & BEZANILLA, F. (1977). Inactivation of the sodium channel. II. Gating current experiments. *Journal of General Physiology* **70**, 567–590.
- ASHMORE, J. F. (1987). A fast motile response in guinea-pig outer hair cells: the cellular basis of the cochlear amplifier. *Journal of Physiology* **338**, 323–347.
- ASHMORE, J. F. (1989). Transducer motor coupling in cochlear outer hair cells. In *Mechanics of Hearing*, ed. KEMP, D. & WILSON, J. P., pp. 107–113. Plenum Press, New York.
- ASHMORE, J. F. (1992). Mammalian hearing and the cellular mechanism of the cochlear amplifier. In *Sensory Transduction*, ed. COREY, D. P. & ROPER, S. D., pp. 395–412. Rockefeller University Press, NY, USA.
- ASHMORE, J. F. & OHMORI, H. (1990). Control of intracellular calcium by ATP in isolated OHCs of the guinea-pig cochlea. *Journal of Physiology* **428**, 109–131.
- BEZANILLA, F. & ARMSTRONG, C. M. (1977). Inactivation of the sodium channel. I. Sodium current experiments. *Journal of General Physiology* **70**, 549–566.
- BEZANILLA, F., TAYLOR, R. E. & FERNANDEZ, J. M. (1982). Distribution and kinetics of membrane dielectric polarization. I. Long-term inactivation of gating currents. *Journal of General Physiology* **79**, 21–40.
- BROWNELL, W. E., BADER, C. R., BERTRAND, D. & DE RIBAUPIERRE, Y. (1985). Evoked mechanical responses of isolated cochlear outer hair cells. *Science* **227**, 194–196.
- CHIEN, S., SUNG, K. L., SKALAK, R., USAMI, S., & TOZEREN, A. (1978). Theoretical and experimental studies on viscoelastic properties of erythrocyte membrane. *Biophysical Journal* **24**, 463–487.
- CODY, A. R. & RUSSELL, I. J. (1985). Outer hair cells in the mammalian cochlea and noise-induced hearing loss. *Nature* **315**, 662–665.
- COLE, K. S. & MOORE, J. W. (1960). Potassium ion current in the squid giant axon: dynamic characteristics. *Biophysical Journal* **1**, 161–202.
- DALLOS, P., HALLWORTH, R. & EVANS, B. (1993). Theory of electrically driven shape changes of cochlear outer hair cells. *Journal of Neurophysiology* **70**, 299–322.
- DALLOS, P., SANTOS-SACCHI, J. & FLOCK, A. (1982). Intracellular recordings from outer hair cells. *Science* **218**, 582–584.
- EHRENSTEIN, D. & IWASA, K. H. (1996). Viscoelastic relaxation in the membrane of the auditory outer hair cell. *Biophysical Journal* **71**, 1087–1094.
- FORGE, A. (1991). Structural features of the lateral walls in mammalian cochlear outer hair cells. *Cell Tissue Research* **265**, 473–483.
- GALE, J. E. & ASHMORE, J. F. (1994). Charge displacement induced by rapid stretch in the basolateral membrane of the guinea pig OHC. *Proceedings of the Royal Society of London B* **255**, 243–249.
- GALE, J. E. & ASHMORE, J. F. (1997). An intrinsic frequency limit to the cochlear amplifier. *Nature* **389**, 63–66.
- HALLWORTH, R. (1995). Passive compliance and active force generation in the guinea pig outer hair cell. *Journal of Neurophysiology* **74**, 2319–2328.
- HOCHMUTH, R. M. (1993). Measuring the mechanical properties of individual human blood cells. *Journal of Biomechanical Engineering* **115**, 515–519.
- HOUSLEY, G. D. & ASHMORE, J. F. (1993). Direct measurement of the action of ACh on isolated OHCs of the guinea pig cochlea. *Proceedings of the Royal Society of London B* **244**, 161–167.
- HUANG, G.-J. & SANTOS-SACCHI, J. (1993). Mapping the distribution of the outer hair cell motility voltage sensor by electrical amputation. *Biophysical Journal* **65**, 2228–2236.
- HUANG, G.-J. & SANTOS-SACCHI, J. (1994). Motility voltage sensor of the outer hair cell resides within the lateral plasma membrane. *Proceedings of the National Academy of Sciences of the USA* **91**, 12268–12272.
- IWASA, K. H. (1993). Effect of stress on the membrane capacitance of the auditory outer hair cell. *Biophysical Journal* **65**, 492–498.
- IWASA, K. H. (1994). A membrane motor model for the fast motility of the OHC. *Journal of the Acoustical Society of America* **96**, 2216–2224.
- IWASA, K. H. & ADACHI, M. (1997). Force generation in the outer hair cell of the cochlea. *Biophysical Journal* **73**, 546–555.
- KAKEHATA, S. & SANTOS-SACCHI, J. (1995). Membrane tension directly shifts voltage dependence of outer hair cell motility and associated gating charge. *Biophysical Journal* **68**, 2190–2197.
- PUSCH, M. & NEHER, E. (1988). Rates of diffusional exchange between small cells and a measuring patch pipette. *Pflügers Archiv* **411**, 204–211.
- RUGGERO, M. A. (1992). Responses to sound of the basilar membrane of the mammalian cochlea. *Current Opinion in Neurobiology* **2**, 449–456.

- SANTOS-SACCHI, J. (1990). Fast outer hair cell motility: how fast is fast? In *The Mechanics and Biophysics of Hearing*, ed. DALLOS, P., GEISLER, C. D., MATTHEWS, J. W., RUGGERO, M. A. & STEELE, C. R., pp. 69–75. Springer-Verlag, Berlin.
- SANTOS-SACCHI, J. (1991). Reversible inhibition of voltage-dependent outer hair cell motility and capacitance. *Journal of Neuroscience* **11**, 3096–3110.
- SANTOS-SACCHI, J. (1992). On the frequency limit and phase of outer hair cell motility: effects of the membrane filter. *Journal of Neuroscience* **12**, 1906–1916.
- SANTOS-SACCHI, J. (1993). Harmonics of outer hair cell motility. *Biophysical Journal* **65**, 2217–2227.
- SANTOS-SACCHI, J. & DILGER, J. P. (1988). Whole cell currents and mechanical responses of isolated outer hair cells. *Hearing Research* **35**, 143–150.
- SANTOS-SACCHI, J., HUANG, G.-J. & KAKEHATA, S. (1994). Variability of voltage dependency of the outer hair cell (OHC) motility voltage sensor. 127th Meeting of the Acoustical Society of America, June.
- SHEPHERD, G. M. & COREY, D. P. (1994). The extent of adaptation in bullfrog saccular hair cells. *Journal of Neuroscience* **14**, 6217–6229.
- SKALAK, R., TOZEREN, A., ZARDA, R. P., & CHEIN, S. (1973). Strain energy function of red blood cell membranes. *Biophysical Journal* **13**, 245–264.
- SRIDHAR, T. S., LIBERMAN, M. C., BROWN, M. C. & SEWELL, W. F. (1995). A novel cholinergic ‘slow effect’ of efferent stimulation on cochlear potentials in the guinea pig. *Journal of Neuroscience* **15**, 3667–3678.
- STEFANI, E., TORO, L., PEROZO, E. & BEZANILLA, F. (1994). Gating of Shaker K⁺ channels: I. Ionic and gating currents. *Biophysical Journal* **66**, 996–1010.
- TOLMEO, J. A. & STEELE, C. R. (1995). Orthotropic piezoelectric properties of the cochlear outer hair cell wall. *Journal of the Acoustical Society of America* **97**, 3024–3029.
- TOLMEO, J. A., STEELE, C. R. & HOLLEY, M. C. (1996). Mechanical properties of the lateral cortex of mammalian auditory outer hair cells. *Biophysical Journal* **71**, 421–429.
- TSCHOEGL, N. W. (1989). *The Phenomenological Theory of Linear Viscoelastic Behavior*. Springer-Verlag, Berlin.

Acknowledgements

This work was supported by NIH-NIDCD grant DC00273 and DC02003 to J.S.S. We thank Margaret Mazzucco for technical help. We also thank Drs Robert Apfel, Hongbo Zhao and Francisco Bezanilla for helpful discussions.

Corresponding author

J. Santos-Sacchi: Surgery (Otolaryngology), BML 244, Yale University School of Medicine, 333 Cedar Street, New Haven, CT 06510, USA.

Email: joseph.santos-sacchi@yale.edu

Fast Electromechanical Amplification in the Lateral Membrane of the Outer Hair Cell

Joseph Santos-Sacchi,* Enrique Navarrete, and Lei Song

Departments of Surgery (Otolaryngology), Cellular and Molecular Physiology, and Neurobiology, Yale University School of Medicine, New Haven, Connecticut 06510

ABSTRACT Outer hair cells provide amplification within the mammalian cochlea to enhance audition. The mechanism is believed to reside within the lateral membrane of the cell that houses an expansive array of molecular motors, identified as prestin, which drives somatic electromotility. By measuring nonlinear capacitance, the electrical signature of electromotility, at kilohertz rates we have uncovered new details of the early molecular events that arise from voltage perturbations of prestin. We show that dynamic changes in motor state probability occur within the kilohertz range, and signify an amplificatory event. Additionally, we show a lack of effect of CI driving force, an absence of cell length effect (indicating that the kinetics does not vary across auditory frequency), and the first demonstration of the time dependence of tension induced amplificatory shifts. The process we have identified, where the stimulus-response function shifts in time along the stimulus axis in a multi-exponential manner, bears similarities to those components of adaptation found in the OHC stereociliar transducer identified recently. As with the forward transducer, the speed of the reverse transducer amplificatory event consequently impacts on high frequency peripheral auditory processing.

INTRODUCTION

The hallmark of mammalian cochlear amplification is a mechanical nonlinearity that is thought to arise from the mechanical activity of outer hair cells (OHC). There are two key nonlinear electro-mechanical systems in OHCs, the stereocilia forward transduction apparatus and lateral membrane reverse transduction apparatus. Each is considered a potential powerhouse for cochlear amplification. These systems transduce acoustically derived electrical energy back into mechanical energy that must finally feedback into the organ of Corti to provide an enhanced drive to the inner hair cells (IHC), which predominately control eighth-nerve afferent activity.

The favored mechanism for fast stereocilia feedback corresponds to events underlying a Ca-dependent adaptation of the hair cell's receptor current (1,2). Owing to tension dependence of the stereocilia channel, insight into channel open/closed state probability derives from inspection of the cell's nonlinear receptor current-bundle displacement (I-X) or conductance-displacement (G-X) relationship, which quantifies the activity of the channels' tension sensors. Positive tension increases the probability that the channels will reside in the open state. During a step bundle displacement, fast adaptation apparently results from the influx and binding of Ca ions to a component of the unidentified transduction channel, somehow closing the channel. At the channel population level, the process is observed as a shift of the channels' Boltzmann distribution along the stimulus axis in the same direction (polarity) as the stimulus (bundle displacement).

Thus, the process of opening transduction channels tends to close those same channels in a time-dependent manner, and the process has been shown recently to operate at the submillisecond timescale (kHz range) in OHCs (3). The resultant, channel-induced bundle movements may provide feedback into the auditory end organ.

The OHC lateral membrane motor, recently identified as prestin (4), is voltage dependent, and has been known for some time to work effectively in the kilohertz range (5,6). One popular model posits that the integral lateral membrane motors fluctuate in area between two states, contracted and expanded, just as bundle channels fluctuate between closed and open states (7,8). Owing to the motor's voltage dependence, insight into motor state probability derives from inspection of the cell's nonlinear charge-voltage (Q-V) or capacitance-voltage (C-V) relationship, which quantifies the activity of the motors' voltage sensors (9,10). Depolarization favors the contracted state. Prestin presents a behavior somewhat akin to, but notably different from the bundle adaptation process. That is, during a step voltage stimulus there is a shift in the motors' Boltzmann distribution along the stimulus axis, but unlike bundle adaptation, the shift is of opposite polarity (11). A negative voltage step will shift the distribution in the positive direction, and visa versa. This necessarily leads to an amplification of the mechanical response, because, for example, the shift caused by a hyperpolarizing voltage stimulus results in an accompanying, time-dependent augmentation in the number of motors in the expanded state at the new voltage (see Fig. 2). Thus, the voltage-dependent process that causes motors to expand tends to recruit more motors into the expanded state, whereas the process that contracts motors tends to recruit additional motors into the contracted state. Whereas the OHC motor can be driven between states at

Submitted June 27, 2008, and accepted for publication October 21, 2008.

*Correspondence: joseph.santos-sacchi@yale.edu

Enrique Navarrete's present address is AutoMate Scientific, Inc., 650 University Ave No. 5, Berkeley, CA 94710.

Editor: Francisco Bezanilla.

© 2009 by the Biophysical Society
0006-3495/09/01/0739/9 \$2.00

doi: 10.1016/j.bpj.2008.10.015

frequencies in excess of 80 kHz (6), the fastest component of the amplificatory shift was shown previously to be ~ 70 ms (11), a timescale well below the kilohertz requirements for an influence on cochlear amplification. We show that just as previous measures of bundle adaptation kinetics were and still may be compromised by the technical problems inherent in studying acoustic rate events (3), our previous measures of amplificatory kinetics were underestimated. We now find components of the amplificatory shift that operate at submillisecond timescales, establishing the significance of this phenomenon in high frequency auditory processing. Additionally, we investigate the influence of Cl^- anions, a recently identified key player in OHC motor activity (12,13), and membrane tension on this amplificatory mechanism.

METHODS

Guinea pigs were decapitated after anesthetic overdose with halothane. Outer hair cells were freshly isolated from the guinea pig cochlea using Dispase (1 mg/ml) followed by trituration, and were whole-cell voltage clamped at room temperature using an Axon 200B amplifier. Membrane voltages were corrected for the effects of residual series resistance, which ranged from 3–5 M Ω . Ionic blocking solutions were used to remove voltage-dependent ionic conductances so that capacitive currents could be analyzed in isolation (10). Extracellular solution included: 100 mM NaCl, 20 mM TEA, 20 mM CsCl, 2 mM CoCl_2 , 1.48 mM MgCl_2 , 2 mM CaCl_2 , 10 mM HEPES, and 5 mM dextrose, adjusted to pH 7.2 with NaOH, and

adjusted to 300 mOsm with dextrose. Pipette solution included: 140 mM CsCl, 10 mM EGTA, 2 mM MgCl_2 , and 10 mM HEPES, adjusted to pH 7.2 with CsOH, and adjusted to 300 mOsm with dextrose (used in Figs. 1 and 3–5). In some cases, TEA, CsCl, CoCl_2 , CaCl_2 , and MgCl_2 were omitted (Figs. 6–8). Gluconate was used to replace chloride (Fig. 6). In some experiments, the extracellular solution was used in patch electrodes. In a few experiments, 50 μM GdCl_3 was included in the extracellular solution to decrease residual currents. At this concentration, gadolinium has an insignificant effect on OHC capacitance (14).

To deliver rapid changes in membrane tension, we used a pressure clamp system from ALA Instruments (Westbury, NY). Pipette tip diameters were increased in size for these experiments (~ 1 M Ω).

Outer hair cell capacitance was measured with a continuous high-resolution two-sine voltage stimulus protocol (20 mV peak at both f_1 and f_2 ; $f_2 = 2 \times f_1$; f_1 ranging up to 3906.3 Hz), and subsequent FFT based admittance analysis (11,15). These small, high frequency sinusoids were superimposed on voltage steps and sinusoids that spanned up to ± 200 mV.

Outer hair cell C-V plots were fitted with the function $C_m = C_{\text{lin}} + C_v$, where C_{lin} is the voltage-independent (linear surface area component) capacitance of the lipid bilayer, and $C_v = dQ_{\text{nonl}}/dV$ is the voltage-dependent component of C_m originating from prestin voltage-sensor activity. The first derivative with respect to V_m of a two-state Boltzmann function $Q = Q_{\text{max}}/(1 + \exp(-ze(V_m - V_{\text{pk}C_m})/k_B T))$ was used to fit the C-V data (10). Q_{max} is total charge moved. The measured apparent valence of prestin voltage-sensor (z) is defined as $z = q \times d$, where d is a normalized perpendicular projection of distance traveled by the voltage sensor charge (q) within the plasma membrane field. $V_{\text{pk}C_m}$ is the membrane potential (V_m) at which prestin molecules are distributed equally between expanded and contracted states. It corresponds to the peak of the C_v function.

All data collection and most analyses were carried out with an in-house developed Windows based whole-cell voltage clamp program, jClamp

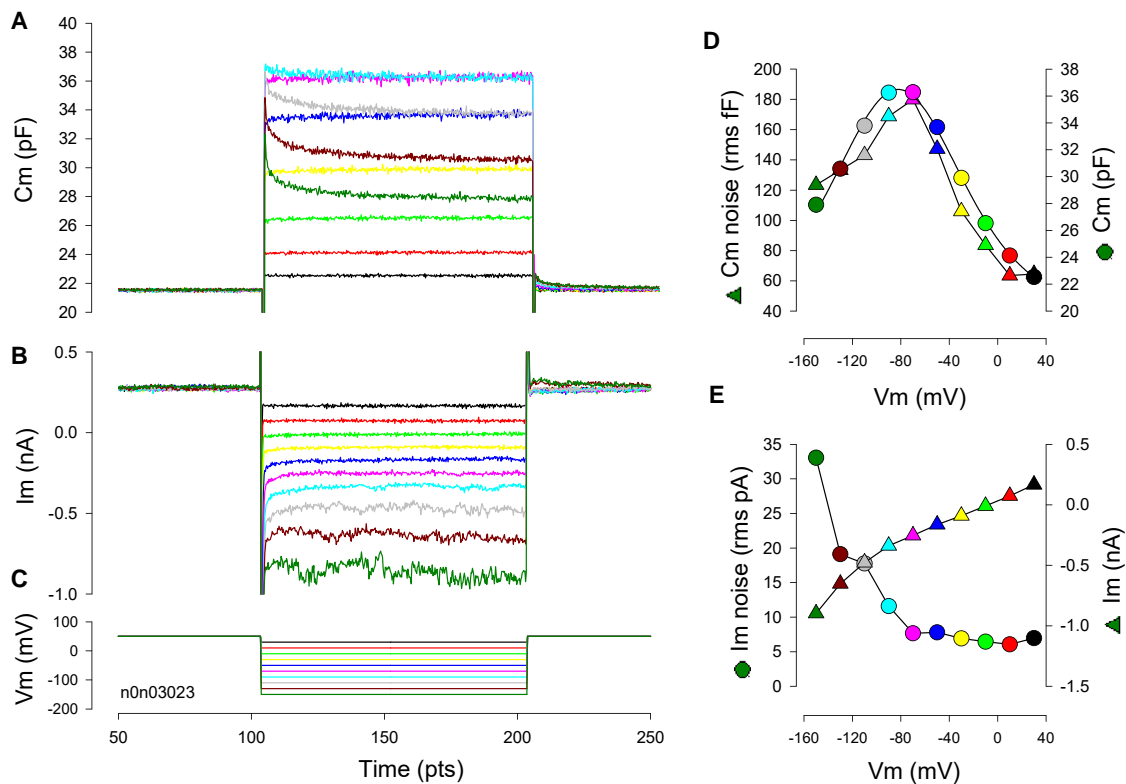


FIGURE 1 Time-dependent changes in NLC at fixed voltages. Capacitance (A), and current (B) in response to voltage steps (C) from +50 mV to -150 mV of 200 ms duration. C_m noise and magnitude (D) values are from the last 35 ms of the C_m traces. Current noise and magnitude (E) values are from the last 35 ms of the current traces.

(www.scisoftco.com), using a Digidata (Axon, CA) 1320 board. MATLAB (The MathWorks, Natick, MA) or SigmaPlot was used for fitting the C_m data.

RESULTS

Voltage steps from a holding potential of +50 mV (Fig. 1 C), a potential chosen because it is in a near-linear region of the OHC Q-V function, induce changes in whole cell current and capacitance (Fig. 1, A and B). The change in steady state current is a monotonic function of voltage (in this case, residual unblocked currents largely representing the activity of G_{metL} (13) (Fig. 1 E), whereas capacitance is a bell-shaped function of voltage (Fig. 1 D). Membrane current noise increases with hyperpolarization level due to activation of membrane conductances, reaching a maximum at the most hyperpolarized level of -150 mV. On the other hand, membrane capacitance noise peaks near the voltage at peak capacitance (V_{pkcm}). This likely results from the cresting chatter of prestin transitions between compact and expanded states at that voltage, because for a molecule that fluctuates between two states, variance of activity will be maximal when state probability is 0.5. Both channel current noise and gating shot noise analyses have been used to garner single channel characteristics (16–18). For the OHC, NLC noise, which is analogous to shot noise, should peak when motor state probability is half, i.e., where NLC is maximal. As far as other possible contributors to the generation of OHC capacitive noise, because the mechanical compliance of the lateral membrane (analogous to behavior hair bundle compliance (19)) is maximal at the midpoint voltage (V_{pkcm}) of the Boltzmann (20), the membrane embedded motors might be more susceptible to mechanical and/or thermal noise influences. It has been shown that motors are quite sensitive to mechanical and thermal perturbations (21–24).

Time-dependent changes in the magnitude of C_m (ΔC_m) at a fixed step occur because the C-V function shifts along the voltage axis as a result of changes from initial voltage conditions (Fig. 1 A). Fig. 2 illustrates a mechanistic account of the observation, and is discussed later. As a methodological control, Dieters' cells, supporting cells from the organ of Corti, were tested. No time-dependent changes in capacitance are observed during step changes in voltage (data not shown).

In our original work on this time-dependent phenomenon, double exponential fits to ΔC_m were made (11)

$$\Delta C_m = C_m(t) = C_0 e^{-t/\tau_0} + C_1 e^{-t/\tau_1} + C_{off}, \quad (1)$$

where C_0 and C_1 are the magnitudes of each of the components of the exponential time courses τ_0 and τ_1 , respectively. C_{off} is an offset, the cell's linear capacitance, required for fitting purposes. An example is shown in Fig. 3 A, using a C_m sampling rate (f1) of 195 Hz, used previously. However, Fig. 3, B and C, shows that the double exponential is not as accurate as the stretched exponential fitting function (25),

$$\Delta C_m = C_m(t) = C_0 \cdot e^{[-(t/\tau)^{1/h}]} + C_{off}, \quad (2)$$

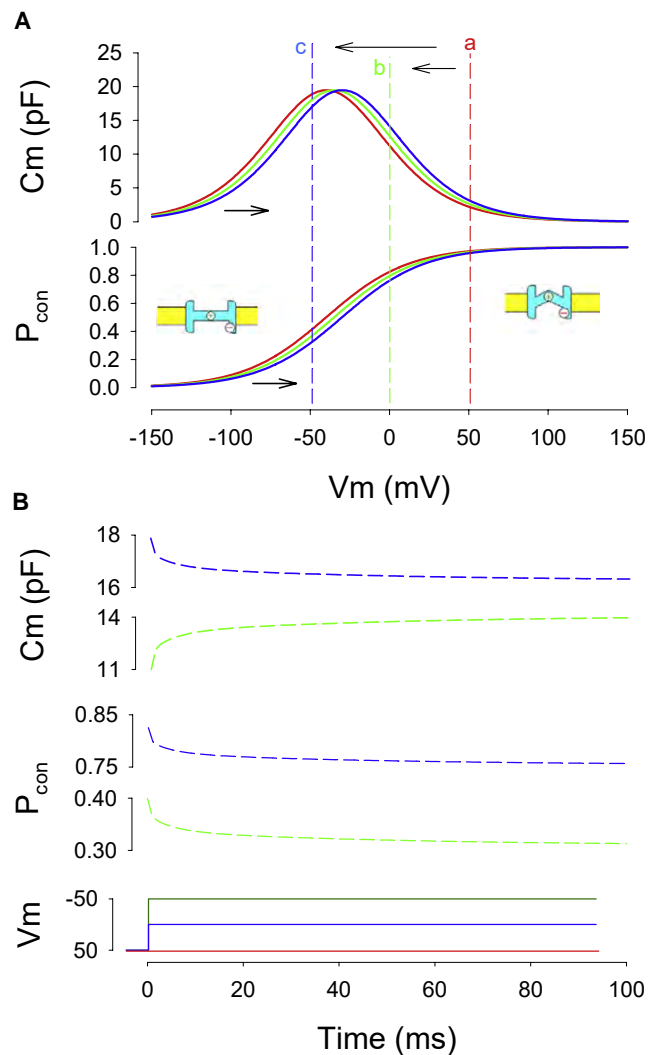


FIGURE 2 NLC shifts report on the conformational state probability of the OHC motor protein. (A) Model NLC and corresponding probability of the motor being in the compact state (P_{con}) versus membrane voltage. Cartoons depict motor in expanded state with anion bound and with positive gating charge on cytoplasmic side, and in contracted state with gating charge displaced toward the extracellular side of the membrane. (B) Corresponding time-dependent changes in state probability and NLC (green traces) during voltage steps from +50 mV to 0 mV ($a \rightarrow b$) or from +50 mV to -50 mV ($a \rightarrow c$; blue traces). Note polarities of relaxations.

where meanings are as above, and h is an indicator of non-homogeneity in the time course of change, the value of 1 reducing to a single exponential distribution. Residuals of the double exponential fit, especially at early times, are larger than those of the stretched exponential fit. The stretched exponential approach has been used to characterize complex relaxations in proteins where the discrete assumptions of single or multi-exponential processes may not hold (26). It can be useful when component rates of a phenomenon are not stationary in time, or when a phenomenon could present multiple components if looked at over a wider timescale. For example, because the apparent viscosity of a medium may

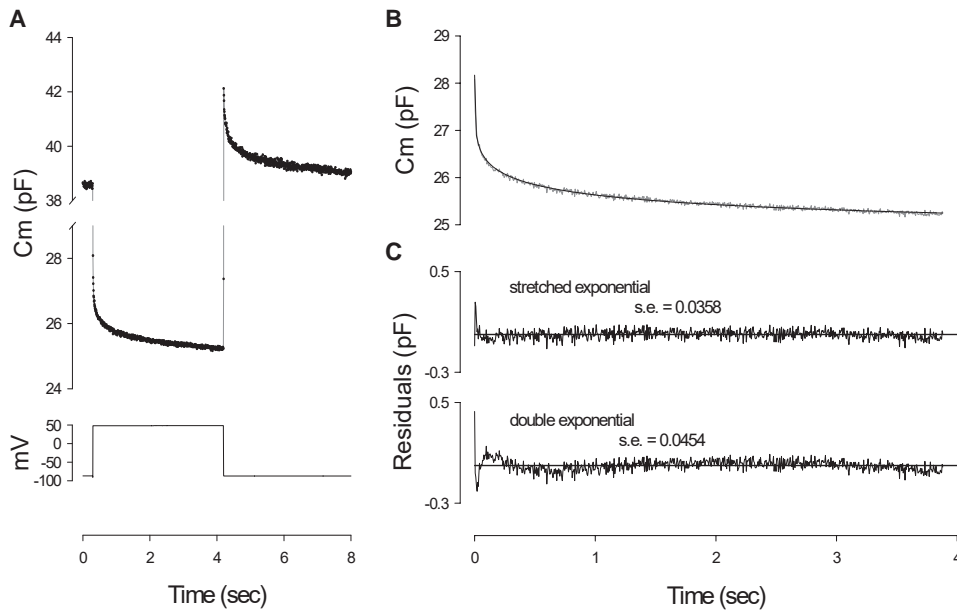


FIGURE 3 Long duration voltage pulse stimulation shows multi-exponential components in the OHC C_m relaxation. (A) C_m response induced by 4 s voltage step from -87 mV to $+53$ mV. (B) C_m trace during pulse fitted with a stretched exponential. Note excellent fit with residuals (C) being greater for the double exponential fit.

depend on rate, duration and magnitude of deformation, such stimulus dependence could be better assessed by a more dynamic fit. Although this type of fitting procedure may be especially important when an extended time course of ΔC_m is inspected, if we focus our attention on short initial time segments during a step in voltage, a double exponential proves adequate to show the fast kinetics of ΔC_m (Fig. 4). To resolve faster components of ΔC_m , sampling frequency was extended to 1.9–3.9 kHz, and step durations were restricted below 100 ms. By increasing sampling frequency from 0.196 to 1.95–3.9 kHz, a significant enhancement in the resolution of early events is obtained, simply because sampling begins at 256 or 512 μ s, rather than 5.12 ms after the onset of the voltage step. Because typically the first few points are discarded because of the transient current response contamination of the FFT, most of our older data (11) were obtained after an initial delay of >10 ms, having clearly biased the analysis toward slower components of ΔC_m . Fig. 4 A illustrates this enhancement in resolution over our previous measurements (11). Fig. 4 B shows the ΔC_m response to a 20-ms step voltage where fits to either a stretched exponential or a double exponential were made and the residuals plotted. Each seems adequate (SE = 0.0326 vs. 0.0337 pF, respectively). The stretched fit gives a time constant of 1.2 ms and h value of 2.2. The first component of the double exponential is well below 1 ms, and the second is an order of magnitude larger (τ_0 : 0.57 ± 0.142 ; τ_1 : 6.38 ± 1.22 ms; A_0 : 1.61 ± 0.3 , A_1 : 1.7 ± 0.41 pF, $n = 6$). These data indicate that early components of the amplificatory shift work in the kilohertz range.

The time course of ΔC_m , and consequently, the shift in V_{pkcm} , is dependent on voltage step magnitude (Fig. 5). Because the clamp time constant (τ_{clamp}) will depend on the step potential when recording from OHCS, as it depends on the sum of linear- and voltage-dependent capacitance, C_m

($\tau_{clamp} = Rs \times Rm / (Rs + Rm) \times C_m$), the time course of capacitance shift was determined at the termination of the voltage step when the holding voltage was reestablished (tail capacitance; Fig. 5 A, inset). The greater the voltage change the faster was the amplificatory shift. This voltage dependence could be due to a variety of voltage-dependent phenomenon in the OHC that may affect prestin, including membrane tension, membrane stiffness (as it can influence tension effects), or transmembrane chloride movements.

Chloride is a major player in prestin activity (12,13,27), and has been shown to permeate the OHC lateral plasma membrane under the control of membrane voltage and tension (13). Because chloride can shift the voltage dependence of NLC (13,28), it is conceivable that chloride influx during step changes in membrane potential could shift V_{pkcm} in a time-dependent manner. However, inspection of currents and capacitance simultaneously evoked by voltage steps (Fig. 1) indicates no correspondence of the two in time. Instead, it is possible that the time course of accumulation or removal of subplasmalemmal intracellular chloride may be the important factor. To evaluate this possibility, we varied the chemical driving force for Cl by changing the concentration of extracellular Cl^- (1, 10, or 140 mM), while using either normal pipettes with 10 mM intracellular Cl^- or perforated patch pipettes to maintain normal low intracellular Cl^- concentrations of ~ 10 mM (27). These manipulations produced neither significant changes in the magnitude nor the time course of the amplificatory shift (Fig. 6). These data indicate that Cl^- in and of itself does not contribute to the timing of the amplificatory process, leaving the possibility that mechanical events, e.g., membrane tension, within the OHC membrane might influence the generation of the shift. We had previously modeled the shift as resulting from relaxations of motor induced membrane tension (11).

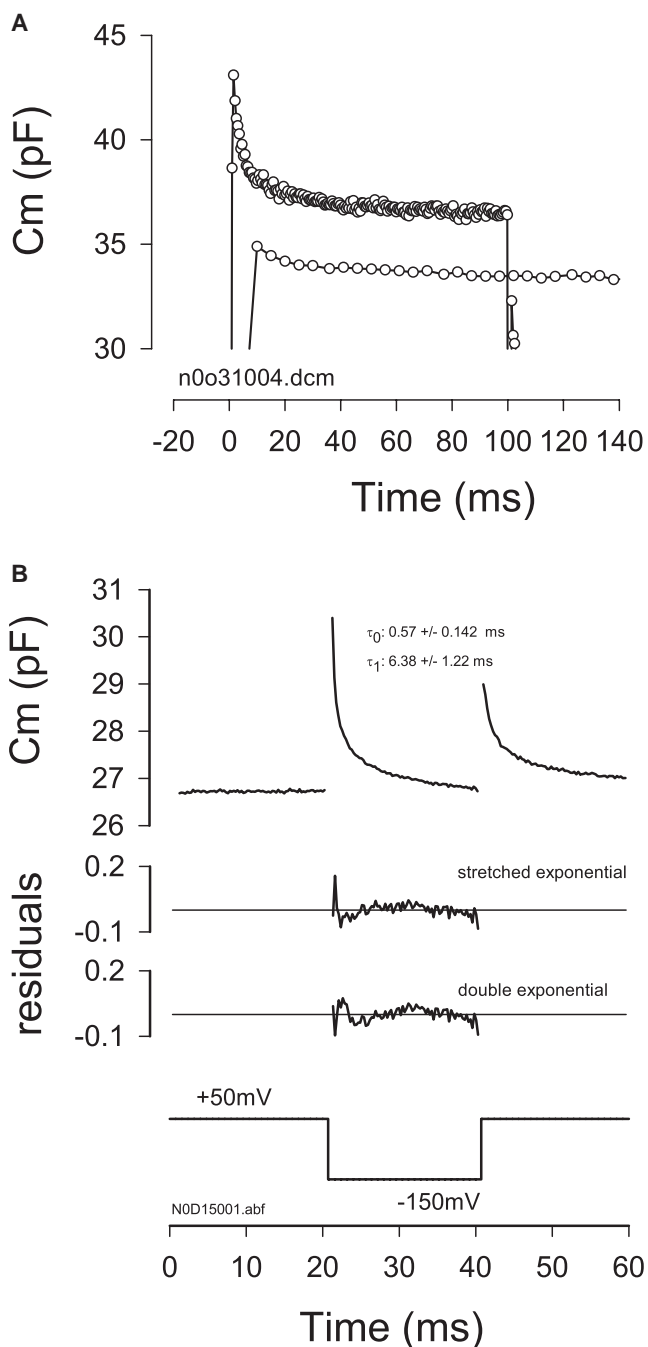


FIGURE 4 Early components of the amplificatory shift are shown with a faster C_m sampling rate. (A) C_m relaxations measured in the same cell in response to a voltage step from +50 mV to -150 mV. Top trace was sampled at 1.96 kHz and bottom trace (shifted down for visibility) was sampled at 196 Hz. Early components are evident with fast sampling. (B) Example of C_m relaxation (averaged traces, $n = 9$) in response to 20 ms voltage step from +50 to -150 mV at a C_m sampling frequency of 3.9 kHz. In this case a double exponential fit and stretched fit provide equally good fits as indicated by residuals. For six cells, τ_0 : 0.57 ± 0.142 τ_1 : 6.38 ± 1.22 ms; A_0 : 1.61 ± 0.3 , A_1 : 1.7 ± 0.41 pF.

The voltage-induced deformations of the lateral membrane must be influenced by the mechanical properties of the cell; for example, the stiffness of the OHC varies with cell length

(30) and whole cell stiffness (that is additionally voltage dependent (31)) might feedback into the active mechanics of the lateral membrane. To see if cell stiffness can influence the shift, we tested whether cell length correlates with the time course of the shift. Fig. 7 shows that cell length does not influence the time course of the amplificatory shift.

Finally, we tested whether rapid changes in membrane tension, which are expected to produce rapid changes in motor state probability (21,22,24), can mimic or interact with the voltage induced amplificatory shift. Fig. 8 shows that rapid changes in membrane tension at a fixed voltage shifts V_{pkcm} in a time-dependent manner, mimicking to some extent the C_m relaxations induced by step voltage changes. The examples shown are two of the best cells obtained in over 30 cells studied. An example of the OHC strain associated with a pressure step (black solid trace) is depicted in Fig. 8 A, and shows that the major strain occurs at the onset of the pressure delivery to the cell. In Fig. 8 B, before step changes in pipette pressure, a voltage ramp (denoted by the numeral 1) was delivered to measure V_{pkcm} . Subsequently, a step in pressure was delivered and after 2 s another voltage ramp (2) was delivered to gauge the shift in V_{pkcm} . Finally, a voltage step from 0 to -50 mV was delivered to observe the voltage-induced C_m relaxation at the stepped pressure. The protocol was repeated after a minute wait for recovery. In this manner, pressure steps up to 2 kPa were delivered. The lowest pressure step depicted (Fig. 8 B, black line) produced no response because cellular material in the pipette tip obstructed flow. With increasing pressures it can be seen that the pipette unplugged at decreasingly shorter times after onset of the pressure step (red, green, dark green, blue, and purple). The last pressure pulse (purple) caused the cell to burst at ~1.75 s after onset. The shift in V_{pkcm} and changes in z are plotted in Fig. 8, C and D. The reduction in z may correspond to the restricted movements of charge that Adachi and Iwasa (33) found on extreme inflation of the trypsinized OHCs. In general, the effects of rapid pressure changes correspond to analogous step changes in voltage; however, the time course of the shifts (compare relaxations due to pressure alone versus the additional voltage step (3)) is slower for pressure changes. One caveat is that intracellular pressure may not be as constant as membrane voltage because OHC strain changes slightly during the constant pipette pressure pulse.

DISCUSSION

By measuring OHC nonlinear membrane capacitance at sub-millisecond resolutions, we have examined the early time course of the dynamic response of the OHC motor to preconditioning membrane voltages and tensions. We show for the first time that this time course is multi-exponential, with the earliest detectable components residing in the kilohertz range, thereby establishing the phenomenon's potential significance in peripheral auditory processing of the mammal. These effects actually extend well into the low frequency range, as well; indeed, altering steady state resting potentials can stably

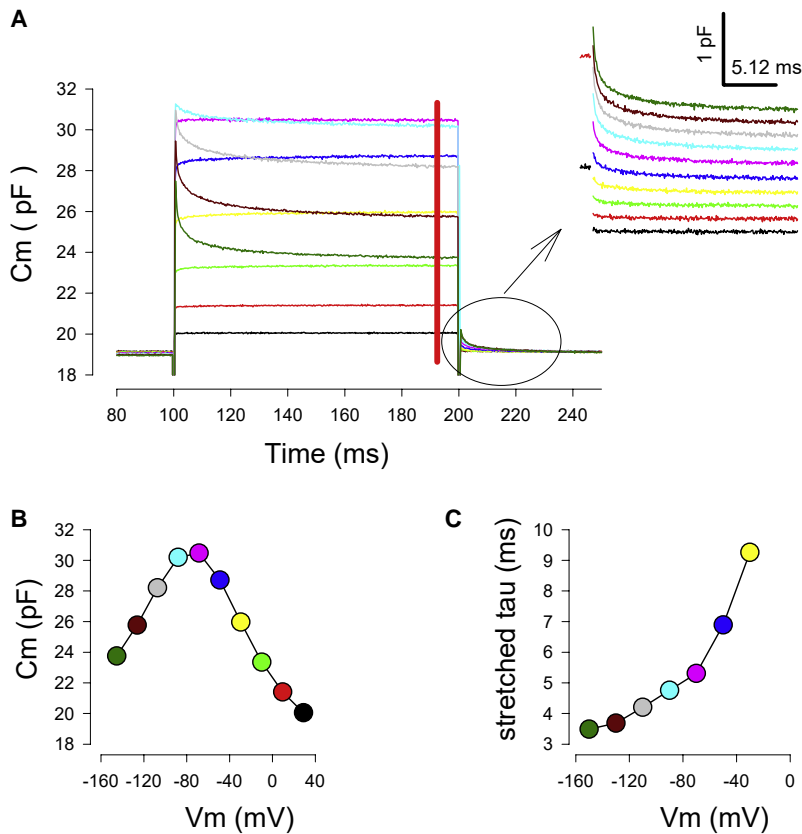


FIGURE 5 Voltage dependence of amplificatory shift. (A) Averaged C_m traces ($n = 9$) in response to voltage steps from +50 mV to -150 mV as in Fig. 1. The red bar indicates the region used to plot the C-V curve (B). Tail capacitance (inset) was used to measure voltage dependent time constants (C).

set the operating point of electromotility to different points along the voltage axis.

Our data, although measuring whole cell capacitance, actually provide insight into the initial condition-dependent conformational states of the motor protein, prestin. As such, the correspondence between voltage-induced ΔC_m and motor state probability can be extracted from the data of Fig. 1, as schematized in Fig. 2. Thus, for voltage steps to potentials positive to V_{pkcm} (Fig. 2 A, $a \rightarrow b$), the magnitude of C_m increases during the step duration, because the rising side of the C-V function moves to the right and the shift eventually halts at a point where capacitance is now larger at the step potential. For steps to potentials negative to V_{pkcm} (Fig. 2 A, $a \rightarrow c$), the magnitude of C_m decreases during the step duration, because the falling side of the C-V function moves to the right and the shift halts at a point where capacitance is now lower at the step potential. Although capacitance may increase or decrease (Fig. 2 B), both correspond to a unidirectional change in motor state probability, as a conversion of capacitance to gating charge would show. Consequently, depolarizing voltages, in addition to causing a near instantaneous redistribution of motors to the compact state, will foster a supplemental recruitment of additional motors into that state, leading to an amplification of the initial response. The same amplification effect holds for hyperpolarizing voltages, where recruitment of motors will be into the expanded state. To reiterate, when OHC holding potential is stepped to a negative potential and maintained there, there will be a shift

in the motor state probability function in the opposite direction to positive potentials. The initial voltage step to a negative potential will immediately cause a set of motors to move to the expanded state. When the motor state probability function moves to positive potentials, at the fixed holding potential more motors will enter the expanded state because the new probability at the fixed holding potential dictates it. From this, it is easy to predict the distortion in the mechanical response that will arise, distortion being the hallmark of mammalian cochlear amplification (34).

It should be emphasized that the amplificatory shift that occurs in the Boltzmann function does not predict a high pass response. In contrast, it is a process that rapidly follows the instantaneous change in motor state probability initiated by a step voltage, and continues over the stretched exponential time course we have described, reaching maximum at steady state. Thus, it is a low pass response where motors are recruited into the same state initially evoked by the onset of the voltage stimulus. We previously modeled the expected response (11), which we and others have observed in OHC mechanical responses. The multi-exponential amplificatory response dictates that the phenomenon will have impact in the acoustic frequency range. To be sure, the most important frequency range for humans is that of the speech frequencies (500–2000 Hz).

Although anions play a major role in NLC generation, our results indicate that modifying the driving force for chloride movement across the OHC lateral membrane through G_{metL}

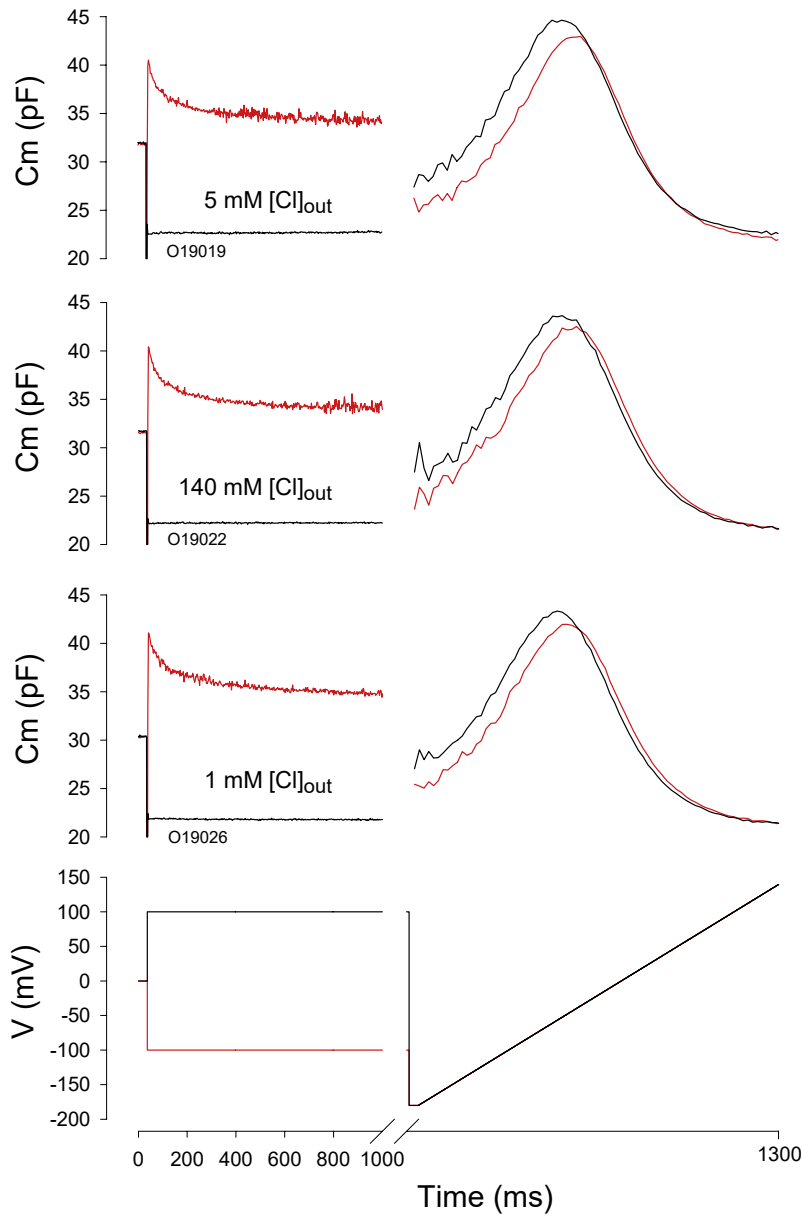


FIGURE 6 Time course and magnitude of amplificatory shift is not dependent on Cl^- driving force. Results from a typical cell clamped with a perforated gramicidin patch to maintain intracellular Cl^- levels. Extracellular Cl^- was altered to 5 mM (top, C_m traces), 140 mM (middle, C_m traces) and 1 mM (bottom, C_m traces). Voltage protocol is shown at bottom. After step jumps to either 100 or -100 mV from 0 mV, a ramp was voltage delivered to gauge the shift of V_{pkcm} . Shifts were -47.8 to -40.9 , -50 to -41.5 , and -54 to -46 for 5, 140, and 1 mM Cl^- , respectively.

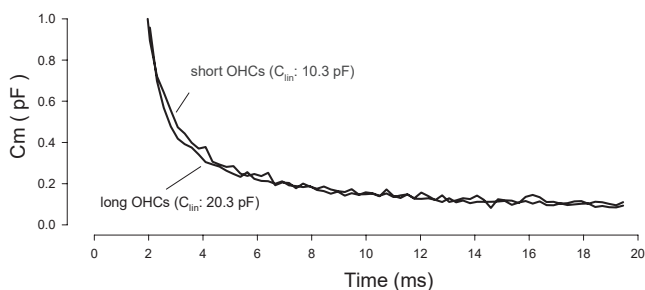


FIGURE 7 Whole cell characteristics do not influence time course of the amplificatory shift. Double exponential fits were made. Short OHC labeled trace is averaged C_m response (return to $+50$ mV from -150 mV) from four short cells ($C_{\text{lin}}: 10.3 \pm 0.69$ pF; $\tau_0: 0.76$; $\tau_1: 4.09$ ms). Long OHC labeled trace is average from five long cells ($C_{\text{lin}}: 20.27 \pm 0.88$; $\tau_0: 0.76$; $\tau_1: 3.98$ ms). Time courses are essentially equal.

(13) does not modify the extent or time course of the amplificatory shift. This is in marked contrast with the effects of altering the driving force for Ca^{2+} on stereociliar adaptation (3). Reducing the entry of Ca^{2+} through the stereociliar channels can remove the tension-induced shift in the forward transducer function along the stimulus axis. Thus, parallels between the two mechanisms (apical stereociliar and lateral prestin motor) are not tight. It should be noted that although driving force for chloride did not significantly affect the amplificatory shift of the motor, the interactions of anions with the motor may still play a role. In this regard, we have found recently that the state probability of prestin influences anion binding affinity (L. Song and J. Santos-Sacchi, unpublished), and that even if concentrations remain the same at the intracellular binding sites of prestin, changes in

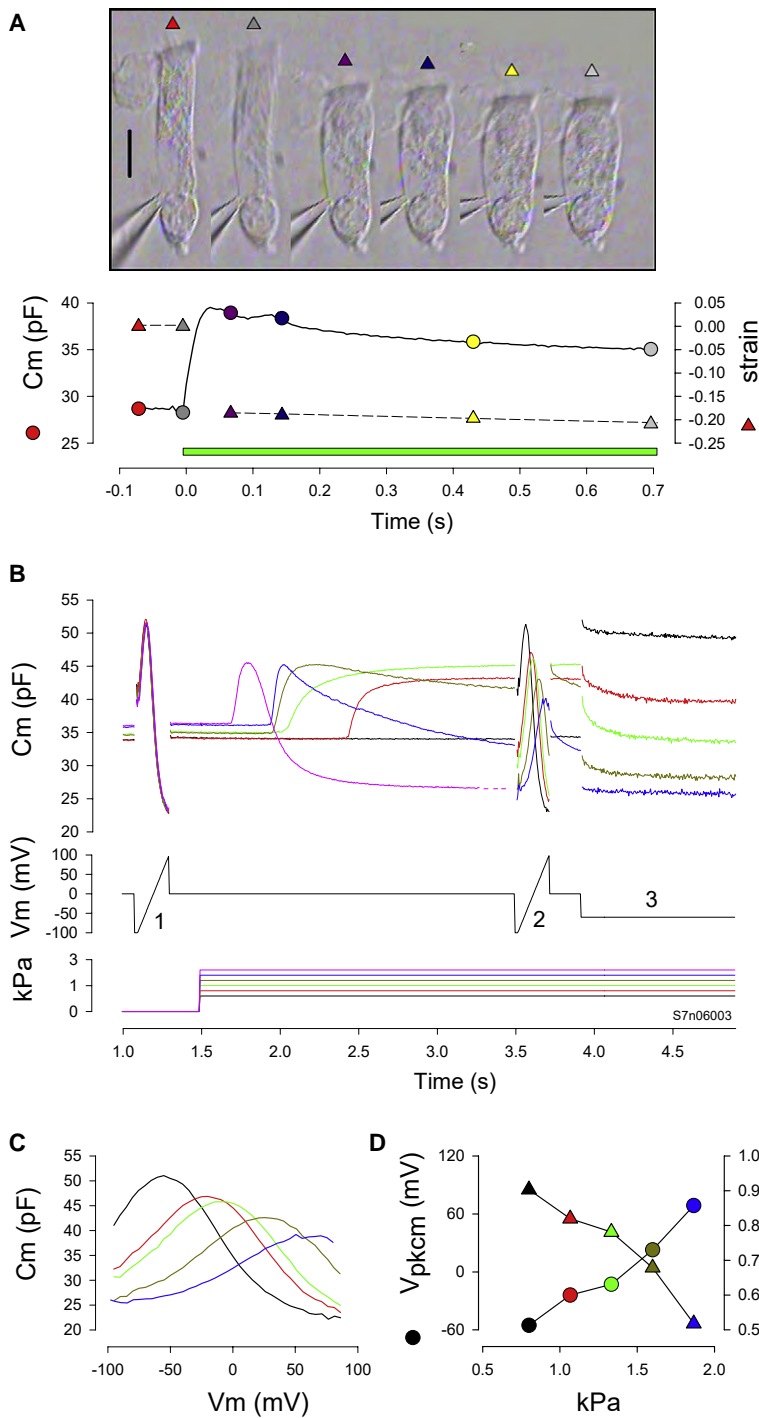


FIGURE 8 Rapid turgor pressure changes induce membrane tension with accompanying relaxations in C_m . (A) Photos of an OHC at different time points during a 1.8 kPa pressure step. C_m relaxation and longitudinal strain ($(L - \delta L)/L$) are plotted beneath. Green bar indicates pressure delivery to the cell. Note the majority of strain occurs before C_m relaxation begins. (B) Another cell. Color coded C_m traces induced by combinations of voltage ramps (1 and 2), voltage steps (3) and pressure steps. Single exponential fits of the C_m relaxations due to 1.4 (dark green), 1.6 (blue), and 1.8 (purple) kPa steps were 1.01, 0.88, and 0.16 s, respectively. (C) C-V plots obtained 2 s after onset of pipette pressure steps. Voltage was corrected for R_s effects that ranged from 1.7–4.5 $M\Omega$ during the pressure changes. (D) Boltzmann parameters V_{pkcm} and z as a function of pressure.

binding site affinity, as can occur with allosteric modulation, could alter energy profiles, resulting in V_{pkcm} shifts. We are exploring such possibilities currently.

Since the initial observations of Iwasa (21), membrane tension effects on the OHC motor have provided important information on surprisingly efficient piezoelectric activity of this protein (35). Because membrane tension can shift V_{pkcm} and, indeed, in extreme applications, restrict conformational activity (33), we had modeled the voltage-induced

amplificatory shift as resulting from motor induced tension (11). In this study we attempted to directly test this by applying rapid changes in membrane tension and seeking C_m relaxations that mimic those induced by voltage steps. Although there are indications of C_m relaxations after rapid tension changes, the time courses of voltage-induced and tension-induced C_m relaxations differ, tension effects being slower. It is possible that during our attempts to alter membrane tension through global changes in OHC structure

we may have been restricted by the viscoelastic properties of the whole cell. For example, Ehrenstein and Iwasa (36) found that mechanical relaxations in the OHC have a time constant on the order of 40 s. However, because the fastest C_m relaxation time constants that we found with pressure steps were ~ 2 orders of magnitude faster than their measured time course, our pressure clamp driver seems to have been quite successful in overcoming this mechanical impediment. We suggest that tension induced by the molecular motors themselves can better bypass this viscoelastic constraint, thereby providing more rapid tensions to evoke fast amplification shifts. Thus, we still view motor-derived membrane tension, possibly through alterations of anion binding affinity, to underlie voltage-induced amplification shifts. Nevertheless, as we have shown previously, the membrane environment of prestin can have profound effects on the magnitude and time course of the amplification shift (37).

In summary, we show remarkably fast changes in the Boltzmann distribution of prestin motor states induced by initial voltage conditions. The shifts along the voltage axis represent amplification supplementation to the voltage-induced mechanical response of the cell, and it is expected that this phenomenon will impact on high frequency peripheral auditory processing.

This study was supported by the National Institute on Deafness and Other Communication Disorders grant DC00273 to J.S.S.

REFERENCES

- Choe, Y., M. O. Magnasco, and A. J. Hudspeth. 1998. A model for amplification of hair-bundle motion by cyclical binding of Ca^{2+} to mechano-electrical-transduction channels. *Proc. Natl. Acad. Sci. USA*. 95:15321–15326.
- Ricci, A. J., A. C. Crawford, and R. Fettiplace. 2000. Active hair bundle motion linked to fast transducer adaptation in auditory hair cells. *J. Neurosci.* 20:7131–7142.
- Kennedy, H. J., M. G. Evans, A. C. Crawford, and R. Fettiplace. 2003. Fast adaptation of mechano-electrical transducer channels in mammalian cochlear hair cells. *Nat. Neurosci.* 6:832–836.
- Zheng, J., W. Shen, D. Z. He, K. B. Long, L. D. Madison, et al. 2000. Prestin is the motor protein of cochlear outer hair cells. *Nature*. 405:149–155.
- Santos-Sacchi, J. 1992. On the frequency limit and phase of outer hair cell motility: effects of the membrane filter. *J. Neurosci.* 12:1906–1916.
- Frank, G., W. Hemmert, and A. W. Gummer. 1999. Limiting dynamics of high-frequency electromechanical transduction of outer hair cells. *Proc. Natl. Acad. Sci. USA*. 96:4420–4425.
- Santos-Sacchi, J. 1993. Harmonics of outer hair cell motility. *Biophys. J.* 65:2217–2227.
- Iwasa, K. H. 1994. A membrane motor model for the fast motility of the outer hair cell. *J. Acoust. Soc. Am.* 96:2216–2224.
- Ashmore, J. F. 1990. Forward and reverse transduction in the mammalian cochlea. *Neurosci. Res. Suppl.* 12:S39–S50.
- Santos-Sacchi, J. 1991. Reversible inhibition of voltage-dependent outer hair cell motility and capacitance. *J. Neurosci.* 11:3096–3110.
- Santos-Sacchi, J., S. Takehata, and S. Takahashi. 1998. Effects of membrane potential on the voltage dependence of motility-related charge in outer hair cells of the guinea-pig. *J. Physiol.* 510:225–235.
- Oliver, D., D. Z. He, N. Klocker, J. Ludwig, U. Schulte, et al. 2001. Intracellular anions as the voltage sensor of prestin, the outer hair cell motor protein. *Science*. 292:2340–2343.
- Rybalchenko, V., and J. Santos-Sacchi. 2003. Cl^- flux through a non-selective, stretch-sensitive conductance influences the outer hair cell motor of the guinea-pig. *J. Physiol.* 547:873–891.
- Takehata, S., and J. Santos-Sacchi. 1996. Effects of salicylate and lanthanides on outer hair cell motility and associated gating charge. *J. Neurosci.* 16:4881–4889.
- Santos-Sacchi, J. 2004. Determination of cell capacitance using the exact empirical solution of dY/dC_m and its phase angle. *Biophys. J.* 87:714–727.
- Crouzy, S. C., and F. J. Sigworth. 1993. Fluctuations in ion channel gating currents. Analysis of nonstationary shot noise. *Biophys. J.* 64:68–76.
- Conti, F., and W. Stuhmer. 1989. Quantal charge redistributions accompanying the structural transitions of sodium channels. *Eur. Biophys. J.* 17:53–59.
- Sigworth, F. J. 1980. The variance of sodium current fluctuations at the node of Ranvier. *J. Physiol.* 307:97–129.
- Howard, J., and A. J. Hudspeth. 1988. Compliance of the hair bundle associated with gating of mechano-electrical transduction channels in the bullfrog's saccular hair cell. *Neuron*. 1:189–199.
- Iwasa, K. H. 2000. Effect of membrane motor on the axial stiffness of the cochlear outer hair cell. *J. Acoust. Soc. Am.* 107:2764–2766.
- Iwasa, K. H. 1993. Effect of stress on the membrane capacitance of the auditory outer hair cell. *Biophys. J.* 65:492–498.
- Gale, J. E., and J. F. Ashmore. 1994. Charge displacement induced by rapid stretch in the basolateral membrane of the guinea-pig outer hair cell. *Proc. R. Soc. Lond. B. Biol. Sci.* 255:243–249.
- Santos-Sacchi, J., and G. Huang. 1998. Temperature dependence of outer hair cell nonlinear capacitance. *Hear. Res.* 116:99–106.
- Takehata, S., and J. Santos-Sacchi. 1995. Membrane tension directly shifts voltage dependence of outer hair cell motility and associated gating charge. *Biophys. J.* 68:2190–2197.
- Laherrere, J., and D. Sornette. 1998. Stretched exponential distributions in nature and economy: “fat tails” with characteristic scales. *Eur. Phys. J. B.* 2:525–539.
- Lee, K. C., J. Siegel, S. E. Webb, S. Leveque-Fort, M. J. Cole, et al. 2001. Application of the stretched exponential function to fluorescence lifetime imaging. *Biophys. J.* 81:1265–1274.
- Santos-Sacchi, J., L. Song, J. Zheng, and A. L. Nuttall. 2006. Control of mammalian cochlear amplification by chloride anions. *J. Neurosci.* 26:3992–3998.
- Song, L., A. Seeger, and J. Santos-Sacchi. 2005. On membrane motor activity and chloride flux in the outer hair cell: lessons learned from the environmental toxin tributyltin. *Biophys. J.* 88:2350–2362.
- Reference deleted in proof.
- He, D. Z., J. Zheng, F. Kalinec, S. Takehata, and J. Santos-Sacchi. 2006. Tuning in to the amazing outer hair cell: membrane wizardry with a twist and shout. *J. Membr. Biol.* 209:119–134.
- He, D. Z., and P. Dallos. 1999. Somatic stiffness of cochlear outer hair cells is voltage-dependent. *Proc. Natl. Acad. Sci. USA*. 96:8223–8228.
- Reference deleted in proof.
- Adachi, M., and K. H. Iwasa. 1999. Electrically driven motor in the outer hair cell: effect of a mechanical constraint. *Proc. Natl. Acad. Sci. USA*. 96:7244–7249.
- Takahashi, S., and J. Santos-Sacchi. 1999. Distortion component analysis of outer hair cell motility-related gating charge. *J. Membr. Biol.* 169:199–207.
- Dong, X. X., M. Ospeck, and K. H. Iwasa. 2002. Piezoelectric reciprocal relationship of the membrane motor in the cochlear outer hair cell. *Biophys. J.* 82:1254–1259.
- Ehrenstein, D., and K. H. Iwasa. 1996. Viscoelastic relaxation in the membrane of the auditory outer hair cell. *Biophys. J.* 71:1087–1094.
- Santos-Sacchi, J., and M. Wu. 2004. Protein- and lipid-reactive agents alter outer hair cell lateral membrane motor charge movement. *J. Membr. Biol.* 200:83–92.

Joseph Santos-Sacchi · Volodymyr Rybalchenko ·
Jun-Ping Bai · Lei Song · Dhasakumar Navaratnam

On the temperature and tension dependence of the outer hair cell lateral membrane conductance G_{metL} and its relation to prestin

Received: 19 December 2005 / Accepted: 20 December 2005 / Published online: 7 March 2006
© Springer-Verlag 2006

Abstract Recently, we identified an outer hair cell (OHC) lateral membrane conductance, G_{metL} , that colocalizes with prestin and passes Cl^- , thereby influencing prestin's (SLC26A5) electromechanical activity. In this study, we report on a comparison of the temperature and tension dependence of G_{metL} and prestin. Though we find significant temperature and tension dependence of each, substantial differences exist which indicate their independent identity. The following data support this conclusion: (1) The voltage dependence of G_{metL} does not follow that of prestin's nonlinear capacitance (NLC) function when the latter is shifted by either temperature or membrane tension; (2) Unlike native OHCs whose NLC can be modulated by influx of extracellular Cl^- , prestin-transfected Chinese hamster ovary (CHO) cells do not show this phenomenon; (3) Stretch-sensitive, single channel currents are not evidenced after prestin transfection in CHO cells; and (4) There is no correlation between prestin expression level (gauged via NLC) and transmembrane current through G_{metL} . Thus, G_{metL} must result from the activity of another molecular species within the lateral membrane of the OHC. A clue to its identity is the conductance's nonlinear temperature dependence in contrast to prestin and other

OHC conductances' linear dependence. Whereas K^+ conductances in OHCs present a uniform Q_{10} close to 1.2, G_{metL} shows a bimodal Q_{10} , with a Q_{10} of 1.5 below 34°C and a Q_{10} of greater than 4 and above. The dissociation of SLC26A5 (prestina) and G_{metL} theoretically provides for a modifiable anionic feedback to prestin via the degree of spatial separation between these interacting partners within the OHC lateral membrane.

Introduction

The outer hair cell (OHC) lateral membrane motor, prestin or SLC26A5 [15, 27, 31], is thought to underlie the mammalian cochlear amplifier [14], and intracellular chloride is known to influence its activity [19, 21, 29]. This motor activity, measured either as a length change of the OHC or as an associated nonlinear capacitance (NLC), has been modeled successfully as a two-state Boltzmann process, with depolarization driving the motor into the compact state [10, 22, 23]. Recently, we discovered a stretch/voltage sensitive conductance (G_{metL}) that nonselectively passes small cations and anions through the OHC lateral membrane [21]. Furthermore, the intracellular accumulation of chloride via this conductance strongly influences prestin activity, increasing the probability of prestin being in the compact state. We found no indication of a conductance similar to G_{metL} in isolated neighboring Deiters' cells, which lack prestin.

G_{metL} shares some properties of prestin, namely, its restricted location within the lateral membrane, tension dependence, and modulation by Cl^- channel blockers [21]. In this regard, it is well established that some transporter family members actually underlie ionic conductances, including, for example, cystic fibrosis transmembrane conductance (CFTR) [8], the sodium/bicarbonate cotransporter, NBCn1 [4], and the glial glutamate transporter EAAT2 [20]. In fact, recently, another SLC26 family member, SLC26A7, has been shown to function as a chloride channel that is regulated by pH [13]. It is interesting to note, whereas SLC26A7 chloride currents are

J. Santos-Sacchi · V. Rybalchenko · J.-P. Bai · L. Song
Department of Otolaryngology,
Yale University School of Medicine,
BML 246, 333 Cedar Street,
New Haven, CT 06510, USA

J. Santos-Sacchi (✉) · D. Navaratnam
Department of Neurobiology,
Yale University School of Medicine,
BML 246, 333 Cedar Street,
New Haven, CT 06510, USA
e-mail: joseph.santos-sacchi@yale.edu
Tel.: +1-203-7855407
Fax: +1-203-7372502

D. Navaratnam
Department of Neurology,
Yale University School of Medicine,
BML 246, 333 Cedar Street,
New Haven, CT 06510, USA

blocked by DIDS, that G_{metL} is actually enhanced by DIDS [21], similar to the Na current associated with NBCn1 expression [4]. It is conceivable that G_{metL} could result from either the expression of prestin itself or through other proteins within the lateral membrane. In this study, we analyze the temperature and tension dependence of G_{metL} and prestin, thereby allowing us to determine whether prestin activity results in or influences Cl^- movements through membranes expressing this protein. Our data indicate that the molecular identity of G_{metL} is distinct from prestin, providing insight into their feedback capabilities.

Materials and methods

General

Guinea pigs were killed with halothane inhalation overdose in accordance with an approved protocol from Yale University's Animal Use and Care Committee. OHCs were freshly isolated from the adult guinea pig organ of Corti by sequential enzymatic (dispase 0.5 mg/mL) and mechanical treatment in Ca-free medium. Currents and capacitance from voltage-clamped cells were recorded at room temperature or at other temperatures (set by a Peltier device controlling the perfusion chamber) using an Axon 200A or 200B amplifier, Digidata 1321A or NI PCI-6052E board (Axon Inst., CA, USA; National Inst., USA), and the software program jClamp (Scisoft, CT, USA). To limit interfering K^+ conductances, the base intra- and extracellular solution was NaCl or TrisCl 140–150, CaSO_4 2.5, MgSO_4 1.2, HEPES 10, pH 7.2, 300 mOsm. Chloride substitutions were made with malate. For K^+ current studies, intracellular solutions were made with KCl. Solutions were delivered to individual cells by Y tube during continuous whole bath perfusion of base extracel-

lular solution. Series resistance effects were corrected offline. Currents were monitored at the fixed holding potential stated in the figure legends. Evaluations of gerbil prestin were made in Chinese hamster ovary (CHO) cells. Transient cotransfection was achieved as described previously [16], with cotransfection of GFP. Data are presented as mean \pm SE.

Nonlinear capacitance

Nonlinear membrane capacitance was evaluated using a continuous high-resolution (2.56 ms sampling), two-sine voltage stimulus protocol (10 mV peak at both 390.6 and 781.2 Hz), with subsequent fast Fourier transform-based admittance analysis as fully described in Santos-Sacchi et al. [24, 26]. These high-frequency sinusoids were superimposed on voltage ramps. To avoid capacitive current contamination (influenced by the cell's voltage-dependent capacitance) of I_{metL} , we used ramps of 1 s duration. Peak nonlinear capacitance was determined by subtracting linear capacitance. $C-V$ data were fit with the first derivative of a two-state Boltzmann function and a constant representing the linear capacitance [22],

$$C_m = Q_{\text{max}} \frac{ze}{kT} \frac{b}{(1+b)^2} + C_{\text{lin}} \quad (1)$$

$$b = \exp\left(\frac{-ze(V_m - V_{\text{pkcm}})}{kT}\right)$$

where Q_{max} is the maximum nonlinear charge moved, V_{pkcm} is voltage at peak capacitance or half maximal nonlinear charge transfer, V_m is membrane potential, C_{lin} is linear capacitance, z is apparent valence, e is electron charge, k is Boltzmann's constant, and T is absolute

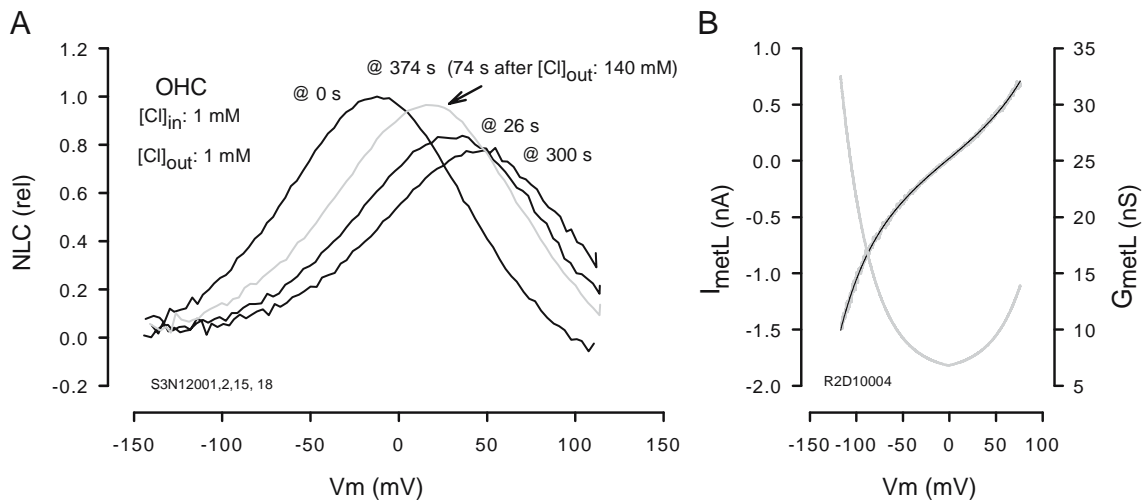


Fig. 1 Chloride enters the OHC through a lateral membrane conductance. **a** After obtaining whole-cell condition with 1 mM intra/extracellular Cl^- (Na-based) solutions, OHC NLC shifts rightward and decreases. NLC reaches steady state at about 2/3 of initial NLC beyond 1 min washout. Subsequently, a switch to 140 mM extracellular Cl^- restores NLC (grey trace), indicating Cl^- influx through G_{metL} . **b** Ionic current of an OHC with 150 mM Cl^- (Tris-based) intra/extracellular solution evoked by a 1 sec voltage ramp. The sigmoidal current is fitted with Eq. 2 (solid line; $V_h: -0.71$ mV) and the slope conductance (grey, V-shaped line) derived from the fit

temperature. A phenomenological equation was devised to fit the sigmoidal V_m dependence of I_{metL} , providing estimates of the midpoint voltage (V_h) of its operating voltage range, which were then compared with the midpoint voltage, V_{pkcm} , of the simultaneously recorded NLC.

$$I = A * dV * \exp(|dV|/b) + off \quad (2)$$

where A is current amplitude, $dV=V_m-V_h$, b is a slope factor, and off is an offset.

Single channel recoding

Prestin-transfected CHO cells and controls were tested for the occurrence of stretch-activated single channel currents. Forty control CHO cells and 55 CHO cells transfected with normal prestin-yellow fluorescent protein were recorded by cell-attach configuration. Some of them were also recorded by inside-out configuration. Patches were made over fluorescent hot spots. Bath solution (mM): 140 NaCl, 2 MgSO₄, 2 CaSO₄, 10 HEPES; pipette solution (mM): 140 NaCl, 2 MgSO₄, 2 CaSO₄, 10 EGTA, 10 HEPES pH 7.2, 300 mOsm.

Results

NLC capacitance in the OHC is a shallow function of voltage (Fig. 1). The magnitude- and voltage-operating range is highly dependent on intracellular chloride levels but is also dependent in the native OHC on extracellular chloride which passes through a lateral membrane conductance. Figure 1a shows that, in the presence of low extracellular chloride (1 mM), washout of intracellular chloride with low chloride containing patch pipette solutions shifts NLC to depolarizing levels and decreases its peak magnitude. After reaching steady state, the introduction of normal extracellular chloride levels (140 mM)

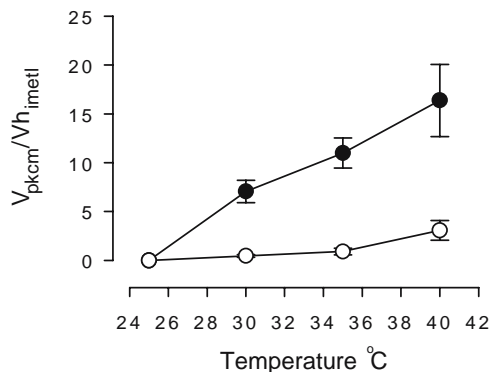


Fig. 2 After obtaining stable whole-cell conditions with 150 mM Cl⁻ (Tris-based) intra/extracellular solutions, bath temperature was altered. V_{pkcm} of the NLC (filled circles) shifted rightward (depolarizing) with increases in temperature; however V_h of I_{metL} (open circles) did not follow, indicating independence of the two simultaneous measures. Plotted is mean±SE, $n=4$

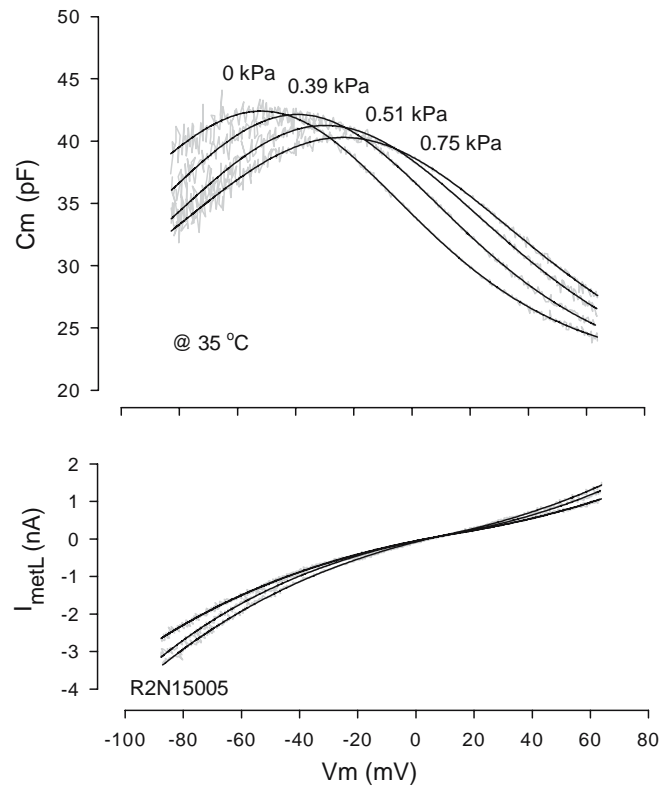


Fig. 3 After obtaining stable whole-cell conditions with 150 mM Cl⁻ (Tris-based) intra/extracellular solutions, tension was applied to the OHC membrane by pipette pressure. NLC shifts rightward and decreases with increasing turgor pressure. Note that I_{metL} increases with increasing membrane tension, but its voltage dependence remains unaltered. V_{pkcm} (mV) vs V_h (mV) with increasing pressure: -49.2/13.9; -39.0/14.2; -30.6/10.4; -23.0/11.3. Indeed, the initial turgor pressure change from 0 to 0.39 kPa produced a NLC shift, but no significant change in current, indicating the independence of the two simultaneous measures. Temperature was 35°C

restores NLC. This restoration is a consequence of a gradient-driven, lateral membrane chloride current, I_{metL} , that has a V-shaped conductance, G_{metL} , and has been shown to be charge nonselective [21]. Fitting the slope conductance of the G_{metL} defines a midvoltage (V_h), where conductance is minimal, and establishes an operating voltage range which can be compared to that of NLC measured in the same cell. To determine whether the underlying molecular structure, prestin, which is responsible for NLC generation, also fosters G_{metL} , we simultaneously compared V_h and V_{pkcm} , under conditions where V_{pkcm} is known to change.

First, we altered bath temperature (from 25 to 40°C), which has been shown to shift V_{pkcm} in the depolarizing direction [17, 25]. Figure 2 shows that whereas the operating voltage range of prestin is altered by temperature, shifting about 1 mV/°C, that of G_{metL} is little affected. Second, we changed intracellular turgor pressure to alter tension on the OHC membrane. As expected, increasing turgor pressure shifted V_{pkcm} to depolarizing levels [6, 9, 11, 27] (Fig. 3); however, the voltage-operating range of G_{metL} is unaffected. These observations were confirmed in more than five OHCs. Finally, we directly tested whether

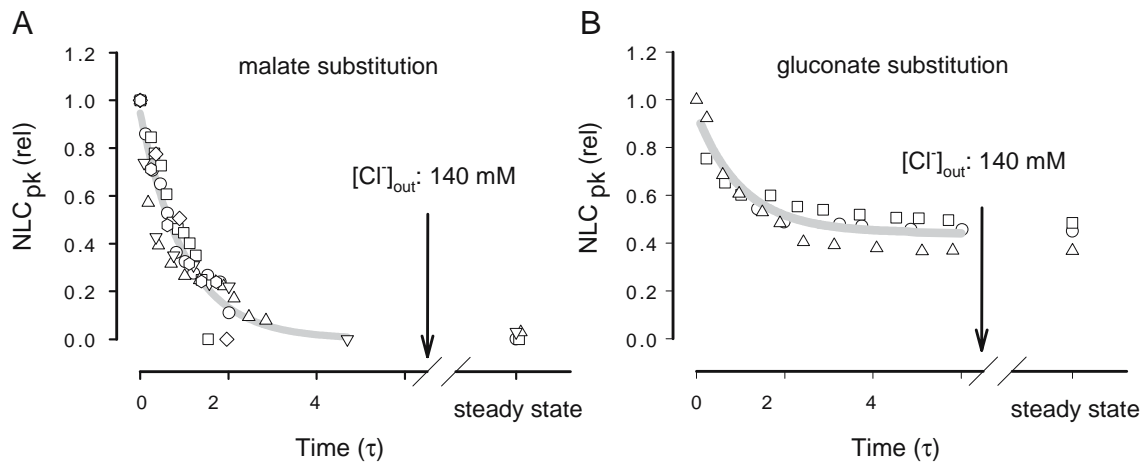


Fig. 4 a, b After obtaining whole cell in prestin-transfected cells with 1 mM intra/extracellular Cl^- (Na-based) solutions, NLC shifts rightward and decreases to barely perceptible levels when malate is the substitute anion. Using gluconate as substitute, reduction is only about 30%, similar to what we find in OHCs [21, 30]. Unlike in OHCs, a subsequent switch to 140 mM extracellular Cl^- does not restore NLC, indicating lack of Cl^- influx. Symbols denote individual cells whose washout effects were corrected for washout rate and plotted against the exponential washout time. The mean (\pm SE) value of τ was 49.18 ± 7.57 s (malate); $\tau = 35.56 \pm 10.00$ s (gluconate)

prestin transfection in nonauditory cells results in the generation of a chloride conductance in addition to NLC. We previously showed that prestin targets the plasma membrane and generates NLC in CHO cells [18]. Now, we find that, as with OHCs in the presence of low extracellular chloride (1 mM), washout of intracellular chloride with low chloride containing patch pipette solutions shifts NLC to depolarizing levels and decreases its peak magnitude (Fig. 4). However, unlike native OHCs, the introduction of normal extracellular chloride levels (140 mM) fails to restore NLC. The degree of reduction in NLC during

washout of chloride is dependent on the substitute anion. For malate, NLC decreases nearly fully (Fig. 4a); however, with gluconate as substitute, about 30% NLC remains (Fig. 4b), similar to what we find in OHCs [21, 29]. For either substitute anion, however, the subsequent reintroduction of high extracellular chloride does not increase NLC. Similar experiments carried out with gramicidin patches to eliminate pipette washout of chloride near the inner aspect of prestin gave the same results (Fig. 5a). On the other hand, when we increased intracellular chloride via the patch pipette after gramicidin patch rupture or when we

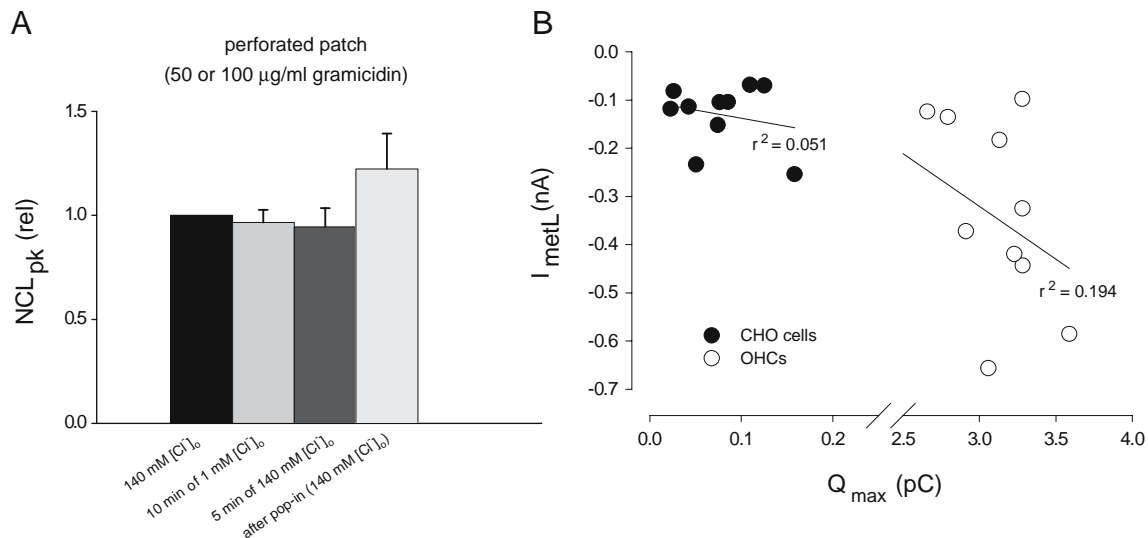


Fig. 5 a Lack of chloride influx in prestin-transfected CHO cells under perforated patch conditions. Prestin-transfected CHO cells were patched with gramicidin pipettes to limit the pipette washout of chloride so that transmembrane chloride flux could be unambiguously determined. In the presence of 140 mM extracellular chloride, relative NLC was determined after series resistance allowed whole-cell measurements. Subsequently, extracellular chloride was altered to see if NLC could be modulated by influx or outflux of chloride. Reductions and reperfusion of chloride had no effect, but NLC was augmented when true whole-cell configuration was established after patch rupture, indicating that chloride did not enter through the membrane. $n=6$ cells. **b** Comparison of G_{metL} and prestin activities shows no correlation in either prestin-transfected CHO cells or OHCs, as might have been expected if the expression level of prestin influenced I_{metL} activity. Symbols denote separate cells

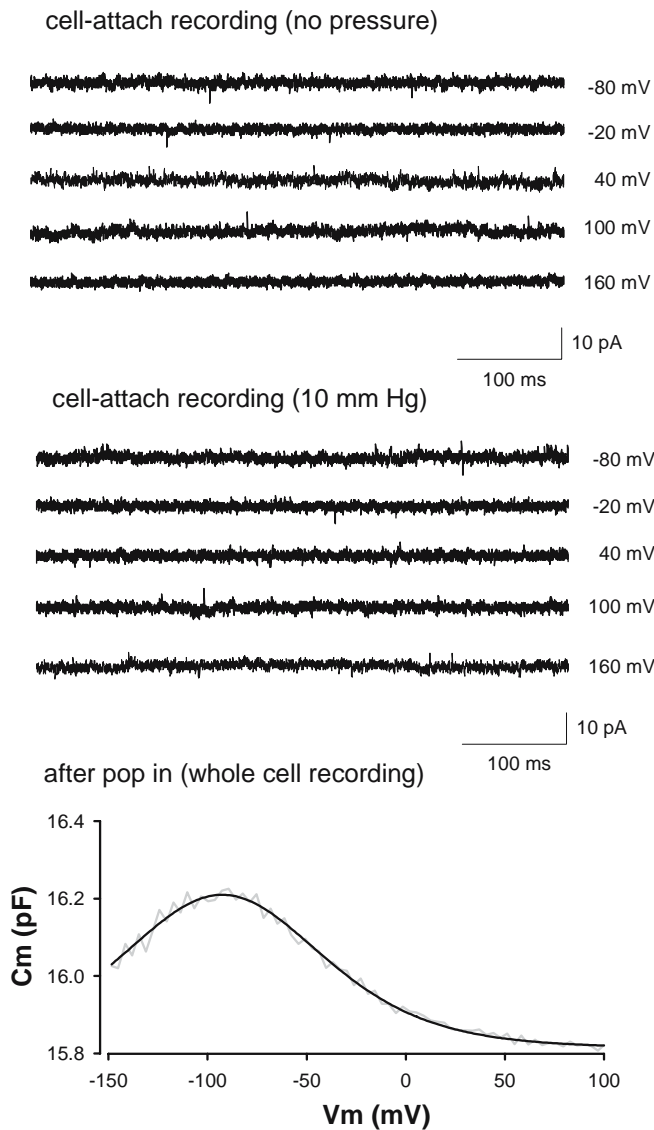


Fig. 7 I_{metL} is bimodally temperature sensitive, showing high sensitivity above 34°C , and typical diffusional sensitivity below that. K^+ current magnitude in OHCs is not temperature sensitive. OHC I_{metL} at -70 mV, circles; OHC I_{K^+} $+30$ mV, triangles. Plotted is mean \pm SE, $n=3-5$. Series resistance correction was performed on a point by point basis ($V_{\text{m}} = V_{\text{command}} - I \cdot R_{\text{s}}$). The progressive limited range of voltages as a function of current magnitude results in the “tilted” appearance of the I - V curves

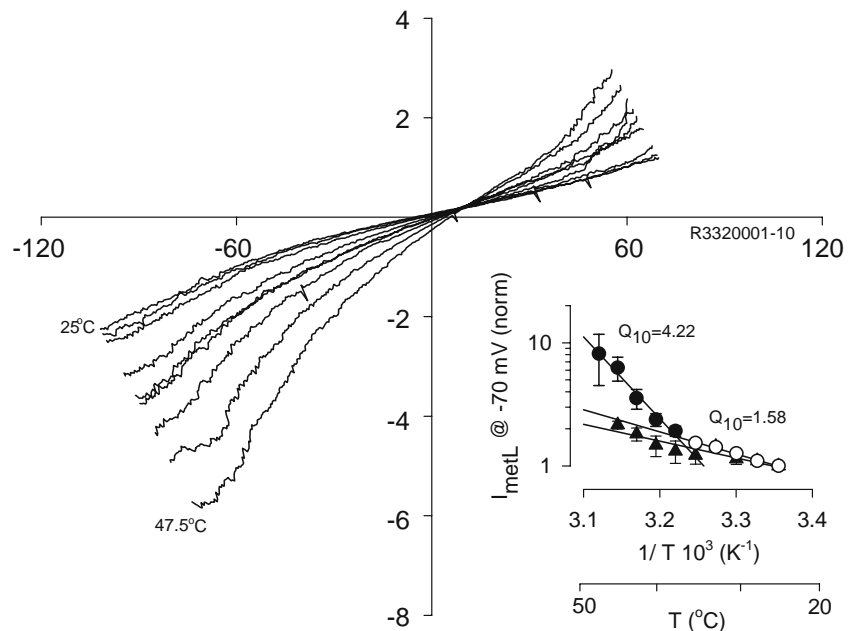


Fig. 6 On cell patch recording of prestin-transfected CHO cells to determine single channel currents [before (*top panel*) and after (*middle panel*) stretch to patch]. In the prestin-transfected cell, shown stretch did not elicit single channel currents (*top and middle panels*). The *bottom panel* NLC was confirmed after patch rupture. Forty cells of control CHO cells and 55 transfected cells of prestin-YFP fusions were recorded by cell-attach configuration. Some of them were also recorded by inside-out configuration. No stretch-sensitive activity was found from the prestin group. In both groups, some non-stretch-activated endogenous currents were recorded. They were activated only at hyperpolarization potentials, i.e., around rest potential (-80 to -60 mV). The numbers are 7 out of 40 from control CHO cells and 5 out of 55 from prestin cells

reintroduced chloride via whole-cell pipette backfill after intracellular washout, NLC increased or recovered, respectively. We also compared prestin activity (Q_{max}) to G_{metL} activity (I_{metL} at -70 mV in symmetrical 140 Cl solutions) to see if there was a correlation between the two (Fig. 5b). In either CHO cells or OHCs, the activities were uncorrelated. In addition, we searched for stretch-dependent, single channel activity that might have arisen following prestin expression in CHO cells and found none (Fig. 6). Taken together, our data show that prestin is not responsible for the chloride conductance, G_{metL} , found in OHCs.

Finally, though we found no change in the voltage-operating range of G_{metL} with temperature (Fig. 2), I_{metL} magnitudes at -70 mV were bimodally temperature sensitive. Figure 7 shows that below about 34°C , the Q_{10} value was 1.58 (open circles, inset), but above that temperature, Q_{10} was 4.22 (closed circles). In comparison, in the absence of ionic-blocking solutions, K^+ currents at $+30$ mV (steady holding level) in OHCs (triangles) show Q_{10} s of less than 1.3.

Discussion

G_{metL} is partially blocked by a few stretch-channel blockers, including gadolinium, tamoxifen, and quinine but is resistant to a host of other channel and transporter blockers [21]. Although the molecular identity of G_{metL} remains unknown, it is clear that G_{metL} and prestin share some characteristics, including restriction to the lateral membrane and sensitivity to chloride channel blockers (e.g., niflumic acid). One possibility is that G_{metL} arises from prestin itself, just as SLC26A7 underlies a chloride conductance [13]. Here, because we hypothesized that G_{metL} could arise from the conformational activity of prestin, we surmised that modulating prestin's voltage dependence with temperature and pressure would necessarily affect G_{metL} 's voltage dependence if the foregoing premise were true. To test whether prestin produces the OHC conductance or whether prestin somehow gates this conductance (possibly via a prestin-induced mechanical activation), we monitored characteristics of G_{metL} while modulating NLC with established techniques, including manipulations of turgor pressure and temperature, to see if each is similarly affected. In addition, we determined whether transfection of prestin into nonauditory cells induces a chloride conductance. The absence of a correspondence between the voltage-operating range of NLC and of G_{metL} in OHCs and an absence of significant Cl^- flux in prestin-transfected cells lead us to conclude that each is independent. This conclusion is further established by the absence of a correlation between Q_{max} and I_{metL} magnitudes in CHO cells and OHCs, and the absence of induced, stretch-dependent single channel activity in prestin-transfected CHO cells.

Another indication of the distinct nature of the two lateral membrane components is the temperature effects we observe on each. Though each is temperature sensitive, a clear breakpoint in sensitivity is evidenced for G_{metL} , where the conductance markedly changes its behavior as a characteristic temperature is crossed; NLC, on the other hand, is monotonically responsive to temperature, and this additionally indicates that possible phase transitions within the lateral membrane do not occur. That is, temperature has its effects on the protein structures underlying NLC and G_{metL} , not the membrane environment. This is not to say that temperature cannot affect prestin via the lipid bilayer, as we have shown that lipid reactive agents and, indeed, temperature can alter the kinetics of voltage- (prepulse) induced shifts in the motor's Boltzmann function along the voltage axis [28].

It is of interest that the temperature dependence of G_{metL} points to a molecular structure whose conformation is switched at a threshold temperature. Again, the absence of such a threshold phenomenon in the K^+ currents of OHCs argues against a nonspecific influence on the membrane. This type of behavior is reminiscent of some temperature sensitive transient receptor potential (TRP) channels [7], where Q_{10} above threshold temperatures, ranging from 30 to 50°C, can switch to greater than 10. It is also interesting that TRP channels can be mechanically sensitive, as is

G_{metL} . Nevertheless, TRP channels are cation selective, and we have previously tested the TRP channel blocker, ruthenium red, without effect [21]. It is interesting that GLUT5 is known to be associated with prestin within the lateral membrane [1]; however, in our preliminary tests, cotransfection of GLUT5 and prestin into CHO cells did not generate chloride fluxes. It may be that I_{metL} may arise from other components within the lateral membrane, including other SLC26 family members whose residence has not yet been determined in the OHC. CFTR has also been found to interact with prestin in OHCs [30], though we have not found electrophysiologic evidence for this or other chloride channels in the OHC [21].

Currently, there are two mechanisms that may contribute to cochlear amplification in mammals. One mechanism involves stereociliary bundle mechanics, driven by ionic flux of Ca^{++} through the, as yet, molecularly unidentified {however, see [5] for a review} stereociliary mechano-electrical transducer (MET) conductance [3, 12]. The other mechanism involves prestin-based electromotility of OHCs [2, 14, 31], which, being anion dependent [19], can be modulated by ionic flux of chloride through the, as yet, molecularly unidentified lateral membrane conductance, the G_{metL} [21, 30]. Our observations indicate that for the latter mechanism, interaction between ion and motor function arises from distinct molecular contributors, namely, prestin and G_{metL} , whereas in the former case, the MET conductance works on itself. This difference between feedback mechanisms may be important in understanding capabilities of each mechanism towards amplification. For example, whereas the molecular colocalization of the stereociliary bundle's feedback mechanism constrains timing of interactions between Ca^{++} and the channel, the distinct identities of prestin and G_{metL} could permit variable interaction delays simply by varying the distances between each within the lateral membrane. It is well known that setting appropriate feedback delays is crucial in nonlinear system performance, and, thus, having a potential means to adjust feedback delays may be viewed as particularly advantageous.

Acknowledgements This research was supported by NIH NIDCD grant DC000273 to JSS and grant K08 DC05352 to DN. We also thank Margaret Mazzucco for the technical help.

References

1. Belyantseva I, Adler HJ, Curi R, Frolenkov GI, Kachar B (2000) Expression and localization of prestin and the sugar transporter GLUT-5 during development of electromotility in cochlear outer hair cells. *J Neurosci* 20:RC116
2. Brownell WE, Bader CR, Bertrand D, de Ribaupierre Y (1985) Evoked mechanical responses of isolated cochlear outer hair cells. *Science* 227:194–196
3. Chan DK, Hudspeth AJ (2005) Ca^{2+} current-driven nonlinear amplification by the mammalian cochlea in vitro. *Nat Neurosci* 8:149–155
4. Choi I, Aalkjaer C, Boulpaep EL, Boron WF (2000) An electroneutral sodium/bicarbonate cotransporter NBCn1 and associated sodium channel. *Nature* 405:571–575

5. Corey DP, Garcia-Anoveros J, Holt JR, Kwan KY, Lin SY, Vollrath MA, Amalfitano A, Cheung EL, Derfler BH, Duggan A, Geleoc GS, Gray PA, Hoffman MP, Rehm HL, Tamasauskas D, Zhang DS (2004) TRPA1 is a candidate for the mechanosensitive transduction channel of vertebrate hair cells. *Nature* 432:723–730
6. Gale JE, Ashmore JF (1994) Charge displacement induced by rapid stretch in the basolateral membrane of the guinea-pig outer hair cell. *Proc R Soc Lond B Biol Sci* 255:243–249
7. Gunthorpe MJ, Benham CD, Randall A, Davis JB (2002) The diversity in the vanilloid (TRPV) receptor family of ion channels. *Trends Pharmacol Sci* 23:183–191
8. Hasegawa H, Skach W, Baker O, Calayag MC, Lingappa V, Verkman AS (1992) A multifunctional aqueous channel formed by CFTR. *Science* 258:1477–1479
9. Iwasa KH (1993) Effect of stress on the membrane capacitance of the auditory outer hair cell. *Biophys J* 65:492–498
10. Iwasa KH (1994) A membrane motor model for the fast motility of the outer hair cell. *J Acoust Soc Am* 96:2216–2224
11. Kakehata S, Santos-Sacchi J (1995) Membrane tension directly shifts voltage dependence of outer hair cell motility and associated gating charge. *Biophys J* 68:2190–2197
12. Kennedy HJ, Evans MG, Crawford AC, Fettiplace R (2003) Fast adaptation of mechano-electrical transducer channels in mammalian cochlear hair cells. *Nat Neurosci* 6:832–836
13. Kim KH, Shcheynikov N, Wang YX, Muallem S (2005) SLC26A7 is a Cl⁻ channel regulated by intracellular pH. *J Biol Chem* 280:6463–6470
14. Liberman MC, Gao J, He DZ, Wu X, Jia S, Zuo J (2002) Prestin is required for electromotility of the outer hair cell and for the cochlear amplifier. *Nature* 419:300–304
15. Ludwig J, Oliver D, Frank G, Klocker N, Gummer AW, Fakler B (2001) Reciprocal electromechanical properties of rat prestin: the motor molecule from rat outer hair cells. *Proc Natl Acad Sci U S A* 98:4178–4183
16. Meltzer J, Santos-Sacchi J (2001) Temperature dependence of non-linear capacitance in human embryonic kidney cells transfected with prestin, the outer hair cell motor protein. *Neurosci Lett* 313:141–144
17. Meltzer J, Santos-Sacchi J (2001) Temperature dependence of non-linear capacitance in human embryonic kidney cells transfected with prestin, the outer hair cell motor protein. *Neurosci Lett* 313:141–144
18. Navaratnam D, Bai JP, Samaranayake H, Santos-Sacchi J (2005) N-terminal-mediated homomultimerization of prestin, the outer hair cell motor protein. *Biophys J* 89:3345–3352
19. Oliver D, He DZ, Klocker N, Ludwig J, Schulte U, Waldegger S, Ruppertsberg JP, Dallos P, Fakler B (2001) Intracellular anions as the voltage sensor of prestin, the outer hair cell motor protein. *Science* 292:2340–2343
20. Otis TS, Jahr CE (1998) Anion currents and predicted glutamate flux through a neuronal glutamate transporter. *J Neurosci* 18:7099–7110
21. Rybalchenko V, Santos-Sacchi J (2003) Cl⁻ flux through a non-selective, stretch-sensitive conductance influences the outer hair cell motor of the guinea-pig. *J Physiol* 547:873–891
22. Santos-Sacchi J (1991) Reversible inhibition of voltage-dependent outer hair cell motility and capacitance. *J Neurosci* 11:3096–3110
23. Santos-Sacchi J (1993) Harmonics of outer hair cell motility. *Biophys J* 65:2217–2227
24. Santos-Sacchi J (2004) Determination of cell capacitance using the exact empirical solution of partial derivative $Y/\text{partial}$ derivative $C-m$ and its phase angle. *Biophys J* 87:714–727
25. Santos-Sacchi J, Huang G (1998) Temperature dependence of outer hair cell nonlinear capacitance. *Hear Res* 116:99–106
26. Santos-Sacchi J, Kakehata S, Takahashi S (1998) Effects of membrane potential on the voltage dependence of motility-related charge in outer hair cells of the guinea-pig. *J Physiol (Lond)* 510(1):225–235
27. Santos-Sacchi J, Shen W, Zheng J, Dallos P (2001) Effects of membrane potential and tension on prestin, the outer hair cell lateral membrane motor protein. *J Physiol* 531:661–666
28. Santos-Sacchi J, Wu M (2004) Protein- and lipid-reactive agents alter outer hair cell lateral membrane motor charge movement. *J Membr Biol* 200:83–92
29. Song L, Seeger A, Santos-Sacchi J (2004) On membrane motor activity and chloride flux in the outer hair cell: lessons learned from the environmental toxin tributyltin. *Biophys J* 88:2350–2362
30. Zheng J, Aguinaga C, Anderson C, Miller K, Dallos P (2005) Prestin's interaction with CFTR enhances its function. Abstract of 28th meeting of the association for research in otolaryngology, New Orleans, LA
31. Zheng J, Shen W, He DZ, Long KB, Madison LD, Dallos P (2000) Prestin is the motor protein of cochlear outer hair cells. *Nature* 405:149–155

Rapid Report

Effects of membrane potential and tension on prestin, the outer hair cell lateral membrane motor protein

Joseph Santos-Sacchi, Weixing Shen*, Jing Zheng* and Peter Dallos*

*Sections of Otolaryngology and Neurobiology, Yale University School of Medicine, New Haven, CT 06510 and *Neurobiology and Physiology, Northwestern University, 2299 N. Campus Drive, Evanston, IL 60208, USA*

(Received 14 December 2000; accepted after revision 25 January 2001)

1. Under whole-cell voltage clamp, the effects of initial voltage conditions and membrane tension on gating charge and voltage-dependent capacitance were studied in human embryonic kidney cells (TSA201 cell line) transiently transfected with the gene encoding the gerbil protein prestin. Conformational changes in this membrane-bound protein probably provide the molecular basis of the outer hair cell (OHC) voltage-driven mechanical activity, which spans the audio spectrum.
2. Boltzmann characteristics of the charge movement in transfected cells were similar to those reported for OHCs ($Q_{\max} = 0.99 \pm 0.16$ pC, $z = 0.88 \pm 0.02$; $n = 5$, means \pm S.E.M.). Unlike that of the adult OHC, the voltage at peak capacitance (V_{pkcm}) was very negative (-74.7 ± 3.8 mV). Linear capacitance in transfected cells was 43.7 ± 13.8 pF and membrane resistance was 458 ± 123 M Ω .
3. Voltage steps from the holding potential preceding the measurement of capacitance–voltage functions caused a time- and voltage-dependent shift in V_{pkcm} . For a prepulse to -150 mV, from a holding potential of 0 mV, V_{pkcm} shifted 6.4 mV, and was fitted by a single exponential time constant of 45 ms. A higher resolution analysis of this time course was made by measuring the change in capacitance during a fixed voltage step and indicated a double exponential shift ($\tau_0 = 51.6$ ms, $\tau_1 = 8.5$ s) similar to that of the native gerbil OHC.
4. Membrane tension, delivered by increasing pipette pressure, caused a positive shift in V_{pkcm} . A maximal shift of 7.5 mV was obtained with 2 kPa of pressure. The effect was reversible.
5. Our results show that the sensitivity of prestin to initial voltage and membrane tension, though present, is less than that observed in adult OHCs. It remains possible that some other interacting molecular species within the lateral plasma membrane of the native OHC amplifies the effect of tension and prior voltage on prestin's activity.

In mammals, two classes of hair cell evolved to meet the requirements of high frequency acoustic reception. The inner hair cell, which is innervated by the majority of eighth-nerve afferents (Spendlin, 1986), is the primary sensory receptor. The outer hair cell (OHC), while capable of generating acoustically evoked receptor potentials (Dallos *et al.* 1982), additionally functions as a mechanical effector that is thought to provide feedback to the basilar membrane to enhance auditory sensitivity and frequency resolving power (Brownell *et al.* 1985; Ashmore, 1987; Dallos, 1992).

The OHC is clearly unique. It alone is capable of voltage-induced mechanical responses ranging up to at least 100 kHz (Frank *et al.* 1999). The lateral membrane of this cylindrical cell houses the molecular machinery responsible for this

response (Dallos *et al.* 1991; Kalinec *et al.* 1992; Huang & Santos-Sacchi, 1993). Recently the gene for a candidate motor protein, prestin, has been cloned (Zheng *et al.* 2000), and this protein is restricted to the lateral membrane of OHCs (Belyantseva *et al.* 2000). Prestin, in addition to enabling voltage-induced mechanical activity in transfected non-auditory cells, was shown to display some of the electrical characteristics of the native OHC sensor/motor, namely gating charge movement or non-linear capacitance that exhibits shallow voltage dependence (Zheng *et al.* 2000).

In this study we explored further the characteristics of prestin's voltage sensor, and found that similar to the native OHC motor, prestin's charge *vs.* voltage (Q – V) function possesses memory (Santos-Sacchi *et al.* 1998) and is

mechanically sensitive (Iwasa, 1993; Gale & Ashmore, 1994; Kakehata & Santos-Sacchi, 1995). That is, the motor molecule's behaviour is influenced by prior voltage conditions and membrane tension.

METHODS

The electrical characteristics of prestin and the native OHC sensor/motor were evaluated under the same conditions. Transient transfection of human embryonic kidney (TSA201) cells with gerbil prestin was performed as previously described (Zheng *et al.* 2000). Co-expression of green fluorescent protein provided visual identification of transfected cells. OHCs were freshly isolated from the cochleae of gerbils, which were killed by decapitation following anaesthetic overdose (100 mg kg⁻¹ Nembutal, i.p.). This method follows the guidelines established by Northwestern and Yale University's Animal Care and Use Committees. Cells were whole-cell voltage clamped with an Axopatch 200B amplifier (Axon

Instruments, CA, USA) at a holding potential of 0 mV. The patch pipette solution contained (mM): 140 CsCl, 2 MgCl₂, 10 EGTA, 10 Hepes; pH 7.2. The external solution contained (mM): 120 NaCl, 20 TEA-Cl, 2 CoCl₂, 2 MgCl₂, 10 Hepes, 5 glucose; pH 7.2. Osmolarity was adjusted to 300 mosmol l⁻¹ with glucose. Current responses were filtered at 5 kHz. Corrections were made for the effects of residual series resistance, which averaged less than 10 MΩ. All data collection and most analyses were performed with a Windows-based whole-cell voltage-clamp program, jClamp (SciSoft, CT, USA), utilizing a National Instruments PCI-6052E 16-bit interface. Matlab (Natick, MA, USA) was used for some analyses. Fits were made with the Levenberg-Marquardt algorithm. Recordings from TSA201 cells that evidenced electrical coupling to adjacent cells were excluded from data analysis. Coupling was assessed with input capacitance measures (Santos-Sacchi, 1991a).

Whole-cell membrane capacitance was measured with two techniques, transient and AC. The former entailed the delivery of a stair-step voltage ranging from -160 to 120 mV, in 14 mV

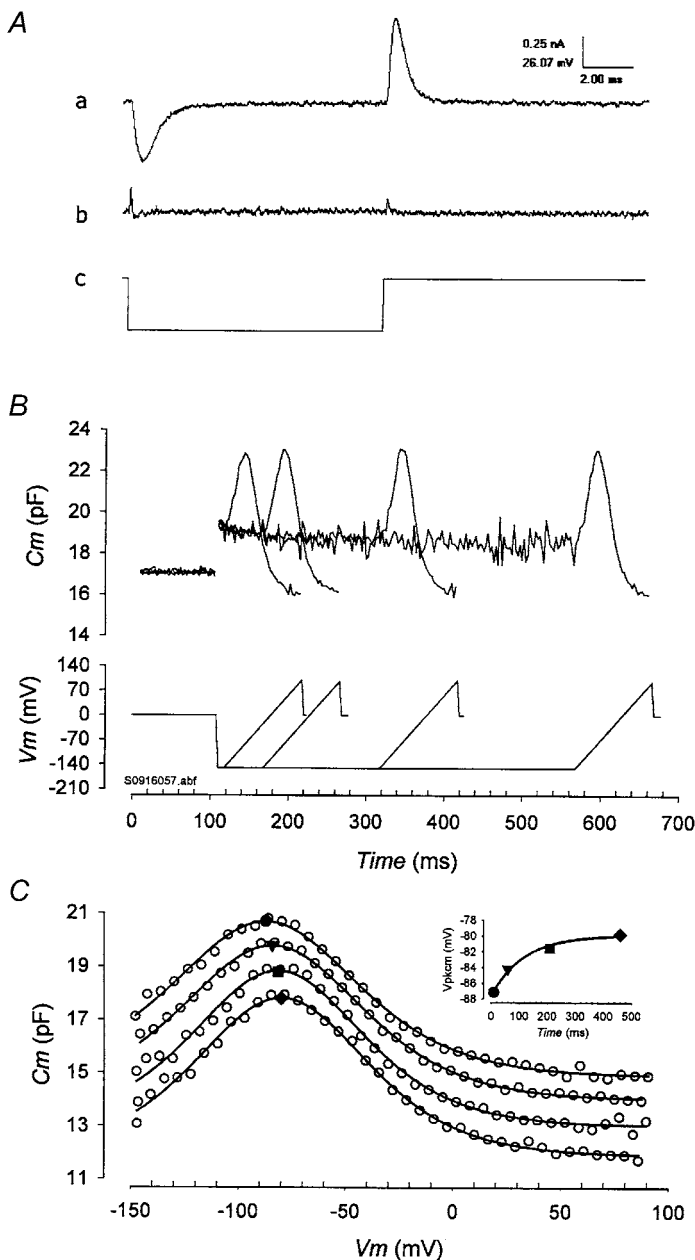


Figure 1. Prestin's charge movement is sensitive to initial voltage

A, gating current (*a*) in a prestin-transfected TSA201 cell induced by a voltage step (*c*) to -100 mV from a holding potential of 0 mV. Non-transfected cells did not produce gating currents (*b*). *P/-4* protocol was used with a subtraction holding potential of +50 mV. *B*, whole-cell C_m determined with dual sinusoidal technique (top panel). The bottom panel shows the voltage protocol. Sinusoids have been removed for visual clarity. Data were obtained from 4 episodes; voltage was stepped to -150 mV with incrementing durations from a holding potential of 0 mV. Five-second intervals at the holding potential were allowed for recovery between episodes. *C*, capacitance data from *B* are plotted vs. ramp voltage. Traces are shifted downward (1 pF decrements) for visual clarity. Fits indicate a shift in V_{pkcm} denoted by ● (V_{pkcm} , Q_{max} , z and C_{in} were, respectively: -87.15 mV, 0.89 pC, 0.66 and 14.7 pF), ▼ (-84.2 mV, 0.91 pC, 0.64 and 15.0 pF), ■ (-81.5 mV, 0.97 pC, 0.61 and 15.0 pF) and ◆ (-79.8 mV, 0.96 pC, 0.63 and 14.9 pF). The same symbols are used in the inset plot to show the time course of the shift. A single exponential fit gave $\tau = 116$ ms.

increments. Transient currents were integrated to obtain cell capacitance (C_m) measurements as previously described (Huang & Santos-Sacchi, 1993). The second technique utilized a continuous high-resolution (2.56 ms sampling) two-sine voltage stimulus protocol (10 mV peak at both 390.6 and 781.2 Hz), with subsequent fast Fourier transform (FFT)-based admittance analysis (Santos-Sacchi *et al.* 1998). These high-frequency sinusoids were superimposed on voltage ramp, step or sinusoidal stimuli. Capacitance data were fitted to the first derivative of a two-state Boltzmann function (Santos-Sacchi, 1991*b*):

$$C_m = Q_{\max} \left(\frac{zeb}{kT(1+b)} \right) + C_{\text{lin}}, \quad (1)$$

$$b = \exp \left(\frac{-ze(V_m - V_{\text{pkcm}})}{kT} \right),$$

where Q_{\max} is the maximum non-linear charge moved, V_{pkcm} is voltage at peak capacitance or half-maximal non-linear charge transfer, V_m is membrane potential, C_{lin} is linear capacitance, z is valency, e is electron charge, k is Boltzmann's constant and T is absolute temperature. Gating currents were obtained as described previously (Santos-Sacchi, 1991*b*). V_{pkcm} was tracked in real time with 2 mV resolution by monitoring the reversal of gating current polarity as fully described previously (Kakehata & Santos-Sacchi, 1995). Pipette pressure was monitored with a solid-state device (WPI, FL, USA) (Kakehata & Santos-Sacchi, 1995).

RESULTS

With ionic currents blocked, transfected TSA201 cells evidenced non-linear gating currents with characteristics similar to those obtained from native OHC lateral membrane sensor/motors (Fig. 1*Aa*). Control cells that were not transfected did not generate such currents (Fig. 1*Ab*). This result confirms the findings of Zheng *et al.* (2000). Transient analysis of the membrane capacitance arising from these gating currents provided estimates of the voltage-dependent Boltzmann characteristics of the charges. In five cells, we obtained values similar to those reported for OHCs, namely $Q_{\max} = 0.99 \pm 0.16$ pC and $z = 0.88 \pm 0.02$ (means \pm S.E.M.). Unlike that of the OHC, however, the voltage at peak capacitance (V_{pkcm}) was very negative (-74.7 ± 3.8 mV) at the outset of whole-cell voltage clamp. Guinea-pig OHCs had their peak non-linear capacitance at -21.5 mV (Kakehata & Santos-Sacchi, 1995). Linear capacitance in transfected cells was 43.7 ± 13.8 pF and membrane resistance was 458 ± 123 M Ω .

Voltage steps from the holding potential preceding the measurement of capacitance *vs.* voltage (C - V) functions caused a time- and voltage-dependent shift in V_{pkcm} . Figure 1*B* illustrates an example utilizing the admittance-based measurement technique. From a holding potential of 0 mV, the cell was stepped to -150 mV for 10, 60, 210 or 460 ms, after which the cell was ramped to 100 mV to obtain the C - V function. The negative prepulse caused a shift in the capacitance function in the depolarizing direction; as prepulse length increased, the magnitude of the shift increased, with a 7.3 mV shift being obtained after 460 ms. The inset in Fig. 1*C* presents the time course of the shift and shows a

single exponential fit with a time constant of 116 ms. Figure 2 presents the average results obtained from such prepulse experiments; a single exponential fit to the averaged data points provided a time constant of 45 ms. In comparison, similar data obtained from native OHCs could be fitted with a time constant of about 200 ms (Santos-Sacchi *et al.* 1998). Additionally, whereas prepulse-induced, steady-state shifts of 14 mV are found in native OHCs (Santos-Sacchi *et al.* 1998), the average shift was 6.4 mV in transfected cells (Fig. 2).

We refined our estimates of the time course of the V_{pkcm} shift by measuring cell capacitance during constant voltage steps. Since a change in voltage induces a shift in the bell-shaped capacitance function along the voltage axis, at any fixed voltage the magnitude of the capacitance will change over time, and will reflect the time course of the shift in V_{pkcm} (Santos-Sacchi *et al.* 1998). Figure 3 illustrates this phenomenon for a transfected cell and a gerbil OHC. During the voltage step, the capacitance magnitudes changed with a double exponential time course. For the transfected cell τ_0 was 51.6 ms and τ_1 was 8.5 s, whereas for the OHC τ_0 was 69.2 ms and τ_1 was 2.79 s. It should be noted that the duration of the step was short relative to the second time constant values. Good fits by eye were obtained by fixing both second time constants at 1.2 s, the second time constant value obtained from OHCs when longer step durations were delivered (Santos-Sacchi *et al.* 1998).

Finally, we evaluated the effects of membrane tension on V_{pkcm} . Membrane tension, applied via pipette or osmotic pressure, is known to shift V_{pkcm} in OHCs (Iwasa, 1993; Gale & Ashmore, 1994; Kakehata & Santos-Sacchi, 1995). Figure 4 shows that changes in pipette pressure can reversibly shift V_{pkcm} in transfected cells. For example, a pipette pressure of 2 kPa resulted in a shift of about 7.5 mV. With pressures larger than 2 kPa cells were blown off the pipette or seals were lost. Changes in the

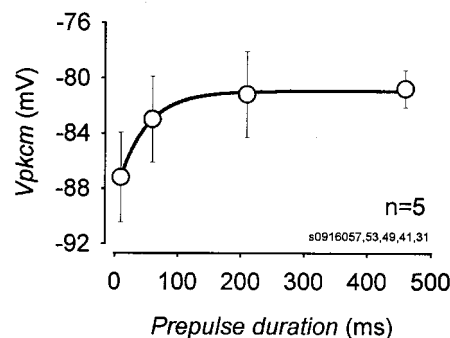


Figure 2. Average V_{pkcm} *vs.* prepulse duration

Data were obtained from experimental protocols as in Fig. 1. Plotted are the means \pm S.E.M. for five transfected cells. The single exponential fit gave $\tau = 45$ ms.

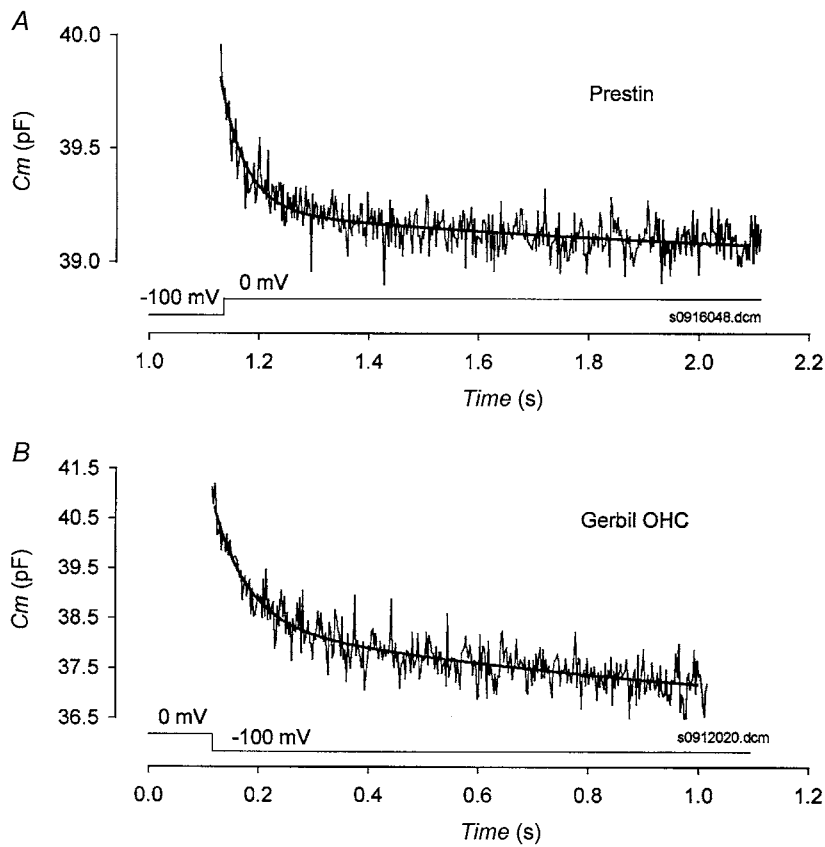


Figure 3. Time course of capacitance change following voltage step

A, transfected cell capacitance decreased with $\tau_0 = 51.6$ ms and $\tau_1 = 8.5$ s indicative of the time-dependent shift in V_{pkcm} . *B*, OHC capacitance decreased with $\tau_0 = 69.2$ ms and $\tau_1 = 2.79$ s. These results are predicted by a visco-elastic model of motor interactions (Santos-Sacchi *et al.* 1998).

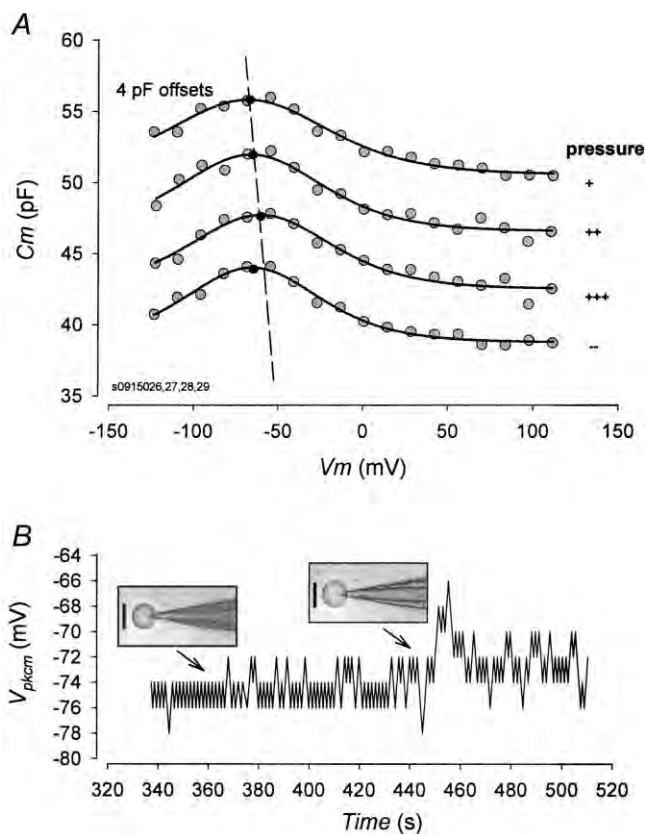


Figure 4. Effects of membrane tension on V_{pkcm}

A, $C-V$ functions were obtained with transient analysis under conditions where pipette pressure was modified. Capacitance functions are offset by -4 pF for visual clarity. ●, fitted V_{pkcm} . A straight line is drawn through the top three values, indicating the depolarizing shift in V_{pkcm} that accompanied pipette pressure increases. Pipette pressure was less than 0 kPa ($-$), ~ 0.6 kPa ($+$), ~ 1.3 kPa ($++$) and ~ 2 kPa ($+++$). When pressure was made negative, V_{pkcm} shifted back in the hyperpolarizing direction. Fits (from top trace to bottom trace) for V_{pkcm} , Q_{max} , z and C_{lin} were, respectively: -68.0 mV, 0.81 pC, 0.66 and 50.6 pF; -66.2 mV, 0.91 pC, 0.60 and 50.6 pF; -60.5 mV, 0.91 pC, 0.58 and 50.5 pF; -65.4 mV, 0.96 pC, 0.55 and 50.8 pF. *B*, V_{pkcm} was tracked during changes in pipette pressure. Photographs of patch-clamped transfected cells correspond to points (arrows) before and after a pressure increase that changed cell diameter by 8%. A slight depolarizing shift in V_{pkcm} was observed during the pressure increase.

dimensions of the cells confirmed that pipette pressure was delivered to the cells (Fig. 4B). The magnitude of the response was small compared to that of OHCs where shifts as large as 50 mV are found (Takehata & Santos-Sacchi, 1995).

DISCUSSION

Non-linearity is the hallmark of the mammalian auditory system's active process whereby near-threshold responses are selectively enhanced. In fact, a variety of non-linear phenomena exist within single OHCs that identify candidate mechanisms likely to underlie the 'cochlear amplifier'. These include non-linearities intrinsic to the mechanics of the cell soma, as well as those of the stereociliary bundle. Within the soma several non-linear, voltage-dependent processes have been studied, including electromotility (Brownell *et al.* 1985; Ashmore, 1987; Santos-Sacchi & Dilger, 1988), stiffness (He & Dallos, 1999) and membrane lipid mobility (Oghalai *et al.* 2000). Recently, we showed that the very same stimulus, i.e. lateral membrane voltage, that evokes OHC somatic mechanical activity influences its form (Santos-Sacchi *et al.* 1998). We successfully modelled the effect as a visco-elastic interaction among lateral membrane motor molecules, where motor-induced membrane tension shifted the cell's C - V function. One of the consequences of this interaction is similar to that occurring within the stereociliary bundle, namely that a shift in the operating point of the transducer function over time provides for differing instantaneous and steady-state responsiveness. Consequently, in the case of the OHC soma, we observe hysteresis in the C - V or Q - V function, the magnitude of which may be frequency dependent (J. Santos-Sacchi & E. Navarrete, unpublished observation). Even at the system level, susceptibility of the motor to membrane tension underlies the generation of non-linearities resulting from mechanical interactions among OHCs within the organ of Corti (Zhao & Santos-Sacchi, 1999). Our present observation that prestin displays the same complex electrical characteristics, and attendant non-linearities, as those of the native OHC motor confirms the identity of this protein. Since prestin presents these qualities in the absence of its normal cellular environment, our work also raises questions about the molecular requirements for full functional activity.

There are several features that differentiate OHCs from other hair cells. Most notably, the OHC possesses an extensive composite lateral wall, consisting of the mechanically active lateral plasma membrane, the cortical cytoskeleton and the subsurface cisternae (Flock *et al.* 1986; Holley *et al.* 1992; Pollice & Brownell, 1993). Structural distinctions such as these probably underscore a functional requirement for unique protein constituents, and indeed, besides prestin, other proteins specific to the OHC are known to exist (Sakaguchi *et al.* 1998; Zheng *et al.* 2000). While it is possible that novel auxiliary protein

subunits act in conjunction with prestin to modify its behaviour, as occurs for ionic channels (Walker & De Waard, 1998), our present results indicate that other unique proteins present in the normal OHC are not required for the generation of voltage-induced or tension-induced shifts in V_{pkem} . We had previous indications of this autonomy, since we demonstrated that neither of the effects was abolished in OHCs by destruction of intracellular constituents with trypsin or pronase (Takehata & Santos-Sacchi, 1995; Santos-Sacchi *et al.* 1998).

Notwithstanding the many electrical properties of the lateral membrane motor that appear intrinsic to prestin, auxiliary subunit contributions cannot be ruled out. In this regard, we found that V_{pkem} values in transfected cells are very negative relative to those found in adult OHCs (-74.7 vs. -21.5 mV; Takehata & Santos-Sacchi, 1995). Two physiological mechanisms that are capable of shifting V_{pkem} are membrane tension (Iwasa, 1993; Gale & Ashmore, 1994; Takehata & Santos-Sacchi, 1995) and phosphorylation (Frolenkov *et al.* 2000). While the voltage dependencies that we found may simply result from differences in resting membrane tension between transfected cells and OHCs, or from differences in the degree of phosphorylation, it is also possible that auxiliary subunits can contribute. Indeed, the voltage-dependent Ca^{2+} channel β subunit is known to shift the voltage dependence of the channel's activation (De Waard *et al.* 1994). Interestingly, during the development of rat OHCs, V_{pkem} shifts from hyperpolarized levels to more depolarized levels as found in adult guinea-pig OHCs over the course of a few days (Oliver & Fakler, 1999). Although Oliver & Fakler (1999) argued in favour of phosphorylation over subunit interaction, the issue remains open. Finally, we note that the magnitude of the effects that we observed in the present study is not as great as that seen in native OHCs (Takehata & Santos-Sacchi, 1995; Santos-Sacchi *et al.* 1998). Thus, while the intrinsic properties of a single protein, prestin, may form the basis of mammalian auditory system responsiveness, it remains possible that some other interacting molecular species within the lateral plasma membrane amplifies the effect of tension and prior voltage on prestin's activity. One such candidate protein is the sugar transporter GLUT-5, which localizes to the OHC lateral membrane and may influence the OHC motor (Géléoc *et al.* 1999; Belyantseva *et al.* 2000). GLUT-5 is not expressed in TSA201 cells (J. Zheng, unpublished data). Notwithstanding this scenario, it should be noted that another possibility, not yet examined, is that intrinsic constituents of the TSA201 cell's plasma membrane could influence the activity of an expressed foreign protein. Nevertheless, it is certainly clear that with the identification of prestin and other novel OHC proteins, the issue of molecular interactions within the OHC's mechanically active lateral plasma membrane can be directly assessed.

- ASHMORE, J. F. (1987). A fast motile response in guinea-pig outer hair cells: the cellular basis of the cochlear amplifier. *Journal of Physiology* **388**, 323–347.
- BELYANTSEVA, I., ADLER, H. J., CURI, R., FROLENKOV, G. I. & KACHAR, B. (2000). Expression and localization of Prestin and the sugar transporter GLUT-5 during development of electromotility in cochlear outer hair cells. *Journal of Neuroscience* **20**, RC116.
- BROWNELL, W. E., BADER, C. R., BERTRAND, D. & DE RIBAUPIERRE, Y. (1985). Evoked mechanical responses of isolated cochlear outer hair cells. *Science* **227**, 194–196.
- DALLOS, P. (1992). The active cochlea. *Journal of Neuroscience* **12**, 4575–4585.
- DALLOS, P., EVANS, B. N. & HALLWORTH, R. (1991). Nature of the motor element in electrokinetic shape changes of cochlear outer hair cells. *Nature* **350**, 155–157.
- DALLOS, P., SANTOS-SACCHI, J. & FLOCK, A. (1982). Intracellular recordings from cochlear outer hair cells. *Science* **218**, 582–584.
- DE WAARD, M., PRAGNELL, M. & CAMPBELL, K. P. (1994). Ca²⁺ channel regulation by a conserved beta subunit domain. *Neuron* **13**, 495–503.
- FLOCK, A., FLOCK, B. & ULFENDAHL, M. (1986). Mechanisms of movement in outer hair cells and a possible structural basis. *Archives of Otorhinolaryngology* **243**, 83–90.
- FRANK, G., HEMMERT, W. & GUMMER, A. W. (1999). Limiting dynamics of high-frequency electromechanical transduction of outer hair cells. *Proceedings of the National Academy of Sciences of the USA* **96**, 4420–4425.
- FROLENKOV, G. I., MAMMANO, F., BELYANTSEVA, I. A., COLING, D. & KACHAR, B. (2000). Two distinct Ca²⁺-dependent signaling pathways regulate the motor output of cochlear outer hair cells. *Journal of Neuroscience* **20**, 5940–5948.
- GALE, J. E. & ASHMORE, J. F. (1994). Charge displacement induced by rapid stretch in the basolateral membrane of the guinea-pig outer hair cell. *Proceedings of the Royal Society B* **255**, 243–249.
- GÉLÉOC, G. S., CASALOTTI, S. O., FORGE, A. & ASHMORE, J. F. (1999). A sugar transporter as a candidate for the outer hair cell motor. *Nature Neuroscience* **2**, 713–719.
- HE, D. Z. & DALLOS, P. (1999). Somatic stiffness of cochlear outer hair cells is voltage-dependent. *Proceedings of the National Academy of Sciences of the USA* **96**, 8223–8228.
- HOLLEY, M. C., KALINEC, F. & KACHAR, B. (1992). Structure of the cortical cytoskeleton in mammalian outer hair cells. *Journal of Cell Science* **102**, 569–580.
- HUANG, G. & SANTOS-SACCHI, J. (1993). Mapping the distribution of the outer hair cell motility voltage sensor by electrical amputation. *Biophysical Journal* **65**, 2228–2236.
- IWASA, K. H. (1993). Effect of stress on the membrane capacitance of the auditory outer hair cell. *Biophysical Journal* **65**, 492–498.
- KAKEHATA, S. & SANTOS-SACCHI, J. (1995). Membrane tension directly shifts voltage dependence of outer hair cell motility and associated gating charge. *Biophysical Journal* **68**, 2190–2197.
- KALINEC, F., HOLLEY, M. C., IWASA, K. H., LIM, D. J. & KACHAR, B. (1992). A membrane-based force generation mechanism in auditory sensory cells. *Proceedings of the National Academy of Sciences of the USA* **89**, 8671–8675.
- OGHALAI, J. S., ZHAO, H. B., KUTZ, J. W. & BROWNELL, W. E. (2000). Voltage- and tension-dependent lipid mobility in the outer hair cell plasma membrane. *Science* **287**, 658–661.
- OLIVER, D. & FAKLER, B. (1999). Expression density and functional characteristics of the outer hair cell motor protein are regulated during postnatal development in rat. *Journal of Physiology* **519**, 791–800.
- POLLICE, P. A. & BROWNELL, W. E. (1993). Characterization of the outer hair cell's lateral wall membranes. *Hearing Research* **70**, 187–196.
- SAKAGUCHI, N., HENZL, M. T., THALMANN, I., THALMANN, R. & SCHULTE, B. A. (1998). Oncomodulin is expressed exclusively by outer hair cells in the organ of Corti. *Journal of Histochemistry and Cytochemistry* **46**, 29–40.
- SANTOS-SACCHI, J. (1991*a*). Isolated supporting cells from the organ of Corti: some whole cell electrical characteristics and estimates of gap junctional conductance. *Hearing Research* **52**, 89–98.
- SANTOS-SACCHI, J. (1991*b*). Reversible inhibition of voltage-dependent outer hair cell motility and capacitance. *Journal of Neuroscience* **11**, 3096–3110.
- SANTOS-SACCHI, J. & DILGER, J. P. (1988). Whole cell currents and mechanical responses of isolated outer hair cells. *Hearing Research* **35**, 143–150.
- SANTOS-SACCHI, J., KAKEHATA, S. & TAKAHASHI, S. (1998). Effects of membrane potential on the voltage dependence of motility-related charge in outer hair cells of the guinea-pig. *Journal of Physiology* **510**, 225–235.
- SPOENDLIN, H. (1986). Receptoneural and innervation aspects of the inner ear anatomy with respect to cochlear mechanics. *Scandinavian Audiology* (suppl.) **25**, 27–34.
- WALKER, D. & DE WAARD, M. (1998). Subunit interaction sites in voltage-dependent Ca²⁺ channels: role in channel function. *Trends in Neurosciences* **21**, 148–154.
- ZHAO, H. B. & SANTOS-SACCHI, J. (1999). Auditory collusion and a coupled couple of outer hair cells. *Nature* **399**, 359–362.
- ZHENG, J., SHEN, W., HE, D. Z., LONG, K. B., MADISON, L. D. & DALLOS, P. (2000). Prestin is the motor protein of cochlear outer hair cells. *Nature* **405**, 149–155.

Acknowledgements

This work was supported by NIH-NIDCD grant DC00273 to J.S.-S. and DC00708 to P.D.

Corresponding author

J. Santos-Sacchi: Surgery (Otolaryngology), BML 244, Yale University School of Medicine, 333 Cedar Street, New Haven, CT 06510, USA.

Email: joseph.santos-sacchi@yale.edu

Control of Mammalian Cochlear Amplification by Chloride Anions

Joseph Santos-Sacchi,^{1,2,3} Lei Song,¹ Jiefu Zheng,⁴ and Alfred L. Nuttall^{4,5}

Sections of ¹Otolaryngology, ²Neurobiology, and ³Cellular and Molecular Physiology, Yale University School of Medicine, New Haven, Connecticut 06510,

⁴Oregon Hearing Research Center, Department of Otolaryngology–Head and Neck Surgery, Oregon Health and Science University, Portland, Oregon 97239-3098, and ⁵Kresge Hearing Research Institute, The University of Michigan, Ann Arbor, Michigan 48109-0506

Chloride ions have been hypothesized to interact with the membrane outer hair cell (OHC) motor protein, prestin on its intracellular domain to confer voltage sensitivity (Oliver et al., 2001). Thus, we hypothesized previously that transmembrane chloride movements via the lateral membrane conductance of the cell, G_{metL} , could serve to underlie cochlear amplification in the mammal. Here, we report on experimental manipulations of chloride-dependent OHC motor activity *in vitro* and *in vivo*. *In vitro*, we focused on the signature electrical characteristic of the motor, the nonlinear capacitance of the cell. Using the well known ototoxicant, salicylate, which competes with the putative anion binding or interaction site of prestin to assess level-dependent interactions of chloride with prestin, we determined that the resting level of chloride in OHCs is near or below 10 mM, whereas perilymphatic levels are known to be ~140 mM. With this observation, we sought to determine the effects of perilymphatic chloride level manipulations of basilar membrane amplification in the living guinea pig. By either direct basolateral perfusion of the OHC with altered chloride content perilymphatic solutions or by the use of tributyltin, a chloride ionophore, we found alterations in OHC electromechanical activity and cochlear amplification, which are fully reversible. Because these anionic manipulations do not impact on the cation selective stereociliary process or the endolymphatic potential, our data lend additional support to the argument that prestin activity dominates the process of mammalian cochlear amplification.

Key words: chloride; hearing; outer hair cell; capacitance; basilar membrane; cochlea

Introduction

Hallowell Davis coined the term “cochlear amplifier” to signify a boost in hearing capabilities near threshold that is provided by the uniquely mammalian outer hair cell (OHC) (Davis, 1983). The subsequent discovery of electrically evoked OHC mechanical activity provided a very attractive substrate for amplification (Brownell et al., 1985). Nevertheless, processes thought to be characteristic of mammalian cochlear amplification (e.g., spontaneous otoacoustic emissions) have been observed in lower vertebrates lacking OHCs (Manley et al., 2001); such observations have fueled the debate over whether the source of amplification in the mammal is the prestin-containing lateral membrane of the OHC or the stereociliary transduction apparatus, each of which can potentially provide feedback into the basilar membrane through accessory structures (Santos-Sacchi, 2003). This debate may frame an evolutionary battle between an anionic based mechanism and a cationic based mechanism, the calcium ion underpinning stereocilia-based feedback (Fettiplace et al., 2001; Chan and Hudspeth, 2005) and the chloride ion underpinning

prestin-based feedback (Oliver et al., 2001; Rybalchenko and Santos-Sacchi, 2003).

The manner whereby stereocilia may provide force feedback during auditory stimulation relies on the intracellular action of calcium ions on either myosin molecules or the transduction channel itself, possibly ankyrin-repeat transient receptor potential cation channel, subfamily A, member 1; both of these actions influence apical bundle mechanics (Yamoah and Gillespie, 1996; Gillespie and Corey, 1997; Fettiplace and Ricci, 2003; Corey et al., 2004). In contrast, the lateral membrane motor, prestin (Zheng et al., 2000), is highly sensitive to intracellular anions (Oliver et al., 2001; Rybalchenko and Santos-Sacchi, 2003; Song et al., 2005), in particular, chloride, which has been shown to pass through a lateral membrane conductance, G_{metL} , in a voltage- and tension-dependent manner (Rybalchenko and Santos-Sacchi, 2003). Both ions respectively alter the steady state energy profile of their corresponding transduction mechanism; calcium shifts the stereociliar channel open probability along the mechanical deflection axis (Kennedy et al., 2003), and chloride shifts the area state probability of prestin along the voltage axis (Rybalchenko and Santos-Sacchi, 2003). These ionic effects contribute to force generation in each system, because, as the data imply, conformational changes in the molecules accompany ion binding.

There have been several reports that have focused on the assignment of amplificatory substrate in the mammal. Notably, a prestin knock-out has provided direct evidence that this unusual motor protein (Zheng et al., 2000) is required for OHC electro-

Received Oct. 24, 2005; revised March 1, 2006; accepted March 3, 2006.

This work was supported by National Institutes of Health—National Institute on Deafness and Other Communication Disorders Grants DC 00141 (A.L.N.) and DC 00273 (J.S.-S.). We thank Margaret Mazzucco for assistance.

Correspondence should be addressed to Joseph Santos-Sacchi, Otolaryngology, Neurobiology, and Cellular and Molecular Physiology, Yale University School of Medicine, Brandy Memorial Laboratory 246, 333 Cedar Street, New Haven, CT 06510. E-mail: joseph.santos-sacchi@yale.edu.

DOI:10.1523/JNEUROSCI.4548-05.2006

Copyright © 2006 Society for Neuroscience 0270-6474/06/263992-07\$15.00/0

mechanical activity and cochlear amplification (Liberman et al., 2002). In contrast, studies on isolated mammalian cochleas, which may retain some residual characteristics of cochlear amplification, point to potential contributions from stereociliary mechanics (Fettiplace et al., 2001; Kennedy et al., 2003; Chan and Hudspeth, 2005).

We report here that modulating chloride activity *in vitro* and *in vivo*, with cochlear amplifier intact, either directly by basolateral perfusion of the OHC with altered chloride content solutions or by the use of tributyltin (TBT), a chloride ionophore (Tosteson and Wieth, 1979; Wieth and Tosteson, 1979; Song et al., 2005), alters OHC electromechanical activity and cochlear amplification in a reversible manner. Because these anionic manipulations do not impact on the cation-selective stereociliary process or the endolymphatic potential, our data lend additional support to the argument that prestin activity dominates the process of mammalian cochlear amplification.

Materials and Methods

In vitro

The methods for single hair cell recordings were the same as those described in detail previously (Song et al., 2005). Hartley albino guinea pigs were killed with halothane. Temporal bones were excised, and the top three turns of the cochleae were dissected with enzyme treatment (0.5 mg/ml Dispase I; 10–12 min). Individual outer hair cells were isolated by gentle trituration. Isolated single outer hair cells were then studied under whole-cell voltage clamp and were held at 0 mV to eliminate the electrical drive for Cl across the lateral membrane; therefore, Cl concentration changes were studied in isolation. A custom made Y-tube perfusion system was used to deliver experimental solutions to isolated OHCs. Perforated patch solutions contained 25 mg/ml gramicidin in 0.25% DMSO (Akaike, 1996).

Nonlinear capacitance (NLC) was measured using a continuous high-resolution (2.56 ms sampling) two-sine stimulus protocol (10 mV peak at both 390.6 and 781.2 Hz) superimposed onto a voltage ramp from –150 to +140 mV (Santos-Sacchi et al., 1998b; Santos-Sacchi, 2004). Capacitance data were fit to the first derivative of a two-state Boltzmann function (Santos-Sacchi, 1991) as follows:

$$C_m = Q_{\max} \frac{ze}{kT} \frac{b}{(1+b)^2} + C_{\text{lin}},$$

where

$$b = \exp\left(\frac{-ze(V_m - V_{\text{pkcm}})}{kT}\right),$$

where Q_{\max} is the maximum nonlinear charge moved, V_{pkcm} (also commonly called V_h) is voltage at peak capacitance or equivalently at half-maximum charge transfer, V_m is membrane potential, z is valence, C_{lin} is linear membrane capacitance, e is electron charge, k is Boltzmann's constant, and T is absolute temperature. NLC was calculated by subtracting linear capacitance (C_{lin}) from peak amplitude ($C_{m,\text{pk}}$).

The base extracellular solution contained the following (in mM): 140 NaCl, 2 CaSO₄, 1.2 MgSO₄, and 10 HEPES. Cl concentration was adjusted from 1 to 140 mM by substituting Cl with gluconate. Final solutions were adjusted to ~300 mOsm with D-glucose and adjusted to pH ~7.2–7.3 with NaOH. Pipette solutions (same as extracellular solution except with the addition of 10 mM EGTA) contained Cl ranging from 1 to 140 mM. This composition permitted us to reduce ionic currents (mainly K currents), which we and others routinely block to measure precisely NLC or gating charge movements (Santos-Sacchi, 1991; Song et al., 2005). The extracellular perfusion solution (1–140 mM Cl) also contained graded concentrations of salicylate (1 μM to 10 mM), with or without the addition of 1 μM TBT. For the gramicidin patch experiments, although we attempted to record cells as soon after the animals were killed as possible, we were limited by time required for dissection and cell

isolation and by the time after seal formation to achieve good whole cell conditions, namely achieving a series resistance of <20 MΩ.

In vivo

Animals and surgery. Pigmented guinea pigs weighing 250–350 g were used in this experiment. After anesthesia, the left bulla was opened via a lateral and ventral approach, and the middle ear muscle tendons were sectioned. A hole (~0.3 × 0.4 mm) in the scala tympani of the cochlea was made for measuring the basilar membrane (BM) velocity.

Basilar membrane velocity measurements. The BM velocity at the site corresponding to the frequency near 17 kHz [the characteristic frequency (CF)] was measured from a gold-coated reflective glass bead (10–30 μm in diameter) on the BM using a laser interferometer (Polytec OFV 1102 Laser Vibrometer; Polytec, Waldbronn, Germany). The BM velocity response was evoked by pure tones (2–24 kHz) delivered through a speaker coupled to the ear canal. The output of the interferometer consists of a voltage proportional to the velocity of the targeted bead. The voltage was measured with a lock-in amplifier and recorded by reading the magnitude and phase by computer query via the serial line output from the lock-in amplifier. The vibration of stapes was measured at the end of each experiment and used to compute the gain of BM motion.

Perilymphatic perfusion. For the perilymphatic perfusion, an inlet hole (diameter, ~90 μm) was made in the scala tympani of the basal turn of the cochlea close to the round window niche, and the hole for BM measurement served as fluid outlet. A polyethylene tube with a fine tip (diameter, ~80 μm) was inserted into the inlet hole, and the other end of this tube was connected to a three-way perfusion system that allowed solution replacement. Perfusion was accomplished using a precision syringe pump. Tributyltin (50 μM), salicylate (1–10 mM), or combinations of the two agents in artificial perilymph (PL) were infused into the scala tympani at the rate of 2 μl/min with the duration of 10–20 min. Similar results were found with 10 μM TBT, but higher concentrations ensured better access across the BM into the spaces of Nuel. The normal artificial perilymph composition is as follows (in mM): 132 NaCl, 3.5 KCl, 25 NaHCO₃, 1.3 CaCl₂, 1.14 MgCl₂ · 6H₂O, 0.51 NaH₂PO₄ · H₂O, 5.0 Tris, 3.3 glucose, and 2.1 urea. For chloride reductions, gluconate substitutions were made. During our treatments, we measured low-frequency cochlear microphonics (CM), a procedure commonly accepted to gauge the OHC stereociliar transducer function (Patuzzi and Moleirinho, 1998) and endolymphatic potential (EP) to evaluate potential effects on supporting cell K recycling, which might be expected to compromise the EP (Wangemann et al., 2004).

Results

Determination of the resting chloride gradient across the OHC membrane

Our first goal was to characterize resting intracellular levels of chloride in OHCs, using the effects of salicylate on NLC as a quantitative measurement tool. The elucidation of the chloride gradient across the OHC basolateral membrane is important in understanding our subsequent *in vivo* manipulations of perilymphatic chloride levels. Peak OHC NLC is reduced in the presence of salicylate (Fig. 1a). The flattening of NLC (and increase at voltages away from the voltage at peak capacitance [V_{pkcm}]) at high salicylate doses occurs because the voltage sensitivity is depressed across a wider voltage range, an observation completely in line with previous work (Tunstall et al., 1995; Kakehata and Santos-Sacchi, 1996; Santos-Sacchi and Navarrete, 2002). Because salicylate competes for the binding site of chloride on prestin (Oliver et al., 2001), increasing the intracellular concentration of chloride should counter the effects of salicylate. Indeed, the addition of TBT to the extracellular solution induces an influx of chloride down its chemical gradient and a restoration of NLC. We have shown previously that TBT only enhances the flux of chloride when there is a chemical gradient of the anion across the OHC plasma membrane. Consequently, we found that the effects of salicylate cannot be countered by TBT when intracellular and

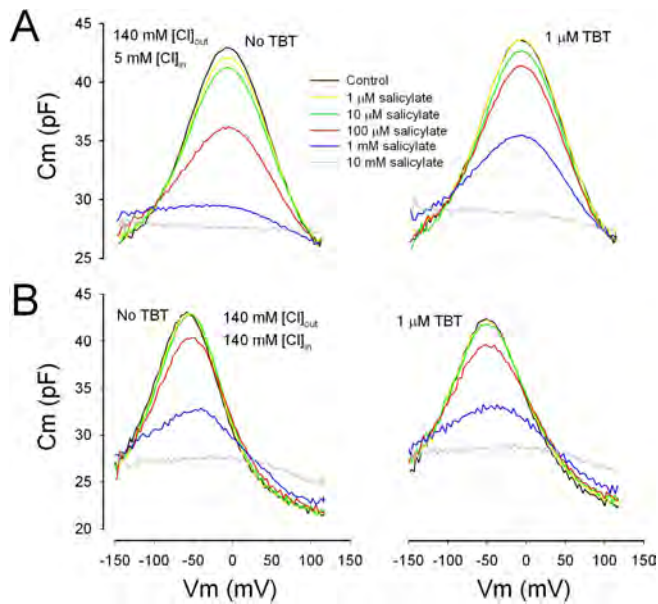


Figure 1. TBT rescues the reduction of salicylate block in NLC under whole-cell voltage clamp. Only in the presence of a chloride gradient can TBT counter this reduction. **A, B**, Effects of graded concentrations of salicylate in the presence of a chloride chemical gradient (**A**) and in the absence of a gradient (**B**). Note also the shifts in operating voltages (V_{pkcm}) that accompany changes in intracellular chloride, an increase shifting NLC to hyperpolarizing voltages. Such shifts directly alter the gain of OHC electromotility at the normal resting potential of the cell (Takehata and Santos-Sacchi, 1996).

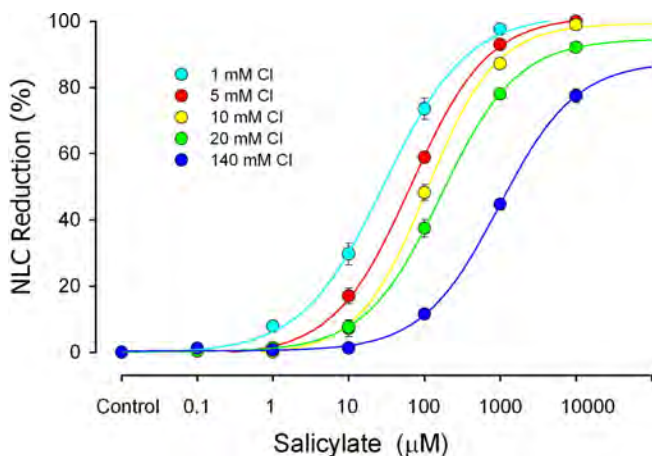


Figure 2. Average dose–response curves (mean \pm SE; $n = 4–5$) for extracellularly applied salicylate block of NLC. Each curve was collected at a different intracellular concentration of chloride. Chloride was unequivocally controlled by matching intracellular and extracellular levels, as we have done previously (Song et al., 2005). Note the leftward shift as intracellular chloride is reduced, indicating a more effective action of salicylate on the motor. Logistic fits provided the following slope and IC_{50Sal} values (1, 5, 10, 20, and 140 mM chloride, respectively): 0.79, 29.5 μ M; 0.83, 77.9 μ M; 0.81, 124.0 μ M; 0.86, 165 μ M; 0.86, 964 μ M. There is no significant difference between slopes at any concentration.

extracellular chloride levels are equal (Fig. 1*b*). From these data, it is clear that the degree of NLC reduction by salicylate is greatly dependent on intracellular Cl level. When we reduce the concentration of Cl on the cytoplasmic aspect of the integral membrane motor protein, the ability of salicylate to reduce remaining NLC increases (Fig. 1*a,b*, compare left panels). To quantify this observation, we constructed average dose–response functions for a range of salicylate and chloride concentrations (Fig. 2). Although salicylate has its effects on the intracellular aspect of the motor

(Takehata and Santos-Sacchi, 1996; Oliver et al., 2001), for these experiments, we needed to unequivocally control intracellular Cl by setting both intracellular and extracellular Cl concentration to the same level under whole-cell voltage clamp; this is an essential approach that we used previously, because the lateral membrane conductance, G_{metL} , efficiently passes Cl ions (Rybalchenko and Santos-Sacchi, 2003; Song et al., 2005). Voltage-dependent NLC was quantified by subtracting linear capacitance from peak capacitance, which directly correlates with estimates of maximum motor charge movement ($Q_{max} = 4kT/ze \times NLC$) (Santos-Sacchi et al., 1998a), determined from fits to the first derivative of a two-state Boltzmann function (see Materials and Methods). IC_{50Sal} for extracellular salicylate action on the motor ranges from 29 μ M for the 1 mM intracellular Cl condition to 964 μ M for the 140 mM Cl condition. From these data, and assuming a salicylate dissociation constant, K_{dSal} of 23.8 mM (Oliver et al., 2001), we can extract an average chloride dissociation constant, $K_{dCl} = [Cl]/(IC_{50Sal}/K_{dSal} - 1)$, of 3.4 ± 0.6 mM (mean \pm SD, from the five tested chloride concentrations), which compares favorably to previous direct estimates of the K_{dCl} of ~ 6 mM of the motor (Oliver et al., 2001; Song et al., 2005). Although this small difference is likely insignificant, the agreement is actually much better considering that our IC_{50Sal} values are based on extracellular concentrations of salicylate, and we previously demonstrated that intracellular levels will be slightly lower than extracellular levels (Takehata and Santos-Sacchi, 1996). With our data serving as a calibration standard, we were able to glean an estimate of the intracellular chloride activity of OHCs, a quantity of which the determination is essential in assessing the significance of the role of this anion in cochlear amplification *in vivo*. Thus, by using the gramicidin patch variant of the whole-cell voltage clamp, we measured the effect of salicylate without perturbing intracellular chloride levels (because gramicidin is impermeant to Cl) in the presence of normal, *in vivo*-like extracellular chloride concentrations, namely 140 mM. Under these conditions, the effectiveness of salicylate on OHCs, which were patched quickly after isolation from the cochlea to abate chloride loading, was similar to that under the 10 mM intracellular Cl condition (Fig. 3*A*), indicating that intracellular chloride rests near 10 mM. OHCs maintained in culture for longer times showed higher chloride levels, and this accumulation of intracellular chloride was accompanied by cell swelling (Fig. 3*B*). The similarity between our estimate of OHC intracellular chloride (~ 10 mM) and the K_{dCl} of OHC (~ 6 mM) (Oliver et al., 2001; Song et al., 2005) and the opposing interactions between salicylate and intracellular chloride levels set predictable outcomes from comparable manipulations *in vivo*, if cochlear amplification arises predominantly from OHC lateral membrane motor activity.

In vivo effects of chloride manipulations

To test for anionic modulation of cochlear amplification, we directly measured BM motion using a laser interferometer in living guinea pigs, the cochleas of which were surgically exposed. Perfusion of artificial PL (see Materials and Methods for compositions) in the scala tympani was accomplished via a local two-port system in the basal turn and permitted basolateral perfusions of OHCs without altering the ionic milieu of endolymph that bathed the apically located stereocilia (Fig. 4*A*). BM motion is sharply tuned to a characteristic frequency determined by place along the cochlea spiral, in our preparation corresponding to $\sim 16–17$ kHz. The tip of the tuning curve is highly vulnerable, and generally any manipulation of the cochlear fluids or homeostatic environment results in a decrease in cochlear amplification.

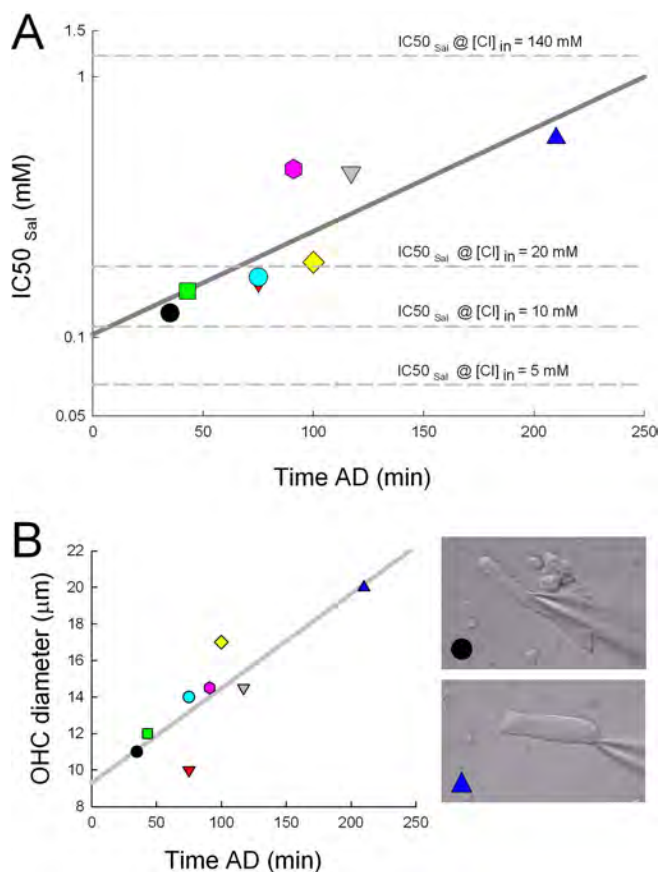


Figure 3. Estimates of OHC intracellular chloride levels using the gramicidin patch method. **A**, IC_{50sal} was determined in the presence of 140 mM extracellular chloride to mimic the *in vivo* condition. It should be stressed that IC_{50sal} measures only evaluate the interactions between intracellular salicylate and chloride on the motor and are not directly influenced by extracellular chloride levels; thus, the IC_{50sal} values determined above in Figure 2A serve as valid calibrations to estimate intracellular chloride levels regardless of extracellular chloride levels. The plot shows that as the length of time after an animal's death (AD) increased, intracellular chloride increased. For the cases in which quick measurements were made, IC_{50sal} was close to that of the value obtained with 10 mM intracellular chloride, indicating that OHC chloride levels are near or possibly <10 mM for cells under *in vivo*-like conditions. **B**, OHC diameter is a sensitive indicator of cell swelling and shows an increase as time AD increased, corresponding with the simultaneous estimates of intracellular chloride above. OHC images show one cell recorded at 30 min and another at 210 min, the latter showing pronounced swelling. The chloride loading after death probably indicates that our measures provide overestimates of intracellular chloride levels. Each symbol in the plots denotes an analysis from an individual cell from different animals ($n = 8$).

Interestingly, to date, no manipulation has been found [other than positive DC electric current (Parthasarathi et al., 2003)] to improve cochlear amplification once compromised. Figure 4B shows BM responses in a sensitive cochlea, where surgical preparation caused minimal loss in sensitivity (<10 dB), as gauged by preoperation and postoperation auditory compound action potential (CAP) measures. After switching perfusion from normal PL to a PL containing TBT (50 μ M), a reduction in BM motion was observed (Fig. 4B). An even larger reduction was brought on by a switch to salicylate containing PL (5 mM) and was reversed by washout. Interestingly, in a cochlea where the preparatory manipulations produced a large decrease in CAP sensitivity (>20 dB), the action of TBT was to augment acoustically evoked BM vibration (Fig. 4C). Peak amplitude (at best frequency) of the BM mechanical tuning (evoked by 40 dB sound pressure level acousti) with artificial perilymph and TBT perfusion into the

scala tympani showed an enhancement of 4.42 ± 1.16 dB (mean \pm SD; $n = 5$; paired t test, $p < 0.001$). In linear terms, this is a >50% increase in response (1.66 ± 0.22). This highly unusual and repeatable finding may indicate that intracellular chloride is normally poised at a level that is optimal, and that changes in intracellular chloride activity can have either positive or negative effects on BM tuning, depending on initial condition of the preparation (i.e., perhaps preparative procedures altered Cl levels and our perfusions re-established preinsult conditions). Again, in this animal, salicylate caused a decrease in BM motion, but the combination of salicylate and TBT resulted in an effect less detrimental than salicylate alone, reminiscent of the rescuing effect of TBT on the block by salicylate of NLC *in vitro*. Finally, we directly tested the effects of low-chloride PL (5 mM; substitution with gluconate) on BM motion. A profound loss of cochlear amplification was found (loss of sharp tip region and shift of CF to lower frequencies), which was fully reversible after reperfusion with normal PL (Fig. 4D). The addition of TBT to the normal perfusion again augmented BM motion above initial conditions. However, TBT was unable to counter the loss induced by low-chloride perfusions, because very little gradient in chloride existed across the OHC plasma membrane. CM at sub-CF frequencies (0.5 kHz), which report on stereociliary forward transduction in OHCs (Patuzzi and Moleirinho, 1998), were unchanged or slightly increased by low chloride or salicylate perfusions, as expected from previous work (Desmedt and Robertson, 1975; Fitzgerald et al., 1993). This implies that our treatments do not affect stereociliary processes, including the transducer Ca sensitivity. Additionally, we measured the EP in three animals under low-chloride conditions and found it to be unaffected (<3 mV variations). Together, the *in vitro* and *in vivo* data indicate the powerful role played by chloride in cochlea amplification and highlight the importance of the prestin-containing lateral membrane and its conductance, G_{metL} .

Discussion

The problem of assignment of cochlear amplification to the apical or lateral membrane of the OHC may reduce to a test of the effects of modulating chloride levels around the basolateral region of the OHCs, a manipulation that should not interfere with the cationic workings of the proposed stereociliary mechanism. Indeed, this general approach has been used to assess the contribution of calcium ion effects on the role of stereocilia in amplification, in which modulation of endolymphatic ionic makeup was performed while maintaining perilymphatic makeup (Chan and Hudspeth, 2005). We approached this issue by directly measuring cochlear amplification on the BM *in vivo*, along with complimentary measures of isolated OHC activity under whole-cell voltage clamp. Thus, *in vitro*, we measured the electromechanical activity of isolated OHCs by gauging the motor-generated NLC of the cell under whole-cell voltage clamp (Santos-Sacchi, 1991), and *in vivo* we measured BM vibratory velocity directly (Nuttall et al., 1991). Interactions among three manipulations of the lateral membrane motor were made using the following: (1) salicylate, a well known ototoxicant that works directly on the motor (Tunstall et al., 1995; Kakehata and Santos-Sacchi, 1996) via its interaction with the chloride binding site of the motor (Oliver et al., 2001); (2) TBT, an ionophore that promotes OHC Cl flux down its chemical gradient (Song et al., 2005); and (3) extracellular chloride levels, which will influence intracellular chloride activity via G_{metL} (Rybalchenko and Santos-Sacchi, 2003; Song et al., 2005). We found that in intact OHCs, intracellular chloride rests at level well below that of extracellular chloride, being ~ 10 mM or

less intracellularly. Manipulations of extracellular chloride, the effects of which arose from the chemical gradient of chloride across the OHC membrane, had pronounced effects on motor charge movement *in vitro* and markedly and reversibly affected cochlear amplification on the basilar membrane.

Our data provide clear evidence that the gain of cochlear amplification is tied directly to the gain of OHC motor activity, the electrical correlates of which are the amount of motor charge moved and the voltage range over which the motors operate, both of which are influenced by intracellular chloride and salicylate (Tunstall et al., 1995; Kakehata and Santos-Sacchi, 1996; Oliver et al., 2001; Rybalchenko and Santos-Sacchi, 2003; Song et al., 2005). Effects on stereociliar transduction and EP were absent, lending support to a direct effect on the OHC lateral membrane motor protein, prestin. Interestingly, although salicylate was found to affect emissions in the Tokay gecko (Stewart and Hudspeth, 2000), the hair cells of which lack prestin, there is no direct action of salicylate on the stereociliar mechano-electrical transducer (MET) channels (Kimitsuki et al., 1994). Although a variety of physiological factors affect the gain of OHC motor activity, including membrane tension (Iwasa, 1993; Gale and Ashmore, 1994; Kakehata and Santos-Sacchi, 1995), temperature (Santos-Sacchi and Huang, 1998), and phosphorylation (Huang and Santos-Sacchi, 1993; Szonyi et al., 1999; Frolenkov et al., 2000; Deak et al., 2005), the recruitment of a ubiquitous anion to drive our exquisite sense of hearing bares an underlying simplicity in design for such a complicated endorgan.

How might chloride work on cochlear amplification?

Clearly, it has been shown that chloride ions have a powerful effect on prestin activity via an intracellular binding or interaction site (Oliver et al., 2001; Rybalchenko and Santos-Sacchi, 2003; Song et al., 2005). The effect may not simply apply to chloride interactions but also to interactions with other anions, for example, sulfate. Interestingly, whereas sulfate was initially found by Oliver et al. (2001) to be ineffective in influencing prestin activity, namely an inability to support NLC, we and others have since found that sulfate can support NLC in intact OHCs while shifting V_h to very depolarized potentials (Rybalchenko and Santos-Sacchi, 2003; Ashmore, 2005; Fettiplace, 2005). Nevertheless, the physiological abundance of chloride indicates that it may be the major player in OHC function.

It is conceivable, however, that manipulating perilymphatic chloride could have effects within the cochlear aside from the OHC lateral membrane. For example, chloride transport is thought to play a role in K recycling within the inner ear (Wangemann et al., 2004). Our observation that the endolymphatic potential is unperturbed during our manipulations rules out such a possibility, because K recycling interference would compromise

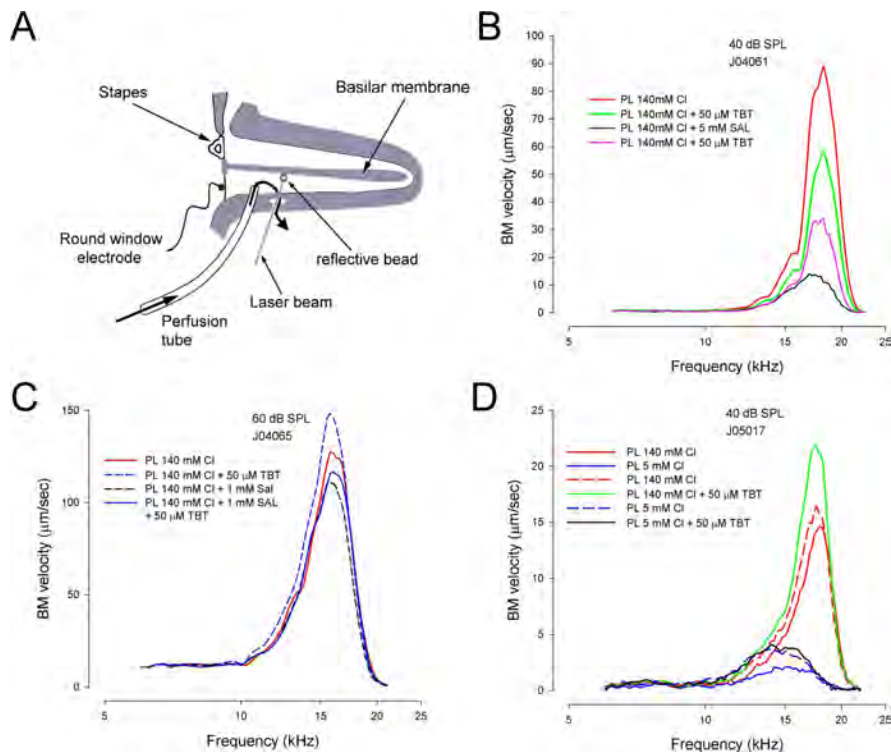


Figure 4. *A*, Schematic of *in vivo* preparation. See Materials and Methods for details. *B*, BM responses to acoustic stimulation during perfusion with artificial PL. The temporal order of listed perfusions is from top to bottom. This was a sensitive cochlea where CAP thresholds were little affected by surgery (<10 dB). In this case, a switch from normal PL to TBT-containing solution causes a decrease in BM motion. Salicylate produces a more pronounced reduction, and recovery follows reperfusion with TBT PL. *C*, This example shows a preparation that was less sensitive; thresholds deteriorated at >20 dB. TBT perfusion, in this case, augmented BM vibration and antagonized the detuning effects of salicylate. *D*, Perfusion of low chloride PL caused a profound loss of cochlear amplification, which was completely reversible. Again, in this animal, TBT increased BM vibration in the presence of normal chloride levels but was ineffective in the presence of low chloride levels, in which a chloride gradient across the OHC membrane would be small or absent. The small difference in the effects of low Cl treatment between the first perfusion and the fourth perfusion may stem from previous TBT treatment or the time between data collections. For visual clarity, sound pressure is plotted on a linear scale; frequency is plotted logarithmically.

the EP. Additionally, it is well known that OHC turgor can be modulated by extracellular chloride manipulations (Cecola and Bobbin, 1992; Song et al., 2005), and that electromotility can be modulated by changes in membrane tension (Iwasa, 1993; Gale and Ashmore, 1994; Kakehata and Santos-Sacchi, 1995). Indeed, we hypothesized that cochlear amplification could be controlled by turgor pressure changes in OHCs (Kakehata and Santos-Sacchi, 1995). Thus, it may be that turgor pressure changes accompanied by chloride flux contributes to our *in vivo* measures (*in vitro* we control turgor pressure and show chloride effects directly). We note, however, that in the absence of a chloride conductance and gradient, such effects on turgor pressure would not arise, because it is the flux of chloride that instigates water movement into and out of the OHC. Interestingly, manipulations of perilymphatic osmolarity *in vivo* have been found to modulate otoacoustic emissions, and the auditory compound action potential (Choi and Spector, 2005). Thus, it may be that two mechanisms known to modulate the OHC lateral membrane may contribute to the chloride effects we observed, although the effects we observe are larger than those observed with osmolarity manipulations.

The lateral membrane as forward and reverse transducer

The apparent voltage-dependent nature of OHC electromotility necessarily encumbers the effectiveness of the presumed stimulus

(receptor potentials) in driving high-frequency mechanical activity. This conundrum derives from the low-pass resistor-capacitor (RC) filter effect of the plasma membrane of the cell (Santos-Sacchi, 1989, 1992; Housley and Ashmore, 1992), estimated to be between 50 and 800 Hz. Consequently, receptor potentials generated by stereociliary transduction elements will be reduced at high acoustic frequency, resulting in diminished feedback into the basilar membrane. Although several proposals have been advanced to understand how the OHC may deal with this difficulty (Santos-Sacchi et al., 1998a; Kakehata and Santos-Sacchi, 1995; Dallos and Evans, 1995; Spector et al., 2003), the issue remains unresolved.

We presented previously a hypothesis that the OHC lateral membrane, with its mechanically active conductance, G_{metL} , may have usurped the role of stereocilia by fluxing anions, rather than cations, during acoustic stimulation (Rybalchenko and Santos-Sacchi, 2003; Santos-Sacchi, 2003). Notably, acoustically driven motions of the organ of Corti have been shown to deform the OHC soma (Fridberger and De Monvel, 2003), potentially gating G_{metL} at acoustic rates. Furthermore, tuned mechanical responses of the isolated OHC induced by water-jet driven mechanical stimulation of the lateral membrane can be blocked by polylysine (Brundin et al., 1989; Brundin and Russell, 1994), a chemical that partially blocks G_{metL} (Rybalchenko and Santos-Sacchi, 2003). Such a cellular adaptation of forward transduction may offer a means to overcome the RC filter problem. Basically, the anion driven conformational state dependence of prestin would be unencumbered by the low-pass filtering effects of the OHC membrane but would only depend on the kinetics of anion current flow and submembranous accumulation and clearing. We have shown mechanical gating of G_{metL} in the kilohertz range (Rybalchenko and Santos-Sacchi, 2003), but additional work on this hypothesis is required.

Although our data provide support for an evolutionary switch from cation to anion control, it was shown recently that manipulations of Ca-dependent stereociliar mechanics altered a remaining nonlinearity present in an *in vitro* explant of the mammalian cochlea, suggesting that bundle mechanics could partly contribute to mammalian cochlear amplification (Chan and Hudspeth, 2005). Thus, it appears that the evolution of the OHC and its mechanically active lateral membrane may have occurred to supplement an already primitive amplificatory system, which, for the mammal, begged an extra boost.

References

- Akaike N (1996) Grammidin perforated patch recording and intracellular chloride activity in excitable cells. *Prog Biophys Mol Biol* 65:251–264.
- Ashmore J (2005) Prestin is an electrogenic anion transporter. Paper presented at 42nd Workshop on Inner Ear Biology, Tubingen, Germany, September.
- Brownell WE, Bader CR, Bertrand D, de Ribaupierre Y (1985) Evoked mechanical responses of isolated cochlear outer hair cells. *Science* 227:194–196.
- Brundin L, Russell I (1994) Tuned phasic and tonic motile responses of isolated outer hair cells to direct mechanical stimulation of the cell body. *Hear Res* 73:35–45.
- Brundin L, Flock A, Canlon B (1989) Sound-induced motility of isolated cochlear outer hair cells is frequency-specific. *Nature* 342:814–816.
- Cecola RP, Bobbin RP (1992) Lowering extracellular chloride concentration alters outer hair cell shape. *Hear Res* 61:65–72.
- Chan DK, Hudspeth AJ (2005) Ca^{2+} current-driven nonlinear amplification by the mammalian cochlea *in vitro*. *Nat Neurosci* 8:149–155.
- Choi C, Spector A, Oghalai J (2005) Perilymph osmolarity modulates cochlear function. Midwinter Meeting of the Association for Research in Otolaryngology, February.
- Corey DP, Garcia-Anoveros J, Holt JR, Kwan KY, Lin SY, Vollrath MA, Amalfitano A, Cheung EL, Derfler BH, Duggan A, Geleoc GS, Gray PA, Hoffman MP, Rehm HL, Tamasauskas D, Zhang DS (2004) TRPA1 is a candidate for the mechanosensitive transduction channel of vertebrate hair cells. *Nature* 432:723–730.
- Dallos P, Evans BN (1995) High-frequency motility of outer hair cells and the cochlear amplifier. *Science* 267:2006–2009.
- Davis H (1983) An active process in cochlear mechanics. *Hear Res* 9:79–90.
- Deak L, Zheng J, Orem A, Du GG, Aguinaga S, Matsuda K, Dallos P (2005) Effects of cyclic nucleotides on the function of prestin. *J Physiol (Lond)* 563:483–496.
- Desmedt JE, Robertson D (1975) Ionic mechanism of the efferent olivocochlear inhibition studied by cochlear perfusion in the cat. *J Physiol (Lond)* 247:407–428.
- Fettiplace R, Ricci AJ (2003) Adaptation in auditory hair cells. *Curr Opin Neurobiol* 13:446–451.
- Fettiplace R, Ricci AJ, Hackney CM (2001) Clues to the cochlear amplifier from the turtle ear. *Trends Neurosci* 24:169–175.
- Fitzgerald JJ, Robertson D, Johnstone BM (1993) Effects of intra-cochlear perfusion of salicylates on cochlear microphonic and other auditory responses in the guinea pig. *Hear Res* 67:147–156.
- Fridberger A, De Monvel JB (2003) Sound-induced differential motion within the hearing organ. *Nat Neurosci* 6:446–448.
- Frolenkov GI, Mammamo F, Belyantseva IA, Coling D, Kachar B (2000) Two distinct Ca^{2+} -dependent signaling pathways regulate the motor output of cochlear outer hair cells. *J Neurosci* 20:5940–5948.
- Gale JE, Ashmore JF (1994) Charge displacement induced by rapid stretch in the basolateral membrane of the guinea-pig outer hair cell. *Proc R Soc Lond B Biol Sci* 255:243–249.
- Gillespie PG, Corey DP (1997) Myosin and adaptation by hair cells. *Neuron* 19:955–958.
- Housley GD, Ashmore JF (1992) Ionic currents of outer hair cells isolated from the guinea-pig cochlea. *J Physiol (Lond)* 448:73–98.
- Huang G-J, Santos-Sacchi J (1993) Metabolic control of OHC function: phosphorylation and dephosphorylation agents shift the voltage dependence of motility related capacitance. Meeting of the Association for Research in Otolaryngology, St Petersburg, FL, February.
- Iwasa KH (1993) Effect of stress on the membrane capacitance of the auditory outer hair cell. *Biophys J* 65:492–498.
- Kakehata S, Santos-Sacchi J (1995) Membrane tension directly shifts voltage dependence of outer hair cell motility and associated gating charge. *Biophys J* 68:2190–2197.
- Kakehata S, Santos-Sacchi J (1996) Effects of salicylate and lanthanides on outer hair cell motility and associated gating charge. *J Neurosci* 16:4881–4889.
- Kennedy HJ, Evans MG, Crawford AC, Fettiplace R (2003) Fast adaptation of mechano-electrical transducer channels in mammalian cochlear hair cells. *Nat Neurosci* 6:832–836.
- Kimitsuki T, Nakagawa T, Hisashi K, Komune S, Uemura T (1994) The effects of ototoxic drugs on mechano-electric transduction channels in chick cochlear hair cells. *Eur Arch Otorhinolaryngol* 251 [Suppl 1]:S53–S56.
- Liberman MC, Gao J, He DZ, Wu X, Jia S, Zuo J (2002) Prestin is required for electromotility of the outer hair cell and for the cochlear amplifier. *Nature* 419:300–304.
- Manley GA, Kirk DL, Koppl C, Yates GK (2001) *In vivo* evidence for a cochlear amplifier in the hair-cell bundle of lizards. *Proc Natl Acad Sci USA* 98:2826–2831.
- Nuttall AL, Dolan DF, Avinash G (1991) Laser doppler velocimetry of basilar-membrane vibration. *Hearing Res* 51:203–213.
- Oliver D, He DZ, Klocker N, Ludwig J, Schulte U, Waldegger S, Ruppertsberg JP, Dallos P, Fakler B (2001) Intracellular anions as the voltage sensor of prestin, the outer hair cell motor protein. *Science* 292:2340–2343.
- Parthasarathi AA, Grosh K, Zheng J, Nuttall AL (2003) Effect of current stimulus on *in vivo* cochlear mechanics. *J Acoust Soc Am* 113:442–452.
- Patuzzi R, Moleirinho A (1998) Automatic monitoring of mechano-electrical transduction in the guinea pig cochlea. *Hear Res* 125:1–16.
- Rybalchenko V, Santos-Sacchi J (2003) Cl^{-} flux through a non-selective, stretch-sensitive conductance influences the outer hair cell motor of the guinea-pig. *J Physiol (Lond)* 547:873–891.
- Santos-Sacchi J (1989) Asymmetry in voltage-dependent movements of isolated outer hair cells from the organ of Corti. *J Neurosci* 9:2954–2962.

- Santos-Sacchi J (1991) Reversible inhibition of voltage-dependent outer hair cell motility and capacitance. *J Neurosci* 11:3096–3110.
- Santos-Sacchi J (1992) On the frequency limit and phase of outer hair cell motility: effects of the membrane filter. *J Neurosci* 12:1906–1916.
- Santos-Sacchi J (2003) New tunes from Corti's organ: the outer hair cell boogie rules. *Curr Opin Neurobiol* 13:459–468.
- Santos-Sacchi J (2004) Determination of cell capacitance using the exact empirical solution of dY/dC_m and its phase angle. *Biophys J* 87:714–727.
- Santos-Sacchi J, Huang GJ (1998) Temperature dependence of outer hair cell nonlinear capacitance. *Hear Res* 116:99–106.
- Santos-Sacchi J, Navarrete E (2002) Voltage-dependent changes in specific membrane capacitance caused by prestin, the outer hair cell lateral membrane motor. *Pflügers Arch* 444:99–106.
- Santos-Sacchi J, Kakehata S, Kikuchi T, Katori Y, Takasaka T (1998a) Density of motility-related charge in the outer hair cell of the guinea pig is inversely related to best frequency. *Neurosci Lett* 256:155–158.
- Santos-Sacchi J, Kakehata S, Takahashi S (1998b) Effects of membrane potential on the voltage dependence of motility-related charge in outer hair cells of the guinea-pig. *J Physiol (Lond)* 510:225–235.
- Song L, Seeger A, Santos-Sacchi J (2005) On membrane motor activity and chloride flux in the outer hair cell: lessons learned from the environmental toxin tributyltin. *Biophys J* 88:2350–2362.
- Spector A, Popel AS, Brownell W (2003) Piezoelectric properties enhance outer hair cell high-frequency response. In: *Biophysics of the cochlea: from molecules to models* (Gummer A, ed), pp 51–54. Singapore: World Scientific Publishing.
- Stewart CE, Hudspeth AJ (2000) Effects of salicylates and aminoglycosides on spontaneous otoacoustic emissions in the Tokay gecko. *Proc Natl Acad Sci USA* 97:454–459.
- Szonyi M, He DZ, Ribari O, Sziklai I, Dallos P (1999) Cyclic GMP and outer hair cell electromotility. *Hear Res* 137:29–42.
- Tosteson MT, Wieth JO (1979) Tributyltin-mediated exchange diffusion of halides in lipid bilayers. *J Gen Physiol* 73:789–800.
- Tunstall MJ, Gale JE, Ashmore JF (1995) Action of salicylate on membrane capacitance of outer hair cells from the guinea-pig cochlea. *J Physiol (Lond)* 485:739–752.
- Wangemann P, Itza EM, Albrecht B, Wu T, Jabba SV, Maganti RJ, Lee JH, Everett LA, Wall SM, Royaux IE, Green ED, Marcus DC (2004) Loss of KCNJ10 protein expression abolishes endocochlear potential and causes deafness in Pendred syndrome mouse model. *BMC Med* 2:30.
- Wieth JO, Tosteson MT (1979) Organotin-mediated exchange diffusion of anions in human red cells. *J Gen Physiol* 73:765–788.
- Yamoah EN, Gillespie PG (1996) Phosphate analogs block adaptation in hair cells by inhibiting adaptation-motor force production. *Neuron* 17:523–533.
- Zheng J, Shen W, He D, Long K, Madison L, Dallos P (2000) Prestin is the motor protein of cochlear outer hair cells. *Nature* 405:149–155.



ELSEVIER

Hearing Research 159 (2001) 69–73

**HEARING
RESEARCH**

www.elsevier.com/locate/heares

Furosemide alters nonlinear capacitance in isolated outer hair cells

Joseph Santos-Sacchi *, Min Wu, Seiji Kakehata

Sections of Otolaryngology and Neurobiology, Department of Surgery (Otolaryngology), BML 244, Yale University School of Medicine, 333 Cedar St., New Haven, CT 06510, USA

Received 19 December 2000; accepted 14 February 2001

Abstract

The outer hair cell (OHC) from the organ of Corti plays a crucial role in hearing through its unique voltage-dependent mechanical responses. Furosemide, one of the loop diuretics, disrupts normal cochlear function. Here we report on direct effects of furosemide on OHC motility-related, voltage-dependent capacitance using the whole-cell patch-clamp technique. Extracellularly applied furosemide reversibly shifted the voltage at peak capacitance (V_{pkC_m}) to positive levels. The shift, whose maximum approached 90 mV, evidenced a Hill coefficient of 1.5 and $K_{1/2}$ of 10 mM. Changes in the magnitude of nonlinear capacitance were not fully reversible. While it is clear that the overwhelming effect of furosemide on hearing results via its effects on the endolymphatic potential, the present results indicate that furosemide directly alters OHC motility and may, in part, contribute to sensory dysfunction. © 2001 Published by Elsevier Science B.V.

Key words: Outer hair cell; Motility; Nonlinear capacitance; Basilar membrane tuning

1. Introduction

The outer hair cell (OHC) from the organ of Corti is believed to provide feedback into the basilar membrane through its unique voltage-dependent mechanical responses (Ashmore, 1987; Brownell et al., 1985; Santos-Sacchi and Dilger, 1988). The feedback sharpens the passive mechanical vibration of the cochlear partition. The OHC has a nonlinear gating charge movement or, equivalently, a voltage-dependent capacitance which presents characteristics similar to those of OHC motility, indicating that membrane-bound voltage sensor-motor elements control OHC length (Ashmore, 1990; Dallos et al., 1993; Santos-Sacchi, 1991, 1993).

Furosemide, one of the loop diuretics, is ototoxic. Systemic or intracochlear administration of furosemide induces changes in receptor potentials (Forge and Brown, 1982), auditory -nerve responses (Evans and Klinke, 1982) and basilar-membrane vibration (Ruggero and Rich, 1991). Furosemide is thought to exert its effects on these stimulus-related responses via inter-

ference with stria vascularis function (Brown and McElwee, 1972; Kusakari et al., 1978; Wangemann, 1995), namely, through a reduction of the positive endolymphatic potential (EP). Ruggero and Rich (1991) suggested that a decrease in basilar membrane vibration at near-characteristic frequencies (CF) results from an indirect action of furosemide on OHCs via a reduction of receptor potentials, the presumed driving force for OHC motility. They concluded that the sensitivity and frequency selectivity of basilar membrane responses are due to the mechanical activity of OHCs. In order to examine whether furosemide may interfere with OHC motility more directly, we studied the effects of furosemide on OHC motility-related nonlinear capacitance using the whole-cell patch-clamp technique.

2. Methods

OHCs were freshly isolated from the organ of Corti of the guinea-pig cochlea, following death by anesthetic overdose with Nembutal. The procedures were in accordance with Yale University's Animal Use And Care Committee guidelines. OHCs were whole-cell voltage clamped using patch pipets with initial resistances of

* Corresponding author. Tel.: +1 (203) 785 7566;

Fax: +1 (203) 737 2502.

E-mail address: joseph.santos-sacchi@yale.edu (J. Santos-Sacchi).

2–3 M Ω . Series resistance ranged from 3 to 5 M Ω . The patch-pipette solution contained (in mM): 140 CsCl, 2 MgCl₂, 10 EGTA and 10 HEPES, with pH 7.2 and 300 mOsm. Ionic blocking solutions were used to remove voltage-dependent ionic conductances so that capacitive currents could be analyzed in isolation. The external solution contained (in mM): 100 NaCl, 20 TEA, 20 CsCl, 2 CoCl₂, 1.52 MgCl₂, 10 HEPES and 5 dextrose, pH 7.2, 300 mOsm. Furosemide was tested in concentrations ranging from 0.5 to 30 mM, with NaCl adjusted to maintain osmolarity. Drugs were applied via cell-chamber perfusion, or in some cases via Y tube. Voltages were corrected for the effects of residual series resistance.

Whole-cell membrane capacitance was measured with two techniques, transient and AC. The former entailed the delivery of a stair-step voltage stimulus. Transient currents were integrated to obtain cell capacitance (C_m) measures as previously described (Huang and Santos-Sacchi, 1993). The latter technique utilized a continuous high-resolution (2.56 ms sampling) two-sine voltage stimulus protocol (10 mV peak at both 390.6 and 781.2 Hz), with subsequent fast Fourier transform-based admittance analysis (Santos-Sacchi et al., 1998). These high-frequency sinusoids were superimposed on voltage-ramp stimuli. Capacitance data were fit to the first derivative of a two-state Boltzmann function (Santos-Sacchi, 1991),

$$C_m = Q_{\max} \frac{ze}{kT} \frac{b}{(1+b)^2} + C_{\text{lin}} \quad (1)$$

$$b = \exp \frac{-ze(V_m - V_{\text{pk}C_m})}{kT}$$

where Q_{\max} is the maximum nonlinear charge moved, $V_{\text{pk}C_m}$ is voltage at peak capacitance or half-maximal nonlinear charge transfer, V_m is membrane potential, C_{lin} is linear capacitance, z is valence, e is electron charge, k is Boltzmann's constant, and T is absolute temperature. $V_{\text{pk}C_m}$ was tracked in real time with 2 mV resolution by monitoring the reversal of gating current polarity as fully described elsewhere (Kakehata and Santos-Sacchi, 1995).

3. Results

The inset of Fig. 1 illustrates the effect of furosemide on $V_{\text{pk}C_m}$ of an isolated OHC utilizing the $V_{\text{pk}C_m}$ tracking procedure. The drug (20 mM) shifted $V_{\text{pk}C_m}$ from a resting value of -65 mV to about $+20$ mV; washout reversed the effect. In order to prevent interference by potential turgor pressure changes (Kakehata and Santos-Sacchi, 1995), the cylindrical cell was collapsed with

negative pipette pressure from the outset of recording. The dose response curve for the shift in $V_{\text{pk}C_m}$ (Fig. 1) indicates a Hill coefficient of 1.5, K_m of 10.06 mM, and maximum shift of 86.9 mV. Significant shifts were seen at low concentrations, i.e. at 1 mM, the average shift was 5.96 ± 1.43 mV ($n = 18$; mean \pm S.E.M.).

Furosemide also reduced the magnitude of nonlinear capacitance in a graded manner (Fig. 2, inset). For the cell depicted in Fig. 2, $C_{m,\text{pk}}$ decreased from 36.2 pF to 35.6, 34.0, 32.3 and 30.9 pF at 0.7, 4, 15 and 20 mM, respectively. The corresponding positive shifts in $V_{\text{pk}C_m}$ were 12, 20.9, 62.4 and 75.6 mV. However, the effects of furosemide on the magnitude and voltage dependence of OHC capacitance were not necessarily correlated. Upon washout, whereas $V_{\text{pk}C_m}$ typically returned to near-initial conditions, nonlinear capacitance usually remained depressed. Since OHC capacitance and mechanical functions coincide (Kakehata and Santos-Sacchi, 1995; Wu and Santos-Sacchi, 1998), this depression corresponds to a change in the form of the OHC electromechanical function.

4. Discussion

A correspondence between OHC nonlinear capacitance and motility indicates that the lateral membrane motor and sensor are tightly coupled or one entity (Santos-Sacchi, 1991; Kakehata and Santos-Sacchi, 1995); the motor is likely the recently identified protein prestin (Zheng et al., 2000; Santos-Sacchi et al., 2001). We demonstrate here that furosemide directly alters the OHC's peak capacitance and $V_{\text{pk}C_m}$, demonstrating that the drug directly affects the mechanical activity of the OHC. The magnitude of its effect is one of the largest of any drug measured to date. Interestingly, the peak capacitance does not recover with the same time course as $V_{\text{pk}C_m}$, indicating that the voltage sensitivity of the mechanical response is more sensitive to furosemide than is its operating point along the voltage axis. It should be noted that the Boltzmann model parameters that describe the nonlinear capacitance are not necessarily linked, and it is not unusual to independently affect one but not another. For example, $V_{\text{pk}C_m}$ could shift simply due to a change in membrane surface potential, while all other parameters remain constant.

The mechanism whereby furosemide affects the OHC motor is not clear. Furosemide, which is a known inhibitor of chloride transport (see Wangemann, 1995), is also reported to block Cl channels, such as γ -aminobutyric acid A (Nicoll, 1978; Pearce, 1993) and Ca²⁺-dependent Cl channels (Evans et al., 1986). Despite the existence of a potentially susceptible Cl channel in the lateral membrane (Gitter et al., 1986; Ohnishi et al., 1993), we have ruled out consequent effects on turgor

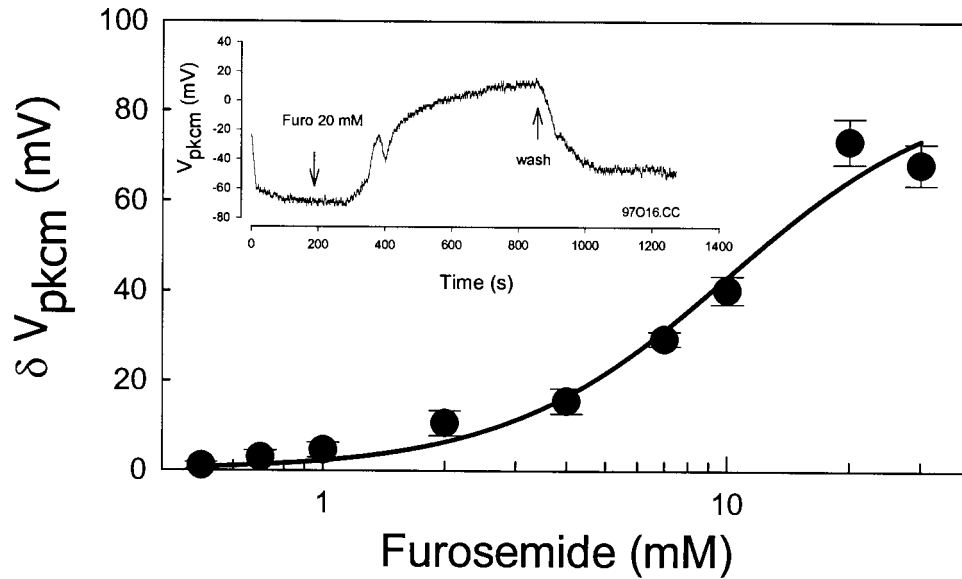


Fig. 1. Effect of furosemide on V_{pkcm} . Inset: V_{pkcm} as a function of time after whole-cell voltage-clamp configuration was obtained with the tracking technique. Furosemide (20 mM) was applied by bath. The delay in response is due to time required for bath solution exchange. Cell was collapsed from the outset of recording. Note reversible shift in V_{pkcm} . The main figure shows three parameter Hill fit giving a Hill coefficient of 1.5, K_m of 10.06 mM, and maximum shift of 86.9 mV. Data points are mean \pm S.E.M., with observation number ranging from 3 to 10.

pressure by collapsing the OHCs. It may be significant that furosemide can also block sulfate transport (Wolpaw and Martin, 1986) and that the recently identified OHC motor protein, prestin, is homologous to sulfate transporters (Zheng et al., 2000).

The predominant ototoxic effects of furosemide on cochlear function are believed to result from a drop

in the EP (Evans and Klinke, 1982; Sewell, 1984; Wangemann, 1995). However, while Ruggero and Rich (1991) conclude that furosemide-induced decreases in basilar membrane vibration at near-CF are via an indirect action of furosemide on OHCs, there is some evidence that furosemide treatments can affect OHCs directly (Comis et al., 1990; Forge and Brown, 1982).

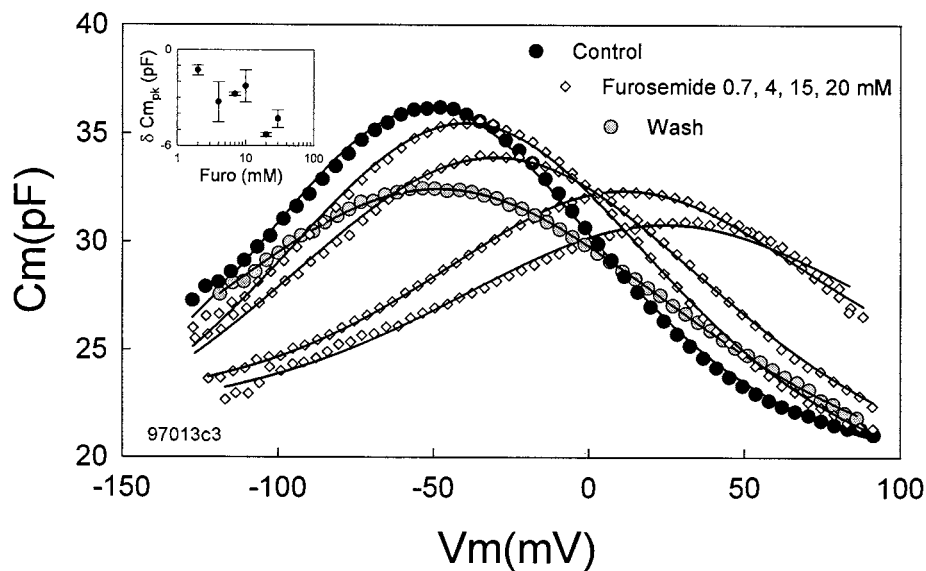


Fig. 2. Effect of furosemide on OHC $C-V$ function. Inset: Change in peak capacitance as a function of furosemide concentration (mean \pm S.E.M.). The main plot shows, for an individual OHC, the effects of 0.7, 4, 15, and 20 mM furosemide (diamonds, successively decreasing peaks) on the cell's $C-V$ function. Control (filled circle) and wash conditions (gray circle) are shown as well. Fits (solid lines) are to Eq. 1. Fitted parameters: control (V_{pkcm} , z , Q_{max} , C_{lin} , respectively): -51.51 , 0.67 , 2.57 , 19.35), 0.7 mM (-39.47 , 0.60 , 2.95 , 18.19), 4 mM (-30.11 , 0.52 , 3.06 , 18.13), 15 mM (11.36 , 0.61 , 1.69 , 22.19), 20 mM (24.67 , 0.53 , 1.76 , 21.51) and wash (-48.44 , 0.48 , 3.03 , 18.09).

Indeed, it has recently been demonstrated that otoacoustic emissions, which are thought to reflect OHC mechanical activity, are capable of recovering from the effects of furosemide treatment prior to the recovery of the EP (Mills et al., 1993). These data indicate that EP alterations may not solely underlie furosemide's effects on cochlear function.

Ostensibly, the strongest argument that intravenous furosemide works solely on the stria vascularis, without direct effects on OHC function, is the rapidity of its adverse effects on eighth-nerve function; perilymphatic perfusion apparently requires longer times and high concentrations, and Evans and Klinke (1982) and Sewell (1984) are frequently quoted in support of this argument. However, Evans and Klinke report only data from one experimental attempt at perilymphatic perfusion, and Sewell cites his unpublished observations. It is invariable that during surgical preparation for perilymphatic perfusion cochlear function is depressed by 20 dB or greater (Sewell, personal communication). Thus, during perilymphatic perfusion of furosemide, if the effects were smaller than 20 dB they would not have been observed. Since we show that the effect of furosemide is immediate on isolated OHCs, we would expect a rapid effect via perilymphatic perfusion of the mid-micromolar concentrations instilled by Evans and Klinke. We conclude that effects were masked by a compromised cochlear.

It is expected that either a shift in the OHC membrane potential or the voltage dependence of the cell's mechanical response may modify the OHC's feedback into the basilar membrane, since the gain of the OHC mechanical response will be modified (Takehata and Santos-Sacchi, 1996). Small changes in feedback can have pronounced effects. For example, the major efferent neurotransmitter, acetylcholine, maximally hyperpolarizes the OHC membrane potential a few millivolts (Housley and Ashmore, 1991). Such an effect may underlie the observation by Dolan et al. (1997) that stimulation of the OHC efferent system is capable of modifying basilar membrane mechanics *in vivo*. How effective might furosemide be in altering OHC activity in the living animal, given its large K_m of 10 mM? Mid-micromolar concentrations of furosemide can shift V_{pkC_m} by about 1 mV. By comparison, salicylate, another ototoxic agent which has measurable consequences at perilymphatic concentrations of 400 μ M (Jastreboff et al., 1986), shifts V_{pkC_m} less than the same concentration of furosemide (Takehata and Santos-Sacchi, 1995). Following intravenous administrations of ototoxic furosemide levels, perilymphatic concentrations are cleared more slowly than in serum, but reach only low micromolar concentrations ($\sim 15 \mu$ M) (Rybak et al., 1979). Interestingly, immature animals accumulate higher perilymphatic levels (Mills et al., 1997).

While the effects of such low furosemide concentrations on cochlear function in the absence of EP effects has yet to be determined, it can be reasonably concluded that a compromised EP, as occurs with intravascular administration, will have a predominant effect on cochlear function.

Acknowledgements

This work was supported by Grant NIDCD DC00273.

References

- Ashmore, J.F., 1987. A fast motile response in guinea-pig outer hair cells: the cellular basis of the cochlear amplifier. *J. Physiol.* 388, 323–347.
- Ashmore, J.F., 1990. Forward and reverse transduction in the mammalian cochlea. *Neurosci. Res.* 12, S39–S50.
- Brown, R.D., McElwee, T.W., Jr., 1972. Effects of intra-arterially and intravenously administered ethacrynic acid and furosemide on cochlear N 1 in cats. *Toxicol. Appl. Pharmacol.* 22, 589–594.
- Brownell, W.E., Bader, C.R., Bertrand, D., de Ribaupierre, Y., 1985. Evoked mechanical responses of isolated cochlear outer hair cells. *Science* 227, 194–196.
- Comis, S.D., Osborne, M.P., Jeffries, D.J., 1990. Effect of furosemide upon morphology of hair bundles in guinea pig cochlear hair cells. *Acta Otolaryngol. (Stockh.)* 109, 49–56.
- Dallos, P., Hallworth, R., Evans, B.N., 1993. Theory of electrically driven shape changes of cochlear outer hair cells. *J. Neurophysiol.* 70, 299–323.
- Dolan, D.F., Guo, M.H., Nuttall, A.L., 1997. Frequency-dependent enhancement of basilar membrane velocity during olivocochlear bundle stimulation. *J. Acoust. Soc. Am.* 102, 3587–3596.
- Evans, E.F., Klinke, R., 1982. The effects of intracochlear and systemic furosemide on the properties of single cochlear nerve fibres in the cat. *J. Physiol.* 331, 409–427.
- Evans, M.G., Marty, A., Tan, Y.P., Trautmann, A., 1986. Blockage of Ca-activated Cl conductance by furosemide in rat lacrimal glands. *Pflug. Arch.* 406, 65–68.
- Forge, A., Brown, A.M., 1982. Ultrastructural and electrophysiological studies of acute ototoxic effects of furosemide. *Br. J. Audiol.* 16, 109–116.
- Gitter, A.H., Zenner, H.P., Fromter, E., 1986. Membrane potential and ion channels in isolated outer hair cells of guinea pig cochlea. *ORL J. Otorhinolaryngol. Relat. Spec.* 48, 68–75.
- Housley, G.D., Ashmore, J.F., 1991. Direct measurement of the action of acetylcholine on isolated outer hair cells of the guinea pig cochlea. *Proc. R. Soc. Lond. Biol. Sci.* 244, 161–167.
- Huang, G., Santos-Sacchi, J., 1993. Mapping the distribution of the outer hair cell motility voltage sensor by electrical amputation. *Biophys. J.* 65, 2228–2236.
- Jastreboff, P.J., Hansen, R., Sasaki, P.G., Sasaki, C.T., 1986. Differential uptake of salicylate in serum, cerebrospinal fluid, and perilymph. *Arch. Otolaryngol. Head Neck Surg.* 112, 1050–1053.
- Takehata, S., Santos-Sacchi, J., 1995. Membrane tension directly shifts voltage dependence of outer hair cell motility and associated gating charge. *Biophys. J.* 68, 2190–2197.
- Takehata, S., Santos-Sacchi, J., 1996. Effects of salicylate and lanthanides on outer hair cell motility and associated gating charge. *J. Neurosci.* 16, 4881–4889.

- Kusakari, J., Ise, I., Comegys, T.H., Thalmann, I., Thalmann, R., 1978. Effect of ethacrynic acid, furosemide, and ouabain upon the endolymphatic potential and upon high energy phosphates of the stria vascularis. *Laryngoscope* 88, 12–37.
- Mills, C.D., Whitworth, C., Rybak, L.P., Henley, C.M., 1997. Quantification of furosemide from serum and tissues using high-performance liquid chromatography. *J. Chromatogr. B Biomed. Sci. Appl.* 701, 65–70.
- Mills, D.M., Norton, S.J., Rubel, E.W., 1993. Vulnerability and adaptation of distortion product otoacoustic emissions to endocochlear potential variation. *J. Acoust. Soc. Am.* 94, 2108–2122.
- Nicoll, R.A., 1978. The blockade of GABA mediated responses in the frog spinal cord by ammonium ions and furosemide. *J. Physiol.* 283, 121–132.
- Ohnishi, S., Hara, M., Inagaki, C., Yamashita, T., Kumazawa, T., 1993. Regulation of Cl⁻ conductance in delayed shortening and shrinkage of outer hair cells. *Acta Otolaryngol. (Stockh.)* 500 (Suppl.), 42–45.
- Pearce, R.A., 1993. Physiological evidence for two distinct GABAA responses in rat hippocampus. *Neuron* 10, 189–200.
- Ruggero, M.A., Rich, N.C., 1991. Furosemide alters organ of Corti mechanics: evidence for feedback of outer hair cells upon the basilar membrane. *J. Neurosci.* 11, 1057–1067.
- Rybak, L.P., Green, T.P., Juhn, S.K., Morizono, T., Mirkin, B.L., 1979. Elimination kinetics of furosemide in perilymph and serum of the chinchilla. *Neuropharmacologic correlates. Acta Otolaryngol. (Stockh.)* 88, 382–387.
- Santos-Sacchi, J., 1991. Reversible inhibition of voltage-dependent outer hair cell motility and capacitance. *J. Neurosci.* 11, 3096–3110.
- Santos-Sacchi, J., 1993. Harmonics of outer hair cell motility. *Biophys. J.* 65, 2217–2227.
- Santos-Sacchi, J., Dilger, J.P., 1988. Whole cell currents and mechanical responses of isolated outer hair cells. *Hear. Res.* 35, 143–150.
- Santos-Sacchi, J., Kakehata, S., Takahashi, S., 1998. Effects of membrane potential on the voltage dependence of motility-related charge in outer hair cells of the guinea-pig. *J. Physiol.* 510, 225–235.
- Santos-Sacchi, J., Shen, W., Zheng, J., Dallos, P., 2001. Effects of membrane potential and tension on prestin, the outer hair cell lateral membrane motor protein. *J. Physiol.* 531, 661–666.
- Sewell, W.F., 1984. The effects of furosemide on the endocochlear potential and auditory-nerve fiber tuning curves in cats. *Hear. Res.* 14, 305–314.
- Wangemann, P., 1995. Comparison of ion transport mechanisms between vestibular dark cells and stria marginal cells. *Hear. Res.* 90, 149–157.
- Wolpaw, E.W., Martin, D.L., 1986. Sulfate-chloride exchange transport in a glioma cell line. *Biochim. Biophys. Acta* 855, 302–311.
- Wu, M., Santos-Sacchi, J., 1998. Effects of lipophilic ions on outer hair cell voltage-dependent capacitance and motility. *J. Membr. Biol.* 166, 111–118.
- Zheng, J., Shen, W., He, D.Z., Long, K.B., Madison, L.D., Dallos, P., 2000. Prestin is the motor protein of cochlear outer hair cells. *Nature* 405, 149–155.

Cell coupling in the supporting cells of Corti's organ: Sensitivity to intracellular H^+ and Ca^{+2}

Yukihiro Sato ^a, J. Santos-Sacchi ^{b,*}

^a Department of Otolaryngology, Kawasaki Medical School, Kawasaki, Japan

^b Sections of Otolaryngology and Neurobiology, Yale Medical School, BML 244, 333 Cedar Street, New Haven, CT 06510, USA

(Received 2 March 1994; revision received 1 June 1994; accepted 5 June 1994)

Abstract

The input capacitance of cell pairs or small groups can be used to gauge the degree of electrical coupling via gap junctions (Santos-Sacchi, 1991). In order to estimate junctional sensitivity to intracellular Ca^{+2} and H^+ concentration, the input capacitance of supporting cell syncytia of the organ of Corti was measured with the whole cell voltage clamp technique, while directly modifying the cation concentrations via the patch pipette. Typically, a pH below 6.5 was capable of uncoupling Hensen cells. On the other hand, pCa levels as low as 3 were ineffective.

Keywords: Gap junctions; Organ of Corti; Supporting cell; Homeostasis; Ionic concentration

1. Introduction

The supporting cells of the organ of Corti not only serve to physically support the hair cells, but probably to maintain the homeostasis of the organ. It is significant, therefore, that the supporting cells are joined together by gap junctions (Jahnke, 1975; Gulley and Reese, 1976; Iurato et al., 1976), and are consequently electrically and metabolically coupled (Santos-Sacchi and Dallos, 1983; Santos-Sacchi, 1986). In our previous work, we demonstrated that uncoupling was induced reversibly by treatments which lead to a rise in $[Ca^{+2}]_i$ or $[H^+]_i$, either by direct intracellular iontophoresis of these ions or in the case of H^+ , by perfusion of the cells with CO_2 saturated media (Santos-Sacchi, 1984, 1985, 1991). During those experiments the degree of intracellular ionic concentration changes was unknown. The present work was carried out in order to estimate the relative uncoupling abilities of these two ions, by intracellular perfusion with known cation concentrations. We report that supporting cell coupling is more sensitive to alterations of $[H^+]_i$.

A preliminary account of this work has been presented previously (Sato and Santos-Sacchi, 1991).

2. Methods

Albino guinea pigs were decapitated under halothane anesthesia. The cochleas were removed, the top two turns separated, and placed in calcium free Leibovitz salt solution containing 1 mg/ml trypsin. The tissue was agitated gently in a modified test tube shaker for about 15 min, where upon isolated cells were harvested and allowed to settle onto the coverslip bottom of a 750 μ l perfusion chamber. The cells were continuously perfused with an ionic blocking solution containing (in mM) 100 NaCl, 20 TEA, 20 CsCl, 2 $CoCl_2$, 1.52 $MgCl_2$, 10 HEPES and 5 dextrose, pH 7.2, 300 mOsm. Patch electrodes contained (in mM) 140 CsCl, 10 HEPES, 10 EGTA, and 2 $MgCl_2$, with the pH ranging from 4.03 to 8.14, adjusted using CsOH. Alternatively, at a fixed pH of 7.2, pCa was altered between 2.3 and 8. EGTA buffering was used only for levels of Ca at and below 1 μ M (Imai and Takeda, 1967). Calcium levels in bulk solution were verified using a Ca-sensitive electrode (Orion Research). Initial resistances of the patch electrodes ranged from 3–4 $M\Omega$. The ionic blocking solution was used to reduce the

* Corresponding author.

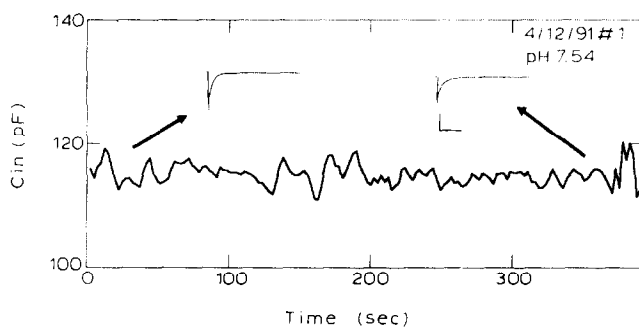


Fig. 1. Group of four cells, one cell of which was whole cell recorded. Pipette pH was 7.54. The input capacitance is stable during the 6.5 min recording, indicating that no uncoupling had occurred. Insets: Capacitive current traces due to -10 mV steps collected at beginning and end of recording session. Changes in trace shape is indicative of changes in cell parameters. Scale: 1.4 nA/4 ms.

voltage dependent ionic conductances so that capacitive currents were recorded in isolation. Blockers of plasmalemma voltage dependent ionic channels do not interfere with junctional communication (Fig. 1; Santos-Sacchi, 1991).

Pairs or small groups of isolated Hensen cells were easily identified under Hoffmann optics and one cell of the pair or group was whole cell voltage clamped. The measurement of input capacitance is a sensitive indicator of cell coupling because by definition the input capacitance will correspond to the amount of electrically contiguous membrane. Changes in input capacitance can therefore indicate the degree of cell coupling (Santos-Sacchi, 1991). However, because the other whole cell parameters (i.e., R_s and R_m) can change as well during alterations in coupling, it is necessary to estimate the input capacitance corrected for these changes. For a single cell the proper method of measuring membrane capacitance can be obtained by modelling the cell-clamp as an electrode resistance (access resistance, R_s) in series with a parallel combination of a membrane resistance (R_m), and a membrane capacitance (C_m). Solving for membrane capacitance (Santos-Sacchi, 1993),

$$C_m = \frac{(R_m + R_s)^2 Q}{R_m^2 V_c} = \frac{(R_{tot})^2 Q}{R_m^2 V_c} \quad (1)$$

The charge (Q) is obtained by integration of the decaying current transient induced by the command voltage step (V_c : 10–20 mV), at a holding potential of -80 mV. R_{tot} is equal to the sum of membrane and electrode resistances, and is obtained from the steady state current response. R_s is estimated from the current decay time constant (Santos-Sacchi, 1993). To a first approximation, for pairs or small groups of cells, R_{in} and C_{in} replaced R_m and C_m , respectively. The capacitance determination is actually only exact when either the cells are highly coupled (if voltage drops are equal in coupled cells) or uncoupled. Nevertheless, the

intermediate capacitance values during uncoupling are useful inasmuch as they reflect changes in cell-to-cell interaction, i.e., in the electrical contiguity between the membranes of adjacent cells. Cell uncoupling was judged to occur if input capacitance values approached single cell levels (25 ± 9 pF; Santos-Sacchi, 1991), within recording periods of 6 min. Syncytia with an initial R_{in} less than 70 M Ω were abandoned. Electronic series resistance compensation was not performed in order to gauge pipette plugging.

The care and use of the animals in this study were approved by the Yale Animal Care and Use Committee under NIH grant DC00273.

3. Results

Whole cell recordings were made 30 min to 2 h after tissue isolation, sufficient time for residual halothane, a potent uncoupler, to be washed away. The input capacitance of a syncytium of supporting cells depends upon the number of coupled cells. In Fig. 1, a group of four Hensen cells, one cell of which was whole-cell recorded, possesses an input capacitance of about 120 pF. This is roughly four times the value of single cells (Santos-Sacchi, 1991). In this case, the pipette solution pH was 7.54, and the Ca concentration was less than 10 nM. The input capacitance is stable during the 6.5 min recording period, indicating that the recorded cell remains coupled to adjacent cells. When pH is lowered below 6.5, an increase in the probability of uncoupling occurs (Figs. 2 and 3). Note in Fig. 2 that the input capacitance begins to decrease during uncoupling before the input resistance changes. This indicates that capacitance measures are more sensitive than DC resistance measures in evaluating junctional conductance changes. Between pH 7 and 8, only one cell uncoupled ($N = 7$), possibly due to injury during recording. Between pH 5 and 7, five cells uncoupled ($N = 13$), and between pH 4 and 5, 6 cells uncoupled ($N = 12$).

Unlike H^+ effects, Ca^{+2} induced uncoupling was observed in only one out of two cases at pCa 2.27 (Fig. 4). At lower concentrations ($N = 18$; pCa 3–8) no uncoupling was observed throughout the recording period, which typically lasted for greater than 6 min. Pooling all data for cells into two groups where pH was either above or below 7, we obtained 2 uncouplings / 26 observations, and 11 uncouplings / 25 observations, respectively. There were significantly fewer uncoupled cells in the high pH condition ($\chi^2 = 6.2$; $P = 0.01$).

4. Discussion

The classic experiments of Loewenstein (e.g., Loewenstein et al., 1967) implicated Ca^{+2} as a control-

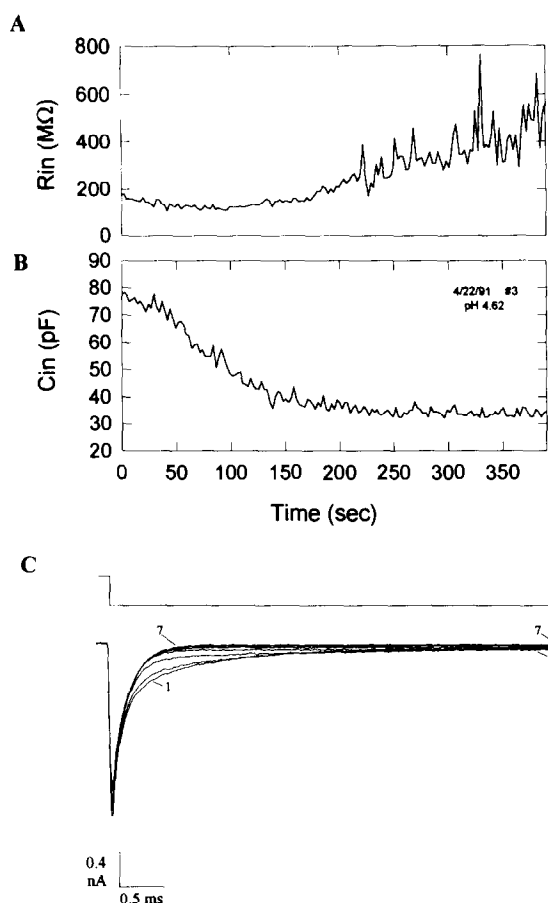


Fig. 2. Two cells with patch pipette at pH 4.62. (A): Input resistance increases as cells uncouple. Note that R_{in} begins to rise following changes in C_{in} . (B): Input capacitance begins to decrease almost immediately after establishment of whole cell configuration. It eventually approaches single cell values as the recorded cell's junctional conductance decreases. (C): Capacitive transients recorded at 50 s intervals (1–7). Note the decrease of steady state values over time indicative of increasing input resistance; the reduction of the charge (area under curves) over time corresponds to the decrease in C_{in} .

ling factor in gap junctional communication. Subsequently, pH was implicated as well (Turin and Warner, 1977). Considerable controversy still exists concerning

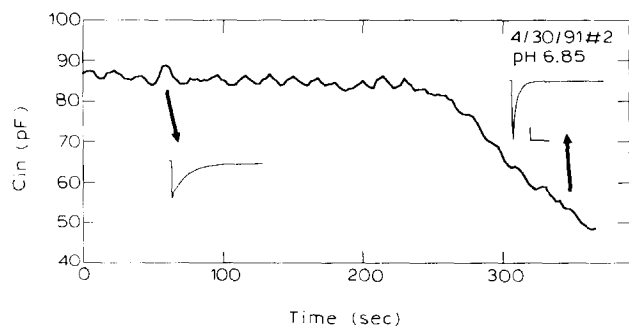


Fig. 3. Two or three cells. Patch pipette pH was 6.85. Cell uncoupling occurred only after prolonged recording. Insets: Capacitive current traces due to -10 mV steps collected at beginning and end of recording. Changes in trace shape is indicative of changes in series resistance, as well as R_{in} and C_{in} . Scale: 0.4 nA/ 0.8 ms.

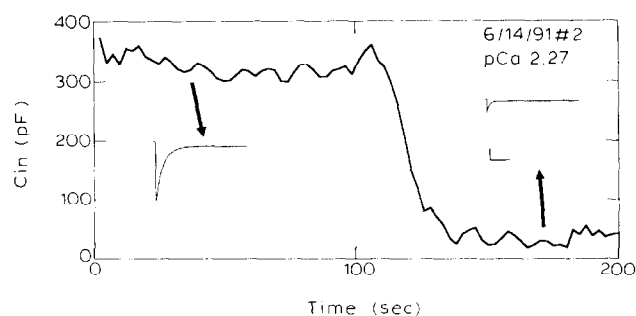


Fig. 4. Large group of cells, one cell of which was whole cell recorded. Pipette pH was 7.2 and pCa was 2.27. The input capacitance drops after one hundred seconds, indicating that uncoupling had occurred due to this high level of Ca^{+2} . Insets: Capacitive current traces due to -10 mV steps collected at beginning and end of recording. Scale: 0.2 nA/ 6 ms.

the sensitivity of gap junctional communication to intracellular Ca^{+2} and H^{+} levels. For example, Spray et al. (1981) found in fish blastomeres that uncoupling due to pH alterations occurred near physiological levels whereas calcium effects were observed only in the millimolar range. Indeed, Ca^{+2} has been shown to permeate both hepatocyte and smooth muscle cell gap junctions (Saez et al., 1989; Christ et al., 1993). On the other hand, others have found that Ca^{+2} can uncouple cells at concentrations approaching physiological levels, viz., in the low to sub-micromolar range (Neyton and Trautmann, 1986; Noma and Tsuboi, 1987; Perachia, 1990). The intracellular regulation of Ca^{+2} and H^{+} are coupled, so that it is important to have control of each ion during experimental manipulations. In the present study, direct perfusion of small Hensen cells with buffered solutions provided a convenient means to study the differential effects of these ions on supporting cell junctional conductance.

It is demonstrated here that an individual Hensen cell is more likely to uncouple from its neighbors during alterations of pH near physiological levels than during alterations of calcium near physiological levels. Indeed, only when calcium levels were clearly pathologic, did uncoupling occur. It should be noted that the ability to maintain the cell's intracellular H^{+} and Ca^{+2} concentrations at that of the electrode's solution depends upon the efficacy of the intracellular perfusion, and intracellular buffering capacity. The latter is an especially important factor at sites proximal to gap junctions which may be distal to the perfusion site. In this regard, it is important to note that Hensen cells are relatively small, with single cell capacitance values of about 25–30 pF (Santos-Sacchi, 1991). Intracellular concentration variability may also occur due to pipette plugging. One difference noted between the two experimental protocols was a greater series resistance for high Ca^{+2} containing pipettes. In the Ca^{+2} modification experiments the average series resistance was 29

$M\Omega$ as compared to $17 M\Omega$ for the H^+ modification experiments. Typically, as the concentration of either ion was increased, the series resistance increased. Nevertheless, there are indications that the experimental differences between H^+ and Ca^{+2} sensitivities are real, and not related to perfusion problems. That is, in a group of cells ($N = 5$) near pH 6, where the probability of uncoupling is great, the series resistance was $21.6 M\Omega$. At a comparable concentration of calcium, (pCa 6 [$N = 5$]), where the probability of uncoupling is negligible, the series resistance was $10.1 M\Omega$. Thus, in cases of similar perfusion efficiencies, intercellular communication in the supporting cells appears more sensitive to the effects of H^+ than Ca^{+2} . Nevertheless, other means of raising intracellular Ca^{+2} levels should be explored.

The supporting cells of the organ of Corti are extensively coupled to one another via gap junctions (Iurato et al., 1976; Jahnke, 1975). It is probable that such coupling is important for sinking of K^+ released during hair cell and neural activity, even in relative quiet. Indeed, it has been shown that Henson cells 'share' ionic channels among each other via gap junctions; in particular, an inward rectifier is active near normal resting potentials (Santos-Sacchi, 1991). The sensitivity of the inner ear to metabolic insult is high and it is likely that resulting H^+ imbalances contribute to this insult by uncoupling supporting cells.

Acknowledgements

Supported by NIH-NIDCD Grant DC00273. We thank Drs. Y. Orita and M. Matsumura and Janet Santos for technical assistance.

References

- Christ, G.J., Moreno, A.P., Gondre, C.M., Roy, C., Campos de Carvalho, A.C., Melman, A. and Spray, D.C. (1993) Gap junctions in human corpus cavernosum vascular smooth muscle: a test for functional significance. *Prog. Cell Res.* 3, 211–217.

- Imai, S. and Takeda, K. (1967) Actions of calcium and certain multivalent cations on potassium contracture of guinea-pig's taccinia coli. *J. Physiology* (London) 190, 155–169.
- Iurato, S., Franke, K., Luciano, L., Werbter, G., Pannese, E. and Reale, E. (1976) Intercellular junctions in the organ of Corti as revealed by freeze fracturing. *Acta Otolaryngol.* 82, 57–69.
- Jahnke, K. (1975) The fine structure of freeze-fractured intercellular junctions in the guinea pig inner ear. *Acta Otolaryngol.* [Suppl] 336.
- Gulley, R.S. and Reese, T.S. (1976) Intercellular junctions in the reticular lamina of the organ of Corti. *J. Neurocytol.* 5, 479–507.
- Lowenstein, W.R., Nakas, M. and Socolar, S.J. (1967) Junctional membrane uncoupling. Permeability transformation at a cell membrane junction. *J. Gen. Physiol.* 50, 1865–1891.
- Neyton, J. and Trautmann, A. (1986) Physiological modulation of gap junction permeability. *J. Exp. Biol.* 124, 93–114.
- Noma, N. and Tsuboi, N. (1987) Dependence of junctional conductance on proton, calcium and magnesium ions in cardiac paired cells of guinea pig. *J. Physiol.* 382, 193–211.
- Peracchia, C. (1990) Effects of caffeine and ryanodine on low pH-induced changes in gap junction conductance and calcium concentration in Crayfish septate axons. *J. Membrane Biol.* 117, 79–89.
- Saez, J.C., Conner, J.A., Spray, D.C. and Bennett, M.V.L. (1989) Hepatocyte gap junctions are permeable to the second messenger, inositol 1,4,5-trisphosphate, and to calcium ions. *Proc. Natl. Acad. Sci. USA* 86, 2708–2712.
- Santos-Sacchi, J. and Dallos, P. (1983) Intercellular communication in the supporting cells of the organ of Corti. *Hear. Res.* 9, 317–326.
- Santos-Sacchi, J. (1984) Increased intracellular H^+ and Ca^{++} uncouples the cells of Corti's organ. *Assoc. Res. Otolaryngol.* Clearwater, FL.
- Santos-Sacchi, J. (1985) The effects of cytoplasmic acidification upon electrical coupling in the organ of Corti. *Hear. Res.* 19, 207–215.
- Santos-Sacchi, J. (1986) Dye coupling in the organ of Corti. *Cell Tissue Res.* 245, 525–529.
- Santos-Sacchi, J. (1991) Isolated supporting cells from the organ of Corti: some whole cell electrical characteristics and estimates of gap junctional conductance. *Hear. Res.* 52, 89–98.
- Santos-Sacchi, J. (1993) Ionic conductances of Type I spiral ganglion cells of the mammalian inner ear. *J. Neurosci.* 13, 3599–3611.
- Sato, Y. and Santos-Sacchi, J. (1992) Calcium and hydrogen ion sensitivity of gap junctional conductance in the supporting cells of the organ of Corti. *Assoc. Res. Otolaryngol.* St. Petersburg, FL.
- Spray, D.C., Harris, A.L. and Bennett, M.V.L. (1981) Gap junctional conductance is a simple and sensitive function of intracellular pH. *Science* 211, 712–715.
- Turin, L. and Warner, A. (1977) Carbon dioxide reversibly abolishes ionic communication between cells of the amphibian embryo. *Nature* 270, 56–57.

Calcium-Dependent Synaptic Vesicle Trafficking Underlies Indefatigable Release at the Hair Cell Afferent Fiber Synapse

Michael E. Schnee,¹ Joseph Santos-Sacchi,³ Manuel Castellano-Muñoz,¹ Jee-Hyun Kong,¹ and Anthony J. Ricci^{1,2,*}

¹Department of Otolaryngology

²Department of Molecular and Cellular Physiology

Stanford University School of Medicine, Stanford, CA 94304, USA

³Department of Surgery (Otolaryngology), Neurobiology and Cellular and Molecular Physiology, Yale University School of Medicine, New Haven, CT 06510, USA

*Correspondence: aricci@stanford.edu

DOI 10.1016/j.neuron.2011.01.031

SUMMARY

Sensory hair cell ribbon synapses respond to graded stimulation in a linear, indefatigable manner, requiring that vesicle trafficking to synapses be rapid and nonrate-limiting. Real-time monitoring of vesicle fusion identified two release components. The first was saturable with both release rate and magnitude varying linearly with Ca^{2+} , however the magnitude was too small to account for sustained afferent firing rates. A second superlinear release component required recruitment, in a Ca^{2+} -dependent manner, of vesicles not in the immediate vicinity of the synapse. The superlinear component had a constant rate with its onset varying with Ca^{2+} load. High-speed Ca^{2+} imaging revealed a nonlinear increase in internal Ca^{2+} correlating with the superlinear capacitance change, implicating release of stored Ca^{2+} in driving vesicle recruitment. These data, supported by a mass action model, suggest sustained release at hair cell afferent fiber synapse is dictated by Ca^{2+} -dependent vesicle recruitment from a reserve pool.

INTRODUCTION

The hair cell afferent fiber synapse maintains a high level of tonic vesicle release and responds to graded input with linear changes in release across a wide range of stimulus frequencies (Furukawa et al., 1978). Information regarding frequency, intensity, and phase of stimulation are transferred across this synapse with high fidelity (Rose et al., 1967, 1971) and mechanisms by which this occurs are the focus of much work (Eisen et al., 2004; Meyer et al., 2009; Neef et al., 2007; Nouvian et al., 2006; Parsons et al., 1994; Schnee et al., 2005). Hair cells have a presynaptic dense body (DB) or synaptic ribbon, as do other sensory cells requiring graded and tonic release (Lagnado, 2003; Parsons and Sterling, 2003; Schnee et al., 2005; von Gersdorff and Matthews, 1997). The functional significance of the DB is unclear but synapses

with DBs have common features including linear release with increasing Ca^{2+} load, high release rates, and limited fatigue. At conventional synapses, vesicle populations are classified based on location and release kinetics, with a readily releasable pool (RRP) of vesicles near the membrane, a more distal recycling pool that communicates with the RRP, and a larger reserve pool whose role varies with synapse type (Rizzoli and Betz, 2005). Physiological investigations with either capacitance measurements or optical techniques find that pools do not strictly adhere to these distributions and that the ability to move between pools varies with synapse type (Rizzoli and Betz, 2004, 2005).

At ribbon synapses, vesicle pools have been classified by position relative to the ribbon and plasma membrane (Nouvian et al., 2006). The locations of vesicles around the ribbons have been correlated with capacitance measurements that identify pools based on release kinetics and saturation (Gomis et al., 1999; Gray and Pease, 1971; Mennerick and Matthews, 1996; Moser and Beutner, 2000; Schnee et al., 2005). Data establishing a direct link between vesicle location and release pools are limited. Furthermore, vesicle populations are often more difficult to observe in auditory hair cells because saturation is less evident and rapid vesicle trafficking appears to create overlap between pools (Schnee et al., 2005).

The role of the DB in regulating synaptic transmission remains unclear. In hair cells lacking DBs because of knockout of the anchoring protein bassoon, sustained exocytosis is maintained but synchronous vesicle release is lost (Khimich et al., 2005). DBs may tether vesicles, clustering them near presynaptic membranes, a hypothesis supported by morphological data (Lenzi et al., 1999; Wittig and Parsons, 2008). The DB may also control release rates, acting as a conveyor belt to rapidly bring vesicles to release sites (Parsons and Sterling, 2003). Causal data to support any specific role is limited (Nouvian et al., 2006).

How vesicles reach synaptic regions is also contentious. In the visual system, vesicles may freely diffuse within the cytosol until affixing to DBs (Holt et al., 2004; LoGiudice and Matthews, 2009). Brownian motion can provide enough DB-vesicle encounters to maintain vesicle availability during long release paradigms (Beaumont et al., 2005). Data from hair cells suggest vesicles are present in a gradient; density is highest near the synapse and lower

away from the synapse (Lenzi et al., 1999; Schnee et al., 2005), intimating a more structured system. Calcium dependence of vesicle trafficking has also been suggested (Spassova et al., 2004).

In this study, we assess synaptic vesicle trafficking and fusion at the hair cell afferent synapse in real time. Our approach has allowed us to separate release into a linear component that does not require recruitment of vesicles and a superlinear component dependent upon vesicle trafficking. We are able to clearly identify pools of depletable vesicles that correspond in size to those vesicles near the DB. Data presented here implicate strong interactions between the RRP and the recycling pool, which together account for the observed linear release component and also demonstrate an ability to rapidly recruit from the reserve pool. Vesicle trafficking is calcium dependent and release of stored calcium may be critical for recruitment of vesicles to the release site from the distant reserve pool.

RESULTS

Ca²⁺ Dependence of Trafficking

At retinal ribbon synapses, paired-pulse experiments identified an RRP that could be depleted (Coggins and Zenisek, 2009). For experiments with turtle auditory hair cells, we designed a protocol to elicit a capacitance change roughly equivalent to release of all vesicles associated with the DB (300 ms pulse to -20 mV, based on previous estimates of vesicle distribution, Schnee et al., 2005) and the interval between pulses was varied from 1 s to 10 ms (Figure 1A). Surprisingly, we did not observe depletion or reduction of release during the second pulse at any interpulse duration (Figure 1B). Rather, as the interpulse interval was reduced, capacitance increased (Figure 1). The increase in release from the second pulse approached that equivalent to a single 600 ms pulse (data not shown). These data suggest that vesicles can be rapidly recruited to release sites faster than they are depleted. To test whether a depletable pool could be observed by altering stimulus duration, we held the interpulse interval at 30 ms and varied stimulus duration between 10 and 300 ms (Figure 1C). Depletion was never observed and again, as stimulus duration was increased, the second response was greater than the first, indicative of rapid vesicle recruitment. Assuming capacitance reflects synaptic vesicle fusion, a change of 400 fF equates to 8000 vesicles (assuming 50 aF per vesicle) or 186 vesicles per synapse (see Figure 4 for synapse counts), more vesicles than previously identified to be near the synapse (Schnee et al., 2005), indicating that rapid vesicle recruitment is required.

To identify discrete pools, it might be necessary to reduce calcium entry as a potential means of slowing release and possibly vesicle trafficking. Additionally, pool populations might be masked by priming of synapses such that the second stimulation might not provide similar information to the initial one. This can be a significant issue when multiple stimulations are required to assess release across a broad time frame. Additionally, both intra- and intercellular variability may make it more difficult to identify discrete vesicle pools.

Two-Sine Measurements

To address these concerns and more directly investigate vesicle trafficking, we developed a method for continually monitoring

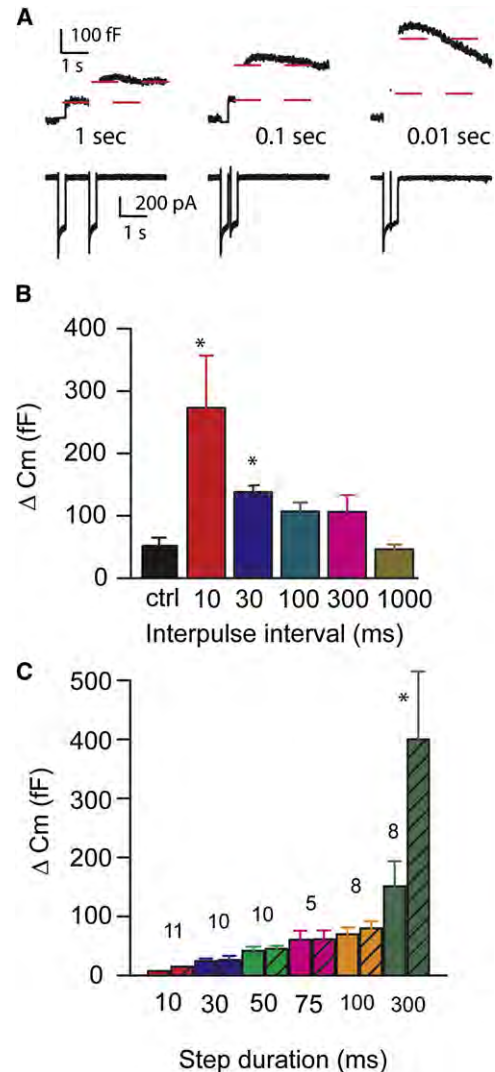


Figure 1. Paired-Pulse Paradigms Suggest Vesicle Trafficking Is Fast, Limiting the Ability to Identify Discrete Pools

(A) Paired pulses of 300 ms duration with interpulse intervals from 1000 to 10 ms, with capacitance shown above and I_{Ca} below. Red lines indicate instantaneous capacitance values, revealing a lack of depletion regardless of interpulse interval (IPI) with short duration IPIs unmasking a facilitatory effect. (B) Summary of data from protocol shown in (A) demonstrating that release from the second stimulus was greater than that observed from the first ($n = 4$). The bar graph represents change in capacitance for the second pulse with IPI given below, ctrl is the average capacitance change for the first stimulus. (C) Summary of release data where the IPI was constant at 30 ms and the stimulus duration varied from 10 to 300 ms. Cross-hatched bars indicate second pulse response, while open bars indicate initial response; n is given above each pair. Asterisks indicate statistical significance at the $p < 0.05$ level.

cell capacitance that simultaneously tracks capacitance and conductance changes. This two-sine technique requires accurate compensation of electrode capacitance and calibration of the recording system (for detailed description of technique see Santos-Sacchi, 2004 and Supplemental Information, Figures S1–S3). With this approach, we could resolve all components of release from a single cell with a single pulse. Importantly,

continuous monitoring of capacitance allowed the use of protocols eliciting submaximal I_{Ca} , thereby slowing Ca^{2+} influx, with the goal of creating separation between individual components of trafficking and release.

Figure 2 provides an example of a cell probed with a depolarization eliciting either 75% or 35% of the maximal Ca^{2+} current. As predicted, strong depolarization compressed release components so that saturable pools were difficult to observe (Figures 2B and 2C, left panel). Surprisingly though, the rate of release increased during the stimulation (Figure 2). We commonly observed a slight delay in release after the stimulus onset that varied with intensity and repetition making it difficult to quantify (Figure 2C). Probably this delay relates to strong calcium clearance mechanisms at the synapse and results from nonphysiological stimulus protocols where cells are held at very hyperpolarized potentials (see Figure 5). Slowing Ca^{2+} entry separated release into at least two clearly identifiable components, an initial shallow component that showed depletion followed by a large, rapid, superlinear component (Figure 2B). These results are in contrast to those from photoreceptors where the initial release was fast, followed by longer but slower release components (Innocenti and Heidelberger, 2008). With slower Ca^{2+} accumulation, the depletable pool size increased from 24 vesicles/synapse to 60 vesicles/synapse (based on 50 aF/vesicle and synapse numbers presented in Figure 4). Therefore, slowing Ca^{2+} entry unmasked a saturable pool of vesicles whose pool size varied with Ca^{2+} load. Depending on stimulus intensity this additional pool could be recruited into the depletable first component (Figure 2D).

Plotting the Ca^{2+} load against capacitance changes corroborated the superlinear nature of the second release component (Figure 2E). Interestingly, the dramatic difference in Ca^{2+} load required to elicit the secondary larger capacitance change depended on the rate of Ca^{2+} entry. Depolarizations closer to the peak elicited the superlinear component with less than 200 pC of Ca^{2+} entry as compared to 600 pC when Ca^{2+} entry was slowed. This may reflect the presence of strong Ca^{2+} clearance mechanisms at the synapse that were overwhelmed with rapid Ca^{2+} entry. Fitting the data in Figure 2E with a Hill equation by using previously determined maximal release values (Schnee et al., 2005) yielded a Hill coefficient of 3.6 ± 0.4 for the high-frequency cells ($n = 14$). The coefficient was not dependent upon level of depolarization as the shift in the capacitance versus Ca^{2+} load with depolarization was parallel (Figure 2E). This value is similar to that obtained when photolysis of caged calcium was used to stimulate release and to that observed in mouse IHCs (Beurg et al., 2010; Beutner et al., 2001). Interestingly, this value is predominated by the superlinear component of release that is at least in part a reflection of vesicle trafficking and not only of release.

The nonlinearity in release differs from previous measurements (Schnee et al., 2005). However, a limitation to those experiments was the use of the single-sine method, which provided no direct kinetic information; rather, kinetics were inferred from responses measured after the pulse by combining responses from multiple cells and/or multiple pulses to individual cells. A comparison of data collected by using the two-sine wave technique to that previously obtained by using the single-sine

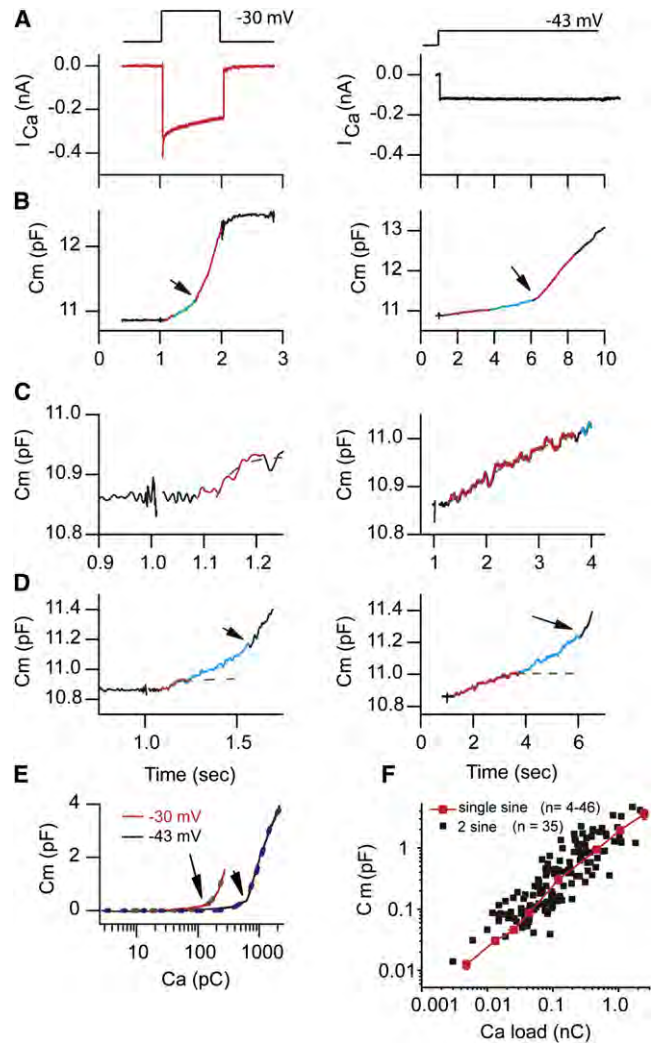


Figure 2. Two Ca^{2+} -Dependent Components of Vesicle Release Were Observed during Hair Cell Depolarization

(A) I_{Ca} elicited in response to membrane depolarization from -85 mV to -30 mV (75% peak, left) or -43 mV (35% of peak, right). (B) Capacitance change elicited in response to I_{Ca} in (A); arrow indicates superlinear onset. Colors show regions where rates are different. (C) Expansion of the axis of (B). Red identifies a saturable pool of vesicles that differs in amplitude between stimulus protocols. Blue indicates an intermediary component that also is saturable depending on Ca^{2+} load and purple represents the superlinear component. (D) Expansion of plots in (B) to illustrate the intermediate component of release where depletion has ended but superlinear response has not started. The dashed line is the exponential fit showing depletion. (E) Capacitance against Ca load (integral of current in A), demonstrating both linear and nonlinear (indicated by arrow) responses. Dashed lines are fit to Hill equation: $Cm = Cm_{(max)} \times x^n / (k^n + x^n)$ where n is Hill coefficient ($r^2 = 0.99$, see text for details). (F) Plot of capacitance change after stimulation from high-frequency (1 mM EGTA internal) cells included in this study for varying intensities and durations of depolarization as compared to previous data obtained with single-sine wave method (Schnee et al., 2005).

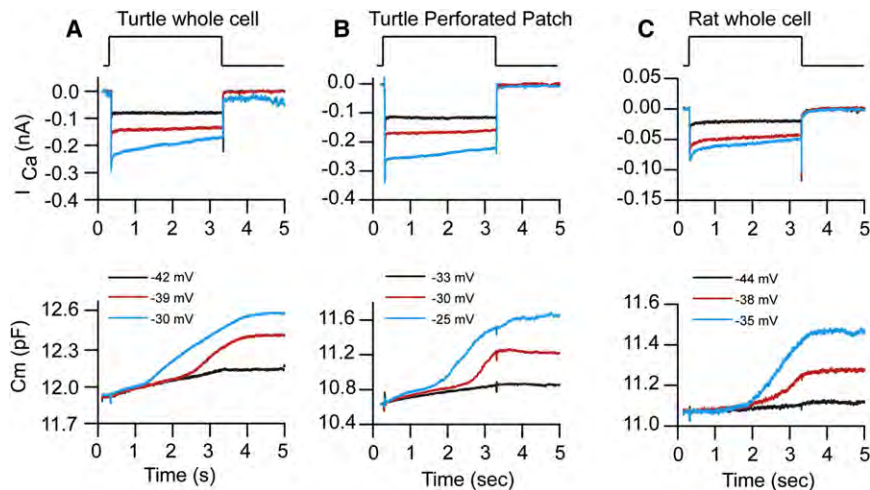


Figure 3. Superlinear Release Is Observed in Whole-Cell and Perforated-Patch Recordings and across Species

(A) The I_{Ca} (above) and capacitance response (below) are presented for a turtle cell recorded in whole-cell mode (1mM EGTA as buffer). A saturating response as well as two superlinear responses are presented in response to different levels of depolarization.

(B) A perforated patch-recording ($n = 4$) presented in a similar manner to (A).

(C) A whole-cell recording from a rat inner hair cell ($n = 16$) with 1 mM EGTA as the buffer. Similar responses were observed from all conditions.

technique confirmed that variability between and within cells may have masked the superlinear behavior of individual cells (Figure 2F). These data point out the limitations of using a technique that requires multiple sampling to intuit kinetic information as compared to direct measurements of kinetics.

To determine whether the superlinear release component was an artifact of whole-cell recording, we performed perforated-patch experiments to maintain endogenous buffering. We observed two release components in both perforated-patch recordings and whole-cell recordings by using 1 mM EGTA (Figure 3), indicating that the observed release properties are not due to the whole-cell recording technique. To ensure that the superlinear release component is not unique to turtle, we recorded from rat and mouse inner hair cells (ages postnatal day P7–P15) and observed two components of release in these preparations (Figure 3C). Previous work in chick auditory hair cells also documented two release components (Eisen et al., 2004), suggesting multiple release components may be a ubiquitous feature of vesicle release in hair cells.

Comparisons between Hair Cells of Different Frequency Locations

Quantitative comparison of release properties between frequency positions requires knowing the number of synapses present. Whole-mount papillae were double labeled with Ctbp2+PSD-95 or Ribeye+PSD-95 antibodies to count the number of functional ribbon synapses at the same tonotopic positions used in the electrophysiological analysis ($n = 6$). Examples from a high-frequency position are shown in Figures 4A–4F. Ribbon synapses were localized in hair cell basolateral regions (Figures 4D and 4E), were scarce above the nucleus and were typically present in series, probably corresponding to the finger-like projections of the afferent fiber (Figures 4D and 4F, inset). No synapses were included that did not positively label adjacent pre- and postsynaptic markers (Figure 4F, inset). PSD-95 puncta that did not have a corresponding Ribeye component accounted for less than 5% of the observed puncta. Frequency histograms are plotted to show the distribution of synapses for both frequency positions (Figure 4G). The low-frequency distribution

was best fit with a normal distribution having a center value of 19.5 ± 0.4 synapses/cell and a full-width at half-maximum value of 9 ($r^2 = 0.92$; $n = 38$

cells). The high-frequency distribution was best fit by the sum of two Gaussians with center peaks of 46 ± 1 and 75 ± 4 , and full-width at half-maximum values of 21 and 9, respectively ($r^2 = 0.92$; $n = 90$ cells). Previous morphological work suggested that at higher frequencies some hair cells are dually innervated (Sneary, 1988). Hypothesizing that dual innervations might account for the bimodal distribution in synapse number and further correlate with I_{Ca} , we plotted the frequency distribution of peak I_{Ca} (Figure 4H), revealing a bimodal distribution. The second population of cells with larger I_{Ca} ($\sim 3\%$ of the total) and those with larger synapse number ($\sim 5\%$ of the total) may represent dual innervations and skew the absolute mean values (Sneary, 1988). Therefore, we used the major peak value in all analyses, rather than the mean of the total population, to ensure similar cell populations were compared between high- and low-frequency cells. I_{Ca} (peak of fit) increased from 313 pA to 586 pA between frequency locations; similarly, synapse number increased from 20 to 46 from low to high frequency such that the Ca^{2+} load per synapse was 16 pA/synapse for low frequency compared to 13 pA/synapse for high frequency. Calcium channels are considered clustered at release sites based on previous measurements in turtle (Tucker and Fettiplace, 1995) and frog (Roberts et al., 1990).

First Release Component: Pool Size

As discussed above, depolarizations elicited two distinct components of release, the first corresponding to a saturable pool whose release rate varied with Ca^{2+} entry and a second component in which the release rate was increased relative to the first component. Sixty-four percent of high-frequency cells and 80% of low-frequency cells had a clearly identifiable saturable vesicle pool. The smallest saturable pool observed (Figures 4K and 4L) had asymptotic capacitance measurements of 48 ± 20 fF ($n = 12$) and 90 ± 35 fF ($n = 9$) for low- and high-frequency cells, respectively. This pool size agrees reasonably well with vesicle numbers under the ribbon closest to the plasma membrane and might represent the RRP (Schnee et al., 2005; Rizzoli and Betz, 2005). The largest saturable pools identified (Figures 4K and 4L) were 145 ± 71 ($n = 11$) for low- and

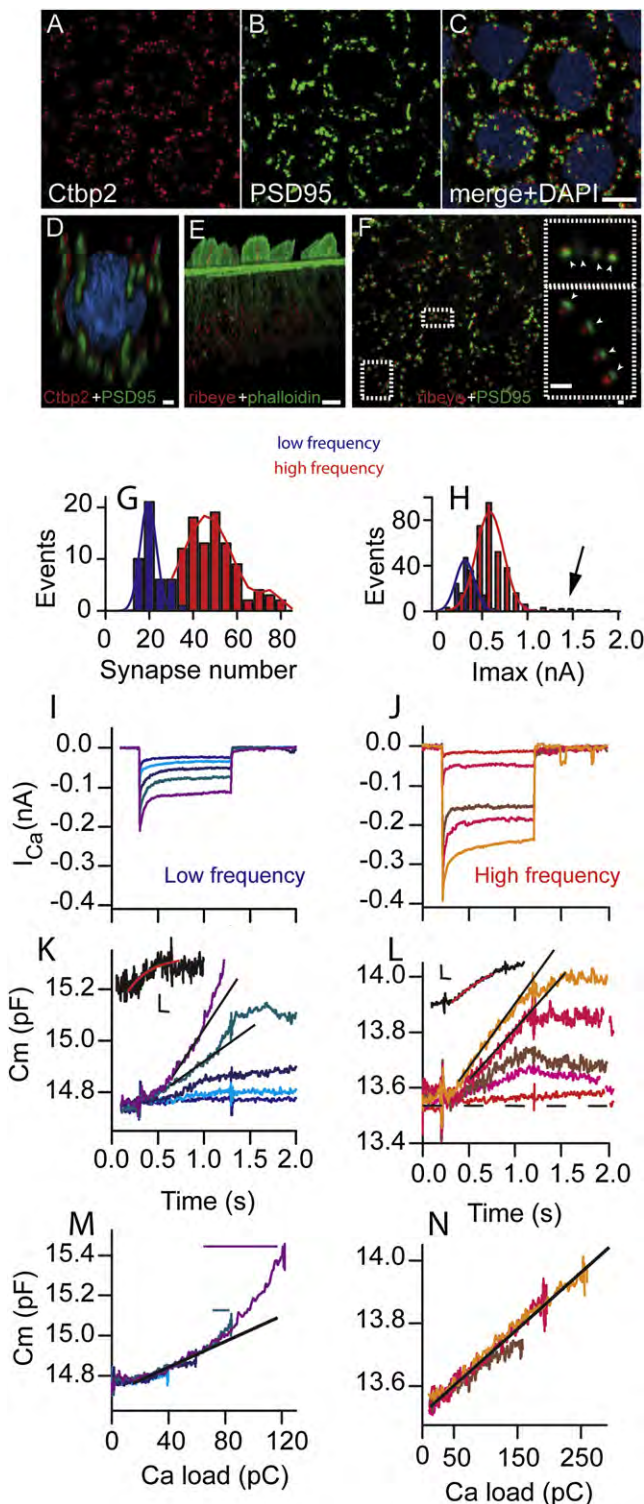


Figure 4. Low-Frequency Cells Release Faster per Synapse Than High-Frequency Cells
(A–C) Maximal-intensity projections of confocal Z-stacks from a whole-mount preparation (high frequency). Immunofluorescence portrays the presence of ribbons (Ctbp2, red) adjacent to postsynaptic densities (PSD95, green).

328 ± 187 fF ($n = 12$) for high-frequency cells. These values are not statistically different from previous morphological measurements estimating vesicles associated with the DB and the total pool may correspond to the recycling pool and the RRP (Rizzoli and Betz, 2005; Schnee et al., 2005). Movement of vesicles within this pool was dependent on the rate of Ca^{2+} entry, suggesting that trafficking of vesicles to release sites is fast and Ca^{2+} dependent and that the ability of vesicles to move between pools is enhanced at auditory ribbon synapses.

First Release Component: Release Rates

Release rates varied linearly with Ca^{2+} load (Figures 4M and 4N). To compare high- and low-frequency cells, we selected stimuli where the Ca^{2+} load was comparable when normalized to synapse number. Rates were estimated by fitting lines to the initial portions of the release plots prior to depletion. The release rate at low-frequency synapses was significantly faster (530 ± 10 vesicles/s/synapse, $n = 14$) than at high-frequency synapses (191 ± 60 vesicles/s/synapse, $n = 11$) ($p < 0.05$, see Figure S6A). We also compared the Ca^{2+} dependence between frequency positions (Figures 4M and 4N). Release varied linearly with Ca^{2+} for the initial release component but the relationship often appeared more exponential in low-frequency cells (Figure 4M), as has been described for mammalian low-frequency cells (Johnson et al., 2008). However, careful inspection reveals encroachment of the superlinear release component (Figures 4K and 4L). No superlinear component is seen in high-frequency cells at these stimulus levels (Figure 4L). The presence of this superlinear component may account for the exponential appearance, suggesting perhaps that vesicle trafficking and not intrinsic

(D) A three-dimensional (3D) reconstruction of a single hair cell with red being Ctbp2, green being PSD95, and blue being DAPI.
(E) A 3D confocal reconstruction showing the presence of ribbons (Ribeye, red) in the basolateral region of hair cells. Hair bundles can be localized with phalloidin staining (green).
(F) A maximum-intensity projection by using Ribeye (red) and PSD95 (green) to colocalize synapses. Insets in F represent regions outlined to better illustrate the coupling of label. Scale bars: C and E, $5 \mu\text{m}$; D and F, $1 \mu\text{m}$. Note that the Ribeye antiserum also labels the kinocilium nonspecifically.
(G) A frequency histogram (blue being low frequency and red high frequency throughout) for the number of synapses per cell with solid lines as Gaussian fits to plots (see text for details).
(H) A plot of the frequency distribution for peak I_{Ca} , again with Gaussian fits to data as solid lines; arrow indicates small peak corresponding to high-frequency cells with twice the I_{Ca} .
(I–N) I_{Ca} (I and J) and capacitance measurements (K and L) in response to different voltage steps (-44 , -41 , -38 , -35 , -43 mV from -80 mV) for low- (blue) and in response to different voltage steps (-50 , -47 , -44 , -41 , -38 mV from -80 mV) for high-frequency (red) cells. Both high-frequency (J, L, and N) and low-frequency (I, K, and M) hair cells show linear, incremental increases in release with increased Ca^{2+} load. Expanding the smallest capacitance response from (K and L) reveals a saturating component (inset, scale bars are 200 ms and 20 fF). Black lines indicate linearity of release for larger depolarizations. (M and N) plot the data from (K and L) against the integral of the corresponding I_{Ca} illustrating the linear relationship between release and Ca^{2+} entry for the first release component. Note that the low-frequency response appears nonlinear because of encroachment of the superlinear component. Encroachment is depicted by horizontal solid lines above traces derived from the point where the capacitance response diverges from linearity (L). Solid black lines in (M and N) point out linearity of response.

differences in Ca^{2+} dependence of release may be responsible for the observed results (Figure 4M). We consistently observed that the superlinear component required less Ca^{2+} influx in low-frequency cells than high-frequency cells, which could create an apparent exponential appearance to the Ca^{2+} dependence.

Superlinear Release Components

The larger superlinear release component was observed in all cells when the Ca^{2+} load was high (Figure 5). The superlinear nature of the response is denoted by a sharp increase in release rate during constant stimulation. As in Figures 3 and 4, capacitance traces elicited by smaller I_{Ca} showed a linear response until reaching a point where release rate dramatically increased. Additional depolarization did not further increase the release rate but rather shortened the onset time of this faster component (Figure 5B). Maximal rates, obtained by fitting a linear equation to the slope of the superlinear component, were 0.9 ± 0.5 pF/s ($n = 13$) and 1.0 ± 0.8 pF/s ($n = 17$) for low- and high-frequency cells, respectively, corresponding to 20,000 vesicles/s and 18,000 vesicle/s or 900 vesicles/s/synapse and 434 vesicles/s/synapse for low- and high-frequency cells, respectively. As with the first release component, low-frequency synapses operated faster than high-frequency synapses, though release rates per cell were comparable. Plotting the change in capacitance against Ca^{2+} load (Figure 5C) shows that the inflection point where the superlinear component began was at the same Ca^{2+} load for the two responses, suggesting the temporal difference in Figure 5B was due to the difference in rate of Ca^{2+} entry. As seen in Figure 2, this onset time for the superlinear component could be varied by altering the Ca^{2+} load. Further inspection of the Ca^{2+} load driving capacitance change (Figure 5D) shows that first component release plateaus just prior to the onset of the superlinear response. Whether initial vesicle pool depletion provides a signal for rapid vesicle recruitment to the synapse remains to be explored.

Functional Relevance of Superlinear Component

The superlinear capacitance changes are paradoxical in that postsynaptic recordings have indicated that release at the hair cell afferent fiber synapse is linear (Keen and Hudspeth, 2006; Li et al., 2009). No physiological experimental data exist that correspond to the superlinear release kinetics, yet large numbers of vesicles must be released continually in order to account for afferent firing properties (Taberner and Liberman, 2005). To address this question, we voltage clamped hair cells at -45 mV, near the expected resting potential (Farris et al., 2006) and then depolarized the cells to the peak I_{Ca} . The response was compared to the conventional experimental protocol in which the cell is held at -85 mV (Figures 5E–5G). At the hair cell's resting potential, where Ca^{2+} channel open probability is nonzero (Figure 5E), the I_{Ca} in response to the depolarization was minimally reduced, yet the capacitance change was dramatically increased (Figure 5F). The capacitance response from -85 mV was small and saturating, indicating that release was depleted and the superlinear component not recruited, while the response at the resting potential was almost linear, more in line with what is expected based on afferent fiber recordings. These data suggest

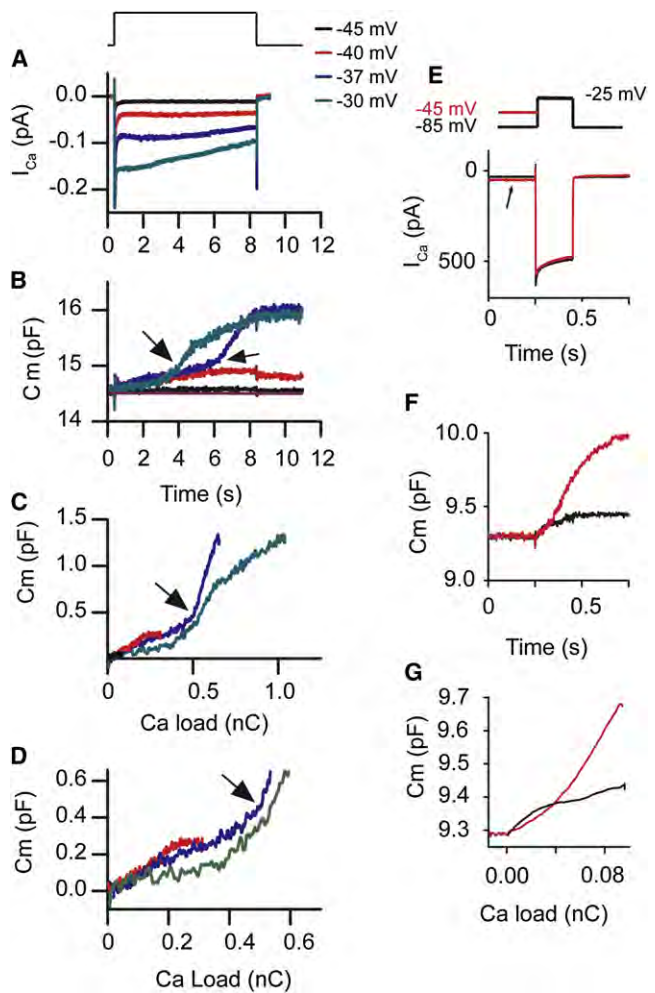


Figure 5. The Superlinear Release Component Onset Is Ca^{2+} Dependent but the Release Rate Is Not

(A) I_{Ca} in response to listed voltage steps from -85 mV. (B) The capacitance responses corresponding to I_{Ca} in (A). In each panel, arrows indicate where release becomes superlinear. (C) A plot of the Ca^{2+} load against the capacitance change; responses are color-coded as in (A) and (B). (D) An expansion of (C) to better exhibit the capacitance results versus Ca^{2+} load. (E) The upper panel shows stimulus and the lower panel presents the I_{Ca} in response to color-coded stimuli where prepulse to -45 mV (red) or -85 mV (black) were presented. (F and G) A plot of the capacitance response against time (F) or Ca^{2+} load (G) for the same stimuli as in (E). Similar results were obtained in 19 cells.

that vesicle release and trafficking kinetics are strongly dependent on calcium homeostasis such that altering homeostasis by hyperpolarizing the cell results in the recruitment of an apparent superlinear process, whereas under physiological conditions release could be maintained for much longer periods of time by the merging of linear and superlinear processes. The magnitude of the release observed with the prepulse requires recruitment of vesicles to release sites (i.e., a superlinear process), suggesting that the prepulse results in the temporal merging of the two release components. Biophysically, it is possible to distinguish

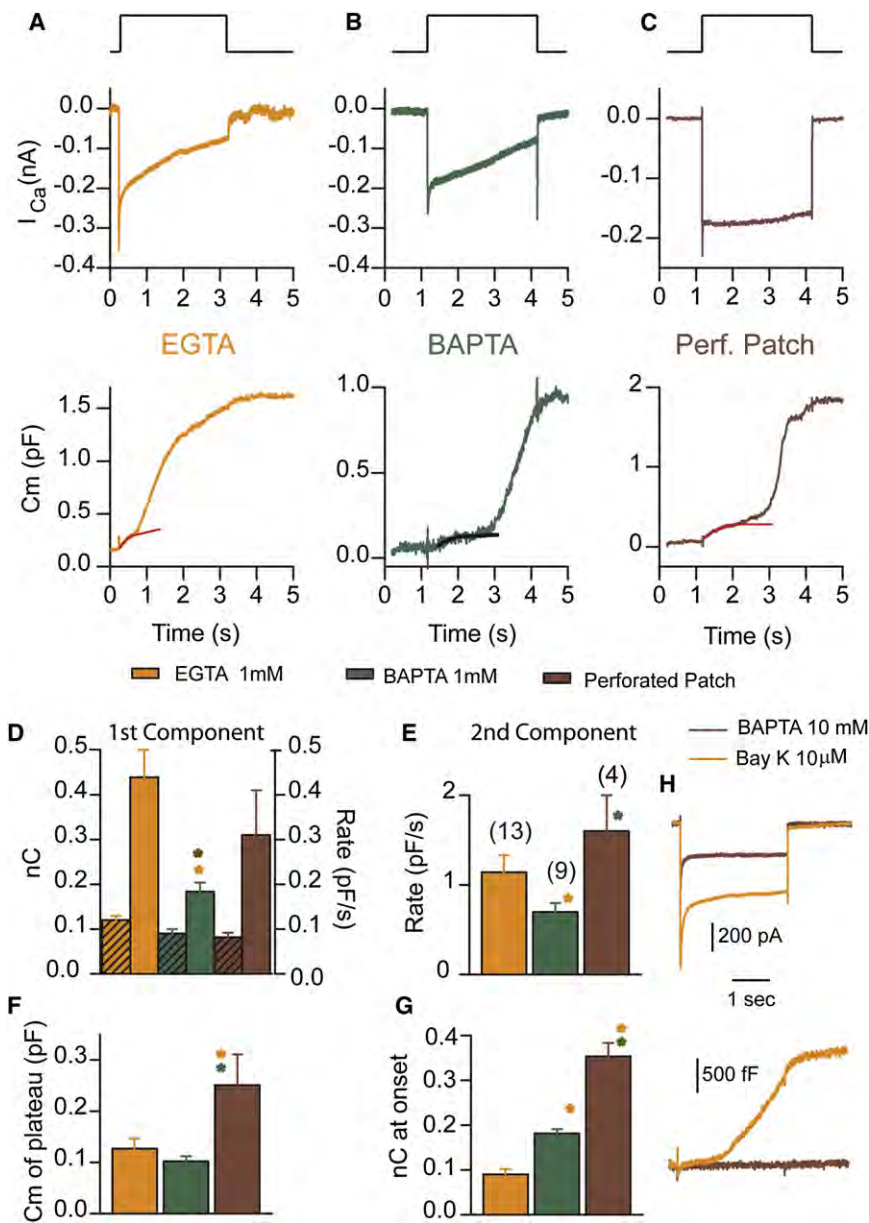


Figure 6. Fast Ca²⁺ Buffers Slow Release Rates and Onset of Release but Pool Size Does Not Change

(A–C) EGTA (tan) at 1 mM (A), BAPTA (green) at 1 mM (B), and perforated patch (purple) (C) with I_{Ca} (upper panels) and capacitance (lower panels) in response to a depolarization eliciting about 60% of the maximal I_{Ca} .

(D) A plot of the Ca²⁺ load (hatched bars) and the release rate for the first component under different internal Ca²⁺ buffering. Asterisks indicate significance at the $p < 0.05$ level against the recording condition indicated by color.

(E–G) Similarly, (E) plots the rate of the superlinear component, (F) plots the capacitance change for the depleted pool, and (G) plots the Ca²⁺ load at the onset of the superlinear response. The number of cells is given in parentheses above bars in (E).

(H) I_{Ca} recorded (upper panel) and capacitance change (lower panel) with 10 mM BAPTA internally in the absence (brown) or presence (tan) of 10 μ M Bay K.

that elicited about 60% of the maximal I_{Ca} (Figures 6A–6C). First, component rates varied with stimulus intensity so rates were compared for a similar Ca²⁺ load (Figure 6D). BAPTA significantly slowed release as compared to EGTA or perforated patch. The perforated-patch recordings suggest an endogenous buffer capacity less than 1 mM BAPTA, but more than 1 mM EGTA, similar to that suggested previously (Moser and Beutner, 2000) and consistent with a release mechanism located near the source of Ca²⁺ influx. A comparison of initial release rates against Ca²⁺ load for individual cells is presented in Figure S6B illustrating how BAPTA reduces release rates. As compared to EGTA, BAPTA also increased the duration of the plateau between the first release component and the onset of the superlinear component, represented by the Ca²⁺ load required

between release and trafficking, but physiologically, the process is created to provide rapid and continual release. The linearity obtained by incorporating the superlinear component is clearly demonstrated by plotting the Ca²⁺ load against capacitance (Figure 5G). This is not unlike arguments made previously when investigating Ca²⁺ dependence of release in hair cells by using caged Ca²⁺ (Beutner et al., 2001). These data suggest multiple sequential first-order processes could account for trafficking and release in the hair cell.

Ca²⁺ Buffering Alters the Two Release Components Differently

The effect of Ca²⁺ buffering on release properties was investigated with EGTA, BAPTA, and perforated patch at stimulations

for the onset of the superlinear release (Figure 6G). In this instance perforated-patch responses suggest endogenous buffering was stronger than either BAPTA or EGTA. This might indicate that the site of action is further removed from the Ca²⁺ source where concentration rather than kinetics is more relevant (Naraghi and Neher, 1997). In contrast, changes in the rate of the superlinear component (Figure 6E) suggest the perforated-patch response was less efficacious than EGTA or BAPTA, supporting the contention that endogenous buffer kinetics are slow. Finally, the difference in Ca²⁺ load required to initiate the superlinear component of release led to an increase in the magnitude of the first component plateau (Figure 6F), supporting the conclusion that vesicle movement to release sites was rapid and Ca²⁺ dependent. The delay between release components also

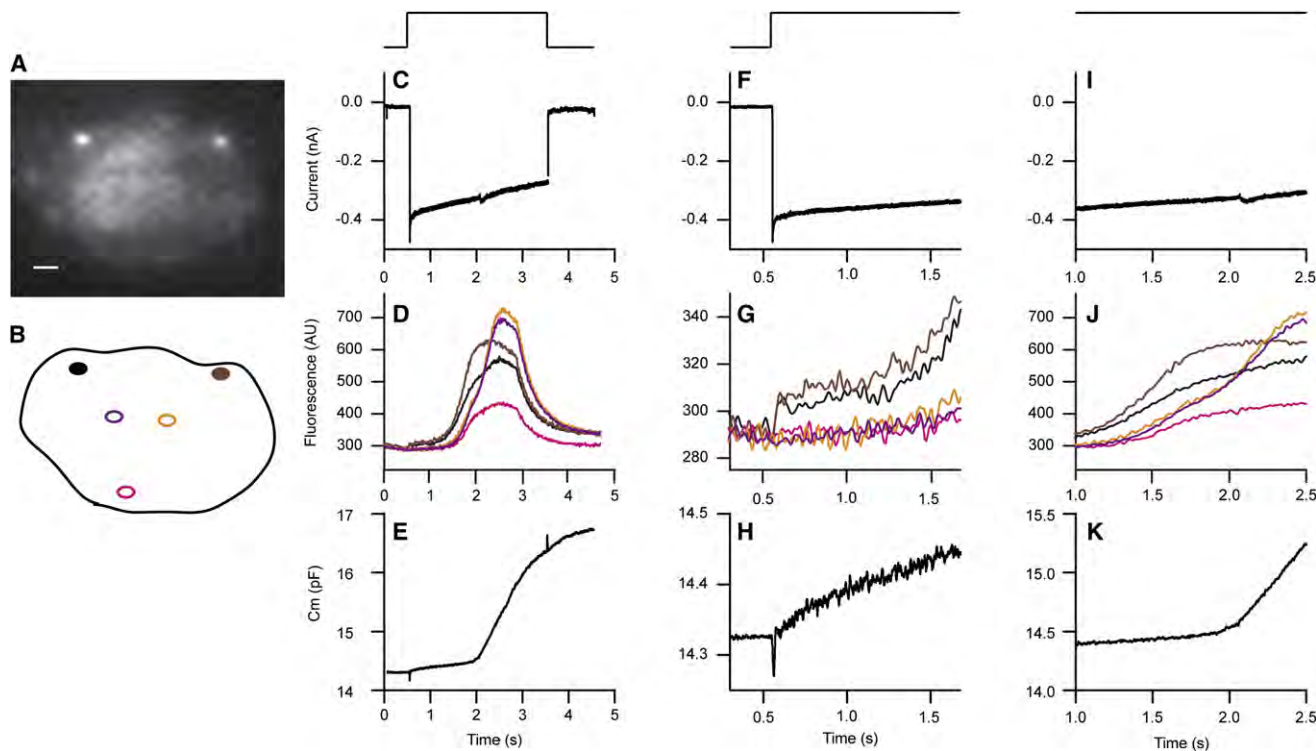


Figure 7. High-Speed Ca^{2+} Imaging Coupled with Continuous Capacitance Measurements Reveals a Nonlinear Increase in Ca^{2+} during Responses with Superlinear Release Properties

(A and B) Fluorescent image (A) of Ctbp2 binding peptide-labeled DBs (scale bar: 1 μm) with schematic in (B) showing regions selected for Ca^{2+} imaging.

(C–E) (C) shows stimulus above which the I_{Ca} response elicits local changes in Ca^{2+} (D) as well as capacitance changes (E).

(F–H) An expansion of the plots from (C–E) in (F–H) focuses on the initial changes in Ca^{2+} current (F), local Ca^{2+} changes (G), and first component of capacitance (H). (I–K) A focus on the onset of the superlinear component again with the Ca^{2+} current (I), local Ca^{2+} signaling (J), and capacitance (K) signals.

supports this conclusion, demonstrating that despite the presence of Ca^{2+} to drive release, depletion persisted for longer periods of time when Ca^{2+} buffering was increased because trafficking was slowed.

An alternative possibility is that vesicle position at the synapse is Ca^{2+} dependent and that greater buffer efficacy leads to diffusion of vesicles away from the synapse. We tested this hypothesis by recording cells with 10 mM BAPTA internally, blocking release at all but maximal stimulus levels, and then increasing Ca^{2+} load by using Bay K (10 μM), which prolongs Ca^{2+} channel open time (Figure 6H). Capacitance changes evoked by Bay K treatment included both linear and superlinear components supporting the hypothesis that vesicle movement toward the synapse is Ca^{2+} dependent and largely unidirectional.

Calcium Imaging Demonstrates Multiple Release Components

It is possible that additional sources of Ca^{2+} , for example Ca^{2+} stores, enhance release during longer stimulations (Lelli et al., 2003). We tested this hypothesis with high-speed confocal Ca^{2+} imaging. Labeling ribbons with a rhodamine-tagged ctbp2-terminal binding peptide in the patch electrode (Zenisek et al., 2003) allowed synapses to be localized during simultaneous Ca^{2+} imaging and capacitance measurements (Figure 7A). The capacitance changes show a typical response with both

release components (Figures 7C–7E). The fluorescent signal, however, is quite complex and not simply the integral of the current, as might be predicted. Rather, the initial response (Figures 7F–7H), representing mostly first component release, shows a rapid increase at the synapse followed by a plateau, similar to that observed in mouse (Frank et al., 2009), indicative of strong Ca^{2+} clearance followed by an integrating increase in signal. Sites distal to the synapse show little change initially, consistent with the source of Ca^{2+} being at a distance, followed by a slow increase. The later signals (Figures 7I–7K), corresponding to the onset of the superlinear response, present a different picture. Ca^{2+} at the synapse shows an abrupt increase in signal, followed by a plateau and decrease in signal even in the face of constant Ca^{2+} entry (Figures 7D and 7J). Ca^{2+} signals away from the synapse show a slower integrating signal followed by a sudden increase in signal whose rate is faster and peak greater than that observed at the synaptic region (Figure 7J). The change in kinetics at these distant sites suggests a secondary source of Ca^{2+} . Similar results were obtained in five cells where the superlinear release component was observed. Smaller depolarizations revealed simple integrating responses that diminished away from the synapse while larger depolarizations yielded similar complex responses (Figure S7). Together these data suggest that Ca^{2+} dynamics are complex, clearance near the synapse is strong, and a second source of Ca^{2+} may play a role in vesicle

trafficking. Also, although the second component of release appears to be superlinear when compared to the Ca^{2+} integral, indicating more release per Ca^{2+} for the second component, when compared to the Ca^{2+} fluorescent signal the opposite is true. By using fluorescence changes at the synapse, the ratio (Cap/Fluor) of the first component divided by the second component provided an indicator of relative efficiency of release and was 1.5 ± 0.4 ($n = 3$), indicating that release was more efficient at lower values of Ca^{2+} .

DISCUSSION

Utilization of a two-sine technique for real-time tracking of vesicle fusion has allowed for more detailed investigation of presynaptic release components at the auditory hair cell-afferent fiber synapse. By using stimuli that did not elicit maximal I_{Ca} , saturable pools were clearly identified, whereas variability between and within cells made this impossible (in turtle) with the single-sine technique (Schnee et al., 2005). A superlinear release component whose onset varied with Ca^{2+} load and correlated with release of an additional source of Ca^{2+} was also revealed. The superlinear component of release is postulated to reflect the ability of hair cells to rapidly recruit vesicles from regions distant from the synapse, which may underlie the inability to deplete vesicle pools and the ability of hair cell synapses to operate at high rates for sustained periods of time.

The first component of vesicle release had a pool size consistent with vesicles within the vicinity of the DB and thus did not require significant vesicle recruitment, though movement of vesicles to release sites on the plasma membrane would be required. The release rate and amplitude of the first component varied linearly with Ca^{2+} entry. Saturable vesicle pools could be observed within this first release component. The size of the saturable pool varied both with frequency position and Ca^{2+} load and could increase significantly if Ca^{2+} entry were slowed, suggesting that additional vesicles could be recruited to release sites faster than the existing pool of vesicles could be released. This vesicle pool may be as small as the vesicle population associated with the plasma membrane and DB to as large as all the vesicles associated with the DB (Figure 8A). This first component of release is very similar to what has been described for ribbon synapses of hair cells and other sensory cells (Beutner et al., 2001; Eisen et al., 2004; Moser and Beutner, 2000; Neef et al., 2007; Neves and Lagnado, 1999; Parsons et al., 1994; Schnee et al., 2005; Thoreson et al., 2004; von Gersdorff and Matthews, 1997).

The second, superlinear component represented a much larger pool of vesicles, requiring trafficking of distant vesicles to the synapse, likely equating to the reserve pool (Figure 8A). It also behaved as if there were a threshold Ca^{2+} load required for onset that was sensitive to factors affecting homeostasis, such as Ca^{2+} buffering and the rate of Ca^{2+} entry. Ca^{2+} imaging experiments suggest a correlation with release of an internal pool of Ca^{2+} , though further studies are needed. Third, the release rate did not increase with Ca^{2+} load; rather, the onset time decreased. These results suggest the superlinear component is more a reflection of vesicle trafficking than vesicle fusion.

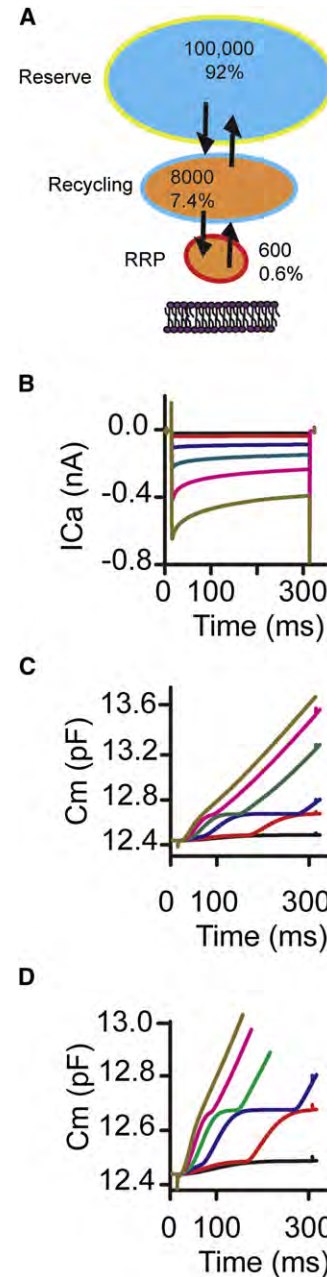


Figure 8. Mass Action Model Incorporating First-Order Ca^{2+} Dependence of Trafficking and Release Reproduces Release Data (A) A schematic representation of a model identifying vesicle pools, rate constants, and Ca^{2+} gradients. (B) A Hodgkin-Huxley model of I_{Ca} in response to increasing depolarizations from -53 in 3 mV increments. (C) Corresponding capacitance changes elicited in response to calcium currents elicited in (B). (D) An expansion of the y axis to better visualize vesicle pools.

One possible mechanism for the increased yet insensitive release rate for the superlinear component is that release sites are not maximally filled at stimulus onset, in a similar manner to the DB being only 50% occupied (Lenzi et al., 1999; Schnee

et al., 2005), but during stimulation the percentage of occupied release sites increases such that the measured release rate increases (vesicle trafficking is faster than vesicle fusion). This would explain the variability in size of depletable vesicle pool with stimulus intensity. The assumption is that the measured release rate is a reflection of the sum of filled and unfilled release sites and the machinery controlling release is operating maximally during stimulus conditions where Ca^{2+} at the release site is saturating. As more sites are filled, the measured release rate increases. When all release sites are full, the release rate will be constant, with the time to achieving this condition varying with Ca^{2+} load.

An alternative hypothesis is that additional synapses are recruited during the stimulation as the Ca^{2+} signal spreads. This seems unlikely, as synapses without Ca^{2+} channels have not been identified in mature hair cells (Frank et al., 2009; Issa and Hudspeth, 1996; Schnee et al., 2005).

Another possibility is that superlinear release does not represent synaptic vesicle fusion, but rather, endosomal fusion or fusion of vesicles at some distant site (Coggins et al., 2007; Zenisek et al., 2000). Direct tests of this possibility are lacking; however, the ability of afferent fibers to operate spontaneously at rates of more than 100 spikes/s and to sustain release in the face of stimulation at rates more than 400 spikes/s argue for the requirement of rapid vesicle replenishment (Lieberman and Brown, 1986; Taberner and Liberman, 2005). The maximal release rate reported here for mammalian inner hair cells when the superlinear component is included is about 307 vesicles/s/synapse (assuming 15 synapses and 50 aF/vesicle) (Meyer et al., 2009), probably underestimating the release required to sustain these large firing rates. Prepulse experiments further illustrate that under more physiological stimulation conditions, release is linear and sustained; neither of these properties would occur without the superlinear component summing with the first release component. Finally, previous experiments have imaged vesicle release in mammalian hair cells at rates higher than reported here for superlinear component of release and also suggested trafficking must be rapid (Griesinger et al., 2005).

Data suggest that low-frequency cells release at faster rates per synapse than high-frequency cells, though the release rate per cell was similar for both components. In turtle, largely one fiber innervates one hair cell, but with multiple synapses it may be the overall release rate that is more significant than release per synapse, in contrast to the mammalian system in which one fiber innervates one synapse. The underlying mechanisms responsible for differences in release per synapse remain to be determined. In contrast, work in mammalian systems (Johnson et al., 2008) has shown a difference in the Ca^{2+} dependence of release. In turtle there was an apparent difference in Ca^{2+} dependence associated with the ability of low-frequency cells to recruit superlinear release with less Ca^{2+} than high-frequency cells. Comparable experiments are needed to test this in mammalian hair cells.

Our data are consistent with the existence of multiple vesicle pools, with the first linear saturable release component including both the RRP and recycling vesicle pools and the superlinear release component corresponding to the reserve pool (Figure 8A). Based on release measurements, we estimated vesicle

pool sizes of 600 vesicles in the RRP (0.6%), 8000 vesicles in the recycling pool (7.4%), and 100,000 vesicles in the reserve pool (92%) (Figure 8A). These sizes are consistent with data from other synapse types (Rizzoli and Betz, 2005), the major difference being the ability of vesicles to be recruited for release from each pool. The rate and extent of Ca^{2+} entry appear to finely regulate the first two pools, while release of intracellular stored Ca^{2+} may be involved in recruitment of the reserve pool of vesicles. At other synapses recruitment of the reserve pool vesicles appears to be limited (Rizzoli and Betz, 2005).

Previous work developed a simple mass action model for vesicle release accounting for observed release properties (Schnee et al., 2005). No specific role for the DB was included and the model did not incorporate Ca^{2+} dependence of release or vesicle trafficking. Alone, this model cannot reproduce superlinear release. Modification of this simple model to include both first-order Ca^{2+} -dependent release and Ca^{2+} -dependent vesicle trafficking reproduced all of the basic release properties reported (Figures 8A–8D, see Supplemental Information for more detailed description). Simulations show both saturable linear release components and a superlinear release component of invariant rate (Figures 8B–8D). Saturating levels correspond well with anticipated pool sizes. Models that did not include Ca^{2+} dependence of vesicle trafficking could not reproduce the superlinear component of release unless higher order release functions were incorporated and even here the superlinear component did not correspond well with available vesicles (data not shown). The model varied from physiological measurements in that the separation between vesicle pools was more sharply defined, probably reflecting the artificial nature of threshold Ca^{2+} levels to recruit vesicle pools. Perhaps vesicle trafficking is uniformly Ca^{2+} dependent and the recruitment depends on the location of vesicles with respect to Ca^{2+} influx, with the Ca^{2+} gradient into the cell dictating the pool size and rate of movement more than the location or specialization of the vesicle. This possibility is consistent with data demonstrating that vesicle movements are similar between different regions of the cell (Zenisek et al., 2000), but is unusual in that it suggests vesicles are tethered in some manner, whether directly associated with the ribbon or not. It is in contrast with arguments that vesicle movement is diffusion based (Holt et al., 2004; LoGiudice and Matthews, 2009), unless diffusion can be regulated via Ca^{2+} levels, but is consistent with recent cryoelectron tomography arguing that all vesicles are tethered by the cytoskeleton (Fernández-Busnadiego et al., 2010). Perhaps the differences in release properties between ribbon synapses in the visual and auditory system, mainly being that release in hair cells is much less defatigable, have more to do with trafficking than with mechanisms of release. Hair cells are required to maintain continual and rapid release in order to maintain high spontaneous activity in the afferent fiber but this is much less of a requirement in the visual system.

Afferent fibers show a pronounced neural adaptation in which firing rates can be reduced by more than 50% during the initial phase of stimulation (Lieberman and Brown, 1986). Data presented here may provide insight into possible mechanisms by which this may happen. We suggest the initial decrease in firing represents the time when vesicles are being released faster than

replenished, so that vesicle trafficking is not maximized. That firing rates do not adapt to zero but rather to a relatively high rate indicates that trafficking (superlinear component) is rapidly accessible under physiological conditions. Similar to the response described in Figure 5, under physiological conditions the processes tend to merge but vesicle release shows a reduction in slope initially that becomes sustained. The level of neural adaptation may in part be determined by how rapidly each synapse is capable of recruiting vesicles between pools—the faster the recruitment, the less adaptation is observed. In fact, it may be argued that steady-state firing requires recruitment of vesicles such that the rate of release at any given synapse may be dictated by access to the reserve pool of vesicles. Thus it may be that spontaneous firing rates are regulated by resting calcium currents and vesicles in the RRP and recycling pool, while stimulated release is more dependent upon vesicle recruitment from the reserve pool and the ability to modulate release of stored calcium (Guth et al., 1991).

In summary, we used real-time capacitance measurements to identify saturable pools of vesicles and discovered a superlinear release component requiring recruitment of vesicles to release sites. We suggest that Ca^{2+} -dependent vesicle trafficking is responsible for this movement, which is required for hair cell synapses to maintain high rates of sustained vesicle fusion. We postulate that the superlinear release component reflects synapses operating at maximal rates of release and trafficking and that release of an as yet undefined internal pool of Ca^{2+} may be required. These characteristics of synaptic vesicle recruitment and release make hair cell ribbon synapses quite unique as compared to other synapses.

EXPERIMENTAL PROCEDURES

Tissue Preparation

The auditory papilla from red-eared sliders (*Trachemys scripta elegans*) were prepared as previously described (Schnee et al., 2005) by using methods approved by the IACUC committee at Stanford University and following standards established by NIH guidelines. Tectorial membranes were removed as previously described by using a hypertonic and hypercalcemic (10 mM Ca^{2+}) solution (Farris et al., 2006). The external recording solution contained 125 mM NaCl, 0.5 mM KCl, 2.8 mM CaCl_2 , 2.2 mM MgCl_2 , 2 mM pyruvate, 2 mM creatine, 2 mM ascorbate, 6 mM glucose, and 10 mM N-(2-hydroxyethyl) piperazine-N'-(2-ethanesulfonic acid) (HEPES) with pH adjusted to 7.6 and osmolality maintained at 275 mosm/kg. One hundred nanometers apamin was included in the external solution to block SK potassium currents (Tucker and Fettiplace, 1996). Cells were imaged with a BX51 fixed-stage upright microscope (Olympus) with bright-field optics. Conventional epifluorescence was used for the Ca^{2+} imaging.

Cochlea from rat pups (ages P7–P10) were dissected into an external solution containing 135 mM NaCl, 5.8 mM KCl, 1.3 mM CaCl_2 , 0.9 mM MgCl_2 , 0.7 mM NaH_2PO_4 , 10 mM HEPES, 5.6 mM glucose, 2 mM pyruvate, and 2 mM creatine. Both stria and spiral ganglia were peeled from the organ of Corti and the remaining epithelium was placed into a glass-bottomed recording chamber. The tectorial membrane was removed and the organ of Corti held in place with single strands of dental floss. Apamin was included at 100 nM to block small conductance calcium-activated potassium currents.

Electrophysiology

Fire-polished borosilicate patch electrodes of resistance 3–5 M Ω were used for all recordings. Unless otherwise stated, the internal solution for turtle contained 110 mM CsCl, 5 mM MgATP, 5 mM creatine phosphate, 1 mM ethylene glycol-bis (β -amino ethyl ether)-N,N,N',N'-tetraacetic acid (EGTA), 10 mM

HEPES, 2 mM ascorbate (pH 7.2). Osmolality was maintained at 255 mosm by adjusting CsCl levels; pH was 7.2. For perforated-patch recordings the internal solution contained 110 mM Cs aspartate, 15 mM CsCl, 3 mM NaATP, 3 mM MgCl_2 , 1 mM BAPTA, and 10 mM HEPES. Amphotericin dissolved in dry DMSO was used as the perforating agent. In several experiments Alexa 488 was included in the recoding pipette to verify the whole-cell mode was not obtained. For rat hair cells the internal solution contained 90 mM Cs methylsulfonate, 20 mM TEA, 1 mM EGTA, 5 mM MgATP, 5 mM creatine phosphate, 3 mM ascorbate, 3 mM MgCl_2 , and 10 mM HEPES. Stimulus protocols were applied 10 min after achieving whole-cell mode to allow equilibration of internal solution and run up of I_{Ca} (Schnee and Ricci, 2003). Hair cells were voltage clamped with a lock-in amplifier (Cairn) allowing for capacitance measurements as initially described by Neher and Marty (1982) and later used for hair cell recordings (Johnson et al., 2002; Schnee et al., 2005). A ± 40 mV sine wave at 1.5 kHz was imposed onto the membrane holding potential, blanked during depolarization that elicited I_{Ca} , and resumed so that capacitance measurements before and after stimulus were obtained. Capacitance data were amplified and filtered at 100 Hz offline. This amplifier was also used initially for validation of the two-sine wave method (see below). The multi-clamp amplifier (Axon Instruments) was also used for capacitance measurements. All data were sampled with a Daq/3000 (IOtech) driven by jClamp software (Scisoft).

Two-Sine Method

Vesicle release was determined by measuring membrane capacitance correlates of surface area change. Capacitance was measured with a dual sinusoidal, FFT-based method (Santos-Sacchi, 2004; Santos-Sacchi et al., 1998) relying on component solutions of a simple model of the patched cell (electrode resistance, R_s , in series with a parallel combination of membrane capacitance, C_m , and membrane resistance, R_m ; see Figure 1 in Santos-Sacchi, 2004). In this RC analysis method, two voltage frequencies, f_1 and f_2 (twice the f_1 frequency) are summed and the real and imaginary components of the current response are used to determine the magnitudes of the three model components. The time resolution of the C_m measurement is the period of f_1 , which we varied from 5.12 to 0.32 ms, corresponding to 195 to 3125 Hz. Comparisons between single-sine and dual-sine-wave methods showed no differences for membrane responses to 100 ms depolarizations to -20 mV. Single-sine values of 90 ± 15 fF ($n = 12$) were obtained as compared to 110 ± 24 fF for dual-sine wave measurements from the same cell population. The same two-sine wave technique (implemented in jClamp) has been used previously, but only as a before and after measurement which gave similar results to the single-sine method (Edmonds et al., 2004; Thoreson et al., 2004). Details of methods and control data are presented in Figures S1–S3. The time between stimuli was varied based on the previous stimulus but was never less than 2 min and typically varied between 5 and 10 min to ensure appropriate time for reaching equilibrium.

Calcium Imaging

Swept-field confocal high-speed (SFC) calcium imaging was performed as previously described (Beurg et al., 2009). The SFC (Prairie Technologies, Middleton WI) was coupled to a Redshirt camera. Fluo 4ff was used as the indicator, chosen to both limit effects on release properties and serve to localize the calcium source. Images were captured at 125 fps with a 35 mm slit. A 100 \times dipping lens with an added 1.25 magnification gave a final pixel size of ~ 350 nm. Ribbons were identified by using the Ctbp2 peptide tagged with rhodamine (Zenisek et al., 2003). Data was analyzed by selecting 3 \times 3 pixel regions uniformly encompassing Ctbp2-labeled regions. Image planes were selected to help isolate individual synapses to ensure individual synapses were being investigated.

Data Analysis

Data were included based on several parameters. Leak currents needed to be less than 50 pA at -85 mV and series resistance (uncompensated) needed to be stable and below 15 M Ω . As electrode capacitance compensation is critical for the accurate use of the two-sine wave methodology, bath height and electrode filling were kept low to limit stray capacitance. Unless otherwise stated, data are presented as mean \pm standard deviation with number of samples (n)

given. Where appropriate Student's *t* tests, two-tailed, were performed to assess significance; *p* values and correlation coefficients (r^2) are listed with data.

Immunofluorescence and Quantification of Synapse Number

Isolated papillae were incubated for 1 hr at 4°C in external solution containing 4% formaldehyde and 0.1% Triton X-100. After washing four times for 10 min at room temperature in external solution containing 0.1% Triton X-100, papillae were incubated for 30 min in the same solution supplemented with 5% bovine serum albumin. Specimens were then incubated with primary antisera diluted at 1:250 to 1:500 in the same solution overnight at 4°C. Antisera included those against Ctbp2 (rabbit polyclonal, #1869), Ribeye (rabbit polyclonal, #1846), and PSD-95 (mouse monoclonal, Abcam #2723, concentrated at 3.3 μg/μl with UPPA-Protein Concentrate Kit, #662120, Calbiochem). After washing five times for 10 min at room temperature, samples were incubated with FITC or TRITC-conjugated secondary antibodies (Invitrogen, Carlsbad, CA) at a dilution of 1:500. Where mentioned, FITC-conjugated phalloidin (#77415, Sigma) was added during the incubation with the secondary antibodies. After washing five times for 10 min at room temperature, specimens were mounted between two coverslips with Vectashield (H1200, Vector Laboratories, Burlingame, CA) and images were acquired with a Zeiss LSM5 Exciter confocal microscope with a 63 × 1.4 NA oil-immersion objective or with a spinning disc confocal by using 100 × 1.4 NA oil-immersion lens. Background noise and contrast enhancement were adjusted with Volocity software (Improvision). Confocal Z-stacks taken with 0.1 μm steps were analyzed by using Volocity software. Ribeye- and PSD95-positive fluorescent objects with 25%–100% intensity were identified on independent channels. Intersecting objects were subsequently selected as potential synaptic ribbons (Figure S5A) and manually confirmed by using the point tool of Volocity (Figure S5B). When two synaptic ribbons were in close proximity, objects were analyzed in the XZ-YZ planes (Figures S5C and S5D) and line intensity profiles were performed (Figure S5E) to identify individual synaptic terminals. The number of peaks, typically one, identified the number of synapses (see Movie S1 and Figure S5).

SUPPLEMENTAL INFORMATION

Supplemental Information includes six figures, Supplemental Experimental Procedures, one table, and one movie and can be found with this article online at doi:10.1016/j.neuron.2011.01.031.

ACKNOWLEDGMENTS

We thank Drs. Revathy Uthaiiah and Jim Hudspeth for providing the Ctbp2 and Ribeye antibodies. The Ctbp2 peptide tagged with rhodamine was generously provided by David Zenisek at Yale University. We thank Medha Pathak, Alan Cheng, the reviewers, and the editorial board for their help with this manuscript. This work was funded by NIDCD grant DC009913 to A.J.R. and J.S.-S. and by core grant P30 44992. M.C.-M. was supported by a Dean's Postdoctoral Fellowship from Stanford School of Medicine and a Cajamadrid Foundation Fellowship.

Accepted: January 19, 2011

Published: April 27, 2011

REFERENCES

- Beaumont, V., Llobet, A., and Lagnado, L. (2005). Expansion of calcium microdomains regulates fast exocytosis at a ribbon synapse. *Proc. Natl. Acad. Sci. USA* 102, 10700–10705.
- Bourg, M., Fettiplace, R., Nam, J.H., and Ricci, A.J. (2009). Localization of inner hair cell mechanotransducer channels using high-speed calcium imaging. *Nat. Neurosci.* 12, 553–558.
- Bourg, M., Michalski, N., Safieddine, S., Bouleau, Y., Schneggenburger, R., Chapman, E.R., Petit, C., and Dulon, D. (2010). Control of exocytosis by synaptotagmins and otoferlin in auditory hair cells. *J. Neurosci.* 30, 13281–13290.
- Butner, D., Voets, T., Neher, E., and Moser, T. (2001). Calcium dependence of exocytosis and endocytosis at the cochlear inner hair cell afferent synapse. *Neuron* 29, 681–690.
- Coggins, M., and Zenisek, D. (2009). Evidence that exocytosis is driven by calcium entry through multiple calcium channels in goldfish retinal bipolar cells. *J. Neurophysiol.* 101, 2601–2619.
- Coggins, M.R., Grabner, C.P., Almers, W., and Zenisek, D. (2007). Stimulated exocytosis of endosomes in goldfish retinal bipolar neurons. *J. Physiol.* 584, 853–865.
- Edmonds, B.W., Gregory, F.D., and Schweizer, F.E. (2004). Evidence that fast exocytosis can be predominantly mediated by vesicles not docked at active zones in frog saccular hair cells. *J. Physiol.* 560, 439–450.
- Eisen, M.D., Spassova, M., and Parsons, T.D. (2004). Large releasable pool of synaptic vesicles in chick cochlear hair cells. *J. Neurophysiol.* 91, 2422–2428.
- Farris, H.E., Wells, G.B., and Ricci, A.J. (2006). Steady-state adaptation of mechanotransduction modulates the resting potential of auditory hair cells, providing an assay for endolymph [Ca²⁺]. *J. Neurosci.* 26, 12526–12536.
- Fernández-Busnadiego, R., Zuber, B., Maurer, U.E., Cyrklaff, M., Baumeister, W., and Lucic, V. (2010). Quantitative analysis of the native presynaptic cytomatrix by cryoelectron tomography. *J. Cell Biol.* 188, 145–156.
- Frank, T., Khimich, D., Neef, A., and Moser, T. (2009). Mechanisms contributing to synaptic Ca²⁺ signals and their heterogeneity in hair cells. *Proc. Natl. Acad. Sci. USA* 106, 4483–4488.
- Furukawa, T., Hayashida, Y., and Matsuura, S. (1978). Quantal analysis of the size of excitatory post-synaptic potentials at synapses between hair cells and afferent nerve fibres in goldfish. *J. Physiol.* 276, 211–226.
- Gomis, A., Burrone, J., and Lagnado, L. (1999). Two actions of calcium regulate the supply of releasable vesicles at the ribbon synapse of retinal bipolar cells. *J. Neurosci.* 19, 6309–6317.
- Gray, E.G., and Pease, H.L. (1971). On understanding the organisation of the retinal receptor synapses. *Brain Res.* 35, 1–15.
- Griesinger, C.B., Richards, C.D., and Ashmore, J.F. (2005). Fast vesicle replenishment allows indefatigable signalling at the first auditory synapse. *Nature* 435, 212–215.
- Guth, P.S., Aubert, A., Ricci, A.J., and Norris, C.H. (1991). Differential modulation of spontaneous and evoked neurotransmitter release from hair cells: Some novel hypotheses. *Hear. Res.* 56, 69–78.
- Holt, M., Cooke, A., Neef, A., and Lagnado, L. (2004). High mobility of vesicles supports continuous exocytosis at a ribbon synapse. *Curr. Biol.* 14, 173–183.
- Innocenti, B., and Heidelberger, R. (2008). Mechanisms contributing to tonic release at the cone photoreceptor ribbon synapse. *J. Neurophysiol.* 99, 25–36.
- Issa, N.P., and Hudspeth, A.J. (1996). Characterization of fluo-3 labelling of dense bodies at the hair cell's presynaptic active zone. *J. Neurocytol.* 25, 257–266.
- Johnson, S.L., Thomas, M.V., and Kros, C.J. (2002). Membrane capacitance measurement using patch clamp with integrated self-balancing lock-in amplifier. *Pflugers Arch.* 443, 653–663.
- Johnson, S.L., Forge, A., Knipper, M., Münkner, S., and Marcotti, W. (2008). Tonotopic variation in the calcium dependence of neurotransmitter release and vesicle pool replenishment at mammalian auditory ribbon synapses. *J. Neurosci.* 28, 7670–7678.
- Keen, E.C., and Hudspeth, A.J. (2006). Transfer characteristics of the hair cell's afferent synapse. *Proc. Natl. Acad. Sci. USA* 103, 5537–5542.
- Khimich, D., Nouvian, R., Pujol, R., Tom Dieck, S., Egner, A., Gundelfinger, E.D., and Moser, T. (2005). Hair cell synaptic ribbons are essential for synchronous auditory signalling. *Nature* 434, 889–894.
- Lagnado, L. (2003). Ribbon synapses. *Curr. Biol.* 13, R631.
- Lelli, A., Perin, P., Martini, M., Ciubotaru, C.D., Prigioni, I., Valli, P., Rossi, M.L., and Mammano, F. (2003). Presynaptic calcium stores modulate afferent release in vestibular hair cells. *J. Neurosci.* 23, 6894–6903.

- Lenzi, D., Runyeon, J.W., Crum, J., Ellisman, M.H., and Roberts, W.M. (1999). Synaptic vesicle populations in saccular hair cells reconstructed by electron tomography. *J. Neurosci.* *19*, 119–132.
- Li, G.L., Keen, E., Andor-Ardó, D., Hudspeth, A.J., and von Gersdorff, H. (2009). The unitary event underlying multiquantal EPSCs at a hair cell's ribbon synapse. *J. Neurosci.* *29*, 7558–7568.
- Lieberman, M.C., and Brown, M.C. (1986). Physiology and anatomy of single olivocochlear neurons in the cat. *Hear. Res.* *24*, 17–36.
- LoGiudice, L., and Matthews, G. (2009). The role of ribbons at sensory synapses. *Neuroscientist* *15*, 380–391.
- Mennerick, S., and Matthews, G. (1996). Ultrafast exocytosis elicited by calcium current in synaptic terminals of retinal bipolar neurons. *Neuron* *17*, 1241–1249.
- Meyer, A.C., Frank, T., Khimich, D., Hoch, G., Riedel, D., Chapochnikov, N.M., Yarin, Y.M., Harke, B., Hell, S.W., Egner, A., and Moser, T. (2009). Tuning of synapse number, structure and function in the cochlea. *Nat. Neurosci.* *12*, 444–453.
- Moser, T., and Beutner, D. (2000). Kinetics of exocytosis and endocytosis at the cochlear inner hair cell afferent synapse of the mouse. *Proc. Natl. Acad. Sci. USA* *97*, 883–888.
- Naraghi, M., and Neher, E. (1997). Linearized buffered Ca²⁺ diffusion in microdomains and its implications for calculation of [Ca²⁺] at the mouth of a calcium channel. *J. Neurosci.* *17*, 6961–6973.
- Neef, A., Khimich, D., Piri, P., Riedel, D., Wolf, F., and Moser, T. (2007). Probing the mechanism of exocytosis at the hair cell ribbon synapse. *J. Neurosci.* *27*, 12933–12944.
- Neher, E., and Marty, A. (1982). Discrete changes of cell membrane capacitance observed under conditions of enhanced secretion in bovine adrenal chromaffin cells. *Proc. Natl. Acad. Sci. USA* *79*, 6712–6716.
- Neves, G., and Lagnado, L. (1999). The kinetics of exocytosis and endocytosis in the synaptic terminal of goldfish retinal bipolar cells. *J. Physiol.* *515*, 181–202.
- Nouvian, R., Beutner, D., Parsons, T.D., and Moser, T. (2006). Structure and function of the hair cell ribbon synapse. *J. Membr. Biol.* *209*, 153–165.
- Parsons, T.D., and Sterling, P. (2003). Synaptic ribbon. Conveyor belt or safety belt? *Neuron* *37*, 379–382.
- Parsons, T.D., Lenzi, D., Almers, W., and Roberts, W.M. (1994). Calcium-triggered exocytosis and endocytosis in an isolated presynaptic cell: Capacitance measurements in saccular hair cells. *Neuron* *13*, 875–883.
- Rizzoli, S.O., and Betz, W.J. (2004). The structural organization of the readily releasable pool of synaptic vesicles. *Science* *303*, 2037–2039.
- Rizzoli, S.O., and Betz, W.J. (2005). Synaptic vesicle pools. *Nat. Rev. Neurosci.* *6*, 57–69.
- Roberts, W.M., Jacobs, R.A., and Hudspeth, A.J. (1990). Colocalization of ion channels involved in frequency selectivity and synaptic transmission at presynaptic active zones of hair cells. *J. Neurosci.* *10*, 3664–3684.
- Rose, J.E., Brugge, J.F., Anderson, D.J., and Hind, J.E. (1967). Phase-locked response to low-frequency tones in single auditory nerve fibers of the squirrel monkey. *J. Neurophysiol.* *30*, 769–793.
- Rose, J.E., Hind, J.E., Anderson, D.J., and Brugge, J.F. (1971). Some effects of stimulus intensity on response of auditory nerve fibers in the squirrel monkey. *J. Neurophysiol.* *34*, 685–699.
- Santos-Sacchi, J. (2004). Determination of cell capacitance using the exact empirical solution of partial differential Y/partial differential Cm and its phase angle. *Biophys. J.* *87*, 714–727.
- Santos-Sacchi, J., Kakehata, S., and Takahashi, S. (1998). Effects of membrane potential on the voltage dependence of motility-related charge in outer hair cells of the guinea-pig. *J. Physiol.* *510*, 225–235.
- Schnee, M.E., and Ricci, A.J. (2003). Biophysical and pharmacological characterization of voltage-gated calcium currents in turtle auditory hair cells. *J. Physiol.* *549*, 697–717.
- Schnee, M.E., Lawton, D.M., Furness, D.N., Benke, T.A., and Ricci, A.J. (2005). Auditory hair cell-afferent fiber synapses are specialized to operate at their best frequencies. *Neuron* *47*, 243–254.
- Sneary, M.G. (1988). Auditory receptor of the red-eared turtle: II. Afferent and efferent synapses and innervation patterns. *J. Comp. Neurol.* *276*, 588–606.
- Spassova, M.A., Avissar, M., Furman, A.C., Crumling, M.A., Saunders, J.C., and Parsons, T.D. (2004). Evidence that rapid vesicle replenishment of the synaptic ribbon mediates recovery from short-term adaptation at the hair cell afferent synapse. *J. Assoc. Res. Otolaryngol.* *5*, 376–390.
- Taberner, A.M., and Lieberman, M.C. (2005). Response properties of single auditory nerve fibers in the mouse. *J. Neurophysiol.* *93*, 557–569.
- Thoreson, W.B., Rabl, K., Townes-Anderson, E., and Heidelberger, R. (2004). A highly Ca²⁺-sensitive pool of vesicles contributes to linearity at the rod photoreceptor ribbon synapse. *Neuron* *42*, 595–605.
- Tucker, T., and Fettiplace, R. (1995). Confocal imaging of calcium microdomains and calcium extrusion in turtle hair cells. *Neuron* *15*, 1323–1335.
- Tucker, T.R., and Fettiplace, R. (1996). Monitoring calcium in turtle hair cells with a calcium-activated potassium channel. *J. Physiol.* *494*, 613–626.
- von Gersdorff, H., and Matthews, G. (1997). Depletion and replenishment of vesicle pools at a ribbon-type synaptic terminal. *J. Neurosci.* *17*, 1919–1927.
- Wittig, J.H., Jr., and Parsons, T.D. (2008). Synaptic ribbon enables temporal precision of hair cell afferent synapse by increasing the number of readily releasable vesicles: A modeling study. *J. Neurophysiol.* *100*, 1724–1739.
- Zenisek, D., Steyer, J.A., and Almers, W. (2000). Transport, capture and exocytosis of single synaptic vesicles at active zones. *Nature* *406*, 849–854.
- Zenisek, D., Davila, V., Wan, L., and Almers, W. (2003). Imaging calcium entry sites and ribbon structures in two presynaptic cells. *J. Neurosci.* *23*, 2538–2548.

Neuron, Volume 70

Supplemental Information

Calcium-Dependent Synaptic Vesicle
Trafficking Underlies Indefatigable Release
at the Hair Cell Afferent Fiber Synapse

Michael E. Schnee, Joseph Santos-Sacchi, Manuel Castellano-Muñoz, Jee-Hyun Kong, and
Anthony J. Ricci

Supplemental Figures S1 and S2 are the control experiments for the two sine wave technology. They are essential to validate the use of the technique for investigating release kinetics and in particular for demonstrating the nonlinear release component is related to vesicle fusion. These figures are essentially the controls for Figures 2, 3, 5, and 7 in the main text.

Supplemental Figure S3 uses a mathematical model, also used in Figure 8 of the text, to corroborate both the methodology used and the underlying conclusions drawn from the data.

Movie S1 (also called Supplemental Figure S4) is the movie illustrating the methodology used to quantify the immunocytochemistry. This movie is available with the article online.

Supplemental Figure S5 also validates the immunohistochemistry methodology used for identifying ribbon synapses.

Supplemental Figure S6 provides the raw data examples of release rates measured between high and low frequency cells and also the effects of different internal calcium buffers on release rates for individual cells.

Supplemental Figure S7 provides calcium imaging data for a cell that with small stimulations did not show superlinear release and with larger stimulations did.

The additional text provides detailed description of the new two sine technology as well as of the modeling used. Figure legends for the supplemental figures are also included. The table included in the text of the supplement provides values for each parameter of the model.

Supplemental Figure S1A gives the basic result from a two sine stimulation where the cell was held at -85 mV, depolarized to -35 mV and then returned to -85 while simultaneously stimulating with the sum of two sine waves. The upper panel provides the deconvolved current elicited from the stimulus while the lower panel reveals multiple kinetically distinct capacitance components. To determine which components were driven by vesicle fusion, Ca^{2+} buffers were increased and results compared. Supplemental Figure S1B demonstrates that with 1 mM EGTA three capacitive components were observed; with 1 mM BAPTA only two components were observed and when 10 mM BAPTA was used only a fast component remained (see arrows). Capacitance measurements before and after the stimulus showed no vesicle fusion with 10 mM BAPTA for this duration stimulus, suggesting the initial fast capacitance change was not release

driven. Most likely this fast component was associated with gating charge for the Ca^{2+} channel (Kilic and Lindau, 2001) or an effect of the probative sine wave on channel activation. To differentiate between possibilities, Cd was used to block the Ca^{2+} current (I_{Ca}) but not gating (Supplemental Figures S2A and S2B). With 10 mM BAPTA in the pipette Cd blocked the initial fast component, implicating activation of I_{Ca} by the sine waves. Supplemental Figure S1C and S1D reveal that as the sine wave frequency was increased the fast capacitive component was reduced, suggesting channel kinetics could not follow higher frequency stimulation. Single sine waves of ± 60 mV, applied in voltage clamp from a holding potential of -85 mV and low pass filtered show the I_{Ca} activation (Supplemental Figures S1E and S1F). Barium was used to increase I_{Ca} without altering gating and Bay K (10 μM) was used to increase the current while slowing gating (Supplemental Figures S2C–S2E). Barium increased the current with a corresponding increase in the fast component, suggesting current and not gating was causal. Bay K increased the current while slowing kinetics, resulting in a decreased fast component. Apparently, slowing the kinetics had a similar effect to increasing the sine wave frequency (Supplemental Figure S2E). And finally, a model incorporating gating currents for the Ca^{2+} channel was used to further validate the analysis program and demonstrate that current activation and not gating was responsible for the initial fast component (Supplemental Figure S3). Together these data demonstrate the fast component is neither due to release nor gating charge movement, but rather a function of current activation by the probative sine wave. Using a 0.32 ms period for the fast sine wave removed the majority of fast component leaving only Ca^{2+} dependent capacitive changes. Remaining artifacts were digitally subtracted. All measurements in main text were done under these conditions. A model was created to test the

accuracy of the JClamp analysis software, to identify the mechanism of the fast non release dependent capacitance change and to investigate mechanisms of vesicle trafficking and release. The model was further probed to demonstrate electrode capacitance altered in a linear manner the fast artifact associated with the measurements. To this end a Hodgkin-Huxley (HH) type of model was created for the I_{Ca} , much like that previously described (Farris et al., 2006; Hudspeth and Lewis, 1988; Zidanic and Fuchs, 1995). The following equations summarize how g_{Ca} was described using a third order HH model.

$$I_{Ca} = g_{Ca} (V_m - E_{Ca}) \quad (1)$$

$$I_{Ca} = g_{Ca} m^3 (V_m - E_{Ca}) \quad (2)$$

$$dm/dt = \alpha_m(1-m) - \beta m \quad (3)$$

$$\alpha_m = \alpha_0 * \exp[-(V_m + V_0)/V_A] + K_A \quad (4)$$

$$\beta_m = \beta_0 * \exp[(V_m + V_0)/V_B] + K_B \quad (5)$$

Where I_{Ca} is calcium current, g_{Ca} maximal Ca^{2+} Conductance when all channels are open, m is the activation probability of the HH model, α_m is the voltage dependent opening rate, β_m is the voltage dependent closing rate, α_0 , K_A , β_0 , and K_B are rate constants and V_0 , V_A and V_B , and V_m are potentials, E_{Ca} is reversal potential for I_{Ca} .

Calcium induced inactivation of the current was implemented simply by scaling m as a function of calcium entry as:

$$m = m - ([Ca]_i/3.5e^{-12})^{1.4} \quad (6)$$

where $[Ca]_i$ is the integral of I_{Ca} .

Release and vesicle trafficking were modeled as described previously (Schnee et al., 2005). This simple mass action model was modified to incorporate a calcium dependence of release as well as Ca^{2+} dependent thresholds for vesicle trafficking. The equations were as follows:

$$dF/dt = K_1 * A(t) \quad (7)$$

$$K_1 = k_1 * [Ca]_i \quad (8)$$

$$dA/dt = k_2 * B(t) * (A_t - A(t))/A_t - K_1 * A(t) \quad (9)$$

$$dB/dt = k_3 * C(t) * ((B_t - B(t))/B_t - k_2 * B(t) * (A_t - A(t))/A_t) \quad (10)$$

$$dC/dt = k_4 * D(t) - k_3 * C(t) * (B_t - B(t))B_t \quad (11)$$

$$dD/dt = -k_4 * D(t) \quad (12)$$

$F(t)$ is the number of vesicles fusing with the membrane and is related to time-dependent capacitance changes by converting with 50 aF/ves. $A(t) - D(t)$ are time dependent number of vesicles in each pool while A_t and B_t are maximal number of vesicles possible in rapid and readily releasable pools. Vesicle numbers were fixed based on morphological counts (Schnee et al., 2005). Calcium-dependent thresholds were set to simulate recruitment of additional pools of vesicles.

Supplemental Table S1 identifies the values used for each model parameter.

Parameter	Value	Parameter	Value
g_{Ca}	6.7 nS	A threshold	4.2×10^{-12}
E_{Ca}	100 mV	B threshold	5.3×10^{-12}
α_0	0.97	C threshold	2.3×10^{-11}
V_0	100 mV	D threshold	3×10^{-11}
V_A	6×10^{-3} mV	K_1	300
K_A	940	K_2	150
β_0	22800	K_3	15
V_B	8×10^{-3}	K_4	3
K_B	510	A_t	1920
Ca channel number	1800	B_t	3720

With this model we were able to probe the validity of our conclusions regarding the nonrelease dependent capacitance change (Figure S3) demonstrating that current activation by the sine wave and not gating charge was responsible. Also remaining artifact was due to electrode capacitance variability. We were also able to demonstrate that JClamp analysis software reproduced expected capacitance changes as defined by the model. And finally, as demonstrated in the main text, the model was capable of reproducing most aspects of measured release.

Fast component artifact that remains at high frequencies appears to be the result of how well electrode compensation was performed and how linear the patch amplifier behaved. Ensuring a linear amplifier and maximal electrode compensations further reduces artifact. Remaining artifacts were linearly subtracted from data. Variations in sine wave amplitude did not alter capacitance responses and any remaining artifact scaled predictably as driven by electrode capacitance.

Figure S1. Two Sine Wave Method for Capacitance Measurements Reveals Multiple Kinetic Components

(A) I_{Ca} , upper, and capacitance, lower panel elicited from a depolarization to -35 mV, from a holding potential of -85 mV with sine waves of 1.56 and 0.8 kHz and amplitude of ± 20 mV superimposed. The capacitance trace reveals three components, a very fast (indicated by arrows), intermediate and slow component.

(B) Ca^{2+} buffers separate capacitance components, where the black trace denotes 1 mM EGTA internally, the red trace 1mM BAPTA, and the green trace 10 mM BAPTA.

(C) Recordings with 10 mM BAPTA where sine wave frequency was varied from a period of 5.12 to 0.32 ms, upper panel is I_{Ca} , lower panel capacitive response.

(D) Summarizes the results in (C) plotting the change in capacitance against sine wave period; the color code for sine wave period is the same for C-F (n=19).

(E) Demonstrates the sine wave stimulus was activating I_{Ca} using a sine wave of ± 60 mV from a -80 mV holding potential.

(F) Low pass filtered responses are plotted in (F) to show current activation (n=8).

Figure S2. Initial Fast Capacitive Component Is Driven by I_{Ca}

(A) Top trace is stimulus, middle trace is I_{Ca} in the absence (black) and presence (red) of Cd and lower trace are capacitance changes (n=5). 10 mM BAPTA was in the pipette to inhibit release.

(B) Plots I_{Ca} (red) and capacitance (black) in the absence (filled) and presence (open) of Cd (1 mM).

(C and D) Upper panel is stimulus, middle I_{Ca} and lower capacitance response in the absence (black) and presence (red) of Bay K (10 μ M) (C) or 5 mM Ca (red) or 5 mM Ba (blue).

(E) Summarizes data from C and D using different probative sine wave frequencies.

Figure S3. Theoretical Reconstruction of Capacitance Components Demonstrates that Fast Initial Component Is Due to Inductive I_{Ca}

(A–D) Left is capacitance and right is I_{Ca} elicited at different voltage steps, top trace represents time course of stimulus. (A) includes I_{Ca} , gating currents and release components, (B) includes I_{Ca} and gating, (C) only current and (D) only gating. Note the scale bar changes.

(E) Represents the sensitivity of the Ca^{2+} current to the sine wave frequency, similar to the data presented in Figure 2. Here a sine wave of increasing frequency is superimposed onto a voltage step to -30 mV. As the frequency increased the Ca^{2+} current decreased. Only low frequency stimulus is shown at top.

Figure S4 (also called Movie S1). Movie of Z-Stack (0.1 μm Sections) Showing psd95 (Green) and Ribeye (Red) Antibody Labeling

Individual synapses are marked for counting. This movie is available with the article online.

Figure S5. Confocal Z-Stacks Taken with 0.1 μm Steps Were Analyzed Using Volocity Software

Ribeye- (red) and PSD95- (green) positive fluorescent objects with 25-100% intensity were identified on independent channels. Intersecting objects were subsequently selected as potential synaptic ribbons (A) and manually confirmed using the *point tool* of Volocity (B). When two synaptic ribbons were in close proximity, objects were analyzed in the XZ-YZ planes (C and D) and line intensity profiles were performed (E) to ascertain the occurrence of individual synaptic terminals.

Figure S6. Release Rates per Synapse Vary between Cells of Different Characteristic Frequencies and Dependent on internal Ca^{2+} Buffering

(A) Plots release rate per synapse, either as capacitance (left axis) or as vesicles (right axis) against Ca^{2+} load per synapse per second. Data were obtained by depolarizing to elicit varying size Ca^{2+} currents, each cell is connected by lines with points reflecting different depolarizing levels.

(B) Plots release rate against Ca^{2+} load for high frequency cells using either 1 mM EGTA (open black circles) or 1 mM BAPTA (filled green squares) against Ca^{2+} load.

Figure S7. High Speed Confocal Ca^{2+} Imaging of Synaptic Zones Reveals Both Linear and Superlinear Changes in Ca^{2+}

(A) Ctbp2 labeling of DB with schematic on right indicating regions that were imaged. Two stimuli were used, one eliciting about 15% (E) of the peak Ca^{2+} current, the other 65% (B) of maximal current. Capacitance responses are given in (C,F) for the different Ca^{2+} loads, (F) eliciting only the first component while (C) eliciting both components. (G) Ca^{2+} imaging experiments reveal a signal that integrates Ca^{2+} with a faster larger response at the synapse, decreasing with distance away from the synaptic zone. (D) finds nonlinear increases in Ca^{2+} signal with rise times and peaks invariant with distance from the synapse but for the furthest distance.

Supplemental References

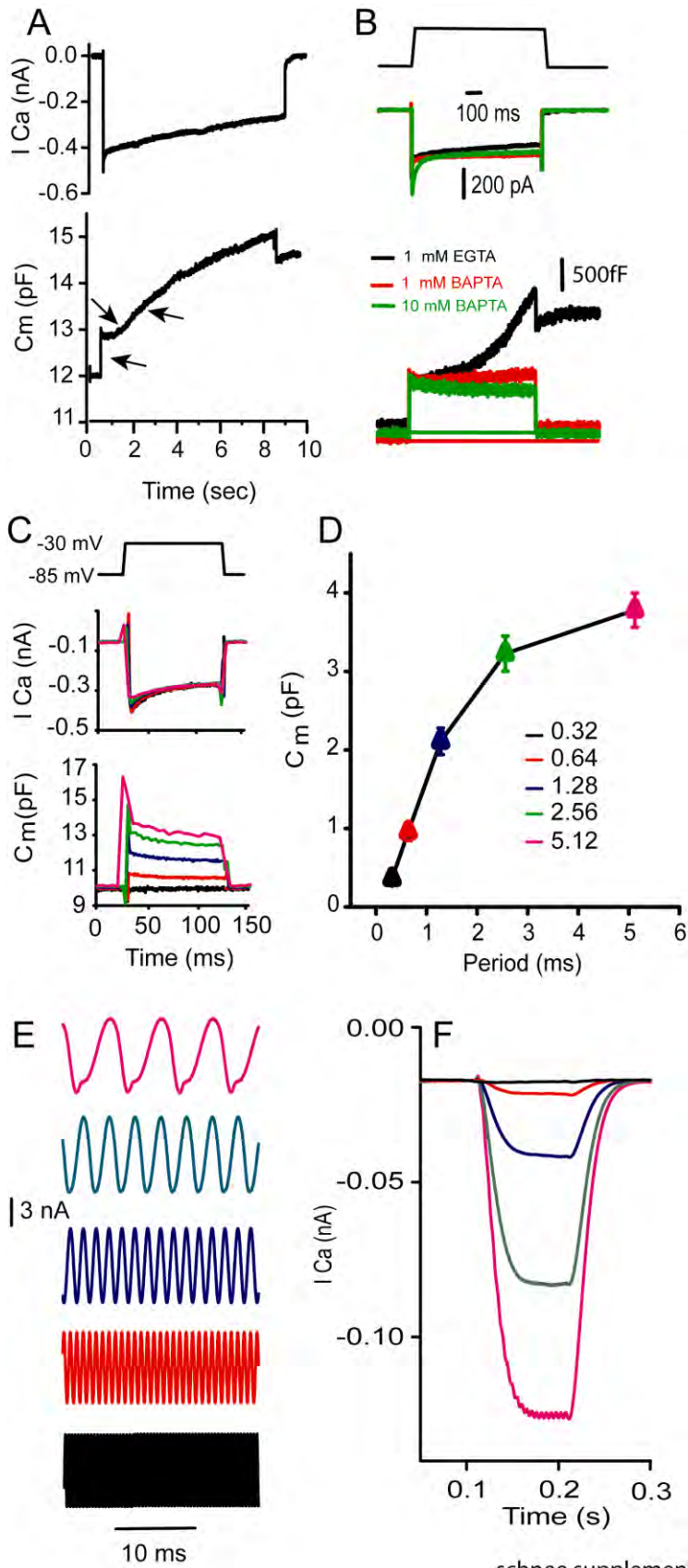
Farris, H. E., Wells, G. B., and Ricci, A. J. (2006). Steady-state adaptation of mechanotransduction modulates the resting potential of auditory hair cells, providing an assay for endolymph $[\text{Ca}^{2+}]$. *J Neurosci* 26, 12526-12536.

Hudspeth, A. J., and Lewis, R. S. (1988). A model for electrical resonance and frequency tuning in saccular hair cells of the bull-frog, *Rana catesbeiana*. *J Physiol (Lond)* 400, 275-297.

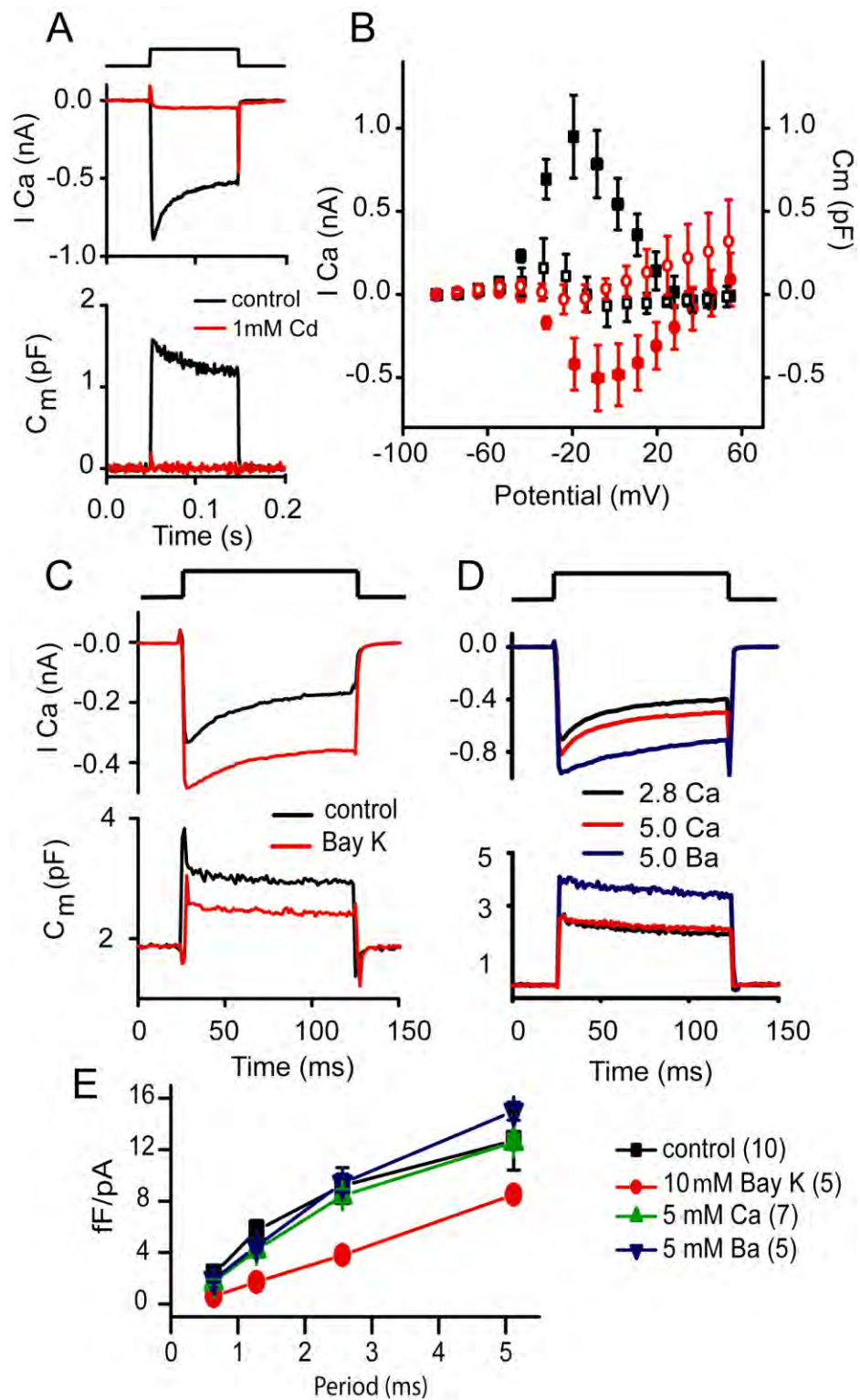
Kilic, G., and Lindau, M. (2001). Voltage-dependent membrane capacitance in rat pituitary nerve terminals due to gating currents. *Biophys J* 80, 1220-1229.

Schnee, M. E., Lawton, D. M., Furness, D. N., Benke, T. A., and Ricci, A. J. (2005). Auditory hair cell-afferent fiber synapses are specialized to operate at their best frequencies. *Neuron* 47, 243-254.

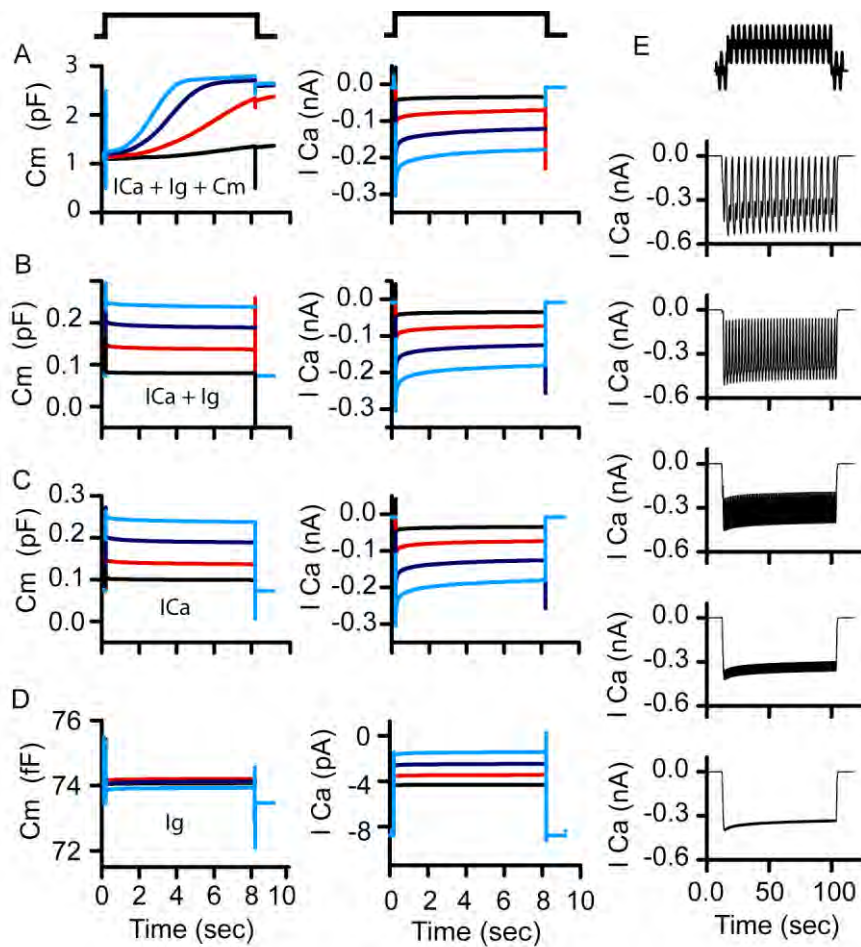
Zidanic, M., and Fuchs, P. A. (1995). Kinetic analysis of barium currents in chick cochlear hair cells. *Biophys J* 68, 1323-1336.



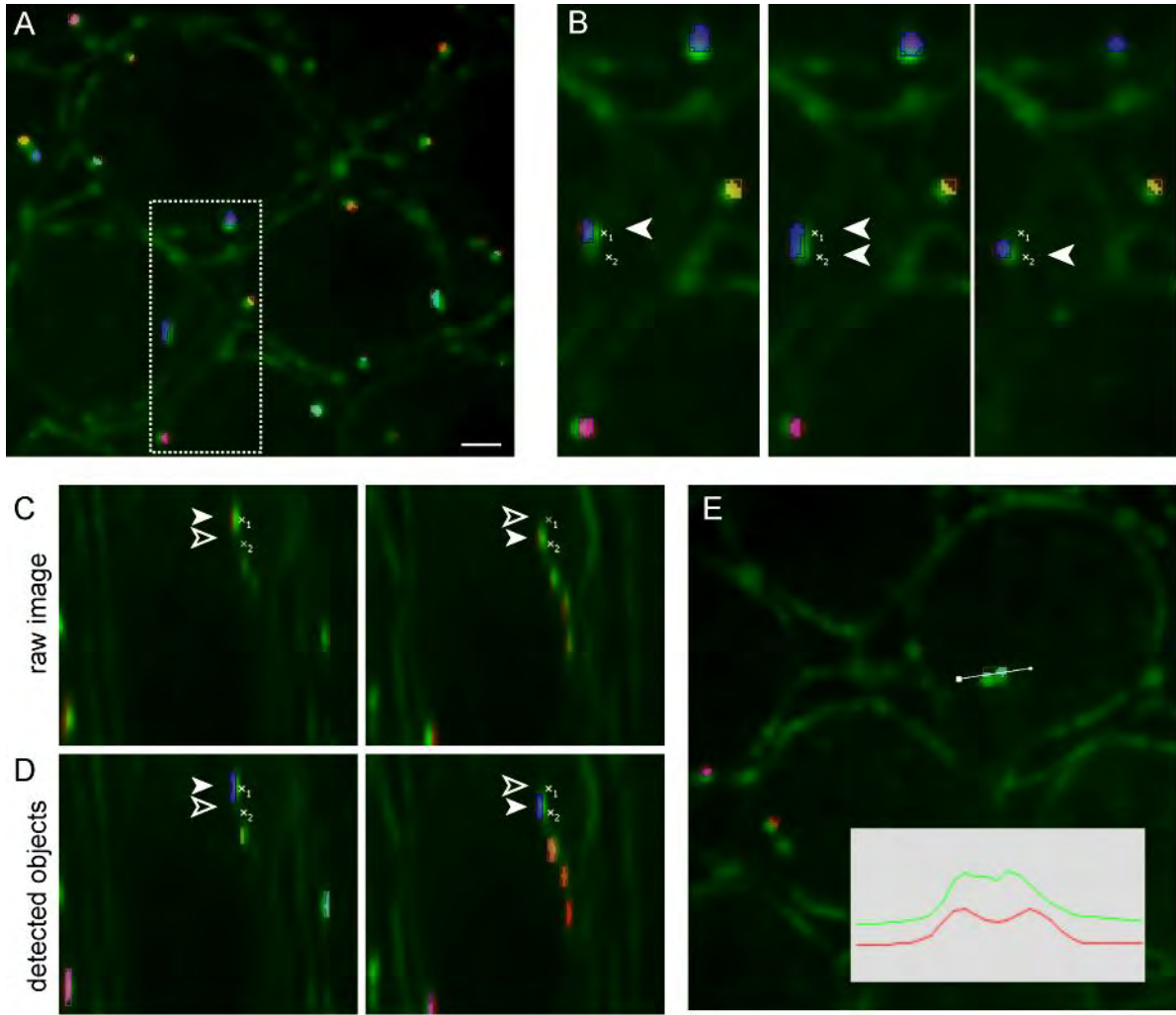
schnee supplemental figure 1



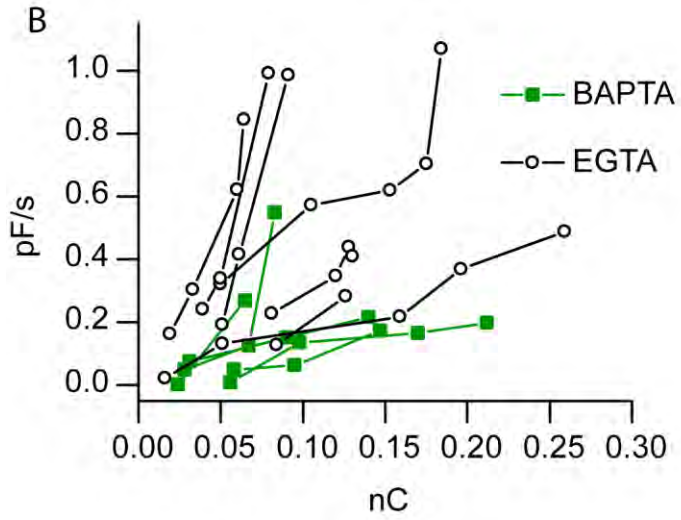
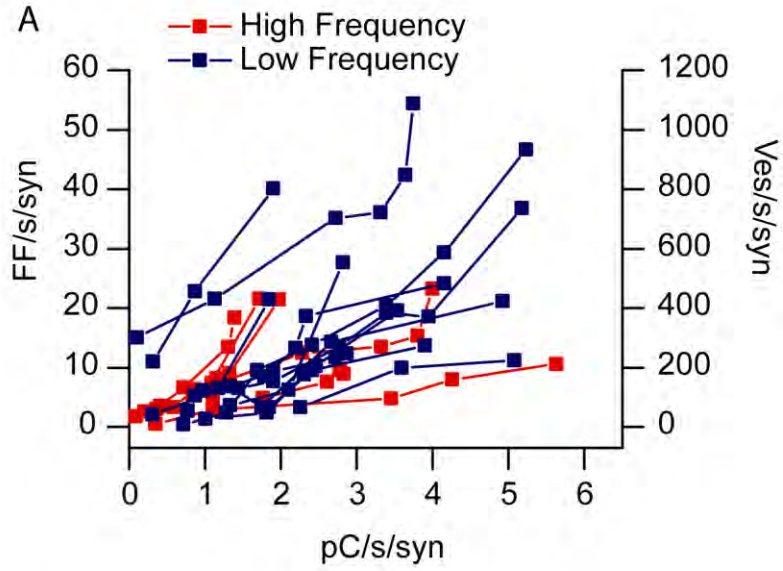
schnee supplemental figure 2



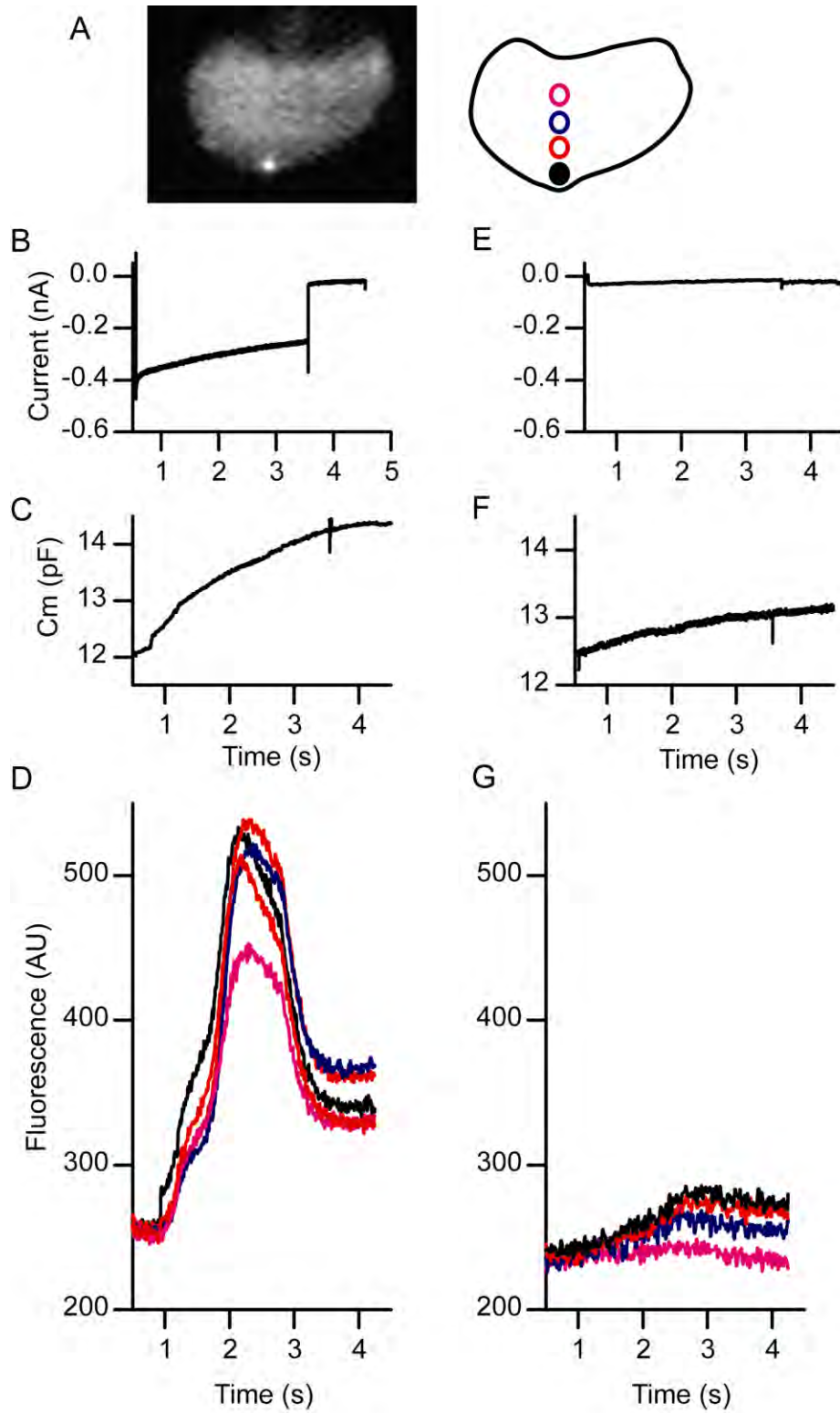
schnee supplemental figure 3



Schnee Supplemental figure 5



schneesupplementalfigure6



schnee supplemental figure 7

Tracking vesicle fusion from hair cell ribbon synapses using a high frequency, dual sine wave stimulus paradigm

Michael E. Schnee,¹ Manuel Castellano-Muñoz,¹ Jee-Hyun Kong,¹ Joseph Santos-Sacchi³ and Anthony J. Ricci^{1,2*}

¹Department of Otolaryngology; ²Molecular and Cellular Physiology; Stanford University School of Medicine; Stanford, CA;

³Department of Surgery (Otolaryngology), Neurobiology and Cellular and Molecular Physiology; Yale University School of Medicine; New Haven, CT USA

Recent experiments describe a technique for tracking membrane capacitance during depolarizations where membrane conductance is varying. This is a major advance over traditional technologies that can only monitor capacitance when conductance is constant because it gives direct information regarding release kinetics from single stimulations. Presented here are additional data supporting the use of this technology with multiple conductances being active including BK-Ca-activated potassium channels, SK Ca-activated potassium conductances and also the rapidly activating sodium conductance. It goes further to illustrate the ability to monitor rapid capacitive changes. And finally, it points out the need to evaluate single step responses because of the use-dependent movement of vesicles.

Ribbon type synapses are commonly found in peripheral sensory cells such as auditory hair cells and photoreceptors, where vesicle fusion is in response to a graded receptor potential.¹ These synapses typically show little fatigue and multiple components of release.² Paired and post synaptic measurements suggest a linear input output function for these synapses, particularly at auditory hair cell afferent fiber synapses.²⁻⁴ Recent evidence suggests that the linearity in release properties arises from the sum of nonlinear processes, the linearity appearing as the processes merge temporally about the hair cell's resting potential.⁵ In that study, two components of release were identified. The first component varied directly in release rate and

magnitude with calcium influx and was saturable with a vesicle population corresponding to those near the synapse. The second 'superlinear' component had a constant rate, was indefatigable and required recruitment of vesicles from more distant pools. These new processes were revealed by the use of a dual sine technique which allows for the continuous monitoring of capacitance changes, even in the face of conductance changes.^{5,6}

Traditionally, a single sine technique has been used to monitor capacitance.⁷ In this case the imaginary component of the complex current correlates to capacitance, as long as there is no conductance change of either membrane or electrode, otherwise the imaginary component reflects both capacitance and conductance in an inseparable manner.⁷ The two sine method allows for the continual tracking of conductance and capacitance and thus the potential ability to separate each.⁶ The added complexity of monitoring capacitance during conductance change is that the sine wave may activate ion channels, with an attendant intrusive inductance that interferes with measures of capacitive current phase, leading to unacceptable errors in capacitance measures.⁵ Sufficiently higher frequency sine wave stimuli can alleviate this problem because channel kinetics will not be able to respond to the rapid cycle by cycle voltage change. **Figure 1** illustrates that the dual sine wave approach can be used to track capacitance in the presence of BK-calcium activated potassium channels, SK-calcium activated potassium channels, as well as rapidly activating and inactivating sodium channels.

Key words: ribbon synapses, hair cells, vesicle trafficking, capacitance measurements

Submitted: 08/19/11

Accepted: 08/22/11

DOI: 10.4161/cib.4.6.17822

*Correspondence to: Anthony J. Ricci;
Email: aricci@stanford.edu

Addendum to: Schnee ME, Santos-Sacchi J, Castellano-Muñoz M, Kong JH, Ricci AJ. Calcium-dependent synaptic vesicle trafficking underlies indefatigable release at the hair cell afferent fiber synapse. *Neuron* 2011; 70:326-38; PMID:21521617; DOI:10.1016/j.neuron.2011.01.031.

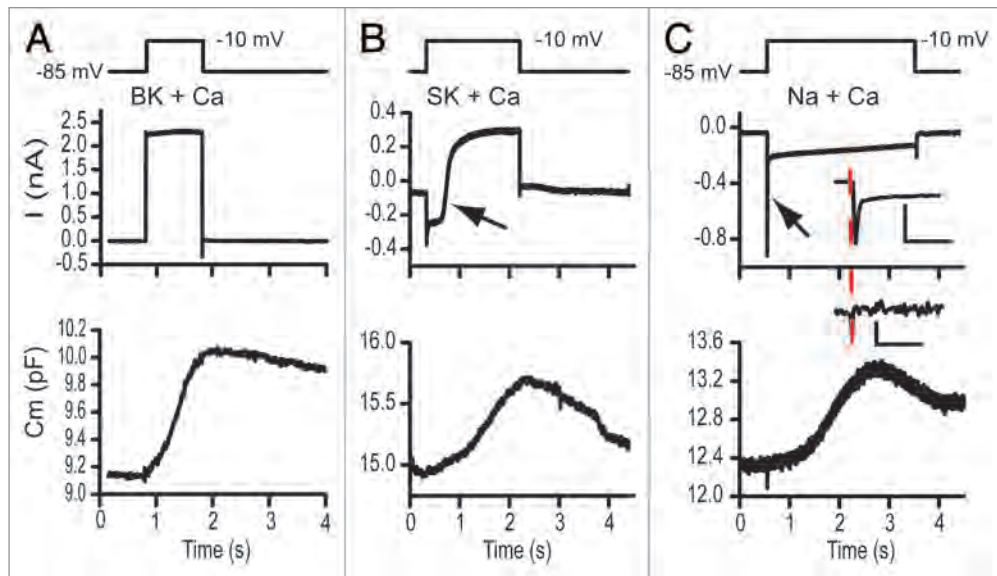


Figure 1. The dual sine wave technology allows for monitoring capacitance concomitantly with the occurrence of voltage or calcium-dependent currents. In each frame the upper panel depicts the stimulus, the middle panel the extracted currents and the lower panels the capacitance measurements. The sine waves are not shown on the stimulus but had frequencies of 6.3 and 9.4 kHz. Stimulus artifacts were digitally removed and data filtered with a Fourier filter to remove high frequency components. Both (A and B) were recordings from turtle hair cells while (C) was from an immature rat hair cell. (A) illustrates capacitance changes measured with a potassium based intracellular solution where the BK calcium activated potassium current activates rapidly in response to a depolarization to -10 mV. (B) Similar records with a cesium based intracellular solution without the presence of apamin externally. The large calcium current activated the SK calcium activated current, indicated by the arrow. SK activation had no effect on capacitance measurements (depolarization to -10 mV). (C) presents capacitance measurements from a postnatal day 8 rat inner hair cell that transiently expressed Na currents. This rapidly activating, rapidly inactivating current, indicated by arrow, also had little effect on the measured capacitance response. The inset expands in time each response with the scale bars reflecting 10 ms and 100 fF and 0.5 nA. The dashed line indicates onset time so that stimulus artifact can be separated from Na current. (A and B) were post filtered, while (C) was not in order to not lose fast components.

In each case rapidly activating L-type calcium channels ($\alpha 1D$) are driving vesicle fusion. The conductance changes do not alter the capacitance measurements.

The high frequency sine wave approach samples capacitance at higher rates than the traditional single sine method. These higher sampling rates allow monitoring of vesicle fusion kinetics at least at the macroscopic level. **Figure 2** depicts release from an auditory hair cell showing a small rapid saturable pool of release, (indicated by the arrow in A) and a larger less saturable pool of recruitable vesicles. Time expansion of (A) reveals the rapid release rise time; release begins immediately at the stimulus onset and continues until saturation. The solid red line is an exponential fit to this small first component of release.

Data using the two sine technology reveals a dynamic equilibrium between vesicles and calcium such that pool sizes are continually in flux between release and recruitment. This dynamic situation makes experiments requiring repetitive stimulation suspect because the baseline

vesicle distribution varies with each stimulation; thus, protocols requiring multiple stimulations may not produce the same response as an individual stimulus. Clearly, this is a major limitation of the single sine technique that provides only single time points for each stimulation, and requires substantial stimulus-response averaging both between and within cells to obtain a time course of release. **Figure 3** provides an example of this problem uncovered with the dual sine technique. A second repetition of the same stimulation results in faster release with an earlier onset to the second release component. Thus, the apparent calcium-dependence of release varies with each voltage pulse, most likely due to reshuffling of vesicle populations (or some biochemical change to the vesicles that makes them more easily released) as dictated by calcium homeostasis.

Data obtained with the dual sine technique provide new insight into how ribbon synapses function. These data also challenge the usefulness of single sine

techniques for understanding the effects of repetitive stimuli. Finally, the ability to measure capacitance in the face of evoked conductances likely will make the dual sine approach useful for the analysis of a variety of model systems.

Acknowledgements

This work was supported by NIDCD RO1 DC009913 to A.J.R. and J.S.S. as well as P30, DC44992.

References

- Zanazzi G, Matthews G. The molecular architecture of ribbon presynaptic terminals. *Mol Neurobiol* 2009; 39:130-48; PMID:19253034; DOI:10.1007/s12035-009-8058-z.
- Schnee ME, Lawton DM, Furness DN, Benke TA, Ricci AJ. Auditory hair cell-afferent fiber synapses are specialized to operate at their best frequencies. *Neuron* 2005; 47:243-54; PMID:16039566; DOI:10.1016/j.neuron.2005.06.004.
- Keen EC, Hudspeth AJ. Transfer characteristics of the hair cell's afferent synapse. *Proc Natl Acad Sci USA* 2006; 103:5537-42; PMID:16567618; DOI:10.1073/pnas.0601103103.
- Li GL, Keen E, Andor-Ardo D, Hudspeth AJ, von Gersdorff H. The unitary event underlying multiquantal EPSCs at a hair cell's ribbon synapse. *J Neurosci* 2009; 29:7558-68; PMID:19515924; DOI:10.1523/JNEUROSCI.0514-09.2009.

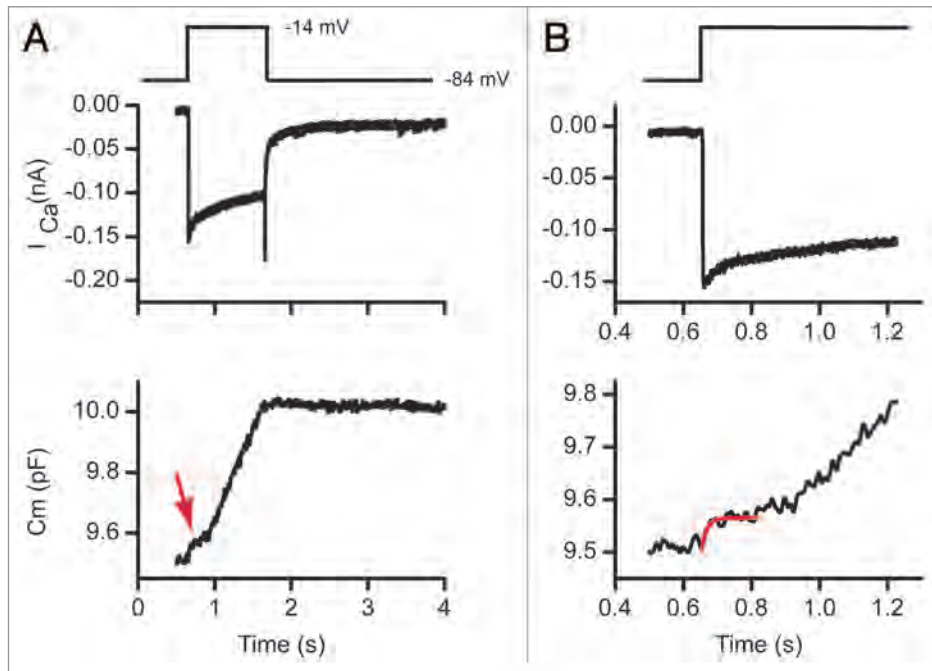


Figure 2. The dual sine wave technique allows for rapid kinetic changes to be monitored. (A) shows a calcium current response and corresponding capacitance change. The capacitance response shows multiple release components. (B) is a time expansion of (A) where the rapid release and then plateau of a small pool of vesicles is observed.

5. Schnee ME, Santos-Sacchi J, Castellano-Munoz M, Kong JH, Ricci AJ. Calcium-dependent synaptic vesicle trafficking underlies indefatigable release at the hair cell afferent fiber synapse. *Neuron* 2011; 70:326-38; PMID:21521617; DOI:10.1016/j.neuron.2011.01.031.
6. Santos-Sacchi J. Determination of cell capacitance using the exact empirical solution of partial differential Y/partial differential Cm and its phase angle. *Biophys J* 2004; 87:714-27; PMID:15240504; DOI:10.1529/biophysj.103.033993.
7. Neher E, Marty A. Discrete changes of cell membrane capacitance observed under conditions of enhanced secretion in bovine adrenal chromaffin cells. *Proc Natl Acad Sci USA* 1982; 79:6712-6; PMID:6959149; DOI:10.1073/pnas.79.21.6712.

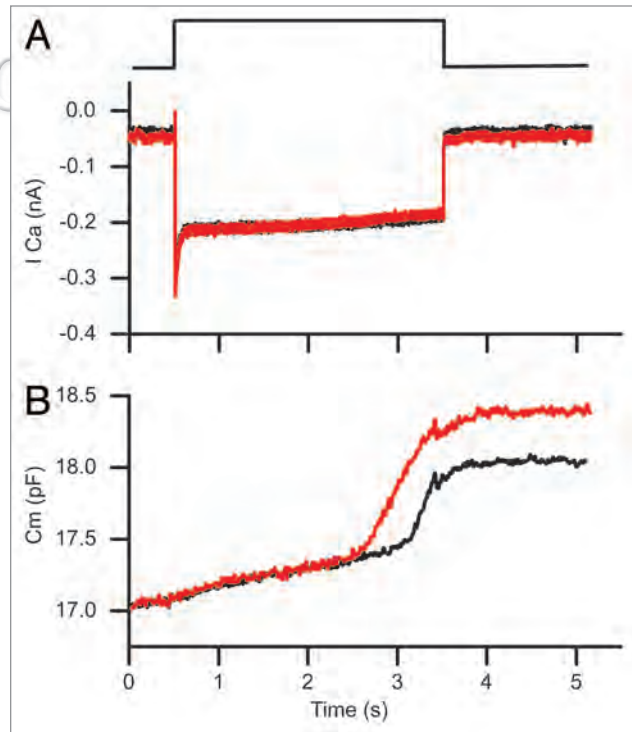


Figure 3. The dual sine technique demonstrates a major flaw with techniques that require repetitive stimulation in that responses are altered by previous stimulations. The black trace was obtained 10 min after breakthrough and is a response to a depolarization to 75% of the peak calcium current. The red trace was obtained 5 min later and shows an increased release with insignificant change in the calcium current. This likely reflects a redistribution of vesicles following the first stimulation. The red trace was offset in the y-axis in order to clearly overlay traces.



Intracellular calcium affects prestin's voltage operating point indirectly via turgor-induced membrane tension

Lei Song and Joseph Santos-Sacchi

Citation: [AIP Conference Proceedings](#) **1703**, 030009 (2015); doi: 10.1063/1.4939324

View online: <http://dx.doi.org/10.1063/1.4939324>

View Table of Contents: <http://scitation.aip.org/content/aip/proceeding/aipcp/1703?ver=pdfcov>

Published by the [AIP Publishing](#)

Articles you may be interested in

[Effect of point and grain boundary defects on the mechanical behavior of monolayer MoS2 under tension via atomistic simulations](#)

J. Appl. Phys. **116**, 013508 (2014); 10.1063/1.4886183

[Basilar Membrane Measurements from Wild Type, Prestin 499, and Prestin KO mice](#)

AIP Conf. Proc. **1403**, 432 (2011); 10.1063/1.3658126

[Understanding anomalous delays in a model of intracellular calcium dynamics](#)

Chaos **20**, 045104 (2010); 10.1063/1.3523264

[Spatiotemporal intracellular calcium dynamics during cardiac alternans](#)

Chaos **19**, 037115 (2009); 10.1063/1.3207835

[Temperature-induced length and tension variations affecting the pitch of a stretched string](#)

J. Acoust. Soc. Am. **66**, S30 (1979); 10.1121/1.2017708

Intracellular Calcium Affects Prestin's Voltage Operating Point Indirectly via Turgor-Induced Membrane Tension

Lei Song* and Joseph Santos-Sacchi^{*,†,**}

*Departments of *Surgery (Otolaryngology), †Cellular and Molecular Physiology, and **Neurobiology
Yale University School of Medicine, New Haven, Connecticut, USA*

Abstract. Recent identification of a calmodulin binding site within prestin's C-terminus indicates that calcium can significantly alter prestin's operating voltage range as gauged by the Boltzmann parameter V_h (Keller et al., J. Neuroscience, 2014). We reasoned that those experiments may have identified the molecular substrate for the protein's tension sensitivity. In an effort to understand how this may happen, we evaluated the effects of turgor pressure on such shifts produced by calcium. We find that the shifts are induced by calcium's ability to reduce turgor pressure during whole cell voltage clamp recording. Clamping turgor pressure to 1kPa, the cell's normal intracellular pressure, completely counters the calcium effect. Furthermore, following unrestrained shifts, collapsing the cells abolishes induced shifts. We conclude that calcium does not work by direct action on prestin's conformational state. The possibility remains that calcium interaction with prestin alters water movements within the cell, possibly via its anion transport function.

INTRODUCTION

Prestin is the protein responsible for OHC electromotility, and forms the molecular basis of mammalian cochlear amplification [4, 13, 23, 26]. The protein is sensitive to a variety of biophysical forces which are capable of shifting its voltage operating range (quantified by the Boltzmann fit parameter, V_h) of the protein. These include initial holding potential [21], intracellular anions [15, 18, 25], temperature [14, 20], and membrane tension [7, 10, 11]. The structural components of prestin responsible for these sensitivities are not known. Recently, Keller et al [12] have shown that structurally disordered elements in the C-terminus of prestin can serve as calmodulin binding sites, and that intracellular calcium can dramatically shift V_h of prestin in the hyperpolarizing direction during wash-in of calcium-containing patch pipette solutions following establishment of whole cell recording. Treatments with trifluoperazine (TFP), a calmodulin inhibitor, or mutations of residues within the calmodulin binding site (R571D, R572D, K573D, R576D, K577D and K580D) abolished the calcium effect. In our hands, those same mutations were shown to shift V_h in the positive direction [2], in line with manipulations that increase membrane tension. Additionally, we had previously shown that negative V_h shifts in NLC occur during wash-in due to reduction of turgor pressure (reduced membrane tension). We wondered if Keller et al. [12] had identified the mechanism of action for membrane tension effects on prestin. To determine if calcium plays this pivotal role we evaluated the effect of turgor pressure using their experimental approach.

METHODS

Isolated OHCs from guinea pigs were whole cell voltage clamped using methodology previously described in detail [22,24]. Briefly, gigohm seals were formed and then ruptured to allow pipette solution wash-in. Wash-in typically takes about 3 minutes [16]. NLC was determined using admittance analysis, with 2 voltage sinusoids at harmonic frequencies superimposed on ramps ranging from -150 to + 100 mV. Detrending of raw currents preceded FFT analysis. Capacitance data were fit to the first derivative of a two-state Boltzmann function [19],

$$C_m = Q_{\max} \frac{ze}{kT} \frac{b}{(1+b)^2} + C_{lin} \quad b = \exp\left(\frac{-ze(V_m - V_h)}{kT}\right) \quad (1)$$

where Q_{\max} is the maximum nonlinear charge moved, V_h is voltage at peak capacitance or equivalently, at half maximum charge transfer, V_m is membrane potential, z is valence, C_{lin} is linear membrane capacitance, e is electron charge, k is Boltzmann's constant, and T is absolute temperature. In addition to determining V_h via voltage ramps

every 30 seconds, V_h was tracked in real time by monitoring the voltage at gating current reversal using the +/-P technique [1], a procedure we previously described in detail [11]. The V_h values determined by either protocol were not statistically different ($p > .05$). Video images were captured during recording to gauge cell swelling.

Solutions were the same as Keller et al. [12]. Intracellular (in mM): 150 CsCl, 2 MgCl₂, 0.1 CaCl₂ (or 10 EGTA), and 10 (or 20) HEPES; extracellular (in mM): 150 NaCl, 2 MgCl₂, 2 CoCl₂, and 10 HEPES. All solutions were adjusted to pH 7.4, and osmolarity to 340 mmol/kg with glucose. Intracellular pressure (i.e., pipette pressure) was either 0 kPa, as per Keller et al. [12], or clamped to 1 kPa. This latter pressure corresponds to normal OHC turgor pressure [17]. TFP (50 μ M), a calmodulin antagonist, was locally perfused in bath solution. Two sided t-tests were used to assess significance.

RESULTS

Figure 1A shows the time course of V_h change following rupture of the OHC patch membrane following seal formation. Initial values of V_h immediately after establishment of whole cell conditions (measured with ramp protocol; *open and filled circles*) quickly shifted to more negative values (about -60 mV, indicated at the onset of successful V_h tracking, *line plot*) regardless of the presence of Ca²⁺. Thereafter, V_h for the Ca²⁺-containing condition shifted over the course of minutes to more negative potentials, whereas in the absence of calcium, a continued depolarizing shift was observed. V_h measures from ramp protocols and tracking paradigm were equivalent (Fig. 1B, C). These changes in V_h are in line with Keller et al. [12].

Figure 2 shows averaged data similarly collected ($n=4-6$ cells), with ΓV_h relative to time after patch rupture shown for comparison. These data confirm that V_h shifts in opposite directions over time depending upon the solution used. Interestingly, we find that in the group lacking Ca²⁺, cells tended to swell during recording. This was not observed in cells recorded with Ca²⁺. Thus, in order to test for turgor pressure effects we measured another calcium group of cells in the presence of a constant 1 kPa pipette pressure. The presence of increased turgor pressure completely countered the calcium effect, showing no statistically significant difference between the V_h values obtained with and without Ca²⁺ (Fig. 2, *down triangles vs. open circles*; p 's > 0.05). Additionally, following V_h tracking for several minutes we collapsed all cells and measured the resulting V_h . No significant differences for all conditions were found compared to the initial V_h values at patch rupture time (Fig. 2, symbols above by *collapsed* label). We conclude that in our experiments turgor pressure changes governed the V_h shifts.

Our results with local perfusion of TFP as per Keller et al. [12] are variable (Fig. 3). In the 2005 MOH meeting proceedings, we published that local perfusion itself can cause rapid (within seconds) shifts in OHC V_h , presumably due to membrane tension effects. Recently, we have further investigated this phenomenon and determined that perfusion-induced shifts are absent following collapse of the OHC. This may impact on our variable results with TFP perfusion, since when cells are deflated TFP has little effect, whereas when cells are inflated there is a depolarizing shift in V_h , which is rapidly reversed upon flow cessation. In addition, we find that even perfusion of normal bath solution will cause a depolarizing shift for the intracellular Ca²⁺ solution condition. Previous studies used prolonged treatments with calmodulin inhibitors such as TFP (>30 min) prior to evaluating effects on cell shape or V_h [5, 6]. In our hands, then, the ability of TFP to work within seconds as a calmodulin inhibitor during acute perfusion is unresolved.

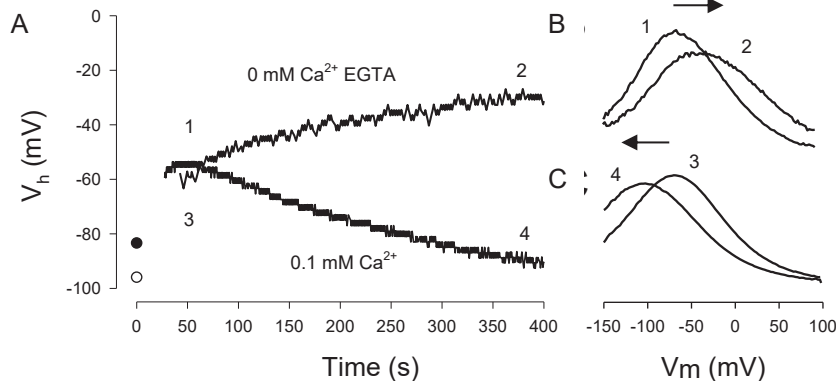


FIGURE 1. NLC V_h tracked in real time during wash-in of indicated solution. (A) Since V_h -tracking takes time to initially find V_h , we also measured NLC with ramps. Symbols indicate V_h immediately after patch rupture (*filled circle*: 0.1 mM Ca²⁺; *open circle*: no Ca²⁺). Numbers 1- 4 also indicate ramp-measured V_h at select times. C_m - V_m functions from those measures are plotted in (B) and (C) (no averaging).

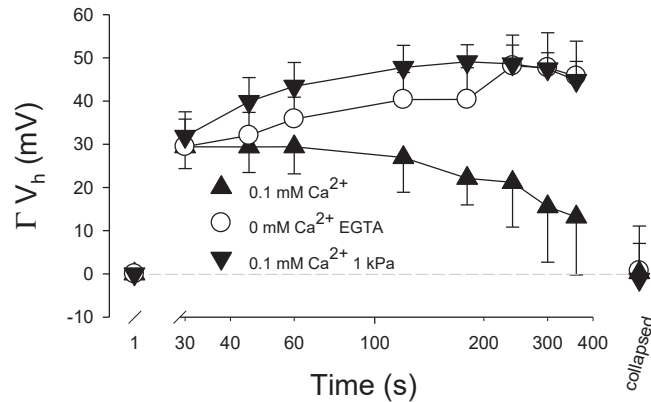


FIGURE 2. Averaged measures of V_h shift. Calcium-induced negative shifts in V_h are absent in the presence of positive intracellular turgor pressure. After recording for several minutes, cells were collapsed with negative pipette pressure, and V_h values for all conditions returned to levels observed at patch rupture.

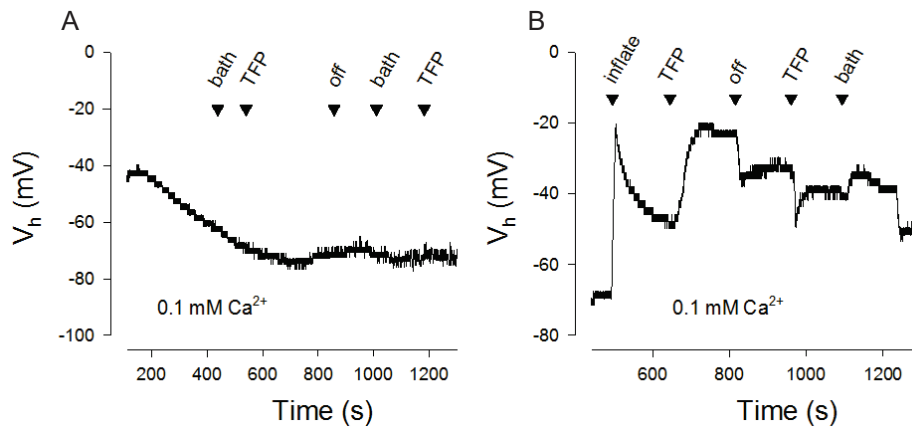


FIGURE 3. Effects of TFP perfusion on V_h shift. Calcium-induced negative shifts were obtained in OHCs and the effects of TFP perfusion and bath perfusion assessed. (A) Deflated cells show no response to perfusions. (B) In another cell, after inflation via positive pipette pressure positive shifts were observed.

DISCUSSION

Here we show that shifts of OHC V_h induced by intracellular solutions in the presence or absence of Ca^{2+} result from alterations in membrane tension caused by changes in turgor pressure. In the absence of Ca^{2+} , cells tend to swell, but in its presence cells do not swell. The OHC is highly sensitive to osmotic influences [3], likely influenced by membrane bound ion transport mechanisms. The shape is normally maintained by a cortical cytoskeleton [8], but cells may swell or collapse during whole cell recording, altering V_h due to prestin's membrane tension sensitivity [11]. Because of this we and others typically evaluate direct effects on prestin by collapsing OHCs to remove these effects.

The action of Ca^{2+} on OHC shape and NLC have been previously evaluated. Dulon et al. [5] used the Ca^{2+} ionophores ionomycin and A23187 to show that increases in intracellular Ca^{2+} induce cell volume decreases by up to 5%. This is in line with our observations. The calmodulin inhibitor TFP was able to block this effect, without altering the induced changes in intracellular Ca^{2+} . Frolenkov et al [6] also used ionophores or ACh to increase intracellular Ca^{2+} ; however, whereas turgor reductions similar to those observed by Dulon et al. [5] were observed, simultaneous measures of NLC showed virtually no changes in V_h . This may not be unusual, since depending on initial V_h , turgor pressure reductions can have a limited effect on V_h shift [11]. Both studies concluded that calcium

can work on cytoskeletal elements via a calmodulin dependent pathway. Interestingly, Frolenkov et al. [6] did determine that agents which alter phosphorylation state can shift V_h in the absence of turgor pressure changes.

How can our results be reconciled with the Ca^{2+} /calmodulin hypothesis of Keller et al. [12]? First, species differences may exist. For example, salicylate sensitivity of mouse prestin is nearly an order of magnitude greater in mouse than guinea pig [9, 22]. Second, Ca^{2+} may be working on cellular mechanisms that influence the generation of water movements, thus turgor changes, in cells. Perhaps even prestin's anion transport function is directly calmodulin dependent, controlling ion fluxes that influence membrane stress that is fed back to prestin's tension sensor. In this scenario, calmodulin inhibitors or mutations of prestin that abrogate calmodulin binding [2, 12] may disrupt the cell's ability to maintain turgor pressure, and thus provide self-control to motor function.

ACKNOWLEDGMENTS

Supported by NIH NIDCD R01 DC000273 to JSS.

REFERENCES

- [1] Armstrong CM, Bezanilla F (1973) Currents related to movement of the gating particles of the sodium channels. *Nature* 242:459–461
- [2] Bai JP, Navaratnam D, Samaranayake H, Santos-Sacchi J (2006) En block C-terminal charge cluster reversals in prestin (SLC26A5): effects on voltage-dependent electromechanical activity. *Neurosci Lett* 404:270–275
- [3] Chertoff ME, Brownell WE (1994) Characterization of cochlear outer hair cell turgor. *Am J Physiol* 266:C467–C479
- [4] Dallos P, Wu X, Cheatham MA, Gao J, Zheng J, Anderson CT, Jia S, Wang X, Cheng WH, Sengupta S, He DZ, Zuo J (2008) Prestin-based outer hair cell motility is necessary for mammalian cochlear amplification. *Neuron* 58:333–339
- [5] Dulon D, Zajic G, Schacht J (1990) Increasing intracellular free calcium induces circumferential contractions in isolated cochlear outer hair cells. *J Neurosci* 10:1388–1397
- [6] Frolenkov GI, Mammano F, Belyantseva IA, Coling D, Kachar B (2000) Two distinct Ca^{2+} -dependent signaling pathways regulate the motor output of cochlear outer hair cells. *J Neurosci* 20:5940–5948
- [7] Gale JE, Ashmore JF (1994) Charge displacement induced by rapid stretch in the basolateral membrane of the guinea-pig outer hair cell. *Proc R Soc Lond B Biol Sci* 255:243–249
- [8] Holley MC, Ashmore JF (1988) A cytoskeletal spring in cochlear outer hair cells. *Nature* 335:635–637
- [9] Homma K, Dallos P (2011) Evidence that prestin has at least two voltage-dependent steps. *J Biol Chem* 286:2297–2307
- [10] Iwasa KH (1993) Effect of stress on the membrane capacitance of the auditory outer hair cell. *Biophys J* 65:492–498
- [11] Kakehata S, Santos-Sacchi J (1995) Membrane tension directly shifts voltage dependence of outer hair cell motility and associated gating charge. *Biophys J* 68:2190–2197
- [12] Keller JP, Homma K, Duan C, Zheng J, Cheatham MA, Dallos P (2014) Functional regulation of the SLC26-family protein prestin by calcium/calmodulin. *J Neurosci* 34:1325–1332
- [13] Liberman MC, Gao J, He DZ, Wu X, Jia S, Zuo J (2002) Prestin is required for electromotility of the outer hair cell and for the cochlear amplifier. *Nature* 419:300–304
- [14] Okunade O, Santos-Sacchi J (2013) IR laser-induced perturbations of the voltage-dependent solute carrier protein SLC26a5. *Biophys J* 105:1822–1828
- [15] Oliver D, He DZ, Klocker N, Ludwig J, Schulte U, Waldegger S, Ruppertsberg JP, Dallos P, Fakler B (2001) Intracellular anions as the voltage sensor of prestin, the outer hair cell motor protein. *Science* 292:2340–2343
- [16] Pusch M, Neher E (1988) Rates of diffusional exchange between small cells and a measuring patch pipette. *Pflugers Arch* 411:204–211
- [17] Ratnanather J, Brownell W, Popel A (1993) Mechanical properties of the outer hair cell. In: Duifhuis H, Horst JW, van Dijk P, van Netten SM (eds) *Biophysics of Hair Cell Sensory Systems*. Singapore: World Scientific, pp. 199–206
- [18] Rybalchenko V, Santos-Sacchi J (2003) Cl^- flux through a non-selective, stretch-sensitive conductance influences the outer hair cell motor of the guinea-pig. *J Physiol* 547:873–891
- [19] Santos-Sacchi J (1991) Reversible inhibition of voltage-dependent outer hair cell motility and capacitance. *J Neurosci* 11:3096–3110
- [20] Santos-Sacchi J, Huang G (1998) Temperature dependence of outer hair cell nonlinear capacitance. *Hear Res* 116:99–106
- [21] Santos-Sacchi J, Kakehata S, Takahashi S (1998) Effects of membrane potential on the voltage dependence of motility-related charge in outer hair cells of the guinea-pig. *J Physiol* 510:225–235
- [22] Santos-Sacchi J, Song L (2014) Chloride and salicylate influence prestin-dependent specific membrane capacitance: support for the area motor model. *J Biol Chem* 289:10823–10830
- [23] Santos-Sacchi J, Song L, Zheng J, Nuttall AL (2006) Control of mammalian cochlear amplification by chloride anions. *J Neurosci* 26:3992–3998
- [24] Song L, Santos-Sacchi J (2013) Disparities in voltage-sensor charge and electromotility imply slow chloride-driven state transitions in the solute carrier SLC26a5. *Proc Natl Acad Sci USA* 110:3883–3888

- [25] Song L, Seeger A, Santos-Sacchi J (2005) On membrane motor activity and chloride flux in the outer hair cell: lessons learned from the environmental toxin tributyltin. *Biophys J* 88:2350–2362
- [26] Zheng J, Shen W, He DZ, Long KB, Madison LD, Dallos P (2000) Prestin is the motor protein of cochlear outer hair cells. *Nature* 405:149–155

COMMENTS AND DISCUSSION

Paul Teal: The argument is mostly convincing.

In the discussion, Frolenkov et al. are cited as finding that increased Ca^{2+} caused turgor reductions similar to those observed by Dulon et al, but simultaneous measures of NLC showed virtually no changes in V_h . Even though there is discussion on possible reconciliation with Keller et al., there is none on reconciliation with this result which seems to be just as significant. Or have I misunderstood? Some clarification might help here.

No doubt displaying my ignorance here but when the pipette pressure in one of the experiments (as per Keller et al) is 0 kPa, how is the solution actually introduced?

Joseph Santos-Sacchi [reply to Paul Teal]: Thanks, Paul.

Positive turgor pressure introduced by pipette pressure changes V_h in the depolarizing direction and shifts will continue until the cell bursts – membranes can only withstand about 5-7% stretch. The effect of negative pressure depends on the initial turgor level. When a cell still appears cylindrical at low pressure, because the cortical cytoskeleton maintains a cylindrical state, it may be possible to reduce pressure and cause cell collapse. We previously showed that there is a limiting hyperpolarizing shift when the cell approaches collapse. Thus, during recording, a negative pressure could produce small to no changes in V_h . I assume that the membrane at that point is lax. Our simple observation in our new MOH paper is that the solutions used with 0 Ca cause increased turgor pressure (thus membrane tension) and positive shifts, which dissipate when the cell is collapsed with all solutions tested.

Pipette pressure, which could cause bulk flow of pipette fluid into the cell, is not necessary to exchange ionic solutes. Indeed, with perforated patch recording (depending on ionophore species used), ionic replacement of cell constituents with that of the pipette is possible. Clearly, pipette pressure cannot be changed during that process else the perforated patch would burst, putting the cell into standard whole cell voltage clamp mode.

Thanks, again.

Andrew Bell: Hello Lei and Joseph:

You have shown that OHCs are very sensitive to changes in osmotic pressure, a result supported by Chertoff & Brownell (your ref. 2). This seems to imply that OHCs are also capable of responding to changes in hydraulic pressure of the cochlear fluids. By extension, this raises the possibility that small changes in intracochlear pressure – due to sound pressure – could also alter the electrical potential of the cell. The implication is that OHCs might react directly to a sound stimulus (Bell 2003) and bending of the stereocilia is not the only possible effective stimulus. Do you consider such a complementary mechanism possible?

Bell, A. (2003). Are outer hair cells pressure sensors? Basis of a SAW model of the cochlear amplifier. In *Biophysics of the Cochlea from Molecules to Models* (ed. A.W. Gummer), pp.429-431.

Joseph Santos-Sacchi [reply to Andrew Bell]: Hi Andrew, thanks. Yes, I agree and we have published on this in abstract and manuscript form (Rybalchenko and Santos-Sacchi 2003 *JPhysiol*). Subsequent papers from our lab also refer to this possibility. The susceptibility to in vivo tensions stems not only from the tension sensitivity of the motor, but also to the tension sensitivity of GmelL, a lateral membrane conductance that permits chloride flux. — Joe

A Walkthrough of Nonlinear Capacitance Measurement of Outer Hair Cells

Lei Song and Joseph Santos-Sacchi

Abstract

Nonlinear capacitance (NLC) measures are often used as surrogate measures of outer hair cell (OHC) electromotility (eM), since the two are commonly thought to share many biophysical features. The measurement of NLC is simpler than direct measurements of eM and, therefore, many investigators have adopted it. A standard patch-clamp hardware configuration is sufficient for recording NLC, given the proper software interface. Thus, the approach is cost effective. We use the software jClamp since it is tailored to capacitance measurement. Here we detail steps that we use to measure NLC. The walk through includes isolation of guinea pig OHCs, building voltage commands, recording, and analysis.

Key words Nonlinear capacitance, Outer hair cells, Electromotility, Prestin, Cochlea, Inner ear

1 Introduction

The OHC lateral membrane protein prestin [1] powers electromotility [2–5], key to mammalian cochlear amplification [6]. Direct measurement of OHC motility requires a number of additional techniques (such as microchamber [7–9] or equipment (such as fast camera [10] or photodiode [7, 8, 11] which are not standard additions to the usual patch clamp [12] setup. For the investigation of prestin function in nonnative cells [13–15], although electromotility measurement is possible, a micro chamber is required to deform the cell [1] and the magnitude of motility is an order of magnitude smaller than that of the native OHC [1, 13–15]. NLC, a surrogate measure of motility, is the electrical signature of prestin activity. NLC can substitute for measures of motility, and can be carried out on a typical patch-clamp setup without additional equipment. The advantage of NLC is more evident in the assessment of prestin function in transfected cell lines which often express much less prestin, but requires relatively fast measures to acquire large number of cells for statistics [13, 14, 16].

Conventional methods for measuring cell capacitance use step-induced transient analysis (charge integration) or the use of a lock-in amplifier to interrogate phase responses to sine wave stimuli [17–19]. Using a phase detector, the phase tracking method follows the current changes attributed to capacitance changes. Limitations include having low and stable membrane conductance, and these measures are subject to influence of fast (stray) capacitance between pipette and bath solution [18, 20]. We use two-sine method where the additional set of recorded parameters from the second sine is used to solve capacitance which is more resistive to fast conductance change. Data analysis can alternatively be performed on one of the recorded sine wave currents if desired so it offers flexibility in data analysis.

Here we introduce the measurement of NLC of OHCs, a procedure that circumvents the mechanical measurement of OHCs. An example of using two types of stimuli (dual-sine and transient step perturbations atop a voltage ramp) on the same OHC is shown (Fig. 1) where a stair-step stimulus we previously used to detect OHC capacitance [9] and a two-sine stimulus are each applied to

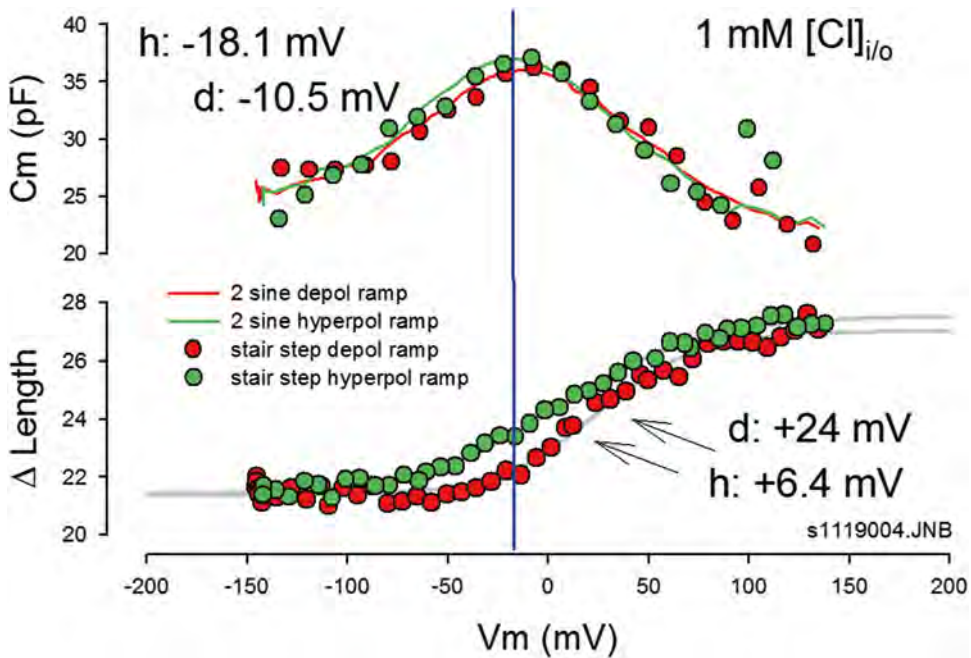


Fig. 1 Example traces of NLC collected from same OHC by using a stair step stimulus (*upper panel, circle*) and 2-sine (*upper panel, solid lines*). Stimulus of either depolarization or hyperpolarization ramp are color coded. In general the two stimulus methods generate NLC curves that are overlapping, except the curves that were generated by using 2-sine are less “noisier” than those acquired by step stimulus. *Bottom panel* shows simultaneous measurement of motility. *Blue line* is the voltage at peak capacitance for a hyperpolarized ramp. A depolarized shift of V_h in motility measurement is marked for each depolarized and hyperpolarized stimulus

the same whole-cell patched OHC. Two-sine analysis is less noisy than that acquired by stair-step stimuli (upper panel, Fig. 1), although mechanical measurement obtained by each ramp stimulus almost overlap (lower panel, Fig. 1). We focus on measuring NLC in OHCs by using the two-sine method. We routinely use the software jClamp (jClamp, www.scisoft.com) in our daily data collection so our introduction is unavoidably based on the operation of that software. However, the basic steps can be replicated by a skilled physiologist/programmer by referring to original publications [21, 22].

We introduce the basic steps for acquiring NLC so a trained electrophysiologist who is familiar with patch clamping can start the measurement with minimal modifications such as the addition of software. Major procedures include isolating OHCs, preparation of the experiment solutions, building stimulus command, and recordings. Some notes are provided to offer tips to acquire high quality data.

2 Materials

2.1 Patch-Clamp Hardware and Software

1. PC running on windows (XP, Vista, Win 7, and Win 8).
2. Pipette puller (Sutter P-2000 or similar) and soft glass thin wall pipette (WPI, Sarasota, FL).
3. Amplifier (Axon 200 series or 700 series) and headstage.
4. D/A converter: Axon 13xx, 14xx series (Molecular Devices, Sunnyvale, CA), National Instrument Austin, TX) or IO Tech (Measurement Computing Corp, Norton, MA).
5. A Windows compatible camera is optional for measuring NLC and electromotility simultaneously, but is also helpful in monitoring OHC conditions.
6. Software: jClamp (*see Note 1*).

2.2 Solutions

All solutions are made in deionized water.

1. Ionic blocking extracellular solutions (mM): Mix 92 NaCl, 20 TEACl, 20 CsCl, 1 CaCl₂, 2 CoCl₂, 1 MgCl₂, 10 HEPES, in 950 mL of H₂O. Use 1–2 M NaOH to adjust pH 7.2–7.4, then top off to 1 L. Use D-Glucose to increase osmolality of solution to ~300 mOsm (*see Note 2*). Store at 4 °C.
2. Intracellular pipette solution (mM): 136 CsCl, 2 MgCl₂, 10 HEPES, 10 EGTA, start from a smaller volume such as 180 mL. Use 1–2 M CsOH to adjust pH 7.2–7.4 as in Subheading 2.2, **step 1**. Then top off to 200 mL (you can make smaller volume based on your consumption of pipette solution). Use D-glucose to adjust osmolality to ~300 mOsm.

Be sure to keep intracellular and extracellular solution to within 2 mOsm. When making “physiological” intracellular chloride concentration, gluconate is used as an anion substitute for chloride (*see Note 3*). Store at 4 °C.

3. Filter all solutions with a 0.22 µm filter after the solution is made.
4. (Dispase I, 10 U/mL, Roche).

2.3 Equipment

1. pH meter (e.g., Corning pH meter 430 or similar).
2. Dissecting tools: Scissor (assorted sizes), hemostat, Malleus Bone Nipper, No. 3, No. 5 and fine forceps.

3 Methods

3.1 Isolating Guinea Pig Outer Hair Cells

All animal protocols should be approved by the institutional animal care and use committee according to NIH guidelines.

1. Euthanize animals with isoflurane overdose.
2. Dissect and isolate temporal bones and place in a petri dish filled with 1x PBS.
3. Refrigerate unused second cochlea at 0–4 °C for later use (up to 4 h).
4. Open bulla with a Malleus Bone Nipper, to expose cochlea and remove ossicles with No. 3 forceps.
5. Press and crack the apical part of the cochlea using blunted or No. 3 forceps. Lift the cracked bone to create an opening.
6. Carefully tuck between the bone and spiral ligament and press toward the bone (outward) using the blunted forceps tip or No. 3 forceps. Cracked bone chips will then be lifted away. Start from the opening and work down toward the base to expose the whole Organ of Corti.
7. Carefully strip off Organ of Corti (*see Note 4*).
8. Place stripped Organ of Corti in either extracellular solution or PBS with Dispase (5 U/mL).
9. Incubate for 10–12 min at room temperature, then transfer the organ of Corti strip to the recording chamber with a few drops of extracellular solution.
10. Gently triturate the Organ of Corti strip using a flame thinned pipette tip (200-µL pipette tip) mounted on a 1 cc syringe (*see Note 5*).
11. Leave the suspension solution in the recording chamber for about 15–20 min for cells to sink and stick to the glass bottom.
12. Fill the dish with extracellular solution and start recording (*see Note 6*).

3.2 Preparing for Whole-Cell Patch Clamping of Outer Hair Cells

1. Prepare a recording pipette with a resistance of 4–6 M Ω . We typically use thin-walled electrodes (TW150-4 from WPI, Sarasota, FL) (*see Note 7*).
2. Use standard whole-cell patch-clamp technique to form a G Ω seal and then rupture membrane to form a whole-cell configuration. OHC membrane tension (evidenced by changes in cell turgor) should be monitored during pipette washout. This is a crucial step to avoid artifacts since NLC is sensitive to turgor pressure-induced membrane tension [23–27] (*see Note 8*).

3.3 Recording Nonlinear Capacitance

1. Prior to building a command file, make sure the system calibration file is correct (*see Note 9*). Always use an electrical cell model to verify that the measurement system is working properly.
2. Build command file in jClamp within the command building utility. We routinely apply two-sine stimulus [21, 22] superimposed onto a voltage ramp. For construction of command, see help file in jClamp (*see Note 10*).
3. Save command file in the quick access RPD (Rapid Parameter Directory) window to allow quick activation of commands during online recording. Once activated, a command window will pop up and stimulus parameters can be modified online.
4. Use “init” button in the command utility window (or the RPD buttons) to start recording (*see Note 11*). Changes of the command are not saved automatically unless the save button is clicked. Nevertheless, each data file possesses the command protocol for reconstruction.
5. Select Cm vs. Vm in Results window. The data will be displayed as NLC curves online following each data collection. Each stimulus condition can be repeated until stabilization of NLC is reached, usually when intracellular pipette solution exchange is accomplished.

3.4 Data Analysis

1. Open Analysis window then select data file by using open folder icon to load raw data.
2. Select part(ition) 3 by clicking “Sel” for the two-sine ramp collection we typically use (Fig. 2). Only part 3 of the command (ramp) is selected and displayed.
3. Select Y axis: Cm in the drop down window and X axis: Voltage to plot NLC curve.
4. Check “Rs” for series resistance correction.
5. Check “DtR” for detrending of data prior to FFTing (optional, *see Note 12*).
6. Fit NLC curve by select fitting icon and move cursor by left clicking and holding.

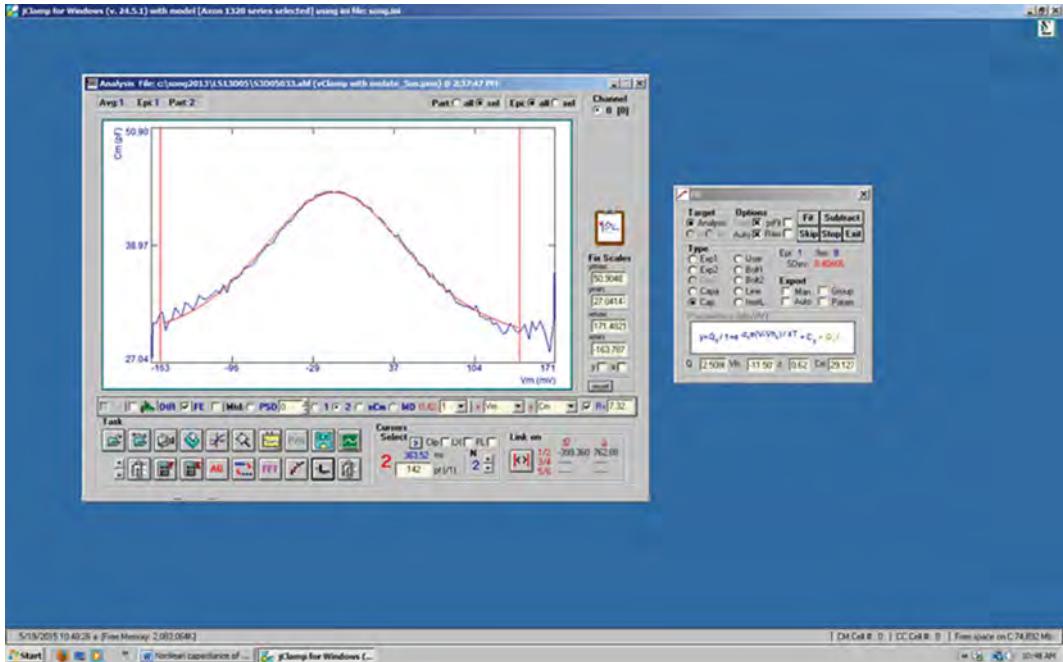


Fig. 2 Screenshot of data analysis window. Red lines/cursors highlight the voltage range fitted. Activate the cursor by clicking the fitting icon on the bottom row of buttons, 7th from the left. Then click each cursor and drag to the proper place. Before fitting, remember to check R_s so the series resistance is corrected. Right window pops up when selecting curve fitting icon. Select Cap and click “fit” button. Fitting parameters are shown in the bottom windows. You can export those fitting parameters by selecting “Param” in “Export” panel (see jClamp help files for more detailed explanations)

7. Select the range for fitting and in the pop up window, select “CAP” fit. Parameters shown in the windows are Q_{max} (total charge moved), V_h (voltage at peak capacitance), z (valence), and C_{in} (linear capacitance) (Fig. 2).
8. Export fitted parameters. Select “Param” and then click “Fit” button. Select “Auto” will include fitted curve in the export file so traces can be used in other plotting software, such as SigmaPlot.
9. Plot NLC curve in supported extremal software. Left click on the software icon and drag to the data analysis window and release. Refer to Help file in jClamp for detailed instructions (see **Note 13**).

4 Notes

1. Although other common software used for patch clamping can also measure NLC, the analyses were very often carried out in a separate program post hoc [28–31]. Our in house developed

software jClamp (distributed through Scisoft, Ridgefield, CT) is by far the easiest software to measure and analyze linear/nonlinear capacitance. The online display of NLC and a number of data analysis features offer handy functions when tracking voltage shifts of NLC. Once an investigator becomes familiar with the program, the data acquisition and analysis are routine.

2. When possible, ionic blocking solutions are used to eliminate current that may interfere with NLC measurements. When “physiological” solutions are needed for your investigation, check the current (by selecting in the analysis window “Vm vs. Im”). If a nonlinear current is present at the voltage where NLC is present, you need to take precaution when interpreting your data, because nonlinear currents can interfere with NLC assessment.
3. Intracellular chloride is the key anion that modulates prestin’s function [32]. When an experiment requires reduction of intracellular chloride, substitute anions often shift NLC curve toward different directions along the voltage axis [32–35]. Errors in fitting for parameters occur if the NLC is moved out of the stimulus voltage range [33, 34]. In general, gluconate substitution maintains NLC curves within the voltage range of the amplifier so that both ends of the curve reach a steady state. Fitting is more reliable under those conditions. When another anion substitution is required, adjust voltage range of stimulation accordingly within the limit of amplifier so that the NLC curve is clearly within the voltage range. Remember, you cannot fit a NLC curve where the peak is not clearly resident, with substantial capacitance measures on either side.
4. Use a forceps to press from under the coiled organ of Corti to break the bone from the modiolus. Start from apex then work down toward base. An alternative is to separate the organ of Corti from the apex and use fine forceps to hold the broken end, while carefully pulling along the spiral of the modiolus.
5. The 200- μ L pipette tips are flame heated in the middle of the taper then pulled to thin the wall. Then trim the base of pipette tip to fit a 1 cc syringe and cut the thinned tube so the opening is just large enough to suck in the strip of the organ of Corti. Metal needles or glass pipettes are not appropriate, as cells tend to adhere to the surface of glass and metal.
6. Fill extracellular (bath) solution gently so OHCs, which adhere to the bottom of the dish, will not float away. An alternative is to use a large opening patch pipette to move an individual OHC settled at the bottom of the dish to the recording chamber.

7. Typical pipette resistances in 140 mM Cl solution are around 4 M Ω . When the gluconate substitute is used, the resistance is raised to 5–6 M Ω in 5 mM Cl pipette solution.
8. Membrane tension: Outer hair cell membrane tension is a strong modulator of NLC [10, 24, 25, 27]. Increased membrane tension (e.g., caused by turgor pressure) can shift NLC curve over 50 mV [10, 25, 26]. Such a shift in V_h may create errors in data interpretation; we strongly recommend investigators to control turgor pressure in OHC recordings during NLC and motility measurements. Tension changes can occur due to a variety of reasons including imbalanced osmolality between intracellular and extracellular solution, higher intracellular chloride levels [36] or influx of chloride [35] or other ions, plugged pipette, and positive pressure clamped to the pipette [10, 24, 26]. Therefore, either controlling or close monitoring of membrane tension is important to obtain unbiased data. We routinely adopt two approaches to reduce artifacts derived from membrane tension changes: (1) to monitor cell turgor/length change with a video camera [36], and (2) to collapse the cell by suctioning the pipette. If turgor tension is not the focus of study, collapsing cells is the best approach to eliminate the problem. When membrane tension is part of the study or a “natural” condition is desired especially in motility measurement, collapse the cell at the end to acquire recordings as a control condition. Capturing images and making measurements of cell length change also gives helpful indications of turgor changes and is highly recommended when a video camera is available.
9. Calibration should be done prior to the experiment and needs to be repeated after some time period, or whenever the system changes—new sampling clock, different filter setting on the amplifier, change in amplifier gain, etc. If the calibration is wrong then the data are WRONG! On the headstage, remove the pipette holder. Insert a 10 M Ω resistor and connect to the ground. Run the calibration according to the menu instruction. This is a step easily ignored by investigators. Do not use wrong calibration files! File names should be saved to contain time and amplifier filter frequency and clock information so that earlier calibration files are all identifiable. Calibrations are saved with data files.
10. Building command file: A command file is built in the Command Utility interface prior to the experiment and a shortcut can be used. Move cursor to the left of screen and point to the command utility icon (6th from the top) and open the panel (shown on the right). Load command protocols by clicking folder icon in Command Utility window and select from the command file folder. If a command is used frequently,

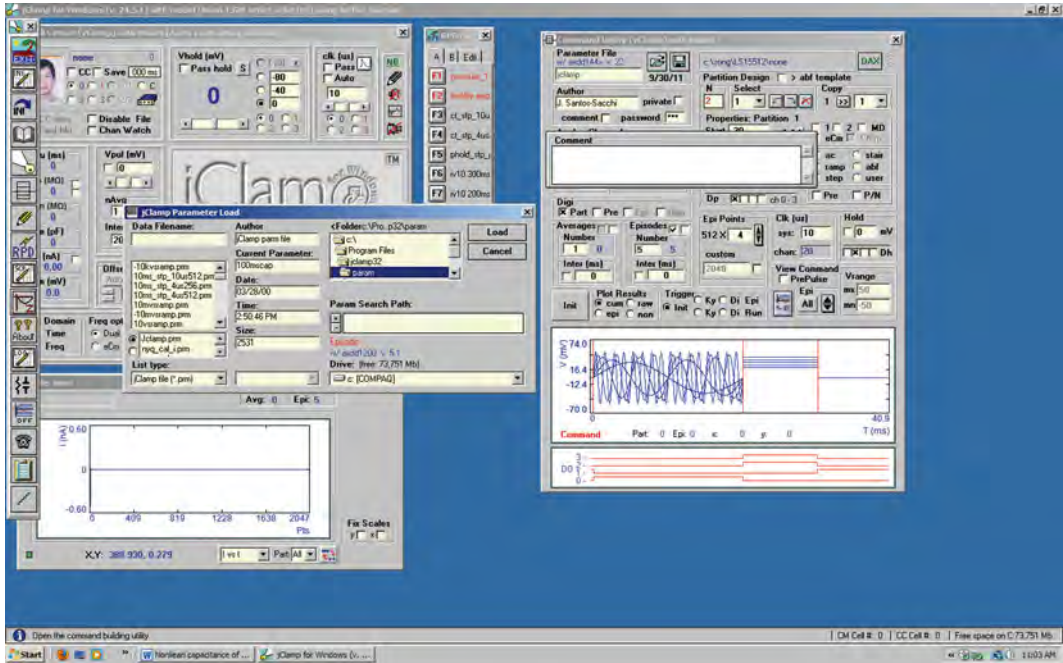


Fig. 3 Screenshot of command building window. Left column is activated by moving cursor to the left. Then select 6th icon from the list to activate command utility window. Click open folder icon to select command file to work on. Command files are saved in “Param” subfolder in jClamp folder

you may save it in the “RPD” window (Shown in small panel with quick access keys, (Fig. 3) to enable quick access. A typical dual-sine ramp command is shown below in command utility window. We use four sections to define the command. The sections 1 and 4 have matching holding potentials. Partition 2 defines the beginning of ramp voltage. Partition 3 is the ramp where the start voltage is at the end of the ramp (-200 mV in the screenshot). Command Cm window needs to be selected and typical resolution is 2.56 ms if two-sine [22, 33] is to be superimposed onto the ramp (Fig. 4).

11. Quick access key (RPD) is the fast approach to activate a saved command file frequently used. We use it only at the beginning of the recording series. Upon activation of a command, the command utility window and Result Window data display will both pop up. Change the data display to V_m vs. C_m in drop down window so the NLC is displayed online. If the command needs repeated, use “init” key to activate the command during the continuous recording of the cell. The advantage of doing so is the ability to keep all the prior NLC curves on the data display window so you can track the changes of NLC online. This is particularly useful in determining the completion of cell dialysis [35] and tracking whether the cell has reached steady

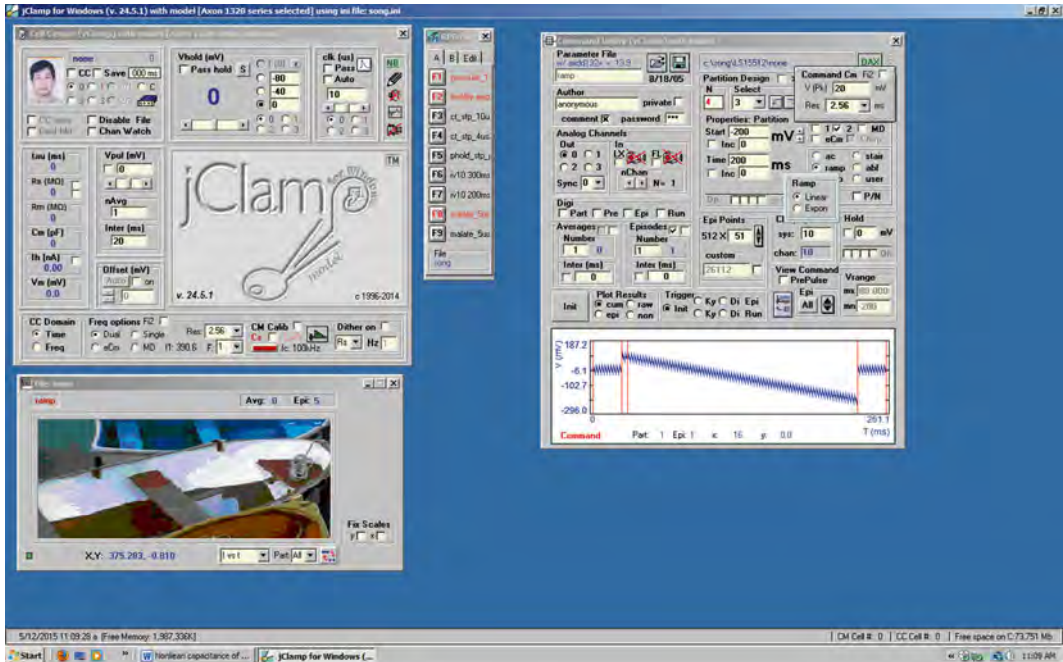


Fig. 4 Screenshot of window when building a ramp command with superimposed two-sine. First check “ramp.” Then move cursor to 2 (two-sine). “Command Cm” box will pop up when box of “2” is checked. Typical two-sine resolution is 2.56 ms and two-sine voltage is 10–20 mV (shown in the figure). Each section has to have 2-sine enabled. Start voltage of the ramp is +80 mV in partition 2 and –200 mV in partition 3. Typical ramp duration is 200–300 ms

state upon various manipulations (perfusion of extracellular solution containing drugs, change holding potential, change membrane tension, etc.). We routinely record NLC online until a few overlapping NLC traces appear before advancing to the next manipulation in the experiment. This is essential in acquiring high quality data.

12. Detrending is a method to properly prepare the data prior to FFT analysis and extraction of NLC. Detrending removes slow changes in the current response but leaves behind clear dual-sine currents, which possess the capacitance information. For example, without detrending, a fast ramp or sine wave superimposed with a two-sine stimulus will erroneously result in NLC peaks larger than slower ramp or sine stimuli. Detrending uses a small scale “piece-wise linear” approach to remove the trend generated by the underlying ramp or sinusoid stimulus. Users may choose to enable “detrending” if the underlying stimulus rate is fast and a small noise increase is not crucial.
13. jClamp can be linked to other data analysis or plotting software such as Excel, SigmaPlot, Matlab, and Origin. You need to

select in the ini file to link the software (*see* jClamp help files for detailed steps). The linked software will appear on the upper right corner in jClamp analysis window (the SigmaPlot icon in the screenshot, (Fig. 2). To export the plot, simply left click and drag the software icon to the NLC curve analysis window and release. A generic plot will automatically be generated in the selected software.

References

- Zheng J, Shen W, He DZ, Long KB, Madison LD, Dallos P (2000) Prestin is the motor protein of cochlear outer hair cells. *Nature* 405:49–155
- Brownell WE, Bader CR, Bertrand D, de Ribaupierre Y (1985) Evoked mechanical responses of isolated cochlear outer hair cells. *Science* 227:194–196
- Ashmore JF (1987) A fast motile response in guinea-pig outer hair cells: the cellular basis of the cochlear amplifier. *J Physiol* 388:323–347
- Santos-Sacchi J, Dilger JP (1988) Whole cell currents and mechanical responses of isolated outer hair cells. *Hear Res* 35:143–150
- Iwasa KH, Kachar B (1989) Fast in vitro movement of outer hair cells in an external electric field: effect of digitonin, a membrane permeabilizing agent. *Hear Res* 40:247–254
- Ashmore J, Avan P, Brownell WE et al (2010) The remarkable cochlear amplifier. *Hear Res* 266:1–17
- Dallos P, Evans BN, Hallworth R (1991) Nature of the motor element in electrokinetic shape changes of cochlear outer hair cells. *Nature* 350:155–157
- He DZ, Evans BN, Dallos P (1994) First appearance and development of electromotility in neonatal gerbil outer hair cells. *Hear Res* 78:77–90
- Huang G, Santos-Sacchi J (1993) Mapping the distribution of the outer hair cell motility voltage sensor by electrical amputation. *Biophys J* 65:2228–2236
- Song L, Santos-Sacchi J (2013) Disparities in voltage-sensor charge and electromotility imply slow chloride-driven state transitions in the solute carrier SLC26a5. *Proc Natl Acad Sci U S A* 110:3883–3888
- Santos-Sacchi J, Song L (2014) Chloride-driven electromechanical phase lags at acoustic frequencies are generated by SLC26a5, the outer hair cell motor protein. *Biophys J* 107:126–133
- Hamill OP, Marty A, Neher E, Sakmann B, Sigworth FJ (1981) Improved patch-clamp techniques for high-resolution current recording from cells and cell-free membrane patches. *Pflugers Archiv* 391:85–100
- Bai JP, Navaratnam D, Samaranayake H, Santos-Sacchi J (2006) En block C-terminal charge cluster reversals in prestin (SLC26A5): effects on voltage-dependent electromechanical activity. *Neurosci Letts* 404:270–275
- Bai JP, Surguchev A, Bian S et al (2010) Combinatorial cysteine mutagenesis reveals a critical intramonomer role for cysteines in prestin voltage sensing. *Biophys J* 99:85–94
- Bian S, Koo BW, Kelleher S, Santos-Sacchi J, Navaratnam DS (2010) A highly expressing Tet-inducible cell line recapitulates in situ developmental changes in prestin's Boltzmann characteristics and reveals early maturational events. *Am J Physiol Cell Physiol* 299:C828–C835
- Bai JP, Surguchev A, Ogando Y, Song L, Bian S, Santos-Sacchi J, Navaratnam D (2010) Prestin surface expression and activity are augmented by interaction with MAP1S, a microtubule-associated protein. *J Biol Chem* 285:20834–20843
- Joshi C, Fernandez JM (1988) Capacitance measurements. An analysis of the phase detector technique used to study exocytosis and endocytosis. *Biophys J* 53:885–892
- Lindau M, Neher E (1988) Patch-clamp techniques for time-resolved capacitance measurements in single cells. *Pflugers Archiv* 411:137–146
- Neher E, Marty A (1982) Discrete changes of cell membrane capacitance observed under conditions of enhanced secretion in bovine adrenal chromaffin cells. *Proc Natl Acad Sci U S A* 79:6712–6716
- Debus K, Hartmann J, Kilic G, Lindau M (1995) Influence of conductance changes on patch clamp capacitance measurements using a lock-in amplifier and limitations of the phase tracking technique. *Biophys J* 69:2808–2822
- Santos-Sacchi J (2004) Determination of cell capacitance using the exact empirical solution

- of partial differential Y /partial differential C_m and its phase angle. *Biophys J* 87:714–727
22. Santos-Sacchi J, Kakehata S, Takahashi S (1998) Effects of membrane potential on the voltage dependence of motility-related charge in outer hair cells of the guinea-pig. *J Physiol* 510:225–235
 23. Santos-Sacchi J, Shen W, Zheng J, Dallos P (2001) Effects of membrane potential and tension on prestin, the outer hair cell lateral membrane motor protein. *J Physiol* 531:661–666
 24. Santos-Sacchi J, Rybalchenko V, Bai JP, Song L, Navaratnam D (2006) On the temperature and tension dependence of the outer hair cell lateral membrane conductance G_{metL} and its relation to prestin. *Pflügers Archiv* 452:283–289
 25. Santos-Sacchi J, Navarrete E, Song L (2009) Fast electromechanical amplification in the lateral membrane of the outer hair cell. *Biophys J* 96:739–747
 26. Song L, Santos-Sacchi J (2010) Conformational state-dependent anion binding in prestin: evidence for allosteric modulation. *Biophys J* 98:371–376
 27. Kakehata S, Santos-Sacchi J (1995) Membrane tension directly shifts voltage dependence of outer hair cell motility and associated gating charge. *Biophys J* 68:2190–2197
 28. Oliver D, Fakler B (1999) Expression density and functional characteristics of the outer hair cell motor protein are regulated during postnatal development in rat. *J Physiol* 519:791–800
 29. Dong XX, Iwasa KH (2004) Tension sensitivity of prestin: comparison with the membrane motor in outer hair cells. *Biophys J* 86:1201–1208
 30. Iwasa KH (1993) Effect of stress on the membrane capacitance of the auditory outer hair cell. *Biophys J* 65:492–498
 31. Muallem D, Ashmore J (2006) An anion antiporter model of prestin, the outer hair cell motor protein. *Biophys J* 90:4035–4045
 32. Oliver D, He DZ, Klöcker N et al (2001) Intracellular anions as the voltage sensor of prestin, the outer hair cell motor protein. *Science* 292:2340–2343
 33. Rybalchenko V, Santos-Sacchi J (2003) Cl^- flux through a non-selective, stretch-sensitive conductance influences the outer hair cell motor of the guinea-pig. *J Physiol* 547:873–891
 34. Rybalchenko V, Santos-Sacchi J (2008) Anion control of voltage sensing by the motor protein prestin in outer hair cells. *Biophys J* 95:4439–4447
 35. Song L, Seeger A, Santos-Sacchi J (2005) On membrane motor activity and chloride flux in the outer hair cell: lessons learned from the environmental toxin tributyltin. *Biophys J* 88:2350–2362
 36. Santos-Sacchi J, Song L, Zheng J, Nuttall AL (2006) Control of mammalian cochlear amplification by chloride anions. *J Neurosci* 26:3992–3998

Article

An Electrical Inspection of the Subsurface Cisternae of the Outer Hair Cell

Lei Song¹ and Joseph Santos-Sacchi^{1,2,3,*}¹Surgery (Otolaryngology), ²Neurobiology, and ³Cellular and Molecular Physiology, Yale University School of Medicine, New Haven, Connecticut

ABSTRACT The cylindrical outer hair cell (OHC) of Corti's organ drives cochlear amplification by a voltage-dependent activation of the molecular motor, prestin (SLC26a5), in the cell's lateral membrane. The voltage-dependent nature of this process leads to the troublesome observation that the membrane resistor-capacitor filter could limit high-frequency acoustic activation of the motor. Based on cable theory, the unique 30 nm width compartment (the extracisternal space, ECS) formed between the cell's lateral membrane and adjacent subsurface cisternae (SSC) could further limit the influence of receptor currents on lateral membrane voltage. Here, we use dual perforated/whole-cell and loose patch clamp on isolated OHCs to sequentially record currents resulting from excitation at apical, middle, and basal loose patch sites before and after perforated patch rupture. We find that timing of currents is fast and uniform before whole-cell pipette washout, suggesting little voltage attenuation along the length of the lateral membrane. Prior treatment with salicylate, a disrupter of the SSC, confirms the influence of the SSC on current spread. Finally, a cable model of the OHC, which can match our data, indicates that the SSC poses a minimal barrier to current flow across it, thereby facilitating rapid delivery of voltage excitation to the prestin-embedded lateral membrane.

INTRODUCTION

The outer hair cell (OHC) provides a unique function for mammalian hearing, underlying a 40–60 decibel boost that enhances our ability to detect and discriminate among sounds, namely, cochlear amplification (1). The structure of the OHC is likewise unique, being cylindrical and ranging in length over tens of micrometers depending on tonotopic location along the cochlea spiral, reaching ~90 μm in the apical OHC of the guinea pig. The lateral wall of the OHC, composed of the lateral plasma membrane, cortical cytoskeleton, and subsurface cisternae (SSC), hosts a restricted subplasmalemmal compartment of 30–50 nm width, termed the extra cisternal space (ECS) (2,3). This ECS is an interesting compartment because prestin, the molecular motor that drives OHC electromotility, resides in the adjacent plasma membrane, with its C- and N-terminals and its anion-binding site projecting into the space (4–6). Prestin contributes to the lateral membrane's capacitance, not only linearly, due to its abundant occupancy increasing surface area (7,8), but nonlinearly because of the electrical signature of prestin activity, namely, nonlinear capacitance (NLC) (9,10). Previous modeling efforts have attributed special electrical characteristics to the ECS (11,12), but they did not include NLC in the lateral plasma membrane.

One recurring concern with the voltage-dependent nature of OHC electromotility is the membrane resistor-capacitor (RC) filter effect on the driving force (sound-induced recep-

tor potentials) for prestin activation. Indeed, it has been estimated that OHC mechanical responses would be 20 dB less than basilar membrane movements at high acoustic frequencies (13). Since then, a number of solutions to the RC problem have been proposed, in an attempt to confirm high frequency, cycle-by-cycle voltage drive for the cochlea amplifier. The presence of the SSC/ECS might also interfere with voltage delivery to the lateral membrane, presenting barriers to receptor current flow. In this report, we directly investigate the influence of the SSC/ECS on OHC electrical behavior. Using dual voltage clamp on isolated OHCs, we find that whole-cell recording via perforated patch records equally fast responses from electrical stimulation of the lateral membrane along its entire length via loose patch. Cable modeling indicates that the SSC barrier does not limit current spread to the ECS, thereby facilitating efficient and rapid delivery of voltage drive to the molecular motors within the lateral membrane.

MATERIALS AND METHODS

Experiment

Electrical measurements were made with modifications to the approach used by Anson and Roberts (14). Three types of electrode arrangements were used—perforated patch whole-cell recording followed by patch rupture into standard whole-cell mode, each accompanied by roving loose patch voltage stimulation. Specifically, two electrodes were patched onto isolated OHCs simultaneously: a perforated patch electrode (gramicidin, 25 or 50 $\mu\text{g}/\text{ml}$) initially served as the recording electrode (holding potential at 0 mV), and a loose patch electrode placed at three locations along the lateral membrane to deliver voltage stimulations. Subsequently, the perforated patch electrode was ruptured to make recordings under standard whole-cell mode. The perforated patch permitted replacement of

Submitted September 11, 2014, and accepted for publication December 8, 2014.

*Correspondence: joseph.santos-sacchi@yale.edu

Editor: Miriam Goodman.

© 2015 by the Biophysical Society
0006-3495/15/02/0568/10 \$2.00

<http://dx.doi.org/10.1016/j.bpj.2014.12.010>



intracellular cations with those of pipette cations, notably Na to inhibit K currents in the basal membrane, thus reducing their effects on our measures of currents and NLC. We view the perforated patch condition as the least intrusive and thus the condition most indicative of normal cellular behavior.

Isolated OHCs from the organ of Corti of guinea pigs were obtained as previously described (15). Long cells (~80 μm long) from apical turns were chosen to allow reliable cable analysis. We used 5 mM chloride to mimic the intracellular chloride concentration of the normal cell that we measured previously (16). Prestin is sensitive only to intracellular chloride, and to clamp intracellular chloride to 5 mM we needed to match inside and outside chloride because the lateral membrane harbors a substantial chloride conductance (6). The bath solution contained, in mM, NaCl 5, Na gluconate 135, CaSO₄ 2, MgSO₄ 1.2, and HEPES 10. Final solutions were adjusted to 300 mOsm with D-glucose and pH 7.2–7.3 with NaOH. The whole-cell patch pipette solution was the same as the extracellular solution except with the addition of 10 mM EGTA. Loose patch electrodes contained the bath solution with resistances near 1 M Ω . Loose patch electrodes served as stimulating electrodes roving along the lateral membrane of OHCs (Fig. 1), positioned ~20, 45, and 70 μm from the base of the cell. To reduce cellular adhesion to the roving pipette, tips were treated with trichlorosilane. Experiments were performed at room temperature (22–23°C). A Nikon Eclipse E600-FN microscope with 40 \times water immersion lens was used to observe cells during the electrical measurements.

Axon 200B amplifiers were used for patch clamping, currents being sampled at 10 μs with an Axon Digidata 1322 using jClamp software (www.scisoftco.com). Voltage steps of 20 ms duration ranging from –160 to +160 mV with 20 mV steps were delivered via a loose patch electrode. Perforated patch electrodes were used to collect current data. Recorded currents were filtered with a 10 kHz 4 pole Bessel filter. Current traces were individually fit with single exponentials in jClamp. Initial electrode resistance was 4–6 M Ω . Gohm seals are reached before decrease of patch resistance due to gramicidin perforation. With pipette backfilling, time for establishing perforated patch whole-cell patch was

around 30–40 min. R_s for the perforated patch electrode was typically 15–25 M Ω , and was reduced by series resistance compensation to maintain a ~10 M Ω resistance. Similarly, after rupture of the perforated patch and establishment of whole-cell recording, R_s was maintained near 10 M Ω . It was important to keep electrode series resistance uniform among cell recordings because time constants are dependent on the series resistance. Amplifier lag controls were not manipulated but were left at minimum levels during R_s compensation. The recording protocol (perforated patch recording with apical, middle, and basal stimulation, followed by whole-cell recording and roving stimulation) was quite demanding so that many cells were lost before completing all recording conditions. Whole-cell NLC was measured with the recording electrode using a 2-sine voltage stimulus atop a voltage ramp with subsequent admittance analysis as previously described (17).

To investigate the effects of subsurface cisternae damage, OHCs were incubated in extracellular solutions that contained 10 mM salicylate for 30–40 min. This time period of exposure has been shown to cause irreversible damage to the subsurface cisternae (3), thereby minimizing contributions of the SSC/ECS to our measures. Washout of salicylate was performed before recording to alleviate its direct reversible effects on prestin's NLC (18,19).

Average responses for stimulation at basal, middle, and apical positions for a range of step voltage commands included three cells where all recording/stimulation configurations were successfully completed. Statistical tests included cells where less than the full paradigm was completed, with numbers ranging from 3 to 10 (see Fig. 4 for numbers of cells used for statistical tests). We were careful to ensure that electrophysiological conditions (especially recording clamp time constants) were similar before and after patch rupture. Results for perforated/whole-cell conditions (with standard –10 mV pulse stimulation via the recording pipette) were (mean \pm SE; $n = 3$): R_s : 10.1 \pm 0.1 M Ω vs. 10.4 \pm 0.2 M Ω ; R_m : 314 \pm 83 M Ω vs. 256 \pm 87 M Ω ; C_m 39.4 \pm 1.15 pF vs. 41.8 \pm 1.9 pF; clamp τ : 375 \pm 12 μs vs. 403 \pm 26 μs . These measures were repeated and remained stable for each roving pipette stimulation configuration. For salicylate-treated cells, perforated/whole-cell conditions were (mean \pm SE; $n=3$): R_s : 10.5 \pm 0.2 M Ω vs. 10.4 \pm 0.2 M Ω ; R_m : 267 \pm 36 M Ω vs. 262 \pm 42 M Ω ; C_m 40.1 \pm 0.2 pF vs. 40.0 \pm 0.4 pF; clamp τ : 401 \pm 9 μs vs. 395 \pm 8 μs .

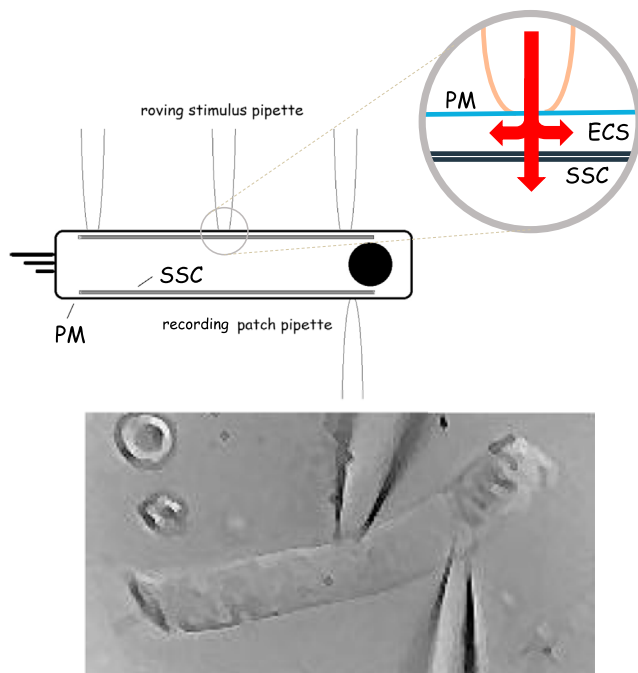


FIGURE 1 Schematic of OHC under voltage clamp with recording patch pipette, while being stimulated with a roving loose patch pipette. The enlarged section shows possible current flow from the loose patch electrode. Beneath is a digitally captured image of an OHC during middle position stimulation. To see this figure in color, go online.

Model

A lumped parameter model and a cable model of 47 sections that helped to understand the data were implemented in MATLAB's Simulink (The MathWorks, Natick, MA) using Simscape and are schematized (see Figs. 5 a and 6 a). The cable model was a standard one-dimensional model similar to that of Halter et al. (11) (see Results below). Though the length of the OHCs that we modeled was short compared to typical cell lengths used for cable analyses, we found it beneficial to analyze in this manner to compare to previous results and help in defining current paths and resistances within the OHC. An automation link between jClamp and MATLAB allowed us to stimulate the model and analyze in jClamp, similar to the biophysical experiments. Parameters were taken from the biophysical data as provided in Results. Both whole-cell and loose patch NLC were modeled as

$$C_m = Q_{\max} \frac{ze}{kT} \frac{b}{(1+b)^2} + C_{lin},$$

$$b = \exp\left(\frac{-ze(V_m - V_h)}{kT}\right),$$

where Q_{\max} is the maximum charge moved, z is valence, C_{lin} is the linear capacitance of the cell membrane and V_h is the voltage at half-maximal charge. e , k , and T have their usual meanings.

To fit current transients to the cable model, we averaged traces across all cells. Because the absolute magnitudes of the currents differed and we were

concerned with maintaining time constant information, we first scaled all currents to unity based on peak current, and then averaged and rescaled to average magnitude. In this way, current shapes (τ) from all traces contributed equally to the averages.

RESULTS

Experiment

We investigated longitudinal charge movement within the cell by recording with perforated patch clamp while simultaneously stimulating along the length of isolated OHCs using a loose patch electrode (Fig. 1), in a manner similar to that of Anson and Roberts (14). Perforated patch recording leaves the plasma membrane unbroken but allows electrical continuity with the whole cell (20). The enlarged, circled section in Fig. 1 indicates possible current flow from the stimulating loose patch electrode into the ECS or across the SSC into the axial core of the cell. We found that loose patch stimulation at all cell positions relative to the recording electrode produced equally fast responses under the perforated recording condition. Interestingly, we only observed single exponential responses. For example, Fig. 2, A–C, shows that time constants of induced current transients were similar with basal, middle, and apical stimulation during perforated patch recording conditions, regardless of voltage stimulation magnitude. These data may indicate that charge movement within and along the ECS is rapid. However, upon perforated patch rupture with suction, and establishment of standard whole-cell recording, time constants showed differences; apical and middle stimulation showed slower responses, and interestingly took on a clear voltage dependence arising from the loose patch's NLC (Fig. 2, D–F). We take this to indicate that the SSC was somehow altered either by washout of

cell constituents or washin of gramicidin, resulting in altered characteristics of the cell's cable properties. Whole-cell NLC measured under these two conditions were similar (Fig. 2, C and F), indicating that the large increase in time constants is not due to a corresponding large increase in NLC of the whole cell. It should be noted that limiting time constants are imposed by the patch clamp (roughly, $R_s C_m$) and in absolute terms do not reflect cell capabilities. We only use these measures as a tool to understand relative timing relationships between conditions and between electrodes.

The incorporation of gramicidin into a membrane is a fairly slow process; for example, up to 45 min is required to obtain good series resistance of the perforated patch electrode before beginning our experiments. Following patch rupture, we required only ~10 min to complete the rest of the experiment, though maintaining the cell for the complete protocol was not guaranteed. Thus, little gramicidin is expected to incorporate with the plasma membrane and this is evidenced by the maintenance of fairly high membrane resistance in whole-cell mode (see Materials and Methods for values). In any case, a reduction in membrane resistance should speed up the electrical response rather than slow it down, as occurred after patch rupture. Thus, we reasoned that establishing the whole-cell condition by pipette suction caused alterations to the SSC during washout/in. To test this hypothesis, we transiently treated cells with salicylate, which has been shown to irreversibly alter SSC ultrastructure (3). The effect of prior salicylate treatment (30–45 min) was to abolish the increase in time constants that occur following patch rupture, as would be expected if the SSC/ECS were altered before patch rupture (Fig. 3, A and B). As with untreated cells, we were careful to ensure that recording conditions were similar before and after patch

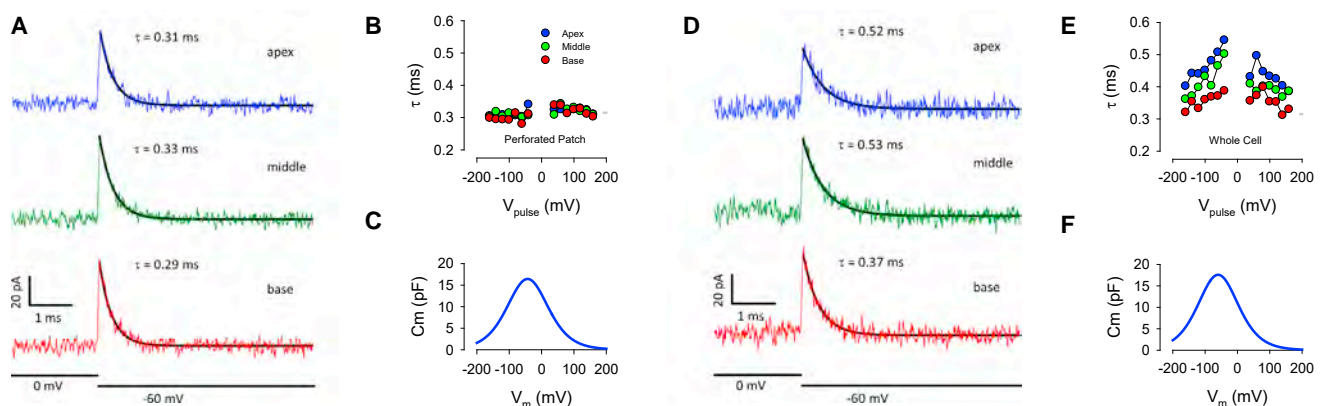


FIGURE 2 Time constants (τ) of current responses induced by step voltages of the roving loose patch electrode before (A–C) and after (D–F) rupture of recording the electrode perforated patch. (A) Traces of currents measured during apical, middle, and basal stimulation. Traces are averages (see Materials and Methods). Note that current responses have similar exponential decays. (B) Average response tau across voltage stimulation magnitude. Circles depict average responses at each voltage for 3–10 cells. (C) NLC based on average fits (see Materials and Methods). Q_{\max} , V_h , z : 2.95 pC, –59.7 mV, 0.61. (D) Traces of currents measured during apical, middle, and basal stimulation following recording electrode patch rupture into standard whole-cell mode. Traces are averages. Note that current responses now have differing exponential decays. (E) Average response tau across voltage stimulation magnitude, showing clear voltage dependence. Circles depict average responses at each voltage. (F) NLC based on average fits. Q_{\max} , V_h , z : 2.81 pC, –43.2 mV, 0.60. To see this figure in color, go online.

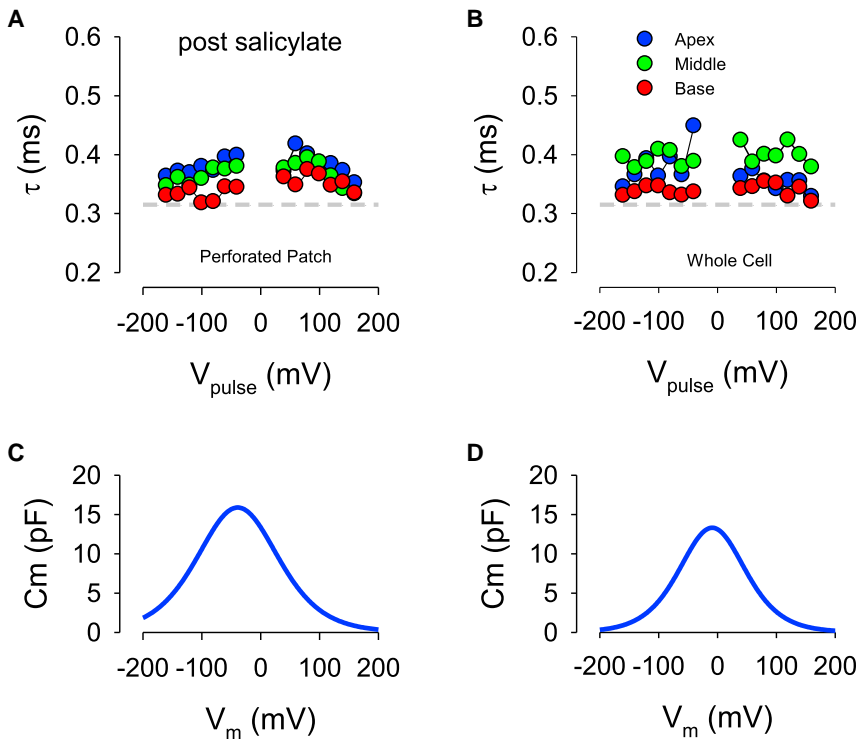


FIGURE 3 Time constants (τ) of perforated (A) and whole-cell (B) patch responses following salicylate treatment induced by step voltages of the roving loose patch electrode. Circles depict average responses at each voltage for three cells. Note similarity of time constants (τ) before and after establishment of whole-cell condition. (C) and (D) show corresponding measures of average NLC measured with whole-cell/perforated patch electrode (Q_{max} , V_h , z : 2.94/2.00 pC, $-39.0/-9.2$ mV, 0.55/0.68). To see this figure in color, go online.

rupture (see Materials and Methods). In these cells, NLC before patch rupture was slightly less than controls not treated with salicylate (compare Fig. 2, C and F with Fig. 3, C and D). After patch rupture, NLC was shifted rightward and decreased somewhat (see figure legends for fits).

Fig. 4, A and B, compare the time constants obtained at -60 mV steps and time to peak current (Tpk) at the 160 mV pulse, each at three locations, before and after

establishing whole-cell conditions for cells without salicylate treatment. Statistically significant differences are found at all stimulation locations (significance is given in plot). The observations on current time constants are to a large extent paralleled by measures of Tpk. That is, although these metrics were stable across stimulus locations for the perforated patch condition, they increased for the whole-cell condition. For example, current spread latency between

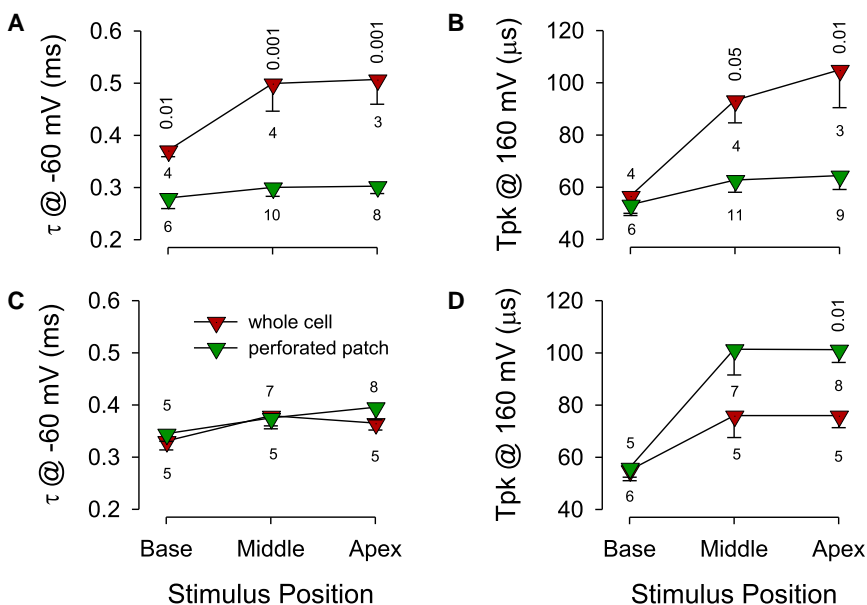


FIGURE 4 (A) Average time constants at -60 mV show little difference among roving patch locations for the perforated patch condition, but significant differences following whole-cell recording. (B) Similarly, times to peak (Tpk) current increase at apical and middle positions following patch rupture. (C) For salicylate-treated cells, time constants show no significant differences between perforated patch and whole-cell conditions. (D) Tpk shows no significant differences at basal and middle positions; however, a difference was observed at the apical position where Tpk was now shorter following patch rupture. Number of cells is noted. Statistical significance ($p < ; t$ -test), where present, between pre- and post-patch rupture is shown for each location. To see this figure in color, go online.

stimulating and recording electrodes based on Tpk between basal and apical stimulation is on the order of only $3.4 \mu\text{s}$ (53.3 ± 3.3 vs. $56.7 \pm 4.0 \mu\text{s}$; $p > 0.05$), whereas following establishment of whole-cell conditions the spread significantly slowed to $41.1 \mu\text{s}$ (105.0 ± 14.5 vs. $64.4 \pm 5.2 \mu\text{s}$; $p < 0.05$). Fig. 4 C shows that no significant differences are found in time constants for the salicylate-treated case, indicating that SSC alterations were present both before and after patch rupture. Tpk for salicylate-treated cells show no differences at basal and middle stimulation locations (Fig. 4 D), but a significant difference is found for the apical stimulation position. However, this difference, namely that Tpk is shortened following rupture, is opposite that observed without salicylate (see Fig. 4 B). This may indicate an interactive action of combined salicylate and gramicidin.

Models

Lumped parameter model

To understand our results, we constructed a lumped parameter model of the OHC, before and after establishing whole-cell configuration (Fig. 5 A). The model parameters are those actual averaged (see above) measures obtained in perforated patch mode (*condition 1*) and whole-cell mode (*condition 2*). C_p , the linear capacitance of the patch, and patch NLC were set to 0.02 of the measured whole-cell values. R_p , the patch resistance that was stimulated, was set based on Halter et al.'s value of lateral membrane conductivity, 0.001 mS/cm^2 (11). This is reasonable, because

we have previously shown that the lateral membrane is devoid of voltage-dependent conductances (21). V_h of the loose patch was set to a 20 mV more depolarized value than whole-cell or perforated patch V_h because the tension provided to the patch ($\sim 1 \text{ kPa}$) to increase loose patch shunt resistance (R_{sh}) is known to shift $V_h \sim 20 \text{ mV/kPa}$ (22). R_{sh} was set to $5.0 \text{ M}\Omega$. R_{sp} was set to $1.8 \text{ M}\Omega$, based on measures of electrode resistance before cell attachment. Stimulation was done as with the biophysical measures using jClamp and Simulink. In the perforated condition, an intervening resistance (R_{inter}) between stimulating and recording electrodes of $10 \text{ M}\Omega$ or less produced results that resembled our data (see below).

Fig. 5 B shows the time constants of evoked currents when the model was simulated with parameters obtained under perforated patch and whole-cell experimental conditions. Though tau were similar in magnitude to our data, no differences in tau are observed between the two conditions, unlike the increase in voltage-dependent tau that we observed experimentally. This means that the differences observed between model and data are not due to the experimentally observed changes in R_s , R_m , C_{lin} , and NLC between the two conditions. Could unrecognized changes in R_{sp} or R_{sh} have influenced our data? In Fig. 5, C and D, we show the effects of altering R_{sp} (1, 5, 10 $\text{M}\Omega$) and R_{sh} (1, 5, 15 $\text{M}\Omega$). No influence on tau was found. Changes in R_{sh} can, however, alter the magnitude of the current response, and thus could underlie differences between current magnitudes found in whole-cell and perforated patch recordings. Finally, we modified R_{inter} (10, 100, 300 $\text{M}\Omega$) and found an increase in voltage-dependent tau as a function

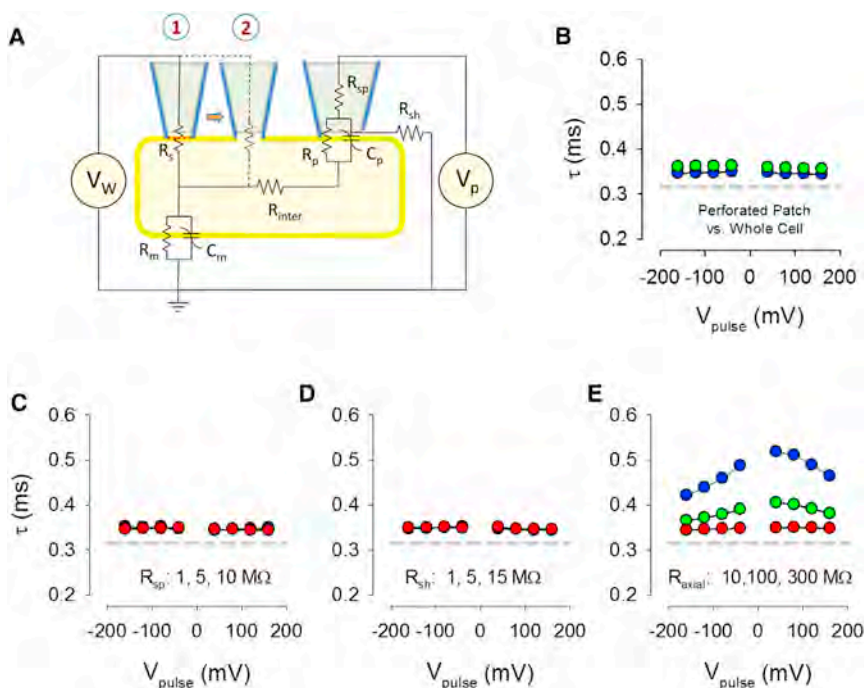


FIGURE 5 Lumped parameter model of OHC under the experimental conditions. (A) Schematic showing circuit and parameters of current measuring and voltage stimulating pipettes. Model was evaluated first under perforated patch (*condition 1*) and then under whole-cell (*condition 2*). See Materials and Methods for details. Right pipette is stimulating pipette. Parameters are taken from actual biophysical data given in Results. (B) With biophysical measures obtained under perforated patch and whole-cell condition, no differences in taus are observed. (C and D) Neither R_{sh} nor R_{sp} affects the evoked current time constants. However, interelectrode resistance has a profound effect on them, producing results similar to the biophysical data, indicating that this resistance must have changed upon entry into whole-cell mode. To see this figure in color, go online.

of increasing resistance (Fig. 5 E). A value between 100 and 300 M Ω was required to simulate our experimental observations. It should be noted that the possibility of an induced cross talk between recording and stimulating electrodes following patch rupture is ruled out, because in the salicylate-treated controls, no increase in tau is found following patch rupture.

Cable model

To hone in on the identity of the intervening resistance, R_{inter} , we assembled a 47 section cable model (Fig. 6 A) similar to the one devised by Halter et al. (11). We kept their basis values for R_L (0.001 mS/cm²), R_{ecs} , R_{ax} (70 Ω cm), and R_{sc} (0.1 mS/cm²); however, in our case we included lateral membrane NLC based on our measurements. Other values were R_s 10 M Ω , R_p 1.8 M Ω , R_{sh} 3–12 M Ω , C_m 0.8 μ F/cm², C_b 3 pF, C_a 2pF, R_{mb} 300 M Ω , and R_{ma} 10 G Ω (high because stereocilia were damaged by trituration during cell isolation). ECS width was set to 30 nm. Similar to our experimental measures, a 10 kHz 4 pole Bessel filter implementation in Simulink was used on model currents.

As noted previously, we only observe single exponential current transients in our experiments. Fig. 6 B shows that

the cable model cannot reproduce our data if we use the R_{sc} value of Halter et al. (11). The resultant pink solid lines are not simple single exponentials, and whole-cell NLC of this model (measured via the recording electrode) was substantially less than our biophysical measurements (Q_{max} : 1.35 pC vs. 2.95 pC). We must increase R_{sc} conductance by three orders of magnitude (0.15 S/cm²) to fit our perforated patch data (black solid lines), and to simultaneously obtain a value matching our normal whole-cell NLC values (Q_{max} : 2.92 pC). This indicates that the SSC are highly conductive, on the order of electroporated membranes (23). To fit the data following patch rupture (Fig. 6 C), the ECS resistivity had to be increased three orders of magnitude (70 k Ω cm); this apparent increase in resistivity could instead indicate that the ECS space had collapsed or the actual ionic strength of the space had decreased. Additionally, R_{sc} conductance was reduced, as well (0.015 S/cm²). Thus, the intervening resistance, R_{inter} , of the lumped parameter model corresponds to the R_{ecs} and R_{sc} components of the cable model. Fig. 7 shows time constants and NLC of the model using the perforated patch and whole-cell parameters obtained by trace fits. Similarity to the biophysical data is clear (compare with Fig. 2). These results

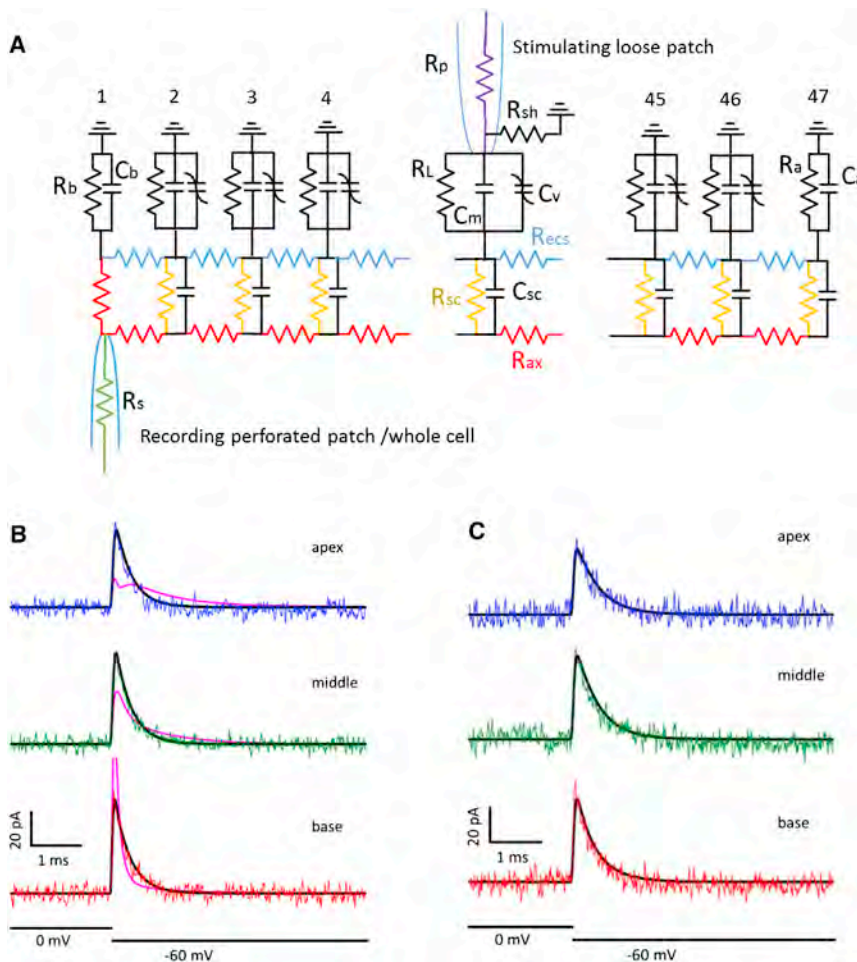


FIGURE 6 (A) Cable model with 47 sections. Roving loose patch electrode was placed at section 2, 22, and 42 to mimic basal, middle, and apical stimulations. See Model Results for parameter values. (B) R_{sc} values based on Halter et al. (11) (0.1 mS/cm²) could not fit data in perforated mode (pink traces); however, a value of 0.15 S/cm² fit the data well (black traces). (C) For the model to fit whole-cell data, R_{ecs} resistivity had to be increased to 70 k Ω cm (black traces), with R_{sc} conductivity set to 0.015 S/cm². To see this figure in color, go online.

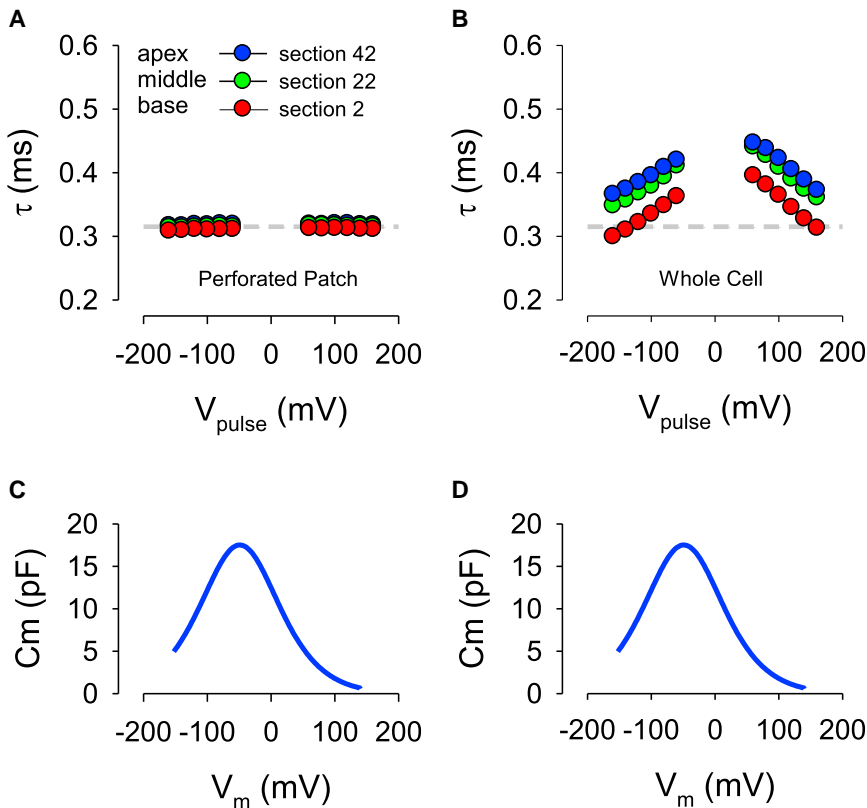


FIGURE 7 Cable model time constants (τ) of perforated (A) and whole-cell (B) patch responses induced by step voltages of the roving loose patch electrode. Note increase in time constants (τ) after change from perforated patch parameters to whole-cell parameters (see Model Results), and an apparent rise in voltage dependency similar to what is seen with the biophysical data. (C) and (D) show corresponding measures of whole-cell NLC measured with recording whole-cell electrode (Q_{max} , V_h , z : 2.78/2.94 pC, $-40.7/-56.3$ mV, 0.60/0.60). Compare to Fig. 2. To see this figure in color, go online.

indicate that under unperturbed conditions, with perforated patch recording intact, the high conductance of the SSC facilitates voltage delivery to the lateral membrane. Cable model results similar to the salicylate experiments were obtained with ECS resistivity set to $70 \text{ k}\Omega \text{ cm}$ and R_{sc} conductivity of 0.03 or 0.026 S/cm^2 for perforated patch or whole-cell condition, respectively (model data not shown).

Finally, to evaluate the influence of SSC conductance on voltage excitation of the lateral membrane, we used our cable model driven by current injection into the cell's apical axial core, mimicking receptor currents (Fig. 8). In the absence of the SSC, frequency response magnitude is maximized, but phase is significantly changing at frequencies below 1 kHz . With R_{sc} conductivity from Halter et al. (11), significant reduction of frequency response magnitude and large phase changes across the spectrum arise. By increasing R_{sc} conductivity frequency response magnitude is enhanced and phase behavior is flattened. Thus, electrical transparency of the SSC tends to facilitate voltage delivery to the lateral membrane.

DISCUSSION

The mammalian OHC functions to enhance perception at acoustic frequencies, even beyond 100 kHz in some mammals. As a result, there is no doubt that the cell can produce mechanical activity at high frequencies (24), nor is there

doubt that the OHC's stereocilia transduction apparatus operates at high frequencies (25–27). Indeed, there is little disagreement that cochlear amplification deriving from OHC electromechanics works most efficiently at high frequencies (28). Nevertheless the conundrum arising from a voltage-dependent basis of amplification continues to garner interest. The problem stems from the observed disparity between OHC resting membrane potential and the voltage where maximal mechanical activity occurs (V_h) (13,27). Should these two voltages overlap there would then be less difficulty with an RC filter. Several mechanisms have been postulated to understand why the RC filter should not interfere with prestin activity at high frequencies. Previously, we envisioned three mechanisms that might help: 1), because turgor pressure within the OHC shifts the voltage dependence of NLC and electromotility (22,29,30), we suggested that alterations in turgor pressure could align V_h and resting potential (22); 2), because prestin charge density increases in high-frequency OHCs (31,32), we reasoned that the rising electrical energy delivered to the lateral membrane could counter the reduced voltage drive; and 3), we reasoned that the flux of chloride through the stretch-activated chloride conductance, G_{metL} , in the lateral membrane could gate prestin's chloride-dependent activity independent of the membrane RC (6). Though the first two possibilities remain tenable, the latter is unlikely, because we have recently discovered that the effects of chloride on prestin are

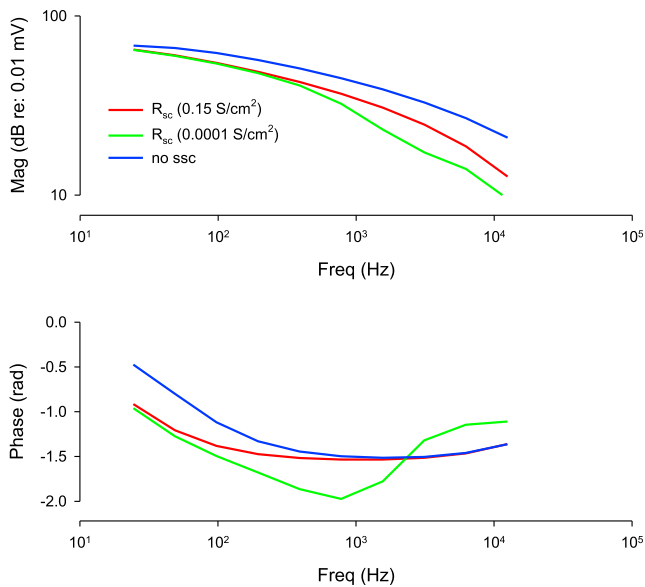


FIGURE 8 Magnitude and phase of voltage drop across section 33 lateral membrane of the cable model induced by 0.1 nA AC injection into the apical axial core. Without SSC frequency response is maximal. Reduction of R_{sc} from value based on Halter et al. (11) (0.1 mS/cm^2) tends to increase frequency response and provide a flat phase response. To see this figure in color, go online.

low-pass filtered by a slow intermediary state transition (33). Others, as well, have developed theories on overcoming the RC problem. These include 1), an intrinsic high pass augmentation of receptor potentials due to prestin's piezoelectricity (34); 2), a reduction of the RC effects by increases in membrane conductance (35); and 3), the observation that OHC resting potential may be more depolarized than the original estimates made in vivo (27,36), thus aligning resting potential and V_h (37).

Beyond the RC problem, however, ultrastructural specializations of the OHC lateral wall, namely the membranous SSC and the restricted, femtoliter space (ECS) it establishes, could provide isolation of the lateral membrane from axial receptor currents. This potentially could lead to reduced voltage drive to prestin motors embedded in the lateral membrane. Our present data directly relate to this issue.

Cable effects of the SSC

There has been a paucity of information on the electrical role of the SSC, mainly arising from modeling results of whole-cell electrical stimulation (11,38). Our experiments were aimed at electrically exploring restricted regions of the cell's lateral wall. Our data and model analyses indicate that the electrical transparency of the SSC promotes uniformly fast stimulus delivery to the lateral membrane motor, and therefore limits time-dependent, potentially nonlinear, activation of the motors. Based on average time to peak current measures between our apical and basal stimulus electrodes in the perforated patch condition

($3.5 \mu\text{s}$; see Results), for a $55 \mu\text{m}$ distance, a conduction velocity $>150 \text{ m/s}$ is obtained, and considering the high resistivity of the lateral plasma membrane, likely promotes isopotential conditions at any given acoustic frequency for the range of OHC lengths found within the cochlea spiral. This possibility was previously suggested because voltage-dependent conductances are absent along the OHC lateral membrane (21). The observation that damage to the SSC alters timing along the length of the OHC may indicate its high conductance is actively maintained. Indeed, the row of mitochondria adjacent to the SSC may play a role, because the washin of gramicidin following perforated patch rupture may uncouple mitochondrial oxidative phosphorylation (39). It is noteworthy that salicylate can also uncouple mitochondrial oxidative phosphorylation (40). We are currently evaluating the effects of other mitochondrial perturbations on SSC conductance.

Interestingly, in the model of Halter et al. (11), ECS current was found to exceed that within the cell's axial core, possibly pointing to unusual differences in resistivity between ECS and axial cytoplasm as also suggested by Fari-nelli et al. (38). Nakagawa and Brownell (12) have used the voltage-dependent dye, di-8-ANEPPS, to observe high frequency phase differences between OHC basal and lateral membrane voltages, which they attribute to the effects of a higher resistance of the axial core than ECS. Of course, this is counter intuitive based on the cross-sectional area of the ECS. Indeed, even fluorescent dye diffusion is somewhat slower in the ECS than in the axial core, though, of course, dye spread may not necessarily correlate with current spread (41). We were able to obtain single-exponential behavior of currents with our cable model if we set R_{ecs} resistivity to $0.7 \Omega \text{ cm}$, while maintaining the higher R_{ax} resistivity at $70 \Omega \text{ cm}$ and R_{sc} conductivity at 0.1 mS/cm^2 . However, typical values of cytosolic resistivity range between ~ 30 and $600 \Omega \text{ cm}$ (42), and considering the geometry of the ECS, this would mean that the ionic strength of the space would be enormous. It could be that the abundance of prestin within the lateral membrane, estimated to be up to 10 million copies based on nonlinear charge movement (43), contributes to a higher ionic strength in the ECS by virtue of its transport capabilities (44–46). Nevertheless, we consider it more reasonable to have the SSC highly conductive, possibly due to fenestrations, or vesiculations that may require work to maintain, because phospholipid bilayers tend to assume planar configurations (47). In this scenario, we might expect the performance of the OHC to be dependent on the energetics required to maintain an unusually high SSC conductivity.

ACKNOWLEDGMENTS

This research was supported by National Institutes of Health (NIH) National Institutes of Deafness and Other Communication Disorders (NIDCD) grant DC00273 to J.S.S.

REFERENCES

1. Ashmore, J., P. Avan, ..., B. Canlon. 2010. The remarkable cochlear amplifier. *Hear. Res.* 266:1–17.
2. Holley, M. C., and J. F. Ashmore. 1988. A cytoskeletal spring in cochlear outer hair cells. *Nature.* 335:635–637.
3. Dieler, R., W. E. Shehata-Dieler, and W. E. Brownell. 1991. Concomitant salicylate-induced alterations of outer hair cell subsurface cisternae and electromotility. *J. Neurocytol.* 20:637–653.
4. Zheng, J., W. Shen, ..., P. Dallos. 2000. Prestin is the motor protein of cochlear outer hair cells. *Nature.* 405:149–155.
5. Oliver, D., D. Z. He, ..., B. Fakler. 2001. Intracellular anions as the voltage sensor of prestin, the outer hair cell motor protein. *Science.* 292:2340–2343.
6. Rybalchenko, V., and J. Santos-Sacchi. 2003. Cl⁻ flux through a non-selective, stretch-sensitive conductance influences the outer hair cell motor of the guinea-pig. *J. Physiol.* 547:873–891.
7. Abe, T., S. Kakehata, ..., H. Shinkawa. 2007. Developmental expression of the outer hair cell motor prestin in the mouse. *J. Membr. Biol.* 215:49–56.
8. Liberman, M. C., J. Gao, ..., J. Zuo. 2002. Prestin is required for electromotility of the outer hair cell and for the cochlear amplifier. *Nature.* 419:300–304.
9. Santos-Sacchi, J. 1991. Reversible inhibition of voltage-dependent outer hair cell motility and capacitance. *J. Neurosci.* 11:3096–3110.
10. Ashmore, J. F. 1990. Forward and reverse transduction in the mammalian cochlea. *Neurosci. Res. Suppl.* 12:S39–S50.
11. Halter, J. A., R. P. Kruger, ..., W. E. Brownell. 1997. The influence of the subsurface cisterna on the electrical properties of the outer hair cell. *Neuroreport.* 8:2517–2521.
12. Nakagawa, T., J. S. Oghalai, ..., W. E. Brownell. 2006. Photometric recording of transmembrane potential in outer hair cells. *J. Neural Eng.* 3:79–86.
13. Santos-Sacchi, J. 1989. Asymmetry in voltage-dependent movements of isolated outer hair cells from the organ of Corti. *J. Neurosci.* 9:2954–2962.
14. Anson, B. D., and W. M. Roberts. 1998. A novel voltage clamp technique for mapping ionic currents from cultured skeletal myotubes. *Biophys. J.* 74:2963–2972.
15. Song, L., and J. Santos-Sacchi. 2010. Conformational state-dependent anion binding in prestin: evidence for allosteric modulation. *Biophys. J.* 98:371–376.
16. Santos-Sacchi, J., L. Song, ..., A. L. Nuttall. 2006. Control of mammalian cochlear amplification by chloride anions. *J. Neurosci.* 26:3992–3998.
17. Santos-Sacchi, J., S. Kakehata, and S. Takahashi. 1998. Effects of membrane potential on the voltage dependence of motility-related charge in outer hair cells of the guinea-pig. *J. Physiol.* 510:225–235.
18. Kakehata, S., and J. Santos-Sacchi. 1996. Effects of salicylate and lanthanides on outer hair cell motility and associated gating charge. *J. Neurosci.* 16:4881–4889.
19. Tunstall, M. J., J. E. Gale, and J. F. Ashmore. 1995. Action of salicylate on membrane capacitance of outer hair cells from the guinea-pig cochlea. *J. Physiol.* 485:739–752.
20. Horn, R., and A. Marty. 1988. Muscarinic activation of ionic currents measured by a new whole-cell recording method. *J. Gen. Physiol.* 92:145–159.
21. Santos-Sacchi, J., G. J. Huang, and M. Wu. 1997. Mapping the distribution of outer hair cell voltage-dependent conductances by electrical amputation. *Biophys. J.* 73:1424–1429.
22. Kakehata, S., and J. Santos-Sacchi. 1995. Membrane tension directly shifts voltage dependence of outer hair cell motility and associated gating charge. *Biophys. J.* 68:2190–2197.
23. Hibino, M., M. Shigemori, ..., K. Kinoshita, Jr. 1991. Membrane conductance of an electroporated cell analyzed by submicrosecond imaging of transmembrane potential. *Biophys. J.* 59:209–220.
24. Frank, G., W. Hemmert, and A. W. Gummer. 1999. Limiting dynamics of high-frequency electromechanical transduction of outer hair cells. *Proc. Natl. Acad. Sci. USA.* 96:4420–4425.
25. Dallos, P. 1985. Membrane potential and response changes in mammalian cochlear hair cells during intracellular recording. *J. Neurosci.* 5:1609–1615.
26. Russell, I. J., A. R. Cody, and G. P. Richardson. 1986. The responses of inner and outer hair cells in the basal turn of the guinea-pig cochlea and in the mouse cochlea grown in vitro. *Hear. Res.* 22:199–216.
27. Dallos, P., J. Santos-Sacchi, and A. Flock. 1982. Intracellular recordings from cochlear outer hair cells. *Science.* 218:582–584.
28. Ruggero, M. A., and N. C. Rich. 1991. Furosemide alters organ of corti mechanics: evidence for feedback of outer hair cells upon the basilar membrane. *J. Neurosci.* 11:1057–1067.
29. Iwasa, K. H. 1993. Effect of stress on the membrane capacitance of the auditory outer hair cell. *Biophys. J.* 65:492–498.
30. Gale, J. E., and J. F. Ashmore. 1994. Charge displacement induced by rapid stretch in the basolateral membrane of the guinea-pig outer hair cell. *Proc. Biol. Sci.* 255:243–249.
31. Santos-Sacchi, J., S. Kakehata, ..., T. Takasaka. 1998. Density of motility-related charge in the outer hair cell of the guinea pig is inversely related to best frequency. *Neurosci. Lett.* 256:155–158.
32. Corbitt, C., F. Farinelli, ..., B. Farrell. 2012. Tonotopic relationships reveal the charge density varies along the lateral wall of outer hair cells. *Biophys. J.* 102:2715–2724.
33. Song, L., and J. Santos-Sacchi. 2013. Disparities in voltage-sensor charge and electromotility imply slow chloride-driven state transitions in the solute carrier SLC26a5. *Proc. Natl. Acad. Sci. USA.* 110:3883–3888.
34. Spector, A. A., W. E. Brownell, and A. S. Popel. 2003. Effect of outer hair cell piezoelectricity on high-frequency receptor potentials. *J. Acoust. Soc. Am.* 113:453–461.
35. Ospeck, M., X. X. Dong, ..., K. H. Iwasa. 2006. Electromotility in outer hair cells: a supporting role for fast potassium conductance. *ORL J. Otorhinolaryngol. Relat. Spec.* 68:373–377.
36. Russell, I. J., and P. M. Sellick. 1983. Low-frequency characteristics of intracellularly recorded receptor potentials in guinea-pig cochlear hair cells. *J. Physiol.* 338:179–206.
37. Johnson, S. L., M. Beurg, ..., R. Fettiplace. 2011. Prestin-driven cochlear amplification is not limited by the outer hair cell membrane time constant. *Neuron.* 70:1143–1154.
38. Farinelli, F., W. Brownell, and B. Farrell. 2010. Evidence that the subsurface cisternae influences the electrical properties of the outer hair cell. Abstracts of the Thirty-Third Annual Midwinter Research Meeting. *Assoc. Res. Otolaryngol.* 33:194–195, Abstract 571.
39. Rottenberg, H., and R. E. Koeppe, 2nd. 1989. Stimulation of cation transport in mitochondria by gramicidin and truncated derivatives. *Biochemistry.* 28:4361–4367.
40. Miyahara, J. T., and R. Karler. 1965. Effect of salicylate on oxidative phosphorylation and respiration of mitochondrial fragments. *Biochem. J.* 97:194–198.
41. Ashmore, J., and J. Gale. 2004. The cochlear amplifier. *Curr. Biol.* 14:R403–R404.
42. Golding, N. L., T. J. Mickus, ..., N. Spruston. 2005. Factors mediating powerful voltage attenuation along CA1 pyramidal neuron dendrites. *J. Physiol.* 568:69–82.
43. Huang, G., and J. Santos-Sacchi. 1993. Mapping the distribution of the outer hair cell motility voltage sensor by electrical amputation. *Biophys. J.* 65:2228–2236.
44. Bian, S. M., B. W. Koo, ..., D. Navaratnam. 2011. Evaluating prestin's changing biophysical attributes in development using a tet-induced cell

- line. What fire is in mine ears. *Progress in Auditory Biomechanics*. 1403:143–147.
45. Bai, J. P., A. Surguchev, ..., D. Navaratnam. 2009. Prestin's anion transport and voltage-sensing capabilities are independent. *Biophys. J.* 96:3179–3186.
46. Mistrik, P., N. Daudet, ..., J. F. Ashmore. 2012. Mammalian prestin is a weak $\text{Cl}^-/\text{HCO}_3^-$ electrogenic antiporter. *J. Physiol.* 590:5597–5610.
47. Graham, T. R., and M. M. Kozlov. 2010. Interplay of proteins and lipids in generating membrane curvature. *Curr. Opin. Cell Biol.* 22:430–436.

Chloride dependent coupling of molecular to cellular mechanics in the outer hair cell of Corti's organ.

Lei Song and Joseph Santos-Sacchi

*Surgery (Otolaryngology), Cellular and Molecular Physiology,
and Neurobiology, Yale University
School of Medicine, New Haven, Connecticut*

Abstract. Within the OHC lateral membrane, conformational changes in the motor protein prestin are driven by voltage induced displacements of intrinsic, charged moieties that can be monitored by measures of the cell's nonlinear capacitance. The cellular expression of these summed molecular events is a robust electromotility of the whole cell. We now find that the coupling of molecular to cellular mechanics is dependent on intracellular chloride levels, where normal levels (<10 mM) do not support tight coupling between the two. Thus, in vivo, electromotility is predicted to be poorly coupled to changes in OHC receptor potentials, whereas molecular conformational change is tightly coupled. We suspect that membrane mechanical characteristics driven by prestin may more significantly govern cochlea amplification than electromotility.

Keywords: chloride, capacitance, prestin, OHC

PACS: 43.64.Ld, 43.64.Kc

INTRODUCTION

Mammalian outer hair cell (OHC) electromotility results from voltage-dependent conformational changes of the membrane protein prestin [1], with the cell's motor charge movement or nonlinear capacitance (NLC) being considered a surrogate measure of electromotility [2,3]. A number of physiological factors shift prestin's voltage dependence, including changes in intracellular Cl and membrane holding potential (pre-pulse effect) [4,5], each presumably affecting electromotility and NLC equivalently.

We have been studying the consequences of combined chloride and pre-pulse manipulations on NLC with simultaneous measurements of electromotility. We find, as expected from our previous work, that OHCs patch clamped with pipettes containing 140 mM intracellular chloride show robust depolarizing shifts of NLC upon negative pre-pulse, with electromotility displaying a similarly coupled shift. However, lower, more physiological levels of intracellular chloride [6], induce an uncoupling of mechanical responses from NLC, evidenced as discordance between the voltage dependence of each. This discordance is also variably affected by polarity and rate of voltage stimulation. Such discordance requires a rethinking of how the OHC may influence basilar membrane mechanics and cochlear amplification, possibly pointing away from previously envisioned mechanisms of mechanical feedback.

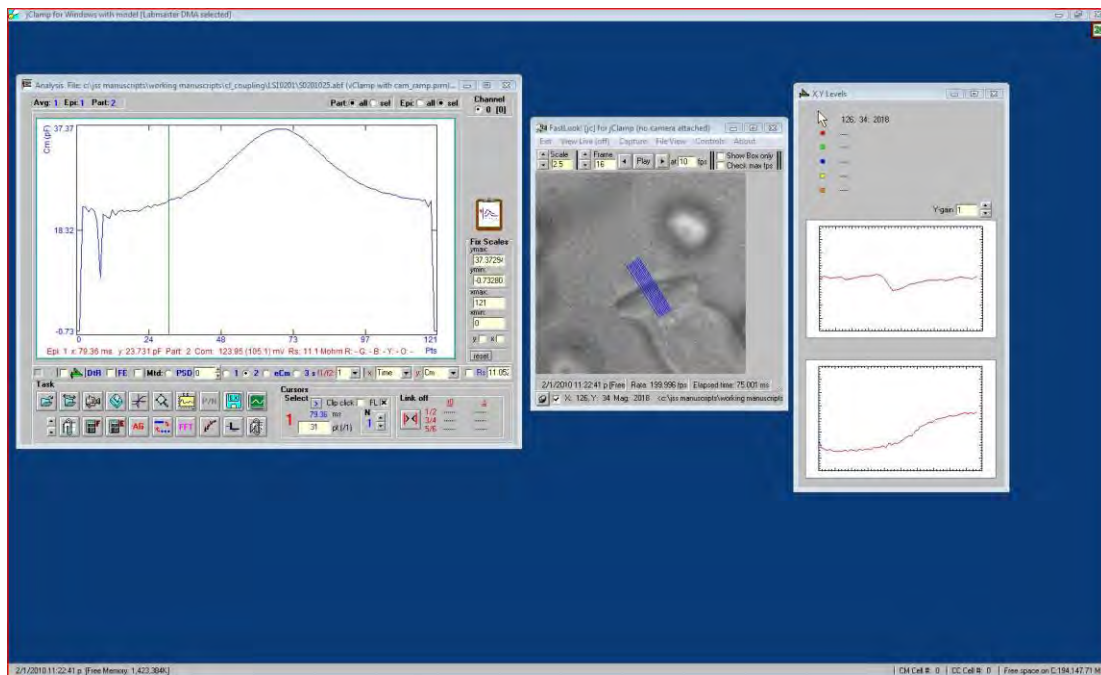


FIGURE 1. jClamp (Scisoftco.com) software was used to simultaneously measure NLC and electromotility. Capacitance measures were synchronized to video frame capture so that voltage dependence of NLC and motility could be compared. Motility functions were obtained by measuring movements of the cuticular plate edge, with the base of the OHC fixed by the patch electrode.

METHODS

OHCs were voltage clamped using an Axon 200B amplifier under jClamp (Scisoftco.com) software control. NLC and mechanical responses were measured simultaneously with depolarizing and hyperpolarizing ramps of 100 ms – 5 sec duration, effectively modulating the rate of voltage change. NLC was measured with a dual sine method [7] with a 390 Hz resolution, and mechanical responses were measured (in pixels; 15 pix/5 μm) from video images (Prosilica GE680 camera) synchronized within jClamp (Fig. 1) to the voltage stimuli. Frame rate was typically set at 200 fps. Solutions were as previously described [8]. Chloride was substituted with gluconate. No averaging was done. V_h (mid- point voltage) for motility functions was determined from midpoint of sigmoidal fits; V_h of NLC from peak capacitance.

RESULTS

Under voltage clamp, OHCs display a nonlinear capacitance that is bell shaped with its peak residing at a voltage (V_h) where motor charge movement is equally distributed on either side (Fig. 2A). Coupled to this nonlinear charge movement is a mechanical response of the whole cell that follows the charge's voltage dependence. Shifts in NLC V_h , induced by changing the long term holding potential (prepulse) of the cell,

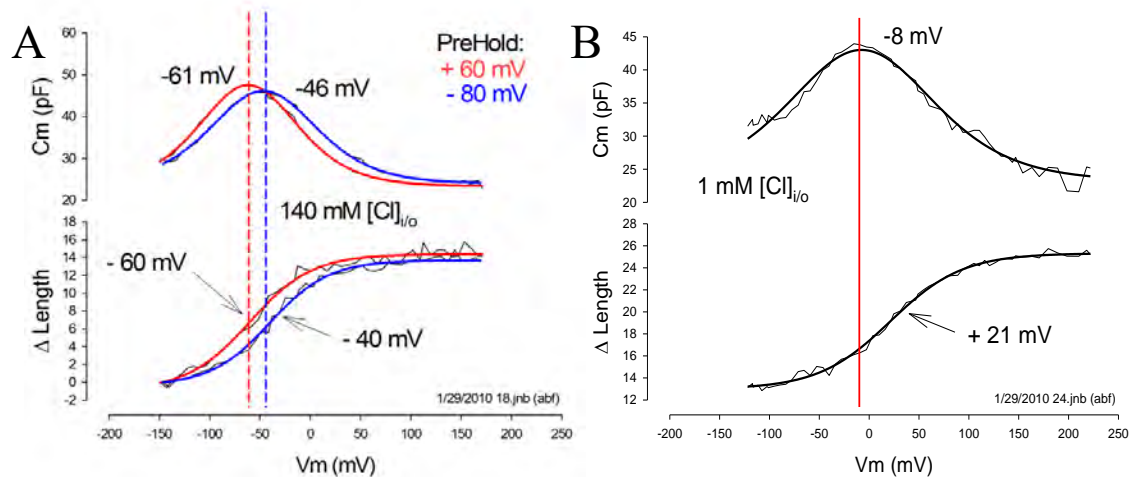


FIGURE 2. OHC NLC and electromotility share a common voltage dependence that changes when holding potential is changed. **A)** NLC and motility before and after holding resting potential for 2 minutes at indicated voltages. This effect is seen regardless of intracellular chloride concentration. **B)** However, when intracellular chloride is set low, NLC and motility voltage dependence are separated.

are accompanied by equivalent shifts in electromotility voltage dependence. This tight coupling between motor conformation and electromotility is seen when intracellular chloride is high, e.g., 140 mM, the typical intracellular level used for experimentation during the last few decades to study OHCs. More recently, normal OHC intracellular chloride levels were found to be < 10 mM [6], and given the significant influence of chloride on OHC motor charge movement [4,8,9], we evaluated the influence of chloride concentration on electromechanical coupling. Surprisingly, electromotility uncoupled from charge movement at low chloride levels (Fig. 2B and 3). We have found disparities in some cells as large as 50 mV between molecular and whole cell mechanical responses.

The disparity is not only chloride dependent, but increases as ramp rate is increased (data not shown). This increase resembles a visco-elastic like behavior. Lowering intracellular chloride changed the rate dependence of the uncoupling - low frequency effects were diminished and high frequency effects were augmented.

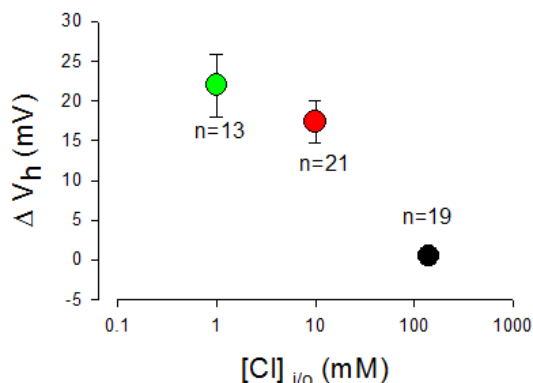


FIGURE 3. Average difference in V_h (ΔV_h) between NLC and mechanical response. No difference is observed when intracellular chloride is clamped to 140 mM. However, at lower levels an uncoupling of voltage dependence is apparent.

We also observed that coupling efficacy was stimulus polarity dependent, and was observable for voltage steps or ramps (Fig. 4). Uncoupling was larger for depolarizing excursions, suggesting work against the OHC cytoskeletal spring [10] during cell contraction. Interestingly, we find that agents which modify the cytoskeleton can

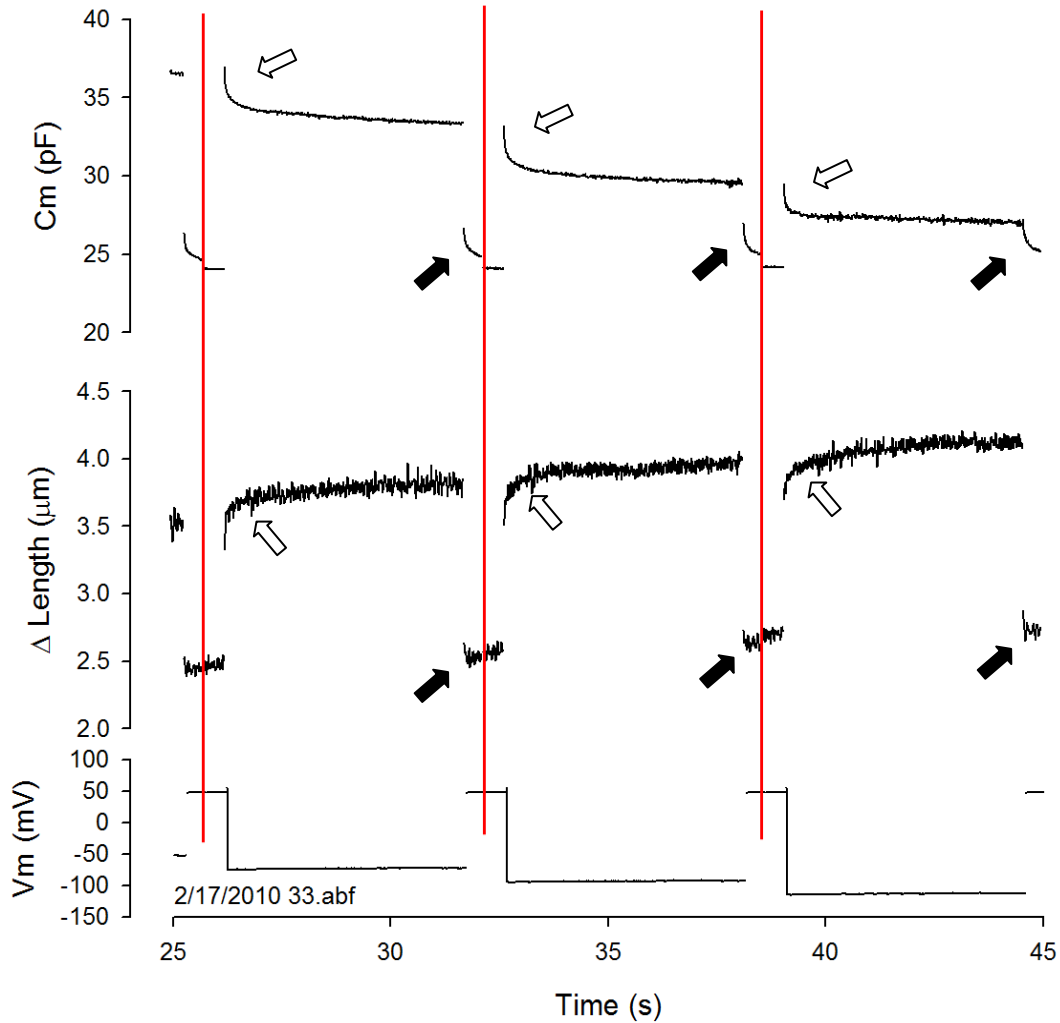


FIGURE 4. Simultaneous changes in OHC capacitance and OHC length during incrementing step changes in voltage, illustrating the polarity dependent coupling between motor charge movement and whole cell mechanical response. Red lines indicate a recovery period (1 sec) at 50 mV between voltage steps to hyperpolarized levels. Note that voltage steps in the hyperpolarizing direction induce synchronous time dependent changes in both NLC and electromotility (white arrows); however, returning depolarizing steps, though inducing similar time dependent changes (of opposite direction) in NLC, corresponding time dependent changes in electromotility are absent (black arrows). This polarity dependent coupling is observable with ramps of opposite polarity, as well (data not shown).

modulate the disparity, further suggesting that chloride influences a cytoskeletal-based coupling between prestin's conformational state and whole cell mechanics.

DISSUSSION

Coupling between the molecular conformation of prestin motors (estimated from nonlinear charge movement or NLC) and OHC whole cell mechanical response (measured directly by video) is not fixed. Depending on intracellular chloride and stimulus conditions, the voltage dependence of NLC and electromotility can vary independently. V_h of NLC is significantly influenced by initial voltage condition, and

has corresponding effects on electromotility. However, electromotility shows augmented effects attributable to degree of electromechanical coupling. Coupling is very tight with high intracellular chloride (140 mM), and at low rates of voltage perturbation. Even with normal low intracellular chloride concentrations (<10 mM, [6]), increases of voltage perturbation rate promotes growing voltage uncoupling of molecular and whole cell mechanical activity. Agents affecting the cortical cytoskeleton alter ramp rate effects, possibly by modifying lateral membrane stiffness/tension. These observations are expected to have considerable consequences *in vivo*; namely, whole cell mechanical activity of the OHC (and feedback into the basilar membrane that it is expected to provide) may not simply follow the membrane potential of the cell.

CONCLUSIONS

The uncoupling we find imposes an additional challenge for the voltage-sensitive protein prestin to drive the cochlear partition during acoustic stimulation, since the whole cell mechanical response will be variably uncoupled from voltage, depending on phase of receptor potential. On the other hand, the molecular conformation of prestin is tightly coupled, implying that membrane characteristics (e.g., changes in membrane stiffness) driven by prestin may more significantly govern “cochlea amplification” than electromotility.

ACKNOWLEDGMENTS

Supported by NIH NIDCD Grant R01 DC 000273 to JSS.

REFERENCES

- [1] Zheng J, Shen W, He DZ, Long KB, Madison LD, Dallos P (2000) Prestin is the motor protein of cochlear outer hair cells. *Nature* 405: 149-155.
- [2] Ashmore JF (1990) Forward and reverse transduction in the mammalian cochlea. *Neurosci Res Suppl* 12: S39-S50.
- [3] Santos-Sacchi J (1991) Reversible inhibition of voltage-dependent outer hair cell motility and capacitance. *J Neurosci* 11: 3096-3110.
- [4] Rybalchenko V, Santos-Sacchi J (2003) Cl⁻ flux through a non-selective, stretch-sensitive conductance influences the outer hair cell motor of the guinea-pig. *J Physiol* 547: 873-891.
- [5] Santos-Sacchi J, Kakehata S, Takahashi S (1998) Effects of membrane potential on the voltage dependence of motility-related charge in outer hair cells of the guinea-pig. *J Physiol* 510 (Pt 1): 225-235.
- [6] Santos-Sacchi J, Song L, Zheng J, Nuttall AL (2006) Control of mammalian cochlear amplification by chloride anions. *J Neurosci* 26: 3992-3998.
- [7] Santos-Sacchi J (2004) Determination of cell capacitance using the exact empirical solution of dY/dCm and its phase angle. *Biophys J* 87: 714-727.
- [8] Song L, Seeger A, Santos-Sacchi J (2005) On membrane motor activity and chloride flux in the outer hair cell: lessons learned from the environmental toxin tributyltin. *Biophys J* 88: 2350-2362.
- [9] Oliver D, He DZ, Klocker N, Ludwig J, Schulte U, Waldegger S, Ruppertsberg JP, Dallos P, Fakler B (2001) Intracellular anions as the voltage sensor of prestin, the outer hair cell motor protein. *Science* 292: 2340-2343.
- [10] Holley MC, Ashmore JF (1988) A cytoskeletal spring in cochlear outer hair cells. *Nature* 335: 635-637.

Conformational State-Dependent Anion Binding in Prestin: Evidence for Allosteric Modulation

Lei Song and Joseph Santos-Sacchi*

Department of Surgery (Otolaryngology), Department of Cellular and Molecular Physiology, and Department of Neurobiology, Yale University School of Medicine, New Haven, Connecticut

ABSTRACT Outer hair cells boost auditory performance in mammals. This amplification relies on an expansive array of intramembranous molecular motors, identified as prestin, that drive somatic electromotility. By measuring nonlinear capacitance, the electrical signature of electromotility, we are able to assess prestin's conformational state and interrogate the effectiveness of anions on prestin's activity. We find that the affinity of anions depends on the state of prestin that we set with a variety of perturbations (in membrane tension, temperature, and voltage), and that movement into the expanded state reduces the affinity of prestin for anions. These data signify that anions work allosterically on prestin. Consequently, anions are released from prestin's binding site during expansion, i.e., during hyperpolarization. This is at odds with the extrinsic voltage sensor model, which suggests that prestin-bound intracellular anions are propelled deep into the membrane. Furthermore, we hypothesize that prestin's susceptibility to many biophysical forces, and notably its piezoelectric nature, may reflect anion interactions with the motor.

INTRODUCTION

Allosteric modulation of protein function is ubiquitous, denoting the control of a protein's conformational state (tensed versus relaxed) and activity by perturbation (via ligand or nonligand mechanisms) of sites distal to the protein's active site (1–4). Monod et al. (3) originally developed a concerted allosteric model to describe the effects of oxygen binding on hemoglobin, but this model has also been shown to be useful for understanding other proteins, including intramembranous proteins. For example, modeling the modulation of Maxi-K channels by voltage and Ca²⁺ has benefited from allosteric theory (5,6). One interesting consequence of allostery is the coupling of the conformational state and ligand-binding affinity, a phenomenon that forms the basis of state-dependent block of ion channels (7).

The conformational state of the outer hair cell (OHC) motor protein, prestin, is primarily driven by voltage. Changes in the conformational state of the molecule can be gleaned from the voltage dependence of its nonlinear charge movement or its equivalent bell-shaped nonlinear capacitance (NLC) (8, 9). Indeed, the voltage at peak capacitance (V_{pkcm}) or, equivalently, the half-maximal charge movement (V_h), is a sensitive indicator of the distribution of motors in the compact or expanded state, according to two-state models of OHC motor activity (10,11). However, the distribution is not fixed; rather, it depends on a host of external influences. Prolonged negative holding potentials (prepulse) (12), positive membrane tension (13–16), and increasing temperature (17,18) can each significantly shift V_{pkcm} rightward, in the depolarizing direction, in a multiexponential,

time-dependent manner (19), indicating a redistribution of compact motors into the expanded state.

Recent observations have established an important role for anions in controlling prestin and OHC function (20–24). Charge movement in prestin is modulated by Cl[−] ions with a $K_{1/2}$ of ~6 mM (21,22). We have argued that the binding of anions works allosterically to modify prestin activity (20,23–26). Here we capitalize on prestin's sensitivity to membrane tension, temperature, and voltage to show that prestin's binding affinity for the anions Cl[−] and salicylate is dependent on motor conformation, confirming an allosteric interaction.

MATERIALS AND METHODS

General preparation and procedure

Hartley albino guinea pigs were overdosed with halothane. The temporal bones were excised and the cochleae were dissected in a calcium-free (no chelator) solution and then treated with enzyme (0.5 mg/mL Dispase I, 10–12 min). Individual OHCs were isolated by gentle trituration. The suspension of cells was then transferred to a petri dish for the cells to settle.

The base extracellular solution contained (in mM) NaCl 132, CaCl₂ 2, MgCl₂ 2, and Hepes 10. The final solutions were adjusted to ~300 mOsm with D-glucose (except for the solutions used for the osmotic challenge experiment, which were adjusted to ~280 mOsm) and pH 7.2–7.3 with NaOH. The intracellular solution was the same as the extracellular solution except for the addition of 10 mM EGTA. Other Cl[−] levels were achieved by replacing Cl[−] with gluconate. Salicylate (10 mM) was added to the base extracellular solution (~300 mOsm, pH 7.2–7.3) and subsequently diluted into concentrations of 0.1, 1, 10, 100, 1000, and 10,000 μ M. Continuous local perfusion was achieved with the use of a custom-made Y-tube. Perfusion of salicylate either as a concentration series or at a single dose were performed with and without positive pressure in the patch pipette (increased tension at ~0.7 kPa). Pipette pressure was monitored via a pressure monitor (PM015R; World Precision Instruments, Sarasota, FL). Whole-cell NLC (see below) recordings were made after the pressure stabilized.

Experiments were performed at room temperature and at 32–35°C. To study the effect of temperature, bath solutions at room temperature were

Submitted August 12, 2009, and accepted for publication October 16, 2009.

*Correspondence: joseph.santos-sacchi@yale.edu

Editor: Tzyh-Chang Hwang.

© 2010 by the Biophysical Society
0006-3495/10/02/0371/6 \$2.00

doi: 10.1016/j.bpj.2009.10.027

exchanged with preheated bath solutions to increase the temperature around the OHC of interest. A temperature probe (model DP26-TC-AP; Omega Engineering) was placed in the bath near the recorded OHC to document the temperature rise. Recordings of NLC were made when the temperature rose $\sim 10^\circ\text{C}$. A Nikon Eclipse E600-FN microscope with a $40\times$ water immersion lens was used to observe cells during electrical measurements. Digital images were taken with a Hamamatsu image processor.

Patch-clamp and stimulus protocols

OHCs were recorded under a whole-cell, patch-clamp configuration. An Axon 200B amplifier was used for data collection. NLC was measured using a continuous high-resolution (2.56 ms sampling) two-sine stimulus protocol (10 mV peak at both 390.6 and 781.2 Hz) superimposed on a 200 ms voltage ramp from -180 to $+200$ mV (12,27). All recordings and analyses were performed using jClamp (SciSoft, Ridgefield, CT; www.scisoftco.com). Capacitance data were fit to the first derivative of a two-state Boltzmann function (8):

$$C_m = Q_{\max} \frac{ze}{kT} \frac{b}{(1+b)^2} + C_{\text{lin}} \text{ where}$$

$$b = \exp\left(\frac{-ze(V_m - V_{\text{pk}C_m})}{kT}\right),$$

where Q_{\max} is the maximum nonlinear charge moved; $V_{\text{pk}C_m}$ or V_h is the voltage at peak capacitance or, equivalently, at half-maximum charge transfer; V_m is the membrane potential; z is the valence; C_{lin} is the linear membrane capacitance; e is the electron charge; k is Boltzmann's constant; and T is the absolute temperature. Q_{sp} , the specific density of charge movement is defined as $Q_{\max}/(C_{\text{lin}} - 6.5 \text{ pF})$; 6.5 pF corresponds to the area in OHCs devoid of prestin NLC (28). Peak NLC was calculated by subtracting the linear capacitance (C_{lin}) from the peak amplitude (C_{mpk}). We used C_{lin} determined from the fit to each individual NLC trace. Paired t -tests were used and reported as the mean \pm SE. Dose response curves were fitted in SigmaPlot (Systat Software) using a four-parameter Hill equation. For the Cl^- dose response curve, the low-concentration end point was fixed to 25% of the maximum charge because we previously determined this asymptote using a full range of Cl concentrations (22).

RESULTS

Membrane tension alters the IC50 of salicylate on NLC

Salicylate is known to block NLC in OHCs via intracellular interactions with the motor (29,30). Recently, it was shown that salicylate competes with Cl^- for prestin's anion-binding site(s) (20,21). We assessed salicylate's relative affinity (competition with Cl^-) by noting the degree of reduction in NLC with intracellular Cl^- fixed at 10 mM, the normal resting level of chloride (20). Fig. 1, A and B, demonstrate that with a fixed extracellular salicylate perfusion of 0.1 mM, tension reduced the effectiveness of the salicylate insult (intra- and extracellular solutions both contained 10 mM Cl). The reduction of nonlinear peak capacitance was 11.22 ± 0.68 pF for collapsed cells and 7.44 ± 1.15 pF for pressurized (~ 0.7 kPa) cells ($n = 4$, $P < 0.01$, paired t -test). In percentage terms, this corresponds to reductions of 22.08% and 16.57%, respectively. Since the perfusion is done extracellularly, it is possible that the manipulation of membrane tension can change membrane properties such that salicylate entry into the cells will be different under the

two conditions. To rule out this possibility, we introduced 0.1 mM salicylate intracellularly via the patch pipette, and obtained comparable significant results. Indeed, even with equal concentrations of salicylate intra- and extracellularly, similar results were obtained. The use of an osmotic challenge (~ 280 mOsm) produced comparable results (data not shown).

Tension effects were explored in greater detail in another set of experiments to measure the IC50 of salicylate. A series of salicylate concentrations (0.1–10,000 μM) were applied to OHCs first under collapsed conditions and then, after complete washout (assessed by the return of NLC to pretreatment conditions), under pressurized conditions (~ 0.7 kPa). Fig. 1 C illustrates the shift in the dose response curve obtained for a single OHC. Data from four cells (with pipette solutions containing 10 mM Cl^-) yielded a shift of IC50 from 144.77 ± 61.33 to 550.05 ± 221.49 mM. This represents an ~ 4 -fold reduction in effectiveness, indicating an equivalent reduction in the affinity of salicylate for prestin. For cells with 140 mM Cl^- in and out, the shift for IC50s for salicylate dose response curves was from 333.89 ± 46.81 to 563.77 ± 27.99 mM ($n = 3$). The smaller shift at higher chloride levels is consistent with our previous finding that salicylate is more effective at lower chloride levels (20).

Membrane voltage prepulse and temperature alter salicylate's effect on NLC

The data obtained so far indicate that increasing membrane tension, which tends to redistribute the motors into the expanded state, reduces the affinity of salicylate for prestin's anion-binding site. If the conformation of prestin were responsible for this effect, we would expect any method we used to redistribute prestin into the expanded state to work similarly. Fig. 2 A confirms that by heating the cells, we diminished the ability of salicylate to reduce NLC. The average reductions of nonlinear peak capacitance for 1 mM salicylate treatment were 9.9 ± 1.00 pF at room temperature and 5.58 ± 0.73 pF after an $\sim 10^\circ\text{C}$ increase in bath temperature ($n = 4$, $P < 0.05$, paired t -test). Intermediate temperatures between room temperature and $+10^\circ\text{C}$ were proportionally effective. The effectiveness of salicylate insult (reduction of NLC) fell at a rate of 0.366 pF/ $^\circ\text{C}$ with increases in temperature (see Fig. S1 in the Supporting Material).

Additionally, Fig. 2 B shows that holding at negative voltages, which redistributes prestin into the expanded state, diminishes the ability of salicylate to reduce NLC. The average reduction of nonlinear peak capacitance for 1 mM salicylate treatment was 10.50 ± 0.16 pF at $\sim +55$ mV holding potential and 6.41 ± 1.05 pF at ~ -75 mV holding potential ($n = 4$, $P < 0.005$, paired t -test). Intermediate holding voltages between $+55$ and -75 mV were proportionally effective. The effectiveness of salicylate insult (reduction of NLC) fell at a rate of 0.029 pF/mV with hyperpolarization (see Fig. S1).

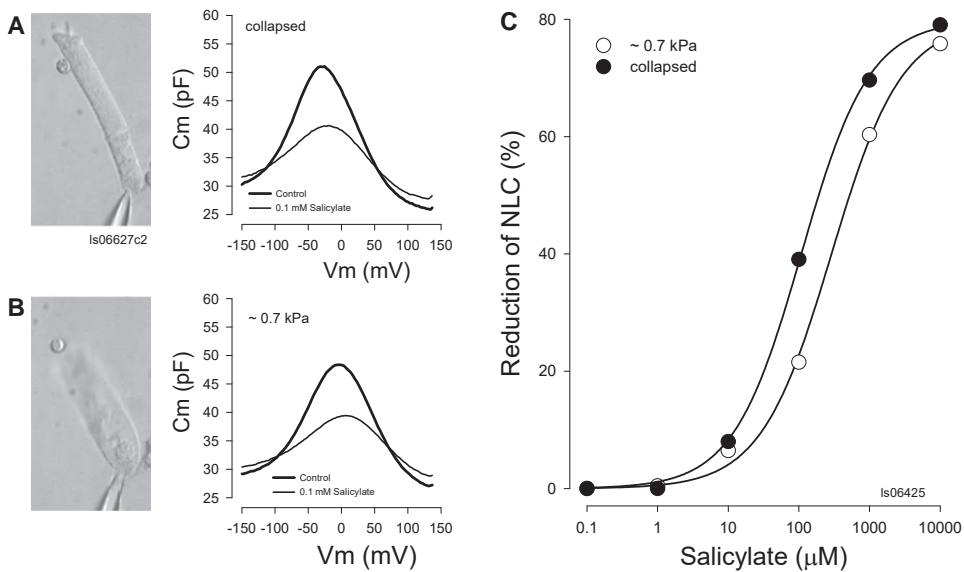


FIGURE 1 Competition between salicylate and chloride for prestin's anion-binding site is dependent on membrane tension. (A) Image of patch-clamped OHC under collapsed conditions and associated NLC traces obtained before (control) and after perfusion with 0.1 mM salicylate. Cell diameter is 10 μm . (B) Corresponding image (note the reduced length and increased diameter of cell) and NLC traces for the same cell after an increase in pipette pressure (0.7 kPa). The averaged reduction of nonlinear peak capacitance due to salicylate perfusion is 11.22 ± 0.68 for collapsed cells and 7.44 ± 1.15 pF ($n = 4$, mean \pm SE, $P < 0.01$, paired t -test). (C) Plot from another cell of the dose response curve for salicylate before and after membrane tension delivery. Averaged results show a shift in IC_{50} from 144.77 ± 61.33 to 550.05 ± 221.49 (mean \pm SE).

Membrane tension reduces chloride's binding affinity for prestin

Finally, we confirmed the generality and physiological significance of our results by testing the effects of membrane tension on Cl-anion affinity. In this series of experiments, the chloride concentration was set to the same level intra- and extracellularly, and the effects of membrane tension on NLC were determined for a range of chloride ion concentrations (1–140 mM). NLC was measured first under collapsed conditions and then under pressurized conditions (~ 0.7 kPa). Fig. 3 A illustrates the average shift ($n = 4$ –5) in the dose response curve. The fitted sigmoidal (Hill) functions indicate a $K_{1/2}$ of 1.68 mM under collapsed conditions, and 4.74 mM under pressurized conditions. The shift of V_{pkcm} due to ~ 0.7 kPa pressurization is ~ 20 mV to the right regardless of chloride concentration (Fig. 3 B), indicating that the results are not due to chloride-dependent changes in the susceptibility to membrane tension.

It is important to note that with each type of manipulation available to us, we had to limit the perturbation magnitude to maintain our cell recordings during the lengthy protocols; therefore, we obtained only a limited interrogation of the changes in binding affinity that might be realized by a complete shift between compact and expanded states.

DISCUSSION

The OHC motor is voltage-dependent (31) and possesses a voltage sensor that controls its conformational state (compact/expanded) at rates in excess of 75 kHz (10,11,32). The voltage dependence of the sensor charge movement is shallow, with a Boltzmann slope factor of ~ 29 mV, and thus very large voltage changes (>200 mV)

are required to fully redistribute motors between its two conformations (compact and expanded) (8, 9). The midpoint voltage (V_{pkcm} or V_h) of this operational range can be modified by several manipulations, including membrane tension, prior (prepulse) holding voltage, and temperature. The effect of tension on V_{pkcm} is on the order of a 20 mV rightward (i.e., depolarizing) shift per kPa of intracellular pressure, with the cell being able to withstand only a few kilopascals before it ruptures (15,16). Changes in the holding potential can shift V_{pkcm} tens of millivolts, with the shift being opposite to the prepulse polarity and having maximum effectiveness near normal resting potentials (12,19). Increases in temperature cause a 20 mV rightward shift per 10°C (17,18).

In this work, we exploited prestin's sensitivity to these biophysical forces to test the hypothesis that anions work allosterically by interrogating the effect of the motor conformational state on anion affinity. Although we were only able to interrogate conformation-dependent binding affinity over a limited population shift between compact and expanded states (see Materials and Methods), each perturbation we made to shift the state dependence of prestin motors from the compact to the expanded state reduced the affinity of the tested anion for the motor. We reason that prestin's anion-binding site, which has been tentatively identified in prestin as homologous to the Cl-binding motif conserved in ClC channels (GXXXP (26,33,34)), is altered during induced conformational change to modify binding affinity for anions. We especially note a parallel in the reciprocal nature of the voltage dependence and tension dependence of prestin (piezoelectricity) and the reciprocal nature of anion binding and the conformational state of prestin (allostery). The piezoelectric nature of prestin was first identified by Iwasa (13), who found that membrane tension can cause

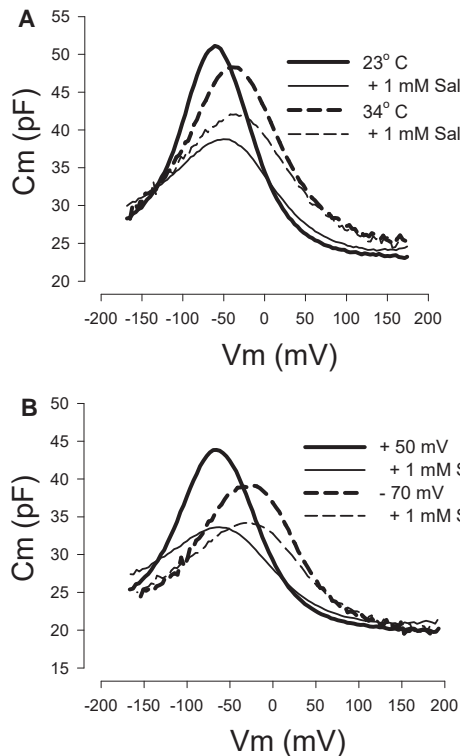


FIGURE 2 Competition between salicylate and chloride for prestin's anion-binding site is dependent on temperature and holding voltage. (A) A representative OHC was whole-cell patched with 140 mM Cl^- in and out, and perfused with 1 mM salicylate first at 23°C (solid lines) and then at 34°C (dashed lines). The reduction of NLC after salicylate perfusion (thin lines) is less under the high-temperature condition. Average reductions of nonlinear peak capacitance for salicylate treatment are 9.9 ± 1.00 pF (mean \pm SE) vs. 5.58 ± 0.73 pF (mean \pm SE) ($n = 4$, $P < 0.05$, paired t -test). (B) A representative OHC was whole-cell patched and perfused with 1 mM salicylate at room temperature. The OHC was held at either -70 mV (dashed lines) or $+50$ mV (solid lines). The reduction of NLC after salicylate perfusion (thin lines) is less at the -70 mV holding potential. The average reduction of nonlinear peak capacitance for salicylate treatment is 10.50 ± 0.16 (mean \pm SE) at positive holding potentials and 6.41 ± 1.05 (mean \pm SE) at negative holding potentials ($n = 4$, $P < 0.005$, paired t -test).

a shift in the voltage dependence of OHC NLC; thus, tension can induce displacement currents in the OHC (14,35). This linkage between deformation and electrical activity is greater in the OHC than in piezoelectric crystals (36), and has been the focus of models that aim to enhance the frequency-dependent effects of electromotility (37). We conjecture that the piezoelectric nature of prestin may ultimately reside in the allosteric action of anions. Furthermore, we hypothesize that the sensitivity of prestin to the range of biophysical perturbations observed to influence the state of the motor may involve anion interactions with the motor. To be sure, the shift magnitudes from membrane tension, temperature, and prepulse are dwarfed by that observed when physiologically tolerable chloride concentrations are changed within the OHC: at the $K_{1/2}$ for the Cl^- -dependent V_{pkcm} shift

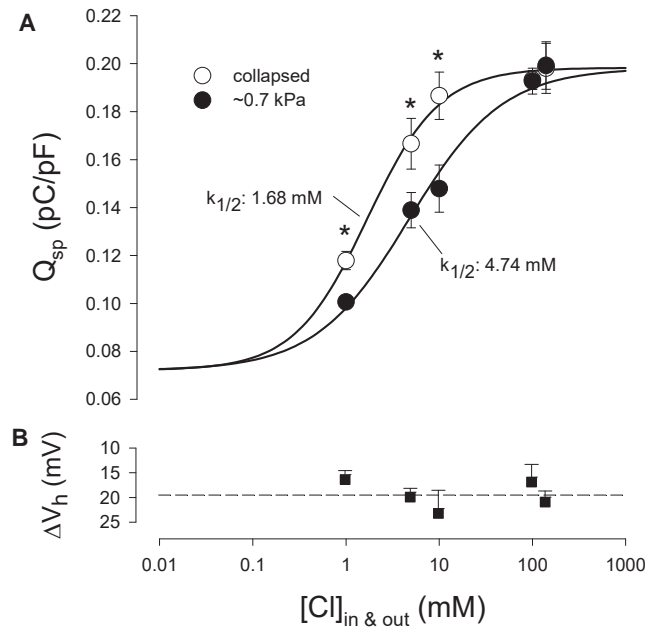


FIGURE 3 Chloride binding to prestin is state-dependent. OHCs were whole-cell patched and NLC was recorded. Chloride concentration was set to the same level intra- and extracellularly, and the effects of membrane tension on NLC were determined for a range of chloride ion concentrations (1–140 mM). NLC was measured first under collapsed conditions and then under pressurized conditions (~ 0.7 kPa). OHC NLC was fitted (Eq. 1) to determine V_h and total nonlinear charge moved (Q_{max}), with Q_{max} normalized to cell surface area (Q_{sp}) for comparison across cells. (A) OHC Q_{sp} is Cl^- -dependent, with $\sim 25\%$ of the charge insensitive to chloride as demonstrated previously (22). Changing prestin's state by application of positive membrane tension shifts the dose response curve to the right. Paired t -test significance (*, $P < 0.05$; $n = 4-5$) is noted in the figure. The fitted sigmoidal (Hill) functions indicate a $K_{1/2}$ of 1.68 mM under collapsed conditions and 4.74 mM under pressurized conditions. (B) The shift of V_h due to ~ 0.7 kPa pressurization is ~ 20 mV to the right regardless of chloride concentration, indicating no chloride-dependent changes in the susceptibility to membrane tension.

(4.8 mM, close to the resting intracellular $[\text{Cl}^-]$ (20)), the shift is ~ 8 mV/mM (22). Thus, we would predict that other perturbations that affect the prestin state, such as changes in the membrane lipid environment of OHCs (38,39) or prestin-transfected cells (40), result from alterations of anion-binding affinity.

The competitiveness of salicylate with chloride for prestin's anion-binding site results from a higher affinity for salicylate over chloride (21). If we assume that chloride and salicylate binding affinity can be manipulated independently, then the reduced binding affinity of chloride by our manipulations could have increased salicylate's effectiveness. This was not the case, and we must conclude that our manipulations affect the binding site in a manner that influences binding of all anions. Thus, the effects of salicylate are direct, and not a result of displacing chloride. This is in line with the variable effects of different species of anions on NLC (25).

In summary, all perturbations that caused V_{pkcm} to shift in the depolarizing direction, i.e., that caused prestin motors to move into the expanded state, reduced prestin's anion-binding affinity. These observations have direct implications for the mechanism of voltage sensing in prestin (Fig. 4). Oliver et al.'s (21) popular model of prestin as a dysfunctional anion transporter, in which an intracellular chloride anion serves as extrinsic voltage sensor, predicts that truncated transport of chloride from its intracellular binding site on prestin to an extracellularly directed intramembranous site within the protein evokes prestin's expanded state. On the contrary, our data necessarily indicate that intracellularly bound anions are released (due to reduced affinity) upon motor expansion, and thus conflict with their model. We maintain that anion binding is associated with motor contraction and OHC shortening, in line with our previous observations that increasing Cl^- intracellularly boosts the number of motors residing in the contracted state (22,23). Of interest, an analysis of a variety of models, including those resulting from intrinsic sensing, extrinsic sensing, and a combination of transporting and sensing mechanisms, found that predicted movements of chloride during transport are associated with the contraction of prestin (41). We believe these fine points of contention with the extrinsic voltage sensor model can be used to argue for a general mechanism of allostery that portrays prestin as a protein of normal character that does not require unusual modes (or models) of action. To be sure, we determined that the sensor charge movement in prestin relies on particular charged residues, as is the case in other voltage-dependent proteins (42), and that prestin's voltage-dependent charge movement can be isolated from its anion transport (26). These data do not imply that models that detect (incorporate) composite charge movement contributions from anions and intrinsic residues are faulty in their

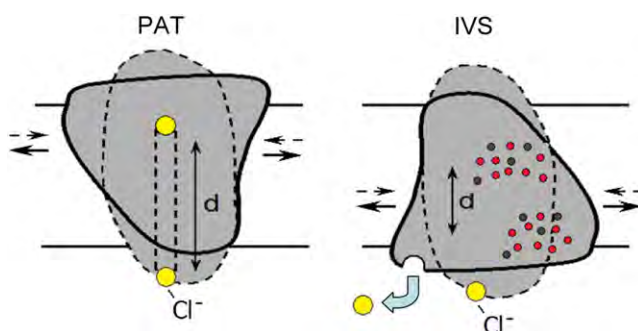


FIGURE 4 Two models representing the events after anion binding to prestin. The left panel depicts the extrinsic voltage sensor model (21), where Cl^- binds and enters the defunct transporter, which in turn triggers an extension of prestin. The right panel depicts the intrinsic voltage sensor model (23–25), where Cl^- binding to prestin allosterically promotes the contracted state, but voltage sensing results from movement of intrinsically charged amino acid residues (red: positive residues; black: negative residues) (26). Our new data confirm that during expansion, anions are released from prestin. (In both panels, d is the perpendicular distance traversed across the membrane field by the voltage sensor.)

assessment of NLC (41,43), as we fully acknowledge that any charged species moving through the membrane field can contribute to NLC. We simply want to point out that the assignment of charge components to effect electromotility or not is not a simple process, and it could be that the movement of a transported anion through prestin (and its resultant displacement current) is unrelated to the mechanism that drives the voltage-dependent mechanical activity of the protein. Thus, the only thing that is absolutely clear to us is that NLC is modulated by anions. Consequently, our new findings and our previous observations that also conflict with the extrinsic voltage sensor model—namely, that 1), changes in the intracellular anion concentration and species shift the voltage dependence of NLC (V_{pkcm}); 2), the anion valence does not correlate with the voltage sensor valence; 3), prestin successfully transports anions; 4), the intrinsic charge contributes to prestin's voltage sensing; and 5), single-site mutations can separate voltage sensing and transport (23,25,26)—lead us to conclude that anions work through an allosteric action on prestin.

SUPPORTING MATERIAL

A figure is available at [http://www.biophysj.org/biophysj/supplemental/S0006-3495\(09\)01669-5](http://www.biophysj.org/biophysj/supplemental/S0006-3495(09)01669-5).

We thank Fred Sigworth for his thoughts on allostery.

This work was supported by grants from the National Institute on Deafness and Other Communication Disorders (DC00273 to J.S.S.) and Oshe grant for Surgical Research at Yale University School of Medicine (to L.S.).

REFERENCES

1. Gunasekaran, K., B. Ma, and R. Nussinov. 2004. Is allostery an intrinsic property of all dynamic proteins? *Proteins*. 57:433–443.
2. Goodey, N. M., and S. J. Benkovic. 2008. Allosteric regulation and catalysis emerge via a common route. *Nat. Chem. Biol.* 4:474–482.
3. Monod, J., J. Wyman, and J. P. Changeux. 1965. On the nature of allosteric transitions: a plausible model. *J. Mol. Biol.* 12:88–118.
4. Koshland, Jr., D. E., G. Némethy, and D. Filmer. 1966. Comparison of experimental binding data and theoretical models in proteins containing subunits. *Biochemistry*. 5:365–385.
5. Cui, J., and R. W. Aldrich. 2000. Allosteric linkage between voltage and Ca^{2+} -dependent activation of BK-type $mslo1$ K^{+} channels. *Biochemistry*. 39:15612–15619.
6. Rothberg, B. S. 2004. Allosteric modulation of ion channels: the case of Maxi-K. *Sci. STKE*. 2004:e16.
7. Ragsdale, D. S., J. C. McPhee, ..., W. A. Catterall. 1994. Molecular determinants of state-dependent block of Na^{+} channels by local anesthetics. *Science*. 265:1724–1728.
8. Santos-Sacchi, J. 1991. Reversible inhibition of voltage-dependent outer hair cell motility and capacitance. *J. Neurosci.* 11:3096–3110.
9. Ashmore, J. F. 1990. Forward and reverse transduction in the mammalian cochlea. *Neurosci. Res. Suppl.* 12:S39–S50.
10. Santos-Sacchi, J. 1993. Harmonics of outer hair cell motility. *Biophys. J.* 65:2217–2227.
11. Iwasa, K. H. 1994. A membrane motor model for the fast motility of the outer hair cell. *J. Acoust. Soc. Am.* 96:2216–2224.

12. Santos-Sacchi, J., S. Kakehata, and S. Takahashi. 1998. Effects of membrane potential on the voltage dependence of motility-related charge in outer hair cells of the guinea-pig. *J. Physiol.* 510:225–235.
13. Iwasa, K. H. 1993. Effect of stress on the membrane capacitance of the auditory outer hair cell. *Biophys. J.* 65:492–498.
14. Gale, J. E., and J. F. Ashmore. 1994. Charge displacement induced by rapid stretch in the basolateral membrane of the guinea-pig outer hair cell. *Proc. R. Soc. Lond. B. Biol. Sci.* 255:243–249.
15. Kakehata, S., and J. Santos-Sacchi. 1995. Membrane tension directly shifts voltage dependence of outer hair cell motility and associated gating charge. *Biophys. J.* 68:2190–2197.
16. Dong, X. X., and K. H. Iwasa. 2004. Tension sensitivity of prestin: comparison with the membrane motor in outer hair cells. *Biophys. J.* 86:1201–1208.
17. Meltzer, J., and J. Santos-Sacchi. 2001. Temperature dependence of non-linear capacitance in human embryonic kidney cells transfected with prestin, the outer hair cell motor protein. *Neurosci. Lett.* 313:141–144.
18. Santos-Sacchi, J., and G. Huang. 1998. Temperature dependence of outer hair cell nonlinear capacitance. *Hear. Res.* 116:99–106.
19. Santos-Sacchi, J., E. Navarrete, and L. Song. 2009. Fast electromechanical amplification in the lateral membrane of the outer hair cell. *Biophys. J.* 96:739–747.
20. Santos-Sacchi, J., L. Song, ..., A. L. Nuttall. 2006. Control of mammalian cochlear amplification by chloride anions. *J. Neurosci.* 26:3992–3998.
21. Oliver, D., D. Z. He, ..., B. Fakler. 2001. Intracellular anions as the voltage sensor of prestin, the outer hair cell motor protein. *Science.* 292:2340–2343.
22. Song, L., A. Seeger, and J. Santos-Sacchi. 2005. On membrane motor activity and chloride flux in the outer hair cell: lessons learned from the environmental toxin tributyltin. *Biophys. J.* 88:2350–2362.
23. Rybalchenko, V., and J. Santos-Sacchi. 2003. Cl⁻ flux through a non-selective, stretch-sensitive conductance influences the outer hair cell motor of the guinea-pig. *J. Physiol.* 547:873–891.
24. Rybalchenko, V., and J. Santos-Sacchi. 2003. Allosteric modulation of the outer hair cell motor protein prestin by chloride. In *Biophysics of the Cochlea: From Molecules to Models*. A. Gummer, editor. World Scientific Publishing, Singapore. 116–126.
25. Rybalchenko, V., and J. Santos-Sacchi. 2008. Anion control of voltage sensing by the motor protein prestin in outer hair cells. *Biophys. J.* 95:4439–4447.
26. Bai, J. P., A. Surguchev, ..., D. Navaratnam. 2009. Prestin's anion transport and voltage-sensing capabilities are independent. *Biophys. J.* 96:3179–3186.
27. Santos-Sacchi, J. 2004. Determination of cell capacitance using the exact empirical solution of dY/dCm and its phase angle. *Biophys. J.* 87:714–727.
28. Santos-Sacchi, J., S. Kakehata, ..., T. Takasaka. 1998. Density of motility-related charge in the outer hair cell of the guinea pig is inversely related to best frequency. *Neurosci. Lett.* 256:155–158.
29. Kakehata, S., and J. Santos-Sacchi. 1996. Effects of salicylate and lanthanides on outer hair cell motility and associated gating charge. *J. Neurosci.* 16:4881–4889.
30. Tunstall, M. J., J. E. Gale, and J. F. Ashmore. 1995. Action of salicylate on membrane capacitance of outer hair cells from the guinea-pig cochlea. *J. Physiol.* 485:739–752.
31. Santos-Sacchi, J., and J. P. Dilger. 1988. Whole cell currents and mechanical responses of isolated outer hair cells. *Hear. Res.* 35:143–150.
32. Frank, G., W. Hemmert, and A. W. Gummer. 1999. Limiting dynamics of high-frequency electromechanical transduction of outer hair cells. *Proc. Natl. Acad. Sci. USA.* 96:4420–4425.
33. Dutzler, R., E. B. Campbell, and R. MacKinnon. 2003. Gating the selectivity filter in CIC chloride channels. *Science.* 300:108–112.
34. Dutzler, R., E. B. Campbell, ..., R. MacKinnon. 2002. X-ray structure of a CIC chloride channel at 3.0 Å reveals the molecular basis of anion selectivity. *Nature.* 415:287–294.
35. Takahashi, S., and J. Santos-Sacchi. 2001. Non-uniform mapping of stress-induced, motility-related charge movement in the outer hair cell plasma membrane. *Pflugers Arch.* 441:506–513.
36. Dong, X. X., M. Ospeck, and K. H. Iwasa. 2002. Piezoelectric reciprocal relationship of the membrane motor in the cochlear outer hair cell. *Biophys. J.* 82:1254–1259.
37. Spector, A. A., W. E. Brownell, and A. S. Popel. 2003. Effect of outer hair cell piezoelectricity on high-frequency receptor potentials. *J. Acoust. Soc. Am.* 113:453–461.
38. Santos-Sacchi, J., and M. Wu. 2004. Protein- and lipid-reactive agents alter outer hair cell lateral membrane motor charge movement. *J. Membr. Biol.* 200:83–92.
39. Rajagopalan, L., J. N. Greeson, ..., W. E. Brownell. 2007. Tuning of the outer hair cell motor by membrane cholesterol. *J. Biol. Chem.* 282:36659–36670.
40. Sfondouris, J., L. Rajagopalan, ..., W. E. Brownell. 2008. Membrane composition modulates prestin-associated charge movement. *J. Biol. Chem.* 283:22473–22481.
41. Muallem, D., and J. Ashmore. 2006. An anion antiporter model of prestin, the outer hair cell motor protein. *Biophys. J.* 90:4035–4045.
42. Bezanilla, F. 2008. How membrane proteins sense voltage. *Nat. Rev. Mol. Cell Biol.* 9:323–332.
43. Sun, S. X., B. Farrell, ..., A. A. Spector. 2009. Voltage and frequency dependence of prestin-associated charge transfer. *J. Theor. Biol.* 260:137–144.

Disparities in voltage-sensor charge and electromotility imply slow chloride-driven state transitions in the solute carrier SLC26a5

Lei Song^a and Joseph Santos-Sacchi^{a,b,c,1}

Departments of ^aSurgery (Otolaryngology), ^bNeurobiology, and ^cCellular and Molecular Physiology, Yale University School of Medicine, New Haven, CT 06510

Edited by Richard W. Aldrich, University of Texas at Austin, Austin, TX, and approved January 25, 2013 (received for review October 24, 2012)

Outer hair cells (OHCs) drive cochlear amplification that enhances our ability to detect and discriminate sounds. The motor protein, prestin, which evolved from the SLC26 anion transporter family, underlies the OHC's voltage-dependent mechanical activity (eM). Here we report on simultaneous measures of prestin's voltage-sensor charge movement (nonlinear capacitance, NLC) and eM that evidence disparities in their voltage dependence and magnitude as a function of intracellular chloride, challenging decades' old dogma that NLC reports on eM steady-state behavior. A very simple kinetic model, possessing fast anion-binding transitions and fast voltage-dependent transitions, coupled together by a much slower transition recapitulates these disparities and other biophysical observations on the OHC. The intermediary slow transition probably relates to the transporter legacy of prestin, and this intermediary gateway, which shuttles anion-bound molecules into the voltage-enabled pool of motors, provides molecular delays that present as phase lags between membrane voltage and eM. Such phase lags may help to effectively inject energy at the appropriate moment to enhance basilar membrane motion.

hearing | molecular motor

Outer hair cells (OHC) foster mechanical feedback within the mammalian cochlear partition that enhances perception of auditory stimuli by 2–3 orders of magnitude; this is known as cochlear amplification (1, 2). Following the molecular identification of prestin (3), an SLC26 family member (a5) that recapitulates the electromechanical properties of the native OHC's voltage sensor/motor (4, 5), a preponderance of evidence pointed to prestin-based electromotility (eM) as the basis of this boost (6, 7). During the last couple of decades, measures of nonlinear charge movement or capacitance (NLC), an electrical correlate of voltage-dependent conformational changes within the motor protein prestin, have served as surrogate, indeed as signature, of voltage-evoked eM of the OHC (8–12). Intracellular chloride plays an important role in prestin function (13), and recent evidence indicates that anions serve a modulatory, allosteric-like role (14–17). For the most part, anion effects, as well as many other influences on prestin, have been limited to the study of NLC, on the assumption that NLC reports on steady-state characteristics of OHC eM. We now show that this assumption is wrong.

Using simultaneous measures of charge movement and eM, we show disparity between deduced characteristics of prestin motor protein conformation. That is, a dissociation in magnitude and voltage dependence of NLC and eM is revealed by lowering intracellular chloride to physiological levels (≤ 10 mM; ref. 6), all previous comparisons having been made with abnormally high intracellular chloride levels. Furthermore, this chloride effect, which presents as a function of rate and polarity of voltage stimulation, uncovers a mechanism predicted to be frequency dependent *in vivo*, and likely plays an important role in frequency selectivity and efficiency of cochlear amplification. A very simple kinetic model, which recapitulates most known behaviors of prestin, indicates that the chloride effect is due to intermediary, non-voltage-dependent transitions, the kinetics of

which are very much slower than those of prestin's chloride-binding or voltage-dependent state transitions. These slow conformational changes likely derive from prestin's lineage as a slow anion transporter, providing lags between voltage stimulation and mechanical activity, possibly contributing to productive cochlear amplification.

Methods

Recordings were made from single isolated OHCs from the organ of Corti. Hartley albino guinea pigs were overdosed with isoflurane, the temporal bones excised, and the top turns of the cochleae dissected free. Enzyme treatment (1 mg/mL Dispase I, 10 min) preceded gentle trituration, and isolated OHCs were placed in a glass-bottom recording chamber. A Nikon Eclipse E600-FN microscope with 40 \times water immersion lens was used to observe cells during voltage clamp. Experiments were performed at room temperature.

Solutions. Chloride levels were set to bracket the intracellular level in intact OHCs, namely ~ 10 mM (6). An ionic blocking solution was used to remove ionic currents, allowing valid measures of membrane capacitance. The base high Cl solution contained (in millimoles): NaCl 100, tetraethyl ammonium-Cl 20, CsCl 20, CoCl₂ 2, MgCl₂ 1, CaCl₂ 1, Hepes 10. Lower chloride concentrations (10 and 1 mM) were achieved by substituting chloride with gluconate. In a subset of experiments, aspartate was used as the substitute. Base intracellular solutions contains (in millimoles): CsCl 140, MgCl₂ 2, Hepes 10, and EGTA 10. The intracellular and extracellular Cl concentration was set the same to guarantee levels in the subplasmalemmal space of the OHC.

Manipulation of the subsurface cytoskeletal integrity was made with diamide and latrunculin. Diamide works on spectrin to unbundle actin filaments and reduce OHC stiffness (18). On the other hand, latrunculin results in actin depolymerization (19). OHCs were treated with 2 mM diamide in extracellular solutions for 30 min before recordings. Latrunculin A (0.01 μ M) was perfused both intracellularly (via patch electrode) and extracellularly during recording. All chemicals used were purchased from Sigma.

Cell Capacitance and Mechanical Response. An Axon 200B amplifier was used for whole cell recording. Coupled voltage ramps (depolarizing followed immediately by hyperpolarizing ramp) of varying durations from 100 to 5,000 ms were delivered to the cells from a holding potential of 0 mV. In a subset of cells, ramp order was reversed after routine collection and comparison of the two yielded no significant differences. The ramp voltage was set between -250 and $+250$ mV maximum, but span was fixed at 360 mV. For each individual cell, the ramp voltage was set according to V_h of NLC permitting responses to reach steady state to ensure good Boltzmann fits. No averaging was done.

Nonlinear capacitance was measured using a continuous high-resolution (2.56-ms sampling) two-sine stimulus protocol (10 mV peak at both 390.6 and 781.2 Hz) superimposed onto the voltage ramp (20, 21). Capacitance data were fit to the first derivative of a two-state Boltzmann function (9) (see *Supporting Information* for equation), providing Q_{max} , the maximum nonlinear charge moved, V_h the voltage at peak capacitance or equivalently,

Author contributions: L.S. and J.S.-S. designed research, performed research, contributed new reagents/analytic tools, analyzed data, and wrote the paper.

The authors declare no conflict of interest.

This article is a PNAS Direct Submission.

¹To whom correspondence should be addressed. E-mail: joseph.santos-sacchi@yale.edu.

This article contains supporting information online at www.pnas.org/lookup/suppl/doi:10.1073/pnas.1218341110/-DCSupplemental.

at half maximum charge transfer, z , the valence, and C_{lin} the linear membrane capacitance.

Simultaneous eM measurements were recorded with a Prosilica GE680 camera (Allied Vision Technologies). Video sampling of 3.3 ms were achieved with binning and reduced region of interest. Video image resolution was 2.83 pixels per micrometer. The eM video recordings were digitally analyzed with jClamp (www.SciSoftCo.com), allowing synchronous assessment of eM and NLC in time and voltage. The edge of the cuticular plate was used to track OHC length change, the patch electrode providing a fixed point at the basal end of the cell. Sigmoidal fits (four parameters) provided estimates of V_h , maximal movement and slope factor b . Shift of motility against NLC is calculated by subtracting NLC V_h from eM V_h .

Model Assessment. The kinetic model was assessed using Matlab Simulink in conjunction with jClamp. jClamp provides an automation link to Matlab, which allows voltage stimuli to be delivered to and current responses to be obtained from Simulink models. The kinetic model was interfaced to jClamp via a model of the patch clamp amplifier and OHC. The linear component of the patch-cell model possessed an R_s of 5 M Ω , R_m of 500 M Ω , and C_{lin} of 15 pF. The nonlinear component, NLC derived from charge movement of the prestin model, parameters laid out in *Results*. The exact same voltage stimuli and exact same analysis of model two-sine currents were performed as with the biophysical data. Mechanical contraction data of the model, namely eM, was taken as the accumulated residence in the C state. Fits of model NLC and eM were performed the same way as the biophysical data.

Although this parallel approach provides for powerful comparisons between model and biophysical data, it is laborious. Thus, only visual “fits” to the data are presented because no automatic iteration is possible. Instead, each set of model parameters was selected and compiled in Matlab. Then jClamp was used to stimulate, collect, and analyze the resulting model data, as was done

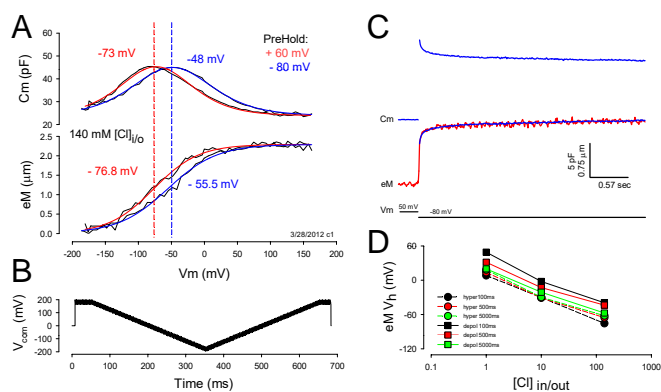


Fig. 1. Nonlinear capacitance and eM are coupled. (A) OHCs possess a capacitance that is nonlinear with voltage. Its peak resides at a voltage, V_h , that changes depending upon holding potential. In this case, V_h is -73 mV after holding the cell at $+60$ mV for one minute (red line). V_h shifts to -48 mV after holding the cell at -80 mV for one minute (blue line). Similar shifts are observed for eM. Fits: (red) NLC V_h -73.10 , z 0.69 , Q_{max} 3.15 , C_{lin} 23.86 ; eM V_h -76.81 , b 33.96 , eM_{max} 2.42 ; (blue) NLC V_h -48.76 , z 0.63 , Q_{max} 3.42 , C_{lin} 23.90 ; eM V_h -55.48 , b 37.13 , eM_{max} 2.41 . (B) Voltage stimulus used for the collection of capacitance and eM. Dual sine superimposed on ramps is used to evaluate C_m (Methods). Measures shown in A were obtained with hyperpolarizing ramps. The effects of ramp duration and polarity are described in subsequent figures. (C) A step voltage from 50 to -80 mV induces an elongation of the OHC (red trace) and simultaneous jump in C_m (blue trace). C_m relaxes with a stretched (multi) exponential time course that is mirrored by eM. The C_m trace was inverted, scaled and overlaid onto the eM trace (blue trace on red), showing similar time courses. (D) eM shifts in the depolarizing direction when intracellular chloride is reduced. The eM and NLC were measured simultaneously with hyperpolarizing and depolarizing ramps at the indicated ramp durations/rates. Regardless of polarity or rate, a large shift of V_h is observed, but the absolute values of V_h are more depolarized with longer depolarizing ramps. Number of cells averaged is the same as indicated in Fig. 3 A–C. SEs are not plotted for clarity. They are for 1, 10, and 140 mM Cl: black squares, 4.5, 3.7, and 3.8 mV; red squares, 5.0, 3.8, and 2.7; green squares, 7.3, 3.8, and 9.6; black circles, 4.6, 4.2, and 3.8; red circles, 3.5, 5.2, and 4.3; and green circles, 5.4, 6.0, and 10.6.

with OHCs. The data were then plotted for comparison with biophysical data, followed by visual determination of goodness of fit. Another choice of model parameters was then made and the process repeated. In consequence, an enormous amount of time was invested in obtaining model data.

Results

Experiment. Under voltage clamp, OHCs display an NLC that is bell shaped with its peak magnitude residing at a voltage (V_h), where prestin’s charge is equally distributed on either side, similar in behavior to an ionic channel’s voltage-sensor charge (22) (Fig. 1A). Coupled to this nonlinear charge movement is a mechanical response of the whole cell (a length change; eM) that follows the charge’s voltage dependence. Shifts in NLC V_h along the voltage axis, known to be induced by changing the long-term holding potential (prepulse) of the OHC or prestin-transfected cells (4, 20, 23), are accompanied by corresponding shifts in eM voltage dependence. In this example (Fig. 1A), a V_h shift of 25 mV for OHC NLC arises, along with a parallel V_h shift of 21.3 mV for eM. Furthermore, Fig. 1C illustrates that the time course of OHC length change follows the time course of NLC during step voltage stimulation, each showing stretched (multi) exponential behavior (23). This tight coupling between NLC and eM is observed when intracellular chloride is high, e.g., 140 mM, the typical intracellular level used for experimentation during the last few decades to study OHCs.

Recently, the level of intracellular chloride was estimated to be ≤ 10 mM in OHCs (6). As noted above with hyperpolarizing prepulses, lowering intracellular chloride is known to shift NLC V_h to depolarized levels (14). We confirm that the same is true for eM (Fig. 1D). Here, voltage ramps (± 180 mV) of different duration/rate (100–5,000 ms or equivalently 4–0.08 mV/ms) and polarity drove eM, while simultaneously summed high-frequency dual-sine stimuli reported on NLC (see *Methods* for details; refs. 20, 21). Although eM V_h shifted to depolarized levels regardless of protocol rate, the faster depolarizing ramps produced a more depolarized V_h . It was surprising that, although lowering intracellular chloride levels shifts both NLC V_h and eM V_h to positive voltages, a disparity between V_h of NLC and eM arises (Fig. 2). As chloride levels reduce, V_h of eM is shifted further to the right than V_h of NLC. In the examples shown, 10 mM chloride produced a disparity of 15.3 mV, and 1 mM chloride produced a disparity of 39.7 mV. This disparity is dependent not only on chloride level, but also on rate and polarity of voltage ramp stimulation (Fig. 3 A–C). Note that there is a chloride-dependent ΔV_h disparity that is greater in the depolarizing ramp direction as rate is increased, reaching an average disparity of about 45 mV with depolarizing 100-ms ramps; but even at very slow ramp rates, a chloride-dependent disparity remains. A large disparity is also observed when we instead use aspartate to replace chloride (Fig. 3C). Finally, there is a decrease in disparity with shorter ramp durations in the hyperpolarizing direction, and with 140 mM chloride, little disparity exists, which accounts for assertions of good electromechanical coupling during the last couple of decades (8–12).

In addition to disparity in voltage dependence, there is disparity in correspondence between maximal charge movement (Q_{max}), estimated from Boltzmann fits to NLC, and maximal eM (eM_{max}), estimated from sigmoidal fits to eM. Q_{max} has been taken to report on the number of elementary charged motors (prestins) in the OHC (8, 9), and consequently, there is a correlation between prestin surface expression and Q_{max} (24). Because it is undisputed that prestin conformational changes drive eM (25), the number of active prestin molecules should correspond to measures of eM, with eM_{max} correlated with Q_{max} . Fig. 3D shows that this is not the case; that is, although chloride reduction significantly reduces Q_{max} , eM does not follow. For example, eM_{max} values (mean \pm SE in micrometers; $n = 9$ –14) for 500-ms hyperpolarizing ramps were 2.19 ± 0.12 @ 1 mM; 2.01 ± 0.20 @ 10 mM; and 2.41 ± 0.28 @ 140 mM chloride. Corresponding Q_{max} values (mean \pm SE in picocoulombs, $n = 9$ –12) were 2.04 ± 0.09 , 2.86 ± 0.09 , and 3.10 ± 0.03 . Neither eM_{max} nor Q_{max} magnitude was significantly different for hyperpolarizing or

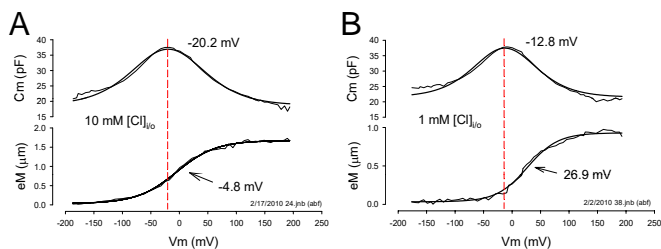


Fig. 2. Reduction of intracellular chloride toward physiological levels reveals disparity in NLC and eM operating voltage range. (A) The 10 mM chloride condition evidences a V_h disparity of 15.3 mV with eM more depolarized than NLC. Fits: NLC V_h , -20.15, z 0.59, q_{max} 3.17, C_{lin} 18.66; eM V_h , -4.87, b 34.58, eM_{max} 1.64. (B) Under 1 mM chloride conditions the disparity is larger, namely, 39.7 mV. Fits: NLC V_h , -12.87, z 0.68, q_{max} 2.38, C_{lin} 21.50; eM V_h , 26.92, b 26.78, eM_{max} 0.9.

depolarizing ramps. The slope factor (b ; *Methods*) of eM with 140 mM at this 500-ms ramp rate was 34.8 ± 0.84 mV, which translates to 17.3 nm/mV maximal sensitivity ($eM_{max}/4b$). This is similar to previously reported values (26, 27).

Iwasa (28) first identified the membrane tension dependence of OHC NLC and introduced a mechanical energy term in the Boltzmann model of prestin (29). In confirmation of its molecular nature, tension dependence was subsequently shown to have direct action on the motor/prestin (4, 5, 10). The susceptibility of fast ramp rate effects to perturbations of whole-cell mechanics is illustrated with turgor pressure manipulations (Fig. 3 E–G). Increasing turgor pressure, which increases membrane tension, eliminates the disparity (ΔV_h) evidenced with 100-ms ramps. Also revealed are disparate changes in V_h of NLC and eM. Whereas, the V_h of NLC shifts in the depolarizing direction during increases in membrane tension regardless of ramp polarity, the direction of V_h shift of eM depends on ramp polarity. That is, hyperpolarizing ramps cause near-equivalent depolarizing shifts in V_h of eM and NLC; depolarizing ramps, on the other hand, cause a hyperpolarizing shift in eM V_h . It is this differing behavior that accounts for the elimination of ΔV_h during increases in membrane tension, and points to a molecular phenomenon.

To ensure that the observations that we observe derive from molecular actions of prestin, rather than mechanical characteristics of the cell, we perturbed the cytoskeleton. We treated OHCs with latrunculin (an agent causing actin depolymerization) and diamide (a spectrin, actin-bundling protein antagonist), each of which is expected to modify the OHC cortical cytoskeleton. Fig. 4 illustrates that only minor changes in the fast rate effects are evident. These small effects we attribute to the influence of the cytoskeleton in controlling tension delivered to the membrane.

Model. In the two-state area motor model of OHC electromotility (29, 30), the accumulation of prestin motors into the contracted state (small surface area) will shorten the cell, and accumulation into the expanded state (large surface area) will lengthen the cell. This two-state model cannot reproduce our data (see below). To understand the molecular events underlying our time- and chloride-dependent observations, we developed an extended, yet very simple kinetic model, schematized in Fig. 5A.

Similar to carbonic anhydrase (31), we assume very fast anion (chloride) binding and unbinding transitions ($X_o \leftrightarrow X_c$). Because the voltage-dependent mechanical activity of prestin is greater than 80 kHz (32), we also assume very fast voltage-dependent conformational transitions ($X \leftrightarrow C$). The transition to state C carries a unit charge, q ; Q_{max} , total charge moved, will reflect the maximal accumulation of motors in that state. The number of motors in state C also equates to magnitude of eM (contraction), providing a Boltzmann-like sigmoidal response. Nestled between the anion-binding and voltage-dependent transitions, resides a non-voltage-dependent transition ($X_c \leftrightarrow X$), which is very much slower than the other two transitions. The kinetics of these slow transitions

is set to have the model resemble prestin's electromechanical behavior. The differential equations describing the model are listed in the *Supporting Information*, where $k_1 = 10^7 * [Cl]_{in}$, $k_2 = 10^7 * k_d$, $\alpha_0 = 75 * \exp(t_m)$, $\beta_0 = 5.58 * 10^8 * \exp(-E_a/RT)$, $\alpha = 10^6 * \exp(zFV_m/2RT)$, $\beta = 583 * 10^9 * \exp(-zFV_m/2RT + t_m/2 - E_a/RT)$, $k_d = 0.001$, $T = 296$ K, $E_a = 38.36 * 10^3$ J/mol, $F = 9.648 * 10^4$ C/mol, $R = 8.315$ J/Kmol, $k = 1.381 * 10^{-23}$ VC/K.

The rates α_0 and β are tension sensitive, because tension is known to increase prestin residence in the expanded (X) state (10, 28), t_m in units kT (eRT/F); rates β and β_0 are equally temperature sensitive, with Arrhenius activation energy, E_a . Here, α and β are voltage dependent, with sensor valence z . At $T = 296$ K, $V_m = 0$ mV, $T_m = 0$ kT, and $[Cl]_{in} = 0.14$ M, initial rates are $k_1 = 1.4e6$, $k_2 = 1e4$, $\alpha_0 = 75$, $\beta_0 = 95$, $\alpha = 1e6$, and $\beta = 1e5$.

Model results recapitulate our biophysical data. Stimulation of the model is with the same voltage protocols used to collect the biophysical data, and analysis is the same. Fig. 5 B–D shows chloride-, rate-, and polarity-dependent disparity similar to the biophysical results illustrated in Fig. 3 A–C. The polarity dependence of the fastest rates with low chloride levels is not as rectified as the biophysical data, the model showing only minor differences, and may result from the extraordinary simplicity of the model. The triangles depict results obtained when intermediary rates, α_0 and β_0 , are set 8 orders of magnitude faster. Under such conditions, the model resembles a fast two-state model, with no disparity between NLC and eM. We reason that at high chloride levels the population of voltage-enabled Cl-bound motors is enriched, and the fast kinetics of the voltage-dependent

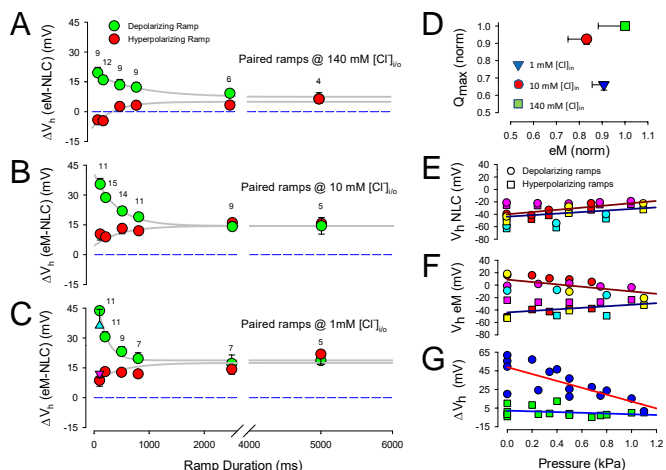


Fig. 3. The eM and NLC are disparate. (A) The eM and NLC operating voltage disparities are dependent on chloride levels, ramp durations/rates, and polarity. With 140 mM chloride intracellular, polarity effects are symmetrical but offset in the depolarizing direction. (B) For 10 mM chloride, the offset is larger, and a depolarizing asymmetry arises at short ramp durations. (C) With 1 mM chloride, the depolarizing offset is larger still, and the depolarizing asymmetry at short ramp durations is also greater. Errors bars are SE and numbers of cells are indicated. Triangles (up, blue: depolarizing ramp; down, purple: hyperpolarizing ramp) depict results obtained with aspartate as the chloride substitute at 100 ms duration ramp. Compare with model results in Fig. 5 B–D. (D) Q_{max} and eM_{max} are not strictly correlated. Normalized Q_{max} and eM_{max} are derived from 500 ms hyperpolarizing ramp data. As chloride levels decrease, Q_{max} decreases, but eM does not follow. Error bars are SE, number as in Fig. 3 A–C. Compare with model results in Fig. 5E. (E) Membrane tension reduces V_h disparity between eM and NLC. V_h of NLC shifts in the depolarizing direction with increase in membrane turgor pressure regardless of ramp polarity. (F) V_h of eM also shifts in the depolarizing direction with hyperpolarizing ramps as tension increases. However, eM V_h shifts in the hyperpolarizing direction when measured with depolarizing ramps. (G) Net effect of shifts in V_h is to reduce V_h disparity as membrane tension increases. ΔV_h obtained by subtraction of data in A and B; $n = 4$. Compare with model results in Fig. 5 F–H.

transitions work on this population to dominate the cell response, thus appearing more similar to a fast two-state process.

Fig. 5E illustrates that the model, similar to the biophysical results in Fig. 3D, exhibits poor correlation between Q_{\max} and magnitude of eM. In this case, Q_{\max} estimates can reduce with essentially no change in eM. Fig. 5 F–H illustrates the effects of tension on kinetic model behavior and shows similarity to the biophysical data of Fig. 3 E–G. Namely, a reduction of the fast ramp (100 ms) ΔV_h disparity results from inverse shifts of polarity dependent eM V_h . NLC V_h , on the other hand, shifts in the depolarizing direction for both polarity ramps. It is important to note that Fig. S1 A–D illustrates that a variety of perturbations to the model recapitulate biophysical behavior of NLC observed during the previous two decades, including prepulse effect, chloride concentration effect, temperature effect, and exponential relaxations of C_m induced by voltage step. The success of the model strongly suggests that an intermediary slow transition governs prestin behavior.

Given that the model recapitulates most of the available biophysical data, we are confident that it can be used to investigate other expected qualities that enable the OHC to function effectively as cochlear amplifier. To this end, we tested the phase characteristics of the model. Fig. S1 E–G shows that (i) eM phase lags that of stimulating membrane potential, (ii) the phase lag is chloride and voltage dependent, and (iii) depending on intermediary gateway kinetics, the phase lag exhibits variable frequency dependence. Fig. S2 confirms that we do find small phase lags in OHC eM.

Discussion

OHC eM is voltage dependent and necessarily coupled to its charged voltage sensor (8, 9, 12, 26, 27, 33). Thus, it is expected that sensor-charge movement, measured as displacement currents or NLC, should correspond to mechanical movements of the cell. In fact, a strict correspondence is predicted based on two-state Boltzmann models that incorporate transition speeds that match the very fast voltage-induced mechanical response (>80 kHz) (32). The incongruence of our data with this scheme, especially at physiological chloride levels, requires rethinking of prestin's molecular mechanism.

Measures of prestin's NLC alone are not sufficient to rule on the existence of kinetic schemes above two states, given that C_m - V_m functions can be fit equally well by two-state Boltzmann or multistate Langevin functions within physiological voltage ranges (34, 35). However, by evaluating simultaneous measures of NLC and eM, we are able to identify at least three state transitions, including fast anion-binding and voltage-dependent ones, and an intermediary slow one. The intermediary state transition controls the delivery of primed (anion bound) motors into a voltage-enabled pool, and likely corresponds to the allosteric-like behavior we have observed previously (16, 17). Thus, rather than a typical allosteric mechanism, chloride binding to the evolutionary

ancient transport-binding site functions to effect a slow conformational change that enables a process (voltage sensing and eM) unrelated to transport per se. We had previously separated NLC and anion transport via mutations in prestin, and identified charged amino residues that contribute to charge movement (36). In consequence, the intermediate transition serves as a gateway controlling the magnitude and voltage dependence of eM, and underlies the disparity between measures of NLC and eM.

We emphasize that our data do not suggest that NLC and eM are intrinsically separable, but that they only appear disparate because our measuring techniques are subject to intermediate rate effects that the disparity highlights. This is somewhat analogous to the recently observed need to integrate sensor charge across long time ranges to reconcile large shifts in the voltage sensor domain Q-V function of Shaker channels (37). Thus, we find that the apparent operating voltage range of prestin depends on the frequency of interrogation of its behavior. With our measures of NLC, we are studying a nonstationary population of voltage-dependent motors, varying according to the kinetics of the intermediary gateway. That is, NLC measures that characterize the voltage-dependent conformational change in prestin at discrete frequencies cannot provide steady-state behavior as previously thought, because we are not dealing with an invariant fast two-state system. The kinetic model starkly illustrates this: when intermediate rates are set very fast, model behavior is similar to fast two-state behavior. As a correspondence, we find that differing V_h is obtained by varying integration times of step-induced charge movement. Thus, past estimates of steady-state prestin behavior have been influenced by this gateway. For example, we and others had assumed that lowering intracellular chloride levels shifts eM correspondingly with NLC in the positive direction along the voltage axis. We now know that eM shift is greater. Physiologically, acoustic frequency stimulation *in vivo* will be influenced by intermediary kinetics corresponding to its equivalent frequency bandwidth. This may underlie some of the differences between low- and high-frequency cochlear behavior. It is important to note that the simple model we provide here has single exponential kinetics, whereas previously observed kinetic characteristics of NLC (e.g., see Fig. 1 NLC time course), which we can now ascribe to this gateway, clearly show that the transition actually has stretched exponential behavior providing control ranging from the submillisecond to the seconds timescale (20, 23). Implementing this kinetic diversity will certainly increase the complexity of the model, but may improve its correspondence with biophysical data. For example, at the present time we needed to decrease the transition rates from the millisecond to the second timescale to obtain the voltage prepulse effect as in Fig. S1A. As noted above, NLC relaxations do have components in this slower time range.

Anions and eM. The operating voltage range of eM is dependent on chloride level (Fig. 1D), showing a greater dependence than that of NLC. In a similar way, Q_{\max} estimates of charge movement do not correlate well with eM. The disparities may be explained because NLC only reports on the voltage-enabled population of motors at interrogation frequencies, whereas eM is evaluated at ramp rates much slower than that of the intermediate transition rates. Still, it is interesting to note that steady-state eM magnitude is little affected by chloride removal. It was previously observed that removal of intracellular chloride abolished eM (13). That observation involved replacement of chloride with pentane sulfonate, which we subsequently showed causes NLC V_h to shift to very hyperpolarized voltages, effectively shifting eM outside practical interrogation voltage ranges (16). In the present study, we successfully evaluate the full range of eM at various chloride levels and show robust mechanical responses, despite large reductions in chloride. We and others have determined the K_d for prestin, ranging from 1 to 6 mM, using measures of NLC (13, 15, 17). Our robust eM observations along with clear indications that NLC measures may not faithfully depict prestin's steady-state

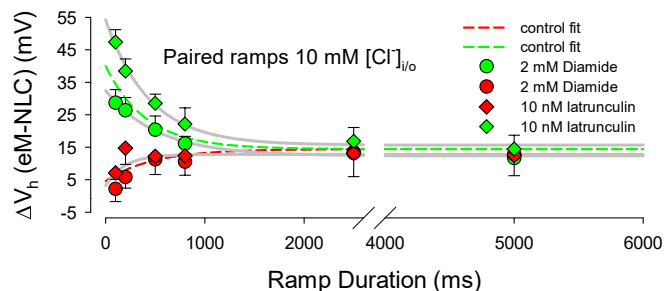


Fig. 4. The eM and NLC V_h disparity is little influenced by cytoskeletal integrity. The dotted lines are fits from the 10 mM chloride plot of Fig. 3B. The effects of diamide and latrunculin are absent with hyperpolarizing ramps (red symbols). On the other hand, diamide slightly reduces and latrunculin slightly increases fast ramp effects.

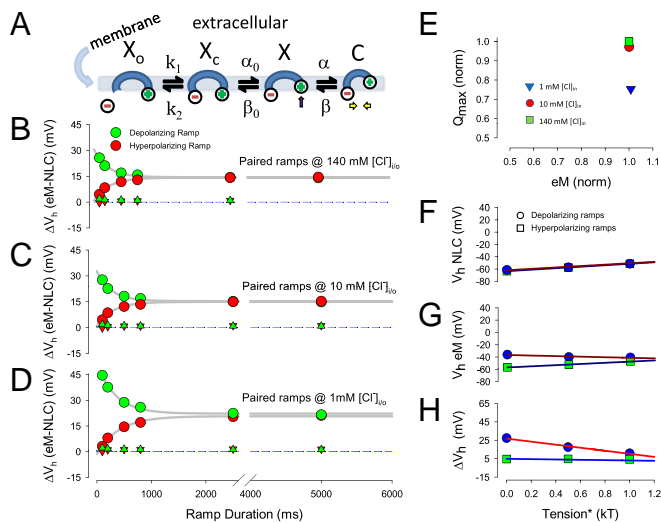


Fig. 5. Kinetic model of prestin. (A) Simple kinetic model of prestin activity within the plasma membrane. X_o state is unbound by anion. The X_c state is bound by anion but intrinsic voltage-sensor charge is not responsive to membrane electric field. Slow conformational transition to X state enables voltage sensing of electric field (arrow depicts positive charged sensor movement into the membrane field). Depolarization moves positive sensor charge outward within the membrane field, simultaneously resulting in compact state C , which corresponds to cell contraction (yellow arrows). (B–D) Kinetic model recapitulates ΔV_h disparity of biophysical data. Plots correspond to those plots of Fig. 3 A–C. Note increasing V_h disparity with chloride reduction and shorter ramp durations. There is a slight asymmetry at fast ramp rates for the 1 mM chloride condition. Triangles depict results obtained when the intermediate transition rates were increased by a factor of $1e8$. No disparity is detected under these conditions, as expected for a simple fast two-state model. (E) Kinetic model recapitulates uncorrelated Q_{max} and eM_{max} of biophysical data. As chloride levels decrease, Q_{max} decreases, but eM does not follow. Compare with biophysical data of Fig. 3D. (F–H) Kinetic model recapitulates membrane tension dependence of biophysical data. Plots correspond to those plots of Fig. 3 E–G. Note similarity of model behavior and biophysical behavior, resulting in reduced ΔV_h disparity as membrane tension increases.

properties indicate that the K_d for prestin mechanical activity needs reassessment.

Models of Prestin. The earliest molecular models of prestin, based on OHC NLC and eM, were simple two-state Boltzmanns (8, 9, 29, 30), corresponding to two area states, compact and expanded. The first observation of tension effects on OHC NLC led to a modified Boltzmann model, where a mechanical energy term supplemented that of electrical energy (28, 29). Those whole-cell experiments correctly implicated a molecular basis, as subsequent experiments revealed (4, 5, 10). Here we find that the disparity between eM and NLC is susceptible to membrane tension, thus directly implicating molecular underpinnings. To be sure, the hallmark of the intermediate transition rate, the C_m relaxation indicative of the shifting Q-V function, is impervious to intracellular pronase treatment (20), does not depend on OHC length (23), and is found in prestin transfected cells (4), as expected for a membrane-based phenomenon. Indeed, the minor effects of present cytoskeletal perturbations on the ΔV_h disparity confirm those observations. In accordance, it must be emphasized that water movements into and out of the OHC that can alter OHC shape are expected to be slow (38), and thus their greatest contribution to the disparity in ΔV_h would be during long ramps, which is just the opposite of what we find. In fact, chloride (water) movement into or out of the cell should depend on ramp polarity but at long durations disparity remains the same for each polarity ramp. In addition, the order of ramp delivery is without effect on the data. We conclude that our results cannot be due to whole-cell mechanical properties or chloride/water movements during

stimulation, and that the success of our model derives from its accurate description of prestin's molecular behavior.

Recently, extensive models, some deriving from OHC measures, incorporating transporter or multistate behavior have been devised to replicate some of the available biophysical data, mostly prestin's anion dependence (39–41). Prestin's anion transporter capabilities are controversial, some groups championing transport, others not (36, 42–44). However, another simple four-state model (sum of two voltage-dependent Boltzmanns) was found to rival an earlier model (45) in goodness of fit of NLC and salicylate's effect on OHC NLC (41). In a subsequent addition (33), the authors suggest that chloride binding could screen intrinsic voltage-sensor charge thus underlying V_h shifts; however, ions of any one polarity are not expected to produce extreme V_h shifts in both positive and negative directions, as has been measured in OHCs (16). In any case, their model cannot reproduce our data, as chloride binding leads directly to fast voltage-dependent reactions. It should be noted, that we previously identified a voltage dependence of NLC relaxations, which could signal that the slow intermediate transition may possess some measure of voltage dependency (23). In subsequent model renditions we intend to evaluate this possibility, and the possible effects of electric field on anion binding. In its present form, however, our simple model derives from typical ligand gated channels (e.g., ACh receptor channels) where fast ligand-binding kinetics leads to very much slower conformational changes that gate open conductance (46, 47). For prestin, the slower, voltage-independent intermediate conformational change enables voltage sensing. It is well known that a voltage-independent transition can affect the characteristics of a linked voltage-dependent one (37, 48, 49). It may be that the other more complicated, although untested (re the host of biophysical data available), models of prestin possess some of the qualities of our model, but to date our model is the simplest capable of recapitulating the widest known set of OHC biophysical data. In league with the transporter models, however, we speculate that the transporter lineage of prestin underlies the slow transition process that controls the fastest known molecular motor.

What Is Required of the OHC as an Amplifier? To provide amplification within the cochlear partition, the OHC must exert its force fast and at the right time. OHCs can respond to sinusoidal voltage stimulation above 80 kHz (32), and although resistor-capacitor (RC) filtering posed initial skepticism due to expected decreases in eM driving force at high acoustic frequencies (26, 50), much work has basically eliminated this concern (14, 51–55). However, one of those potential mechanisms that we envisioned to overcome the RC problem does not survive tests with our model. We previously suggested (14) that should chloride levels fluctuate at acoustic rates near prestin (analogous to stereocilia mechano-electrical transducer Ca^{2+} flux effects on bundle mechanics), this could drive high-frequency mechanical responses, bypassing an RC limit. Our observations indicate that such fluctuations are of limited effect because prestin's intermediary rates will low pass filter responses, with the intermediate transition imposing its time dependence on chloride-driven eM. Nonetheless, chloride flux at rates at or below intermediary rates could significantly affect eM.

Some cochlea models require a phase lag between OHC voltage and OHC force, typically 1.57 rad, thereby delivering force to the basilar membrane at an appropriate phase angle to cancel viscous drag (56–58). This requires a delay between receptor potential and activation of eM. Although various mechanisms have been invoked to establish phase lags in cochlear models, none have been based on intrinsic biophysical mechanisms of the OHC motor. We suggest that the disparity that we observe between NLC and eM may represent a delay proffered by the additional states required to replicate the biophysical data. To this end, we find in the model that phase lags between membrane voltage and eM are generated by the intermediary gateway, and that chloride level and membrane resting potential control lag magnitude (Fig. S1). It must also be remembered that

the gateway is actually multiexponential, thus in addition the model can generate frequency-dependent phase delays depending on the kinetics of the gateway. However, we find that model lag magnitudes are a fraction of 1.57 rad. Indeed, we find a small phase lag in our physiological measures of eM (Fig. S2), thus contributing to those model phase requirements. It should be mentioned, however, that more recent models of OHC-based amplification do not have lags required of older models (59). Based on new concepts, it is not OHC action on the basilar membrane, but instead on the fluid micromechanics of the

subtectorial membrane space that affords amplification (60, 61). Although our data are in harmony with the phase-lag requiring models, it remains to be seen how our predicted phase characteristics of the OHC motor impact on newer models, and whether the throttling kinetics of prestin's intermediary gateway can influence amplification.

ACKNOWLEDGMENTS. This research was supported by National Institutes of Health National Institute on Deafness and other Communication Disorders Grant DC00273 (to J.S.-S.).

- Brownell WE, Bader CR, Bertrand D, de Ribaupierre Y (1985) Evoked mechanical responses of isolated cochlear outer hair cells. *Science* 227(4683):194–196.
- Ashmore J, et al. (2010) The remarkable cochlear amplifier. *Hear Res* 266(1–2):1–17.
- Zheng J, et al. (2000) Prestin is the motor protein of cochlear outer hair cells. *Nature* 405(6783):149–155.
- Santos-Sacchi J, Shen W, Zheng J, Dallos P (2001) Effects of membrane potential and tension on prestin, the outer hair cell lateral membrane motor protein. *J Physiol* 531(Pt 3):661–666.
- Ludwig J, et al. (2001) Reciprocal electromechanical properties of rat prestin: The motor molecule from rat outer hair cells. *Proc Natl Acad Sci USA* 98(7):4178–4183.
- Santos-Sacchi J, Song L, Zheng J, Nuttall AL (2006) Control of mammalian cochlear amplification by chloride anions. *J Neurosci* 26(15):3992–3998.
- Dallos P, et al. (2008) Prestin-based outer hair cell motility is necessary for mammalian cochlear amplification. *Neuron* 58(3):333–339.
- Ashmore JF (1990) Forward and reverse transduction in the mammalian cochlea. *Neurosci Res Suppl* 12:539–550.
- Santos-Sacchi J (1991) Reversible inhibition of voltage-dependent outer hair cell motility and capacitance. *J Neurosci* 11(10):3096–3110.
- Takehata S, Santos-Sacchi J (1995) Membrane tension directly shifts voltage dependence of outer hair cell motility and associated gating charge. *Biophys J* 68(5):2190–2197.
- Takehata S, Santos-Sacchi J (1996) Effects of salicylate and lanthanides on outer hair cell motility and associated gating charge. *J Neurosci* 16(16):4881–4889.
- Wang X, Yang S, Jia S, He DZ (2010) Prestin forms oligomer with four mechanically independent subunits. *Brain Res* 1333:28–35.
- Oliver D, et al. (2001) Intracellular anions as the voltage sensor of prestin, the outer hair cell motor protein. *Science* 292(5525):2340–2343.
- Rybalchenko V, Santos-Sacchi J (2003) Cl⁻ flux through a non-selective, stretch-sensitive conductance influences the outer hair cell motor of the guinea-pig. *J Physiol* 547(Pt 3):873–891.
- Song L, Seeger A, Santos-Sacchi J (2005) On membrane motor activity and chloride flux in the outer hair cell: Lessons learned from the environmental toxin tributyltin. *Biophys J* 88(3):2350–2362.
- Rybalchenko V, Santos-Sacchi J (2008) Anion control of voltage sensing by the motor protein prestin in outer hair cells. *Biophys J* 95(9):4439–4447.
- Song L, Santos-Sacchi J (2010) Conformational state-dependent anion binding in prestin: Evidence for allosteric modulation. *Biophys J* 98(3):371–376.
- Adachi M, Iwasa KH (1997) Effect of diamide on force generation and axial stiffness of the cochlear outer hair cell. *Biophys J* 73(5):2809–2818.
- Morton WM, Ayscough KR, McLaughlin PJ (2000) Latrunculin alters the actin-monomer subunit interface to prevent polymerization. *Nat Cell Biol* 2(6):376–378.
- Santos-Sacchi J, Takehata S, Takahashi S (1998) Effects of membrane potential on the voltage dependence of motility-related charge in outer hair cells of the guinea-pig. *J Physiol* 510(Pt 1):225–235.
- Santos-Sacchi J (2004) Determination of cell capacitance using the exact empirical solution of dY/dCm and its phase angle. *Biophys J* 87(1):714–727.
- Bezanilla F (2008) How membrane proteins sense voltage. *Nat Rev Mol Cell Biol* 9(4):323–332.
- Santos-Sacchi J, Navarrete E, Song L (2009) Fast electromechanical amplification in the lateral membrane of the outer hair cell. *Biophys J* 96(2):739–747.
- Bian S, Koo BW, Kelleher S, Santos-Sacchi J, Navaratnam DS (2010) A highly expressing Tet-inducible cell line recapitulates in situ developmental changes in prestin's Boltzmann characteristics and reveals early maturational events. *Am J Physiol Cell Physiol* 299(4):C828–C835.
- Liberman MC, et al. (2002) Prestin is required for electromotility of the outer hair cell and for the cochlear amplifier. *Nature* 419(6904):300–304.
- Ashmore JF (1987) A fast motile response in guinea-pig outer hair cells: The cellular basis of the cochlear amplifier. *J Physiol* 388:323–347.
- Santos-Sacchi J, Dilger JP (1988) Whole cell currents and mechanical responses of isolated outer hair cells. *Hear Res* 35(2–3):143–150.
- Iwasa KH (1993) Effect of stress on the membrane capacitance of the auditory outer hair cell. *Biophys J* 65(1):492–498.
- Iwasa KH (1994) A membrane motor model for the fast motility of the outer hair cell. *J Acoust Soc Am* 96(4):2216–2224.
- Santos-Sacchi J (1993) Harmonics of outer hair cell motility. *Biophys J* 65(5):2217–2227.
- Prabhananda BS, Rittger E, Grell E (1987) Kinetics and mechanism of anionic ligand binding to carbonic anhydrase. *Biophys Chem* 26(2–3):217–224.
- Frank G, Hemmert W, Gummer AW (1999) Limiting dynamics of high-frequency electromechanical transduction of outer hair cells. *Proc Natl Acad Sci USA* 96(8):4420–4425.
- Homma K, Dallos P (2011) Dissecting the electromechanical coupling mechanism of the motor-protein prestin. *Commun Integr Biol* 4(4):450–453.
- Huang G, Santos-Sacchi J (1993) Mapping the distribution of the outer hair cell motility voltage sensor by electrical amputation. *Biophys J* 65(5):2228–2236.
- Scherer MP, Gummer AW (2005) How many states can the motor molecule, prestin, assume in an electric field? *Biophys J* 88(5):L27–L29.
- Bai JP, et al. (2009) Prestin's anion transport and voltage-sensing capabilities are independent. *Biophys J* 96(8):3179–3186.
- Lacroix JJ, Labro AJ, Bezanilla F (2011) Properties of deactivation gating currents in Shaker channels. *Biophys J* 100(5):L28–L30.
- Ashmore J (2008) Cochlear outer hair cell motility. *Physiol Rev* 88(1):173–210.
- Muallem D, Ashmore J (2006) An anion antiporter model of prestin, the outer hair cell motor protein. *Biophys J* 90(11):4035–4045.
- Schaechinger TJ, et al. (2011) A synthetic prestin reveals protein domains and molecular operation of outer hair cell piezoelectricity. *EMBO J* 30(14):2793–2804.
- Homma K, Dallos P (2011) Evidence that prestin has at least two voltage-dependent steps. *J Biol Chem* 286(3):2297–2307.
- Schaechinger TJ, Oliver D (2007) Nonmammalian orthologs of prestin (SLC26A5) are electrogenic divalent/chloride anion exchangers. *Proc Natl Acad Sci USA* 104(18):7693–7698.
- Tang J, Pecka JL, Tan X, Beisel KW, He DZ (2011) Engineered pendrin protein, an anion transporter and molecular motor. *J Biol Chem* 286(35):31014–31021.
- Schänzler M, Fahlke C (2012) Anion transport by the cochlear motor protein prestin. *J Physiol* 590(Pt 2):259–272.
- Santos-Sacchi J, Navarrete E (2002) Voltage-dependent changes in specific membrane capacitance caused by prestin, the outer hair cell lateral membrane motor. *Pflügers Arch* 444(1–2):99–106.
- Del Castillo J, Katz B (1957) Interaction at end-plate receptors between different choline derivatives. *Proc R Soc Lond B Biol Sci* 146(924):369–381.
- Osterrieder W, Noma A, Trautwein W (1980) On the kinetics of the potassium channel activated by acetylcholine in the S-A node of the rabbit heart. *Pflügers Arch* 386(2):101–109.
- Colquhoun D (1998) Binding, gating, affinity and efficacy: The interpretation of structure-activity relationships for agonists and of the effects of mutating receptors. *Br J Pharmacol* 125(5):924–947.
- Shirokov R (2011) What's in gating currents? Going beyond the voltage sensor movement. *Biophys J* 101(2):512–514, discussion 515–516.
- Santos-Sacchi J (1989) Asymmetry in voltage-dependent movements of isolated outer hair cells from the organ of Corti. *J Neurosci* 9(8):2954–2962.
- Santos-Sacchi J, Takehata S, Kikuchi T, Katori Y, Takasaka T (1998) Density of motility-related charge in the outer hair cell of the guinea pig is inversely related to best frequency. *Neurosci Lett* 256(3):155–158.
- Ospeck M, Dong XX, Fang J, Iwasa KH (2006) Electromotility in outer hair cells: A supporting role for fast potassium conductance. *ORL J Otorhinolaryngol Relat Spec* 68(6):373–377.
- Spector AA, Brownell WE, Popel AS (2003) Effect of outer hair cell piezoelectricity on high-frequency receptor potentials. *J Acoust Soc Am* 113(1):453–461.
- Johnson SL, Beurg M, Marcotti W, Fettiplace R (2011) Prestin-driven cochlear amplification is not limited by the outer hair cell membrane time constant. *Neuron* 70(6):1143–1154.
- Corbitt C, Farinelli F, Brownell WE, Farrell B (2012) Tonotopic relationships reveal the charge density varies along the lateral wall of outer hair cells. *Biophys J* 102(12):2715–2724.
- Neely ST (1993) A model of cochlear mechanics with outer hair cell motility. *J Acoust Soc Am* 94(1):137–146.
- Markin VS, Hudspeth AJ (1995) Modeling the active process of the cochlea: Phase relations, amplification, and spontaneous oscillation. *Biophys J* 69(1):138–147.
- Geisler CD (1993) A realizable cochlear model using feedback from motile outer hair cells. *Hear Res* 68(2):253–262.
- Yoon YJ, Steele CR, Puria S (2011) Feed-forward and feed-backward amplification model from cochlear cytoarchitecture: An interspecies comparison. *Biophys J* 100(1):1–10.
- Nowotny M, Gummer AW (2011) Vibration responses of the organ of Corti and the tectorial membrane to electrical stimulation. *J Acoust Soc Am* 130(6):3852–3872.
- Guinan JJ, Jr (2012) Mechanical excitation of IHC stereocilia: An attempt to fit together diverse evidence. *What Fire Is in Mine Ears: Progress in Auditory Biomechanics*, eds Shera C, Olson E (American Institute of Physics, Melville, NY), pp 90–96.

Supporting Information

Song and Santos-Sacchi 10.1073/pnas.1218341110

Equations

Capacitance data were fit to the first derivative of a two-state Boltzmann function

$$C_m = Q_{\max} \frac{ze}{kT} \frac{b}{(1+b)^2} + C_{lin}, \quad b = \exp\left(\frac{-ze(V_m - V_h)}{kT}\right),$$

where Q_{\max} is the maximum nonlinear charge moved, V_h is voltage at peak capacitance or equivalently, at half maximum charge transfer, V_m is membrane potential, z is valence, C_{lin} is linear membrane capacitance, e is electron charge, k is Boltzmann's constant, and T is absolute temperature.

Model differential equations are

$$X_o \xrightleftharpoons[k_2]{k_1} X_c \xrightleftharpoons[\beta_0]{\alpha_0} X \xrightleftharpoons[\beta]{\alpha} C$$

$$\frac{dX_o}{dt} = X_c \cdot k_2 - X_o \cdot k_1$$

$$\frac{dX_c}{dt} = X_o \cdot k_1 + X \cdot \beta_0 - X_c \cdot \alpha_0 - X_c \cdot k_2$$

$$\frac{dX}{dt} = X_c \cdot \alpha_0 + C \cdot \beta - X \cdot \alpha - X \cdot \beta_0$$

$$\frac{dC}{dt} = X \cdot \alpha - C \cdot \beta.$$

On Membrane Motor Activity and Chloride Flux in the Outer Hair Cell: Lessons Learned from the Environmental Toxin Tributyltin

Lei Song,^{*‡} Achim Seeger,[‡] and Joseph Santos-Sacchi^{*†‡}

Otolaryngology,^{*} Neurobiology,[†] and Surgery,[‡] Yale University School of Medicine, New Haven, Connecticut

ABSTRACT The outer hair cell (OHC) underlies mammalian cochlea amplification, and its lateral membrane motor, prestin, which drives the cell's mechanical activity, is modulated by intracellular chloride ions. We have previously described a native nonselective conductance (G_{metL}) that influences OHC motor activity via Cl flux across the lateral membrane. Here we further investigate this conductance and use the environmental toxin tributyltin (TBT) to better understand Cl-prestin interactions. Capitalizing on measures of prestin-derived nonlinear capacitance to gauge Cl flux across the lateral membrane, we show that the Cl ionophore TBT, which affects neither the motor nor G_{metL} directly, is capable of augmenting the native flux of Cl in OHCs. These observations were confirmed using the chloride-sensitive dye MQAE. Furthermore, the compound's potent ability, at nanomolar concentrations, to equilibrate intra- and extracellular Cl concentrations is shown to surpass the effectiveness of G_{metL} in promoting Cl flux, and secure a quantitative analysis of Cl-prestin interactions in intact OHCs. Using malate as an anion replacement, we quantify chloride effects on the nonlinear charge density and operating voltage range of prestin. Our data additionally suggest that ototoxic effects of organotins can derive from their disruption of OHC Cl homeostasis, ultimately interfering with anionic modulation of the mammalian cochlear amplifier. Notably, this observation identifies a new environmental threat for marine mammals by TBT, which is known to accumulate in the food chain.

INTRODUCTION

Sensitive hearing in mammals relies on cochlear amplification, and is thought to result from the voltage-dependent motor activity of outer hair cells (OHCs) (Brownell et al., 1985; Ashmore, 1987; Santos-Sacchi and Dilger, 1988). The motor protein prestin, which resides exclusively in the lateral membrane (Belyantseva et al., 2000), is likely key to this process (Zheng et al., 2000; Liberman et al., 2002). Recent studies suggest that prestin activity is highly dependent on the intracellular chloride (Cl) anion. Oliver et al. (2001) found that removing intracellular Cl abolishes the motor's nonlinear charge movement (or nonlinear capacitance, NLC), thereby blocking OHC motility. However, the story is actually more complicated than initially thought, since we discovered that some effects of Cl removal result from induced shifts in prestin's operating voltage range, and not from elimination of motor charge movement (Rybalchenko and Santos-Sacchi, 2003a,c; Santos-Sacchi, 2003). Indeed, substitution of intracellular Cl with other anions, such as sulfonate derivatives or malate, results in a shift of motor function along the voltage axis, the direction of which depends on the substituted anion (Rybalchenko and Santos-Sacchi, 2003b,c): the voltage at peak NLC (V_{pkcm}) ranges from -180 mV for pentane-sulfonate substitution to $+100$ mV for malate substitution. Since Cl is the physiologically abundant intracellular anion, it probably sets the operating

position of NLC and motor function in the OHC. This operating position hovers around the physiological resting potential, namely ~ -70 mV (Dallos et al., 1982).

Considering the importance of Cl ions in OHC function, regulation of Cl transport across the lateral membrane is paramount. Little is known about processes that control chloride flux in OHCs (Gitter et al., 1986; Kawasaki et al., 1999; Rybalchenko and Santos-Sacchi, 2003a,c), though we have identified an unusual stretch-sensitive conductance localized to the lateral membrane, G_{metL} , that passes chloride and consequently can modulate prestin activity. A more detailed understanding of chloride's role in intact OHCs is needed, and could help in understanding normal as well as pathological cochlear function.

The organotin compounds trimethyl (TMT) and triethyl (TET) tin are known to cause auditory dysfunction, which has been attributed to disrupted calcium homeostasis (Clerici et al., 1991; Fechter et al., 1986, 1992; Liu and Fechter, 1995). Indeed, the effects of organotins on other physiological processes also have been linked to their untoward influence on Ca mechanisms (Kishimoto et al., 2001). Interestingly, though, organotin compounds can act as Cl ionophores (Tosteson and Wieth, 1979; Wieth and Tosteson, 1979), with tributyltin (TBT) being three orders of magnitude more effective than TMT at promoting anion exchange diffusion. The halides and hydroxyl anions can participate in heteroexchange with Cl across the membranes of red cells and mitochondria, as well as artificial bilayers (Motais et al., 1977; Selwyn et al., 1970; Wieth and Tosteson, 1979; Tosteson and Wieth, 1979). Intrinsic chloride conductance of the membrane is unaffected, and at concentrations below a few micromolar the intrinsic membrane dipole is unperturbed

Submitted September 27, 2004, and accepted for publication November 29, 2004.

Address reprint requests to Joseph Santos-Sacchi, Sections of Otolaryngology and Neurobiology, Yale University School of Medicine, BML 246, 333 Cedar St., New Haven, CT 06510. Tel.: 203-785-5407; Fax: 203-737-2502; E-mail: joseph.santos-sacchi@yale.edu.

© 2005 by the Biophysical Society

0006-3495/05/03/2350/13 \$2.00

doi: 10.1529/biophysj.104.053579

(Tosteson and Wieth, 1979). Because TBT readily promotes Cl flux, it is routinely used to equilibrate intracellular and extracellular Cl to calibrate chloride-sensitive fluorescent dyes, such as MQAE (*N*-(ethoxycarbonylmethyl)-6-methoxyquinolinium bromide) (Verkman, 1990; Marandi et al., 2002). Among the organotins, TBT in particular is an internationally recognized environmental threat to marine life since it accumulates in the food chain, and remains a commonly used antifouling compound for large boat bottoms (U.S. Environmental Protection Agency, 2004).

Here we study the effects of TBT on Cl exchange across the OHC lateral membrane to gain insight into the function of the anion's natural pathway, G_{metL} , and assure ourselves of uncompromised control of Cl on both sides of the OHC's lateral membrane. We find rapid and profound effects of TBT on OHC NLC, which are directly related to the toxin's ability to transport Cl across the OHC membrane. Consequently, we have been able to obtain definitive and quantitative information on Cl-prestin interactions in native, intact OHCs. We also conclude that organotin ototoxicity ultimately results from interference with the anionic control of mammalian cochlear amplification, and, accordingly, we identify the marine mammal's auditory periphery as an especially susceptible target for the pervasive environmental toxin TBT.

MATERIALS AND METHODS

Hartley albino guinea pigs were overdosed with halothane. Temporal bones were excised and the organ of Corti was exposed under a dissection microscope in calcium-free extracellular medium. The top three turns of the organ of Corti were dissected from the cochlea, and the dissected segments were digested with dispase I (0.5 mg/ml) in a nominally (no chelator) calcium free extracellular medium for 10–12 min. After resuspension in 1 mM chloride extracellular medium (see below), cells were isolated by gentle trituration. The solution was then placed in a plastic petri dish to allow OHCs to settle. A Nikon Eclipse E600-FN microscope with Hoffmann optics was used to observe cells during the electrical measurements.

The base extracellular solution contained NaCl (140 mM), CaSO₄ (2 mM), MgSO₄ (1.2 mM), and Hepes (10 mM). The intracellular solution contained NaCl (140 mM), CaSO₄ (2 mM), MgSO₄ (1.2 mM), Hepes (10 mM), and EGTA (10 mM). Cl concentrations were 0.1, 0.2, 0.5, 1, 5, 10, 20, 40, 80, 140, and 200 mM. Cl concentration was adjusted by substituting Cl with the divalent anion malate. In a subset of experiments, gluconate was the major substitute. Final solutions were adjusted to ~300 mOsm (except for the solutions that contain 200 mM Cl) with dextrose and adjusted to pH 7.2–7.3 with NaOH. A stock solution of TBT (200 mM) was made in ethyl alcohol (EtOH) and then diluted in extracellular medium to obtain the desired concentrations. To dissociate the effect of TBT from EtOH, in a subset of experiments, TBT was directly mixed with extracellular medium to obtain desired concentrations (under the assumption that TBT totally dissolves in the alcohol-free solution). In these control experiments, the actual concentration of TBT is undetermined but likely to be lower than those equivalent solutions prepared using EtOH stock solution.

A custom-made Y-tube perfusion system was used for the delivery of experimental solutions to individual OHCs during continuous chamber wash with control extracellular solution. Perfusions were made with a range of chloride concentrations in combination with varying TBT levels. For the first set of experiments, we used either 5 or 140 mM Cl extracellular solution with varying TBT concentrations (0.01, 0.1, 1, 10, and 50 μM). In the next set of experiments, TBT concentrations were fixed at 1 μM , but Cl

concentrations were varied (1, 5, 10, 20, 40, 80, 140, and 200 mM). NLC was permitted to reach steady state before any subsequent manipulation. Perfusion speed through the Y-tube was 20 $\mu\text{l}/\text{min}$ with the tip placed 150–200 μm away from the patched cells. In this setup, junction potentials (calculated with Jpcalc; Axon Instruments, Union City, CA) associated with malate are small, and not corrected [<9 mV absolute for the largest changes from 1-mM to 140-mM Cl solutions, assuming a mobility for malate of 0.4 relative to Cl; direct measures of junction potentials were much smaller (2–3 mV)]. For the quantitative analysis of chloride level effects on motor activity, solutions were matched intracellularly and extracellularly (except that intracellular solutions had an additional 10 mM EGTA; see above), thus avoiding junctional potential effects.

Single OHCs were studied under whole-cell voltage clamp. An Axon 200B amplifier was used to hold the cell at 0 mV to remove the electrical drive for Cl ion flux. Thus, the effects of our imposed Cl concentration gradients were studied in isolation. Initial pipette resistances were 4–7 M Ω . Series resistances, which ranged from 5 to 20 M Ω , remained uncompensated for C_m measurements. Before establishing whole-cell configuration, gigohm seals were obtained (1.5–3.5 G Ω), and stray pipette capacitance was neutralized. All data acquisition and analysis was performed with a Windows-based patch-clamp program jClamp (www.SciSoftCo.com). Voltage was corrected offline for the effects of series resistance.

NLC was calculated using a continuous high-resolution (2.56-ms sampling) two-sine stimulus protocol (10 mV peak at both 390.6 and 781.2 Hz) superimposed onto a voltage ramp (200-ms duration) from either –200 to +80 mV or –160 to +120 mV (Santos-Sacchi et al., 1998b). Capacitance data were fit to the first derivative of a two-state Boltzmann function (Santos-Sacchi, 1991),

$$C_m = Q_{\text{max}} \frac{ze}{kT} \frac{b}{(1+b)^2} + C_{\text{lin}}, \quad (1)$$

where

$$b = \exp\left(\frac{-ze(V_m - V_{\text{pkcm}})}{kT}\right),$$

Q_{max} is the maximum nonlinear charge moved, V_{pkcm} is voltage at peak capacitance or, equivalently, at half maximum charge transfer, V_m is membrane potential, z is valence, C_{lin} is linear membrane capacitance, e is electron charge, k is Boltzmann's constant, and T is absolute temperature.

Q_{sp} (specific nonlinear charge) was calculated as $Q_{\text{max}}/(C_{\text{lin}} - 6.5)$, where C_{lin} is the linear capacitance, a measure of surface area, obtained from Boltzmann fits (Santos-Sacchi and Navarrete, 2002). A value of 6.5 pF in linear capacitance is the estimated contribution of apical and basal ends of the OHC, and therefore is subtracted to provide only that lateral membrane area that contains prestin (Huang and Santos-Sacchi, 1993; Santos-Sacchi, 2004). To determine unbiased estimates of linear capacitance we employed the following logic and strategy. The capacitance of the OHC is an asymmetric bell-shaped function due to motor surface area change; on average the left side of the function asymptotes at a value 3.5 pF greater than the right asymptote (Santos-Sacchi and Navarrete, 2002). C_{lin} is defined as the minimum capacitance, that is, when all the motors are in the compact state (right side of function). However, since the NLC curve shifts depending on intracellular Cl concentration and substitute anion, in some cases C_{lin} was not directly measurable because the right side was truncated. To assure accurate estimates of C_{lin} across cells with different intracellular Cl concentrations, all cells were first fitted only to the left half of the NLC curve to obtain an initial estimate of Q_{max} and z . Q_{max} and z were then used to estimate motor number ($N = Q_{\text{max}}/ze$), and the offset capacitance proportional to motor surface area change was determined from Fig. 4 c in Santos-Sacchi and Navarrete (2002). By subtracting this offset from the left-side asymptote of the NLC function we obtained an unbiased estimate of C_{lin} . It should be noted, however, that all final estimates of Q_{max} and z reported in this manuscript were determined from fits of Eq. 1 to full NLC datasets. All curve fitting was performed offline with jClamp and derived

parameters were analyzed in Excel and Sigma Plot (Jandel Scientific, San Rafael, CA). Plots were generated by using Sigma Plot. Standard errors are reported.

Chloride flux experiments were performed using fluorescence imaging of OHCs loaded with the Cl-sensitive dye MQAE, obtained from Molecular Probes (Eugene, OR). Isolated OHCs incubated in 1 mM Cl extracellular solution were placed onto coverslips coated with Cell-Tak (BD Biosciences, San Jose, CA). Cells were then moved to a thermostatically controlled microperfusion chamber, and incubated with 10 mM MQAE dye in the dark for 30 min. After excess dye was flushed off the coverslips, cells were examined under an inverted microscope with 60 \times magnification (IX70, Olympus, Tokyo, Japan) and images were captured through a Photometrics (Tucson, AZ) cooled CCD camera and analyzed with the program Metafluor (Universal Imaging, Downingtown, PA). The bath solutions were then changed in the following order: 1 mM Cl, 145 mM Cl, 1 mM Cl with 10 μ M TBT, 145 mM Cl with 10 μ M TBT and 145 mM Cl. The solution exchange rate was 4 ml/min by gravity flow into a 0.6-ml chamber. Measurements were carried out with excitation at 350 \pm 10 nm and emission at 450 \pm 10 nm. For presentation, noncellular background fluorescence, measured simultaneously, was subtracted from cellular responses. Photobleaching of the dye was insignificant on the timescale of our measurements; this is indicated by the return of fluorescence to the same 1 mM Cl pretreatment level after exposure to 145 mM Cl (see Fig. 1).

RESULTS

TBT promotes chloride flux across the OHC membrane

It is firmly established that TBT promotes Cl exchange across membranes (Motais et al., 1977; Selwyn et al., 1970; Wieth and Tosteson, 1979; Tosteson and Wieth, 1979; Verkman, 1990). However, to confirm that TBT also enhances Cl flux in OHCs, experiments were carried out with the use of the Cl-

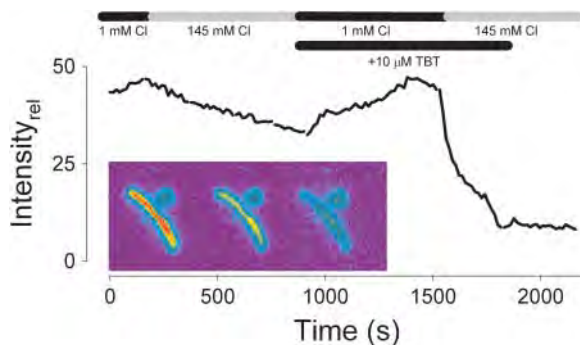


FIGURE 1 TBT promotes enhanced Cl flux across the OHC lateral membrane as measured by the fluorescent, chloride-sensitive dye MQAE. A dye-loaded OHC was perfused with the following solutions (indicated by the bars in the figure): 1 mM Cl, 145 mM Cl, 1 mM Cl with 10 μ M TBT, 145 mM Cl with 10 μ M TBT, and 145 mM Cl. Emission light intensity drops when the intracellular dye is quenched due to an increase in intracellular chloride. The chloride flux during the initial chloride gradient step, i.e., through G_{metL} , is less than that during a subsequent gradient step in the presence of TBT. Time resolution was 7.5 s. (Inset) Another example of an OHC showing fluorescence image changes. Cell width is 10 μ m. At zero time (left panel), the OHC bath was switched from 1 mM to 140 mM Cl extracellular solution. (Middle panel) At 360 s after, and (right panel) 945 s after switch. Flux is through G_{metL} alone, since TBT is absent in this case. The quenching of fluorescence (red \rightarrow green) indicates an increase in intracellular Cl.

sensitive fluorescent dye MQAE. In MQAE-loaded isolated OHCs that were preincubated in 1 mM chloride extracellular solution, a switch to 145 mM extracellular chloride solution caused a quenching of the dye's fluorescence, indicating that an increased chloride gradient resulted in an influx of chloride via the OHC's native conductance G_{metL} (Fig. 1). The addition of TBT markedly enhanced the influx of chloride. Thus, the OHC membrane is no different in its susceptibility to TBT than the other membranes previously studied.

TBT affects NLC only in the presence of a chloride gradient across the OHC

To further study the effect of TBT on OHC chloride flux during perfusion of TBT, we monitored NLC, which we and others have shown to be a very sensitive indicator of intracellular chloride levels (Oliver et al., 2001; Rybalchenko and Santos-Sacchi, 2003c). In the steady-state presence of a chemical gradient of Cl across the OHC lateral membrane (140 mM outside, 5 mM inside), and in the absence of TBT, V_{pkcm} is stable near -10 mV (Fig. 2 A, rightmost trace). This stability under these recording conditions arises from a net balance of Cl movements via G_{metL} and the patch pipette, resulting in a stable Cl activity at the intracellular aspect of prestin. However, in the presence of extracellular TBT, V_{pkcm} shifts leftward (hyperpolarizing direction) and the absolute magnitude of the shift increased with increasing TBT concentration (Fig. 2, A and C, solid symbols). This incrementing shift arises from the enhanced Cl exchange, which more effectively counters pipette washout, since, as we show below, TBT has no effect on prestin itself. At high levels (>10 μ M), TBT caused membrane instability and loss of recordings; we therefore limited most of our work to a 1- μ M concentration.

It is conceivable that TBT may directly interfere with Cl-prestin interactions, thereby contributing to the observed results. To rule out this possibility, we compared the effects of TBT on NLC in the absence of a driving force for Cl transport (5 mM inside, 5 mM outside; Fig. 2 B). In the absence of a gradient, there cannot be a diffusion-based net movement of Cl. However, if TBT were to alter the interaction between Cl and prestin, there would be a dose-dependent effect of TBT upon NLC measures. We chose to use 5 mM intrapipette Cl to ensure that prestin works in the midrange of its dose-response curve (Oliver et al., 2001), allowing alterations in prestin activity to be easily discerned. Under these conditions, perfusion of TBT at varying concentrations did not induce significant shifts of V_{pkcm} or changes in peak capacitance (Fig. 2, B and C, open symbols).

TBT does not directly affect prestin or G_{metL}

Since chloride affects the state probability of prestin (Rybalchenko and Santos-Sacchi, 2003c), it is possible that a chloride gradient can set prestin into a permissive state

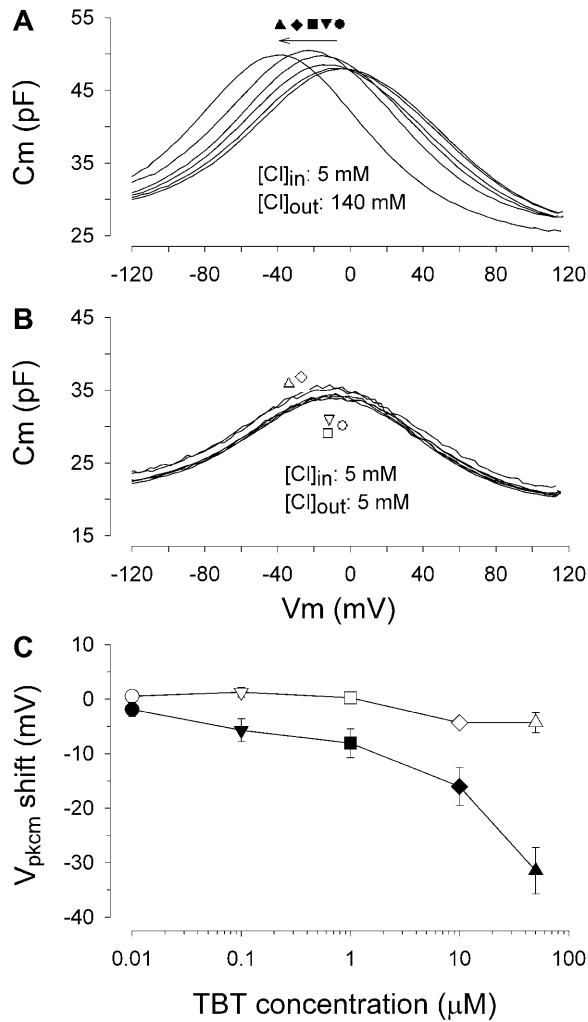


FIGURE 2 Effects of TBT upon V_{pkcm} depend on the chloride concentration gradient across the OHC membrane. (A) A representative cell with the pipette solution containing 5 mM Cl and the extracellular solution containing 140 mM Cl. The NLC curve shifts left with increasing extracellular TBT concentration (from right to left: 0 (rightmost trace), 0.01 (solid circle), 0.10 (solid upside-down triangle), 1.0 (solid square), 10 (solid diamond), and 50 (solid triangle) μM), as the Cl exchange more effectively counters pipette washout. (B) A representative cell with both the pipette and extracellular solution containing 5 mM Cl. Regardless of TBT concentration, the NLC remains virtually unchanged. (C) Average responses of two groups as in A and B ($n = 5-8$); each cell in a group was exposed to the full concentration range. Open and solid symbols represent cells bathed in the extracellular media containing 5 and 140 mM Cl, respectively. Gluconate was used to substitute for Cl in bath solution. Symbol types correspond to different TBT concentrations (as used in A, above). TBT effects were statistically significant (paired t -test; $p < 0.05$) for all concentrations except 10 nM.

whereby TBT could directly act on the protein, in analogy to well known state-dependent effects of blockers on ion channels. To evaluate this possibility, we directly probed the state dependence of TBT effects on prestin by driving the motor into predominantly the expanded or compact state with voltage (-50 and $+50$ mV; no chloride gradient, 140 mM in/out), while noting the effects of TBT on NLC (Fig.

3). The overlapping NLC traces at either holding voltage in the presence or absence of TBT indicates that any state dependence of direct TBT effects on the motor is absent. The difference in the traces obtained at either holding voltage is due to the effect of prior voltage on NLC that we thoroughly described previously (Santos-Sacchi et al., 1998b). In a similar fashion, we also tested nonsaturating chloride conditions (5 mM in, 140 mM out) to determine whether chloride interactions with prestin might be modified by TBT. The basic results were the same—there was no differential action on motor activity by TBT at either holding potential. These data confirm that TBT does not directly affect prestin or its interaction with chloride.

Another possibility that could account for shifts in V_{pkcm} is a direct action of TBT on G_{metL} , which naturally would only be effective in the presence of a Cl gradient. To rule out this possibility, we measured OHC membrane conductance directly during treatments with TBT in the presence of a Cl

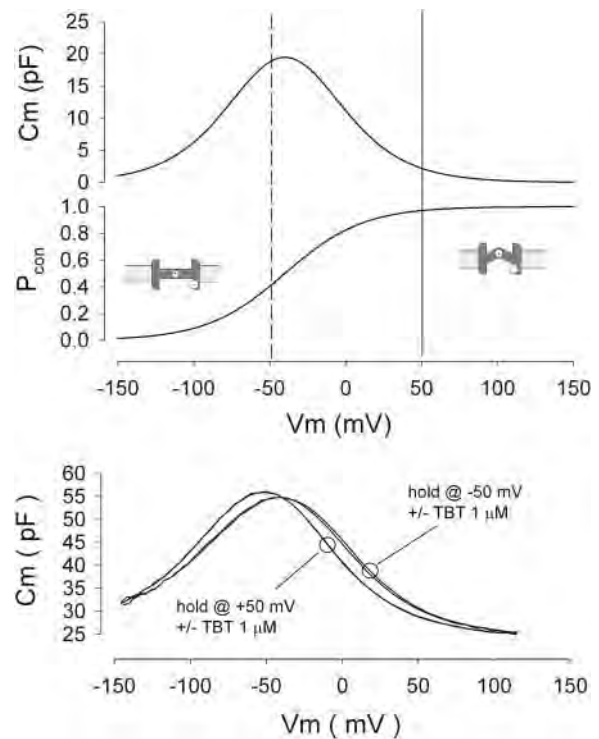


FIGURE 3 TBT does not work on the motor directly in a state-dependent manner. The top two panels indicate the relationship between NLC and motor-state probability, or population distribution of the motors into either the compact or expanded state. Hyperpolarization increases the number of motors in the expanded state. At the two vertical lines the number of motors in each state markedly differs. The lower panel shows four NLC traces. The overlapping traces obtained at $+50$ mV with and without 1 mM TBT test to see if TBT works selectively on the motors when predominantly in the expanded state; those traces obtained under the same conditions except at -50 mV test the effects of TBT when most motors are in the compact state. No Cl gradient is present (140 mM in/out). The overlap of the traces at either holding voltage indicates a lack of a state-dependent effect of TBT directly on the motors. The difference between the traces at each holding potential is fully a result of prior voltage effects on NLC (Santos-Sacchi et al., 1998b).

gradient (5 mM in/ 140 mM out). Fig. 4, *A* and *B*, shows that membrane resistance actually increases slightly, i.e., G_{metL} , which we measure directly, decreases during perfusions with TBT, whereas NLC shows typical effects of Cl modulation (Fig. 4 *C*). Under our ionic recording conditions (see Methods) G_{metL} is mainly responsible for setting R_m . Additionally, the inset of Fig. 4 *A* shows the percent change in membrane resistance caused by 1 μM TBT in the absence of a chloride gradient for different Cl concentrations. TBT decreases conductance by a few percent. These data indicate that TBT does not induce Cl movements by activating G_{metL} or any another conductance.

The effects of TBT on NLC depends on the magnitude and direction of the chloride gradient

Taken together our data thus far, namely, the direct measure of chloride flux with MQAE, the absence of direct effects of

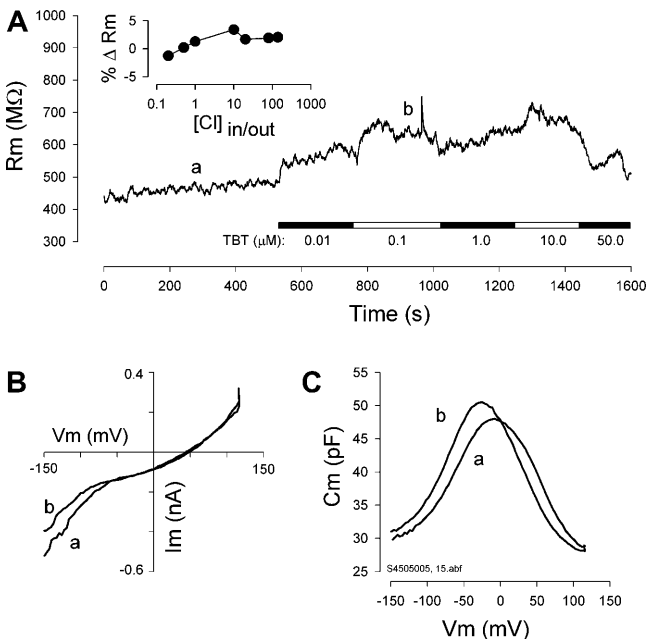


FIGURE 4 TBT does not activate the native Cl pathway, G_{metL} . (A) Continuous measures of R_m (determined with 10 mV step hyperpolarizations at 0 mV holding potential) were made during local perfusion of an OHC with different TBT concentrations with a chloride gradient similar to what we expect in vivo, namely, 140 mM outside/5 mM inside. (Inset) The plot shows the percent change in membrane resistance caused by 1 μM TBT in the absence of a chloride gradient for different Cl concentrations. TBT decreases conductance by a few percent. (B) $i-v$ curves from positions *a* and *b* marked in A. Slope resistance of each curve (*a* and *b*) at 0 mV differs by $\sim 30\%$ as indicated in A. (C) NLC obtained simultaneously at *a* and *b*. During the first 8–9 min, in the absence of TBT, the NLC stabilized, as depicted in C (trace *a*). Upon addition of TBT, membrane conductance actually decreased and is indicated by the $i-v$ curve in B, indicating a reduction of Cl movements through G_{metL} ; however, despite the reduction of Cl movement via membrane conductance, the increase in intracellular Cl via anion exchange diffusion via TBT causes a negative shift in NLC (C, trace *b*). Similar results were obtained in eight cells. These data indicate that TBT does not work by nonselectively increasing membrane conductance or by increasing G_{metL} .

TBT on prestin and G_{metL} , and the requirement for a chloride gradient, strongly indicate that TBT works simply by augmenting the flux of Cl into and out of the OHC in a manner that we have previously shown to occur via G_{metL} (Rybalchenko and Santos-Sacchi, 2003c). The following observations, which show directional and magnitude sensitivity of the chloride gradient on NLC, confirm this conclusion and support the similar conclusions of others (Tosteson and Wieth, 1979; Wieth and Tosteson, 1979; Marandi et al., 2002).

OHCs bathed in 1 mM Cl medium for extended periods of time (up to 2 h) retain a significant concentration of Cl intracellularly, based on initial whole-cell measures of NLC (Fig. 5). The retention of higher chloride levels is likely because the cells are collapsed under this condition, and the stretch-activated G_{metL} is not fully activated. Immediately after establishing whole-cell configuration, V_{pkcm} hovered around -40 mV (Fig. 5 *A*, leftmost NLC curve). At the start of cytoplasmic washout with pipette solutions containing 1 mM Cl, recordings made every 25 s revealed that V_{pkcm} shifted to the right as intracellular Cl levels dropped. Accompanying the shift was a reduction of Q_{max} . Eventually steady-state conditions were reached, indicated by the accumulation of overlapping NLC curves (Fig. 5 *A*). The time course of the pipette washout process was exponential, with time constants of 80.44 ± 7.3 s for V_{pkcm} and 44.87 ± 5.5 s for Q_{max} (mean \pm SE; paired t -test, $p = 0.004$; Fig. 5, *B* and *C*), the difference in time constants possibly indicating independence of the underlying mechanisms responsible for each of the parameters. However, changes in the Boltzmann fit during the shift, resulting from truncations of tail regions of the NLC function due to voltage limitations, conceivably could contribute to this difference. Steady-state levels were reached in 3–5 min, as expected for washout through patch pipettes (Pusch and Neher, 1988); the reason for this stabilization may be that the intracellular Cl concentration finally matched the extracellular concentration or, as noted above, that a stable Cl activity at the intracellular aspect of prestin was achieved. These possibilities are evaluated below.

Since it appears that the impact of TBT on prestin derives from its ionophore effect (Figs. 2–4), a change in the driving force for Cl, namely a change in the mismatch between intra- and extracellular Cl concentrations, should substantially modulate prestin activity, just as occurs with the native conductance G_{metL} (Rybalchenko and Santos-Sacchi, 2003c). To evaluate this possibility, we studied the consequences of changes in extracellular Cl levels with or without the addition of TBT. After steady-state intracellular washout with 1-mM Cl solutions (as in Fig. 6), perfusion of extracellular solutions with graded Cl concentrations (5–140 mM in the absence of TBT) shifted NLC functions back to the left, with a slight change in Q_{max} (Fig. 6, *A*, *C*, and *E*). However, even with the highest Cl concentration extracellularly, V_{pkcm} did not shift more than -20 mV. Furthermore, above 80 mM extracellular Cl, effects seem to saturate (Fig. 6, *A* and *C*),

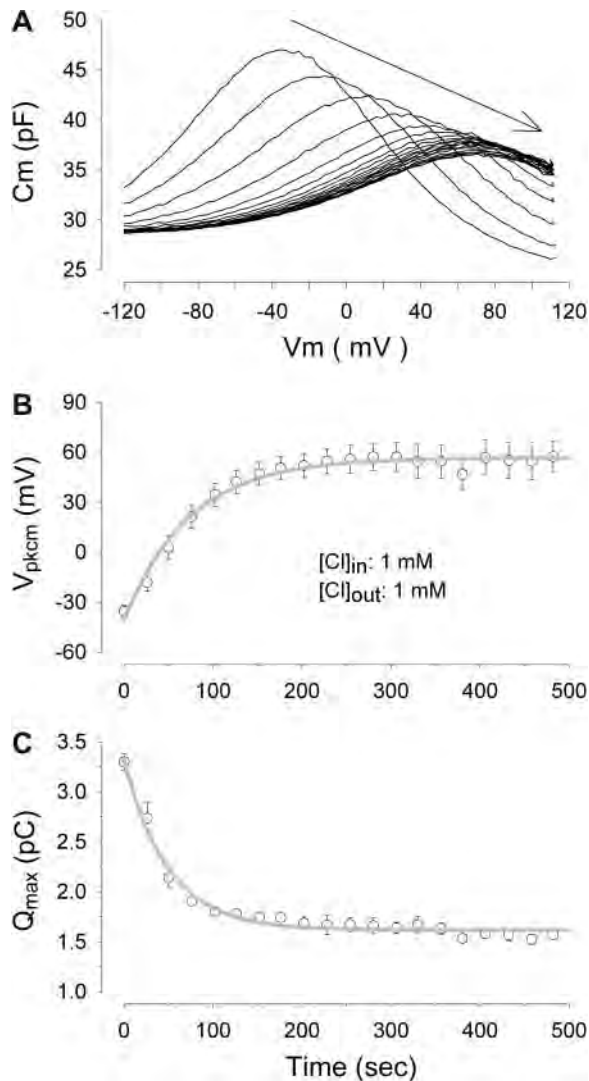


FIGURE 5 Effects of intracellular chloride washout on NLC. Cells were bathed in 1 mM Cl extracellular solutions for up to 2 h to reach steady state. The initial recordings were obtained within 5–10 s after establishment of whole-cell configuration with pipette solutions containing 1 mM Cl. (A) A representative cell with an initial V_{pkcm} near -40 mV. Recordings were made every 25 s until steady state was reached. The NLC curve shifted quickly to the right with the reduction of magnitude. At steady state, NLC curves overlapped. (B and C) Averaged V_{pkcm} and Q_{max} derived from four cells with complete data sets. The thick lines are fits to averaged data and averaged time constants are 80.44 ± 7.3 s for V_{pkcm} , and 44.87 ± 5.5 s for Q_{max} .

indicating the limited capability of the native Cl conductance, G_{metL} , to overcome the continuous pipette-mediated cell washout of Cl (i.e., given a finite G_{metL} (Rybalchenko and Santos-Sacchi, 2003c)).

As we anticipated, the addition of TBT in the perfusion medium augments Cl influx, which is clearly indicated by measures of prestin activity (Fig. 6B). Shown in Fig. 6B are the responses from the same cell depicted in Fig. 6A but now reperfused (after a steady-state return to 1 mM Cl extracellular solutions) with identical Cl concentration steps

containing 1 μ M TBT. In the presence of TBT, V_{pkcm} continuously shifted leftward and Q_{max} increased as extracellular Cl concentration was increased (Fig. 6, B, D, and F). In fact, the initial V_{pkcm} (dashed line, similar to leftmost curve in Fig. 5A but showing a more positive potential due to the delayed start of the initial recording) was recovered when extracellular Cl reached 140 mM, which corresponds to a >-50 mV shift. When the extracellular Cl concentration was increased further to 200 mM (~ 380 mOsm, an unnatural osmolarity and Cl concentration), an additional V_{pkcm} shift of -13 mV was observed (Fig. 6B, leftmost curve). These data clearly show that TBT provides an additional route for Cl influx, whose efficiency, unlike that of the cell's natural Cl conductance, G_{metL} , can more effectively counter the continuous consequences of pipette washout. During the resultant changes in intracellular chloride levels, OHC shape is expected to change as V_{pkcm} shifts; for example, at a fixed holding voltage, a hyperpolarizing shift in V_{pkcm} will be sensed as a depolarizing stimulus by the voltage sensors of the lateral membrane motors. This we observed as a contraction of OHCs when local extracellular Cl perfusion was switched from 1 mM to 80 mM in the presence of TBT, as illustrated in Fig. 7. The magnitude of this contraction indicates that in addition to a voltage-induced contraction, water influx additionally shortens the cell (see Discussion).

We were able to use TBT to study Cl efflux as well as influx, since the compound works by diffusional exchange (Tosteson and Wieth, 1979; Wieth and Tosteson, 1979). In this case, we observed recovery from extracellular perfusions of high Cl concentrations in the presence and absence of TBT (Fig. 8). Initially, cells were patched with 1 mM Cl intra- and extracellularly, and NLC was allowed to reach steady-state conditions, as in Fig. 5. Then cells were loaded with Cl by perfusing with high extracellular Cl in the absence of TBT (either 80 or 140 mM), and allowed to reach steady state again. Upon returning to 1-mM Cl extracellular solutions in the absence of TBT, V_{pkcm} and Q_{max} recovered only partially toward the initial low Cl, control condition (Fig. 8). The subsequent addition of 1 μ M TBT into the extracellular solution quickly completed the recovery toward the control condition (Fig. 8). The inability of G_{metL} to foster a recovery to the same conditions as it permitted before loading may indicate that the conductance is rectified. Alternatively, the conductance may have changed during the intervening time during perfusions (see Discussion).

The chloride- Q_{max} and chloride- V_{pkcm} dose-response function in the intact OHC

NLC in OHCs is clearly influenced by intracellular Cl concentration, and its magnitude and voltage dependence are determined by prestin's Cl dose-response function (Oliver et al., 2001; Rybalchenko and Santos-Sacchi, 2003c). When pipette solutions contain 20 mM Cl, perfusions of higher

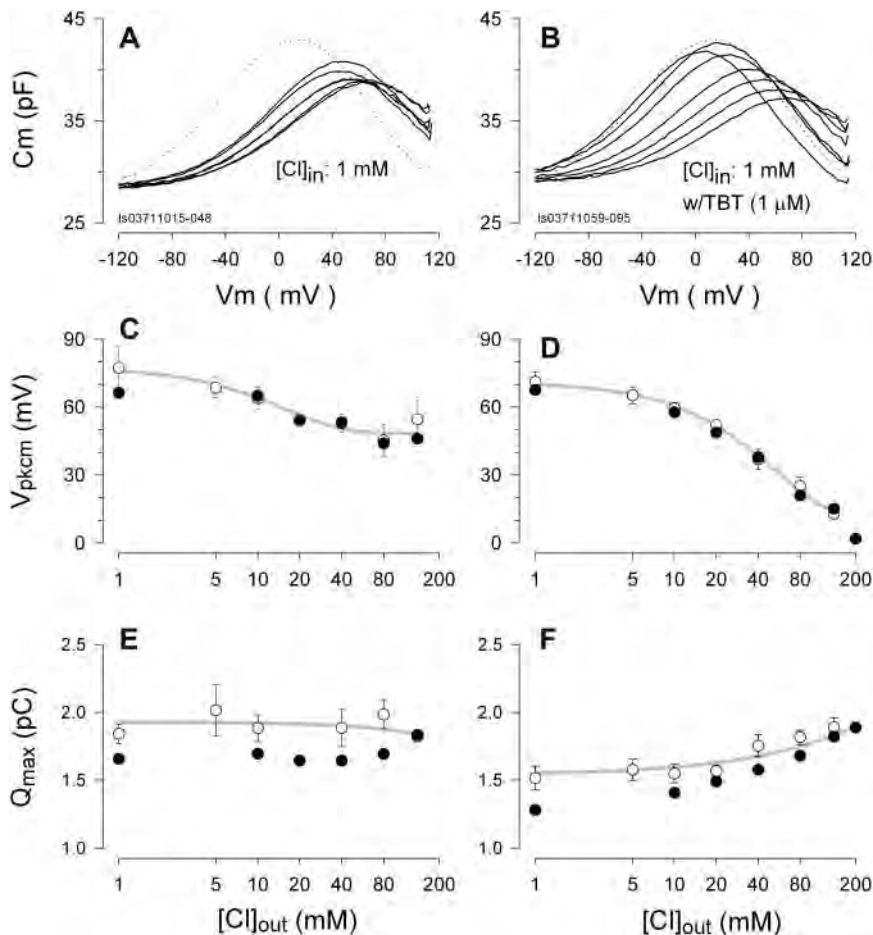


FIGURE 6 Reperfusion of high chloride extracellular solutions recovers prestin activity. (A and B) Response from the same representative cell. With the reperfusion of high Cl extracellular solution, either in the presence or absence of TBT, NLC shifts back toward the original condition (i.e., the first NLC trace measured upon whole-cell pop-in, plotted as *dashed line*, similar to leftmost trace in Fig. 5 A). However, in the absence of TBT, G_{metL} is unable to provide a sufficiently rapid Cl influx to overcome the effects of continuous pipette washout of Cl; the shift of V_{pkcm} did not recover beyond +40 mV (A). With the addition of TBT (1 μM ; B), NLC shifts back to the control level. Derived V_{pkcm} and Q_{max} are plotted in panels (C–F) Solid circles represent the results from the sample cell. Open circles are averages \pm SE.

concentrations of extracellular Cl, with or without TBT, do not significantly shift NLC functions (data not shown), suggesting that Cl - prestin interactions are nearly saturated at this concentration. Oliver et al. (2001) found a $K_{1/2}$ for intracellular Cl of 6.3 mM based on Q_{max} estimates in membrane patches. We measured the NLC functions of intact OHCs under symmetrical intracellular and extracellular Cl concentrations of 0.2, 0.5, 1, 5, 10, 20, 80, and 140 mM. To ensure symmetrical conditions, TBT was used in a subset of experiments, but no statistically significant differences were noted. For example, comparing TBT versus no TBT at 1 mM Cl, Q_{max} was 1.64 ± 0.07 vs. 1.69 ± 0.04 pC (mean \pm SE; $n = 12$, $n = 27$; $p = 0.53$); similarly, for V_{pkcm} , 73.34 ± 4.99 vs. 63.96 ± 3.55 mV ($n = 12$, $n = 27$; $p = 0.14$). As another example, at 80 mM Cl comparisons showed 3.17 ± 0.22 vs. 3.20 ± 0.14 pC ($n = 5$, $n = 10$; $p = 0.94$) and -54.63 ± 6.85 vs. -52.38 ± 5.47 mV ($n = 5$, $n = 10$; $p = 0.80$), respectively. This absence of effects is in line with the data from Fig. 2, and confirmed that the intracellular and extracellular concentrations of Cl were truly equilibrated. Thus, data were pooled, and using a logistic fit, our estimated $K_{1/2}$ for Q_{sp} (Santos-Sacchi et al., 1998a) is 6.06 ± 2.34 mM and slope is 1.02 ± 0.5 (Fig. 9 A); a similar fit was made to the V_{pkcm} data giving 4.48 ± 0.77 and 0.94 ± 0.17 ,

respectively (Fig. 9 B). A significant proportion of motor charge was insensitive to Cl. That is, $\sim 36\%$ of the nonlinear charge movement remained intact in the absence of Cl. It is important to note that the anion used to replace Cl influences V_{pkcm} and Q_{max} (Rybalchenko and Santos-Sacchi, 2003c), and that the insensitive proportion of motor charge can be much larger for other anion substitutes. For example, intracellular washout with malate substitution at 5 mM Cl stabilizes at a Q_{sp} of 0.13 ± 0.005 pC ($n = 19$), whereas substitution with gluconate provides a Q_{sp} of 0.18 ± 0.006 pC ($n = 17$). This difference corresponds to an equivalent shift along the concentration axis of $\sim +9$ mM Cl for malate-based solutions. In other words, the Q_{sp} value with 5 mM Cl in gluconate-based solutions equals the Q_{sp} value measured from 16 mM Cl in malate-based solutions.

The ethanol vehicle for TBT delivery does not influence NLC

In the preparation of TBT stock solution, ethyl alcohol (EtOH) was used to dissolve TBT that otherwise would have been incompletely dissolved in water-based solutions. To evaluate the impact of EtOH, in a subset of experiments, OHCs were perfused with graded concentrations of EtOH

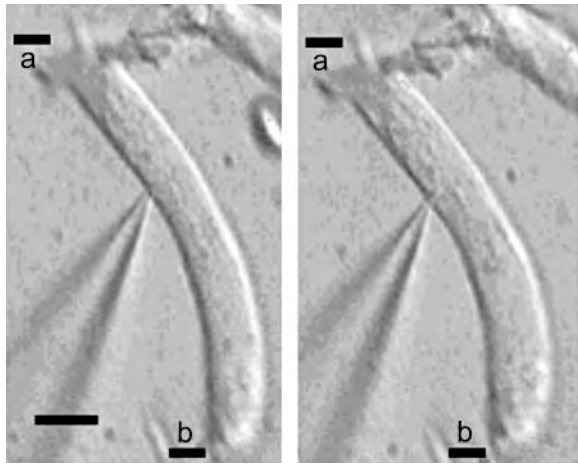


FIGURE 7 Influx of Cl causes OHC contraction. A representative OHC was locally perfused with extracellular medium that contained 1 mM (*left*) and 80 mM (*right*) Cl. TBT (1 μ M) is present in both cases. The fiducial mark is the pipette tip, which remains fixed. Pipette solution contained 1 mM Cl. Small debris are inescapably disturbed by the constant flow. Scale bar (*bottom left*) is 10 μ m. *a*, line at cell apex; *b*, line at cell base.

(Fig. 10). An effect of EtOH on NLC was evident only when the EtOH levels were >1%. In the routine preparation of perfusion solutions that contained TBT, EtOH levels were <0.025%. In the solutions that contained 1 μ M TBT, EtOH level was 0.0005%.

Although a low level of EtOH by itself did not cause significant changes in NLC, it is still possible that EtOH may work synergistically with TBT, as has been demonstrated for other ototoxic agents (Loquet et al., 2000). Therefore in a separate set of experiments, TBT was dissolved in the absence of EtOH. In those cases, the actual concentration of TBT is undetermined but is known to be lower than the amount added (in each of three experiments it was <10 μ M, <1 μ M, and <0.5 μ M). The results were similar to those experiments that employed EtOH as solvent for TBT, indicating that the TBT effect is independent of, and not enhanced by, EtOH.

DISCUSSION

In 1991, we showed that the lanthanide, Gd³⁺, could reversibly block OHC NLC and motility (Santos-Sacchi, 1991); aside from agents that irreversibly damage electromotility (Kalinec and Kachar, 1993), few agents, including salicylate, other lanthanides, and furosemide, have been found to reversibly interfere with lateral membrane motor activity (Dieler et al., 1991; Santos-Sacchi, 2003; Santos-Sacchi et al., 2001; Kakehata and Santos-Sacchi, 1996; Tunstall et al., 1995). After the identification of chloride's preeminent role in promoting prestin activity (Oliver and Fakler, 1999) and the identification of a native pathway for Cl flux within the lateral membrane (Rybalchenko and Santos-Sacchi, 2003c), underlying mechanisms for these

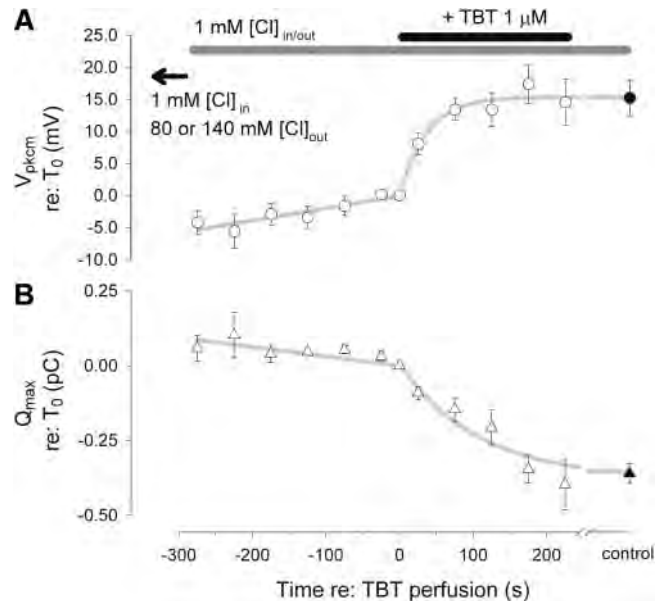


FIGURE 8 TBT enhances Cl efflux. (*A* and *B*) Averages ($n = 7$) of relative V_{pkcm} and Q_{max} during a switch from high to low extracellular Cl. Cells were previously loaded (to steady state) with Cl under high-Cl (80 or 140 mM) extracellular perfusion. Then cells were perfused (starting at -300 s) with 1 mM Cl extracellular medium to unload intracellular Cl. The 0-s mark indicates the beginning of TBT perfusion. Time resolution is 50 s (bin width). During the washout, R_s remained unchanged. The averaged values at the beginning of washout, beginning of TBT perfusion (T0), and the end of washout are 13.2, 12.9, and 13.0 M Ω , respectively. Solid symbols represent control values (1 mM intra/extracellular) before Cl loading. The bars on top show the perfusion strategy. The gray lines are fits to the data; straight line fits were made for the section before TBT, and exponential fits (τ : V_{pkcm} , 35.71 s; Q_{max} , 105.4 s) during TBT perfusion. The control values were used as steady-state end points for the fits.

blocking agents' actions on OHCs have been revealed. Thus, salicylate, though previously shown to have worked intracellularly in its charged form (Kakehata and Santos-Sacchi, 1996), is now known to interfere with the interaction of Cl and prestin (Oliver et al., 2001); the other agents, in addition to possible direct effects on the motor, may interfere with Cl flux across the lateral membrane (Rybalchenko and Santos-Sacchi, 2003c). These observations have been very helpful in understanding the molecular mechanism responsible for cochlear amplification in mammals (see Santos-Sacchi, 2003).

In this study, we report several new observations that have important consequences for understanding OHC function, and how cochlear amplification may be compromised. First, we show that the ionophore TBT can seriously disrupt chloride homeostasis in the mammalian OHC. Direct measures of chloride flux with the chloride-sensitive dye MQAE, as well as direct measures of chloride-sensitive prestin activity, provide strong evidence for this conclusion. To be sure, TBT was without direct effect on the motor and G_{metL} ; the effects were only observed in the presence of a chloride gradient across the OHC membrane, and the

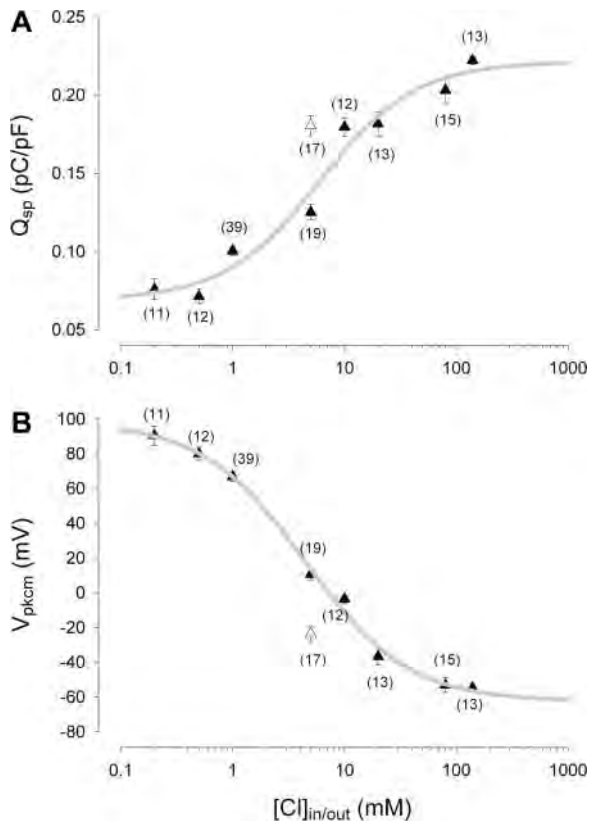


FIGURE 9 Prestin-Cl dose-response relationship. Nonlinear charge density, Q_{sp} and V_{pkcm} as a function of intracellular subplasmalemmal Cl concentrations, are fitted with logistic Hill function (solid triangles, malate as substitute anion). Each point represents the average (\pm SE; numbers in parentheses) from pooled recordings with or without TBT, since no statistically significant differences were found. Q_{sp} and V_{pkcm} were measured after pipette washout reached steady state. $K_{1/2}$ for Q_{sp} is 6.06 ± 2.34 mM and slope is 1.02 ± 0.50 (A); $K_{1/2}$ for V_{pkcm} data is 4.48 ± 0.77 mM, and slope is 0.94 ± 0.17 (B). Open triangles represent values from 5 mM Cl intracellular/extracellular with gluconate as substitute anion. Q_{sp} at steady state is 0.18 as compared to 0.13 in the case of malate substitution, a value that is equivalent to ~ 16 mM Cl inside with malate substitution.

magnitude of effects depended on the magnitude of the chloride gradient, with the direction of effects dependent on the direction of the gradient. This behavior was expected from previous work with this agent (Tosteson and Wieth, 1979; Wieth and Tosteson, 1979), and indeed, TBT is used to equilibrate intra- and extracellular chloride for estimation of chloride levels when using chloride-sensitive dyes such as MQAE (Verkman, 1990; Marandi et al., 2002). Second, given TBT's overwhelming effects we were able to compare the efficacy of G_{metL} in permitting chloride flux across the OHC membrane; NLC measures showed that native flux via this conductance is far less efficient than the flux provided by TBT, indicating that G_{metL} contributes to a regulated mechanism for chloride homeostasis within the OHC. Given such an effective agent as TBT, we were able to confirm uncompromised control over intracellular chloride levels and this allowed us, for the first time, to investigate prestin-

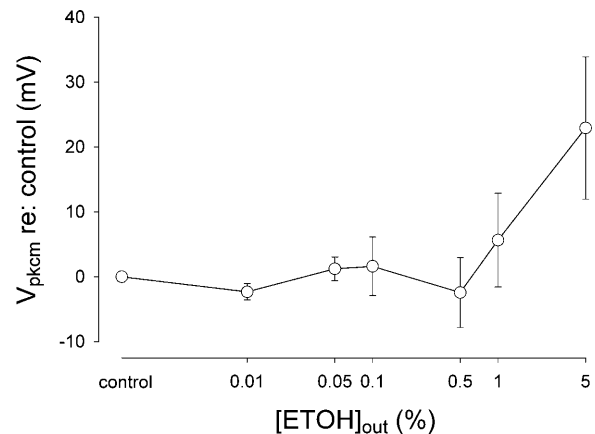


FIGURE 10 Ethyl alcohol shifts the NLC curve to the right at concentrations above 1%. Mean \pm SE of V_{pkcm} shift relative to the control are plotted as the function of EtOH concentration. Intracellular Cl is 5 mM in all cases. Q_{max} (not shown) did not change.

chloride interactions in the intact OHC. Finally, because of TBT's continued presence within marine environments and its accumulation in the food chain, we identify it as a potential hazard for marine mammals.

The operating range of prestin and lateral membrane Cl flux

Under typical whole-cell voltage-clamp conditions, where 140 mM Cl is perfused intra- and extracellularly, V_{pkcm} resides between -40 and -70 mV (Kakehata and Santos-Sacchi, 1995). This operating position is not fixed, since several fundamental biophysical forces have been shown to shift the NLC function along the voltage axis, i.e., to alter the steady-state energy profile of the lateral membrane motor. These forces include membrane tension (Iwasa, 1993; Gale and Ashmore, 1994; Takahashi and Santos-Sacchi, 2001; Kakehata and Santos-Sacchi, 1995), temperature (Meltzer and Santos-Sacchi, 2001; Santos-Sacchi and Huang, 1998), and voltage (Santos-Sacchi et al., 1998b). Recently, we found that alterations of intracellular Cl concentration can do the same, a decrease in concentration causing a shift in the depolarizing direction (Rybalchenko and Santos-Sacchi, 2003c). Depending on the substitute anion, the position of V_{pkcm} can vary between -180 and greater than $+100$ mV.

In the absence of TBT, chloride can permeate the lateral membrane through the stretch-activated conductance, G_{metL} . Under whole-cell voltage clamp, however, the effectiveness of this native conductance in modulating intracellular levels of chloride, in the face of changes in the extracellular Cl driving force depends on the pipette washout rate. Thus, after achieving steady-state conditions in the presence of 1 mM Cl within the patch pipette and extracellularly, an increase in extracellular Cl levels leads to a hyperpolarizing shift in V_{pkcm} , demonstrating that intracellular Cl increases as a result

of the imposed chemical driving force. However, the shift in V_{pkcm} does not recover to initial levels, and indicates that G_{metL} -mediated Cl flux is not sufficient to counteract the continuous washout of Cl by intracellular pipette perfusion. Clearly, if G_{metL} were to provide no barrier to the passage of Cl, the OHC could not use this ion as a modulator of prestin. The limiting nature of this native conductance was confirmed by treatment with TBT, which augmented Cl flux and returned V_{pkcm} further back toward initial conditions. Washout of cellular constituents via pipette is an efficient process, with replacements typically occurring within a few minutes (Pusch and Neher, 1988). It is surprising, therefore, that TBT can work so efficiently against pipette washout of Cl, and it may be possible that the restricted nature of the lateral subplasmalemmal space (LSpS) aids this process (see discussion in Rybalchenko and Santos-Sacchi, 2003c). Of course, in the intact OHC, G_{metL} will not have to struggle against such a powerful buffering mechanism as artificial pipette washout.

In our experiments on efflux of Cl from the OHC, we found a barrier to the complete washout of Cl from the LSpS, after Cl loading (Fig. 8). Whereas the influx of Cl during perfusion of high extracellular Cl competes with pipette washout, the efflux of Cl during perfusion of low extracellular Cl levels should be augmented by pipette washout. Despite this, TBT was required to fully allow Cl efflux, and may indicate some type of rectification of the native conductance, G_{metL} . However, our direct electrophysiological evaluation of G_{metL} showed no rectification near our holding potential of 0 mV (Rybalchenko and Santos-Sacchi, 2003c). Instead, we suspect that the conductance magnitude of G_{metL} may have changed during the shifts between low and high chloride. Perhaps lateral membrane tension was altered, thus altering the activation state of the pathway. Alternatively, exposure of G_{metL} to low Cl levels may have altered its activity, as has been found to occur in K channels (Loboda et al., 2001; Melishchuk et al., 1998).

Anion effects on motor charge movement— Q_{max}

In vivo, the flux of Cl across the lateral membrane through G_{metL} will be governed by membrane potential, membrane tension, and chloride's chemical driving force (Rybalchenko and Santos-Sacchi, 2003c). We have estimated intracellular Cl levels to be <9 mM at the normal in vivo resting potential (see Rybalchenko and Santos-Sacchi, 2003c), which places the cell in a maximally responsive region of the Q_{max} -Cl curve (Fig. 9). Interestingly, we again obtain a Q_{max} -Cl relationship in intact OHCs that differs substantially from that obtained by Oliver et al. in membrane patches (Oliver et al., 2001). Previously, we obtained an estimate of the Q_{max} -Cl function from OHCs by utilizing the conductive power of G_{metL} to control Cl on either side of the lateral membrane (Rybalchenko and Santos-Sacchi, 2003c). In those experiments, Cl concentration ranges from zero to 140 mM were evaluated, but we found that peak NLC could not be decreased below

~0.4 of control levels. This contrasted with the results of Oliver et al. (2001), where even 1-mM concentrations of Cl reduced Q_{max} to 0.15 of control values. In this set of experiments, to ensure against noise and drift caused by zero Cl levels, we did not lower Cl below 0.2 mM and employed TBT to ensure robust control of Cl concentration on either side of the lateral membrane. Nevertheless, we were unable to reduce motor charge movement (Q_{max}) to those levels found by Oliver et al. (2001); our Q_{max} levels at 0.2 mM Cl remain at 0.36 (1.15 ± 0.09 pC; $n = 11$) of saturated values (Fig. 9). Thus, ~36% of motor charge movement is insensitive to Cl, and reinforces our prior suggestions that Cl does not simply serve as prestin's extrinsic voltage sensor (Rybalchenko and Santos-Sacchi, 2003a,c). For that fraction of charge that is regulated by Cl, we find a $K_{1/2}$ (6.06 mM) and slope (1.02) that closely correspond to those measures of Oliver et al. (2001). It should be noted that the other physiological anion that affects prestin is bicarbonate, whose $K_{1/2}$ is 44 mM (Oliver et al., 2001), and which, under our intracellular and extracellular perfusion conditions, cannot reasonably account for the Cl-insensitive component of Q_{max} .

How is it that Cl is only partially responsible for charge movement of the OHC motor? It may be that prestin presents characteristics substantially similar to those of other transporters capable of charge movement under appropriate conditions, as evidenced by presteady-state currents (which are equivalent to an NLC) (Sacher et al., 2002; Hazama et al., 1997). Thus, in the absence of substrate, transporters such as mGAT3 and SGLT1 produce voltage-dependent displacement currents which may depend upon ion binding/dissociation or intrinsic conformational change. Interestingly, the GABA transporter's charge-movement dependence on Cl is not absolute (Sacher et al., 2002). We reason that the OHC motor likely possesses intrinsic charge movement due to conformational change, induced either by voltage or tension. Notably, those displacement currents displayed by transporters are typically abolished by saturating concentrations of appropriate substrate. Are we unaware of a natural substrate for prestin (SLC26a5), which normally works to dilute OHC NLC and motor activity?

Cl effect on OHC mechanics

NLC and electromotility are inextricably related; namely, shifts in V_{pkcm} along the voltage axis are mirrored in the mechanical activity of the OHC (Wu and Santos-Sacchi, 1998; Kakehata and Santos-Sacchi, 1995, 1996; Santos-Sacchi, 1991). Thus, OHC length is expected to change as V_{pkcm} shifts during intracellular chloride modulation simply because the drive to prestin is governed by the position of its Q - V or NLC function along the voltage axis. At a fixed holding voltage, a hyperpolarizing shift in V_{pkcm} will be sensed as a depolarizing stimulus by the lateral membrane motors, causing the cell to contract, as we illustrated (Fig. 7). Viewed as a population of motors, the percentage of motors

occupying the contracted state will increase; or for a given motor, the probability that that motor will reside in the contracted state will increase. A similar effect will also occur when Cl is modulated by pipette perfusion. In addition to direct effects of Cl on the motor, another possible mechanism could contribute to changes in cell length within the timescale that we worked under whole-cell voltage clamp, namely, water uptake after Cl influx. The expected magnitude of the voltage-induced contraction is easily calculated based on known OHC length- V_m functions. The contraction due to water movement can be quite large, and may overwhelm that induced by a perceived change in voltage. The cell in Fig. 7 shows a contraction of 4.4 μm . The average change in V_{pkcm} during a change from 1 mM extracellular solution to a saturating Cl solution (namely, 80 mM or above in 1 μM TBT's presence; Fig. 8) is ~ 15 mV. Given the largest measured mechanical response of 30 nm/mV (Santos-Sacchi and Dilger, 1988), we calculate that a half-micrometer contraction must occur. So in addition to an expected half-micrometer voltage-induced response, we likely have an additional 4 μm response due to water movements.

Based on these results, it is imperative that the consequences of chloride-induced shifts in V_{pkcm} and water movements be considered when evaluating effects of Cl manipulations on OHC mechanical characteristics. For example, OHC stiffness, which has been shown to be voltage-dependent in a manner that mimics electromotility (He and Dallos, 2000), will necessarily change when Cl-induced changes in V_{pkcm} occur, even if motor charge movement remains unaltered. Thus, it is not at all clear whether changes in voltage drive to the motor or changes in motor sensitivity underlie the effects of Cl manipulations on OHC stiffness (He et al., 2003). Indeed, controlling for these shifts is especially important when using anion substitutes such as pentane sulfonate (He and Dallos, 2000), which can cause V_{pkcm} to shift to very negative potentials (Rybalchenko and Santos-Sacchi, 2003b,c). Such a shift would cause the OHC to respond as it would to a depolarizing stimulus, namely, with a decrease in the cell's stiffness. In such a case, evaluations made across a full range of voltages are required for proper assessments of Cl's role.

The ototoxic effect of organotins

In this study we have shown that TBT functions as an ionophore that can bypass the native Cl pathway, G_{metL} . In effect, prestin is no longer subject to Cl modulation, and thus cochlear amplification will likely suffer. Whereas the other organotins, TET and TMT, have been shown to reduce auditory sensitivity in mammals (Clerici et al., 1991; Fechter et al., 1986, 1992; Liu and Fechter, 1995), their major action is considered to be at the inner hair cell/spiral ganglion cell level, and involve disruption of Ca homeostasis.

The ineffectiveness of TBT in the absence of a chloride gradient between intra and extracellular spaces indicates that

TBT does not affect the motor directly, and that any other possible intermediary effect on the motor resulting from TBT treatment is absent within our experimental timeframe; this precludes possible Ca effects as well. Additionally, the observed rapid effects of TBT (within seconds) differs from the slow (>30 min) cell shortening action of other trialkyltins on OHCs (Clerici et al., 1991; Fechter et al., 1986, 1992; Liu and Fechter, 1995). Indeed, Frolenkov et al (2000) showed that intracellular Ca increases caused by ionomycin or ACh, with or without perforated patch, produced no changes in OHC NLC. They did find, however, that phosphorylating and dephosphorylating agents, after 30–60 min incubation, resulted in V_{pkcm} shifts but had no effect on Q_{max} . To be sure, these results cannot be reconciled with our data on TBT effects, which show 1), a requirement for a Cl gradient; 2), simultaneous effects on both V_{pkcm} and Q_{max} ; 3), a dependence on magnitude and direction of the chloride gradient; that is, relative to initial conditions, the degree of V_{pkcm} shift and magnitude of Q_{max} depend on the magnitude of the Cl gradient, and the direction of V_{pkcm} shift depends on the direction of the Cl gradient; 4), rapid onset, within seconds; and 5), insensitivity to intracellular Ca buffer (10 mM EGTA). These observations indicate that the effects of TBT on the OHC result from Cl effects and not those of Ca. Interestingly, though, our results that organotins foster chloride flux across the OHC membrane may partially underlie their observed ability to shorten OHCs (Clerici et al., 1993), since, as we discussed above, binding of chloride ions to prestin increases the probability of the motor's residence in the contracted state.

Finally, we believe that the marine pollutant TBT poses a serious threat to marine mammals in particular, since they share with us the benefits of cochlear amplification. There are a growing number of studies linking TBT to untoward effects on mammalian cellular processes. For example, Akaike's group (Kishimoto et al., 2001) has found that environmentally relevant concentrations (30–100 nM) influence GABAergic neurotransmission, and suggested that some marine food sources which can accumulate TBT at levels of 100 nM or more pose a human health risk. Marine mammals likewise are exposed to this risk, perhaps more so. It will be important to assess the impact of TBT exposure on marine mammal communication.

We thank Dr. John Geibel (Yale Dept. of Surgery) for help with the MQAE dye experiments and the use of his equipment. We also thank Margaret Mazzucco for technical help.

This research was supported by National Institutes of Health National Institute on Deafness and Other Communication Disorders grant DC000273 to J.S.S.

REFERENCES

- Ashmore, J. F. 1987. A fast motile response in guinea-pig outer hair cells: the cellular basis of the cochlear amplifier. *J. Physiol.* 388:323–347.
- Belyantseva, I. A., H. J. Adler, R. Curi, G. I. Frolenkov, and B. Kachar. 2000. Expression and localization of prestin and the sugar transporter

- GLUT-5 during development of electromotility in cochlear outer hair cells. *J. Neurosci.* 20:RC116.
- Brownell, W. E., C. R. Bader, D. Bertrand, and Y. de Ribaupierre. 1985. Evoked mechanical responses of isolated cochlear outer hair cells. *Science.* 227:194–196.
- Clerici, W. J., M. E. Chertoff, W. E. Brownell, and L. D. Fechter. 1993. In vitro organotin administration alters guinea pig cochlear outer hair cell shape and viability. *Toxicol. Appl. Pharmacol.* 120:193–202.
- Clerici, W. J., B. Ross, Jr., and L. D. Fechter. 1991. Acute ototoxicity of trialkyltins in the guinea pig. *Toxicol. Appl. Pharmacol.* 109:547–556.
- Dallos, P., J. Santos-Sacchi, and A. Flock. 1982. Intracellular recordings from cochlear outer hair cells. *Science.* 218:582–584.
- Dieler, R., W. E. Shehata-Dieler, and W. E. Brownell. 1991. Concomitant salicylate-induced alterations of outer hair cell subsurface cisternae and electromotility. *J. Neurocytol.* 20:637–653.
- Fechter, L. D., W. J. Clerici, L. Yao, and V. Hoeffding. 1992. Rapid disruption of cochlear function and structure by trimethyltin in the guinea pig. *Hear. Res.* 58:166–174.
- Fechter, L. D., J. S. Young, and A. L. Nuttall. 1986. Trimethyltin ototoxicity: evidence for a cochlear site of injury. *Hear. Res.* 23:275–282.
- Frolenkov, G. I., F. Mammano, I. A. Belyantseva, D. Coling, and B. Kachar. 2000. Two distinct Ca(2+)-dependent signaling pathways regulate the motor output of cochlear outer hair cells. *J. Neurosci.* 20:5940–5948.
- Gale, J. E., and J. F. Ashmore. 1994. Charge displacement induced by rapid stretch in the basolateral membrane of the guinea-pig outer hair cell. *Proc. R. Soc. Lond. B. Biol. Sci.* 255:243–249.
- Gitter, A. H., H. P. Zenner, and E. Fromter. 1986. Membrane potential and ion channels in isolated outer hair cells of guinea pig cochlea. *ORL J. Otorhinolaryngol. Relat. Spec.* 48:68–75.
- Hazama, A., D. D. Loo, and E. M. Wright. 1997. Presteady-state currents of the rabbit Na⁺/glucose cotransporter (SGLT1). *J. Membr. Biol.* 155:175–186.
- He, D. Z., and P. Dallos. 2000. Properties of voltage-dependent somatic stiffness of cochlear outer hair cells. *J. Assoc. Res. Otolaryngol.* 1:64–81.
- He, D. Z., S. Jia, and P. Dallos. 2003. Prestin and the dynamic stiffness of cochlear outer hair cells. *J. Neurosci.* 23:9089–9096.
- Huang, G., and J. Santos-Sacchi. 2003. Motility voltage sensor of the outer hair cell resides within the lateral plasma membrane. *Proc. Natl. Acad. Sci. USA.* 91:12268–12275.
- Iwasa, K. H. 1993. Effect of stress on the membrane capacitance of the auditory outer hair cell. *Biophys. J.* 65:492–498.
- Kakehata, S., and J. Santos-Sacchi. 1995. Membrane tension directly shifts voltage dependence of outer hair cell motility and associated gating charge. *Biophys. J.* 68:2190–2197.
- Kakehata, S., and J. Santos-Sacchi. 1996. Effects of salicylate and lanthanides on outer hair cell motility and associated gating charge. *J. Neurosci.* 16:4881–4889.
- Kalinec, F., and B. Kachar. 1993. Inhibition of outer hair cell electromotility by sulfhydryl specific reagents. *Neurosci. Lett.* 157:231–234.
- Kawasaki, E., N. Hattori, E. Miyamoto, T. Yamashita, and C. Inagaki. 1999. Single-cell RT-PCR demonstrates expression of voltage-dependent chloride channels (CIC-1, CIC-2 and CIC-3) in outer hair cells of rat cochlea. *Brain Res.* 838:166–170.
- Kishimoto, K., S. I. Matsuo, Y. Kanemoto, H. Ishibashi, Y. Oyama, and N. Akaike. 2001. Nanomolar concentrations of tri-n-butyltin facilitate gamma-aminobutyric acidergic synaptic transmission in rat hypothalamic neurons. *J. Pharmacol. Exp. Ther.* 299:171–177.
- Lieberman, M. C., J. Gao, D. Z. He, X. Wu, S. Jia, and J. Zuo. 2002. Prestin is required for electromotility of the outer hair cell and for the cochlear amplifier. *Nature.* 419:300–304.
- Liu, Y., and L. D. Fechter. 1995. Trimethyltin disrupts loudness recruitment and auditory threshold sensitivity in guinea pigs. *Neurotoxicol. Teratol.* 17:281–287.
- Loboda, A., A. Melishchuk, and C. Armstrong. 2001. Dilated and defunct K channels in the absence of K⁺. *Biophys. J.* 80:2704–2714.
- Loquet, G., P. Campo, R. Lataye, B. Cossec, and P. Bonnet. 2000. Combined effects of exposure to styrene and ethanol on the auditory function in the rat. *Hear. Res.* 148:173–180.
- Marandi, N., A. Konnerth, and O. Garaschuk. 2002. Two-photon chloride imaging in neurons of brain slices. *Pflugers Arch.* 445:357–365.
- Melishchuk, A., A. Loboda, and C. M. Armstrong. 1998. Loss of shaker K channel conductance in 0 K⁺ solutions: role of the voltage sensor. *Biophys. J.* 75:1828–1835.
- Meltzer, J., and J. Santos-Sacchi. 2001. Temperature dependence of non-linear capacitance in human embryonic kidney cells transfected with prestin, the outer hair cell motor protein. *Neurosci. Lett.* 313:141–144.
- Motais, R., J. L. Cousin, and F. Sola. 1977. The chloride transport induced by trialkyl-tin compound across erythrocyte membrane. *Biochim. Biophys. Acta.* 467:357–363.
- Oliver, D., and B. Fakler. 1999. Expression density and functional characteristics of the outer hair cell motor protein are regulated during postnatal development in rat. *J. Physiol. (Lond).* 519:791–800 In press.
- Oliver, D., D. Z. He, N. Klocker, J. Ludwig, U. Schulte, S. Waldegger, J. P. Ruppersberg, P. Dallos, and B. Fakler. 2001. Intracellular anions as the voltage sensor of prestin, the outer hair cell motor protein. *Science.* 292:2340–2343.
- Pusch, M., and E. Neher. 1988. Rates of diffusional exchange between small cells and a measuring patch pipette. *Pflugers Arch.* 411:204–211.
- Rybalchenko, V., and J. Santos-Sacchi. 2003a. Allosteric modulation of the outer hair cell motor protein prestin by chloride. In *Biophysics of the Cochlea: From Molecules to Models*. A. Gummer, editor. World Scientific Publishing, Singapore. 116–126.
- Rybalchenko, V., and J. Santos-Sacchi. 2003b. Modulation of the outer hair cell motor by sulfonate-containing anions. *Assoc. Res. Otolaryngol. Abs.* 209.
- Rybalchenko, V., and J. Santos-Sacchi. 2003c. Cl⁻ flux through a non-selective, stretch-sensitive conductance influences the outer hair cell motor of the guinea-pig. *J. Physiol.* 547:873–891.
- Sacher, A., N. Nelson, J. T. Ogi, E. M. Wright, D. D. Loo, and S. Eskandari. 2002. Presteady-state and steady-state kinetics and turnover rate of the mouse gamma-aminobutyric acid transporter (mGAT3). *J. Membr. Biol.* 190:57–73.
- Santos-Sacchi, J. 1991. Reversible inhibition of voltage-dependent outer hair cell motility and capacitance. *J. Neurosci.* 11:3096–3110.
- Santos-Sacchi, J. 2003. New tunes from Corti's organ: the outer hair cell boogie rules! *Curr. Opin. Neurobiol.* In press.
- Santos-Sacchi, J. 2004. Determination of cell capacitance using the exact empirical solution of partial differential Y/partial differential C_m and its phase angle. *Biophys. J.* 87:714–727.
- Santos-Sacchi, J., and J. P. Dilger. 1988. Whole cell currents and mechanical responses of isolated outer hair cells. *Hear. Res.* 35:143–150.
- Santos-Sacchi, J., and G. Huang. 1998. Temperature dependence of outer hair cell nonlinear capacitance. *Hear. Res.* 116:99–106.
- Santos-Sacchi, J., S. Kakehata, T. Kikuchi, Y. Katori, and T. Takasaka. 1998a. Density of motility-related charge in the outer hair cell of the guinea pig is inversely related to best frequency. *Neurosci. Lett.* 256:155–158.
- Santos-Sacchi, J., S. Kakehata, and S. Takahashi. 1998b. Effects of membrane potential on the voltage dependence of motility-related charge in outer hair cells of the guinea-pig. *J. Physiol (Lond).* 510:225–235.
- Santos-Sacchi, J., and E. Navarrete. 2002. Voltage-dependent changes in specific membrane capacitance caused by prestin, the outer hair cell lateral membrane motor. *Pflugers Arch.* 444:99–106.
- Santos-Sacchi, J., M. Wu, and S. Kakehata. 2001. Furosemide alters nonlinear capacitance in isolated outer hair cells. *Hear. Res.* 159:69–73.
- Selwyn, M. J., A. P. Dawson, M. Stockdale, and N. Gains. 1970. Chloride-hydroxide exchange across mitochondrial, erythrocyte and artificial

- lipid membranes mediated by trialkyl- and triphenyltin compounds. *Eur. J. Biochem.* 14:120–126.
- Takahashi, S., and J. Santos-Sacchi. 2001. Non-uniform mapping of stress-induced, motility-related charge movement in the outer hair cell plasma membrane. *Pflugers Arch.* 441:506–513.
- Tosteson, M. T., and J. O. Wieth. 1979. Tributyltin-mediated exchange diffusion of halides in lipid bilayers. *J. Gen. Physiol.* 73:789–800.
- Tunstall, M. J., J. E. Gale, and J. F. Ashmore. 1995. Action of salicylate on membrane capacitance of outer hair cells from the guinea-pig cochlea. *J. Physiol.* 485:739–752.
- U.S. Environmental Protection Agency. 2004. Notice of availability of final aquatic life criteria document for tributyltin (TBT). *Fed. Regist.* 69:342–343 (USA).
- Verkman, A. S. 1990. Development and biological applications of chloride-sensitive fluorescent indicators. *Am. J. Physiol.* 259:C375–C388.
- Wieth, J. O., and M. T. Tosteson. 1979. Organotin-mediated exchange diffusion of anions in human red cells. *J. Gen. Physiol.* 73:765–788.
- Wu, M., and J. Santos-Sacchi. 1998. Effects of lipophilic ions on outer hair cell membrane capacitance and motility. *J. Membr. Biol.* 166:111–118.
- Zheng, J., W. Shen, D. Z. He, K. B. Long, L. D. Madison, and P. Dallos. 2000. Prestin is the motor protein of cochlear outer hair cells. *Nature.* 405:149–155.

BASIC–LIVER, PANCREAS, AND BILIARY TRACT

Glibenclamide Stimulates Fluid Secretion in Rodent Cholangiocytes Through a Cystic Fibrosis Transmembrane Conductance Regulator–Independent Mechanism

CARLO SPIRÌ,^{*,†,§} ROMINA FIOROTTO,^{*,†} LEI SONG,[¶] JOSEPH SANTOS–SACCHI,[¶] LAJOS OKOLICSANYI,^{||} SARA MASIER,^{*} LORETTA ROCCHI,[#] MARIA PIA VAIRETTI,^{**,§} MARINA DE BERNARD,^{†,††} SAIDA MELERO,^{||} TULLIO POZZAN,[†] and MARIO STRAZZABOSCO^{*,†,§}

^{*}Department of Medical and Surgical Sciences, University of Padova, Padova, Italy; [†]Venetian Institute of Molecular Medicine, Padova, Italy; [§]Division of Gastroenterology and Center for Liver Research, Ospedali Riuniti di Bergamo, Bergamo, Italy; [¶]Departments of Surgery and Neurobiology, Yale University School of Medicine, New Haven, Connecticut; ^{||}Department of Surgical and Gastroenterological Sciences, University of Padova, Padova, Italy; [#]Department of Forensic Medicine, University of Pavia, Pavia, Italy; ^{**}Department of Internal Medicine and Medical Therapy, University of Pavia, Pavia, Italy; and ^{††}Department of Biology, University of Padova, Padova, Italy

Background & Aims: Progressive liver disease is a severe complication of cystic fibrosis, a genetic disease characterized by impaired epithelial adenosine 3',5'-cyclic monophosphate–dependent secretion caused by mutations in the cystic fibrosis transmembrane conductance regulator (CFTR). In the liver, CFTR is expressed in cholangiocytes and regulates the fluid and electrolyte content of the bile. Glibenclamide, a sulfonylurea and a known CFTR inhibitor, paradoxically stimulates cholangiocyte secretion. We studied the molecular mechanisms underlying this effect and whether glibenclamide could restore cholangiocyte secretion in cystic fibrosis. **Methods:** NRC-1 cells, freshly isolated rat cholangiocytes, isolated rat biliary ducts, and isolated biliary ducts from CFTR-defective mice (Cftr^{tm1Unc}) were used to study fluid secretion (by video-optical planimetry), glibenclamide-induced secretion (by high-performance liquid chromatography in cell culture medium), intracellular pH and intracellular Ca²⁺ concentration transients [2'7'-bis(2-carboxyethyl)-5,6-carboxyfluorescein-acetoxymethylester and Fura-2 f-AM (5-Oxazolecarboxylic acid, 2-(6-(bis(2-((acetyloxy)methoxy)-2-oxoethyl)amino)-5-(2-(2-(bis(2-((acetyloxy)methoxy)-2-oxoethyl)amino)-5-methylphenoxy)ethoxy)-2-benzofuranyl)-, (acetyloxy)methyl ester) microfluorometry], gene expression (by reverse-transcription polymerase chain reaction), and changes in membrane capacitance (by patch-clamp experiments). **Results:** Stimulation of cholangiocyte secretion by glibenclamide and tolbutamide required Cl[–] and was mediated by the sulfonylurea receptor 2B. Glibenclamide-induced secretion was blocked by inhibitors of exocytosis (colchicine, wortmannin, LY294002, and N-ethylmaleimide) and by inhibitors of secretory granule acidification (vanadate, bafilomycin A1, and niflumic acid) but was Ca²⁺ and depolarization independent; membrane capacitance measurements were consistent with stimulation of vesicular transport and fusion. Glibenclamide, unlike secretin and

forskolin, was able to stimulate secretion in Cftr^{tm1Unc} mice, thus indicating that this secretory mechanism was preserved. **Conclusions:** The ability of glibenclamide to stimulate secretion in CFTR-defective mice makes sulfonylureas a model class of compounds to design drugs useful in the treatment of cystic fibrosis with liver impairment and possibly of other cholestatic diseases.

The intrahepatic biliary epithelium extensively modifies hepatocellular bile by increasing its water content and HCO₃[–] concentration. Fluidification of bile and its alkalization are required to meet digestive needs and to facilitate the flux of bile. This function of the biliary epithelium is regulated by gastrointestinal hormones and by paracrine signals that act either through the adenosine 3',5'-cyclic monophosphate (cAMP)/protein kinase A pathway (secretin) or via Ca²⁺ signaling (purinergic receptors).¹

Ductal cholestasis, ie, reduced fluid and electrolyte transport by cholangiocytes, is a central step in the pathogenetic sequence of biliary tree diseases, as exemplified by the progressive liver disease associated with cystic fibrosis (CF), a common genetic defect in which a

Abbreviations used in this paper: BCECF, 2'7'-bis(2-carboxyethyl)-5,6-carboxyfluorescein-acetoxymethylester; bp, base pair; CF, cystic fibrosis; CFTR, cystic fibrosis transmembrane conductance regulator; C_m, membrane capacitance; DIDS, 4,4'-diisothiocyanato-stilbene-2,2'-disulfonic acid; DMSO, dimethyl sulfoxide; IBDU, isolated bile duct unit; Kir, inward rectifier K⁺ channel; MEM, minimal essential medium; NEM, N-ethylmaleimide; NKCC1, Na-K-2Cl cotransporter isoform 1; NRC-1, normal rat cholangiocyte cell line; pH_i, intracellular pH; RT-PCR, reverse-transcription polymerase chain reaction; SUR, sulfonylurea receptor; TEA, tetraethylammonium.

© 2005 by the American Gastroenterological Association
0016-5085/05/\$30.00

doi:10.1053/j.gastro.2005.03.048

failure of cAMP-regulated Cl^- transport (CF transmembrane conductance regulator; CFTR) causes a secretory failure in a number of epithelia, including the biliary tree.^{2,3} Recently, it was shown that glibenclamide stimulates bile flow at the level of the bile duct epithelium,⁴ a result in apparent contradiction to the known inhibitory effects of glibenclamide on CFTR. Progressive pulmonary disease is the leading cause of death in CF, but as the life expectancy for these patients is extended through improved pulmonary, nutritional, and general medical care, hepatobiliary complications become more frequent and have a negative effect on survival. As a consequence of the ductal cholestasis that results from defective biliary Cl^- and fluid transport, liver inflammation, cholangiocyte damage, and portal fibrosis progressively occur.² Pharmacological improvement of ductal secretion may help to reverse this series of events.

Sulfonylureas are widely used in the treatment of non-insulin-dependent diabetes mellitus (type 2 diabetes) because of their ability to stimulate insulin secretion from pancreatic β -cells.⁵ In this study, we investigated the molecular mechanisms that underlie the recently reported choleric effects of glibenclamide on the bile duct epithelium and its possible exploitation in CF. Our results indicate that in isolated bile duct units (IBDUs), sulfonylureas stimulate fluid secretion by a mechanism that is independent of Ca^{2+} and cAMP signaling but involves vesicle transport and fusion. The glibenclamide effect is maintained in cholangiocytes isolated from CFTR knockout mice. The stimulatory effect of glibenclamide on cholangiocyte secretion in cells lacking CFTR makes this class of compounds an attractive tool to stimulate fluid secretion in CF liver disease, a prototypic cholangiopathy present in up to 30% of CF patients that seriously affects morbidity and mortality.

Materials and Methods

Chemicals and Solutions

Epidermal growth factor, dexamethasone, triiodothyronine, ethylenediaminetetraacetic acid, collagenase IV, collagenase XI, pronase, hyaluronidase, deoxyribonuclease, forskolin, insulin, diethylpicrocarbonate, glibenclamide, 4,4'-diisothiocyanato-stilbene-2,2'-disulfonic acid (DIDS), diazoxide, tolbutamide, tetraethylammonium (TEA), niflumic acid, vanadium oxide, wortmannin, LY294002, colchicine, γ -lumicolchicine, TRI Reagent (Sigma Chemical Company, Milan, Italy), barium- Cl^- , adenosine triphosphate (ATP), diButyryl (dB)-cAMP, bafilomycin A1, and nocodazole were purchased from Sigma. Culture media, α -minimal essential medium (MEM), Dulbecco's MEM, Ham's F12, fetal bovine serum, MEM nonessential amino acid solution, MEM vitamin solutions, glyceryl monostearate, chemically defined lipid concentrate, soybean trypsin inhibitor, penicillin/streptomycin,

gentamicin, trypsin/ethylenediaminetetraacetic acid, and glutamine were purchased from Gibco (Life Technology, Milano, Italy). NuSerum and bovine pituitary extract were obtained from Becton Dickinson (Milan, Italy). Membrane inserts were purchased from Nunc (Mascia Brunelli, Milan, Italy), and Dynabeads M-450 rat anti-mouse immunoglobulin M was purchased from Deutsche Dynal GmbH (Hamburg, Germany). 2'7'-Bis(2-carboxyethyl)-5,6-carboxyfluorescein-acetoxymethylester (BCECF) and Fura-2 were purchased from Molecular Probes (Eugene, OR). Moloney murine leukemia virus reverse transcriptase was obtained from Perkin Elmer (Milan, Italy), whereas a Qiagen QIAquick PCR Purification Kit and Qiagen QIAquick Gel Extraction Kit were purchased from Qiagen GMBM (Ilden, Germany). Anti-*Taq* DNA polymerase antibody was obtained from Clontech (Milano, Italy). The composition of perfusion buffers used was essentially as described previously.^{3,6} In HEPES used to acid load cells, 20 mmol/L NH_4Cl was substituted for equal amounts of NaCl. BCECF, Fura-2-AM, glibenclamide, diazoxide, bafilomycin A1, wortmannin, and LY294002 were prepared as a 1 mmol/L stock solution dissolved in dimethyl sulfoxide (DMSO), whereas nigericin was solubilized in ethanol.

Glibenclamide Secretion in NRC-1 Cell Culture and in Isolated and Perfused Rat Liver

NRC-1 is a well-differentiated normal rat cholangiocyte cell line that maintains a polarized distribution of membrane markers and ion transporters and has been extensively characterized and used.⁷⁻⁹ Cells were grown as previously described⁷⁻⁹ over collagen-coated semipermeable membrane inserts (Nunc, Mascia-Brunelli, Milano, Italy). Experiments were performed in cells cultured for 1 week after they reached confluence and had a transepithelial resistance $>1000 \Omega/\text{cm}^2$ (Millicell-ERS System; Millipore Co, Bedford, MA).⁷ NRC-1 monolayers were exposed to glibenclamide from basolateral side, and at different times, apical supernatant was collected.

Animals received care according to the principles outlined in the *Guide for the Care and Use of Laboratory Animals* (National Academy Press, 1996, 7th edition), and the following protocols were approved by the University of Padua Institutional Veterinary Medicine Service. Sprague-Dawley rats were anesthetized with pentobarbital (50 mg/kg body weight); procedures for isolated and perfused rat liver and setup were performed as previously described.¹⁰ Bile flow was measured gravimetrically in preweighted tubes, and perfusion pressure was monitored continuously. Liver viability was ascertained by monitoring perfusion pressure and oxygen consumption during the course of the experiment and by determining trypan blue distribution on completion.

Glibenclamide and its 2 major metabolites (4-*trans*- and 3-*cis*-hydroxyglibenclamide) were measured by high-performance liquid chromatography in the bile collected from isolated and perfused rat liver or in the supernatant of NRC-1 cell line. Gliclazide (0.1–10 μg) was used as an internal standard. Sulfuric acid 1N was added to bile or to cell overnatant, and, after the addition of *N*-hexane/ethyl acetate (3:1, vol/vol), the

organic phase was dried, dissolved in mobile phase, and injected into a liquid chromatographic system (Agilent Series 1100; Hewlett-Packard, Palo Alto, CA). The analytical column was a reversed-phase LiChrospher RP-Select B obtained from Merck (Darmstadt, Germany). Calibration standard samples were prepared by adding glibenclamide or metabolites to "blank" bile or, in the case of cell overnatants, to a buffer solution. Calibration lines of all analytes were linear in the range investigated: correlation coefficient values (r^2) were consistently >0.9834 . The mobile phase (flow at 1 mL/min) consisted of a mixture of acetonitrile and water (50:50, vol/vol) containing sodium dodecylsulfate (0.01 mol/L) and glacial acetic acid (0.5% vol/vol). The UV detection wavelength was 230 nm.

Intrahepatic Rat Bile Duct Units and Immunopurified Bile Duct Cells

Rats and mice were anesthetized as described previously. IBDUs (ie, sealed fragments of isolated bile ductules in short-term culture that have retained polarity and secrete into a closed lumen) were prepared and purified as previously described^{6,11,12}; they were plated for 24 hours over a thin layer of Matrigel (Collaborative Research Products, Bedford, MA) as previously described.^{6,11,12} Immunomagnetic isolation of cholangiocytes was performed as previously described¹³ by using the OC-2 primary antibody (1:1000; a kind gift of Dr D. Hixson, Brown University, Providence, RI). Histochemical assays for γ -glutamyltranspeptidase indicated purity values of $>95\%$ in all cholangiocyte preparations used. Viability was evaluated by trypan blue exclusion.

Assessment of Ductular Secretion in Intrahepatic Rat Bile Duct Units by Video-optical Planimetry

Expansion of the IBDU lumen over time was quantified by video-optical planimetry as a measure of the ductular secretion rate, as previously described.^{6,11,12} After a 5-minute baseline period, IBDUs were exposed to glibenclamide (100 μ mol/L), to tolbutamide (100 μ mol/L), or to glibenclamide and different inhibitors; the luminal area was then measured every 5 minutes for up to 30 minutes. Serial images of the IBDU were acquired by a JVC TKC 1380 video camera (Galileo Siscam, Firenze, Italy); luminal areas were determined from the recorded images by using an image processor (Arkon; Nikon; Firenze, Italy).

Measurement of Na-K-2Cl Cotransporter Isoform 1 Activity

The effects of glibenclamide on the activity of the $\text{Na}^+/\text{K}^+/\text{2Cl}^-$ cotransporter was assessed by measuring the recovery of intracellular pH (pHi) from NH_4Cl^- -induced alkalization by using the cell-permeant fluorescent pHi indicator BCECF/AM (12 μ mol/L). BCECF loading procedures of IBDU, the microscopic setup, and the measurement and calibration procedures have already been described.¹⁴ Acid and

base fluxes were calculated by using cellular intrinsic and total buffering powers (β_i and β_{tot} , respectively), values previously measured.^{6,11} The rates of pHi changes ($\delta\text{pHi}/\delta t$) were calculated as previously described.^{6,11} The effects of glibenclamide on $\text{Na}^+/\text{K}^+/\text{2Cl}^-$ activity were assessed by measuring the rate of pHi recovery from an alkaline load induced by 20 mmol/L NH_4^+Cl^- .^{6,15} The $\text{Na}^+/\text{K}^+/\text{2Cl}^-$ cotransporter can transport NH_4^+ in stoichiometrical substitution of K^+ . When cells are exposed to NH_4Cl , NH_3 enters the cells by nonionic diffusion and leads to cytoplasmatic alkalization. The subsequent cellular uptake of NH_4^+ by Na-K-2Cl cotransporter isoform 1 (NKCC1) causes pHi acidification, and NKCC1 activity can be measured from the initial phase of the acidification slope.^{6,15}

Measurement of Intracellular Ca^{2+}

Intracellular Ca^{2+} transients were measured by using Fura-2-AM. IBDUs were loaded in tissue culture medium for 20–30 minutes at room temperature with Fura-2-AM (5 μ mol/L). Coverslips with dye-loaded cells were mounted into a heated metal flow-through perfusion chamber, placed on the stage of an inverted Olympus IX 70 microscope (Milano, Italy), and perfused by gravity feed at 1.5–2 mL/min. After a 3-minute baseline period, cells were exposed to glibenclamide (100 μ mol/L) for 10 minutes, and at the end of the experiment, ATP (10 μ mol/L) was used as an internal control. Emitted fluorescence was measured in response to alternate pulses of excitation light (10 milliseconds long) at 340 and 380 nm. The emitted fluorescence (510 nm) was focused on a photomultiplier tube, amplified, digitally converted, and analyzed with Till Vision software (Till Photonics, Martinsried, Germany). Images of the IBDU were acquired by a charge-coupled device camera. The ratio of emitted light from the 2 excitation wavelengths (340 and 380 nm) of Fura-2 provides a measure of ionized cytoplasmic $[\text{Ca}^{2+}]$.¹⁶

Sulfonylurea Receptor, Inward Rectifier K^+ Channel 6.x, and chloride channels (CLC)-3 Gene Expression

Sulfonylurea receptor (SUR) and inward rectifier K^+ channel (Kir) 6.x isoforms and chloride channels (CLC)-3 gene expression were assessed by reverse-transcription polymerase chain reaction (RT-PCR). SUR1 messenger RNA (mRNA) was detected by using the primers 5'-GCAGCCGAGAGCGAGGAA-GATGA-3' and 5'-ACAGCCAGGGCGGAGACACAGAGT-3', which amplified a 539-base pair (bp) fragment. SUR2 mRNA was amplified by using the primers 5'-CGCGGCGGT-CATCGTGCTC-3' and 5'-CGCCGCGCCTGCTCGTAGTT-3', which amplified a 603-bp fragment. SUR2AB mRNA was detected by using the primers 5'-GACAGCCTTTGCG-GATCG-3' and 5'-GCATCGAGACACAGGTGCTG-3', which amplified a 387-bp fragment for SUR2A and a 211-bp fragment for SUR2B. CLC-3 mRNA was detected by using the primers 5'-GCGAGAAAAGTGTAAAGGAC-3' and 5'-TCAAAGC-CCAAAAGATGTA-3', which amplified a 377-bp fragment; Kir 6.1 mRNA was detected by using the primers 5'-TTCTGCG-TTTCTCTTCTCCATCG-3' and 5'-GGGGCTACGCTTAT-

CAATCACAT-3', which amplified a 445-bp fragment. Kir 6.2 mRNA was detected by using the primers 5'-GGAGAG-GAGGGCCCGCTTCGTGTC-3' and 5'-GGCGTAATGAT-CATGCTTTTCGGAGGTC-3', which amplified a 553-bp fragment; 28S mRNA was detected by using the primers 5'-AGAAGGGCAAAGCTCGCTT-3' and 5'-AGCAGGAT-TACCATGGCAAC-3', which amplified a 288-bp fragment. Total RNA was isolated from OC-2 using the TRI Reagent solution (Sigma), according to the manufacturer's instructions. One microgram of total RNA was reverse-transcribed with Moloney murine leukemia virus reverse transcriptase (2.5 U/ μ L). PCR was performed in a thermocycler M. J. Research (M-Medical, Firenze, Italy) with AmpliTaq Gold polymerase and 1 \times GeneAmp buffer (Applied Biosystems Inc, Foster City, CA). PCR was initiated by hot start, followed by 40 cycles of 94°C for 1 minute, 50°C–74°C for 1 minute, and 72°C for 1 minute and by a final extension at 72°C for 10 minutes. Contamination by genomic DNA was ruled out by running samples without a previous RT-PCR phase. Preliminary kinetic analysis was performed to position amplification cycles on the exponential phase of the reaction. Amplification products were electrophoresed on 7% acrylamide gel, visualized by ethidium bromide, and then silver-stained. Purified PCR products were sequenced on an ABI 373A Stretch automated sequencer (Perkin-Elmer, Milan, Italy) to verify the identity.

Patch-Clamp Experiments

Immunopurified cholangiocytes were identified with a Nikon Eclipse E600FN microscope by visualizing antibody-coated magnetic beads (4.5 μ m) bound to the cell-surface antigens. The cells were whole-cell voltage-clamped with an Axopatch 200B amplifier and Digidata 1320A board (Axon Instruments, Union City, CA) by using solutions modified from Barg et al.¹⁷ Extracellular medium contained (mmol/L) NaCl 138, KCl 5, MgCl₂ 1.2, CaCl₂ 2.6, and HEPES 5. The pH was adjusted to 7.4 with NaOH, and osmolarity was adjusted to 310 mOsm with D-glucose. Pipette solution contained (mmol/L) K⁺-gluconate 125, KCl 10, NaCl 10, MgCl₂ 1, HEPES 5, ethylene glycol-bis(β -aminoethyl ether)-N,N,N',N'-tetraacetic acid 10, CaCl₂ 5 (170 nmol/L free Ca²⁺), and Mg-ATP 3; pH was adjusted to 7.15 with KOH. The solution had an osmolarity of approximately 310 mOsm. DMSO was used to dissolve tolbutamide and nocodazole before their addition into the pipette solution. γ -Lumicolchicine was prepared in chloroform. The final concentration of DMSO and chloroform in pipette solutions was 0.1%. Some cells were pretreated with colchicine (50 μ mol/L), γ -lumicolchicine (50 μ mol/L), and nocodazole (10 μ mol/L) in extracellular medium for 30, 30, and 60 minutes, respectively.

Membrane capacitance (C_m) measurements were begun immediately after the establishment of a whole-cell recording condition. Holding potentials of -40 and -80 mV did not provide stable recordings, and it proved difficult to hold the cells for the required prolonged recording periods. Consequently, cells were typically held at 0 mV during C_m measurements. The initial pipette resistance was 4–7 M Ω . Gigohm seals were obtained (1.5–3.5 G Ω), and stray capaci-

tance was compensated before the rupture of the cell membrane. Uncompensated series resistances ranged from 10 to 30 M Ω and remained uncompensated, because the capacitance measurement algorithm is sensitive to introduced system lag. Corrections for series resistance were subsequently made off-line. Capacitance was tracked (every 150 milliseconds) with a high-resolution dual sinusoidal (10-mV peak at both 390.6 and 781.2 Hz) stimulus paradigm.^{18,19} Simultaneously, membrane resistance, series resistance, and holding current were recorded. Transient analysis measurements with 10-mV steps were confirmatory. During our measurements, we were careful to record from isolated single cells because cell groups could have been coupled by gap junctions. It is well known that recordings from single cells in a group of coupled cells present an inflated syncytial capacitance, which could be voltage dependent.²⁰ Another reason for avoiding coupled cell groups is that the use of standard single- and dual-sine measurement approaches is invalidated by a model other than a single resistance-capacitance compartment.¹⁹

For a subset of cells, current voltage relations were investigated with a voltage step series (-100 to $+40$ or 50 mV; 200-millisecond step duration; holding potential of -60 mV) that was delivered to cells near the beginning and several times during the continuous monitoring of C_m . Current voltage (I-V) plots were derived from the last 50 milliseconds of current response. C_m recordings were made until C_m stabilized; typical durations ranged from 10 to 20 minutes. Statistical comparisons were made at steady state. A 4-pole Bessel filter at 10 kHz was used. All data acquisition and analyses were performed with the Windows-based voltage clamp software jClamp (SciSoft, New Haven, CT). Digital photos were captured with jClamp.

Cystic Fibrosis Transmembrane Conductance Regulator Knockout Mice

Congenic B6.129P2-Cftr^{tm1Unc} mice, which possess the S489X mutation that blocks transcription of CFTR,²¹ were used. Heterozygous breeding pairs were obtained from Jackson Laboratories (Bar Harbor, ME) and then bred in our animal facility. Genotypes for each mouse were determined by PCR with DNA isolated from tail clips by following Jackson Laboratories' instructions. Mice were maintained on a liquid elemental diet (Peptamen; Nestle, Milan, Italy) to prevent the intestinal obstruction associated with the CFTR mutation. Wild-type mice received regular solid mouse chow.²¹ Autoclaved tap water in bottles with sipper tubes was provided ad libitum. Mice selected for the experiments reported here were 7 to 8 weeks old without obvious signs of disease or discomfort (average weight, 18 ± 2.3 g for CFTR^{-/-} and 22 ± 1.7 g for their normal (CFTR^{+/+} and CFTR^{+/-}) littermates. For experiments with isolated perfused mouse liver, animals were anesthetized with pentobarbital sodium (50 mg/kg body weight). The abdomen was opened, and the gallbladder was cannulated after distal ligation of the common bile duct.²² The liver was perfused in situ at 5 mL/min with oxygenated HCO₃⁻-containing Ringer buffer and maintained at 37°C. Bile sampling

was started after a stabilizing period of 10 minutes after cannulation. Bile flow was determined gravimetrically, assuming a density of 1 g/mL for bile.

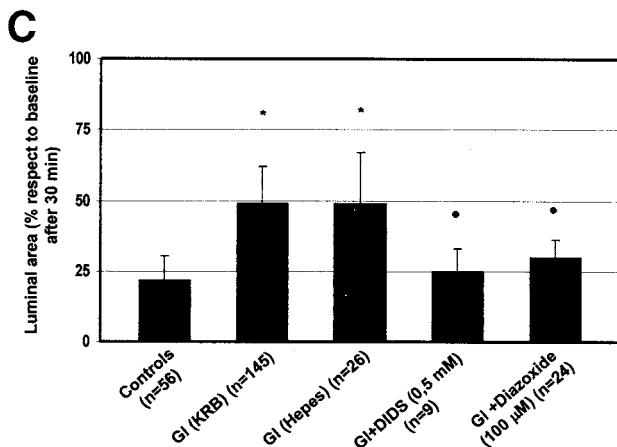
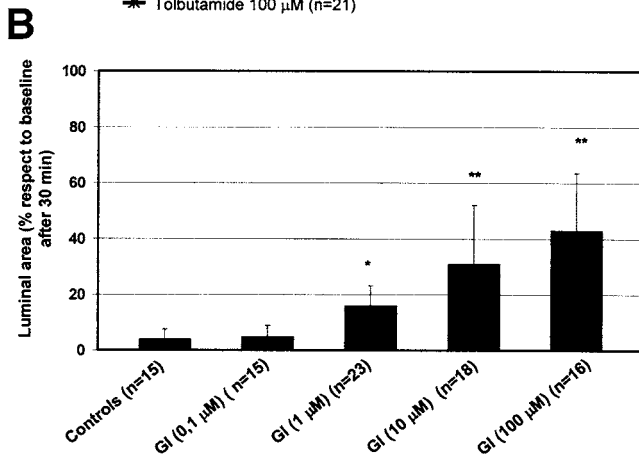
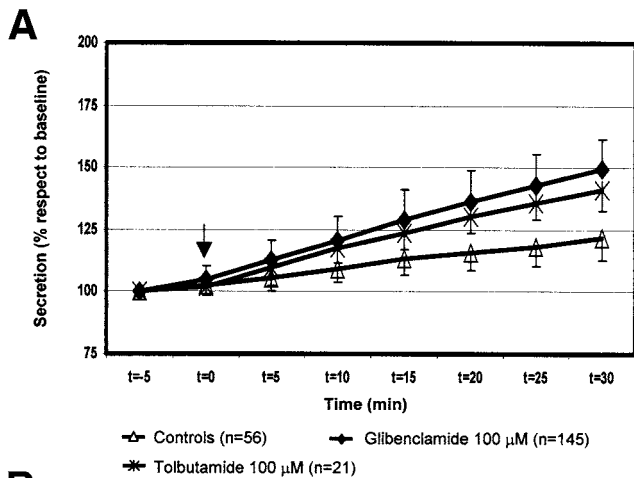
Statistical Analysis

Results are shown as mean ± SD. Statistical comparisons were made with Student *t* tests or analysis of variance, with Tukey post hoc tests where appropriate. GraphPad software (Biosoft, Cambridge, UK) was used; *P* values <.05 were considered significant.

Table 1. Luminal Area Expansion (Percentage With Respect to Baseline) in IBDUs

Variable	Changes (30 min)	n	<i>P</i>
Controls (KRB)	21 ± 9	56	
Controls (HEPES)	21 ± 11	30	
Glib (KRB)	49 ± 13	145	<.001 vs control
DIDS + glib	24 ± 8	9	<.005 vs glib
Glibenclamide (HEPES)	49 ± 18	26	<.001 vs control
Tolbutamide	41 ± 9	20	<.001 vs control
Diazoxide + glib	30 ± 6	24	<.005 vs glib
Colchicine + glib	24 ± 5	24	<.001 vs glib
γ-Lumilcolchicine + glib	47 ± 7	31	NS vs glib
Wortmannin + glib	21 ± 9	22	<.001 vs glib
LY294002 + glib	19 ± 7	13	<.001 vs glib
NEM + glib	17 ± 7	11	<.01 vs glib
Barium	19 ± 13	12	NS vs control
Tea	22 ± 9	32	NS vs control
Bafilomycin + glib	17 ± 6	8	<.01 vs glib
Vanadate + glib	29 ± 6	20	<.01 vs glib
Niflumic acid	16 ± 5	13	<.001 vs glib

KRB; HCO₃⁻ containing Ringer buffer; NS; not significant; glib, glibenclamide.



Results

Glibenclamide-Induced Fluid Secretion in Isolated Bile Duct Units

Cholangiocyte secretion was measured, as previously described,⁴ from the change in luminal area induced by exposure of rat intrahepatic bile duct units to glibenclamide (Figure 1A and Table 1). Administration of glibenclamide induced a dose-dependent (0.1–100 μmol/L) increase in luminal area with respect to controls. The increase in luminal area was 16% ± 7% (*P* < .05) at 1 μmol/L and reached the maximal effect at 100 μmol/L: 45% ± 20% (expressed as percentage increase with respect to baseline after 30 minutes; *P* < .01;

Figure 1. Sulfonylureas-stimulated secretion in IBDUs is dose dependent, HCO₃⁻ independent, and Cl⁻ dependent. (A) IBDUs were examined under control conditions for 10 minutes and then for an additional 30 minutes after the administration of glibenclamide or tolbutamide (arrow). Both sulfonylureas induced a significant (*P* < .001) increase in the luminal area. (B) Glibenclamide stimulates secretion in IBDUs in a dose-dependent manner. Columns represent the percentage of luminal area expansion with respect to baseline after 30 minutes of glibenclamide administration (mean ± SD). **P* < .05 and ***P* < .01 vs controls. (C) Perfusion with HCO₃⁻-free buffer (HEPES) did not affect the increase in luminal area induced by glibenclamide, which is inhibited by the Cl⁻ transporter inhibitor DIDS. Diazoxide inhibits the choleric effect of glibenclamide. Columns represent the percentage of luminal area expansion with respect to baseline after 30 minutes of glibenclamide administration (mean ± SD). **P* < .001 vs controls; ●*P* < .05 vs glibenclamide. KRB, HCO₃⁻-containing Ringer buffer; GI, glibenclamide.

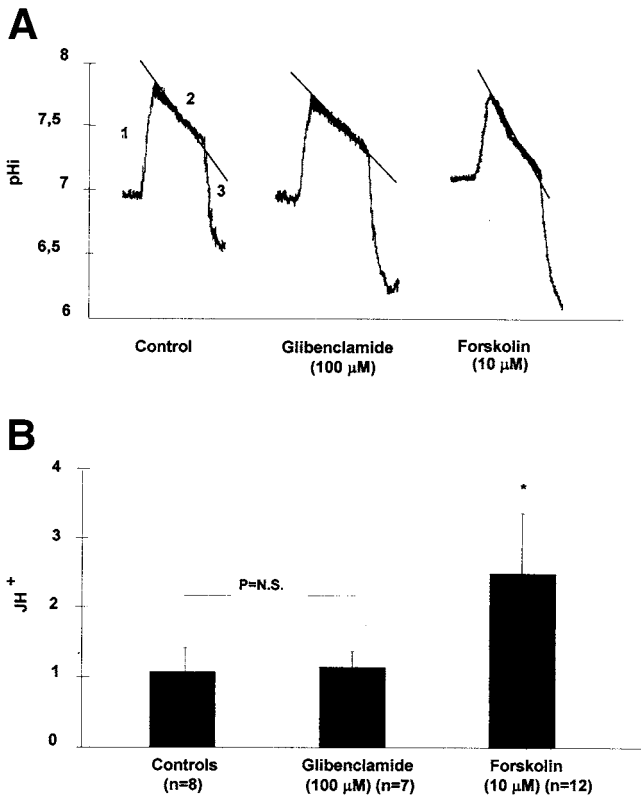


Figure 2. Glibenclamide-stimulated secretion in IBDUs does not involve stimulation of the $\text{Na}^+\text{-K}^+\text{-2Cl}^-$ cotransporter. (A) $\text{Na}^+\text{-K}^+\text{-2Cl}^-$ activity was measured by using the NH_4Cl^- (20 mmol/L) pulse technique¹⁵ (which exploits the ability of NKCC1 to transport NH_4^+ in stoichiometrical substitution of K^+) from the initial rate of acidification (120 seconds) (2) after the NH_3 -induced alkalinization (1); rapid acidification occurred after NH_4Cl withdrawal (3). (B) The graph bars show the transmembrane H^+ fluxes (J_{H^+}) calculated as $\delta\text{pHi}/\delta t \times \beta_i$ (intrinsic buffering power) at pH 7.5. Columns represent the mean \pm SD. * $P < .01$ vs controls. N.S., not significant.

Figure 1B). Glibenclamide-induced choleresis was Cl^- dependent: it was blocked by bumetanide,⁴ an NKCC1 inhibitor, and by DIDS (0.5 mmol/L), a general inhibitor of Cl^- -dependent transport (Table 1). Omission of HCO_3^- from the perfusate (HEPES buffer), conversely, did not inhibit glibenclamide choleresis (Figure 1C and Table 1), thus indicating that, in contrast to secretory events that depend on cAMP or Ca^{2+} signaling,^{3,23} HCO_3^- transport is likely not involved in glibenclamide choleresis. Contrary to a previous hypothesis based on bumetanide inhibition,⁴ direct measurement of NKCC1 activity (Figure 2) showed that glibenclamide did not stimulate NKCC1; on the other hand, forskolin (10 $\mu\text{mol/L}$) administration induced the expected stimulatory effect. NKCC1 activity was as follows: transmembrane H^+ fluxes (J_{H^+}) = 1.08 ± 0.26 $\text{mmol} \cdot \text{L}^{-1} \cdot \text{min}^{-1}$, $\delta\text{pH}/\delta t = 0.08 \pm 0.01/\text{min}$ (pH 7.5; $n = 7$) in controls; $\text{J}_{\text{H}^+} = 2.5 \pm 0.88$ $\text{mmol} \cdot \text{L}^{-1} \cdot \text{min}^{-1}$, $\delta\text{pH}/\delta t = 0.171 \pm 0.06/\text{min}$ (pH

7.5; $n = 12$) in IBDU treated with forskolin (10 $\mu\text{mol/L}$); and $\text{J}_{\text{H}^+} = 1.15 \pm 0.23$ $\text{mmol} \cdot \text{L}^{-1} \cdot \text{min}^{-1}$, $\delta\text{pH}/\delta t = 0.074 \pm 0.01/\text{min}$ (pH 7.5; $n = 8$; not significant vs controls) in IBDU treated with glibenclamide.

Glibenclamide Is Not Secreted by Cholangiocytes

Many drugs induce osmotic bile secretion after their active transport and concentration into the bile. Therefore, we measured the concentration of glibenclamide and of its metabolites 3-*cis*-hydroxyglibenclamide and 4-*trans*-hydroxygliburide in the bile collected from isolated rat livers perfused with 100 $\mu\text{mol/L}$ glibenclamide for 30 minutes and compared it with the concentrations found in the apical overnatant of rat cholangiocyte monolayers after the administration of 100 $\mu\text{mol/L}$ glibenclamide from the basolateral side. The glibenclamide concentration in bile collected from isolated rat livers was 127 ± 21 $\mu\text{mol/L}$ ($n = 4$), whereas that of its metabolites 3-*cis*-hydroxygliburide and 4-*trans*-hydroxygliburide was 490 ± 113 $\mu\text{mol/L}$ and 311 ± 86 $\mu\text{mol/L}$, respectively. Conversely, after basolateral administration of glibenclamide (100 $\mu\text{mol/L}$) to polarized NRC-1 cholangiocyte monolayers, no metabolites were detected in the apical medium, and the glibenclamide concentration linearly increased, reaching only 32.5 $\mu\text{mol/L}$ after a 2-hour incubation (data not shown). This is consistent with diffusion rather than active transport by cholangiocytes. Thus, an osmotic effect by glibenclamide and its metabolites may only partially account for stimulation of hepatocellular bile flow in the isolated perfused rat liver, but not for the secretory effects induced by glibenclamide in isolated cholangiocyte units that are not capable of secreting glibenclamide or its metabolites into the lumen.

Stimulation of Ductal Choleresis Is a Property of Sulfonylurea Compounds and Is Mediated by Interaction With Cholangiocyte Sulfonylurea Receptor 2B

Similarly to glibenclamide, the administration of another sulfonylurea, tolbutamide (100 $\mu\text{mol/L}$), was able to stimulate fluid secretion in IBDUs (Figure 1A and Table 1). Preincubation with diazoxide (100 $\mu\text{mol/L}$), a classic SUR inhibitor, inhibited glibenclamide-stimulated secretion (Figure 1C and Table 1), consistent with the functional involvement of the SUR. Indeed, RT-PCR of mRNA extracted from immunopurified cholangiocytes revealed gene expression of SUR2B, the most widely expressed SUR isoform (Figure 3A), and of Kir 6.1 (Figure 3B), a protein belonging to a family of K^+_{ATP} channels associated with SUR.

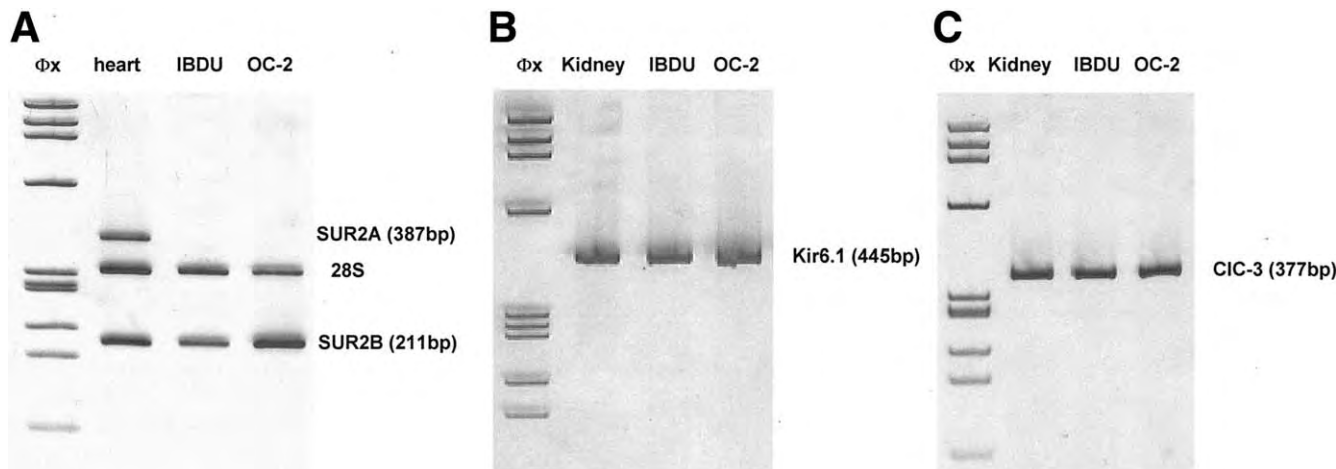


Figure 3. Gene expression of the SUR2B receptor, of the Kir 6.1 K^+_{ATP} channel, and of the CLC-3 Cl^- channel in IBDUs and in immunopurified rat cholangiocytes (OC-2). (A) SUR2AB primers were designed to cross the 177-bp insert in the SUR2A DNA sequence that gives rise to alternative spliced SUR2 variants (the primer pairs should generate PCR fragments of 211 bp for rSUR2B and 387 bp for rSUR2A. In the heart (control tissue), both SUR2 variants are expressed, whereas in IBDUs and OC-2 only the SUR 2B variant is expressed; the ribosomal fraction 28S was used as a housekeeping gene. (B) Kir 6.1, but not Kir 6.2 (data not shown), isoform PCR products are present in IBDUs and OC-2 cells. (C) The CLC-3 Cl^- channel is expressed in IBDUs and OC-2 cells; kidney tissue was used as a positive control.

Stimulation of Ductal Choleresis in Cholangiocytes Is Independent From Depolarization and Stimulation of Ca^{2+} Transients

In β -cells, sulfonylureas trigger insulin secretion by stimulating exocytotic events. Therefore, we tested the effects of several agents known to inhibit vesicular transport in the liver^{24–26} on glibenclamide-mediated choleresis: the microtubule-disrupting agent colchicine (50 μ mol/L; but not the inactive analogue γ -lumicolchicine), 2 phosphoinositol-3' kinase inhibitors (wortmannin 100 nmol/L and LY294002 50 μ mol/L), and *N*-ethylmaleimide (NEM; 1 mmol/L; an inhibitor of Soluble *N*-ethylmaleimide-sensitive factor attachment protein receptor (SNARE) proteins required to permit vesicles to fuse with plasma membrane). All significantly inhibited glibenclamide-induced secretion in IBDUs (Figure 4A and Table 1). Taken together, these results indicate that glibenclamide stimulates vesicle exocytosis in cholangiocytes.

In pancreatic β -cells, the binding of glibenclamide to SUR inhibits the function of K^+_{ATP} channels. The resulting cell depolarization causes Ca^{2+} influx through L-type Ca^{2+} channels, and the increase in intracellular $[Ca^{2+}]$ stimulates exocytosis of insulin. However, in IBDUs, cell depolarization induced by depolarizing concentrations of extracellular K^+ (40 mmol/L)⁴ or by barium (5 mmol/L) and TEA (10 mmol/L) (2 well-known K^+ -channel inhibitors) did not stimulate secretion in IBDUs (Figure 5A and Table 1). Furthermore, neither glibenclamide nor membrane depolarization increased

Ca^{2+} in IBDUs (Figure 5B), whereas after ATP (10 μ mol/L) treatment, the expected Ca^{2+} response was recorded. The mechanism responsible for glibenclamide-induced secretion in cholangiocytes seems, therefore, to be similar to the Ca^{2+} -independent pathway that represents an additional mechanism through which sulfonylureas stimulate insulin secretion in pancreatic β -cells.²³ In this case, exocytosis of insulin-containing granules is dependent on the binding of glibenclamide to granular binding sites and is triggered by increasing osmotic forces inside the secretory granules induced by the cooperation of a V-type H^+ -adenosine triphosphatase (ATPase) and an accompanying shunt conductance provided by a CLC-3 Cl^- channel. Consistent with the predictions of this latter model, glibenclamide-induced fluid secretion was inhibited by V-type H^+ -ATPase inhibitors such as bafilomycin A (1 μ mol/L) and vanadate (100 μ mol/L; Figure 4B and Table 1). Also, glibenclamide-induced secretion was inhibited by niflumic acid, an inhibitor of Cl^- channels, including CLC-3, the gene expression of which was detected by RT-PCR in immunopurified cholangiocytes (Figure 3C).

Capacitance and Conductance Measurements on Isolated Cholangiocytes

To directly assess the possibility of vesicular release, we performed patch-clamp experiments on immunopurified cholangiocytes. Single cells measuring on average $7.06 \pm 1.3 \mu$ m in diameter ($n = 28$) were studied; this size equates to a simple spherical membrane surface area of 156μ m² (Figure 6A). Our measured diameter is

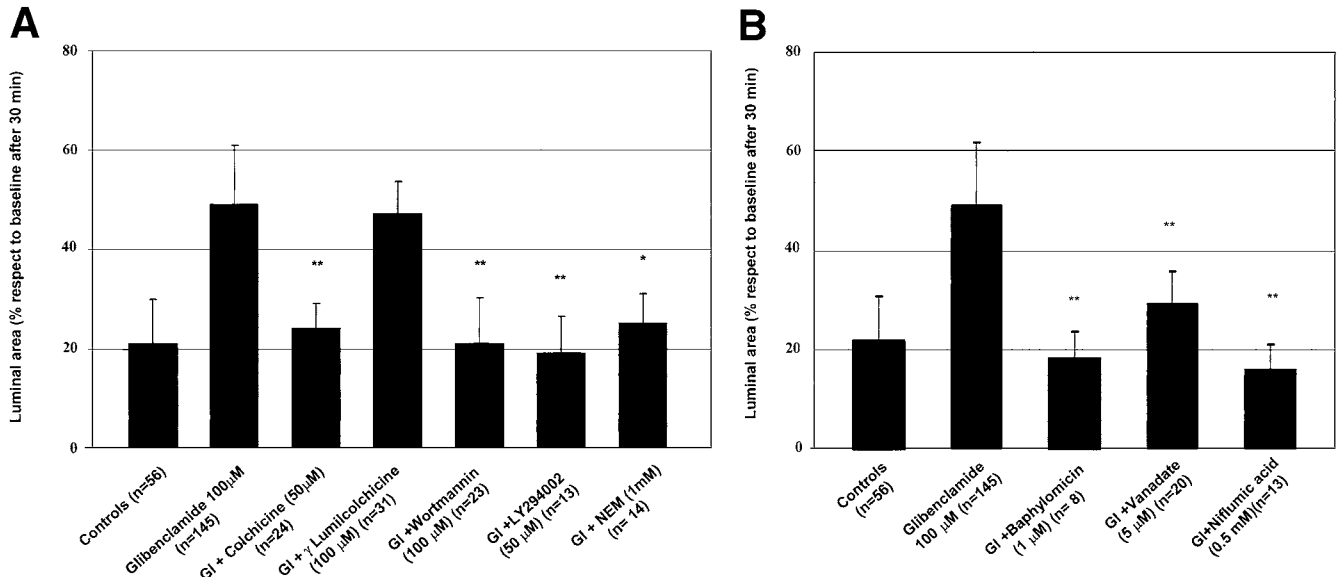


Figure 4. The choleric effect of glibenclamide in IBDUs is mediated by vesicular transport and is inhibited by V-type H⁺ ATPase and CLC-3 Cl⁻ channel blockers. (A) Inhibition by colchicine, phosphoinositol-3' kinase inhibitors (wortmannin and LY294002), and the SNARE inhibitor NEM. (B) Inhibition by V-type H⁺ ATPase inhibitors (bafilomycin and vanadate) and of CLC-3 inhibitors (niflumic acid). Columns represent the percentage of luminal area expansion with respect to baseline 30 minutes after the administration of glibenclamide (mean ± SD). *P < .01; **P < .001 vs glibenclamide. Gl, glibenclamide.

smaller than that found in other reports²⁷ that used cholangiocytes isolated from bile duct-ligated rats, rather than from normal ones, and is consistent with the size reported by Kanno et al¹³ for small duct cholangiocytes. The initial control cell diameter was 7.47 ± 0.91

μm, and C_m was 2.22 ± 1.1 pF (n = 5). On the basis of recent estimates of specific C_m (0.005 pF/μm²),²⁸ this C_m measurement exceeds the expected value of 0.87 pF and indicates that substantial cell membrane folding exists. Even with the more commonly used translation factor of

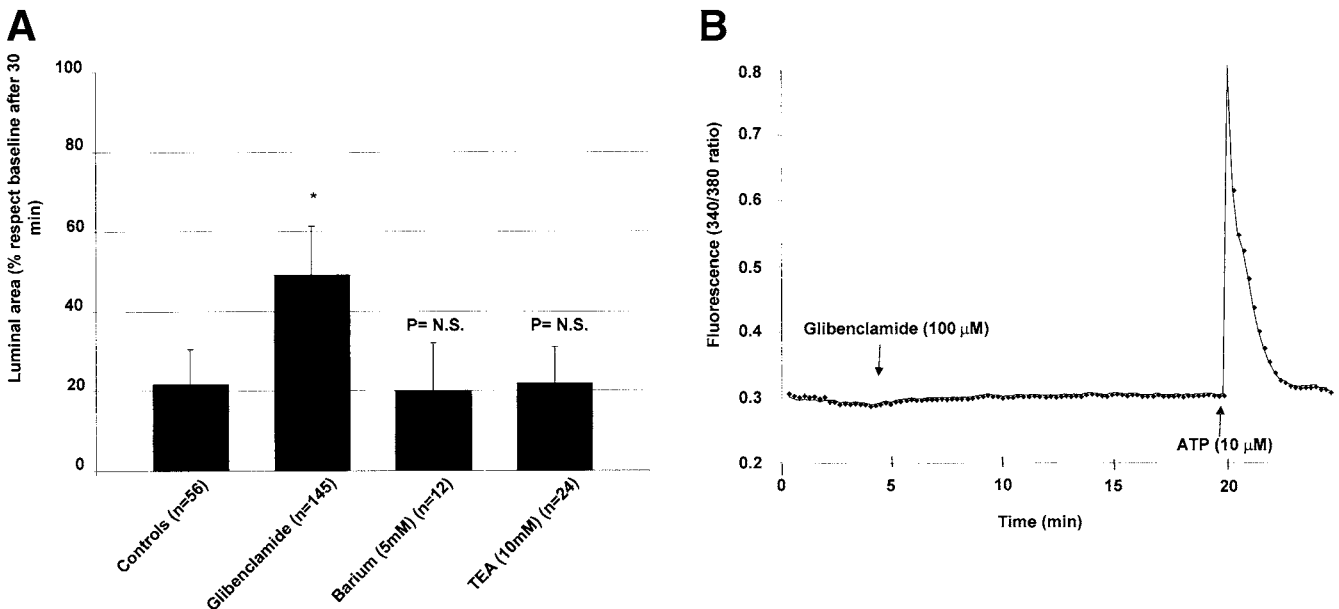


Figure 5. (A) Effects of depolarization on luminal expansion in IBDUs. Depolarizing concentrations of barium and of TEA did not stimulate secretion in IBDUs. Columns represent the percentage of luminal area expansion with respect to baseline after 30 minutes of stimulus administration (mean ± SD). (B) Effect of glibenclamide on intracellular Ca²⁺ levels. A representative tracing is shown of 22 similar experiments showing changes in the ratio of the 2 wavelengths of FURA-2 induced by the administration of glibenclamide. Glibenclamide did not increase intracellular [Ca²⁺] in IBDUs, whereas administration of ATP induced the expected Ca²⁺ increase. Similar experiments (n = 10) were performed by depolarizing the cells with TEA (10 mmol/L), and no significant changes in intracellular [Ca²⁺] were found. N.S., not significant.

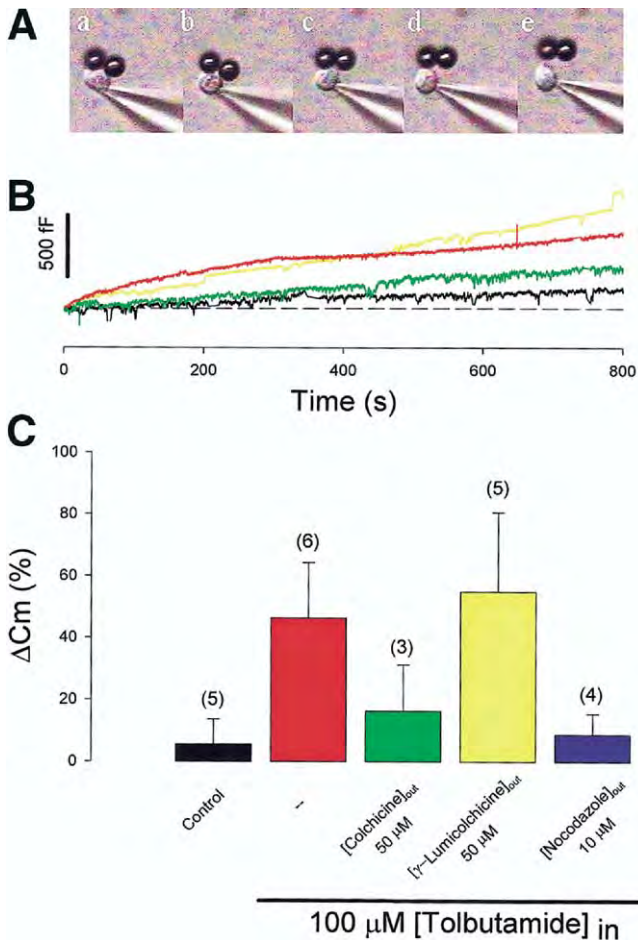


Figure 6. Whole-cell capacitance measurements in cholangiocytes. (A) Isolated cholangiocyte with 2 magnetic beads (diameter, 4.5 μm) attached to the cell membrane. Images a–e were captured at 5 minutes 12 seconds, 7 minutes 10 seconds, 10 minutes 24 seconds, 13 minutes 3 seconds, and 16 minutes 34 seconds after the establishment of whole-cell conditions, respectively. Note the gradual upward shift of beads as the cell swells. The change in surface area is smaller than it appears. This can be appreciated as follows. The initial diameter of the cell at 5 minutes 12 seconds is 7 μm , giving an apparent area of 153 μm^2 ; the final diameter is 10.7 μm , giving an area of 373 μm^2 . The initial capacitance is 1.12 pF, which equates to 224 μm^2 . Thus, the membrane at the beginning is highly folded, and the diameter is underestimated.²⁸ The capacitance at 16 minutes 34 seconds is 1.81 pF, which equates to 362 μm^2 and corresponds well to the measured diameter of the inflated cell. (B) Example C_m recordings for 4 different cells after the establishment of whole-cell conditions; colors correspond to color-coded treatments in (C). Initial capacitance for individual cells was as follows: black, 1.611 pF; yellow, 0.716 pF; red, 1.655 pF; and green, 1.152 pF. (C) Bar graph depicting average results (with SD error lines) for the different cell treatments. See Materials and Methods for details. The number of cells is indicated. Tolbutamide significantly enhanced C_m increases over control-level increases ($P < .05$). Colchicine and nocodazole treatment significantly suppressed C_m changes compared with tolbutamide and γ -lumicolchicine treatment ($P < .05$).

0.01 pF/ μm^2 , C_m measurements suggest significant membrane folding that is not resolved at the light-microscopic level. C_m measurements in control cells were quite stable for tens of minutes (Figure 6B).

After establishment of whole-cell recording with pipettes containing tolbutamide (100 $\mu\text{mol/L}$), C_m increased over the course of several minutes (Figure 6B). Concomitantly, cells swelled; this was easily discerned by the movement of the membrane-bound magnetic beads that followed the contour of the expanding cell outline (Figure 6A). C_m eventually leveled off; at steady state, increases of 56% and 50% were found (Figure 6C). The preincubation of cholangiocytes with either colchicine (50 $\mu\text{mol/L}$ for 30 minutes) or nocodazole (10 $\mu\text{mol/L}$ for 60 minutes) blocked the increase in capacitance caused by tolbutamide. However, an inactive form of colchicine, namely, γ -lumicolchicine (50 $\mu\text{mol/L}$; 30 minutes), was unable to block the effects of tolbutamide (Figure 6C). We also found cells to swell during these treatments, so the increase in cell size (and, possibly, surface area) may not solely underlie the capacitance increases that we found (see Discussion).

Membrane conductance and holding current remained stable during recordings of control cells and cells treated with tolbutamide. Current–voltage relations showed linear, time-invariant currents (Figure 7), which in the example cell actually decreased slightly during tolbutamide treatments. For 6 cells, the membrane conductance at 0 mV was unaffected by tolbutamide during the time when C_m levels significantly increased (0 minutes, 0.985 ± 0.23 nS; 10 minutes, 1.15 ± 0.3 nS; paired t test; $P = .158$). Thus, in our isolated cholangiocytes, we

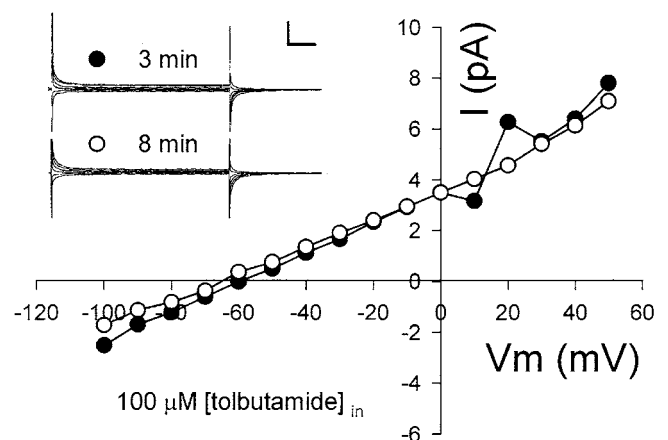


Figure 7. Whole-cell conductance measurements in cholangiocytes. I–V curves at 3 minutes (●) and 8 minutes (○) after the establishment of whole-cell conditions with 100 $\mu\text{mol/L}$ tolbutamide-containing pipette solution. Only a slight decrease in chord conductance was observed in this example. (Inset) Corresponding current traces at selected voltages (200-millisecond pulse duration) of -100, -70, -40, -10, 20, and 50 mV. Note linear, time-independent currents. Voltage at 0 current was stable and negative, near -60 mV; calculated reversal potentials for K and Cl were -86 and -34 mV, respectively. Scale: 40 pA, 31 milliseconds. Traces were filtered at 500 Hz with a digital gaussian filter.

found no evidence for a plasma membrane Cl^- conductance augmented by the increase in C_m .

Glibenclamide Stimulates Bile Flow in Isolated Perfused Mouse Liver and Fluid Secretion in Isolated Bile Duct Units From Cystic Fibrosis Transmembrane Conductance Regulator Knockout Mice

Because glibenclamide is a known CFTR inhibitor, our data thus far suggest that the choleric effect of glibenclamide is mediated by a CFTR-independent mechanism that would likely be maintained in CF. To address this possibility, we tested the effect of glibenclamide in isolated perfused mouse liver and in IBDUs from mice knocked out for CFTR (B6.129P2-Cftr^{tm1Unc}). In isolated perfused mouse liver, glibenclamide increased bile flow in wild-type mice as well as in CFTR knockout mice, and, interestingly, the increase in bile flow was significantly higher in CFTR knockout mice (Figure 8). In IBDUs isolated from 4 wild-type and 4 heterozygous mice, the administration of forskolin (10 $\mu\text{mol/L}$) or secretin (50 nmol/L) significantly increased the luminal area (wild-type—forskolin, $68\% \pm 19\%$, $n = 42$; secretin, $62\% \pm 17\%$, $n = 39$, $P < .01$ vs controls, $12\% \pm 6\%$, $n = 36$; heterozygous—forskolin, $58 \pm 13\%$, $n = 51$; secretin, $57\% \pm 20\%$, $n = 24$; $P < .01$ vs controls, $14\% \pm 6\%$, $n = 31$). In IBDUs isolated from 5 homozygous CFTR knockout mice ($-/-$), the effects of forskolin and of secretin were significantly inhibited

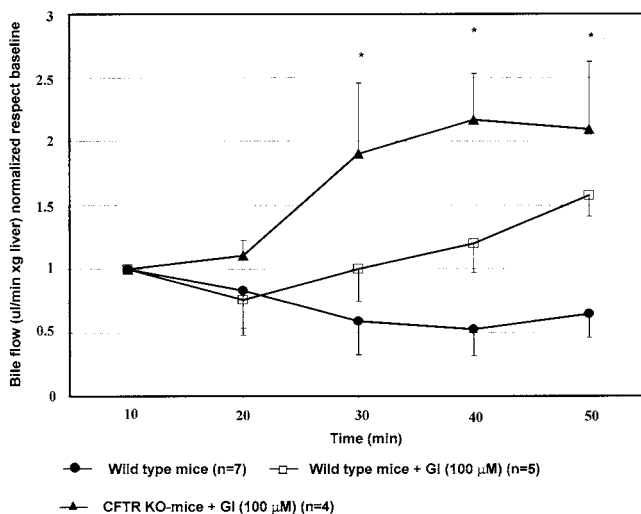


Figure 8. Glibenclamide stimulates bile flow in wild-type and CFTR knockout mice. Glibenclamide stimulates bile flow in isolated perfused mouse livers from wild-type and CFTR knockout mice. Bile flow was significantly increased ($*P < .001$) in wild-type and CFTR knockout mouse livers perfused with glibenclamide (100 $\mu\text{mol/L}$) with respect to wild-type mice. Bile flow is expressed as microliters of bile secreted in 1 minute and normalized for liver weight. Gl, glibenclamide.

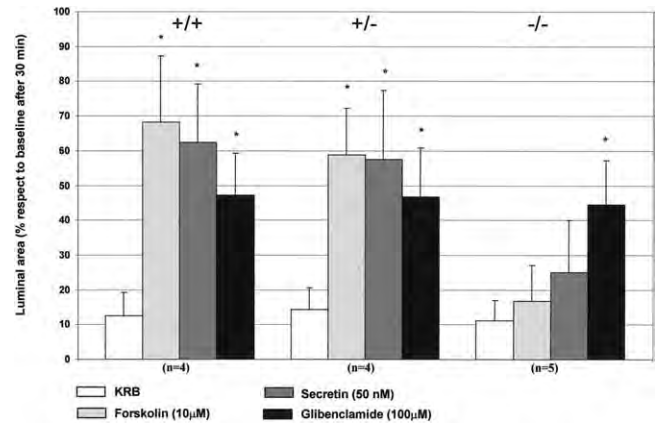


Figure 9. The choleric effect of glibenclamide is maintained in IBDUs isolated from CF mice. IBDUs were examined under control conditions for 10 minutes and then for an additional 30 minutes after the administration of glibenclamide, forskolin or secretin, or vehicle. Each luminal area was normalized by its initial value. Glibenclamide significantly ($*P < .01$ vs controls) stimulated secretion in IBDUs isolated from wild-type (+/+), heterozygous (+/-), and homozygous (-/-) mice. Forskolin and secretin were able to significantly ($*P < .01$) stimulate secretion only in wild-type and heterozygous, but not in homozygous, mice. KRB, HCO_3^- -containing Ringer buffer.

(forskolin, $17\% \pm 10\%$, $n = 54$; secretin, $25\% \pm 17\%$, $n = 41$; $P < .001$ vs wild-type and heterozygous), thus indicating that the fundamental CF secretory defect was maintained in the liver of homozygous mice. Conversely, in CFTR knockout mice, the secretory effect of glibenclamide was maintained and was equal to that recorded in wild-type and heterozygous animals (Figure 9).

Discussion

Strategies aiming at directly stimulating fluid secretion by cholangiocytes may be a useful approach to treat cholestasis in biliary tract diseases,² particularly in CF, in which reduced Cl^- and fluid secretion into the lumen causes inspissation of bile and chronic liver damage. To this end, we have studied the molecular mechanisms underlying the choleric effects of glibenclamide. The interest in this compound derives from previous studies by Nathanson et al,⁴ which showed that glibenclamide, a known CFTR inhibitor, paradoxically stimulates bile flow at the level of cholangiocytes.

Because the mechanism of glibenclamide-induced choleresis was not clarified, we sought to investigate these mechanisms in more detail. Given the inhibitory effects of bumetanide on glibenclamide-induced cholangiocyte secretion, a direct stimulation of Cl^- uptake by the NKCC1 cotransporter¹⁵ was proposed as a possible explanation.⁴ In this study, we have measured the effects of glibenclamide on $\text{Na}^+/\text{K}^+/\text{2Cl}^-$ activity, and, contrary to the previous hypothesis,⁴ we could find no

evidence of NKCC1 stimulation. Our data also show that polarized cholangiocytes⁷⁻⁹ are not able to transport glibenclamide into the apical lumen and that this stimulation of secretion is not due to an osmotic choleresis.

After binding to a specific receptor (SUR), sulfonylureas stimulate an exocytotic release of insulin from pancreatic β -cells.^{5,29} The following observations suggest that the choleric effect of glibenclamide on cholangiocytes may also be due to a receptor-mediated mechanism: (1) tolbutamide, another sulfonylurea, was able to induce luminal expansion in IBDUs to a similar extent; (2) the mRNA for SUR2B was expressed in immunopurified cholangiocytes; and (3) diazoxide, a known SUR inhibitor, significantly inhibited the secretory effect of glibenclamide. Our data also indicate that, similar to their effects on pancreatic β -cells,^{17,29} sulfonylureas are likely to stimulate fluid secretion via vesicular transport in cholangiocytes. In fact, tolbutamide induced an increase in C_m in immunisolated cholangiocytes; in addition, glibenclamide-induced secretion and/or the increase in C_m was inhibited by compounds known to block vesicular transport in the liver, such as colchicine, nocodazole, and wortmannin,²⁴⁻²⁶ and by NEM. These compounds act through different mechanisms; whereas colchicine and nocodazole are microtubule inhibitors, wortmannin is a phosphoinositol-3' kinase inhibitor, and NEM blocks the NEM-sensitive fusion protein.^{30,31} Although none of them can be considered a specific inhibitor of vesicular exocytosis, their consistent inhibitory effect on glibenclamide choleresis and on C_m changes provides strong evidence that glibenclamide stimulates vesicle exocytosis in cholangiocytes.

In the pancreatic β -cell, SUR complexes with Kir 6.x (a Kir sensitive to intracellular concentration of ATP [ATP]_i). In these cells, closure of the K_{ATP} channel induced by glibenclamide interaction with SUR depolarizes the cell, favoring Ca^{2+} influx via L-type Ca^{2+} channels.³² Although expression of the mRNA of the Kir 6.1 K_{ATP} channel isoform was detectable in immunopurified cholangiocytes (Figure 3B), neither the K^+ channel inhibitor TEA nor maneuvers aimed at inducing membrane depolarization in cholangiocytes (barium or high K^+)⁴ were able to induce luminal expansion in IBDUs. Also, in patch-clamp experiments, depolarization did not induce vesicular release; furthermore, neither the administration of glibenclamide nor membrane depolarization increased intracellular Ca^{2+} levels. This is in clear contrast to the 450 nmol/L intracellular [Ca^{2+}] increase induced by depolarization in β -cells.³³ Altogether, these data suggest that, in cholangiocytes, glibenclamide stimulates secretion via a mechanism that is independent from depolarization and Ca^{2+} transients.

In pancreatic β -cells, sulfonylureas are also able to potentiate insulin secretion by acting directly on the exocytotic machinery. Ninety percent of the high-affinity sulfonylurea binding sites in the β -cell are intracellular and seem to colocalize with the insulin-containing secretory granules.^{25,26} Recent studies have also shown that recombinant green fluorescent protein-tagged SUR and Kir colocalize with fluorescent glibenclamide in insulin-containing granules.³⁴ Furthermore, it has been shown that sulfonylureas, being weak acids, can cross biological membranes by diffusion,³⁵ thus inducing a pHi decrease similar to the one originally described by Nathanson et al⁴ in cholangiocytes. Several studies have provided evidence indicating that intracellular binding of sulfonylureas activates a DIDS- and niflumic acid-sensitive CLC-3 Cl^- channel operating in conjunction with a bafilomycin-sensitive V-type H^+ -ATPase. The resulting Cl^- and H^+ influx stimulates the exocytotic machinery and insulin discharge in a depolarization and Ca^{2+} independent way.^{17,36,37} In fact, a low granular pH promotes conformational changes in SNARE proteins, making them more fusogenic.²⁹ Our data in cholangiocytes are consistent with this mechanism; in fact, (1) glibenclamide administration does not increase intracellular [Ca^{2+}] levels; (2) membrane depolarization does not stimulate cholangiocyte secretion; (3) CLC-3 mRNA was detected in cholangiocytes; (4) DIDS, a generic inhibitor of Cl^- channels, and niflumic acid, which inhibits CLC-3, blocked the choleric response to glibenclamide; and (5) the V-type H^+ -ATPase inhibitors bafilomycin A1 and vanadate significantly reduced the secretory response to glibenclamide. Altogether, these data suggest the presence in cholangiocytes of a cAMP- and Ca^{2+} -independent secretory mechanism that is stimulated by sulfonylureas and requires functional exocytotic machinery.

Our capacitance measurements provide further evidence that tolbutamide promotes an increase in cell-surface area; the dependence of this effect on microtubule stability argues for vesicular fusion with the plasma membrane.³⁸ Increases in C_m of approximately 50% were found, similar to our luminal area measurements in IBDUs, and although this may seem large, a complete vesicular release in bile ductal cells of the pig increased the membrane surface area by >100%.³⁹ Actually, an increase in capacitance may arise from several sources, including an increase in membrane surface area due to vesicular fusion and swelling of the cell with attendant thinning of the membrane and unraveling of membrane folds (eg, microvilli). Thinning of the membrane caused by membrane stretch is expected to increase specific C_m , and the resulting increase in whole-cell capacitance can-

not be distinguished electrically from actual membrane accrual. Additionally, tight folding of the membrane may initially limit the accessibility of voltage perturbation across those membranes, and after cell swelling and unraveling, these membranes may then be fully excited and contribute more to C_m measurements. We found that cells readily swelled during our recording and, indeed, shifted the attached magnetic beads (Figure 6A). Although the microtubule destabilizers may be thought to specifically inhibit vesicular release in cholangiocytes,³⁸ they may also somehow affect the other potential mechanisms of C_m increase. Thus, we cautiously hypothesize that at least a component of C_m increase results from vesicular fusion.

Usually we held the cell membrane potential at zero voltage during capacitance measurements, because we observed that cells were not maintained for prolonged periods of time when they were held at negative potentials. Despite this depolarized holding potential, control cells did not show capacitance increases as might have occurred if an influx of extracellular Ca^{2+} via voltage-gated Ca^{2+} channels could induce exocytosis. Indeed, under our recording conditions, measurements do not show inward currents typical of non-inactivating L-type Ca^{2+} channels.

We did not find significant changes in membrane conductance during tolbutamide treatments. Indeed, our isolated cells, before and after these treatments, showed only small linear, time-independent currents, similar to 1 pattern of 3 found by Fitz et al.²⁷ Perhaps our isolation technique favored a particular cell subpopulation. The holding current was remarkably stable during our treatments, and current-voltage relations confirmed these measurements, showing that changes in ionic conductance did not necessarily accompany C_m increases. Although we observed that secretion in IBUs could be inhibited by Cl^- channel blockers, it should be noted that our whole-cell voltage-clamp measurements are unable to assess channel activity within intracellular membrane compartments, such as vesicles; of course, blockers may work at this level. As already shown,^{37,40} CLC-3 channels provide an electrical shunt pathway that permits vesicle acidification by the vacuolar pump before vesicular release. This scenario favors a fluid-phase type of secretory activity in our cholangiocyte preparation.

The transport functions of the biliary epithelium are regulated by different gastrointestinal hormones that stimulate either secretory or absorptive mechanisms.¹ Secretin, the principal stimulatory hormone, increases ductular choleresis through cAMP/protein kinase A-dependent stimulation of Cl^- efflux and HCO_3^- secretion

through the coordinated actions of CFTR and the anion exchanger isoform 2 Cl^-/HCO_3^- exchanger, both located at the apical pole of the cells.^{41,42} Cl^- efflux into the bile can also be mediated by Ca^{2+} -dependent Cl^- channels stimulated by binding of extracellular ATP to P2Y2 purinergic receptors located at the apical pole of cholangiocytes.^{3,23} In addition, a substantial amount of evidence indicates that stimulation of vesicular transport and fusion plays a role in cholangiocyte secretion. In vivo and in vitro studies using fluid-phase markers have shown that cholangiocytes are capable of microtubule-dependent fluid-phase transcytotic transport from the basolateral to the apical domains.^{10,38,43} Furthermore, cholangiocytes possess a dense population of subapical vesicles that undergo a high rate of constitutive exocytosis⁴⁴ that can be stimulated by osmotic stress and by cAMP. Cyclic AMP stimulates the exocytosis of acridine orange in cholangiocytes³⁸ and the apical insertion of vesicles containing aquaporins and ion transporters (such as CFTR and anion exchanger isoform 2) as a means of achieving rapid regulation of biliary ion and fluid transport.⁴⁵

The choleric effect of glibenclamide is a paradox; in fact, because it is a known inhibitor of CFTR, one would expect glibenclamide to inhibit secretion. Thus, the major finding of our study, which is of potential therapeutic relevance, is that sulfonylureas possess the ability to stimulate cholangiocyte secretion, thus promoting a novel cAMP-, Ca^{2+} -, and depolarization-independent exocytotic mechanism, and that this effect is preserved and even more active in experimental animals defective for CFTR. An important line of research in CF aims at finding small molecules able to stimulate fluid secretion in CFTR-defective cells and focuses on compounds able to function as molecules that (1) can serve as chaperones for CFTR, (2) can activate the mutated CFTR, and (3) can stimulate Ca^{2+} -dependent Cl^- conductances.

Direct transfer of these observations to human therapy is not likely, because the K_d for the choleric effects of glibenclamide is approximately 9 $\mu\text{mol/L}$,⁴ a concentration that may result in hypoglycemia. However, our data represent an important proof of concept; the identification of a compound able to stimulate bile secretion independently of CFTR and the 2 major signaling pathways (Ca^{2+} and cAMP) is of major general interest. Sulfonylureas may thus represent model compounds to design drugs for conditions characterized by a failure in cAMP-dependent secretion (such as CF-related liver disease) and possibly other cholestatic conditions in which a defect in Ca^{2+} signaling is present.⁴⁶

References

- Strazzabosco M. New insights into cholangiocyte physiology. *J Hepatol* 1997;27:945–952.
- Ferenchak AP, Sokol RJ. Cholangiocyte biology and cystic fibrosis liver disease. *Semin Liver Dis* 2001;21:471–487.
- Zsembery A, Jessner W, Spirli C, Strazzabosco M, Graf J. Correction of CFTR malfunction and stimulation of Ca^{2+} -activated Cl^- channels restore HCO_3^- secretion in cystic fibrosis bile ductular cells. *Hepatology* 2002;35:95–104.
- Nathanson MH, Burgstahler AD, Mennone A, Dranoff JA, Rios-Velez L. Stimulation of bile duct secretion by glibenclamide in normal and cholestatic rat liver. *J Clin Invest* 1998;101:1–12.
- Doyle ME, Egan JM. Pharmacological agents that directly modulate insulin secretion. *Pharmacol Rev* 2003;55:105–131.
- Spirli C, Nathanson MH, Fiorotto R, Duner E, Denson LA, Sanz JM, Di Virgilio F, Casagrande F, Strazzabosco M. Pro-inflammatory cytokines inhibit secretion in rat bile duct epithelium. *Gastroenterology* 2001;121:156–169.
- Spirli C, Granato A, Zsembery A, Anglani F, Okolicsanyi L, La Russo NF, Crepaldi G, Strazzabosco M. Functional polarity of Na^+/H^+ and $\text{Cl}^-/\text{HCO}_3^-$ exchangers in a rat cholangiocytes cell line. *Am J Physiol* 1998;275:G1236–G1245.
- Vroman B, La Russo NF. Development and characterization of polarized primary cultures of rat intrahepatic bile duct epithelial cells. *Lab Invest* 1996;74:303–313.
- Lazaridis KN, Pham L, Vroman B, de Groen PC, LaRusso NF. Kinetic and molecular identification of sodium-dependent glucose transporter in normal rat cholangiocytes. *Am J Physiol* 1997;272:G1168–G1174.
- Benedetti A, Marucci L, Bassotti C, Mancini R, Contucci S, Jezequel AM, Orlandi F. Tubulovesicular transcytotic pathway in rat biliary epithelium: a study in perfused liver and isolated intrahepatic bile duct. *Hepatology* 1993;18:422–432.
- Mennone A, Alvaro D, Cho W, Boyer JL. Isolation of small polarized bile duct units. *Proc Natl Acad Sci U S A* 1995;92:6527–6531.
- Spirli C, Fabris L, Duner E, Fiorotto R, Ballardini G, Roskams T, La Russo NF, Sonzogni A, Okolicsanyi L, Strazzabosco M. Cytokine-stimulated, nitric oxide production inhibit adenylyl cyclase and cAMP-dependent secretion in cholangiocytes. *Gastroenterology* 2003;124:737–753.
- Kanno N, Le Sage G, Glaser S, Alvaro D, Alpini G. Functional heterogeneity of the intrahepatic biliary epithelium. *Hepatology* 2000;31:555–561.
- Strazzabosco M, Mennone A, Boyer JL. Intracellular pH regulation in isolated rat bile duct epithelial cells. *J Clin Invest* 1991;87:1503–1512.
- Insering P, Jacoby SC, Payne JA, Forbush B III. Comparison of Na-K-Cl cotransporters. *J Biol Chem* 1998;273:11295–11301.
- Brini M, De Giorgi F, Murgia M, Marsault R, Massimino ML, Cantini M, Rizzuto R, Pozzan T. Subcellular analysis of Ca^{2+} homeostasis in primary cultures of skeletal muscle myotubes. *Mol Biol Cell* 1997;8:129–143.
- Barg S, Renstrom E, Berggren PO, Bertorello A, Bokvost K, Braun M, Eliasson L, Holmes WE, Kohler M, Rorsman P, Thevenod F. The stimulatory action of tolbutamide on Ca^{2+} -dependent exocytosis in pancreatic β cells is mediated by a 65-kDa mdr-like P-glycoprotein. *Proc Natl Acad Sci U S A* 1999;96:5539–5544.
- Santos-Sacchi J, Kakehata S, Takahashi S. Effects of membrane potential on the voltage dependence of motility-related charge in outer hair cells of the guinea-pig. *J Physiol* 1998;510:225–235.
- Santos-Sacchi J. Determination of cell capacitance using the exact empirical solution of dY/dC_m and its phase angle. *Biophys J* 2004;87:714–727.
- Santos-Sacchi J. Isolated supporting cells from the organ of Corti: some whole cell electrical characteristics and estimates of gap junctional conductance. *Hear Res* 1991;52:89–98.
- Snouwaert JN, Brigman KK, Latour AM, Malouf NN, Boucher RC, Smithies O, Koller BH. An animal model for cystic fibrosis made by gene targeting. *Science* 1992;257:1083–1088.
- Oude-Elferink RPJ, Ottenhoff R, van Wijland M, Smit JJM, Schinkel AH, Groen AK. Regulation of biliary lipid secretion by mdr2 P-glycoprotein in the mouse. *J Clin Invest* 1995;95:31–38.
- Zsembery A, Spirli C, Granato A, LaRusso NF, Okolicsanyi L, Crepaldi G, Strazzabosco M. Purinergic regulation of acid/base transport in human and rat biliary epithelial cell lines. *Hepatology* 1998;28:914–920.
- Dallenbach A, Renner EL. Colchicine does not inhibit secretin-induced choleresis in rats exhibiting hyperplasia of bile ductules: evidence against a pivotal role of exocytotic vesicle insertion. *J Hepatol* 1995;22:338–348.
- Sato SB, Taguchi T, Yasmashina S, Toyama S, Wortmannin and Li^+ specifically inhibit clathrin-independent endocytic internalization of bulk fluid. *J Biochem* 1996;119:887–897.
- Folli F, Alvaro D, Gigliozzi A, Bassotti C, Kahn RC, Pontiroli AE, Capocaccia L, Jezequel AM, Benedetti A. Regulation of endocytic-transcytotic pathways and bile secretion by phosphatidylinositol 3-kinase in rats. *Gastroenterology* 1997;113:954–965.
- Fitz JG, Basavappa S, McGill J, Melhus O, Cohn JA. Regulation of membrane chloride currents in rat bile-duct epithelial-cells. *J Clin Invest* 1993;91:319–328.
- Solsona C, Innocenti B, Fernandez JM. Regulation of exocytotic fusion by cell inflation. *Biophys J* 1998;74:1061–1073.
- Thevenod F. Ion channels in secretory granules of the pancreas and their role in exocytosis and release of secretory proteins. *Am J Physiol* 2002;283:C651–C672.
- Galli T, Zahraoui A, Vaidyanathan VV, Raposo G, Tian JM, Karin M, Niemann H, Louvard D. A novel tetanus neurotoxin-insensitive vesicle-associated membrane protein in SNARE complexes of the apical plasma membrane of epithelial cells. *Mol Biol Cell* 1998;9:1437–1448.
- Xu T, Ashery U, Burgoyne RD, Neher E. Early requirement for α -SNAP and NSF in the secretory cascade in chromaffin cells. *EMBO J* 1999;18:3293–3304.
- Ashcroft FM, Gribble FM. Tissue-specific effects of sulfonylureas: lessons from studies of cloned K_{ATP} channels. *J Diabetes Complications* 2000;14:192–196.
- Abrahamsson H, Berggren PO, Rorsman P. Direct measurements of increased free cytoplasmic Ca^{2+} in mouse pancreatic beta-cells following stimulation by hypoglycemic sulfonylureas. *FEBS Lett* 1985;190:21–24.
- Geng X, Lehong L, Watkins S, Robbins PD, Drain P. The insulin secretory granule is the major site of K_{ATP} channels of the endocrine pancreas. *Diabetes* 2003;52:767–776.
- Kamp F, Kizilbash N, Corkey B, Berggren PO, Hamilton J. Sulfonylureas rapidly cross phospholipid bilayer membranes by a free-diffusion mechanism. *Diabetes* 2003;52:2526–2531.
- Renstrom E, Barg S, Thévenod F, Rorsman P. Sulfonylurea-mediated stimulation of insulin exocytosis via an ATP-sensitive K^+ channel-independent action. *Diabetes* 2002;51:S33–S36.
- Barg S, Huang P, Eliasson L, Nelson DJ, Obermuller S, Rorsman P, Thevenod F, Renstrom E. Priming of insulin granules for exocytosis by granular Cl^- uptake and acidification. *J Cell Sci* 2001;114:2145–2154.
- Kato A, Gores GJ, LaRusso NF. Secretin stimulates exocytosis in isolated bile duct epithelial cells by a cyclic AMP-mediated mechanism. *J Biol Chem* 1992;267:15523–15529.
- Buanes T, Grotmol T, Landsverk T, Raeder MG. Secretin empties bile-duct cell cytoplasm of vesicles when it initiates ductular HCO_3^- secretion in the pig. *Gastroenterology* 1988;95:417–424.

40. Hara-Chikuma M, Yang B, Sonawane ND, Sasaki S, Uchida S, Verkman AS. ClC-3 chloride channels facilitate endosomal acidification and chloride accumulation. *J Biol Chem* 2005;280:1241–1247.
41. Cohn JA, Strong TV, Picciotto MR, Nairn AC, Collins FS, Fitz JG. Localization of the cystic fibrosis transmembrane conductance regulator in human bile duct epithelial cells. *Gastroenterology* 1993;105:1857–1864.
42. Martinez-Ansò E, Castillo JE, Diaz J, Medina JF, Prieto J. Immunohistochemical detection of Cl⁻/HCO₃⁻ anion exchanger in human liver. *Hepatology* 1994;19:1400–1406.
43. Benedetti A, Marucci L, Bassotti C, Guidarelli C, Jezequel AM. Brefeldin A inhibits the transcytotic vesicular transport of horseradish peroxidase in intrahepatic bile ductules isolated from rat liver. *Hepatology* 1995;22:194–201.
44. Doctor B, Dahl R, Fouassier L, Kilic G, Fitz JG. Cholangiocytes exhibit dynamic, actin-dependent apical membrane turnover. *Am J Physiol Cell Physiol* 2002;282:C1042–C1052.
45. Tietz PS, Marinelli RA, Chen XM, Huang B, Cohn J, Kole J, McNiven MA, Alper S, LaRusso NF. Agonist-induced coordinated trafficking of functionally related transport proteins for water and ions in cholangiocytes. *J Biol Chem* 2003;278:20413–20419.
46. Shibao K, Hirata K, Robert ME, Nathanson MH. Loss of inositol 1,4,5-trisphosphate receptors from bile duct epithelia is a common event in cholestasis. *Gastroenterology* 2003;125:1175–1187.

Received April 8, 2004. Accepted March 16, 2005.

Address requests for reprints to: Mario Strazzabosco, MD, PhD, Division of Gastroenterology, Ospedali Riuniti di Bergamo, Largo Barozzi, 1, 24128 Bergamo, Italy. e-mail: mstrazzabosco@ospedaliriuniti.bergamo.it; fax: (39) 035-26-6818.

Supported by Telethon (Grant E-873), by the Italian Cystic Fibrosis Research Foundation (Grant 2003) with the contribution of Fondazione Cariverona, by Ministero dell'Istruzione, Università e Ricerca (MIUR; cofinanziamento 2003; Grant 2003060498-001), by Fondazione San Martino, and by National Institutes of Health NIDCD Grant DC 000273 (J.S.-S.).

Distortion Component Analysis of Outer Hair Cell Motility-Related Gating Charge

S. Takahashi, J. Santos-Sacchi

Sections of Otolaryngology and Neurobiology, Yale University School of Medicine, New Haven, CT 06510, USA

Received: 31 December 1998/Revised: 12 March 1999

Abstract. The underlying Boltzmann characteristics of motility-related gating currents of the outer hair cell (OHC) are predicted to generate distortion components in response to sinusoidal transmembrane voltages. We studied this distortion since it reflects the mechanical activity of the cell that may contribute to peripheral auditory system distortion. Distortion components in the OHC electrical response were analyzed using the whole-cell voltage clamp technique, under conditions where ionic conductances were blocked. Single or double-sinusoidal transmembrane voltage stimulation was delivered at various holding voltages, and distortion components of the current responses were detected by Fourier analysis. Current response magnitude and phase of each distortion component as a function of membrane potential were compared with characteristics of the voltage-dependent capacitance, obtained by voltage stair-step transient analysis or dual-frequency admittance analysis. The sum distortion was most prominent among the distortion components at all holding voltages. Notches in the sum (f_1+f_2), difference (f_2-f_1) and second harmonic ($2f$) components occur at the voltage where peak voltage-dependent capacitance resides (V_{pkCm}). Rapid phase reversals also occurred at V_{pkCm} , but phase remained fairly stable at more depolarized and hyperpolarized potentials. Thus, it is possible to extract Boltzmann parameters of the motility-related charge movement from these distortion components. In fact, we have developed a technique to follow changes in the voltage dependence of OHC motility and charge movement by tracking the voltage at phase reversal of the f_2-f_1 product. When intracellular turgor pressure was changed, V_{pkCm} and distortion notch voltages shifted in the same direction. These data have important implications for understanding cochlear nonlinearity, and more generally, indicate the use-

fulness of distortion analysis to study displacement currents.

Key Words: Outer hair cell — Distortion — Gating charge — Membrane capacitance — Turgor pressure

Introduction

In linear systems, input and output signals contain the same in-phase frequency components. In nonlinear systems, stimulus frequencies (single: f_1 ; two-tone: f_1, f_2) produce harmonic and combination distortion components, such as nf_1 , $(n+1)f_1-nf_2$ and $(n+1)f_2-nf_1$ ($n = 1, 2, 3, \dots$). Distortion is readily perceived by the auditory system despite the purity of acoustic stimuli (Goldstein, 1967). Physiological correlates of the perceived distortion exist in responses of auditory nerve fibers (Goldstein & Kiang, 1968; Kim, Molinar & Matthews, 1980), inner hair cells (Nuttall & Dolan, 1990), and basilar membrane vibration patterns (Robles, Ruggero & Rich, 1991, 1997). Such distortion, which is dependent upon normal outer hair cell (OHC) function, clearly reveals the nonlinear nature of peripheral auditory processing. OHCs are the primary source of distortion components in mammals.

The OHC produces voltage-dependent mechanical responses that provide feedback into the basilar membrane, thereby sharpening the passive mechanical vibration of the cochlear partition (Brownell et al., 1985; Ashmore, 1987; Santos-Sacchi & Dilger, 1988; Ruggero, 1992). The cell also possesses a nonlinear gating charge movement or correspondingly, a voltage-dependent capacitance, which correlates well with its mechanical activity (Ashmore, 1989; Santos-Sacchi, 1990, 1991). The underlying nonlinear Boltzmann characteristics of the charge movement and mechanical response are predicted to generate distortion components in the response to single and dual sinusoidal transmembrane volt-

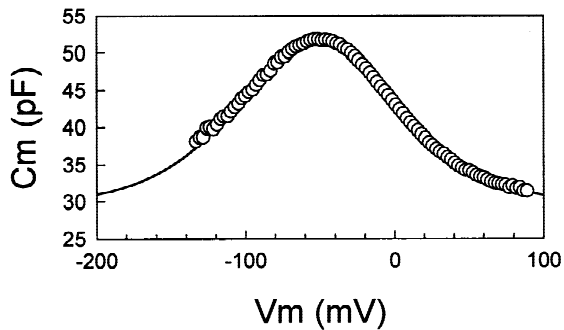


Fig. 1. Outer hair cell voltage-dependent capacitance determined from FFT-based dual-sinusoidal technique (Santos-Sacchi et al., 1998). Fit to Eq. 1 indicates V_{pkC_m} : -52.6 mV; z : 0.71; Q_{max} : 3.22 pC; and C_{lin} : 29.6 pF.

ages. Indeed, OHCs generate mechanical distortions when stimulated under voltage clamp (Santos-Sacchi, 1993) or transcellularly within a pipette microchamber (Hu et al., 1994). The purpose of the present experiments is to describe the features of OHC electrical distortion components that arise from motility-related charge movement. These electrical distortion components reflect the mechanical activity of the OHC and thus are useful in understanding the generation of mechanical distortion that is present in the peripheral auditory system. While the data have important implications for understanding cochlear nonlinearity, more generally, they illustrate the type of behavior expected from nonlinear membrane charge movement regardless of source (e.g., from ionic channels).

A preliminary presentation of these data has been made (Takahashi & Santos-Sacchi, 1997).

Materials and Methods

GENERAL

OHCs and supporting cells were freshly isolated from the organ of Corti of the guinea-pig cochlea and transferred to a $700 \mu\text{l}$ perfusion chamber (Kakehata et al., 1995) filled with an external standard solution. The external standard solution contained (in mM): 142 NaCl, 5.37 KCl, 1.25 CaCl_2 , 1.48 MgCl_2 , 10 HEPES and 5 dextrose, pH 7.2 , 300 mOsm. OHCs were whole-cell voltage clamped using an Axon 200B amplifier with patch pipettes having initial resistances of 2 – 3 $\text{M}\Omega$. Residual series resistance ranged from 3 – 7 $\text{M}\Omega$. To remove voltage-dependent ionic conductances, the external standard solution was replaced with an ionic blocking solution during electrical recording. The external ionic blocking solution contained (in mM): 100 NaCl, 20 TEA, 20 CsCl, 2 CoCl_2 , 1.52 MgCl_2 , 10 HEPES and 5 dextrose, pH 7.2 , 300 mOsm (adjusted with dextrose). The patch pipette solution contained (in mM): 140 CsCl, 2 MgCl_2 , 10 EGTA and 10 HEPES, with pH 7.2 and osmolarity 300 mOsm (adjusted with dextrose). Thus, capacitive currents could be analyzed in isolation (Santos-Sacchi, 1991; Huang & Santos-Sacchi, 1993; Kakehata & Santos-Sacchi, 1995). Salicylate (10 mM) or lutetium chloride (3 mM) was used to reduce

motility related gating charge movement in some experiments (Kakehata & Santos-Sacchi, 1996).

Pipette pressure was modified with a syringe connected to the Teflon tubing attached to the patch pipette holder. Pressure was monitored via a T-connector to a pressure monitor (WPI, Sarasota, FL). δz , longitudinal strain, a unit-less metric, was calculated as $\Delta L/L_0$, where ΔL is the change of cell length due to turgor pressure change and L_0 is the original cell length. All experiments were performed at room temperature (-23°C).

EVALUATION OF MEMBRANE CAPACITANCE

Detailed evaluation of membrane capacitance was made at different potentials by transient analysis of currents induced by a voltage stair step stimulus (-150 to $+50$ mV, 10 mV increments; Huang & Santos-Sacchi, 1993), or by FFT-based admittance analysis of dual voltage sinusoidal stimulation (Santos-Sacchi et al., 1998); the capacitance data were fit to the first derivative of a two state Boltzmann function relating nonlinear charge to membrane voltage (Santos-Sacchi, 1991),

$$C_m = C_v + C_{lin} = Q_{max} \frac{ze}{kT} \frac{b}{(1+b)^2} + C_{lin} \quad \text{Eq (1)}$$

where

$$b = \exp\left(\frac{-ze(V_m - V_{pkC_m})}{kT}\right)$$

Q_{max} is the maximum nonlinear charge moved, V_{pkC_m} is voltage at peak capacitance or equivalently, at half maximal nonlinear charge transfer, V_m is membrane potential, z is valence, C_{lin} is linear membrane capacitance, e is electron charge, k is Boltzmann's constant, and T is absolute temperature. Series resistance, R_s , was estimated from the decaying time constant and integrated charge of the voltage step-induced current, as fully described elsewhere (Huang & Santos-Sacchi, 1993). Membrane resistance, R_m , was evaluated from steady state current. C_{lin} was estimated from the fit to above capacitance (C_m) equation, and indicates the intrinsic linear capacitance of the membrane upon which rides the bell-shaped voltage-dependent capacitance (C_v).

DISTORTION MEASUREMENT

To evoke distortion components, single or two summed sinusoidal membrane voltages were delivered to OHCs under whole-cell voltage clamp at various holding potentials. Peak amplitude of input stimuli was set between 5 and 26 mV. Input stimulus frequencies and frequency ratios (f_2/f_1) were also varied. The AC stimulus duration was fixed at 51.2 msec, with the sampling at $10 \mu\text{sec}$. Data were filtered at 5 kHz (4-pole Bessel). Steady-state current responses were analyzed by Fast Fourier Transform (FFT) to extract the magnitude and phase of distortion components at $2f_1 \pm f_2$, $2f_2 \pm f_1$, $f_2 \pm f_1$, $2f_1$, and $3f_1$. All data collection and analysis were performed with an in-house developed Window's based whole-cell voltage clamp program, jClamp (www.med.yale.edu/surgery/otolar/santos/jclamp.html), utilizing a Digidata 1200 board (Axon, CA).

Results

After blocking nonlinear conductances in the OHC, the predominant electrical nonlinearity that remains is a voltage-dependent capacitance, which derives from motility-

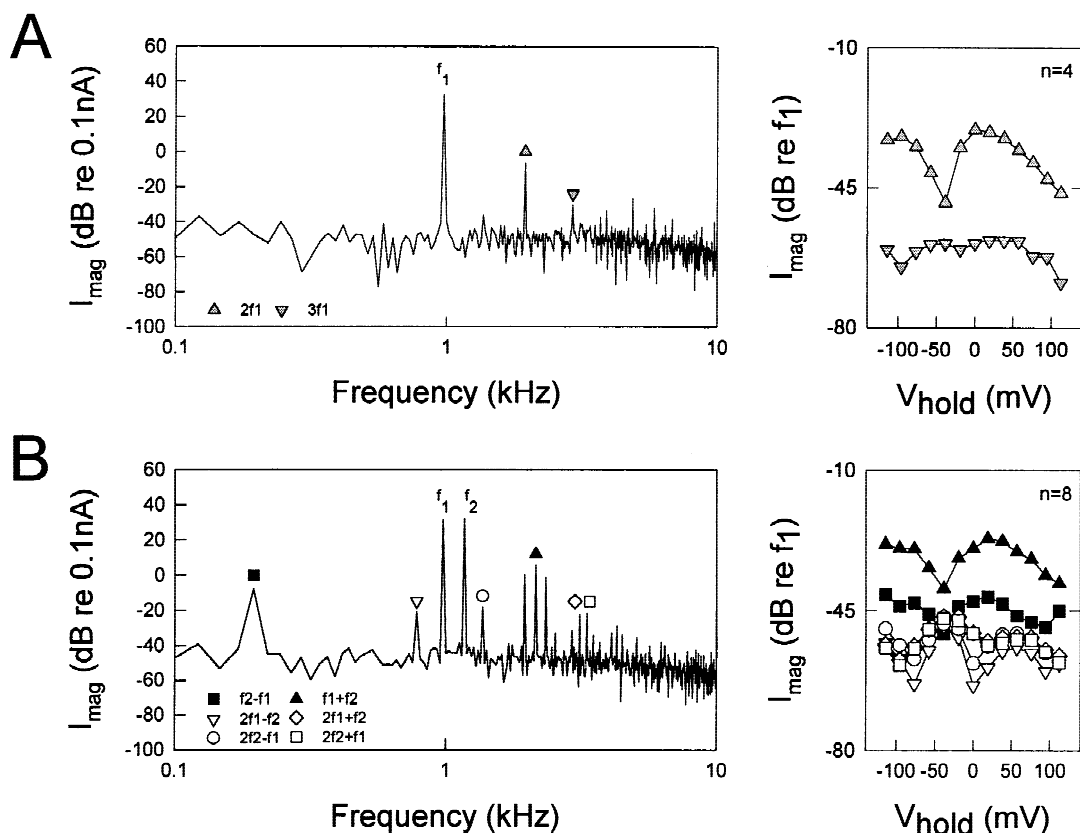


Fig. 2. *Left panels:* Typical frequency spectra of OHC current responses to AC transmembrane voltage stimuli measured under whole cell voltage clamp. Spectra were obtained by fast Fourier transform. Input stimulus frequencies were set at 963 Hz (f_1) and 1156 Hz (f_2); magnitudes were 25 mV peak. Induced currents contained (A) harmonic distortion components ($2f_1$, $3f_1$) and (B) combination distortion components (f_2-f_1 , f_1+f_2 , $2f_1-f_2$, $2f_2-f_1$), as well as peaks at the primary frequencies. The *right panels* illustrate the average effects of holding voltage (-120 to 120 mV, in 20 mV increments) on distortion component magnitudes (dB re: magnitude at f_1). Averaged series and membrane resistances were 4.0 and 259 $m\Omega$, respectively.

related nonlinear charge movement (Fig. 1). Due to this nonlinearity, delivery of single or dual sinusoidal voltages across the OHC membrane elicits current responses that contain the original frequency components as well as distortion components. Fig. 2 (*left panels A and B*) shows typical spectra obtained by FFT analysis of current responses evoked by 25 mV AC transmembrane voltage stimuli (f_1 : 963 Hz and f_2 : 1156 Hz). In addition to the peaks at the input stimulus frequencies (f_1 , f_2), quadratic distortions ($f_2 \pm f_1$), cubic distortions ($2f_1 \pm f_2$, $2f_2 \pm f_1$), and second and third harmonic distortions ($2f_1$, $3f_1$) were detected above the noise floor. The noise floor associated with our measuring system averaged approximately -46.7 dB re 0.1 nA in the 5 kHz bandwidth. Second harmonic, sum (f_1+f_2) and difference (f_2-f_1) distortion components were largest. For example, the largest sum component averaged 27 dB down from f_1 response magnitude. The *right panels* in Fig. 2 show averaged magnitude responses as a function of holding potential. Second harmonic, sum and difference distortion components exhibit magnitude notches near -40

mV, whereas notches in the other distortion component magnitudes appear at voltages above and below that voltage.

Distortion in cochlear supporting cells, e.g., Deiters cells, which lack the voltage-dependent capacitance characteristic of OHCs, was close to the noise floor (Fig. 3), supporting the view that the extensive distortion arising within the OHC is related to its lateral membrane sensor-motors. Indeed, the voltage dependence of distortion components derives from the Boltzmann characteristics of the robust OHC motility-related nonlinear charge movement and is evident in the representative data ($n = 10$) of Fig. 4 where voltage-dependent capacitance is plotted along with distortion component magnitude and phase. The voltage where magnitude minima are observed in second harmonic, sum and difference components corresponds to the voltage at peak capacitance (V_{pkcm}). Associated with the magnitude minima are abrupt phase reversals. The other distortion component minima are also associated with abrupt phase reversals. Changes in stimulus frequencies (f_2 : 0.6–1.4 kHz)

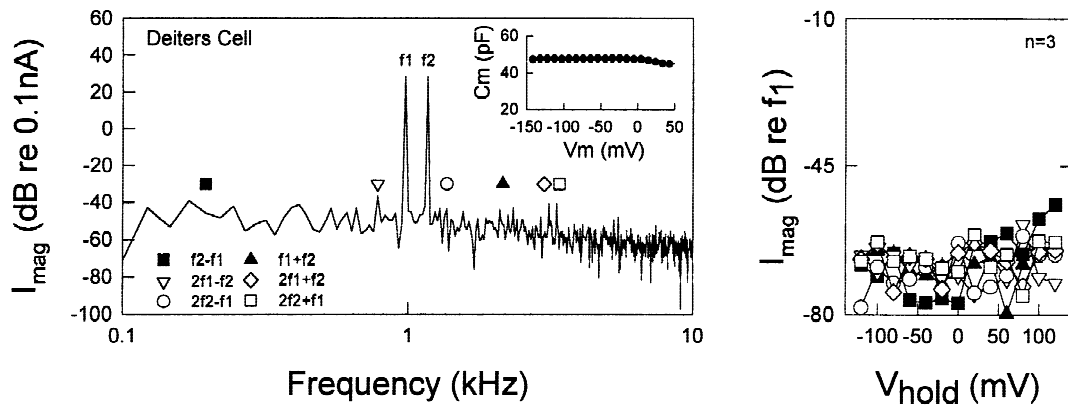


Fig. 3. Distortion components generated in a Deiters supporting cell obtained as in Fig. 2. *Left panel* shows distortion components close to the noise floor. Inset illustrates the linear capacitance of the cell. The *right panel* shows the effect of holding potential. It is clear that supporting cells do not present the degree of nonlinearity that characterizes the OHC.

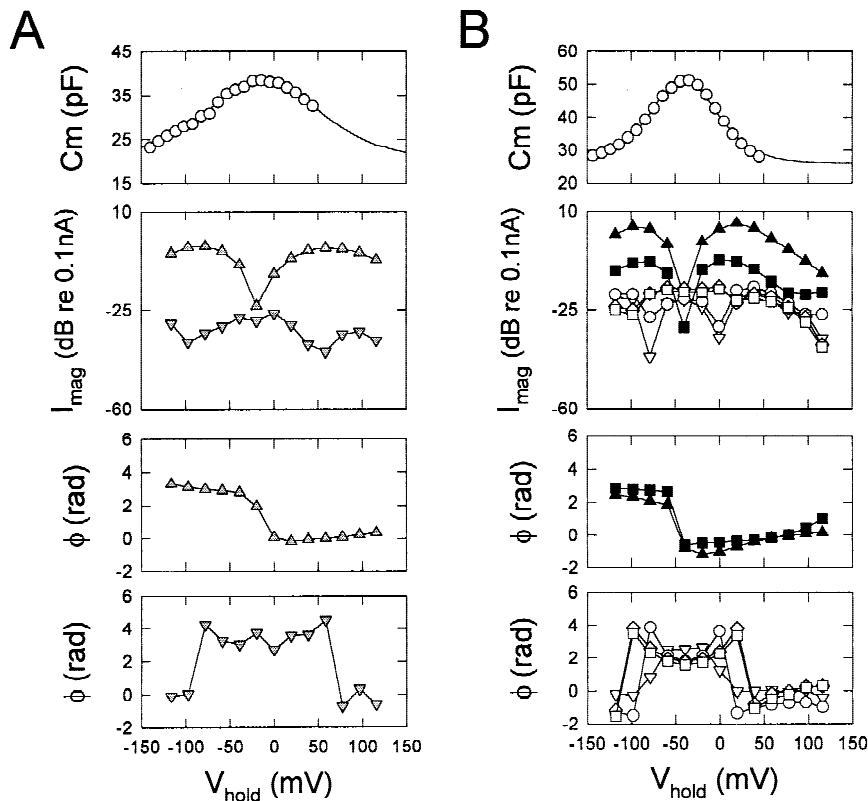


Fig. 4. Relationship between nonlinear capacitance and distortion component magnitude and phase. (A) OHC capacitance was determined by the stair step technique. The solid line indicates a fit of this cell's capacitance to Eq. 1: V_{pkCm} : -12.0 mV; z : 0.59 ; Q_{max} : 3.17 pC; and C_{lin} : 20.3 pF. The bottom panels plot the magnitude and phase of the second and third harmonic. Lines are only connections between symbols. Symbols are as in Fig. 2A. Note that the minima in magnitudes correspond to abrupt phase reversals. (B) The solid line indicates a fit of this cell's capacitance to Eq. 1: V_{pkcm} : -40.6 mV; z : 1.0 ; Q_{max} : 2.61 pC; and C_{lin} : 26.0 pF. The bottom panels plot the magnitude and phase of the combination distortion components. Symbols are as in Fig. 2B. As above, magnitude minima correspond to abrupt phase reversals.

or frequency ratios (f_2/f_1 : 1.1–1.4) did not alter distortion components. Figure 5 shows the intensity functions for the sum and difference components at three holding potentials, -60 , 0 and 60 mV. Distortion decreased at a rate greater than stimulus intensity. Other distortion components showed similar decreases, but in the low range of stimulus intensities disappeared into the noise floor.

Further evidence implicating OHC motility-related

nonlinear charge movement as the source of distortion is derived from charge blocking experiments. Both lanthanides and salicylate blocked voltage-dependence capacitance and distortion. Figure 6 illustrates the effects of 3 mM lutetium chloride on nonlinear capacitance and distortion products. The drop in capacitance is mirrored by a decrease in all distortion components. In the case of salicylate, the reductions were reversible (*data not shown*). The correspondence between distortion prod-

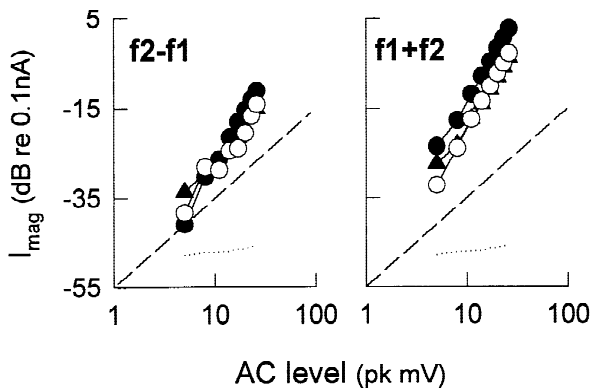


Fig. 5. Sum and difference distortion magnitude as a function of AC stimulus level. Results at three holding potentials are plotted: -60 mV, closed triangles; 0 mV, filled circles; 60 mV, open circles. Both components decrease at a rate greater than the stimulus. The dashed line illustrates a linear relationship. The dotted line is the noise floor.

ucts and nonlinear capacitance can be used to predict alterations in the Boltzmann characteristics. Figure 7 shows the utilization of $f2-f1$ phase reversal to track peak capacitance and V_{pkcm} during changes in OHC turgor pressure. As intracellular pressure is decreased, indicated by the change in OHC longitudinal strain (δz), C_m increases and V_{pkcm} shifts in the negative direction as observed previously using other techniques (Kakehata & Santos-Sacchi, 1995).

Discussion

The present results indicate that membrane-bound nonlinear charge movement, in this case due to motility voltage sensors residing in the OHC lateral membrane, can lead to distortion component generation under whole cell voltage clamp. Classical studies have used linearized impedance analysis to characterize ionic channel gating charge movement (Fishman, Moore & Ponssart, 1977; Takashima, 1978; Bezanilla et al., 1982; Fernandez, Bezanilla & Taylor, 1982). Indeed, similar analyses have been made on OHC motility-related gating charge (Santos-Sacchi, 1991). However, those studies did not evaluate distortion generation. In the OHC, single frequency voltage stimulation generates harmonic distortion and two-frequency stimulation generates combination distortion in the current responses. The largest components were at the second harmonic ($2f$), sum ($f1+f2$) and difference ($f2-f1$) frequencies, but significant responses were obtained at the more complex combination frequencies. The voltage dependence of the distortion component magnitude and phase derive from the Boltzmann characteristics of the OHC's motility-related gating charge. Thus, it was possible to track changes in V_{pkcm} , or equivalently V_h , the voltage at half-maximal charge

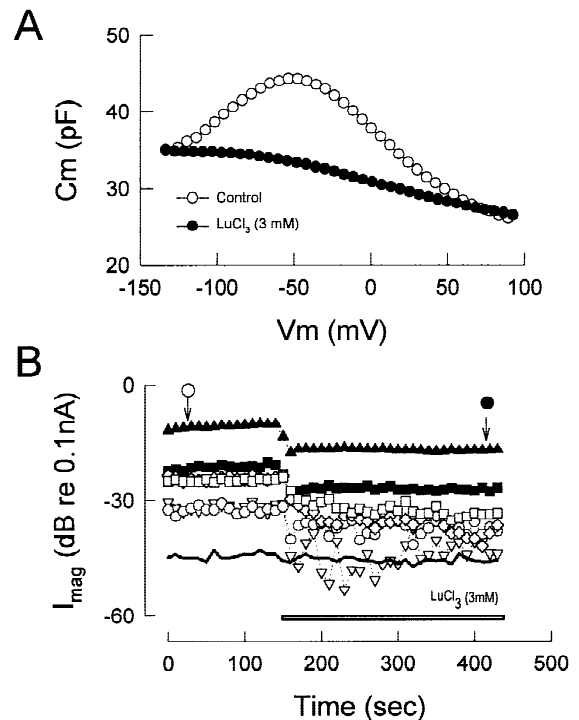


Fig. 6. Effects of charge blocking lutetium chloride on OHC capacitance and distortion. (A) Capacitance (measured with dual frequency admittance technique) of OHC before and after 3 mM LuCl_3 . Fit of control capacitance to Eq. 1 indicates V_{pkcm} : -53.3 mV; z : 0.59 ; Q_{max} : 3.68 pC; and C_{lin} : 23.4 pF. After treatment the function could not be fit reliably, however, at -60 mV nonlinear capacitance is halved by the treatment. (B) After treatment, distortion components measured at a holding potential of -60 mV were down about 6 dB (halved). Symbols are the same as in Fig. 2B.

displacement, by monitoring the phase reversal of the $f2-f1$ distortion component.

The magnitude and phase data are readily predicted from an electrical model of the OHC-patch-clamp system, which includes an electrode resistance in series with a parallel combination of membrane resistance and capacitance, the capacitance being comprised of a linear and voltage-dependent component (*see* Santos-Sacchi, 1993 for details). The voltage-dependent capacitance component is the only nonlinearity in the system. Figure 8 illustrates the response of the model to the same protocols, i.e., single- and two-frequency voltage stimulation, that we used in the experiments on OHCs and supporting cells. The fitted parameters of the two OHCs depicted in Fig. 4 were used in the model to generate the distortion components. The model response compares favorably with the biophysical data (*compare* Figs. 4 and 8), confirming that distortion magnitude minima and phase reversals result from the characteristics of the nonlinear capacitance function, or equivalently, the nonlinear $Q-V$ function. Notably, the nonlinearity in the OHC that we studied is similar to that of ionic channel gating,

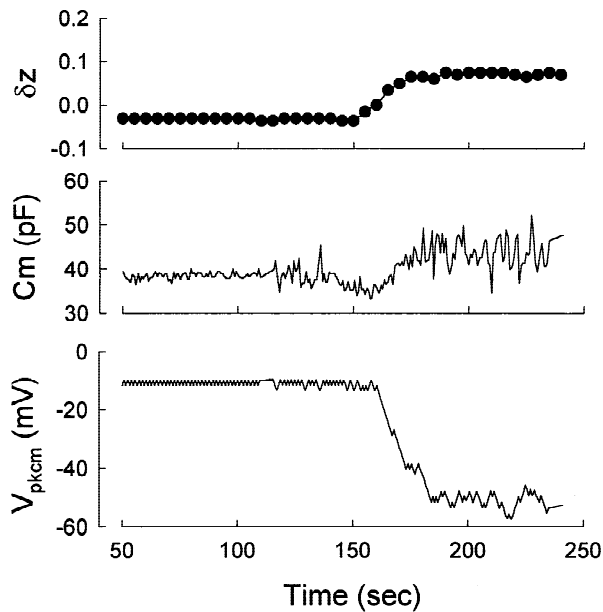


Fig. 7. Utilization of phase data to track changes in Boltzmann characteristics of OHC capacitance. The voltage at which f_2 - f_1 phase reversed (V_{pkcm}) was tracked by altering holding potential in 2 mV increments until a phase reversal occurred, whereupon holding potential was decremented until reversal occurred. The tracking process was continuous while OHC turgor pressure was altered. When turgor pressure was reduced, indicated by an increase in longitudinal strain (δz), C_m increased and V_{pkcm} shifted in the negative direction, in line with previous studies (Kakehata & Santos-Sacchi, 1995).

and therefore it is expected that channel gating will possess a distortion signature that characterizes its voltage-dependent behavior. Indeed, the small distortion components detected in supporting cells may arise from gating of ionic channels. A more selective and detailed analysis directed within an ionic channel's activation voltage range may prove more revealing.

Intermodulation distortion characteristics derived from the form of the mathematical function describing the excited nonlinearity; the magnitudes and phases of distortion are given by the Fourier expansion of the excitation products and are predictable (Dallos, 1973). In the case where a function can be expressed mathematically as a polynomial, AC distortions correspond to the order of the polynomial. Functions of quadratic order produce "quadratic distortions," namely (for dual excitation) $f_2 \pm f_1/2$, and those of cubic order produce "cubic distortions," namely, $2f_1 \pm f_2$, $2f_2 \pm f_1$. Since our data show both types of distortion, it is clear that the two-state Boltzmann function can be characterized by the sum of polynomials with even and odd orders, the relative contribution depending on the holding potential level. Thus, the distortion that we obtained empirically and verified through modeling and experimental perturbation with charge blockers is simply a consequence of the form of an OHC's Q-V function. It should be noted, however,

that memory-less characterizations such as this, as in our model, do not take into account the recently observed dependence of the Q-V function on initial voltage conditions (Santos-Sacchi et al., 1998). Thus, the slight differences between model and data may arise from this dependence.

Our data also indicate the need for caution when performing dual sinusoidal capacitance measures (Rohlicek & Rohlicek, 1993; Donnelly, 1994). Because of the large AC voltages typically used with these techniques, it is possible that distortion generated by membrane nonlinearities can interfere with capacitance measures. We used an FFT-based variation of this technique (Santos-Sacchi et al., 1998), but our signal levels were at 10 mV pk, where little distortion was generated in the OHC.

RELEVANCE TO THE AUDITORY SYSTEM

In the mammal, the range of auditory sensitivity spans greater than 100 dB. In order to process this immense range, the system response (e.g., basilar membrane amplitude) grows nonlinearly with stimulus level. As a result, distortion is generated and is the hallmark of the normal auditory system response; it is indicative of an active process that enhances the mammal's ability to detect and analyze spectral content in the environment, especially near threshold, at high acoustic frequencies (>10 kHz; see Ruggero and Santos-Sacchi (1997) for review). Damage to OHCs interferes with this process, and reduces system nonlinearities.

It is widely held that the active process involves voltage-driven mechanical responses of OHCs which provide feedback into the basilar membrane (Dallos, 1996). The molecular motors that reside in the lateral membrane of the OHC are bidirectional inasmuch as either membrane voltage or tension can evoke gating currents (Santos-Sacchi, 1991; Iwasa, 1993; Gale & Ashmore, 1994; Kakehata & Santos-Sacchi, 1995; Takahashi & Santos-Sacchi, 1998). Furthermore, the cell's voltage-dependent capacitance correlates well with its mechanical activity (Ashmore, 1989; Santos-Sacchi, 1990, 1991). It is expected, then, that nonlinear distortions that characterize the motility-related gating currents also describe concurrent mechanical responses. Indeed, harmonic mechanical responses and harmonic current responses have been observed in response to single sinusoidal stimulation of the OHC under whole cell voltage clamp (Santos-Sacchi, 1993).

Two-frequency evoked distortion components have been measured in the force of stereociliar bundles of Bullfrog saccular hair cells (Jaramillo, Markin & Hads-peth, 1993). From the bundle's resting position, AC stimulation produced distortion responses that were similar to those reported here. Sum and difference compo-

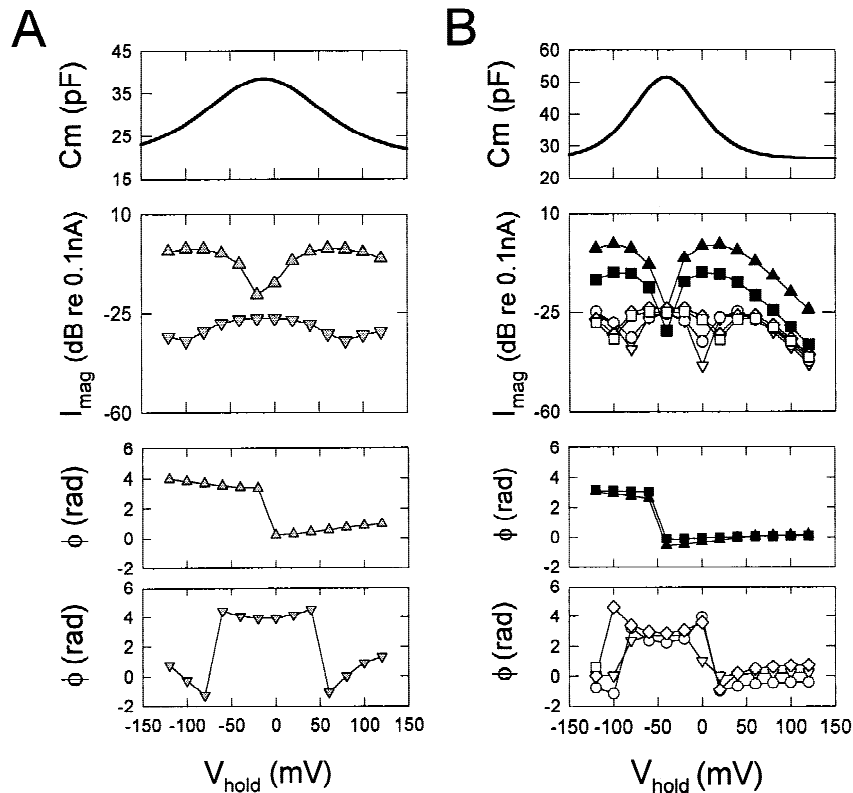


Fig. 8. Model simulation of OHCs under voltage clamp. The model consisted of an electrode resistance (R_s) in series with a parallel combination of membrane resistance (R_m) and capacitance (C_m), the capacitance being comprised of a linear (C_{lin}) and voltage-dependent component (C_v). The panels A and B correspond to those of Fig. 4, whose fitted cell parameters were used to generate the model distortion products shown here. Data were generated using the same stimulus protocols as in Fig. 4. In panel A, the membrane capacitance was modeled as in Eq. 1 with V_{pkcm} : -12.0 mV; z : 0.59; Q_{max} : 3.17 pC; and C_{lin} : 20.3 pF. R_s was 5 M Ω and R_m was 180 M Ω . In panel B, the membrane capacitance was modeled as in Eq. 1 with V_{pkcm} : -40.6 mV; z : 1.0; Q_{max} : 2.61 pC; and C_{lin} : 26.0 pF. R_s was 7 M Ω and R_m was 160 M Ω . The top panels illustrate the capacitance of each model cell, taken from Fig. 4 top panel fits. The symbols of the bottom panels show the generated distortion components as in Fig. 4. The lines simply connect the symbols. Note the similarities between model and biophysical data (Fig. 4).

nents were greatest in magnitude. It might be expected that in an analogous manner to the holding voltage manipulations reported here, stereocilia bundle biasing would produce magnitude and phase alterations in the force distortion components. Since the characteristics of OHC stereociliar bundles are basically the same as those of the lower vertebrate (Russell, Kossl & Richardson, 1992), it is expected that OHC stereocilia will likewise support distortion generation.

Despite the generation of distortion in single hair cells, significant differences exist between the characteristics of single cell distortion and distortion found in the intact auditory system. Indeed, while OHCs may ultimately underlie distortion found in the basilar membrane, inner hair cells and neural elements of the auditory system, it is unlikely that any single nonlinearity in a single hair cell can fully and simply account for the level and frequency-dependent behavior of distortion in the intact system. For example, in the basilar membrane, distortion levels decrease as the f_2/f_1 ratio is increased (Robles et al., 1997), but this ratio dependence is absent in isolated cells. One simple explanation for the *in vivo* dependence, alluded to by Robles et al. (1997) is the requirement for the two frequencies to reside within the excitation region of the cell. Thus, while delivery of disparate frequencies to single isolated cells is guaranteed experimentally, delivery to a single cell *in vivo* depends on the tuning characteristics of the basilar mem-

brane. Only when frequencies are close enough to be within the excitatory bandwidth at a given stimulus level will an OHC receive two-tone stimulation. Another difference between system and cell is that distortion *in vivo* is robust at low stimulus levels. Nonlinearities in single cells are measured and predicted to decrease precipitously as stimulus levels decrease (Santos-Sacchi, 1993). This is shown here for the sum and difference distortion components (Fig. 5), where the rate of drop in magnitude is greater than that of the stimulating frequencies. Essentially, nonlinearities vanish at very small signal levels. In this regard, it should be stressed that the stereocilia transduction (displacement to receptor potential) function has a more significant nonlinearity near threshold than does the OHC motility function, indicating that the former is more likely to underlie the generation of nonlinearities in OHC mechanical responses that impinge on the basilar membrane (Santos-Sacchi, 1993). Thus, stereocilia may dominate distortion product generation whether or not stereocilia themselves are capable of mechanically influencing the cochlear partition. It is certainly conceivable, however, that alteration in the OHC motility nonlinearity may be observable in distortion components should the stereociliar nonlinearity remain stable. That is, modifications to the OHC lateral membrane motor alone will likely influence system nonlinearities.

Finally, a difference between single cell and basilar

membrane distortion that cannot be easily explained is the difference in the magnitude of distortion components. While the simple difference and sum components (f_1+f_2 , f_2-f_1) were greatest in our single cell data, the stereociliar force production data (Jaramillo et al., 1993), and the OHC motility data (Hu et al., 1994), the greatest responses observed on the basilar membrane were the combination components, $2f_2-f_1$ and $2f_1-f_2$. Additionally, single cell distortion products were over an order of magnitude less than the stimulus frequency responses, while basilar membrane distortion could be greater — a result dependent upon tuning characteristics of the basilar membrane (Robles et al., 1997). Thus, it may be argued that the observed differences between intact system and single cell distortion call for an interaction of OHC assemblies to account for system nonlinearity characteristics. In line with this concept, we have recently shown that intact adjacent OHCs are mechanically coupled through supporting cells (Zhao & Santos-Sacchi, 1998). Furthermore, under dual voltage clamp, independent single sine wave stimulation in each cell generates combination distortion components in both cells (Zhao & Santos-Sacchi, 1999). In vivo, the extent of basilar membrane excitation distributions in the high frequency region of the cochlear can be taken to support interaction within OHC assemblies (Russell & Nilsen, 1997).

This work was supported by NIH-NIDCD grant DC00273 to JSS. We thank Margaret Mazzucco for technical help.

References

- Ashmore, J.F. 1987. A fast motile response in guinea-pig outer hair cells: the cellular basis of the cochlear amplifier. *J. Physiol.* **388**:323–347
- Ashmore, J.F. 1989. Transducer motor coupling in cochlear outer hair cells. In: *Mechanics of Hearing*. D. Kemp and J.P. Wilson, editors. pp. 107–113. Plenum Press, New York
- Bezanilla, F., Taylor, R.E., Fernandez, J.M. 1982. Distribution and kinetics of membrane dielectric polarization. I. Long-term inactivation of gating currents. *J. Gen. Physiol.* **79**:21–40
- Brownell, W.E., Bader, C.R., Bertrand, D., de Ribapierre, Y. 1985. Evoked mechanical responses of isolated cochlear outer hair cells. *Science* **227**:194–196
- Dallos, P. 1973. *The Auditory Periphery: Biophysics and Physiology*. Academic Press, New York
- Dallos, P. 1996. Overview. In: P. Dallos, A.N. Popper and R.R. Fay, editors. pp. 1–43. *The Cochlea*, Springer, New York
- Donnelly, D.F. 1994. A novel method for rapid measurement of Membrane Resistance, capacitance, and access resistance. *Biophys. J.* **66**:873–877
- Fernandez, J.M., Bezanilla, F., Taylor, R.E. 1982. Distribution and kinetics of membrane dielectric polarization. II. Frequency domain studies of gating currents. *J. Gen. Physiol.* **79**:41–67
- Fishman, H.M., Moore, L.E., Poussart, D. 1977. Asymmetry currents and admittance in squid axons. *Biophys. J.* **19**:177–183
- Gale, J.E., Ashmore, J.F. 1994. Charge displacement induced by rapid stretch in the basolateral membrane of the guinea pig OHC. *Proc. Roy. Soc. Lond. B* **255**:243–249
- Goldstein, J.L. 1967. Auditory nonlinearity. *J. Acoust. Soc. Am.* **41**:676–689
- Goldstein, J.L., Kiang, N.Y.S. 1968. Neural correlates of the aural combination tone $2f_1-f_2$. *Proc. IEEE* **56**:981–992
- Hu, X.T., Evans, B.N., He, Z.Z., Dallos, P. 1994. Distortion products in electromotile responses of isolated outer hair cells. Abstracts of the Mid-winter Meeting of the Association for Research in Otolaryngology, St. Petersburg, FL, February
- Huang, G., Santos-Sacchi, J. 1993. Mapping the distribution of the outer hair cell motility voltage sensor by electrical amputation. *Biophys. J.* **65**:2228–2236
- Iwasa, K.H. 1993. Effect of stress on the membrane capacitance of the auditory outer hair cell. *Biophys. J.* **65**:492–498
- Jaramillo, F., Markin, V.S., Hudspeth, A.J. 1993. Auditory illusions and the single hair cell. *Nature* **364**:527–529
- Kakehata, S., Santos-Sacchi, J. 1995. Membrane tension directly shifts voltage dependence of outer hair cell motility and associated gating charge. *Biophys. J.* **68**:2190–2197
- Kakehata, S., Santos-Sacchi, J. 1996. Effects of salicylate and lanthanides on outer hair cell motility and associated gating charge. *J. Neurosci.* **16**:4881–4889
- Kim, D.O., Molnar, C.E., Matthews, J.E. 1980. Cochlear mechanics: nonlinear behavior in two-tone responses as reflected in cochlear-nerve-fiber responses and in ear canal sound pressure. *J. Acoust. Soc. Am.* **67**:1704–1721
- Nuttall, A.L., Dolan, D.F. 1990. Inner hair cell responses to the $2f_1-f_2$ intermodulation distortion product. *J. Acoust. Soc. Am.* **87**:782–790
- Robles, L., Ruggero, M.A., Rich, N.C. 1991. Two-tone distortion in the basilar membrane of the cochlear. *Nature* **349**:413–414
- Robles, L., Ruggero, M.A., Rich, N.C. 1997. Two-tone distortion on the basilar membrane of the chinchilla cochlear. *J. Neurophysiol.* **77**:2385–2399
- Rohlicek, V., Rohlicek, J. 1993. Measurement of membrane capacitance and resistance of single cells using two frequencies. *Physiol. Res.* **42**:423–428
- Ruggero, M.A. 1992. Responses to sound of the basilar membrane of the mammalian cochlea. *Neurobiology* **2**:449–456
- Ruggero, M.A., Santos-Sacchi, J. 1997. Cochlear mechanics and biophysics. In: *Handbook of Acoustics*. M.J. Croker, Editor. John Wiley & Sons
- Russell, I.J., Kossel, M., Richardson, G.P. 1992. Nonlinear mechanical responses of mouse cochlear hair bundles. *Proc. Roy. Soc.* **50**:217–227
- Russell, I.J., Nilsen, K.E. 1997. The location of the cochlear amplifier: spatial representation of a single tone on the guinea pig basilar membrane. *Proc. Natl. Acad. Sci. USA* **94**:2660–2664
- Santos-Sacchi, J., Dilger, J.P. 1988. Whole cell currents and mechanical responses of isolated outer hair cells. *Hearing Res.* **35**:143–150
- Santos-Sacchi, J. 1990. Fast outer hair cell motility: how fast is fast? In: *The Mechanics and Biophysics of Hearing*. P. Dallos, C.D. Geisler, J.W. Matthews, M.A. Ruggero, and C.R. Steele, editors. pp. 69–75. Springer-Verlag, Berlin
- Santos-Sacchi, J. 1991. Reversible inhibition of voltage dependent outer hair cell motility and capacitance. *J. Neurosci.* **11**:3096–3110
- Santos-Sacchi, J. 1993. Harmonics of outer hair cell motility. *Biophys. J.* **65**:2217–2227

- Santos-Sacchi, J., Kakehata, S., Takahashi, S. 1998. The outer hair cell membrane potential directly affects the voltage dependence of motility — related gating charge. *J. Physiol.* **510**:225–235
- Takahashi, S., Santos-Sacchi, J. 1998. Tension-induced OHC gating currents are restricted to the cell's mid region. Abstracts of the Mid-winter Meeting of the Association for Research in Otolaryngology, St. Petersburg, FL, February
- Takahashi, S., Santos-Sacchi, J. 1997. Distortion product analysis of outer hair cell motility-related gating currents. Abstracts of the Mid-winter Meeting of the Association for Research in Otolaryngology, St. Petersburg, FL, February
- Takashima, S. 1978. Frequency domain analysis of asymmetry current in squid axon membrane. *Biophys. J.* **22**:115–119
- Zhao, H.B., Santos-Sacchi, J. 1998. Mechano-electrical coupling among outer hair cells of Corti's organ. *Biophys. J.* **74**:A246 (Abstr.)
- Zhao, H.B., Santos-Sacchi, J. 1999. Auditory collusion and a coupled couple of outer hair cells. *Nature (in press)*

Shin Takahashi · Joseph Santos-Sacchi

Non-uniform mapping of stress-induced, motility-related charge movement in the outer hair cell plasma membrane

Received: 21 July 2000 / Received after revision: 24 August 2000 / Accepted: 18 September 2000 / Published online: 7 November 2000
© Springer-Verlag 2000

Abstract There is a growing consensus that outer hair cell (OHC) electromotility underlies the mammalian cochlear amplifier. This voltage-dependent motility is mirrored by a gating current, which along with motility can be altered by tension applied to the cell's plasma membrane. We used localized tension application along the length of the OHC to induce gating currents from membrane microdomains; with this information we mapped the distribution of the OHC's sensitivity to membrane stress before and after disrupting the cytoskeleton with intracellular Pronase. Mechanically induced gating currents, which were susceptible to salicylate, lanthanides and turgor pressure, evidenced a bell-shaped distribution that was restricted to the lateral membrane where the electromotile response resides. After Pronase treatment, gating currents remained intact and restricted. These results confirm that the molecular motors are intrinsically and bi-directionally susceptible to voltage and tension, and provide evidence for limited mobility of OHC motors within the cell's lateral membrane.

Keywords Gating charge · Membrane capacitance · Membrane tension · Outer hair cell · Turgor pressure

Introduction

In mammals, the outer hair cell (OHC) provides mechanical feedback into the basilar membrane which enhances auditory sensitivity and frequency resolving power [7, 29]. The likely underlying cellular mechanism is a unique voltage-dependent somatic mechanical response

that can be driven at acoustic rates [3, 5, 13, 15, 31, 32]. The mechanical response of the OHC is mirrored by an electrical signature, a motility-related gating current, reminiscent of the gating currents that regulate ion channel conductance [4, 30]. This gating current or charge movement can equivalently be measured as a nonlinear, voltage-dependent capacitance whose cellular location maps to the lateral membrane along the central extent of the cylindrical OHC [19]. This is precisely where the elusive molecular motors responsible for the OHC length change reside [8]. In fact, the lateral membrane harbors, almost exclusively, those sensor/motors that drive somatic motility; voltage-dependent ionic channels are largely absent, and reside in the basal membrane [33]. Beneath the motor-containing lateral membrane lies a well-developed cortical cytoskeleton that maintains the cylindrical shape of the cell [17, 37], and may function to limit the lateral diffusion of intramembranous motors.

One of the most notable features of the OHC is its piezoelectric-like behavior; under voltage clamp, not only do voltage perturbations induce mechanical responses and associated gating currents, but mechanical perturbations of the plasma membrane can induce gating currents as well [4, 14, 21, 22, 30]. Indeed, in the intact sensory epithelium, as a consequence of mechanical coupling through supporting Deiters' cells, the mechanical activity of any one OHC can induce gating currents in adjacent OHCs [41]. The susceptibility of OHC mechanical and electrical activity to membrane stress has been surmised to arise from an action on lateral membrane sensor/motors. Here we utilize this phenomenon to assess the extent of motor activity along the longitudinal axis of the OHC. Our data show that the susceptibility to membrane stress is restricted to the same cellular region that harbors the high density of sensor/motors, confirming the hypothesis that rapid changes in OHC membrane tension induce conformational changes in the molecular sensor/motor elements that are measurable as gating charge movements. Furthermore, the nonuniform distribution that we find provides evidence for limited mobility of OHC motors within the cell's lateral membrane.

J. Santos-Sacchi (✉)
Surgery (Otolaryngology), BML 244,
Yale University School of Medicine, 333 Cedar St.,
New Haven, CT 06510, USA
Tel.: +1-203-7857566

S. Takahashi · J. Santos-Sacchi
Sections of Otolaryngology and Neurobiology,
Yale University School of Medicine,
New Haven, CT 06510, USA

Materials and methods

General preparation

Guinea pigs were overdosed with pentobarbital. The temporal bones were removed and OHCs were isolated from cochleas by gentle pipetting of the isolated top two turns of organ of Corti in Ca-free medium with collagenase (0.3 mg/ml). The cell-enriched supernatant was then transferred to a 700- μ l perfusion chamber, and the cells were permitted to settle onto the coverglass bottom. All experiments were performed at room temperature ($\approx 23^\circ\text{C}$). A Nikon Diaphot inverted microscope with Hoffmann optics was used to observe the cells during electrical recording. A modified Lebovitz medium (NaCl, 142.2 mM; KCl, 5.37 mM; CaCl_2 , 1.25 mM; MgCl_2 , 1.48 mM; HEPES, 10 mM; dextrose, 5 mM; adjusted to pH 7.2 with NaOH, and adjusted to 300 mosmol/l with dextrose) was used as the standard perfusion solution.

Electrical recordings

Cells were whole-cell voltage clamped with an Axopatch 200B amplifier (Axon Instruments, Calif., USA). Gigaohm seals were obtained at the supra-nuclear region of the OHC membrane prior to whole-cell recording. Patch electrodes had initial resistances of 3–5 M Ω , corresponding to tip sizes of approximately 1–2 μm . The series resistance typically ranged from 8 to 15 M Ω . No series resistance compensation was performed, as this interferes with admittance-based capacitance measures (see below). Pipette solutions were composed of 140 mM CsCl, 10 mM EGTA, 2 mM MgCl_2 , and 10 mM HEPES (buffered to pH 7.2 with CsOH, and adjusted to 300 mosmol/l with dextrose). In order to evaluate non-linear capacitive gating currents in the absence of confounding ionic currents, the standard perfusion solution was replaced with an ionic blocking solution following seal formation {NaCl, 100 mM; tetraethylammonium (TEA), 20 mM; CsCl, 20 mM; CoCl_2 , 2 mM; MgCl_2 , 1.48 mM; HEPES, 10 mM; dextrose, 5 mM; adjusted to pH 7.2 with NaOH, and adjusted to 300 mosmol/l with dextrose; [19, 30]}. In some cases, the extracellular solution contained 10 mM sodium salicylate (replacing NaCl). Additionally, in some cases intracellular Pronase (500 $\mu\text{g}/\text{ml}$), a wide spectrum proteolytic enzyme, was added to the pipette solution to destroy the cortical cytoskeleton [20, 22, 24, 35]. All chemicals were purchased from Sigma (USA). OHCs were held at 0 mV. Currents were recorded as averages of ten responses. Data collection and analysis were performed with a Window's based whole-cell voltage-clamp program, jClamp (<http://www.med.yale.edu/surgery/otolar/santos/jclamp.html>), utilizing a Digidata 1200 board (Axon Instruments, Calif., USA). Patch pipette pressure was modified with a syringe connected to the Teflon tubing attached to the patch pipette holder and monitored via a T-connector to a pressure monitor (WPI, Florida, USA). All experiments were video taped.

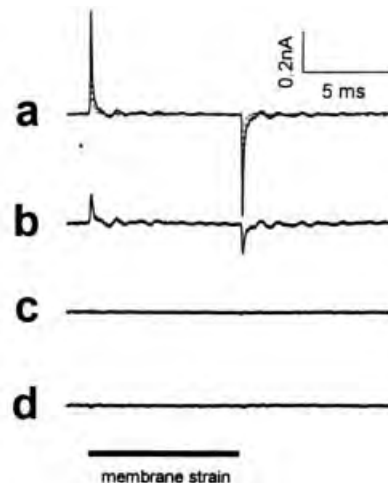
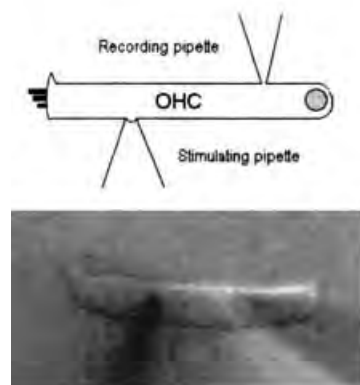
Membrane capacitance and mechanically evoked gating currents

Voltage-dependent OHC capacitance was measured with a continuous high-resolution two-sine voltage stimulus protocol (10 mV peak at both 390.6 and 781.2 Hz) [35]. Sinusoids were superimposed on voltage ramps.

Restricted regions of the OHC lateral membrane were stressed using a micropipette aspiration technique. This technique has been used extensively to study the mechanical properties of membrane, notably by Evans and associates [10]. In fact, Brownell and colleagues [25] have used it to study the mechanical properties of the OHC lateral membrane through aspiration-evoked deformation.

Aspiration was delivered through a solution-filled glass pipette fitted to a computer-controlled piezoelectric device (PZL, Burleigh Instruments, N.Y., USA) within an in-house-designed pipette holder. The pipette tip was heat polished to a final inner diameter of 2.5 μm . The pipette contained bath solution that interfaced with mineral oil in the fluid-tight, rigid plastic pipette holder. Piezoelectrically driven piston movements within the mineral oil were delivered to the pipette solution. To maintain a tight seal between the pipette tip and the cell membrane, the tip was placed on the cell surface at right angles and slight negative pressure was applied. Tip placement by the micromanipulator was visually observed, and recorded on videotape for later measurement. Membrane deformation was induced by movements of the driver's piston stepped in the negative direction (producing suction) in the range of 200 to 800 nm, controlled by the voltage magnitude delivered to the piezoelectric. For the mapping studies, one fixed voltage was used along the cell length. The spatial pattern of stress delivery along the length of the cell was random; that is, there was no particular path along the cell length that was followed. Additionally, since we found that cell collapse altered the magnitude of mechanically evoked gating currents, we maintained the cylindrical shape of the OHC with small pipette pressures for those cells

Fig. 1A–D On the *left* is a schematic and digitally captured image of isolated outer hair cell illustrating the patch pipette at the supra nuclear region and stimulating pipette. **A** Whole-cell current induced by discrete mechanical stimulation of the lateral plasma membrane. The *Solid line* depicts raw current and the *dotted line* shows the transient current artifact with the stimulating pipette off the cell. **B** Mechanically induced current obtained by subtracting current artifact from the raw current response. **C** As in **B**, except the driving piston in the stimulating pipette was absent, and consequently mechanical stimulation of the membrane was lacking. Under this condition, however, the piezoelectric driver was still activated and transient current artifacts were still generated. **D** Absence of response following the stimulation of the supporting Deiters cell membrane. *Black bar* indicates the duration of mechanical stimulus (see text)



used for mapping experiments (see [22] for details). In some cells, repeat measures were made following mapping, and responses were within 10% of initial ones, indicating that delivery of the stimulus was uniform and repeatable along the length of the cell.

Data are derived from cells in the low frequency region of the organ of Corti, 60–70 μm long. These cells were chosen over shorter, high frequency cells so that the distribution within the lateral membrane could be mapped with increased resolution over our previous electrical amputation method [19]. A particular stimulation location was binned within one of ten equally spaced (6–7 μm) regions along the cell length, providing relative measures of response distribution. Eight of those regions corresponded to the lateral membrane (see Results, and schematic of Fig. 4). If we had chosen smaller cells, the number of regions would have been smaller (given our aspiration pipette size).

Oscillations in the current response were generated by a mechanical resonance in the stimulus delivery system, as has been described previously [14]. The magnitude and frequency of the resonance depended on the piezoelectric device and pipette/membrane seal combination. Resonances around 1 kHz were observed and could be reduced by filtering the command voltage to the piezoelectric. These oscillatory currents are real motor-generated currents, and are differentiated from a concurrent electrical artifact (initial few microseconds – see Results). Such high frequency responses are not unusual since the frequency responsiveness of OHC charge movement extends into the tens of kilohertz range [15]. Membrane currents were quantified by either measuring the RMS value during the extent of the mechanical stimulus, or by integrating the current response over that same period. The latter technique was employed when under some experimental conditions exponentially decaying currents possessed minimal oscillations, so that gating charge estimates could be made. Either measure produced quantitatively similar mapping patterns.

Results

Restricted tension application evokes motility-related gating currents

Under whole-cell voltage clamp with ionic currents blocked, discrete mechanical stimulation of the OHC lateral plasma membrane evokes an initial transient followed by small oscillatory currents (Fig. 1). The piezoelectric-driven aspiration pipette that we use to apply membrane stress contributes a short-lived electrical artifact at the onset (dotted line, Fig. 1A) that is subtracted from the raw response to obtain membrane currents (Fig. 1B). In the absence of the aspiration pipette's driving piston, no membrane currents are elicited (Fig. 1C). Supporting cells do not generate membrane currents when stimulated mechanically (Fig. 1D). Digestion of the subsurface cytoskeleton with intracellular Pronase (500 $\mu\text{g}/\text{ml}$) did not abolish mechanically evoked gating currents, similar to results with voltage-induced charge movement [20].

Further evidence indicating that these discretely generated currents derive from OHC sensor/motors residing in the lateral membrane is obtained from the current's sensitivity to agents that block voltage-induced OHC motility and capacitance. Figure 2A shows that salicylate blocks the mechanically elicited membrane current. Additionally, the currents show a bell-shaped voltage dependence that is expected based on macroscopic methods of mechanical stimulation of the OHC [14, 41]. Pan-

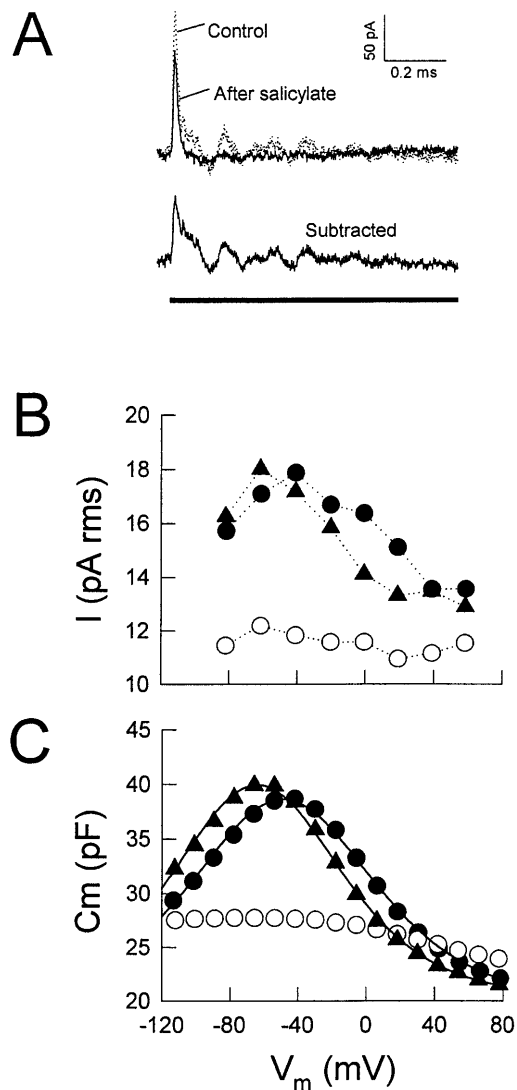


Fig. 2 **A** Dotted line illustrates the raw whole-cell current induced by discrete mechanical stimulation of the lateral plasma membrane. The solid line is the response after perfusing the cell with 10 mM salicylate. Beneath, the subtracted current represents that current sensitive to salicylate. The black bar indicates the duration of mechanical stimulus. **B** Mechanically induced gating current magnitude versus holding membrane potential. Solid circles indicate responses before salicylate (10 mM) treatment, open circles during salicylate treatment, and solid triangles following salicylate washout. **C** Corresponding membrane capacitance as a function of membrane potential. Symbols are as in **B**. Fits to the capacitance data were obtained using the following formula:

$$C_m = C_v + C_{lin} = Q_{max} \frac{zeb}{kT(1+b)^2} + C_{lin}$$

$$b = \exp\left(\frac{-ze(V_m - V_{pkcm})}{kT}\right)$$

where Q_{max} is the maximum nonlinear charge moved, V_{pkcm} is voltage at peak capacitance or half-maximal nonlinear charge transfer, V_m is membrane potential, C_{lin} is linear capacitance, z is valence, e is electron charge, k is Boltzmann's constant, and T is absolute temperature. Before salicylate – Q_{max} : 2.56 pC, V_{pkcm} : -63.7, z : 0.78, C_{lin} : 20.4; after washout – Q_{max} : 2.64 pC, V_{pkcm} : -48.8, z : 0.72, C_{lin} : 20.1. The data during salicylate treatment could not be fit reliably

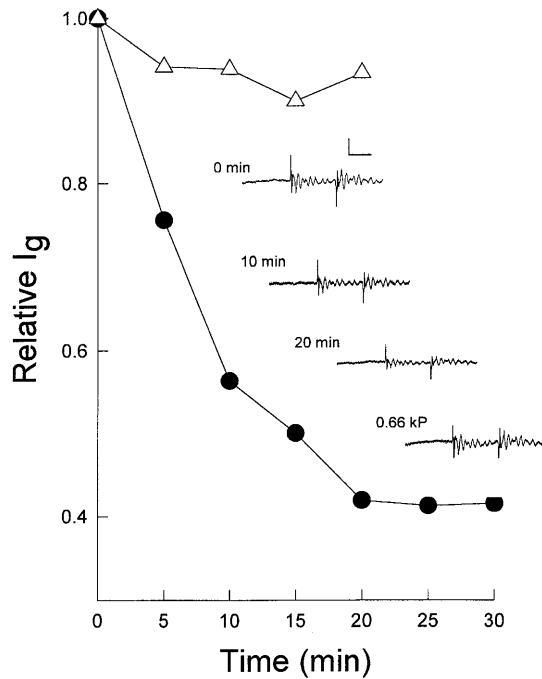


Fig. 3 Mechanically induced gating current magnitude depends on intracellular turgor pressure. Average ($n=3$) relative gating current magnitude is plotted as a function of time after establishment of whole-cell recording (filled circles). The magnitude decreases to less than half of the initial level within 20 min and remains stable after that time. Following stabilization, positive pressure delivered via the patch pipette (≈ 0.6 kPa) increased the average relative gating magnitude to 0.81. The inset depicts mechanically induced gating currents from a single cell during the course of recording. Scale 80 pA, 5 ms. In another five cells (open triangles), positive pipette pressure delivered throughout the recording period blocked the decrease in gating current magnitude

els B and C of Fig. 2 illustrate the voltage-dependent magnitude of the cell's membrane capacitance and mechanically evoked membrane currents. Each is reversibly reduced by salicylate. The shift in the voltage at peak capacitance (V_{pkcm}) evident after washout is possibly due to a reduction of OHC turgor pressure during the recording. This shift is observable in the current-voltage ($I-V$) function as well. Gating currents arise from the small area within the orifice of the stimulating pipette; this was confirmed by treatments with lutetium, a known blocker of motility and nonlinear capacitance that works solely on the extracellular aspect of the lateral plasma membrane [23]. When lutetium was placed within the solution of the stimulating pipette nearly all gating current was abolished; however, when lutetium was placed within the bath solution, gating current was little affected, since the blocking agent could not reach the mechanically activated site (data not shown).

Turgor pressure modulates gating current magnitude

The effect of turgor pressure on the mechanically elicited membrane current was studied in detail. It is known that

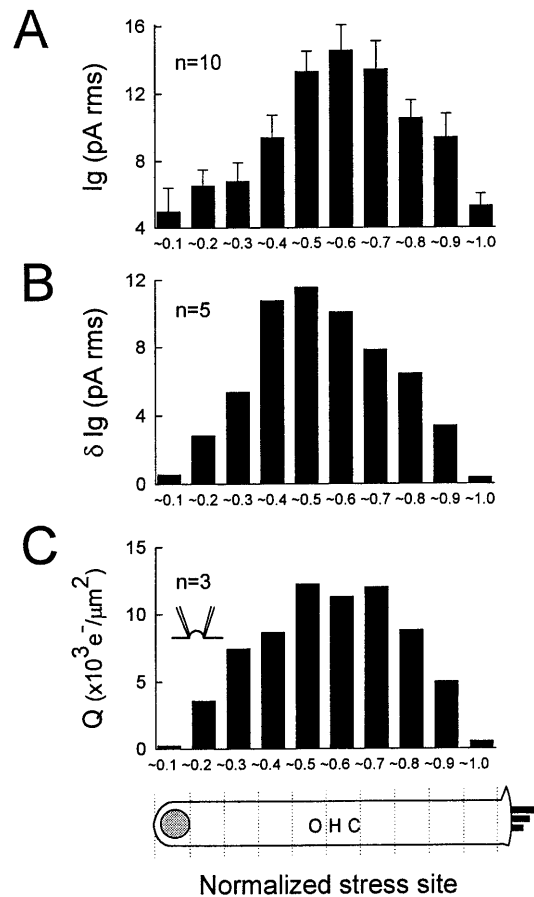
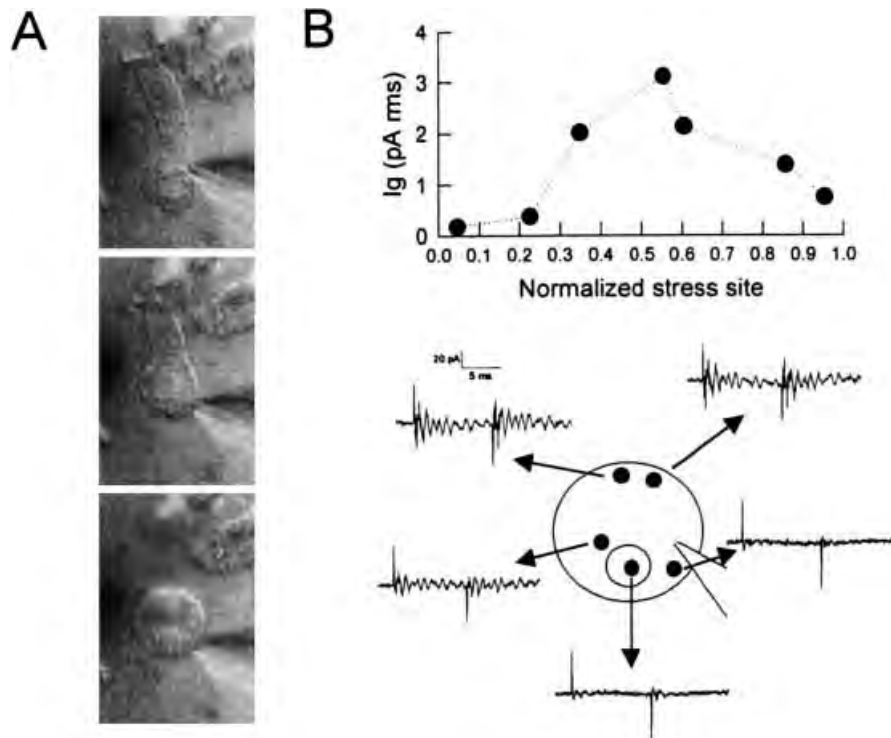


Fig. 4A–C Mechanically induced gating currents are restricted to the lateral membrane of the OHC. **A** Average (\pm SE; $n=10$) gating currents as a function of normalized stress site. **B** Five of the cells in **A** were subsequently treated with 10 mM salicylate, and the salicylate-sensitive gating current obtained through subtraction is displayed. Note minimal currents at cell extremes. **C** In three additional cells, where the exponentially decaying gating current dominated the mechanically evoked response, gating charge was determined via integration. Membrane surface area under the stimulating pipette was calculated based on tip diameter and an assumed hemispheric profile. Charge density is similar to that obtained via voltage stimulation paradigms

the intracellular pressure of the OHC dissipates following establishment of whole-cell voltage clamp [22]. During that time V_{pkcm} shifts in the negative direction and peak capacitance increases. Figure 3A shows that after the establishment of the whole-cell configuration, mechanically elicited membrane currents (filled circles) decrease in size over a time course similar to the known effects on OHC capacitance [22]. Indeed, simultaneously, V_{pkcm} shifts in the negative direction (data not shown). Applying positive pressure through the patch pipette prevents the decrease in gating current magnitude (open triangles). The current trace insets depict, for a single cell, the decrease in gating current magnitude over the course of 20 min; at that time a positive pressure of 0.66 kPa applied to the patch pipette reestablished the initial magnitude of the mechanically evoked current.

Fig. 5A, B Mechanically induced gating currents remain intact and restricted following cytoskeletal disruption. **A** Digitally captured images of an OHC during recording with Pronase-containing intracellular solution. *Top* – after 9 min; during this time control measurements were made. *Middle* – cell is beginning to form a sphere as the cytoskeleton is disrupted. *Bottom* – after 13 min the cell is fully spherical. Diameter is 24 μm . The cuticular plate is on the underside of the cell. **B** Plot shows restricted gating currents obtained while the cell was still cylindrical. The *bottom schematic* illustrates the cell after the cytoskeleton was destroyed. Gating currents were measured at the regions marked by *filled circles*. Note the absence of response over the nuclear region which was determined from video to correspond to the basal membrane



Tension-induced gating currents map to the lateral membrane in a nonuniform manner

Having confirmed that the membrane aspiration-induced currents derive from OHC motors, we used this method to map the distribution of stress sensitivity within the OHC plasma membrane. Single cells were subjected to multiple discrete mechanical stimulations along the length of the cell. Figure 4A shows the average RMS gating current magnitude along the normalized length of the OHC. The response is clearly largest in the central region of the cell, which corresponds to that region where OHC voltage-dependent capacitance and motility reside [8, 19]. Figure 4B plots the extent of the gating current that is susceptible to salicylate; negligible mechanical sensitivity resides at the extremes of the cell. In three cells it was possible to determine gating charge via integration since an exponentially decaying gating current dominated the mechanically evoked response. In Fig. 4C we plot the average gating charge density from these cases and show that the average density within the central portion of the cell membrane, about $10,000 e/\mu\text{m}^2$, is similar to the charge density obtained by voltage stimulation protocols [19].

Motor distribution is maintained following cytoskeletal disruption

Finally, we examined the effects of destroying the OHC's cortical cytoskeleton on the generation and distribution of stress-induced gating currents. In two cells we were able to perfuse intracellularly with 500 $\mu\text{g}/\text{ml}$ Pron-

ase via the patch pipette and map the distribution before and after cytoskeletal disruption. Figure 5 shows an example. Over the course of about 10–15 min, OHCs lose their cylindrical shape and form spheres (Fig. 5A) [20, 22, 24]. In the process, the cortical cytoskeleton is disrupted, leaving free plasma membrane [20]. Before disruption occurred, the cells showed typical distributions of stress-induced gating currents (Fig. 5B, top panels). Following cytoskeletal disruption, gating currents were still evoked by membrane stress, and surprisingly remained restricted in their distribution (Fig. 5B, bottom panels). Having videotaped the experiments, we were able to track and conclusively identify the cell's basal membrane as it changed shape. Over the time course of the experiments (≈ 20 –30 min), lateral diffusion of the molecular motors into the basal plasma membrane did not occur.

Discussion

The OHC is a highly partitioned cell whose sensory activity is augmented by voltage-dependent mechanical activity. OHCs possess a mechano-electrical transduction mechanism within the apical membrane – the stereociliar bundle, and synaptic machinery in the basal membrane. This basic polarization, found in all vertebrate hair cells, has evolved in the OHC, since, additionally, molecular motors responsible for the cell's electro-mechanical transduction are restricted to the lateral membrane [8, 19, 20, 24]. The membrane area comprising the cylindrical cell's lateral membrane can range up to nearly four times that of the combined apical and basal membrane

(e.g., given a 90- μm -long OHC, apical and basal surface area is estimated to be about 750 μm^2 , whereas lateral membrane area is about 2700 μm^2).

The OHC lateral plasma membrane displays an unusually dense population of tightly packed 8- to 10-nm particles that probably represent protein motors embedded in the lipid bilayer [12, 16, 24, 34]. Densities up to 6000/ μm^2 have been reported. Electrophysiological experiments similarly provide motor density estimates ranging from 2500 to 7500/ μm^2 based on voltage-induced gating charge densities from low frequency OHCs [4, 15, 19, 30]. Despite this good correspondence, we have recently shown that the correlation between ultrastructural and electrophysiological estimates of motor density may not hold for high frequency OHCs, where charge density increases more so than membrane particle density [34]. Nevertheless, all estimates clearly indicate that the molecular motors dominate the makeup of the lateral membrane. We now show that the density of mechanically induced charge movement, while not uniform, is similar to those estimates determined through whole-cell voltage stimulation. An average density of 10,000 e-/ μm^2 was found, assuming a hemispherical insertion of the membrane into the aspiration pipette. Oghalai et al. [25] have shown that upon slight suction, this type of membrane deformation is expected with an aspiration pipette of our size. Thus, the co-localization of voltage- and mechanical-sensitive charge movement to the lateral plasma membrane that we report here strongly suggests that we are observing intrinsic piezoelectric-like activity of integral membrane motors. That is, voltage and mechanical sensitivity are features of one molecular entity – the motor, and independent of cytoskeletal requirements, since cytoskeletal disruption with Pronase leaves charge movement intact.

The nonuniform distribution of stress sensitivity along the lateral membrane may arise from a true motor distribution pattern or regional differences in the efficacy of mechanical stimulation due, for example, to membrane stiffness gradients along the cell length. It is clear from the turgor results that changes in the mechanical properties of the membrane can influence the magnitude of charge movements, yet it is not obvious from ultrastructural studies that the lateral wall structure harbors such longitudinal mechanical gradients [28]. However, it is clear that abrupt mechanical changes probably arise at the apical and basal terminal borders of the subsurface cytoskeleton and cisternae that lie beneath the lateral plasma membrane. Nevertheless, the changes in charge density are clearly more gradual. Previously, we had mapped the distribution of voltage-induced charge movement using an electrical amputation technique [19]. In order to evaluate our data that were admittedly limited in spatial resolution we modeled the motor density as evenly distributed along the lateral membrane, and concluded that the apical and basal poles of the OHC were devoid of sensor / motors. While our present data confirm the virtual absence of motors in the apical and basal poles, it appears that a uniform distribution is unlikely.

This is corroborated to some extent by the findings of Zajic and Schacht [40], who showed that in response to K depolarization mechanical responses in the middle of the OHC are larger than at its apical and basal regions. We conclude that the nonuniform distribution of motors is real and must be an expression of restricted lateral mobility within the plane of the cell's plasma membrane.

The OHC's cortical cytoskeleton is extensive; structural similarities have been found between it and the peripheral cytoskeleton of other cell types, including muscle cells and red blood cells [11, 17, 24, 37]. In the red blood cell, band 3 membrane proteins are restricted in their lateral movements by interactions with the subsurface cytoskeleton (see Edidin [9] for review). Agents that disrupt the cytoskeleton can increase lateral mobility by about two orders of magnitude. In the OHC, the cortical cytoskeleton lies beneath that region of the membrane where the dense array of membrane particles resides, and it is possible that interactions with the motors restrict their diffusion to basal and apical compartments of the cell. We have evidence that protein motors are indeed able to diffuse laterally within the lateral membrane itself [36]. Utilizing microdomain photoinactivation of motor charge movements (i.e., voltage-dependent capacitance), we showed that photo exposure of dye marked OHC lateral membrane for extended periods of time irreversibly depleted whole-cell charge movement beyond that expected for an immobile population in the exposed area. Nevertheless, the present data indicate that diffusion of motors into regions normally devoid of motors, viz. the apical and basal regions, does not occur within the time frame of our experiments. For a typical diffusion coefficient of membrane protein untethered by cytoskeleton, e.g., 1 e-9 cm²/s [2], we might have expected to observe gating charge movements in the basal region after 10–20 min. For example, if we assume that the molecular motors within the Pronase-treated spherical OHC are initially restricted to one hemisphere then the time to redistribute the motors equally within the sphere would be:

$$\tau = r_o^2/2D$$

where r_o is the cell radius, and D is the diffusion coefficient [18]. With $r_o=12 \mu\text{m}$ (Fig. 5A), and $D=1\text{e-}9 \text{ cm}^2/\text{s}$, we obtain τ of about 12 min. Clearly, this redistribution did not occur. In fact, τ is an overestimate since the motors in our treated cells occupy far greater than 50% of the membrane surface area. Furthermore, motors would only need to diffuse a few microns in order to occupy the basal membrane. It is not unusual for mobilities to vary within different membrane microdomains. For example, voltage-gated Na channels in neuronal soma diffuse more readily than in the axon hillock (one to two orders of magnitude difference in diffusion coefficients) [2]. Indeed, there is a barrier to the diffusion of Na channels between the two regions of neuronal membrane. Tethering by ankyrin probably plays a role in clustering Na channels at the axon hillock [43], and, interestingly, Winckler et al. [39] suggest that this type of interaction

between membrane protein and the cytoskeleton provides a diffusion barrier for other membrane proteins in the neuron as well. Our data, however, suggest that this type of cytoskeletal barrier is not acting to limit the diffusion of lateral membrane motors into the basal membrane region. The story may be different for voltage-gated ion channels that are restricted to the basal membrane of the OHC [32]. Though it cannot be dismissed that their clustering relies on cytoskeletal elements, as do Na channels, the highly organized nature of the subsurface cytoskeleton found in the lateral membrane is absent in the basal membrane. One further means of restricting ionic channel movements to the basal membrane could arise from the high density of molecular motors within the lateral membrane, which would effectively provide a barrier to diffusion into the motor region from the basal membrane. Indeed, the high density may also limit lateral diffusion within the lateral membrane itself. Recently, Oghalai et al. [26, 27] have shown that lipid mobility in the lateral membrane is quantitatively similar to that of other cell types but is dependent upon membrane voltage and tension, as might be expected if the state of the molecular motors, in addition to their density, were influential.

The susceptibility of mechanically induced gating currents to salicylate is understandable since the drug is capable of blocking the OHC's voltage-dependent charge movement (or capacitance) within seconds of application [23, 38]; a mechanically induced shift of the charge-voltage ($Q-V$) function along the voltage axis is thought to give rise to mechanically induced gating currents [14, 22, 41]. Indeed, for this reason, the mechanically evoked currents possess a bell-shaped voltage dependency. However, while some common characteristics of mechanically and voltage-evoked gating currents, e.g., block by salicylate and lanthanides, are readily explainable, the effect of cell turgor on mechanically evoked gating current magnitude is not simply explained, and deserves some discussion. OHCs normally possess a positive intracellular pressure that helps maintain the cylindrical shape of the cell [6]. Steady state decreases in OHC turgor pressure cause negative dc shifts of the $Q-V$ or capacitance function along the voltage axis until a limiting V_{pkcm} , near -70 mV, is attained [22]. At that point, tension changes have little effect on V_{pkcm} . This phenomenon may play a role in reducing mechanically generated gating currents when the cell is collapsed from its cylindrical shape; however, from our data it appears that mechanically evoked gating currents are reduced in a graded fashion as intracellular pressure is decreased. Even more confounding is the observation that Q_{max} derived from voltage stimulation appears to *decrease* as intracellular pressure is *increased* [14, 22] until, under extreme conditions, charge movement can be blocked substantially [1]. Of course, these findings might suggest an opposite result from what we found. It should be noted, however, that the changes in turgor pressure that we encountered amount to changes of less than 1 kPa, and, within that range, with an intact cytoskeleton, quite

small changes in Q_{max} are expected [22]. Finally, it may simply be that the efficacy of a given stimulus delivered to the membrane patch under the stimulating pipette depends on the degree of resting membrane tension. This might occur if membrane deformation or bending were the effective stimulus. In this regard, we have suggested that after cytoskeletal destruction, the membrane is more sensitive to turgor pressure, as though the cytoskeleton were impeding membrane deformation [22]. This is borne out by independent studies on the stiffness of the OHC lateral wall (combination of the plasma membrane, cortical cytoskeleton and subsurface cisternae) [25], where the component stiffness of the lateral membrane was found to be less than that of the combined cytoskeleton and subsurface cisternae. We can also conclude from these data of Oghalai et al. [25] that our small deformations of the intact lateral wall would not have independently stimulated the lateral membrane, in contrast to the case following Pronase treatment.

The co-localization of a bi-directional voltage/mechanical sensitivity to the lateral plasma membrane underscores an intrinsic feedback mechanism that exists not only within single OHCs but also among OHCs residing within the normally functioning organ of Corti [41]. Just as the motor is restricted to one region of the OHC, the cellular expression of the motor is restricted to only one hair cell type in the mammalian sensory epithelium, viz the OHC. Recently, Dallos and coworkers [42] have identified a protein unique to the OHC which when expressed in nonauditory cells bears the mechanical and electrical signatures of the OHC motor. From this discovery, we can expect more detailed examinations and understanding of the mechanisms responsible for the segregation and mobility of this unique protein within the OHC plasma membrane.

Acknowledgements This work was supported by NIH-NIDCD grant DC00273 to J.S.S. We thank Margaret Mazzucco for technical help.

References

1. Adachi M, Iwasa KH (1999) Electrically driven motor in the outer hair cell: effect of a mechanical constraint. *Proc Natl Acad Sci USA* 96:7244–7249
2. Angelides KJ, Elmer LW, Loftus D, Elson E (1988) Distribution and lateral mobility of voltage-dependent sodium channels in neurons [published erratum appears in *J Cell Biol* 1989 May 108(5): preceding 2001]. *J Cell Biol* 106:1911–1925
3. Ashmore JF (1987) A fast motile response in guinea-pig outer hair cells: the cellular basis of the cochlear amplifier. *J Physiol (Lond)* 388:323–347
4. Ashmore JF (1989) Transducer motor coupling in cochlear outer hair cells. In: Kemp D, Wilson JP (eds) *Mechanics of hearing*. Plenum, New York, pp 107–113
5. Brownell WE, Bader CR, Bertrand D, de Ribaupierre Y (1985) Evoked mechanical responses of isolated cochlear outer hair cells. *Science* 227:194–196
6. Chertoff ME, Brownell WE (1994) Characterization of cochlear outer hair cell turgor. *Am J Physiol* 266:C467–C479
7. Dallos P (1996) Overview: cochlear neurobiology. In: Dallos P, Popper A, Fay R (eds) *The cochlea*. Springer, Berlin Heidelberg New York, pp 1–43

8. Dallos P, Evans BN, Hallworth R (1991) Nature of the motor element in electrokinetic shape changes of cochlear outer hair cells. *Nature* 350:155–157
9. Edidin M (1987) Rotational and lateral diffusion of membrane proteins and lipids: phenomena and function. *Curr Topics Membr Transp* 29:91–127
10. Evans EA (1973) New membrane concept applied to the analysis of fluid shear- and micropipette-deformed red blood cells. *Biophys J* 13:941–954
11. Flock A, Flock B, Ulfendahl M (1986) Mechanisms of movement in outer hair cells and a possible structural basis. *Arch Otorhinolaryngol* 243:83–90
12. Forge A (1991) Structural features of the lateral walls in mammalian cochlear outer hair cells. *Cell Tissue Res* 265:473–483
13. Frank G, Hemmert W, Gummer AW (1999) Limiting dynamics of high-frequency electromechanical transduction of outer hair cells. *Proc Natl Acad Sci USA* 96:4420–4425
14. Gale JE, Ashmore JF (1994) Charge displacement induced by rapid stretch in the basolateral membrane of the guinea-pig outer hair cell. *Proc R Soc Lond B Biol Sci* 255:243–249
15. Gale JE, Ashmore JF (1997) An intrinsic frequency limit to the cochlear amplifier. *Nature* 389:63–66
16. Gulley RS, Reese TS (1977) Regional specialization of the hair cell plasmalemma in the organ of Corti. *Anat Rec* 189:109–124
17. Holley MC, Ashmore JF (1988) A cytoskeletal spring in cochlear outer hair cells. *Nature* 335:635–637
18. Huang HW (1973) Mobility and diffusion in the plane of cell membrane. *J Theor Biol* 40:11–17
19. Huang G, Santos-Sacchi J (1993) Mapping the distribution of the outer hair cell motility voltage sensor by electrical amputation. *Biophys J* 65:2228–2236
20. Huang G, Santos-Sacchi J (1994) Motility voltage sensor of the outer hair cell resides within the lateral plasma membrane. *Proc Natl Acad Sci USA* 91:12268–12272
21. Iwasa KH (1993) Effect of stress on the membrane capacitance of the auditory outer hair cell. *Biophys J* 65:492–498
22. Kakehata S, Santos-Sacchi J (1995) Membrane tension directly shifts voltage dependence of outer hair cell motility and associated gating charge. *Biophys J* 68:2190–2197
23. Kakehata S, Santos-Sacchi J (1996) Effects of salicylate and lanthanides on outer hair cell motility and associated gating charge. *J Neurosci* 16:4881–4889
24. Kalinec F, Holley MC, Iwasa KH, Lim DJ, Kachar B (1992) A membrane-based force generation mechanism in auditory sensory cells. *Proc Natl Acad Sci USA* 89:8671–8675
25. Oghalai JS, Patel AA, Nakagawa T, Brownell WE (1998) Fluorescence-imaged microdeformation of the outer hair cell lateral wall. *J Neurosci* 18:48–58
26. Oghalai JS, Tran TD, Raphael RM, Nakagawa T, Brownell WE (1999) Transverse and lateral mobility in outer hair cell lateral wall membranes. *Hear Res* 135:19–28
27. Oghalai JS, Zhao HB, Kutz JW, Brownell WE (2000) Voltage- and tension-dependent lipid mobility in the outer hair cell plasma membrane. *Science* 287:658–661
28. Pollice PA, Brownell WE (1993) Characterization of the outer hair cell's lateral wall membranes. *Hear Res* 70:187–196
29. Ruggero MA, Rich NC (1991) Furosemide alters organ of corti mechanics: evidence for feedback of outer hair cells upon the basilar membrane. *J Neurosci* 11:1057–1067
30. Santos-Sacchi J (1991) Reversible inhibition of voltage-dependent outer hair cell motility and capacitance. *J Neurosci* 11:3096–3110
31. Santos-Sacchi J (1992) On the frequency limit and phase of outer hair cell motility: effects of the membrane filter. *J Neurosci* 12:1906–1916
32. Santos-Sacchi J, Dilger JP (1988) Whole cell currents and mechanical responses of isolated outer hair cells. *Hear Res* 35:143–150
33. Santos-Sacchi J, Huang GJ, Wu M (1997) Mapping the distribution of outer hair cell voltage-dependent conductances by electrical amputation. *Biophys J* 73:1424–1429
34. Santos-Sacchi J, Kakehata S, Kikuchi T, Katori Y, Takasaka T (1998) Density of motility-related charge in the outer hair cell of the guinea pig is inversely related to best frequency. *Neurosci Lett* 256:155–158
35. Santos-Sacchi J, Kakehata S, Takahashi S (1998) Effects of membrane potential on the voltage dependence of motility-related charge in outer hair cells of the guinea-pig. *J Physiol (Lond)* 510:225–235
36. Santos-Sacchi J, Zhao HB (1999) Green card motors: OHC lateral membrane molecular motors may travel. Midwinter Meeting of the Association for Research in Otolaryngology
37. Tolomeo JA, Steele CR, Holley MC (1996) Mechanical properties of the lateral cortex of mammalian auditory outer hair cells. *Biophys J* 71:421–429
38. Tunstall MJ, Gale JE, Ashmore JF (1995) Action of salicylate on membrane capacitance of outer hair cells from the guinea-pig cochlea. *J Physiol (Lond)* 485:739–752
39. Winckler B, Forscher P, Mellman I (1999) A diffusion barrier maintains distribution of membrane proteins in polarized neurons [see comments]. *Nature* 397:698–701
40. Zajic G, Schacht J (1991) Shape changes in isolated outer hair cells: measurements with attached microspheres. *Hear Res* 52:407–410
41. Zhao HB, Santos-Sacchi J (1999) Auditory collusion and a coupled couple of outer hair cells. *Nature* 399:359–362
42. Zheng J, Shen W, He D, Long K, Madison L, Dallos P (2000) Prestin is the motor protein of cochlear outer hair cells. *Nature* 405:149–155
43. Zhou D, Lambert S, Malen PL, Carpenter S, Boland LM, Bennett V (1998) AnkyrinG is required for clustering of voltage-gated Na channels at axon initial segments and for normal action potential firing. *J Cell Biol* 143:1295–1304

ORIGINAL RESEARCH COMMUNICATION

Novel Role of the Mitochondrial Protein Fus1 in Protection from Premature Hearing Loss *via* Regulation of Oxidative Stress and Nutrient and Energy Sensing Pathways in the Inner Ear

Winston J.T. Tan,^{1,*} Lei Song,^{2-4,*} Morven Graham,⁵ Amy Schettino,⁶ Dhasakumar Navaratnam,^{7,8} Wendell G. Yarbrough,^{1,9} Joseph Santos-Sacchi,^{1,8,10} and Alla V. Ivanova¹

Abstract

Aims: Acquired hearing loss is a worldwide epidemic that affects all ages. It is multifactorial in etiology with poorly characterized molecular mechanisms. Mitochondria are critical components in hearing. Here, we aimed to identify the mechanisms of mitochondria-dependent hearing loss using Fus1 KO mice, our novel model of mitochondrial dysfunction/oxidative stress.

Results: Using auditory brainstem responses (ABRs), we characterized the Fus1 KO mouse as a novel, clinically relevant model of age-related hearing loss (ARHL) of metabolic etiology. We demonstrated early decline of the endocochlear potential (EP) that may occur due to severe mitochondrial and vascular pathologies in the Fus1 KO cochlear stria vascularis. We showed that pathological alterations in antioxidant (AO) and nutrient and energy sensing pathways (mTOR and PTEN/AKT) occur in cochleae of young Fus1 KO mice before major hearing loss. Importantly, short-term AO treatment corrected pathological molecular changes, while longer AO treatment restored EP, improved ABR parameters, restored mitochondrial structure, and delayed the development of hearing loss in the aging mouse.

Innovation: Currently, no molecular mechanisms linked to metabolic ARHL have been identified. We established pathological and molecular mechanisms that link the disease to mitochondrial dysfunction and oxidative stress.

Conclusion: Since chronic mitochondrial dysfunction is common in many patients, it could lead to developing hearing loss that can be alleviated/rescued by AO treatment. Our study creates a framework for clinical trials and introduces the Fus1 KO model as a powerful platform for developing novel therapeutic strategies to prevent/delay hearing loss associated with mitochondrial dysfunction. *Antioxid. Redox Signal.* 27, 489–509.

Keywords: Fus1/Tusc2, age-related hearing loss, stria vascularis, spiral ganglion neurons, mitochondria, antioxidants

¹Department of Surgery, Section of Otolaryngology, Yale University School of Medicine, New Haven, Connecticut.

²Department of Otolaryngology-Head and Neck Surgery, Ninth People's Hospital, Shanghai Jiao Tong University School of Medicine, Shanghai, China.

³Ear Institute, Shanghai Jiao Tong University School of Medicine, Shanghai, China.

⁴Shanghai Key Laboratory of Translational Medicine on Ear and Nose Diseases, Shanghai, China.

⁵CCMI EM Core Facility, Yale University School of Medicine, New Haven, Connecticut.

⁶Yale School of Medicine, New Haven, Connecticut.

Departments of ⁷Neurology, ⁸Neuroscience, ⁹Pathology, and ¹⁰Cellular and Molecular Physiology, Yale University School of Medicine, New Haven, Connecticut.

*These authors contributed equally to this work.

Innovation

Age-related hearing loss is a serious health problem with few efficient therapies due to its multifactorial etiology and poorly characterized molecular mechanisms. We present evidence that mitochondrial dysfunction/oxidative stress, often associated with inflammatory or mitochondrial diseases, result in a special type of progressive hearing loss manifested by mitochondrial and vascular degeneration in the cochlear stria vascularis, a decrease in endocochlear potential, and early alterations in aging-associated molecular pathways in the inner ear. Remarkably, antioxidant supplementation corrects these electrophysiological, mitochondrial, and molecular pathologies resulting in a significant delay in hearing decline and suggesting approaches to alleviate this type of hearing loss.

Introduction

ACCORDING TO THE World Health Organization (WHO), 360 million people worldwide live with disabling hearing loss (www.who.int/mediacentre/factsheets/fs300/en). The prevalence of hearing loss increases with age; thus, in children it is 1.7%, in adults aged 15 years or more it is about 7%, and it rapidly increases to almost one in three in adults older than 65 years (www.who.int/pbd/deafness/estimates/en). Besides aging (32), a number of other risk factors have been identified, including noise exposure (27, 28, 60, 74), ototoxic drugs (57), hypertension (1), diabetes (26), and smoking (10).

Unrecognized or untreated hearing loss results in widespread effects from difficulties in communicating, and affects productivity and quality of life. It may lead to social isolation, depression, and cognitive decline (2). Uncovering and detailed characterization of the mechanisms of premature hearing decline would provide a foundation for tailored prevention or treatment plans based on “individual broken systems.”

One of the critical components of hearing function is mitochondrial health. The mitochondrion is a versatile energy-producing organelle that regulates vital cellular processes, such as metabolism, calcium and redox signaling, and apoptosis. Mitochondrial involvement in auditory function was recognized by hearing impairment in many patients with mitochondrial diseases and *via* identification of mutations in mitochondrial DNA in patients with maternally inherited deafness (12). Mitochondrial dysfunction-mediated hearing impairment can be inborn or progressive when induced by aminoglycosides, sound exposure, or aging.

Mitochondria contain more than 1500 proteins, but only 14 are encoded by mitochondrial DNA while the rest are nuclear encoded (33). Therefore, one would expect that abnormal activities/loss of many of these mitochondria-residing proteins could affect hearing. However, the significance of nuclear-encoded mitochondrial proteins in hearing is poorly understood with only several hearing loss-linked mutations characterized in humans (73, 17).

In mice, the most extensively studied model is the so-called mtDNA-mutator mouse bearing a mutation in the mitochondrial polymerase gene (Polg) (69) that exhibits a significant elevation of auditory brainstem response (ABR) thresholds at low to middle frequencies by 9–10 months of

age (63). Two other mouse models that lack the antioxidant (AO) enzymes, Gpx1 or Sod1, show enhanced susceptibility to noise-induced hearing loss (45). Scavenging of mitochondrial reactive oxygen species (ROS) by targeting an AO protein catalase to mitochondria in MCAT transgenic mice alleviates hearing loss in aging MCAT mice compared to age-matched WT mice (58, 59).

Recently, our group characterized a transgenic mouse strain that robustly overexpresses the mitochondrial methyltransferase TFB1M (Tg-mtTFB1 mice) and exhibits progressive hearing loss most likely of strial etiology; however, no obvious signs of strial atrophy were detected. Hearing loss in this model was rescued by genetically reducing AMPK α 1 activity (38). While these few models provide strong evidence that mitochondria and mitochondria-generated ROS play essential roles in progressive hearing loss, additional mouse models are required to characterize the spectrum of auditory system pathologies inflicted by mitochondrial dysfunction-induced oxidative stress and inflammation.

Our early studies showed that mitochondrial dysfunction and oxidative stress are the primary pathogenic mechanisms in Fus1-deficient cells and mice. In our KO model (22), loss of mitochondrial protein Fus1 profoundly affects several mitochondrial parameters, such as ROS production, calcium uptake, mitochondrial membrane potential (MMP), respiratory reserve, and mitochondrial fusion (70, 71). As we demonstrated, the perturbed mitochondrial homeostasis/oxidative stress in Fus1 KO mice affect steady-state mitochondrial activities and severely compromise stress response on exposure to asbestos, radiation, infection, or immune stimulation (20, 70, 71, 76). Therefore, we hypothesized that Fus1 KO mice may experience either an inborn hearing defect or develop early progressive age-related hearing loss (ARHL) and that this pathology may be alleviated by improving the redox state in the cochlea.

Here, we established that Fus1 KO mice suffer from the least characterized type of ARHL of strial origin, making this model a valuable tool for studying mitochondrial/oxidative mechanisms of age-related hearing decline. Using this model, we establish and characterize in detail the phenotypic manifestations of premature hearing loss of strial etiology based on Fus1 loss-mediated mitochondrial dysfunction, and identify the target cells and tissues in the inner ear that are most vulnerable to such dysfunction. We also identify molecular pathways responsible for early hearing loss, and explore an AO approach to slow down hearing loss and development of molecular defects in cochlear tissues associated with mitochondrial dysfunction/oxidative stress.

Results

Fus1 KO mice show early-onset progressive hearing loss

Our earlier studies showed that Fus1 KO cells and tissues are characterized with high levels of ROS and insufficient AO machinery (70, 71, 77). Considering the detrimental effects of oxidative stress on hearing (19), we hypothesized that Fus1 KO mice may have progressive hearing loss. We used ABRs to measure hearing levels in Fus1 WT and KO mice of different ages. We found that while young 2-month-old KO mice had similar hearing thresholds to WT mice at middle

frequencies, and slightly elevated thresholds at low and high frequencies (Fig. 1A), 4–5-month-old KO mice had moderately elevated thresholds over the 2–32 kHz frequency range, and 8–10-month-old KO mice had substantial threshold elevations of up to 50 dB across all frequencies. Hearing de-

cline continued further in 12–13-month-old KO mice (Fig. 1A). Age-matched WT mice over the same time period showed no significant changes in thresholds at middle frequencies and a slight threshold elevation at high and low frequencies (Fig. 1B). Hearing decline in WT mice was slow

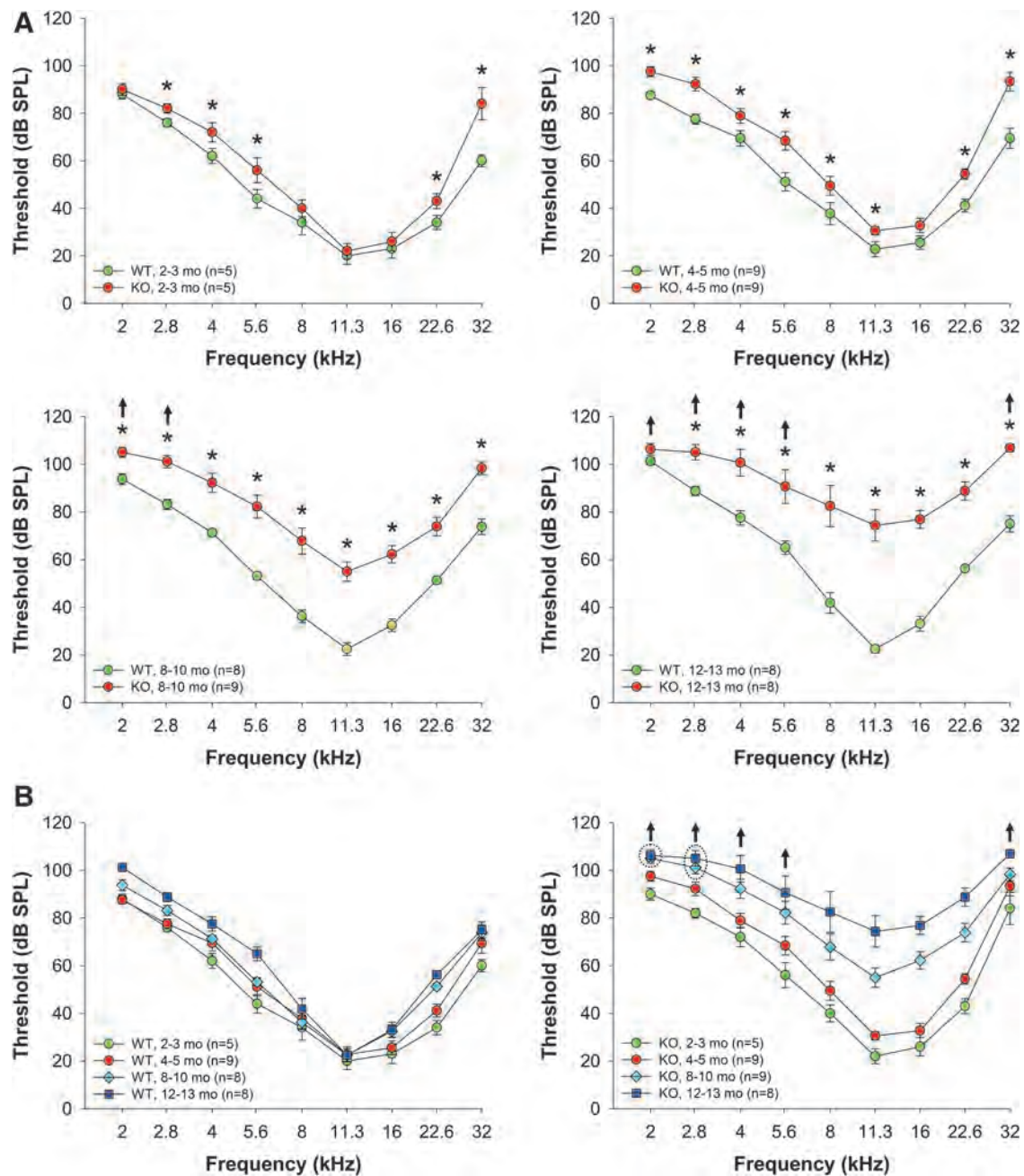


FIG. 1. Age-related changes in hearing thresholds in WT and *Fus1* KO mice. (A) The graphs illustrate hearing thresholds (dB SPL) defined *via* measuring ABRs in WT (green circles) and *Fus1* KO (red circles) mice of different age groups. Fast dynamics of progressive hearing loss is observed in *Fus1* KO mice, which have similar thresholds to WT mice at 2 months of age, significant moderate threshold elevations compared to WT mice at 4–5 months of age, and drastically elevated thresholds at 8–10 months of age. Hearing sensitivity further declined in 12–13-month-old KO mice. (B) The graphs illustrate age-dependent threshold changes in WT and *Fus1* KO mice. In contrast to KO mice, WT mice showed no significant changes in thresholds at midfrequencies with age and only a slight threshold increase at low and high frequencies. Data presented as mean \pm SEM. * $p < 0.05$ (Student's *t*-test, unpaired). \uparrow These data points include mice that showed no response at 110 dB SPL, the upper limit of the ABR recording. Number of mice with “no response” thresholds: 8–10-month-old KO mice at 2 kHz = 2, 2.8 kHz = 1; 12–13-month-old KO mice at 2 kHz = 6, 2.8 kHz = 5, 4 kHz = 2, 5.6 kHz = 1, 32 kHz = 3. ABR, auditory brainstem response. To see this illustration in color, the reader is referred to the online version of this article at www.liebertpub.com/ars

and even 15–18-month-old WT mice had much better hearing than 8-month-old KO mice. Thus, systemic loss of *Fus1* affects hearing at all frequencies starting from 4 to 5 months of age and results in rapid progression of hearing loss thereafter.

Young Fus1 KO mice have robust ABR wave I amplitude that rapidly diminishes with age

Amplitudes and latencies of the initial four ABR waves were analyzed. These waves are the response to 3 ms pips that represent sequential temporal events along the auditory ascending pathway. The amplitude of the waves reflects the number of activated neurons and synchrony of firing, while latency, the elapsed time from sound delivery, reflects the timing of synaptic transmission and nerve conduction. Amplitude and latency analysis of the ABR waves provides information on the integrity of auditory periphery and brainstem pathways. In humans, aging substantially reduces the amplitudes of all principal ABR waves producing significant latency shifts in waves I and III (25).

We compared ABR wave latencies and amplitudes in cohorts of 2- and 8–10-month-old WT and KO mice (Fig. 2). In young WT and KO mice, wave I latencies were similar at the majority of sound levels (Fig. 2B). Strikingly, in 8–10-month-old *Fus1* KO mice, wave I latencies were profoundly delayed with the largest difference at 65–70 dB SPL (sound pressure level) (Fig. 2A).

Interestingly, in young KO mice, wave I amplitude tended to be higher than in WT mice at all analyzed sound intensities and was significantly higher at 60–80 dB SPL (Fig. 2B). However, with age, wave I amplitude became profoundly lower in *Fus1* KO mice (Fig. 2A, B), consistent with the correlation between hearing loss and decrease in wave I amplitude in humans (25). Figure 2C shows further deterioration of wave I parameters along with profound interindividual heterogeneity reflecting variations in the onset of ARHL in 12–13-month-old KO mice. Note that age-matched WT mice still show normal wave I parameters and low interindividual heterogeneity.

Latencies and amplitudes of waves II–IV in *Fus1* KO mice were similar to wave I patterns (Supplementary Fig. S1; Supplementary Data are available online at www.liebertpub.com/ars).

Thus, analysis of the adult *Fus1* KO ABR waveforms reveals profound early changes in the integrity of auditory periphery and brainstem pathways similar to the changes that occur in aged people. These data are consistent with premature aging of the auditory system in *Fus1* KO mice.

Signs of chronic inflammation in the inner ear of aging Fus1 KO mice

In our early studies, we established that *Fus1* loss results in augmented/skewed innate and adaptive inflammatory responses, suggesting a preactivated state of the immune cells in KO mice (20, 70). Thus, we hypothesized that *Fus1* KO mice may have low-grade chronic inflammation in cochlear tissues and surroundings that could affect auditory performance.

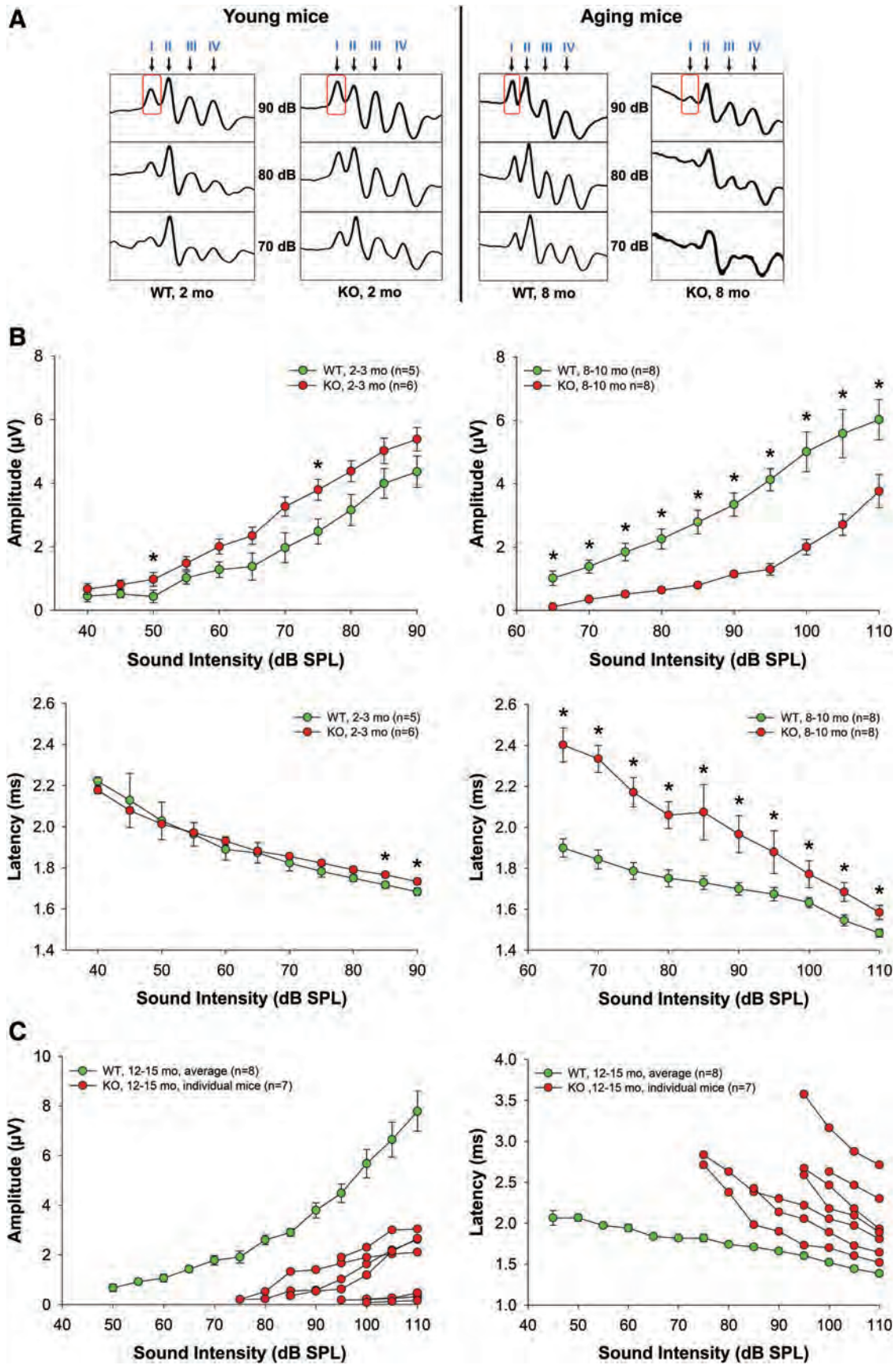
Indeed, hematoxylin and eosin (H&E) staining of bone marrow (BM) cells in the temporal bone surrounding the cochlea showed that in older KO mice, the BM is more hypercellular and myeloid predominant than in age-matched WT mice (Fig. 3A, lower panel). This type of BM histology is often observed in patients with low-grade chronic inflammation that results in an increased systemic level of inflammatory cytokines (68). Staining of BM with Iba-1, a microglia/macrophage-specific calcium-binding protein up-regulated during macrophage activation, confirmed this finding (Fig. 3B, upper panel). BM from temporal bones of young WT and KO mice was phenotypically indistinguishable, suggesting that development of this pathology is age dependent. Staining of cochlear tissues with Iba-1 revealed that the number of activated cochlear macrophages is also higher in KO mice supporting the hypothesis of chronic inflammatory processes in the aging *Fus1* KO cochlea (Fig. 3B, lower panel).

Aging KO mice with severe hearing loss have slight or no changes in auditory sensory and neuronal cell counts but showed reduced number of inner hair cell synapses and type IV fibrocytes in the cochlea

We investigated morphological changes of three major cochlear cell types that could have major effects on hearing: outer hair cells (OHCs), inner hair cells (IHCs), and spiral ganglion neurons (SGNs). Hair cells are the sensory receptors of the mammalian auditory system located within the organ of Corti. The spiral ganglion is a group of nerve cells that receive inputs from hair cells and serve to transfer these signals to auditory brainstem nuclei. Damage to any of these cells results in decreased hearing sensitivity, and because regeneration is absent, this damage is permanent (15, 42, 60).

For IHC and OHC counts, we stained the organ of Corti dissected from the cochleae of 11-month-old mice using the nuclear dye DAPI. Nuclei with uniform size, shape, and staining intensity are characteristic of healthy inner and OHCs (Fig. 3C). Despite the considerable hearing loss in KO mice, both WT and KO mice had mostly intact inner and

FIG. 2. ABR wave I amplitudes and latencies in young (2 months) and old (8–10 months) WT and *Fus1* KO mice at 16 kHz. (A) A schematic of representative ABR waveforms in aging *Fus1* KO mice showing rapid deterioration in wave amplitudes (wave I obtained at 90 dB is boxed for easier comparison) (B) The graphs illustrate the amplitudes (μV , microvolts) and latencies (ms, milliseconds) of ABR wave I as a function of sound intensity (dB SPL) at 16 kHz in young and old WT (green circles) and *Fus1* KO (red circles) mice. At 2 months of age, amplitudes were higher in KO than in WT mice, however, this was reversed at 8–10 months with KO mice having significantly lower amplitudes. Latencies were similar in young WT and KO mice, but were significantly delayed in old KO mice compared with WT mice. The other ABR waves (II, III, and IV) displayed similar changes (data presented in Supplementary Fig. S1). (C) The graphs illustrate prominent interindividual heterogeneity in wave I amplitudes and latencies in old *Fus1* KO mice (red circles). Data for age-matched WT mice (green circles) are averaged with no prominent heterogeneity at the analyzed ages observed. Data presented as mean \pm SEM. * $p < 0.05$ (Student's *t*-test, unpaired). To see this illustration in color, the reader is referred to the online version of this article at www.liebertpub.com/ars



OHCs, and, in general, a well-preserved cochlear structure. SGN count in H&E-stained cochlear sections showed only a marginal, although statistically significant, decrease in the number of SGNs in the KO mouse cochlea (Fig. 3D). It is worth noting, however, that this slight decrease in the number of SGNs could not be responsible for the severe age-related elevation of hearing thresholds and delay in the absolute wave latencies in *Fus1* KO mice.

SGNs are connected to auditory hair cells *via* multiple synapses (65). Recent data have suggested IHC synaptic loss as an important mechanism of hearing loss after auditory damage and aging (28). We immunostained cochlear tissue sections with antibodies to CtBP2/Ribeye, a principal component of the presynaptic ribbon, to compare the numbers of IHC synapses in aging cochleae (60) with young animals that have 14–18 synapses/cell (Fig. 3E). We found an age-related decrease in all three cochlear turns with a more prominent loss in the apical turn in both WT and KO mice. However, the synaptic loss was significantly greater in KO mice (Fig. 3E).

Another histopathological change that was observed in 11-month-old KO mice but not in WT mice was the loss of a small spatially distinct class of fibrocytes (type IV) within the inferior region of the spiral ligament (SL) (Fig. 3F), which is vulnerable to sound exposure and aging. However, the impact of this type of pathology alone on hearing is inconclusive since the presence or absence of type IV fibrocytes does not completely correlate with the degree of hearing threshold shift (74, 27).

EM analysis points to the stria vascularis as the primary target tissue most vulnerable to mitochondrial damage and oxidative stress in aging Fus1 KO mice

Aging (senescence) is characterized by progressive accumulation of macromolecular damage, thought to be due to continuous minor oxidative stress associated with mitochondrial respiration. Earlier we showed that *Fus1*-deficient cells and tissues experience severe oxidative stress (70, 71, 76, 77). Thus, we hypothesized that accumulation of oxidative damage to macromolecules followed by loss of their

function is the underlying cause of premature hearing loss in *Fus1* KO mice. We performed transmission electron microscopy (TEM) analysis to identify cochlear cells dependent on *Fus1* and mitochondrial activities. Cochleae were isolated from 12-month-old WT and KO mice, the age when KO mice have almost no hearing, while WT mice still maintain a robust auditory response (Fig. 1). We performed comparative analysis of four types of cells/tissues that are known to play major roles in ARHL.

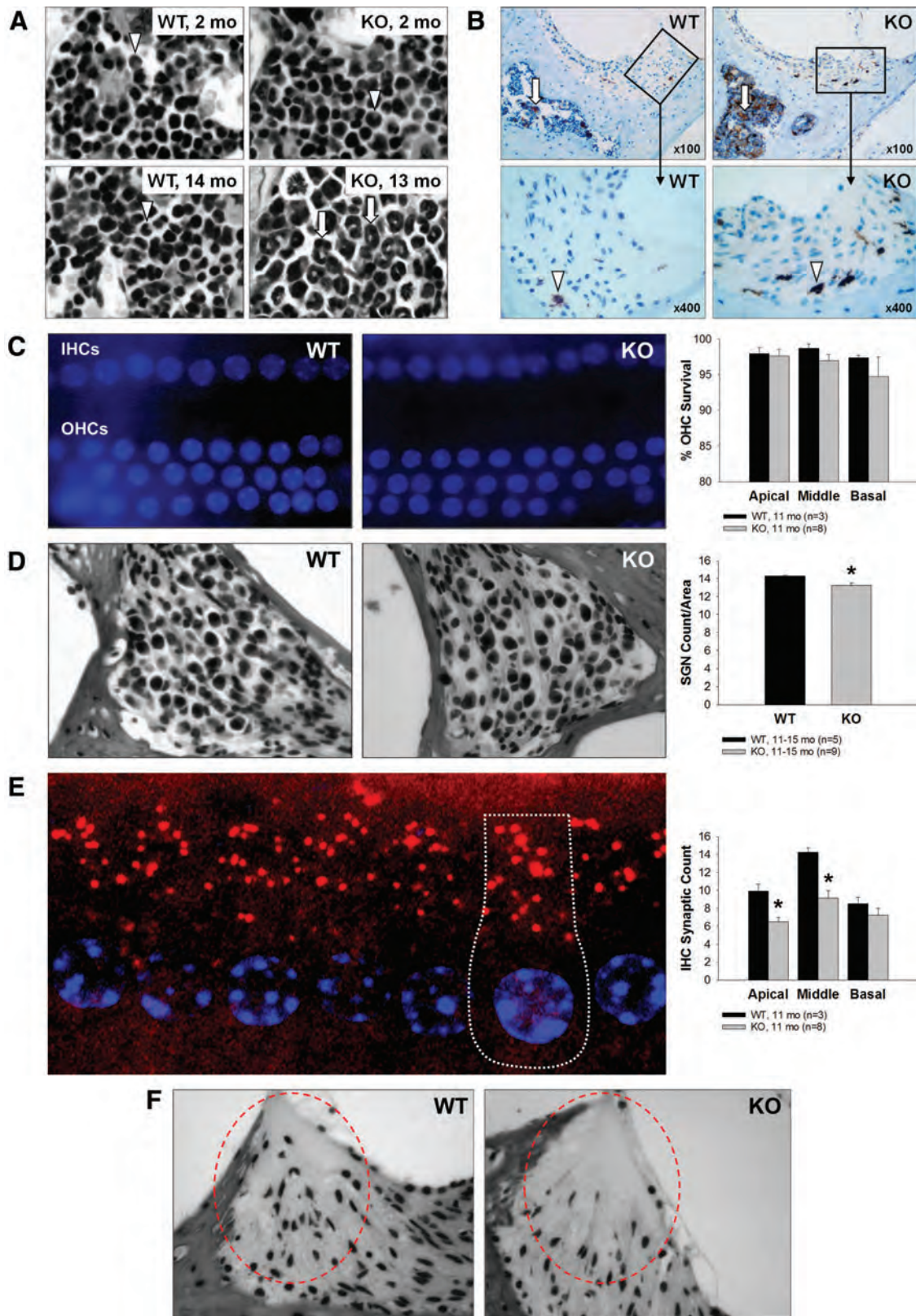
Outer hair cells. In KO OHCs, we did not observe significant deviation from the WT morphology or innervation (data not shown). Also, no difference in mitochondrial morphology was observed between WT and KO OHCs (Fig. 4A).

Inner hair cells. The general morphology of WT and KO IHCs was similar (data not shown). We also observed no difference in the number and structure of mitochondria between WT and KO IHCs (Fig. 4A).

Spiral ganglion neurons. In KO SGNs, we observed modest pathological alterations such as occasional myelin sheath splits (Fig. 4B-I) and areas of nerve fiber degeneration (Fig. 4B-II). At higher magnification, the differences in the morphological structure and sizes of WT and KO mitochondria were easily discernable. Mitochondria in KO SGNs were considerably larger in size and were mostly round in shape. Many of them had electron-lucent content and partially or fully disrupted cristae architecture indicative of mitochondrial pathology/degeneration (Fig. 4B-III).

Stria vascularis and SL. The SV has a dense capillary network and an exceptionally high metabolic rate, the highest of all cochlear tissues (34). The main role of the SV is to produce endolymph, the fluid within the scala media, and generate the endocochlear potential (EP) *via* activation of $\text{Na}^+\text{-K}^+\text{-ATPase}$ pumps for ion balance maintenance. As this process requires a continuous energy supply, the SV has an extensive capillary network and numerous mitochondria

FIG. 3. Chronic inflammation and sensory hair cell, spiral ganglion neuron and inner hair cell synaptic count, and type IV fibrocytes in the cochleae of 12-month-old *Fus1* KO mice. (A) Hematoxylin and eosin-stained cochlear sections showing predominance of activated myeloid progenitor cells (*arrows*) in the bone marrow of the otic capsule in aging *Fus1* KO mice. In contrast, young KO mice and young/old WT mice have compact, undifferentiated myeloid cells (*arrowheads*). (B) Staining with Iba-1, a marker of microglia/activated macrophages, confirmed this finding in the bone marrow (*arrows*), and also revealed an increased infiltration of activated macrophages (*arrowheads*) in the inferior region and along the lateral edge (adjacent to the otic capsule) of the spiral ligament. (C) The images show DAPI-stained IHCs and OHCs from the middle turn of an 11-month WT and *Fus1* KO cochlea. The nuclei (*blue*) are all uniform in size, shape, and staining intensity, which is characteristic of healthy inner and outer hair cells. The graph illustrates the percentage survival of OHCs in the apical, middle, and basal cochlear turns of 11-month-old WT and KO mice. There was no significant loss of OHCs in all three cochlear turns in both WT and KO mice. (D) The representative images and graph illustrate the average number of spiral ganglion neurons in the cochleae of 11-month-old WT and KO mice. There was a marginal but significant decrease in the number of spiral ganglion neurons in the *Fus1* KO cochlea compared with the WT cochlea. (E) Confocal image of IHCs from a 2-month WT cochlea with the nuclei stained with DAPI (*blue*) and presynaptic ribbons stained with CtBP2 (*red*), showing a normal number (14–18) of synapses per IHC. A single IHC is outlined with dotted lines. The graph illustrates the average number of CtBP2-positive IHC presynaptic ribbons on the IHCs from the apical, middle, and basal cochlear turns of 11-month-old WT and *Fus1* KO mice. *Fus1* KO mice had significantly less synaptic ribbons compared to WT mice in the apical and middle turns. (F) Light microscopic images showing substantial loss of type IV fibrocytes in the inferior region of the spiral ligament (*circled*) in 12-month-old *Fus1* KO mice compared with age-matched WT mice. Data presented as mean \pm SEM. * $p < 0.05$ (Student's *t*-test, unpaired). Magnification $\times 400$. IHC, inner hair cell; OHC, outer hair cell. To see this illustration in color, the reader is referred to the online version of this article at www.liebertpub.com/ars



Downloaded by YALE UNIVERSITY from www.liebertpub.com at 08/22/18. For personal use only.

inside marginal cell (MC) processes that interdigitate with intermediate cells (IC) (46). The SL is a dense layer of vascular connective tissue that participates in EP generation (46). The EP enhances the sensitivity of hair cells and, thus, is essential for audition.

TEM analysis showed no abnormality in the SV of aging WT mice while multiple signs of deterioration were observed in the KO SV and SL. First, MC of the SV contained multiple lipofuscin-like dark inclusions (Fig. 4D) that usually correlate positively with oxidative stress and mitochondrial

damage (67). Second, the majority of mitochondria in MCs showed different degrees of pathological changes such as swelling, rounded shape, electron-lucent cytoplasm, as well as partially or entirely disrupted cristae architecture. Many mitochondria were drastically enlarged forming so-called giant mitochondria indicative of defective fission (Fig. 4D). Third, large mitochondria in KO SV were not surrounded by double-layered membrane, characteristic of autophagosomes, and therefore, not targeted for degradation *via* autophagy-like mitochondria in WT SV (Fig. 4E). Fourth, the SV appeared devoid of MC/IC interdigitations, possibly indicating a reduction in IC number, which has been shown to adversely affect EP production (24).

Another layer of pathological change was observed in the SV capillary network. Many capillaries in Fus1KO SV were occluded, filled with electron-dense material and dying blood cells (Fig. 4F). Neither endothelial nor pericapillary cells of KO vessels contained functional mitochondria (Fig. 4F), while WT mitochondria were easily discernable in cells of the capillary wall (data not shown). Moreover, while WT capillaries in SV were surrounded by numerous morphologically normal mitochondria, the KO capillary surroundings consisted of mostly swollen dysfunctional mitochondria and vacuolar structures (Fig. 4F). This suggests that occlusion and degeneration of capillaries in KO SV occur due to capillary cell energy crisis. It is noteworthy that the basal lamina was abnormally thick in KO capillaries compared to WT mice (Fig. 4F). Interestingly, these severe pathological changes were characteristic only for the SV capillaries, while capillaries located in the spiral ganglion from the same cochlea appeared normal reflecting a lower energy demand of this cell type compared to the SV network (Supplementary Fig. S2B).

The KO SL also showed multiple signs of deterioration/ degradation. For example, the type IV fibrocyte area in the SL contained only a few normal fibrocytes while most of them had already been degenerated (Fig. 4G), which is consistent with our light microscopy data. The same type IV fibrocyte area in KO mice showed degenerating vessels, while WT vessels had normal morphology (Fig. 4G).

Thus, based on TEM examination, we concluded that the SV and SL, which showed signs of severe deterioration, are

most likely the primary cause of premature hearing loss in Fus1 KO mice. However, pathological changes in IHCs and SGNs may be contributing factors.

Reduced EP in young adult Fus1 KO mice

The SV and fibrocytes of the SL play major roles in the generation and maintenance of the EP *via* constant ion transport to the endolymphatic space of the cochlea. The EP plays a critical role in maintaining normal hearing sensitivity (4, 61). In view of our EM data showing severe pathology in the SV of KO mice (Fig. 4), we hypothesized that premature loss of hearing in Fus1 KO mice was linked to altered EP. Thus, we measured EPs in 4–5-month-old WT and KO mice (Fig. 5). Representative EP recordings from WT and KO mice are shown in Figure 5B. EP measured in WT mice averaged 101.8 ± 2.1 mV ($n=3$) (Fig. 5C), which is similar to published values. In contrast, the average EP in KO mice was 59.9 ± 7.6 mV ($n=3$), 41.9% lower than in WT mice, $p=0.026592$ (Fig. 5C), which directly demonstrates the importance of SV integrity/functionality for establishing the high EP.

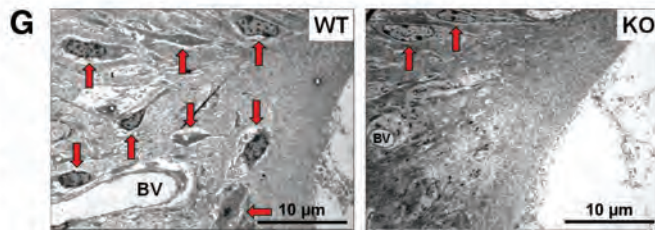
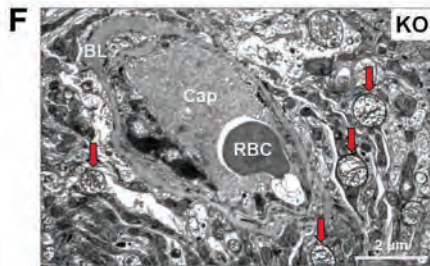
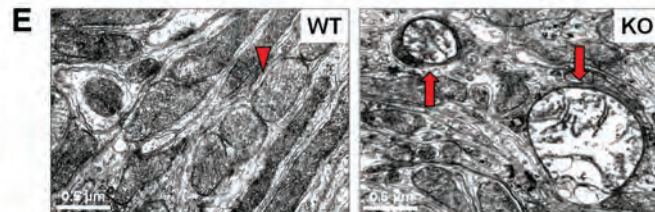
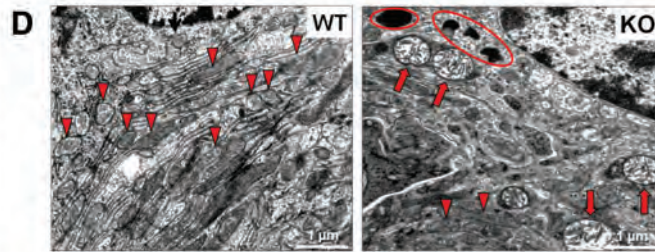
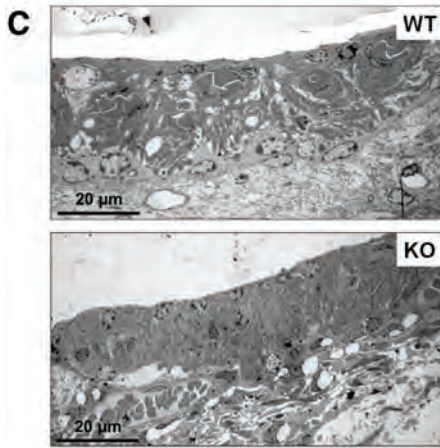
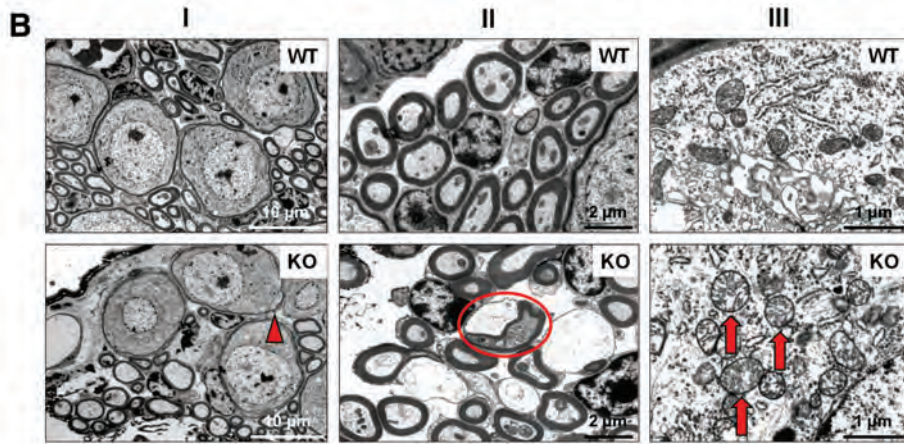
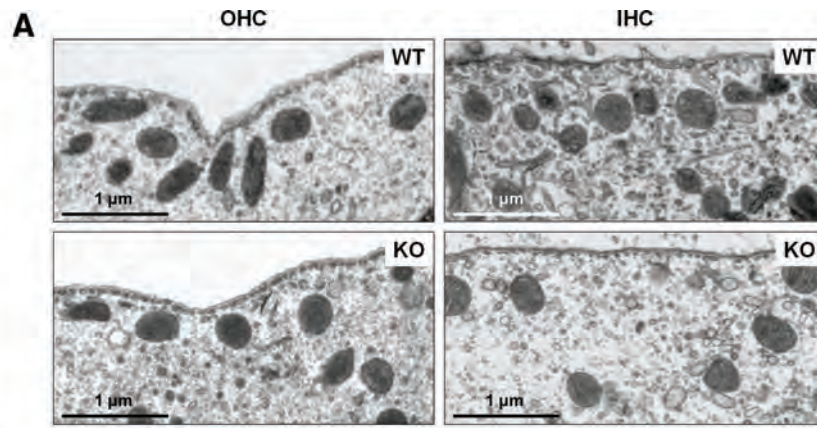
These data suggest that the major mechanism of premature ARHL in Fus1 KO mice is an inability to maintain EP due to, most likely, mitochondrial dysfunction-caused energy crisis in cells of the SV and SL.

Cochlear tissues of 3-month-old Fus1 KO mice show pathological molecular changes in aging-associated pathways, antioxidant and autophagy machineries

To determine the molecular alterations in the KO mouse cochlea that initiate progressive hearing loss, we performed immunoblot analysis focusing on aging-associated pathways. To capture the onset of pathological changes, we analyzed proteins from cochleae of 1- and 3.5-month-old WT and KO mice. Cochleae extracted from five mice per group were pooled together to obtain sufficient protein amounts.

Starting from 1 month of age, we detected potentially detrimental molecular alterations in Fus1 KO mice (Fig. 6 and Supplementary Figure S3A, B). Among proteins of AO machinery, an increase in PRDX1 and a pathological

FIG. 4. TEM analysis of cochlear tissue from 12-month-old Fus1 KO mice. (A) Mitochondria of WT and KO inner and outer hair cells. The number and morphology of mitochondria in the IHCs and OHCs of the organ of Corti are similar in WT and Fus1 KO mice. (B) Spiral ganglion cells in the Fus1 KO cochlea. Pathological signs of degeneration are observed in some regions of the KO cochlea but not in the WT cochlea, such as myelin sheath splits (I, arrowhead), nerve fiber degeneration (II, circled), and abnormal mitochondria in SGNs (III, arrows). KO mitochondria are considerably larger in size, mostly round in shape, and have electron-lucent content and partially or fully disrupted cristae architecture. (C) Stria vascularis of WT and Fus1 KO mice, low magnification. The stria vascularis of the KO cochlea is considerably atrophied compared to that of the WT cochlea. The MC/IC interdigitations present in the WT are not apparent in the KO, possibly indicating IC loss. (D) Comparison of WT and Fus1 KO marginal cells of the SV at higher magnification. Note the mitochondrion-rich cytoplasm (arrowheads) in WT marginal cells, while in KO cells, there are fewer normal mitochondria (arrowheads), presence of multiple swollen “giant” mitochondria (arrows), and numerous electron-dense lipofuscin-like pigment inclusions (circled). (E) Mitochondria of WT and KO marginal cells, high magnification. Note that in the KO cell, large abnormal mitochondria are not a part of autophagosomes (arrows). (F) Vascular pathology in Fus1 KO stria vascularis. Strial capillaries (Cap) in the KO cochlea are occluded, filled with electron-dense gray material and dying RBC. The BL is abnormally thick and there is a lack of functional mitochondria in the capillary wall. Moreover, the area surrounding the blood vessels consists of many swollen and dysfunctional mitochondria (arrows) and vacuolar structures. (G) Inferior region of the spiral ligament in the WT and Fus1 KO cochlea. There is a substantial loss of type IV fibrocytes (arrows) in the KO spiral ligament, and BV also appears to be degenerated. RBC, red blood cell; BL, basal lamina; BV, blood vessels; SGN, spiral ganglion neuron; TEM, transmission electron microscopy. To see this illustration in color, the reader is referred to the online version of this article at www.liebertpub.com/ars



decrease in mitochondrial Sod2 levels were observed (Fig. 6A). Autophagy marker LC3-II showed a Fus1-dependent decrease pointing to an early onset of autophagy dysregulation (Fig. 6D). The most dramatic and consistent changes were found in the PTEN/AKT pathway where total PTEN levels were decreased, while phosphorylation of AKT, a substrate for PTEN phosphatase activity, was increased (Fig. 6B). The level of the mitochondrial kinase PINK1, a mitochondrial quality control protein and PTEN substrate, was also noticeably downregulated (Fig. 6A).

In the adult KO mouse cochlea (3.5 months), we detected escalation of molecular changes observed in younger mice as well as new critical changes (Fig. 6 and Supplementary Fig. S3A, B). The most unexpected change was a dramatic decrease/loss in total AKT levels in 3.5-month-old KO mice in contrast to 1-month-old KO mice that had increased AKT phosphorylation but no changes in total level of AKT (Fig. 6B). This suggests the existence of pathological factors other than PTEN dysregulation that affect AKT translation/degradation in adult KO cochleae. Along with dysregulation of AKT pathway, we observed an apparent mTOR activation (ppS6) in KO cochleae (Fig. 6C). It is noteworthy that mTOR activation (pS6 increase) was observed at both total and phosphorylated levels indicating that Fus1 affects different levels of protein regulation. We also found a further decrease in the levels of AO molecules and a decrease in the level of OxPhos I, a member of mitochondrial respiratory complex I (Fig. 6A). Further decrease in LC3-II levels suggested accumulation of dysfunctional mitochondria due to defective autophagy (Fig. 6D). The PTEN and Pink1 levels in both KO age groups were consistently lower than in WT mice (Fig. 6A, B).

Interestingly, some aging-associated signaling hubs, such as MAPK42/44 and STAT3 (Fig. 6E), as well as apoptotic proteins with the exception of Bax (Fig. 6D) showed no or marginal changes between KO and WT mice in young or adult mice, thus suggesting Fus1 deficiency specifically targets the PTEN/AKT and mTOR/autophagy axes.

Short-term AO supplementation alleviates/corrects pathological molecular changes in cochlear tissues of adult Fus1 KO mice

All molecular pathways analyzed in the present study are mitochondria/energy dependent. In our earlier studies and here

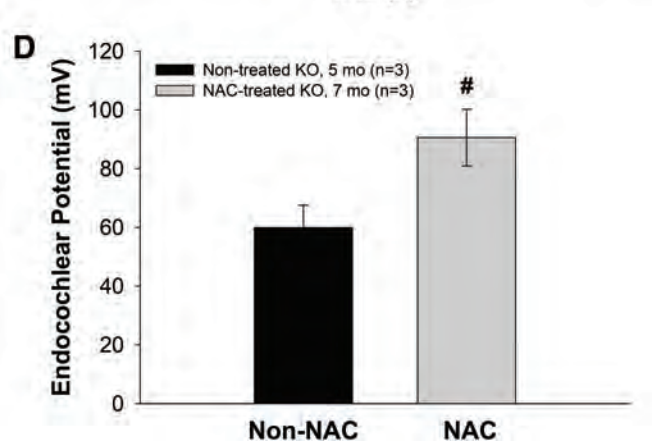
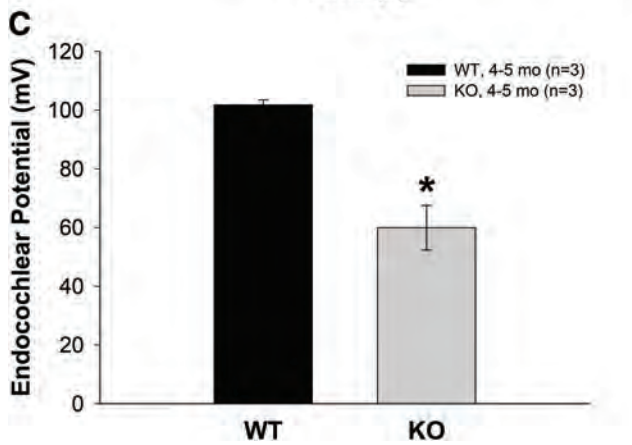
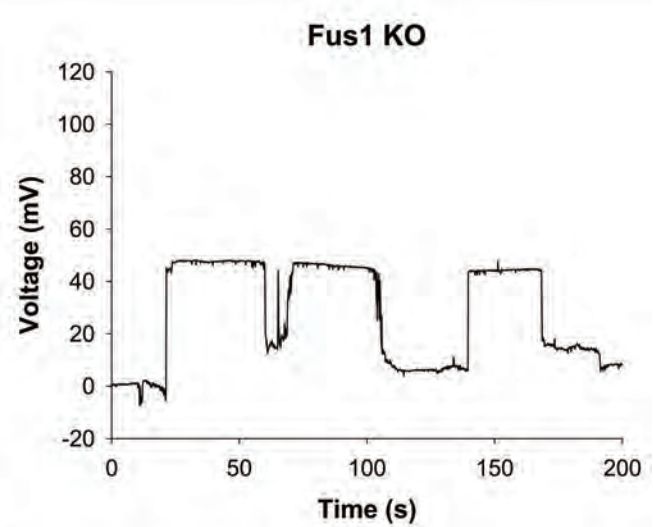
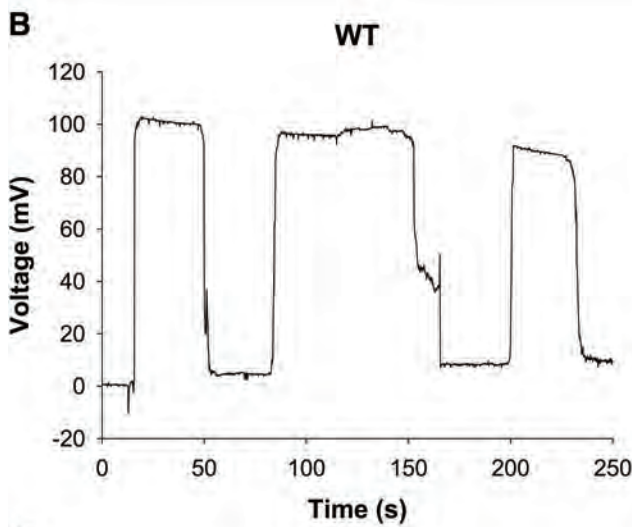
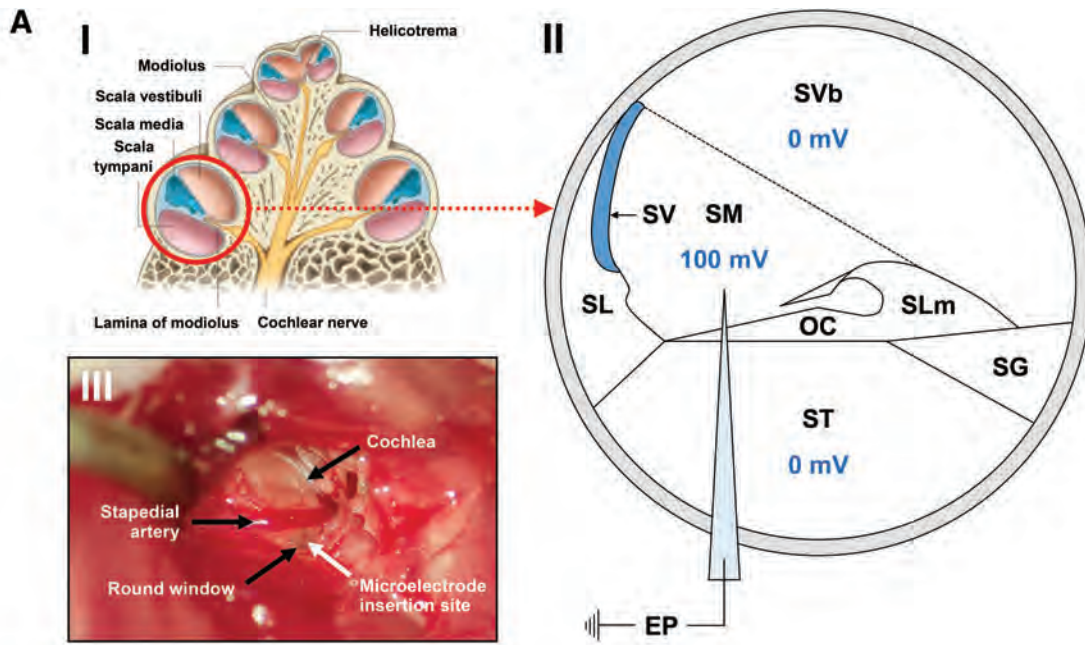
(70, 71, 77) (Fig. 6 and Supplementary Fig. S3A, B), we showed that Fus1-deficient tissues experience chronic oxidative stress that may be detrimental for mitochondria and tissues with high-energy demand such as the cochlea. We hypothesized that relief of oxidative stress may improve mitochondrial activities, alleviate molecular pathology, and slow down hearing loss. To validate this hypothesis, 30 mM N-acetyl cysteine (NAC), an AO compound, was provided in drinking water to 3.5-month-old WT and KO mice for 30 days. Our choice of AO was substantiated by several data sets. First, NAC was one of the three AO supplements that was reported to alleviate hearing pathology in B6 mice when provided for 11 months in a study that tested the long-term effect of 17 different AO compounds (62). Second, NAC was shown to be able to penetrate the blood-brain barrier (BBB) (13), and third, it was shown to prevent mitochondria from oxidative injury, which is critical for our model of mitochondrial dysfunction (29).

To confirm that NAC relieves oxidative stress in the cochleae of KO mice, we compared the levels of AO proteins and found that PRDX1 and OxPhos I level 39 kDa were completely rescued in the cochleae of NAC-treated KO mice compared to WT mice (Fig. 6A). Remarkably, NAC treatment normalized or alleviated Fus1-dependent pathological changes in other aging-related proteins such as autophagy marker LC3-II and proteins from the nutrient (mTOR) and energy (PTEN/AKT) sensing pathways (Fig. 6, red arrows). Interestingly, not all proteins in the analysis were equally sensitive to NAC treatment. Thus, we did not observe significant NAC effects on mitochondrial proteins SOD2 or Pink1 (Fig. 6A), while levels of total and phosphorylated AKT, S6, and PTEN were drastically improved (Fig. 6B, C). This discordant response to AO intervention suggests that NAC may not efficiently penetrate mitochondria, or that in addition to oxidative stress, other pathological processes are associated with Fus1 loss in the cochlea.

Short-term antioxidant (NAC) supplementation prevents progression of hearing loss, improves ABR wave amplitudes, restores EP levels, and improves mitochondrial morphology in SV cells and SGNs in Fus1 KO mice

To determine the effect of AO treatment on progression of hearing loss in KO mice, we treated 4-month-old mice

FIG. 5. Endocochlear potential (EP) measurements in WT and Fus1 KO mice. (A) (I) Drawing of cross section of a cochlea showing the apical, middle and basal (*circled*) turn. (II) Schematic diagram of the cross section of the basal cochlear turn illustrating the method of EP measurement. A 3 M KCl-filled microelectrode was inserted into the perilymph-filled scala tympani (0 mV) from the round window and then advanced into the endolymph-filled scala media (100 mV in a WT mouse) to record the EP. (III) Photograph of a surgically exposed cochlea before EP measurement showing the location of the round window below the stapedial artery (*black arrows*) and the insertion site of the microelectrode (*white arrow*). (B) Representative EP recordings from a 4–5-month-old WT and Fus1 KO mouse. The traces show the voltage (mV) of the scala media as a function of time (s). The electrode was advanced into the scala media, withdrawn back into the scala tympani, advanced again back into the scala media, and further into the scala vestibuli, and then retracted back into the scala tympani, giving three peaks in the trace. (C) The graph illustrates a significant 41.9% reduction in the EP in 4–5-month-old Fus1 KO mice (59.9 ± 7.6 mV) compared with age-matched WT (101.8 ± 1.7 mV) mice. (D) The graph illustrates a 1.5-fold increase in EP in Fus1 KO mice treated with NAC for 3 months (90.6 ± 9.6 mV) relative to non-NAC-treated Fus1 KO mice (59.9 ± 7.6 mV), which is almost a complete restoration of EP to that of WT mice. Data presented as mean \pm SEM ($n = 3$). * $p < 0.05$ (Student's *t*-test, unpaired). # $p = 0.07$ (Student's *t*-test, unpaired). (Fig. A–I reproduced and modified from Drake *et al.* (11a)). OC, organ of Corti; SG, spiral ganglion; SL, spiral ligament; SLm, spiral limbus; SM, scala media; ST, scala tympani; SV, stria vascularis; SVb, scala vestibuli. To see this illustration in color, the reader is referred to the online version of this article at www.liebertpub.com/ars



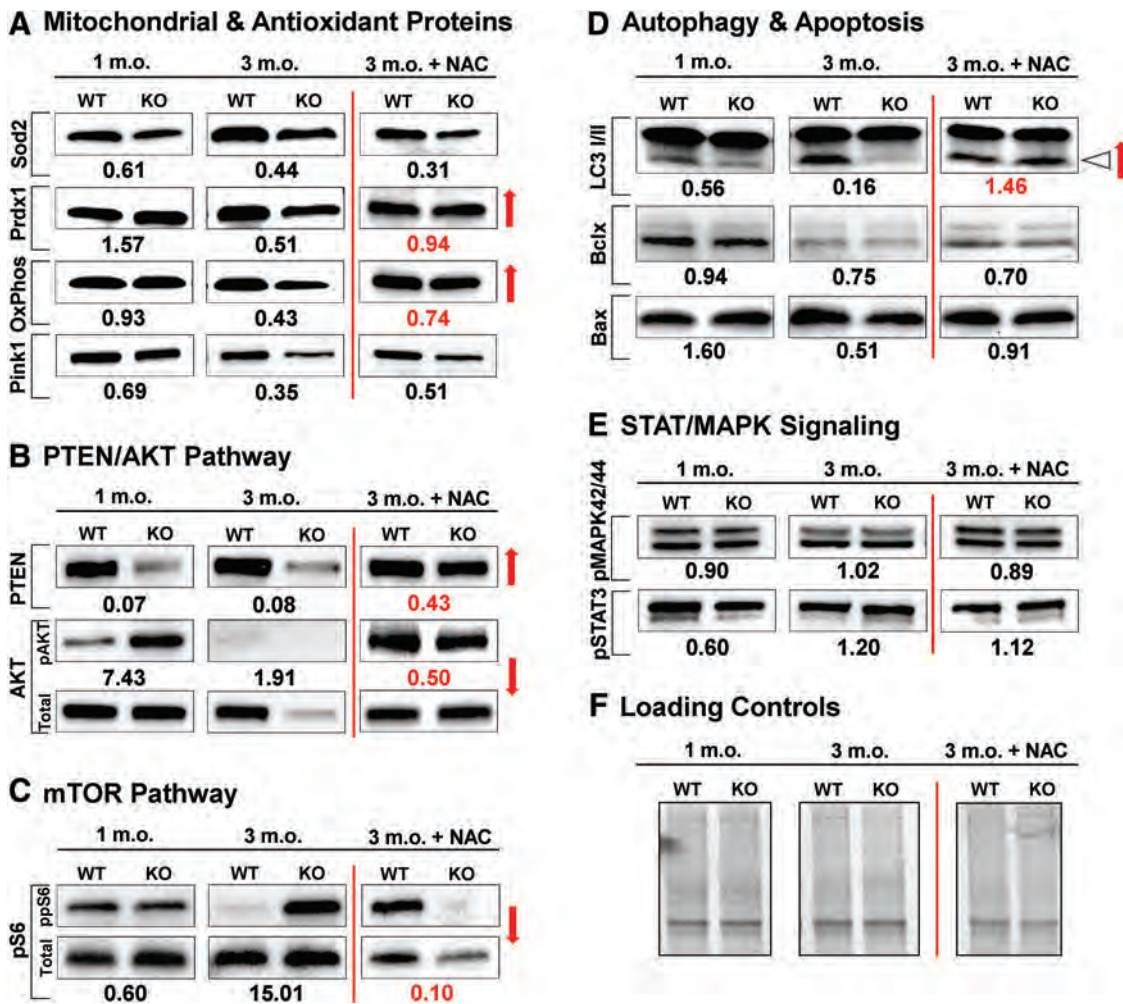


FIG. 6. Dynamic changes in aging-related proteins in the cochlea of young and adult WT and *Fus1* KO mice and NAC-mediated changes in these pathways. The results of Western blot analysis are presented as a relative expression or phosphorylation index of several aging-associated groups of proteins in *Fus1* KO compared to WT cochlea. (A) Mitochondrial proteins and antioxidant machinery, (B) PTEN/AKT pathway, (C) mTOR pathway, (D) autophagy and apoptosis, and (E) STAT/MAPK signaling in WT and *Fus1* KO mice at 1 month and 3 months of age were analyzed. The last panel shows relative changes in the analyzed proteins induced by 30 days of NAC supplementation to 3-month-old mice. The number below the bands represents the fold change in protein expression or phosphorylation index in the KO cochlea relative to the WT cochlea. Phosphorylation index is the ratio of phosphorylated protein intensity over total protein band intensity. Loading controls are shown in (F). Red arrows indicate correction of pathological changes in KO cochlea induced by 30 days of NAC supplementation compared to nontreated 3-month-old KO mice. Triangle arrow in (D) points to LC3-II isoform involved in autophagy. To see this illustration in color, the reader is referred to the online version of this article at www.liebertpub.com/ars

with NAC for 3 months. NAC supplementation significantly retarded hearing loss in KO mice making the ABR threshold levels of 7-month-old KO mice comparable to WT mice, while nontreated control KO mice of similar age had profound hearing loss (Fig. 7A). Moreover, NAC prevented both the reduction of wave I amplitudes (Fig. 7B) and the delay in wave I latencies (Fig. 7C), and almost restored the EP in KO mice to the level of 4–5-month-old WT mice (Fig. 5D).

In addition, the effect of NAC at the ultrastructural level in the cochlea of KO mice was examined by TEM analysis (Fig. 8). In nontreated 5–6-month-old *Fus1* KO mice, SV cells and SGNs had swollen mitochondria with disrupted cristae architecture, similar to that observed in 12-month-old KO mice, but not as severe. NAC supplementation of 4-month-old KO mice for 2 months significantly improved the

morphology of mitochondria in SV cells and SGNs completely restoring cristae architecture. These results, therefore, suggest that oxidative stress is one of the major causative mechanisms of ARHL in *Fus1* KO mice.

Discussion

Mitochondria present a unique and crucial set of key intracellular functions (72). The critical role of mitochondria in auditory function and ARHL began to emerge some time ago but is still understudied and underestimated (5). With regard to oxidative stress and mitochondrial function, only a few genes and loci linked to ARHL have been proposed as a result of candidate gene-based association human studies. Among them are AO enzymes superoxide dismutases (SODs) and

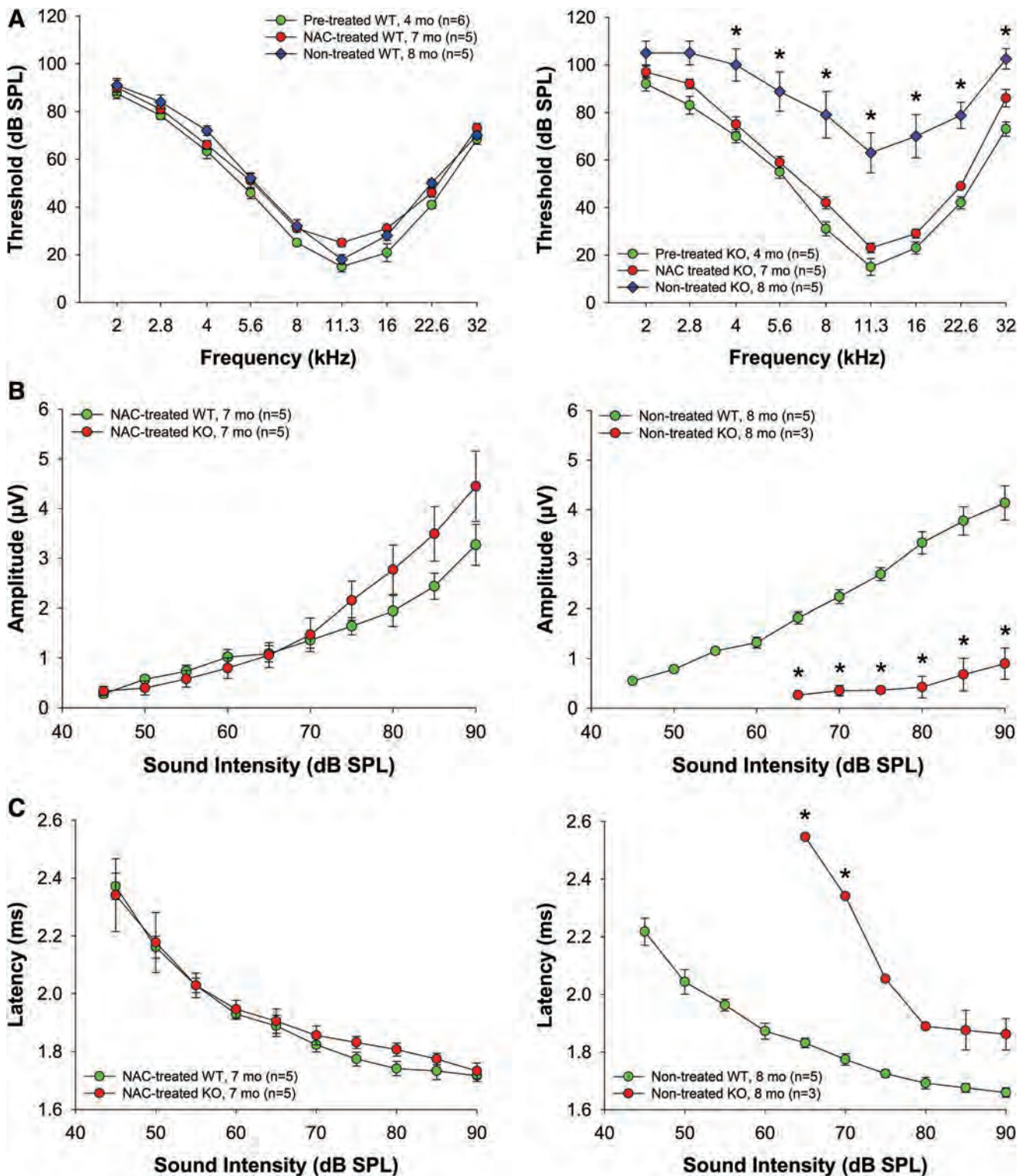


FIG. 7. Effect of NAC supplementation on hearing thresholds and ABR wave I amplitudes in WT and *Fus1* KO mice. (A) The graphs illustrate ABR thresholds in nontreated and NAC-treated WT and *Fus1* KO mice. NAC supplementation for 3 months (red circles) significantly improved the thresholds across all frequencies in *Fus1* KO mice but not in WT mice. (B, C) The graphs illustrate the amplitudes (μ V) and latencies (ms) of ABR wave I as a function of sound intensity (dB SPL) at 16 kHz in nontreated and NAC-treated WT and *Fus1* KO mice. NAC prevented the reduction and delay of wave I amplitudes and latencies, respectively. Data presented as mean \pm SEM. * p < 0.05 (Student's *t*-test, unpaired). To see this illustration in color, the reader is referred to the online version of this article at www.liebertpub.com/ars

glutathione S-transferases (GSTs), and mitochondrial uncoupling proteins (UCPs) that reduce the MMP in mammalian cells (16). Deletions/mutations in mitochondrial DNA or reduced expression of genes from mtDNA has also been associated with ARHL in humans (3, 35, 14). Animal studies largely confirmed the conclusion that oxidative stress, altered levels of AO enzymes, decreased activity of I, II, IV complexes/ altered respiration, and increased mtDNA mutation rate lead to premature hearing loss (23, 37, 39, 48, 63, 69).

Types of mitochondrial dysfunction are defined by the activities of the mitochondrial protein(s) or mitochondrial hub(s) that are defective in a specific tissue. In addition to ATP production, other mitochondrial functions may define the type of dysfunction, such as maintaining calcium concentration within cellular compartments, calcium signaling that mediate responses to outside signals, regulation of the

membrane potential, AO function, apoptosis, and regulation of cellular metabolism (44). It would be logical to suggest that mitochondrial impact on hearing is defined by the type of mitochondrial dysfunction. Thus, additional models of premature hearing loss linked to various mitochondrial activities are urgently needed to understand the basic mitochondrial mechanisms of ARHL and counteract them.

In the current study, we characterized a novel model of ARHL mediated by the loss of the mitochondrial protein Fus1 and determined its molecular mechanisms. In our earlier studies, we established Fus1 as one of the few regulators of mitochondrial calcium handling (71, 72). However, Fus1 KO cells were presented with dysregulation not only in calcium accumulation/distribution but also in calcium-coupled mitochondrial parameters (*via* so-called metabolic coupling), such as ROS production, mitochondrial potential, GSH content, mitochondrial fusion, and calcium signaling mediated *via* NF κ B/NFAT axis. We hypothesized then that disruption of metabolic coupling in mitochondria may result in multiple cellular and systemic pathologies (71, 72).

Indeed, in this study, we provide multiple lines of evidence that Fus1 KO mice are a mechanistically novel, convenient, and clinically relevant model of premature ARHL. We found that besides early and fast progressing hearing decline (Fig. 1), young Fus1 KO animals have paradoxically increased ABR wave amplitudes (Fig. 2). Higher amplitudes normally reflect increased number of firing neurons or higher synchrony of firing. We speculate that higher ABR wave amplitudes in young KO mice may be a result of higher ROS production or altered intracellular calcium/signaling.

In our early work, we established that immune cells from young Fus1 KO mice are chronically activated, which could benefit young mice by better protecting them from acute infection, but may play a detrimental role during aging (20, 71). Here we suggest that heightened ABR responses in the young KO inform a higher metabolic demand, and may underlie the drastic drop of amplitudes and hearing later in life as we observed in aging KO mice (8–10 months) but not in age-matched WT mice (Fig. 2). We did not find that this phenotype is gender specific.

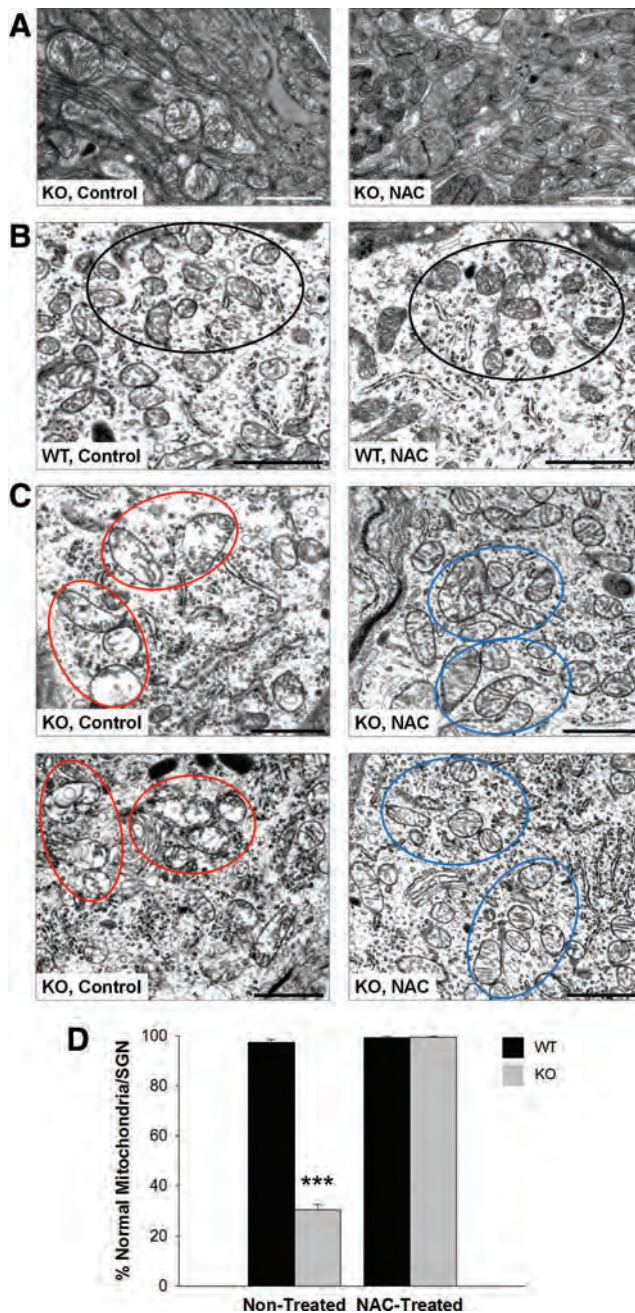


FIG. 8. Transmission electron microscopy (TEM) analysis of cochlear tissue from 5- to 6-month-old non-treated and NAC-treated Fus1 KO mice. (A) Comparison of mitochondria in stria vascularis cells between nontreated and NAC-treated Fus1 KO mice. **(B)** Mitochondria of SGNs from nontreated and NAC-treated WT mice. **(C)** Mitochondria of two representative SGNs from nontreated and NAC-treated Fus1 KO mice. NAC treatment of 4-month-old Fus1 KO mice for 2 months significantly improved the morphology of mitochondria (reduced size and improved cristae architecture) in SV cells and SGNs. Clusters of representative mitochondria are circled in the micrographs. **(D)** The graph illustrates the percentage of morphologically normal mitochondria in SGNs of WT and Fus1 KO cochleae before and after NAC treatment. The number of normal and abnormal mitochondria was counted in each spiral ganglion cell (6–10 microscope fields/cell) and the average percentage of normal mitochondria per SGN calculated. Scale bar = 1 μ m. Data presented as mean \pm SEM. *** p = 0.0000474 (Student's t -test, unpaired). To see this illustration in color, the reader is referred to the online version of this article at www.liebertpub.com/ars

The patterns of ABR wave deterioration in adult KO mice are very similar to the data obtained from studies on aging individuals (25), suggesting that the Fus1 KO mouse is a clinically relevant model of ARHL, and therefore studying the molecular mechanisms of hearing loss in Fus1 KO mice as well as approaches for its prevention could be applicable to humans.

We ruled out death of sensory cells as a primary cause that often underlies age-related sensorineural hearing loss (75). The absence of mitochondrial pathology in OHCs and IHCs also suggests preservation of their bioenergetics levels in Fus1 KO organ of Corti. Although based on the slight but significant decrease in the number of SGNs and IHC synapses as well as on prominent mitochondrial swelling and morphological abnormalities in SGNs corrected by antioxidant treatment, we cannot exclude neural cell involvement at some stages of hearing pathology in KO mice.

However, the severe vascular and mitochondrial structural changes in the SV and SL, with reduced MC/IC interdigitations, strongly suggest that the basis of ARHL in Fus1 KO mice is of metabolic nature. The significant pathological changes of strial capillaries may cause a restrained cochlear blood flow, which can lead to mitochondria-mediated insufficiency in energy production that is needed to maintain ion pumping to the endolymph. The SV is critical for the generation and maintenance of the EP. Reduction in the EP results in a loss of electrical driving force for hair cell transduction current (4, 61). EP measurement in 4–5-month-old mice revealed a significant 41.9% reduction in KO mice (59.9 ± 7.6 mV) compared with WT mice (101.8 ± 2.1 mV) demonstrating that strial dysfunction contributes to cochlear pathology underlying progressive hearing loss in Fus1 KO mice.

Metabolic (based on strial pathology) ARHL is the least studied pathology (4, 64). No human genes that promote strial presbycusis have been identified nor is its pathophysiology well understood (45, 46). Although extensive strial degeneration coincides with hearing loss, EPs have never been measured in humans due to the absence of technology for this invasive measurement. In animal studies, until recently, only two well-studied models, Mongolian gerbils and *Tyrp1*(B-It) mice (8), were known to undergo age-associated EP reduction. Recently, four other strains with modest to severe EP reduction during aging (C57BL/6-Tyr(c-2J) (50), BALB/cJ (47), CBA/CAJ, and NOD.NON-H2(nbl)/LtJ (49)) were described. So far, only one individual gene *Tyrp1*, which codes for tyrosinase-related protein (56), has been linked to age-related EP decline in these strains, although several candidate protein classes had been suggested such as AO machinery, ion channels, exchangers and pumps, immune-related genes, and cell repair genes (6, 46).

Therefore, our novel Fus1 KO model of mitochondrial dysfunction that affects the performance of AO machinery (76, 77), intracellular calcium distribution (71), and immune response (20, 70) may be of a great value for studying the etiology and molecular mechanisms of age-related strial degeneration.

To pinpoint the molecular basis of strial degeneration, we analyzed protein alterations in cochlear tissue of Fus1 KO mice. We used a *logical* candidate-based approach when choosing the proteins for analysis, including pathways and processes linked to (i) nutrient sensing and energy expenditure (PTEN/AKT and mTOR); (ii) mitochondrial activities; (iii) oxidative stress; (iv) apoptosis and autophagy. Our main quest was to identify primary Fus1-dependent molecular

changes that drive other molecular and pathological changes later in life. Therefore, we compared protein levels and their phosphorylation/activation in the cochlea of 1- and 3.5-month-old animals. The most consistent and early alterations were observed in the PTEN/AKT pathway as well as the proteins of AO machinery, allowing us to consider them as the primary molecular events. Phosphatase and tensin homolog (PTEN) is involved in numerous important systemic functions, including anti-aging activities. It was shown to positively regulate longevity (51). Recently, a new metabolic role of PTEN as a positive regulator of energy expenditure through increased oxidative phosphorylation was revealed (52). ROS have been shown to oxidize the active site cysteine on PTEN (Cys124), resulting in inactivation of PTEN and perpetual activation of the AKT pathway (30). Moreover, mitochondrial ROS specifically were shown to inhibit PTEN and activate AKT (9), which is consistent with the molecular events we observed in young Fus1 KO mice.

Based on the ROS scavenging effects in Fus1 KO mice that resulted in rescue of PTEN/AKT pathway, we believe that consistently decreased PTEN levels and activation of AKT in the Fus1 KO cochlea are due to pathologically high levels of ROS. However, the exact nature of PTEN decrease in Fus1 KO cochlea is yet to be confirmed since PTEN is regulated by multiple mechanisms, including but not limited to phosphorylation, oxidation, binding to different partners, and transcriptional regulation (31). Considering the importance of PTEN in aging and hearing, there is no doubt that PTEN regulation is one of the key molecular mechanisms of Fus1 action in protection from premature hearing loss. It is worth noting that in our earlier work we showed that Fus1 is also involved in PTEN regulation in lungs during bacteria-induced inflammatory response (20).

Another important alteration we observed in 3.5-month-old KO mice is the decreased levels of OxPhos 39 kDa, a subunit of mitochondrial respiratory Complex I, a component of the oxidative phosphorylation chain. This decrease was rescued by AO treatment. Low levels of Complex I indicate low ATP levels in KO cochlear tissue since ATP is produced during oxidative phosphorylation. ATP deficiency may lead to an energy crisis and strial malfunction.

In line with PTEN inactivation/pAKT activation in young KO mice, in adult mice we observed activation of the mTOR pathway measured by ribosomal protein S6 phosphorylation, a downstream target of mTOR. mTOR lies at the heart of a nutrient-sensing signaling network that controls cellular metabolism and, thus, aging (21). mTOR activation has been linked to aging in multiple studies [(18), and reviewed in (53)]. It was suggested that aberrant mTOR activation in aging is a response to mitochondrial stress in cells (41), which is consistent with the processes that may take place in the Fus1-deficient cochlea.

Interestingly, in 1- and 3.5-month-old KO cochlea, we observed negative age-related dynamics in accumulation of the autophagy marker LC3-II. Autophagy is an evolutionarily conserved catabolic process that targets proteins and organelles to lysosomes for degradation, followed by recycling of free amino acids and ATP for biosynthesis (68). Autophagy mediates cytoprotective effects (40). During autophagy a cytosolic form of LC3 (LC3-I) is converted *via* conjugation to phosphatidylethanolamine to LC3-II, which is recruited to autophagosomes. High levels of LC3-II reflect a higher autophagy rate and *vice versa*. In our study, based on LC3-II and

Pink1 decrease and accumulation of large swollen mitochondria, we concluded that Fus1 KO cochlear tissues are deficient in autophagy/mitophagy. Moreover, in line with deficient autophagy, we registered activation of mTOR in 3.5-month-old KO mice, which has been shown to suppress autophagy and, thus, promote aging [(43) and references therein]. Normalization of LC3-II levels in Fus1 KO cochleae after AO treatment confirms the link of oxidative stress and autophagy.

Finally, in line with all the data pointing to deficient autophagy/mitophagy in KO cochleae, we showed downregulation of PINK1 (PTEN-induced putative kinase 1) protein in 1- and 3-month-old KO mice. The mitochondrial protein PINK1 is a PTEN-induced putative kinase regulating mitochondrial quality control *via* activation of mitophagy (36). It is a critical protector from age-related diseases linked to dysfunctional mitochondria (7, 54). In the Fus1 KO setting, decreased levels of PINK1 are in line with decreased levels of its upstream regulator PTEN (Fig. 6). In terms of long-term consequences for tissue integrity, PINK1 deficiency could be detrimental for aging Fus1 KO tissues as it leads to inability to withstand oxidative and environmental stress due to defective mitochondrial quality control resulting in accumulation of dysfunctional mitochondria and deterioration of tissues due to energy crisis as we observed in the SV of aging 8–11-month-old Fus1 KO mice.

Apoptotic markers that we used to monitor cell death in young Fus1 KO cochlear tissues showed little difference in expression between KO and WT mice (Fig. 6D, Bcl-X, and Bax), suggesting that deficiency in autophagy may result in other types of cell death in the cochlea (55).

It was also interesting to find, in terms of Fus1 biology, that crucial signaling hubs such as STAT3 (11) and MAPK42/44

(66) showed no major perturbations, suggesting that the antiaging effect of Fus1 is promoted specifically through PTEN/AKT/mTOR pathways partially mediated through control of oxidative stress.

Simple supplementation of the AO NAC to Fus1 KO mice for 1 month increased the level of AO enzymes, normalized PTEN/AKT and mTOR pathways, and protected mitochondria from dysfunction and degradation. Based on our early studies of Fus1 protein biology (70–72), we suggest that normalization of ROS levels in Fus1-deficient tissues helps in recovering mitochondrial integrity, MMP and mitochondrial calcium transport across the membrane and, thus, improve mitochondrial activities, including ATP production and Ca^{2+} distribution, dynamics, and calcium signaling. These changes in different mitochondrial processes could explain the multitude of effects of NAC-mediated ROS scavenging in the Fus1 KO cochlea.

Importantly, NAC supplementation for 3 months produced several highly beneficial changes in hearing of Fus1 KO mice, including prevention of age-related hearing decline, normalization of ABR peak amplitudes, and rescue of the EP. WT mice did not show significant auditory changes in response to NAC treatment at this age, most likely due to the absence of degenerative processes in auditory system at the analyzed age. Short-term NAC treatment also significantly improved the morphology of mitochondria in cells of the SV and SGNs. These results strongly suggest that oxidative stress is one of the major pathogenic factors in ARHL in Fus1 KO mice. It is likely that more potent AOs that specifically target mitochondrial ROS and have better efficacy would produce even more robust rescuing effects in Fus1 KO mice.

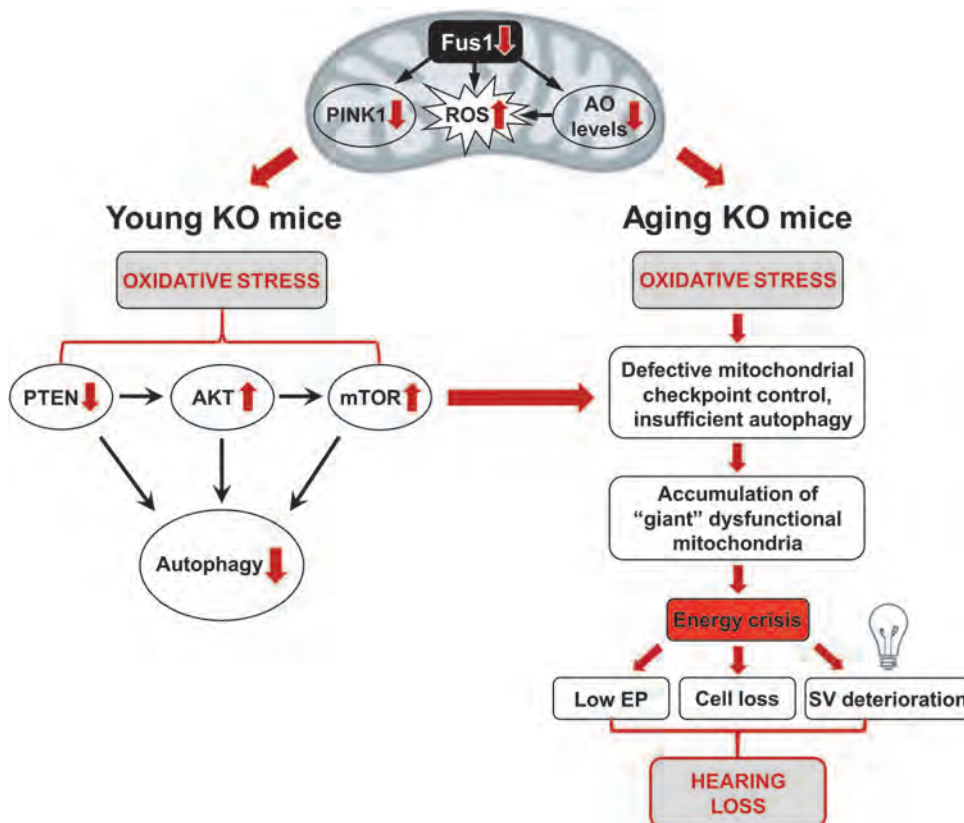


FIG. 9. Hypothetical scheme of molecular and cellular events in the cochleae of young (left) and old (right) Fus1 KO mice leading to premature hearing loss. This model represents a hypothetical pathological chain of events in the cochleae of young and old Fus1 KO mice compared to age-matched WT mice. This scheme was deduced from ABR, TEM, and Western blot analysis of Fus1 KO mouse cochlear tissues. To see this illustration in color, the reader is referred to the online version of this article at www.liebertpub.com/ars

A schematic illustration of our data presented in Figure 9 suggests how loss of *Fus1* results in premature hearing loss that begins with molecular changes in the cochleae of very young *Fus1* KO mice. Our data suggest that efficient targeting of mitochondrial dysfunction-mediated premature hearing loss may require combinatorial approaches that will include AO, anti-inflammatory, anti-TOR, calcium balancing, and other therapies.

Materials and Methods

Fus1 KO mouse model

Fus1 KO mice generated by Dr. A Ivanova (22) were backcrossed to 129sv background in the laboratory of Dr. S Anderson (NCI-Frederick). All animal experiments were performed according to a protocol approved by the Yale University Institutional Animal Care and Use Committee (IACUC) and the animals were cared for according to the recommendations in the “Guide for the Care and Use of Laboratory Animals” (National Institutes of Health). The mice were fed with a standard diet, housed in standard cages (five per cage), and maintained in a 12-h light–12-h dark cycle. They had *ad libitum* access to drinking water and normal diet throughout the experiment. Mice of both genders were used in the study.

NAC supplementation

In all experiments described (30 and 90 days of treatment), N-acetyl cysteine (NAC) (Cat# A7250; Sigma-Aldrich, Inc.) was dissolved in drinking water (30 mM) and supplied *ad libitum* to the mice. For the first 2 days, mice were provided with 15 mM NAC water to acclimate them to the taste and then it was replaced with 30 mM NAC for the remainder of the experiment. NAC water was the only source of drinking water during the experiments. NAC water was changed twice a week.

Auditory brainstem responses

ABR represents the activity of the auditory nerve and the central auditory pathways in response to sounds. ABR measurements were carried out within a sound attenuating booth (Industrial Acoustics Corp.). Mice were first anesthetized with chloral hydrate (480 mg/kg i.p.) and then placed onto a heating pad to maintain body temperature at 37°C. Subdermal needle electrodes (Rochester Electro-Medical, Inc.) were placed at the vertex (active, noninverting), the infraauricular mastoid region (reference, inverting), and the neck region (ground). The acoustic stimuli for ABR were produced and the responses recorded using a customized TDT3 system (Tucker-Davis Technologies, Inc.) controlled by BioSig (TDT), digital signal processing software. Differentially recorded scalp potentials were bandpass filtered between 0.05 and 3 kHz over a 15-ms epoch. A total of 400 trials were averaged for each waveform for each stimulus condition. ABRs were elicited with digitally generated (SigGen; TDT, Inc.) pure tone pips presented free field *via* a speaker (TDT, Inc.; Part FF1 2021) positioned 10 cm from the vertex. Symmetrically shaped tone bursts were 3 ms long (1 ms raised cosine on/off ramps and 1 ms plateau) and were delivered at a rate of approximately 20 per second. Stimuli were presented at frequencies between 2 and 32 kHz and in 5 dB decrements of sound intensity from 90 dB SPL (or

110 dB SPL if thresholds exceeded 90 dB SPL). The ABR threshold was defined as the lowest intensity (to the nearest 5 dB) capable of evoking a reproducible, visually detectable response.

Amplitudes (μ V) and latencies (ms) of the initial four ABR peaks (waves I, II, III, and IV) were then determined at 16 kHz. The most sensitive frequency range of hearing in mice is 11.3–22.6 kHz, and 16 kHz is half octave in-between, so was therefore chosen for analysis. The analysis was carried out offline in BioSig on traces with visible peaks by setting cursors at the maxima and minima (trough) of the peaks. Latency was determined as the time from the onset of the stimulus to the peak, while amplitude was measured by taking the mean of the Δ V of the upward and downward slopes of the peak.

EP measurement

EP was measured in nontreated and NAC-treated WT and *Fus1* KO mice. The method of EP measurement is illustrated in Figure 5A. Mice were deeply anesthetized with sodium pentobarbital (45 mg/kg, i.p.) and placed onto a heating pad to maintain body temperature at 37°C. Animals were then secured onto a stereotaxic mouse head holding adaptor (MA-6 N; Narishige) mounted onto a ball-and-socket stage (Model M-RN-50; Newport Corporation) and a magnetic base (Model 100; Newport Corporation). A silver–silver chloride reference electrode was placed under the skin of the chest. A tracheotomy was first performed and then the round window of the cochlea was exposed *via* a ventral approach by opening the auditory bulla of the temporal bone. A microelectrode (5–15 M Ω 1B150F-4; World Precision Instruments, Sarasota, FL) filled with 3 M KCl was positioned in the round window using a micromanipulator with a pulse motor driving unit (PF5-1; Narishige). An Axon 200A patch clamp amplifier was used for current clamp recording with an Axon Digidata 1321A and jClamp software version 22.8.4 (Scisoft, Inc.). When the microelectrode was inserted into the perilymph of the scala tympani, the voltage was balanced to 0 mV and then the microelectrode was advanced in 5 μ m steps through the basilar membrane and into the endolymph of the scala media to measure the EP. For confirmation of the EP recording, the microelectrode was withdrawn back into the scala tympani, advanced again into the scala media, and continued further into the scala vestibuli, and then retracted back again into the scala tympani. After the EP measurement, the animals were euthanized with an overdose of sodium pentobarbital.

Confocal immunofluorescence

Cochleae were extracted from the temporal bones of 11-month-old WT and *Fus1* KO mice, perfused, fixed for 1 h in 4% paraformaldehyde (PFA) in phosphate-buffered saline (PBS), then washed, and stored in PBS at +4°C. The bony capsule, lateral wall, and modiolus were removed under a dissection microscope using fine forceps. The cochleae were incubated with 5% goat serum in 0.1% Triton/PBS for 30 min at room temperature followed by incubation overnight with mouse monoclonal CTBP2 primary antibody (Cat# 612044; BD Biosciences, Inc.) diluted 1:500 in 2% goat serum/antibody diluent (Cat # S202230-2; Dako, Inc.). The next day, the cochleae were washed thrice in 0.1% Triton X-100/PBS followed by incubation with the secondary antibody Alexa Fluor 568-conjugated rabbit (Cat # A-11011; Thermo Fisher

Scientific, Inc.) at room temperature for 1 h. Mounting on glass slide was done in the DAPI mounting solution (Cat# H-1200; Vector Laboratories, Inc.). During mounting, SLs were dissected away to allow good exposure of the organ of Corti, and the cochleae were separated into three parts, the apical turn (corresponding to frequencies between 200–1.5 kHz), middle turn (1.5–16 kHz), and basal turn (>16 kHz). DAPI-labeled IHCs, OHCs, and IHC synaptic ribbons were visualized with a Zeiss LSM410 laser confocal microscope (Carl Zeiss Microscopy). Sensory hair cell loss was quantitatively evaluated by counting missing hair cells in the apical, middle, and basal turns of the cochlea. Images were collected and analyzed with a ZEN camera and ZEN software. CTBP2-positive synaptic ribbons were counted per IHC (3–5 fields per region, 10–12 IHC per field) and then averaged/region.

H&E staining and immunohistology

Cochleae were fixed in 4% PFA in PBS for 12–48 h, washed in PBS, decalcified in 0.1 M EDTA for 3–4 days, dehydrated through an ethanol gradient, and then embedded in paraffin. Sections of 5 μ m thick in the midmodiolar, vertical plane were stained with H&E, then analyzed using a Nikon Eclipse 80i Microscope (Nikon Instruments, Inc.). The SGN density (cells in 3–5 areas were counted and averaged) in Rosenthal's canal of the basal turn was counted. Immunostaining with rabbit anti-Iba1 antibodies (Wako Chemicals, Inc.) on thin sections was performed using automatic Omni Multimer detection. Statistical analysis was performed using the Student's t-test to compare KO genotype and WT groups.

Cochlear protein lysate preparation and Western blot analysis

Both cochleae from each mouse were harvested, and one was immersed in 4% PFA in 0.1 M phosphate buffer (PB; fixative solution; pH 7.4) and used for immunohistochemical staining. The contralateral cochlea was placed in lysis buffer (RIPA plus protease inhibitor cocktail), perfused with the lysis buffer through the oval and round windows, snap-frozen, and kept at -80°C until required for lysate preparation. For protein lysate preparation, five cochleae from five WT or KO animals were pooled into an Eppendorf tube, 100 μ L of lysis buffer was added to the tube, and the cochlear tissues were homogenized using a plastic mini-pestle. Lysates were sonicated and cleared *via* 15 min of centrifugation at 14,000 rpm in a microcentrifuge (Eppendorf). The supernatants were then transferred to a fresh tube. Western blot analysis of cochlear tissues was performed as described in our previous articles (76, 77).

Antibodies for Western blot analysis

The following antibodies were used in the study: rabbit anti-Sod2 (Cat# ab13533; Abcam), rabbit anti-PRDX1 (Cat# HPA007730; Sigma-Aldrich, Inc.), mouse anti-OxPhos 39 kDa (Cat# 45-8199; Thermo Fisher Scientific, Inc.), and mouse anti-Pink1 (Cat# NBP2-36488; Novus Biologicals). The following antibodies were bought from Cell Signaling Technology, Inc.: rabbit anti-AKT total and pAKT (Cat# 9272 and 3787), mouse anti-pS6 total (Cat# 2317), rabbit anti-ppS6 (Cat# 2221), rabbit anti-pSTAT3 (Cat# 9131), rabbit anti-pMAPK42/44 (Cat# 4695), rabbit anti-Bax (Cat#

5023), mouse anti-BclX (Cat# 2764), and mouse anti-PTEN (Cat# 9552).

TEM analysis

Cochleae from 5–6 month-old and 12-month-old WT and KO mice were extracted and deboned as described above and fixed in 2.5% glutaraldehyde and 2% PFA in 0.1 M sodium cacodylate buffer pH 7.4 for 1 h. After fixation, the cochleae were rinsed in cacodylate buffer, then postfixed in 1% osmium tetroxide in cacodylate, and en bloc stained in 2% aqueous uranyl acetate for a further hour each. The samples were well rinsed, followed by dehydration in an ethanol series, infiltrated with epoxy resin Embed 812 (Electron Microscopy Sciences), and baked overnight at 60°C . Hardened blocks were cut using a Leica UltraCut UC7. Sections (60 nm) were collected on formvar/carbon-coated grids and contrast stained using 2% uranyl acetate and lead citrate. The sample sections were viewed using an FEI Tecnai Biotwin Transmission Electron Microscope (FEI, Hillsboro, OR) at 80Kv. Images were taken using MORADA CCD and iTEM (Olympus) software.

Acknowledgments

This work was supported by grants R21 DC014357-02 to A.I. and R01 000273 and 008130 to J.S., all from NIDCD, National Institutes of Health, USA and OSHE grant to L.S. I apologize to those colleagues whose work I could not cite owing to space limitations. The authors of this article declare no conflicts of interest or competing financial interests.

Author Disclosure Statement

No competing financial interests exist.

References

1. Agarwal S, Mishra A, Jagade M, Kasbekar V, and Nagle SK. Effects of hypertension on hearing. *Indian J Otolaryngol Head Neck Surg* 65: 614–618, 2013.
2. Agrawal Y, Platz EA, and Niparko JK. Risk factors for hearing loss in US adults: data from the National Health and Nutrition Examination Survey, 1999 to 2002. *Otol Neurotol* 30: 139–145, 2009.
3. Bai U, Seidman MD, Hinojosa R, and Quirk WS. Mitochondrial DNA deletions associated with aging and possibly presbycusis: a human archival temporal bone study. *Am J Otol* 18: 449–453, 1997.
4. Boettcher FA. Presbycusis and the auditory brainstem response. *J Speech Lang Hear Res* 45: 1249–1261, 2002.
5. Bottger EC and Schacht J. The mitochondrion: a perpetrator of acquired hearing loss. *Hear Res* 303: 12–19, 2013.
6. Bowl MR and Dawson SJ. The mouse as a model for age-related hearing loss - a mini-review. *Gerontology* 61: 149–157, 2015.
7. Bueno M, Lai YC, Romero Y, Brands J, St Croix CM, Kanga C, Corey C, Herazo-Maya JD, Sembrat J, Lee JS, Duncan SR, Rojas M, Shiva S, Chu CT, and Mora AL. PINK1 deficiency impairs mitochondrial homeostasis and promotes lung fibrosis. *J Clin Invest* 125: 521–538, 2015.
8. Cable J, Jackson IJ, and Steel KP. Light (Blt), a mutation that causes melanocyte death, affects stria vascularis function in the mouse inner ear. *Pigment Cell Res* 6: 215–225, 1993.

9. Connor KM, Subbaram S, Regan KJ, Nelson KK, Mazurkiewicz JE, Bartholomew PJ, Aplin AE, Tai YT, Aguirre-Ghiso J, Flores SC, and Melendez JA. Mitochondrial H₂O₂ regulates the angiogenic phenotype via PTEN oxidation. *J Biol Chem* 280: 16916–16924, 2005.
10. Dawes P, Cruickshanks KJ, Moore DR, Edmondson-Jones M, McCormack A, Fortnum H, and Munro KJ. Cigarette smoking, passive smoking, alcohol consumption, and hearing loss. *J Assoc Res Otolaryngol* 15: 663–674, 2014.
11. Demaria M, Camporeale A, and Poli V. STAT3 and metabolism: how many ways to use a single molecule? *Int J Cancer* 135: 1997–2003, 2014.
- 11a. Drake RL, Vogl AW, and Mitchell AWM. Gray's Anatomy for Students, 2nd Edition. Philadelphia, PA: Churchill Livingstone/Elsevier, 2009.
12. Estivill X, Govea N, Barcelo E, Badenas C, Romero E, Moral L, Scozzari R, D'Urbano L, Zeviani M, and Torroni A. Familial progressive sensorineural deafness is mainly due to the mtDNA A1555G mutation and is enhanced by treatment of aminoglycosides. *Am J Hum Genet* 62: 27–35, 1998.
13. Farr SA, Poon HF, Dogrukol-Ak D, Drake J, Banks WA, Eyerman E, Butterfield DA, and Morley JE. The antioxidants alpha-lipoic acid and N-acetylcysteine reverse memory impairment and brain oxidative stress in aged SAMP8 mice. *J Neurochem* 84: 1173–1183, 2003.
14. Fischel-Ghodsian N, Bykhovskaya Y, Taylor K, Kahen T, Cantor R, Ehrenman K, Smith R, and Keithley E. Temporal bone analysis of patients with presbycusis reveals high frequency of mitochondrial mutations. *Hear Res* 110: 147–154, 1997.
15. Francis HW, Ryugo DK, Gorelikow MJ, Prosen CA, and May BJ. The functional age of hearing loss in a mouse model of presbycusis. II. Neuroanatomical correlates. *Hear Res* 183: 29–36, 2003.
16. Fujimoto C and Yamasoba T. Oxidative stresses and mitochondrial dysfunction in age-related hearing loss. *Oxid Med Cell Longev* 2014: 582849, 2014.
17. Gispert S, Parganlija D, Klinkenberg M, Drose S, Wittig I, Mittelbronn M, Grzmil P, Koob S, Hamann A, Walter M, Buchel F, Adler T, Hrabe de Angelis M, Busch DH, Zell A, Reichert AS, Brandt U, Osiewicz HD, Jendrach M, and Auburger G. Loss of mitochondrial peptidase Clpp leads to infertility, hearing loss plus growth retardation via accumulation of CLPX, mtDNA and inflammatory factors. *Hum Mol Genet* 22: 4871–4887, 2013.
18. Harrison DE, Strong R, Sharp ZD, Nelson JF, Astle CM, Flurkey K, Nadon NL, Wilkinson JE, Frenkel K, Carter CS, Pahor M, Javors MA, Fernandez E, and Miller RA. Rapamycin fed late in life extends lifespan in genetically heterogeneous mice. *Nature* 460: 392–395, 2009.
19. Henderson D, Bielefeld EC, Harris KC, and Hu BH. The role of oxidative stress in noise-induced hearing loss. *Ear Hear* 27: 1–19, 2006.
20. Hood MI, Uzhachenko R, Boyd K, Skaar EP, and Ivanova AV. Loss of mitochondrial protein Fus1 augments host resistance to *Acinetobacter baumannii* infection. *Infect Immun* 81: 4461–4469, 2013.
21. Howell JJ and Manning BD. mTOR couples cellular nutrient sensing to organismal metabolic homeostasis. *Trends Endocrinol Metab* 22: 94–102, 2011.
22. Ivanova AV, Ivanov SV, Pascal V, Lumsden JM, Ward JM, Morris N, Tessarolo L, Anderson SK, and Lerman MI. Autoimmunity, spontaneous tumorigenesis, and IL-15 insufficiency in mice with a targeted disruption of the tumour suppressor gene Fus1. *J Pathol* 211: 591–601, 2007.
23. Keithley EM, Canto C, Zheng QY, Wang X, Fischel-Ghodsian N, and Johnson KR. Cu/Zn superoxide dismutase and age-related hearing loss. *Hear Res* 209: 76–85, 2005.
24. Kim HJ, Gratton MA, Lee JH, Perez Flores MC, Wang W, Doyle KJ, Beermann F, Crognale MA, and Yamoah EN. Precise toxicogenic ablation of intermediate cells abolishes the “battery” of the cochlear duct. *J Neurosci* 33: 14601–14606, 2013.
25. Konrad-Martin D, Dille MF, McMillan G, Griest S, McDermott D, Fausti SA, and Austin DF. Age-related changes in the auditory brainstem response. *J Am Acad Audiol* 23: 18–35; quiz 74–75, 2012.
26. Konrad-Martin D, Reavis KM, Austin D, Reed N, Gordon J, McDermott D, and Dille MF. Hearing Impairment in Relation to Severity of Diabetes in a Veteran Cohort. *Ear Hear* 36: 381–394, 2015.
27. Kujawa SG and Liberman MC. Acceleration of age-related hearing loss by early noise exposure: evidence of a mis-spent youth. *J Neurosci* 26: 2115–2123, 2006.
28. Kujawa SG and Liberman MC. Synaptopathy in the noise-exposed and aging cochlea: primary neural degeneration in acquired sensorineural hearing loss. *Hear Res* 330: 191–199, 2015.
29. Kuo HT, Lee JJ, Hsiao HH, Chen HW, and Chen HC. N-acetylcysteine prevents mitochondria from oxidative injury induced by conventional peritoneal dialysate in human peritoneal mesothelial cells. *Am J Nephrol* 30: 179–185, 2009.
30. Lee SR, Yang KS, Kwon J, Lee C, Jeong W, and Rhee SG. Reversible inactivation of the tumor suppressor PTEN by H₂O₂. *J Biol Chem* 277: 20336–20342, 2002.
31. Leslie NR, Batty IH, Maccario H, Davidson L, and Downes CP. Understanding PTEN regulation: PIP2, polarity and protein stability. *Oncogene* 27: 5464–5476, 2008.
32. Lin FR, Thorpe R, Gordon-Salant S, and Ferrucci L. Hearing loss prevalence and risk factors among older adults in the United States. *J Gerontol A Biol Sci Med Sci* 66: 582–590, 2011.
33. Lopez MF, Kristal BS, Chernokalskaya E, Lazarev A, Shestopalov AI, Bogdanova A, and Robinson M. High-throughput profiling of the mitochondrial proteome using affinity fractionation and automation. *Electrophoresis* 21: 3427–3440, 2000.
34. Marcus DC, Thalman R, and Marcus NY. Respiratory rate and ATP content of stria vascularis of guinea pig in vitro. *Laryngoscope* 88: 1825–1835, 1978.
35. Markaryan A, Nelson EG, and Hinojosa R. Quantification of the mitochondrial DNA common deletion in presbycusis. *Laryngoscope* 119: 1184–1189, 2009.
36. Matsuda S, Kitagishi Y, and Kobayashi M. Function and characteristics of PINK1 in mitochondria. *Oxid Med Cell Longev* 2013: 601587, 2013.
37. McFadden SL, Ding D, Burkard RF, Jiang H, Reaume AG, Flood DG, and Salvi RJ. Cu/Zn SOD deficiency potentiates hearing loss and cochlear pathology in aged 129,CD-1 mice. *J Comp Neurol* 413: 101–112, 1999.
38. McKay SE, Yan W, Nouws J, Thormann MJ, Raimundo N, Khan A, Santos-Sacchi J, Song L, and Shadel GS. Auditory Pathology in a Transgenic mtTFB1 Mouse Model of Mitochondrial Deafness. *Am J Pathol* 185: 3132–3140, 2015.
39. Menardo J, Tang Y, Ladrech S, Lenoir M, Casas F, Michel C, Bourien J, Ruel J, Rebillard G, Maurice T, Puel JL, and Wang J. Oxidative stress, inflammation, and autophagic stress as the key mechanisms of premature age-related hearing loss in SAMP8 mouse Cochlea. *Antioxid Redox Signal* 16: 263–274, 2012.

40. Moreau K, Luo S, and Rubinsztein DC. Cytoprotective roles for autophagy. *Curr Opin Cell Biol* 22: 206–211, 2010.
41. Nacarelli T, Azar A, and Sell C. Aberrant mTOR activation in senescence and aging: a mitochondrial stress response? *Exp Gerontol* 68: 66–70, 2015.
42. Nadol JB, Jr. Hearing loss. *N Engl J Med* 329: 1092–1102, 1993.
43. Ng S, Wu YT, Chen B, Zhou J, and Shen HM. Impaired autophagy due to constitutive mTOR activation sensitizes TSC2-null cells to cell death under stress. *Autophagy* 7: 1173–1186, 2011.
44. Nicholls DG. Mitochondrial function and dysfunction in the cell: its relevance to aging and aging-related disease. *Int J Biochem Cell Biol* 34: 1372–1381, 2002.
45. Ohlemiller KK. Contributions of mouse models to understanding of age- and noise-related hearing loss. *Brain Res* 1091: 89–102, 2006.
46. Ohlemiller KK. Mechanisms and genes in human strial presbycusis from animal models. *Brain Res* 1277: 70–83, 2009.
47. Ohlemiller KK, Lett JM, and Gagnon PM. Cellular correlates of age-related endocochlear potential reduction in a mouse model. *Hear Res* 220: 10–26, 2006.
48. Ohlemiller KK, McFadden SL, Ding DL, Lear PM, and Ho YS. Targeted mutation of the gene for cellular glutathione peroxidase (Gpx1) increases noise-induced hearing loss in mice. *J Assoc Res Otolaryngol* 1: 243–254, 2000.
49. Ohlemiller KK, Rice ME, and Gagnon PM. Strial microvascular pathology and age-associated endocochlear potential decline in NOD congenic mice. *Hear Res* 244: 85–97, 2008.
50. Ohlemiller KK, Rice ME, Lett JM, and Gagnon PM. Absence of strial melanin coincides with age-associated marginal cell loss and endocochlear potential decline. *Hear Res* 249: 1–14, 2009.
51. Ortega-Molina A, Efeyan A, Lopez-Guadamillas E, Munoz-Martin M, Gomez-Lopez G, Canamero M, Mulero F, Pastor J, Martinez S, Romanos E, Mar Gonzalez-Barroso M, Rial E, Valverde AM, Bischoff JR, and Serrano M. Pten positively regulates brown adipose function, energy expenditure, and longevity. *Cell Metab* 15: 382–394, 2012.
52. Ortega-Molina A and Serrano M. PTEN in cancer, metabolism, and aging. *Trends Endocrinol Metab* 24: 184–189, 2013.
53. Perl A. mTOR activation is a biomarker and a central pathway to autoimmune disorders, cancer, obesity, and aging. *Ann N Y Acad Sci* 1346: 33–44, 2015.
54. Pickrell AM and Youle RJ. The roles of PINK1, parkin, and mitochondrial fidelity in Parkinson's disease. *Neuron* 85: 257–273, 2015.
55. Ryter SW, Mizumura K, and Choi AM. The impact of autophagy on cell death modalities. *Int J Cell Biol* 2014: 502676, 2014.
56. Sarangarajan R and Boissy RE. Tyrp1 and oculocutaneous albinism type 3. *Pigment Cell Res* 14: 437–444, 2001.
57. Schacht J, Talaska AE, and Rybak LP. Cisplatin and aminoglycoside antibiotics: hearing loss and its prevention. *Anat Rec (Hoboken)* 295: 1837–1850, 2012.
58. Schriener SE and Linford NJ. Extension of mouse lifespan by overexpression of catalase. *Age (Dordr)* 28: 209–218, 2006.
59. Schriener SE, Linford NJ, Martin GM, Treuting P, Ogburn CE, Emond M, Coskun PE, Ladiges W, Wolf N, Van Remmen H, Wallace DC, and Rabinovitch PS. Extension of murine life span by overexpression of catalase targeted to mitochondria. *Science* 308: 1909–1911, 2005.
60. Sergeenko Y, Lall K, Liberman MC, and Kujawa SG. Age-related cochlear synaptopathy: an early-onset contributor to auditory functional decline. *J Neurosci* 33: 13686–13694, 2013.
61. Sewell WF. The effects of furosemide on the endocochlear potential and auditory-nerve fiber tuning curves in cats. *Hear Res* 14: 305–314, 1984.
62. Someya S, Xu J, Kondo K, Ding D, Salvi RJ, Yamasoba T, Rabinovitch PS, Weindruch R, Leeuwenburgh C, Tanokura M, and Prolla TA. Age-related hearing loss in C57BL/6J mice is mediated by Bak-dependent mitochondrial apoptosis. *Proc Natl Acad Sci U S A* 106: 19432–19437, 2009.
63. Someya S, Yamasoba T, Kujoth GC, Pugh TD, Weindruch R, Tanokura M, and Prolla TA. The role of mtDNA mutations in the pathogenesis of age-related hearing loss in mice carrying a mutator DNA polymerase gamma. *Neurobiol Aging* 29: 1080–1092, 2008.
64. Spicer SS and Schulte BA. Pathologic changes of presbycusis begin in secondary processes and spread to primary processes of strial marginal cells. *Hear Res* 205: 225–240, 2005.
65. Spoenclin H. Innervation densities of the cochlea. *Acta Otolaryngol* 73: 235–248, 1972.
66. Steelman LS, Chappell WH, Abrams SL, Kempf RC, Long J, Laidler P, Mijatovic S, Maksimovic-Ivanic D, Stivala F, Mazzarino MC, Donia M, Fagone P, Malaponte G, Nicoletti F, Libra M, Milella M, Tafuri A, Bonati A, Basecke J, Cocco L, Evangelisti C, Martelli AM, Montalto G, Cervello M, and McCubrey JA. Roles of the Raf/MEK/ERK and PI3K/PTEN/Akt/mTOR pathways in controlling growth and sensitivity to therapy-implications for cancer and aging. *Aging (Albany NY)* 3: 192–222, 2011.
67. Terman A, Gustafsson B, and Brunk UT. The lysosomal-mitochondrial axis theory of postmitotic aging and cell death. *Chem Biol Interact* 163: 29–37, 2006.
68. Travlos GS. Histopathology of bone marrow. *Toxicol Pathol* 34: 566–598, 2006.
69. Trifunovic A, Wredenberg A, Falkenberg M, Spelbrink JN, Rovio AT, Bruder CE, Bohlooly YM, Gidlof S, Oldfors A, Wibom R, Tornell J, Jacobs HT, and Larsson NG. Premature ageing in mice expressing defective mitochondrial DNA polymerase. *Nature* 429: 417–423, 2004.
70. Uzhachenko R, Issaeva N, Boyd K, Ivanov SV, Carbone DP, and Ivanova AV. Tumour suppressor Fus1 provides a molecular link between inflammatory response and mitochondrial homeostasis. *J Pathol* 227: 456–469, 2012.
71. Uzhachenko R, Ivanov SV, Yarbrough WG, Shanker A, Medzhitov R, and Ivanova AV. Fus1/Tusc2 is a novel regulator of mitochondrial calcium handling, Ca²⁺-coupled mitochondrial processes, and Ca²⁺-dependent NFAT and NF- κ B pathways in CD4⁺ T cells. *Antioxid Redox Signal* 20: 1533–1547, 2014.
72. Uzhachenko R, Shanker A, Yarbrough WG, and Ivanova AV. Mitochondria, calcium, and tumor suppressor Fus1: at the crossroad of cancer, inflammation, and autoimmunity. *Oncotarget* 6: 20754–20772, 2015.
73. von Arnim S, Wang G, Boulouiz R, Rutherford MA, Smith GM, Li Y, Pogoda HM, Nurnberg G, Stiller B, Volk AE, Borck G, Hong JS, Goodyear RJ, Abidi O, Nurnberg P, Hofmann K, Richardson GP, Hammerschmidt M, Moser T, Wollnik B, Koehler CM, Teitel MA, Barakat A, and Kubisch C. A mutation in PNPT1, encoding mitochondrial-RNA-import protein PNPase, causes hereditary hearing loss. *Am J Hum Genet* 91: 919–927, 2012.

74. Wang Y, Hirose K, and Liberman MC. Dynamics of noise-induced cellular injury and repair in the mouse cochlea. *J Assoc Res Otolaryngol* 3: 248–268, 2002.
75. Wong AC and Ryan AF. Mechanisms of sensorineural cell damage, death and survival in the cochlea. *Front Aging Neurosci* 7: 58, 2015.
76. Yazlovitskaya EM, Uzhachenko R, Voziyan PA, Yarbrough WG, and Ivanova AV. A novel radioprotective function for the mitochondrial tumor suppressor protein Fus1. *Cell Death Dis* 4: e687, 2013.
77. Yazlovitskaya EM, Voziyan PA, Manavalan T, Yarbrough WG, and Ivanova AV. Cellular oxidative stress response mediates radiosensitivity in Fus1-deficient mice. *Cell Death Dis* 6: e1652, 2015.

Address correspondence to:

Dr. Lei Song
 Department of Otolaryngology-Head and Neck Surgery
 Ninth People's Hospital
 Shanghai Jiao Tong University School of Medicine
 Shanghai 200011
 China

E-mail: lei.song@yale.edu; lei.song@vip.126.com

Prof. Joseph Santos-Sacchi
 Department of Surgery, Section of Otolaryngology
 Yale University School of Medicine
 New Haven, CT 06510

E-mail: joseph.santos-sacchi@yale.edu

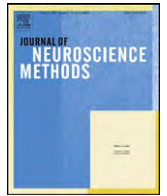
Dr. Alla V. Ivanova
 Department of Surgery, Section of Otolaryngology
 Yale University School of Medicine
 New Haven, CT 06510

E-mail: alla.ivanova@yale.edu

Date of first submission to ARS Central, August 10, 2016; date of final revised submission, January 20, 2017; date of acceptance, January 26, 2017.

Abbreviations Used

ABR = auditory brainstem response
 AO = antioxidant
 ARHL = age-related hearing loss
 BBB = blood–brain barrier
 dB = decibel
 EP = endocochlear potential
 IHC = inner hair cell
 IC = intermediate cell
 MC = marginal cell
 NAC = N-acetyl cysteine
 OHC = outer hair cell
 ROS = reactive oxygen species
 SGN = spiral ganglion neuron
 SPL = sound pressure level
 SV = stria vascularis
 SL = spiral ligament
 TEM = transmission electron microscopy



Patch-clamp amplifiers on a chip

Pujitha Weerakoon^{a,1}, Eugenio Culurciello^b, Youshan Yang^c,
Joseph Santos-Sacchi^{c,d,e}, Peter J. Kindlmann^b, Fred J. Sigworth^{a,c,*}

^a Department of Biomedical Engineering, Yale University, New Haven, CT 06520, United States

^b Department of Electrical Engineering, Yale University, New Haven, CT 06520, United States

^c Department of Cellular and Molecular Physiology, Yale University, New Haven, CT 06520, United States

^d Department of Neurobiology, Yale University, New Haven, CT 06520, United States

^e Department of Surgery (Otolaryngology), Yale University, New Haven, CT 06520, United States

ARTICLE INFO

Article history:

Received 18 May 2010

Accepted 28 June 2010

Keywords:

Patch-clamp
Amplifier
Series resistance
Integrated circuit
Voltage clamp

ABSTRACT

We present the first, fully integrated, two-channel implementation of a patch-clamp measurement system. With this “PatchChip” two simultaneous whole-cell recordings can be obtained with rms noise of 8 pA in a 10 kHz bandwidth. The capacitance and series-resistance of the electrode can be compensated up to 10 pF and 100 M Ω respectively under computer control. Recordings of hERG and Na_v 1.7 currents demonstrate the system’s capabilities, which are on par with large, commercial patch-clamp instrumentation. By reducing patch-clamp amplifiers to a millimeter size micro-chip, this work paves the way to the realization of massively parallel, high-throughput patch-clamp systems for drug screening and ion-channel research. The PatchChip is implemented in a 0.5 μ m silicon-on-sapphire process; its size is 3 \times 3 mm² and the power consumption is 5 mW per channel with a 3.3 V power supply.

© 2010 Elsevier B.V. All rights reserved.

1. Introduction

The patch-clamp amplifier is a ubiquitous tool for characterizing ion-channel activity. For the screening of pharmaceutical compounds or the characterization of expressed channels, high-throughput patch-clamp systems are being developed, where recordings are made from cells in each well of a 96- or 384-well plate. In these systems the recording is made not with a glass pipette, but from a planar electrode at the bottom of each well (Fig. 1). An important part of such highly-parallel recording systems is a high-density array of patch-clamp amplifiers. We present here a highly miniaturized patch-clamp amplifier with complete whole-cell measurement capabilities.

Important constraints in building massively parallel patch-clamp systems have been the size and cost of the amplifiers, heat dissipation – which restricts the proximity of the amplifiers to the cells – and cross-talk between channels. The integrated “PatchChip” amplifier presented in this paper solves all of these design requirements, and is based on experience from our prototypes (Weerakoon et al., 2009, 2007a,b; Laiwalla et al., 2006a,b,c).

The dual-channel patch-clamp system occupies 3 \times 3 mm² of area and consumes just 5 mW of power per channel. It is fabricated using a standard silicon-on-sapphire fabrication process, which allows parasitic capacitances and cross-talk effects to be minimized.

2. Materials and methods

Fig. 2 shows a block diagram of one channel of the PatchChip system. The two channels of the system are identical. The main signal path is from the electrode current I_{in} to the monitor voltage output $V_{out} = I_{in}R_f$, through operational amplifiers A1, A2, and A3.

Cells are stimulated by controlling the voltage $V_p = V_{clamp}$ at the electrode and measuring the resultant ionic current I_{in} . The goal of the compensation circuits is to allow step changes to be applied to the cell membrane potential V_m while the ionic current I_i is measured. The cell membrane can be modeled as a capacitance C_m in parallel with the membrane resistance R_m . The headstage of the patch-clamp recording system consists of a current-to-voltage transimpedance amplifier A1. The feedback resistor R_f is selectable in eight steps from 50 k Ω to 10 M Ω . Small shunt capacitors stabilize the feedback loop while yielding a bandwidth of a minimum of 300 kHz (with $R_f = 10$ M Ω) when the total capacitance on the input node is 30 pF. A difference amplifier A2 subtracts V_{clamp} from the transimpedance output. The resultant output voltage V_{out} is proportional to the input current, I_{in} .

The output filter A3 represents two poles of a three-pole, 20 kHz anti-aliasing filter. The third pole is presented by an external capac-

* Corresponding author at: Yale University, Department of Cellular and Molecular Physiology, 333 Cedar Street, New Haven, CT 06520, United States.

Tel.: +1 203 785 5773.

E-mail address: fred.sigworth@yale.edu (F.J. Sigworth).

¹ Present address: Boston Scientific Neuromodulation Corp., 25155 Rye Canyon Loop, Valencia, CA 91355, United States.

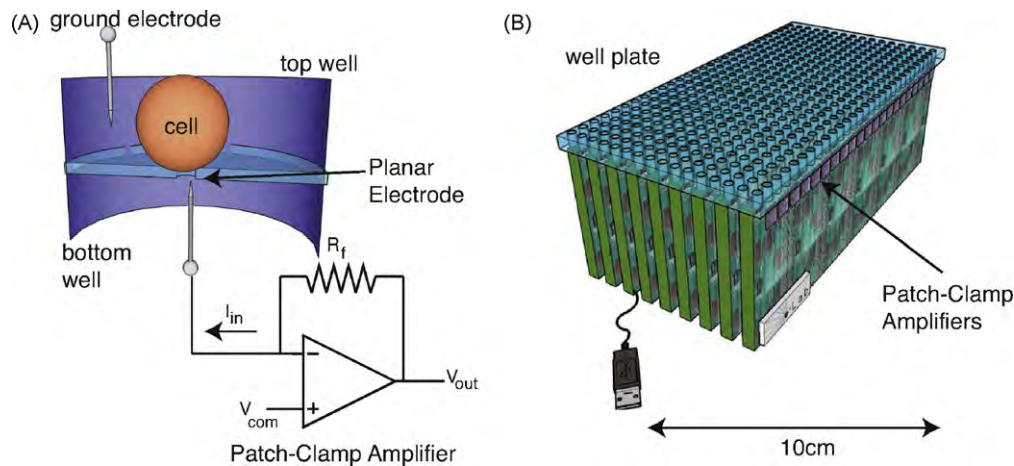


Fig. 1. (A) Patch-clamp amplifier performing whole-cell membrane current recording using a planar electrode. The planar electrode replaces the traditional glass micro-pipette with a micron sized-aperture that is topologically equivalent to the glass tip of the pipette. Cells are introduced into well, and when suction is applied, the cells seal into the aperture. Further suction is applied to rupture the cell so that a whole-cell configuration is established. (B) Using the amplifiers presented in this paper, it is possible to design a high-throughput, automatic patch-clamp system that operates on entire 384-well plates. The wells on B are identical to the one in (A). Requirements for the amplifier are millimeter-size dimensions and minimized heat dissipation, cross-talk and low fabrication cost.

itor and is the only “glue” component required for the analog interface between the PatchChip and the external A–D converter. Similarly, the two-pole input reconstruction filter A6, critically damped with a time constant of $2 \mu\text{s}$, smooths the input command signal V_{com} delivered directly from an external D–A converter and prevents rapid steps from causing nonlinearities and slew-limiting in the other amplifiers of the system.

2.1. Electrode compensation circuitry

The system compensates for the difference between the actual membrane voltage V_m and the clamping voltage V_{clamp} due to the voltage drop across the pipette electrode series resistance R_s . The circuit also compensates for the current i_{prs} drawn by the electrode parasitic capacitance C_{prs} and by the seal leakage-resistance R_L . R_s

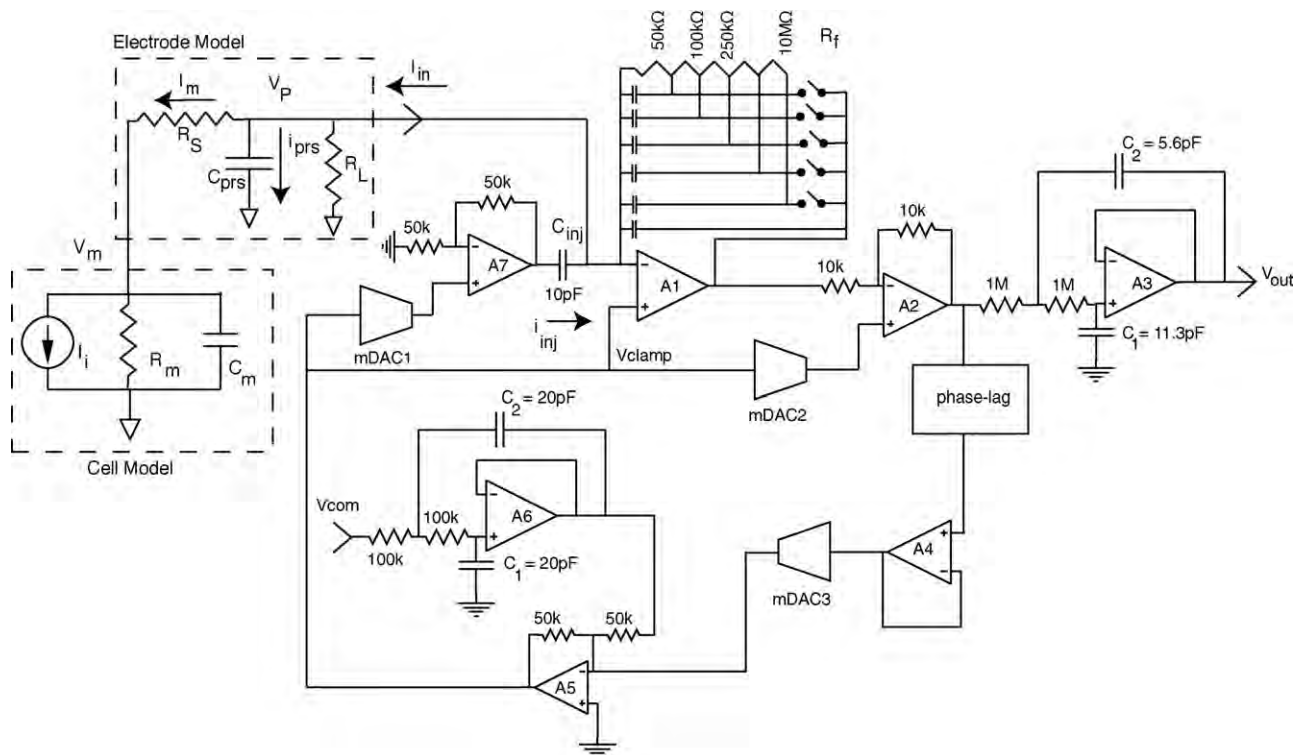


Fig. 2. One channel of the two-channel integrated patch-clamp system and the electrical model of a cell and pipette electrode. The main signal path is from the electrode current I_{in} to the monitor voltage output $V_{out} = I_{in}R_f$, through operational amplifiers A1, A2 and A3. Multiplying digital to analog converter mDAC1 controls the parasitic capacitive compensation, mDAC2 provides leak subtraction, mDAC3 and the phase-lag controller circuit provides series resistance compensation. Input reconstruction and output anti-aliasing filters are also integrated. mDAC1 and mDAC2 are voltage-mode, R-2R DACs with $R = 50\text{k}\Omega$, minimum gains of 0.5, and resolutions of 8 and 10 bits, respectively. mDAC3 is a 9-bit hybrid transconductance-mode DAC with a maximum transconductance of 0.2 mS . Typical values of the electrode and cell elements are $C_{prs} = 5\text{ pF}$, $R_L = 100\text{ M}\Omega$, $R_s = 10\text{ M}\Omega$, $C_m = 30\text{ pF}$, $R_m = 100\text{ M}\Omega$ and peak values of I_i are 1–10 nA.

compensation is necessary for two reasons. First, it allows accurate voltage clamping of the membrane by reducing the errors from the voltage drop across the series access resistance R_s . Second, the compensation reduces the time needed to charge C_m enabling the circuit to monitor ion-channel events occurring immediately after changes in V_{com} is applied (Sigworth, 1995b). The drop across R_s is predicted by adding a fraction of V_{out} to the applied membrane-command potential V_{com} by means of amplifier A5, to obtain V_{clamp} . The fraction of compensated series-resistance is determined by the 9-bit mDAC3, which at full-scale yields compensation for a resistance of $10 \times R_f$. mDAC3 was designed as a hybrid weighted-resistor and R-2R device to minimize the noise gain of the A5 stage. A passive phase-lag compensation circuit is included in the positive-feedback loop if desired, to improve stability when a high percentage of R_s , e.g. more than 90%, is compensated.

For effective R_s compensation the measured current must be equal to the current I_m flowing through R_s . The charging current of the parasitic electrode capacitance C_{prs} and the current through the leakage conductance R_l therefore must first be subtracted from the measurement of I_m . The capacitive-current subtraction is done by injecting a current i_{inj} through an integrated capacitor C_{inj} of 10 pF. The gain α_{inj} of the amplifier A7 is determined by the 8-bit mDAC1 to be between 1 and 2. The compensated capacitance is equal to $(\alpha_{inj} - 1)C_{inj}$.

The differential amplifier A2 is unbalanced when the voltage-output mDAC2 is set to a gain different from its minimum value of 0.5. As its gain increases, subtraction is provided for the excess I_m on the input. The maximum gain of the 10-bit mDAC2 is unity, allowing for compensation of a leakage resistance as high as R_f . All three compensation circuits are controlled using a serial digital control bus. A 64-bit shift register and buffer register store the bit patterns for the mDACs and various switches in one patch-clamp channel.

2.2. Voltage swings and R_f

Modern patch-clamp amplifiers contain an additional ‘‘C-Slow’’ compensation circuit to remove the large current transients due to the charging of the membrane capacitance C_m , which is typically in the range of 20–40 pF. These circuits have been implemented as a first-order state-variable filter (Sigworth, 1995a,b) in which the time constant is roughly 100 μ s to 1 ms. Due to the limited capacitor sizes, and therefore short time constants, that can be realized in a monolithic circuit, we decided not to provide this ‘‘slow capacitance’’ compensation. Instead, this compensation will be provided in software. We rely on the use of a 16-bit or higher resolution A–D converter to digitize the current-monitor signal V_{out} so that the large charging transients can be subtracted digitally.

In the absence of slow-capacitance compensation, the entire charging current of the membrane capacitance must be injected through the feedback resistor R_f . Thus the voltage swing available at the output of amplifier A1 becomes an important issue. We have used a 3.3 V silicon-on-sapphire (SOS) process, so that the analog power-supply voltages are ± 1.6 V. Although the typical membrane-potential excursions are only in the range ± 150 mV, when R_s compensation is in use the excursions of V_p can be an order of magnitude larger.

Consider the case in which a fraction k of the series resistance is compensated. When a voltage step of magnitude ΔV_{com} is applied to V_{com} the effect of the R_s compensation feedback is to produce an initial step $\Delta V_p = \Delta V_{com} / (1 - k)$. For example, a 150 mV step with $k = 0.8$ (80% compensation) yields an initial step of 750 mV. Even ignoring the current through R_l the initial current will be $I_m = \Delta V_p / R_s$ and will have to be sourced through the feedback resistor R_f . Thus the initial voltage at the output of A1 ($V_{out,A1}$) will need

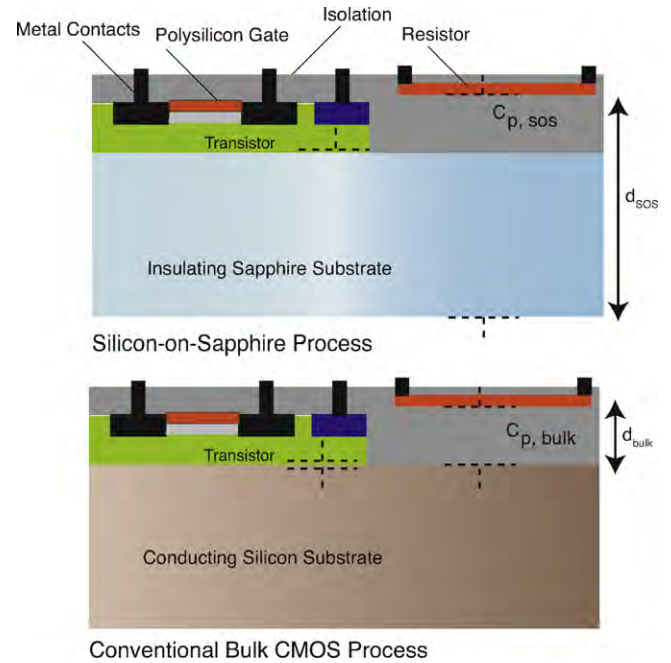


Fig. 3. The patch-clamp system was implemented using silicon-on-sapphire (SOS) technology. The insulating substrate in SOS (top) reduces parasitic capacitance and allows fabrication of large resistors to implement R_f with no degradation in frequency response. The insulating substrate reduces cross-talk between channels and allows devices to operate at faster speeds than conventional bulk CMOS technology (bottom).

to be

$$V_{out,A1} = \frac{\Delta V_{com}(R_s + R_f)}{(1 - k)R_s} \quad (1)$$

If R_f is chosen to be equal to R_s in this example, the initial value of $V_{out,A1}$ must be 1.5 V, very close to the available supply voltage of 1.6 V. To avoid amplifier saturation therefore, two steps must be taken. First, R_f must be kept to a low value, typically 5–10 M Ω in cases where R_s is in this resistance range. Second, amplifier A1 (and also other amplifiers in the circuit) must have a rail-to-rail output swing capability. The characteristics of the operational amplifiers are described in Section 2.4.

The low value of the feedback resistor R_f means that the current-monitor signal of the PatchChip will have a substantial contribution from the resistor’s thermal noise; in a 10 kHz bandwidth this noise is 4 pA rms when $R_f = 10$ M Ω . The thermal noise arising in R_s is also large, and when its value is equal to R_f , its noise is equal to that from R_f at high frequencies $f > f_c$, where $f_c = 1 / (2\pi R_s C_m)$. When R_s compensation is in use, which in effect increases the recording bandwidth beyond f_c , the two resistances R_f and R_s make nearly equal contributions to the noise variance. Thus the low value of R_f does result in increased noise, but the increase is moderate, about a factor of $\sqrt{2}$ over the theoretical minimum noise due to R_s alone.

2.3. Silicon-on-sapphire technology

The PatchChip was implemented using the silicon-on-sapphire (SOS) technology. SOS offers several advantages over conventional bulk CMOS technology, as is illustrated in Fig. 3. First, the absence of a conducting substrate greatly reduces parasitic capacitance and allows the fabrication of large, nearly ideal resistors. In conventional bulk-CMOS processes the source and drain of each transistor is isolated from the substrate by a reverse-biased diode; these diodes contribute a considerable capacitance to each such node in

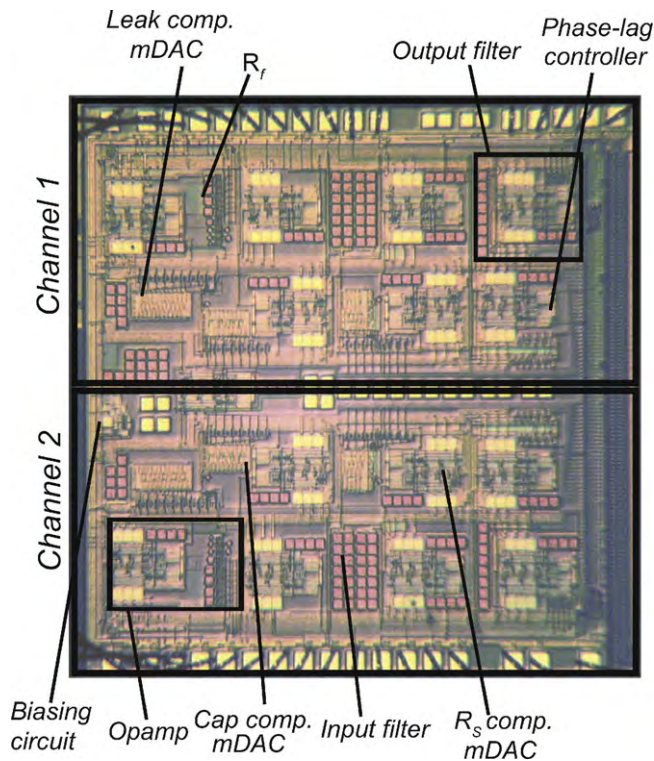


Fig. 4. A micrograph of the test circuit in silicon-on-sapphire technology. The fabricated die contained two channels and occupied just $3 \times 3 \text{ mm}^2$. Each channel has series resistance, parasitic capacitance and leak compensation capability. After initial setup expenditures, each amplifier costs just a few dollars to manufacture.

the circuit. Even resistor elements, which are isolated from the bulk silicon by oxide layers, show considerable parasitic capacitance because the oxide layers are relatively thin. In SOS on the other hand, transistors and resistors are fabricated on top of the thick sapphire substrate (Fig. 3) and therefore experience vastly smaller parasitic capacitances (Culurciello et al., 2007). Second, the non-conducting substrate provides a better means of isolating devices on the substrate, yielding better cross-talk performance between patch-clamp channels. Third, the insulating substrate allows the power supplies for digital and analog parts of this mixed-signal circuit to be separated to obtain better noise performance. Fourth, the lower parasitic capacitance allows SOS devices to perform at faster speeds and lower power than those made using conventional bulk CMOS technology (Culurciello, 2010). The final layout of the microchip implementing the two-channel patch-clamp system is shown in Fig. 4. This layout is the physical implementation of the circuits reported in Fig. 2.

2.4. High-performance operational amplifier design

A low-noise, rail-to-rail, constant-transconductance operational amplifier was designed specifically for this system (Weerakoon et al., 2010). SOS transistors have low output resistance and therefore yield low voltage gains; we therefore made extensive use of cascode circuits, obtaining with this three-stage design a DC gain of 75 dB and a gain-bandwidth product of 12 MHz for unity-gain operation. Fig. 5 shows the fabricated operational amplifier, which occupies an area of less than 0.1 mm^2 . Rail-to-rail operation of the amplifier is needed to maximize voltage swings with the small power-supply voltages. The amplifier reported a $3 \text{ nV}/\sqrt{\text{Hz}}$ of input-referred voltage noise in a bandwidth of 10 kHz, and $<1 \text{ mV}$ of input-referred offset, while consuming 1.4 mW of power. Table 1 reports a summary of the amplifier characteristics.

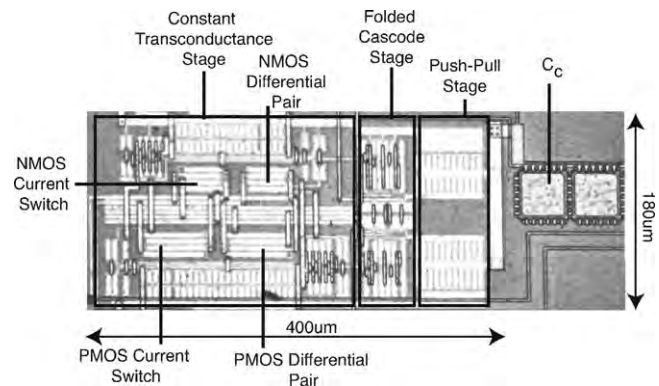


Fig. 5. A die micrograph of the fabricated operational amplifier. The operational amplifier occupies an area of 0.08 mm^2 providing rail-to-rail output voltage and constant gain-bandwidth product over the entire rail-to-rail common-mode range. The capacitor C_c is the frequency-compensation capacitor.

3. Results

We have extensively tested the electrical properties of the two-channel patch-clamp system, and its functionality in patch-clamp recordings from cells. In these tests the system was controlled and data were acquired using the JClamp patch-clamp software (www.scisoftco.com). The results are comparable to those from commercial non-integrated patch clamp amplifiers.

Fig. 6 shows the measured step responses of the series resistance compensation circuit. The time constant τ associated with charging the membrane capacitance C_m through a compensated resistance ($R_S - R_{comp}$) when a step V_{com} is applied (inset), is given by $\tau = C_m(R_S - R_{comp})$. Increasing compensation, R_{comp} approaches R_S and τ decreases, increasing recording bandwidth. Using the series resistance compensation circuit, we compensated 3–4 M Ω of the 4 M Ω electrode series resistance, decreasing the time needed to charge C_m from $\tau = 200$ to $50 \mu\text{s}$ (75% compensation) and about $120 \mu\text{s}$ (100% compensation). Full resistance compensation can only be obtained with the phase-lag compensation circuit, which yields complete compensation at low frequencies but slows the settling time of the system.

Fig. 6 shows the measured step response of the electrode capacitive compensation circuit. When uncompensated, the headstage provides the current i_{prs} needed to charge the parasitic capacitance. This current appears as spikes in the current-monitor signal with the same polarity as V_{com} . When properly compensated, the spikes are greatly reduced in size.

Fig. 7 shows measured simultaneous data from both channels of the system. We applied a large voltage step (100 mV) to one channel with a model cell connected to its input terminal. The cross-talk on the adjacent non-measuring channel is 40 dB lower even with 80% series resistance compensation in use.

Table 1

Measurement results for the operational amplifier designed for the patch-clamp system. A load resistance of 15 k Ω and a 3.3 V power supply was used in the measurements. The operational amplifier met all design specifications.

Die area	0.08 mm ²
Open loop gain	75 dB
Gain-bandwidth product	12 MHz
Input-referred offset voltage	0.4 mV
Input common-mode range	0–3.3 V
Output swing	0–3.3 V
Slew rate	10 V/ μs
Input-referred voltage noise at 10 kHz	$3 \times 10^{-9} \text{ V}/\sqrt{\text{Hz}}$
Quiescent current	430 μA
Input capacitance	2.6 pF

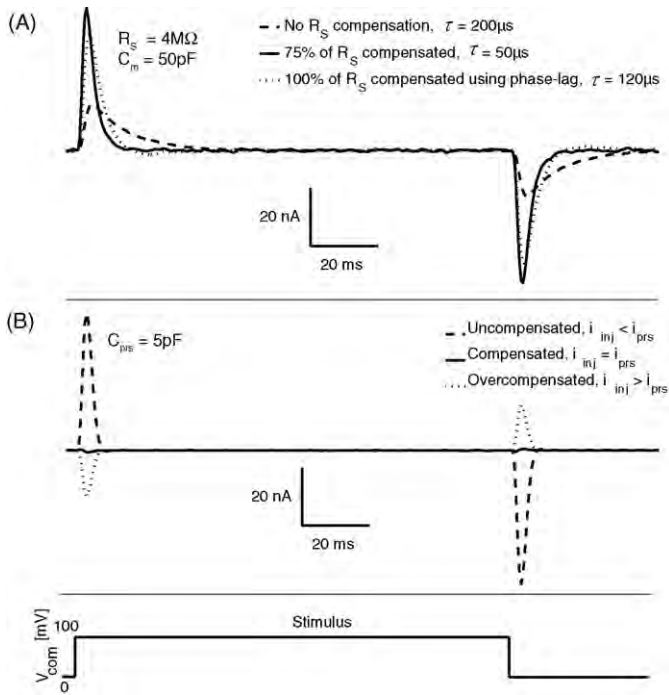


Fig. 6. (A) Measured response of the series resistance compensation circuit when compensating a 4 MΩ electrode series resistance. The time needed to charge C_m was reduced from $\tau=200$ to $50 \mu\text{s}$ (75% compensation) and $120 \mu\text{s}$ (100% compensation with phase-lag). (B) Measured step response of the electrode capacitive compensation circuit when compensating 5 pF at the input. When uncompensated, the headstage provides the current $i_{\text{pr}s}$ needed to charge the parasitic capacitance. This current appears as spikes in the current–monitor signal. When properly compensated, $i_{\text{pr}s} = i_{\text{inj}}$ and the spikes do not appear. When overcompensated, $i_{\text{inj}} > i_{\text{pr}s}$ and the spikes reverse polarity.

Fig. 8 shows a whole-cell recording from an HEK293 cell expressing hERG channels. We compensated the 6.5 pF parasitic capacitance, and 80% of the 4.2 MΩ series resistance present at the input. R_f was set to 5 MΩ. The peak tail current curve in (C) shows the standard voltage dependence of inactivation and activation in the channels.

Sodium-channel currents present a particularly demanding test for a whole-cell recording system. The rapid kinetics and negative-resistance characteristic of these currents requires good R_s compensation. Fig. 9 shows single-sweep recordings from an

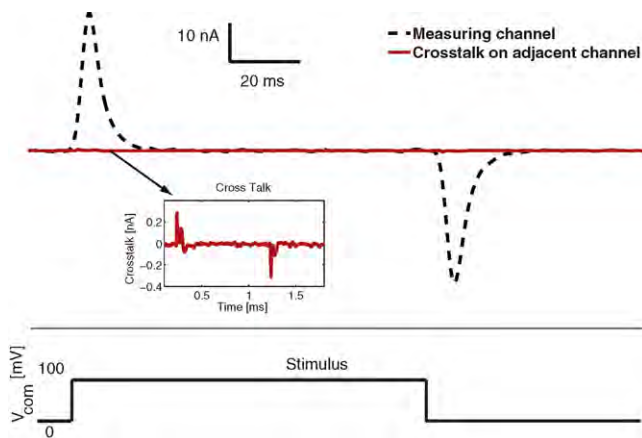


Fig. 7. Measured cross-talk between channels. A voltage step of 100 mV was applied to one channel, which was driving a model circuit with 80% series-resistance compensation. The current–monitor signal in the adjacent non-measuring channel is at least 40 dB lower.

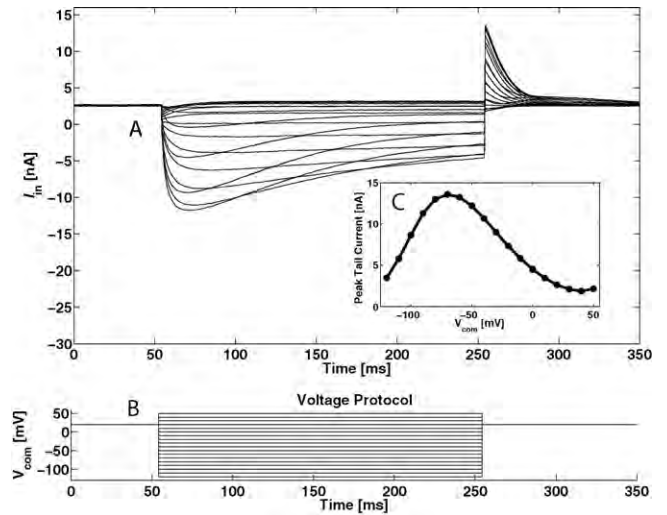


Fig. 8. (A) Single-sweep responses from an HEK 293 cell expressing hERG channels. R_s was 4.2 MΩ of which 80% was compensated. $C_{\text{pr}s}$ of 6.5 pF was fully compensated. C_m was 40 pF. (B) The cells were held at 20 mV and stepped to potentials of -130 mV to 50 mV in 10 mV increments for 200 ms. (C) The tail currents at +20 mV are plotted vs. V_{com} from A. The extracellular solution contained (mM) 117 NaCl, 13 KCl, 10 HEPES, and 5 EGTA. The pipette solution contained 160 KCl, 1 EGTA, and 10 HEPES. Currents were sampled at 100 kHz and filtered at 10 kHz.

HEK293 cell expressing $\text{Na}_v 1.7$ channels. Linear leak and residual capacitance artifacts were subtracted using the $-P/6$ method. This protocol (using six inverted pulse sequences scaled down by a factor of 6, delivered at negative membrane potentials) increases the net rms noise in the traces about threefold. Despite the large cell capacitance ($C_m = 40$ pF) the clamp time constant was 40 μs, giving a faithful current time course. The peak current–voltage curve (Fig. 9) shows steep activation of the channel currents with no evidence of series-resistance error (Estacion et al., 2008).

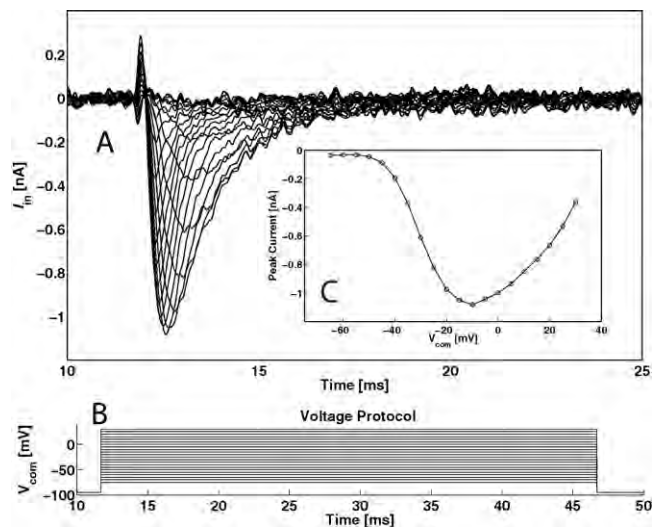


Fig. 9. (A) Single-sweep responses of HEK 293 cells expressing $\text{Na}_v 1.7$ sodium channels, after linear leak subtraction using the $-P/6$ protocol. The leak subtraction increases the net rms noise in the traces about threefold. R_s was 4.5 MΩ of which 80% was compensated. $C_{\text{pr}s}$ of 7 pF was fully compensated. C_m was 40 pF. (B) To generate activation curves, the cells were held at -100 mV and stepped to potentials of -75 to 30 mV in 5 mV increments for 35 ms. (C) The peak currents vs. V_{com} from (A). The current–monitor signal was filtered at 10 kHz and sampled at a 100 kHz rate. The recording was made at room temperature. The extracellular solution contained (in mM) 127 NaCl, 13 KCl, and 10 HEPES. The pipette solution contained 10 NaCl, 140 CsF, 10 HEPES, and 1 EGTA.

Table 2
Key features of the two-channel patch-clamp system.

Technology	0.5 μm silicon-on-sapphire
Number of channels	2 per die
Silicon area	$3 \times 3 \text{ mm}^2$ per die
	$1.5 \times 3 \text{ mm}^2$ per channel
Power consumption	5 mW per channel at 3.3 V
Capacitive compensation	10 pF max
Series resistance compensation	80% up to $10 \times R_f$, or 100% with phase-lag compensation
Leak compensation	Conductance up to $1/R_f$
Current noise	8 pA rms input-referred in a 10 kHz bandwidth ($R_f = 10 \text{ M}\Omega$)
Variable feedback resistor R_f	50, 100, 250, 500 k Ω 1, 2.5, 5, 10 M Ω
Dynamic range	$\pm 20 \mu\text{A}$
Reconstruction filter	2 poles, 60 kHz cutoff
Anti-aliasing filter	3 poles, 20 kHz cutoff
Nonlinearity	<0.1%
Cross-talk between adjacent channels	-40 dB (at 80% series resistance channels compensation)

Table 2 summarizes the key features of the PatchChip. The two-channel system occupies $3 \times 3 \text{ mm}^2$ of area and consumes 5 mW of power per channel. The low power consumption allows the amplifiers to be placed in close proximity to the cells under test. The input-referred noise is 8 pA rms at 10 kHz bandwidth.

4. Discussion

We have implemented a two-channel patch-clamp system in silicon-on-sapphire on a $3 \times 3 \text{ mm}^2$ chip area. The system reports below -40 dB of cross-talk between adjacent channels and the input-referred current noise of the system is 8 pA rms in a 10 kHz bandwidth. The appropriate setting of the feedback resistor, 5–10 M Ω for typical whole-cell recordings, means that the resistor's thermal noise makes a contribution; however this contribution is moderate in comparison to the thermal noise from the series resistance of the electrode-and-cell combination. The system is able to compensate series resistances and parasitic capacitances up to 100 M Ω and 10 pF respectively. The power consumption of the device is 5 mW per channel at 3.3 V. This accurate, low-noise system with electrode compensation can replace a commercial rack-mounted patch-clamp system; more importantly it can also be integrated into a massively parallel, high-throughput, patch-clamp

system that can significantly advance the state-of-the-art in drug screening and ion-channel research.

Acknowledgements

The authors are grateful to Yangyang Yan and Mark Estacion for their assistance with the cell lines; also to John Keeler of Warner Instruments, and Victor Pantani, Henrik Abildgaard, Hazael Montanaro and Andrew Kunil Choe for their assistance in preparing the hardware test-bed. This project was funded in part by NIH R42NS062408, NSF IDBR DBI-0649349 and ONR N00014-08-1-0065.

References

- Culurciello E, Pouliquen P, Andreou A. A digital isolation amplifier in silicon-on-sapphire CMOS. *Electronics Letters* 2007;43(8):451–2.
- Culurciello E. *Silicon-on-sapphire circuits and systems*. 1st edition McGraw-Hill; 2010.
- Estacion M, Dib-Hajj S, Benke P, te Morsche R, Eastman E, Macala L, et al. Na_v1.7 gain-of-function mutations as a continuum: A1632E displays physiological changes associated with erythromelalgia and paroxysmal extreme pain disorder mutations and produces symptoms of both disorders. *Journal of Neuroscience* 2008;28(43):11079–88.
- Laiwalla F, Klemic K, Sigworth F, Culurciello E. An integrated patch-clamp amplifier in silicon-on-sapphire CMOS. *IEEE Transactions on Circuits and Systems, TCAS-I, Special Issue on Life Science and Applications* 2006a;53(11):2364–70.
- Laiwalla F, Klemic K, Sigworth F, Culurciello E. An integrated patch-clamp amplifier in silicon-on-sapphire CMOS. In: *IEEE international symposium on circuits and systems, ISCAS'06, IEEE; 2006b*. p. 4054–7.
- Laiwalla F, Klemic K, Sigworth F, Culurciello E. An integrated silicon-on-sapphire patch-clamp amplifier. In: *IEEE/NLM life science systems and application workshop, IEEE; 2006c*.
- Sigworth F. Design of the EPC-9, a computer-controlled patch-clamp amplifier. 1. Hardware. *Journal of Neuroscience Methods* 1995a;56:195–202.
- Sigworth F. Electronic design of the patch-clamp. In: Sakmann B, Neher E, editors. *Single-channel recording*. 2nd edition New York: Plenum Press; 1995b [Chapter 4].
- Weerakoon P, Klemic K, Sigworth F, Culurciello E. An integrated patch-clamp amplifier for high-density whole-cell recordings. In: *IEEE international symposium on circuits and systems, ISCAS'07, IEEE; 2007a*. p. 1205–9.
- Weerakoon P, Sigworth F, Klemic K, Culurciello E. Integrated patch-clamp biosensor for high-density screening of cell conductance. *IEEE Electron Device Letters* 2007b;44(2):81–2.
- Weerakoon P, Culurciello E, Klemic K, Sigworth F. An integrated patch-clamp potentiostat with electrode compensation. *IEEE Transactions on Biomedical Circuits and Systems* 2009;3:117–25.
- Weerakoon P, Sigworth F, Kindlmann P, Culurciello E. A 3 nV/ $\sqrt{\text{Hz}}$ rail-to-rail operational amplifier in silicon-on-sapphire with constant transconductance. *Analog Integr Circ Sig Process* 2010; doi:10.1007/s10470-010-9484-6.

Effects of Lipophilic Ions on Outer Hair Cell Membrane Capacitance and Motility

M. Wu, J. Santos-Sacchi

Sections of Otolaryngology and Neurobiology, Yale University School of Medicine, New Haven, Connecticut 06510, USA

Received: 14 May 1998/Revised: 24 August 1998

Abstract. The outer hair cell (OHC) from the mammalian organ of Corti possesses a bell-shaped voltage-dependent capacitance function. The nonlinear capacitance reflects the activity of membrane bound voltage sensors associated with membrane motors that control OHC length. We have studied the effects of the lipophilic ions, tetraphenylborate (TPB^-) and tetraphenylphosphonium (TPP^+), on nonlinear capacitance and motility of isolated guinea-pig OHCs. Effects on supporting cells were also investigated. TPB^- produced an increase in the peak capacitance ($C_{m_{pk}}$) and shifted the voltage at peak capacitance (V_{pkCm}) to hyperpolarized levels. Washout reversed the effects. Perfusion of 0.4 μM TPB^- caused an average increase in $C_{m_{pk}}$ of 16.3 pF and V_{pkCm} shift of 13.6 mV. TPP^+ , on the other hand, only shifted V_{pkCm} in the positive direction, with no change in $C_{m_{pk}}$. The contributions from native OHC and TPB^- -induced capacitance were dissected by a double Boltzmann fitting paradigm, and by blocking native OHC capacitance. While mechanical response studies indicate little effect of TPB^- on the motility of OHCs which were in normal condition or treated with salicylate or gadolinium, the voltage at maximum mechanical gain ($V_{\delta L_{max}}$) was shifted in correspondence with native V_{pkCm} , and both changed in a concentration-dependent manner. Both TPB^- -induced changes in $C_{m_{pk}}$ and V_{pkCm} were affected by voltage prepulses and intracellular turgor pressure. TPB^- induced a voltage-dependent capacitance in supporting cells whose characteristics were similar to those of the OHC, but no indication of mechanical responses was noted. Our results indicate that OHC mechanical responses are not simply related to quantity of nonspecific nonlinear charge moved within the membrane, but to the effects of motility voltage-

sensor charge movement functionally coupled to a mechanical effector.

Key words: Cochlea — Gating current — Tetraphenylborate — Motility — Capacitance

Introduction

Acoustic signal processing by the mammalian cochlea is accomplished by two classes of sensory hair cells: the inner hair cells (IHCs) and outer hair cells (OHCs). IHCs are solely mechano-electrical transducers, while OHCs function, in addition, as mechanical effectors. It is believed that the unique voltage-dependent mechanical response of the OHC provides feedback into the basilar membrane, thereby sharpening the passive mechanical vibration of the cochlear partition (Brownell et al., 1985; Ashmore, 1987; Santos-Sacchi & Dilger, 1988; Ruggero, 1992). The OHC demonstrates a nonlinear gating charge movement or, correspondingly, a voltage-dependent capacitance that has characteristics similar to those of OHC motility, indicating that membrane-bound voltage sensor/motor elements control OHC length (Santos-Sacchi, 1990, 1991, 1993; Ashmore, 1989, 1992; Dallos et al., 1991; Iwasa, 1994).

The causal relation between OHC nonlinear charge movement and mechanical response is an important feature in theories of OHC motility where voltage-dependent conformational changes in putative lateral membrane molecular motors fluctuate between two areal states (Santos-Sacchi, 1993; Huang & Santos-Sacchi, 1994; Iwasa, 1994). Accordingly, intrinsic gating charge movement represents the reorientation of charged moieties within a membrane-bound, protein motor molecule. Only this charge movement should be coupled to OHC mechanical activity. Membrane bound charge movement associated with extraneous sources, e.g., the cell's

normal complement of voltage-gated ionic channels or exogenous membrane bound charge, should neither effect nor directly affect OHC motility. Furthermore, blockade of motility-related gating charge should be sufficient to block motility.

To evaluate these predictions, we attempted to induce additional nonlinear charge movement within the OHC plasma membrane with the exogenous hydrophobic ions, tetraphenylborate (TPB^-) and tetraphenylphosphonium (TPP^+). Furthermore, salicylate and Gd^{+3} , known blockers of OHC motility and charge movement (Santos-Sacchi, 1991; Shehata, Brownell & Dieler, 1991; Tunstall, Gale & Ashmore, 1995; Kakehata & Santos-Sacchi, 1996), were evaluated to dissect out contributions of native nonlinear charge movement during hydrophobic ion treatment. Hydrophobic ions such as TPB^- or dipicrylamine have been used to amplify small capacitive signals of secretory vesicle release (Oberhauser & Fernandez, 1995). The ions have also been used as probes of tight junctions (Turin et al., 1991), and membrane structure (Benz & Läuger, 1977; Benz & Nonner, 1981; Dilger & Benz, 1985; Smejtek & Wang, 1991) and function (Reyes & Latorre, 1979; Fernandez, Bezanilla & Taylor, 1982). The TPB^- -induced current is similar, in some ways, to that which arises from voltage-dependent ionic channel gating (Benz & Nonner, 1981).

We report here that TPB^- augments native OHC nonlinear capacitance and produces a negative shift of the equivalent voltages at peak capacitance (V_{pkC_m}) and maximal mechanical gain (V_{dLmax}), but does not enhance the mechanical response. TPP^+ only causes a shift in the voltage dependencies. Such results might be expected from simple charge screening. These data highlight the specific and causal relationship between the native nonlinear capacitance and the mechanical activity of the OHC.

Materials and Methods

METHODS

Guinea pigs were anesthetized with halothane and killed by cervical dislocation. OHCs and supporting cells were isolated enzymatically with dispase I (0.5 mg/ml for 10 min followed by gentle trituration through a polyethylene pipette) in a modified Leibovitz medium which contained (in mM): NaCl 142, KCl 5.37, MgCl_2 1.47, HEPES 5, CaCl_2 2 and dextrose 5; 300 mOsm, pH 7.2. The cells were then transferred to a 700- μl perfusion chamber. All experiments were conducted at room temperature ($\sim 23^\circ\text{C}$). A Nikon Diaphot inverted microscope with Hoffmann optics was used to observe the cells during electrical recording. All experiments were videotaped.

Single OHCs and supporting cells were studied under whole cell voltage-clamp conditions using an Axon 200A amplifier at a holding potential of -80mV . Initial resistances of patch pipettes were 2–3 M Ω , corresponding to tip sizes of 1–2 μm (Hamill et al., 1981). Residual series resistance ranged from 3 to 7 M Ω . All data collection and analysis were performed with an in-house developed Windows-based pro-

gram, **jClamp** (www.med.yale.edu/surgery/otolar/santos/jclamp.html). Ionic blocking solutions were used to remove voltage-dependent ionic conductances so that capacitive currents could be analyzed in isolation (Santos-Sacchi, 1991; Huang & Santos-Sacchi, 1993). The patch pipette solution contained (in mM): CsCl 140, MgCl_2 2, EGTA 10, HEPES 5, with pH 7.2 and osmolarity 300 mOsm (adjusted with dextrose). The external ionic blocking solution contained (in mM): BaCl_2 10, CoCl_2 2, MgCl_2 1.47, NaCl 100, CaCl_2 2, HEPES 5, with pH 7.2 and osmolarity 300 mOsm (adjusted with dextrose). In this solution BaCl_2 replaced the usually employed blockers, CsCl and TEA (Huang & Santos-Sacchi, 1993), because both caused precipitation with sodium tetraphenylboron. The reagents ($\text{Na}^+ \text{TPB}^-$ and $\text{TPP}^+ \text{Cl}^-$) were freshly prepared and applied using the Y-tube method (Murase et al. 1990) at a rate of 0.3 to 0.65 ml/min. These two hydrophobic ions were chosen for their opposite charges, which we presumed might provide for differing effects. We reasoned that the effectiveness in influencing capacitance and motility might depend on the sign of the hydrophobic ion relative to that of the native charge. Whole chamber perfusion was continuous.

A tracking procedure was used to continuously monitor the voltage at peak capacitance (V_{pkC_m}) after obtaining whole-cell configuration (Kakehata & Santos-Sacchi, 1995). Membrane potential was corrected for the effects of residual series resistance. Peak capacitance ($C_{m, pk}$) values were also monitored during the tracking procedure using transient analysis of capacitive currents induced by a -10mV step. Detailed evaluation of total membrane capacitance was made at different potentials by transient analysis of currents induced by a voltage stair step stimulus, and the capacitance function was fit to the first derivative of a two state Boltzmann function relating nonlinear charge to membrane voltage (dQ/dV ; Santos-Sacchi, 1991; Huang & Santos-Sacchi, 1993)

$$C_m = Q_{max} \frac{ze}{kT} \frac{b}{(1+b)^2} + C_{lin}$$

where

$$b = \exp\left(\frac{-ze(V - V_{pkcm})}{kT}\right)$$

Q_{max} is the maximum nonlinear charge moved, V_{pkC_m} is voltage at peak capacitance or equivalently, at half-maximal nonlinear charge transfer, V_m is membrane potential, z is valence, C_{lin} is linear membrane capacitance, e is electron charge, k is Boltzmann's constant, and T is absolute temperature.

Pipette pressure was monitored via a T-connector to a pressure monitor (WPI, Sarasota, FL), and modified when required with a syringe connected to the Teflon tubing attached to the patch pipette holder (Kakehata & Santos-Sacchi, 1995). The cylindrical shape of OHCs was maintained during data collection. Measures of voltage-induced (-160 to 40mV , 20mV increment) mechanical responses were made off the video monitor during playback with a differential opto-resistor technique (Santos-Sacchi, 1989; 1991). Mechanical data were fit to a two state Boltzmann function to determine the voltage at maximum mechanical gain (V_{dLmax}).

Dose-response data (charge vs. hydrophobic ion concentration) were averaged and are given as mean \pm SE. A fit was made according to a modified Michaelis-Menten equation with the use of a least-squares routine (Sigma Plot, CA),

$$Q = Q_{max} \frac{C^n}{(C^n + K_b^n)}$$

where Q is the charge induced by the hydrophobic ion, C is hydropho-

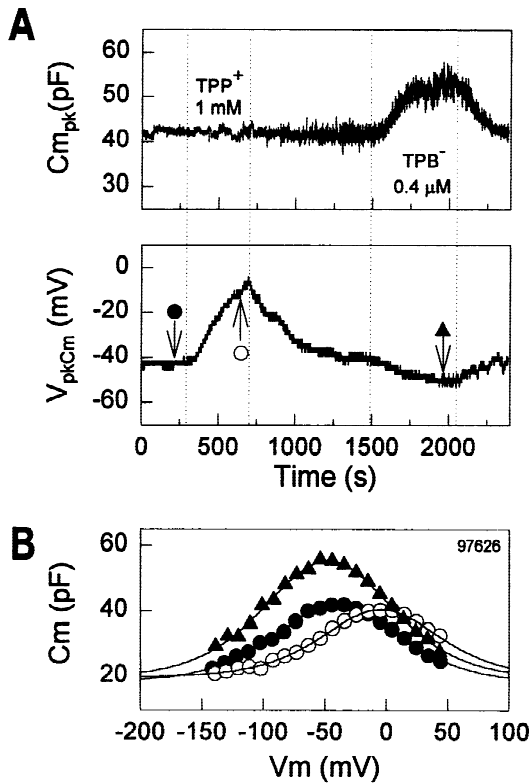


Fig. 1. Effects of TPP^+ and TPB^- on $C_{m_{pk}}$ and V_{pkCm} of an OHC obtained by the tracking technique (A) and the voltage stair step technique (B). (A) After $C_{m_{pk}}$ and V_{pkCm} stabilized, TPP^+ (1 mM) was applied extracellularly at the first dotted line. V_{pkCm} shifted to depolarized levels with no change in $C_{m_{pk}}$. Washout at the second dotted line caused recovery. TPB^- (0.4 μM) was applied extracellularly at the third dotted line. V_{pkCm} shifted slightly to hyperpolarized levels with an increase in $C_{m_{pk}}$. Washout following TPB^- treatment started from the 4th line. Arrows indicate points at which capacitance functions were determined by the voltage stair step technique for the same cell. (B) Fits (solid lines) for the capacitance data indicate $C_{m_{pk}}$, V_{pkCm} , Q_{max} and z of 42.1 pF, -40.2 mV, 3.26 pC and 0.75 (closed circles, control); 40.6 pF, -4.4 mV, 2.69 pC and 0.79 (open circles, TPP^+ treatment); 55.7 pF, -47.4 mV, 5.08 pC and 0.73 (closed triangles, TPB^- treatment).

bic ion concentration, K_D is the dissociation constant, and n is the Hill coefficient.

Results

OHCs possess a capacitance that depends upon transmembrane voltage, and which derives from motility-related gating currents (Fig. 1). Membrane-bound, charged molecules from external sources can also contribute to membrane capacitance. This is illustrated in Fig. 1 where the effects of TPB^- and TPP^+ on $C_{m_{pk}}$ and V_{pkCm} are monitored with the tracking technique described in the methods (Fig. 1A); in addition, a more detailed analysis of membrane capacitance is provided by the stair step protocol (Fig. 1B). Under our experi-

mental conditions, TPP^+ had no effect on $C_{m_{pk}}$, but shifted V_{pkCm} to depolarized levels. In contrast, TPB^- increased $C_{m_{pk}}$ and shifted V_{pkCm} to hyperpolarized levels. Washout reversed the effects (Fig. 1A). The average onset and recovery time constant for 0.4 μM TPB^- was 102.2 ± 25.91 sec ($n = 5$) and 184 ± 60.74 sec ($n = 4$), respectively.

The average steady state shift of V_{pkCm} induced by 1 mM TPP^+ was 33.9 ± 1.7 mV (mean \pm SE; $n = 10$; stair analysis). The difference in $C_{m_{pk}}$ before and during TPP^+ treatment was 0.57 ± 0.3 pF. Higher concentrations of TPP^+ , up to 10 mM, were equally ineffective in altering $C_{m_{pk}}$. On the other hand, the average elevation of $C_{m_{pk}}$ and shift of V_{pkCm} induced by 0.4 μM TPB^- were 16.3 ± 2.7 pF and -13.6 ± 3.04 mV ($n = 15$), respectively.

To study the concentration effects of TPB^- on OHC nonlinear capacitance, TPB^- was applied by 'Y-tube' in increasing concentrations ranging from 0.2 μM to 1 μM , without intermittent washing. Tracking commenced immediately after whole cell configuration, and stair step analysis was performed after V_{pkCm} reached steady state at each concentration. Figure 2A illustrates the TPB^- concentration dependence of OHC $C_{m_{pk}}$ and V_{pkCm} . By gradually increasing the concentration of TPB^- , correspondingly larger increases in $C_{m_{pk}}$ and V_{pkCm} shifts were elicited. Concentrations greater than 1 μM could induce very large capacitances, which compromised the effectiveness of our voltage clamp.

Contributions to the voltage-dependent capacitance observed in Fig. 2A are derived from two distinct sources of nonlinear charge movement (native and TPB^- -induced), which theoretically should be separable analytically. Unfortunately, it is clear from the data that the characteristics of native and TPB^- -induced charge movement are not disparate enough to produce a bimodal capacitance function, which could easily be fit by the sum of two Boltzmann functions. Nevertheless, we have devised a procedure which estimates the TPB^- contribution assuming that in addition to augmenting charge, TPB^- causes a shift in the voltage dependence of OHC native charge movement, as occurred in the presence of TPP^+ . Thus, we first obtained fits (single Boltzmann) of OHC native capacitance prior to TPB^- treatment and used these parameters (all fixed except for V_{pkCm} which was permitted to vary) in subsequent fits (sum of two Boltzmanns) of capacitance in the presence of TPB^- . Figure 2B illustrates the result, and indicates that, opposite to the effects TPP^+ , the native OHC capacitance function is shifted in the negative direction by the negatively charged TPB^- .

This shift in V_{pkCm} was independently confirmed in a group of OHCs where the effects of TPB^- on OHC motility and capacitance were studied in concert. Before and during TPB^- treatment, voltage-induced OHC move-

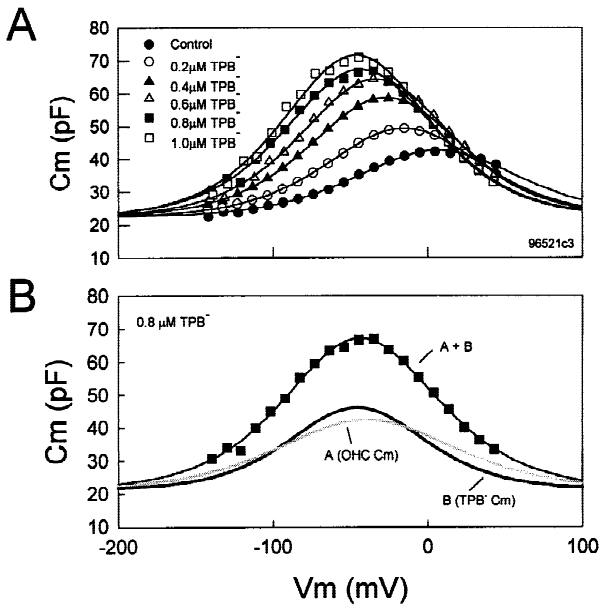


Fig. 2. (A) Concentration dependence of TPB^- effects on $C_{m_{pk}}$ and V_{pkCm} of an OHC. $C_{m_{pk}}$ increased and V_{pkCm} shifted to hyperpolarized levels in a concentration-dependent manner. Fits (solid lines) for capacitance indicate $C_{m_{pk}}$, V_{pkCm} , Q_{max} and z of 42.5 pF, 6.5 mV, 2.89 pC and 0.72 (closed circles, control), 49.4 pF, -15.3 mV, 3.61 pC and 0.77 (open circles, 0.2 μM TPB); 58.8 pF, -26.8 mV, 4.81 pC and 0.78 (closed triangles, 0.4 μM TPB); 64.4 pF, -33.4 mV, 5.48 pC and 0.79 (open triangles, 0.6 μM TPB); 67.2 pF, -43.1 mV, 5.85 pC and 0.79 (closed squares, 0.8 μM TPB) and 71.6 pF, -46.1 mV, 6.26 pC and 0.81 (open squares, 1 μM TPB). (B) Example of extraction technique used to assess the individual contributions of TPB^- -induced and native OHC capacitance to the overall capacitance function. A, native capacitance of OHC; B, TPB^- -induced capacitance; A + B, total capacitance with 0.8 TPB^- treatment. See text for details.

ment and voltage-dependent capacitance were obtained by voltage steps (-160 to 40 mV, 20 mV increment) and stair step analysis, respectively. As shown in Fig. 3A and B, TPB^- had a significant effect on the magnitude of $C_{m_{pk}}$ but little effect on the magnitude of voltage-dependent movement. The ratio of total Q_{max} in the presence of TPB^- to Q_{max} in its absence was 1.71, whereas the corresponding ratio of δL_{max} was 1.06 ($n = 7$). These results indicate that an increase in OHC nonlinear capacitance by an external source does not result in significant enhancement of cell movement. Although TPB^- does not alter the magnitude of OHC motility, its voltage dependence is susceptible. In fact, the effect on $V_{\delta L_{max}}$ corresponds to the effect on the extracted value of native OHC V_{pkCm} (Fig. 3C); both shift in the hyperpolarizing direction in a concentration-dependent manner. This is expected since the voltage dependencies of OHC motility and nonlinear capacitance are known to coincide (Kakehata & Santos-Sacchi, 1995). Within a limited concentration range of TPB^- (0.2–1.0 μM), the response slope is $-32 \text{ mV}/\mu\text{M}$ ($n = 3$). The dose-response data

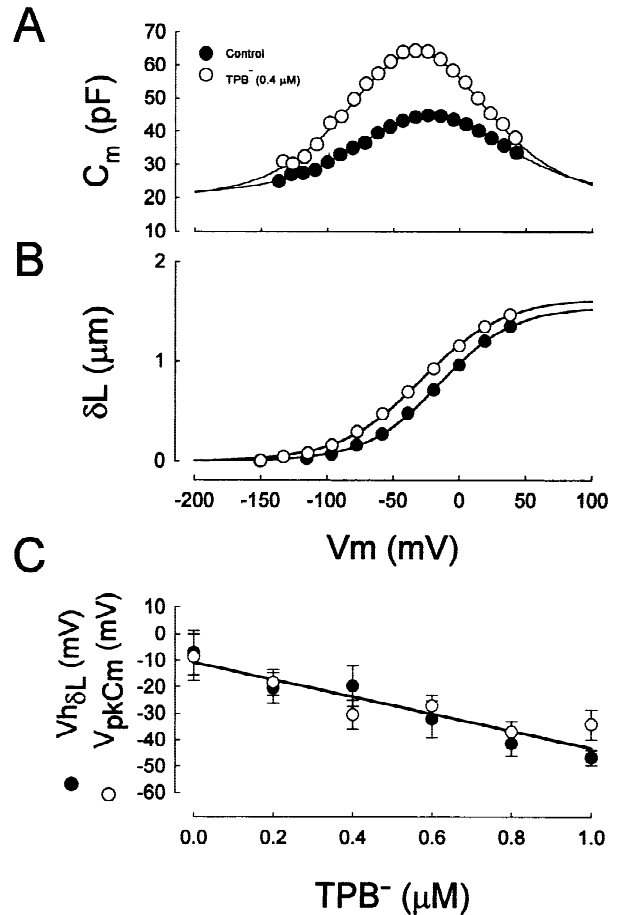


Fig. 3. (A) Voltage-dependent capacitance and (B) voltage-induced length change of seven OHCs measured before and during TPB^- treatment. Length changes induced by 20 mV steps from -160 to 40 mV, but corrected for series resistance. Fits for average overall capacitance data indicate $C_{m_{pk}}$, V_{pkCm} , Q_{max} and z of 44.8 pF, -21.9 mV, 3.69 pC and 0.67 (closed circles, control); 63.9 pF, -32.3 mV, 6.3 pC and 0.72 (open circles, 0.4 μM TPB). Fits for average mechanical data indicate $V_{\delta L_{max}}$ and z of -14.9 mV and 0.9 (closed circles, control); -28.5 mV and 0.81 (open circles, 0.4 μM TPB). Cell length was $64.29 \pm 1.44 \mu\text{m}$ (mean \pm SE; $n = 7$). (C) Correspondence between shifts in extracted OHC V_{pkCm} (determined as in text) and $V_{\delta L_{max}}$ of OHCs treated with TPB^- as a function of concentration. Each point is the mean \pm SE ($n = 3$).

indicate a Hill coefficient of 1.85 ± 0.10 , Q_{max} of $5.38 \pm 0.23 \text{ pC}$, and K_d of $0.50 \pm 0.03 \mu\text{M}$.

Other ways to dissociate the two components of nonlinear charge movement may include delivery of pre-pulse voltages (Santos-Sacchi, Kakehata & Takahashi, 1997, 1998; Santos-Sacchi, 1997), alterations of lateral membrane tension (Iwasa, 1993; Gale & Ashmore, 1994; Kakehata & Santos-Sacchi, 1995), and treatments with salicylate (Tunstall et al., 1995; Kakehata & Santos-Sacchi, 1996) or Gd^{3+} (Santos-Sacchi, 1991), since these manipulations may selectively influence native OHC charge movement.

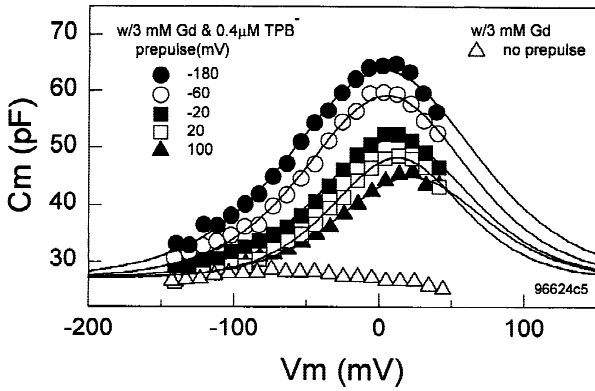


Fig. 4. Effects of 1-sec voltage prepulse on $C_{m_{pk}}$ and V_{pkC_m} of an OHC treated with gadolinium and TPB^- . Once reduction of OHC nonlinear capacitance by Gd^{+3} (3 mM) reached steady state (reduction of $C_{m_{pk}}$ from 41.2 to 28.2 pF), TPB^- (0.4 μ M) was added to the solution. Control capacitance function (open triangles, 3 mM Gd^{+3} , no prepulse) could not be reliably fit. After the appearance of TPB^- -induced capacitance, prepulse effects were studied. $C_{m_{pk}}$, V_{pkC_m} , Q_{max} and z were 63.7 pF, 2.8 mV, 6.28 pC and 0.60 (closed circles, -180 mV prepulse); 59.2 pF, 5.3 mV, 4.86 pC and 0.68 (open circles, -60 mV prepulse); 51.6 pF, 10.3 mV, 3.46 pC and 0.73 (closed squares, -20 mV prepulse); 48.3 pF, 12.5 mV, 2.57 pC and 0.85 (open square, 20 mV prepulse) and 44.9 pF, 22.1 mV, 2.42 pC and 0.76 (closed triangles, 100 mV prepulse).

In the untreated OHC, negative prepulse voltages shift V_{pkC_m} in the positive direction and visa versa, with little effect on $C_{m_{pk}}$ (Santos-Sacchi et al., 1997, 1998). In the TPB^- treated OHC, changes in V_{pkC_m} and $C_{m_{pk}}$ were found (*data not shown*) and could not be accounted for by effects on native charge alone; indeed, these data suggested that TPB^- induced charge movement was susceptible to prepulse effects, as well. To confirm this, gadolinium (3 mM) was first used to block intrinsic OHC nonlinear capacitance, so that TPB^- charge movement could be studied in isolation. Figure 4 illustrates the effects of prepulses on the voltage dependence of the isolated TPB^- -induced nonlinear capacitance. As the prepulse potential decreased from 100 to -180 mV, TPB^- -induced nonlinear capacitance progressively increased in magnitude and V_{pkC_m} became more negative. This is distinctly different from prepulse effects on the intrinsic nonlinear capacitance of the OHC (Santos-Sacchi et al., 1997, 1998).

Positive turgor pressure shifts OHC V_{pkC_m} to depolarized levels and reduces $C_{m_{pk}}$ (Iwasa, 1993; Gale & Ashmore, 1994; Kakehata & Santos-Sacchi, 1995). However, in OHCs treated with TPB^- , whereas positive intracellular pressure also shifts V_{pkC_m} to depolarized levels, $C_{m_{pk}}$ increases (Fig. 5). With 0.4 μ M TPB^- treatment, $C_{m_{pk}}$ and V_{pkC_m} of the cell shown in Fig. 5A were 53.3 pF and -27.2 mV at steady state. Positive intracellular pressure (1.35 kPa pipette pressure) increased $C_{m_{pk}}$ by 6.1 pF and shifted V_{pkC_m} in the depolarized direction by 17.6 mV. The average elevation of

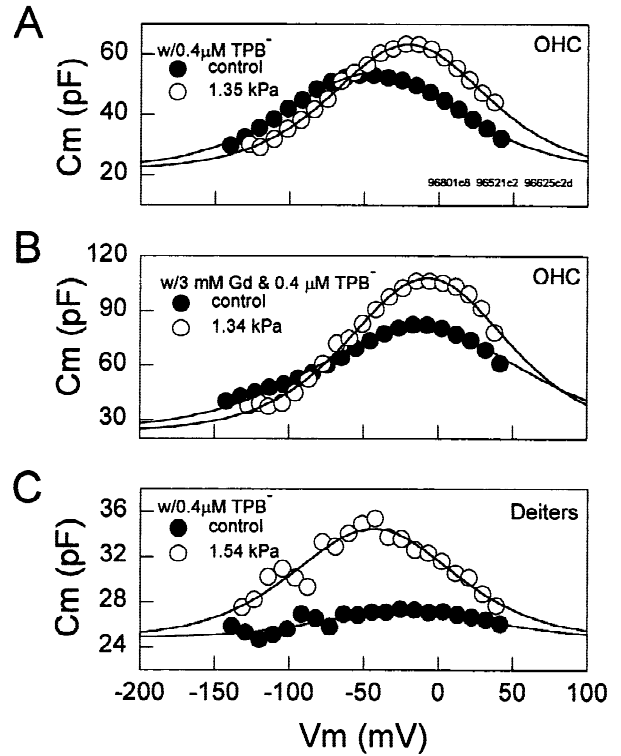


Fig. 5. Effects of positive intracellular pressure on C_m of OHCs (A, B) and Deiters cells (C). (A) After OHC C_m was increased by 0.4 μ M TPB^- and reached steady state, positive intracellular pressure caused a positive shift in overall V_{pkC_m} and increase in $C_{m_{pk}}$. (B) OHC nonlinear capacitance was blocked with Gd^{+3} , and followed by treatment with TPB^- . After $C_{m_{pk}}$ reached steady state, increased intracellular pressure caused a positive shift in V_{pkC_m} and an increase in $C_{m_{pk}}$. (C) TPB^- (0.4 μ M) induced a nonlinear capacitance in Deiters cells. In this case, after reaching steady state, positive pressure caused a negative shift in V_{pkC_m} and an increase in $C_{m_{pk}}$.

$C_{m_{pk}}$ and shift of V_{pkC_m} induced by positive pipette pressure (0.95 \pm 0.14 kPa) was 6.1 \pm 1.35 pF ($n = 4$) and 15.5 \pm 3.66 mV ($n = 4$), respectively. After intrinsic OHC nonlinear capacitance was blocked by gadolinium (3 mM), positive intracellular pressure still increased TPB^- -induced capacitance and shifted V_{pkC_m} in the depolarized direction (Fig. 5B). However, there was a greater increase in $C_{m_{pk}}$ and smaller shift in V_{pkC_m} . Under this condition, the average elevation of capacitance and shift of V_{pkC_m} caused by positive pressure (1.23 \pm 0.16 kPa) was 14.8 \pm 3.74 pF and 5.35 \pm 1.97 mV ($n = 4$), respectively. Positive intracellular pressure affected supporting cells in a similar way (Fig. 5C). The average increase in capacitance was 5.5 \pm 0.83 pF ($n = 4$) by positive pressure (1.37 \pm 0.26 kPa). Similar results were obtained by changing intracellular pressure with hypotonic solutions (*data not shown*).

Salicylate blocks OHC voltage-dependent capacitance and decreases the cell's mechanical response (Kakehata & Santos-Sacchi, 1996). We found that the pres-

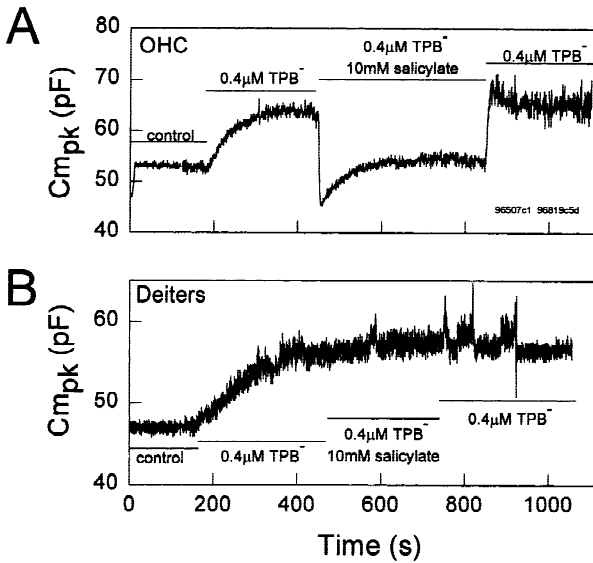


Fig. 6. Effects of salicylate on intrinsic and TPB^- induced nonlinear capacitance. $C_{m_{pk}}$ of (A) an OHC and (B) a Deiters cell monitored by the V_{pkCm} tracking technique. Same treatments were used for both cells. Salicylate specifically blocks intrinsic OHC nonlinear capacitance. Salicylate (10 mM) had no effect on $C_{m_{pk}}$ of the Deiters cell.

ence of TPB^- molecules does not affect the reduction of OHC nonlinear capacitance caused by salicylate. In Fig. 6, $C_{m_{pk}}$ of an OHC and supporting cell were monitored. TPB^- (0.4 μM) increased $C_{m_{pk}}$ of the OHC (top trace) to a steady-state value of 63.8 pF. Subsequent treatment with salicylate (10 mM), reduced $C_{m_{pk}}$ to 45.6 pF, with a time constant of 1.69 sec. The average time constant was 3.79 ± 0.94 sec (mean \pm SE, $n = 8$). This rate is faster than that observed by Kakehata and Santos-Sacchi (1996), and may be due to the presence of TPB^- or the higher perfusion rate used here. Although $C_{m_{pk}}$ recovered partially over the course of salicylate perfusion, reaching 52 pF, no recovery of mechanical response was noted. After removal of salicylate, $C_{m_{pk}}$ increased again due to the reversible effect of salicylate on OHC nonlinear capacitance. The same treatment used for OHCs was applied to supporting cells (Fig. 6, bottom). TPB^- also increased $C_{m_{pk}}$ of Deiters cells, but to a lesser and more variable degree. The average elevation of $C_{m_{pk}}$ by 0.4 μM TPB^- was 9.5 ± 1.2 pF for OHCs ($n = 15$) and 5.5 ± 1.0 pF for Deiters cells ($n = 11$). The latter figure does not include another 11 Deiters cells whose capacitance did not show an increase by at least 5 min after onset of TPB^- treatment. No effect of salicylate on $C_{m_{pk}}$ was found and no mechanical response was detected for TPB^- -treated Deiters cells.

The effects of salicylate (or gadolinium) on OHC motility are not alleviated by TPB^- treatment (Fig. 7). The figure illustrates the effects of TPB^- on C_m and movement of an OHC whose nonlinear capacitance was blocked by intracellular salicylate. Simultaneous mea-

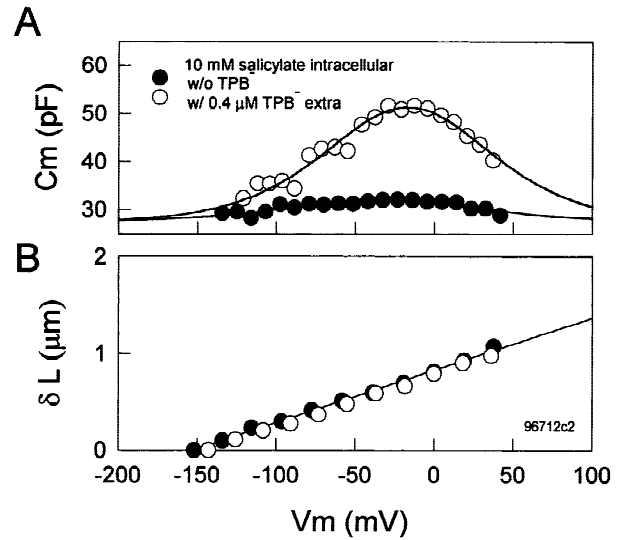


Fig. 7. Effects of TPB^- on (A) capacitance and (B) movement of OHCs whose nonlinear capacitance was blocked by salicylate. Length changes were induced by 20-mV steps from -160 to 40 mV and series resistance was corrected. Capacitance was evaluated with the stair step protocol. Fits (solid lines) for capacitance data indicate $C_{m_{pk}}$, V_{pkCm} , Q_{max} , and z of 32.1 pF, -31.8 mV, 0.82 pC and 0.59 (closed circles, w/o TPB^-); 51.4 pF, -16.9 mV, 2.43 pC and 0.72 (open circles, w/ 0.4 μM TPB^-). Fits for mechanical data indicate $V_{\delta L_{max}}$ and z of 119 mV and 0.091 (closed circles, w/o TPB^-); -9.1 mV and 0.1213 (open circles, w/ 0.4 μM TPB^-). Despite the induction of a prominent nonlinear capacitance by TPB^- , no recovery of the mechanical response was observed. Cell length: 71 μm .

ures of capacitance and voltage dependent movement were made before and during extracellular application of 0.4 μM TPB^- . For this cell, $C_{m_{pk}}$ was reduced to a steady-state level of 32.1 pF by 10 mM salicylate, which is consistent with the results of Kakehata and Santos-Sacchi (1996). During TPB^- treatment, peak capacitance increased to 51.7 pF. Although TPB^- -induced an additional nonlinear capacitance of 19.64 pF and shifted overall V_{pkCm} from -31.83 to -16.28 mV, the difference in maximum length change was only 0.09 μm . The average difference in maximum length change for 3 cells was 0.03 ± 0.02 μm .

Discussion

The present results show that the hydrophobic ion, TPB^- , but not TPP^+ , increases nonlinear charge movement, as evidenced through capacitance measures, in OHCs and supporting cells from the organ of Corti. The enhancement of nonlinear charge movement, which is accompanied by a concentration-dependent shift in the voltage at peak capacitance, is greater for OHCs than for supporting cells. This suggests that membrane structural parameters such as thickness, dielectric constant, dipole poten-

tial, or the degree of the lipid hydrocarbon chain order (Ketterer, Randic & Läuger, 1971; Benz & Läuger, 1977; Reyes & Latorre, 1979; Fernandez et al., 1982) may be different between the two types of cells; another clear difference between the cells is the existence of intrinsic voltage-sensor/motor elements in OHCs. The latter difference is exemplified by the results from salicylate treatments. Salicylate reduced OHC membrane capacitance attributable to intrinsic lateral membrane sensor/motors, which is in agreement with earlier studies (Tunstall et al., 1995; Kakehata & Santos-Sacchi, 1996), but did not reduce the TPB⁻-induced capacitance of supporting cells or OHCs. This evidence further supports the notion that salicylate directly and specifically acts on the sensor/motor of the OHC (Kakehata & Santos-Sacchi, 1996), and not via some nonselective mechanism to impede all charge movement within the membrane.

The characteristics of TPB⁻-induced nonlinear capacitance are similar in some ways to those of the OHC intrinsic capacitance, namely, each has a shallow voltage dependence and is affected by voltage prepulse and membrane tension. However, there are obvious differences which are readily revealed when the OHC's intrinsic nonlinear capacitance is blocked. Whereas the OHC nonlinear capacitance shifts its voltage dependence in the negative direction with positive prepulse (Santos-Sacchi, Kakehata & Takahashi, 1998), the voltage dependence of TPB⁻-induced capacitance does the opposite. Also, whereas positive intracellular pressure decreases OHC peak capacitance (Gale & Ashmore, 1994; Kakehata & Santos-Sacchi, 1995), TPB⁻-induced peak capacitance increases. The reasons for these differences are not obvious, but may possibly relate to differences in sign of the mobile charged species.

Despite some similarities between TPB⁻-induced nonlinear charge movement and OHC intrinsic nonlinear charge movement, the former cannot effect mechanical responses, indicating that TPB⁻ charge movement does not alter lateral membrane motor conformation. Similarly, in frog myelinated nerve, lipophilic dipicrylamine ions did not interact with Na channels (Benz & Nonner, 1981). However, we found that TPB⁻-induced shifts in OHC intrinsic V_{pkCm} which are mirrored by similar shifts in V_{dLmax} . Since TPB⁻ does not directly alter the magnitude of OHC motility, it is probable that the ion's effects on motility are via electrostatic interactions with the motility voltage sensor; that is, the voltage dependence of intrinsic OHC capacitance is likely shifted by TPB⁻, just as it is by TPP⁺.

A variety of evidence indicates that the OHC's native nonlinear charge movement is causally related to the cell's mechanical response. First, blockers of OHC nonlinear capacitance cause reductions in OHC motility (Santos-Sacchi, 1991; Tunstall et al., 1995; Kakehata & Santos-Sacchi, 1996). Second, the kinetics of charge

movement and mechanical response coincide (Santos-Sacchi, 1990, 1991; Gale & Ashmore, 1997). Third, treatments which induce shifts in the voltage dependence of nonlinear charge movement or capacitance similarly shift that of the mechanical response (Fig. 3C; Kakehata & Santos-Sacchi, 1995). Fourth, mechanical stimulation of the lateral membrane elicits the salicylate blockable motility-related gating charge movement (Gale & Ashmore, 1994; Takahashi & Santos-Sacchi, 1997). Finally, the present data indicate that induced nonspecific charge movement cannot evoke or recover blocked mechanical responses.

The apparent discrepancy between the degree of salicylate-induced reduction in capacitance and mechanical response indicated by the closed symbols in Fig. 7, and noted previously (Kakehata & Santos-Sacchi, 1996) may be readily accounted for. First, the relative decrease in capacitance and motility is not known since the pipette contained the drug and the effect is near immediate (Kakehata & Santos-Sacchi, 1996); no pre-drug measures are available. Second, the native nonlinear charge movement is not completely abolished, and in fact may be extended over a wider voltage range than under normal conditions (reduced z), so that measurement could be limited by our ability to deliver extreme voltages. Furthermore, we have previously shown that when the nonlinear capacitance remaining after salicylate treatment is blocked by Gd³⁺, the mechanical response is fully abolished (Kakehata & Santos-Sacchi, 1996). Third, the whole-cell mechanical response magnitude may be dependent upon many physical criteria, including turgor pressure (Shehata et al., 1991; Santos-Sacchi, 1991), whole-cell stiffness (Dallos et al., 1997), and possibly membrane visco-elasticity (Santos-Sacchi et al., 1997, 1998). The linearity of the residual mechanical response may be an expression of a reduction in z which would necessarily provide an apparent linearization within a restricted voltage range.

In summary, TPB⁻ ions increase the magnitude of nonlinear capacitance and modify V_{pkCm} and V_{dLmax} of OHCs. TPB⁻-induced nonlinear capacitance is independent of OHC intrinsic nonlinear capacitance. We conclude that the OHC mechanical response is not simply related to quantity of nonspecific nonlinear charge moved within the membrane, but to the effects of motility voltage-sensor charge movement functionally coupled to a mechanical effector.

This work was supported by NIH-NIDCD grant DC00273 to JSS. We thank Margaret Mazzucco for technical help.

References

- Ashmore, J.F. 1987. A fast motile response in guinea-pig outer hair cells: the cellular basis of the cochlear amplifier. *J. Physiol.* **338**:323–347

- Ashmore, J.F. 1989. *In: Mechanics of Hearing*, D. Kemp and J.P. Wilson, editors. pp. 107–113. Plenum, New York
- Ashmore, J.F. 1992. Mammalian hearing and the cellular mechanism of the cochlear amplifier. *In: Sensory Transduction*. D.P. Corey and S.D. Roper, editors. pp. 395–412. Rockefeller University Press, New York
- Benz, R., Lauger, P. 1977. Transport kinetics of dipicrylamine through lipid bilayer membrane: effects of membrane structure. *Biochem. Biophys. Acta* **455**:245–258
- Benz, R., Nonner, W. 1981. Structure of the axolemma of frog myelinated nerve: relaxation experiments with a lipophilic probe ion. *J. Membrane Biol.* **59**:127–134
- Brownell, W.E., Bader, C.R., Bertrand, D., de Ribaupierre, Y. 1985. Evoked mechanical responses of isolated cochlear outer hair cells. *Science* **227**:194–196
- Dallos, P., Evans, B.N., Hallworth, R. 1991. On the nature of the motor element in cochlear outer hair cells. *Nature* **350**:155–157
- Dallos, P., He, D.Z., Lin, X., Sziklai, I., Mehta, S., Evans, B.N. 1997. Acetylcholine, outer hair cell electromotility, and the cochlear amplifier. *J. Neurosci.* **17**(6):2212–2226
- Dilger, J.P., Benz, R. 1985. Optical and electrical properties of thin monoolein lipid bilayers. *J. Membrane Biol.* **85**:181–189
- Fernandez, J.M., Bezanilla, R., Taylor, R.E. 1982. Effect of chloroform on charge movement in the membrane. *Nature* **297**:150–152
- Gale, J.E., Ashmore, J.F. 1994. Charge displacement induced by rapid stretch in the basolateral membrane of the guinea pig OHC. *Proc. R. Soc. Lond. B. Biol. Sci.* **255**:243–249
- Gale, J.E., Ashmore, J.F. 1997. An intrinsic frequency limit to the cochlear amplifier. *Nature* **389**:63–66
- Hamill, O.P., Marty, A., Neher, E., Sakmann, B., Sigworth, F.R. 1981. Improved patch-clamp techniques for high-resolution currents recording from cells and cell-free membrane patches. *Pfluegers Arch.* **391**:85–105
- Haydon, D.A., Hladky, S.B. 1972. Ion transport across thin lipid membranes: a critical discussion of mechanisms in selected systems. *Q. Rev. Biophys.* **5**(2):187–282
- Huang, G.-J., Santos-Sacchi, J. 1993. Mapping the distribution of the outer hair cell motility voltage sensor by electrical amputation. *Biophys. J.* **65**:2228–2236
- Huang, G.-J., Santos-Sacchi, J. 1994. Motility voltage sensor of the outer hair cell resides within the lateral plasma membrane. *Proc. Natl. Acad. Sci. USA* **91**:12268–12272
- Iwasa, K.H. 1993. Effect of stress on the membrane capacitance of the auditory outer hair cell. *Biophys. J.* **65**:492–498
- Iwasa, K.H. 1994. A membrane motor model for the fast motility of the OHC. *J. Acoust. Soc. Am.* **96**:2216–2224
- Kakehata, S., Santos-Sacchi, J. 1995. Membrane tension directly shifts voltage dependence of outer hair cell motility and associated gating charge. *Biophys. J.* **68**:2190–2197
- Kakehata, S., Santos-Sacchi, J. 1996. Effects of salicylate and lanthanides on outer cell motility and associated gating charge. *J. Neurosci.* **16**(16):4881–4889
- Ketterer, B., Neumcke, B., Lauger, P. 1971. Transport mechanism of hydrophobic ions through lipid bilayer membranes. *J. Membrane Biol.* **5**:225–245
- Murase, K., Randic, M., Shirasaki, T., Nakagawa, T., Akaike, N. 1990. Serotonin suppresses N-methyl-D-aspartate responses in acutely isolated spinal dorsal horn neurons. *Brain Res.* **525**:84–91
- Oberhauser, A.F., Fernandez, J.M. 1995. Hydrophobic ions amplify the capacitive currents used to measure exocytotic fusion. *Biophys. J.* **69**:451–459
- Reyes, J., Latorre, R. 1979. Effect of the anesthetics benzyl alcohol and chloroform on bilayers made from monolayers. *Biophys. J.* **28**:259–280
- Ruggero, M.A. 1992. Responses to sound of the basilar membrane of the mammalian cochlea. *Neurobiology* **2**:449–456
- Santos-Sacchi, J. 1989. Asymmetry in voltage dependent movements of isolated outer hair cells from the organ of Corti. *J. Neurosci.* **9**:2954–2962
- Santos-Sacchi, J. 1990. Fast outer hair cell motility: how fast is fast? *In: The Mechanics and Biophysics of Hearing*. P. Dallos, C.D. Geisler, J.W. Matthews, M.A. Ruggero and C.R. Steele, Editors. pp. 69–75. Springer-Verlag, Berlin
- Santos-Sacchi, J. 1991. Reversible inhibition of voltage-dependent outer hair cell motility and capacitance. *J. Neurosci.* **11**:3096–3110
- Santos-Sacchi, J. 1993. Harmonics of outer hair cell motility. *Biophys. J.* **65**:2217–2227
- Santos-Sacchi, J. 1997. Voltage-induced tension can account for membrane potential effects on OHC capacitance. Abstracts of the 34th Workshop on Inner Ear Biology, Rosa Marina, Italy
- Santos-Sacchi, J., Dilger, J.P. 1988. Whole cell currents and mechanical responses of isolated outer hair cells. *Hear. Res.* **35**:143–150
- Santos-Sacchi, J., Kakehata, S., Takahashi, S. 1997. Voltages past: The outer hair cell has memory. The 20th Midwinter Research Meeting of the Association for Research in Otolaryngology, St. Petersburg Beach, FL
- Santos-Sacchi, J., Kakehata, S., Takahashi, S. 1998. Effects of membrane potential on the voltage dependence of motility-related charge in outer hair cells of the guinea pigs. *J. Physiol.* **510**:225–235
- Shehata, W.E., Brownell, W.E., Dieler, R. 1991. Effects of salicylate on shape, electromotility and membrane characteristics of isolated outer hair cells from guinea pig cochlea. *Acta Otolaryngol* **111**:707–18
- Smejtek, P., Wang, S. 1991. Domains and anomalous adsorption isotherms of dipalmitoylphosphatidylcholine membranes and lipophilic ions: pentachlorophenolate, tetraphenylborate, and dipicrylamine. *Biophys. J.* **59**:1064–1073
- Takahashi, S., Santos-Sacchi, J. 1998. Tension-induced OHC gating currents are restricted to the cell's mid region. Abstracts of the Mid-winter Meeting of the Association for Research in Otolaryngology, St. Petersburg, FL
- Tunstall, M.J., Gale, L.E., Ashmore, J.F. 1995. Action of salicylate on membrane capacitance of outer hair cells from the guinea-pig cochlea. *J. Physiol.* **485**:739–752
- Turin, L., Behe, P., Plonsky, I., Dunina-Barkovskaya, A. 1991. Hydrophobic ion transfer between membranes of adjacent hepatocytes: a possible probe of tight junction structure. *Proc. Natl. Acad. Sci. USA* **88**:9365–9369



Research paper

Effect of capsaicin on potassium conductance and electromotility of the guinea pig outer hair cell

T. Wu^a, L. Song^b, X. Shi^a, Z. Jiang^a, J. Santos-Sacchi^b, A.L. Nuttall^{a,c,d,*}^a Oregon Hearing Research Centre, NRC04, Department of Otolaryngology/Head & Neck Surgery, Oregon Health & Sciences University, 3181 S.W. Sam Jackson Park Rd., Portland, OR 97239, United States^b Otolaryngology, Neurobiology, and Molecular and Cellular Physiology, Yale University School of Medicine, New Haven, CT 06510, United States^c Kresge Hearing Research Institute, The University of Michigan, 1301 East Ann Street, Ann Arbor, MI 48109-0506, United States^d Department of Otolaryngology, Renji Hospital, Shanghai Jiao Tong University, Shanghai, China

ARTICLE INFO

Article history:

Received 23 August 2010

Received in revised form

21 October 2010

Accepted 21 October 2010

Available online 31 October 2010

ABSTRACT

Capsaicin, the classic activator of TRPV-1 channels in primary sensory neurons, evokes nociception. Interestingly, auditory reception is also modulated by this chemical, possibly by direct actions on outer hair cells (OHCs). Surprisingly, we find two novel actions of capsaicin unrelated to TRPV-1 channels, which likely contribute to its auditory effects *in vivo*. First, capsaicin is a potent blocker of OHC K conductances (I_K and $I_{K,n}$). Second, capsaicin substantially alters OHC nonlinear capacitance, the signature of electromotility – a basis of cochlear amplification. These new findings of capsaicin have ramifications for our understanding of the pharmacological properties of OHC I_K , $I_{K,n}$ and electromotility and for interpretation of capsaicin pharmacological actions.

© 2010 Elsevier B.V. All rights reserved.

1. Introduction

The mammalian cochlea contains two types of hair cells with distinct functions. Inner hair cells (IHCs) are responsible for sound detection and its conversion to electrical signals. Whereas, outer hair cells (OHCs) additionally amplify sound stimulus by increasing both the amplitude and frequency selectivity of basilar membrane (BM) vibration. Electrically evoked OHC mechanical activity, whose electrical signature is a nonlinear capacitance (NLC), is a basis of this cochlear amplification (Dallos et al., 2008; He et al., 2006; Santos-Sacchi, 2003; Santos-Sacchi et al., 2006; Zheng et al., 2003). I_K and $I_{K,n}$ are the two major K conductances in OHCs (Housley and Ashmore, 1992, 2006; Mammano and Ashmore, 1996; Santos-Sacchi and Dilger, 1988). I_K activates at potentials more positive than -35 mV and its identity and role is still unclear. $I_{K,n}$, which activates at hyperpolarized potentials, is carried by KCNQ4 channels and controls the resting potential of OHCs (Chambard and Ashmore, 2005; Holt et al., 2007; Kharkovets et al., 2000, 2006; Wu et al., 2010;

Xu et al., 2007). The resting potential is an important component of the driving force for OHC electromotility.

Capsaicin, the natural product of capsicum pepper, is an active ingredient of many spicy foods. Capsaicin selectively activates TRPV-1, a non-selective cation channel (NSCC) in primary sensory neurons, initiating nociception through its depolarizing effects. This is the classical action of capsaicin (Caterina et al., 1997; Szallasi and Blumberg, 1999). Interestingly, we showed that capsaicin reduced cochlear amplification, resulting in an elevation in the threshold of the auditory nerve compound action potential in an *in vivo* study (Zheng et al., 2003). Furthermore, we and others have observed TRPV-1 immunolabeling in OHCs (Ishibashi et al., 2008; Mukherjea et al., 2008; Zheng et al., 2003). From these data, we hypothesized that OHCs were the major target of capsaicin, and activation of TRPV-1 would result in OHC depolarization leading to a reduction in both receptor potential and evoked OHC motility. Therefore, it is of particular interest to understand the action of capsaicin on OHCs at the cellular level.

In this study, we whole-cell voltage clamped isolated OHCs. Surprisingly, capsaicin did not elicit characteristic TRPV-1 currents in the OHCs. Unexpectedly, we found that capsaicin is a potent blocker of OHC K conductances (I_K and $I_{K,n}$) and alters NLC substantially. These novel pharmacological effects of capsaicin have never been reported before and likely contribute to the drug's detrimental action on cochlear amplification *in vivo*.

* Corresponding author. Oregon Hearing Research Center, NRC04, Department of Otolaryngology/Head & Neck Surgery, Oregon Health & Science University, 3181 S.W. Sam Jackson Park Rd. Portland, OR 97239, United States. Tel.: +1 503 4948032. E-mail address: nuttall@ohsu.edu (A.L. Nuttall).

2. Materials and methods

2.1. OHC preparation

Adult guinea pigs (250–350 g) with positive Preyer's reflex were anesthetized by intramuscular injection of an anesthetic mixture (60 mg/ml ketamine, 2.4 mg/ml xylazine, and 1.2 mg/ml acepromazine in saline) at a dose of 1 ml kg⁻¹ and were then killed by decapitation. The cochleae were rapidly removed from the bulla and dissected in a Petri dish filled with a standard artificial perilymph composed of (mM): NaCl 144, KCl 4, CaCl₂ 1.3, MgCl₂ 0.9, Na₂HPO₄ 0.7, HEPES 10 and glucose 5.6. The osmolarity of the solution was adjusted to 304 mosmol/l with glucose and the pH was adjusted to 7.40 with NaOH. All procedures were performed at room temperature. The organ of Corti dissected from the apical two cochlear turns was digested with dispase I (1.0 mg/ml) for 12 min. Dissociated OHCs, obtained by gentle titration, were placed in a Petri dish and allowed to settle onto the glass bottom. They were continuously perfused with the artificial perilymph. OHCs with lengths ranging from 72 to 75 μm (the upper 3rd turn, used in most of experiments unless otherwise specified) and 48–55 μm (the lower 2nd turn) were chosen for patch recordings. All procedures in this study were approved by the Institutional Animal Care and Use Committee of Oregon Health & Science University.

2.2. Solutions for OHC recordings

All reagents were from Sigma–Aldrich. In the bath solutions, agents were added as 1000 X concentrates. Capsaicin was pre-dissolved in dimethylsulfoxide (DMSO), which was used at a final concentration of 0.1% DMSO. BaCl₂ and 4-AP were pre-dissolved in water. The drugs were gravity delivered at a rate of (0.35 ml min⁻¹) through an array of parallel polyethylene tubes with an inner diameter of ~280 μm at the distal end, which was positioned ~350 μm next to the OHCs. Rapid switching of two different solutions was performed by shifting loaded tubes.

a) Solutions for current recordings: Bath solution contained (in mM): NaCl 142, KCl 5, CaCl₂ 1.5, MgCl₂ 2, Hepes 10 and D-glucose 5.6. The pH was adjusted to 7.40 with NaOH and the osmolarity to 304 mosmol/l with D-glucose. Pipette solution (mM) contained (in mM): KCl 148, CaCl₂ 0.5, MgCl₂ 2, Hepes 10 and EGTA 1. The pH was adjusted to 7.40 with KOH and the osmolarity to 298 mosmol/l with D-glucose.

b) Solutions for NLC recordings: Bath solution (mM) was NaCl 132, CaCl₂ 2, MgCl₂ 2, and Hepes 10. Pipette solution was the same except with EGTA 10. In a subset of experiments, Ca was removed from both intracellular and extracellular solutions by substituting NaCl. The extracellular solution contained 3, 10, 30, 100, 300 and 1000 μM capsaicin. The pH was adjusted to 7.20 with NaOH and the osmolarity to 300 mosmol/l with D-glucose. We have previously shown that DMSO and ethanol at the concentrations used in this report do not affect measures of NLC (Rybalchenko and Santos-Sacchi, 2003; Song et al., 2005).

2.3. Whole-cell recordings of OHCs

In regular current detection procedures, an Axopatch 1-D amplifier (Axon Instruments) was used with its low-pass filter bandwidth set to 1 kHz (four-pole Bessel). Membrane currents were recorded with a Digidata 1322A (Axon Instruments) interface and pCLAMP 8 software (Axon Instruments) at a sampling rate of 10 kHz for episodic I–V commands and with Minidigi digitizer and Axoscope 9.2 software (Axon Instruments) for simultaneous gap-free recording at a sampling rate of 50 Hz. The whole-cell configuration was achieved by rupturing the cell membrane with suction after achieving a high-resistance seal (>1.5 gohm). Stability of the patch was ascertained by monitoring

gap-free recording and cell parameters (cell capacitance (C_{cell}), membrane resistance (R_m) and series resistance (R_s)) during the recordings. The patch pipettes were pulled in four steps from borosilicate capillaries (WPI, 1B150F-4) using a puller (P80/PC Sutter Instrument). In a regular Na⁺ rich bath and K⁺ rich pipette solution, the initial pipette resistance was 6–7 MΩ. The uncompensated R_s (MΩ) were off-line corrected with the equation $V_c = V_u - I \times R_s$ (V_c , corrected clamping voltage; V_u , uncorrected clamping voltage; I , current) in Excel sheets and Origin 7.5 (OriginLab Technical) files. In order to stabilize the liquid junction potential (LJP), a salt bridge (3 M NaCl) with a ceramic tip was used as a reference electrode. The LJP (actual measurement) was 3 mV in the regular Na⁺ rich bath and K⁺ rich pipette solutions. The LJP was corrected in the Excel sheets and Origin 7.5 (OriginLab Technical) files. Data were analyzed by clampfit 9.0 (Axon Instruments) and Origin 7.5 (OriginLab Technical).

2.4. Nonlinear capacitance measurements

OHC capacitance was measured with a continuous high-resolution (2.56 ms) two-sine voltage stimulus protocol (10 mV peak at both 390.6 and 781.2 Hz), and subsequent FFT based admittance analysis as fully described previously (Santos-Sacchi et al., 1998). These small, high frequency sinusoids were superimposed on voltage ramps that spanned ±180 mV. All data collection and most analyses were performed with an in-house developed Windows based whole-cell voltage clamp program, jClamp (www.scisoft.com), utilizing a Digidata 1320 board (Axon, CA). Matlab (Natick, MA) or SigmaPlot was used for fitting the C_m data.

C – V data were fit with the first derivative of a two-state Boltzmann function and a constant representing the linear capacitance (Santos-Sacchi, 1991),

$$C_m = Q_{\text{max}} \frac{ze}{kT} \frac{b}{(1+b)^2} + C_{\text{lin}} \quad (1)$$

$$b = \exp\left(\frac{-ze(V_m - V_{\text{pkcm}})}{kT}\right)$$

where Q_{max} is the maximum nonlinear charge moved, V_{pkcm} is voltage at peak capacitance or half-maximal nonlinear charge transfer, V_m is membrane potential, C_{lin} is linear capacitance, z is apparent valence, e is electron charge, k is Boltzmann's constant, and T is absolute temperature.

2.5. TRPV1 immunofluorescence labeling in OHCs of guinea pigs and *Trpv1*^{-/-} mice

The cochleae of guinea pigs, *Trpv1*^{-/-} mice, and the wild type control mice with the same background (Jackson Lab) were dissected and fixed in 4% paraformaldehyde solution overnight. After being washed in 0.02 M phosphate-buffered saline (PBS) for 30 min, the tissues were permeabilized in 0.5% Triton X-100 (Sigma) for 1 h (h) and incubated in 10% goat serum and 1% bovine serum in 0.02 M PBS for 1 h. The tissues were incubated overnight in primary anti-TRPV1 (rabbit polyclonal, RA10110, Neuromics, Edina, MN, USA) diluted to 1:500 with 1% BSA-PBS. After being washed in 1% BSA-PBS for 30 min, the tissues were incubated in Alexa fluor 488 anti-rabbit IgG (diluted to 1:100) and Alexa fluor 568 phalloidin (diluted to 1:50, Invitrogen, Eugene, OR, USA) for 1 h and Hoechst (1 μg/ml, Invitrogen, Eugene, OR, USA) for 15 min. After being washed in 0.02 M PBS for 30 min, the tissues were mounted and observed on a Nikon Eclipse TE 300 inverted microscope fitted with an Olympus Fluview confocal laser microscope system. Negative controls were 1) tissue incubated with 1% BSA-

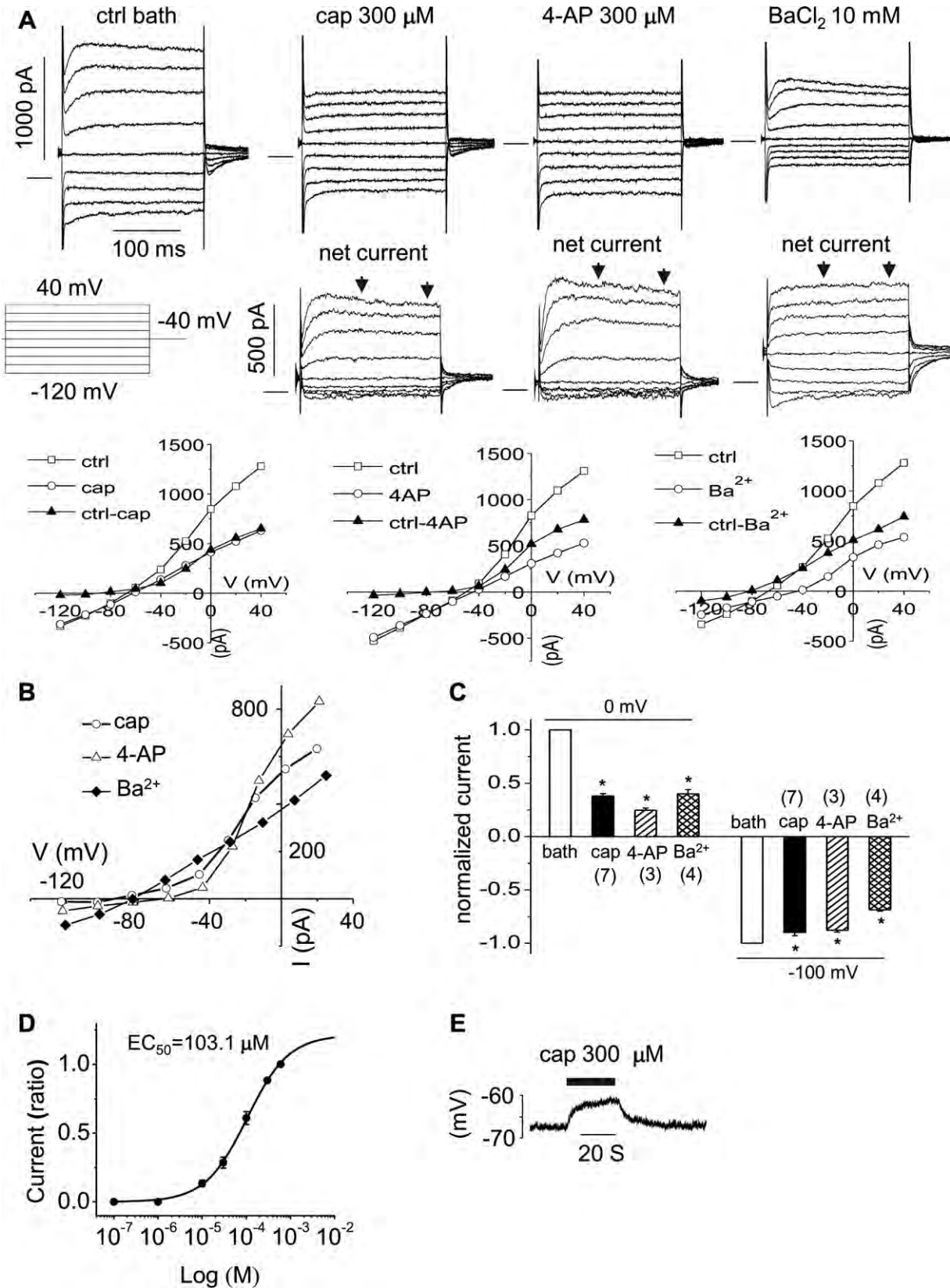


Fig. 1. Capsaicin blocks I_K and I_{Kn} of OHCs from the upper third turn. **A.** Representative currents (of 72 μM OHC) induced by step voltage commands following application of capsaicin (cap), 4-AP and BaCl_2 . Net currents (cap, 4-AP and Ba^{2+} sensitive current) are after subtraction from control (ctrl) currents in bath. The ctrl current in the figure is for capsaicin and the ctrl for 4-AP and BaCl_2 are not shown here. The zero current is shown as a solid horizontal bar preceding the step currents. Representative I–V plots were produced for each original recordings **B.** Representative I–V plots of net currents in **A.** The current for each voltage (V) is the 100 ms average bounded by the arrows. **C.** Bar graph summary: 300 μM capsaicin, 300 μM 4-AP and 10 mM BaCl_2 blocked outward currents at 0 mV and inward currents at -100 mV. Currents were normalized by the currents in ctrl bath. * $P < 0.05$. **D.** Dose response curve of capsaicin-sensitive current at 0 mV ($n = 5$). Current (ratio): currents normalized by the current at 600 μM capsaicin. **E.** Representative recording of membrane potential with 300 μM capsaicin.

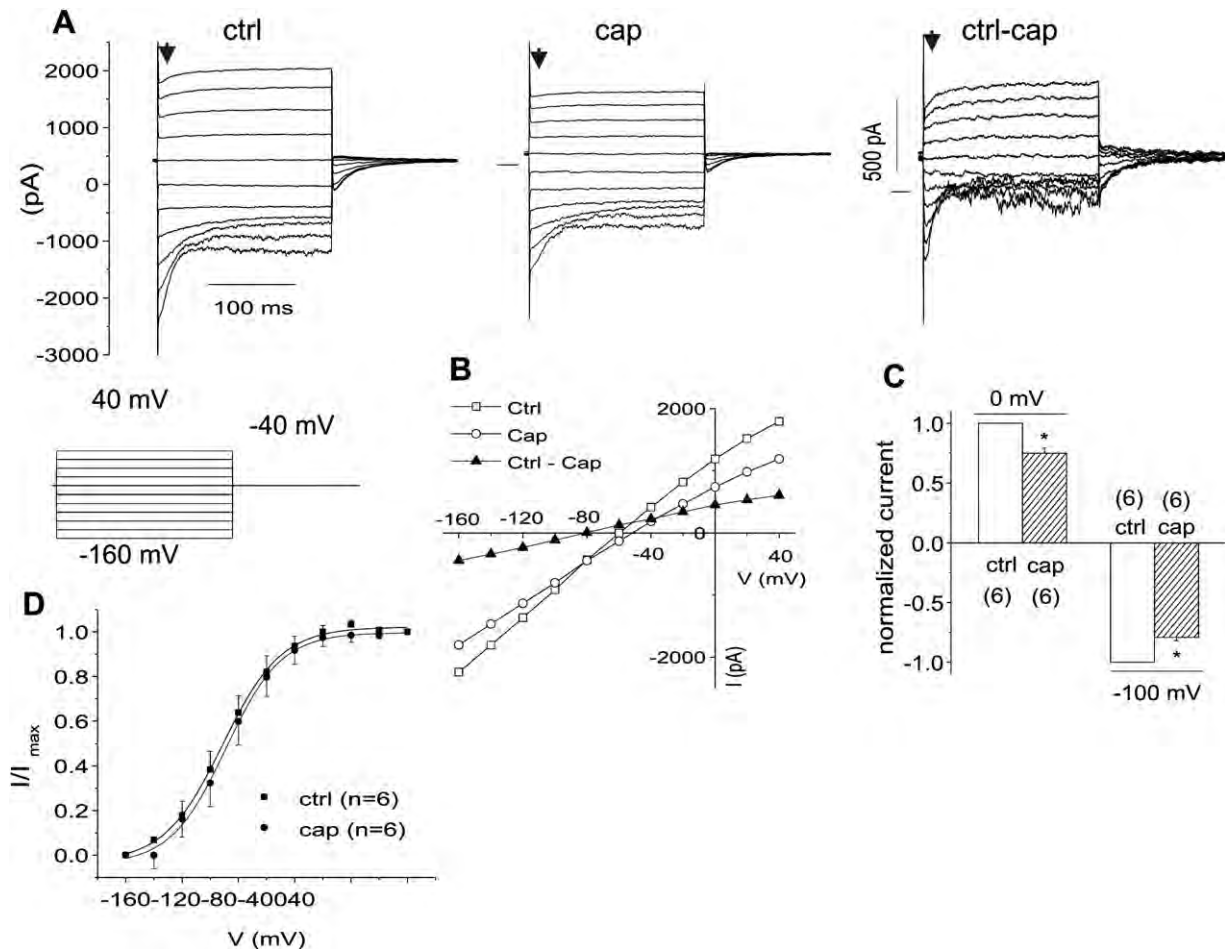


Fig. 2. Capsaicin blocks $I_{K,n}$ of OHCs from the lower 2nd turn. A. Representative currents in control (ctrl) bath and following application of 300 μM capsaicin (cap). Net currents (ctrl-cap) are after subtraction from control (ctrl) currents in bath. B. Representative I - V plots of the currents in A. C. Bar graph summary: 300 μM cap blocked outward currents at 0 mV and inward currents at -100 mV. Currents were normalized by the currents in ctrl. * $P < 0.05$. D. Effect of cap (0.1 mM) on steady state activation curve of $I_{K,n}$. Normalized tail-current amplitudes versus prepulse potentials were fitted with a first-order Boltzmann function ($n = 6$): $I = I_{\text{max}} / (1 + \exp((V - V_{\text{half}}) / S))$, where I_{max} is the fully activated current amplitude at the tail-current potential, V_{half} is the potential at half-maximal activation, V is prepulse potentials and S is the slope factors.

PBS to replace the primary antibody, 2) tissue with the primary antibody (TRPV-1) and its blocking peptide (10^4 M) (Neuromics, Edina, MN, USA), and 3) tissues from the *Trpv1*^{-/-} mice.

2.6. Statistics

Data are presented as means \pm SE from n observations. Student's t -test (paired or non-paired as appropriate) was performed using Microsoft Excel software; $p \leq 0.05$ represents a significant difference.

3. Results

3.1. Capsaicin blocks two types of potassium currents in OHCs, I_K and $I_{K,n}$

In our standard Na^+ rich bath and K^+ rich pipette solutions, upper 3rd turn OHCs presented two previously described K^+ currents (Fig. 1A) (Housley and Ashmore, 1992); I_K , a slowly developing outward current showing slight inactivation (activated above -40 mV), and $I_{K,n}$, an inward current which relaxes during large hyperpolarizing steps (-120 mV). Capsaicin (300 μM) reversibly abolished I_K and slightly reduced $I_{K,n}$. The effects are analogous to the previously observed actions of 4-AP (300 μM) (Mammano and Ashmore, 1996) (Fig. 1A). In comparison, Ba^{2+} (10 mM) blocked most of $I_{K,n}$, without a significant block of I_K . The reversal potential

(V_r) of the capsaicin-sensitive current was -83.6 ± 4.3 ($n = 7$), which is comparable to that of the 4-AP and barium-sensitive current (-70.5 ± 0.5 ($n = 3$) and -82.5 ± 0.8 ($n = 4$), respectively), suggesting a high selectivity to K^+ (Fig. 1B) (The K^+ equilibrium potential (E_K) was -88 mV). From step protocols, average reductions in steady state outward currents at 0 mV for capsaicin, 4-AP, and Ba^{2+} were 62.1%, 75.2%, and 59.9%, respectively ($n = 4-7$; $p < 0.05$; Fig. 1C). Average reductions in steady state inward currents at -100 mV for capsaicin, 4-AP, and Ba^{2+} were 10.1%, 12.2%, and 31.2%, respectively ($n = 3-7$; $p < 0.05$; Fig. 1C). The capsaicin elicited reduction in the outward current was concentration-dependent with $\text{EC}_{50} = 103.1$ μM when held at 0 mV (Fig. 1D). Capsaicin depolarized OHCs by 4.005 mV (Fig. 1E), shifting the resting potential, which is driven by $I_{K,n}$ (Housley and Ashmore, 1992), from -67.9 ± 1.5 to -63.9 ± 1.8 mV ($n = 7$, $p < 0.05$), which is consistent with a small but significant inhibition of $I_{K,n}$ by capsaicin.

To further study the effect of capsaicin on $I_{K,n}$, we used lower 2nd turn OHCs, which presented much larger $I_{K,n}$, but little I_K (Fig. 2A). We found that Capsaicin (300 μM) partially inhibited $I_{K,n}$ (Fig. 2A). The I - V plot showed that capsaicin caused a current reduction in the whole range of voltage commands with V_r of capsaicin-sensitive current at ~ -80 mV (Fig. 2B). Average reductions in steady state inward currents for capsaicin are 25.1% (at 0 mV) and 20.9% (at -100 mV) (Fig. 2C). Fig. 2D shows the effect of capsaicin (300 μM) on the steady state activation curve of $I_{K,n}$,

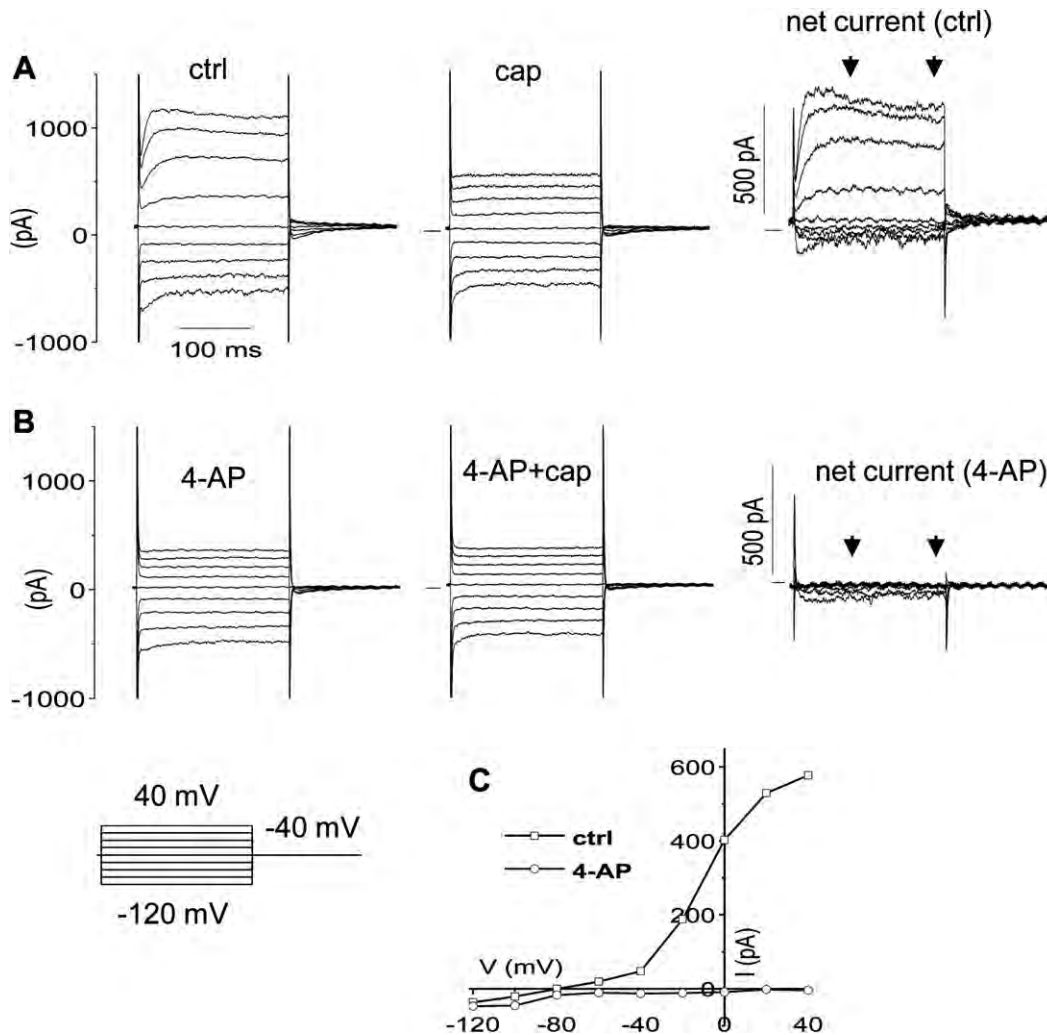


Fig. 3. 4-AP blocks the net capsaicin currents. A. Representative currents in ctrl bath and following application of 300 μM capsaicin (cap). Net currents (ctrl-cap) are after subtraction from ctrl currents in bath. B. Representative currents in 4-AP (300 μM) bath and following application of 300 μM cap. Net currents (cap-sensitive currents) are after subtraction from the currents in 4-AP bath. C. Representative I–V curves of net currents in A and B. The current for each V is the 100 ms average bounded by the arrows.

which was determined from tail currents with the voltage protocol in Fig. 2A. Capsaicin did not significantly shift the V_{half} . The V_{half} (mV) and slope factor (S) (mV) are -91.2 ± 2.3 ($n = 6$) and 20.8 ± 2.1 ($n = 8$), respectively for capsaicin treatment, versus -88.9 ± 2.1 (V_{half}) and 19.7 ± 1.9 (S) for control. The V_{half} of $I_{K,n}$ was consistent with previous findings (Housley and Ashmore, 1992; Jagger and Ashmore, 1999b).

Consistent with the above findings, capsaicin-sensitive currents (the upper 3rd turn OHCs) were blocked by 4-AP (300 μM) and BaCl_2 (10 mM). 4-AP (300 μM) blocked all capsaicin-sensitive outward currents in step protocols ($n = 3$) (Fig. 3). In Fig. 4A, when held at -44 mV (where $I_{K,n}$ is predominantly activated), OHCs presented a net outward current, i.e. a positive current above zero, in continuous gap-free recordings. Capsaicin (300 μM) reversibly inhibited the outward current by shifting it negatively. The shift was reduced in the presence of BaCl_2 (10 mM). In step protocols (Fig. 4. B, C, D, E), BaCl_2 (10 mM) reduced the capsaicin-sensitive current at -40 mV by 89.6% ($n = 3$, $p < 0.05$) and at 0 mV by 55.7% ($n = 3$, $p < 0.05$).

We also tested the effect of capsaicin on I_K and $I_{K,n}$ at the concentration used in our previous *in vivo* study (Zheng et al., 2003). Consistent with that study, 20 μM capsaicin produced a small but significant reduction of I_K and $I_{K,n}$. From step protocols

(shown in Fig. 1), average reductions in steady state outward currents for capsaicin (20 μM) were 8.4% at 0 mV ($p < 0.05$, $n = 10$) and 6.5% at -100 mV ($p < 0.05$, $n = 10$) (Fig. 5).

3.2. Capsaicin alters electromotility

Application of extracellular capsaicin altered OHC nonlinear capacitance, the electrical signature of electromotility. Fig. 6A shows the effects of increasing concentrations on the C–V function. The drug shifted V_{pkcm} to the left and reduced peak capacitance for concentrations over 30 μM . The shifts of V_{pkcm} for concentrations 30, 100, 300 and 1000 μM capsaicin perfusions were 1.67 ± 0.34 , 4.98 ± 1.01 , 25.03 ± 1.34 and 29.94 ± 1.16 mV, respectively (se, $n = 5$, $p < 0.05$). Reductions in nonlinear peak capacitance for concentrations 30, 100, 300 and 1000 μM capsaicin perfusions were 1.21 ± 0.35 , 2.03 ± 0.49 , 3.81 ± 0.58 and 3.39 ± 0.55 pF, respectively (se, $n = 5$, $p < 0.05$). No significant differences were found when cells were held at 0 or -70 mV. The concentration dependence of the V_{pkcm} shift is shown in Fig. 6B. A Hill fit gives a half maximal shift (EC_{50}) at 158 μM ($n = 8$). Removing Ca^{2+} , both extracellular and intracellular, reduced the V_{pkcm} shift at the two highest concentrations, namely -17.3 mV at 300 μM ($p = 0.04$) and -22.3 mV at 1000 μM ($p = 0.07$). This resulted in an increase in the

EC₅₀ to 204 μM. Reducing intracellular and extracellular chloride levels to 1 mM did not alter the ability of capsaicin to shift the V_{pkcm}.

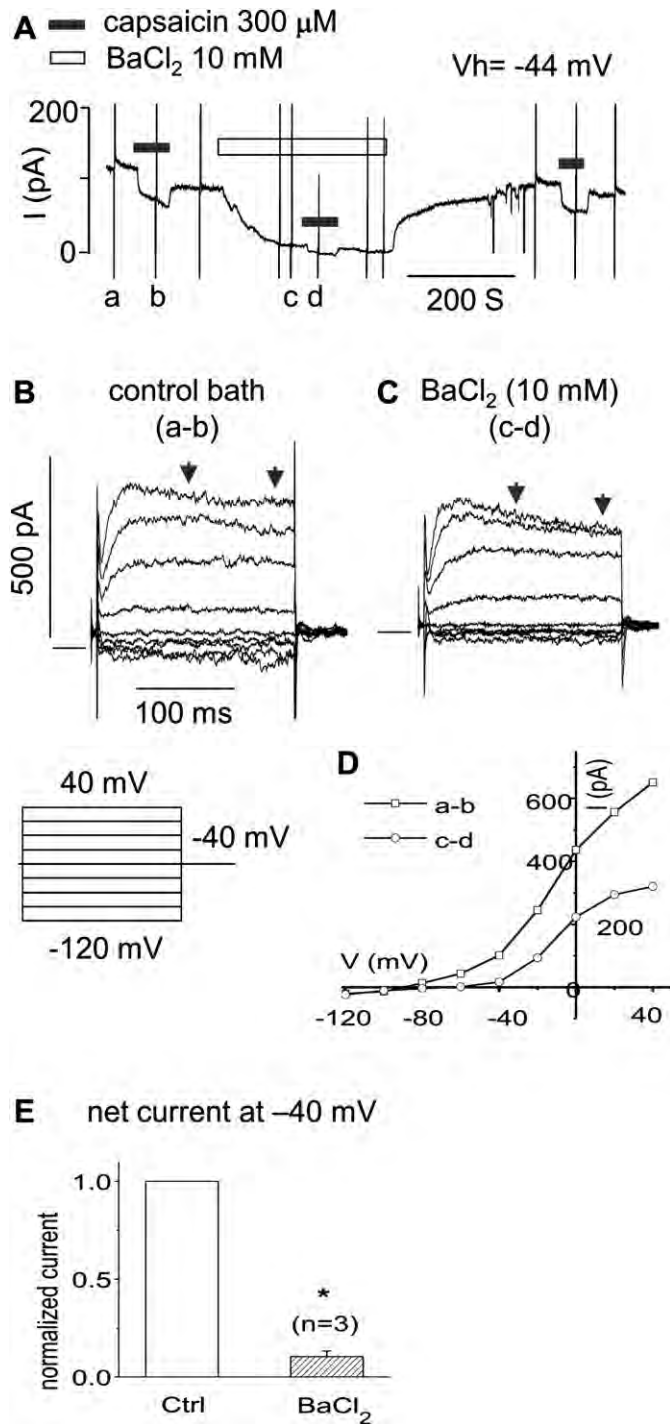


Fig. 4. BaCl₂ partially blocks the net capsaicin currents. **A.** Representative current in gap-free mode at holding voltage of -44 mV. The vertical spike currents, such as a, b, c and d, were caused by the I–V step voltage commands as shown in **B**. **B.** Net capsaicin (300 μM) currents (a–b) in control bath. The zero current was shown as a solid horizontal bar preceding the step currents in **B** and **C**. **C.** Net capsaicin (300 μM) currents (c–d) in the bath with 10 mM BaCl₂. **D.** Representative I–V curves of net currents in **B** and **C**. The current for each V is the 100 ms average bounded by the arrows. **E.** Bar graph summary: the net capsaicin currents at V_h of -40 mV in the control (ctrl) and BaCl₂ (10 mM) bath. The currents were normalized by the currents of ctrl. *P < 0.05, n = 3.

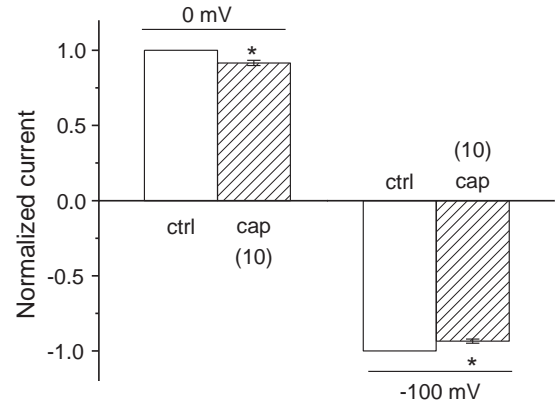


Fig. 5. Capsaicin blocks I_K and I_{K,N} at the concentration (20 μM) used in previous *in vivo* studies. Bar graph summary: 20 μM capsaicin (cap) (n = 10) significantly blocked outward currents at 0 mV and inward currents at -100 mV with step protocols (shown in Fig. 1). Currents were normalized by the currents in ctrl bath. *P < 0.05.

3.3. TRPV1 immunofluorescence labeling in OHCs of guinea pigs and Trpv1^{-/-} mice

TRPV-1 labeling was found in the basolateral membrane of the OHCs and IHCs of the guinea pigs (Fig. 7A) and Trpv1^{+/+} mice

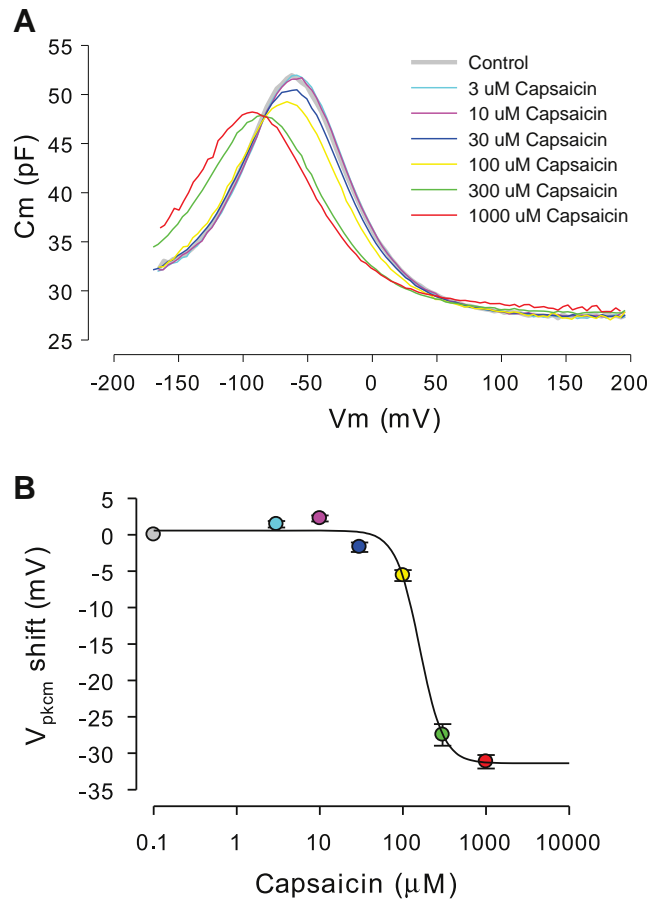


Fig. 6. Representative effects of capsaicin on OHC NLC. **A.** Cm–Vm plots for increasing concentrations of capsaicin. Both a decrease in peak capacitance and shift in voltage at peak capacitance result from drug exposure. **B.** Dose response function with standard errors, showing an IC₅₀ of 158 μM (n = 8). The data are statistically significant at 10uM and above (p < 0.013), showing a biphasic response shift at low concentrations. Peak NLC reduction is significant at 30 μM and above (p < 0.05).

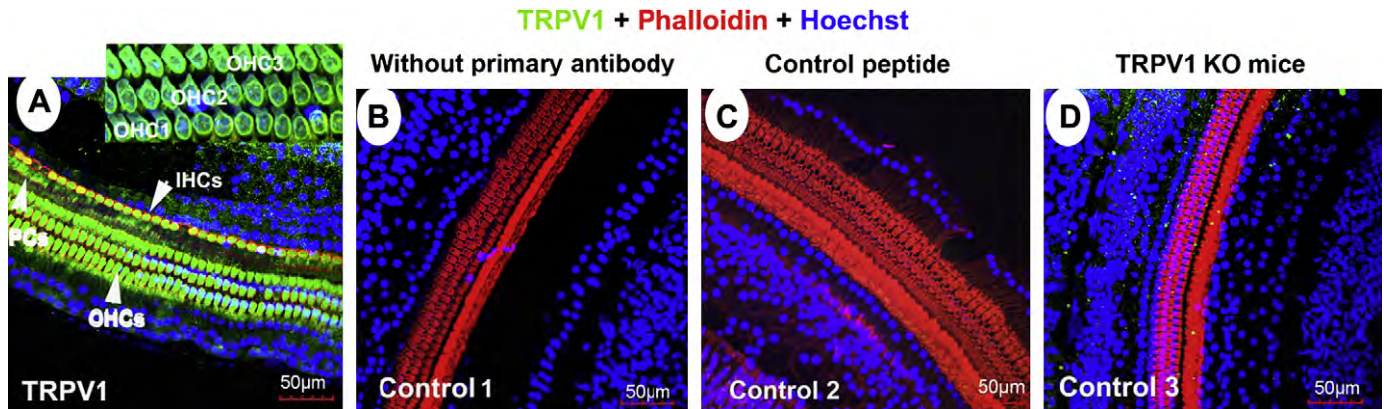


Fig. 7. TRPV1 immunofluorescence labeling of guinea pig and *Trpv1*^{-/-} mice. A, a representative confocal projection image showing TRPV1 immunolabelling in OHCs, IHCs and pillar cells of guinea pigs. The insert shows that TRPV1 is expressed in the basolateral membrane of OHCs. No significant labeling was found in OHCs, IHCs and PCs of negative controls including 1) primary antibody only (B), 2) with control peptide (C) and 3) *Trpv1*^{-/-} mice (D). TRPV1 labeling of *Trpv1*^{+/+} mice is similar to guinea pigs (data not shown).

(similar to guinea pigs, data not shown). No significant TRPV-1 labeling was found in the OHCs and IHCs in the negative controls including 1) primary antibody only (Fig. 7B), 2) with control peptide (Fig. 7C), and 3) the *Trpv1*^{-/-} mice (Fig. 7D). TRPV-1 labeling was also found in supporting cells including pillar cells and Hensen's cells (Fig. 7A).

4. Discussion

4.1. Capsaicin blocks I_K and $I_{K,n}$

There are several types of K currents expressed in adult guinea pig OHCs, I_K and $I_{K,n}$ being the two major ones (Housley and Ashmore, 1992, 2006; Mammano and Ashmore, 1996; Santos-Sacchi and Dilger, 1988). I_K , which activates at potentials more positive than -35 mV, is most prominent in the apical turn (Housley and Ashmore, 1992) and is specifically blocked by 4-AP (Mammano and Ashmore, 1996). $I_{K,n}$, which activates at hyperpolarized potentials more negative than -40 mV, is most prominent in the basal turn and is more susceptible to barium (10 mM) (Mammano and Ashmore, 1996). $I_{K,n}$ is carried by KCNQ4 channels (Chambard and Ashmore, 2005; Holt et al., 2007; Kharkovets et al., 2000, 2006) and dominates the OHC membrane conductance at the resting potential. These conductances are restricted to the basal pole of the OHC (Santos-Sacchi et al., 1997).

Our findings indicate that capsaicin is a potent I_K blocker; 300 μ M capsaicin, similar to 300 μ M 4-AP, abolished most of the current (Fig. 1). The reversal potential (V_r) of the capsaicin-sensitive current (-83.6 mV) was close to that expected for a K conductance (-88 mV), suggesting most of the capsaicin-sensitive current under these conditions was carried by potassium. That 4-AP completely blocked the outward capsaicin-sensitive current in step protocols is another piece of evidence that capsaicin and 4-AP work similarly (Fig. 3). The potency of capsaicin was slightly less than 4-AP; the outward current at 0 mV was reduced by 62.1% for capsaicin (300 μ M) and by 75.2% for 4-AP (300 μ M). Unlike $I_{K,n}$ (KCNQ4), the molecular identity of I_K has not been successfully discovered, although some candidates have been proposed and some efforts have been made (Ashmore and Meech, 1986; Jagger and Ashmore, 1999a).

Capsaicin also reduced $I_{K,n}$. This conclusion is supported by the following findings in the upper 3rd turn OHCs. 1) Capsaicin slightly depolarized OHCs by 4 mV. 2) At -44 mV, where $I_{K,n}$ is the dominant current, capsaicin caused a considerable negative shift of an outward current in gap-free recording (Fig. 4A). 3) The shift caused

by capsaicin was blocked by barium (10 mM). 4) In step protocols, barium (10 mM) significantly blocked the capsaicin-sensitive current (Fig. 4B–E). However, the reduction of $I_{K,n}$, though statistically significant ($p < 0.05$), was quite small for capsaicin (300 μ M), with a reduction of inward current at -100 mV by 12.2%. In comparison, barium (10 mM) reduced the inward current by 31.2%. In the short OHCs (the lower 2nd turn) with larger $I_{K,n}$, capsaicin reduced more inward current (by 20.9% at -100 mV).

Our study is the first to report the blocking effects of capsaicin on K conductances in cochlear hair cells. Capsaicin has been previously reported to block voltage gated K currents in a variety of different cells including Schwann cells, dorsal root ganglion cells, T cells, vertebrate axons, and some mammalian cell lines with an IC_{50} ranging from 23 to 158 μ M (Grissmer et al., 1994). These values are comparable to our observation of 103.1 μ M. More interestingly, capsaicin was found to block a KCNQ current in the vestibular type II hair cells of the gerbil (Rennie et al., 2001) and a delayed rectifier K⁺ current in the vestibular hair cells of frog semicircular canals (Marcotti et al., 1999). Analogous to our findings in guinea pig OHCs, the K conductance of the frog vestibular hair cells was also pharmacologically separated into two complementary components: a capsaicin-sensitive current and a barium-sensitive current (Marcotti et al., 1999).

4.2. Capsaicin alters OHC electromotility

The electrically evoked OHC mechanical response underlies mammalian cochlear amplification (Brownell, 1984; Liberman et al., 2002; Santos-Sacchi et al., 2006). Here we show that capsaicin can significantly reduce NLC and shift its operating voltage range. Changes in NLC are known to correspond to changes in electromotility (see Kakehata and Santos-Sacchi, 1995), and shifts in the operating range are predicted to alter the cell's mechanical gain. We show that capsaicin is not working through changes in intracellular chloride levels, which are known to be important for OHC motor function (Oliver et al., 2001; Rybalchenko and Santos-Sacchi, 2003; Santos-Sacchi, 2003; Song et al., 2005), but may work directly on the motor protein, prestin. It is the first study to report that capsaicin has a direct action on OHC electromotility.

4.3. TRPV-1 considerations

We confirmed that TRPV-1 immunolabeling is observed in normal guinea pig and mouse OHCs, IHCs, and supporting cells (pillar cells

and Hensen's cells), as previously shown by us and others (Ishibashi et al., 2008; Mukherjea et al., 2008; Zheng et al., 2003). However, immunolabeling is absent in *Trpv1*^{-/-} mice. Given these strong data, it is surprising that we did not see characteristic TRPV-1 currents in isolated OHCs at capsaicin concentrations ranging from 0.1 to 600 μ M. There are a couple of possibilities for this quandary. First, it is possible that the native TRPV-1 is functional *in vivo*, but was inactivated during the relatively harsh OHC isolation procedure. It has been reported that isolated OHCs are loaded with more Ca^{2+} and Na^{+} and have less polarized resting potential and significantly reduced input resistance (Mammano et al., 1995). Second, it may be possible that the native TRPV-1 expressed in OHCs is non functional, similar to normal TRPLM3 (Grimm et al., 2007). Consequently, in the first case, the *in vitro* action of capsaicin on I_K , $I_{K,n}$ and NLC of OHCs would be unmasked by block of TRPV-1 resulting from the harsh isolation. The *in vivo* effect of capsaicin on I_K , $I_{K,n}$ and NLC would augment any direct effect of capsaicin on TRPV-1 in accounting for our previous *in vivo* finding of reduced amplification. To be sure, the capsaicin concentration of our *in vivo* study (20 μ M) was found to produce a significant reduction of I_K , $I_{K,n}$ (Fig. 5) and a significant shift of NLC (Fig. 6). Nevertheless, we cannot rule out that capsaicin's action on IHCs and supporting cells may also have contributed to our *in vivo* findings.

In summary, we hypothesize that the reduction of I_K and $I_{K,n}$ by capsaicin led to a depolarization of OHCs, which consequently decreased the driving force for transduction current. The resulting reduced drive for OHC electromotility in combination with the direct action of capsaicin on electromotility was likely causal in reducing cochlear amplification. The possible contributory role of supporting cells and IHCs remains under investigation.

Acknowledgments

NIH grants DC 005983, DC 000141 (ALN), DC 000273 (JSS), DC 008130 (JSS), DC 004716 (JZG) DC 010844 (XS), DC 008888-02(XS), DC 008888-02S1 (XS).

References

- Ashmore, J.F., Meech, R.W., 1986. Ionic basis of membrane potential in outer hair cells of guinea pig cochlea. *Nature* 322, 368–371.
- Brownell, W.E., 1984. Microscopic observation of cochlear hair cell motility. *Scan. Electron Microsc.* 3, 1401–1406.
- Caterina, M.J., Schumacher, M.A., Tominaga, M., Rosen, T.A., Levine, J.D., Julius, D., 1997. The capsaicin receptor: a heat-activated ion channel in the pain pathway. *Nature* 389, 816–824.
- Chambard, J.M., Ashmore, J.F., 2005. Regulation of the voltage-gated potassium channel KCNQ4 in the auditory pathway. *Pflugers Arch.* 450, 34–44.
- Dallos, P., Wu, X., Cheatham, M.A., Gao, J., Zheng, J., Anderson, C.T., Jia, S., Wang, X., Cheng, W.H.Y., Sengupta, S., He, D.Z.Z., Zuo, J., 2008. Prestin-based outer hair cell motility is necessary for mammalian cochlear amplification. *Neuron* 58, 333–339.
- Grimm, C., Cuajungco, M.P., van Aken, A.F., Schnee, M., Jörs, S., Kros, C.J., et al., 2007. A helix-breaking mutation in TRPML3 leads to constitutive activity underlying deafness in the varitint-waddler mouse. *Proc. Natl. Acad. Sci. U.S.A.* 104, 19583–19588.
- Grissmer, S., Nguyen, A.N., Aiyar, J., Hanson, D.C., Mather, R.J., Gutman, G.A., Karmilowicz, M.J., Auperin, D.D., Chandy, K.G., 1994. Pharmacological characterization of five cloned voltage-gated K⁺ channels, types Kv1.1, 1.2, 1.3, 1.5, and 3.1, stably expressed in mammalian cell lines. *Mol. Pharmacol.* 45, 1227–1234.
- He, D.Z., Zheng, J., Kalinec, F., Kakehata, S., Santos-Sacchi, J., 2006. Tuning in to the amazing outer hair cell: membrane wizardry with a twist and shout. *J. Membr. Biol.* 209, 119–134.
- Holt, J.R., Stauffer, E.A., Abraham, D., Geleoc, G.S., 2007. Dominant-negative inhibition of M-like potassium conductances in hair cells of the mouse inner ear. *J. Neurosci.* 27, 8940–8951.
- Housley, G.D., Ashmore, J.F., 1992. Ionic currents of outer hair cells isolated from the guinea-pig cochlea. *J. Physiol. (Lond)* 448, 73–98.
- Housley, G.D., Marcotti, W., Navaratnam, D., Yamoah, E.N., 2006. Hair cells – beyond the transducer. *J. Membr. Biol.* 209, 89–118.
- Ishibashi, T., Takumida, M., Akagi, N., Hirakawa, K., Anniko, M., 2008. Expression of transient receptor potential vanilloid (TRPV) 1, 2, 3, and 4 in mouse inner ear. *Acta Otolaryngol.* 128, 1286–1293.
- Jagger, D.J., Ashmore, J.F., 1999a. The fast activating potassium current, I(K, f), in guinea-pig inner hair cells is regulated by protein kinase A. *Pflugers Arch.* 427, 368–371.
- Jagger, D.J., Ashmore, J.F., 1999b. Regulation of ionic currents by protein kinase A and intracellular calcium in outer hair cells isolated from the guinea-pig cochlea. *Pflugers Arch.* 437, 409–416.
- Kakehata, S., Santos-Sacchi, J., 1995. Membrane tension directly shifts voltage dependence of outer hair cell motility and associated gating charge. *Biophys. J.* 68, 2190–2197.
- Kharkovets, T., Hardelin, J.P., Safieddine, S., Schweizer, M., El-Amraoui, A., Petit, C., Jentsch, T.J., 2000. KCNQ4, a K⁺ channel mutated in a form of dominant deafness, is expressed in the inner ear and the central auditory pathway. *Proc. Natl. Acad. Sci. U S A* 97, 4333–4338.
- Kharkovets, T., Dedek, K., Maier, H., Schweizer, M., Khimich, D., Nouvian, R., Vardanyan, V., Leuwer, R., Moser, T., Jentsch, T.J., 2006. Mice with altered KCNQ4 K⁺ channels implicate sensory outer hair cells in human progressive deafness. *EMBO J.* 25, 642–652.
- Liberman, M.C., Gao, J., He, D.Z., Wu, X., Jia, S., Zuo, J., 2002. Prestin is required for electromotility of the outer hair cell and for the cochlear amplifier. *Nature* 419, 300–304.
- Mammano, F., Ashmore, J.F., 1996. Differential expression of outer hair cell potassium currents in the isolated cochlea of the guinea-pig. *J. Physiol.* 496 (Pt 3), 639–646.
- Mammano, F., Kros, C.J., Ashmore, J.F., 1995. Patch clamped responses from outer hair cells in the intact adult organ of Corti. *Pflugers Arch.* 430, 745–750.
- Marcotti, W., Russo, G., Prigioni, I., 1999. Inactivating and non-inactivating delayed rectifier K⁺ currents in hair cells of frog crista ampullaris. *Hear. Res.* 135, 113–123.
- Mukherjea, D., Jajoo, S., Whitworth, D., Bunch, J.R., Turner, J.G., Rybak, L.P., Ramkumar, V., 2008. Short interfering RNA against transient receptor potential vanilloid 1 attenuates cisplatin-induced hearing loss in the rat. *J. Neurosci.* 28, 13056–13065.
- Oliver, D., He, D.Z., Klocker, N., Ludwig, J., Schulte, U., Waldegger, S., Ruppersberg, J.P., Dallos, P., Fakler, B., 2001. Intracellular anions as the voltage sensor of prestin, the outer hair cell motor protein. *Science* 292, 2340–2343.
- Rennie, K.J., Weng, T., Correia, M.J., 2001. Effects of KCNQ channel blockers on K(+) currents in vestibular hair cells. *Am. J. Physiol. Cell Physiol.* 280, C473–C480.
- Rybalchenko, V., Santos-Sacchi, J., 2003. Cl⁻ flux through a non-selective, stretch-sensitive conductance influences the outer hair cell motor of the guinea-pig. *J. Physiol.* 547, 873–891.
- Santos-Sacchi, J., 1991. Reversible inhibition of voltage-dependent outer hair cell motility and capacitance. *J. Neurosci.* 11, 3096–3110.
- Santos-Sacchi, J., 2003. New tunes from Corti's organ: the outer hair cell boogie rules. *Curr. Opin. Neurobiol.* 13, 459–468.
- Santos-Sacchi, J., Dilger, J.P., 1988. Whole cell currents and mechanical responses of isolated outer hair cells. *Hear Res.* 35, 143–150.
- Santos-Sacchi, J., Huang, G.J., Wu, M., 1997. Mapping the distribution of outer hair cell voltage-dependent conductances by electrical amputation. *Biophys. J.* 73, 1424–1429.
- Santos-Sacchi, J., Kakehata, S., Takahashi, S., 1998. Effects of membrane potential on the voltage dependence of motility-related charge in outer hair cells of the guinea-pig. *J. Physiol.* 510 (Pt 1), 225–235.
- Santos-Sacchi, J., Song, L., Zheng, J., Nuttall, A.L., 2006. Control of mammalian cochlear amplification by chloride anions. *J. Neurosci.* 26, 3992–3998.
- Song, L., Seeger, A., Santos-Sacchi, J., 2005. On membrane motor activity and chloride flux in the outer hair cell: lessons learned from the environmental toxin tributyltin. *Biophys. J.* 88, 2350–2362.
- Szallasi, A., Blumberg, P.M., 1999. Vanilloid (capsaicin) receptors and mechanisms. *Pharmacol. Rev.* 51, 159–212.
- Wu, T., Lv, P., Kim, H.J., Yamoah, E.N., Nuttall, A.L., 2010. Effect of salicylate on KCNQ4 of the guinea pig outer hair cell. *J. Neurophysiol.* 103, 1969–1977.
- Xu, T., Nie, L., Zhang, Y., Mo, J., Feng, W., Wei, D., Petrov, E., Calisto, L.E., Kachar, B., Beisel, K.W., Vazquez, A.E., Yamoah, E.N., 2007. Roles of alternative splicing in the functional properties of inner ear-specific KCNQ4 channels. *J. Biol. Chem.* 282, 23899–23909.
- Zheng, J., Dai, C., Steyger, P.S., Kim, Y., Vass, Z., Ren, T., Nuttall, A.L., 2003. Vanilloid receptors in hearing: altered cochlear sensitivity by vanilloids and expression of TRPV1 in the organ of Corti. *J. Neurophysiol.* 90, 444–455.

RESEARCH ARTICLE

Tyrosine motifs are required for prestin basolateral membrane targeting

Yifan Zhang^{1,*}, Iman Moeini-Naghani^{1,*}, JunPing Bai^{1,*}, Joseph Santos-Sacchi^{3,4} and Dhasakumar S. Navaratnam^{1,2,3,‡}

ABSTRACT

Prestin is targeted to the lateral wall of outer hair cells (OHCs) where its electromotility is critical for cochlear amplification. Using MDCK cells as a model system for polarized epithelial sorting, we demonstrate that prestin uses tyrosine residues, in a YXXΦ motif, to target the basolateral surface. Both Y520 and Y667 are important for basolateral targeting of prestin. Mutation of these residues to glutamine or alanine resulted in retention within the Golgi and delayed egress from the Golgi in Y667Q. Basolateral targeting is restored upon mutation to phenylalanine suggesting the importance of a phenol ring in the tyrosine side chain. We also demonstrate that prestin targeting to the basolateral surface is dependent on AP1B (μ1B), and that prestin uses transferrin containing early endosomes in its passage from the Golgi to the basolateral plasma membrane. The presence of AP1B (μ1B) in OHCs, and parallels between prestin targeting to the basolateral surface of OHCs and polarized epithelial cells suggest that outer hair cells resemble polarized epithelia rather than neurons in this important phenotypic measure.

KEY WORDS: Golgi, Hair cell, Tyrosine, Cell polarity, Protein sorting

INTRODUCTION

The cochlear amplifier is responsible for the exquisite sensitivity of mammalian hearing (Davis, 1983). There is considerable experimental data implicating electromotility of outer hair cells as integral to this process (Ashmore, 1987; Brownell et al., 1985; Dallos and Evans, 1995; Geisler, 1993; Geisler and Sang, 1995; Russell and Nilsen, 1997; Santos-Sacchi, 2003). Electromotility in outer hair cells is brought about by prestin, a transmembrane protein of the SLC26 family (Zheng et al., 2000), and molecular evidence has now confirmed its importance to cochlear amplification (Gao et al., 2007; Liberman et al., 2002; Mellado Lagarde et al., 2008). The localization of prestin along the lateral wall of these elongated cylindrical cells is critical to

electromotility (Dallos et al., 1991; Hallworth et al., 1993; Huang and Santos-Sacchi, 1993; Kalinec et al., 1992; Yu et al., 2006; Zheng et al., 2000). The presence of prestin along the lateral wall of the cell brings about the voltage mediated elongation and shortening of outer hair cells along its longitudinal axis. How prestin is targeted to the lateral wall of the cell has been indeterminate.

Hair cells are specialized epithelial cells that show features of both epithelial cells as well as neurons. Individual cells form apically located tight junctions with other cells and have apically located stereocilia that are analogous to apically located microvilli (Leonova and Raphael, 1997; Mahendrasingam et al., 1997). Hair cells resemble neurons in containing unstable membrane potentials that result from a plethora of voltage and mechanically sensitive ion channels. These channels are sharply segregated in the cell with mechanically sensitive channels located in stereocilia (Fettiplace, 2009). In contrast many of its voltage and ligand gated ion channels are located at the basolateral surface of the cell (Housley et al., 2006). Inner hair cells, in addition, have synaptic apparatus that is located at its basal pole (Glowatzki et al., 2008).

A large body of work in polarized epithelial cells has shown the segregation of proteins to the basolateral and apical ends of the cell that results in a segregation of function (Farr et al., 2009; Rodriguez-Boulan et al., 2005). This segregation of proteins occurs by sorting of proteins after exit from the Golgi. Since neurons demonstrate a similar segregation of function, it has been proposed that dendritic and axonal compartments are analogous to the basolateral and apical surface respectively of polarized epithelial cells (Bradke and Dotti, 1998; Dotti et al., 1991; Dotti and Simons, 1990; Pietrini et al., 1994). Hair cells, however, pose a dilemma since they have features of both epithelial cells and neurons. Critically, the dendritic and axonal ends of a hair cell are at opposite ends to the expected basolateral and apical ends of the cell. Thus mechanosensitive channels that serve as its receptors are present in stereocilia and not at the basolateral surface as would be expected by its dendritic extrapolation. Similarly, the synaptic apparatus of inner hair cells is located at the basal pole and not at the stereociliary apical end as would be expected by its axonal extrapolation.

A collation of previous experimental data would suggest that protein sorting in hair cells resembles that of polarized epithelial cells rather than neurons. Thus, prior work has shown the basolateral localization of a number of proteins that are classically sorted to the basolateral surface of polarized epithelial cells. These proteins include E-cadherin, β-catenin and Na/K ATPase in mammalian, chicken and zebrafish hair cells (Bian et al., 2011; Clemens Grisham et al., 2013; Leonova and Raphael, 1997; Mahendrasingam et al., 1997). Moreover, AP1B

¹Department of Neurology, Yale School of Medicine, New Haven, CT 06510, USA.

²Department of Neurobiology, Yale School of Medicine, New Haven, CT 06510, USA.

³Department of Surgery, Yale School of Medicine, New Haven, CT 06510, USA.

⁴Department of Cellular and Molecular Physiology, Yale School of Medicine, New Haven, CT 06510, USA.

*These authors contributed equally to this work

‡Author for correspondence (Dhasakumar.Navaratnam@Yale.Edu)

This is an Open Access article distributed under the terms of the Creative Commons Attribution License (<http://creativecommons.org/licenses/by/3.0>), which permits unrestricted use, distribution and reproduction in any medium provided that the original work is properly attributed.

(μ 1B), a protein subunit in the AP1B clathrin protein complex integral to the basolateral sorting apparatus, is present in hair cells and its loss is important for the sorting of Na/K ATPase to the basolateral surface of hair cells (Clemens Grisham et al., 2013). This protein subunit, which was identified as critical to hair cell function in a forward screening of hair cell dysfunction mutants in zebrafish, is normally present only in epithelial cells and not in other cell types including neurons (Ohno et al., 1999).

In this paper we demonstrate that prestin, the protein responsible for outer hair cell electromotility, is localized along the basolateral surface of polarized epithelial cells using a tyrosine signal motif that is dependent on the AP1B (μ 1B) subunit. These data further support an emerging concept that in hair cells protein sorting resembles that of epithelial cells rather than neurons. Previous work in other polarized CL4 epithelial cells have shown a similar sorting of two proteins, Espin and myosin Xa, associated with the stereociliary apparatus to the apical surface of the cell and prestin to the basolateral surface of the cell. The implications to this concept are significant.

MATERIALS AND METHODS

cDNA constructs and generation of mutants

Single or multiple amino acid substitutions were generated using QuickChange II or QuickChange II Multi site-directed mutagenesis kits (Stratagene, La Jolla, CA) with a gerbil prestin-YFP in pEYFPN1 vector (Clontech, Mountain View, CA) as a template. All mutations were confirmed by DNA sequencing, including the entire coding region.

Antibody labeling

Cells were fixed in 4% formaldehyde, washed in PBS 0.05% Tween 20, 0.05% Triton-X 100 (incubation buffer) three times, and incubated with primary antibody in incubation buffer overnight at 4°C. The primary antibodies were goat anti-prestin antibody (1:500, N-20 prestin, Santa Cruz, CA) mouse anti- β -catenin (1:50, Becton Dickinson), mouse anti-Na/K ATPase (1:20, Affinity Bioreagents), and goat anti-AP1B (μ 1B) (1:100, Santa-Cruz). After three washes in incubation buffer the cells/tissue was incubated with secondary antibody in incubation buffer for 1 hour at room temperature. Secondary antibodies used included goat anti-mouse Alexa 647 (1:200, Becton Dickinson) and Donkey anti-goat (Beckton-Dickinson, 1:200). Actin was detected using Phalloidin Alexa 546 (1:200, Beckton-Dickinson) added to the secondary antibody. Cells were washed in incubation buffer mounted in Vectashield and viewed using a Zeiss 510 laser scanning microscope.

Cochlea processing

Tissue from 3+ week old mice (C57BL/6) were obtained after animals were euthanized using CO₂ asphyxiation in accordance with Yale University IACUC protocol. The temporal bones were isolated and placed in 4% formaldehyde overnight after opening the round and oval windows. Cochlea were removed after micro-dissection of the temporal bones washed in incubation buffer three times and processed for immunostaining as described above.

Cell transfection and imaging

MDCK and LLC-PK cells were a gift from Dr Michael Caplans lab, Yale University (in turn obtained from ATCC) and cells were not subject to STR profiling. MDCK and LLC-PK cells plated on glass coverslips (or where applicable HEK cells and CHO cells) were transiently transfected with constructs using Fugene6 according to the manufacturer's instructions (Promega, Madison, WI). Cells were plated at 100% confluency to ensure polarization, and transfected 36 hours after plating. Cells were fixed at 30 hours after transfection unless otherwise indicated. Cells were imaged by confocal microscopy using a Zeiss LSM 510/510 meta after fixation as previously described (Bai et al., 2011). Image parameters (scan time per pixel, pixel density, z step) were kept constant in a given experimental paradigm to allow reliable comparison.

In siRNA experiments, MDCK cells were electroporated with Prestin YFP and siRNA to the medium subunit of AP1B (μ 1B) as previously described (Gravotta et al., 2007). We used a previously proven siRNA to μ 1B siRNA (μ 1B-M16 sequence 5'-AACAAAGCTGGTACTGGCAAAA-3' (Gravotta et al., 2007)] and a control chicken β -4 siRNA (chick KCNMB4, (Bai et al., 2011)) that were custom synthesized (Dharmacon, Lafayette, CO). Briefly, μ 1B siRNA (or chick KCNMB4 siRNA in control experiments) at 5 nM and PrestinYFP plasmid at 10 nM was resuspended with 1 million trypsinized MDCK cells in 100 μ l of DMEM. Cells were electroporated using a square wave pulse with the following parameters: 300 V for 100 μ s \times 1 and 25 V for 20 ms \times 11 with a 100 ms pause in between. The entire electroporation protocol was repeated once. Cells were incubated on ice for 30 minutes and plated in prewarmed complete medium in 24 well plates on glass coverslips at a density of 350,000 cells per well (100% confluency). The medium was changed daily and cells were fixed and imaged 72 hours later.

Sixteen bit Images were acquired on a Zeiss 510 laser scanning microscope using a 63 \times water immersion lens (N.A 1.4), with fixed laser settings, a scan rate of 6.4 μ s per pixel, a pinhole aperture of 1.0 Airy units, and fixed detector gain. Regions of interest were identified and fluorescence data extracted. We established that the fluorescence intensity was within the linear range and used mean fluorescence density as a measure of protein concentration.

Gated STED

Gated STED, a new method of super resolution confocal microscopy, was used to visualize prestin expression in OHCs. Mouse cochlea were dissected and incubated with anti-prestin antibody (1:100 goat anti-prestin, Santa Cruz, CA) in incubation buffer overnight at 4°C. Tissue was washed three times with incubation buffer and then incubated with donkey anti-goat Oregon Green 488 (1:100, Beckton Dickinson) at room temperature for 1 hour. Cells were washed three times in incubation buffer followed by two washes in PBS. Tissue was mounted in Prolong Gold (Invitrogen) and viewed using a Leica TCS SP8 Gated STED microscope (Vicidomini et al., 2011).

Image processing and data analysis

Images were processed after acquisition using Volocity software (Perkin Elmer, CA). Pearson's correlation was calculated after automated thresholding using the method of Costes et al. (Costes et al., 2004). All results are given as mean \pm s.e.m. Where appropriate, ANOVA with Bonferroni Multiple Comparisons test was used to test for significance in differences (Instat3, CA).

Electrophysiological recording

For electrophysiological recordings 100,000 Chinese hamster ovary (CHO) cells were transfected in 24-well plates using Lipofectamine (Invitrogen, Carlsbad, CA) as previously described (Bai et al., 2011).

Cells were recorded by whole-cell patch clamp configuration at room temperature using an Axon 200B amplifier (Axon Instruments, CA), as described previously (Bai et al., 2011). Cells were recorded 24–48 hours after transfection to allow for stable measurement of non-linear capacitance. Ionic blocking solutions were used to isolate capacitive currents. The bath solution contained (in mM): TEA 20, CsCl 20, CoCl₂ 2, MgCl₂ 1.47, Hepes 10, NaCl 99.2, CaCl₂·2H₂O 2, pH 7.2, and the pipette solution contained (in mM): CsCl 140, EGTA 10, MgCl₂ 2, Hepes 10, pH 7.2. Osmolarity was adjusted to 300 \pm 2 mOsm with dextrose. Command delivery and data collections were carried out with a Windows-based whole-cell voltage clamp program, jClamp (Scisoft, New Haven, CT), using a Digidata 1322A interface (Axon Instruments, CA).

Capacitance was evaluated using a continuous high-resolution 2-sine wave. Capacitance data were fitted to the first derivative of a two-state Boltzmann function:

$$C_m = Q_{max} \frac{ze}{kT} \frac{b}{(1+b)^2} + C_{lin},$$

where

$$b = \exp\left(\frac{-ze(V_m - V_h)}{kT}\right).$$

Q_{\max} is the maximum nonlinear charge transfer, V_h the voltage at peak capacitance or half-maximal nonlinear charge transfer, V_m the membrane potential, C_{lin} linear capacitance, z the valence (a metric of voltage sensitivity), e the electron charge, k the Boltzmann's constant and T the absolute temperature. Q_{\max} is reported as Q_{sp} the specific charge density, i.e. total charge moved normalized to linear capacitance. A student's t -test was used to evaluate the effects of mutants on the different parameters of NLC.

RESULTS

OHCs express prestin and other basolateral markers along baso-lateral wall, and express the AP1B ($\mu 1\beta$) subunit

Previous theoretical treatments confirmed by electrophysiological and immunolocalization experiments have demonstrated the localization of prestin along the lateral wall of OHCs. We sought to further confirm these data using high resolution confocal microscopy. Adult mice cochlea were stained with anti-prestin antibodies and visualized using gated STED microscopy. As shown in Fig. 1 prestin is sharply localized along the lateral wall of the OHCs. The protein staining was uniform through the lateral wall. At the basolateral pole of the cell however, there was a patchy clustering of prestin. In contrast, there was a gradual tapering of prestin staining at the apical end of the cell.

The localization of prestin to the basolateral surface of outer hair cells led us to reason that outer hair cells are analogous to polarized epithelial cells with anatomical and functional segregation of the cell into an apical and basolateral compartments. The apical segregation of the stereociliary apparatus and the basolateral segregation of the cochlear amplifier are consistent with this separation. Prior work in hair cells of different species has shown the presence of β -catenin and Na/K ATPase, two proteins identified as classically localized in the basolateral compartment of polarized epithelial cells, to be present in the basolateral surface of hair cells. As shown in Fig. 1 these two proteins – β -catenin and Na/K ATPase – were found to segregate along the basolateral surface of outer hair cells (Fig. 1), further confirming similarities between outer hair cells and polarized epithelial cells. We also determine that OHCs express the AP1B ($\mu 1\beta$) subunit that has been shown to be important for basolateral sorting of proteins in polarized epithelial cells (Fig. 1).

Prestin has several tyrosine residues within a basolateral targeting sequence of which Y520 and Y667 are important for basolateral sorting

In order to establish an experimental model system to tease apart the mechanisms underlying prestin's basolateral targeting, we expressed it in MDCK cells. These cells have a long history of being used as a model system for studying polarized sorting in epithelial cells. As shown in Fig. 2 prestin tagged with YFP at its C-terminus is targeted to the basolateral surface of MDCK cells. The protein shows a similar pattern of distribution to β -catenin and Na/K ATPase, both well known basolaterally targeted proteins. Prestin lacking a YFP tag showed similar targeting to the basolateral membrane (data not shown).

A number of sequence motifs in a protein are important for the targeting of a protein to the basolateral surface of polarized epithelial cells. Prestin has several tyrosine residues contained within a YXX Φ motif in its C-terminus, and lacks other targeting motifs classically associated with basolateral targeting (including

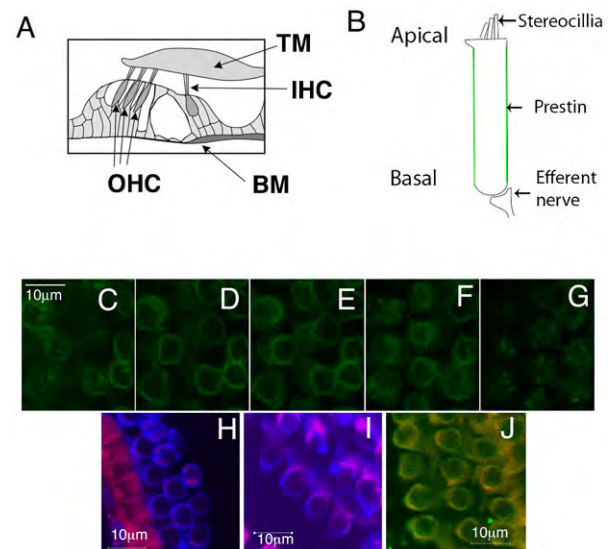


Fig. 1. Prestin in mouse outer hair cells is localized along the lateral wall of the cell along with β -catenin and Na/K ATPase. Shown are cartoons of the organ of Corti (A) and its contained outer hair cells. TM, tectorial membrane; BM Basilar membrane; IHC, inner hair cell; OHC Outer hair cell. (B) A model of an outer hair cell in which prestin is shown lining its lateral wall (green). (C–G) The figure shows serial X-Y sections of mouse outer hair cells labeled with an anti-prestin antibody and then visualized using a Leica gated STED microscope. The sections start at the apical end (left) and end at the basal end (right). There is a uniform labeling of prestin along the lateral wall of the cell (middle three panels). Prestin labeling at the apical end of the cell tapers (C). Similarly, there is a patchy clustering of prestin at the basal pole of the cell (G). Mouse outer hair cells immunostained with antibodies to the basolateral markers β -catenin (H) and Na/K ATPase (I), and demonstrates the localization of these proteins (blue) along the lateral wall of the cell. The cells were counterstained with phalloidin Alexa 546 (red), which shows the presence of the sub cortical lattice of actin along the lateral wall of the cell. (J) The AP1 μ 1B subunit (green) is present in outer hair cells evidenced by antibody labeling of these cells. The figure shows co labeling of these cells with Na/K ATPase (red). Scale bar is 10 microns. These experiments were repeated five times.

dileucine motifs, NPxY) (Brewer and Roth, 1991; Cancino et al., 2007; Gonzalez and Rodriguez-Boulan, 2009; Gravotta et al., 2007; Hunziker et al., 1991; Lin et al., 1997; Matter et al., 1992; Rodriguez-Boulan and Gonzalez, 1999; Weisz and Rodriguez-Boulan, 2009). These include the tyrosine residues Y520, Y526, Y616 and Y667 (shown in cartoon form in the two alternative membrane spanning models of prestin in supplementary material Fig. S1). In order to ascertain the importance of these residues for basolateral targeting, we individually mutated these residues and determined their basolateral localization. As shown in Fig. 2 mutation of Y520Q, and to a lesser extent Y667Q, resulted in a reduced expression of prestin on the basolateral surface of the cell. There was both increased intracellular retention (Fig. 2) of the protein as well as targeting to the apical surface of the cell (Fig. 3).

In order to further confirm that the effects of these mutations were specific in bringing about deficient basolateral targeting we sought to determine the effects of these mutations on the surface expression of prestin in non-polarized HEK and CHO cells. As shown in Fig. 4 wt type prestin and prestin with mutations at Y520 and Y667 were both targeted to the cell surface. However, both these mutations affected the function of the molecule. In CHO cells expressing these mutant proteins, an increase in non-linear

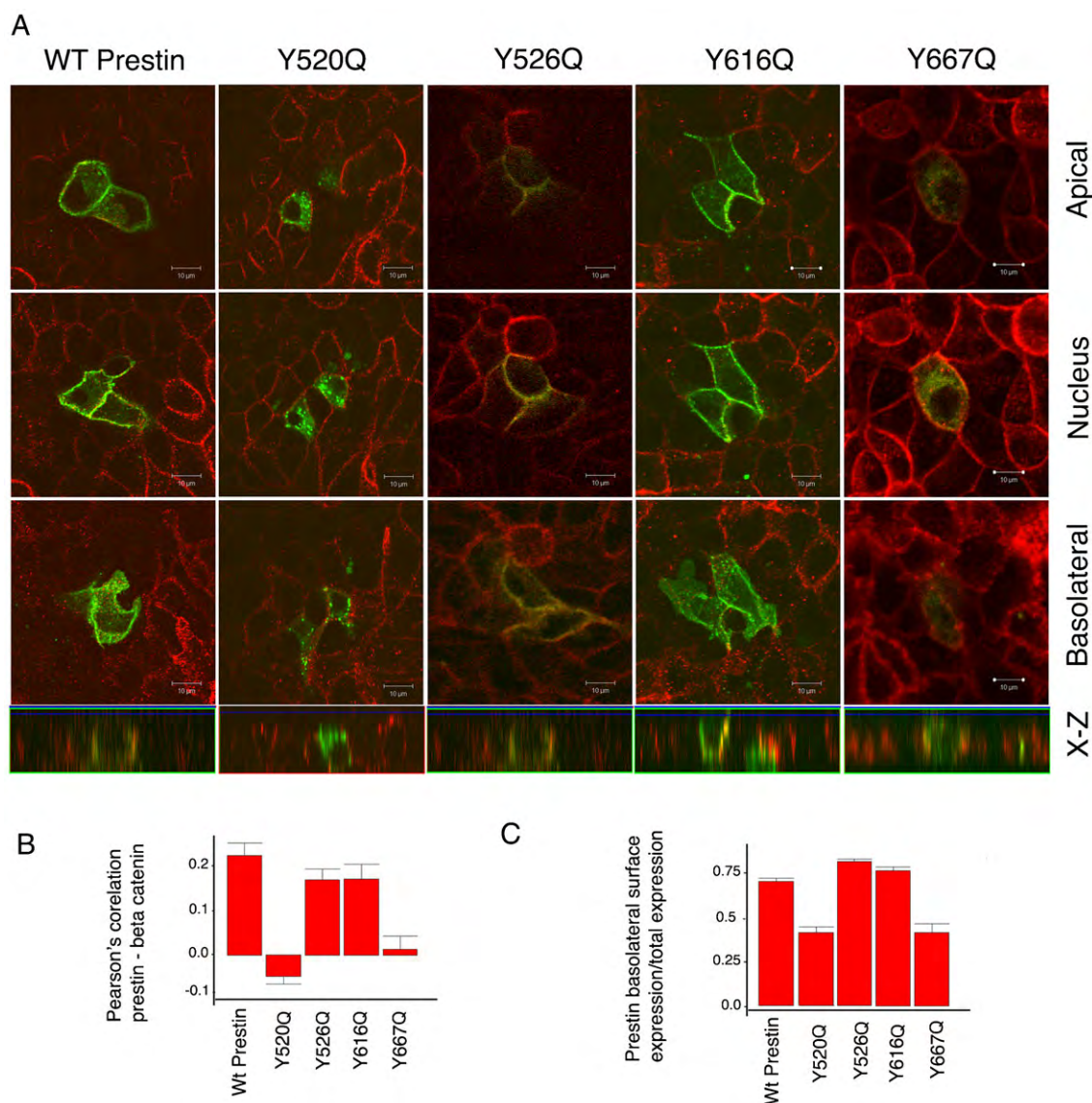


Fig. 2. Y520 and Y667 contained within the YXX Φ motif are important for basolateral targeting of prestin in MDCK cells. The figure shows MDCK cells transiently transfected with wild type prestin and mutations of prestin: Y520Q, Y526Q, Y616Q and Y667Q. The cells were fixed after 36 hours. Prestin was tagged with YFP at its C-terminus (green) and the cells were stained with an antibody to β -catenin. Shown are serial X-Y confocal sections along the z axis (A). The corresponding X-Z sections are shown at the bottom. Mutations at Y520 and Y667 result in a failure to target the basolateral surface of the cell along with intracellular retention of the protein and apical trafficking. (B,C) Pearson's correlation of prestin with β -catenin and a ratio of prestin fluorescence on the surface of the cell compared to the total in the cell. The mean Pearson's correlation values were: wt 0.23 (\pm 0.028SE, $n=7$); Y520Q -0.045 (\pm 0.016 SE, $n=7$); Y526Q 0.17 (\pm 0.025 SE, $n=14$); Y616Q 0.175 (\pm 0.033 SE, $n=14$); Y667Q 0.01386 (\pm 0.03 SE, $n=10$). The differences between wt and Y520Q and Y667Q were considered significant. A one way ANOVA (parametric) with Bonferroni post test comparison yielded a p value of <0.001 for wt vs Y520Q and wt vs Y667Q; wt vs Y616Q and Y667Q were not significant. The mean surface to total ratios were: wt 0.67 (\pm 0.016 SE, $n=22$); Y520Q -0.39 (\pm 0.0129 SE, $n=20$); Y526Q 0.78 (\pm 0.013 SE, $n=13$); Y616Q 0.73 (\pm 0.02 SE, $n=13$); Y667Q 0.40 (\pm 0.044 SE, $n=13$). Here too the differences between wt and Y520Q and Y667Q were significant. A one-way ANOVA (parametric) with Bonferroni post-test comparison yielded a p value of <0.001 for wt vs Y520Q and wt vs Y667Q. The scale bar is 10 microns.

capacitance, the widely accepted functional surrogate for electromotility, was absent with Y520Q and markedly diminished with Y667Q. Supplementary material Table S1 shows the parameters for NLC in these mutants.

The phenol ring within the tyrosine residues (Y520 and Y667) are important for basolateral targeting

We sought to determine the importance of the stereo chemical properties of the tyrosine residue at position 520 and 667 to ascertain its effects on targeting to the basolateral surface of

MDCK cells. We mutated individual tyrosine residues to serine or phenylalanine to mimic the effects of the side chain hydroxyl group and phenol ring respectively. We determined that substitution of tyrosine with phenylalanine at Y520 resulted in near complete recovery in basolateral targeting (Fig. 5). In contrast, mutation of Y520 to a serine residue (to mimic the side chain OH group) resulted in poor delivery of the protein to the basolateral surface (Fig. 5). Similarly, it is unlikely that the effects of these other mutations are mediated by their size or hydrophilicity since mutation of Y520 to alanine failed to restore

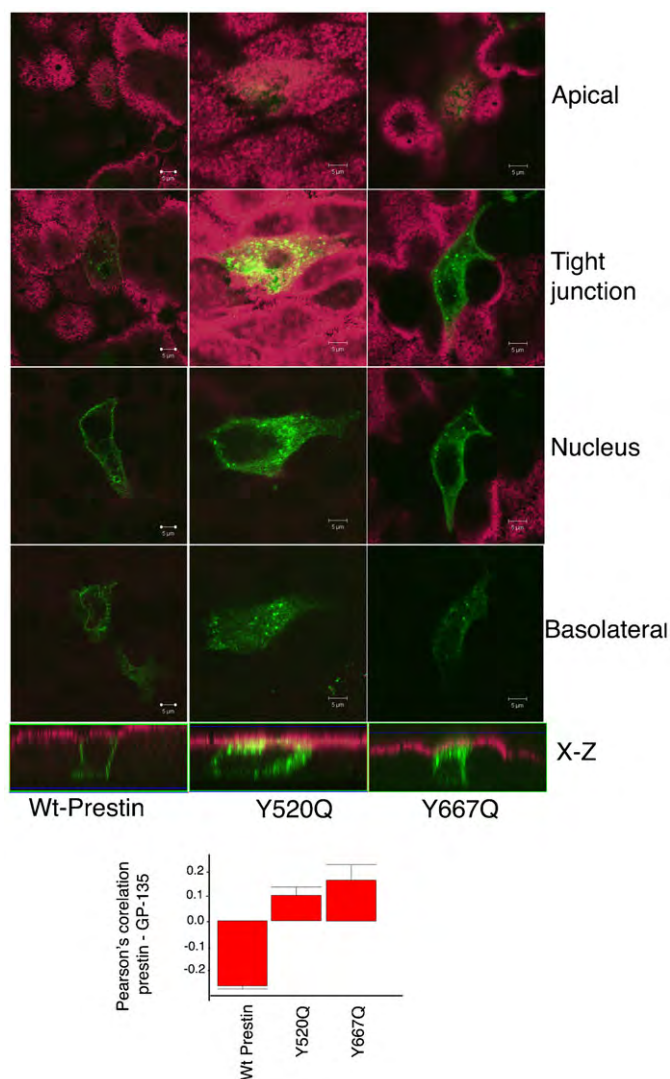


Fig. 3. Mutation of Y520 and Y667 result in increased delivery of prestin to the apical surface of MDCK cells. MDCK cells transiently transfected with wt prestin YFP and the two constructs Y520Q prestin YFP, and Y667Q prestin YFP were fixed at 36 hours and stained with antibody to the apical marker GP130 (podohexin). There is significant apical targeting of Y520Q and Y667Q evident in the serial X-Y sections along the z axis and the corresponding X-Z sections at the bottom. The bottom panel shows Pearson's correlation of prestin YFP and GP130 confirming absent apical targeting of the wild type construct and apical targeting of Y520Q and Y667Q. The mean Pearson's correlation values were: wt -0.027 (± 0.011 SE, $n=7$); Y520Q 0.105 (± 0.035 SE, $n=5$); Y667Q 0.17 (± 0.063 SE, $n=11$). The differences between wt prestin and Y520Q and wt prestin and Y667Q were significant. A one-way ANOVA (parametric) yielded a p value of <0.01 between wt prestin and Y520Q, and a p value of <0.001 between wt prestin and Y667Q. The scale bar is 5 microns.

basolateral targeting of prestin (Fig. 5). Similar effects were seen with mutation of Y667.

Mutation of Y520 and Y667 residues results in retention within the Golgi

Previous experiments in other proteins targeted to the basolateral surface have shown that sorting of proteins is determined at the Golgi. We hypothesized that mutation of tyrosine residues at Y520 and Y667 would result in retention of the protein within the Golgi

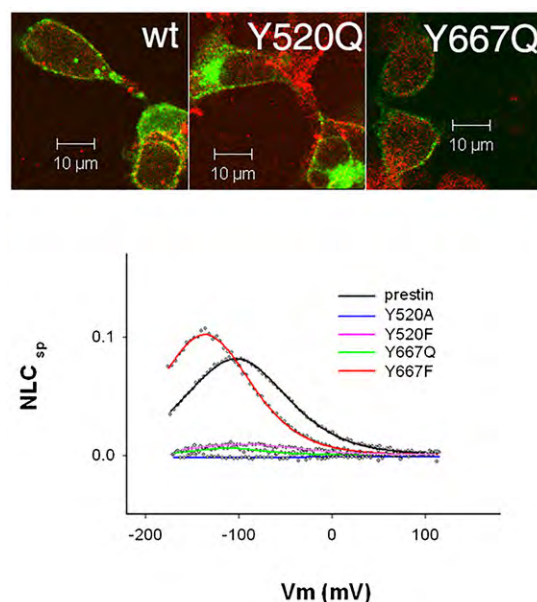


Fig. 4. Mutation of Y520Q and Y667Q results in targeting of prestin to the plasma membrane of HEK cells, and presence of NLC in Y667Q, Y520F and Y667F. The upper panels show HEK cells transfected with wild type prestin-YFP, and the two constructs Y520Q prestin YFP, and Y667Q prestin YFP that were fixed 48 hours after transfection. Cells were stained with antibodies to Na/K ATPase and visualized by confocal microscopy. Wild type prestin YFP, Y520Q prestin YFP and Y667Q prestin YFP all target the plasma membrane as evidenced by its co-localization with plasma membrane Na/K ATPase. The lower panel shows NLC traces of different mutations at Y520 and Y667. The actual values of NLC parameters along with cell numbers are given in supplementary material Table S1. The scale bar is 10 microns.

(and could explain at least partially, the increased amounts of the mutated protein retained within the cell). MDCK cells transfected with prestin YFP, Y520Q, or Y667Q were fixed at different times after transfection and retention within the Golgi determined by co-localization with the Golgi specific protein Giantin (Fig. 6) (Deborde et al., 2008). We determined that mutation of Y520Q resulted in a persistent retention of prestin within the Golgi. In contrast, Y667Q showed retention of prestin within the Golgi, which improved with time. Thus, Y667Q was localized within the Golgi at 12, 20 and 30 hours after transfection but demonstrated increasing efflux from the Golgi at 40 hours. In contrast, wt prestin had made a near complete exit from the Golgi by 20 hours. Y520Q showed little egress from the Golgi with continued retention within that organelle even at 40 hours.

Prestin exit from the Golgi to the plasma membrane is mediated by early recycling endosomes

We then sought to determine the identity of organelles responsible for movement of prestin from the Golgi to the plasma membrane. For these experiments we transfected prestin YFP into MDCK cells. Transfected cells were kept at 19°C to allow accumulation of protein within the Golgi (Golgi block) (Bian et al., 2013). Cells were incubated with transferrin Alexa 647 applied to cells for 10 minutes to label early/recycling endosomes. The cells were then immersed in fresh culture medium and fixed at different time points after raising the temperature to 37°C to release proteins from Golgi block. As shown in Fig. 7 there was co-localization of vesicles containing

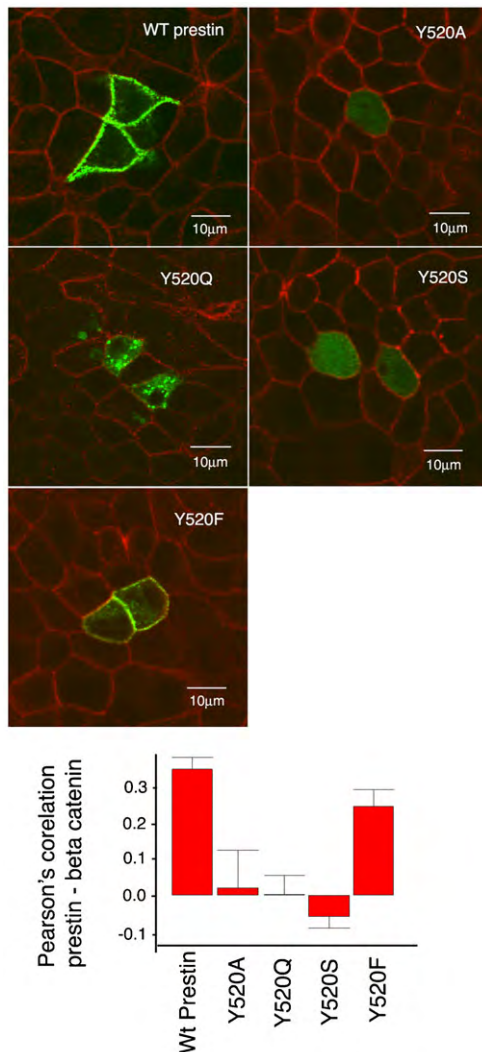


Fig. 5. The phenol ring in the tyrosine residue is critical for the targeting of prestin to the basolateral surface of MDCK cells. MDCK cells transiently transfected with prestin YFP and the mutations Y520Q, Y520A, Y520S and Y520F were fixed 36 hours after transfection and imaged by confocal microscopy. The basolateral wall of the cell was visualized by immunostaining with anti- β -catenin antibody. The mutations Y520A, Y520Q, and Y520S failed to target the basolateral surface of the cell, while Y520F was targeted to the basolateral surface of the cell. Pearson's correlation between prestin YFP and β -catenin confirm the observed co-localization of wild type prestin-YFP with β -catenin and Y520F with β -catenin. The mean Pearson's correlation values were: wt prestin 0.34 (\pm 0.033 SE, $n=8$); Y520A 0.019 (\pm 0.10 SE, $n=5$); Y520Q 0.002 (\pm 0.052 SE, $n=5$); Y520S -0.05 (\pm 0.03, $n=6$); Y520F 0.25 (\pm 0.045 SE, $n=6$). A one way ANOVA revealed significant differences between wt prestin and Y520A ($P<0.01$), wt prestin and Y520Q ($P<0.001$), and wt prestin and Y520S ($P<0.001$). The differences between wt prestin and Y520F were not significant. The scale bar is 10 microns.

both prestin YFP and transferrin Alexa 647. We interpret this data to suggest that prestin YFP use early/recycling endosomes to reach the basolateral surface of the cell.

Prestin targeting to the basolateral surface also involves the AP1B (μ 1B) pathway

In other systems the use of tyrosine motifs for basolateral sorting in polarized epithelial cells has been shown to involve the AP1B

(μ 1B) pathway. We sought to ascertain if AP1B (μ 1B) was important for sorting prestin to the basolateral surface of polarized epithelial cells. In initial experiments we used LLC-PK cells, which lack the AP1B (μ 1B) subunit. In these cells Prestin YFP shows decreased targeting to the basolateral surface of the cell (supplementary material Fig. S2). We then used siRNA knockdown of AP1B (μ 1B) to determine targeting of prestin YFP in MDCK cells. In these cells knock down treatment with siRNA to AP1B (μ 1B) resulted in apical targeting of the protein and reduced expression of the protein on the basolateral surface of the cell (Fig. 8).

DISCUSSION

In this paper we show for the first time that prestin is sorted to the basolateral surface of polarized epithelial (MDCK) cells using a tyrosine motif. We identified two tyrosine residues contained in the cassette YXX Φ motif that are likely important for its localization to the basolateral surface of the cell. Mutation of one of these residues Y520 resulted in apical targeting and intracellular retention of the protein. A second mutation of Y667 resulted in delayed exit from the Golgi to the basolateral surface with initial targeting to the apical surface of the cell and intracellular retention. With increasing time, however, there was progressive localization of this mutant at the basolateral surface of the cell. We believe mutation of these residues resulted in specific loss of basolateral targeting since the mutant protein was targeted to the apical surface of MDCK cells and since the protein showed plasma membrane targeting in non-polarized CHO and HEK cells. Nevertheless, it still remains a possibility that the loss of basolateral targeting resulted from a subtle misfolding of the protein that also affected its normal function. We were unable to demonstrate normal function as measured by the presence of non-linear capacitance in these mutants expressed in CHO cells (Y520Q showed absent NLC while Y667Q showed diminished NLC). In this context, it should be noted that several mutations that also affected prestin function by subtle alterations in its folding, show normal basolateral targeting in MDCK cells (data not shown). We would also like to note previous experiments by Zheng et al. (Zheng et al., 2005), in which mutation of Y520 and Y526 together failed to show targeting to the surface of TSA and OK cells. We do not have an explanation for the discordance in our data although the experiments are not strictly comparable since Zheng et al. (Zheng et al., 2005) were describing the targeting of a double mutant (Y520A and Y526A) while we describe the targeting of single mutations (Y520 or Y667).

Our interpretation that prestin is sorted to the basolateral surface of cells using a tyrosine motif is further substantiated by two other related findings. First, we demonstrate that AP1B (μ 1B) is important for basolateral targeting, since expression of prestin in LLC-PK cells that lack this subunit resulted in decreased basolateral targeting. Moreover knockdown of AP1B (μ 1B) in MDCK cells also resulted in increased apical targeting of prestin with deficient basolateral targeting of the protein. It is now believed that the tyrosine residues are critical for direct interaction with AP1B (μ 1B) and bringing about basolateral targeting of proteins (Bonifacino and Dell'Angelica, 1999; Carvajal-Gonzalez et al., 2012; Fields et al., 2007). We also demonstrate using Golgi block experiments that prestin uses recycling endosomes as a post Golgi transport intermediate to transit from the Golgi to the basolateral plasma membrane. The use of AP1B (μ 1B) has been demonstrated by several other proteins using tyrosine residues contained in a YXX Φ motif to

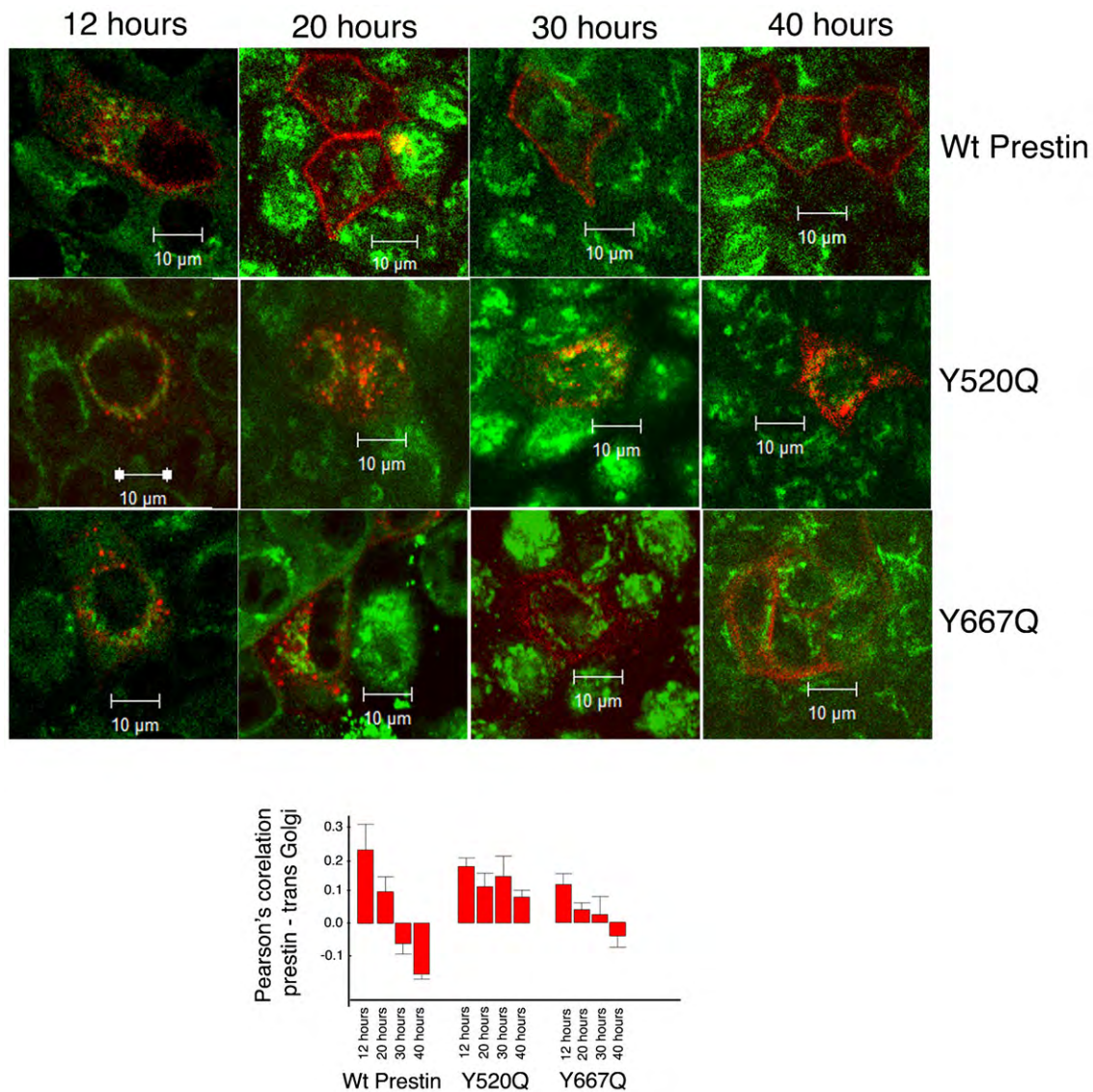


Fig. 6. Egress from the Golgi is poor/absent in Y520Q and delayed in Y667Q. MDCK cells transiently transfected with prestin YFP, and the mutations Y520Q and Y667Q contained in the prestin YFP cassette were fixed after 12, 20, 30 and 40 hours after transfection. The cells were then stained with antibodies to the Golgi protein Giantin. While prestin YFP exits the Golgi at 20 hours, Y520Q does not egress from the Golgi and Y667Q leaves the Golgi after 40 hours. A graphical form of Pearson's correlation between prestin YFP and Giantin at the different time points is shown below. For wt prestin there was a significant difference on one way ANOVA between the Pearson's correlation between prestin and Giantin at all times compared to 12 hours: 12 hours vs 20 hours, $P < 0.05$; 12 hours vs 30 hours, $P < 0.001$; and 12 hours vs 40 hours $P < 0.001$. In contrast, the differences in Pearson's correlation between Y520Q and Giantin at all times compared to 12 hours were not significantly different ($P > 0.05$ on one way ANOVA). For Y667Q the Pearson's correlation with Giantin was significantly different on one way ANOVA between 12 hours and 40 hours ($P < 0.05$), while the remaining two time points were not significantly different (12 hours vs 20 hours, $P > 0.05$; 12 hours vs 30 hours, $P > 0.05$). The mean values for the different time points were as follows: wt prestin 12, 20, 30 and 40 hours: 0.23 (± 0.08 SE, $n=5$), 0.09 (± 0.04 SE, $n=10$), -0.06 (± 0.03 SE, $n=12$), -0.162 (± 0.02 SE, $n=13$); Y520Q 12, 20, 30 and 40 hours: 0.17 (± 0.02 SE, $n=5$), 0.114 (± 0.04 SE, $n=6$), 0.145 (± 0.06 SE, $n=13$), 0.08 (± 0.02 SE, $n=8$); Y667Q 12, 20, 30 and 40 hours: 0.112 (0.03 SE, $n=13$), 0.04 (± 0.02 SE, $n=9$); 0.026 (± 0.05 SE, $n=8$) and -0.04 (± 0.03 SE, $n=8$). The scale bar is 10 microns.

target the basolateral membrane (Adair-Kirk et al., 2003; Ang et al., 2004; Duffield et al., 2004; Fields et al., 2007; Fölsch et al., 1999; Fölsch et al., 2003; Gravotta et al., 2007; Sugimoto et al., 2002). Moreover, the use of transferrin containing endosomes has been shown with basolateral proteins that use a tyrosine motif to exit the Golgi (Ang et al., 2004; Donoso et al., 2009). In prior experiments membrane targeting to the surface of CL4 cells, which are derived from LLC-PK1 cells have been

observed (Zheng et al., 2010). In the absence of data on the expression of AP1B ($\mu 1B$) in CL4 cells used for these experiments or the relative surface expression of prestin in these cells, it is difficult to comment on the significance of these data (Zheng et al., 2010).

The implications to our data are greatest to hair cells. Our data further suggest that hair cells are similar to polarized epithelial cells with differential sorting of proteins to the apical

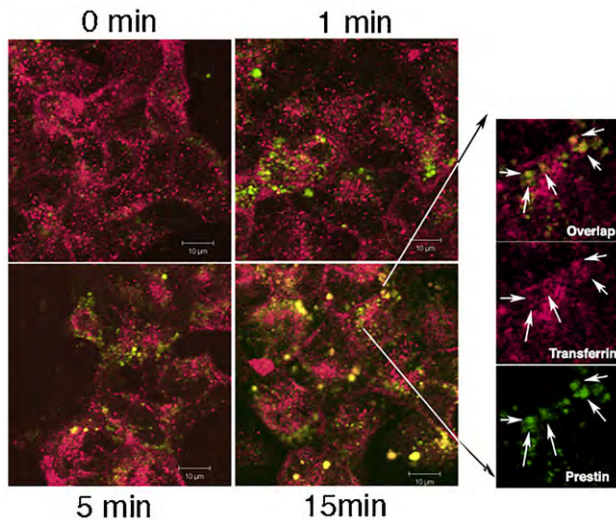


Fig. 7. Prestin YFP uses transferrin containing endosomes to transit from the Golgi to the basolateral membrane. MDCK cells were transiently transfected with prestin-YFP and kept at 19°C to induce Golgi block. Cells were incubated with transferrin - Alexa 647 for 10 minutes. The incubation temperature was raised to 37°C after which cells were fixed at 0, 1 minute, 5 minutes, 10 minutes and 15 minutes. Cells were then imaged with confocal microscopy. Shown are confocal images in the X-Y plane at the basolateral Z axis of the cell that were fixed at different times after raising the temperature to 37°C. With increasing time there is co-localization of prestin-YFP exiting the Golgi with transferrin - Alexa 647. The right hand panels shows merged and individual Alexa 647 and prestin-YFP images of an enlarged area at 15 minutes after raising the temperature to 37°C. Co-localization of prestin YFP and transferrin 647 is demonstrated. The scale bar is 10 microns.

and basolateral surface of the cell. Hair cells could be thought of as having different compartments – an apical surface important for transducing sound and a basal pole that is important for synaptic transmission in inner hair cells and a basolateral pole that is important for housing the cochlear amplifier and its processes. Our data suggest that integral to this segregation of function is the segregation of proteins to different apical and basal compartments of the cell along the lines demonstrated in polarized epithelial cells. Other work has also shown the apical sorting in CL4 cells of proteins identified as important for stereociliary and transduction function in hair cells (Zheng et al., 2010). At least in the context of protein sorting, hair cells seem to have retained features of polarized epithelial cells rather than neurons. The expected segregation of proteins along a dendritic and axonal separation would result in a reversal of the observed localization of proteins in hair cells. Perhaps one explanation for this unexpected finding is that hair cells resemble epithelial cells more than they do neurons. Importantly, hair cells are derived from the embryonic otic placode, a thickened segment of the cranial ectoderm that invaginates separately from the neural tube to form the otocyst. Consistent with its epithelial phenotype, hair cells express the clathrin adaptor protein AP1B (μ 1B) subunit that is present only in polarized epithelial cells and lacking in neurons. Significantly, this subunit is important for the localization of several proteins that, like prestin, use a tyrosine motif to target to the basolateral surface of the cell. It remains to be established if prestin uses tyrosine residues and /or the AP1B (μ 1B) subunit to target to the lateral wall of outer hair cells.

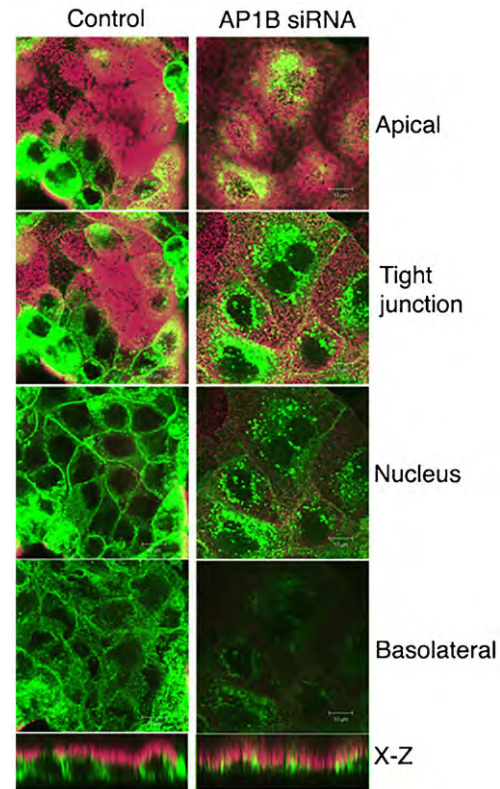


Fig. 8. Targeting of prestin YFP to the basolateral membrane requires AP1B (μ 1B). MDCK cells were electroporated with prestin YFP plasmid and siRNA to AP1B (μ 1B). Cells were plated at confluent density and fixed after 30 hours. Cells were stained with antibodies to the apical marker GP130 and visualized by confocal microscopy. Shown are X-Y images along the z axis of transfected cells. The lowest panel shows the corresponding X-Z sections. Transfection of MDCK cells with siRNA to AP1B (μ 1B) resulted in an apical localization of prestin YFP and near absence in targeting to the basolateral surface. In contrast, cells co-transfected with control siRNA (chicken KCNMB4) resulted in basolateral targeting of prestin YFP. The scale bar is 10 microns.

Acknowledgements

We wish to thank Dr Michael Caplan for critical reading of the manuscript.

Competing interests

The authors declare no competing or financial interests.

Author contributions

YZ, IMN, JPB, JSS and DSN conceived, designed, executed and interpreted the experiments. YZ, IMN, JPB, JSS and DSN drafted and revised the paper.

Funding

This work was funded by the National Institute on Deafness and Other Communication Disorders (NIDCD; National Institutes of Health) [grant number RO1 DC 008130].

References

- Adair-Kirk, T. L., Dorsey, F. C. and Cox, J. V. (2003). Multiple cytoplasmic signals direct the intracellular trafficking of chicken kidney AE1 anion exchangers in MDCK cells. *J. Cell Sci.* **116**, 655-663.
- Ang, A. L., Taguchi, T., Francis, S., Fölsch, H., Murrells, L. J., Pypaert, M., Warren, G. and Mellman, I. (2004). Recycling endosomes can serve as intermediates during transport from the Golgi to the plasma membrane of MDCK cells. *J. Cell Biol.* **167**, 531-543.
- Ashmore, J. F. (1987). A fast motile response in guinea-pig outer hair cells: the cellular basis of the cochlear amplifier. *J. Physiol.* **388**, 323-347.
- Bai, J. P., Surguchev, A. and Navaratnam, D. (2011). β 4-subunit increases Slo responsiveness to physiological Ca^{2+} concentrations and together with β 1 reduces surface expression of Slo in hair cells. *Am. J. Physiol.* **300**, C435-C446.

- Bian, S., Bai, J. P., Chapin, H., Le Moellic, C., Dong, H., Caplan, M., Sigworth, F. J. and Navaratnam, D. S. (2011). Interactions between β -catenin and the HSlo potassium channel regulates HSlo surface expression. *PLoS ONE* **6**, e28264.
- Bian, S., Navaratnam, D. and Santos-Sacchi, J. (2013). Real time measures of prestin charge and fluorescence during plasma membrane trafficking reveal sub-tetrameric activity. *PLoS ONE* **8**, e66078.
- Bonifacino, J. S. and Dell'Angelica, E. C. (1999). Molecular bases for the recognition of tyrosine-based sorting signals. *J. Cell Biol.* **145**, 923-926.
- Bradke, F. and Dotti, C. G. (1998). Membrane traffic in polarized neurons. *Biochim. Biophys. Acta* **1404**, 245-258.
- Brewer, C. B. and Roth, M. G. (1991). A single amino acid change in the cytoplasmic domain alters the polarized delivery of influenza virus hemagglutinin. *J. Cell Biol.* **114**, 413-421.
- Brownell, W. E., Bader, C. R., Bertrand, D. and de Ribaupierre, Y. (1985). Evoked mechanical responses of isolated cochlear outer hair cells. *Science* **227**, 194-196.
- Cancino, J., Torrealba, C., Soza, A., Yuseff, M. I., Gravotta, D., Henklein, P., Rodriguez-Boulan, E. and González, A. (2007). Antibody to AP1B adaptor blocks biosynthetic and recycling routes of basolateral proteins at recycling endosomes. *Mol. Biol. Cell* **18**, 4872-4884.
- Carvajal-Gonzalez, J. M., Gravotta, D., Mattered, R., Diaz, F., Perez Bay, A., Roman, A. C., Schreiner, R. P., Thuenauer, R., Bonifacino, J. S. and Rodriguez-Boulan, E. (2012). Basolateral sorting of the coxsackie and adenovirus receptor through interaction of a canonical YXX Φ motif with the clathrin adaptors AP-1A and AP-1B. *Proc. Natl. Acad. Sci. USA* **109**, 3820-3825.
- Clemens Grisham, R., Kindt, K., Finger-Baier, K., Schmid, B. and Nicolson, T. (2013). Mutations in ap1b1 cause mistargeting of the Na⁺/K⁺-ATPase pump in sensory hair cells. *PLoS ONE* **8**, e60866.
- Costes, S. V., Daelemans, D., Cho, E. H., Dobbin, Z., Paviaklis, G. and Lockett, S. (2004). Automatic and quantitative measurement of protein-protein colocalization in live cells. *Biophys. J.* **86**, 3993-4003.
- Dallos, P. and Evans, B. N. (1995). High-frequency motility of outer hair cells and the cochlear amplifier. *Science* **267**, 2006-2009.
- Dallos, P., Evans, B. N. and Hallworth, R. (1991). Nature of the motor element in electrokinetic shape changes of cochlear outer hair cells. *Nature* **350**, 155-157.
- Davis, H. (1983). An active process in cochlear mechanics. *Hear. Res.* **9**, 79-90.
- Deborde, S., Perret, E., Gravotta, D., Deora, A., Salvarezza, S., Schreiner, R. and Rodriguez-Boulan, E. (2008). Clathrin is a key regulator of basolateral polarity. *Nature* **452**, 719-723.
- Donoso, M., Cancino, J., Lee, J., van Kerkhof, P., Retamal, C., Bu, G., Gonzalez, A., Cáceres, A. and Marzolo, M. P. (2009). Polarized traffic of LRP1 involves AP1B and SNX17 operating on Y-dependent sorting motifs in different pathways. *Mol. Biol. Cell* **20**, 481-497.
- Dotti, C. G. and Simons, K. (1990). Polarized sorting of viral glycoproteins to the axon and dendrites of hippocampal neurons in culture. *Cell* **62**, 63-72.
- Dotti, C. G., Parton, R. G. and Simons, K. (1991). Polarized sorting of glypiated proteins in hippocampal neurons. *Nature* **349**, 158-161.
- Duffield, A., Fölsch, H., Mellman, I. and Caplan, M. J. (2004). Sorting of H,K-ATPase beta-subunit in MDCK and LLC-PK cells is independent of mu 1B adaptin expression. *Traffic* **5**, 449-461.
- Farr, G. A., Hull, M., Mellman, I. and Caplan, M. J. (2009). Membrane proteins follow multiple pathways to the basolateral cell surface in polarized epithelial cells. *J. Cell Biol.* **186**, 269-282.
- Fettiplace, R. (2009). Defining features of the hair cell mechano-electrical transducer channel. *Pflügers Arch.* **458**, 1115-1123.
- Fields, I. C., Shteyn, E., Pypaert, M., Proux-Gillardeaux, V., Kang, R. S., Galli, T. and Fölsch, H. (2007). v-SNARE cellubrevin is required for basolateral sorting of AP-1B-dependent cargo in polarized epithelial cells. *J. Cell Biol.* **177**, 477-488.
- Fölsch, H., Ohno, H., Bonifacino, J. S. and Mellman, I. (1999). A novel clathrin adaptor complex mediates basolateral targeting in polarized epithelial cells. *Cell* **99**, 189-198.
- Fölsch, H., Pypaert, M., Maday, S., Pelletier, L. and Mellman, I. (2003). The AP-1A and AP-1B clathrin adaptor complexes define biochemically and functionally distinct membrane domains. *J. Cell Biol.* **163**, 351-362.
- Gao, J., Wang, X., Wu, X., Aguinaga, S., Huynh, K., Jia, S., Matsuda, K., Patel, M., Zheng, J., Cheatham, M. et al. (2007). Prestin-based outer hair cell electromotility in knockin mice does not appear to adjust the operating point of a cilia-based amplifier. *Proc. Natl. Acad. Sci. USA* **104**, 12542-12547.
- Geisler, C. D. (1993). A realizable cochlear model using feedback from motile outer hair cells. *Hear. Res.* **68**, 253-262.
- Geisler, C. D. and Sang, C. (1995). A cochlear model using feed-forward outer-hair-cell forces. *Hear. Res.* **86**, 132-146.
- Glowatzki, E., Grant, L. and Fuchs, P. (2008). Hair cell afferent synapses. *Curr. Opin. Neurobiol.* **18**, 389-395.
- Gonzalez, A. and Rodriguez-Boulan, E. (2009). Clathrin and AP1B: key roles in basolateral trafficking through trans-endosomal routes. *FEBS Lett.* **583**, 3784-3795.
- Gravotta, D., Deora, A., Perret, E., Oyanadel, C., Soza, A., Schreiner, R., Gonzalez, A. and Rodriguez-Boulan, E. (2007). AP1B sorts basolateral proteins in recycling and biosynthetic routes of MDCK cells. *Proc. Natl. Acad. Sci. USA* **104**, 1564-1569.
- Hallworth, R., Evans, B. N. and Dallos, P. (1993). The location and mechanism of electromotility in guinea pig outer hair cells. *J. Neurophysiol.* **70**, 549-558.
- Housley, G. D., Marcotti, W., Navaratnam, D. and Yamoah, E. N. (2006). Hair cells – beyond the transducer. *J. Membr. Biol.* **209**, 89-118.
- Huang, G. and Santos-Sacchi, J. (1993). Mapping the distribution of the outer hair cell motility voltage sensor by electrical amputation. *Biophys. J.* **65**, 2228-2236.
- Hunziker, W., Harter, C., Matter, K. and Mellman, I. (1991). Basolateral sorting in MDCK cells requires a distinct cytoplasmic domain determinant. *Cell* **66**, 907-920.
- Kalinec, F., Holley, M. C., Iwasa, K. H., Lim, D. J. and Kachar, B. (1992). A membrane-based force generation mechanism in auditory sensory cells. *Proc. Natl. Acad. Sci. USA* **89**, 8671-8675.
- Leonova, E. V. and Raphael, Y. (1997). Organization of cell junctions and cytoskeleton in the reticular lamina in normal and ototoxically damaged organ of Corti. *Hear. Res.* **113**, 14-28.
- Liberman, M. C., Gao, J., He, D. Z., Wu, X., Jia, S. and Zuo, J. (2002). Prestin is required for electromotility of the outer hair cell and for the cochlear amplifier. *Nature* **419**, 300-304.
- Lin, S., Naim, H. Y. and Roth, M. G. (1997). Tyrosine-dependent basolateral sorting signals are distinct from tyrosine-dependent internalization signals. *J. Biol. Chem.* **272**, 26300-26305.
- Mahendrasingam, S., Katori, Y., Furness, D. N. and Hackney, C. M. (1997). Ultrastructural localization of cadherin in the adult guinea-pig organ of Corti. *Hear. Res.* **111**, 85-92.
- Matter, K., Hunziker, W. and Mellman, I. (1992). Basolateral sorting of LDL receptor in MDCK cells: the cytoplasmic domain contains two tyrosine-dependent targeting determinants. *Cell* **71**, 741-753.
- Mellado Lagarde, M. M., Drexler, M., Lukashkina, V. A., Lukashkin, A. N. and Russell, I. J. (2008). Outer hair cell somatic, not hair bundle, motility is the basis of the cochlear amplifier. *Nat. Neurosci.* **11**, 746-748.
- Ohno, H., Tomemori, T., Nakatsu, F., Okazaki, Y., Aguilar, R. C., Foelsch, H., Mellman, I., Saito, T., Shirasawa, T. and Bonifacino, J. S. (1999). Mu1B, a novel adaptor medium chain expressed in polarized epithelial cells. *FEBS Lett.* **449**, 215-220.
- Pietrini, G., Suh, Y. J., Edelmann, L., Rudnick, G. and Caplan, M. J. (1994). The axonal gamma-aminobutyric acid transporter GAT-1 is sorted to the apical membranes of polarized epithelial cells. *J. Biol. Chem.* **269**, 4668-4674.
- Rodriguez-Boulan, E. and Gonzalez, A. (1999). Glycans in post-Golgi apical targeting: sorting signals or structural props? *Trends Cell Biol.* **9**, 291-294.
- Rodriguez-Boulan, E., Kreitzer, G. and Müsch, A. (2005). Organization of vesicular trafficking in epithelia. *Nat. Rev. Mol. Cell Biol.* **6**, 233-247.
- Russell, I. J. and Nilsen, K. E. (1997). The location of the cochlear amplifier: spatial representation of a single tone on the guinea pig basilar membrane. *Proc. Natl. Acad. Sci. USA* **94**, 2660-2664.
- Santos-Sacchi, J. (2003). New tunes from Corti's organ: the outer hair cell boogie rules. *Curr. Opin. Neurobiol.* **13**, 459-468.
- Sugimoto, H., Sugahara, M., Fölsch, H., Koide, Y., Nakatsu, F., Tanaka, N., Nishimura, T., Furukawa, M., Mullins, C., Nakamura, N. et al. (2002). Differential recognition of tyrosine-based basolateral signals by AP-1B subunit mu1B in polarized epithelial cells. *Mol. Biol. Cell* **13**, 2374-2382.
- Vicidomini, G., Moneron, G., Han, K. Y., Westphal, V., Ta, H., Reuss, M., Engelhardt, J., Eggeling, C. and Hell, S. W. (2011). Sharper low-power STED microscopy by time gating. *Nat. Methods* **8**, 571-573.
- Weisz, O. A. and Rodriguez-Boulan, E. (2009). Apical trafficking in epithelial cells: signals, clusters and motors. *J. Cell Sci.* **122**, 4253-4266.
- Yu, N., Zhu, M. L. and Zhao, H. B. (2006). Prestin is expressed on the whole outer hair cell basolateral surface. *Brain Res.* **1095**, 51-58.
- Zheng, J., Shen, W., He, D. Z., Long, K. B., Madison, L. D. and Dallos, P. (2000). Prestin is the motor protein of cochlear outer hair cells. *Nature* **405**, 149-155.
- Zheng, J., Du, G. G., Matsuda, K., Orem, A., Aguiñaga, S., Deák, L., Navarrete, E., Madison, L. D. and Dallos, P. (2005). The C-terminus of prestin influences nonlinear capacitance and plasma membrane targeting. *J. Cell Sci.* **118**, 2987-2996.
- Zheng, L., Zheng, J., Whitton, D. S., García-Añoveros, J. and Bartles, J. R. (2010). Targeting of the hair cell proteins cadherin 23, harmonin, myosin XVa, espin, and prestin in an epithelial cell model. *J. Neurosci.* **30**, 7187-7201.

Supplementary Material

Yifan Zhang et al. doi: 10.1242/bio.201410629

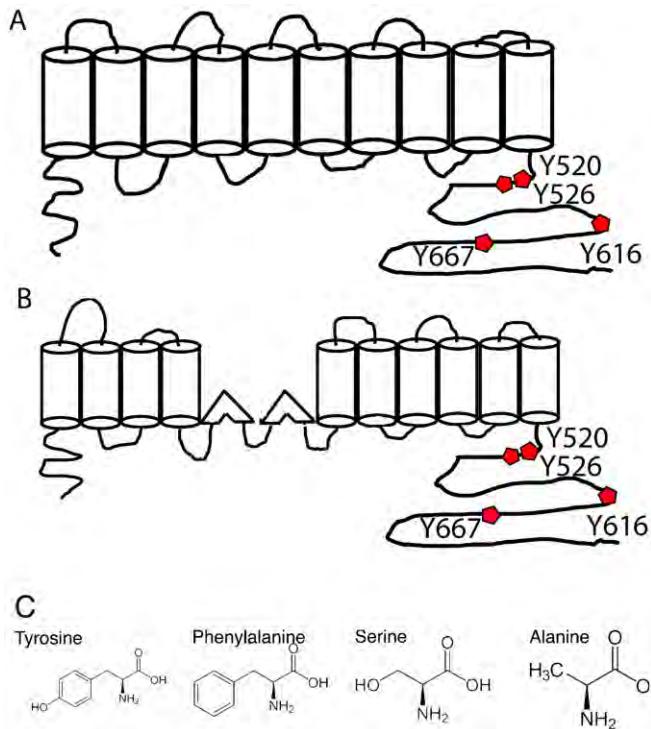


Fig. S1. A cartoon of the localization of individual C-terminal tyrosine residues within the 10 (A) and 12 (B) transmembrane models of prestin are shown. (C) The structure of individual residues including phenylalanine, serine and alanine used to substitute for individual tyrosine residues are compared.

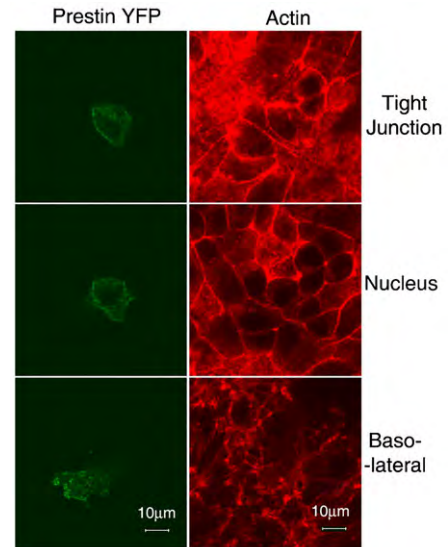


Fig. S2. LLC-PK cells show deficient basolateral targeting of prestin YFP. Confluent polarized LLC-PK1 cells were transfected with prestin YFP (green) and imaged by confocal imaging after fixation 72 hours later. Shown are serial X-Y sections along the z axis of a transfected cell (at the level of the tight junction, nucleus and basolateral surface). The actin cytoskeleton was stained with Phalloidin Alexa 647 (red). There is reduced targeting of prestin at the basolateral surface of the cell.

Table S1. Parameters of non linear capacitance in prestin and specific tyrosine mutants

	Q_{sp} (fC/pF)	V_h (mV)	z	n
Prestin	10.73±1.02	-115.44±4.32	0.78±0.02	7
Y667F	17.57±3.56	-149.18±8.34	0.82±0.02	5
Y667Q	0.92±0.24	-103.39±8.73	0.81±0.05	5
Y520F	2.75±0.75	-97.62±6.03	0.81±0.03	6

Measures of NLC in different mutants of prestin at Y667 and Y520 are compared. Other mutations at these sites did not show NLC. Note that substitution of Y520 and Y667 with a phenyl alanine residue resulted in divergent effects on V_h with the former causing a mild depolarization shift while the latter caused a marked hyperpolarization shift. The latter was also associated with an increase in Q_{sp} .

Effect of Membrane Tension on Gap Junctional Conductance of Supporting Cells in Corti's Organ

HONG-BO ZHAO and J. SANTOS-SACCHI

From the Sections of Otolaryngology and Neurobiology, Yale University School of Medicine, New Haven, Connecticut 06510

ABSTRACT The effects of turgor pressure-induced membrane tension on junctional coupling of Hensen cell isolates from the inner ear were evaluated by input capacitance or transjunctional conductance measurement techniques. Turgor pressure was altered by changing either pipette pressure or the osmolarities of extracellular solutions. Both positive pipette pressure and extracellular applications of hypotonic solutions, which caused cell size to concomitantly increase, uncoupled the cells as indicated by reduced input capacitance and transjunctional conductance. These changes were, in many cases, reversible and repeatable. Intracellular application of 50 μ M H-7, a broad-based protein kinase inhibitor, and 10 mM BAPTA did not block the uncoupling effect of positive turgor pressure on inner ear gap junctions. The transjunctional conductance at a holding potential of -80 mV was 53.6 ± 5.8 nS (mean \pm SEM, $n = 9$) and decreased $\sim 40\%$ at a turgor pressure of 1.41 ± 0.05 kPa. Considering the coincident kinetics of cell deformation and uncoupling, we speculate that mechanical forces work directly on gap junctions of the inner ear. These results suggest that pathologies that induce imbalances in cochlear osmotic pressure regulation may compromise normal cochlear homeostasis.

KEY WORDS: cochlea • membrane tension • turgor pressure • gap junctions • Hensen cells

INTRODUCTION

The supporting cells of the organ of Corti are structurally and electrically coupled together by gap junctions (Jahnke, 1975; Gulley and Reese, 1976; Iurato et al., 1976; Hama and Saito, 1977; Santos-Sacchi and Dallos, 1983; Kikuchi et al., 1995). Such gap junctional coupling among the supporting cells provides for electrical and metabolic uniformity; cochlear homeostasis is believed to rely on intercellular coupling (Santos-Sacchi, 1985, 1986, 1991; Kikuchi et al., 1995).

Gap junction channels are distinguished from other ionic channels since the integration of two aligned hemichannels from adjacent cells is required for normal function. In early work, hypertonic solutions, which cause cell and tissue shrinkage, were found to uncouple gap junctions in several different preparations (Barr et al., 1965, 1968; Goodenough and Gilula, 1974; Loewenstein et al., 1967). More recently, hypotonic treatments, which cause cell swelling, were determined to either increase (Kimelberg and Kettenmann, 1990) or decrease (Ngezahayo and Kolb, 1990) gap junctional coupling. These effects could have been due

to a variety of factors, including direct mechanical influences, changes in nonjunctional resistance, and modulation of intracellular factors that are known to uncouple cells. In the study of Ngezahayo and Kolb (1990), where junctional conductance was studied directly, the decrease in coupling was abolished by 5 mM EGTA in nominally Ca^{2+} -free internal solutions, and was linked to the activity of PKC. In the present report, we used the whole-cell voltage clamp technique to examine the effects of turgor pressure on junctional coupling of isolated pairs or small groups of cochlear supporting cells. Both input capacitance (Santos-Sacchi, 1991; Bigiani and Roper, 1995) and transjunctional conductance measures were used to gauge intercellular communication. We report that data obtained with both techniques indicate that positive intracellular pressure, which is known to induce membrane tension, uncouples gap junctions of supporting cells in Corti's organ.

METHODS

Detailed experimental methods can be found in previous reports (Santos-Sacchi, 1991; Sato and Santos-Sacchi, 1994). In brief, isolated supporting cells or cell aggregates were freshly obtained from the organ of Corti of the guinea pig cochlea by shaking for 5–15 min in nominally Ca^{2+} -free Leibovitz medium containing 1 mg/ml trypsin. To reduce the voltage-dependent ionic currents from nonjunctional membrane during double voltage clamp experiments, cells were perfused with an ionic blocking solution containing (mM): 100 NaCl, 20 TEA, 20 CsCl, 1.25 CoCl_2 , 1.48 MgCl_2 , 10 HEPES, pH 7.2, 300 mosM. In initial experiments, a modified Leibovitz medium was used for measurement of input

Portions of this work were previously published in abstract form (Zhao, H.B., and J. Santos-Sacchi. 1997. *Assoc. Res. Otolaryngol.* St. Petersburg, FL, pp. 15).

Address correspondence to Joseph Santos-Sacchi, Ph.D., Professor, Surgery (Otolaryngology), BML 244, Yale University School of Medicine, 333 Cedar St., New Haven, CT 06510. Fax: 203-737-2245; E-mail: joseph.santos-sacchi@yale.edu

capacitance (C_{in})¹ with a single pipette voltage clamp containing (mM): 136.9 NaCl, 5.37 KCl, 1.25 CaCl₂, 1.48 MgCl₂, 10 HEPES, pH 7.2, 300 mosM. Pipette solutions were composed of (mM): 140 KCl, 10 EGTA or BAPTA, 2 MgCl₂, and 10 HEPES, pH 7.2. For double voltage clamp recording, 140 mM KCl was replaced with 140 mM CsCl. Patch electrodes had initial resistances of 2.5–4 MΩ, corresponding to 1–2 μm in diameter. Series resistance (R_s) after whole cell configuration was estimated from the current in response to 10-mV steps (Huang and Santos-Sacchi, 1993). In single Hensen cells, where R_s could be unequivocally determined after whole cell configuration, the average value was 7.16 ± 0.43 MΩ (mean \pm SEM, $n = 48$). Cells were typically held at -80 mV, within the Hensen cell's linear current-voltage range (Santos-Sacchi, 1991). Currents were filtered at 10 kHz with a four-pole Bessel filter (Axon Instruments, Foster City, CA). Intracellular pressure was modified either through the patch pipette with a syringe connected to the Teflon[®] tubing attached to the patch pipette holder or by changing osmolarity with "Y-tube" bath perfusion. Pipette pressure was monitored via a T-connector to a pressure monitor (World Precision Instruments, Inc., Sarasota, FL). All experiments were video tape recorded and performed at room temperature.

Since the input capacitance can be measured by a single pipette voltage clamp and is correlated with junctional conductance (Santos-Sacchi, 1991; Bigiani and Roper, 1995), it can be conveniently used to study gap junctional coupling under conditions of less cellular damage than the double voltage clamp technique. Input capacitance, in conjunction with input resistance (R_{in}), was continually measured on line to monitor junctional coupling. C_{in} and R_{in} were determined from the transient charge and steady state current, respectively, induced by small (-10 mV) test pulses with duration of $18\times$ the clamp time constant at the holding potential; measures were made at ~ 1 – 3 Hz (Santos-Sacchi, 1991).

$$C_{in} = \frac{Q_{in}}{V_{test}} \quad (1)$$

$$R_{in} = \frac{V_{test}}{\Delta I_{\infty}} \quad (2)$$

where

$$Q_{in} = \int_0^{\infty} I_c dt \quad (3)$$

Q_{in} is the charge moved, V_{test} is the voltage of the test pulse, I_c is the capacitive current induced by the test pulse, and ΔI_{∞} is the current difference between the steady state current induced by the test pulse and the holding current at the holding potential.

For the double voltage clamp, each cell in a cell pair was separately voltage clamped using 200A and 200B patch clamps (Axon Instruments). Both cells were clamped at the same holding potentials and a test pulse (10 mV, 10 ms) superimposed only on cell 1. The transjunctional current (I_j) is equal to the current difference (ΔI_2) in cell 2 caused by the test pulses applied to cell 1. The transjunctional conductance (G_j) can be calculated by:

$$G_j = \frac{-\Delta I_2}{V_{test}} \quad (4)$$

where V_{test} is the test pulse voltage applied to cell 1. Data collection and analysis were performed with an in-house developed

windows-based whole-cell voltage clamp program, jClamp (<http://www.med.yale.edu/surgery/otolar/santos/jclamp.html>), using a Digidata 1200 board (Axon Instruments). In some experiments, G_j was measured online at 2–4 Hz and the corresponding video images of recorded cells were digitally captured every 5–10 s under software (jClamp) control. The captured images were printed at $\sim 1,700\times$ and the plane cell areas calculated. To gauge membrane stress, area strain ($\Delta A/A_0$) was calculated, where ΔA is the change of cell area after pressure or osmotic treatment and A_0 is the original cell area.

RESULTS

Hensen cells can be easily distinguished from other inner ear supporting cells by their prominent lipid vacuoles. The number of cells comprising isolates of Hensen cells can be determined under the light microscope, and corresponds to the isolate's C_{in} since Hensen cells are well coupled electrically. Although the size of Hensen cells is variable, the distributions of C_{in} for one, two, and three Hensen cells, whose numbers were visually confirmed, were quite distinct (Fig. 1 A). At the

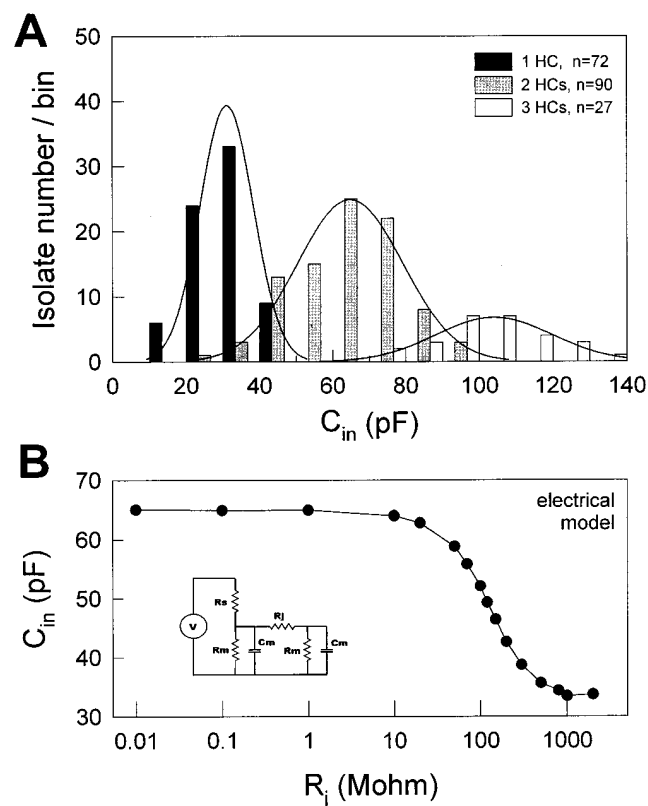


FIGURE 1. (A) The distributions of C_{in} of Hensen cell (HC) isolates. The cell numbers (1, 2, or 3) in the isolates were determined under the light microscope, and the C_{in} was obtained at the holding potential -80 mV. Each bar represents the number of isolates within a bin width of 10 pF. The lines plotted over each histogram represent the fitted Gaussian distribution for the three isolate groups. (B) C_{in} was measured for a coupled two-cell electrical model as transjunctional resistance (R_j) was changed. R_s , 4.7 MΩ; R_{in} , 500 MΩ; C_m , 33 pF. (inset) Coupled two-cell electrical model.

¹Abbreviations used in this paper: C_{in} , input capacitance; G_j , transjunctional conductance; OHC, outer hair cell; R_{in} , input resistance; R_s , series resistance.

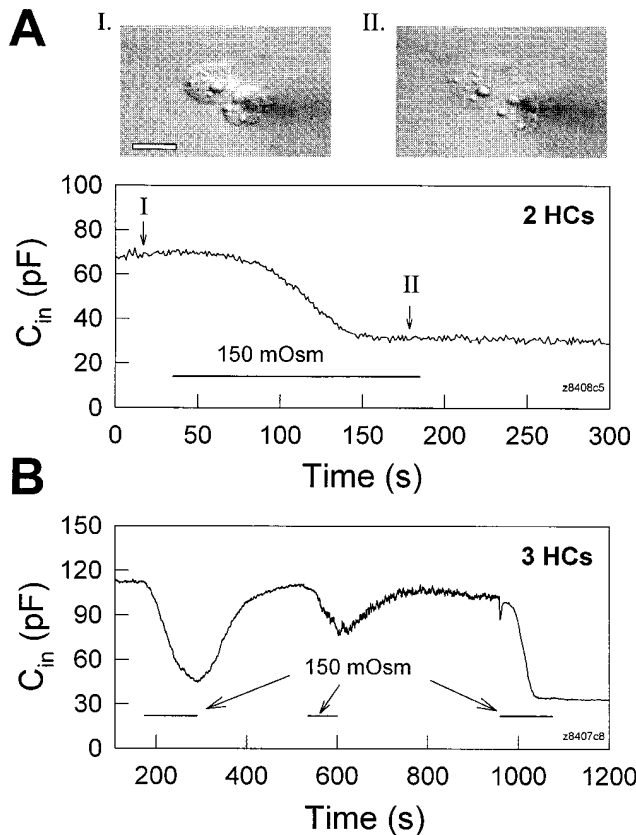


FIGURE 2. Osmolarity-induced turgor pressure increase uncouples Hensen cells. Both bath solution and electrode solution were 300 mosM. (A) When an extracellular 150 mosM solution was perfused (indicated by the horizontal bar) the cell pair swelled (see insets). Concomitantly, C_{in} decreased to half value due to cell uncoupling. R_s , 6.5 M Ω . (insets) Captured cell images before and during the perfusion of the hypo-osmotic solution. The white scale bar represents 20 μ m. (B) Decreases of C_{in} due to hypo-osmotic challenge were reversible and repeatable. In this case, the cells finally fully uncoupled and C_{in} remained at the single cell capacitance level. R_s , 3.8 M Ω .

holding potential of -80 mV, the peaks of the isolate distributions were clearly separated at 31.03 ± 0.86 , 64.75 ± 1.5 , and 103.9 ± 3.05 pF, corresponding to one, two, and three cell contributions, respectively. The number of cells within isolates can also be confirmed using uncoupling agents, such as CO_2 , octanol, or, as we now find, positive turgor pressure, to uncouple the cells. When cells fully uncoupled, C_{in} reached single cell capacitance levels (e.g., Figs. 2 and 3). The correlation of C_{in} with degree of cell coupling is illustrated by real measures of C_{in} in a coupled two-cell electrical model (Fig. 1 B). C_{in} of the electrical model was a monotonic function of transjunctional resistance or conductance, indicating the validity of C_{in} as an indicator of cell coupling.

Positive turgor pressure induced either by osmolarity changes or directly via the patch pipette decreased C_{in}

of cell pairs or three-cell groups (Figs. 2 and 3), but did not reduce single cell capacitance (Fig. 4). This indicates that positive turgor pressure uncouples gap junctions between adjacent Hensen cells.

In Fig. 2 A, bath application of hypo-osmotic solution (150 mosM) caused a Hensen cell pair to swell (insets) and decreased C_{in} of the pair to single cell levels. The uncoupling induced by increased turgor pressure is reversible since return to normal osmolarity solution often restored initial C_{in} values; subsequent reperfusion with hypo-osmotic solution remained effective as an uncoupling stimulus (Fig. 2 B). In single cells, while the same hypo-osmotic treatment caused cell swelling, C_{in} remained stable (Fig. 4 B).

Fig. 3 illustrates the uncoupling effect of cell turgor pressure change induced by patch pipette pressure. As turgor pressure was directly increased to ~ 1.2 kPa via the patch pipette, C_{in} decreased to almost single cell levels (after an initial delay possibly due to pipette plugging), and immediately began to return when the pressure was released (Fig. 3 A). The cells could be permanently uncoupled during the application of prolonged, continuous positive pressure (Fig. 3 B). The uncoupling effect of positive turgor pressure was found in 40 of 42 cell pairs, or three-cell groups. As with osmolarity change, direct application of positive turgor pressure via the patch pipette also did not decrease the measured capacitance in single Hensen cells despite cell swelling (Fig. 4 A, insets).

Although C_{in} can be easily measured by single pipette voltage clamp to gauge the degree of cell coupling, transjunctional conductance cannot be measured directly since transjunctional voltage and current are unknown. Additionally, a quantitative estimate of degree of coupling based on C_{in} is not easily established since C_{in} is a nonlinear function of transjunctional conductance (see Fig. 1 B and DISCUSSION). To further investigate the uncoupling effect of positive turgor pressure on gap junctions in Hensen cells, the transjunctional conductance was directly assessed with a double voltage clamp technique, and corresponding changes of the cell plane surface areas ($\Delta A/A_0$) (i.e., an indicator of membrane strain) were simultaneously measured.

Figs. 5 and 6 illustrate the results of such experiments. Cell areas increased in concert with decreases of transjunctional conductance as positive turgor pressure was delivered to the cells. The changes in cell area were observable before gap junctional uncoupling and occurred faster than G_j decay (Figs. 5 and 6). However, unlike pressure changes induced by pipette pressure, hypo-osmotic shocks produced changes in G_j and cell areas that were quite fast. With extracellular perfusion of a 150-mosM solution, the time constant for G_j decay was 9.53 s in Fig. 6 B, and the average value was 5.1 ± 1.86 s ($n = 6$). In Fig. 6 B, the rise time constant of

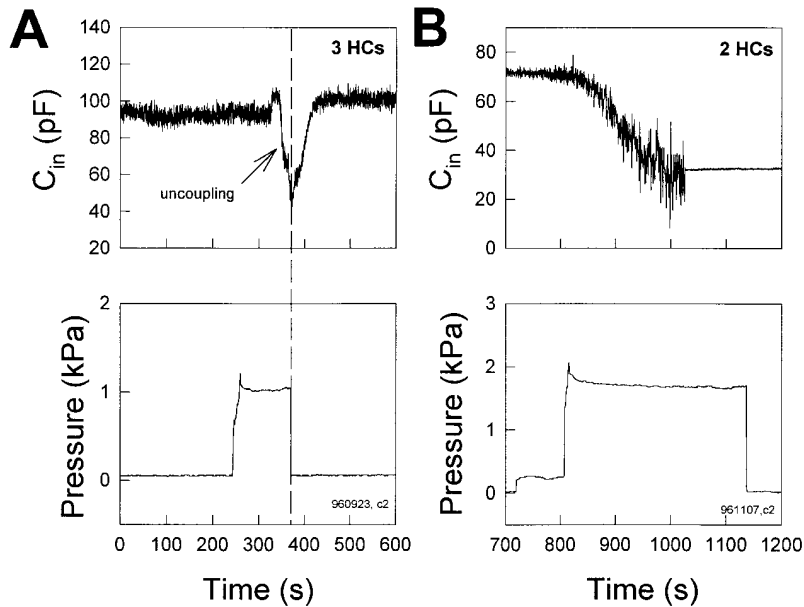


FIGURE 3. Hensen cells uncouple as turgor pressure is directly increased via the patch pipette. (A) In this example, increased pipette pressure caused C_{in} to decrease to single cell levels after an initial delay (possibly due to pipette plugging), but returned to the original level soon after pipette pressure was released. R_s , 9.76 M Ω . (B) A Hensen cell pair uncoupled after prolonged application of pressure. C_{in} decreased from 71.2 pF to a single cell level of 34.7 pF. R_s , 8.5 M Ω .

membrane strain was 4.43 s. The average rise time constant of membrane strain is estimated to be close to or less than that of the average G_j decay since in most cases the swelling fully occurred within the 5–10-s video capture rate. In most, but not all, cases, it was noted that after membrane tension stabilized, transjunctional conductance likewise stabilized (Fig. 5). The correlated and reciprocal changes in G_j and membrane strain

($\Delta A/A_0$) were reversible and repeatable (Fig. 6 A), strongly indicating that G_j decreases were relative to increases of membrane strain; i.e., membrane tension. It should be noted that the latency to G_j change after $\Delta A/A_0$ change is possibly due to the absence of significant membrane stress during the initial cell inflation, which clearly (based on the magnitude of cell enlargement) was accompanied by membrane unfolding.

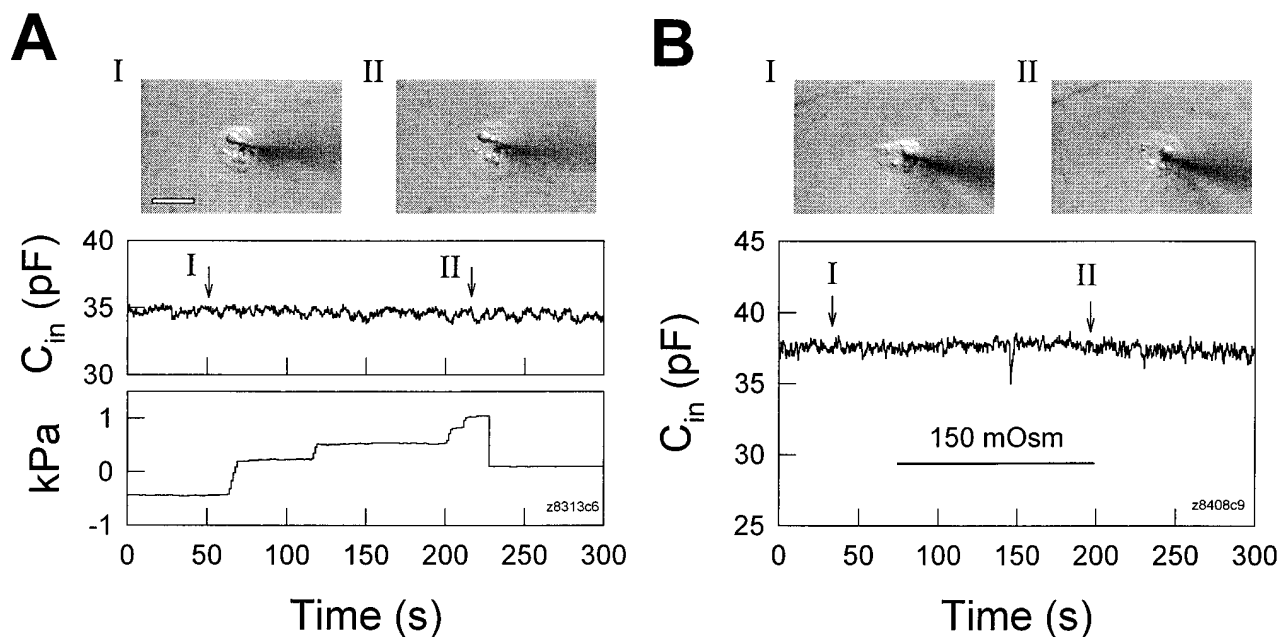


FIGURE 4. Changes of turgor pressure caused either directly via the patch pipette (A) or by perfusion of hypo-osmotic solutions (B) do not decrease the measured capacitance in a single Hensen cell. (insets) Captured cell images before and during applications of positive intracellular pressure. Cell swelling was visible as turgor pressure increased. The white scale bar represents 20 μ m. R_s : (A) 8.4 M Ω , (B) 4.4 M Ω .

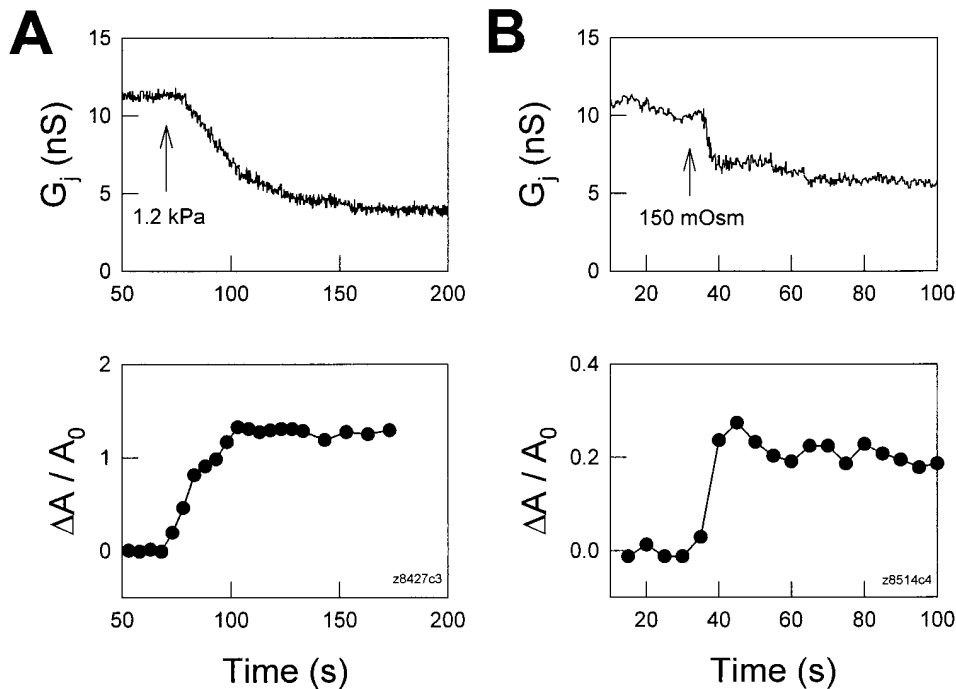


FIGURE 5. Positive turgor pressure-induced reduction in transjunctional conductance is correlated with increases in membrane strain ($\Delta A/A_0$). Transjunctional conductance was measured with a double voltage clamp technique, and membrane strains were calculated from captured images (see METHODS). Each cell in a Hensen cell pair was separately held at -40 mV. The continuous treatments used to increase intracellular pressure began at the arrows. (A) Positive pipette pressure induced an increase in membrane strain and concomitantly reduced G_j . (B) Perfusion of 150 mosM solution also induced an increase in membrane strain and concomitantly reduced G_j . The pipette solution contained $50 \mu\text{M}$ H-7.

Uncoupling of Hensen cell gap junctions by membrane stress was not inhibited by using pipette solutions containing $50 \mu\text{M}$ H-7 (dihydrochloride; Calbiochem Corp., La Jolla, CA), a broad-based serine/threonine kinase inhibitor (Boulis and Davis, 1990) (Figs. 5 B and 6 B). These data imply that the uncoupling effect of positive turgor pressure on inner ear gap junctions is independent of protein kinases, and that the effect is different from previous observations that cell volume changes induced uncoupling of gap junctions via the PKC pathway (Ngezahayo and Kolb, 1990). Nevertheless, cell swelling induced by hypo-osmotic shocks has been linked to increases of another uncoupling agent, intracellular Ca^{2+} (Hoffmann and Simonsen, 1989; Suzuki et al., 1990). However, uncoupling by Ca^{2+} , which occurs at millimolar intracellular concentrations in Hensen cells (Sato and Santos-Sacchi, 1994), can be ruled out since pipette solutions contained 10 mM BAPTA, a fast highly selective calcium chelating reagent, and extracellular and intracellular solutions were nominally Ca^{2+} free. Considering all evidence, the observed uncoupling effect of positive turgor pressure on inner ear gap junctions, which is fast (within seconds), correlated with changes of membrane strain, and independent of protein kinases and Ca^{2+} , is likely to occur via direct mechanical effects on the plasmalemma; i.e., membrane tension.

The effect of membrane tension on gap junctional conductance was further studied by increasing turgor pressure in cell 1 and measuring I_j in cell 2 at different membrane potentials (Fig. 7). Gap junctional conduc-

tance in Hensen cells at a holding potential of -80 mV was $52.9 \pm 12.1 \text{ nS}$ ($n = 51$). As the turgor pressure in cell 1 was increased, I_j decreased (Fig. 7 A). The junctional conductance at different membrane potentials reduced in parallel when the turgor pressure was increased. In those cell pairs where turgor pressure alterations were successfully applied without losing the cells, G_j at -80 mV holding potential decreased $38.3 \pm 9.5\%$ from $50.5 \pm 14 \text{ nS}$ ($n = 9$) at a turgor pressure of $1.41 \pm 0.05 \text{ kPa}$. The V_m dependence of G_j is also visible in Fig. 7. In this case, as the cells were depolarized, G_j decreased (Fig. 7 B). Other V_m dependencies of transjunctional conductance were also found, including V_m insensitivity and an increase with depolarization. Pressure did not alter voltage-dependent behaviors.

DISCUSSION

We provide evidence, based on input capacitance and double voltage clamp measures, that junctional coupling is sensitive to positive turgor pressure-induced membrane tension. Turgor pressure has been used to induce membrane tension in a wide variety of cells, including the outer hair cell (OHC), where it has been shown that motility and motility-related gating current characteristics are directly altered (Iwasa, 1993; Gale and Ashmore, 1994; Takehata and Santos-Sacchi, 1995). Membrane tension (possibly acting via cytoskeletal interactions) is also known to gate stretch-activated ionic channels (Yang and Sachs, 1989), which have been observed in outer hair cells (Ding et al., 1991; Iwasa et al.,

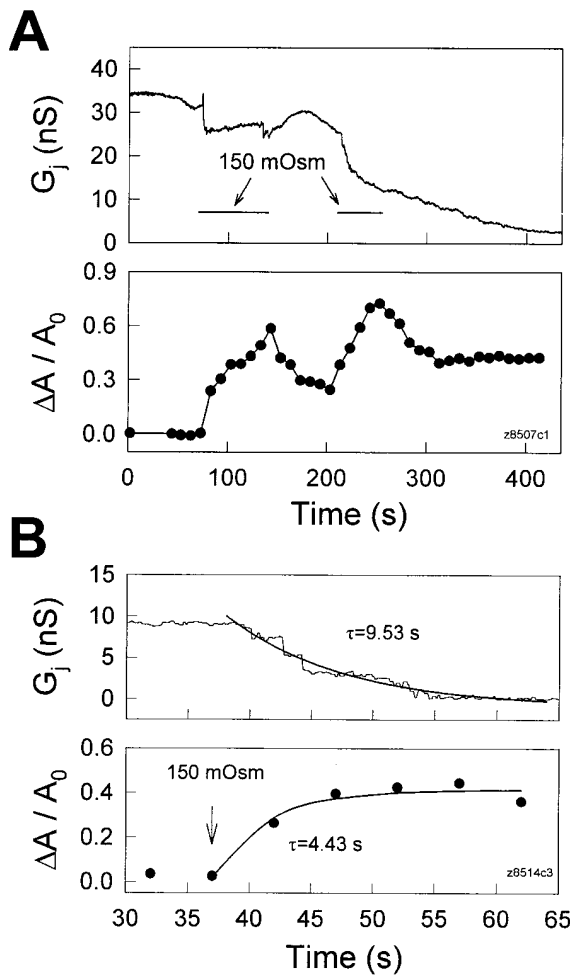


FIGURE 6. (A) Hypo-osmotic solutions induced reversible, concomitant changes in transjunctional conductance and membrane strain. Both cells were held at -40 mV. Repeated applications of 150 mosM solution are indicated by the horizontal bars. (B) The time course of the uncoupling effect caused by hypo-osmotic shock is compared with the increase of membrane strain. The beginning of treatment is indicated by an arrow and continued during the observed period. Thick solid lines represent single exponential fits. Membrane strain appears to have increased before the decrease of G_j . Pipettes contained $50 \mu\text{M}$ H-7.

1991). It is possible that membrane tension also alters gating characteristics of supporting cell gap junctions. We show, however, that unlike stretch channels, inner ear gap junctional conductance decreases with membrane stress. Recently, it has been postulated that gap junction channels possess two distinct gating mechanisms, namely, a voltage gating mechanism and a chemical gating mechanism (Bukauskas et al., 1995; Bukauskas and Peracchia, 1997; Bukauskas and Weingart, 1994). Chemical uncoupling agents, such as CO_2 , H^+ , and Ca^{2+} , may act on sensor elements from the cytoplasmic side. Supporting cell coupling has been shown to be sensitive to a variety of chemical uncoupling agents (Santos-Sacchi, 1985; 1991), and we now

report that supporting cell coupling is voltage dependent as well. The existence of voltage-dependent gap junctional conductance may account in part for previous reports of temperature-induced depolarization on supporting cell coupling ratios (Santos-Sacchi, 1986). Interestingly, junctional voltage dependence is unaffected by concomitant tension-induced junctional conductance change, possibly indicating that an independent tension gating mechanism may exist.

Gap junctions consist of two aligned transmembrane hemichannels (connexons), one from each cell (Revel et al., 1984; Goodenough et al., 1988; Bennett et al., 1991). Each of these hemichannels is formed by six connexin subunits (Kumar and Gilula, 1996; Perkins et

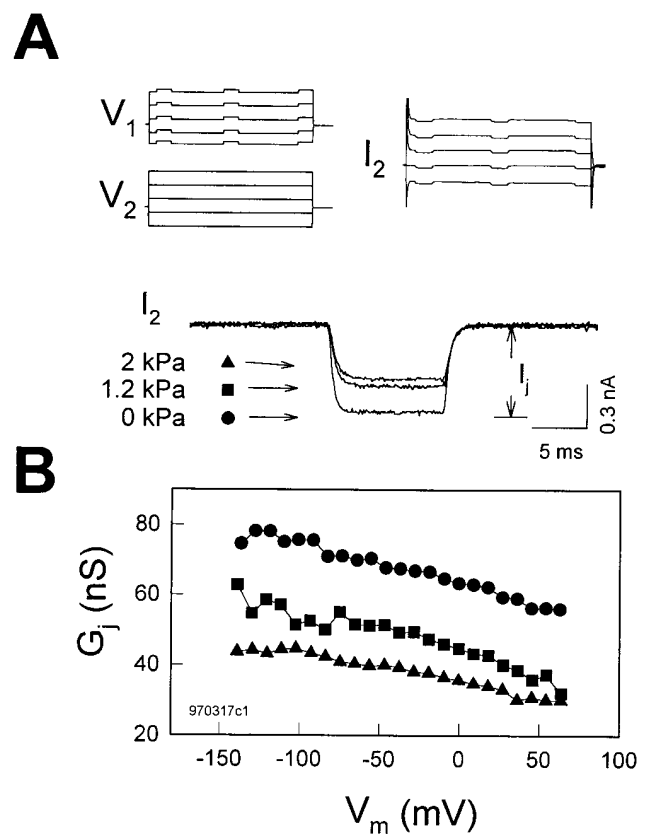


FIGURE 7. Turgor pressure does not affect membrane potential (V_m or V_{i-o}) dependence of gap junctions in Hensen cells. (A) Voltage stimulus protocols for each cell and current trace recorded in cell 2 are plotted (only five traces are shown for clarity). Each cell in a Hensen cell pair was separately voltage clamped at the same holding potential of -80 mV. Voltage steps from -140 to 70 mV for 100 ms in 10 -mV increments were simultaneously delivered into both cells except for 10 mV, 10 -ms test pulses superimposed on cell 1 only. Transjunctional current (I_j) is measured in cell 2. The turgor pressure of cell 1 was directly changed by the patch pipette. Three current traces from cell 2 at different pressures were zeroed and superimposed in the middle. (B) Positive turgor pressure decreased G_j at all membrane potentials. Note G_j decrease as the cells were depolarized. R_i at 0 kPa, 12.5 M Ω ; at 1.2 kPa, 12.7 M Ω ; at 2 kPa, 12.2 M Ω .

al., 1997). Our data indicate that membrane stress acts on inner ear gap junctions in a manner independent of Ca^{2+} , pH, and protein kinases. The rapid and reversible nature of the uncoupling also indicates that the mechanism is not due to some sort of mechanical destruction of the channels. While there may be other unknown links between membrane stress and junctional conductance, it is conceivable that tension may gate gap junction channels by a conformational change in connexon structure, possibly causing only the stressed membrane's hemichannel to close.

Gap junction connexins represent a family of homologous proteins that have differing voltage gating characteristics (Harris et al., 1981; Spray et al., 1981; Bennett et al., 1991; Dahl, 1996). Using immunocytochemistry and transmission electron microscopy, Cx26 was found in gap junctions of the rat (Kikuchi et al., 1995) and gerbil (Forge et al., 1997) organ of Corti. More recently, Cx26, Cx30, Cx32, and Cx43 have been localized to supporting cell regions of the rat cochlea (Lautermann et al., 1997). Such diversity of connexins within the organ may provide for a variety of junctional communication characteristics; for example, rectifying junctional conductance. Indeed, in addition to our direct observation that voltage-dependent junctional communication exists in the supporting cells, we have preliminary evidence that junctional rectification occurs. Directional flow of ions mediated by rectified gap junctions may be crucial for normal cochlea homeostasis (see below).

Since the mid 1980's, gap junctional coupling has usually been studied with double voltage clamp. However, input capacitance and resistance reflect the degree of electrical coupling and can be conveniently measured using a single voltage clamp (Santos-Sacchi, 1991; Sato and Santos-Sacchi, 1994; Bigiani and Roper, 1995). Based on a coupled two-cell model (see Fig. 1 B, inset), and assuming that the individual cells have the same input impedance, the following equations are obtained (Bigiani and Roper, 1995),

$$C_{in} = \frac{(2R_m R_j + 2R_m^2 + R_j^2) R_m^2}{(2R_m R_s + R_m^2 + R_s R_j + R_m R_j)^2} C_m, \quad (5)$$

$$R_{in} = \frac{R_s R_j + 2R_s R_m + R_j R_m + R_m^2}{R_j + 2R_m}, \quad (6)$$

where R_s and R_m are electrode series resistance and nonjunctional membrane resistance, respectively, and C_m is single cell capacitance (see Fig. 1 B, inset). Since R_m is not readily available from recordings, we can solve Eqs. 5 and 6 to remove R_m . R_j can be finally expressed:

$$R_j = \left| \frac{C_{in} R_{in}^2 + 4C_m R_s R_{in} - 2C_m R_s^2 - 2C_m R_{in}^2}{\sqrt{2C_m^2 R_s R_{in} + C_{in} C_m R_{in}^2 - C_m^2 R_s^2 - C_m^2 R_{in}^2}} \right|. \quad (7)$$

C_{in} , R_{in} , and R_s are readily obtained from recordings. Fig. 8 illustrates the measurement of these parameters during an uncoupling event, and the bottom panel shows the estimated G_j based on those data. Changes in estimated G_j mirror pressure-induced changes in C_{in} . It should be noted that R_s changes can also produce changes in C_{in} and R_{in} . For example, to obtain the observed maximum change in C_{in} , an order of magnitude increase of R_s would be required in this case. In our experiments, changes solely in R_s required to produce a comparable change in C_{in} were not observed. Series resistance remained constant, being $7.79 \pm 0.49 \text{ M}\Omega$ ($n = 7$) for cell pairs that were well coupled and $6.34 \pm 1.13 \text{ M}\Omega$ after those same cells were uncoupled with positive pipette pressure.

Finally, how might the turgor pressure dependence of junctional coupling in the organ of Corti affect coch-

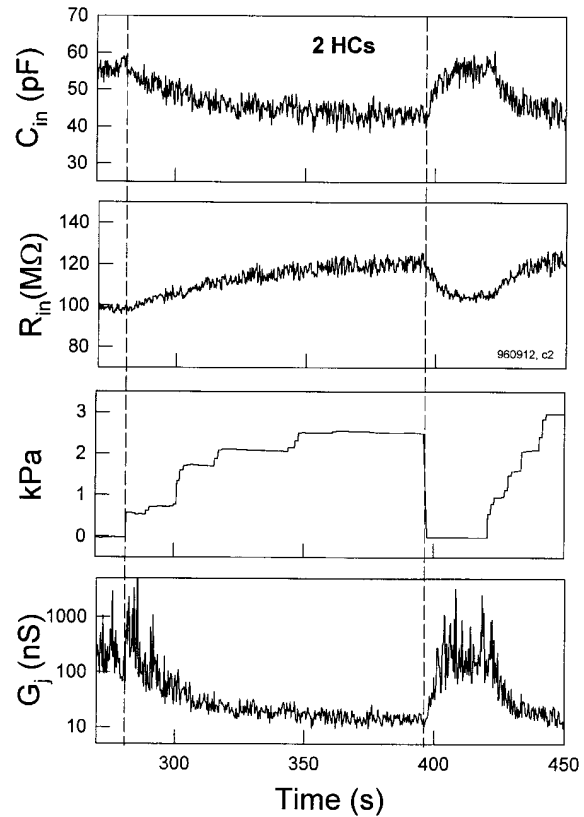


FIGURE 8. Transjunctional conductance is estimated by C_{in} and R_{in} in single pipette voltage clamp. (top) C_{in} decreased and R_{in} simultaneously increased as turgor pressure increased. C_{in} and R_{in} followed changes in pressure. R_s , $8.73 \text{ M}\Omega$. (bottom) G_j is estimated from C_{in} and R_{in} measurements from the cell pair data based on the coupled two-cell model. C_m was set as half of C_{in} , 27.5 pF , at zero applied pressure, and R_s was $8.5 \text{ M}\Omega$. The change in estimated G_j corresponds well to changes in C_{in} . The magnitude of G_j is larger than the largest obtained under double voltage clamp ($\sim 500 \text{ nS}$), and may be due to the fact that cell impedances are not actually identical as required in the model.

lear function? In vivo, the organ of Corti, comprising hair cells and supporting cells, is bathed in two different media, high K^+ endolymph apically and low K^+ perilymph basally. Since the receptor current through hair cells is predominantly carried by K^+ , an accumulation of K^+ within the perilymphatic space along the basolateral region of the hair cells is unavoidable. This would potentially depolarize hair cells with disastrous consequences for both forward and reverse sensory transduction. In the mammal, forward transduction (gating of stereociliar transduction channels) relies on the large driving force present across the hair cell's apical plasma membrane. Voltage gradients across the apical membranes of inner and outer hair cells (i.e., endolymphatic potential minus membrane potential) range from 125 to 150 mV, and drive the K^+ -based receptor currents. Reduction of this gradient (e.g., by membrane depolarization) will reduce the magnitude of receptor potentials and synaptic output. Reverse transduction is a phenomenon that is restricted to the outer hair cell and is believed to provide for the enhanced high frequency selectivity and sensitivity enjoyed by mammals. OHCs, which are additionally mechanically active, possess lateral membrane motors that are driven by voltage (Santos-Sacchi and Dilger, 1988); the cell's mechanical response provides feedback into the basilar membrane, thereby enhancing the stimulus to the primary receptor cells, the inner hair cells (for review see Ruggero and Santos-Sacchi, 1997). Not only will depolarization of the OHC alter the driving force for the mechanical response, but the function relating mechanical response to voltage will be shifted along the voltage axis as well, resulting in an altered gain for the "cochlear amplifier" (Santos-Sacchi et al., 1998). Some mechanisms must prevent such an undesirable scenario. A nutritive and K^+ sinking role for gap junctions

in the avascular organ of Corti has been proposed (Santos-Sacchi, 1985, 1991; Santos-Sacchi and Dallos, 1983). Inner ear supporting cells have been shown to "share" plasmalemmal voltage-dependent conductances due to the high degree of cell coupling (Santos-Sacchi, 1991). The magnitude and stability of their resting potentials is pronounced (close to -100 mV), and likely depends on cell coupling since isolated cell resting input conductance is only ~ 1 nS. At the normal resting potential of this cellular syncytium, an inward rectifier appears continuously activated and may result in K^+ removal from perilymphatic spaces. It should be noted that the large perilymphatic fluid spaces may provide little support in sinking K^+ or directing its movement, since hair cell regions that are likely to experience K^+ elevations are not directly exposed to those spaces. Inner hair cells are closely surrounded by supporting cells, and the region of the OHCs that possesses voltage-dependent conductances (e.g., outward K^+) is restricted to the basal pole of the cell (Santos-Sacchi et al., 1997), which is surrounded by a Deiters cell cup. Recently, Kikuchi et al. (1995) provided morphological evidence detailing epithelial and connective tissue gap junctional systems within the cochlea that may complete the mechanism responsible for recycling K^+ from the perilymphatic space near hair cells to the K^+ -rich endolymph via the stria vascularis. The maintenance of normal fluid space architecture within the inner ear requires fine osmotic control; imbalances can lead to serious auditory and vestibular problems (e.g., Meniere's disease). While at present we do not know the normal physiological significance of tension-dependent gap junctional communication, it is likely that fluid balance disorders in the inner ear will affect gap junctional communication, thus compromising sensory function by indirectly modifying hair cell activity.

We thank Margaret Mazzucco for technical help.

This work was supported by National Institute on Deafness and Other Communication Disorders grant DC00273 to J. Santos-Sacchi.

Original version received 12 January 1998 and accepted version received 24 July 1998.

REFERENCES

- Barr, L., W. Berger, and M.M. Dewey. 1968. Electrical transmission at the nexus between smooth muscle cells. *J. Gen. Physiol.* 51:347–368.
- Barr, L., M.M. Dewey, and W. Berger. 1965. Propagation of action potentials and the structure of the nexus in cardiac muscle. *J. Gen. Physiol.* 48:797–823.
- Bennett, M.V.L., L.C. Barrio, T.A. Bargiello, D.C. Spray, E. Hertzberg, and J.C. Saez. 1991. Gap junctions: new tools, new answers, new questions. *Neuron.* 6:305–320.
- Bigiani, A., and S.D. Roper. 1995. Estimation of the junctional resistance between electrically coupled receptor cells in *Necturus* taste buds. *J. Gen. Physiol.* 106:705–725.
- Boulis, N.M., and M. Davis. 1990. Blockade of the spinal excitatory effect of cAMP on the startle reflex by intrathecal administration of the isoquinoline sulfonamide H-8: comparison to the protein kinase C inhibitor H-7. *Brain Res.* 525:198–204.
- Bukauskas, F.F., C. Elfgang, K. Willecke, and R. Weingart. 1995. Biophysical properties of gap junction channels formed by mouse connexin40 in induced pairs of transfected human HeLa cells. *Biophys. J.* 68:2289–2298.
- Bukauskas, F.F., and C. Peracchia. 1997. Two distinct gating mechanisms in gap junction channels: CO_2 -sensitive and voltage-sensitive. *Biophys. J.* 72:2137–2142.
- Bukauskas, F.F., and R. Weingart. 1994. Voltage-dependent gating

- of single gap junction channels in an insect cell line. *Biophys. J.* 67:613–625.
- Dahl, G. 1996. Where are the gates in gap junction channels? *Clin. Exp. Pharmacol. Physiol.* 23:1047–1052.
- Ding, J.P., R.J. Salvi, and F. Sachs. 1991. Stretch-activated ion channels in guinea pig outer hair cells. *Hear. Res.* 56:19–28.
- Forge, A., D. Becker, and W.H. Evans. 1997. Gap junction isoforms in the inner ear of gerbils and guinea pigs. *Br. J. Audiol.* 31:76–77.
- Gale, J.E., and J.F. Ashmore. 1994. Charge displacement induced by rapid stretch in the basolateral membrane of the guinea-pig outer hair cell. *Proc. R. Soc. Lond. B Biol. Sci.* 255:243–249.
- Goodenough, D.A., and N.B. Gilula. 1974. The splitting of hepatocyte gap junctions and zonulae occludentes with hypertonic disaccharides. *J. Cell Biol.* 61:575–590.
- Goodenough, D.A., D.L. Paul, and L. Jesaitis. 1988. Topological distribution of two connexin32 antigenic sites in intact and split rodent hepatocyte gap junctions. *J. Cell Biol.* 107:1817–1824.
- Gulley, R.S., and T.S. Reese. 1976. Intercellular junctions in the reticular lamina of the organ of Corti. *J. Neurocytol.* 5:479–507.
- Hama, K., and K. Saito. 1977. Gap junctions between the supporting cells in some acousticovestibular receptors. *J. Neurocytol.* 6:1–12.
- Harris, A.L., D.C. Spray, and M.V.L. Bennett. 1981. Kinetic properties of a voltage-dependent junctional conductance. *J. Gen. Physiol.* 77:95–117.
- Hoffmann, E.K., and L.O. Simonsen. 1989. Membrane mechanisms in volume and pH regulation in vertebrate cells. *Physiol. Rev.* 69:315–382.
- Huang, G., and J. Santos-Sacchi. 1993. Mapping the distribution of the outer hair cell motility voltage sensor by electrical amputation. *Biophys. J.* 65:2228–2236.
- Iurato, S., K. Franke, L. Luciano, G. Wermber, E. Pannese, and E. Reale. 1976. Intercellular junctions in the organ of Corti as revealed by freeze fracturing. *Acta Otolaryngol.* 82:57–69.
- Iwasa, K.H., M.X. Li, M. Jia, and B. Kachar. 1991. Stretch sensitivity of the lateral wall of the auditory outer hair cell. *Neurosci. Lett.* 133:171–174.
- Iwasa, K.H. 1993. Effect of stress on the membrane capacitance of the auditory outer hair cell. *Biophys. J.* 65:492–498.
- Jahnke, K. 1975. The fine structure of freeze-fractured intercellular junctions in the guinea pig inner ear. *Acta Otolaryngol. Suppl. (Stockh).* 336:1–40.
- Takehata, S., and J. Santos-Sacchi. 1995. Membrane tension directly shifts voltage dependence of outer hair cell motility and associated gating charge. *Biophys. J.* 68:2190–2197.
- Kikuchi, T., R.S. Kimura, D.L. Paul, and J.C. Adams. 1995. Gap junctions in the rat cochlea: immunohistochemical and ultrastructural analysis. *Anat. Embryol.* 191:101–118.
- Kimelberg, H.K., and H. Kettenmann. 1990. Swelling-induced changes in electrophysiological properties of cultured astrocytes and oligodendrocytes. I. Effects on membrane potentials, input impedance and cell–cell coupling. *Brain Res.* 529:255–261.
- Kumar, N.M. and N.B. Gilula. 1996. The gap junction communication channel. *Cell.* 84:381–388.
- Lautermann, J., W.-J.F. ten Cate, K. Jahnke, P. Altenhoff, O. Traub, and E. Winterhager. 1997. Expression pattern of different gap-junction connexins in the rat cochlea. 34th Workshop on Inner Ear Biology. Rosa Marina, Italy. pp. 59. (Abstr.).
- Loewenstein, W.R., M. Nakas, and S.J. Socolar. 1967. Junctional membrane uncoupling: permeability transformations at a cell membrane junction. *J. Gen. Physiol.* 50:1865–1891.
- Ngezahayo, A., and H.A. Kolb. 1990. Gap junctional permeability is affected by cell volume changes and modulates volume regulation. *FEBS Lett.* 276:6–8.
- Perkins, G., D. Goodenough, and G. Sosinsky. 1997. Three-dimensional structure of the gap junction connexon. *Biophys. J.* 72:533–544.
- Revel, J.-P., B.J. Nicholson, and S.B. Yancey. 1984. Molecular organization of gap junctions. *Fed. Proc.* 43:2672–2677.
- Ruggero, M.A., and J. Santos-Sacchi. 1997. Cochlear mechanics and biophysics. In *Handbook of Acoustics*. M.J. Croker, editor. John Wiley & Sons Inc., New York. 1357–1369.
- Santos-Sacchi, J. 1985. The effects of cytoplasmic acidification upon electrical coupling in the organ of Corti. *Hear. Res.* 19:207–215.
- Santos-Sacchi, J. 1986. The temperature dependence of electrical coupling in the organ of Corti. *Hear. Res.* 21:205–211.
- Santos-Sacchi, J. 1991. Isolated supporting cells from the organ of Corti: some whole cell electrical characteristics and estimates of gap junction conductance. *Hear. Res.* 52:89–98.
- Santos-Sacchi, J., and P. Dallos. 1983. Intercellular communication in the supporting cells of the organ of Corti. *Hear. Res.* 9:317–326.
- Santos-Sacchi, J., and J.P. Dilger. 1988. Whole cell currents and mechanical responses of isolated outer hair cells. *Hear. Res.* 35:143–150.
- Santos-Sacchi, J., G.J. Huang, and M. Wu. 1997. Mapping the distribution of outer hair cell voltage-dependent conductances by electrical amputation. *Biophys. J.* 73:1424–1429.
- Santos-Sacchi, J., S. Takehata, and S. Takahashi. 1998. The outer hair cell membrane potential directly affects the voltage dependence of motility-related gating charge. *J. Physiol. (Camb.)* 510:225–235.
- Sato, Y., and J. Santos-Sacchi. 1994. Cell coupling in the supporting cells of Corti's organ: sensitivity to intracellular H⁺ and Ca⁺⁺. *Hear. Res.* 80:21–24.
- Spray, D.C., A.L. Harris, and M.V.L. Bennett. 1981. Equilibrium properties of a voltage-dependent junctional conductance. *J. Gen. Physiol.* 77:77–93.
- Suzuki, M., K. Kawahara, A. Ogawa, T. Morita, Y. Kawaguchi, S. Kurihara, and O. Sakai. 1990. [Ca²⁺]_i rises via G protein during regulatory volume decrease in rabbit proximal tubule cells. *Am. J. Physiol.* 258:F690–F696.
- Yang, X.C., and F. Sachs. 1989. Block of stretch-activated ion channels in *Xenopus* oocyte by gadolinium and calcium ions. *Science.* 243:1068–1070.

show a characteristic 'U' shape (Fig. 5a). This gives rise to a remarkable chaotic travelling-wave structure which may be seen in the eight lattice 'snapshots' of Fig. 5b–i. Population abundances in the meta-community remain chaotic, but periodic circular waves continuously expand and contract radially as they spread in time across the spatial landscape. Field and model population studies of the Canadian hare–lynx cycle and European vole cycles have found similar travelling-wave structures with spatially distributed U-shaped phase lags^{10,25–27}. Different types of realistic diffusion barrier were introduced into the model but, in general, they failed to destroy the spatial circular wave structure (B.B. *et al.*, manuscript in preparation).

The spatio-temporal structures associated with phase synchronization have important implications for conservation ecology. Even if a disturbance perturbs a local patch population to the brink of extinction, the periodicity of spatial phase synchronization guarantees the recurring arrival of wave fronts in which new colonizers will buffer the endangered population. In contrast to the common view of population synchronization as a cause of global population extinctions¹⁴, it appears that phase synchronization can be important for maintaining species persistence. Our findings indicate that synchronization is a powerful process that has the potential to shape the distribution and abundance of species over all scales, from local to continental. We expect that the complex synchronization phenomena identified here will provide new insight into the dynamics of spatial ecologies and will have important applications to the study of biological rhythms in general. □

Received 22 January; accepted 29 March 1999.

1. Elton, C. & Nicholson, M. The ten-year cycle in numbers of the lynx in Canada. *J. Anim. Ecol.* **11**, 215–244 (1942).
2. May, R. M. *Stability and Complexity in Model Ecosystems* (Princeton University Press, Princeton, 1973).
3. Keith, L. B. *Wildlife's 10-year cycle* (University of Wisconsin Press, Madison, 1963).
4. Hanski, I., Turchin, P., Korpimäki, E. & Henttonen, H. Population oscillations of boreal rodents: regulation by mustelid predators leads to chaos. *Nature* **364**, 232–235 (1993).
5. Sinclair, A. R. E. *et al.* Can the solar cycle and climate synchronize the snowshoe hare cycle in Canada? Evidence from tree rings and ice cores. *Am. Nat.* **141**, 173–198 (1993).
6. Royama, T. *Analytical Population Dynamics* (Chapman & Hall, London, 1992).
7. Moran, P. A. P. The statistical analysis of the Canadian lynx cycle. *Aust. J. Zool.* **1**, 291–298 (1953).
8. Bulmer, M. G. A statistical analysis of the 10-year cycle in Canada. *J. Anim. Ecol.* **43**, 701–718 (1974).
9. Korpimäki, E. & Krebs, C. J. Predation and population cycles of small mammals. A reassessment of the predation hypothesis. *BioScience* **46**, 754–764 (1996).
10. Ranta, E., Kaitala, V. & Lundberg, P. The spatial dimension in population fluctuations. *Science* **278**, 1621–1623 (1997).
11. Schaffer, W. Stretching and folding in lynx fur returns: Evidence for a strange attractor in nature? *Am. Nat.* **124**, 798–820 (1984).
12. Rosenblum, M. G., Pikovsky, A. S. & Kurths, J. Phase synchronization of chaotic oscillators. *Phys. Rev. Lett.* **76**, 1804–1807 (1996).
13. Schäfer, C., Rosenblum, M. G., Kurths, J. & Abel, H. Heartbeat synchronized with ventilation. *Nature* **392**, 239–240 (1998).
14. Earn, D. J. D., Rohani, P. & Grenfell, B. Persistence, chaos and synchrony in ecology and epidemiology. *Proc. R. Soc. Lond. B* **265**, 7–10 (1998).
15. May, R. M. Simple mathematical models with very complicated dynamics. *Nature* **261**, 459–467 (1976).
16. Stone, L. Period-doubling reversals and chaos in simple ecological models. *Nature* **365**, 617–620 (1993).
17. Blasius, B., Neff, R., Beck, F. & Lüttge, U. Oscillatory model of Crassulacean acid metabolism with a dynamic hysteresis switch. *Proc. R. Soc. Lond. B* **266**, 93–101 (1999).
18. Gurney, W. S. C., Crowley, P. H. & Nisbet, R. M. Locking life-cycles on to seasons: circle-map models of population dynamics and local adaptation. *J. Math. Biol.* **30**, 251–279 (1992).
19. Hastings, A. & Powell, T. Chaos in a three-species food chain. *Ecology* **72**, 896–903 (1991).
20. Gilpin, M. E. Spiral chaos in a predator–prey model. *Am. Nat.* **107**, 306–308 (1979).
21. Vandermeer, J. Seasonal isochronic forcing of Lotka Volterra equations. *Progr. Theor. Phys.* **71**, 13–28 (1996).
22. Gotelli, N. J. *A Primer of Ecology* (Sinauer, Massachusetts, 1995).
23. Pecora, L. M. & Carroll, T. L. Synchronization in chaotic systems. *Phys. Rev. Lett.* **64**, 821 (1990).
24. Cohen, A. H., Holmes, P. J. & Rand, R. H. The nature of the coupling between segmental oscillators of the lamprey spinal generator for locomotion: a mathematical model. *J. Math. Biol.* **13**, 345–369 (1982).
25. Ranta, E. *et al.* Solar activity and hare dynamics: A cross-continental comparison. *Am. Nat.* **149**, 765–775 (1997).
26. Sinclair, A. R. E. & Gosline, M. Solar activity and mammal cycles in the northern hemisphere. *Am. Nat.* **149**, 776–784 (1997).
27. Ranta, E. & Kaitala, V. Travelling waves in vole population dynamics. *Nature* **390**, 456 (1997).
28. Stenseth, N. C., Falck, W., Bjørnstad, O. N. & Krebs, C. J. Population regulation in snowshoe hare and Canadian lynx: Asymmetric food web configurations between hare and lynx. *Proc. Natl Acad. Sci. USA* **94**, 5147–5152 (1997).
29. O'Donoghue, M. *et al.* Functional response of coyotes and lynx to the snowshoe hare cycle. *Ecology* **79**, 1193–1208 (1998).
30. Wolf, J. B., Swift, H. L. & Vastano, J. A. Determining Lyapunov exponents from a time series. *Physica D* **16**, 285–317 (1982).

Supplementary information is available on Nature's World-Wide Web site (<http://www.nature.com>) or as paper copy from the London editorial office of Nature.

Acknowledgements. We thank MINERVA for their award of a Fellowship to B.B., and H. Bhasin for her comments on the manuscript.

Correspondence and requests for materials should be addressed to L.S. (e-mail: lewi@lanina.tau.ac.il).

Auditory collusion and a coupled couple of outer hair cells

Hong-Bo Zhao & J. Santos-Sacchi

Sections of Otolaryngology and Neurobiology, Yale University School of Medicine, 333 Cedar Street, New Haven, Connecticut 06510, USA

The discrepancies between measured frequency responses of the basilar membrane in the inner ear and the frequency tuning found in psychophysical experiments led to Békésy's idea of lateral inhibition in the auditory nervous system¹. We now know that basilar membrane tuning can account for neural tuning², and that sharpening of the passive travelling wave depends on the mechanical activity of outer hair cells (OHCs)³, but the mechanism by which OHCs enhance tuning remains unclear. OHCs generate voltage-dependent length changes at acoustic rates^{4–8}, which deform the cochlear partition^{9–11}. Here we use an electrical correlate of OHC mechanical activity, the motility-related gating current, to investigate mechano-electrical interactions among adjacent OHCs. We show that the motility caused by voltage stimulation of one cell in a group evokes gating currents in adjacent OHCs. The resulting polarization in adjacent cells is opposite to that within the stimulated cell, which may be indicative of lateral inhibition. Also such interactions promote distortion and suppression in the electrical and, consequently, the mechanical activity of OHCs. Lateral interactions may provide a basis for enhanced frequency selectivity in the basilar membrane of mammals.

The mechanical response of the OHC is mirrored by an electrical signature, a motility-related charge movement, similar to the gating charge movements that control ion-channel conductance^{12,13}. Both gating currents arise from a redistribution of charged voltage sensors across the membrane. The magnitude of the gating current reflects the rate of charge redistribution. In the OHC, the redistribution of motility-related charge is controlled by both voltage and membrane tension; consequently, either can evoke gating currents^{14–16}. Within the organ of Corti, OHCs are indirectly mechanically coupled to each other through contacts with supporting Deiters' cells. The apical regions of OHCs and Deiters' cells are joined by tight junctions and form the plate-like reticular lamina. Basally, the OHCs sit in the cups of Deiters' cells, and the strength of these attachments varies along the length of the basilar membrane¹⁷. This morphology makes it likely that the voltage-induced mechanical responses of one OHC will affect surrounding OHCs. Determining the nature of this interaction may provide insight into the process of fine frequency tuning by OHCs. We studied this interaction by simultaneously recording from adjacent OHCs under dual whole-cell voltage and current clamp.

In isolated pieces of Corti's organ, where cellular relations remain intact, voltage stimulation of an OHC induces mechanical responses and gating currents in that cell (Fig. 1). Transient outward currents are generated by the onset of depolarization, which causes the cell to contract (Fig. 1b). These currents correspond to the displacement of positive charge to the extracellular aspect of the lateral plasma membrane, which holds motility/voltage sensors^{18,19}. The charge–voltage ($Q-V$) function is well described by a two-state

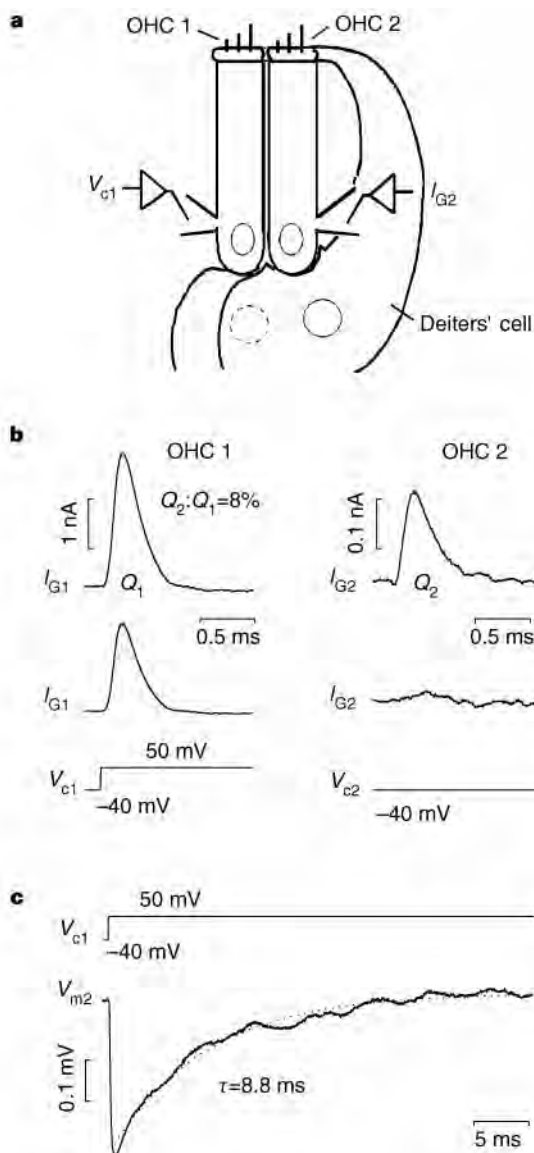


Figure 1 Adjacent OHCs are mechano-electrically coupled. **a**, Schematic illustrating two adjacent OHCs mechanically coupled through Deiters' cells and the recording configuration. **b**, Each cell in a pair was whole-cell voltage clamped to -40 mV. Depolarization of OHC 1 to 50 mV (V_{c1}) generates outward transient currents in both OHC 1 and OHC 2 (I_{G1} , I_{G2} , respectively; top two traces). The charge ratio (Q_2/Q_1) is 0.08 . Following application of negative pressure (~ -0.5 kPa; middle two traces) to the patch pipette of OHC 1, the response in OHC 2 was abolished. The response in the voltage-stimulated cell is decreased somewhat, as expected, owing to a negative shift in its Q - V function¹⁶. **c**, OHC 1 was held under voltage clamp and OHC 2 under current clamp. As a consequence of the impulsive gating current evoked in OHC 2, a negative voltage is developed across its membrane. The trace depicts the average induced potential ($n = 7$) in OHC 2. Dotted line: single exponential fit of 8.8 ms.

Boltzmann function^{12,13}:

$$Q(V) = \frac{Q_{\max}}{1 + b} \quad (1)$$

$$b = \exp\left(\frac{-ze(V_m - V_h)}{kT}\right)$$

where Q_{\max} is the maximum nonlinear charge moved, V_h is the voltage at half-maximal gating-charge transfer, V_m is the membrane potential, z is the valence, e is the electron charge, k is Boltzmann's constant and T is the absolute temperature.

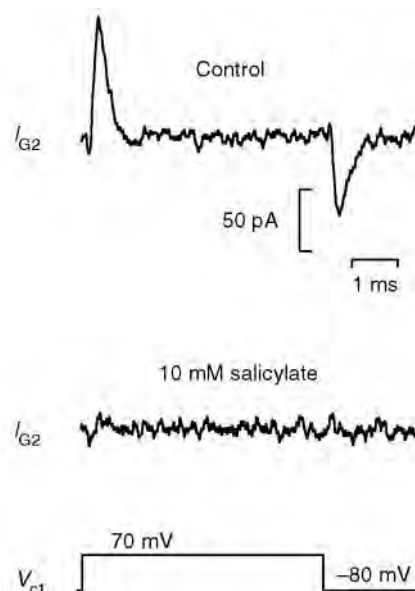


Figure 2 Both OHCs were voltage clamped to -80 mV, and OHC 1 was stepped to 70 mV (V_{c1}). The top trace shows the gating current (I_{G2}) evoked in OHC 2. Perfusion of the cells with 10 mM salicylate abolishes the gating current.

When the stimulated OHC (OHC 1) is depolarized, gating currents are seen in the adjacent OHC (OHC 2). The ratio of charge movement (Q_2/Q_1) in adjacent OHCs can be up to 0.1 . The induced gating current in OHC 2 is not generated by electrical interactions between the cells. Individually isolated cells that are positioned to touch each other do not show this charge coupling. Furthermore, collapse of OHC 1 by negative pipette pressure (-0.25 to -0.5 kPa), which abolishes the cell's normal mechanical activity¹³, eliminates gating currents in adjacent OHCs (Fig. 1b).

As in OHC 1, the magnitude of the gating currents in OHC 2 reflects the rate of charge redistribution; in this case, however, the rate mirrors that of the deformation of OHC 2. This is indicated by the significant correlation between the OHC 1 clamp time constant (which controls the rate of the OHC mechanical response under whole-cell voltage clamp⁶) and gating current magnitude in OHC 2 ($r^2 = 0.63$; $n = 21$). This is expected, because the OHC gating-current magnitude resulting from stretch is related to the velocity of stretch¹⁵. The charge redistribution in OHC 2 generates a voltage with a time course that depends on the cells' membrane time constant ($\tau_m = R_m \times C_m$). We looked at this induced voltage under current clamp. In seven cells, the average time constant of voltage decay induced by the impulsive gating current was 8.8 ms. The average membrane resistance of these cells was 272 ± 28 M Ω (mean \pm s.e.), the membrane capacitance (at the holding potential) was 35.1 ± 2.02 pF and, consequently, $\tau_m = 9.5$ ms. The initial voltage magnitudes were up to 1.2 mV. The polarity of the induced voltage was negative, corresponding to the movement of positive charge to the outside of the cell membrane. The polarity of the voltage change in mechanically coupled cells is opposite to that of the electrically stimulated cell. Direct currents (d.c.) were not observed in adjacent OHCs, confirming the absence of gap-junction-mediated electrical coupling.

Additional evidence indicates that the transient currents and voltages in adjacent OHCs result from mechanical coupling between OHCs, and that these electrical responses are generated by the displacement of motility/voltage sensors. Figure 2 shows that salicylate, a known blocker of OHC gating currents and motility^{20,21}, abolishes the gating currents in adjacent OHCs. In our experiments, salicylate probably has two effects: it blocks both the mechanical response of the stimulated cell and the charge movement in the

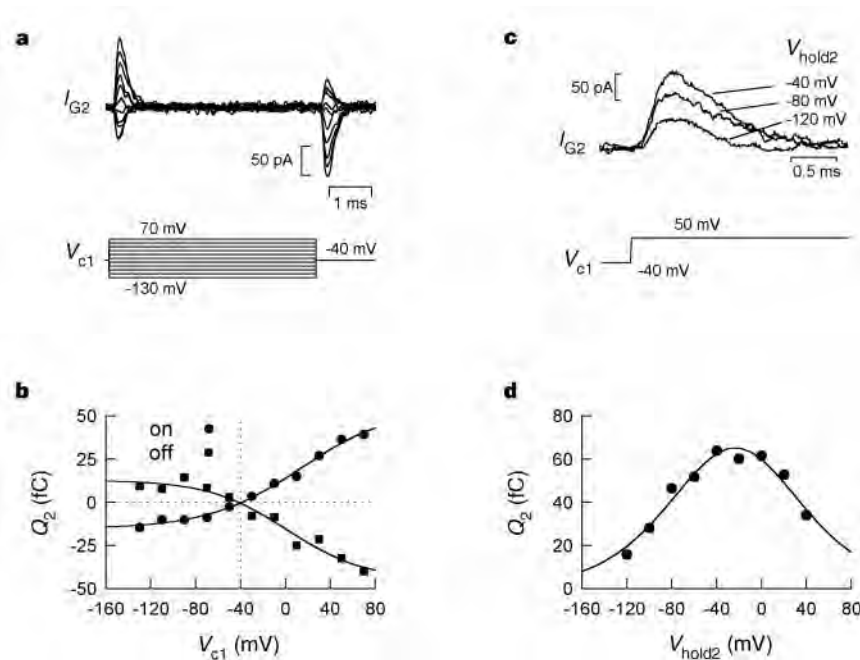


Figure 3 Gating currents are a function of both OHCs' holding potential. **a**, Both OHCs were voltage clamped to -40 mV, and OHC 1 was stepped for 5 ms from -130 to 70 mV (V_{c1}) in 20 mV steps. Gating currents (I_{G2}) in an adjacent OHC are shown in the top trace. The polarity of the currents depends on that of the stimulus voltage in OHC 1. **b**, the Q - V plot (on and off charge in OHC 2 versus voltage of OHC 1) shows a reversal of gating charge sign at the OHC 1 holding potential. The nonlinearity of the response partially reflects the nonlinear nature of the motility

function. **c**, The magnitude of gating current (I_{G2} , top traces) in OHC 2 induced by a fixed voltage step in OHC 1 depends on the membrane (holding) potential of OHC 2. **d**, The Q - V plot (on charge in OHC 2 versus holding voltage of OHC 2) shows that charge magnitude is a bell-shaped function of OHC 2 holding potential. The data were fit (solid line) to equation (2) with Q_{max} (prior determination from Q_2 - V_{c2} function) fixed at 2.99 pC. $\delta V_h = 2.5$ mV; $V_h = -23.5$ mV; $z = 0.65$.

adjacent cell. Further evidence derives from the polarity of the gating currents in adjacent cells (Fig. 3a, b). As expected for a process dependent on the stimulated OHC's mechanical response, the gating current polarity of the adjacent cell reverses at the holding potential of the stimulated cell; depolarization from this potential causes contraction of the cell, whereas hyperpolarization produces elongation. The deformation of adjacent cells will alter the tension on their lateral membranes. Reduced tension effectively shifts the voltage dependence of the Q - V function in the negative direction, and will evoke a positive gating current¹⁶. This agrees with the effects measured in adjacent OHCs. The magnitude of charge movement induced by this shift depends on the adjacent cell's membrane (holding) potential and is given by the difference between the two shifted Boltzmann functions¹⁵:

$$Q(V) = -Q_{max} \delta V_h \frac{ze}{kT(1+b)^2} \quad (2)$$

where δV_h is the magnitude of the V_h shift induced by a change in membrane tension, and b is as in equation (1).

Indeed, this behaviour is seen in our experiments (Fig. 3c, d). The magnitude of gating charge in the adjacent OHC depends on its holding potential, and the bell-shaped function of equation (2) satisfactorily describes the relationship. As the Q - V function mirrors the OHC's motility function¹⁶, the mechanical activity of coupled OHCs will be affected similarly.

Our data show that, as a result of OHC mechanical activity, lateral interactions exist within the organ of Corti that may significantly affect its responsiveness to sound. We have explored some of the consequences of these interactions. When two pure-tone frequencies are presented to a subject, auditory illusions of additional tonal frequencies and measurable physiological counterparts result^{22,23}. Additionally, one tone can be suppressed by another. This distortion arises from nonlinearities in the peripheral auditory system, and in the mammal it results from OHC activity^{24,25}. Even within single isolated hair cells, distortion evoked by two-frequency stimulation

can be generated by nonlinearities of the stereociliar transducer or by OHC motility²⁶⁻²⁸. We tested whether this type of distortion can arise from interactions between OHCs by simultaneously and independently stimulating each cell of coupled pairs with differing voltage frequencies (OHC 1, $f_1 = 813.8$ Hz; OHC 2, $f_2 = 976.5$ Hz) and observing nonlinear interactions. Under these stimulation conditions, both frequencies are present in the current responses of each cell (Fig. 4). The magnitude of the mechanically induced frequency component (for example, f_2 in OHC 1) is a bell-shaped function of holding potential, indicating, as above, that this component is generated by frequency-following shifts in the voltage dependence of the Q - V function of the cell. Furthermore, this mechanically generated frequency component suppresses the voltage-evoked frequency component by up to 10%. Finally, the interaction of the two frequency components gives rise to nonlinear intermodulation distortion in each cell (Fig. 4b). The sum and difference distortion components ($f_2 + f_1, f_2 - f_1$) can be observed as little as 20 dB below the mechanically induced primary.

Our data show that nonlinear mechanical interactions occur among OHCs within Corti's organ, and that these interactions generate distortion and suppression that are similar to those found in the intact organ. The generated distortion, seen only in coupled OHCs, may arise not only from the interaction of intrinsic cellular nonlinearities^{27,28}, but also from nonlinearity in the visco-elastic coupling between cells. The mechanical coupling strength, based on ratios of charge or current, is up to 10%. However, the degree of mechano-electrical coupling among OHCs may be greater *in vivo* than is demonstrated here, as physical coupling in our preparations was probably compromised by the isolation procedure.

It is believed that passive basilar-membrane tuning is enhanced by feedback from OHC mechanical activity³; however, based solely on mechanical activity evoked by passive tuning, sharpening would not be expected. The consequence of OHC coupling is twofold for adjacent cells; the voltage dependence of motility is altered, and a voltage of opposite phase is evoked. These mechanically generated

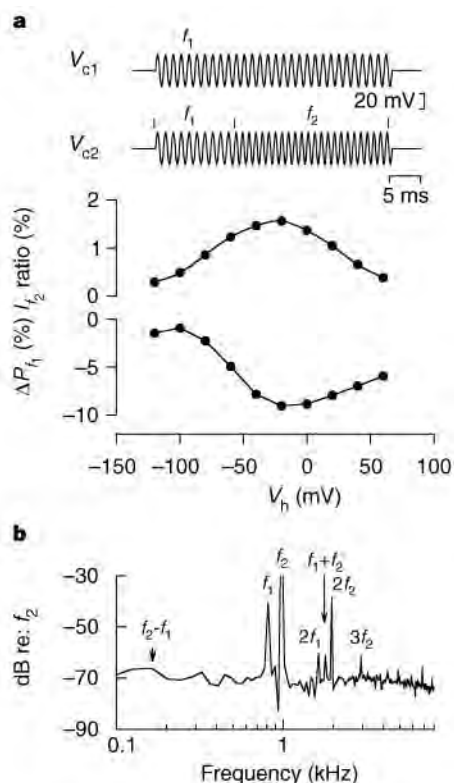


Figure 4 Both OHCs were voltage clamped to -40 mV and independently stimulated with pure sine-wave voltages. **a**, The upper two traces show the voltage stimuli delivered independently to each cell. During the initial part of the stimulus duration, each cell received a 20 mV peak sine wave at $f_1 = 813.8$ Hz; in the latter three-quarters of the stimulus duration, the OHC 2 frequency was switched to 976.5 Hz. Fast Fourier transform analysis was limited to the last half of stimulus duration to avoid transient responses. Comparisons were made before and after uncoupling by collapsing OHC 2. The upper plot shows the ratio of mechanically induced f_2 current (I_{f_2}) in OHC 1 due to f_2 voltage stimulation in OHC 2. The ratio of the power of the f_1 component in the response of OHC 1 before and after OHC 2 was collapsed was also obtained. The change in this ratio (ΔP_{f_1}) is shown in the lower plot. Negative percentage means that the f_1 response after collapse of OHC 2 was larger than that before; in other words, the mechanically induced f_2 component in OHC 1 suppressed the f_1 response in OHC 1. **b**, The spectrum of current response in OHC 2. The magnitude (in dB) is referenced to f_2 magnitude. Besides harmonic distortion products, the peak of sum frequency distortion ($f_1 + f_2$) is clearly visible.

lateral interactions may allow basilar membrane motion to be selectively enhanced at a particular location where passive vibration is maximal. In nonlinear systems, 10% feedback can have enormous consequences. The likely increase in OHC coupling with increasing frequency, supported by morphological evidence¹⁷, may explain the finding that tuning is sharper at higher characteristic frequencies. In this model, distortion in the cochlea arises from the very process that promotes greater frequency resolution. □

Methods

Pieces of the organ of Corti, containing between 3 and more than 50 OHCs with associated Deiters' cells, were freshly isolated from the guinea-pig cochlea, and adjacent OHCs were separately whole-cell voltage clamped at room temperature using an Axon 200A and 200B amplifier. Membrane voltages were corrected for the effects of residual series resistance, which ranged from 3 to 7 M Ω . We used ionic blocking solutions to remove voltage-dependent ionic conductances so that capacitive currents could be analysed in isolation²⁹. Gating currents were extracted using the P/4 technique³⁰. Pipette crosstalk artefacts at the onset of traces (first 50 μ s) were subtracted from the data, using the artefacts obtained in the absence of mechanical coupling. All data collection

and most analyses were performed with an in-house-developed, Windows-based whole-cell voltage-clamp program, jClamp (www.med.yale.edu/surgery/otolar/santos/jclamp.html), using a Digidata 1200 board (Axon).

Received 29 January; accepted 1 April 1999.

1. von Békésy, G. *Experiments in Hearing* (McGraw-Hill, New York, 1960).
2. Narayan, S. S., Temchin, A. N., Recio, A. & Ruggero, M. A. Frequency tuning of basilar membrane and auditory nerve fibers in the same cochlea. *Science* **282**, 1882–1884 (1998).
3. Dallos, P. The active cochlea. *J. Neurosci.* **12**, 4575–4585 (1992).
4. Brownell, W. E., Bader, C. R., Bertrand, D. & de Ribaupierre, Y. Evoked mechanical responses of isolated cochlear outer hair cells. *Science* **227**, 194–196 (1985).
5. Santos-Sacchi, J. & Dilger, J. P. Whole cell currents and mechanical responses of isolated outer hair cells. *Hear. Res.* **35**, 143–150 (1988).
6. Santos-Sacchi, J. On the frequency limit and phase of outer hair cell motility: effects of the membrane filter. *J. Neurosci.* **12**, 1906–1916 (1992).
7. Dallos, P. & Evans, B. N. High frequency motility of outer hair cells and the cochlear amplifier. *Science* **267**, 2006–2009 (1995).
8. Gale, J. E. & Ashmore, J. F. An intrinsic frequency limit to the cochlea amplifier. *Nature* **389**, 63–66 (1997).
9. Xue, S., Mountain, D. C. & Hubbard, A. E. Electrically evoked basilar membrane motion. *J. Acoust. Soc. Am.* **97**, 3030–3041 (1995).
10. Nuttall, A. L. & Ren, T. Electromotile hearing: evidence from basilar membrane motion and otoacoustic emissions. *Hear. Res.* **92**, 170–177 (1995).
11. Mammano, F. & Ashmore, J. F. Reverse transduction measured in the isolated cochlea by laser Michelson interferometry. *Nature* **365**, 838–841 (1993).
12. Ashmore, J. F. Forward and reverse transduction in the mammalian cochlea. *Neurosci. Res. (suppl.)* **12**, 39–50 (1990).
13. Santos-Sacchi, J. Reversible inhibition of voltage dependent outer hair cell motility and capacitance. *J. Neurosci.* **11**, 3096–3110 (1991).
14. Iwasa, K. H. Effect of stress on the membrane capacitance of the auditory outer hair cell. *Biophys. J.* **65**, 492–498 (1993).
15. Gale, J. E. & Ashmore, J. F. Charge displacement induced by rapid stretch in the basolateral membrane of the guinea-pig outer hair cell. *Proc. R. Soc. Lond. B* **255**, 243–249 (1994).
16. Kakehata, S. & Santos-Sacchi, J. Membrane tension directly shifts voltage dependence of outer hair cell motility and associated gating charge. *Biophys. J.* **68**, 2190–2197 (1995).
17. Vater, M., Lenoir, M. & Pujol, R. Ultrastructure of the horseshoe bat's organ of Corti. II. Transmission electron microscopy. *J. Comp. Neurol.* **318**, 380–391 (1992).
18. Huang, G.-J. & Santos-Sacchi, J. Mapping the distribution of the outer hair cell motility voltage sensor by electrical amputation. *Biophys. J.* **65**, 2228–2236 (1993).
19. Huang, G.-J. & Santos-Sacchi, J. Motility voltage sensor of the outer hair cell resides within the lateral plasma membrane. *Proc. Natl Acad. Sci. USA* **91**, 12268–12272 (1994).
20. Tunstall, M. J., Gale, J. E. & Ashmore, J. F. Action of salicylate on membrane capacitance of outer hair cells from the guinea-pig cochlea. *J. Physiol. (Lond.)* **485**, 739–752 (1995).
21. Kakehata, S. & Santos-Sacchi, J. Effects of lanthanides and salicylate on outer hair cell motility and associated gating charge. *J. Acoust. Soc. Am.* **41**, 676–689 (1967).
22. Goldstein, J. L. Auditory nonlinearity. *J. Acoust. Soc. Am.* **41**, 676–689 (1967).
23. Goldstein, J. L. & Kiang, N. Y. S. Neural correlates of the aural combination tone 2f₁-f₂. *Proc. IEEE* **56**, 981–992 (1968).
24. Dallos, P. & Harris, D. In *Psychophysics and Physiology of Hearing* (eds Evans, E. F. & Wilson, J. P.) 147 (Academic, London, 1977).
25. Dallos, P., Harris, D. M., Relkin, E. & Cheatham, M. A. in *Psychophysical Physiological and Behavioural Studies in Hearing* (eds van den Brink, G. & Bilsen, F. A.) 242–249 (Delft Univ. Press, Holland, 1980).
26. Jaramillo, F., Markin, V. S. & Hudspeth, A. J. Auditory illusions and the single hair cell. *Nature* **364**, 527–529 (1993).
27. Takahashi, S. & Santos-Sacchi, J. Distortion component analysis of outer hair cell motility-related gating charge. *J. Membr. Biol.* (in the press).
28. Santos-Sacchi, J. Harmonics of outer hair cell motility. *Biophys. J.* **65**, 2217–2227 (1993).
29. Santos-Sacchi, J., Kakehata, S. & Takahashi, S. The outer hair cell membrane potential directly affects the voltage dependence of motility-related gating charge. *J. Physiol. (Lond.)* **510**, 225–235 (1998).
30. Bezanilla, F. & Armstrong, C. M. Inactivation of the sodium channel. I. Sodium current experiments. *J. Gen. Physiol.* **70**, 549–566 (1977).

Acknowledgements. We thank M. Mazzucco for technical help. This work was supported by a grant from NINCDS to J.S.S.

Correspondence and requests for materials should be addressed to J.S.S. (e-mail: joseph.santos-sacchi@yale.edu).

Signals from the reproductive system regulate the lifespan of *C. elegans*

Honor Hsin & Cynthia Kenyon

Department of Biochemistry and Biophysics, University of California at San Francisco, San Francisco, California 94143-0448, USA

Understanding how the ageing process is regulated is a fascinating and fundamental problem in biology. Here we demonstrate that signals from the reproductive system influence the lifespan of the nematode *Caenorhabditis elegans*. If the cells that give rise to the germ line are killed with a laser microbeam, the lifespan of the

Voltage Gating of Gap Junctions in Cochlear Supporting Cells: Evidence for Nonhomotypic Channels

H.B. Zhao,* J. Santos-Sacchi

Sections of Otolaryngology and Neurobiology, Yale University School of Medicine, New Haven, CT 06511, USA

Received: 17 September 1999/Revised: 12 January 2000

Abstract. The organ of Corti has been found to have multiple gap junction subunits, connexins, which are localized solely in nonsensory supporting cells. Connexin mutations can induce sensorineural deafness. However, the characteristics and functions of inner ear gap junctions are not well known. In the present study, the voltage-dependence of gap junctional conductance (G_j) in cochlear supporting cells was examined by the double voltage clamp technique. Multiple types of asymmetric voltage dependencies were found for both nonjunctional membrane voltage (V_m) and transjunctional (V_j) voltage. Responses for each type of voltage dependence were categorized into four groups. The first two groups showed rectification that was polarity dependent. The third group exhibited rectification with either voltage polarity, i.e., these cells possessed a bell-shaped G_j - V_j or G_j - V_m function. The rectification due to V_j had fast and slow components. On the other hand, V_m -dependent gating was fast (<5 msec), but stable. Finally, a group was found that evidenced no voltage dependence, although the absence of V_j dependence did not preclude V_m dependence and vice versa. In fact, for all groups V_j sensitivity could be independent of V_m sensitivity. The data show that most gap junctional channels in the inner ear have asymmetric voltage gating, which is indicative of heterogeneous coupling and may result from heterotypic channels or possibly heteromeric configurations. This heterogeneous coupling implies that single connexin gene mutations may affect the normal physiological function of gap junctions that are not limited to homotypic configurations.

Key words: Voltage dependence — Gap junction — Hybrid coupling — Supporting cell — Inner ear — Hearing loss

Introduction

Connexins, the basic protein subunits of vertebrate gap junction channels, derive from a homologous gene family. More than 15 connexin genes have been cloned. Gap junctions comprised of different members of the connexin family have differing voltage gating properties either to transjunctional voltage (V_j) or to membrane potential (V_m or V_{i-o}) (*see* reviews: Bennett et al., 1991; Dahl, 1996; Kumar & Gilula, 1996). Each gap junction channel is composed of two hemichannels (connexons) and each hemichannel is composed of six connexin subunits (Perkins et al., 1997). A homotypic channel consists of two identical connexons and has symmetric voltage gating on either side owing to its symmetric structure. A heterotypic channel is formed by two different connexons and its voltage gating can be asymmetrical owing to its asymmetrical constitution (Barrio et al., 1991; Rubin et al., 1992a; Verselis et al., 1994; White et al., 1994a). A heteromeric channel possesses hemichannels formed by different connexin subunits and little is known about its voltage gating (Brink et al., 1997; Lee & Rhee, 1998).

Physiological and anatomical evidence for gap junctional coupling among the supporting cells of Corti's organ has been obtained both in vivo and in vitro (Jahnke, 1975; Gulley & Reese, 1976; Iurato et al., 1976; Hama & Saito, 1977; Santos-Sacchi & Dallos, 1983; Santos-Sacchi, 1987; Zwislocki et al., 1992; Kikuchi et al., 1995; Forge et al., 1997; Zhao & Santos-Sacchi, 1998). Connexin 26 (Cx26) is extensively distributed among cochlear nonsensory cells, including the supporting cells of Corti's organ (Kikuchi et al., 1995; Forge et

* Present address: Department of Otorhinolaryngology and Communicative Science NA 500, Baylor College of Medicine, Houston Texas 77030, USA

al., 1997). More recently, Lautermann et al. (1998) reported that cochlear supporting cells also contained Cx30 and Cx43; moreover, Cx30 was extensively expressed in a pattern similar to that of Cx26. Ultrastructural, immunohistochemical and physiological studies have found no evidence indicating that sensory cells (inner and outer hair cells) have gap junctions. However, mutations of connexin genes, for example, *GJB2* which encodes Cx26, have been identified in association with a high incidence of nonsyndromic sensorineural deafness (Kelsell et al., 1997; Denoyelle et al., 1998; Estivill et al., 1998; Xia et al., 1998). Little is known about the mechanism by which such a mutation may cause deafness. To some extent, the lack of a complete characterization of the biophysical properties of inner ear gap junctions limits our understanding.

Inner ear gap junctions can be modified by a variety of treatments, such as altering the intracellular activities of Ca^{++} and H^+ , temperature and membrane tension (Santos-Sacchi, 1985, 1986, 1991; Sato & Santos-Sacchi, 1994; Zhao & Santos-Sacchi, 1998). In the present report, the effects of voltage on inner ear gap junctions were explored by a double voltage clamp technique. The principal finding is that cochlea supporting cells display a variety of voltage dependencies, typified by asymmetrical rectification. The variety of asymmetrical voltage gating is indicative of complex heterotypic and/or heteromeric coupling. This heterogeneous coupling implies that single connexin gene mutations may affect the normal physiological function of gap junctions that are not limited to homotypic configurations.

Preliminary accounts of this work have been presented (Zhao & Santos-Sacchi, 1997, 1999).

Materials and Methods

The guinea pig's organ of Corti was freshly isolated and subsequently dissociated by shaking for 5–15 min in nominally Ca^{++} -free Leibovitz medium containing 1 mg/ml of trypsin. The dissociated cells were transferred into a recording chamber. Hensen cells are distinguishable by their bright lipid vacuoles under Hoffman optics (Fig. 1A). A classical double voltage-clamp technique was used to measure transjunctional conductance (G_j). Each cell in a Hensen cell pair was separately voltage-clamped using an Axopatch 200A and 200B (Axon, CA) (Fig. 1A). Test voltages were applied to one cell (cell 1) and transjunctional current (I_j) was measured in the adjacent cell (cell 2). To accurately obtain G_j -voltage relations, calculations were made with corrections for electrode access resistance (R_s) and nonjunctional membrane resistance (R_m) (Neyton & Trautmann, 1985):

$$V_j = V_{c1} - V_{c2} - (\Delta I_1 R_{s1} - \Delta I_2 R_{s2}) \quad (1)$$

$$G_j = \frac{I_j}{V_j} = \frac{-\Delta I_2 \left(1 - \frac{R_{s2}}{R_{m2}}\right)}{V_j} \quad (2)$$

Where V_{c1} and V_{c2} are the clamp voltages applied to cell 1 and cell 2, respectively; ΔI_1 and ΔI_2 are the holding current changes in cell 1 and

cell 2 caused by the test voltage in cell 1. R_{m2} is the nonjunctional membrane resistance of cell 2, where I_j was measured (Fig. 1A). It is clear from recent work that in cases where R_m is greater than 500 m Ω , R_s dominates errors in junctional estimates (Van Rijen et al., 1998), and is readily corrected for. Our residual series resistance is quite small and stable, and membrane resistance is typically greater than 1 G Ω (*see below*). Furthermore, cell pairs that had G_j greater than 20 nS were not included in the data analysis. Data collection and analysis were performed with an in-house developed Window's based whole-cell voltage clamp program, **jClamp** (<http://www.med.yale.edu/surgery/otolar/santos/jclamp.html>), utilizing a Digidata 1200 board (Axon, Foster City, CA.) All experiments were tape recorded and performed at room temperature.

To limit interference from nonjunctional voltage-dependent ionic currents, cells were continuously perfused by an extracellular ionic blocking solution that was composed of (in mM): NaCl 100, TEA 20, CsCl 20, CoCl_2 1.25, MgCl_2 1.48, HEPES 10, pH 7.2 and osmolarity 300 mOsm (Santos-Sacchi, 1991; Zhao & Santos-Sacchi, 1998). Patch pipettes were filled with an intracellular solution that contained (in mM): 140 CsCl, 5 EGTA, 2 MgCl_2 , and 10 HEPES, pH 7.2. After blocking nonjunctional voltage dependent ionic channels, Hensen cells had linear I - V relationships and high membrane resistances ($R_m > 1$ G Ω) (Fig. 1C).

Patch pipettes (Borosilicate Glass, MTW150-4, World Precision, FL) were pulled by a laser, based pipette puller (P-2000, Sutter, CA). A pair of pulled pipettes was used in each double voltage-clamp recording to promote symmetrical recording conditions. Pipettes had initial resistance of 2.5–3.5 M Ω in bath solution. After whole cell configuration was established, the residual series resistance of the electrode was in a range of 3.9–9.8 M Ω , which was measured by the peak of the uncompensated whole cell capacitance current (Huang & Santos-Sacchi, 1993) as both cells were simultaneously stimulated by an identical test pulse. R_s was stable and was 6.09 ± 0.22 M Ω and 6.23 ± 0.34 M Ω (mean \pm SE, $n = 64$) before and after experiments, respectively. In 11 cell pairs, R_s was further validated after one cell of the cell pairs was broken or pulled away by an electrode so that R_s could be unequivocally determined under single whole cell configuration. The measured R_s was 6.17 ± 0.62 M Ω consistent with those values which were determined under double voltage-clamp configuration.

Results

Gap junctions in Hensen cells had asymmetric responses to positive and negative transjunctional voltages (V_j). Macroscopic transjunctional currents were both time and voltage dependent (Fig. 1), and consequently, nonlinear I_j - V_j relationships were obtained at voltage onset and steady state. G_j - V_j relations could be classified into four groups, including one with no apparent voltage-dependence (Fig. 2D). The purpose of our categorizing junctional (and nonjunctional—*see below*) voltage dependencies was to simplify our dealings with the data, emphasize the diversity of response, and make some comparisons to published data.

Two basic asymmetrical V_j -dependencies were identified which showed opposite polarity sensitivities. The one whose conductance increased as V_j was made positive (Fig. 2A) is similar to that obtained from heterotypic channels containing Cx26 components (Barrio et al., 1991; Rubin et al., 1992a,b; Verselis et al., 1994; Dahl et

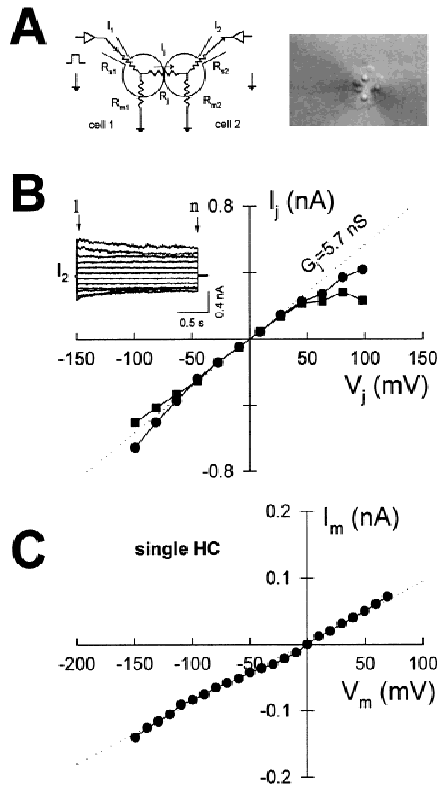


Fig. 1. (A) Schematic drawing and video-captured image illustrate the double voltage-clamp recording in a Hensen cell pair. Scale bar is 20 μ m. Both cells were initially voltage-clamped at -40 mV. V_j was produced by 2 sec voltage steps (V_{c1}) applied to cell 1 in 20 mV increments from -150 to $+70$ mV and cell 2 (V_{c2}) continuously held at -40 mV; the change in V_j is equal to ± 110 mV. Depolarization of the stepped cell corresponds to positive V_j and produces a downward current in cell 2 (I_2). (B) Transjunctional currents in response to V_j stimulation were obtained from a Hensen cell pair. Initial and steady-state transjunctional currents (I_j) were measured at onset (5 msec) and end (2 sec) of voltage steps and are represented by solid circles and squares, respectively. Initial I_j as well as steady-state I_j increased nonlinearly for V_j s greater than $+50$ mV. The dotted line indicates a conductance of 5.7 nS. (C) Typical example of membrane current (I_m) of single isolated Hensen cell as a function of membrane potential (V_m) obtained with the ionic blocking solutions used for coupling studies (see Materials and Methods). Membrane resistance is greater than 1 $\text{G}\Omega$, and the $I_m - V_m$ curve is linear.

al., 1996). The other had a conductance that decreased with positive V_j but changed less with negative V_j (Figs. 1 and 2B). The last group evidenced a slightly asymmetric bell-shaped $G_j - V_j$ relationship (Fig. 2C). While V_j -induced G_j changes typically ranged between 40–50%, in some cases G_j decreased below 20%; this variability probably reflects the heterogeneity of the channel population.

In most cell pairs, the V_j asymmetry was characterized by alternating the stimulus configuration, such that transjunctional conductance was measured in both directions between a cell pair (cell 1 \rightarrow cell 2 and cell 2 \rightarrow

cell 1). An example is shown in Fig. 3. When cell 1 of the pair was stepped to positive potentials, while holding cell 2 constant, steady-state transjunctional conductance, G_{jss} , decreased. On the other hand, when cell 2 was stepped to negative potentials, G_{jss} decreased. Unlike the asymmetry of G_{jss} , G_{j0} was insensitive to V_j gradients. These data illustrate that the asymmetric response to V_j in this cell pair resulted from a junctional conductance decrease only when cell 1 was depolarized, a clear transjunctional effect, and not due to possible asymmetric recording conditions. Furthermore, the conductance plots are nearly mirror images of each other, indicating an absence of V_m contribution in this case. This V_m insensitivity was independently verified by direct measures (see below).

To rule out fast gating effects, we determined the ratio of G_{jss}/G_{j0} in all cells that showed V_j dependence (Fig. 2 A–C). From these cells we found indications of slow (steady state) rectification in 9 out of the 28 cell pairs (Fig. 4). The ratio shows no voltage dependence until positive V_j values are reached, whereupon the ratio falls. This type of behavior strongly indicated that Hensen cells have heterotypic gap junctions, such as those containing Cx26 subunits as observed in oocyte pairs (Barrio et al., 1991; Rubin et al., 1992a,b; Verselis et al., 1994; Dahl et al., 1996).

Interestingly, Hensen cells demonstrate rapid voltage sensitivity of gap junctional coupling with the V_j protocol (Figs. 1 and 2). $V_j - G_j$ functions obtained from onset currents displayed the same asymmetrical behavior as steady state functions. In fact, in some cell pairs, no slow V_j -sensitive gating was observed, and it should be noted that nonlinear onset responses such as these might result not only from V_j sensitivity, but also from V_m sensitivity. This is further investigated below.

V_m -dependent gating was found in most (29/45) Hensen cell pairs (Figs. 5 and 6). In Fig. 5, G_j changes occurred within 5 msec or less after altering V_m , and remained stable for the full recording period. Slow V_m -dependent gap junction gating was never detected in Hensen cells. However, we only explored time periods up to 5 sec.

As with the V_j dependent conductance data, V_m -dependent junctional sensitivities could be categorized into four groups, including one that showed no dependence (Fig. 6). One group showed a decrease in coupling upon depolarization, while another showed the opposite effect (Fig. 6 A and B). The third group demonstrated a bell shaped $G_j - V_m$ function (Fig. 6C).

V_m gating was independent of V_j -gating. This is illustrated in Fig. 7, where comparisons between V_j and V_m dependence are made within the same cell pairs. Figure 7A shows data from a cell pair that lacked V_j -dependent gating; neither G_{j0} nor G_{jss} showed V_j sensitivity. However, G_{jm} decreased with cell depolarization. In another

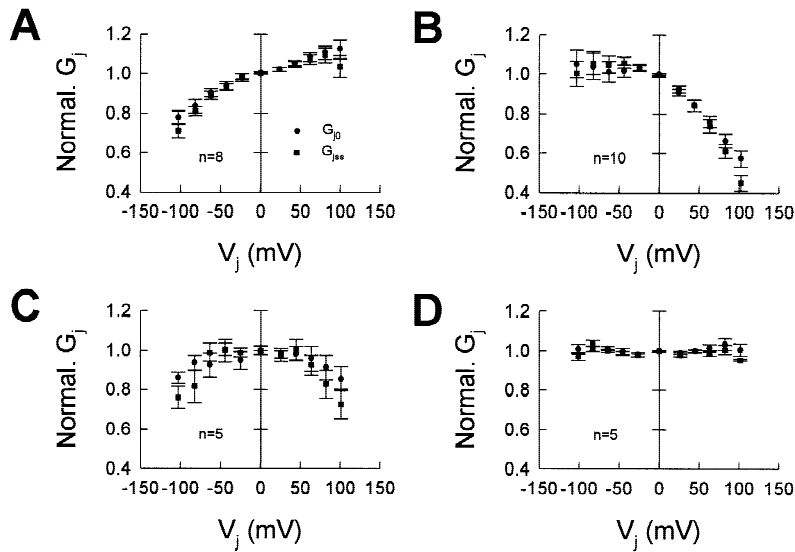


Fig. 2. Gap junctional coupling of Hensen cells presented differing voltage sensitivities for V_j stimulation. Initial transjunctional conductance (G_{j0}) and steady state conductance (G_{jss}) were normalized to the mean conductance at the average of V_j at ± 10 mV. G_j (mean \pm SE; $n = 28$) was 11.8 ± 1.31 nS. Cell pairs that had G_j greater than 20 nS were not included. Holding potential was -40 mV. Error bar represents SE.

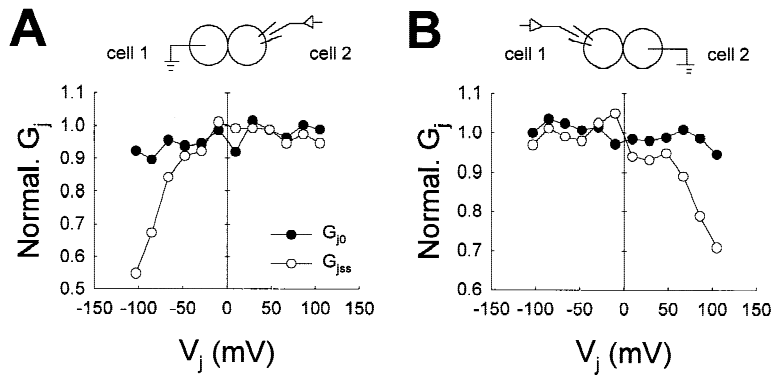


Fig. 3. V_j applied to either cell in the same cell pair identified rectified V_j -dependence. Positive V_j polarity corresponds to depolarization in the stepped cell. (A) Cell 1 was held and cell 2 was voltage-stepped. Rectification occurred at negative V_j , i.e., during cell 2 hyperpolarization. (B) Voltage steps were delivered to cell 1 while cell 2 voltage was held constant. At positive V_j (cell 1 depolarized), G_{jss} decreased. In this cell pair, G_{jss} always rectified at relatively positive polarity of V_j referring to cell 1. For each case onset conductance was fairly stable across voltage. The transjunctional conductance in this cell pair was about 13 nS. $R_{s1} = 4.3$ M Ω , $R_{s2} = 4.9$ M Ω , $R_{m1} = 1591$ M Ω , and $R_{m2} = 962$ M Ω .

cell pair the opposite behavior is illustrated (Fig. 7B). In this case, transjunctional conductance exhibited an asymmetric V_j -dependence, but was insensitive to V_m . Additionally, slow V_j -sensitive gating was undetectable since G_{jss} mirrored G_{j0} ; this further indicates that only a pure fast V_j -dependent gating is present.

Discussion

The most pronounced property of gap junctional voltage gating within cochlear supporting cells is its diverse asymmetry. This asymmetric gating is likely indicative of asymmetric channel structure within each cell, i.e., heterotypic and/or heteromeric junctional channels. Evidence is mounting that nonsyndromic deafness is associated with connexin gene mutations, such as Cx26 (Kelsell et al., 1997; Denoyelle et al., 1998; Estivill et al., 1998; Xia et al., 1998). While a variety of connexin types are present in supporting cells (Lautermann et al., 1998), functional impairments induced by single gene

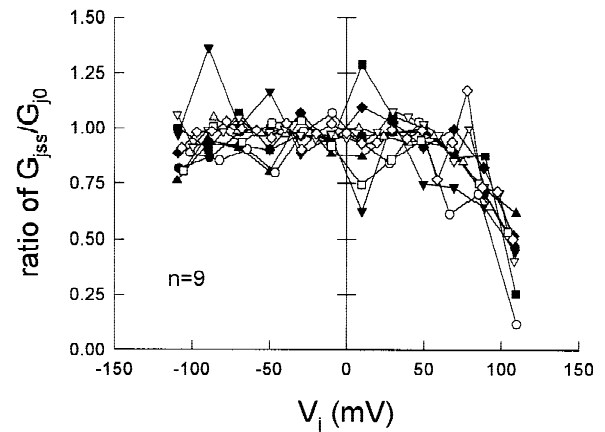


Fig. 4. Ratio of $G_{jss}:G_{j0}$ indicates slow V_j -dependent gating in response to V_j stimulation. Each symbol and line represents a cell pair.

mutations can not be rescued by other coexisting connexins. Our data provide evidence for the occurrence of hybrid gap junction channels in cochlea supporting cells,

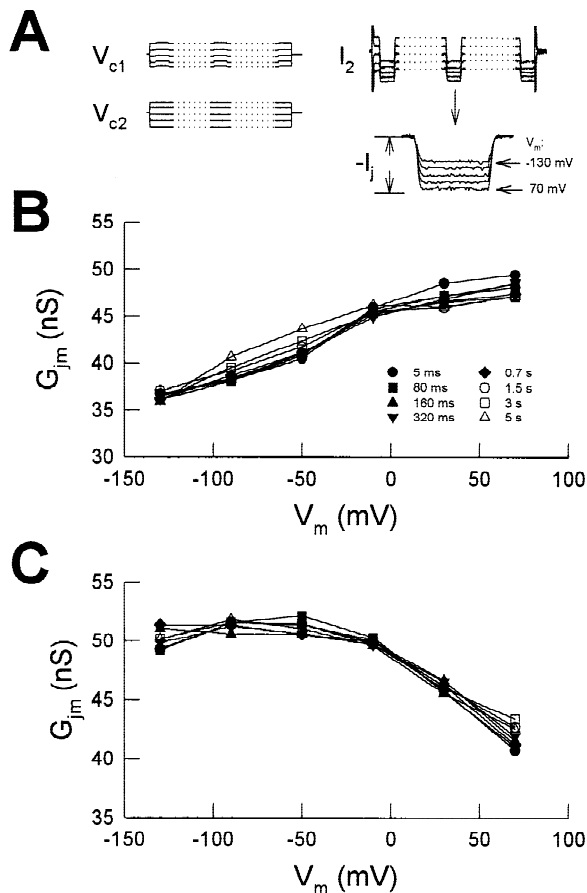


Fig. 5. Gap junction channels in Hensen cells are sensitive to membrane potential (V_m or V_{i-o}). **A** Voltage protocols. Both cells were simultaneously stimulated with voltage steps (V_{c1} and V_{c2}) from -130 to $+70$ mV in 40 mV increments, for a 5 sec duration. A test pulse (10 mV, 10 msec) was superimposed on cell 1 at different times to elicit transjunctional current. For clarity, the full length of waveforms is not shown. Example current traces at different membrane potentials are zeroed and superimposed. **(B and C)** V_m -dependent transjunctional conductance (G_{jm}) at different times is plotted. G_{jm} of the cell pair in panel **B** increased as the cells were depolarized, whereas in panel **C** G_{jm} decreased as the cells depolarized. Despite the opposite polarity dependence of the two coupled pairs, G_{jm} remained stable throughout the recording period.

and indicate that single gene mutations will impair more than just those channels destined to be homotypic. In heterotypic or heteromeric channels, the presence or absence of a single subunit type can have dramatic effects on junctional voltage dependence (Dahl et al., 1996; Brink et al., 1997; He et al., 1999; Li & Simard, 1999) and possibly other gating characteristics (Lee & Rhee, 1998). Thus, the potentially pervasive influence of single connexin gene mutations on diverse gap junction channel types may contribute to its devastating effects on hearing. This indicates, as well, that the diversity of channel types is important for cochlea function.

Cx26 and Cx30 are colocalized in cochlear support-

ing cells (Lautermann et al., 1998). In the paired oocyte expression system, Cx26 can form heterotypic gap junction channels with Cx30 (Dahl et al., 1996). The voltage gating of this heterotypic channel demonstrates remarkable differences from those of the corresponding homotypic channels (Jarillo et al., 1995; Dahl et al., 1996). One of the most distinguishable properties of this heterotypic channel is its slow V_j -dependent gating, rectifying with positive V_j on the Cx30 side of the junction (Dahl et al., 1996). It is likely that this type of heterotypic channel exists in the organ of Corti, since we find similar gating characteristics in cochlear supporting cells (Figs. 1, 3 and 4).

However, in addition to characteristics that are found in known heterotypic channels, we observed properties that are atypical, possibly indicating the existence of heteromeric channels. Although few physiological studies have suggested the existence of heteromeric channels (Brink et al., 1997; Lee & Rhee, 1998), biochemical analyses clearly reveal their presence (Stauffer, 1995; Jiang & Goodenough, 1996; Brink et al., 1997). In our experiments, several observed gating properties might arise from heteromeric channel behavior. First, the existence of fast asymmetric V_j -dependent gating that is distinct from slow V_j -dependent gating and V_m -dependent gating (Figs. 2 and 7B) is inconsistent with behaviors of known heterotypic and homotypic channels (Rubin et al., 1992a,b; Verselis et al., 1994). Second, the occurrence of multiple V_m -sensitivities found in coupled Hensen cells is unusual. While a depolarization-induced increase in conductance (as in Fig. 6A) has been observed in oocyte preparations of vertebrate Cx26 connexins (Rubin et al., 1992a,b), decreases in conductance, as in Fig. 6B, are only seen in insect preparations (Obaid et al., 1983; Verselis et al., 1991; Bukauskas et al., 1992). Bell-shaped V_m dependencies (Fig. 6C) have never been previously reported. Finally, the independence of V_m and V_j gating within the same cell pair is unique (Fig. 7). Considering this evidence and the high probability of heteromeric connexon formation within supporting cells (since at least Cx26, 30 and 43 are coexpressed), heteromeric channels likely exist in inner ear gap junctions.

Although contrary evidence initially existed (Spray et al., 1984, 1986; Riverdin & Weingart, 1988), it is currently accepted that vertebrate gap junctions are gated by voltage, either V_j or V_m (Moreno et al. 1991; 1992; Kumar & Gilula, 1996). Interestingly, although most Hensen cells present voltage-gated junctional conductances, we find an absence of voltage dependence, either to V_j or V_m , in a large proportion of Hensen cells. While this might be expected for coupling derived from cytoplasmic bridges between cells, we typically find that Hensen cell coupling is sensitive to agents that uncouple gap junctions, e.g., octanol or low pH (Santos-Sacchi, 1985; 1991; Sato & Santos-Sacchi, 1994). It should also

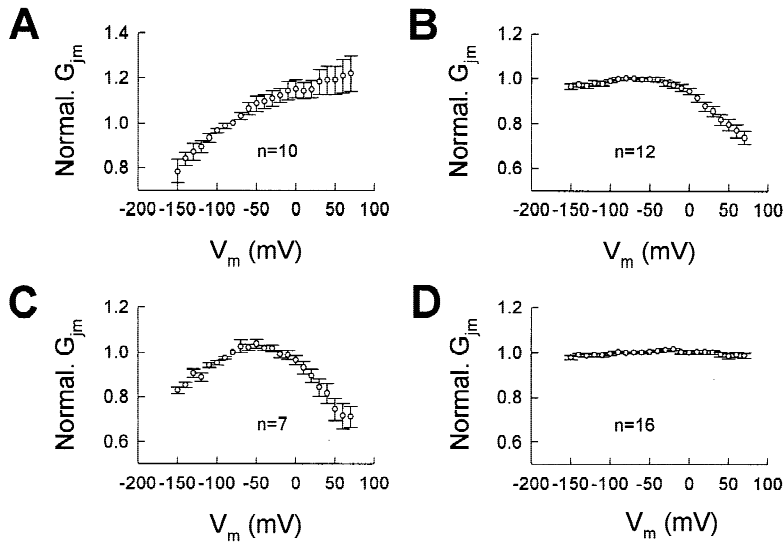


Fig. 6. Coupling of Hensen cells showed multiple V_m -dependences. V_m -dependent G_{jm} was normalized to that at the Hensen cell's holding potential of -80 mV. Error bar represents SE. (A) Conductance increases during depolarization. (B) Above -40 mV, conductance decreases. (C) Conductance is a bell-shaped function of membrane voltage.

be noted that we have used techniques (*see* Materials and Methods) that enable us to accurately deliver voltage and assess its delivery to the cells, so that we can be sure that voltage-clamp problems are minimized. The voltage-gating properties of homotypic and heterotypic channels comprised of connexins identified in supporting cells (Cx26, 30 and 43) show clear voltage dependence. Channels derived from Cx26 and 30 exhibit marked V_j -dependence, whereas homotypic channels derived from Cx43 exhibit weak steady-state voltage dependence (Moreno et al., 1992; Veenstra et al., 1992; Miyoshi et al., 1996). In the inner ear, the expression of Cx43 in cochlear supporting cells was described as relatively weak (Lautermann et al., 1998). Indeed, Forge et al. (1997) did not detect Cx43 antibody labeling in the supporting cell region in gerbil and guinea pig cochlea. Thus, the lack of voltage dependence in many supporting cells is possibly due to either the summed opposed characteristics of the channel populations found in the cell pair or due to heteromeric configurations. Voltage sensitivity may be modulated by allosteric interactions between opposing connexons (White et al., 1994a). It may also be that voltage sensitivity can be modulated by heteromeric interactions within a connexon.

It is well established that V_m -sensitive gating occurs in invertebrate gap junctions (Obaid et al., 1983; Verselis et al., 1991; Bukauskas et al., 1992). Only recently, however, has V_m -dependence been documented in vertebrate gap junctions either in natural tissues (Verselis et al., 1993) or in the paired oocyte expression system (Barrio et al., 1991, 1997; Rubin et al., 1992a; White et al., 1994b; Jarillo et al., 1995). The conductance of channels possessing Cx30 and 43 decreases with depolarization (White et al., 1994b; Jarillo et al., 1995), similar to what we observed in Hensen cells. A V_m dependent conductance also arises when channels possess either Cx26 or

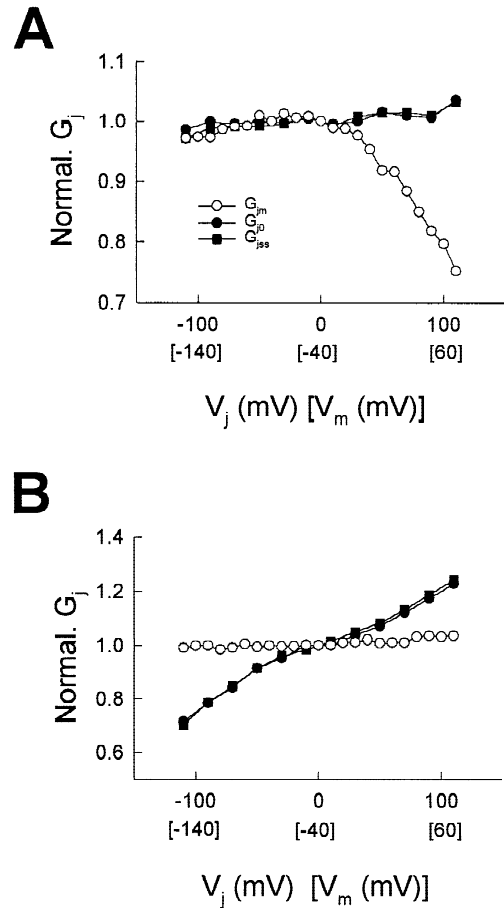


Fig. 7. Voltage-dependent Hensen cell coupling shows independent V_j and V_m sensitivities. (A) In the same cell pair, V_m depolarization reduced junctional conductance but V_j was without effect. (B) In this cell pair the sensitivity is reversed. Coupling was sensitive to V_j stimulation but insensitive to V_m (or V_{i-o}). Note that this pair had fast V_j -dependent gating, but no slow V_j -dependent gating.

45; however, conductance increases upon depolarization (Barrio et al., 1991, 1997; Rubin et al., 1992a). Some Hensen cell pairs have similar gating characteristics to that of Cx26 and 45 (Figs. 5B and 6A). However, while the voltage sensitivity expressed in Hensen cells is greater than that of Cx26, it is quite similar to that of Cx45 (Barrio et al., 1997). Whether Cx45 is present in the inner ear remains to be seen; nevertheless, mutation studies indicate that connexins other than those already identified histochemically also exist (*see below*).

Hensen cells, *in vivo*, are bathed in different media, endolymph (high K^+ and +80 mV) apically and perilymph (low K^+ and 0–10 mV) basally. They contribute to a barrier against ionic diffusion from the endolymph to perilymph caused by the gradients of ions and voltage. These gradients are vitally important for normal sensory function, and it has been proposed, though still remains unproved, that supporting cells help maintain these gradients by sinking K^+ released during hair cell and neural excitation (Santos-Sacchi, 1987; 1991). Recently, an anatomical substrate for the directional sinking of ions through gap junctions has been proposed (Kikuchi et al., 1995). It is currently held that differing connexins may contribute to the formation of functional junctional pathways with variable gating sensitivities and permeabilities (Elfgang et al., 1995; Mills & Massey, 1995; Brink, 1996; Trexler et al., 1996). In fact, non-uniform, directionally limited dye spread in the intact organ of Corti has been found (Santos-Sacchi, 1986; Oberoi & Adams, 1998). Our data that establishes the likelihood of hybrid gap junction channels underscores the possibility of functional pathways within the organ of Corti. It may be that the nonsyndromic hearing loss that arises from connexin mutations occurs because functional pathways are disturbed. So far, three connexin genes, *GJB1* (encoding Cx32), *GJB2* (encoding Cx26) and *GJB3* (encoding Cx31), have been identified in association with hearing impairment (Bergoffen et al., 1993; Kelsell et al., 1997; Denoyelle et al., 1998; Estivill et al., 1998; Xia et al., 1998). These data indicate that the potential variability in heteromeric combinations is even greater than the immunohistochemical data suggest. Furthermore, it is likely that mutations of Cx30 and 43 could also alter heterotypic- or heteromeric-like gap junctional coupling in the inner ear, thus leading to hearing impairment.

This work was supported by NIDCD grant DC 00273 to JSS. We thank Margaret Mazzucco for technical help.

References

Barrio, L.C., Capel, J., Jarillo, J.A., Castro, C., Revilla, A. 1997. Species-specific voltage-gating properties of connexin45 junctions expressed in *Xenopus* oocytes. *Biophys. J.* **73**:757–769

Barrio, L.C., Suchyna, T., Bargiello, T., Xu, L.X., Roginski, R.S., Bennett, M.V.L., Nicholson, B.J. 1991. Gap junctions formed by

connexins 26 and 32 alone and in combination are differently affected by applied voltage. *Proc. Natl. Acad. Sci. USA* **88**:8410–8414

Bennett, M.V.L., Barrio, L.C., Bargiello, T.A., Spray, D.C., Hertzberg, E., Saez, J.C. 1991. Gap junctions: New tools, new answers, new questions. *Neuron* **6**:305–320

Bergoffen, J., Scherer, S.S., Wang, S., Scott, M.O., Bone, L.J., Paul, D.L., Chen, K., Lensch, M.W., Chance, P.F., Fischbeck, K.H. 1993. Connexin mutations in X-linked Charcot-Marie-Tooth disease. *Science* **262**:2039–2042

Brink, P.R. 1996. Gap junction channel gating and permselectivity: Their roles in coordinated tissue function. *Clin. Exp. Pharmacol. Physiol.* **23**:1041–1046

Brink, P.R., Cronin, K., Banach, K., Peterson, E., Westphale, E.M., Seul, K.H., Ramanan, S.V., Beyer, E.C. 1997. Evidence for heteromeric gap junction channels formed from rat connexin43 and human connexin37. *Am. J. Physiol.* **273**:C1386–C1396

Bukauskas, F.F., Kempe, C., Weingart, R. 1992. Electrical coupling between cells of the insect *Aedes albopictus*. *J. Physiol.* **448**:321–337

Dahl, E., Manthey, D., Chen, Y., Schwarz, H.J., Chang, Y.S., Lalley, P.A., Nicholson, B.J., Willecke, K. 1996. Molecular cloning and functional expression of mouse connexin-30, a gap junction gene highly expressed in adult brain and skin. *J. Biol. Chem.* **271**:17903–17910

Dahl, G. 1996. Where are the gates in gap junction channels? *Clin. Exp. Pharmacol. Physiol.* **23**:1047–1052

Denoyelle, F., Lina-Granade, G., Plauchu, H., Bruzzone, R., Chaïb, H., Lévi-Acobas, F., Weil, D., Petit, C. 1998. Connexin26 gene linked to a dominant deafness. *Nature* **393**:319–320

Elfgang, C., Eckert, R., Lichtenberg-Frate, H., Butterweck, A., Traub, O., Klein, R.A., Hulser, D.F., Willecke, K. 1995. Specific permeability and selective formation of gap junction channels in connexin-transfected HeLa cells. *J. Cell. Biol.* **129**:805–817

Estivill, X., Fortina, P., Surrey, S., Rabionet, R., Melchionda, S., D'Agruma, L., Mansfield, E., Rappaport, E., Govea, N., Milà, M., Zelante, L., Gasparini, P. 1998. Connexin-26 mutations in sporadic and inherited sensorineural deafness. *Lancet* **351**:394–398

Forge, A., Becker, D., Evans, W.H. 1997. Gap junction connexin isoforms in the inner ear of gerbils and guinea pigs. *Brit. J. Audiol.* **31**:76–77

Gulley, R.S., Reese, T.S. 1976. Intercellular junctions in the reticular lamina of the organ of Corti. *J. Neurocytol.* **5**:479–507

Hama, K., Saito, K. 1977. Gap junctions between the supporting cells in some acousticovestibular receptors. *J. Neurocytol.* **6**:1–12

He, D.S., Jiang, J.X., Taffet, S.M., Burt, J.M. 1999. Formation of heteromeric gap junction channels by connexins 40 and 43 in vascular smooth muscle cells. *Proc. Natl. Acad. Sci. USA* **96**:6495–6500

Iurato, S., Franke, K., Luciano, L., Wermber, G., Pannese, E., Reale, E. 1976. Intercellular junctions in the organ of Corti as revealed by freeze fracturing. *Acta Otolaryngol.* **82**:57–69

Jarillo, J.A., Barrio, L.C., Gimlich, R.L. 1995. Different voltage dependence of *Xenopus* connexin 30 and rat connexin 32 junctional channels expressed in oocyte pairs. In: Intercellular Communication Through Gap Junctions. Y. Kanno, K. Kataoka, Y. Shiba, Y. Shibata, T. Shimazu, editors. pp. 399–402. Elsevier, New York

Jiang, J.X., Goodenough, D.A. 1996. Heteromeric connexons in lens gap junction channels. *Proc. Natl. Acad. Sci. USA* **93**:1287–1291

Jahnke, K. 1975. The fine structure of freeze-fractured intercellular junctions in the guinea pig inner ear. *Acta Otolaryngol. [Suppl]* **336**

Kelsell, D.P., Dunlop, J., Stevens, H.P., Lench, N.J., Liang, J.N., Parry,

- G., Mueller, R.F., Leigh, I.M. 1997. Connexin 26 mutations in hereditary nonsyndromic sensorineural deafness. *Nature* **387**:80–83
- Kikuchi, T., Kimura, R.S., Paul, D.L., Adams, J.C. 1995. Gap junctions in the rat cochlea: immunohistochemical and ultrastructural analysis. *Anat. Embryol.* **191**:101–118
- Kumar, N.M., Gilula, N.B. 1996. The gap junction communication channel. *Cell* **84**:381–388
- Lautermann, J. ten Cate, W.J.F., Altenhoff, P., Grümmer, R., Traub, O., Frank, H.G., Jahnke, K., Winterhager, E. 1998. Expression of the gap-junction connexins 26 and 30 in the rat cochlea. *Cell Tissue Res.* **294**:415–420
- Lee, M.J., Rhee, S.K. 1998. Heteromeric gap junction channels in rat hepatocytes in which the expression of connexin26 is induced. *Molecules & Cells* **8**:295–300
- Li, X., Simard, J.M. 1999. Multiple connexins form gap junction channels in rat basilar artery smooth muscle cells. *Circ. Res.* **84**:1277–1284
- Mills, S.L., Massey, S.C. 1995. Differential properties of two gap junctional pathways made by AII amacrine cells. *Nature* **377**:734–737
- Miyoshi, H., Boyle, M.B., MacKay, L.B., Garfield, R.E. 1996. Voltage-clamp studies of gap junctions between uterine muscle cells during term and preterm labor. *Biophys. J.* **71**:1324–1334
- Moreno, A.P., Campos de Carvalho, A.C., Verselis, V., Eghbali, B., Spray, D.C. 1991. Voltage-dependent gap junction channels are formed by connexin32, the major gap junction protein of rat liver. *Biophys. J.* **59**:920–925
- Moreno, A.P., Fishman, G.I., Spray, D.C. 1992. Phosphorylation shifts unitary conductance and modifies voltage-dependent kinetics of human connexin43 gap junction channels. *Biophys. J.* **62**:51–52
- Neyton, J., Trautmann, A. 1985. Single-channel currents of an intercellular junction. *Science* **317**:331–335
- Obaid, A.L., Socolar, S.L., Rose, M. 1983. Cell to cell channels with two independently regulated gates in series: Analysis of junctional conductance modulation by membrane potential, Calcium, and pH. *J. Membrane Biol.* **73**:69–89
- Oberoi, P., Adams, J.C. 1998. In vivo measurements of dye-coupling among nonsensory cells in the organ of Corti. *Assoc. Res. Otolaryngol.* St. Petersburg, FL, <http://www.aro.org/abstracts/abstracts.html>
- Perkins, G., Goodenough, D., Sosinsky, G. 1997. Three-dimensional structure of the gap junction connexon. *Biophys. J.* **72**:533–544
- Riverdin, E.C., Weingart, R. 1988. Electrical properties of the gap junctional membrane studied in rat liver cell pairs. *Am. J. Physiol.* **254**:C226–C234
- Rubin, J.B., Verselis, V.K., Bennett, M.V.L., Bargiello, T.A. 1992a. Molecular analysis of voltage dependence of heterotypic gap junctions formed by connexins 26 and 32. *Biophys. J.* **62**:183–195
- Rubin, J.B., Verselis, V.K., Bennett, M.V.L., Bargiello, T.A. 1992b. A domain substitution procedure and its use to analyze voltage dependence of homotypic gap junctions formed by connexins 26 and 32. *Proc. Natl. Acad. Sci. USA* **89**:3820–3824
- Santos-Sacchi, J., Dallos, P. 1983. Intercellular communication in the supporting cells of the organ of Corti. *Hear. Res.* **9**:317–326
- Santos-Sacchi, J. 1985. The effects of cytoplasmic acidification upon electrical coupling in the organ of Corti. *Hear. Res.* **19**:207–215
- Santos-Sacchi, J. 1986. The temperature dependence of electrical coupling in the organ of Corti. *Hear. Res.* **21**:205–211
- Santos-Sacchi, J. 1987. Cell coupling differs in the in vitro and in vivo organ of Corti. *Hear. Res.* **25**:227–232
- Santos-Sacchi, J. 1991. Isolated supporting cells from the organ of Corti: Some whole cell electrical characteristics and estimates of gap junction conductance. *Hear. Res.* **52**:89–98
- Sato, Y., Santos-Sacchi, J. 1994. Cell coupling in the supporting cells of Corti's organ: Sensitivity to intracellular H⁺ and Ca⁺⁺. *Hear. Res.* **80**:21–24
- Spicer, S.S., Schulte, B.A. 1994. Differences along the place-frequency map in the structure of supporting cells in the gerbil cochlea. *Hear. Res.* **79**:161–177
- Spray, D.C., Ginzberg, R.D., Morales, E.A., Gatmaitan, Z., Arias, I.M. 1986. Electrophysiological properties of gap junctions between dissociated pairs of rat hepatocytes. *J. Cell. Biol.* **103**:135–144
- Spray, D.C., White, R.L., Campos de Carvalho, A.C., Bennett, M.V.L. 1984. Gating of gap junction channels. *Biophys. J.* **45**:219–230
- Stauffer, K.A. 1995. The gap junction proteins B1-connexin (connexin32) and B2-connexin (connexin26) can form heteromeric hemichannels. *J. Biol. Chem.* **270**:6768–6772
- Trexler, E.B., Bennett, M.V.L., Bargiello, T.A., Verselis, V.K. 1996. Voltage gating and permeation in a gap junction hemichannel. *Proc. Natl. Acad. Sci. USA* **93**:5836–5841
- Van Rijen, H.V., Wilders, R., Van Ginneken, A.C., Jongsma, H.J. 1998. Quantitative analysis of dual whole-cell voltage-clamp determination of gap junctional conductance. *Pfluegers Arch.* **436**:141–151
- Veenstra, R.D., Wang, H.Z., Westphale, E.M., Beyer, E.C. 1992. Multiple connexins confer distinct regulatory and conductance properties of gap junctions in developing heart. *Circ. Res.* **71**:1277–1283
- Verselis, V.K., Bargiello, T.A., Rubin, J.B., Bennett, M.V.L. 1993. Comparison of voltage-dependent properties of gap junctions in hepatocytes and in *Xenopus* oocytes expressing Cx32 and Cx26. In: Gap Junctions. J.E. Hall, G.A. Zampighi, R.M. Davis, editors. pp. 105–112. Elsevier, New York
- Verselis, V.K., Bennett, M.V.L., Bargiello, T.A. 1991. A voltage-dependent gap junction in *Drosophila melanogaster*. *Biophys. J.* **59**:114–126
- Verselis, V.K., Ginter, C.S., Bargiello, T.A. 1994. Opposite voltage gating polarities of two closely related connexins. *Nature* **368**:348–351
- White, T.W., Bruzzone, R., Goodenough, D.A., Paul, D.L. 1994a. Voltage gating of connexins. *Nature* **371**:208–209
- White, T.W., Bruzzone, R., Wolfram, S., Paul, D.L., Goodenough, D.A. 1994b. Selective interactions among the multiple connexin proteins expressed in the vertebrate lens: the second extracellular domain is a determination of compatibility between connexins. *J. Cell. Biol.* **125**:879–892
- Xia, J.H., Liu, C.Y., Tang, B.S., Pan, Q., Huang, L., Dai, H.P., Zhang, B.R., Xie, W., Hu, D.X., Zheng, D., Shi, X.L., Wang, D.A., Xia, K., Yu, K.P., Liao, X.D., Feng, Y., Yang, Y.F., Xiao, J.Y., Xie, D.H., Huang, J.Z. 1998. Mutations in the gene encoding gap junction protein β -3 associated with autosomal dominant hearing impairment. *Nature Genet.* **20**:370–373
- Zhao, H.B., Santos-Sacchi, J. 1997. Fast voltage dependence of gap junctions in cochlear supporting cells. *Society for Neuroscience, 27th Annual Meeting.* p 461. New Orleans, LA
- Zhao, H.B., Santos-Sacchi, J. 1998. Effect of membrane tension on gap junctional conductance of supporting cells in Corti's organ. *J. Gen. Physiol.* **112**:447–455
- Zhao, H.B., Santos-Sacchi, J. 1999. Multiple and rectifying voltage dependence of gap junctional channels in cochlear supporting cells. *Assoc. Res. Otolaryngol.* St. Petersburg, FL. <http://www.aro.org/abstracts/abstracts.html>
- Zwislocki, J.J., Slepecky, N.B., Cefaratti, L.K., Smith, R.L. 1992. Ionic coupling among cells in the organ of Corti. *Hear. Res.* **57**:175–194



Seeing the long tail: A novel green fluorescent protein, SiriusGFP, for ultra long timelapse imaging

Sheng Zhong^{a,e}, Felix Rivera-Molina^b, Alberto Rivetta^d, Derek Toomre^b,
Joseph Santos-Sacchi^{a,c,d}, Dhasakumar Navaratnam^{a,c,e,*}

^a Dept. of Surgery (Otolaryngology), Yale University School of Medicine, New Haven, CT, 06511, United States

^b Dept. of Cell Biology, United States

^c Dept. of Neuroscience, United States

^d Dept. of Cellular and Molecular Physiology, United States

^e Dept. of Neurology, United States

ARTICLE INFO

Keywords:

SiriusGFP

GFP

Fluorescence

4D confocal

Structured Illumination Microscopy

Photostable

ABSTRACT

Background: Fluorescent proteins (FPs) have widespread uses in cell biology. However, the practical applications of FPs are significantly limited due to their rapid photobleaching and misfolding when fused to target proteins. **New Method:** Using a combination of novel and known mutations to eGFP, we developed a well folded and very photostable variant, SiriusGFP.

Results: The fluorescence spectrum indicated that the excitation and emission peaks of SiriusGFP were red-shifted by 16 and 8 nm, respectively. Co-operative effects of two key mutations, S147R and S205V, contribute to its photostability. SiriusGFP tagged to the mitochondrial outer membrane protein Omp25 showed sustained fluorescence during continuous 3D-scanning confocal imaging (4D confocal) compared to eGFP-tagged Omp25. Furthermore, with super-resolution structured illumination microscopy (SIM) we demonstrate marked improvements in image quality and resolution (130 nm in XY axis, and 310 nm in Z axis), as well as, decreased artifacts due to photobleaching.

Comparison with Existing Method(s): Compared to eGFP, SiriusGFP shows a 2-fold increase in photostability in vitro, and folds well when fused to the N- and C- termini of cytoplasmic and membrane proteins. While its quantum yield is ~3 fold lower than eGFP, its decreased brightness was more than compensated by its increased photostability in different experimental paradigms allowing practical experimentation without dynamic adjustment of light intensity or fluorescence sampling times.

Conclusions: We have developed a variant of eGFP, SiriusGFP, that shows over a two fold increase in photostability with utility in methods requiring sustained or high intensity excitation as in 4D confocal or SIM imaging.

1. Introduction

Fluorescent proteins (FPs) are widely used in cellular imaging for recording subcellular events and detailed dynamic processes, including *in vivo* imaging. In the nervous system, fluorescent proteins have been used for temporospatial migration of individual cells and to ascertain numerous physiological phenomena including changes in membrane potential and Ca²⁺ and Cl⁻ levels (Baker, Mutoh et al. 2008; Chen, Wardill et al. 2013; Zhong, Navaratnam et al. 2014). Compared to chemical dyes, genetically encoded FPs have many benefits including 1) precise targeting with fusion proteins 2) avoidance of chemical loading/labelling with consequent cell toxicity and dye leakage/

delocalization. Perhaps the most distinguishing advantage of FPs is genetic labeling that allows potential development of cell-lines and transgenic animals with the gene-editing tool CRISPR/Cas9 and tissue-specific gene expression.

Recently, the expansion in 3D time-lapse (4D) confocal imaging of cells during development and super-resolution microscopic technologies have required brighter, photostable fluorophores for imaging. Photobleaching is one of the major problems for FPs, which limits their applications in biological investigation. Reduced light emission due to photobleaching can be compensated by increases in excitation light intensity and exposure time. These two compensatory mechanisms also accelerate photobleaching (Cranfill, Sell et al. 2016). Moreover, these

* Corresponding author at: Dept of Neurology, Yale School of Medicine, New Haven, Connecticut, 06511, United States.

E-mail address: dhasakumar.navaratnam@yale.edu (D. Navaratnam).

<https://doi.org/10.1016/j.jneumeth.2018.12.008>

Received 6 November 2018; Received in revised form 11 December 2018; Accepted 11 December 2018

Available online 19 December 2018

0165-0270/ © 2018 The Authors. Published by Elsevier B.V. This is an open access article under the CC BY-NC-ND license (<http://creativecommons.org/licenses/by-nc-nd/4.0/>).

compensatory mechanisms are not possible for the fast imaging times used in modern fluorescence imaging techniques. For confocal microscopy and almost all superresolution microscopy methods, photostability is as important a factor as brightness for imaging quality. For super-resolution structured illumination microscopy (SIM), in particular, the requirement of at least 15 frames (3 angles and 5 phases per angle) to generate a single image makes it more sensitive to photobleaching than conventional confocal microscopy (Rego and Shao, 2015; Hong, Wilton et al. 2017).

The green fluorescent protein (GFP) and its variants derived from jellyfish *Aequorea victoria* are the most extensively used FPs. eGFP is the most widely used FP, but has significant drawbacks in biological applications. The chromophore in GFPs, *para*-hydroxybenzylidene-imidazolinone (*p*-HBDI), is formed by sequential autocatalytic cyclization and dehydration/oxidation, after initial folding of the polypeptide chain into a β -barrel conformation. For *p*-HBDI, the *Z-E* isomerization on the exocyclic double bond is the major internal conversion pathway, the non-fluorescent alternative pathway of energy dissipation of the excited fluorophore. The fluorescence quantum yield (ϕ_f) of *p*-HBDI (without the surrounding β -barrel) is < 0.001 in gas phase (Huang, Cheng et al. 2013), and even lower (~ 0.0001) in solvents, while the quantum yield (ϕ_{ZE}) of *Z-E* isomerization is ~ 0.5 (Yang, Huang et al. 2008; Chatterjee, Mandal et al. 2015). The β -barrel scaffold of GFP provides hydrophobic isolation and a rigidly constrained environment for the chromophore, functioning as a protective nest for efficient production of fluorescence. As a result, the quantum yield of GFP can reach up to 0.77 (as reference, 0.80 for frozen *p*-HBDI at 77 K, where the internal conversion pathway is almost eliminated) (Niwa, Inouye et al. 1996; Nielsen, Lapierre et al. 2001).

How irreversible photobleaching of the chromophore in FPs occurs is not clear, although oxygen concentration dependence on photobleaching has been confirmed in many GFP-like FPs. The destruction of chromophores in chemical dyes is preceded by ROS formation from redox reactions with the excited chromophore. The formation of ROS is, in turn, strongly dependent on the local redox environment. The damage to the chromophore in GFP is likely caused by endogenous and exogenous singlet oxygen. For wtGFP or eGFP, self-generated endogenous singlet oxygen (1O_2) occurs when exposed to illumination (Greenbaum, Rothmann et al. 2000; Jimenez-Banzo, Nonell et al. 2008; Bogdanov, Bogdanova et al. 2009). The formation of superoxide was postulated to be the gateway initiating a series of chemical reactions leading to the destruction of the chromophore (Chatterjee, Mandal et al. 2015). Furthermore, solvated electrons produced from solvent radiolysis outside the β -barrel can migrate to the chromophore cavity through a water tunnel near residue His148. Therefore, it is possible to reduce photosensitized 1O_2 by limiting the accessibility of molecular oxygen to the chromophore; a tighter β -can or an allosteric block are two potential ways.

Based on the knowledge of fluorophore photochemistry, we developed a series of eGFP derivatives to increase photostability that can tolerate higher intensity illumination and longer exposure. The best variant, SiriusGFP, contains several folding mutations and two key mutations, S147R and S205V, both of which contribute to significant improvement in photostability over eGFP. Although SiriusGFP has reduced brightness compared to eGFP, it is more than compensated for by an increase in photostability. Practically, this allowed for improved 4D confocal imaging as it eliminated dynamic adjusting of exposure time. Furthermore, SIM images with SiriusGFP show resolution improvement, especially in the Z axis. The optical properties were determined with purified protein of SiriusGFP, and compared to eGFP. The photobleaching mechanism of SiriusGFP was determined to be oxygen-dependent under oxygen-depletion in both high and low intensity illumination. This contrasts with eGFP that shows different mechanisms and sensitivities to oxygen with high and low laser power. Our new green FP, SiriusGFP, provides improved capabilities for superresolution and time-lapse microscopy.

2. Methods

2.1. Gene construct and mutations & cell culture

Mutagenesis was performed using the Quick Change method adapted from Stratagene QC protocol. Mutations were verified by DNA sequencing the entire gene. We used eGFP-N1 as the backbone vector. HEK-293 and HeLa cells were cultured in Dulbecco's modified Eagle's medium (DMEM, high glucose) containing 50 U/ml penicillin and streptomycin (1%), 10% fetal bovine serum (FBS) at 37 °C in a CO₂ incubator (5%).

The sequences of SiriusGFP and the intermediates of SG205 and SG147 are as followed.

SG205: eGFP-S205V/A206K

SG147: eGFP-S147R/A206K

SiriusGFP: eGFP-S30R/Y39N/F99S/N105T/S147R/M153T/V163A/S205V/A206K

2.2. Fluorescent protein extraction from cell lysis

Cultured HEK-293 cells were grown in 10 cm dishes and transiently transfected with eGFP and SiriusGFP plasmid, respectively. After 48 h of incubation, the cells were scraped with a plastic scraper after a brief rinse in DPBS. Cells were resuspended in 200 μ l of EBC buffer (50 mM Tris, 120 mM NaCl, 0.5% NP40, pH 7.5) containing Protease Inhibitor cocktail (ThermoFisher, PI-88665), vortexed at 4 °C for 15 min to lyse the cells, and then centrifuged at 14,000 rpm for 20 min (4 °C). The supernatant containing solubilized fluorescent proteins was aspirated and used for further experimentation.

2.3. Expression and purification of eGFP and SiriusGFP

SiriusGFP and eGFP proteins were expressed in *E. coli* and purified by immobilized metal ion affinity chromatography. eGFP and SiriusGFP genes were subcloned in the pQE-801 vector (Qiagen) using BamHI and HindIII restriction sites. The vector is designed to provide a six-histidine tag on the N-terminus of the expressed eGFP and SiriusGFP for affinity purification. The complete tag sequence fused to the actual eGFP and SiriusGFP proteins was MRGSHHHHHHGS. The constructs were transformed in *E. coli* BL21(DE3), spread on LB plates containing 100 μ g/ml ampicillin (LBA), and incubated overnight at 37 °C. A single colony from each construct was inoculated in 50 ml LBA and incubated for 16 h at 37 °C without shaking. The resulting seed culture was added to 500 ml LBA in a 2-liter baffled Erlenmeyer flask, and incubated at 37 °C in an orbital shaker (150 rpm) until OD₆₀₀ reached 0.6–0.7. The flasks were quickly cooled under running tap water and the cultures injected with 0.5 mM isopropyl β -D-1-thiogalactopyranoside (IPTG) to induce protein expression. The cultures were incubated with shaking (150 rpm) for a further 22 h at 15 °C until it reached a final density OD₆₀₀ \sim 5. Cells were pelleted by centrifugation (4000 g/10 min) and the pellets resuspended in 40 ml Buffer A: 50 mM NaH₂PO₄ (titrated to pH 8 with NaOH), 300 mM NaCl. Temperature was kept at 4 °C throughout cell lysis and purification steps. After addition of protease inhibitor cocktail (10 μ g/ml each of aprotinin, leupeptin, pepstatin, chymostatin) and 10 mM imidazole, the cell slurry was sonicated using a Bredson digital sonifier (6 cycles of 30 s each, at 67% amplitude). Cell lysates were centrifuged for 40 min at 15,000 g, and the supernatant added to a 1 ml bed volume of Ni-NTA agarose resin (Qiagen) and gently nutated for 1 h. The resin was loaded on a column and sequentially washed with 10 ml Buffer A plus 10 mM imidazole, and 10 ml Buffer A plus 20 mM imidazole. Fluorescent proteins were eluted using Buffer A containing 250 mM imidazole and dialyzed against 1 L of 20 mM Tris (titrated to pH 7.5 with HCl) and 150 mM NaCl. Protein concentration was measured with the Bradford method (Bradford, 1976; ThermoScientific/Pierce Coomassie Protein Assay Kit), using bovine serum albumin as a calibration standard. Both eGFP and SiriusGFP proteins ran as a single band

at ~25 kDa molecular weight on SDS-PAGE gel (Bio-Rad Mini-Protean TGX gel, 4–15%). Typical protein yields for both eGFP and SiriusGFP were about 40 mg per liter of culture.

2.4. Optical properties

The absorbance spectroscopy of purified FPs was performed in 150 mM NaCl, 20 mM Tris, pH 7.5 with an Agilent 8453 UV–vis spectroscope. The fluorescence spectra of purified FPs was obtained in the same buffer in a FluoroMax-3 (Jobin Yvon Horiba). The quantum yields were calculated from the spectral readout.

2.5. Wide-field photobleaching on live cells

The cultured cells were grown on glass coverslips (No.1, 0.13–0.16 mm thick, 15 mm round, Warner Instr., USA). Transient transfection with the plasmid of interest was performed using lipofectamine-2000 (Invitrogen, Life technologies). After transfection, the coverslips were mounted on a quick change chamber and platform (RC-42LP and QE-1, Warner Instr., USA). Fluorescence images were acquired using an oil-immersion objective (N.A. = 1.30, Plan Fluor 100× Objective, Nikon, Japan) with a Nikon Eclipse Ti equipped with a 200 W metal-halide lamp (Lumen200, Prior Scientific, USA) as the fluorescence illumination source. Shutter and filter wheel (Lambda10-3 optical filter changer with smart shutter, Sutter Instr., USA) were connected between the microscope and the illumination source, in which Semrock ET430/24x-32 was used as the excitation filter for CFP, Semrock ET500/20x-32 as the excitation filter for YFP and Chroma HQ520LP as the emission filter. A 14-bit back-illuminated EMCCD camera system (128 × 128 pixels, 24 μm array, Andor iXon^{EM} + DU-860E, USA) was used to record the fluorescence images under 430 or 500 nm excitation. All peripheral hardware control, image acquisition and image processing were achieved and/or synchronized on a PC computer via a 16-bit/1-MHz USB Data Acquisition System (Personal Daq/3000 Series, IOtech, USA) by using customized software (jClamp & FastLook, SciSoft, USA; www.SciSoftCo.com). Photobleaching data and fluorescence images were achieved with our ratiometric imaging system controlled by jClamp & FastLook. Photobleaching efficiency at a wavelength of 430 nm is higher than at 500 nm, although the absorption at 430 nm is much lower than 500 nm. Because of this enhanced bleaching capability and to optimize our identification of photostable products, we bleached GFP variants at 430 nm (approximately 1 mW with the 100X objective). Stable optical power at the utilized wavelengths was confirmed using an analog optical power meter (ThorLabs PM30-130, w/ S130 A Slim Sensor). The 430 nm filter was used for 60 ms at the beginning of each episode and then the filter changed to 500 nm, an image acquired, and then the filter changed back to 430 nm for bleaching for a further 2 s. This procedure was performed reiteratively for 400 episodes. Filter changes required 100 ms. There is a 200 ms interval time between two successive episodes, and the excitation filter remained at 430 nm between successive episodes. The photobleaching curves were measured in GFP variants expressed in the cytosol of HEK-293 cells. The average fluorescence intensity of regions of interest (ROI) was measured, and the background fluorescence was subtracted using FastLook and ImageJ. Data were analyzed with Matlab, Origin 2016 and SigmaPlot 10.0.

2.6. Confocal photobleaching on live cells

The photobleaching of live HeLa cells was performed on a Zeiss LSM 710 duo confocal scanning microscope with an OPSS laser at 489 nm (100 mW at maximum power). HeLa cells were grown on 35 mm glass-bottom culture petri dishes (P35GC-1.0-14-C, MatTek, USA), and transfected with eGFP/SG205/SG147/SiriusGFP plasmids using Lipofectamine 2000 (Invitrogen, USA) followed by 24 h incubation at 37 °C. Before imaging, culture media in petri dishes was changed to a

neutral buffer of 0.2 mM NaCl, 100 mM sodium Malate, 300 mOsm, pH 7.20 after a rinse with PBS. All photobleaching data were fit by a single exponential decay function, $Y = Y_0 + Ae^{-x/t}$, where Y_0 is the constant offset representing the residual fluorescence after photobleaching reaching a steady state (R^2 ranged from 0.97–0.99). The laser power was measured with an analog optical power meter (ThorLabs PM30-130, w/ S130 A Slim Sensor).

2.7. Oxygen-depletion photobleaching

The photobleaching of PFA-fixed HeLa cells are performed in the same Zeiss LSM 710 duo confocal microscope. The oxygen-depletion buffer containing COT was prepared as previously described (Olivier, Keller et al. 2013). Mercaptoethylamine (MEA, Sigma-Aldrich 30,070) was dissolved in deionized water as 1 M stock solution, then adjusted to pH 8 by glacial acetic acid (Avantor Performance Materials). The stock solution was stored at 4 °C and used within a week. β-mercaptoethanol (BME, Sigma M3148) was used without dilution as a 14.3 M solution. Cyclooctatetraene (COT, Sigma-Aldrich 138,924) was diluted in DMSO as 200 mM stock solution and stored at 4 °C. Protocatechuic acid (PCA, Sigma-Aldrich 37,580) was dissolved in deionized water as 100 mM stock solution, then adjusted to pH 9 with KOH aq. The stock solution was stored at 4 °C and used within a month. Protocatechuic acid 3,4-dioxygenase from *Pseudomonas* sp. (PCD, Sigma-Aldrich P8279) was dissolved in 100 mM Tris–HCl (pH 8) containing 50 mM KCl, 1 mM EDTA and 50% glycerol as 5 μM stock solution, and stored at –20 °C.

Before oxygen-depletion treatment and confocal imaging, HELA cells transfected with eGFP-Omp25 or SiriusGFP-Omp25 were fixed with 4% PFA for 10 min, and the coverslips rinsed with PBS 3 times. Cells were treated with 0.2% Triton X-100 in PBS for 15 min to permeabilize cell membranes. Coverslips were rinsed with PBS 3 times. Confocal imaging was performed with a Zeiss LSM710 Duo confocal scanning microscope in freshly made oxygen-depletion solution of 10 mM PBS-Tris (pH 7.5) containing 10% (w/v) glucose, 10 mM MEA, 50 mM BME, 2 mM COT, 2.5 mM PCA and 50 nM PCD. This oxygen-depletion solution was abbreviated as pcaPCD in the Fig. 2. Controls were in 10 mM PBS-Tris buffer containing 10% glucose. The maximum optical power of the OPSS laser is 100 mW, and 5% (low intensity) and 50% (high intensity) were the percentage of laser power used for photobleaching.

2.8. Photobleaching on purified protein embedded in gel

Photobleaching rates on purified proteins of GFPs embedded in polyacrylamide gel were measured by Zeiss LSM710 laser-scanning confocal microscopy, following a previously described protocol (Cranfill, Sell et al. 2016). This experiment was designed to produce a homogenous population of immobilized protein of known concentration which was photobleached. Briefly, 20% polyacrylamide-1 μM FP solution was polymerized by addition of ammonium persulfate and TEMED. The 20% polyacrylamide-1 μM FP solution was then injected into a space between a coverslip and glass slide. After polymerization of the acrylamide the outside edges of the coverslip were sealed with Cytoseal to prevent dehydration around the edges. The slides were maintained in the dark at 4 °C overnight before photobleaching and imaging.

2.9. Confocal 4D imaging

Confocal 4D imaging of live HeLa cells transfected with eGFP-Omp25 and SiriusGFP-Omp25, respectively. We used a Yokogawa CSU-X1 spinning disc confocal microscope for image acquisition. The 3D confocal Z-stack scanning was done continuously to maximize photobleaching.

2.10. Structured illumination microscopy (SIM)

HEK-293 or HeLa cells were transfected with eGFP-Omp25 or SiriusGFP-Omp25, and incubated at 37 °C in a CO₂ incubator (5%). The targeting protein embedded in the outer membrane of mitochondria in HEK-293 or HeLa cells. Before imaging, cells were fixed with 4% PFA and then rinsed with PBS buffer. Structured Illumination Microscopy (SIM, DeltaVision-OMX, Applied Precision, GE life) was performed in PBS. The XY and Z resolution were measured with the lines perpendicularly across individual mitochondrial membranes at XY and XZ/YZ axes, respectively. Gaussian fitting of the readout traces gives full width at half maximum (FWHM) of each peak. Averages of over 100 peaks in SIM images were measured to ascertain the resolution of the imaging technique.

3. Results

3.1. Optical properties of SiriusGFP

Mutations of F99S/M153 T/V163 A in Cycle3 GFP help folding and maturation by avoiding aggregation traps (Fukuda, Arai et al. 2000), and S30R/Y39 N/N105 T help fast folding in super-folder GFP/YFP (Pedelacq, Cabantous et al. 2006; Andrews, Schoenfish et al. 2007; Ottmann, Weyand et al. 2009). A206 K mutation makes GFP fully monomeric even at high concentrations (Zacharias, Violin et al. 2002), which eliminates the multimerization/ aggregation of GFP in fusion proteins.

Upon illumination, the neutral chromophore HBDI of wtGFP is excited and converted to the anion excited state, via excited state proton transfer (ESPT), in the picosecond timescale. It was reported that the mutant S205 V of wtGFP has ESPT 30 times slower than in wtGFP through an alternative proton wire via T203 to E222 (Shu, Leiderman et al. 2007; Fang, Frontiera et al. 2009). And ESPT in S205 A is 15 times slower than wtGFP (Erez, Gepshtein et al. 2011; Wineman-Fisher, Simkovitch et al. 2014). Our previous work on chloride-sensitive YFP also indicated that S205 V in eYFP substantially increased the photostability (Zhong, Navaratnam et al. 2014). However, the double mutant of eGFP-T203 V/S205 V is still fluorescent when excited at 488 nm (data not shown), confirming that the majority of its chromophore stays in the anionic state, and ESPT is not necessary for fluorescence emission in eGFP.

Currently, Emerald GFP is the most photostable GFP variant, but exhibits a very fast initial fluorescence decay to about 50% before reaching a photostable state (Tsien, 1998; Cubitt, Woollenweber et al. 1999). This fast decay component makes Emerald less ideal for long term imaging or superresolution imaging. The key mutation in Emerald GFP is N149 K. We tested this mutation based on SG205 (S205 V/A206 K) by generating several mutants including N149 K, S147 H/N149 K, and Y145 F/S147 P/N149 K, respectively. However, all of these mutants still showed the fast initial decay (data not shown).

Based on the photobleaching results of the intermediate mutant SG147 (S147R/A206 K), we generated a mutation S147R that also increased both fluorescence lifetime (Tau) and residual fluorescence after photobleaching (Y₀). The increased Tau and Y₀ may be attributed to the protective effect of charge repulsion of positive ions (including protons) by the bulky Arginine side chain. Consistent with this possibility SiriusGFP has a pK_a of 5.29 that also implies a proton repulsion effect of S147R near the phenolic group of the chromophore (Fig. S1D).

The UV-VIS spectroscopy of purified FPs revealed that SiriusGFP has a major excitation peak at 504 nm and a minor peak at 396 nm (Fig. 1A), indicating that the chromophore has two protonation states of the phenolic group, and that the protonated state is responsible for the minor peak. The extinction coefficient of SiriusGFP and eGFP are not significantly different (56,600 M⁻¹ cm⁻¹ at 504 nm for SiriusGFP, compared to 55,000 M⁻¹ cm⁻¹ at 488 nm for eGFP). The emission peak of SiriusGFP is at 516 nm (with a shoulder at ~550 nm) instead of

508 nm for eGFP (with a shoulder at ~540 nm). When excited at 400 nm SiriusGFP has the same emission peak at 516 nm (Fig. S1E), implying that ESPT occurs in SiriusGFP. Since the main proton pathway via Ser205 to Glu222 for ESPT was blocked by the mutation of S205 V, the alternative pathway via T203 is probably involved in ESPT of SiriusGFP. A proportion of Glu222 in SiriusGFP should be in the anionic state as a proton acceptor, while the majority of molecules maintains its chromophore in an anionic state along with a neutral Glu222. The ratio between the absorption intensities of the bands A:I in SiriusGFP (peak at 396 and 504 nm, respectively) is 1:3.75, whereas this ratio is 4 : 1 in wtGFP (peak at 400 nm and 488 nm). The fluorescence quantum yield (φ_f) of SiriusGFP is significantly reduced compared to eGFP (0.214 for SiriusGFP and 0.60 for eGFP) (Fig. S1C). Thus, the brightness (extinction coefficient X quantum yield) of SiriusGFP is 12,112 M⁻¹ cm⁻¹, while eGFP is 33,000 M⁻¹ cm⁻¹. These results imply that there are more competing pathways for deactivation of the excited state of SiriusGFP than that of eGFP. The decreased φ_f could be attributed to the increased τ-torsion on the chromophore by an absence of a constrained H-bond between Ser205 and the phenolic group of p-HBDI, which makes the phenolic group in SiriusGFP more flexible than that in eGFP. The τ-torsion (less than 90°) on the methylene bridge (the only exocyclic double bond) facilitates internal conversion and deactivation to ground state (Huang, Cheng et al. 2013) that can compete with the radiative relaxation as fluorescence.

The excitation and emission peak are both red-shifted from eGFP (Ex 488 nm, Em 508 nm) to SiriusGFP (Ex 504 nm, Em 516 nm), implying that the energy gap in SiriusGFP is narrower than that of eGFP and has more vibration levels in the S₀ and S₁ state.

When photobleaching transfected HeLa cells with a scanning laser at 489 nm (~1500 μW at the objective) in a confocal microscope, exponential decay curves with different lifetimes (Tau) and residue offsets Y₀ were noted, and shown in Fig. 1B. The average lifetime (Tau) of SiriusGFP (118.3 s) is more than twice that of eGFP (50.1 s), with the intermediate mutants having values that lay between (Tau of SG205 is 104.4 s and SG147 is 76.3 s (Fig. 1C)). An ANOVA analysis on fluorescence lifetimes (Tau) among the four GFP variants indicates highly significant differences (p < 0.01). Thereafter, using Tukey-Kramer Multiple Comparisons Test for Tau pairwise comparison, Q values were 23.4 for eGFP and SiriusGFP, 19.2 for eGFP and SG205, 8.6 for eGFP and SG147, 5.1 for SiriusGFP and SG205, 13.7 for SiriusGFP and SG147, and 9.3 for SG205 and SG147. Note that a Q value of 3.6 or greater denotes a significant difference. Y₀ is the offset value with single exponential decay fitting, and represents the residual steady state fluorescence after photobleaching. Y₀ for SiriusGFP is 15.1% and is three fold that of eGFP (5.1%). Similar to Tau, the intermediate mutants had values that lay between that of eGFP and SiriusGFP (7.2% for SG205 and 12.5% for SG147 (Fig. 1C, D)). An ANOVA analysis on Y₀ among the four GFP variants also indicates significant differences (p < 0.01). As with Tau, these intermediate values resulted in a smaller degree of confidence in statistical differences of Y₀ between the SiriusGFP and the intermediate mutants when compared to SiriusGFP and eGFP. The Q values for Y₀ pairwise comparison were 36.7 for eGFP and SiriusGFP, 8.2 for eGFP and SG205, 27.6 for eGFP and SG147, 27.8 for SiriusGFP and SG205, 8.9 for SiriusGFP and SG147, 18.9 for SG205 and SG147. These data suggest that mutation of S205 V and S147R both contribute to the increase of Tau and Y₀. The combination of S205 V and S147R makes SiriusGFP superior to eGFP, although with a tradeoff in φ_f.

To compare brightness and photostability with the same amount of eGFP and SiriusGFP, the normalized photobleaching curves showed that the two variants have different rates of decay, and intersect at 167 s under constant laser power (~1500 μW) (Fig. 1E). The integrated area under curves are 423 for eGFP and 437 for SiriusGFP. The residual fluorescence of SiriusGFP is near four-fold higher than that of eGFP at the end of the long tail. With greater light intensity, the decay curves intersect at a shorter time point. Thus, for experiments requiring high

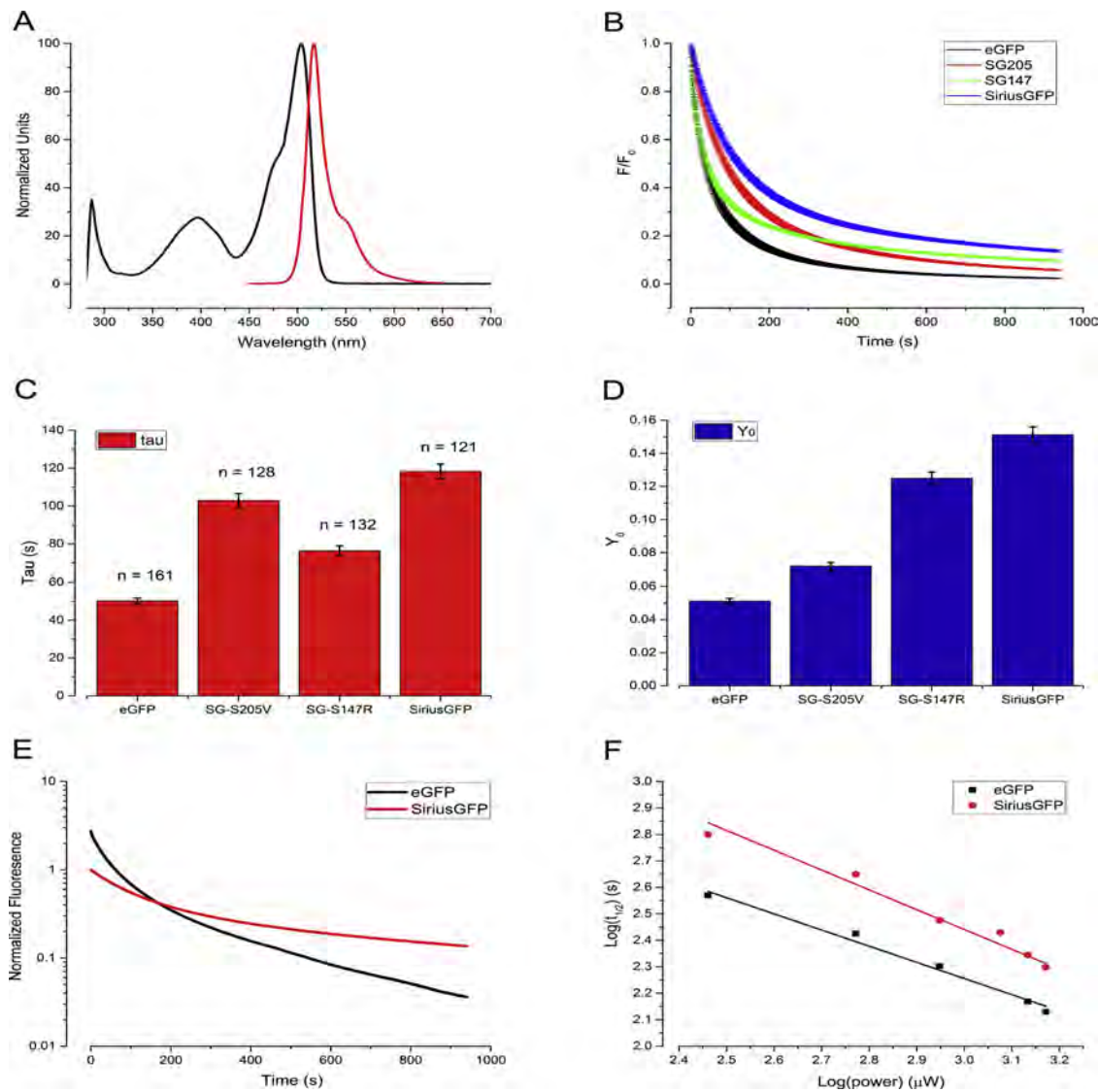


Fig. 1. Optical properties of SiriusGFP compared to eGFP. **(A)** The UV-vis spectrum of SiriusGFP indicates that the protonate chromophore exists in a minor proportion. Shown is the UV-vis absorbance and fluorescent spectrum of purified SiriusGFP in a buffer of 150 mM NaCl, 20 mM Tris, pH7.5. SiriusGFP has a major excitation peak at 504 nm and a minor peak at 396 nm, implying that the protonated chromophore exists in minor proportion. **(B)** SiriusGFP is more photostable than eGFP. Shown are the photobleaching curves of eGFP, SG205, SG147, and SiriusGFP expressed in HeLa cells. Fluorescence was detected by laser irradiation of live cells at 489 nm on a Zeiss confocal microscope (Zeiss LSM 710 duo). We determined that the photostability of SiriusGFP is > 2.4 fold higher than that of eGFP. The ratio of integrated areas under the curves is 1 : 1.99 : 1.88 : 3.34 for eGFP : SG205 : SG147 : SiriusGFP. The optical power of scanning laser at 489 nm was \sim 1500 μ W. Each curve is the average of > 100 cells with standard error accounting for the variability in the thickness of each line. **(C)** SiriusGFP shows increased photobleaching time constants compared to eGFP. Photobleaching data can be fit by a single exponential decay function, $Y = Y_0 + Ae^{-x/t}$, where Y_0 is the constant offset representing the residual fluorescence after photobleaching reached a steady state (R^2 ranged from 0.97–0.99). The single exponential fitting on photobleaching curves determined that the lifetime (Tau) of SiriusGFP is 118.3 s, 102.9 s for SG205, 76.3 s for SG147, compare to 50.1 s for eGFP under the same photobleaching conditions. The cell numbers (n) are shown on the top of each sample. The error bar is standard error. ANOVA analysis of Tau values shows high confidence in statistically significant differences (p -value 2.42×10^{-50}). **(D)** Residual fluorescence in SiriusGFP is greater than eGFP after prolonged photobleaching. Y_0 represents the residual fluorescence after photobleaching; 15.1% for SiriusGFP compared to 12.5% for SG147, 7.2% for SG205 and 5.1% of eGFP. The error bar is standard error. **(E)** The choice of eGFP and SiriusGFP depends on the intended duration of an experiment. The normalized photobleaching curves with the same amount of eGFP and SiriusGFP show the two curves crossing at 167 s. At the end of long tail, the residual fluorescence of SiriusGFP is 3.76-fold higher than that of eGFP. The integrated area is 423.4 for eGFP, and 437.6 for SiriusGFP, confirming that SiriusGFP emits more photons upon prolonged exposure. Conversely, the number of photons emitted in short durations is greater in eGFP, which is therefore preferred in experiments with short fluorescence emission. **(F)** Across a range of light intensities SiriusGFP maintains its superior photobleaching characteristics compared to eGFP. Shown is a log-log plot of photobleaching rates versus illumination laser power of the laser-scanning confocal microscope using purified SiriusGFP and eGFP embedded in polyacrylamide (see method section). SiriusGFP shows slower rates of photobleaching at different light intensities compared to eGFP. Data were fitted to the equation $\log(F) = -\alpha \log(P) + c$, where F is the photobleaching half-time constant and P is the illumination power, α is 0.61 for eGFP and 0.75 for SiriusGFP, while c is 4.1 for eGFP and 4.7 for SiriusGFP.

intensity light SiriusGFP offers significantly greater advantages when longer exposures are required. These data also indicate that SiriusGFP emits more photons during long exposures or under high power illumination, although less than eGFP at the onset of exposure. In fact, at a given light intensity, the longer the exposure time the greater the

differential advantage in photons emitted by SiriusGFP.

We also measured the photobleaching rates of GFPs with purified proteins embedded in polyacrylamide gel by laser-scanning confocal microscopy (Fig. 1F). This log-log plot of photobleaching rates versus illumination power showed nearly linear relationships that indicates an

accelerated photobleaching of eGFP and SiriusGFP (Cranfill, Sell et al. 2016). The decay slope of SiriusGFP is similar to that of eGFP, but the lifetime is almost doubled. The photobleaching results measured with purified FPs in gel are similar to that in transfected cells.

Due to the long fluorescence tail of SiriusGFP, normal 3D confocal microscopy or superresolution microscopy, such as SIM, imaging quality can benefit.

3.2. Oxygen-depletion photobleaching

To explore the mechanisms of photobleaching in SiriusGFP we carried out photobleaching experiments with confocal microscopy under conditions of oxygen depletion. HELA cells separately transfected with eGFP-Omp25 and SiriusGFP-Omp25 were fixed in 4% PFA followed by oxygen-depletion treatment. Omp25 is a mitochondrial outer membrane protein, localized to the mitochondrial outer membrane anchoring by a single transmembrane segment at the C-terminal. Overexpression of OMP25 results in perinuclear clustering of mitochondria in transfected cells (Nemoto and De Camilli, 1999). eGFP and SiriusGFP were fused on the N terminus of Omp25. Photobleaching of eGFP and SiriusGFP was performed under aerobic and anaerobic conditions at low and high laser power. When photobleaching with low laser power (~150 μ W) both eGFP and Sirius GFP show sensitivity to oxygen. In contrast, at high laser power (~1500 μ W) photobleaching of eGFP is not oxygen dependent, while SiriusGFP shows oxygen-dependence (Fig. 2). In all these conditions SiriusGFP remained more photostable than eGFP. It is believed that GFP's differential sensitivity to oxygen under differing intensities of light points to different mechanisms of photobleaching (Tsien, 1998; Greenbaum, Rothmann et al. 2000; Jimenez-Banzo, Nonell et al. 2008; Grigorenko, Nemukhin et al. 2015). High photon flux may lead to higher-order photobleaching due to a multi-photon effect (Chen, Zeng et al. 2002). Our data indicate that the photobleaching mechanisms of SiriusGFP are different from that in eGFP, particularly in high intensity light. We infer that SiriusGFP is resistant to high-order photobleaching in high intensity light.

3.3. Practical applications 1. 4D confocal scanning

To test the performance of SiriusGFP in confocal microscopy, we

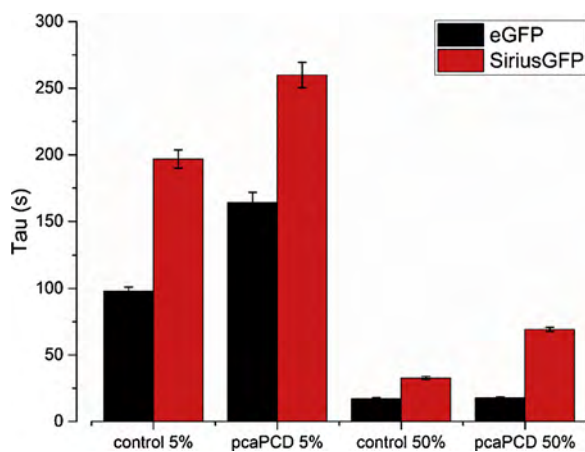


Fig. 2. Photobleaching of SiriusGFP-Omp25 is oxygen dependent across a range of light intensities and contrasts with eGFP-Omp25. Shown are the photobleaching time constants of eGFP and SiriusGFP in PFA-fixed HeLa cells with (pcaPCD – see section 7 in Methods) and without (control) oxygen-depletion solution under low and high optical power illumination, respectively. The percentage of laser power (5% and 50%) at 489 nm used for photobleaching corresponded to measured light intensities of 150 μ W (5%) and 1500 μ W (50%) at the objective. The error bar is standard error. At high and low intensity light, photobleaching of SiriusGFP is oxygen dependent. In contrast, eGFP is oxygen dependent only in low intensity light.

carried out an experiment with 4D confocal imaging on live HeLa cells. Cells were transfected with eGFP-Omp25 and SiriusGFP-Omp25 and imaged live in PBS (Fig. 3). In this experiment, 3D confocal Z-stacking scanning was done in continuous mode to maximize photobleaching. The 4D confocal imaging results indicate a dramatic improvement of image clarity due to the photostability of SiriusGFP (more than 30 min) compared to eGFP (~10 min). Indeed, after longer exposure (60 min) under the same conditions, SiriusGFP-Omp25 cells continued to exhibit vivid images of intracellular mitochondria (Fig. S3). For instance, the outline of mitochondria were not visible after 60 min of continuous imaging of OMP25 eGFP, but were clearly visible with Sirius GFP.

3.4. Practical applications 2. Structured illumination microscopy (SIM)

We sought to ascertain if SiriusGFP improved the quality of super-resolution microscopy, where the demands on photostability are pronounced. We used structured illumination microscopy (SIM) to explore the advantages of SiriusGFP. The SIM images of fixed HEK-293 cells expressing SiriusGFP-Omp25 was compared to eGFP-Omp25. The image resolution of SIM with SiriusGFP was significantly improved (Fig. 4).

Quantitative measures in Z planes, in particular, show marked improvement in image quality. We repeated the SIM imaging of fixed HeLa cells expressing SiriusGFP-Omp25 and eGFP-Omp25, respectively. Peak to peak Gaussian fitting of over 100 peaks showed an XY resolution of SiriusGFP-Omp25 to be 130 ± 1.4 nm, similar to eGFP-Omp25 with an XY resolution of 131 ± 1.8 nm ($p = 0.546$). In contrast, the Z axis resolution of SiriusGFP-Omp25 was 310 ± 4.6 nm and significantly improved ($p = 0.0017$) over that of eGFP-Omp25 at 335 ± 5.6 nm. These values of SiriusGFP are approaching the limit of SIM resolution (Gustafsson, 2000; Heintzmann and Huser, 2017). Both total photon number and point of spread function (PSF) are key determinants of image quality and resolution. The increased resolution in the Z axis indicates that more photons were collected by the photoelectronic detector with SiriusGFP-Omp25 compared to eGFP-Omp25 since the PSF should be similar.

Although the XY resolution is similar by analysis of profile peaks after the Gaussian fitting of SIM, absent in the quantitative assessment were the qualitative differences in these two FPs. The majority of mitochondria using eGFP-Omp25 demonstrated absent membrane segments on the Z reconstructions (top and bottom profiles) while those using SiriusGFP-Omp25 were much more integrated (Fig. 4). In the XY plane, the mitochondrial membrane labeled with SiriusGFP-Omp25 showed very clear and detailed images; for instance, fission-fusion processes and twisted structures under stress. In contrast, many parts of the mitochondrial membrane labeled with eGFP-Omp25 showed broken/ discontinuous profiles that are likely artifacts from photobleaching (Fig. 5) (Figure.S4). The slower photobleaching of SiriusGFP made superresolution imaging better with more detailed information of subcellular organelles, and also produced less imaging artifacts than eGFP.

4. Discussion

We have developed an improved version of eGFP, named SiriusGFP, that shows a more than 2-fold increase in photostability compared to eGFP and is able to fold well with both N and C terminal fusion proteins. Prestin-SiriusGFP with SiriusGFP fused to the C-terminus of prestin, and SiriusGFP-Omp25 with SiriusGFP fused to the N-terminus of Omp25 both fold well. We have confirmed the obvious biological applicability of SiriusGFP using SIM and 4D confocal microscopy, and explored photobleaching mechanisms for SiriusGFP and eGFP. A number of points about the mechanism of photostability bear discussion below.

In GFPs, there is a seesaw-like action on protonation between the chromophore (p-HBDI) and Glu222. In wtGFP, the chromophore is

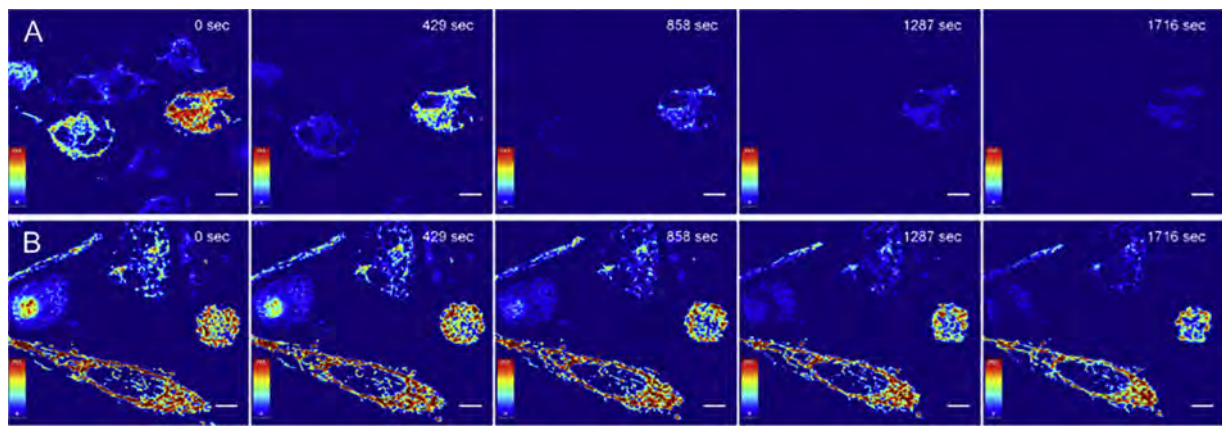


Fig. 3. Continuous confocal 4D imaging of live HeLa cells, in PBS, transfected with eGFP-Omp25 (A, upper panel) and SiriusGFP-Omp25 (B, lower panel), respectively. The confocal Z-stack scanning was continuous, and lasted 30 min. The color table for intensity is shown in the images. The data show SiriusGFP to be significantly resistant to photobleaching with markedly improved image quality even at 30 min. In contrast eGFP shows rapid degradation of image quality owing to photobleaching even at 7 min (429 s). The scale bar is 15 μm .

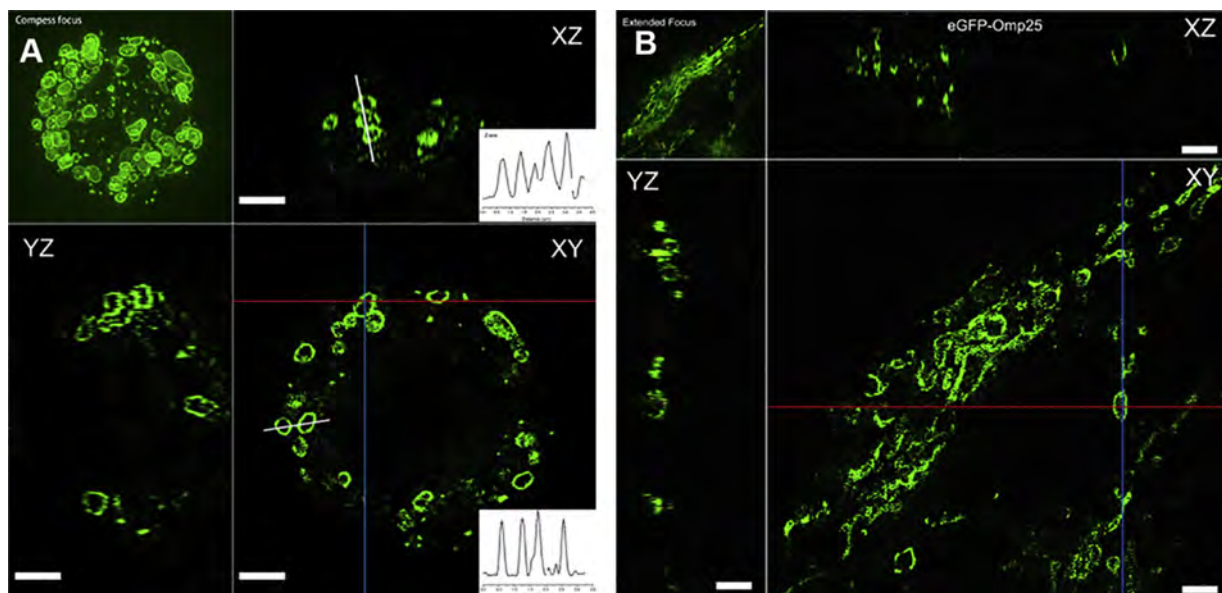


Fig. 4. SiriusGFP enhances SIM image quality, particularly in the Z axis. (A) Shown is the XYZ profile of SiriusGFP-Omp25 transfected HEK-293 cells captured by Structured Illumination Microscopy (SIM, DeltaVision-OMX, Applied Precision, GE life). The blue and red lines indicate the locations where the YZ (upper panel) and XZ (left panel) profiles were obtained. One can distinguish individual mitochondria even from Z axis images. The same image with extended focus has been attached to the left-upper corner. Two line measurements (white line) were performed on individual mitochondria in the Z and XY axes (right inset), respectively. We then used Gaussian fitting of the readout traces to obtain estimates of full width at half maximum (FWHM). (B) Shown is the XYZ profile of eGFP-Omp25. Many of Z profile of mitochondrial outer membrane were missing, and even some of XY profile also showed many discontinuous lines. The scale bar in A is 2.5 μm and B is 2.2 μm .

mainly protonated (80% in neutral state), while Glu222 is correspondingly in a deprotonated anion state. This proton movement is brought about by excited state proton transfer (ESPT). In contrast, the chromophore of eGFP is deprotonated (anion state) while Glu222 is protonated (neutral) at physiological pH (Bettati, Pasqualetto et al. 2011). In SiriusGFP, the chromophore is mixed with the major deprotonated (anion state) and the minor protonated form at a ratio of 4:1 (80% in anion state), and the same emission peak can be observed when excited at ~ 398 nm, indicating ESPT exists in SiriusGFP. But the minor protonated population that absorbs at 396 nm may not be the reason why SiriusGFP is more photostable than eGFP because wtGFP has larger absorption peak at 400 nm, while it is less photostable than eGFP.

Photobleaching in GFPs induced by UV/visible light or X-ray was determined to be related to Glu222 decarboxylation as a point of primary damage and the consequent rearrangement of the H-bond network (van Thor et al., 2002; Bell, Stoner-Ma et al. 2003; Royant and Noirclerc-Savoie, 2011; Arpino, Rizkallah et al. 2012). Glu222

contributes to the rigidity of the chromophore cavity by H-bonding adjacent residues and a cluster of water molecules. The decarboxylation of Glu222 results in the collapse of the H-bonding network next to the chromophore, and further promotes non-irradiative relaxation to the ground state or chromophore destruction (Royant and Noirclerc-Savoie, 2011). Still, there is a gap in our understanding of Glu222 decarboxylation and final chromophore destruction.

Light or X-ray irradiation on FPs can produce radical species by electron transfer (ET) from the excited chromophore. It was suggested that in wtGFP and PA-GFP the excitation of chromophore may promote charge transfer from Glu222 to the chromophore. This induces a biradical state that then relaxes back to the ground state or occasionally leads to decarboxylation of Glu222 that, in turn, leads to permanent chromophore destruction (Adam, Carpentier et al. 2009). The Kolbe mechanism was proposed to be responsible for the photoinduced decarboxylation of Glu222 in wtGFP (van Thor et al., 2002). However, after ultrafast ESPT in femtosecond scale the excited chromophore is

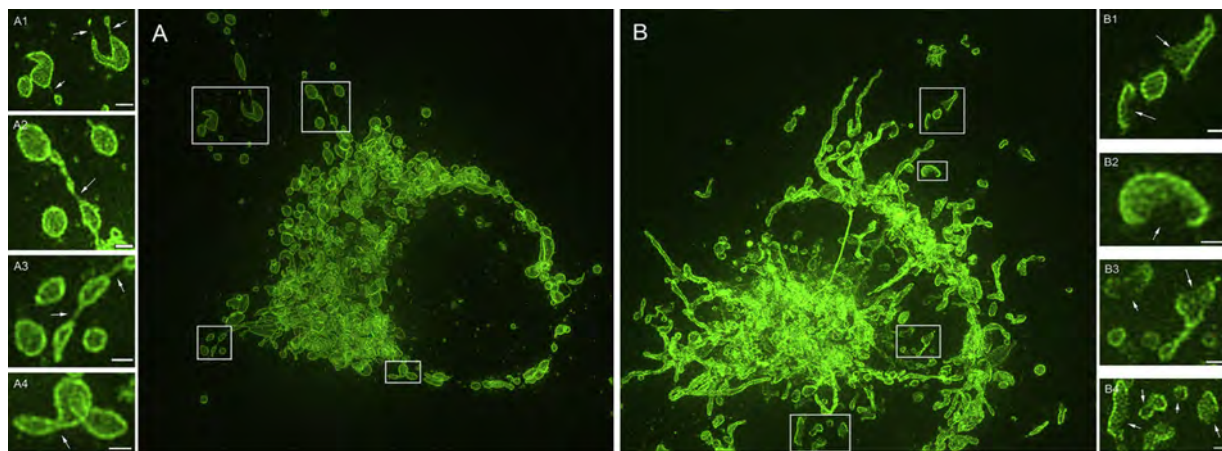


Fig. 5. (A) SiriusGFP shows qualitative enhancement in SIM images in the XY plane. A SIM image of SiriusGFP-Omp25 in HeLa cells. This sample was fixed with 4% PFA and imaged in PBS. The insets are the enlarged area of the white boxes. The uniformity of the mitochondrial outer membrane and the z-axis accumulation was very well achieved. A number of details can be discerned in the high quality images including mitochondrial fusion/fission (A1-3, arrows) and bended/twisted (A-4, arrows) structures shown in the insets.

(B) In the XY plane of eGFP is qualitatively inferior to SiriusGFP in SIM imaging. A SIM image of eGFP-Omp25 in HeLa cells. This sample was fixed with 4% PFA and imaged in PBS. The insets are the enlarged area of the white boxes. The uniformity of the mitochondrial outer membrane was interrupted by obvious breaks (B1-4, arrows) and the Z-axis accumulation cannot be well achieved due to the photobleaching of eGFP. The patchy depletion of the mitochondrial outer membranes are notable (B, B1-4). These images are in contrast to those obtained with SiriusGFP, where mitochondrial outer membranes show consistent and uniform patterns with no artifactual loss (A, A1-4). The scale bars are 0.5 μm .

turned to an anionic state that may not be able to be an electron acceptor. Moreover, in eGFP the chromophore is dominantly in the anion state. Another photophysical pathway had been proposed that triggers redox reactions inside GFP (Bochenkova, Klaerke et al. 2014), in which the chromophore anion HBDI⁻ undergoes a photodetachment upon absorption of one-photon UV or multi-photon visible light to produce a solvated electron and a radical chromophore. Thereafter, the photo-oxidized radical chromophore can accept an electron as an oxidant in Glu222 decarboxylation.

The interruption of the proton wire between HBDI and Glu222 by S205 V may hinder the electron transfer, therefore reducing the possibility of the biradical state and further chromophore destruction. However, the double mutant of eGFP-T203 V/S205 V that lacks both possible pathways of ESPT also shows photobleaching (data not shown), implying that the photobleaching pathway may not be limited by Glu222 damage.

4.1. Z-E isomerization

Upon excitation of chromophore *p*-HBDI of GFPs, the Z-E isomerization undergoes the τ -torsion around the only exocyclic double bond with a τ angle smaller than 90°, followed by internal conversion (IC) mostly to the ground state of Z isomers. The τ -torsion transiently disrupts the conjugated π -electron system for reversible loss in fluorescence, which could be the major non-radiative decay channel for the excited state S_1 of *p*-HBDI in GFPs (Chatterjee, Mandal et al. 2015).

In eGFP, the first excited state S_1 deactivates mainly via fluorescence with high quantum yield (~0.60) attributed to limiting τ -rotation around the only exocyclic double bond by H-bond network.

That the quantum yield ϕ_f of SiriusGFP is smaller than that of eGFP is probably due to less constraints on the phenolic group of *p*-HBDI; the lack of H-bond binding on Ser205 facilitates τ -torsion and thereby could increase internal conversion by facilitating τ -torsion along the methylene bridge between imidazolinone and phenolate moieties. Meanwhile, the τ -torsion with less constraints in SiriusGFP may also increase the possibility of internal conversion from S_n to S_{n-1} (e.g., $S_1 \leftarrow S_2$ or $S_2 \leftarrow S_3$). This in turn can decrease the possibility of electron-detachment and subsequent chromophore destruction. Quantum yield is proportional to brightness, but may not directly affect photostability.

That is, lower quantum yield does not mean higher photostability. For instance, most red FPs have low quantum yield (< 0.20) but are still easily photobleached (Cranfill, Sell et al. 2016). The electron transfer during deactivation may be the critical step for chromophore damage.

The methylene bridge between imidazolinone and phenolate moieties can perform τ -torsion for internal conversion or lead to Glu222 decarboxylation and chromophore destruction, depending on how many photons are absorbed by the chromophore and if ROS or solvated electrons nearby are available. A nearby oxygen can accept a photoelectron from the anionic GFP chromophore to form superoxide radicals on the exocyclic methylene bridge of the chromophore. This superoxide radical consequently undergoes a further series of chemical reactions resulting in the cleavage of the exocyclic bridging bond of the chromophore resulting in permanent bleaching (Grigorenko, Nemukhin et al. 2015). The electron transfer in eGFP may occur from the chromophore anion to external oxidants via an intermediate aromatic residue, Tyr145 (Bogdanov, Acharya et al. 2016). Substitution of key residues controlling electron transfer to external oxidants would be expected to increase photostability, although the detailed effects on different substituted residues need further investigation (Hosoi, Hazama et al. 2015). We tested mutation of Y145I and Y145E in eGFP and SiriusGFP. Both mutants showed dimmed fluorescence (data not shown), perhaps due to the over 3-fold decrease in the extinction coefficients of Y145I or Y145E (Bogdanov, Acharya et al. 2016). S147R associating with H148 at the entrance of access to the phenolic group of the chromophore may help block exterior ROS. Both its positive charge and bulky side chain could contribute to the photostability without the fast decay phase seen in N149K in Emerald-GFP. The photobleaching results (Fig. 1B) suggest that S147R may play an important role in blocking the entrance of external oxidants or, alternatively, affecting the electron transfer efficiency to external oxidants.

In summary, photobleaching is one of the major problems for genetically encoded FPs, which limits their application in biological investigations. We have developed a FP, SiriusGFP, that shows significant improvement in photostability over eGFP in high and low intensity illumination. While Sirius GFP has reduced brightness compared to eGFP, its 2-fold increase in photostability allows for much improved imaging requiring high or prolonged intensity light. In practical terms this gain in stability allows imaging without a dynamic adjustment in

exposure time and light intensity with increasing experimental time. Our new FP will provide improved capabilities for superresolution and time-dependent confocal microscopy.

Acknowledgement

We would like to thank Dr. Lena Schroeder for kindly sharing eGFP-Omp25 plasmid with us.

This work was funded by the National Institute of Health grant, NIDCD R01 DC 000273 and NIDCD R01 DC 016318 to J.S.S., R01 DC 008130 to J.S.S. and D.S.N., and R01 DC 007894 to D.S.N.

Appendix A. Supplementary data

Supplementary material related to this article can be found, in the online version, at doi:<https://doi.org/10.1016/j.jneumeth.2018.12.008>.

References

- Adam, V., Carpentier, P., Violot, S., Lelimosin, M., Darnault, C., Nienhaus, G.U., Bourgeois, D., 2009. Structural basis of X-ray-induced transient photobleaching in a photoactivatable green fluorescent protein. *J. Am. Chem. Soc.* 131 (50), 18063–18065.
- Andrews, B.T., Schoenfish, A.R., Roy, M., Waldo, G., Jennings, P.A., 2007. The rough energy landscape of superfolder GFP is linked to the chromophore. *J. Mol. Biol.* 373 (2), 476–490.
- Arpino, J.A., Rizkallah, P.J., Jones, D.D., 2012. Crystal structure of enhanced green fluorescent protein to 1.35 Å resolution reveals alternative conformations for Glu222. *PLoS One* 7 (10) e47132.
- Baker, B.J., Mutoh, H., Dimitrov, D., Akemann, W., Perron, A., Iwamoto, Y., Jin, L., Cohen, L.B., Isacoff, E.Y., Pieribone, V.A., Hughes, T., Knopfel, T., 2008. Genetically encoded fluorescent sensors of membrane potential. *Brain Cell Biol.* 36 (1–4), 53–67.
- Bell, A.F., Stoner-Ma, D., Wachter, R.M., Tonge, P.J., 2003. Light-driven decarboxylation of wild-type green fluorescent protein. *J. Am. Chem. Soc.* 125 (23), 6919–6926.
- Bettati, S., Pasqualetto, E., Lolli, G., Campanini, B., Battistutta, R., 2011. Structure and single crystal spectroscopy of Green Fluorescent Proteins. *Biochim. Biophys. Acta* 1814 (6), 824–833.
- Bochenkova, A.V., Klaerke, B., Rahbek, D.B., Rajput, J., Toker, Y., Andersen, L.H., 2014. UV excited-state photoresponse of biochromophore negative ions. *Angew. Chem. Int. Ed. Engl.* 53 (37), 9797–9801.
- Bogdanov, A.M., Bogdanova, E.A., Chudakov, D.M., Gorodnicheva, T.V., Lukyanov, S., Lukyanov, K.A., 2009. Cell culture medium affects GFP photostability: a solution. *Nat. Methods* 6 (12), 859–860.
- Bogdanov, A.M., Acharya, A., Titelmayer, A.V., Mamontova, A.V., Bravaya, K.B., Kolomeisky, A.B., Lukyanov, K.A., Krylov, A.I., 2016. Turning On and Off Photoinduced Electron Transfer in Fluorescent Proteins by pi-Stacking, Halide Binding, and Tyr145 Mutations. *J. Am. Chem. Soc.* 138 (14), 4807–4817.
- Chatterjee, T., Mandal, M., Gude, V., Bag, P.P., Mandal, P.K., 2015. Strong electron donation induced differential nonradiative decay pathways for para and meta GFP chromophore analogues. *Phys. Chem. Chem. Phys.* 17 (32), 20515–20521.
- Chen, T.S., Zeng, S.Q., Luo, Q.M., Zhang, Z.H., Zhou, W., 2002. High-order photobleaching of green fluorescent protein inside live cells in two-photon excitation microscopy. *Biochem. Biophys. Res. Commun.* 291 (5), 1272–1275.
- Chen, T.W., Wardill, T.J., Sun, Y., Pulver, S.R., Renninger, S.L., Baohan, A., Schreiter, E.R., Kerr, R.A., Orger, M.B., Jayaraman, V., Looger, L.L., Svoboda, K., Kim, D.S., 2013. Ultrasensitive fluorescent proteins for imaging neuronal activity. *Nature* 499 (7458), 295–300.
- Cranfill, P.J., Sell, B.R., Baird, M.A., Allen, J.R., Lavagnino, Z., de Gruiter, H.M., Kremers, G.J., Davidson, M.W., Ustione, A., Piston, D.W., 2016. Quantitative assessment of fluorescent proteins. *Nat. Methods* 13 (7), 557–562. <https://doi.org/10.1038/nmeth.3891>. Epub 2016 May 30. PMID: 27240257.
- Cubitt, A.B., Woollenweber, L.A., Heim, R., 1999. Understanding structure-function relationships in the *Aequorea victoria* green fluorescent protein. *Methods Cell Biol.* 58, 19–30.
- Erez, Y., Gepshtein, R., Presiado, I., Trujillo, K., Kallio, K., Remington, S.J., Huppert, D., 2011. Structure and excited-state proton transfer in the GFP S205A mutant. *J. Phys. Chem. B* 115 (41), 11776–11785.
- Fang, C., Frontiera, R.R., Tran, R., Mathies, R.A., 2009. Mapping GFP structure evolution during proton transfer with femtosecond Raman spectroscopy. *Nature* 462 (7270), 200–204.
- Fukuda, H., Arai, M., Kuwajima, K., 2000. Folding of green fluorescent protein and the cycle3 mutant. *Biochemistry* 39 (39), 12025–12032.
- Greenbaum, L., Rothmann, C., Lavie, R., Malik, Z., 2000. Green fluorescent protein photobleaching: a model for protein damage by endogenous and exogenous singlet oxygen. *Biol. Chem.* 381 (12), 1251–1258.
- Grigorenko, B.L., Nemukhin, A.V., Polyakov, I.V., Khrenova, M.G., Krylov, A.I., 2015. A Light-Induced Reaction with Oxygen Leads to Chromophore Decomposition and Irreversible Photobleaching in GFP-Type Proteins. *J. Phys. Chem. B* 119 (17), 5444–5452.
- Gustafsson, M.G., 2000. Surpassing the lateral resolution limit by a factor of two using structured illumination microscopy. *J. Microsc.* 198 (Pt 2), 82–87.
- Heintzmann, R., Huser, T., 2017. Super-resolution structured illumination microscopy. *Chem. Rev.* 117 (23), 13890–13908.
- Hong, S., Wilton, D.K., Stevens, B., Richardson, D.S., 2017. Structured illumination microscopy for the investigation of synaptic structure and function. *Methods Mol. Biol.* 1538, 155–167.
- Hosoi, H., Hazama, S., Takeda, Y., 2015. Smaller 145th residue makes fluorescent protein non-fluorescent: Fluorescence lifetimes of enhanced yellow fluorescent protein (eYFP) Y145 mutants and H148 mutants. *Chem. Phys. Lett.* 618, 186–191.
- Huang, G.J., Cheng, C.W., Hsu, H.Y., Prabhakar, C., Lee, Y.P., Diau, E.W., Yang, J.S., 2013. Effects of hydrogen bonding on internal conversion of GFP-like chromophores. I. The para-amino systems. *J. Phys. Chem. B* 117 (9), 2695–2704.
- Jimenez-Banzo, A., Nonell, S., Hofkens, J., Flors, C., 2008. Singlet oxygen photosensitization by EGFP and its chromophore HB1. *Biophys. J.* 94 (1), 168–172.
- Nemoto, Y., De Camilli, P., 1999. Recruitment of an alternatively spliced form of synaptotagmin 2 to mitochondria by the interaction with the PDZ domain of a mitochondrial outer membrane protein. *EMBO J.* 18 (11), 2991–3006.
- Nielsen, S.B., Lapiere, A., Andersen, J.U., Pedersen, U.V., Tomita, S., Andersen, L.H., 2001. Absorption spectrum of the green fluorescent protein chromophore anion in vacuo. *Phys. Rev. Lett.* 87 (22) 228102.
- Niwa, H., Inouye, S., Hirano, T., Matsuno, T., Kojima, S., Kubota, M., Ohashi, M., Tsuji, F.I., 1996. Chemical nature of the light emitter of the *Aequorea* green fluorescent protein. *Proc. Natl. Acad. Sci. U. S. A.* 93 (24), 13617–13622.
- Olivier, N., Keller, D., Gonczy, P., Manley, S., 2013. Resolution doubling in 3D-STORM imaging through improved buffers. *PLoS One* 8 (7).
- Ottmann, C., Weyand, M., Wolf, A., Kuhlmann, J., Ottmann, C., 2009. Applicability of superfolder YFP bimolecular fluorescence complementation in vitro. *Biol. Chem.* 390 (1), 81–90.
- Pedelacq, J.D., Cabantous, S., Tran, T., Terwilliger, T.C., Waldo, G.S., 2006. Engineering and characterization of a superfolder green fluorescent protein. *Nat. Biotechnol.* 24 (1), 79–88.
- Rego, E.H., Shao, L., 2015. Practical structured illumination microscopy. *Methods Mol. Biol.* 1251, 175–192.
- Royant, A., Noirclerc-Savoye, M., 2011. Stabilizing role of glutamic acid 222 in the structure of enhanced Green Fluorescent Protein. *J. Struct. Biol.* 174 (2), 385–390.
- Shu, X., Leiderman, P., Gepshtein, R., Smith, N.R., Kallio, K., Huppert, D., Remington, S.J., 2007. An alternative excited-state proton transfer pathway in green fluorescent protein variant S205V. *Protein Sci.* 16 (12), 2703–2710.
- Tsien, R.Y., 1998. The green fluorescent protein. *Annu. Rev. Biochem.* 67, 509–544.
- van Thor, J.J., Gensch, T., Hellingwerf, K.J., Johnson, L.N., 2002. Phototransformation of green fluorescent protein with UV and visible light leads to decarboxylation of glutamate 222. *Nat. Struct. Biol.* 9 (1), 37–41.
- Wineman-Fisher, V., Simkovitch, R., Shomer, S., Gepshtein, R., Huppert, D., Saif, M., Kallio, K., Remington, S.J., Miller, Y., 2014. Insight into the structure and the mechanism of the slow proton transfer in the GFP double mutant T203V/S205A. *Phys. Chem. Chem. Phys.* 16 (23), 11196–11208.
- Yang, J.S., Huang, G.J., Liu, Y.H., Peng, S.M., 2008. Photoisomerization of the green fluorescence protein chromophore and the meta- and para-amino analogues. *Chem. Commun. (Camb.)* (11), 1344–1346.
- Zacharias, D.A., Violin, J.D., Newton, A.C., Tsien, R.Y., 2002. Partitioning of lipid-modified monomeric GFPs into membrane microdomains of live cells. *Science* 296 (5569), 913–916.
- Zhong, S., Navaratnam, D., Santos-Sacchi, J., 2014. A genetically-encoded YFP sensor with enhanced chloride sensitivity, photostability and reduced pH interference demonstrates augmented transmembrane chloride movement by gerbil prestin (SLC26a5). *PLoS One* 9 (6) e99095.



A Genetically-Encoded YFP Sensor with Enhanced Chloride Sensitivity, Photostability and Reduced pH Interference Demonstrates Augmented Transmembrane Chloride Movement by Gerbil Prestin (SLC26a5)

Sheng Zhong¹, Dhasakumar Navaratnam^{1,2,3}, Joseph Santos-Sacchi^{1,3,4*}

1 Dept. of Surgery (Otolaryngology), Yale University School of Medicine, New Haven, Connecticut, United States of America, **2** Dept. of Neurobiology, Yale University School of Medicine, New Haven, Connecticut, United States of America, **3** Dept. of Neurology, Yale University School of Medicine, New Haven, Connecticut, United States of America, **4** Dept. of Cellular and Molecular Physiology, Yale University School of Medicine, New Haven, Connecticut, United States of America

Abstract

Background: Chloride is the major anion in cells, with many diseases arising from disordered Cl⁻ regulation. For the non-invasive investigation of Cl⁻ flux, YFP-H148Q and its derivatives chameleon and Cl-Sensor previously were introduced as genetically encoded chloride indicators. Neither the Cl⁻ sensitivity nor the pH-susceptibility of these modifications to YFP is optimal for precise measurements of Cl⁻ under physiological conditions. Furthermore, the relatively poor photostability of YFP derivatives hinders their application for dynamic and quantitative Cl⁻ measurements. Dynamic and accurate measurement of physiological concentrations of chloride would significantly affect our ability to study effects of chloride on cellular events.

Methodology/Principal Findings: In this study, we developed a series of YFP derivatives to remove pH interference, increase photostability and enhance chloride sensitivity. The final product, EYFP-F46L/Q69K/H148Q/I152L/V163S/S175G/S205V/A206K (monomeric Cl-YFP), has a chloride K_d of 14 mM and pK_a of 5.9. The bleach time constant of 175 seconds is over 15-fold greater than wild-type EYFP. We have used the sensor fused to the transmembrane protein prestin (gerbil prestin, SLC26a5), and shown for the first time physiological (mM) chloride flux in HEK cells expressing this protein. This modified fluorescent protein will facilitate investigations of dynamics of chloride ions and their mediation of cell function.

Conclusions: Modifications to YFP (EYFP-F46L/Q69K/H148Q/I152L/V163S/S175G/S205V/A206K (monomeric Cl-YFP) results in a photostable fluorescent protein that allows measurement of physiological changes in chloride concentration while remaining minimally affected by changes in pH.

Citation: Zhong S, Navaratnam D, Santos-Sacchi J (2014) A Genetically-Encoded YFP Sensor with Enhanced Chloride Sensitivity, Photostability and Reduced pH Interference Demonstrates Augmented Transmembrane Chloride Movement by Gerbil Prestin (SLC26a5). PLoS ONE 9(6): e99095. doi:10.1371/journal.pone.0099095

Editor: Stefan Strack, University of Iowa, United States of America

Received: December 23, 2013; **Accepted:** May 12, 2014; **Published:** June 5, 2014

Copyright: © 2014 Zhong et al. This is an open-access article distributed under the terms of the Creative Commons Attribution License, which permits unrestricted use, distribution, and reproduction in any medium, provided the original author and source are credited.

Funding: Support was provided by National Institutes of Health National Institute on Deafness and Other Communication Disorders grants DC 000273 (to J.S.S.). The funders had no role in study design, data collection and analysis, decision to publish, or preparation of the manuscript.

Competing Interests: The authors have declared that no competing interests exist.

* E-mail: joseph.santos-sacchi@yale.edu

Introduction

Chloride is the major anion in cells, and plays various physiological roles. For example, chloride is a key determinant of intestinal fluid secretion and cell volume primarily through affecting osmotic gradients [1–3]. Chloride is also important in setting neuronal resting membrane potential through a number of chloride channels and inhibitory neurotransmitter receptors that have chloride conductance [4]. As a natural consequence of affecting these diverse phenomena many diseases result from disordered Cl⁻ regulation [5]. These diverse effects of chloride underscore the need to accurately and dynamically measure physiological intracellular chloride concentration.

While many proteins work to regulate intracellular Cl⁻, others are regulated by intra- and extracellular Cl⁻. For example, the unique membrane protein prestin in outer hair cells (OHCs),

SLC26a5, functions as an ultrafast molecular motor, converting electrical to mechanical energy. This protein is thought to bring about cochlear amplification in mammals, which is responsible for the exquisite sensitivity of mammalian hearing. Intracellular chloride ions in the 0–10 mM range regulate the behavior of prestin, shifting its voltage responsiveness by –2 mV per mM of chloride (with gluconate as the counter anion). These *in vitro* findings have been supported by *in vivo* experiments demonstrating effects of chloride on cochlear amplification [6]. Hence, dynamic monitoring of intracellular Cl⁻ concentrations near prestin's intracellular chloride binding site will aid in understanding chloride's role in cochlear amplification. We previously have used the fluorescent dye MQAE to measure chloride flux in OHCs [7], but the technical problems with this approach are overwhelming. Consequently, we have worked to develop a genetically encoded

chloride sensor that can be tagged on the intracellular C-terminus of prestin, sensing chloride fluctuation during prestin activity.

Over the last decade, engineered fluorescent proteins (FPs) were developed as genetically encoded indicators allowing non-invasive monitoring of intracellular ion fluctuations, such as Cl^- [8–11], pH [12,13], and Ca^{2+} [14–16]. FPs are also quite useful for measuring membrane potential [17–19] and other cell biological phenomena. Most of them are GFP-based variants or FRET pair probes, like CFP-YFP.

EYFP, GFP-S65G/V68L/S72A/T203Y, has proven to respond rapidly and reversibly to concentration changes of halides, which enables YFPs to be genetically encoded Cl^- sensors in living cells. YFP-H148Q and its derivatives [8], including CFP-YFP-based Clomeleon [9], were introduced as genetically encoded chloride indicators, in which H148Q enhances the halide affinity due to better binding cavity access via a solvent channel, thereby favoring chromophore protonation following halide binding to reduce fluorescence [20]. The K_d of YFP at pH 7.5 is 777 mM, and 154 mM for YFP-H148Q, far removed from intracellular $[\text{Cl}^-]$ under physiological conditions. In the YFP-H148Q library, I152L and V163S exhibit higher chloride affinity with a K_d of 88 mM and 62 mM, respectively [10,21,22]. The triple mutant of YFP-H148Q/I152L/V163S was adopted in the CFP-YFP-based emission ratiometric Cl^- indicator (Cl-sensor) [11]. In Cl-sensor, the real sensor for chloride is the YFP mutant itself with $K_d \sim 30$ mM, instead of requiring a peptide linker between CFP and YFP, or an extrinsic sensor such as calmodulin in Cameleon [23]. In YFPs, the halide-binding cavity near the chromophore has the ability to modulate the protonation state of the chromophore, and this is the basis of YFP's chloride sensitivity. In the CFP-YFP based indicator, CFP is insensitive to halides, providing an *in situ* ratiometric calibration for YFP.

Compared to calcium FP-sensors, the YFP-based chloride sensor has less sensitivity (high mM scale instead of μM or nM), less photostability and is usually accompanied by significant, confounding pH effects near physiological pH. To date, YFP-based Cl^- indicators are limited in their application because of these three reasons. In this study, we developed a series of YFP mutants extending previous work. We introduced a positive charged residue, Q69K, into the halide-binding cavity to decrease pK_a , and two folding mutations, F46L/S175G, to enhance folding. Furthermore, we uncovered a key mutation in the proton delivery pathway, S205V, which 1) increased the time constants of photobleaching 15-fold greater than wild-type EYFP, 2) lowered the pK_a away from physiological pH, and 3) enhanced the chloride sensitivity to 14 mM. These improvements provide for a superior chloride sensor. Finally, using this new enhanced chloride sensor, we demonstrate dynamic flux of chloride in the mM range into prestin expressing HEK cells.

Results

ClSM, a YFP Modification with Intermediate Chloride Sensitivity and pH Dependence

In designing a chloride sensitive YFP we evaluated and adopted a number of amino acid changes that had previously been shown to enhance fluorescence and stability. The maturation of YFP includes two phases, peptide chain folding and chromophore formation. F46L significantly accelerates chromophore oxidation, while the well-known folding mutations of F64L, M153T, V163A and S175G facilitate the folding process of the peptide chain [20,24]. These mutations that affect folding and the rate limiting chromophore oxidation step also affect chloride sensitivity. F64L counteracts the conformational change in orientation caused by

V68L in the YFP variant Venus, and also induces reduced halide sensitivity by preventing halide ion access to its binding site [24]. V68L is included in native EYFP, and we therefore opted to not include F64L in our new Cl^- sensor. Since V163A may also be involved in eliminating chloride sensitivity in Venus by presumed shortening of the side chain, we introduced V163S, with a longer side chain that enhances halide sensitivity [10] while simultaneously maintaining photostability. Similarly, S175G that breaks an existing hydrogen bond network facilitates folding and enhances fluorescence intensity of Venus [24,25] and ECFP [25], and was incorporated in our constructs. M153T by virtue of its smaller side chain and increased flexibility [26] has also been shown to facilitate folding and increase fluorescence intensity. However, this mutation seemed to affect the expression of YFP in several of our constructs and was therefore not incorporated in our final constructs.

There are nine residues in the halide-binding cavity near the chromophore of YFP that have direct interaction or a distance of less than 5 Å from the binding halide anion, namely, Q69, R96, V150, I152, V163, F165, Q183, L201 and Y203 [20]. T203Y is the key mutational difference between YFP and GFP, and I152L/V163S already exist in the sequence of EYFP-H148Q/I152L/V163S from which we began our development effort. Q69 is fairly close to the chromophore anion inside the β -barrel of YFP. It was previously reported that Q69K could promote the anionic form of the chromophore to hinder its protonation, and therefore reduce the apparent pK_a to 6.1, with little effect on its other sensitivities [27]. But we found that the mutant Q69K when added to EYFP-H148Q/I152L/V163S folds poorly at 37°C, which was previously reported in EYFP-V68L/Q69K [27], possibly resulting from the extra length of the Lysine side chain and disturbing the hydrogen-bond network in the halide-binding cavity. Fortunately, this folding problem of Q69K can be compensated by the folding mutation of F46L. F46L can greatly accelerate the oxidation of the chromophore at 37°C, the rate-limiting step of maturation of chromophore, without changing the pK_a of EYFP [24]. The new construct, EYFP-F46L/Q69K/H148Q/I152L/V163S, which we term **ClSM**, expressed very well in HEK-293 cells, showing bright fluorescence. The pK_a of **ClSM** was reduced to 6.5~7.1 and was dependent on the chloride concentration (0.2 mM and 140 mM, respectively). The chloride sensitivity of **ClSM** remained at ~ 30 mM (data not shown). Interestingly, the alternative replacement of Q69 with arginine could barely fold to exhibit fluorescence in transiently transfected HEK-293 cells, probably because of the large side chain of the arginine residue. In this study, all further mutants are made based on **ClSM**.

Mutations to Reduce pH Sensitivity Resulted in Enhanced Photostability and Further Increased Chloride Sensitivity

Positive charges in the halide-binding cavity close to the YFP chromophore not only increase the affinity of halide binding, but also promote the anion state of the chromophore, which in turn can reduce the pK_a of the chromophore by dispersing negative charge over the conjugated structure of the chromophore. So our first strategy for improvement was introducing more positively charged residues into the halide-binding cavity.

We evaluated the addition of another positive charge besides Q69K into the halide-binding cavity of **ClSM** attempting to reduce confounding pH effects by single-site mutation of the individual residues V150, F165, Q183, L201 to lysine or arginine. However, all of the double-charge mutants (V150K/R, F165K/R, Q183K/R, L201K/R, each in combination with Q69K) could not fold to exhibit fluorescence, even in the presence of two additional folding mutations of M153T and S175G, as well as

F46L. The double-charge mutants of Q69K/F165K and Q69K/L201K express somewhat better, but still showed lower than normal YFP fluorescence. We concluded that the double-charge residues in the halide-binding cavity can significantly affect the folding of YFP. We speculate that this could result from difficulty in burying an extra positive charge (in addition to R96 and Q69K) into the cavity proximal to the chromophore, due either to excess electrostatic forces or cavity size limitations.

The other strategy to lower the pK_a of the YFP-based chloride sensor is to set a barrier within the proton delivery pathway to the phenolate anion of the chromophore, which is protonated via a hydrogen bond network composed of the main chain of residue N146, the side chain of S205 and a bridging water molecule linked with a surface water molecule. The protons are delivered from the external solvent into the YFP β -barrel through this hydrogen bond network. If the proton delivery pathway is blocked or impeded, lower pH (higher $[H^+]$) is needed to overcome the obstructed proton access, indicating that pK_a is reduced. We chose S205 as the essential target site to impede proton access. S205 was substituted with other neutral residues without hydroxyl groups, such as alanine, leucine, isoleucine, and valine. Interestingly, we found that in addition to its influence in altering pK_a , S205 substitutions also enhanced photostability. Valine substitution of S205 has the best photostability. The percentage of residual fluorescence after photobleaching is the highest with this mutant S205V. Thus, the time constant of fluorescence photobleaching is 175 s compared to the **Cl₅M** bleaching time constant of ~ 10 s (**Fig. 1**). Note that the folding mutations S175G or M153T does not enhance photostability.

Work from the Tsien laboratory has shown that the tendency for YFP dimerization can be greatly reduced or eliminated by mutating the hydrophobic amino acids in the dimerization interface to positively charged residues [28]. The order of effectiveness is A206K>L221K>F223R. The dissociation constant K_d of mYFP-A206K derived from the association constant (K_a) is much higher than that of mYFP-L221K and mYFP-F223R

[29]. Because prestin can oligomerize, we included the A206K mutation into the construct to make a monomeric version that will avoid aggregation when making fusion proteins with a targeting protein. Therefore, EYFP-F46L/Q69K/H148Q/I152L/V163S/S175G/S205V and its monomeric version with A206K, now termed **Cl-YFP** and **mCl-YFP (or mClY for short)**, respectively, were characterized in detail to determine their pK_a and chloride sensitivity.

Cl-YFP and mCl-YFP are significantly less pH sensitive than Cl₅M, with a pK_a of ~ 5.3 for Cl-YFP (data not shown) and a pK_a of ~ 5.9 for mCl-YFP (**Fig. 2A**), both of which are far removed from physiological pH conditions. The pK_a of mCl-YFP is slightly higher than that of Cl-YFP, indicating better access for protons to reach the chromophore. This is likely due to a smaller steric barrier on the dimer interface. Although Cl-YFP and mCl-YFP have similar time constants for photobleaching, about 175 s, the percentage of residual fluorescence after bleaching was different; 50% and 65%, respectively (**Fig. 1**). Finally, mCl-YFP has a higher chloride sensitivity of 14.4 mM (**Fig. 2B**) compared to the previously reported best value of ~ 30 mM for all YFP variants [11]. It should be noted that the larger reduction in fluorescence (F/F_0) for low pH (**Fig. 2A**) versus high chloride (**Fig. 2B**) likely arises because protonation of the chromophore directly quenches the fluorescence of YFP, while chloride binding would change the proton affinity of chromophore, consequently reducing fluorescence intensity. Residual fluorescence that we measure likely depends on the oxidation equilibrium of fluorophor under the given spectrum and level of illumination such as optical power. It might be that if we changed these photobleaching conditions or solution pH that these asymptotic levels would differ. The point that we make is that under the same photobleaching conditions the relative response differs among mutations, with our mCl-YFP showing the best bleaching time constant, best pK_a and best K_d for chloride as well as the strong capability of removing YFP dimerization. The important point about bleaching is that it is minimized during the course of an experiment.

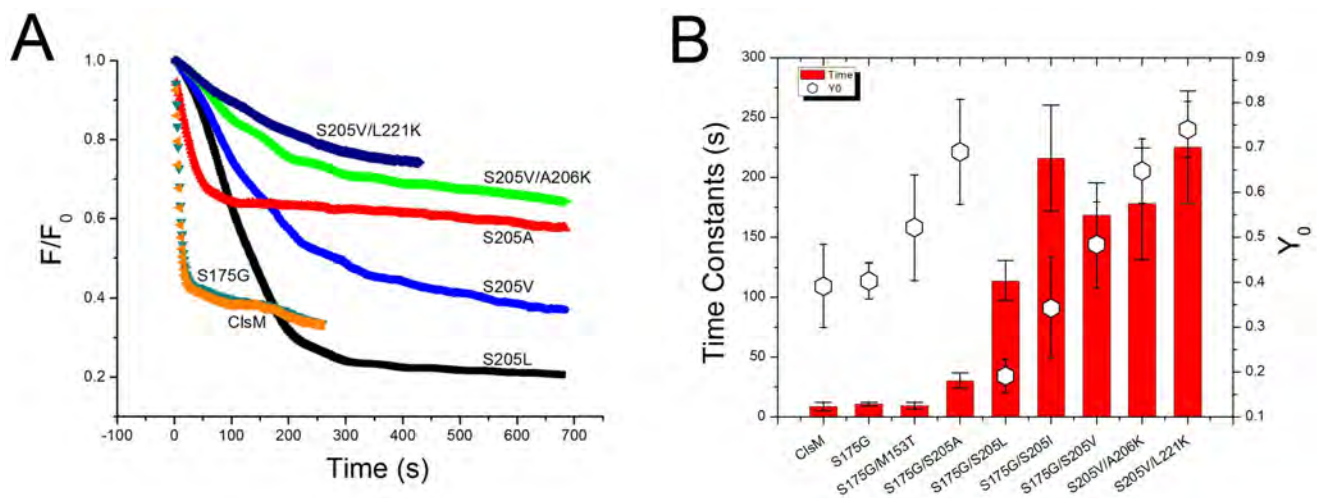


Figure 1. Photobleaching dynamics of YFP chloride sensor mutations. (A) Representative traces of some YFP variants photobleached at 430 nm. All variants are based on the EYFP-F46L/Q69K/H148Q/I152L/V163S (**Cl₅M**). Photobleaching data were fit by a single exponential decay function, $Y = Y_0 + Ae^{-x/t}$, where Y_0 is the constant offset representing the residual fluorescence after photobleaching (R^2 ranged from 0.96–0.99). It is notable that the mutant Cl₅M-S175G/S205V/A206K (mClY, green curve) has a long time constant of 175 s under our photobleaching conditions, which is much longer than wild-type YFP and **Cl₅M** each at ~ 10 s. **(B)** The red columns are the time constants of fluorescence decay during photobleaching, and Y_0 is the constant offset of fluorescence exponential decay by photobleaching, representing the residual fluorescence when photobleaching reached a stable state. The folding mutations of S175G and M153T did not enhance the photostability of **Cl₅M**, while the mutations of S205 did increase the time constants of fluorescence decay.
doi:10.1371/journal.pone.0099095.g001

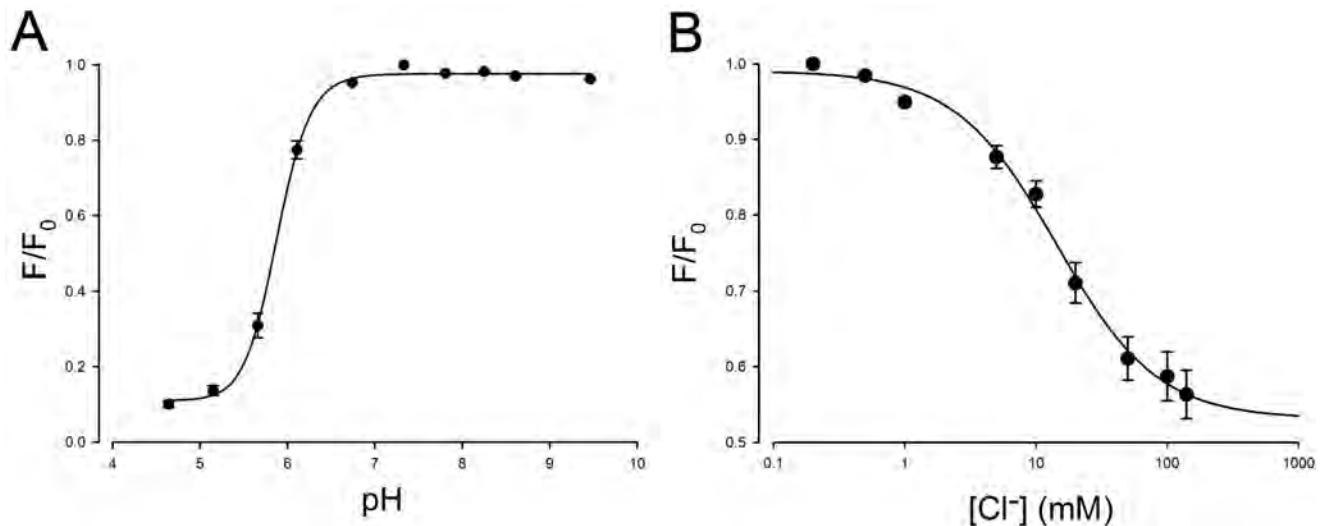


Figure 2. pH-sensitivity and chloride sensitivity of mCl-YFP measured by local perfusion of individual cells. (A) The pH-sensitivity of mCl-YFP fluorescence with a pK_a of 5.88 calibrated with a fixed 0.2 mM Cl^- solution containing 100 μ M TBT and 50 μ M Nigericin. F_0 is the initial fluorescence at pH 7.20. For each data point, fluorescence data of more than 35 cells were averaged. Note in each case that the pK_a is far removed from physiological pH. (B) The chloride sensitivity of mCl-YFP with a K_d of 14.4 mM at a fixed 0.2 mM Cl^- solution using 100 μ M TBT and 50 μ M nigericin at pH 7.20. F_0 is the initial fluorescence under 0.2 mM Cl^- . For each data point, fluorescence data of more than 25 cells were averaged. The sensitivity is doubled compared to previous YFP-based Cl^- sensors, and within the physiological range of cellular Cl^- changes. doi:10.1371/journal.pone.0099095.g002

The Outer Hair Cell Protein Prestin Shows Dynamic Chloride Movement that is Demonstrable with the Enhanced Chloride Sensor

To test our improved chloride sensor, mCl-YFP was fused to the C-terminus of the OHC motor protein, prestin, and transfected the construct into HEK-293T cells. After 24 hrs of incubation, chloride flux into the transfected cells was monitored during changes in extracellular chloride from 0.2 mM Cl^- to 140 mM Cl^- (Fig. 3). The standard bath solution contained 0.2 mM chloride. Upon perfusion with higher chloride solutions, the fluorescence dropped immediately demonstrating chloride influx. The most sensitive response was near the K_d of the sensor. Standard calibration of the sensor with 100 μ M TBT and 50 μ M nigericin provides a translation of fluorescence response to chloride concentrations. TBT and nigericin are ionophores that allow Cl^- and H^+ ions to pass freely through the cell membrane.

In experiments using prestin-mClY, we noted a decrease in fluorescence upon exposure to increasing concentrations of extracellular chloride, compared to mCl-YFP fused to the control membrane protein CD80 (a B cell protein, the extracellular portion of which acts as a co-stimulatory molecule of T cells, and has no known chloride transport function). The relative reduction in fluorescence was proportional to the concentration of extracellular chloride applied to the cell. Although the differences in individual mean fluorescence did not reach statistical significance, the rates of change per extracellular Cl^- were significantly different (slope difference: 0.02 unit/100 mM Cl^- ; $p < 0.05$), and indicates a more rapid transmembrane flux of Cl^- with prestin when extracellular Cl^- increases. The dilution of sub-membranous Cl^- into the cytosolic pool of Cl^- likely limits the accumulation of the anion near the plasmalemma. Importantly, prestin-mClY demonstrated unchanged prestin function evidenced in parameters of charge movement in the membrane (non-linear capacitance, data not shown). Moreover, there was tight correlation between estimates of intracellular chloride concentration determined by changes in voltage at peak capacitance (V_h) [7,30]

and decrease in fluorescence intensity in prestin-mClY. Both methods of estimating Cl^- concentration are concordant with a rise in intracellular peri-membranous Cl^- concentration of < 10 mM, when cells were perfused with 140 mM Cl^- . Note that there was an increase in intracellular chloride concentrations with both prestin-mClY and CD80-mClY, although the reduction in fluorescence with prestin was more marked. We interpret these data to suggest that prestin enhances a basal Cl^- influx into the cell. The rise in intracellular juxta-membrane chloride concentration is due to a complex contribution from prestin activity (conductance or transport), native channels and transporters in the HEK cell, and diffusional dilution into the cytoplasm away from the plasma membrane. Resolving these issues will require additional work.

Discussion

Here we report the development of a powerful fluorescent chloride sensor that displays 1) superior photostability, 2) reduced susceptibility to $[H^+]$ fluctuations near physiological pH, and 3) enhanced chloride sensitivity to permit assessment of low-level physiological changes in $[Cl^-]$. For example, the K_d estimates of Prestin sensitivity to chloride range from 1–6 mM [7,31,32], and the fused Prestin/mCl-YFP sensor will be ideal for monitoring chloride levels in the OHC sub-plasmalemmal compartment where chloride concentrations have been speculated to fluctuate and affect prestin function [33–35]. Additionally, we demonstrate here dynamic changes in intracellular chloride concentration in response to changes in extracellular chloride that we attribute to prestin. It is unclear if this increase in intracellular chloride concentration is a result of transporter activity or a more channel-like conductance [36–38]. We are confident that the benefits of the probe will extend to other physiological preparations, as well.

Protonation & Cl^- Binding

We used known characteristics of YFP and previous iterations of other chloride sensor homologues to engineer our new sensor. In

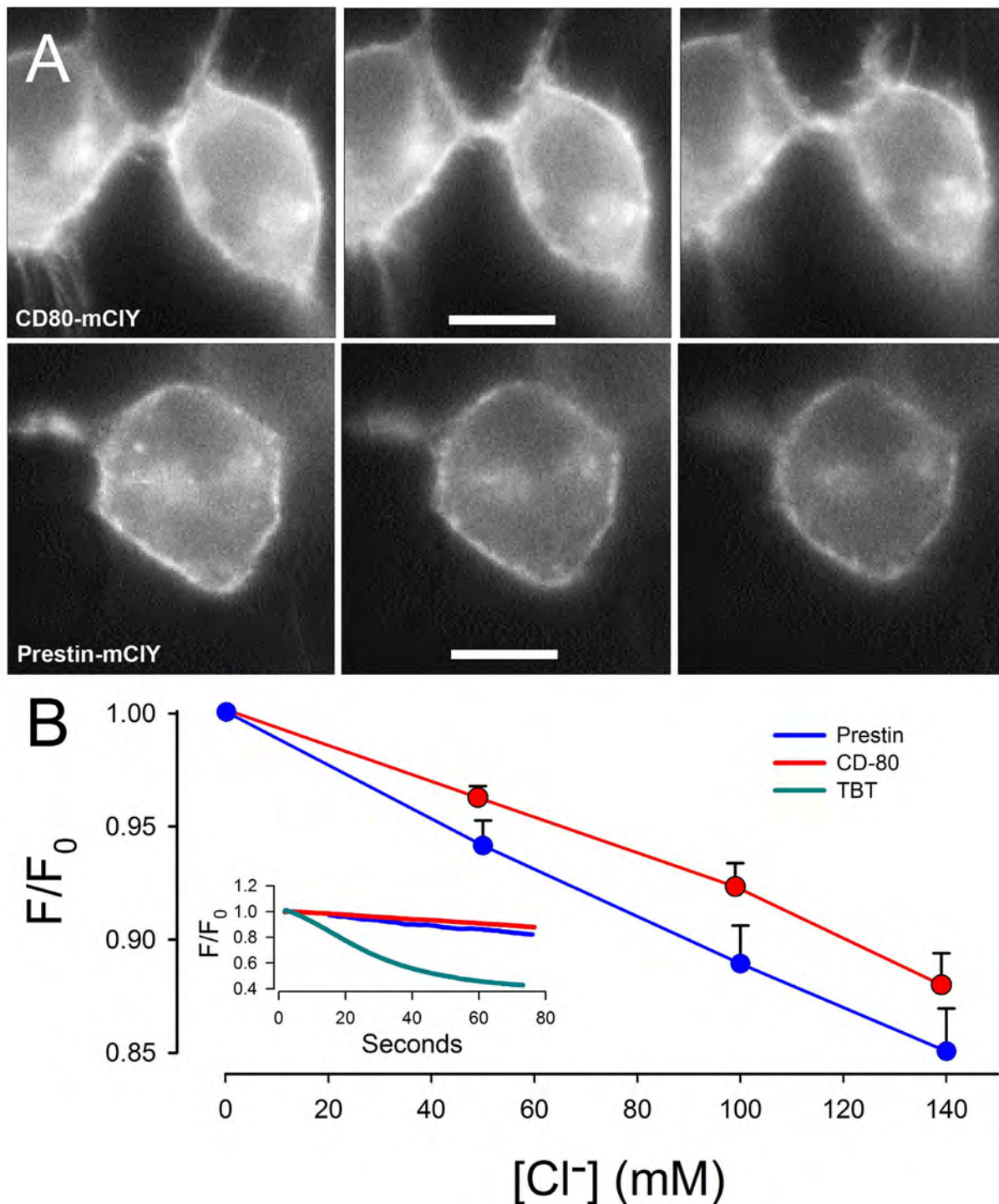


Figure 3. Prestin dependent Cl^- flux in HEK-293T cells. (A) Two panels show representative fluorescence change on HEK-293T cells transiently transfected with CD80-mClY (upper) and Prestin-mClY (lower), respectively, under local perfusion of high K^+ solution with different Cl^- concentration, indicating a chloride flux into the cells. In the image panel, the perfused chloride concentration was $<0.2\text{ mM}$ (left), 50 mM (middle), and 140 mM (right). All images were acquired at the same time. The bar in middle lane was $10\text{ }\mu\text{m}$. These three lanes were in the same time scale. (B) The graph illustrates the effects on mean (\pm se, standard error) YFP fluorescence intensity upon local perfusion by High K^+ (Na^+ -deficient) solution with different Cl^- concentrations (19 cells expressing Prestin-mClY and 12 cells expressing CD80-mClY). The decrease in YFP fluorescence is more marked in cells expressing Prestin-mClY than CD80-mClY. All data have been compensated for photobleaching according to the photobleaching curve that was measured just prior to perfusion. Inset shows YFP fluorescence changes in two typical cells expressing Prestin-mClY and CD80-mClY, when perfused with $140\text{ mM } Cl^-$ from the bath solution containing $0.2\text{ mM } Cl^-$. This active but slower movement of Cl^- is contrasted with the rapid passive equilibration of intracellular Cl^- achieved by the addition of the ionophores TBT ($100\text{ }\mu\text{M}$) and nigericin ($50\text{ }\mu\text{M}$) while perfusing with 140 mM extracellular Cl^- .
doi:10.1371/journal.pone.0099095.g003

previous published YFP variants, alterations in the Cl^- sensitivity is usually accompanied by alterations in confounding pH effects because halide binding promotes the protonation of the chromophore, and vice versa [8,11,20]. The relationship of pK_a and halide sensitivity of YFP variants exhibits features that imply positive cooperativity of protonation and halide-binding [8,39]. In some variants of GFP, pH-sensitivity is exploited to measure compartmental pH [12,40], but for FRET-based studies, the sensitivity of YFP to environmental pH is highly undesirable because it can interfere with the interpretation of the energy transfer efficiency or distance estimation between donor and acceptor. Indeed, YFP variants with low pH and halide sensitivity have been developed, namely Venus [24,25] and Citrine [27]. Despite the apparent interdependence of pH and halide sensitivity, each can be separated.

In YFP, pK_a is mainly determined by two factors: the negative charge density on the phenolic oxygen of the chromophore and the local proton availability in the surrounding environment. The negative charge of chromophore anion mainly distributes on the phenolic oxygen or the carbonyl oxygen of imidazolinone as two major resonance structures. If the phenolate negative charge can delocalize over the conjugated skeleton to the carbonyl oxygen of imidazolinone, the phenolic oxygen would have less negative charge to attract protons for protonation, indicating that the pK_a would decrease. Our first strategy to decrease pK_a was to introduce as many positive charged residues as possible into the halide-binding cavity that is adjacent to the carbonyl oxygen of imidazolinone. Positive charges can help maintain the chromophore's anionic state, and also likely provide a large fraction of anion-binding energy for increasing halide sensitivity. In our study, Q69K decreased the pK_a to 6.5–7.1 from 7.1–8.0 depending on the chloride concentration, and F46L resolved the folding problem caused by Q69K.

The local proton availability around the phenolic group of chromophore is proportional to the pH value of the external solution depending on proton accessibility. If the proton has unencumbered access to the phenolic anion of the chromophore, the pK_a will be higher. When proton access along the proton delivery pathway is encumbered, the pK_a value will decrease, indicating that a higher H^+ concentration is needed to overcome the more difficult delivery. Therefore, the other strategy to decrease the pK_a was to identify mutations of some key residues that can block or raise the barrier within the proton delivery pathway to the phenol group of the chromophore. In the proton delivery pathway from the external solvent to the phenolic group of the chromophore, a water molecule adjacent to the chromophore phenolate forms H-bonds with the side chain of S205 and the main chain of N146, linking the chromophore phenolate with a surface water molecule within H-bond range (Fig. 4). Upon binding a halide ion, the distance between the bridging water molecule and the nearest surface water molecule increases to 4.7 Å, likely due to conformational rearrangement. S205 is the only residue that can be mutated to affect the bridging water molecule linked with a surface water molecule. Interestingly, S205 plays an important role for photostability, as it links E222 and the chromophore. In keeping with this possibility we also found that S205 mutations affect the photostability of the fluorophore, in addition to its effects on pK_a .

Photostability

Using selective screening assays and directed evolution strategies, highly photostable variants of mOrange and TagRFP were developed by Tsien's group [41]. Nevertheless, the YFP photobleaching mechanism and details of the photo-reactive process

remain poorly understood. We tried to endow our chloride sensor with higher photostability using a structure-guided strategy.

As noted above, we view S205 as being important for both proton delivery and photostability because of the hydrogen-bond chain network between the chromophore phenolate, S205 and E222 (Fig. 4B). Both GFP and YFP show decarboxylation of E222, evidenced as a loss of 44 Daltons (CO_2), upon intense illumination, and in the case of YFP it is associated with photobleaching [42–44]. Continuous illumination irreversibly photobleaches YFP into a weakly fluorescent species, which absorbs at 390 nm and fluoresces at 460 nm, similar to its spectroscopic properties as free chromophore [42]; this behavior indicates that the photon-induced chemical destruction happens within the chromophore via excited states, while the protein is partially unfolding and aggregating [43,44]. Though the detailed mechanism of how the E222 decarboxylation of YFP induces chromophore destruction remains to be determined, it could involve the hydrogen bond network between the chromophore and E222. In YFP-H148Q, E222 could be either H-bonded to S205 or to the nitrogen on the imidazole ring of the chromophore, but not to both at the same time (Fig. 4).

We found that the mutation S205V increased YFP photostability (bleach tau = ~175 s) more than 15 fold over wild-type YFP or C1sM. In fact, not only is its photostability enhanced, but the possible H-bond network rearrangement afforded by the mutation of S205 reduces pK_a , and improves chloride sensitivity, indicating that a new equilibrium was reached between the chromophore protonation and halide-binding. S205A, S205L and S205I similarly cannot support proton transfer in the absence of a hydrogen bond donor or acceptor at position 205. S205A, which is less bulky than S205V, provides a bleach time constant of ~30 s. S205L and S205I, which have larger side chains than S205V, show bleach time constants of ~110 s and ~220 s, respectively. This may indicate that side chain size or rotational freedom of residue 205 is important for photostability.

Interestingly, it was reported that wtGFP-S205V and wtGFP-S205A slow down the travel time through the excited-state proton transfer pathway (ESPT) from several tens of picoseconds to a few nanoseconds by rearranging E222 and Thr203 to form an alternative ESPT pathway without S205 [45,46]. It is unlikely that this would occur in YFP because it lacks the corresponding neutral form of the chromophore that wtGFP possesses, and the orientation of Y203 in YFP cannot permit its phenolic group to interact in an alternative H-bonding network for proton transfer. Furthermore, any potential effects of these mutations on GFP photobleaching were not reported.

In summary, we have developed an YFP-based chloride sensor that has enhanced chloride sensitivity and photostability, while possessing reduced confounding pH effects. We have used it to measure sub-membranous chloride flux in HEK cells when fused to the transmembrane protein prestin, and show that it is capable of monitoring changes in intracellular chloride at levels expected to have physiological impact. We also note that the stability of our YFP mutants could be useful in studies where photobleaching plays a key role, for example in single molecule [47] and superresolution microscopy [48] methodologies.

Methods

1. Gene Construct and Mutations

Mutagenesis was performed using the Quick Change method adapted from Stratagene QC protocol. Mutations were verified by sequencing the entire gene. The vector is EYFP-N1. The

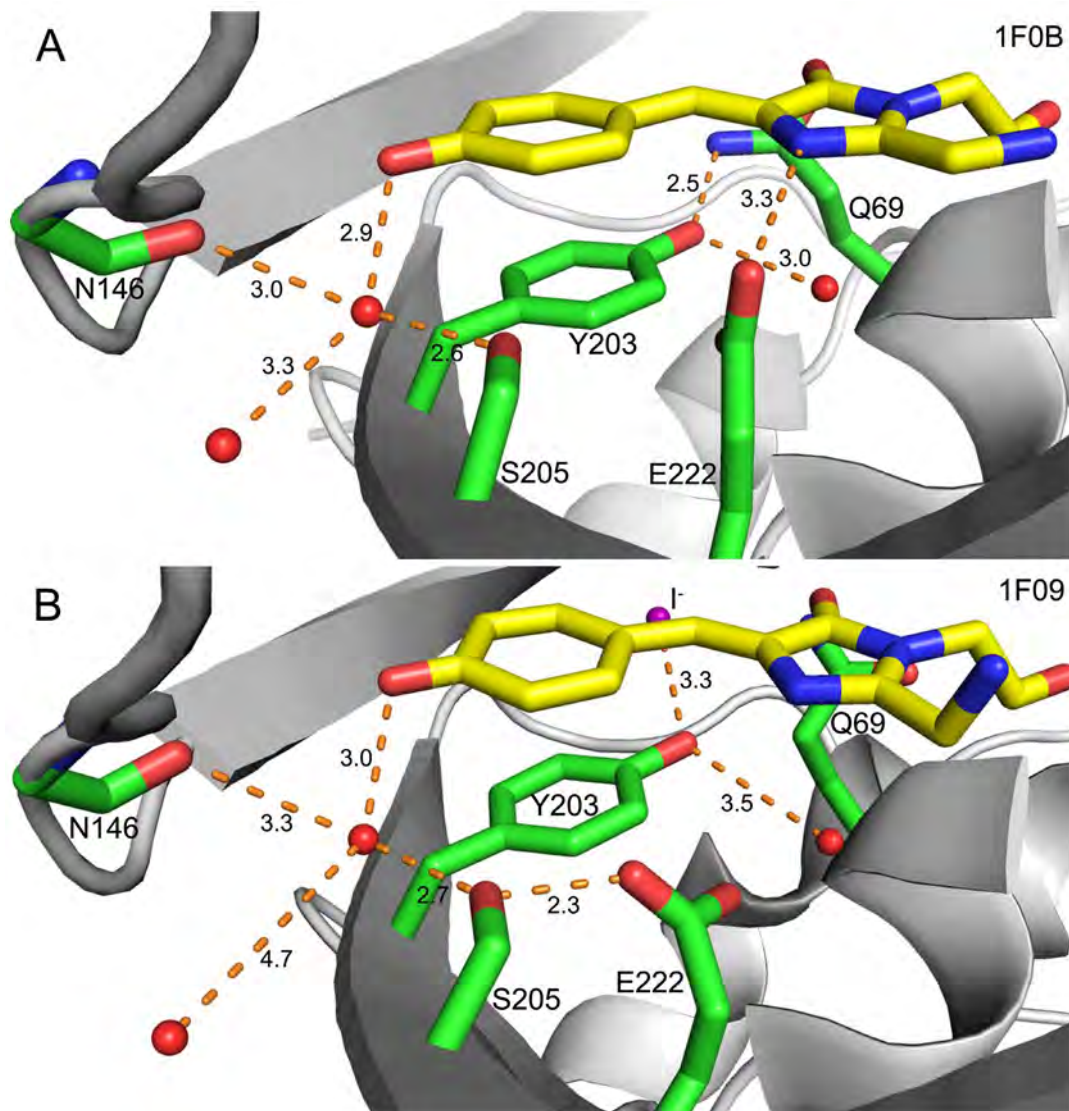


Figure 4. The H-bond network comprising the proton transfer pathway within the chromophore (in Yellow) of YFP-H148Q drawn with PyMol. Water molecules displayed as red balls. **(A)** YFP-H148Q without halide-binding (PDB: 1F0B). The phenolic oxygen of the chromophore is H-bonded to a water molecule that is also H-bonded to the side chain of S205 and the main chain of N146; additionally, there is a H-bond to a surface water molecule that is exposed to exterior solvent. E222 is H-bonded to the nitrogen on the imidazole ring, indicating that E222 is protonated, while the phenolic group of Y203 forms H-bond with Q69 and a nearby water molecule. Notably, there is no H-bond between S205 and E222 whose nearest distance is 3.9 Å. **(B)** iodide-bound YFP-H148Q (PDB: 1F09). The water molecule H-bonded to N146, S205 and the phenolic oxygen of the chromophore was separated away from the surface water molecule, whose distance increased to 4.7 Å. The deprotonated E222 forms H-bond to S205 that is in the H-bond chain with protonated chromophore, while the phenolic group of Y203 is near H-bonding distance with iodide, which may be a reason why YFPs are halide-sensitive since Y203 is the unique residue of YFP from GFP.
doi:10.1371/journal.pone.0099095.g004

sequences of EYFP-H148Q/152L/V163S and ClsM were synthesized by GeneWiz (USA).

2. Cell Culture & Excitation Ratiometric Imaging System

HEK-293T cells were cultured on glass coverslips (No. 1, 0.13–0.16 mm thick, 15 mm round, Warner Instr., USA), which were mounted on a quick change chamber and platform (RC-42LP and QE-1, Warner Instr., USA). Transient transfection with the plasmid of interest was done using lipofectamine-LTX with Plus Reagent (Invitrogen, Life technologies). Fluorescence images were acquired using an oil-immersion objective (N.A. = 1.30, Plan Fluor 100× Objective, Nikon, Japan) with a Nikon Eclipse Ti equipped with a 200W metal-halide lamp (Lumen200, Prior Scientific, USA)

as the fluorescence illumination source. Shutter and filter wheel (Lambda10–3 optical filter changer with smart shutter, Sutter Instr., USA) were connected between the microscope and the illumination source, in which Semrock ET430/24x-32 was used as the excitation filter for CFP, Semrock ET500/20x-32 as the excitation filter for YFP and Chroma HQ520LP as the emission filter. A 14-bit back-illuminated EMCCD camera system (128×128 pixels, 24 μm array, Andor iXon^{EM+} DU-860E, USA) was used to record the fluorescence images under CFP or YFP excitation. All peripheral hardware control, image acquisition and image processing were achieved and/or synchronized on a PC computer via a 16-bit/1-MHz USB Data Acquisition System (Personal Daq/3000 Series, IOtech, USA) by using customized

software (jClamp & FastLook, SciSoft, USA; www.SciSoftCo.com). The average fluorescence intensity of regions of interest (ROI) was measured, and the background fluorescence was subtracted using ImageJ. The excitation ratios (F_{500}/F_{430}) of fluorescence intensity were then determined. The emission spectrum of mCl-YFP has the same shape as wt-YFP, with the peak around 527 nm. This was determined at an excitation of 485 nm using a microplate reader (TECAN infinity M1000 Pro). The determinations of photobleaching, pK_a and chloride sensitivity were made using HEK-293 cells expressing YFP mutants directly in the cytosol, and not with membrane bound fusion proteins, which avoids the possibility of confounding results caused by limited expression or dim fluorescence. Data were analyzed with Matlab, Origin 8.0 and SigmaPlot 10.0.

3. Photobleaching

Photobleaching data and fluorescence images were achieved with our ratiometric imaging system controlled by jClamp & FastLook. Photobleaching efficiency at a wavelength of 500 nm is lower than at 430 nm, although the absorption at 430 nm is much lower than 500 nm. Because of this enhanced bleaching capability and to optimize our identification of photostable products, we bleached at the CFP excitation wavelength of 430 nm (approximately 17 μ W). At the beginning of every episode, the excitation filter was changed to the YFP filter (500 nm) by the filter wheel and an image was captured by the camera and then the excitation filter was changed back to CFP filter (430 nm) for bleaching until the next acquisition. Filter change and acquisition took about 100 ms. The protocol includes 400 episodes and 200 ms interval time between each episode. CFP excitation remained on during intervals. Stable optical power at the utilized wavelengths was confirmed using an analog optical power meter (ThorLabs PM30–130, w/S130A Slim Sensor). Photobleaching of mCl-YFP did not shift its emission peak.

4. pK_a Measurement

The pK_a of the YFP mutants were directly measured from the fluorescence change of the transfected HEK-293T cells under local perfusion (Y-tube) with low $[Cl^-]$ solutions (0.2 mM Cl^-) at different pH values containing 50 μ M nigericin and 100 μ M TBT, which eliminates pH and Cl^- gradients across the cell membrane, respectively. A Hill function (SigmaPlot, unconstrained, 4 parameters, $y = y_0 + \frac{ax^b}{c^b + x^b}$) was fitted to the data points to calculate the apparent pK_a .

5. Chloride Sensitivity Calibration

The chloride sensitivity of YFP mutants was measured from the fluorescence change of the transfected HEK-293T cells under local perfusion (Y-tube) with near neutral solutions (pH 7.20) of

different $[Cl^-]$ containing 50 μ M nigericin and 100 μ M TBT, according to the standard nigericin-tributyltin equilibrating protocol. A Hill function (SigmaPlot, unconstrained, 4 parameter) was fitted to the data points to calculate the apparent K_d . Local perfusion were performed with high K^+ solution (Na^+ -deficient) to minimize any pH effect on the chloride sensor by native membrane Na^+/H^+ exchanger.

6. Chloride Flux Promoted by Local Perfusion

The chloride flux into HEK-293 cells expressing prestin-mClY or CD80-mClY was measured by fluorescence change during local perfusion using high K^+ solutions containing different chloride concentrations at pH 7.20. Photobleaching compensation was corrected based on the photobleaching time constant that was measured prior to Cl^- perfusions. ImageJ was used to define a region of interest around membrane sections that were free from movement artifact in which fluorescence intensity changed with perfusion with different Cl^- concentrations. Perfusion data were analyzed using mixed model repeated measurements with a group-specified compound symmetry structure within SAS software. The repeated-measures design was used for the experiment of comparing the Cl^- influx pattern between prestin and CD80 constructs. Since each cell was perfused with a series concentration of extracellular Cl^- , fluorescence measured within each cell was correlated. A repeated measures analysis using the procedure of Proc Mixed in SAS software (Cary, NC) was performed to model the change of fluorescence per extracellular Cl^- . The dependency between repeated measures for same cell was incorporated into analysis by using a group specified compound symmetry covariance structure, which assumes common variance and covariance within group and accounts for the heterogeneous structure between groups. The interaction between group and concentration of Cl^- was included in the model to examine the difference of rate of change in fluorescence between groups [49,50].

7. Data Availability Statement

All data are supplied in the manuscript, including information on point mutations. Further requests can be made to the corresponding author.

Acknowledgments

We thank Mr. Fangyong Lian for help with statistical analysis, and thank Dr. John P Geibel in Yale School of Medicine for helpful discussion. Gerbil prestin was kindly provided by Dr. Peter Dallos and Dr. Jing Zheng.

Author Contributions

Conceived and designed the experiments: SZ JSS. Performed the experiments: SZ. Analyzed the data: SZ JSS. Contributed reagents/materials/analysis tools: DN. Wrote the paper: SZ DN JSS.

References

- Baumgarten CM, Clemler HF (2003) Swelling-activated chloride channels in cardiac physiology and pathophysiology. *Prog Biophys Mol Biol* 82: 25–42.
- Murek M, Kopic S, Geibel J (2010) Evidence for intestinal chloride secretion. *Exp Physiol* 95: 471–478.
- Okada Y, Shimizu T, Maeno E, Tanabe S, Wang X, et al. (2006) Volume-sensitive chloride channels involved in apoptotic volume decrease and cell death. *J Membr Biol* 209: 21–29.
- Jentsch TJ, Stein V, Weinreich F, Zdebik AA (2002) Molecular structure and physiological function of chloride channels. *Physiol Rev* 82: 503–568.
- Planells-Cases R, Jentsch TJ (2009) Chloride channelopathies. *Biochim Biophys Acta* 1792: 173–189.
- Santos-Sacchi J, Song L, Zheng J, Nuttall AL (2006) Control of mammalian cochlear amplification by chloride anions. *J Neurosci* 26: 3992–3998.
- Song L, Seeger A, Santos-Sacchi J (2005) On membrane motor activity and chloride flux in the outer hair cell: lessons learned from the environmental toxin tributyltin. *Biophys J* 88: 2350–2362.
- Jayaraman S, Haggie P, Wachter RM, Remington SJ, Verkman AS (2000) Mechanism and cellular applications of a green fluorescent protein-based halide sensor. *J Biol Chem* 275: 6047–6050.
- Kuner T, Augustine GJ (2000) A genetically encoded ratiometric indicator for chloride: capturing chloride transients in cultured hippocampal neurons. *Neuron* 27: 447–459.
- Galletta LJ, Haggie PM, Verkman AS (2001) Green fluorescent protein-based halide indicators with improved chloride and iodide affinities. *FEBS Lett* 499: 220–224.

11. Markova O, Mukhtarov M, Real E, Jacob Y, Bregestovski P (2008) Genetically encoded chloride indicator with improved sensitivity. *J Neurosci Methods* 170: 67–76.
12. Mahon MJ (2011) pHluorin2: an enhanced, ratiometric, pH-sensitive green fluorescent protein. *Adv Biosci Biotechnol* 2: 132–137.
13. Li Y, Tsien RW (2012) pHTomato, a red, genetically encoded indicator that enables multiplex interrogation of synaptic activity. *Nat Neurosci* 15: 1047–1053.
14. Palmer AE, Tsien RY (2006) Measuring calcium signaling using genetically targetable fluorescent indicators. *Nat Protoc* 1: 1057–1065.
15. Mank M, Griesbeck O (2008) Genetically encoded calcium indicators. *Chem Rev* 108: 1550–1564.
16. Perez Koldenkova V, Nagai T (2013) Genetically encoded Ca indicators: Properties and evaluation. *Biochim Biophys Acta*.
17. Perron A, Mutoh H, Akemann W, Gautam SG, Dimitrov D, et al. (2009) Second and third generation voltage-sensitive fluorescent proteins for monitoring membrane potential. *Front Mol Neurosci* 2: 5.
18. Siegel MS, Isacoff EY (2010) Green fluorescent proteins (GFPs) for measuring voltage. *Cold Spring Harb Protoc* 2010: pdb top76.
19. Jin L, Han Z, Platasa J, Wooltorton JR, Cohen LB, et al. (2012) Single action potentials and subthreshold electrical events imaged in neurons with a fluorescent protein voltage probe. *Neuron* 75: 779–785.
20. Wachter RM, Yarbrough D, Kallio K, Remington SJ (2000) Crystallographic and energetic analysis of binding of selected anions to the yellow variants of green fluorescent protein. *J Mol Biol* 301: 157–171.
21. Rhoden KJ, Cianchetta S, Duchi S, Romeo G (2008) Fluorescence quantitation of thyrocyte iodide accumulation with the yellow fluorescent protein variant YFP-H148Q/I152L. *Anal Biochem* 373: 239–246.
22. Cianchetta S, di Bernardo J, Romeo G, Rhoden KJ (2010) Perchlorate transport and inhibition of the sodium iodide symporter measured with the yellow fluorescent protein variant YFP-H148Q/I152L. *Toxicol Appl Pharmacol* 243: 372–380.
23. Truong K, Sawano A, Mizuno H, Hama H, Tong KI, et al. (2001) FRET-based in vivo Ca²⁺ imaging by a new calmodulin-GFP fusion molecule. *Nat Struct Biol* 8: 1069–1073.
24. Nagai T, Ibata K, Park ES, Kubota M, Mikoshiba K, et al. (2002) A variant of yellow fluorescent protein with fast and efficient maturation for cell-biological applications. *Nat Biotechnol* 20: 87–90.
25. Rekas A, Alattia JR, Nagai T, Miyawaki A, Ikura M (2002) Crystal structure of venus, a yellow fluorescent protein with improved maturation and reduced environmental sensitivity. *J Biol Chem* 277: 50573–50578.
26. Battistutta R, Negro A, Zanotti G (2000) Crystal structure and refolding properties of the mutant F99S/M153T/V163A of the green fluorescent protein. *Proteins* 41: 429–437.
27. Griesbeck O, Baird GS, Campbell RE, Zacharias DA, Tsien RY (2001) Reducing the environmental sensitivity of yellow fluorescent protein. Mechanism and applications. *J Biol Chem* 276: 29188–29194.
28. Zhang J, Campbell RE, Ting AY, Tsien RY (2002) Creating new fluorescent probes for cell biology. *Nat Rev Mol Cell Biol* 3: 906–918.
29. Zacharias DA, Violin JD, Newton AC, Tsien RY (2002) Partitioning of lipid-modified monomeric GFPs into membrane microdomains of live cells. *Science* 296: 913–916.
30. Rybalchenko V, Santos-Sacchi J (2003) Cl⁻ flux through a non-selective, stretch-sensitive conductance influences the outer hair cell motor of the guinea-pig. *J Physiol* 547: 873–891.
31. Oliver D, He DZ, Klocker N, Ludwig J, Schulte U, et al. (2001) Intracellular anions as the voltage sensor of prestin, the outer hair cell motor protein. *Science* 292: 2340–2343.
32. Song L, Santos-Sacchi J (2010) Conformational state-dependent anion binding in prestin: evidence for allosteric modulation. *Biophys J* 98: 371–376.
33. Rybalchenko V, Santos-Sacchi J (2003) Cl⁻ flux through a non-selective, stretch-sensitive conductance influences the outer hair cell motor of the guinea-pig. *J Physiol* 547: 873–891.
34. Rybalchenko V, Santos-Sacchi J (2008) Anion control of voltage sensing by the motor protein prestin in outer hair cells. *Biophys J* 95: 4439–4447.
35. Song L, Seeger A, Santos-Sacchi J (2005) On membrane motor activity and chloride flux in the outer hair cell: lessons learned from the environmental toxin tributyltin. *Biophys J* 88: 2350–2362.
36. Bai JP, Surguchev A, Montoya S, Aronson PS, Santos-Sacchi J, et al. (2009) Prestin's anion transport and voltage-sensing capabilities are independent. *Biophys J* 96: 3179–3186.
37. Mistrik P, Daudet N, Morandell K, Ashmore JF (2012) Mammalian prestin is a weak Cl⁻/HCO₃⁻ electrogenic antiporter. *J Physiol* 590: 5597–5610.
38. Schanzler M, Fahlke C (2012) Anion transport by the cochlear motor protein prestin. *J Physiol* 590: 259–272.
39. Wachter RM, Remington SJ (1999) Sensitivity of the yellow variant of green fluorescent protein to halides and nitrate. *Curr Biol* 9: R628–629.
40. Morimoto YV, Kojima S, Namba K, Minamino T (2011) M153R mutation in a pH-sensitive green fluorescent protein stabilizes its fusion proteins. *PLoS One* 6: e19598.
41. Shaner NC, Lin MZ, McKeown MR, Steinbach PA, Hazelwood KL, et al. (2008) Improving the photostability of bright monomeric orange and red fluorescent proteins. *Nat Methods* 5: 545–551.
42. McAnaney TB, Zeng W, Doe CF, Bhanji N, Wakelin S, et al. (2005) Protonation, photobleaching, and photoactivation of yellow fluorescent protein (YFP 10C): a unifying mechanism. *Biochemistry* 44: 5510–5524.
43. Bell AF, Stoner-Ma D, Wachter RM, Tonge PJ (2003) Light-driven decarboxylation of wild-type green fluorescent protein. *J Am Chem Soc* 125: 6919–6926.
44. van Thor JJ, Gensch T, Hellingwerf KJ, Johnson LN (2002) Phototransformation of green fluorescent protein with UV and visible light leads to decarboxylation of glutamate 222. *Nat Struct Biol* 9: 37–41.
45. Erez Y, Gepshtein R, Presiado I, Trujillo K, Kallio K, et al. (2011) Structure and excited-state proton transfer in the GFP S205A mutant. *J Phys Chem B* 115: 11776–11785.
46. Shu X, Leiderman P, Gepshtein R, Smith NR, Kallio K, et al. (2007) An alternative excited-state proton transfer pathway in green fluorescent protein variant S205V. *Protein Sci* 16: 2703–2710.
47. Ulbrich MH, Isacoff EY (2007) Subunit counting in membrane-bound proteins. *Nat Methods* 4: 319–321.
48. Lau L, Lee YL, Matis M, Axelrod J, Stearns T, et al. (2011) STED Super-resolution Microscopy in Tissue and in Mammalian Cells. *Proc Soc Photo Opt Instrum Eng* 7910.
49. Sullivan LM (2008) Repeated measures. *Circulation* 117: 1238–1243.
50. Little R, Milliken G, Stroup W, Wolfinger R, Schabenberger O (2006) SAS for mixed models. Cary, NC: SAS Institute Inc.